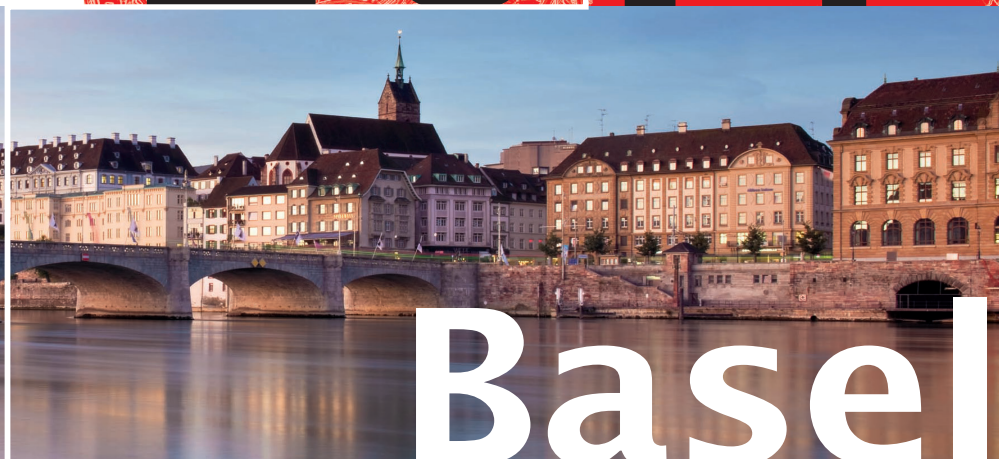


FEL 2014



Basel

36th International Free Electron Laser Conference

25-29 August 2014
Congress Center Basel, Switzerland
www.fel2014.ch

International Executive Committee:

I. Ben-Zvi, *BNL & Stony Brook University*
M.-E. Couprie, *Synchrotron SOLEIL*
J.N. Galayda, *SLAC*
L. Giannessi, *ENEA & ELETTRA-Sincrotrone Trieste*
A. Gover, *Tel Aviv University*
H. Hama, *Tohoku University*
K.-J. Kim, *ANL & The University of Chicago*
V.N. Litvinenko, *Stony Brook University & BNL*
E.J. Minehara, *JAEA & WERC*

G.R. Neil, *Jefferson Lab.*
C.W. Roberson, *ONR (ret.)*
J. Rossbach, *DESY & Hamburg University*
T.I. Smith, *Stanford University*
H. Tanaka, *RIKEN Spring-8*
A.F.G van der Meer, *FELIX Facility, Radboud University*
N.A. Vinokurov, *BINP & KAERI*
R.P. Walker, *Diamond Light Source*
Z.T. Zhao, *SINAP*

International Program Committee

S. Reiche, *PSI (Chair)*
E. Allaria, *Elettra*
S. Benson, *Jlab*
S. G. Biedron, *CSU*
J. Byrd, *LBL*
B. E. Carlsten, *LANL*
S. di Mitri, *Elettra*
M. Ferrario, *INFN*
J. C. Frisch, *SLAC*
G. Geloni, *XFEL*
F. Grüner, *UNI HH*
J.-H. Han, *PAL*
T. Hara, *RIKEN*
Z. Huang, *SLAC*
R. Ischebeck, *PSI*
Y. U. Jeong, *KAERI*
H.-S. Kang, *PAL*
M. Labat, *Soleil*

U. Lehnert, *HZDR*
J. W. Lewellen, *LANL*
Y. Li, *XFEL*
H. Loos, *SLAC*
A. Meseck, *HZB*
P. Musumeci, *UCLA*
B. Patterson, *PSI*
S. Schreiber, *DESY*
C. B. Schroeder, *LBL*
O. A. Shevchenko, *BINP*
T. Tanaka, *RIKEN*
N. Thompson, *ASTEC*
K. Tiedtke, *DESY*
D. Wang, *SINAP*
S. Werin, *Maxlab*
M. Yabashi, *RIKEN*
A. A. Zholents, *ANL*

Organizing Committee:

H.-H. Braun, *PSI (Conference Chair)*
R. Ganter, *PSI (Local Organizing Committee Chair)*

Contact: fel2014@psi.ch



Preface
Group Picture

Foreword

The international community of experts, students and enthusiasts in the field of Free-electron lasers met from August 25th to 29th 2014 at the Basel Congress Center, Switzerland, for the 36th International Free Electron Laser Conference, FEL2014. A total of 424 participants from 23 countries attended the event, which was hosted by the Paul Scherrer Institute, PSI.

The modern conference venue provided a state-of-the-art auditorium for the Oral Sessions and an extensive lobby that hosted lively Poster Sessions and an Industrial Exhibition. The exhibition allowed fruitful contacts to be made between FEL scientists and suppliers of sophisticated FEL equipment. The program included a reception in the historic Safran Zunft of Basel and a visit to PSI that encompassed a tour of the SwissFEL construction site, the SwissFEL Injector Test Facility and the Swiss Light Source. The excursion concluded with a traditional Swiss banquet held at PSI's renowned restaurant.

In the opening session, a talk by Dr. Li-Hua Yu commemorated the life and achievements of FEL pioneer Dr. Samuel Krinsky, who sadly passed away earlier in 2014. The program of scientific talks consisted of 34 invited and contributed talks on various FEL topics, ranging from FEL theory to the many operational and technical aspects of FEL accelerators, through to end-user applications. Furthermore two presentations were given by this year's FEL prize winners, and two first FEL lasing announcements were made, namely from FLASH II at DESY, Hamburg and the SwissFEL Injector Test Facility at PSI. Three excellent tutorial sessions were also offered to the delegates.

Notable highlights from the program were the recent results from the existing X-ray FEL facilities LCLS, SACLA and Fermi. These accelerators have now advanced beyond their commissioning phase. In addition to routine user operation, they provide important tests of novel ideas in beam dynamics and FEL physics. Multi-color operation with a single beam line and bandwidth control in the hard and soft X-ray regime have both been demonstrated, paving the way towards a technical maturity that will improve the beam quality to beyond basic SASE operation.

Another trend made apparent from the contributions is the research towards compact light sources. Alternative electron sources, new acceleration concepts and compact radiators aim to reduce the spatial footprint of intense, femtosecond X-ray light sources. Certain technologies, such as plasma bunch generation and acceleration, have advanced to a level that envisages a compact FEL to be driven in the foreseeable future.

We would like to thank the many participants who presented and shared their ideas and research, the Program Committee for formulating an interesting and varied scientific program, and the Local Organizing Committee for putting together a most professional event that, in true Swiss tradition, ticked like clockwork! Finally, a special thanks to the JACoW editorial team for their meticulous efforts in processing the manuscripts and ensuring the timely release of these Proceedings.



Sven Reiche
Scientific Program Chair



Hans-Heinrich Braun
Conference Chair

November 2014

Committees

International Executive Committee

I. Ben-Zvi	BNL and Stony Brook University, USA
M.-E. Couprie	Synchrotron SOLEIL, France
J.N. Galayda	SLAC, USA
L. Giannessi	ENEA and Elettra-Sincrotrone Trieste, Italy
A. Gover	Tel Aviv University, Israel
H. Hama	Tohoku University, Japan
K.-J. Kim	ANL and University of Chicago, USA
V.N. Litvinenko	Stony Brook University and BNL, USA
E.J. Minehara	JAEA and WERC, Japan
G.R. Neil	Jefferson Lab, USA
C.W. Roberson	ONR (ret.), USA
J. Rossbach	DESY and Hamburg University, Germany
T.I. Smith	Stanford University, USA
H. Tanaka	RIKEN SPring-8, Japan
A.F.G. van der Meer	FELIX Facility, Radboud Uni., Netherlands
N.A. Vinokurov	BINP, Russia and KAERI, Korea
R.P. Walker	Diamond Light Source, UK
Z.T. Zhao	SINAP, China

Local Organizing Committee

H.-H. Braun	PSI	Conference Chair
S. Reiche	PSI	IPC Chair
R. Ganter	PSI	LOC Chair
J. Chrin	PSI	Proceedings
S. Bacher	PSI	Conference Secretariat
L. Adrion	PSI	Social Events
F. Reiser	PSI	Budget and Social Events
H. Schori	PSI	Presentations Officer
C. Rosenberg	PSI	Poster Officer

Editorial Board

J. Chrin	PSI
S. Reiche	PSI
V. RW Schaa	GSI

International Programme Committee

E. Allaria	Elettra, Italy
S. Benson	JLAB, USA
S. Biedron	CSU, USA
J. Byrd	LBL, USA
B. Carlsten	LANL, USA
S. di Mitri	Elettra, Italy
M. Ferrario	INFN, Italy
J. Frisch	SLAC, USA
G. Geloni	XFEL, Germany
F. Grüner	Hamburg Uni., Germany
J.-H. Han	PAL, Korea
T. Hara	RIKEN, Japan
Z. Huang	SLAC, USA
R. Ischebeck	PSI, Switzerland
Y.-U. Jeong	KAERI, Korea
K.-S. Kang	PAL, Korea
M. Labat	SOLEIL, France
U. Lehnert	HZDR, Germany
J. Lewellen	LANL, USA
Y. Li	XFEL, Germany
H. Loos	SLAC, USA
A. Meseck	HZB, Germany
P. Musumeci	UCLA, USA
B. Patterson	PSI, Switzerland
S. Schreiber	DESY, Germany
C. Schroeder	LBL, USA
O. Shevchenko	BINP, Russia
T. Tanaka	RIKEN, Japan
N. Thompson	ASTEC, UK
K. Tiedtke	DESY, Germany
D. Wang	SINAP, China
S. Werin	Maxlab, Sweden
M. Yabashi	RIKEN, Japan
A. Zholents	ANL, USA

Contents

Preface	i
Group Picture	i
Foreword	iii
Committees	iv
Contents	v
Papers	1
MOA01 – Remembering Samuel Krinsky	1
MOA03 – First Lasing at FLASH2	7
MOB01 – Pulse Control in a Free Electron Laser Amplifier	9
MOB02 – Small-scale Accelerator-based Radiation Sources and Their Applications	14
MOB03 – Phase Space Manipulations in Modern Accelerators	16
MOP001 – Particle Tracking Simulations for EXFEL Complex shape Collimators	22
MOP003 – Helical Undulator Radiation in Internally Coated Metallic Pipe	26
MOP007 – High Accuracy Shimming Technique for the Phase Shifters of the European XFEL	29
MOP008 – Temperature Effects of the FLASH2 Undulators	34
MOP010 – The Photon Beam Loss Monitors as a Part of Equipment Protection System at European XFEL	37
MOP012 – Implementation Phase of the European XFEL Photon Diagnostics	41
MOP014 – X-ray Photon Temporal Diagnostics for the European XFEL	45
MOP015 – A Power Switching Ionization Profile Monitor (3D-IPM)	47
MOP017 – Measurement of the Output Power in Millimeter Wave Free Electron Laser using the Electro Optic Sampling Method	50
MOP018 – Conceptual Study of a Self-seeding Scheme at FLASH2	53
MOP019 – Double-grating Monochromator for Ultrafast Free-electron Laser Beamlines	58
MOP020 – Compact Spectrometer for Single Shot X-ray Emission and Photon Diagnostics	62
MOP021 – Commissioning of a Dual-sweep Streak Camera with Applications to the ASTA Photoinjector Drive Laser	66
MOP022 – Pulse by Pulse Electron Beam Distribution for Multi-beamline Operation at SACLA	71
MOP023 – Development of a Magnetic System to Cancel the Attractive Force toward Structural Reform of Undulators	75
MOP028 – Field Integral Measurement System and Optical Alignment System for HUST THz-FEL	80
MOP030 – Performance Analysis of Variable-Period Helical Undulator with Permanent Magnet for a KAERI THz FEL	84
MOP032 – PAL-XFEL Magnet Power Supply System	87
MOP033 – Design, Fabrication, and Performance Tests of Dipole and Quadrupole Magnets for PAL-XFEL	90
MOP036 – Estimating Effect of Undulator Field Errors using the Radiation Hodograph Method	93
MOP037 – Modeling and Design of the Variable Period and Pole Number Undulator for the Second Stage of the Novosibirsk FEL	96
MOP038 – Characterization of the Undulator Magnetic Field Quality by the Angle Averaged Radiation Spectrum	100
MOP039 – High Stability Resonant Kicker Development for the SwissFEL Switch Yard	103
MOP040 – General Strategy for the Commissioning of the ARAMIS Undulators with a 3 GeV Electron Beam	107
MOP041 – Summary of the U15 Prototype Magnetic Performance	111
MOP043 – Magnetic Design of an Apple III Undulator for SwissFEL	116
MOP044 – A Stripline Kicker Driver for the Next Generation Light Source	121
MOP045 – Phase Shifter Design for iSASE	123
MOP046 – Undulator Radiation Damage Experience at LCLS	127
MOP047 – A 200 μm -period Laser-driven Undulator	131
MOP049 – Oxygen Scintillation in the LCLS	137
MOP052 – Update on FEL Performance for SwissFEL	140
MOP053 – SASE FEL Performance at the SwissFEL Injector Test Facility	144
MOP054 – Harmonic Lasing Options for LCLS-II	148
MOP055 – Start-to-End Simulations for IR/THz Undulator Radiation at PITZ	153
MOP056 – SASE Characteristics from Baseline European XFEL Undulators in the Tapering Regime	159
MOP057 – Proposal to Generate 10 TW Level Femtosecond X-ray Pulses from a Baseline Undulator in Conventional SASE Regime at the European XFEL	164

MOP058 – Purified SASE Undulator Configuration to Enhance the Performance of the Soft X-ray Beamline at the European XFEL	169
MOP059 – Beam Dynamic Simulations for Single Spike Radiation with Short-Pulse Injector Laser at FLASH . .	173
MOP060 – Demonstration of SASE Suppression Through a Seeded Microbunching Instability	177
MOP061 – Electron Beam Delays for Improved Temporal Coherence and Short Pulse Generation at SwissFEL	181
MOP062 – FEL Proposal Based on CLIC X-Band Structure	186
MOP063 – A Novel Modeling Approach for Electron Beams in SASE FELs	190
MOP064 – Statistical Properties of the Radiation from SASE FEL Operating in a Post-saturation Regime with and without Undulator Tapering	194
MOP065 – Optimization of a High Efficiency FEL Amplifier	199
MOP066 – An Overview of the Radiation Properties of the European XFEL	204
MOP067 – Prospects for CW Operation of the European XFEL in Hard X-ray Regime	210
MOP068 – Suppression of the Fundamental Frequency for a Successful Harmonic Lasing in SASE FELs . . .	215
MOP070 – Design Study for the PEHG Experiment at SDUV-FEL	219
MOP075 – Laser Seeding Schemes for Soft X-rays at LCLS-II	223
MOP077 – Measurements of the FEL-bandwidth Scaling with Harmonic Number in a HGHG FEL	227
MOP078 – Measurements of FEL Polarization at FERMI	231
MOP079 – Generation of Multiple Coherent Pulses in a Superradiant Free-Electron Laser	233
MOP082 – Perspectives for Imaging Single Protein Molecules with the Present Design of the European XFEL .	238
MOP083 – Start-to-End Simulation for FLASH2 HGHG Option	244
MOP084 – Enhancing Coherent Harmonic Generation using Tilted Laser Wavefronts	248
MOP086 – Broadly Tunable THz FEL Amplifier	252
MOP087 – Upgrade Plans for the Short-pulse Facility at DELTA	255
MOP088 – High Repetition Rate Energy Modulator System Utilizing a Laser Enhancement Cavity	260
MOP090 – Soft X-ray Self-seeding Simulation Methods and their Application for LCLS	264
MOP092 – X-ray Monochromators for Self-seeding XFELs in the Photon Energy Range Starting from 1.5 keV .	269
MOP094 – Indirect Measurements of NIR and UV Ultrashort Seed Laser Pulses using a Transverse Deflecting RF-Structure	272
MOP095 – HGHG AND EEHG MICROBUNCHES WITH CSR AND LSC	275
MOP096 – Enhancing the Harmonic Content of an HGHG Microbunch	281
MOP097 – A Concept for Seeding 4-40 nm FEL Radiation at FLASH2	286
MOC01 – Circular Polarization Control by Reverse Undulator Tapering	297
MOC03 – Radiation Properties of Tapered Hard X-ray Free Electron Lasers	300
MOC04 – Chirped and Modulated Electron Pulse Free Electron Laser Techniques	303
TUA02 – A Review of High Power OPCPA Technology for High Repetition Rate Free-Electron Lasers	310
TUA03 – A GaAs Photoemission DC Gun for CAEP High-average-power THz FEL	318
TUA04 – Status of the SwissFEL C-band Linac	322
TUB01 – Review of Coherent SASE Schemes	327
TUB02 – Generation of Intense XVUV Pulses with an Optical Klystron Enhanced Self- amplified Spontaneous Emission Free Electron Laser	332
TUB03 – FEL Overcompression in the LCLS	337
TUB04 – Operation of FLASH with Short SASE-FEL Radiation Pulses	342
TUP002 – Characterization of Partially Coherent Ultrashort FEL Pulses	346
TUP003 – Quantum FEL II: Many-electron Theory	348
TUP004 – Quantum FEL I: Multi-mode Theory	353
TUP006 – Two-color Free-electron Laser via Two Orthogonal Undulators	358
TUP007 – Spectral Limits and Frequency Sum-rule of Current and Radiation Noise Measurement	362
TUP008 – An Analysis of Optimum Out-coupling Fraction for Maximum Output Power in Oscillator FEL	368
TUP009 – A Simple Method for Generating a Few Femtosecond Pulses in Seeded FELs	371
TUP012 – Numerical Simulation of a Super-radiant THz Source Driven by Femtosecond Electron Bunches . .	374
TUP013 – X-Ray Smith-Purcell Radiation from a Beam Skimming a Grating Surface	378
TUP014 – Forward X-Ray and Ultraviolet Smith-Purcell Radiation for FEL	384
TUP015 – Radiation and Interaction of Layers in Quasi-plane Electron Bunches Moving in Undulators	388
TUP016 – Quasi-optical Theory of Terahertz Superradiance from an Extended Electron Bunch	391
TUP017 – Using Lorentz Transformations for Simulations of Wiggler Superradiance from the Picosecond Electron Bunches	395

TUP018 – Sensitivity Study of a Tapered Free-Electron Laser	399
TUP019 – Update on the FEL Code Genesis 1.3	403
TUP020 – MINERVA, a New Code to Model Free-Electron Lasers	408
TUP021 – Recent Updates to the Optical Propagation Code OPC	412
TUP022 – The Implementation of 3D Undulator Fields in the Unaveraged FEL Simulation Code Puffin	416
TUP023 – Modeling CSR in a Vacuum Chamber by Partial Fourier Analysis and the Discontinuous Galerkin Method	419
TUP025 – TW X-ray Free Electron Laser Optimisation by Transverse Pulse Shaping	425
TUP026 – Transverse Coherence Properties of a TGU-based FEL	429
TUP027 – Initial Value Problem for an FEL Driven by an Asymmetric Electron Beam	433
TUP028 – Mode Contents Analysis of a Tapered Free Electron Laser	437
TUP029 – iSASE Study	442
TUP030 – Mode Component Evolution and Coherence Analysis in Terawatt Tapered FEL	446
TUP031 – FEL Code Comparison for the Production of Harmonics via Harmonic Lasing	451
TUP032 – FEL Simulation and Performance Studies for LCLS-II	456
TUP033 – Broadly Tunable Free-Electron Laser for Four-wave Mixing Experiments with Soft X-ray Pulses	461
TUP035 – Investigation of Reverse Taper to Optimize the Degree of Polarization for the Delta Undulator at the LCLS	465
TUP036 – Observation of Smith-Purcell Radiation at 32 GHz from a Multi-channel Grating with Sidewalls	470
TUP040 – Flying RF Undulator	474
TUP042 – High Efficiency Lasing with a Strongly Tapered Undulator	478
TUP045 – IFEL Driven Micro-Electro-Mechanical System Free Electron Laser	481
TUP046 – Terahertz FEL based on Photoinjector Beam in RF Undulator	485
TUP047 – Chirped Pulse Superradiant Free-electron Laser	489
TUP049 – Storage Ring XFEL with Longitudinal Focusing	492
TUP054 – Status of Electron Beam Slicing Project at NSLS-II, BNL	496
TUP057 – Development of Compact THz-FEL System at Kyoto University	501
TUP060 – Potential Photochemical Applications of the Free Electron Laser Irradiation Technique in Living Organisms	505
TUP064 – Narrow Linewidth, Chirp-Control and Radiation Extraction Optimization in an Electrostatic Accelerator FEL Oscillator	509
TUP066 – Facility for Coherent THz and FIR Radiation	512
TUP069 – Cavity Length Change vs. Mirror Steering in a Ring Confocal Resonator	516
TUP070 – Numerical Calculation of Diffraction Loss for Characterisation of a Partial Waveguide FEL Resonator	521
TUP072 – Present Status of Coherent Electron Cooling Proof-of-principle Experiment	524
TUP073 – High Power Operation of the THz FEL at ISIR, Osaka University	528
TUP074 – High Power Coupled FEL Oscillators for the Generation of High Repetition Rate Ultrashort Mid-IR Pulses	532
TUP075 – Commissioning Status of the ASTA Facility at Fermilab	537
TUP077 – Characteristics of Transported Terahertz-wave Coherent Synchrotron Radiation at LEBRA	541
TUP079 – A Swedish Compact Linac-based THz/X-ray Source at FREIA	545
TUP080 – Towards an X-ray FEL at the MAX IV Laboratory	549
TUP081 – Configuration and Status of the Israeli THz Free Electron Laser	553
TUP082 – Coherent Harmonic Generation at the DELTA Storage Ring: Towards User Operation	556
TUP083 – ALPHA – The THz Radiation Source based on AREAL	561
TUP085 – FERMI Status Report	564
TUP086 – Experiment Preparation Towards a Demonstration of Laser Plasma Based Free Electron Laser Amplification	569
TUP087 – The Status of LUNEX5 Project	574
TUP088 – Free Electron Lasers in 2014	580
TUP089 – The Turkish Accelerator and Radiation Laboratory in Ankara (TARLA) Project	585
TUP091 – Developments in the CLARA FEL Test Facility Accelerator Design and Simulations	589
TUP093 – A Beam Test of Corrugated Structure for Passive Linearizer	593
TUP095 – Design of a Compact Light Source Accelerator Facility at IUAC, Delhi	596
TUP097 – Fast, Multi-band Photon Detectors based on Quantum Well Devices for Beam-monitoring in New Generation Light Sources	600
TUC01 – Hard X-ray Self-Seeding Setup and Results at SACLA	603
TUC03 – Generation of Optical Orbital Angular Momentum Using a Seeded Free Electron Laser	609

WEA04 – First Lasing from a High Power Cylindrical Grating Smith-Purcell Device	611
WEB02 – Beam Operation of the PAL-XFEL Injector Test Facility	615
WEB03 – European XFEL Construction Status	623
WEB04 – The New IR FEL Facility at the Fritz-Haber-Institut in Berlin	629
WEB05 – FLASH: First Soft X-ray FEL Operating Two Undulator Beamlines Simultaneously	635
THA01 – THz Streak Camera for FEL Temporal Diagnostics: Concepts and Considerations	640
THA02 – Experimental Characterization of FEL Polarization Control with Cross Polarized Undulators	644
THA03 – A Plan for the Development of Superconducting Undulator Prototypes for LCLS-II and Future FELs	649
THB01 – Simultaneous Measurement of Electron and Photon Pulse Duration at FLASH	654
THB02 – Experimental Results of Diagnostics Response for Longitudinal Phase Space	657
THB03 – Femtosecond-Stability Delivery of Synchronized RF-Signals to the Klystron Gallery over 1-km Optical Fibers	663
THB04 – Electron Beam Diagnostics and Feedback for the LCLS-II	666
THP002 – Beam Energy Management and RF Failure Compensation Scenarios for the European XFEL	672
THP003 – Two Charges in the Same Bunch Train at the European XFEL	678
THP004 – Start-to-End Error Studies for FLUTE	682
THP006 – Optimization of the PITZ Photo Injector Towards the Best Achievable Beam Quality	685
THP007 – Recent Electron Beam Optimization at PITZ	689
THP008 – Evolution of a Warm Bunched Electron Beam in a Free Drift Region	692
THP010 – Analysis of Beam Stability in the KAERI Ultrashort Pulse Accelerator	697
THP011 – Beam Measurement of Photocathode RF-gun for PAL-XFEL	699
THP012 – Error Analysis for Linac Lattice of Hard X-ray FEL Line in PAL-XFEL*	703
THP013 – Slice Emittance Measurement using RF Deflecting Cavity at PAL-XFEL ITF	707
THP014 – Cyclotron-Undulator Cooling of a Free-Electron-Laser Beam	710
THP016 – Optimization of FEL Performance by Dispersion-based Beam-tilt Correction	714
THP018 – The Seed Laser System for the Proposed VUV FEL Facility at NSRRC	718
THP019 – Higher-Order Moment Models of Longitudinal Pulse Shape Evolution in Photoinjectors	722
THP020 – Electron Beam Dynamics Optimization Using A Unified Differential Evolution Algorithm	726
THP022 – Theoretical Investigation of Coherent Synchrotron Radiation Induced Microbunching Instability in Trans- port and Recirculation Arcs	730
THP023 – Simulation of Alpha Magnet Elements in Dipole-only Tracking Codes	735
THP024 – High-gradient Cathode Testing for MaRIE	739
THP025 – Linear Accelerator Design for the LCLS-II FEL Facility	743
THP026 – Design Study of LCLS Chirp-Control with a Corrugated Structure	748
THP027 – LCLS-II Bunch Compressor Study: 5-Bend Chicane	755
THP029 – MOGA OPTIMIZATION DESIGN OF LCLS-II LINAC CONFIGURATIONS	763
THP030 – Recent Photocathode R&D for the LCLS injector	769
THP031 – Further Understanding the LCLS Injector Emittance	774
THP032 – Effects of Potential Energy Spread on Particle Dynamics in Magnetic Bending Systems	779
THP033 – Mechanical Design for a Corrugated Plate Dechirper System for LCLS	785
THP034 – Further Analysis of Corrugated Plate Dechirper Experiment at BNL-ATF	788
THP035 – Relativistic Effects in Micro-bunching	790
THP036 – Benchmark and Simulation Design of a Low Energy Bunch Compressor	795
THP037 – Beam Performance of the Photocathode Gun for the Max IV Linac	799
THP039 – Commissioning of the Photo-Cathode RF Gun at APS	803
THP040 – Status of Pump-probe Laser Development for the European XFEL	807
THP041 – Development of All-metal Stacked-double Gate Field Emitter Array Cathodes for X-ray Free-electron Laser Applications	811
THP042 – The LCLS-II Injector Design	815
THP043 – Model-based Klystron Linearization in the SwissFEL Test Facility	820
THP044 – RF Pulse Flattening in the SwissFEL Test Facility based on Model-free Iterative Learning Control	824
THP045 – Development of Photocathode Drive Laser System for RF Guns in KU-FEL	828
THP046 – Cu and Cs ₂ Te Cathodes Preparation and QE History at the SwissFEL Injector Test Facility.	832
THP047 – Photoemission Studies of Niobium and Lead Photocathodes Using Picosecond UV Laser	836
THP048 – Formation of the Electron Bunch Longitudinal Profile for Coherent Electron Cooling Experiment	840
THP049 – High Power RF Test and Analysis of Dark Current in the SwissFEL-gun	843

THP051 – Thyatron Replacement	847
THP052 – Affordable Short Pulse Marx Modulator	849
THP053 – Steady State Multipacting in a Micro-pulse Electron Gun	851
THP054 – Dark Current Studies at the APEX Photoinjector	855
THP056 – The SwissFEL C-band RF Pulse Compressor: Manufacturing and Proof of Precision by RF Measurements	859
THP057 – Longitudinal and Transverse Optimization for a High Repetition Rate Injector	864
THP058 – Solid-State Switch for a Klystron Modulator for Stable Operation of a THz- FEL	868
THP059 – The Laser Heater System of SwissFEL	871
THP060 – Design of a Spatio-temporal 3-D Ellipsoidal Photo Cathode Laser System for the High Brightness Photo Injector PITZ	878
THP061 – Commissioning of an Improved Superconducting RF Photo Injector at ELBE	881
THP063 – Production of C-band Disk-loaded type CG Accelerating Structures	885
THP064 – High Repetition Rate S-band Photoinjector Design for the CLARA FEL	889
THP069 – Performance Study of High Bandwidth Pickups Installed at FLASH and ELBE for Femtosecond-Precision Arrival Time Monitors	893
THP070 – A Tool for Real Time Acquisitions and Correlation Studies at FERMI	898
THP073 – Optics Measurements at FLASH2	902
THP074 – Infrared Diagnostics Instrumentation Design for the Coherent Electron Cooling Proof of Principle Experiment	905
THP075 – Design of TDS-based Multi-screen Electron Beam Diagnostics for the European XFEL	909
THP076 – Measurements of the Timing Stability at the FLASH1 Seeding Experiment	913
THP080 – A Low-Cost, High-Reliability Femtosecond Laser Timing System for LCLS	917
THP082 – Measurements of Compressed Bunch Temporal Profile using Electro-Optic Monitor at SITF	922
THP083 – Coherent Radiation Diagnostics for Longitudinal Bunch Characterization at European XFEL	925
THP084 – Longitudinal Diagnostics of RF Electron Gun using a 2-cell RF Deflector	929
THP085 – Commissioning and Results from the Bunch Arrival-time Monitor Downstream the Bunch Compressor at the SwissFEL Test Injector	933
THP087 – Electron Beam Diagnostics for COXINEL	937
THP088 – Comparison of Quadrupole Scan and Multi-screen Method for the Measurement of Projected and Slice Emittance at the SwissFEL Injector Test Facility	941
THP090 – Femtosecond Timing Distribution for the European XFEL	945
THP091 – Design and Test of Wire-Scanners for SwissFEL	948
THP092 – Transition Radiation of an Electron Bunch and Imprint of Lorentz-Covariance and Temporal-Causality	952
THP093 – Coherent Electron Cooling Proof of Principle Phase 1 Instrumentation Status	956
THP095 – Evolvment of the Laser and Synchronization System for the Shanghai DUV-FEL Test Facility	960
THP097 – Longitudinal Response Matrix Simulations for the SwissFEL Injector Test Facility	964
THP098 – CameraLink High-Speed Camera for Bunch Profiling	968
THC02 – Thermal Emittance Measurements at the SwissFEL Injector Test Facility	970
THC03 – Suppression of the CSR-induced Emittance Growth in Achromats using Two-dimensional point-kick Analysis	976
THC04 – Beam Simulations of High Brightness Photocathode DC Gun and Injector for High Repetition FEL Light Source	980
FRA02 – Wave-Mixing Experiments with Multi-colour Seeded FEL Pulses	985
FRA04 – Optimization of High Average Power FEL Beam for EUV Lithography Application	990
FRB02 – A Collinear Wakefield Accelerator for a High Repetition Rate Multi-beamline Soft X-ray FEL Facility	993
FRB04 – Divergence Reduction and Emittance Conservation in a Laser Plasma Acceleration Stage	999
Appendices	1003
List of Authors	1003
Institutes List	1017
Participants List	1034

REMEMBERING SAMUEL KRINSKY

L.H. Yu, BNL, Upton, NY 11973, USA

Abstract

This year, we lost our colleague Samuel Krinsky. Sam has made many important contributions to very broad field of accelerator physics. In remembrance of his life and achievements, we will review his contributions to the field of free electron lasers. In particular, we will concentrate on his contributions to the foundation of the theory of high gain FELs, and his managerial and experimental contributions to pioneer work on x-ray FEL development.



Figure 1: Sam Krinsky January 14, 1945 - April 26, 2014.

SAM'S CONTRIBUTIONS

Sam has made contributions in accelerator physics covering very broad areas. Among many of these contributions to accelerator physics, we focus on the following:

- NSLS X-ray ring (1978) design and commissioning
- First short-period in-vacuum undulator at NSLS (1987)
- First global orbit feedback system at NSLS
- Design NSLS-II storage ring (2014)
- Important contributions to studies of impedances and collective effects including the theory on coherent synchrotron radiation and micro-bunching in electron beams.
- Founded Source Development Laboratory at BNL

We will not be able to cover such broad areas of research works in these proceedings. Instead, we shall concentrate on his contributions to free electron laser physics.

Among many other contributions made by Sam, we would like to highlight his most important seminal contributions to the FEL community. We shall categorize these contributions in two aspects: theoretical basis for high gain FEL, and leading experimental and managerial roles.

Among Sam's many contributions to the theoretical basis of high gain FEL physics:

- Universal gain scaling function [1]
- 3-D SASE start-up noise [2]
- Effect of wiggler errors [3]
- Average spacing of peaks in SASE spectrum [4]

We also recognize among many of his leading experimental and managerial roles:

With his managerial skill and foresight, Sam contributed decisively to the formation of FEL team. This led to the creation and successful execution of FEL projects at Brookhaven National Laboratory during his tenure as deputy chairman of the NSLS department, paving the way toward many accomplishments with important impacts on the worldwide short wavelength FEL development. Here we highlight some of the most significant of these:

- Facilitated the 1990 Sag Harbor "Prospects for a 1 Å Free Electron Laser" Workshop with R. Palmer.
- 1997-1999 ATF HGHG Experiment at 5 μm:
Sam was instrumental in getting the NSLS to provide resources to the BNL Accelerator Test Facility to complete R&D on the photo-injector and to carry out the HGHG proof-of-principle experiment in the infrared.
- Leading role in the construction of the DUVFEL at the SDL for 2000 -2003 HGHG Experiment at 266 nm.

SCALING FUNCTION OF GAIN

In 1990, collaborating with L. H. Yu and R. Gluckstern, Sam derived an FEL integral differential equation describing evolution of the electric field strength E in an undulator, taking into account of diffraction, optical guiding, energy spread, emittance, detuning, focusing and betatron oscillation [1]:

$$(\Delta_{\perp}^2 + \Omega)E(\vec{r}) = \frac{i}{2}(2\rho\gamma_0)^3 \int \frac{d\gamma}{\gamma^2} h'(\gamma) \int d^2p \int_{-\infty}^0 ds e^{-i\alpha s} u(p^2 + \kappa^2 r^2) E[\vec{r} \cos(\kappa s) + \frac{\vec{p}}{\kappa} \sin(\kappa s)]. \quad (1)$$

This equation has many eigen-solutions, each representing an eigen-mode of the optical guiding, giving the gain of the

ISBN 978-3-95450-133-5

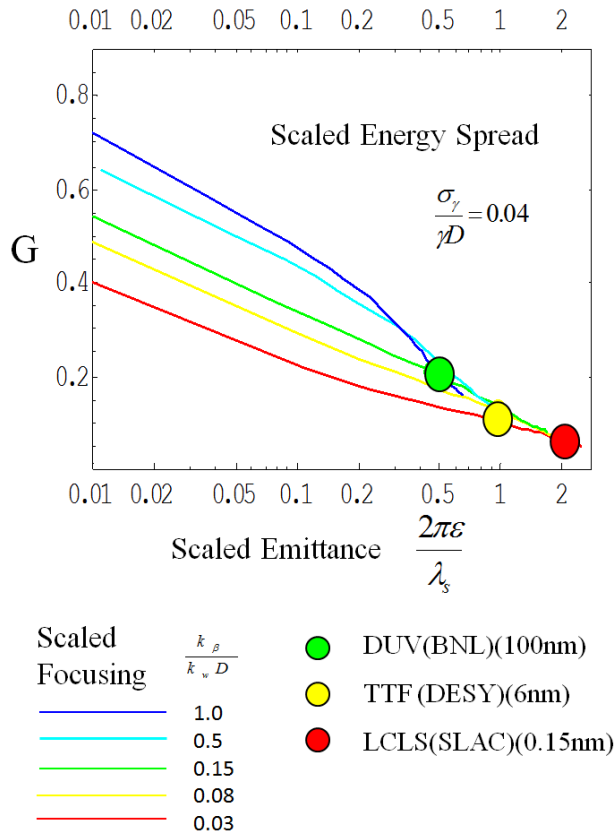


Figure 2: Scaling gain function showing the parameters of 3 FEL facilities.

electric field strength E . The mode with the highest growth rate dominates and gives scaling gain as function of the scaled emittance, energy spread, beta function, and detuning. The scaled gain can be represented by two different forms. The first form is:

$$\frac{1}{2k_w L_G^{3D} \rho} = \frac{\text{Im}\Omega}{\rho} \equiv G(\tilde{a}, \frac{\sigma}{\rho}, k_s \epsilon, \frac{\omega - \omega_s}{\omega_s \rho}), \quad (2)$$

In the second form, it is:

$$\frac{1}{2k_w L_G^{3D} D} = \frac{\text{Im}\Omega}{D} \equiv F(k_s \epsilon, \frac{\sigma}{D}, \frac{k_\beta}{k_w D}, \frac{\omega - \omega_s}{\omega_s D}), \quad (3)$$

The first form scaled with the FEL parameter ρ , is suitable for comparison with 1-D theory, showing the deviation from the 1-D theory for a perfect beam due to the diffraction, finite emittance, detuning, and energy spread.

The second form scaled with the scaling parameter D , which is determined only by the current and the energy of the electron beam, hence is independent from current density or beam size. As we can see in the following, this second form is suitable for scaling down from long wavelength to short wavelength FEL.

Sam, R. Gluckstern and I calculated the Scaling function using variational method and checked with codes from Los

Alamos and Lawrence-Livermore. We found excellent agreements with the codes, with errors within few percents which is determined mostly by the simulation itself. Later when we compared the scaled parameters for several FEL projects, we found we can put them on one plot. Even though the wavelengths of these FELs change by several orders of magnitudes, the scaled parameters are not very far from each other on the plot. In Fig. 2, we plot the scaled parameters for DUVFEL of BNL, the TTF FEL of DESY, and for LCLS.

The scaling function provides fast calculation of gain length, and as a benchmark vs. codes, it serves as the basis for high gain FEL calculations

Two years later, in 1992, Ming Xie fit our scaling function formula to polynomials, which is widely used in world FEL community, and known as "Ming Xie's formula".

1990 SAG HARBOR "PROSPECTS FOR A 1 Å FREE ELECTRON LASER" WORKSHOP

When we worked out the scaling function for FEL gain, we were equipped with a powerful tool to scan large parameter space to find the optimized FEL gain for short wavelength. Sam then initiated a discussion with R. Palmer (BNL's Dir. Office). The goal was very clear: we would like to inform our lab's management office of the potential of x-ray FEL, and influence the future development direction. We worked out a table on a blackboard, which listed the parameters of several X-ray FELs (see Fig. 3). R. Palmer recognized the importance of this new trend immediately, and decided to organize a workshop on x-ray FEL. The workshop is the 1990 Sag Harbor "Prospects for a 1 Å Free Electron Laser" Workshop. The table we generated on the blackboard has been published in the proceedings of this workshop, and is copied here as Fig. 3:

We can see that the LCLS parameters (proposed after 1992) is quite close to the last column of this table, apparently off by a factor 2. Notice that the last column of the table is for a 1 angstrom x-ray FEL while LCLS design goal is 1.5 angstrom. Also notice that in 1990 our assessment was that the normalized emittance of 2 mm-mrad was achievable by RF photo-cathode gun in the foreseeable future, hence we used the normalized emittance of 2 mm-mrad instead of the 1 mm-mrad which later appeared in LCLS design report. Hence the difference between the LCLS and our last column of the table in 1990 is within even less than a factor of 2.

We copied the front page and the contents of the 1990 Sag Harbor "Prospects for a 1 Å Free Electron Laser" Workshop in Fig. 4.

During the workshop, C. Pellegrini first presented a general talk about SASE and x-ray FELs. Then I presented a paper about the scaling relations and the parameters for 1 angstrom FEL, with the table of Fig. 3 included in the paper, which is just the table we established on the blackboard during the discussion with R. Palmer, as we mentioned before. Then a paper authored by a group including H. Winick and C. Pellegrini was presented about a 40 angstrom FEL based

E(GeV)	0.25	5	1.67	50	28
K	1	1	1	5.2	3.7
B _w	1.07	1.07	10.7	0.8	1
λ(Angstrom)	400	1	1	1	1
λ _w (cm)	1	1	0.1	7	4
ε _n (mm-mrad)	4	0.2	0.07	2	2
σ(x10 ⁻³)	1	1	1	1	1
I(Amp)	100	2000	670	10360	10360
power gain length (m)	1.73	1.73	0.17	12.1	9.9
λ _β (m)	6.28	6.28	0.628	44	26
natural λ _β (m)	6.9	140	4.8	1860	830

Figure 3: Table of parameters for several FELs, copied from Sag Harbor workshop proceedings.

TABLE OF CONTENTS	
BNL--52273 DE91 007631	PREFACE iii
PROCEEDINGS OF THE WORKSHOP PROSPECTS FOR A 1 Å FREE-ELECTRON LASER SAG HARBOR, NEW YORK April 22-27, 1990 Juan C. Gallardo, Editor	SECTION I: Free-Electron Laser Theory, Scaling Relations and Simulations
	SASE and Development of an X-Ray FEL 3 C. Pellegrini
	Scaling Relations and Parameters for 1 Å FEL 13 L.-H. Yu
	Three-Dimensional Simulations of the Generation of One-Angstrom Radiation by a Self-Amplified Spontaneous Emission Free-Electron Laser 31 J.C. Goldstein, C. J. Elliott and M. J. Schmitt
	A 40-Å FEL on the PEP Storage Ring 41 A. Fisher, S. Baird, H.-D. Nuhn, R. Tatchyn, H. Winick and C. Pellegrini
	80 mm FEL Design in an Oscillator Amplifier Configuration 57 R. Barbini, F. Ciocci, G. Dattoli, A. DiPace, L. Giannessi, G. Maino, C. Mari, A. Marino, C. Ronsaville, E. Sabia and A. Torre
	SECTION II: Micro-Wigglers
	The Performance of a Superconducting Micro-Undulator Prototype 65 I. Ben-Zvi, Z. Y. Jiang, G. Ingold, L. H. Yu and W. B. Sampson
	Fast Excitation Wiggler Development 79 A. van Steenberg, J. C. Gallardo, T. Romano and M. Woodle
	Strong Betatron Focusing in Linearly Polarized Wigglers 94 J. Claus
	SECTION III: Photocathode and Switched Power Gun
	Note on RF Photo-Cathode Gun 121 K.-J. Kim
	Correction of Induced Emittance Growth in Photocathode Guns 136 J. C. Gallardo and R. B. Palmer
	Switched Power Gun 149 W. Willis and R. C. Fernow
CENTER FOR ACCELERATOR PHYSICS BROOKHAVEN NATIONAL LABORATORY UPTON, LONG ISLAND, NEW YORK 11973	

Figure 4: Contents of Sag Harbor 1 Å Free Electron Laser Workshop

on PEP storage ring. K.J.Kim also gave a talk about RF photo-cathode gun in the workshop.

This workshop clearly has an important impact on the future development of x-ray FELs. We quote from E-mail of H. Winick to A. Sessler on May 9, 2013:

'The 1990 Sag Harbor workshop on "Prospects for a 1 Å Free-Electron Laser" was a very important event. I point this out in my talks and recently received several copies of the proceedings from Gallardo, which I distribute to those interested.'

Two years later, in 1992, H. Winick organized the workshop "1992 Workshop on Fourth Generation Light Sources, SLAC". This workshop also had important impact on the later development of LCLS. Two papers generated during this workshop are directly related to LCLS: one is a paper by W. Barletta, A. Sessler, L.H. Yu, "Using the SLAC Two Mile Accelerator for Powering An FEL", SLAC-PUB-15126,

1992, the other is a paper by C. Pellegrini "A 4 to 0.1 nm FEL based on the SLAC Linac", Proceedings Workshop on Fourth Generation Light Sources, 1992. We represent the connection of these two workshops to the advent of LCLS as in Fig. 5. A photo taken during the 1990 Sag Harbor workshop on "Prospects for a 1 Å Free-Electron Laser" is given in Fig. 6.

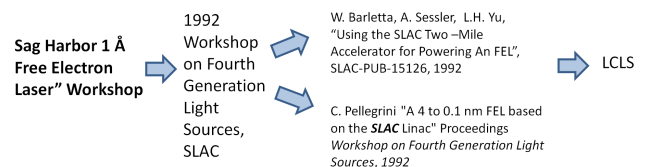


Figure 5: Connection of two workshops with LCLS.



Figure 6: Photo taken during the 1990 Sag Harbor workshop on "Prospects for a 1 Å Free-Electron Laser".

FEL EXPERIMENTS AT ATF AND SDL

With his managerial skill and foresight, Sam contributed decisively to the formation of FEL team, the creation and successful execution of FEL projects at Brookhaven National Laboratory during his tenure as deputy chairman of the NSLS department, which led to many important accomplishments with important impact on the worldwide short wavelength FEL development.

In particular, Sam's support of the first HGHG experiment to generate 5 micron FEL output from 10 μm seed from a 10 μm CO₂ laser at ATF was critically important for its success. The work generated a publication in the journal "Science" in 2000 [5]. With Sam's support we were able to develop BNL RF-photo-cathode gun at the ATF and achieved emittance at 1 mm-mrad at 0.7 nC, a significant achievement at that time. In Fig. 7 we show the photo taken during the acquisition of "Cornell Wiggler A" for 1997-1999 ATF HGHG Experiment at 5 μm , where Sam was standing in the front, with full energy and spirit.



Figure 7: Photo taken during the acquisition of "Cornell Wiggler A" for 1997-1999 ATF HGHG Experiment at 5 μm .

Following this experiment, Sam started the organization of Source Development Laboratory (SDL). Sam's leading role in the construction of SDL was again crucially important for the success of the DUVFEL. The success of HGHG at 266 nm with more than 130 micro joules with seed at 800 nm shows high stability and Fourier transform limited spectrum. In Fig. 8 we show the HGHG spectrum with a comparison of the SASE spectrum. The experiment demonstrated the basic principle of the HGHG.

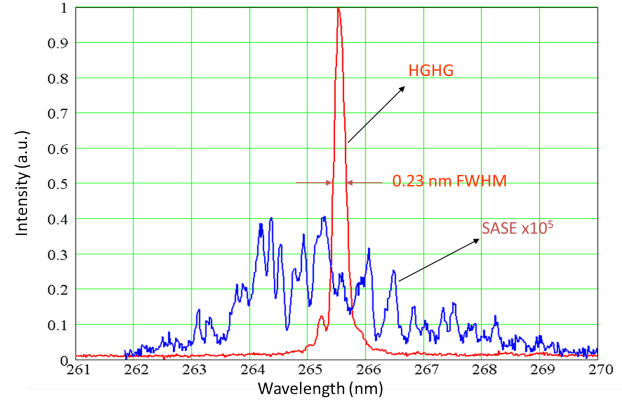


Figure 8: HGHG spectrum with a comparison of the SASE spectrum

Both these two experiments have important impact on the later development of coherent FEL based on the HGHG principle.

EFFECT OF WIGGLER ERRORS

Another of Sam's contribution to high gain FEL theory is the theory on the effect of wiggler errors [3]. It seems to be a rather complicated problem at first. However, we were able to reduce this problem to the solution of a rather simple equation:

$$y''' - i(\delta'y)'' = i(2\rho k_\omega)^3 y, \quad (4)$$

where δ is the phase error due to wiggler errors. The analysis of this equation shows that the condition for the damaging effect of the wiggler error to be small is the phase error accumulated in one gain length should be much smaller than 1 radian.

Another interesting conclusion from the solution of this equation using Born approximation is that the criterion on the peak to peak amplitude error is largely relaxed, the criterion for negligible gain reduction is

$$\frac{2\pi}{9\sqrt{3}} \frac{K_0^4}{(1 + K_0^2/2)^2} \frac{(\Delta B/B)_{\text{rms}}^2}{\rho} \ll 1. \quad (5)$$

This result means that $(\Delta B/B)_{\text{rms}}^2$ should be smaller than ρ , the FEL parameter. Before the derivation of this equation and its solution, the intuition seems to be that we should require $(\Delta B/B)_{\text{rms}} \ll \rho$, which is a much more stringent condition. For example, for LCLS, $\rho \sim 10^{-4}$. Thus the

first impression is we require $(\Delta B/B)_{\text{rms}} \ll 10^{-4}$. However this work about wiggler error points to the requirement of $(\Delta B/B)_{\text{rms}}^2 \ll 10^{-4}$, i.e., $(\Delta B/B)_{\text{rms}} \ll 10^{-2}$, a much more relaxed condition.

As a result of this, the work emphasizes the importance of phase error in one gain length dominated by error of mean value in one gain length and the trajectory deviation from the axis, and prescribes the alignment tolerance as:

$$P = P_0 e^{-\left(\frac{x_{\text{rms}}}{x_{\text{tol}}}\right)^4}, \quad (6)$$

where P_0 is the FEL power without wiggler error, while P is the power with wiggler error in the linear exponential regime.

When the distance between the correction station $L_s \ll$ the gain length L_G , we have the tolerance of trajectory within a gain length as:

$$x_{\text{tol}} = \left(\frac{L_s}{L_G}\right)^{\frac{3}{4}} \times 0.266 \sqrt{\lambda_s L_G} \left(\frac{L_G}{z}\right)^{\frac{1}{4}}. \quad (7)$$

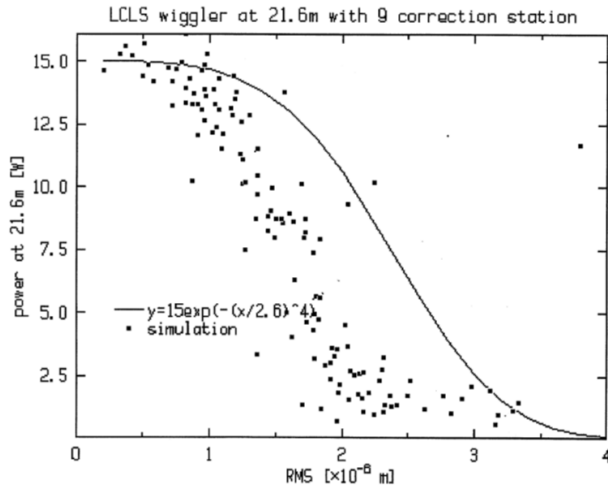


Figure 9: Power versus RMS trajectory errors obtained by the above formula and simulation.

For LCLS, we find $x_{\text{tol}} = 2.6 \mu\text{m}$. In Fig. 9, we compare the power as function of RMS trajectory error obtained from the above formula and simulation result. The result shows the simulation result indicated is a little more stringent than our result.

AVERAGE SPACING BETWEEN PEAKS IN SASE SPECTRUM [4]

Another example of Sam's work is very useful during experiment. This is the work on the statistical properties of SASE radiation. Even though the analysis of the SASE spectrum has been carried out previously, Sam's analysis provides a very simple way to obtain the length of the electron bunch. Once we see the SASE spectrum, we can use

the average spacing between the peaks in the spectrum to deduce the pulse length. We choose a section of the spectrum, and count the number of peaks in the section to calculate the average spacing between the peaks to be about 0.35nm during one of the SASE experiment at SDL as shown in Fig. 10. The formula then gives:

$$T_b = \frac{\lambda^2}{0.64 c \Delta \lambda} = \frac{(266\text{nm})^2}{0.64 \times 3 \times 10^8 \text{m/s} \times 0.35\text{nm}} \approx 1\text{ps}. \quad (8)$$

This result is in good agreement we obtained using zero phasing method during the experiment. This is typical of Sam's theoretical works: it is tightly connected to experiments.

Due to the limited space and time, some of Sam's important works were not described here. For example, the work on 3-D SASE start up noise [2] described in details about how the noise is amplified and how it creates many competing modes, how and under what condition these modes are finally dominated by a single fastest growing mode, how the transverse coherence is developed during this process, and how these modes are related to the the spontaneous radiation of the first two gain lengths of the undulator, how much of this radiation is coupled into the different transverse modes, etc. Hence the theory is directly related to the saturation length, the coherence properties of the output radiation, etc.

Finally, I would like to thank Faith Krinsky for providing the video of Sam's conversation.

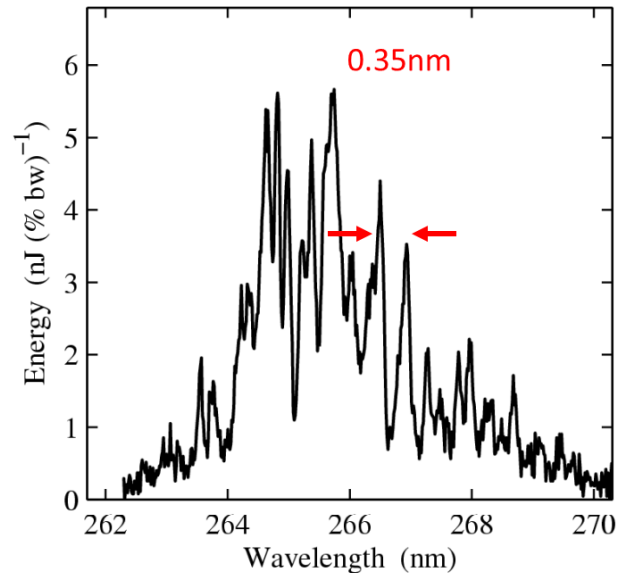


Figure 10: Intensity spiking in the frequency domain (arbitrary units). In the single-shot spectrum, the width of the peaks is inversely proportional to the electron bunch duration T_b .

REFERENCES

- [1] L.H. Yu, S. Krinsky, R.L. Gluckstern, "Calculation of universal scaling function for free-electron-laser gain" Phys. Rev. Lett. **64**, 3011 (1990)

- [2] L.H. Krinsky, S. Yu, “Output power in guided modes for amplified spontaneous emission in a single-pass free-electron-laser” *Phys. Rev. A.* **35**, 3406-3422 (1987)
- [3] L.H. Yu, S. Krinsky, R.L. Gluckstern, et al., “Effect of wiggler errors on free-electron-laser gain” *Phys. Rev. A.* **45**, 1163-1174 (1992)
- [4] S. Krinsky, R.L. Gluckstern, “Analysis of statistical correlations and intensity spiking in the self-amplified spontaneous-emission free-electron laser” *Phys. Rev. ST Accel. Beams* **6**, 050701 (2003)
- [5] L.H. Yu, M. Babzien, I. Ben-Zvi, et al., “High-Gain Harmonic-Generation Free-Electron Laser” *Science* **289**, 932-934 (2000)

FIRST LASING AT FLASH2

S. Schreiber*, B. Faatz, DESY, Hamburg, Germany[†]

Abstract

FLASH, the free-electron laser user facility at DESY (Hamburg, Germany), has been upgraded with a second undulator beamline FLASH2. The installation of the FLASH2 electron beamline, including twelve variable gap undulators, was finalized early 2014, and beam commissioning of the new beamline started in March 2014. We announce first lasing at FLASH2 achieved at a wavelength of 40 nm on August 20, 2014.

INTRODUCTION

FLASH [1–5], the free-electron laser (FEL) user facility at DESY (Hamburg), delivers high brilliance XUV and soft X-ray FEL radiation for photon experiments. FLASH is a user facility since 2005.

FLASH is a linear accelerator with a photoinjector followed by a superconducting linac. The maximum electron beam energy is 1.25 GeV, allowing lasing down to 4.1 nm with its fixed gap undulators. This undulator beamline (FLASH1) is in operation since 2004. More details on the FLASH facility and its present status can be found in these proceedings [5].

As FLASH, all high gain FEL's in the soft and hard X-ray range are driven by a linear accelerator. Therefore, beam can only be delivered to one experiment at a given time. FLASH has five experimental beamlines, so that usually two or sometimes three experiments can be set-up in parallel. But, they usually receive beam by a day to day basis, not at the same time.

Fortunately, the superconducting accelerating technology of FLASH allows to accelerate several thousand electron bunches per second. The bunches come in bursts with a repetition rate of 10 Hz. The maximal burst length is 0.8 ms, the smallest distance between single bunches is 1 μ s allowing a maximum number of 800 bunches per burst.

Since years, beam time for users is overbooked by a factor of about four. Therefore, a second undulator beamline FLASH2 has been constructed in 2011–14. The burst of electron bunches is now shared between two undulator beamlines, such that two experiments receive beam simultaneously with 10 Hz each. Sharing is possible for pairs of experiments requiring together at maximum the full burst duration of 0.8 ms, minus a transition time of 30 μ s for the kicker-septum system to divide the pulse train burst.

An additional important and unique feature is, that beam parameters and bunch pattern can vary for the two undulator beamlines, so that two experiments with different wavelengths, pulse durations, and pulse pattern are possible at the same time. The flexibility is realized with three main

features. Firstly, variable gap undulators allow to adjust the wavelength for FLASH2 experiments, while the beam energy is determined by the wavelength required for FLASH1. Secondly, two different laser systems operated in parallel at the photoinjector allow different charges, different pulse pattern, and to create a variable gap between the sub-bursts for FLASH1 and FLASH2. Thirdly, the low-level RF control of the accelerating structures are able to adjust phases and amplitudes – to a certain extend – independently for both beamlines, thus making different compression schemes possible.

For details on FLASH2 photon beam parameters the reader is referred to [6].

COMMISSIONING AND FIRST LASING

Mounting the FLASH2 electron beamline, including 12 undulator modules (Fig. 1), was finished in January 2014. The official permission of FLASH2 beam operation was given in early February, and the beam commissioning started in March.



Figure 1: FLASH2 undulator beamline with twelve variable gap undulators.

Due to FLASH1 user operation, dedicated beam time for FLASH2 had been restricted to a few days only until simultaneously operation was established end of May. Starting with June, the FLASH2 beam commissioning has taken place, whenever possible, parallel to FLASH1 user operation. This increased significantly the time available for FLASH2 commissioning with beam.

The first electron beam was transported into the FLASH2 extraction beamline on March 4, 2014, and beam transport up to the dump was achieved on May 23, 2014. In order to avoid radiation damage on the permanent undulator magnets, the first beam operation has been carried out with open undulator gaps.

* siegfried.schreiber@desy.de

[†] for the FLASH team

After a thorough preparation of the electron beam up to the FLASH2 dump, the undulator gaps of the last four undulators have been closed for the first time in August 20, 2014 resulting immediately in a first signal of SASE radiation. The signal was optimized by adjusting the phase shifters between the modules together with a slight orbit correction.

Figure 2 shows the first SASE photon beam seen on a Ce:YAG screen in the photon beamline, about 18 m distant from the end of the undulators. The estimated photon wavelength was 40 nm, determined by the undulator gap of 9.5 mm and the beam energy of 680 MeV. The spot size in Fig. 2 is about 3 mm FWHM yielding in an opening angle of 80 μ rad. This is expected for SASE radiation; spontaneous radiation would have a spot size of 60 mm. Also the fluctuation of the pulse energy is in agreement with the typical SASE fluctuations for high-gain, but not saturated lasing.

A few days later, the photon spectrum could be measured with two different undulator gap settings giving photon wavelengths of 42 nm and 23.5 nm.

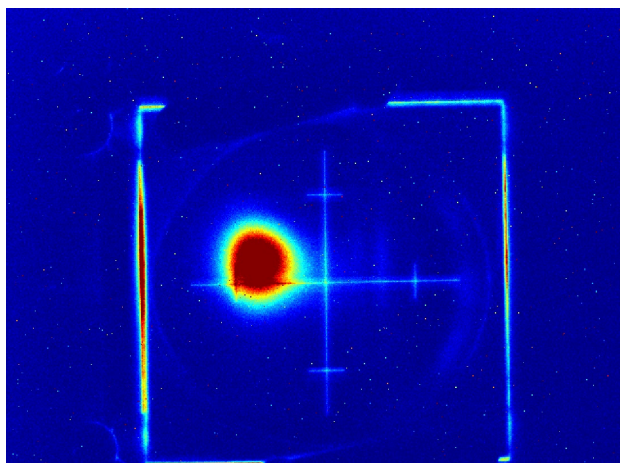


Figure 2: Photon beam on the Ce:YAG screen of the FLASH2 beamline. The distance of the cross marker to the center is 5 mm. The distance undulators – screen is about 18 m.

Of uttermost importance for the two beamline scheme is, that first lasing of FLASH2 has been achieved while FLASH1 was running SASE with 250 bunches in the burst at a wavelength of 13.5 nm prepared for a user experiment.

This is the first time that a soft X-ray FEL facility has operated successfully two undulator beamlines driven by the same accelerator simultaneously.

SUMMARY AND OUTLOOK

The FLASH2 beam commissioning started in March 2014 and the first lasing was achieved on August 20, 2014. The FLASH2 commissioning continues mainly in parallel to the FLASH1 user operation. The first FLASH2 pilot photon experiments are expected in 2015, and regular user operation in 2016.

ISBN 978-3-95450-133-5

With FLASH2 in operation, the user capacity of FLASH will be significantly increased. The variable gap undulators ease photon wavelength changes in FLASH2, and, together with two injector lasers and the flexible LLRF system, allow parallel operation of FLASH1 and FLASH2 with to a certain extent independent parameters.

ACKNOWLEDGMENT

We like to thank all colleagues participating in the construction and commissioning of FLASH2. Your devoted involvement has been indispensable and highly appreciated.

REFERENCES

- [1] W. Ackermann *et al.*, “Operation of a free-electron laser from the extreme ultraviolet to the water window”, *Nature Photonics* **1**, 336 (2007).
- [2] K. Tiedtke *et al.*, “The soft x-ray free-electron laser FLASH at DESY: beamlines, diagnostics and end-stations”, *New J. Phys.* **11**, 023029 (2009).
- [3] K. Honkavaara *et al.*, “Status of the FLASH Facility”, in *Proc. 35th Free-Electron Laser Conf.*, New York, 2013, pp. 550-553.
- [4] M. Vogt *et al.*, “Status of the Free Electron Laser User Facility FLASH”, in *Proc. 5th Int. Particle Accelerator Conf.*, Dresden, 2014, pp. 938-940.
- [5] K. Honkavaara *et al.* “FLASH: First Soft X-ray FEL Operating Two Undulator Beamlines Simultaneously”, in *These Proceedings: Proc. 36th Int. Free-Electron Laser Conf.*, Basel, 2014, WEB05.
- [6] B. Faatz *et al.*, “FLASH II: Perspectives and challenges”, *Nucl. Instr. Meth. A* **635**, S2 (2011).

PULSE CONTROL IN A FREE ELECTRON LASER AMPLIFIER

Luca Giannessi, ENEA C. R. Frascati and Elettra-Sincrotrone Trieste, Italy

Abstract

A significant progress has been made in controlling the properties of the radiation emitted by a FEL amplifier. Experiments have demonstrated the possibility both to increase the temporal coherence and to reduce the amplifier length to reach saturation, by seeding it with an external source. This may be a solid state, short pulse, laser (Ti:Sa,OPA..), doubled or tripled in a crystal, or a high order harmonic pulse generated in gas. The coherence improvement and the increased compactness of the source are only the first beneficial offspring of this marriage between the optical laser world and that of FELs. Non-linear effects in the seeded FEL dynamics may be exploited to shorten the pulse length beyond that allowed by the FEL natural gain bandwidth. Multiple seed pulses can be used to generate pulses whose temporal distance and properties are also controlled. Similarly, the FEL gain can be adapted to match the seed properties by tailoring the electrons phase space to generate ultra-short output pulses at unparalleled intensities.

INTRODUCTION

The free electron laser is a very special laser amplifier relying on a quasi “medium-free” amplification mechanism. The active medium is indeed constituted by electrons interacting with the ponderomotive potential made by the undulator and the laser field itself. This fact allows great control on the resonances coming into play and the amplification process may be designed in an extremely wide spectral range. Single pass FELs operate in mirrorless configurations where the radiative interaction of electrons is mainly that with the laser optical electromagnetic wave at the resonant frequency, permitting the lasing process down to the VUV or X-ray spectral range. FEL light sources dedicated to user experiments are fully functional both in the hard X-rays, such as LCLS and SACLA [1, 2], and in the soft X-rays, as FLASH and FERMI [3–5]. After a first phase where the main scientific and technical challenge was that of achieving sufficient gain to reach saturation, the problem shifted to that of gaining full control of the properties of the emitted radiation. We are now learning how to influence the amplification process and modify the properties of radiation according to the needs of experiments where the FEL light is the investigation tool. Several experiments have demonstrated the possibility of both increasing the temporal coherence and reducing the amplifier length required to reach saturation, by seeding the amplifier with an external source. The electron beam, can be shaped to influence the gain spectrum and effectively modify the gain frequency bandwidth to generate ultrashort pulses, even beyond the limit posed by the intrinsic gain bandwidth of the FEL process. Other experiments have shown the ability of the FEL to act as harmonic converter, extending to very high order the emission of harmonics. In this contribu-

tion we have reviewed some of the experiments carried out at SPARC and FERMI, that were done within this specific scientific framework.

SEEDING AND HARMONIC GENERATION

The FEL conversion from electron kinetic energy to energy of the optical wave has the typical behavior of an instability, with an exponential growth regime followed by a saturation process [6–9]. The gain of the instability, as resulting from the one-dimensional theory and in the cold beam limit, is described by the universal scaling parameter ρ_{fel} [9], related to the power e-folding (gain) length L_G by the relation $L_G = \lambda_u / (4\pi \sqrt{3} \rho_{fel})$. When the process starts from the electronic noise, after an exponential growth over a distance $L_{sat} \sim 20 L_G$ the signal saturates at a power $P_{sat} \sim \rho_{fel} P_{beam}$ where $P_{beam} = I_{peak} \gamma m_0 c^2 / e_0$ is the power carried by the electron beam. The natural line width of the output radiation from the SASE process in the classical regime is of the order of the parameter ρ_{fel} . The frequency spectrum of the emitted radiation corresponds to the white noise associated to the initial electron random distribution, filtered by the FEL gain bandwidth. Self amplified spontaneous emission output usually has poor longitudinal coherence, with a temporal and spectral structure consisting of a series of spikes uncorrelated in phase or amplitude [10–12].

This natural evolution of the FEL process may be influenced at startup by seeding the amplifier with an external source. The coherence properties of the seed are transferred to the electron modulation, leading to coherent emission at the undulator resonance and at its harmonics. The input seed, in order to be effective, must be intense enough to dominate the beam shot noise associated intensity, which may be derived according to the model in [13] and is given by $I_{sn} \approx 3 \omega \gamma m_0 c^2 \rho_{fel}^2$, where ω is the FEL resonant frequency.

Harmonic generation in gas [14] is one of the most promising methods to generate radiation in the VUV region of the spectrum, and this method was used at different facilities to seed directly an FEL amplifier at wavelengths ranging from 160 nm down to 38 nm [15–19]. Seeding at the shortest wavelengths has pointed out the increasing difficulty in overcoming the electron beam associated shot noise power, which is linearly proportional to the photon energy. An alternative is to seed the FEL at longer wavelengths and exploit the harmonic generation mechanism to reach the desired spectral range. The first idea on implementing an FEL as an harmonic converter appeared in [20]. Afterwards different schemes involving higher order harmonic bunching and harmonic generation were proposed and studied both theoretically and experimentally by several authors [21–27]. Harmonic generation combined with a high gain FEL am-

plifier (HGHG [26]) was investigated in two experiments done at Brookhaven [28, 29] that are considered important milestones in the development path of seeded FELs amplifiers. This development led to the design and construction of FERMI, the first seeded FEL user facility, that produced the first light in 2010. The HGHG cascade scheme is implemented in FERMI FEL-1, to generate fully coherent radiation pulses in the VUV spectral range [4]. The seed signal, continuously tuneable typically in the range 230-260 nm, is obtained from a sequence of nonlinear harmonic generation and mixing conversion processes from an optical parametric amplifier. The radiation resulting from conversion in the FEL up to the 13th harmonic is routinely delivered to user experiments [30]. The HGHG cascade may also be seeded by two temporally separated pulses. The FEL produces multiple, virtually jitter free, VUV pulses which may be separated in frequency within the FEL amplifier bandwidth. The generation of two-colour extreme ultraviolet pulses of controlled wavelengths, intensity and timing was demonstrated in a pioneering experiment where the time evolution of a titanium-grating diffraction pattern was studied by tuning the two coherent pulses to the titanium M-resonance [31].

With a double conversion stage based on the fresh bunch injection technique concept [32, 33] FERMI FEL-2 [5] extends the spectral range of the seeded FEL facility down to 4 nm at the first harmonic of the final radiator, providing radiation to experimental stations in the soft-X ray region of the spectrum.

SHAPING THE FEL GAIN

Single Spike

Tailoring the longitudinal properties of the electron beam distribution is another method of controlling the output characteristics of the FEL pulse. An example is provided by the “single-spike” operation where lasing is enabled in a region of the bunch comparable or shorter than the FEL cooperation length [34, 35]. Some pulse shortening methods rely upon purposeful degradation of the FEL gain outside a small temporal region; after several gain lengths, this region will dominate the FEL output [36]. However, the single-spike approach may be characterized by a very short gain length, due to the high brightness beams achievable when the bunch charge is reduced (< 10 pC) to shorten the pulse length. This generally implies an efficient radiation production, but also a relatively small absolute pulse energy. On the other hand, an alternative option consists in introducing a linear correlation (chirp) in the electron longitudinal phase space and in tapering the undulator to enable the preservation of FEL gain along a determined spatio-temporal path [37, 38]. This scheme combines therefore electron beam energy chirp with a judiciously-chosen undulator-field taper, i.e., a smooth variation of peak magnetic field along the beam propagation axis. The scheme was demonstrated at SPARC [39], where it was shown the possibility of generating isolated radiation spikes in a single pass FEL operating in SASE mode, without an increase in the gain length or a loss of efficiency, but

in fact with an increase by a factor of 20 in the pulse energy. This was due to the involvement in the gain process of a longitudinal extension of the e-beam comparable to the slippage length. This efficiency improvement was accompanied by a narrowing of the spectral width in a single moded spectral shape. The properties of the radiation in these conditions were further investigated in [40] where a FROG diagnostic was implemented to simultaneously measure the temporal and spectral content of the radiation along with the pulse's phase information. A time bandwidth product of about 1.2 was measured, with a pulse duration of about 100fs (fwhm), compatible with the spectral width independently measured.

Chirped Pulse Amplification

An alternative way to obtain ultrashort pulses, while preserving the FEL interaction over a longitudinally extended region of the electron bunch, is by optically compressing the radiation after amplification. An electron beam with a nonzero energy chirp, seeded by a properly chirped optical pulse, may generate a radiation pulse which may be then compressed in an additional optical stage (the compressor). This method corresponds to the chirped pulse amplification technique implemented in solid state lasers. Here the issue is not that of reducing the peak power in an active medium, but to allow the use of an extended electron beam longitudinal region, increasing the active bunch charge, without compressing the electrons to the ultimate limit. Chirped pulse amplification (CPA) in FEL amplifiers was proposed originally in [41] and further studied in the framework of a SASE amplifier in [42]. Critical is the efficiency of the optical compressor which has also to be tunable in the wavelength region of interest.

Generation of Trains of Ultrashort Pulses

Different techniques relying on concepts adapted to FELs from mode-locked cavity lasers, have been proposed for modifying the characteristic time scales of x-ray pulses beyond the FEL bandwidth limitation [43–45]. These methods foresee the generation of trains of high peak coherent power flashes with large contrast ratio by applying a series of spatiotemporal shifts between the co-propagating radiation and the electron bunch. This undulator configuration corresponds to a multiple resonances-undulator [46, 47], and from the point of view of the spectral gain distribution, it has some analogies to the gain distribution of a double-peaked electron energy distribution. An experiment was carried out at the SPARC FEL [48], where the double-peaked electron energy spectrum was obtained by the laser comb technique, in the velocity bunching regime [49, 50]. The electron beam, constituted by two short and balanced bunches, is extracted from the linac accelerating section near the maximum compression. At this point, the two beamlets, temporally superimposed in the longitudinal phase space, are characterized by a different value of the mean energy. The SASE emission corresponds to that of the two simultaneously lasing ultra-short electron bunches in single spike regime, separated in resonant frequency by a relative distance larger than

the ρ_{fel} parameter. The output radiation corresponding to the optical interference of the two pulses, was measured by a FROG diagnostics, and presented the expected comb temporal distribution with a corresponding spectral structure broader than the single beam amplifier bandwidth [51]. This method, which has been tested at SPARC FEL in the infrared, could be extrapolated in the production of sub-femtosecond pulses in the X-rays.

SATURATION AND SUPER-RADIANCE

At radiation saturation, the exponential gain process is replaced by a cyclic energy exchange between the electron beam and FEL radiation, with the period corresponding to that of the longitudinal synchrotron oscillation of those electrons trapped in the ponderomotive well. We may distinguish between a situation where the radiation pulse length is much longer than the slippage distance covered during one period of synchrotron oscillation, and the situation where the pulse length is comparable or shorter than this distance. In both cases the pulse shape is strongly affected by saturation effects.

Small Slippage: Pulse Splitting

In the first case we may neglect the fact that radiation slips over the electron current. Saturation effects, intended as over-bunching in the longitudinal phase space, may be induced in a HGHG FEL already at the entrance of the final radiator, by increasing the seed power or by increasing the dispersion in the chicane after the modulator. In these conditions the temporal distribution of the modulated electrons goes through a wave-breaking process at the central peak, while the temporal edges where the seed power is lower, may contain the correct density modulation at entrance to the radiator to produce two satellite pulses which are amplified in the radiator. This regime of operation was originally investigated in [52] and studied in combination of a frequency chirped seed pulse in [53]. In this configuration, the FEL is seeded by a powerful laser pulse carrying a significant frequency chirp. As a result, the output FEL radiation is split in two pulses, separated in time (as in the previous case) and having different central wavelengths. The spectral and temporal distances between FEL pulses can be independently controlled, providing the possibility of using the FEL at the same time as a pump and as a probe with multicolor synchronized pulses, where the two output pulses can be independently diagnosed with dispersive optics [54].

Large Slippage: Super-radiance and Harmonic Heneration

In the mid 1990s a number of papers analyzed theoretically and numerically the consequences of the slippage on the pulse evolution in a FEL amplifier [55–57]. It was pointed out the existence of a super-radiant regime where a short optical pulse slips over the electron beam and increases its energy while keeping a self-similar shape. In this regime, the radiation pulse has a peak power increasing with the

square of the distance along the undulator and a longitudinal width decreasing with the inverse square root of this distance. The radiated power is proportional to the square of the electron current. The pulse spectral bandwidth increases and the pulse undergoes longitudinal focusing. This regime was studied at BNL in an experiment where the NISUS undulator was seeded by an infrared Ti:Sa laser of 150 fs of pulse duration [58]. Pulse shortening down to about 82 fs was observed, and the pulse energy scaling vs distance along the undulator was verified. Another important feature of this regime is in the generation of harmonics of high orders and the behavior in a cascaded FEL configuration [59]. In a cascaded FEL operating in the super-radiant regime the distinction between the modulator and the radiator typical of common HGHG-FEL schemes is no longer appropriate: the steps of energy modulation, density modulation and emission take place simultaneously at different locations along the optical pulse. As in steady state FEL dynamics, the density modulation induces intense emission of radiation at higher order harmonics, but this occurs during the pulse propagation along all the undulator. When the electron beam passes from one stage of a cascade to the next, the region of high density modulation will emit a short pulse of coherent radiation at the new resonant wavelength. This pulse slips on a fresh portion of the electron beam and may be amplified in the exponential gain regime or, as happens in most cases, may be intense enough to saturate and enter the super-radiant regime.

The behavior of the single-pass FEL in deep saturation has been studied at SPARC by seeding the entire amplifier with six undulators tuned at 400 nm with short laser pulses with peak power of the same order of the FEL saturation power. The observation of harmonic emission up to the 11th order was reported in [60]. Later on the behavior of the system in a HGHG configuration was also studied at SPARC [61]. In a FEL cascade, at the transition from a modulator to a radiator, the high frequency components in the leading edge of the pulse are expected to induce the growth of a new super-radiant pulse at the harmonic frequency, which then grows, according to the scaling relations, in the next undulator. The six SPARC undulators were configured to establish an HGHG FEL, with the first undulator tuned with the resonance at 400 nm, playing the role of modulator, and the other five tuned at 200 nm, as radiators. The evolution of the pulse in the radiator was studied by measuring its energy and spectral properties. Energy per pulse substantially larger than the FEL saturation energy, without applying any undulator taper, was observed. An energy scaling vs the longitudinal position along the undulator of the type $E \propto z^{3/2}$ was measured, in satisfactory agreement with the theoretical model and simulations. Successful generation of high harmonic radiation output in a harmonic cascade configuration [62] has been recently accomplished at FERMI, both in FEL-1 [63] and FEL-2 [64] and harmonics up to order 65 and 192 of the input seed were respectively observed.

ACKNOWLEDGMENTS

I wish to thank my wife and my family for tolerating and being supportive of my bi-laboratory existence during all these years. All this would not have been possible if not for hard work, persistence and cooperation among the researchers from the teams I had the pleasure, honor and luck to work with, at both SPARC and FERMI. I gratefully extend my sincerest appreciation to my colleagues who have shared with me the excitement for the work done. With the wish to continue ...

REFERENCES

- [1] P. Emma et al., Nat. Photon. 176, 1038 (2010).
- [2] Ishikawa T. et al. Nat. Photon. 6, 540–544 (2012).
- [3] Ackermann, W. et al. Nat. Photon. 1, 336–342 (2007).
- [4] E. Allaria et al., Nat. Photon. 6, 699 (2012).
- [5] E. Allaria et al., Nat. Photonics 7, 913 (2013).
- [6] A.M. Kondratenko, E.L. Saldin, Particle Accelerators 10, 207 (1980).
- [7] H. Haus, IEEE Journal of Quantum Electronics 17(8), 1427 (1981).
- [8] G. Dattoli, A. Marino, A. Renieri, F. Romanelli, IEEE Journal of Quantum Electronics 17(8), 1371 (1981).
- [9] R. Bonifacio, C. Pellegrini, L. Narducci, Optics Communications 50(6), 373 (1984).
- [10] K.J. Kim, Phys. Rev. Lett. 57, 1871 (1986).
- [11] R. Bonifacio, L. De Salvo, P. Pierini, N. Piovella, C. Pellegrini, Phys. Rev. Lett. 73, 70 (1994).
- [12] E. Saldin, E. Schneidmiller, M. Yurkov, Optics Communications 148(4-6), 383 (1998).
- [13] M. Couprie, L. Giannessi, Seeding Free Electron Lasers with High Order Harmonics generated in Gas, submitted for publication (Springer).
- [14] P.B. Corkum, Phys. Rev. Lett. 71, 1994 (1993).
- [15] G. Lambert, T. Hara, D. Garzella, T. Tanikawa, M. Labat, B. Carre, H. Kitamura, T. Shintake, M. Bougeard, S. Inoue, et al., Nature Physics 4(4), 296 (2008).
- [16] L. Giannessi et al. FEL experiments at SPARC: Seeding with harmonics generated in gas, Proceedings of FEL 2010 Conference, Malmo, August 2010, TUPB18 (2010), <http://www.JACoW.org>
- [17] M. Labat, M. Bellaveglia, M. Bougeard, B. Carré, F. Ciocci, E. Chiadroni, A. Cianchi, M.E. Couprie, L. Cultrera, M. Del Franco, G. Di Pirro, A. Drago, M. Ferrario, D. Filippetto, F. Frassetto, A. Gallo, D. Garzella, G. Gatti, L. Giannessi, G. Lambert, A. Mostacci, A. Petralia, V. Petrillo, L. Poletto, M. Quattromini, J.V. Rau, C. Ronsivalle, E. Sabia, M. Serluca, I. Spassovsky, V. Surrenti, C. Vaccarezza, C. Vicario, Phys. Rev. Lett. 107, 224801 (2011).
- [18] T. Togashi, E.J. Takahashi, K. Midorikawa, M. Aoyama, K. Yamakawa, T. Sato, A. Iwasaki, S. Owada, T. Okino, K. Yamanouchi, F. Kannari, A. Yagishita, H. Nakano, M.E. Couprie, K. Fukami, T. Hatsui, T. Hara, T. Kameshima, H. Kitamura, N. Kumagai, S. Matsubara, M. Nagasono, H. Ohashi, T. Ohshima, Y. Otake, T. Shintake, K. Tamasaku, H. Tanaka, T. Tanaka, K. Togawa, H. Tomizawa, T. Watanabe, M. Yabashi, T. Ishikawa, Optics Express 19, 317 (2011).
- [19] S. Ackermann, A. Azima, S. Bajt, J. Bödwadt, F. Curbis, H. Dachraoui, H. Delsim-Hashemi, M. Drescher, S. Düsterer, B. Faatz, M. Felber, J. Feldhaus, E. Hass, U. Hipp, K. Honkavaara, R. Ischebeck, S. Khan, T. Laarmann, C. Lechner, T. Maltezopoulos, V. Miltchev, M. Mittenzwey, M. Rehders, J. Rönsch-Schulenburg, J. Rossbach, H. Schlarb, S. Schreiber, L. Schroedter, M. Schulz, S. Schulz, R. Tarkeshian, M. Tischer, V. Wacker, M. Wieland, Phys. Rev. Lett. 111, 114801 (2013).
- [20] I. Boscolo, V. Stagno, Il Nuovo Cimento 58, 271 (1980).
- [21] B. Girard, Y. Lapierre, J.M. Ortega, C. Bazin, M. Billardon, P. Elleaume, M. Bergher, M. Velghe, Y. Petroff, Phys. Rev. Lett. 53, 2405 (1984).
- [22] R. Prazeres, J. Ortega, C. Bazin, M. Bergher, M. Billardon, M. Couprie, M. Velghe, Y. Petroff, Nuclear Instruments and Methods in Physics Research Section A: Accelerators, Spectrometers, Detectors and Associated Equipment 272(1-2), 68 (1988).
- [23] R. Barbini, F. Ciocci, G. Dattoli, A. Dipace, L. Giannessi, G. Maino, C. Mari, C. Marina, C. Ronsivalle, E. Sabia, A. Torre, in Proceedings of the Prospects for a 1 A Free Electron Laser, Sag Harbor, New York, April 22-27, J. C. Gallardo Editor (BNL 52273) (1990).
- [24] R. Bonifacio et al. NIM A 296 (1990).
- [25] R. Prazeres, P. Guyot-Sionnest, J. Ortega, D. Jaroszynski, M. Billardon, M. Couprie, M. Velghe, Y. Petroff, Nuclear Instruments and Methods in Physics Research Section A: Accelerators, Spectrometers, Detectors and Associated Equipment 304(1-3), 72 (1991).
- [26] L. H. Yu PRA 44, 5178 (1991).
- [27] F. Ciocci et al. IEEE JQE31, 1242 (1995).
- [28] L. H. Yu et al. Science 289 (2000).
- [29] L.H. Yu, L. DiMauro, A. Doyuran, W.S. Graves, E.D. Johnson, R. Heese, S. Krinsky, H. Loos, J.B. Murphy, G. Rakowsky, J. Rose, T. Shafter, B. Sheehy, J. Skaritka, X.J. Wang, Z. Wu, Phys. Rev. Lett. 91, 074801 (2003).
- [30] E. Allaria et al., New J. Phys. 14, 113009 (2012).
- [31] E. Allaria et al., Nature Communications 4, 2476 (2013).
- [32] I. Ben-Zvi, K.M. Yang, L.H. Yu, Nuclear Instruments and Methods in Physics Research A 318, 726 (1992).
- [33] L.H. Yu, I. Ben-Zvi, Nuclear Instruments and Methods in Physics Research A 393, 96 (1997).
- [34] J. Rosenzweig et al., Nuclear Instruments and Methods in Physics Research A 593, 39 (2008).
- [35] Y. Ding et al., Phys. Rev. Lett. 102, 254801 (2009).
- [36] P.J. Emma et al., Phys. Rev. Lett. 92, 074801 (2004).
- [37] E.L. Saldin, E.A. Schneidmiller, and M.V. Yurkov, Phys. Rev. ST Accel. Beams 9, 050702 (2006).
- [38] W. Fawley, Nuclear Instruments and Methods A 593, 111 (2008).
- [39] L. Giannessi et al. Phys. Rev. Lett. 106, 144801 (2011).

- [40] G. Marcus et al., Appl. Phys. Lett. 101, 134102 (2012).
- [41] L.H. Yu et al., Phys. Rev. E 49 (1994).
- [42] F. Frassetto et al. NIM A 593, 14 (2008).
- [43] N.R. Thompson and B. W. J. McNeil, Phys. Rev. Lett. 100, 203901 (2008).
- [44] D. J. Dunning, B. W. J. McNeil, and N. R. Thompson, Phys. Rev. Lett. 110, 104801 (2013).
- [45] E. Kur, D. J. Dunning, B.W.J. McNeil, J. Wurtele and A. Zholents, New Journal of Physics, 13, 063012(2011).
- [46] G. Dattoli et al., NIM A 495 48 (2002).
- [47] F. Ciocci et al., Phys. Rev. E 47, 2061 (1993).
- [48] L. Giannessi, D. Alesini, P. Antici, et al., Phys. Rev. ST Accel. Beams 14, 060712 (2011).
- [49] M. Ferrario et al., Phys. Rev. Lett. 104, 054801 (2010).
- [50] M. Ferrario et al., Nucl. Instrum. Methods Phys. Res., Sect. A 637, S43 (2011).
- [51] V. Petrillo et al., Phys. Rev. Lett. 111, 114802 (2013).
- [52] M. Labat et al., Phys. Rev. Lett. 103, 264801 (2009).
- [53] G. De Ninno et al., Phys. Rev. Lett. 110, 064801 (2013).
- [54] B. Mahieu et al, Optics Express 21, 22730 (2013).
- [55] R. Bonifacio et al. Riv. N. Cim. 13, 1 (1990).
- [56] R. Bonifacio, L. De Salvo, P. Pierini, and N. Piovella, Nucl. Instrum. Methods Phys. Res. A 296, 358 (1990).
- [57] R. Bonifacio, N. Piovella, and B. W. J. McNeil, Phys. Rev. A 44, R3441 (1991).
- [58] T. Watanabe et al. PRL 98, 034802 (2007).
- [59] L. Giannessi, P. Musumeci, S. Spampinati, JAP 98, 043110 (2005).
- [60] L. Giannessi et al., Phys. Rev. Lett. 108, 164801 (2012).
- [61] L. Giannessi et al., Phys. Rev. Lett. 110, 044801 (2013).
- [62] L. Giannessi, P. Musumeci New Journal of Physics 8, 294 (2006).
- [63] L. Giannessi et al. First Lasing of FERMI FEL-2 (1st stage) and FERMI FEL-1 recent results, Proceedings of FEL 2012 Conference, Nara, August 2012, MOOB06 (2012), <http://www.JACoW.org>
- [64] In preparation.

SMALL-SCALE ACCELERATOR-BASED RADIATION SOURCES
AND THEIR APPLICATIONS

Young Uk Jeong, KAERI, Daejeon, Korea

Abstract

Small-scale accelerator-based radiation sources can be used more widely for developing advanced technologies and exploring new science with high convenience and low cost. Sometimes they are competitive comparing with giant facilities like X-ray free-electron lasers (X-FELs). We have developed a table-top terahertz (THz) FEL for substituting X-ray or millimeter-wave-based security imaging technologies (body scanners) and a laboratory-scale ultrashort electron accelerator for investigating femtosecond dynamics of atoms or molecules with pump-probe experiments. I will present on the status of the development of the small-scale radiation sources and plans for the pump-probe experiments. Additionally recent research results on biological study with the operating KAERI (Korea Atomic Energy Research Institute) THz FEL will be given with the information of the references.

THZ FREE-ELECTRON LASER DRIVEN
BY MAGNETRON-BASED MICROTRON

We have developed a laboratory-scale terahertz (THz) free-electron laser by using a compact conventional microtron with a magnetron RF generator. The brief history and references of the developments are listed as follows.

- FIR FEL Development (1995-1998) [1-3]
 - Target wavelength of 30-40 μm with a 12.5-mm-period undulator
 - Failed in FEL lasing
- THz FEL Development (1998-2007) [4-16]
 - Target wavelength of 100-300 μm with a 25-mm-period period
 - First lasing at the end of 1999 ($\lambda=100\text{-}170\text{ }\mu\text{m}$)
 - FEL & beam dynamics study
 - System stabilization & upgrade ($\lambda=100\text{-}300\text{ }\mu\text{m}$)
- THz Applications (2004-present) [17-23]
 - THz imaging, spectroscopy, meta-material study, THz-bio interaction, & so on
- Table-top THz FEL Development (2008-present) [24-27]
 - Rack-type FEL for security inspection (dimensions of $1.5\text{ x }2.5\text{ m}^2$)
 - Target wavelength of 300-600 μm with the average power of 0.1-1 W

ULTRAFAST ELECTRON DIFFRACTION
FACILITIES

An RF-photogun-based linear accelerator for ultrafast pump-probe research is under construction [28]. The layout of the KAERI ultrashort accelerator is shown in

Fig. 1. This system has four beamlines. Two of them are for ultrafast electron diffraction (UED) experiments on solid and gas targets. The main target parameters of the UED beamlines are listed on the Table 1. The electron bunch duration and timing jitter of the UED beamlines are designed to be less than 50 fs in FWHM and 30 fs in rms. The UED beamlines can perform single-shot measurement with a temporal accuracy less than 100 fs. This small-scale facility can be used for investigating time-resolved diffraction experiments with samples of gas, liquid, solid, and surface. The performance of the UED for those samples can compete with that of the X-FEL facilities. The details on the facility will be shown in these Proceedings [29].

The application experiments of the UED beamlines will be performed by the collaboration with universities in Korea. We are planning to investigate the reaction dynamics of gas-phase samples of pyridine and cyclohexadiene (CHD) with higher temporal resolutions than those of previous studies.

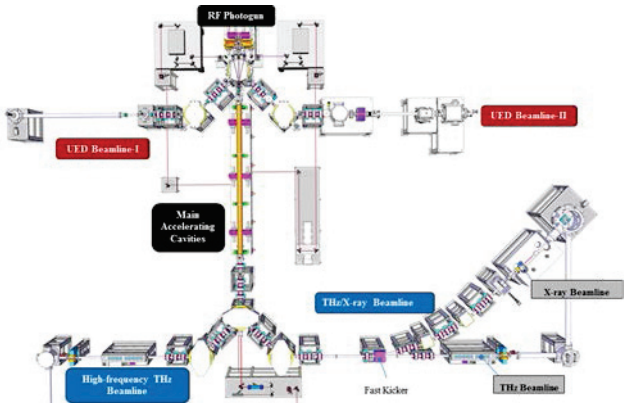


Figure 1: Layout of the KAERI ultrashort accelerator for femtosecond pump-probe experiments.

Table 1: Simulated Beam Parameters of The KAERI UED

Bunch Charge	1 pC
Beam Energy	2.6 MeV
Bunch Length (FWHM)	< 50 fs
Norm. Emittance	0.3 mm mrad
Energy Spread (r.m.s.)	0.3%

ACKNOWLEDGMENT

This work was supported by the World Class Institute program (WCI 2011-001) of the National Research Foundation of Korea funded by the Ministry of Science, ICT and Future Planning.

REFERENCES

- [1] R. Akberdin, et al., Nucl. Instr. Meth. A 405, 195 (1998).
- [2] Y. U. Jeong, et al., Nucl. Instr. Meth. A 407, 396 (1998).
- [3] J. Lee, et al., Nucl. Instr. Meth. A 407, 161 (1998).
- [4] Y. U. Jeong, et al., Nucl. Instr. Meth. A 475, 47 (2001).
- [5] G. M. Kazakevitch, et al., Nucl. Instr. Meth. A 475, 599 (2001).
- [6] Y. U. Jeong, et al., Nucl. Instr. Meth. A 483, 195 (2002).
- [7] Y. U. Jeong, et al., Nucl. Instr. Meth. A 483, 363 (2002).
- [8] G. M. Kazakevitch, et al., Nucl. Instr. Meth. A 483, 331 (2002).
- [9] G. M. Kazakevitch, et al., Nucl. Instr. Meth. A 507, 146 (2003).
- [10] Y. U. Jeong, et al., Nucl. Instr. Meth. A 507, 125 (2003).
- [11] Y. U. Jeong, et al., Nucl. Instr. Meth. A 528, 88 (2004).
- [12] G. M. Kazakevitch, et al., Nucl. Instr. Meth. A 528, 115 (2004).
- [13] Y. U. Jeong, et al., J. Kor. Phys. Soc., 51, 416 (2007).
- [14] G. M. Kazakevitch, et al., J. Appl. Phys., 102, 034507 (2007).
- [15] G. M. Kazakevitch, et al., Phys. Rev. ST Accel. Beams 12, 040701 (2009).
- [16] G. M. Kazakevitch, et al., Nucl. Instr. Meth. A 647, 10 (2011).
- [17] V. V. Kubarev, et al., Nucl. Instr. Meth. A 507, 523 (2003).
- [18] Y. U. Jeong, et al., Nucl. Instr. Meth. A 543, 90 (2005).
- [19] G. D. Bogomolova, et al., Nucl. Instr. Meth. A 543, 96 (2005).
- [20] G. N. Zhizhin, et al., Infra. Phys. Tech. 49, 108 (2006).
- [21] H. J. Cha, et al., J. Kor. Phys. Soc. 49, 354 (2006).
- [22] Y. U. Jeong, et al., Nucl. Instr. Meth. A 575, 58 (2007).
- [23] Y. Hwang, et al., Optics Express, 22, 11465 (2014).
- [24] Y. U. Jeong, et al., J. Kor. Phys. Soc., 59, 3251 (2011).
- [25] N. A. Vinokurov, Y. U. Jeong, Phys. Rev. Lett. 110, 064805 (2013).
- [26] J. Mun, et al., Phys. Rev. ST Accel. Beams 17, 080701 (2014).
- [27] K. Lee, et al., submitted to Nucl. Instr. Meth. A (2014).
- [28] N. Vinokurov, et al., Proceedings of the 35th International Free Electron Laser Conference, New York, USA, 2013, p. 287.
- [29] H. W. Kim, et al., Proceedings of the 36th International Free Electron Laser Conference, Basel, Switzerland, 2014.

PHASE SPACE MANIPULATIONS IN MODERN ACCELERATORS*

Dao Xiang[†], Shanghai Jiao Tong University, Shanghai, China

Abstract

Beam manipulation is a process to rearrange beam's distribution in 6-D phase space. In many cases, a simple phase space manipulation may lead to significant enhancement in the performance of accelerator based facilities. In this paper, I will discuss various beam manipulation techniques for tailoring beam distribution in modern accelerators to meet the requirements of various applications. These techniques become a new focus of accelerator physics R&D and hold great promise in opening up new opportunities in accelerator based scientific facilities.

INTRODUCTION

The ability to tailor a beam's 6-D phase space to meet the demands of various applications is of fundamental interest in accelerator physics. For instance, the electron bunch length typically needs to be reduced in FELs to drive the exponential growth process while it may need to be increased in storage rings to increase beam life time. Beam manipulations include a wide array of techniques that use rf cavities, dispersive elements, lasers, etc. to rearrange beam distribution in 6-D phase spaces. On the one hand, one has the freedom to use many elements to design a beam for a specific application (see. e.g. [1]); on the other hand, beam manipulation has to obey some basic rules (e.g. the emittances of the subspaces cannot be partially transferred from one plane to another if the beam is uncoupled before and after the transformation [2]). Here I will discuss a few representative beam manipulation techniques and show how they may enhance the capabilities of modern accelerators.

GENERAL DISCUSSIONS

In transverse plane, dipoles are used to bend the beam and quadrupoles are used to focus the beam. When they are integrated in a suitable way, they can form a closed loop (an electron storage ring) which allows the beam to circulate for millions of thousands turns. While it appears trivial to control the transverse beam size with quadrupoles, focusing the beam to extremely small size requires special efforts. For instance, a ~ 500 m final focus beam line is needed to focus the electron beam to nanometer (nm) level in linear colliders [3]; another extreme is electron microscope where the spherical aberration is corrected up to the 5th order to provide sub-50 pm resolution which allows one to see individual Hydrogen atom [4].

In longitudinal plane, beam phase space manipulation typically requires an element to change beam energy and a dispersive element to change beam path length. This is be-

cause relativistic electrons travel more or less with the speed of light (e.g., for 1 GeV electron, $1 - v/c \approx 1.3 \cdot 10^{-7}$). As a result, for modern beams with typical small energy spreads, the relative longitudinal velocities of electrons are so small that they do not change their relative positions when the beam travels along a straight line in a drift. With a dispersive element, one can force the particles to follow different paths and the beam longitudinal distribution can be readily shaped.

BEAM MANIPULATION FOR FELS

So far most of the high-gain FELs in the short wavelength (VUV to hard x-ray regime) have operated in the SASE mode in which radiation from the electron beam shot noise is exponentially amplified to the GW level. While a SASE FEL has excellent transverse coherence, its temporal coherence is rather limited (noisy in temporal profile and spectrum). In this section we discuss several beam manipulation techniques that may improve temporal coherence of FELs by providing coherent bunching to seed the FEL amplification process.

To provide bunching at short wavelength, fine structures in beam current distribution have to be created. The creation of a charge density modulation at sub-optical wavelengths in an electron beam with lasers is analogous to the manipulation of the electron bunch length in a magnetic bunch compressor. The difference is that the energy chirp (correlation between a particle's energy and its longitudinal position) is imprinted by lasers rather than RF cavities. The process of longitudinal bunch compression, to the first order, can be described as a linear transformation where the bunch length is reduced while the energy spread (conservation of phase space area) and peak current (conservation of charge) are both increased. This is achieved by first accelerating the beam off-crest in RF cavities to establish a correlated energy chirp (e.g. with bunch head having a slightly lower energy than the bunch tail), and then sending the beam through a dispersive chicane. The particles with lower energy are bent more in the chicane and therefore tra-

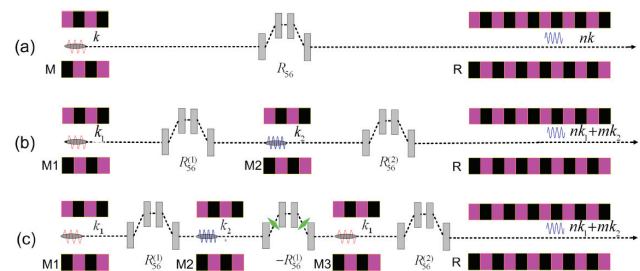


Figure 1: Various harmonic generation schemes for seeding FELs.

* Work supported by the National Natural Science Foundation of China under Grants No. 11327902.

[†] dxiang@sjtu.edu.cn

verse a longer path length than the higher energy particles that are bent less. As a result, the low energy electrons slip back longitudinally while the high energy electrons catch up, which leads to bunch compression.

Replacing the RF cavity with a laser allows one to create much finer structures in beam phase space without changing the overall bunch length. This is because the laser wavelength is typically much shorter than the electron beam duration, so the laser does not give beam a net energy chirp. As a result, after dispersion the overall bunch duration is kept constant. Instead, the time-varying laser field imprints a sinusoidal energy chirp (called an energy modulation) on the beam phase space which leads to varying local compression/decompression of the beam current on the scale of the laser wavelength after dispersion. The result is a density modulation in the current distribution of the beam, both at the laser frequency and at its harmonics.

For example, the phase space evolution in high-gain harmonic generation (HGHH [5]) scheme (Fig. 1a) is shown in Fig. 2. A laser is first used to interact with the beam in a modulator to produce sinusoidal energy modulation in beam phase space (Fig. 2b). After passing through a chicane, half of the particles that have the negative energy chirp (blue particles in Fig. 2b and Fig. 2c) are compressed, while the other half with the positive energy chirp (red particles in Fig. 2b and Fig. 2c) are decompressed. As a result of this transformation, the energy modulation is effectively converted into a density modulation (see Fig. 2d where the beam density consists of many spikes equally separated by the laser wavelength) that contains harmonic frequency components of the laser fundamental frequency.

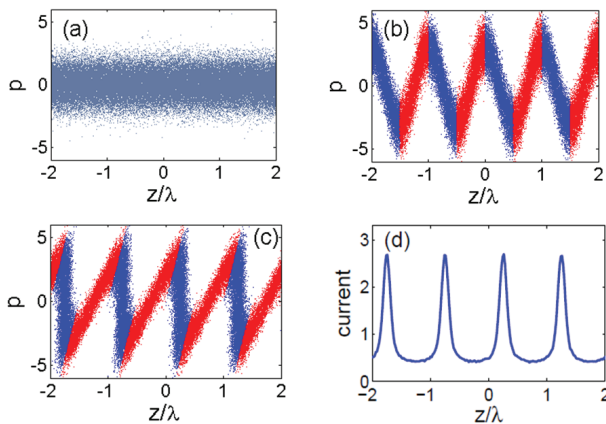


Figure 2: Evolution of the phase space in HGHH scheme. (a) before the modulator; (b) after the modulator; (c) after the chicane; (d) density distribution after the chicane normalized to the initial beam current. The horizontal axis is the beam longitudinal position normalized to the laser wavelength and the vertical axis is particle's energy deviation with respect to the reference particle normalized to the rms slice energy spread of the beam. The energy modulation is three times larger than the beam energy spread.

Analysis shows that the width of the current spike normalized to the laser wavelength is approximately $1/A$, where $A = \Delta E/\sigma_E$ is the ratio of energy modulation amplitude ΔE to the beam energy spread σ_E . Therefore, in general generation of the h th harmonic requires the energy modulation to be approximately h times larger than beam energy spread, an undesired consequence for FEL applications where the increased energy spread may significantly reduce the FEL gain. Another undesired consequence for HGHH is that if the h th harmonic is to be achieved, the peak current of the bump is also increased by about h times (as can be seen in Fig. 1d), which may cause undesirable collective effects. Furthermore, the spectrum of the bunching is found to be sensitive to beam imperfections such as nonlinear beam energy chirps that may easily broaden the bunching spectrum by changing the separation of the current spikes [6, 7].

These limitations can be overcome with the echo-enabled harmonic generation (EEHG [8, 9]) scheme in the double modulator-chicane system (Fig. 1b). In EEHG the beam is also first energy modulated by a laser in the first modulator. But quite differently, the first chicane is chosen to have a large momentum compaction such that after passing through the strong chicane the density modulation is macroscopically smeared (Fig. 3a). Simultaneously, complicated fine structures (e.g. 'energy banding') are introduced into the phase space, which has been recently observed experimentally [10]. A second laser is then used to further modulate the beam energy in the second modulator (Fig. 3b) to imprint additional correlations in phase space. A second weaker chicane orients these correlations vertically in the energy space, which yields a charge density modulation at very high harmonic frequencies. As a result of this nonlinear process, the harmonic bunching structure emerges as a recoherence effect after a short disappearance, like an echo

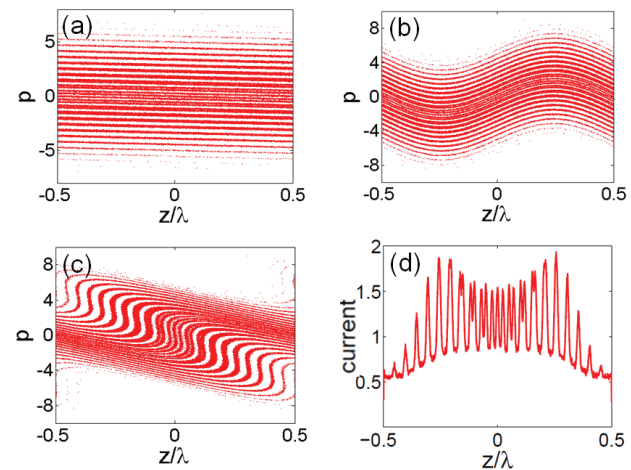


Figure 3: Evolution of the longitudinal phase space in EEHG scheme. (a) after the first strong chicane; (b) after the second modulator; (c) after the second weak chicane; (d) density distribution after the second chicane.

(Fig. 3c and Fig. 3d). The first stage of EEHG may also be understood as bunch local decompression such that the spread of each energy band is reduced compared to the initial energy spread; and the second stage of EEHG is then similar to HHG.

The key advantage of EEHG technique is that it can generate very high harmonics with harmonic number much larger than the ratio of energy modulation to energy spread. This makes it possible to generate very high frequency bunching while simultaneously keeping the beam energy spread small, which allows the generation of soft x-rays from a UV seed laser in a single stage. Another advantage of EEHG is that by splitting the single current bump into many bumps per wavelength, the peak current of each current bump can be significantly reduced, which mitigates the potential collective effects related to the high peak current. For instance, as seen in Fig. 3d, with the energy modulation three times larger than the beam energy spread, the peak current is only increased by a factor of 2 while the harmonic number is extended to ~ 20 . Even higher harmonics can be produced by increasing the momentum compaction of the first chicane while keeping the energy modulation amplitudes essentially unchanged. Furthermore, due to the highly nonlinear phase space gymnastics that decompress local regions of the beam, the spectrum of the bunching is made to almost immune to the phase space imperfections. This allows the generation of transform-limited highly coherent radiation in realistic conditions when the beam has considerable nonlinear chirps [11].

To push the harmonic number to beyond 100, very recently a novel seeding scheme that uses a triple modulator-chicane (TMC) system has also been proposed [12]. This scheme is schematically shown in Fig. 1c where the first and second chicanes have opposite momentum compaction and the first and third lasers have the same wavelength and π phase shift. To illustrate the physics behind the TMC scheme, the evolution of the beam longitudinal phase space is shown in Fig. 4. For simplicity, in Fig. 4 the lasers have the same wavelength in the three modulators and only the phase space within one wavelength region is shown.

The beam phase space after interaction with the first laser is shown in Fig. 4a where the energy modulation is 3 times larger than the beam slice energy spread. Similar to the EEHG scheme, separated energy beamlets are generated (Fig. 4b) after the beam passes through the first chicane with a moderate R_{56} as a result of bunch decompression with a decompression factor D . After interaction with the second laser of which the energy modulation is 20 times smaller than beam slice energy spread, the beam phase space evolves to that in Fig. 4c. Because the energy modulation is much smaller than beam's initial energy spread, it is actually very difficult to see the difference between Fig. 4b and Fig. 4c. The second chicane with opposite momentum compaction ($R_{56}^{(2)} = -R_{56}^{(1)}$) compresses the beamlets by a factor of D and amplifies the modulation imprinted in M2. The resulting beam phase space is shown in Fig. 4d which is similar to that in Fig. 4a. If no modulation is imposed

in M2, the second chicane will restore beam phase space to the same distribution as that before the first chicane, because the transfer matrix from the exit of M1 to the exit of the second chicane is unity. With a small energy modulation in M2, the second chicane will transform the beam phase space to a distribution similar to that before the first chicane with the presence of energy modulation from M2 superimposed on the modulation from M1 (Fig. 4d).

The laser in M3 is chosen to give the beam the same modulation amplitude as that in M1, but with π phase shift, so that the overall energy modulation in M1 is canceled in M3. After the cancellation, the modulation from M2 becomes dominant, as shown in Fig. 4e. The wavelength of the modulation in Fig. 4e is roughly D times shorter than that in M2. A third chicane with small R_{56} further converts the energy modulation into density modulation (Fig. 4f). By integrating the modulators and chicanes in a clever way, the 22nd harmonic is generated with a modulation in M2 that is 20 times smaller than beam slice energy spread and the final energy spread growth is only about 15%.

The unique advantages of TMC scheme that only a small energy modulation is needed in M2 and the second chicane compresses the modulation imprinted in M2 to shorter wavelength opens new opportunities for using low power high-order harmonic generation (HHG) source (see, for example [13]) at short wavelength to seed x-ray FELs. As an example, in [12] the feasibility of generating significant bunching at 1 nm and below from a low power (100 kW) HHG seed at 20 nm assisted by two moderate power UV lasers at 200 nm while keeping the energy spread growth within 40% has been shown. The supreme up-frequency conversion efficiency of the TMC scheme together with its unique advantage in maintaining beam energy spread opens new opportunities for generating fully coherent x-rays at sub-nanometer wavelength from external seeds.

Both HHG and EEHG have been demonstrated experimentally. So far the record for HHG is the 60th harmonic obtained in a two-stage configuration [14] and that

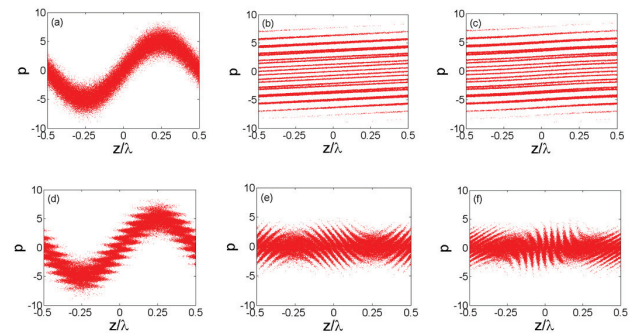


Figure 4: Evolution of the longitudinal phase space in TMC scheme. (a)-After the first modulator; (b)-After the first chicane; (c)-After the second modulator; (d)-After the second chicane; (e)-After the third modulator; (f)-After the third chicane.

for EEHG in a single stage is 15th harmonic [15]. While the EEHG is still in the early experimental development stage [15–18], the two distinct advantages of EEHG, i.e. high frequency up-conversion efficiency and insensitivity to electron beam phase space imperfections have both been demonstrated. For instance, Fig. 5 shows the radiation spectra of HGHG and EEHG produced with a 2.4 micron seed laser when the beam has considerable quadratic energy chirp. The beam is accelerated at an off-crest phase (about 2.5 degrees from on-crest phase) to imprint a positive energy chirp and the exact energy chirp is varying from the fluctuation of timing jitter and RF phase jitter. From the results, one can see that while the radiation from HGHG has large fluctuations in the central wavelength and relatively large bandwidth, that from EEHG is essentially unchanged with a much narrower bandwidth. These results should forward the development of future seeded x-ray FELs that aim to produce laser-like x-rays.

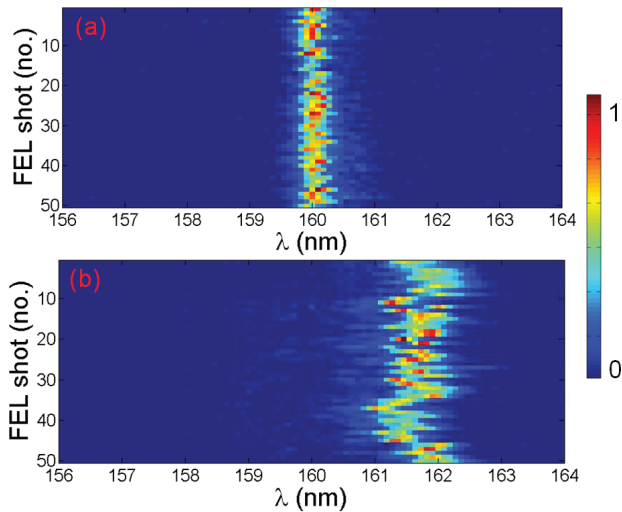


Figure 5: Fifty consecutive radiation spectra for EEHG (a) and HGHG (b) with a chirped beam. Note, the central wavelength of HGHG signal is shifted by the linear chirp and the bandwidth of the HGHG signal is increased by the nonlinear chirp, while those for EEHG are essentially unaffected.

BEAM MANIPULATION FOR THZ RADIATION

For structures at THz wavelength and above, the drive laser as required in a photocathode rf gun may be shaped accordingly to generate the desired pattern in beam current distribution, taking advantage of the promptness of the photoemission process [19–21]. Alternatively, one may use two lasers to manipulate the beam longitudinal phase space for generation of charge density modulation at THz frequency. For instance, in the scheme proposed in [22] a laser is used to generate energy modulation in the beam phase space in the first undulator; after interacting with the second laser, the beam phase space consists of fast modulation at the

sum frequency and a slow modulation at the difference frequency (see Fig. 6). After passing through a chicane, the energy modulation at the difference frequency can be converted to density modulation. If the frequencies of the two lasers are close to each other, the difference frequency will be much lower than the laser frequency. In this case the relativistic electron beam is used as the nonlinear medium to down-convert the frequency of two optical lasers to THz range, and therefore one can generate long-scale periodic structures in electron beam through short-scale laser modulations.

This technique has been demonstrated at SLAC's NLCTA where density modulation around 10 THz was generated by down-converting the frequencies of an 800 nm laser and a 1550 nm laser [23]. One of the many advantages of this technique is the flexibility it offers to tune the central frequency of the modulation, which can be achieved through tuning of laser wavelengths, beam energy chirp, and chicane momentum compaction. In principle, this allows one to generate coherent narrow-band THz radiation covering the whole THz range. A variant of this scheme that allows one to use two lasers with the same wavelength to produce THz using the EEHG setup has also been briefly discussed in [23] and studied in detail in [24]. Here an energy chirp is used to produce a slight shift of the wavelength of the modulation from the first laser, which also leads to density modulation at THz frequency when superimposed with the second laser modulation. This scheme removes the need of an OPA for producing lasers with different wavelengths for THz generation.

It is also possible to use a transverse mask to generate fine structures in beam transverse distribution, and then use emittance exchange technique [25–27] to convert the spatial structures into time structures [28]. For a beam line that couples the beam dynamics in x and z planes, analysis shows if its 4 by 4 transfer matrix has such a form that it is 2 by 2-block antidiagonal, then a particle's final transverse

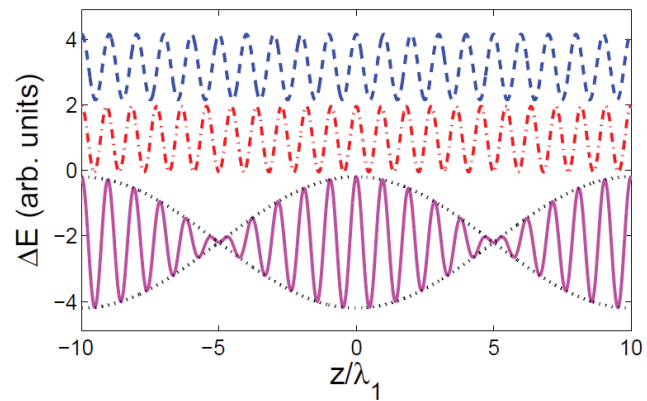


Figure 6: Energy modulation with a laser at λ_1 (blue line) and at $0.9\lambda_1$ (red line); a combination of the two energy modulations (magenta line); the black dotted line illustrates the envelope of the slow modulation at the difference frequency of the two lasers.

coordinates will only depend on its initial longitudinal coordinates, and vice versa. As a result, beam's transverse and longitudinal degrees of freedom will be exchanged after the beam passes through the beam line. The first beam line for transverse-to-longitudinal EEX proposed in 2002 consists of a RF deflecting cavity in the center of a chicane [25]. This scheme is easy to implement, but the exchange is not complete. Later a complete EEX beam line was found in which the deflecting cavity is put between two identical doglegs [26]. However, this scheme introduces offset in beam trajectory which might be undesirable in some cases. Recently a chicane type exact EEX beam line was also proposed [27] where a pair of quadrupoles is used to form a negative unity transfer matrix for the transverse plane in the chicane. The negative unity section reverses the dispersion of the first half of the chicane, which is optically equivalent to flipping the sign of a dogleg. This beam line also provides exact EEX and may be easier to implement because it doesn't introduce offset, and turning off the quadrupoles and deflecting cavity makes the beam line a simple chicane. Because the transverse and longitudinal phase space are exchanged, one can produce tailored beam distribution in longitudinal plane by shaping the initial beam distribution in transverse plane [28].

BEAM MANIPULATION FOR ADVANCED ACCELERATORS

Advanced accelerators driven by laser and electron beam hold great promise in downsizing accelerator based scientific facilities through the orders of magnitude higher acceleration gradient. With a special mask, one may generate a beam with linearly ramped current [29] through emittance exchange that will significantly increase the transformer ratio in electron beam driven advanced accelerators.

Here I will focus on how one may enhance the performance of inverse FEL (IFEL) where a high power laser is used to boost beam energy in an undulator. In rf accelerators, the electron bunch is much shorter than the wavelength of the rf field, and therefore a monoenergetic beam can be routinely obtained. However, obtaining a monoenergetic beam in laser accelerators is not trivial, because typically the electron bunch length is much longer than laser wavelength and different particles would see different phases (some get accelerated while others are decelerated). One promising way to obtain monoenergetic beams in laser accelerators is to first use a laser to generate microbunches, and then put the bumps at the acceleration phase so that most of the particles see more or less the same field which will lead to net acceleration. This has been demonstrated both at FIR wavelength [30] and optical wavelength [31].

As shown in Fig. 7, with the electron bunch being much longer than laser wavelength, in a single stage IFEL half of the electrons are accelerated while the other half decelerated (middle). In a cascaded IFEL, much more electrons can be accelerated by a strong laser pulse after being packed into optical microbunches by a weaker initial laser pulse

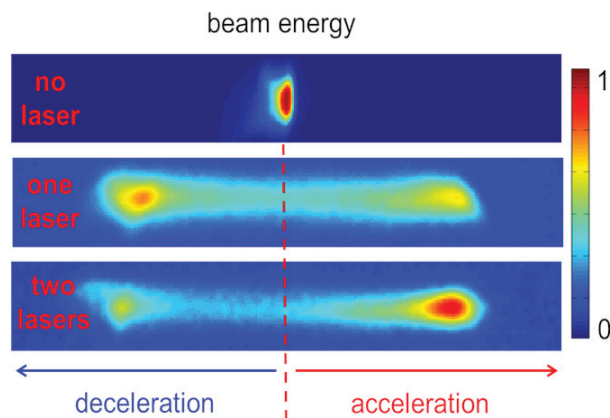


Figure 7: Benefits of cascading in an optical IFEL: a relativistic electron beam with small energy spread (top) can be accelerated with a co-propagating laser (middle), or with two lasers in sequence (bottom).

(bottom), which leads to reduced beam energy spread and higher trap efficiency.

BEAM MANIPULATION FOR UED/UEM

Accelerator based ultrafast electron diffraction (UED [32–34]) and ultrafast electron microscopy (UEM [35–37]) facilities are complementary to FELs and may also provide both high temporal and spatial resolution in probing matter at extremely high precision. In UEDs, one of the main challenges is how to produce beam with ~ 10 fs duration and sufficient number of electrons (say $\sim 10^6$). The beam at the exit of the photocathode rf gun typically has a positive energy chirp from the longitudinal space charge force, which would further increase bunch length in the following drift. One solution is to use an rf cavity to reverse the energy chirp and then the bunch length may be reduced in a drift or chicane. The other is to use an Alpha magnet that has positive R_{56} to compress the beam. With these manipulation in longitudinal plane, one may realize ~ 10 fs resolution in UED.

In UEMs, one of the main challenges is to produce beam with energy spread below 10^{-4} and normalized emittance below 0.1 micron [36, 37]. To reduce beam emittance, the beam charge needs to be reduced and bunch length needs to be increased to mitigate the space charge effect. However, as bunch length increases, the nonlinear rf curvature tends to increase the beam global energy spread. This can be compensated for with a harmonic cavity, similar to that in FELs where harmonic cavities are used to linearize the beam longitudinal phase space to enhance the performance of bunch compressors. For instance, as shown in Fig. 8, with the compensation in the harmonic cavity, beam energy spread can be reduced from 10^{-3} to below 10^{-4} .

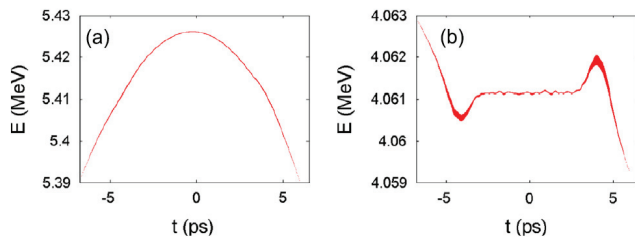


Figure 8: Beam longitudinal phase space at the exit of the s-band photocathode rf gun (a) and at the exit of the c-band harmonic cavity (b).

SUMMARY

In this paper, various techniques for manipulating beam distribution in phase space are discussed. I focused on the techniques that I'm most familiar with. There are many techniques not included in the discussion, such as beam conditioning, emittance partitioning, etc., and the interested readers can find more information elsewhere. For readers particularly interested in beam manipulation with lasers, more information can be found in the review article [1]. These techniques become a new focus of accelerator physics R&D and I believe very likely these advanced concepts will open up new opportunities in accelerator based scientific facilities and the science enabled by them.

ACKNOWLEDGMENT

I want to thank my SLAC colleagues: A. Chao, G. Stupakov, T. Raubenheimer, K. Bane, Y. Cai, Y. Ding, M. Dunning, P. Emma, W. Fawley, C. Hast, E. Hemsing, X. Huang, Z. Huang, A. Marinelli, C. Pellegrini, F. Wang, J. Wang, S. Weathersby, J. Wu etc. for many useful collaborations and discussions. I am also grateful to M. Couprie, C. Behrens, H. Deng, C. Feng, P. Musumeci, G. Penn, S. Reiche, W. Wan, D. Wang, Z. Zhao, A. Zholents, etc. for useful international collaborations and discussions. I want to thank the support from DOE Early Career Award from 2012 to 2014.

REFERENCES

- [1] E. Hemsing, G. Stupakov, D. Xiang and A. Zholents, *Rev. Mod. Phys.* 86, 897 (2014).
- [2] E. Courant, *Conservation of phase space in Hamiltonian systems and particle beams*, in *Perspectives in Modern Physics, Essays in Honor of Hans A. Bethe*, edited by R. E. Marshak (Interscience Publishers, New York), p. 257.
- [3] P. Raimondi and A. Seryi, *Phys. Rev. Lett.* 86, 3779 (2001).
- [4] R. Erni *et al.*, *Phys. Rev. Lett.* 102, 096101 (2009).
- [5] L.-H. Yu, *Phys. Rev. A* 44, 5178 (1991).
- [6] T. Shafan and L.-H. Yu, *Phys. Rev. E* 71, 046501 (2005).
- [7] A. Marinelli, C. Pellegrini, L. Giannessi and S. Reiche, *Phys. Rev. ST Accel. Beams* 13, 070701 (2010).
- [8] G. Stupakov, *Phys. Rev. Lett.* 102, 074801 (2009).
- [9] D. Xiang and G. Stupakov, *Phys. Rev. ST Accel. Beams* 12, 030702 (2009).
- [10] E. Hemsing *et al.*, *Phys. Rev. ST Accel. Beams* 17, 010703 (2014).
- [11] Z. Huang *et al.*, in *Proceedings of FEL 09* (Liverpool, 2009), p.127.
- [12] D. Xiang and G. Stupakov, *New J. Phys.* 13, 093028 (2011).
- [13] T. Popmintchev *et al.*, *Nature Photon.* 4, 822 (2010).
- [14] E. Allaria *et al.*, *Nature Photonics* 7, 913 (2013).
- [15] E. Hemsing *et al.*, *Phys. Rev. ST Accel. Beams* 17, 070702 (2014).
- [16] D. Xiang *et al.*, *Phys. Rev. Lett.* 105, 114801 (2010).
- [17] D. Xiang *et al.*, *Phys. Rev. Lett.* 108, 024802 (2012).
- [18] Z. Zhao *et al.*, *Nature Photon.* 6, 360 (2012).
- [19] J. Neumann *et al.*, *J. Appl. Phys.* 105, 053304 (2009).
- [20] P. Musumeci, R.K. Li and A. Marinelli, *Phys. Rev. Lett.* 106, 184801 (2011).
- [21] Y. Shen *et al.*, *Phys. Rev. Lett.* 107, 204801 (2011).
- [22] D. Xiang and G. Stupakov, *Phys. Rev. ST Accel. Beams* 12, 080701 (2009).
- [23] D. Dunning *et al.*, *Phys. Rev. Lett.* 109, 074801 (2012).
- [24] Z. Wang *et al.*, *Echo-enabled tunable terahertz radiation generation with a laser-modulated relativistic electron beam*, *Phys. Rev. ST Accel. Beams*, in press (2014).
- [25] M. Cornacchia and P. Emma, *Phys. Rev. ST Accel. Beams* 5, 084001 (2002).
- [26] P. Emma *et al.*, *Phys. Rev. ST Accel. Beams* 9, 100702 (2006).
- [27] D. Xiang and A. Chao, *Phys. Rev. ST Accel. Beams* 14, 114001 (2011).
- [28] Y.-E. Sun *et al.*, *Phys. Rev. Lett.* 105, 234801 (2010).
- [29] P. Piot *et al.*, *Phys. Rev. ST Accel. Beams* 14, 022801 (2011).
- [30] W. Kimura *et al.*, *Phys. Rev. Lett.* 86, 4041 (2001).
- [31] D. Dunning *et al.*, *Phys. Rev. Lett.* 110, 244801 (2013).
- [32] X. Wang, D. Xiang, T. Kim, and H. Ihee, *Potential of Femtosecond Electron Diffraction Using Near-Relativistic Electrons from a Photocathode RF Electron Gun*, *Journal of the Korean Physical Society*, 48, 390 (2006).
- [33] J. Hastings *et al.*, *Appl. Phys. Lett.* 89, 184109 (2006).
- [34] P. Musumeci *et al.*, *Appl. Phys. Lett.* 97, 063502 (2010).
- [35] J. Yang *et al.*, *Proc. of IPAC14*, p.2205 (2014).
- [36] D. Xiang *et al.*, *Nucl. Instrum. Methods Phys. Res., Sect. A* 759, 74 (2014).
- [37] R. Li and P. Musumeci, *Phys. Rev. Applied*, 2, 024003 (2014).

PARTICLE TRACKING SIMULATIONS FOR EXFEL COMPLEX SHAPE COLLIMATORS

V.G. Khachatryan*, V.H. Petrosyan, T.L. Vardanyan, CANDLE SRI, Yerevan 0040, Armenia

Abstract

The study sets the objective to investigate through numerical simulation the produced secondary radiation properties when the electron beam particles hit collimator walls. Using particle tracking simulation code FLUKA, the European XFEL electron beam as well as beam halo interaction with the collimator were simulated [1,2]. The complex geometrical shape and material composition of the collimator have been taken into account. Absorbed dose spatial distribution in the material of the collimators and particle fluencies from the downstream surface of the collimator were simulated for the total secondary radiation and its main components.

INTRODUCTION

The beam halo consists of particles per bunch with large betatron or energy amplitudes. Evaluation of the number of large-amplitude particles which can be expected due to the scattering processes, wakefields, and magnet nonlinearities is a difficult task. The beam collimation systems are applied to get rid of beam halo. description of collimators with the picture of general view and the photo of “Collimators Block” unit is provided Nina Golubeva [3] The XFEL main collimator CL.COLM (4 collimators) is a system consisting of 4 Titanium alloy tubes (diameters are 4, 6, 8 and 20 mm) distributed vertically, internal pure Al block and outer Copper block (length=50cm) with brazed cooling tubes[4]. Collimator with its movers will be located inside the steel housing (length=1m), in vacuum. In numerical calculations with FLUKA only the main characteristics of geometry has been taken into account. Therefore, somewhat simplified geometry was used in calculations which includes only main collimator block, steel housing and beam pipe (with 40.5mm diameters). The thickness of the titanium tubes and beam pipe wall is 2 mm. All tubes (0.5m long) are not tapered. Vertical direction movers enable the usage of any of four aperture of the collimator. The general view does not correspond to the exact final design. EXFEL linear accelerator beam main parameters are specified in Table 1 [2].

Table 1: Beam Parameters at Undulators

Energy	17.5 GeV
Emittance (normalized)	≤ 1.4 mm-mrad
Beta function	≈ 220 m
Spot size	9×10^{-5} m

*Khachatryan@asls.candle.am

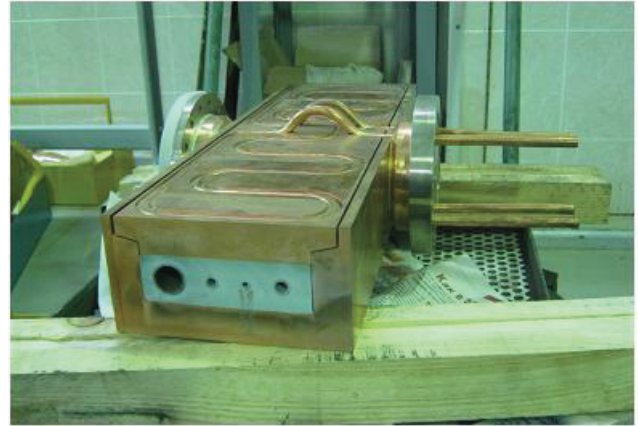


Figure 1: The photo of “Collimators Block” unit (The photo is provided by N. Golubeva) [3].

BEAM IMPACT ON COLLIMATOR WALL

At the undulator the beam size corresponds to the beta function value 220 m [3]. We took 17.5 GeV for the beam energy and 1.4 mm-mrad for the beam normalized emittance.

Bending or corrector magnets supply current values deviations from the stationary ones deflect the beam to the collimator wall. The simulation of the beam impact on the collimator is important from the radiation protection point of view, since high rate of the radiation produced can be harmful for both humans and sensitive equipment. Spatial distribution of the radiation field downstream collimator may indicate where an additional shielding would be useful. We assume that miss-struck beam hits the front wall of the titanium tube at the coordinates $x=0$, $y=0.4$ cm. Electromagnetic cascade has been developed in the body of the titanium tube and then the shower spreads out to the neighbouring volumes (Figure 2). All the plots shown in Figures 2 and 3 are normalized to one of the primary particle. One can see that downstream to collimator outside beam pipe dose rate (Dose-Equivalent) reaches to a few Pico Sievert (≤ 10 pSv) per primary electron. That corresponds to 0.06 Sieverts per 1nC. Plots in the Figure 2 (right column) depict dose distribution [pSv] along the channel with maximum value. A full scale electromagnetic shower developments starts at the middle of the collimator. Figure 3 shows particle fluencies from the downstream surface of the collimator [$\text{GeV}^{-1} \text{ cm}^{-2}$]. Note that the Fluence from the surface of the housing flange prevails in the low energy region while at higher energies most radiation passes through the beam pipe cross sectional area.

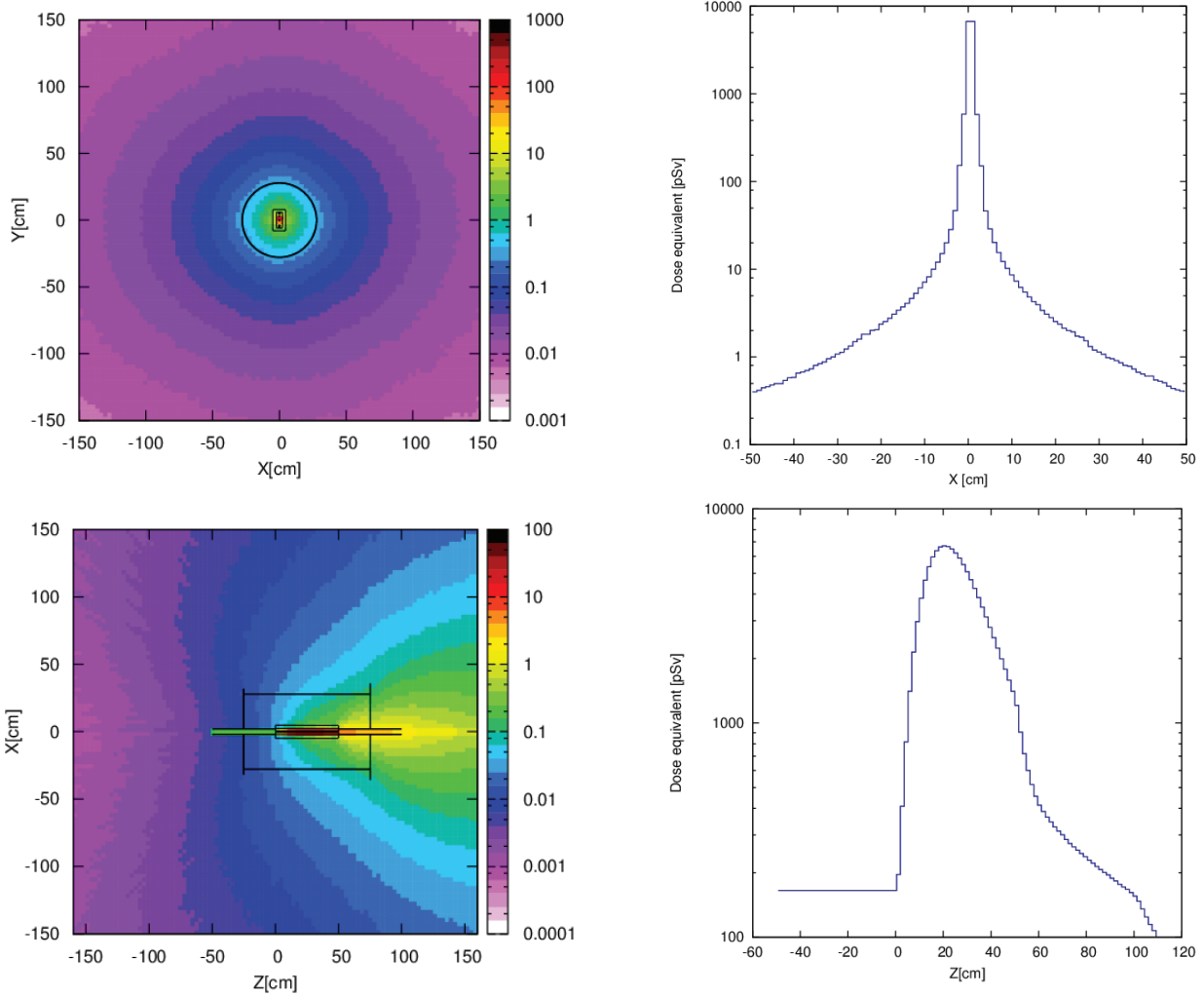


Figure 2: Dose distribution in picoSieverts (left column). Dose distribution in picoSieverts along channel with maximum value (right column).

Beam electrons lose their energy in the volume of the collimator mainly through electromagnetic showers ($\sim 75.6\%$), (Table 2). Hadron and muon energy loss channels compose only 0.1% of the total energy loss. Unwanted hazardous radiation accounts for 24% of incident beam energy carried by the particles escaping the collimator.

Table 2: The energy available per beam particle in GeV and percentage of total energy loss is divided into several prompt radiation channels

	GeV	Percent
Hadron and muon energy loss	2.5×10^{-2}	0.1
Electro-magnetic showers	1.32	75.6
Nuclear recoils and fragments	1.3×10^{-3}	0.0
Low energy neutrons	4.6×10^{-4}	0.0
Particles escaping the system	4.20	24
Energy per beam particle	16.5	100

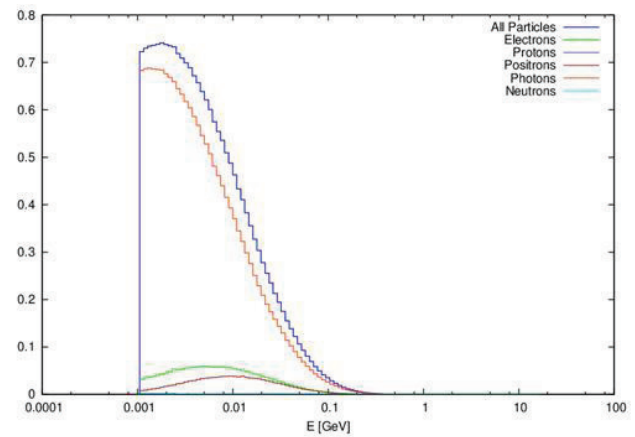


Figure 3: Particle fluencies from the downstream surface of the collimator [$\text{GeV}^{-1} \text{cm}^{-2}$].

BEAM HALO INTERACTION WITH COLLIMATOR

When radiation detectors indicate that the electron beam hits collimator wall, the beam will be steered to the dump quickly enough to avoid significant damage by the radiation. Thus that mechanism cannot be considered as a halo source. Besides, the produced particles are widely spread over energy, spatial and angular ranges and the magnetic lattice will draw them promptly out of the beam orbit.

The peripherals of the beam starts just from the beam gun and part of it passes through the magnetic lattice and reaches undulators. The particles of the beam halo are being lost continuously in interactions with the beam pipe walls. The most efficient way to get rid of the beam halo is collimation. In the result of the halo particles impacts on the collimator walls, a secondary particles coming out of collimator volume are being produced (Photons, electrons, positrons, neutrons, etc.). The dominating component of the secondary radiation is the gamma component. They are insensitive to the magnetic field of lattice and keep their direction of the motion becoming part of the general radiation background. Part of the electrons can contribute to the beam halo.

Since some processes (energy spread, lattice imperfections, interactions with the beam diagnostic equipment, various types of beam instabilities etc.) contribute to the beam halo continuously, further collimation is necessary. Therefore, four collimators of the same type will be installed in EXFEL collimator section.

Input and Output Files Description

To make use of beam transport codes or just lattice transfer matrices it is convenient to rely on the FLUKA capabilities to take beam input and output files as an ASCII table with the particle parameters presented in the separate columns.

In order to do calculations from the custom beam distribution, the user should give the ASCII file. A layout of the data is organized as a table with 9 columns (ID, X,Y, Z, COSX, COSY, COSZ, E), where ID is a type of particle (for example 3 for electrons), X,Y,Z are coordinates in [cm], COSX, COSY, COSZ are the cosines of moving direction with respect to axes and E is the energy in GeV. It is possible to give input file with the mixture of different particles using IDs of particles.

Output files are given in the same format as input files and are written to the different files depending on particle types. For electrons, positrons, protons, photons, neutrons individual output files are created and data of other particles are written in the same file as the mixture of particles. The program is flexible enough to give output files with different formats and any customization is possible if desired. Data organization in that format make possible to use transfer matrices from the magnetic lattice description to transport beam parameters between the individual collimators.

ISBN 978-3-95450-133-5

Initial Halo Types

Two options of the beam halo particles spatial distribution inside beam pipe have been considered:

- 1) Particles are normally distributed along radial direction with the maximum at the beam pipe axis;
- 2) Particles distances from the beam pipe axis are uniformly distributed.

Divergence angles are chosen to be correlated with the particle distance from the axis, in a way that $xx' \sim \epsilon$, where $\epsilon = 0.41 \times 10^{-10}$ is the beam natural emittance.

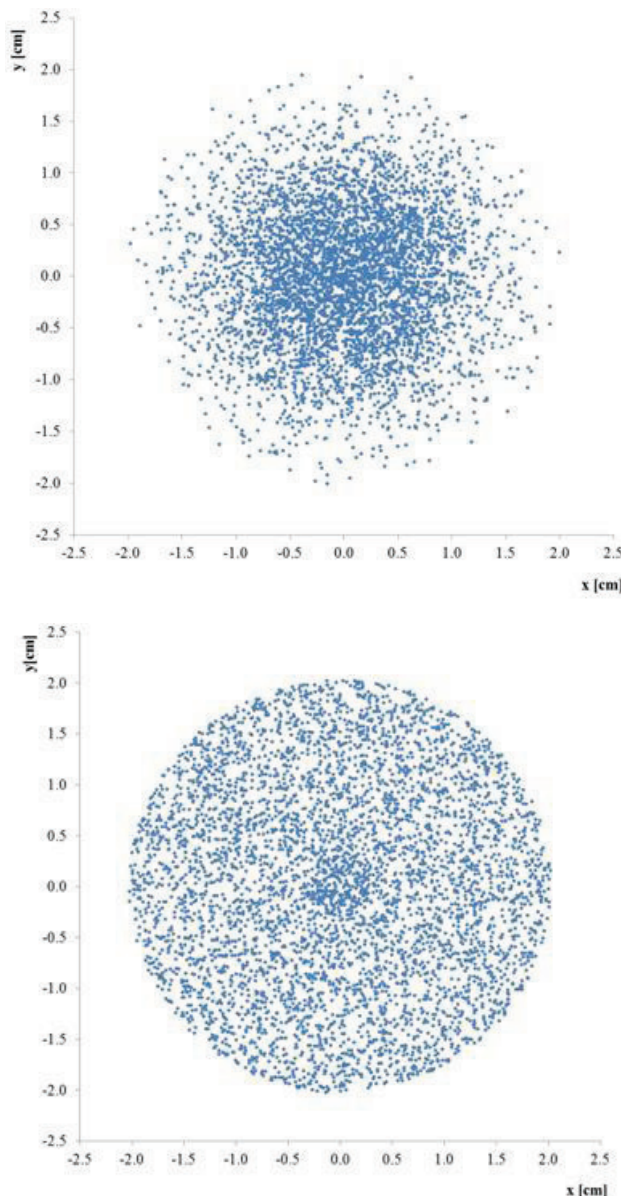


Figure 4: Beam halo particles spatial distribution (5 000 entries) at the entrance (top) and exit (bottom) of the first collimator.

Halo at the First Collimator Exit

Beam halo particles spatial distribution at the entrance and exit of the first collimator is presented in Figure 4.

When the beam halo consisting of the normally distributed within inner area of the beam pipe interacts with the first collimator, the halo coming out from downstream surface of the collimator in the beam pipe region is dominated by the photons (Figure 5). The majority of the electrons and positrons have the energy close to core value 17.5 GeV are being driven by the magnetic lattice to the 2nd collimator entrance while almost all photons are being lost because of the dogleg shape of the undulator section.

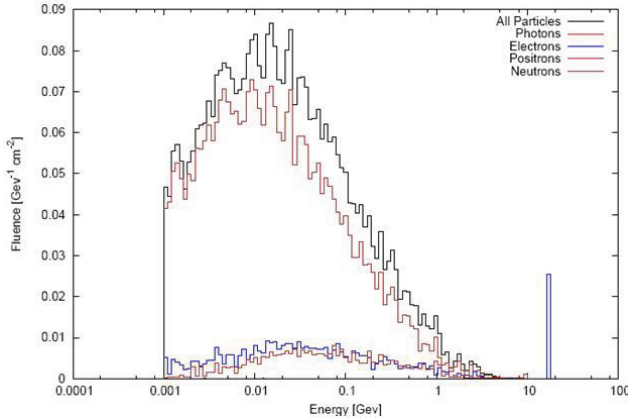


Figure 5: Particle fluencies from the beam pipe region of the 1st collimator surface (Particles per primary electron) produced by the beam halo.

FLUKA simulations show that interaction of the beam halo with the first two collimators significantly reduces halo population (Tables 3, 4). If one assumes that halo particles mean energy is about 17.5 GeV, then 43% of halo energy is absorbed in the first collimator volume, while the mean energy of halo particles incident on the second collimator becomes 1.2 GeV, 24% of which is being lost there.

Table 3: Particle fluencies from the beam pipe region of the collimator surface (Particles per cm² per primary electron). Surface area is 12.87 cm²

Particle Type	Collimator1	Collimator2
All Particles	0.38	0.21
Electrons	4.06 10 ⁻²	2.31 10 ⁻²
Positron	2.8 10 ⁻²	1.57 10 ⁻²
Photons	0.31	0.177
Neutrons	1.7 10 ⁻⁵	1.77 10 ⁻⁷

Table 4: Particle fluencies from the collimator-housing surface (Particles per cm² per primary electron). Surface area is 50265.48 cm²

Particle Type	Collimator1	Collimator2
All Particles	11.57	6.59
Electrons	1.21	0.70
Positron	0.81	0.47
Photons	9.54	5.41
Neutrons	5.63 10 ⁻³	2.26 10 ⁻⁴

SUMMARY AND CONCLUSION

Using particle tracking simulation code FLUKA, the European XFEL electron beam as well as the beam halo interaction with the collimator were simulated. The XFEL main collimator CL.COLM (4 collimators) is a system of four collimators inserted into dogleg shape collimator section. In numerical calculations with FLUKA the characteristics of geometry have been taken into account using SIMPLE GEO package.

We took 17.5 GeV for the beam energy and 1.4 mm-mrad for the beam normalized emittance. Beta function is ≈ 220 m (Spot size (σ_x) is 9×10^{-5} m) at the collimator. The beam halo consists of particles per bunch with large betatron or energy amplitudes. Two types of beam halo filling the inner volume of the beam pipe were simulated.

Bending or corrector magnets supply current values deviations from the stationary ones can deflect the beam to the collimator wall. The simulation of the beam impact on the collimator wall is important from the radiation protection point of view, since high rate of the radiation produced can be harmful both for humans and sensitive equipment. The results of the simulations of the beam impact on the collimator wall show that downstream to collimator outside beam pipe dose rate (Dose-Equivalent) reaches to a few Pico Sieverts (≤ 10 pSv) per primary electron.

To find the effectiveness of the collimator in reducing a beam halo the interaction of the two different types of halo with the collimator were simulated. The parameters of the electrons coming out from the downstream surface of the collimator were transferred to the entrance of the next collimator at the EXFEL collimator section using linear transfer matrices.

The study of the beam halo dynamics is in progress including the evaluation of the number of large-amplitude particles which can be expected due to the scattering processes, wakefields, and magnet nonlinearities [5].

ACKNOWLEDGMENT

The authors are grateful to Nina Golubeva and Vladimir Balandin (DESY) for the essential information and useful discussions.

REFERENCES

- [1] A. Ferrari, P.R. Sala, A. Fassò, J. Ranft, "FLUKA: a multi-particle transport code", CERN 2005-10 (2005), INFN/TC_05/11, SLAC-R-773.
- [2] M. Altarelli *et al.*, XFEL: The European X-Ray Free-Electron Laser, Technical Design Report, DESY 2006-097, Hamburg, 2006.
- [3] Nina Golubeva, Vladimir Balandin, private communication.
- [4] FEL Beam Dynamics Group Home Page: <http://www.desy.de/fel-beam/>
- [5] P. Tenenbaum, T.O. Raubenheimer, M. Woodley, Sources Of Beam Halo In The Next Linear Collider Main Linac, SLAC-PUB-8935 July, 2001, p. 4.

HELICAL UNDULATOR RADIATION IN INTERNALLY COATED METALLIC PIPE*

T. Vardanyan[#], A. Grigoryan, L. Hovakimyan, M. Ivanyan, A. Tsakanian, V. Tsakanov,
CANDLE SRI, Yerevan, Armenia

Abstract

The vacuum chambers of many advanced undulator sources are coated internally in order to reduce the impedance of the vacuum chamber or improve the vacuum performance. Although the impedances and radiation properties of the internally coated metallic pipes for straightforward moving charge are well studied, the peculiarities of the particles wiggling motion on the radiation characteristics in such structure are missed. In this paper we obtain exact expressions for the fields of a particle moving along a spiral path, as in the single-layer resistive as well as in the two-layer metallic waveguides, modelling NEG coating of the waveguide walls. Based on these results, it will be possible to obtain the necessary characteristics of the radiation of helical undulators, very close to reality. The solution is obtained as a superposition of a particular solution of inhomogeneous Maxwell's equations in a waveguide with perfectly conducting walls, and the solutions of the homogeneous Maxwell equations in the single-layer and double-layer resistive waveguides. Solution in the form of the multipole expansion for inhomogeneous Maxwell's equations for a waveguide with perfectly conducting walls, are also obtained in this study.

INTRODUCTION

We consider the spiral motion of a point charge in a resistive circular waveguide, modeling the charge motion in the vacuum chamber of a helical undulator. Helical undulator radiation, which has a number of important specific properties (axial symmetry of the distribution of the radiation power and its narrow directional and narrow band character) is widely used in modern synchrotron radiation sources [1,2].

The problem was considered earlier in the approximation of the spiral motion of the bunch in the free space [3] and in the presence of cylindrical [3-5] or rectangular [6] vacuum chamber with perfectly conducting walls. Limitation on the transverse dimensions of the vacuum chamber by the magnet poles causes a significant impact on the character of the chamber wall radiation. In connection with this it is necessary to take into account the finite conductivity of vacuum chamber walls, which is made in this paper. In this paper we consider also the case of a two-layer metal vacuum chamber, the presence of which, under certain conditions, causes the presence of narrow-band resonance of wakefield radiation in case of rectilinear motion of a

particle [7].

In this paper, the method of expansion of the field in multipoles [8,9] is used, in contrast to the method of eigenfunction expansion of the waveguide, used previously to solve similar problems. The work examines the particle radiation, moving along a spiral trajectory in perfectly conducting cylindrical waveguide, in the resistive cylindrical waveguide and in the two-layer metal waveguide.

RADIATION IN A PERFECTLY CONDUCTING CIRCULAR WAVEGUIDE

Density distribution of charge and current in a cylindrical coordinate system in time domain are represented as follows:

$$\begin{aligned}\rho(z, r, \varphi, t) &= \frac{1}{\sqrt{ra}} \delta(r-a) \delta(\varphi - \omega_b t) \delta(z - vt), \\ j(z, r, \varphi, t) &= (v \vec{e}_z + \omega_b a \vec{e}_\varphi) \rho(z, r, \varphi, t)\end{aligned}\quad (1)$$

and in frequency domain:

$$\begin{aligned}\tilde{\rho}(\omega, r, \varphi, t) &= \frac{1}{2\pi\sqrt{ra}} \delta(r-a) \exp\{j(z - vt + \varphi - jn\omega_b t)\} \\ \tilde{j}(\omega, r, \varphi, t) &= (v \vec{e}_z + \omega_b a \vec{e}_\varphi) \tilde{\rho}(\omega, r, \varphi, t), \quad n = 1, 2, 3, \dots\end{aligned}\quad (2)$$

Here a is the radius of the helical curve, ω_b the gyroscopic rotation frequency, v the longitudinal velocity of the particle, $\vec{e}_z, \vec{e}_\varphi$ the unit vectors of cylindrical coordinate system. Solutions for the radiation fields are searched using the pair of combinations of vector-valued functions [8,9]:

$$\vec{e}_{I,K}(\alpha) = \exp\{j(z - vt + \varphi - jn\omega_b t)\} \begin{Bmatrix} nI_n(\alpha r)/\alpha r, & jI'_n(\alpha r), & 0 \\ nK_n(\alpha r)/\alpha r, & jK'_n(\alpha r), & 0 \end{Bmatrix}\quad (3)$$

Here I_n, K_n are the modified Bessel functions of the first and second kind, respectively and $\alpha = k/\gamma$, where γ is a Lorentz factor and $k = \omega/v$ with frequency ω .

With the help of these functions solutions of the inhomogeneous Maxwell's equations for the radiation fields in the waveguide with a perfectly-conducting walls can be constructed. The result is a combination of TM ($H_z \equiv 0$) and TE ($E_z \equiv 0$) waves:

$$\vec{E}^i = \vec{E}^{TM} + \vec{E}^{TE}\quad (4)$$

with

*This work was supported by State Committee of Science MES RA, in frame of the research project № SCS 13YR-1C0056
#tvardanyan@asls.candle.am

$$\begin{aligned}
 \vec{E}^{TM} &= \begin{cases} -jA_1 Z_0 k^{-1} \text{rot } \vec{e}_I(\alpha), & 0 \leq r \leq a \\ -jA_2 Z_0 k^{-1} \text{rot } \{\vec{e}_K(\alpha) + u\vec{e}_I(\alpha)\}, & a \leq r \leq b \end{cases} \\
 \vec{H}^{TM} &= \begin{cases} A_1 k^{-2} \text{rot rot } \vec{e}_I(\alpha), & 0 \leq r \leq a \\ A_2 k^{-2} \text{rot rot } \{\vec{e}_K(\alpha) + u\vec{e}_I(\alpha)\}, & a \leq r \leq b \end{cases} \\
 u &= -K_n(\alpha a) / I_n(\alpha a) \\
 \vec{E}^{TE} &= \begin{cases} -jB_1 Z_0 \vec{e}_I(\alpha), & 0 \leq r \leq a \\ -jB_2 Z_0 \{\vec{e}_K(\alpha) + u\vec{e}_I(\alpha)\}, & a \leq r \leq b \end{cases} \\
 \vec{H}^{TE} &= \begin{cases} B_1 k^{-1} \text{rot } \vec{e}_I(\alpha), & 0 \leq r \leq a \\ B_2 k^{-1} \text{rot } \{\vec{e}_K(\alpha) + u\vec{e}_I(\alpha)\}, & a \leq r \leq b \end{cases} \quad (5) \\
 u &= -K_n(\alpha a) / I'_n(\alpha a)
 \end{aligned}$$

Coefficients u are determined from the condition of the zero-equal tangential component of the electric field on the waveguide surface: $E_z = E_\phi = 0$ at $r = a$ (a is a waveguide radius). The case $u = 0$ corresponds to the free space. Amplitudes $A_{1,2}$ and $B_{1,2}$ are determined from the condition of continuity of the magnetic components H_r^{TM} and H_r^{TE} at $r = a$ and from the discontinuity of component H_ϕ^{TM} and H_z^{TE} , equal to $gv/2\pi$ and $g\omega_b a/2\pi$, (g is the normalization factor) respectively, for the same value of radius,

$$\begin{aligned}
 A_1 &= -j \exp\{-jn\omega_b t\} \frac{g\alpha v}{\pi\beta^2} (K_n(\alpha a) + uI_n(\alpha a)), \\
 A_2 &= -j \exp\{-jn\omega_b t\} \frac{g\alpha v}{\pi\beta^2} I_n(\alpha a), \quad (6) \\
 B_1 &= j \exp\{-jn\omega_b t\} \frac{gka\omega_b}{\pi} (K'_n(\alpha a) + uI'_n(\alpha a)), \\
 B_2 &= j \exp\{-jn\omega_b t\} \frac{gka\omega_b}{\pi} I'_n(\alpha a).
 \end{aligned}$$

Thus, the longitudinal component of the current generates TM wave, while the transverse ones generates TE mode.

RADIATION IN RESISTIVE-WALL CIRCULAR WAVEGUIDE

The electromagnetic properties of the metal walls of the waveguide are characterized by the metal conductivity σ and its dielectric permittivity $\varepsilon = \varepsilon_0 - j\sigma/\omega$. The radius of the waveguide is still b , and the wall thickness is considered infinite. The solution is sought in the form of a sum of the particular solution \vec{E}^i of inhomogeneous Maxwell equations (4)-(6), obtained for a waveguide with perfectly conducting walls, and the general solution \vec{E}^r of the homogeneous Maxwell equations for the resistive-wall waveguide:

$$\vec{E} = \vec{E}^r + \vec{E}^i \quad (7)$$

Partial solutions for the internal region within the waveguide ($0 \leq r \leq b$) and in its walls ($b \leq r < \infty$) can be written as follows:

for $0 \leq r \leq b$:

$$\vec{E} = C_1 \vec{E}_0^{TM} + C_2 \vec{E}_0^{TE} + \vec{E}^i, \quad \vec{H} = C_1 \vec{H}_0^{TM} + C_2 \vec{H}_0^{TE} + \vec{H}^i \quad (8)$$

where

$$\begin{aligned}
 \vec{E}_0^{TM} &= -jZ_0 k^{-1} \text{rot } \vec{e}_I(\alpha), \quad \vec{E}_0^{TE} = -jZ_0 \vec{e}_I(\alpha), \\
 \vec{H}_0^{TM} &= k^{-2} \text{rot rot } \vec{e}_I(\alpha), \quad \vec{H}_0^{TE} = k^{-1} \text{rot } \vec{e}_I(\alpha). \quad (9)
 \end{aligned}$$

For $b \leq r < \infty$:

$$\vec{E} = D_1 \vec{E}_1^{TM} + D_2 \vec{E}_1^{TE}, \quad \vec{H} = D_1 \vec{H}_1^{TM} + D_2 \vec{H}_1^{TE}, \quad (10)$$

where

$$\begin{aligned}
 \vec{E}_1^{TM} &= -jZ_0 k^{-1} \text{rot } \vec{e}_K(\delta), \quad \vec{E}_1^{TE} = -jZ_0 \vec{e}_K(\delta), \\
 \vec{H}_1^{TM} &= k^{-2} \text{rot rot } \vec{e}_K(\delta), \quad \vec{H}_1^{TE} = k^{-1} \text{rot } \vec{e}_K(\delta). \quad (11)
 \end{aligned}$$

Here $\delta = \alpha^2 - j\omega\sigma\mu_0$ with μ_0 magnetic permeability of vacuum.

Amplitudes $C_{1,2}$ and $D_{1,2}$ are determined from the condition of continuity of the tangential component of the electric and magnetic fields (8) and (10) on the boundary between two media (at $r = b$).

We write down the value of the tangential component of the radiation fields in an ideal waveguide on the boundary between two media (at $r = b$):

$$\begin{aligned}
 E_\phi^i &= E_z^i = 0, \quad H_\phi^i = -j \frac{\beta^2 A_2}{ab I_n(ab)} + j \frac{n B_2}{\alpha^2 b^2 I'_n(ab)}, \\
 H_z^i &= j \frac{B_2}{bk I'_n(ab)} \quad (12)
 \end{aligned}$$

In matrix form, the system of equations for amplitudes written as follows:

$$\begin{pmatrix} \frac{Z_0 n I_n}{\alpha b} & Z_0 I'_n & -\frac{Z_0 n K_n}{\delta b} & -Z_0 K'_n \\ \frac{Z_0 I_n \alpha}{k} & 0 & -\frac{Z_0 K_n \delta}{k} & 0 \\ j \frac{(k^2 - \alpha^2) I'_n}{k^2} & j \frac{n I_n}{\alpha b} & j \frac{(k^2 - \delta^2) K'_n}{k^2} & -j \frac{n K_n}{\delta b} \\ 0 & j \frac{\alpha I_n}{k} & 0 & -j \frac{\delta K_n}{k} \end{pmatrix} \cdot \begin{pmatrix} C_1 \\ C_2 \\ D_1 \\ D_2 \end{pmatrix} = \begin{pmatrix} 0 \\ 0 \\ -H_{\phi,b}^i \\ -H_{z,b}^i \end{pmatrix} \quad (13)$$

Here $I_n = I_n(ab)$, $K_n = K_n(\delta b)$, $I'_n = I'_n(ab)$, $K'_n = K'_n(\delta b)$.

Thus, the problem reduces to solving a linear system of four algebraic equations with four unknown amplitudes.

RADIATION IN THE TWO LAYER RESISTIVE-WALL CIRCULAR WAVEGUIDE

Here we consider the spiral motion of a particle in a two-layer circular waveguide. Ideally conducting waveguide walls are coated from inside with a non-magnetic metal layer. The inner radius of the waveguide and electromagnetic parameters of the inner coating are the same as in the previous case. An additional parameter $b_1 = b + d$ is the outer radius of the inner coating, where d is its thickness. Solution is sought, as before, by the method of partial waves. In this case, there are two boundaries between media: at $r = b$ and $r = b_1$.

Field inside the waveguide (at $0 \leq r \leq b$, as in the previous case, is defined by expressions (6) - (9), while the field inside the metal coating ($b \leq r \leq b_1$), in addition to the modified Bessel functions of the second kind $K_n(\delta r)$ also contains the modified Bessel functions of the first kind $I_n(\delta r)$:

$$\begin{aligned}\vec{E}' &= D_1 \vec{E}_1^{TM} + D_2 \vec{E}_1^{TE} + F_1 \vec{E}_2^{TM} + F_2 \vec{E}_2^{TE}, \\ \vec{H}' &= D_1 \vec{H}_1^{TM} + D_2 \vec{H}_1^{TE} + F_1 \vec{H}_2^{TM} + F_2 \vec{H}_2^{TE},\end{aligned}\quad (14)$$

$$\hat{D} = \begin{pmatrix} \frac{Z_0 n I_n(ab)}{ab} & Z_0 I_n'(ab) & \frac{Z_0 n K_n(\delta b)}{\delta b} & -Z_0 K_n'(\delta b) & -\frac{Z_0 n I_n(\delta b)}{Z_0 \delta I_n(\delta b)} & -Z_0 I_n'(\delta b) \\ \frac{Z_0 \alpha I_n(ab)}{k} & 0 & -\frac{Z_0 \delta K_n(\delta b)}{k} & 0 & -\frac{Z_0 \delta I_n(\delta b)}{k} & 0 \\ j \frac{(k^2 - \alpha^2) I_n'(ab)}{k^2} & j \frac{n I_n(ab)}{ab} & -j \frac{(k^2 - \alpha^2) K_n'(ab)}{k^2} & -j \frac{n K_n(\delta b)}{\delta b} & -j \frac{(k^2 - \alpha^2) I_n'(ab)}{k^2} & -j \frac{n I_n(\delta b)}{\delta b} \\ 0 & j \frac{\alpha I_n(ab)}{k} & 0 & -j \frac{\delta K_n(\delta b)}{k} & 0 & -j \frac{\delta I_n(\delta b)}{k} \\ 0 & 0 & \frac{Z_0 n K_n(\delta b_1)}{\delta b_1} & Z_0 K_n'(\delta b_1) & \frac{Z_0 n I_n(\delta b_1)}{\delta b_1} & Z_0 I_n'(\delta b_1) \\ 0 & 0 & \frac{Z_0 \delta K_n(\delta b_1)}{k} & 0 & \frac{Z_0 \delta I_n(\delta b_1)}{k} & 0 \end{pmatrix} \quad (18)$$

where

$$\begin{aligned}\vec{E}_2^{TM} &= -j Z_0 k^{-1} \text{rot } \vec{e}_l(\delta), \quad \vec{E}_2^{TE} = -j Z_0 \vec{e}_l(\delta), \\ \vec{H}_2^{TM} &= k^{-2} \text{rot rot } \vec{e}_K(\delta), \quad \vec{H}_2^{TE} = k^{-1} \text{rot } \vec{e}_l(\delta).\end{aligned}\quad (15)$$

Six equations for the amplitudes $C_{1,2}$, $D_{1,2}$ and $F_{1,2}$ determined from the matching conditions of the tangential electric and magnetic components of fields (8) and (14) on the vacuum-metal boundary ($r = b$) and the condition of zero-equal tangential electric field components (14) at the metal-perfect conductor boundary ($r = b_1$):

$$\begin{aligned}E_\varphi &= E'_\varphi, E_z = E'_z, \quad H_\varphi = H'_\varphi, H_z = H'_z \quad \text{at } r = b, \\ E'_\varphi &= 0, E'_z = 0, \quad \text{at } r = b_1.\end{aligned}\quad (16)$$

In matrix form, the system of equations for amplitudes may be written as follows:

$$\hat{D} \cdot \hat{X} = \hat{A} \quad (17)$$

where

and two single-column matrixes \hat{X} and \hat{A} :

$$\begin{aligned}\hat{X} &= \{C_1, C_2, D_1, D_2, F_1, F_2\} \\ \hat{A} &= \{0, 0, -H_{\varphi,b}^i, -H_{z,b}^i, 0, 0\}\end{aligned}\quad (19)$$

CONCLUSION

Expressions are obtained for the radiation fields in the ideal-conductive, resistive, and double-layer metal waveguides for a charged particle moving along a spiral trajectory coaxial with the axis of the waveguide.

The form in which the solutions are obtained (superposition of solutions for inhomogeneous and homogeneous Maxwell equations) allows ones to select part of the radiation due to the resistivity of the walls of the waveguide, and to investigate its effect on the undulator radiation.

REFERENCES

- [1] M. Ivanyan et al., ICFA Beam Dynamics Newsletter 45:125-138, 2008.
- [2] M. Altarelli, The European XFEL TDR, DESY 2006-097, (2007).
- [3] H. Wiedemann, Synchrotron Radiation, Springer, Berlin, 2003.
- [4] V.P. Dokuchaev, Izv. VUZ-ov, Radiofizika, vol. 44, no. 7, 587-591 (2001).
- [5] T. Vardanyan et al, in *Proc. 5th Int. Particle Accelerator Conf.*, 2014, Dresden, Germany, WEP0022.
- [6] Y. H. Chin, LBL-29981, DE91 007744 (1990).
- [7] M. Ivanyan, PRST-AB, 17, 021302 (2014).
- [8] A. Piwinski, DESY HERA 92-11 (1992).
- [9] M. Ivanyan et al., PRST-AB, 11, 084001 (2008).

HIGH ACCURACY SHIMMING TECHNIQUE FOR THE PHASE SHIFTERS OF THE EUROPEAN XFEL

Yuhui Li, Joachim Pflueger, The European XFEL, Notkestr 85, 22607 Hamburg, Germany

Abstract

For the European XFEL 91 phase shifters are needed, which have to fulfil stringent field integral specifications: There should be no observable beam deflection when the strength, i.e. the magnetic gap is changed

In order to facilitate the mass production of 91 phase shifters within the tough XFEL schedule a shimming technique was developed. It is based on measured shim signatures and is straight forward and fast to apply. The method is described and results are presented demonstrating that all requirements can be fulfilled.

INTRODUCTION

The undulator systems of the European XFEL need a total of 91 phase shifters. They should be transparent to the electron beam: This means that there should be no detectable effect by changing their strength i.e. their magnetic gap. As a consequence the gap dependent first field integrals error of a phase shifter must not exceed 0.004Tmm (4Gcm) for phase shifter gaps > 16mm. For smaller gaps tolerances can be relaxed as shown in table 1. In addition these requirements must be fulfilled in a good field region in the horizontal plane ± 0.5 mm around the device axis limiting allowed integrated gradient to below 0.004T. A summary is given in table 1.

These tolerances are tight. The magnetic design has a high magnetic symmetry to eliminate any systematic gap dependency due to geometry [1]. Nevertheless small effects may arise due to imperfections in the magnetic material and errors in the pole contours. From observations made on the first prototype [1] it became clear that the gap dependence cannot be compensated by the pole height tuning as applied to the XFEL undulators [2]. By placing shims on poles and/or magnets gap dependent effects can be compensated. Moreover a smart strategy can also provide a good field region of ± 0.5 mm in the horizontal plane to facilitate alignment. Therefore a systematic method was developed which allows the determination of shim parameters to compensate any measurable gap dependency and to provide a sufficient good field region.

Table 1: Gap dependent Tolerance Specifications

Gap (mm)	>16	15	14	13	12	10.5
Spec (Gcm)	± 4	± 7	± 10	± 13	± 16	± 18
Good field range (mm)	± 0.5					

On the other hand, a fast and effective tuning procedure is a key issue for an economic and timely production of a large number of phase shifters. This paper explains a fast

and systematic shimming technique to obtain the required gap dependent field integral specification and simultaneously a small enough gradient to have the required good field range. Measured results are presented.

MAGNETIC MOMENT IN SHIMS

A shim is made from highly permeable such as low carbon iron. When placed on a pole or magnet the external magnetic field induces a magnetic moment in the shim. Its effects are similar but not identical to that of an additional small permanent magnet.

Fig. 1 explains the effect and shows a schematic cut through a hybrid type magnet structure as are used for the Phase Shifters [1]. The magnetization of the magnets is parallel/antiparallel to the beam axis. The flux is redirected perpendicular to the axis by the poles. If a shim is placed on a magnet besides a pole the magnetic moment vector in the shim is mainly parallel to axis and only a small contribution is perpendicular to the axis. In contrast a shim on a pole mainly induces a perpendicular contribution and acts similar to a pole shift.

The magnetic field \vec{B} of a magnetic moment \vec{m} at position \vec{r} is given by:

$$\vec{B}(\vec{r}) = \frac{\mu_0}{4\pi} \left[\frac{3\vec{r}(\vec{m} \cdot \vec{r})}{r^5} - \frac{\vec{m}}{r^3} \right]. \quad (1)$$

Therefore the field integral caused by \vec{m} perpendicular to the axis is given by:

$$\int_{-\infty}^{+\infty} B_{\perp} dz = \int_0^{\pi} \frac{m_{\perp} (3 \sin^2 \theta - 1) + 3 m_{\parallel} \sin \theta \cos \theta}{r^3} d\theta. \quad (2)$$

$$= \frac{28 m_{\perp}}{15 d^3}$$

Where m_{\parallel} and m_{\perp} represent the magnet moment parallel and perpendicular to phase shifter axis, respectively. d is the distance from the magnetic moment to the axis as shown in Fig. 1. According to Eq. 2 only m_{\perp} contributes to the vertical field integral and m_{\parallel} does not. The induced magnetic moment of shims on poles is mainly m_{\perp} and by shims on magnet is predominantly m_{\parallel} . So shims on poles are clearly more efficient. Unfortunately they eat up the effective phase shifter gap and are not self-adhesive by magnetic forces and therefore need to be restrained (glued). In contrast shims on magnet don't narrow the gap due to a 0.5mm pole overhang with respect to magnets. Experimental tests have demonstrated that in contrast to Eq. 2 magnet shims still give a small strength suitable for weak corrections. They stay on magnets firmly. They are a convenient choice Phase Shifters shimming.

The field induced by the shim on the beam axis depends on the distance d . Therefore by changing the transverse dimensions and positions of the shims the gap dependent contribution to the field integral is changed. So different gap dependencies may be created with different shim geometries.

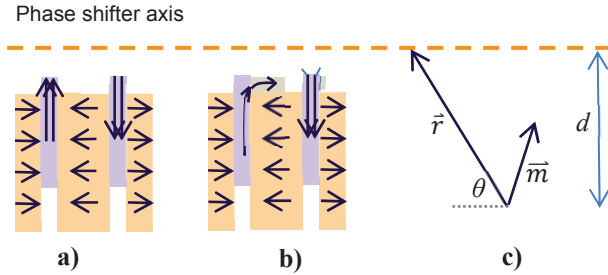


Figure 1: a): Magnetic moments in magnets and poles in a hybrid undulator. b) Magnetic moments in shims on magnets and poles. c) The orientation of a magnet moment vector and its contribution to the field in a point.

SYSTEMATIC TUNING STRATEGY

Two Basic Assumptions

Field integrals and transverse field integral gradients are changed by shims. A systematic tuning technique must determine shim geometry and placement. To do so two assumptions are essential [3,4]:

1. **Linearity principle:** The contribution of any shim is proportional to its thickness.

2. **Superposition principle:** The contribution of a combination of several shims equals to the sum up of the contributions of the individual shims.

It was demonstrated by RADIA simulations as well as by measurements that for the magnet shimming these assumptions hold fairly well [3,4]. In practice the shim thickness varies from 0.1mm to 0.5mm.

Geometry

Fig. 2 illustrates the magnet configuration of a Phase Shifter: It is comprised by four identical magnet modules. Each contains one full magnet and two half magnets. Fig. 2 defines 32 different positions where shims can be placed. Symmetry requires that shims on different positions function accordingly. Experience has shown, that the symmetry principle for half and full magnets needs to be applied differently. Accordingly the 32 different positions can be grouped in two types: Shims on half magnets and shims on full magnets. In each group the function of the shim follows the symmetry properties.

Without loss of generality position 1 in Fig. 2 is selected to represent the “original” position “O” for half magnets and position 3 as the original position for full magnets.

Positions opposite to the original positions on the X axis such as 2, 4 are named “mirror” positions, “M”. Positions on poles with opposite sign are named as “reversed” position “R”. There are positions which are both opposite

to the original position and on the reversed poles. They are named “MR”.

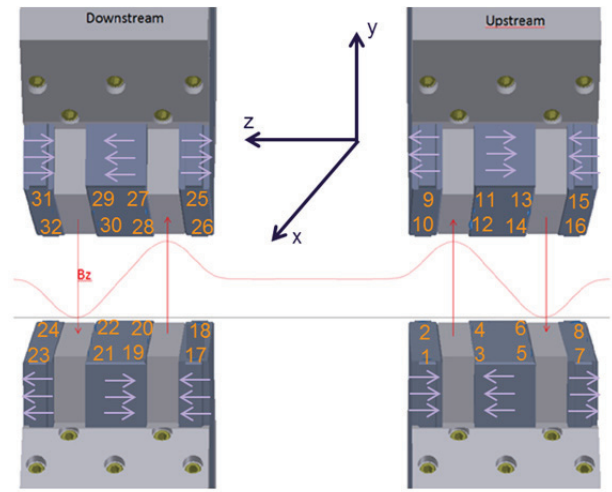


Figure 2: Illustration of the four modules of a phase shifter and definition of the 32 different magnet positions.

Table 2: Combination of Shims and Functions

Combination Type	Expression	Function
“O”+“O”	$2f(x)$	Integral doubles, gradient doubles;
“O”+“M”	$f(x)+f(-x)$	Integral doubles, gradient eliminates
“O”+“R”	$f(x)-f(-x)=0$	Integral eliminates, gradient eliminates
“O”+“MR”	$f(x)-f(-x)$	Integral eliminates, gradient doubles
“M”+“M”	$2f(-x)$	Integral doubles, gradient double & reverse
“M”+“R”	$f(-x)-f(x)$	Integral eliminates, gradient double & reverse
“M”+“MR”	$f(-x)-f(-x)=0$	Integral eliminates, gradient eliminates
“R”+“R”	$-2f(x)$	Integral double & reverse, gradient double & reverse
“R”+“MR”	$-f(x)-f(-x)$	Integral doubles & reverse, gradient eliminate
“MR”+“MR”	$-2f(-x)$	Integral doubles & reverse, gradient double

The field integral induced by a shim on an “O” position as a function of the transverse position x is described by a function of $f(x)$, $x = 0$ is the axis position. Here $f(x)$ can stand for horizontal or vertical field integral. The contributions by shims on the other symmetry positions can be described using $f(x)$ and applying the according symmetry operation: For “M” shims it goes like $f(-x)$, for “R” shims like $-f(x)$ and for “MR” shims like $-f(-x)$. These relationships regularize important geometric properties for a combination of shims on different positions in terms of both gap dependent field integrals and transverse gradients. Table 2 summarizes the combination function of shims at two different

positions. Two things need to be emphasized: 1.) The symmetry operations apply only to shims which have identical geometry. 2.) The shims may be distributed over different locations i.e. on different sides of a pole and/or on poles with different polarity so each position gives a contribution to the field integral.

Full and half magnets are not equivalent and need to be distinguished. In addition each shim produces both a horizontal and vertical field integral.

So there are four cases, which need to be considered separately: Shims on half/full magnets and their effects to vertical/horizontal field. For each case there are the “O”, “M”, “R” and “MR” positions. The magnet positions related to Fig. 2 for these cases are different.

The magnet positions the “O”, “M”, “R” and “MR” positions for the four cases are summarized in Table 3.

Table 3: Magnet Positions with “O”, “M”, “R”, “MR” Symmetry for Horizontal/Vertical Field Integrals and Half/Full Magnets

Magnet & work direction	Symmetry Group	Positions Labelled in Fig. 2
Half magnet & Vertical field	“O”	1, 9, 17, 25
	“M”	2, 10, 18, 26
	“R”	7, 15, 23, 31
	“MR”	8, 16, 24, 32
Full magnet & Vertical field	“O”	3, 11, 19, 27
	“M”	4, 12, 20, 28
	“R”	5, 13, 21, 29
	“MR”	6, 14, 22, 30
Half magnet & Horizontal field	“O”	1, 15, 17, 32
	“M”	8, 10, 24, 26
	“R”	7, 9, 23, 25
	“MR”	2, 16, 18, 32
Full magnet & Horizontal field	“O”	3, 13, 19, 29
	“M”	6, 12, 22, 28
	“R”	5, 12, 21, 27
	“MR”	4, 14, 20, 30

The symmetry relations described in Table 2 and Table 3 are the basis for the shimming technique:

According to Table 2 the effect of two shims can be eliminated and according to Table 3 the symmetry group for horizontal or vertical field contains different positions. It allows to combine shims to correct the field error in one direction without changing the other direction. On the other hand, according to Table 2 the compensation to gap dependent field and gradient errors can also be separated. So small gap dependent field integral and gradient errors can be compensated at the same time.

In order to demonstrate the strategy by using symmetry groups of “O”, “M”, “R”, “MR” in Table 3 the impact of a shim of dimension 36x8x0.4mm placed on a full magnet was measured.

Following Table 3 eight different positions 3, 4, 5, 6, 11, 12, 13, 14 out of the 16 allowed for the vertical field integrals of full magnet were selected for the test. Fig. 3 demonstrates the results. Fig. 3 top shows the original

data for these eight measurements. Sign and dependence depends on the symmetry group. Two measurements were made on each symmetry position “O” at 3, 11; “M” at 4, 12; “R” at 5, 13; “MR” at 6, 14. All pairs are in good agreement. In Fig. 3 bottom the curves are transformed back to “O”. Using the relations of table 3 and table 2 the overlap of these curves is quite good demonstrating that the assumptions on symmetry hold well.

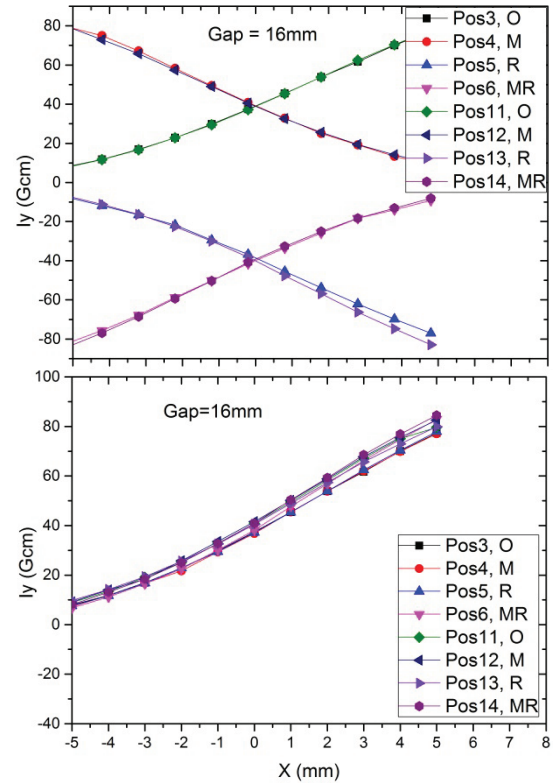


Figure 3: Measurements for test the positions in groups of “O”, “M”, “R” and “MR”. Top: Impact on the vertical field integral of a shim of 36x8x0.4mm on 8 different positions. Bottom: Data transformed back using the symmetry group in Table 3.

FIELD INTEGRAL TUNING

For the large scale production of the 91 Phase Shifters a fast tuning method was developed. It is based on: a) measured signatures of a selection of 5 types of shims with different geometries on half and full magnets, b) the consequent use of the symmetry properties described in tables 2 and 3, c) the application of the linearity and superposition principle and finally d) the numerical optimization using superposition of combinations of shims and their signatures by trial and error with subsequent evaluation of field integrals and gradients. Discrete steps were selected for the thickness of the shims: 50, 100, 200, 300, 400 and 500µm.

Shimming Signatures

For the numerical optimization the dependence of horizontal/vertical field integrals and on-axis gradient on the Phase Shifter gap needs to be known for different

shim geometries and for full and half magnets. A linear dependency on thickness is assumed. These dependencies are called “Signatures”. Many different shim geometries were investigated. Five shims with different dimensions and positions were selected for further work. The criterion was that their signatures were quite different. Fig. 4 top illustrates the gap dependence of the horizontal field integral for these five shims. Fig. 4 bottom shows the dependency of the vertical field integrals on x at a Phase Shifter gap of 10.5mm. At this gap field integrals and gradients are highest. The gradient for the optimization is represented by the slope at $x=0$.

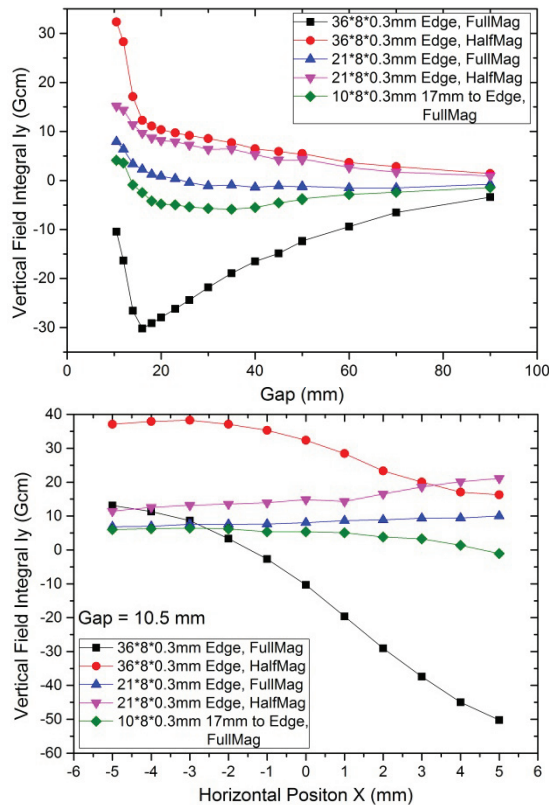


Figure 4: Signatures of the five types of shims selected for the tuning. Top: Signatures for gap dependent field integrals. Bottom: the signature for the gradient was evaluated from the slope of the Field integral vs. x at $x=0$. Shim dimensions are given. The positions with respect magnet edges are indicated.

Tuning Results

Results for the vertical field integrals and gradients are shown in Fig. 5. One of the prototype phase shifter was used for demonstration of these results. Fig. 5 top demonstrates the efficiency of the tuning. A large deviation, especially at large gaps, could be reduced so that it fits into the specs window, see table 1. The gradient is low enough that these specs are preserved inside the good field area of ± 0.5 mm around the axis. This is explicitly shown in Fig. 5 bottom by the dependence on x at the minimum gap of 10.5mm before and after tuning.

SUMMARY

A systematic strategy for the field integral tuning for the phase shifter of the European XFEL was developed. It is based on measured signatures of a set of known shims using the linearity and superposition principle. A shim configuration, which minimizes field integral errors and transverse gradient, is found by numerical simulation on a large number using a numerical trial and error method. This is a fast method to tune the field integrals and gradients for the Phase Shifters for the European XFEL to specifications or even below. It is being now used for the mass production of these devices.

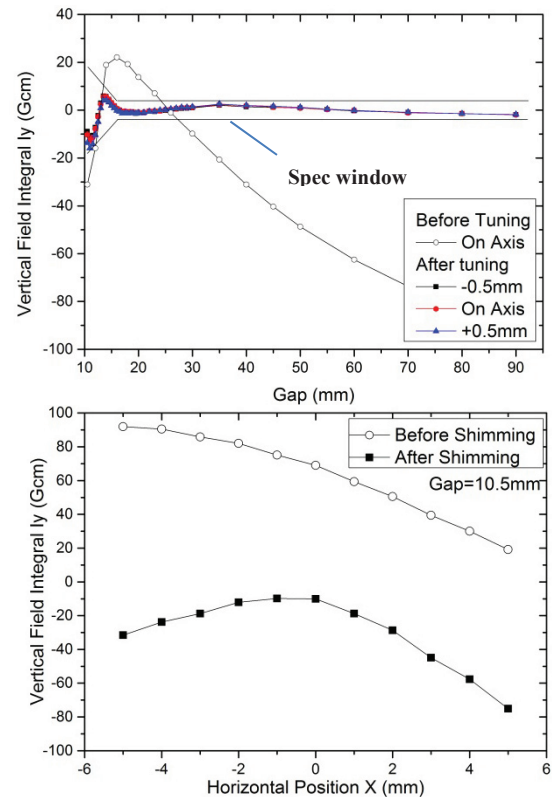


Figure 5: Demonstration of the tuning of the vertical field integrals. Top: Open symbols, status as found. Full symbols: Field integral after tuning: On axis red and at ± 0.5 mm blue, black. The specs window, see table 1, is indicated for comparison. Bottom: The low gradient is demonstrated by the X -dependence at 10.5mm gap before and after tuning.

REFERENCES

- [1] H. Lu, Y. Li, J. Pflueger, “The permanent magnet phase shifter for the European X-ray free electron laser” Nucl. Instr. And Meth. A605 (2009), 399.
- [2] J. Pflüger, H. Lu, T. Teichmann “Field optimization by pole height adjustments”, Nucl. Instr. and Meth. A429 (1999) 386.
- [3] Y. Li, J. Pflueger, “Compensation of gap dependent kicks by applying shims”, Internal XFEL.EU report WP71/2012/15, unpublished.

- [4] Y. Yang, Y. Li, H. Lu, F. Wolff-Fabris J. Pflueger,
 “Shimming Strategy for the Phase Shifters used in
 the European XFEL”, TUPSO42, Proceedings of the
 FEL2013, Aug 25-30, 2014 New York City, USA.

TEMPERATURE EFFECTS OF THE FLASH2 UNDULATORS

M. Tischer*, A. Schöps, P. Vagin, DESY, Hamburg, Germany

Abstract

FELs are very sensitive to small changes in the resonance condition of the emitted radiation. As a consequence, permanent magnet undulators in FELs usually require extensive temperature control in order to assure stable operation conditions. In principle, the temperature dependence of permanent magnet material is well known but more things need to be considered like different thermal expansion of various mechanical parts or thermally induced deformation which do not only affect the K parameter but also the field quality. We have performed temperature dependent magnetic measurements in a range from 19 to 28 degrees Celsius and have analyzed the magnetic performance of the undulator. The results of this case study can be transferred to all FLASH2 undulators and shall allow for a simple temperature dependent gap correction in order to make the spectral properties insensitive to temperature changes of the insertion devices.

MAGNET MATERIAL REMANENCE

The temperature coefficient for the remanent magnetization of the magnet material VACODYM 776AP used for the FLASH2 undulators is -1100ppm/K [1]. For determining the effects of changes in the remanence on the magnetic field amplitude in a complex structure like a hybrid undulator, also the geometry and the saturation of the poles have to be taken into account.

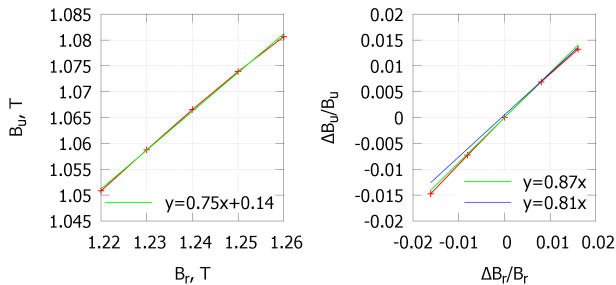


Figure 1: Calculated undulator magnetic field amplitude B_u versus magnet material remanence B_r (left) and $\Delta B_u/B_u$ versus $\Delta B_r/B_r$ normalized for $B_r = 1.24 \dots 1.26$ T (right).

The dependence of the magnetic field B_u on the remanence of the magnet material B_r was calculated using Radia [2]. For the FLASH2 pole and magnet geometry, it can be described as: $B_u(B_r) = 0.75 \cdot B_r + 0.14$ T (Fig. 1). Therefore the expected relative change in magnetic field $\Delta B_u/B_u$ due to the temperature-induced change in the remanent magnetization B_r , normalized for $B_r = 1.24 \dots 1.26$ T, is $\Delta B_u/B_u = -1100 \text{ ppm/K} \cdot 0.87 \dots 0.81 = -960 \dots -890 \text{ ppm/K}$.

* markus.tischer@desy.de

MAGNETIC MEASUREMENTS

Recently temperature effects have also been studied for XFEL undulators [3]. For the FLASH2 undulators, magnetic field maps were measured with different methods for crosschecking that the temperature dependence of the field sensors is properly compensated. The field was measured by a Hall probe, a pick-up coil and a stretched wire. The Hall probe and coil gain were calibrated by an NMR magnetometer in a 0.4 T permanent magnet at each temperature change. This single point calibration was used for the Hall probe as mainly its gain and offset change with temperature, and changes of a higher order nonlinearity could be neglected. For the coil, the gain of the whole measurement system was calibrated, not just the coil area, as the coil and the integrator input resistances are also temperature dependent.

The alignment of the bench scan axis with respect to undulator magnetic axis was performed at each temperature change by magnetic measurements, in order to compensate probe displacement caused by thermal expansion of the undulator and the measurement bench.

In contrast to the Hall probe which has a small sensitive area with a width of $100 \mu\text{m}$, the coil measures a field which is averaged over its size of 3 mm. For a sinusoidal magnetic field of an undulator with a period of 31.4 mm, such an averaging reduces the measured field amplitude by up to 1% [4]. This gain error for the sensitivity of the coil would be the same for different temperatures, and the relative temperature dependence of the field amplitude could still be measured with a such sensor even without any gain compensation.

The stretched wire for the field integral measurements was installed transversely to the magnet structure, instead of the usual orientation along the undulator. This way, by moving the wire along the magnet structure, it measures the vertical field, averaged transversely over the whole pole width. Therefore the measured field could not be compared directly to the Hall probe and coil measurements on the beam axis. However, the temperature dependence of the average field should be the same as the temperature dependence of the field on beam axis. Also, only a small part of the magnet structure could be measured due to the limited range the moving stages of 100 mm, covering only few undulator periods. The stretched wire setup was not calibrated. With 1 mm wire step size, its gain is defined by the mechanical accuracy and temperature stability of the linear stages.

The measured temperature dependence for the magnetic field amplitude shows a linear behaviour with a temperature coefficient of $-885 \pm 3 \text{ ppm/K}$ (Fig. 2). The 3 different measurement methods obtain this value in almost perfect agreement. The measured value compares very well to the calculated value of the B_r -induced temperature dependence. This indicates that other effects like thermal expansion of the support structure should be smaller than 80 ppm/K.

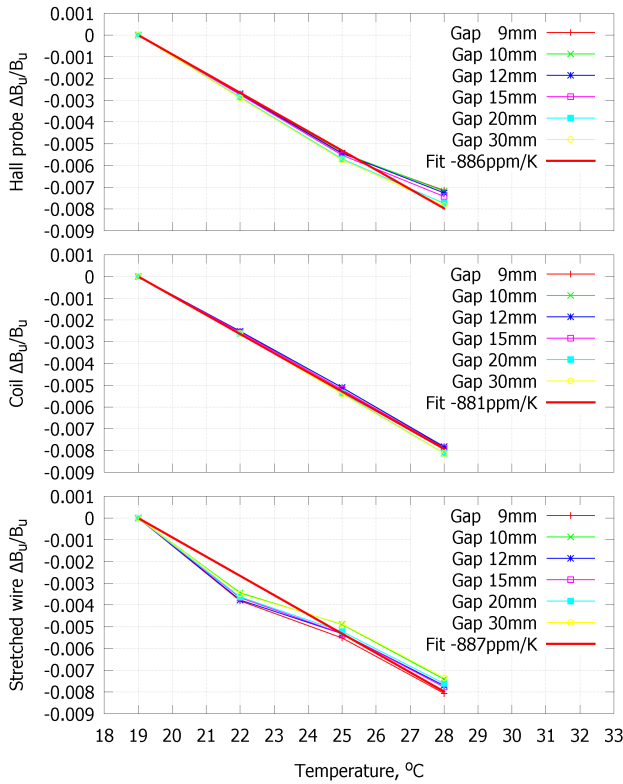


Figure 2: Measured undulator magnetic field amplitude vs temperature for different gap settings, measured with the Hall probe (top), coil (middle), and stretched wire (bottom), normalized to the field amplitude at 19°C. The measured temperature coefficient is -885ppm/K with excellent agreement between the three different measurement methods.

UNDULATOR GAP

The time-dependence of several sensor readings during the change of the ambient temperature was studied in order to reveal the time constants for the thermal behavior of different components. In this case, the readings of the temperature sensors at the magnet girders, the air temperature and the readings of the motor's rotary encoders have been monitored. Since the control system uses the additional linear encoders mounted on the magnet girders as a feedback for position control to maintain a constant magnetic gap, the changes of the rotary encoder readings at the motor axes reflect the thermal behavior of the support structure.

Figures 3 and 4 show that the readings of the rotary encoders follow the air temperature while the actual girder temperature adapts to the ambient conditions with a much longer time constant of about 10 hours. This behaviour can be explained by the fact that the caliper arms for the encoder systems have 25 times less mass than the magnet girders and a surface to volume ratio which is approximately 2.5 times higher. As pointed out clearly in Fig. 4, they adapt much faster to changes of the ambient temperature and cause the control system to correct for their length variation long before the actual gap has also adapted to the temperature changes.

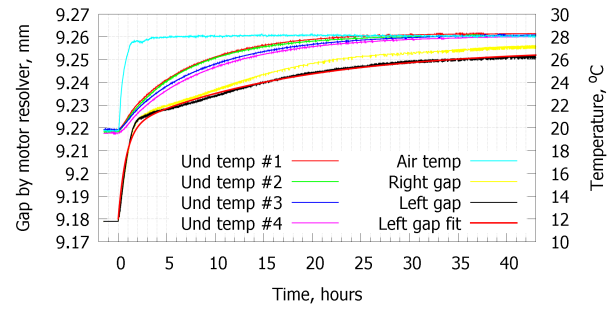


Figure 3: Motor rotary encoder reading and undulator temperature settling after a step change from 19.7°C to 28.1°C. The undulator temperature is measured by four Pt100 temperature sensors placed on the magnet girders. There are two processes, a fast change because of the encoder caliper arm expansion, which almost follows the air temperature change during the first hour, and then a slow temperature settling of the massive girders and the support structure.

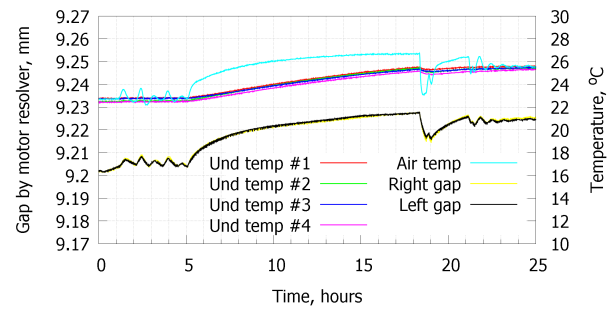


Figure 4: Motor rotary encoder reading during temperature changes. The temperature oscillations and instability are due to a single event failure of the temperature stabilization. This is a good illustration of the fast temperature response of the linear encoders compared to the undulator temperature.

Fitting the gap correction over time (Fig. 3) with

$$g(t) = g_0 + a_0(1 - e^{-t/t_0}) + a_1(1 - e^{-t/t_1})$$

provides $g_0 = 9.18\text{mm}$, $a_0 = 40\mu\text{m}$, $t_0 = 0.8\text{h}$, $a_1 = 35\mu\text{m}$, $t_1 = 10.7\text{h}$. A total gap change of $40+35=75\mu\text{m}$ per 8.4K corresponds to $9\mu\text{m/K}$ gap correction by linear encoders.

UNDULATOR SUPPORT STRUCTURE

The distance between the bearings for upper and lower spindles at the support is 1360mm (Fig. 5). It is made of steel type S235JR with a thermal expansion coefficient of 12ppm/K. The spindles themselves are made from a high-grade steel with similar thermal expansion coefficient and an effective length of 368mm each at a gap of 9mm. Therefore the girder fixation points have a thermal expansion coefficient of $1360\text{mm} \cdot 12\text{ppm/K} - 736\text{mm} \cdot 12\text{ppm/K} = 7.5\mu\text{m/K}$. The linear encoder caliper arms are made from aluminum with an expansion coefficient of 25ppm/K and a length of 625mm; the related thermal expansion is $-625\text{mm} \cdot 25\text{ppm/K} = -15.6\mu\text{m/K}$. Therefore the linear encoders should measure

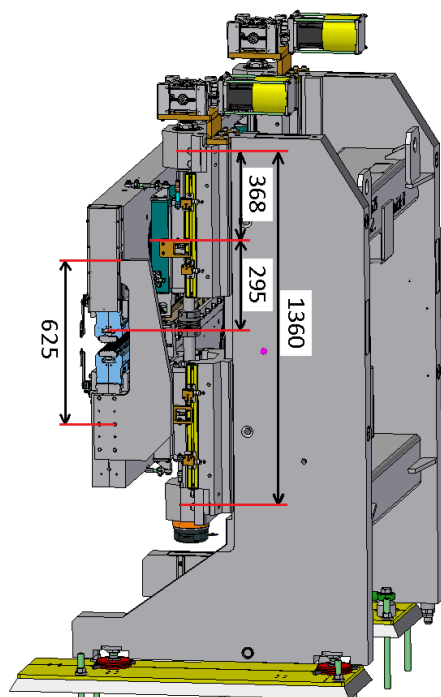


Figure 5: Undulator support structure with the dimensions of relevant parts in mm.

and compensate $7.5 - 15.6 = -8.1 \mu\text{m/K}$. Which is in a good agreement with the measured value of $9 \mu\text{m/K}$ (Fig. 3) of the correction by control the system with opposite sign.

With a closed loop feedback for the undulator gap by linear encoders, the thermal expansion of the support structure does not affect the actual gap setting, as it is measured and controlled directly by linear encoders. Both the encoder caliper arms and the magnet girders are made of aluminum. Thus their thermal expansions almost fully compensate each other. Only the air gap between poles is not compensated. It corresponds to an effective length of about 30mm of aluminum with the thermal expansion coefficient of 25ppm/K providing $30\text{mm} \cdot 25\text{ppm/K} = 0.75 \mu\text{m/K}$ undulator gap temperature dependence. For the minimum undulator gap of 9mm and 1T field, an increase in gap of $1 \mu\text{m}$ would result in a magnetic field change of $-100 \mu\text{T}$. The thermal expansion of the undulator gap of $0.75 \mu\text{m/K}$ corresponds to a magnetic field change of -75ppm/K .

UNDULATOR PERIOD

From the measured magnetic field maps it is possible to extract longitudinal positions of the magnetic field maxima. By calculating the average difference between them, it is possible to find the temperature changes of the undulator period. The measured value is $+18\text{ppm/K}$. Its sign is opposite to the magnetic field amplitude temperature dependence, but being 50 times smaller it can not compensate the latter in the emitted wavelength or undulator K parameter, which is a product of undulator period and field amplitude.

UNDULATOR AXIS VERTICAL OFFSET

The vertical $\cosh(y)$ dependence of the undulator's magnetic field could be approximated by a parabola with a 2nd order coefficient of $2.57\%/ \text{mm}^2$ at a gap of 10mm. With a beam height of 1.4m and a thermal expansion coefficient of 12ppm/K for the steel support structure, the undulator magnetic axis vertically drifts by $17 \mu\text{m/K}$. Therefore an on-axis field change of $+7\text{ppm/K}^2$ is expected. Due to its parabolic dependence it should be considered in case of temperature changes above a few degrees.

The measured mechanical offset drift of the undulator magnetic axis is $11 \mu\text{m/K}$, which is smaller than calculated for the undulator support structure, however the granite measurement bench also has its own temperature expansion that partly compensates the measured thermal drift of the undulator's magnetic axis in these measurements. In the tunnel, the vertical drift of the undulator's magnetic axis relative to the beam position should be considered.

CONCLUSION

In order to apply gap corrections to compensate temperature changes, several effects should be considered:

The temperature dependence of the undulator gap, which includes two parts: the thermal expansion of the linear encoders' caliper arms, which should be corrected based on air temperature or additional temperature sensors on the linear encoders; and the thermal expansion of the girders and support structure with a time constant of about 10 hours.

The temperature dependence of the magnetic field amplitude due to the remanence change of the magnet material, which should be compensated based on the temperature of the undulator girders.

With the known temperature dependence of the magnetic field and an exponential approximation for the field amplitude versus gap behavior, the required correction for a given gap value and temperature can be calculated.

Operation without linear encoders, using only motor encoders, requires not only a gap correction of the support structure deformation under magnetic forces, but also a compensation of the support structure's thermal expansion.

REFERENCES

- [1] Vacuumschmelze, "Rare-Earth Permanent Magnets VACODYM & VACOMAX", http://www.vacuumschmelze.com/fileadmin/Medienbibliothek_2010/Downloads/DM/Vdym_Vmax_en.pdf
- [2] O. Chubar, et al., Journal of Synchrotron Radiation 5 (1998), pp. 481-484. <http://www.esrf.eu/Accelerators/Groups/InsertionDevices/Software/Radia>
- [3] Y. Liu, S. Karabekyan, "Temperature change compensation by means of undulator gap correction", E-XFEL WP71 Report, WP71/2014/05, 2014
- [4] P. Vagin, M. Tischer, P. Neumann, "Magnetic Measurement Developments for Undulators", IPAC14 Proceedings, Dresden, 2014, WEP0034.

THE PHOTON BEAM LOSS MONITORS AS A PART OF EQUIPMENT PROTECTION SYSTEM AT EUROPEAN XFEL

N. Gerasimova[#], H. Sinn, European XFEL GmbH, Hamburg, Germany
S. Dziarzhytski, R. Treusch, DESY, Hamburg, Germany

Abstract

For the X-ray beam transport systems, the problem of potential damage to the equipment by mis-steered photon beam emerged with advent of powerful X-ray Free-Electron-Lasers (FELs). In particular high repetition rate machines as European XFEL, where not only focused beam can produce ablation, but even unfocused beam can melt the beamline components while machine operates in multibunch mode, demand for implementation of equipment protection. Here we report on development of photon beam loss monitors at European XFEL facility. The photon beam loss monitors will react on the mis-steered photon beam and interface the machine protection system. The prototype comprises the vacuum chamber with fluorescence crystals positioned outside the photon beampath. The fast sub-hundred ns fluorescence induced by mis-steered beam can be detected by photomultiplier tube allowing for intra-train reaction of machine protection system. First tests have been carried out at FLASH and shown the feasibility of detection based on PMT-detected fluorescence. In addition to the efficient YAG:Ce crystal, the robust low-Z material as CVD microcrystalline diamonds has shown a potential to be used as fluorescence crystals.

INTRODUCTION

The high energy and high intensity accelerator facilities use the beam loss detection systems to react on losses of the particle beam and prevent radiation damage to the equipment. Different types of such beam loss monitors exist (see, for instance, [1]). The beam loss detection becomes an essential part of the machine protection system in case of superconducting linacs.

In case of photon beam transport systems, the problem of potential damage to the equipment was not considered till very recently. The total energy of a particle beam is usually much higher than the energy of produced by it photon beam. However with advent of highly brilliant X-ray Free-Electron-Lasers the potential danger of damage to the photon beam transport systems has been realised. Focused X-rays can ablate components of the beam transport systems. And in case of high repetition rate machines as European XFEL, trains of photon pulses capable to melt the beamline components even in case of unfocused beam [2]. In order to prevent such damage, we propose to introduce photon beam loss monitors reacting on mis-steered beams and interfacing the machine protection system in a way similar to electron (particle)

beam loss monitors. To our knowledge the development presented in this paper is the first attempt to introduce a protection system for the photon beamlines.

DETECTION SCHEME

The kind of potential damage to the photon beam transport system differs from those in case of a particle beam. While highly energetic particles escape the vacuum chamber of the accelerator, and beam losses are usually detected outside the vacuum, the X-ray beam, in particular of low photon energies, is potentially capable to produce highly localized damage to the vacuum chamber itself or to the components inside the vacuum. This leads to necessity of introducing a detection system reacting on losses of photon beam into the vacuum of the beamline. The possible realization of such detection will be presented in following subsections. As for electronics and interface to machine protection system, this part of beam loss detection system can be in high degree adopted from the beam loss monitors for the particle beam. In our case, the systems developed for the electron beam loss detection at European XFEL [3] will be used.

Conceptual Scheme

The conceptual scheme of proposed photon beam loss monitors is presented in Fig. 1. As discussed above, the main task of the photon beam loss monitors is to prevent hitting of the beamline components by the photon beam. To react on mis-steering of the photon beam, some 'screen' can be introduced into vacuum vessel around the nominal beam path (represented in yellow in Fig. 1). This 'screen' converts the X-rays into visible light. The conversion of photons into visible range enables relatively easy detection, since many types of detectors are available

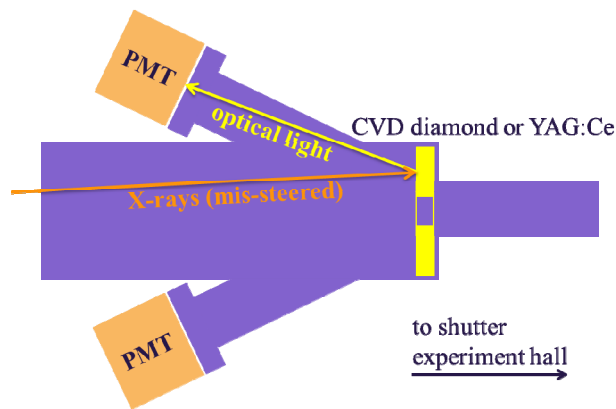


Figure 1: Conceptual scheme of the photon beam loss monitor (see text).

[#]natalia.gerasimova@xfel.eu

and positioning of detector outside the vacuum vessel is possible. Types of converting screens will be discussed in next subsection, and a detector for visible light will follow. Among the requirements to the detection system comprising converting screen and detector of visible light is a fast response allowing to react within the pulse train and to stop machine (or reduce number of bunches in train) in order to prevent damage. The maximal repetition rate of photon pulses at European XFEL of 4.5 MHz results on desirable detection response < 220 ns. Another important issue is a radiation hardness of the 'screen' in order not to be destroyed by the X-ray beam. And finally, since the beam loss monitors interface the machine protection system, the detection scheme should provide clean, highly reliable signal of high signal-to-noise ratio.

Conversion of X-rays into Visible Light

Conversion of intense X-ray radiation into visible light can be realized either by using luminescent material or by detecting thermal light. These two possibilities have its advantages and disadvantages. While luminescence response is strongly material dependent property, thermal light is less material dependent and would be induced in any material due to the temperature increase after absorption of intense X-ray pulses. Thus, in case of thermal light, one can choose almost any radiation stable material, for instance B_4C – material, which, due to high damage threshold, will be used at European XFEL for the slits and dumps in photon beamlines. In contrast to thermal light, the choices of luminescent material are much more limited. However, though not in any arbitrary material, the luminescence response reaches much higher spectral brightness, allowing, thus, for much easier detection. Taking this into account, we decided to start the development using the luminescent materials for conversion of X-rays into visible light.

The two luminescent materials have been chosen to be tested in the prototype of the photon beam loss monitors: monocrystalline YAG:Ce and polycrystalline CVD diamonds.

YAG:Ce is well known scintillator material and is widely used to convert energy of the particles and X-rays into visible light. The light yield of YAG:Ce luminescence of about 8 photons/keV is high. The fast, < 100 ns, time response makes YAG:Ce attractive to applications demanding for time resolution. The yellow characteristic luminescence of Ce in YAG falls into the wavelength range corresponding to maximal sensitivity of conventional detectors as PMT. All these properties make YAG:Ce a good candidate for a fast and efficient convertor of X-rays into visible light. Indeed, the monocrystalline YAG:Ce is widely used to image X-rays at XUV/X-ray FELs as FLASH and LCLS. However, the applications of YAG:Ce at these powerful machines are limited by the damage threshold of YAG, which demands for high attenuation or / and reducing number of pulses in train. The problem of relatively low damage threshold holds for most of well-known scintillator materials, since the scintillators are usually used to detect a weak signal

and have been optimized for highest possible absorption, corresponding to high-Z materials. While to reduce the damage threshold, one should aim for low-Z materials in order to minimize absorption and thus reduce the density of excitations in material. This means that new luminescent materials should be developed for high-intensity applications.

CVD diamonds: The low-Z material known for its superior properties relative to any kind of damage is diamond. The damage threshold in diamonds, exposed to X-ray beam of European XFEL, is expected to be by two orders of magnitude higher than in YAG. The monocrystalline diamonds are excessively expensive for the presented here project (in total, several tens of large, of few cm^2 surface, crystals are needed). However, polycrystalline CVD diamonds, which are available for a much lower price, are still very robust materials. The high penetration depth of X-rays in diamonds reduces the excitation density and increases single shot damage threshold, while high thermal conductivity helps to sustain long pulse trains.

The light yield of CVD diamond luminescence is known to be very weak compared to YAG:Ce luminescence, - the best reported yield in CVD diamonds is by two orders of magnitude lower than in YAG:Ce. Still, due to high intensities of FEL radiation, this yield can be acceptable, in particular taking into account that only the integral signal, without spatial resolution, is to be detected by the beam loss monitors.

Another particularity of luminescence from diamonds is its spectral signature. In YAG:Ce the spectral content of luminescence is well-defined and almost does not depend on growth conditions, due to its origin in Ce atoms which are embedded in YAG in very low concentration of typically 0.2%. In contrast, the defects responsible for the luminescence in diamonds are strongly dependent on preparation conditions. More than a hundred of different luminescent centres in diamonds have been reported.

Finally, the decay time of X-ray induced luminescence in diamonds is about 10 fs, which is even faster than in YAG:Ce.

In summary, the CVD diamonds would be preferable convertor into visible light, provided that the luminescent signal can be clearly detected. Finally, one more property of luminescence should be investigated and taken into account for applications with intense X-ray beams, namely saturation. This phenomenon is known to be limiting the signature of YAG:Ce luminescence, in particular for lower photon energies, when the penetration depth decreases and the density of excitations in material increases.

Detection of Visible Light

Among existing detectors for visible light, the photo-multiplier tube (PMT) is sufficiently fast for our application, with typical time response of few ns. The high sensitivity and the high dynamic range make the PMT a good candidate to be used in photon beam loss monitors. Moreover, the PMT is often used for the beam

loss monitoring in accelerators. In latter case, the PMT faces directly the surface of the medium transporting visible light: glass or fiber transporting Cherenkov radiation, or scintillator transporting luminescence. Such geometry allows for easy optical shielding from the ambient light. For the case discussed here, namely detecting the light induced by photon beam in the luminescent screen (or screen producing thermal light), a direct contact between the screen and the PMT is hardly possible. Being located at some distance from the screen (preferable realization would be outside the vacuum chamber), the PMT, due to its high sensitivity, can ‘see’ even very weak light coming through the beam transport system. If light, coming from the outside of the vacuum chamber, can be eliminated by optical shielding of the vacuum chamber, the light, coming along the beamline, is a more challenging obstruction. In particular, being originated from the same bunches as the FEL light, bending magnet radiation of the electron dump system and spontaneous radiation in undulators (in contrast to ambient light) cannot be filter out by the nanosecond timing response of the PMT. Thus, the problem of signal to noise ratio can question the feasibility of the PMT detector in case of weak signals. Additional filtering by spectral filters is possible in case of luminescence, since the spectral response is well defined (in contrast to thermal light, which spectral response is wide and strongly temperature dependent). This possibility to clean the signal favours the luminescent screen versus the thermal one. The sensitivity range of the detector should be considered as well. Though the detectors of high sensitivity in IR range are available nowadays, they are more expensive than those for visible light and usually exhibit lower signal-to-noise ratio. This fact favours again luminescence, in particular with spectral response in the middle of visible range, versus thermal light. Lastly, since the PMTs are used for the electron beam loss monitors at European XFEL [3], implementing the same detector type for the photon beam loss monitors would be a cost effective solution allowing for easy integration.

FEASIBILITY TESTS AT FLASH

To check on proposed detection scheme comprising the luminescent screen and the PMT detector, the feasibility tests have been carried out at FLASH.

The prototype of the photon beam loss monitor, presented in Fig. 2, has been constructed in a way to optimize detection of weak luminescent (or thermal light) signal. Since both types of radiation, luminescence and thermal light, are emitted into entire solid angle of 4π sr, the closest possible distance between the screen and the detector (or lens, focusing onto detector) ensures maximal angular collection of the visible light. In the simplest case of the detector located outside the vacuum vessel, the geometry was optimized to reduce distance from the beam axis to the window flanges, where the detector is attached. The feedthroughs will allow to position 4 screens: from sides, from above and from below, in order to confine the photon beam path according to

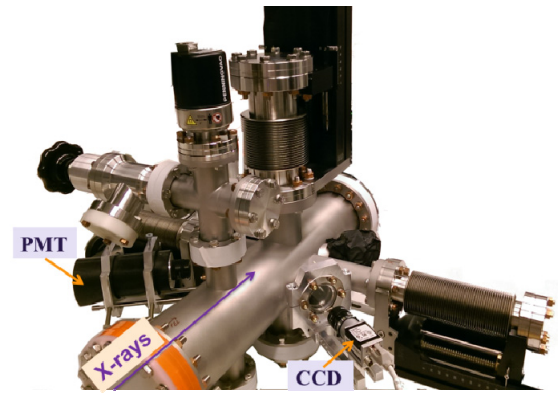


Figure 2: Prototype of a photon beam loss monitor used for the feasibility tests at FLASH.

the photon energy and the beam loss monitor location in the beamline. In tests, presented below, the feedthroughs were used only for positioning of the test samples into the beam. The HAMAMATSU R7600U-00-M4 PMT has been attached to one of optical windows directed to the luminescent screen. Due to large effective area of the PMT of 18 mm x 18 mm, no lens has been used to focus collected light onto PMT. Such a lens can increase the collection angle of the visible light and can be introduced if required. Neutral density and bandpass filters can be attached to the PMT depending on signal level and spectral content of luminescence. The PMT maximum sensitivity is in the range 300 – 500 nm. The chamber was optically shielded when the PMT was in operation. In order to check the origin of detected by PMT signal, a Basler acA640-120gm CCD equipped with RICOH FL-HC1214-2M lens has been attached to the second window flange. Images of the spot on sample, recorded with the CCD, provided a resolution of 8.5 pix / mm in horizontal direction and 12 pix / mm in vertical direction.

FLASH was operating at 7 nm (corresponding to the photon energy of 177 eV). The measurements were done behind the focus at the PG2 beamline. The spot size on sample was about 0.85 mm x 1.75 mm. The beam of an average energy of about 50 μ J per pulse has been transmitted onto the sample. The single pulse measurements have been performed with the repetition rate of 10 Hz.

Several polycrystalline CVD diamonds from different producers (from Diamond Materials, Germany, from General Institute of Physics, Russia and from TISNUM, Russia) have been investigated. The samples have been produced under different conditions and are characterized by different content of impurities as nitrogen and boron. The thickness of the CVD diamond samples were in the range 50 – 300 μ m, which is much higher than penetration depth for 177 eV photons of about 0.4 μ m. Thus all the XUV photons were absorbed in the samples. Similar in case of YAG:Ce with penetration depth of below 0.07 μ m and the sample thickness of 500 μ m. The reference YAG:Ce samples have been produced by Crytur Ltd., Czech Republic, and by Academy of Science of Armenia.

The signal from all the samples has been detected by both PMT and CCD detectors. The PMT high voltage has been set to 340 V in case of YAG:Ce and to 600 V in case of diamonds. In both cases the neutral density filter on the PMT was attenuating the signal by two orders of magnitude. The signal from YAG:Ce was of the same level and spectral content for the samples from different producers, while the signal from CVD diamonds differs strongly from sample to sample. The light yield in diamonds has been estimated 2 – 3 orders of magnitude lower than in YAG for the measurement conditions.

The CCD was used to check on the origin of the signal. While moving the samples through the beam, both PMT signal and CCD images were taken simultaneously. The PMT signal was appearing only when the beam spot was seen by CCD on the sample. An example of simultaneous measurements by PMT and CCD is presented in Fig. 3. One can see the clear signature of luminescence in one of the CVD diamond samples.

This is a very encouraging result demonstrating that not only luminescence from YAG:Ce, but from polycrystalline CVD diamonds as well, can be used for the photon beam loss monitors. Indeed, for the presented system, even by several magnitude lower signal can be clearly detected due to possibility of increasing the gain of PMT by more than order of magnitude and removing two orders of magnitude attenuation filters from the PMT.

The fluctuations of the PMT signal have been observed. By correlating the PMT signal with the FEL intensity measurements by the gas monitor detector (Fig. 4), it can be demonstrated that the fluctuations reflect the SASE fluctuations. The amplitude of fluctuations in the PMT signal is lower than in gas monitor detector, which indicates some degree of saturation in diamond luminescence. The saturation effects are to be investigated, and present measurements indicate even higher saturation in YAG:Ce. At higher photon energies of the European XFEL operation range, the density of excitations will be by several orders of magnitude reduced resulting much higher saturation threshold.

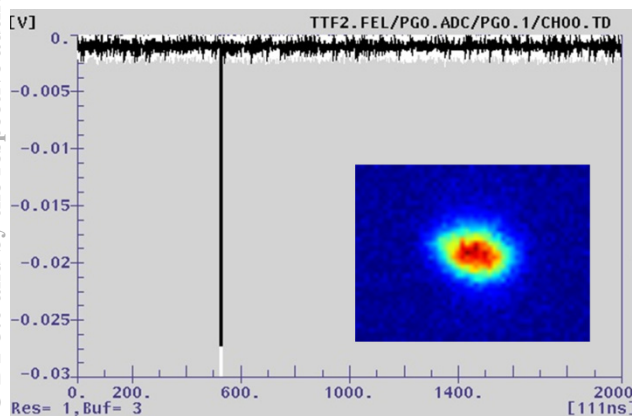


Figure 3: Signal from the CVD diamond, recorded with PMT (main panel), and simultaneously recorded by CCD image (insertion).

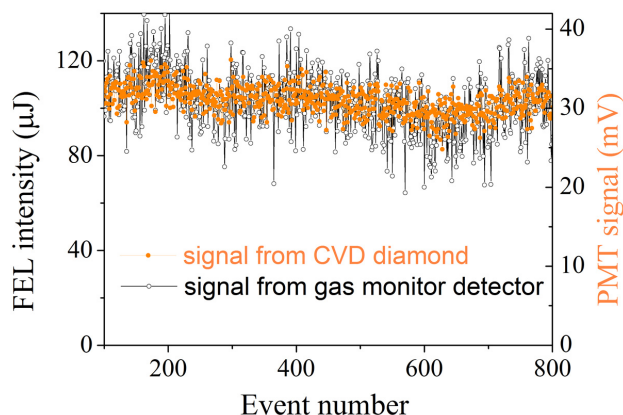


Figure 4: Signal from the CVD diamond measured with PMT compared to the signal from gas monitor detector.

CONCLUSION

The concept of novel photon beam loss monitors for the European XFEL is proposed. The induced by mis-steered X-ray beam luminescence in CVD diamonds can be detected by PMT, interfacing the machine protection system. The feasibility of such a detection has been proved at FLASH.

ACKNOWLEDGMENT

Authors are grateful to A. Kaukher and D. Noelle (DESY) for sharing their experience on the beam loss monitors for the electron beam at European XFEL and for lending of the PMT assembly; to A. Parenti (European XFEL) and to V. Rybnikov (DESY) for support with data acquisition, to B. Dickert and X. Dong (European XFEL) for technical support. The authors are thankful to Eckhard Wörner (Diamond Materials, Freiburg), Victor Ralchenko (General Institute of Physics, Moscow), Sergey Terent'ev (TISNUM, Russia) and Ashot Petrosyan (Academy of Science of Armenia) for providing test samples. Scientific and technical team at FLASH is greatly appreciated for the delivery of the FEL beam.

REFERENCES

- [1] K. Wittenburg, "Beam Loss Monitoring and Control", in *Proc. 8th European Particle Conf.*, Paris, 2002, pp. 109-113.
- [2] H. Sinn, *et al.*, "Technical Design Report: X-Ray Optics and Beam Transport", XFEL.EU TR-2012-006, 2012.
- [3] A. Kaukher, *et al.*, "XFEL Beam Loss Monitor System", in *Proc. 15th Beam Instrumentation Workshop*, Newport News, 2012, pp. 35-37.

IMPLEMENTATION PHASE OF THE EUROPEAN XFEL PHOTON DIAGNOSTICS

Jan Grünert, Jens Buck, Wolfgang Freund, Andreas Koch, Marc Planas, Florian Dietrich,
European XFEL GmbH, Hamburg, Germany

Abstract

The European XFEL facility with 3 undulators and initially 6 experimental end-stations requires an extensive set of photon beam diagnostics for commissioning and user operation, capable of handling the extreme brilliance and its inherent damage potential, and the high intra bunch train repetition rate of 4.5 MHz, potentially causing additional damage by high heat loads and making shot-to-shot diagnostics very demanding [1].

After extensive design [2-5] and prototype studies, in 2014 the installation of the photon beam devices starts with the equipment in the first photon tunnel XTD2 which is where the SASE1 hard X-ray undulator is located. This contribution reports on the device construction progress by focusing on the XTD2 tunnel devices and their implementation into the tunnel environment.

OVERVIEW

The photon part of the European XFEL facility is here defined as starting from the undulators, followed by the photon transport system leading into the experimental hall with the experimental endstations. The photon transport system contains beam transporting and shaping X-ray optics as well as X-ray photon diagnostics and is located in the photon tunnels XTD1 through XTD10. The hard X-ray undulator SASE1 is located in tunnel XTD2 which is also the first tunnel in the installation sequence to be equipped with the machine. As an example of the photon diagnostics devices in the overall facility, in this article we will describe the devices in XTD2 and their current implementation.

After definition of the overall diagnostics layout [1], long design phases of the individual devices, prototyping and production, most devices for XTD2 are ready for installation. Their implementation into the tunnel is prepared, which means that their design was accommodated to the space restrictions at their particular tunnel position, possible collisions were checked, infrastructure interfaces defined, and where required special infrastructure such as the rare-gas supply was designed.

Implementation

A particular feature of the XTD1 and XTD2 tunnels and an example of the tunnel implementation difficulties is that here the photon beamline is at a different and varying height – up to 2.65 m above the tunnel floor, whereas in all other tunnels there is a standard beamline height of

1.4 m. These two tunnels containing the undulators SASE2 and SASE1 respectively have downward slopes towards their ends in order to allow for transport paths crossing underneath the photon and electron beamlines when approaching the shaft buildings which are the branching points of tunnels and connect the incoming tunnel to the subsequent two outgoing tunnels. Due to this feature it was decided to build concrete platforms for the devices bringing the floor up so that the devices and their mounts can be built for the standard beamline height, avoiding special versions of the devices which are present in all tunnels. One such platform can be seen in Fig. 7.

Installation Sequence

The sequence of tunnel installations of infrastructure and also photon transport and diagnostics was fixed in the same order as the future commissioning sequence: first SASE1, then SASE3, and finally SASE2 will be installed. SASE1 is the hard X-ray beamline with a directly linear transport of the electron beam into the undulator - in SASE2 the electrons need to pass a bend before entering into the undulator which is an additional complication. Once electrons are transported through SASE1 they necessarily pass through the soft X-ray undulator SASE3 on their way to one of the two available main dumps, which is why the SASE3 area is installed next after SASE1.

DEVICES

This proceedings paper focuses on the photon diagnostics devices in XTD2 which is a representative subset of all diagnostics. In this conference the temporal diagnostics will be presented in another contribution (MOP014), as well as more details on the undulator commissioning spectrometer (MOP009) and details about the imagers (MOP013).

The photon diagnostics devices in XTD2 are all downstream of the separation point where the electron beam is separated from the photon beam. The first device, pushed as far as spatially possible towards the source, towards this separation, is a filter chamber and the transmissive imager. The space is very limited since the electron beamline is still very close, branching off at only a small angle.

The **Filter chamber**, see Fig. 1, is the most upstream photon diagnostics component and allows for initial spectroscopy by selecting and inserting X-ray filters, using characteristic K-lines of metals, and it contains absorbers for synchrotron radiation during undulator commissioning.

*corresponding author, contact jan.gruenert@xfel.eu

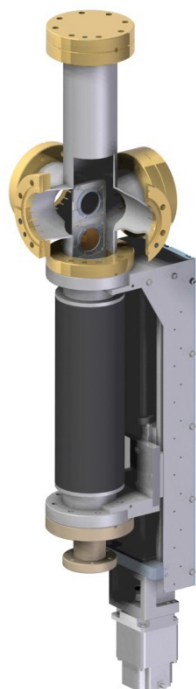


Figure 1: Filter chamber.

The **Transmissive Imager** will deliver the most upstream photon beam image, with the largest possible unobstructed view on the undulator radiation before any X-ray optics. With light transmitted to a second, downstream imager one can determine undulator beam pointing. It's an OTR screen from the electron beam diagnostics work-package converted for X-ray use.

Next in line is the **undulator commissioning spectrometer** or **K-monochromator** which is used during commissioning for tuning the gaps and phases of individual undulator segments. It can operate in 2-bounce or 4-bounce mode and requires either photodiodes or the 2D-imager-SR downstream for detection. It rests on a fully motorized support structure and can be completely retracted from the beam [4], see Figs. 6,7 and poster MOP009.

After a set of differential pumps, the X-ray beam enters the **X-ray Gas Monitor (XGM)**, see Fig. 2, which non-destructively delivers absolutely calibrated per-pulse intensity and also x/y-beam position data, using photoemission in rare gases. It consists of four UHV chambers on a common girder, resting on two steel pillars. Each chamber is equipped with a split electrode and can therefore deliver beam position in one transverse direction. Two chambers per direction are needed because one measures an absolute intensity calibrated at a synchrotron, but is averaging over many photon pulses, while the other chamber contains a very sensitive large area custom built electron multiplier which delivers a relative intensity value for every shot in the pulse trains, even at harder X-ray energies beyond 20 keV where rare gas cross sections become challenging small. The XGM is

a contribution by DESY, and it's implemented together with WP74. To provide the support up to the girder, WP74 performed FE-analysis of possible vibrations and determined that good stability could be obtained with two separated hollow steel pillars with rectangular shape, which rest on the ground on manually adjustable threaded rods and are then fixed to the floor by grouting.

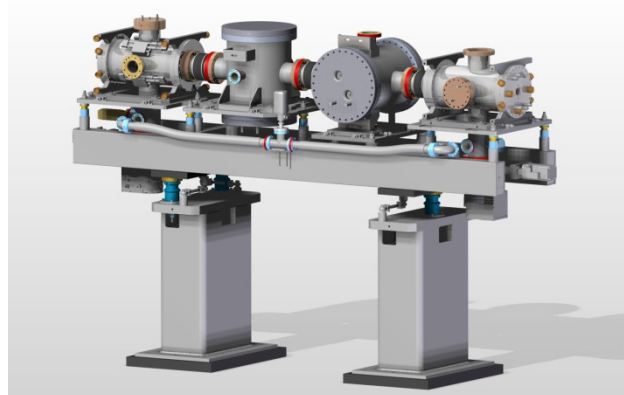


Figure 2: X-ray gas monitor.

The next monitoring device is the **Photoelectron Spectrometer (PES)**, see Fig. 3, which delivers non-destructively the FEL spectrum and polarization on a shot-to-shot basis. It requires high-speed DAQ electronics, an elaborate frame motion, magnetic field compensation, and rare gas supply. This device [2] is developed together with the P04 team at PETRA3.

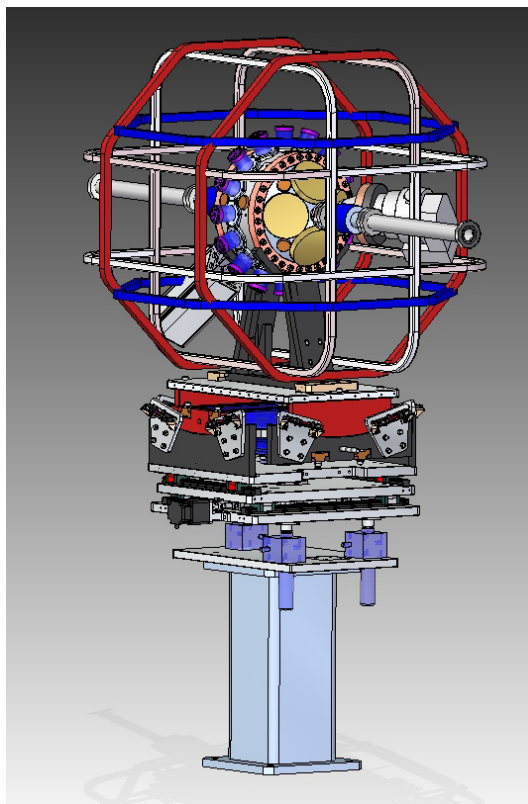


Figure 3: Photoelectron spectrometer.

Differential Pumping Units are inserted in the photon transport between the XGM and PES to separate the gas environments of these two devices. Changing pressure or type of gas in one device will therefore not affect the operation and accuracy of the other, which is especially important to guarantee the absolute calibration of the XGM intensity data.

The **2D-imager-FEL** (Fig. 4) is the main device to determine the FEL beam shape and important for commissioning and FEL optimization [3]. Several scintillators and a photodiode can be inserted into the beam. In combination with the transmissive imager, it allows to determine the beam pointing.

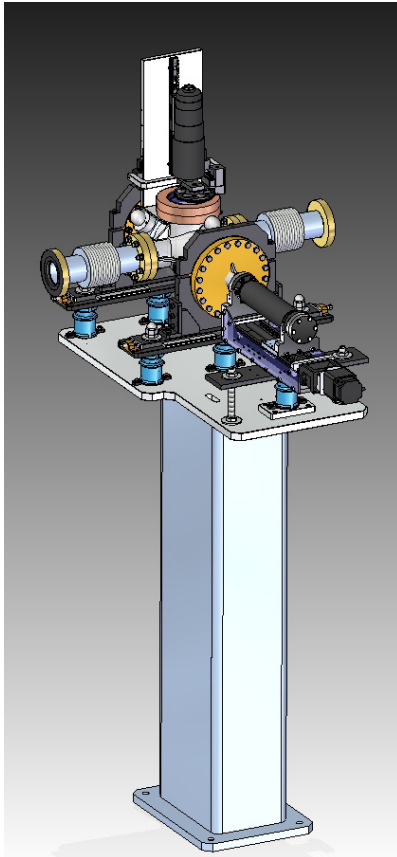


Figure 4: 2D-imager-FEL.

After passing across the two offset mirrors, the beam arrives at the **MCP-based detector** (Fig. 5) which records X-ray intensities from the spontaneous level (\sim nJ) all the way up to FEL in saturation (\sim mJ), in order to establish lasing at the critical intensity threshold and to study and optimize the gain curve. Built-in redundancy by installing three MCPs in the device ensures commissioning reliability. This contribution by JINR / Dubna has a long history at FLASH, and was tested at DORISIII with hard X-ray synchrotron radiation [5]. It has a basic aluminium frame since the position accuracy requirements are low compared to the devices that were placed on grouted steel pillars.

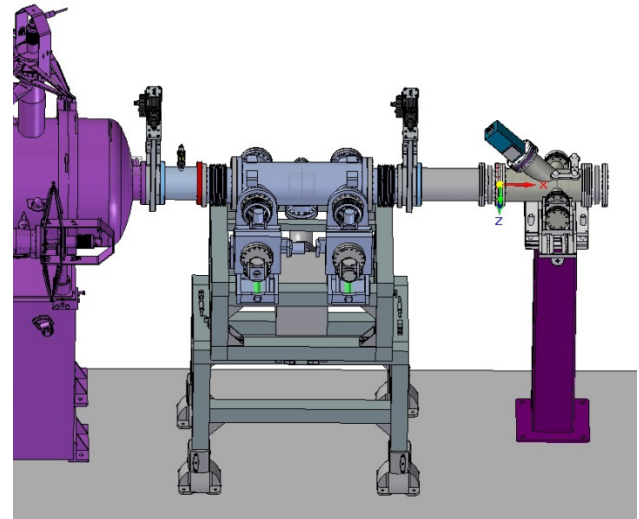


Figure 5: MCP-based detector (center) and Pop-in monitor type II-45° (right). On the left, the chamber of the second offset mirror can be seen, which is very close in order to minimize the required transverse motion of the MCPs for different photon energies and their corresponding mirror angle settings.

The X-rays arrive finally at the last diagnostics device in XTD2, the **Pop-in Monitor**. This Imaging Station is required to find and adjust the FEL beam downstream of X-ray optics in general and here in particular for the two offset mirrors. The Pop-in monitors currently come in four types (here it's a type II-45°) to cover different field of view ranges depending on their location in the beamline.

Table 1 lists the complete sequence of photon diagnostics devices in XTD2 along with their positions in tunnel coordinates.

Table 1: Sequence of Photon Diagnostics Devices in XTD2 (positions are given as distances from the FEL origin in the undulator)

Position [m]	Device name
180.3 m	Filter chamber
181.3 m	Transmissive Imager
200.3 m	K-monochromator system, incl. 2D-imager-SR
209.7 m	X-ray gas monitor (XGM)
216.6 m	Differential Pumping by WP74
220.0 m	Photoelectron spectrometer (PES)
242.5 m	2D-imager-FEL
259.6 m	MCP detector
261.1 m	Pop-in Monitor Type II-45°

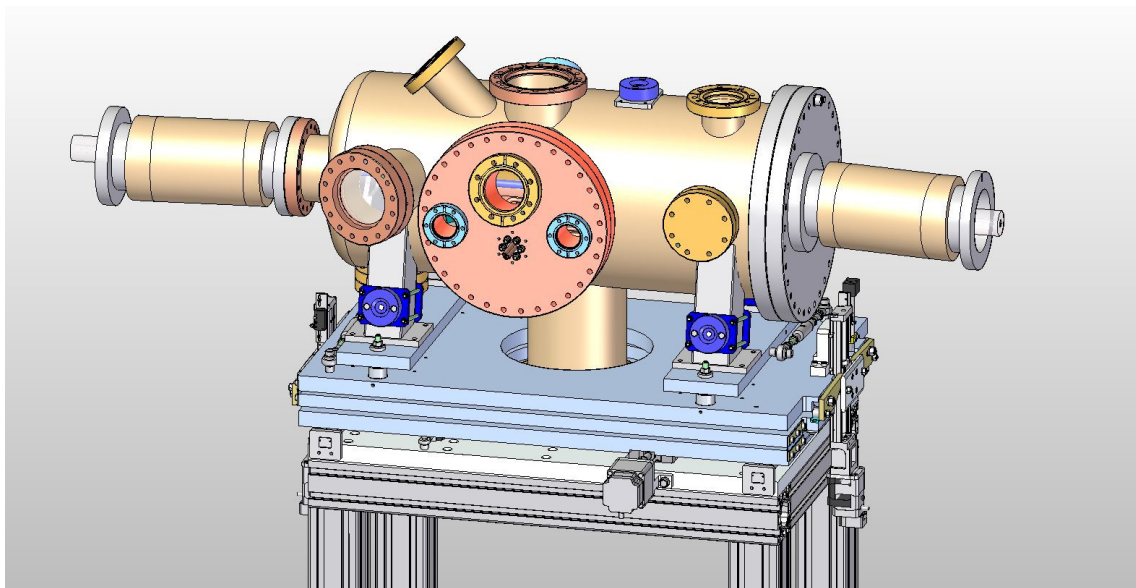


Figure 6: K-monochromator.

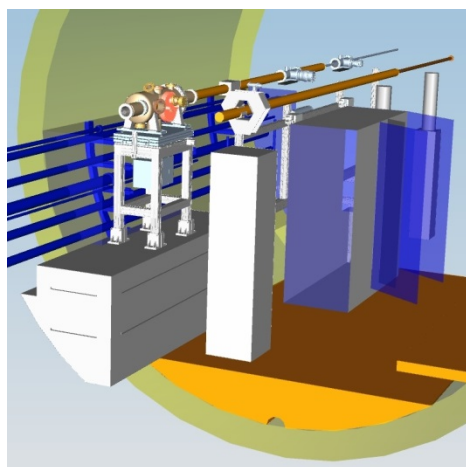


Figure 7: K-monochromator on concrete pedestal.

Research (JINR), Dubna, Russia, who also provided the final devices. The X-ray gas monitors are a development of the FLASH photon diagnostics team of K. Tiedke at DESY, Hamburg, Germany. The undulator commissioning spectrometer was built within WP74 with support by A. Erko and J. Rehanek from Helmholtz-Zentrum Berlin (HZB), Berlin, Germany, who also contributed to the design of the hard X-ray high-resolution single-shot spectrometer. C. David group at Paul-Scherrer-Institute (PSI), Villigen, Switzerland, worked with us on the single-shot spectrometer and on wavefront sensing with grating interferometers. The development of an online photoelectron spectrometer is a close collaboration with the PETRA3-P04 team of J. Viehhaus at DESY. The work on diamond detectors is a collaboration with M. Pomorski at Commissariat à l'Energie Atomique (CEA), Saclay, France.

CONCLUSION

The X-ray photon diagnostics devices were designed and produced for the tunnel XTD2, and their implementation in terms of collision checks, infrastructure planning etc. has progressed to a point that they are ready for installation. Most devices will be reproduced for the SASE2 beamline and with modifications for the soft X-ray beamline SASE3. Additional devices not described here are located in downstream photon tunnels and in the experimental hall, most notably all diagnostics of temporal pulse properties.

ACKNOWLEDGMENT

Most of the photon diagnostics devices were developed and produced in collaboration with external institutes, which we wish to acknowledge here: the MCP-based detectors were developed and prototypes tested together with E. Syresin group at the Joint Institute for Nuclear

REFERENCES

- [1] J. Grünert, "Conceptual Design Report: Framework for X-Ray Photon Diagnostics at the European XFEL", XFEL.EU technical report TR-2012-003, April 2012, doi:10.3204/XFEL.EU/TR-2012-003
- [2] J. Buck, "Online Photoemission Time-of-Flight Spectrometer for X-ray Photon Diagnostics", TR-2012-002, 06/2012.
- [3] C. Ozkan, "Conceptual design report for Imaging Stations at the European XFEL", TR-2012-004, February 2012.
- [4] W. Freund, "The European XFEL Undulator Commissioning Spectrometer", XFEL.EU technical report, May 2011.
- [5] E. Syresin et al., "Technical Design of the XFEL-MCP-Based Detectors", XFEL report EDMS-D3595161, 12/2012.

X-RAY PHOTON TEMPORAL DIAGNOSTICS FOR THE EUROPEAN XFEL

Jia Liu^{*}, Jens Buck, Florian Dietrich, Wolfgang Freund, Jan Grünert, Michael Meyer,
European XFEL GmbH, Hamburg, Germany

Abstract

The European XFEL facility (XFEL.EU), which will be commissioned starting 2016 shows exceptional features with its high delivery rate of light pulses and extremely high average brilliance. Characterizing the temporal properties of the FEL pulses on a shot-to-shot basis is important and challenging. Here we report about the concept and recent progress concerning temporal diagnostics for XFEL.EU. Spectral encoding and THz-streaking are the techniques which will be implemented to deliver arrival time and pulse duration monitoring while coping with the high repetition rate and high brilliance of XFEL.EU.

INTRODUCTION

European XFEL (XFEL.EU) will be commissioned in 2016 and become operational in 2017. Its most prominent advantages will be its extremely high number of light pulses per second (27000 p/s) and two or three orders higher average brilliance than other FEL facilities. The FEL pulses in XFEL.EU are produced in 10 Hz bunch trains that contain up to 2700 individual pulses within the 600 μ s time of one bunch train, corresponding to a pulse separation of 220 ns between individual light pulses or a 4.5 MHz repetition rate, as illustrated in the conceptual (CDR) and technical design reports (TDR) [1-5].

When choosing and designing the timing tools for XFEL.EU, the extremely high peak brilliance and high repetition rate must be addressed. A universal independent shot-to-shot temporal tool shall be developed, which is expected to be applicable in a broad range of x-ray photon energies and with various x-ray pulse lengths under different operation modes.

Adapted from attosecond (as) metrology, where the as XUV pulses generated via high harmonic generation (HHG) are characterized by using a few-cycle near Infrared laser pulse [6-8], the x-ray THz streaking technique was experimentally successfully employed for single shot soft x-ray temporal diagnostic [9-12], utilizing THz radiation from a THz undulator or an external laser based THz source. Very recently, hard x-ray streaking was successfully demonstrated as an arrival time monitor and pulse length monitor in SACLA across a broad photon energy range of 5 to 12 keV.

Independent photon arrival time monitoring based on spectral encoding was first demonstrated by LCLS and is also planned for XFEL.EU. It needs to be shot-to-shot burst mode compatible, and ideally permit extraction of a veto signal. Since spectral encoding was demonstrated so far only for repetition rates of 10 Hz to 120 Hz, an

extension to MHz repetition rates for XFEL.EU has yet to be studied and developed.

STREAKING ELECTRONS WITH THZ RADIATION

The energy distribution of photoelectrons ejected from noble gases ionized by x-ray pulses can be broadened and shifted by an external optical field depending on its ionization time instant, and the temporal properties of the x-ray pulse are then mapped onto the kinetic energies of the photoelectrons. One can thus uniquely determine the relative time delay between x-ray and external field as well as the pulse length of the x-ray pulse by comparing the photoelectron energy with and without external streaking field.

Long wavelength THz pulses are chosen to get rid of the intrinsic time jitter of the x-rays since longer wavelength streaking fields give rise to a larger linear streaking region which is less sensitive to the x-ray time jitter.

A single-cycle THz pulse, generated by tilted pulse front pulses in a Lithium Niobate (LN) crystal, with zero crossing temporal duration of \sim 600 fs to 1 ps, will be implemented [13]. An example of a THz pulse, generated from 2.5 mJ, 1 kHz, 800 nm is illustrated in Fig. 1. The THz radiation has a central frequency of 0.65 THz and extends up to 3 THz, with the electric field strength of 130 kV/cm. More effect will be studied and further optimizations to the THz pulse shape and field strength will be done, e.g. by cooling down the LN crystal or using organic crystals like DAST for higher frequency and higher field strength THz generation [14].

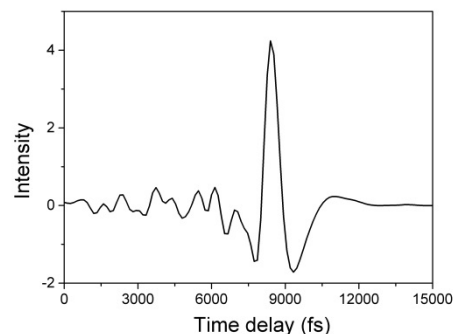


Figure 1: Typical single-cycle THz pulse from LN using the tilted pulse front method.

It should be pointed out that the temporal resolution of THz streaking is related to the THz field strength and the initial photoelectron energies and is limited to the bandwidth of the x-ray pulse, the energy resolution of the electron time of flight (eTOF) spectrometer and shot-to-

^{*}corresponding author, contact jia.liu@xfel.eu

shot time jitter. The temporal resolution can be improved by either applying a more intense THz field or streaking higher energetic electrons for a given eTOF spectrometer.

We performed a theoretical analysis of THz streaking for different photon energies, pulse durations and temporal jitter using the THz field shown in Fig. 1 with a peak electric field of 200 kV/cm. Examples of the Kr 2p streaking traces below photon energy of 2 keV with different pulse length and time jitter can be found in the left column of Fig. 2. Each energy spectrum is an average of 50 shots, and 300 corresponding shot-to-shot photoelectron energy spectra can be found in the right column of Fig. 2 for the fixed time delay of zero delay.

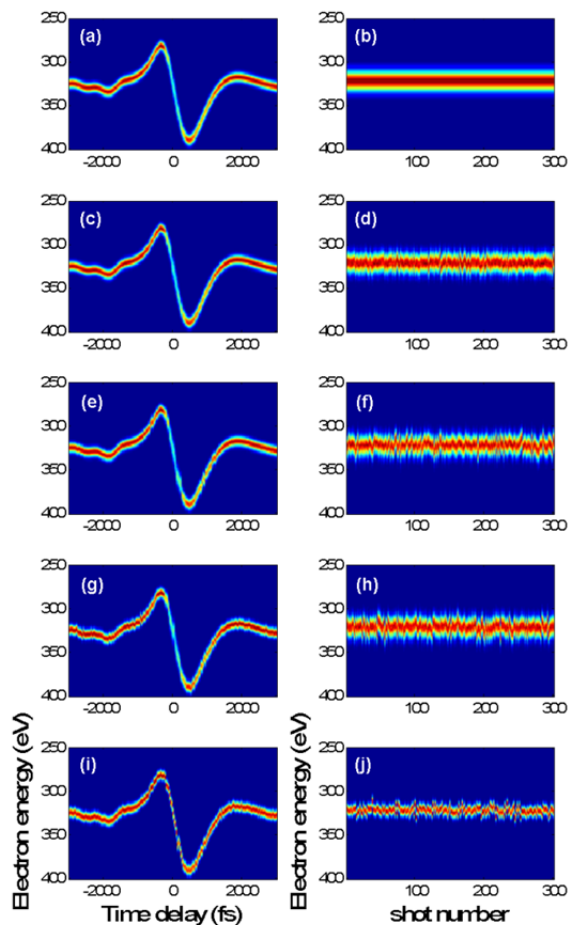


Figure 2: Simulation results of streaking Kr 2p electrons below 2 keV x-ray photon energy by assuming (a) 35 fs, 0 fs time jitter, 0 eV photon jitter, (c) 35 fs, 50 fs time jitter, 0 eV photon jitter, (e) 35 fs, 100 fs time jitter, 0 eV photon jitter, (g) 35 fs, 100 fs time jitter, 5 eV photon jitter, (i) 10 fs, 100 fs time jitter, 5 eV photon jitter; in the right column corresponding shot-to-shot photoelectron spectra are shown with the fixed zero delay.

One can directly see how the streaking trace changes with different x-ray pulse input parameters, and this in turn provides the possibility of reconstruct the x-ray pulse information by recording streaking traces. In principle, the energy jitter contribution can be eliminated from the single-shot spectrometer data and the arrival time of each

shot can be determined by mapping the center of mass photoelectron energy into time. Together with the shot-to-shot energy spectral bandwidth and shape, one can calculate the pulse length and profiles in a shot-to-shot basis [10-12].

As mentioned above, an independent photon arrival time monitor based on spectral encoding will also be developed for XFEL.EU. To ensure operation at the high repetition rates in the MHz range, there is a number of issues that have to be studied ranging from fast data acquisition to fast relaxation material, heat load and damage control, as well as MHz white-light generation and characterization [15].

CONCLUSION

In this paper, potential fundamental shot-to-shot x-ray photon temporal diagnostic methods for XFEL.EU are discussed. The THz streaking and spectral encoding techniques will be implemented in view of the high repetition rate in the MHz range and the high brilliance of XFEL.EU. A laser-based THz generation prototype and simulations of THz streaking of x-ray induced photoelectrons are presented as examples.

REFERENCES

- [1] T. Tschentscher, Layout of the X-Ray Systems at the European XFEL XFEL.EU TN-2011-001.
- [2] J. Grünert, Frame work for X-Ray Photon Diagnostics at the European XFEL, TR-2012-003.
- [3] J. Buck, Online Photoemission Time-of-Flight Spectrometer for X-ray Photon Diagnostics, TR-2012-003.
- [4] B. Li, X-Ray Photon Temporal Diagnostics for European XFEL, TN-2012-002-01.
- [5] T. Mazza, et. al., Scientific Instrument SQS, TR-2012-007.
- [6] J. Itatani, et. al., Attosecond Streak Camera, Phys. Rev. Lett. **88**, 173903 (2002).
- [7] F. Krausz, M.Y. Ivanov, Attosecond physics, Rev. Mod. Phys. **81**, 163 (2009).
- [8] P.B. Corkum, et. al., Attosecond science, Nat. Phys. **3**, 381 (2007).
- [9] F. Tavella, et. al., Few-femtosecond timing at fourth-generation X-ray light sources, Nat. Photonics **5**, 162 (2011).
- [10] U. Fröhling, et. al., Single-shot terahertz-field-driven X-ray streak camera, Nat. Photonics **3**, 523 (2009).
- [11] I. Grguraš, et. al., Ultrafast X-ray pulse characterization at free-electron lasers, Nat. Photonics **6**, 852 (2012).
- [12] U. Fröhling, Light-field streaking for FELs, J. Phys. B: At. Mol. Opt. Phys. **44**, 243001 (2011).
- [13] J. Hebling, et.al., Velocity matching by pulse front tilting for large-area THz-pulse generation, Opt. Express **10**, 1161 (2002).
- [14] X.C. Zhang, et. al., Terahertz optical rectification from a nonlinear organic crystal, Appl. Phys. Lett., **61**, 3080 (1992).
- [15] J. Liu, et. al., Supercontinuum pulse measurement by molecular alignment based cross-correlation frequency resolved optical gating, Opt. Express **19**, 40 (2011).

A POWER SWITCHING IONIZATION PROFILE MONITOR (3D-IPM)

H. Breede, L. V. Vu, M. Sachwitz, H. Grabosch, DESY, Zeuthen, Germany

Abstract

FLASH at DESY in Hamburg is a linear accelerator to produce soft x-ray laser light ranging from 4.1 to 45 nm. To ensure the operation stability of FLASH, monitoring of the beam is mandatory. Two Ionization Profile Monitors (IPM) detect the lateral x and y position and profile changes of the beam. The functional principle of the IPM is based on the detection of particles, generated by interaction of the beam with the residual gas in the beam line. The newly designed IPM enables the combined evaluation of the horizontal and vertical position as well as the profile. A compact monitor, consisting of two micro-channel plates (MCP) is assembled on a conducting cage along with toggled electric fields in a rectangular vacuum chamber. The particles created by the photon beam, drift in the homogenous electrical field towards the respective MCP, which produces an image of the beam profile on an attached phosphor screen. A camera for each MCP is used for assessment. This indirect detection scheme operates over a wide dynamic range and allows the live detection of the clear position and the shape of the beam. The final design is presented.

INTRODUCTION

To ensure a smooth operation of the free electron laser FLASH at DESY Hamburg, numerous detectors for the precise measurement of the electron and laser beam are necessary. The great advantage of the here described Ionization Profile Monitor (IPM) is an undisturbed determination of the position and intensity distribution of the laser beam.

MEASURING PRINCIPLE OF AN IONIZING PROFILE MONITOR (IPM)

The FLASH laser beam with a variable wavelength from 4.1 to 45 nm is located in an Ultra High Vacuum (UHV) beam pipe. Despite the vacuum a certain amount of residual gases still exist. If the laser beam hits a residual gas atom, it becomes ionized and charged electrons and ions are created. By means of a homogeneous electric field, these electrons and ions can be deflected in a rectilinear way towards the micro-channel plate (MCP). Here, the impacting particles create an avalanche of secondary electrons in the micro tubes of the MCP and are being visualized on the phosphor-screen see Figure 1). These results in an image of the intensity-dependent laser beam profile (see Figure 2).

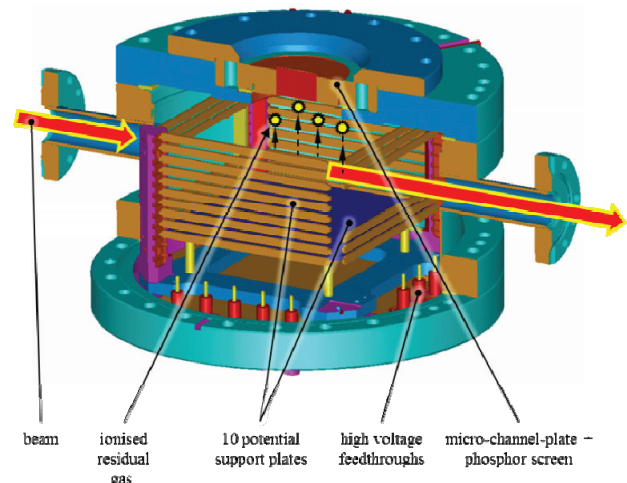


Figure 1: Conventional set up [1].

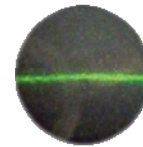


Figure 2: Image of the FLASH laser beam [1] [2].

CONVENTIONAL SET UP

Figure 2 shows an IPM module for the laser beam position measurement as implemented in FLASH [1] [2]. Problems and disadvantages of this design are the following:

- The large size of the monitor (approx. 400 mm x 300 mm x 200 mm) results in an insufficient homogeneity of the electrical field applied. Therefore the exact path of the electrons or ions from the origin of creation to the MCP is unknown and the spatial resolution is in the order of about ± 50 microns.
- The size makes the IPM harder to manufacture and more expensive due to the high number of high voltage feedthroughs.
- To detect the horizontal and vertical parameters of the laser beam (3D) two consecutive detectors have to be implemented with perpendicular orientation to each other demanding large space.
- To take a look at the single bunches rather than just examining the whole train, the IPM needs a time resolution of at least 100 ns, the conventional set is not capable of.

A NEW DESIGN OF THE IONIZATION PROFILE MONITOR

In order to tackle the challenges described above the following design is proposed:

- Unification of the separate horizontal and vertical monitors with an alternating homogeneous electric field.
- A special cage protects the area of interest from electrical stray fields to ensure an optimal homogenous electric field.
- Decreasing the size of the device to 203 mm × 218 mm × 246 mm while at the same time reducing the applied electrical voltage with the appropriate low cost feedthroughs.
- With the Finite Element Method (FEM) a comparison of different residual gas particles is performed concerning their trajectories in the electric field.
- This procedure offers an optimization of the design by simulating the trajectory of the particles in the electrical field with the deflection caused by the inhomogeneity of the field. Varying the CAD monitor model helps finding out the best possible determination of the laser beam position.

Following the principles described above in figure 3 the resulting new design of a 3D detector is presented. The inner cage with a measure of 100 mm × 100 mm × 100 mm consists of equally sized pads, plates and two 28 mm diameter holes for the passage of the beam. Figure 3 shows that 30 different electrical potentials are needed to achieve a homogeneous field in two directions.

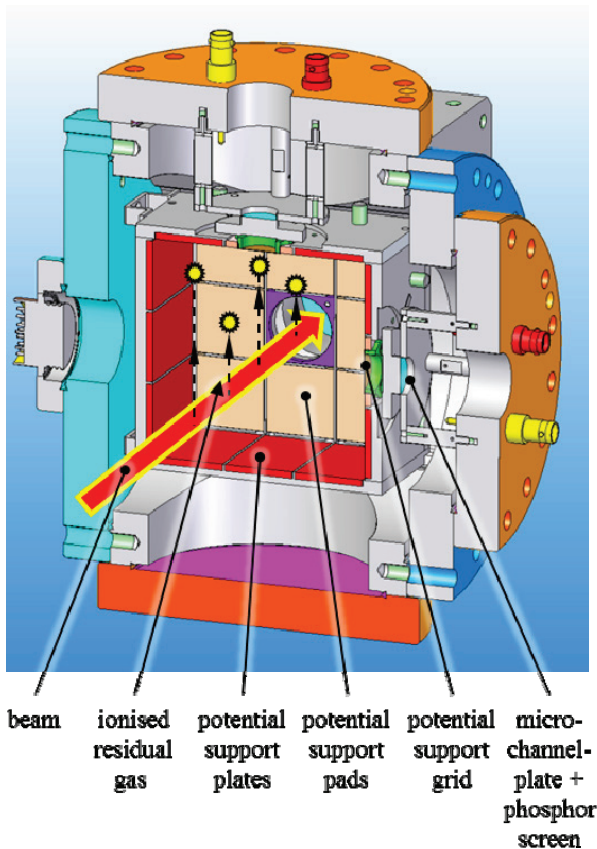


Figure 3: Design of the 3D ionization profile monitor.

Device Specifications

The following special components were chosen:

- 1x stainless steel block with measures 140 mm × 203 mm × 203 mm
- 1× 41-time electrical feedthroughs with plugs and cables
 - W-MPC2-41-DE-CE-SSG [3]
- 2x grid bonded in a ring washer by Precision Eforming
 - MN49 bonded to 20mm SS Frame [4]
- potential support plates and pads consisting of stainless steel
- an inner retainer of the cage consisting of MACOR by MCI UG [5]
- a pulse generator for generating an alternating orthogonal electrical field
 - A-GBS-MATRIXPULS 1×25 by GBS ELEKTRONIK GmbH
 - with a frequency of 100 kHz [6]
- 2x micro-channel-plate and P47 phosphor screen assembly by HAMAMATSU
 - F2222-27P227 [7]
 - Emission range 375 - 600 nm
- 2x special coated sight glasses for optimal transmission
 - VPCF40DUVQ-L-BBAR2 [3]
 - Fused Silicia with anti-reflective coating
- a Camera especially for the emission range of the phosphorscreen
 - Basler acA2500-14gm with an Aptina CMOS MT9P
- an Objective especially for the emission range of the phosphorscreen and the small distance to this screen
 - Schneider Kreuznach Makro-Symmar 5.8/80

The time difference between a photo of the horizontal and the vertical view should be as fast as possible in order to get a complete snapshot of the beam profile at a specific moment.

Temporal Resolution

The selected camera offers a shutter frequency of 12 pictures. This means that 12 times per second the position and the profile of the beam can be measured. The time between the horizontal and the vertical measurements of the profile is limited to the time of fly of the ions and the intensity of light of the screen. A N^{2+} Ion needs 1 μ s from the middle of the assembly to the screen. The intensity of the light is unknown and it has to be tested. Certainly, the shutter time is much longer than the time of fly. But a shutter time of 400 μ s is realistic, resulting in a complete profile measurement of the beam every Millisecond.

Optical Limits of Measurements

In order to have a very short shutter time a special optical system is needed. Different lenses, glasses and cameras were compared. The following Table 1 shows the relative spectral emission, transmission and spectral response of the chosen parts and the optical system.

Table 1: Signal Intensity of the Optical System

Phosphor-screen Hamamatsu F2222-27P227	Inspection Glass Vacom	Objektive Schneider Kreuznach Makro-Symmar 5.8/80	Camera Basler acA2500-14gm	relative Light- absorption with Makro- Symmar and AcA2500-14gm
wave-length in nm	rel. spectral emission in 1	rel. transmission in 1	rel. spectral response in 1	rel. trans- mission of light relating 25 nm
350	0,00	0,90	0,00	0,00
375	0,10	0,90	0,66	0,00
400	0,70	0,90	0,85	6,43
425	0,95	0,90	0,95	11,37
450	0,95	0,90	0,95	12,18
475	0,80	0,90	0,96	10,54
500	0,70	0,90	0,97	9,32
525	0,55	0,90	0,97	7,20
550	0,35	0,90	0,97	4,43
575	0,22	0,90	0,97	2,64
600	0,12	0,90	0,97	1,31

Relative signal intensity of the
beam photo relating to the sender: 48,11%

The chosen parts leads to a signal intensity of 48,11% because of unavoidable transmission and response losses. Semiconductor detectors these avoid.

FEM ANALYSIS

To analyse the homogeneity of the electric field and to determine the trajectory of different particles obtained with the design described above, a FEM analysis was carried out using ANSYS 14 modules workbench [8] and classic [8]. In the simulations different variations and possible future developments of the design were included directly from the CAD-model.

Potential Ratios

Simulation studies performed with the ANSYS 14.5 workbench module package proved the potential ratios, as can be seen in Figure 4, to be optimal for a homogeneous electric field and hence for a straight flight of particles. Since the MCP has a diameter of merely 20 mm, only in the marked "area of interest" the electric field must be homogeneous. Also, the expected beam variation in X or Y is below ± 5 mm. Homogeneity in a larger space does not result in a higher spatial resolution.

The electrically conductive potential supporting points are assumed as being an ideal conductor with equal

potential at any point. The permittivity of the ceramic was assigned to $\epsilon = 6$ and of the vacuum to $\epsilon = 1$.

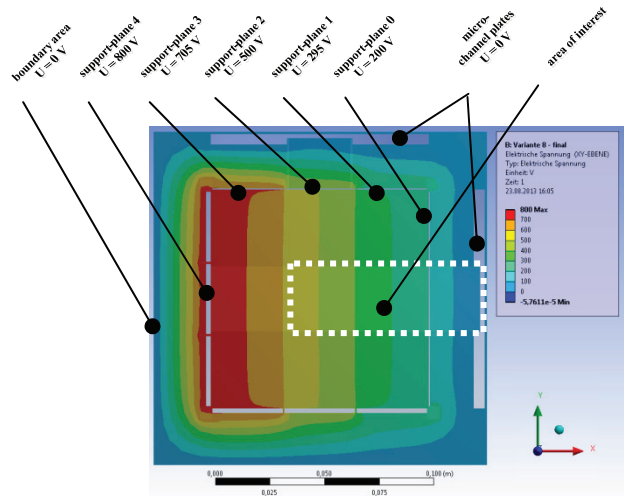


Figure 4: Equipotential lines of the electrical field [8].

CONCLUSION

The first prototype of a 3D-IPM is currently under construction and will be completed and tested in 2014. Before any test with a toggling electrical field, there will be tests with a rigid field. First practice tests are planned in 2015 at FLASH in DESY Hamburg site.

REFERENCES

- [1] Miesner, J., Sachwitz, M., Markert, M., Sternberger, R., Tiedtke, K., Hofmann, A., „An Ionization Profile Monitor for the determination of the FLASH photon beam parameter“, Nucl. Instr. and Meth. A 635, S104-S107 (2011).
- [2] M. Sachwitz, A. Hofmann, S. Pauliuk, K. Tiedtke, H. Wabnitz, “Proc. of EPAC08”, 1266-1268 (2008).
- [3] VACOM Vakuum Komponenten & Messtechnik GmbH, www.vacom.de
- [4] Phosphor-screen P47, Hamamatsu Photonics Company, www.hamamatsu.com
- [5] MCI UG, <http://www.mc-i.de>
- [6] GBS ELEKTRONIK GmbH, <http://www.gbs-elektronik.de>
- [7] Precision Eforming LLC, <http://www.precisioneforming.com>
- [8] ANSYS 14 Workbench und Classic, www.ansys.de

MEASUREMENT OF THE OUTPUT POWER IN MILLIMETER WAVE FREE ELECTRON LASER USING THE ELECTRO OPTIC SAMPLING METHOD

A. Klein[#], A. Abramovich, D. Borodin, A. Friedman, H. Marks,

Department of Electrical and Electronic Engineering, Ariel University, Ariel, Israel

Abstract

In this experimental work an electro optic (EO) sampling method was demonstrated as a method to measure the output power of an Electrostatic Accelerator Free Electron Laser (EA-FEL). This 1.4 MeV EA-FEL was designed to operate at the millimeter wavelengths and it utilizes a corrugated waveguide and two Talbot effect quasi-optical reflectors with internal losses of ~30%. Millimeter wave radiation pulses of 10 μ s at a frequency of about 100 GHz with peak power values of 1-2 kW were measured using conventional methods with an RF diode. Here we show the employment of an electro-optic sampling method using a ZnTe nonlinear crystal. A special quasi optical design directs the EA-FEL power towards the ZnTe nonlinear crystal, placed in the middle of a cross polarized configuration, coaxially with a polarized HeNe laser beam. The differences in the ZnTe optical axis due to the EA-FEL power affects the power levels of the HeNe laser transmission. This was measured using a polarizer and a balanced amplifier detector. We succeeded in obtaining a signal which corresponds to the theoretical calculation.

INTRODUCTION

Continue Wave (CW) and pulsed millimeter wavelength (MMW) and Terahertz (THz) radiation have many applications in medicine, industry, military and security [1]. In order to realize those applications, knowledge of the MMW or THz beam properties such as beam power, beam diameter and beam cross section pattern are required. For the MMW Electrostatic Accelerator-Free Electron Laser (EA-FEL) operating at 100 GHz we used heterodyne detection and received good results [2]. For higher frequency radiation and pulsed sources, photoconductive antennas and far-infrared interferometric techniques are used [3, 4]. Photoconductive antennas have higher responsivity, and their signal-to-noise ratios are better than liquid helium cooled bolometers. Their detection bandwidth with a short dipole length can exceed 1-3 THz. The drawback of those photoconductive antennae is the resonant behavior and the limited operating bandwidth. Interferometric techniques provide an autocorrelation of terahertz pulses but important parameters of the beam are lost and it is complicated to realize. In this study, we report the use of an alternative optoelectronic method, free-space electro-optic sampling [5], to characterize freely propagating terahertz bandwidth CW or pulsed electromagnetic

radiation. The advantages of this method are the sensitivity and speed of response allowing the identification of a short pulse envelope. Also this method can detect the cross-section of the THz beam radiation. In this work we demonstrated power measurements of single pulses and in-the future we intend to image the cross sectional pattern of MMW and THz pulses. Our detection is independent of the source of MMW and we use inexpensive components, which include a HeNe CW laser, detector, optical components and two off-axis parabolic mirrors (OPM) to focus the MMW beam onto the ZnTe Electro-Optic (EO) crystal cross section (see Fig. 1).

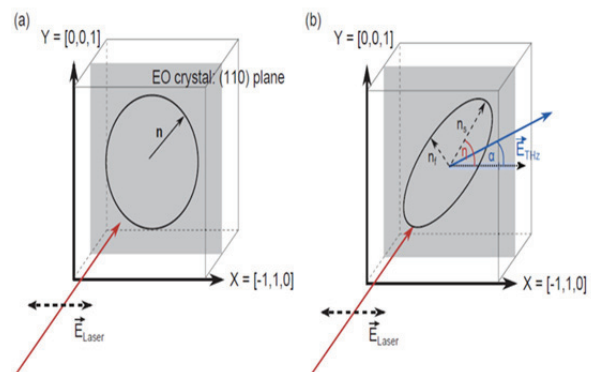


Figure 1: Refractive index ellipsoid of ZnTe Electro Optic crystal (a) Symmetric ellipsoid, without electric field and (b) The directions and the magnitudes of the main axes are changed, when an electric field is applied.

THEORY

Electro-Optic Effect in ZnTe [6, 7]

The EO crystal ZnTe exhibits a birefringence, which means a different refractive index property along the propagating direction of a laser beam. Each refractive index is linear dependent on the electric field's strength. This effect is called Pockels effect.

The direction of the axes and the dependency of each refractive index can be calculated by considering the constant energy surface of the electric displacement vector space and the impermeable tensor which is linear in the electric field. The main refractive indices can be known from the refractive index ellipsoid equation by a principal-axis transformation. For a ZnTe crystal cut in the 110 plane, polarized laser light enters the crystal with amplitude equal to the two main axis, the different refractive index in each one cause to different phase between them [3].

[#]klenavi1@gmail.co.il

$$\cos(2\eta) = \frac{\sin(\alpha)}{\sqrt{1+3\cos^2\alpha}} \quad (1)$$

where α is the angle between Electric THz field to X axis, η is the angle that determine the new primary axes of refractive indexes.

$$\Gamma = \frac{w_0 d}{c} (n_1 - n_2) = \frac{\pi d}{\lambda} n_0^3 r_{41} E_a \sqrt{1 + 3\cos^2\alpha} \quad (2)$$

$$\text{For ZnTe, } r_{41} \cong 4.04 \cdot 10^{-12} \frac{\text{m}}{\text{v}} \quad (3)$$

where λ is the wave length of the laser beam, d is the crystal thickness, n_0 is the initial refractive index, r_{41} is the electro-optic constant and E is the electric field strength.

The difference of the propagating speed due to different refractive indexes, changes the polarization of the incident laser beam. This difference can be represented as a relative phase shift between the two components of the new primary axes directions.

The output power in the cross polarizer scheme is:

$$\Delta I = I_0 \sin^2\left(\frac{\Gamma}{2}\right) \quad (4)$$

EXPERIMENTAL SETUP

A block diagram of MMW radiation power measurements based on the EO sampling method is shown in Fig. 2. The EO sampling is based upon a ZnTe EO crystal (see Fig. 1). A polarized MMW beam from the EA-FEL is transferred to the input aperture. A 1.2 mW CW HeNe laser operating at 633 nm is used as a probe beam. The laser beam is polarized by an input polarizer and it is perpendicular to the EA-FEL beam. The laser beam is focused on a ZnTe crystal, coaxially with the measured EA-FEL 100 GHz beam. An off axis parabolic mirror (OPM) is used to focus the EA-FEL beam on the crystal. The laser beam is transferred through a hole in the OPM. The ZnTe crystal cut is 110 and its size is 10*10*1 mm (see Fig. 1). The laser beam after the analyzer is directed to one of the photo diodes in the balanced detector. The photodiode signal is measured using an oscilloscope.

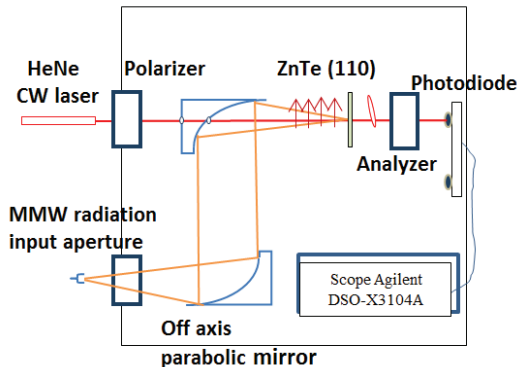


Figure 2: Experimental set-up for measuring the pulsed beam radiation using EO crystal ZnTe.

EXPERIMENTAL RESULTS

The power results measurement of the FEL power are shown in Fig. 3 for three consecutive pulses. The pulse duration was measured to be 6 μs with power of about 1-2 kW. In the top graph the results of measurements with the EO detector and in the bottom graph for the same pulses the power profiles measured by an RF diode.

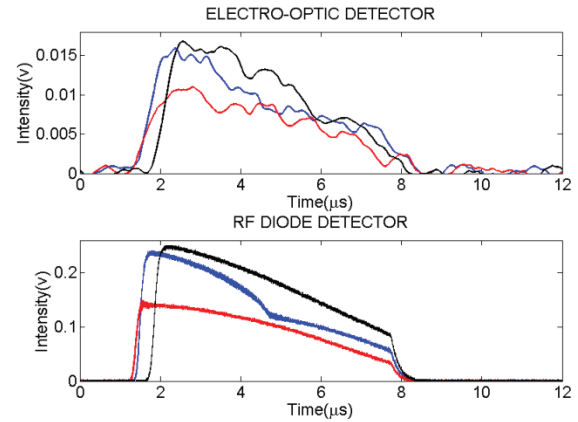


Figure 3: Experimental results for measuring the pulsed beam radiation using the EO crystal ZnTe (top graph) using the configuration of Fig. 2. for comparison the same pulses were measured simultaneously using an RF diode.

The experimental results of the RF diode confirm the correctness of the power measurements using the EO sampling method.

FUTURE FOLLOW-UP EXPERIMENT

Our next step is to obtain a cross sectional image of the EA-FEL beam pattern. For that we have to expand the detection system by using higher power laser and beam expander to overlap the MMW beam from the EA-FEL. The influences of the MMW beam cross section on the ZnTe crystal properties and consequently on the laser beam will be captured using sensitive CCD camera.

SUMMARY AND CONCLUSION

For 100 GHz, 2-10 μs pulse with about 1-2KW of input power, a good electro-optic signal was obtained. The signal was compared with a signal from a well-known RF Diode detector. The EO sampling method provides the ability to measure much shorter pulses due to the fast response of the ZnTe crystal. Imaging of the cross section of the EA-FEL MMW beam can be carried-out. Unlike RF diode detectors, no RF attenuators are required. The power measurements demonstrated in this study are broadband, mobile and independent of the MMW or THz source.

REFERENCES

- [1] Masayoshi Tonouchi, "Cutting-edge THz technology," Nature Technology, vol 1, p. 97 2007.
- [2] A. Abramovich, et. Al., "First operation of the Israeli Tandem Electrostatic Accelerator Free-Electron

- Laser,” Nuclear Instruments and Methods in Physics Research A, 407, 16-20, 1998.
- [3] Q. B. B. Hu, J. T. Darrow, X.-C. Zhang, D. H. Auston, and P. R. Smith, “Optically steerable photoconducting antennas,” Appl. Phys. Lett. 56, 886, 1990.
 - [4] S. E. Ralph and D. Grischkowsky, "THz spectroscopy and source characterization by optoelectronic interferometry," Appl. Phys. Lett. 60, 1070, 1992.
 - [5] Q. Wu and X. C. Zhang, “Free space electro optic sampling of terahertz beams,” Appl. Phys. Lett. 67, 3523 , 1995.
 - [6] S. Casalbuoni, H. SchlarbB. SchmidtB, Steffen P.Schmuser A. Winter, “Numerical Studies on the Electro-Optic Sampling of Relativistic Electron Bunches,” TESLA Report 2005-01.
 - [7] G. Berden , Nieuwegein, F.J.P Wijnen, H. van der Pluijm, R.T. Jongma, Radboud University, Nijmegen, The Netherlands “A Simple spectral calibration technique for terahertz free electron laser radiation,” Proceedings of FEL2011, Shanghai, China.

CONCEPTUAL STUDY OF A SELF-SEEDING SCHEME AT FLASH2

T. Plath, L. L. Lazzarino, Universität Hamburg, Hamburg, Germany
K. E. Hacker, T.U. Dortmund, Dortmund, Germany

Abstract

We present a conceptual study of a self-seeding installation at the new FEL beamline, FLASH2, at the free-electron laser at DESY, Hamburg. For self-seeding, light from a first set of undulators is filtered by a monochromator and thus acts as a seed for the gain process in the main undulator. This scheme has been tested at LCLS at SLAC with a diamond monochromator for hard X-rays and with a grating monochromator for soft X-rays covering energies between 700 and 1000 eV. For such a design to offer benefits at FLASH2, it must be modified to work with X-rays with wavelength of about 5 nm (248 eV) where the damage threshold of the monochromator in the setup and the divergence at longer wavelengths become an issue. An analysis of the potential performance and limitations of this setup is performed using GENESIS 1.3 and a method developed for the soft X-ray self-seeding experiment at the European XFEL.

With a total of 9 undulators in the first stage and 8 undulators after the monochromator, a pulse energy contrast ratio of 3.3 was simulated with an initial peak current of 2.5 kA.

INTRODUCTION

Starting the lasing process in Free-Electron Lasers (FELs) from noise limits the longitudinal coherence and shot-to-shot wavelength stability of the FEL radiation. To overcome the limitations of self amplified spontaneous emission (SASE) operation, the FEL process can be initiated by an external light field from either a tabletop laser or from an upstream FEL. When the seed light comes from an upstream FEL, the process is called self-seeding.

Self-seeding, originally proposed by [1], describes a seeding scheme in which the light from a first set of radiators is sent through a monochromator and used to seed a second set of radiators. It has been experimentally demonstrated at LCLS for hard X-rays [2] and soft X-rays with energies from 500-1000 eV [3, 4].

This is a study of a soft X-ray self-seeding design for FLASH2 [5]. An FEL energy of 248 eV was chosen because this is close to the high energy limit of operation. Our design is based on the one used at LCLS [4]. The simulation methods are adapted from the ones used for the European XFEL [6].

Our studies show that tolerances on the electron bunch are very tight due to the space constraints of FLASH2. To generate sufficient pulse energies in both, the first and the second undulator stage, the electron peak current has to be about 2.5 kA with an emittance of 1.5 mm mrad and a slice energy spread of 200 keV at an electron bunch energy of 1.1 GeV. These conditions are estimated through simulation alone and are not based on past performance at FLASH2. Achieving a slice energy spread of 200 keV with 2.5 kA peak

current would be challenging. A larger energy spread would decrease the performance and self-seeding operation under the given space constraints would no longer be possible.

While losses in the monochromator are comparable to the LCLS and European XFEL designs, the divergence of the beam is larger due to the longer wavelength operation regime, leading to lower intensity and a best predicted pulse energy contrast between the seed and SASE background of 3.3.

Hardware Setup at FLASH2

FLASH2 is the second FEL beamline at FLASH, the Free-Electron Laser at DESY in Hamburg. In this paper we describe a rearrangement of the 12 existing undulator modules as well as the addition of 7 further modules and a 3 m long chicane for self-seeding and study the performance given the space constraints.

Altogether there are 21 open spaces for the self-seeding undulators and chicane, 18 of which are filled in this design.

MONOCHROMATOR AND CHICANE

Monochromator Design

The monochromator shown in Fig. 1 consists of a variable line spacing (VLS) toroidal grating followed by a plane mirror (M1), a cylindrical mirror (M2) and another plane mirror (M3). Between the first and the second mirror, a slit is located: it allows for the selection of the transmitted bandwidth, stray light reduction and much easier alignment of the optics. The VLS grating focuses the dispersed wavelengths into lines at the slit position, while the grating sagittal curvature and M2 tangential curvature focus them in the middle of the first undulator module of the seeded undulator stage.

The monochromator parameters can be found in table 1 for a minimum of 200 eV (6.2 nm) and a maximum of 350 eV (3.5 nm) photons. The working point for the FEL simulations in this paper lies at 248 eV (5 nm).

Chicane Design

The chicane delay and the monochromator delay need to be approximately equal so that the longitudinal overlap with the radiation is preserved. The chicane additionally destroys the micro-bunching from the first undulator stage leaving a smeared out longitudinal charge density to be seeded in the main undulator.

The chicane as shown in Fig. 1 consists of 4 steering dipoles with 300 mm yoke length. The magnetic length of each magnet is given by 330 mm with a maximum possible magnetic field of 0.25 T. The FODO structure of FLASH2 limits the overall chicane length to about 3.2 m. The chicane parameters can be found in table 2 for the minimum and

Table 1: Monochromator Parameters for Two Different Photon Energies of Photons (200 eV and 350 eV are the minimum and maximum values for the chicane. The working point for this paper will be 248 eV.)

Parameter	200 eV	350 eV
Grating		
position (z) [mm]	791	
line density [1/mm]	1000	
linear coeff [1/mm ²]	4.08	
quadratic coeff [1/mm ³]	0.0034	
tangential radius [m]	120	
sagittal radius [m]	0.200	
diffraction order	1	
incident angle [deg]	1	
exit angle [deg]	6.462	4.898
incident radiation peak intensity [GW/cm ²]	16	
M1		
position (z) [mm]	819.7	827.4
incident angle [deg]	3.731	2.949
Slit		
position (z) [mm]	2373	
width [μm]	3	
M2		
position (z) [mm]	2423	
incident angle [deg]	3	
tangential radius [m]	1.863	
M3		
position (z) [mm]	2459	
width [μm]	3	
transmission [%]	6.1	6.6

maximum photon energies of the monochromator. Since the delay of the monochromator changes with the wavelength of the photons, the magnetic fields of the chicane dipoles has to be adjusted to change its delay accordingly.

While traversing the chicane, the electrons are not only influenced by linear optics, but are also subject to coherent synchrotron radiation (CSR). To estimate the energy spread blow-up induced by CSR, simulations with the particle tracking code CSRtrack [7] have been done. The total energy spread of the electron bunch increases from about $\Delta\gamma = 0.44$ before the chicane to $\Delta\gamma = 0.74$ after the chicane.

Table 2: Chicane Parameters for Two Different Photon Energies of Photons (200 eV and 350 eV are the minimum and maximum values for the chicane. The working point for this paper will be 248 eV.)

Parameter	200 eV	350 eV
distance D ₁₂ [mm]	900	
distance D ₂₃ [mm]	200	
magnetic field [T]	0.2344	0.2207
deflection angle [deg]	1.10	1.03
R ₅₆ [mm]	0.808	0.717
horizontal offset h [mm]	23.0	21.7
horizontal offset after dipole h _I [mm]	2.88	2.71
timing difference Δt [ps]	1.469	1.302

In comparison to the 200 keV used in the simulation, an initial 500 keV keV slice energy spread based on measured performance at FLASH1 would increase the gain length in the first stage and a tenth undulator would be required to still achieve sufficient seed power for the second undulator stage. The CSR in the chicane would however increase this energy spread further. At an energy spread of about 1 MeV at the entrance of the second undulator stage, the saturation length of such an electron beam would exceed the space available at FLASH2.

Resolving Power

While the monochromator setup does employ an optional slit, there is a lower limit to the resolving power, R , the monochromator can operate with: the electron bunch itself acts as a slit since it is only in overlap with a specific fraction of the light pulse. This allows for coupling of a certain spectral range only and determines the amount of power coupling to the electrons. From this, an instrumental function for the monochromator and the second undulator stage describing the coupling factor of the seed radiation as a function of its wavelength can be calculated. To estimate this resolving power the method proposed in [6] has been followed.

The monochromator gives a horizontal offset to different wavelengths at the point of interaction with the electron bunch in the second undulator stage. The overlap of the light pulse and the electron bunch will therefore get worse with higher $\Delta\lambda$ and thus diminish the coupling of the light to the electrons.

The results of the Genesis 1.3 [8] simulations are shown in Fig. 2. The input coupling factor is given by the peak power of the FEL pulse after a few gain lengths and is normalized to the peak power at perfect overlap. The resolving power of the setup is then given by the FWHM of the shown curve $R = \frac{\lambda}{\Delta\lambda} = 17500$.

Figure 3 shows the spectrum of the first undulator stage with the window that will be cut out by the monochromator

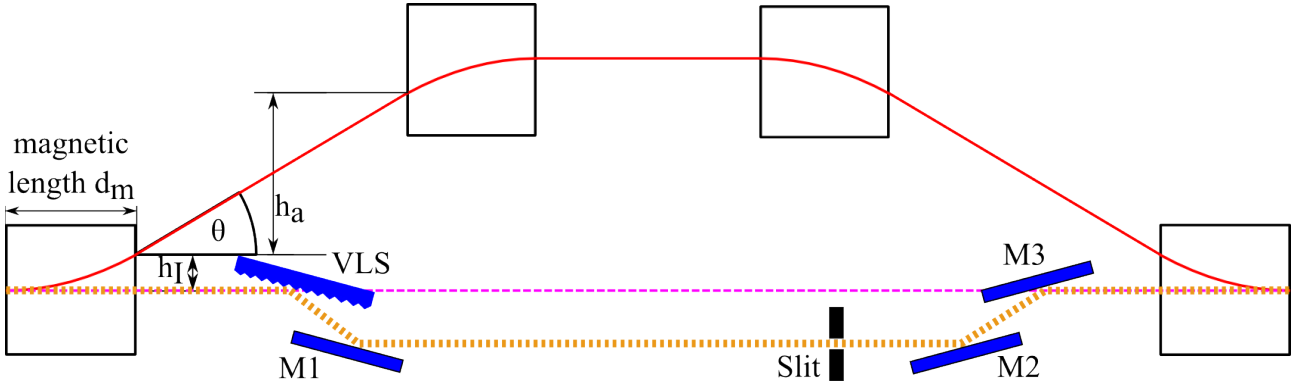


Figure 1: Drawing of the chicane between first and second undulator stage and monochromator. The red line shows the orbit of the electrons, while the yellow dotted line shows the path of the light pulse. Blue elements are optical element while the quadratic white boxes are the chicane dipoles.

with the electron bunch acting as a slit. This window can be moved on the wavelength axis by rotating the M1 mirror.

The resolution is given after 2-3 gain lengths after which the seed radiation coupled to the electron bunch.

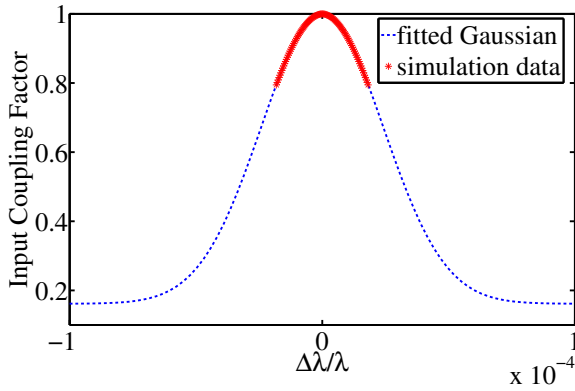


Figure 2: Input coupling factor as a function of wavelength difference of the incoming seed radiation. While the red crosses show Genesis 1.3 simulation results, the blue dashed line is the Gaussian Fit, giving the resolving power.

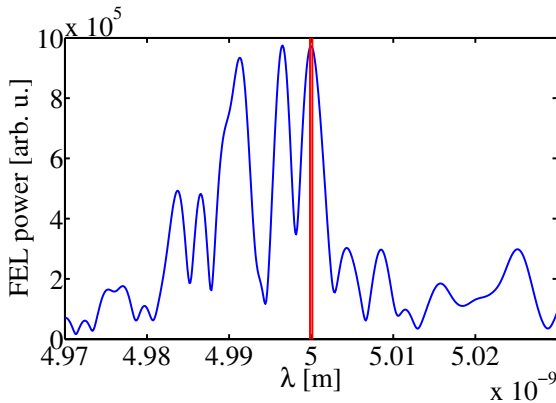


Figure 3: Spectral output of the first undulator stage. The blue lines show the fraction cut out by the resolving power of the electron bunch.

This resolving power is, however, a local property since $\frac{d\lambda}{dx}$ increases linearly with the z position along the undulator.

FEL SIMULATIONS

First Undulator Stage

The first undulator stage of the self-seeding setup has to deliver enough input power to successfully seed the second stage with the monochromator losses and resolving power taken into account. A Genesis 1.3 simulation for the SASE case at 5 nm for FLASH2 has given the properties of the FEL pulse after different numbers of FLASH2 undulator modules.

Table 3: Photon Pulse Properties After Different Number of Undulator Modules for the First Undulator Stage (divergence and beam size of the light pulse are given at the maximum power along the undulator axis)

Undulator Modules:	7	8	9
photon pulse energy [μJ]	0.282	1.020	3.939
divergence [mrad]	0.7	0.7	0.6
beam size (rms) [mm]	0.18	0.14	0.12
SASE bandwidth $(\Delta\lambda/\lambda)_{\text{SASE}}$	1.75%	1.59%	1.46%
resolving power R_m	17500	17500	17500
photon pulse energy monochromator [pJ]	55	229	924

Table 3 shows the resulting photon pulse properties and the estimated results for the pulse after the monochromator. The photon pulse energy after the monochromator is estimated by

$$E_{\text{in}}^{(2)} = \frac{T_m}{R_m(\Delta\lambda/\lambda)_{\text{SASE}}} E_{\text{out}}^{(1)}, \quad (1)$$

where $E_{\text{in}}^{(2)}$ denotes the input pulse energy of the second undulator stage, $E_{\text{out}}^{(1)}$ the output pulse energy of the first

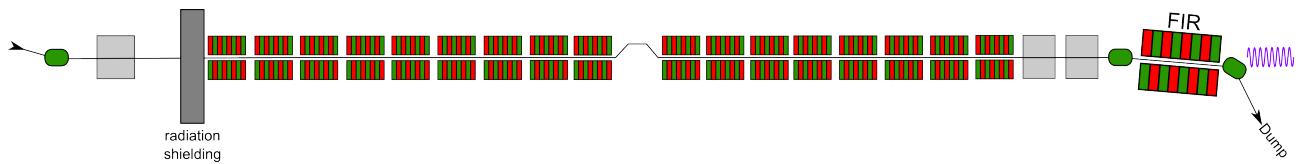


Figure 4: FLASH2 layout for a possible self-seeding scheme at 5 nm. The grey boxes show places where additional undulators could be installed if required. The last space was reserved for either a transverse deflecting structure or afterburner. The space before the radiator could be used for a seeding scheme.

undulator stage, T_m the transmission of the monochromator, R_m its resolving power.

From this we recommend a total of 9 undulators in front of the monochromator to have sufficient seed pulse energy of about 924 pJ with a pulse length of 129 fs and from this a peak power of about 6 kW for the second stage.

According to the simulations the laser beam on the grating will have a peak fluence of $12 \mu\text{J}/\text{cm}^2$, that is 4 orders of magnitude lower than the expected damage threshold of about $1\text{J}/\text{cm}^2$ while repetition rate does not exceed 120 Hz [3].

Seeded Undulator Stage

The Genesis 1.3 simulations for the undulators after the monochromator employ Gaussian electron and seed pulses only. The properties of the electron beam are derived from the first stage and the chicane effects (such as CSR), the properties of the seed pulse are defined by the first stage and the above discussed influence of the monochromator. It is, however, not the same electron distribution, but a newly generated one that goes into this simulation. From the properties of the first undulator stage and the monochromator an input seed pulse energy of 924 pJ and a pulse length of 129 fs can be expected.

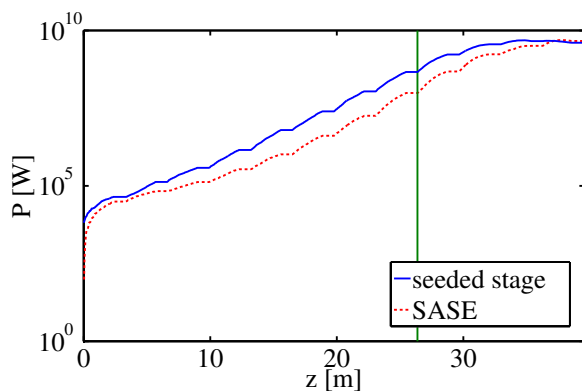


Figure 5: FEL gain curves for a 6 kW seeded electron bunch, compared to a SASE case. The green vertical line shows the end of the 4th FODO cell and with this the 8th undulator modules. The energy contrast ratio between the seeded light pulse to the SASE background is about 3.3.

Figure 5 shows FEL peak powers for a 6 kW seed compared to the SASE case. It can be seen that the seeded run reaches saturation after 9 undulators at about 30 m. To

measure the performance of a self-seeding, experiment not only the peak power of the FEL light, but also the spectral brightness and contrast to the SASE case is important.

Figure 6 shows the spectral profiles of the FEL pulse after 8 undulator modules compared to the SASE case. The energy contrast of the seeded FEL pulses compared to SASE pulses is about 3.3. When using 9 undulators for the second stage this contrast decreases by a factor of 2 which is why this study recommends 8 undulator modules for the second radiator stage with a final peak power of $P_{\text{Peak}} \approx 0.5 \text{ GW}$.

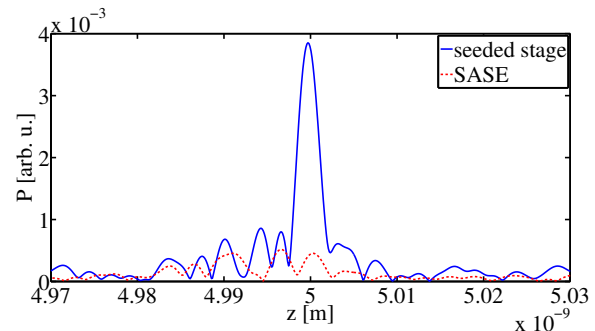


Figure 6: Spectral power profile of FEL pulses 8 undulators. The red line shows the SASE background and the blue line the seeded FEL pulse.

Its bandwidth is estimated by a Gaussian fit to be $(\Delta\lambda/\lambda)_{\text{seeded}} \approx 7.5 \cdot 10^{-4}$. This is a factor of about 20 narrower than the SASE bandwidth. Given this bandwidth a transform limited pulse would have a length of $\Delta t \approx 9.1 \text{ fs}$, while the FEL pulse from the simulation has a length of $\Delta t \approx 18.3 \text{ fs}$ and thus close to Fourier limited.

Figure 4 shows the proposed arrangement of undulators and the chicane for a possible self-seeding setup at 5 nm.

CONCLUSION

A possible self-seeding setup at the FLASH2 facility has to deal with tight space constraints and has thus to run at high peak currents of about 2.5 kA to be able to generate seeded FEL pulses close to saturation with a bandwidth about 20 times narrower than the SASE pulse.

While the calculations show a peak power of 6 kW after the monochromator, it might be very challenging to achieve this performance from both the monochromator and the first undulator stage, since this study has been taken out with ideal Gaussian bunches and pulses. Less power from the first stage would lead to a worse energy contrast and less

peak power of the final FEL pulse. All calculations have to be redone with a full start-to-end simulation and based on experience at FLASH2 in order to determine the tolerances more accurately.

Additionally the monochromator needs to be further optimized to allow a lower resolving power and thus leading to more energy in a shorter light pulse with a reasonable divergence and focus point.

The present simulation shows that a self-seeding scheme at 5 nm would use 9 undulator modules in the first stage, a 3 meter chicane spanning only one undulator slot and 8 undulator modules for the second set of radiators. There are 21 available slots for hardware, 18 of which are used up in this design. To account for the possibility of poorer performance in this first undulator stage, an additional radiator would be recommended, leaving 2 open slots, one at the end for a TDS or afterburner, and one at the beginning for a compact external seeding concept.

ACKNOWLEDGMENT

The authors of this paper would like to thank Svitozar Serkez for helpful discussions and feedback. Supported by Federal Ministry of Education and Research of Germany under contract No. 05K1GU4 and 05K10PE1 and the German Research Foundation program graduate school 1355.

REFERENCES

- [1] J. Feldhaus *et al.*, "Possible application of X-ray optical elements for reducing the spectral bandwidth of an X-ray SASE FEL", *Optics Communications* 140, 1997, 341-352.
- [2] J. Amann *et al.*, "Demonstration of self-seeding on a hard-X-ray free-electron laser", *Nature Photonics* 6, 2012, 693-698.
- [3] D. Ratner, "Soft X-ray Self Seeding Current Status", *Advanced X-ray FEL Workshop*, Hamburg, 2012.
- [4] Y. Feng *et al.*, "System Design for Self-Seeding the LCLS at Soft X-Ray Energies", *Proceedings of FEL2012, Nara, Japan*, 2012, pp- 205-212.
- [5] B. Faatz *et al.*, "FLASH II: Perspectives and challenges", *Nuclear Instruments and Methods A* 635 (2011), S2-S5.
- [6] S. Serkez *et al.*, "Grating monochromator for soft X-ray self-seeding the European XFEL", *DESY Report* 13-04, arXiv:1303.1392v1, 2013.
- [7] M. Dohlus and T.Limberg, "CSRtrack: Faster Calculation of 3-D CSR Effects", *Proceedings of 2004 FEL Conference*, Trieste, Italy, 2004, pp. 18-21.
- [8] S. Reiche, "GENESIS 1.3: a fully 3D time-dependent FEL simulation code", *Nuclear Instruments and Methods A* 429, 1999, pp. 243-248.

DOUBLE-GRATING MONOCHROMATOR FOR ULTRAFAST FREE-ELECTRON-LASER BEAMLINES

F. Frassetto, L. Poletto[#], CNR-IFN, Padova, Italy
E. Ploenjes, M. Kuhlmann, DESY, Hamburg, Germany

Abstract

We present the design of an ultrafast monochromator explicitly designed for extreme-ultraviolet FEL sources, in particular the upcoming FLASH II at DESY. The design originates from the variable-line-spaced (VLS) grating monochromator by adding a second grating to compensate for the pulse-front tilt given by the first grating after the diffraction. The covered spectral range is 6–60 nm, the spectral resolution is in the range 1000–2000, while the residual temporal broadening is lower than 15 fs. The proposed design minimizes the number of optical elements, since just one grating is added with respect to a standard VLS monochromator and requires simple mechanical movements, since only rotations are needed to perform the spectral scan.

INTRODUCTION

One of the most demanded features for free-electron-laser beamlines is the possibility to monochromatize the FEL beam even beyond the intrinsic FEL resolution. Grating monochromators are used both at FLASH [1, 2] and LCLS [3, 4]. Unfortunately, especially for operation in the extreme-ultraviolet region of FLASH, the monochromator temporal response strongly affects the pulse duration, because of the pulse-front tilt introduced by the grating after the diffraction [5]. The full exploitation of the ultrashort temporal characteristics of a FEL source requires the use of a grating monochromator that compensates for the pulse-front tilt, that we define Compensated Monochromator (CM). The design consists in using two gratings in compensated configuration, i.e., the second grating compensates for the pulse-front tilt introduced by the first one [6–10]. CMs have been realized and used in high-order laser harmonics ultrafast beamlines, giving at the output pulses as short as 8 to 10 fs in the 20–45 nm region [11–14]. A CM for FEL has to be designed taking into account the peculiar parameters of the source, particularly the peak intensity, and the different requirements, particularly the definitely larger size of the optics.

Here we present the design of a CM explicitly tailored for extreme-ultraviolet FEL sources, in particular the upcoming FLASH II. The driving parameters for the design are: a) spectral range 6–60 nm; b) spectral resolution in the 1000–2000 range; c) time response shorter than 50 fs; d) minimum lateral displacement to let

space to adjacent beamlines; e) minimum vertical displacement to reduce the change of the beam height; f) mirror length shorter than 500 mm; g) grating length shorter than 300 mm.

The monochromator design originates from the variable-line-spaced (VLS) grating monochromator that is already used at LCLS (see Ref. 2) by adding a second grating to compensate for the pulse-front tilt.

BEAMLINE DESIGN

The design originates from the variable-line-spaced (VLS) grating monochromator, that has been adopted for synchrotron radiation beamlines [15], high-order laser harmonics [16] and FELs (see Ref.s 3 and 4). The light coming from the source is focused by a concave mirror, that produces a converging beam. This is intercepted by a VLS plane grating, that diffracts the radiation onto the exit slit. The variable groove spacing of the grating provides the additional free parameters to keep the focal distance almost constant as a function of the wavelength and to compensate for high-order aberrations. The VLS monochromator is also rather simple mechanically in that only two optical elements are required and the photon energy is scanned by a single rotation of the grating around an axis passing through its center.

The CM is realized by adding a second section with an identical VLS plane grating illuminated by the diverging monochromatic light coming out from the slit and mounted in a compensated geometry with respect to the first grating, i.e., internal and external diffraction orders are splitted between the two gratings.

The design has been specialized to the requirements of FLASH II:

- The monochromator works without an entrance slit, being the FEL itself the source point (as the case of the monochromator at LCLS).
- An additional plane mirror is inserted between the two gratings to fold the beam and give very low displacement of the output beam with respect to the input.
- Horizontal and vertical foci are kept separated to reduce the radiation density on the slit blades, due to high peak intensity. In particular, the first mirror, that is demanded to illuminate the grating in converging light, is a plane-elliptical one, therefore the focus on the intermediate slit is astigmatic, i.e., the beam is focused only in the spectral direction.

The optical layout is shown in Fig. 1. The FEL beam is focused by the plane-elliptical mirror M1 toward the plane VLS grating G1. The latter diffracts the radiation toward the intermediate slit, where the beam is

[#]luca.poletto@ifn.cnr.it, National Research Council of Italy, Institute of Photonics and Nanotechnologies, via Trasea 7, I-35131 Padova (Italy)

monochromatized. The plane mirror M2 is used to fold the beam, therefore reducing the lateral displacement of the beamline. The grating G2 has the same groove-space-variation parameters as G1 and is mounted to realize the compensated configuration. The diverging radiation coming out from G2 is finally focused to the sample area by two plane-elliptical mirrors in Kirkpatrick-Baez configuration.

The whole beamline consists of four mirrors and two gratings. With respect to a standard VLS monochromator beamline, only two optical elements, the grating and the plane folding mirror, have been added to obtain the ultrafast response.

With respect to the monochromator beamline at FLASH, which has five mirrors and one grating (see Ref. 1), the total number of optical elements is the same. With respect to the monochromator beamline at LCLS, which has three mirrors and one grating (see Ref. 3), one additional grating and the plane folding mirror have been added.

The spectral dispersion plane is assumed to be the side view, i.e., the radiation is dispersed in the vertical plane. The incidence angle on the last focusing mirror has been chosen to have the output beam parallel to the input beam in the vertical plane. The displacement of the output beam with respect to the input is kept very low in the vertical plane: the output is parallel to the input and just ≈ 20 cm higher. The lateral displacement with respect to the entrance direction is also ≈ 20 cm.

The direction of the output beam with respect to the horizontal axis may be exchanged just choosing a different incident angle on the mirror M4. Therefore, the angle on M4 may be selected to have the output of the CM beamline parallel to the other beamlines. This will give the additional advantage to have all the beamline output axes parallel, therefore it will be easy to use the same experimental chambers in different beamlines.

The beamline parameters are resumed in Tab. 1. Two sets of gratings are used to cover the 6 - 60 nm spectral region. The FLASH II source has been assumed to have size of 200 μ m FWHM and divergence of 75 μ rad FWHM at 40 nm, that scales as $\lambda^{3/4}$. Given the limited size of the optical elements, a partial cut of the beam occurs at wavelengths longer than 40 nm. The vignetting is 4% at 40 nm, 6% at 50 nm, 20% at 60 nm.

Table 1: Beamline Parameters

M1	Plane-elliptical
Entrance arm	60 m
Exit arm	3 m
Incidence Angle	87°
Size	500 mm \times 40 mm
M2	Plane
Incidence Angle	88.5°
Size	400 mm \times 40 mm
M3	Plane-Elliptical
Entrance Arm	67.5 m
Exit Arm	2 m
Incidence Angle	87°
Size	500 mm \times 30 mm
M4	Plane-elliptical
Entrance Arm	5 m
Exit Arm	1.5 m
Incidence Angle	85.5°
Size	400 mm \times 25 mm
G1A-G2A	VLS plane grating
Spectral region	6-20 nm
Central groove density	600 gr/mm
Deviation angle	168°
Size	250 mm \times 20 mm
G1B-G2B	VLS plane grating
Spectral region	20-60 nm
Central groove density	200 gr/mm
Deviation angle	168°
Size	300 mm \times 40 mm

The optical performances have been simulated by a ray-tracing program that is able to calculate the pulse-front tilt after the grating diffraction. G1 is operated in the internal spectrum, i.e., $\beta_{G1} < \alpha_{G1}$, to have the incident angle on G1 higher than 84°: $85.0^\circ < \alpha_{G1} < 87.3^\circ$. On the contrary, G2

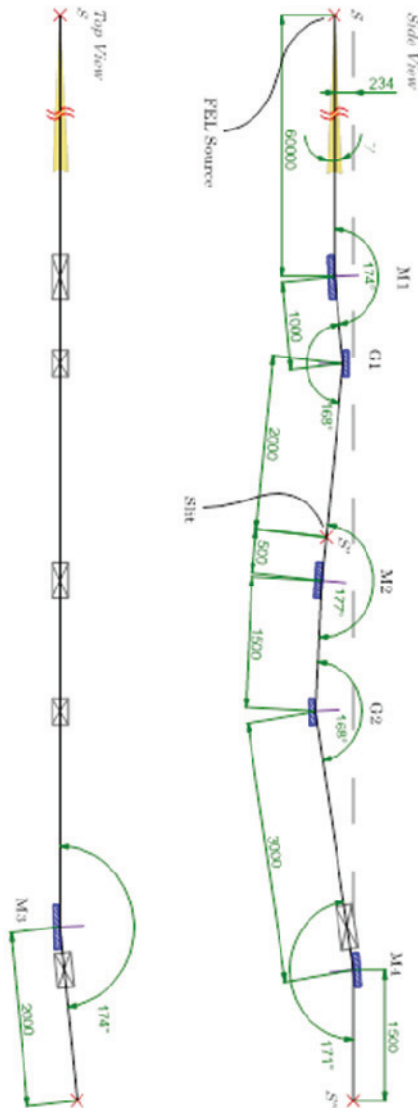


Figure 1: Beamline layout. Distances are in millimetres.

is operated in the external spectrum to realize a compensated configuration, i.e., $\beta_{G2} > \alpha_{G2}$, which results in $80.7^\circ < \alpha_{G2} < 83.0^\circ$. The use of G1 at incident angles higher than 85° makes it safer to operate the grating under the intense FEL beam. G2 is illuminated at incident angles lower than 83° , but being it located after the intermediate slit, the FEL beam intensity is much lower than at G1.

The resolution is shown in Fig. 2 for a 50- μm -wide slit. It has been calculated as $\lambda/\Delta\lambda_{\text{FWHM}}$, where λ is the wavelength and $\Delta\lambda_{\text{FWHM}}$ the full-width-at-half-maximum bandwidth that is transmitted through the intermediate slit. The resolution is higher than 1000 in the whole spectral range of operation, according to the requirements.

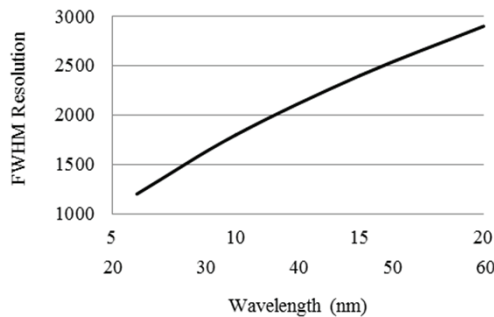


Figure 2: Resolution, $\lambda/\Delta\lambda$, 50- μm slit.

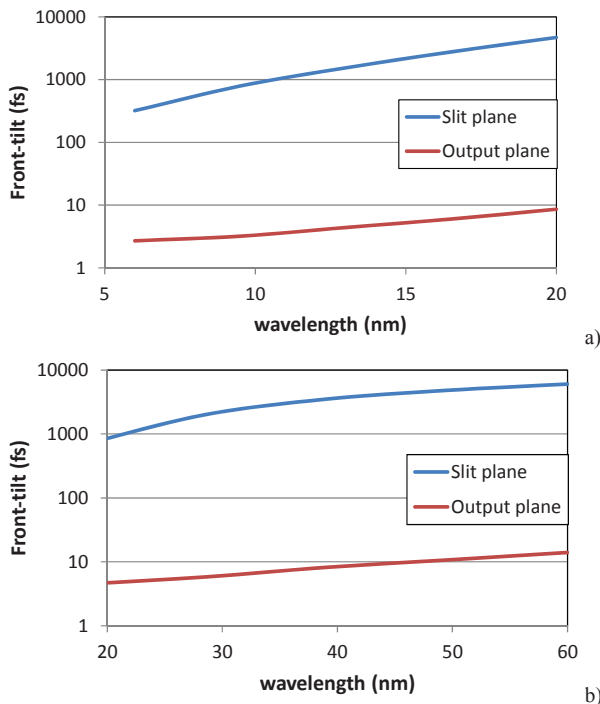


Figure 3: Pulse-front tilt at the intermediate plane and at the output: a) 600 gr/mm grating; b) 200 gr/mm grating.

As already outlined, there is no stigmatic focus within the optical path of the monochromator, with the exception of the end focus. In particular, the spot is astigmatic on the intermediate slit, to reduce the radiation density on the

slit blades. The spot is focused only in the direction perpendicular to the slit by M1 and G1. In the direction parallel to the slit, there is no focusing power, therefore the size of the spot depends from the source divergence. It is 6 mm FWHM at 40 nm and scales as $\lambda^{3/4}$, therefore 8 mm at 60 nm, 3.6 mm at 20 nm and 2.1 mm at 10 nm.

The FWHM pulse-front tilt in the intermediate plane and at the output is shown in Fig. 3. The double-grating configuration is really effective in compensating the pulse-front tilt, being able to reduce it from the picosecond time scale down to few femtoseconds. Therefore, the temporal resolution of the beamline is increased by two to three orders of magnitudes.

Finally, the FWHM spot size is shown in Fig. 4. It ranges in the 10-15 μm interval.

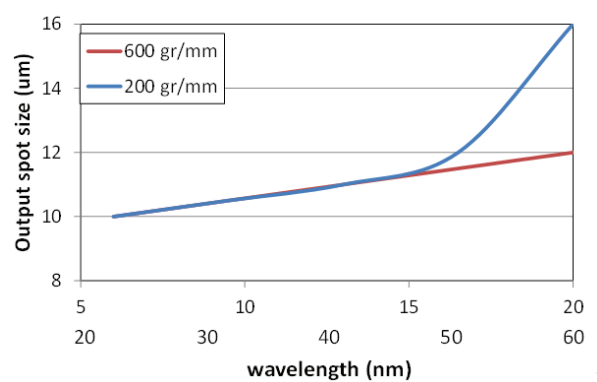


Figure 4: FWHM spot size in the focal plane.

The total efficiency of the beamline is mainly determined by the efficiency of the gratings, since there are two of them. The efficiency curve are strongly dependent on the available grating profiles. At present, VLS gratings for the extreme-ultraviolet are realized with laminar profile. The efficiency curve of the VLS plane grating (Jobin-Yvon, France) that has been used to realize the spectrometer-monochromator described in Ref. [17] is ranging in the 6-16% interval in the 5-20 nm spectral region. Taking these as typical values, the efficiency of the CM beamline is expected to be 5-15 times lower than the efficiency of a standard VLS grating beamline.

CONCLUSION

We have presented the design of an ultrafast monochromator explicitly tailored for extreme-ultraviolet FEL sources, in particular the upcoming FLASH II at DESY (Hamburg). The configuration here presented shows that a CM beamline may be realized in a relatively simple configuration, extending the VLS-plane-grating monochromator configuration to the use with ultrashort pulses. Only six optical elements are required: four mirrors and two gratings. The mechanical complexity is rather reduced, since only two rotations are required to perform the spectral scan. Furthermore, the temporal resolution of the beamline is increased by almost three orders of magnitudes with respect to a single-grating monochromator. Indeed, the proposed configuration

minimizes the number of optical elements, since just one grating is added with respect to a standard VLS monochromator beamline, gives very low displacement of the output beam with respect to the input, and guarantees high focusing properties in the whole spectral range of operation.

It is worth to note that, although being tailored to the FLASH II requirements, the proposed concept can be extended to any extreme-ultraviolet FEL.

REFERENCES

- [1] M. Martins et al, "Monochromator beamline for FLASH," *Rev. Sci. Instr.* 77, 115108 (2006).
- [2] N. Guerasimova et al, "The monochromator beamline at FLASH: performance, capabilities and upgrade plans," *J. Mod. Opt.* 58, 1480 (2011).
- [3] P. Heimann et al, "Linac Coherent Light Source soft x-ray materials science instrument optical design and monochromator commissioning," *Rev. Sci. Instr.* 82, 093104 (2011).
- [4] W. F. Schlotter et al, "The soft x-ray instrument for materials studies at the linac coherent light source x-ray free-electron laser," *Rev. Sci. Instr.* 83, 043107 (2012).
- [5] L. Poletto and F. Frassetto, "Time-preserving grating monochromators for ultrafast extreme-ultraviolet pulses," *Appl. Opt.* 49, 5465 (2010).
- [6] L. Nugent-Glandorf et al, "A laser-based instrument for the study of ultrafast chemical dynamics by soft x-ray-probe photoelectron spectroscopy," *Rev. Sci. Instr.* 73, 1875 (2002).
- [7] J. Norin et al, "Design of an extreme-ultraviolet monochromator free from temporal stretching," *Appl. Opt.* 43, 1072 (2004).
- [8] L. Poletto, "Time-compensated grazing-incidence monochromator for extreme-ultraviolet and soft X-ray high-order harmonics," *Appl. Phys. B* 78, 1013 (2004).
- [9] L. Poletto and P. Villoresi, "Time-compensated monochromator in the off-plane mount for extreme-ultraviolet ultrashort pulses," *Appl. Opt.* 45, 8577 (2006).
- [10] L. Poletto, F. Frassetto and P. Villoresi, "Ultrafast Grating Instruments in the Extreme Ultraviolet," *J. Sel. Top. Quant. Electron.* 18, 467 (2012).
- [11] L. Poletto et al, "Intense femtosecond extreme ultraviolet pulses by using a time-delay compensated monochromator," *Opt. Lett.* 32, 2897 (2007).
- [12] L. Poletto et al, "Time-delay compensated monochromator for the spectral selection of extreme-ultraviolet high-order laser harmonics," *Rev. Sci. Instrum.* 80, 123109 (2009).
- [13] M. Ito et al, "Spatiotemporal characterization of single-order high harmonic pulses from time-compensated toroidal-grating monochromator," *Opt. Express* 18, 6071 (2010).
- [14] H. Igarashi et al, "Pulse compression of phase-matched high harmonic pulses from a time-delay compensated monochromator," *Opt. Express* 20, 3725 (2012).
- [15] J. H. Underwood and J. A. Koch, "High-resolution tunable spectrograph for x-ray laser linewidth measurements with a plane varied-line-spacing grating," *Appl. Opt.* 36, 4913 (1997).
- [16] L. Poletto, G. Tondello, and P. Villoresi, "Optical design of a spectrometer-monochromator for the extreme-ultraviolet and soft-x-ray emission of high-order harmonics," *Appl. Opt.* 42, 6367 (2003).
- [17] L. Poletto, S. Bonora, M. Pascolini and P. Villoresi, "Instrumentation for analysis and utilization of extreme-ultraviolet and soft X-ray high-order harmonics," *Rev. Sci. Instr.* 75, 4413 (2004).

COMPACT SPECTROMETER FOR SINGLE SHOT X-RAY EMISSION AND PHOTON DIAGNOSTICS

L. Poletto[#], F. Frassetto, P. Miotti, CNR-IFN, Padova, Italy
 P. Finetti, E. Giangrisostomi, R. Mincigrucci, E. Principi, Sincrotrone Elettra, Trieste, Italy
 C. Grazioli, Department of Chemical and Pharmaceutical Sciences, Trieste, Italy
 A. Kivimäki, CNR-IOM, Trieste, Italy
 A. Di Cicco, F. Iesari,
 University of Camerino, School of Science and Technology, Camerino (MC), Italy
 S. Stagira, Department of Physics, Politecnico di Milano, Milano, Italy
 M. Coreno, CNR-ISM, Trieste, Italy

Abstract

The design and characterization of a compact spectrometer realized for photon in-photon out experiments (in particular X-Ray Emission Spectroscopy), conceived to be used at the FERMI free-electron-laser (FEL) at ELETTRA (Italy) is here presented. The instrument can be easily installed on different end stations at variable distances from the target area both at synchrotron and FEL beamlines. Different input sections can be accommodated in order to fit the experimental requests. The design is compact in order to realize a portable instrument within an overall size of less than one square meter. The spectrometer covers the 25-800 eV spectral range, with spectral resolution better than 0.2%. The characterization on Gas Phase @ ELETTRA as instrument for XES and some experimental data of the FEL emission acquired at EIS-TIMEX @ FERMI, where the instrument has been used for photon beam diagnostics, are introduced.

INTRODUCTION

X-ray emission spectroscopy (XES) is a well-established method in surface and solid-state investigations at third generation synchrotron radiation sources [1-2]. The instrument presented here is designed for photon in-photon out experiments, in particular XES, at synchrotron and FEL beamlines. The equipment is intended to be used at the LDM (Low-Density-Matter) [3] and EIS-TIMEX (Elastic and Inelastic Scattering - Time-resolved studies of Matter under EXtreme and metastable conditions) [4] beamlines of FERMI. Additionally, it can be used as a diagnostic tool for the real-time shot-to-shot acquisition of the FERMI spectral content (both fundamental and high-harmonics) and of the shot-to-shot fluctuations beam characteristics, especially at energies above 250 eV, where it could be complementary to the existing spectrometer used as a diagnostic of FERMI [5]. Two selectable gratings are used to cover the 25-800 eV energy range with a spectral resolution higher than 0.2% and an acceptance angle as high as 1.7×10^{-4} rad. Different input sections, with/without an entrance slit and

with/without an additional relay mirror can be attached to the spectrometer to adapt it to the size of the experimental chamber.

INSTRUMENT DESIGN

The optical design of the instrument is well established both for FELs [6] and high-order laser harmonics [7,8] and has been presented elsewhere [9]. It consists of an entrance slit, a grazing-incidence spherical diffraction grating with variable groove spacing and a detector. The 25-800 eV range is covered by gratings (Hitachi cod. 001-0437, 1200 gr/mm and cod. 001-0450, 2400 gr/mm). An EUV-enhanced back-illuminated CCD camera (Princeton Instruments PIXIS-XO 400B, 1340×400 pixel, 20- μ m pixel size), is mounted on a motorized linear translation stage and is connected to the grating stage by a bellows. Since the length of his focal curve is longer than the detector size, the latter is moved by means of a motorized stage to cover the whole spectral region. Three configurations have been realized by connecting three different input stages to the grating block. Configuration A is shown in Fig. 1. It has a variable-width entrance slit. Configuration B, shown in Fig. 2, has an additional cylindrical mirror acting as a relay section between the slit and the grating. In this way, the distance between the input and the grating is increased. Configurations A and B were tailored to the needs of the experimental chambers of the Gas Phase beamline of Elettra and the LDM beamline of FERMI and were designed for measurements on gas samples. Configuration C, shown in Fig. 3, is mainly planned to be used in chambers for measurements on solid targets. It is operated without an entrance slit, since the FEL focal spot on the sample acts as point-like source of the instrument. Again, a cylindrical mirror was added to the configuration, acting as a relay section between the source and the grating to adapt the envelope of the instrument to the size of the TIMEX experimental chamber. To maintain the pressure gradient between the inner and outer parts of the shield that contains the instrument, a pumping system is connected via a dedicated pumping flange to the spectrometer.

The spectral resolving element of the instrument, defined as the energy dispersion on the 20- μ m detector pixel, is shown in Fig. 4. The global response of the

[#]luca.poletto@ifn.cnr.it, National Research Council of Italy, Institute of Photonics and Nanotechnologies

instrument, in terms of counts per input photon, is presented in Fig. 5.

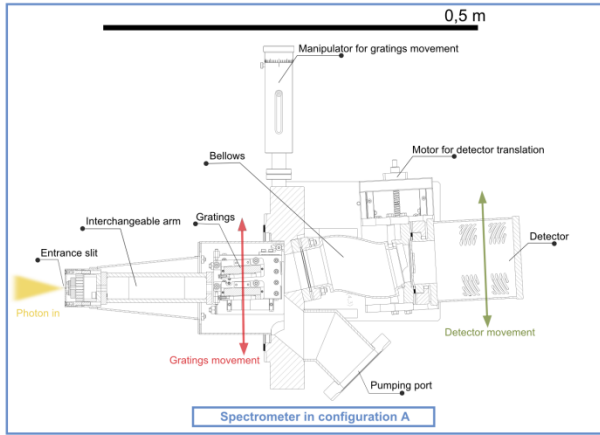


Figure 1: Spectrometer in configuration A.

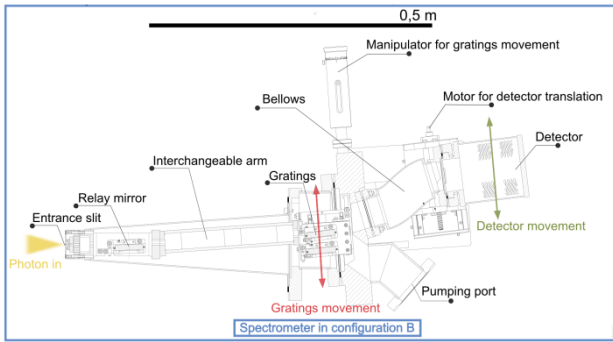


Figure 2: Spectrometer in configuration B.

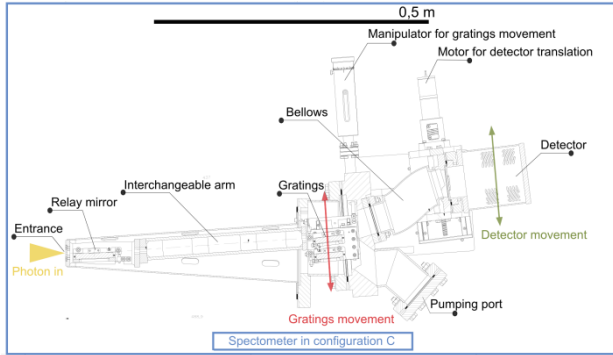


Figure 3: Spectrometer in configuration C.

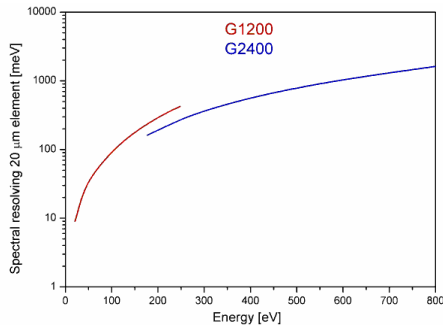


Figure 4: Spectral resolving element of the instrument.

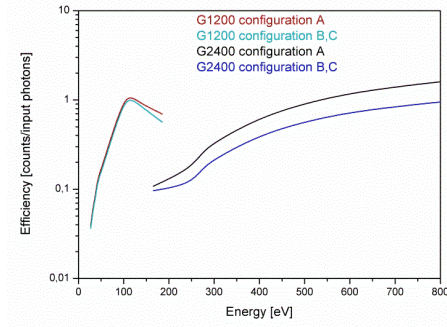


Figure 5: Global response of the spectrometer. It is defined as the product of the efficiency that has been measured for each component, namely the gratings, the detector and the mirrors.

The instrumental parameters of the instrument are finally summarized in Table1.

The collection angle in the direction of the spectral dispersion is limited by the angular acceptance of the gratings, which is 10 mrad for G1200 and 5 mrad for G2400. In the direction perpendicular to the dispersion, the collection angle is limited by the size of the detector, being in the range of 9-17 mrad depending on the instrument configuration.

Table 1: Instrumental Parameters

Grating G1200		Spherical VLS
Central groove density	1200	mm ⁻¹
Photon energy range	25-250	eV
Incidence angle	87	deg
Grating G2400		Spherical VLS
Central groove density	2400	mm ⁻¹
Photon energy range	180-800	eV
Incidence angle	88.7	deg
Grating entrance arm	237	mm
Grating-to-detector distance	235	mm
CCD detector		
Format	1340 × 400	
Pixel size	20 × 20	μm
Detector area	26.8 × 8	mm
Configuration A: entrance slit + grating		
Slit-to-grating distance	237	mm
Configuration B: entrance slit + relay mirror + grating		
Slit-to-grating distance	457	mm
Configuration C: relay mirror + grating		
Source-to-grating distance	637	mm

INSTRUMENT AS X-RAY EMISSION SPECTROMETER

The spectrometer as instrument for X-ray emission experiments was fully characterized at the low-energy branch of the Gas Phase beamline of Elettra synchrotron by acquiring fluorescence spectra from solid and gas targets. The instrument was assembled in configuration A and mounted perpendicular to the direction of the synchrotron beam with the entrance slit 10 mm away from the focal point and opening of 200 μm. The photon

flux on the sample was in the 10^9 - 10^{11} ph/s range, with the lower flux measured above 150 eV, where the plane mirror of the branch line has its cut-off in reflectivity.

Fluorescence from Solid Target

Measurements on solid targets were performed on silicon and on boron or boron nitride powder. The samples were positioned on the focus of the branch line at an incidence angle variable in the range 60-80 deg, in order to have the elastic contribution out of the spectrometer. A Si fluorescence spectrum taken at the Si L-edge is shown in Fig. 6. The spectrum is in overall agreement with literatures on crystalline Si films [10]. B and BN fluorescence spectra have been taken at the B K edge. In Fig. 7 the main emission peak due to a B(2p)-B(1s⁻¹) transition is presented for B, in agreement with the data in the literature [11].

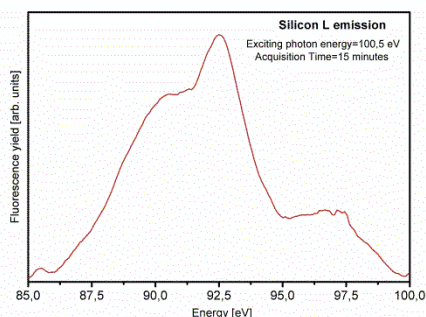


Figure 6: Si L emission fluorescence spectrum for crystalline Si.

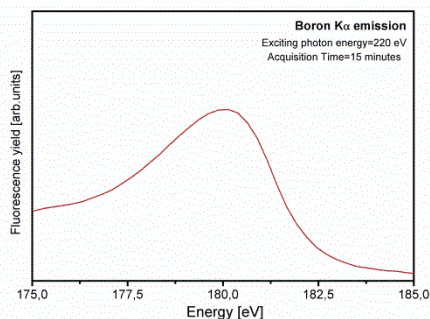


Figure 7: B Kα emission fluorescence spectra.

Fluorescence from Gas-Phase Targets

To measure fluorescence from gas targets, a suitable gas cell was mounted close to the entrance slit of the spectrometer, having entrance and exit holes for the synchrotron beam and a lateral slit (120-μm wide and 5-mm long) parallel to the entrance slit of the spectrometer, to maximize the throughput of the fluorescence that is collected by the instrument. The pressure in the experimental chamber was measured to be few- 10^{-3} mbar with a pressure inside the gas cell in the several- 10^{-1} mbar range.

He fluorescence spectra emitted when the exciting photon energy was fixed either to the (3,0) resonance at 64.118 eV or to the (4,-1) resonance at 64.133 eV are shown respectively in Fig. 8 and in Fig. 9. The emission lines observed in the different experimental conditions are in agreement with the literature [12]. When exciting at 64.118 eV, a peaked photon emission due to the (2p3d)¹P-(1s3d)¹D transition is measured, whereas the emission at 40.81 eV is due to He photoionization from higher-orders synchrotron light. The emission spectrum changes appreciably when different resonances of He are populated, as in the case of the (4,-1) resonance at 64.133 eV. Fluorescence emission from Kr excited at the $M_{4,5}$ edge was also measured. Fig. 10 shows the spectrum with exciting photon energy at the Kr 3d_{5/2}→5p resonance (91.2 eV). The Kr transitions 3d_{5/2}⁻¹ 5p_{3/2} (J=1) – 4p_{3/2}⁻¹ 5p_{3/2} (J=0,2) are clearly visible around 80 eV.

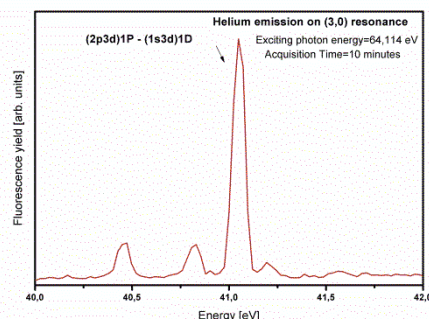


Figure 8: He fluorescence spectrum on (3,0) resonance at 64.114 eV.

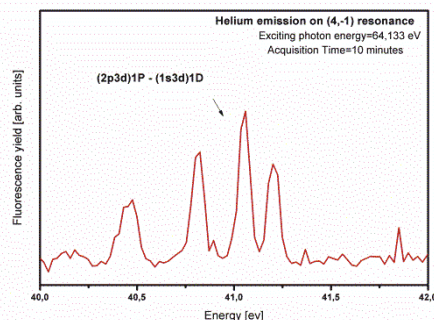


Figure 9: He fluorescence spectrum on (4,-1) resonance at 64.133 eV.

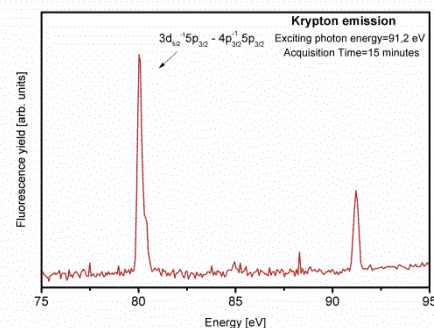


Figure 10: Krypton fluorescence spectrum with 91.2 eV exciting photon energy.

INSTRUMENT AS A TOOL FOR FEL DIAGNOSTICS

The instrument in configuration C has been interfaced to the EIS-TIMEX chamber to perform diagnostics on the FERMI beam. Single-shot spectra have been acquired successfully. Some of the single-shot spectra acquired at the 9th harmonic (35,97 nm) are shown in Fig. 11. The intensity fluctuations reflect the shot-to-shot variations in the photon-beam parameters and are in agreement with the typical pulse-to-pulse distribution of the FEL pulse energy. The FEL emission has also been tuned over 100 eV, where the expected photon fluxes are lower. The capability to acquire single-shot spectra at this energies confirms the high sensitivity of the instrument to very low photon fluxes. The net counts per shot on the CCD camera at 103.3 eV are ≈ 55000 counts. Considering the CCD conversion factor (2 e⁻/count) and efficiency (13 e⁻/ph), the grating efficiency (0.17) and the reflectivity of the Si mirror that was used to redirect the light into the instrument ($4 \cdot 10^{-5}$ at 103.3 eV), the flux entering into the TIMEX chamber at 103,3 eV is $1,2 \cdot 10^9$ ph/pulse.

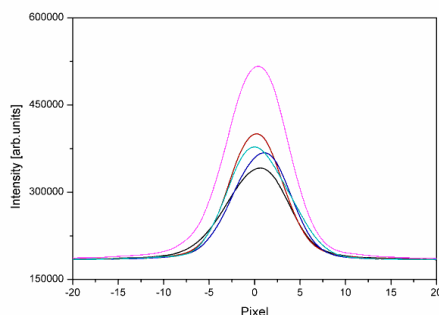


Figure 11: Single shot spectra acquired at the 9th harmonic of the seed laser set at 323.7 nm.

CONCLUSION

The portable and compact photon spectrometer to be used for X-ray emission experiments and photon diagnostics at FERMI has been presented. The spectrometer was fully characterized by measuring fluorescence spectra from solid and gas targets with synchrotron radiation at Gas Phase @ ELETTRA. The collected spectra are in full agreement with data reported in the literature, in particular the fluorescence spectra from gas targets have a signal-to-noise ratio that is higher than the data available in the literature, opening the way to the use of the spectrometer for specific gas targets where experimental data are missing. Single-shot FEL emissions have been measured at EIS-TIMEX @ FERMI. High resolution in a wide spectral region, high sensitivity and high dynamic have been tested for single-shot acquisition of the FEL beam. This opens to the possibility to use the instrument as an on-line instrument for the inspection of the spectral content of the FEL emission, complementary to the high-resolution spectrometer presently available at FERMI. Furthermore, the possibility to use the instrument at energies up to 800 eV

opens perspectives to test and characterize new configurations of the FERMI FEL acceleration sections.

ACKNOWLEDGMENT

The authors would like to thank Dr. Monica De Simone (CNR-IOM) for the help in the preparation of the experiment at Gas Phase and Dr. Carlo Callegari (Elettra) for the support in defining the interface of the instrument to LDM at FERMI.

This work was supported by the project “Single-shot X-ray emission-spectroscopy experiments”, funded by the Italian Ministry for Education and Research as In-Kind Project for the EuroFEL consortium.

REFERENCES

- [1] U. Bergmann and P. Glatzel, “X-ray emission spectroscopy,” *Photosynth. Res.* 102, 255 (2009)
- [2] J. Yano and V.K. Yachandra, “X-ray absorption spectroscopy,” *Photosynth. Res.* 102, 241 (2009)
- [3] A. Di Cicco et al., “Probing matter under extreme conditions at Fermi@Elettra: the TIMEX beamline,” in *Damage to VUV, EUV, and X-ray Optics III*, SPIE Proc. 8077, 807704 (2011)
- [4] V. Lyamayev et al., “A modular end-station for atomic, molecular, and cluster science at the low density matter beamline of FERMI@Elettra,” *J. Phys. B* 46, 164007 (2013)
- [5] M. Zangrando et al., “The photon analysis, delivery, and reduction system at the FERMI@Elettra free electron laser user facility,” *Rev. Sci. Instr.* 80, 113110 (2009)
- [6] F. Frassetto et al., “Extreme-ultraviolet compact spectrometer for the characterization of the harmonics content in the free-electron-laser radiation at FLASH,” *J. Synchrotron Radiation* 19, 596 (2012)
- [7] L. Poletto et al., “Grazing-incidence flat-field spectrometer for high-order harmonic diagnostics,” *Opt. Eng.* 40, 178 (2001)
- [8] L. Poletto et al., “High-order laser harmonics detection in the EUV and soft X-ray spectral regions,” *Rev. Sci. Instr.* 72, 2868 (2001)
- [9] L. Poletto et al., “Instrument for single-shot X-ray emission-spectroscopy experiments”, in *Advances in X-ray Free-Electron Lasers II: Instrumentation*, SPIE Proc. 8778, 87780W (2013)
- [10] J. A. Carlisle et al., “Soft-x-ray fluorescence study of buried silicides in antiferromagnetically coupled Fe/Si multilayers,” *Phys. Rev. B* 53, 14 (1996)
- [11] Y. Muramatsu et al., “Resonant x-ray Raman scattering in B K α emission spectra of boron oxide (B₂O₃) excited by undulator radiation,” *Phys. Rev. Lett.* 71, 3 (1993)
- [12] K.-H. Scharfner et al., “Radiative cascades from doubly excited He states,” *Phys. Rev. A* 64, 040501 (2001)

COMMISSIONING OF A DUAL-SWEEP STREAK CAMERA WITH APPLICATIONS TO THE ASTA PHOTOINJECTOR DRIVE LASER*

A. H. Lumpkin[#], D. Edstrom, J. Ruan, and J. Santucci
Fermi National Accelerator Laboratory, Batavia, IL 60510, USA

Abstract

Following re-commissioning of the dual-sweep streak camera with a Gig-E readout CCD camera, a comprehensive set of measurements has been performed on the ASTA drive laser beam components with respect to bunch length, phase stability, and multiplicity of peaks. The multi-pass amplifier was identified as the primary source of the longer UV component bunch length at 4 ps and peak multiplicity. This amplifier was replaced with three single-pass amplification stages and tests indicate clean micropulses and bunch lengths of about 3.6 ps sigma.

INTRODUCTION

The high-power electron beams for the Advanced Superconducting Test Accelerator (ASTA) facility [1] will be generated in a photoinjector based on a UV drive laser and the L-band rf photocathode (PC) gun cavity. Initially, the laser was composed of a Calmar Yb fiber oscillator and amplifier, a multi-pass YLF-based amplifier (MPA), three single-pass YLF-based amplification stages, and two frequency-doubling stages that result in a UV component at 263 nm with a 3 MHz micropulse repetition rate [2]. The initial objectives of these studies were: 1) to evaluate the amplified UV component's bunch length and phase stability and 2) to commission the laser room Hamamatsu C5680 streak camera system. A Prosilica GC1380 digital CCD with Gig-E readout was used for streak camera readout as it was compatible with our image processing tools. In the following sections, the process of characterizing the UV beam using the streak camera is described. This includes identification of a UV micropulse length longer than expected, multiplicity within the bunch structure, steps taken to mitigate these issues, and UV beam characterizations following these steps. We have systematically investigated the issues of whether the multiplicity was with each micropulse of the 3 MHz train (using the gated MCP), if any multiplicity is on different cycles of the 81.25 MHz rf (using dual-sweep streak images), and the origin in the laser system of the longer bunch length and the multiplicity. We describe our extensive investigations that indicated both issues originated in the multi-pass amplifier.

EXPERIMENTAL ASPECTS

A request to have the streak camera readout camera be compatible with the Gig-E vision protocol has been addressed by selection of the Prosilica 1.3 Mpixel camera

with 2/3" format. We have then used both the online Java-based ImageTool and the offline MATLAB-based ImageTool processing programs [3,4] in the commissioning of the system. Initial measurements of the UV component indicated the bunch length Gaussian fit sigma was closer to 4 ps, and there was evidence of more-than-expected peak multiplicity near the 3 MHz main peaks with spacing of 65-70 ps. Initially timing effects between the controls group 3 MHz source and that derived from the master oscillator were detected, but these were ultimately ruled out as the source of the peak multiplicity through a process of selection of individual pulses by gating the streak camera MCP and employing the dual-sweep synchroscan functions of the streak camera. Unless noted otherwise, the streak camera's synchroscan unit was phase locked to the master oscillator, which operationally provides the rf sync for the linac and rf gun. We provide a description of the commissioning of the streak camera system and image acquisition tools and the application to the drive laser.

The Drive Laser

The drive laser (Fig. 1) was based on an Yb fiber laser oscillator running at 1.3 GHz that was then divided down to 81.25 MHz and amplified. The four-stage origination and amplification was a set of commercial components from Calmar collectively referred to as the seed laser in the context of ASTA. The 81.25 MHz packets of infrared (IR) laser, at a wavelength of 1054 nm was initially directed into a YLF-based multi-pass amplifier (MPA), at 3MHz, selected by a Pockels cell referred to as the pulse picker. A number of pulses was selected using two pulse cleaner Pockels cells, while three YLF-based single-pass amplifiers (SPA) and a Northrup-Grumman SPA (NGA) boost the intensity as high as 50 μ J per pulse before the two doubling crystal stages generate the green and then the UV components at 3 MHz [2]. The UV component was transported from the laser lab through the UV transport line to the photocathode of the gun for generation of the photoelectron beams for use in the SC rf accelerator [2].

The multi-pass amplifier is a cavity that allows the amplification of the IR macropulse dependent on the timing of a fourth Pockel's cell (Conoptics 350-105) referred to as the Q-Switch. In combination with a Brewster plate, the IR beam is injected into the MPA cavity and is amplified using an YLF solid state amplifier, similar to those used in the single-pass amplification stages, until the Q Switch triggers, directing the amplified beam back out by means of the same Brewster plate, collinear with its injection trajectory. The round trip time for laser within the cavity is 12 ns, and several roundtrips-

*Work supported under Contract No. DE-AC02-07CH11359 with the United States Department of Energy.
#lumpkin@fnal.gov

generally between 8 and 14 for the purposes of these studies- are made, each resulting in a net amplification. The number of roundtrips made is adjusted by means of a T560 timing-module trigger to the Q-Switch timing. The MPA has been replaced by three single pass amplifiers.

Prosilica 1.3-Mpix Gig-E vision digital CCD which is thus compatible with the video acquisition [3,4] designed for all of the RadiaBeam beamline imaging stations. The commissioning of this readout camera as well as the image analysis tools was a primary goal of these studies.

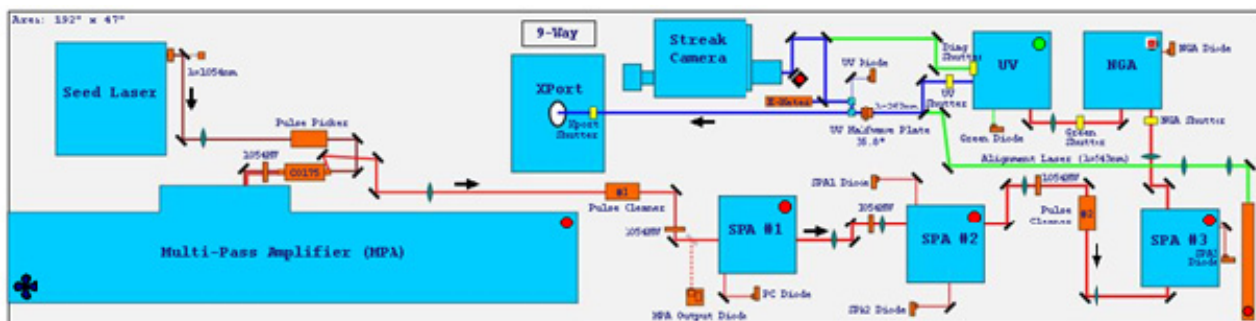


Figure 1: Schematic of the ASTA drive laser optical layout showing the seed laser, MPA, SPAs, and the streak camera.

The Hamamatsu C5680 Streak Camera System

Commissioning of the streak camera system was facilitated through a new suite of controls centered around ACNET, the Fermilab accelerator controls network. This suite included operational drivers to control and monitor the streak camera as well as Synoptic displays to facilitate interface with the driver and Java-based ImageTool programs to retrieve images from the readout camera. This commissioning period allowed for a number of improvements to be made to all aspects of interfacing with the streak camera, both in terms of front-end and back-end software, and hardware.

The streak camera consists of a Hamamatsu C5680 mainframe with S20 PC streak tube and can accommodate a vertical sweep plugin unit and either a horizontal sweep unit or blanking unit. The UV-visible input optics allow the assessment of the 263-nm component as well as the amplified green component or IR components converted to green by a doubling crystal. We started the studies with the M5675 synchroscan unit with its resonant circuit tuned to 81.25 MHz and the blanking unit. The low level rf is amplified in the camera to provide a sine wave deflection voltage for the vertical plates that results in low jitter (~ 1 ps) of the streak camera images and allows synchronous summing of a pulse train. The temporal resolution is about 1.5 ps FWHM, or 0.6 ps sigma, for NIR photons at 800 nm. When combined with the C6878 phase locked loop (PLL) delay box we can track phase effects at the ps level over several minutes (and even hours as long as the unit phase balance is stable) and within the macropulse to about 200 fs. As a point of comparison, the M5676 vertical fast sweep unit has about 20-ps internal trigger jitter in addition to the nominal 100-ps trigger jitter of the DG535 delay units. This would mean the streak image would jitter in and out of the frame when running on the fastest sweep range with a full scale range of about 150 ps, illustrating the critical advantage of the synchroscan mode. We have replaced the Hamamatsu Peltier-cooled firewire CCD readout camera with a

There is a fundamental reduced sensitivity issue of the Prosilica camera compared to the cooled CCD camera that may push us towards the streak tube space-charge limited regime. The concept of the streak tube's using the 81.25 MHz rf from the master oscillator to generate the vertical deflection voltages with the phase-locked delay box was critical. This combination enabled a new series of experiments at A0PI [5] and will also apply at ASTA. A second set of deflection plates provides the orthogonal deflection for the slower time axis in the 100-ns to 10-ms regime. These plates are driven by the dual-axis sweep unit which was also commissioned during these studies.

In order to assess the sources of the peak multiplicity, we anticipated the use of both the streak tube's MCP gate option for the single micropulse selection and the dual sweep mode for isolating the 81.25 MHz cycles of the synchroscan sampling mode. To examine the latter, the blanking unit was replaced with an M5679 Dual Timebase Extender unit. This unit provided a ramped horizontal deflection similar to the fast vertical deflection unit, but works over a considerably longer time-frame. The full-amplitude range for the dual-sweep unit is 0.1 μ s to 100 ms. The diagram of the final streak camera configuration in Fig. 2 is representative of all studies noted hereafter, except for the gating study, where gating around one or more micropulses was selected using a DG535. In this exception, the C5680 Gate Trigger In was connected to a DG535 TTL output with the correct gating time.

Streak camera calibrations were performed with the new Prosilica readout camera through use of a Colby delay unit (PN109122; SN#8081195) to provide discrete and known ps-regime delay changes. Initially, noticeable jitter was seen on the image position with the PLL on in R1, but we took 10-, 20-, and 30-ps steps and averaged the mean positions of the images. The resulting calibration factors with 1x1 pixel binning in the CCD were: R4: 2.0 ± 0.1 ps/pixel, R3: 1.0 ± 0.1 ps/pixel, R2: 0.45 ± 0.03 ps /pixel, R1: 0.15 ± 0.03 ps/pixel. After reducing the jitter in the system, we adjusted the R1 calibration factor's measured value.

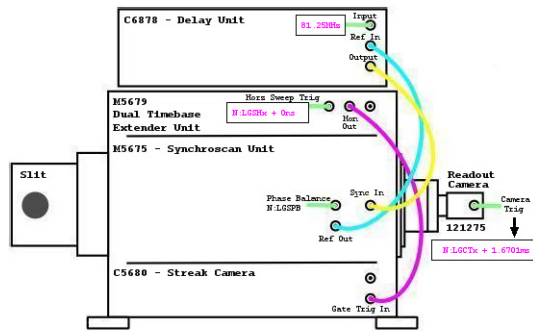


Figure 2: A streak camera wiring diagram. N:LGSHx and N:LGCTx are ACNET names for beam-synchronized VME-based timers. The 81.25MHz is derived from the Master Oscillator (MO) and an additional cable delay of 120 ns was added to N:LGSHx for the purposes of the dual sweep studies.

EXPERIMENTAL RESULTS

Initial Amplified UV

Our laser studies began with the evaluation of the amplified UV component of the drive laser at the point before it is transmitted to the UV transport line to the rf PC gun. This is the bunch length that will determine the initial photoelectron bunch length in the gun cavity. We were aware of the possibility for space-charge effects in the streak tube with the lower Q.E of the tube PC and the lower sensitivity of the readout camera that would combine to require more input signal for the same output signal. We were able to attenuate the UV signal input to obtain focus mode slit images with a 20- μm tall slit at the 6-pixel level sigma. This value is higher than the white light (4.2 pixel) or green component value and was attributed to the inherently larger photoelectron energy spread within the tube from UV photon conversion and possibly some input optics focus. As shown in Fig. 3, the main peak was accompanied by a second peak 70 ps away in time. The assessment of whether the multiplicity was with each micropulse or just in the synchronous sum was pursued.

It was recognized that one could use the external gate mode on the streak camera which would localize the recorded image to one 300-ns interval and confirm if the multiple pulses observed are *associated with the single selected UV pulse*. Alternatively, the dual-sweep mode can be used to ascertain if any of the 5 pulses arrive on other rf cycles than one sweep. (The single sweep unit has internal trigger jitter plus DG535 trigger jitter, but in principle could be timed for one UV pulse interval). As a followup, we recorded a set of gated MCP images while running in synchroscan mode. As shown in Fig. 4, we set the gate width to 250 ns, and then the gate delay was set to include only the first of five micropulses. We observed the doublet image with only the first micropulse gated and the 7.5 ns timing shift. The gate width was progressively

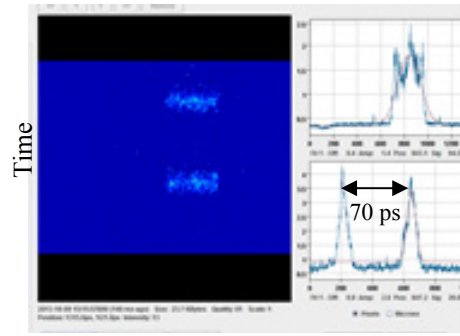


Figure 3: Example of UV multiplicity in the streak image on the left and the vertical (time) profile at lower right.

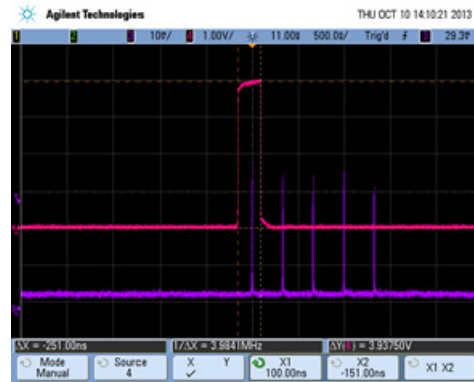


Figure 4: Screen captures of scope trace and MCP gate (250 ns) and the 5 laser micropulses detected by the photodiode. The gate width was stepped in 333-ns steps to include 1 to 5 micropulses.

increased, and we generated a plot of the Gaussian fits to the amplitudes of the two peaks with doublet timing on the laser as a function of the streak camera MCP gate width for micropulses 1-5 as shown in Fig. 5. The first peak is also seen with normal timing of the laser. This monotonic increase of intensity with micropulse number as the MCP gate width was incremented in 333-ns steps confirms the assignment of the second peak to each micropulse interval.

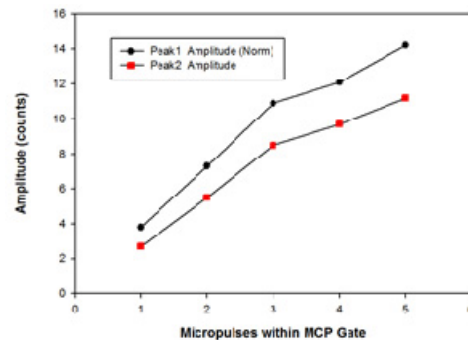


Figure 5: Plot of the two peak intensities with MCP gate width showing the doublet peak 2 tracks with each micropulse.

Amplified Green Component

An additional optical transport path was added at the location of the amplified green component to bring it to the entrance of the streak camera. Investigations of the parameters of the green component were done. With OD5.5 the focus image size was reduced to a reasonable 5.9 ± 0.2 pixels, but this is still larger than the white light value. We then proceeded to streak mode and immediately saw the multiplicity of peaks, 6-9, in the green with about 63 ± 2 ps separation on range 2. In this case the offline MATLAB program does fit the baseline even with the multiple peaks. The image bunch lengths on range 1, SS1 are longer at 40 and 37 pixels in the image below than our UV component data at ~ 28 pixels sigma. This is plausible with the nonlinear aspect in the frequency doubling crystal process.

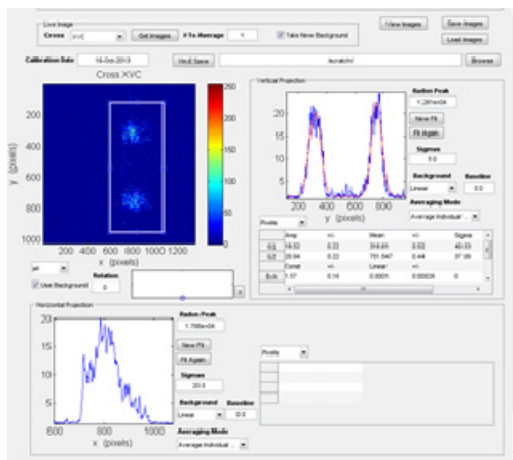


Figure 6: Amplified green component with streak camera range R1. The offline MATLAB program fit each of the peaks to Gaussians and provided amplitude, centroid, and sigma values.

Green Converted MPA Component

After confirming the seed laser output seemed nominal with 2.3-ps bunch lengths, we moved to the MPA output. As a final step, we investigated the output of the MPA after converting the IR to 527-nm light with a BBO doubling crystal. The repetition rate is 3 MHz and the signal is stronger after the MPA than the converted seed laser signal. The principal peak is about 29 pixels sigma as shown in Fig. 7 with offline analysis, so we again are in the 4.2-ps sigma bunch length regime. We adjusted the trigger timing and actually used a cable length added into the delay line to shift the trigger by 120 ns and allow clear display of the R3-100 ns image with external gate applied. The unique image is shown in Fig. 7 (upper-left quadrant). There, we still see the isolated multiplets, but the horizontal-sweep profile below the image shows three steps in the 10-image sum. Some of the peaks arrive 12.4 or 2×12.4 ns later to the right of the first sweep cycle. There are at least 3 rf cycles represented with peaks 2 and 5 from the bottom being the brightest and usually on the same rf cycle and ~ 200 ps apart. This said, the pulse

cleaners should suppress 3-MHz pulses on the adjacent rf cycles. The sum image in 8-bit scale actually has some saturation in the two brightest peaks so the relative amplitudes and the sigmas of those are overestimated.

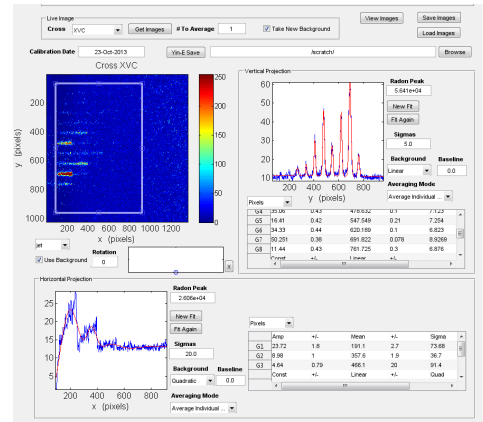


Figure 7: Dual-sweep image (R3-100ns) of the MPA output converted to green showing different intensity multiplets for different rf cycles.

UV Component with Preamp Installed

Having reviewed the data from the MPA source, we replaced the MPA with three single pass amplifiers to act as a preamp. The UV was evaluated again, and in a 200 micropulse R1 synchronous sum, we observe a bunch length of about 25.3 pixels or 3.6 ps (sigma) after subtracting in quadrature the estimated resolution term for the focus mode as shown in Fig. 8. The micropulse sum also appears clean of secondary peaks. There is a slight x-t tilt which contributes to the total bunch length.

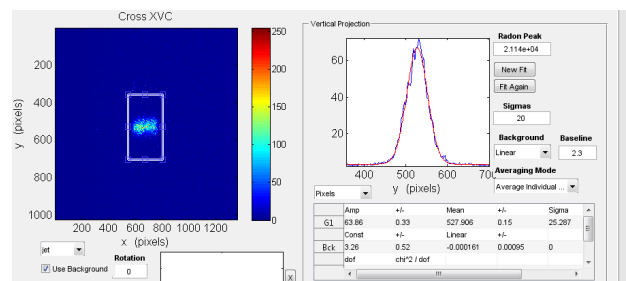


Figure 8: Synchronous UV streak image using R1 showing the reduced bunch length of 3.6 ps (sigma).

SUMMARY

In summary, we have described a series of commissioning results using the laser lab Hamamatsu streak camera with the new Prosilica Gig-E readout camera including: image processing, streak range calibrations, system phase jitter, rf phase locking, and streak-camera-based measurements of the ASTA drive laser with the multipass amplifier. We assessed the amplified UV and green, and the converted IR components from the seed laser at 81.25 MHz and the MPA output at 3 MHz. We observed a bunch-length

sigma of 4.2 ps from the MPA vs. 2.3 ps from the seed laser, and the multiplicity at 65-70 ps originating in the MPA. Implementing the preamplifier in the chain to replace the MPA mitigated these effects, and the UV laser stands ready to support the first electron beam to the 50-MeV beam dump.

ACKNOWLEDGMENTS

The authors acknowledge the acquisition of the Prosilica CCD camera for this application by Amber Johnson; the generation of ACNET streak camera, CCD, and delay box controls by C. Briegel; the development of the Java-based ImageTool code by J. Diamond, the revisions of the Matlab-based code by R. Thurman-Keup; the 81.25 MHz rf source provided by B. Chase, and the support of Elvin Harms and Nathan Eddy, all at Fermilab.

REFERENCES

- [1] The ASTA User Facility Proposal, Fermilab-TM-2568, October 2013.
- [2] J. Ruan, M. Church, D. Edstrom, T. Johnson, J. Santucci, "Commission of the Drive Laser System for Advanced Superconducting Test Accelerator", In *Proc. 4th Int. Particle Accelerator Conf.*, Shanghai, China, 2013, pp. 3061-3063
- [3] J. Diamond, FNAL, online Java-based ImageTool, (2013).
- [4] R Thurman-Keup, FNAL, offline MATLAB based. ImageTool, (2011).
- [5] A.H. Lumpkin, J. Ruan, and R. Thurman-Keup, Nucl. Instr. and Meth. **A687**, 92-100 (2012).

PULSE BY PULSE ELECTRON BEAM DISTRIBUTION FOR MULTI-BEAMLINE OPERATION AT SACLA

Toru Hara*, Hideki Takebe, Takahiro Inagaki, Chikara Kondo, Yuji Otake, Hitoshi Tanaka,
RIKEN SPring-8 Center, Sayo-cho, Hyogo 679-5198, Japan
Kenji Fukami,
JASRI, Sayo-cho, Hyogo 679-5149, Japan

Abstract

In SACLA, the second undulator beamline (BL2) is installed during the 2014 summer shutdown. The beamlines are initially switched by a DC switching magnet for the commissioning. Then the DC switching magnet will be replaced by a kicker and a DC twin-septum magnet and the pulse by pulse operation will start in January 2015. The kicker magnet is driven by a 60 Hz trapezoidal current waveform. In the pulse by pulse multi-beamline operation of XFEL, the electron beam energy should be optimized for the laser wavelengths of each beamline from bunch to bunch. To control the beam energy of the electron bunches, the multi-energy operation of the linac has been proposed and demonstrated at SACLA. The pulse by pulse operation will be also applied for the beam injection to the upgraded low-emittance ring of SPring-8 (SPring-8-II) in future. Since the SPring-8-II storage ring has a small dynamic aperture, low emittance is required for the injection beam. In addition, the use of SACLA as a low-emittance injector enables to save the running cost of the injector system during top-up operation.

INTRODUCTION

In order to meet the increasing demand for XFEL user operation, the second undulator beamline (BL2) is installed during the 2014 summer shutdown at SACLA. Different from the storage ring based synchrotron radiation facilities, the linac of XFEL can not simultaneously operate plural beamlines. However, quasi-simultaneous pulse by pulse operation by distributing the electron beam to the beamlines on a bunch-to-bunch basis improves efficiency and usability of the facility.

The undulator hall of SACLA is designed to accommodate five XFEL beamlines, and a DC switching magnet located at the end of the linac currently switches the beamlines (see Fig. 1) [1]. For the pulse by pulse operation, this DC switching magnet will be replaced by a kicker magnet and a DC twin-septum magnet in January 2015. The electron beam is deflected into three directions at 60 Hz by the kicker, which is the maximum beam repetition at SACLA, and then the DC twin-septum magnet augments the deflection angles. Since the stability of the electron beam orbit is crucially important for XFEL, high stability is required, particularly, for the kicker magnet power supply.

In the XFEL operation, the electron beam energy is

normally optimized for the laser wavelength requested from the user. But in case of the multi-beamline operation, the wavelengths can be different between the beamlines. Although the wavelength can be adjusted by changing the undulator gap, the tuning range is limited and small K-values result in drop of laser intensity. In order to avoid these limitations on the user experiments, it is necessary to control the beam energy from bunch to bunch in the multi-beamline operation.

The method to control the electron bunch energy in the linac has been proposed and demonstrated at SACLA by changing the repetition of a certain number of RF units [2]. In the pulse by pulse multi-beamline operation of SACLA, the multi-energy operation of the linac is planned to be used in combination with the electron bunch distribution to provide the electron beam having the optimized energy to the laser wavelength of each beamline.

ELECTRON BUNCH DISTRIBUTION

Although the maximum beam repetition of SACLA is 60 Hz, lower repetitions are sometimes used for user experiments due to the time necessary to exchanging samples. Also to save the time for preparation and removal of experimental instruments, the multi-beamline operation contributes to improve the efficiency and usability of the facility.

The schematic of SACLA is shown in Fig. 1. After the acceleration and longitudinal compression of the electron bunches in the linac, the DC switching magnet currently switches the beamlines by deflecting the beam orbit by ± 3 degrees (± 52 mrad). For the electron bunch distribution, this DC switching magnet will be replaced by the kicker magnet and the DC twin-septum magnet as shown in Fig. 2. In order to minimize the orbit fluctuation of the deflected beam by the kicker magnet, the deflection angle of the kicker is kept small as ± 9 mrad and the rest of the angle is given by the DC twin-septum magnet (± 43 mrad).

The yoke of the kicker is 0.4 m long made of laminated silicon steel plates with 0.35 mm thickness and 20 mm gap, and its maximum field is 0.67 T (see Fig. 3). The power supply of the kicker is a PWM (Pulse Width Modulation) type using 8 FET units connected in parallel. The power supply generates a 60 Hz trapezoidal current waveform and its amplitude and polarity can be arbitrarily changed according to the beam energy and an electron bunch distribution pattern.

Figure 4 is an example of the distribution pattern of the electron bunches. The arrival timing of the electron

*toru@spring8.or.jp

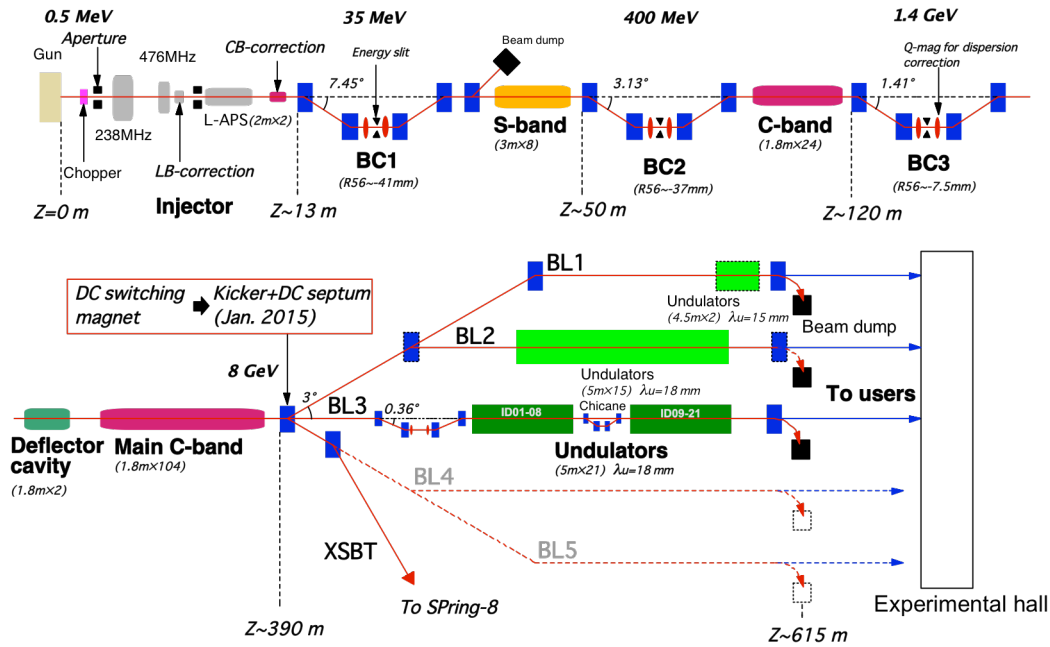


Figure 1: Schematic of SACLA.

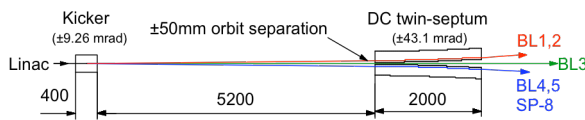


Figure 2: Configuration of a kicker magnet and a DC twin-septum magnet. The unit of the lengths is mm.



Figure 3: Kicker magnet made of 0.35 mm laminated silicon steel plates.

bunches is set at the end of the flat top of the trapezoidal waveform. When the kicker current is zero, the electron bunch goes straight through the kicker and takes the orbit to BL3. The electron bunch is deflected to BL2 for a positive current and to BL4 for a negative current. In this example, the pulse repetition of BL3 is twice higher than those of BL2 and BL4.

The DC twin-septum magnet consists of two 2 m-long septum magnets with the septum sides facing to each other. Figure 5 is the cross section of its upstream end.

The electron beam orbits are horizontally separated by ± 50 mm at the entrance of the twin-septum. While the electron beam for BL3 goes straight between the septums, the beam orbits for BL2 and BL4 are further deflected by ± 43 mrad. The magnetic field leakage on the center straight orbit is expected to be about 0.2 G, which can be further reduced by turning on both septums owing to the cancellation of two leak fields with opposite signs.

The fabrication of the kicker magnet and its power supply have been already completed. The stability and reproducibility are checked with a DCCT and a gated NMR. The gated NMR is specially designed to measure pulsed magnetic fields developed by ECHO DENSHI Co., Ltd. As shown in Fig. 6, the resonant frequency is scanned during the gate opened for 0.6 ms. From the results of the magnetic field measurements, we confirmed that the stability of the kicker fields is better than 30 ppm (p-p). The DC twin-septum and its power supply are under fabrication.

MULTI-BEAMLINE OPERATION AT SACLA

The beam orbit to the BL2 undulators passes through a dogleg after the end of the linac. The electron beam is deflected by 3 degrees (52 mrad) by the kicker and the DC twin septum magnets, and then deflected back to parallel with BL3 (see Fig.1) by a DC bending magnet. In order to cancel R_{56} and keep achromatic and isochronous conditions, two small inversed bending magnets will be introduced in the dogleg. This is necessary to avoid unwanted bunch length change at the dogleg and keep the accelerator operation conditions the same for BL2 and BL3.

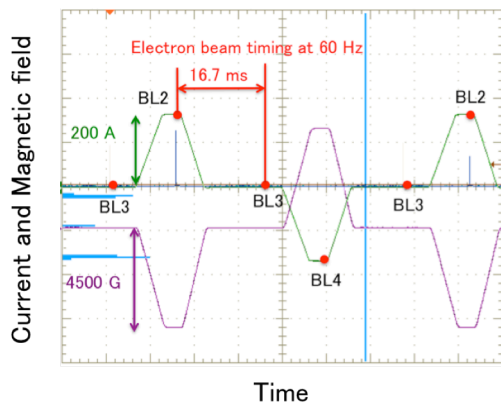


Figure 4: Measured current waveform (green line) and magnetic fields (purple line) of the kicker magnet. Red circles on the green line correspond to the beam arrival timing at 60 Hz.

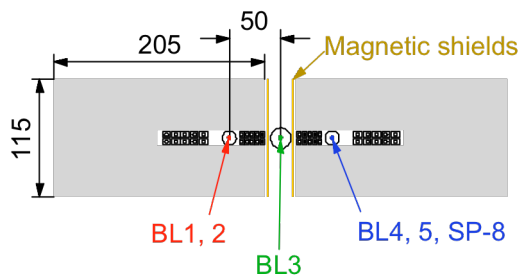


Figure 5: Cross sectional view of the DC twin-septum magnet (upstream end). The unit of the lengths is mm.

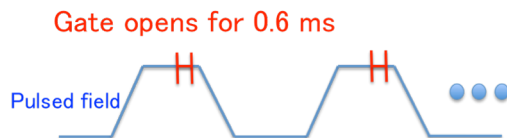


Figure 6: Gated NMR scans the resonant frequency and measures the magnetic fields for 0.6 ms-long gate duration shown in red.

There are three bending magnets on the electron beam orbit to BL2, which are the kicker, the DC twin-septum and the DC bending magnet. The expected stabilities of these magnets are 30 ppm (p-p) for the kicker, 10 ppm (p-p) for the twin-septum and 3 ppm (p-p) for the DC bending magnet. Compared to the current electron beam orbit stability of SACLA, which is about 1 μ rad (p-p), the electron bunch distribution will increase the beam orbit fluctuation by 10-20 %, but it will not cause serious degradation of the pointing stability or the performance of the laser currently achieved at SACLA.

The in-vacuum undulators installed in BL2 are the same as those of BL3, whose periodicity is 18 mm. The user experiments will be allocated to these two beamlines not by the wavelength range, but by the type of the experiments. So in order to perform two user experiments in parallel, the laser wavelengths should be independently adjusted for these two beamlines. Since the tuning range

of the undulator is limited within 30 % at SACLA, a large difference in wavelengths between the beamlines should be covered by changing the beam energy from bunch to bunch.

By operating some RF units at subharmonics of the bunch repetition, the number of accelerating structures effectively used for acceleration can be adjusted from bunch to bunch. Figure 7 is an example of accelerator setup for the multi-energy operation. All electron bunches are accelerated to 6.8 GeV at 60 Hz in the upstream part of the linac. By operating 4 RF units at 30 Hz and another 2 units at 15 Hz in the last part of the linac, half of the electron bunches pass through these 6 RF units without being accelerated, so the beam energy stays at 6.8 GeV. A quarter of the electron bunches are accelerated to 7.6 GeV by the 4 RF units working at 30 Hz. The last quarter of the bunches are further accelerated by the 2 RF units working at 15 Hz, thus the final beam energy reaches 8.0 GeV. By properly choosing the combination of the number and repetition of the RF units, the electron beam energy can be controlled from bunch to bunch.

Figure 8 shows an example of the multi-energy operation demonstrated at SACLA. The repetition of the electron bunch was 10 Hz and 8 RF units were operated at 5 Hz. The beam energy of the electron bunches were measured at a chicane located upstream of the BL3 undulators. Since the beam energy gain of one RF unit is about 130 MeV, the beam energy is alternately changed from bunch to bunch between 8.0 GeV and 6.9 GeV as expected.

Figure 9 is the SASE spectrum obtained from three-energy bunches measured by a monochromator. The repetition of the electron beam was 10 Hz, and 2 RF units were operated at 5 Hz and one RF unit at 1 Hz in Fig. 9. Consequently the SASE pulses were observed at 10 keV, 9.35 keV and 8.7 keV at the repetitions of 1 Hz, 4 Hz and 5 Hz respectively.

In the multi-beamline operation of SACLA, the beam energy of the electron bunches will be accelerated to the optimum energies for the laser wavelength of each beamline. Then the electron bunches are distributed to the beamlines pulse by pulse using the kicker and the DC twin-septum magnets located at the end of the linac.

ELECTRON BEAM INJECTION TO SPRING-8-II

SPRING-8-II is the upgrade plan of the SPRING-8 storage ring aiming at low emittance, which is currently scheduled around 2020 [3]. In this upgrade plan, SACLA is considered to be used as a low emittance injector for achieving good injection efficiency, low operation cost and minimum energy consumption. The SPRING-8-II storage ring requires a low-emittance injection beam due to its small dynamic aperture. Since the emittance of a synchrotron booster is determined from its equilibrium state of the circulating electron beam, it is hard to obtain a low-emittance beam with the existing SPRING-8 injector system composed of a linac and a FODO synchrotron

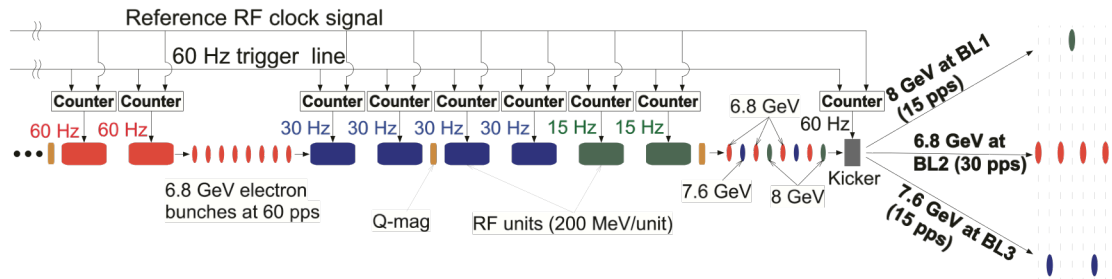


Figure 7: Example of the RF setup for the multi-energy operation.

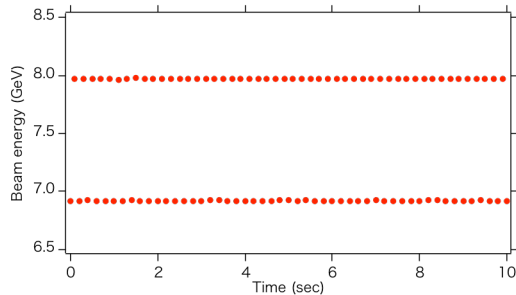


Figure 8: Electron bunch energies measured at the chicane in front of the BL3 undulators during the multi-energy operation.

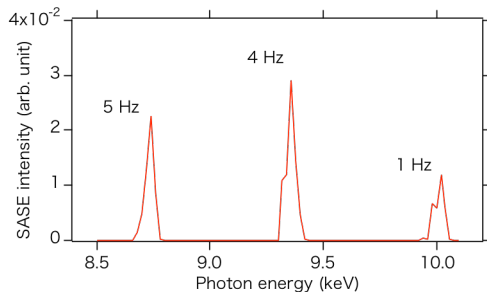


Figure 9: Spectra of SASE measured by a monochromator. The electron bunch repetition was 10 Hz and the beam energies of the electron bunches were changed between 7.3, 7.55 and 7.8 GeV.

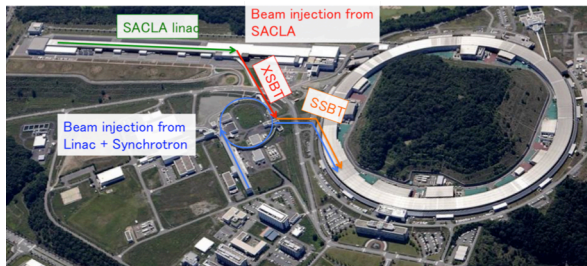


Figure 10: Beam transport line from SACLA to SPring-8 (XSBT and SSBT).

booster. In addition, despite of a low injection frequency during top-up operation, it is necessary to maintain the injector system in a warmed-up condition. Consequently it results in an increase of operation cost and energy consumption. On the other hand, SACLA is an

independent user facility from SPring-8-II and its linac is always running. Therefore the beam injection from SACLA will enable to save the energy consumption and operation cost necessary for idling the accelerator.

The nominal beam energy of SPring-8-II is expected to be 6 GeV, while the beam energies used for the XFEL operation are around 5~8.5 GeV depending on the laser wavelength. The electron bunches are highly compressed and its peak current reaches several kA for the XFEL operation, but such high peak current is not necessary or even harmful for the beam injection due to the emittance degradation at a beam transport line. To achieve the parallel operation of XFEL and the beam injection to SPring-8-II, not only the beam energy but also the peak current should be controlled from bunch to bunch.

The beam transport line from SACLA to the exit of the existing synchrotron booster, which is called XSBT (XFEL to Synchrotron Beam Transport) in Fig. 10, had been constructed together with the SACLA facility. The electron beam of SACLA has already been successfully transported to the exit of XSBT. Further beam transport to the storage ring and the evaluation of the beam emittance are planned before the construction of SPring-8-II.

SUMMARY

Following the installation of the BL2 undulators, the pulse by pulse operation of multi-beamline will start in January 2015 at SACLA. For the beam injection to SPring-8-II, it is necessary to elongate the bunch length, which is possible by controlling the RF phase to reduce the energy chirp at the bunch compressors. Also since the electron beam is injected to the storage ring on-demand during top-up operation, the parameter of the RF units should be changed at arbitrary timing. For those features, a new timing and low-level RF systems are planned to be developed by 2020.

REFERENCES

- [1] T. Ishikawa, et al., Nat. Photon. 6, 540 (2010).
- [2] T. Hara, et al., Phys. Rev. ST Accel. Beams 12, 080706 (2013).
- [3] H. Tanaka, et al., to be published in Synchrotron Radiation News.

DEVELOPMENT OF A MAGNET SYSTEM TO CANCEL THE ATTRACTIVE FORCE TOWARD STRUCTURAL REFORM OF UNDULATORS

R. Kinjo and T. Tanaka, RIKEN SPring-8 Center, Sayo, Hyogo, Japan

T. Seike and A. Kagamihata, JASRI, Sayo, Hyogo, Japan

S. Yamamoto, KEK Photon Factory, Tsukuba, Ibaraki, Japan

Abstract

Toward realization of a new undulator concept based on a much more compact and lightweight structure than conventional ones, cancellation of a magnetic attractive force is being studied, which significantly relaxes the requirements for the undulator mechanical design and reduces the cost and lead time of construction and installation. We have proposed to add periodically-magnetized monolithic magnets beside the main magnets generating the undulator field and attractive force, which are expected to generate a repulsive force having the same gap-dependency as the attractive force in a cost-effective way. The present status of the development of the force cancellation system is presented, with a focus on the result of preliminary experiments using the periodically-magnetized magnets. Also introduced is a development plan for the compact and lightweight undulator based on the cancellation system.

INTRODUCTION

It is well known that a large attractive force is generated between the top and bottom magnetic arrays of undulators, if the gap in between is relatively narrow. For example, a typical undulator in SPring-8 having the Halbach configuration with the period of 32 mm and the total length of 4.5 m has the attractive force of about 3 tons at the gap of 8 mm. The undulator in SACLA having the hybrid configuration with the period of 18 mm and the total length of 5 m has the attractive force of around 9 tons at the gap of 3 mm. To control the magnet gap precisely against the large attractive force, the undulators usually require rigid mechanical components and frames. Moreover, a large number of components are necessary to distribute the mechanical load along the undulator axis and avoid deformation of the magnetic arrays. Such a conventional undulator design gives rise to structural issues that most of the weight, dimension and cost of the undulator are attributable to the auxiliary apparatus but not to the core part, i.e. the magnetic arrays.

The above discussion in turn gives us a new concept of undulator design; if the attractive force is cancelled out, the heavy and large base frame is no longer required, and then the undulator can be much more lightweight and compact. As a result, the cost and lead time of construction, transportation and installation are significantly reduced.

Up to now, two different methods have been developed to cancel the attractive force. One is the mechanical system composed of a number of springs having different

lengths and coefficients attached to the both sides of the main magnets, which was applied to an in-vacuum wiggler developed at Synchrotron SOLEIL [1]. The other is the magnetic system composed of two rows of magnet array generating a repulsive force attached to the both sides of the main magnets, which is applied to the in-vacuum revolver undulator (IVRU) developed at SPring-8 [2]. Although both systems worked well for their own purposes, they may not be applicable to the new undulator concept.

In the former method, the precise magnetic measurement indispensable for undulator field correction is not possible with the conventional instrument, and the gap-dependency of the repulsive force generated by the springs is somewhat different from that of the attractive force. In the latter method, the number of magnets and magnet holders is three times as large as that of the main magnetic array, which increases the cost and time and effort for manufacturing.

As an alternative to the above two methods, R&Ds are under progress in SPring-8, toward realization of a cost-effective force cancellation system, which are reported in this paper.

BASIC CONCEPT

The cancellation system under development is based on the magnetic system applied to IVRU, which is schematically illustrated in Fig. 1. The point is that to generate repulsive force the magnets arrays which has the same structure with the main magnets are used in IVRU, while multipole monolithic magnets (MMMs) are discussed in this paper, which may be more cost-effective and easier fabricable than the IVRU type.

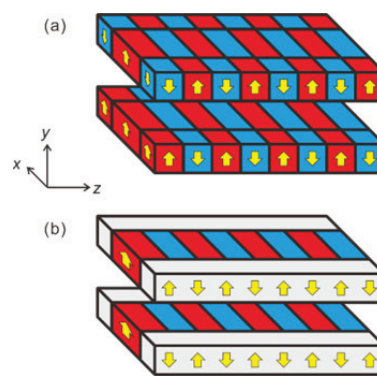


Figure 1: Conceptual drawing of force cancellation system (a) by normal magnets applied to IVRU and (b) by MMMs discussed in this paper.

ISBN 978-3-95450-133-5

The magnetic system to cancel the attractive force is required to generate the repulsive force having the gap dependence identical to the attractive force. It is well known that the magnetic field of the undulator, and thus the attractive force F , depend exponentially on the gap,

$$F \propto \left[\sum_n \alpha_n \exp \left(-n\pi \frac{g}{\lambda_u} \right) \right]^2.$$

i.e., where n is an integer indicating the harmonic number of the undulator field and α_n indicates the coefficient depending on the period and the remanent magnetic field, and so on.

In order to reduce the cost and effort for construction of the repulsive array, we are exploring the applicability of the multi-pole magnetizing method, which has been originally proposed by one of the authors (S. Y.) to facilitate the construction of extremely short-period undulators [3,4]. By using this method, the repulsive force having the same gap-dependence will be generated in a cost-effective way.

PRELIMINARY EXPERIMENT

Outline

The goal of the preliminary experiment is to demonstrate that the repulsive force by the MMMs has the same gap-dependence as the attractive force by the main magnets, and to acquire the data necessary to design the force cancellation system in the prototype of the compact and lightweight undulator.

Measurement of Field on Multipole Monolithic Magnet

The monolithic blocks are magnetized by the pulse magnetization and feed system shown in Fig. 2. The specification of the monolithic block and the system are listed in Table 1. The monolithic blocks have the length of 150 mm, the width of 30 mm, and the thickness of 4 or 8 mm. The pulse current and duration are 15 kA and 0.3 ms (FWHM), respectively. The pulse magnetic field were 2.49 T and 1.13 T at the gap of $G = 4$ mm and $G = 8$ mm, respectively, which were measured by the air-core pickup coil. The magnetization heads are for 15 mm period. The block are magnetized and fed by the stroke of 15 mm, iteratively.

The measured magnetic field on MMM are shown in Fig. 3. In the upper figure, the z -direction distributions of B_y at $x = 0$ mm and $y = 2$ mm are shown. The blue and red lines indicate the field distributions of 4 mm-thick and 8 mm-thick MMM, respectively. In the middle figure, the x -direction distribution of B_y at $z = 3.75$ mm (at the peak position) and $y = 2$ mm is shown. The maximum deviation of the peak amplitude along z except the both ends was less than 0.2%, which shows that a good-quality sinusoidal field was obtained. The lower figure shows the y -direction distributions of B_y , which corresponds to the gap-dependence of the peak field.

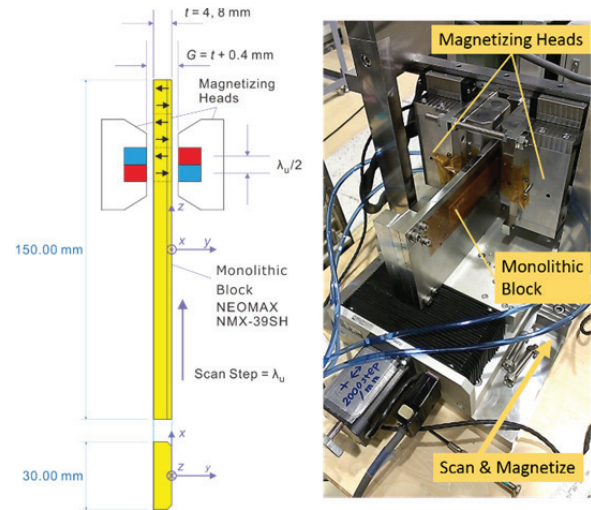


Figure 2: Magnetization system for MMM.

The above measurement results show that the magnetic field generated by the 8 mm-thick MMM was higher than that by the 4 mm-thick MMM. This sounds plausible if we assume that both MMMs were magnetized with the same pulse field. In practice, however, this is not true: the pulse field with $G = 8$ mm is much lower than that with $G = 4$ mm. We thus need to investigate the magnetization of the both MMMs to examine if all the experimental results are consistent.

Estimation of Magnetization in Multipole Monolithic Magnet

To estimate the magnetization in the MMM, the numerical results using the magnetization model as shown in the upper figure of Fig. 4 were compared with the experimental results. In the model, we have assumed that the magnetization profile is trapezoidal along the longitudinal axis and is composed of the flat-top region with the height of M_{top} and the transition domain with the length of d .

After numerical trials, it has been found that $M_{\text{top}} = 1.15$ T and $d = 1$ mm reproduces the experimental results for the 4 mm-thick MMM, and $M_{\text{top}} = 1.11$ T and $d = 1.25$ mm reproduces those for the 8 mm-thick MMM. The difference between the two conditions comes from the difference in the gap between the magnetization heads.

Table 1. Magnetization Experiment Setup

Period	15 mm
Periodic Number	10
Block Size	L150 mm, W30 mm, 4mmt / 8 mmt
Block Material	NMX-39SH (Hitachi Metals, Ltd.) ($B_r = 1.2 - 1.28$ T)
Pulse Current	15 kA, 0.3 ms (FWHM)
Pulse Field	2.49 T (4 mm), (Gap Center)
	1.13 T (8 mm)

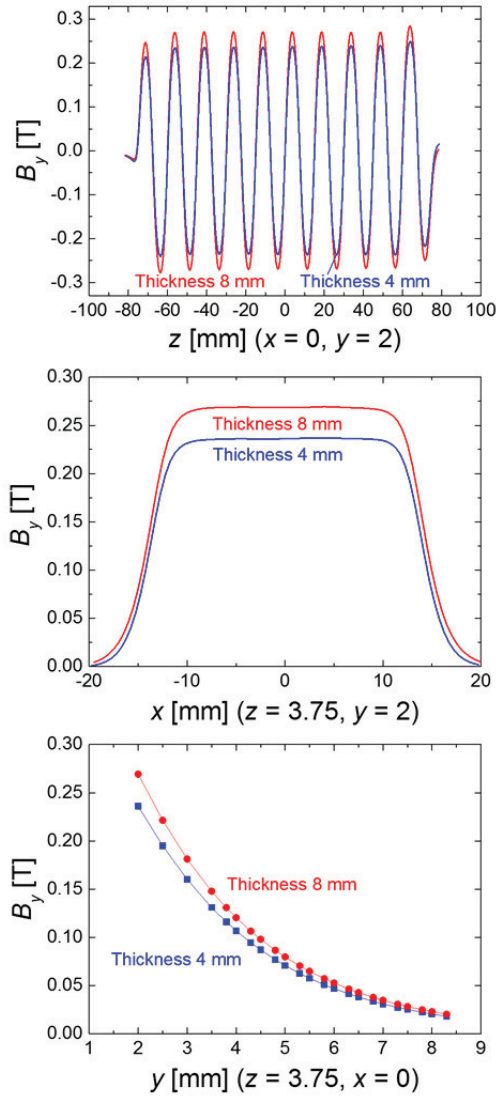


Figure 3: Field distribution of MMM.

The above values of M_{top} are almost the same as the magnetization including the diamagnetic effect for the magnets having $B_r = 1.2$ T and $B_r = 1.13$ T, respectively. Although M_{top} for the 4 mm-thick MMM reaches B_r of NMX-39SH (block material), that for the 8 mm-thick MMM is limited by the strength of the pulse field, 1.13 T, at the gap of the magnetization heads of 8 mm. If a cooling capacity of the magnetization heads is enhanced and the pulse current is increased, the 8 mm-thick MMM will be fully magnetized as well as the 4 mm-thick MMM.

Measurement of Attractive / Repulsive Force

Having verified that the MMM generate the sinusoidal field as expected, the repulsive force created by them, as well as the attractive force created by the main undulator magnets, have been measured with the measurement setup shown in Fig. 5. The main magnets having the Halbach configuration with the period of 15 mm, width of 20 – 25 mm, height of 8 mm and total length of 600 mm,

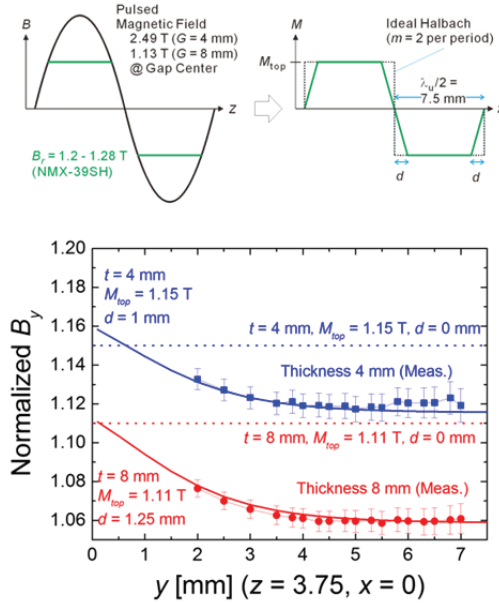


Figure 4: Modelling and numerical computation of magnetization in MMM.

were mounted on the copper magnet beams. Each magnet block is made of NMX-50BH (Hitachi Metals, Ltd.) which has a high remanent field of 1.36 T. Each magnet beam was connected to the undulator base frame using 4 load cells, which were calibrated for both the forces of compression and tension within an accuracy of 0.5 kg. The gap between the magnetic arrays was measured by several linear gauges.

The MMMs are attached on both sides of the main magnets using the stainless-steel supports. The gap between the MMMs was adjusted to coincide with the gap

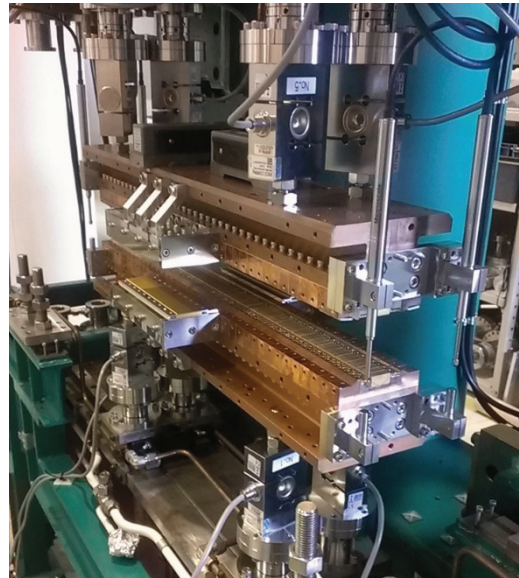


Figure 5: Gap-force measurement system. The force between the upper and lower magnets is measured by 8 strain-gauge-type load cells which supports the magnets. The real gap between them is measured by 4 linear gauges.

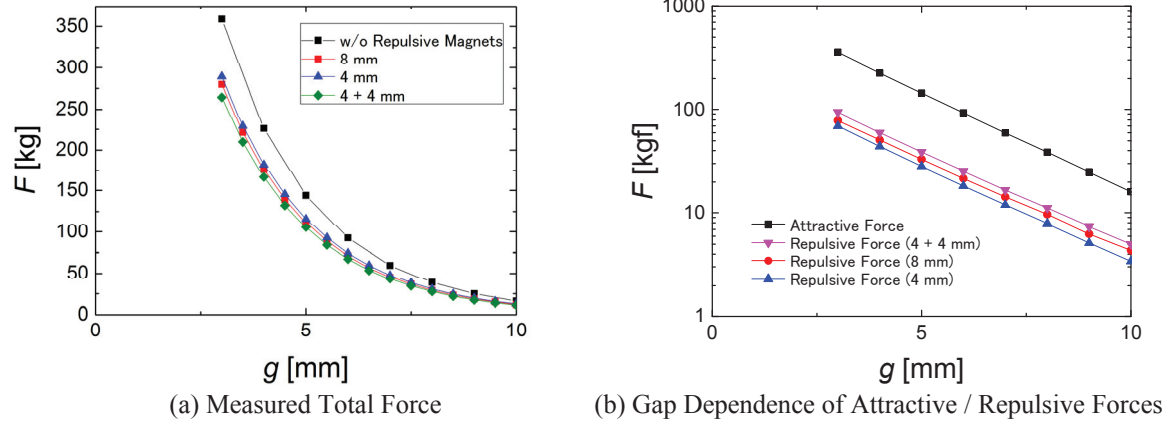


Figure 6. Measured force in preliminary experiment. The force is measured (1) without MMM (black square line), (2) with 4 mm-thick MMM (red circle line), (3) with 8 mm-thick (blue upper triangle line), (4) with two-ply 4 mm-thick (pink lower triangle line).

between the main magnets. Measurements were performed in the conditions (1) without the MMMs, (2) with the 4 mm-thick MMMs, (3) with the 8 mm-thick MMMs, (4) with the two-ply 4 mm-thick MMMs.

Results and Discussions for Force Measurement

The attractive forces measured as a function of the gap are shown in Fig. 6 (a) for various conditions. The black square line, the red circle line, the blue upper triangle line, and the pink lower triangle line indicate the measured forces at the conditions (1) – (4) mentioned above, respectively. The repulsive forces generated by the MMMs, which are retrieved from the experimental results, are plotted as a semi-logarithmic scale in Fig. 6 (b) as well as the attractive force. The gradients of the repulsive force in the all conditions were the same as that of the attractive force, which means that the gap-dependence of the repulsive force is coincident with the attractive force by the Halbach array. This is an encouraging result, because the absolute value of the repulsive force is adjustable by designing the size and B_r of the MMMs. Then we conclude that the attractive force can be fully cancelled out by the scheme presented in this paper.

Note that the repulsive forces are much smaller than the attractive force even though the repulsive magnets are twice wider than the main magnets. Of course, there is a difference in the lengths of the main magnets ($L = 600$ mm) and the MMMs ($L = 150$ mm). The remains is quantitatively explicable by the differences in B_r , height (thickness), the number of magnets in one period, and the distribution of the magnetization. To compensate those disadvantage in the MMMs, one can make the width or B_r of the multipole monolithic magnet large, or make the gap between the multipole monolithic magnets small.

Comparison of Experiment and Calculation

In Fig. 7, the experimental and calculated data are compared under an assumption that the total length of the MMMs is the same as that of the main magnets (600 mm).

Namely, the experimental data were reconstructed by subtracting 4 times (= 600 mm/150 mm) the repulsive force from the attractive force. In the numerical calculation, the values of M_{top} and d derived above were used.

The calculation well reproduced the experiment data for condition (1). However, from the results for conditions (2) – (4), we found non-negligible discrepancies between the experimental and numerical data of the repulsive forces. More detailed data showed that within the gap from 3 mm to 10 mm, there are around 20% differences in conditions (2) and (4), and around 15% difference in condition (3). This means that the numerical model of the MMM does not reflect the reality well. Not only z -direction distribution of the magnetization in multipole monolithic magnets, but also the y -direction distribution should be introduced in the future work.

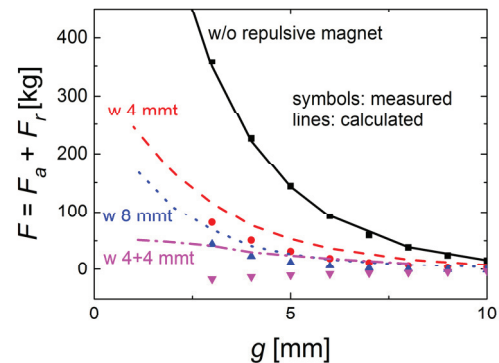


Figure 7: Measured and calculated force. The force is measured and numerically calculated (1) without MMM (black square, solid line), (2) with 4 mm-thick MMM (red circle, dashed line), (3) with 8 mm-thick (blue upper triangle, dotted line), (4) with two-ply 4 mm-thick (pink lower triangle, chain line).

DEVELOPMENT PLAN FOR COMPACT AND LIGHTWEIGHT UNDULATOR

In parallel to the development of the force cancellation system, the prototype of a compact and lightweight undulator based on the force cancellation system is being developed in SPring-8. The conceptual drawing of the prototype is introduced in Fig. 8.

We plan to measure the field distribution in the prototype at the gap of around 1 mm and check the suppression of the phase errors in the undulator field caused by the deflection of the magnet beam due to large attractive force. To measure the field at the very narrow gap, the gap between the multipole monolithic magnets is designed to be the same as the gap of main magnets. Two types of monolithic magnet with two different B_r are selected. The repulsive forces are mainly tuned by the width of the multipole monolithic magnets.

Because the numerical calculation have not reproduced the experimental repulsive forces well, the experimental data is also used to design the prototype. The adjustment mechanism for the repulsive force by means of phasing the multipole monolithic magnets is under discussion.

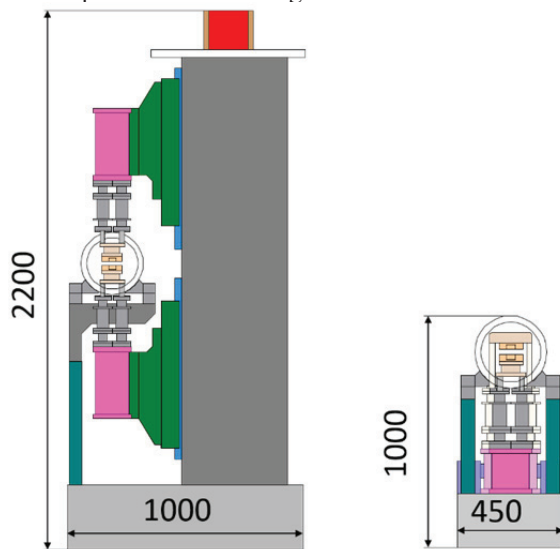


Figure 8: Conceptual drawing of conventional (LEFT) and lightweight compact & cost-effective (RIGHT) undulator.

CONCLUSION

Activities in SPring-8/SACLA toward a new undulator concept were introduced. To achieve the cost-effective force cancellation system which can generate the repulsive force having the same gap-dependence as the attractive force, we discussed the usage of the multipole monolithic magnets as the repulsive magnet. The preliminary experimental results showed that the multipole monolithic magnet can generate the repulsive force having the same gap-dependence with the attractive force by the main magnets. The development plan for the prototype of the lightweight and compact undulator based on the cancellation system was introduced.

REFERENCES

- [1] O. Marcouill , “Production of High Flux Hard X-ray Photons at SOLEIL”, in Proc. Int. Particle Accelerator Conf., Kyoto, Japan, 2010, WEPD009, <http://accelconf.web.cern.ch/AccelConf/IPAC10/papers/wepd009.pdf>
- [2] T. Bizen et al., “Development of In-vacuum Revolver Undulator”, in Proc. 8th Int. Conf. Synchrotron Radiation Instrumentation, San Francisco, USA, 2003, pp. 175–178.
- [3] S. Yamamoto, “A Novel Attempt to Develop Very Short Period Undulators”, J. Phys.: Conf. Series 425, (2013) 032014, doi:10.1088/1742-6596/425/3/032014
- [4] S. Yamamoto, “Development of the Very Short Period Undulators”, in Proc. Int. Particle Accelerator Conf. Dresden, Germany, 2014, WEOAA02, <http://accelconf.web.cern.ch/AccelConf/IPAC2014/papers/weoaa02.pdf>

FIELD INTEGRAL MEASUREMENT SYSTEM AND OPTICAL ALIGNMENT SYSTEM FOR HUST THz-FEL

B. Qin, K.F. Liu, X.L. Liu, Y.B. Wang, X. Lei, X. Liu, Q.S. Chen, Z. Ouyang, Q. Fu, L. Yang, T.N. Hu, J. Yang, P. Tan, Y.Q. Xiong, M.W. Fan, HUST, Wuhan 430074, China
Y.J. Pei, USTC/NSRL, Hefei 230026, China

Abstract

A Free Electron Laser oscillator with radiation wavelength 50–100 μm is under construction in Huazhong University of Science and Technology (HUST). The linear polarization undulator with $K=1.0\text{--}1.25$ has been designed and manufactured by Kyma s.r.l., by using a pure permanent magnet scheme. Acceptance test has been performed in Kyma factory with well controlled phase error and field integrals for all gaps. This paper introduces the development of an online field integrals measurement system for the undulator, using the stretched wire method. The design and considerations of the optical alignment system is described as well.

INTRODUCTION

High average power and continuous tunable terahertz (THz) sources based on low gain FEL oscillator scenario have widely applications covering materials, security inspection, molecule imaging etc.

A compact THz FEL oscillator for prototype study was proposed by Huazhong University of Science and Technology (HUST) and National Synchrotron radiation Laboratory (NSRL/USTC), which is designed to generate 50–100 μm coherent radiation with Watt level average power at initial stage [1, 2]. The general view is shown in Fig. 1, with the main parameters listed in Table 1. For the injector, a thermionic electron gun with an independently tunable cell (ITC) was chosen as the electron beam source for simplicity, and a S-band linac with traveling wave structure will accelerate the beam to range of 6 MeV to 14 MeV [3]. The macro pulse duration 5 μs is long enough for the power build up process which is around 1 μs . A 2.93m symmetrical near-concentric optical cavity is formed by two gold-coated copper toroid mirrors and a rectangular partial waveguide installed with the range covering the undulator, with estimated 15% total round trip loss [4]. The schematic view of this facility is shown in Fig. 1, with main specifications in Table 1.

STATUS OF THE PLANAR UNDULATOR

A pure permanent planar undulator with a moderate K is adopted, and design considerations were described in Ref. [2]. We signed contract with Kyma s.r.l. for design and manufacturing of the undulator, and the assembly was accomplished in November 2013, as shown in Fig. 2.

Main characteristics of this undulator are:

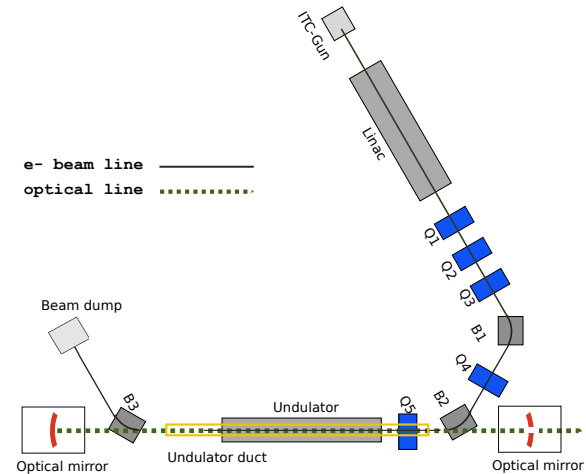


Figure 1: Schematic view of HUST THz-FEL oscillator.

Table 1: Parameters of HUST THz FEL Oscillator

Beam energy	8–12 MeV
Radiation wavelength, λ_r	50–100 μm
Bunch charge	≥ 200 pC
Bunch length (FWHM), σ_s	5–10 ps
Energy spread (FWHM)	0.3%
Macro pulse duration	4–6 μs
Repetition rate	10–200 Hz
Number of the full strength period, N_u	30
Undulator period, λ_u	32 mm
Undulator parameter, K	1.0–1.25
Optical cavity length	2.93 m
Peak power	0.5–1 MW

- Total length 1.03 m, with $N_u = 30$, $L_u = 32\text{mm}$; N_u is optimized by balancing the single pass gain and the natural extraction efficiency ($\approx 1/4N_u$)
- Pure permanent magnet (PPM) structure was chosen, and some techniques such as pre-sorting in block modules and "virtual shimming" [5] are used for controlling the field homogeneity and phase error. To achieve designed K for short period, high coercivity grades ($H_{cj} > 20\text{kOe}$) of NdFeB material was chosen; and the deviation of polarization and spread of the remanent field B_r were controlled within 1% level (rms)
- $K = 1.0 - 1.35$, by varying the gap from 19mm to 16mm, and two pair of independent controlled correction coils are installed in the transverse side of the undulator end, to correct the first and second field integrals both in vertical and horizontal directions



Figure 2: Linear polarization undulator, manufactured by Kyma s.r.l.

Acceptance tests for magnetic field and mechanical characteristic have been performed in Kyma Tehnologjia laboratory, Sezana. Figures 3 and 4 show the K value and rms phase error corresponding to varying gaps, calculated from the mapping result using the hall probe. The phase error is well controlled within required 2 degrees. First field integrals $I_z < \pm 5Gs \cdot cm$, using a flip coil system with $2.5Gs \cdot cm$ repeatability. Second field integrals $II_z < 0.08Gs \cdot m^2$ from hall probe mapping with $0.025Gs \cdot m^2$ repeatability. These can be corrected by using correction coils based on beam alignment process.

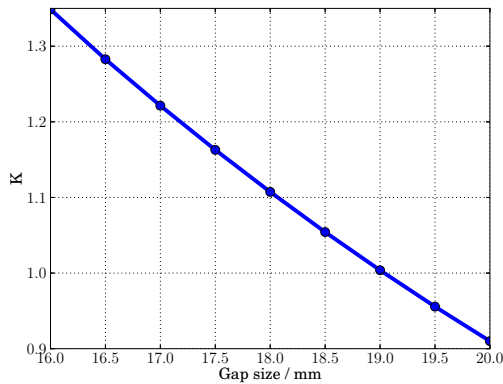


Figure 3: K value with variable gaps, $K=0.91$ - 1.35 for gap between 16 mm to 20 mm, and $K=1.25$ @ gap=16.77 mm, $K=1.0$ @ gap=19.04 mm.

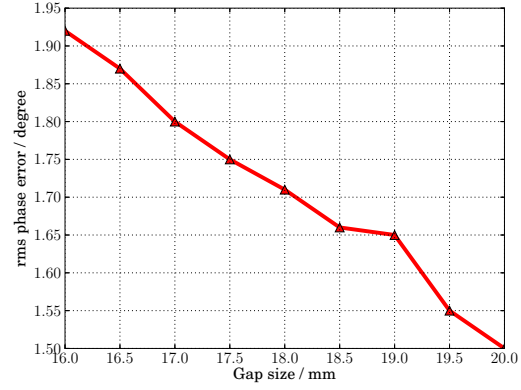


Figure 4: rms phase error with variable gaps.

DEVELOPMENT OF ONLINE FIELD MAPPING SYSTEM

A high precision Cartesian mapping system using Group3 MPT-141 Hall probe and DTM-151 Teslameter was developed in HUST [6], originally used for field mapping of a 10 MeV compact cyclotron. However the maximum range of this system is about 0.9 m, which can't cover HUST undulator. Kyma's mapping result can be trusted, but we decide to make an online integral field mapping system for commissioning and reference of beam alignment.

For fast online integral field measurement, some existing methods are considered and stretched wire method (SWM) [7] was chosen due to its simplicity and stability. Figure 5 shows the experiment setup for the SWM for field integral measurement. A 7.5 period test undulator with hybrid permanent magnet structure was used for experiment study, and the field distribution along the beam axis was measured by the hall probe system, with 1mm step and total 640 mm length. A 1.1 m stretched wire is wound in series by 50 turns Elekrisola Litz wire with 80 μm diameter, to enhance the integrated voltage signal due to first field integral I_y :

$$\int V \cdot dt = N \cdot \Delta x \cdot I_y \quad (1)$$

For the movement platform with synchronous horizontal / vertical motion to measure I_y , I_x , II_y , II_x , Kohzu positioning stages XA10A-L2 / ZA16A-X1 are combined to fulfill 2D positioning, and SC410 Motion Controller was chosen to provide maximum 4 axis synchronous motion control, with high repetitive positioning precision 2 μm . Agilent 3458A 8.5 digits multimeter is used for voltage integration. A Labview code was written to control the synchronous motion of the positioning stages, and trigger 3458A to record the voltage signal induced by wire movement, by serial GPIB interface (see Fig. 6). A soft trigger is used for timing between the stage motion and the multimeter's recording.

Figure 7 shows 5 sample signals of the voltage and its integration on time, for the same position $x=0$ mm. The stretched wire is moved from -2 mm to +2 mm in horizontal direction, with 2mm/s speed, and then return to original

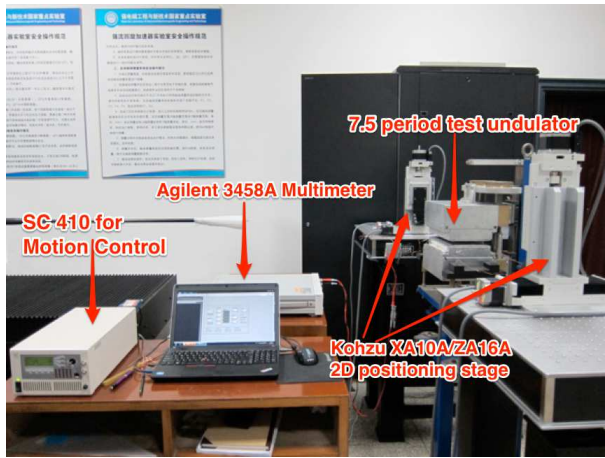


Figure 5: Experiment setup for online field integral measurement with stretch wire method.

-2 mm after 4 seconds. The voltage integrals have been corrected by removing the accumulated background error, by assuming the final voltage integral to be zero when returning to the original point. To improve the repeatability accuracy of the measurement, 20 sets of measurements were used for one position, and the repeatability (rms error) is better than $2.5\text{Gs} \cdot \text{cm}$.

As shown in Table 2, four times of measurement were taken within 40 days, with the reproducibility of $5\text{Gs} \cdot \text{cm}$. The difference between the SWM and hall probe mapping is about $20\text{Gs} \cdot \text{cm}$, which is mainly caused by the earth field integrals introduced by the longer 1.1 m stretched wire (hall probe only covers 0.64 m). For the second field integrals, the signal to noise ratio is much lower due to the cross movement of the stretched wire, which increases the repeatability error to about 5%.

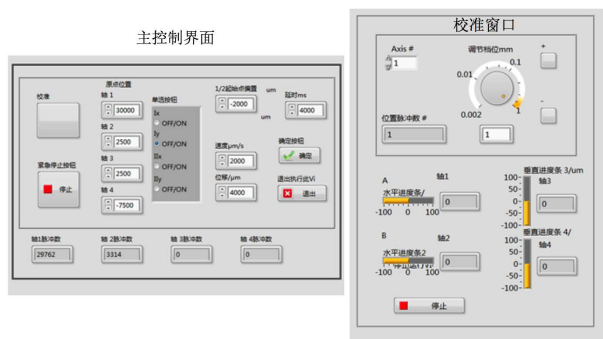


Figure 6: Labview GUI for integral field measurement.

Based on this SWM field integral measurement system, another system using pulsed wire method (PWM) is under development. The main challenge for PWM is its high sensitivity and dependence on circumference factors and configuration of wire characteristics. A good point for PWM is that the field distribution can be extracted from the distributed second field integrals.

ISBN 978-3-95450-133-5

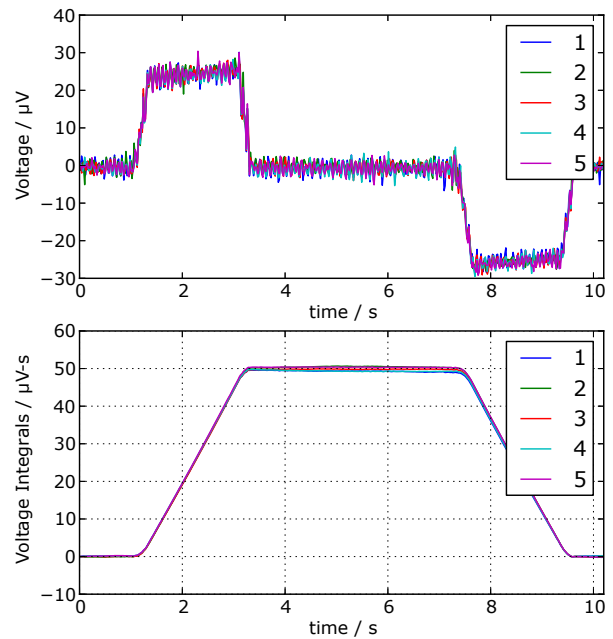


Figure 7: Voltage and voltage integral during horizontal movement from -2 mm to +2 mm. (5 times).

ALIGNMENT SYSTEM FOR OPTICAL CAVITY

To achieve optimum lasing performance, it is important to align three axes: the optical axis, the electron beam axis, and the magnetic axis in the undulator. An elaborate scenario applied in ALICE IR-FEL [8] was adopted, but with some modifications.

The overall view of the optical cavity alignment is shown in Fig. 8. Since the optical cavity of HUST THz-FEL is only 1/3 compared to ALICE case, only one central wedge is used. The wedge has two functions: a 1 mm hole is used for angle correction of optical mirrors by using two independent HeNe laser beam, which are installed in the bottom of 45 degree pop-in mirrors; YAG:Ce crystal is embedded in the wedge tip for monitoring the electron beam. This wedge can be remotely controlled by a staging platform with $5\mu\text{m}$ repeatability precision.

The reference axis will be established by align the wedge hole, centers of two YAG screens to the magnetic axis of the undulator by telescope survey; then the optical axis is aligned to adjusting two optical mirrors by HeNe auxiliary laser, with goal of observing centered diffraction pattern at the central wedge using CCD camera; and by using steering magnets, the electron beam can be centered at both YAG screens and pass through the wedge hole.

CONCLUSION

The THz-FEL facility in HUST is under installation in the new experimental hall, and the commissioning of the injector was initiated. The acceptance test of the planar undulator was performed, with all required specifications

Table 2: Measurement Results of First Field Integral with SWM (Unit: Gs · cm)

Date	x=-5 mm	x=0 mm	x=+5 mm
2013.10.06	$I_y = 199.76, \sigma = 1.36$	$I_y = 222.63, \sigma = 2.05$	$I_y = 249.47, \sigma = 1.36$
2013.10.18	$I_y = 196.93, \sigma = 1.64$	$I_y = 218.64, \sigma = 2.37$	$I_y = 245.78, \sigma = 2.09$
2013.10.22	$I_y = 196.18, \sigma = 1.34$	$I_y = 220.80, \sigma = 1.70$	$I_y = 249.76, \sigma = 1.87$
2013.11.11	$I_y = 194.46, \sigma = 1.32$	$I_y = 217.20, \sigma = 1.68$	$I_y = 246.32, \sigma = 1.72$
Hall probe mapping	$I_y = 170.28$	$I_y = 200.34$	$I_y = 234.42$

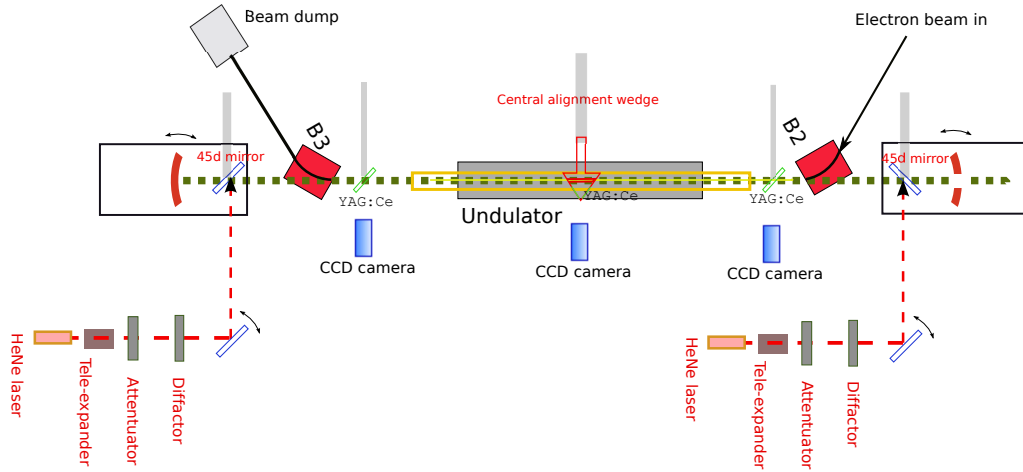


Figure 8: Schematic view of the optical alignment system.

passed. This undulator has been delivered to HUST, and will be installed after completion of the injector commissioning. A fast online integral field measurement system using the stretched wire method was developed, with repeatability of 2.5Gs · cm for the first field integrals. The alignment scheme is determined for optimizing the performance of FEL lasing.

ACKNOWLEDGMENT

We would like to thank Mauro Zambelli, Raffaella Geometrante, Mirko Kokole and Luka Belingar in Kyma s.r.l. for design and manufacturing the high performance linear polarization undulator.

We express our thanks to George Neil, Stephen Benson and Shukui Zhang in Jlab, for their very helpful advises and discussions.

We also thank Ping Lu, Baogen Sun and Xiaoye He in USTC/NSRL, for their helps and suggestions on optical/beam alignment.

REFERENCES

- [1] Xiong Yong-Qian, Qin Bin, Feng Guang-Yao et al. Chinese Physics C, 2008, **32**, supplement I, Mar.
- [2] B. Qin, P. Tan, L. Yang and X.L. Liu, Design considerations of a planar undulator applied in a terahertz FEL oscillator, Nucl. Instrum. Meth. A 727 (2013) 90-96.
- [3] Y.J. Pei et al., Design of 14 MeV Linac for THz source based FEL, IPAC 13, WEPWA023.
- [4] P. Tan et al., Optical cavity losses calculation and optimization of THz FEL with a waveguide, FEL 13, WEP069.
- [5] Kyma internal report, 2013.
- [6] J. Yang et al., Magnetic field measurement system for CYCHU-10, PAC 09, MO6PFP021.
- [7] D. Zangrando and R.P. Walker, Nucl. Instr. and Meth. in Phys. Res. A, 776 (1996) 275-282.
- [8] D.J. Dunning et al., First lasing of the ALICE IR-FEL at Daresbury Laboratory, FEL 2011, MOOA2.

PERFORMANCE ANALYSIS OF VARIABLE-PERIOD HELICAL UNDULATOR WITH PERMANENT MAGNET FOR A KAERI THz FEL

Jungho Mun^{1,2}, Young Uk Jeong^{1,#}, Nikolay Vinokurov¹, Kitae Lee¹, Seong Hee Park¹,
Kyu-Ha Jang¹, Min Yong Jeon²

¹WCI Center for Quantum-Beam-based Radiation Research, Korea Atomic Energy Research Institute, 1045 Daedeok, Yuseong-gu, Daejeon, 305-353, Korea

²Department of Physics, Chungnam National University,
99 Daehak-ro, Yuseong-gu, Daejeon, 305-764, Korea

Abstract

We could realize a variable-period (V-P) permanent-magnet helical undulator, which shows strong (~ 1 T) and constant field for the whole range of undulator period-length from 23 to 26 mm. This new compact and strong undulator will be used for developing a table-top high-power terahertz (THz) free-electron laser (FEL).

INTRODUCTION

A common way of tuning the undulator radiation wavelength is by varying the magnetic field of the undulator, which changes the K value. For a permanent-magnet undulator, the magnetic field strength is adjustable by changing the gap between the parts of the undulator. Another solution for wavelength tuning is variation of the undulator period-length [1, 2]. Recently, a V-P undulator was proposed with a planar structure using a split-pole structure of a hybrid permanent-magnet undulator [3]. The V-P undulator gives almost constant field strength at different periods, which results in less variations of a gain and radiation power for a given wavelength tuning range as compared with those for variable-gap undulators. The V-P undulator has a far less stringent dimensional tolerance and less driving force as compared to those for the variable-gap undulator, as it is shown in Ref. 3.

DESIGN AND FABRICATION

The concept of the design is based on the structure of the hybrid permanent-magnet planar undulator.

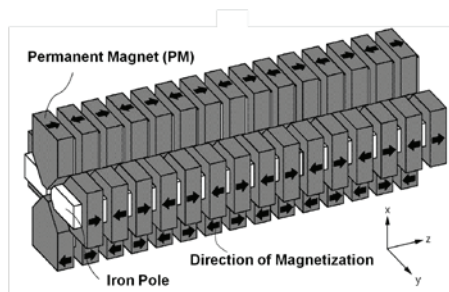


Figure 1: Magnetic design of the V-P helical permanent-magnet undulator [4].

Table 1: Main Parameters of the V-P Helical Permanent Magnet Undulator for a Compact THz FEL [4].

Gap	5 mm
Number of periods	30
Length of period	23-26 mm
Peak magnetic field	1 T

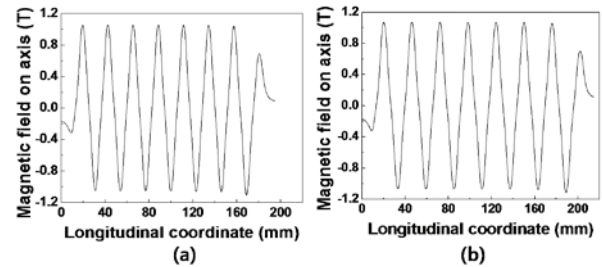


Figure 2: Calculated vertical component of the on-axis magnetic field of the V-P helical undulator. (a) $\lambda_w = 23$ mm and (b) $\lambda_w = 26$ mm. The calculated peak magnetic field is about 1 T [4].

This helical undulator is a combination of two planar undulators. A three-dimensional (3-D) simulation of the V-P helical undulator using the CST code [5] for different undulator period lengths was carried out. Table 1 shows the main parameters of our V-P helical undulator for a compact THz FEL. Figure 1 shows the structure of the V-P helical undulator, consisting of permanent magnets and iron poles. A short undulator with seven periods was then simulated for $\lambda_w = 23$ mm and 26 mm, where λ_w is the undulator period-length. In this simulation, the sizes of the magnets and poles were fixed. Only the period length of the undulator was varied. Figure 2 shows the simulated vertical component of magnetic field on the axis of the V-P helical undulator. According to the results of the simulation, the peak magnetic field on the undulator axis almost does not depend on the period length. Thus, the V-P helical undulator enables us to tune FEL wavelength without significant degrading the FEL gain.

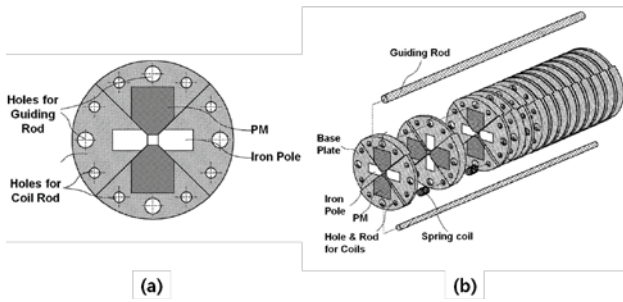


Figure 3: (a) Schematics of a basic module of the V-P helical permanent-magnet undulator. The module contains two permanent magnets and two iron poles. (b) Assembly configuration of the undulator [4].

A magnetic basic module composes of two permanent magnets and two iron poles on a non-magnetic plate, which corresponds to the 1/4 of the undulator period, as shown in Fig. 3. The using permanent magnets are NdFeB which has the remanent flux density of about 1.2 T. The modules are successively installed with the rotation by of 90-degree. Four such rotated modules form one period of the undulator. The basic modules are set through the guiding non-magnetic rods. Each modular plate has longitudinal repulsive force by the bigger permanent magnets than iron poles and also, we strengthen the force with the aid of spring coils between the modular plates. By simply controlling the longitudinal position of one end modular plate of the undulator by using a linear moving stage, we can change the period of the undulator because all modular plates are spaced regularly by the repulsive force. The period lengths of the undulator can change by using a mechanical motorizing system.

FIELD DISTRIBUTION AND PERIODICITY MEASUREMENTS

For the analysis of the field distribution and periodicity of the V-P helical undulator, the field measurement was performed by using a transverse Hall sensor (Lakeshore Inc.). Figure 4 shows the measured values of the vertical field component on the undulator axis at a period length of 26 mm. The measured and simulated values are in good agreement. The measured average peak magnetic field is 0.96 T. The difference of this value from the calculated one is less than the uncertainty of the permanent-magnet magnetization.

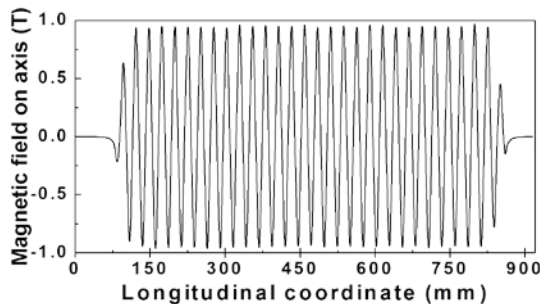


Figure 4: Measured vertical component of field on the undulator axis at the period length of 26 mm.

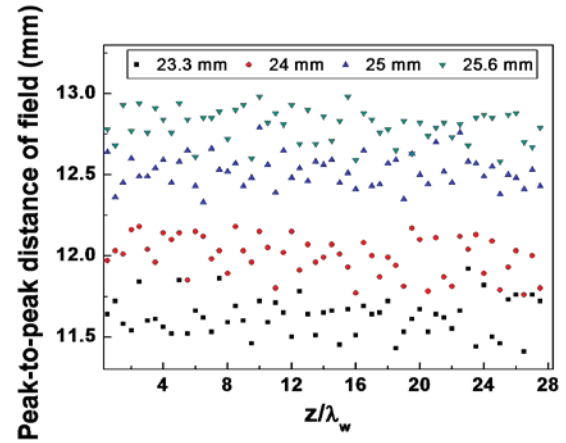


Figure 5: Measured peak-to-peak distances for four undulator periods [4].

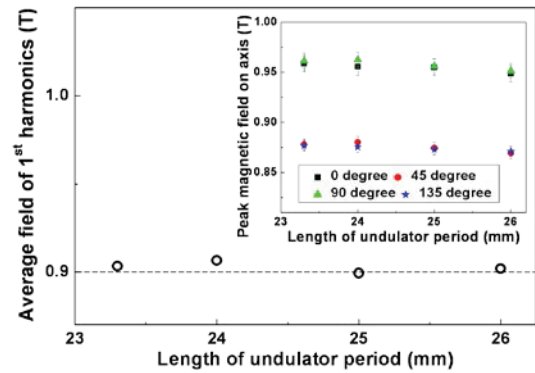


Figure 6: Dependence of the average fundamental harmonics of magnetic field on the period length of the V-P helical undulator. The inset graph of the figure shows the peak magnetic field on the undulator axis [4].

The new feature of this V-P undulator is the variable positions of poles and magnets. Therefore, it was interesting to measure the corresponding aperiodicity of the field. Figure 5 shows the periodicity measurements of the V-P helical undulator for period lengths of 23.3, 24, 25, and 25.6 mm. We estimated the period through the analysis of distances between the maxima of the measured magnetic field component. The r. m. s. deviation of the peak-to-peak length in each case was less than 1%. Figure 6 shows the dependence of the average fundamental harmonics of magnetic field on the period length of the V-P helical undulator. The inset graph of the figure shows the deviation of the peak magnetic field along the undulator axis for each period length. The r. m. s. deviation of the peak field module for each period length was measured to be less than 0.7%. The first and the second field integrals and the corresponding radiation Fourier harmonics [6] were calculated. Calculated ratio of the maximum spectral intensity of radiation to the ideal one and r. m. s. phase errors are presented in Table 2.

Table 2: Spectral Intensity, normalized to the ideal one, and r. m. s. phase errors for different undulator periods [4].

Period (mm)	Spectral intensity ratio (%)	R.m.s. phase errors (degree)
23.3	98	2.7
24	95	8.0
25	98	3.6
25.6	97	3.7

The reproducibility of the phase error was checked by measuring the field six times at 25.6 mm period after random shifts of undulator sections. The mean value of the r. m. s. phase errors is 3.7. The results of these calculations show, that the field errors are within the tolerances for a table-top THz FEL.

CONCLUSION

This undulator has several advantages as below. First, tuning of the radiation wavelength without decrease of the undulator field is possible by adjusting the undulator period. Second, the helical permanent magnet undulator can generate strong field on the undulator axis. Third, realization of a compact and mechanically simple system is possible. Fourth, the V-P undulator enables us to tune the FEL wavelength and to reduce the size of the undulator without degrading the FEL gain. Consequently, this strong and compact undulator may be a useful technology for the development of a new FELs and cost effective insertion devices for synchrotron radiation sources.

ACKNOWLEDGMENT

This work was supported by the World Class Institute (WCI) Program of the National Research Foundation of Korea (NRF) funded by the Ministry of Science, ICT and Future Planning. (NRF Grant Number: WCI 2011-001)

REFERENCES

- [1] R. Z. Bachrach, R. D. Bringans, B. B. Pate and R. G. Carr, Proc. of SPIE 582, 251 (1985).
- [2] G. Isoyama, S. Yamamoto, T. Shioya, J. Ohkuma, S. Sasaki, T. Mitsuhashi, T. Yamakawa and H. Kitamura, Rev. Sci. Inst. 60, 1863 (1989).
- [3] N. A. Vinokurov, O. A. Shevchenko, and V. G. Tcheskidov, Phys. Rev. ST Accel. Beams 14, 040701 (2011).
- [4] J. Mun, Y. U. Jeong, N. A. Vinokurov, K. Lee, K.-H. Jang, S. H. Park, M. Y. Jeon, and S.-I. Shin, Phys. Rev. ST Accel. Beams 17, 080701 (2014).
- [5] CST EM Studio ®, © 2005 CST - Computer Simulation Technology, Wellesley Hills, MA, USA, www.cst.com.
- [6] E. Levichev and N. Vinokurov, Rev. Accel. Sci. Technol. 3, 203 (2010).

PAL-XFEL MAGNET POWER SUPPLY SYSTEM

Seong Hun Jeong[#], Ki-Hyeon Park, Hyung Suck Suh, Sang-Bong Lee, Bongi Oh, Young-Gyu Jung, Hong-Gi Lee, Dong Eon Kim, Heung-Sik Kang and In Soo Ko
PAL, Pohang, Republic of Korea

Abstract

This paper presents an overview of the magnet power supply (MPS) for the PAL-XFEL. The number of total MPS is up to 624 and they will be installed along the accelerator and the undulator sections. The power capacity of the MPS was ranging from about 1 A to 300 A. These MPSs were required to meet the high stability that was subjected from the beam dynamics specifications. This paper described the overall MPS requirements, MPS assembling, test process, control scheme, installation plan and so on.

INTRODUCTION

The PAL-XFEL is the 4th-generation light source, base on a single pass FEL, under constructing at Pohang Accelerator Laboratory in Korea. This project aims at the generation of X-ray FEL radiation in the range of 0.1 to 10 nm for users. The machine consists of 10 GeV linear accelerator and hard and soft X-ray undulator beamlines. The accelerator will operate at a 60 Hz and will be extended to 120 Hz [1]. Total 624 set of MPS are used for beam orbit correction and maintained for the beam trajectory. To reach the best performances expected from a 4th-generation source, very demanding specifications have been targeted notably on magnetic field stability and reproducibility of the various magnets, hence on the currents delivered by the power supplies. The power supplies have ratings which range from about 1 A to 300 A. The topologies of the MPSs are buck and H-bridge chopper type. This paper describes the MPS developing status and installing plan and so on.

MAGNET POWER SUPPLY SPECIFICATIONS

Table 1 describes the specifications of the three kinds - quadrupole, dipole and corrector - magnet power supplies for the PAL-XFEL.

Table 1: Total MPSs Number for PAL-XFEL

Magnet	MPS type	Qty	Stability(ppm)
Corrector	Digital	283	10 & 50
	Analog	108	50
Quadrupole	Unipolar	122	100
	Bipolar	86	
Dipole	Unipolar	20	20
	Bipolar	2	
Solenoid	Bipolar	3	20

*Work supported by Ministry of Science, ICT & Future Planning of Korea, #jsh@postech.ac.kr

Based on the maximum operating current and voltage, 213 quadrupole magnets are divided into 11 families, 48 dipole magnets are 7 families. The 391 corrector magnets are grouped 3 families base on the current rating and stability. The power supplies can be categorized as unipolar and bipolar power supplies.

HARDWARE STRUCTURE AND CONTROL SCHEME

The basic structure of a power supply with controller, ADC and interface to the control system is shown in figure 1. The topologies of the converters are either buck or H-bridge. It is based for the unipolar of dipole and quadrupole MPS on the following chain of elements: 12-phase transformer, rectifier, input filter, energy storage, switching device and output filter.

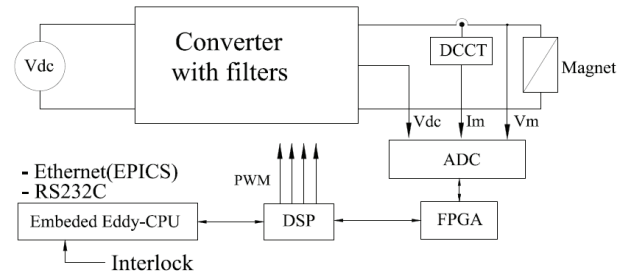


Figure 1: PS control structure overview.

The transformers adapted to the higher power capacity have two secondary windings, one delta-connected and the other wye-connected to configure the 12 phase rectifier in order to reduce the AC ripple on the DC link of the power supply. The bandwidth of the input filter should be less than 30 Hz to have a good output performance. A freewheeling diode and an L-C filter are put across the output stage. The cut-off frequency of output L-C filter is about 5 kHz. It gives a good dynamic control performance. A soft charge circuit on the rectifier limits the inrush current during power on.

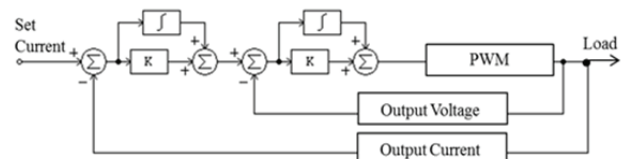


Figure 2: Control loop structure.

Figure 2 shows the control loop structure of MPS. The control loops for the switching mode power supply are consisted of a cascaded current and voltage feedbacks, the inner loop controls the output voltage, and outer loop

controls the output current [2]. The control loops are executed at every PWM switching frequency.

Since the introduction of digital signal processor, a fully digital-controlled MPS has many advantages over the analog one. Its output characteristics are less sensitive to noise and less susceptible to parameter variations from thermal and aging effects. Also, it has flexibility in control system [3]. Digital control processing for MPS will be built on the DSP TMS320F28335 from TI Co. It has 6 enhanced PWM modules with 150 ps micro edge positioning [4]. The uC5282 embedded microprocessor module from Arcturus Co. was assembled into the DSP board to support Ethernet.

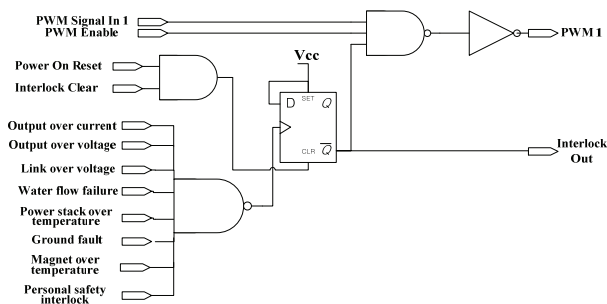


Figure 3: Logic diagram of Interlock signal process.

Interlock signal process is shown in figure 3. All MPS are equipped with latched interlocks to detect abnormal MPS and magnet conditions such as shown in figure 3. When interlock is occurred, MPS output is blocked by hardware logic and it transfer the state to control room. In this time, interlock state is latched and it was returned to normal state by reset switch or consol command.

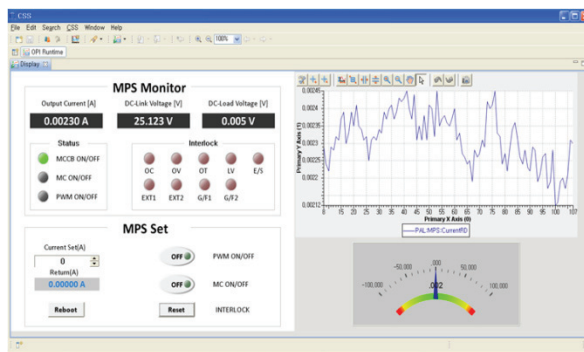


Figure 4: MMI display at computer.

Figure 4 shows the MMI (Man Machine Interface) example of MPS. This panel is made by CSS tools [5]. The EPICS IOC was embedded in the uC5282 board of the MPS controller. The MPS also included the RS232C port to interface in the front of the MPS site. These MPSs included the small web server to make easy maintenance.

MAGNET POWER SUPPLY ASSEMBLING

There is a lot of numbers MPS assembling. Whole power supply should be modularized to install in 19' rack

size. Figure 5 shows an example of the corrector MPS installation diagram.

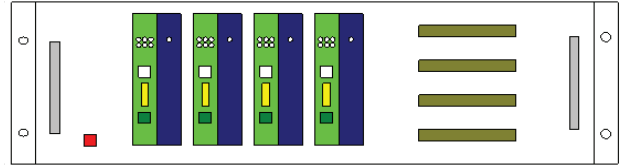


Figure 5: Corrector MPS mounting diagram.

We plan the 4 - corrector MPSs (below 400W) is installed in 3U unit of standard 19' rack. These corrector MPS has independent controller, but communication module is shared by 2 MPS. The switching frequency of these 4 corrector MPS should be design to synchronize. The size of quadrupole MPS for less than 400W is 1/2 of 4U unit. All MPS cabinets have safety ground which was connected to the distribution board.

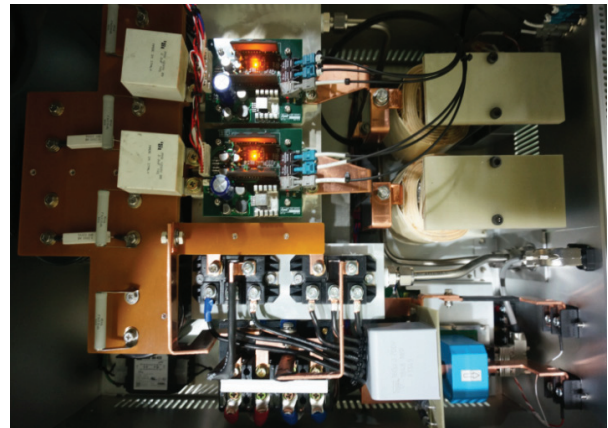


Figure 6: Power stack of 90A Bipolar MPS.

Figure 6 shows the power stack of 90A bipolar MPS. The left side is source input and right side is output. It shows the IGBT modules and input, output filters.

TEST PROCESS

In factory stage, the acceptance test will focused on the power circuit. During the 8 hour's operation at 100% normal current, DC link capacitor bank and IGBT module temperatures will be checked.

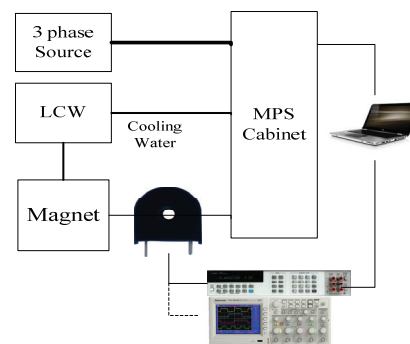


Figure 7: MPS performance test scheme.

Figure 7 shows the MPS performance test scheme. For the measurement of DC output current, digital volt meter (DVM), HP3458A, and external high precision DCCT MACC150 from HITEC are used and output ripple voltage is measured by oscilloscope [6]. The DVM has an 8 1/2 digit resolution, and 0.6 ppm accuracy [7]. To measure the insulation resistance, mega ohm tester is used. All data is acquired by computer to verify the MPS performance.

Figure 8 shows the performance test result of prototype power supply and magnet for PAL-XFEL. The short term stability of the MPS is below 5 ppm for 30 minute at full output power.

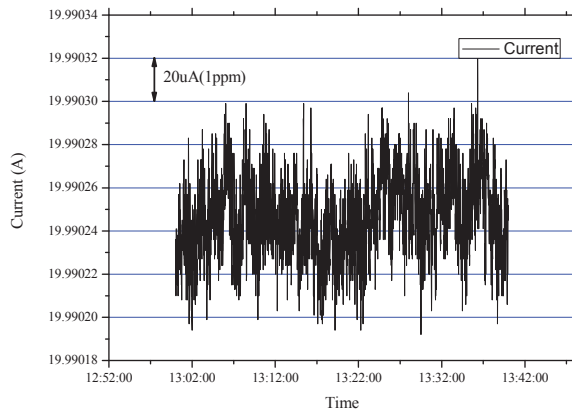


Figure 8: Current stability for 30 minute at 20A and 5V output.

Figure 9 shows the reproducibility test results. The current was set to 10 A and 8A repeatedly by 5 times. It shows the difference of output is less than 2.5 ppm.

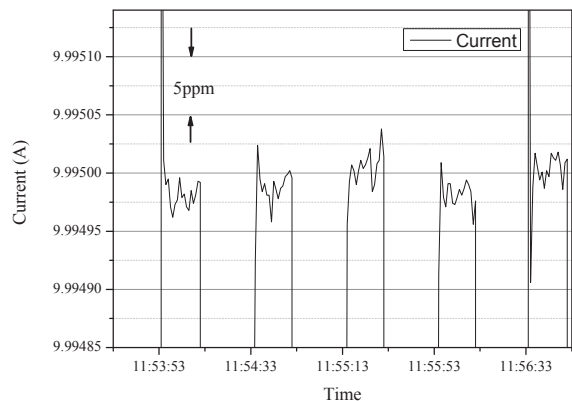


Figure 9: Reproducibility test result.

INSTALLATION PLAN

We will prepare the installation plan and verify the schedule and procedure. All assembled MPSs are evaluated the performance at before installation. To remove the interference between the accelerator devices and MPSs, 3D model drawing of magnet and MPS rack will be draw. The output cables of MPS are non-radioactive and current capacity is 1.5 A/mm² for above 100A and 2 A/mm² for below 100A. When the devices are installed in site, field tests are done for verifying the performance. The MPS will be begin to install in March and ended in June 2015. The whole MPS site tests will be carried out for 3 months from July 2015. We hope all errors are cleared out and keep for normal status for the best beam commissioning.

CONCLUSION

This paper described the overall MPS requirements, control scheme, MPS assembling, test process, installation plan for PAL-XFEL. In factory stage, the acceptance test will focused on the power circuit. After the 8 hour's operation at 100% normal current, DC link capacitor bank and power stack temperature will be checked. These MPS included the small web server to make easy maintenance. The MPS will be installed from March 2015 and operation tests will begin July 2015.

REFERENCES

- [1] Heung-Sik Kang, et al., "Current Status of PALXFEL Project", IPAC2013, Shanghai, May 2013, WEODB103, p.2074 (2013).
- [2] H. Jin, S.B. Dewan, "A Combined Feed-Forward and feedback Control Scheme for Low-Ripple Fast-Response Switch-mode Magnet Power Supply", IEEE Trans. On Magnetics, Vol.30, No.2, July 1994, P.1801.
- [3] J. Carwardine and F. Lenkszus, "Trends in the use of digital technology for control and regulation of power supplies", In *Int. Conf. on Accelerator and Large Experimental Physics Control System*, Trieste, Italy, 1999, p. 171
- [4] Texas Instruments Co., www.ti.com
- [5] <http://ics-web.sns.ornl.gov/css>
- [6] K. H. Park, et al., "The development of high stability magnet power supply", Cyclotrons2013, Vancouver, April 2013, TUPSH012
- [7] <http://www.agilent.com>

DESIGN, FABRICATION, AND PERFORMANCE TESTS OF DIPOLE AND QUADRUPOLE MAGNETS FOR PAL-XFEL*

Hyung Suck Suh[#], Bongi Oh, Dong Eon Kim, Heung-Sik Kang, Hong-Gi Lee, In Soo Ko, Ki-Hyeon Park, Moo Hyun Cho, Sang-Bong Lee, Seong Hun Jeong, Young-Gyu Jung
PAL, Pohang, Republic of Korea

Abstract

PAL(Pohang Accelerator Laboratory)-XFEL is now being constructed in Pohang, Korea. This facility will consist of a 10 GeV linac and five undulator beamlines. As the first phase we will construct one hard X-ray and one soft X-ray beamlines which require 6 different families of dipole magnets, and 11 families of quadrupole magnets. We have designed these magnets with considering the efficient production and the proper power supplies. In this presentation, we describe the design features of the magnets, the manufacturing, and the thermal analysis with the test results.

INTRODUCTION

The PAL-XFEL is a 0.1-nm hard X-ray FEL project starting from 2011. Three hard X-ray and two soft X-ray branches are planned. As the first phase of this project, one hard X-ray (HX1) and one soft X-ray (SX1) which consist of 51 dipole and 208 quadrupole magnets will be constructed [1].

We have designed all magnets on our own by using OPERA and ANSYS codes [2, 3]. We tried to reduce the number of coil types and the number of the power supply types for the convenient production. Every magnet is designed to maintain the maximum temperature rise of coils below 20 K for about 120% of the rated currents. In the process of the design, it was helpful to parameterize the main figures of the magnets in a spread sheet for easy estimation by changing some parameter often. Now we are manufacturing them and testing the prototype magnets.

DIPOLE MAGNETS

The dipole magnets were classified into 6 kinds according to the pole gap, the effective magnetic length, and the maximum magnetic field. The results of the classification are listed in Table 1.

Dipole magnets have the same pole gaps of 30 mm except D6 of 15 mm for the self-seeding. D1, D2, and D4 have H-type core shape, and D3, D6, and D7 have C-type. All dipole magnets of D1~D6 for the bunch compressor, the chicane, and the self-seeding have the trim coils with 1% of the main field.

The pole profiles of magnets are optimized by the small bumps at the tip of the pole for the field uniformity. The requirements for the field uniformity are different from each magnet, e.g. in the case of H-type dipole magnet D1,

$\Delta B/B_0 < 1.0E-4$ for ± 17 mm, $\Delta B/B_0 < 5.0E-4$ for ± 41 mm in 3D calculation.

Table 1: The Families of Dipole Magnets (D5 was Replaced with D2)

Family	Magnetic length [m]	Max. field [T]	Qty	Position
D1	0.20	0.80	6	BC1
D2	0.70	1.00	18	BC2,BC3, BAS1
D3	1.50	1.30	11	BAS2,3,4
D4	0.17	0.30	4	Laser Heater
D6	0.30	0.485	4	Self seeding
D7	0.75	1.164	2	Tune-up dump

So the pole contour of D1 is made like Fig. 1 where the a-b line has a slight slope. The 2D/3D field uniformities of the calculation results are shown in Fig. 2.

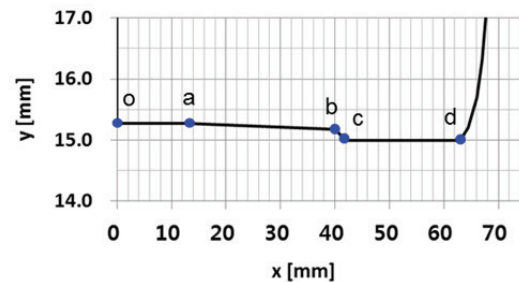


Figure 1: Pole contour of H-type dipole magnet D1.

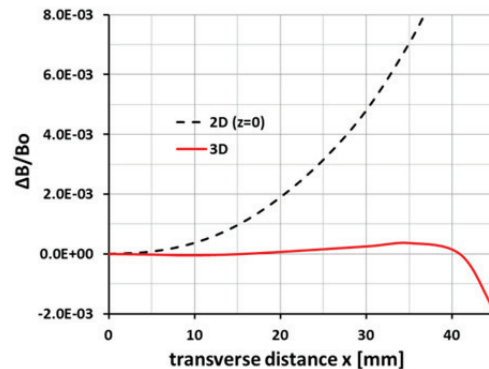


Figure 2: Calculated 2D/3D field uniformities of dipole magnet D1.

The laminated cores are used for the magnets D2 and D3 which quantities are more than 10 magnets, and the solid cores are used for the rest of the dipole magnets.

*Work supported by Ministry of Science, ICT and Future Planning of Korea, #suhhs@postech.ac.kr

We measured the magnetic field of D4 dipole magnet that has four coils per magnet for the space in the middle (see Fig. 3). The 3D results of the field uniformity satisfied the requirement that is less than $1.0E-4$ within ± 9 mm as shown Fig. 4. But now we are analysing the multipole components along the beam trajectory.

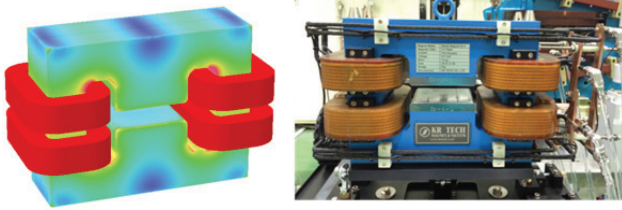


Figure 3: The FEM model and the prototype of dipole magnet D4.

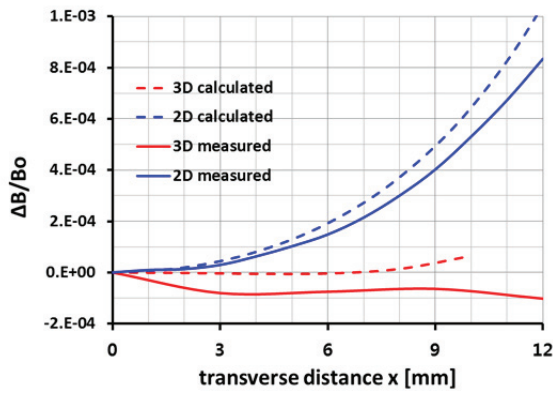


Figure 4: Field uniformity comparison of D4 magnet.

QUADRUPOLE MAGNETS

The quadrupole magnets are classified into 11 kinds according to the aperture diameter, the effective length, and the maximum field gradient. The results of the classification are listed in Table 2.

Table 2: The Families of Quadrupole Magnets

Family	Aperture diameter [mm]	Magnetic length [m]	Max. gradient [T/m]	Qty
Q1	30	0.065	15	18
Q2	30	0.13	25	60
Q3	30	0.18	25	18
Q4	44	0.20	25	7
Q5	22	0.40	35	14
Q6	16	0.13	40	31
Q7	80	0.50	18	3
Q8	22	0.25	30	19
Q9	16	0.08	32	18
Q10	44	0.50	25	4
Q11	44	0.10	10	16

There are the horizontal and vertical steering functions in some quadrupole magnets (Q1, Q2, Q3, Q6, and Q9) for the bunch compressors and the inter-undulator.

The multipole components were calculated by using an equation, the radial component: $B_r(r_0, \phi) = \sum_n \{A_n \sin(n\phi) + B_n \cos(n\phi)\}$, where r_0 is the reference radius that is the good field radius. All magnets are optimized to have the relative multipole components less than $1.0E-4$ in 3D calculations. Fig. 5 shows the half pole contour. In this figure the o-m line follows along an ideal hyperbola, the m-n is a straight line and an arc after n point. We could satisfy the multipole requirements by manipulating the position and the length of the straight section.

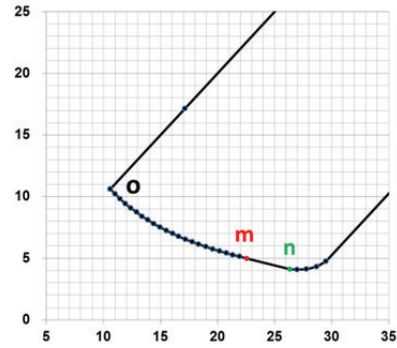


Figure 5: The half pole of quadrupole magnet.

The indirect cooling system (heat sink) for the quadrupole magnets (Q1, Q2, Q3, Q5, Q6, Q8, and Q9) was adopted. Fig. 7 shows the cross section of the conductor and the temperature distribution of quadrupole magnet Q2. We used the effective thermal conductivity: $1/k_{eff} = \sum v_i/k_i$ for the turn insulation and the ground insulation, where v_i is the volume fraction.

We made two kinds of prototype quadrupole magnet of Q2 and Q5, and measured the magnetic field with a hall probe and the temperature rise (see Fig. 6 and Table 3).

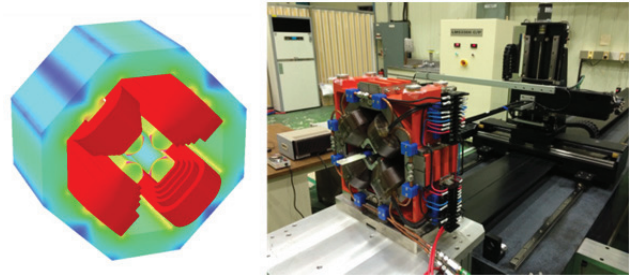


Figure 6: FEM model and field measurement scene of a quadrupole magnet.

Table 3: The Calculated and Measured Temperature Rise

Magnet	Calculated	Estimated (by resistance)	Measured
Q2	11	16	14
Q5	10	15	17

The relative deviation of the field gradient $\Delta B'/B'$ for Q2 was shown as $1.2E-3$ within ± 10 mm on the mid-plane. We prepare the field clamp to shield the leakage field from quadrupole magnets. The field clamp of 1 mm

thickness can reduce the leakage field to less than 5 Gauss beyond this clamp. But this field clamps reduce the magnetic length by about 1% for Q2.

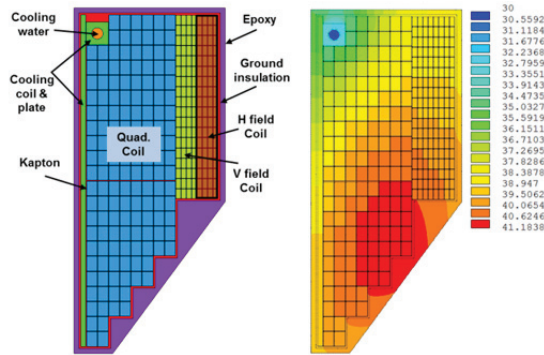


Figure 7: The conductor cross section and the temperature distribution of quadrupole magnet Q2 with a heat sink.

CORRECTOR MAGNETS

The dipole magnets and the quadrupole magnets for the chicanes and the beam analysing have the trim coils or the horizontal/vertical steering coils respectively. Beside these, we prepare the independent corrector magnets of 49 that are composed of 35 with iron core and 14 with air core. The other correctors with iron core have the heat sink system similar to Fig. 7 for the narrow space. The main parameters of the corrector magnets are shown in Table 4.

Table 4: The Main Parameters of Corrector Magnets

Corrector type	C1	C2	C3
Core	iron	iron	air
Cooling type	air	heat sink	air
Field integral [Gcm]	5000	5000	1000
Magnet length [mm]	295	144	200
Current density [A/mm ²]	1.1	2.6	0.9
Temperature rise [K]	16	12	18
Quantity	35	6	14

CONCLUSION

When we classified the magnets and determined the coil sizes, we should consider the connection condition of magnets in series or stand alone, the electrical properties of magnets, and the number of cooling circuit. If the number of cooling circuits is increased in order to reduce the temperature rise, then the magnets become more complicate with the risk of leakage [4].

We have designed almost all magnets, and are testing the prototype magnets now. The results of tests are not bad until now. But we have to modify magnets if it is necessary after analysing the magnetic field and the temperature rise.

REFERENCES

- [1] PAL-XFEL, Beam Optics and Parameter Design, Heung-Sik Kang, 2012.
- [2] Vector Fields Software, <http://www.cobham.com>
- [3] ANSYS, <http://www.ansys.com>
- [4] Jack T. Tanabe, "Iron Dominated Electromagnets", 2005, pp. 113-126.

ESTIMATING EFFECT OF UNDULATOR FIELD ERRORS USING THE RADIATION HODOGRAPH METHOD

N.A. Sokolov[#], Budker INP, Novosibirsk, Russia
N. Vinokurov, Russia, and KAERI, Daejeon, Rep. of Korea

Abstract

Spatially-periodic magnetic structures are widely used for generation of high-brilliance radiation in storage rings, sources of synchrotron radiation and free electron lasers. In 1947, V.L. Ginzburg suggested the first undulator scheme.

An alternating magnetic field created by a planar undulator makes electrons oscillate in the transverse direction, with interference of radiation emitted from separate parts of the trajectory. The spectrum of the forward emitted radiation is enhanced due to constructive interference.

The undulator is made of the magnetized bars that are not perfect and their magnetization differs. Therefore, the electron trajectory is not purely sinusoidal and, as a result, the spectral intensity fades. The task was to find out if the precision of magnet manufacturing is sufficient.

This paper presents modelling of electron motion in the measured magnetic field of the new (third) free electron laser at the Siberian Synchrotron Radiation Centre. We have managed to estimate the effect of the field errors through comparison of the resulting emitted field amplitude with the amplitude from ideal magnet bars using the hodograph method.

CALCULATING MAGNETIC FIELD OF UNDULATOR

The undulator under study consists of two rows of magnetized bricks with $1.5 \times 1.5 \text{ cm}^2$ square cross-section, a width w of 9 cm and alternating magnetization directions as shown in Fig. 1. A brick is characterized by homogeneous magnetization M and the brick shorter side b . The vertical component of the field of a brick, centered at the origin is given by two expressions for contributions of vertical M_y and horizontal M_z components of magnetizations. Now the undulator field can be calculated as the sum of the fields of all its bricks (Eq. 1):

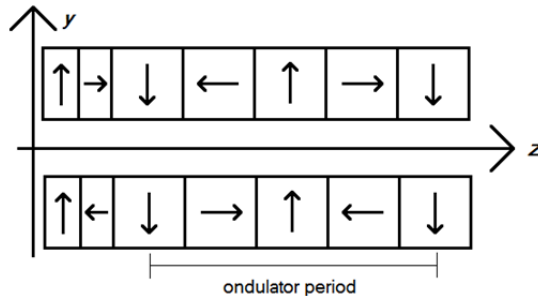


Figure 1: Scheme of permanent magnet undulator.

$$B_y(z) = 2 \sum_n \left[B_v(0, g, z - nb) \cos \frac{\pi n}{2} + B_h(0, g, z - nb) \sin \frac{\pi n}{2} \right], \quad (1)$$

where g is the distance between the undulator axis and the brick centres, and $M_y = M_z = M$. It should be taken into account that the undulator begins and ends with two pairs of halved bricks for the average angle of particle trajectory and the transverse coordinate to be the same at the undulator ends. The fields of these termination bricks were calculated with formula, similar to Eqs. 2 and 3. The contribution of termination bricks is skipped in Eq. 1, but was taken into account in field and trajectory calculations. Bricks with vertical (along the OY axis) magnetization change the particle transverse angle, while bricks magnetized horizontally along the OZ axis change the transverse coordinate of particle.

This results, for a magnetic field of ideal bricks, in an electron trajectory which is close to the undulator axis and has close-to-zero transverse angle and coordinate (see Fig. 2).

Since the average magnetization of brick M is not known precisely, let select it such that the ideal undulator field is close to the measured undulator field, shown in Fig. 3. We obtained an average magnetization of 1.076 kG using the method of standard deviations. The field errors, shown in Fig. 4, apparently do not exceed 5 % of the field maximum.

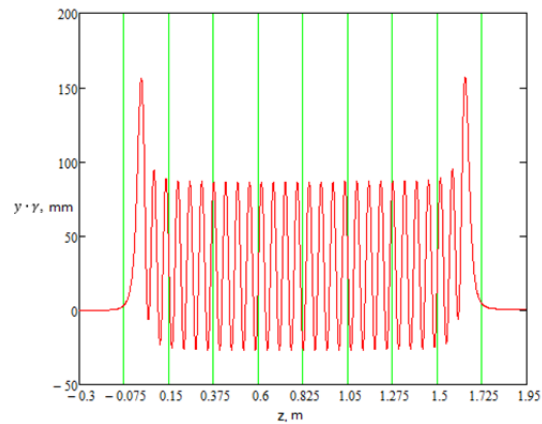


Figure 2: Electron trajectory in the field of the ideal undulator.

[#]faucet@gmail.com

$$B_y(x, y, z) = -M_y \operatorname{atan} \frac{(y - y') \sqrt{(x - x')^2 + (y - y')^2 + (z - z')^2}}{(x - x')(z - z')} \bigg|_{x'=-w/2}^{x'=w/2} \bigg|_{y'=-b/2}^{y'=b/2} \bigg|_{z'=-b/2}^{z'=b/2}, \quad (2)$$

$$B_h(x, y, z) = M_z \ln \frac{\sqrt{(x - x')^2 + (y - y')^2 + (z - z')^2} - x + w/2}{\sqrt{(x - x')^2 + (y - y')^2 + (z - z')^2} - x - w/2} \bigg|_{y'=-b/2}^{y'=b/2} \bigg|_{z'=-b/2}^{z'=b/2}. \quad (3)$$

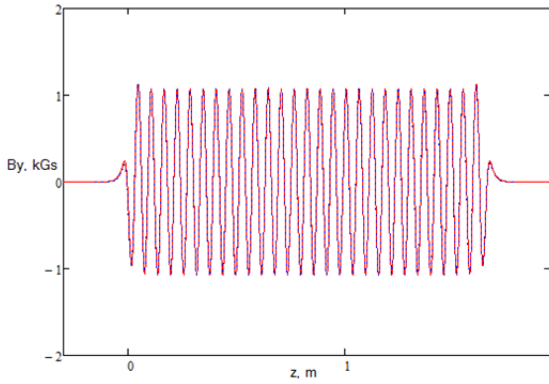


Figure 3: Measured undulator magnetic field.

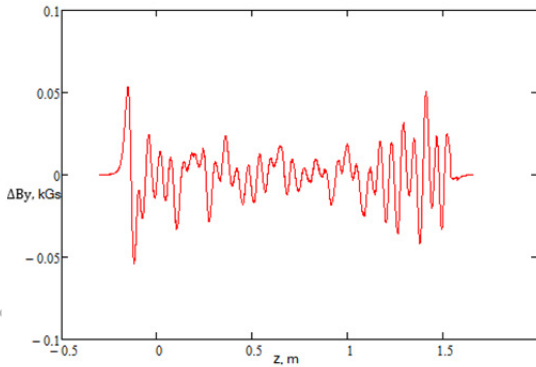


Figure 4: Difference in the fitted ideal and measured magnetic fields.

RADIATION HODOGRAPH METHOD

For a planar undulator the Fourier-harmonics of forward emitted radiation at frequency ω is proportional to [1]:

$$\int_{-\infty}^{\infty} e^{i\omega t(z) - i\omega z/c} \frac{dx}{dz}(z) dz, \quad (4)$$

where c is the velocity of light. Eq. 4 shows that it is sum of contributions of all segments of the particle trajectory. In a good undulator at some frequency phases of contributions of different segments are the same, and the modulus of the radiation Fourier-harmonics is maximum.

To visualize contributions of different parts of the undulator one can take the integral Eq. 4 from the undulator entrance to some current point z_1 . Calculating arrival time $t(z)$ and small deflection angle dx/dz through the measured field we define the hodograph function [2, 3] as

$$G(z_1) = \int_0^{z_1} I_{1y}(z) \exp\{-i\kappa[z + \int_0^z I_{1y}^2(z') dz']\} dz, \quad (5)$$

where the $I_{1y}(z)$ is the first integral of the magnetic field:

$$I_{1y}(z) = \frac{e}{mc^2} \int_0^z B_y(0, 0, z') dz', \quad (6)$$

and $\kappa = \omega/(2\gamma^2 c)$. We can use this expression to estimate the magnetic field error if we draw the curve consisting of points with coordinates $\operatorname{Re}G(z_1)$, $\operatorname{Im}G(z_1)$.

CALCULATION OF MEASURED FIELD RADIATION HODOGRAPH

Let apply the hodograph formula Eq. 5 to the measured field of the undulator and then compare with the case of ideal field. We can calculate the particle trajectory with a 1 mm step in the z coordinate (see Fig. 5).

Let's calculate the hodograph applying the formula to these trajectories. The results are shown in Figs. 6 and 7.

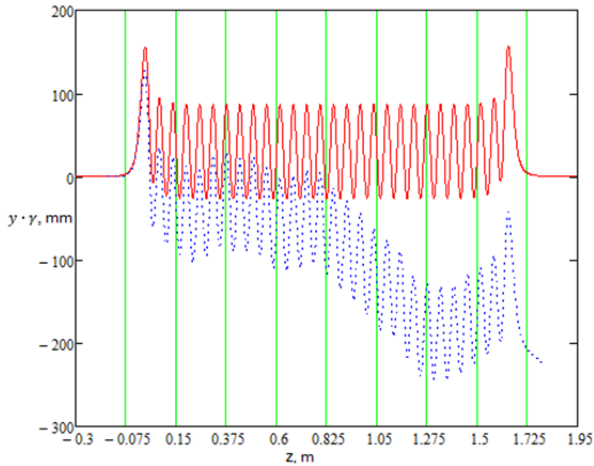


Figure 5: Particle transverse deviations multiplied by gamma. The red line represents trajectory in the ideal field; the blue line is for the measured field.

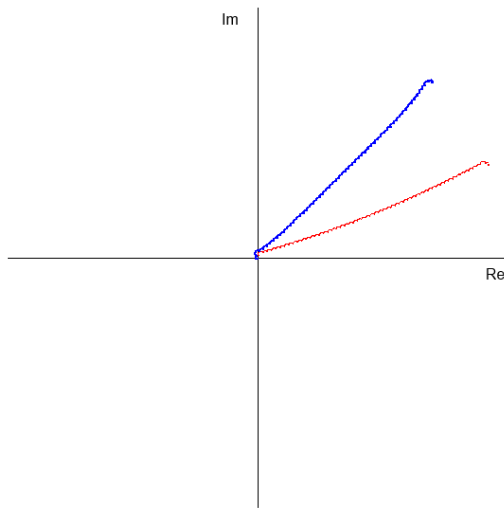


Figure 6: Measured and ideal field hodographs. Blue line: measured field, red line: ideal field.

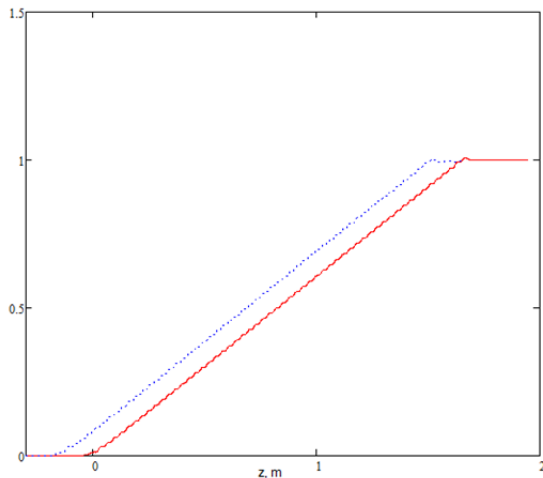


Figure 7: Hodographs' absolute value increments.

RESULTS

We can reach the emitted field amplitude maximums at $\kappa = 88.65m^{-1}$ and $88.61m^{-1}$ for ideal and measured fields accordingly. Maximum amplitude for a measured field is equal 0.995 of a maximum amplitude for an ideal field.

Building the emitted amplitude spectrum (Fig. 8), we can estimate the relative width of main peak equal 3.2%.

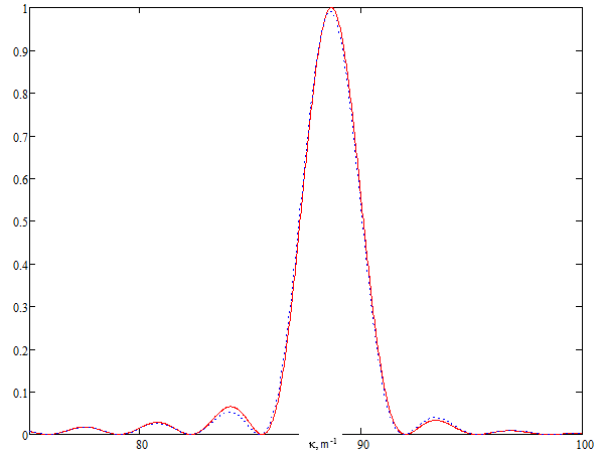


Figure 8: Radiation spectrum for measured (red) and ideal (blue) fields.

From comparing the amplitudes' maxima for the measured and ideal fields, it follows that we cannot enhance the spectral intensity in maximum more than by 1% neither by increasing the precision of magnet manufacturing, neither by increasing the precision of their spatial placement. That means that the measured field is good enough for generation of a monochromatic terahertz radiation.

ACKNOWLEDGMENT

This work is supported by Russian Science Foundation (project 14-12-00480).

REFERENCES

- [1] L.D. Landau and E.M. Lifshitz, *The Classical Theory of Fields*, Oxford, New York, Toronto, Sidney, Braunschweig: Pergamon Press, 1971, 172.
- [2] E. Gluskin et al., Nucl. Instr. And Meth. A475 (2001) 323.
- [3] E. Levichev and N. Vinokurov, Rev. Accel. Sci. Technol. **3** (2010) 203.

MODELING AND DESIGN OF THE VARIABLE PERIOD AND POLE NUMBER UNDULATOR FOR THE SECOND STAGE OF THE NOVOSIBIRSK FEL*

O.A. Shevchenko, V.G. Tcheskidov, N.A. Vinokurov, BINP, Novosibirsk, Russia
I. Davidyuk[#], Novosibirsk State University, Novosibirsk, Russia

Abstract

The concept of the permanent magnet variable period undulator (VPU) has been proposed just several years ago and there are few examples of its implementation yet. The VPUs have several advantages compared to conventional undulators. One of them is wider radiation wavelength tunability range and another one is an option to increase the number of poles for shorter periods. Both these advantages will be realized in VPU which is being developed now at Budker INP. In this paper, we present the 2-D and 3-D magnetic field simulation results and discuss the design features of this VPU.

INTRODUCTION

Tuning of the radiation wavelength is one of the basic FEL advantages which differs them from conventional lasers. Wide tunability range is desirable for many applications. Therefore its increasing is important goal of the FEL design optimization. As the wavelength in FEL depends on several parameters it can be tuned several ways. Each of them has its own advantages and disadvantages. But from the point of view of the maximum tunability range the best way of wavelength tuning is based on the varying of the undulator period.

The concept of the variable period undulator (VPU) has been proposed just recently [1] and it has very few implementations yet. There are several types of the VPU design. One of them proposed in [2] is similar to conventional hybrid undulator in which the iron poles are divided in two halves. This type of VPU is composed from separate magnet blocks which can move freely along longitudinal axis. Each block includes one permanent magnet and two iron plates. At fixed positions of the outer blocks the inner blocks distribute evenly in longitudinal direction due to the repulsive forces and the period of this distribution can be adjusted by moving of the outer blocks. This design allows to change number of blocks so, that at fixed space allocated for undulator one can have larger number of periods for shorter wavelength.

The variable period undulator for the NovoFEL is being developed now at Budker INP. It will replace electromagnetic undulator of the second stage FEL which is installed on the bypass of the second horizontal track [3]. The tunability range of the existing FEL is 35 - 80 microns. Application of VPU will allow to shift the short wavelength boundary to 15 microns (see simulation

results below). By now design of the VPU magnetic block has been already developed and small prototype which has only six blocks is being manufactured now. In this paper we discuss undulator design and its magnetic field properties.

UNDULATOR GEOMETRY AND FIELD SIMULATION RESULTS

To find the optimal undulator geometry and investigate the magnetic field properties 2-D and 3-D simulations were carried out. For 2-D simulations we used code FEMM [4] which runs quite fast therefore we could calculate magnetic field for the total number of undulator periods (about 50). The final 3-D geometry is presented in Fig. 1. It was simulated by CST Studio [5].

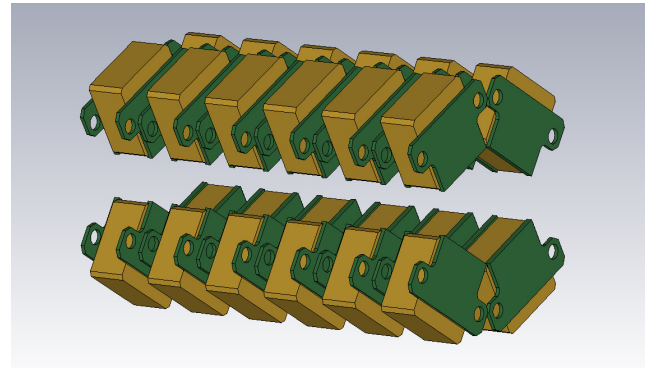


Figure 1: Undulator geometry used in 3-D simulations. Yellow blocks – permanent magnets, green plates – iron poles.

The undulator transverse aperture was chosen to be 50 mm. This value cannot be significantly reduced because of electron and optical beam losses. The minimal undulator period 48 mm is limited by the aperture. For the smaller periods the undulator deflection parameter and consequently the FEL gain become too small (see Fig. 6,8).

Each undulator block consists of one permanent magnet and two iron plates. The opposite plates of two blocks adjacent in longitudinal direction form one pole. Two blocks at the top as well as two blocks at the bottom are combined in one unit which moves as a whole. Top and bottom units are not connected. The blocks in one unit are tilted with respect to each other. This configuration provides the growth of the field amplitude with the distance from the central axis in all directions. As the

*Work supported by Russian Science Foundation (project 14-12-00480).
[#]daveduke@outlook.com

result this undulator will focus electron beam horizontally as well as vertically.

The permanent magnets are supposed to be made of NdFeB. In simulations we used permanent magnet with magnetization value 1.3T. Dimensions of the magnets and iron plates were optimized to obtain the maximal field amplitude at minimal period.

Transverse cross-sections of the iron plate and permanent magnet with final dimensions are presented in Fig. 2.

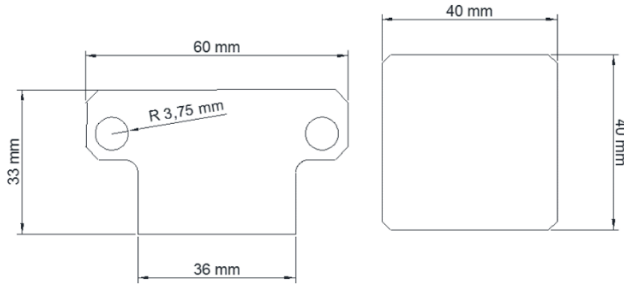


Figure 2: Transverse cross-sections of the iron plate (left) and permanent magnet (right).

Full 3-D simulations of the undulator regular part were used to obtain the dependences of the basic undulator parameters on the period. The results are presented below. Dependences of the field amplitude and K parameter on the period are shown in Fig. 3 and 4. It is seen that variation of the period in VPU does not lead to the so significant change of the field amplitude as variation of the gap does in variable gap undulators (VGU).

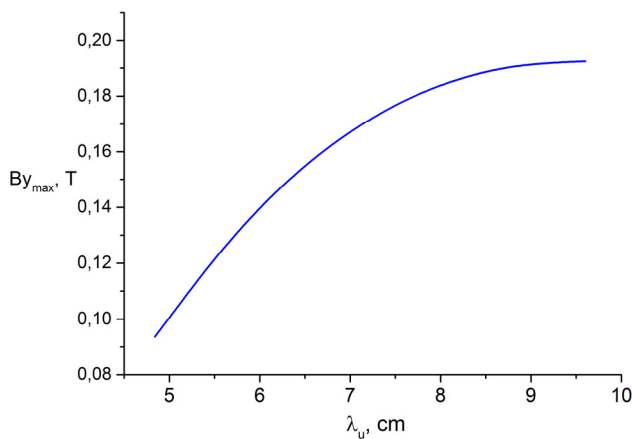


Figure 3: Dependence of the field amplitude on the undulator period.

In Fig.5 one can see the normalized amplitude of the third harmonic. In VPU it cannot be minimized for all periods but for our FEL application its value is small enough in the whole range.

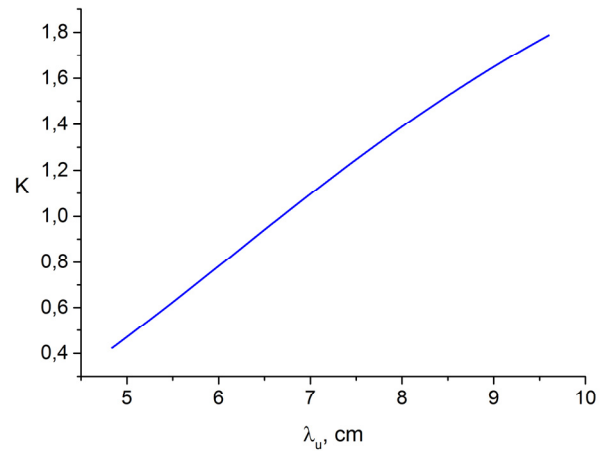


Figure 4: Undulator deflection parameter.

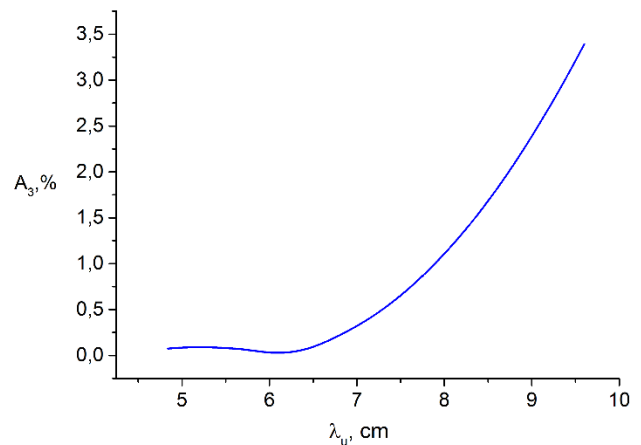


Figure 5: The third harmonic of the undulator magnetic field normalized to the first harmonic amplitude.

Tolerance Requirements

In the considered type of VPU design longitudinal positions of the magnetic blocks in the regular part of undulator are not fixed mechanically and in principal may have some essential errors. This fact is often used as an argument against feasibility of the VPU concept. Therefore this problem has to be investigated.

There are two types of position errors – random deviation from regular positions and systematic change of the distance between adjacent blocks which leads to slow linear tapering of undulator period. The last one is most dangerous. This type of errors can appear due to friction forces or due to the tilt of undulator from horizontal plane.

To find acceptable spread of longitudinal positions for our undulator we made 2-D simulations of undulator with 50 periods for both types of errors. The linear tapering for systematic error simulations was 10 μm per period. Undulator performance was characterized by spectrum of spontaneous emission at zero angle. The results are presented in Fig. 6.

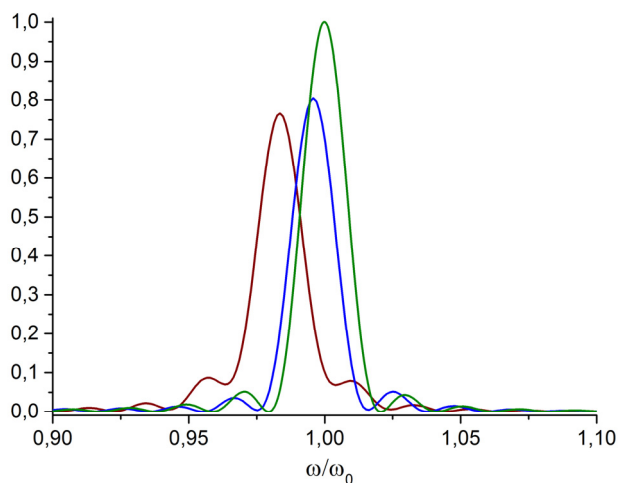


Figure 6: Spectrums of spontaneous emission. Green one – ideal undulator, blue – random block shift with amplitude 1.5 mm, red – systematic 5 μm block shift.

It seen that acceptable random spread is more than 1 mm while systematic shift should not exceed several microns which at first sight does not look very realistic. But 3-D calculations showed that restoring force acting on one unit at 5 microns shift is 0.2 N. The weight of one unit block is less than 1 kg and vertical magnetic force acting on the unit is about 40 N. Therefore to avoid the problem with systematic shift one has to provide the value of the friction coefficient less than $4 \cdot 10^{-3}$ and the value of the tilt angle less than 0.02 which looks feasible.

Terminations Field Correction

In the regular part of undulator electron beam has to move along the central axis. This condition is required to provide overlap of electron beam with the optical cavity mode as well as to avoid betatron oscillations induced by strong undulator focusing. The standard way to provide this condition consists in decreasing of the strength of two magnets at undulator entrance. By proper choice of the decreasing coefficients one can easily compensate the first and the second field integrals at given undulator period. Varying of the period in principle can lead to violation of this compensation but according to our undulator simulations for the considered range of periods (from 4.8 to 9.6 cm) this violation is not very significant.

Undulator Focusing

Electron beam in Novosibirsk FEL has low energy therefore undulator focusing plays significant role. As it was mentioned earlier the undulator geometry provides focusing in both vertical and horizontal directions. In Fig. 7 one can see the dependence of the matched horizontal and vertical β - functions on the undulator period.

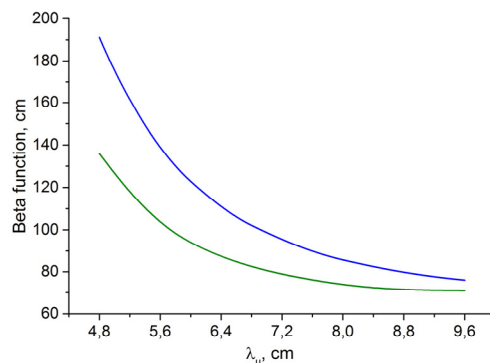


Figure 7: Dependence of the matched horizontal (blue) and vertical (green) β - functions on the undulator period.

FEL Tunability Range

According to the simulation results the developed undulator allows to increase the wavelength tunability range of the Novosibirsk FEL. As it is well known the lasing in FEL oscillator is possible when the FEL gain increases the round trip radiation losses in optical cavity. In Fig. 8 one can see the gain and losses [6] of the second stage Novosibirsk FEL for different wavelengths and for different types of undulators. The gain was calculated for the following electron beam parameters: energy – 22 MeV, energy spread – 0.5 %, peak current – 40 A. Gain calculation for the VPU case takes into account increasing of the number of periods for shorter wavelengths. Together with VPU plot one plot for the VGU with comparable tuning range and one plot for the currently installed EM undulator are presented. Advantage of the VPU becomes evident from comparison these plots.

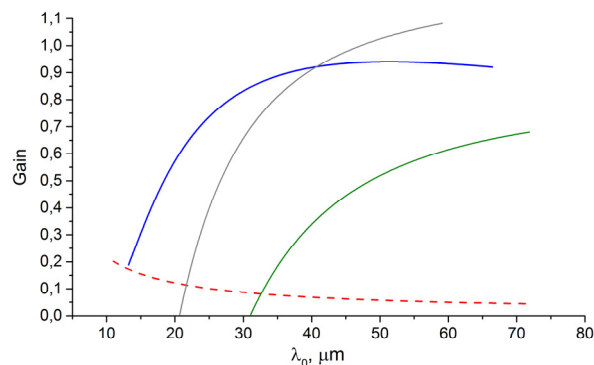


Figure 8: The FEL gain (blue – VPU, gray – VGU, green – electromagnetic undulator) and optical cavity losses (red dashed) for different radiation wavelengths.

MECHANICAL DESIGN

The undulator mechanical design is presented in Fig 9.

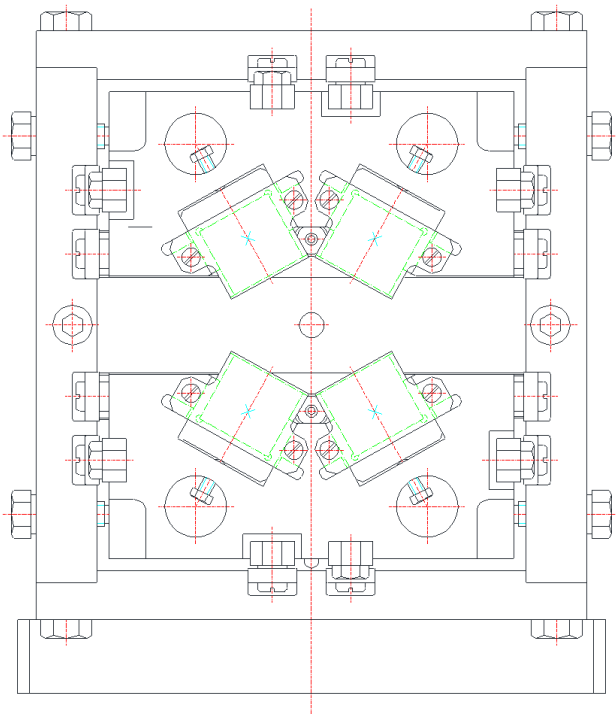


Figure 9: Undulator mechanical design.

To provide small friction coefficient the units, which contain magnet blocks are placed on the bearings. In present design the number of periods is changed manually but the period itself can be varied remotely by special mechanism.

CONCLUSION

The variable period undulator developed for the Novosibirsk FEL provides a wavelength tuning range about 13 – 76 μm while the tuning range of existing FEL based on electromagnetic undulator is only 37 – 80 μm . Thus the proposed undulator replacement will essentially reduce the short wavelength limit that will make Novosibirsk FEL more powerful research instrument.

REFERENCES

- [1] G. K. Shenoy et al., J. Synchrotron Rad. (2003). 10, p. 205-213.
- [2] N.A. Vinokurov et al., Phys. Rev. ST Accel. Beams 14, 040701 (2011).
- [3] O.A. Shevchenko et al., "The Novosibirsk terahertz FEL facility – current status and future prospects", FEL 2012, Nara, Japan (2012)
- [4] <http://www.femm.info/wiki/HomePage>.
- [5] <https://www.cst.com/Products/CSTEMS>
- [6] V.V. Kubarev, Quantum Electronics 39 (3) p. 235 - 240 (2009).

CHARACTERIZATION OF THE UNDULATOR MAGNETIC FIELD QUALITY BY THE ANGLE AVERAGED RADIATION SPECTRUM*

O. A. Shevchenko[#], Budker INP SB RAS, Novosibirsk, Russia

N. Vinokurov, Budker INP SB RAS, Novosibirsk, Russia, and KAERI, Daejeon, Rep. of Korea

Abstract

The real undulator magnetic field always contains errors which influence undulator performance. The effect of these errors is usually characterized by broadening of the spontaneous emission spectrum at zero angle and corresponding reduction of the spectral intensity. This approach works very well for the phase errors while it does not take into account transversal trajectory displacements. The integrated over the angles radiation spectrum contains more complete information about the undulator field quality but its calculation requires more effort. Therefore the spectral density of emitted radiation (the total number of emitted photons with given energy) can be considered as a figure of merit for an undulator. In this paper we derive analytical formula for this spectrum suitable for doing efficient numerical calculations and demonstrate its application to the case of some typical undulator field errors.

INTRODUCTION

Real undulators differ from ideal ones. The common way of the characterization of this difference is comparison of calculated spectral intensities of their radiation in forward direction and trajectories (see, e. g., [1]). For good undulator the reduction of spectral intensity is small and the trajectory deviation is less than the radius of first Fresnel zone divided by 2π , $\sqrt{\lambda L}/(4\pi)$, where L is the undulator length, and λ is the radiation wavelength. These two conditions are independent. Indeed, let us consider an undulator with parallel shift of electron trajectory in the middle (see below). The reduction of the forward-direction spectral intensity can be fully compensated by proper phase shift of radiation from the second half of the undulator (for example, by proper longitudinal shift of the second half). In this case we return constructive interference of the radiation from the undulator halves. But, in other but forward directions the path difference differs and spectral intensity will remain less than an ideal one. Therefore the total (integrated by angles) spectral power of radiation in this example is reduced. In this paper we consider the use of the spectral density of emitted radiation (the total number of emitted photons with given energy) as a figure of merit for an undulator. We derive analytical formula for this spectrum suitable for doing efficient numerical calculations and demonstrate its application for simple examples.

*Work supported by Russian Science Foundation (project 14-12-00480).
#O.A.Shevchenko@inp.nsk.su

SPECTRUM FORMULA

Let electron with charge e and coordinate \mathbf{r}_0 moves at velocity $\mathbf{v} = d\mathbf{r}_0/dt$. The Fourier harmonics of the radiation vector potential is [2]

$$\mathbf{A}_\omega(\mathbf{r}) = e \frac{e^{ikr}}{cr} \int_{-\infty}^{\infty} \mathbf{v}(t) e^{i\omega t - i\mathbf{k}\mathbf{r}_0(t)} dt, \quad (1)$$

where $k = \omega/c$, $\mathbf{r} = \mathbf{n}r$, $\mathbf{k} = \mathbf{n}k$. The spectral intensity (energy, radiated to the solid angle $d\omega$ and frequency interval $d\omega/(2\pi)$) is

$$dE_\omega = \frac{ck^2}{2\pi} |\mathbf{n} \times \mathbf{A}_\omega|^2 r^2 d\omega \frac{d\omega}{2\pi} = \frac{e^2 k^2}{2\pi c} \int_{-\infty}^{\infty} \int_{-\infty}^{\infty} [\mathbf{v}(t_1) \cdot \mathbf{v}(t_2) - \mathbf{n} \cdot \mathbf{v}(t_1) \mathbf{n} \cdot \mathbf{v}(t_2)] e^{i\omega(t_1-t_2) - i\mathbf{k}[\mathbf{r}_0(t_1) - \mathbf{r}_0(t_2)]} dt_1 dt_2 d\omega \frac{d\omega}{2\pi} \quad (2)$$

Integration over the angles gives the total energy, radiated to the frequency interval $d\omega/(2\pi)$, or the spectral power,

$$dW_\omega = \int_{4\pi} dE_\omega = 2 \frac{e^2 k^2}{c} \int_{-\infty}^{\infty} \int_{-\infty}^{\infty} e^{i\omega(t_1-t_2)} \left[\mathbf{v}(t_1) \cdot \mathbf{v}(t_2) \left\langle e^{-i\mathbf{k}\mathbf{n}[\mathbf{r}_0(t_1) - \mathbf{r}_0(t_2)]} \right\rangle - v_p(t_1) v_q(t_2) \left\langle n_p n_q e^{-i\mathbf{k}\mathbf{n}[\mathbf{r}_0(t_1) - \mathbf{r}_0(t_2)]} \right\rangle \right] dt_1 dt_2 \frac{d\omega}{2\pi} \quad (3)$$

where

$$\left\langle e^{-i\mathbf{a}\mathbf{n}} \right\rangle = \frac{1}{4\pi} \int_{4\pi} e^{-i\mathbf{a}\mathbf{n}} d\omega = \quad (4)$$

$$\frac{1}{4\pi} \int_0^\pi e^{-ia \cos \theta} 2\pi \sin \theta d\theta = \frac{\sin a}{a},$$

$$\left\langle n_p n_q e^{-i\mathbf{a}\mathbf{n}} \right\rangle = \left(\frac{\sin a}{a^3} - \frac{\cos a}{a^2} \right) \delta_{pq} + \left(\frac{\sin a}{a} - 3 \frac{\sin a}{a^3} + 3 \frac{\cos a}{a^2} \right) \frac{a_p a_q}{a^2}, \quad (5)$$

$$\text{and } \mathbf{a} = k[\mathbf{r}_0(t_1) - \mathbf{r}_0(t_2)].$$

Taking into account that

$$k^2 \mathbf{n} \cdot \mathbf{v}(t_1) \mathbf{n} \cdot \mathbf{v}(t_2) e^{-ik[\mathbf{r}_0(t_1) - \mathbf{r}_0(t_2)]} = \frac{d}{dt_1} \frac{d}{dt_2} e^{-ik[\mathbf{r}_0(t_1) - \mathbf{r}_0(t_2)]}$$

and integrating Eq. 3 by parts one can also obtain

$$dW_\omega = \frac{2e^2 k^2}{c} \int_{-\infty}^{\infty} \int_{-\infty}^{\infty} [\mathbf{v}(t_1) \cdot \mathbf{v}(t_2) - c^2] \left\langle e^{-ik[\mathbf{r}_0(t_1) - \mathbf{r}_0(t_2)]} \right\rangle e^{i\omega(t_1 - t_2)} dt_1 dt_2 \frac{d\omega}{2\pi} \quad (6)$$

Plugging Eqs. 4, 5 into Eqs. 3, 6 gives Eq. 7:

$$2\pi \frac{dW_\omega}{d\omega} = 2 \frac{e^2 k^2}{c} \int_{-\infty}^{\infty} \int_{-\infty}^{\infty} [\mathbf{v}(t_1) \cdot \mathbf{v}(t_2) - c^2] \frac{\sin a}{a} e^{i\omega(t_1 - t_2)} dt_1 dt_2 \quad (7)$$

Since $v_z dt = dz$, in paraxial $|x_1 - x_2|, |y_1 - y_2| \ll |z_1 - z_2|$ and ultrarelativistic $\gamma \gg 1$ approximation

$$ct_1 - ct_2 \approx z_1 - z_2 + \frac{z_1 - z_2}{2\gamma^2} + \int_{z_2}^{z_1} \frac{x'^2 + y'^2}{2} dz, \quad (8)$$

Eq. 7 can also be written as shown in Eq. 9:

$$2\pi \frac{dW_\omega}{d\omega} = 2 \frac{e^2 k^2}{c} \int_{-\infty}^{\infty} \int_{-\infty}^{\infty} \left[1 + x'_1 x'_2 + y'_1 y'_2 - \frac{1}{\beta_{z1} \beta_{z2}} \right] \frac{\sin a}{a} \cos[\omega(t_1 - t_2)] dz_1 dz_2 \approx \frac{e^2 k}{2c} \int_{-\infty}^{\infty} \int_{-\infty}^{\infty} \frac{(x'_1 - x'_2)^2 + (y'_1 - y'_2)^2}{s} \sin \frac{k}{2\gamma^2} \left[s + \gamma^2 \int_{z-s/2}^{z+s/2} (x'^2 + y'^2) dz' - \gamma^2 \frac{(x_1 - x_2)^2 + (y_1 - y_2)^2}{s} \right] ds dz +, \quad (9)$$

$$\frac{e^2 k}{\gamma^2 c} \int_{-\infty}^{\infty} \left\{ \int_{-\infty}^{\infty} \sin \frac{k}{2\gamma^2} \left[s + \gamma^2 \int_{z-s/2}^{z+s/2} (x'^2 + y'^2) dz' - \gamma^2 \frac{(x_1 - x_2)^2 + (y_1 - y_2)^2}{s} \right] \frac{ds}{s} - \frac{\pi}{2} \right\} dz$$

where $s = z_1 - z_2$ and $z = (z_1 + z_2)/2$. This integral does not contain fast-oscillating terms and can be calculated numerically for any paraxial trajectory. Now we will demonstrate the use of Eq. 9 for the simplest case of helical undulator and for planar undulator with parallel shift of electron trajectory.

IDEAL HELICAL UNDULATOR

For an ideal helical undulator

$$x = \frac{K}{\gamma k_u} \cos k_u z, \quad y = \frac{K}{\gamma k_u} \sin k_u z \quad (10)$$

for $0 < z < L$. Then for long ($k_u L = 2\pi N \gg 1$) undulator

$$2\pi \frac{dW_\omega}{d\omega} \approx \frac{e^2 k K^2 L}{\gamma^2 c} \int_{-\infty}^{\infty} \frac{1 - \cos u}{u} \sin \left\{ \frac{k}{2\gamma^2 k_u} \left[u(1 + K^2) - 2K^2 \frac{1 - \cos u}{u} \right] \right\} du + \frac{e^2 k L}{\gamma^2 c} \left\{ \int_{-\infty}^{\infty} \sin \left\{ \frac{k}{2\gamma^2 k_u} \left[u(1 + K^2) - 2K^2 \frac{1 - \cos u}{u} \right] \right\} \frac{du}{u} - \frac{\pi}{2} \right\} \quad (11)$$

For weak ($K \ll 1$) undulator integral in (11) can be taken easily, and one obtains well-known result [3]

$$2\pi \frac{dW_\omega}{d\omega} \approx \frac{\pi e^2 k K^2 L}{\gamma^2 c} \left[1 - 2 \frac{k}{2\gamma^2 k_u} \left(1 - \frac{k}{2\gamma^2 k_u} \right) \right] \mathcal{G}(2\gamma^2 k_u - k) \quad (12)$$

where $\mathcal{G}(x)$ is Heaviside step function, $\mathcal{G}(x) = 1$ for $x \geq 0$, $\mathcal{G}(x) = 0$ for $x < 0$.

UNDULATOR WITH PARALLEL SHIFT OF TRAJECTORY

Now we will compare the undulator with parallel shift of electron trajectory (see Fig. 1) with an ideal one.

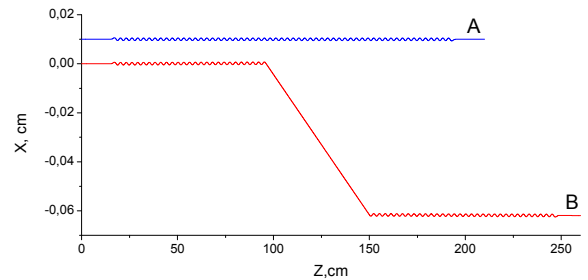


Figure 1: Calculated trajectories in ideal (A) and disturbed (B) undulators.

The calculated with Eq. 2 spectral intensities of forward-direction radiation (Fig. 2) at the frequency of interest are the same.

The corresponding total spectral powers, obtained with Eq. 9, are shown in Fig. 3.

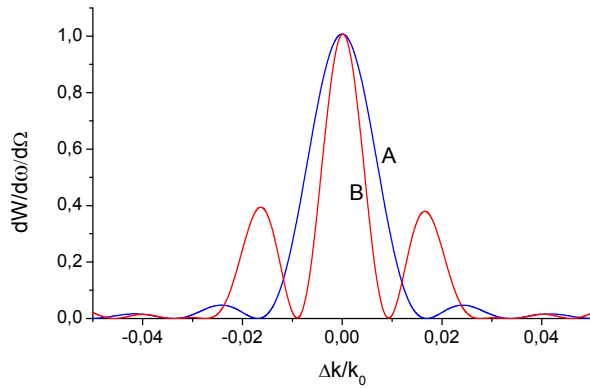


Figure 2: Spectral intensities of forward-direction radiation for ideal (A) and disturbed (B) undulators.

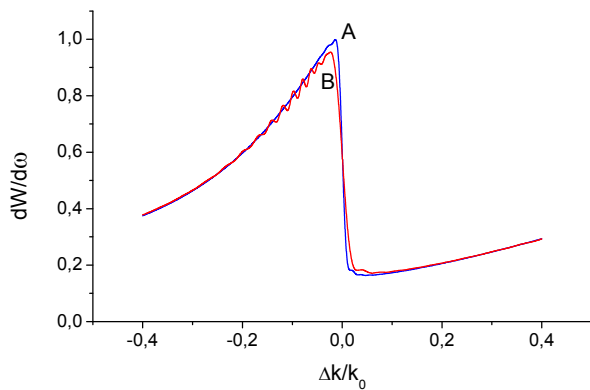


Figure 3: Total spectral powers for ideal (A) and disturbed (B) undulators.

CONCLUSION

In this paper we have shown, that the total spectral power of undulator radiation can be used to characterize the undulator quality. This quantity is less sensitive to the most of field disturbance than the forward-direction spectral intensity. On the other hand, in contrary to the forward-direction spectral intensity it is sensitive to all kinds of imperfections. Therefore instead of two figures of merit (forward-direction spectral intensity and trajectory straightness) one can optimize one only. Moreover, the corresponding variational problem for undulator field optimization can be considered.

ACKNOWLEDGMENT

This work is supported by Russian Science Foundation (project 14-12-00480).

REFERENCES

- [1] E. Levichev and N. Vinokurov, *Rev. Accel. Sci. Technol.* **3**, 203-220 (2010).
- [2] L.D. Landau and E.M. Lifshitz, *The Classical Theory of Fields*, Oxford, New York, Toronto, Sidney, Braunschweig: Pergamon Press, 1971, 172.
- [3] J.D. Jackson *Classical Electrodynamics, 3rd Edition*, John Wiley & Sons, Inc., 1999, 690.

HIGH STABILITY RESONANT KICKER DEVELOPMENT FOR THE SwissFEL SWITCH YARD

M. Paraliev[#], C. Gough, S. Dordevic, H. Braun,
Paul Scherrer Institut, Villigen PSI, Switzerland

Abstract

The SwissFEL is a linac-based X-ray free electron laser facility under construction at the Paul Scherrer Institute. The facility will provide femtosecond, high brightness X-ray pulses for fundamental and applied science research. To increase facility efficiency, a double bunch operation is planned to serve simultaneously two experimental stations at the full linac repetition rate. The main linac will accelerate two electron bunches spaced 28 ns apart and a fast and stable deflecting system will be used to separate the two bunches into two different undulator lines. The deflecting system uses a novel concept based on resonant kicker magnets. A prototype kicker magnet and its control system were designed and built. Since stability is crucial, the stability performance of the prototype was studied. The peak to peak amplitude stability of ± 11 ppm (3.5 ppm rms) was achieved, which is well within the FEL tolerance of ± 80 ppm. The layout of the deflecting system and the key design parameters are also presented.

INTRODUCTION

The Swiss X-ray Free Electron Laser (SwissFEL) [1] is a 4th generation light source under construction at Paul Scherrer Institute (Switzerland). It is based on a linear electron accelerator with maximum energy of 5.8 GeV and will be a user operated facility. It will produce short (2 to 20 fs) and high brightness (up to $6 \cdot 10^{35}$ photons \cdot mm⁻² \cdot mrad⁻² \cdot s⁻¹) X-ray pulses covering the spectral range from 1 to 70 Å [2]. In order to make the facility more efficient the main linac operates in two electron bunch mode. Each RF pulse will accelerate two electron bunches, separated in time by 28 ns. At 3.0 GeV beam energy a high stability deflector system separates

them and sends them to two additional linacs and respectively to two undulator lines. This allows simultaneous operation of two experimental stations at the full repetition rate of the machine (100 Hz). The SwissFEL layout is schematically presented in Fig. 1.

RESONANT KICKER SCHEME

A novel approach using fast high Q-factor resonant deflecting magnets is being used for high stability, reliable and fast bunch separation. The main component of the deflecting system is the composite kicker magnet. It consists of two vertical resonant kicker magnets (kickers) and three compensating vertical DC dipole magnets (dipoles). The two kickers are high Q-factor LC resonators tuned to frequency with half period equal to the bunch separation time (17.857 MHz). They are synchronously excited and after they reach their nominal current amplitude (500 A peak-to-peak) the two electron bunches arrive and are deflected up and down ($\sim \pm 1$ mrad) by the positive and negative maximum of the magnetic field created by the oscillating magnet current. This process is illustrated in Fig. 2. The three compensating dipoles steer the “down deflected” beam (straight beam) back to the machine axis. After some drift distance (with quadrupole magnets) the “up deflected” beam (deflected beam) enters a DC septum magnet 10 mm off axis [3]. The DC septum is a Lambertson type dipole magnet that bends the deflected beam 2° in the horizontal plane and creates the final angular separation between them. A system of DC dipole magnets brings the deflected beam back into the machine horizontal plane and steer it parallel to the machine axis at 3.75 m distance.

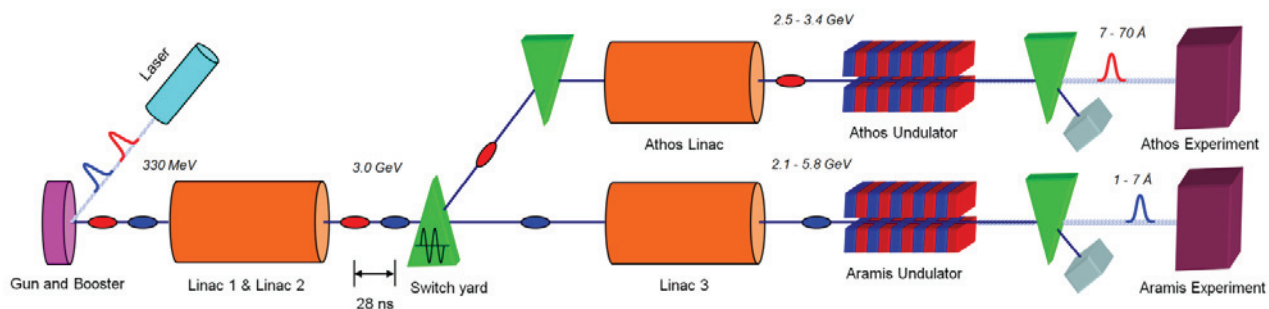


Figure 1: Schematic representation of SwissFEL double bunch operation scheme.

[#]martin.paraliev@psi.ch

In order to ensure the required beam position stability the shot-to-shot stability requirement for the entire system is set to be better than ± 5 ppm of the total 2° deflection. This sets the stability requirement for the composite kicker to be better than ± 80 ppm [3].

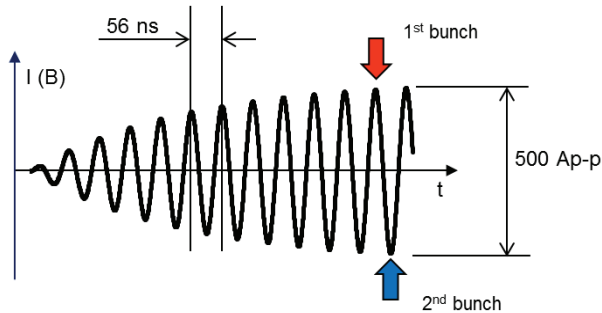


Figure 2: Deflecting current is slowly excited in the resonant deflecting magnet. The two bunches arrive at the positive and negative maximum of the resonating current.

BEAM TRAJECTORIES

Since the total angular separation provided by the composite kicker (K1 and K2) is only in the order of ± 1 mrad the two beams continue to travel very close to the machine axis down to the entrance of the septum magnet (S). They share the same machine optics components and travel in the same vacuum chamber. The three compensating dipoles (D1, D2 and D3) are set in order to steer the straight beam back to the machine axis. In this way the machine optics components do not introduce significant trajectory changes to the straight beam.

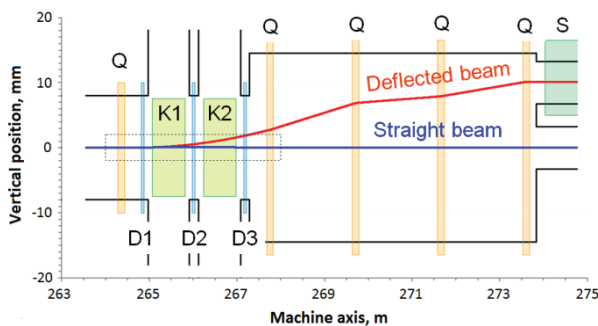


Figure 3: Beam trajectories of the straight and deflected beam. The color rectangles represent the corresponding magnet field regions.

However this is not the case for the deflected beam. It diverges slightly from the machine axis and its trajectory is altered by the quadrupole magnets (Q). The net result is that the total deflection of the beam is reduced by about 30%. Figure 3 shows the beam trajectories through the composite kicker and down to the septum. Figure 4 gives an enlarged view of the beam trajectories in the composite

kicker region (the area indicated by dotted line rectangle in Fig. 3).

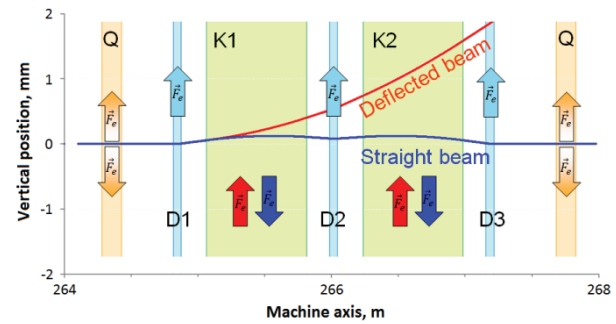


Figure 4: Enlarged view of the trajectories through K1 and K2 region. The color rectangles represent the corresponding magnets' field regions and the arrows represent the direction of the electron deflection force.

OPERATION MODES

Using different settings of the composite kicker components it could be operated in different modes. The operation modes are divided in two groups: "Operation" and "Diagnostics". In the "Operation" modes the beams are separated and delivered to the two different beam lines. In the "Diagnostics" modes the two bunches are not separated. Certain components are turned off to enable machine tests or development. The figures below give a schematic view of the beam trajectories and the spatial constraints along the composite kicker region. The horizontal and the vertical axis units are arbitrary. The numbers above each particular component gives its relative deflection strength.

Operation Modes

Figure 5 and Figure 6 illustrate the two main operation modes. In this case the beams are delivered to the corresponding beam lines. A phase inversion of the kickers allows to control which beam is deflected and which goes straight.

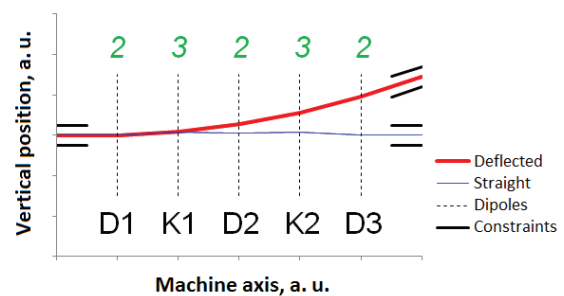


Figure 5: Main operation mode. The beams are separated and delivered to the corresponding beam lines. The numbers above each particular component gives its relative deflection strength.

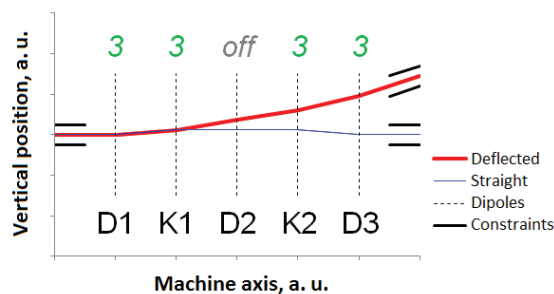


Figure 6: Alternative operation mode with the middle of the compensating dipole magnets off.

Diagnostics Modes

The set of diagnostic modes enables jitter measurements by sending both bunches to only one beam line. Since the stability of the system is crucial these modes can be used to identify instability in different parts of the composite kicker as well as to further develop and upgrade the machine.

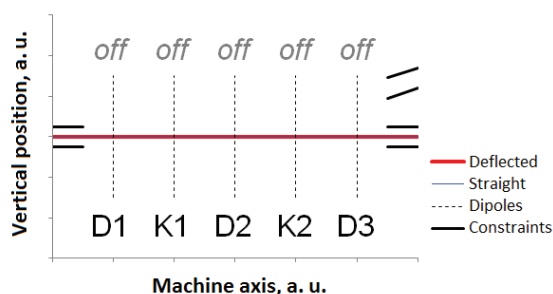


Figure 7: All magnets off. No beam deflection. Both bunches go straight.

Figure 7 shows a “trivial” state of the deflection system (all magnets off). In this mode the residual beam instability (not driven by the deflection system) can be evaluated. As well, this mode could be used for testing of the straight beam line (Aramis).

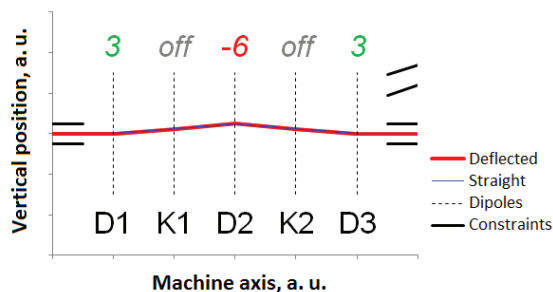


Figure 8: All kickers off. Chicane formed by the compensating dipoles. Both bunches go straight.

The mode in Fig. 8, permits a stability measurement of the compensating dipoles.

Figure 9 shows the mode that could send both bunches to the second beam line. As well, this mode could be used for testing of the second beam line (Athos).

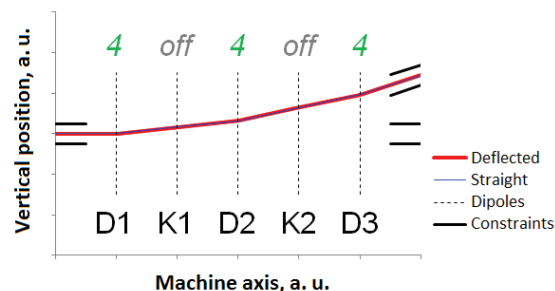


Figure 9: All kickers off. The deflection is provided by the compensating dipoles. Both bunches are deflected.

This list of modes is not exhaustive. The modes above illustrate the operation flexibility of the composite kicker.

KICKER MAGNET PROTOTYPE

A prototype kicker and its control system was built and tested.

Resonance systems can convert phase noise into amplitude noise. In order to have stable operation of the resonant kicker a low phase noise driver was designed. The driver supply voltage is controlled with 1 ppm resolution. In order to avoid radiation concerns all the active electronics will be outside of the beam tunnel.

Figure 10 shows the prototype kicker in the lab.

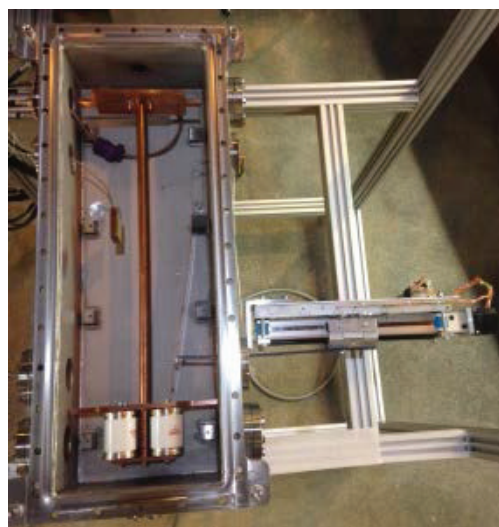


Figure 10: Prototype kicker resonator in the vacuum tank.

The prototype kicker magnet was tested for amplitude and phase stability. This system also provided a test bed for temperature, resonance tunability and mechanical vibration stability studies.

CALIBRATION AND STABILITY MEASUREMENTS

A high precision amplitude measurement system was developed in order to evaluate the stability of the kicker magnet. It is based on balanced measurement method and it is capable of measuring the amplitude stability of the kicker down to several ppm. The performance of a balanced system depends strongly on the used reference. A high stability voltage source was developed with stability of 0.35 ppm rms for more than 80 h [3]. Care was taken to ensure the proper measurement sensitivity since the incremental sensitivity could significantly differ from the full-range sensitivity. Figure 11 shows the calibration of the measurement system using 50 ppm incremental steps.

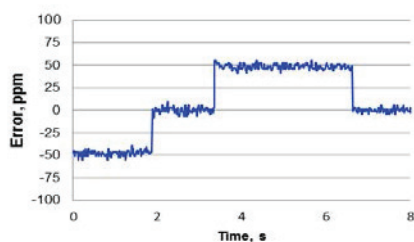


Figure 11: Calibration of the measurement system using 50 ppm incremental steps.

The shot-to-shot amplitude stability of the kicker prototype was measured to be ± 9 ppm (3.0 ppm rms) and 11 ppm (3.5 ppm rms) with the slow amplitude feedback respectively *off* and *on* [3]. The results are shown in Fig. 12 and Fig. 13.

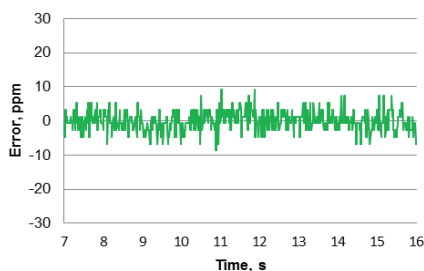


Figure 12: Kicker prototype amplitude shot-to-shot stability ± 9 ppm (3.0 ppm rms) with slow feedback *off*.

Measured time jitter of the kicker resonance waveform was ± 25 ps peak-to-peak corresponding to ± 2 ppm peak-to-peak amplitude jitter. This value is small compared to the amplitude jitter, thus the time jitter contribution could be neglected [3].

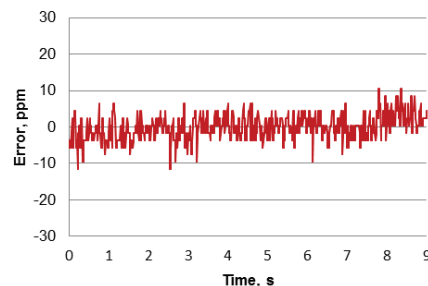


Figure 13: Kicker prototype amplitude shot-to-shot stability ± 11 ppm (3.5 ppm rms) with slow feedback *on*.

SUMMARY

In order to increase the facility efficiency the SwissFEL will operate in double bunch operation accelerating two electron bunches 28 ns apart in one RF pulse. A novel high precision beam deflecting system based on high Q-factor resonant kicker magnets separates the bunches and sends them to two independent beam lines. The shot-to-shot stability of the resonant kicker magnets is crucial. A prototype kicker magnet was built and characterized. The measured shot-to-shot stability of the prototype was ± 9 ppm and ± 11 ppm peak-to-peak with slow feedback respectively *off* and *on*. Both results are well within SwissFEL tolerances (± 80 ppm peak-to-peak). This gives confidence that this novel design approach is viable for the SwissFEL project.

REFERENCES

- [1] SwissFEL website: <http://www.psi.ch/swissfel>
- [2] "SwissFEL Conceptual Design Report", PSI Bericht Nr. 10-04, April 2012, ftp://ftp.psi.ch/psi/SwissFEL_CDR/SwissFEL_CDR_V20_23.04.12.pdf
- [3] M. Paraliiev, C. Gough, "Stability Measurements of SwissFEL Resonant Kicker Prototype", *Proc. 2014 IEEE Int. Power Modulator and High Voltage Conf.*, Santa Fe, NM, USA, 2014

GENERAL STRATEGY FOR THE COMMISSIONING OF THE ARAMIS UNDULATORS WITH A 3 GeV ELECTRON BEAM

M. Calvi, M. Aiba, M. Brügger, S. Danner, Th. Schmidt, R. Ganter, L. Patthey, Th. Schietinger, R. Ischebeck, PSI, Villigen, Switzerland

Abstract

The commissioning of the first SwissFEL undulator line (Aramis) is planned for the beginning of 2017. Each undulator is equipped with a 5-axis camshaft system to remotely adjust its position in the micrometer range and a gap drive system to set K-values between 0.1 and 1.8. In the following paper the beam-based alignment of the undulator with respect to the golden orbit, the definition of look-up tables for the local correction strategy (minimization of undulator field errors), the fine-tuning of the K-values as well as the setting of the phase shifters are addressed. When applicable both electron beam and light based methods are presented and compared.

INTRODUCTION

The large number of undulator modules required in a free electron laser (FEL) makes the commissioning of a beamline more involved than in a synchrotron where the light source consists (regularly) of a single device. Thirteen U15 modules (assuming to use also the spare unit), each 4 m long, will be operated together in the first SwissFEL hard X-ray line (called Aramis). It requires a precise control of the K-value of each unit within 100 ppm, a steering of the electron beam trajectory better than 2 μm RMS and a phase error of less than 5° RMS over a 4 m long unit.

All the SwissFEL undulators will be tested and optimized in the PSI magnetic measurement laboratory before the installation in the accelerator tunnel, see [1]. Nevertheless residual field errors together with the tight tolerances indicate the need of commissioning individual undulator modules directly with the beam as already experienced in comparable facilities [2]. Additional correction magnets are installed between undulator units and procedures are defined to improve the performance of the FEL during the commissioning and operation time.

In the following the different measurements together with the correction strategy are presented in the preliminary sequence planned for the commissioning of the beamline at the starting electron energy of 3.0 GeV.

UNDULATOR E-BEAM BASED ALIGNMENT

When the electron beam energy of at least 3 GeV (5.8 GeV is the nominal energy) is attained in the linac and transported to the undulators, the commissioning of the line can technically start. During the beam-based alignment (BBA) the undulators are set at open gap where the low magnetic field should minimize the orbit errors.

An alternative candidate for the BBA is the nominal gap where the undulator is magnetically optimized.

Definition of the Reference Orbit

The first step is the definition of a reference orbit using BBA technique. For the SwissFEL a novel approach has been developed, as described in details in [3]. The proposed algorithm is based on the minimization of the deviation of the correction required to steer the beam to BPMs (beam position monitors) centers.

The BBA method in operation at the LCLS [4] is considered a valuable back up in case the baseline solution will not give satisfactory results. It is established on the BPMs reading at different beam energies (dispersion measurements) but the algorithm is rather complex and the full procedure is time consuming [5].

Once this phase is completed the undulators have to be aligned to the reference orbit as described in the following.

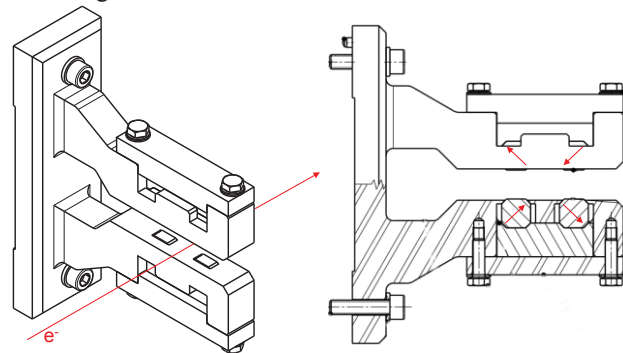


Figure 1: Alignment quadrupoles, on the left the 3D drawing with the detail of the beam axis, on the right the front view with the details of the magnets and magnetization directions.

Alignment Quadrupoles Technique

The axis of a planar undulator (light linear horizontal polarized) is the region where the vertical field (B_y) is minimum and where the longitudinal field (B_s) is zero. This definition identifies clearly the axis on the vertical plane while leaves some margin in the horizontal where a mechanical reference is used.

Taking the axis as a reference has the advantage to reduce the requirements on the alignment accuracy ($dBy/dy=0$) and to minimize the kicks due to the natural focusing on the vertical plane. Choosing a reference injection orbit with specific magnetic properties simplifies the challenging task of matching the field of different undulator modules which shall work together as a single device to make the FEL lasing.

On the Hall sensor bench in the PSI magnetic measurement laboratory [1] the undulator axis is measured and transferred to an external reference. Two small permanent quadrupole magnets (called Qal, see Fig. 1) are used for this purpose, one upstream and one downstream the undulator, to outline the undulator axis through their magnetic centers.

Once installed in the beamline, the undulators can be then beam based aligned as follow. Starting from the reference orbit with all Qal off, the upstream alignment quadrupole of a generic unit is activated and the undulator is moved both horizontally and vertically. Monitoring the downstream BPMs, the center is defined where the reference orbit reading is recovered. After removing the upstream quadrupole, the same procedure is applied to the downstream quadrupole. Once these two points of the axis are measured, it is possible to calculate the height and the horizontal position together with the correct pitch and yaw angles and to align the undulator with a 5-axis camshaft mover system.

The alignment quadrupoles are used only during the alignment phase and they are taken off during the operation of the FEL. They are made of permanent magnets and they are removed by mean of a pneumatic system remotely controlled from the control room.

IN SITU CORRECTION OF MAGNETIC FIELD ERRORS

Once the alignment is completed the residual field errors shall be measured. A set of corrector magnets with a strength up to $200 \text{ G}\cdot\text{cm}$ can be used to compensate both the first and second field integrals.

Originally this was planned only for the horizontal plane where systematic kicks are expected. A hybrid magnetic structure, made of permanent magnet and iron poles, can be optimized only for a given gap and it shows residual field errors at different apertures. Nevertheless the experience with the U15 prototype indicates that field errors of the same strength are also present in the vertical plane.

Finally, four magnets, two dipoles upstream and two downstream, have been organized for the correction of the residual field errors in both planes.

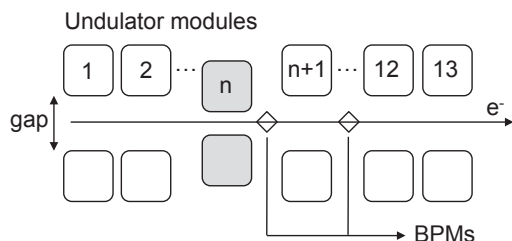


Figure 2: Measurements of the residual field errors with the help of the two downstream BPMs.

Starting with all modules opened, the BPM readings are recorded while the undulators are closed one by one, see Fig. 2. To simplify the data analysis, the quadrupole downstream the tested module shall be switched off. In

case this creates problem for the transport to the beam dump, it is enough to switch off the first quadrupole (better the first two) after the undulator. This guarantees at least two “clean” BPMs for the analysis of the field error. Once the position at the BPMs is recorded, it is fairly simple to estimate the residual field integrals as a function of the gap. With an electron beam energy of 3.0 GeV, a BPM resolution of $1.0 \mu\text{m}$ and a distance between BPMs of about 4.7 m, it is possible to estimate the first field integral with a resolution better than $5 \text{ G}\cdot\text{cm}$, enough to produce accurate look-up tables for the operation. But in case higher resolution is required, the electron energy can be further reduced.

After implementing the new look-up table, it is important to check the impact on the alignment, repeating the procedure described in the previous section before proceeding with further tests.

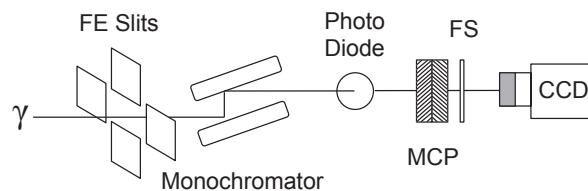


Figure 3: Schematic view of the photon diagnostic required for the commissioning of the U15 modules.

PHOTON BASED FINE-TUNING

For the commissioning of the undulator line a photon diagnostic section is required. As schematically represented in Fig. 3 the minimum requirements consist of a pair of front end slits to shape the beam, a double crystal monochromator with a selectivity better than 10^{-4} , a photodiode to measure the intensity and a MCP (micro-channel plates) followed by a fluorescent screen to image the beam profile on a CCD camera. The first measurement planned concerns the adjustment of the K-value as described in the following.

K-value in-Situ Calibration

The requirement (given by the FEL bandwidth) of a K-value uniformity among the modules of 10^{-4} is very challenging and cannot be easily achieved relying only on the magnetic measurements. The reproducibility of the Hall sensor bench is well within this range but the absolute accuracy is not better than 0.25%. In case the probe has to be changed or simply recalibrated during the test campaign, this would not guarantee enough homogeneity among the magnetic model of individual modules.

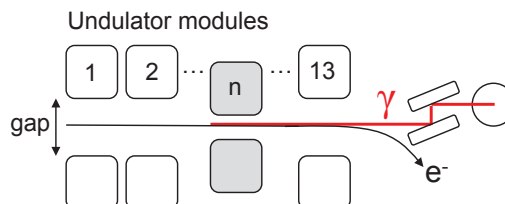


Figure 4: The calibration of the K-value is schematically represented for the n^{th} undulator module (grey).

The in-situ measurement of the K-value shall be done at the beginning around the nominal value of 1.2 for all the modules. The monochromator is set to the photon energy of 3.3 keV and the K-value is changed between 1.18 and 1.22 in steps of 10^{-4} while the intensity of the monochromatic radiation is measured on a photodiode and recorded (see Fig. 4). To accurately compare the results from different undulators, the impact of the different undulator locations (estimated in 0.1%) shall be taken into account. To overcome this difficulty it is possible to measure directly the total flux, i.e. the flux integrated over the full solid angle. It requires a sufficiently large aperture before the monochromator, in general about $3/\gamma \times L$, where L is the longest distance from the source, see Fig. 5 (calculations performed with the computer code SPECTRA [6]). A more detailed discussion about the advantages of measuring the total flux can be found in [2].

This procedure shall be repeated for the full operational range of K between 1.0 and 1.8 in steps of 0.1. With these data, look-up tables can be produced that allow a reliable operation of the undulator. Before completing this task, it is better to verify the undulator alignment (height and pitch).

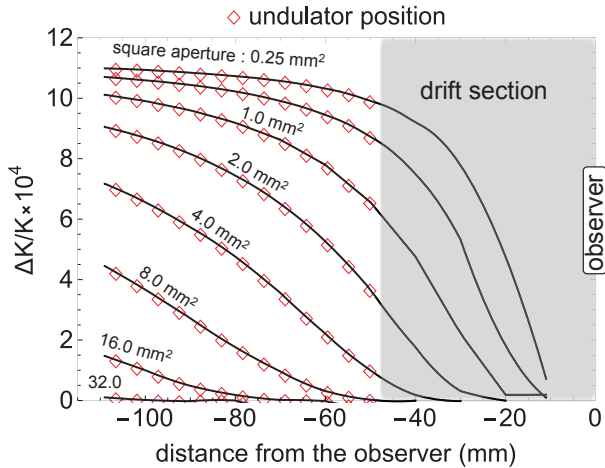


Figure 5: The position of the blue edge of the spectra in units of K-value for different square apertures.

Height and Pitch Adjustment

If an undulator module is misaligned and operated out of the axis, it is visible in the spontaneous radiation. When the electron bunch crosses the undulator parallel but above (or below) the axis, the energy of the photon is reduced. A simple way to measure the vertical offset, is to fix the monochromator energy at the nominal value and scan remotely the height. The maximum flux is at the position of the correct height.

The pitch of the undulator can also be optimized looking at the slope of the flux in the blue edge side. Electrons, which cross the undulator axis with a pitch angle, experience different K-values thus increasing the spectral width. Maximizing the slope is an effective way to get rid of the undesired pitch.

In the soft X-ray line, Athos, where Apple III undulators will be implemented [7], the same procedure can be used to align them also in the horizontal plane and in the yaw angle.

Correction of the Pointing Direction

After applying all the corrections previously described, the electron beam trajectory over the undulator line should be straight. Nevertheless it is considered safer to have the possibility to cross check it also versus the pointing direction of the spontaneous light. For this measurement all the undulator modules have to be prepared in lasing operating conditions but it is better without a lasing signal. This configuration is easily achieved: it is enough to close all modules at the same gap and leaving the phase shifter in random configuration to minimize the synchronization between modules. This last operation is not strictly required but it helps to improve the measurement quality, reducing the background.

Undulator modules

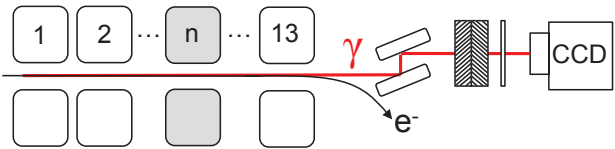


Figure 6: Schematic view of the measurement of the pointing direction of the n^{th} undulator module (grey).

Then, one by one, each undulator module has to be detuned from the others changing its K-value of few percent while locking the monochromator at this new energy, see Fig. 6. The photon beam at the exit of the monochromator carries only information about the selected module. Imaging the mono-beam with the help of a MCP and a CCD camera gives its pointing direction. Repeating this procedure for each module and using the upstream dipole corrector to change the injection angle, the different spots from the different modules can be forced to overlap and new look-up table can be produced.

Undulator modules

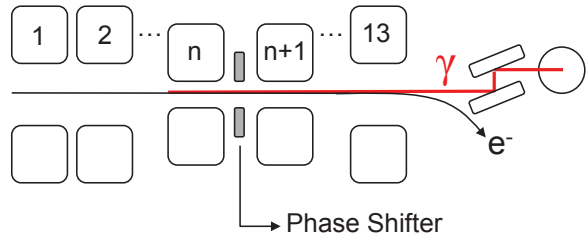


Figure 7: Schematic view of the setting-up of the n^{th} phase shifter. In the picture there is represented only the phase shifter under test.

Setting Up of the Phase Shifters

To achieve lasing the spontaneous radiation of different modules have to be in phase. Between modules a compact (few centimeter long) variable strength magnetic chicane (phase shifter) is installed to precisely delay the electron

in order to tune the phase of the radiation in the downstream module. They are designed to rotate the phase of more than 4π for any K-value. There are both available simulations and magnetic measurements to calibrate the field of the phase shifter but it requires also a precise knowledge of the longitudinal position of each modules. At nominal K-value (1.2) an error of 1 mm introduces a phase of about 14° . More precise survey measurement and alignment of the modules can simplify the setting of the phase shifter but an in-situ calibration helps to optimize the intensity in case the nominal performances are not achieved. The radiation out of two neighboring modules, previously tuned to operate at the same K-value, has to be measured while the phase (the strength of the phase shifter) is changing, see Fig. 7. The recorded intensity signal changes periodically and the phase correlating to the maximum intensity has to be retained. This procedure has to be repeated for all K-values.

Measuring the Wakefield

The electron bunch loses energy while traveling across the undulator chain. There are two main mechanisms involved; the first concerns the energy radiated by the FEL process, the second one concerns the energy radiated because of the wakes. This last effect is expected to be the largest in the SwissFEL because of the small undulator aperture, and it is difficult to quantitative estimate its impact.

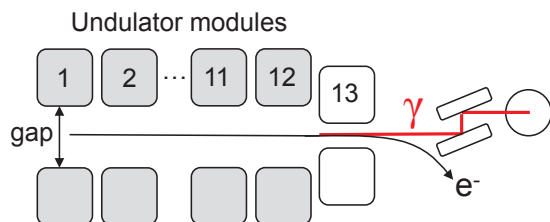


Figure 8: Measurement of the energy loss produced by the wakefield in the first 12 undulator units.

Making use of the correlation between photon energy and electron energy, it is possible to measure the losses produced by the wakefield during the machine commissioning. Starting with all undulators opened but the last one (the 13th), the intensity after the monochromator can be measured around the nominal K-value of the 13th, see Fig. 8. After defining this baseline, the gap of the first 12 undulators can be closed in steps while the intensity is recorded.

Two effects can be measured; the first is the shift of the blue edge due to energy losses and the second one a change in the blue edge slope due to the increase of the energy spread.

An estimation of the impact of the wakefield on the electron beam is very important in the commissioning phase where the lack of a lasing signal could make any

optimization very difficult. When a lasing signal is established, it can be optimized empirically changing the taper value and/or trying different tapering schema.

CONCLUSION

A consistent set of measurements has been identified for the commissioning of the undulator in the machine. Electron and photon diagnostic are both key instruments in the proposed framework. Sometimes they are used to check the quality of the magnetic measurements like the BPMs versus field errors, sometimes they are used for redundancy like in the alignment procedure where both electron and photon diagnostic are implemented. In the last example, the two approaches are only similar and they might give different results in case the straightness of the trajectory inside a module is not within the tolerances. The complexity of the machine requires a high flexibility in the diagnostic tools to speed up the commissioning and to reach the designed parameters.

ACKNOWLEDGMENT

We would like to acknowledge H. H. Braun and R. Abela for the constant support during the project and to H. Tanaka and the operation team for giving us the chance to participate in the commissioning of SACLA.

REFERENCES

- [1] M. Calvi et al., "Summary of the U15 Prototype Magnetic Performance", in These Proceedings: 36th Int. Free-Electron Laser Conf. , Basel, 2014, MOP041.
- [2] T. Tanaka et al., "In-situ Undulator Field Measurement with the SAFALI System", in Proc. 29th Int. Free-Electron Laser Conf. , Novosibirsk, 2008, pp. 467-471.
- [3] M. Aiba and M. Böge, "Beam based alignment of an X-FEL undulator section utilizing the corrector pattern", in Proc. 34th Int. Free-Electron Laser Conf. , Nara, 2012, pp. 293-296.
- [4] P. Emma, R. Carr, H.-D. Nuhn, "Beam-based alignment for the LCLS FEL undulator", Nucl. Instrum. and Methods in Physics Research A (1999), 407-413.
- [5] H. Loos, "Operational experience at the LCLS", in Proc. 33th Int. Free-Electron Laser Conf. , Shanghai, 2011, pp.166-172.
- [6] T. Tanaka and H. Kitamura, "SPECTRA: a synchrotron radiation calculation code", J. Synchrotron Radiation, Vol. 8, 2001, pp.1221-1228.
- [7] Th. Schmidt et al. "Magnetic design of an Apple III undulator for SwissFEL", in These Proceedings: 36th Int. Free-Electron Laser Conf., Basel, 2014.

SUMMARY OF THE U15 PROTOTYPE MAGNETIC PERFORMANCE

M. Calvi, M. Aiba, M. Brügger, S. Danner, R. Ganter, C. Ozkan, Th. Schmidt,
PSI, Villigen, Switzerland

Abstract

The first undulator prototype for SwissFEL (U15) was assembled and magnetically tested. The measurement instrumentations and the algorithms developed for the undulator optimization are presented and a comparison among different approaches is reviewed. The magnetic measurement results before and after the installation of the vacuum components are discussed. The summary of the undulator test with 100 MeV electron beam is presented and the impact of the radiation on the magnetics is addressed.

INTRODUCTION

The U15 design has been developed specifically for the SwissFEL project. Both the hard and the soft X-ray lines will be equipped with undulators built with the same frame and gap drive system.

To optimize the undulator stiffness and its dimensions a close frame has been implemented. This feature makes the undulator more compact but it required the development of a new magnetic measurement bench to optimize the structure.

Two new benches were developed based on SAFALI system [1]: the first is used without the vacuum chamber during the optimization phase and the second one with the vacuum chamber for phase adjustment and final checks before the installation in the tunnel.

The large number of undulator modules required per beamline (12 for Aramis I) increases substantially the effort associated with the magnetic shimming compared to a synchrotron where a beamline consists usually of a single module. To mitigate this issue and the cost associated, the support of the magnetics has been designed more flexible. It is now possible to precisely adjust the pole heights in the range of micrometers by means of a flexor driven by a wedge-screw system.

Before the series production a prototype was built to validate the new design approach. It was extensively tested and magnetically optimized before the installation into the SwissFEL Injector Test Facility of PSI. This last activity aimed to a better integration of the undulator hardware within the rest of the accelerator components as well as to test the field quality directly with the electron beam. The impact of the radiation on both the magnetics and electronics was monitored. In the following all these activities are discussed in view of the series production.

MAGNETIC MEASUREMENT INSTRUMENTATION

There are two main systems used for the magnetic measurements of the undulators, the Hall sensors and the moving wire. The first is used to estimate the field profile

and to calculate the trajectory and the phase error; the second is needed to measure the field integrals and the earth field in the laboratory (this measurement is performed before installing the undulator). The first field integral and the earth field are also used to calibrate the data measured with the Hall sensors. A zero Gauss chamber is planned for a systematic cross check during the production phase. A third system, the so-called pulsed wire, is also available but it is not planned to be used on a regular basis and it is not discussed in the following.

Hall Sensor Measurement Benches

A Hall probe is used to measure the magnetic field profile along or parallel to the undulator axis. The probe is built of three Hall sensors to measure the three components of the field. They are embedded in a ceramic support and aligned to the direction of the measurement axis and spaced of 2 mm.

To precisely follow the undulator axis the probe is guided with lasers. The two beams pass through two pinholes attached to the probe. The transmitted light carries the information about its position. This information is detected by two position sensitive diodes (PSD) and used to correct the trajectory of the probe. This logic is implemented in a feedback loop and optimized to decrease the measurement noise produced by the vibrations.

As already previously mentioned there are two different Hall sensor benches with two specific applications.

The one used for the optimization (bench A) is not constrained by the vacuum chamber and its implementation is more comfortable. A linear motor is used to displace the probe and the electronics. This last feature has the advantage to reduce the cable length and to have a fix connection between the probe and the ADC.

The measurements after the installation of the vacuum chamber (bench B) require more integration efforts. A piezoelectric-motor has been implemented in place of the linear motor because of the reduced dimensions. These actuators are usually made for travel shorter than a meter and the ceramic supports where the two piezoelectric legs actually “walk” are produced only for short length. Custom manufacture is possible but expensive and fragile. The solution implemented consists of several ceramic supports glued along the measuring bench and a piezoelectric motor with four legs to easily overcome the junction region between ceramic modules.

Moving Wire Bench

The moving wire bench has been modified and improved with respect to the system available at the SLS. A set of servomotors has been implemented in place of the steppers used previously to move the stages. This

choice allowed higher speed and smoother motion (i.e. more uniform velocity). A Keithley nano-volt meter is now used to read out the induced voltage while the wire is moving. The integral (Bdl) is then simply equal to the voltage divided by the speed in each instantaneous wire position.

OPTIMIZATION ALGORITHMS

The optimization of the magnetic structure can start when all the data available from the measurement campaign are ready and analysed. There are no direct specifications on the field profile and it is easier and more convenient to operate directly on the trajectory and phase errors. The shimming is based on the individual pole height adjustment applied by means of a robot. A second and coarser knob is the adjustment of the columns height to locally tune the field strength, i.e. the phase error.

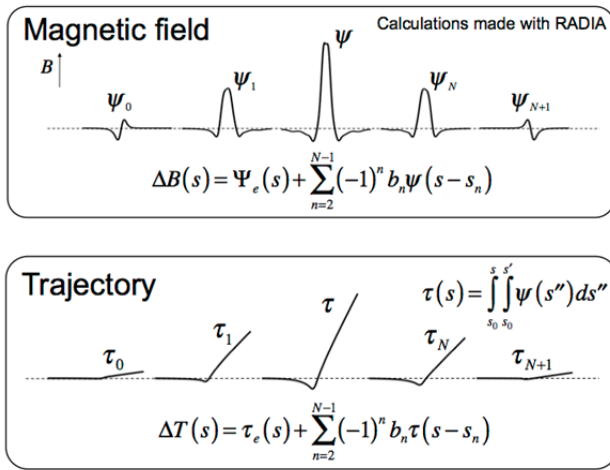


Figure 1: On the upper picture the calculated field variation (RADIA code) due to pole height variations and on the bottom the correspondent trajectory corrections. On the centre of both pictures it is represented the changes in the periodic part of the array, on the sides the impact of the poles in the extremities (the last two screws in both sides).

Trajectory Optimization

Integrating twice the magnetic field profile along the longitudinal coordinate gives, after an appropriate normalization, the trajectory. The straightness of the trajectory is one of the main requirements for a FEL to guarantee the overlap between electrons and photons. For the SwissFEL, a maximum trajectory deviation of 2 μm RMS is specified.

The straightness is an intuitive requirement and it can be also quantified. The electron wiggling around a straight line represents the ideal trajectory and any deviation is accounted as an error. One of the ways to estimate the deviation is to convolute the calculated trajectory with a window function with a width equal to the undulator period length. This approach is very effective for the majority of the trajectory but it fails in giving an accurate estimation in the end regions where

there is no periodicity. For the first and last period the optimization was done following a more pragmatic approach, calibrating this knob experimentally and finding the right correction with an iterative procedure.

An algorithm estimates the local pole height corrections. It requires first the knowledge of the field change caused by the local corrections. These are calculated with the computer code RADIA, see Fig. 1. In the limit of small corrections (field change < 1%) the hypothesis of linear superposition is accurate and it simplifies the optimization process. Knowing the trajectory deviation, it is then possible to calculate the full set of adjustments.

Phase Optimization

A perfect trajectory is not enough to fulfill the requirement of a FEL and the phase error, which measures the accuracy of the electron-photon resonance condition, should also be taken into account. The phase error calculation is quite standard and it can be found in any textbook on the subject [2]. To reduce ambiguity it is relevant to highlight that the deviation from the ideal synchronization is estimated only for the photons which correspond to the zeros of the first field integral. As discussed previously for the trajectory, it is also possible to estimate the impact of each pole height change on the phase and sum them up with some approximations. In Fig. 2 the local phase correction is calculated for a pole height change. When the local field is increased the phase undergoes a local step function plus an oscillating tail.

The height of the columns can also be changed to correct the phase error. It is a coarser correction than the pole height correction because it is localized over a region of about half a meter. The optimization algorithm previously described is also used to estimate the column adjustment, based on the ANSYS calculation of the deformation induced.

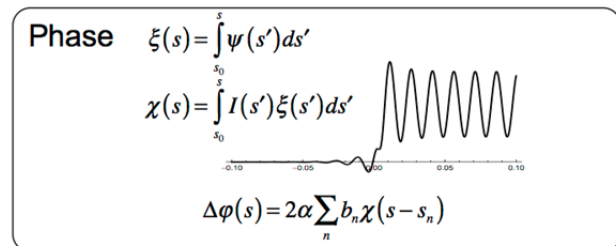


Figure 2: The phase change due to pole height variation, this calculation is relevant only for the periodic part of the undulator field.

MAGNETIC MEASUREMENT RESULTS

The U15 prototype was an important test for the new set of magnetic measurement benches and optimization procedure in view of the series production.

The assembly of the magnetic array into the frame is completed at PSI before moving the undulator to the bench A. There the undulator is aligned mechanically to the bench by mean of 5-axis movers. The height and the

pitch are further aligned based on magnetic field measurements. Then the undulator is optimized at the nominal gap ($K=1.2$) and then the magnetic field is measured for all gaps. The trajectories and the phase errors are calculated to check how they scale with gap and if further correction actions are required. Then the undulator is moved out of the bench and the magnetic array disassembled from the frame. The vacuum components are installed around the array and moved back to the frame. The completed undulator assembly is then moved to the measuring bench B for the phase error optimization and final characterization. This last action requires the same environmental conditions experienced in the tunnel to produce reliable data to be used later in the machine operation.

In the following the results of the first complete measurement campaign are reported with some additional information concerning the qualification of the measuring systems.

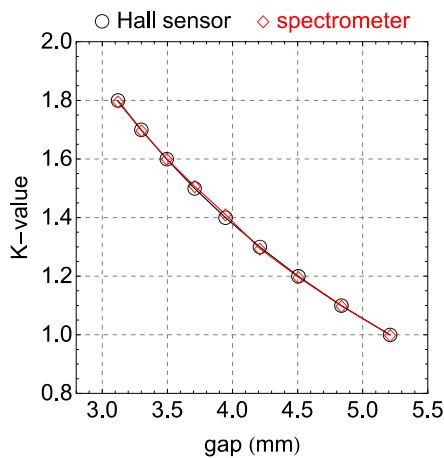


Figure 3: The K-value is measured as a function of the gap with two independent systems: in black the values estimated with the magnetic measurements (Hall sensors) and in red the value measured with the spectrometer during the test in the SwissFEL injector accelerator.

K-value versus Gap Measurements

The first parameter to be verified is the K-value; in Fig. 3 the K-value versus gap is reported. The curve is fitted with the standard function used for hybrid structure. The reproducibility of the measurement is better than 0.01% while the absolute accuracy of the probe is 0.25%.

Trajectory Measurements

In the optimization procedure selected for the prototype, the trajectory is the first parameter that shall be optimized. In Fig. 4 an example of the results obtained after a single correction is presented where no further iterations are required. This is feasible because of the accuracy of the magnetic model and the precision of the applied corrections, only conceivable with the help of an angular encoder. This successful result is valid only for the nominal gap while in Fig. 5 the trajectory for all operational relevant gaps ($K>1$) is reported. The

corrections applied do not scale ideally for all gaps but the results are well within the specifications.

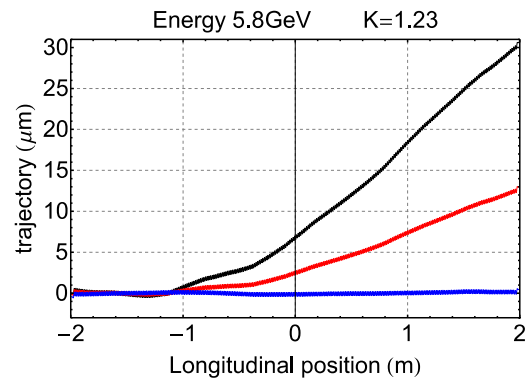


Figure 4: The trajectory measurements before (black), during (red) and after the optimization (blue) for nominal gap.

The trajectories after the assembling of the vacuum components show some changes. For instance the first field integral is 200 G×cm different and this requires further investigations. The preliminary conclusion is that the assembly work had a negligible impact and the main perturbation comes from the magnetic field produced in the magnets present in the vacuum pumps. It was demonstrated that it is possible to minimize this impact with an appropriate swapping of those magnets. This is a time consuming procedure and it should be as much as possible avoided. The layout of the vacuum chamber has been redesigned and now it allows moving the pumps further out from the beam axis if necessary.

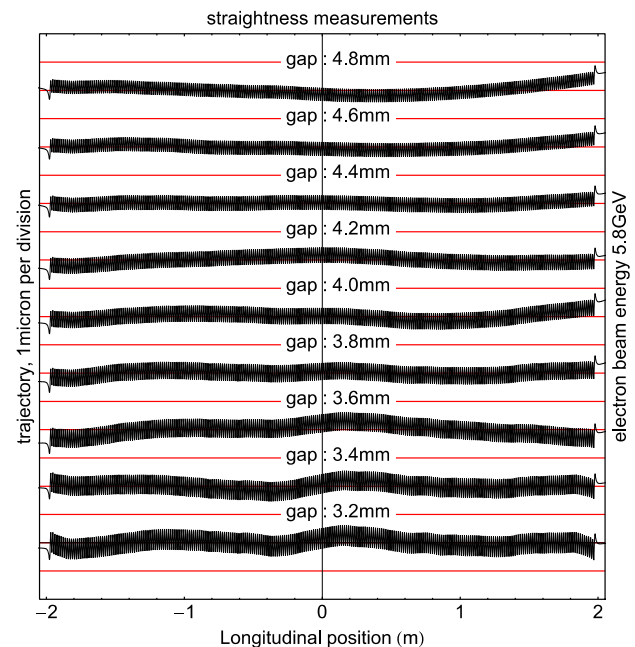


Figure 5: The trajectory straightness for different gaps. Residual entrance and exit kicks are not represented in this picture.

Phase Error Measurements

The phase was optimized after the correction of the trajectory, starting with the coarse knob represented by the column height adjustment. This was enough to minimize the RMS phase error well below the requirements. To investigate the limit of the approach the phase was further improved using pole height adjustment. At the end of this campaign the RMS phase error was about 2.3 at nominal gap. This was an excellent result and very encouraging towards the series production. Unfortunately the corrections did not last while changing the gap. After a “field cycle” (nominal gap, fully open gap, fully close gap, nominal gap) the phase was changing up to unacceptable values (measured up to 14°). This problem is now identified and well understood: it is originated in the locking mechanism. The height of the columns is adjusted by mean of a differential screw and then locked with a counter nut. In the original design only one counter nut was foreseen which is not enough to block the play in both sides of the screw. A second nut was then designed and a fully column assembly tested. The two sides of the device are now behaving as a single solid object. The final test of the undulator with the new columns is planned for the end of 2014.

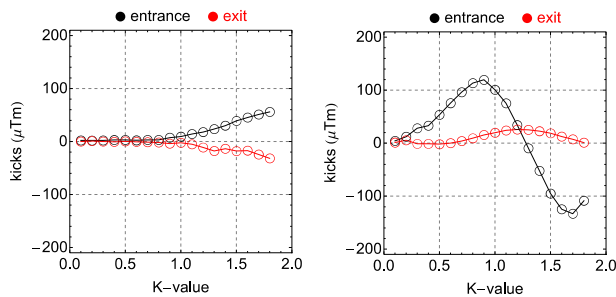


Figure 6: On the left side equivalent the entrance and exit kicks on the horizontal plane and on the right on the vertical plane.

TEST IN THE INJECTOR

The U15 prototype was tested also with a low energy electron beam (maximum 250 MeV) at the PSI injector test facility. The layout of the accelerator was adapted to this test, one 5 m long girder was removed to gain space for the undulator and the adjacent girders reshuffled to allocate the instrumentation. In the following only the tests and results relevant to evaluate the magnetic performance are presented.

Two upstream BPMs and two downstream BPMs are installed to monitor the position and angle of the beam before and after the undulator. A spectrometer for visible light is installed downstream the undulator to measure the photon energy (this test was performed at a reduced electron energy of 100 MeV).

The first action is the definition of a reference orbit, followed by the beam-based alignment of the undulator by mean of two dedicated quadrupoles. These last are pre-aligned during the magnetic measurement and keep track

of the undulator axis: one is just at the entrance of the undulator and one at the exit.

BPMs

The first and second field integrals of the undulator can be estimated from the orbit measurements. The BPMs are sorted for this convenience and to simplify the task all quadrupole in between the BPMs are switched off and only corrector up-stream the undulator are used to keep a constant injection orbit. The analysis of the data is summarized in Fig. 6, where the first and second field integrals are represented as an equivalent entrance and exit kick (assuming no kick for fully open gap).

The results for the horizontal plane show the signature of the central symmetry of the field profile, which is not shadowed by the field error. The kick magnitude is comparable to the calculated values and the results of the magnetic measurements.

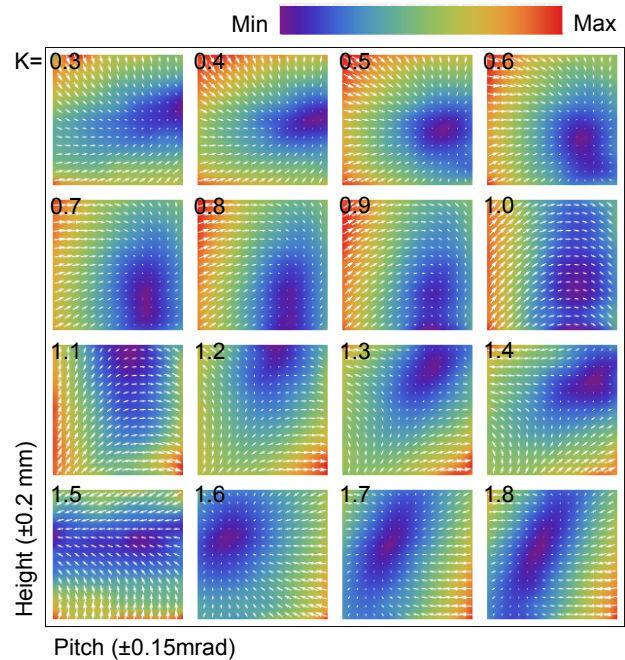


Figure 7: The center (deep purple colored) of the vertical quadrupole component for different K-values, starting from the top left with K=0.3, down to the right bottom with K=1.8. The individual plots represent the first and second field integral (the x and y components of the white arrows respectively) as a function of the undulator pitch and height.

On the vertical plane this preliminary analysis shows kicks larger than expected. The functional relation between the field errors and the K-values carries the signature of the quadrupole component. The undulator vertical focusing cannot be neglected at the operating energy of the injector and extra set of data is produced to better characterize this feature and as far as possible to disentangle the two effects. The estimation of the vertical kicks is repeated for different undulator height and pitch and several K-values, see Fig. 7. In this plane (pitch-

height) the quadrupole component displays very clearly and the phase advance changes for different K-value.

The axis of the quadrupole component moves for different K-values and this can be explained only by field errors. The dynamic described by the center indicates also that the field errors change with the gap.

Spectrometer

Operating the injector at 100 MeV produces photons in the visible and it gives the opportunity to use a simple spectrometer in air to characterize the radiation energy/wavelength. As presented in Fig. 3 this measurement provides the opportunity to cross check the estimation of K-values versus gap previously estimated with the hall sensors in the laboratory. The good agreement confirms the magnetic design and the quality of the new magnetic measurement bench.

Radiation Measurements

The radiation level was constantly monitored during the entire test. This information was available in the control

room and used to minimize the dose on the hardware. After the 3 months period the integrated dose absorbed was estimated to be about 100 Gray and there was no impact observed neither in the magnetics nor in the electronics.

CONCLUSION

The test of the U15 prototype was an important milestone for the SwissFEL project. The original design was assessed, some residual problems were discovered and working solution implemented.

REFERENCES

- [1] T. Tanaka et al., "In-situ Undulator Field Measurement with the SAFALI System", in Proc. 29th Int. Free-Electron Laser Conf. , Novosibirsk, 2008, p. 467-471.
- [2] J. A. Clarke, "The Science and Technology of Undulators and Wigglers", Oxford Science Publications, 2004.

MAGNETIC DESIGN OF AN APPLE III UNDULATOR FOR SWISSFEL

Th. Schmidt, A. Anghel, P. Böhler, M. Brügger, M. Calvi, S. Danner, P. Huber, A. Keller,
M. Locher, PSI, Villigen, Switzerland

Abstract

For the SwissFEL at PSI beside the hard x-ray beamline to start with a soft x-ray line is planned to cover the wavelength between 0.7 and 7.0nm. For full control of the polarization of the FEL light, APPLE undulators are foreseen. In this paper the design of these devices is introduced and the preliminary magnetic configuration together with the optimization strategy is presented in details.

INTRODUCTION

The SwissFEL free-electron laser currently under construction is designed with two beamlines: the hard x-ray beamline Aramis will be driven by the in-vacuum undulator U15 and will start operation with commissioning in summer 2016 being ready for user operation in 2017. The soft x-ray beamline Athos will be constructed in a second phase from 2017 to 2020. Both beamlines will have a self-seeding option [1].

While the U15 is trimmed to shortest period length, the focus on the soft x-ray undulator lies on a full polarization control by the users, that is circular, elliptical and linear polarizations to be rotatable from 0° to 180°.

The 5.8GeV SwissFEL shall accelerate two successive bunches in any of the rf – buckets coming with up to 100Hz. At an electron energy of 3 GeV the second bunch is extracted and sent into the Athos beamline where another linac can accelerate or decelerate the electrons by another 400MeV, so that the electron energy can be varied independently from the hard x-ray line within 2.6 – 3.4GeV. The wavelength range for the soft x-ray beamline shall be 0.7nm – 7nm (177eV – 1800eV). To reach with the 3.4GeV electron energy the minimum wavelength with a minimum K-value of 1 the period length is determined to 40mm. Accordingly to reach the 7nm with 2.6GeV a K-value of 4 is required.

The self-seeding chicane divides the undulator into two stages which allows to use planar devices before and for full flexibility APPLE type undulators in all modules of the second stage. The position of the self-seeding chicane has been optimized to be after 4 modules [2], which will result in 4 planar U40 and 8 APPLE type UE40 undulator modules.

The undulator design for SwissFEL is based on a modular support structure. One single frame is designed to support all kind of undulator types, planar in and out of vacuum [3] as well as APPLE undulator with their more complex forces. So for the UE40 only the shiftable magnet arrays, the magnets and their keeper have to be designed. The support structure with gap drive, the mover, the transport infrastructure and cabling etc. remains the same (see Fig. 1).

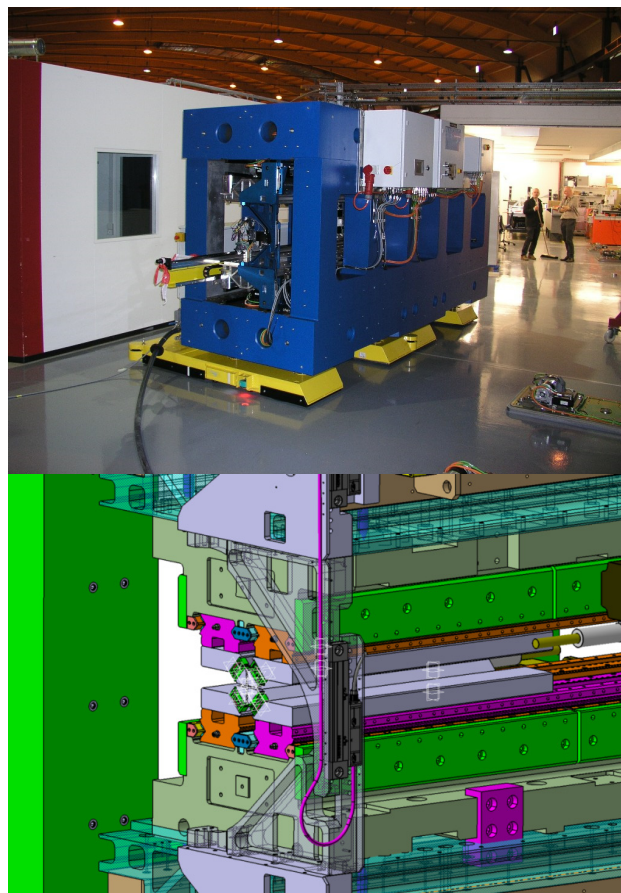


Figure 1: Modular support structure of the SwissFEL undulator series. This support structure out of cast mineral with a wedge based gap drive system can be equipped with planar in and out of vacuum magnet structures or APPLE magnet arrays.

As the APPLE undulators have to be properly aligned in vertical and horizontal direction, the mover system is a camshaft design with 5 degrees of freedom. Based on a SLAC design [4] these movers have already been used at PSI for the SLS girder and in-vacuum undulators. The movers have been reinforced and the drive system has been optimized so that they now allow the remote alignment of the undulator with μm precision. The alignment will be done by beam-based alignment with dedicated alignment quadrupoles. These are fixed quadrupoles made of permanent magnets, which are moved in and out by a simple pneumatic system. The system has been successfully tested with the prototype U15 undulator in the SwissFEL test injector [3].

Following the concept of the U15 the magnetic optimization of the UE40 shall also be based on adjustable keeper with a flexor design. Therefore the

magnet design foresees the orientation of the magnets by 45° which allows the magnetic field optimization with a 1-dim flexor. However because of the 3-dim forces carefully FEM calculation are mandatory. Essential - especially with such flexible keeper - is to minimize the forces generated by the magnet structure. It helps that the UE40 has to be designed for a single pass FEL. As for the U15 the field (-integral) quality needs to be optimized only on axis without the need to take care on the halo particles especially during injection in storage rings.

In this paper the current magnet design for the UE40 will be presented. The existing designs will be discussed as well as the different magnet material options, and the optimization strategy including the vacuum chamber design. This paper will be the basis for a proper prototype design.

MAGNET DESIGN

Discussion of APPLE Designs

The development of undulators with variable polarization has seen beside the original APPLE II design by Shigemi Saski in 1993 [5] various add-ons in functionality or specializations, especially for single pass accelerators. The APPLE II design is the working horse in storage rings because it has no limitations for the horizontal dimension of the vacuum chamber. This and also a sufficient large good field integral region is an issue, especially for top-up injection. In addition it has maximum space for magnetic measurements with Hall-probes. APPLE II designs exist with variable gap but also in fixed gap implementations at Swiss Light Source (SLS) and Pohang Light Source (PLS). Fixed gap operation is more problematic because of problems which occur from transverse field gradients along the beam axis [6]. For linac driven undulators there are more options. In the APPLE III design by Johannes Bahrtdt are the magnets magnetized under 45°. Only in the center the room for a round vacuum chamber is given, to the sides the magnets enclose the vacuum chamber giving room only for magnetic measurements [7]. This design increases the fields, which in return allows for shorter periods. A fixed gap design is the more recent DELTA design by Alexander B. Temnykh, where triangle magnets are soldered on a copper keeper allowing the most compact design [8]. Like in the classical Onuki undulator [9] the horizontal fields are generated with a horizontal magnetized magnet array pair (see Fig. 2). However for the price of limited access for magnetic optimization and the need for fixed gap operation.

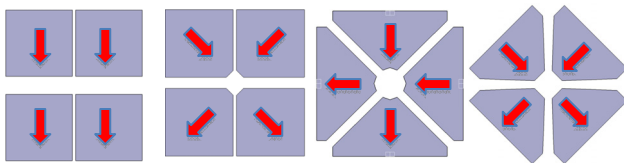


Figure 2: APPLE Designs: APPLE II, APPLE III [7], DELTA [8], proposed SwissFEL UE40.

The proposed design for the SwissFEL APPLE undulator is a APPLE III type with 45° magnetized magnets which like in the DELTA design have a triangle shape.

The triangle shape makes use of the fact that the contribution to the field from the magnet material which is cut away in anyhow negligible. Second, this shape allows an easier adaption to the keeper. New is that the shimming of the magnets is not 2-dimensional in horizontal and vertical direction but only 1-dimensional under 45° and so in parallel to the magnetization direction. This allows the adaptation of the flexor design used already in the U15, with some modifications, of course.

Gap Requirements

The minimum allowed gap is strongly related to the vacuum chamber design. Vacuum requirements as well as beam dynamic considerations in terms of wake-fields due to the geometry and surface roughness of the vacuum chamber. The design presented here assumes that a round vacuum pipe made of copper with an outer diameter of 6mm and inner diameter larger than 5.5mm could be sufficient. Assuming the APPLE III approach the minimum gap is beside the space for the vacuum pipe in the center only limited by the space requirements for the Hall-probe measurement system, which is currently in minimum 2.5mm.

Magnetic Materials

The standard permanent magnet materials used for undulators are various grades of NdFeB. With various stabilization techniques they can be used up to a remanence of $B_r=1.25T$, used i.e. in the SwissFEL U15. However, beside NdFeB there is also the older SmCo option. SmCo exists in two stoichiometries, $SmCo_5$ and Sm_2Co_{17} . The remanence of the SmCo magnets is weaker so that for the same field larger magnets or smaller gap is needed. But their temperature dependency is by a factor of 2 to 3 better, which is useful as the Athos undulators are positioned just beside linac 3 for the hard x-ray beamline in the same tunnel. In addition for $SmCo_5$ the susceptibilities are smaller, which results in smaller shift dependent kicks on the electron trajectory. The coercivity determines the radiation stability, which is reasonable for all these materials.

Table 1: Remanence, coercivity, temperature dependency and susceptibility parallel and transverse to the magnetization direction for Samarium Cobalt and Neodymium Iron Boron magnets. SmCo magnets are weaker but have lower temperature dependency and in case of $SmCo_5$ lower nonlinearities

	B_r [T]	H_{cj} [kA/m]	dB/dT [%]	$X_{ /\perp}$
$SmCo_5$	1.0	2400	0.05	0.01 / 0.04
Sm_2Co_{17}	1.1	2000	0.035	0.06 / 0.15
NdFeB	1.25	2300	0.1	0.06 / 0.15

Energy Range for Various Polarizations

The energy range for APPLE undulator beamlines needs some special care. Often the maximum photon energy range specified can only be reached in linear horizontal mode. This is because in standard APPLE geometry the vertical field is stronger than the horizontal one by up to 30%. User might be interested to measure over the full range with horizontal and vertical polarization which means $K_z = K_x$. Circular light is required only for the K- α edges of the transition metals at around 700eV which is not critical. Only in inclined modes the field is weaker, because some flux is directed in the longitudinal field components. The design for the UE40 foresees to reach the K of 4 not only for the horizontal polarization but also for the vertical polarization. The stronger vertical field would then only increase the forces without benefit for user operation. Hence the design foresees a symmetric magnetic design with the minimum gap being equal to the fixed slit between the magnet rows on the left and the right side.

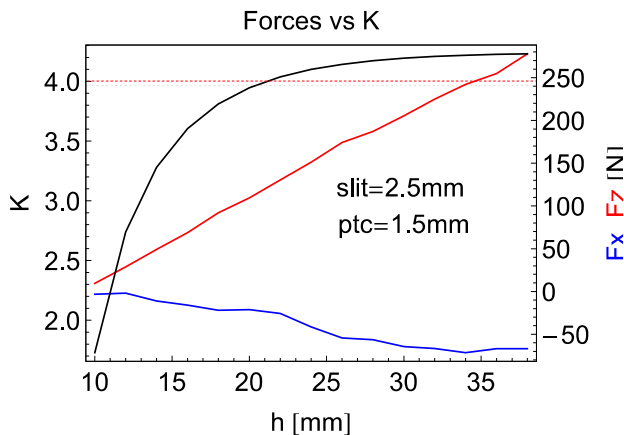


Figure 3: K-value and forces as function of magnet dimension. A diagonal h of 20mm allows already $K = 4$.

UE40 Design

Taking into account all the above remarks the following design for the UE40 is proposed: The magnets are fully symmetric at the minimum gap, magnetized under 45° . In addition the magnets could have a small angle of 2° , which further helps to reduce the forces and moments on the flexible keeper. The minimum photon energies are in this design equal for LH, LV and circular and reach the minimum value of 180eV. Only in inclined mode the minimum photon energies are larger, i.e. at an angle of 45° 330eV.

The forces scale linearly with the magnet dimensions while the field and hence the K-value saturates at a given magnet size. Therefore it is preferable to optimize the magnet dimensions to reach just the required K-value. To reach the required $K = 4$ at a gap and slit of 2.5mm with SmCo magnets a height of the diagonal of 20mm is sufficient which results in forces of up to 10kg on a single magnet holder. However, with the stronger magnet

materials a K value of 4.3 and 4.8 could be reached in this configuration. For the vacuum chamber a diameter of 6.5mm is available. With a gap-slit combination of 3mm and a smaller chamfer at the center of 1mm only with SmCo a height of 25mm would be required (Fig. 3) and the free space for the vacuum chamber is with only 0.3mm less practically similar. With NdFeB 4mm gap-slit and 10mm diameter for a vacuum chamber are possible. This needs to be optimized including FEM calculations of the flexor keeper system described in the following.

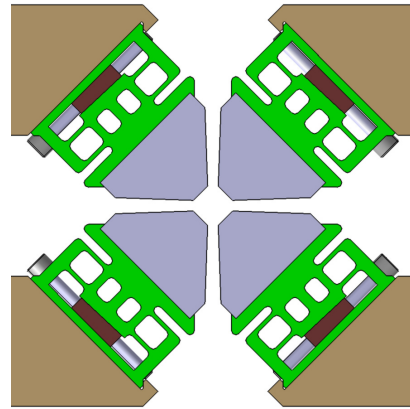


Figure 4: Radia model of UE40 magnet structure. The minimum gap is equal to slit width. Shimming like magnetization with 45° angle.

Flexor Keeper

The magnets are kept not in massive keeper but in an extruded aluminium profile which allows the shimming of the magnets parallel to the magnetization direction under 45° . The magnet position can be adjusted with μm precision by moving a 2° and hence self-locking wedge inside the keeper. A vertical kick is produced by shimming all four keepers identical with the same sign, a horizontal kick by shimming with alternating sign. Figure 4 shows a starting layout, used for FEM studies to optimize the geometries. Shimming with $30\mu\text{m}$ would result in a local field change of 0.07%, which produces a kick of 50Gcm. The maximum allowed shimming depends on the forces and the design of the keeper. In case of the U15 the preload of the keeper with the wedge is $60\mu\text{m}$ and the shim range is $\pm 30\mu\text{m}$.

For APPLE undulators beside the vertical field variation also the horizontal field variation needs to be considered. Figure 5 shows the variation in circular and inclined mode. The good field region is with $50\mu\text{m}$ and $60\mu\text{m}$ to $80\mu\text{m}$ comparable to the vertical one. As a result the alignment specifications in both vertical and horizontal are very tight but can be handled with the cam-shaft movers in a remote controlled way.

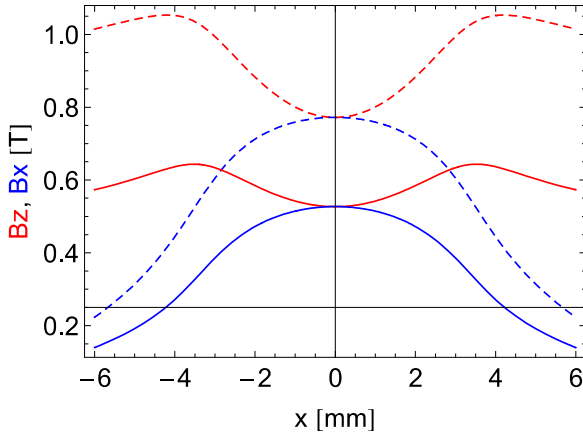


Figure 5: Transverse variation of the peak fields in inclined and circular (dashed) mode. The good field region of 10^{-4} is $50\mu\text{m}$ for the vertical field and $60\text{--}80\mu\text{m}$ for the horizontal.

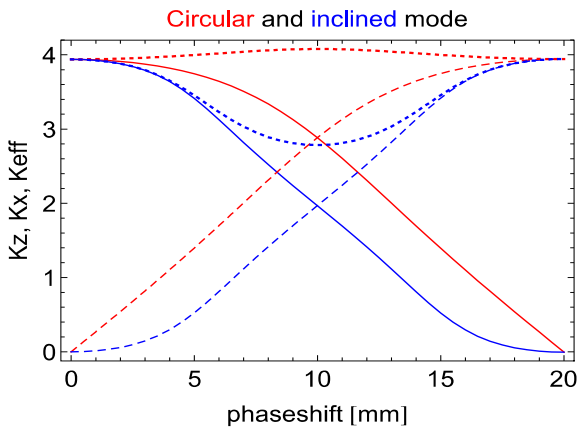


Figure 6: Shift dependent variation of K_z (solid), K_x (dashed) and K_{eff} (dotted) for circular and inclined polarization. The 45° magnetization and slit = gap_{min} result in this symmetric plot.

The symmetric changes the shift variation, because both vertical and horizontal K-values are the same. As a result, the effective K-value in circular mode is even slightly larger and only the minimum effective K-value in inclined mode is smaller with the corresponding minimum reachable photon energy of 330eV (see Fig. 6).

OPERATIONAL ASPECTS

APPLE undulators are normally operated with gap and shift variation. However it is also possible to run them in fixed gap mode like the UE40 undulator for the ADDRESS beamline at SLS. In fixed gap mode, there are field gradients at the nominal beam axis which may affect the operation. At the ADDRESS beamline, the spectra in circular mode were found to be smeared out at their blue edge. The spectra could be recovered by changing the operating conditions: Instead of changing the energy by a relative shift of top versus bottom magnet arrays, the same energy can be set with a shift left versus

right magnet arrays (Fig. 7). The reason is the relative large horizontal beam size in a storage ring while the vertical beam size is only 1% or less.

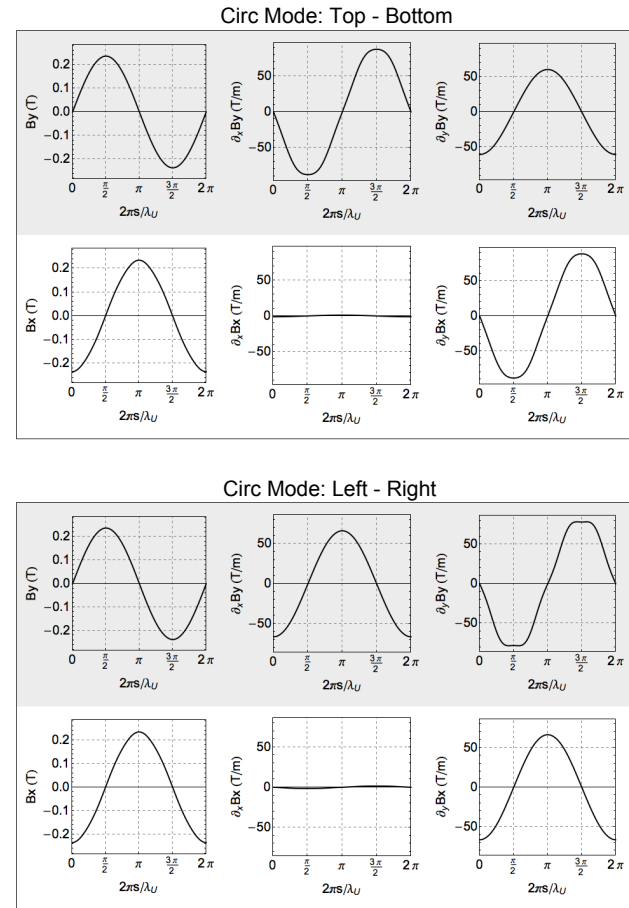


Figure 7: Field gradients in fixed gap APPLE operation with energy shift in Top - Bottom and Left - Right configuration.

For FELs with their small emittance the impact is appropriate small but should be noticed. For more flexibility and the common support structure, the APPLE undulator for SwissFEL will have shift and gap variation.

CONCLUSION

The soft x-ray line for SwissFEL shall provide full polarization control for the users. The presented UE40 design considerations propose the availability of all the major polarization states LH, LV and circular over the entire photon energy range. The design integrates the best of former designs and allows in addition the use of the flexor keeper design from the U15 undulator for an in-situ and automatized shimming under 45° . A horizontal field of 1.05T ($K=4$) for the horizontal field is pretty demanding. Small gaps are required and it is mandatory to optimize the forces wherever possible. Therefore magnet material is removed wherever possible which results in the delta shape of the magnets, the large slit width with its additional angle and the symmetric design.

REFERENCES

- [1] SwissFEL website: <http://www.psi.ch/swissfel>
- [2] E. Prat, S. Reiche, “Self Seeding design for SwissFEL”, FEL2012, Nara, August 2012, pp. 281-284.
- [3] M. Calvi et al. “Comissioning of U15”, These Proceedings: FEL2014, Basel, 2014.
- [4] A. Streun, “Algorithms for dynamic alignment of the SLS storage ring girders”, PSI, Report SLS-TME-TA-2000-0152.
- [5] S. Sasaki et al, “Design of a new type of planar undulator fo generating variable polarized radiation”, Nucl. Instr. And Meth. A 331, pp.77-82 (1994).
- [6] Th. Schmidt, M. Calvi et al, “Operation experience of the UE44 fixed gap APPLE II at PSI”, SRI2012, Lyon, 2012.
- [7] J. Bahrtdt et al., “Undulators for the BESSY Soft X-Ray-FEL”, FEL2004, Trieste, 2004 , pp.610-613.
- [8] A. Temnykh, “Delta undulator for Cornell energy recovery linac”, Physical Review Special Topics – Accelerators and Beams 11, 120702 (2008).
- [9] H. Onuki, “Progress Report on recent research with polarizing undulator”, SPIE Vol.2873 (1996).

A STRIPLINE KICKER DRIVER FOR THE NEXT GENERATION LIGHT SOURCE*

Fred Niell, Dr. Neal Butler, Dr. Marcel P.J. Gaudreau, PE, Michael Kempkes,
Diversified Technologies, Inc., Bedford, MA 01730, USA

Abstract

Diversified Technologies, Inc. (DTI) has designed, built, and demonstrated a prototype stripline kicker driver capable of less than 10 ns rise and fall time, ~40 ns pulse length, and peak power greater than 1.7 MW/pulse.

INTRODUCTION

Diversified Technologies, Inc. (DTI), under an SBIR grant from the U.S. Department of Energy, assembled a prototype pulse generator capable of meeting the original specifications for the Next Generation Light Source (NGLS) fast deflector. The ultimate NGLS kicker driver must drive a 50 Ω load (a 50 Ω terminated Transverse Electromagnetic (TEM) deflector blade) at 10 kV, with flat-topped pulses according to the NGLS pulsing protocol and a sustained repetition rate of 100 kHz. Additional requirements of the specification include a 2 ns rise time (10 to 90%), a highly repeatable flat-top with pulse width from 5 – 40 ns, and a fall time (90% to .01%) less than 1 μ s. The driver must also effectively absorb high-order mode signals emerging from the deflector itself.

STRIPLINE KICKER DRIVERS

The ultimate size, and hence cost, of any damping ring strongly depends on the speed of the kickers. It is envisioned that a scintilla of deflection will be imparted by a symmetric pair of shaped parallel deflection blades, pulsed in opposition at 10 kV. Within the guide, comprised of the two deflector blades and their environment, each TEM wave produced by the two pulse generators traverses the guide synchronously with the selected (relativistic) charge packet. Various system designs were explored for producing the desired pulse wave forms. The options included a direct series high voltage switch, solid-state Marx bank, inductive adder, or more conventional pulse transformers and transmission-line adders, several of which were considered in detail. The inductive adder was ultimately selected as the preferred development path for the remainder of the program.

The DTI team has designed and demonstrated the key elements of a solid-state kicker driver capable of meeting the NGLS requirements, with possible extension to a wide range of fast-pulse applications. The current iteration employs compensated-silicon MOSFETs with a charge-

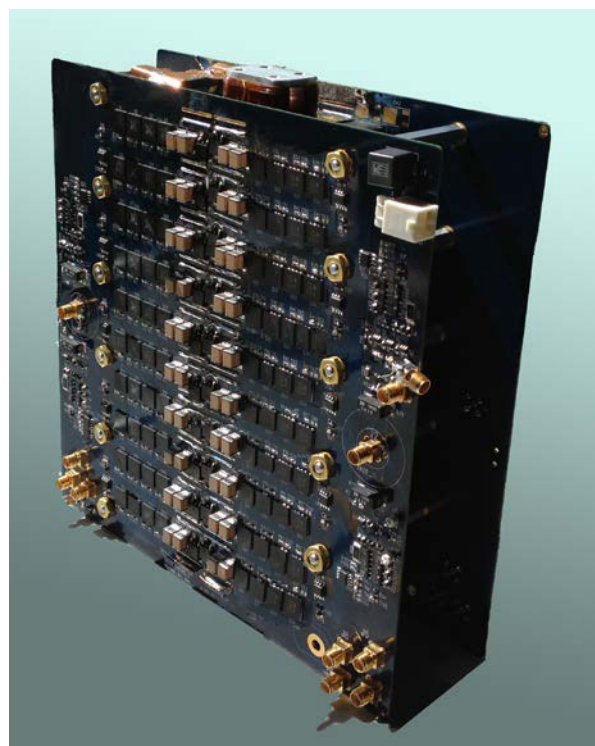


Figure 1: The dual-board pulser, displaying top and bottom boards with central output busbar.

pump gate drive arrangement (Figure 1). Two of these transistor-gate driver modules are used to drive opposite ends of the primary winding of an inductive adder transformer in a Marx-derived topology, achieving 1 kV per stage with transistors rated for 650 V. The high voltage gate-drive technique speeds up switching by quickly charging the power transistor gate capacitance in spite of significant internal gate resistance and package inductance. This can be considered a Marx generator-type circuit because two capacitors are charged from the prime power in parallel and discharged in series.

HYBRID MARX-INDUCTIVE ADDER

The inductive adder functions by applying several separately-powered primary circuits, each with its own ferrite coupling transformer core, to a single shared secondary circuit. In this manner, the voltages of all the primaries add together, creating one large output pulse. The output pulse voltage is simply the applied voltage, minus any forward drop in the switching circuitry, across the “T” model of the output transformer. The current

*Work supported by U.S. Department of Energy SBIR Award DE-SC0004255

through the magnetizing inductance is chosen to be very small compared to the main pulse current, perhaps 1/100th of the main pulse current. This way, the clamp diodes across the primaries are not dissipating too much power on each pulse. The transformer leakage inductances then primarily set the rise and fall time of the system. Currently, no efforts have been made to optimize the primary-referred secondary inductances as 7-10 nH was achieved with simple methods.

In Figure 2, the green line shows the flow of current during the “charging” phase. The capacitors $C_1 - C_n$ are charged through the resistors to the nominal 500 V bus voltage. The blue line shows the flow of current during the “on” state of the transistors. The various blocking inductances and snubber diodes are not shown in the interest of clarity.

RESULTS

The fully populated (dual-board) pulser with low inductance output structure is shown in Figure 1, while Figure 3 displays pulser performance. Note the arrangement of both sides to drive the common output busbar. The busbar was designed to fit snugly inside the core structure with enough clearance for 6 layers of 0.005” Kapton sheet as insulation. The bar was rounded on the edges to relieve electrical stress on the insulation, but the radius was simply 1/8” instead of an actual Rogowski profile. The output was terminated into 100 ohms (two Bourns 50-ohm RF terminator resistors), with two boards operating in bipolar mode (± 2.5 kV). Future designs will incorporate some impedance control on the secondary winding.

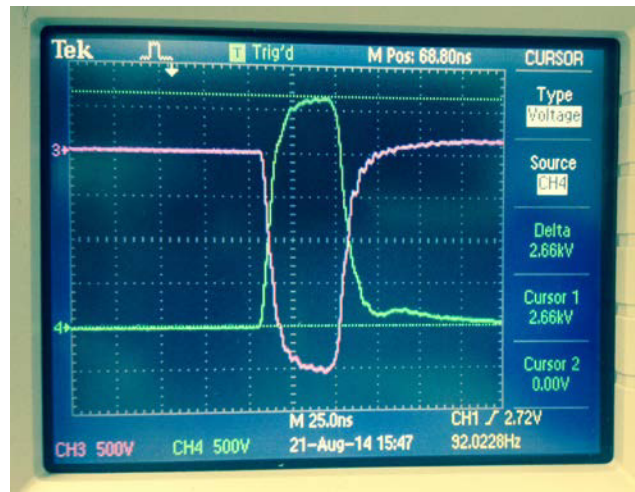


Figure 3: Output of two boards into 100 ohms operating in bipolar mode. 5 kV (± 2.5 kV), 5 ns 10 – 90% risetime, 25 ns pulsewidth.

FUTURE EFFORTS

Within the remainder of the project, effort level will remain high, as the initial challenge of circuit selection and demonstration is over. The hardware to test our theories has been built and proven to the 1 MW level. Testing of the hardware will continue, comparing the results with the initial PSPICE simulations and extending to 2 MW/pulse. Changes will be made to improve rise time and fall time by altering the physical form of the secondary windings and materials of the coupling transformers. Cooling options will be studied, and appropriate adjustments will be made to the design in order to complete a lab-bench prototype of the pulser that will support full voltage and current at the required PRF cooling.

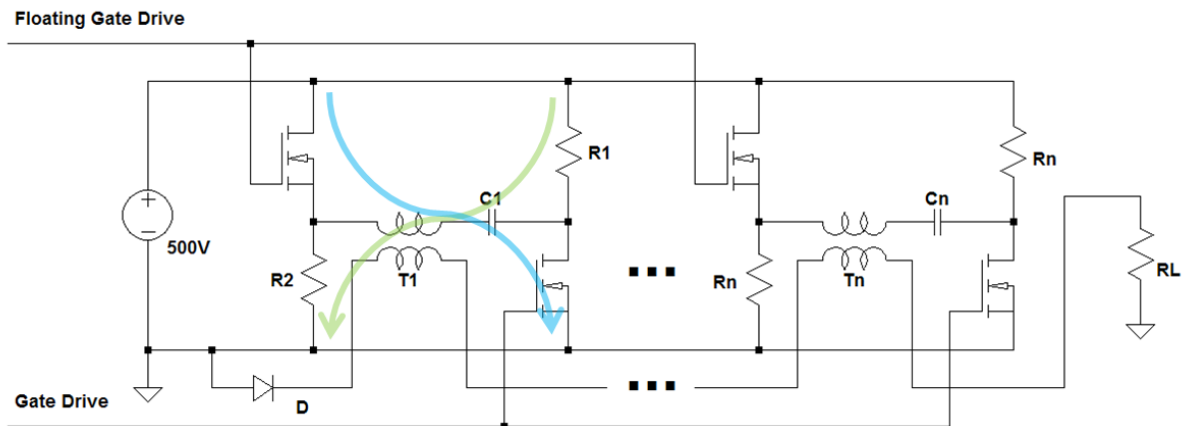


Figure 2: Electrical schematic of two stages showing main pulse current path in blue and charging current path in green. The floating gate drive is referenced to the source leads of the “flying” transistors. For clarity, snubbers and clamp diodes are not shown.

PHASE SHIFTER DESIGN FOR ISASE

S.D. Chen, K. Fang, L. Zhu, H.-D. Nuhn, C. Pellegrini, J. Wu, SLAC, CA 94025, USA

S.D. Chen, C.S. Hwang, NCTU, Hsinchu 30076, Taiwan

C.S. Hwang, NSRRC, Hsinchu 30076, Taiwan

Abstract

A phase shifter to generate an additional phase advance of the spontaneous light versus the electron beam was designed for the iSASE scheme. The iSASE mechanism is for reducing the bandwidth further from SASE FEL process. A large phase advance about $1600 \times 2\pi$ as the FEL operating at wavelength 0.8 nm was needed according to the simulation of iSASE process. Since the iSASE is thought to implement into LCLS II project, the space limitation causing by LCLS II should be considered when designing the phase shifter. An optimized three-pole electric phase shifter with 7.3 mm gap has the center field of 1.8 T. The vanadium steel was considered as pole material and the magnet physical length is 260 mm, meanwhile the water-cooling type copper coil was adopted. The temperature increment, force analysis, low field operation mode concept, and preliminary tolerance study were discussed.

INTRODUCTION

Improved SASE (iSASE) [1,2] was proposed to reduce the SASE bandwidth. In iSASE scheme, several phase shifters with large phase delay are inserted to increase the coherence length. In this scheme, the phase shifters should be placed in linear growth region, for example in our layout: five phase shifter was inserted into LCLS-II lattice, and the phase shifter for phase matching at local place [3,4] will be replaced.

In our case, five phase shifters divide the linear growth region into six sections. Looking into the details of how the mechanism works: as electron beam passing through the first section, the electric field (light field) grows up and contains the informations of structure of local electron beam; after going through the first phase shifter, the electric field got a further phase advance and located at a new position inside the electron bunch; in the second section, the electric field can stimulate the new local electrons as a seed; in the following sections, same thing happens that the electric field will be placed at a new position by large phase delay caused by phase shifter and works as a seeding stimulating local electrons at new position. The coherence length was hence increased.

The scheme was first studied by a fundamental set up of five phase shifter with 100, 200, 400, 800, $1600 \times 2\pi$ phase delay, at wavelength 0.8 nm. The largest phase shifter, $1600 \times 2\pi$, which is the hardest one to be achieved, was first designed and presented in this paper. Restricted by the space limitation from LCLS-II undulator hall, the length of phase shifter should be less than 260 mm, which forces the magnetic field high as 1.8 T to generate such a large phase delay.

A permanent magnet can not afford the requirement; an electric magnet with pole material of the vanadium steel, which has a high saturation field of 2.4 T, was chosen. Meanwhile the water-cooling type copper coil was adopted to eliminate the Joule heat from copper wire.

This paper was organized as following: the specifications of magnet were first presented, then the water cooling system and evaluation of phase delay were described; the requirement of fringe field and remanence field were also discussed; the preliminary tolerance study was mentioned; the conclusion was in the end.

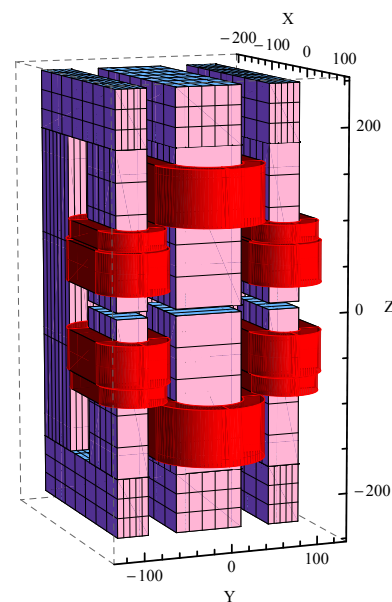


Figure 1: Magnet model plotted by Radia.

DESIGN OF THE MAGNET

The model displayed herein is a preliminary design, but can be the proof of the feasibility of producing $1600 \times 2\pi$ phase delay under space limitation, which is that physical length is less than 260 mm, gap is 7.3 mm, and physical height is less than 500 mm. To make the model practical, the details of manufacturing of the magnet and the effects on neighbor magnets as inserting into undulator hall were integrally considered. The model was designed by Radia associated with Mathematica; the diagram of model is in Figure 1 and the specifications were in Table 1. The pole will be sliced and glued to prevent strong eddy current and reduce the charging time. The minimum bending radius of copper wire is considered. The transverse good filed region is now 10 times larger than requirement, however the saturation

ISBN 978-3-95450-133-5

Table 1: Specifications

Items	Value	Unit
Physical length	258.9	mm
Physical height	487.3	mm
gap	7.3	mm
Magnetic field center/side	1.795/-1.780	T
$\Delta B/B$ along X	< 0.2% in 15 mm	-
wire type	5.6mm x 5.6mm copper, rectangular $\phi 3$ mm hollowed	-
Main current	273	A
Material of pole	vanadium steel	
temperature increase on coil	1.87 / 1.86	°C
Vertical force Center/Side	0.77 / 0.35	tons
1st Integral field	-20.0	μTm
2nd Integral field	-1.5	μTm^2

issue is the priority of optimizing the transverse width of poles. The temperature increase on the surface of magnet is required to be lower than 2°C, so the 2-in-2-out cycling water circuit is adopted to the coil of main pole (detailed in next section.) The field along the beam trajectory is in Figure 2. The saturation analysis inside the pole is plotted in Figure 3. It shows the corner of the pole material is highly saturated; More design work on the shape of pole can improve the efficiency of this magnet. The total force between upper and bottom part was analyzed and is about 1.4 tons. Considering the strong force and the assembling of magnet, the C-frame design should be replaced by H-frame.

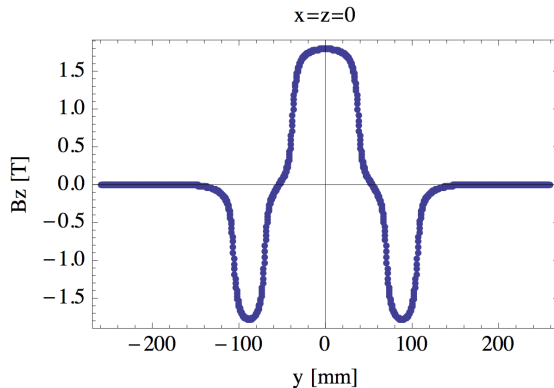


Figure 2: Field along the beam trajectory.

TRANSVERSE GOOD FIELD REGION

The required horizontal good field region is mainly determined by beam dynamic. It should be wider than wiggle amplitude as the electron beam passing through phase shifter. The maximum value of second integral of magnetic field is $4600 \mu\text{Tmm}^2$. The amplitude can be calcu-

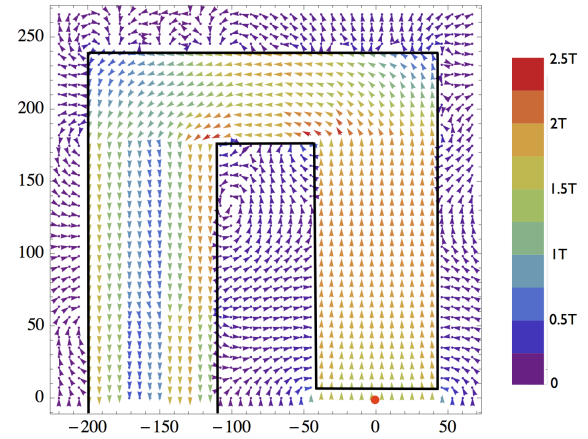


Figure 3: Field inside the pole.

lated by $\int \int B_z d^2 y / \bar{B} \rho$, where $\bar{B} \rho$ is beam rigidity. With beam energy 4 GeV, the maximum amplitude is calculated as $345.1 \mu\text{m}$. Beam size should be also considered; for β -function equal to 20 m, $\sigma_x = \sqrt{\epsilon \beta}$ is around $20 \mu\text{m}$. The jitter from shut to shut increases the required width too. It is about 10 % of beam size and is $2 \mu\text{m}$. The field error from the misalignment of phase shifter should be prevented. To be safe, the quantity of misalignment is estimated about 0.5 mm. Combining all mentioned issues, the horizontal good field region is around $\pm 1 \text{ mm}$, of which the field variation is 6.2×10^{-5} .

WATER COOLING SYSTEM

There are 4 Side-Coil and 2 Center-Coil, and it is 1-in-1-out for side coil and 2-in-2-out for center coil. Waterways of all 8 coil sections are in parallel connection. The water pressure is at 5 atm, and the required total flow rate is 27 Liter per minute. The temperature raise on magnet is under 2°C by the design in Table 2, however, the flow velocity is too high; empirically 2.5~4 m/sec is proper number to have better efficiency. More optimization work were needed for cooling system. On the other hand, the cooling water itself of cooling system in LCLS-II has a temperature vibration about 2°C. This will be considered in following work.

Table 2: Cooling Water System

Items	Value	Unit
Cooling water pressure	5	atm
sections per coil (Center/Side)	2/1	-
Flow velocity (Center/Side)	7.95/7.98	m/sec
Flow rate of each coil (Center/Side)	6.74/3.38	Liter/Min
Total flow rate	27.0	Liter/Min

PHASE DELAY

Refer to the field along the beam trajectory in Figure 2, the phase delay can be integrated by formula

$$PI = \int_{-\infty}^{\infty} \left(\left(\int_{-\infty}^z B_x(z') dz' \right)^2 + \left(\int_{-\infty}^z B_y(z') dz' \right)^2 \right) dz,$$

where B_x and B_y are the field of two transverse direction. The integrated PI along the beam trajectory is plotted in Figure 4. The number of phase delay can be calculated by

$$\Delta\varphi = \frac{\pi}{\lambda_\gamma} \frac{e^2}{\gamma^2 m_e^2 c^2} PI.$$

The total $\Delta\varphi$ is $1653 * 2\pi$, which is 3% more than expectation. The small amount excessive give more flexibility for engineering tolerance.

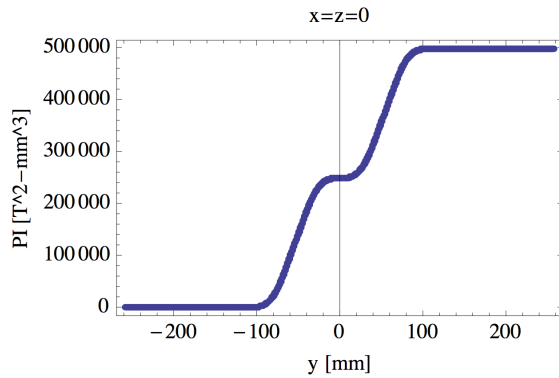


Figure 4: Phase delay.

FRINGE FIELD ANALYSIS

There are a undulator and a quadrupole at the downstream and upstream of phase shifter, respectively. The both two magnets are about 10 cm far from the side of phase shifter, so the fringe field on the transverse plane was analyzed and shown in Figure 5. The result shows that the fringe field is up to 75 Gauss, which is much higher than requirement, 0.5 Gauss. The magnetic shielding was needed to be inserted between phase shifter and neighbor magnets.

REMANENCE FIELD

In LCLS-II, iSASE scheme should be remain optional. Once the iSASE mechanism is turned off, the phase shifter should work as a normal phase shifter for phase matching between undulators. At such situation, few number of phase delay with high precision of around 3° was needed. However, it's hard for a magnet, which is optimized for such a large phase delay, to offer a small and precise magnetic field. The remanence field is the first priority problem. As long as the remanence field is low enough, there is a chance to operate this phase shifter for phase matching. Unfortunately, the actual remanence field and result of the degaussing process can only be discovered experimentally. So, it was planed

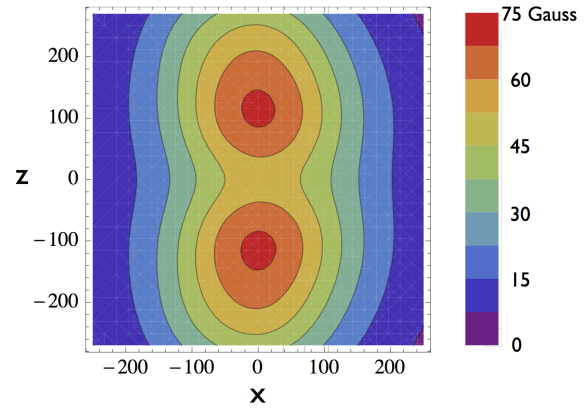


Figure 5: Fringe field at 10 cm far from phase shifter.

to do the remanence field analyzation after the prototype constructed. If there are no chance to operate the phase shifter for phase matching, a moving stage carrying two phase shifter, one is for iSASE scheme and another is for phase matching, will be adopted to solve the problem.

PRECISION OF POWER SUPPLY

The variation of power supply causes additional phase error on phase shifter. If the phase error is demanded lower than 10° , the power supply should have a precision of $3 * 10^{-5}$ for the largest phase shifter. Supposing the presented design is adopted for all 5 phase shifter, the current and the required precision of power supply were simulated and listed in Table 3; how the B-field various is plotted as a function of current in Figure 6. The designed phase shifter is optimized for the $1600 * 2\pi$, and only one power supply was needed for all three poles. If this design is going to be adopting on other smaller phase shifter, the center and side poles should be charged by two different power supplies for compensating the 1st and 2nd integral field. The high precision of power supply is achievable when using proper power supply associated with 16-bit control system; the current facility in LCLS-II can match the requirement. However, the phase error of 10° is only a naive assumption; further tolerance study is needed.

Table 3: Precision of All Phase Shifter.

$\Delta\phi$	Current(A)	$\Delta I/I$	ΔI (mA) for $\Delta\phi = 10^\circ$
1600	272.92	$3 * 10^{-5}$	8.2
800	136.46	$3 * 10^{-5}$	4.1
400	71.48	$6.2 * 10^{-5}$	4.43
200	48.74	$8 * 10^{-5}$	3.9
100	38.01	$1.5 * 10^{-4}$	5.7

PRELIMINARY TOLERANCE STUDY

The physical requirement of how precise the phase shifter for iSASE scheme is preliminary studied. An modified GENESIS code [5] was developed to simulate iSASE scheme [6],

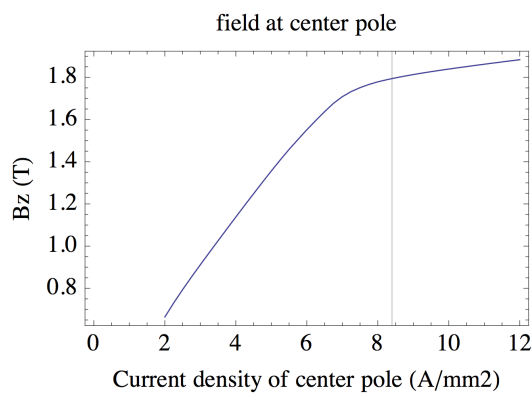


Figure 6: B-field various with exciting current.

and the phase error from phase shifter can also be simulated by the developed code. Various phase errors were adopted to the largest phase shifter, and the trend of variation of bandwidth was plotted in Figure 7. For each case of phase error, 20 cases of random seed were used for simulating the shot noise. The result shows that only in some few shots the bandwidth goes up. The trend of with different phase error tells that if the phase delay by the phase shifter is not an integer, the bandwidth does not affected. Note that this is only for the largest phase shifter with $1600 \times 2\pi$ phase delay. So the tolerance of the largest phase shifter in this configuration is quit flexible.

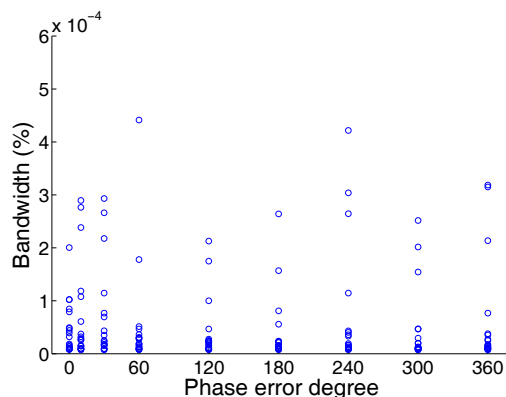


Figure 7: The phase error of 0° – 360° were adopted to the 5th phase shifter, and the bandwidths were plotted.

CONCLUSION

A phase shifter for iSASE scheme with a large enough phase delay is proved achievable within space limitation by LCLS-II. The efficiency of this magnet, which is judged by saturation field analyzation, can be improved further. The magnetic shielding is needed for minimizing the cross-talk effect. Remanence field analyzation is hard topic, but an alternative method is planed if the remanence field is too high. There is only preliminary study for the tolerance about physical requirement; in the future, the fully tolerance study of physical requirement will be focused and the result is quite important to the study of iSASE scheme.

ACKNOWLEDGMENT

The authors would like to thank Amann, John W. and Wolf, Zachary R. of SLAC for many engineering discussions. The work was supported by the US Department of Energy (DOE) under contract DE-AC02-76SF00515 and the US DOE Office of Science Early Career Research Program grant FWP-2013-SLAC-100164. The work of K.F. was also supported by the US DOE grant DE-FG02-12ER41800 and National Science Foundation grant NSFPHY-1205431.

REFERENCES

- [1] J. Wu et al., "Generation of longitudinally coherent ultra high power X-Ray FEL pulses by phase and amplitude mixing", in *Proceedings of the 32th International Free Electron Laser Conference, Nara, Japan, 2012*, JACoW, p. 237 (2012).
- [2] J. Wu et al., "X-Ray spectra and peak powr control with iSASE" in *Proceedings of the 4th International Particle Accelerator Conference, Shanghai, China, 2013* (JACoW), p. 2068 (2013).
- [3] Heinz-Dieter Nuhn et al., "LCLS-II Undulator Phase Shifter-Physics Requirement Document", SLAC Report, SLAC-I-060-103-083-00-R001 (2013).
- [4] Wolf Zackary R. et al., "LCLS-II Undulator Phase Shifter-Engineering Specifications Document", SLAC Report, SLAC-I-060-102-121-00-R000 (2013).
- [5] S. Reiche, "GENESIS 1.3: a fully 3D time-dependent FEL simulation code", *Nucl. Instrum. Methods A*, **429**, 243 (1999).
- [6] K. Fang, "iSASE study", TUPO029, Proceeding of FEL2014, Basel, Switzerland (2014).

UNDULATOR RADIATION DAMAGE EXPERIENCE AT LCLS*

H.-D. Nuhn[#], R.C. Field, S. Mao, Y. Levashov, M. Santana, J.N. Welch, Z. Wolf
SLAC National Accelerator Laboratory, Menlo Park, CA 94025, U.S.A

Abstract

The SLAC National Accelerator Laboratory has been running the Linac Coherent Light Source (LCLS), the first x-ray Free Electron Laser since 2009. Undulator magnet damage from radiation, produced by the electron beam traveling through the 133-m long straight vacuum tube, has been and is a concern. A damage measurement experiment has been performed in 2007 in order to obtain dose versus damage calibrations. Radiation reduction and detection devices have been integrated into the LCLS undulator system. The accumulated radiation dose rate was continuously monitored and recorded. In addition, undulator segments have been routinely removed from the beamline to be checked for magnetic (50 ppm, rms) and mechanic (about 0.25 μm , rms) changes. A reduction in strength of the undulator segments is being observed, at a level, which is now clearly above the noise. Recently, potential sources for the observed integrated radiation levels have been investigated. The paper discusses the results of these investigation as well as comparison between observed damage and measured dose accumulations and discusses, briefly, strategies for the new LCLS-II upgrade, which will be operating at more than 300 times larger beam rate.

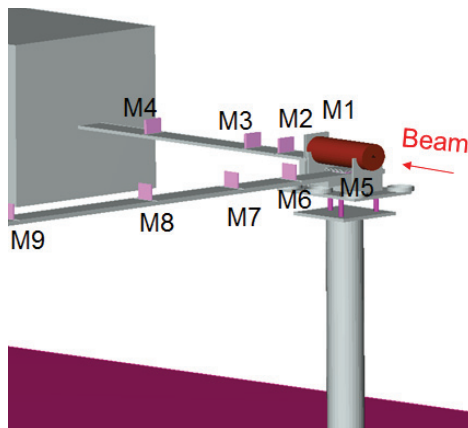


Figure 1: Layout of the SLAC End-Station A (ESA) undulator magnet block damage experiment. M1 to M9 indicate the placement of the individual magnet blocks relative to the copper cylinder. M5 is located underneath the copper cylinder.

INTRODUCTION

The Linac Coherent Light Source (LCLS) has been delivering intense ultra-short x-ray beams to international users at the SLAC National Accelerator Laboratory (SLAC) since 2009 [1]. These x-ray beams are generated

* Work was supported by U.S. Department of Energy, Office of Basic Energy Sciences, under Contract DE-AC02-76SF00515.

[#] nuhn@slac.stanford.edu

with fixed, canted gap hybrid ($\text{Nd}_2\text{Fe}_{14}\text{B}$) permanent magnet undulators [2].

MAGNET DAMAGE CALIBRATION

In July 2007, a radiation damage experiment was conducted on nine LCLS-I type ($\text{Nd}_2\text{Fe}_{14}\text{B}$) permanent magnet blocks, mounted well separated from one another, behind a solid Cu cylinder, which was bombarded with a 13.6-GeV electron beam (see Figure 1). The experiment was located inside SLAC's ESA (End-Station A) enclosure. During the 12 days of irradiation the magnet blocks stayed at a temperature of $23.8^\circ\text{C} \pm 0.8^\circ\text{C}$. The estimated accumulated maximum radiation doses in each block, based on a FLUKA [3,4] model, ranged from about 1500 kGy to less than 1 kGy and the corresponding measured reduction in total magnetic moment from about 9.6% to less than 0.1%. In fact, the two magnet blocks with the lowest amount of accumulated radiation dose showed a slight increase in total magnetic moment. Linear fitting resulted in a scaling factor of 70 kGy/%. This simple scaling seems not to describe the low-dose behaviour with sufficient detail. Other radiation damage studies and experiments have been conducted in other laboratories around the world, answering a wider range of questions with more detail [5,6,7].

LCLS UNDULATOR RADIATION DOSE MEASUREMENTS

A record of the integrated radiation dose, as actually received by the LCLS undulator magnets, has been kept over the entire operational period with the help of thermoluminescent dosimeters (TLDs). The TLDs have been shielded in small Pb-casings and were mounted in front of each undulator segment with the sensitive element about 25 mm above and horizontally centered on the beam axis. The Pb-casings were added in order to filter out the low energy and non-damaging radiation background coming from synchrotron radiation during the FEL process. Each TLD is left in place for some time (originally several weeks, now several months), before it is replaced by a fresh TLD. Some of the readings are shown in Figure 2 versus the total amount of beam energy that passed through the beam pipe during the same time period. Beam energy is the integral of the product of particle energy, number of particle per bunch and bunch repetition rate. The figure shows a fairly consistent loss rate over about a 3-year period. Three different regions along the undulator line (girder numbers) can be distinguished. The higher levels in the front end (girders 1-10) come from LTU scattering events from inserted wires, screens or the tune-up stopper (TDUND). The higher levels at the back end of the undulator line (girders 17-33) come from events within the undulator vacuum chamber, especially from a

misaligned vacuum chamber in the HXRSS chicane that was in place between January and October 2012. The low level part in the center (girders 10-16) is attributed to a general loss of halo particles.

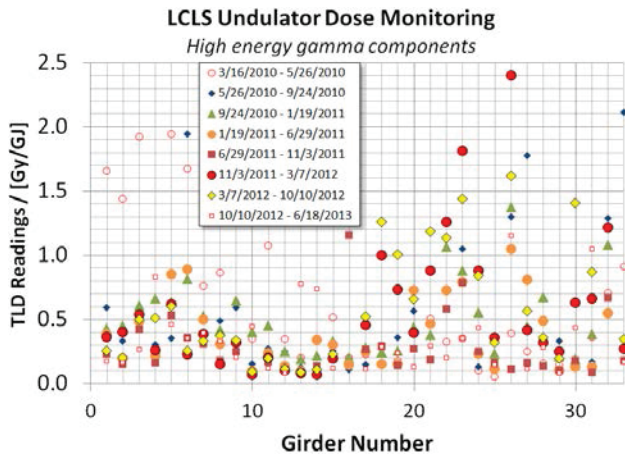


Figure 2: Radiation dose measurements by Pb-cased TLDs placed in front of each LCLS undulator segment. The readings are plotted against the beam energy passed through the undulator beam pipe during the same period. Note: 2 readings for girder 32: 4.9 Gy/GJ and 4.0 Gy/GJ for the last 2 periods, respectively, are cut off.

While TLDs are quite reliable in accumulating dose, they are not readily available for investigating the sources of radiation events. Recently, remotely readable electronic dosimeters (RADFETs) [8] have been installed together with Lucite detectors. Following a small experimental installation of RADFETs, a more extensive installation has been made in 2014, and this time the units were biased to enhance their sensitivity and further reduce their already slow rate of fade. Since readings are made every 10 minutes, it has been possible to follow the influence of beam conditions on the dose rate. Downstream of the self-seeding chicanes, it has been noticed that, when operating with higher energy electron beams (9 – 15 GeV), the dose rate is higher than typically seen with beams at 4 – 5 GeV. Upstream of the chicanes, the tendency, if anything, is reversed. The relative amplitudes of the beam losses can also be measured pulse by pulse with an array of acrylic Cherenkov counters using photomultiplier tubes, installed along the undulator. Some are distributed to intercept the off-axis radiation away from the undulator segments; others monitor the showers close to the vacuum chamber and the undulator material. A few hours of beam time have been available for an initial study of the settings of the machine's collimators with respect to their effect on these counters. Adjusting the collimators for then-current beam conditions has shown the potential for reducing the dose accumulation by factors of ~ 10 at the upstream end of the undulator, but no dose reduction was observed further downstream along the undulator. The RADFET dose rates corroborated these observations. Further work is anticipated.

LCLS UNDULATOR K MONITORING AND RECALIBRATION

The LCLS undulator segments have been designed to be easily removed and reinstalled on any of the girders without the need for special alignment. This was done by machining the individual feet blocks for each undulator such that one of the blocks' vertical surfaces and the bottom surfaces are machined to have fixed distances to the magnetic axis of the undulator segment. Segments have been removed from the tunnel and replaced with standby segments at a rate of roughly 1 segment per month since the end of commissioning.

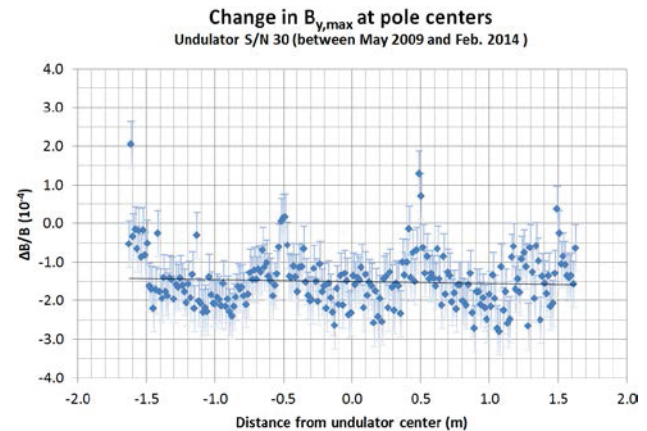


Figure 3: Differences between two Hall probe measurements (taken in 5/09 and in 2/14) of the absolute on-axis peak magnetic fields at 218 core poles (of the total 226 poles) of LCLS undulator segment SN30.

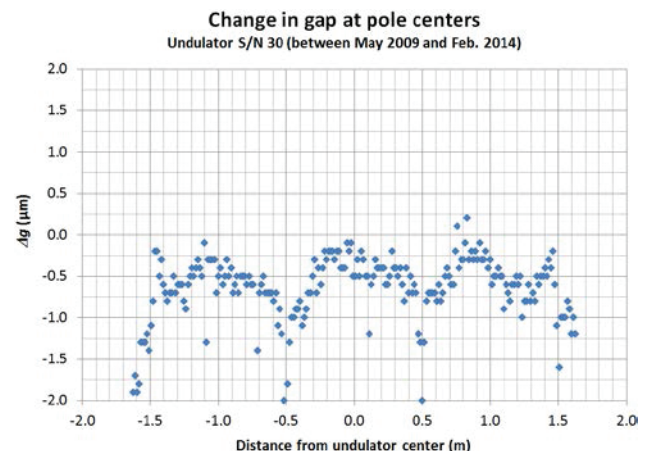


Figure 4: Differences between two CMM measurements (taken in 5/09 and in 2/14) of the gap heights at 218 core poles (of the total 226 poles) of LCLS undulator segment SN30 at the same x location relative to the eight device tooling ball sockets. At each pole, the value shown in the graph is based on an average over 8 – 10 individual measurements taken at horizontally different locations.

These segments have been re-measured in the LCLS magnet measurement facility and compared with earlier measurements for changes in $\Delta K/K$ ($\sigma = 6 \times 10^{-5}$) (see

example in Figure 3), phase shake and total phase ($\sigma=0.1$ degXray), field integrals ($\sigma=5$ G cm), and gap changes ($\sigma=0.25$ μm) (see example in Figure 4). The latter is done in the same x-z plane as earlier, defined by the 8 tooling ball sockets that are part of each segment, using a large coordinate measurement machine (CMM). A detailed description of the measurement technique is given in a different paper [9].

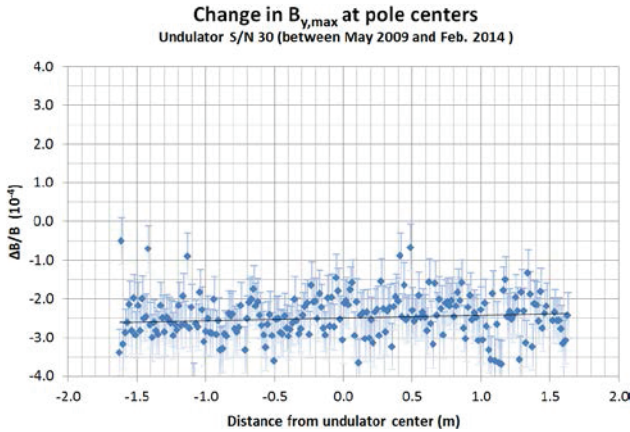


Figure 5: Magnetic field measurements shown in Figure 4 after correction by the CMM gap measurements shown in Figure 5. The remaining change in relative field amplitude is $-(2.5 \pm 0.5) \times 10^{-4}$.

Both, changes in $\Delta K/K$ and in gap height have been observed. The former have been corrected by the latter, using the known dependence of relative undulator strength, $\Delta K/K$, on small undulator gap changes, Δg : $\Delta K/K/\Delta g = -(1.46 \pm 0.15) \times 10^{-4}/\mu\text{m}$, for the LCLS undulator segments (see example in Figure 5).

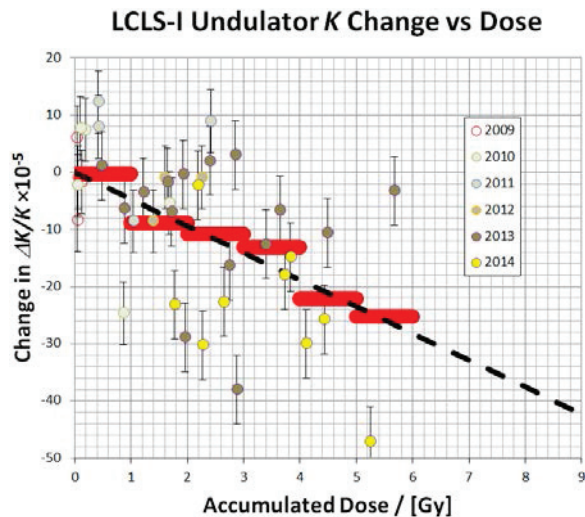


Figure 6: Change in the strength ($\Delta K/K$) of undulator segments vs. the amount of beam energy transported through the beam pipe during the periods in which they were installed in the beam line.

The corrected values of $\Delta K/K$ have been attributed to radiation damage. Note: One undulator has been kept inside the magnet measurement facility since it first

finished tuning in 2007. It has been regularly measured over the years as a reference of the measurement process. This reference undulator does not show the reduction in $\Delta K/K$ as observed on the undulator segments that have spent time in the radiation environment. The averages for the individual undulator segments are plotted in Figure 6 against the radiation dose as accumulated by the TLDs. (see above). In spite of the large spread in the data points, a reduction in segment strength with increased accumulated radiation dose can be seen. Whenever an LCLS undulator segment is re-measured it is recalibrated, i.e., the K polynomials, which translate between the horizontal (x) positions of the canted undulator segments and the K values, are recalculated based on the new measurements. This simple recalibration technique works because of the observed homogeneous z-profile of the K value reduction (see Figure 5).

LCLS ELECTRON BEAM COLLIMATION

Collimator systems appear to be the essential tool for reducing average radiation dose. They remove beam halo, i.e., the large-emittance background that accompanies the electron bunches. Collimators need to be carefully designed and strategically placed to remove out-of-core particles in 5 phase space dimensions (x, x', y, y', E), i.e., transverse (horizontal, x, x' , and vertical, y, y') and energy, E .

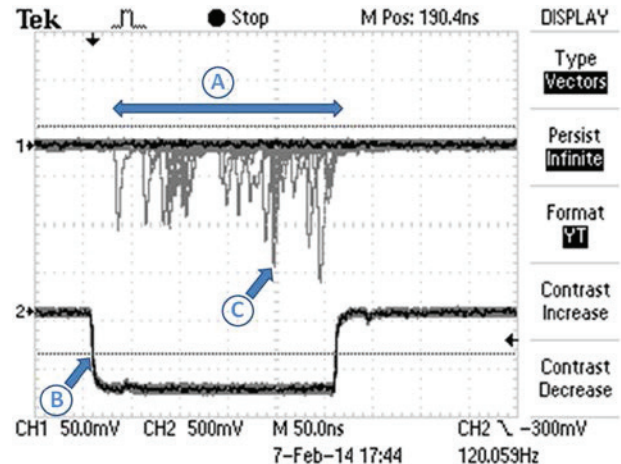


Figure 7: Lost particles from dark current pulses (A) and from the laser driven beam (C) observed at a position along the undulator by a beam loss detector (accumulated over about 500 beam pulses), showing the time spread loss events relative to the true beam time. The lower signal is the oscilloscope trigger from the accelerator timing system (B). The full width of the plot is 500 ns. The rf bucket separation is 0.3 ns.

Recent analysis has shown problems with the current LCLS collimator system. One of the problems is that the LCLS collimators are too short (3 X0), the the LCLS-II collimators will be 15 radiation lengths (X0). Another problem comes from the fact that collimators both remove and create halo. The creation comes from converting core particles that interact with the collimator but are not

removed from the beam by the collimator, itself, to halo particles. A third problem comes from the fact that halo reduction requires the collimator jaws to get quite close to the beam core such that changes in steering and/or beam optics matching can result in transmission rate changes for core particles. For each of the two transverse planes there need to be two collimators separated by 90 degrees of betatron phase advance. The energy collimator needs to be located at a position of high dispersion (such as inside a chicane or a dogleg). In order to avoid that halo particles, produced by the collimation system, will be able to reach the undulator segments, multiple collimation systems will be used and positioned such that there is at least one dipole between the last collimator and the first undulator segments.

A significant source of radiation can come from dark current in out-of-time buckets, i.e., that are generated in the RF photocathode gun when the electric field is right for acceleration but no laser pulse is present. Those losses have been detected along the LCLS undulator beam pipe (Figure 7). It has been shown that the losses, shown in the figure, can be suppressed by switching the gun rf to be out of time with the accelerator rf; they were not much affected by removing the drive laser, which generates the desired bunches, from the gun. In operation, the dark current bunches could be removed by a fast kicker system that should be located after the first accelerator section (L0) when the electron beam energy is still low. Such a kicker system does not exist for LCLS-I but is planned for LCLS-II, for which it is considered essential because of the much larger number of extra rf bucket due to the DC mode of beam operation.

LCLS-II UNDULATOR RADIATION ISSUES

While LCLS operates currently at a maximum beam power of 324 W, (120 Hz, 15 GeV, 180 pC), LCLS-II is being designed for a maximum beam power of 120 kW (100 kHz, 4 GeV, 300 pC) or (1 MHz, 4 GeV, 30 pC), i.e., a beam power increase by a factor 370.

A new LCLS-II collimation system is being designed, incorporating the lessons learned on LCLS-I, including:

1. LCLS-I halo collimators are too short and close to the undulator line.
2. The radiation produced by halo collimators (including gamma and neutron radiation) must be deflected and shielded, i.e., For example, there must be a dipole between halo collimators and undulator segments. Shielding must be added around the halo collimators.
3. Use of beam intercepting devices in front of the undulator line must be limited to low rep-rate operation. They must be fully retrieved from the beam path when not used.
4. A sensitive machine protection monitoring system with correct trip threshold will need to be developed.
5. The understanding of dark current from the gun and L0 during LCLS-II operation needs to be improved.

It will be necessary to add a fast kicker in injector area, right after the first linac section.

It is expected that the new system will result in reduction of radiation dose by orders of magnitude compared to the present system for the same beam power. This should allow keeping the segment recalibration rate at roughly 1 segment per month. Initially, LCLS-II will run in mixed-rate operation to keep the average beam power much lower than the planned 120 kW. The average beam power will be slowly increased based on radiation detector readings as halo reduction is improved. This approach will allow high repetition rate to occur early during the start of LCLS-II operations but at a reduced duty cycle.

CONCLUSION

Reduction in magnetic field strength ($\Delta K/K$) as a function of accumulated radiation dose has been observed for the LCLS undulator segments. The existing halo collimation system was found to have a number of insufficiencies. Significant (sometimes the majority of) beam loss comes from out-of-time buckets. Lessons learned with LCLS-I are being used for the design of the LCLS-II undulator radiation protection system at more than 300 times higher beam power levels.

REFERENCES

- [1] P. Emma, *et al.*, "First Lasing and Operation of an Ångström-Wavelength Free-Electron Laser", *Nature Photonics* **4**, 641. doi:10.1038/nphoton.2010.176
- [2] I.B. Vasserman *et al.*, "LCLS Undulator Design Development", *FEL2004*, 367-370
- [3] G. Battistoni, S. Muraro, P.R. Sala, F. Cerutti, A. Ferrari, S. Roesler, A. Fasso', J. Ranft, "The FLUKA code: Description and benchmarking" Proceedings of the Hadronic Shower Simulation Workshop 2006, Fermilab 6-8 September 2006, M. Albrow, R. Raja eds., AIP Conference Proceeding 896, 31-49, (2007)
- [4] A. Ferrari, R.R. Sala, A. Fasso, J. Ranft *et al.*, "FLUKA: a Multi-Particle Transport Code", CERN-2005-10 (2005), INFN/TC_05/11, SLAC-R-773
- [5] Y. Asano, T. Bizen, and X. Marechal, "Analyses of the factors for the demagnetization of permanent magnets caused by high-energy electron radiation," *J. Synchrotron Rad.* **16** (2009), 317-324
- [6] A.B. Temnykh, "Measurement of NdFeB permanent magnets demagnetization induced by high energy electron radiation", *Nuclear Instruments and Methods in Physics Research A* **587** (2008) 13-19
- [7] S. Anderson *et al.*, "Fast Neutron Damage Studies on NdFeB materials", PAC05, Knoxville, TN, May 16-20, 2005
- [8] REM Oxford Ltd., Witney, England; A. Holmes-Siedle.
- [9] Z. Wolf, Y. Levashov, "Reference Undulator Measurement Results", LCLS-TN-09-3 (2009)

A 200 μm -PERIOD LASER-DRIVEN UNDULATOR*

F. Toufexis, T. Tang, S.G. Tantawi, SLAC, Menlo Park, CA 94025, USA

Abstract

To reduce the linac energy required for a given synchrotron radiation wavelength, and hence the size of the device, a smaller undulator period with sufficient field strength is needed. In this work, a microfabricated, laser-driven undulator with 200 μm undulator period is proposed. A transverse electric (TE) wave that co-propagates with the electron beam is excited between two polysilicon thin films, having a gap of 16.5 μm . The mode that is excited is a deflecting mode and causes the electron beam to wiggle. The device is fabricated on a silicon wafer, using conventional silicon micromachining techniques. A single polysilicon thin film is supported on a silicon chip, which has a slit from the back to allow delivery of the laser beam. Two such chips are bonded together to form a 16.5 μm gap, within which the electron beam passes through. The final device has dimensions 1cm x 1cm x 1.1mm and has approximately 35 undulator periods. In this paper, the model, design, fabrication, and cold measurements of the device are reported.

INTRODUCTION

Traditionally, coherent emission of short wavelength electromagnetic radiation employed undulators – devices that generate a periodic magnetic field – made of permanent magnets. Such undulators present several limitations on how short their period can be, while maintaining reasonable field strength and beam aperture. These limitations, along with the resonance condition between the electrons' oscillatory motion, including relativistic and Doppler effects, and the wavelength of the emitted light, require very high-energy beams, making a tabletop free electron laser (FEL) prohibitive. In order to shrink an FEL, a smaller linac and therefore lower beam energy is required. A smaller undulator period is therefore required, while maintaining sufficient field strength. However, the undulator wavelength cannot be too small – for example using directly a laser beam – because the emittance requirements make it infeasible to operate as a laser [1]. Alternatives to traditional undulators are superconducting magnet-based undulators [2], photonic crystal undulators [3], and microwave undulators [4]. Recently laser driven undulators have been developed [5–8].

In this work, a novel laser-driven undulator is proposed. Figure 1a outlines the principle of operation of the proposed device. A parallel plate dielectric waveguide is used as the interaction region. A TE wave is excited with a 10.6 μm silicon dioxide (CO₂) laser. The angle of incidence is chosen so that a specific undulator wavelength is produced. The electron bunch co-propagates with the TE wave, producing an effective undulator wavelength that is larger than the

excitation wavelength. The waveguide is formed by two thin polycrystalline silicon (p-Si) films, supported on two single crystal silicon (SCS) dies that are bonded together, as shown in Figure 1b. A thicker epitaxially grown polycrystalline silicon (epi p-Si) layer, along with sacrificial silicon oxide (SiO₂) layers are used to define the gap between the two plates of the waveguide, as well as assist in etching the backside trench, without affecting the plates of the waveguide. Figure 1c shows the two sides of a single die before assembly. Note that in Figure 1c, the SiO₂ has not been etched, and the thin film covering the trench has been removed, for better visibility. The devices were fabricated in the Stanford Nanofabrication Facility (SNF) [9].

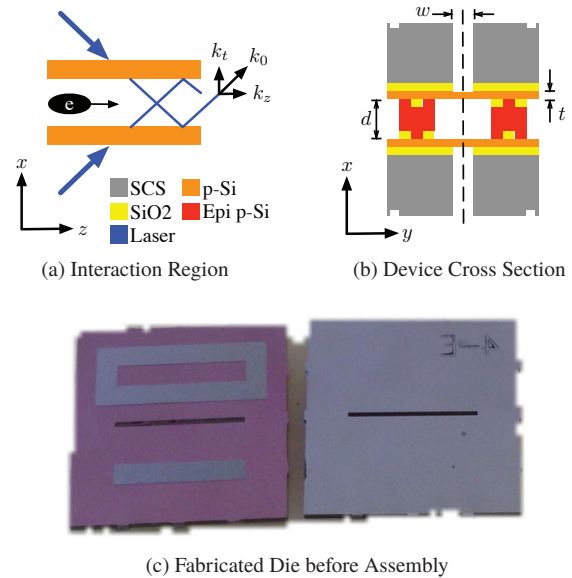


Figure 1: Proposed Device Overview.

ANALYTICAL MODEL & DESIGN

Eigen Modes in Infinite Metallic Parallel Plate Waveguide

In this section, solutions to the Time Harmonic Maxwell's equations are sought for the case of the infinite parallel metallic plate waveguide. Analysis starts with this structure, since it is a very good approximation of the fields inside the interaction region of the undulator. The structure has a finite height d in the x -direction, is infinite in y and z -directions, and waves travel along the z direction. Fields are assumed to vary with time as $e^{-j\omega t}$, and therefore, a field propagating in the positive z direction has a z -dependence of the form $e^{jk_z z}$, where $\omega = \frac{2\pi c}{\lambda_0}$ is the field angular frequency, $k_0 = \frac{2\pi}{\lambda_0}$ is the free space propagation constant, $k_z = \frac{2\pi}{\lambda_G}$ is the propagation

* This project was funded by U.S. Department of Energy under Contract No. DE-AC02-76SF00515 and the DARPA AXIS program.

constant in z -direction, $k_t = \frac{\pi}{d} = \sqrt{k_0^2 - k_z^2}$ is the transverse propagation constant, λ_0 is the free space wavelength, and λ_G is the wavelength inside the waveguide.

Following the methodology in [10], the eigen modes of this waveguide can be split into TE and transverse magnetic (TM) fields. Analysis begins by separating the transverse and longitudinal to z fields, and replacing $\frac{\partial}{\partial z} = jk_z$. TE solutions are found by finding an expression for H_z that satisfies the wave equation, and replacing it in Maxwell's equations along with $E_z = 0$:

$$H_z = jE_0 \frac{k_t}{\omega\mu} \sin(k_t x) e^{-j(\omega t - k_z z)} \quad (1)$$

$$\mathbf{H}_t^{TE} = j \frac{k_z}{k_t^2} \nabla_t H_z = -\hat{x} E_0 \frac{k_z}{\omega\mu} \cos(k_t x) e^{-j(\omega t - k_z z)} \quad (2)$$

$$\mathbf{E}_t^{TE} = -j \frac{\omega\mu}{k_t^2} (\hat{z} \times \nabla_t H_z) = \hat{y} E_0 \cos(k_t x) e^{-j(\omega t - k_z z)} \quad (3)$$

TM solutions are found by finding an expression for E_z that satisfies the wave equation, and replacing it in Maxwell's equations along with $H_z = 0$:

$$E_z = jE_0 \frac{k_t}{k_z} \cos(k_t x) e^{-j(\omega t - k_z z)} \quad (4)$$

$$\mathbf{E}_t^{TM} = j \frac{k_z}{k_t^2} \nabla_t E_z = \hat{x} E_0 \sin(k_t x) e^{-j(\omega t - k_z z)} \quad (5)$$

$$\mathbf{H}_t^{TM} = j \frac{\omega\epsilon}{k_t^2} (\hat{z} \times \nabla_t E_z) = \hat{y} E_0 \frac{\omega\epsilon}{k_z} \sin(k_t x) e^{-j(\omega t - k_z z)} \quad (6)$$

Comparing Equations (3) and (5), in TE modes, the electric field on the walls of the waveguide is zero, while in TM modes the electric field is maximum. Therefore the TE modes are the most suitable for an undulator since the peak electric fields is in the center of the waveguide.

Undulating Mechanism

The basic theory of a microwave undulator cavity was presented in [11]. When electrons interact with a forward and backward wave, the equivalent undulator wavelength is given by:

$$\lambda_u = \frac{\lambda_0}{1 \pm \frac{\lambda_0}{\lambda_G}} \quad (7)$$

where the plus sign corresponds to the electromagnetic (EM) wave counter-propagating with the electrons, and the minus sign corresponds to the EM wave co-propagating with the electrons. These two cases are referred to as short-period and long-period undulation respectively. Therefore in order to have an undulator wavelength longer than the EM wave wavelength, the wave must co-propagate with the electrons.

For a relativistic electron, the equation of motion is given by:

$$\mathbf{F} = -q_e [\mathbf{E} + \beta c (\hat{z} \times \mathbf{B})] \quad (8)$$

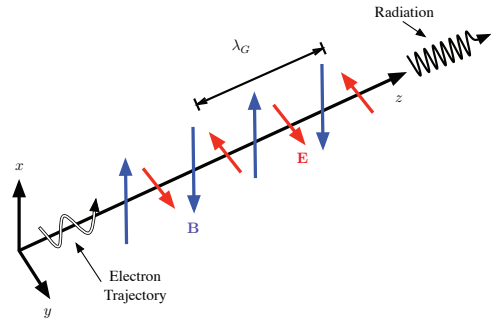


Figure 2: Electron Trajectory in TE Wave, adapted from [11].

Replacing (1), (2), and (3) into (8) yields:

$$\mathbf{F} = -\hat{y} q_e E_0 \left(1 - \beta \frac{\lambda_0}{\lambda_G} \right) \cos(k_t x) \cos\left(2\pi \frac{z}{\lambda_u}\right) \quad (9)$$

The wiggling is a result of both the electric and magnetic field, which although mostly cancel each other, given a large E_0 , the interaction is still significant. Comparing Equation (9) with the traditional permanent magnet undulator [11], yields an equivalent magnetic field:

$$B_{eq} = \frac{E_0}{\beta c} \left(1 - \beta \frac{\lambda_0}{\lambda_G} \right) \approx \frac{E_0}{c} \left(1 - \frac{\lambda_0}{\lambda_G} \right) \quad (10)$$

Equation (9) therefore describes the motion inside an undulator with:

$$\lambda_u = \frac{\lambda_0}{1 - \frac{\lambda_0}{\lambda_G}} \quad K = \frac{q_e E_0 \lambda_u}{2\pi c^2 m_0} \left(1 - \frac{\lambda_0}{\lambda_G} \right) \quad (11)$$

Figure 2 shows an overview of the electron trajectory and field configuration of the proposed device.

TE Modes in Parallel Plate Dielectric Waveguide

Figure 3a presents the optical model of the proposed undulator. A laser beam hits the top of the waveguide at an angle θ_0 . Part of it gets transmitted in region II and the rest gets reflected in region I. The transmitted beam travels in region II with a different propagation constant and angle, because of the change in refractive index, and gets partially reflected and partially transmitted at the boundary between regions II and III. Depending on the choice of dimensions, the structure in Figure 3a can behave as a waveguide in z -direction, operating at a weakly confined TE eigen mode.

For a given undulator wavelength, the corresponding waveguide wavelength from Equation (11) is obtained, that determines $k_z = \frac{2\pi}{\lambda_G}$. Also given the excitation free space wavelength λ_0 , the propagation constant $k_0 = \frac{2\pi}{\lambda_0}$ is determined. Therefore, to achieve a given undulator wavelength, the angle the laser beams forms with the surface is $\theta_0 = \arccos\left(\frac{k_z}{k_0}\right)$. In order for the structure of Figure 3a to behave as a waveguide in z -direction, the waves in all three areas have to travel with the same propagation constant k_z . For a given medium with refractive index n_i , the

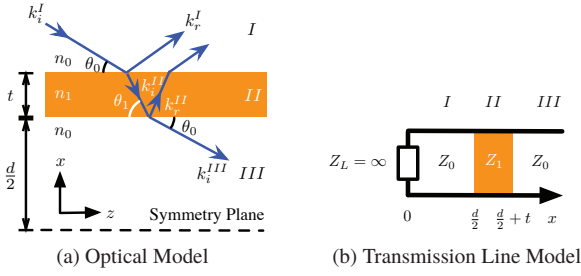


Figure 3: Parallel Plate Dielectric Waveguide Model.

transverse to z propagation constant k_t^i can then be determined from $k_t^i = \sqrt{k_i^2 - k_z^2}$, where $k_i = n_i k_0$ represents the propagation constant in that medium. In that medium $\theta_i = \arccos\left(\frac{k_z}{k_i}\right) = \arccos\left(\frac{k_z}{n_i k_0}\right)$.

The problem can be analysed separately in x and z coordinates. In the z -direction a TE wave – of some distribution in x – travels with a propagation constant k_z . In the x -direction, standing waves are formed in each region, that satisfy the boundaries between regions. In each region, the standing wave is formed by a forward and backward in the x -direction wave, that travels in region i with a propagation constant k_t^i . The symmetry plane $x = 0$ is a perfect magnetic wall for the eigen mode of interest, since it has maximum tangential electric field and zero tangential magnetic field. The waveguide can therefore be analysed in the x -direction as a transmission line problem, where the voltage represents the electric field E_y and the current represents the magnetic field H_z . Each region with a refractive index n_i has a wave impedance Z_i , and the system is terminated at $x = 0$ with a $Z_L = \infty$. The transmission line equivalent model of the undulator is shown in Figure 3b. Using transmission line theory, the transverse to x fields in each region can be written as:

$$\begin{bmatrix} E_y^I(x) \\ H_z^I(x) \end{bmatrix} = \mathbf{M}(x; k_t^0; Z_0) \begin{bmatrix} E_0 \\ 0 \end{bmatrix} \quad (12a)$$

$$\begin{bmatrix} E_y^{II}\left(\frac{d}{2} + x\right) \\ H_z^{II}\left(\frac{d}{2} + x\right) \end{bmatrix} = \mathbf{M}(x; k_t^1; Z_1) \begin{bmatrix} E_y^I\left(\frac{d}{2}\right) \\ H_z^I\left(\frac{d}{2}\right) \end{bmatrix} \quad (12b)$$

$$\begin{bmatrix} E_y^{III}\left(\frac{d}{2} + t + x\right) \\ H_z^{III}\left(\frac{d}{2} + t + x\right) \end{bmatrix} = \mathbf{M}(x; k_t^0; Z_0) \begin{bmatrix} E_y^{II}\left(\frac{d}{2} + t\right) \\ H_z^{II}\left(\frac{d}{2} + t\right) \end{bmatrix} \quad (12c)$$

where

$$\mathbf{M}(x; k_t^i; Z_i) = \begin{bmatrix} \cos(k_t^i x) & -j Z_i \sin(k_t^i x) \\ -j \frac{\sin(k_t^i x)}{Z_i} & \cos(k_t^i x) \end{bmatrix} \quad (13)$$

is the transmission matrix,

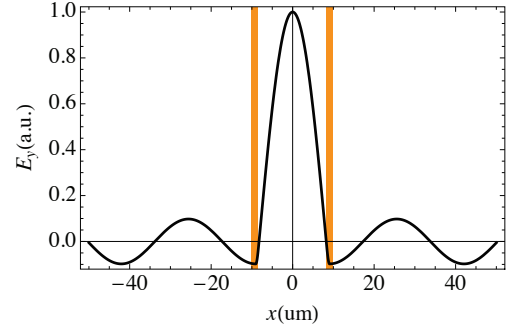
$$Z_i = \frac{\omega \mu_0}{k_t^i} \quad (14)$$

are the wave impedances, and

$$k_t^0 = \frac{2\pi}{\lambda_0} \sin \theta_0 = k_0 \sin \theta_0 \quad (15)$$

$$k_t^1 = \sqrt{k_1^2 - k_z^2} = k_0 \sqrt{n_1^2 - \cos^2 \theta_0} \quad (16)$$

are the transverse propagation constants for a given excitation k_0 and angle of incidence θ_0 .


 Figure 4: Electric field distribution in x .

Design

The input parameters are the laser wavelength $\lambda_0 = 10.6 \mu\text{m}$, and the desired undulator wavelength $\lambda_u = 200 \mu\text{m}$. Using those parameters, Equation (11) is solved for the waveguide wavelength $\lambda_G = 11.19 \mu\text{m}$. All propagation constants can now be fully determined, and the incidence angle is:

$$\theta_0 = \arccos\left(\frac{k_z}{k_0}\right) = 18.73^\circ \quad (17)$$

A choice for the distance d between the two thin p-Si films can be calculated such that the interface behaves as a perfect conducting surface:

$$d = \frac{\pi}{k_t^0} = 16.5 \mu\text{m} \quad (18)$$

A choice for the p-Si film thickness, is such that the reflected power from the thin film is maximised. The ray that is reflected from the boundary between region I and region II changes polarity because the light travels from a medium with low refractive index, to a medium with high refractive index. To maximise reflected power, the reflected wave from the boundary between region II and region III has to interfere constructively with the reflection from the boundary between region I and region II. The condition for this is $2tk_t^1 = \pi$, which yields:

$$t = \frac{\pi}{2k_t^1} = 806 \text{ nm} \quad (19)$$

Now, the design is fully specified, the transverse field profile can be calculated using Equations (12), which is shown in Figure 4. The peak electric field is limited by the dielectric strength of polysilicon which is 400 MV/m, [12]. The maximum peak field in the center is 4.09 GV/m, which from Equation (11) yields $K = 0.013$. Using a material with a higher dielectric strength as the optical layer, will help increase K .

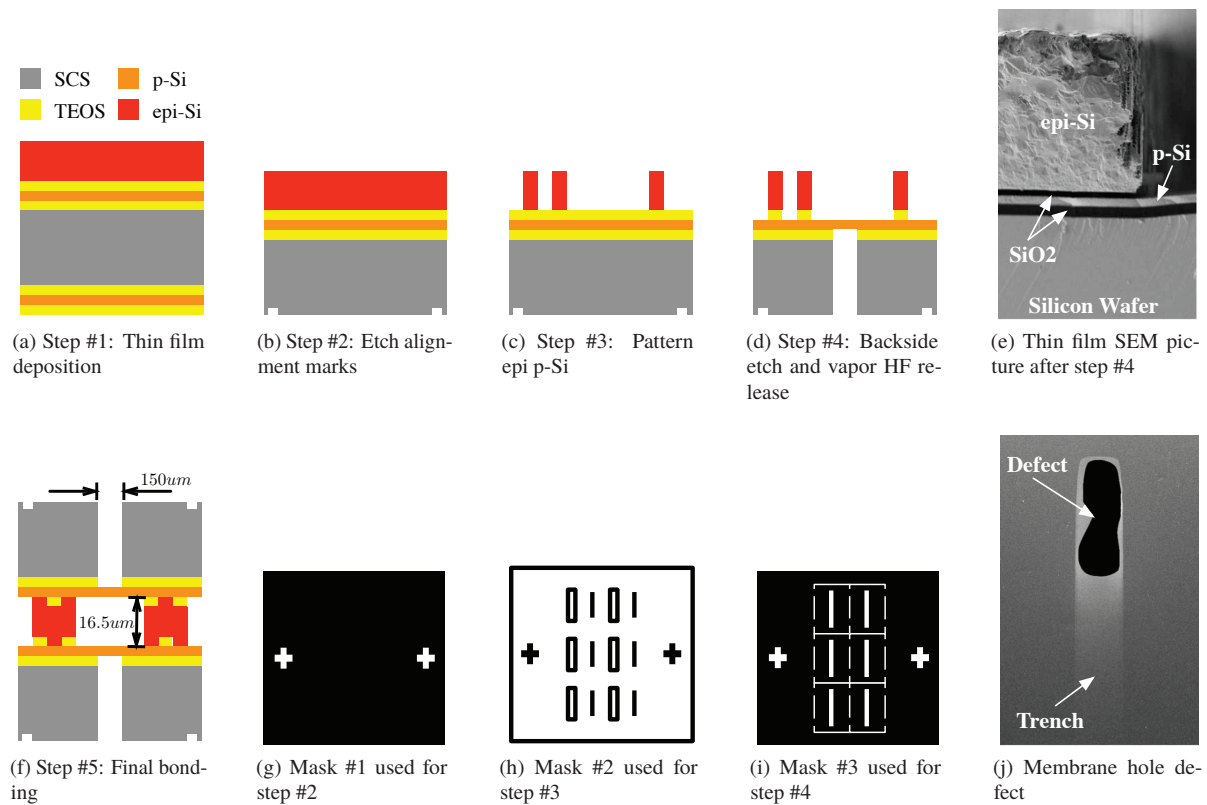


Figure 5: Fabrication diagram and process characterisation.

DEVICE FABRICATION

Fabrication Process

The device is fabricated on <100> SCS wafers (WRS Materials, R-Prime Wafers). After a standard pre-diffusion clean, wafers are coated with 1 μm of sacrificial SiO_2 in a tetraethyl orthosilicate (TEOS) furnace (Tylan), running the standard TEOS process. The wafers are then coated with 806nm of p-Si, in an low pressure chemical vapor deposition (LPCVD) furnace (Thermco Systems), followed by coating with another 0.5 μm of sacrificial TEOS oxide. On the front side of the wafers, a 16 μm -thick epi p-Si layer, is grown at 1080°C using dichlorosilane (DCS) in an epitaxial reactor (Applied Materials Centura). The epi p-Si growth is done in 5 steps, because the maximum allowed growth thickness between two chamber cleans is 3 μm . This stage of the wafer processing is depicted in Figure 5a.

Subsequently, the two TEOS oxide layers and the p-Si layer are removed from the backside of the wafers using dry etching (Applied Materials Precision 5000). The wafers go through a standard piranha clean, followed by a 30 seconds HF dip to clean the surface for lithography. Subsequently, the surface is vapor-primed with hexamethyldisilazane (HMDS) in a 150°C oven (Yield Engineering Systems), and the back side is coated with 1 μm positive tone photoresist (Shipley 3612). The back side is exposed in a contact aligner (Electronic Visions 620), using the first mask to pattern alignment marks. A simplified model of the mask is depicted in Fig-

ure 5g. The photoresist is developed using the standard recipe for this photoresist, and the exposed area is etched 500nm deep, using dry etching (Applied Materials Precision 5000), to form the alignment marks for subsequent lithography steps. The photoresist is removed in microwave oxygen plasma (Gasonics Aura Asher). This stage of the wafer processing is depicted in Figure 5b.

The wafers go again through the standard piranha clean, 30 seconds HF dip, and HMDS oven, to prepare for lithography. The front side is coated with 1.6 μm positive tone photoresist (Shipley 3612) and the wafers are exposed, aligning the second mask to the alignment marks on the backside. The second mask is used to pattern the epi p-Si, and a model of the mask is shown in Figure 5h. The photoresist is developed using the standard recipe for this photoresist, and the exposed area is etched all the way until the sacrificial TEOS oxide, in a deep reactive ion etching (DRIE) tool (Surface Technology Systems Inductively Coupled Plasma), and the photoresist is removed in microwave oxygen plasma. This stage of the wafer processing is depicted in Figure 5c. Figure 5e shows a cross section of the films at this stage of processing from a wafer that was cleaved.

The wafers go again through the standard Piranha clean, 30 seconds HF dip, and HMDS oven, to prepare for lithography. The back side is coated with 7 μm positive tone photoresist (SPR 220-7) and processing is stopped for at least 24 hours, for the resist to outgas. The wafers are then exposed, aligning the third mask to the alignment marks on

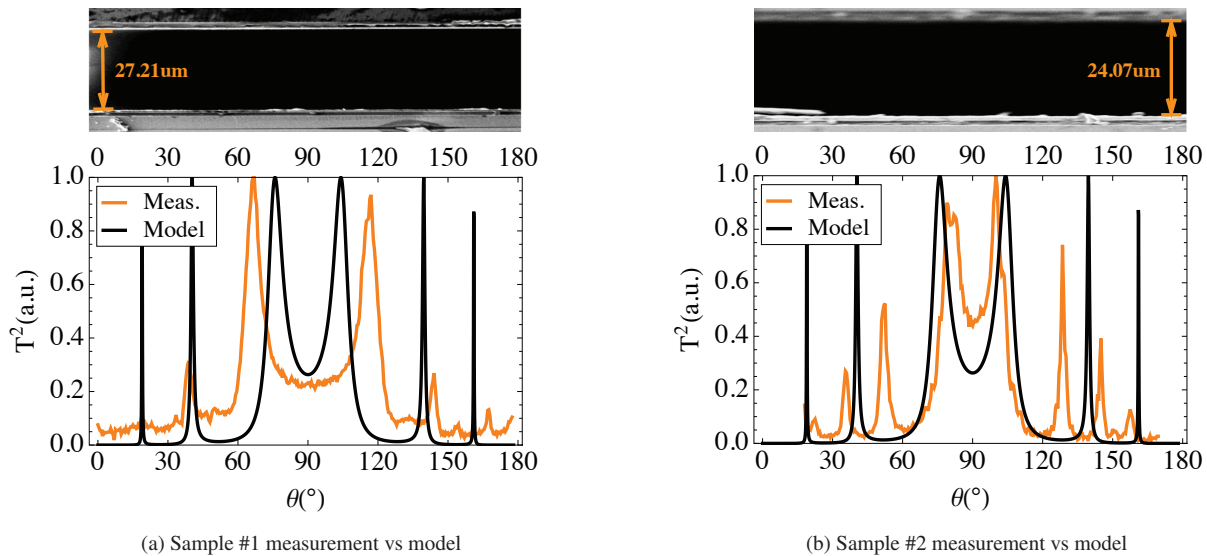


Figure 6: Sample measurements (inset shows the SEM measured gap between the dielectric plates).

the backside. The third mask is used to define the trench opening, and a model of the mask is shown in Figure 5i. The photoresist is developed using the standard recipe for this photoresist, and the exposed area is etched all the way until the sacrificial TEOS oxide, in a DRIE tool. At this point the wafer is almost etched through, and has many pieces connected together with small silicon bridges. These bridges are cracked manually to dice the wafer. The photoresist is removed from the backside of the pieces in microwave oxygen plasma, using a carrier wafer that has a pocket etched. Subsequently, the sacrificial TEOS oxide is removed from all open areas using anhydrous vapor HF and ethanol (SPTS uEtch). This stage of processing is depicted in Figure 5d. Finally, the pieces are taken out of the cleanroom and assembled together. Epoxy is applied on the sides of the stack to keep the pieces together. The final devices are depicted in Figure 5f

Choice of Materials & Processes Discussion

The fabrication process was significantly affected by the availability of materials and tools at SNF. For the substrate, silicon was chosen in order to simplify the fabrication, since SNF is mainly a silicon laboratory. Other options such as germanium or cadmium telluride, that are transparent in the wavelength of interest, were more expensive, and would create complications for processing in SNF. However because silicon is not entirely transparent, it follows that a backside trench must be formed in order to deliver most of the light to the waveguide. For the optical layer, polycrystalline silicon was chosen since it is transparent and has low absorbance in the wavelength of interest, unlike silicon oxide and silicon nitride. Other materials that are suitable for this application, like titanium dioxide, could only be deposited with atomic layer deposition (ALD) tools, thus limiting the thickness to less than 50nm, which is far from what is required for

this device. The epi p-Si layer was used, since it was the only process available that could deposit a 16 μm -thick layer to be used as a spacer. This layer was etched in a DRIE tool, because it was the only available tool, that could etch 16 μm of silicon, without burning the photoresist.

The greatest issue that was encountered during fabrication, was the stress between the two sacrificial layers and p-Si layer that caused it to crack. Initially thermal oxide was used as the first sacrificial layer. After the DRIE step to open the backside trench, most of the epi p-Si membranes on the top of the trench were either completely gone, or cracked. The membranes that were left, were destroyed in the subsequent dicing of the wafer – due to vibrations – and removal of the sacrificial layers. Low stress silicon nitride was also investigated as an alternative, since it is very strong material and indeed all membranes were intact after the DRIE step. However, removing the silicon nitride – which is very absorbing material – with dry etching caused the membranes to crack. TEOS oxide has very low stress since it is deposited at low temperature and more than 70% of the membranes survived the DRIE and wafer dicing steps. Finally removing the sacrificial layers with vapor HF, instead of wet or dry etching with plasma, allowed around 50% total yield. In some of the successfully fabricated devices, there are still some minor cracks at the edges of the trench, however, that position is shaded by the height of the trench, and therefore does not affect operation. Such a defect is shown in Figure 5j.

Another issue, was that the pieces did not correctly align during the last assembly step, resulting in larger gaps, and not perfectly parallel plates. The reasons for that were big silicon particles from the dicing of the wafer, and tolerances in the patterning of the epi p-Si layer, in which a transparency mask was used.

COLD TESTS

To validate the presented model of the undulator, optical power transmission measurements were performed at different angles of incidence. The device was mounted on a rotating stage, as shown in Figure 7. The output of an optical parametric amplifier (OPA), tuned at $10.6\mu\text{m}$ to emulate a carbon dioxide (CO₂) laser, was focused on the sample slit, and the transmitted power was measured at the detector. The entire transmission model for different angle of incidence θ_0 can be obtained using Equations (12), (13), (14), (15), and (16):

$$\begin{bmatrix} (1+R) E_i \\ (1-R) \frac{E_i}{Z_0} \end{bmatrix} = \mathbf{M}_t \begin{bmatrix} T E_i \\ T \frac{E_i}{Z_0} \end{bmatrix} \quad (20a)$$

$$\mathbf{M}_t = \mathbf{M}(t; k_t^1; Z_1) \mathbf{M}(d; k_t^0; Z_0) \mathbf{M}(t; k_t^1; Z_1) \quad (20b)$$

where R and T are the field reflection and transmission coefficients. Equations (20) are solved for T , and the total power transmission coefficient is T^2 .

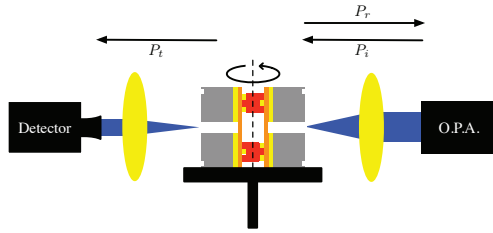


Figure 7: Transmission Measurement Setup.

Two undulators were assembled, and optical transmission measurements were performed using the setup in Figure 7. The measurements from the two samples are shown in Figure 6. The measurements were normalised to the maximum power measurement, since a fraction of power was not transmitted due to poor focusing and shading at the backside trench. The samples were also analysed under SEM, in order to measure the gap and film thickness. The measured thickness was 872 nm, which is in good agreement with the design value in Equation (19), given that the fabrication occurred in an experimental facility. The measured gaps however, deviated significantly because of alignment issues. Overall, the measurements are in agreement with the model in terms of the number of peaks and their relative positions, however there are differences because of the dielectric plates not being parallel.

CONCLUSION

In this work, a novel laser-driven undulator with $200\mu\text{m}$ undulator wavelength was proposed, and the analytical model for the undulator was derived. The fabrication process was presented, and optical transmission measurements in fabricated devices were performed to validate the model. Certain parts of the fabrication process need to be re-worked, before proceeding to hot tests.

ISBN 978-3-95450-133-5

ACKNOWLEDGMENT

Work was performed in part at the Stanford Nanofabrication Facility which is supported by National Science Foundation through the NNIN under Grant ECS-9731293. This project was funded by U.S. Department of Energy under Contract No. DE-AC02-76SF00515 and the DARPA AXiS program. The authors would like to thank the SNF staff, especially Mahnaz Mansourpour, and Maurice Stevens for their assistance in critical parts of the fabrication process, Joseph Robinson for assisting with the optical measurements, and Chris Pearson for assisting with the SEM imaging.

REFERENCES

- [1] Z. Huang and K.-J. Kim, "Review of x-ray free-electron laser theory," *Phys. Rev. ST Accel. Beams*, vol. 10, p. 034801, Mar 2007.
- [2] Y. Ivanyushenkov *et al.*, "Development of a superconducting undulator for the aps," *Journal of Physics: Conference Series*, vol. 425, no. 3, p. 032007, 2013.
- [3] S. Bellucci *et al.*, "Experimental study for the feasibility of a crystalline undulator," *Phys. Rev. Lett.*, vol. 90, p. 034801, Jan 2003.
- [4] S. Tantawi *et al.*, "Experimental demonstration of a tunable microwave undulator," *Phys. Rev. Lett.*, vol. 112, p. 164802, Apr 2014.
- [5] R. J. Loewen, "A compact light source: Design and technical feasibility study of a laser-electron storage ring x-ray source," Ph.D. dissertation, Stanford University, 2003.
- [6] A. Debus *et al.*, "Traveling-wave thomson scattering and optical undulators for high-yield euv and x-ray sources," *Applied Physics B*, vol. 100, no. 1, pp. 61–76, 2010.
- [7] V. Karagodsky and L. Schächter, "High efficiency x-ray source based on inverse compton scattering in an optical bragg structure," *Plasma Physics and Controlled Fusion*, vol. 53, no. 1, p. 014007, 2011.
- [8] T. Plettner and R. L. Byer, "Proposed dielectric-based microstructure laser-driven undulator," *Phys. Rev. ST Accel. Beams*, vol. 11, p. 030704, Mar 2008.
- [9] Stanford nanofabrication facility website. [Online]. Available: <http://snf.stanford.edu>
- [10] S. F. Mahmoud, *Electromagnetic Waveguides: theory and applications*. IET, 1991.
- [11] T. Shintake, "Experimental results of microwave undulator," *Proc. SPIE*, vol. 0582, pp. 336–343, 1986.
- [12] R. J. England *et al.*, "Manufacture and testing of optical-scale accelerator structures from silicon and silica," *Proc. 3rd Int. Particle Accelerator Conf.*, 2012.

OXYGEN SCINTILLATION IN THE LCLS*

J.L. Turner, R.C. Field, SLAC NAL, Menlo Park, CA 94025, U.S.A.

Abstract

Oxygen was tested as a replacement for nitrogen in the Gas Detector system in the Linac Coherent Light Source (LCLS) X-ray Free Electron Laser (FEL) at the SLAC National Accelerator Center. The attenuation and pulse-to-pulse intensity monitors for LCLS use nitrogen, but for experiments at the nitrogen K 1S energy of about 410eV this functionality is gone due to energy fluctuations above and below the K-edge. Oxygen was tested as a scintillating gas at 400 eV and 8.3 keV.

INTRODUCTION

In the LCLS X-ray beam, a length of the beam transport line is filled with low pressure nitrogen. One use of the gas is to attenuate the X-ray intensity as needed [1]. The gas pressure in a 4 meter section is controlled at pressures of up to 20 Torr to implement this, and it is useful up to X-ray energies of about 1.5 keV. Additional short sections before and after the attenuator section have independent pressure controls for up to 2 Torr, and are used to monitor the X-ray laser beam intensity. They function by making use of the excitation of the nitrogen molecules by the X-ray beam. As the nitrogen de-excites, a fraction of the energy is emitted in spectral lines in the range 300 to 430 nm, corresponding to both excited and ionized molecular transitions. Some of this light is detected through sapphire beam windows by photomultiplier tubes.

THE BEAMLINE AND NITROGEN

The beam chamber for these devices contains a series of 4 mm diameter beam apertures with differential pumping between them, to reach the base level at E-8 Torr beyond the device. Ion-pumps, turbo-pumps backed by scroll-pumps and Roots pumps are used.

The nitrogen K-edge occurs at about 410 eV (Fig. 1). When the LCLS is tuned to operate at this energy, the nitrogen gas systems are not useful because their response varies wildly as the beam energy fluctuates within its intrinsic width.

For the occasions when users need X-ray energies in the nitrogen K-edge range, a solution is to use an alternative gas. The practical requirements are that the pumping system can maintain the upstream and downstream base pressures, while delivering a useful range of pressures for the attenuator and detectors (Fig. 2), and that the de-excitation light should be detectable with the present vacuum windows and photomultiplier system.

Light noble gases would be considerably more difficult

to pump, and, with the exception of helium, their reported light emission wavelengths are too deep in the ultraviolet. Oxygen is the nearest analogue to nitrogen as far as gas handling and pumping is concerned.

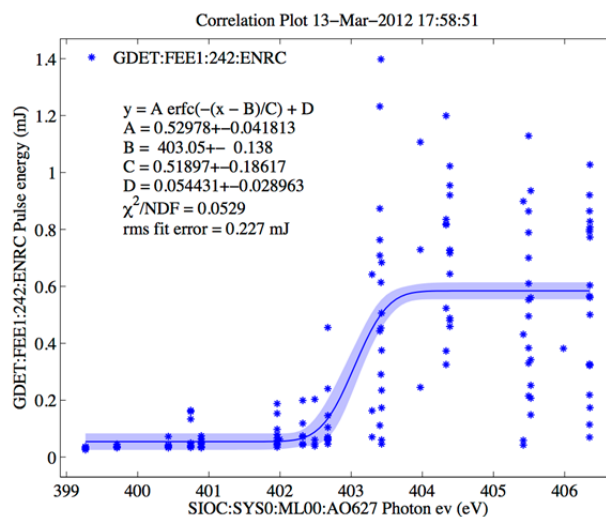


Figure 1: X-ray energy on the horizontal axis, vertical is nitrogen response as a function of the energy fluctuating under and over and spanning the K 1S edge.

THE BEAMLINE AND OXYGEN

Oxygen Concerns

With oxygen, no changes to the pumps are needed, and the switch over from one gas to the other is fairly simple. Since it is used at very low pressures, there is no significant combustion safety issue, except for normal oxygen precautions for the source and regulator. The chemical activity of atomic oxygen and ozone generated in the beam pipe has been considered. Most of it is, of course, intercepted by the walls and aperture plates, and the concentration downstream is too small to be of concern. B4C, which is often used as an absorber for X-rays, is known to be etched by ozone in the presence of strong UV illumination. Based on this, an upper limit on the etching rate on B4C components in the ~10 Torr oxygen environment shows surface loss too small to be significant.

Oxygen Utility

The oxygen K-edge is at 530 eV, and so, used at near 409 eV, its absorption would be relatively low, comparable to that of nitrogen at 1095 eV. This improves resolution, and operability at low pressure, of the controls of the gas system. For example, a pressure of 0.05 Torr used in nitrogen at 415 eV would be matched by 0.6 Torr using oxygen.

* This work was supported by U.S. Department of Energy, Office of Basic Energy Sciences, under Contract DE-AC02-76SF00515

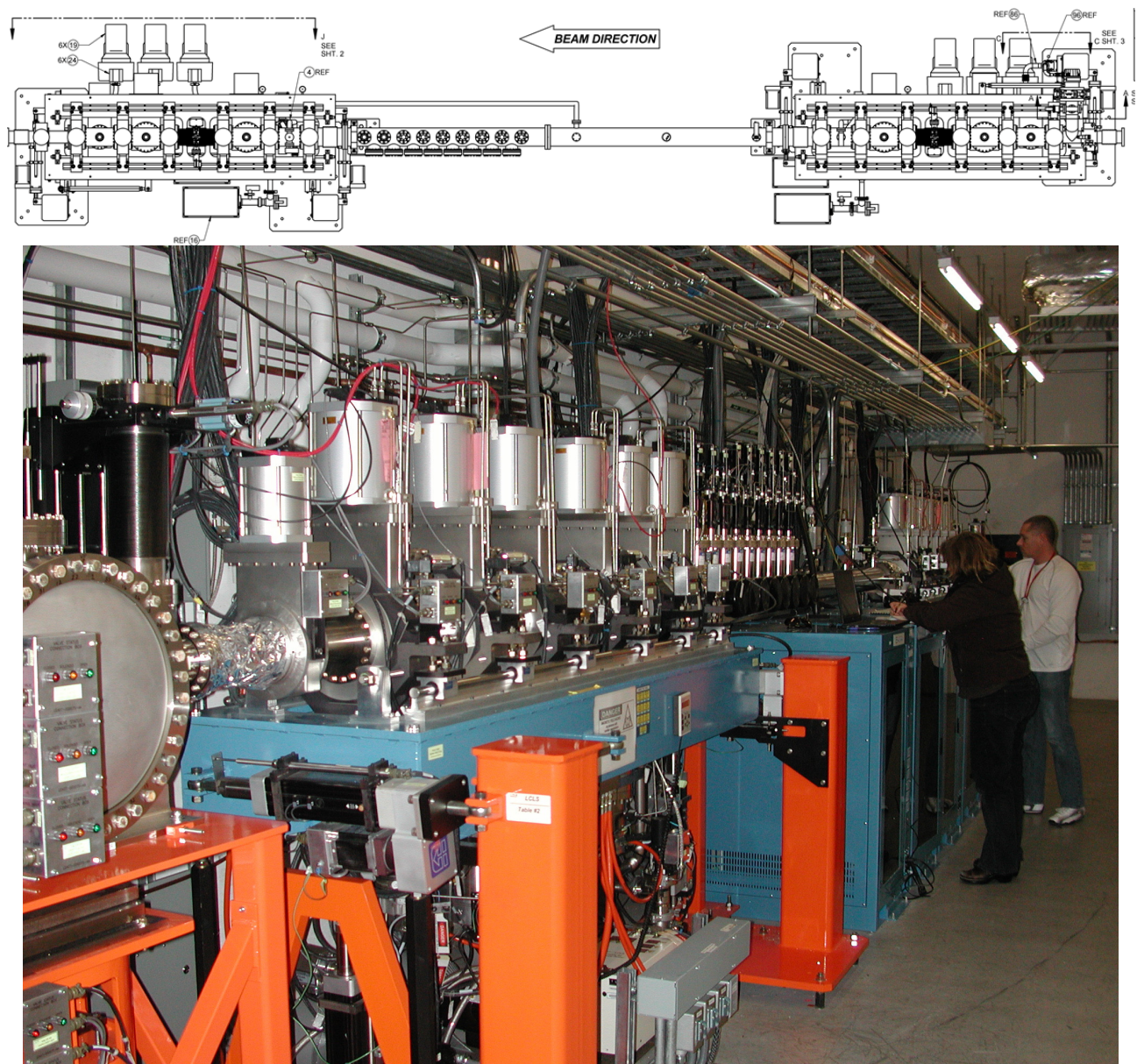


Figure 2: Gas Attenuator installation drawing and photograph. Gas Detector 2 Differential Pumping Assembly is centered, the gas attenuator is above the blue instrumentation and control racks right of center, and the initial Differential Pumping Assembly in the right distance.

Oxygen Literature

On the other hand, the light emission of oxygen is not as well understood as is that of nitrogen. Nitrogen has been studied in detail since, for example, it produces effectively all the atmospheric fluorescence that is used to measure extensive showers from cosmic ray interactions. Oxygen's effect in suppressing the nitrogen fluorescence is also well measured.

A relevant measurement, where gas at near 1 atmosphere was excited by charged particles, and the fluorescence light detected by a photomultiplier tube, reported [2] that the oxygen light emission is approximately 1% of the nitrogen output. However, at

low pressures, the de-excitation processes for the different excitation bands change by a large amount from the 1 atmosphere values, and it is not possible to extrapolate. There are some spectra from low pressure oxygen that can be found in the literature. Some of these have evidence of nitrogen contamination. However, there are some reported emission lines in the UV-blue range, extending to longer wavelengths than for nitrogen.

Customizing the System

The wavelength range originally used for the light from nitrogen used optical filters to cut off light at wavelengths longer than about 385 nm. This was done to strongly reduce broadband light that is occasionally encountered

from coherent emission processes associate with the electron beam far upstream. To accommodate the weak emission from oxygen, the optical filters have been replaced and the pass-band has been extended up to 450 nm. (This also increases the signal from nitrogen.) The occasional effects of coherent light are removed by a timing cut on the pulse profile.

Beam Tests

The use of oxygen has been tested with the X-ray beam. As expected, it was found that gas handling was similar to the use of nitrogen. The largest uncertainty was in the light emission, and signals were indeed detected. The de-excitation time in this environment was much shorter than for nitrogen, with 90 % amplitude reduction in less than 100 nsec. In Fig 3 and 4, pulse profiles from nitrogen and oxygen are illustrated.

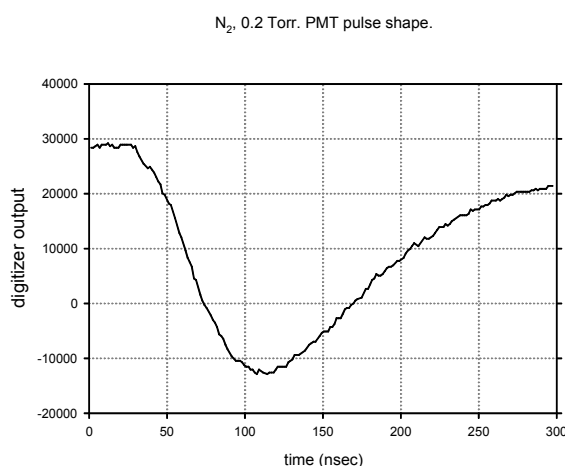


Figure 3: Nitrogen de-excitation time.

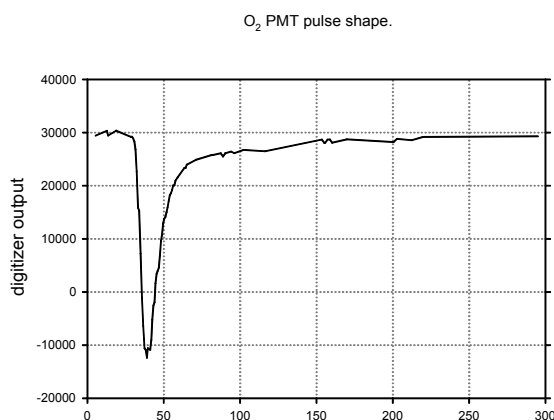


Figure 4: Oxygen de-excitation time.

The hard X-ray operability was tested with 1.5 millijoules at 8.3 keV. Using 2.0 Torr of oxygen, the PMT (photomultiplier tube) high voltages had operational headroom indicating capability at higher energies.

Solenoids surrounding the chambers optimized roughly at the same fields as used with nitrogen.

The pulse amplitude fluctuations were consistent with expected fluctuations of the beam, and photon counting statistics were adequate for the device's normal use as a tuning and monitoring tool. A correlation between signals from two PMTs, measured on the same pulses, showed an RMS spread of 1.0 %, indicating that the beam intensity measurement could be made to 0.5 % on a pulse-by-pulse basis by averaging the two PMT signals.

CONCLUSION

LCLS gas detectors were tested using oxygen at soft X-rays (near the nitrogen K edge) and at hard X-rays (8.3 keV). The most notable difference to nitrogen was in pulse duration and subsequent gating. With oxygen however, the gas detectors were clearly operable as a relative intensity monitor at both energies tested with capability to go to higher energy.

REFERENCES

- [1] Ultrafast x-ray-matter interaction at LCLS, Stefan P. Hau-Riege, Advanced Instrumentation Seminar (AIS) SLAC NAL 2008, <https://www-group.slac.stanford.edu/ais/listPastSeminars.asp>
- [2] J. Heintze et al., Nucl. Instr. and Meth. 138 (1976) 641.

UPDATE ON FEL PERFORMANCE FOR SWISSFEL

E. Prat and S. Reiche, PSI, Villigen, Switzerland

Abstract

The SwissFEL project under construction at the Paul Scherrer Institute foresees for 2017 the realization of an X-ray FEL with a photon wavelength down to 1 Å. In this paper we present the expected SASE performance for SwissFEL based on input distributions obtained from detailed start-to-end simulation results. The effects of the longitudinal wakefields due to resistive wall and surface roughness in the undulator beamline have been taken into account. We have studied and optimized the impact on the FEL performance of different factors like the electron focusing or the undulator tapering. Results for the standard cases with 200 pC and 10 pC electron bunch charge are shown.

INTRODUCTION

The SwissFEL facility, presently under construction at the Paul Scherrer Institute, will provide SASE and self-seeded FEL radiation at a hard (1-7 Å) and soft (7-70 Å) X-ray FEL beamlines [1]. SwissFEL will operate with electron beam charges varying between 10 and 200 pC and beam energies from 2.1 to 5.8 GeV. Two standard operational modes are foreseen: 1) the long-pulse (LP) mode to maximize the FEL output energy, with an electron beam charge of 200 pC and a rms bunch length of 18.4 fs; and 2) the short-pulse (SP) mode with 10 pC beam charge and 2.5 fs pulse duration.

In this document we present the SASE simulation results for the hard X-ray beamline and the two described operational modes. We have done the calculations for the shortest and longest radiation wavelengths, i.e. 1 Å and 7 Å. We have optimized the average β -function along the undulator beamline as well as the undulator tapering. We present the effects of the wakefields in the undulator beamline, showing that tapering can be employed to reduce the wakefields impact to a negligible level.

LAYOUT AND SIMULATIONS SETUP

The present design lattice for the hard X-ray beamline consists of 12 undulator modules. Each of them is 4 m long, has a period length of 15 mm and a variable gap with a nominal value of 4.2 mm. The distance between modules is 0.75 m. In addition we have reserved the space corresponding to an undulator module to place a magnetic chicane and a Bragg crystal to be used for self-seeding [2]. The facility is able to accommodate up to seven more modules for potential future upgrades such as long post-saturation tapering. A quadrupole magnet in the middle of each section between undulators is employed for beam focusing.

Figure 1 shows the properties of the electron beam distributions that we used as input for the FEL simulations for 1 Å. The distributions have been obtained

by tracking with the simulation codes *ASTRA* [3] and *elegant* [4].

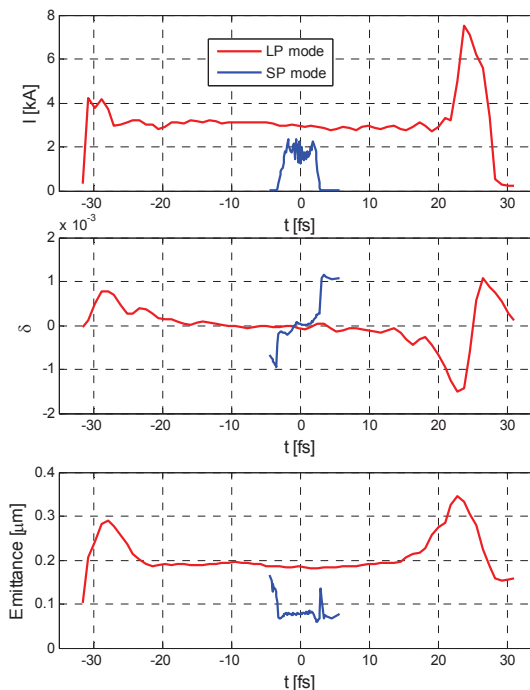


Figure 1: Electron beam slice properties at the undulator entrance for the LP mode (red) and SP mode (blue). Current profile (top), relative energy deviation (center) and normalized emittance (bottom). The emittance is defined as the geometrical average of the horizontal and vertical emittances.

The lasing at a radiation wavelength of 1 Å is obtained when the electron beam has a maximum energy of 5.8 GeV, which corresponds to an undulator parameter K of about 1.2. For the long wavelength (7 Å) we choose the undulator parameter as large as possible to maximize the beam energy and, as a consequence, to enhance the FEL output power. The maximum K is about 1.5, which corresponds to a beam energy of about 2.4 GeV. The particle distributions for 7 Å are obtained simply by scaling the distributions at 1 Å. This scaling is valid since the difference between the two configurations is only the energy provided by the last part of the linac, while keeping the same compression setup. The FEL interaction is simulated with *Genesis* [5].

FOCUSING OPTIMIZATION

We have analyzed how the FEL performance varies as a function of the focusing along the undulator for the LP mode. Figure 2 shows the relative FEL power at saturation as a function of the β -function for the two

radiation wavelengths. For 1 Å, the best SASE performance is obtained when the average β -function along the undulator is 10-11 m. For the 7 Å case the optimum β -function would be smaller or equal to 9 m, which is the minimum value that can be obtained in our lattice. For the SP mode we expect to have smaller optimum β -functions, since the emittances for this mode are also smaller. We have chosen for all succeeding simulations an average β -function along the undulator of 10 m, a compromise between the different optimums.

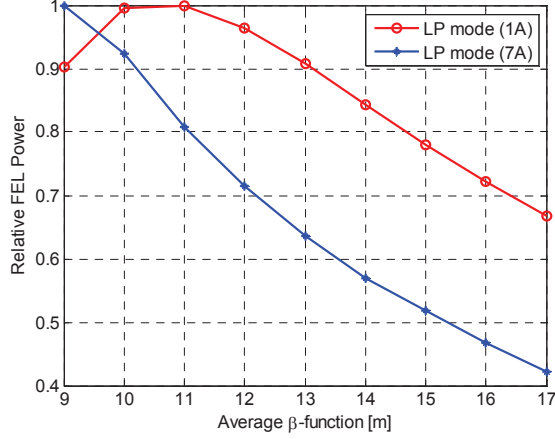


Figure 2: Relative FEL power at saturation as a function of the β -function along the undulator for the LP mode for a radiation wavelength of 1 Å and 7 Å.

FEL PERFORMANCE

Tapering the undulator helps to improve the FEL performance because it compensates the energy loss of the electrons due to lasing. For the two modes we have applied two stages of linear tapering: pre-saturation taper to optimize the gain length in the exponential regime and post-saturation taper to maximize the FEL power at the end of the undulator beamline. As an illustration example, Figure 3 shows the FEL macropulse energy at the end of the undulator as a function of the post-saturation taper amplitude for the LP mode at a radiation wavelength of 1 Å.

Table 1 shows the SASE properties at the undulator exit for the studied cases, namely the FEL macropulse energy, the FEL pulse duration (rms), the spectrum bandwidth (rms), the radiation divergence (rms) and the effective source point. These results correspond to only one shot noise seed. Due to the stochastic nature of the SASE process, the output energy fluctuates roughly proportionally to $n_s^{-1/2}$, being n_s the number of spikes of the SASE pulse. According to this, the FEL energy fluctuations are expected to be the following: about 38 % for the SP mode at 7 Å (7 spikes), about 17 % for the SP mode at 1 Å (35 spikes), and better than 10 % for the LP mode (more than 100 spikes).

Figures 4 and 5 show the FEL energy along the undulator beamline and the radiation spectrum, respectively, for the optimum case for all the considered configurations.

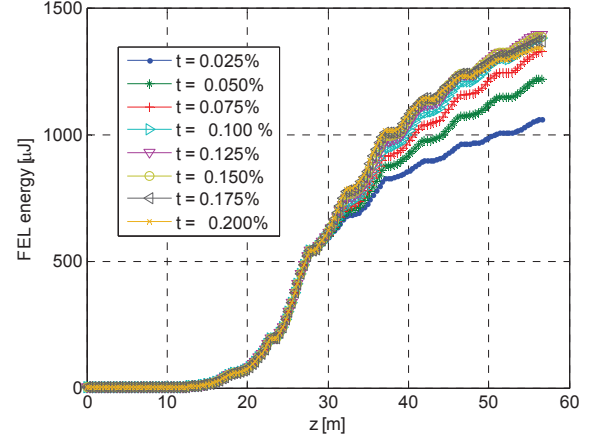


Figure 3: FEL macropulse energy for different post-saturation tapers. The maximum FEL energy is around 1.4 mJ and corresponds to a linear taper amplitude of 0.125% per undulator module.

Table 1: FEL Properties for the Different Studied Cases

	FEL Energy [μJ]	Rms length [fs]	Rms Spect. Band.	Rms div. [μrad]	Source point [m]
LP / 1 Å	1390	17.7	0.21%	2.0	20.4
LP / 7 Å	1650	17.0	0.45%	9.8	~10
SP / 1 Å	108	1.5	0.12%	1.6	24.2
SP / 7 Å	78	1.7	0.35%	8.5	~10

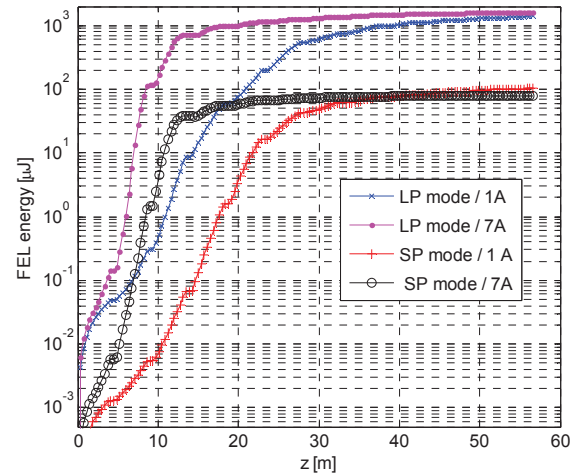


Figure 4: FEL macropulse energy along the undulator beamline for the different operational modes. The simulations are done per each case with the optimum focusing and undulator tapering.

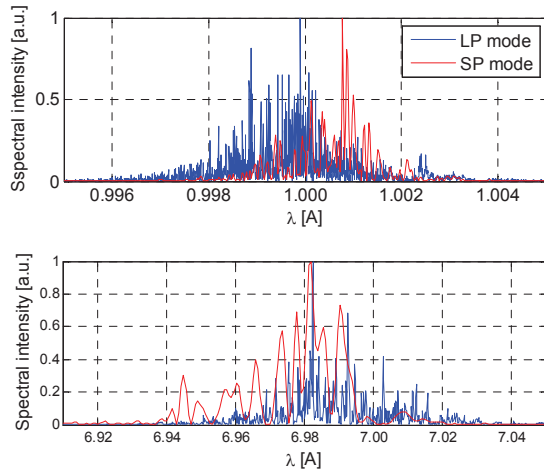


Figure 5: Radiation spectrum for the different operational modes for a wavelength of 1 Å (top) and 7 Å (bottom). The simulations are done with the optimum focusing and undulator tapering.

As an example, Figure 6 shows the divergence and the effective waist position along the undulator beamline for the LP mode at a radiation wavelength of 1 Å. The source position is calculated following the procedure described in Ref. [6]. For 7 Å we could not follow this procedure mostly due to slippage effects. For this case we have estimated the source point to be at about 2 gain lengths before saturation, i.e. at around 10 m.

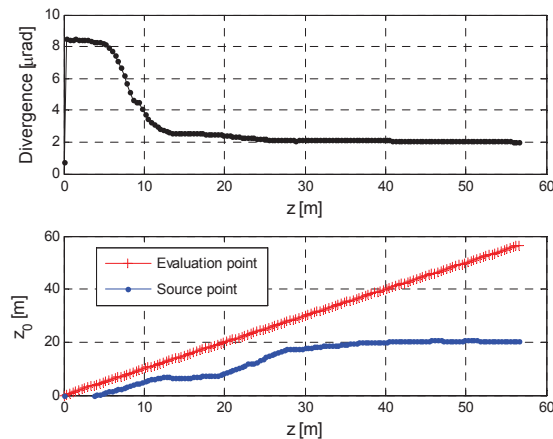


Figure 6: Radiation divergence (top) and effective source position (bottom, blue) along the undulator for the LP mode at a radiation wavelength of 1 Å. The red curve of the bottom plot indicates the point where the evaluation is done ($z_0 = z$).

WAKEFIELD EFFECTS

Longitudinal wakes in the undulator can modify the energy of the electrons and therefore degrade the FEL performance by shifting the resonance condition. We have studied the wake effects due to resistive wall and surface roughness for the LP mode and a radiation wavelength of 1 Å. For the calculation of the wakes we

follow the procedure of Refs. [7, 8] and we assume the parameters indicated in Table 2.

Table 2: Parameters for the Wakefield Calculations

Material	Copper
Separation of parallel plates	4.4 mm
Corrugation amplitude	100 nm
Corrugation period	10 μm

Figure 7 shows the wake along the bunch ($\zeta = 0$ indicates the head of the bunch). The current profile as well as the contributions of the resistive wall and the surface roughness are indicated. Although the current profile is slightly different than the one showed in Figure 1, the results are expected to be equivalent. We note that the final wake does not depend significantly on the current spike in the head of the bunch and on the visible ripples in the current profile. The ripples are due to the low number of particles used in the start-to-end simulations in that case, which yield a larger shot-noise level for the longitudinal space-charge calculations in the elegant tracking.

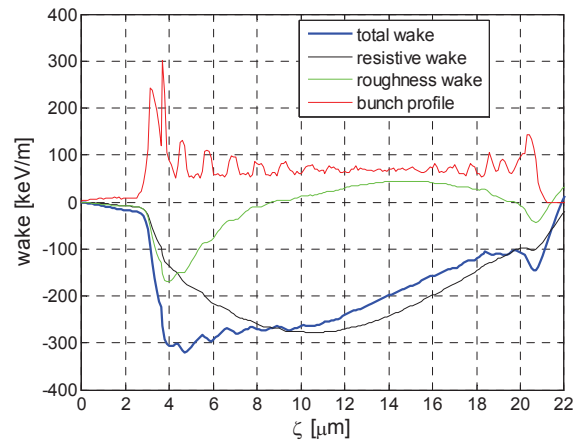


Figure 7: Undulator wakes along the bunch for the LP mode (the beam charge is 200 pC).

The effect of the wakes can be compensated by tapering the undulator. Figure 8 shows the relative macropulse FEL energy at the end of the undulator for different linear pre-saturation taper amplitudes, with and without considering the wakes. In this case we did not optimize the post-saturation tapering. Without tapering, the FEL energy decreases by a factor of 2 due to the wakes. The optimum tapering without considering the wakes is about 0.05 %. In the presence of wakes, the taper amplitude has to be further increased to about 0.096 % to compensate for the additional energy loss due to wakes. The final FEL performance is not significantly degraded due to wakes: the optimum FEL performance for the 2 cases differ only for about 5%.

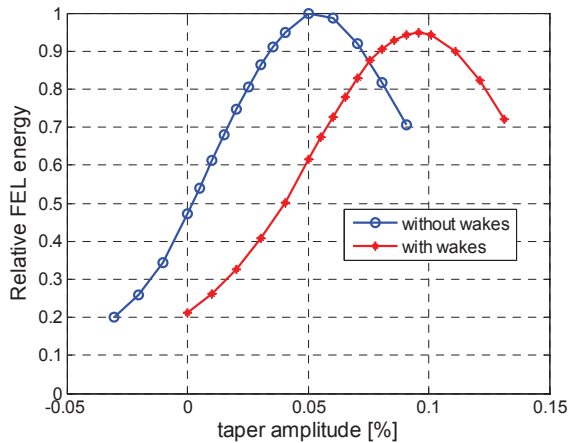


Figure 8: FEL relative pulse energy vs taper gradients. Tapering reduces the wakefield effects to a ~5 % level.

CONCLUSIONS AND OUTLOOK

We have presented the expected SASE performance for the hard X-ray beamline of SwissFEL based on electron distributions obtained from start-to-end simulations. The FEL macropulse energy is significantly higher than the one obtained with the design parameters and presented in Ref. [1] – for example for the LP mode, we expect to obtain about 1.5 mJ of FEL energy, a factor of ~10 higher than with the design parameters. The improvement can be explained by three factors: smaller normalized emittances, a better β -function along the undulator optimized for such emittances, and undulator tapering. Based on our slice and thermal emittance measurements at the SwissFEL Injector Test Facility [9, 10] we presently expect to obtain significantly smaller emittances than the design ones – for instance, for the LP mode the design emittance is $0.43 \mu\text{m}$ and the currently expected is about $0.20 \mu\text{m}$.

For the LP mode, the spike at the head of the bunch (see Figure 1) contributes to the FEL performance. In the start-to-end simulations we have considered 1D CSR effects in the bunch compressors and longitudinal space-charge along the linac. We will perform more advanced calculations to benchmark our 1D simulation results.

Apart from the two standard operation modes, SwissFEL will have two additional special configurations: a large-bandwidth mode with 200 pC charge in which the FEL bandwidth will reach the few-percent level, and a ultra-short pulse mode that will generate attosecond pulses with three compression stages. Detailed start-to-end simulations for these modes will be presented in a future opportunity.

ACKNOWLEDGMENTS

We thank Simona Bettoni and Bolko Beutner for the work to generate the particle distributions that we used as input for the FEL simulations.

REFERENCES

- [1] R. Ganter et al, PSI Report No. 10-04, 2012.
- [2] G. Geloni et al, DESY report 10-053, 2010.
- [3] K. Floettmann, *ASTRA - A Space Charge Tracking Algorithm*. DESY, Hamburg, Germany.
- [4] M. Borland, Advanced Photon Source Report No. LS-287, 2000.
- [5] S. Reiche, NIM A **429**, 243, 1999.
- [6] S. Reiche. Proceedings of the FEL'06, Berlin, Germany, 126-129 (2006).
- [7] K. L. F. Bane and G. Stupakov SLAC Report N0. SLAC-PUB-10707, 2004.
- [8] G. Stupakov and S. Reiche. Proceedings of the FEL'13, New York, USA, 127-131 (2013).
- [9] E. Prat et al. Proceedings of the FEL'13, New York, USA, 200-204 (2013).
- [10] E. Prat et al. Proceedings of this conference.

SASE FEL PERFORMANCE AT THE SWISSFEL INJECTOR TEST FACILITY

S. Reiche *on behalf of the SwissFEL Team* – Paul Scherrer Institut, Villigen, Switzerland

Abstract

A 4 m long prototype of the SwissFEL undulator module with an undulator period length of 15 mm was installed at the SwissFEL Injector Test Facility and tested with a 200 MeV electron beam in the beginning of 2014. We observed FEL lasing in SASE mode in the wavelength range from 70 to 800 nm, tuning the wavelength by energy and gap. The measurements of the FEL performance are reported.

INTRODUCTION

Hard X-ray FEL facilities rely very heavily on cutting-edge technology for RF, diagnostics, insertion devices, and X-ray optics such that building these facilities would represent a high risk without a prior test of the key components. This was the main purpose of various test facilities around the world, such as GTF [1] for LCLS, PITZ [2] for the European XFEL, or SCSS [3] for SACLA. The SwissFEL [4], currently under construction at the Paul Scherrer Institute (PSI), is based on the results of the SwissFEL Injector Test Facility [5], also hosted by the PSI. The test facility has been in operation since August 2010 and will be decommissioned in fall 2014 to move parts over to the SwissFEL building for installation. The start of commissioning of SwissFEL is foreseen for 2015 with a duration of two years.

Like SACLA, SwissFEL will utilize in-vacuum undulators to minimize the undulator period and thus the required electron energy to reach one Angstrom as the resonant wavelength of the FEL. Due to the technical challenge to construct 12 modules of 4 m each a test with an electron beam is highly beneficial to discover possible limitations in the performance of the undulator prototype module. For that an undulator module was installed at the test facility in the early months of 2014. Demonstrating SASE performance was one of the goals for this measurement series and the results are reported in this paper.

THE SWISSFEL INJECTOR TEST FACILITY

The SwissFEL Injector Test Facility (SITF) is a platform to test key components for SwissFEL as well as to demonstrate the beam parameters of the electron beam to successfully operate SwissFEL at its shortest wavelength of 1 Angstrom.

The RF gun is a 2.5 cell photo RF gun [6], operating at European S-band frequency of 2.998 GHz, which has recently replaced the 3rd generation CLIC Test Facility (CTF3) Gun in spring 2014. The former CTF3 gun was sufficient to demonstrate the key beam parameters for a 200 pC beam and a slice emittance of about 200 nm [7]. The gun is followed

by two 4 m long S-band traveling wave accelerating structures, boosting the electron energy up to 130 MeV. They are enclosed by focusing solenoids to keep the beam size and Twiss parameter within reasonable limits. An additional S-band RF station feeds two S-Band structures to increase the energy up to 250 MeV and to apply a chirp for compression. However running off-crest to generate the chirp yields less beam energy at a level of about 220 MeV. An X-band RF structure linearizes the energy chirp for a better control on the current profile after compression.

The 11 m long bunch compressor is movable to have variable R_{56} from 0 to 70 mm while keeping the vacuum chamber small. This allows for precise BPM readings in the dispersive section of the bunch compressor as well as the installation of quadrupoles and skew quadrupoles to correct for linear tilts in the electron beam distribution in both transverse planes [8].

A diagnostic section follows the bunch compressor for current profile, projected and slice emittance, and longitudinal phase space measurements (the last in the dispersive part of the beam dump). The key component is a S-band transverse deflecting cavity, streaking the beam in the vertical direction. Initially a FODO section was foreseen to measure the beam size at various positions along several cells of the FODO lattice and reconstruct the beam emittance values from it. In practice quad scans and multi-knob measurements with a dedicated high resolution YAG screen at the end of the beam line were more robust and easier to use [9]. The center part of the FODO section could therefore be modified for other tests.

One important test involved the in-vacuum undulator prototype: a 4 m long undulator with a period length of 15 mm and a tunable undulator parameter K between 1.0 and 1.7. The main study was the entrance and exit kick of the undulator on the electron beam and the alignment strategy of the module by means of alignment quadrupoles [10]. The orbit within the undulator is checked with the spontaneous radiation (or FEL beam) on various screens after the undulator and compared to the electron BPM reading.

With the installation of an undulator the expectation for a SASE signal comes naturally. In particular the narrow opening angle of the FEL signal would yield better resolution in the angle between light cone and electron beam than the rather broad and weak signal of the spontaneous undulator radiation.

The general layout of the SwissFEL Injector Test Facility is shown in Fig. 1.

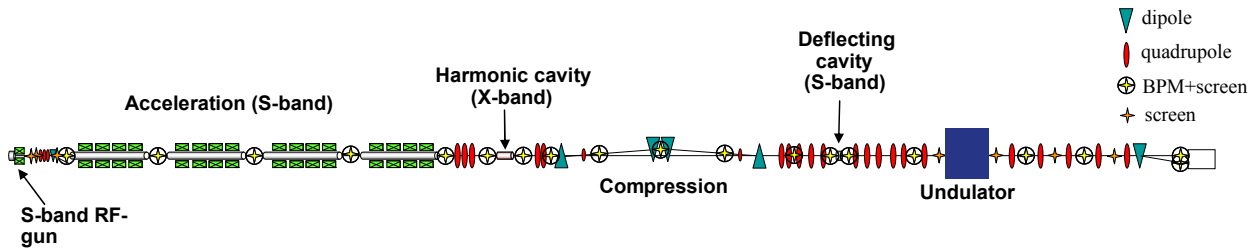


Figure 1: Schematic Layout of the SwissFEL Injector Test Facility.

SASE FEL MEASUREMENTS

In this section we report the measurements of the FEL performance. In the same measurement period from January to April 2014 other studies have been carried out, such as the orbit response measurement of the U15 undulator module, which are reported elsewhere [10] and not directly related to the FEL performance.

Within two days of restarting the test injector after shut-down we observed a bright signal on a YAG screen after the undulator in addition to the electron spot. However the spot exhibited diffraction like patterns and could not be propagated beyond the first screen. Also the statistical distribution of the FEL pulse intensity didn't follow the expected Gamma distribution [11] but had a significant enhancement at very low pulse energies. The suspicion that we have observed only a reflection of the FEL beam was confirmed by increasing the aperture of the vacuum chamber after the undulator

and the analysis of the orbit response measurements indicating a very strong downward kick of the electron beam by the fringe fields of the undulator field [10].

After the modification we observed an almost round spot on various screens after the undulator. With a pair of corrector magnets right after the undulator module the FEL signal was separated from the electron beam. A special YAG screen with a hole in the lower half allowed bypassing the electron beam without generating scintillating light in the case that the FEL signal would be weak. However the intensity of the spot was bright enough that a normal YAG screen could be used. Figure 2 shows a series of FEL spots on the YAG screen, 1 m behind the undulator module, taken for the statistical analysis of the FEL energy.

The measurement of the intensity fluctuation can give information on the pulse length of the FEL pulse. The less it fluctuates the longer the FEL pulse is because more spikes are present in the pulse reducing the fluctuation in the summation over all spikes per pulse. To check the behavior we configured the FEL for two different electron bunch lengths and compared with numerical simulations, using the FEL code Genesis 1.3 [12]. For the simulations we didn't fit any beam parameter. Instead the beam properties were derived from the measurement of the electron beam parameters at the test facility, such as bunch length, charge, emittance and energy chirp.

The results of measurements and simulations are shown in Fig. 3 and are in reasonably good agreement. Assuming a Gamma distribution as the underlying distribution the only free parameter is M and has fit values of $M = 136$ and $M = 208$ for the measurement and simulation, respectively. The beam energy was 100 MeV and a peak current of 20 A, resulting in a radiation wavelength of 300 nm.

The pulse was compressed by applying a chirp with the X-band cavity because at the time of the measurement the RF station for the last two accelerating S-band structures, controlling the chirp and boosting the beam energy to 250 MeV, was not operational. The values in the fluctuation of the FEL energy in measurements and simulations were $M = 28$ and $M = 20$, respectively.

The fitting of the Gamma distribution to the measurement results were challenging because a background value has to be subtracted. A slight change in that value has a strong impact on the fit value, in particular for distributions, where the spread is small compared to the mean value (e.g. the long

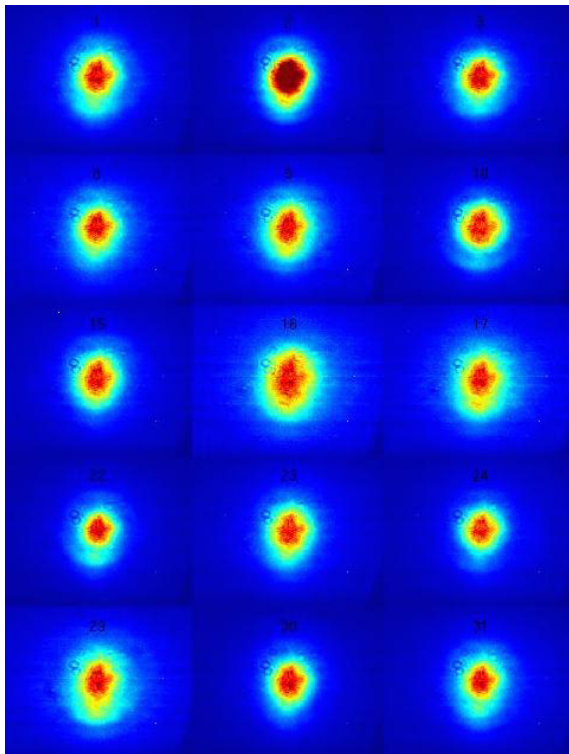


Figure 2: Various FEL spots on a YAG screen 1 m after the undulator.

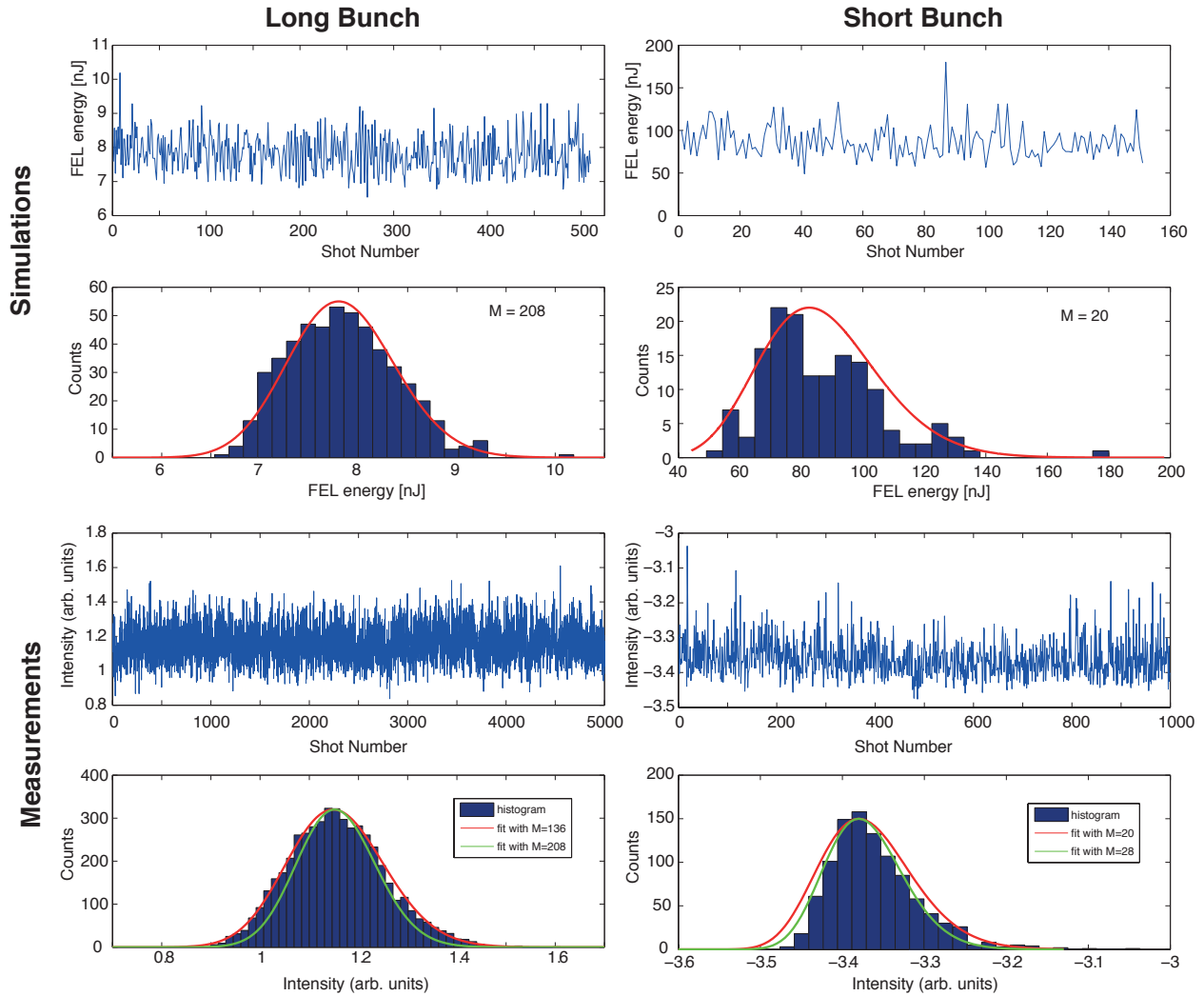


Figure 3: Statistical fluctuation of the FEL signal in simulations and measurements for a long and short bunch (left and right plots, respectively). For comparison the fit from the simulation has been overlaid in the distribution of the measurements.

bunch case with a value of $M = 136$). We measured the base

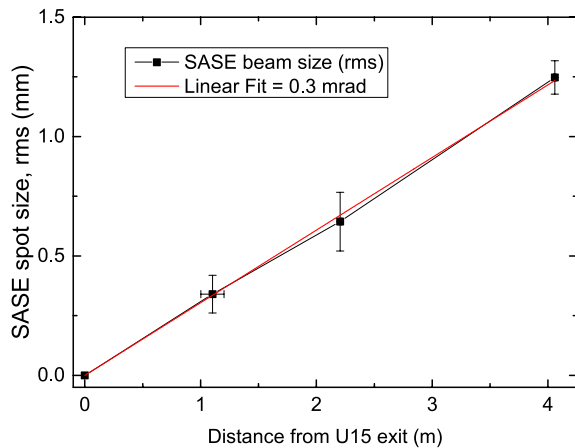


Figure 4: RMS FEL beam size at various screens after the undulator.

level by disabling the electron bunch generation and thus the FEL pulse, while keeping the region of interest constant. The fit of the Gamma distribution to the measurement is reasonably good although the base level may have been influenced by the stray light of the YAG screen, generated by the electron beam itself.

With the ability to measure the FEL spot on three different screens the divergence of the FEL beam can be determined and compared to simulations (see Fig. 4). The measurements yield a value of 0.3 mrad while the simulations produce a divergence of 0.38 mrad. As for the fluctuation of the FEL pulse energy the simulations are based on measured electron beam parameters and not matched to fit the result. For this measurement the beam was compressed to a peak current of 200 A at a beam energy of 130 MeV. The lower value in the measurement indicates that the FEL amplification was lower than in simulation and that gain guiding is weaker. The resulting larger FEL mode size yield less diffraction and thus smaller divergence.

Tunability of the SASE FEL wavelength can be achieved by opening and closing the gap with a tuning range up to a factor 2 with respect to the shortest wavelength. This corresponds to undulator parameter values of 1.0 and 1.7. The measurements were done at a low beam energy of around 120 MeV with a resonance wavelength in the visible spectrum, because a spectrometer was available for that spectral range. In Fig. 5 two different spectra are shown. The overall tuning range in this measurement was between 500 and 1000 nm. There is also a visible signal of the 3rd harmonic, which shifts according to the resonance condition of the FEL. Note that the spectrometer hasn't been calibrated so that the shown signals do not correspond to the spectral intensity. A calibration would indicate much higher intensities towards longer wavelengths and the ratio between first and third is on a percent level at maximum. The spectrum is broader because the electron beam has a residual chirp due to compression. The measurement of the actual SASE bandwidth would have required an uncompressed beam with low beam current, resulting in a theoretical bandwidth smaller than the resolution of the spectrometer.

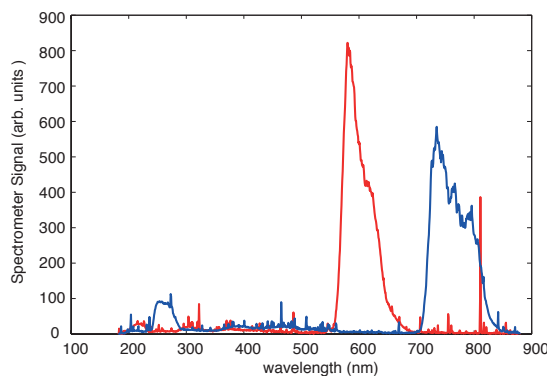


Figure 5: FEL spectra for an undulator gap of 4 and 5 mm (blue and red curve, respectively).

CONCLUSION

Installing a 4 m long in-vacuum undulator in the Swiss-FEL Injector Test Facility has successfully demonstrated

SASE operation, though no saturation has been achieved. The measurements of the divergence angle and the SASE fluctuation agree quite well with simulation based on the measurements of the slice electron beam parameters using a transverse deflector.

Besides some strong kicks in the entrance and exit of the undulator, which had not been anticipated but could be compensated with a larger aperture succeeding the undulator, the field quality of the undulator is sufficient for operating a VUV and visible undulator. The more stringent undulator field requirements for a hard X-ray FEL could not be verified experimentally.

REFERENCES

- [1] J.F. Schmerge *et al*, Nucl. Instr. & Meth. **A 483** (2002) pp. 301-304.
- [2] S. Rimjaem *et al*, Nucl. Instr. & Meth. **A 671** (2012) pp. 62-75.
- [3] T. Shintake *et al*, Nucl. Instr. & Meth. **A 507** (2003) pp. 382-387.
- [4] R. Ganter *et al*, PSI-Bericht 10-04.
- [5] M. Pedrozzi *et al*, "250 MeV Injector Test Facility for the SwissFEL Project" in *Proc. 31st Int. Free-Electron Laser Conf.*, Liverpool, 2009, pp. 321-324
- [6] J.Y. Raguin and M. Bopp, "The Swiss FEL C-Band Accelerating Structure: RF Design and Thermal Analysis" in *Proc. 26th Int. Linear Accelerator Conf.*, Tel Aviv, 2012, pp. 501-503
- [7] E. Prat *et al*, "Slice Emittance Optimization at the SwissFEL Injector Test Facility" in *Proc. 35th Int. Free-Electron Laser Conf.*, New York, 2013, pp. 200-204
- [8] M. Guetg, B. Beutner, E. Prat, S. Reiche, "Dispersion Based Beam Tilt Correction" in *Proc. 35th Int. Free-Electron Laser Conf.*, New York, 2013, pp. 267-270
- [9] E. Prat, Nucl. Instr. & Meth. **A 743** (2014) pp. 103-108.
- [10] M. Calvi *et al*, "Summary of the U15 Prototype Magnetic Performance", presented at this conference: *36th Int. Free-Electron Laser Conf.*, Basel, 2014, MOP041.
- [11] E.L. Saldin, E.A. Schneidmiller, and M.V. Yurkov, Opt. Comm. **148** (1998) pp. 383-403
- [12] S. Reiche, Nucl. Instr. & Meth. **A 429** (1999) 243.

HARMONIC LASING OPTIONS FOR LCLS-II

G. Marcus, Y. Ding, Z. Huang, T. Raubenheimer, SLAC, Menlo Park, CA 94025, USA
G. Penn, LBNL, Berkeley, CA 94720, USA

Abstract

Harmonic lasing can be a cheap and relatively efficient way to extend the photon energy range of a particular FEL beamline. Furthermore, in comparison to nonlinear harmonics, harmonic lasing can provide a beam that is more intense, stable, and narrow-band. This paper explores the application of the harmonic lasing concept at LCLS-II using various combinations of phase shifters and attenuators. In addition, a scheme by which individual undulator modules are tuned to amplify either the third or fifth harmonic in different configurations is presented in detail.

INTRODUCTION

Harmonic lasing in FELs, where the collective electron beam/radiation instability of odd harmonics in a planar undulator evolve independently of the fundamental resonant radiation, has generated much recent interest and potentially offers many benefits over nonlinear harmonic generation [1–3]. Some of these benefits include a more intense, stable, and narrow-band radiation pulse. Harmonic lasing can also be a relatively efficient way of extending the photon energy range of a particular FEL beamline.

The performance of harmonic lasing schemes is contingent on the successful suppression of the fundamental radiation. In this way, incoherent energy spread that is associated with the growth of the fundamental does not interrupt linear growth of the target harmonic, allowing it to reach full saturation. A variety of methods have been proposed to suppress the fundamental radiation including, but not limited to: introducing periodic phase shifts between the field and the electron beam such that the fundamental experiences a non-integer 2π phase shift while the desired harmonic experiences an integer 2π shift; periodically filtering the fundamental with a spectral attenuator while allowing the desired harmonic to pass and simultaneously debunching the electron beam in a bypass chicane; using a combination of detuned/retuned undulators such that the desired harmonic is resonant at different harmonic numbers (third, fifth, etc.) for contiguous undulator sections. This paper explores the application of each of these methods (and combinations thereof) in the case of the LCLS-II design study to not only extend the tuning range of individual beamlines, but to also increase the performance of the hard x-ray (HXR) and soft x-ray (SXR) beamlines at the high end of the tuning range [4]. The performance is illustrated through numerical particle simulations using the FEL code GENESIS [5] where we focus primarily on lasing at the third harmonic.

PARAMETERIZATION

The eigenvalue equation for a high-gain FEL with all of the relevant three-dimensional effects included was first generalized to the case of harmonics in [6]. More recently [2], Ming Xie fitting formulas for the power gain length [7,8] were also generalized to harmonic lasing:

$$\frac{L_{1d}^{(h)}}{L_g^{(h)}} = \frac{1}{1 + \Lambda(\eta_d^{(h)}, \eta_\epsilon^{(h)}, \eta_\gamma^{(h)})}$$

$$L_{1d}^{(h)} = \left(\frac{A_{JJ1}^2}{h A_{JJh}^2} \right)^{1/3} L_{1d}$$

$$\eta_d^{(h)} = \left(\frac{A_{JJ1}^2}{h A_{JJh}^2} \right)^{1/3} \frac{\eta_d}{h} \quad (1)$$

$$\eta_\epsilon^{(h)} = \left(\frac{A_{JJ1}^2}{h A_{JJh}^2} \right)^{1/3} h \eta_\epsilon \quad (2)$$

$$\eta_\gamma^{(h)} = \left(\frac{A_{JJ1}^2}{h A_{JJh}^2} \right)^{1/3} h \eta_\gamma$$

The Xie approach to parameterizing the power gain length is useful for quickly estimating three-dimensional effects using scaled parameters that represent essential system features. Using this formalism, it is possible to quickly estimate electron beam and undulator parameters that are suitable for optimizing harmonic lasing. For instance, it offers a quick estimate on the distance between phase shifters necessary to effectively suppress the fundamental. It is also useful for determining if harmonic lasing is viable for given electron beam and undulator parameters. The harmonics can be extremely sensitive to the slice energy spread and emittance. The Xie formalism quickly quantifies this sensitivity and can illuminate how high in harmonics (and photon energy) the harmonic lasing concept can be pushed.

Table 1: Nominal Electron Beam and Undulator Parameters for the Baseline LCLS-II Scenario

Paramter	Symbol	Value SXR(HXR)	Unit
e-beam energy	E	4.0	GeV
emittance	ϵ	0.45	μm
current	I	1000	A
energy spread	σ_E	500	keV
beta	$\langle\beta\rangle$	12(13)	m
undulator period	λ_u	39(26)	mm
segment length	L_u	3.4	m
break length	L_b	1.0	m
# segments	N_u	21(32)	-
total length	L_{tot}	96(149)	m

An example of this optimization is illustrated in Figure 1, which shows the dependence on the slice energy spread and normalized emittance (at constant current) of the retuned fundamental gain length (top left), the third harmonic gain length (top right) and their ratio (bottom) for the nominal LCLS-II parameters (see Table 1) for lasing at $E_\gamma = 5$ keV in the presence of three-dimensional effects. The bottom plot illustrates that the third harmonic at 5 keV has a shorter gain length than the fundamental tuned to produce 5 keV photons (through undulator parameter K tuning) regardless of the slice energy spread or emittance around the LCLS-II design point. The middle plot illustrates, however, that these parameters must be reasonably controlled in order for the harmonic to reach saturation within the undulator length constraints. It also shows that the third harmonic is far more sensitive to an increase in the slice energy spread than the fundamental.

PHASE SHIFTERS

Phase shifters are present in gap tunable undulators in order to maintain a 2π phase shift between the FEL radiation and electron beam during the break sections that host strong focusing quadrupoles. If, however, these phase shifters are tuned such that the electron's phase delay is either $2\pi/3$ or $4\pi/3$, the third harmonic stays resonant while the fundamental radiation is suppressed.

Figure 2 shows the power gain curves for an ideal electron beam specified by the parameters in Table 1 comparing the production of $E_\gamma = 5$ keV photons through nonlinear harmonics (brown), harmonic lasing (cyan) and the retuned, using K, fundamental (blue) for the LCLS-II baseline scenario in the HXR beamline. Here, we have included additional phase shifters for illustrative purposes in the harmonic lasing scenario that are not in the current iteration of the undulator lattice but are nonetheless needed to effectively suppress the fundamental. We have found that the phase shifter spacing should be less than the fundamental power gain length. The phase shifter distribution is the optimized recipe reported in [3]. As one can see, harmonic lasing saturates at a higher average power than the nonlinear harmonics. While it saturates at about the same power as the retuned fundamental, it does so at a much earlier location, which leaves significant room for post saturation tapering. The current LCLS-II baseline barely reaches saturation at the fundamental at $E_\gamma = 5$ keV. Among other advantages, harmonic lasing enables the consideration of self-seeding at 5 keV with the electron beam from the superconducting linac. Furthermore, the RMS bandwidth of the harmonic lasing photon beam is roughly two times smaller than that coming from the fundamental, producing an overall brighter beam.

While the primary aim of the phase shifters is to suppress the fundamental radiation by shifting its phase relative to the electrons, what actually ends up happening for self-amplified spontaneous emission is the amplification of well separated frequency bands. The goal of the phase shifters, then, is to

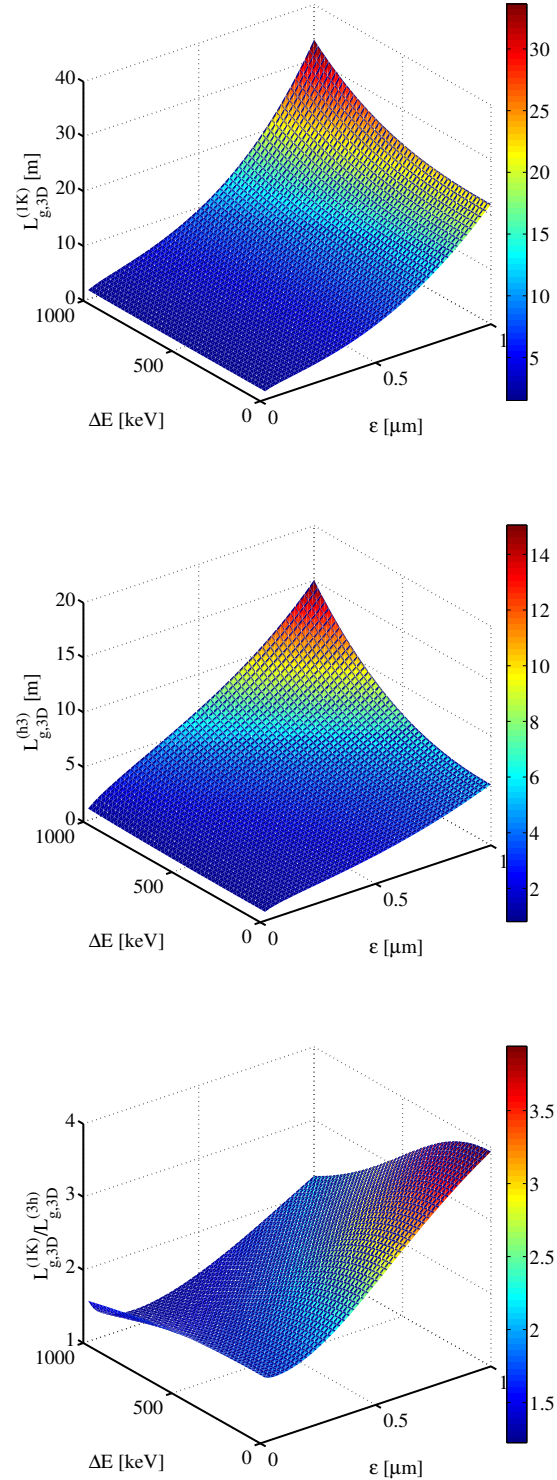


Figure 1: Surface plots illustrating the dependence on the slice energy spread and normalized emittance (at constant current) of the retuned fundamental (using undulator K, denoted (1K)) gain length (top), the third harmonic gain length (middle) and their ratio (bottom) for the nominal LCLS-II parameters for lasing at $E_\gamma = 5$ keV.

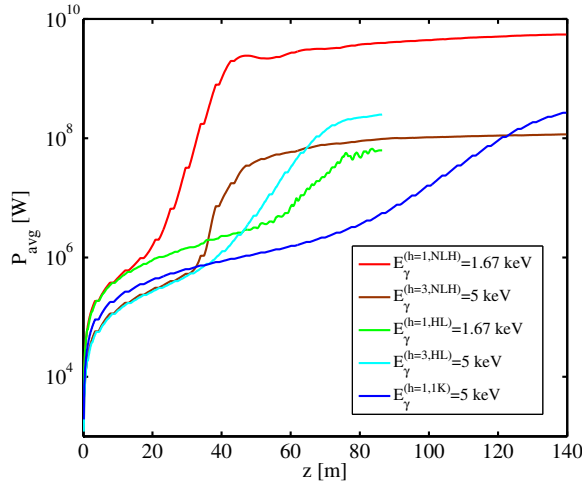


Figure 2: The average power gain curves for the fundamental tuned to $E_\gamma = 1.67$ keV (red), which drives the third harmonic through nonlinear harmonic interaction (brown); The suppressed fundamental (by phase shifters) tuned to $E_\gamma = 1.67$ keV (green) and the third harmonic from harmonic lasing (cyan); the retuned fundamental at $E_\gamma = 5$ keV (blue).

increase the bandwidth of the fundamental by filling these sidebands non-preferentially. While the optimized recipe provided in [3] strategically fills these sidebands, and certainly works for most scenarios, randomized phase shifter recipes can also produce the desired effect. This is illustrated in Figure 3. The top plot shows the fundamental and third harmonic using the optimized phase shifter recipe (blue and green respectively) as well as the fundamental and third harmonic (cyan and red) from a completely random distribution of phase shifters. In this case, the performance is almost identical, with the randomized distribution doing slightly better at saturation. Randomized distributions, however, are often inconsistent in their results as illustrated in the bottom plot for a different random distribution.

INTRAUNDULATOR SPECTRAL FILTERING

As previously mentioned, the LCLS-II does not have the necessary phase shifter period to effectively suppress the fundamental radiation when the third harmonic is tuned to amplify 5 keV photon. Other methods, however, can be used in concert with the given number of phase shifters to optimize the performance. The results of including several stages of spectral filtering (shown here using a crude model where the filters perfectly absorb the fundamental while passing the third harmonic), along with using the available phase shifters in a randomized fashion, is shown in Figure 5. The filters have to be placed frequently enough such that the fundamental does not increase the energy spread as it amplifies. The top plot shows the average power gain curves for the

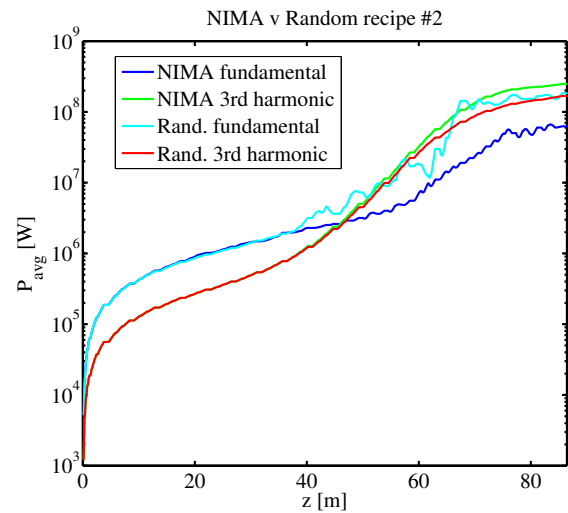
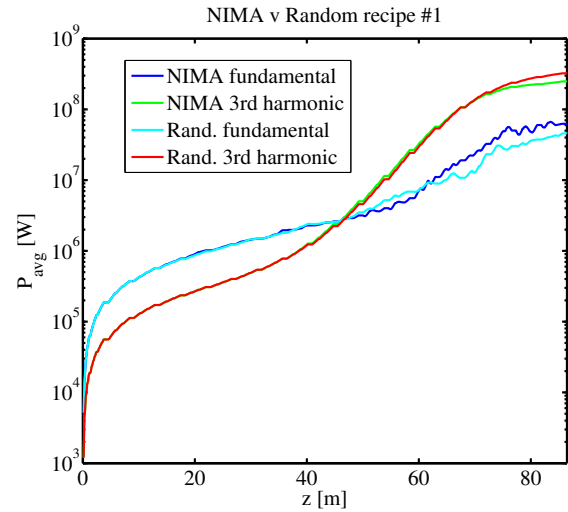


Figure 3: Comparison of the optimized phase shifter recipe detailed in [3] with two independent random phase shifter recipes. The top plot shown a comparable (or even slightly better) performance while the bottom plot shows a clearly worse performance for the random recipes.

third harmonic tuned to 5 keV (green) and the fundamental (blue) using two spectral filters and compares the results to the nominal performance of 5 keV at the fundamental using a retuned undulator (red). The slice emittance, energy spread, and beam matching for this particular study were for slightly more pessimistic LCLS-II parameters than what is listed in Table 1, which explains the slightly longer third harmonic saturation length. The third harmonic (green) clearly outperforms the retuned fundamental (red). The addition of a third spectral filter allows for the amplification of 7 keV photons at the third harmonic close to saturation. This photon energy is current beyond the reach of the fundamental in the baseline LCLS-II case.

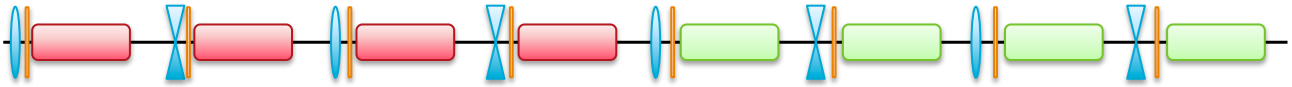


Figure 4: The split undulator scheme where the first half of the undulator (red segments) has the desired photon energy at the third harmonic while the second half of the undulator (green segments) has the desired photon energy at the fifth harmonic. Quadrupoles are shown in blue while adjustable phase shifters are shown in orange.

DETUNED AND RETUNED UNDULATORS

More exotic methods of harmonic lasing have also been proposed [9, 10]. If the undulator parameter K is large enough, individual undulator sections can be tuned such that the desired photon energy is resonant at either the third or fifth harmonic (or higher). The scheme presented here uses the first half of the LCLS-II SXR undulator such that the third harmonic is tuned to produce $E_\gamma = 4.1$ keV photons while the existing phase shifters attempt to suppress the fundamental as efficiently as possible (see Figure 4). The second half of the undulator is tuned such that the fifth harmonic is resonant at 4.1 keV. Here, the fundamental radiation from the first half of the undulator is not resonant with any harmonic. The phase shifters are used in an attempt to suppress both the fundamental and third harmonic radiation while allowing the fifth harmonic to continue to grow. Figure 6 illustrates the performance of the undulator under these conditions.

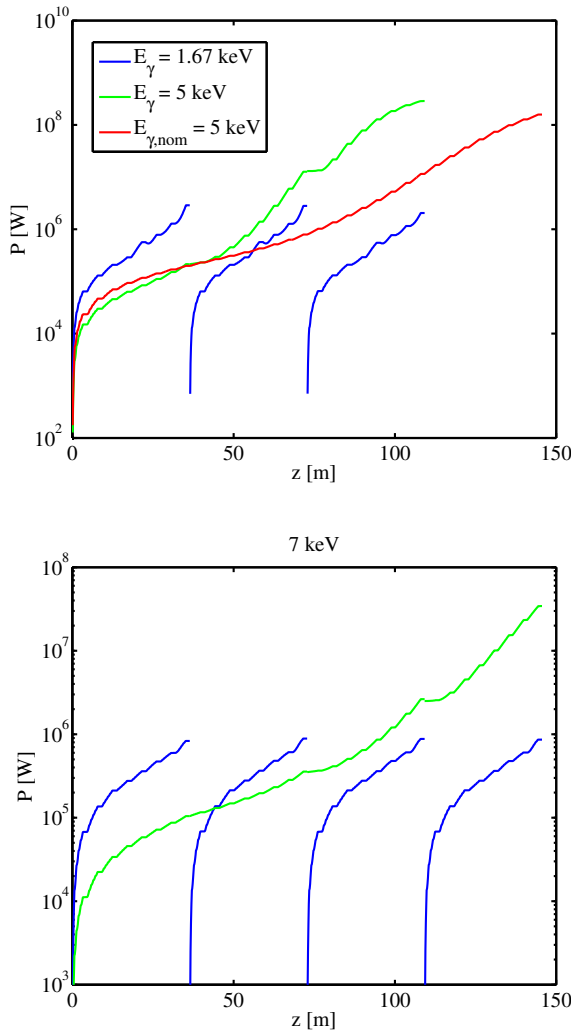


Figure 5: The average power gain curves for the third harmonic tuned to 5 keV (green) and the fundamental (blue) using two spectral filters compared to the nominal performance of 5 keV at the fundamental (red).

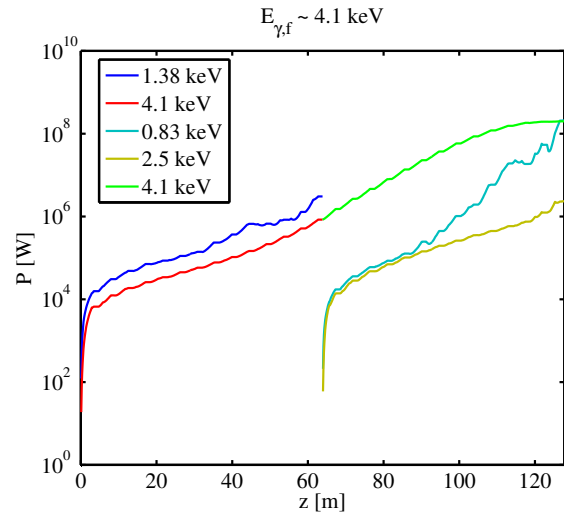


Figure 6: Harmonic lasing scheme where the first.

It should be noted that the FEL resonance condition requires an electron beam energy greater than 4 GeV to produce 4.1 keV photons from the fundamental in the SXR beamline, which is beyond the baseline scenario. It is also clear that the phase shifters in both the first and second half of the undulators are not sufficient to suppress the undesired harmonics completely. However, by the time the fundamental radiation in the second undulator (0.83 keV) begins to amplify, the fifth harmonic at the desired energy has nearly

saturated. Of course, ever more complicated arrangements of undulator segments is being explored.

DISCUSSION

Harmonic lasing using clever combinations of phase shifters, attenuators and detuned/retuned undulators offers an attractive option to both improve the performance of undulator beamlines at the high end of their tuning range and to fully extend the tuning range altogether. Useful formulas exist for quickly estimating the necessary harmonic lasing method needed to reach a desired performance level. However, detailed numerical particle simulations are typically needed to evaluate the efficacy of the implementation [11]. This paper details an initial harmonic lasing performance study in the context of the LCLS-II project. It is worth emphasizing that even though harmonic lasing nominally requires a large number of phase shifters to effectively suppress the fundamental radiation, more exotic methods of suppression using detuned and retuned undulators work for the baseline LCLS-II beamlines without any additional components. More realistic physical models of the spectral filters and chicanes, as was done in [12], will be included in future studies. For the moment, however, it has been shown that the LCLS-II should benefit greatly from these concepts.

ACKNOWLEDGMENT

The authors would like to thank E. A. Schneidmiller and M. V. Yurkov for many helpful and insightful discussions. This work was supported by U.S. Department of Energy Contract No. DE-AC02-76SF00515 and No. DE-AC02-05CH11231.

REFERENCES

- [1] B.W.J. McNeil *et al.*, *Phys. Rev. Lett* **96**, 084801 (2006).
- [2] E. A. Schneidmiller *et al.*, *Phys. Rev. ST Accel. Beams* **15**, 080702 (2012).
- [3] E. A. Schneidmiller *et al.*, *Nucl. Instr. Met. Phys. Res. Sect. A* **717**, 37 (2013).
- [4] G. Marcus *et al.*, “FEL Simulation and Performance Studies for LCLS-II”, in *These Proceedings: Proc. 36th Int. Free-Electron Laser Conf.*, Basel, 2014, TUP032.
- [5] S. Reiche, *Nucl. Instr. Meth. Phys. Res. Sect. A* **429**, 243 (1999).
- [6] Z. Huang *et al.*, *Phys. Rev. E* **62**, 5 (2000).
- [7] M. Xie, *Nucl. Instrum. Methods Phys. Res. Sect. A* **445**, 59 (2000).
- [8] Z. Huang, Private Communication.
- [9] R. Brinkmann *et al.*, DESY-14-025 (2014).
- [10] G. Penn, Private Communication.
- [11] G. Marcus *et al.*, “FEL Code Comparison for the Production of Harmonics via Harmonic Lasing”, in *These Proceedings: Proc. 36th Int. Free-Electron Laser Conf.*, Basel, 2014, TUP031.
- [12] D. Ratner *et al.*, “Harmonic Lasing at the LCLS”, in *Proc. 35th Int. Free-Electron Laser Conf.*, New York, 2013, WEPSO53.

START-TO-END SIMULATIONS FOR IR/THZ UNDULATOR RADIATION AT PITZ

P. Boonpornprasert*, M. Khojoyan, M. Krasilnikov, F. Stephan, DESY, Zeuthen, Germany
B. Marchetti, E. Schneidmiller, M. Yurkov, DESY, Hamburg, Germany
S. Rimjaem, Chiang Mai University, Chiang Mai, Thailand

Abstract

High brightness electron sources for modern linac-based Free-Electron Lasers (FELs) have been characterized and optimized at the Photo Injector Test facility at DESY, Zeuthen site (PITZ). Since the time structure of the electron bunches at PITZ is identical to those at the European XFEL, the PITZ accelerator is being considered as a proper machine for the development of an IR/THz source prototype for pump and probe experiments planned at the European XFEL. Tunable IR/THz radiation sources using synchrotron radiation from a dipole magnet, transition radiation, high gain FELs and coherent radiation of tailored or premodulated beams are currently under consideration. This work describes start-to-end simulations for generating the FEL radiation using an APPLE-II undulator with electron beams produced by the PITZ accelerator. Analysis of the physical parameter space has been performed with tools of the FAST program code package. Electron Beam dynamics simulations were performed by using the ASTRA code, while the GENESIS 1.3 code was used to study the SASE process. The results of these studies are presented and discussed in this paper.

INTRODUCTION

The concept of generating IR/THz radiation by electron bunches from a linear accelerator for pump and probe experiments at the European XFEL was presented in Ref. [1]. One of the important requirements for the IR/THz pulse is the possibility for a precise synchronization with the x-ray pulse. A way to meet this requirement is generating the IR/THz pulse from the same type of electron source which serves the European XFEL and therefore can provide the same time structure and repetition rate as those of the x-ray pulses.

The Photo Injector Test facility at DESY, Zeuthen site (PITZ) has been established to develop, study and optimize high brightness electron sources for modern linac-based short-wavelength Free-Electron Lasers (FELs) like FLASH [2] and the European XFEL [3]. The photocathode laser system at PITZ has the essential feature to be able to produce various temporal pulse shapes [4]. The flat-top temporal profile with a FWHM length of 20-22 ps and ~2 ps rise/fall times is usually used for the operation. The electron bunch charge can be varied from a few pC to 4 nC and the beam can be accelerated up to ~22 MeV/c.

Since PITZ serves as the facility for commissioning and optimizing RF guns for the European XFEL [5,6] the same characteristics (time structure and beam quality) of the elec-

tron beam from the RF gun at PITZ is available as it will be at the European XFEL. In addition, the site of a PITZ-like setup is small enough to fit in the experimental hall for the European XFEL users so that the transport of the IR/THz radiation to the user experiments is very short. From these advantages, PITZ can be considered as an ideal machine for the development of a prototype IR/THz source for pump-probe experiments at the European XFEL.

With the current techniques for the production of electron beam at PITZ and different means for radiation generation (dipole magnet, transition radiation, high gain FELs, coherent radiation of tailored or premodulated beams, etc), it will be possible to cover wavelengths in the whole radiation spectrum from IR (μm) to THz (cm) wavelengths with a variety of field patterns (from single-cycled to narrow-band), and with a high level of the peak and average radiation power [1].

As the PITZ beamline has limited possibilities to install additional components, a preliminary layout for the IR/THz radiation source was developed and is presented in Fig. 1. Preliminary studies by using this layout have been done in order to get benchmark results for actual beamline modifications and further studies. The layout consists of a 1.6-cell L-band photo RF gun surrounded by main and bucking solenoids, a cut disk structure (CDS) booster, a c-shape chicane bunch compressor (D1 to D4), quadrupole magnets (Q1 to Q11), screen stations (S1 to S5) and an APPLE-II type undulator [7]. The components and their positions in this layout from the RF gun to the screen S1 are similar to those of the current PITZ layout. With this preliminary layout, we plan to study the radiation generation with 2 procedures: (i) Self-Amplification of Spontaneous Emission Free-Electron Lasers (SASE FELs) in the undulator using an uncompressed, high charge electron bunch and (ii) Coherent Transition Radiation (CTR) using an ultra-short electron bunch which is compressed by the chicane bunch compressor. The SASE radiation is anticipated to cover radiation wavelengths of 20-100 μm while radiation wavelengths above 100 μm are expected from the CTR.

This paper presents start-to-end (S2E) numerical simulations for the SASE FEL radiation in the wavelength range of 20-100 μm . An uncompressed electron beam with 4 nC bunch charge and the APPLE-II type undulator were used in the simulations. Calculation of the saturation characteristics has been performed with tools of the FAST program code package [8-10]. Beam dynamics simulations were performed by using A Space charge TRacking Algorithm (ASTRA) code [11], while the GENESIS1.3 code [12] was used to study the SASE process.

* prach.boonpornprasert@desy.de

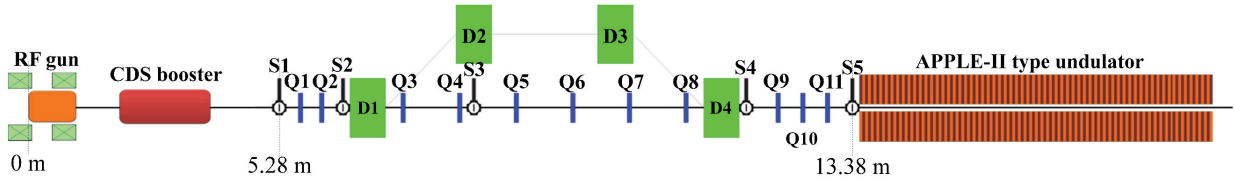


Figure 1: Preliminary schematic layout of the IR/THz facility at PITZ. Here S, Q and D represent screen stations, quadrupole magnets and dipole magnets, respectively.

CONSIDERATIONS OF UNDULATOR PERIOD LENGTH AND ELECTRON BEAM MOMENTUM

The objectives of this section are to determine the undulator period length and the electron beam momentum for generating radiation wavelengths of 20 μm and 100 μm . The undulator used in this study is an APPLE-II type undulator in circular polarization mode. Its peak magnetic field (B_0) and undulator parameter (K) can be calculated by using the following equations [13, 14]:

$$B_0 = 1.54 \exp \left(-4.46 \frac{g}{\lambda_u} + 0.43 \left(\frac{g}{\lambda_u} \right)^2 \right), \quad (1)$$

$$K = \frac{e B_0 \lambda_u}{2 \pi m_e c}, \quad (2)$$

where g is the undulator gap, λ_u is the undulator period length, e is the electron charge, m_e is the electron mass and c is speed of light. The goal FEL radiation wavelength (λ_{rad}) can be calculated by the well-known undulator equation:

$$\lambda_{rad} = \frac{\lambda_u}{2\gamma^2} (1 + K^2), \quad (3)$$

where γ is the Lorentz factor of the electron beam.

In order to achieve the shortest FEL saturation length, the shortest period length of the undulator is expected. The minimum gap is chosen to be 10 mm for sufficient space for the beam pipe. In order to avoid strong space-charge effects during the beam transportation, the minimum electron beam momentum is limited to 15 MeV/c and the beam momentum needs to be as high as possible for each radiation wavelength. However, the maximum electron beam momentum is limited at 22 MeV/c which is the practical maximum momentum used at PITZ. Figure 2 presents the calculated beam momentum as a function of the undulator gap for each case of radiation wavelength and undulator period length. Under the above mentioned conditions, the proper period length is 40 mm, from which follows that the radiation wavelengths of 20 μm and 100 μm can be generated with beam momenta of 22 MeV/c and 15 MeV/c, and gap widths of ~ 16.5 mm and ~ 10 mm, respectively.

OVERVIEW OF THE PARAMETER SPACE

An analysis of the parameter space of the SASE FEL at PITZ is performed for two cases of radiation: 100 μm wavelength using a 15 MeV/c electron beam and 20 μm wavelength using a 22 MeV/c electron beam. It is performed

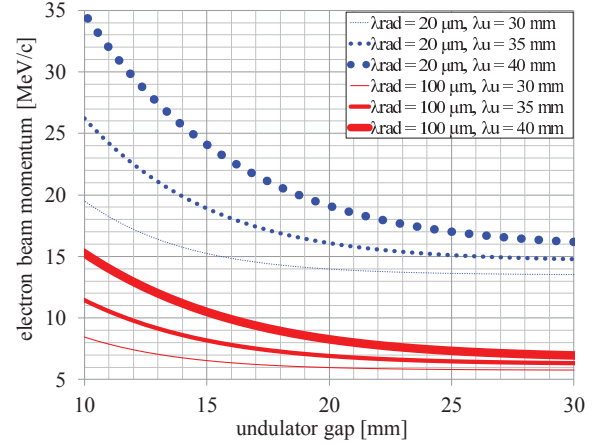


Figure 2: Electron beam momenta for radiation wavelengths of 20 μm and 100 μm as a function of the undulator gap for the different period lengths of the undulator.

by means of tools implemented in the code package FAST [8–10]. We assume natural focusing properties of the helical undulator, thus the remaining parameters of the problem are photon wavelength, energy of the electron beam, peak current, emittance, and energy spread. The numerical solution of the corresponding eigenvalue equation [8, 10] shows that the main physical effects defining the operation of the FEL amplifier are the diffraction effects and the space charge effects. The influence of the longitudinal velocity spread due to emittance and energy spread is negligible.

Figures 3 and 4 show an overview of the saturation characteristics of the SASE FEL versus peak current and emittance. The gray circles at these plots denote the points in the parameter space which we analyze below with detailed numerical simulations with the code GENESIS 1.3. An important feature of the physical parameter space is the small value of the diffraction parameter and the large value of the space charge parameter [8]. In the largest fraction of the parameter space we observe pretty slow dependence of the saturation characteristics on the emittance which reflects the feature of the logarithmic dependence of the FEL gain for small values of the diffraction parameter [8]. At small emittances we see degradation of the FEL gain due to strong space-charge fields. Strong diffraction effects are important also as a factor for a significant reduction of the slippage of the radiation with respect to the kinematic slippage due to the fact that the group velocity of the amplified wave, $\partial\omega/\partial k$,

is less than the velocity of light (c) [8]. This effect allows effective operation of the FEL amplifier driven by short electron pulses. Analysing the influence of the peak current shows that operation at higher currents is more preferable for a reduction of the saturation length and an increase of the peak radiation power. Note that the parameter space of the PITZ FEL is pretty close to that of the first SASE FEL by the UCLA/LANL/RRCKI/SLAC group [8, 15, 16].

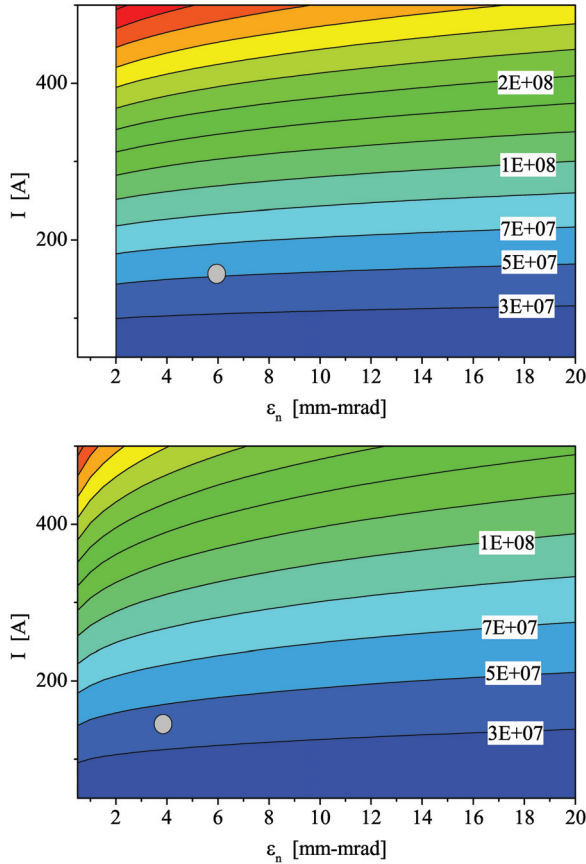


Figure 3: Contour plot for the saturation power [W] versus peak current [A] and emittance [mm-mrad]. Top and bottom plots correspond to the cases of 100 μm using a 15 MeV/c electron beam and 20 μm using a 22 MeV/c electron beam, respectively. The calculations have been performed with the code FAST.

BEAM DYNAMICS SIMULATIONS

Beam dynamics simulations using the ASTRA code were performed in order to deliver an uncompressed 4 nC electron beam from the cathode to the undulator entrance. Space-charge calculations were included in the simulations. The beam transport line layout used in these simulations follows the schematic diagram in Fig. 1. A flat-top cathode laser pulse with a FWHM length of 20 ps and ~ 2 ps rise/fall times was used. In order to ensure that the rms laser spot size is big enough for generating 4 nC bunch charge, the rms laser spot size was set to 1 mm which is close to the maximum size from the practical point of view. The peak electric field

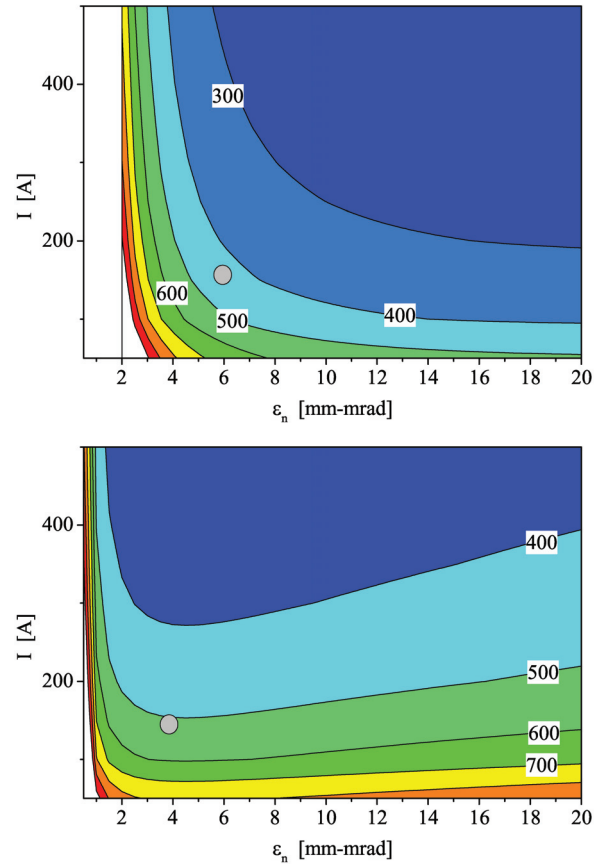


Figure 4: Contour plot for the saturation length [cm] versus peak current [A] and emittance [mm-mrad]. Top and bottom plots correspond to the cases of 100 μm using a 15 MeV/c electron beam and 20 μm using a 22 MeV/c electron beam, respectively. The calculations have been performed with the code FAST.

at the cathode was fixed at 60 MV/m and the booster peak electric fields were set to 10 and 18 MV/m for the beam momenta of 15 MeV/c and 22 MeV/c, respectively.

The contour plots in the previous section indicate that the emittance values at the undulator entrance should be large enough in order to get rid of strong space-charge fields. However, if one realizes beams with high bunch charge and quite low momentum, a huge increase of the emittance during the beam transport can be expected. For this reason, the main solenoid current at the gun was optimized for minimum beam emittance values at the first screen station (S1) for both cases of beam momenta. Figure 5 shows the normalized transverse emittance as a function of the main solenoid current. The minimum emittance values were obtained at the main solenoid current of 388 A and 390 A for the cases of beam momenta of 15 MeV/c and 22 MeV/c, respectively.

Simulations using the optimized main solenoid current were done from the cathode to the undulator entrance. The quadrupole magnets Q1 to Q10 were used for beam transport and matching. The matching strategy is that the transverse size is slightly focused during the transport in order to have a

compromise between the smallest beam size and the weakest beam divergence at the undulator entrance. Figure 6 shows the evolutions of rms beam sizes and the emittance values through the RF gun, the booster cavity and the matching section (S1 to S5). The simulation results show that the growth of emittance in vertical plane is bigger than that of the horizontal plane for both cases of beam momenta. For the case of 15 MeV/c, the emittance growth from the begin to the end of the matching section is about a factor 3 while it is about a factor 2 for the case of 22 MeV/c. The asymmetry of the emittance values between vertical and horizontal planes is due to asymmetric quadrupole focusing strength between two planes [17]. The final transverse parameters and longitudinal profiles of the beams at the undulator entrance are shown in Table 1 and Fig. 7, respectively. Parameters denoted by the gray circles in Fig. 3 and Fig. 4 are illustrated for these final beam profiles. Saturation power of more than 30 MW and a saturation length around 5 m can be expected. The strategies of beam optimization and matching still have to be improved in order to deliver beams which allow for shorter saturation length.

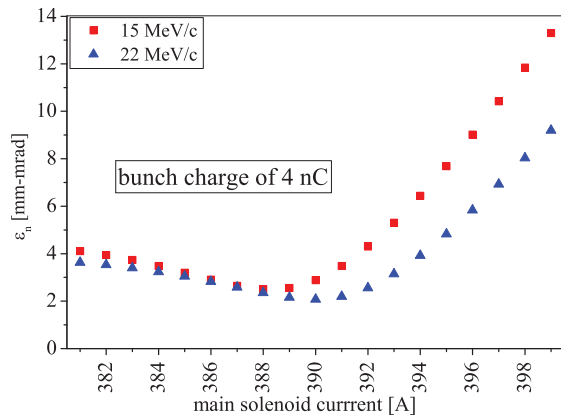


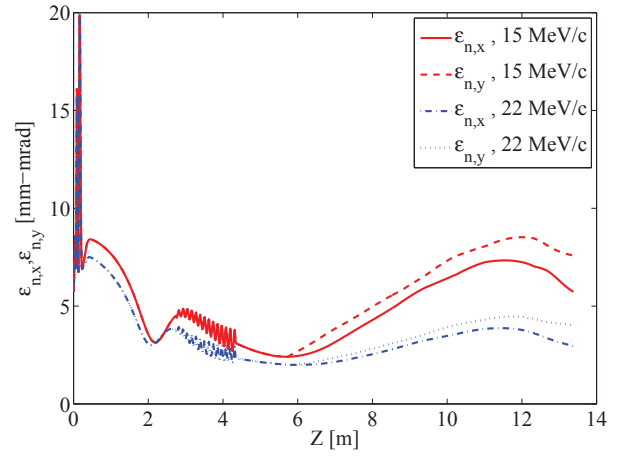
Figure 5: Simulated normalized transverse emittance at the screen S1 as a function of main solenoid current.

Table 1: Transverse Parameters of the Matched Beams at the Undulator Entrance

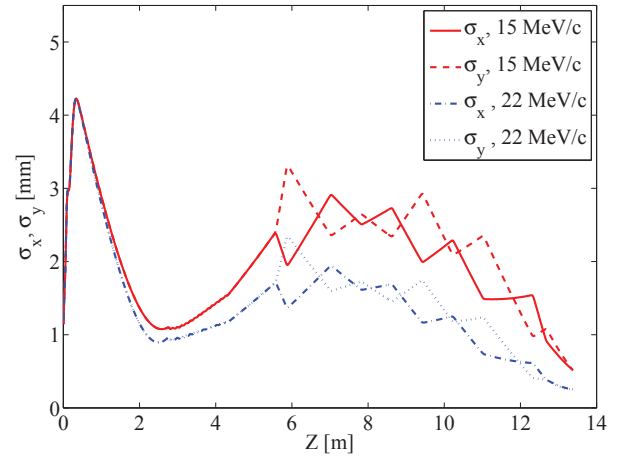
Parameters	15 MeV/c	22 MeV/c
σ_x [mm]	0.36	0.25
σ_y [mm]	0.36	0.25
$\varepsilon_{n,x}$ [mm-mrad]	6.34	2.95
$\varepsilon_{n,y}$ [mm-mrad]	7.16	3.98
α_x	0.62	0.20
α_y	1.36	-0.03

FEL SIMULATIONS

Simulations of the FEL radiation were performed using the GENESIS 1.3 code. The calculations in time-dependent mode including space-charge effects were used in the simulations. The simulations were performed for both cases of radi-



(a) Normalized transverse emittance.



(b) Transverse rms size.

Figure 6: Evolutions of the transverse emittances ($\varepsilon_{n,x}$, $\varepsilon_{n,y}$) and transverse rms sizes ($\sigma_{n,x}$, $\sigma_{n,y}$) of the electron beams from the cathode to the undulator entrance.

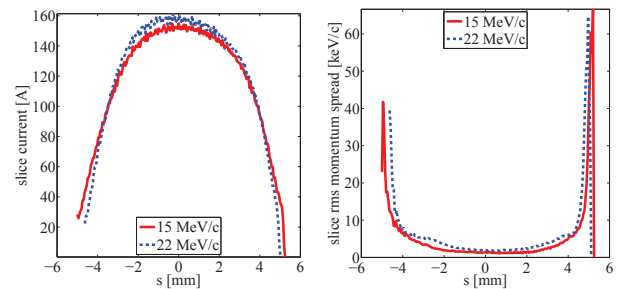


Figure 7: The slice current (left) and the slice rms momentum spread (right) of the matched beams at the undulator entrance.

ation: 20 μm and 100 μm . The matched beams from the previous section were used as the input beams for GENESIS 1.3. The undulator period length was set to 40 mm and the undulator length is assumed to be 7 m (175 periods) in order to be long enough to reach the saturation points for the both cases. In this preliminary simulation, the grid size for the field calculation was set to be larger than the transverse radi-

ation size along the entire undulator length in order to avoid complication of the boundary conditions.

Figure 8 presents the peak power along the undulator. The saturation lengths are 4.12 m (103 periods) and 5.60 m (140 periods) for the radiation wavelengths of 100 and 20 μm , respectively. Figure 9 presents the temporal and spectral structures of the radiation pulses at the points of saturation. For 100 μm , the saturation power is about 90 MW while a spectrum bandwidth of the main peak is about 3 %. For 20 μm , the saturation power is about 130 MW with a bandwidth of the main peak in the spectrum spectrum is less than 1 %. By comparing these results with the results from the code FAST in Fig. 3 and Fig. 4, the saturation lengths from the simulations are corresponding well to the results from those contour plots. In contrast, the saturation powers from the simulations are higher than those in the contour plots for the both cases.

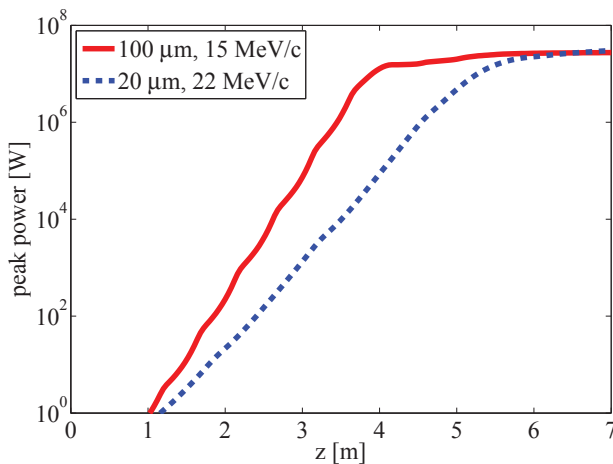
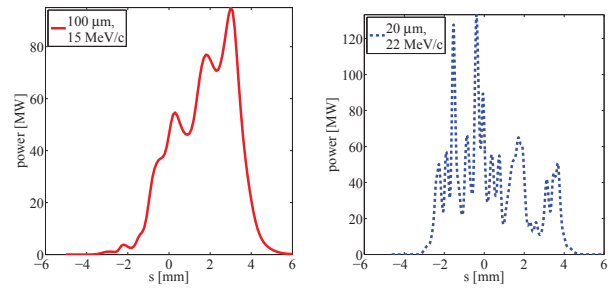


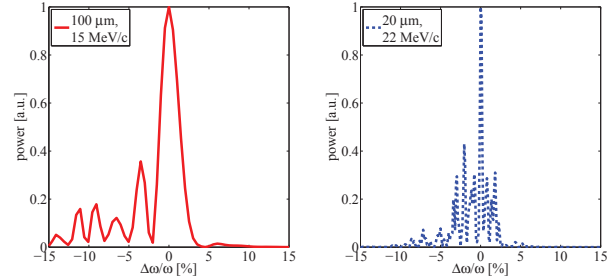
Figure 8: Output peak power along the undulator axis for the cases of 100 μm using a 15 MeV/c electron beam and 20 μm using a 22 MeV/c electron beam.

CONCLUSION AND OUTLOOK

The parameter space of a new IR/THz source based on PITZ setup was studied. Analysis of the physical parameter space was done using the FAST code and preliminary start-to-end simulations of the SASE FEL were performed using the ASTRA and the GENESIS 1.3 codes. The results show that a radiation peak power of more than 90 MW with a narrow bandwidth below 3 % can be achieved. However, the strategies of electron beam optimization and matching still can be improved in order to enhance the FEL performance. In a next step, FEL simulations including waveguide boundary conditions will be studied and performed. Already now this case study shows interesting options for a tunable, synchronized IR/THz source for pump-probe experiment at the European XFEL.



(a) Temporal profiles of the radiation pulses.



(b) Spectral profiles of the radiation pulses.

Figure 9: Temporal and spectral profiles of the radiation pulses at the saturation points. Left and right plots correspond to the case of 100 μm using a 15 MeV/c electron beam and 20 μm using a 22 MeV/c electron beam, respectively.

ACKNOWLEDGMENT

The authors would like to thank colleagues at PITZ for the useful comments and discussions.

REFERENCES

- [1] E. Schneidmiller et al., “Tunable IR/THz source for pump probe experiment at European XFEL”, in *Proc. 34th Int. Free-Electron Laser Conf.*, Nara, Japan, 2012, pp. 503-506.
- [2] W. Ackermann et al., “Operation of a free-electron laser from the extreme ultraviolet to the water window” *Nature Photon.*, vol. 1, pp. 336-342, 2007.
- [3] M. Altarelli et al., “The European x-ray free-electron laser technical design report”, DESY, Hamburg Report No. DESY 2006-097, 2007.
- [4] I. Will and G. Klemz, “Generation of flat-top picosecond pulses by coherent pulse stacking in a multicrystal birefringent filter”, *Optics Express*, vol. 16, pp. 14922-14937, 2008.
- [5] I. Isaev et al., “Conditioning status of the first XFEL gun at PITZ”, in *Proc. 35th Int. Free-Electron Laser Conf.*, New York, 2013, pp. 283-286.
- [6] M. Otevrete et al., “Report on gun conditioning activities at PITZ in 2013”, in *Proc. 5th Int. Particle Accelerator Conf.*, Dresden, Germany, 2014, pp. 2962-2964.
- [7] S. Sasaki, “Analyses for a planar variably-polarizing undulator”, *Nucl. Instrum. and Methods A*, vol. 347, pp. 83-86, 1994.
- [8] E.L. Saldin, E.A. Schneidmiller and M.V. Yurkov, *The Physics of Free Electron Lasers*. Berlin, Germany: Springer, 2000.

- [9] E.L. Saldin, E.A. Schneidmiller and M.V. Yurkov, "FAST: a three-dimensional time-dependent FEL simulation code", *Nucl. Instrum. and Methods A*, vol. 429, pp. 233-237, 1999.
- [10] E.L. Saldin, E.A. Schneidmiller and M.V. Yurkov, "The general solution of the eigenvalue problem for a high-gain FEL", *Nucl. Instrum. and Methods A*, 475, pp. 86-91, 2001.
- [11] K. Flöttmann, ASTRA particle tracking code. Available: <http://www.desy.de/~mpyf1o/>.
- [12] S. Reiche, "GENESIS 1.3: a fully 3D time-dependent FEL simulation code", *Nucl. Instrum. and Methods A*, vol. 429, pp. 243-248, 1999.
- [13] C.J. Boccheta et al., "Conceptual Design Report (CDR) for the FERMI@Elettra project", Sincrotrone Trieste, Trieste, ST/F-TN-07/12, 2007.
- [14] P. Schmüser et al., *Ultraviolet and soft x-ray free-electron lasers*, Berlin, Germany: Springer, 2008, pp. 58-59.
- [15] M. Hogan et al., "Measurements of gain larger than 10^5 at 12 μm in a self-amplified spontaneous-emission free-electron laser", *Phys. Rev. Lett.*, vol. 81, pp. 4867-4870, 1998.
- [16] E.L. Saldin, E.A. Schneidmiller and M.V. Yurkov, "Numerical simulations of the UCLA experiments on a high gain SASE FEL", *AIP Conference Proceedings*, vol. 468, 321-333, 1999.
- [17] G. Kourkafas et al., "Emittance increase and matching along the tomography module at PITZ", in *Proc. 5th Int. Particle Accelerator Conf.*, Dresden, Germany, 2014, pp. 1144-1146.

SASE CHARACTERISTICS FROM BASELINE EUROPEAN XFEL UNDULATORS IN THE TAPERING REGIME

I. Agapov*, G. Geloni, European XFEL GmbH, Hamburg, Germany
G. Feng, V. Kocharyan, E. Saldin, S. Serkez, I. Zagorodnov, DESY, Hamburg, Germany

Abstract

The output SASE characteristics of the baseline European XFEL, recently used in the TDRs of scientific instruments and X-ray optics, have been previously optimized assuming uniform undulators without considering the potential of undulator tapering in the SASE regime. Here we demonstrate that the performance of European XFEL sources can be significantly improved without additional hardware. The procedure consists in the optimization of the undulator gap configuration for each X-ray beamline. Here we provide a comprehensive description of the X-ray photon beam properties as a function of wavelength and bunch charge. Based on nominal parameters for the electron beam, we demonstrate that undulator tapering allows one to achieve up to a tenfold increase in peak power and photon spectral density in the conventional SASE regime.

INTRODUCTION

The output SASE characteristics of the baseline European XFEL have been previously optimized assuming uniform undulator settings and used in the design of scientific instruments [2–4]. In order to enable experiments over a continuous photon energy range, European XFEL undulators have adjustable gap [1]. The availability of very long tunable gap undulators provides a unique opportunity for an up to tenfold increase in spectral density and peak output power (up to the TW-level) for nominal electron beam parameter sets. [5] provides an overview of the design considerations and the general layout of the X-ray instrumentation of the European XFEL sources, beam transport systems and instruments. Baseline parameters for the electron beam have been defined and presented in [6, 7]. These parameters have been used for simulating FEL radiation characteristics and saturation lengths relevant to the European XFEL SASE undulators [8]. A well-known way to enhance the SASE efficiency is to properly configure undulators with variable gap [9–12]. In [13] it has been studied on an example of a particular working point how a tapering procedure, i.e. a slow reduction of the field strength of the undulator in order to preserve the resonance wavelength, while the kinetic energy of the electrons decreases due to the FEL process, can be used to significantly improve performance of the European XFEL sources without additional hardware. In present article we demonstrate that tapering allows one to achieve up to a tenfold increase in output for all achievable photon energies and all nominal electron bunch charges. A new set of baseline parameters of the electron beam for the

European XFEL has been recently updated [6, 7] and was used in present work.

In the following we assume that SASE1 operates at the photon energy of 12 keV, and the FEL process is switched off for dedicated SASE3 operation with the help of a beta-tron switcher [14]. The energy spread due to spontaneous radiation emission in SASE1 is accounted for. We highlight operation of SASE3 for the electron energy of 14 GeV as the most probable working energy. Optimal tapering is found by numerical optimization using a piecewise-quadratic law. The Genesis 1.3 code [15] has been used for our FEL studies. Benchmarks have been performed with another FEL code ALICE [13, 16]. More details on the simulation procedure can be found in [17] and up-to-date parameters will be maintained on the XFEL.EU photon beam parameter web page [18].

PHOTON BEAM PROPERTIES

At the European XFEL facility three photon beamlines will be delivering X-ray pulses to six experimental stations. For fixed electron and photon energy, five working points are foreseen, corresponding to bunch charges of 0.02 nC, 0.1 nC, 0.25 nC, 0.5 nC, 1 nC, and resulting in pulse durations of roughly 2 fs, 8 fs, 20 fs, 40 fs and 80 fs. The hard X-ray undulators SASE1/2 are 250m long producing 4keV-25keV photons, and the soft X-ray undulator SASE3 is 120 m with photon energy range of 0.25-3 keV. We will focus on a more comprehensive description of SASE3 parameters, with the performance of SASE1 discussed more shortly. The improvement in SASE1 performance is comparable to that of SASE3. Moreover, a self-seeding setup [19] is foreseen for SASE1 from the beginning, which makes the high power extraction in the SASE mode more attractive in the soft X-ray range.

The source properties: size, divergence, radiation pulse energy, and maximum photon spectral density depend on photon energy, bunch charge, and electron energy. The pulse energies and the number of photons per pulse are shown in Fig. 1 for the tapered mode and in Fig. 2 for the saturation mode as functions of photon energy and bunch charge. In the tapered mode, pulse energy (or, equivalently, number of photons) increases by up to ten times compared to saturation, depending on the bunch charge and radiation wavelength. For short bunches (e.g. corresponding to 0.02 nC) the tapering efficiency drops since the radiation slips forward relative to the electron bunch and stops being amplified.

Figures 3 and 4 show comparisons of peak power and photon spectral density produced in the standard SASE mode

* ilya.agapov@xfel.eu

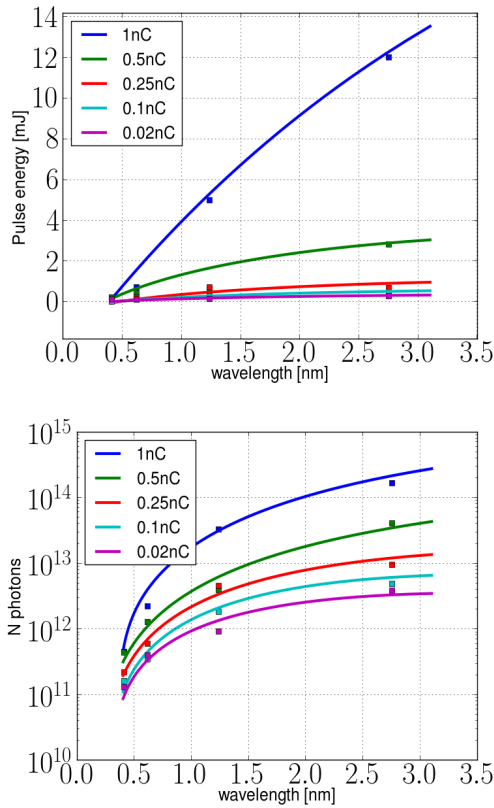


Figure 1: SASE3 baseline for 14 GeV electron energy: (top) pulse energy and (bottom) number of photons per pulse as a function of photon energy and bunch charge in the SASE saturation mode of operation.

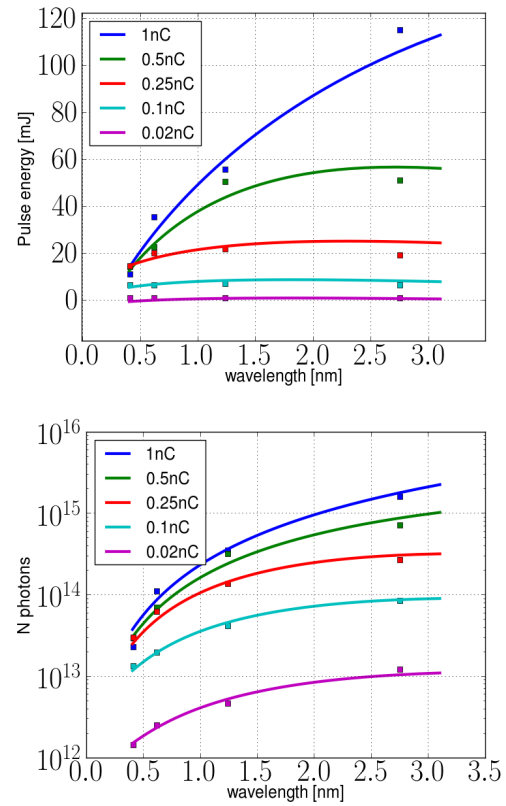


Figure 2: SASE3 baseline for 14 GeV electron energy: (top) pulse energy and (bottom) number of photons per pulse as a function of photon energy and bunch charge in the SASE tapering mode of operation.

at saturation and in the tapered mode. Also in this case, up to tenfold increase in these parameters is observed.

For soft X-rays produced at SASE3 a grating monochromator will be used in order to reduce the bandwidth of FEL radiation for spectroscopy applications. This monochromator provides resolution better than 10^{-4} and is able to accept the high power level of the XFEL radiation [5]. Since the monochromator bandwidth is much narrower than the SASE FEL bandwidth, in order to predict the monochromator output in terms of number of photon per pulse it is convenient to describe the calculated spectral distribution by the maximum photon spectral density of the source.

The source divergence is the most important parameter for the layout of the X-ray beam transport system. Figure 5 shows X-ray pulse divergence in terms of the FWHM of the angular distribution of X-ray pulse energy as a function of photon energy and bunch charge, for saturation and tapered modes respectively. The source divergence is largest for the smallest photon energies and the lowest bunch charges. Since one needs to minimize diffraction from the optics aperture and preserve the radiation wavefront, any optical elements should ideally have an aperture size large enough to accept at least 4σ tails. The (horizontal) offset mirrors of the SASE3 beamline are placed about 300 m behind the

undulator exit. This mirror system can be adjusted between 6 mrad and 20 mrad incidence angle. The X-ray optics and transport group is planning to implement offset mirrors with clear aperture of 800 mm [4]. With these parameters, using Fig. 5, one obtains that the transverse clear aperture of the offset mirrors is in principle enough to fulfill the 4σ requirement for the SASE tapering mode of operation.

Figure 6 shows the evolution of the output energy in the photon pulse and of the variance of the energy fluctuation as a function of the distance inside the undulator, including tapering. Figures 7 and 8 show a comparison of power and spectrum produced in the standard SASE mode at saturation and power and spectrum produced in the SASE mode including post-saturation tapering.

Similar results can be obtained for the hard X-ray undulator SASE1 (see Fig. 9). Moreover, here, due to the shorter radiation wavelength, the radiation slippage does not cause the decrease in tapering efficiency for shorter pulses.

The photon beam quality in the saturation and tapered regime need not be the same. It is best to study such quality by propagation of the photon pulse through the X-ray optics and looking at the distribution of the photon field at the experiment. Simulations with SRW [20] show that for the SPB line [4], the beamline for coherent imaging where smallest

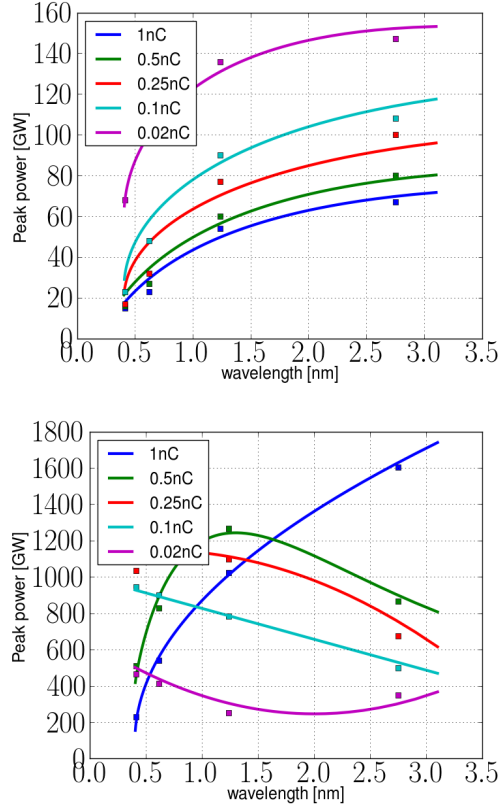


Figure 3: SASE3 baseline for 14 GeV electron energy: peak power in saturation (top) and tapering (bottom) mode.

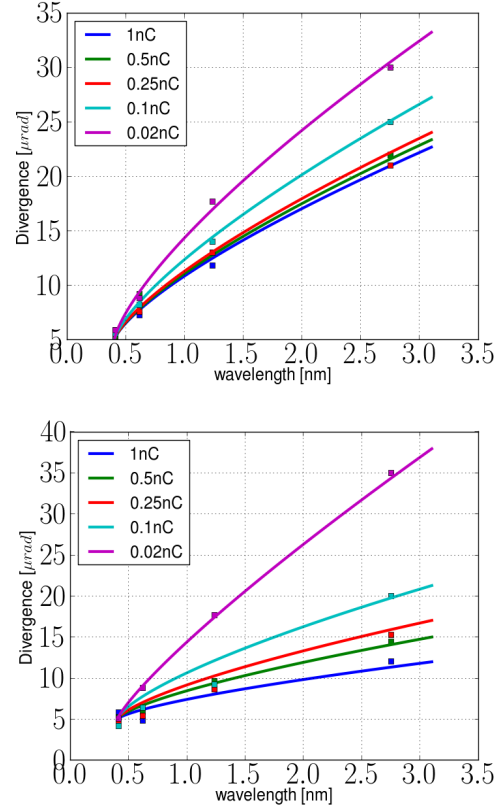


Figure 5: SASE3 baseline for 14 GeV electron energy: FWHM of angular distribution of X-ray pulse energy as a function of photon energy and bunch charge in SASE saturation mode (top) and in tapered mode (bottom).

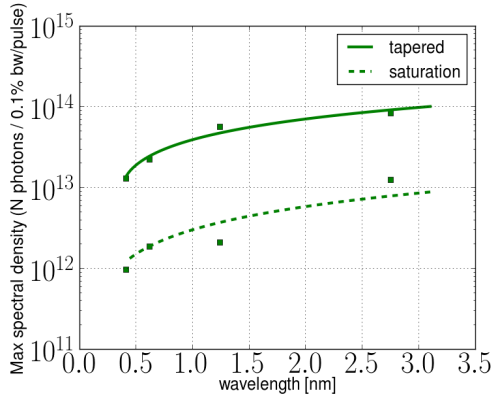


Figure 4: SASE3 baseline for 14 GeV electron energy: Maximum of average spectral density, for 0.5 nC electron beam.

spot size is possible, 100nm focusing can be achieved both with the saturation and tapered parameters (see Fig. 10), which demonstrates that the photon beam quality does not deteriorate. A more detailed analysis of the photon beam quality will be done elsewhere.

CONCLUSION

In this article we demonstrated that the potential of the European XFEL in the standard SASE mode has been underestimated up to the present day. The output X-ray pulse

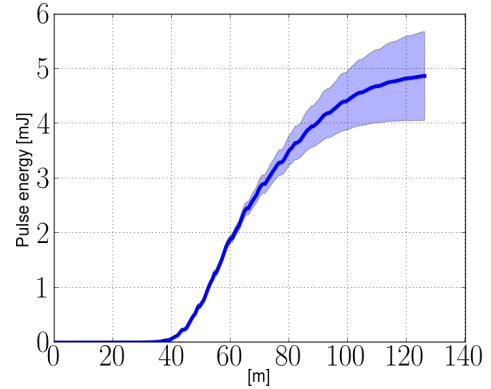


Figure 6: SASE3 baseline for 14 GeV electron energy, 0.1nC bunch charge, 1keV photon energy: Pulse energy evolution

parameters indicated in the design reports of scientific instruments and X-ray beam transport system are far from the optimum found in this paper. Based on start-to-end simulations it has been shown that tapering of baseline undulators for both hard and soft X-rays provides an additional factor of ten increase in spectral density and output power (up to TW-level) for a baseline electron beam parameter set.

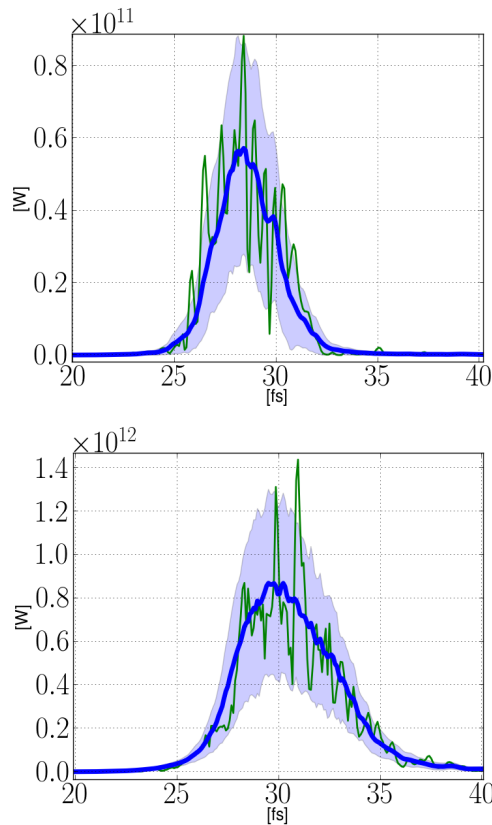


Figure 7: SASE3 baseline for 14 GeV electron energy, 0.1nC bunch charge, 1keV photon energy. Pulse shape: mean (blue), rms (shaded), and median (green). Saturation (top) and tapered (bottom).

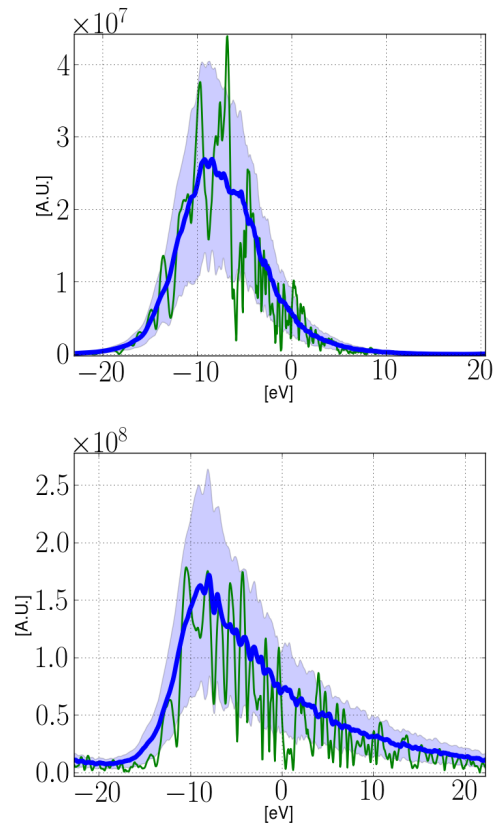


Figure 8: SASE3 baseline for 14 GeV electron energy, 0.1nC bunch charge, 1keV photon energy. Spectrum: mean (blue), rms (shaded), and median (green). Saturation (top) and tapered (bottom).

REFERENCES

- [1] M. Altarelli et al. (eds.), "The European X-Ray Free-Electron Laser : Technical design report", DESY 2006-097 (2006).
- [2] A. Scherz et al., "Scientific Instrument Spectroscopy and Coherent Scattering (SCS): Conceptual Design Report", XFEL.EU TR-2013-006 (2013).
- [3] T. Mazza, H. Zhang and M. Meyer, "Scientific Instrument SQS: Technical Design Report", XFEL.EU TR-2012-007 (2012).
- [4] H. Sinn et al., "X-Ray Optics and Beam Transport: Technical Design Report", XFEL.EU TR-2012-006 (2012).
- [5] Th. Tschentscher, "Layout of the X-Ray Systems at the European XFEL", Technical Report 10.3204/XFEL.EU/TR-2011-001 (2011).
- [6] I. Zagorodnov, <http://www.desy.de/xfel-beam/s2e> (2011).
- [7] G. Feng et al., "Beam Dynamics Simulations for European XFEL", TESLA-FEL 2013-04 (2013).
- [8] E. Schneidmiller and M. Yurkov, "Photon beam properties at the European XFEL", DESY 11-152 (2011).
- [9] A. Lin and J.M. Dawson, "High-Efficiency Free-Electron Laser", Phys. Rev. Lett. 42 1670 (1979).
- [10] P. Sprangle, C.M. Tang and W.M. Manheimer, "Nonlinear Formulation and Efficiency Enhancement of Free-Electron Lasers", Phys. Rev. Lett. 43 1932 (1979).

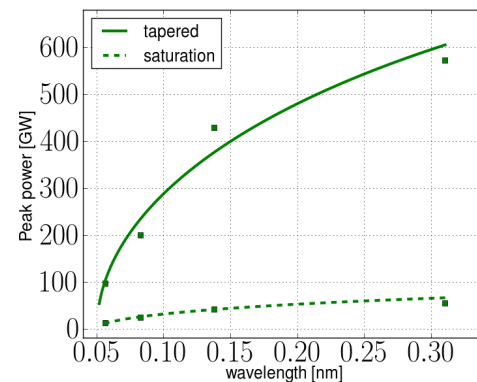


Figure 9: Peak power as a function of photon energy for SASE1 baseline for 14 GeV electron energy, 0.1nC bunch charge

- [11] N.M. Kroll, P. Morton and M.N. Rosenbluth, "Free-Electron Lasers with Variable Parameter Wiggles", IEEE J. Quantum Electron., QE-17, 1436 (1981).
- [12] T.J. Orzechowski et al., "High-Efficiency Extraction of Microwave Radiation from a Tapered-Wiggler Free-Electron Laser", Phys. Rev. Lett. 57, 2172 (1986).

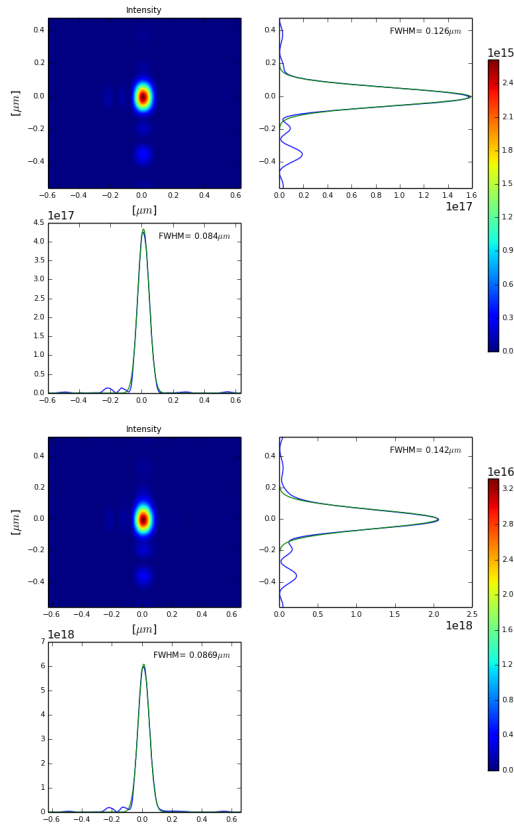


Figure 10: Photon beam distribution at the focus of the SPB instrument, 9keV. Saturation (top) and tapered (bottom) regime.

- [13] S. Serkez et al., "Nonlinear undulator tapering in conventional SASE regime at baseline electron beam parameters as a way to optimize the radiation characteristics of the European XFEL", DESY 13-162 (2013).
- [14] R. Brinkman et al., "Possible operation of the European XFEL with ultra-low emittance beams", DESY 10-011 (2010).
- [15] S. Reiche et al., "GENESIS 1.3: a fully 3D time-dependent FEL simulation code", Nucl. Instr. and Meth. A 429, 243 (1999).
- [16] I. Zagorodnov and M. Dohlus, "Numerical FEL studies with a new code ALICE", in Proceedings of FEL 2009 MOPC16 (2009), I. Zagorodnov, "Numerical Modeling of Collective Effects in Free Electron Laser", in Proceedings of ICAP 2012 TUAC11 (2012).
- [17] I. Agapov et al., "The Full Potential of the Baseline SASE Undulators of the European XFEL", DESY 14-047 (2014).
- [18] <ftp://ftp.desy.de/pub/exfel-wp72/repository/fel/index.html>
- [19] G. Geloni et al., "Scheme for generation of highly monochromatic X-rays from a baseline XFEL undulator", DESY 10-033 (2010).
- [20] O. Chubar and P. Elleaume, "Accurate and efficient computation of synchrotron radiation in the near field region", in Proceedings of EPAC98, Stockholm, Sweden (1998).

PROPOSAL TO GENERATE 10 TW LEVEL FEMTOSECOND X-RAY PULSES FROM A BASELINE UNDULATOR IN CONVENTIONAL SASE REGIME AT THE EUROPEAN XFEL

Svitozar Serkez, Vitali Kocharyan, Evgeni Saldin, Igor Zagorodnov
Deutsches Elektronen-Synchrotron (DESY), Hamburg, Germany
Gianluca Geloni
European XFEL GmbH, Hamburg, Germany

Abstract

Output characteristics of the European XFEL have been previously studied assuming an operation point at 5 kA peak current. Here we explore the possibility to go well beyond such nominal peak current level. We consider a bunch with 0.25 nC charge, compressed up to a peak current of 45 kA. An advantage of operating at such high peak current is the increase of the x-ray output peak power without any modification to the baseline design. Based on start-to-end simulations, we demonstrate that such high peak current, combined with undulator tapering, allows one to achieve up to a 100-fold increase in a peak power in the conventional SASE regime, compared to the nominal mode of operation. In particular, we find that 10 TW-power level, femtosecond x-ray pulses can be generated in the photon energy range between 3 keV and 5 keV, which is optimal for single biomolecule imaging. Our simulations are based on the exploitation of all the 21 cells foreseen for the SASE3 undulator beamline, and indicate that one can achieve diffraction to the desired resolution with 15 mJ (corresponding to about $3 \cdot 10^{13}$ photons) in pulses of about 3 fs, in the case of a 100 nm focus at the photon energy of 3.5 keV.

INTRODUCTION

Imaging of single molecules at atomic resolution using radiation from the European XFEL facility would enable a significant advance in structural biology, because it would provide means to obtain structural information of large macromolecular assemblies that cannot crystallize, for example membrane proteins. The imaging method “diffraction before destruction” [1]- [5] requires pulses containing enough photons to produce measurable diffraction patterns, and short enough to outrun radiation damage. The highest signals are achieved at the longest wavelength that supports a given resolution, which should be better than 0.3 nm. These considerations suggest that the ideal energy range for single biomolecule imaging spans between 3 keV and 5 keV [6]. The key metric for optimizing a photon source for single biomolecule imaging is the peak power. Ideally, the peak power should be of the order of 10 TW [7].

The baseline SASE undulator sources at the European XFEL will saturate at about 50 GW [8]. While this limit is very far from the 10 TW-level required for imaging single biomolecules, a proposal exists to improve the output power at the European XFEL by combining self-seeding [9]- [28],

emittance spoiler foil [29]- [31], and undulator tapering techniques [32]- [42]. However, the realization of such proposal requires installing additional hardware in the undulator system and in the bunch compressor [7]. Here we explore a simpler method to reach practically the same result without additional hardware. This solution is based on the advantages of the European XFEL accelerator complex, which allows one to go well beyond the nominal 5 kA peak current.

The generation of x-ray SASE pulses at the European XFEL using strongly compressed electron bunches has many advantages, primarily because of the very high peak power, and very short pulse duration that can be achieved in this way [43]. Considering the baseline configuration of the European XFEL [8], and based on start-to-end simulations, we demonstrate here that it is possible to achieve a 100-fold increase in peak power by strongly compressing electron bunches with nominal charge. In this way we show that 10 TW power level, 3 fs-long pulses at photon energies around 4 keV can be achieved in the SASE regime. This example illustrates the potential for improving the performance of the European XFEL without additional hardware.

The solution to generate 10 TW power level proposed in this article is not without complexities. The price for using a very high peak-current is a large energy chirp within the electron bunch, yielding in its turn a large (about 1%) SASE radiation bandwidth. However, there are very important applications like bio-imaging, where such extra-pink x-ray beam has a sufficiently narrow bandwidth to be used as a source for experiments without further monochromatization.

In order to enable high focus efficiency with commercially available mirrors (80 cm-long) at photon energies around 4 keV, the undulator source needs to be located as close as possible to the bio-imaging instrument. With this in mind we performed simulations for the baseline SASE3 undulator of the European XFEL at a nominal electron beam energy of 17.5 GeV. We optimized our setup based on start-to-end simulations for an electron beam with 0.25 nC charge, compressed up to 45 kA peak current [44]. In this way, the SASE saturation power could be increased to about 0.5 TW.

In order to generate high-power x-ray pulses we exploit undulator tapering. Tapering consists in a slow reduction of the field strength of the undulator in order to preserve the resonance wavelength, while the kinetic energy of the electrons decreases due to the FEL process. The undulator taper can be simply implemented as discrete steps from one undulator segment to the next, by changing the undulator

Table 1: European XFEL Parameters Used in this Paper

	Units	
Undulator period	mm	68
Periods per cell	-	73
Total number of cells	-	21
Intersection length	m	1.1
Energy	GeV	17.5
Charge	nC	0.25

gap. In this way, the output power of the SASE3 undulator could be increased from the value of 0.5 TW in the SASE saturation regime to about 5 TW. The SASE3 undulator with 21 cells consists of two parts. The first is composed by an uniform undulator, the second consists of a tapered undulator. The SASE signal is exponentially amplified passing through the first uniform part. This is long enough, 9 cells, in order to reach saturation, which yields about 0.5 TW power. Finally, in the second part of the undulator the SASE output is enhanced up to 5 TW by taking advantage of magnetic field tapering over the last 12 cells.

From all applications of XFELs for life sciences, the main expectation and the main challenge is the determination of 3D structures of biomolecules and their complexes from diffraction images of single particles. Parameters of the accelerator complex and availability of long baseline undulators at the European XFEL offer the opportunity to build a beamline suitable for single biomolecular imaging experiments from the very beginning of the operation phase. In the next decade, no other infrastructure will offer such high peak current (up to about 50 kA) and high electron beam energy (up to about 17.5 GeV) enabling 10 TW mode of operation in the simplest SASE regime.

FEL STUDIES

We present a feasibility study of the setup described above with the help of the FEL code Genesis 1.3 [45] running on a parallel machine. Results are presented for the SASE3 FEL line of the European XFEL, based on a statistical analysis consisting of 100 runs. The overall beam parameters used in the simulations are presented in Table 1.

The beam parameters at the entrance of the SASE3 undulator, and the resistive wake inside the undulator are shown in Fig. 1, see also [44]. Full tracking calculations were used to find a new set of electron bunch parameters at the entrance of baseline undulators. The main effects influencing the electron beam acceleration and transport, such as space charge force, rf wakefields and coherent synchrotron radiation (CSR) effects inside magnetic compressors have been included. Our calculations account for both wakes and quantum fluctuations in the SASE1 undulator.

Using a bunch with larger slice emittance and energy spread, but also higher peak current, does not necessarily complicates reaching SASE saturation, because the increased peak current eases the effects of the increased longitudinal velocity spread. For example, the final normalized

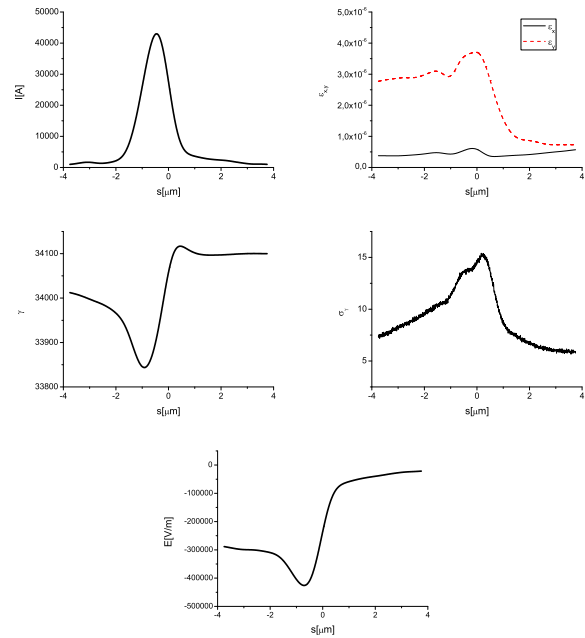


Figure 1: Results from electron beam start-to-end simulations at the entrance of SASE3. (First Row, Left) Current profile. (First Row, Right) Normalized emittance as a function of the position inside the electron beam. (Second Row, Left) Energy profile along the beam. (Second Row, Right) Electron beam energy spread profile. (Bottom row) Resistive wakefields in the SASE3 undulator.

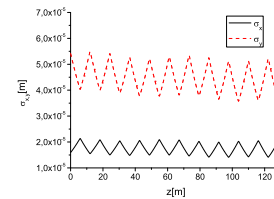


Figure 2: Evolution of the horizontal and vertical dimensions of the electron bunch as a function of the distance inside the SASE3 undulator. The plots refer to the longitudinal position inside the bunch corresponding to the maximum current value.

slice emittance in the 45 kA case studied here is about 4 μm , but the SASE saturation length is in the very safe range of 9 undulator cells at photon energies around 4 keV. The extreme working point at 45 kA peak current is very interesting, because the radiation peak power at saturation is ten-fold increased up to about 0.5 TW. The problem with operation at higher peak current is that wake fields become larger and, therefore, the energy chirp within the electron bunch becomes in its turn more and more important. In our case of interest, the variation in the electron energy within the bunch can be large compared to the Pierce parameter ρ (i.e. with the slice gain-bandwidth) [44], but this does not result in gain reduction (in order to incur in gain reduction, one should have a relative variation in the electron beam

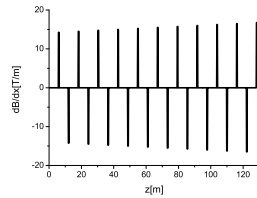


Figure 3: Quadrupole strength along the undulator.

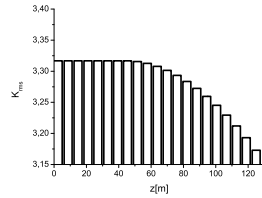


Figure 4: Tapering law.

energy comparable or larger than the Pierce parameter ρ within a cooperation length). Specifically, simulations show that the large energy chirp along the electron bunch only yields a large (about 1%) output radiation bandwidth.

Due to collective effects in the bunch compression system, emittances in the horizontal and vertical directions are significantly different. As a result, the electron beam looks highly asymmetric in the transverse plane: in the horizontal direction $\sigma_x \sim 20 \mu\text{m}$, while in the vertical direction $\sigma_y \sim 50 \mu\text{m}$. The evolution of the transverse electron bunch dimensions are plotted in Fig. 2. The evolution of the transverse electron bunch dimensions is plotted in Fig. 2, and the correspondent quadrupole strength is shown in Fig. 3. The undulator is tapered according to the law in Fig. 4. The quadrupole strength and the tapering have been optimized to maximize the final output power.

The output characteristics, in terms of power and spectrum, are plotted in Fig. 5. Inspection of the plots shows that one can reach 5 TW pulses with a bandwidth of about 1%. Fig. 6 shows the distribution of the radiation pulse energy per unit surface and angular distribution of the exit of the setup. Finally, in Fig. 7 we plot the evolution of the output energy in the photon pulse and of the variance of the energy fluctuation as a function of the distance inside the output undulator.

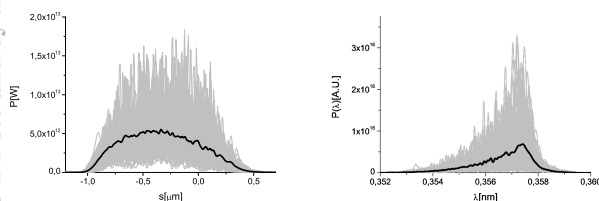


Figure 5: Power and spectrum produced in the SASE mode with undulator tapering. Grey lines refer to single shot realizations, the black line refers to the average over a hundred realizations.

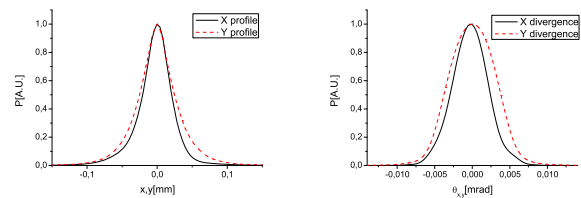


Figure 6: Distribution of the radiation pulse energy per unit surface and angular distribution of the exit of the setup.

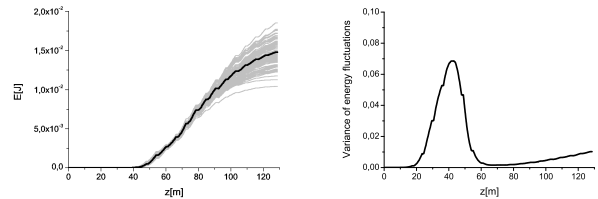


Figure 7: Evolution of the output energy in the photon pulse and of the variance of the energy fluctuation as a function of the distance inside the output undulator, with tapering. Grey lines refer to single shot realizations, the black line refers to the average over a hundred realizations.

CONCLUSIONS

The nominal design parameters for the European XFEL for a 0.25 nC electron bunch, which allow for SASE saturation with $0.4 \mu\text{m}$ normalized slice emittance and 5 kA peak current are described in [46]. In this article we note that the European XFEL accelerator complex is flexible enough to be reconfigured for much higher bunch peak-current. In this case, the new beam parameters are simply set in the control room, and do not require hardware modifications in the tunnel. This flexibility is demonstrated by studying the new acceleration and compression parameters required over a wide range of a peak current values well beyond the nominal 5 kA [44]. For each case, full tracking calculations were used to find a new set of electron bunch parameters at the entrance of baseline undulators. In this paper we considered the extreme working point at 45 kA peak current, where the radiation peak power at saturation is ten-fold increased up to about 0.5 TW. This approach allows one to increase the peak power to 5 TW by taking advantage of an undulator magnetic-field taper over the baseline SASE3 undulator.

REFERENCES

- [1] J. Hajdu, "Single-molecule X-ray diffraction", *Curr. Opin. Struct. Biol.*, vol. 10, pp. 569-573, (2000).
- [2] R. Neutze et al., "Potential for biomolecular imaging with femtosecond X-ray pulses", *Nature*, vol. 406, pp. 752-757, doi:10.1038/35021099, (2000).
- [3] H. Chapman et al., "Femtosecond diffractive imaging with a soft-X-ray free-electron laser", *Nat. Phys.*, vol. 2, pp. 839-843, doi:10.1038/nphys461, (2006).
- [4] K. J. Gaffney and H. N. Chapman, "Imaging Atomic Structure and Dynamics with Ultrafast X-ray Scattering", *Science*, vol.

- 316, no. 5830, pp. 1444-1448, doi:10.1126/science.1135923, (2007).
- [5] M. M. Seibert et al., "Single mimivirus particles intercepted and imaged with an X-ray laser", *Nature*, vol. 470, pp. 78-81, doi:10.1038/nature09748, (Feb. 2011).
- [6] S. Baradaran et al., *LCLS-II New Instruments Workshops Report*, pp. 66-72, (2012).
- [7] S. Serkez et al., "Proposal for a scheme to generate 10 TW-level femtosecond x-ray pulses for imaging single protein molecules at the European XFEL", DESY 13-101, (2013).
- [8] Th. Tschentscher, "Layout of the x-Ray Systems at the European XFEL", Technical Report 10.3204/XFEL.EU/TR-2011-001, Hamburg, doi:10.3204/XFEL.EU/TR-2011-001, (2011).
- [9] J. Feldhaus et al., "Possible application of X-ray optical elements for reducing the spectral bandwidth of an X-ray SASE FEL" *Optics. Comm.*, vol. 140, pp. 341-352, (1997).
- [10] E. Saldin et al., "X-ray FEL with a meV bandwidth", *NIM, ser. A*, vol. 475, pp. 357-362, (Dec. 2001).
- [11] E. Saldin et al., "Optimization of a seeding option for the VUV free electron laser at DESY", *NIM, ser. A*, vol. 445, pp. 178-182, (May 2000).
- [12] R. Treusch et al., "The seeding project for the FEL in TTF phase II", DESY Ann. report, (2001).
- [13] A. Marinelli et al., "Comparative study of nonideal beam effects in high gain harmonic generation and self-seeded free electron lasers", *Phys. Rev. ST Accel. Beams*, vol. 13, p. 070701, (Jul 2010).
- [14] G. Geloni et al., "Scheme for generation of highly monochromatic X-rays from a baseline XFEL undulator", DESY 10-033, (2010).
- [15] Y. Ding et al., "Two-bunch self-seeding for narrow-bandwidth hard x-ray free-electron lasers" *Phys.Rev.ST Accel.Beams*, vol. 13, p. 060703, (2010).
- [16] G. Geloni et al., "A simple method for controlling the line width of SASE x-ray FELs", DESY 10-053, (2010).
- [17] G. Geloni et al., "A Cascade self-seeding scheme with wake monochromator for narrow-bandwidth x-ray FELs", DESY 10-080, (2010).
- [18] G. Geloni et al., "Cost-effective way to enhance the capabilities of the LCLS baseline", DESY 10-133, (2010).
- [19] J. Wu et al., "Staged self-seeding scheme for narrow bandwidth , ultra-short X-ray harmonic generation free electron laser at LCLS", *Proc. 34th Int. Free-Electron Laser Conf., Malmo, TUPB08*, (2010).
- [20] G. Geloni et al., "Generation of doublet spectral lines at self-seeded X-ray FELs", DESY 10-199, 2010, and *Optics Commun.*, vol. 284, p. 3348, (2011).
- [21] G. Geloni et al., "Production of transform-limited X-ray pulses through self-seeding at the European X-ray FEL", DESY 11-165, (2011).
- [22] G. Geloni et al., "A novel self-seeding scheme for hard X-ray FELs", *J. of Modern Optics*, vol. 58, p. 1391, (2011).
- [23] J. Wu et al., "Simulation of the Hard X-ray Self-seeding FEL at LCLS", *Proc. 33rd Int. Free-Electron Laser Conf., Shanghai, MOPB09*, (2011).
- [24] J. Amann et al., "Demonstration of self-seeding in a hard-X-ray free-electron laser", *Nature Photonics*, vol. 6, pp. 693-698, DOI:10.1038/NPHOTON.2012.180, (2012).
- [25] Yu. Shvyd'ko, R. Lindberg, "Spatiotemporal response of crystals in x-ray Bragg diffraction", *Phys. Rev. ST Accel. Beams*, vol. 15, p. 100702, (Oct. 2012).
- [26] Y. Feng et al., "System design for self-seeding the LCLS at soft X-ray energies", *Proc. 34th Int. Free-Electron Laser Conf., Nara, Japan, TUOB10*, (2012).
- [27] S. Serkez et al., "Grating monochromator for soft X-ray self-seeding the European XFEL", DESY 13-040, Available: <http://arxiv.org/abs/1303.1392>, (2013).
- [28] G. Geloni et al., "Wake monochromator in asymmetric and symmetric Bragg and Laue geometry for self-seeding the European XFEL", DESY 13-013, (2013).
- [29] P. Emma et al., "Femtosecond and Subfemtosecond X-Ray Pulses from a Self-Amplified Spontaneous-Emission-Based Free-Electron Laser", *Phys. Rev. Lett.*, vol. 92, p. 074801-1, (2004).
- [30] P. Emma et al., "Attosecond X-ray pulses in the LCLS using the slotted foil method", *Proc. 26th Int. Free-Electron Laser Conf., Trieste, TUBIS01*, (2004).
- [31] Y. Ding et al., "Femtosecond X-Ray Pulse Characterization in Free-Electron Lasers Using a Cross-Correlation Technique", *Phys. Rev. Lett.*, vol. 109, p. 254802, (2012).
- [32] A. Lin and J. M. Dawson, "High-Efficiency Free-Electron Laser", *Phys. Rev. Lett.*, vol. 42, p. 1670, (1979).
- [33] P. Sprangle et al., "Nonlinear Formulation and Efficiency Enhancement of Free-Electron Lasers", *Phys. Rev. Lett.*, vol. 43, p. 1932, (1979).
- [34] N. M. Kroll et al., "Free-Electron Lasers with Variable Parameter Wigglers", *IEEE J. Quantum Electron.*, vol. QE-17, no. 8, p. 1436, (1981).
- [35] T. J. Orzechowski et al., "High-Efficiency Extraction of Microwave Radiation from a Tapered-Wiggler Free-Electron Laser", *Phys. Rev. Lett.*, vol. 57, p. 2172, (1986).
- [36] W. Fawley et al., "Tapered undulators for SASE FELs", *NIM, ser. A*, vol. 483, p. 537, (2002).
- [37] M. Cornacchia et al., "Future possibilities of the Linac Coherent Light Source" *J. Synchrotron rad.* vol. 11, pp. 227-238, (2004).
- [38] X. Wang et al., "Efficiency and Spectrum Enhancement in a Tapered Free-Electron Laser Amplifier" *Phys. Rev. Lett.*, vol. 103, p. 154801, (2009).
- [39] G. Geloni et al., "Scheme for generation of fully coherent, TW power level hard x-ray pulses from baseline undulators at the European XFEL", DESY 10-108, (2010).
- [40] W. M. Fawley et al., "Toward TW-level LCLS radiation pulses", *Proc. 33rd Int. Free-Electron Laser Conf., Shanghai, TUOA4* (2011).
- [41] Y. Jiao et al., "Modeling and multidimensional optimization of a tapered free electron laser", *Phys. Rev. ST Accel. Beams*, vol. 15, p. 050704, (2012).
- [42] S. Serkez et al., "Perspectives of Imaging of Single Protein Molecules with the Present Design of the European XFEL", presented at this conference: 36th Int. Free-Electron Laser Conf., Basel, MOP082 (2014).

- [43] T. Limberg et al., "Optimized bunch compressor system for the European XFEL", Proc. of Particle Accelerator Conference, Knoxville, TN, pp. 1236-123, (2005).
- [44] I. Zagorodnov, "Compression scenarios for the European XFEL" [Online], http://www.desy.de/fel-beam/data/talks/files/Zagorodnov_ACC2012_ready_new.pptx (2012).
- [45] S. Reiche et al., "GENESIS 1.3: a fully 3D time-dependent FEL simulation code", Nucl. Instr. and Meth., ser. A, vol. 429, pp. 243-248, (1999).
- [46] I. Zagorodnov, "Beam Dynamics simulations for XFEL" [Online], Available: <http://www.desy.de/fel-beam/se/> (2011).

PURIFIED SASE UNDULATOR CONFIGURATION TO ENHANCE THE PERFORMANCE OF THE SOFT X-RAY BEAMLINE AT THE EUROPEAN XFEL

Svitozar Serkez, Vitali Kocharyan, Evgeni Saldin, Igor Zagorodnov
Deutsches Elektronen-Synchrotron (DESY), Hamburg, Germany
Ilya Agapov, Gianluca Geloni
European XFEL GmbH, Hamburg, Germany

Abstract

The purified SASE (pSASE) undulator configuration recently proposed at SLAC promises an increase in the output spectral density of XFELs. In this article we study a straightforward implementation of this configuration for the soft x-ray beamline at the European XFEL. A few undulator cells, resonant at a subharmonic of the FEL radiation, are used in the middle of the exponential regime to amplify the radiation, while simultaneously reducing the FEL bandwidth. Based on start- to-end simulations, we show that with the proposed configuration the spectral density in the photon energy range between 1.3 keV and 3 keV can be enhanced of an order of magnitude compared to the baseline mode of operation. This option can be implemented into the tunable-gap SASE3 baseline undulator without additional hardware, and it is complementary to the self-seeding option with grating monochromator proposed for the same undulator line, which can cover the photon energy range between about 0.26 keV and 1 keV.

INTRODUCTION

The SASE3 beamline at the European XFEL will be operated in the photon energy range between 0.26 keV and at least 3 keV. A high level of longitudinal coherence is the key to upgrade the baseline performance. Self-seeding is a promising approach to significantly narrow the SASE bandwidth and to produce nearly transform-limited pulses [1]-[20]. The implementation of this method in the soft x-ray wavelength range necessarily involves gratings as dispersive elements, which may be installed in the SASE3 undulator without perturbing the electron focusing system and could cover the spectral range between about 0.26 keV and 1 keV [18]- [19]. In order to provide a high level of longitudinal coherence in the photon energy range between 1 keV and 3 keV, proposals exist to narrow the SASE bandwidth at the European XFEL by combining self-seeding and fresh bunch techniques. However, this requires installing additional hardware in the undulator system [21, 22]. Here we explore a simpler method to reach practically the same result without further changes in the undulator system. The solution is based in essence on the purified SASE (pSASE) technique proposed at SLAC [23], and naturally exploits the gap tunability of the SASE3 undulator. In the pSASE configuration, a few undulator cells resonant at a subharmonic of the FEL radiation, called altogether the "slippage-boosted

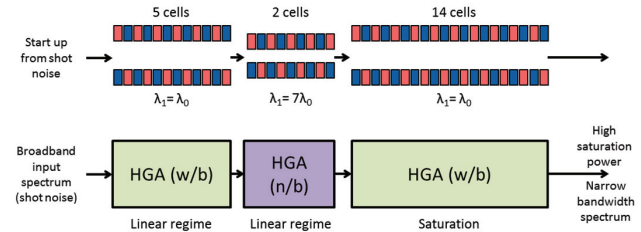


Figure 1: The pSASE undulator configuration proposed for the SASE3 beamline, which is expected to operate in the photon energy range between 1.3 keV and 3 keV.

section", are used in the high-gain linear regime to reduce the SASE bandwidth. The final characteristics of a pSASE source are a compromise between high output power, which can be reached with a conventional SASE undulator source resonant at the target wavelength, and narrow bandwidth, which can be reached with harmonic lasing [24]- [28]. We demonstrate that it is possible to cover the energy range between 1.3 keV and 3 keV using the nominal European XFEL electron beam parameters, and to reduce the SASE bandwidth by a factor 5, still having the same output power as in the baseline SASE regime. Note that the slippage-boosted section is tuned to a subharmonic (the fifth, or the seventh) of the FEL radiation. Therefore, the choice of the lowest pSASE photon energy considered in this article, 1.3 keV, is dictated by the minimal photon energy (0.26 keV) that can be reached in the conventional SASE regime.

A more detailed treatment can be found in [29].

FEL STUDIES

A schematic layout of the proposed pSASE configuration for the SASE3 undulator at the European XFEL is illustrated in Fig. 1 and consists of three parts which will be called U1 (5 cells), U2 (2 cells) and U3 (14 cells). We performed a feasibility study of the pSASE setup with the help of the FEL code Genesis 1.3 [30] running on a parallel machine. Results are presented for the SASE3 FEL line of the European XFEL, based on a statistical analysis consisting of 100 runs. The overall beam parameters used in the simulations are presented in Table 1.

The nominal beam parameters at the entrance of the SASE3 undulator, and the resistive wake inside the undulator are shown in Fig. 2, see also [31]. The evolution of the transverse electron bunch dimensions is plotted in Fig. 3.

Table 1: European XFEL Parameters Used in this Paper

	Units	
Undulator period	mm	68
Periods per cell	-	73
Total number of cells	-	21
Intersection length	m	1.1
Energy	GeV	10.5
Charge	nC	0.1

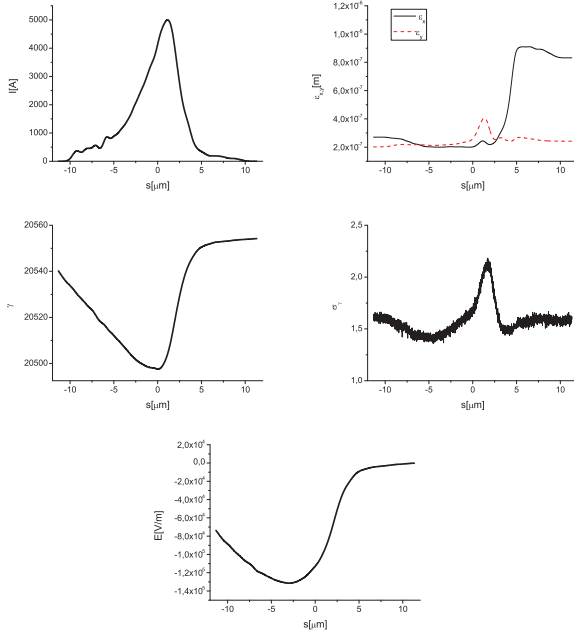


Figure 2: Results from electron beam start-to-end simulations at the entrance of SASE3. (First Row, Left) Current profile. (First Row, Right) Normalized emittance vs. position inside the electron beam. (Second Row, Left) Energy profile along the beam. (Second Row, Right) Electron beam energy spread profile. (Bottom row) Resistive wakefields in the SASE3 undulator.

The number of cells in the undulator U1 should be equal to five in order to optimize the final characteristics of the radiation pulse. The output power and spectrum after the first undulator tuned to 0.6 nm (the corresponding rms K value is 2.54) is shown in Fig. 4 for 100 runs. The average behavior

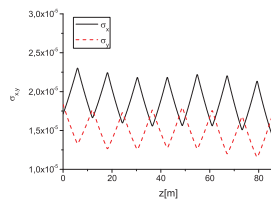


Figure 3: Evolution of the horizontal and vertical dimensions of the electron bunch (at maximum current value) vs. distance inside the SASE3 undulator.

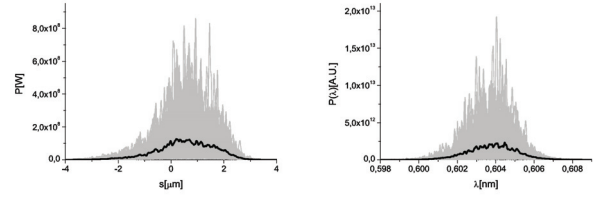


Figure 4: Power distribution and spectrum of the SASE soft x-ray radiation pulse at the exit of the first undulator part U1. Grey lines: single shot realization, black line: average over 100 realizations.

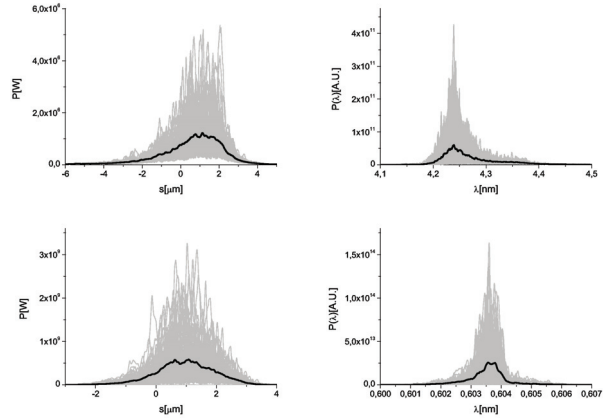


Figure 5: SASE radiation power and spectrum at the exit of the second undulator part U2 (slippage-booster section). The SASE radiation generated in U1 is purified in U2, which consists of 2 cells resonant at 4.2 nm. The fundamental radiation at 4.2 nm is seeded by shot noise. The harmonic radiation is seeded by that produced in U1. Top row: Results of numerical simulations for radiation at the fundamental produced in U2. Bottom row: Results of numerical simulations for harmonic radiation amplified in U2. Grey lines refer to single shot realizations, the black line refers to the average over a hundred realizations.

is rendered in black. The radiation field is first dumped at the exit of U1, and then further imported in the Genesis code for simulating the 7th harmonic interaction in U2, which is resonant at a fundamental of 4.2 nm. Together with the radiation pulse, also electron beam file generated using the values of energy loss and energy spread at the exit of U1 is fed in the simulation of the second undulator part. The Genesis 7th harmonic field and particle file are downloaded at the exit of the U2 undulator and used as input file for the Genesis simulations of the U3 undulator. As explained in the previous section, the length of the booster U2 is chosen to make sure that the FEL power at the fundamental wavelength is much lower than that at the chosen harmonic. The output power and spectrum of fundamental and harmonic radiation pulse after the U2 undulator tuned to 4.2 nm (the corresponding rms K value is 7.16, and can be achieved by reducing the undulator gap), that is the seventh subharmonic of the target wavelength, are shown in the left and right plot

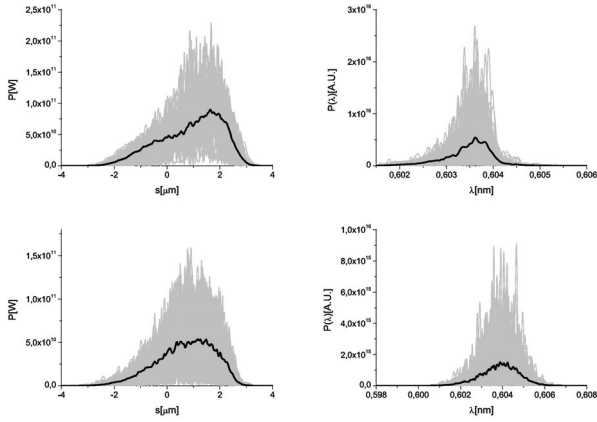


Figure 6: Power and spectrum produced in the pSASE mode (top row) and in the standard SASE mode (bottom row) at saturation without undulator tapering. Grey lines: single shot realization, black line: average over 100 realizations.

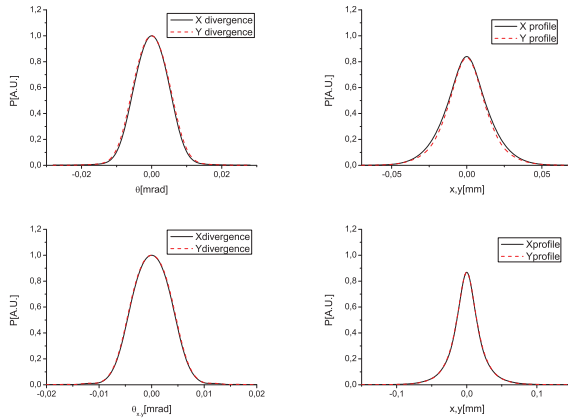


Figure 7: Distribution of the radiation pulse energy per unit surface and angular distribution of the pSASE radiation pulse energy at saturation (top row) and at the exit of the setup, including tapering (bottom row).

of Fig. 5. Since the FEL power at the fundamental wavelength of 4.2 nm, which is about 1 MW, is much lower than that at 0.6 nm, which is about 1 GW, phase shifters are not needed to suppress the lasing at fundamental harmonic.

The output undulator U3 consists of two sections. The first section is composed by a uniform undulator, the second section by a tapered undulator. The purified pulse is exponentially amplified passing through the first uniform

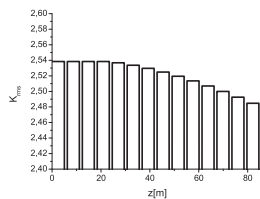


Figure 8: Tapering law.

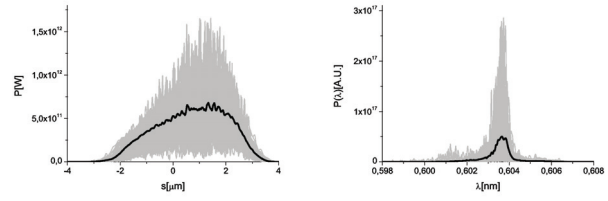


Figure 9: Power distribution and spectrum of the purified SASE soft x-ray radiation pulse at the exit of the setup, with tapering. Grey lines refer to single shot realizations, the black line refers to the average over a hundred realizations.

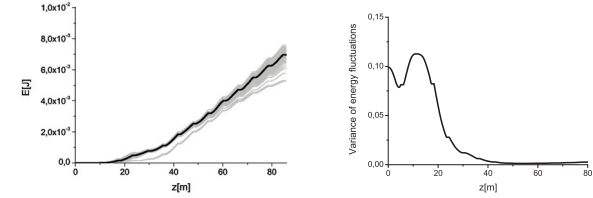


Figure 10: Evolution of the output energy in the photon pulse and of the variance of the energy fluctuation as a function of the distance inside the output undulator, with tapering. Grey lines refer to single shot realizations, the black line refers to the average over a hundred realizations.

part of the output undulator. This section is long enough, 5 cells, in order to reach saturation, which yields about 50 GW power Fig. 6 (top row). The radiation power profile and spectra for SASE3 undulator beamline working in the nominal SASE mode is shown in Fig. 6 (bottom row). As seen before, the power level for both modes of operation are similar, but the spectral density for the pSASE case is significantly higher than for the nominal SASE case. The size and divergence of the pSASE radiation pulse at saturation are shown in Fig. 7 (top row). In the second part of the output undulator U3, the purified FEL output is enhanced up to about 0.6 TW taking advantage of a taper of the undulator magnetic field over the last 9 cells after saturation. The tapering law is shown in Fig. 8. The output power and spectrum of the entire setup, at the exit of U3, is shown in Fig. 9. The size and divergence of the pSASE radiation pulse at the exit of the setup including undulator tapering are shown in the bottom row of Fig. 7. By inspection, one can see that the difference with the pSASE setup at saturation, shown in the top row of the same figure, is minimal. The evolution of the output energy in the photon pulse as a function of the distance inside the output undulator is reported in Fig. 10. The photon spectral density for the output TW-level pulse is about 30 times higher than that for the nominal SASE pulse at saturation.

CONCLUSIONS

We studied the simple scheme proposed in [23] to significantly enhance the spectral brightness of a SASE FEL with the help of numerical simulations. Using the param-

eters for the soft x-ray beamline SASE3 at the European XFEL and a nominal electron bunch parameter set, we show that the SASE bandwidth at saturation can be reduced by a factor of five with respect to the proposed configuration of the baseline, variable gap SASE3 undulator. In addition to the example studied in [23], the purified radiation after saturation is further significantly amplified (we report an order of magnitude increase in power) in the last tapered part of SASE3 undulator. With this configuration, a pSASE FEL reaches TW peak power level with significantly enhanced brightness (about one order of magnitude) compared with the nominal SASE regime [32].

REFERENCES

- [1] J. Feldhaus et al., "Possible application of X-ray optical elements for reducing the spectral bandwidth of an X-ray SASE FEL" *Optics. Comm.*, vol. 140, pp. 341-352, 1997.
- [2] E. Saldin et al., "X-ray FEL with a meV bandwidth", *NIM, ser. A*, vol. 475, pp. 357-362, Dec. 2001.
- [3] E. Saldin et al., "Optimization of a seeding option for the VUV free electron laser at DESY", *NIM, ser. A*, vol. 445, pp. 178-182, May 2000.
- [4] R. Treusch et al., "The seeding project for the FEL in TTF phase II", *DESY Ann. report*, 2001.
- [5] A. Marinelli et al., "Comparative study of nonideal beam effects in high gain harmonic generation and self-seeded free electron lasers", *Phys. Rev. ST Accel. Beams*, vol. 13, p. 070701, Jul 2010.
- [6] G. Geloni et al., "Scheme for generation of highly monochromatic X-rays from a baseline XFEL undulator", *DESY 10-033*, 2010.
- [7] Y. Ding et al., "Two-bunch self-seeding for narrow-bandwidth hard x-ray free-electron lasers" *Phys. Rev. ST Accel. Beams*, vol. 13, p. 060703, 2010.
- [8] G. Geloni et al., "A simple method for controlling the line width of SASE x-ray FELs", *DESY 10-053*, 2010.
- [9] G. Geloni et al., "A Cascade self-seeding scheme with wake monochromator for narrow-bandwidth x-ray FELs", *DESY 10-080*, 2010.
- [10] G. Geloni et al., "Cost-effective way to enhance the capabilities of the LCLS baseline", *DESY 10-133*, 2010.
- [11] J. Wu et al., "Staged self-seeding scheme for narrow bandwidth, ultra-short X-ray harmonic generation free electron laser at LCLS", *Proc. 34th Int. Free-Electron Laser Conf., Malmo, 2010, TUPB08*.
- [12] G. Geloni et al., "Generation of doublet spectral lines at self-seeded X-ray FELs", *DESY 10-199*, 2010, and *Optics Commun.*, vol. 284, p. 3348, 2011.
- [13] G. Geloni et al., "Production of transform-limited X-ray pulses through self-seeding at the European X-ray FEL", *DESY 11-165*, 2011.
- [14] G. Geloni et al., "A novel self-seeding scheme for hard X-ray FELs", *J. of Modern Optics*, vol. 58, p. 1391, 2011.
- [15] J. Wu et al., "Simulation of the Hard X-ray Self-seeding FEL at LCLS", *Proc. 33rd Int. Free-Electron Laser Conf., Shanghai, 2011, MOPB09*.
- [16] J. Amann et al., "Demonstration of self-seeding in a hard-X-ray free-electron laser", *Nature Photonics*, vol. 6, pp. 693-698, DOI:10.1038/NPHOTON.2012.180, 2012.
- [17] Yu. Shvyd'ko, R. Lindberg, "Spatiotemporal response of crystals in x-ray Bragg diffraction", *Phys. Rev. ST Accel. Beams*, vol. 15, p. 100702, Oct. 2012.
- [18] Y. Feng et al., "System design for self-seeding the LCLS at soft X-ray energies", *Proc. 34th Int. Free-Electron Laser Conf., Nara, Japan, 2012, TUOBIO*.
- [19] S. Serkez et al., "Grating monochromator for soft X-ray self-seeding the European XFEL", *DESY 13-040*, Available: <http://arxiv.org/abs/1303.1392>, 2013.
- [20] G. Geloni et al., "Wake monochromator in asymmetric and symmetric Bragg and Laue geometry for self-seeding the European XFEL", *DESY 13-013*, 2013.
- [21] G. Geloni et al., "Conceptual design of an undulator system for a dedicated bio-imaging beamline at the European x-ray FEL", *DESY 12-082*, 2012, Available: <http://arxiv.org/abs/1205.6345>.
- [22] G. Geloni et al., "Optimization of a dedicated bio-imaging beamline at the European x-ray FEL", *DESY 12-159*, 2012, Available: <http://arxiv.org/abs/1209.5972>.
- [23] D. Xiang et al., "Purified self-amplified spontaneous emission free-electron lasers with slippage-boosted filtering", *Phys. Rev. ST Accel. Beams*, vol. 16, p. 010703, 2013.
- [24] R. Bonifacio et al., "Large harmonic bunching in a high-gain free-electron laser", *Nucl. Instrum. Methods Phys. Res., Sect. A*, vol. 293, pp. 627-629, 1990.
- [25] Z. Huang and K. Kim, "Three-dimensional analysis of harmonic generation in high-gain free-electron lasers", *Phys. Rev. E*, vol. 62, p. 7295, 2000.
- [26] J. B. Murphy et al., "Collective instability of a free electron laser including space charge and harmonics", *Opt. Commun.*, vol. 53, p. 197, 1985.
- [27] B. W. J. McNeil et al., "Harmonic Lasing in a Free-Electron-Laser Amplifier", *Phys. Rev. Lett.*, vol. 96, p. 084801, 2006.
- [28] E. A. Schneidmiller and M. V. Yurkov, "Harmonic lasing in x-ray free electron lasers", *Phys. Rev. ST Accel. Beams*, vol. 15, p. 080702, 2012.
- [29] S. Serkez et al., "Purified SASE undulator configuration to enhance the performance of the soft x-ray beamline at the European XFEL", *DESY 13-135*, 2013, Available: <http://arxiv.org/abs/1308.0172>.
- [30] S. Reiche et al., "GENESIS 1.3: a fully 3D time-dependent FEL simulation code", *Nucl. Instr. and Meth., ser. A*, vol. 429, pp. 243-248, 1999.
- [31] I. Zagorodnov. (2011). "Beam Dynamics simulations for XFEL" [Online], Available: <http://www.desy.de/fel-beam/s2e>. and "Compression scenarios for the European XFEL" [Online], Available: http://www.desy.de/fel-beam/data/talks/files/Zagorodnov_ACC2012_ready_new.pptx, 2012.
- [32] Th. Tschentscher, "Layout of the x-Ray Systems at the European XFEL", *Technical Report 10.3204/XFEL.EU/TR-2011-001*, Hamburg, 2011, doi:10.3204/XFEL.EU/TR-2011-001

BEAM DYNAMIC SIMULATIONS FOR SINGLE SPIKE RADIATION WITH SHORT-PULSE INJECTOR LASER AT FLASH*

M. Rehders[†], J. Roensch-Schulenburg, Hamburg University and CFEL, Hamburg, Germany
J. Rossbach, Hamburg University, Hamburg, Germany
S. Schreiber, DESY, Hamburg, Germany

Abstract

This paper discusses the generation of single spike SASE pulses at soft x-ray wavelength at the free-electron laser FLASH by using very short electron bunches of only a few micrometer bunch length. In order to achieve these extremely short bunch lengths, very low bunch charges (in the order of 20 pC) and short electron bunches exiting the photo-injector are required. For this, a new short-pulse injector laser with adjustable rms pulse duration in the range of 0.7 ps to 1.6 ps and bunch charges up to 200 pC was installed, extending the electron beam parameter range before bunch compression in magnetic chicanes. Beam dynamic studies have been performed to optimize the injection and compression of low-charge electron bunches by controlling the effect of coherent synchrotron radiation and space-charge induced bunch lengthening and emittance growth. Optimization includes the pulse parameters of the injector laser. The simulation codes ASTRA, CSRtrack and Genesis 1.3 were employed.

MOTIVATION

The Free-Electron Laser in Hamburg (FLASH) is a high-gain SASE FEL user facility offering highly brilliant radiation pulses in the XUV- to soft x-ray range with a typical pulse duration between <50 and 200 fs (FWHM) [1]. Amongst the variety of user experiments that are performed at FLASH there are many pump-probe experiments where the time resolution is limited by the XUV pulse duration. These experiments would greatly benefit from being provided with shorter SASE pulses. In principle, the shorter the SASE pulses that can be offered to the users, the shorter the time scales that can be studied and the better the time resolution for a given process to be investigated. FEL facilities around the world are investigating on the generation of extremely short SASE pulses. A relatively straight-forward method is the generation of SASE pulses from very short electron bunches (see e.g. [2–4]).

Due to the relatively low energies of only a few mega electron volt, space charge forces still play a major role at the injector. Therefore the high peak current and short bunch duration required for the production of short SASE pulses cannot be created at the injector. Instead bunch compression is achieved at higher energies, typically in magnetic chicanes. Strong compression in magnetic chicanes requires very tight RF tolerances in the accelerating structure used to apply the

required energy chirp on the bunch. The main challenge for the generation of very short electron bunches is therefore the tolerance of the accelerating RF fields.

At FLASH an additional injector laser has been installed to produce shorter bunches already at the injector. This short pulse injector laser reduces the bunch compression required in the magnetic chicanes for low charge electron bunches, relaxing the RF tolerances for short pulse SASE operation [5].

SASE pulses typically consist of many longitudinal optical modes in the power distribution and spectrum. These individual spikes are typically separated by the cooperation length L_{coop} [6]. The shortest possible SASE pulse consists of only a single mode. This single spike operation constitutes a special mode of operation for FELs. For single spike radiation the bunch length σ_z has to approximately obey $\sigma_z \leq 2\pi L_{\text{coop}}$ [2, 6]. At FLASH this means that the bunch length has to be in the order of only a few micrometers.

Beam dynamic simulations have been performed to achieve a detailed understanding of single spike operation at FLASH. A start-to-end simulation for single spike radiation with the short-pulse injector laser is presented that is very close to machine settings used for standard short pulse operation at FLASH.

SHORT PULSE OPERATION AT FLASH

FLASH has an RF photo-injector consisting of a 1.5 cell L-band gun and two solenoids for emittance compensation. Seven superconducting accelerating modules accelerate the bunch to energies of up to 1.25 GeV. Four third harmonic cavities upstream of the first bunch compressor are used to linearize the longitudinal phase space distribution. Two magnetic bunch compressors situated at 150 MeV and at 450 MeV are used to longitudinally compress the bunch to peak currents and bunch lengths required for SASE operation. Recently FLASH has been upgraded to have a second undulator beamline (FLASH2) that is currently being commissioned [1]. A schematic overview of FLASH is given in Fig. 1. The simulations presented in this paper have been performed for the original undulator beamline, FLASH1.

In order to adjust the SASE pulse duration to the needs of each specific user experiment, the bunch length at the undulator section is set accordingly. This is done by a combination of two methods. First, the bunch length can be scaled by adjusting the bunch compression applied in the magnetic chicanes. Second, especially for the shortest SASE pulses, the bunch length is additionally reduced already at the injector. This is done by scaling of the bunch charge

* The project has been supported by the Federal Ministry of Education and Research of Germany (BMBF) under contract No. 05K10GU2 and FSP301

[†] Marie.Rehders@desy.de

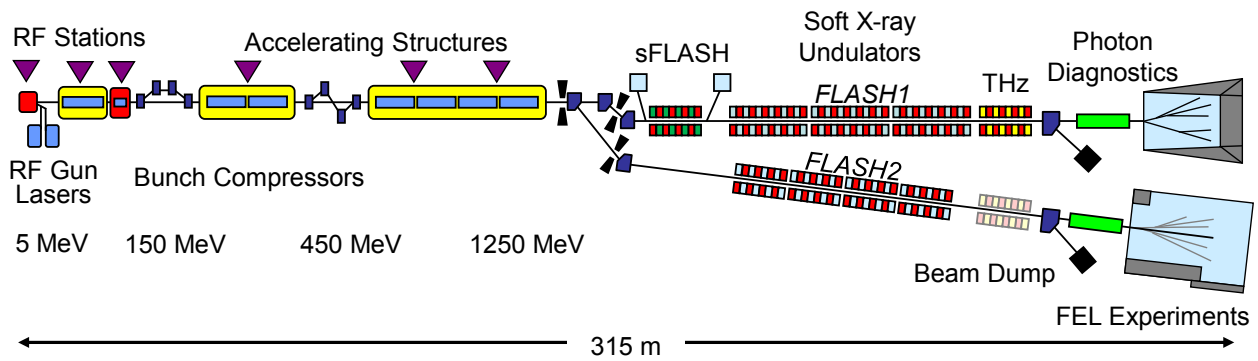


Figure 1: Schematic overview of FLASH. The simulations presented here have been performed for FLASH1.

and thus of the space charge forces that act on the electron bunch at the low energies present at the injector. Thus a small bunch charge in combination with a very strong bunch compression is used to produce the shortest SASE pulses of less than 50 fs (FWHM).

The initial bunch length of very low charge electron bunches where longitudinal space charge forces do not play a role any more at RF photo-injectors is given by the pulse duration of the injector laser. Bunch compression in magnetic chicanes is limited by RF tolerances. Thus a limit is given for the minimum SASE pulse duration that can be reached by this means and for stable SASE operation.

Short Pulse Injector Laser

While the standard injector laser at FLASH has a fixed pulse duration of 6.5 ps (rms), the pulse duration of the short-pulse injector laser can be adjusted between 0.7 ps and 1.6 ps (rms). By this means, the total bunch compression that has to be applied to the bunch for single spike radiation can be reduced by a factor 3–5.

Bunch charges of up to 200 pC can be produced with the short-pulse laser. The transverse spot size on the photocathode can be chosen by selecting a specific aperture from a set with different radii that can be imaged onto the cathode. The parameters laser pulse duration, bunch charge and spot size on cathode can be set independently for each laser.

START-TO-END SIMULATION

A start-to-end simulation for an example of standard short pulse operation at 13.5 nm can be found at [7]. The simulation is based on a machine setting from March 2012 that was used to produce SASE pulses with a pulse duration of 50 fs (FWHM) for a dedicated comparison of various different techniques for SASE pulse characterization. The bunch charge was 150 pC. This simulation has been used as a basis for a start-to-end simulation with the short pulse laser that is demonstrated in this paper.

It is important to note that no theoretical design optics was used but instead the optics used for the simulations is the exact optics that was in use in the machine during this specific run.

A combination of the particle tracking codes ASTRA [8] and CSRtrack [9] has been used for the simulations to include collective effects such as space charge forces and coherent synchrotron radiation (CSR). Wakefields have been added analytically.

Start-to-end Simulation with Short Pulse Injector Laser

A start-to-end simulation has been performed based on machine settings for standard short pulse operation at FLASH, but now for the short pulse injector laser. For the simulation, only parameters that are independent for each laser have been altered and the RF phase of the first accelerating module after the gun has been scanned for optimum bunch compression. Apart from this the machine setting is exactly the same for both simulations.

The bunch charge has been chosen to be 20 pC in order to be suited for single spike radiation at FLASH. The laser-dependent parameters for both simulations are given in Table 1.

Table 1: Laser-dependent parameters used for the start-to-end simulation for standard short pulse operation at FLASH [7] (standard laser) and the simulation with the short-pulse injector laser based on it that is presented in this paper.

parameter	standard laser	short-pulse laser
pulse duration	15 ps FWHM	2.8 ps FWHM
spot diameter	1.2 mm	1.0 mm
bunch charge	150 pC	20 pC

A comparison of the longitudinal current profile after the gun for both simulations is given in Fig. 2. The parameters chosen for the short pulse injector laser result in a reduction of the bunch duration by a factor 4 to 0.41 mm rms. The core slice emittance is 0.26 mm mrad and the slice energy spread 1.6 keV. The focussing strength of the solenoid has not been optimized for emittance compensation but is fixed to the value from the specific machine run described above.

The RF phase of the first accelerating module (ACC1) after the gun has been adjusted by 0.6° for optimum bunch

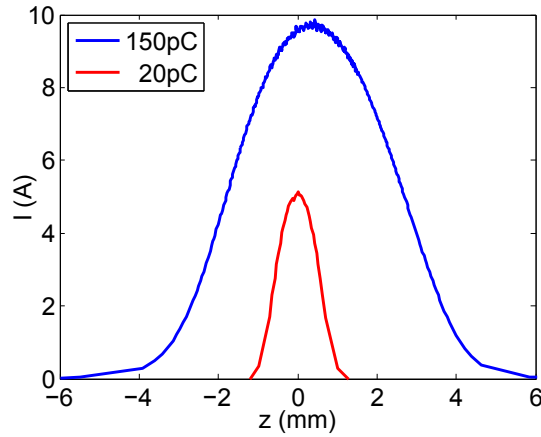


Figure 2: Longitudinal current profile after the gun for the standard injector laser (150 pC) and for the short pulse injector laser (20 pC) corresponding to the parameters in Table 1. The head of the bunch is to the right.

compression. Non of the other phases or gradients have been altered. The longitudinal phase space distribution of the bunch is well linearized upstream of the first magnetic chicane. The bunch is slightly over-compressed in the second bunch compressor.

Space charge forces acting on the bunch after compression lead to a double structure in the longitudinal current profile of the bunch, as can be seen in Fig. 3 at the beginning of the undulator. The rms bunch length at the undulator is $3.6 \mu\text{m}$, while the individual widths of the two spikes can be fitted by a Gaussian to be $0.5 \mu\text{m}$ (trailing spike) and $0.6 \mu\text{m}$ (leading spike). The slice emittance is 0.8 mm mrad (horizontal) and 1.2 mm mrad (vertical) for the trailing and 0.2 mm mrad (hor.) and 0.5 mm mrad (ver.) for the leading spike, while the energy spread is 1.6×10^{-3} and 5.1×10^{-4} respectively.

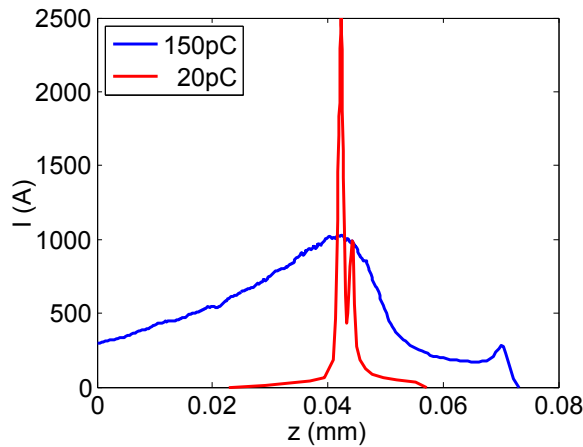


Figure 3: Longitudinal current profile at the beginning of the undulator section for the standard injector laser (150 pC) and for the short pulse injector laser (20 pC). The head of the bunch is to the right.

SASE Simulation

The SASE process has been simulated with the 3D time dependent code Genesis1.3 [10]. Longitudinal space charge forces have not been taken into account in the SASE simulation.

The longitudinal SASE profile and spectrum after 15 m of the undulator section is shown in Fig. 4 for four different statistical seeds. The SASE pulse duration is 2–3 fs FWHM corresponding to the individual seeds. 2–3 modes are visible in the spectrum of the SASE simulation, indicating that the SASE pulse shown is not yet a perfect single spike.

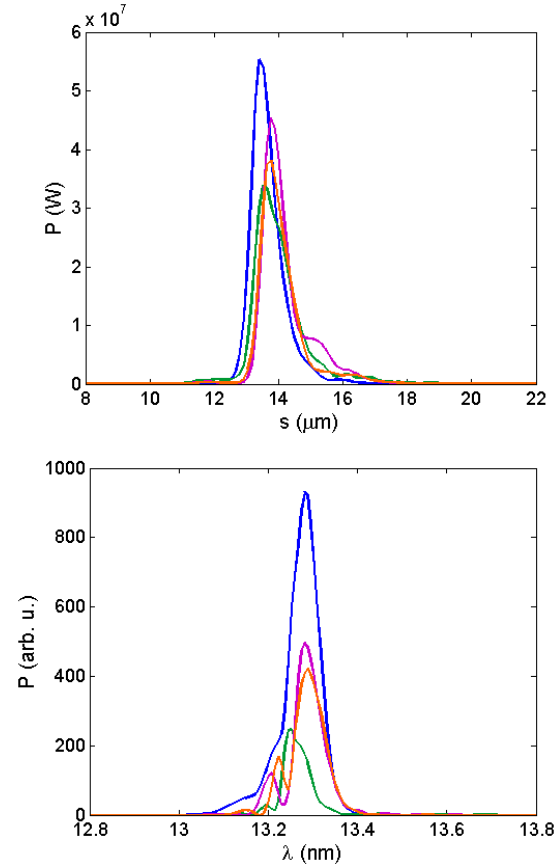


Figure 4: Longitudinal SASE profile (top) and spectrum (bottom) at 15 m of the undulator section for four different statistical seeds.

The double structure from the current profile of the bunch is not visible in the longitudinal SASE profile. This is due to the difference in the slice parameters of the two current spikes. While the trailing spike of the bunch has the highest peak current of 2.5 kA, its slice emittance and slice energy spread are much worse than those of the leading spike. The trailing spike therefore doesn't contribute much to the lasing process. Instead the single spike that is seen in the longitudinal current profile is produced by the smaller leading spike. The peak current of the leading spike of 1.1 kA is still high enough for SASE operation. It is comparable to the peak current for the case of standard short pulse operation as described above and in [7].

CONCLUSION

Start-to-end simulations demonstrate that single spike SASE FEL radiation can be achieved with the short-pulse injector laser for machine settings that are almost identical to standard short pulse operation (with the standard injector laser) at FLASH.

The machine parameters that have to be adapted to achieve this are only those that solely depend on the injector laser that is in use – laser pulse duration, spot size and bunch charge – and the RF phase of one single accelerating module to optimize bunch compression.

As a result, if the machine is well set up, very little time is needed to switch between standard short pulse operation and single spike operation mode by switching between the standard and short-pulse injector laser.

Recently very short SASE pulses with only one to four spikes in the spectrum (an average of only 1.5 spikes within the FWHM) have been achieved with the short pulse injector laser at FLASH (see [5]).

REFERENCES

- [1] K. Honkavaara et al., “FLASH: First Soft X-Ray FEL Operating Two Undulator Beamlines Simultaneously”, in *These Proceedings: Proc. 36th Int. Free-Electron Laser Conf.*, Basel, 2014, WEB05.
- [2] J.B. Rosenzweig et al., “Generation of ultra-short, high brightness electron beams for single-spike SASE FEL operation”, NIM A 593 (2008) 39-44.
- [3] S. Reiche et al., “Development of ultra-short pulse, single coherent spike for SASE X-ray FELs”, NIM A 593 (2008) 45-48.
- [4] B. Marchetti et al., “Preliminary Study of Single Spike SASE FEL Operation at 0.26nm Wavelength for the European XFEL”, proceedings of the ICAP 2012.
- [5] J. Rönsch-Schulenburg et al., “Operation of FLASH with Short SASE-FEL Radiation Pulses”, in *These Proceedings: Proc. 36th Int. Free-Electron Laser Conf.*, Basel, 2014, TUB04.
- [6] R. Bonifacio et al., “Spectrum, Temporal Structure and Fluctuations in a High-Gain Free-Electron Laser Starting from Noise”, PRL 73 (1994) 70.
- [7] S. Düsterer et al., “Development of experimental techniques for the characterization of ultrashort photon pulses of XUV free-electron lasers”, to be published.
- [8] K. Flöttmann, “ASTRA A Space Charge Tracking Algorithm”, Manual, Version 3.0, Oct. 2011, <http://desy.de/mpyflo/>
- [9] M. Dohlus and T. Limberg, “CSRtrack Version 1.2 User's Manual”, <http://www.desy.de/xfel-beam/csrtrack/>
- [10] S. Reiche, Genesis 1.3, <http://genesis.web.psi.ch/index.html>

DEMONSTRATION OF SASE SUPPRESSION THROUGH A SEEDED MICROBUNCHING INSTABILITY*

C. Lechner[†], A. Azima, M. Drescher, L.L. Lazzarino, Th. Maltezopoulos, V. Miltchev, T. Plath, J. Rönsch-Schulenburg, J. Rossbach, University of Hamburg, Hamburg, Germany
K. E. Hacker, S. Khan, R. Molo, DELTA, TU Dortmund University, Dortmund, Germany
S. Ackermann, J. Bödewadt, G. Brenner, M. Dohlus, N. Ekanayake, T. Golz, E. Hass, K. Honkavaara, T. Laarmann, T. Limberg, E. Schneidmiller, N. Stojanovic, M. Yurkov, DESY, Hamburg, Germany

Abstract

Collective effects and instabilities due to longitudinal space charge and coherent synchrotron radiation can degrade the quality of the ultra-relativistic, high-brightness electron bunches needed for the operation of free-electron lasers. In this contribution, we demonstrate the application of a laser-induced microbunching instability to selectively suppress the SASE process. A significant decrease of photon pulse energies was observed at the free-electron laser FLASH in coincidence with overlap of 800 nm laser pulses and electron bunches within a modulator located approximately 40 meters upstream of the undulators. We discuss the underlying mechanisms based on longitudinal space charge amplification (LSCA) [1] and present measurements.

INTRODUCTION

Microbunching instabilities driven by longitudinal space charge (LSC) forces occurring in linear accelerators driving free-electron lasers (FELs) affect electron beam diagnostics as well as FEL operation. For instance, emission of coherent optical transition radiation (COTR) was observed at several facilities and it has to be mitigated for accurate measurements of the transverse beam profile [2–5]. The concept to use these instabilities for short-wavelength radiation production was proposed as longitudinal space charge amplifier (LSCA) in [1]. As illustrated in Fig. 1, an LSCA comprises multiple amplification “cascades”, each one consisting of a focusing channel (an electron beamline with quadrupole magnets) followed by a dedicated dispersive element. In the focusing channel, the electrons in the higher-density regions

expand longitudinally introducing an energy change. The R_{56} value of the dispersive element (we consider chicanes here) converts these energy changes into a density modulation. Starting from shot noise, a strong density modulation can be achieved in two to four cascades.

LSCA effects were studied experimentally at the Next Linear Collider Test Accelerator (NLCTA) at SLAC, where the impact of compression changes on spontaneous undulator radiation was measured [6]. At the National Synchrotron Light Source Source Development Laboratory (SDL) at Brookhaven National Laboratory (BNL), a modulated current profile was generated at the photoinjector with a modulated laser pulse. Microbunching gain was observed at wavelengths suitable for THz generation [7]. In [8] it is proposed to use longitudinal space charge effects to reduce the slice energy spread in HHG seeding applications.

In this contribution, we give an overview of LSCA studies at FLASH in which the amplification process was initiated by modulating the electron bunch by means of an external laser pulse. The amplified energy modulation is shown to suppress the lasing process.

EXPERIMENTAL SETUP

The measurements presented in this contribution were performed at the FEL user facility FLASH at DESY, Hamburg [9]. The schematic layout of the facility is shown in Fig. 2. The superconducting linear accelerator (linac) driving the FEL delivers high-brightness electron bunches with energies up to 1.25 GeV. At a repetition rate of 10 Hz, bunch trains consisting of up to 800 bunches at a 1 MHz repetition rate can be produced. The facility has been upgraded by a second undulator beamline FLASH2, which is currently under commissioning. The hardware (fast kickers and a septum) needed for the distribution of electron bunches into the two undulator beamlines has been installed downstream of the linear accelerator.

The hardware used in the measurements is located in the FLASH1 electron beamline between the collimation section and the undulator system, compare Fig. 3. The electron bunches arriving from the collimation section of FLASH1 are modulated in an electromagnetic undulator (5 periods of 20 cm, $K_{\max} = 10.8$) by the $\lambda = 800$ nm laser pulses arriving from the seeding laser system. After the modulator, chicane C_1 with variable R_{56} is installed. For studies of the LSCA, we use a combination of a transverse-deflecting structure (TDS) and a dipole spectrometer installed about

* Work supported by Federal Ministry of Education and Research of Germany under contract No. 05K10PE1, 05K10PE3, 05K13GU4, and 05K13PE3 and the German Research Foundation programme graduate school 1355.

[†] christoph.lechner@desy.de

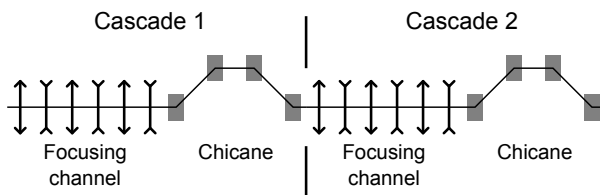


Figure 1: Schematic layout of an LSCA configuration with two cascades [1].

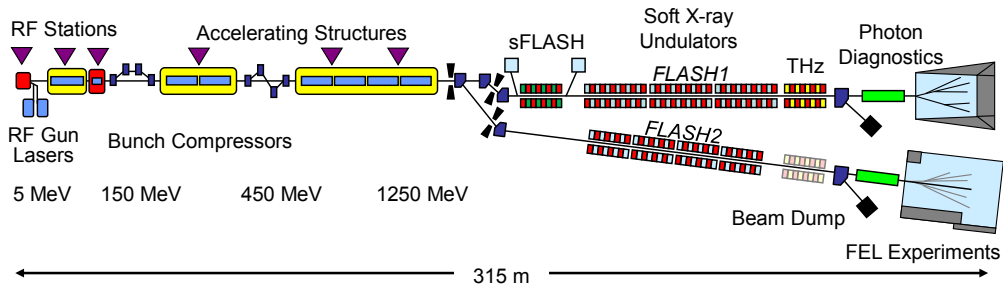


Figure 2: Schematic layout of the FLASH facility.

TexText font size 1.5

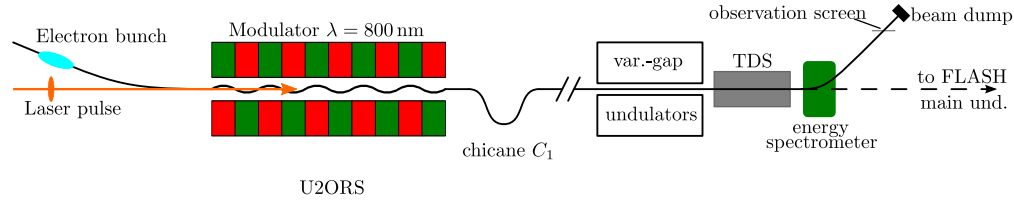


Figure 3: Hardware used in the LSCA measurements. The electron bunch arrives from the collimation section of the FLASH1 beamline, the 800 nm pulse from the laser system. In the modulator, the electron-light interaction imprints an energy modulation into the bunch that is converted into a density modulation in the subsequent chicane C_1 . We do not use the variable-gap undulators of the seeding experiment.

13 m upstream of the FLASH1 SASE undulators. First, an arrival-time dependent transverse kick is applied in the TDS, an RF structure operated at 2856 MHz. After this conversion of longitudinal to spatial position, the contents of the longitudinal phase space can be measured on the observation screen in the dispersive section downstream of the energy spectrometer.

For the measurements with SASE, the TDS and the energy spectrometer have to be disabled to allow for transport of the density modulated electron bunches to the FLASH1 main undulator. To measure the energy of the XUV pulses, the gas-monitor detector (GMD) was used. Additionally, spectra of XUV photon pulses were measured with a high-resolution spectrometer. On its way to the beam dump, the electron bunch traverses the THz undulator. Emission from this undulator was also sent to a spectrometer.

PHYSICS OF LSCA

The electron bunches arriving from the FLASH collimation section are energy-modulated by interacting with laser pulses in the near-infrared ($\lambda = 800$ nm). A chicane at the exit of the modulator transforms this energy modulation into a density modulation. As this current-modulated electron bunch is injected into a focusing beamline, an oscillation of the longitudinal charge density is initiated. The wavelength of this longitudinal plasma oscillation is [1]

$$\Lambda = \sqrt{\frac{I_A}{I} \frac{Z_0}{|Z'|} \frac{\lambda \gamma^3}{2}}. \quad (1)$$

Here $I_A = 17$ kA is the Alfvén current, I the current of the electron bunch, $Z_0 = 377 \Omega$ is the free-space impedance, λ is the wavelength of the modulation, γ is the Lorentz factor,

and Z' is the LSC impedance per unit length. Electrons in regions of higher charge density expand longitudinally and an increase of the energy modulation amplitude may be the result while the current modulation becomes smaller. The maximum energy modulation amplitude, which is larger than the initial one, is achieved after drifting for $\Delta z = \Lambda/4$. This is the optimal position for the chicane of the next cascade of the amplifier.

We simulated the transport of the modulated electron bunch with the 3-D periodic space charge solver QField [10]. At the position of the modulator, we prepare a one-period long central slice of the modulated electron bunch. This slice is then tracked through the quadrupole optics assuming periodic conditions. To account for the impact of the chicane on the longitudinal phase space, a 2×2 matrix is applied at a dedicated longitudinal position.

OVERVIEW OF MEASUREMENTS

Investigation of Space Charge Amplification

For the studies of laser-induced longitudinal space charge amplification, we used mildly compressed electron bunches with a peak current of 0.3 kA and an rms bunch duration of 0.3 ps. The energy of the electron bunches was 700 MeV. These electron bunches are modulated by the $\lambda = 800$ nm laser and in chicane C_1 the bunching is generated. The electron beamline from this chicane to the TDS, which we use for measurements of the longitudinal phase space, is configured as a drift space of about 24 m length.

Using the TDS, the effect of variations of the laser pulse energy (pulse duration 60 fs FWHM) as well as R_{56} variations of chicane C_1 was studied in the longitudinal phase space.

SASE Suppression

With the FLASH1 FEL beamline in SASE operation at $\lambda \approx 13$ nm, we re-established the temporal overlap between laser pulses and electron bunches. The energy of the XUV photon pulses was measured with the “gas-monitor detector” (GMD), a gas-filled volume in the XUV photon beamline leading to the FLASH experimental hall. There, the photons ionize gas atoms and the ion and electron currents indicate the FEL pulse energy.

As for the studies of LSCA, we used external laser pulses to generate an initial density modulation in the electron bunch. Propagating to the SASE undulator, the energy modulation amplitude grows at the expense of bunching. This degradation of the electron bunch parameters results in a reduction of the XUV photon pulse energy, as shown in Fig. 4. We studied this SASE suppression effect for different laser pulse energies and electron beamline configurations.

High-resolution spectra of the FEL radiation were recorded for several laser pulse energy settings. Finally, we acquired spectra of the emission of the electron bunches in the THz undulator, which was tuned to 800 nm for these measurements.

We reported on first SASE suppression results already in [11]. These results were obtained before the FLASH 2013 shutdown with the injection beamline constructed for the study of direct-HHG seeding at 38 nm [12]. The suppression results summarized in this section have been obtained after the shutdown with a different laser beamline [13] that will be used to study the high-gain harmonic generation (HHG) and echo-enabled harmonic generation (EEHG) seeding options [14].

SUMMARY

We successfully reproduced the SASE suppression effect after the FLASH 2013 shutdown with a different laser injection beamline. The laser-induced density modulation

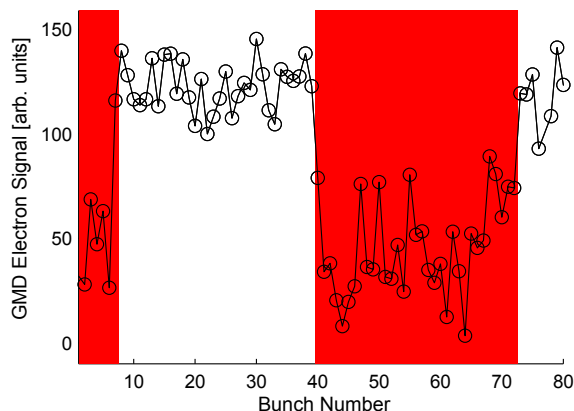


Figure 4: Impact of the amplified laser modulation on SASE energy. With laser switched on (red background), a significant reduction of the XUV photon pulse energy is observed, as compared to SASE with laser off.

initiates a growth of the energy modulation amplitude, hampering the FEL process and significantly reducing the XUV photon pulse energy. This process was studied for different laser and electron beamline configurations. Furthermore, in this contribution, we reported on measurements of the underlying laser-seeded LSCA mechanism. The detailed data analysis is still on-going and the final results will be presented in [15].

ACKNOWLEDGEMENTS

We thank DESY and the FLASH team for the opportunity to perform our experiment. Supported by Federal Ministry of Education and Research of Germany under contract No. 05K10PE1, 05K10PE3, 05K13GU4, and 05K13PE3 and the German Research Foundation programme graduate school 1355.

REFERENCES

- [1] E.A. Schneidmiller and M.V. Yurkov, *Using the longitudinal space charge instability for generation of vacuum ultraviolet and x-ray radiation*, Phys. Rev. ST Accel. Beams 13, 110701 (2010).
- [2] H. Loos, et al., *Observation of coherent optical transition radiation in the LCLS linac*, Proc. 30th Int. Free-Electron Laser Conf., Gyeongju, Korea, 2008, 485–489.
- [3] S. Wesch, et al., *Observation of coherent optical transition radiation and evidence for microbunching in magnetic chicanes*, Proc. 31st Int. Free-Electron Laser Conf., Liverpool, UK, 2009, 619–622.
- [4] C. Behrens, et al., *Electron beam profile imaging in the presence of coherent optical radiation effects*, Phys. Rev. ST Accel. Beams 15, 062801 (2012).
- [5] S. Matsubara, et al., *Improvement of screen monitor with suppression of coherent-OTR effect for SACLA*, Proc. of 1st Int. Beam Instrumentation Conf., Tsukuba, Japan, 2012, 34–37.
- [6] A. Marinelli, et al., *Generation of Coherent Broadband Photon Pulses with a Cascaded Longitudinal Space-Charge Amplifier*, Phys. Rev. Lett. 110, 264802 (2013).
- [7] S. Seletskiy, et al., *Seeding, Controlling, and Benefiting from the Microbunching Instability*, Phys. Rev. Lett. 111, 034803 (2013).
- [8] K. Hacker, *HHG and EEHG microbunches with CSR and LSC*, These Proceedings: Proc. 36th Int. Free-Electron Laser Conf., Basel, 2014, MOP095.
- [9] K. Honkavaara, et al., *FLASH: First Soft X-ray FEL Operating Two Undulator Beamlines Simultaneously*, These Proceedings: Proc. 36th Int. Free-Electron Laser Conf., Basel, 2014, WEB05.
- [10] M. Dohlus, Ch. Henning, *Particle Tracking with Periodic Poisson Solver*, to be published.
- [11] J. Bödeadt and C. Lechner, *Results and perspectives on the FEL seeding activities at FLASH*, Proc. 35th Int. Free-Electron Laser Conf., New York, NY, USA, 2013, 491–495.
- [12] S. Ackermann, et al., *Generation of Coherent 19- and 38-nm Radiation at a Free-Electron Laser Directly Seeded at 38 nm*, Phys. Rev. Lett. 111, 114801 (2013).

- [13] K. Hacker, et al., *Progress Towards HGHG and EEHG at FLASH*, Proc. 34th Int. Free-Electron Laser Conf., Nara, Japan, 2012, 257–260.
- [14] J. Bödewadt, et al., *Overview of FEL Seeding Activities at FLASH*, These Proceedings: Proc. 36th Int. Free-Electron Laser Conf., Basel, 2014, MOP089.
- [15] C. Lechner, et al., *in preparation*

ELECTRON BEAM DELAYS FOR IMPROVED TEMPORAL COHERENCE AND SHORT PULSE GENERATION AT SWISSFEL

N.R. Thompson, ASTeC, STFC Daresbury Laboratory, UK
S. Reiche, PSI, Villigen, Switzerland

Abstract

Proposals have been made for the introduction of magnetic electron beam delays in between the undulator modules of a long sectional FEL undulator - these can be used for the generation of trains of FEL pulses which can individually be shorter than the FEL cooperation time [1] or to greatly improve the temporal coherence of the FEL output compared to the nominal SASE configuration [2–4]. This paper comprises a feasibility study of the application of these techniques to a future SwissFEL hard X-Ray beamline. Three-dimensional simulations are used to investigate the potential photon output.

INTRODUCTION

SwissFEL, the X-ray free electron laser at the Paul Scherrer Institut, is currently under construction with planned operation from the end of 2016. The facility comprises a FEL named Aramis operating from 1–7Å and a second FEL named Athos operating from 7–70Å. Both FELs will operate in SASE and self-seeding modes. Space is reserved in the undulator hall for the future addition of a second hard X-ray FEL. In this paper we investigate the potential performance of two proposed novel FEL schemes, the Mode-Locked Amplifier FEL [1] and the High-Brightness SASE FEL [2–4] if implemented on this future beamline. The two schemes are considered together because they utilise common hardware.

The Mode-Locked Amplifier FEL

In the Mode-Locked Amplifier FEL electron beam delay chicanes are introduced between the modules of a long FEL undulator. By delaying the electrons, the emission from each undulator module is delayed with respect to the emission from the previous undulator module. If the undulator modules are relatively short, such that the electron bunch microstructure does not evolve much from one undulator module to the next, the total field builds up as a series of delayed, overlapped, fields of similar phase and amplitude leading to interference. In the frequency domain the field comprises a spectral comb centred on the resonant wavelength $\lambda_r = \lambda_w(1 + \bar{a}_w^2)/2\gamma^2$ with an overall envelope given by the spontaneous emission spectrum of a single undulator module with FWHM bandwidth $\Delta\lambda/\lambda \approx 1/N_w$. Here λ_w is the undulator period, \bar{a}_w is the rms undulator deflection parameter, γ is the electron relativistic factor and N_w is the number of periods in one undulator module. The wavelength spacing between the sideband modes is given by $\Delta\lambda = \lambda_r^2/s$ where $s = \delta + N_w\lambda_r$ is the total slippage between radiation and electrons in one combined undulator+delay module with δ the applied delay in the chicane and $N_w\lambda_r$ the slippage in

one undulator module. The spectrum is equivalent to that of a laser ring cavity of length s —in effect a very short laser cavity has been synthesised via the use of the macroscopic electron beam delays. Viewed in the temporal domain the radiation intensity builds up into a sequence of non-identical spikes of separation s modulated by the normal SASE envelope, which due to the increased slippage itself becomes stretched temporally by the slippage enhancement factor $S_e = s/N_w\lambda_r$. The shape of the spikes evolves along the pulse because the radiation sideband modes are not phase locked. To lock the modes a technique analogous to that used in conventional lasers cavity is adopted—a modulation is added to the system with a frequency equal to the mode spacing, or equivalently a period of s . In the FEL this is done by adding a modulation of period s to the electron beam energy. In the time domain the FEL pulse is then seen to comprise a series of cleanly separated, similar radiation spikes where the length of each spike is approximately equal to the slippage $N_w\lambda_r$ in each undulator module.

The mode-locked amplifier FEL is thus a method for producing a train of separated ultrashort radiation pulses. In addition, because the bandwidth is inversely proportional to the module length when the modules are shorter than a gain length it is possible, by using very short undulators, to produce radiation output pulses with a bandwidth significantly broader than that of a SASE FEL.

The High Brightness SASE FEL

The High Brightness SASE (HB-SASE) FEL utilises the same hardware. The SASE radiation coherence length is artificially extended by using electron beam delays to increase the relative slippage between radiation and electrons. For equal delays s a modal structure is created in the radiation spectrum, as in the Mode-Locked FEL. In the time domain this gives a pulse strongly modulated with period s . It has been found that in this case the increase in radiation coherence length is limited. However, because the mode spacing depends on the delay s then by making all the delays different it can be arranged that the sideband modes are unique for every delay s_i so that there are no modes which are continually amplified. Only the central resonant mode reaches saturation, giving a narrow bandwidth pulse with a smooth temporal structure. For the simulations in this paper the delays are based on prime number sequences [4], but good results have been observed in other studies using delays which are random [2] or steadily increasing by a common factor [3]. Studies of the evolution of the radiation coherence length l_{coh} through the system show that it grows exponentially for a distance of several gain lengths through the undulator and at saturation, for both prime number and

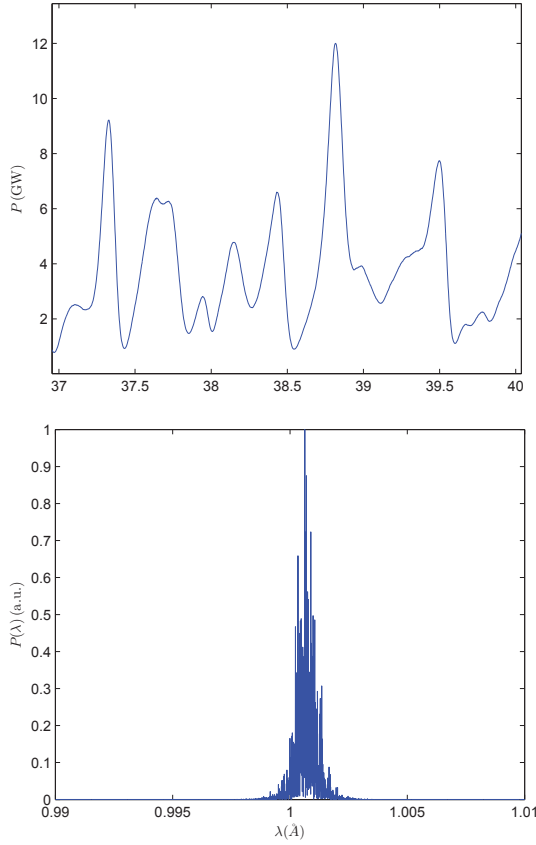


Figure 1: SASE control case for Long Pulse parameters. A 3 fs section of the radiation pulse and spectrum of the whole pulse are shown, at saturation which occurs at 37 m.

random delays, $l_{\text{coh}} \approx 0.35S$ where $S = \sum s_i$ is the total slippage between radiation and electrons.

OUTLINE OF SIMULATION STUDIES

Both schemes were studied using version 3.0 of the 3D simulation code Genesis 1.3 [5] and the results compared with control simulations of standard SASE, the results of which are shown in Figure 1. The parameters were based on the nominal parameters for the SwissFEL accelerator operating in Long Pulse mode at a resonant wavelength of 0.1 nm, and are given in Table 1. The approach taken was to determine the minimum changes required to the standard lattice, as utilised in the Aramis beamline, in order for the two schemes to demonstrate effective performance. The nominal undulator length for Aramis is $N_w = 265$ periods—this was used as a starting point then the length reduced to 130 periods, then 65 periods. The intra-undulator gap length of 0.6 m was kept constant and the FODO quadrupole gradient also kept constant to maintain the same average β -function. For each undulator length the schemes were simulated with standard 4-dipole chicanes, in which the appropriate R_{56} term corresponding to the delay was calculated (and implemented via the `itram56` input parameter in Genesis 1.3), then also with isochronous chicanes ($R_{56} = 0$). For the

studies of Mode-Locking the full amplitude of the applied energy modulation $\Delta\gamma/\gamma$ was varied between 3.8×10^{-4} ($\approx \rho$) to 14.8×10^{-4} ($\approx 4\rho$), and slippage enhancement factors of $S_e = 3.0$ and $S_e = 6.0$ were used. For HB-SASE no energy modulation is required because the modes are suppressed and do not therefore require locking.

Table 1: Electron Beam and Undulator Parameters Used for Simulations

Parameter	Value
Beam Energy E	5.8 GeV
Peak Current I	3 kA
Normalised Emittance ε_n	0.3 mm-mrad
Energy Spread σ_γ/γ	6×10^{-5}
Undulator Period λ_w	15 mm
Undulator parameter \bar{a}_w	0.848

Results for Mode-Locking

It was found that for $N_w = 265$ it was not possible to produce a clean temporal or spectral structure, for any combination of energy modulation, slippage enhancement factor or chicane type. The best results for this undulator length (not shown) were for $R_{56} = 0$, $S_e = 6$ and $\Delta\gamma/\gamma = 3.8 \times 10^{-4}$ for which there was observed a strong regular modulation in the pulse profile and clear spectral modes, but neither the temporal spikes or modes were clearly separated.

However, far improved results were obtained for shorter undulator modules—the cleanest pulse profiles and spectra results for the four permutations of $N_w = 130$, $N_w = 65$, $R_{56} = 0$ and $R_{56} \neq 0$ are shown in Figures 2-5. The caption for each plot gives the parameters and N_{mod} is the undulator module after which the results are shown. The ranges on the x -axes of these plots are the same as the SASE control case shown in Figure 1 to allow easy comparison with the SASE case. For $N_w = 130$ the FWHM duration of the temporal spikes is ≈ 70 as and this reduces to ≈ 30 as for $N_w = 65$. It is also seen that the full bandwidths of the mode-locked output are significantly broader than the SASE control—for SASE $(\Delta\lambda)_{\text{FULL}} \sim 0.003 \text{ \AA}$ which approximately doubles for $N_w = 130$ to $\sim 0.007 \text{ \AA}$ and doubles again to $\sim 0.014 \text{ \AA}$ for $N_w = 65$. Comparison of the results using standard and isochronous chicanes shows that the spectra are less well defined for standard chicanes but that the temporal structures are comparable. It should also be noted that using standard chicanes the required number of undulator modules is nearly halved, due to the enhancement of the FEL bunching in the chicanes.

Results for HB-SASE

Summary results for HB-SASE are encapsulated in Figure 6 which shows, for $N_w = 265$, $N_w = 130$ and $N_w = 65$ the rms bandwidth, normalised to that of the SASE control, for $R_{56} = 0$ and $R_{56} \neq 0$, as a function of the slippage enhancement S_e . Also shown in the figure, for reference, is the reciprocal of the slippage enhancement factor S_e . Here S_e is defined slightly differently because each delay is dif-

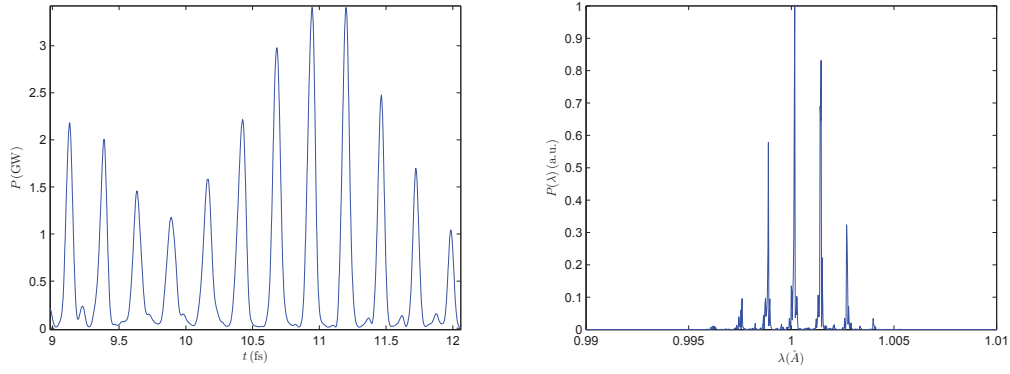


Figure 2: $N_w = 130$, $R_{56} = 0$, $\Delta\gamma/\gamma = 7.4 \times 10^{-4}$, $N_{\text{mod}} = 14$.

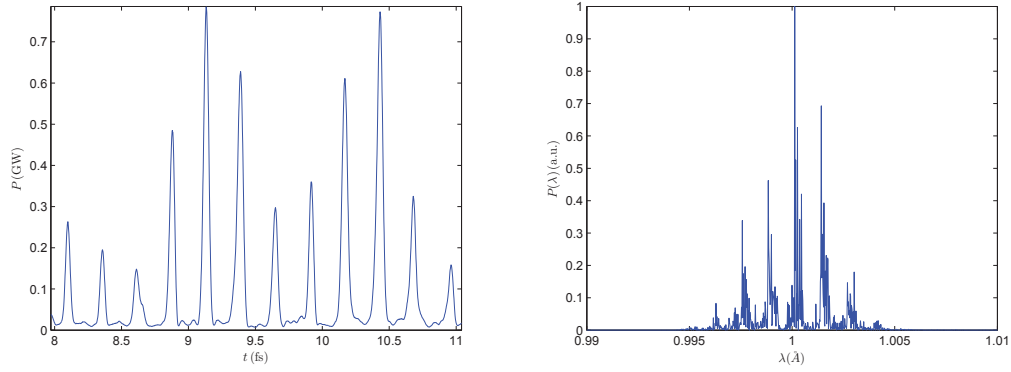


Figure 3: $N_w = 130$, $R_{56} \neq 0$, $\Delta\gamma/\gamma = 3.8 \times 10^{-4}$, $N_{\text{mod}} = 8$.

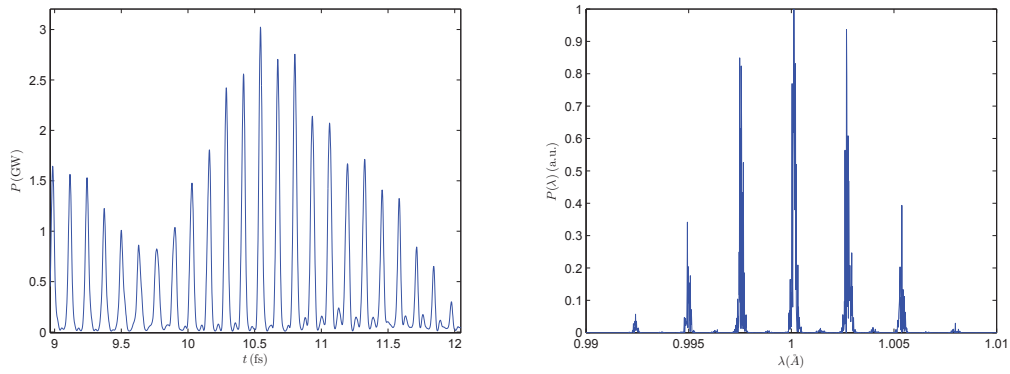


Figure 4: $N_w = 65$, $R_{56} = 0$, $\Delta\gamma/\gamma = 7.4 \times 10^{-4}$, $N_{\text{mod}} = 28$.

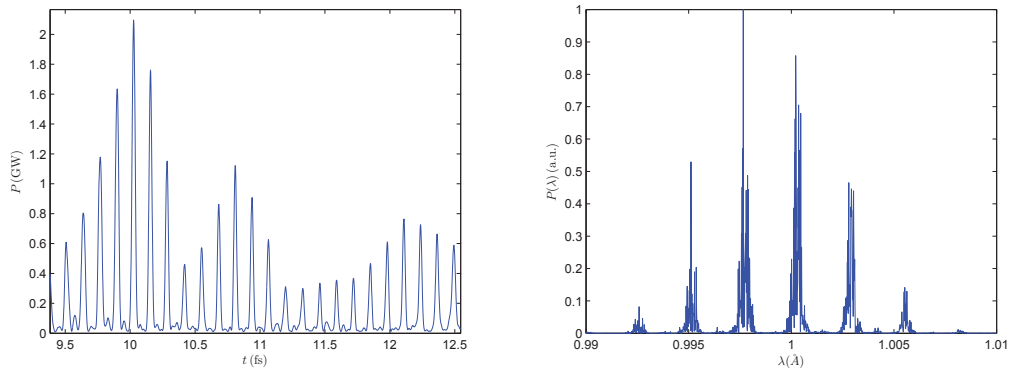


Figure 5: $N_w = 65$, $R_{56} \neq 0$, $\Delta\gamma/\gamma = 3.8 \times 10^{-4}$, $N_{\text{mod}} = 19$.

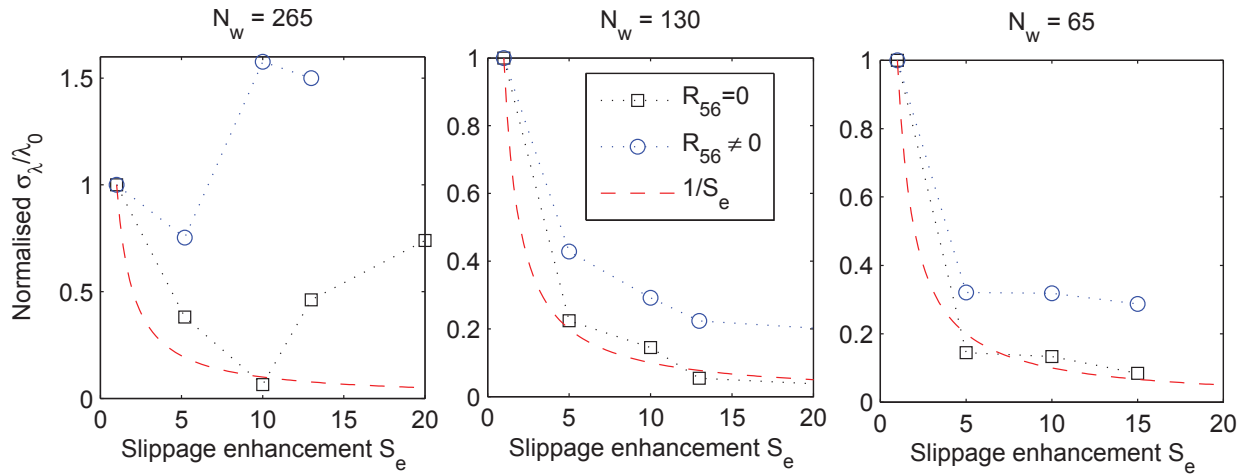


Figure 6: Summary of HB-SASE results, showing for $N_w = 265$, $N_w = 130$ and $N_w = 65$ the rms bandwidth, normalised to that of the SASE control, for $R_{56} = 0$ and $R_{56} \neq 0$, as a function of the slippage enhancement S_e .

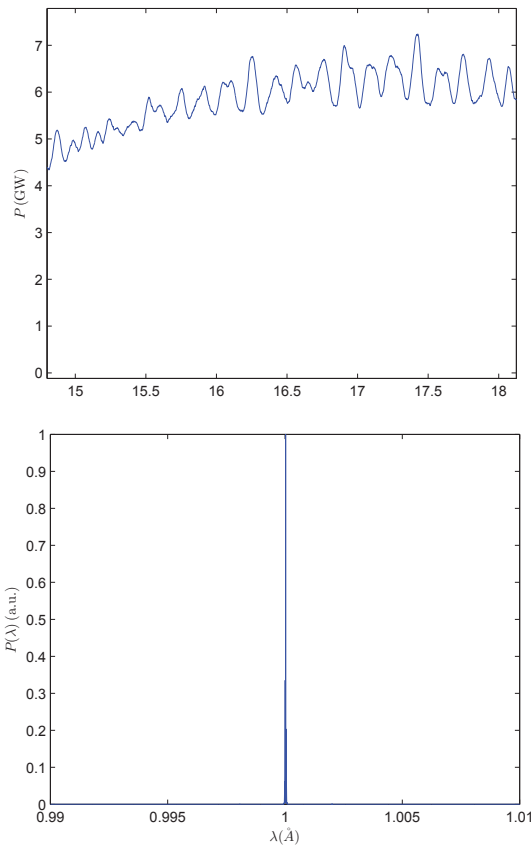


Figure 7: Example HB-SASE result, with $N_w = 130$, $S_e = 21$, $N_{\text{mod}} = 17$.

ferent, so $S_e = (\sum_{i=1}^n s_i)/nN_w\lambda_r$ is the total accumulated slippage divided by the total slippage within the undulator modules. The results show that for $N_w = 265$ the bandwidth, compared to SASE, can be reduced by a factor of 15 using isochronous chicanes, but no reduction is possible with standard chicanes. For the shorter undulator modules a bandwidth reduction of up to a factor of 5 can be achieved using standard chicanes, and a reduction of a factor of 30 can

be achieved with isochronous chicanes. Further reduction may be possible for larger values of S_e . Comparison of the measured bandwidths with $1/S_e$ shows that for isochronous delays, and the shorter undulators, the bandwidth reduction is approximately proportional to S_e . Example output is shown in Figure 7 in which the axes scalings are the same as previously. The parameters for this example are $N_w = 130$, $S_e = 21$, $N_{\text{mod}} = 17$ and the rms bandwidth of the pulse is $\sigma_\lambda/\lambda_0 = 1.6 \times 10^{-5}$.

CONCLUSION

It was found that for Mode-Locking the undulator modules should have length shorter than $N_w = 130$ periods and the beam delays could be implemented as dipole only chicanes. To extend the output bandwidth further than the factor of four enhancement demonstrated here the undulator modules should be reduced to even shorter than $N_w = 65$. Future work will push this limit as far as possible to determine the broadest possible bandwidth.

For HB-SASE it was found that for $N_w = 265$ the bandwidth can be reduced by a factor of 10 using isochronous chicanes, but not at all with standard chicanes. Shorter undulator modules are required to see an effect using standard chicanes but for significant bandwidth reduction isochronous chicanes are needed. A factor of 30 reduction is already observed, which is sufficient to generate transform limited output for the 10pC mode of operation of the SwissFEL accelerator—first results for this option confirm this, but space restrictions in this paper do not permit them to be included. In future the HB-SASE work will be extended to higher slippage enhancement factors. It may also be possible to use delay sequences using mostly standard chicanes, but bring forward to earlier in the sequence some of the larger delays and implement these with special chicanes with an R_{56} of the *opposite sign* to cancel the R_{56} accumulated to that point. These delays would require more space and require the use of quadrupoles, so diffraction issues may be relevant, but this will be another interesting topic for future study.

REFERENCES

- [1] N. R. Thompson and B. W. J. McNeil, 'Mode-Locking in a Free-Electron Laser Amplifier', *Phys. Rev. Lett.*, 100:203901, 2008.
- [2] N. R. Thompson et al., 'Improved Longitudinal Coherence in SASE FELs', in *Proc. 1st Int. Particle Accelerator Conf.*, Kyoto, 2010, pp.2257-2259.
- [3] J. Wu, A. Marinelli, and C. Pellegrini. 'Generation of Longitudinally Coherent Ultra High Power X-Ray FEL Pulses by Phase and Amplitude Mixing', in *Proc. 34th Int. Free-Electron Laser Conf.*, Nara, 2012, pp. 237-240.
- [4] B. W. J. McNeil, N. R. Thompson and D. J. Dunning, 'Transform-Limited X-Ray Pulse Generation from a High-Brightness Self-Amplified Spontaneous Emission Free-Electron Laser', *Phys. Rev. Lett.* 110:134802, 2013.
- [5] S. Reiche, 'Genesis 1.3: a fully 3D time-dependent FEL simulation code', *Nucl. Instrum. Methods Phys. Res. Sect. A*, 429, p243, 1999, code available at <http://genesis.web.psi.ch/>

FEL PROPOSAL BASED ON CLIC X-BAND STRUCTURE

A. Aksoy*, Ö. Yavaş, Institute of Accelerator Technologies, Ankara, Turkey
 D. Schulte, A. Latina, W. Wuensch, A. Grudiev, I. Syratchev, CERN, Geneva, Switzerland
 Z. Nergiz, Nigde University Physics Department, Nigde, Turkey
 M. Jacewicz, R. Ruber, V. Ziemann, Uppsala University, Uppsala, Sweden
 G. D'auria, S. Di Mitri, Elettra, Trieste, Italy
 M. J. Boland, T. Charles, R. Dowd, G. LeBlanc, Australian Synchrotron, Clayton, Australia
 Q. Gu, W. Fang, Shanghai Institute of Applied Physics, Shanghai, China
 J. Clarke, D. Angal-Kalinin, STFC, Daresbury Laboratory Cockcroft Institute, Daresbury, UK
 E. Gazis, A. Charitonidis, National Technical University of Athens, Greece
 E. Adli, University of Oslo Department of Physics, Oslo, Norway

Abstract

A linear accelerating structure with an average loaded gradient of 100 MV/m at X-Band frequencies has been demonstrated in the CLIC study. Recently, it has been proposed to use this structure to drive an FEL linac. In contrast to CLIC the linac would be powered by klystrons not by an RF source created by a drive beam. The main advantage of this proposal is achieving the required energies in a very short distance, thus the facility would be rather compact. In this study, we present the structure choice and conceptual design parameters of a facility which could generate laser photon pulses below Angstrom. Shorter wavelengths can also be reached with slightly increasing the energy.

INTRODUCTION

X-band accelerator development has gained improvement within last ten years, motivated by the need for high-gradient accelerators for the future linear colliders in high-energy physics research [1]. Studies on accelerating structures operating at 11.4 GHz were made at SLAC and KEK, in the last two decades of the nineteen (up to 2004), for the development of a TeV-scale high energy Linear Collider, and led to achieve 65-70 MV/m accelerating gradients [2]. Design of accelerator cells [3], manufacturing [4], and characterization technique [5] have been developed. Later, significant progress have been achieved by the CERN CLIC (Compact Linear Collider) Collaboration, that has recently demonstrated the possibility to operate 12 GHz accelerating structures with an average loaded gradient higher than 100 MV/m [6], values far beyond those reached with the present S and C band technology. The development of power sources for x-band structures [7] gives opportunity this technology may represent an useful solution to get very compact and cost effective linacs for multi-GeV electron beams. More recently, after the successful operation of the new FEL light sources like LCLS, SACLA, FERMI, a stronger and more vigorous interest in X-band technology has arose. The demand for new FEL facilities is worldwide continuously increasing, spurring plans for new dedicated machines. This led to a general reconsideration of costs and spatial issues,

particularly for the hard X-ray sources, driven by long and expensive multi-GeV NC linacs. For these machines the use of X-band technology can greatly reduce costs and capital investment, reducing the linac lengths and the size of buildings. To pursue this objectives, a scientific collaboration has recently been established among several laboratories, interested in FEL developments, aimed at validating the use of X-band technology for FEL based light sources [8]. The specific objectives of the collaboration will include the design, assembly and high power tests of an X-band accelerating module for FEL applications, made up of two accelerating structures, RF pulse compression and a waveguide distribution systems. Special care will be given to the operating gradients, RF breakdown fault rate, alignment issues, wake fields, and operating stabilities. The overall objective of the collaboration is to support the feasibility studies of new research infrastructures and/or the major upgrading of existing ones, using X-band technology. The work program foresees a strong interaction between FEL scientists, FEL designers and accelerator experts. Starting from the FEL output specification, a fully self consistent FEL facility design will be established (in terms of accelerator layout, major hardware choices, and FEL

MACHINE DESCRIPTION

The proposed facility is a two-stage 6 GeV linac, consisting of an S-Band injector and high-gradient X-band linac which can deliver a high-repetition rate low-emittance beam, one or several undulator sections and photon beam lines with a user facility. The proposed layout is given with Fig. 1. Expected facility length is about 550 m and basic parameters of facility is given in Table 1.

Injector

The injector is proposed to be similar to the injector at SwissFEL [9]. It is based on S-band RF gun operating at about 100 MV/m gradient and standard S-band structures operating at about 20 MV/ gradient.

Main Accelerator

The X-band accelerating structures developed for CLIC project [10] are planned to be used in main accelerating sec-

* avniaksoy@ankara.edu.tr

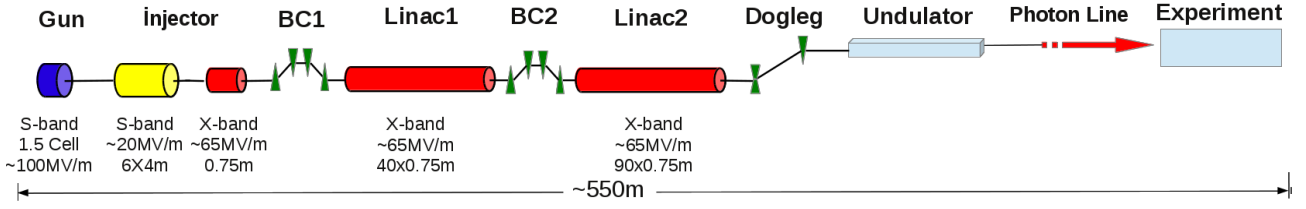


Figure 1: Layout of proposed facility.

Table 1: Basic Parameters of an X-FEL Facility Based on X-band Linac

	Parameter	Unit	Value
Main Linac	Energy	GeV	6
	Bunch Charge	pC	250
	Normalized emittance	μrad	<0.5
	RF pulse length at structure	ns	150
	Pulse repetition rate	Hz	50-100
	Number of bunches per pulse	#	1-3
	Linac frequency	GHz	12
	No of structures per RF module	#	10
	Total (effective) module length	m	10 (7.5)
	Number of RF modules needed	#	12
	Linac gradient	MV/m	65
	No of klystrons per RF module	#	2
	Klystron output power	MW	50
	Klystron output pulse length	μ	1.5
	Total (effective) linac length	m	150 (100)
Injector	Energy	MeV	300
	Linac frequency	GHz	3
	Linac gradient	MV/m	20
	Number of klystrons	#	5
	Klystron output Power	MW	50
	Total (effective) injector length	m	50 (25)

tion. In order to define structure parameters initially we have the impact of single bunch wake field along the main linac. As the beam traverses down along the linac, the head of a single bunch undergoes an unperturbed transverse motion. On the other hand the tail, experiences deflection due to the wake excited by the preceding particles. The amplitude of the deflection in normalized transverse coordinates so called amplification factor will be

$$A = \frac{Ne^2}{2} \int_0^L \frac{\beta(s)}{E(s)} W_{\perp}(s) ds \quad (1)$$

where N is number of particles per bunch, β is beta function along the linac, E is energy and W_{\perp} is the transverse wake potential of the structures [11]. Figure 2 shows the curves of maximum amplifications of $\max[\frac{A_x}{A_{x0}}] = 0.1$ and 0.4 versus gradient of two different CLIC structure (CLIC-502 [10], CLIC-G [12]). As it can be seen on the figure in order to get $\max[\frac{A_x}{A_{x0}}] = 0.4$ the gradient of CLIC-G structure must be more than 110 MV/m while the gradient above 35 MV/m is acceptable for CLIC-502 type of structure. Both structure do not allow to get $\max[\frac{A_x}{A_{x0}}] = 0.1$ amplification.

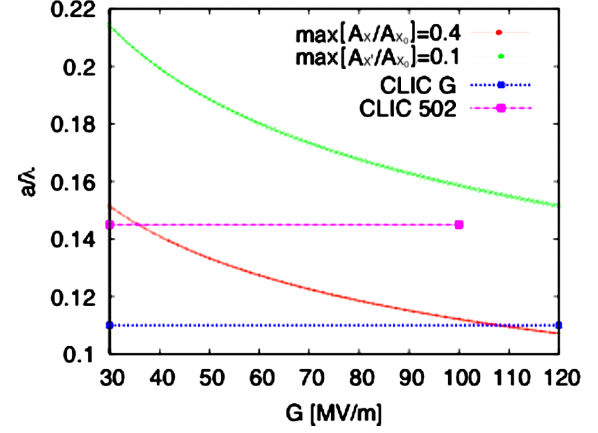

 Figure 2: Amplification factor of a single bunch versus gradient and a/λ of structures.

Figure 3 shows the amplification of slices along a Gaussian bunch using CLIC-502 structure with structure parameter of $a/\lambda = 0.15$ and gradient of $G = 65$ MV/m. In the calculation simplified wake model for CLIC structure has been used. As it can be on the figure the amplification of tail in real coordinates is below 0.2 but the angle reaches 1.6.

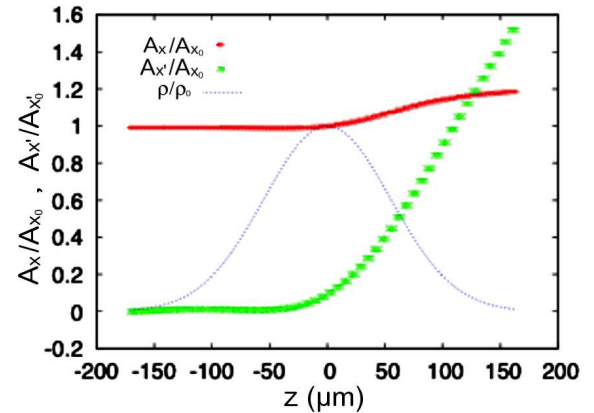


Figure 3: Deflection of slices along Gaussian bunch.

Cost estimation has been done using the structure database of CLIC taking into account wake field effect and

- Structure; a/λ , gradient, length, input power
- Module; pulse compressor, number of structure per module

and the cost has been compared between each other. The summary of cost estimation is given with Table 2

Table 2: Summary of Basic Parameters of Cost Optimization

Parameter	CLIC-502		Optimum
Structures per RF unit	12	16	10
Klystrons per RF unit	2	2	2
Structure length (m)	0.23	0.23	0.75
a/λ	0.145	0.145	0.125
Allowed gradient (MV/m)	100	100	>80
Operating gradient (MV/m)	77	67.5	65
Energy gain per RF unit (MeV)	213	248	488
RF units needed	27	23	12
Total klystrons	54	46	24
Linac active length (m)	74	84	88
Cost estimate (a.u.)	76.2	71.5	51.7

Pulse Compressor and RF Module Layout

Using the results given in Table 2, 10 structures will be installed on one RF module and fed by one RF station which is essentially is combination two klystrons. Schematic view of the module and power combination/distribution system is given with Fig. 4.

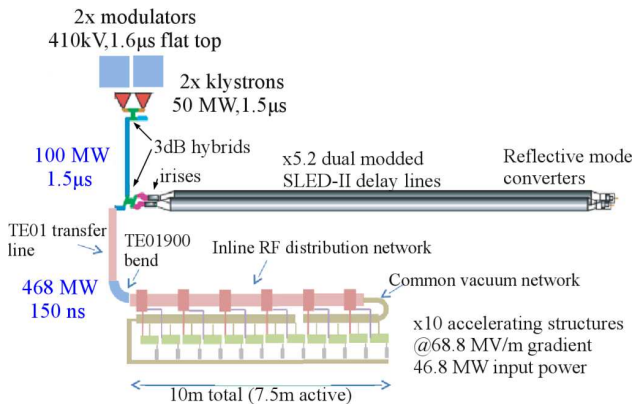


Figure 4: Layout of proposed facility.

Two klystron that each has power of 50 MW and pulse length of 1.5 μ s will be driven by two individual modulator. The RF pulses will be combined with hybrids combiners. Single RF pulse that has 100 MW power and 1.5 μ s length will be compressed to 150 ns by SLED-II delay lines [13]. After compression expected RF power is 468 MW. The compressed power will be distributed by an RF network to each structure evenly which means each structure will be fed by 46.8 MW power yielding 68.8 MV/m gradient.

SIMULATIONS

Preliminary simulations has been performed for the injector, main accelerating section and FEL generation.

Injector

Similar to LCLS [14] a 1.5 cell photo cathode RF gun operating 100 MV/m gradient at 3 GHz is proposed for the electron source. The cathode of the gun is assumed to deliver 250 pC bunch charge and 9 ps full width half maximum

bunch length. Travelling wave accelerating structures that are operating with 20 MV/m gradient at 3 GHz are followed the RF gun similar to SwissFEL. Astra code [15] has been used for simulations and optimization injector section. The beam size and emittance along the RF gun and two RF structures of injector is given with Figs. 5. As it can be seen the projected normalized emittance ϵ_x is below 0.5 mm.mrad.

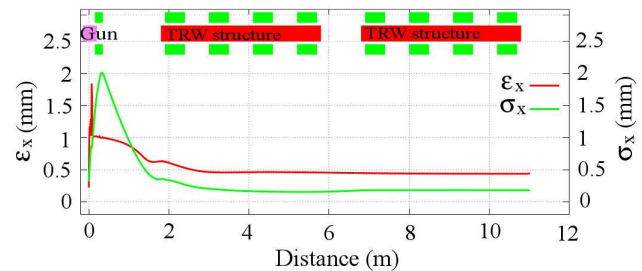


Figure 5: Emittance and horizontal beam size through the injector.

Main Accelerating Section

The injector is followed by an X-Band structure as a chirp linearizer in order to perform better bunch compression. A bunch compressor is located after the linearizer structure afterward two stage main accelerating section separated with bunch compressor is proposed for the main accelerating section (see Fig. 1). FODO type of lattice is proposed for beam transport and Elegant code [16] has been used for tracking.

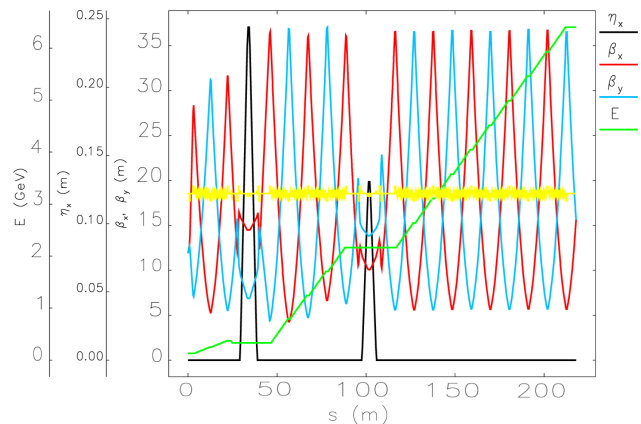


Figure 6: Beam energy, and Twiss functions along the main linac.

Figures 6 and 7 show the beam energy and Twiss functions along the linac and final longitudinal phase space of the bunch. As it can be seen on Fig. 7 the bunches are compressed down to $\sigma_t = 26$ fs ($\sigma_z = 8 \mu$ m) and RMS energy spread at the end of linac is $\sigma_E/E = 0.06\%$

Lasing Section

For the lasing section it is proposed that planar undulators each has about 4.2 m length are located on FODO type of

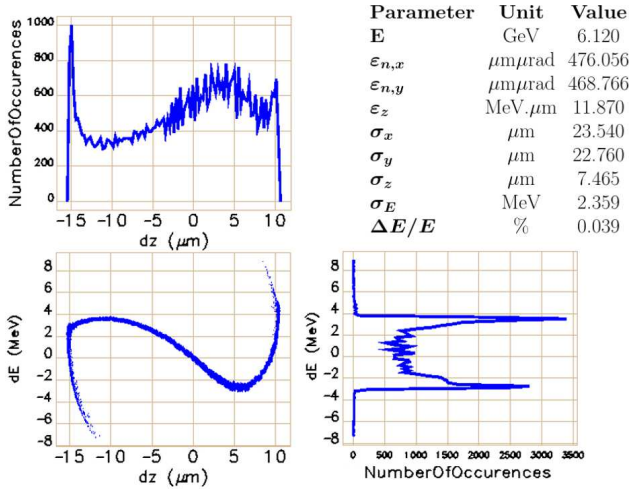


Figure 7: Longitudinal phase space of bunch at the end of linac.

lattice. Free electron laser (FEL) at very small wavelength range can be produced with a single-pass devices in the Self Amplified Spontaneous Emission (SASE) mode. The resonant wavelength of radiation produced from a undulator is given by

$$\lambda = \frac{\lambda_u}{2\gamma^2} (1 + K_{\text{RMS}}^2), \quad (2)$$

where λ_u is the undulator period, K_{RMS} is the RMS undulator strength and γ is the relativistic factor. Figure 8 shows saturation process of FEL at 1 Å resonant wavelength for beam energy of 6 GeV and undulator period of $\lambda_u = 15$ mm and undulator strength of $K_{\text{RMS}} = 1$. As it can be seen the power saturates around 50 m.

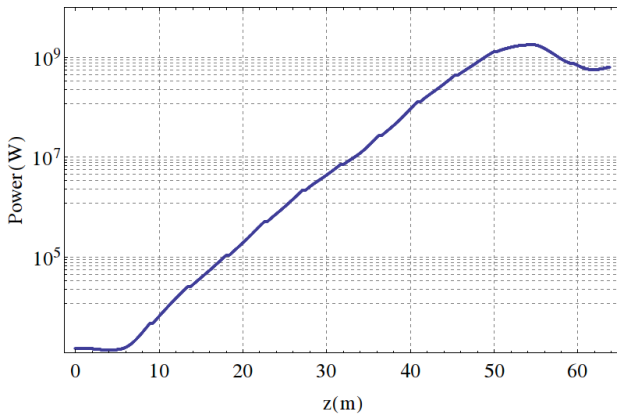


Figure 8: Power growth along the lasing section.

CONCLUSION

In this paper we focused on feasibility of usage of CLIC X-Band structures driving an FEL facility. We described preliminary simulations. It is shown that the radiation below 1 Å can be produced in SASE mode. The self seeding and tapered undulator options should be studied in future work.

REFERENCES

- [1] J.W. Wang et al., "Accelerator Structures R&D for Linear Colliders", Proceedings of the 1999 Particle Accelerator Conference, New York (1999).
- [2] C. Adolphsen, SLAC-Pub 11224 (2005).
- [3] J. Klingmann et al., "Fabrication of DDS-3, an 11.4 GHz Damped-Detuned Structure", Proceedings of the 1999 Particle Accelerator Conference, New York (1999).
- [4] Z. Li, "RDDS Cell Design and Optimization for the NLC Linac", Proceedings of the 1999 Particle Accelerator Conference, New York (1999).
- [5] S.M. Hanna et al., "Development of Characterization Techniques for X-Band Accelerator Structures", Proc. Of the 1997 IEEE PAC (1997).
- [6] M. Aicheler et al., "A Multi-TeV Linear Collider Based on CLIC Technology : CLIC Conceptual Design Report", ERN-2012-007 ; SLAC-R-985 ; KEK-Report-2012-1 ; PSI-12-01 ; JAI-2012-001 (2012).
- [7] J. Kovermann et al., "Commissioning of the first klystron-based x-band power Source at CERN", Proceedings of IPAC2012, New Orleans, Louisiana, USA (2012).
- [8] A. Aksoy et al., IPAC 2014, Dresden, Germany, (2013).
- [9] R. Ganter, "SwissFEL Conceptual Design Report", PSI Bericht 10-04 (2012).
- [10] A. Grudiev, D. Schulte, "The Accelerating Structure for A 500 GeV CLIC", LINAC'10, Tsukuba, (2010).
- [11] A. Aksoy et al., "Beam dynamics simulation for the Compact Linear Collider drive-beam accelerator", Phys. Rev. ST Accel. Beams, v:14, i:8, p:84402, (2011).
- [12] J. Shi et al. "Tuning of CLIC Accelerating Structure Prototypes at CERN", Proceedings of Linear Accelerator Conference LINAC2010, Tsukuba, Japan, (MOP022), (2010).
- [13] C. Nantista et al., "High-Power RF Pulse Compression with SLED-II at SLAC", SLAC-PUB 6145 (1993) EPAC'96.
- [14] C. Limborg et al., "RF Design of the LCLS Gun", LCLS-TN-05-3, (2006).
- [15] K. Floettmann, "ASTRA User Manual", (2011).
- [16] M. Borland, "User's Manual for Elegant", (2013).

A NOVEL MODELING APPROACH FOR ELECTRON BEAMS IN SASE FELs

P. Niknejadi and J.M.J. Madey

University of Hawai'i at Manoa, Honolulu, HI 96822, USA

Abstract

We have recently shown that the Wheeler-Feynman analysis of the interaction of a moving charge with distant absorbers provides a perfect match to the energy radiated by two coherently oscillating charged particles (a heretofore unsolved problem in classical electrodynamics). Here we explain the need to include the Wheeler-Feynman coherent radiation reaction force as an integral part of the solution to the boundary value problem for free electron lasers (FELs) that radiate into "free space". We will also discuss how the advanced field of the absorber can interact with the radiating particles at the time of emission. Finally we will introduce and explore the possibility of improving the temporal coherence of self amplified spontaneous emission (SASE) FELs as well as the possibility of optimizing the spectrum of their emitted radiation via altering the structure of their targets by using the Wheeler-Feynman coherent radiation reaction force in the analysis of FEL operation.

INTRODUCTION

In the past few years the successful operation of x-ray FELs based on the SASE principle has made them a powerful new tool for addressing fundamental questions in biology, chemistry and nano-technology [1]. On the other hand the fundamental principle that the SASE FEL's rely on, the theory of radiation in classical electrodynamics, has a few unresolved questions of its own. For instance, since classical field theory has, for about a century, failed to provide a non-diverging solution and origin for the radiation reaction field, our understanding of the process of coherent radiation in the classical limit with respect to conservation of energy is not complete. The radiation reaction field is the electric field responsible for energy conservation in the process of radiation.

The analysis provided by Wheeler and Feynman, in their 1945 paper "Interaction with the Absorber as the Mechanism of Radiation," for the first time yields an exact match between the radiated power of oscillating particles and the rate of change of the particle's kinetic energy [2]. The conceptual backbone of the Wheeler and Feynman model has been debated for many years and raises a number of questions about the nature of interactions of fields and particles. But it has been shown that the model is consistent with the quantum electrodynamics [3] and Dirac's theory of single particle radiation reaction force [4]. In their paper, Wheeler and Feynman did not consider the coherent radiation emitted by multiple accelerated charges. However, we have shown that the Wheeler-Feynman derivation for a moving charge interacting with the absorber also provides a perfect match

to the radiated energy in the case of two or more coherently oscillating charged particles [5].

These developments seem likely to clarify our understanding and contribute to the further advancement of FEL light sources, and possibly improve the temporal coherence of SASE FELs. With the rapid advancement and reliance upon these sources, this is a good time to consider the effect of the Wheeler-Feynman approach on current technology. We also hope that this approach will provide further insight into physics underlying the behavior of the of these powerful devices as well as additional means to control the spectral intensity and bandwidth in addition to the operating wavelength.

The description of advanced interactions as set forth in the Wheeler Feynman paper has led us to explore both the engineering implications for the design of SASE FEL systems and possible new approaches for the investigation of the distribution of distant matter in the universe as well [6].

APPLYING WHEELER FEYNMAN ANALYSIS TO COLLECTION OF COHERENTLY OSCILLATING PARTICLES

Wheeler and Feynman were able to demonstrate that, when formulated in the language of covariant action-at-a-distance, the solution to the boundary value problem corresponding to an oscillating particle within a spherical absorbing shell of arbitrary density is dominated by the interference of the retarded and advanced forces originating in the accelerated and absorbing particles. This leads to a force on the accelerated particle exactly equal to that needed to match the power carried by radiation to the particles in the absorbing shell. In their 1949 paper, their quantitative findings also show that these interactions are only evident in the immediate vicinity of the radiating/absorbing charges, and converge to the conventional retarded electrodynamics at larger distances from the radiating charge [7].

Case of Two Coherently Oscillating Particles

Consider two coherently oscillating charged particles displaced by distance " r " in an arbitrary direction. If the displacement r has an angle α with respect to the direction of motion of the coherently oscillating charged particles, the integral of Poynting vector (the radiated power) is defined Equation 1. When the charges oscillate perpendicular to the direction of their separation vector, $\alpha = \pi/2$, the power radiated is given by Equation 2.

$$P_{\text{Radiated}}(\alpha) \propto 2 \int_0^{2\pi} \int_0^\pi \sin^3(\theta) \cos^2 \times \left(\frac{kr(\cos(\theta) \cos(\alpha) + \sin(\theta) \sin(\alpha) \cos(\phi))}{2} \right) d\theta d\phi \quad (1)$$

and $P_{\text{Radiated}}(\alpha = \pi/2) \propto$

$$2 \int_0^{2\pi} \int_0^\pi \sin^3(\theta) \cos^2 \left(\frac{kr(\sin(\theta) \cos(\phi))}{2} \right) d\theta d\phi \quad (2)$$

The work done on the radiating charges by the electric field they generate must equal the radiated power calculated by Poynting's vector in Equation 1 and Equation 2.

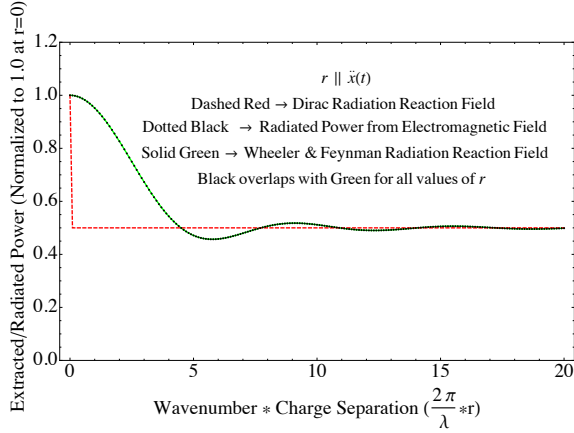


Figure 1: Comparison of the power extracted by the Dirac coherent radiation force and amplitude of the Wheeler-Feynman coherent radiation force with the power radiated by the two oscillating charged particles' for displacements parallel to their vector accelerations. The non-local component of the Dirac coherent radiation reaction force falls to zero for any finite displacement of the two charges along this direction, leaving only each particle's single point radiation reaction force to oppose their oscillating velocities (adapted from Reference [5]).

As indicated in Figure 1 and 2, the Wheeler and Feynman model is particularly useful when dealing with coherently radiating particles in free-space. Figure 3 compares the radiated power and energy extracted by the Wheeler-Feynman coherent radiation reaction force for all angles of α .

Case of Coherent Beams in SASE FELs

The coherent radiation emitted by tightly bunched electron beams plays a critical role in the analysis and operation of free electron lasers. For conducting or reflecting (resonator mirror) FELs, a normal mode analysis of operation already includes the relevant boundary conditions. However, in order to arrive at a comprehensive first-principles field-based analysis of the intense of radiation emitted into free-space by devices that work based on the SASE principle, including all target interactions, we also need to include the effect of boundary condition at the target.

Kimel and Elias [8] were able to show it is possible to use the Lienard-Wiechert description of FEL interaction to

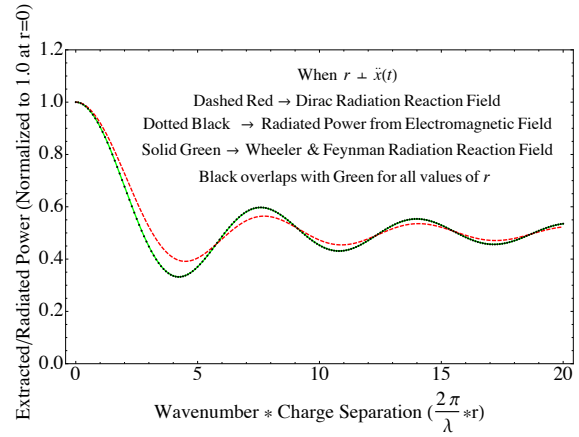


Figure 2: Comparison of the power extracted by the Dirac coherent radiation force and the amplitude of the Wheeler-Feynman coherent radiation force with the power radiated by the two oscillating charged particles' for displacements perpendicular to their vector accelerations (adapted from Reference [5]).

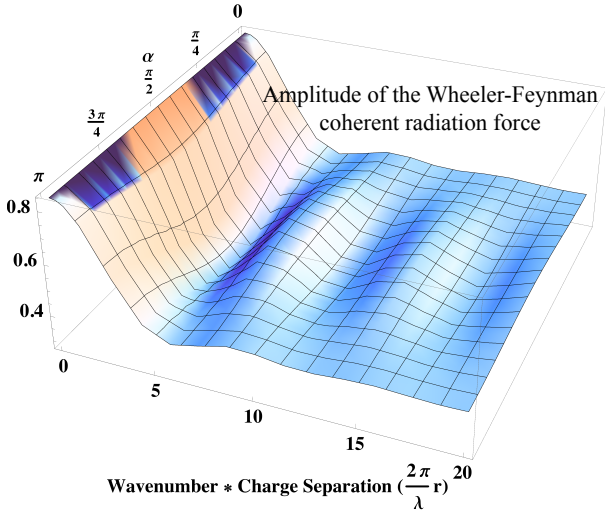


Figure 3: Amplitude of the Wheeler-Feynman coherent radiation reaction force for two oscillating charged particles' with displacement r and angle α (between the displacement and direction of oscillation).

include a viable model the coherent radiation reaction in covariant form valid for radiation into free-space.

In the Wheeler Feynman model, to calculate the effect of absorber in vicinity of an accelerating source charge, the retarded field of the source charge traveling outbound is first used to calculate the motions of absorber particles. Then the sum of the absorber's advanced fields near the source is calculated. Finally it is shown that the addition of this field to the half advanced plus half retarded field of the source gives the expected fully retarded field of the source, while also producing the correct radiation reaction force.

Applying the same principle to the beam traveling in a SASE FEL, we start by considering both the advanced and

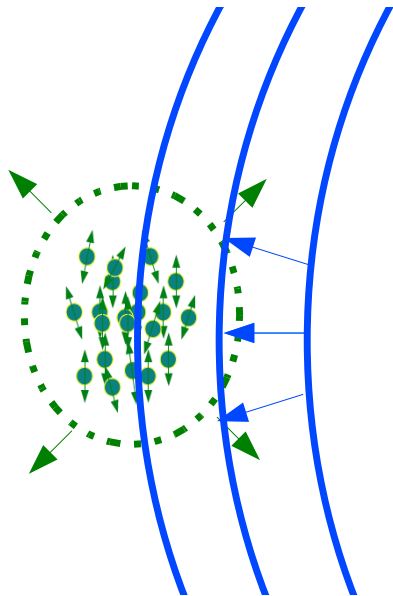


Figure 4: Diagram showing the advanced field (solid blue) of the absorber due to retarded field (dashed green) of emitting electrons acting on the oscillating electrons.

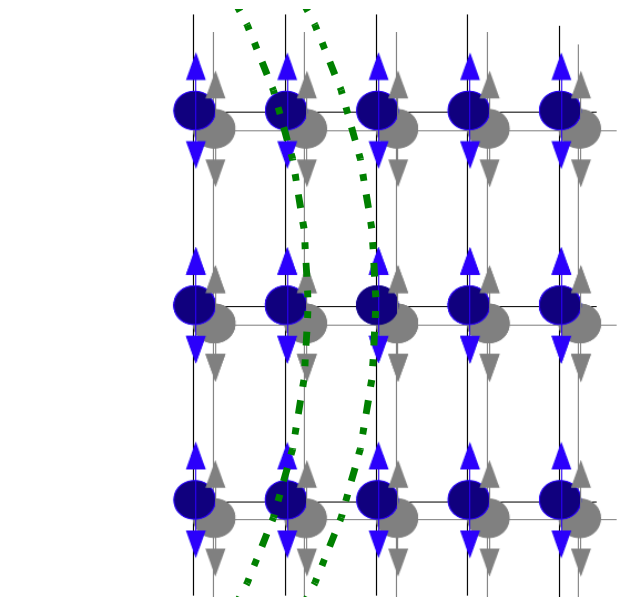
retarded field/potential of both the target (the absorber) and the electrons (the emitter). Now we must include half the retarded (outgoing) field of the emitters and the half the advanced (incoming) field of the target. The interaction of the advanced field of the target with the radiating electrons will insure energy conservation on the one hand, and on the other hand imposes the fields and forces initiated from the target on the source (Figure 4).

This feature allows for improving the spectral bandwidth and temporal coherence of the output of SASE FELs by manipulation of the target, as long as the target can resonate with the source and impose higher degrees of coherence.

MÖSSBAUER EFFECT

In order to measure and check the validity of this model it is essential to have a target that can verify the role of the absorber. In the past century, the Mössbauer effect has been used to investigate special electronic structures in matter, as well as biology and chemistry. In recent years, Mössbauer spectrometry has also been utilized for measurement of coherent scattering and diffraction of nuclear radiation [9]. Due to its nature, the Mössbauer absorber can be approximated stationary oscillating dipoles (Figure 4).

Since the energy distribution of the utilized radiation is extremely narrow, a Mössbauer absorber, for instance Fe^{57} above the Curie point [10], is an effective tool for high energy resonance spectroscopy. Including a Mössbauer absorber as part of the target of the SASE FEL will allow the advanced field of the target to have interactions with the emitting electrons and yield a narrow spectral bandwidth. Further analysis on use of Mössbauer solids as target for SASE FELs discusses the characteristic and advantages of concave target, one similar to the concave resonator mirrors



of a cavity FEL, for measurement of the coherence in these sources [11].

CONCLUSION

Here we discussed the results and implications of Wheeler-Feynman analysis of the interaction of a moving charge with distant absorbers. We showed that it provides a perfect match to the energy radiated by two coherently oscillating charged particles, and described the reasoning behind including the Wheeler-Feynman coherent radiation reaction force as an integral part of the solution of the boundary value problem of FELs that radiate into free-space. Finally we conclude that the Wheeler-Feynman model enables the development of a transparent first principles model of the instantaneous effects of boundary conditions on the radiation emitted by oscillating charges in systems subject to those boundary conditions enabling both the attainment of energy conservation and the modification of the relevant boundary conditions to optimize system performance.

ACKNOWLEDGMENT

We like to thank Eric B. Szarmes, Jeremy M. D. Kowalczyk, Nicholas A. Wisniewski and Ian Howe for many fruitful conversations and Graduate Student Organization at University of Hawai'i at Manoa and FEL Conference for their supplementary grants.

REFERENCES

- [1] J. Amann, W. Berg, V. Blank et al., Nature Photonics, vol. 6, pp. 693-698, Aug. 2012.
- [2] J. A. Wheeler, R. P. Feynman, Rev. Mod. Phys. 17, 157 (1945).
- [3] J. G. Cramer Rev. Mod. Phys. 58, 647 (1986).

- [4] P. A. M. Dirac, "Classical Theory of Radiating Electrons", *Proceedings of the Royal Society A: Mathematical, Physical and Engineering Sciences*, vol. 167, no. 929, pp. 148-169, Aug. 1938.
- [5] P. Niknejadi et al., "Energy Conservation of Coherently Oscillating Charged Particles in Classical Electrodynamics" (submitted for publication).
- [6] J.M.J. Madey et al., "Conceptual and experimental implications of advanced interactions in electrodynamics and cosmology", (to be published).
- [7] J.A. Wheeler, R.P. Feynman, *Rev. Mod. Phys.* 21, 425 (1949).
- [8] I. Kimel, L. Elias, *Nuclear Instruments and Methods in Physics Research Section A: Accelerators, Spectrometers, Detectors and Associated Equipment* 375, 565 (1996).
- [9] B. Flutz, "Mössbauer Spectrometry" in *Characterization of Materials*, New York: Wiley, 2002.
- [10] T. A. Kovats, J. C. Walker, *Phys. Rev.* 181, 610 (1969).
- [11] P. Niknejadi et al. "Analysis for a concave Mössbauer solid as a resonating SASE FEL target". (to be published).

STATISTICAL PROPERTIES OF THE RADIATION FROM SASE FEL OPERATING IN A POST-SATURATION REGIME WITH AND WITHOUT UNDULATOR TAPERING

E.A. Schneidmiller, M.V. Yurkov, DESY, Hamburg, Germany

Abstract

We describe statistical and coherence properties of the radiation from x-ray free electron lasers (XFEL) operating in the post-saturation regime. We consider practical case of the SASE3 FEL at European XFEL. We perform comparison of the main characteristics of X-ray FEL operating in the post-saturation regime with and without undulator tapering: efficiency, coherence time and degree of transverse coherence.

INTRODUCTION

Radiation from Self Amplified Spontaneous Emission Free Electron Laser (SASE FEL) [1, 2] has limited spatial and temporal coherence. This happens due to start-up of the amplification process from the shot noise in the electron beam. The fluctuations of the electron beam density are uncorrelated in time and space, and many radiation modes are excited at the initial stage of amplification. As a rule, ground spatial TEM₀₀ mode with highest gain dominates, and the degree of transverse coherence grows in the exponential amplification stage. Radiation wave slips forward with respect to the electron beam by one wavelength per one undulator period. This relative slippage on the scale of the field gain length gives an estimate for coherence length. Both, degree of transverse coherence and coherence time reach maximum value in the end of the exponential regime of amplification, and then degrade visibly in the nonlinear regime. Maximum degree of transverse coherence of about 0.95 is reached for the values of diffraction parameter about 1. For large values of the diffraction parameter the degree of transverse coherence falls down due to poor mode selection, i.e. mode degeneration takes place. For small values of the diffraction parameter the degree of transverse coherence falls down due to more poor longitudinal coherence [3–6].

Radiation from SASE FEL with planar undulator contains visible contribution of odd harmonics. Parameter range where intensity of higher harmonics is defined mainly by nonlinear beam bunching in the fundamental harmonic has been intensively studied in refs. [7–16]. Comprehensive studies of the nonlinear harmonic generation have been performed in [16] in the framework of the one-dimensional model. General features of harmonic radiation have been determined. It was found that coherence time at saturation falls inversely proportional to harmonic number, and relative spectrum bandwidth remains constant with harmonic number. Comprehensive study of the coherence properties of the odd harmonics in the framework of 3D model have been performed in [17]. We considered parameter range when intensity of higher harmonics is mainly defined by

nonlinear harmonics generation mechanism. The case optimized XFEL has been considered. Using similarity techniques we present universal dependencies for the main characteristics of the SASE FEL covering all practical range of optimized X-ray FELs.

Application of the undulator tapering [18] allows to increase conversion efficiency to rather high values [19–27]. New wave of interest to the undulator tapering came with x-ray free electron lasers [28–32] (see [33–36] and references therein). It is used now not only as demonstration tool [37], but as a routine tool at operating x-ray FEL facilities LCLS and SACLA.

There are several reasons why we performed the present study. The first reason is that SASE3 FEL at the European XFEL operating at long wavelengths can not be tuned as optimized FEL [4] due to limitation on minimum value of the focusing beta function, and dedicated study is required for description of coherence properties. Another reason is that in the parameter range of SASE3 FEL linear mechanism of harmonic generation is essential which results in much higher power of higher odd harmonic with respect to the case of nonlinear harmonic generation [33, 38]. Finally, we compare coherence properties for both, fundamental and the third harmonic for the case of untapered undulator and undulator with optimized tapering. We show that the brilliance of the fundamental harmonic of the radiation from SASE FEL with optimized tapering can be increased by a factor of 3 with respect to untapered case.

GENERAL DEFINITIONS AND SIMULATION PROCEDURE

The first-order transverse correlation function is defined as

$$\gamma_1(\vec{r}_\perp, \vec{r}'_\perp, z, t) = \frac{\langle \tilde{E}(\vec{r}_\perp, z, t) \tilde{E}^*(\vec{r}'_\perp, z, t) \rangle}{\left[\langle |\tilde{E}(\vec{r}_\perp, z, t)|^2 \rangle \langle |\tilde{E}(\vec{r}'_\perp, z, t)|^2 \rangle \right]^{1/2}},$$

where \tilde{E} is the slowly varying amplitude of the amplified wave. For a stationary random process γ_1 does not depend on time, and the degree of transverse is:

$$\zeta = \frac{\int |\gamma_1(\vec{r}_\perp, \vec{r}'_\perp)|^2 I(\vec{r}_\perp) I(\vec{r}'_\perp) d\vec{r}_\perp d\vec{r}'_\perp}{\left[\int I(\vec{r}_\perp) d\vec{r}_\perp \right]^2},$$

where $I(\vec{r}_\perp) = \langle |\tilde{E}(\vec{r}_\perp)|^2 \rangle$. The first order time correlation function, $g_1(t, t')$, is calculated in accordance with the definition:

$$g_1(\vec{r}, t - t') = \frac{\langle \tilde{E}(\vec{r}, t) \tilde{E}^*(\vec{r}, t') \rangle}{\left[\langle |\tilde{E}(\vec{r}, t)|^2 \rangle \langle |\tilde{E}(\vec{r}, t')|^2 \rangle \right]^{1/2}},$$

For a stationary random process time correlation functions are functions of the only argument, $\tau = t - t'$. The coherence time is defined as $\tau_c = \int_{-\infty}^{\infty} |g_1(\tau)|^2 d\tau$. Peak brilliance is defined as a transversely coherent spectral flux:

$$B = \frac{\omega d \dot{N}_{ph}}{d\omega} \frac{\zeta}{(\lambda/2)^2}.$$

If one traces evolution of the brilliance of the radiation along the undulator length there is always the point, which we define as the saturation point, where the brilliance reaches maximum value [4].

Simulations have been performed with three-dimensional, time-dependent FEL simulation code [4, 17, 39] tracing actual number of electrons. In our simulation procedure particles correspond to real electrons randomly distributed in full 6D phase space. This allows us to avoid any artificial effects arising from standard procedures of macroparticle loading as we described earlier [4]. Simulations of the FEL process have been performed for the case of a long bunch with uniform axial profile of the beam current. Such a model provides rather accurate predictions for the coherence properties of the XFEL, since typical radiation pulse from the XFEL is much longer than the coherence time. Output of the simulation code are arrays containing complex values of the radiation field amplitudes. Then we apply statistical analysis, and calculate physical values as it has been defined in this section.

RESULTS

We perform comparative analysis of tapered and untapered case for parameters of the SASE3 undulator of the European XFEL. Undulator period is 6.8 cm, electron energy is 14 GeV, radiation wavelength is 1.55 nm. Undulator consists of 21 modules, each is 5 meters long with 1.1 m long intersections between modules. Parameters of the electron beam correspond to 0.25 nC case of the baseline parameters of the electron beam: emittance 0.6 mm-mrad, rms energy spread 2.5 MeV, peak beam current 5 kA [33]. Average focusing beta function is equal to 15 m. The value of the diffraction parameter is $B = 1.1$ which is close to optimum conditions for reaching maximum value of the degree of transverse coherence [4]. Two cases were simulated: untapered undulator, and undulator optimized for maximum FEL efficiency [40].

Plots in Fig. 1 show evolution along the undulator of the radiation power, degree of transverse coherence, coherence time, and brilliance for the fundamental harmonic. Power, coherence time, and brilliance are normalized to the values

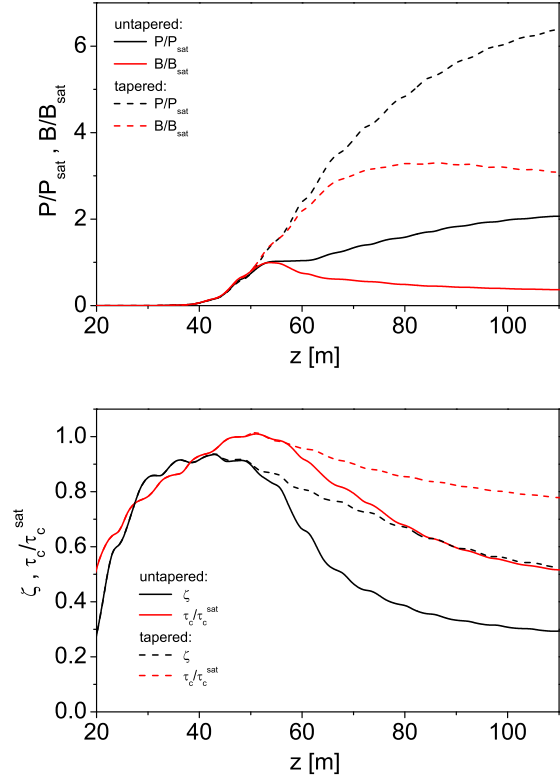


Figure 1: Fundamental harmonic: evolution of the radiation power and brilliance (top plot) and of coherence time and degree of transverse coherence (bottom plot) along the undulator for untapered (solid curves) and optimized tapered case (dashed curves).

of the fundamental harmonic in the saturation point. Saturation length for the fundamental harmonic is equal to 53 m. Absolute values in the saturation point are: radiation power is 108 GW and 6.6 GW; coherence time is 1.2 fs and 0.5 fs; degree of transverse coherence is 0.86 and 0.72 for the fundamental and the 3rd harmonic, respectively. Brilliance of the fundamental harmonic in the saturation point is equal to 3.8×10^{22} photons/sec/mm²/rad²/0.1% bandwidth. Now we compare behavior of the radiation properties for the tapered and untapered case. Growth of the radiation power is higher for the tapered case. We also obtain less intensive degradation of the coherence properties of the radiation. However, brilliance of the radiation for tapered saturates at the undulator length of 80 m, and then drops down gradually. Benefit of the tapered case against untapered case in terms of the radiation brilliance is factor of 3. It is mainly reached by the increase of the radiation power by a factor of 5. Coherence properties of the radiation in the point of maximum brilliance are worse than those of the untapered SASE FEL in the saturation point: 0.86 to 0.68 for the degree of transverse coherence, and 1 to 0.86 in terms of coherence time. Figure 2 presents normalized spectral power of the fundamental harmonic for untapered (black) and tapered (red) case. Output points correspond to the maximum

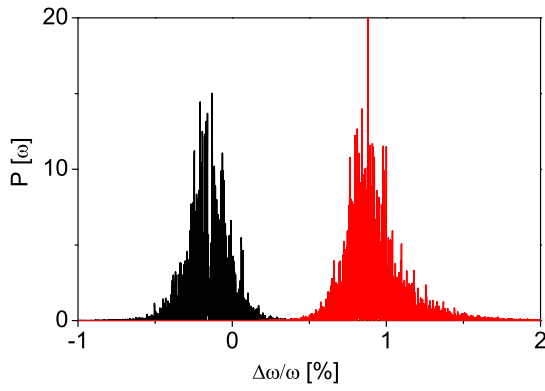


Figure 2: Normalized spectral power of the fundamental harmonic for untapered (black) and tapered (red) case. Output points correspond to the maximum brilliance: $z = 53$ m and $z = 80$ m for untapered and tapered case, respectively. Spectrum of untapered case is shifted by 1% to the right-hand side.

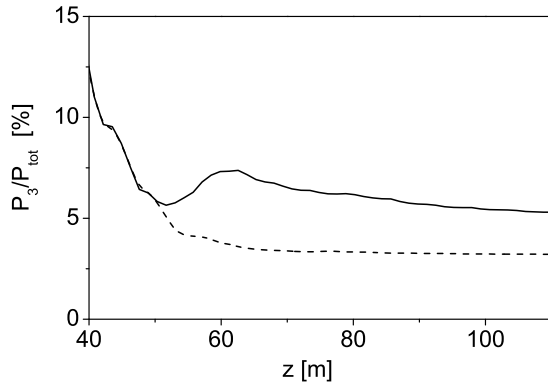


Figure 3: Contribution of the 3rd harmonic radiation power to the total radiation power for untapered (solid curves) and optimized tapered case (dashed curves).

brilliance: $z = 53$ m and $z = 80$ m for untapered and tapered case, respectively. It is seen that spectrum of the untapered case is more narrow and does not contain spanning tails.

We already mentioned that parameters of SASE3 FEL are such that we expect significant increase of the radiation power in the higher odd harmonics due to mechanism of linear harmonic generation. This happens due to small value of the diffraction parameter and high quality of the electron beam (small emittance and energy spread) [38]. Results of numerical simulations presented in Fig. 3 shows that for untapered case contribution of the 3rd harmonic to the total power is about 6% in the saturation point. Note that mechanism of nonlinear harmonic generation results in the value of 2% only. High value of the 3rd harmonic radiation power should be the subject of concern for the planned user experiments. It can constitute harmful background, or can be used in pump-probe experiments. Mechanisms to control 3rd harmonic contribution are now the subject of dedicated studies [41].

ISBN 978-3-95450-133-5

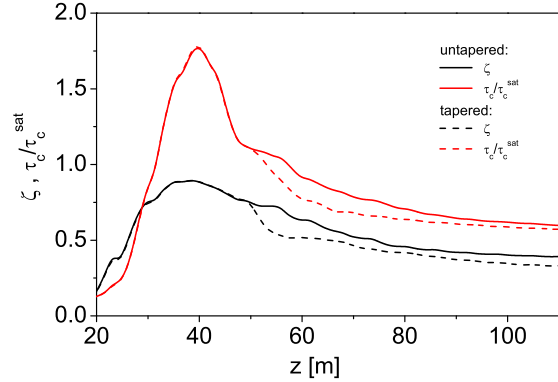
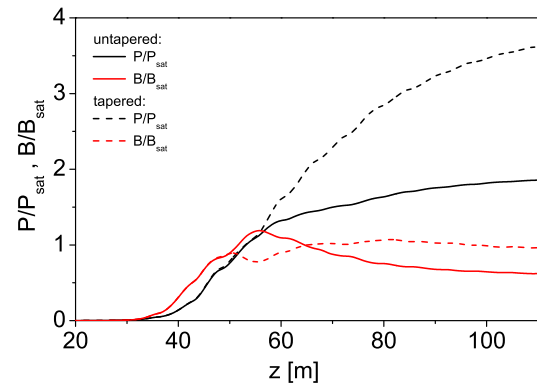


Figure 4: 3rd harmonic: evolution of the radiation power and brilliance (top plot) and of coherence time and degree of transverse coherence (bottom plot) along the undulator for untapered (solid curves) and optimized tapered case (dashed curves).

Plots in Fig. 4 show evolution along the undulator of the radiation power, degree of transverse coherence, coherence time, and brilliance for the 3rd harmonic. Power, coherence time, and brilliance are normalized to the values of the 3rd harmonic in the saturation point of the fundamental harmonic. Absolute numbers were introduced above. There is interesting observation that brilliance of the radiation of the 3rd harmonic does not differ significantly for untapered and tapered cases. In the case of optimized tapered undulator relative contribution of the 3rd harmonic to the total power is visibly less while absolute power is higher than for untapered case. Coherence properties of the 3rd harmonic for untapered case are a bit better than those of the tapered case.

To make our paper complete, we conclude with presenting in Fig. 5 of the evolution along the undulator of the FWHM spot size and FWHM angular divergence of the radiation in the far zone. Cone of the fundamental harmonic radiation in the far zone is visibly wider for the tapered case. Also, phase front of the radiation is quite different for tapered and untapered case. This is a hint for careful design of the optical transport system capable effectively handle both, untapered and tapered options.

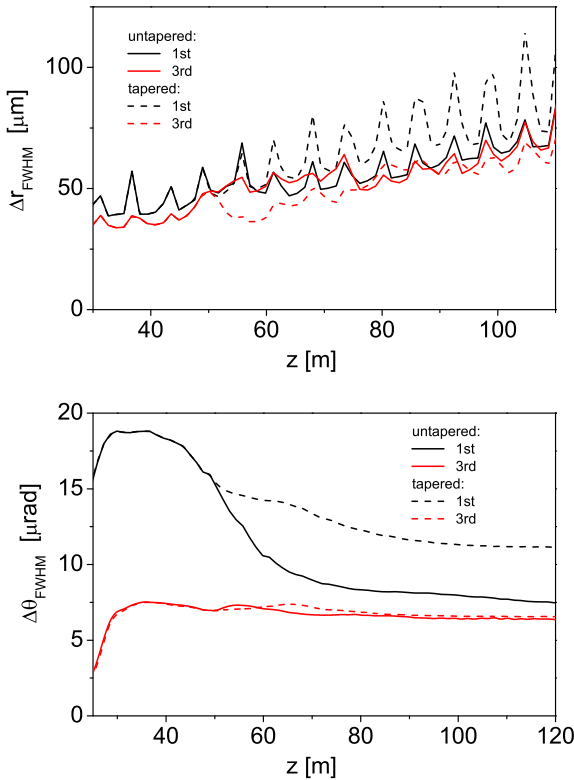


Figure 5: Evolution along the undulator of the FWHM spot size (top plot) and FWHM angular divergence of the radiation in the far zone (bottom plot) for untapered (solid curves) and optimized tapered case (dashed curves). Black and red colors correspond to the fundamental and the 3rd harmonic, respectively.

SUMMARY

Application of undulator tapering has evident benefit for SASE3 FEL operating in the wavelength range around 1.6 nm. It is about factor of 6 in the pulse radiation energy with respect to the saturation regime, and factor of 3 with respect to the radiation power at full length. General feature of tapered regime is that both, spatial and temporal coherence degrade in the nonlinear regime, but a bit slowly than for untapered case. Peak brilliance is reached in the middle of tapered section, and exceeds by a factor of 3 the value of the peak brilliance in the saturation regime. Degree of transverse coherence in the saturation for untapered case is 0.86. Degree of transverse coherence for maximum brilliance of tapered case is 0.66. Coherence time falls by 15%. At the exit of the undulator degree of transverse coherence for tapered case is 0.6, and coherence time falls by 20%. 3rd harmonic in the nonlinear regime for both, untapered and tapered cases, exhibit nearly constant brilliance and nearly constant contribution to the total power. Coherence time of the 3rd harmonic for the tapered case approximately scales inversely proportional to harmonic number, as in untapered case.

REFERENCES

- [1] Ya.S. Derbenev, A.M. Kondratenko, and E.L. Saldin, Nucl. Instrum. and Methods 193 (1982) 415.
- [2] J.B. Murphy and C. Pellegrini, Nucl. Instrum. and Methods A237 (1985) 159.
- [3] E.L. Saldin, E.A. Schneidmiller, and M.V. Yurkov, Opt. Commun. **186** (2000) 185.
- [4] E.L. Saldin, E.A. Schneidmiller, and M.V. Yurkov, Opt. Commun. 281 (2008) 1179.
- [5] E.L. Saldin, E.A. Schneidmiller, and M.V. Yurkov, Opt. Commun. 281 (2008) 4727.
- [6] E.L. Saldin, E.A. Schneidmiller, and M.V. Yurkov, New J. Phys. 12 (2010) 035010, doi: 10.1088/1367-2630/12/3/035010.
- [7] M. Schmitt and C. Elliot, Phys. Rev. A, 34 (1986) 6.
- [8] R. Bonifacio, L. De Salvo, and P. Pierini, Nucl. Instr. Meth. A 293 (1990) 627.
- [9] W.M. Fawley, Proc. IEEE Part. Acc. Conf., 1995, p. 219.
- [10] H. Freund, S. Biedron and S. Milton, Nucl. Instr. Meth. A 445 (2000) 53.
- [11] H. Freund, S. Biedron and S. Milton, IEEE J. Quant. Electr. 36 (2000) 275.
- [12] S. Biedron et al., Nucl. Instr. Meth. A 483 (2002) 94.
- [13] S. Biedron et al., Phys. Rev. ST 5 (2002) 030701.
- [14] Z. Huang and K. Kim, Phys. Rev. E, 62 (2000) 7295.
- [15] Z. Huang and K. Kim, Nucl. Instr. Meth. A 475 (2001) 112.
- [16] E.L. Saldin, E.A. Schneidmiller and M.V. Yurkov, Phys. Rev. ST-AB 9 (2006) 030702
- [17] E.A. Schneidmiller and M.V. Yurkov, Proc. 2012 FEL Conference, Nara, Japan, 2012, p. 65.
- [18] N.M. Kroll, P.L. Morton, and M.N. Rosenbluth, IEEE J. Quantum Electron. 17, 1436 (1981).
- [19] T.J. Orzechowski et al., Phys. Rev. Lett. 57, 2172 (1986).
- [20] R.A. Jong, E.T. Scharlemann, W.M. Fawley Nucl. Instrum. Methods Phys. Res. A272, 99 (1988).
- [21] W.M. Fawley, Nucl. Instrum. Methods Phys. Res. A375, 550 (1996).
- [22] W.M. Fawley et al., Nucl. Instrum. Methods Phys. Res. A483, 537 (2002).
- [23] E.L. Saldin, E.A. Schneidmiller and M.V. Yurkov, Opt. Commun. 95, 141 (1993).
- [24] Review by E.T. Scharlemann in Laser Handbook, Volume 6, Free electron lasers, eds. W.B. Colson, C. Peilegrini and A. Renieri (North Holland, Amsterdam, 1991).
- [25] E.L. Saldin, E.A. Schneidmiller and M.V. Yurkov, Physics Reports 260, 187 (1995).
- [26] E.L. Saldin, E.A. Schneidmiller, M.V. Yurkov, "The Physics of Free Electron Lasers" (Springer-Verlag, Berlin, 1999).
- [27] E.A. Schneidmiller, V.F. Vogel, H. Weise and M.V. Yurkov, Journal of Micro/Nanolithography, MEMS, and MOEMS 11(2), 021122 (2012).
- [28] P. Emma et al., Nature Photonics **4** (2010) 641.

- [29] T. Ishikawa et al., *Nature Photonics* **6** (2012) 540.
- [30] M. Altarelli et al. (Eds.), *XFEL: The European X-Ray Free-Electron Laser. Technical Design Report, Preprint DESY 2006-097*, DESY, Hamburg, 2006 (see also <http://xfel.desy.de>).
- [31] R. Ganter (Ed.), *Swiss FEL Conceptual Design Report*, PSI Bericht Nr. 10-04, April 2012.
- [32] H.S. Kang, K.W. Kim, I.S. Ko, *Current Status of PAL-XFEL Project. Proc. IPAC 2014 Conf.*, paper THPRO019 (2014).
- [33] E.A. Schneidmiller and M.V. Yurkov, *Preprint DESY 11-152*, Hamburg, 2011.
- [34] Y. Jiao et al. *Phys. Rev. ST Accel. Beams* **15**, 050704 (2012).
- [35] G. Geloni, V. Kocharyan, and E. Saldin, *DESY Report 11-049*, 2011.
- [36] I. Agapov et al., *Proc. 2014 FEL Conference, Basel, Switzerland, 2014*, MOP056.
- [37] Y. Hidaka et al., *Proceedings of 2011 Particle Accelerator Conference, New York, NY, USA, THP148* (2011).
- [38] E.A. Schneidmiller and M.V. Yurkov, *Phys. Rev. ST-AB* **15** (2012) 080702.
- [39] E.L. Saldin, E.A. Schneidmiller, and M.V. Yurkov, *Nucl. Instrum. and Methods A* **429** (1999) 233.
- [40] E.A. Schneidmiller and M.V. Yurkov, *Proc. 2014 FEL Conference, Basel, Switzerland, 2014*, MOP065.
- [41] E.A. Schneidmiller and M.V. Yurkov, *Proc. 2014 FEL Conference, Basel, Switzerland, 2014*, MOP068.

OPTIMIZATION OF A HIGH EFFICIENCY FEL AMPLIFIER

E.A. Schneidmiller, M.V. Yurkov, DESY, Hamburg, Germany

Abstract

The problem of an efficiency increase of an FEL amplifier is now of great practical importance. Technique of undulator tapering in the post-saturation regime is used at the existing x-ray FELs LCLS and SACLA, and is planned for use at the European XFEL, Swiss FEL, and PAL XFEL. There are also discussions on the future of high peak and average power FELs for scientific and industrial applications. In this paper we perform detailed analysis of the tapering strategies for high power seeded FEL amplifiers. Application of similarity techniques allows us to derive universal law of the undulator tapering.

INTRODUCTION

Efficiency of FEL amplifier with untapered undulator is defined by the value of the FEL parameter ρ . Application of the undulator tapering [1] allows to increase conversion efficiency to rather high values. In the framework of the one-dimensional theory the status of the problem of tapering has been settled, and it is generally accepted that optimum law of the undulator tapering is quadratic with the linear correction for optimization of the particle's capture in the decelerating potential [2–7]. Similar physical situation occurs in the FEL amplifier with waveguide with small waveguide parameter. In this case radiation is confined with the waveguide. Physical parameters of FEL amplifiers operating in infrared, visible, and x-ray wavelength range are such that these devices are described in the framework of three dimensional theory with an “open” electron beam, i.e. physical case of pure diffraction in a free space. In this case diffraction of the radiation is essential physical effect influencing optimization of the tapering process. Discussions and studies on optimum law of the undulator tapering in 3D case are in the progress for more than 20 years. Our previous studies were mainly driven by occasional calculations of perspective FEL systems for high power scientific (for instance, FEL based $\gamma\gamma$ - collider) and industrial applications (for instance, for isotope separation, and lithography [8–10]). New wave of interest to the undulator tapering came with x-ray free electron lasers. It is used now not only as demonstration tool [11], but as a routine tool at operating x-ray FEL facilities LCLS and SACLA.

During an intermediate physical discussion on the subject of tapering we pointed out that asymptotical law of the undulator tapering for FEL amplifier with “open” beam should be linear in terms of the detuning parameter [7]. The origin for this statement is that radiation power of the bunched electron beam grows linearly with the undulator length for very long undulator. However, the problem of optimum matching of the electron beam into the regime of coherent deceleration is still open. Practical calculations of specific systems yielded in several empirical laws using dif-

ferent polynomial dependencies, application of tricks with detuning jumps, etc (see [12, 13] and references therein).

In this paper we perform global analysis of the parameter space of seeded FEL amplifier and derive universal law of the undulator tapering defined by the only diffraction parameter.

BASIC RELATIONS

We consider axisymmetric model of the electron beam. It is assumed that transverse distribution function of the electron beam is Gaussian, so rms transverse size of matched beam is $\sigma = \sqrt{\epsilon\beta}$, where $\epsilon = \epsilon_n/\gamma$ is rms beam emittance, γ is relativistic factor, and β is focusing beta-function. In the following we consider rectified case of the “cold” electron beam and neglect space charge effects. Under this assumptions the FEL amplifier is described by the diffraction parameter B [7], and detuning parameter \hat{C} :

$$B = 2\Gamma\sigma^2\omega/c, \quad \hat{C} = C/\Gamma, \quad (1)$$

where $\Gamma = [I\omega^2\theta_s^2 A_{JJ}^2 / (I_A c^2 \gamma_z^2 \gamma)]^{1/2}$ is the gain parameter, $C = 2\pi/\lambda_w - \omega/(2c\gamma_z^2)$ is the detuning of the electron with the nominal energy \mathcal{E}_0 . In the following electron energy is normalized as $\hat{P} = (E - E_0)/(\rho E_0)$, where $\rho = c\gamma_z^2\Gamma/\omega$ is the efficiency parameter¹. The following notations are used here: I is the beam current, $\omega = 2\pi c/\lambda$ is the frequency of the electromagnetic wave, $\theta_s = K_{rms}/\gamma$, K_{rms} is the rms undulator parameter, $\gamma_z^{-2} = \gamma^{-2} + \theta_s^2$, $k_w = 2\pi/\lambda_w$ is the undulator wavenumber, $I_A = 17$ kA is the Alfvén current, $A_{JJ} = 1$ for helical undulator and $A_{JJ} = J_0(K_{rms}^2/2(1 + K_{rms}^2)) - J_1(K_{rms}^2/2(1 + K_{rms}^2))$ for planar undulator. Here J_0 and J_1 are the Bessel functions of the first kind.

Equations, describing motion of the particles in the ponderomotive potential well of electromagnetic wave and undulator get simple form when written down in normalized form (see, e.g. [7]):

$$\frac{d\Psi}{d\hat{z}} = \hat{C} + \hat{P}, \quad \frac{d\hat{P}}{d\hat{z}} = U \cos(\phi_U + \Psi), \quad (2)$$

where $\hat{z} = \Gamma z$, and U and ϕ_U are amplitude and phase of effective potential. Energy change of electrons is small in the exponential stage of amplification, $\hat{P} \ll 1$, and process of electron bunching in phase Ψ lasts for long distance, $\hat{z} \gg 1$. Situation changes drastically when electron energy change \hat{P} approaches to the unity. The change of phase on the scale of $\Delta\hat{z} \approx 1$ becomes to be fast, particles start to slip in phase Ψ which leads to the debunching of the electron beam modulation, and growth of the radiation power is saturated. operation. Undulator tapering [1], i.e. adjustment of the detuning

¹ Note that it differs from 1-D definition by the factor $B^{1/3}$ [7].

according to the energy loss of electrons, $\hat{C}(\hat{z}) = -\hat{P}(\hat{z})$, allows to keep synchronism of electrons with electromagnetic wave and increase output power.

Radiation of Modulated Electron Beam

FEL radiation is coherent radiation of the electron beam which is modulated at the resonance wavelength during amplification process. It is reasonable here to remember properties of the radiation of the modulated electron beam. Radiation power of modulated beam in helical undulator is given by [14]:

$$P = \frac{\pi \theta_s^2 \omega I_0^2 a_{in}^2 z}{4\pi c^2} \left[\arctan\left(\frac{1}{2N}\right) + N \ln\left(\frac{4N^2}{4N^2 + 1}\right) \right], \quad (3)$$

where a_{in} is amplitude of modulation of the electron beam current ($I(z, t) = I_0[1 + a_{in} \cos \omega(z/v_z - t)]$), and $N = k\sigma^2/z$ is Fresnel number. We note here that expression (3) is a crucial element for understanding the optimum law of the undulator tapering. Indeed, in the deep tapering regime some fraction of the particles is trapped in the regime of coherent deceleration. Thus, beam modulation is fixed, and asymptotically radiation power should be described by (3). One can easily find that both asymptotes of undulator tapering discussed in the introductory section: 1D model of (wide electron beam), and thin beam asymptote are well described by this expression. Asymptote of wide electron beam corresponds to large values of Fresnel number N , and it follows from (3) that radiation power scales as $P \propto z^2$. Asymptote of thin electron beam corresponds to small values of the Fresnel Number N , and radiation power becomes linearly proportional to the undulator length, $P \propto z$. Undulator tapering should adjust detuning according to the energy loss by electrons, and we find that tapering law should be quadratic for the case of wide electron beam, $C \propto -P \propto z^2$, and linear - for the case of thin electron beam, $C \propto -P \propto z$.

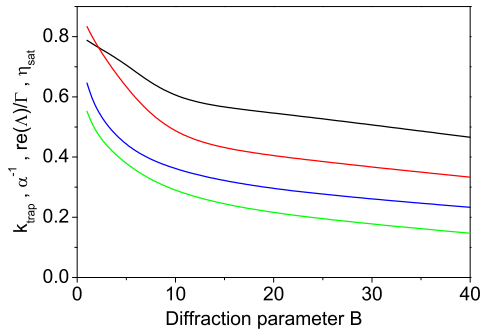


Figure 1: Universal characteristics of FEL amplifier. Color codes are: black - trapping efficiency K_{trap} for globally optimized undulator; red - fitting coefficient of global optimization α_{tap}^{-1} ; blue - FEL field gain $\text{Re } \Lambda/\Gamma$; green - FEL efficiency in the saturation, $\eta_{sat} = P_{sat}/(\rho P_b)$.

GLOBAL OPTIMIZATION

We start with global optimization of the parameter space. Simulations have been performed with three-dimensional, time-dependent FEL simulation code [15]. In the framework of the accepted model (cold electron beam) both, field gain $\text{Re } \Lambda/\Gamma$ and efficiency in the saturation, $\eta_{sat} = P_{sat}/(\rho P_b)$ of the FEL amplifier tuned to exact resonance are defined by the only diffraction parameter B (see Fig.1). Operation of the FEL amplifier before saturation is also defined by the diffraction parameter B . One can clearly observe this from Fig. 2. Here longitudinal coordinate is normalized to the gain length $L_g = 1/(\text{Re } \Lambda/\Gamma)$, and radiation power is normalized to the saturation power. When amplification process enters nonlinear stage, output power is function of two parameters, diffraction parameter and reduced undulator length.

Now we come to the problem of efficiency increase with undulator tapering. First, we solve this problem using approach of straightforward global optimization. The function of optimization is to find maximum of the output power at the undulator length exceeding ten field gain lengths. We divide undulator into many pieces and change detuning of all pieces independently. We apply adiabatic (smooth) tapering, i.e. we prevent jumps of the detuning on the boundary of the sections. Number of sections is controlled to be large enough to provide the result which is independent on the number of sections. Then we choose tapering law $C(B, z)$ corresponding to the maximum power at the exit of the whole undulator. This global optimization procedure has been performed in the practically important range of diffraction parameters from $B = 1$ to $B = 40$. Results of this global optimization are summarized in Fig. 3. Ratio of the normalized power to the normalized detuning gives us the value of trapping efficiency of electrons into the regime of coherent deceleration, $K_{trap} = \hat{P}/\hat{C}$. This universal function of diffraction parameter B is plotted on Fig. 1. We find that optimum trapping factor approaches values of 80% for $B = 1$, and falls down to 45% for $B = 40$. It is interesting to notice that for $B \gtrsim 5$ it scales roughly as $B^{-1/3}$, similar

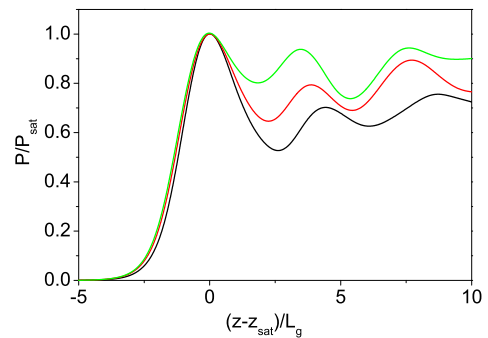


Figure 2: Evolution of the radiation power along the undulator (untapered case). Color codes: black, red, green curves correspond to the value of diffraction parameter $B = 1, 10$, and 40.

to other FEL characteristics like FEL gain and saturation efficiency.

It comes from global optimization that in the whole parameter range undulator tapering starts from the value of $\Delta z \approx 2L_g$ before saturation. This is not surprising if we look on Fig. 2. Optimum undulator tapering should compensate loss of the electron energy which is in fact follows identical parametric dependence on the gain L_g for all values of diffraction parameter. Next observations come from the analysis of the beam modulation. The first observation is that the beam modulation at the initial stage of the non-linear regime follows similar behavior for all diffraction parameters (see Fig. 4). This gives a hint that initial capture of the particles is performed in a similar way in the whole parameter range. The second observation is that the beam modulation after trapping of the electrons to the coherent deceleration process remains constant along the undulator, and it is universal function of the diffraction parameter B (see Fig. 4). This gives us the main hint which we discussed in the previous section. I.e., excluding trapping transition stage, we deal with radiation of the modulated electron beam (3). Main essence of our study is to apply para-

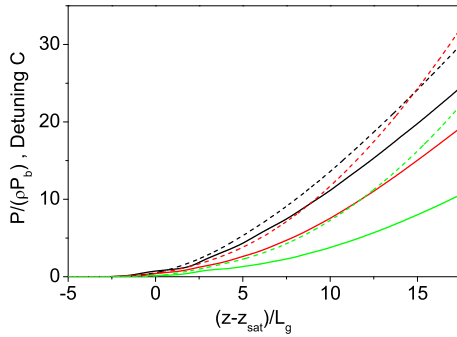


Figure 3: Evolution along the undulator of the output power (solid curves) and detuning (dashed curves) for FEL amplifier with global optimization of the undulator tapering. Color codes: black, red, green curves correspond to the value of diffraction parameter $B = 1, 10$, and 40 .

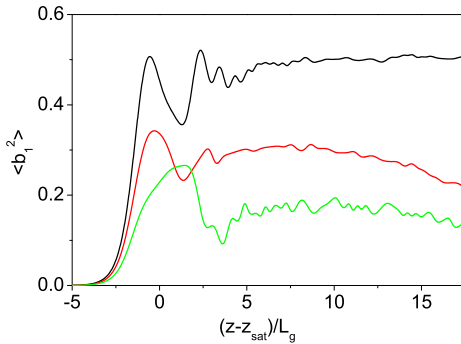


Figure 4: Evolution along the undulator of the squared value of the beam bunching for FEL amplifier with global undulator tapering. Color codes: black, red, green curves correspond to the value of diffraction parameter $B = 1, 10$, and 40 .

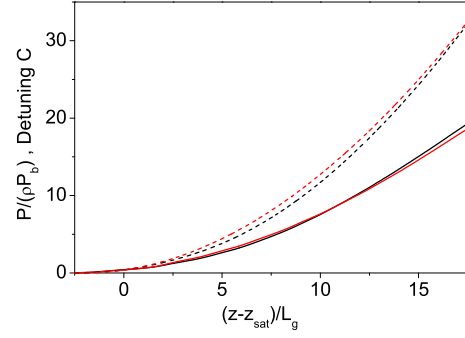


Figure 5: Evolution along the undulator of the output power (solid curves) and detuning (dashed curves) Color codes: black - FEL with global optimization of undulator tapering, red - fit with formula (4). Here the value of diffraction parameter is $B = 10$.

metrical dependence like (3) to fit optimum detuning pattern in Fig. 3 such that condition of optimum tapering is preserved:

$$\hat{C} = \alpha_{tap}(\hat{z} - \hat{z}_0) \left[\arctan\left(\frac{1}{2N}\right) + N \ln\left(\frac{4N^2}{4N^2 + 1}\right) \right], \quad (4)$$

with Fresnel number N fitted by $N = \beta_{tap}/(\hat{z} - \hat{z}_0)$. Thus, we try to fit optimum detuning with three parameters: z_0 , α_{tap} and β_{tap} . Here undulator length is normalized to the gain parameter, $\hat{z} = \Gamma z$. One parameter of this fit, start of the undulator tapering z_0 is firmly fixed by the global optimization procedure, $z_0 = z_{sat} - 2L_g$. Another parameter of the problem, β_{tap} , is rather well approximated with the linear dependency on diffraction parameter, $\beta_{tap} = 10 \times B$. Remaining parameter, α_{tap} is plotted in Fig. 1. It is slow function of the diffraction parameter B , and scales approximately to $B^{1/3}$ as all other important FEL parameters presented in Fig. 1. Thus, application of similarity techniques gives us an elegant way for general parametrical fit of such complicated phenomena as optimum undulator tapering. Actually, accuracy of this fit is pretty good giving the results for optimum detuning which are close to the global optimum. We illustrate with Fig. 5 tapering law (4) for specific value of the diffraction parameter $B = 10$. Curves in black color are normalized power and detuning derived from global optimization. Red dashed curve is detuning \hat{C} given by (4) with $\alpha_{tap} = 2.2$ (see Fig. 1, and $\beta_{tap} = 100$ (according to relation $\beta_{tap} = 10 \times B$). The solid curve in red color is normalized FEL efficiency simulated using detuning (4). We see good agreement of the fit with global optimization. The same situation occurs in the whole range of traced values of diffraction parameter B . Such a good agreement is not surprising since fitting is based on very clean parametric dependencies, and numerical simulations just provided relevant numerical factors.

We finish our paper with illustration of the trapping process. Trapping efficiency $K_{trap} = \hat{P}/\hat{C}$ is plotted in Fig. 1. Trapping efficiency falls down with diffraction parameter B .

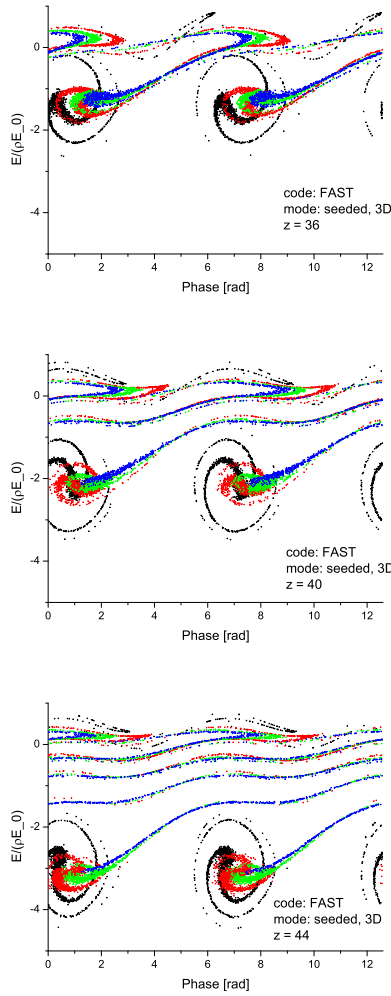


Figure 6: Phase space distribution of electrons at different stages of trapping process. Color codes correspond to different location of the particles in the beam (black - core of the beam, blue - edge of the beam). Here diffraction parameter is $B = 10$. Top, middle, and bottom plots correspond to $(z - z_{sat})/L_g = 2.5, 3.9$ and 5.3 , respectively (see Fig. 5).

This is natural consequence of diffraction effects discussed earlier (see, e.g. [7], Chap. 4). For small value of the diffraction parameter B gradient of the field of the beam radiation mode across the electron bunch is smaller than for large values of diffraction parameter. In the latter case we obtain situation when electrons located in the core of the electron beam are already fully bunched while electrons on the edge of the beam are not bunched yet. As a result, number of electrons with similar positions on the energy-phase plane falls down with the growth of the diffraction parameter, as well as trapping efficiency into the regime of coherent deceleration. The trapping process is illustrated with phase space plots presented on Fig. 6 for the value of diffraction parameter $B = 10$. Top, middle, and bottom plots correspond to the points of $(z - z_{sat})/L_g = 2.5, 3.9$ and 5.3 on Fig. 3. Different color codes (black to blue) correspond to differ-

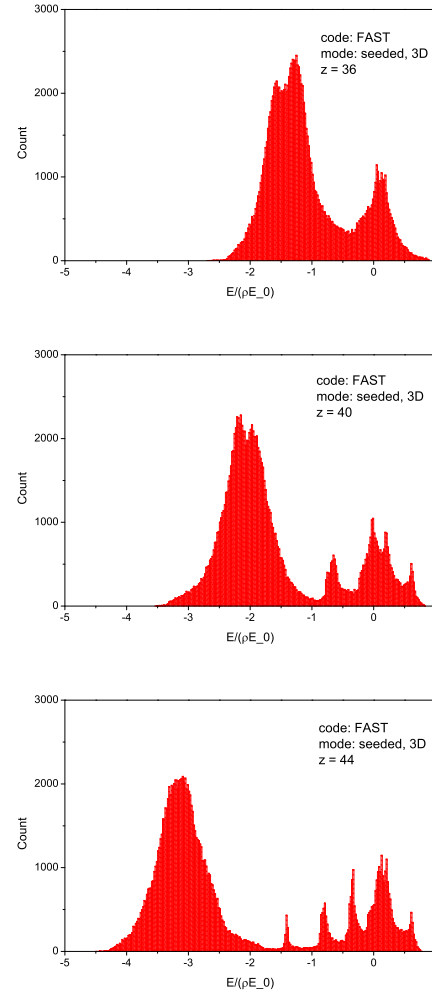


Figure 7: Population of electrons in energy at different stages of trapping process. Color codes correspond to different location of the particles in the beam (black - core of the beam, blue - edge of the beam). Here diffraction parameter is $B = 10$. Top, middle, and bottom plots correspond to $(z - z_{sat})/L_g = 2.5, 3.9$ and 5.3 , respectively (see Fig. 5).

ent locations of the particles across the beam (core to edge). We see that particles in the core of bunch (black points) are trapped most effectively. Nearly all particles located in the edge of the electron beam (blue points) leave stability region very soon. Trapping process lasts for several field gain length when trapped particles become to be isolated in the trapped energy band for which undulator tapering is optimized further. For specific value of the diffraction parameter $B = 10$ it is not finished even at three field gain lengths after saturation, and non-trapped particles continue to populate low energy tail of the energy distribution (see Fig. 7). Recently we have been invited to the discussion on the details of trapped particles distribution in the phase space observed experimentally at LCLS [16]. Graphs presented in Figs. 6 and 7 give a hint on the origin of energy bands which are formed by non-trapped particles. This is consequence

of nonlinear dynamics of electrons leaving the region of stability. Actually, similar effect can be seen in the early 1D studies [5, 6].

DISCUSSION

In this paper we derived general law for optimum undulator tapering in the presence of diffraction effects. Purified case of “cold” electron has been considered. This allowed us to isolate diffraction effects in the most clear form. It has been found that universal function of the undulator tapering depends on the only diffraction parameter. Tapering law is described with simple analytical expression with two fitting coefficients. Extension of this approach to practical life (including energy spread and emittance) is pretty much straightforward and will result in corrections to the fitting coefficients without changing general law given by (4). The same law is evidently applicable to SASE FEL as well with relevant correction of fitting coefficients.

ACKNOWLEDGEMENT

We are grateful to Vadim Banine and Vivek Bakshi, contacts with them and other members of industrial community stimulated our interest to the development of high power FEL systems. We thank Christopher Behrens for attracting our attention to deeper analysis of the trapping process (energy bands) and for useful discussions.

REFERENCES

- [1] N.M. Kroll, P.L. Morton, and M.N. Rosenbluth, IEEE J. Quantum Electron. 17, 1436 (1981).
- [2] T.J. Orzechowski et al., Phys. Rev. Lett. 57, 2172 (1986).
- [3] R.A. Jong, E.T. Scharlemann, W.M. Fawley Nucl. Instrum. Methods Phys. Res. A272, 99 (1988)
- [4] W.M. Fawley et al., Nucl. Instrum. Methods Phys. Res. A483, 537 (2002)
- [5] Review by E.T. Scharlemann in Laser Handbook, Volume 6, Free electron lasers, eds. W.B. Colson, C. Peilegrini and A. Renieri (North Holland, Amsterdam, 1991).
- [6] E.L. Saldin, E.A. Schneidmiller and M.V. Yurkov, Physics Reports 260, 187 (1995).
- [7] E.L. Saldin, E.A. Schneidmiller, M.V. Yurkov, “The Physics of Free Electron Lasers” (Springer-Verlag, Berlin, 1999).
- [8] E.L. Saldin, V.P. Sarantsev, E.A. Schneidmiller and M.V. Yurkov, Nucl. Instrum. and Methods A339. 583 (1994).
- [9] C. Pagani, E.L. Saldin, E.A. Schneidmiller and M.V. Yurkov, Nucl. Instrum. and Methods A455, 733 (2000).
- [10] E.A. Schneidmiller, V.F. Vogel, H. Weise and M.V. Yurkov, Journal of Micro/Nanolithography, MEMS, and MOEMS 11(2), 021122 (2012).
- [11] Y. Hidaka et al., Proceedings of 2011 Particle Accelerator Conference, New York, NY, USA, THP148 (2011). <https://JACoW.org/PAC2011/papers/thp148.pdf>
- [12] Y. Jiao et al. Phys. Rev. ST Accel. Beams 15, 050704 (2012).
- [13] G. Geloni, V. Kocharyan, and E. Saldin, DESY Report 11-049, 2011.
- [14] E.L. Saldin, E.A. Schneidmiller and M.V. Yurkov, Nucl. Instrum. and Methods A539, 499 (2005).
- [15] E.L. Saldin, E.A. Schneidmiller, and M.V. Yurkov, Nucl. Instrum. and Methods A 429, 233 (1999).
- [16] C. Behrens, Talk at the Workshop on Advanced X-Ray FEL Development, May 23, 2014, Hamburg.

AN OVERVIEW OF THE RADIATION PROPERTIES OF THE EUROPEAN XFEL

E.A. Schneidmiller, M.V. Yurkov, DESY, Hamburg, Germany

Abstract

We present an overview of the radiation properties of the European XFEL based on recently accepted strategy of operation at the fixed set of electron energies (8.5 GeV, 12 GeV, 14 GeV, and 17.5 GeV), baseline parameters of the electron beam, and new set undulator parameters. We also discuss potential extension of the parameter space which does not require new hardware and can be realized at a very early stage of the European XFEL operation.

INTRODUCTION

Construction of the European XFEL [1] entered final stage: underground tunnels and infrastructure are ready, and first pieces of the equipment has been already installed [2]. Superconducting accelerator will provide energy of electrons up to 17.5 GeV. It operates in the burst mode with 10 Hz repetition rate of 0.6 ms pulse duration. Each pulse brings train of up to 2700 electron bunches (4.5 MHz repetition rate). Three undulators will be installed at the first stage: SASE1, SASE2, and SASE3. SASE3 undulator is placed sequentially after SASE1 undulator in the same electron beamline. All undulators have similar mechanical design. Length of the undulator module is equal to 5 meters. Length of undulator intersection is equal to 1.1 m. undulators SASE1 and SASE2 are identical: period length is 40 mm, number of modules is 35, range of gap variation is 10 to 20 mm. Undulator SASE3 has period of 68 mm, 10 to 25 mm gap tunability range, and consists of 21 module. Most portion of the undulator modules has been manufactured, and magnetic measurements and tuning are going on [3]. Design and construction of user's end station (instruments) is on track as well. Requirements by users are summarized and analyzed in a proper way to provide maximum opportunities for every instrument and experiment [4].

BASELINE PARAMETERS

Baseline parameters of the European XFEL passed two major corrections: in 2006 [1] and 2010 [4–6]. Operating range for bunch charge is from 20 pC to 1 nC, peak current is 5 kA, and normalized rms emittance is between 0.3 mm-mrad and 1 mm-mrad depending on bunch charge [5]. There are two changes in the baseline option since last update in 2010. Tunability range of undulators has been corrected on the base of magnetic measurements [3], and in terms of undulator parameter is 1.65 - 4 and 4 - 9 for SASE1/2 and SASE3, respectively. Tunability range in terms of $\lambda_{\max}/\lambda_{\min}$ is 3.5 for SASE1/2 and 4.6 for SASE3. Reduction of tunability range caused the change of operating energies providing required flexibility for simultaneous operation of different beamlines and instruments. Now four

operating points in the electron energy are fixed: 17.5 GeV, 14 GeV, 12 GeV, and 8.5 GeV [7]. Figures 1 and 2 show an overview of the main photon beam properties of the European XFEL for two values of the baseline parameters for the bunch charge of 0.1 nC and 1 nC. Calculations have been performed with FEL simulation code FAST [8]. Left and right columns in these plots correspond SASE1/2 and SASE3 undulator, and allow visual tracing of the operating wavelength bands, pulse energy, and brilliance as function of the electron energy. General tendencies are that operation with higher charges provides higher pulse energy and higher average brilliance. Qualitative difference in the behavior of the brilliance at 0.1 nC and 1 nC for SASE1/2 requires some clarification. It originates from two reasons. The first reason relates to optimization procedure which corresponds to the choice of optimum focusing beta function providing maximum power gain [9, 10]. Optimization procedure suggests smaller values of focusing beta function for smaller emittances. However, there is always technical limitation on the minimum focusing beta function (15 m in our case). As a result, SASE3 and 0.1 nC option of SASE1 operate with beta function defined by technical limit of 15 m, while optimum beta function for high charge (1 nC) option of SASE1 is above 15 m, and its values depend on operating point in the radiation wavelength and in the electron energy. Another factor defining peculiar behavior of brilliance at high charge and small wavelength relates to degradation of coherence properties of the radiation due to large value of the emittance [10]. This effect is responsible for the reduction of the brilliance for 1 nC case at short wavelengths.

Detailed parameters of the radiation together with 3D field maps are being compiled in the photon data base of the European XFEL [11, 12]. Currently this data base is used in the test mode for optimization of the photon beam transport and imaging experiment [13, 14]. When user interface will be finally settled, photon data base will be open for free external access, and can be used by users for planning experiments.

Operation of SASE3

Properties of the radiation from SASE3 presented in Figs. 1 and 2 assume that electron beam is not disturbed by FEL interaction in the SASE1 undulator. Decoupling of SASE3 and SASE1 operation can be performed with an application of betatron switcher [6, 15] (see Fig. 3). Feedback kickers can be used to test and operate this option at the initial stage. In case of positive results dedicated kickers need to be installed [5].

Operation of SASE3 as an afterburner of SASE1 is also possible, but with reduced range of accessible wavelengths, and reduced power (see Fig. 4). General problem is that

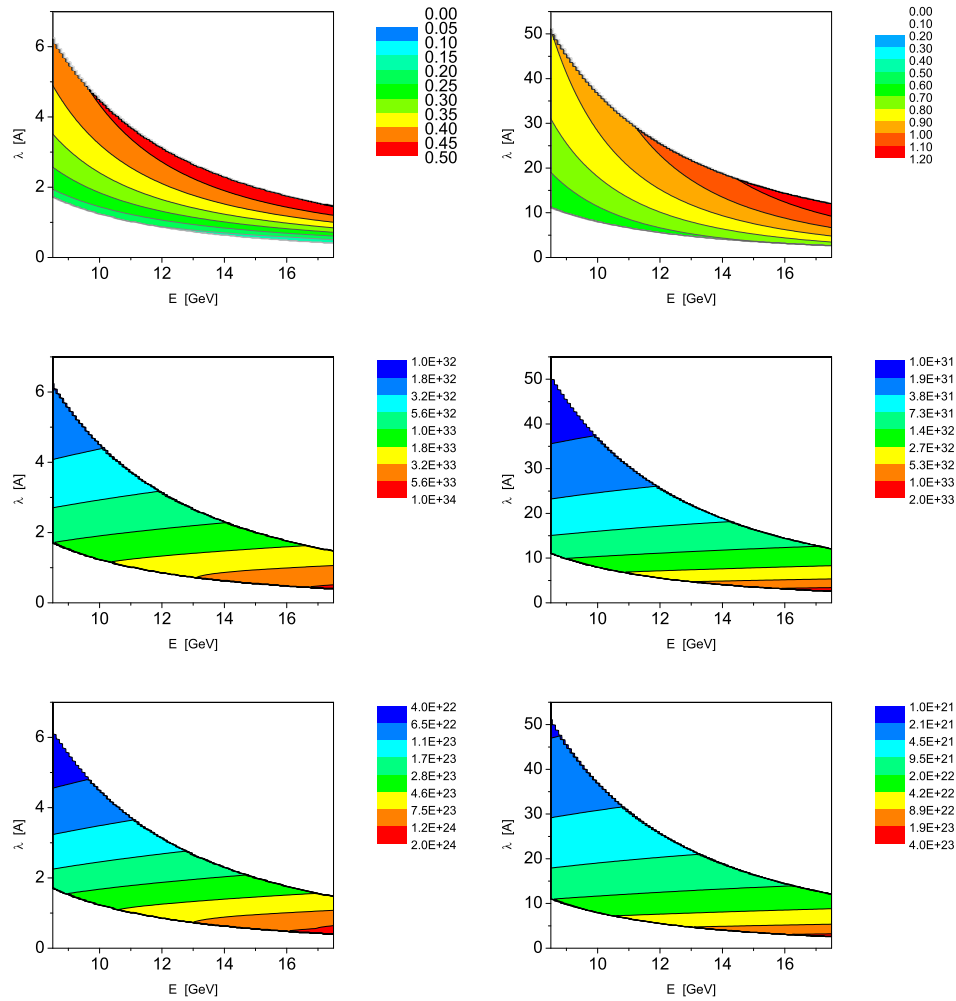


Figure 1: An overview of main photon beam properties of the European XFEL for SASE1/2 (left column) and SASE3 (right column). Contour plots present pulse energy (top row), peak brilliance (middle row), and average brilliance (lower row). Units for the pulse energy and brilliance are mJ and photons/sec/mm²/rad²/0.1% bandwidth, respectively. Bunch charge is equal to 0.1 nC. Calculations have been performed with FEL simulation code FAST [8].

tuning of SASE1 to higher pulse energies leads to higher induced energy spread in the electron beam, and to degradation of the SASE3 performance. For instance, operation of SASE3 at the energy of 17.5 GeV is impossible at any wavelength if wavelength of SASE1 is longer than 0.1 nm, and radiation power of SASE1 is tuned by a factor of 1.5 above saturation power.

POTENTIAL EXTENSIONS BEYOND BASELINE OPTION

There are several potential extensions beyond baseline option which can be realized at a very early stage of the European XFEL operation without additional hardware, or by means of extensions of the functions of the present hardware. Some ideas are pretty old, and some other appeared just recently. Some proposal rely on parameters of the electron beam beyond baseline option. Several groups perform theoretical and simulation studies of different options.

There is also experimental activity at FLASH and LCLS on verification of advanced concepts. Here we briefly highlight several extensions related to the European XFEL with references to the most fresh publications.

Efficiency Increase by Undulator Tapering

Undulator tapering will allow to increase significantly FEL power. Many studies on this subject have been performed for the parameters of the European XFEL (see [1, 6, 16, 17] and references therein). Benefit in the photon flux can be pretty high. For instance, it can be up to one order of magnitude for SASE3 operating in the wavelength range above 1 nm. However, coherence properties of the radiation degrade with respect to SASE FEL operating in the saturation with untapered undulator. Increase of the brilliance is visibly less than increase of the radiation power [17]. Users relying just on photon flux will have

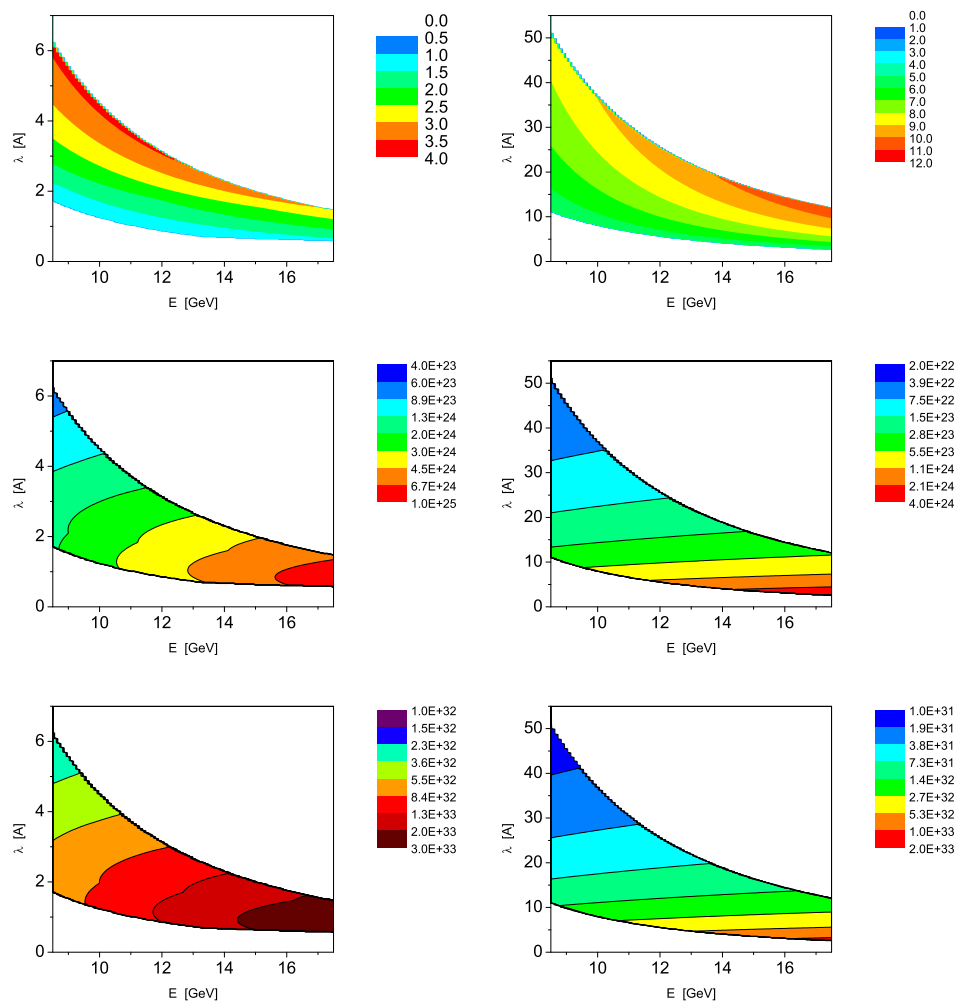


Figure 2: An overview of photon beam properties of the European XFEL for SASE1/2 (left column) and SASE3 (right column). Contour plots present pulse energy (top row), peak brilliance (middle row), and average brilliance (lower row). Units for the pulse energy and brilliance are mJ and photons/sec/mm²/rad²/0.1% bandwidth, respectively. Bunch charge is equal to 1 nC. Calculations have been performed with FEL simulation code FAST [8].

profit from the undulator tapering. Note that undulator tapering is routine procedure at LCLS [18].

Extended Range of Electron Beam Parameters

Several options are under consideration exploiting higher peak currents, and higher bunch charges to increase pulse energy and peak power (see [6, 19] and references therein). Dedicated activity on simulation, production and characterization of high charge bunches in XFEL-type electron gun is ongoing at PITZ [20, 21]. Another direction of studies is production of ultrashort pulses. This activity also involves both, simulation studies for XFEL and experimental studies at FLASH (see [22–24] and references therein). For instance, use of higher charges in combination with tapering will allow to generate sub-Joule energies in the radiation pulse [6]. Note that there can be some technical complications for operation with charges which are not in the gate of baseline parameters [5]. It is our experience of FLASH

operation with small charges that limitations of the electron beam diagnostic are not a stopovers, but they significantly complicate tuning, since some feedback system stop to work because of noisy measurements.

Multicolor Mode of Operation

Betatron switcher [15] mentioned in the previous section can be used in long undulators for providing multi-color operation. Different parts of the undulator are tuned to different resonance wavelength. Fast kicker and steerer force lasing of selected bunch in specific part of the undulator similar to that described in the caption to Fig. 3.

Harmonic Generation

Contrary to nonlinear harmonic generation, harmonic lasing in a high-gain FEL can provide much more intense, stable, and narrow-band FEL beam which is easier to handle if the fundamental is suppressed [25]. At the European XFEL

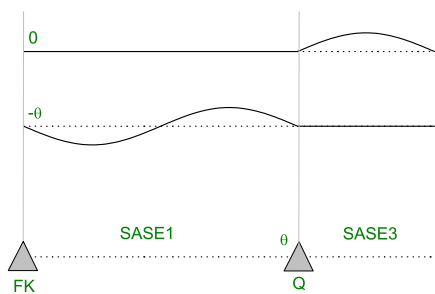


Figure 3: A schematic illustration of the betatron switcher for decoupling of operation of SASE1 and SASE3 [6, 15]. Here "FK" stands for a fast kicker (giving different kicks to selected bunches) and "Q" for a quadrupole or a static steer (giving the same static kick to all bunches). Lasing to saturation takes place only on straight sections of beam orbit. Bunches not disturbed by fast kicker lase only in SASE1 (top curve), while those deflected by fast kicker lase in SASE3 only (bottom curve).

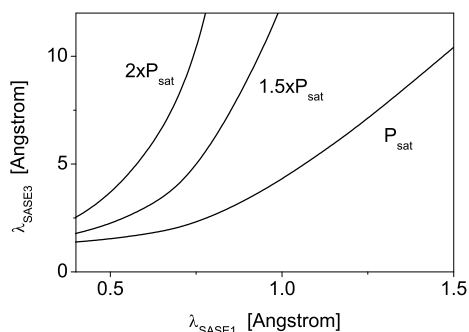


Figure 4: Minimum wavelength of SASE3 versus operating wavelength of SASE1. Electron energy is 17.5 GeV, bunch charge is 1 nC. Minimum wavelength is defined by the condition of saturation at the length of SASE3 undulator of 100 meters. P_{sat} , $1.5 \times P_{\text{sat}}$, and $2 \times P_{\text{sat}}$ denote power of SASE1 in terms of saturation power. Operation of SASE3 in saturation is possible for the wavelengths above the curves. Calculations have been performed with FEL simulation code FAST [8].

the harmonic lasing would allow to extend operating range ultimately up to 100 keV. Currently this option is studied for implementation in the MID instrument [26]. Dedicated experimental program on harmonic generation is ongoing at LCLS [27].

"Pink" Photon Beam

Some user application require "pink" photon beam with spectrum width of several per cent. Two options of spectrum increase has been considered so far: formation of the energy chirp in the bunch train [5], and formation of the energy chirp within electron bunch [28].

Harmonic Lasing Self-Seeded FEL

A concept of a harmonic lasing self-seeded FEL (HLSS) has been proposed recently [25]. A gap-tunable undulator is divided into two parts by setting two different undulator parameters such that the first part is tuned to a sub-harmonic of the second part. Harmonic lasing occurs in the exponential gain regime in the first part of the undulator, also the fundamental stays well below saturation. In the second part of the undulator the fundamental mode is resonant to the wavelength, previously amplified as the harmonic. The amplification process proceeds in the fundamental mode up to saturation. In this case the bandwidth is defined by the harmonic lasing (i.e. it is reduced by a significant factor depending on harmonic number) but the saturation power is still as high as in the reference case of lasing at the fundamental in the whole undulator, i.e. the spectral brightness increases. Application of the undulator tapering in the deep nonlinear regime would allow to generate higher peak powers approaching TW level [29]. Modification of the HLSS scheme, named purified SASE - pSASE [30], is under consideration as well [31].

Afterburners and Polarization Control

Baseline design of a typical X-ray FEL undulator assumes a planar configuration which results in a linear polarization of the FEL radiation. However, many experiments at X-ray FEL user facilities would profit from using a circularly polarized radiation. As a cheap upgrade one can consider an installation of a short helical (or cross-planar) afterburner, but then one should have an efficient method to suppress linearly polarized background from the main undulator. An elegant technique for such a suppression has been proposed recently: an application of the reverse taper in the main undulator [32]. In this case the density modulation (bunching) is practically the same as in the case of non-tapered undulator while the power of linearly polarized radiation is suppressed by orders of magnitude. Then strongly modulated electron beam radiates at full power in the afterburner. Technique for the suppression of the output power with negative tapering has been successfully demonstrated recently at LCLS [33].

The proposed method is rather universal, i.e. it can be used at SASE FELs and seeded (self-seeded) FELs, with any wavelength of interest, in a wide range of electron beam parameters, and with any repetition rate. Considering SASE3 undulator of the European XFEL as a practical example, it has been demonstrated that soft X-ray radiation pulses with peak power in excess of 100 GW and an ultimately high degree of circular polarization can be produced [32]. This option has been granted high priority as the first upgrade of the European XFEL [5].

Self-Seeding Option

Self-seeding option [34] has also high priority as the first upgrade of the European XFEL (see [5, 35–37] and references therein). Both, hard and soft x-ray options are un-

der consideration with optimization on dedicated beamline for bio-imaging [38]. As soon as fine measurements of the electron beam and FEL parameters will be performed, an upgrade for self-seeding option will be launched [5].

Longitudinal Space Charge Amplifier

Longitudinal space charge instability can be used in the schemes for generation of vacuum ultraviolet (VUV) and X-ray radiation [39]. A typical longitudinal space charge amplifier (LSCA) consists of few amplification cascades (drift space plus chicane) with a short undulator behind the last cascade. If the amplifier starts up from the shot noise, the amplified density modulation has a wide band, on the order of unity. The bandwidth of the radiation within the central cone is given by inverse number of undulator periods. A wavelength compression could be an attractive option for LSCA since the process is broadband, and a high compression stability is not required. LSCA can be used as a cheap addition to the existing or planned short-wavelength FELs. In particular, it can produce the second color for a pump-probe experiment. It is also possible to generate attosecond pulses in the VUV and X-ray regimes [40]. Some user experiments can profit from a relatively large bandwidth of the radiation, and this is easy to obtain in LSCA scheme. Recently LSCA scheme has been successfully demonstrated at SLAC [41].

ACKNOWLEDGMENTS

Results presented in this paper have been discussed at the meetings devoted to revision of parameter space and discussion of potential extensions of the European XFEL. We are grateful to our colleagues from DESY and European XFEL for fruitful collaboration during this work: M. Altarelli, C. Bressler, R. Brinkmann, W. Decking, J. Gaudin, N. Gerasimova, J. Gruenert, T. Limberg, A. Madsen, A. Mancuso, M. Meyer, S. Molodtsov, J. Pflueger, L. Samoylova, A. Schwarz, H. Sinn, T. Tschentscher, and H. Weise. We thank our colleagues from the Beam Dynamics Group for providing us with parameters of the electron beam: M. Dohlus, G. Feng, I. Zagorodnov. We are grateful to M. Krasilnikov and F. Stephan for fruitful collaboration on high charge option. We thank R. Brinkmann for fruitful collaboration and support of our work.

REFERENCES

- [1] M. Altarelli et al. (Eds.), XFEL: The European X-Ray Free-Electron Laser. Technical Design Report, Preprint DESY 2006-097, DESY, Hamburg, 2006. (see also <http://xfel.desy.de>).
- [2] W. Decking and F. Le Pimpec, Proc. FEL 2014 Conference, Basel, Switzerland, 2014, WEBO3.
- [3] J. Pflueger et al., Status of the undulator systems for the European x-ray free electron laser, Proc. FEL2013, New York, USA, 2013, TUPS060.
- [4] T. Tschentscher, Layout of the X-Ray Systems at the European XFEL, Technical Report (2011) [10.3204/XFEL.EU/TR-2011-001] XFEL.EU TR-2011-001.
- [5] W. Decking, T. Limberg, European XFEL Post-TDR Description, XFEL.EU Technical Note 1-22 (2013) XFEL.EU TN-2013-004
- [6] E.A. Schneidmiller and M.V. Yurkov, Preprint DESY 11-152, DESY, Hamburg 2011.
- [7] Decision of the working group of the European XFEL and DESY.
- [8] E.L. Saldin, E.A. Schneidmiller and M.V. Yurkov, Nucl. Instrum. and Methods A 429 (1999) 233.
- [9] E.L. Saldin, E. A. Schneidmiller, and M.V. Yurkov, Opt. Commun. 235(2004)415.
- [10] E.L. Saldin, E.A. Schneidmiller, and M.V. Yurkov, Opt. Commun. 281(2008)1179.
- [11] E.A. Schneidmiller and M.V. Yurkov, An update of the photon beam properties of the European XFEL, in preparation.
- [12] An activity on generation of photon data base at the European XFEL is performed by L. Samoylova, C.H. Yoon, J. Szuba, K. Wrona, et al.
- [13] H. Sinn et al., Technical Design Report: X-Ray Optics and Beam Transport, Technical Report (2012) [10.3204/XFEL.EU/TR-2012-006] XFEL.EU TR-2012-006.
- [14] A.P. Mancuso et al., Report (2013) Technical Design Report: Scientific Instrument Single Particles, Clusters, and Biomolecules (SPB), XFEL.EU Technical Report 1-232 (2013) [10.3204/XFEL.EU/TR-2013-004] XFEL.EU TR-2013-004.
- [15] R. Brinkmann, E.A. Schneidmiller and M.V. Yurkov, Nucl. Instrum. and Methods A 616 (2010) 81.
- [16] I. Agapov et al., Proc. FEL 2014 Conference, Basel, Switzerland, 2014, MOP056.
- [17] E.A. Schneidmiller and M.V. Yurkov, Proc. FEL 2014 Conference, Basel, Switzerland, 2014, MOP065.
- [18] H. Loos, Proc. FEL2011 Conference, Shanghai, China, 2011, TIOB13.
- [19] S. Serkez et al., Proc. FEL 2014 Conference, Basel, Switzerland, 2014, MOP057.
- [20] M. Krasilnikov et al., Proc. FEL2011 Conference, Shanghai, China, 2011, THPA08.
- [21] G. Vashchenko et al., Proc. IPAC2011, San Sebastian, Spain, 2011, THPC115.
- [22] I. Zagorodnov, Proc. FEL 2010 Conference, Malmö, Sweden, 2010, WE0B12.
- [23] B. Marchetti et al., Physica Procedia 52 (2014) 80.
- [24] J. Roensch-Schulenburg, Proc. FEL 2014 Conference, Basel, Switzerland, 2014, TUB04.
- [25] E.A. Schneidmiller and M.V. Yurkov, Phys. Rev. ST Accel. Beams 15(2012)080702
- [26] A. Madsen et al., Technical Design Report: Scientific Instrument MID, XFEL.EU Technical Report 1-191 (2013) [10.3204/XFEL.EU/TR-2013-005] XFEL.EU TR-2013-005.

- [27] D.F. Ratner et al, Proc. FEL2013 Conference, New York, USA, 2013, WEPSO53.
- [28] S. Serkez et al., Proc. FEL2013 Conference, New York, USA, 2013, WEPSO63.
- [29] E.A. Schneidmiller and M.V. Yurkov, Proc. FEL2013 Conference, New York, USA, 2013, WEPSO78.
- [30] D. Xiang et al., Phys. Rev. ST Accel. Beams 16 (2013)010703
- [31] S. Serkez et al., preprint DESY-13-135, DESY, Hamburg, 2013.
- [32] E.A. Schneidmiller and M.V. Yurkov, Phys. Rev. ST Accel. Beams 16 (2013) 110702.
- [33] J.P. MacArthur et al., Proc. FEL 2014 Conference, Basel, Switzerland, 2014, MOP082.
- [34] J. Feldhaus et al., Optics. Comm. 140, 341 (1997).
- [35] G. Geloni, V. Kocharyan and E.L. Saldin, Journal of Modern Optics 58 (2011) 1391.
- [36] G. Geloni, V. Kocharyan and E.L. Saldin, Preprint DESY 12-034, DESY, Hamburg, 2012.
- [37] S. Serkez et al., Preprint DESY 13-101, DESY, Hamburg, 2013.
- [38] G. Geloni, V. Kocharyan and E.L. Saldin, Preprint DESY 12-082, DESY, Hamburg, 2012.
- [39] E.A. Schneidmiller and M.V. Yurkov, Phys. Rev. ST Accel. Beams 13 (2010) 110701.
- [40] E.A. Schneidmiller and M.V. Yurkov, Phys. Rev. ST Accel. Beams 14 (2011) 090702.
- [41] A. Martinelli et al., Phys. Rev. Lett. 110 (2013) 264802.

PROSPECTS FOR CW OPERATION OF THE EUROPEAN XFEL IN HARD X-RAY REGIME

R. Brinkmann, E.A. Schneidmiller, J. Sekutowicz, M.V. Yurkov, DESY, Hamburg, Germany

Abstract

The European XFEL will operate nominally at 17.5 GeV in SP (short pulse) mode with 0.65 ms long bunch train and 10 Hz repetition rate. A possible upgrade of the linac to CW (continuous wave) or LP (long pulse) modes with a corresponding reduction of electron beam energy is under discussion since many years. Recent successes in the dedicated R&D program allow to forecast a technical feasibility of such an upgrade in the foreseeable future. One of the challenges is to provide sub-Ångstrom FEL operation in CW and LP modes. In this paper we perform a preliminary analysis of a possible operation of the European XFEL in the hard X-ray regime in CW and LP modes with the energies of 7 GeV and 10 GeV, respectively. We show that, with reasonable requirements on electron beam quality, lasing on the fundamental will be possible in sub-Ångstrom regime. As an option for generation of brilliant photon beams at short wavelengths we also consider harmonic lasing that has recently attracted a significant attention.

INTRODUCTION

The European XFEL [1] will be the first hard X-ray FEL user facility based on superconducting accelerator technology, and will provide unprecedented average brilliance of photon beams. The XFEL linac will operate nominally at 17.5 GeV in a burst mode with up to 2700 bunches within a 0.65 ms long bunch train and 10 Hz repetition rate. Even though the RF pulses are much longer than those available at X-ray FEL facilities, based on normal conducting accelerators, in the context of this paper we will call this SP (short pulse) mode of operation.

In order to cope with high repetition rate within a pulse train, special efforts are being made to develop fast X-ray instrumentation [2]. Still, many user experiments would strongly profit from increasing distance between X-ray pulses while lengthening pulse trains and keeping total number of X-ray pulses unchanged (or increased). Such a regime would require an operation of the accelerator with much longer RF pulses (LP, or long pulse mode), or even in CW (continuous wave) mode as a limit. A possible upgrade of the XFEL linac to CW or LP modes with a corresponding reduction of electron beam energy is under discussion since many years [3]. Recent successes in the dedicated R&D program [4] allow to forecast a technical feasibility of such an upgrade in the foreseeable future.

One of the main challenges of CW upgrade is to provide sub-Ångstrom FEL operation which is, obviously, more difficult with lower electron energies. One can consider improving the electron beam quality as well as reducing the undulator period as possible measures. An additional possi-

bility is a harmonic lasing [5–8] that has recently attracted a significant attention [8]. Harmonic lasing can extend operating range of an X-ray FEL facility and provide brilliant photon beams of high energies for user experiments.

CW UPGRADE OF THE LINAC

A possible upgrade of the XFEL linac to CW or LP modes holds a great potential for a further improvement of X-ray FEL user operation, including a more comfortable (for experiments) time structure, higher average brilliance, improved stability etc. The drawbacks are a somewhat smaller peak brilliance and a reduced photon energy range, both due to a lower electron beam energy. Both disadvantages can, however, be minimized by an improvement of the electron beam quality and application of advanced FEL techniques. Moreover, one can keep a possibility to relatively quickly switch between SP and CW modes thus greatly improving the flexibility of the user facility.

For a CW upgrade of the linac, the following main measures will be needed [4]:

- i) Upgrade of the cryogenic plant with the aim to approximately double its capacity;
- ii) Installation of new RF power sources: compact Inductive Output Tubes (IOTs);
- iii) Exchange of the first 17 accelerator modules by the new ones (including a larger diameter 2-phase helium tube, new HOM couplers etc.) designed for operation in CW mode with a relatively high gradient (up to 16 MV/m). This ensures that the beam formation system (up to the last bunch compressor) operates with a similar energy profile as it does in SP mode. Then 12 old accelerating modules are relocated to the end of the linac;
- iiii) Installation of a new injector generating a high-brightness electron beam in CW mode.

The first two items can be realized in a straightforward way; the third one is based on the steady progress of the TESLA technology [9] and is not particularly challenging. Until recently the main uncertainty was connected with the absence of CW injectors providing a sufficient quality of electron beams. However, last year there was an experimental demonstration of small emittances (for charges below 100 pC) at a CW photoinjector using a DC gun followed immediately by acceleration with superconducting cavities [10]. The measured parameters are already sufficient for considering this kind of injector as a candidate for CW upgrade of the XFEL linac (although the operation would be limited to low charge scenarios). As an alternative one can consider a superconducting RF gun that can potentially produce also larger charge bunches with low emittances (the progress reports can be found in [11, 12]) or even a normal conducting

Table 1: Main Assumptions for CW/LP Upgrade of the XFEL Facility

Parameter	Unit	Value
Beam		
Maximum charge per bunch	[nC]	0.5
Time between subsequent bunches	[μ s]	4
Average current	[mA]	0.125
Maximum beam energy in CW mode	[GeV]	7.8
Main Linac		
Number of 8-cavity cryomodules	-	96
1.8K cryogenic dynamic load per cryomodule	[W]	16
1.8K cryogenic static load per cryomodule	[W]	4
Q_0 of cavities	-	2.8×10^{10}
Maximum E_{acc} for CW mode	[MV/m]	7.3
Q_{load} of input coupler	-	2×10^7
Mean RF-power per cavity	[kW]	< 2.5
Assumed microphonics: (peak-peak)/2	[Hz]	32
Injector Section up to 2 GeV		
Number of 8-cavity cryomodules in linacs L0 / L1 / L2	-	1 / 4 / 12
Maximum E_{acc} for CW mode in linacs L0 / L1 / L2	[MV/m]	16 / 11 / 15
1.8K total cryogenic load per cryomodule in linacs L0 / L1 / L2	[W]	91 / 45 / 80
Q_0 of cavities	-	2.5×10^{10}

RF gun [13]. In the latter case a special regime can, in principle, be organized when a continuous sequence of short RF pulses is used [14] instead of powering the gun in true CW mode.

In this paper we do not present a comprehensive technical description of the CW upgrade, it will be published elsewhere [15]. Here we only summarize some technical details in Table 1.

To predict a possible electron energy range in CW and LP modes, and to test the XFEL cryomodules in these regimes, a series of measurements is being performed at DESY [4]. The measurements demonstrate stable behavior of the modules in these regimes, and allow to conservatively predict that the energy can reach 7 GeV in CW mode, and 10 GeV in LP mode with 35% duty factor [4]. Recent measurements of a cryomodule equipped with large grain Nb cavities and improved HOM couplers demonstrated even better performance, and allow for more optimistic forecasts (as it is reflected in Table 1). Moreover, all these measurements have been done with pre-series XFEL cryomodules which have not yet reached an ultimate performance. In other words, one can hope for higher electron energies after CW upgrade. Nevertheless, in this paper we conservatively consider electron energy range between 7 GeV and 10 GeV.

LASING IN THE BASELINE UNDULATOR

Apart from the standard regime of the FEL operation, namely lasing at the fundamental wavelength to saturation, in this paper we will also consider harmonic lasing as an option for reaching short wavelengths. Harmonic lasing in single-pass high-gain FELs [5–8] is the radiative instabil-

ity at an odd harmonic of the planar undulator developing independently from lasing at the fundamental. Contrary to nonlinear harmonic generation (which is driven by the fundamental in the vicinity of saturation), harmonic lasing can provide much more intense, stable, and narrow-band FEL beam if the fundamental is suppressed. The most attractive feature of saturated harmonic lasing is that the brilliance of a harmonic is comparable to that of the fundamental. Indeed, a good estimate for the saturation efficiency is $\lambda_w / (hL_{sat})$, where λ_w is the undulator period, L_{sat} is the saturation length, and h is harmonic number. At the same time, the relative rms bandwidth has the same scaling. If we consider lasing at the same wavelength on the fundamental and on a harmonic (with the retuned undulator parameter K), transverse coherence properties are about the same since they are mainly defined by emittance-to-wavelength ratio. Thus, also the brilliance is about the same in both cases. In many cases, however, the saturation length for harmonics can be shorter than that of the fundamental at the same wavelength. As a consequence, for a given undulator length one can reach saturation on harmonics at a shorter wavelength. It was shown in a recent study [8] that the 3rd and even the 5th harmonic lasing in X-ray FELs is much more robust than usually thought, and can be widely used at the present level of accelerator and FEL technology.

In the following we will consider the range of beam energies from 7 to 10 GeV, assuming that the former can be achieved in CW mode, and the latter - in LP mode with about 35% duty factor [4]. The hard X-ray undulators SASE1 and SASE2 of the European XFEL have 4 cm period, and the largest K-value of 3.9 is achieved at the gap of 10 mm. The

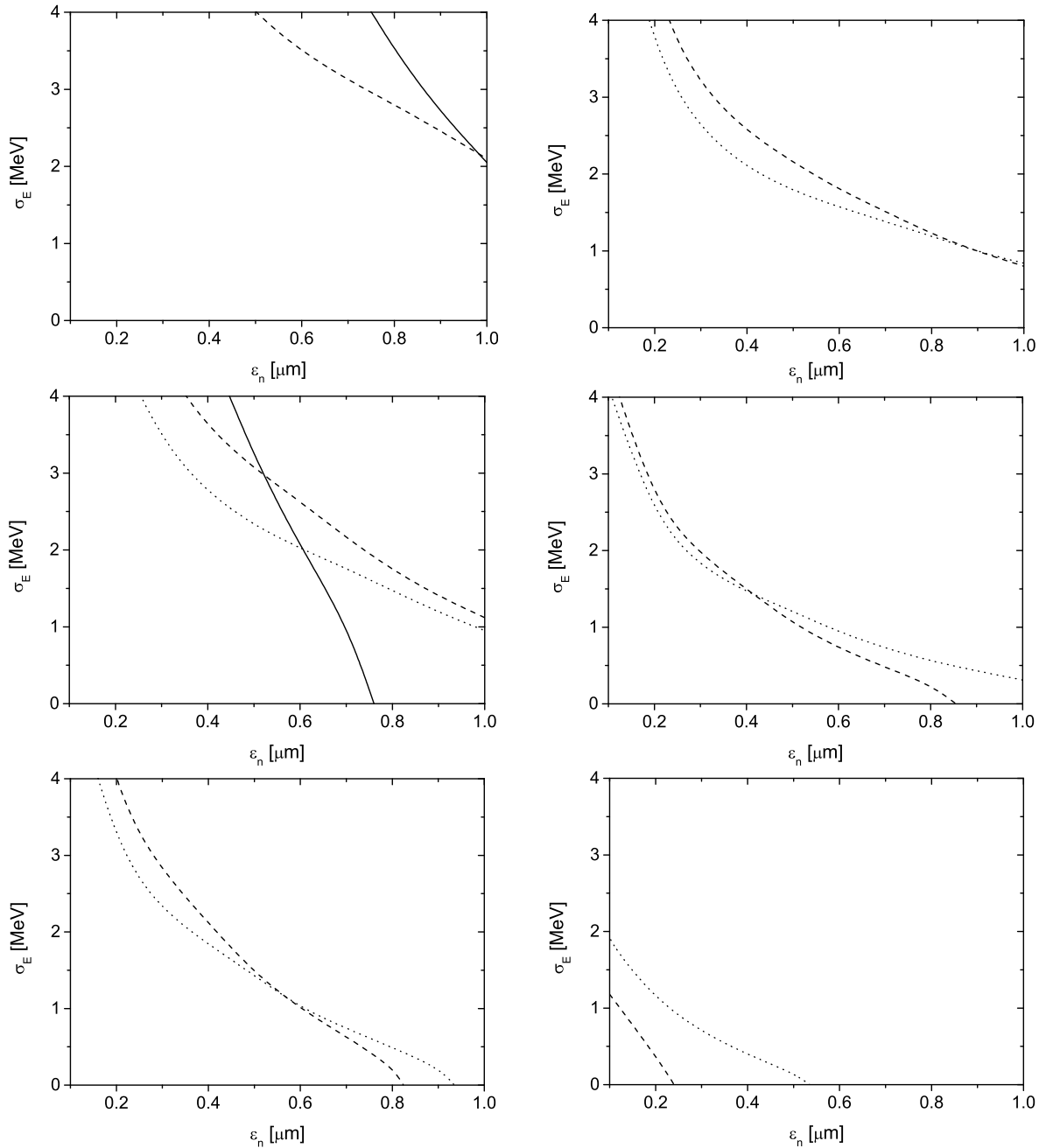


Figure 1: Energy spread versus normalized emittance for which the saturation in SASE1 undulator is possible at 1 Å (upper graphs), 0.75 Å (middle graphs), and 0.5 Å (lower graphs). The beam energy is 10 GeV (left column) and 7 GeV (right column), and the peak current is 5 kA. Beta-function is optimized for the highest gain when the optimum is larger than 15 m, otherwise beta-function is 15 m. Solid, dash, and dot curves correspond to the 1st, the 3rd, and the 5th harmonic lasing, correspondingly.

net magnetic length of the undulator is 175 m. Our task is to define the range of achievable photon energies depending on electron beam quality. We consider lasing on the fundamental as well as on the 3rd and the 5th harmonics. The formulas from [8] are used to calculate the saturation length. We assume that the peak current is 5 kA in all considered cases (different compression scenarios we leave for future studies). We optimize beta-function in the undulator for the

shortest gain length. However, when the optimum beta is smaller than 15 m (which we assume as a technical limit), we set it to 15 m.

In Fig. 1 we present energy spread versus normalized emittance for which the saturation is possible at 1 Å, 0.75 Å, and 0.5 Å for the electron energies of 7 and 10 GeV. The corresponding photon energy range is 12.4–24.8 keV. In the case of 10 GeV the lasing at 1 Å is not possible on the fifth

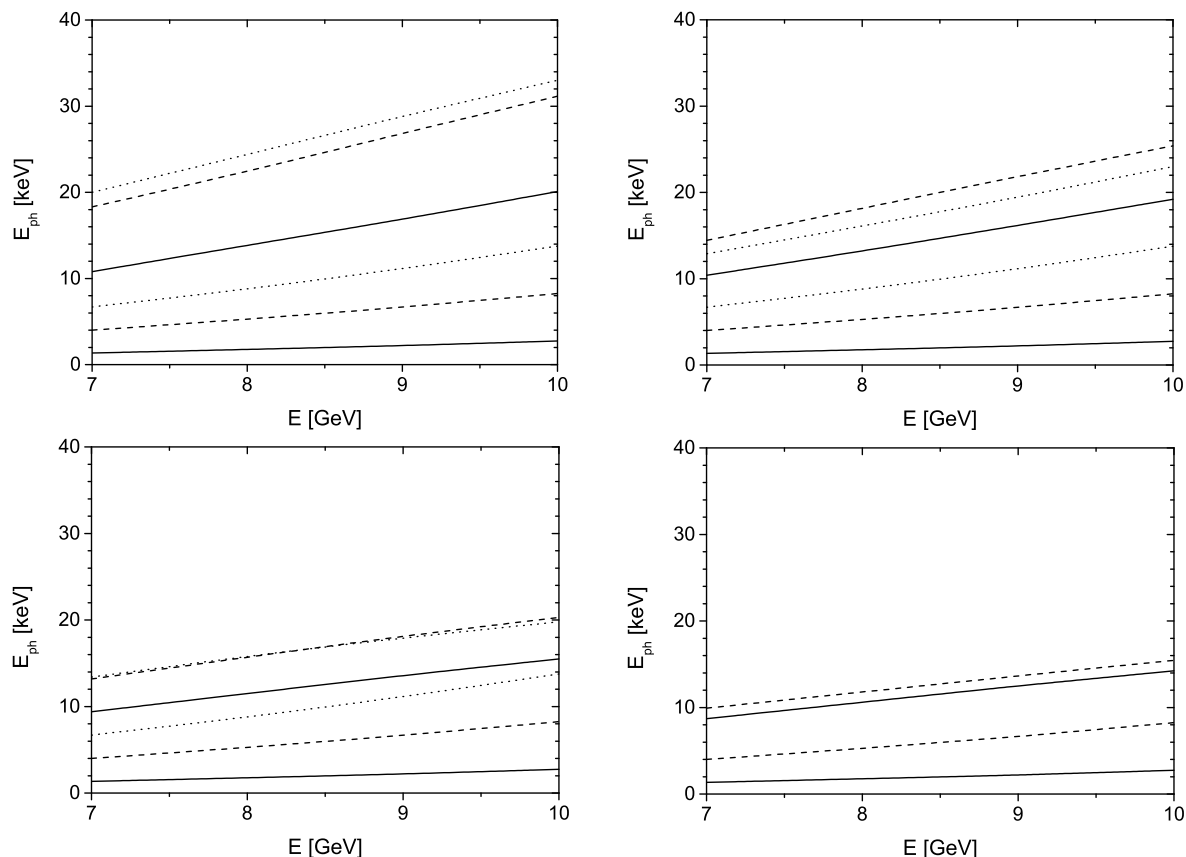


Figure 2: Range of photon energies accessible with the fundamental (between the solid lines), the third harmonic (between the dash lines), and the fifth harmonic (between the dot lines). Upper left: $\epsilon_n = 0.4 \mu\text{m}$, $\sigma_E = 1 \text{ MeV}$, upper right: $\epsilon_n = 0.4 \mu\text{m}$, $\sigma_E = 2 \text{ MeV}$, lower left: $\epsilon_n = 0.8 \mu\text{m}$, $\sigma_E = 1 \text{ MeV}$, lower right: $\epsilon_n = 0.8 \mu\text{m}$, $\sigma_E = 2 \text{ MeV}$. The undulator period is 4 cm, maximum K is 3.9, the peak current is 5 kA. Beta-function is optimized for the highest gain when the optimum is larger than 15 m, otherwise beta-function is 15 m.

harmonic because K is not sufficiently large. However, lasing to saturation on the fundamental and on the 3rd harmonic is possible practically for any reasonable beam quality. Resonance at 0.5 \AA cannot be achieved on the fundamental, but lasing to saturation on the 3rd and on the 5th harmonics is possible for a sufficiently bright electron beam. In the case of 7 GeV the resonance at 1 \AA and at shorter wavelengths is not possible on the fundamental. However, lasing to saturation on the 3rd and the 5th harmonics in sub-Ångstrom regime is possible (although at 0.5 \AA it would require extremely bright electron beams).

We can also calculate photon energy range that can be achieved in the considered electron energy range depending on electron beam quality. In Fig. 2 we present the results for four different combinations of slice emittance and energy spread ranging from $0.4 \mu\text{m}$ and 1 MeV (upper left plot) to $0.8 \mu\text{m}$ and 2 MeV (lower right plot). One can see that harmonics have a significant advantage over the fundamental only if the electron beam is bright enough. One can notice that, for example, lasing on the 5th harmonic is not possible for the most pessimistic parameter set.

Finally, let us note that the baseline undulator with a relatively large period and large K value has an advantage of a

big tunability range, as one can see from Fig. 2. Moreover, one can keep the usual operation range after switching back to the SP mode. Another advantage is that keeping a relatively large gap (10 mm) is favorable in the context of CW operation with a high average power of the electron beam. However, we have also considered a scenario with a shorter period undulator, the results can be found in [16].

REFERENCES

- [1] M. Altarelli et al. (Eds.), XFEL: The European X-Ray Free-Electron Laser. Technical Design Report, Preprint DESY 2006-097, DESY, Hamburg, 2006 (see also <http://xfel.desy.de>).
- [2] A. Koch et al., J. Phys.: Conf. Ser. **425**(2013)062013
- [3] R. Brinkmann, Proc. of the LINAC2004 Conference, Lübeck, Germany, MO102, [<http://www.jacow.org>]
- [4] J. Sekutowicz et al., Proc. of the FEL2013 Conference, New York, USA, p. 189, [<http://www.jacow.org>]
- [5] J.B. Murphy, C. Pellegrini and R. Bonifacio, Opt. Commun. **53**(1985)197
- [6] Z. Huang and K. Kim, Phys. Rev. E, **62**(2000)7295.
- [7] B.W.J. McNeil et al., Phys. Rev. Lett. **96**, 084801 (2006)

- [8] E.A. Schneidmiller and M.V. Yurkov, Phys. Rev. ST-AB **15**(2012)080702
- [9] R. Brinkmann et al. (Eds.), TESLA technical design report, Part II: Accelerator. Preprint DESY 2001-11, Hamburg, 2001.
- [10] C. Gulliford et al., Phys. Rev. ST-AB **16**(2013)073401
- [11] S.A. Belomestnykh, Proc. of the FEL2013 Conference, New York, USA, p. 176, [<http://www.jacow.org>]
- [12] M. Schmeisser et al., Proc. of IPAC2013 Conference, San Sebastian, Spain, p. 3146, [<http://www.jacow.org>]
- [13] C.F. Papadopoulos et al., Proc. of the FEL2013 Conference, New York, USA, p. 391, [<http://www.jacow.org>]
- [14] V. Vogel et al., Proc. of IPAC2011 Conference, Shanghai, China, p. 282, [<http://www.jacow.org>]
- [15] J. Sekutowicz et al., "Duty factor upgrade of the XFEL linac", to be published.
- [16] R. Brinkmann, E.A. Schneidmiller, J. Sekutowicz, M.V. Yurkov, report DESY-14-025, March 2014; arXiv:1403.0465

SUPPRESSION OF THE FUNDAMENTAL FREQUENCY FOR A SUCCESSFUL HARMONIC LASING IN SASE FELS

E.A. Schneidmiller, M.V. Yurkov, DESY, Hamburg, Germany

Abstract

Harmonic lasing in X-ray FELs has recently attracted a significant attention and is now seriously considered as a potential method for generation of brilliant photon beams at short wavelengths. It is clear, however, that for a successful harmonic lasing one has to suppress the fundamental. In this paper we discuss different methods for such a suppression: phase shifters, intraundulator spectral filtering, and switching between the 3rd and the 5th harmonics.

INTRODUCTION

Harmonic lasing in single-pass high-gain FELs [1–7] is the radiative instability at an odd harmonic of the planar undulator developing independently from lasing at the fundamental. Contrary to nonlinear harmonic generation (which is driven by the fundamental in the vicinity of saturation), harmonic lasing can provide much more intense, stable, and narrow-band FEL beam if the fundamental is suppressed. The most attractive feature of saturated harmonic lasing is that the brilliance of a harmonic is comparable to that of the fundamental. Indeed, a good estimate for the saturation efficiency is $\lambda_w/(hL_{\text{sat}})$, where λ_w is the undulator period, L_{sat} is the saturation length, and h is harmonic number. At the same time, the relative rms bandwidth has the same scaling. If we consider lasing at the same wavelength on the fundamental and on a harmonic (with the retuned undulator parameter K), transverse coherence properties are about the same since they are mainly defined by emittance-to-wavelength ratio. Thus, also the brilliance is about the same in both cases. In many cases, however, the saturation length for harmonics is significantly shorter than that of the fundamental at the same wavelength. As a consequence, for a given undulator length one can reach saturation on harmonics at a shorter wavelength. It was shown in a recent study [6] that the 3rd and even the 5th harmonic lasing in X-ray FELs is much more robust than usually thought, and can be widely used at the present level of accelerator and FEL technology.

For a successful harmonic lasing the fundamental mode must be suppressed. Otherwise it saturates earlier and spoils the longitudinal phase space of the electron beam thus preventing further exponential growth of harmonics. In this paper we discuss and compare different methods of suppression.

PHASE SHIFTERS

An elegant method to disrupt the fundamental without affecting the third harmonic lasing was suggested in [4]: one can use phase shifters between undulator modules. If phase shifters are tuned such that the phase delay is $2\pi/3$ (or $4\pi/3$)

Table 1: Parameters of Electron Beam and Undulator

Electron beam	Value
Energy	1.25 GeV
Charge	150 pC
Peak current	2.5 kA
Rms normalized slice emittance	0.5 μm
Rms slice energy spread	250 keV
Rms pulse duration	24 fs

Undulator	Value
Fundamental wavelength	3.9 nm
Period	2.3 cm
K_{rms}	1
Beta-function	7 m
Net magnetic length	25 m

for the fundamental, then its amplification is disrupted. At the same time the phase shift is equal to 2π for the third harmonic, i.e. it continues to get amplified without being affected by phase shifters. We define phase shift in the same way as it was done in [4] in order to make our results compatible with the previous studies. For example, the shift $2\pi/3$ corresponds to the advance of a modulated electron beam with respect to electromagnetic field by $\lambda/3$.

Since there are two possible phase shifts, one can consider different ways of their distributions along the undulator. Here we compare four strategies studied in the literature [4–6, 8] by performing simulations with the code FAST [9]. For the sake of comparison we take a set of parameters from a proposal for FLASH upgrade for harmonic lasing up to 1 keV [7]. The parameters of the beam and the undulator are summarized in Table 1. The undulator is supposed to be made of 3 m long segments with integrated phase shifters (in addition to phase shifters between the segments) such that the distance between the phase shifters is 0.5 m.

In the following we present the results of simulations with four different ways of distribution of phase shifters.

Consecutive Use of the Same Phase Shifts

This variation of the phase shifters method was considered in [4]. The simulations in [4] were done for the case of a monochromatic seed, and the results cannot be applied for a SASE FEL. The reason is that in the latter case the amplified frequencies are defined self-consistently, i.e. there is frequency shift (red or blue) depending on positions and magnitudes of phase kicks. This leads to a significantly weaker suppression effect. We illustrate this for the SASE FEL with the parameters from Table 1.

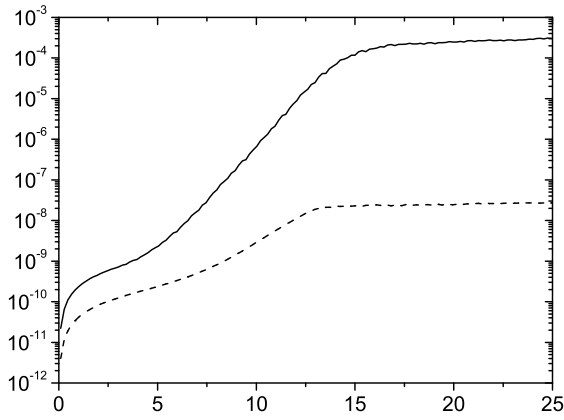


Figure 1: Pulse energy versus magnetic length of the undulator for the fundamental (solid) and the 3rd harmonic (dash). Electron beam and undulator parameters are given in Table 1. Phase shifters are located after every 0.5 m long section of the undulator. All the phase shifts are set to $2\pi/3$.

In Fig. 1 we present the gain curve for the case of using only $2\pi/3$ phase shifters (the case of only $4\pi/3$ phase shifters look similar). One can see that the method is inefficient. The saturation of the fundamental is delayed by about 20%, which is not sufficient for letting the third harmonic reach saturation. Instead, at the position $z \simeq 13$ m in the undulator the fundamental enters nonlinear regime and spoils the longitudinal phase space such that the exponential growth of the third harmonic is stopped. It is interesting to notice that there is no nonlinear harmonic generation which is usually expected to result in emission of radiation on the 3rd harmonic at the level of 1% of the fundamental. This effect is explained in [7].

We can conclude that the version of the phase shifter method, considered in [4], is inefficient in suppression of the fundamental in the case of SASE FELs (although it works well in the case of a monochromatic seed, see [4]) even if the number of phase shifters is very large.

Alternation of Phase Shifts $2\pi/3$ and $4\pi/3$

The second version of the phase shifter method was proposed in [5]: one should use an alternation of $2\pi/3$ and $4\pi/3$ phase shifters. In this case two frequency bands are generated at the fundamental, and the gain is reduced. We have simulated this configuration with the same parameters of the beam and the undulator. The results are shown in Fig. 2. One can see that this modification of the method works better, i.e. the saturation of the fundamental is delayed more significantly. However, this is still not sufficient to provide the 3rd harmonic lasing up to its saturation in the considered case.

Piecewise Use of Phase Shifts $2\pi/3$ and $4\pi/3$

In [6] we proposed another modification of phase shifters method that works better in the case of a SASE FEL. In the following we assume that a distance between phase shifters is shorter than the gain length of the fundamental harmonic.

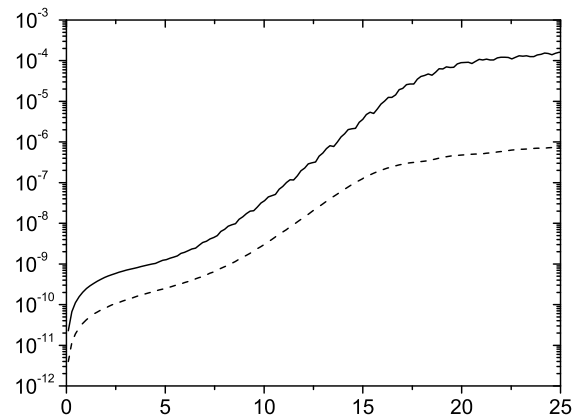


Figure 2: Pulse energy versus magnetic length of the undulator for the fundamental (solid) and the 3rd harmonic (dash). Electron beam and undulator parameters are given in Table 1. Phase shifters are located after every 0.5 m long section of the undulator, the phase shifts are $2\pi/3$ for the even phase shifters, and $4\pi/3$ for the odd ones.

Our method of disrupting the fundamental mode can be defined as a piecewise use of phase shifters with the strength $2\pi/3$ and $4\pi/3$. For example, in the first part of the undulator (consisting of several segments with phase shifters between them) we introduce phase shifts $4\pi/3$. A red-shifted (with respect to a nominal case without phase shifters) frequency band is amplified starting up from shot noise. In the following second part of the undulator we use $2\pi/3$ phase shifters, so that the frequency band, amplified in the first part, is practically excluded from the amplification process. In a realistic 3D case, the radiation is diffracted out of the electron beam, and the density and energy modulations within this frequency band are partially suppressed due to emittance and energy spread while the beam is passing the second part of the undulator (although the suppression effect is often not strong). Instead, a blue-shifted frequency band is amplified in the second part of the undulator, starting up from shot noise. Then, in the third part we change to no phase shifts case, then again to $4\pi/3$ in the fourth part, etc. A more complicated optimization can include using one or two $2\pi/3$ shifts in the first part with $4\pi/3$ phase shifters, and so on. The efficiency of the method strongly depends on the ratio of the distance between phase shifters and the gain length of the undisturbed fundamental mode. The smaller this ratio, the stronger suppression can be achieved after optimization of phase shifts distribution.

In Fig. 3 we present the results of simulations with the parameters from Table 1 and optimized distribution of phase shifts. One can see that the piecewise method works well in the considered case, i.e. it allows to suppress the fundamental such that the third harmonic reaches saturation while the fundamental is still well below its saturation.

We can simply generalize the method to the 5th harmonic lasing. One can introduce a piecewise combination of some of the phase shifts $2\pi/5$, $4\pi/5$, $6\pi/5$, or $8\pi/5$ (for the fundamental frequency). In this case also the third harmonic will

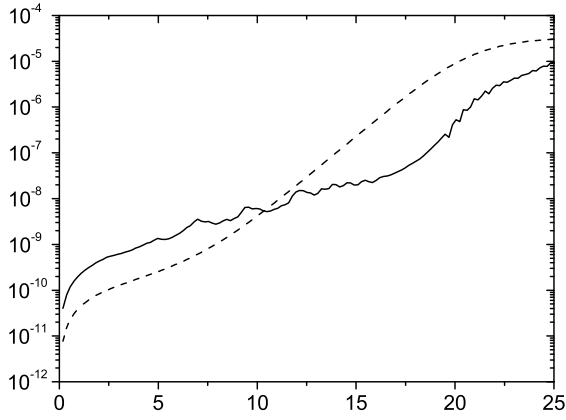


Figure 3: Pulse energy versus magnetic length of the undulator for the fundamental (solid) and the 3rd harmonic (dash). Electron beam and undulator parameters are given in Table 1. Phase shifters are located after every 0.5 m long section of the undulator. The phase shift is $4\pi/3$ after sections 1-4, 6-9, 11-13, 18, 23, 39-49, and $2\pi/3$ after sections 5, 10, 14-17, 19-22, 24-27.

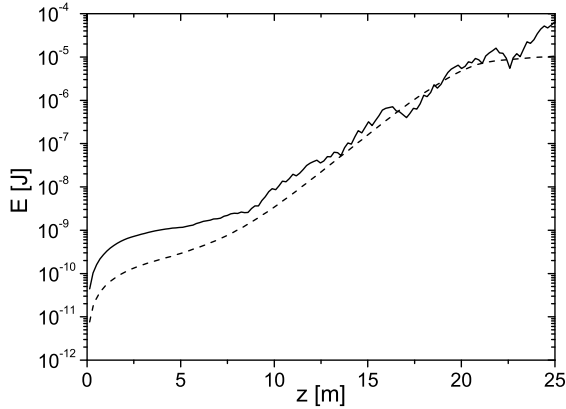


Figure 4: Pulse energy versus magnetic length of the undulator for the fundamental (solid) and the 3rd harmonic (dash). Electron beam and undulator parameters are given in Table 1. Phase shifters are located after every 0.5 m long section of the undulator. A choice between phase shifts $2\pi/3$ and $4\pi/3$ is randomly generated.

see the disrupting shifts, while the fifth harmonic will not be affected. If the number of phase shifters is sufficient, the fundamental mode and the third harmonic can be strongly suppressed.

Random Distribution of Shifts $2\pi/3$ and $4\pi/3$

This variation of phase shifters method is proposed in [8]. We simulated this method using the parameters from Table 1 again. We tried 5 different random realizations of phase shifts, the best result is shown in Fig. 4. One can notice that the approach with random distributions promises better suppression than the first two approaches using regular distributions. However, it looks somewhat less effective than the optimized piecewise distribution.

At the end of our studies of the phase shifters method, we can conclude that the method works but one needs a lot of phase shifters and a fancy way of their distribution.

INTRAUNDULATOR SPECTRAL FILTERING

The method was proposed in [6], its idea is simple: at a position in the undulator where the fundamental harmonic is in the high-gain linear regime (well below saturation), the electron beam trajectory deviates from a straight line, and a filter is inserted that strongly suppresses the fundamental mode but only weakly affects the third harmonic. As a simple bending system one can use, for example, a chicane that substitutes one of the undulator segments as it is done at LCLS [10] for operation of the self-seeding scheme [11]. A possible alternative is to make a closed bump with the help of moving quadrupoles of the undulator focusing system (quadrupoles are usually placed after each undulator segment, so that in this case two segments are excluded from lasing). Although the main purpose of the bending system is to provide an offset for insertion of a filter, it has to satisfy two other requirements: on the one hand a delay of the bunch with respect to a radiation pulse must be smaller than the bunch length; on the other hand, the R_{56} (equal to the double delay) should be sufficient for smearing of energy and density modulations at the fundamental wavelength: $2\pi\sigma_\gamma R_{56}/(\gamma\lambda_1) \gg 1$. Both conditions can be easily satisfied simultaneously in most cases. The active length of the first part of the undulator is chosen such that, on the one hand, the highest possible gain is achieved; on the other hand, energy modulations, induced by the FEL interaction at the fundamental wavelength (and converted to uncorrelated energy spread through the chicane), should be sufficiently small to avoid a significant increase of gain length of the third harmonic in the second part of the undulator.

We present here a numerical example for third harmonic lasing at LCLS at the photon energy of 25 keV with a significant power and a relatively narrow intrinsic bandwidth. LCLS undulator consists of 33 identical 3.4-m-long segments, undulator period is 3 cm, and the peak undulator parameter is 3.5 (rms value of K is 2.5). The 16th segment is replaced with a chicane (hard X-ray self-seeding, or HXRSS chicane) for operation of the self-seeding scheme [11]. As a possible realization of the filter we propose here a silicon crystal that is not supposed to spoil phase front of the third harmonic radiation while attenuating the fundamental harmonic by orders of magnitude. A thickness of the crystal is defined by a required attenuation factor and an expected photon energy range. As an example we consider here the thickness of 600 μm and third harmonic lasing at 25 keV. Attenuation length at 8.3 keV is $\mu^{-1} = 73 \mu\text{m}$, and at 25 keV it is $\mu^{-1} = 1.85 \text{ mm}$ [12], so that the corresponding transmission factors are 2.7×10^{-4} and 0.72. With a given thickness of the crystal the scheme would work well in the range 20-30 keV, and for lower photon energies of the third harmonic a thinner crystal would be needed.

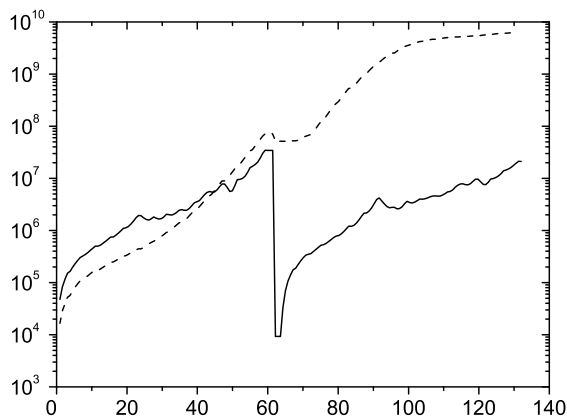


Figure 5: Averaged peak power for the fundamental harmonic (solid) and the third harmonic (dash) versus geometrical length of the LCLS undulator (including breaks). The wavelength of the third harmonic is 0.5 \AA (photon energy 25 keV). Beam and undulator parameters are in the text. The fundamental is disrupted with the help of the spectral filter (see the text) and of the phase shifters. The phase shifts are $4\pi/3$ after segments 1-5 and 17-22, and $2\pi/3$ after segments 6-10 and 23-28. Simulations were performed with the code FAST.

In the considered parameter range the spectral filtering method alone is not sufficient, therefore we suggest to combine it with the phase shifters method. We propose to install phase shifters with the shift $4\pi/3$ after undulator segments 1-5 and 17-22, and with the shift $2\pi/3$ after segments 6-10 and 23-28. Let us consider a specific parameter set for third harmonic lasing at 0.5 \AA (photon energy 25 keV). The electron beam parameters are as follows: energy is 13.6 GeV (the fundamental wavelength is 1.5 \AA), peak current is 3 kA , normalized slice emittance is 0.3 \mu m , uncorrelated energy spread is 1.4 MeV . The beta-function in the undulator is 30 m . In our simulations we do not consider a specific bunch length, so that our result is the peak power of the third harmonic radiation in the part of the pulse that overlapped with the electron beam after the chicane. We performed simulations with the code FAST [9], the results are presented in Fig. 5. The averaged peak power of the third harmonic radiation is 6 GW , and an intrinsic bandwidth is 3×10^{-4} (FWHM). The power incident on the crystal is in the range of tens of megawatts, and should not be problematic from the point of view of peak and average power load.

It was suggested [13] to perform a test experiment at 18 keV with the filter installed in the soft X-ray self-seeding (SXRSS) chicane and without phase shifters (using only HXRSS chicane as a phase shifter). If this experiment will be successful, one can think of installation of an additional filter in HXRSS chicane and/or phase shifters.

SWITCHING BETWEEN THE 3RD AND THE 5TH HARMONICS

This method was proposed at DESY [14] and independently by SLAC/LBNL group [8]. The method is based on

the observation that in some practical cases the gain lengths of the 3rd and the 5th harmonics are close to each other [14]. Thus, the following trick is possible. Imagine, we aim at lasing at 1 \AA . We tune the first part of the undulator to the resonance with 5 \AA , so that we are interested in the 5th harmonic lasing. The fundamental and the third harmonic are suppressed by the piecewise combination of (some of the) phase shifters $2\pi/5$, $4\pi/5$, $6\pi/5$, and $8\pi/5$ such that they stay well below saturation in the first part of the undulator. Then, in the second part we reduce parameter K such that the resonance at 3 \AA is achieved. Now the fifth harmonic from the first part continues to get amplified as the third harmonic (while the first and the third ones are off resonance). The fundamental in the second part is suppressed with the help of piecewise distribution of phase shifters $2\pi/3$ and $4\pi/3$. If necessary, one can later switch back to a resonance with 5 \AA , and so on. Also, a use of many pieces with 5th and 3rd harmonic lasing without phase shifters might be possible. Moreover, the scheme can be generalized to the case of even higher harmonics.

CONCLUSION

There exist different methods for suppression of the fundamental to provide conditions for harmonic lasing. There is also a hope that more methods will be invented as soon as the interest to this mode of operation will grow.

REFERENCES

- [1] J.B. Murphy, C. Pellegrini and R. Bonifacio, *Opt. Commun.* **53**(1985)197
- [2] R. Bonifacio, L. De Salvo, and P. Pierini, *Nucl. Instr. Meth.* **A293**(1990)627.
- [3] Z. Huang and K. Kim, *Phys. Rev. E*, **62**(2000)7295.
- [4] B.W.J. McNeil et al., *Phys. Rev. Lett.* **96**, 084801 (2006)
- [5] G. Parisi et al., *Proc. of the FEL2005 Conference*, Stanford, California, USA, p. 187, [<http://www.jacow.org>]
- [6] E.A. Schneidmiller and M.V. Yurkov, *Phys. Rev. ST-AB* **15**(2012)080702
- [7] E.A. Schneidmiller and M.V. Yurkov, *Nucl. Instr. Meth.* **A717**(2013)37.
- [8] G. Marcus, Z. Huang, T. Raubenheimer, and G. Penn, "Harmonic Lasing Options for LCLS-II", presented at this Conference, MOP054, *Proc. of the FEL2014 Conference*, Basel, Switzerland.
- [9] E.L. Saldin, E.A. Schneidmiller and M.V. Yurkov, *Nucl. Instrum. and Methods A* **429**(1999)233
- [10] P. Emma et al., *Nature Photonics* **4**(2010)641
- [11] G. Geloni, V. Kocharyan and E. Saldin, preprint DESY-10-133, August 2010
- [12] www.csrrri.iit.edu/mucal.html
- [13] D. Ratner et al., *Proc. of the FEL2013 Conference*, New York, USA, p. 623, [<http://www.jacow.org>]
- [14] R. Brinkmann, E.A. Schneidmiller, J. Sekutowicz and M.V. Yurkov, preprint DESY-14-025, March 2014; arXiv:1403.0465

DESIGN STUDY FOR THE PEHG EXPERIMENT AT SDUV-FEL*

C. Feng, H.X. Deng[#], M. Zhang, T. Zhang, X.T. Wang, W. Zhang, B. Liu, D. Wang, Z.T. Zhao
Shanghai Institute of Applied Physics, CAS, Shanghai 201800, China

Abstract

In this paper, design studies for the proof-of-principle experiment of the recently proposed phase-merging enhanced harmonic generation (PEHG) mechanism are presented. A dogleg and a new designed transverse gradient undulator should be added in the undulator system of SDUV-FEL to perform the phase-merging effect. With the help of 3D simulation codes, we show the possible performance of PEHG with the realistic parameters of SDUV-FEL.

INTRODUCTION

High-gain seeded FEL schemes have been developed for producing stable and fully temporal coherence laser pulse from deep UV down to the x-ray regime. The most famous frequency up-conversion scheme is so called the high-gain harmonic generation (HGHG) [1], which uses an external laser pulse to interact with the electron bunch for the generation of coherent micro-bunching. The property of HGHG output is a direct map of the seed laser's attributes, which ensures high degree of temporal coherence and small pulse energy fluctuations with respect to self-amplified spontaneous emission (SASE) [2]. However, significant bunching at higher harmonics usually needs to strengthen the energy modulation in HGHG, which will result in a degradation of the amplification process of FEL. Thus the requirement of FEL amplification on the beam energy spread prevents the possibility of reaching short wavelength in a single stage HGHG.

Recently, a novel seeded FEL scheme termed phase-merging enhanced harmonic generation (PEHG) [3, 4], has been proposed for significantly improving the frequency up-conversion efficiency of harmonic generation FELs. Generally, a transversely dispersed electron beam and a transverse gradient undulator (TGU) [5] are needed in PEHG for performing the phase-merging effect purpose: when the transversely dispersed electrons passage through the TGU, around the zero-crossing of the energy modulation, electrons with the same energy will merge into a same longitudinal phase.

Several ways have been proposed [3, 4, 6] for performing the phase-merging effect as shown in Fig. 1, where doglegs are added before modulators for transversely dispersing the electron bunch. Fig. 1(a) shows the initial proposed PEHG scheme, where a short TGU is used for the energy modulation and to precisely manipulate the electrons in the horizontal dimension. It is found later that these two functions of TGU can be separately performed by employing a modified design, as shown in Fig. 1 (b). In this scheme, a normal modulator is

used for the energy modulation, and the TGU is responsible only for transverse manipulation of the electrons, a design that will be much more flexible for practical operation. Fig. 1(c) shows a much simpler scheme that adopts a normal modulator and a wave-front tilted seed laser pulse to realize the phase-merging effect. Analytical and numerical investigations indicate that all these three schemes have the potential of generating ultra-high harmonic bunching factor with a relatively small energy modulation. To demonstrate these theoretical predictions, a proof-of-principle experiment for PEHG has been planned at Shanghai deep ultraviolet free-electron laser facility (SDUV-FEL) [7, 8]. In this paper, we present the design studies for this experiment.

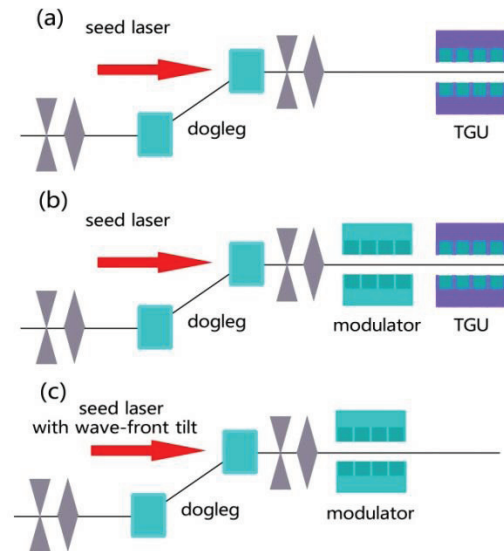


Figure 1: Modulation schemes for PEHG.

LAYOUT AND MAIN PARAMETERS

The SDUV-FEL is an integrated multi-purpose test facility for seeded FEL principles, capable of testing various seeded FEL working modes. A new beam line will be added after the linac of SDUV-FEL for the PEHG and Thomson scattering experiments in this year. The layout of the PEHG experiment is shown in Fig. 2. A dogleg is adopted for switching the electron bunch and introducing a large transverse dispersion into the electron beam. After that, a conventional modulator and a new designed TGU, as shown in Fig. 3, are employed for energy modulation and manipulating the electron beam. The energy modulation will be converted to density modulation by the dispersion section (DS). Then the coherently bunched beam is sent through the radiator for high harmonic radiation.

*Work supported by National Natural Science Foundation of China (11475250, 11175240, 11322550 and 11205234)
[#]denghaixiao@sinap.ac.cn

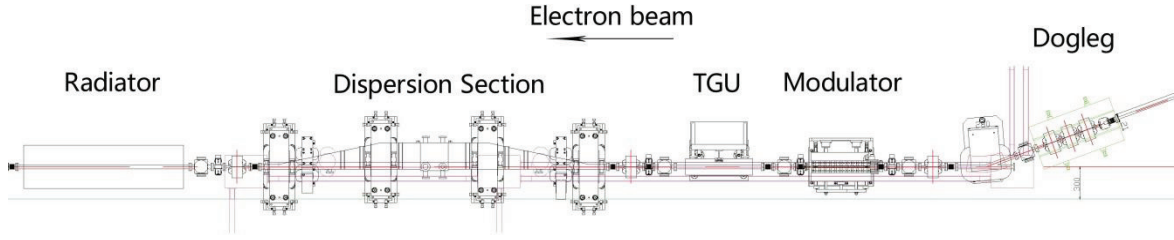


Figure 2: Layout for the PEHG experiment at SDUV-FEL.

One can find that the undulator beam line in Fig. 2 is suitable for testing all the three modulation schemes in Fig. 1. Here we only present the design and simulation results for the second scheme (Fig. 1(b)), which is the most flexible scheme for PEHG.

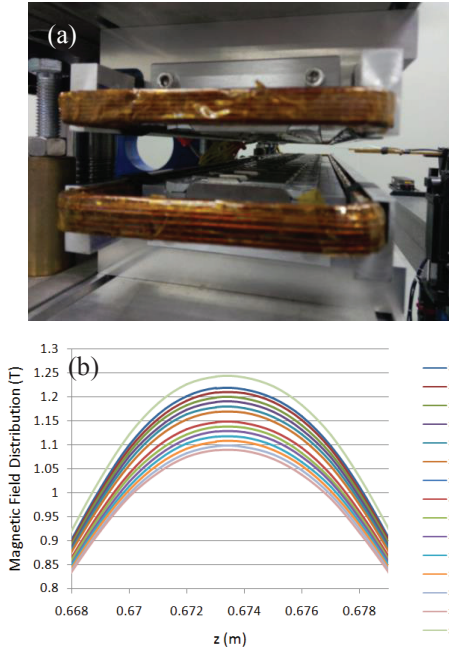


Figure 3: (a) The TGU for PEHG experiment. (b) Measurement results of magnetic field distributions for different transverse position of TGU.

To roughly estimate the optimal parameters of the PEHG experiment, here we adopt the 4-dimensional linear beam transport matrix in the x - z plane, i.e., (x, x', z, δ) is used in the following. The 4×4 beam transport matrix for the dogleg is

$$R_D = \begin{pmatrix} 1 & L_D & 0 & \eta \\ 0 & 1 & 0 & 0 \\ 0 & \eta & 1 & \xi_D \\ 0 & 0 & 0 & 1 \end{pmatrix}, \quad (1)$$

where L_D is the length of the dogleg, η and ξ_D are, respectively, the dispersion and the momentum compaction generated in the dogleg. We ignore the effects of ξ_D hereafter.

When an electron beam with central beam energy γ_0 is sent through a TGU with total length L_T , transverse

gradient α and central undulator parameter K_0 , the transport matrix of the short TGU approximately reads:

$$R_T \approx \begin{pmatrix} 1 & L_T & 0 & 0 \\ 0 & 1 & 0 & -\tau \\ \tau & \tau L_T / 2 & 1 & 0 \\ 0 & 0 & 0 & 1 \end{pmatrix}, \quad (2)$$

where $\tau = L_T K_0^2 \alpha / 2\gamma_0^2$ is the transverse gradient parameter of the TGU. Then the transport matrix for the whole beam line including all components shown in Fig. 1(b) can be written as

$$R = \begin{pmatrix} k_1 & k_2 & 0 & a_2 \eta \\ k_3 & k_4 & -h\tau & c_2 \eta - \tau \\ k_1 \tau + c_1 \eta (1 + h\xi_c) & k_2 \tau + d_1 \eta (1 + h\xi_c) & 1 + h\xi_c & \xi_c + a_2 \eta \tau \\ c_1 h \eta & d_1 h \eta & h & 1 \end{pmatrix}, \quad (3)$$

where a , b , c , d are beam matching parameters, $k_1 = a_1 a_2 + b_2 c_1$, $k_2 = a_2 b_1 + b_2 d_1$, $k_3 = a_1 c_2 + c_1 d_2 - c_1 h \eta \tau$, $k_4 = b_1 c_2 + d_1 d_2 - d_1 h \eta \tau$, $a_1 d_1 - b_1 c_1 = 1$, $a_2 d_2 - b_2 c_2 = 1$, h is the seed laser induced energy chirp around the zero-crossing of the energy modulation and ξ_c is the momentum compaction of the DS. For simplify, we choose $a_1 = a_2 = d_1 = d_2 = 1$ and $b_1 = b_2 = c_1 = c_2 = 0$ here, then the Eq. (3) can be re-written as

$$R = \begin{pmatrix} 1 & 0 & 0 & \eta \\ 0 & 1 - h \eta \tau & -h\tau & -\tau \\ \tau & \eta (1 + h\xi_c) & 1 + h\xi_c & \xi_c + \eta \tau \\ 0 & h \eta & h & 1 \end{pmatrix}, \quad (4)$$

The density modulation of a high harmonic generation scheme is an optical-scale micro-bunch compression process. To maximize the high harmonic bunching factor, $1 + h\xi_c = 0$ should be satisfied first, and the optimized condition for the phase-merging effect is $\xi_c + \eta \tau = 0$. Under these optimized conditions, the bunching factor will be only affected by the product of τ and the initial horizontal beam size σ_x according to Eq. (4). From Eq. (3), one can also find that the required value of η and τ for performing the phase-merging effect can be significantly reduced by changing the values of a_1 and a_2 . The optimal parameters for the PEHG experiment are summarized in Table 1.

Table 1: Main Parameters for PEHG Experiment

Parameters	Value
Beam energy	160 MeV
Slice energy spread	48 keV
Normalized emittance	3 μmrad
Bunch charge	300 pC
Peak current	100 A
η of dogleg	1 m
Seed wavelength	2500 nm (from OPA)
Seed pulse length	1 ps (FWHM)
Period of TGU	60 mm
L_r of TGU	0.6 m
α of TGU	-43.5 m^{-1}
K_0 of TGU	5
ξ_c of DS	1 mm
Radiation wavelength	250 nm
Period of radiator	25 mm
Length of radiator	1.5 m

SIMULATIONS

With parameters shown in Table 1, we carried out 3D simulations for the PEHG experiment. ASTRA [9] is used for tracking the particle from the cathode to the injection point to the linac. Then the electron beam is tracked through the main accelerator with help of ELEGANT [10] taking into account of the CSR and the space charge effects. The energy of the electron beam is around 160 MeV at the exist of the linac, the peak current after bunch compression is about 100 A, and the slice energy spread in the central part of the electron beam is around 2 keV. This kind of small energy spread will result in a large bunching factor at low harmonic numbers for both HGHG and PEHG.

The key advantage of the PEHG is that it can generate very high harmonics with harmonic number much larger than the ratio of energy modulation to energy spread. This makes it possible to generate very high frequency bunching while simultaneously keeping the beam energy spread small. However, limited by the beam energy and period length of the radiator, generation of ultra-high harmonic radiation is not possible at SDUV-FEL. An alternative way to demonstrate the superiority of PEHG over HGHG is to increase the initial slice energy spread. In this design, we adopt a Nd:YLF laser at 1047 nm to heat the electron beam energy spread before the dogleg. After this laser heater, the slice energy spread is increased to about 48 keV.

The energy and density modulation processes are tracked with a modified version of GENESIS [11]. For comparison purpose, we carried out simulations for both HGHG and PEHG. The only difference for these two simulations is set $\alpha = 0$ or $\alpha = -43.5 \text{ m}^{-1}$. The longitudinal

phase space distributions in a small fragment of the electron bunch are shown in Fig. 4. Different from a conventional HGHG, most of the electrons are compressed into a small region around the zero-phase in PEHG, which indicates that the density modulation has been significantly enhanced for high harmonics, as shown in Fig. 5. The 10th harmonic bunching factor of HGHG is at the shot noise level.

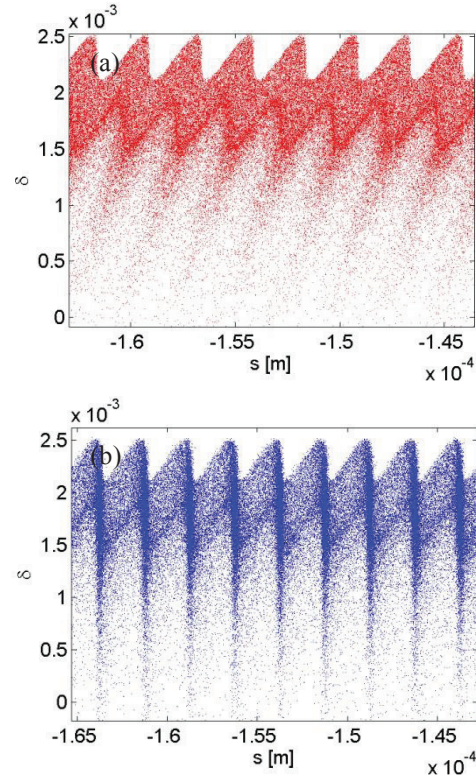


Figure 4: Phase space distributions in the central part of electron beam for (a) HGHG and (b) PEHG.

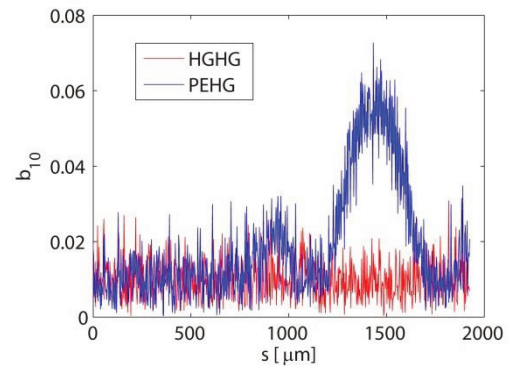


Figure 5: Comparison of 10th harmonic bunching factor distributions along the electron bunch for HGHG and PEHG.

The bunched electron beams are then sent through a short radiator resonant at 250 nm for the generation of coherent signals at 10th harmonic of the seed. Simulations results of the radiation pulses and single-shot spectra for HGHG and PEHG are shown in Fig. 6. The output pulse

energy of PEHG is much higher than HGHG at 10th harmonic and the spectrum bandwidth of PEHG is quite close to the transform limit.

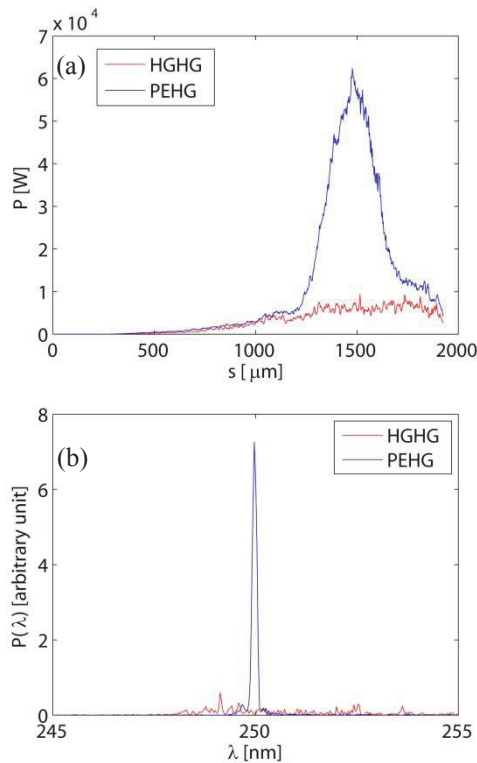


Figure 6: Comparisons of 10th harmonic radiation pulses (a) and spectra (b) for HGHG and PEHG.

CONCLUSION

In conclusion, we present design studies of a proof-of-principle experiment for PEHG based on the upgraded SDUV-FEL. With a new designed dogleg and a TGU, all the three modulation schemes for PEHG can be demonstrated at SDUV-FEL. Theoretical analysis and numerical simulations are given to show the parameter optimization method and possible performance of PEHG. The coherent signal of PEHG at 250 nm with pulse energy much larger than HGHG can be obtained by properly choosing the parameters of the machine. The upgrade of SDUV-FEL will be finished in this year and the commissioning of PEHG will be started in the next year.

REFERENCES

- [1] L.H. Yu, Phys. Rev. A, 44, 5178 (1991).
- [2] A. M. Kondratenko, E. L. Saldin, Part Accel. 10, 207 (1980).
- [3] H. Deng, C. Feng, Phys. Rev. Lett. 111, 084801 (2013).
- [4] C. Feng, H. Deng, D. Wang, Z. Zhao, New J. Phys. 16, 043021 (2014).
- [5] Z. Huang, Y. Ding, C.B. Schroeder, Phys. Rev. Lett. 109, 204801 (2013).
- [6] C. Feng, T. Zhang, H. Deng, Z. Zhao Phys. Rev. ST Accel. Beams 17, 070701 (2014).
- [7] Z. Zhao, *et al.* Nucl Instr Meth A, 528, 591 (2004).
- [8] H. Deng, Nucl. Sci. Tech. 25, 010101 (2014).
- [9] K. Floettmann, ASTRA User's Manual.
- [10] M. Borland, Phys. Rev. STAccel. Beams 4, 070701 (2001).
- [11] S. Reiche, Nucl Instr Meth A, 429, 243–248 (1999).

LASER SEEDING SCHEMES FOR SOFT X-RAYS AT LCLS-II

G. Penn, LBNL, Berkeley, CA, USA

P. Emma, E. Hemsing, G. Marcus, T.O. Raubenheimer, L. Wang, SLAC, Menlo Park, CA, USA

Abstract

The initial design for LCLS-II incorporates both SASE and self-seeded configurations. Increased stability and/or coherence than is possible with either configuration may be provided by seeding with external lasers followed by one or more stages of harmonic generation, especially in the soft x-ray regime. External seeding also allows for increased flexibility, for example the ability to quickly vary the pulse duration. Studies of schemes based on high-gain harmonic generation and echo-enabled harmonic generation are presented, including realistic electron distributions based on tracking through the injector and linac.

INTRODUCTION

In addition to SASE [1] and self-seeding [2, 3] schemes, LCLS-II [4] may also incorporate seeding using external lasers. Benefits include more control over the x-ray pulse, better shot-to-shot stability, and possibly a narrower spectrum. The use of external lasers may have an impact on repetition rate and tends to reduce the energy of the final x-ray pulse. In addition, upshifting by very large harmonics from the laser wavelength introduces new challenges. Here we discuss designs for both the two-stage high-gain harmonic generation (HG) and single-stage echo-enabled harmonic generation (EEHG) seeding schemes, and compare their performance. Two-stage HG with a fresh-bunch delay has been demonstrated at FERMI@Elettra [5] with excellent performance down to the 65th harmonic (4 nm). EEHG has been demonstrated at NLCTA [6] up to the 15th harmonic (160 nm).

ELECTRON BEAM AND UNDULATOR PARAMETERS

The simulations shown below use particles obtained from two start-to-end (S2E) simulations of the linac accelerating the beam to 4 GeV. One simulation uses a 100 pC bunch and the other a 300 pC bunch. Not all aspects of longitudinal dynamics have been modelled, however. The nominal parameters for the electron beam and the main undulator sections for producing radiation are given in Table 1. Local parameters will vary with position along the bunch. The longitudinal phase space of the beams are shown in Fig. 1, and the current profiles are shown in Fig. 2. Compared to the 100 pC bunch, the 300 pC bunch is longer, has a larger emittance and a slightly lower peak current.

The final undulators have a period of 39 mm and cover the desired tuning range from 250 eV to 1.3 keV. Here, we focus on producing radiation at 1 nm, which is the most challenging part of the tuning range. The external laser is

fixed at a wavelength of 260 nm. The large overall harmonic jump presents certain challenges which will be noted below.

Table 1: Beam and Undulator Parameters for Soft X-ray Production at LCLS-II

Parameter	Symbol	Value
Electron Beam:		
Bunch charge	Q	100 — 300 pC
Electron energy	E	4 GeV
Peak current	I	1 kA
Emittance	ϵ_N	0.3 — 0.43 μm
Energy spread	σ_E	0.5 MeV
Beta function	β	15 m
Final undulators:		
Undulator period	λ_u	39 mm
Undulator segment length	L_{seg}	3.4 m
Break length	L_b	1.2 m
Min. magnetic gap	g_{min}	7.2 mm
Max. undulator parameter	K_{max}	5.48
Max. resonant wavelength	λ_{max}	5.1 nm

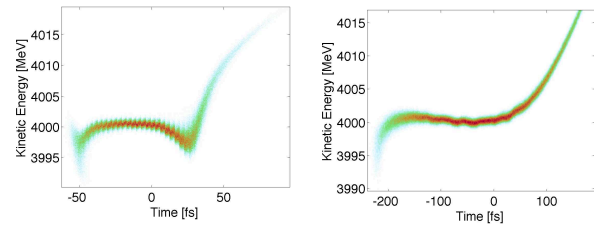


Figure 1: Longitudinal phase space for 100 pC (left) and 300 pC (right) electron bunches.

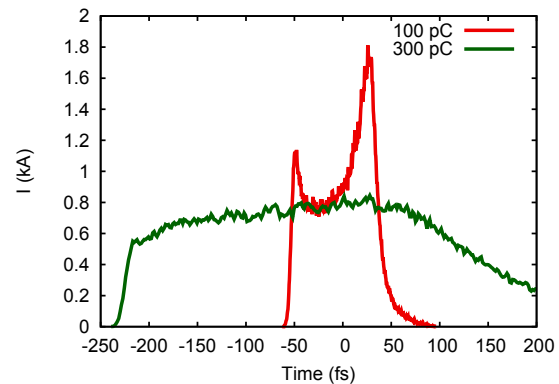


Figure 2: Current profiles for 100 pC and 300 pC electron bunches.

HGHG AND EEHG SCHEMES

The layouts for the two main schemes are shown in Fig. 3. Additional undulator sections may be placed at the end, tuned to a shorter wavelength. FEL simulations were performed using GENESIS [7]. These and other schemes have previously been considered in Chapter 18 of the LCLS-II Conceptual Design Report [8] for idealized beams and with a focus on producing radiation at 2 nm.

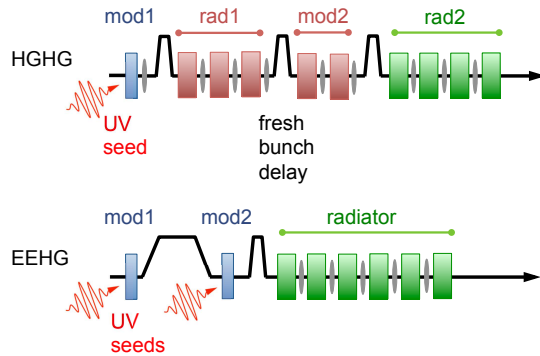


Figure 3: Beamline layouts using EEHG (top) and two-stage HGHG with a fresh bunch delay (bottom).

HGHG Design and Layout

The initial HGHG design uses one laser with a 260 nm wavelength. One stage of harmonic generation is followed by a fresh-bunch delay and a second stage of harmonic generation to reach wavelengths as low as 1 nm. The nominal peak power to reach 1 nm is 800 MW, but the laser power has to be adjusted differently for the two beams because radiation production at the intermediate wavelength is sensitive to the electron properties. Because of the fresh-bunch delay the pulse duration must be short in order to have the two stages fit within the core of the electron bunch.

The undulator used for the initial modulation has a period of 100 mm and is 3.2 m long. The resulting energy modulation can be as large as 6 MeV. The next five undulator sections have a period of 80 mm, each 3.2 m long. These undulators have helical polarization to increase the coupling at the intermediate wavelength; all other undulators have planar polarization. The first three are used to radiate through the narrow bunching produced at a 260 nm wavelength. This is followed by a delay chicane, and the next two undulator sections modulate electrons in a region which is located further to the head of the bunch. The large total undulator length is required to be able to reach a final wavelength of 1 nm. The intermediate wavelength in that case is 13 nm, the 20th harmonic.

The third chicane yields bunching at 1 nm of the order of 1%. The final set of undulators, with a 39 mm period, radiate at this wavelength to saturation. The final stage of harmonic generation must produce significant bunching at the 13th harmonic, so the energy modulation must be quite large as well, but at the same time radiation at 1 nm will be

suppressed if the energy spread grows beyond around 3 MeV. Note that both bunches have a minimum energy spread of 0.5 MeV.

The chicanes are fairly modest, and are all about 2 m in length. The first chicane has $R_{56} = 22 \mu\text{m}$. The fresh-bunch delay can be as small as 25 fs, corresponding to $R_{56} = 15 \mu\text{m}$, in order to fit the entire process into the 100 pC bunch length. For the 300 pC bunch, the delay could be as large as 100 fs. The weaker end of this range for the delay chicane is not enough to suppress bunching at the intermediate wavelength. The bunching towards the tail of the bunch will radiate in the undulator sections immediately following the fresh bunch delay, although not enough to produce significant bunching after next stage of harmonic generation.

EEHG Design and Layout

Echo-enabled harmonic generation (EEHG) [9] operates through a form of wave-mixing, where two energy modulations are used instead of one for standard HGHG. The first modulation is followed by a chicane which strongly over-bunches the modulation, creating well-separated bands in longitudinal phase space. Each band has a reduced energy spread. The second modulation is also followed by a chicane but in this case they are tuned so as to perform a standard phase rotation of each band. The overall bunching factor can be significant even at very high harmonics.

For the EEHG example, we consider two seed lasers both with a wavelength of 260 nm. The first undulator section is 3.2 m long, with a period of 0.1 m, identical to the first undulator used for HGHG. The laser pulse going into this undulator has a peak power of 47 MW, and generates an energy modulation of 1.5 MeV. This is followed by a chicane with $R_{56} = 14.37 \text{ mm}$. The second undulator is also 3.2 m long but with a period of 0.4 m. The laser pulse going into this undulator has a peak power of 900 MW, and generates an energy modulation of 2 MeV. Both lasers have a Rayleigh length of 1 m. The pulse duration can be anywhere from 10s to 100s of fs. This is followed by a chicane with $R_{56} = 53 \mu\text{m}$. Bunching is generated directly at 1 nm.

The reason for the difference in undulator periods is that in the second undulator the phase space bands in the beam are particularly sensitive to energy scattering. Increasing the period lowers the magnetic field and reduces incoherent synchrotron radiation (ISR). For the same reason, the large dispersion required for the first chicane is obtained by increasing the length of the magnets rather than increasing the magnetic field. Thus, the first chicane is 9 m long with 2 m dipole magnets, while the second chicane is only 2 m long. Even without magnetic fields, there is intra-beam scattering (IBS) which pushes the design towards being as short as possible. The combined effect of both ISR and IBS reduces the bunching factor at 1 nm from an ideal value of 5.2% to roughly 1.4%. Without taking into effect the impact of scattering, the optimal bunching parameter would be given

by the magnitude of

$$\hat{b} = \sum_{\substack{m, p \\ k_X = k_2 p - k_1 m}} e^{i(p\psi_2 - m\psi_1)} (-1)^p \quad (1)$$

$$\times J_p(C_2 \eta_{m2}) J_m(C_1 \eta_{m1}) e^{-iC_1 \bar{\eta}} e^{-C_1^2 \sigma_{\eta}^2 / 2},$$

where $C_1 = k_X R_2 - k_1 m R_1$, $C_2 = k_X R_2$, $\psi_{1,2}$ are the laser phases, $k_{1,2}$ are the laser wavenumbers, and k_X is the target output wavenumber. The relative energy spread $\sigma_{\eta} = \sigma_E/E$, the relative height of the two energy modulations are η_{m1} and η_{m2} , and $\bar{\eta}$ is the local relative energy offset. Usually only one term in the summation contributes significantly to the bunching, and this term is generally selected to correspond to $m = 1$. Note that normally $|C_1| \ll |C_2|$, which results in reduced sensitivity to both energy spread and energy chirps.

After the bunching is generated, the electron beam goes directly into undulator sections with a 39 mm undulator period. Radiation is produced at 1 nm and amplified to saturation.

SIMULATION RESULTS

We show results for producing radiation at 1 nm. Shorter wavelengths and higher harmonics are in general more challenging. Performance improves dramatically for longer wavelengths, but 1 nm (1.2 keV) has been selected because it is the upper end of the tuning range for soft x-rays at LCLS-II.

For two-stage HGHG, we present results when going from a 260 nm external laser to a 13 nm intermediate wavelength to 1 nm. The final x-ray properties are shown in Fig. 4 for both 100 pC and 300 pC bunches. The output pulse energy at 1 nm is 7 μ J for the 100 pC bunch and 4 μ J for the 300 pC bunch. There are several major differences in the parameter settings for these examples. The 100 pC bunch offers a very short interval in which to perform each stage of harmonic generation, thus the fresh-bunch delay is set to only 25 fs. Even with a short pulse duration, the external laser tends to blow up the energy spread in the second half of the bunch. Therefore, a super-Gaussian distribution is used with power $\propto \exp(-t^4/t_0^4)$ having a fwhm duration of 20 fs. For the 300 pC bunch, the fresh bunch delay can be increased to 100 fs, and the external laser is a regular Gaussian with 40 fs fwhm. Because the 300 pC bunch has larger transverse emittances and suffers from more longitudinal variations than the 100 pC bunch, the peak power must be increased to 900 MW to compensate.

In both examples, short pulses are generated, although the 300 pC case shows significant SASE background occurring in those regions where the energy spread has not been increased. If the beamline were made longer, the total pulse energy would increase but the contrast becomes significantly worse. Figure 5 shows step-by-step profiles of the radiation at different wavelengths in the various stages of the FEL. The importance of slippage and the motivation for using a super-Gaussian external laser can be clearly seen in this example.

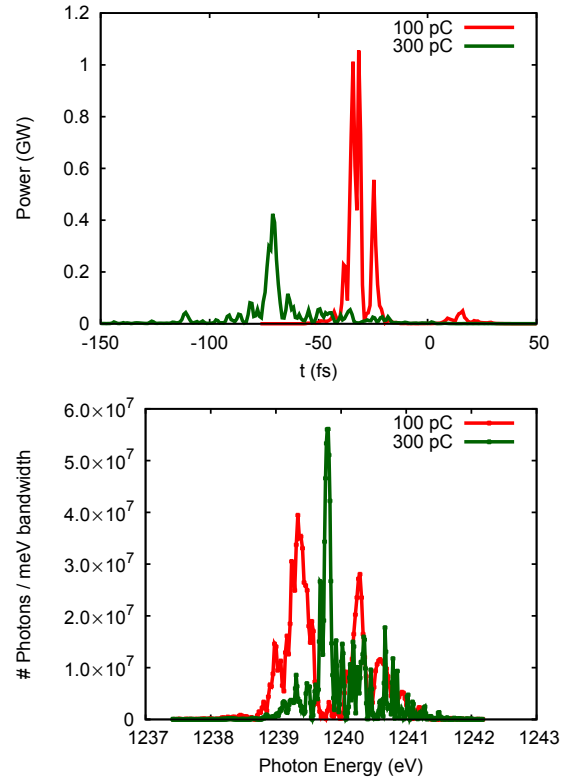


Figure 4: Power and spectral profiles of the final x-ray pulses for HGHG.

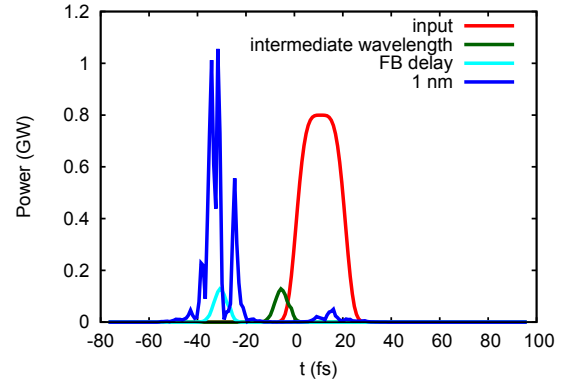


Figure 5: Power profile of the radiation at various stages in the HGHG beamline, for a 100 pC electron bunch.

The spectrum is quite broad in both cases, many times more than the transform limit. This is partially due to SASE background. More importantly, the large harmonic jump makes the beamline highly sensitive to any longitudinal variations in the electron beam. The performance improves greatly at wavelengths 2 nm or longer.

For EEHG going from a 260 nm external laser directly to 1 nm, the final x-ray properties are shown in Fig. 6 for both 100 pC and 300 pC bunches. Here, the configuration was not changed at all except for the external lasers, which have a 100 fs fwhm duration for the 100 pC bunch and a 200 fs fwhm duration for the 300 pC bunch, in order to take

advantage of the longer bunch length. For the 100 pC bunch the output pulse energy at 1 nm is 18 μ J with a 22 fs fwhm duration. The fwhm bandwidth is 0.13 eV, which is about 1.5 times the bandwidth limit. For the 300 pC bunch the output pulse energy at 1 nm is 25 μ J with a 45 fs fwhm duration. The fwhm bandwidth is 0.07 eV, which is also less than a factor of 2 from the transform limit. In both cases, the ratio of the duration of the output pulse to that of the second seed laser is roughly $1.4(\lambda_2/\lambda_X)^{1/3}$.

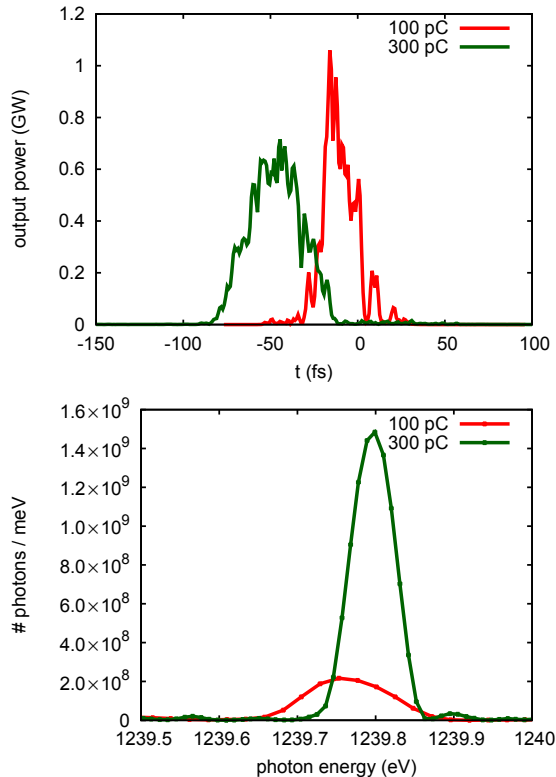


Figure 6: Power and spectral profiles of the final x-ray pulses for EEHG.

CONCLUSION

The main limitation of the HGHG scheme is that the current bunch profile barely has enough length to support a fresh-bunch delay. However, pulses with several fs duration can be produced even for the 100 pC bunch. Longer bunches should allow for longer pulses. Further study is needed to determine what minimum bandwidth can be achieved; at 1 nm it may be only a modest reduction compared to SASE.

The EEHG seeding scheme should produce long pulses with good coherence, assuming that the second seed laser can be tightly controlled. The parameter settings, especially the chicane strengths, must be carefully set but are not depend much on the electron bunch properties. Not only small variations in beam quality but even large changes, such as in the bunch charge, should be able to be accommodated without re-adjustment. However, commissioning may be challenging, especially to reach 1 nm.

ISBN 978-3-95450-133-5

In both the two-stage HGHG and single-stage EEHG schemes, the energy spread is increased to above 2 MeV. The minimum energy spread generated in the seeded portion of the beam grows as the target wavelength is reduced. At the same time, the FEL bandwidth decreases. This increases the required undulator length to reach saturation, and reduces the final peak power. Competition with SASE from unseeded portions of the bunch also becomes a concern.

For the EEHG scheme, 1 nm seems to be approaching the limit for using EEHG. The two-stage HGHG scheme with a fresh bunch delay more sensitive to pre-existing energy chirps and energy modulations than the EEHG scheme. Therefore, for HGHG 1 nm may be at or even past the limit for producing pulses with stable temporal structure shot-to-shot. If stable or narrow spectral structure is required as well, that limit may be closer to 2 nm.

ACKNOWLEDGMENT

This work was supported by the Director, Office of Science, Office of Basic Energy Sciences, of the U.S. Department of Energy under Contract Nos. DE-AC02-05CH11231 and DE-AC02-76SF00515.

REFERENCES

- [1] R. Bonifacio, L. De Salvo, P. Pierini, N. Piovella, and C. Pellegrini. Spectrum, temporal structure, and fluctuations in a high-gain free-electron laser starting from noise. *Phys. Rev. Lett.*, 73:70–73, 1994.
- [2] J. Feldhaus, E.L. Saldin, J.R. Schneider, E.A. Schmeidmiller, and M.V. Yurkov. Possible application of x-ray optical elements for reducing the spectral bandwidth of an x-ray SASE FEL. *Optics Commun.*, 140:341–352, 1997.
- [3] G. Geloni, V. Kocharyan, and E. Saldin. A novel self-seeding scheme for hard x-ray FELs. *Journal of Modern Optics*, 58:1391–1403, 2011.
- [4] G. Marcus et al. FEL simulation and performance studies for LCLS-II. In *These Proceedings: Proc. 36th Int. Free Electron Laser Conf. JACoW, Basel, Switzerland, 2014*. TUP032.
- [5] E. Allaria, R. Appio, L. Badano, W.A. Barletta, S. Bassanese, S.G. Biedron, A. Borgia, E. Busetto, D. Castronovo, P. Cinquegrana, et al. Highly coherent and stable pulses from the fermi seeded free-electron laser in the extreme ultraviolet. *Nature Photonics*, 6:699–704, 2012.
- [6] E. Hemsing, M. Dunning, C. Hast, T.O. Raubenheimer, S. Weathersby, and D. Xiang. Highly coherent vacuum ultraviolet radiation at the 15th harmonic with echo-enabled harmonic generation technique. *Phys. Rev. ST Accel. Beams*, 17:070702, 2014.
- [7] S. Reiche. GENESIS 1.3: a fully 3D time-dependent FEL simulation code. *Nucl. Instr. Meth. A*, 429:243–248, 1999.
- [8] LCLS-II Design Study Group. LCLS-II conceptual design report. Report LCLSII-1.1-DR-0001-R0, SLAC, January 2014.
- [9] G. Stupakov. Using the beam-echo effect for generation of short-wavelength radiation. *Phys. Rev. Lett.*, 102:074801, 2009.

MEASUREMENTS OF THE FEL-BANDWIDTH SCALING WITH HARMONIC NUMBER IN A HGHG FEL *

Enrico Allaria[#], Miltcho B. Danailov, William M. Fawley,
Elettra-Sincrotrone Trieste S.C.p.A., Basovizza, Italy

Luca Giannessi,

Elettra-Sincrotrone Trieste S.C.p.A., Basovizza, Italy and ENEA C.R. Frascati, Frascati (Roma), Italy

Eugenio Ferrari,

Elettra-Sincrotrone Trieste S.C.p.A., Basovizza, Italy and Università degli Studi di Trieste, Trieste, Italy

Abstract

In this work we report recent measurements done at FERMI showing the dependence of the FEL bandwidth with respect to the seed laser harmonic at which the FEL is operated. Comparison of FEL spectra for different Fourier-limit seed and chirp pulses is also reported.

need of the FERMI user to have complete tunability of the FEL or not the seed pulses can be obtained either by using the third harmonic of a Ti:Sapphire laser (THG), or by the use of an Infrared Optical Parametric Amplifier (OPA) with consequent frequency up-conversion to UV. Main parameters for the two possible configurations are reported in Table 1 and Table 2.

THE HGHG FEL AT FERMI

FERMI is the seeded FEL system in operation at Trieste and running for user's experiment that can use high power pulses in the VUV – soft X-ray spectral range characterized by a high degree of coherence [1,2] and also variable polarization [3]. The two FELs, in operation at FERMI, in order to cover the spectral range that goes from 100 nm down to 4 nm are based on the high gain harmonic generation scheme [4]; this uses an external laser in the UV to initiate the coherent emission at his harmonics that is then amplified by the FEL process. Since the external coherent seed imposes an exact phase relation between various electrons participating to the FEL emission, the seeding is crucial for improving the longitudinal coherence. However, it has been pointed out that the method is affected, like other frequency multiplication processes, by the phase noise amplification [5]. As a consequence of the harmonic conversion, a small residual phase noise in the seeding signal could significantly deteriorate the phase of FEL radiation up to the point to destroy the longitudinal coherence.

Recently a series of numerical simulation have been done for a simplified HGHG FEL showing that as a consequence of the nonlinear process of the bunching creation the time-bandwidth product deterioration due to residual chirp in the seed laser is partially mitigated [6].

By measuring the dependency of the FEL bandwidth as a function of the FEL harmonic and of the seed laser residual chirp, we experimentally investigate the phase noise amplification process in a seeded FEL.

The Seed Laser

Since the FEL process is initiated by the seed laser and the properties of the FEL depend on the quality of the laser a lot of effort has been dedicated at FERMI to guarantee a high performance of the seed laser system, a detailed description can be found in [7]. Depending on the

Table 1: Seed Laser Parameters for the THG

Parameter	
Pulse length (FWHM)	120 fs
Bandwidth (FWHM)	~0.8 nm
Central Wavelength	261 nm ± 1 nm
Energy per pulse	10-100 µJ

It should be noted that in the case of THG seeding the available UV pulse energy allows to use a grating compressor and compensate the linear chirp introduced by the rather complex beam-transport. However, in the case of OPA seeding at present the seed pulses cannot be compressed and contain a residual positive chirp.

Table 2: Seed Laser Parameters for the OPA in the Most Frequently Used 230-262 nm Seed Wavelength Range

Parameter	
Pulse length (FWHM)	120-150 fs
Bandwidth (FWHM)	1-1.1 nm
Central Wavelength	230-262 nm
Energy per pulse	7-50 µJ

The Electron Beam

Because electrons are the medium used in the FEL amplification, it is clear that the quality of the electron beam is another crucial parameter. In particular it has been shown how possible modulation in the longitudinal phase space can deteriorate the FEL bandwidth. For this reason the typical electron beam used for normal operations at FERMI has a moderate compression and a lot of effort is done in order to linearize the longitudinal phase space [8] and suppress the microbunching [9].

*Work partially supported by the Italian Ministry of University and Research under grants FIRB-RBAP045JF2 and FIRB-RBAP06AWK3
#enrico.allaria@elettra.eu

The electron beam parameters used during these measurements are reported in Table 3.

Table 3: Electron Beam Parameters

Parameter	
Peak current (A)	~500
Charge (pC)	500
Energy (GeV)	1.2
Energy spread (keV)	150
Emittance (mm mrad)	1
Beam size (mm)	0.15

MEASUREMENTS

For this experiment the FEL has been characterized looking at the spectra that can be acquired with the available diagnostic at FERMI [10]. FEL spectra are measured acquiring the images of the energy dispersed FEL radiation on a YAG. The acquisition done through the FERMI control system allows one to acquire either the full CCD image or only the signal projected along the wavelength axis. In this work, we mainly acquired the simple projections but in few cases the full images have been acquired, like the case showed in Fig. 1.

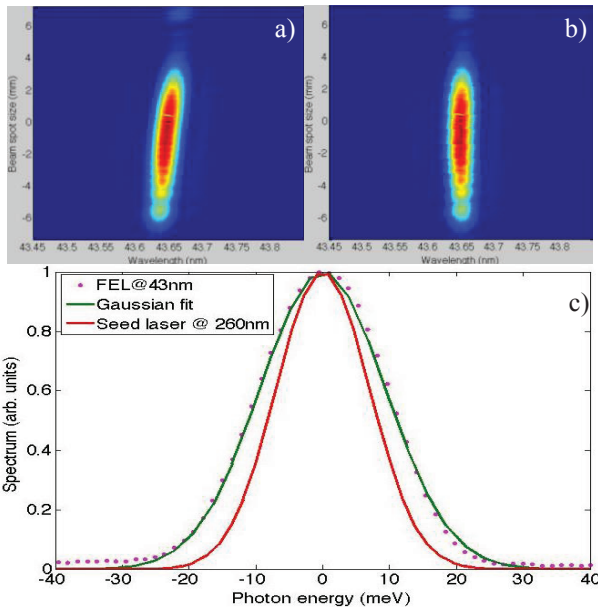


Figure 1: a) direct image of the acquired FEL spectra at 43 nm; b) a numerical correction is applied in order to remove the small residual tilt due to the CCD. c) The projection of the image along the horizontal axis is used to obtain the FEL spectrum to be compared to the seed laser spectrum.

For each studied configuration we acquired long sequences of spectra that has been statistically analysed and whose typical distribution for the FEL bandwidth is

reported in Fig. 2 showing the case of 43 nm obtained with the THG seed laser.

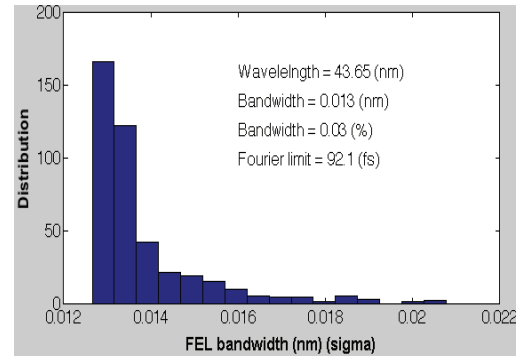


Figure 2: Distribution of the FEL bandwidth at 43 nm.

The data present an asymmetric distribution with a peak toward narrow bandwidth and a long tail to large bandwidths. Such a distribution can be explained taking into account that the timing jitter between the electron beam and the seed laser can occasionally place the seed laser far from the good region where the phase space distortions of the electron beam deteriorate the FEL spectra. This fact is confirmed by looking at the correlation between the FEL spectra and the compression signal that is known to be related to the electron beam arrival time (Figure 3).

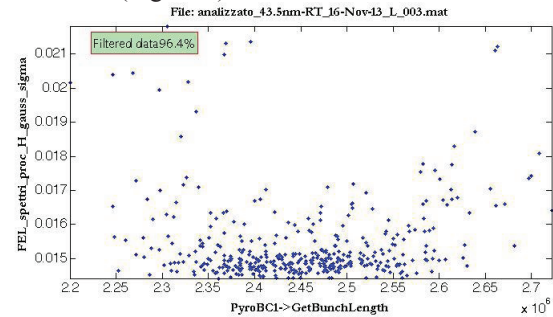


Figure 3: Correlation curve between the FEL spectrum and the electron beam compression signal.

Given that the tail in the distribution is coming from the electron beam properties, in order to characterize the impact of the seed on the FEL spectra and his dependence with the harmonic number we discard those shots characterized by a too large bandwidth.

Using the same seed laser and the same electron beam scan of the FEL wavelength from 23 to 62 has been done changing the FEL harmonic from the 4th to the 11th. For every FEL wavelength in addition to change the undulator resonance, the seeding power and the strength of the dispersive section where slightly optimized.

In figure 4 the evolution of the FEL bandwidth as a function of the FEL harmonic is shown both in absolute and relative scale (Fig. 4-a,b). In order to take into account the small contribution to the bandwidth coming from the CCD tilt, when possible the bandwidth has been measured from the rotated images as in Fig. 1b. When this was not possible we apply a similar correction to the bandwidth obtained from the non-corrected images.

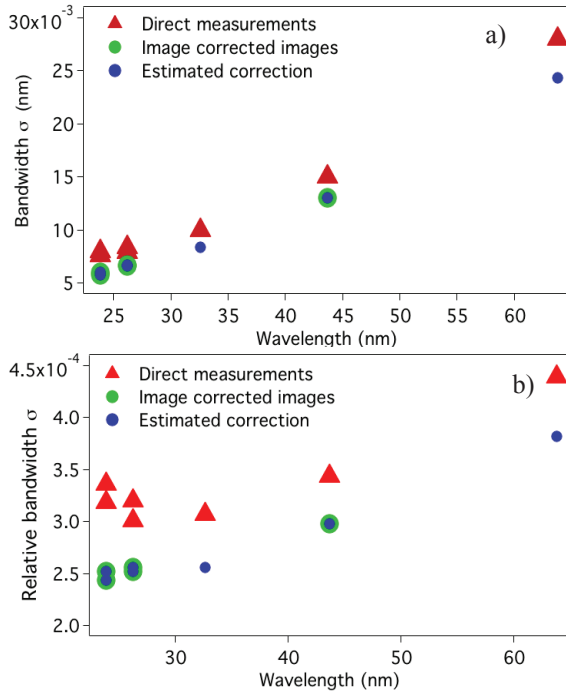


Figure 4: Measured FEL bandwidth for different harmonics in nm (a) and normalized to the FEL wavelength (b).

The FEL Pulse Shortening

Because the measured spectra are well fitted by a Gaussian curve we can estimate the FEL pulse length from the spectrum with the equation:

$$\Delta t_{FWHM} = \frac{0.44}{\Delta \omega_{FWHM}}. \quad (1)$$

This easy calculation for the FEL pulse length makes the strong assumption that FEL pulses are fully coherent and no chirp or phase noise is present. Given the already mentioned phase noise amplification, such a hypothesis is expected to be less valid as we go toward shorter wavelength (higher harmonics). But in any case this approximation allow to calculate the lower limit for the pulse lengths at various harmonics, indeed shorter pulses would necessarily imply a bandwidth larger than the one measured.

Using the data for the FEL bandwidth reported in Figure 4 with Eq. (1) we obtain the expected evolution of the pulse length as a function of the wavelength and harmonic (Figure 5).

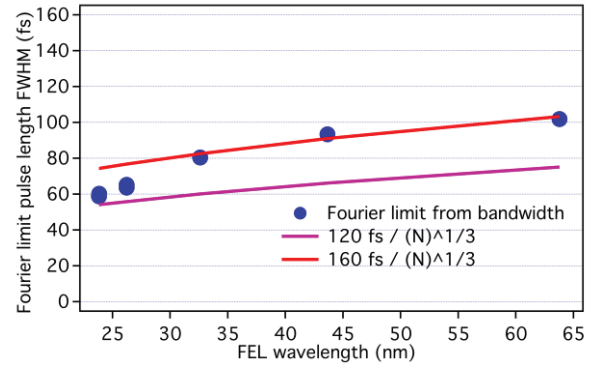


Figure 5: Calculated pulse length from the measured spectral bandwidth (blue dots) and estimated pulse length assuming the scaling law with the harmonic described by Eq. (2) [6].

The calculated pulse length can be compared with the one that can be calculated according to the theory presented in [6] that predict scaling law for the FEL pulse with respect to the harmonic that can be described by:

$$\Delta t^{FEL} = \frac{\Delta t^{seed}}{\sqrt[3]{N_H}}. \quad (2)$$

where, Δt^{seed} , is the pulse length of the seed laser, and N_H is the harmonic at which the FEL is operated.

Equation (2) is used with the nominal seed laser pulse length (120 fs) for the magenta curve in Figure 5, in addition a curve for a seed laser of 160 fs has been also plotted.

Because our measurements set the lower limit for the real FEL pulse length we see that the data can not be fitted with the pulse shortening scaling law predicted in [6] if one consider the seed laser pulse length that has been measured in the laser table (taking into account the effects for all the optics driving the laser into the FEL). Experimental measurements and theoretical prediction would better fit if one considers a seed laser 160 fs long (red curve in Figure 5). In this case there is a good agreement for the longer wavelengths (lower harmonics) where we expect the bandwidth degradation due to the phase noise multiplication to be limited. A virtual shortening (due to a bandwidth enlargement) of the points at shorter wavelengths could be the results of a reduced longitudinal coherence and an increase of the phase noise for this high harmonic cases.

FEL Bandwidth Degradation due to Seed Pulse Residual Phase Curvature

A second experiment has been done by changing the seeding properties while keeping other parameters (FEL wavelength, harmonic, electron beam) constant. We note that when OPA is used for seeding, the pulses arriving in the undulator have a non-negligible residual phase curvature (both linear and higher order terms). The non-flat phase comes from the OPA scheme (which involves chirped white light continuum for the OPA seeding), the frequency up-conversion to UV where GVM effects are

non-negligible, and from the beam transport optics containing a number of reflections on broadband UV multilayer mirrors as well as propagation in about 12 mm of fused silica. In the case of THG seeding, the linear chirp (i.e. second order phase) caused by the beam transport can be pre-compensated by the use of a dedicated UV grating compressor.

To understand the influence of this difference on the generated FEL light quality we compare the FEL spectra at 23 nm (11th harmonic) generated first with seeding in THG mode and then in OPA mode where both were set at about the same wavelength (262 nm) and had bandwidths of 0.8 and 1 nm, respectively. As it can be seen from the cross-correlation traces shown on Fig. 6, the OPA pulse is longer and has nearly two times higher time-bandwidth product due to an estimated uncompensated GDD of about $2.5 \times 10^3 \text{ fs}^2$.

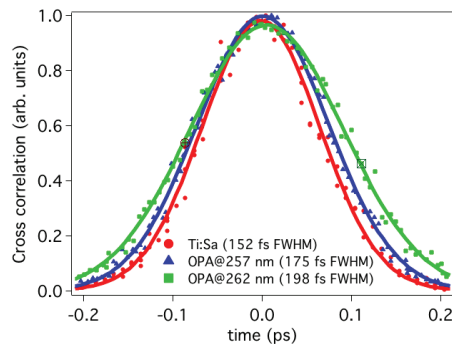


Figure 6: Cross correlation curves of the seed laser in the THG and OPA configurations.

The effect of the seed laser chirp has been measured looking at relatively short wavelengths (high harmonics) where the effect is expected to be stronger.

Figure 7 shows a comparison between what is measured using the THG seed laser and the OPA at 262 nm.

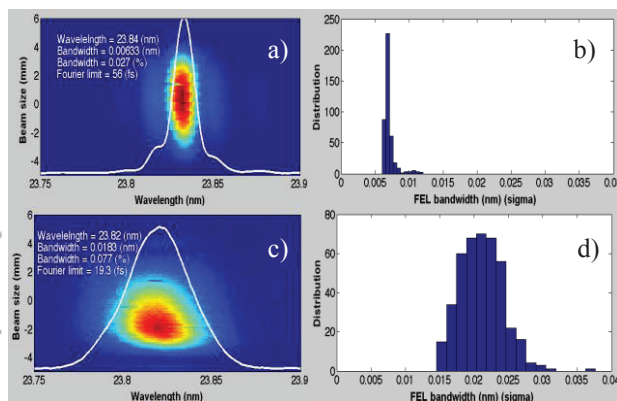


Figure 7: FEL spectrum and his distribution for the FEL at 23 nm using the THG (a,b) and the OPA (c,d) as a seed.

Our results show that when operating at relatively high harmonics ($N_H = 11$) a small change in the seed laser coherence properties has a strong impact in the FEL pulse length and bandwidth as expected from the phase noise frequency multiplications.

CONCLUSION

In the reported measurements we have shown the bandwidth properties of the FEL in seeded HGHG configuration both as a function of the FEL harmonic and of the seed laser quality. The influence of the seed laser pulse phase distortions on the FEL spectrum quality is significant at high harmonic and may spoil the seeding benefits at very short wavelength. It is therefore planned to dedicate an additional effort (e.g. by implementing an adaptive seed pulse shaping) for providing a better control on the UV pulse quality in both THG and OPA mode. Moreover further FEL studies combining spectral properties to FEL pulse length would give more information about the effective pulse shortening and bandwidth degradation occurring in the harmonic generation.

ACKNOWLEDGMENT

We are pleased to acknowledge the extensive assistance we have received from the FERMI commissioning and the laser teams during the operation of the FEL during the dedicated measurements.

REFERENCES

- [1] E. Allaria *et al.*, Nat. Photon. **6**, 699 (2012).
- [2] E. Allaria *et al.*, Nat. Photon. **7**, 913 (2013).
- [3] E. Allaria *et al.*, submit.
- [4] L.H. Yu, Phys. Rev. A **44**, 5178–5193 (1991).
- [5] E.L. Saldin *et al.*, Opt. Commun. **281**, 1179–1188 (2008).
- [6] D. Ratner *et al.*, Phys. Rev. ST Accel. Beams **15**, 030702 (2012).
- [7] M.B. Danailov *et al.*, Proceedings of FEL conference 2011, TUOC4, Shanghai (China) 2011.
- [8] G. Penco *et al.*, FEL conference 2013, TUOCNO01, New York (USA) 2013.
- [9] S. Spampinati *et al.* in preparation.
- [10] M. Zangrando *et al.*, Rev. Sci. Instrum. **80**, 113110 (2009).

MEASUREMENTS OF FEL POLARIZATION AT FERMI

Enrico Allaria, Elettra-Sincrotrone Trieste S.C.p.A., Basovizza, Italy

Abstract

We report detailed quantitative characterization of different polarization states of a single-pass, externally-seeded FEL operating with variable polarization undulators in the VUV spectral range. The experiment has been performed at FERMI FEL-1 operated in the 52–26 nm wavelength range. Three different, independent polarimeter setups, installed at the end of experimental beamlines, have been used to characterize the four “pure” polarization states: horizontal, vertical, right-circular and left-circular. The impact of downstream transport optics upon the radiation polarization has been assessed; at longer wavelengths, dichroism effects lead to a non-negligible ellipticity for an originally circularly polarized state. The results from the different polarimeter setups validate each other and allow a cross-calibration of the instruments.

INTRODUCTION

FERMI user facility relies on two different seeded FELs to cover the spectral range from 100 nm down to 4 nm using a common linear accelerator. The first FEL, namely FEL-1, has been designed for the long wavelength spectral range (100 – 20 nm) and is in operation since late 2010 [1]. The second FEL, FEL-2, is based on a double high gain harmonic generation scheme to cover the spectral range from 20 down to 4 nm [2] and user dedicated experiments will start in 2015 [3]. In order to allow the FERMI users to control the radiation polarization, FERMI uses APPLE-II type undulators [4] for the FELs. Because FERMI is the first FEL user facility in the soft-x ray spectral range allowing polarization control through the use of variable polarization undulators it is important the characterization of the degree of polarization produced.

In order to allow a detailed characterization of the degree of polarization, a collaboration has been setup between the FERMI team and other laboratories to perform dedicated experiments. In the framework of this collaboration three different polarimeters have been installed at FERMI and used during one week of dedicated beamtime. The “FERMI polarization measurements” collaboration involved in addition to the FERMI commissioning team; a team from LOA and collaborators responsible for the VUV optical polarimeter [5]; a team from DESY-XFEL and collaborators responsible for the e-TOF polarimeter [6]. In addition to the to aforementioned polarimeters a third polarimeter based on polarized fluorescence has been setup by the LDM team at FERMI and collaborators [7].

In this work we briefly report about the measurement setup. For a discussion about the results of the polarization measurements we refer to the dedicated paper recently published [8].

THE LOA POLARIMETER

The LOA polarimeter is an all-optical device based on the principle described by Schäfers et al. in [9]. The system uses a polarizer followed by an analyser. The polarizer relies on the fact that, at each reflection onto optics, the s and p components of the electric field are characterised by a different delay and a different reflectivity. Both the polarizer and the analyser can be rotated independently around the propagation axis of the input light. A polarization measurement is done by scanning one of the two angles and measuring the detected signal on the analyser.

THE E-TOF POLARIMETER

The e-TOF polarimeter uses angle resolved electron spectroscopy in order to measure the degree of linear polarization of the FEL radiation. It is based on 16 independent electron time-of-flight (e-TOF) spectrometers mounted in a plane perpendicular to the FEL beam. This configuration allows one to accurately determine the angular distribution of the photoelectrons emitted by the ionizing radiation.

THE FLUORESCENCE POLARIMETER

Polarization measurements with the fluorescence polarimeter have been carried out taking advantage of the intrinsic polarization properties of fluorescence light from resonantly excited atoms. This scheme uses the conversion of polarized VUV radiation into longer wavelength radiation that has the same polarization parameters. The scheme has the advantage to allow a polarization measurement in the visible where suitable optics are easily available and has been previously used in an experiment on synchrotron radiation [10].

CONCLUSION

A dedicated experiment has been organized at FERMI for the detailed characterization of the produced radiation. The experiment involved different groups from LOA, DESY, XFEL and SLAC. Results, recently published [8] have shown the FERMI capability of producing high degree and variable polarization.

ACKNOWLEDGMENT

The Author is thankful to all the people involved in the experiment for their effort in allowing the success of the measurement campaign. Author is also indebt with the FERMI team and management for supporting the experiment.

REFERENCES

- [1] E. Allaria *et al.*, “*Highly coherent and stable pulses from the FERMI seeded free-electron laser in the extreme ultraviolet*”, *Nat. Photonics* **6**, 699 (2012).
- [2] E. Allaria *et al.*, “*Two-stage seeded soft-x-ray free-electron laser*”, *Nat. Photonics* **7**, 913 (2013).
- [3] M. Svandrlik *et al.*, “*FERMI Status Report*”, *Proceeding of the 36th International Free Electron Laser Conference FEL 2014*, **TUP085**, Basel, Switzerland (2014).
- [4] S. Sasaki, “*Analyses for a planar variably- polarizing undulator*”, *Nucl. Instrum. Meth. Phys. Res. A* **347**, 83 (1994).
- [5] B. Vodungbo, A. Barszczak Sardinha, J. Gautier, G. Lambert, C. Valentin, M. Lozano, G. Iaquaniello, F. Delmotte, S. Sebban, J. Luning, *et al.*, “*Polarization control of high order harmonics in the EUV photon energy range*”, *Opt. Expr.* **19**, 4346 (2011).
- [6] J. Viefhaus, F. Scholz, S. Deinert, L. Glaser, M. Ilchen, J. Seltmann, P. Walter, and F. Siewert, “*The variable polarization XUV beamline p04 at PETRA III: Optics, mechanics and their performance*”, *Nucl. Instrum. Meth. Phys. Res. A* **710**, 151 (2013).
- [7] P. Finetti *et al.*, in preparation.
- [8] E. Allaria *et al.*, “*Control of the polarization of a vacuum-ultraviolet, high-gain, free-electron laser*”, to be published in *Phys. Rev. X* (2014).
- [9] F. Schafers *et al.*, “*Soft-x-ray polarimeter with multi-layer optics: Complete analysis of the polarization state of light*”, *Appl. Opt.* **38**, 4074 (1999).
- [10] C.J Latimer, M.A MacDonald, and P Finetti, “*A new method for polarization analysis in the VUV*” *J. Electron Spectrosc. Relat. Phenom.* **101-103**, 875–878 (1999).

GENERATION OF MULTIPLE COHERENT PULSES IN A SUPERRADIANT FREE-ELECTRON LASER

X. Yang, S. Seleskiy

National Synchrotron Light Source, Brookhaven National Laboratory, Upton, NY 11973, USA
L. Giannessi, Elettra-Sincrotrone, Trieste, S.C.p.A., Basovizza, and ENEA C.R. Frascati, Italy

Abstract

We analyze the structure of the tail of a superradiant pulse, which is constituted by a train of trailing-pulses with decaying amplitudes. We show how a trailing pulse, with phase advance from the leading pulse, is generated at the falling edge of the leading pulse, where the corresponding phase space is deeply saturated and the electrons become de-trapped by the reduced ponderomotive potential. Once the trailing pulse gains enough energy, it generates a second trailing pulse, and the process takes place again. By performing detailed simulations of the resulting electron phase space distribution and the FEL pulse spectral and temporal structure with PERSEO, we confirm that the deformation and re-bunching of the longitudinal phase space create a sequence of pulses.

INTRODUCTION

The free-electron laser (FEL) is a tunable source of coherent radiation, ranging from terahertz (THz) waves to hard X-rays, with the capability for femtosecond time resolution. Progress was made recently in single-pass FELs in moving toward the X-ray region of the spectrum, such as the self-amplified spontaneous emission (SASE) FEL that successfully lased from soft X-rays down to 1.5Å [1,2], and the high-gain harmonic generation (HG) FEL [3] pioneered at Brookhaven [4] and now implemented in a facility at Elettra-Sincrotrone Trieste, where FERMI [5,6] provides radiation for user experiments in the VUV and soft X-ray wavelength range. One of the main advantages of the HG and laser-seeded FEL over the SASE FEL is that they produce not only transversely, but also temporally coherent pulses. In contrast, SASE radiation starts from the initial shot-noise of the electron beam, so that the resulting radiation exhibits excellent spatial-, but a rather poor temporal-coherence.

In this report, we present numerical evidence for a slippage-dominant superradiance FEL interaction regime, wherein the emitted main FEL pulse is followed by multiple trailing pulses, which we dubbed a “trailing-pulse regime”. This dynamic behavior is guaranteed in the circumstance of an ultra-short seed pulse with the power beyond saturation [7,8]; it may be important for the existing and next-generation short-wavelength-seeded FELs, such as the FERMI, and the LCLS-II [9]. A deep understanding and controlling of these regimes are essential for optimizing the power as well as the quality of FEL sources, features demanded by the user communities. Using the Perseo simulation [10], we investigated the

behaviors of the seeded FEL, and obtained new insights on the trailing pulse generation that we interpreted in terms of the fragmentation of the most significantly bunched electrons by the main radiation pulse in the longitudinal phase (LPS) into new buckets, which are responsible for the trailing pulses. Here, the term “bucket” denotes the electric field of a radiation pulse that assures longitudinal focusing, thereby constraining the electron’s motion to a stable region in LPS.

The mechanism of FEL amplification commonly is analyzed in three steps: energy modulation, exponential growth, and saturation. In the first step, energy is exchanged between the electrons and the radiation, leading to an energy modulation, and further, to a density modulation (microbunching) of the electrons at the resonant wavelength $\lambda_r = \lambda_w(1+K^2/2) / (2\gamma_r^2)$, determined by the electron beam’s energy $E_r = mc^2\gamma_r$. $K = eB_w/mck_w$ is the dimensionless undulator parameter, and λ_w , k_w , and B_w are, respectively, the undulator’s wavelength, wave number, and magnetic field [11]. Initiating the FEL process with a coherent seed allows to lock in the phase of the microbunches and to achieve an improved temporal coherence. Afterwards, the FEL enters the second evolutionary step: radiation power increases exponentially to the detriment of the electron beam’s kinetic energy. The strong energy losses, corresponding to a redshift of λ_r , thereafter disable the electron-radiation field’s interaction. In the so called steady state regime, the FEL power reaches a maximum and saturates. However, where pulse propagation effects are considered, the radiation pulse is simultaneously dominated by saturation and slippage [12], and its evolution is characterized by the propagation of a solitary wave with the peak power growing quadratically with time and the pulse length decreasing [12,13,14]. In this regime the main pulse propagates at the velocity of light over the electron current leaving highly bunched electrons after its passage. These electrons in the trailing edge coherently radiate into a new trailing pulse. Here, the trailing-pulse regime can be extended over the entire slippage distance along the electron bunch (Fig. 1). Numerical studies reveal that LPS fragmentation and the formation of new buckets are core ingredients of the trailing-pulse dynamics. In these circumstances, an ultra-short seed-pulse induces microbunching when it slips over the electrons at $v_g \sim c$ [14,15]. Microbunching induces coherent emission of the electrons, forming the main radiation pulse and leaving behind those highly bunched electrons with large energy spread. Due to the energy transfer from electrons to the main radiation pulse, the low-energy part ($p < 0$) carries the larger part of charge ($\geq 70\%$, obtained by counting the

number of macro-particles in the low-energy part vs. the total number of particles distributed within $(-\pi, \pi)$, and accordingly, a larger bunching coefficient than the high-energy part. It therefore, emits coherent light with a redshift λ_r to become a new trailing pulse. Here, $p = (E - E_0) / \rho \cdot E_0$ is the energy variation with respect to the reference particle E_0 , and ρ is the FEL Pierce parameter [16] characterizing the gain of the FEL. This process occurs again in the trailing edge of this second pulse, but with a smaller fraction of trapped charge, due to the increasing energy spread caused by the interaction with the previous pulses (a fraction $\leq 50\%$, similarly obtained by counting the particles). Additional trailing pulses are generated.

In this paper we numerically explore the generation and suppression of multiple trailing superradiance pulses in a single-pass FEL amplifiers. We analyze FEL evolution from the viewpoint of electron longitudinal phase-space, showing the relation between the synchrotron oscillation and the structure of the radiation pulse. We support our analysis via simulations obtained with the well-known and established simulation code Perseo [10], employing it to resolve the one-dimensional (1D) FEL model, including the high-order harmonics described by the one-dimension Colson model [11]:

$$\frac{\partial \phi_j}{\partial z} = p_j, \quad 1(a)$$

$$\frac{\partial p_j}{\partial z} = -[A(\bar{z}, \tau) e^{i\phi_j} + c.c.], \quad 1(b)$$

$$\left(\frac{\partial}{\partial z} + \frac{\partial}{\partial \tau} \right) A(\bar{z}, \tau) = \chi(\tau) b(\bar{z}, \tau). \quad 1(c)$$

Each particle $j, j=1 \dots N_e$ wherein N_e , the total number of electrons in the optical field A , is followed in the phase space using ϕ_j , the particle's relative phase, and p_j , the particle's relative energy, both normalized to the reference particle. The variables ϕ_j, p_j , and A are functions of the longitudinal coordinates τ along the electron bunch, and \bar{z} along the undulator. τ is defined within $0 < \tau < L_e$, with L_e the electron bunch's length, and \bar{z} is defined within $0 < \bar{z} < L_w$, with L_w the undulator length. All dimensions are in cooperation length [12,17] units: $l_c = \lambda/4\pi\rho$. χ is the macroscopic electronic-density normalized to 1, and $b(\bar{z}, \tau)$ is the bunching coefficient: $b(\bar{z}, \tau) = (1/N) \sum e^{i\phi_j}$. Eq 1(a) and 1(b) describe the particle's dynamics, while Eq. 1(c) includes the pulse's propagation.

SIMULATION

The initial condition for the slippage-dominant superradiance regime is defined more precisely in scaled units using $S_{seed} (=4\pi\rho N_w/L_{seed})$, the ratio of the slippage length to the duration of the seed pulse, $S_e (=4\pi\rho N_w/L_e)$, the ratio of the slippage length to the electron-bunch's length [18], and $F_{seed} (= \Delta f_{FWHM}/f_0 \cdot \rho)$, the ratio of the seed's spectral bandwidth and the FEL-gain's bandwidth. Within the limit of the short-seed pulse, ($S_e \ll 1$) is

chosen to have a nearly constant electron current in the simulation window, while ($S_{seed} \gg 1$) and ($F_{seed} \gg 1$) satisfy the slippage-dominant superradiance condition, where the bandwidth of the seed laser is much larger than that of the FEL gain. Therefore when the seed pulse slips over the electron bunch at $v_g \sim c$, it only microbunches the electrons [13].

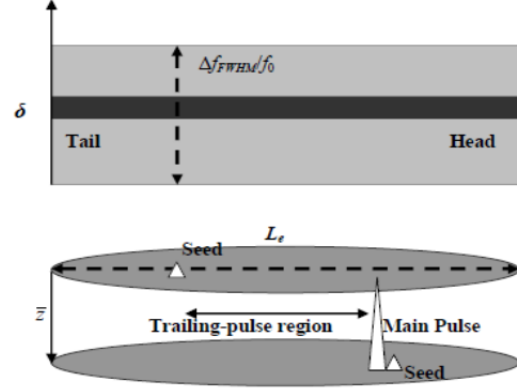


Figure 1: Schematic of the seeded-FEL's initial parameters. \bar{z} is the longitudinal coordinate along the undulator. L_e and $\delta = (E - E_r) / \rho \cdot E_r$ are, respectively, the electron bunch's length and energy detuning. Here, $E_r = E_0$. Δf_{FWHM} is bandwidth of the seed laser.

Eq. 1 is used to simulate the evolution of the FEL in the regime of a long electron bunch and slippage-dominant superradiance, i.e., $S_e \ll 1$, $S_{seed} \gg 1$, and $F_{seed} \gg 1$. Figure 2 illustrates the dynamics of the FEL pulse via 2D diagrams with the longitudinal coordinate along the electron bunch, τ , is plotted in the horizontal axis and the coordinate along the undulator \bar{z} in the vertical axis.

Figure 2(a) depicts the evolution of the FEL into the superradiance regime [15,19,20]. The seed pulse provides microbunching to the electrons when it slips over them at $v_g \sim c$, and maintains its pulse shape in the undulator. Microbunching emits coherent light that grows exponentially to become the main pulse. At the end of exponential growth and in the beginning of superradiance ($\bar{z} \approx 2.6$ in the undulator), the main pulse slips as in the exponential regime ahead of the electron bunch at $v_g \sim c$ instead of at $\sim 3c/(1+2\beta_z^{-1})$ [21], whilst the length of the pulse decreases and the amplitude increases quadratically with the distance in the undulator. Simultaneously, it induces strong microbunching of the electrons. At a given delay in time, the 1st trailing pulse appears weaker in amplitude compared to the main pulse, similar to the case for the 2nd trailing pulse.

To investigate the origin of multiple trailing pulses, we studied the evolution of the particle's relative longitudinal position (phase). A new trailing pulse appears at the π phase shift with respect to the radiation pulse ahead of it. For FELs, the gain medium consists of relativistic electrons, whilst how well the phase of the microbunches is locked and sheared along the undulator determines the optical field's temporal profile. The phase shift is caused by the energy modulation and FEL's intrinsic dispersion.

The original reference particle, corresponding to the original bucket center, and also being the reference for the simulation, is fixed in LPS due to the zero energy offset $\delta_0 (= (E_0 - E_r) / \rho \cdot E_r) = 0$. Here, the bucket center refers to the stable fixed point in the LPS [22]. However, this is not the case for the new reference particle, corresponding to the new bucket center. Rather, it is fixed inside the new bucket but not in the LPS because it has a negative energy-offset ($\delta < 0$) with respect to the original reference particle. It drifts toward the direction of the main pulse's tail. Whenever it varies the phase $\Delta\phi$ across an integer of π , a new trailing pulse appears. $\Delta\phi_n \approx n \cdot \pi$, $n = 1, 2, \dots$, corresponds, respectively, to the 1st, 2nd, ..., trailing pulse. As confirmation, Figure 2(b) presents the LPS of the electrons at the newly formed buckets corresponding to the 1st and 2nd trailing pulses at the undulator distance, $\bar{z} = 12.8$; their phase-changes relative to reference particle are equivalent to $\sim\pi$ and 2π , as indicated by the black dashed lines; this confirms that the π -phase relationship is coincident with the formation of a new trailing pulse. The dephasing of the bunched electrons with the field of the main pulse, causes first the drop of the field amplitude at the trailing edge of the pulse, and then a change of sign of the field which grows with the new phase, shifted of π . The time separation, Δt_n , between the n^{th} trailing pulse and the main pulse is estimated using Eq. 2, derived straightforwardly from Eq. 1(a).

$$\Delta t_n = n \cdot \lambda_r / 2 \cdot \delta_n \cdot c \quad (2)$$

As an example (Fig. 2(c)), the FEL Pierce parameter $\rho = 0.004$ and $\lambda_r = 800\text{nm}$, for $n = 1$, $\delta_1 \approx 5.0$ (Fig. 2(b)), the Δt_1 calculated using Eq. 2 is $\sim 65\text{fs}$, which is consistent with the result $\sim 66\text{fs}$ obtained from the simulation.

Further understanding of the physical mechanism behind the trailing-pulse regime also is gained by analyzing the electron's LPS at different positions along the radiation pulse. At the undulator position $\bar{z} = 12.8$, we obtained the LPS of the electron beam (top), and the overlapping radiation pulse (bottom), as shown in Fig. 2(c). At position A, we show the LPS of the electrons that the seed pulse reaches and they only have the energy modulation. At position B, the effect of the interaction with the optical pulse is evident, such that a strong modulation in energy and density has occurred. On average, the electrons lose energy that is absorbed by the main radiation pulse. At position C, corresponding to the peak of the main pulse, the electrons have reached the bottom of the bucket in phase space, and begin to gain energy from the laser field of the main pulse. Therefore, the power of the laser starts to drop and reaches a minimum at position D, where the corresponding phase space appears deeply saturated and the electrons start to become detrapped by the reduced ponderomotive potential. The strong optical field of the main pulse maximizes microbunching, and also causes a $\sim 5\%$ ($\rho = 0.004$) spread in the beam's energy. At position E, the electrons are detrapped from the bottom energy after the

passage of the main pulse, and are free to start a new process of FEL amplification. Those electrons close to the energy bottom form a new bucket in the series (black dashed circle) that is responsible for generating the new pulse. In addition to the drift in phase brought about by the energy spread and intrinsic dispersion, the majority of the electrons in new buckets arriving at the energy bottom after losing energy to the new pulse generate the peak of the new pulse (see position F). Similar to the main pulse, the electrons already at the bottom of the bucket start to gain energy from the optical field of the new pulse. The energy of the new pulse starts to fall, and reaches a minimum at position G.

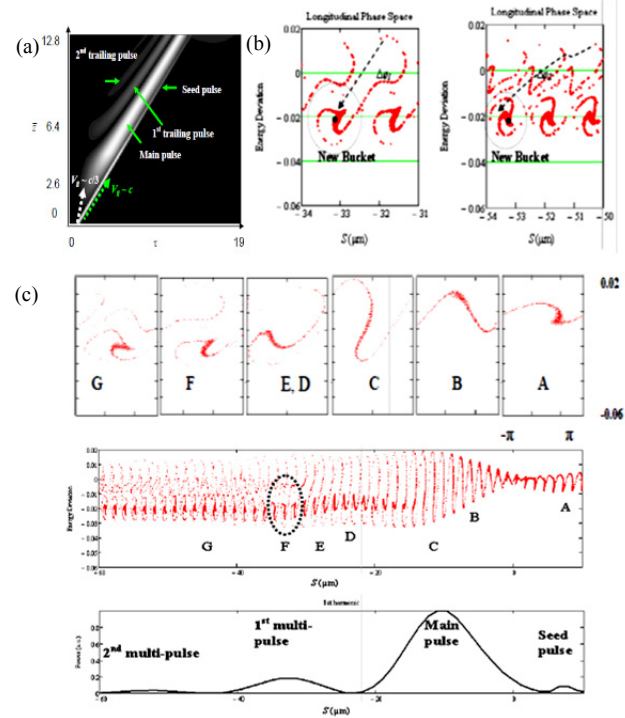


Figure 2: (a) Normalized longitudinal profile of the radiation power along the electron's coordinate, τ , as it evolves along the undulator with coordinate \bar{z} . Seed parameters: $S_{\text{seed}} = 21$ (with Gaussian shape, $\sigma_{\text{seed}} = 0.26$), and $F_{\text{seed}} = 25$ ($A_{\text{FWHM}}/f_0 = 0.1$, $\rho = 0.004$). Maximum seed field amplitude at $\bar{z} = 0$: $A_0 = 20$. Initially: θ_j uniformly distributed within $[-\pi, \pi]$ and p_j following a normal distribution center around zero with standard deviation 0.01%-RMS. $L_e = 88$, corresponding to $S_e = 0.06$. (b) At $\bar{z} = 12.8$ in the undulator, the LPS of the electrons at the positions where the peaks of the 1st (left) and 2nd (right) trailing pulses are. $\Delta\phi_1 \approx \pi$, and $\Delta\phi_2 \approx 2\pi$. (c) At $\bar{z} = 12.8$ in the undulator, the LPS of the electron bunch (top), and the temporal profile of the radiation field along the electron coordinate (bottom). Separation between the main and 1st trailing pulses is $\sim 65\text{fs}$, and between 1st and 2nd pulses it is $\sim 70\text{fs}$. The dashed oval signifies the buckets responsible for generating the 1st trailing pulse. In (b) and (c), energy deviation is calculated using the formula $(E - E_0)/E_0$, and the horizontal axis is the longitudinal position S in units of μm .

Overmodulation is the signature of local saturation; the bunch slices initially under the peak of the main pulse, modulated via the highest optical field, reach saturation in the undulator, and afterwards are detrapped due to the decrease in intensity at the main pulse's tail edge. Electrons, detrapped from original bucket, shearing in z , and retrapped to new bucket, are responsible for generating the new pulse. Since the electrons carry on their rotation in LPS within the optical pulse's electric field, the process is repeated: Additional pulses still are generated. The radiation power of the trailing pulses continuously degrades to weaker levels, $P_n \approx a \cdot P_{n-1}$ ($a \leq 0.25$), only a fraction of the low-energy portion of the electrons ($\leq 50\%$) participates in the generation of the new pulse, as shown in Figs. 2(a) - (c). The output power is proportional to the square of the beam's current ($P \sim I^2$) in the superradiance regime. Here, P_n is the FEL power integrated over the n^{th} pulse, and I is the electron-beam's current that contributes to the FEL output.

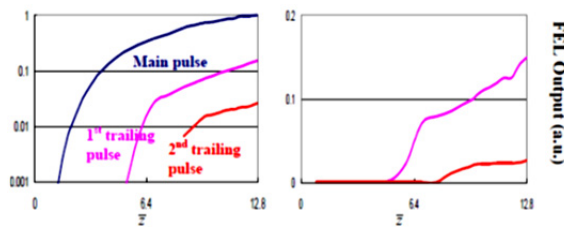


Figure 3: (a) (left) (color online) Evolution of the intensity of the FEL pulse along the undulator calculated using Eq. 1. Intensity integrated over the main pulse (blue), 1st trailing pulse (magenta), and 2nd trailing pulse (red). (b) (right) (color online) Evolution of the FEL pulse intensity normalized by the main pulse along the undulator. 1st trailing pulse (magenta) and 2nd trailing pulse (red).

Figure 3(a) illustrates the evolution of the FEL power (integrated over the radiation pulse) along the undulator for three individual pulses, the main pulse (blue), the 1st trailing pulse (magenta), and the 2nd trailing pulse (red). It confirms that for each radiation pulse, the FEL power first increases exponentially and does not saturate: Its amplification proceeds, power increases as \bar{z}^2 [12,14,19,20]. The slippage propels the main pulse forward into the “fresh” electron region that maintains the feeding of the pulse. However, a similar slippage only pushes a trailing pulse forward into the region where the electrons already have lost energy to the radiation pulses ahead of it. Therefore, the output power of each trailing pulse is weaker than that of the pulse ahead of it. Figure 3(b) shows the evolution of the FEL power along the undulator for the 1st and 2nd trailing pulses, normalized by the main pulse. A strong optical field enhances microbunching; therefore, as the intensity of the main pulse rises, that of the 1st pulse increases faster. The undulator \bar{z} position where the FEL process being terminated can be used as a control parameter to choose between moderately higher radiation output (larger \bar{z}

(>5.12) is better) or suppression of the trailing pulses after the main pulse ($\bar{z} \leq 5.12$).

In conclusion, depending on the initial conditions (the parameters of the electron beam, the undulator, and the seed laser), a short-pulse-seeded FEL can be driven into various regimes with different temporal- and intensity-behaviors. We addressed a new regime for the deeply saturated slippage-dominant FELs, wherein the multiple trailing superradiance pulses following the main pulse can be either enhanced or suppressed. We showed that trailing pulse generation results from the fragmentation of the LPS into new buckets. Furthermore, we numerically and analytically demonstrated that the formation of a new pulse is closely related to the π phase-change ($\Delta\phi_n \approx n \cdot \pi$, $n = 1, 2, \dots$) between the original bucket center and the newly developed bucket center. Therefore, the separation Δt between two adjacent pulses can be controlled via the Pierce parameter and (or) the parameters of the seed laser since they both can alter the energy spread of the electron beam. While trailing pulses enhance FEL power by a small amount (<10%), such a phenomenon might spoil the temporal profile of the radiation. We can avoid trailing pulses by modifying the parameters of the electron beam and undulator. We will compare these results with 3D simulations using the FEL code GENESIS 1.3 in the future.

We gratefully acknowledge useful discussions with S. Hulbert, B. Podobedov, and A. Woodhead. We are thankful for support from the NSLS. This work is supported in part by U. S. Department of Energy (DOE) under contract No. DE-AC02-98CH1-886.

REFERENCES

- [1] P. Emma (LCLS team), *Nature Photonics* **4**, 641 (2010).
- [2] W. Ackermann *et al.*, *Nat. Photon.* **1**, 336 (2007).
- [3] L. H. Yu, *Phys. Rev. A* **44**, 5178 (1991).
- [4] L. H. Yu *et al.*, *Science* **289**, 932-934 (2000).
- [5] E. Allaria *et al.*, *Nat. Photonics* **6**, 699 (2012).
- [6] E. Allaria *et al.*, *Nat. Photonics* **7**, 913 (2013).
- [7] L. Giannessi *et al.*, *Phys. Rev. Lett.* **108**, 164801 (2012).
- [8] L. Giannessi *et al.*, *Phys. Rev. Lett.* **110**, 044801 (2013).
- [9] P. Emma (LCLS team), *Nat. Photon.* **4**, 641 (2010).
- [10] L. Giannessi, *Proceedings of FEL 2006*, (BESSY, Berlin, Germany, 2006), p. 91.
- [11] W. B. Colson, *IEEE J. Quantum Electron.* **17**, 1417 (1981).
- [12] R. Bonifacio *et al.*, *Phys. Rev. A* **44**, 3441 (1991).
- [13] R. Bonifacio *et al.*, *Nucl. Instrum. Methods Phys. Res. A* **296**, 358 (1990).
- [14] L. Giannessi *et al.*, *J. Appl. Phys.* **98**, 043110 (2005).
- [15] X. Yang *et al.*, *Phys. Rev. E* **85**, 026404 (2012).
- [16] R. Bonifacio *et al.*, *Opt. Commun.* **50**, 373 (1984).
- [17] W. B. Colson, *Phys. Lett. A* **59**, 187 (1976).
- [18] M. Labat *et al.*, *Phys. Rev. Lett.* **103**, 264801 (2009).
- [19] D. A. Jaroszynski *et al.*, *Phys. Rev. Lett.* **78**, 1699 (1997).

- [20] T. Watanabe *et al.*, Phys. Rev. Lett. 98, 034802(2007).
- [21] R. Bonifacio *et al.* Rivista del Nuovo cimento 13, 1 (1990).
- [22] S. Y. Lee, Accelerator Physics, World Scientific Publishing Co. Pte. Ltd. (1999).

PERSPECTIVES FOR IMAGING SINGLE PROTEIN MOLECULES WITH THE PRESENT DESIGN OF THE EUROPEAN XFEL

Svitozar Serkez, Vitali Kocharyan, Evgeni Saldin, Igor Zagorodnov
Deutsches Elektronen-Synchrotron (DESY), Hamburg, Germany

Gianluca Geloni

European XFEL GmbH, Hamburg, Germany

Oleksandr Yefanov

Center for Free-Electron Laser Science, Hamburg, Germany

Abstract

European XFEL aims to support imaging and structure determination of biological specimens between less than 0.1 microns and 1 micron size with working photon energies between 3 keV and 16 keV. This wide operation range is a cause for challenges to the focusing optics. A long propagation distance of about 900 m between x-ray source and sample leads to a large lateral photon beam size at the optics. Due to the large divergence of nominal X-ray pulses with durations shorter than 10 fs, one suffers diffraction from mirror apertures, leading to a 100-fold decrease in fluence at photon energies around 4 keV, which seem ideal for imaging of single biomolecules. Moreover, the nominal SASE1 is very far from the level required for single particle imaging. Here we show how it may be possible to optimize the SPB instrument for single biomolecule imaging with minimal additional costs and time, achieving diffraction without destruction at near-atomic resolution with 10^{13} photons in a 4 fs pulse at 4 keV photon energy and in a 100 nm focus, corresponding to a fluence of 10^{23} ph/cm². This result is exemplified using the RNA Pol II molecule as a case study.

INTRODUCTION AND REQUIREMENTS

Imaging of single molecules at near-atomic resolution is expected to result in a significant advance in structural biology. One could obtain structural information of large macromolecular assemblies that cannot crystallize, like membrane proteins. In this contribution we study possibilities and opportunities in this field of science, which will be enabled by applying advanced FEL techniques to the SPB (Single Particle and Biomolecule) instrument to be installed in the European XFEL baseline¹ [1, 2]. In order to perform single molecule imaging, a straightforward “diffraction before destruction” method has been proposed [3]- [6]. A great number of single molecules with the same structure are injected into vacuum and interact with ultrashort X-ray pulses, before being completely destroyed. A sufficient number of diffraction patterns is recorded, with unknown orientation. Next, the relative orientations of the different images is determined, so that a 3D diffraction pattern can be assembled in the reciprocal space [7]- [11]. The 3D electron density of the molecule is obtained from the 3D diffraction pattern with

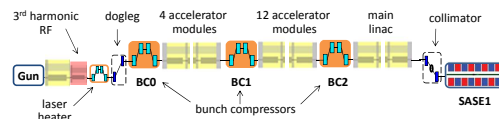


Figure 1: Sketch of the European XFEL, SASE1.

the help of a phase retrieval method. An important parameter of the problem is the number of scattered photons per effective Shannon pixel. For biological material, the photon count per shot per pixel of solid angle Ω_p , averaged over shells of wavenumber q is proportional to the wavelength λ^2 [13]. Lower photon energies result in a stronger diffraction signal, but a limit is dictated by the resolution that one needs to achieve, a balance being in the range between 3 keV and 5 keV. The FWHM focal spot size should be roughly between 5 and 10 times larger than the sample size to grant good photon beam quality within the interaction area. For example, a spot size of 100 nm is good for sample sizes of 10 - 20 nm [14]. We find therefore that a biomolecule of around 15 nm diameter, with $N_{\text{atom}} \sim 30000$, requires a pulse fluence of about 10^{13} ph/(100 nm)², for an average of $\langle N_p \rangle \sim 1.5$ photons per Shannon pixel at a photon energy of 4 keV. This signal level is higher than what is required by usual methods of pattern orientation determination. Photons have to be delivered in extremely short X-ray pulses to limit radiation-induced changes during the exposure. Estimations indicate that an X-ray pulse duration shorter than about 4 fs is needed [15]- [19]. The key metric for optimizing a photon source for single biomolecule imaging is then the peak power. Ideally, the peak power in our case of interest should be more than 1 TW. For example, we note that 10^{13} photons at 4 keV correspond to an energy of about 6 mJ which yields, in 4 fs, a peak power of about 1.5 TW. It is worthwhile to mention that 1 TW at 4 keV gives the same signal per Shannon pixel as 27 TW at 12 keV (assuming a fixed pulse duration).

TW SOURCE FOR THE SPB LINE

The SPB instrument at the European XFEL will be located at the SASE1 undulator line [1, 2]. Figure 1 shows this line from the injector up to the SASE1 undulator. Our scheme for an X-ray source suitable for the SPB instrument is heavily based on the use of a slotted spoiler foil in the last bunch compressor chicane, a method devised and ex-

¹ A much more fleshed-out report can be found in [12], where the reader is also addressed to for a more complete list of references.

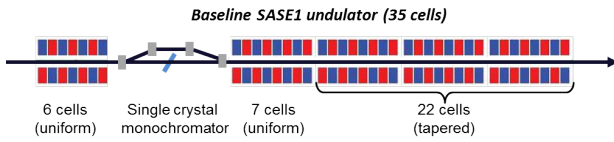


Figure 2: Scheme for a 1 TW-level source for the SPB beam-line. It combines emittance spoiler, self-seeding and post-saturation tapering techniques.

perimentally proved at the LCLS [20]- [22]. The last linac section before the third bunch compressor BC2 is set at an off-crest accelerating rf phase, so that a $y-t$ bunch tilt is present at the center of BC2. A thin foil with a narrow slot at its center is placed in the beam path. Coulomb scattering of the electrons passing through the foil increases the emittance of most of the beam, but leaves a thin unspoiled slice, where the beam passes through the slit, thus allowing for an x-ray FEL pulse much shorter than the FWHM electron bunch duration. The minimum duration of the unspoiled slice of the electron bunch measured at the LCLS is about 3 fs. A design of a self-seeding setup based on the undulator system for the European XFEL is sketched in Fig. 2. We exploit a combination of a self-seeding scheme [23]- [42] with an undulator tapering technique [43]- [51] consisting in a slow reduction of the field strength of the undulator in order to preserve the resonance wavelength, while the kinetic energy of the electrons decreases due to the FEL process. Highly monochromatic pulses generated with the self-seeding technique make the tapering more efficient than in the SASE case. Here we study a scheme for generating 1 TW-level X-ray pulses in the SASE1 tapered undulator. We optimize our setup based on start-to-end simulations for 14 GeV electron beam with 1 nC charge compressed up to 10 kA peak current. In this way, the output power of the SASE1 undulator could be increased from the value of 100 GW in the SASE regime to about 1.5 TW at the photon energy range around 4 keV. For self-seeding we consider a single-crystal scheme, with a crystal identical to that installed at the LCLS, allowing for exploitation of different reflections. In Fig. 3 we show scattering geometry, amplitude and phase of the transmittance for the C(111) asymmetric Bragg reflection at 4.1 keV [38], [42]. The monochromatic seed signal is exponentially amplified passing through the first 7 uniform cells of the output undulator and reaches saturation with about 100 GW power. In a second part of the output undulator the monochromatic FEL signal is enhanced up to 1.5 TW by taking advantage of the undulator magnetic field taper over the last 22 cells.

OPTICS LAYOUT FOR THE SPB LINE

The SPB optical layout [1, 2] is sketched in Fig. 4. The first upstream optical element is a Horizontal Offset Mirror (HOM) pair with a clear aperture along the mirror surface of 800 mm [52]. For the maximal incident angle $\theta = 3.6$ mrad, one achieves an overall high-reflectivity close to 100% over the photon energy range between 3 keV and 5 keV. It can be

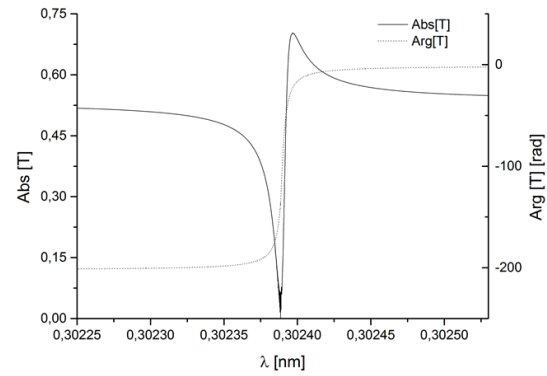


Figure 3: Modulus and phase of the transmittance for the C(111) asymmetric Laue reflection at 4.1 keV.

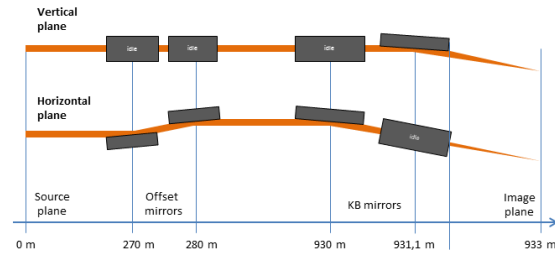


Figure 4: Sketch of optical components for the SPB line [1, 2].

shown that in our case of interest the HOMs are expected to preserve the radiation wavefront. Once the radiation pulse enters the experiment area, it is focused by a KB mirror system to about 100 nm size [2]. A baseline layout for KB system is shown in Fig. 4. Two elliptical mirrors with a 950 mm clear aperture along the mirror surface and a fixed incidence angle of 3.5 mrad are assumed in the vertical and horizontal direction in order to achieve high efficiency at high photon energies. Considering a 950 mm clear aperture and a 3.5 mrad reflection angle, one obtains a lateral aperture of 3.3 mm. However, the about 900 m-long propagation distance from source to sample leads to a large lateral beam size at the focusing optics. In fact, accepting 4σ of the beam, for a photon energy of 4 keV the desired lateral aperture for the ultra-short pulse case is about 8 mm. As a result, due to the large divergence of a nominal X-ray pulse shorter than 10 fs, one suffers major diffraction effects from the KB mirror aperture, leading to about a hundred-fold decrease in fluence at photon energies around 4 keV. However, it is possible to obtain an X-ray source capable of producing X-ray pulses with smaller angular divergence of about $2\mu\text{rad}$ and, simultaneously, a few fs duration, by taking advantage of a minimal modification in the accelerator complex, amounting to the introduction of a slotted foil in the last electron bunch compressor.

RADIATION FROM SASE1

We consider current profile, normalized emittance, energy spread profile, electron beam energy spread and wakefields

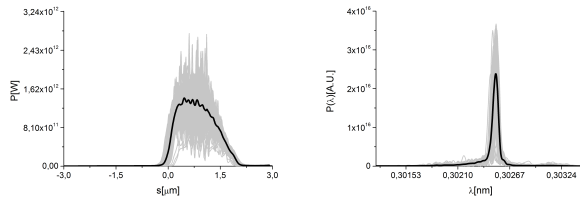


Figure 5: Power distribution and spectrum of the output radiation pulse for the case of short (4 fs) pulse mode of operation.

from start-to-end simulations for the European XFEL at 14 GeV [53]. The electron beam charge is 1 nC, and the peak current is 10 kA. Detailed computer simulations with $2 \cdot 10^5$ macroparticles have been carried out to evaluate the performance of the slotted spoiler using the tracking code ELEGANT [54]. They include multiple Coulomb scattering in a $2 \mu\text{m}$ thin aluminum foil for two case studies referring to pulse length of 12 fs and 4 fs. A slit full-width of 0.7 mm selects a small fraction of electrons, about 20%, and produces an unspoiled electron bunch slice after BC2. Self-seeding and post-saturation tapering simulations were performed with the help of the FEL code Genesis [55]. The output power and spectrum of the entire setup, that is after the second part of the output undulator for the 4 fs case, are shown in Fig. 5.

NANO-SCALE FOCAL SPOT

We carried out wavefront propagation simulations to investigate the evolution of the radiation beam profile through the SPB optics. Our wave optics analysis takes into account aberrations and errors from each optical element. In our case of interest, a reflection from the mirror becomes similar to the propagation through a transparency at the mirror position, which just changes the phase of the reflected beam without changing its amplitude. Applying the Marechal criterion, i.e. requiring a Strehl ratio larger than 0.8, and treating the errors from the different optics independently, we conclude that an height error $h_{\text{rms}} < 1.5 \text{ nm}$ should be sufficiently small for diffraction-limited propagation through the SBP beamline at a photon energy of 4 keV. In fact, the SPB instrument designers are planning to use mirrors capable to preserve the geometrical focus properties at much shorter wavelength range. The effects of the horizontal offset mirrors in the X-ray beam transport are modeled using the code SRW [56] as a combination of two apertures with sizes determined by the mirror length (800 mm in our case) and two phase shifters describing the mirror surface errors. The SRW code has further the capability of modeling the KB optics by elliptical mirrors (with length 950 mm in our case) and to account for all aberrations. The KB mirror surface errors are simulated by two phase shifters, similar to the case of offset mirrors. The plot in Fig. 6 shows the intensity profile at the focus, integrated over the radiation pulse. This is thus a simulation of the energy profile per unit surface

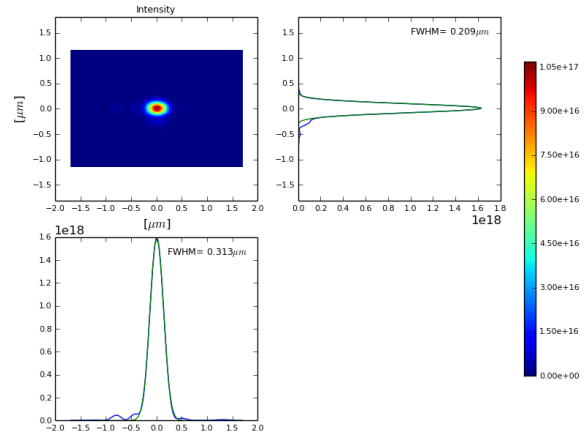


Figure 6: Distribution of the radiation pulse energy per unit surface in the plane placed in the focus, integrated over the radiation pulse.

that can be measured by a detector that integrates over a single radiation pulse, placed in the plane of interest. The maximal fluence in the focus may now be obtained from $F = N_p/S$, where N_p is the number of photons into the radiation pulse and S is the effective focal spot squared. We found that $1/S \sim 1.5 \cdot 10^9 \text{ cm}^{-2}$. For 10^{13} photons per pulse, which can be achieved as discussed previously, this amounts to a fluence of about $1.5 \cdot 10^{22} \text{ photons/cm}^2$. This result can be achieved without additional cost for the baseline optical layout of the SPB beamline, and with very moderate costs for the installation of the slotted foil setup into the beam formation system. The X-ray optical layout of the SPB instrument provides an option of operation with an intermediate source point in the horizontal plane allowing for a fluence of about $0.5 \cdot 10^{23} \text{ photons/cm}^2$. In order to achieve additional tightening of the focusing, pending feasibility study, one might also additionally install two vertical refocusing mirrors. In this way, with a moderate additional cost, a higher fluence of about $10^{23} \text{ photons/cm}^2$ is within reach.

NOISY X-RAY DIFFRACTION PATTERNS

The calculations in this article were carried out for a photon energy of 4.1 keV, corresponding to a wavelength $\lambda = 0.3 \text{ nm}$. For reference, note that in order to reach the resolution $d = 2\pi/(0.4 \text{ nm})$ with a 200 mm by 200 mm detector, the sample to detector distance needs to be as short as 10 cm. For this resolution, and for a molecule size of $w = 10 \text{ nm}$, we estimate the requirement for the number of Shannon pixels as $N_s = 4w/d = 100$. The Adaptive Integrating Detector (AGIPD) [57], which will be installed at the SPB instrument features a pixel size of 0.2 mm and frame of 1 megapixel, amounting to a total lateral size $D = 200 \text{ mm}$. In this case, the average size of a Shannon pixel can be estimated as $D/N_s = 2 \text{ mm}$. However, our calculations assume that the detector can be placed at the necessary propagation distance (10 cm) to realize the desirable resolution. The numerical simulations carried out here are based on

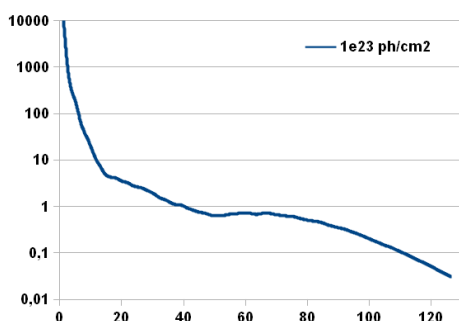


Figure 7: Radial average of the photon counts per pixel vs. position along the detector in mm, starting from the center of the detector.

some simplifying assumptions. In particular, noise is only considered in terms of photon noise, i.e. we assume Poisson shot noise. No additional sources of noise such as detector readout noise are considered. A quantum efficiency of about 85% is assumed for the AGIPD detector, for standard window and at the photon energy of 4 keV. Concerning issues related with detector electronics it can be shown that the expected number of false hits per detector pixel (0.2 mm by 0.2 mm) can be neglected. We simulated 30000 randomly oriented diffraction patterns for the RNA Pol II structure. The plot in Fig. 7 shows the radial average of the photon count. The simulated array size was 200 by 200 pixels, with sampling ratio per dimension of $s = 2$, and binning $b = 5$. Note that larger molecules do not necessarily give larger signals; there are a fixed number of photons per pulse and larger molecules require a proportionally larger focal spot size, hence giving a lower fluence. The plot in Fig. 7 demonstrates that a signal of the order of 0.1 photons per pixel, corresponding to 0.4 photons per Shannon angle can be achieved. A typical diffraction pattern from a single FEL pulse as seen by AGIPD detector is shown in Fig. 8. A difficulty to be considered is that the 6 mm gap width between two detector modules corresponds, in our case of single biomolecule imaging, to the size of three Shannon pixels.

DISCUSSIONS AND CONCLUSIONS

The imaging method “diffraction before destruction” promises to be a revolutionary technique for protein determination, capable of resolving the structure of molecules that cannot crystallize. Here we propose a cost-effective proof-of-principle experiment, aiming to demonstrate the actual feasibility of a single molecule diffraction experiment using the baseline European XFEL accelerator complex and the SPB beamline hardware, with minimal modifications only. More specifically, we want to determine the structure of a relatively small (about 30000 non-hydrogen atoms), well-known protein molecule and compare it with results in the protein data bank. We developed a complete package of computational tools for start-to-end simulations predicting the performance of this experiment. Its composition is

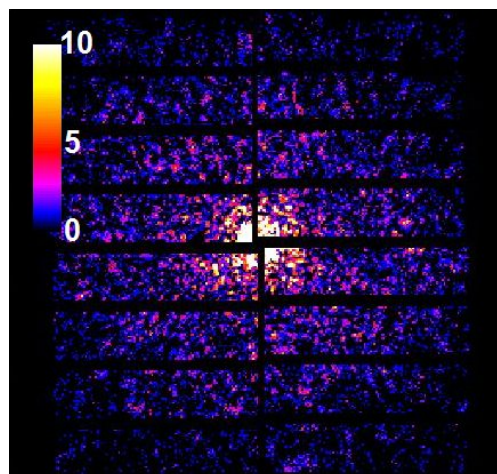


Figure 8: Simulated diffraction pattern from the RNA pol II test object as seed by AGIPD detector at a fluence of 10^{23} photons/cm².

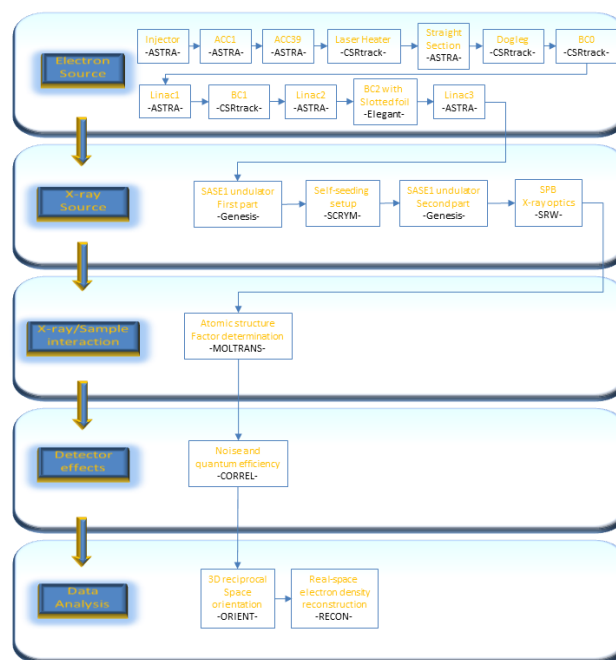


Figure 9: Organization of start-to-end simulation program. See [54]- [56], [58]- [64] and refer to [12] for a more detailed description.

sketched in Fig. 9. In this paper we reported about detailed simulations from the photocathode of the European XFEL injector up to the collection of noisy 2D diffraction data set. Several issues are discussed. As a follow-up of this work, we will perform image reconstruction up to the determination of the electron density distribution, after image orientation and assembly of the 3D diffraction data set.

REFERENCES

- [1] A. Mancuso et al., Scientific Instrument Single Particles, Clusters, and Biomolecules (SPB) CDR, XFEL.EU, TR-2011-007, 2011.

- [2] A. Mancuso et al., The Single Particles, Clusters and Biomolecules (SPB) Instrument TDR, XFEL.EU, TR-2013-004, 2013.
- [3] J. Hajdu, "Single-molecule X-ray diffraction", *Curr. Opin. Struct. Biol.*, vol. 10, pp. 569-573, 2000.
- [4] R. Neutze et al., "Potential for biomolecular imaging with femtosecond X-ray pulses", *Nature*, vol. 406, pp. 752-757, 2000, doi:10.1038/35021099.
- [5] K. J. Gaffney and H. N. Chapman, "Imaging Atomic Structure and Dynamics with Ultrafast X-ray Scattering", *Science*, vol. 316, no. 5830, pp. 1444-1448, 2007, doi:10.1126/science.1135923.
- [6] M. M. Seibert et al., "Single mimivirus particles intercepted and imaged with an X-ray laser", *Nature*, vol. 470, pp. 78-81, Feb. 2011, doi:10.1038/nature09748.
- [7] G. Huldt et al., "Diffraction imaging of single particles and biomolecules", *J. Struct. Biol.*, vol. 144, pp. 219-227, 2003.
- [8] G. Bortel and G. Faigel, "Classification of continuous diffraction patterns: a numerical study", *J. Struct. Biol.*, vol. 158, p. 10, 2007.
- [9] R. Fung et al., "Structure from fleeting illumination of faint spinning objects in flight", *Nature Physics*, vol. 5, pp. 64-67, 2009.
- [10] N. D. Loh et al., "Publisher's Note: Cryptotomography: Reconstructing 3D Fourier Intensities from Randomly Oriented Single-Shot Diffraction Patterns", *Phys. Rev. Lett.*, vol. 104, p. 225501, 2010.
- [11] S. Ikeda and H. Kono, "Phase retrieval from single biomolecule diffraction pattern", *Optics Express*, vol. 20, p. 3375, 2012.
- [12] S. Serkez et al., "Perspectives of Imaging of Single Protein Molecules with the Present Design of the European XFEL. - Part I - X-ray Source, Beamline Optics and Instrument Simulations", DESY 14-137, Available: <http://arxiv.org/abs/1407.8450>, 2014.
- [13] A. Guinier, "X-Ray Diffraction in Crystals, Imperfect Crystals, and Amorphous Bodies.", W. H. Freeman and Company, San Francisco and London, 1963.
- [14] S. Baradaran et al., LCLS-II New Instruments Workshops Report, pp. 66-72, 2012.
- [15] H. Chapman, "Coherent Imaging with X-ray Free Electron Lasers", Lecture Notes of the 43rd IFF Spring School "Scattering Methods for Condensed Matter Research: Towards Novel Applications at Future Sources", Forschungszentrum Juelich, 2012.
- [16] U. Lorenz et al., "Impact of ultrafast electronic damage in single-particle x-ray imaging experiments", *Phys. Rev. E*, vol. 86, p. 051911, 2012.
- [17] B. Ziaja et al., "Limitations of coherent diffractive imaging of single objects due to their damage by intense x-ray radiation", *New J. of Phys.*, vol. 14, p. 115015, 2012, doi:10.1088/1367-2630/14/11/115015.
- [18] S. Schorb et al., "Size-Dependent Ultrafast Ionization Dynamics of Nanoscale Samples in Intense Femtosecond X-Ray Free-Electron-Laser Pulses", *Phys. Rev. Lett.*, vol. 108, p. 233401, 2012.
- [19] S.-K. Son et al., "Impact of hollow-atom formation on coherent x-ray scattering at high intensity", *Phys. Rev. A*, vol. 83, p. 033402, 2011.
- [20] P. Emma et al., "Femtosecond and Subfemtosecond X-Ray Pulses from a Self-Amplified Spontaneous-Emission-Based Free-Electron Laser", *Phys. Rev. Lett.*, vol. 92, p. 074801-1, 2004.
- [21] P. Emma et al., "Attosecond X-ray pulses in the LCLS using the slotted foil method", *Proc. 26th Int. Free-Electron Laser Conf., Trieste, 2004*, TUBIS01.
- [22] Y. Ding et al., "Femtosecond X-Ray Pulse Characterization in Free-Electron Lasers Using a Cross-Correlation Technique", *Phys. Rev. Lett.*, vol. 109, p. 254802, 2012.
- [23] J. Feldhaus et al., "Possible application of X-ray optical elements for reducing the spectral bandwidth of an X-ray SASE FEL" *Optics. Comm.*, vol. 140, pp. 341-352, 1997.
- [24] E. Saldin et al., "X-ray FEL with a meV bandwidth", *NIM, ser. A*, vol. 475, pp. 357-362, Dec. 2001.
- [25] E. Saldin et al., "Optimization of a seeding option for the VUV free electron laser at DESY", *NIM, ser. A*, vol. 445, pp. 178-182, May 2000.
- [26] R. Treusch et al., "The seeding project for the FEL in TTF phase II", *DESY Ann. report*, 2001.
- [27] A. Marinelli et al., "Comparative study of nonideal beam effects in high gain harmonic generation and self-seeded free electron lasers", *Phys. Rev. ST Accel. Beams*, vol. 13, p. 070701, Jul 2010.
- [28] G. Geloni et al., "Scheme for generation of highly monochromatic X-rays from a baseline XFEL undulator", *DESY 10-033*, 2010.
- [29] Y. Ding et al., "Two-bunch self-seeding for narrow-bandwidth hard x-ray free-electron lasers" *Phys.Rev.ST Accel.Beams*, vol. 13, p. 060703, 2010.
- [30] G. Geloni et al., "A simple method for controlling the line width of SASE x-ray FELs", *DESY 10-053*, 2010.
- [31] G. Geloni et al., "A Cascade self-seeding scheme with wake monochromator for narrow-bandwidth x-ray FELs", *DESY 10-080*, 2010.
- [32] G. Geloni et al., "Cost-effective way to enhance the capabilities of the LCLS baseline", *DESY 10-133*, 2010.
- [33] J. Wu et al., "Staged self-seeding scheme for narrow bandwidth, ultra-short X-ray harmonic generation free electron laser at LCLS", *Proc. 34th Int. Free-Electron Laser Conf., Malmo, 2010*, TUPB08.
- [34] G. Geloni et al., "Generation of doublet spectral lines at self-seeded X-ray FELs", *DESY 10-199*, 2010, and *Optics Commun.*, vol. 284, p. 3348, 2011.
- [35] G. Geloni et al., "Production of transform-limited X-ray pulses through self-seeding at the European X-ray FEL", *DESY 11-165*, 2011.
- [36] G. Geloni et al., "A novel self-seeding scheme for hard X-ray FELs", *J. of Modern Optics*, vol. 58, p. 1391, 2011.
- [37] J. Wu et al., "Simulation of the Hard X-ray Self-seeding FEL at LCLS", *Proc. 33rd Int. Free-Electron Laser Conf., Shanghai, 2011*, MOPB09.

- [38] Yu. Shvyd'ko, R. Lindberg, "Spatiotemporal response of crystals in x-ray Bragg diffraction", *Phys. Rev. ST Accel. Beams*, vol. 15, p. 100702, Oct. 2012.
- [39] J. Amann et al., "Demonstration of self-seeding in a hard-X-ray free-electron laser", *Nature Photonics*, vol. 6, pp. 693–698, DOI:10.1038/NPHOTON.2012.180, 2012.
- [40] Y. Feng et al., "System design for self-seeding the LCLS at soft X-ray energies", *Proc. 34th Int. Free-Electron Laser Conf.*, Nara, Japan, 2012, TUOBIO.
- [41] S. Serkez et al., "Grating monochromator for soft X-ray self-seeding the European XFEL", DESY 13-040, Available: <http://arxiv.org/abs/1303.1392>, 2013.
- [42] G. Geloni et al., "Wake monochromator in asymmetric and symmetric Bragg and Laue geometry for self-seeding the European XFEL", DESY 13-013, 2013.
- [43] A. Lin and J. M. Dawson, "High-Efficiency Free-Electron Laser", *Phys. Rev. Lett.*, vol. 42, p. 2172, 1986.
- [44] P. Sprangle et al., "Nonlinear Formulation and Efficiency Enhancement of Free-Electron Lasers", *Phys. Rev. Lett.*, vol. 43, p. 1932, 1979.
- [45] N. M. Kroll, P. Morton and M.N. Rosenbluth, "Free-electron lasers with variable parameter wigglers" *IEEE J. Quantum Electron.*, vol. 17, pp. 1436-1468, 1981.
- [46] T. J. Orzechowski et al., "High-Efficiency Extraction of Microwave Radiation from a Tapered-Wiggler Free-Electron Laser", *Phys. Rev. Lett.*, vol. 57, p. 2172, 1986.
- [47] W. Fawley et al., "Tapered undulators for SASE FELs", *NIM*, ser. A, vol. 483, p. 537, 2002.
- [48] X. Wang et al., "Efficiency and Spectrum Enhancement in a Tapered Free-Electron Laser Amplifier" *Phys. Rev. Lett.*, vol. 103, p. 154801, 2009.
- [49] G. Geloni et al., "Scheme for generation of fully coherent, TW power level hard x-ray pulses from baseline undulators at the European XFEL", DESY 10-108, 2010.
- [50] W. M. Fawley et al., "Toward TW-level LCLS radiation pulses", *Proc. 33rd Int. Free-Electron Laser Conf.*, Shanghai, 2011, TUOA4.
- [51] Y. Jiao et al., "Modeling and multidimensional optimization of a tapered free electron laser", *Phys. Rev. ST Accel. Beams*, vol. 15, p. 050704, 2012.
- [52] H. Sinn et al., "X-Ray Optics and Beam Transport, Conceptual Design Report", XFEL.EU TR-2011-002, 2011.
- [53] I. Zagorodnov, "Compression scenarios for the European XFEL" [Online], Available: http://www.desy.de/fel-beam/data/talks/files/Zagorodnov_ACC2012_ready_new.pptx, 2012.
- [54] M. Borland, "Elegant" [Online], Available: http://www.aps.anl.gov/Accelerator_Systems_Division/Accelerator_Operations_Physics/software.shtml#elegant
- [55] S. Reiche et al., "GENESIS 1.3: a fully 3D time-dependent FEL simulation code", *Nucl. Instr. and Meth., ser. A*, vol. 429, pp. 243-248, 1999.
- [56] O. Chubar et al., "Phase analysis and focusing of synchrotron radiation", *Nucl. Instr. and Meth. Phys. Res. A*, vol. 435, p. 495, 1999.
- [57] J. Becker et al., "The single photon sensitivity of the Adaptive Gain Integrating Pixel Detector", *Nucl. Instr. and Meth. Phys. Res. A*, vol. 694, pp. 82-90, 2012.
- [58] K. Flottmann, "ASTRA documentation" Available: http://www.DESY.de/~mpyflo/Astra_dokumentation/
- [59] M. Dohlus et al., "CSRtrack: Faster Calculations of 3d CSR Effects", *Proc. 26th Int. Free-Electron Laser Conf.*, Trieste, 2004, MOCOS05.
- [60] SCRYM, Inhouse code written by V. Kocharyan and G. Geloni, partly based on xframework routines by I. Agapov, available on request only.
- [61] MOLTRANS, Inhouse code written by E. Weckert, available on request only.
- [62] CORREL, Inhouse code written by E. Weckert, available on request only.
- [63] ORIENT, Inhouse code written by O. Yefanov, available on request only.
- [64] RECON, Inhouse code written by O. Yefanov, available on request only.

START-TO-END SIMULATION FOR FLASH2 HGHG OPTION

Guangyao Feng[#], Igor Zagorodnov, Martin Dohlus, Torsten Limberg, Winfried Decking,
Jörn Boedewadt, Yauhen Kot, Matthias Scholz, Sven Ackermann, DESY, Hamburg, Germany
Kirsten Hacker, Technische Universität Dortmund, Germany
Tim Plath, University of Hamburg, Germany

Abstract

The Free-electron laser in Hamburg (FLASH) is the first FEL user facility to have produced extreme ultraviolet (XUV) and soft X-ray photons. In order to increase the beam time delivered to users, a major upgrade of FLASH named FLASH II is in progress. The electron beamline of FLASH2 consists of diagnostic and matching sections, a seeding undulator section and a SASE undulator section. In this paper, results from a start-to-end simulation for a FLASH2 High-Gain Harmonic Generation (HGHG) option are presented. For the beam dynamics simulation, space charge, coherent synchrotron radiation (CSR) and longitudinal cavity wake field effects are taken into account. In order to get electron beam bunches with small correlated and uncorrelated energy spread, RF parameters of the accelerating modules have been optimized as well as the parameters of the bunch compressors. Radiation simulations for the modulator and the radiator have been done with code Genesis 1.3 by using the particle distribution generated from the beam dynamics simulation. The results show that for a single stage HGHG, 33.6 nm wavelength FEL radiation can be seeded at FLASH2 with a 235 nm seeding laser.

INTRODUCTION

FLASH has been an FEL user facility since 2005 which can produce XUV and soft X-ray radiation in the wavelength range from 4.1 nm to 45 nm [1, 2]. In order to increase the beam time, a major upgrade, FLASH II is in progress which will provide seeded FEL radiation as well as SASE FEL radiation [3]. At the exit of the existing linear accelerator, as the extension of FLASH, FLASH2 was built in a separate tunnel. With fast kickers and a DC Lambertson septum, parts of the electron bunch trains generated from the main linac can be extracted into the FLASH2 arc and then pass through the undulator sections. The undulator sections will consist of the seeding undulator section and the SASE undulator section. The layout of the seeding undulator section will be installed between the extraction arc and the SASE undulator section allows for different seeding schemes, like HHG, HGHG and several combinations of those [4]. The SASE undulator can also be used as the final radiator for the cascaded HGHG scheme and as the amplifier for a direct seeding with HHG. For independent operation of FLASH1 and FLASH2, all FLASH2 undulators will have variable gap to relax the dependency of the radiation wavelength on the electron beam energy.

In this paper, some results of a start-to-end simulation for FLASH2 single stage HGHG option are presented. The injector, the accelerator, the bunch compressors and the extraction arc are studied with help of the codes ASTRA [5] and CSRTrack [6]. Space charge, CSR and longitudinal cavity wake field effects have been taken into account in the beam dynamics simulation. FEL simulations in the modulator and the radiator have been done with Genesis 1.3 [7] by using the particle distribution generated from the beam dynamics simulation. In order to consider the space charge and CSR impacts in the seeding section, the dispersive chicane and the straight beamline between the modulator and the radiator have been simulated with CSRTrack and ASTRA respectively.

LAYOUT OF FLASH

The injector of FLASH consists of a RF gun, an L-band accelerating section and a third-harmonic accelerating section. Electron bunches are generated from a photo cathode by the laser beam and accelerated to 5 MeV by a normal conducting 1.3 GHz RF gun. After the gun, the electron bunches are accelerated in a single TESLA type module named ACC1 [8]. Downstream of ACC1 section a third-harmonic (3.9 GHz) RF system named ACC39 can linearize the RF curvature distortion and minimize the beam tails in the next chicanes [9]. In the L-band superconducting linear accelerator, there are two accelerating sections named L1 and L2 with 1.3 GHz. These two sections are separated by a bunch compressor. L1 has 2 modules (ACC2-3) and L2 has 4 (ACC4-7). There are two bunch compressor chicanes in horizontal plane along the main linac. The first bunch compressor BC2 is located downstream of ACC39. The second bunch compressor BC3 is placed after ACC3 which has an S-type structure (Figure 1).

Behind the main linac of FLASH, three fast vertical kickers and a DC Lambertson-Septum distribute the beam either to the dogleg section of FLASH1 or to the new extraction arc of FLASH2. There are four horizontal bending magnets in the extraction arc of FLASH2 and the arc section is achromatic in horizontal plane. The vertical dispersion caused by the kickers is closed with two vertical bending magnets at the end of the extraction arc. The first order compaction factor (R_{56}) becomes zero at the end of last dipole magnet by using a reverse bending magnet and the proper distribution of dispersion function in the extraction arc section [10]. The undulator

[#] guangyao.feng@desy.de

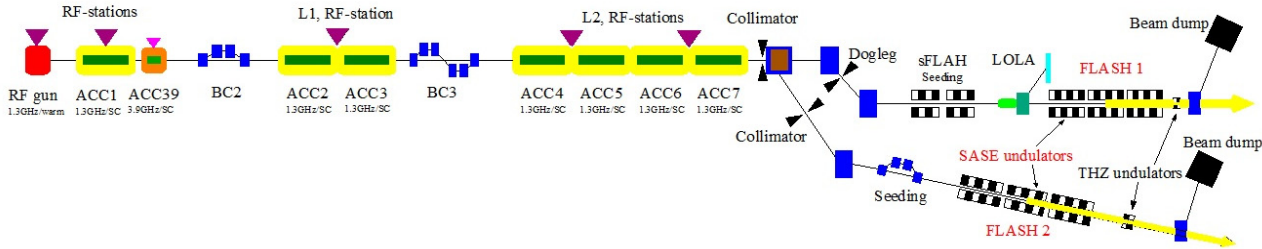


Figure 1: Schematic layout of FLASH facility.

system of FLASH2 will include a seeding undulator section and a SASE undulator section.

BEAM DYNAMICS SIMULATION

The optimization and simulation for a single stage HGHH for FLASH2 have been done. The single stage HGHH section consists of two undulator sections and a dispersive chicane. In the first undulator section, the modulator, a seed laser modulates the electron energy distribution. In the dispersive chicane, the energy modulation is transformed into a density modulation: microbunching. Because the microbunching can have a significant harmonic content, the second undulator section, the radiator, can be tuned to a higher harmonic of the seed wavelength. When the bunched electron beam enters the radiator, it can emit coherent, intense FEL radiation.

The seed laser which will be used for HGHH is a Ti:Sapphire laser at a repetition rate of 100 kHz. After frequency up conversion, the seeding wavelength ranges from 200 nm to 270 nm [11]. In this simulation the electron beam energy is 1 GeV and the seeding laser has wavelength of 235 nm, pulse duration of 30 fs and peak power of 125 MW. In order to avoid particle loss in terms of FEL bandwidth, the energy modulation in the modulator is limited to less than 3 MeV (peak-to-peak). Figure 2 gives the estimation of the bunching factor as a function of harmonics of the seed wavelength for different initial uncorrelated energy spread. One can see at the 7th harmonic, the bunching factor can reach 0.2 in 100 keV slice energy spread case.

For FLASH, it is possible to obtain an electron beam bunch with an uncorrelated energy spread in the range of 100 to 150 keV, when the peak current is about 1.5 kA. Therefore, the peak current of the electron beam is limited to about 1.5 kA and the radiator is tuned to the 7th harmonic of the seed wavelength.

An example of the electron beam bunch from start-to-end simulations, with 0.5 nC charge, is shown below. The beam energy is 1.0 GeV and the peak current is about 1.5 kA. The technical constraints on the RF voltage for the accelerating modules have been considered for the RF parameter settings [12].

For the 0.5 nC case, the initial peak current at the gun is about 26 A and a global compression factor [13], C , of 58 is used. Referring to [1], BC2 is typically operated with a bending angle of 18°. So the curvature radius of the reference trajectory (r_1) in BC2 has been set to 1.618 m.

In order to reduce the space charge effects between the BC2 and BC3, a not strong compression ($C_1=4.7$) in BC2

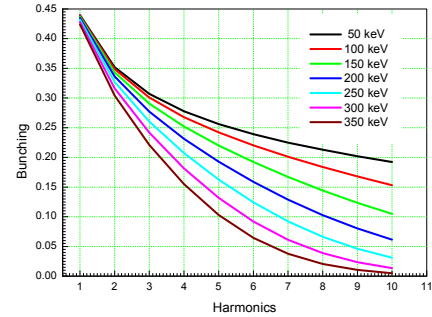


Figure 2: Bunching factor for HGHH with different initial slice energy spreads.

has been used in the simulation. Parameter settings for the bunch compressors are shown in Table 1. During parameter selection, the restriction of curvature radius ($1.4 \text{ m} \leq r_1 \leq 1.93 \text{ m}$, $5.3 \text{ m} \leq r_2 \leq 16.8 \text{ m}$) [13] has been taken into account.

Since the RF parameters of ACC1 and ACC39 are sensitive to the global compression and the current density distribution, we don't want to adjust them once they have been optimized for a linear longitudinal phase space. In order to get HGHH radiation with high monochromaticity, electron beam bunches with small energy chirp are needed. For this purpose, smaller phase shift of L1 has been used to reduce the voltage requirement on L2. Additionally, L2 phase adjustment is helpful to obtain bunches with small energy chirp at the end of the linac.

In reality the RF parameters solution obtained from the relation among the RF parameters, the beam energy and the global compression functions cannot produce the required compression because of the collective effects [13]. In order to take these effects into account a fast tracking code written in the MATLAB language has been used. The RF parameter settings for the accelerating modules are shown in Table 2.

Beam dynamics simulation from the gun to the entrance of the modulator has been done for the 0.5 nC case. For all of the arc sections, like BC2, BC3 and the extraction arc, CSRTrack code is used. The beam tracking in the straight sections (including RF accelerating modules) with space charge effects is simulated with ASTRA code. For the ASTRA simulation, the 3D calculation has been used in order to get results with higher credibility. The

Table 1: Parameter Settings for the Bunch Compressors

Charge Q, nC	Curvature radius in BC2, r_1 [m]	$R_{56,BC2}$ [mm]	Compr. In BC2	Curvature radius in BC3, r_2 [m]	$R_{56,BC3}$ [mm]	Total compr. C
0.5	1.618	180.7	4.7	6.18	72.8	58

Table 2: RF Parameter Settings for the Accelerating Modules

V_{acc1} [MV]	Φ_{acc1} [deg]	V_{acc39} [MV]	Φ_{acc39} [deg]	$V_{acc2,3}$ [MV]	$\Phi_{acc2,3}$ [deg]	$V_{acc4,5,6,7}$ [MV]	$\Phi_{acc4,5,6,7}$ [deg]
159.5	2.4	19.8	162.6	323.3	19.0	623.0	-28.0

longitudinal cavity wake field effects [14, 15] have been taken into account at the exit of each accelerating section by using matlab scripts. A million particles are used in the simulation. The model of the RF gun which generates the Gaussian distribution current profile is from [16].

Beam bunch properties (longitudinal phase space, current profile, slice emittances and slice energy spread) at the entrance of the modulator section are shown in Figure 3. The maximum slice energy spread is about 100 keV. The projected emittance is $1.18 \mu\text{m}$ in horizontal plane and $1.16 \mu\text{m}$ in vertical plane.

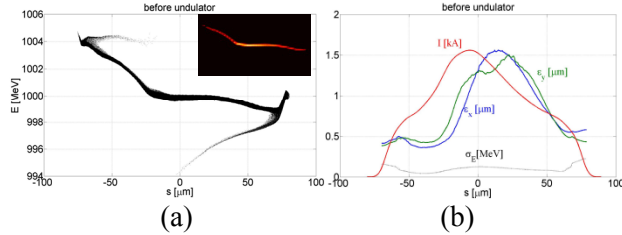


Figure 3: Beam bunch properties before the modulator section for 0.5 nC case. (a) Longitudinal phase space. (b) Current profile, slice emittances and slice energy spread.

RADIATION SIMULATION FOR HGHG

Figure 4 gives a schematic layout of the seeding undulator section. The period length of the modulator is 6.7 cm and the total number of periods is 30. In the dispersive chicane, there are four dipole magnets. The length of the magnet is 0.1 m, with the same length as FLASH correctors. The distance between the first two dipole magnets is 0.5 m. The radiator has the period length of 3.14 cm and the number of periods is 152. It is separated into 2 parts by using one quadrupole magnet. The particle distribution can be up converted to the 7th harmonic of the seeding wavelength in the radiator. There are spaces reserved for installation of a fresh bunch chicane, a second modulator and a second dispersive chicane for a cascaded HGHG option.

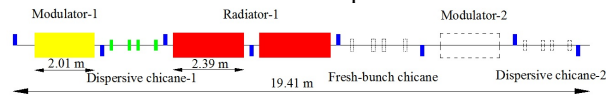


Figure 4: Schematic layout of the seeding undulator section.

An alternating gradient quadrupole lattice provides the electron beam focusing. According to the design optics for FLASH2 SASE option [17], beam optics matching has been done before the SASE undulator section (the second radiator) by using the quadrupole magnets in the seeding

undulator section. Betatron functions are shown in Figure 5. One can see the average beta function in the undulator section is approximately 10 meters.

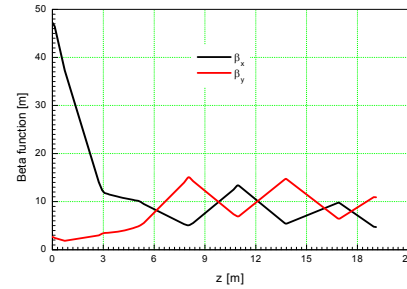


Figure 5: Betatron function in the seeding undulator section.

Particle distribution generated from the above beam dynamics simulation is used for the radiation simulation. Simulation in the modulator and the radiator has been done with Genesis 1.3. In order to take into account the space charge and CSR impacts, we use ASTRA and CSRTrack codes to do the beam dynamics simulation for the beamline between the modulator and the radiator. To obtain the input particle files, particle distribution conversion between ASTRA and Genesis 1.3 has been done by using matlab scripts.

At the exit of the modulator, the longitudinal phase space is shown in Figure 6 from which one can see the energy modulation. An adjustment has been done to shift the seeding laser with respect to the electron bunch.

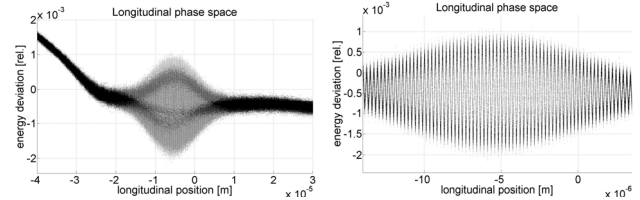


Figure 6: Longitudinal phase space after the modulator.

From the above pictures one can see there is an amplitude distribution of the energy modulation. In order to get FEL radiation with high energy, the R_{56} parameter in the chicane has been scanned. Figure 7 gives the radiation energy at the exit of the radiator for different R_{56} parameters. The energy can reach maximum value when the R_{56} parameter is $41.6 \mu\text{m}$. Therefore the following simulation results are given for this case. The bunching factor (the 7th harmonic of seeding wavelength) at the entrance of the radiator and the bunching distribution along the radiator are shown in Figure 8. One can see the

over compression in the middle of the bunch. At the exit of the radiator, the radiation with peak power about 3.3 GW has high monochromaticity (Figure 9). Figure 10 gives the radiation energy along the radiator. The energy is about 118 μJ after the radiator.

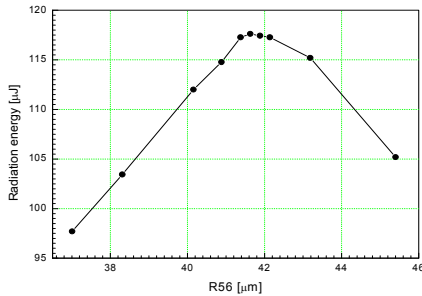


Figure 7: Radiation energy at the exit of the radiator as a function of R_{56} in the chicane.

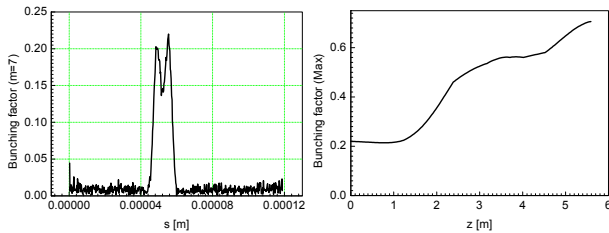


Figure 8: Bunching factor at the entrance of the radiator (left), Bunching vs. z in the radiator (right).

Due to the density modulation, the space charge impact after the dispersive chicane is important because it can cause distortion of the bunch distribution. In this simulation strong space charge impact can not be seen at the entrance of the radiator because of the short distance between the chicane and the radiator. The simulations above are aimed at the cascaded option. If one intends for the HGHG option to operate in a stand-alone fashion, in order to obtain FEL beam with optimal performance delivered to users, maybe it is necessary to let the microbunched beam drift over a significant distance to reach the last radiator section prior to the user beamline. Some issues like LSC, CSR, R_{53} and R_{54} impacts should be considered for that option [18].

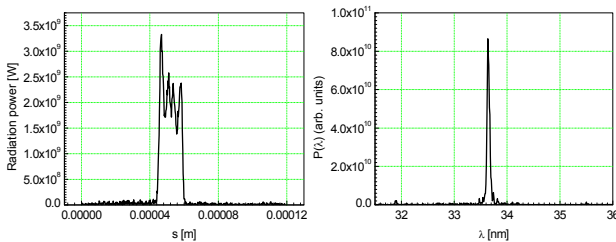


Figure 9: Radiation power at the exit of the radiator (left) and the spectrum (right).

CONCLUSION

FLASH2 will be used as a seeded FEL source. One feasible scheme for single stage HGHG option is given in this paper. In order to get HGHG radiation with several

GW power and with high monochromaticity, parameter settings for the accelerating modules and the bunch compressors have been optimized. Space charge, CSR and longitudinal cavity wake field impacts are taken into account in the start-to-end simulation. The results show that 33.6 nm wavelength FEL radiation can be seeded at FLASH2 with a 235 nm seeding laser.

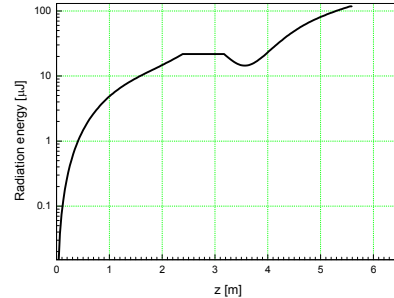


Figure 10: Radiation energy along the radiator.

ACKNOWLEDGMENT

We are grateful to Bart Faatz, Sven Reiche, Velizar Miltchev, Sascha Meykopff for their support and help for this work.

REFERENCES

- [1] M. Vogt, B. Faatz, et al., "Status of the free electron laser FLASH at DESY", Proceedings of IPAC, Spain (2011).
- [2] M. Vogt, B. Faatz, et al., "The free electron laser FLASH at DESY", Proceedings of IPAC, China (2013).
- [3] B. Faatz, et al., "FLASH II: A seeded future at FLASH", Proceedings of IPAC, Kyoto, Japan (2010).
- [4] K. Hacker, "A Concept for Seeding 4-40 nm FEL Radiation at FLASH2", TESLA-FEL, 2013-01.
- [5] K. Floettmann, "ASTRA", DESY, Hamburg, <http://www.desy.de/~mpyflo/>, (2011).
- [6] M. Dohlus, T. Limberg, "CSRtrack: faster calculation of 3D CSR effects", Proceedings of FEL, Italy (2004).
- [7] S. Reiche, "GENESIS 1.3", NIM A 429 (1999) 243.
- [8] J. Iversen, R. Bandelmann, et al., "A Review of the 1.3GHz Superconducting 9-cell cavity Fabrication for DESY", Proceedings of LINAC Conference, Tsukuba (2010).
- [9] M. Dolus, "FLASH beam dynamics issues with 3rd harmonic system", MAC meeting, DESY (2009).
- [10] M. Scholz, W. Decking, et al., "Extraction arc for FLASH II", Proceedings of FEL, Japan (2012).
- [11] T. Tanikawa, "Seeding Preparation at the FLASH2 Beamline", presented at this conference.
- [12] <http://www.desy.de/fel-beam/s2e/flash/Information/RF.txt>
- [13] I. Zagorodnov, M. Dohlus, "A semi-Analytical Modelling of Multistage Bunch Compression with Collective Effects", Physical Review STAB 14 (2011).
- [14] T. Weiland, I. Zagorodnov, "TESLA cryomodule wake", TESLA Report 2003-19, DESY (2003)
- [15] I. Zagorodnov, T. Weiland, M. Dohlus, "ACC39 wake", TESLA Report 2004-01, DESY (2004)
- [16] http://www.desy.de/fel-beam/s2e/flash/Information/astra_simu_flash.html
- [17] M. Scholz, FLASH-lattice files, http://www.desy.de/fel-beam/flash2_elegant_2012_09_19.zip
- [18] K. Hacker, "Longitudinal Space Charge and Seeded Microbunches", presented at this conference.

ENHANCING COHERENT HARMONIC GENERATION USING TILTED LASER WAVEFRONTS*

S. Khan[†], Center for Synchrotron Radiation (DELTA),
TU Dortmund University, 44227 Dortmund, Germany

Abstract

Coherent Harmonic Generation (CHG) to produce ultra-short pulses of synchrotron radiation is based on the interaction of relativistic electrons in a storage ring with femtosecond laser pulses in an undulator. The resulting periodic energy modulation is converted into a density modulation by a dispersive chicane, giving rise to coherent emission at harmonics of the laser wavelength in a second undulator. If the first undulator is in a section with non-zero dispersion, the density modulation can be enhanced using tilted laser wavefronts, thus delaying the phase-space distributions of electrons with different energy with respect to each other. The most simple way to produce a wavefront tilt would be a small crossing angle between the electron and laser beam. Details are discussed for the case of the CHG short-pulse facility at DELTA, a 1.5-GeV synchrotron light source at the TU Dortmund University, but HHG and EEHG seeding of free-electron lasers could also be enhanced this way.

INTRODUCTION

Synchrotron radiation with short wavelength is the standard tool to study the structure of matter on the atomic level. However, synchrotron radiation pulses with a duration of 30 to 100 ps (FWHM) are insufficient to study dynamic processes such as chemical reactions, phase transitions, fast magnetic changes, lattice vibrations etc. which take place on the sub-picosecond scale. The femtosecond regime, on the other hand, has been made available by mode-locked lasers at wavelengths (e.g. 800 nm in the case of titanium-doped sapphire lasers) which are unsuitable to probe inner atomic shells or to provide spatial resolution on the atomic scale.

The need for radiation with short wavelength *and* short pulse duration has prompted new developments in laser physics, such as high-harmonic generation (HHG), as well as in accelerator physics, notably free-electron lasers (FELs) providing extremely brilliant short-wavelength radiation with femtosecond pulse duration. To date, only four linac-based FEL facilities at short wavelengths are in user operation (in chronological order: FLASH, LCLS, SACLA, and FERMI) while more than 50 synchrotron light sources worldwide [1] provide up to 40 beamlines simultaneously with brilliant and tunable radiation. It is therefore worthwhile to study methods which allow to generate conventional synchrotron radiation with shorter pulse duration.

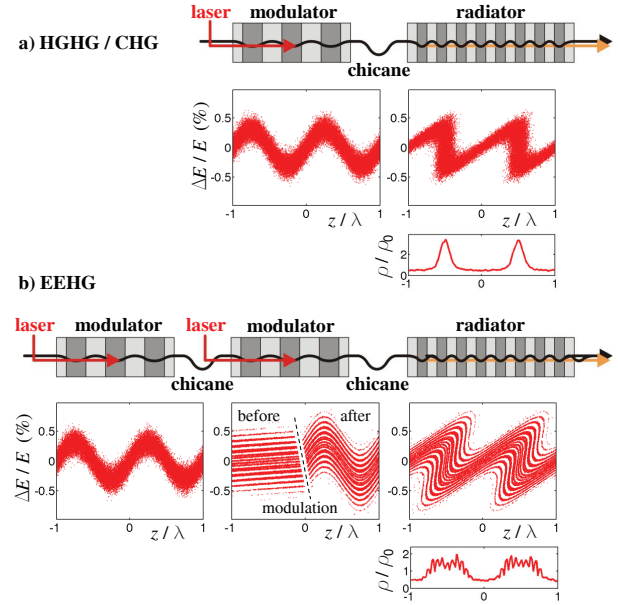


Figure 1: Setup for seeding schemes: a) HHG or CHG and b) EEHG with respective electron distributions in phase space, i.e. longitudinal coordinate z , here normalized to the laser wavelength λ , versus relative energy deviation $\Delta E/E$.

SHORT-PULSE GENERATION

Some methods to generate sub-ps radiation pulses at storage rings are borrowed from FEL seeding schemes using a femtosecond laser pulse to modulate the energy of electrons at the center of a long electron bunch. FEL seeding aims at assisting a positive feedback loop of exponentially growing microbunching and coherent radiation. In a storage ring, on the other hand, the laser pulse is used to define a short "slice" within the electron bunch. A short radiation pulse is emitted by the energy-modulated electrons together with a long pulse from the rest of the bunch. Off-energy electrons can be transversely displaced by dispersion in order to separate the short and long components of incoherent undulator radiation spatially – this scheme is known as "femtosing" [2]. Alternatively, a magnetic chicane may convert the energy modulation into a density modulation giving rise to a short pulse of coherent radiation at harmonics of the laser wavelength, which is brighter than the long incoherent pulse. As long as the signal-to-background ratio

$$\frac{P_{\text{short}}}{P_{\text{long}}} = \frac{n_{\text{short}}^2 b_h^2}{n_{\text{long}}} = f^2 n_{\text{long}} b_h^2 \quad \text{with} \quad f \equiv \frac{n_{\text{short}}}{n_{\text{long}}} \quad (1)$$

is tolerable, no geometric separation is required. Here, $f \approx 10^{-3}$ is the ratio between the number of electrons in the slice

* Work supported by BMBF (contract 05K13PE3)

[†] shaukat.khan@tu-dortmund.de

and in the bunch, and b_h is the bunching factor given by the Fourier transform of the longitudinal charge distribution at the h th harmonic of the laser wavelength. With $n_{\text{long}} = 10^{10}$, to give an example, $b_h = 0.1$ would yield an excellent signal-to-background ratio of 10^2 .

The standard scheme of short-pulse generation by laser-induced energy modulation in an undulator (the "modulator"), microbunching in a magnetic chicane, and coherent emission in a second undulator (the "radiator") is known as coherent harmonic generation (CHG, top part of Fig. 1) [3] and bears a close similarity to an FEL seeding scheme called high-gain harmonic generation (HHG) [4]. Here, the bunching factor decreases with increasing harmonics as $b_h \sim \exp(-h^2)$. In the same way, echo-enabled harmonic generation (EEHG, bottom part of Fig. 1) [5] involving a two-fold energy modulation in order to reach higher harmonics with $b_h \sim h^{-1/3}$ can be used for FEL seeding as well as for short-pulse generation in a storage ring.

TILTED LASER WAVEFRONTS

A primary goal in using CHG or EEHG is to reach high harmonics, i.e. short wavelengths, to extend the range of scientific applications of the short-pulse source. One of the limitations is the finite length of the microbunches given by the sinusoidal nature of the energy modulation and by the electron energy spread σ_E . It may be possible to linearize the energy modulation in a sawtooth-like fashion by seeding with several laser harmonics simultaneously [6, 7], but a given laser pulse energy is usually better invested in obtaining a high modulation amplitude $\Delta E_{\text{max}}/\sigma_E$ rather than in additional harmonic generation. The effect of the energy spread can be reduced if there is a correlation between the energy offset ΔE of each electron and another parameter. The obvious candidate for such a parameter is the transverse coordinate x in the presence of dispersion $D(s)$. In a storage ring, dispersion is introduced in the horizontal plane by the dipole magnets and its value at a particular position, e.g. at the CHG or EEHG modulator, depends on the quadrupole settings. The ΔE - x correlation is to good approximation linear, i.e. $x = D \cdot \Delta E/E$, but is smeared out by the emittance-dependence of the horizontal beam size

$$\sigma_x(s) = \sqrt{\varepsilon_x \beta_x(s) + D^2(s) \sigma_E^2/E^2}, \quad (2)$$

where ε_x is the horizontal beam emittance and $\beta_x(s)$ is the beta function. Reference [8] suggests to use an undulator with transverse gradient as modulator in which the phase advance with respect to the laser field depends on the transverse position. Another and even more simple possibility to make use of the ΔE - x correlation is to seed with tilted laser wavefronts as recently proposed by [9] for FEL seeding. This way, a phase shift of the energy modulation is introduced which depends on x and thus also on ΔE .

An example is shown in Fig. 2 with $D = 0.5$ m, $\sigma_E/E = 8 \cdot 10^{-4}$, $\varepsilon_x = 15$ nm rad, and $\beta_x = 2$ m. In this case, the optimum wavefront tilt is 0.1 mrad and the bunching factor is roughly doubled.

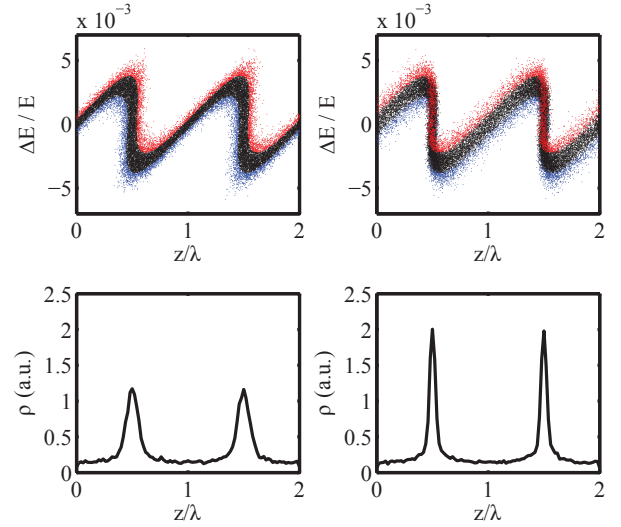


Figure 2: Energy and density modulation without (left) and with (right) wavefront tilt. The top figures show the phase space distribution, the bottom figures the longitudinal electron density. Electrons with an original energy deviation of $\Delta E > \sigma_E$ (and $\Delta E < -\sigma_E$) are shown in red (and blue).

Table 1: Parameters of the Storage Ring DELTA

beam energy	1.5 GeV
circumference	115.2 m
beam current (multibunch)	130 mA
beam current (single bunch)	20 mA
horizontal emittance	15 nm rad
min. horizontal beta function @CHG	2 m
min. vertical beta function @CHG	20 m
horizontal dispersion @CHG	-0.1 m
relative energy spread	0.0008
bunch length (rms)	13 mm

CHG AT DELTA

The 1.5-GeV electron storage ring DELTA with parameters as shown in Table 1 is operated as a synchrotron light source by the TU Dortmund University. In 2011, a short-pulse facility based on CHG was constructed in order to provide ultrashort coherent synchrotron radiation pulses in the VUV and THz regimes for users [10, 11], and an extension based on EEHG including a femtoslicing source is planned [12]. The bunch length corresponds to a pulse duration of 100 ps (FWHM) while the CHG pulse length is below 100 fs. For a typical single-bunch current of 10 mA, the number of electrons is $N_{\text{long}} = 2.4 \cdot 10^{10}$ and the ratio f (cf. Eq. 1) is below 10^{-3} . Seeding is presently performed using Ti:sapphire laser pulses at 800 nm or frequency-doubled pulses thereof, and a signal-to-background exceeding 10^2 is routinely observed for low harmonics [10]. The beam size is $\sigma_x \approx 170 \mu\text{m}$ according to the first term of Eq. 2 while the second term with $D = -0.1$ m in the CHG section amounts only to 80 μm .

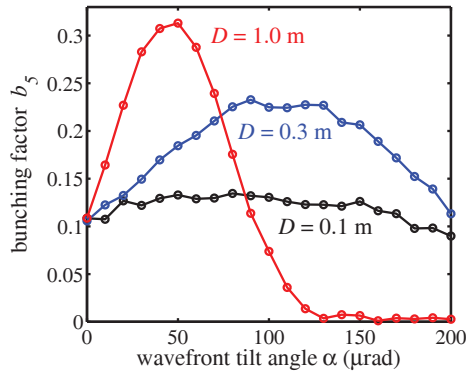


Figure 3: Bunching factors calculated for CHG at the 5th harmonic with the beam parameters of DELTA and different values of dispersion D at the modulator. The laser field is assumed to consist of plane waves arriving under a tilt angle α with respect to the electron beam.

The example shown in Fig. 2 was based on the DELTA parameters except for an increased dispersion value of $|D| = 0.5$ m, which can in principle be achieved by modifying the quadrupole settings of the storage ring, and work to this end is in progress in order to perform an experimental investigation of the tilted-wavefront effect. Calculated bunching factors for different dispersion values are shown in Fig. 3 as function of the tilt angle. As expected, the improvement with $|D| = 0.1$ m is marginal while an experiment with $|D| = 0.3$ m might already yield an observable effect.

A wavefront tilt can be obtained by simply introducing a small crossing angle between the electron and laser beam axes. A tilt produced by other means, e.g. by passing through a prism, will result in a wavefront rotation at the laser waist [13] which is not desired here. A crossing angle of the order of 0.1 mrad is well controllable by the motorized mirrors upstream of the modulator (an electromagnetic undulator with 7 periods of 25 cm length) and would result in an offset of 90 μ m at either end of the modulator, which is small compared to the laser beam size. A variation of the incident laser beam angle presently exhibits a broad maximum of the CHG yield. With larger dispersion, the tilted-wavefront effect is expected to result in a more pronounced optimum angle.

In CHG operation, coherent THz radiation is generated over several turns due to the fact that the energy-modulated electrons leave a gap in the longitudinal charge distribution [14]. This gap gives rise to coherent radiation at wavelengths above ~ 50 μ m and should be insensitive to the sub- μ m effects of tilted wavefronts. Since the absolute crossing angle is not easily determined, an offset between the optimum laser angle for CHG and for THz may be the most obvious signature for the tilted-wavefront effect for a fixed dispersion value. If D can be tuned on the fly, an improvement of the CHG signal with increasing dispersion should be observed.

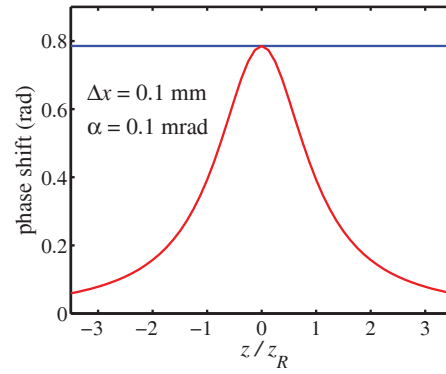


Figure 4: Phase shift of energy modulation for a transverse displacement of $\Delta x = 0.1$ mm and a wavefront tilt angle of $\alpha = 0.1$ mrad as function of longitudinal coordinate z , normalized to the Rayleigh length z_R , for the case of a plane wave (blue) and a Gaussian laser waist at $z = 0$ (red).

MORE REALISTIC WAVEFRONTS

Distortions of the laser wavefronts have not been studied so far but are likely to occur due to the passage of the laser pulses through air and glass (lenses and vacuum windows). Furthermore, even idealized wavefronts of a Gaussian laser beam are curved. Up to now, plane waves were tacitly assumed leading to a constant phase shift of the energy modulation given by

$$\Delta\varphi = \frac{2\pi\alpha}{\lambda}\Delta x \quad (3)$$

for a transverse displacement Δx , a tilt angle α , and a laser wavelength λ . For a Gaussian beam, the wavefront is flat at the center of the laser waist, such that Eq. 3 holds, but nearly spherical in the far field, where $\Delta\varphi$ reduces to zero. In between, the radius of curvature at a distance z from the waist is

$$R(z) = z + \frac{z_R^2}{z} \quad \text{with} \quad z_R \equiv \frac{\pi w_0^2}{\lambda} \quad (4)$$

in paraxial approximation [15], where z_R is the Rayleigh length and w_0 is the $1/e^2$ waist radius. As shown in Fig. 4, the resulting phase shift decreases with increasing distance z . At $z = \pm z_R$, for example, it is only half of the maximum value. Thus, making use of the tilted-wavefront effect may require to increase the Rayleigh length which corresponds to reducing the electric field acting on the electrons. According to theory [16], the Rayleigh length for maximum energy modulation on the beam axis is about 1/4 of the modulator length, but this condition will usually be relaxed due to the finite electron beam size. For the case of DELTA, an optimized value of z_R is 1/2 of the modulator length or even larger [12].

The reduced phase shift due to curved laser wavefronts can be compensated by an increased crossing angle. Since the phase shift is now a function of the position z along the modulator, the improvement of the bunching factor depends on several parameters, such as the undulator length, the

Rayleigh length, the tilt angle etc., and its prediction requires an integration of the laser-electron energy exchange over z . Furthermore, the electric field of the laser pulse and thus the amount of energy modulation is a function of all coordinates. If the chicane is set for optimum bunching at the center of the laser pulse, electrons at any other longitudinal or transverse position will contribute less to the coherent emission of radiation.

SUMMARY

A crossing angle between laser and electron beam can improve the bunching factor for FEL seeding or for the generation of ultrashort pulses in a storage ring via CHG or EEHG, provided the modulator is placed in a section with significant dispersion. The smaller the beam emittance, the larger is the effect of tilted wavefronts for a given dispersion value. It may therefore be advantageous to introduce vertical dispersion. In the case of DELTA, however, vertical dispersion would require additional magnets while horizontal dispersion can be created by changing the quadrupole setting. For this and other reasons (larger vertical beta function, larger horizontal aperture), first experimental investigations of the tilted-wavefront effect will be under horizontal crossing angles only. General statements on the result can only be given in the crude approximation of plane waves and an infinite laser beam size. More realistic predictions require a thorough simulation and are only valid for a particular set of parameters.

ACKNOWLEDGEMENTS

The frequent and very useful discussions with my colleagues at DELTA, TU Dortmund, are gratefully acknowledged. The work on "energy-spread cooling" [8] was brought to my attention by Guanglei Wang, SINAP. Sincere thanks also to Chao Feng, SINAP, for pointing out his recent work on wavefront tilting [9].

REFERENCES

- [1] For a list of synchrotron radiation sources see e.g. <http://www.lightsources.org>
- [2] A.A. Zholents and M.S. Zolotarev, "Femtosecond X-Ray Pulses of Synchrotron Radiation", *Phys. Rev. Lett.* 76, p. 912, 1996.
- [3] R. Coisson and F.D. Martini, "Free-electron relativistic scatterer for UV-generation", in *Physics of Quantum Electronics IX*, edited by S. F. Jacobs et al., Addison-Wesley, 1982.
- [4] L.H. Yu, "Generation of Intense UV Radiation by Subharmonically Seeded Single-Pass Free-Electron Lasers", *Phys. Rev. A* 44, p. 5178, 1991.
- [5] G. Stupakov, "Using the Beam-Echo Effect for Generation of Short-Wavelength Radiation", *Phys. Rev. Lett.* 102, p. 074801, 2009.
- [6] D. Ratner, A. Chao, "Seeded Radiation Sources with Sawtooth Waveforms", *Proc. 33th Free-Electron Laser Conf.*, Shanghai/China, 2011, pp. 53-56.
- [7] G. Stupakov, M.S. Zolotarev, "Using Laser Harmonics to Increase Bunching Factor in EEHG", *Proc. 33th Free-Electron Laser Conf.*, Shanghai/China, 2011, pp. 45-48.
- [8] H. Deng, C. Feng, "Using Off-Resonance Laser Modulation for Beam-Energy-Spread Cooling in Generation of Short-Wavelength Radiation", *Phys. Rev. Lett.* 111, p. 084801, 2013.
- [9] C. Feng, T. Zhang, H. Deng, Zh. Zhao, "Three-dimensional manipulation of electron beam phase space of seeding soft x-ray free-electron lasers", *Phys. Rev. ST - Accel. Beams* 17, p. 070701, 2014.
- [10] S. Khan, F. Bahnsen, S. Cramm, S. Döring, J. Greve, M. Höner, H. Huck, M. Huck, R. Molo, P. Ungelenk, L. Plucinski, A. Schick, C. M. Schneider, "Generation of Ultrashort and Coherent Synchrotron Radiation Pulses at DELTA", *Synch. Rad. News* 26(3), p. 25, 2013.
- [11] A. Meyer auf der Heide, S. Hilbrich, M. Höner, H. Huck, M. Huck, S. Khan, C. Mai, R. Molo, H. Rast, A. Schick, P. Ungelenk, "Coherent Harmonic Generation at the DELTA Storage Ring: Towards User Operation", in these Proceedings: *Proc. 36th Free-Electron Laser Conf.*, Basel/Switzerland, 2014, TUP082.
- [12] S. Hilbrich, M. Höner, H. Huck, M. Huck, S. Khan, C. Mai, A. Meyer auf der Heide, R. Molo, H. Rast, A. Schick, P. Ungelenk, "Upgrade Plans for the Short-Pulse Facility at DELTA", in these Proceedings: *Proc. 36th Free-Electron Laser Conf.*, Basel/Switzerland, 2014, MOP087.
- [13] S. Akturk, X. Gu, P. Bowlan, R. Trebino, "Spatio-Temporal Couplings in Ultrashort Laser Pulses", *J. Opt.* 12, p. 093001, 2010.
- [14] P. Ungelenk, M. Bakr, M. Höner, H. Huck, S. Khan, R. Molo, A. Nowaczyk, A. Schick, M. Zeinalzadeh, "Recent Developments at the DELTA THz Beamline", *Proc. Int. Part. Accel. Conf.*, New Orleans/LA/USA, 2012, pp. 768-770.
- [15] A.E. Siegman, "Lasers", University Science Books 1986.
- [16] A.A. Amir, Y. Greenzweig, "Three-dimensional Theory of the Free-Electron Laser", *Phys. Rev. A* 34, p. 4809, 1986.

BROADLY TUNABLE THZ FEL AMPLIFIER*

Chia-Hsiang Chen,[#] Yu-Chung Chiu, Kuan-Yan Huang, Institute of Photonics, Technologies/Department of Electrical Engineering, National Tsinghua University, Hsinchu 30013, Taiwan

Yi-Kai Gan, Fu-Han Chao, Yi-Chu Wang, Department of Physics, National Tsing Hua University, Hsinchu 30013, Taiwan

Yen-Chieh Huang, Institute of Photonics Technologies/Department of Electrical Engineering, National Tsinghua University, Hsinchu 30013, Taiwan and Department of Physics, National Tsing Hua University, Hsinchu 30013, Taiwan

Abstract

In this paper we present a broadly tunable high-power THz FEL amplifier driven by a photoinjector with a seed source tunable between 0.7-2.0 THz. A fully synchronized THz seed pulse is provided by an optical parametric amplifier pumped by the very driver laser of the electron injector. The FEL amplification gain is almost 3000 at 2 THz for nominal input beam parameters.

INTRODUCTION

In the THz region, high power radiation sources are scarce. A free electron laser is known to be high-power and tunable over a wide spectral range. In the past, FEL oscillators were often built generate high-repetition-rate [1,2] or quasi-CW [3] THz radiation. With rapid advancement on high-brightness photoinjectors, single-pass FELs are playing a crucial role in generating high-peak-power laser radiation through self-amplified spontaneous emission (SASE) [4]. Unfortunately a low-energy beam is susceptible to the space charge effects and makes a SASE THz FEL more difficult to realize. In addition, it is well known that the noisy spectral and temporal output of a SASE FEL is suitable for applications requiring high spectral and temporal purity. Recently, kW-level tunable THz radiation sources are becoming available from optical technologies. A possible path to realizing a MW-level tunable narrow-line THz source is to seed an FEL amplifier with a fully tunable optical THz source. This idea was studied in the past with a limited wavelength-tunability from a CO₂-laser pumped THz different frequency generator (DFG) using GaAs as its gain material [5]. In this paper, we present a design for a high-power tunable THz FEL seeded by an all-solid-state THz parametric amplifier (TPA) broadly tunable between 0.7 and 2 THz.

SYSTEM LAYOUT

Figure 1 shows the design concept of the proposed FEL amplifier to generate fully tunable, narrow-line, high-power THz radiation. The proposed THz FEL system comprises two major components, the FEL amplifier and the THz seed. The FEL beamline consists of a high-

brightness photoinjector and an undulator. The THz seed is a tunable TPA using a lithium niobate (LiNbO₃, LN) crystal as its gain material. One unique design that greatly simplifies the operation of the system is to use the driver laser of the photoinjector to pump the TPA and generate a fully synchronized seed THz pulse for the FEL. First, a Nd:YVO₄ mode-locked laser at 1064 nm is sent into a Nd:YAG regenerative amplifier to gain tens of mJ pulse energy. The laser pulse is then divided into two parts; the first part is frequency-quadrupled to ultraviolet to drive the photoinjector and the other is sent to pump the TPA to generate a THz seed pulse to the undulator. As will be shown below, this TPA is capable of generating a kW THz pulse with tunability between 0.7 and 2.0 THz.

Figure 2 shows the hardware arrangement of the proposed single-pass THz FEL amplifier, including a photoinjector, a solenoid, and an undulator. The total length of the setup is about 3.5 m. The accelerator is a 2.856-GHz BNL/SLAC/UCLA type photoinjector [6], generating a 3-5 MeV electron beam with 0.5-nC charge. A solenoid magnet following the gun compensates the emittance growth of electron bunch and focuses the electron beam to the undulator. Installed between the solenoid and the undulator is an input mirror for the THz seed. To keep the whole system compact, the mirror has an aperture to transmit the electrons.

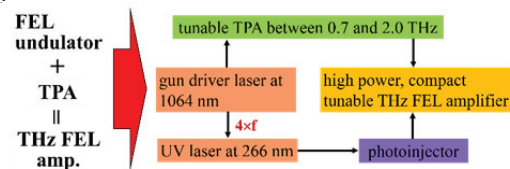


Figure 1: The design concept of the proposed high-power tunable THz FEL amplifier.

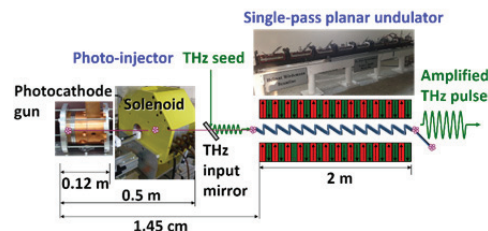


Figure 2: The hardware arrangement of the proposed THz FEL amplifier (planar undulator).

*Work supported by MoST under NSC 102-2112-M-007-002-MY3
#chiahsiang@mx.nthu.edu.tw

THZ PARAMETRIC AMPLIFIER

Among various optical THz technologies, nonlinear frequency mixing is known to offer an effective means to generate coherent THz-wave radiations at room temperature. One notable example is the THz optical parametric generation from LN. This nonlinear optical material is relatively stable, low-cost, and high-gain. In the nonlinear wavelength conversion process, birefringence phase matching in LN requires the THz wave to propagate away from the nearly co-directional optical pump and signal beams at about a 65° angle. In the past we have demonstrated efficient, narrow-line THz-wave generation from optical parametric oscillations in LN waveguides [7, 8]. Recently, using the same material, Minamide *et. al* further demonstrated kW THz radiation from a sub-ns TPA [9]. The proposed THz FEL amplifier, driven by a ps electron bunch, is to radiate a ps THz pulse. We therefore propose a TPA pumped by the ps driver laser of the photoinjector to seed the FEL amplifier with a fully synchronized THz pulse. Figure 3 depicts the schematic of our kW TPA seed source, wherein a pulse laser at 1064 nm pumps an LN crystal to amplify a weak signal tunable around 1070 nm and generate a tunable THz idler wave through difference frequency generation. The driver laser of the injector is an amplified mode-locked Nd:YVO₄ laser producing 10-mJ, 12-ps pulses at 1064 nm with a 10-Hz repetition rate. Approximately 1-mJ pulse energy is split from the gun driver laser to pump the TPA. The pumping intensity in an LN crystal can reach a few GW/cm² with a millimetre pump laser radius. Figure 4 shows the calculated parametric gain of LN over a frequency range between 0.5 and 2.5 THz based on a pump intensity of 1 GW/cm² [10]. For a parametric gain coefficient of 12 cm⁻¹, it is sufficient to generate 1 kW THz radiation from a 1-W seeded TPA with a LN crystal length of 1 cm. The 1-W signal seed to the TPA can be obtained by amplifying an external-cavity tunable diode laser (ECDL) at ~ 1070 nm in a Yb fiber laser amplifier. An ECDL laser usually has a MHz line width. Pumped by a transform-limited Nd laser at 1064 nm and seeded by a MHz line-width signal, the TPA is expected to generate a transform-limited THz seed pulse for the FEL amplifier.

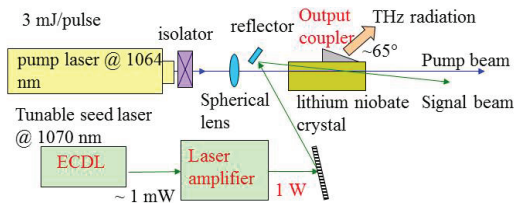


Figure 3: Configuration of a proposed TPA to seed the FEL undulator. The pump laser, derived from the gun driver laser, is focused into an LN gain crystal to amplify a laser signal tunable around 1070 nm and generate a tunable THz radiation.

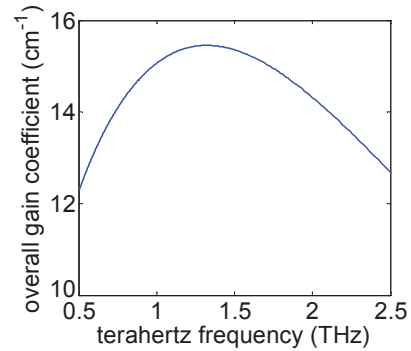


Figure 4: Calculated gain coefficient for the proposed TPA with 1 GW/cm² pumping intensity at 1064 nm. Such gain is sufficient to generate 1 kW power at THz from 1-cm long LN TPA with 1-W seed power at about 1070 nm.

THZ FEL AMPLIFIER

We simulated the acceleration and propagation of the electrons by using the simulation code ASTRA. By varying the peak acceleration gradient of the photoinjector from 72 to 120 MV/m, the electron output energy varies from $\gamma = 6.41$ to 10.76, respectively. Assuming an undulator period of 18 mm and undulator parameter of 0.98, the radiation frequency is in the range of 0.7 to 2 THz. The solenoid after the gun provides a peak magnetic field adjustable between 1.4-2.1 kG to compensate emittance growth at different beam energies. From our stimulation study, the optimized beam parameters at the undulator entrance are: electron bunch length = 10 ps, transverse beam width = 0.5 mm, normalized emittance = 3.5π mm-mrad.

The electrons form microbunches when interacting with the seed THz field in the undulator. Therefore bunching factor in the undulator is an important indication for the FEL amplification gain. Figure 5 shows the bunching factors of the electrons obtained from time-dependent GENESIS simulations with 1 kW seed power at 0.7, 1.4, and 2.0 THz in the 2-m long undulator. The corresponding beam energies are $\gamma = 6.41, 9.06$ and 10.76 for the 0.7, 1.4, and 2.0 THz radiations, respectively. Since a higher energy beam suffers less from the space charge effects, the bunching factor of the 2-THz case is evidently higher than the others. As will be seen below, this higher bunching factor helps the FEL power to build up at 2 THz.

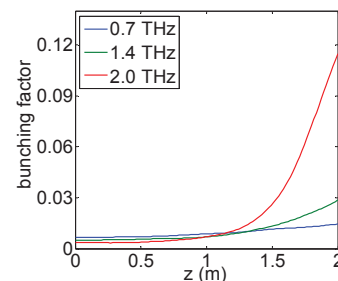


Figure 5: Variation of the bunching factors in the undulator with 1 kW seed power at 0.7, 1.4, and 2.0 THz. (Results obtained from simulation in GENESIS).

Figure 6 shows the FEL power versus undulator length, obtained from our GENESIS simulation. The FEL output power varies between 0.013 – 2.74 MW for the frequency range between 0.7 – 2.0 THz. The amplification gain at 2.0 THz is almost 3000.

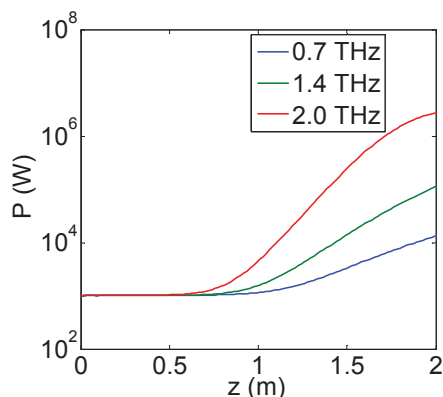


Figure 6: Radiation power vs. undulator length at 0.7, 1.4, and 2.0 THz with 1 kW seeding power.

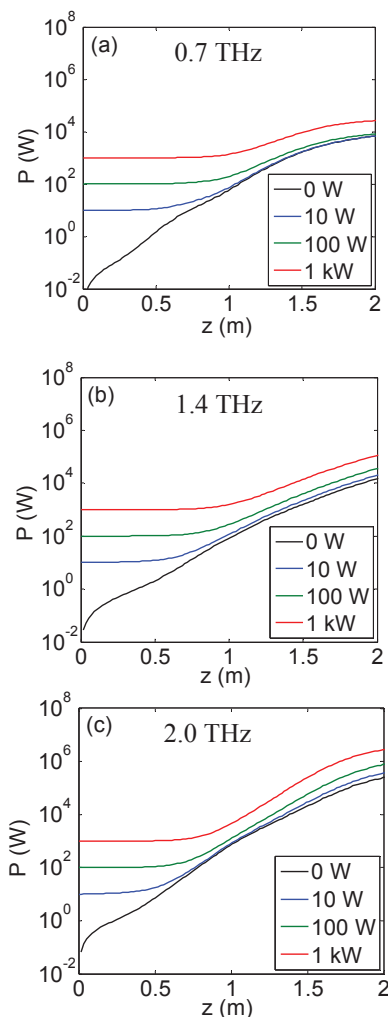


Figure 7: Build-up of FEL powers at (a) 0.7, (b) 1.4, and (c) 2.0 THz with different seeding powers to the undulator. A higher seeding power helps to quickly build up the FEL output.

ISBN 978-3-95450-133-5

In Fig. 7, we compare the radiation powers of the FEL amplifiers at (a) 0.7, (b) 1.4, and (c) 2.0 THz with different seed powers. The 0-W case is equivalent to a SASE FEL, which is known to give a noisy output. It is seen from the figures that a high seed power helps to quickly build up the FEL power, in addition to ensuring the spatial and temporal coherence of the output.

CONCLUSION

We have presented a compact, high-power FEL amplifier broadly tunable between 0.7 and 2.0 THz. The FEL amplifier consists of a 3-5 MeV photoinjector, an emittance compensating coil, a 2-m long undulator, and a kW tunable seed source at THz frequencies. A unique feature of this FEL amplifier is to convert part of the gun driver laser pulse to a fully synchronized THz pulse to seed the FEL amplifier, permitting generating of amplified coherent tunable radiation at the output with a power range between 13 kW and 3 MW.

REFERENCES

- [1] J.S. Sokolowski *et al.*, “First lasing of the Israeli tandem electrostatic accelerator free electron laser”, PAC’97, p. 906, (1997).
- [2] G.N. Kulipanov *et al.* Terahertz Science and Technology 1, 107 (2008).
- [3] Ailin Wu *et al.*, “The parameter study of terahertz free-electron laser oscillator based on electrostatic accelerator”, WEPD51, PAC’11 (2011).
- [4] Website: <http://sbfel3.ucsb.edu/ctst/Top.html/>
- [5] C. Sung *et al.*, “High-gain seeded FEL amplifier tunable in the terahertz range”, FEL’05 (2005).
- [6] D.T. Palmer *et al.*, “Emittance studies of the BNL/SLAC/UCLA 1.6 cell photocathode gun”, PAC’97, p. 2687, (1997).
- [7] A.C. Chiang *et al.*, “Enhanced terahertz-wave parametric generation and oscillation in lithium niobate waveguides at terahertz frequencies”, Opt. Lett. 30, 3392 (2005).
- [8] T.D. Wang *et al.*, “Low-threshold, narrow-line THz-wave parametric oscillator with an intra-cavity grazing-incidence grating”, Opt. Express 16, 12571 (2008).
- [9] Hiroaki Minamide *et al.*, “Kilowatt-peak terahertz-wave generation and sub-femtojoule terahertz-wave pulse detection based on nonlinear optical wavelength-conversion at Room temperature”, Journal of Infrared, Millimeter, and Terahertz Waves 35, 25 (2014).
- [10] S.S. Sussman, *Microwave Lab. Report*, (Stanford University, Stanford, Calif, 1970), 1851.

UPGRADE PLANS FOR THE SHORT-PULSE FACILITY AT DELTA*

S. Hilbrich[†], M. Höner, H. Huck, M. Huck, S. Khan, C. Mai,
A. Meyer auf der Heide, R. Molo, H. Rast, P. Ungelenk,

Center for Synchrotron Radiation (DELTA), TU Dortmund University, Dortmund, Germany

Abstract

The synchrotron light source DELTA comprises a short-pulse facility based on coherent harmonic generation (CHG) to generate coherent radiation with wavelengths in the VUV regime. Even shorter wavelengths can be produced using the echo-enabled harmonic generation (EEHG) technique. An upgrade of the storage ring is planned to install an EEHG as well as a femtoslicing short-pulse source.

INTRODUCTION

The 1.5-GeV synchrotron light source DELTA, operated by the TU Dortmund University, is shown schematically in Fig. 1. Besides dipole magnets as radiation sources, DELTA comprises two undulators (U55, U250) and a superconducting asymmetric wiggler (SAW). The pulse duration of the synchrotron radiation is about 100 ps (FWHM) given by the bunch length. Shorter radiation pulses with durations in the sub-100-fs range can be generated with commercially available laser systems, but with wavelengths in the near-visible range. In the following, three techniques to combine the advantages of both radiation source types in order to produce radiation with short wavelengths as well as short pulse duration are described.

Coherent Harmonic Generation (CHG)

The CHG technique [1] is based on an interaction between a short laser pulse and an electron bunch. The setup consists of two undulators and a dispersive magnetic chicane between them. A detailed description of the CHG setup at DELTA can be found in [2]. The interaction occurs in the first undulator, the so-called modulator, and leads to a sinusoidal modulation of the electron energy with the periodicity of the

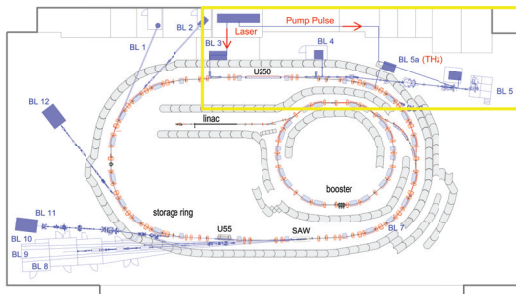


Figure 1: Sketch of the DELTA synchrotron radiation facility. The yellow frame marks the CHG facility in the northern part of the storage ring.

* Work supported by DFG, BMBF, FZ Jülich, and by the Federal State NRW.

[†] svenja.hilbrich@tu-dortmund.de

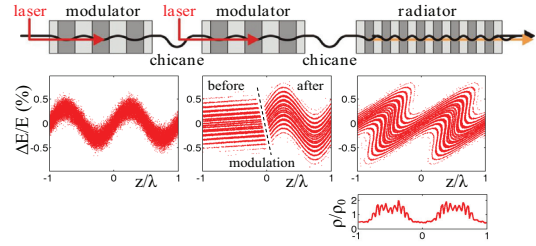


Figure 2: Top: Sketch of the magnetic setup for EEHG. Center: The longitudinal phase space before the first magnetic chicane, before and after the second modulator, and after the second chicane. Bottom: The longitudinal electron density after the second chicane.

laser wavelength within a short "slice" at the center of the bunch. The magnetic chicane converts the energy modulation into a density modulation known as microbunching. In the second undulator, the radiator, the microbunches radiate coherently at the laser wavelength and harmonics thereof with a much higher intensity than the incoherent undulator radiation.

The power of the CHG radiation at the n th harmonic of the laser wavelength is [3]

$$P_n \propto N^2 b_n^2 \quad (1)$$

with N being the number of modulated electrons and the so-called bunching factor

$$b_n \propto e^{-n^2} \quad (2)$$

decreasing exponentially with the harmonic number n .

Echo-enabled Harmonic Generation (EEHG)

The FEL seeding scheme EEHG [4] has been successfully tested at SLAC in Menlo Park (USA) [5] and SINAP in Shanghai (China) [6] and can also be applied at storage rings to generate ultrashort coherent pulses. Compared to CHG, it uses an additional undulator and chicane. As in the case of CHG, the electron energy is sinusoidally modulated in the first modulator, but the first chicane has a larger R_{56} value, such that the electron distribution in the longitudinal phase space is strongly sheared while the density distribution is flat. In the second modulator, the electron energy is modulated by a second laser pulse. In a following magnetic chicane with a moderate R_{56} value, a density modulation with a high content of harmonics is generated (see Fig. 2). The optimized bunching factor for EEHG, i.e., with optimum settings for each harmonic, scales as [7]

$$b_n(\lambda) \propto n^{-\frac{1}{3}} \quad (3)$$

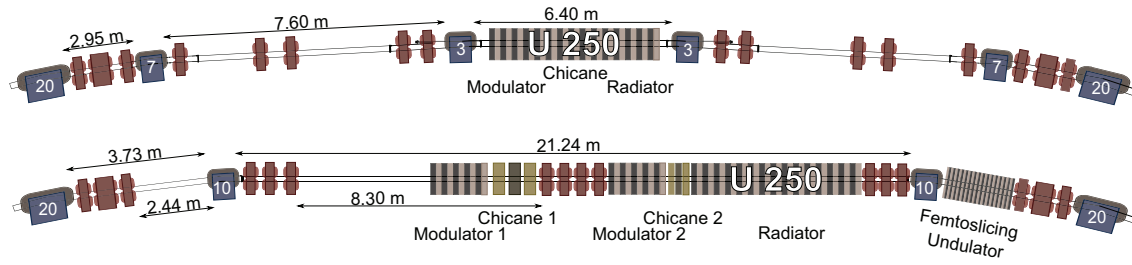


Figure 3: Top: Present magnetic setup in the northern part of DELTA. Bottom: Planned magnetic setup for the implementation of EEHG and femtoslicing in which two 3- and 7-degree dipole magnets are replaced by two 10-degree dipoles.

thus allowing the generation of higher harmonics with reasonable intensity compared to CHG.

Femtosing

In contrast to CHG and EEHG, femtoslicing [8] utilizes a geometrical separation of incoherent radiation from modulated and unmodulated electrons. Downstream of the modulator, a dispersive magnetic element, like a dipole magnet, creates the spatial separation of the electrons. In a following radiator, the off-energy electrons radiate incoherently at wavelengths to which the radiator is tuned. Femtoslicing is routinely performed at the ALS [9], at BESSY [10] and at the SLS [11].

DESIGN CONSIDERATIONS

In order to implement EEHG at DELTA, the CHG facility in the northern part of the storage ring will be replaced by a new magnetic setup. The most challenging task for a successful operation of EEHG is to retain the resulting microbunches until they reach the radiator. Since dipole magnets would smear out the phase space structure, all EEHG components will be placed in one straight section. For that purpose, the 3- and 7-degree dipole magnets will be exchanged by a 10-degree dipole magnet resulting in a long

Table 1: Lattice Properties of the Present and EEHG Configuration. Parameters labeled by an asterisk (*) refer to the CHG/EEHG section

Parameter	Present	EEHG
circumference	115.20 m	115.21 m
straight sections*	1 x 6.40 m	2 x 8.30 m
horizontal displacement*	0.00 m	0.24 m
max. horizontal beta function	41 m	20 m
max. vertical beta function	101 m	25 m
max. horizontal dispersion	1.05 m	1.05 m
min. horizontal beta function*	0.5 m	0.5 m
min. vertical beta function*	2 m	3 m
min. horizontal dispersion*	-0.09 m	-0.01 m
horizontal tune	9.20	9.14
vertical tune	3.37	3.64

straight section with enough space for three undulators and two chicanes as shown in Fig. 3. In addition, there will be enough space for a femtoslicing undulator downstream of the 10-degree dipole magnet following the radiator.

Optical Functions

The new arrangement of the magnetic dipoles and quadrupoles leads to the optical functions shown in Fig. 4. Simulations were performed using a modified version of the code *elegant* [12]. The optical functions of the storage ring outside the range shown in Fig. 4 are identical to the present ones. Table 1 shows the properties of the lattices of the present and EEHG configuration. Another issue taken into consideration is to minimize the change of the circumference. For DELTA, a change of 1 cm is tolerable resulting in a horizontal displacement of the U250 axis by 24 cm towards the ring center (see Table 1).

Second-Order Effects

Considering an rms angular deviation of $\sigma' = \sqrt{\epsilon_x/\beta_0}$, where ϵ_x is the beam emittance and β_0 the beta function at

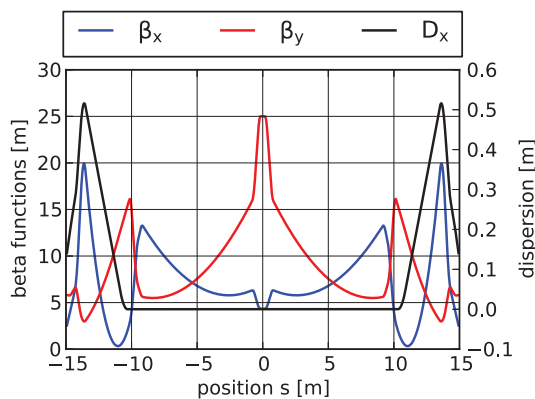


Figure 4: Horizontal and vertical beta function and horizontal dispersion versus longitudinal position s (EEHG lattice).

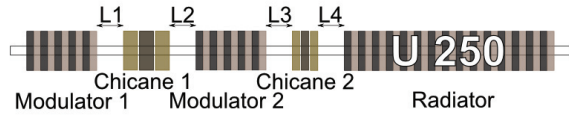


Figure 5: Schematic view of the lengths L1 to L4 between the components used for the EEHG setup.

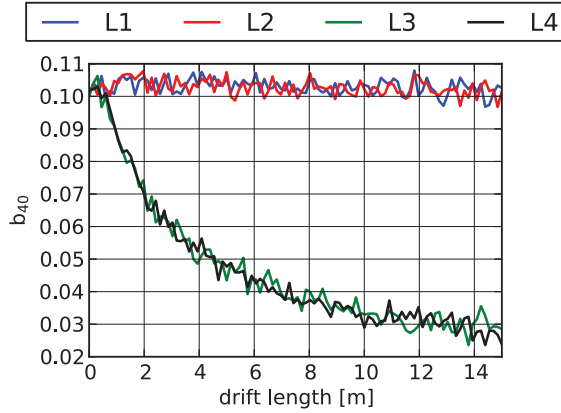


Figure 6: Bunching factor for $n = 40$ versus the variation of the distances L1 to L4 shown in Fig. 5.

the beam waist, the resulting variation of path-lengths is [13]

$$\Delta L = \frac{1}{2} \epsilon_x \frac{L}{\beta_0} \quad (4)$$

in a drift space of length L . This effect can destroy the microbunching due to the various angular deviations of the electrons. For the planned EEHG setup at DELTA, the influence of a variation of the distances L1 to L4 (see Fig. 5) between the undulators and chicanes on the bunching factor was simulated using a self-written code. Each of the distances was varied from 0 to 13 m while the other ones remained zero. The calculation was performed for a horizontal beta function at the beam waist of 5 m and an emittance of 15 nm rad. As shown in Fig. 6, only the distance between the second undulator and the radiator (L3 + L4) has an influence on the transport of the microbunches as predicted by [14]. To reduce this effect, the second modulator and chicane will be placed as close as possible to the radiator.

NEW COMPONENTS

To implement EEHG at DELTA, two additional undulators and chicanes are required if the present U250 is used as radiator.

Undulators

Two new undulators (Fig. 7) were designed based on those used at FLASH for the ORS experiment [15]. The undulators are ordered and will be delivered this year. The design parameters of the new undulators and the U250 are listed in Table 2.

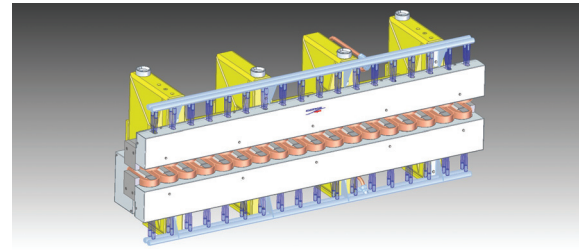


Figure 7: Sketch of the new undulators used in the EEHG setup (courtesy Scanditronix Magnet AB, Vislanda, Sweden).

Table 2: Parameters of the Undulators used in the Future EEHG Setup at DELTA

Parameter	Modulators	U250
pole gap	40 mm	50 mm
total length	1.85 m	4.85 m
period length	0.20 m	0.25 m
number of periods	7	17
magnetic peak field	0.62 T	0.76 T

Chicanes

The strength of the second chicane is similar to that of the chicane in the present CHG setup while the first chicane has a much larger R_{56} value of the order of 1 mm. A sketch with the dimensions of the first chicane is shown in Fig. 8. The parameters for both chicanes are listed in Table 3, and Fig. 9 shows the dependence of the R_{56} value and the horizontal excursion dx on the magnetic field B .

Table 3: Parameters of the Chicanes in the EEHG Setup

Parameter	Chicane 1	Chicane 2
total length	1.5 m	0.9 m
length of single dipoles	0.30 m	0.15 m
distance between dipoles	0.15 m	0.15 m
max. R_{56}	1.6 mm	0.3 mm
max. magnetic field	0.8 T	0.8 T
offset dx	21 mm	7 mm

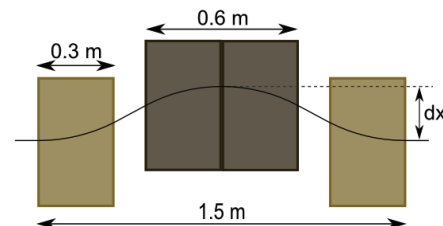


Figure 8: Schematic view of the first chicane.

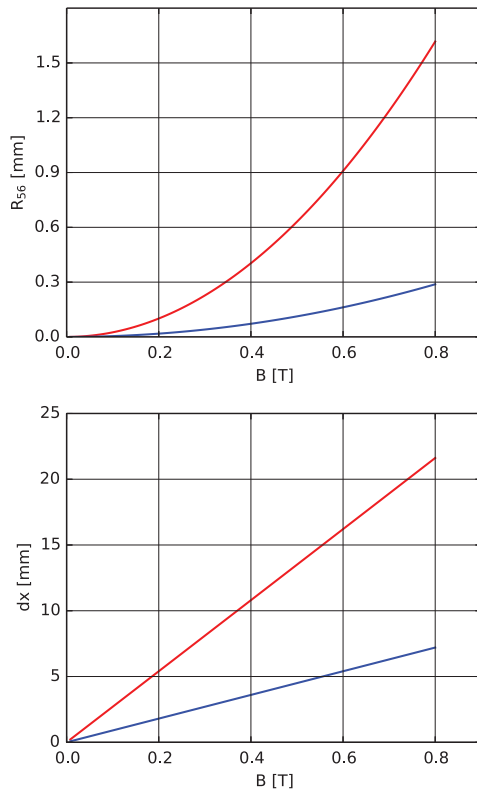


Figure 9: Chicane strength R_{56} and horizontal excursion dx versus the magnetic field for the first (red) and second (blue) chicane in the new EEHG setup.

OPTIMUM LASER WAIST

In order to simulate the energy modulation of the electrons in the modulators, the propagation of the laser light can be described by a Gaussian beam determined by the wavelength λ , the waist position z_0 , the Rayleigh length z_r and the beam quality factor M^2 [16] which is 1 for the fundamental Gaussian mode and larger in the presence of higher-order modes. By varying the waist position and Rayleigh length the energy modulation can be optimized.

Given an undulator of length L and a laser beam waist centered at the undulator, a Rayleigh length of $z_r \approx L/4$ would maximize the energy modulation of an electron on the beam axis [17]. In order to include the M^2 factor and the finite electron beam size, the average energy modulation of the electrons was simulated with the code *elegant* [12], which was modified to include an M^2 factor larger than unity [18]. The simulation was performed assuming an infinitely long laser pulse with the power corresponding to the peak power of a realistic laser pulse. The waist of the laser beam was located at the center of the undulator and the energy modulation was determined under variation of the $1/e^2$ laser waist radius w_0 , which is related to the Rayleigh length z_r by

$$z_r = \pi w_0^2 / (\lambda M^2). \quad (5)$$

For the planned EEHG setup at DELTA, this dependency is shown in Fig. 10 for both modulators. The laser parameters

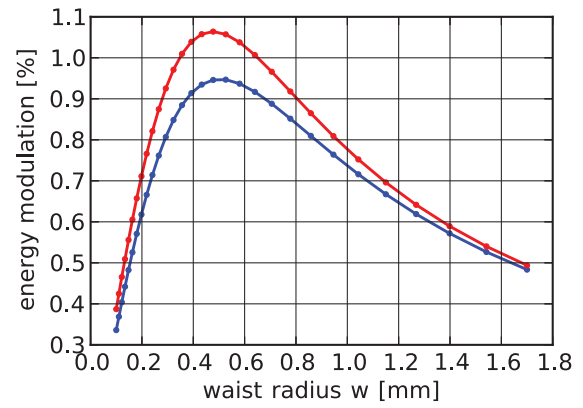


Figure 10: Energy modulation of the electrons versus laser waist radius (blue: first modulator, red: second modulator).

chosen for the simulation were an M^2 factor of 1.1, a laser wavelength of 800 nm, a laser pulse energy of 4 mJ and a pulse length (FWHM) of 60 fs. For both undulators, the maximum energy modulation occurs for a waist radius of about 500 μm . Since the two modulators will be installed at locations with different optical functions (see Fig. 3 and Fig. 4), the energy modulation in the second modulator is about 10% higher. Given the optical functions, the simulation result shows that the Rayleigh length should be $z_r \approx L/1.6$.

OUTLOOK

Since the positions of the undulators, chicanes and quadrupoles are specified, the next step will be to determine the position of BPMs and steerer magnets. A new vacuum chamber design is under development, which will reuse as much as possible of the present chamber in order to minimize the costs.

ACKNOWLEDGMENT

It is a pleasure to thank our colleagues at DELTA and the faculty of Physics of the TU Dortmund University for their support. This work was supported by BMBF (05K13PE3), by the DFG (INST 212/236-1 FUGG), by the Helmholtz ARD Initiative, by the FZ Jülich and by the Federal State NRW.

REFERENCES

- [1] R. Prazeres et al., "Coherent harmonic generation in the vacuum ultraviolet spectral range on the storage ring ACO", *Nucl. Instr. and Meth. A* 272, pp. 68-72, 1988.
- [2] S. Khan et al., "Generation of Ultrashort and Coherent Synchrotron Radiation Pulses at DELTA", *Synch. Rad. News* 26, pp. 25-29, 2013.
- [3] L.H. Yu, "Generation of intense uv radiation by subharmonically seeded single-pass free-electron lasers", *Phys. Rev. A* 44, pp. 5178-5193, 1991.
- [4] G. Stupakov, "Using the Beam-Echo Effect for Generation of Short-Wavelength Radiation", *Phys. Rev. Lett.* 102, pp. 074801 ff., 2009.

- [5] D. Xiang et al., "Demonstration of the Echo-Enabled Harmonic Generation Technique for Short-Wavelength Seeded Free Electron Lasers", *Phys. Rev. Lett.* 105, pp. 114801 ff., 2010.
- [6] Z.T. Zhao et al., "First lasing of an echo-enabled harmonic generation free-electron laser", *Nature Photonics* 6, pp. 360-363, 2012.
- [7] D. Xiang et al., "Echo-enabled harmonic generation free electron laser", *PRSTAB* 12, pp. 030702 ff., 2009.
- [8] A.A. Zholents, M.S. Zolotarev, "Femtosecond X-Ray Pulses of Synchrotron Radiation", *Phys. Rev. Lett.* 76, pp. 912-915, 1996.
- [9] R.W. Schoenlein et al., "Generation of Femtosecond Pulses of Synchrotron Radiation", *Science* 287, pp. 2237-2240, 2000.
- [10] S. Khan et al., "Femtosecond Undulator Radiation from Sliced Electron Bunches", *Phys. Rev. Lett.* 97, pp. 074801 ff., 2006.
- [11] P. Beaud et al., "Spatiotemporal Stability of a Femtosecond Hard-X-Ray Undulator Source Studied by Control of Coherent Optical Phonons", *Phys. Rev. Lett.* 99, pp. 174801 ff., 2007.
- [12] M. Borland, Advanced Photon Source LS-287, 2000.
- [13] R. Molo et al., "EEHG and Femtoslicing at DELTA", in *Proc. 35th Int. Free-Electron Laser Conf.*, New York, 2013, pp. 594-597.
- [14] G. Penn, NGLS Technical Note 35, 2014.
- [15] G. Angelova et al., "Results from the Optical Replica Experiment in FLASH", in *Proc. 11th Europ. Particle Accelerator Conf.*, Genoa, 2008, pp. 1332-1334.
- [16] A.E. Siegmann, *Lasers*, ISBN: 978-0935702118, Univ. Science Books, 1986.
- [17] A. Amir, Y. Greenzweig, "Three-dimensional free electron laser gain and evolution of optical modes", *Nucl. Instr. and Meth. A* 250, pp. 404-412, 1986.
- [18] R. Molo, "Investigation of Short-Pulse Radiation Sources at DELTA Based on Coherent Harmonic Generation and Echo-Enabled Harmonic Generation", Diploma Thesis, faculty of Physics, TU Dortmund, Germany, 2011.

HIGH REPETITION RATE ENERGY MODULATOR SYSTEM UTILIZING A LASER ENHANCEMENT CAVITY *

Y. Honda[†], KEK, Tsukuba, Ibaraki, Japan

Abstract

In order to realize a high repetition rate seeded coherent radiation source, it is necessary to develop a seeding system which works in a continuous mode. Utilizing the longitudinal electric field in a higher transverse mode laser stored in an optical cavity, it is possible to introduce an energy modulation in an electron bunch. Through acceleration and dispersion handling, the modulation at laser wavelength can be converted into a finer density structure. It can be used as a seed of coherent radiation. We are developing a laser system to be used in the laser modulator system.

INTRODUCTION

Recent linear accelerators can realize an electron beam of high brightness and small energy spread. Based on such a high quality electron beam, SASE FEL has been realized and it has been provided as an user machine at various laboratories. At the next stage, temporal coherence and high averaged power are expected as additional characteristics to be developed. For temporal coherence, seeding scheme can be used. And for high averaged power, multiple bunch operation and/or energy recovery scheme with a superconducting cw accelerator can be used. But in order to realize the two items at the same time, a seeding system which can work at high repetition rate is necessary. Usually, seeding is done with a high peak power laser system which can work only at a low repetition rate. Here, we propose an optical cavity system which can realize a high enough electric field at ~100 MHz repetition of continuous operation. This can be used to directly modulate electron beam energy in the scale of optical wavelength. Combining the laser modulation with the bunch compression in the following stage, it can seed shorter wavelength radiation.

ACCELERATION BY AN ELECTRIC FIELD OF LASER

We would like to use an electric field of a laser for electron beam acceleration [1] [2]. Usually, it is not possible because the electric field of a plane wave is in transverse direction. Here we think a TM-wave laser beam which transfers in z -direction. The electric field is mainly in x -direction, and the magnetic field is zero in z -direction. Directly from Maxwell's equation, the following relation,

$$ikE_z = \frac{\partial E_x}{\partial x} \quad (1)$$

is obtained. Variation of transverse electric field results in a longitudinal electric field. Transferring an electron beam

along with the laser beam, the longitudinal component of the field can accelerate or decelerate the electron beam. It introduces energy modulation in the period of laser wavelength.

A higher order transverse mode, TEM₁₀-mode, is one of such a laser beam. The field profile is shown in Fig. 1. Its transverse field varies and zero-crosses at the center area of the profile. It means there is a longitudinal field at the center.

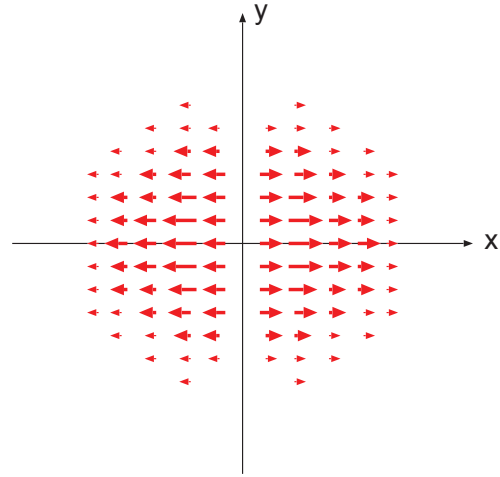


Figure 1: Profile of the higher transverse mode laser.

The x -component of the electric field can be written as,

$$E_{10}^x = A \cdot x \exp\left(-\frac{x^2}{w^2}\right) \exp(i(\omega t - kz + 2\phi(z))). \quad (2)$$

where $\phi(z)$ is Gouy phase, $\phi(z) = \tan^{-1}(\frac{z}{z_0})$, z_0 is Rayleigh length ($z_0 = \frac{\pi w_0^2}{\lambda}$). Simplifying this, the transverse electric field E_x is

$$E_x = x e^{-x^2}. \quad (3)$$

And the longitudinal electric field E_z is

$$E_z = \frac{(1 - 2x^2)e^{-x^2}}{k}. \quad (4)$$

These are shown in Fig. 2.

It can be written using laser power P as,

$$E_z = \frac{1}{2z_0} \sqrt{\frac{P}{c\epsilon_0}}. \quad (5)$$

Laser beam diverges and the phase shifts in the distance of z_0 . So, the effective accelerating distance is $2z_0$. Energy gain G is then,

$$G = E_z \times 2z_0 = e \sqrt{\frac{P}{c\epsilon_0}}. \quad (6)$$

* Work supported by KAKENHI

[†] yosuke@post.kek.jp

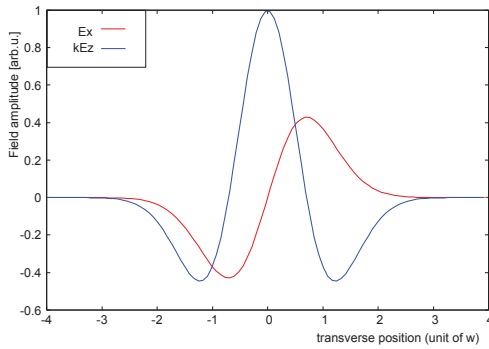


Figure 2: Transverse and Longitudinal field distribution of TEM₁₀ mode.

This does not depend on z_0 and laser spot size w_0 .

For example, at 1 MW of laser peak power, G is estimated to be 20 keV. This seems to be strong enough to introduce an energy modulation comparable with the original energy spread for 100 MeV class electron beam.

Recently, a high averaged power laser beam of 100 kW has been realized inside an optical enhancement cavity [3]. Such a development is done mainly for the photon target of laser Compton scattering sources (LCSS) [4]. Assuming a mode-locked laser pulse of ~ 10 ps duration to be stored in a ~ 100 MHz cavity at an average power of 100 kW, the peak power exceeds 10 MW. Excitation of the higher order transverse mode is also a proven technique. The finer spatial structure of the TEM₀₁ mode than that of the lowest gaussian mode has been used for measuring a small beam size of a low emittance storage ring [5].

Schematic setup of the laser modulator is shown in Fig. 3. An enhancement cavity is excited by a TEM₁₀-like beam, which is converted from a gaussian laser beam. The electron beam goes along the laser pulse inside the cavity in the same direction. It is then accelerated/decelerated by the longitudinal electric field of the laser, results in an energy modulation at the period of laser wavelength.

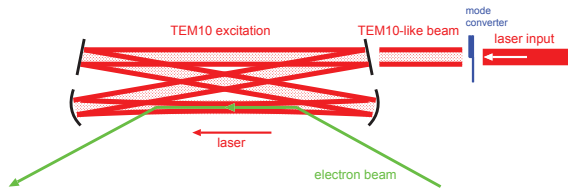


Figure 3: Schematic setup of the laser energy modulator.

REALIZATION OF A DENSITY MODULATION

A test accelerator for an energy recovery linac has been constructed and commissioned at KEK. It can be upgraded to be a 200 MeV class two-loop system in a future. Here, we assume the laser energy modulator system with the future plan. Our target is to realize ~ 30 nm scale of micro-structure

which can work as a seed of coherent radiation at an undulator.

Figure 4 shows the layout. The laser modulator cavity is installed in the inner loop. At the first turn of the inner loop, the laser field introduces an energy modulation at laser wavelength in the electron bunch. The distribution of longitudinal phase space can be controlled in the following beam line. First, at the return arc of the inner loop, by controlling the dispersion $R_{56}^{(1)}$, the phase space is stretched as shown in Fig. 5. This is for realizing density modulation after the following bunch compression. The second turn at the accelerator section is at an off-crest phase to introduce an energy chirp in the whole bunch. Then, the bunch is compressed using the dispersion at the arc of the outer loop $R_{56}^{(2)}$. By controlling the two dispersion parameters, $R_{56}^{(1)}$ and $R_{56}^{(2)}$, the imprinted energy modulation by the laser can be realized as a compressed density modulation at the final point.

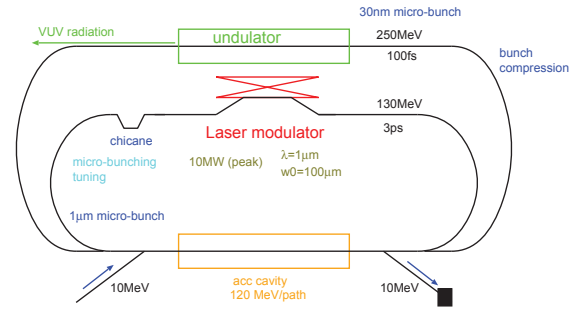


Figure 4: Layout at 2-loop ERL scheme.

Figure 5 shows an example one dimensional calculation. The laser wavelength is $1 \mu\text{m}$ and introduced energy modulation is $\Delta\gamma/\gamma = 1 \times 10^{-4}$. The accelerator RF frequency is 1.3 GHz, the energy gain is 130 MeV/path. The off-crest acceleration phase at the 2nd path is at 30 degree. It is shown that the modulated phase space distribution is stretched at first, then is recovered as a compressed density modulation. In this case, a factor 5 smaller structure than the initial laser wavelength is obtained.

Trying to have a finer structure, Fig. 6 shows the case of a factor 9 compression. Due to the non-linearity of the accelerator RF curve, it shows that a roundness remains in the final distribution, and it limits realization of a clear density modulation. One possible idea for realizing a finer structure is the EEHG scheme, which uses 2 stages of laser modulator as shown in Fig. 7. It can produce 20 nm scale structures in the bunch (Fig. 8).

DEVELOPMENT OF A LASER MODULATOR

We have been developing the laser modulator system. It stores a ~ 10 MW peak power in a ~ 100 MHz repetition enhancement cavity. We used to develop a system with a Nd based laser of 10 ps duration. Recently, we started a test with a Yb based laser of wider band width which is possible to have a shorter pulse and have an advantage to

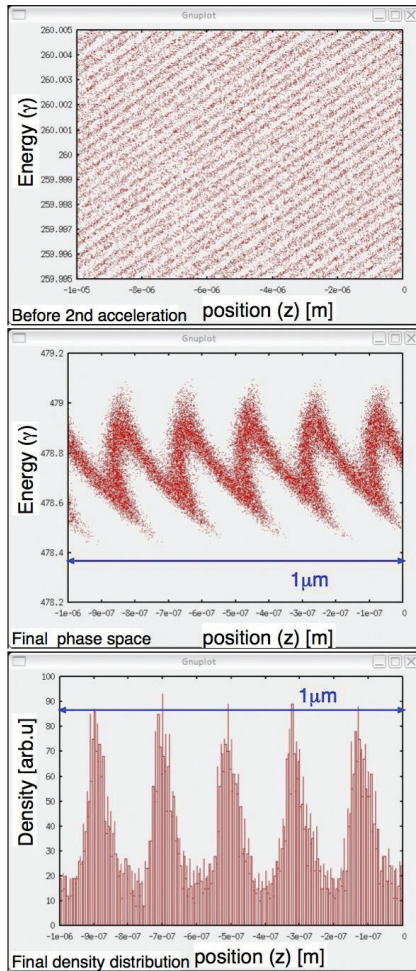


Figure 5: Longitudinal phase space (compression 1/5).

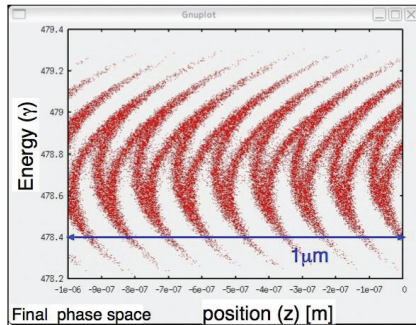


Figure 6: Longitudinal phase space (compression 1/9).

save the average power while keeping the peak power. As a first step, we made a low power test bench to test basic characteristics of the Yb based system. Figure 9 shows the Yb fiber laser oscillator used in this test. It is based on the non-linear polarization rotation mode-lock system. It also include a saturable absorption semiconductor mirror as a self-starter, and an EO modulator for fast controlling cavity resonance condition. The repetition rate is 38 MHz, and the RMS pulse duration is 120 fs.

It is known that one important problem to store a wide band laser in an enhancement cavity is carrier envelope

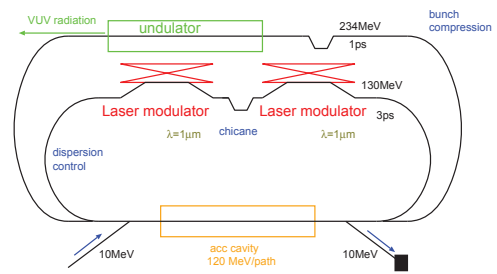


Figure 7: Layout of 2-stage system

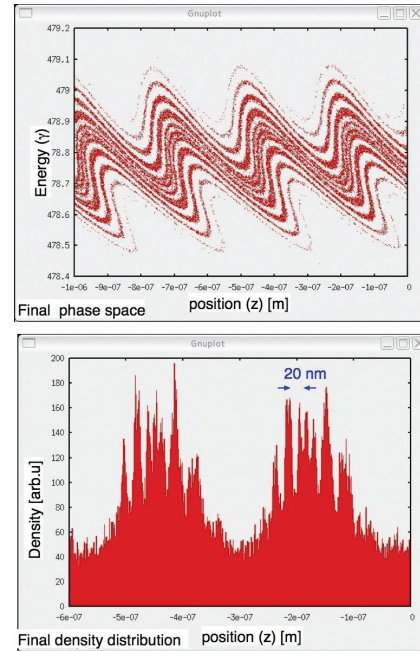


Figure 8: Longitudinal phase space of 2 stage system.

phase offset (CEO). It is the optical phase difference between pulses. When stacking many pulses in an optical cavity, they can not be stacked constructively if there is a finite CEO. It limits the enhancement gain. The effect can be seen when measuring resonance peaks of the cavity while scanning the cavity length as schematically shown in Fig. 10. In the case of zero CEO, the resonance peaks appears symmetrically

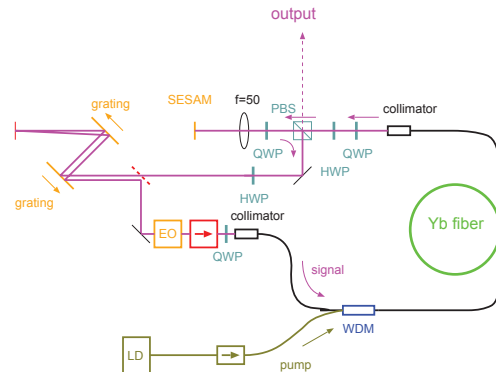


Figure 9: Schematics of the Yb fiber mode-lock oscillator.

and there is the maximum peak which can resonate in a good efficiency. But if there is a finite CEO, the structure becomes asymmetric and the efficiency drops from the ideal case. The efficiency drops considerably in the case of high enhancement gain.

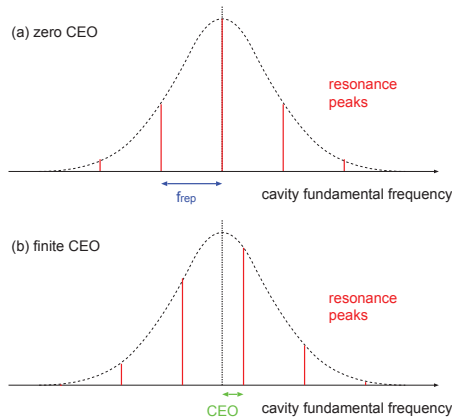


Figure 10: Effect of CEO in the structure of cavity resonances.

One way to control the CEO is to shift the laser wavelength with an Acousto-Optic modulator. The setup is shown in Fig. 11. AOM is used in a double-path layout. By controlling the driving RF frequency, it changes the laser wavelength keeping the repetition rate. It corresponds to giving an optical phase shift in the frequency domain. An experimental result with a test cavity setup of Fig. 12 is shown in Fig. 13. The Yb mode-locked laser pulse first goes through the AOM system, and then injected to the 4-mirror optical cavity of 78 MHz. The transmission signal of one of the mirrors is measured with a photo-diode while sweeping the cavity length. By adjusting the driving frequency of the AOM, the structure of resonance peaks can be controlled. This test shows that there is a simple way to control CEO when we try to use Yb based laser in a high enhancement gain cavity. Our next test item is to dynamically keep the CEO in a long period with a much higher enhancement gain.

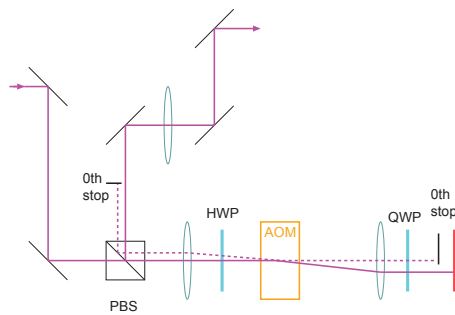


Figure 11: Setup of AOM.

SUMMARY

We propose to use a longitudinal field of a higher transverse mode laser to introduce an energy modulation for

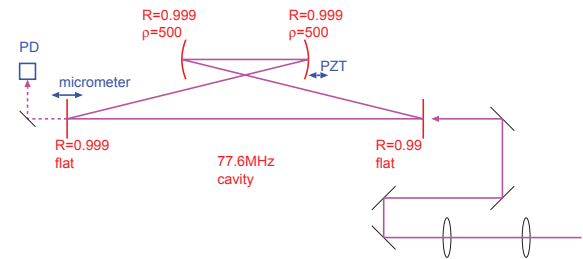


Figure 12: Setup of the enhancement cavity used in this test.

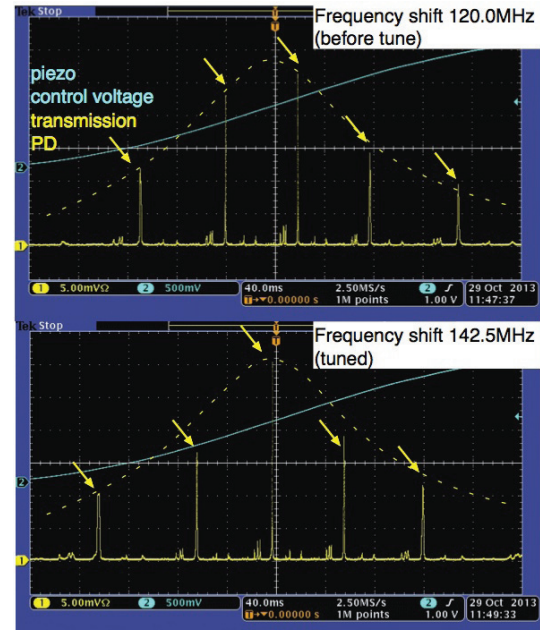


Figure 13: Experimental result of CEO control.

seeded coherent radiation. Combining with a bunch compression scheme, it can realize a finer density structure than the initial wavelength. Applying the optical cavity technique, it is possible to develop a system which works at continuous or multiple bunch operation.

We have started a basic experimental test on the laser system of the enhancement cavity.

REFERENCES

- [1] M. O. Scully, et al., "Simple laser accelerator: Optics and particle dynamics", Phys. Rev. A, vol. 44, 2656 (1991)
- [2] F. Caspers, et al., "Particle acceleration with the axial electric field of a TEM10 mode laser beam", CERN/PS 89-60 (RF/OP) (1989)
- [3] H. Carstens, et al., "Megawatt-scale average-power ultrashort pulses in an enhancement cavity", Opt. Lett. 39, vol. 44, 2595-2598 (2014)
- [4] T. Akagi, et al., "Development of a three dimensional four mirror optical cavity for laser-Compton scattering", Nucl. Instrum. Meth. A 724 63-71 (2013)
- [5] Y. Honda, Kyoto university doctor thesis (2004)

SOFT X-RAY SELF-SEEDING SIMULATION METHODS AND THEIR APPLICATION FOR LCLS

Svitozar Serkez

Deutsches Elektronen-Synchrotron (DESY), Hamburg, Germany

Jacek Krzywinski, Yuantao Ding, Zhirong Huang

SLAC, Menlo Park, California, USA

Abstract

Self-seeding is a promising approach to significantly narrow the Self-Amplified Spontaneous Emission (SASE) bandwidth of XFELs to produce nearly transform-limited pulses. We study radiation propagation through the grating monochromator installed at Linac Coherent Light Source (LCLS). The monochromator design is based on a toroidal Variable Line Spacing (VLS) grating working at a fixed incidence angle mounting without an entrance slit. It covers the spectral range from 500 eV to 1000 eV. The optical system was studied using wave optics method to evaluate the performance of the self-seeding scheme. Our wave optics analysis takes into account the finite size of the coherent source, third-order aberrations and height error of the optical elements. Wave optics is the only method available, in combination with FEL simulations, to simulate performance of the monochromator without exit slit. Two approaches for time-dependent simulations are presented, compared and discussed.

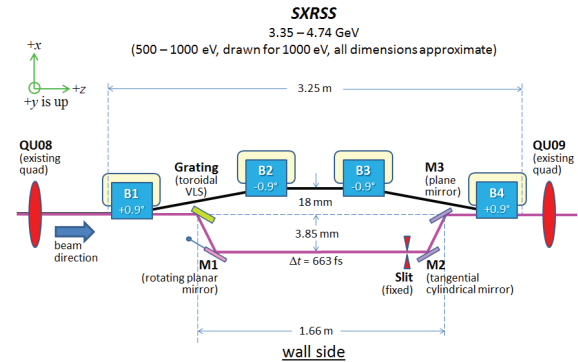


Figure 1: The compact soft x-ray self-seeding system to be located in U9. The grating is a toroidal VLS grating, M1 is a rotating plane mirror, M2 a tangential cylindrical mirror, and M3 a plane mirror used to steer the beam. Adapted from [13].

LCLS SOFT X-RAY SELF-SEEDING SETUP LAYOUT

INTRODUCTION

Self-seeding is a promising approach to significantly narrow the SASE bandwidth and to produce a nearly transform-limited pulses [1]- [10]. Recently a soft X-ray Self-seeding setup was installed in LCLS [11]- [15] and is currently under commissioning [16].

In general, a self-seeding setup consists of two undulators separated by a photon monochromator and an electron bypass, normally a four-dipole chicane (see Fig. 1). Both undulators are resonant at the same radiation wavelength. The SASE radiation generated by the first undulator (SASE undulator) passes through the narrow-band monochromator. A monochromatic pulse is created, which is used as a coherent seed in the second undulator (seeded undulator). Chromatic dispersion effect in the bypass chicane smears out the microbunching in the electron bunch produced by the SASE lasing in the SASE undulator. The electrons and the monochromatized photon beam are recombined at the entrance of the seeded undulator, and the radiation is amplified by the electron bunch until saturation is reached. The required seed power at the beginning of the seeded undulator must dominate over the shot noise power within the gain bandpass, which is order of a kW in the soft X-ray range.

The overall self-seeding setup consists of three parts: the SASE undulator, the self-seeding grating monochromator and the output seeded undulator in which the monochromatic seed signal is being amplified. The seeded undulator consists of two sections. The first section is composed by an uniform undulator, and the second section - by a tapered undulator. The transform-limited seed pulse is exponentially amplified passing through the first uniform part of the seeded undulator. Finally, in the second part of the seeded undulator the monochromatic FEL output is enhanced after saturation.

The Soft X-ray Self-Seeding (SXRSS) monochromator for LCLS was introduced in [13] and is based on a toroidal variable-line-spacing (VLS) grating, a steering plane mirror, a slit, a spherical mirror and another plane mirror (Fig. 1).

The toroidal VLS grating is illuminated by a SASE FEL radiation produced by the SASE undulator with the source in undulator sections 7 or 8 (depends on set-up). Transverse coherence of a SASE FEL allows one to avoid installation of an entrance slit. The plane mirror M1 is used to steer the certain wavelength of an angularly dispersed radiation to the slit. The spherical mirror M2 re-images the radiation from the slit position to the re-imaging point at the entrance to the seeded undulator. The plane mirror M3 reflects the radiation to the seeded undulator, allowing two additional

degrees of freedom for an overlap of the electron beam and the monochromatic radiation.

OPTICS MODELING

In order to simulate transformation of the radiation after passing the entire optical system of the monochromator, we model an effect of a different optical components. Propagation is carried out through an every component sequentially, as the radiation approaches them. Drift spaces are simulated in between. Simulation is based on a single frequency beam propagation method. Fresnel propagator is used to simulate drift spaces (e.g. [17]) and phase shifter method - to simulate optical elements. [18]. A phase-shifter model is used to simulate a focusing effect of the toroidal grating, M2 mirror and contribution of height errors of an optical element surfaces. This model implies an introduction of a shift to a phase of radiation $\Delta\Phi(x, y)$. This shift is dependent on a transverse position at radiation distribution and only changes the phase of the reflected beam without changing its amplitude. It allows one to change the wavefront curvature, therefore field behavior after propagation. In practice, $\Delta\Phi$ represents the deformation of the wavefront in propagation direction divided by the wavelength.

Free Space Propagation

Let's consider electric field in a space-time domain $\vec{E}(t, x, y)$ expressed in Cartesian coordinate system. In this domain radiation is exported from the FEL simulation code GENESIS [19]. Applying temporal and frequency Fourier transforms one obtains the electric field in inverse space-frequency domain - $\vec{E}(\omega, k_x, k_y)$.

Radiation distribution with frequency $\omega = k_0 c$ at a distance z after free space propagation one can calculate with a spatial-frequency response function in paraxial approximation [17]:

$$H(\omega, k_x, k_y, z) \simeq \exp[ik_0 z] \exp\left[-\frac{iz}{2k_0}(k_x^2 + k_y^2)\right],$$

$$\vec{E}(\omega, k_x, k_y, z) = \vec{E}(\omega, k_x, k_y, 0) \cdot H(\omega, k_x, k_y, z). \quad (1)$$

Grating Modeling

We model the toroidal VLS grating as a sum of independent contributions of a sagittal focusing element, a tangential focusing element, C_{12} and C_{30} aberrations, a surface height error and a wavelength-dependent tilt, responsible for angular dispersion. Also, asymmetry of incidence and diffraction angles has to be accounted. Since angles of incidence and diffraction from a grating are not equal, a radiation is re-sized transversely in dispersive dimension by the grating asymmetry parameter $b = \sin \theta_i / \sin \theta_d$.

Radiation distribution at any optical component in our simulation is modified by a phase-shifter in the following way:

$$\vec{E}(\omega, x, y) = \vec{E}_0(\omega, x, y) \exp[i\Delta\Phi(x, y, \dots)] \quad (2)$$

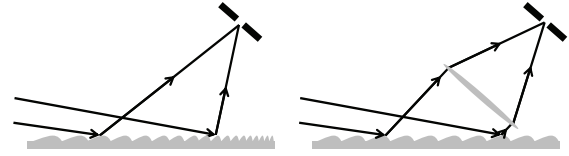


Figure 2: Schematic diagram of a VLS grating element. The VLS grating (left) is represented by a contribution of a planar grating with fixed line spacing and a thin lens (right).

Here $\Delta\Phi$ is a phase shift that depends on various parameters, depending on effect we want to model.

Tangential and sagittal curvatures of the toroidal grating act as an independent cylindrical lenses with the following curvature-determined focal lengths:

$$f_{tang}^{curv} = \frac{R_{tang}}{1/\theta_d + \theta_i/\theta_d^2},$$

$$f_{sag}^{curv} = \frac{R_{sag}}{\theta_i + \theta_d}. \quad (3)$$

Here R_{tang} and R_{sag} are tangential and sagittal radii of curvature, θ_i and θ_d are incidence and diffraction angles respectively. Eq. 3 shows that focal lengths are wavelength-dependent, since $\theta_d = \arccos(\cos \theta_i - \lambda D_0)$, accordingly to the grating equation.

Beside a toroidal curvature, the grating has a variable line spacing with the following line density: $D = D_0 + D_1 l + D_2 l^2$ [lines/mm], where l is a length along the grating.

The VLS focusing contribution may be modeled via introduction of another focusing element in a tangential plane [20] with the following focal length [21]:

$$f_{tang}^{vls} = \frac{\sin^2 \theta_d}{D_1 \lambda}. \quad (4)$$

Toroidal reflecting surfaces introduce aberrations. Two most important contributions are determined by twofold astigmatism and coma aberrations with C_{12} and C'_{30} coefficients correspondingly [22], [21]:

$$C_{12} = -\frac{1}{2} \left(-\frac{\sin \theta_i \cos \theta_i}{R_{sag} z_1} + \frac{\cos \theta_i}{z_1^2} + \frac{\sin \theta_d \cos \theta_d}{R_{sag} z_2} - \frac{\cos \theta_d}{z_2^2} \right),$$

$$C'_{30} = \frac{\lambda n D_2}{3} + \left(\frac{\sin^2 \theta_i}{z_1} - \frac{\sin \theta_i}{R_{tang}} \right) \frac{\cos \theta_i}{2z_1} - \left(\frac{\sin^2 \theta_d}{z_2} - \frac{\sin \theta_d}{R_{tang}} \right) \frac{\cos \theta_d}{2z_2}. \quad (5)$$

Here z_1 and z_2 are distances from an optical element [grating] to an object and an image correspondingly and n is a diffraction order which our case is equal to unity. The quadratic VLS coefficient D_2 introduces a phase shift, that is proportional to x^3 , therefore it is used to compensate the effect of C'_{30} aberration term.

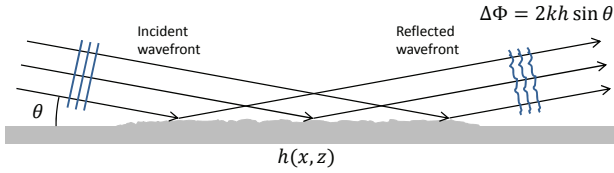


Figure 3: Thin-shifter-like effect of surface height errors for a small mean square of surface displacement, concept adapted from [23].

Aberrations are eliminated when $C'_{30} = 0$ and $C_{12} = 0$ criteria are fulfilled.

In order to simulate time-dependent phenomena of the grating's resolving power one needs to take into account grating dispersion. We propose to induce a wavefront tilt, according to an angular dispersion of the grating. Each wavelength is reflected from the grating at a different angle. Having an ensemble of wavelengths we can choose a principle ray wavelength λ that will propagate downstream with no wavefront tilt. Other wavelengths will propagate from the grating at certain angles from the principle ray, determined by a grating angular dispersion, e.g. $\lambda_0 + \Delta\lambda$ will be tilted by:

$$\Delta\theta = \frac{\Delta\lambda D_0}{\theta_d}, \quad (6)$$

where $\theta_d = \arccos(\cos \theta_i - \lambda D_0)$.

In this case a linear phase tilt should be applied with respect to the principal ray frequency ω_0 :

$$\Delta\Phi(x, y, \omega_0, \Delta\omega) = -\frac{2\pi x \Delta\theta}{\lambda_0} = \frac{2\pi x \Delta\omega D_0}{\omega_0 \theta_d}. \quad (7)$$

Finally, cumulative effect of the grating modeling may be written as

$$\begin{aligned} \vec{E}(\omega, x, y) &= \vec{E}_0(\omega, x, y) \exp[i\Delta\Phi], \\ \Delta\Phi &= k \left(-\frac{f_{iang} x^2 - f_{sag} y^2}{2} + \frac{C_{30} x^3}{\theta_d^3} \right. \\ &\quad \left. + \frac{C_{12} x y^2}{\theta_d} + \frac{2\pi x \Delta\omega D_0}{k \omega \theta_d} \right). \end{aligned} \quad (8)$$

Focusing with Mirrors

In SXRSS setup another optical element, where tangential curvature is present is M2 mirror. In this case simulation is similar to the grating, but D_0 , D_1 and D_2 VLS coefficients are equal to zero, $\theta_i = \theta_d$, and no field resizing should be applied.

Mirror Surface Height Errors Simulation

A very important issue is to keep track of the radiation quality degradation caused by reflections from optical elements with imperfect surfaces. Phase-shifter model was used to simulate this effect, [23] (see Fig. 3). The height error

δh on an optical surface will perturb the radiation wavefront with a phase shift $\Delta\Phi$ in the following way:

$$\Delta\Phi = \frac{4\pi\delta h}{\lambda} \sin \theta, \quad (9)$$

where θ is the radiation's angle of incidence with respect to the surface. In the case of a grating, the phase shift can be expressed in terms of incidence and diffraction angles:

$$\Delta\Phi = 2\pi(\sin \theta_i + \sin \theta_d) \frac{\delta h}{\lambda}. \quad (10)$$

SIMULATION DETAILS AND APPROACHES

SASE FEL distribution at the end of the last section of SASE undulator is obtained with the GENESIS software. It is dumped in a space-time domain. We apply a temporal Fourier transform, and once obtained the radiation distribution in a space-frequency domain, transverse distributions for an every calculated discrete frequency are treated separately. We apply a Fresnel propagator from Eq. (1) with z equal to a distance between the end of the undulator and the hit point at the grating. The phase shifter, described in Eq. (8) is used to simulate focusing of the beam by the toroidal VLS grating. Tilt is introduced accordingly to a difference $\Delta\omega$ between the frequency being currently propagated and the frequency that is chosen to be a principle ray of dispersed radiation (Eq. 7). After the grating, beam is propagated to M1 position, then to M2 mirror with multiplication by it's focusing phase shifter, then to M3 following with the final propagation to the entrance of the seeded undulator. At the every reflecting optical element a height error phase shifter (Eq. 10) with a certain height error profile is applied. This propagation is applied for an every frequency, therefore we may obtain a space-time domain of the dispersed radiation (Fig. 4) with an inverse temporal Fourier transform and use it as a seed in a GENESIS simulations of the seeded undulator. We call this approach the "direct" one.

On the other hand, one may characterize the monochromator performance by calculation of it's instrumental function (Fig. 5). It can be achieved by propagation of a certain typical transverse distribution with a different tilts that correspond to a different wavelengths (Eq. 7). At the entrance to the seeded undulator these distributions will have a varying transverse offset and after amplification simulation in linear mode one will obtain an amplified power as a function of a wavelength. If that power is normalized by the input coupling factor at 1-to-1 imaging from the end of the SASE undulator to the entrance to the seeded undulator it can be interpreted as an instrumental function of the monochromator at a given set-up (wavelength, FEL gain length, etc.) It allows one to avoid propagation of every pulse by only multiplying radiation distribution in space-frequency domain at the end of the SASE undulator by the instrumental function of monochromator. This way one obtains the radiation distribution at

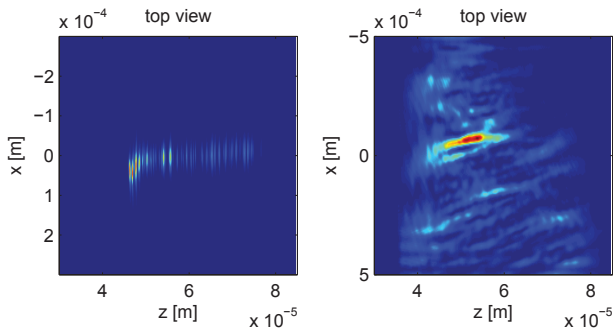


Figure 4: An example of dispersive projection of the radiation distribution in a space-time domain for the FEL pulse before the monochromator (left) and the dispersed radiation distribution after the monochromator (right). Here “x” is a dispersive dimension, and “z” is a dimension along the pulse propagation direction.

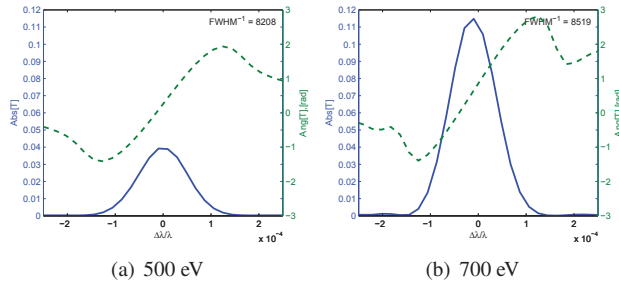


Figure 5: An example of monochromator instrumental functions for a different photon energies. Physical slit is not inserted. An inverse full width at half maximum can be interpreted as an effective resolving power of the monochromator.

the entrance to the seeded undulator. We call this approach the “phenomenological” one. The phase of the instrumental function is obtained with Kramers-Kronig relations (this approach was also used for Hard X-Ray Self Seeding (HXRSS) setup simulation in e.g. [8], [9]). In this case the transverse distribution of the radiation doesn’t change after passing the undulator, which does not correspond to reality, but this distribution is amplified in seeded undulator the same way as one obtained with “direct” approach (Fig. 6) yielding the same radiation properties after amplification (Fig. 7).

CONCLUSIONS

This article describes a way to numerically simulate a propagation of the radiation through the optical system of the Soft X-ray Self Seeding Monochromator. The propagated field is used as a seed for a GENESIS simulations downstream the monochromator allowing one to investigate the FEL beamline performance after the monochromator installation. The monochromator’s optical elements are represented as a transverse phase shifters, allowing to

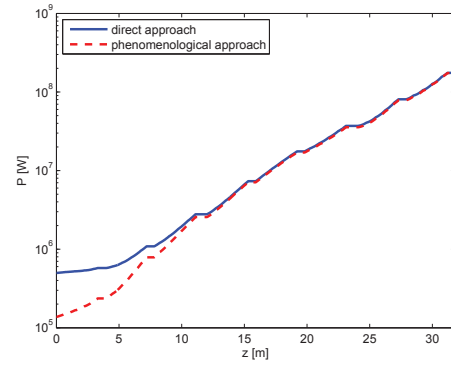


Figure 6: Power of the radiation in the seeded undulator. The radiation was propagated through the seeded undulator with the direct (solid line) and the phenomenological (dashed line) approaches. Pulse energy is 1000 eV.

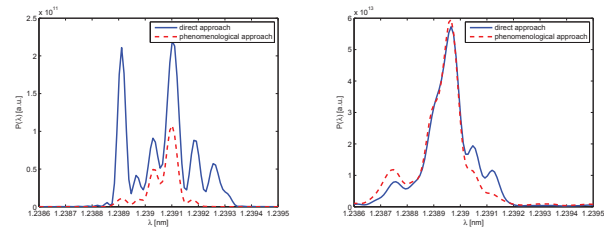


Figure 7: Spectra of the radiation at the seeded undulator entrance (left figure) and exit (right figure). The radiation was propagated through the seeded undulator with the direct (solid line) and the phenomenological (dashed line) approaches. Pulse energy is 1000 eV.

modify the radiation wavefront accordingly to curvatures, positions and height errors of mirrors and aberrations introduced by them. Propagation of the radiation between optical elements is done with Fresnel propagator. The monochromator radiation transport simulation allows one to study the monochromator performance in the beamline, such as effective resolving power of the monochromator without the exit slit, the input coupling factor, or effectiveness of a tapering. Two approaches described above allow one to fill the gap in numerical simulations of FEL performance with SXRSS monochromator.

Based on simulations, we found that resolving power of the LCLS SXRSS monochromator operating without the exit slit varies from 5400 to 8500, that is close to resolving power with $3\mu\text{m}$ exit slit inserted [13]. Resolving power along with input coupling factor are affected by the choice of source position in the SASE undulator. Surface height errors of installed optics have shown no significant effect on the monochromator performance. More detailed study is to be published [24].

REFERENCES

- [1] J. Feldhaus et al., "Possible application of X-ray optical elements for reducing the spectral bandwidth of an X-ray SASE FEL" Optics. Comm., vol. 140, pp. 341-352, 1997.
- [2] E. Saldin et al., "X-ray FEL with a meV bandwidth", NIM, ser. A, vol. 475, pp. 357-362, Dec. 2001.
- [3] E. Saldin et al., "Optimization of a seeding option for the VUV free electron laser at DESY", NIM, ser. A, vol. 445, pp. 178-182, May 2000.
- [4] R. Treusch et al., "The seeding project for the FEL in TTF phase II", DESY Ann. report, 2001.
- [5] A. Marinelli et al., "Comparative study of nonideal beam effects in high gain harmonic generation and self-seeded free electron lasers", Phys. Rev. ST Accel. Beams, vol. 13, p. 070701, Jul 2010.
- [6] G. Geloni et al., "Scheme for generation of highly monochromatic X-rays from a baseline XFEL undulator", DESY 10-033, 2010.
- [7] Y. Ding et al., "Two-bunch self-seeding for narrow-bandwidth hard x-ray free-electron lasers" Phys.Rev.ST Accel.Beams, vol. 13, p. 060703, 2010.
- [8] G. Geloni et al., "A simple method for controlling the line width of SASE X-ray FELs", DESY 10-053, 2010.
- [9] G. Geloni et al., "Cost-effective way to enhance the capabilities of the LCLS baseline", DESY 10-133 2010.
- [10] G. Geloni et al., "A novel Self-seeding scheme for hard X-ray FELs", Journal of Modern Optics, vol. 58, issue 16, pp. 1391-1403, DOI:10.1080/09500340.2011.586473, 2011.
- [11] Y. Feng et al., "Optics for Self-Seeding Soft X-ray FEL Undulators", Proc. 34th Int. Free-Electron Laser Conf., Malmo, Sweden, 2010, TUPB10.
- [12] Y. Feng et al., "Compact Grating Monochromator Design for LCLS-I Soft X-ray Self-Seeding", Available: https://slacportal.slac.stanford.edu/sites/lcls_public/lcls_ii/Lists/LCLS_II_Calendar/Physics_Meetings.aspx, May 2011 and <https://sites.google.com/a/lbl.gov/realizing-the-potential-of-seeded-fels-in-the-soft-x-ray-regime-workshop/talks>, Oct. 2011.
- [13] Y. Feng et al., "System design for self-seeding the LCLS at soft X-ray energies", Proc. 34th Int. Free-Electron Laser Conf., Nara, Japan, 2012, TUOB10.
- [14] D. Cocco et al. "The optical design of the soft x-ray self seeding at LCLS ", Proc. SPIE, vol. 8849, p. 88490A, doi:10.1117/12.2024402, Available: <http://dx.doi.org/10.1117/12.2024402>, Sep. 2013.
- [15] D. Cocco, private communication, 2013.
- [16] D. Ratner, "Soft X-ray Self-Seeding Setup and Results at LCLS", talk at this conference: 36th Int. Free-Electron Laser Conf., Basel, 2014, to be published.
- [17] T. Poon and T. Kim, "Engineering optics in Matlab", World Scientific, 2006, pp. 73-78.
- [18] D. G. Voelz, "Computational Fourier Optics: A Matlab Tutorial", SPIE Press, Washington, 2011, pp. 89-98.
- [19] S. Reiche et al., "GENESIS 1.3: a fully 3D time-dependent FEL simulation code", Nucl. Instr. and Meth., ser. A, vol. 429, pp. 243-248, 1999.
- [20] M. Itou et al., "Soft x-ray monochromator with a varied-space plane grating for synchrotron radiation: design and evaluation", Applied Optics, vol. 28, pp. 146-153, 1989.
- [21] S. Serkez et al., "Grating monochromator for soft X-ray self-seeding the European XFEL", DESY 13-040, Available: <http://arxiv.org/abs/1303.1392>, 2013.
- [22] T. Harada et al., "Design of a high-resolution extreme-ultraviolet imaging spectrometer with aberration-corrected concave gratings", Applied optics, vol. 37, pp. 6803-6810, 1998.
- [23] A. Barty et al., "Predicting the coherent X-ray wavefront focal properties at the Linac Coherent Light Source (LCLS) X-ray free electron laser", Optics Express, vol. 17, pp. 15508-15519, 2009.
- [24] S. Serkez et al., "Soft X-ray Self-Seeding simulation methods and their application for LCLS", to be published.

X-RAY MONOCHROMATORS FOR SELF-SEEDING XFELs IN THE PHOTON ENERGY RANGE STARTING FROM 1.5 keV

Yuri Shvyd'ko*

Advanced Photon Source, Argonne National Laboratory, Argonne, Illinois 60439, USA

Abstract

Self-seeding of FELs with photon energies below 1 keV can be performed using grating monochromators [1]. Forward Bragg diffraction (FBD) monochromators [2] were instrumental for achieving self-seeding in hard x-ray FELs in the photon energy range from 5 to 10 keV [3]. Large photo-absorption in the monochromator crystal at lower photon energies makes extension into lower photon energy range difficult. Here an alternative scheme of x-ray monochromatization is introduced which may enable self-seeding in a yet inaccessible spectral range starting from 1.5 keV, and thus to bridge the gap between the soft and hard x-ray self-seeding.

The new scheme uses grazing-incidence Bragg diffraction under specular reflection conditions [4]. Specular reflection mitigates the problem of photo-absorption, as in this case the FBD radiation is reflected from a very thin crystal surface layer. Application of quartz (SiO_2) instead of diamond crystals, makes feasible Bragg diffraction and therefore monochromatization of x-rays starting from 1.457 keV.

INTRODUCTION

A new scheme of x-ray monochromatization is proposed here, which may enable self-seeding in a yet inaccessible spectral range starting from 1.5 keV, and thus to bridge the existing gap between the soft and hard x-ray self-seeding. The scheme uses grazing-incidence Bragg diffraction under specular reflection conditions [4], as shown in Figure 1.

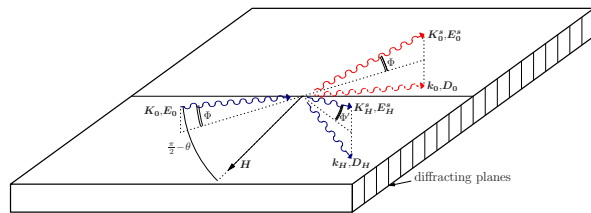


Figure 1: Schematic of grazing incidence x-ray Bragg diffraction in non-coplanar geometry under specular reflection conditions [4].

X-RAY DIFFRACTION UNDER SPECULAR REFLECTION CONDITIONS

Diffracting atomic crystal planes are perpendicular to the crystal surface. Incident x-rays with the wave-vector K_0 are at a very small glancing angle of incidence Φ to the crystal surface, and at a Bragg angle θ to the diffracting

atomic crystal planes (π/θ angle with diffraction vector H). Under these conditions, the Bragg diffracted x-rays propagate at a very small glancing angle of reflection to the crystal surface Φ' . K_H^s , E_H^s are the wave-vector and the amplitude of the specularly reflected Bragg diffracted beam. Another Bragg diffracted component propagates inside the crystal with the wave-vector k_H , and amplitude D_H . Similarly, there are two components of x-rays associated with forward Bragg diffraction (FBD). First, there is an in-crystal component with wave-vector k_0 , D_0 . Second, K_0^s , E_0^s are the in-vacuum wave-vector and the amplitude of the specularly reflected forward Bragg diffracted beam (S-FBD), with the specular reflection angle Φ . Dynamical theory of Bragg diffraction in such scattering geometry has been developed by Afanasev-Melkonyan (1983). For the x-ray monochromator application we will be interested in the S-FBD beam E_0^s .

Specular reflection mitigates the problem of photo-absorption, as in this case the FBD radiation is reflected from a very thin crystal surface layer. Application of quartz (SiO_2) instead of diamond crystals, makes feasible Bragg diffraction and therefore monochromatization of x-rays starting from $\hbar\omega_H = 1.457$ keV, the photon energy for backscattering from the atomic planes with diffraction vector $H = (10\bar{1}0)$. The nominal energy $\hbar\omega_0$ of photons involved in Bragg diffraction is defined as usually by Bragg's angle θ through Bragg's law: $\hbar\omega_0 = \hbar\omega_H / \sin \theta$.

SELF-SEEDING SCHEME

The x-ray FEL self-seeding scheme is shown in Figure 2. X-rays from the first half of the magnetic undulator system

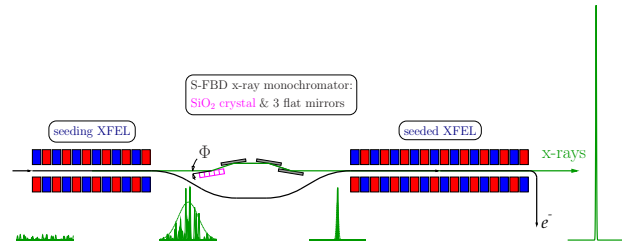


Figure 2: X-ray FEL self-seeding scheme with the S-FBD x-ray monochromator.

(seeding XFEL) are used to seed the electron bunch in the second half (seeded XFEL) via an x-ray monochromator consisting of a SiO_2 crystal and three flat grazing incidence mirrors, used to correct the trajectory of photons. The monochromator produces a delayed monochromatic seed through grazing incidence forward Bragg diffraction under specular reflection (S-FBD) conditions, with a small specular reflection angle $\Phi \lesssim 25$ mrad, see Fig. 1 for details. The

* shvydko@aps.anl.gov

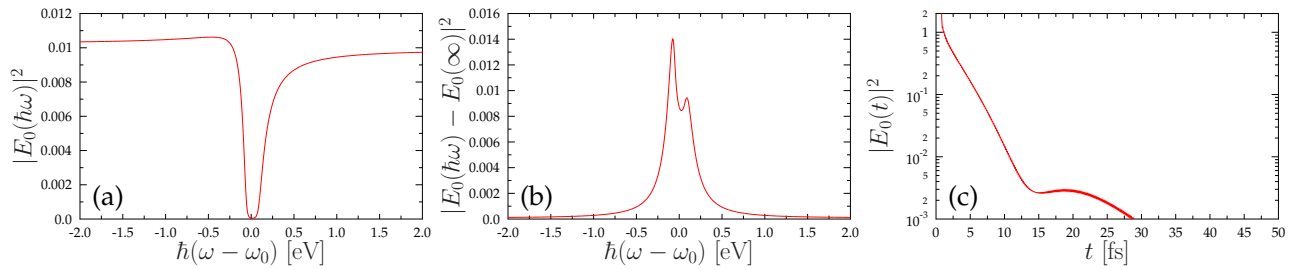


Figure 3: Forward Bragg diffraction (FBD) of 1.46-keV x-rays from a 10- μm SiO_2 crystal, the (1010) Bragg reflection: (a) spectral dependence of x-ray transmissivity $|E_0(\hbar\omega)|^2$; (b) spectral dependence of forward Bragg diffraction $|E_0(\hbar\omega) - E_0(\infty)|^2$; (c) time dependence $|E_0(t)|^2$ of FBD. FBD is more than an order of magnitude weaker than the S-FBD signal, see Fig. 4(c), because of the strong photo-absorption in SiO_2 .

small specular reflection angle Φ and a small spatial off-set of the mirrors $H \simeq 0.2$ mm ensures almost forward Bragg scattering with a small additional delay $\tau = 2\Phi H/c \simeq 30$ fs, due to a slightly detoured flight-path via the SiO_2 crystal and flat mirrors, assuming $\Phi = 22$ mrad.

S-FBD MONOCHROMATOR PERFORMANCE

Performance of the S-FBD monochromator is demonstrated in Fig. 4 by spectral and time dependencies of forward Bragg diffraction under specular reflection conditions (S-FBD) in SiO_2 for x-rays with photon energies $\hbar\omega$ in the vicinity of $\hbar\omega_0 = 1.46$ keV, the nominal energy of the (10 $\bar{1}$ 0) Bragg diffraction at $\theta = 86.14^\circ$.

Spectral dependencies of S-FBD reflectivity for different glancing angles of incidence Φ , in the vicinity of photon energy $\hbar\omega_0 = 1.46$ keV, are shown in Fig. 4(a). At large deviations of photon energies from $\hbar\omega_0$ the reflectivity is flat, and corresponds to pure grazing incidence specular reflectivity with close to zero Bragg diffraction contribution. They correlate with the data for the angular dependence of the specular reflectivity of 1.46 keV photons from SiO_2 at grazing incidence angle Φ , shown in Fig. 4(d).

Spectral dependencies of the delayed part of S-FBD, with a prompt pure specular reflection component subtracted, are presented in Fig. 4(b). These dependencies represent time-averaged spectra of the monochromatic seed, which can be generated through S-FBD. Typical spectral widths are about 100-meV, suitable for seeding FEL pulses with a duration of a few tenths of fs. The peak value of the S-FBD intensity is at the critical angle of total reflection $\Phi = 22$ mrad, see also Fig. 4(d).

Time dependencies of S-FBD, representing the intensity of the monochromatic seed at different delays, are presented in Fig. 4(c), for different glancing angles of incidence Φ . At a 20-fs delay, typically used for self-seeding, the intensity of S-FBD in $\text{SiO}_2(10\bar{1}0)$ is comparable to the intensity of FBD in $\text{C}(004)$ for 8.3 keV x-rays [3], maybe a factor 4 lower. Still, it is two orders of magnitude higher than what one could obtain from a 10- μm thick SiO_2 crystal in FBD mode at the same time delays, as can be seen from in Fig. 3(c).

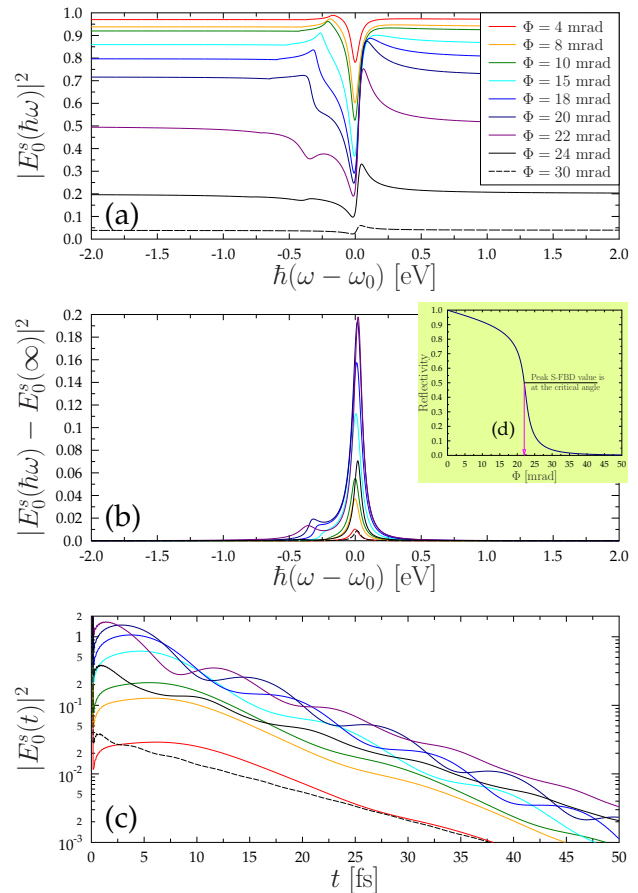


Figure 4: Spectral (a)-(b) and time (c) dependencies of forward Bragg diffraction under specular reflection conditions (S-FBD) in SiO_2 for x-rays with photon energies $\hbar\omega$ in the vicinity of $\hbar\omega_0=1.46$ keV, the nominal energy of the (10 $\bar{1}$ 0) Bragg diffraction at $\theta = 86.1^\circ$.

REFERENCES

- [1] J. Feldhaus, E.L. Saldin, J.R. Schneider, E.A. Schneidmiller, and M.V. Yurkov. *Opt. Commun.*, 140:341, 1997.
- [2] Gianluca Geloni, Vitali Kocharyan, and Evgeni Saldin. A novel self-seeding scheme for hard x-ray FELs. *Journal of Modern Optics*, 58:1391–1403, 2011.
- [3] J. Amann, W. Berg, V. Blank, F.-J. Decker, Y. Ding, P. Emma, Y. Feng, J. Frisch, D. Fritz, J. Hastings, Z. Huang, J. Krzywinski, R. Lindberg, H. Loos, A. Lutman, H.-D. Nuhn,

D. Ratner, J. Rzepiela, D. Shu, Yu. Shvyd'ko, S. Spampinati, S. Stoupin, S. Terentiev, E. Trakhtenberg, D. Walz, J. Welch, J. Wu, A. Zholents, and D. Zhu. Demonstration of self-seeding in a hard-x-ray free-electron laser. *Nature Photonics*, 6, 2012.

[4] A. M. Afanas'ev and M. K. Melkonyan. X-ray diffraction under specular reflection conditions. Ideal crystals. *Acta Cryst.*, A39:207–210, 1983.

INDIRECT MEASUREMENTS OF NIR AND UV ULTRASHORT SEED LASER PULSES USING A TRANSVERSE DEFLECTING RF-STRUCTURE

Nagitha Ekanayake, Sven Ackermann, DESY, Hamburg, Germany

Kirsten Elaine Hacker, DELTA, Dortmund, Germany

Christoph Lechner, Theophilos Maltezopoulos, Tim Plath, University of Hamburg, Germany

Abstract

Seeding of free-electron lasers (FELs) using external coherent optical pulses recently became an area of interest as users demand spectrally and temporally coherent FEL radiation which is not achievable in traditional self-amplified spontaneous emission operation mode. Since temporal and spectral properties of the seed laser pulses are directly imprinted on the electron bunch, a proper characterization of these seed pulses is needed. However, the lack of any measurement technique capable of characterizing ultrashort seed laser pulses at the laser-electron interaction region is a primary drawback. In this paper we report indirect measurements of seed laser pulses in an undulator section using a transverse deflecting RF-structure (TDS) at the free-electron laser FLASH at DESY. Temporally chirped and unchirped seed pulse length measurements will be compared with second-harmonic generation frequency-resolved optical gating measurements and theoretical simulations. Using this technique we will demonstrate that pulse artifacts such as pre- and post-pulses in the seed pulse in the femtosecond and picosecond timescales can be identified without any temporal ambiguity.

INTRODUCTION

External seeding techniques such as High Gain Harmonic Generation (HG) [1] and Echo-Enabled Harmonic Generation (EEHG) [2] have been demonstrated recently. Proper characterization of seed laser pulses in the interaction region, namely the undulator, is important for successful operation of such seeding schemes. However, to best of our knowledge, currently there is no technique available to directly measure the pulse duration of the seed laser pulses inside the undulator. In this study we provide indirect measurements of ultrashort laser pulses, using a technique which utilizes the energy modulation of an electron bunch due to seed laser beam, observed using a transverse deflecting RF-structure.

EXPERIMENTAL SETUP

Seed Laser System

The seed laser system (Fig. 1) employed in the FLASH1 seeding project is a solid-state, commercial, Ti:sapphire system based on chirped pulse amplification technique (CPA). The 108.3 MHz optical oscillator is synchronized to the master laser oscillator (MLO) via a RF-based link with a 50 fs rms jitter. A two-stage amplifier section is used to amplify the pulse energy up to

50 mJ/pulse at 10 Hz repetition rate and 800 nm centre wavelength. Amplified pulses are then extracted from the cavity and compressed down to 50 fs full width at half maximum (FWHM) duration. Pulse duration is measured using a commercial GRENOUILLE setup [3]. After compression, the pulse energy is 35 mJ/pulse with $\pm 2\%$ rms stability.

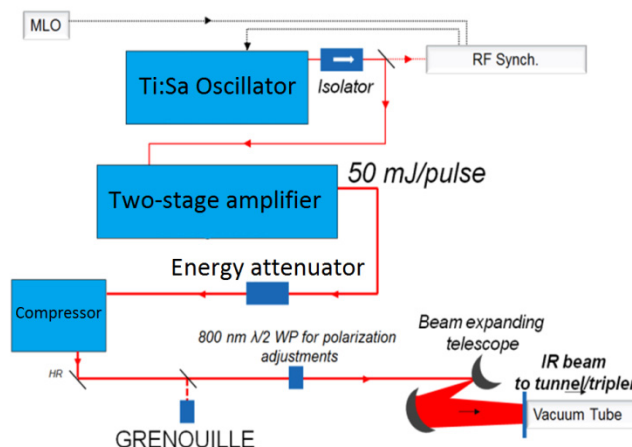


Figure 1: Schematic of the seed laser system at FLASH1.

Beam Delivery

The fundamental 800 nm beam is then delivered to a frequency tripler unit in order to generate the third harmonic of the fundamental beam for seeding. The in-coupling beam line consists of 3 m of air and 1 mm thick fused silica window prior to a high vacuum region of 10^{-6} mbar and 9 m in length. To keep the B-integral below unity the beam diameter is expanded by a factor of 3, from 6 mm FWHM after the amplifier to 18 mm FWHM after the beam expander.

Frequency Upconversion and Injection

Frequency tripling is performed using two β -Barium borate (BBO) crystals. First BBO crystal converts the fundamental frequency to its second harmonic and subsequent α -BBO delay plate adds a temporal delay to the fundamental pulse as both pulses need to be temporally overlapped in the second β -BBO crystal for efficient third harmonic generation. Polarization state of the fundamental beam is adjusted using a quartz waveplate $\lambda/2$ @ 800 nm and λ @ 400 nm. The conversion efficiencies for the second and third harmonics are approximately 20 % and 9%, respectively (Fig. 2). Estimated pulse duration of the third harmonics is approximately 150 fs FWHM.

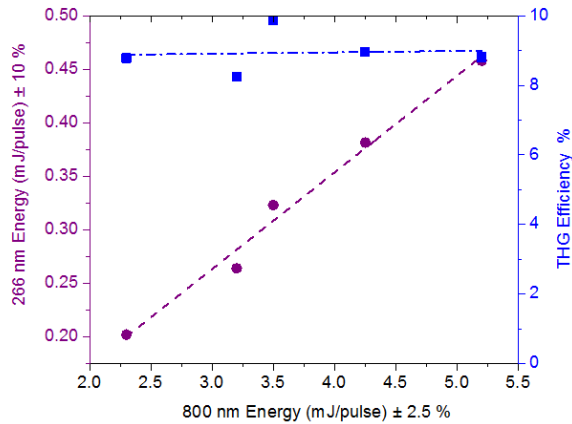


Figure 2: Measured third harmonic pulse energy (left axis, •) and conversion efficiency (right axis, ■) as a function of fundamental pulse energy. Due to generation of non-linear effects the fundamental beam energy is kept below 5 mJ/pulse.

The frequency upconverted seed beam is delivered to the electron beam trajectory using three-wavelength (800, 400, and 266 nm) mirrors. All three wavelengths are injected due to ease of obtaining the laser-electron overlap and the possibility of using the same setup for the SASE suppression experiment [4].

Electron Beam

A single bunch electron beam at 10 Hz repetition with a root mean square (rms) length of few picoseconds is used for at the initial stage to achieve proper overlap between the electron bunch and the seed laser pulse. Electron energy is 700 MeV with a peak current of 300 A.

Spatial and Temporal Overlap

Metal, Ce:YAG, and OTR screens are used for the transverse overlap. Course temporal overlap between laser and electron beam is first observed using a photo multiplier tube with a few hundred picoseconds accuracy and then using a streak camera with an accuracy of few tens of picoseconds. In order to achieve the overlap, the timing of the seed laser oscillator is shifted by means of a vector modulator. Final overlap is established using a transverse deflection structure (LOLA-TDS).

LOLA-TDS at FLASH

The LOLA transverse deflection structure at FLASH consists of a transverse RF deflector to project the longitudinal electron bunch into transverse coordinates and a magnetic dipole to resolve the energy, thus providing an image of energy deviation of the electron bunch as a function of longitudinal position inside the bunch [5, 6]. The location of the hardware is shown in Fig. 3. With proper calibration this image can be converted into energy deviation as a function of time. Once the longitudinal and transverse overlap between the two beams is established the seed laser provides an energy modulation to the electron bunch which can be observed in the LOLA image as a peak structure. As the width of this energy modulation depends on the seed laser pulse duration this image is used in our experiment to estimate the pulse duration of the seed laser inside the undulator section.

EXPERIMENTAL OBSERVATIONS

Fig. 4(a) indicates an energy modulated electron bunch due to overlap with the 800 nm seed pulse of 200 fs where Fig. 4(b) indicates an energy modulation due to 60 fs FWHM pulse. Once the images are calibrated (Fig. 4(c)) this indicates approximately 90 FWHM pulse duration inside the undulator. This pulse broadening is due to slippage and dispersive elements after the tripler such as vacuum window and mirrors. Also, pulse artefacts, such as pre- and post-pulses in the seed laser beam are clearly visible in these images which are not measurable without a temporal ambiguity using a standard ultrashort pulse measurement technique based on second order non-linear effects. Moreover, this technique could be utilized to simultaneously measure the pulse duration of seed laser pulses with different wavelengths.

SUMMARY AND OUTLOOK

In this paper we demonstrated that the LOLA-TDS at FLASH can be used to indirectly measure the ultrashort seed pulse duration inside the laser-electron interaction region. This is important for seeding experiments as there is no other measurement technique available to make such a measurement inside an undulator. This technique is being further investigated as a diagnostic for improving the efficiency of external seeding schemes.

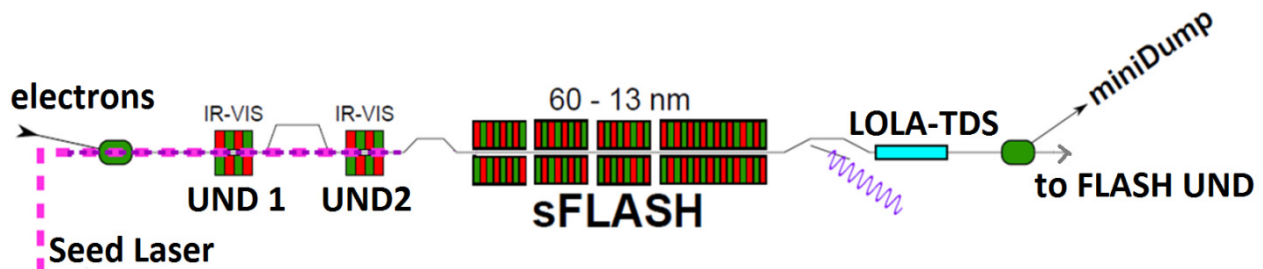


Figure 3: Arrangement of the FLASH1 seeding section.

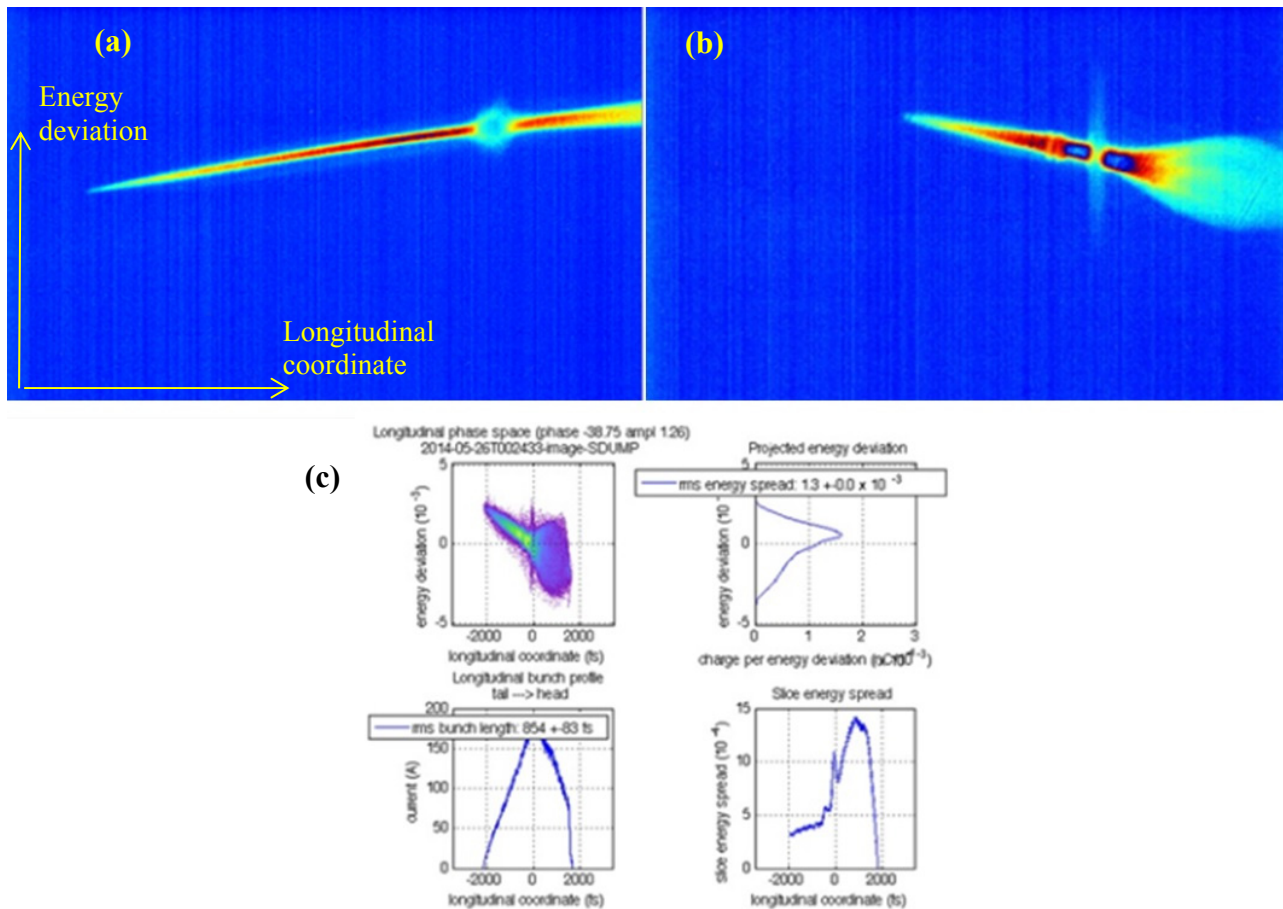


Figure 4: Retrieved images of LOLA-TDS structure once the laser-electron overlap is established. (a) Compressed electron bunch modulated by an 800 nm seed laser pulse of 200 fs FWHM measured after the tripler. (b) Modulation with 800 nm laser with 60 fs duration. Width of the large amplitude spike (3.5 MeV modulation) is related to the seed laser pulse duration. The calibrated image gives laser pulse duration of approximately 90 fs FWHM. Right side of the image indicates the front of the electron bunch. The smaller modulation of 100 keV is visible in the image and corresponds to a post laser pulse. (c) A calibrated LOLA image.

ACKNOWLEDGEMENTS

The authors acknowledge the support received from the FLASH team and many groups at DESY in preparation and commissioning of experiments. We thank our colleagues in the FLASH seeding team for their support.

This work is supported by ARD grant number E.56607 (Laserstrahlkontrolle) and Federal Ministry of Education and Research of Germany under contract numbers 05K13GU4, 05K13PE3, 05K10PE1, and the German Research Foundation programme graduate school 1355.

REFERENCES

- [1] E. Allaria, *et al.*, Nature Photonics **6**, 699 (2012)
- [2] Z. T. Zhao, *et al.*, Nature Photonics **6**, 360 (2012)
- [3] R. Trebino, *Frequency-Resolved Optical Gating: The Measurement of Ultrashort Laser Pulses* (Kluwer Academic Publishers, Norwell, MA, 2002), 1st Edition.
- [4] C. Lechner, *et al.*, “Demonstration of SASE Suppression Through a Seeded Microbunching Instability”, In *These Proceedings: 36th Int. Free Electron Laser Conf.*, Basel, Switzerland, 2014, MOP060
- [5] Christopher Behrens, Dissertation, Fachbereich Physik der Universität Hamburg, 2012
- [6] Behrens, C. *et al.*, Phys. Rev. ST Accel. Beams **15**, 030707 (2012)

HGHG AND EEHG MICROBUNCHES WITH CSR AND LSC*

Kirsten Hacker, TU Dortmund, Germany

Abstract

Longitudinal space charge (LSC) forces in a drift and coherent synchrotron radiation (CSR) in a chicane are relevant for high gain harmonic generation (HGHG) and echo enabled harmonic generation (EEHG) seeding designs. These factors determine whether or not the modulator can be located significantly upstream of the radiator. The benefits and dangers of having a drift in between the radiator and the modulator are investigated and a measurement of the LSC enabled reduction of the energy spread of a seeded beam is presented.

INTRODUCTION

The length of a seeded microbunch determines the harmonic content and the harmonic content together with the energy spread determines the shortest wavelength which the system can seed [1-3]. For a given initial uncorrelated energy spread, the length of a microbunch can be reduced by increasing the modulation amplitude, but when the modulation amplitude becomes too great, the energy spread of the microbunches will be too large to lase in the radiator [4]. In addition, microbunches with high peak currents will be subject to significant coherent synchrotron radiation (CSR) in the chicane and longitudinal space charge (LSC) forces in the drift [5,6]. For FLASH2 seeding, a decision about where an HGHG modulator should be placed is determined by how these factors influence the behavior of an HGHG microbunch in a drift. This material was first presented in [7,8]. It represents an initial investigation into this design issue for FLASH2. The full-bunch simulation methods from [9] would be used in a final design study.

Two possible configurations of a FLASH2 seeding installation are drawn in Fig. 1. Option (a.) has the HGHG modulator in the middle of the radiator, minimizing the drift of the microbunched electrons and option (b.) has the modulator at the beginning of the radiator, necessitating a 20 meter drift of an energy modulated electron bunch prior to beginning the radiation process. This drift is required due to the short length of undulator required to achieve saturation in a seeded FEL and due to the necessity of keeping the saturation point at a fixed point in the radiator for longer wavelengths. If the beam saturates too early in the radiator, then the 20-30 nm FEL light cannot be transported to the users.

In order to determine which option is superior, longitudinal dispersion, longitudinal-transverse coupling, coherent synchrotron radiation (CSR), and longitudinal space charge (LSC) all need to be addressed. The conclusion from a study of these issues is that option (a.), with the modulator in the middle of the radiator, suffers

* work supported by BMBF grant 05K10PE1 and DESY

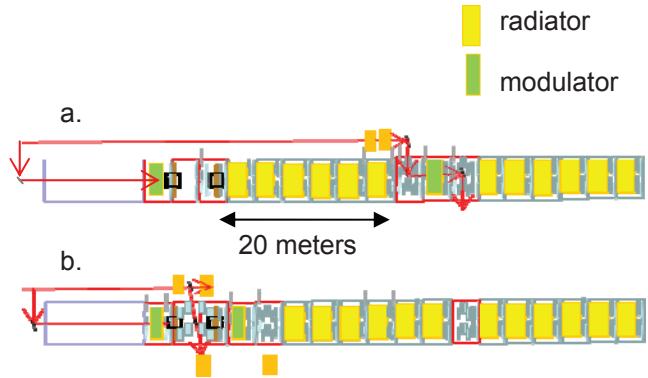


Figure 1: Two possible locations for an HGHG modulator in a FLASH2 seeding installation. Option (a.) shows it in the middle of the radiator in a design which is only suitable for HGHG and option (b.) shows it prior to the radiator in a design which is suitable for a wider range of seeding schemes. The additional, upstream modulator is envisioned for EEHG.

most from CSR, while option (b.), given more ample seed laser intensity, can exploit LSC forces in a beneficial manner, using them to reduce the net energy spread of the microbunches. Measurements and simulations of this LSC enabled increase of the microbunch energy spread concept are presented. Conversely, measurements of the LSC enabled enhancement of a microbunch energy spread are presented in [10] with a different application. Whether or not the LSC force enhances or reduces the microbunch energy spread depends on whether the microbunch is undercompressed or overcompressed at the entrance of a drift.

DISPERSION

The energy modulated beam is affected by dispersion from the chicanes, from the modulator, from mis-aligned magnets or beam trajectories, and from the velocity bunching in the drift itself. Higher order dispersion becomes relevant for large energy modulations in terms of its effect on coupling between longitudinal and horizontal dispersion for non-closed orbit bumps. It will be discussed in the section on 3-D effects. A table summarizing the first-order dispersion ($R_{56} = -2\Delta s$) contributions for a 20 meter drift is given below (Table 1).

Table 1: A summary of the contributions to the dispersion over a 20 meter drift for a beam energy of 700 MeV and a trajectory mis-alignment of 100 μm and modulator with 30 periods.

velocity	$L_{\text{drift}} / \gamma^2$	15 μm
mis-alignment	$L_{\text{drift}} \theta^2$	5 nm
modulator	$2N_{\text{periods}} \lambda_{\text{seed}}$	16 μm
chicane	$(L_{\text{chicane}} - 3L_{\text{bend}}) \theta^2$	0-200 μm

For an overly large, 4 MeV energy modulation, the dispersion required to fully bunch the beam is about 20 μm , while for a more reasonable, 2 MeV energy modulation, the dispersion required for full compression is 50 μm . Since the dispersion in the drift is sufficient to compress a beam with a larger energy modulation, for option (a.), the CSR of the chicane will be dominant, while for option (b.), the LSC of the drift dominates.

CSR AND LSC

Analytic equations [5,6] for CSR and LSC forces can be added to a quick 1-D tracking code by applying the forces to a few microbunches and tracking the particle motion over a drift. The CSR wakes are calculated for the last dipole in the chicane prior to the radiator and the LSC forces are calculated for a given distance, using an interval of 1 meter per re-calculation.

To determine the fraction of the last dipole which is relevant for the CSR calculation, the point at which transverse smearing becomes small must be identified. The metric is that when the longitudinal-transverse smearing ($\sigma_{x,y}$) times R_{53} is larger than the length of the microbunch, then the peak current of the microbunch is low and the CSR can be ignored. Plotting the smearing and the R_{53} along the chicane shows that for $\beta=20$ m, $\varepsilon=1.5$, and a 100 μm (rms) beam radius, $\sigma_{x,y} \cdot R_{53} = 6$ nm at the dipole entrance, implying that the entire length of the last dipole is relevant for a 10 nm long HHG microbunch. Only the last half would be relevant for a shorter, EEHG microbunch (Fig. 2).

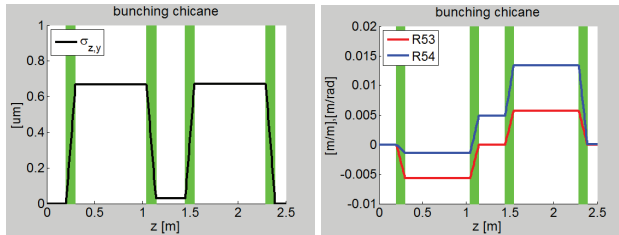


Figure 2: Longitudinal-transverse smearing ($\sigma_{x,y}$) and R_{53} along the chicane. This shows that for a 10 nm microbunch, only the last half of the last dipole is relevant for a CSR calculation.

In option (a.), the bunching is accomplished primarily through the chicane directly after the modulator, making CSR the primary concern whereas, in option (b.), the compression is done mostly through dispersion in the drift making LSC a larger concern. For option (a.), CSR from an electron bunch with an energy modulation of 2 MeV in the last dipole of a 45 μm chicane is studied after a drift of 4 meters with an average beam radius of 100 μm (rms). This gives a picture of the microbunch after the exit of the first radiator segment. For option (b.), the impact of LSC is studied over a drift of 20 meters with an average beam radii of 100 μm (rms) and 200 μm (rms). 2 MeV and 4 MeV energy modulations are compared for a beam energy of 600 MeV and 1 kA initial peak current.

In Fig. 3, the longitudinal phase space of the electrons in a microbunch for option (a.) is plotted along with the projection onto the longitudinal axis. The 2 sigma energy spread limits of the radiator are depicted by dashed lines. The background particles in blue show the conditions prior to the application of CSR and LSC. The foreground, red particles show the bunch after CSR and LSC and 4 meters of drift. The green line shows the LSC force per meter.

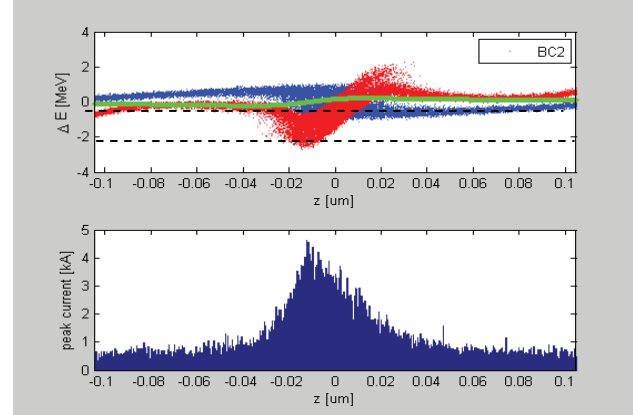


Figure 3: LSC and CSR on a microbunch after 4 meters of drift and an R_{56} of 45 μm . Dashed lines represent the bandwidth of the radiator. The background particles in blue show the conditions prior to the application of CSR or LSC. The foreground, red particles show the bunch after CSR and LSC and 4 meters of drift. The green line gives the LSC potential per meter. This is done for a 700 MeV beam energy, 1 kA initial peak current, 2 MeV (pp) energy modulation and a chicane R_{56} of 45 μm . The harmonic content of the microbunch was unaffected, but the energy spread was increased.

In contrast to the case of option (a.) plotted above in Fig. 3, option (b.) would send the energy modulated beam through a drift of 20 meters prior to the bunching chicane. If the beam radius is 100 μm in the drift, then the LSC wake will completely erase, or even reverse a 2 MeV initial energy modulation (Fig. 4) making seeding impossible with this amount of energy modulation and LSC potential.

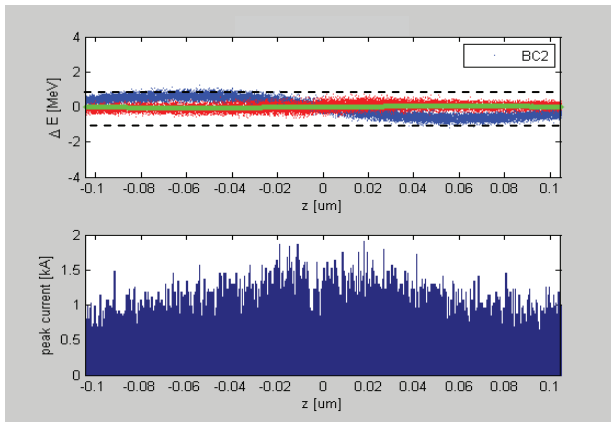


Figure 4: For a 100 μm (rms) radius, 1 kA electron bunch with a beam energy of 700 MeV and an initial energy modulation of 2 MeV (pp), the LSC potential completely removes the initial energy modulation after 20 meters of drift (blue \rightarrow red). LSC potential per meter is green.

If, however, the initial energy modulation is increased to 4 MeV, then one observes an LSC plasma oscillation which bunches the beam in the drift alone (Fig. 5).

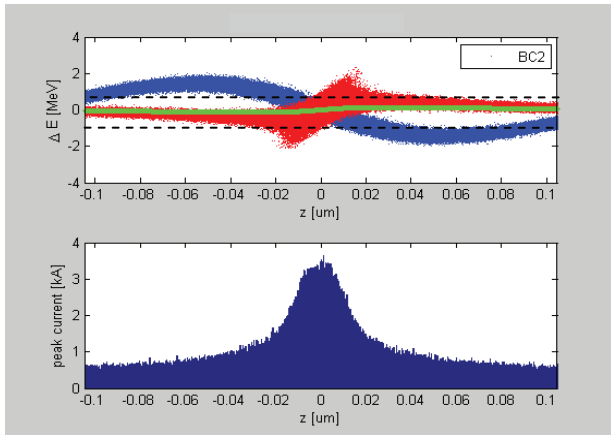


Figure 5: Instead of compression through a chicane, the energy modulated beam develops microbunches as a result of the LSC potential along the drift. The average rms beam radius in the 20 meter drift was 100 μm for a 1 kA initial peak current.

Such an LSC compressed microbunch would have a high enough peak current to radiate in an FEL were it not for the fact that the chirp is positive instead of negative, meaning that any amount of dispersion will blow the microbunch apart. This is not a workable scheme.

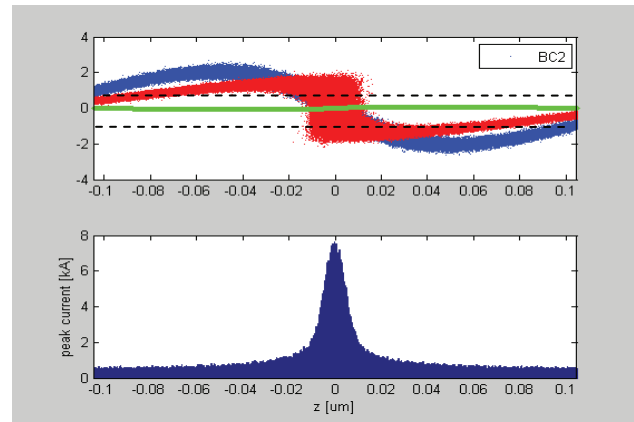


Figure 6: By increasing the beam radius in the 20 meter drift to 200 μm (rms) so that the time-of-flight compression dominates over the LSC force, a microbunch with a reduced peak-to-peak energy modulation is produced.

If the average beam radius in the drift is increased to 200 μm from 100 μm , so that the compression through the time-of-flight in the drift dominates over the effect of the LSC force, then an ideal condition appears to be realized. The beam is compressed without CSR and with an LSC enabled reduction of the peak-to-peak energy modulation (Fig. 6). This reduction of the seeded beam's energy spread improves the performance in FEL radiator, reducing the gain length and increasing the maximum power radiated.

An important tolerance for microbunch compression in a drift is the dispersion leakage in the drift. If the R_{53} and R_{54} are non-zero in the drift, as in a closed orbit bump, then the microbunches will be transversely smeared out in the drift and the effect of the LSC force will be dramatically attenuated. With this in mind, the strength of the LSC wake might be fine-tuned through closed orbit bumps instead of by tuning the beam size in the drift.

3-D SIMULATIONS

All of the previous results are merely 1-D simulations with an LSC force which is calculated from the longitudinal charge density. Simulations that calculate the forces between particles with a Green's function algorithm in 3-D [11] show some additional smearing effects which are not present in the 1-D simulations from Figs. 5 and 6. The effects shown in Fig. 5 and 6 are reproduced in 3-D but with a reduction in the peak current of the microbunch compared to the 1-D results (Fig. 7).

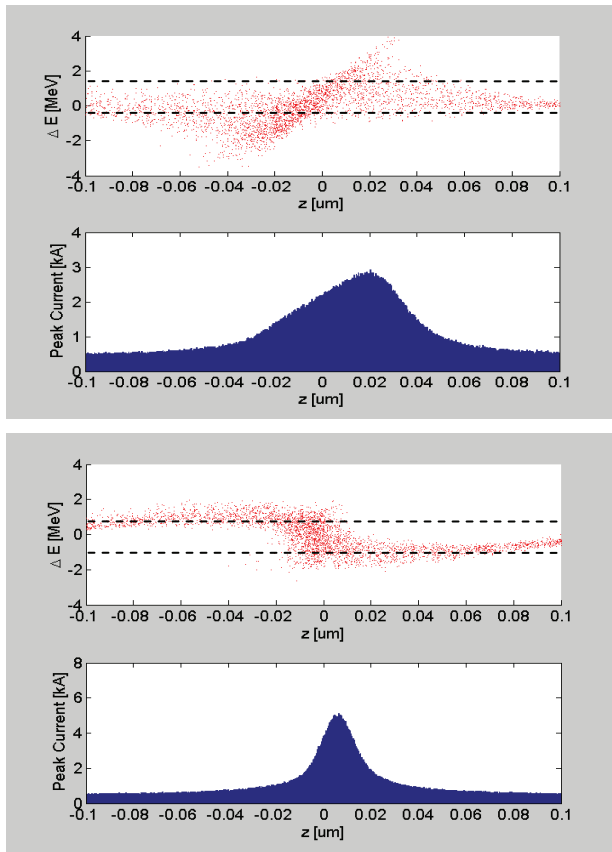


Figure 7: 3-D simulation of conditions from Figs. 5 and 6. The same mechanism is observed, but, due to 3-D smearing effects in the simulation, less impressive peak current is seen. (a.) has a beam radius of 100 μm in the drift and (b.) has a beam radius of 200 μm in the drift

The harmonic content of the microbunch in Fig. 7, representative of option (b.) is sufficient for seeding up to the 12th harmonic of 266 nm, while the harmonic content of the microbunch from Fig. 3, representative of option (a.) has comparable harmonic content. Each result is consistent with the observation of seeding up to the 12th harmonic of 266 nm at ELETTRA with an initial slice energy spread of 150 keV [12]. This allows us to draw a conclusion for HHG that given ample seed intensity, option (a.) is inferior to option (b.) since the energy spread of the microbunches is larger. However, given limited seed intensity, option (a.) is superior for HHG. EEHG requires different considerations.

EEHG

A comparison of option (a.) and option (b.) should also be done with respect to their compatibility with EEHG. Based on Fig. 8, an EEHG folded and energy modulated beam with 1 kA of initial peak current and a 100 μm average radius cannot tolerate the 20 meters of drift required by option (b.). Blue represents a slice of the seeded electron beam prior to the drift and red is after the drift.

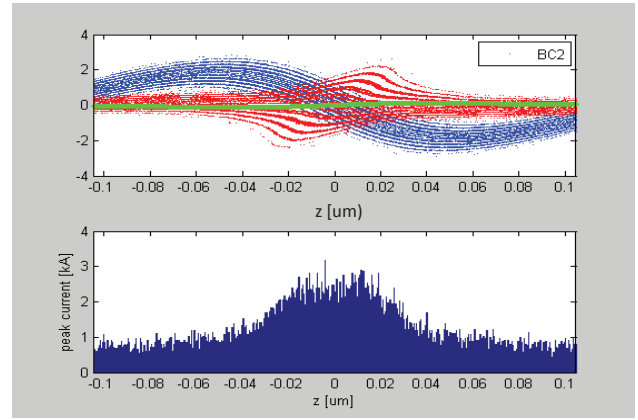


Figure 8: An EEHG folded and energy modulated 1 kA beam cannot be transported over 20 meters of drift in option (b.). The average transverse beam radius for this simulation was 100 μm . Blue represents a slice of the seeded electron beam prior to the drift and red is after the drift.

To avoid the problem with option (b.) shown in Fig. 8, the EEHG microbunches could be compressed directly after modulation, keeping the distance between the chicane exit and the radiator entrance as small as possible. Then, a split radiator scheme would be used in order to transport the FEL radiation to the users. Alternatively, the microbunches might be transported in a closed orbit bump which uses the R_{53} and R_{54} to keep the charge density transversely smeared out so that the LSC wake cannot have the effect shown in Fig. 8.

In option (a.), the folded beam would be transported over the 20 meter drift without the second stage energy modulation shown in blue in Fig. 8. In this case, due to inhomogeneities in the longitudinal charge density which are present after the initial EEHG folding (Fig. 9), effects akin to the LSC-EEHG described in [13] could occur and ruin the effectiveness of the EEHG seeding process.

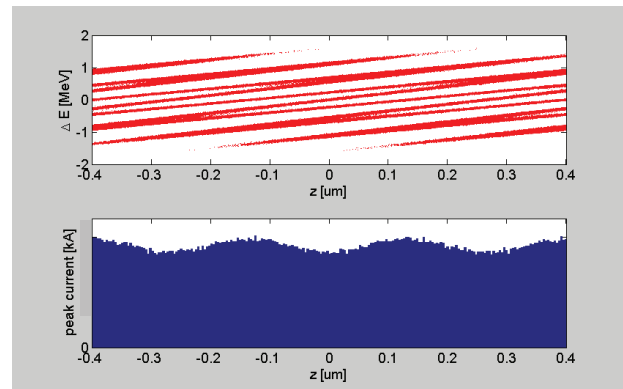


Figure 9: Folded beam distribution in longitudinal phase space. For option (a.), the small variations in the peak current after the first EEHG modulation and folding would introduce distortions due to the LSC force in a long drift.

For option (a.) or (b.), the average beam radius, R_{53} and R_{54} in the drift could be increased to avoid the damaging LSC effects for EEHG. However, only option (b.) offers

the possibility to avoid the LSC problem through a split radiator concept. Only option (b.) is consistent with a fresh-bunch cascade technique.

MEASUREMENT

Measurements of the LSC enabled reduction of the energy spread of a microbunched portion of the beam were performed at FLASH during shifts for a study of SASE lasing suppression [10,14]. The shift conditions used 300 A instead of the 1 kA from simulations shown above and simulations and measurements of longitudinal phase space of the un-bunched, under-bunched, and bunched conditions of the seeded beam are shown in Fig. 10.

The longitudinal phase space measurement was conducted with an RF deflecting structure which streaks out the longitudinal structure of the electron bunch in the vertical direction. A dipole magnet streaks out the energy of the bunch in the horizontal direction. The data analysis tool prepared by [15] was used to interpret the images.

The R_{56} of the chicane directly after the modulator was scanned from zero up to 100 μm . For R_{56} s below 50 μm , the energy modulation was a constant 2 MeV (pp) (Fig. 10a), but at 50 μm a transition occurred. The energy modulation disappeared at $R_{56}=50 \mu\text{m}$ (Fig. 10b). This is due to the LSC potential acting to reduce the energy spread of the microbunches as described in the simulation shown in Fig. 4. As the R_{56} was increased above 50 μm , the energy modulation returned, but in a new form (Fig. 10c). Three regions of streaked charge are observed, while in Fig. 10a, only one region is present. This is due to the fact that the peak current of the microbunches varies more along the seeded portion of 10c, leading to different amounts of LSC potential and modification of the microbunch energy spread along the drift.

CONCLUSION

The issues of LSC in a drift and CSR in a chicane are relevant for HGHG and EEHG seeding designs. Based on a comparison of two designs: one with the HGHG modulator in the middle of the radiator and one with it prior to the radiator, the favored design puts the modulator prior to the radiator due to increased flexibility in operation techniques including a split radiator concept, a fresh bunch cascade concept. The primary benefit may be the possibility of an LSC assisted energy spread reduction concept for HGHG.

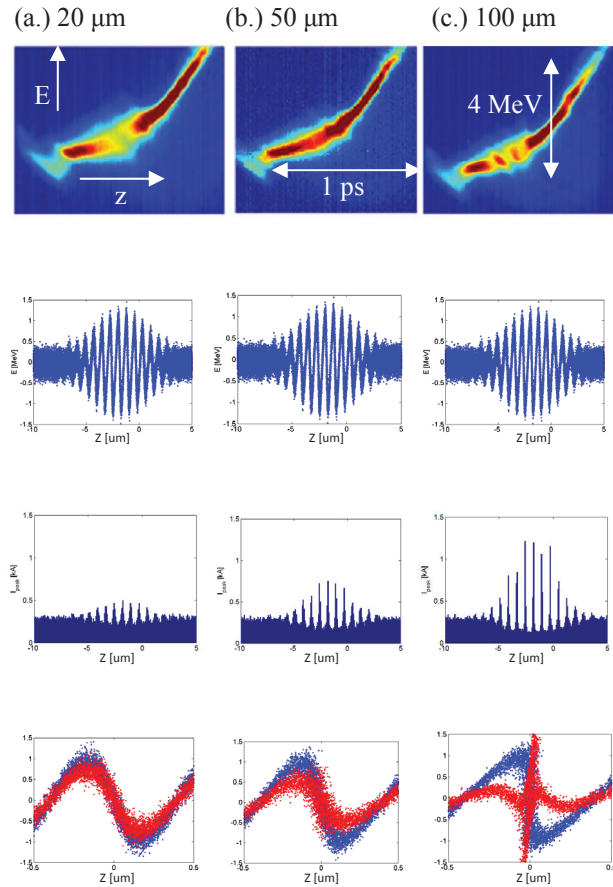


Figure 10: The longitudinal phase space for 3 different chicane R_{56} s measured with RF deflecting structure. The beam energy was 700 MeV and the peak current was 300 A. In (a), the microbunch is only slightly compressed, in (b), the microbunch is almost fully compressed, and in (c), the microbunch is over-compressed in the center of the seed. Simulations of the seeded microbunches are shown below. The seed pulse length has been shortened by a factor of 6 in the simulation, so that the individual bunches are visible. Red dots are after the drift, blue dots are before the drift.

ACKNOWLEDGEMENTS

The author would like to thank Bart Faatz for information about the FLASH2 layout, Velizar Miltchev for his perspective on FLASH2 design, Martin Dohlus for his 3-D LSC code, Holger Schlarb for initial education on several topics, and the operations team [9] for allowing the measurement during beam time allocated for another purpose.

REFERENCES

- [1] L.H. Yu, Phys.Rev. A 44,5178 (1991).
- [2] V.V. Goloviznin and P.W. van Amersfoort, Phys.Rev.E 55, 6002 (1997).
- [3] H.X. Deng and Z.M. Dai, Chinese Phys. C 34, 1140 (2010).
- [4] P. Schmueser, et al., Springer (2008).

- [5] E.L. Saldin, E.A. Schneidmiller, and M.V. Yurkov, DESY Reports, TESLA-FEL 1996-14
- [6] Z. Huang, et al., Phys. Rev. STAB 7, 074401 (2004).
- [7] K. Hacker, “Seeding FLASH between 4 and 40 nm”, FLASH seminar 2013 (Nov, 12 2013).
- [8] K. Hacker, DESY Reports, TESLA-FEL 2013-01.
- [9] G. Feng, et al., These Proceedings: Proc. 36th Int. Free-Electron Laser Conf., Basel, 2014, MOP083.
- [10] C. Lechner et al., These Proceedings: Proc. 36th Int. Free-Electron Laser Conf., Basel, 2014, MOP060.
- [11] M. Dohlus, “Q-solver”, DESY FEL beam dynamics group webpage, <http://www.desy.de/fel-beam/>.
- [12] E. Allaria et al., Nat. Photon. 7, 913 (2013).
- [13] K. Hacker, to-be-published, PRST-AB Sept. 2014.
- [14] Operators for Measurements: S. Ackermann, J. Boedewadt, N. Ekanayake, K. Hacker, C. Lechner, T. Maltezopelous.
- [15] Christopher Behrens, Dissertation, Fachbereich Physik der Universität Hamburg, 2012.

ENHANCING THE HARMONIC CONTENT OF AN HGHG MICROBUNCH

Kirsten Hacker, TU, Dortmund, Germany

Abstract

High Gain Harmonic Generation (HGHG) seeding has been demonstrated in the visible and ultraviolet, but it is limited in performance at high harmonics of the seed by the initial uncorrelated energy spread of the electron beam. A recent proposal from SINAP using a chirped electron beam and a canted pole undulator has suggested a new mechanism for reducing the length of the seeded microbunches in order to improve the performance of HGHG seeding at high harmonics. This note reviews the mechanism, the limitation of the concept and extrapolates to some new concepts using analogous mechanisms derived from transverse gradients of the laser properties. The impact of CSR wakes on the vanishingly short microbunches produced by the methods are also investigated.

INTRODUCTION

Seeded electron beams benefit from a small uncorrelated energy spread of the electron beam because it reduces the length of the seeded microbunches. For High Gain Harmonic Generation (HGHG) seeding, the bunching factor as a function of harmonic number n is given in terms of the uncorrelated energy spread, δ , by [1]

$$b_n = e^{-(nD\delta)^2/2} J_n(nD\Delta\gamma) \quad (1)$$

where $\Delta\gamma$ is the energy modulation, n is the harmonic number, $D=2\pi R_{56}/\lambda_s\gamma_0$ where R_{56} is the dispersion of the chicane and J_n is a Bessel function of order n . When the bunching factor is plotted for a range of slice energy spreads, it is apparent that the seeding method could be extended to shorter wavelengths if a technique could reduce or cool the slice energy spread, δ , prior to or during seeding (Fig. 1).

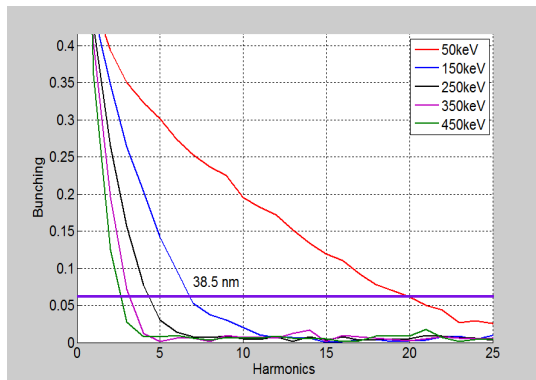


Figure 1: Bunching factor as a function of harmonics for a range of initial uncorrelated energy spreads for a 270 nm HGHG seeded beam.

*work supported by BMBF grant 05K10PE1 and DESY.

Several ideas have been proposed to cool the slice energy spread of an electron beam prior to seeding. The least invasive strategy involves reducing the compression and charge of the electron bunch so that it is easier to transport without suffering from the nonlinearities introduced by various wakefields which scale with the peak current. In simulations, this alone is enough to achieve a 100 keV slice energy spread at FLASH2 [2]. In practice, this is less certain. This strategy also reduces the FEL peak power, since the peak power scales with the peak current.

The next strategy employs a laser heater in the first bunch compressor of the accelerator in order to increase (heat) the uncorrelated energy spread early in the machine and smear out random fine structures in the electron bunch which get amplified as they propagate over large distances [3,4]. The combination of low-charge, weak compression, and laser heating has been shown to reduce the slice energy spread of the Elettra at FERMI beam to ~150 keV for a 500 nC bunch with 500 A of peak current prior to the seeding section [4].

An untried strategy from SINAP uses a canted pole undulator with a transversely chirped electron bunch in order to reduce the effective length of HGHG microbunches [1]. In this note, simulation predictions from seeding with SINAP's canted pole undulator are duplicated and extrapolated to alternatives utilizing novel laser conditions like a transverse intensity gradient, a wavefront rotation, and a transverse chirp as an alternative to the canted undulator pole. The benefits and problems associated with these alternatives are described.

CANTED POLE SEEDING

The SINAP HGHG proposal is to send a transversely chirped electron bunch through an undulator with transversely canted poles (Fig. 2).

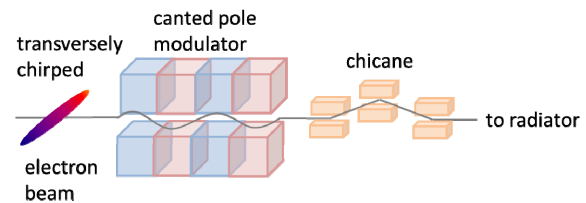


Figure 2: SINAP HGHG proposal sends a transversely chirped electron bunch through an undulator with transversely canted poles.

The mechanism was described by SINAP in the language of off-resonance seed laser modulation for cooling the beam energy spread. This note investigates the mechanism in the language of path length changes and energy transfer from the laser to the electron beam. It then extrapolates to scenarios with transverse variations of

ISBN 978-3-95450-133-5

laser properties in place of a transverse undulator gradient.

The longitudinal displacement of an electron traveling through an undulator magnet is given by [4]

$$z(t) = \bar{v}_z t - \frac{cK^2}{8\gamma^2\omega_u} \sin(2\omega_u t), \quad (2)$$

where

$$\bar{v}_z = 1 - \frac{1}{2\gamma^2} \left(1 + \frac{K^2}{2} \right). \quad (3)$$

Substitute in the time-of-flight through the modulator, $\Delta t = N\lambda_u/c$ and the angular frequency $\omega_u = 2\pi/\lambda_u$ to get

$$z(\Delta t) = \frac{\bar{v}_z N\lambda_u}{c} - \frac{c\lambda_u K^2}{16\gamma^2\pi} \sin(4\pi N/c).$$

Now, substituting in the x dependent portion of v_z and writing $z(x)$ for the canted poles and transversely chirped electron beam gives

$$z(x) = \frac{K(x)^2 N\lambda_u}{4\gamma(x)^2 c} - \frac{c\lambda_u K(x)^2}{16\gamma(x)^2 \pi} \sin(4\pi N/c).$$

Separating out the x dependent terms and writing the longitudinal coordinate for the left and right sides of the beam gives

$$z(x_{left}) = \frac{K(x_{left})^2}{\gamma(x_{left})^2} \left(\frac{N\lambda_u}{4c} - \frac{c\lambda_u \sin(4\pi N/c)}{16\pi} \right)$$

$$z(x_{right}) = \frac{K(x_{right})^2}{\gamma(x_{right})^2} \left(\frac{N\lambda_u}{4c} - \frac{c\lambda_u \sin(4\pi N/c)}{16\pi} \right).$$

Let us call the constant on the right, C , so that the difference in the longitudinal position across the transversely chirped electron bunch in the canted undulator pole is written

$$\Delta z = C \left(\frac{K_{left}^2}{\gamma_{left}^2} - \frac{K_{right}^2}{\gamma_{right}^2} \right) \quad (4)$$

If Δz goes to zero, the microbunch still has a length determined by the uncorrelated energy spread. This microbunch length can be written in terms of the transfer matrix element for dispersion as

$$\Delta z = R_{56} \frac{\Delta E}{E}, \quad (5)$$

where the R_{56} of an undulator is [5,6]

ISBN 978-3-95450-133-5

$$R_{56} = \frac{N\lambda_u}{\gamma_0^2} \left(1 + \frac{3K^2}{2} \right). \quad (6)$$

Equating Eq. 3 and 4 gives the condition for a minimum microbunch length.

The entire energy modulated waveform on the right side of the electron bunch starts out earlier and arrives later than the entire waveform on the left and this happens for a special combination of γ and K which is given in terms of the resonance condition by Eq. 6 of SINAP's paper [7] and, equivalently, in terms of path lengths, by Eq. 3 and 4, above.

Using the SINAP conditions as an example, Eq. 3 and 4 can be used to reproduce the phenomenon in simulation. The beam energy was 0.84 GeV with 84 keV (rms) slice energy spread (0.01%), 600 A peak current, modulator period length of 80 mm, and period number of 12. The induced energy modulation was 500 keV with a 265 nm seed. These conditions can be replicated in a simulation with a beam made up of two stripes of different energies which differ from the reference energy by 0.01%. In Fig. 3, the beam is given an energy modulation and is bunched through the R_{56} term alone.

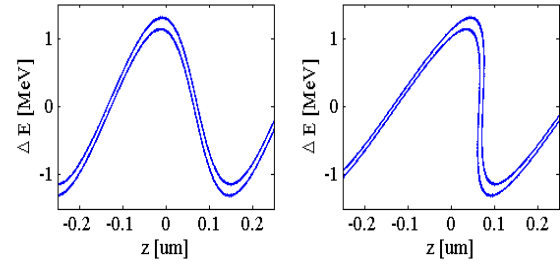


Figure 3: Stripes of charge with different energies in longitudinal phase space modulated with a sinusoidal pattern and then bunched in a chicane.

By varying K by $\pm 0.07\%$ in Eq. 3, the SINAP results are reproduced as shown in Fig. 4.

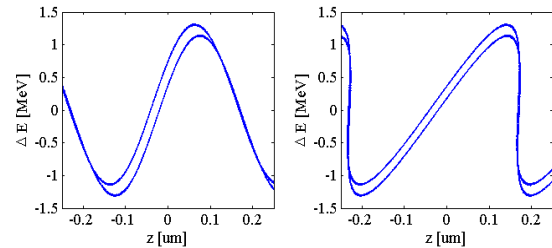


Figure 4: Eq. 4 reproduces the SINAP result with the canted pole undulator and transversely chirped electron bunch.

The same effect can be generated by shifting one curve longitudinally by 10 nm according to $R_{51} \Delta x = 10$ nm. While the R_{56} does vary transversely across the transversely chirped bunch, the effect is negligible compared to the non-energy-dependent path length changes from the R_{51} .

The magnetic field tolerances of the method depend on the energy spread and dispersion of the electron bunch. For the SINAP example, where the K needs to vary by $\pm 0.07\%$, a gap, $g=10$ mm, would need to vary by $13 \mu\text{m}$ over 2σ of the electron beam according to Eq. 63 of [7],

$$\frac{dg}{dx} \Delta x = -\frac{\Delta K}{K} \frac{\lambda_u}{\pi} \coth^{-1}(\pi g / \lambda_u).$$

Another important tolerance evolves around coherent synchrotron radiation (CSR) and longitudinal space charge (LSC). The compression in the above simulations was done in 1-D through R_{56} alone and does not take into account the impact of CSR and LSC. The high peak currents of vanishingly short microbunches can dramatically increase the energy spread and influence the charge distribution after a chicane and a drift [8] and increasing the peak current by shortening the length of the microbunch with this canted pole method could, therefore, be counterproductive. Compression through a drift alone would avoid the CSR and might provide a preferable mode of compression [8]. The drawback of producing a spatially chirped FEL beam should also be considered.

LASER COOLED SEEDING

An alternative to the canted pole technique exploits an analogous mechanism with laser techniques. Tolerances for these techniques are described.

In the case of a tilted laser wavefront produced by giving the trajectory of the laser pulse through the modulator an angle, the condition plotted in Fig. 4 could theoretically be reproduced using the laser wavefront rotation in lieu of the canted undulator pole. The wavefront rotation method would offer superior tunability compared to the canted pole undulator method at a cost of increased sensitivity to a coupled, unstable, and difficult to measure laser parameter (Fig. 5).

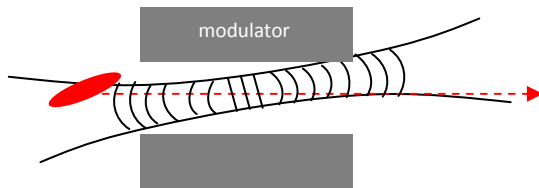


Figure 5: Wavefront rotation due to diagonal trajectory through the modulator. The dashed line is the trajectory of the electrons while the solid lines represent the laser waist and wavefronts. If the waist of the seed is too small, curvature of the wavefronts can complicate the technique along with coupling between modulation amplitude and trajectory.

The wavefront angle required by such a technique is determined by the energy spread which requires correction. If the 84 keV slice energy spread from the SINAP example is used, the laser wavefront would need to arrive 10 nm earlier on the left compared to the right.

For an electron beam which is dispersed by 1 mm at the entrance to the modulator, this corresponds to an angle of $10 \mu\text{rad}$ of the laser wavefront with respect to the electron beam trajectory. Pointing jitter of an injected beam after 20 meters of transport would be on this level, but fast steering correction systems are technically possible. With more electron beam dispersion or slice energy spread, the tolerances on the laser pointing jitter are relaxed. For example, at DELTA, the electron beam could be streaked by 1 cm and require $100 \mu\text{rad}$ of wavefront rotation to demonstrate the effect [9].

Since the transverse overlap in the modulator is coupled to the seed trajectory, this technique can be complicated by coupling between energy modulation amplitude and wavefront tilt. Especially for longer, 2 meter modulators, it could be difficult to distinguish which change in the harmonic content is due to the wavefront rotation change and which is due to the modulation amplitude. However, when the seed spot diameter is a few times larger than that of the electron beam, this coupling effect is tiny.

An alternative way to apply tilted wavefronts is to place the modulator off-center with respect to the laser waist and then misalign the seed pulse compressor so that a wavefront rotation is produced in the modulator (Fig. 6). Compressor misalignments would change the steering into the modulator unless a steering feedback is used to correct the orbit, but there are commercial systems which can do this. Away from the waist, the wavefront rotation disappears and becomes a pulse-front tilt (variation in the arrival time of the intensity fronts), but on-average, the wavefront would be rotated in a single direction and it could be tuned without impacting the overlap. The pulse length, however would be sensitive to large changes in compressor alignment. If the compressor alignment changes are small, then the impact of pulse length changes on the energy modulation should be small.

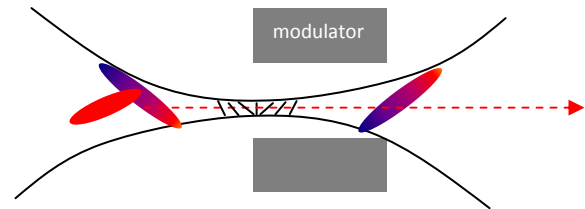


Figure 6: Wavefront rotation produced through compressor misalignment. The pulse has wavefront rotation at the waist and pulse front tilt away from the waist. It has spatial chirp throughout. The dashed line is the trajectory of the electrons while the solid lines represent the laser waist and wavefront rotation.

The impact of the spatial chirp which accompanies the compressor misalignment could be significant (Fig. 6). To remove the effect of an 85 keV electron bunch slice energy spread with a spatially chirped laser pulse, the laser would need to be chirped from 395 nm on one side to 405 nm on the other. This is possible with the bandwidth of the current sFLASH laser system and the

sFLASH modulators, however, to correct for a larger, 400 keV energy spread, a 40 nm bandwidth of a 270 nm seed would be required. This verges on the impossible with known techniques. A spatially chirped laser pulse would necessarily have a significant pulse front tilt and the waist would need to be placed away from the modulator in order to avoid the influence of wavefront rotation which occurs near the waist. The pulse front tilt would also complicate longitudinal overlap with the electron bunch since the electron bunch would need to be chirped in the same plane as the pulse front tilt (Fig. 7).

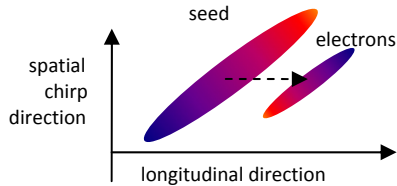


Figure 7: Longitudinal and spatial overlap of chirped electron and chirped seed. Since the seed must be larger than the electron bunch to ensure a flat intensity profile, this method presents challenging overlap and bandwidth considerations.

With an offset from the center of the laser spot, the electron beam will see a slightly tilted wavefront and an intensity gradient (Fig. 8). For large laser spots, the intensity gradient would be the dominant effect and could be used to cool the energy spread.

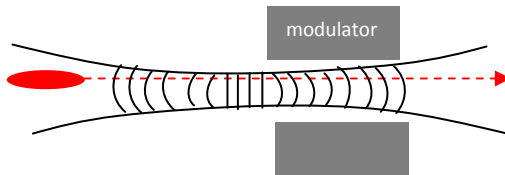


Figure 8: Transverse intensity gradient and wavefront rotation due to offset relative to center of laser spot.

Compared to the wavefront rotation, the intensity gradient is the dominant effect whenever the electron beam is off center from the laser spot and when the compressor is not misaligned. The effect of this intensity gradient on the longitudinal phase space is shown below in Fig. 9. The two particle trajectories come closer together for negative energies but grow further apart for positive energies. The area between the two curves remains constant, per Liouville's theorem.

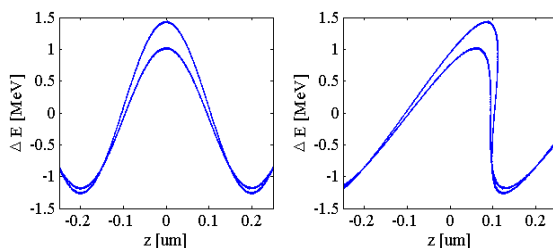


Figure 9: The effect of a transverse laser intensity gradient which transversely varies the energy transferred from the seed to the transversely chirped electron bunch.

The tolerances of such a technique would require a precise laser intensity gradient to be matched to a precise electron beam energy chirp. While tuning the slope of the laser gradient by increasing and decreasing the laser pulse energy could be simple, the energy modulation would also increase and decrease, complicating the method.

A beneficial operation point is found when the transverse gradient technique is combined with a CSR wake from the last dipole of the bunching chicane. While a symmetrically compressed bunch would become chirped by the CSR wake, so that low energy particles get bunched more than the high energy particles, if this is combined with the transverse laser gradient technique and a slightly over compressed bunch, a more dramatic spike in the peak current could be achieved.

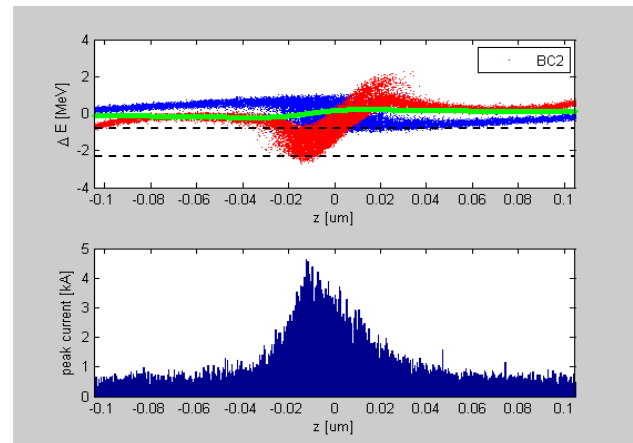


Figure 10: Impact of LSC and CSR on a microbunch after 4 meters of drift and an R_{56} of 45 μm . Dashed lines represent the bandwidth of the radiator. The background particles in blue show the conditions prior to the application of CSR or LSC. The foreground, red particles show the bunch after CSR and LSC and 4 meters of drift. The green line gives the LSC potential per meter. This is done for a 700 MeV beam energy, 1 kA initial peak current, and 2 MeV (pp) energy modulation. The harmonic content of the microbunch was unaffected, but the energy spread was increased.

CONCLUSION

The canted pole undulator technique has tight tolerances on the gap and tunability. Alternatives which combine a dispersed electron bunch with different laser properties in the modulator could be used to produce a similar effect with more tunability, however, each alternative introduces undesirable byproducts in terms of coupled parameters and sensitivity to unstable laser parameters. The most promising technique appears to be to use a transverse laser intensity gradient with a transversely chirped electron bunch. It has reasonable tolerances and provides a mechanism for increasing the microbunch peak current by making use of a CSR wake. For the other methods, CSR destroys the quality of the microbunch, but for the transverse intensity gradient, it enhances it.

REFERENCES

- [1] H. Deng and C. Feng, PRL 111, 084801 (2013).
- [2] G. Feng, et al., These Proceedings: Proc. 36th Int. Free-Electron Laser Conf., Basel, 2014, MOP083.
- [3] Z. Huang, et al., PRST-AB 13, 020703 (2010).
- [4] E. Allaria et al., Nat. Photonics 7, 913 (2013).
- [5] P. Schmueser, et al., Springer (2008).
- [6] Y. Li and J. Pflueger, Proc. FEL 2010, 37 (2010).
- [7] Z. Wolf, “Algorithms To Automate LCLS Undulator Tuning” April 10, 2006, LCLS-TN-06-8, page 26.
- [8] K. Hacker, These Proceedings: Proc. 36th Int. Free-Electron Laser Conf., Basel, 2014, MOP095.
- [9] S. Khan, These Proceedings: Proc. 36th Int. Free-Electron Laser Conf., Basel, 2014, MOP084.

A CONCEPT FOR SEEDING 4-40 nm FEL RADIATION AT FLASH2

Kirsten Hacker[#], TU, Dortmund, Germany

Abstract

This note describes a scheme to seed the FLASH2 FEL over a range of 4-40 nm without impacting SASE capabilities. This scheme combines multiple seeding techniques, builds on current infrastructure and offers a maximized range of performance with higher pulse energies than what are available at lower-peak current facilities. The concept relies on Echo Enabled Harmonic Generation (EEHG), cascaded seeding, and Second Harmonic Afterburners (SHAB) while maintaining the possibility to operate with High Gain Harmonic Generation (HHHG) seeding at >30 nm wavelengths.

INTRODUCTION

High Gain Harmonic Generation (HHHG) and an HHHG cascade have demonstrated seeding at FERMI down to 19 nm with HHHG alone and 4 nm in an HHHG cascaded configuration [1,2]. FERMI operates with low-charge, 400-600 A peak current and weak compression. They have a laser heater and no space for a long, SASE undulator. All of these conditions are the opposite of those presently available at FLASH. In order for FLASH2 to offer a competitive seeding program to users while maintaining SASE capability

- the facility must be compatible with SASE
- first few years of operation without a laser heater
- seeding should work at short, 4 nm wavelengths
- seeding should work over the entire bunch-train
- design must be flexible in order to accommodate different electron beam conditions.

To fulfill these criteria, the seeding methods used at FLASH2 should be High Gain Harmonic Generation (HHHG) down to 40 nm, Echo-Enabled Harmonic Generation (EEHG) down to 7 nm, and an EEHG cascade down to 4 nm and below. Any of these seeding methods can be used with a Second Harmonic After-Burner (SHAB) to reach shorter wavelengths [3]. An HHHG cascade could be attempted, but the tolerances are not generous.

Simulations will show the limitations of each of these radiation (CSR), and laser pulse distortions using 1-D

tracking and analytic estimates for 3-D effects. The full-bunch simulation methods from [4] would be used in a final design study.

Each of the seeding concepts, excluding the afterburner, could be tested in FLASH1 in 2014 [5, 6]. The hardware required for these tests has already been commissioned and experts are available for the operation.

Through the FLASH2 configuration shown in Fig. 1, individual commissioning of HHHG, EEHG and an EEHG cascade could be accomplished in a stepwise fashion, allowing for work starting with proven concepts at 40 nm and ending with seeding at 4 nm. 2 nm could potentially be seeded given an afterburner [3]. HHHG could also be incorporated into the setup in an EEHG-HHHG configuration, but this concept is an add-on of research interest for compact schemes and it is not essential to the design for user operation.

An item which is essential for seeding is the Transverse Deflector Structure (TDS) drawn at the end of the FEL radiator. Aside from providing an unparalleled diagnostic of the overlap of the seed with the electron bunch, this X-band longitudinal beam diagnostic would be shared with the LAOLA plasma wakefield acceleration experiment in FLASH3 [7] and provide information on the FEL pulse length to users.

This paper includes brief descriptions of

- electron beam and laser parameter ranges
- TDS design and resolution
- chicane, modulator and laser injection design
- impacts of electron bunch compression schemes
- impacts of laser parameters
- a simulation of HHHG and EEHG
- the conditions for EEHG cascade and SHAB

The conclusion is that by building a flexible, staged design which has the potential to seed the shortest possible wavelengths for the maximum 1.3 GeV FLASH electron beam energy, a competitive program can be developed for FLASH2 to deliver the benefits of external seeding to the FEL users in terms of longitudinal coherence, increased intensity, direct control over pulse properties and spectral stability.

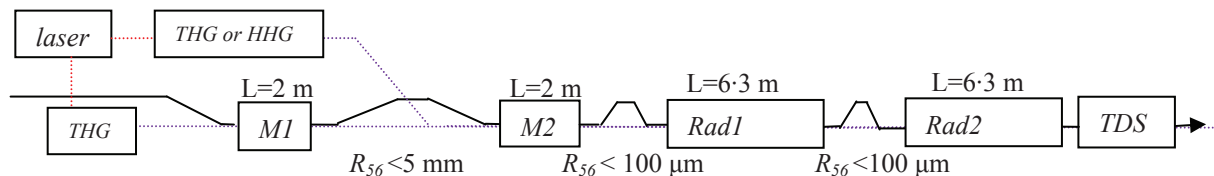


Figure 1: A flexible design for FLASH2 allowing for SASE, HHHG, EEHG, EEHG-HHHG, HHHG and an EEHG cascade, facilitating seeding between 4 and 40 nm. Harmonics of the Ti:sapphire laser pulse can be generated through Third Harmonic Generation (THG) or High Harmonic Generation (HHG). Two modulators (M1, M2) could be used to facilitate a flexible seeding program, while a Transverse Deflecting Structure (TDS) could diagnose the longitudinal profile and energy spread of the electron beam.

[#]*kirsten.hacker@cfel.de

ELECTRON BUNCH

The electron bunch can be compressed and shaped in many different ways. An example of a reasonable electron bunch for seeding is shown with images from a measurement done by C. Behrens using a Transverse Deflector Structure (TDS) to streak out the electron bunch longitudinally (Fig. 2) [8]. The basic constraints of the electron bunch parameter space for seeding are given in Table 1.

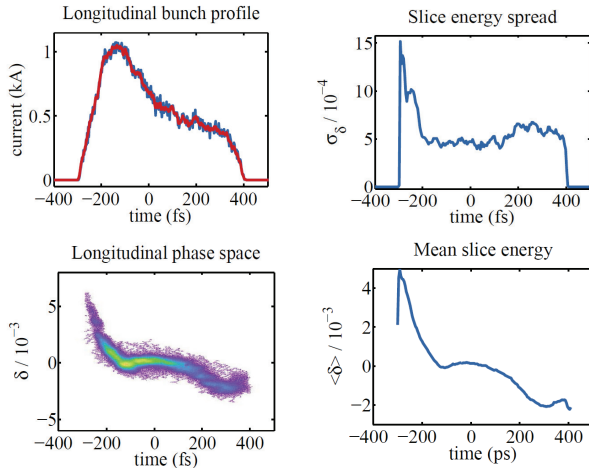


Figure 2: Measured slice energy spread (left), and deviation of the slice energy from the nominal (right). At 1 GeV and with 1 kA. From C. Behrens [8].

Table 1: Electron Bunch Parameters for Seeding

Electron bunch for seeding	
Bunch length	~50 μm (rms)
Energy	<1.3 GeV
Emittance	1.5 mm mrad
Peak current	1-2 kA
Slice energy spread (rms)	100-500 keV

Looking at the electron beam in Fig. 2, one sees that the properties are not uniform along the bunch and that only a small fraction will have the high peak current and low slice energy spread for seeding to be successful. While an uncorrelated energy spread of 50 keV can be simulated for the FLASH2 beamline, such performance has never been observed in FLASH1.

Since the portion of the bunch which has the appropriate properties for seeding is only ~50 fs (rms) (Fig. 2), the synchronization with the ~20 fs (rms) duration of an external laser pulse necessitates the 25 fs (rms) performance of the intra-bunch train feedback and optical synchronization system [9]. It also requires an accurate diagnostic of the longitudinal overlap between seed and electron bunch. This is why a TDS diagnostic installed after the radiator is needed for a successful seeding program.

A TDS streaks the electron bunch out longitudinally so that when it is impinged upon a screen, the charge density as a function of longitudinal position is depicted. After a dispersive section, the energy spread of the electron bunch

is given as a function of the longitudinal position along the bunch. When such a diagnostic is installed after a radiator, the increase in the energy spread of the electron bunch is indicative of energy loss due to radiation of photons in the FEL process. By comparing FEL-on to FEL-off images, one can use the measurement of the energy lost during radiation as a measurement of the longitudinal profile of the FEL light pulse. This has been done at SLAC with a 2 meter long X-band TDS which has gotten 4 fs (rms) resolution with a 13 GeV beam and a 25 MW klystron [10].

A similar cavity, with a smaller, L6145 6 MW klystron, could be used to generate comparable performance with FLASH's 1.3 GeV beam. It could be installed in a 3 meter long section after the last SASE undulator in FLASH II and it would be useful for

- giving users information about the longitudinal profile of the FEL pulse for each bunch train
- R&D for LAOLA ultra-short bunch diagnostics
- commissioning the FLASH II extraction line
- operating any seeding experiments

The slice energy spread increases caused by a seed can be observed on the longitudinal phase space of the electron bunch and allow for optimization of the overlap. While this would be useful for HHG, it would be indispensable for EEHG because it clearly facilitates the longitudinal overlap of two seed pulses with the seedable portion of the electron bunch.

For a beam energy of 1 GeV, a frequency of 9.3 GHz, and a normalized emittance of 1.5 μm (rms), the temporal resolution of an X-band TDS in FLASH II would be

$$\tau[\text{fs}] = 474 / (V[\text{MV}] \cdot \sqrt{\beta[\text{m}]} \cdot \sin(\vartheta))$$

where V is the deflection voltage, β is the beta function at the deflector and ϑ is the phase advance between the deflector and the screen. For example, for $V = 20$ MV, $\beta = 16$ m, $\vartheta = \pi/2$, then 6 fs (rms) resolution should be expected. For FLASH3 (LAOLA) [7], a larger beta function could be used with their smaller emittance in order to approach the sub-fs resolution which they require. For FLASH2, the smaller, 16 m beta function is needed in order to avoid impacting more than two SASE undulators with a large β and in order to maintain a 90 degree phase advance to the dump screen.

The 2 meter long X-band cavity is only marginally more compact than a 2.856 GHz S-band cavity, but due to the shorter wavelength, it offers 3 times the streaking strength so that a weaker klystron can be used. Instead of a 20 MW S-band klystron with a 2.44 meter long LOLA structure, a 6 MW X-band klystron could be used with a 2 m long 9.3 GHz structure to generate 20 MV of streaking voltage. By adding a pulse compressor to the 6 MW klystron, 12 MW would be available to the cavity, further improving the resolution. By sharing the FLASH2 klystron and modulator with the plasma wakefield experiment in FLASH3 and collaborating with XFEL and

other groups on the LLRF development, efficiencies could be exploited.

SEED LASER

The OPCPA seed laser system for FLASH2 produces pulse trains of tunable 740-800 nm with 1 mJ per pulse in the train. These pulses can be compressed to 30-40 fs (FWHM) [11]. The seed pulse trains are designed to seed every 10th bunch in the electron bunch train. The laser can also be operated in single-pulse (10Hz) operation, without pulse trains but with more energy per pulse (Table 2). Another option is to send the 500 mJ 800 nm laser from the plasma wakefield experiment into the FLASH2 tunnel. This laser would provide more power than is required for HHG or EEHG, but it could be used to produce a powerful HHG beam for seeding.

Table 2: IR Laser Parameters for Generating a UV Seed

IR laser options	Pulse-train (100 kHz)	Single-pulse (10Hz)
Wavelength (nm)	740-800	740-800
Peak power (GW)	1.75	30
Pulse energy (mJ)	1	20
FWHM duration (fs)	40	40

The ~800 nm pulses from these different laser configurations can be converted into ~270 nm through frequency multiplication in BBO crystals or they can be frequency multiplied through HHG in a gas jet to make much shorter wavelengths with dramatically reduced conversion efficiency. The frequency multiplied pulses could be injected in either the last bend of the dogleg or in the first EEHG chicane as seeds for the electron bunch.

The 270 nm seed for the first modulator would be injected after the last vertical bend of the extraction line, 11 meters prior to the modulator. There is enough offset at the bend for a 25 mm mirror to inject a beam with a maximum size of 9 mm FWHM on the mirror. The seed for the second and third modulators could be injected in the first chicane where space for an injection mirror is not limited. The injection point in the chicane could be used to deliver the 270 nm seed to the second modulator, located upstream of the first radiator section. It would be compatible with HHG injection but this is only a research option and not central to the concept.

Since a minimum 1:3 ratio in the diameter of the electron beam compared to the seed beam is desirable to avoid degradation of the bunching from the non-uniformity of the transverse laser intensity profile [12], the minimum seed waist which would be desirable for a 50-100 μm (rms) electron bunch would be 350-800 μm (FWHM).

The optimal electron bunch waist is determined by the type of modulator which is used. A short modulator with four 0.1 m long periods could be used with a small electron beam size if the primary goal is to seed with the shortest possible pulses. Such a modulator would minimize the slippage, but it would not make the most

efficient use of a limited amount of laser power and it would not smear out unwanted correlated phase errors in the seed pulse [13]. A longer modulator of 2 meters with 30 periods would allow for a more efficient use of the seed laser power and it is the preferred modulator in this design. The laser parameters for this modulator are in Table 3.

Correlated longitudinal phase errors or chirp do not directly shorten the portion of the seeded beam which will radiate in the FEL as was claimed [14,15]. Instead, the slippage in the modulator averages out the error and makes it possible to seed nearly transform limited FEL pulses [13]. The correlated phase error (α) does, however increase the peak field requirement of the seed (E_0) according to a calculation of the energy modulation along the bunch where $p(t)$ is the position of the seed with respect to the electron beam, k is the wavenumber, σ_s , is the seed pulse length, and L_m is the length of the modulator [13],

$$\gamma_m(s) = \int_0^{L_m/c} \frac{e}{m_e c^2} E_0 e^{-[s-p(t)]^2/4\sigma_s^2} e^{i\left\{k[s-p(t)] + \alpha[s-p(t)]^2 + \phi\right\}} \cdot v_x(t) dt$$

Table 3: Seed Parameters in Modulators for Seed Generated through THG in BBO Crystals

THG seed for EEHG/HHG modulators	
Seed wavelength	250-270 nm
Peak power	<175 MW
Pulse energy	<100 μJ
FWHM pulse duration	40 fs
Seed waists	350-800 μm (FWHM)
Electron beam waist	50-100 μm (rms)

To analytically describe the influence of a distorted seed wavefront in the second undulator on the EEHG bunching factor, one can calculate the bunching factor suppression as a function of distortions of the 270 nm seed (λ_s) [4],

$$\frac{b_{\text{error}}}{b_{\text{noerror}}} = e^{-2\pi^2 a^2 \left(\frac{\sigma_{\lambda_s}}{\lambda_s}\right)^2} \quad (1)$$

where a is the harmonic number. The suppression factor for a range of harmonics of 270 nm and wavefront distortions is plotted in Fig. 3.

CHICANE DESIGN

The first chicane, responsible for folding the beam in EEHG, should be made as long and gentle as space allows with the shortest possible dipoles. Since it would also be used to do a fraction of the final compression of the electron bunch, the beam size should be smallest at the last dipole in the plane of deflection [16]. Given the current FLASH2 lattice with 3.3 m between quadrupoles in a FODO cell, a chicane length of 3 m would fit, however, given the planned 350 mm long dipoles, this

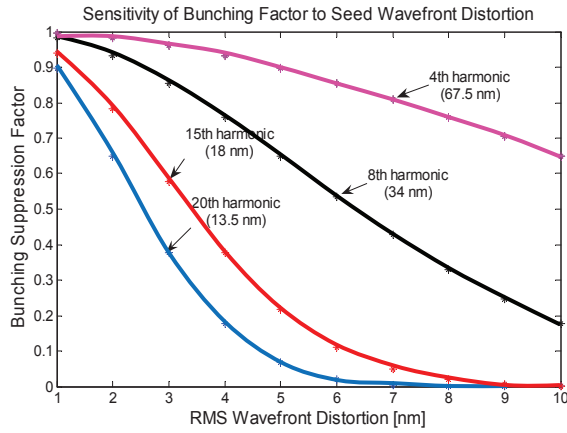


Figure 3: The bunching suppression factor for a range of harmonics and wavefront distortions.

would not leave enough space for incoupling a seed and one would need to build a second chicane for that purpose. The alternative is to turn a 6.6 m FODO cell with two chicanes into just a FO containing one longer chicane with 300 mm long HERA dipoles. The longer chicane reduces the energy spread increase due to CSR in the folding and incoupling chicane by an amount described by the worst-case, steady-state estimates in Table 4 below.

Table 4: Worst-Case CSR Energy Loss for a Gaussian Bunch with 50 μm (rms) Length and 1.2 kA of Peak Current in the EEHG Folding and Injection Chicane in the case that the 6.6 m FODO cell is preserved with two short chicanes or if it is converted into a 6.6 m FO cell with 3 meters between the dipoles

Dispersion	FODO chicanes	FO chicane
1 mm	2 MeV	0.8 MeV
5 mm	2.9 MeV	1.4 MeV
10 mm	3.5 MeV	1.7 MeV

The energy loss due to CSR from the macrobunch is not a big problem for seeding because, while it is non-linear, the seed is very short relative to the scale of the nonlinearities, so the seeded portion experiences this macrobunch CSR as a change in linear energy chirp.

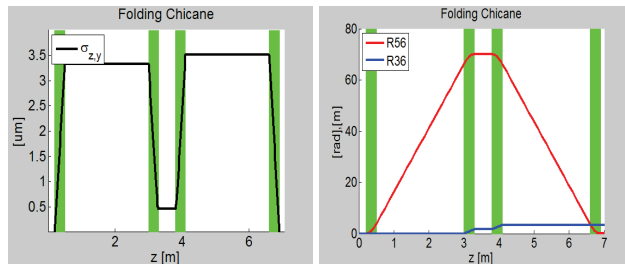


Figure 4: Transverse smearing of charge due to tilt as a function of longitudinal position in folding chicane. Green boxes represent magnet locations. Peak current is highest between the first two dipoles, ruling out danger of microbunch CSR.

The CSR for the seeded microbunch is a different problem. As long as the high peak currents in the EEHG folding process only occur in the first chicane in regions with significant transverse smearing (z,y tilt), disastrous CSR effects in the first chicane can be avoided. To check this, the location of maximum compression was calculated and compared to the smearing plotted in Fig. 4.

The largest effect of micro-bunch CSR arises at the exit of the chicane which is used to do the final bunching as shown with the CSR wake [17] in Fig. 5. This is, however, an over-estimate of the wake, since the full compression is not reached until the last fraction of the dipole and there is significant transverse smearing at the entrance to the dipole which is not included in the calculation. If the final compression is accomplished through the velocity bunching of a 30 m drift, then CSR can be avoided completely.

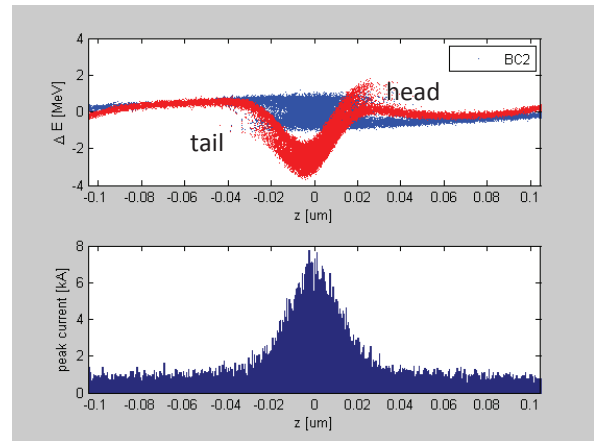


Figure 5: An HGHG microbunch (blue) under the influence of a worst-case steady-state CSR wake (red) in a 100 mm long dipole. The head of the bunch is to the right.

Table 5: Folding and Bunching Chicane Parameters

<i>First chicane at 1GeV</i>	
Pole Gap	40 mm
Magnetic field	280 mT
Physical length	300 mm
Magnetic length	360 mm
Deflection angle	<30 mrad
Dist. btw. dipoles	3 m
Dispersion (R_{56})	<2.7 mm
Max current	3.5 A
Vacuum chamber	100 mm
<i>Second and third chicanes at 1GeV</i>	
Pole Gap	40 mm
Magnetic field	300 mT
Physical length	100 mm
Deflection angle	9 mrad
Dist. btw. dipoles	0.75 m
Dispersion (R_{56})	130 μm
Max current	3.5 A
Vacuum chamber radius	17 mm

The parameters of the chicanes are in Table 5. The first chicane uses HERA magnets fitted with 40 mm pole shoes and the second chicane uses FLASH correctors.

LONGITUDINAL SPACE CHARGE

Incoming density modulations are transformed into an energy modulation ($\Delta\gamma$) in the presence of impedance (Z) [17].

$$\Delta\gamma = \frac{|Z(k)|}{Z_0} \frac{I_0}{I_A} \rho_i \quad (2)$$

where $Z_0 = 377 \Omega$ is the impedance of free-space, $I_A = 17 \text{ kA}$ is the Alfen current, and ρ_i is a small current perturbation at some wavenumber k . This energy modulation is transformed into bunching in a dispersive section. CSR, Longitudinal Space Charge (LSC), geometric wakes, and Coherent Edge Radiation (CER) all contribute. Together they accumulate to create the Micro-Bunching Instability (MBI). The largest contribution by far is made by LSC because it accumulates along the entire machine. The other effects are stronger, but they accumulate over shorter distances.

While FLASH does not have a laser heater to reduce the LSC induced microbunching instability, a special setup of the machine can potentially reduce the microbunching gain by orders of magnitude compared to its manifestation for a typical SASE setup of the machine. By using the 1 ps short-pulse injector laser instead of the 6.4 ps SASE injector laser, one can avoid using the first bunch compressor. Although the energy spread will be more non-linear, the peak current will be smaller through the following acceleration stages, thereby reducing the growth of the microbunching instability. A simulation of a FLASH-like machine done in [18] showed that the microbunching gain with single-stage compression is an order of magnitude smaller than with two-stage compression. The start-to-end simulations done in [4] are consistent with this strategy.

Aside from setup of the accelerator and bunch compressors, the setup of the seeding section undulators and chicanes has an impact on the MBI. For example, if a fully compressed microbunch is transported over 4 meters, the energy chirp reverses and the peak current is reduced (Fig. 6). If, however, the seeded microbunches are transported in an undercompressed state over a few meters, the LSC wake has a beneficial effect: it acts to reduce the energy spread of the microbunch [19-21]. If the length L of the drift is too long or the LSC potential is too strong, then the microbunches will be destroyed. An optimal condition is achieved when the the $R_{56}=L/\gamma^2$ velocity bunching dominates.

There are significant differences between the shape and magnitude of LSC wakes for EEHG microbunches and HGHG microbunches as shown in Fig. 7 for $kr_b < \gamma/2$,

$$Z_{LSC}(k) = \frac{iZ_0}{\pi k r_b^2} \left[1 - \frac{k r_b}{\gamma} K\left(\frac{k r_b}{\gamma}\right) \right] \quad (3)$$

where $r_b = 0.85(\sigma_x + \sigma_y)$ is the radius of a uniform, round beam with radius 100 μm , K is a modified Bessel function, and γ is the Lorentz factor [22]. Note that when the microbunch becomes shorter than the transverse size of the beam, as in the EEHG case, the LSC potential assumes the form of an error function. The potentials from neighboring microbunches cancel each other out except for on the ends. This means that for EEHG, each burst of microbunches will have distortions on the ends and for HGHG and EEHG there will be distortions due to the Gaussian profile of the seed. Imperfect cancellation of these potentials in the tails could lead to shorter than expected seeded FEL pulses.

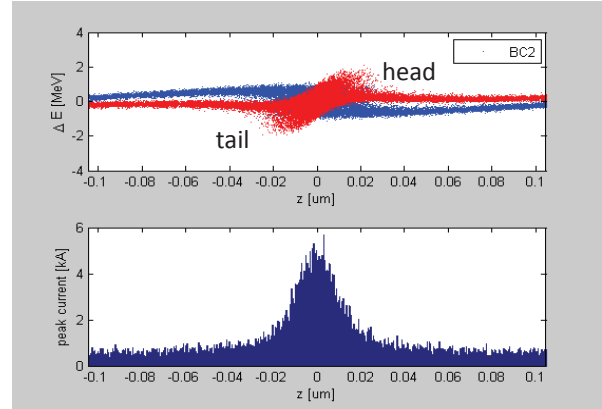


Figure 6: The effect of the LSC potential on a 100 μm (rms) radius HGHG microbunch transported by 4 meters. Blue is the unaffected distribution and red includes the LSC wake.

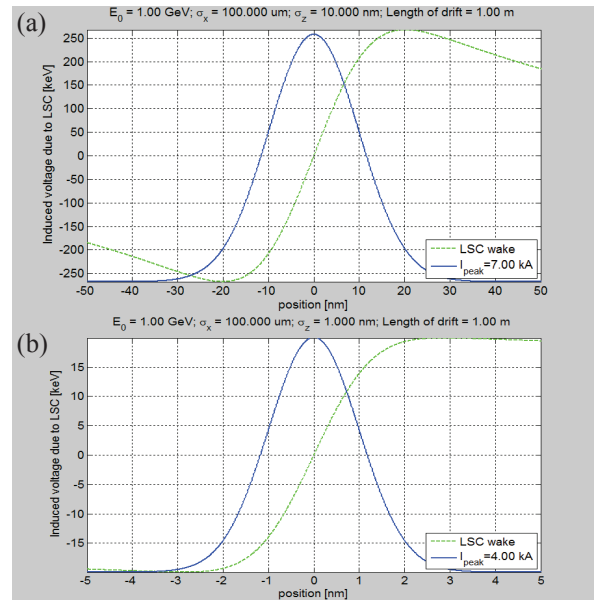


Figure 7: LSC wake per meter for (a.) HGHG microbunch with length of 10 nm (rms) and peak current of 7 kA and (b.) EEHG microbunch with a length of 1 nm (rms) and peak current of 4 kA. The beam radius is 100 μm (rms). The rms length excludes particles surrounding the microbunch and that wakes of neighboring microbunches impact the tails but not the slope of the wake.

HGHG OPERATION

HGHG was proposed in 1980 [23] and it relies on energy modulation of the electron bunch produced through interaction with a seed laser in an undulator tuned to the seed wavelength. Microbunches with the periodicity of the seed laser are then produced through the energy dependent path length differences in a chicane (Figs. 8, 9). The radiator undulator is tuned to a seed harmonic.

HGHG can be used as a low-risk first attempt at seeding in FLASH2. It can also be done with the high repetition rate configuration of the seed laser with an ample overhead in the laser power budget. The 1 mJ, 40 fs 800 nm laser pulses can be converted into 100 μ J, 40 fs 270 nm seed laser pulses through frequency tripling in BBO crystals giving a maximum of 175 MW. This seed would be injected in the first chicane in the seeding section and it would be used to seed in the second modulator (M2) with a waist of 700 μ m (FWHM) over 30 periods. The energy modulation would be 2 MeV (peak-to-peak) with a 40 MW peak power seed out of an available 175 MW. Above this amount of energy modulation, the gain of the FEL decreases. A 50 μ m R_{56} bunches the modulated beam and the beam energy is 700 MeV.

A complication arises with transporting a bunched beam to the radiator undulators at the end of the machine. In the absence of LSC, one should expect $R_{56} = L/\gamma^2 = 15$ μ m of dispersion over the $L=26$ meters from the exit of the modulator to the entrance to the last radiator segment (Rad2) and the net R_{56} required to bunch the beam for 2 MeV energy modulation is ~ 50 μ m. One can use the chicane between the two radiator sections to do the final bunching so that the distance that the bunched beam travels to the radiator is minimized. A small, beneficial reduction in the energy spread of the microbunch is facilitated through the LSC potential in the drift when the beam radius is ~ 200 μ m (rms), but if the beam radius is smaller, then LSC destroys the bunching [19-21].

By taking the Fourier transform of the longitudinal charge density distribution (Fig. 9), the bunching factor as a function of harmonics of the seed wavelength can be calculated for a range of initial slice energy spreads (Fig 10). Since a 1.5 kA beam with a bunching factor of <0.06 (represented by the purple line) will not reach saturation in less than four U32 undulator segments [5], one can use Fig. 10 to make a prediction of the minimum wavelength which can be seeded with HGHG at FLASH2. When CSR and LSC are taken into account, they will suppress the bunching factor for smaller energy spreads. Figure 10 does not take this into account. It can be compared with Fig. 2 of [4] in which a larger energy modulation was used.

Using 150 keV as a reasonable prediction of the likely energy spread for a 1.5 kA electron bunch [4], 38.5 nm could be seeded at FLASH II with a 270 nm seed. Since the 800 nm laser is tunable down to 740 nm, one could extrapolate that the tripled beam would have a wavelength

of 247 nm and it could seed down to 35 nm. If two additional U32 undulators are used as an SHAB, the seeded wavelength could be divided by two.

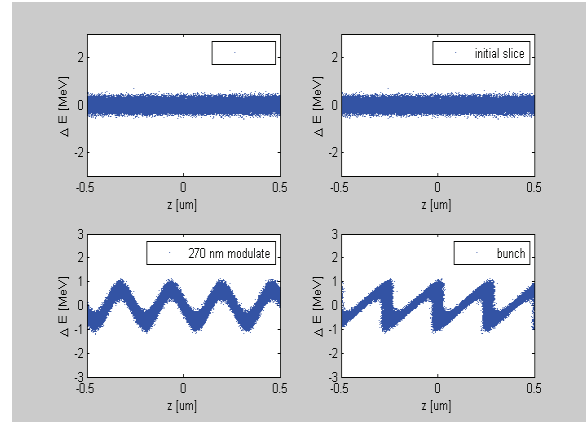


Figure 8: Longitudinal phase space of slice of electron bunch before and after energy modulation with external seed and bunching in a magnetic chicane. A seed with 40 MW of 270 nm and a 700 μ m (FWHM) diameter was used with an electron beam with 150 keV (rms) initial slice energy spread.

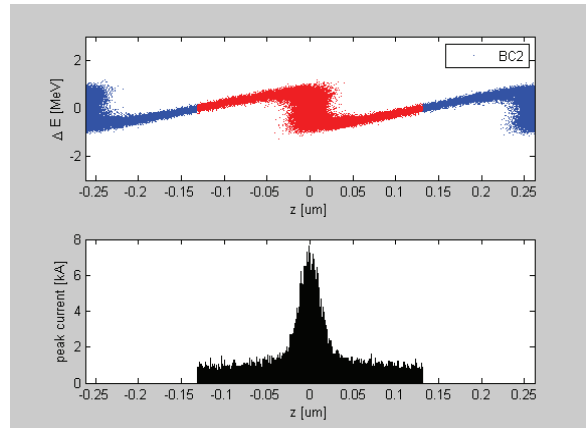


Figure 9: Projection of electrons in longitudinal phase space is used to calculate the peak current of the microbunches for a 1.5 kA initial peak current beam.

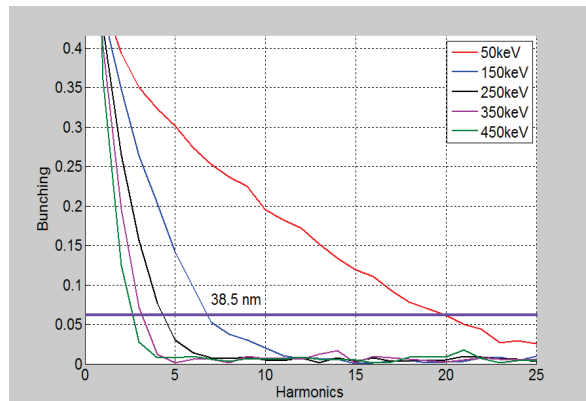


Figure 10: Bunching factor for HGHG with different initial slice energy spreads. The minimum wavelength

which can be seeded with 270 nm and a 150 keV energy spread is 38.5 nm.

EEHG OPERATION

EEHG was proposed in 2008 to overcome the limitations of HGHG in terms of electron beam energy spread tolerances and harmonic number [12]. It calls for the co-propagation of an electron bunch and laser pulse through an -undulator, chicane, undulator, chicane- series. Through interaction with a seed laser, the electron beam develops an energy modulation in an undulator which is then over-compressed in a chicane, creating horizontal bands of charge with discrete energies. The electron bunch is then modulated again in a second undulator and compressed in a second chicane, resulting in vertical stripes of charge with a period consistent with a harmonic of the seed laser wavelength. It has so far been demonstrated by SLAC in the NLCTA facility at the 14th harmonic of the seed [24, 25] and at the DUV-FEL at SINAP [26].

One could seed the entire bunch train with 1 mJ, 40 fs (FWHM) of 800 nm converted into 100 μ J of 270 nm (175 MW). Splitting the seed laser pulses transversely into two beams with ~ 50 μ J in each seed, one injects the seeds at two locations: the dogleg and the first EEHG chicane. This would allow one to use smaller, 500 μ m (FWHM) waists in both 2 meter long modulators. With such conditions, one could achieve the bunching shown in Figs. 11-13 with 20 MW in each modulator, out of an available 175 MW. The dispersion for folding and compression was 1 mm in the first chicane and 60 μ m in the second chicane.

It is important to have a laser power overhead because if the laser pulse has a chirp, the energy modulation will be smaller than for the transform limited pulses which were used in these simulations [13]. 20 meter drifts of the energy modulated yet unbunched beam are also dangerous in the presence of LSC. If a large, 200 μ m beam radius is not enough to remove the LSC problem in the 20 m drift, the modulated beam should be bunched immediately after the modulator and sent directly into the radiator. If the radiator is too far from the user extraction, then a split-radiator scheme should be used.

In 2010, SINAP did start-to-end simulations of EEHG for FLASH2 [27] and the configuration shown here is, in large part, similar to the SINAP configuration. Their investigations done through GENESIS and CSR Track are still valid. They predicted seeding down to 7 nm through EEHG with 1.2 GW of 270 nm focused to 700 μ m (FWHM). The electron beam energy was 700 MeV and the $R_{56}=1$ mm in the folding chicane. They also predicted seeding at 4 nm using the same laser conditions, but with a 1.22 GeV beam energy and a 5.5 mm R_{56} in the folding chicane, but the tolerance of CSR and other distortions becomes more difficult than at 7 nm.

A study of EEHG tolerances for FLASH1 was done in [5]. It tolerates electron beam and laser pulse intensity jitter well. Compared to HGHG it tolerates a very large

slice energy spread, but the trade-off is tight tolerances on the magnetic fields leading up to the radiator.

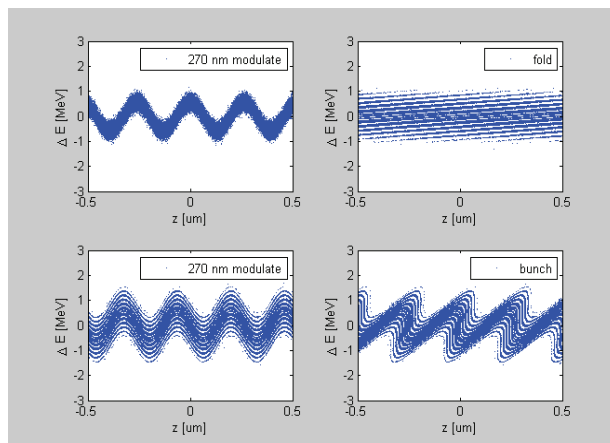


Figure 11: Folding and bunching in longitudinal phase space using a 20 MW 270 nm seed with a 700 μ m (FWHM) waist. 150 keV is the initial slice energy spread.

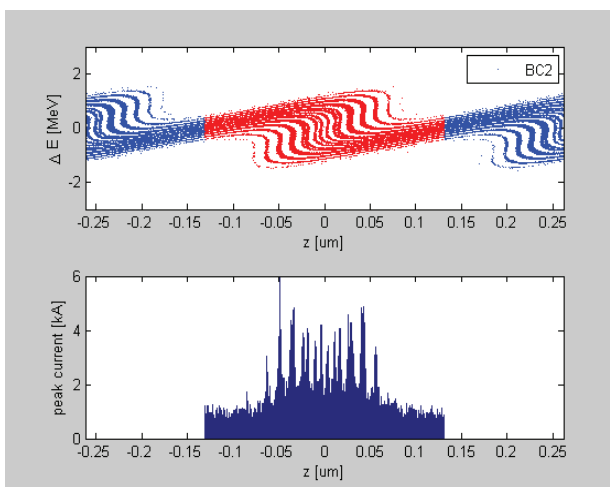


Figure 12: Projection of electrons in longitudinal phase space is used to calculate the peak current of the microbunches.

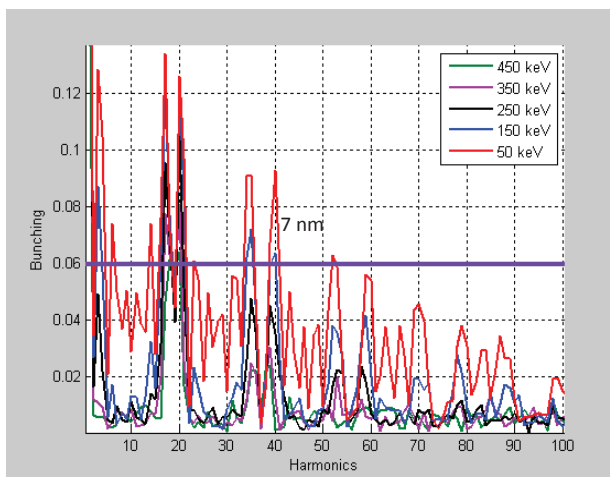


Figure 13: Bunching factor for EEHG with different initial slice energy spreads. The minimum wavelength which can be seeded with 270 nm and a reasonable, 150 keV energy spread is 7 nm.

EEHG-HHG OPERATION

EEHG-HHG (Figs 14-16) uses an HHG beam to seed in the second EHG stage. It uses the same layout as regular EHG, but it is more suitable for seeding on the few-nm scale. It was briefly proposed in 2011 for SWISS-FEL seeding at 1 nm, but it was rejected in favor of self-seeding due to concerns about synchronization and risk [28]. The biggest concern about such a scheme at FLASH is the intensity and quality of the HHG seed pulse required to generate the 250 keV to 500 keV of energy modulation necessary for this scheme to work. A peak power of 250-500 kW with a waist of 350 μm (FWHM) in a 2 meter long undulator with 30 periods is required by this scheme. For a 30 fs pulse length, the pulse energy would need to be 15 nJ.

This would not be a first-line method to attempt seeding at 4 nm. The EHG cascade would have looser tolerances for the seed, but EHG-HHG is interesting research because of its potential for use in compact FEL designs. The HHG mechanism in a gas is fundamentally different from the THG which occurs in a BBO crystal and one can imagine potential advantages in terms of the seed wavefront quality of an HHG pulse compared to a THG pulse.

With a loosely focused, phase matched HHG arrangement at sFLASH, 30 fs long 20 mJ pulses of 800 nm were used to produce up to 35 nJ of 38.1 nm with $M_x^2 = 9.5 \pm 3.1$, and $M_y^2 = 4.4 \pm 2.7$. After 95% losses in transport and 75% losses through overlap, only a fraction of a nanojoule was coupled into the electron beam [29,30]. This is consistent with other literature and optimized coupling of the seed energy into the electron beam, but it is a confusing contrast with literature describing 10 μJ produced at 73.6 nm, 4.7 μJ at 62 nm, 1 μJ at 54 nm, 330 nJ at 29.6 nm and 25 nJ at 13 nm with a 30 fs 16 mJ wavefront shaped IR beam [31,32]. These higher conversion efficiencies are representative of the energy scaling of HHG for different wavelengths, but they were achieved through looser focusing than what sFLASH can use. sFLASH has to use a smaller focus so that the focal spot in the undulator will be matched to the electron bunch. Two-mirror telescopes with direct incidence of XUV light cannot be used because they have unacceptable losses. Capillaries and phase matched cells do not come into consideration because they don't work well for wavelengths longer than 20 nm.

By putting a loosely focused source adjacent to the FLASH II injection, and injecting it with a pair of grazing incidence mirrors, minimal losses can be expected compared to the 95% losses in sFLASH transport, but the 800 nm laser for FLASH II has 95% less peak power than the sFLASH laser, making the expectation of an improvement in the HHG seed power at 38.5 nm compared to sFLASH unrealistic. However, by using 60 nm or 70 nm instead of 38.1 nm, one might expect 10-20 times more conversion efficiency for an expected output of 30-60 nJ for a 1 mJ input pulse. This would be 2-4 times the 15 nJ EHG-HHG requirement.

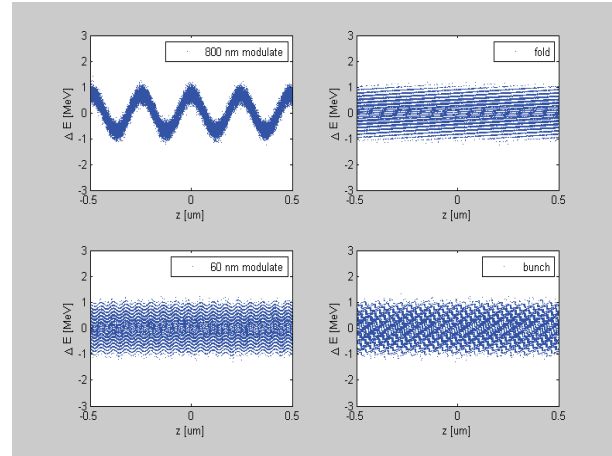


Figure 14: Folding and bunching in longitudinal phase space using a 40 MW 246 nm seed with a 700 μm (FWHM) waist and a 500 kW 61.6 nm seed with a 350 μm (FWHM) waist. 150 keV is the initial slice energy spread.

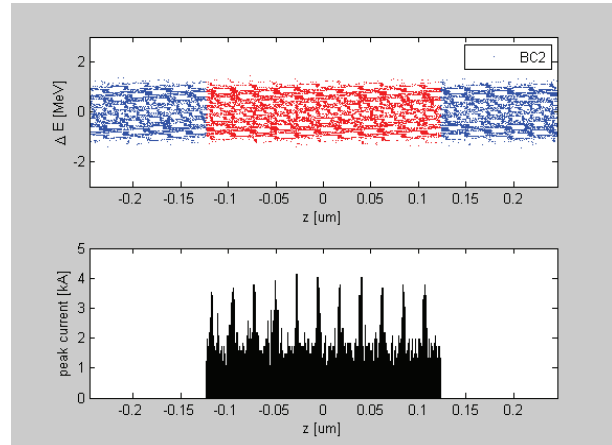


Figure 15: Projection of electrons in longitudinal phase space is used to calculate the peak current of the microbunches.

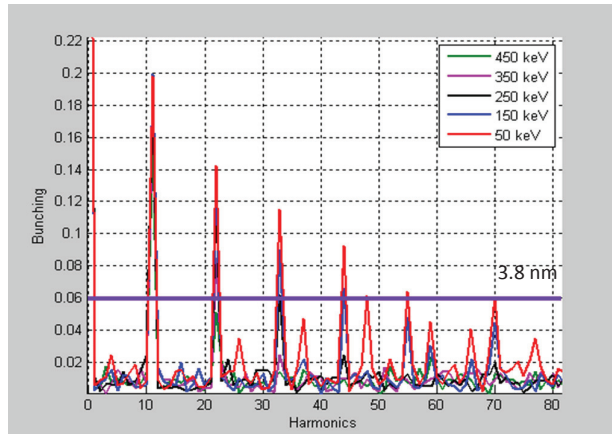


Figure 16: Bunching factor for EHG with different initial slice energy spreads. The minimum wavelength which can be seeded with 270 nm and a 150 keV energy spread is 7 nm.

CASCADED OPERATION

A major benefit of a cascade is the wavefront quality that the seed in the second stage gains by saturating in the first radiator stage. This makes it possible to reach shorter wavelengths with a cascade than are possible through a single-stage seeding scheme which is limited by the seed laser quality (Fig. 3).

The idea behind a fresh-bunch cascade technique is that the portion of the bunch which was seeded in the first radiator (Rad1) is too heated to be used to radiate in a second undulator stage (Rad2), so the radiation from the first stage must be positioned over a fresh, un-modulated portion of the bunch in the second stage [33]. The challenge of the technique is to overlap the radiation from the tail of the bunch with an appropriate portion of the head of the bunch by using a small chicane to delay the electron bunch relative to the light.

An HGHG fresh-bunch cascade has been used at FERMI to seed 4 nm [2] but a similar, three-stage cascade cannot fit into FLASH unless SASE operation is sacrificed, due to space constraints. Another critical difference is that the FERMI cascade is not separated from the linac by a dogleg, as is the case for FLASH2. Coupled with the lack of a laser heater at FLASH, even with the low-charge, weak compression scheme used at FERMI, identical performance should not be expected.

A two-stage, fresh-bunch cascade (Fig. 1) can, however, be used in FLASH2. When used with an HGHG seed, it would be limited to a minimum of 10 nm (the 3rd harmonic of 30 nm) and it would require a small, 150 keV (rms) slice energy spread. An EEHG cascade could, however, tolerate a large, 450 keV (rms) slice energy spread and seed 4 nm (the 3rd harmonic of 12 nm). This tolerance makes an EEHG cascade more suitable for a SASE machine setup and it could facilitate a seeded beam with a higher charge and therefore higher output power than what can be accomplished through a low-charge FERMI-like design.

For a two-stage, fresh-bunch cascade to work, the radiation intensity from the first radiator stage (Rad. 1) must be sufficient to seed in the second radiator stage (Rad. 2). Based on GENESIS simulations [4], the radiated 14 nm beam size at the exit of 3 U32 undulators after reaching saturation would be $\sim 100 \mu\text{m}$ (rms) and the divergence would be $\sim 20 \mu\text{rad}$ (rms). The peak power for a 1.5 kA electron bunch would be 1 GW. The 3rd harmonic of 14 nm would have a smaller divergence and power. One can derive an expression for a harmonic's power from the spectral density per electron of the radiation emitted in the forward direction for the m^{th} harmonic [34],

$$\frac{d^2 U_m}{d\Omega d\omega} = \frac{e^2 \gamma^2 m^2 K^2}{4\pi} \cdot \frac{\sin^2(\pi N_u (\omega - \omega_m) / \omega_1)}{\sin^2(\pi (\omega - \omega_m) / \omega_1)} \cdot |JJ|^2$$

where

$$JJ = J_n \left(\frac{mK^2}{4 + 2K^2} \right) - J_{n+1} \left(\frac{mK^2}{4 + 2K^2} \right), m=2n+1.$$

The radiated power for a given harmonic is proportional to the spectral energy [31],

$$U_m(\omega) = \frac{d^2 U_m}{d\Omega d\omega} \Delta\Omega_m \quad (4)$$

contained in the solid angle $\Delta\Omega_m = 2\pi\sigma_{\theta,m}$. If one plots U_m as a function of radiated wavelength for 3 U32 undulators with $K=2.66$, one sees that the 3rd harmonic has about half of the spectral energy of the fundamental radiation within the solid angle defined by Eq. 4 (Fig. 17).

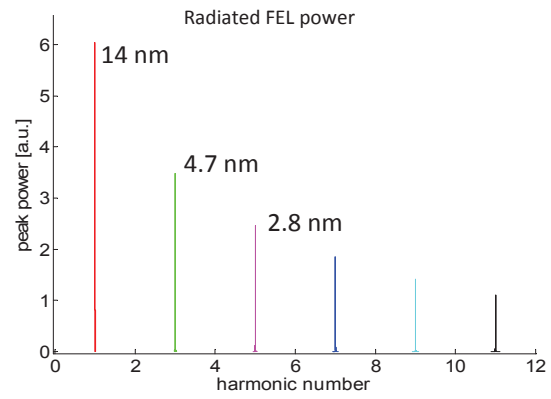


Figure 17: The radiated power of the m^{th} harmonic emitted into the solid angle $\Delta\Omega_m$. The Lorentz factor $\gamma = 2250$, the undulator period $\lambda_u = 3.14 \text{ cm}$, and the K parameter is 2.66.

Based on Fig. 17, one would expect the 3rd harmonic to have half of the 1 GW peak power of the fundamental for a 1.5 kA electron beam and 1/3 of the $\sim 30 \mu\text{rad}$ (rms) divergence. If the peak intensity coming directly out of the first radiator stage is then 1.1 GW/cm^2 , 20 meters downstream, it would have an intensity of 0.25 GW/cm^2 .

1 GW/cm^2 for seeding at $\sim 5 \text{ nm}$ is the seed intensity required to suppress fluctuations of the higher harmonics and it is several orders of magnitude higher than the intensity required to merely establish temporal coherence [35]. From this criteria, one could conclude that if EEHG seeding at $< 20 \text{ nm}$ is successful in the first radiator stage (Rad1), fresh-bunch cascading in the second radiator section (Rad2) is possible with a significant safety margin. To suppress fluctuations of the higher harmonics in order to incorporate a $< 4 \text{ nm}$ afterburner, the distance between the two radiator stages would need to be minimized.

The conditions described above could be achieved in an EEHG cascade starting with 10-20 nm in the first stage. For an HGHG cascade, the wavelength in the first radiator would be longer (30-40 nm) and the divergence and beam size would be about a factor of 2 larger, reducing the intensity in the second radiator stage compared to the

EEHG cascade, but the intensity threshold for establishing temporal coherence is about 0.5 GW/cm^2 lower for the longer wavelengths used in an HGHG cascade.

In conclusion, an EEHG or HGHG cascade could work at the 3rd harmonic. An EEHG cascade is a much more robust option in terms of slice energy spread tolerance compared to an HGHG cascade, however, the tolerance of magnetic field errors in the first-stage of EEHG seeding is tighter than for HGHG.

SUMMARY OF OPERATION MODES

Several different operation modes were outlined in the preceding sections. Each mode has a different tolerance of the initial slice energy spread of the electron beam. Plots summarizing the ranges of operation for a best-case 150 keV slice energy spread are drawn below (Fig. 18). The EEHG options offer more robust performance under poor, 450 keV slice energy spreads.

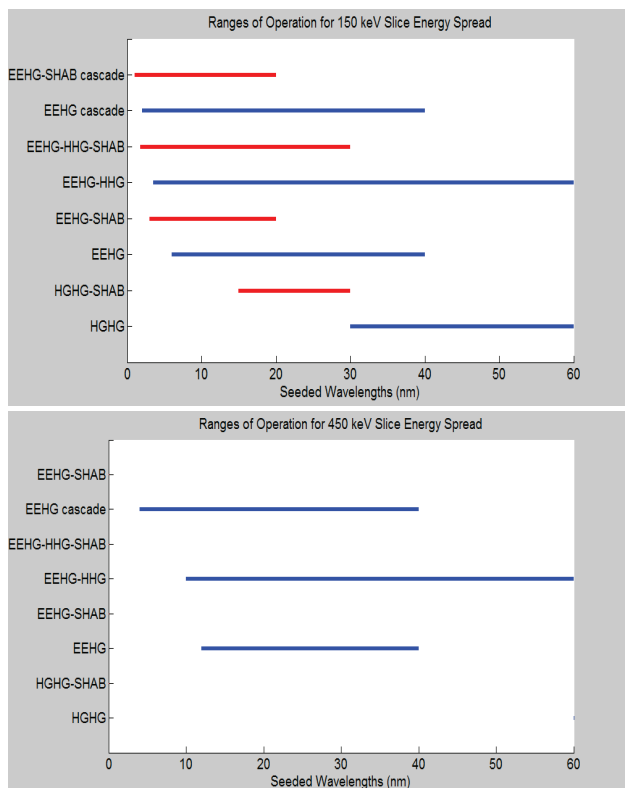


Figure 18: Summary of minimum wavelengths for different types of seeding configurations for the best-case 150 keV (rms) uncorrelated energy spread which has been measured at FLASH and for a poor, 450 keV (rms) uncorrelated energy spread.

CONCLUSION

The concept outlined in this note would allow for a conservative startup at FLASH2 using HGHG with parallel progress towards sub-4 nm seeding using EEHG techniques. All of the concepts illustrated here can be first tested in FLASH1 in 2014, allowing for design work to conclude in 2015 and purchase to proceed in 2016. Prior

to seeding purchases, TDS purchases should commence as soon as possible, for installation in 2015, so that the diagnostic will be available for extraction line commissioning.

ACKNOWLEDGEMENTS

Thank you to Bart Faatz for information on the FLASH II layout and plans and to Joerg Rossbach and Shaukat Khan for reviewing the document.

REFERENCES

- [1] E. Allaria, et al., Nat. Photon. 6, 699 (2012).
- [2] E. Allaria, et al., Nat. Photon. 7, 913 (2013).
- [3] V. Vardaanyan, et al., TESLA-FEL-2012-03.
- [4] G. Feng, et al., These Proceedings: Proc. 36th Int. Free-Electron Laser Conf., Basel, 2014, MOP083.
- [5] K. Hacker, H. Schlarb TESLA-FEL-2011-04.
- [6] K. Hacker, et al., TESLA-FEL-2011-05.
- [7] <http://laola.desy.de/>
- [8] C. Behrens, DESY-THESIS-2012-03.
- [9] I. Grguras et al., Nat. Photon. 6, 852–857 (2012).
- [10] C. Behrens et al., Nat. Comm. 5, 3762 (2014).
- [11] T. Tanikawa et al., These Proceedings: Proc. 36th Int. Free-Electron Laser Conf., Basel, 2014, MOP081.
- [12] D. Xiang and G. Stupakov, SLAC-PUB-13644, 2009.
- [13] C. Feng, et al., Phys. Rev. ST Accel. Beams 16, 060705 (2013).
- [14] D. Ratner, et al., Phys. Rev. STAB 15, 030702(2012).
- [15] G. Geloni, et al., arXiv: 1111.1615v1.
- [16] E.L. Saldin, E.A. Schneidmiller, and M.V. Yurkov, TESLA-FEL 1997-08.
- [17] E.L. Saldin, E.A. Schneidmiller, and M.V. Yurkov, TESLA-FEL 1996-14.
- [18] R.A. Bosch, K.J. Kleman, and J. Wu, Phys. Rev. STAB 11, 090702 (2008).
- [19] K. Hacker, FLASH seminar 2013 (Nov, 12 2013).
- [20] K. Hacker, DESY Reports, TESLA-FEL 2013-01.
- [21] K. Hacker, These Proceedings: Proc. 36th Int. Free-Electron Laser Conf., Basel, 2014, MOP095.
- [22] Z. Huang, et al., Phys. Rev. STAB 7, 074401 (2004).
- [23] I. Boscolo, V. Stago, Nuovo Cimento B 58 (1980) 267.
- [24] E. Ferrari, et al., Proc. 35th Int. Free-Electron Laser Conf. Manhattan, 2013, THOANO03.
- [25] D. Xiang et al., Proc. 35th Int. Free-Electron Laser Conf. Manhattan, 2013, THOANO02.
- [26] H. Deng et al., Nature Photonics 6, 360 (2012).
- [27] H. Deng, et al., DESY Report, DESY-11-034.
- [28] E. Prat et al., Proc. 33rd Int. Free-Electron Laser Conf. Shanghai, 2011.
- [29] Th. Maltezopoulos et al., Appl. Phys. B, doi: 10.1007/s00340-013-5571-6 (2013).
- [30] S. Ackermann et al., Phys. Rev. Lett. 111 114801 (2013).
- [31] E. Takahashi et al., Phys. Rev. Lett. A, 66 021802(R) (2002).
- [32] E. Takahashi et al., Appl. Phys. Lett., Vol. 84, Num. 1, (2004).

- [33] I. Ben-Zvi, K.M. Lang, L.H. Yu, Nucl. Instrum. and Meth. A 318, p. 726 (1992).
- [34] P. Schmueser, et al., "Ultraviolet and Soft X-Ray Free-Electron Lasers," Springer p.14-16 (2008).
- [35] L. Giannessi, Proc. of FEL 2004 Trieste, Italy.

CIRCULAR POLARIZATION CONTROL BY REVERSE UNDULATOR TAPERING

E.A. Schneidmiller, M.V. Yurkov, DESY, Hamburg, Germany

Abstract

Baseline design of a typical X-ray FEL undulator assumes a planar configuration which results in a linear polarization of the FEL radiation. However, many experiments at X-ray FEL user facilities would profit from using a circularly polarized radiation. As a cheap upgrade one can consider an installation of a short helical (or cross-planar) afterburner, but then one should have an efficient method to suppress powerful linearly polarized background from the main undulator. We propose a new method [1] for such a suppression: an application of the reverse taper in the main undulator. The method is free and easy to implement, it can be used at different X-ray FEL facilities, in particular at LCLS after installation of the helical afterburner in the near future. The theoretical background of the method as well as detailed numerical simulations are presented in [1]. In this note we discuss qualitatively the physics of the effect discovered in [1].

METHOD DESCRIPTION

In a short-wavelength SASE FEL the undulator tapering is used for two purposes: to compensate an electron beam energy loss in the undulator due to the wakefields and spontaneous undulator radiation; and to increase FEL power (post-saturation taper). In both cases the undulator parameter K decreases along the undulator length. The essence of our method is that we use the opposite way of tapering: parameter K increases which is usually called reverse (or negative) taper. We discovered [1] that in some range of the taper strength, the bunching factor at saturation is practically the same as in the reference case of the non-tapered undulator, the saturation length increases slightly while the saturation power is suppressed by orders of magnitude. Therefore, our scheme is conceptually very simple (see Fig. 1): in a tapered main (planar) undulator the saturation is achieved with a strong microbunching and a suppressed radiation power, then the modulated beam radiates at full power in a helical afterburner, tuned to the resonance.

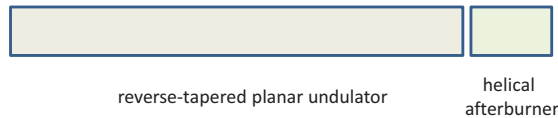


Figure 1: Conceptual scheme for obtaining circular polarization at X-ray FELs.

QUALITATIVE DISCUSSION

The theoretical background of the method as well as detailed numerical simulations are presented in [1]. Here we would like to discuss qualitatively the physics of the considered effect assuming that the reader is familiar with the main results of Ref. [1].

We will characterize the strength and the sign of linear taper by the taper strength parameter:

$$\beta = -\frac{\lambda_w}{4\pi\rho^2} \frac{K(0)}{1+K(0)^2} \frac{dK}{dz}. \quad (1)$$

Here z is the coordinate along the undulator length, ρ is the well-known FEL parameter, λ_w is the undulator period, and K is the undulator parameter with its initial value denoted as $K(0)$.

When the undulator parameter decreases along the undulator length, β is positive and we deal with a standard (positive) taper. In the opposite case the taper is reverse (or negative). Note that there were already two proposals for making use of the reverse taper in FELs: to improve the efficiency of FEL oscillators [2], and to use it in combination with an energy chirp in order to produce attosecond X-ray pulses [3]. Here we discuss a new useful feature of the reverse taper: a possibility to generate a strongly modulated electron beam at a pretty much reduced level of the radiation power.

As for the magnitude of $|\beta|$, one can consider two asymptotes. When $|\beta|$ is small, the undulator tapering leads to a small correction to the FEL gain length which was studied in [4]. Note that the tendency we would like to demonstrate (low power at strong bunching) is not seen in this regime. For this reason we will consider the asymptote of large $|\beta|$ in our qualitative discussion (even though in practical examples we deal with intermediate values of $|\beta|$).

Let us consider the high gain linear regime of the FEL operation and make the following consideration:

i) Consider the evolution of the SASE FEL frequency band which should depend on the sign and the magnitude of β . It was found in [4] that for small $|\beta|$, the central frequency of the amplified band moves half as fast as does the resonance frequency (corresponding to the current value of the undulator parameter K). We have found that situation is quite different in the case of strong taper, i.e. when $|\beta| \gg 1$. In the case of positive β the central frequency completely follows the changes of K , while in the case of a reverse taper, $\beta < 0$, the central frequency remains to be close to the resonance at the beginning of the undulator, i.e. it does not follow the changes of K at all. In other words, in the latter case the detuning from resonance continuously increases along

the undulator length, and the detuning parameter \hat{C} [1, 5] has a large absolute value and is negative.

ii) For a better understanding it is instructive to consider a steady-state FEL amplifier with a large constant negative detuning rather than SASE FEL with a linearly changing detuning. In the former case one can relatively easily solve an initial value problem [1, 5]. Here we can discuss the main results. At the resonance the normalized field gain length (inverse normalized growth rate [5]) is close to one. In the considered asymptote (large negative detuning) it is much larger and scales as $\sqrt{|\hat{C}|}$, as one can find from the solution of the eigenvalue equation. Thus, the field of the electromagnetic wave has more time to modulate the beam in energy, and the latter is larger than the former by the factor $\sqrt{|\hat{C}|}$ when we consider the properly scaled quantities [5] (in contrast, at the resonance they have comparable magnitudes). The energy modulations are converted into density modulations also on the scale of the gain length, so that the ratio between the latter and the former is again $\sqrt{|\hat{C}|}$. Therefore, the ratio between the bunching amplitude and field amplitude (using the standard scaling of these quantities) is given by $|\hat{C}|$. Closing the picture, the constructive interference from the retarded positions of particles happens on the scale of $1/|\hat{C}|$ due to the large offset from resonance, so that the effective formation length is much smaller than the gain length (in contrast with the resonance case). Thus, the solution of the initial value problem gives us a consistent picture. Note also that the phasors of the field amplitude and of the bunching are almost orthogonal in the considered asymptote of a large negative detuning which indicates a weak energy exchange between the beam and the electromagnetic field. Finally, let us note that the ratio between squared bunching and the normalized FEL power [5] (what counts in the end) scales as $|\hat{C}|^2$.

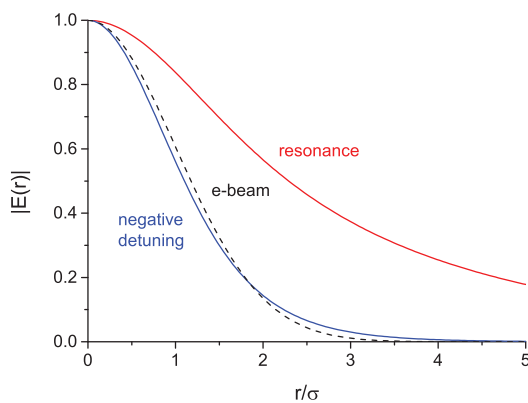


Figure 2: Field distribution of the FEL eigenmode at the exact resonance (red) and at a large negative detuning (blue). The diffraction parameter [5] equals 0.1. The detuning parameter for the blue curve equals -20 in 3D notations [5]. Dashed curve shows the electron beam profile.

iii) From the consideration in ii) it might not be clear why the field efficiently modulates the beam in energy despite a large detuning from the resonance. The explanation of this fact is as follows. From the eigenvalue equation we can find not only the real part of the eigenvalue (or, the inverse field gain length) but also an imaginary part that is responsible for the effective change of the wavenumber. The ratio of the frequency (which is given) and the wavenumber is the phase velocity. In the considered case of a large negative detuning we have found from the solution of the eigenvalue equation that the change of the wavenumber is such that the phase velocity slows down, and, as a result, the synchronism between particles and the amplified wave effectively exists in the high gain linear regime (or, the exponential gain regime).

iv) Let us now return to the SASE FEL case. As we know from i), in the case of a large negative β the central frequency of the amplified band remains to be close to the resonance at the beginning of the undulator, i.e. the detuning from resonance continuously moves towards large negative values as the undulator K increases along the undulator length. Thus, the situation is similar to the case discussed in ii). We have found that the main result is also similar: the ratio between the ensemble averaged squared modulus of the bunching factor and the ensemble averaged normalized power is approximately given by the squared modulus of the detuning parameter at a given position along the undulator length. We should also note that the FEL gain length is short initially, but then it increases as square root of the undulator length. Thus the total increase of the saturation length in case of the SASE FEL is smaller than in case of the FEL amplifier operating in steady-state regime with a constant negative detuning.

v) Up to now we have discussed the considered effect in the frame of 1D theory. It is interesting to note that 3D simulations give us even stronger suppression of FEL power (at the same level of bunching) than one could anticipate from 1D theory. The 3D "bonus" can be explained as follows. In the case when diffraction plays a significant role (i.e. when the diffraction parameter B [5] is smaller than one), the radiation mode size is larger than the electron beam size when an FEL operates close to the resonance (see Fig. 2). However, the field distribution shrinks in the case of a large negative detuning (this can be explained by a shorter effective formation length, see ii)). As a result, for the same FEL power, the field acting on the beam is stronger in the latter case, i.e. it leads to a stronger energy modulation, and, therefore, to a stronger density modulation (bunching) - in addition to the 1D effect discussed in ii).

vi) We have discussed here the high gain linear regime. However, the numerical simulations, performed in [1], confirm that the main effect of the reverse taper (strong bunching at a pretty much reduced radiation power) also takes place at the FEL saturation. In particular, one can have the situation when the bunching is about the same as in the reference case of no taper, the FEL power is suppressed by two orders of magnitude (or more), and the increase of the

saturation length is about 20-30 %. Thus, the effect is not only very attractive for the polarization control as discussed above but can also be efficiently used in other FEL schemes.

REFERENCES

- [1] E.A. Schneidmiller and M.V. Yurkov, Phys. Rev. ST-AB **16** (2013) 110702.
- [2] E.L. Saldin, E.A. Schneidmiller and M.V. Yurkov, Opt. Commun. **103** (1993) 297.
- [3] E.L. Saldin, E.A. Schneidmiller and M.V. Yurkov, Phys. Rev. ST Accel. Beams **9** (2006) 050702.
- [4] Z. Huang and G. Stupakov, Phys. Rev. ST Accel. Beams **8** (2005) 040702.
- [5] E.L. Saldin, E.A. Schneidmiller and M.V. Yurkov, "The Physics of Free Electron Lasers", Springer, Berlin, 1999.

RADIATION PROPERTIES OF TAPERED HARD X-RAY FREE ELECTRON LASERS*

C. Emma, C. Pellegrini, UCLA, Los Angeles, CA, USA
J. Wu, K. Fang, S. Chen, SLAC, Menlo Park, CA, USA
S. Serkez, DESY, Hamburg, Germany

Abstract

We perform an analysis of the transverse coherence of the radiation from a TW level tapered hard X-ray Free Electron Laser (FEL). The radiation properties of the FEL are studied for a Gaussian, parabolic and uniform transverse electron beam density profile in a 200 m undulator at a resonant wavelength of 1.5 Å. Simulations performed using the 3-D FEL particle code GENESIS show that diffraction of the radiation occurs due to a reduction in optical guiding in the tapered section of the undulator. This results in an increasing transverse coherence for all three transverse electron beam profiles. We determine that for each case considered the radiation coherence area is much larger than the electron beam spot size, making coherent diffraction imaging experiments possible for TW X-ray FELs.

INTRODUCTION

Self Amplified Spontaneous Emission X-ray Free Electron Lasers (SASE X-FELs) [1–3] have been used to study structures and dynamical processes with spatial resolution of 1 Å and temporal resolution of 1 fs. This has had a particularly significant impact in the field of bio imaging where X-FELs have been used to push the frontiers of what can be done with diffraction based imaging techniques [4–6]. Future research in this field will benefit from a larger number of coherent photons/pulse, a factor of ten to one hundred larger within a pulse duration of 10-20 fs corresponding to a peak output power of 1 TW or more.

Together with high peak power, coherent X-ray diffraction imaging experiments require the radiation to be sufficiently longitudinally and transversely coherent at the sample position [7]. The longitudinal coherence can be improved by seeding or self-seeding the FEL amplifier [8–10]. Tapering the XFEL after self-seeding presents a promising solution to achieving TW power pulses with adequate longitudinal coherence. In this work we examine the transverse coherence properties of the radiation from a seeded and tapered hard X-ray FEL and determine whether the radiation is sufficiently transversely coherent to serve as an adequate source for diffraction based imaging experiments.

RADIATION PROPERTIES

FEL Radiation in a Tapered Undulator

We analyze the case of a hard X-ray tapered FEL with electron beam and undulator parameters similar to those of the LCLS-II upgrade project. The FEL is formed of

Table 1: GENESIS Simulation Parameters

Parameter Name	Parameter Value
Beam energy E_0	13.64 GeV
Beam peak current I_{pk}	4000 A
Normalized emittances $\epsilon_{x,n}/\epsilon_{y,n}$	0.3/0.3 $\mu\text{m rad}$
Electron bunch length l_b	16.4 fs
Peak radiation power input P_{in}	5 MW
Undulator period λ_w	32 mm
Normalised undulator parameter a_w	2.3832
Radiation wavelength λ_r	1.5 Å
FEL parameter ρ	7.361×10^{-4}

3.4 m long undulator sections with 1m breaks for a total length of 200 m. The system is simulated using the fully 3-dimensional FEL particle code GENESIS in both single frequency and time dependent simulations (see table 1 for parameters). The magnetic field and the quadrupole focusing is optimized to yield the maximum output following the work of Ref. [11]. The simulations are performed for three different transverse electron beam distributions: uniform, parabolic and Gaussian. After the initial saturation and exponential gain regime the FEL process is dominated by refractive guiding of the radiation by the electron beam. This can be described by considering the complex refractive index of the electron beam [12]

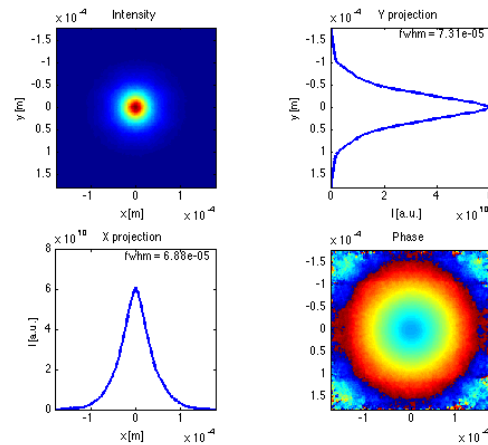


Figure 1: Amplitude and phase of the radiation field at the undulator exit ($z=200$ m) for a Gaussian transverse electron beam distribution obtained from time independent GENESIS simulation

* Work supported by: DOE Grant Number DE-SC0009983

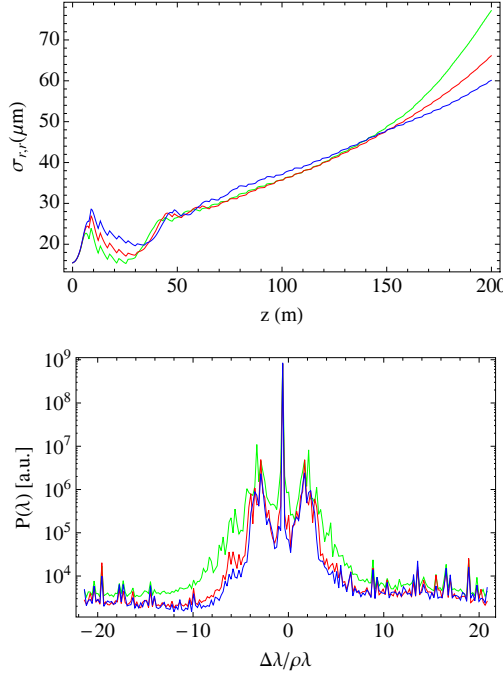


Figure 2: Radiation beam size evolution (top) and spectrum (bottom) at $\lambda_r = 1.50078 \text{ \AA}$ for a seeded hard X-ray tapered FEL at the undulator exit ($z=200\text{m}$) for Gaussian (green), parabolic (red) and uniform (blue) transverse electron distributions.

$$n = 1 + \frac{\omega_p^2}{\omega_s^2} \frac{r_{b0}^2}{r_b^2} \frac{a_w}{2|a_s|} [JJ] \left\langle \frac{e^{-i\Psi}}{\gamma} \right\rangle \quad (1)$$

where ω_p is the electron plasma frequency, ω_s is the radiation frequency and r_b is the electron beam radius. Quantities with subscript 0 refer to initial parameters and the symbol $[JJ] = J_0(x) - J_1(x)$ for a planar undulator and $[JJ] = 1$ for a helical undulator, where $x = a_w^2/2(1 + a_w^2)$. The average term in square brackets is over the beam electrons where Ψ is the electron phase relative to the ponderomotive potential.

The electron beam microbunching $\langle e^{-i\Psi} \rangle$ decays in the tapered section of the undulator and leads to diffraction of the radiation. This is observed in time steady (Fig. 1) and time dependent simulations for a 16 fs electron bunch length at a resonant wavelength of $\lambda_r = 1.50078 \text{ \AA}$ (see Fig. 2). For all three transverse electron distributions the radiation size increases by a factor 3-4 compared to the input seed. The effect is most enhanced for the Gaussian transverse distribution and causes an early saturation of the output power as discussed in Ref. [11]. The radiation spectra at $\lambda_r = 1.50078 \text{ \AA}$ for each of the three cases are also shown in Fig. 2. The effects of the sideband instability [13, 14] on the tapered FEL cause a spectral broadening of the radiation which results in bandwidths of $\Delta\lambda/\lambda \sim 20\rho$. The flatter transverse profiles of the parabolic and uniform distributions mitigate the detrimental effects of the sideband instability more effectively. Integrating the power deposited in the

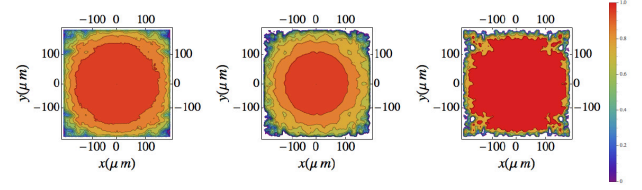


Figure 3: Modulus of the radiation complex coherence factor at the undulator exit ($z=200 \text{ m}$). Results are shown for Gaussian (left), parabolic (center) and uniform (right) transverse electron beams and a bunch length of 16.4 fs

sidebands at $\lambda_r = 1.50078$ we notice a reduction in sideband energy of 61 % for the parabolic case and 72 % for the uniform beam as compared to the Gaussian.

Transverse Coherence

We examine the transverse coherence properties of the output radiation for the three different transverse distributions at a resonant wavelength $\lambda_r = 1.5 \text{ \AA}$ and a bunch length of 16.4 fs. To compute the coherence area we first consider the mutual coherence function [15]:

$$\Gamma(\tau) = \left\langle \vec{E}(\vec{r}_1, t + \tau) \vec{E}^*(\vec{r}_2, t) \right\rangle \quad (2)$$

where the electric field is sampled at two transverse locations and the angle brackets denote the average over the time t . In a self-seeded tapered X-FEL we may apply the *quasimonochromatic* approximation [15] which allows us to define the mutual optical intensity function $J_{12} \equiv \Gamma(0)$. Normalization of the mutual intensity removes the amplitude information of the field and gives a measure of the phase relation between two transverse locations. This defines the complex coherence factor μ_{12} :

$$\mu_{12} = \frac{J_{12}}{\sqrt{J_{11}J_{22}}} \quad (3)$$

where $|\mu_{12}| = 0$ corresponds to vanishing transverse coherence and $|\mu_{12}| = 1$ total transverse coherence. While both the mutual intensity function and the complex coherence factor are 4-dimensional quantities we can obtain a quantitative value of the degree of coherence if we fix a single point \vec{r}_1 in our calculation to be the center of the beam. From μ_{12} we can then calculate the coherence area A_c :

$$A_c = \int \mu_{12} dA \quad (4)$$

The degree of transverse coherence is now quantified by computing the coherence area at various z locations in the undulator and comparing it to the radiation beam spot size. A necessary condition for diffraction imaging applications is that the coherence area be much larger than the beam spot size at the undulator exit. As can be seen by comparing the final beam sizes (Fig. 2) and the coherence areas (Fig. 3) this is indeed the case for all three transverse distributions. The coherence area grows in the tapered undulator due to diffraction of the radiation. For all three distributions at the

undulator exit the radiation beam spotsize σ_r^2 is $O(10^{-3})$ mm² while the calculated coherence area A_c is $O(10^{-1})$ mm².

CONCLUSION

We performed an analysis of the radiation properties of tapered hard X-ray FELs. The tapering strategy used was that described in Ref. [11] which maximises the output radiation power in order to reach TW level peak power or greater. The analysis was performed using the 3-dimensional particle code GENESIS in time independent and time dependent simulations. The spectral properties of the radiation were investigated for three different transverse electron beam distributions: Gaussian, parabolic and uniform. Time dependent simulations show that the radiation spectra at the undulator exit exhibit a broad bandwidth $\Delta\lambda/\lambda \sim 20\rho$. This broadening is caused by the sideband instability and is mitigated more effectively by the flatter transverse electron density profiles. Results show a reduction in sideband energy of 61 % for the parabolic case and 72 % for the uniform beam as compared to the Gaussian for a resonant wavelength $\lambda_r = 1.50078 \text{ \AA}$.

A quantitative study of the transverse coherence properties of the radiation from optimized X-FELs has also been carried out. Results from time dependent simulations show that the transverse coherence area A_c is larger than the beam spotsize σ_r^2 by two orders of magnitude for all electron beam transverse distributions, suggesting that the radiation from a tapered X-FEL can be used in imaging and X-ray diffraction experiments.

ACKNOWLEDGMENT

The authors are grateful to Dr. S. Reiche for helpful discussion and reference to previous work.

REFERENCES

- [1] R. Bonifacio, C. Pellegrini, L. Narducci, Optics Communications, vol. 50, no. 6, p. 373, 1984
- [2] J.B. Murphy, C. Pellegrini, J. Opt. Soc. Am. B, vol. 2, p. 259, 1985
- [3] A. Kondratenko, E. Saldin, Part. Accel., vol. 10, p. 207, 1980
- [4] M. Seibert, et al, Nature, vol. 470, p. 78, 2011
- [5] H. Chapman, et al, Nature, vol. 470, p. 73, 2011
- [6] J.S. Richardson, D. C. Richardson, Biophysical Journal, vol. 106, p. 510, 2014
- [7] L.W. Whitehead, et. al., Phys. Rev. Lett., vol. 103, p. 103, 1009
- [8] J. Feldhaus, E.L. Saldin, J.R. Schneider, E.A. Schneidmiller, M.V. Yurkov, Optics Communications, vol. 140, p. 341, 1997
- [9] G. Geloni, V. Kocharyan, E. Saldin, DESY 10-053, 2010
- [10] Y. Ding, Z. Huang, R.D. Ruth, Phys. Rev. ST. AB., vol. 13, 2010
- [11] Y. Jiao, et. al., Phys. Rev. ST. AB., vol. 15, p. 050704, 2012
- [12] D. Proznitz, A. Szoke, V.K. Neil, Phys. Rev. A., vol. 24, p. 1436, 1981
- [13] T. Yang, et. al., Phys. Fluid. B, vol. 2, p. 2456, 1990
- [14] R.C. Davidson, et. al., Phys. Fluid, vol. 30, p. 557, 1987
- [15] J.W. Goodman, Statistical Optics, (New York, Wiley 2000), 180

CHIRPED AND MODULATED ELECTRON PULSE FREE ELECTRON LASER TECHNIQUES

J. R. Henderson¹, L.T. Campbell^{1,2,3,4}, and B.W.J. McNeil¹

¹SUPA, Department of Physics, University of Strathclyde, Glasgow, UK

²ASTeC, STFC Daresbury Laboratory and Cockcroft Institute, Warrington, UK

³Center for Free-Electron Laser Science, Notkestrasse 85, Hamburg, Germany

⁴Institut für Experimentalphysik, Universität Hamburg, Hamburg, Germany

ABSTRACT

A potential method to improve the free electron laser's output when the electron pulse has a large energy spread is investigate and results presented. A simplified model is the first given, in which there are a number of linearly chirped beamlets equally separated in energy and time. By using chicanes, radiation from one chirped beamlet is passed to the next, helping to negate the effect of the beamlet chirps and maintaining resonant interactions. Hence the addition of chicane allow the electrons to interact with a smaller range of frequencies ($\Delta\omega < 2\rho\gamma_r$), sustaining the FEL interaction. One method to generate such a beamlet structure is presented and is shown to increase FEL performance by two orders of magnitude.

INTRODUCTION

Free Electron Lasers are already important research tools and have started to unlock many new areas of science in diverse fields such as; Warm-Dense matter studies, short pulse protein diffraction and medicine/surgery. Current Free Electron Lasers rely on linear accelerators to provide the electron bunch, for an x-ray FEL the accelerator can be kilometres long. The potential for plasma-wakefield accelerators to drive the Free Electron Laser has been of theoretical and experimental interest for many years. Plasma accelerators generate accelerating gradients on the order of 10^3 times greater traditional linear accelerators, which offers the potential to reduce the total length of the FEL. Electron pulses used in free electron lasers can exhibit a large energy chirp (greater than 1 % of mean electron beam energy) which can degrade the FEL interaction. Linear energy chirps have been previously studied in [1] the results of this work have been recreated here using Puffin [2] an unaveraged 3D parallel FEL simulator. The results of these chirped pulse simulations are in good agreement with [1] showing the flexibility of Puffin. Electron pulses from plasma accelerators are limited by a large energy spread, this is also issue with older accelerators where energy spread is sacrificed for a larger rho (a measure of FEL efficiency) and higher pulse energies. A method that may allow the free electron laser to operate with a large energy spread is proposed, simulations were performed using Puffin. In this method a chirped electron pulse is split in a number of chirped electron beams or beamlets. To sustain the FEL interaction radiation is passed from beamlet to beamlet by applying a series of chicane slip-

page sections. By making the slippage in undulator-chicane module equal the beam separation the radiation pulse will continuously interact with electrons within the same energy range. One method to generate a similar beamlet structure, the beamlet method, is presented. In the beamlet method a modulator-chicane section is used to generate a set of beamlets which have a smaller local (slice) energy spread than the initial electron pulse. Radiation is then passed from these areas of reduced energy spreads to sustain the FEL interaction. This method shows an approximate two-fold improvement in the radiation field intensity and a four-fold improvement when the radiation field is filtered around the resonant frequency.

SINGLE CHIRPED PULSE

When an electron pulse is given an energy chirp, the effects can be both beneficial and detrimental to the FEL interaction depending upon the gradient of the chirp [1].

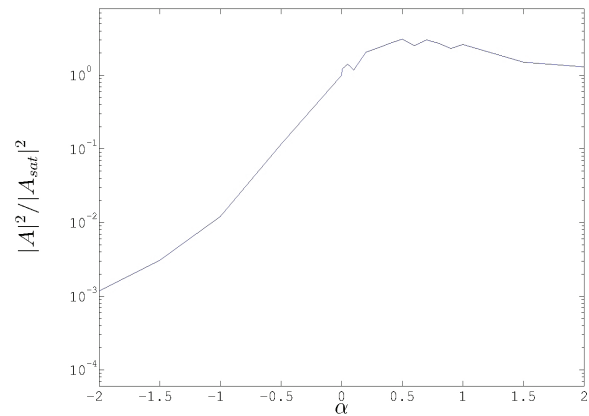


Figure 1: Chirped electron pulse: the scaled saturation power $|A|^2$ is plotted as a function of the energy chirp, the energy chirp parameter [1] is given by $\hat{\alpha} = -\frac{2}{\rho\gamma_r} \frac{d\gamma}{dz_2}$, where $|A_{sat}|^2$ is the saturation intensity at $\hat{\alpha} = 0$. This agrees with Figure 2 of [1] where matching parameters parameters have been used. $|A|^2/|A_{sat}|^2$ is equivalent to η from [1].

The results of [1] are reproduced using Puffin. Puffin uses the scaled notation of [3,4], where \bar{z}_2 defines a position in the electron bunch and is given by $\bar{z}_2 = (ct - z)/l_c$ where the cooperation length is defined as $l_c = \lambda_r/4\pi\rho$. The scaled radiation field is given by, $A_{\perp} = \frac{eu\bar{a}_u l_g}{2\sqrt{2}\gamma_r^2 mc^2 \rho} E_{\perp}$, where u

describes the undulator polarization (i.e. $u = 1$ planar or $u = \sqrt{2}$ helical), which in this case is helical. At saturation in the free electron laser exhibits temporal spikes of the order $A_{\perp} A_{\perp}^* = |A|^2 = 1$.

Figure 1 shows the normalised saturation power ($|A|^2/|A_{sat}|^2$) against energy chirp parameter $\hat{\alpha}$, where $|A_{sat}|^2$ is the average radiation field at saturation for the unchirped electron pulse. The resonant energy is defined as the initial average energy $\gamma_r = \langle \gamma_j \rangle|_{\bar{z}=0}$ and the gain length is defined as $l_g = \lambda_u/4\pi\rho$. The saturation length for various chirps was estimated from Figure 1 of [1]. It should be noted that extending the simulation along a long undulator can generate large power spikes of $|A|^2 = 25$ (see Figure 2). This result was not included in [1]. The electron pulse's energy chirp is beneficial, with a flat-top (non-chirped) electron pulse, the electron pulse loses energy as the radiation field grows after a number of undulator periods the electrons are no longer resonant with the initial radiation field (i.e. the electron pulse can now only amplify radiation at a lower frequency). With a chirped pulse the interaction can be sustained, when the radiation pulse propagates through the electron pulse it will find electrons at a higher energy (which are not resonant with it) and electrons that have lost energy which are now resonant with this radiation pulse. This technique is similar to undulator tapering, wherein the undulator's magnetic field is longitudinally tapered to maintain a resonant interaction along the undulator. The resonant FEL interaction continues as the radiation pulse propagates through the electron pulse allowing the generation of large radiation spikes.

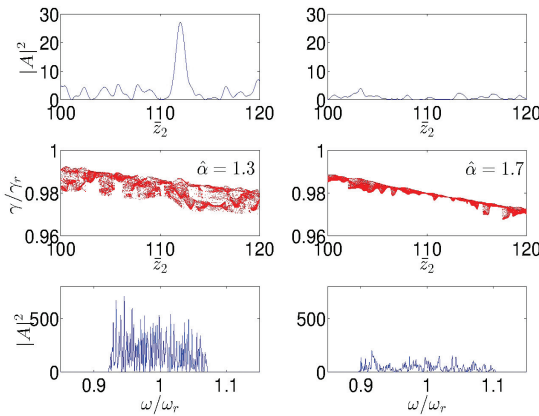


Figure 2: Comparison of chirped electron pulses with different gradients at $\bar{z} = 25$, for $\hat{\alpha} = 1.3$ larger radiation spikes are generated. The energy chirp is beneficial to the FEL interaction because the energy chirp is matched to the rate of energy loss by the electrons so maintaining resonance as the spike propagates through the electron pulse. Larger radiation spikes are present when $\hat{\alpha} = 1.3$ because as the radiation pulse as propagates through the electron pulse it will interact with more electrons within it's FEL bandwidth than it will with a larger energy chirp.

MULTIPLE CHIRPED PULSES - BEAMLETS

In this Section multiple chirped pulses equally spaced in energy are presented. We call this a system of 'beamlets'. Five beamlets are linearly chirped in energy and then equispaced in energy. A schematic of the chirped beamlets is shown in Figure 3. The energy separation of $\Delta\gamma = 2.5\rho\gamma_r$ with a gradient $\frac{d\gamma}{dz_2} = \rho\gamma_r$.

In Puffin each macroparticle is given a macroparticle charge weight χ_j defined as $\chi_j = n_j/n_p$ [2], n_j is the macroparticle charge density and n_p is peak macroparticle density of the electron beam. In the beamlet model here, the chi-value of each macroparticle is given by $\chi_n = \chi_j/N_b$ where N_b is the number of electron beams and χ_j is the chi-value if only one beam were modelled. Therefore if all the electron pulses have the same resonant energy (i.e. $\Delta\gamma = 0$) and then the pulses would be indistinguishable.

Table 1 lists all the relevant simulation parameters.

The Model - Multiple Chirped Pulses

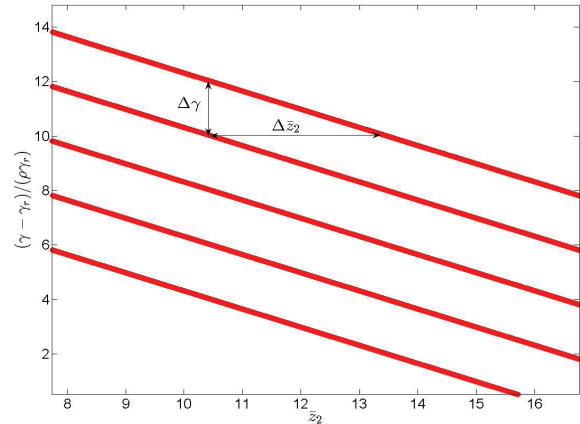


Figure 3: This diagram shows the initial electron pulse phase space. Five cold electron pulses with a linear energy chirp are overlapped and separated in energy by $2.5\rho\gamma_r$. The chirp gradient is $\frac{d\gamma}{dz_2} = \gamma_r\rho$ and the temporal separation is $2.5 l_g$.

The basic principle of this model is to pass radiation from beamlet to beamlet. This is achieved by using a undulator-chicane lattice, the range of electron energies experienced by a radiation pulse can be controlled by changing number of undulator periods per undulator-chicane module.

Standard mode-locking free electron laser theory [5,6] states that an undulator-chicane lattice will amplify modes which are separated by $\Delta\omega/\omega_r = 4\pi\rho/\bar{s}$, where \bar{s} is the scaled slippage in an undulator-chicane module $\bar{s} = s/l_c$. The undulator-chicane slippage is the sum of slippages in the undulator \bar{l} and chicane $\bar{\delta}$ i.e. $\bar{s} = \bar{l} + \bar{\delta}$. The beamlets are separated by $\Delta\gamma$ in energy which can be rewritten as a frequency difference of $\Delta\omega/\omega_r \approx 2\Delta\gamma\gamma_r$ using the resonance condition. To lock the modes these two frequencies are equated; $2\Delta\gamma/\gamma_r \approx 4\pi\rho/\bar{s}$. The chirp gradient is given

by the ratio of the beamlets energy and temporal separation. In this case the temporal separation is given by \bar{s} to ensure that the radiation always interacts with electrons of the same energy range. Therefore the electron chirp gradient is given as,

$$\begin{aligned} \frac{d\gamma}{d\bar{z}_2} &= \frac{\Delta\gamma}{\Delta\bar{z}_2} = \frac{4\pi\rho\gamma_r}{2\bar{s}} \frac{1}{\bar{s}} \\ \frac{d\gamma}{d\bar{z}_2} &= \frac{2\pi\rho\gamma_r}{\bar{s}^2}. \end{aligned} \quad (1)$$

In Figure 3 the initial electron pulse phase space is shown, the cold beam approximation is made, the beamlets are separated by $2.5\rho\gamma_r$ and have energy chirp such that $\frac{d\gamma}{d\bar{z}_2} \leq \rho\gamma_r$. This condition ensures that for $1l_g$ (gain-length) of interaction the radiation field only interacts with electrons within the FEL bandwidth, a value of $\frac{d\gamma}{d\bar{z}_2} = \rho\gamma_r$ was chosen. Temporally the beams are now separated by $2.5l_c$. By using an undulator-chicane lattice radiation can be passed from one beamlet to the next. The undulator-chicane slippage is set equal to the temporal separation of the beamlets, by doing so the radiation pulse at the start of each undulator module can interact with electrons of the same energy. This allows the radiation field to continuously interact with electrons of the same energies sustaining the FEL interaction.

An electron pulse with a linear energy chirp will have an energy dependent slippage length, s_γ , because electrons travelling at different speeds will arrive at the end of the undulator at different times. Therefore the separation of the modes amplified by an undulator-chicane lattice will be energy dependent $\Delta\omega/\omega_r = 4\pi\rho/\bar{s}_\gamma$, where $\bar{s}_\gamma = \bar{l}_\gamma + \bar{\delta}_\gamma$. Here \bar{l}_γ and $\bar{\delta}_\gamma$ are the energy dependent slippages in the undulator and chicane respectively. The energy dependent slippage can be written as,

$$\bar{s}_\gamma = (\bar{l} + D)p_{2j} - D + \bar{\delta} \quad (2)$$

were $p_{2j} \approx 1 - 2(\gamma_j - \gamma_r)/\gamma_r$, or in terms of γ_j ,

$$\bar{s}_\gamma = 2 \left(\frac{\gamma_r - \gamma_j}{\gamma_r} \right) (\bar{l} + D) + \bar{s} \quad (3)$$

As the modal separation of the undulator-chicane modes is now energy dependent this can reduce the mode visibility for large energy chirps and long undulators. It is possible to overcome this by applying a negative dispersion in the chicane, when $D = -\bar{l}$ the effect of the energy dependent slippage is negated (i.e. $\bar{s}_\gamma = \bar{s}$). Equation 3 also explains why using a long undulator (large \bar{l}) can destroy the mode-locking by increasing the energy dependence of the slippage length. Similarly a large dispersion D also increases the effect of the energy dependent slippage.

Results - Multiple Chirped Pulses

The simulations that follow were performed using Puffin with the parameters stated in Table 1. Numerous simulations were performed to demonstrate the effects of changing the

Table 1: Simulation Parameters for Multiple Chirped Pulses

Parameter	Value	description
Q	3E-12 C	charge per electron pulse
ρ	0.001	FEL parameter
γ_r	176.2	mean energy of beamlets
l_b	$80 l_c$	bunch length
a_w	0.511	undulator parameter
$\Delta\gamma$	$2.5 \rho\gamma_r$	beam separation in energy
$\Delta\bar{z}_2$	2.5	beam separation in time
$\frac{d\gamma}{d\bar{z}_2}$	$-\rho\gamma_r$	linear electron pulse chirp
α	2	Saldin chirp parameter

undulator-chicane configuration. The effect of the energy dependent slippage is demonstrated, by destruction of the modes when increasing \bar{l} and D (see equation 3). It is will also be shown that modes normally destroyed by a long undulator (large \bar{l}) can be recovered by applying a negative dispersion such that each undulator-chicane module has zero dispersion, i.e. $D = -\bar{l}$, in accordance with equation 3. In addition to this previous unknown chicane modes are generated after the undulator-chicane modes are destroyed. The additional modes are generated by a slippage only chicane.

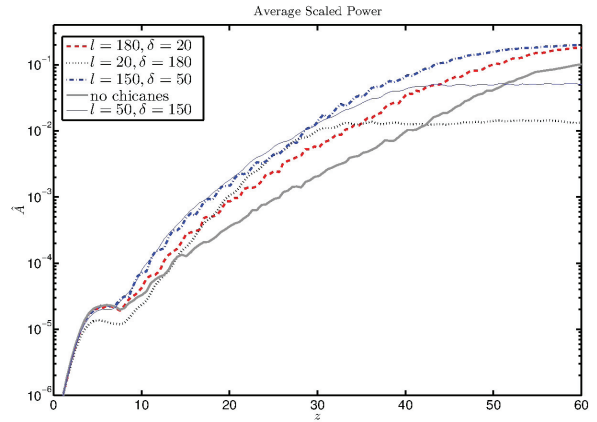


Figure 4: Comparison of a simulation using chicane slippage sections to a simulation without chicane sections. The average radiation power is plotted against \bar{z} (i.e. undulator position). For a large section of the FEL interaction the average radiation power is a factor of ten greater when chicane slippage sections are used.

Figure 4 shows that the average power from beamlets is dependent on the undulator-chicane lattice step-up, increasing the undulator length (while decreasing the chicane slippage) produces higher radiation powers, as happens in normal mode-locking free electron lasers.

In Figure 5 five beamlets are sent through an undulator-chicane lattice. This lattice amplifies modes that are separated by $\Delta\omega/\omega_r = 4\pi\rho/\bar{s} = 0.005$ where \bar{s} is the scaled slippage in an undulator-chicane module. Electron pulses with an energy chirp have an energy dependent slippage (equation 3), i.e. higher energy electrons slip less than low

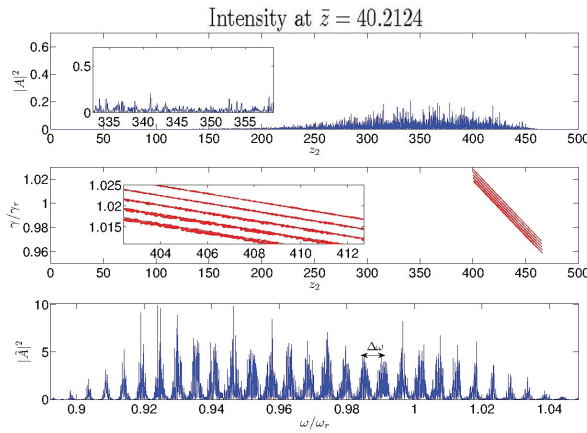


Figure 5: At $\bar{z} = 40$ the radiation is high (top panel), electron microbunching is well developed (middle), the spectrum of the field is shown in the bottom panel. In this case $\bar{l} = 0.2513$, $\bar{\delta} = 2.2619$. Giving a modal separation is given by $\Delta\omega/\omega_r = 4\pi\rho/\bar{\delta} = 0.005$, which matches the numerical result well.

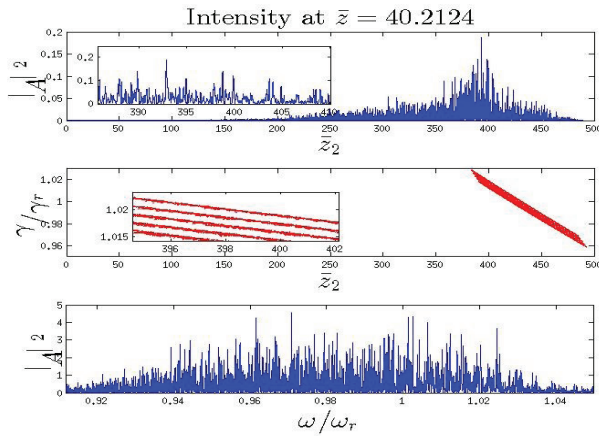


Figure 6: This simulation is identical to Figure 5, expect that the chicanes now apply a small dispersion to the electron pulse which disrupts mode formation. The reason for this is that an electron pulse with such a large energy chirp will have an energy dependent slippage length. For example the slippage of a low energy electron will be greater than that of a higher energy electron. Using a dispersive chicane will increase the difference in slippage lengths between high and low energy electrons. Therefore modes generate at the head of the pulse will have different \bar{s} than at the tail and hence a different $\Delta\omega/\omega_r = 4\pi\rho/\bar{\delta}$ (see Eq. 3), such that the modes start overlapping each other. However using a non-dispersive chicane means that the difference in modal separation is due solely to undulator dispersion, which is small enough to allow the modes to form.

energy electrons. The result of this is that any mode-locking that occurs at the high energy part of the pulse will involve a different set of modes than low energy part of the pulse. The energy dependent slippage (equation 3) can counteracted

by using a short-undulator and a slippage only chicane as is seen Figure 5. However using a dispersive chicane will increase the effect of this energy slippage (equation 3), as higher higher electrons will propagate more than low energy electrons increasing the difference in their slippage lengths. This difference in slippage lengths means that radiation field cannot be passed to the same energy range from one electron pulse to the next. The combination of these effects destroys the modes as is shown in Figure 6. The modes are also destroyed when using a long undulator (Figure 7), as the undulator dispersion over a large number of periods is significant enough to disrupt the mode formation.

In Figure 7 a dispersionless chicane generates an extra set of modes separated by $\delta\omega = 4\pi\rho/\bar{\delta} = 0.02$, these modes are generated because the beamlets will produce a radiation pulse before and after the dispersionless chicane that are similar (nearly identical), therefore the only modes

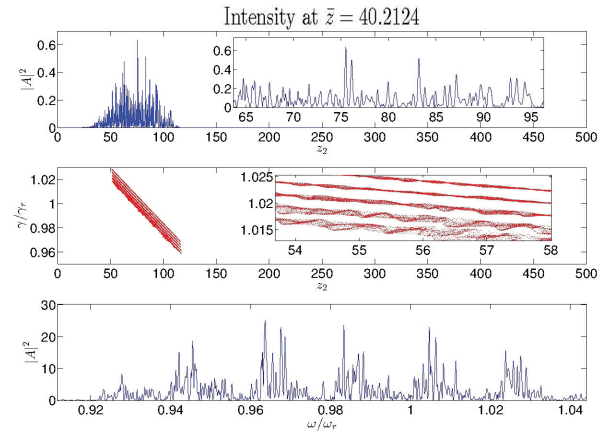


Figure 7: In this simulation longer undulator modules are used, $\bar{l} = 1.885$, $\bar{\delta} = 0.6283$ and slippage only chicanes. Using a longer undulator will produce more dispersion in the electron pulse, this makes the energy dependent slippage between electron of various energies greater. Therefore the radiation modes now overlap. However the slippage only chicanes will produce modes separated $\delta\omega/\omega_r = 4\pi\rho/\bar{\delta}$, this because the electron pulse will produce similar (nearly identical) radiation pulse before and after the slippage only chicane. Therefore the only modes that can survive the U-CS-U section are given by $\delta\omega/\omega_r = 4\pi\rho/\bar{\delta} = 0.02$.

that can survive this chicane slip are those separated by $\delta\omega = 4\pi\rho/\bar{\delta} = 0.02$. These modes can be replaced by the original modes by applying a negative dispersion in the chicanes (Figure 8), the dispersion is in a chicane is such that the total dispersion by an undulator-chicane module is now zero. Having zero-dispersion undulator-chicane modules negates the effects of the energy dependent slippage (see equation 3); as energy dependent slippage and dispersion are the same thing. Using zero-dispersion undulator-chicane modules hinders the development of the bunching, reducing the radiation intensity. The modes of Figure 7 can also be generated by using a short undulator (U), a dispersion only

chicane (CD) and a slippage only (dispersionless) chicane (CS). For this simulation (Figure 9) of an undulator-chicane lattice was constructed from modules of U-CD-U-CS, where each undulator has half the number of periods (10 periods) of the undulator used in Figure 5. The dispersion only chicane will supply the equivalent of 130 periods of undulator dispersion. This gives a total dispersion of 150 periods per module just as in Figure 7 and then the slippage only chicane generates modes separated by $\delta\omega = 4\pi\rho/\delta = 0.02$.

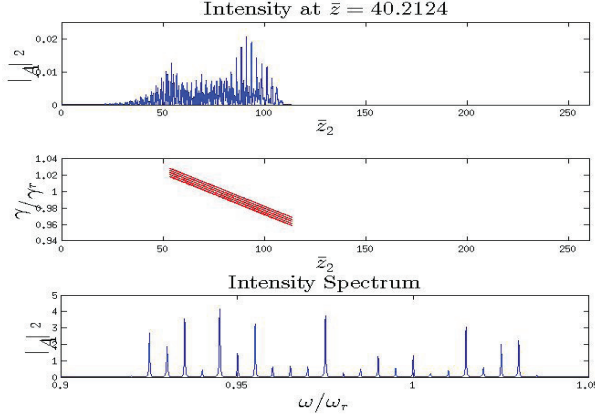


Figure 8: The modes that were destroyed in Figure 7, can be restored by using a chicane that applies a negative dispersion. The magnitude of dispersion applied is equal to the amount dispersion experienced in the preceding undulator section, therefore in an undulator-chicane module there is effectively zero dispersion. In this simulation $\bar{l} = 1.885$, $\delta = 0.6283$. The modes are more clear in this case because of the zero dispersion undulator-chicane modules, where as in Figure 7 the undulator dispersion causes a differential slippage whereby the mode separation varies with energy. Note the reduced radiation intensities, which is due to the negative dispersion chicane that prevents the formation of microbunches.

A full understanding of the interaction of multiple electron pulses (beamlets) is important when modelling more advanced 'novel' FEL schemes. The effect of undulator length, energy dependent slippage and dispersion has been analysed, and will impact different FEL schemes where large variation in electron energies are present.

BEAMLETS

In this section a technique to generate chirped electron pulses from a single electron pulse is presented. The beamlet technique is a two stage method which involves an undulator and a chicane. The electron pulse is modulated in energy and then dispersed. This generates a series of beamlets with reduced local energy spreads, passing radiation from beamlet to beamlet can sustain the FEL interaction.

The Model - Beamlets

The electron pulse is first modulated in an undulator and then dispersed by a chicane section, these transformations

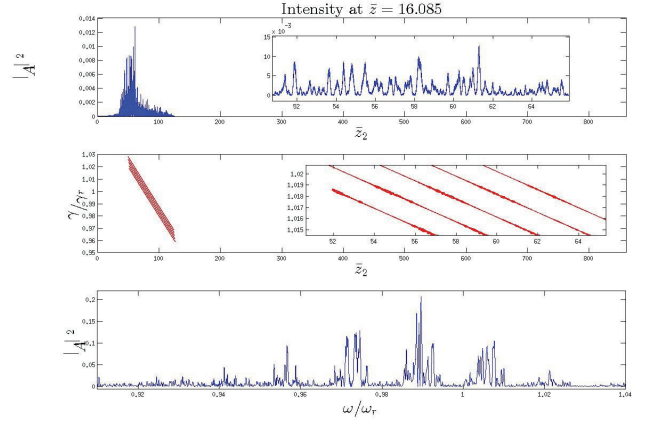


Figure 9: Using a unique undulator-chicane lattice, consisting of dispersion only chicanes (CD) and slippage only chicanes (CS). The lattice is constructed from blocks of U-CD-U-CS arranged in series. In the undulator $\bar{l} = 0.1257$ (10 periods), in the dispersion only chicane (CD) the equivalent of $\delta = 1.6336$ (130 periods) of dispersion is applied and in the slippage only chicane (CS) a slippage of $\delta = 0.6283$ (50 periods) is used. Therefore the dispersion is the same per module as it is in Figure 7. As in Figure 7 the slippage only chicane generates modes given by $\delta\omega/\omega_r = 4\pi\rho/\delta = 0.02$.

are performed by applying the point-transforms given below,

$$\gamma_j = \gamma_j + \gamma_m \sin\left(\frac{\bar{z}_{2j}}{2\rho}\right) \quad (4)$$

$$\bar{z}_{2j} = \bar{z}_{2j} + 2D\left(\frac{\gamma_j - \gamma_r}{\gamma_r}\right). \quad (5)$$

Upon exiting the chicane the electron pulse has a unique phase-space structure. In Figure 10 this phase space structure is shown and is similar to series of chirped electron pulse or beamlets. After the undulator-chicane section the beamlets are passed through an undulator-chicane lattice, this allows radiation to be passed from beamlet to beamlet, similar to the chirped electron pulses method present earlier, sustaining the FEL interaction throughout the electron pulse. The slippage in a undulator-chicane module is therefore equal to the period of energy modulation. A modulation amplitude of $\gamma_m = 0.04\gamma_r$ and dispersion of $D = 200$ was selected.

Results - Beamlets

An electron pulse with a large energy spread and Gaussian current profile is initially generated ($\sigma_\gamma \approx 2.5\gamma_r\rho$, where $\rho = 0.01$). Applying a Gaussian distribution in energy and space will reduce the charge density at the electron pulse corners (in phase space) see Figure 10. Macroparticles with such a low weight are eliminated by Puffin, consequently the electron pulse's phase space is rounded. The electron pulse's Gaussian current profile generates coherent emission at the lower frequencies consequently this radiation has been filtered out. Due to the electron pulse's large energy spread

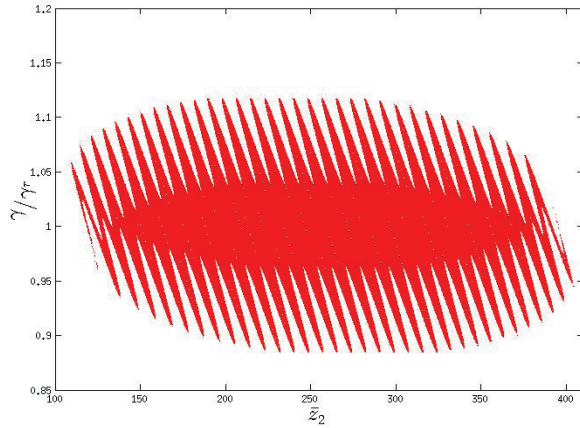


Figure 10: The EEHG beamlet scheme, an electron pulse of a large energy spread is energy modulated ($\gamma_m = 0.04\gamma_r$) and dispersed ($D = 200$) by applying transform 4 and 5. This results in the formation of beamlets with a reduced local energy spread. Radiation can then be passed from beamlet to beamlet sustaining the FEL interaction. The electron pulse was given gaussian distribution in space to cut down on coherent emission from the pulse edges. The macroparticle model of Puffin eliminates macroparticles whose weight is below a certain threshold, as such the particles at the corners of the pulse (in phase space) have the lowest weight and are eliminated. This leaves the outer beamlets less dense and therefore less able to contribute to the FEL interaction.

it cannot produce and amplify FEL radiation to useful intensities, at $\bar{z} = 40$ generally consider to beyond saturation significant radiation is not present (Figure 11). However by applying equations 4 and 5 the electron pulse is transformed into beamlets. These beamlets (at $\bar{z} = 40$) show an approximately two-orders of magnitude improvement as can be seen in Figures 12 and 11. For these simulations $\rho = 0.01$ and the undulator-chicane lattice had 50 undulator periods per module ($\bar{l} = 6.2832$) and 18 chicane ($\bar{\delta} = 2.2619$) slippage periods. In Figure 13 a comparison is made between the beamlet case and the original beam, the radiation field has been filtered around the resonant frequency $0.8 < \omega/\omega_r < 1.2$.

CONCLUSION

The interaction of multiple electron pulses has been analysed and this understanding should prove useful when designing more novel FEL techniques. A potential scheme for generating radiation from an electron pulse of large energy spread has been demonstrated. However many improvement (optimisations) should be possible. Using dispersive chicanes further along the undulator-chicane lattice may help improve the FEL interaction. Due the energy dependent slippage of the beamlets, it may be useful (when using large undulator sections) to match the slippage of various sections of the beam. For example decreasing the slippage per module to counteract the increased slippage for lower en-

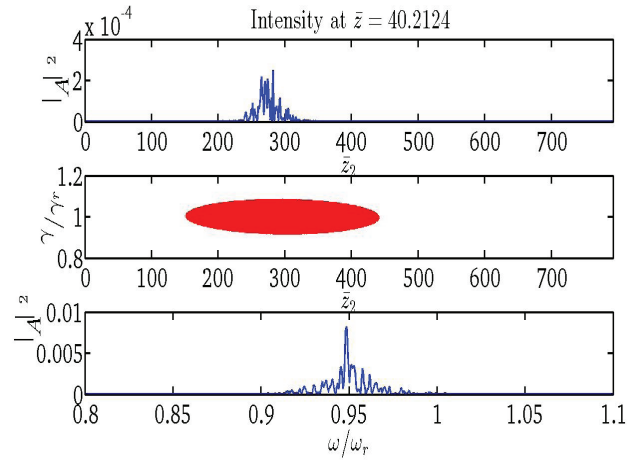


Figure 11: An electron pulse with a large energy spread that exceeds the FEL operational range. This pulse also has a gaussian distribution in space, this was done to minimize coherent spontaneous from the pulse edges.

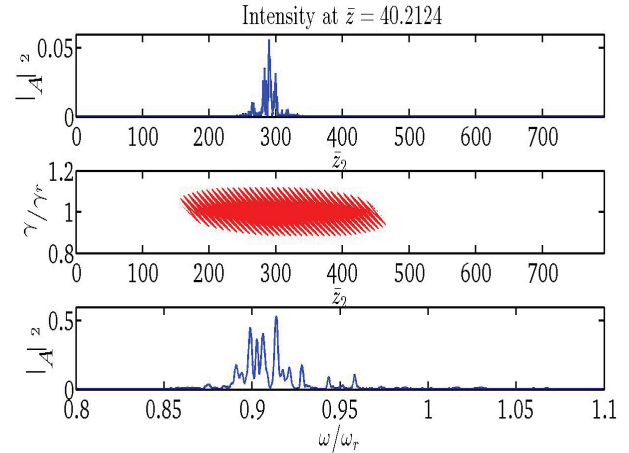


Figure 12: Beamlets near saturation, the radiation field is approaching saturation and the electron microbunching highly developed. Comparing with Figure 11 shows an increase in peak field intensity of 200.

ergy electrons may prove beneficial. The modulation and dispersion parameters of the beamlets scheme can also be optimised and requires further study. The use of the two-colour FEL technique to preferentially amplify modes from the high and low energy regions of the pulse may produce higher radiation powers.

ACKNOWLEDGEMENTS

We gratefully acknowledge support of Science and Technology Facilities Council Agreement Number 4163192 Release #3; ARCHIE-WeSt HPC, EPSRC grant EP/K000586/1; John von Neumann Institute for Computing (NIC) on JUROPA at Jlich Supercomputing Centre (JSC), under project HHH20.

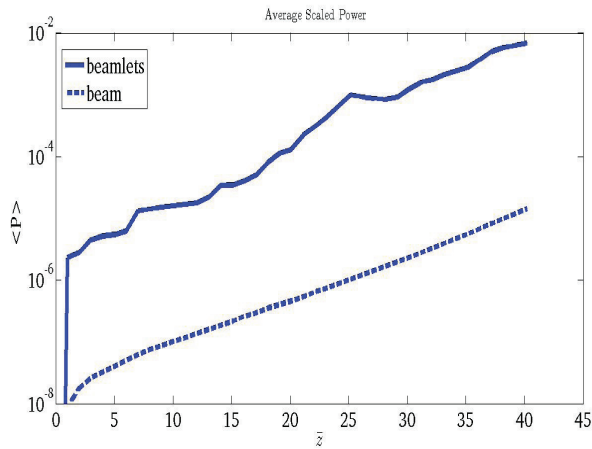


Figure 13: A comparison of the average filtered power of beamlet and original beam is given above. The radiation is filtered around the resonant frequency, $0.8 < \omega/\omega_r < 1.2$. Around 2-3 orders of magnitude improvement has been achieved and may be further optimized.

REFERENCES

- [1] Saldin, E., Schneidmiller, E., and Yurkov, M. (2006). Self-amplified spontaneous emission FEL with energy-chirped electron beam and its application for generation of attosecond x-ray pulses. *Physical Review Special Topics - Accelerators and Beams*, 9(5), 050702.
- [2] Campbell, L. T., and McNeil, B. W. J. (2012). Puffin: A three dimensional, unaveraged free electron laser simulation code. *Physics of Plasmas*, 19(9), 093119. doi:10.1063/1.4752743.
- [3] R. Bonifacio et. el. *Physics of the High-Gain FEL and Super-radiance* (1990).
- [4] R. Bonifacio et. el. *New Effects in the Physics of High-Gain Free-Electron Laser* (1992).
- [5] N. R. Thompson and B. W. J. McNeil *Phys Rev Let*, **100** 203901 (2008).
- [6] B. W. J. McNeil, N. R. Thompson D. J. Dunning and B. Sheehy *J. Phys. B: At. Mol. Opt. Phys.* **44** (2001) 065404.

A REVIEW OF HIGH POWER OPCPA TECHNOLOGY FOR HIGH REPETITION RATE FREE-ELECTRON LASERS*

M. J. Prandolini[†], R. Riedel, Helmholtz-Institut Jena, Fröbelstieg 3, D-07743 Jena, Germany

M. Schulz, Deutsches Elektronen-Synchrotron DESY, Notkestrasse 85, D-22607 Hamburg, Germany

F. Tavella[‡], SLAC National Accelerator Laboratory, 2575 Sand Hill Rd., CA 94025, USA

Abstract

High repetition rate free-electron lasers (FEL) require the development of new laser systems that have the ability to operate at high average power. Optical parametric chirped-pulse amplification (OPCPA) is presently the most promising method to fulfill these requirements. This technique has been used to demonstrate amplification up to tens of watts with a repetition rate in the range between tens of kHz to MHz in burst and continuous mode. We review the current OPCPA technology for systems operating around 800 nm; this includes various frontend options, pump amplifier technology and latests results, and we discuss the important requirements for achieving high power lasers in both burst and continuous operation.

INTRODUCTION

High repetition rate FELs present some unique challenges for laser developers. Superconducting cavities, developed at DESY [1], allow a much higher repetition rate than conventional accelerator technologies; however, they have a burst mode structure. For example, FLASH at Hamburg has a maximum repetition rate of 1 MHz within a burst structure of 800 μ s at 10 Hz [2, 3]. This presents major challenges for the design and operation of FEL seeding and pump-probe lasers operating in burst mode. At lower repetition rates, conventional Ti:sapphire lasers are currently used in FELs [4]. However, in the last years there has been remarkable progress in high average power OPCPA systems (Fig. 1). Currently, the high repetition rate and high power OPCPAs have been demonstrated at an average power of 11.4 W at 3.25 MHz [5] and 22 W at 1 MHz [6], and in a burst operation of 38.5 W at 27.5 kHz within a burst structure similar to FLASH [7]. For the amplification of high power, few-cycle, optical pulses, OPCPA is the leading technology [6, 8–10], due to the inherent bandwidth limitations of Ti:sapphire technology [11].

A comparison of a Ti:sapphire amplifier and a non-collinear optical parametric amplifier (OPA) is schematically shown in Fig. 2. In a Ti:sapphire amplifier, the pump pulses are used to create a population inversion, where the pump energy is stored in the gain material itself before being transferred to the signal via stimulated emission. The quantum defect for Ti:sapphire is 34%, the resulting energy difference

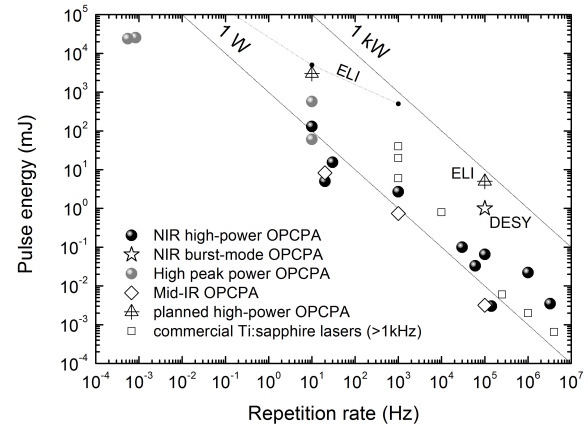


Figure 1: Current and planned high average power laser systems: ELI - Extreme Light Infrastructure; DESY - Deutsches Elektronen-Synchrotron

goes into heating of the gain material, which therefore has to be cooled. In contrast in a noncollinear OPA, the energy of the pump wave (ω_P) is transferred, via a second order nonlinear effect within the gain material, into signal (ω_S) and idler (ω_I) waves. Thereby, energy conservation is maintained between the three waves ($\omega_I = \omega_P - \omega_S$). For certain applications the idler wave can be used, but in general it is discarded. Nevertheless, a small amount of linear absorption from the pump, signal and idler does occur, which starts to become noticeable at around tens of watts of output energy.

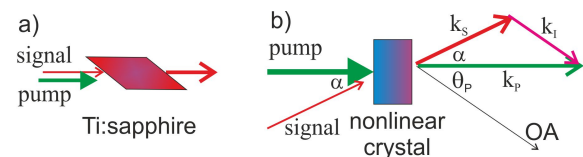


Figure 2: A comparison of laser amplifier technologies: (a) The Ti:sapphire amplifiers operate using the conventional population inversion within the gain material created by a pump pulse. (b) In noncollinear OPA, the energy of the pump is transferred, via a second order nonlinear effect within the gain material, into signal and idler waves: α - non-collinear angle; θ_P - angle between the pump wavevector (k_P) and the optical axis (OA); k_S and k_I - wavevectors of the signal and idler, respectively.

* Work supported by the Helmholtz Institute Jena and the Deutsches Elektronen-Synchrotron DESY in Hamburg. The authors would also like to thank the Helmholtz Association for their support for the spin-off project *Class 5 Photonics*.

[†] mark.prandolini@desy.de

[‡] Formally at DESY

Another important concept is the use of chirped-pulsed amplification (CPA). In CPA, the signal pulses are first temporally stretched to obtain lower signal intensities before being amplified, thereafter the signal pulses must be compressed. This technique lowers the peak intensity during the amplification phase in order to avoid nonlinear propagation effects and material damage issues. The first realization of an optical parametric chirped-pulse amplifier (OPCPA) was performed by Dubietis et al. [12] in 1992. It was recognized quite early that OPCPA has the potential to overcome the limitations imposed on conventional laser amplifier technologies (Ross et al. [13]). Reviews of the progress are given in [14–16]

This remarkable progress has been made possible through the development of high average power pump amplifier technology. Pump pulse durations should ideally be in the sub/few picosecond range providing tens to hundreds of millijoules of energy. Short pump pulses not only reduce the required stretching and compression of the ultrabroadband signal pulse, but also allow for higher pump intensities in the nonlinear crystals before the damage threshold is reached [17]. These laser parameters can potentially be achieved using Yb-doped solid-state laser technology. A typical system usually consists of a Yb-doped fiber amplifier as a frontend combined with, for example, a Yb:YAG (YAG – yttrium aluminium garnet) Innoslab amplifier system [18] and/or a Yb:YAG thin-disk amplifier for low gain, high average power amplification [19]. Presently, commercial OPCPA-pump amplifiers operating in the tens of kilowatt level do not exist, but are planned for the near future. In the design of an ultrabroadband, high power OPCPA system, the OPCPA-pump will be the most costly and energy consuming part of the system. Therefore, the design of an OPCPA should try to optimize the use of the available pump energy. This also keeps initial and running costs to a minimum, and additionally, by reducing the total pump power requirements, the total thermal load and heat dissipation are also minimized.

The outline of this review is as follows. First a general layout of an OPCPA system is discussed, including various frontend options. Then pump amplifier technologies are discussed. Thereafter a review of the OPCPA methods for systems around 800 nm are discussed, including typical nonlinear crystals, thermal effects and a selection of results from both burst and continuous mode OPCPA.

GENERAL LAYOUT AND OPCPA FRONTENDS

The general layout of a high repetition rate OPCPA is shown in Fig. 3. It consists of a frontend, which supplies a narrow band OPCPA-pump pulse (centered at 1030 nm) to the Yb-doped OPCPA-pump system and a broadband signal pulse (centered at 800 nm) to be amplified. In the case shown in Fig. 3, the frontend is a Ti:Sa oscillator, which has enough energy at 1030 nm to simultaneously seed both pump and OPCPA systems. In this example, both the pump and signal

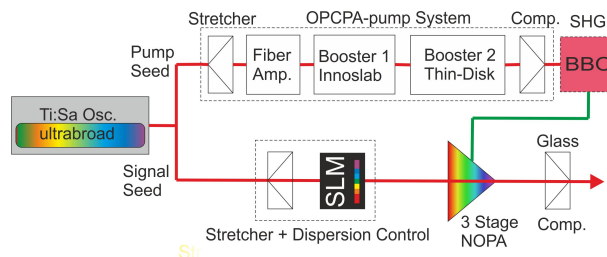


Figure 3: Layout of an OPCPA: Osc. - Laser Oscillator; SLM - spatial light modulator; Comp. - optical compressor; SHG - second harmonic generation; NOPA - non-collinear optical parametric amplifier; BBO - β -barium borate (BaB_2O_4), an example of a nonlinear doubling crystal.

pulses undergo CPA. The OPCPA-pump system consists of a stretcher and a number of amplifier stages (discussed in the next section) followed by second harmonic generation (SHG) to produce pump pulses at 515 nm. Typical SHG nonlinear doubling crystals at these wavelengths are BBO – β -barium borate or LBO – lithium triborate. On the signal side, the signal seed requires a careful dispersion management. In the case shown in Fig. 3, the pulses are first stretched with negative dispersion, so that they match the pulse duration of the pump pulse. Additionally, for short pulses (below 10 fs) the phase of the pulses can be modified by a spatial light modulator (SLM). Thereafter the signal pulses are amplified in a three stage non-collinear OPA. Finally, a compressor consisting of glass and if necessary chirped mirrors is used to produce Fourier-limited pulses.

OPCPA Frontends

The aim of the frontend is to provide a broadband seed pulse to the non-collinear OPA stages centered at 800 nm and a narrow band seed pulse to the OPCPA-pump system at 1030 nm. One possibility would be to use two (master and slave) oscillators electronically (or optically) synchronized together; however, this arrangement not only increases the complexity of the setup, it also adds jitter between OPCPA-seed and OPCPA-pump pulses at the non-collinear OPA stages. This is particularly critical when using Yb-YAG technology, where the pump pulse durations are usually below 1 ps. A better arrangement would be to use a single oscillator to seed both simultaneously, as shown in Fig. 3. Commercial, ultrabroadband, Ti:Sa oscillators centered at 800 nm now exist, where there is enough energy at the pump wavelength of 1030 nm so that it can be filtered out and used as the pump seed pulse (for example, see Venteon Laser Technologies GmbH). If the Ti:Sa oscillator does not have enough energy at the pump wavelength, a fraction of the oscillator pulses can be coupled into a photonic crystal fiber (for example, 20 cm long NKT NL-890 nm) and frequency shifted to the Yb-gain region, as was done in [6,9]. However, this option adds complexity and adds potential long-term instability to the system. In general, the stability of commercial, ultrabroadband Ti:Sa oscillators has greatly improved in the last years. For ultrashort pulses and in cases which

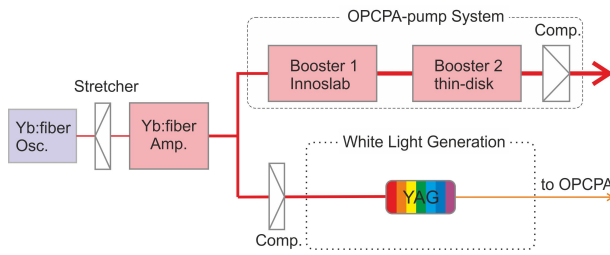


Figure 4: Frontend of an OPCPA using Yb:fiber oscillator (Onefive GmbH) to seed a Yb:fiber amplifier (Active Fiber Systems GmbH), which is used as seed for both the OPCPA-pump system and the dedicated WLG.

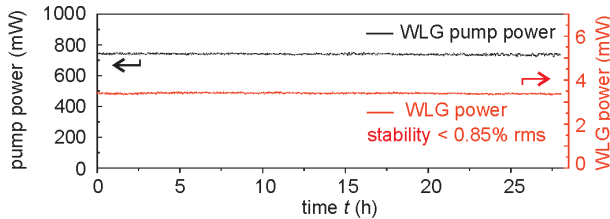


Figure 5: Stability test of the WLG: pump power (black) and WLG power (red), measured over 28 hours. The investigated WLG spectral region ranged from 650 nm to 950 nm.

require carrier envelope phase (CEP) stability, CEP stable Ti:Sa oscillators are still a viable option for OPCPA frontends. However, for maintenance-free, continuous operation over days other options can be explored.

White light continuum generation (WLG), based on “turn-key”, stable fiber lasers, is one potential frontend solution for providing maintenance-free, continuous operation [7, 18]. YAG crystals have been extensively tested at these wavelengths for generating OPCPA seed signals [7, 18]. Other host materials have been reviewed in [20]. YAG requires pulse durations below 1 ps and pulse energies between 1–10 μ J, depending on the experimental conditions [18]. Depending on the exact details of the stretcher/compressor OPCPA-pump system and/or the stability of the booster amplifiers, a fraction of the pump pulse can be used for WLG.

Another possibility would be to use a dedicated WLG using a stable fiber amplifier, with a compacter stretcher/compressor configuration. An example is shown in Fig. 4, where a Yb:fiber oscillator is used to seed a fiber amplifier providing both the OPCPA-pump seed and a dedicated WLG seed. This system was extensively tested in continuous mode [7] and was shown to have good stability over days of operation (Fig. 5).

PUMP AMPLIFIER TECHNOLOGIES

High power, ultrabroadband OPCPA currently use pump amplifier technologies based on Yb-doped solid-state amplifiers, which support a larger bandwidth, and therefore shorter pulses, compared to Nd-doped laser systems. Short pump pulses are important because the amplification of ultrabroadband signal pulses requires high pump intensities in

the OPCPA nonlinear crystals. The damage threshold scales proportional to $\sqrt{\tau}$ with slight deviation from this scaling below 20 picoseconds [17]; for slightly below 1 ps this scaling factor can be considered as an upper limit. Therefore the intensity at which damage occurs scales as $\sim 1/\sqrt{\tau}$.

The CPA is the basis of all OPCPA-pump amplifier technologies, and is used for similar reasons as discussed above for OPCPA. Another important aspect of high average power systems is thermal management. Presently, there are three types of technologies, with three different corresponding geometries, that dissipate the high thermal load in the gain materials. First, Yb-doped rod-type fiber amplifier systems can reach kW-level but are limited in pulse energy extraction [21]. This boundary can be overcome by coherently combining individually cooled fiber rods [22]. Second, slab type geometries can be used, such as Innoslab technology [23]. In this case, cooling occurs on both sides of the slab (gain material) resulting in thermal lensing for the beam propagating between the walls of the cooling surfaces; this effect is used as an integral part of the pulse propagation. Third, thin-disk amplifiers cool only on one side of a thin disk [24]; the pump seed propagates perpendicular to the surface of the thin disk and is reflected on the heat sink. This geometry avoids thermal lensing, if the disk is thin compared to its diameter, but results in a small gain per single pass. The latter two technologies can potentially reach the multi-kW-level at high pulse energies without the need to coherently combine.

In our work, we have combined all three technologies, for example a fiber amplifier can be used as a seed for further amplification with a single stage thin-disk amplifier, or with a combined Innoslab and thin-disk amplifiers. Our OPCPA-pump development concentrated on thin-disk multipass amplifiers, as this technology offers the best possibility for both high energy as well as high power scaling. In an initial development, we have demonstrated kilowatt level output powers in a single stage thin-disk multipass amplifier, in the burst operation mode [19]. This was achieved with a 50 W fiber amplifier (Helmholtz Institute Jena) and optionally a 500 W Innoslab amplifier (AMPHOS GmbH) as seed source for the thin-disk multipass amplifier. The thin-disk amplifier head was provided by TRUMPF GmbH + Co. KG.

In a second setup, a total output power of 14 kW was achieved in a burst operation mode from a 2-stage cascaded Yb:YAG thin-disk multipass amplifier [25]. This yielded a pulse energy of 140 mJ at 100 kHz in burst mode. A block diagram of the pump amplifier setup is shown in Fig. 6a. The seed for the entire amplifier system was generated in a 10 W fiber amplifier system. This was further amplified in an Innoslab amplifier with 500 W output power and a subsequent Innoslab booster amplifier with 1.5 kW output power. After spatial filtering, a total intra-burst output power of 1 kW could be used to seed the thin-disk amplifiers. The multipass setups were conceived for 7 passes through each amplifier. In the first thin-disk amplifier, an output burst energy of 5.4 J was achieved, corresponding to an intra-burst output power of 7 kW. The second thin-disk amplifier increased the output burst energy to 11.2 J, which corresponds to an intra-

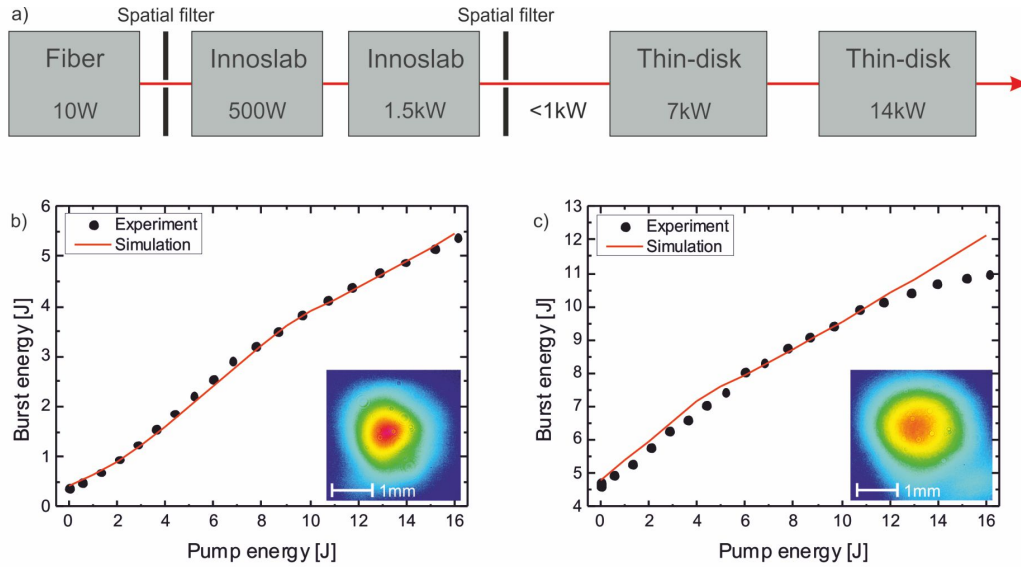


Figure 6: (a) Block diagram of the amplifier setup with a fiber amplifier as seed source for further amplification with two Innoslab booster stages and two thin-disk stages. Experimental (black) and simulated (red) characteristics of the thin-disk amplifier for b) the first amplifier stage and c) the second amplifier stage.

burst output power of 14 kW. The resulting energetics of the two thin-disk amplifiers with analytical simulations are displayed together with the output beam profiles in Fig. 6b and Fig. 6c. Additionally, the spectral bandwidth of the output pulses supports compression to pulse durations below one picosecond. These pulse properties make the amplifier system very interesting as a pump amplifier for a high energy, high repetition rate OPCPA system.

The above mentioned thin-disk amplifier development was carried out in a burst mode operation, which was dictated by the burst structure of the FEL pulse train using superconducting acceleration cavities. This creates both new challenges and benefits. In general, the most important problem to solve with high average power lasers is the induced heat load. However, burst-mode laser amplifiers combine high pulse energies at high repetition rates with the low average power on the sample due to a low duty cycle. Thus, a high thermal load on the sample can be avoided keeping the beneficial effect of the high intra-burst power. The challenges with burst mode amplifiers is providing a 'flat' burst profile, with respect to pump-pulse characteristics, over the selected signal pulses to be amplified. To create a flat burst requires a delicate balance of the timing between the arrival time of the seed pulses and the timing of the diode pulses [19]. In the case of the Innoslab amplifier, we have observed a small pointing error and beam profile deviations within the first $\sim 100 \mu\text{s}$ of the burst. This results from the time required to form a stable thermal lensing for correct beam propagation within the amplifier.

There is currently rapid progress with all three technologies and commercial options exist for moderate power levels. We have made a subjective comparison between the various pump technologies (Table 1), with the restriction that

Table 1: Comparison of Three Types of Pump Amplifiers: rod-type fiber, Innoslab and multipass thin-disk amplifiers (++ very good; + good; o average; - poor; -- very poor).

	Fiber	Innoslab	Thin-Disk
Average Power	o	++	++
Pulse Energy	o	+	++
Single Pass Gain	++	+	--
Pointing Stability	++	+	-
Energy Scaling	--	+	++

coherent combining for rod-type fiber systems was not considered and the multipass thin-disk was not optimized for stability [25]: for example, no relay imaging was used and the amplifier was not in a sealed environment.

OPTICAL PARAMETRIC CHIRPED-PULSE AMPLIFICATION (OPCPA)

At the core of an OPCPA system is the optical parametric amplification (OPA). OPA is related to difference frequency generation (DFG), where a three wave mixing process takes place in an optical crystal as a second-order nonlinear effect. At the wavelengths considered here, the material response to a nonlinear optical excitation is instantaneous. Figure 2b shows the principle of non-collinear three wave mixing, which involves a strong pump wave, a signal wave and a third wave, the idler. The pump, signal and idler waves must firstly fulfill the energy conservation condition, $\omega_I = \omega_P - \omega_S$, where the suffixes P , S and I refer to pump, signal and idler waves, respectively. A second important condition is momentum conservation (or the phase matching condition): $\delta \mathbf{k}(\theta_P, \lambda_P, \lambda_S) = \mathbf{k}_P(\theta_P, \lambda_P) - \mathbf{k}_S(\lambda_S) - \mathbf{k}_I$.

Table 2: Properties of Nonlinear Crystals: d_{eff} effective nonlinear optical coefficient, ρ walk-off angle, TT temperature tolerance, AT angular tolerance. Values given for $\lambda_{\text{pump}} = 515$ nm and $\lambda_{\text{signal}} = 800$ nm. These values are taken from [26].

	d_{eff} [pm/V]	ρ [mrad]	TT [K cm]	AT [mrad cm]
BBO	2.0	55.8	39.7	0.56
LBO	1.0	7.06	6.8	4.54
BIBO	3.0	25.0	2.74	1.15
YCOB	0.36	32.1	110.9	0.94

In high power applications, the pump is narrow band and it is desirable to amplify a broadband signal. Therefore, for a fixed λ_P , there is generally one combination of θ_P and λ_S that satisfies the phase matching condition exactly (i.e. $\delta \mathbf{k} = 0$). To achieve broadband phase matching, and therefore broadband amplification, another parameter needs to be introduced. One option is to introduce a non-collinear angle (α) between the pump and signal [15]. Additionally, the gain bandwidth ($\Delta \nu$) also depends on the crystal length L , the pump intensity I_P and the effective nonlinear coefficient d_{eff} :

$$\Delta \nu = 0.53 \sqrt{\Gamma/L} |u_{SI}| / c, \quad (1)$$

where $1/u_{SI} = 1/u_S - 1/u_I$ is the group-velocity mismatch between the signal and idler pulses and the gain Γ is given by

$$\Gamma = d_{\text{eff}} \sqrt{\frac{2\omega_S \omega_I I_P}{\epsilon_0 n_S n_I n_P c^3}}. \quad (2)$$

Therefore, additional conditions to achieve broadband signal pulses are short nonlinear crystals and high pump intensities.

For high power applications centered at 800 nm, β -barium borate (BBO) and lithium triborate (LBO) are well-established materials [26, 27], which are used in the OPCPA of ultrabroadband, high repetition rate lasers. Other crystals worth mentioning are bismuth triborate (BIBO) and yttrium calcium oxyborate (YCOB) [28]. A summary of some important parameters is given in Table 2. Compared to BBO and LBO, BIBO has a larger nonlinear coefficient (d_{eff}), but also has significant nonlinear absorption at 515 nm [27], making it unsuitable for high power applications. YCOB is presently not commercially available. It has a smaller nonlinear coefficient and the gain bandwidth is not as large as BBO and LBO. But because its temperature tolerance is large (Table 2) and therefore insensitive to temperature changes, it might be useful for narrow band, high power applications.

The aim of the dispersion management is to achieve maximum OPA efficiency of the signal pulse, by temporally stretching the signal pulse to match the pump pulse. Thereafter, the signal pulses must be compressed to their Fourier-limit. Compared to older OPCPA systems based on Nd-doped amplifiers, Yb:YAG offers much shorter pump pulses, and therefore, the required matching signal

stretcher/compressor pairs are compacter, making a smaller footprint on the optical table and increasing the overall stability. The signal pulses can be stretched using a prism pair [7] (chirped mirrors are also an option). After amplification the pulses can be compressed in glass. For signal pulses under 10 fs, it is necessary to control the higher order dispersion using an SLM as shown in Fig. 3.

For high power (mJ pulse energy) OPCPA applications, a three stage OPCPA setup is generally optimal (Fig. 7). The first stage brings the signal pulses from the nJ to the μJ level. This reduces the amplified parametric fluorescence in the second and third stages, where more than 90% of the pump energy is used [7]. The gain in this first stage is between 10^4 and 10^5 . The next two stages provide gain in the range 50-100 and 2 for the second and third stages, respectively. An example of a three-stage broadband amplification of a 800 μs burst is shown in Fig. 8 (taken from [7]). Note: for applications involving tens of millijoules, more stages might be considered, for lower energies (μJ -level range) one to two OPCPA stages are sufficient.

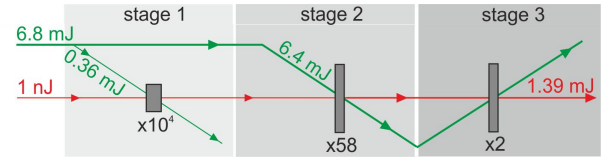


Figure 7: Schematic of a three-stage OPCPA: pump pulses (green) and signal pulses (red). As an example, energies and gains are taken from [7].

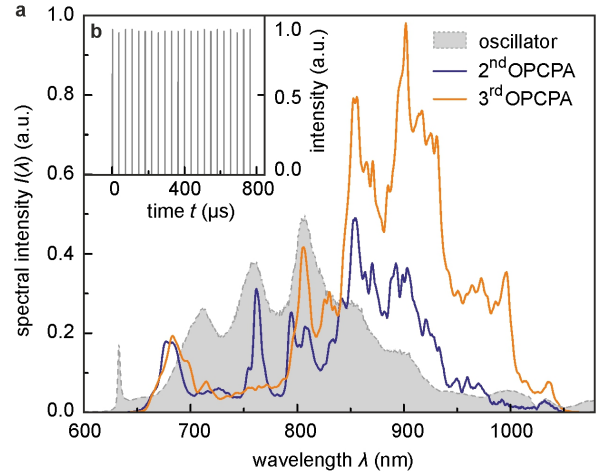


Figure 8: Three-stage broadband OPCPA [7]: (a) Spectral intensity of the Ti:sapphire oscillator (grey shaded), amplified spectra after the second (blue line) and third OPCPA stage (orange line). The amplified spectral bandwidth is $\Delta \nu = 168$ THz at $1/e^2$ ($\Delta \lambda = 360$ nm at $\lambda_c = 800$ nm), with a Fourier-limited pulse duration of 6.4 fs. (b) Inset: Typical pulse train during the burst-mode operation.

For a designer of a high power OPCPA system, one of the most important considerations is the pump-to-signal

conversion efficiency, because typically the pump amplifier dominates the costs of the complete system. As an example, an overall efficiency of 10.2% was achieved from the infrared pump to the signal output [7]. The contributions to this value were from the SHG and the three-stage OPCPA (see Fig. 7):

$$13.2 \text{ mJ} \xrightarrow{\text{SHG } 51\%} 6.8 \text{ mJ} \xrightarrow{\text{OPCPA } 20\%} 1.4 \text{ mJ}. \quad (3)$$

Power Scaling in Continuous Mode

The previous discussed results were carried out in burst mode. However, in continuous mode and at such high average powers, the linear absorption of optical power within the crystals cannot be neglected. This leads to inhomogeneous heating of the nonlinear optical crystal and results in spatial temperature changes. Spatially inhomogeneous refractive index changes can occur, which lead to spatially varying phase-matching conditions, limiting the attainable average power, the spectral bandwidth [29], and the beam quality [26]. Previously, the literature values for the linear absorption coefficients (α_{515}) at the OPCPA-pump wavelength at values near 515 nm were given as upper limit estimates: for example, $\alpha < 10^4 \text{ ppm cm}^{-1}$ at 532 nm for BBO, and $\alpha < 10^3 \text{ ppm cm}^{-1}$ at 532 nm for LBO [30]. Older techniques for measuring very small linear absorption coefficients were based on resonator methods, which suffer from misinterpreting scatter or reflection loss for absorption.

In a recent work [27], we have provided up-to-date measurements of the absorption coefficients at 515 nm using the photothermal common-path interferometry (PCI) method [31,32]. The results demonstrate a large variation of absorption values within and on the surface of the crystals (for an example see Fig. 9 with an average absorption coefficient of $37.33 \text{ ppm cm}^{-1}$ in volume). Additionally, in the case of BBO there would appear to be a large variation between manufacturers. Compared to older literature values, these new values are 1-2 orders of magnitude lower. There are two possible explanations for this discrepancy: (i) improved crystal growing and handling methods, and (ii) the accuracy of the PCI method. These new results show that for high power applications and for large bandwidth amplification, BBO and LBO are still the best crystals for these wavelengths. The application of BIBO for high powers is limited by two-photon absorption at 515 nm.

Another important consideration for high power OPCPA is the correct choice of the signal center frequency and bandwidth. Not only is it important to consider the absorption of the narrow band pump pulse, but the signal and idler pulses can also have significant contributions [29]. Figure 10 shows the optical transmission dependence on wavelength for both LBO and BBO; additionally, simulated signal spectra for LBO and BBO centered at 810 nm with a bandwidth supporting sub-7.0 fs (Fourier-limited) signal pulses and corresponding idler spectra are shown (taken from [26]). The idler spectrum is dependent on the pump wavelength and the broadband signal wavelengths through $1/\lambda_I = 1/\lambda_P - 1/\lambda_S$. In both cases, the signal spectrum must be cut off below

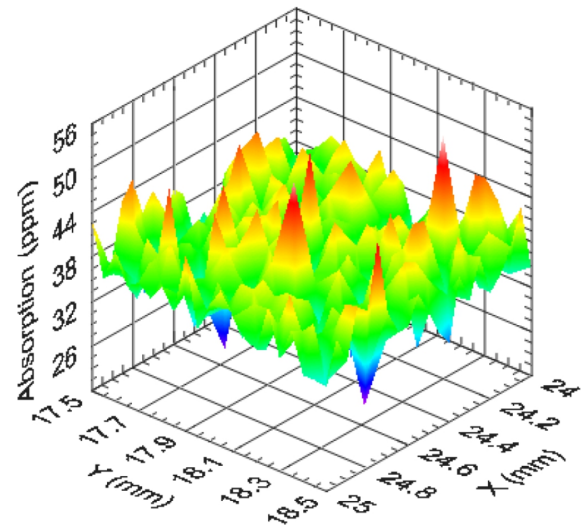


Figure 9: An example measurement of the volume absorption of an LBO sample using the common-path interferometry method (taken from [27]).

700 nm to prevent a strong idler infrared absorption within the range between 2000 and 3000 nm. Given the newly measured absorption coefficients and careful selection of the signal bandwidth, few-cycle laser pulses could be generated with above kW-level of average power [27]. A detailed discussion of thermal effects for high power OPCPA applications, including other parasitic waves, is given in [26,27].

In order to demonstrate the flexibility of OPCPA and the power scaling limits, we realized a compact wavelength-tunable sub-30 fs amplifier with 11.4 W of average power with 20.7% pump-to-signal conversion efficiency at a repetition rate of 3.25 MHz [5]. The broadband signal was generated in a YAG crystal and the complete OPCPA setup was demonstrated on a bread board $80 \times 80 \text{ cm}^2$. The OPCPA pump source was an Innoslab amplifier (AMPHOS, [33]). The OPCPA results are shown in Fig. 11. First, the OPCPA was optimized for broadband amplification. The average output power was 11.4 W (pulse energy of 3.5 μJ) with a spectrum supporting a Fourier-limited pulse of 6 fs FWHM (Fig. 11a). Second, a wavelength-tunable option was tested with a central wavelength between 700 and 900 nm (spectra shown in Fig. 11b). As an example, an autocorrelation measurement of a compressed pulse at center wavelength of 800 nm, with pulse duration of 29.1 fs FWHM was demonstrated (Fig. 11c). For more details see [5].

CONCLUSION

In this review, we discussed some of the technological developments for achieving high power OPCPA pumped at 515 nm using Yb-doped solid-state lasers in both burst mode and continuous mode. These developments have important applications for high repetition rate FELs. Compared to Ti:sapphire amplifiers, OPCPA technology has a number of advantages. First, OPCPA is scalable to high powers [27];

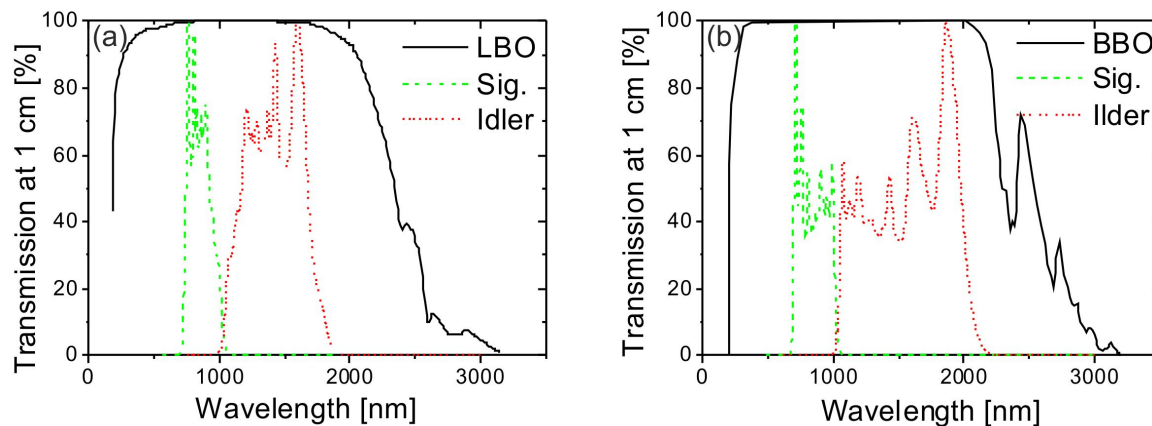


Figure 10: Optical transmission in dependence on wavelength [34], and spectra of signal and idler pulses at the end of the second stage for both LBO (a) and BBO (b) (taken from [26]).

second, OPCPA can amplify a broader bandwidth at high powers [5–7], thereby producing shorter pulses; and third, OPCPA is a wavelength tunable amplifier at high powers [5]. These new developments have been made possible by advances in Yb-doped solid-state laser technology, which

also has the potential to be scalable to high powers. For example, 14 kW burst average power has been demonstrated from a 2-stage Yb:YAG thin-disk multipass amplifier [25]. Finally, since OPCPA does not require sophisticated cooling, it is possible to achieve a compact design, allowing reduced laboratory space and better stability [5].

REFERENCES

- [1] L. Lilje et al., "Achievement of 35 MV/m in the superconducting nine-cell cavities for TESLA", Nucl. Instr. Meth. Phys. Res. A **524**, 1–12 (2004).
- [2] J. Feldhaus, "FLASH – the first soft x-ray free electron laser (FEL) user facility", J. Phys. B: At. Mol. Opt. Phys. **43**, 194002 (2010).
- [3] B. Faatz et al., "Flash II: Perspectives and challenges", Nucl. Instr. Meth. Phys. Res. A **635**, S2–S5 (2011).
- [4] H. Redlin et al., "The FLASH pump-probe laser system: Setup, characterization and optical beamlines", Nucl. Instr. Meth. Phys. Res. A **635**, S88–S93 (2011).
- [5] R. Riedel et al., "Power scaling of supercontinuum seeded megahertz-repetition rate optical parametric chirped pulse amplifiers", Opt. Lett. **39**, 1422–1424 (2014).
- [6] J. Rothhardt et al., "Octave-spanning OPCPA system delivering CEP-stable few-cycle pulses and 22 W of average power at 1 MHz repetition rate", Opt. Express **20**, 10870–10878 (2012).
- [7] R. Riedel et al., "Long-term stabilization of high power optical parametric chirped-pulse amplifiers", Opt. Express **21**, 28987–28999 (2013).
- [8] F. Tavella et al., "90 mJ parametric chirped pulse amplification of 10 fs pulses", Opt. Express **14**, 12822–12827 (2006).
- [9] F. Tavella et al., "Fiber-amplifier pumped high average power few-cycle pulse non-collinear OPCPA", Opt. Express **18**, 4689–4694 (2010).
- [10] J. Rothhardt et al., "High average and peak power few-cycle laser pulses delivered by fiber pumped OPCPA system", Opt. Express **18**, 12719–12726 (2010).

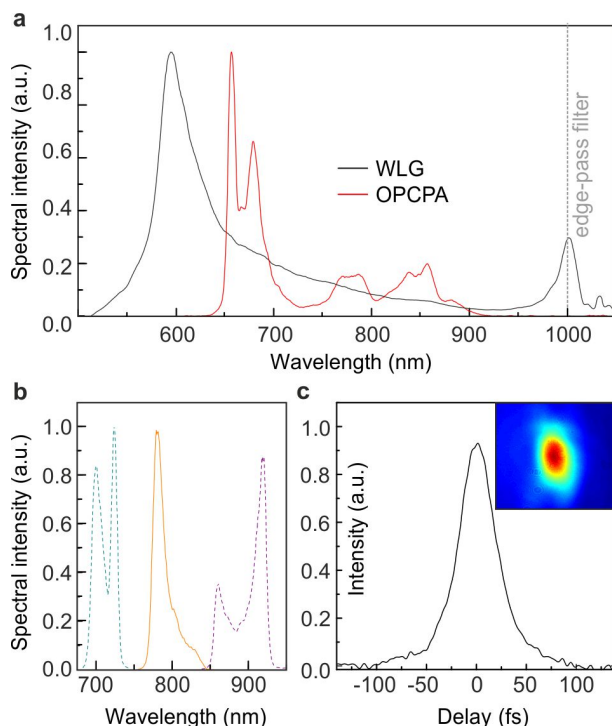


Figure 11: High-power OPCPA [5]: a) Broadband amplified signal (OPA, red) with $\Delta\lambda = 238$ nm at 5% intensity maximum; WLG spectrum (WLG, grey line). b) Selected tunable narrow-band spectra between 700–900 nm, with $\Delta\lambda = 54$ nm bandwidth at 10% intensity maximum. c) Autocorrelation (black line) at 800 nm (orange spectrum in (b)), with a pulse duration of 29.1 fs FWHM. Inset: amplified signal beam profile.

- [11] M. Lenzner et al., "Sub-20-fs, kilohertz-repetition-rate Ti:sapphire amplifier", *Opt. Lett.* **20**, 1397–1399 (1995).
- [12] A. Dubietis, G. Jonušauskas and A. Piskarskas, "Powerful femtosecond pulse generation by chirped and stretched pulse parametric amplification in BBO crystal", *Opt. Commun.* **88**, 437–440 (1992).
- [13] I. N. Ross et al., "The prospects for ultrashort pulse duration and ultrahigh intensity using optical parametric chirped pulse amplifiers", *Opt. Commun.* **144**, 125–133 (1997).
- [14] G. Cerullo and S. De Silvestri, "Ultrafast optical parametric amplifiers", *Rev. Sci. Instrum.* **74**, 1–18 (2003).
- [15] R. Butkus et al., "Progress in chirped pulse optical parametric amplifiers", *Appl. Phys. B* **79**, 693–700 (2004).
- [16] A. Dubietis, R. Butkus and A. P. Piskarskas, "Trends in chirped pulsed optical parametric amplification", *IEEE J. Sel. Topics Quantum Electron.* **12**, 163–172 (2006).
- [17] B. C. Stuart et al., "Laser-induced damage in dielectrics with nanosecond to subpicosecond pulses", *Phys. Rev. Lett.* **74**, 2248–2251 (1995).
- [18] M. Schulz et al., "Yb:YAG Innoslab amplifier: efficient high repetition rate subpicosecond pumping system for optical parametric chirped pulse amplification", *Opt. Lett.* **36**, 2456–2458 (2011).
- [19] M. Schulz et al., "Pulsed operation of a high average power Yb:YAG thin-disk multipass amplifier", *Opt. Express* **20**, 5038–5043 (2012).
- [20] M. Bradler, P. Baum and E. Riedle, "Femtosecond continuum generation in bulk laser host materials with sub- μ J pump pulses", *Appl. Phys. B* **97**, 561–574 (2009).
- [21] T. Eidam et al., "Femtosecond fiber CPA system emitting 830 W average output power", *Opt. Lett.* **35**, 94–96 (2010).
- [22] J. Limpert et al., "Performance Scaling of Ultrafast Laser Systems by Coherent Addition of Femtosecond Pulses", *IEEE J. Sel. Topics Quantum Electron.* **20**, 0901810 (2014).
- [23] P. Russbuehler et al., "Compact diode-pumped 1.1 kW Yb:YAG Innoslab femtosecond amplifier", *Opt. Lett.* **35**, 4169–4171 (2010).
- [24] A. Giesen and J. Speiser, "Fifteen Years of Work on Thin-Disk Lasers: Results and Scaling Laws", *IEEE J. Sel. Topics Quantum Electron.* **13**, 598–609 (2007).
- [25] M. Schulz et al., "14 kilowatt burst average power from 2-stage cascaded Yb:YAG thin-disk multipass amplifier", in *Frontiers in Optics 2013*, I. Kang, D. Reitze, N. Alic, and D. Hagan, eds., OSA Technical Digest (Optical Society of America, 2013), paper FTu4A.2. <http://www.opticsinfobase.org/abstract.cfm?URI=FiO-2013-FTu4A.2>
- [26] M. J. Prandolini et al., "Design considerations for a high power, ultrabroadband, optical parametric chirped-pulse amplifier", *Opt. Express* **22**, 1594–1607 (2014).
- [27] R. Riedel et al., "Thermal properties of borate crystals for high power optical parametric chirped-pulse amplification", *Opt. Express* **22**, 17607–17619 (2014).
- [28] Z. M. Liao et al., "Energy and average power scalable optical parametric chirped-pulse amplification in yttrium calcium oxyborate", *Opt. Lett.* **31**, 1277–1279 (2006).
- [29] J. Rothhardt et al., "Thermal effects in high average power optical parametric amplifiers", *Opt. Lett.* **38**, 763–765 (2013).
- [30] D. N. Nikogosyan, *Nonlinear Optical Crystals: A Complete Survey* (Springer Science+Business Media, Inc., 2005).
- [31] A. Alexandrovski et al., "Photothermal common-path interferometry (PCI): new developments", *Proc. SPIE 7193, Solid State Lasers XVIII: Technology and Devices*, 71930D (2009); doi:10.1117/12.814813.
- [32] B. Gronloh et al., "Green sub-ps laser exceeding 400 W of average power", *Proc. SPIE 8959, Solid State Lasers XXIII: Technology and Devices*, 89590T (2014); doi:10.1117/12.2041288.
- [33] T. Mans et al., "Highly flexible ultrafast laser system with 260 W average power", *Proc. SPIE 7912, Solid State Lasers XX: Technology and Devices*, 79120M (2011); doi:10.1117/12.874417.
- [34] A.V. Smith, *SNLO nonlinear optics code (Ver. 60)*, AS-Photonics, Albuquerque, USA (2013).

A GAAS PHOTOEMISSION DC GUN FOR CAEP HIGH-AVERAGE-POWER THz FEL*

Hanbin Wang[#], Kai Li, Ming Li, Dai Wu, Dexin Xiao, Xingfan Yang
Institute of Applied Electronics, CAEP, China.

Abstract

FEL-THz plays an important role in THz science and technology research, for high power output and tunable wavelength, which is indispensable to material, biology, medical research. Now, the construction is underway at China Academy of Engineering Physics (CAEP) on high-average-power FEL THz source, and the demonstration of stable, reliable, high brightness, high power electron source operation is one of key issues. The components of the system were constructed and the performance tests are still on. The lifetime of the Negative Electron Affinity (NEA) surface is about 40 hours, which is limited mainly by vacuum. Up to now, the gun can supply 5mA beam current and has been employed for preliminary experiments. In this paper, the design considerations and present status are given.

INTRODUCTION

FEL-THz source is a strong candidate among THz sources in THz application researches, and now a high-average-power FEL-THz source is under construction in CAEP. The key component of the facility is a high average current, low emittance electron source, which should deliver about 100pC/bunch (the average current of 5mA). To fulfil the requirements, the DC gun become a leading choice for better technical maturity[1]. Since the gun can offer excellent vacuum, we use a NEA GaAs photocathode, which has a relatively high quantum efficiency (QE) and practical operating wavelength.

The construction of a DC gun is still careful to do, despite its technical maturity and there are two items to consider. One is how to achieve the extra-high vacuum, NEA GaAs is chemically reactive and is degraded by a small fraction of H₂O or CO₂. Photo-cathode's QE can be degraded by ion back bombardment, independent of the gas species forming the ion. the other is how to realize high voltage stable operation, the field emission is a principal challenge[2], which arising from the cathode electrode and its support structure may result in voltage breakdown across the cathode-anode gap, or a punch-through failure of the insulator holding off the cathode potential, and directly affects operation.

The very successful Jlab IR FEL operates based on a photocathode dc gun[3]. The gun design started as a 500 kV gun with a peak electric field of 10 MV/m at the surface of the cathode in the beginning of 1990's[4]. Due to field emission from the electrode structures encountered during the 1kW IR Demo's commissioning,

the gun has been modified to a lower gradient at the cathode achieved by lowering the operating voltage to 320kV and by increasing the cathode-anode gap (6 MV/m at 500 kV)[5]. The 500kV operation is realized until 2011[6]. So, it should be envisioned that the high voltage operation must circumvent many obstacles. We consult the experiences from other lab and ours, and the design incorporates some features of the existing DC gun. In the following sections, the component solutions adopted and the CAEP DC gun status are given.

DESIGN OF CAEP DC GUN

High QE cathode must be prepared and transferred under vacuum. The existing photoemission DC guns can be classified two types; one prepare cathodes in situ in the electron guns, the other transfer cathodes under vacuum from a separate preparation chamber by a load-lock.

As Fig. 1 shows, the CAEP DC gun adopts a load-lock design too, which consists of three components (photocathode load-lock system, main gun chamber and mode lock laser). The following describes a design on the major points of interest about each component.

PHOTOCATHODE LOAD LOCK SYSTEM

The photocathode load lock system includes three chambers as shown in Fig. 1, where the function is realized of cathode puck introduction, preparation and storage.

The beginning part is an introduction chamber, and the primary function is to introduce pucks and store them for succedent processing. The first processing is atomic hydrogen cleaning, which provides a means to clean exotic photocathode materials for which wet chemistry techniques are incapable. A KYKY F700 turbo-pump is used during atomic hydrogen cleaning where typical values for temperature and pressure near the sample are 200 C and 2E-3 Pa respectively. During the process, a ceramic heater is used to raise sample temperature for atomic hydrogen cleaning.

The middle part is a preparation chamber, where the heating and activation processing are completed. A magnet manipulator transfers a puck from introduction chamber to preparation chamber after atomic hydrogen cleaning process. Same to the heating process in the introduction chamber, a ceramic heater is used to heat the wafer to about 450 C at a ramp rate up and down of 1 C per second, and the ramp down control is aided by an active cooler. The preparation chamber is a stainless steel chamber with eighteen ports placed around the circumference, which contains all of the components to produce NEA photocathodes: a channel cesiator, a NF₃ or

*Work supported by the ministry of science and technology
#wanghanbin@caep.cn

O₂ oxidizer, a ring anode, an optical window for light, 100 l/s sputter ion pump, CapaciTorr D3500 SAES NEG. In addition, a residual gas analyzer (RGA) and an extractor gauge used for vacuum diagnostics.

The last part is a storage chamber, which allows us to activate several wafers during an accelerator maintenance day and store them for future use. The three chambers are separated by a 2.5-inch VAT ultra high vacuum metal sealed valve.

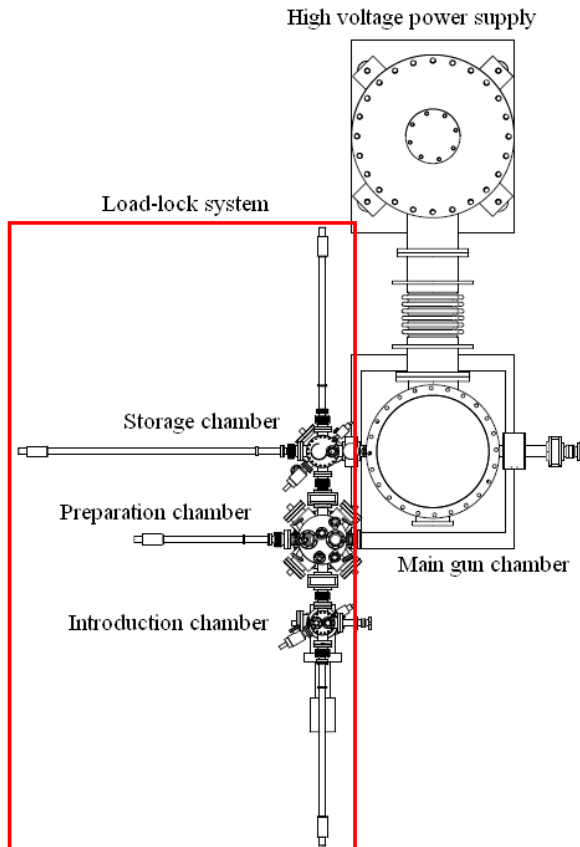


Figure 1: Layout of the photoemission DC gun.

MAIN GUN CHAMBER

The main gun chamber consists of ceramic insulator, stainless steel chamber and electrodes, which provides superb vacuum for NEA photocathode and isolated insulation between high voltage and earth potential.

Design of Extreme-high-vacuum

The operation of high average power FEL-THz requires higher QE photocathodes, but to date they are readily poisoned by small quantities of chemically active gases such as water, oxygen and carbon dioxide[7]. Relatively inert gases such as hydrogen, methane, nitrogen and carbon monoxide have small to negligible poisoning effects on these cathodes, but they can be ionized by electrons traversing cathode-anode gap, and are accelerated back to the photocathode to cause QE degradation. So we must take measures to achieve

extreme high vacuum. The vacuum pump scheme is with triple-ion-pump and non-evaporable getter (NEG) pump, which are well suited for pumping CO, CO₂ and greatly enhanced the pumping speed for hydrogen[8], the dominant gas species in the extreme high vacuum systems.

The original pumping system of the gun chamber was designed to have a 800l/s triple ion pump and three 1300l/s NEG pump[9]. The total pressure were monitored by a B-A ion gauge, and the vacuum pressure falls down to 6.0E-9 Pa after bake-out of the gun chamber at 200°C for about 96 hours and ramps up to 1.2E-8Pa during 5mA operation. In this case, the cathode operation lifetime is so short to make the facility use efficiency too low.

To get longer operation lifetime, we make some improvements on the basis of practice of our lab and experience of other laboratories.

- The internal walls of the chamber were vacuum fired to 500C to decrease the hydrogen load in the bulk material.
- All viton-seal valves used in the gun chamber were replaced by metal-seal to be baked at higher temperature ($\leq 300^\circ\text{C}$).
- The total pumping speed of NEG pumps was reinforced up to 20,000l/s and a 100l/s ion pump was redeployed for inert gas pumping.

Design of High Voltage Parts

The DC gun's high voltage parts include two ceramic insulators, potential dividers, cathode electrodes and their support structure, as shown in Fig. 2. The principal technology challenge is still the field emission from the cathode electrode and its support structure.

The DC gun insulator works in high voltage, high vacuum and high pressure. The voltage holdoff capability of a high voltage ceramic insulator in vacuum is poor compared to that of the ceramic material or the vacuum itself. Field emission originating at the triple junction of ceramic-metal-vacuum is a well-understood cause of internal surface flash-over, and is controlled by reducing the field on the junction with electrostatic shields. The external ceramic surface is usually corrugated to inhibit flashover. But it is unavoidable that the inner surface of ceramic intercepts electrons field-emitted from support tube or meso-potential electrode. Aiming at former problem, the ceramic adopts charge-dissipative type, which provides some surface conduction to bleed off accumulated surface charge and so as to suppress the surface flashover.

The field uniformity can improve the stability and reliability of the DC gun on the surface of a ceramic insulator. We adopted shielding rings which distribution is non-proportional spacing to obtain comparatively equal electric field on the insulator surface, and the potential between rings is controlled by a high-Ohmic divider.

During design of electrodes, the choice of material is a very important ingredient for high potential gradient operation of DC gun. In the foregone experiments, the titanium alloy exhibits better high voltage performance

than stainless steel[10], and the design adopts titanium alloy to make electrodes and tee support. In a pierce gun, the peak field on the electrode is two to three times higher than the field on the cathode, so we adopt flat cathode surface, which produce a high degree of electric field uniformity over the emitting area and have lower peak electric field than pierce type cathode electrode ensuring the emitting field.

To lower the peak electric field of the support tube, a meso-potential electrode is adopted in DC gun, and the peak electric field on the support tube is just 70 percent of field strength without meso-potential electrode, which can effectively decrease the field-emitted currents in the high voltage operation.

The high voltage is supplied by a nominal voltage of 400kV and the maximum current of 10mA. The high voltage power supply is located in a pressure vessel holding 0.6MPa of SF₆, which is connected with the insulator pressure vessel by bellows.

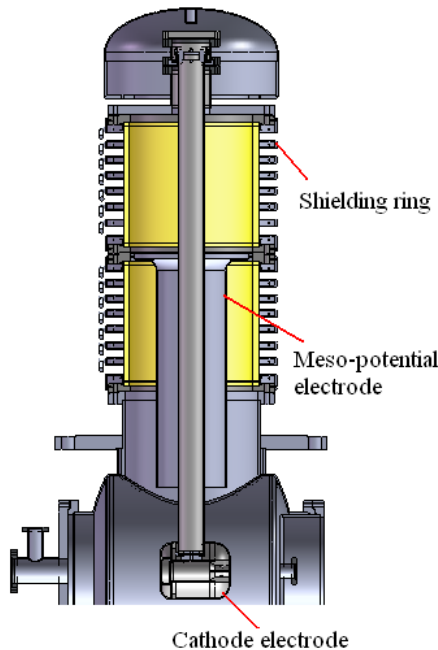


Figure 2: Scheme of the gun high voltage parts.

MODE-LOCK LASER

As drive laser for NEA photocathode, a frequency doubled, mode-locked Nd:YAG laser (GKML-532) is used[11]. The laser generates pulses at a maximum repetition rate of 54.17 MHz in CW mode and up to 3 W of SHG power (on cathode surface) at 532 nm. A maximum current of 5mA can be obtained still, even if the QE of photocathode is low to 0.4%.

PRELIMINARY RESULTS AND WORK SCHEDULE

The new gun is debugging based on the forementioned design thoughts, and the vacuum performance steps up

more than an order of magnitude as compared with original design, new design is about 7E-9Pa while the original 1.5E-7Pa, being pumped only by ion pump.

Proof experiments have been done on the original gun. The gun can operate at 320kV stably, but the current of 5mA (10 ms-long pulses at 10 Hz) just continue about 5 hours for poor vacuum of 1.2E-8Pa, when it is a precondition that maximum power of the drive laser is constant. At the same time, the QE measurements show lifetime (Cs-O activation) is about 40 hours in preparation chamber, where it is measured intermittently, i.e. so-called dark-lifetime. The term lifetime is defined as the time that QE fell to 1/e from the initial value takes, and the QE change with time is shown in Fig. 3. Compared with the results of dark-lifetime from other labs[2], we must realize the space for improvement is so large still and there are many things to do.

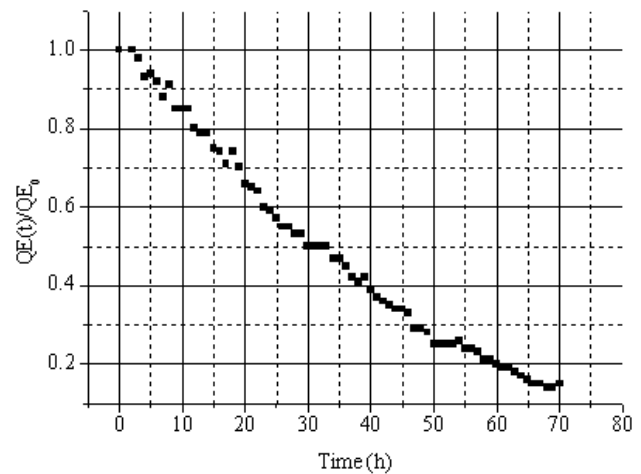


Figure 3: Preliminary result of dark-lifetime measurement.

To make the CAEP FEL-THz facility more practical, we hope upgrade the current continuance of 5 mA by an order of magnitude at least. The superb vacuum of the gun can be realized absolutely, and the ultimate pressure approaching 1E-10 Pa should be possible. According to the work schedule, the new gun can be completed in the end of 2014. With the advance on the technology of preparing NEA GaAs cathode, the target can be realized of elevating 5 mA continuance by order of magnitude.

REFERENCES

- [1] Triveni Rao and David H.Dowell, "DC/RF injectors," in *An engineering guide to photoinjectors*, CreateSpace, 2013.
- [2] Charles K.sinclair, "DC photoemission electron guns as ERL sources," *Nucl. Instr. and Meth. A*, vol. 557, pp. 69-74, 2006.
- [3] C.Hernandez-Garcia et al., "A high average current DC GaAs photocathode gun for ERLs and FELs," in *2005 Particle Accelerator Conference*, Knoxville, Tennessee, 2005, pp. 3117-3119.

- [4] Charles K. Sinclair, "A 500 kV photoemission electron gun for the CEBAF FEL," *Nucl. Instr. and Meth. A*, vol. 318, pp. 410-414, 1992.
- [5] Byung C. Yunn, "High brightness injectors based on photocathode DC Gun," in *2001 Particle Accelerator Conference*, Chicago, Illinois, 2001, pp. 2254-2256.
- [6] Spencer Acberman, Available: <http://www.wired.com/danger-room/2011/02/unexpectedly-navys-superlaser-blasts-away-a-record/>
- [7] G. Suberlucq, "Technological challenges for high brightness photo-injectors," in *European Particle Accelerator Conference 2004*, Lucerne, Switzerland, 2004, pp. 64-68.
- [8] SAES homepage, Available: <http://www.Saesgetters.com/default.aspx?idPage=125>
- [9] WANG Hanbin et al., "DC high voltage photoemission electron gun for CAEP FEL," in *33th International Free Electron Laser Conference*, Shanghai, China, 2011, pp. 598-600.
- [10] T. Nakanishi et al., "An electrode with molybdenum-cathode and titanium-anode to minimize field emission dark currents," in *2004 Linear Accelerator Conference*, Lübeck, Germany, 2004, pp. 645-647.
- [11] GK Laser homepage, Available: <http://www.gklaser.com/en/index.html>

STATUS OF THE SwissFEL C-BAND LINAC

F. Loehl, J. Alex, H. Blumer, M. Bopp, H. Braun, A. Citterio, U. Ellenberger, H. Fitze,
H. Joehri, T. Kleeb, L. Paly, J.-Y. Raguin, L. Schulz, R. Zennaro, C. Zumbach,
Paul Scherrer Institut, Villigen PSI, Switzerland

Abstract

The linear accelerator of SwissFEL will be based on C-band technology. This paper summarizes the latest results that were achieved with the first prototype components. Furthermore, the progress and plans of the series production are discussed.

INTRODUCTION

The hard x-ray free-electron laser facility SwissFEL [1] is currently under construction at the Paul Scherrer Institute. In the main linear accelerator (Linac) of SwissFEL, the electron bunches are accelerated from an energy of 350 MeV to a final energy of up to 5.8 GeV. For this, the Linac is divided into three segments (see Fig. 1): Linac 1, Linac 2, and Linac 3. After Linac 1, the electron bunches are compressed in a magnetic bunch compressor chicane BC2 at an intermediate energy of 2.1 GeV - the first bunch compressor BC1 is located within the injector at an energy of ~350 MeV. After Linac 2, at an energy of 3.0 GeV, a switch-yard [2] is installed with which electron bunches can be sent either straight into Linac 3 and consequently the hard x-ray Aramis line, or into a future soft x-ray line called Athos. At the end of Linac 3, transversely deflecting structures will be located that will allow for measurements of the longitudinal charge profile with a resolution of a few femtoseconds.

C-BAND MODULE

The C-band modules for SwissFEL consists of four C-band structures that are installed onto two granite girders (see [3] for a schematic). A module is fed by a single RF source with up to 50 MW of RF power. The RF pulse is compressed using a barrel open cavity (BOC) pulse compressor [4], and the compressed pulse is distributed to the four accelerating structures using a wave-guide network that is installed on the side of the girders. That way, the entire linac module can be pre-assembled and complete modules can be brought into the SwissFEL facility, which simplifies the assembly procedure of the 26 modules.

The accelerating modules can be operated in two different modes that are defined by how the pulse compressor is operated. In mode I, a 180° phase jump is applied towards the end of the RF pulse, yielding an RF pulse with more than 300 MW of peak power. The pulse is, however, not flat (see [4]). In mode II, a phase modulation is applied that yields a flat RF pulse at the cost of a significantly reduced RF power.

At an RF power from the klystron of 50 MW, the expected on-crest energy gain of a module is around 220 MeV when a flat RF pulse is applied and 275 MeV with the phase jump

mode. In SwissFEL, it is planned to operate the klystrons at up to 40 MW which yields on-crest energy gains of close to 200 MeV and 250 MeV in both modes. When two or more bunches are accelerated within the same RF bunch, as planned for the parallel operation of the hard and soft x-ray lines Aramis and Athos, a flat RF pulse might provide better stability and simplify the operation in Linac 1, where the beam is accelerated off-crest. In Linacs 2 & 3, where the beam is accelerated on-crest, it is planned to operate in the phase jump mode in order to maximize the energy gain.

C-band High Power Test Stand

In order to test RF components, PSI operates a C-band test stand that provides two test benches: a component test bench and a test bench for a complete linac module. All test results that are discussed here are obtained within the component test bench. The second test bench with a complete Linac module is currently being setup and expected to become operational end of this year. The current state of the first prototype module is depicted in Fig. 2. The picture shows the module in beam direction with the accelerating structures and the wave-guide network already in place. On top of the linac module, the water distribution is visible that is also prototyped. The pulse compressor is not yet installed but the support is already visible right at the beginning of the module.

RF Source

The C-band RF pulses with a power of up to 50 MW and a duration of 3 μ s are generated by Toshiba klystrons of type E37212 that are driven by solid-state pre-amplifiers and solid-state modulators. In order to save energy, the collectors of the klystrons will be operated at a temperature of 80 °C so that part of the energy can be recovered to heat buildings on the PSI campus. This scheme was successfully tested in the high power test stand. The first klystrons for SwissFEL are already delivered to PSI, and the delivery of the complete set of klystrons will be completed ahead of schedule.

In order to validate their performance, different pre-amplifiers have been characterized in the test stand, showing that the required phase and amplitude stability can be reached. The tender process for the SwissFEL series will start end of this year.

Of major importance for SwissFEL are the modulators that drive the klystrons. The C-band test stand was operated until now with a ScandiNova K2 modulator. Since this modulator does not fulfill the requirements for SwissFEL in terms of reliability and stability, two prototype solid-state modulators were ordered at two companies last year. The first modulator is built by Scandinova, the second one by

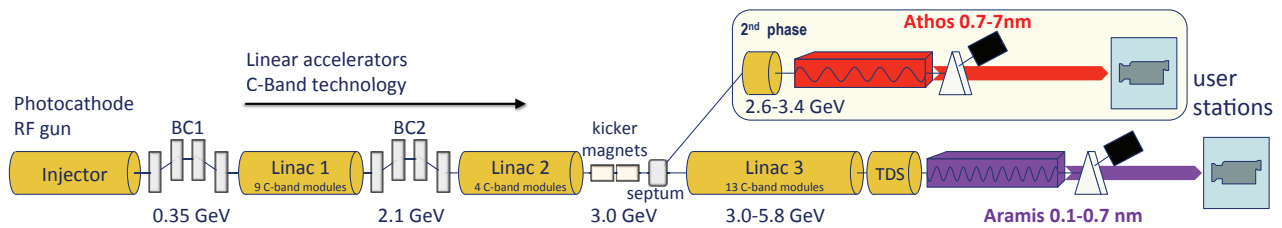


Figure 1: Schematic layout of the SwissFEL facility. It consists of an S-band injector, a C-band linear accelerator, and two undulator lines.

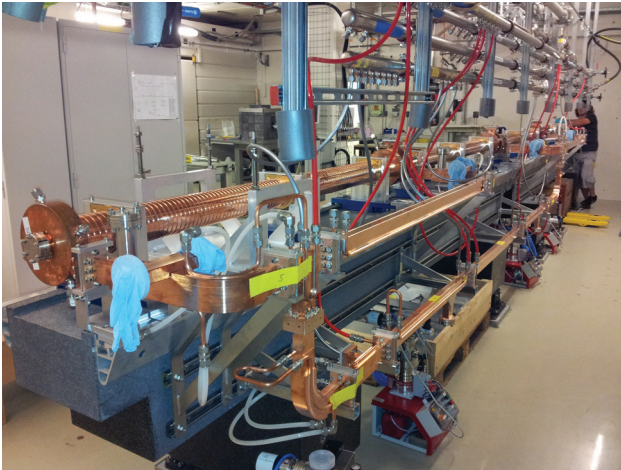


Figure 2: Picture of the first C-band prototype module in the high power test stand.

Ampegon. PSI is in close contact with both companies to support these developments. The delivery of both modulators is expected later this year and it is planned to extensively test both modulator types in the C-band test stand before the order for the SwissFEL series will be placed.

Waveguide Network

There are two main challenge for the waveguide network of the C-band modules. The first one is the length tolerance on the entire horizontal network of only ± 0.2 mm due to the fact that the waveguides are attached directly to the girders. The second challenge is the high RF power of up to 300 MW after the pulse compressor.

Many waveguide components from various manufactures as well as in-house developments of directional couplers, H-splitters, and E-splitter were tested in the C-band test stand prior to a tender process for the SwissFEL series. The winner of this tender is Mitsubishi Heavy Industries (MHI) and MHI already started with the manufacturing of a prototype waveguide network that will be delivered in December this year and consequently tested in the C-band test stand. Another prototype waveguide network was built by TEL Mechatronics based on PSI designs. This waveguide network is currently installed at the prototype C-band module and used to test assembly and tuning procedures. The RF loads were also part of the tender process, and we decided to use water loads manufactured by CML.

Pulse Compressor

The first results that were obtained with the barrel open cavity (BOC) type pulse compressor that was designed at PSI were already presented in [3, 4]. The prototype used during the previously presented measurements was built by VDL. The series for SwissFEL – a total of 26 BOCs are needed for the C-band linac and another one for the transversely deflecting C-band structures at the end of Linac 3 – will be built in house at PSI. The first four BOCs were already completed, and BOCs 5-8 are currently under production (see [5]).

We conducted first measurements of the break-down rates for the BOC manufactured by VDL and for the first BOC from PSI. The VDL BOC was operated in both the phase jump mode at an RF power of 35 MW from the klystron and the phase modulation mode with 40 MW of power from the klystron. The measured break-down rates were $3 \cdot 10^{-8}$ and $2 \cdot 10^{-8}$, respectively. For SwissFEL, a break-down rate of below $4 \cdot 10^{-8}$ is desired under nominal conditions, and with the presently assumed energy gains of the C-band modules, an RF power of 40 MW will be required for Linac 1 (phase modulation) and less than 35 MW for Linac 2 & 3. The measured break-down rates are therefore already in the region that is envisioned for SwissFEL. Recently, initial break-down measurements were performed with the first BOC that was manufactured at PSI, and these yielded a break down rate of $1 \cdot 10^{-7}$ in phase jump mode for 40 MW of RF power. This is an even better result than the one obtained for the VDL prototype. After the excellent break-down results that were obtained for the first C-band structure (see [3]), however, the BOCs still remain the most critical components in terms of break-downs.

A major source of contamination of the copper surface within the first BOCs resulted from the fact that the BOCs had to be tuned after the final brazing step. This involved the application of grease during the machining process, and it is difficult to clean the BOCs afterwards. Due to the good results with the first BOCs that were machined, the manufacturing process was meanwhile adapted such that the BOCs are machined on-frequency without involving an additional tuning step. This way, the BOCs will stay clean after the final brazing step, and it is expected that this will improve the break-down rate further. The first of these BOCs that involves this manufacturing procedure will be tested together with the linac module prototype beginning of next year.



Figure 3: New clean area to perform vacuum leak tests and RF bead-pull measurements. The space is next to the stacking and brazing area.



Figure 4: Transport girder for the transfer of structures from the brazing area on the PSI campus to the external storage area.

Accelerating Structures

The 2 m long accelerating structures have been designed at PSI [6], and meanwhile a total of 5 structures was successfully brazed. The manufacturing process is described in detail in [7].

The structures consist out of 108 copper discs and a J-coupler at both ends. Since the structures are built on-frequency without the possibility for tuning, the parts have to be machined with micrometer precision.

For the J-couplers, various companies were qualified before the tender process for the SwissFEL series was launched. The winner of this tender process is VDL, and the production process has already started. The first batch of coupler parts will be delivered to PSI in October. The brazing of the couplers takes place at PSI.

The main provider for the copper discs is TEL Mechatronics. PSI qualified TEL Mechatronics to build the discs according to a production scheme developed at PSI. Earlier this year, TEL Mechatronics delivered the cups for a first structure to PSI, and after brazing the structure delivered excellent RF bead-pull results. The series production has meanwhile started at TEL Mechatronics, and the delivery of discs will start beginning of September this year.

Since the production of the C-band structures is delayed with respect to the project schedule, PSI ordered C-band discs also from VDL, and the discs for one structure were already delivered earlier this month. The orders foresee a delivery of cups for a total of 4 structures from VDL and of 13 structures from TEL Mechatronics until the end of this year.

The structures are stacked and brazed at PSI (see [3, 5]). In order to be able to deal with the amount of structures that will be brazed at PSI – a total of 104 structures are required for SwissFEL – the area in which the stacking and brazing takes place was meanwhile extended by a new clean area. This space will be used to perform leak-tests of the brazed structures as well as bead-pull measurements to characterize

the RF performance. Figure 3 shows a picture of the new clean area.

The following issue in the manufacturing process is still not entirely understood: Out of the five structures that were brazed so far, 3 had a vacuum leak after they were brazed. In a second repair-brazing step, all three structures could be repaired, but we aim to prevent these repair steps during series production. From the five structures that were brazed, the first two had an initial vacuum leak. For the next three structures, the amount of brazing alloy was increased, and structure 3 & 4 were vacuum tight after they were brazed the first time. The same procedure, however, was applied to structure 5, and this structure required a repair step. There are various possible sources for this that we are looking at. Two of them are the fact that the copper discs for structure 5 were stored a long time under normal atmosphere, and some of the discs were stored on latex rubber mats, and it appears that the discs that came into contact with the latex material showed color changes near the contact areas. These two aspects will be taken care of in the series production by storing the discs under nitrogen atmosphere and by removing the latex material. In order to understand better the amount of brazing alloy that is optimum, additional brazing tests with different amounts of brazing alloy will be performed.

Production of C-band Modules

Once the structures are brazed, leak-checked, and a bead-pull measurement was performed, the structures are transported into a storage hall that PSI has rented for the duration of the SwissFEL project. This happens using special transport girders as shown in Fig. 4. In the storage hall, depicted in Fig. 5, an area is reserved in which the structures can be transferred onto the final granite girders. A set of multiple granite girders will be used as a buffer before the assembly of a linac module takes place. This allows to sort the structures by frequency. Since the structures are fine-tuned in frequency using the temperature of the cooling water, and in

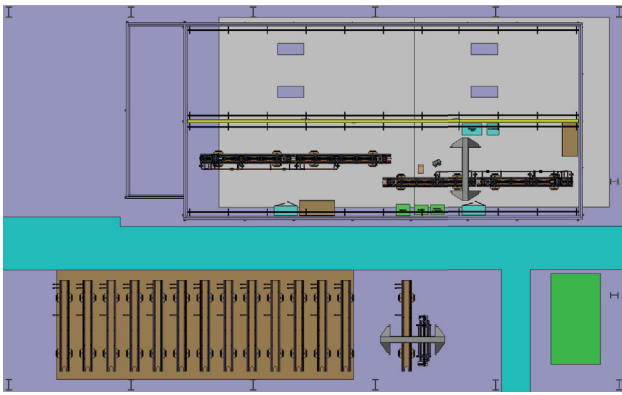


Figure 5: Schematic showing the storage area for the C-band structures (bottom) and the clean room (top) in which the module assembly will take place. Up to two modules can be assembled in parallel.



Figure 6: Clean room that will be used for the assembly of the C-band modules as well as for other girders for SwissFEL.

SwissFEL all four structures of a linac module share a common cooling system, this is a way to increase the efficiency of the linac modules.

When a matching pair of two girders with four structures is available, the girders are transferred into a big clean room (see Fig. 6), where the module assembly takes place. This includes the installation of the pulse compressors, the wave-guide network including its tuning, and components such as quadrupole magnets and diagnostics (BPMs, wire-scanners). The assembled linac modules are then either stored again outside of the clean room, or transported directly into the SwissFEL accelerator tunnel (see Fig. 7).

Temperature Regulation

In reference [3], a first prototype for the BOC temperature regulation system was presented. With this system, a temperature stability of 3 mK was reached. A disadvantage of the presented system was that the time required to reach a steady-state after a distortion happened was rather long with around 4 to 5 minutes. In order to speed up the regulation, a number of steps were taken. The most important ones



Figure 7: Picture of the empty SwissFEL accelerator tunnel.

were the replacement of the heater against a model with an increased heat transfer, the installation of the heater very close to the pulse compressor in order to reduce the dead-time, and the adaption of the regulation algorithm. Besides several other additions, the new algorithm now has a very large gain when the BOC temperature deviation exceeds a desired temperature band. With all these changes, it now takes around 40 seconds until the BOC temperature is stable again when a distortion happens or a step in the temperature set-point is applied.

As a prototype for SwissFEL, the C-band module in the test stand is equipped with a complete SwissFEL cooling station. This station will regulate the temperature of the modulator body, the klystron collector, the BOC, and the four accelerating structures, and we will use it to test and optimize the SwissFEL cooling stations.

SUMMARY AND OUTLOOK

Many prototypes for the SwissFEL C-band Linac have been built and tested, and most of them show the desired performance. Meanwhile, we launched the series production for many components including the C-band structures, the BOC RF pulse compressors, and the wave-guide network. Two prototype solid-state modulators are ordered and will be delivered to PSI in the second half of this year. The next steps include validating the performance of the two modulators before the SwissFEL series can be ordered, and the test of a complete C-band module in the high power RF test stand.

REFERENCES

- [1] R.Ganter (ed.), "SwissFELConceptualDesignReport," „PSI Bericht, 10-04, 2010.
- [2] M. Paraliiev *et al.*, "High stability resonant kicker development for the SwissFEL switch yard," in *These Proceedings: Proc. 36th Int. Free-Electron Laser Conf.*, Basel, 2014, MOP039.
- [3] F. Loehl *et al.*, "Status of the SwissFEL C-band linear accelerator," in *Proc. 35th Int. Free-Electron Laser Conf.*, New York, USA, 2013, pp. 317–321.

- [4] R. Zennaro *et al.*, "C-band RF pulse compressor for SwissFEL," in *Proc. of the IPAC 2013 Conf.*, Shanghai, China., 2013, pp. 2827–2829.
- [5] U. Ellenberger *et al.*, "The SwissFEL pulse compressor BOC: manufacturing and proof of precision by RF measurements," in *These Proceedings: Proc. 36th Int. Free-Electron Laser Conf.*, Basel, 2014, THP056.
- [6] J.-Y. Raguin and M. Bopp, "The SwissFEL C-band accelerating structure: RF design and thermal analysis," in *Proc. of the Linac 2012 Conf.*, Tel-Aviv, Israel, 2012, pp. 501–503.
- [7] U. Ellenberger *et al.*, "Status of the manufacturing process for the SwissFEL C-band accelerating structures," in *Proc. 35th Int. Free-Electron Laser Conf.*, New York, USA, 2013, pp. 245–249.

REVIEW OF COHERENT SASE SCHEMES

B.W.J. McNeil¹, L.T. Campbell^{1,2}, D.J. Dunning^{1,2}, J.R. Henderson¹ and N.R. Thompson²

¹SUPA, Department of Physics, University of Strathclyde, Glasgow, UK

²ASTeC, STFC Daresbury Laboratory, Warrington, UK

Abstract

A review is presented of some of the methods and their origins that have recently been proposed to improve the temporal coherence of SASE output. These methods do not require any external laser seed field, or the use of the so-called self-seeding methods, where the SASE radiation is optically filtered and improved at an early stage of the interaction before re-injection and amplification to saturation. By using methods that introduce an additional relative propagation between the electron beam and the radiation field, the localised collective interaction, which leads to the formation of the ‘spiking’ associated with normal SASE output, is removed. The result is output pulses which are close to the fourier transform limit without the need for any external seeds or intermediate optics.

INTRODUCTION

This review presents the work of several different authors and closely follows the oral presentation presented at the 36th International Free Electron Laser Conference, Basel, August 25-29, 2014. An historical perspective is given of some methods proposed to improve the temporal coherence properties of SASE output. It is hoped this perspective will demonstrate how some of the quite complex, perhaps non-intuitive, departures from a simple FEL interaction evolved.

SASE

The problem with normal SASE output from a FEL is that it has relatively poor temporal coherence. At shorter wavelengths, the electron pulse length can be significantly greater length than the relative propagation, or slippage, of a light wavefront through the pulse to saturation. As the SASE interaction starts from noise, this itself would limit the temporal coherence length to the slippage length. However, a more fundamental length that limits the temporal coherence length is the cooperation length l_c [1]. This is the length that a light wavefront propagates, or slips, through the electron pulse in one gain length l_g through the undulator. As each region of length $\sim l_c$ starts from noise, this leads to a spiking behaviour in the light intensity with spikes separated by $\sim 2\pi l_c$ [2]. A similar noisy spectrum results which gives a relatively large time-bandwidth product $\Delta\nu\Delta t \gg 1$ with typical simulated output in the X-ray shown in slide 3. A closer look at the phase of the light in slide 4, again from simulations, shows that the phase of each of the radiation ‘spikes’ is uncorrelated. i.e. each spike appears to have evolved independently from the others from noise.

DIRECT SEEDING

One method to improve this noisy output is to inject a resonant coherent seed light field coincident with the electron pulse at the start of the FEL interaction. If the seed is of sufficient intensity to dominate that due to the spontaneous noise, then the interaction can progress with a well-defined phase imposed by the seed through to saturation. This was first performed at short wavelengths at ~ 53 nm [3] as shown in slide 6. Unfortunately, no such seeds yet exist in the X-ray.

INDIRECT SEEDING

An alternative to direct seeding at the desired wavelength is to first prepare the electron beam by seeding at a longer wavelength where a suitable seed with good temporal coherence properties is available. The bunched electrons will inherit the coherence properties of the seed and will also have strong coherent bunching components at higher harmonic wavelengths. The electrons can subsequently be injected into an undulator resonant at these shorter harmonic wavelengths [4,5] where lasing may continue (slide 8) in a process sometimes called ‘High Gain Harmonic Generation’. The electron bunching may be enhanced between undulators by using a dispersive chicane. In principle this process can be ‘cascaded’ to shorter wavelengths as demonstrated experimentally [6] and shown in slide 9. Unfortunately (slide 10), the phase noise amplification is multiplied by a factor of the square of the frequency increase through the cascaded system, and with current seeds available this method cannot yet be used to reach X-ray wavelengths [7].

An alternative to HGHG is the Echo Enabled Harmonic Generation, first described in [8,9] and experimentally observed in [10] (slide 13). Interesting variations of the method are also being pursued [11] (slide 14), which may offer scope for further development. The EEHG method is described schematically in slide 15 and involves a preparation of the electron beam by: energy modulation - dispersion - energy modulation - dispersion. This introduces an electron bunching at an harmonic of the energy modulation period which will then emit radiation superradiantly on entering an undulator tuned to the electron bunching period. The limit as to how high the harmonic can be pushed probably remains unresolved, although good progress is being made experimentally with the 15th harmonic emission demonstrated [12]. The work of [13] suggests that the upper harmonic limit will be due to fluctuations in the modulating laser phase and intensity.

It is interesting to note that the final electron bunching spectrum of the EEHG is a comb of modes about the final harmonic with mode separation of the initial modulation

frequency [14] and that emission from each of these modes can be obtained (slides 16-18) using a mode-locked amplifier FEL (see later slides 38-40).

SELF-SEEDING

Self-seeding is a method first proposed in [15] which allows the SASE interaction to develop from noise (slide 20). The light is then filtered pre-saturation to reduce the large noise bandwidth before re-commencing the FEL interaction to saturation. In this way the FEL ‘self-seeds’ from the clean, filtered spectrum. The method of [15], which uses an optical monochromator with grazing incidence optics, has been improved by using a much simpler filtering method [16] that utilises a coherent wake that occurs when X-rays are passed through a diamond crystal (slide 21) instead of the more complex grazing incidence optics. The use of the diamond crystal wake self-seeding has been shown to work successfully in experiments performed at the LCLS [17] (slide 22). While these results are very encouraging, the robustness of this method, e.g. to high rep-rates and re-tuning demands in a user facility such as the EU XFEL, remains to be tested.

HB-SASE, ISASE, PSASE (‘HIBP-SASE’)

The methods of improving the temporal coherence properties of SASE above all require either the use of an external coherent source to dominate the intrinsic noise of the SASE process (a coherent seed) and/or the filtering of the SASE light to remove the noise at some intermediate point between start-up and saturation. In this section, a description is given of methods that do not require either a seed or any filtering. These have been termed variously High-Brightness, Improved and Purified SASE [18–20] - see slide 23 for a conjoining of these terms. (For the authors of this paper, the process of arriving at such methods was mainly one of discovery using numerical experiments to see what could be achieved when ‘playing about’ with the FEL interaction. Some interesting, unexpected effects arose from this process and a short historical perspective is presented. Hopefully, students will be encouraged to similarly experiment and discover.)

The authors’ path towards HB-SASE [18] began by considering the effects of a series of relative phase shifts between the light and electrons as the FEL interaction progresses through the undulator [21].

Phase Shifting

A phase shift can be considered as a shifting of the electrons with respect to a resonant wavefront by a distance less than the resonant wavelength λ_r . This can be achieved by delaying the electrons in a chicane placed between undulator modules - slides 26 & 27.

If a π phase shift (electron delays of $\lambda_r/2$) occurs, electrons that were gaining energy from the field begin to lose energy to the field and visa-versa (slide 26). The effect is to reduce the electron energy spread induced by the interaction

while maintaining the electron bunching process. Note there is little net gain or loss in the field energy as the FEL interaction is being continually interrupted. This π -shifting process can be repeated along the undulator, bunching the electrons while keeping the energy spread relatively small. Slide 28 plots $|b|/\sigma_p$ as a function of the distance along the undulator, where $|b|$ is the bunching factor and $\sigma_p = \sigma_\gamma/\rho\gamma$ is the scaled energy spread. Without phase shifting it is seen the bunching-to-spread ratio saturates at $|b|/\sigma_p \approx 0.7$, whereas with the π phase shifting this is increased to $|b|/\sigma_p \approx 2.5$ demonstrating a larger bunching per unit energy spread.

If the interaction is in a planar undulator and the interaction is also considered at the 3rd harmonic say, then introduction of $2\pi/3$ or $4\pi/3$ phase shifts will disrupt the interaction at the fundamental wavelength. However, the 3rd harmonic will see no net phase shift and can continue an un-interrupted FEL interaction to saturation (slides 29 & 30). This effect of suppressing the fundamental while allowing an harmonic to lase has been termed ‘harmonic lasing’ [22, 23].

Large Integer Wavelength Shifts

The ideas of phase shifting were then extended as part of post-graduate research [24] (slide 32) to introduce much larger relative phase shifts of $n2\pi$, where the integer $n \gg 1$ - i.e. multiple resonant wavelength shifts. By adding these extra integer resonant wavelength shifts, the simplistic idea was that light temporal phase profile and so the SASE spiking would be extended temporally so increasing the temporal coherence (slide 33). As above, the shifts can be achieved using chicanes placed between undulator modules as shown in slide 34. Note that near dispersionless chicanes can be designed so that the electrons receive the same relative shift with respect to the light field irrespective of their energy [25]. The slippage in units scaled with respect to the cooperation length l_c , of a resonant wavefront through the electron pulse within an undulator module is \bar{l} and that in the chicane $\bar{\delta}$. The total slippage in one undulator-chicane module is then $\bar{s} = \bar{l} + \bar{\delta}$. The bottom of slide 34 shows schematically the light field propagation (colour-coded with respect to the undulators above) through the electrons at the end of each undulator-chicane section. The enhancement in the slippage introduced by the chicanes is measured by the enhancement factor $S_e = \bar{s}/\bar{l}$ defined in slide 35. Initial results in slide 35 plot the mean separation of the light spikes as a function of S_e . It is seen that the separation of the spikes Δs , increases from the SASE value of $2\pi l_c$ in a quasi-linear way for the case of dispersionless chicanes ($D = 0$), and it is concluded that the cooperation length of the FEL interaction, and so the temporal coherence of the light, has increased by the slippage enhancement factor S_e . This is seen more clearly in slide 36 which shows the spike separation increasing as increasing $\Delta s \approx S_e \times 2\pi l_c$. Note that for values of $S_e > 2$ (written as S^* in the slide), there is a modulation in the light intensity. This is due to the formation of light modes directly analogous to the modes formed in a ring cavity and discussed in the following section.

It should be noted that around the same time as this research was being conducted, that other researchers hypothesised a similar approach [26] (slide 37).

Mode Generation

The modulations in the light intensity observed in slide 36 can be explained by considering the repeated equal extra slippages introduced by the chicanes - slide 39. The undulator-chicane slippage length s defines a characteristic length within which the light-electron interaction must evolve. Only wavelengths which have an integer number fitting into this length will survive the interferences caused by the repeated chicane slippage. This then defines a set of modes which are calculated in slide 39. The modal spectrum is the formally identical to that of a ring cavity of length s , the total slippage in each undulator/chicane module. This length, in units of the resonant wavelength, is of the order of a few times the number of undulator periods in a module, and can be very small, so that the mode spacing $\Delta\omega_s = 2\pi c/s$, can be much larger than that normally associated with a conventional cavity laser. Similar to mode-locking in conventional cavity lasers, the modes can be locked by introducing a modulation (here to the electron beam) at the mode spacing [27, 28] and may be able to generate few-cycle pulses in the hard X-ray and beyond [29].

HB-SASE

The introduction of extra equal slippage between undulator modules was seen to increase the cooperation length (and so temporal coherence and hence spectral brightness), but also to introduce a set of modes into the light output. If the modes surrounding the fundamental wavelength can be removed or suppressed, so that only the fundamental remains, and the increase in the cooperation length remains, then the objective of increasing the temporal coherence of the SASE output will have been met. This was achieved and then improved upon in two stages.

The first stage removed the modes about the fundamental by changing the total slippage for each undulator-chicane module. This causes the mode separation $\Delta\omega_s$ to change for each undulator-chicane module (slides 42 & 43) so that only the fundamental, central mode, receives sustained amplification. In the first stage, the chicanes introduced a slippage randomised about a mean value [30]. Slide 43 shows how the SASE spike-to-spike separation varies proportionally to, and the light bandwidth is inversely proportional to the mean slippage enhancement factor S_e . This now occurs without any modes evolving.

The second stage [18], slides 44-51, developed this method by introducing a series of increasing chicane slippages. Furthermore, the length l of each undulator module is chosen so that $l < l_g$, the gain length of the FEL interaction. The increasing slippage of each successive chicane should increase the temporal coherence in a non-linear way. The choice of undulator length $l < l_g$, ensures that a wavefront of the light never propagates through the electron pulse further than one cooperation length before being slippaged

by a chicane to another part of it. With the successively increasing slippage, this ensures a wavefront never interacts within a cooperation length range of any part of the electron pulse following a chicane slip. In this way, the localised FEL interaction that causes the spiking in the SASE output should be eliminated. The FEL interaction is de-localised.

In [18], the sequence of prime numbers was used to successively increase the slippage (slide 44 & 45). This ensures that the sideband modes associated with each successive chicane never repeat and only the fundamental mode receives gain. Slide 45 shows a schematic of a wavefront as it propagates through the series of undulators ($l < l_g$) and chicanes of increasing strength.

The rate at which the temporal coherence increases is determined by the rate at which a common phase ϕ of the light field is established throughout the interaction. slide 46 demonstrates how the rate of change of the light phase effectively evolves as $|b|/a$ where b is the electron bunching and a is the scaled field magnitude (see e.g. [31]). In the pre-saturation, linear region of evolution $|b| \sim a$, so that the phase can evolve rapidly from one undulator-chicane module to the next. A common phase can therefore propagate throughout the interaction to establish good temporal coherence and hence high spectral brightness.

Slide 47 shows the results of simulations for an electron pulse of length 4000 cooperation lengths and undulator modules of one half a gain length with the prime number sequence of increasing chicane shifts. Comparison is made against an equivalent SASE interaction (i.e. without chicanes). A relatively small increase in the saturation length is observed from 12 gain lengths for SASE to 14.5 gain lengths for HB-SASE, with no effective difference between the saturation intensities $|A|^2$. The difference between the coherence lengths though is significant, with the HB-SASE coherence length (red-squares) being just over two orders of magnitude greater than that of the SASE case (black-diamonds). Notice that at saturation, the coherence length is approximately half that of the total slippage of a light wavefront through the interaction, the maximum possible coherence length due to causality. Furthermore, in slide 48 summarising this result, it is seen that the coherence length growth rate is exponential in the linear regime prior to saturation.

A comparison of the numerical simulations to linear theory shows that the spectra at excellent agreement (slide 49) for a system operating at a wavelength of 1.24 nm. The modal structures are removed by the increasing prime slippages and the spectrum narrows as the phase information propagates through the pulse as the interaction progresses. (Note the change in frequency scale between the two plots.) Slide 50 shows a comparison between a SASE and an equivalent HB-SASE 3D simulation operating in the hard X-ray. It is seen the the HB-SASE output is close to being fourier transform limited. More detailed plots of the 1.24 nm simulations are shown in slide 51 which compare the SASE and HB-SASE output, with the notable difference being the relatively slowly changing radiation phase over the pulse in the HB-SASE case resulting in the much narrower spectrum.

iSASE

Contemporaneous research to that of HB-SASE [18], called iSASE [19], developed a similar method by using a geometrically increasing series of chicane induced slippages between the co-propagating electrons and light instead of the prime number increase as discussed above (slide 52). Undulator modules were also assumed to be greater than a gain length so that localised cooperative effects occur. The improvements in coherence that was observed in simulations was attributed to a ‘mixing’ of the light amplitudes and phases rather than the de-localisation of the FEL interaction and propagation of phase information throughout the interaction as discussed above. The authors highlight the increased stability of the iSASE method over that of self-seeding (slides 20-22) and the potential problems with crystal vibration and heating in self-seeded high rep-rate facilities. The iSASE method was extended into a tapered undulator. The tapered interaction with improved temporal coherence light enables hard X-ray powers towards TW levels to be extracted.

The above theoretical research led to an experiment at LCLS [32] which tested the basic concept of introducing extra electron-light slippage to increase temporal coherence. Instead of using chicanes to introduce the extra slippage, which were not available, alternate undulator modules were detuned far from resonance so that the light and electrons effectively propagated without interaction through these modules. The extra slippage introduced in these detuned undulator modules are approximately equal. In this respect, the experiment more closely models the earlier work of [30] than that of [18, 19] where the slippage increases in successive chicanes as the interaction progresses. Slides 53 & 54 show the undulator tunings and the output X-ray spectrum which clearly shows a narrowing in the ‘iSASE’ case. (Note that the detuned undulators in slide 54 are those with a small horizontal bar through the vertical yellow bar denoting the undulator parameter strength K .)

pSASE

A similar method of improving the temporal coherence of SASE to those described above is that of ‘purified SASE’ (pSASE). Instead of using chicanes to introduce extra slippage, pSASE (slide 55) replaces a few undulator modules in the middle of the exponential gain regime by ‘slippage boosted’ modules that are resonant at a sub-harmonic of the fundamental wavelength. The fundamental is then an harmonic in these modules and the slippage is increased by the harmonic factor. When planar undulators are used, the light also continues an harmonic gain process. This harmonic gain assists in the FEL guiding to reduce diffractive losses. Simulations demonstrating pSASE bandwidth reduction are seen in slide 55.

HB-SASE Practical Issues

Some practical and limiting issues have been identified relating to the introduction of chicanes into the HB-SASE-type undulator module lattice (slide 56).

Firstly, the undulator modules should ideally be less than a gain length. As discussed above, this stops localised collective effects (spiking) and, as seen in the table enumerating the fractional increase in temporal coherence length l_{coh} of HB-SASE over SASE, is necessary to attain the large increases of $\sim 10^2$ that may be possible. Furthermore, use of near-isochronous chicanes [25] is also desirable. Simple dipole non-isochronous chicanes limit improvements to a factor $\lesssim 10$. Alternative electron delay methods, such as using simple chicanes together with some more complex types with negative R_{56} , may be an alternative but have not yet been investigated. Electron beam jitter may pose problems when used with isochronous chicanes. While the wavelength jitters, the electron delay due to the chicanes will remain constant and may cause phase mis-matching between undulator modules [33]. For example, for typical hard X-ray parameters, and for the largest chicane delay in an HB-SASE system to remain phase matched to $\lambda/4$, the relative electron beam energy jitter should be $\Delta\gamma/\gamma \lesssim 5 \times 10^{-5}$.

Further work with more detailed modelling of such effects is required. However, it is felt this is certainly justified given the potential benefits as summarised in slide 57.

CLARA

Finally, a proposed facility where many of the principles presented above may be tested was discussed. The CLARA proposal [34] (Compact Linear Accelerator for Research and Applications), is for a dedicated, flexible FEL Test Facility, operating with a maximum beam energy of ~ 250 MeV which will be able to test several of the most promising of the new FEL schemes, including those discussed here. The CLARA layout and outline of the methods that require testing is shown in slides 58 - 61. The wavelength range chosen for the CLARA FEL is 400 - 100 nm, which is appropriate for the demonstration of concepts on a relatively low energy accelerator. This wavelength range benefits from good diagnostics to allow characterisation and optimisation of the methods being tested. It is intended that CLARA will help inform the designs of a new generation of FEL facilities where the FEL interaction is pushed to its theoretical limits.

CONCLUSION

It is hoped that this review gives an insight into how research developed towards the concept of the title of this work ‘Coherent SASE Schemes’. The research route, at least for these authors, was not due to any single insight, but developed via collaboration over a decade of research that left some interesting concepts in its wake that may inform future FEL experiments and facility designs. Hopefully, some of these concepts may be able to be tested at a UK FEL test facility, CLARA. It is felt that the wait for such a facility

in the UK will have been worth it if such new concepts can realised.

ACKNOWLEDGMENTS

We gratefully acknowledge the Science and Technology Facilities Council Agreement Number 4163192 Release #3; the John von Neumann Institute for Computing (NIC) for time on JUROPA at Jülich Supercomputing Centre (JSC), under project HHH20; and ARCHIE-WeSt High Performance Computer, EPSRC grant no. EP/K000586/1.

REFERENCES

- [1] R. Bonifacio, B.W.J. McNeil, and P. Pierini, Phys. Rev. A **40**, 4467 (1989)
- [2] R. Bonifacio *et al.*, Phys. Rev. Lett. **73**, 70 (1994)
- [3] G. Lambert *et al.*, Nature Physics **4**, 296-300 (2008)
- [4] R. Bonifacio, L. De Salvo Souza, P. Pierini, and E.T. Scharlemann, NIM A **296**, 787 (1990)
- [5] L.-H. Yu *et al.*, Science **289**, 932 (2000).
- [6] E. Allaria *et al.*, Nature Photon. **7**, 913-918 (2013)
- [7] E.L. Saldin, E.A. Schneidmiller and M.V. Yurkov, Optics Commun., **202**, 169-187 (2002)
- [8] G. Stupakov, Phys. Rev. Lett. **102**, 074801 (2009)
- [9] D. Xiang and G. Stupakov, Phys. Rev. ST AB **12**, 030702 (2009)
- [10] Z.T. Zhao *et al.*, Nature Photon. **6**, 360-363 (2012)
- [11] E. Hemsing *et al.*, Phys. Rev. ST Accel. Beams **17**, 010703 (2014)
- [12] E. Hemsing *et al.*, Phys. Rev. ST Accel. Beams **17**, 070702 (2014)
- [13] Gianluca Geloni, Vitali Kocharyan and Evgeni Saldin, Analytical studies of constraints on the performance for EEHG FEL seed lasers, arXiv:1111.1615 [physics.acc-ph]
- [14] J.R. Henderson and B.W.J. McNeil, EPL, **100**, 64001 (2012)
- [15] J. Feldhaus *et al.*, Opt. Commun. **140**, 341-352 (1997)
- [16] Gianluca Geloni, Vitali Kocharyan and Evgeni Saldin, Journal of Modern Optics, **58**, 1391-1403 (2011)
- [17] J. Amann *et al.*, Nature Photon. **6**, 693 (2012)
- [18] B.W.J. McNeil, N.R. Thompson and D.J. Dunning, Phys. Rev. Lett., **110**, 134802 (2013)
- [19] J. Wu, A. Marinelli and C. Pellegrini, Proc. of 34th Int. FEL Conf., Nara Japan, TUPD07, 237-240 (2012)
- [20] Dao Xiang *et al.*, Phys. Rev. ST Accel. Beams **16**, 010703 (2013)
- [21] B.W.J. McNeil, G.R.M. Robb and M.W. Poole, Proc. of 2005 Particle Accel. Conf., Knoxville, Tennessee, 1718-120 (2005)
- [22] B.W.J. McNeil, G.R.M. Robb and M.W. Poole, and N.R. Thompson, Phys. Rev. Lett. **96**, 084801 (2006)
- [23] E.A. Schneidmiller and M.V. Yurkov, Phys. Rev. ST Accel. Beams **15**, 080702 (2012)
- [24] N.R. Thompson, 'An Investigation of the Physics of Relativistic Electron Beam Interactions with Electromagnetic Radiation', Ph.D. dissertation, Dept. of Physics, Univ. of Strathclyde, Glasgow, Scotland (2013)
- [25] J.K. Jones, J.A. Clarke and N.R. Thompson, Proc. of IPAC 2012, New Orleans, Louisiana, TUPPP069, 1759-1761 (2012)
- [26] Avi Gover and Egor Dyunin, Proc. of FEL 2006, BESSY, Berlin, Germany, MOAAU01, 1-13 (2006)
- [27] N.R. Thompson and B.W.J. McNeil, Phys. Rev. Lett. **100**, 203901 (2008)
- [28] E. Kur *et al.*, New Journal of Physics **13**, 063012 (2011)
- [29] D.J. Dunning, B.W.J. McNeil and N.R. Thompson, Phys. Rev. Lett., **110**, 104801 (2013)
- [30] N.R. Thompson, D. J. Dunning and B.W.J. McNeil, Proc. of IPAC 2010, Kyoto, Japan, TUPE050, 2257-2259 (2010)
- [31] Brian W.J. McNeil and Neil R. Thompson, Nature Photon., **4**, 814-821 (2010)
- [32] J. Wu *et al.*, Proc. of IPAC 2013, Shanghai, China, WEODB101, 2068-2070 (2013)
- [33] T. Tanaka, H. Kitamura and T. Shintake, Phys. Rev. ST Accel. Beams **5**, 040701 (2002)
- [34] J.A. Clarke *et al.*, Journal of Instrumentation, **9**, T05001 (2014)

GENERATION OF INTENSE XVUV PULSES WITH AN OPTICAL KLYSTRON ENHANCED SELF-AMPLIFIED SPONTANEOUS EMISSION FREE ELECTRON LASER

G. Penco^{#1}, E. Allaria¹, G. De Nino¹, E. Ferrari^{1,2}, L. Giannessi^{1,3}

¹Elettra-Sincrotrone Trieste S.C.p.A., Basovizza, Italy

²Università Degli Studi di Trieste, Dipartimento di Fisica (Trieste), Italy

³ENEA C.R. Frascati, Frascati (Roma), Italy

Abstract

Fermi is a seeded FEL operating in high-gain harmonic generation mode. The FEL layout is constituted by a modulator and six radiators separated by a dispersive section. The modulator and the radiators can be tuned to the same resonant frequency to set up an asymmetric optical klystron configuration where self-amplified spontaneous emission can be generated and studied. This paper presents the experiment consisting in the analysis of the enhancement of the self-amplified spontaneous emission (SASE) radiation by the dispersion in the optical klystron. The FEL pulses produced with the optical klystron configuration are several orders of magnitude more intense than in pure SASE mode with the dispersion set to zero. The experimental observations are in good agreement with simulation results and theoretical expectations. A comparison with the typical high-gain harmonic generation seeded FEL operation is also provided.

INTRODUCTION

The optical klystron (OK) concept was proposed by Vinokurov and Skrinsky in 1977 [1] to enhance the gain of a multi-pass free electron laser (FEL) driven by a storage ring. The basic scheme consists of two undulators separated by a dispersive section, which converts the beam energy modulation produced in the first undulator in density modulation, enhancing the electron bunching at the radiation wavelength and speeding up the FEL process in the second undulator. The first experimental demonstration of the optical klystron FEL was performed in 1979 at the VEPP-3 storage ring of the Budker Institute of Nuclear Physics (BINP, Novosibirsk, Russia) [2], obtaining an initial gain of 0.5% at 630 nm and improving it subsequently up to 2.5% per pass [3]. Afterwards, other FEL oscillator facilities implemented the optical klystron scheme, such as ACO SR FEL (LURE, France), which lased at 635 nm in 1983 [4] and at 463 nm in 1987 [5]. Improvements in the optical cavity mirror coatings made it possible to lase in the ultra-violet at 240 nm in 1989 (OK-4/VEPP-3 storage ring FEL [6]) and step by step down to 193 nm in 1999 (OK-4 Duke SR FEL [7]). In 2000, the ELETTRA storage ring FEL lased at 217.9 nm [8].

The gain of the optical klystron dramatically decreases with decreasing wavelength, while the optical cavity mirrors losses increase, and this has constituted a strong constrain in reaching emission at shorter wavelengths. A

distributed optical klystron (DOK) was proposed by Litvinenko [9] to increase the gain and the first successful experiment was conducted in the DOK-1 FEL, at Duke University [10], obtaining a gain of about 48% per pass.

The progress of linac technologies has allowed generating very high brightness electron beams, able to drive single-pass high-gain FELs, providing intense radiation in the XVUV [11-13] and in the X-ray regimes [14,15]. A very common high-gain FEL mode is the self-amplified spontaneous emission (SASE) FEL, that is based on driving a high brightness electron beam through a long undulator tuned at a predetermined wavelength λ_r . The initially incoherent spontaneous radiation emitted by the beam couples with the electron beam itself and is then exponentially amplified, developing energy and density modulation at the wavelength λ_r , and finally emitting intense and coherent radiation. However, to reach the FEL intensity saturation in the extreme VUV and in the X-ray, it is necessary to have a long undulator chain, typically in the order of ~ 100 m, so alternative schemes have been studied in the past years in order to speed up the amplification process. In the following section we provide a short review of the 1-D theory describing the application of the OK concept to the SASE FEL.

OPTICAL KLYSTRON SASE FEL 1-D THEORY

The possibility to apply the optical klystron concept to high-gain FEL amplifiers has been faced in several papers [16-23]. An important result of these studies is that the klystron high-gain FEL performance is strongly influenced by the electron beam relative uncorrelated energy spread (δ), that is required to be much lower than the FEL Pierce parameter ρ [24,25]. In the following we briefly recall the 1-D theory developed in [20,23] that provides an approximated expression for the gain factor G of the optical klystron relative to the “pure” SASE mode, i.e. dispersive section turned off.

We consider an undulator resonating at the frequency $\omega_r = 2\pi / \lambda_r$. The optical klystron enhancement factor to the radiation electric field E at the scaled frequency $v = \omega / \omega_r$ can be written as follows:

$$R(v) = \frac{E_v^{OK}}{E_v^{SASE}} = \frac{1 - \int d\xi \frac{dV(\xi)}{(\mu - \xi)^2} \frac{e^{-i\rho k_r R_{SG}\xi} e^{ik_r v R_{SG}/2}}{d\xi}}{1 + 2 \int d\xi \frac{V(\xi)}{(\mu - \xi)^3}} \quad (1)$$

where $\xi = \delta/\rho$, μ is the complex growth rate of the radiation field in each undulator and $V(\xi)$ is the normalized energy distribution of the electron bunch. Integrating the enhancement factor $R(\nu)$ over the SASE spectrum $S(\nu)$ one can obtain the OK power gain factor G as:

$$G = \int d\nu |R(\nu)|^2 S(\nu) \quad (2)$$

Assuming a Gaussian SASE spectrum having a rms bandwidth equal to ρ , and considering $\sigma_\xi \ll 1$, the gain factor G can be well approximated by the following equation:

$$G \approx \frac{1}{9} \left[5 + D^2 e^{-D^2 \sigma_\xi^2} + 2\sqrt{3} D e^{-\frac{D^2 \sigma_\xi^2}{2}} + \left((4 + \sqrt{3} D) e^{-\frac{D^2 \sigma_\xi^2}{2}} \cos\left(\frac{D}{2\rho}\right) - D e^{-\frac{D^2 \sigma_\xi^2}{2}} \sin\left(\frac{D}{2\rho}\right) \right) e^{-\frac{D^2 \sigma_\xi^2}{8\rho^2}} \right] \quad (3)$$

where $D = k_r R_{56} \rho$.

When the dispersive section R_{56} is low, the chicane works as a phase shifter and the effect of the OK on FEL gain is mainly interferential.

By further increasing the chicane strength, the microbunching induced by the OK dominates and the gain factor G increases progressively up to the maximum FEL intensity, that occurs when $k_r R_{56} \sigma_\delta \sim 1$.

Since $\sigma_\delta \ll \rho$, when the R_{56} is close to the optimum value, D is much larger than 1 so that eq. (3) reduces to:

$$G \approx \frac{1}{9} \left(5 + D^2 e^{-D^2 \sigma_\xi^2} + 2\sqrt{3} D e^{-\frac{D^2 \sigma_\xi^2}{2}} \right) \quad (4)$$

OK-FEL DEMONSTRATION AT FERMI

FERMI is a single-pass S-band linac-driven FEL, based on the High Gain Harmonic Generation (HGHH) principle [26] and operating in the XVUV range (100 – 4 nm) [12,13]. In this scheme an external laser modulates in energy the electron beam passing in an undulator, called modulator, and a subsequent dispersive section converts this energy modulation in density modulation. The beam is then driven in an undulator chain, called radiator, tuned at a higher harmonic of the initial seed laser frequency, emitting coherent and intense radiation.

Nevertheless, by turning off the seed laser, the FERMI layout, and in particular the FEL-1 line (see Fig.1) has been found to be very suitable to realize an optical klystron in a high-gain FEL, by simply tuning both the modulator and the radiators at the same wavelength and exploiting the dispersive section to enhance the bunching induced by the spontaneous emission produced in the modulator. The wavelength tuning for both modulator and radiators is realized by changing the undulator gap [27,28].

As mentioned in the previous section, the ratio between the relative slice energy spread of the electron beam and the ρ parameter strongly affect the OK-FEL performance. The nominal FERMI electron beam has a very small δ ,

typically in the order of 10^{-4} , while the ρ parameter is more than one order of magnitude larger than δ for the usual wavelengths of operation ($\lambda > 10$ nm).

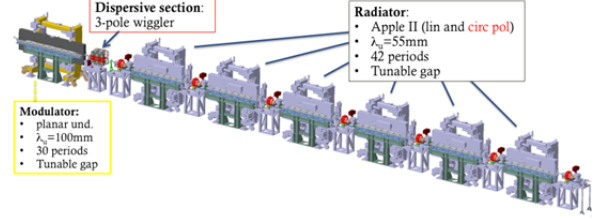


Figure 1: FERMI FEL-1 layout, including the modulator, the dispersive section and the six radiators.

In our experiment, we used a 1.058 GeV-500A electron beam, with a slice energy spread of about 90 keV (rms) and a normalized emittance of about 1.2 mm mrad. Both modulator and radiators have been tuned at 43 nm (the latter in circular polarization) and without activating the dispersive section, i.e. $R_{56} = 0$ μ m, the FEL energy per pulse was measured to be only few micro-Joules (“pure” SASE mode). Then, the dispersive section R_{56} has been progressively increased, while detecting the output FEL intensity. The experimental results are reported in Fig. 2: the radiation intensity has been enhanced by more than an order of magnitude with respect to the “pure” SASE. A more detailed post-processing analysis will be provided in a paper ready to be published [29].

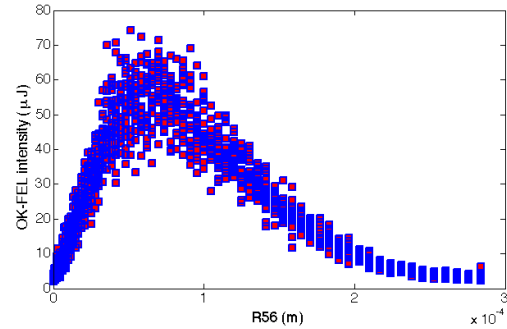


Figure 2: OK-FEL intensity versus the chicane R_{56} .

BEAM SLICE ENERGY SPREAD CONTROL

Since the beam slice energy spread is so important for the efficiency of the OK-FEL, we have modified it by acting on the laser heater system [30-31]. The latter is installed at the end of the linac injector [32], at about 100 MeV, and it is routinely exploited to slightly increase the very small natural intrinsic energy spread at the gun (typically in the order of 3-5 keV [33]) in order to suppress the microbunching instabilities driven by collective effects, such as coherent synchrotron radiation in the magnetic bunch compressor [34] and space charge effects along the linac [35]. The theoretical induced uncorrelated energy spread as a function of the laser heater intensity for the nominal 500 pC FERMI electron bunch has been calculated and is plotted in Figure 3.

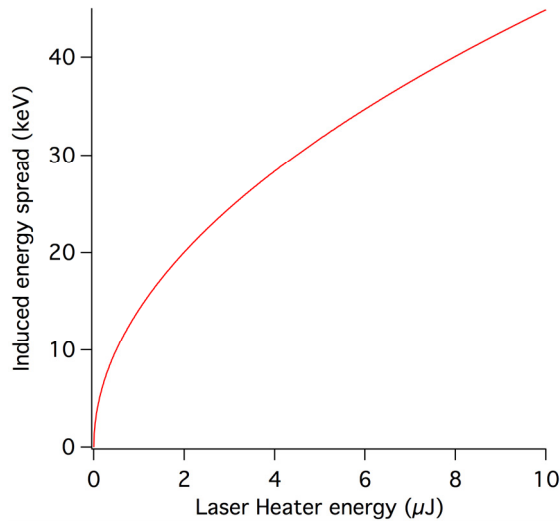


Figure 3: Induced slice energy spread versus laser heater intensity calculated for a 97 MeV electron bunch, with a transverse spot size of 0.1 mm, assuming a 0.2 mm laser heater transverse spot size in the overlapping region.

Figure 4 shows the typical measured slice energy spread at the end of the linac [36] as a function of the laser heater intensity, after the electron beam is compressed by almost a factor 10 to obtain a peak current of 500A. One can observe that increasing the laser heater intensity from 0 to about 1 μJ leads to a decrease of the slice energy spread at the end of the linac thanks to the efficient microbunching suppression, down to a minimum value of about 85 keV. However for larger laser heater intensities, the larger induced energy spread at the injector is translated in an increment of the slice energy spread at the end of the linac.

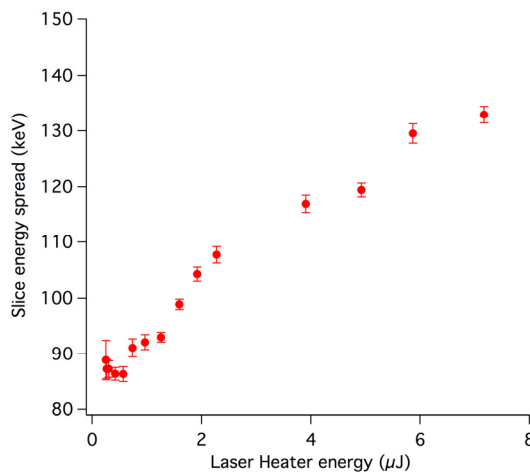


Figure 4: Uncorrelated energy spread versus laser heater intensity measured at the end of the linac by using a transverse deflecting cavity coupled with an electron energy spectrometer.

We have repeated the measurements of the OK-FEL intensity as a function of the dispersive section R_{56} for different value of the laser heater energy, i.e. for different

values of the induced slice energy spread. For higher laser heater energy, the larger induced energy spread depletes the optical klystron FEL gain and as expected its maximum value is obtained for smaller values of R_{56} . In particular increasing the uncorrelated energy spread from about 90 keV to 120 keV reduced the maximum OK-FEL intensity by about a factor 2 [29].

We have then fitted the aforementioned experimental behaviour of the OK-FEL versus R_{56} with the theoretical factor gain curve of eq. (4). A good agreement has been observed for value of the R_{56} smaller or close to the optimum value, while for larger R_{56} the measured OK-FEL intensity is larger than expected by the 1-D theory. The latter in fact makes the strong assumption that electrons have a constant Gaussian slice energy distribution along the bunch while the real bunch presents a non-uniform longitudinal phase space [36]. Even when the laser heater is tuned to optimize the OK-FEL performance, residual microbunching structures are anyway present and can give some contributions to the enhancement of the optical klystron also for large value of R_{56} . A more detailed analysis of the experimental results is going to be provided in a subsequent paper [29].

We have exploited the optical klystron setup to enhance the SASE also at 32.4 nm and at 20 nm, obtaining a gain factor of about 20 and 10 respectively (with proper tuning of the dispersive section).

We have measured the gain curve of the OK-FEL operating at 32.4 nm by progressively opening the radiators gap for three different value of the dispersive section R_{56} . The OK-FEL gain length measured in each case is listed in Table 1.

Table 1: OK-FEL Gain Length at 32.4 nm as Measured for Three Values of the Chicane R_{56}

Chicane R_{56} (μm)	Gain Length (m)
16	1.16 ± 0.03
26	1.19 ± 0.03
63	1.23 ± 0.02

OK-FEL GAIN LENGTH

We have simulated the experiment conducted on FEL-1 at 32.4 nm with GENESIS 1.3 [37] comparing the optical klystron case with the “pure” SASE; the results are plotted in Figure 5.

The optical klystron does not change the FEL gain length that is very similar to the “pure” SASE mode, but it speeds up the process: the bunching induced after the dispersive section enhances the radiation after the first radiator ($z=2.3\text{m}$) by almost two orders of magnitude. The total saturation length could be therefore reduced by about 20%.

As expected the OK-FEL gain length, see Table 1, is independent from the chicane R_{56} and the results are in very good agreement with the GENESIS simulations.

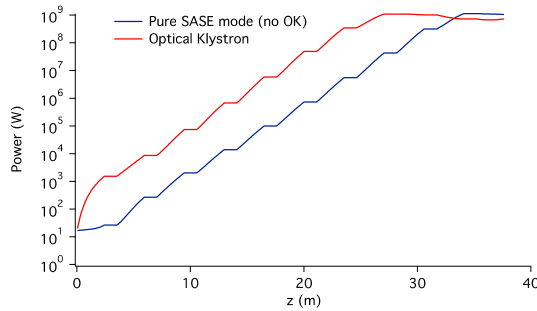


Figure 5: GENESIS simulations results of the FEL power gain curve at 32.4 nm for the OK-FEL and the “pure” SASE mode. The starting point ($z=0$) corresponds to the exit of the dispersive section.

CONCLUSION

The optical klystron enhancement to SASE FEL has been experimentally demonstrated at FERMI down to 20 nm on FEL-1 and at 12 nm on FEL-2. Our experiments have confirmed that the Optical Klystron FEL performance is strongly influenced by the electron beam relative uncorrelated energy spread, that must be much smaller than the FEL ρ parameter.

1-D theory present in literature can reproduce the experimental results when microbunching structures in the longitudinal phase space are fully suppressed and the intrinsic energy spread is similar to the “FEL-slice” energy spread. Otherwise, it would be better to include the non-uniformity of the longitudinal phase space and distinguish between the intrinsic uncorrelated energy spread on the radiation wavelength λ_r scale and the energy spread on the FEL cooperation length scale.

Measurements of the OK-FEL gain curve have confirmed that the gain length is independent on the dispersive section as expected by simulations.

FERMI has been demonstrated to be able to operate also in SASE mode by taking advantage of the optical klystron setup: with this scheme it is capable to provide several tens of μJ in XVUV wavelength range.

ACKNOWLEDGMENT

This work was funded by the FERMI project of Elettra-Sincrotrone Trieste, partially supported by the Ministry of University and Research under grant numbers FIRB-RBAP045JF2 and FIRB-RBAP06AWK3.

The authors thank the whole FERMI Commissioning Team for operating the machine and the PADReS team for the help in delivering the radiation to the end-station.

REFERENCES

- [1] N.A. Vinokurov and A. N. Skrinsky, Budker Institute for Nuclear Physics Report No. BINP 77-59, Novosibirsk, 1977.
- [2] A.S. Artamonov et al., Nucl. Instrum. and Methods **177**, 247-252 (1980).
- [3] G.A. Korniyukhin et al., Nucl. Instrum. and Methods A **237**, 281 (1985).

- [4] M. Billardon et al., Phys. Rev. Lett. **51**, 1652 (1983).
- [5] M. Billardon et al., Europhys. Lett. **3**, 689 (1987).
- [6] I.B. Drobyazko et al., Nucl Instrum and Meth. A **282**, 424 (1989).
- [7] V.N. Litvinenko et al., Nucl Instrum and Meth. A **475**, 195-204 (2001).
- [8] R. Walker et al., Nucl Instrum and Meth. A **475**, 20-27 (2001).
- [9] V.N. Litvinenko et al., Nucl Instrum and Meth. A **304**, 463 (1991).
- [10] Y.K. Wu et al., Phys. Rev. Letters **96**, 224801 (2006).
- [11] W. Ackermann et al. Nature Photonics **1**, 336 (2007).
- [12] E. Allaria et al., Nature Photonics **6**, 699 (2012).
- [13] E. Allaria et al., Nature Photonics **7**, 913 (2013).
- [14] P. Emma et al., Nature Photonics **4**, 641 (2010).
- [15] T. Ishikawa et al., Nature Photonics **6**, 540 (2012).
- [16] R. Bonifacio et al. Phys. Rev. A **45**, 4091 (1992).
- [17] P. Dattoli et al., Nucl. Instrum. and Meth. A **333**, 589 (1993).
- [18] N.A. Vinokurov et al. Nucl. Instrum and Meth. A **375**, 264 (1996).
- [19] S.J. Hahn and K.H. Pae, Journal of the Korean Phys. Soc. **31**, 856 (1997).
- [20] K.J. Kim, Nucl. Instrum. and Meth. A **407**, 126 (1998).
- [21] G.R. Neil and H.P. Freund, Nucl Instrum. and Meth. A **475**, 381 (2001).
- [22] E.L. Saldin, E.A. Schneidmiller and M.V. Yurkov, arXiv:physics/0308060v1 [physics.acc-ph] 14 Aug 2003. DESY 03-108 DESY 03-108 (2003).
- [23] Y. Ding et al., Phys. Rev. ST Accel. and Beams **9**, 070702 (2006).
- [24] W. Colson. “The nonlinear wave equation for higher harmonics in free- electron lasers”. In: IEEE J. Quantum Electron. **17.8** (1981), pp. 1417–1427.
- [25] R. Bonifacio F. Casagrande G. Cerchioni L. De Salvo Souza P. Pierini N. Piovella. “Physics of the high-gain FEL and superradiance”. In: Riv. Nuovo Cimento **13.9** (1990).
- [26] L.H. Yu et al., Phys. Rev. Lett. **91**, 074801 (2003).
- [27] S. Sasaki K. Miyata T. Takada. “A new undulator for generating variably polarized radiation”. In: Jpn. J. Appl. Phys. **31** (1992), pp. L1794–L1796.
- [28] E. Allaria et al., New J. Phys. **14**, 113009 (2012).
- [29] In preparation.
- [30] Z. Huang et al., Phys. Rev. Special Topics Accel. Beams **7**, 074401 (2004).
- [31] S. Spampinati et al., in Proc. of the 2013 Free-Electron Laser Conf., NY, USA, p. 177-180.
- [32] G. Penco et al., Journal of Instrumentation **8**, P05015 (2013).
- [33] M. Hüning and H. Schlarb, in Proc. of the 2003 Particle Accelerator Conf., Portland, OR, 2003 (IEEE, Piscataway, NJ, 2003), p. 2074.
- [34] S. Heifets, G. Stupakov and S. Krinsky, Phys Rev. Special Topics Accel. Beams **5**, 064401 (2002).
- [35] E. L. Saldin, E. A. Schneidmiller, and M. V. Yurkov, Nucl. Instrum. Methods Phys. Res., Sect. A **528**, 355 (2004).

- [36] G. Penco et al., in Proc. of the 2012 Free-Electron Laser Conf., Nara, Japan, p. 417-420.
- [37] S. Reiche, Nucl. Instrum. Methods Phys Res., Sect A **429**, 243 (1999).

FEL OVERCOMPRESSION IN THE LCLS*

J.L. Turner, F.-J. Decker, Y. Ding, Z. Huang, R. Iverson, J. Krzywinski, H. Loos, A. Marinelli, T. Maxwell, H.-D. Nuhn, D. Ratner, T. Smith, J. Welch, F. Zhou,
SLAC NAL, Menlo Park, CA 94025, U.S.A.

Abstract

Overcompression of the Linac Coherent Light Source (LCLS) x-ray Free Electron Laser (FEL) at the SLAC National Accelerator Laboratory is studied. The studies and some operational implications are summarized here.

INTRODUCTION

The needs of XFEL users lead to exploring the LCLS parameter space. Some experiments benefit from a broad spectrum x-ray beam. Inducing projected energy spread across the electron bunch leads to a transformation into broader photon spectrum. Overcompression, is where in the second bunch compressor the head of the bunch slips back behind the tail, adding to the wake induced energy spread in subsequent L3 linac. This induces a relatively large energy deviation along the bunch typically leading to broader spectrum at the cost of reduced x-ray intensity. A method is being developed where performance can be improved by lasing using only the core of the electron beam.

DIAGNOSTICS

Two very useful pulse-to-pulse diagnostics are relied upon in these studies: a hard x-ray single-shot spectrometer (HXSSS) [1] (Figure 1), and an x-band transverse deflecting RF cavity (XTCAV) [2].

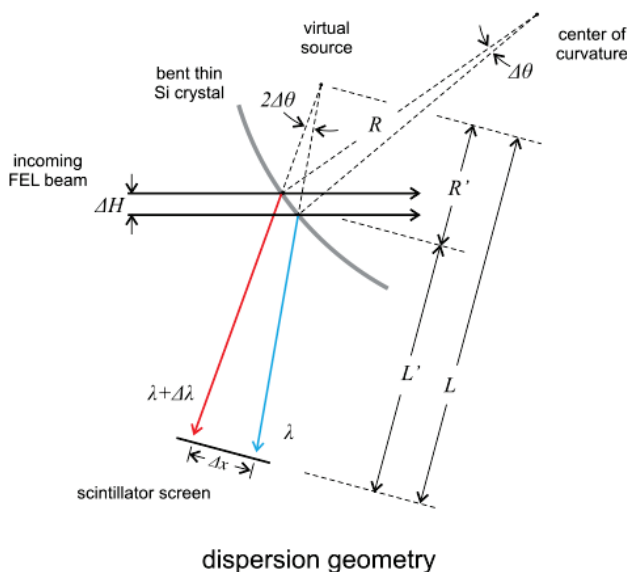


Figure 1: X-ray beam comes in from the left, a small percentage is dispersed by different energies having different Bragg angles from the bent Si crystal. Figure from Ref. [1].

* This work was supported by U.S. Department of Energy, Office of Basic Energy Sciences, under Contract DE-AC02-76SF00515

The cylindrically bent Si(1 1 1) transmissive crystal membrane spectrometer [1] samples different energies across the beam vertical profile, you get amplitude response which is a function of the Gaussian beam profile. To the extent that the beam is larger than the area sampled this makes the response more uniform. In any case, this can be accounted for by nearby beam profile measurement. What you see is the SASE lines in a spectrograph. (Figure 2). The full bandwidth for the data taken was about 120 eV with resolution down to about 1 eV.

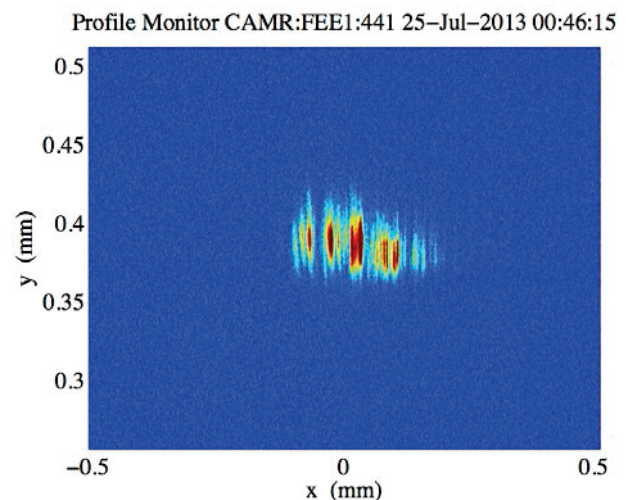


Figure 2: The SASE spikes can be seen dispersed in energy by the spectrometer crystal which in this case is Si(1 1 1). The imaged is rotated, so energy is on the X axis.

The XTCAV

After the electrons exit the undulator, the XTCAV streaks the beam in the horizontal plane, then beam become dispersed in the final bend magnets (Figure 3). The result is an image on a YAG screen which has time for a horizontal axis and energy on the vertical. By taking a non-lasing pulse for reference, images of the electrons during lasing can be used for temporal reconstruction of the x-ray pulse (Figure 3).

REFERENCE DATA

Typical LCLS machine running is undercompressed (see Figure 4) where the LCLS compression scheme leads to the development of high peak current at the head and tail of the beam that are apparent with the temporal reconstruction of the x-rays.

Empirical tuning of the FEL intensity can lead to beta-match and undulator taper match to either the ends or the

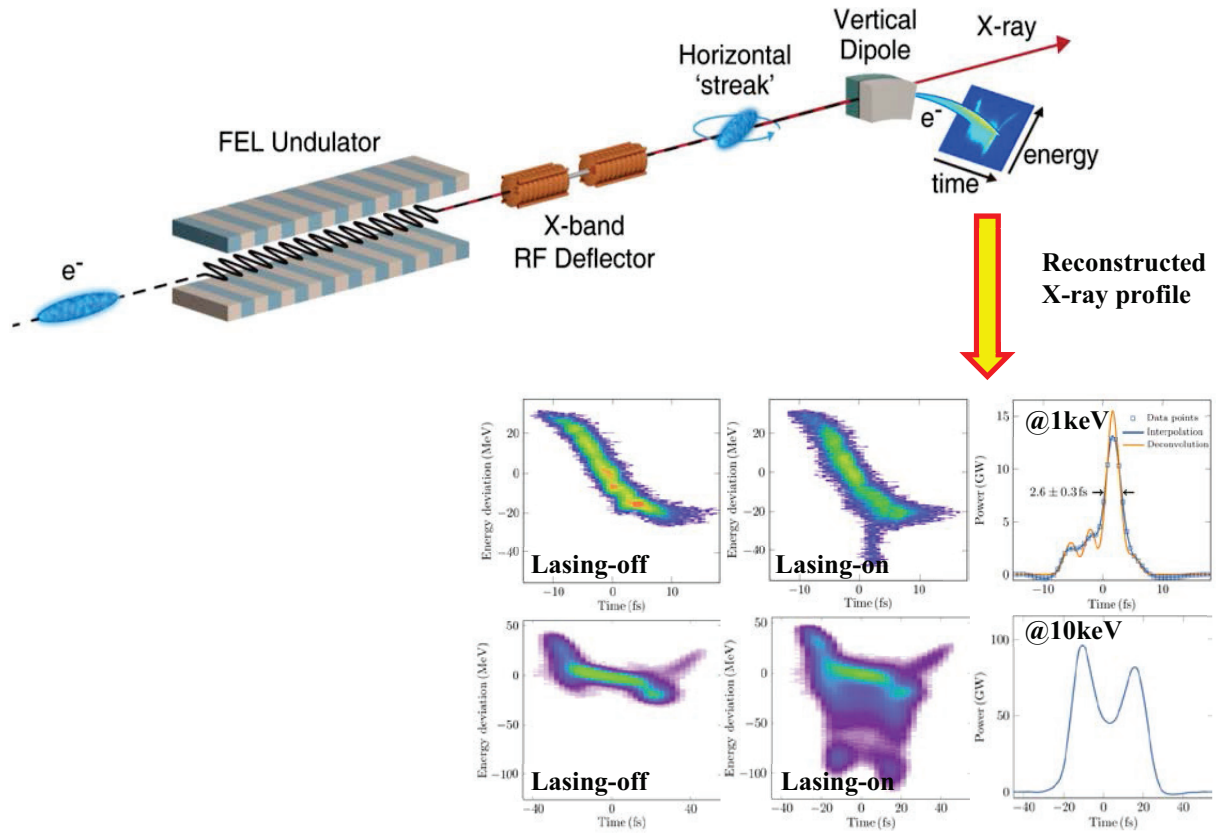


Figure 3: The XTCAV setup. Electrons pass through the undulator, then land on the zero-crossing of the x-band RF creating a horizontal streak. They are then bent and dispersed in the vertical plane. In plots below, reference “lasing off” on the left where 1 keV case is on top and 10 keV case is on bottom. Middle plots are lasing on and right is x-ray temporal reconstruction. Figure from Ref. [2].

center of the beam, or some combination. This can be seen clearly on the XTCAV diagnostic as lasing in the center or the beginning and/or end (see Figure 3, 1 keV “Lasing-on” where lasing is at the end of the pulse).

In Figure 4, see typical good case where the ends and center are lasing, with ends somewhat more than center.

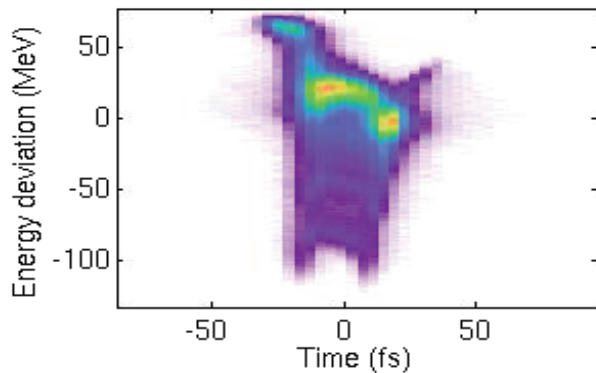


Figure 4: XTCAV data, 8.3 keV, 180 pC, undercompressed (nominal)

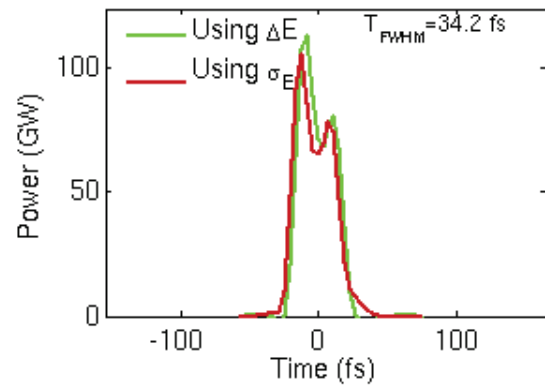


Figure 5: XTCAV data, same conditions as Figure 4.

Figure 5 shows the results of two methods of calculating the x-ray power profile, one using the centroid energy loss of each slice [3] (Equation 1), and a second using the change in the energy spread of each slice (Equation 2).

$$P_{\text{FEL}}(t) = [\langle E \rangle_{\text{FEL off}}(t) - \langle E \rangle_{\text{FEL on}}(t)] \times I(t) \quad (1)$$

$$P_{\text{FEL}}(t) \propto [\sigma^2_{E, \text{FEL on}}(t) - \sigma^2_{E, \text{FEL off}}(t)] \times I^{2/3}(t) \quad (2)$$

The spectrum for this nominal 8.3 keV x-ray beam (Figure 6) is fitted with a Gaussian and has a FWHM of 20 eV.

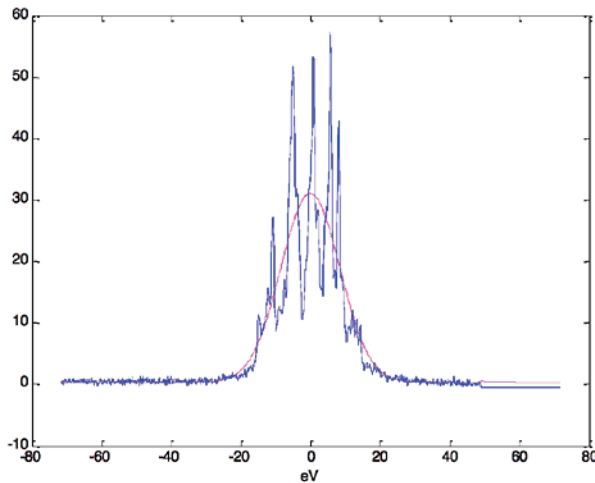


Figure 6: Nominal 8.3 keV undercompressed spectrum, fitted with a Gaussian. FWHM is 20.0 eV for this shot.

OVERCOMPRESSION 250 PC

Inducing projected energy spread across the electron bunch leads to a transformation into broader photon spectrum. Overcompression, as employed here, where in the second bunch compressor the head and tail switch places, induces a relatively large energy deviation along the bunch. The injector current is raised at this point in the experiment to 250 pC away from the nominal 180 pC. This also contributes to the spectral broadening.

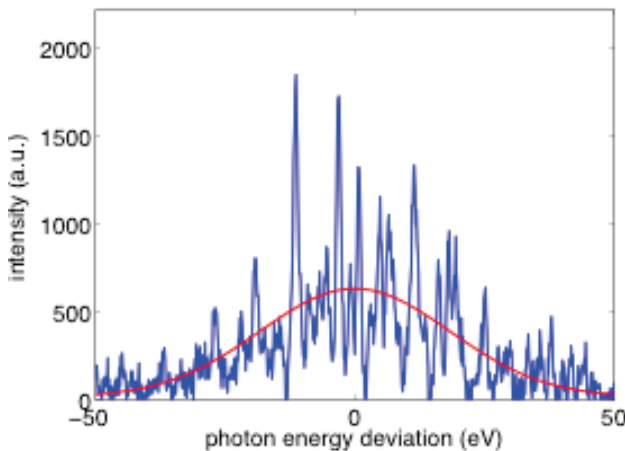


Figure 7: , Fitted FWHM = 44 eV from the spectrometer. 250 pC throughout the LCLS at 8.3 keV nominal energy,

Figure 7 shows the x-ray spectrum is double the nominal with overcompression at 250 pC. This is a single shot, but the average fitted value for about 4000 shots is 43 eV FWHM (not shown).

Lasing top of Figure 8 is clearly in the middle of the beam pulse. Power is ~170 GW.

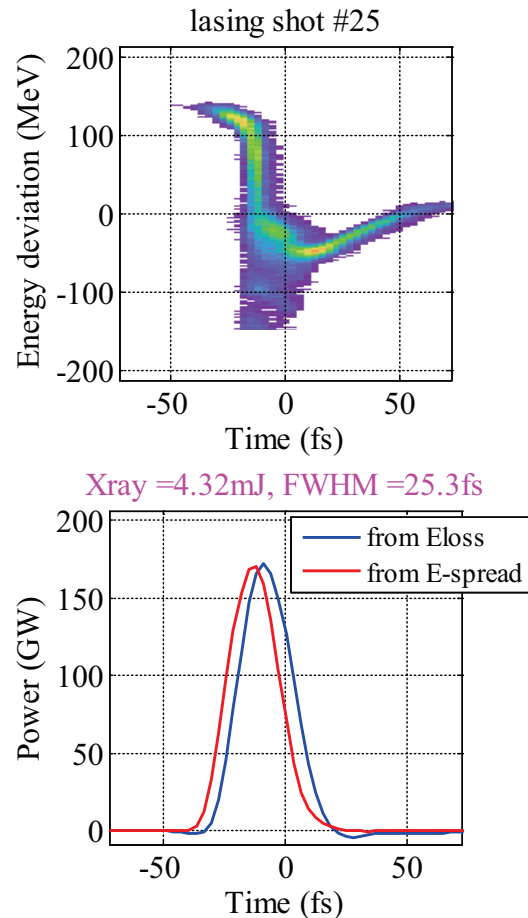


Figure 8: Top is from XTCV where lasing is clearly only in the middle of the bunch. 4.32 mJ in 25.3 fs is ~170 GW.

CUTTING 250 TO 170 PC

Simulation Cutting to 150 pC Undercompressed

Simulation in 2011 by Yuantao Ding shows that cutting the head and tail (“horns”) of the temporal distribution will allow stronger compression in the second bunch compressor (BC2) due to less CSR effects hence a higher peak current in the core is achievable (see Figure 9). The cut is by collimation in the first bunch compressor (BC1).

In this simulation, 5kA is anticipated in the cut core at 13.6 GeV, 8.3 keV.

Experiment Cutting from 250 to 170 pC in BC1

Figure 10 shows the profile monitor at high dispersion in the middle of BC1 and the actual cut to match the simulation.

Experiment Undercompressed Cut Beam

The XTCV data shows the peak power attained in simulation could be realized in experiment. Figure 11 left bottom shows 5 kA could indeed be realized. See the upper left “baseline” shot where lasing is suppressed and the linearity of the core, then the upper right where the energy drop of the electrons show lasing across the core. 4mJ in 21fs, is 200GW. The measured spectrum is also

reduced to about 12 eV FWHM for this horn-cut beam at undercompression. This is to compare the regular undercompressed beam shown in Figure 6.

Experiment Overcompressed Cut Beam

We can also operate the cut beam in an overcompression mode. In this way, a very high peak current over 7 kA has been measured, which helps further improve the FEL peak power. Figure 12 on the right is the spectrum at 40.3 eV FWHM. Figure 12 left 4 blocks are XTCAV data showing 5.36 mJ in 13.8 fs for a peak 350 GW were obtained in experiment. Lasing of the core after linearizing longitudinal phase space by cutting off the head and tail is key here since both the undulator taper match and betatron match can be more uniform across the beam

CONCLUSION

Excellent pulse to pulse diagnostics such as the HXSSS and XTCAV with guidance by simulation can change your direction of study and broaden FEL capabilities. We achieve a factor of 2 increase in bandwidth as simulated.

Overcompression after cutting “horns” off of the core has great potential, and further studies are planned. Because of the large projected energy spread, dispersion after BC2 (Second Bunch Compressor), any downstream chromaticity, and divergence correction at the last bend in BC2 are issues to pursue.

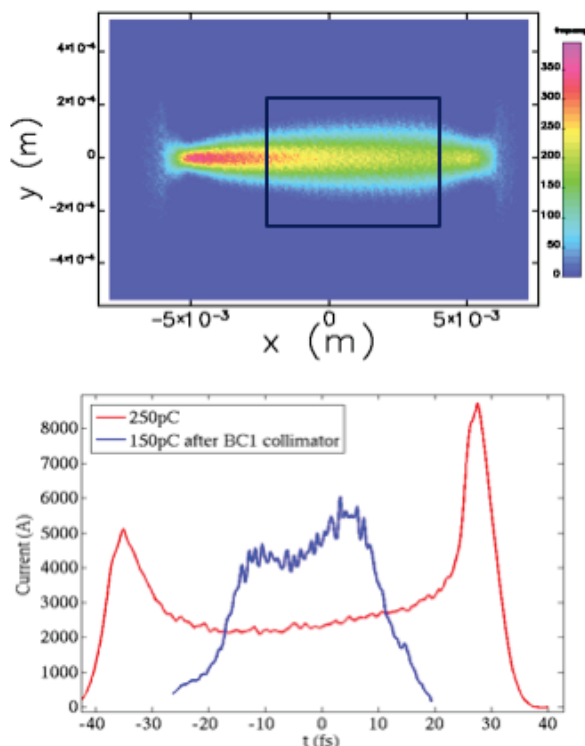


Figure 9: Simulation at BC1 of the cut to achieve the simulated 5 kA (top). This is an asymmetric cut of 6.4 mm offset by +1mm. Result of Elegant runs (bottom) before and after optimizing L2 chirp in each case.

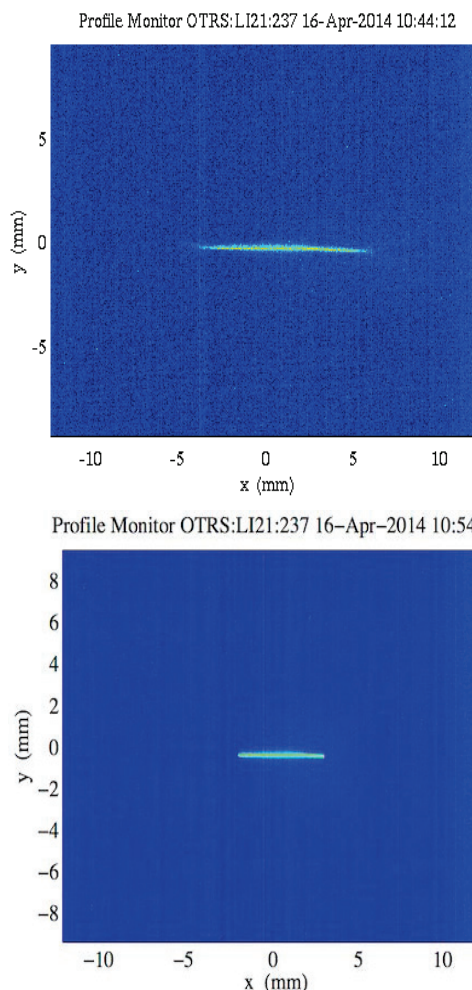


Figure 10: Experimental cut applied in BC1. The profile monitor is in the middle of the chicane just beyond the collimators employed. Top is before, bottom after

REFERENCES

- [1] D. Zhu, M. Cammarata, J. M. Feldkamp, D. M. Fritz, J. B. Hastings, S. Lee, H. T. Lemke, A. Robert, J. L. Turner, and Y. Feng, Applied Physics Letters 101, 034103 (2012), URL <http://scitation.aip.org/content/aip/journal/apl/101/3/10.1063/1.4736725>.
- [2] “Few-femtosecond time-resolved measurements of X-ray free-electron lasers”, C. Behrens, F.-J. Decker, Y. Ding, V. A. Dolgashev, J. Frisch, Z. Huang, P. Krejcik, H. Loos, A. Lutman, T. J. Maxwell, J. Turner, J. Wang, M.-H. Wang, J. Welch & J. Wu, Nature Communications 5, Article number: 3762 doi:10.1038/ncomms4762 30 April 2014 <http://www.nature.com/ncomms/2014/140430/ncomms4762/abs/ncomms4762.html>
- [3] “Femtosecond-scale X-ray FEL Diagnostics with the LCLS X-band Deflector” T. J. Maxwell, C. Behrens, Y. Ding, Z. Huang, P. Krejcik, A. Marinelli, L. Piccoli and D. Ratner, SPIE Optics & Photonics 2014, Diagnostics and Instrumentation II, Paper 9210-19

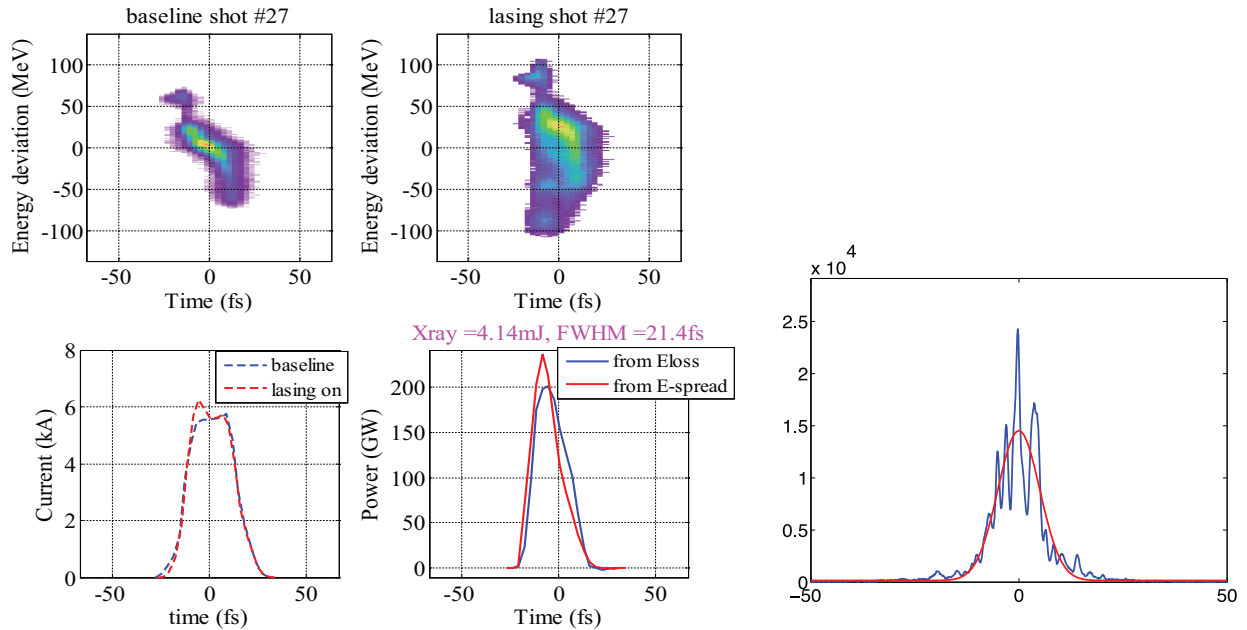


Figure 11: The actual result from XTCav data, Top left is non-lasing reference, center top is lasing, bottom left is peak current profile and bottom center is peak power. 4mJ in 21fs, 200GW. Spectrum is shown on the right and fitted to be 11.9 eV FWHM.

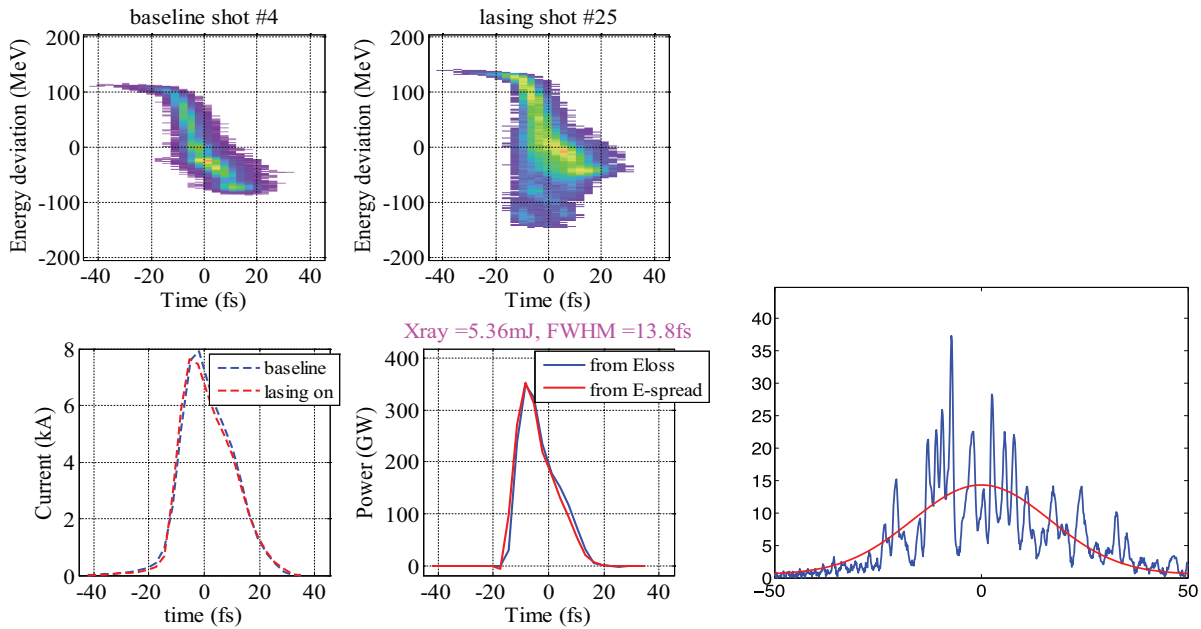


Figure 12: Cut horns (250 pC to 170 pC), overcompressed, 8.3 keV with 5.36 mJ in 13.8 fs is about 350 GW. On the right is the spectrum fitted at 40.3 eV.

OPERATION OF FLASH WITH SHORT SASE-FEL RADIATION PULSES*

J. Rönsch-Schulenburg[#], E. Hass, N.M. Lockmann, T. Plath, M. Rehders, J. Roßbach,
Hamburg University & CFEL, Hamburg, Germany

G. Brenner, S. Dziarzhytski, T. Golz, H. Schlarb, B. Schmidt, E. Schneidmiller, S. Schreiber, B. Steffen, N. Stojanovic, S. Wunderlich, M. Yurkov, DESY, Hamburg, Germany

Abstract

This paper describes the experimental activity on the generation of very short FEL pulses in the soft x-ray range in the SASE-mode at the high-gain free-electron laser FLASH [1, 2]. The key element, a photo-injector laser which is able to generate laser pulses of about 2 ps FWHM has been optimized and commissioned. It allows the generation of shorter bunches with low bunch charge (of up to 200 pC) directly at the photo-cathode. Initially shorter injector laser pulses and thus shorter bunches eases the required bunch compression factor for short pulses below 10 fs duration which makes operation of the electron beam formation system to be more robust with respect to jitters and collective effects. As a result, overall stability of SASE FEL performance is improved. In the optimal case single-spike operation can be achieved. In this paper the experimental results on production of short electron bunches and the SASE performance using the new injector laser will be shown and the measured electron bunch and FEL radiation properties are discussed. In addition, optimizations of bunch diagnostics for low charge and short bunches are discussed.

MOTIVATION

Several user-oriented free-electron laser (FEL) facilities aim for very short vacuum ultraviolet (VUV), extreme ultraviolet (XUV) and X-ray pulses which allow to study ultra-fast processes in different areas of science. In order to achieve such short bunches several schemes have been proposed. The most robust method to generate pulses of a few femtoseconds at FELs is to create a short electron bunch. In the most extreme case the lasing part of the bunch is as short as one longitudinal optical mode and thus the electron bunch length (σ_b) has to fulfill the condition $\sigma_b \leq 2\pi L_{\text{coop}}$ [3, 4], with L_{coop} the cooperation length. These so-called single-spike SASE pulses [3, 4] are bandwidth limited, longitudinally coherent and compared to seeding concepts no long background disturbs the signal. At FLASH [1, 2] single-spike operation requires bunches whose lasing part have a duration of a few fs. To mitigate space charge forces, this can only be achieved by applying low bunch charges of about 20 pC.

SHORT PULSE PHOTO INJECTOR LASER

As discussed already in detail in [5] such a short bunch would require a very strong compression (about 2000) in the two bunch compressors at FLASH when applying the standard photo injector laser with an rms laser pulse duration of 6.5 ps, which is optimized for 1 nC. Such a strong compression would lead to strong instabilities in the accelerator caused by small phase fluctuations. Therefore a new photo injector laser with a reduced pulse duration was commissioned [6, 7, 8]. It is optimized for variable pulse length from 0.7 to 1.7. The laser system consists of an oscillator and a Yb:YAG amplifier [9]. In the infrared an average output power of up to 7 W has been achieved, which corresponds to a single pulse energy of about 7 μJ .

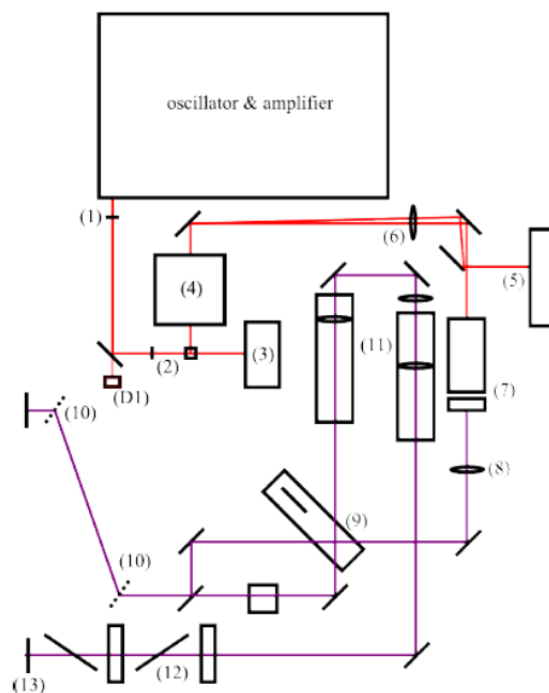


Figure 1: Scheme of the photo injector Laser beamline [8] with the following components: half-wave plate (1); photo diode (D1); beam splitter (2); power meter (3); acousto-optical modulator (AOM) (4); Beam-Dump (5); IR-lens, $f = 300$ mm (6); LBO-crystal and BBO-crystal (7); collimating UV-lens (8); remote controllible mirror for incoupling into the stretcher (9); pulse-stretcher (10); telescope (11); attenuator (12); aperture (13).

*The project has been supported by the Federal Ministry of Education and Research of Germany (BMBF) under contract No. 05K10GU2 and FSP301.

[#]juliane.roensch@desy.de

Figure 1 shows a schematic layout of the optical beamline of the photo injector laser. An AOM (marked with (4) in Fig. 1) allows for arbitrary pulse picking to choose the pulse train length as it is typical at FLASH. The frequency is converted into its fourth harmonic by two non-linear crystals (marked with (7) in Fig. 1). In order to adapt the bunch length at the cathode to the charge, one can stretch the laser pulse with an optical stretcher consisting of two transmissive gratings with 4000 lines per cm. With the current setup, we are able to vary the distance of the gratings between about 50 to 450 mm and thus choose an arbitrary pulse duration between 0.7 to 1.7 ps rms [8].

In order to monitor the laser parameters and correlate those with the corresponding properties of the electron bunch, additionally new diagnostics have been installed. These include a set of quadrant diodes to monitor the transverse laser stability of single pulses in a train, a UV camera to optimize the laser position of all three injector lasers available at FLASH and a UV spectrometer [6, 7].

SHORT PULSE OPERATION

First SASE performance using the new photo injector laser could be demonstrated in January 2013 at a wavelength of 13 nm and a bunch charge of 35 and 80 pC [5].

Another measurement performed in May 2014 will be presented in this section. SASE was optimized for a bunch charge of 110 pC and afterwards it was stepwise reduced down to 55 pC. The laser pulse duration was chosen with 1 ps rms, which means the pulse during the measurements presented in this section is about six times shorter than in standard operation. The transverse distribution of the laser at the photo cathode was a truncated Gaussian [6, 7, 10] with a diameter of 1 mm. These parameters are chosen in such a way that at a bunch charge of about 50 pC the charge density at the photo cathode is comparable to the density at FLASH standard operation.

The spectral FEL pulse distribution has been measured by high resolution monochromator [11, 12]. Figure 2 shows six randomly chosen examples of single shot FEL-spectra measured at a bunch charge of 80 pC. The spectra typically show a few spikes. An analysis of 1768 events has counted in average 3.8 spikes and 2.7 within the FWHM.

An additional measurement of the FEL pulse length with the optical afterburner [13, 11] has been performed under the same conditions. An analysis of the data led to the conclusion, that the upper limit for the pulse duration is 30 fs. An exact value could not be determined due to low statistics during the measurement. In order to shorten the bunch even more, the bunch charge was reduced further down to 55 pC; the machine parameters were readjusted and the spectrum was measured again. Figure 3 shows six randomly chosen examples of single shot spectra measured at a bunch charge of 55 pC.

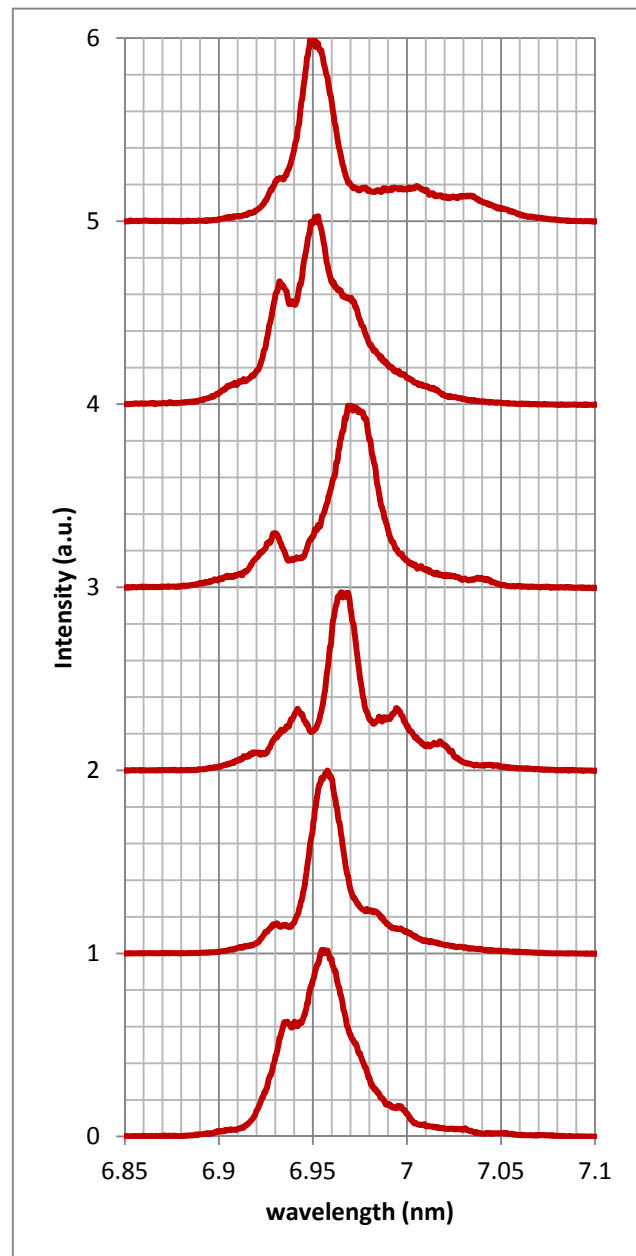


Figure 2: Six typical examples of FEL-spectra measured at FLASH, when the short-pulse laser was applied at a bunch charge of 80 pC.

The analyzed spectra at 55 pC show less spikes, than in the 80 pC case, typically only one or two of the spikes is strongly emphasized. Here an average of 1.5 spikes within the FWHM has been determined. The reduction of the number of spikes with the bunch charge in the FEL spectra may presume also a reduction of the FEL pulse duration. Assuming a bandwidth of 0.4% and a Gaussian electron bunch distribution would lead to an rms FEL-pulse duration of 2.4 ± 0.2 fs. But a lower bandwidth and thus a longer pulse length might be possible.

According to beam dynamics studies a further reduction of the bunch charge should allow the generation of a pure single spike. The experiment will be carried on soon.

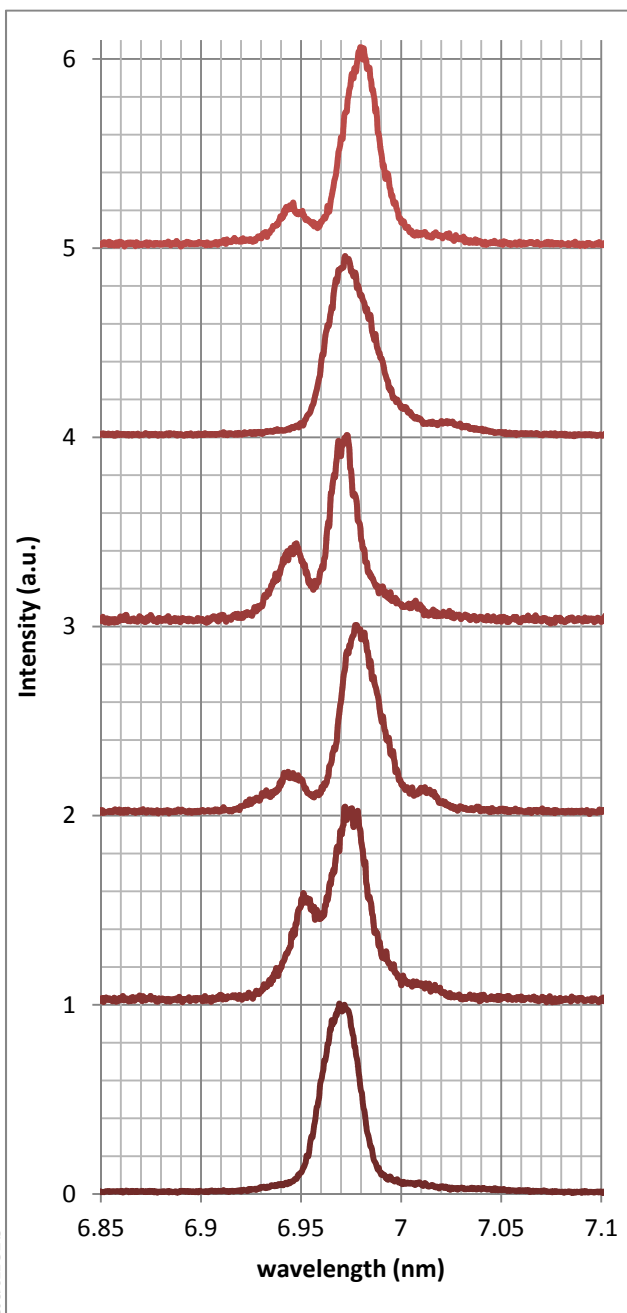


Figure 3: Six typical examples of single shot FEL-spectra measured at FLASH, when the short-pulse laser was applied at a bunch charge of 55 pC.

Start-to-End Simulations

A start-to-end simulation for single spike FEL radiation based on real machine settings for standard short pulse operation at FLASH is presented in [14]. The results of the measurement presented above are currently used as a basis for a start-to-end beam dynamics simulation with the codes ASTRA, CSR-Track and Genesis 1.3. Additionally an optimization of these machine parameters is foreseen in order to achieve pure single-spike pulses in the next experimental run.

DIAGNOSTICS

In order to achieve short bunches and understand the beam dynamics of low charge bunches reasonable diagnostics elements are mandatory. Therefore different types of optics and cameras have been studied in order to optimize the readout system of the transverse deflecting cavity [15]. Additionally also the bunch arrival time monitor [16] and the THz-Spectrometer for bunch length measurement [17] have been redesigned for the operation at low charge. Also the measurements of the duration of the FEL pulses are an important challenge which has been studied in detail in [11].

CONCLUSION

The generation of short FEL pulses, close to single spike in the VUV and soft x-ray range in the SASE-mode at the high-gain free-electron laser FLASH using a short photo-injector laser pulse has been achieved. At a bunch charge of 55 pC the spectra of the SASE pulse with one to four spikes only, in average 1.5 spikes within the FWHM has been observed. Taking into account a coherence length of about 3 fs (measured at a wavelength of 8 nm) at FLASH [18, 19] an FEL pulse duration of only some fs can be assumed. With further optimization of low charge operation, single spike SASE is within reach.

ACKNOWLEDGMENT

The authors would like to thank the whole FLASH team for their support of this project.

REFERENCES

- [1] W. Ackermann et al., "Operation of a free-electron laser from the extreme ultraviolet to the water window", *Nature Photonics* 1, 336 - 342 (2007)
- [2] K. Honkavaara et al., "FLASH: First Soft X-Ray FEL Operating two undulator beamlines simultaneously", WEB05, these proceedings, FEL'14, BASEL, Switzerland (2014).
- [3] R. Bonifacio et al. *PRL* 73 (1994) 70
- [4] J.B. Rosenzweig et al., "Generation of ultra-short, high brightness electron beams for single-spike SASE FEL operation", *Nuclear Instruments and Methods in Physics Research A*, 593, 39-44 (2008).
- [5] J. Rönsch-Schulenburg et al., "Short SASE-FEL Pulses at FLASH", TUPS064, FEL'13, New York, NY, USA (2013).
- [6] T. Plath, "A New Photo-Injector Laser for the Generation of ultra-short Electron Bunches at FLASH", Master Thesis, Hamburg, Germany (2013)
- [7] T. Plath et al., "Commissioning and Diagnostics Development for the New Short-Pulse Injector Laser at FLASH", TUPC03, IBIC'13, Oxford, UK (2013).
- [8] N. M. Lockmann, "Commissioning and Characterization of a Stretcher for a Photo-Cathode Laser System at FLASH and its Influence on the Electron Bunch Properties", Bachelor Thesis, Hamburg, Germany (2014).

- [9] P. Russbuedt et al., “400 W Yb:YAG Innoslab fs-amplifier”, Optics Express, Vol. 17, Issue 15, pp. 12230-12245 (2009).
- [10] F. Zhou et al., “Impact of the spatial laser distribution on photocathode gun operation”, Phys. Rev. ST Accel. Beams, Vol. 15, (2012).
- [11] S. Düsterer et al., , “Development of experimental techniques for the characterization of ultrashort photon pulses of XUV free-electron lasers”, to be published, (2014).
- [12] N. Gerasimova et al., “The monochromator beamline at FLASH: performance, capabilities and upgrade plans”, Journal of Modern Optics, January 2011, Volume 58, Issue 16, 2011.
- [13] M. Först et al., “Optical Afterburner for a SASE FEL: First Results from FLASH“, THPC84, IPAC2011, San Sebastián, Spain (2011).
- [14] M. Rehders et al., “Beam Dynamic Simulations for Single Spike Radiation with Short-Pulse Injector Laser at FLASH”, MOP059, these proceedings, FEL’14, BASEL, Switzerland (2014)
- [15] F. Müller, “Optimization of LOLA Measurements for the Operation of FLASH at Low Charges”, Bachelor Thesis, Hamburg, Germany (2013)
- [16] A. Kuhl et al., “Comparative Analysis of Different Electro-Optical Intensity Modulator Candidates for the New 40 GHz Bunch Arrival Time Monitor System for FLASH and European XFEL”, WEPC41, IBIC 2013; Shanghai, China (2013)
- [17] S. Wunderlich et al., ”A Double-Prism Spectrometer for the Longitudinal Diagnosis of Femtosecond Electron Bunches with Mid-Infrared Transition Radiation”, MOPOD004, to be published at IBIC’14.
- [18] A. Singer et al., ”Spatial and temporal coherence properties of single free-electron laser pulses,” Opt. Express 20, 17480 (2012).
- [19] S. Roling et al., ”Temporal and spatial coherence properties of free-electron-laser pulses in the extreme ultraviolet regime”, Phys. Rev. ST Accel. Beams 14, 080701 (2011)

CHARACTERIZATION OF PARTIALLY COHERENT ULTRASHORT FEL PULSES

C. Bourassin-Bouchet, M.-E. Couprie, Synchrotron SOLEIL, Saint Aubin, France
C. Evain, Laboratoire PhLAM/CERLA, Villeneuve d'Ascq, France

Abstract

The lack of longitudinal coherence, that is shot-to-shot fluctuations, of Free-Electron Lasers (FEL) has prevented so far their full amplitude and phase temporal characterization. To sort out this issue, we propose a solution inspired from attosecond metrology, where XUV pulse measurement techniques already exist, and from coherent diffraction imaging, where numerical solutions have been developed for processing partially coherent diffraction patterns. The experimental protocol implies the measurement of photoelectron spectra obtained through XUV-laser photoionisation. The spectra are then processed with an algorithm in order to retrieve the partially coherent FEL pulse. When applied to SASE FELs, the technique gives access to the full statistics of the emitted pulses. With seeded-FELs, the pulse shape becomes stable from shot-to-shot, but an XUV-laser time jitter remains. In that case, the technique enables the joint measurement of the FEL pulse shape (in amplitude and phase) and of the laser/FEL jitter envelope.

ADAPTING FROG TO FREE-ELECTRON LASERS

Temporal metrology is a major need for emerging ultrashort Extreme Ultraviolet and X-ray (XUV) sources, such as attosecond ($1 \text{ as} = 10^{-18} \text{ s}$) sources based on high-harmonic generation [1, 2] or free electron lasers (FEL) [3, 4]. In attosecond metrology, the most mature technique for temporal characterization is known as the FROG-CRAB technique (*Frequency-Resolved Optical Gating for Complete Reconstruction of Attosecond Bursts*) [5], adapted from the FROG technique used in conventional near-visible ultrafast laser metrology [6]. By sending the XUV pulse through a gas jet in the presence of a laser field, two-color XUV+IR photoionisation is induced. Measuring the spectrum of the produced photoelectrons while varying the IR/XUV delay gives a two dimensional trace called a spectrogram. Such a spectrogram can then be processed with a phase-retrieval algorithm in order to obtain the temporal profile of the XUV pulse.

Ideally, one would like to transpose directly the FROG-CRAB technique to FELs. However, for FELs relying on Self-Amplified Spontaneous Emission (SASE), the XUV pulse changes on a shot-to-shot basis. With seeded FELs, the pulse shape becomes stable from shot to shot, but the synchronization of FEL pulses with an external laser source remains challenging, so that in practice an optical/XUV jitter of a few tens of femtoseconds is often present. For these reasons, FELs have remained incompatible with FROG-CRAB measurements so far. The problem can be understood by considering the XUV pulse as partially coherent, and by

seeing the shot-to-shot fluctuations as the source of decoherence in the experiment. As modern ultrafast metrology relies on the hypothesis that the pulse to measure is fully coherent, it fails in the presence of partial coherence.

FEL PULSE MEASUREMENT IN THE PRESENCE OF PARTIAL COHERENCE

To overcome this problem, we propose a solution based on the recent advances in the domain of coherent diffraction imaging (CDI). This microscopy technique consists in reconstructing an object by processing numerically the diffraction patterns that it produces in the far field. The key is to illuminate the object with a fully coherent light beam, and the imaging quality is rapidly degraded as the degree of coherence decreases. However, strong efforts have been made to enable sample reconstructions even with a partially coherent beam [7, 8], simply by adapting the numerical processing used for the inversion of the diffraction patterns.

By adapting algorithms used in CDI, we have developed a numerical treatment for FROG spectrograms that enables the reconstruction of ultrashort pulses even in the presence of partial coherence [9]. In the case of SASE FELs, the statistics of SASE waveforms (temporal intensity and phase) accumulated during the measurement is recovered. Moreover in the case of seeded FELs, this statistics takes a very specific form, since the waveform is constant from shot to shot up to a random arrival time. It is then possible to recover both the XUV pulse shape and the form of the optical/XUV jitter envelope.

CONCLUSION

This work will also benefit to other domains where the FROG technique is used. In attosecond metrology, it will become possible to determine up to which extent the coherence of an optical wave packet, that is the XUV light pulse, is transferred to the electron wave packet during photoionisation [10]. But FROG is mainly used for the metrology of near visible pulses. One can for example expect applications for the coherent control in molecules [11]. This will also enable one to probe the coherence of complex nonlinear processes, such as the generation of supercontinuum pulses from photonics crystal fibers [12].

REFERENCES

- [1] P. M. Paul *et al.*, "Observation of a Train of Attosecond Pulses from High Harmonic Generation", *Science* **292**, 1689-1692 (2001)
- [2] M. Hentschel *et al.*, "Attosecond Metrology", *Nature* **414**, 509-513 (2001).

- [3] P. Emma *et al.*, “First lasing and operation of an angstrom-wavelength free-electron laser”, *Nat. Photon.* **4**, 641-647 (2010).
- [4] E. Allaria *et al.*, “Highly coherent and stable pulses from the FERMI seeded free-electron laser in the extreme ultraviolet”, *Nat. Photon.* **6**, 699-704 (2012).
- [5] Y. Mairesse and F. Quéré, “Frequency-resolved optical gating for complete reconstruction of attosecond bursts”, *Phys. Rev. A* **71**, 011401(R) (2005).
- [6] R. Trebino *et al.*, “Measuring ultrashort laser pulses in the time-frequency domain using frequency-resolved optical gating”, *Rev. Sci. Instrum.* **68**, 3277-3295 (1998).
- [7] P. Thibault and A. Menzel, “Reconstructing state mixtures from diffraction measurements”, *Nature* **494**, 68-71 (2013).
- [8] J. N. Clark *et al.*, “Dynamic Imaging Using Ptychography”, *Phys. Rev. Lett.* **112**, 113901 (2014).
- [9] C. Bourassin-Bouchet and M.-E. Couprie, “Partially coherent ultrafast spectrography”, (submitted).
- [10] M. Schultze *et al.*, “Delay in Photoemission”, *Science* **328**, 1658-1662 (2010).
- [11] N. Dudovitch *et al.*, “Single-pulse coherently controlled non-linear Raman spectroscopy and microscopy”, *Nature* **418**, 512-514 (2002).
- [12] J. M. Dudley *et al.*, “Supercontinuum generation in photonic crystal fiber”, *Rev. Mod. Phys.* **78** 1135-1184 (2006).

QUANTUM FEL II: MANY-ELECTRON THEORY

P. Kling, Helmholtz-Zentrum Dresden-Rossendorf eV, D-01328 Dresden, Germany
 and Institut für Quantenphysik, Universität Ulm, D-89069 Ulm, Germany
 R. Endrich, E. Giese, Institut für Quantenphysik, Universität Ulm, D-89069 Ulm, Germany
 R. Sauerbrey, Helmholtz-Zentrum Dresden-Rossendorf eV, D-01328 Dresden, Germany
 W. P. Schleich, Institut für Quantenphysik and Center for Integrated Quantum Science
 and Technology (IQST), Universität Ulm, D-89069 Ulm, Germany;
 Texas A&M University Institute for Advanced Study (TIAS),
 Institute for Quantum Science and Engineering (IQSE),
 and Department of Physics and Astronomy,
 Texas A&M University, College Station, Texas 77843, USA

Abstract

We investigate the emergence of the quantum regime of the FEL when many electrons interact simultaneously with the wiggler and the laser field. We find the Quantum FEL as the limit where only two momentum states are populated by the electrons. Moreover, we obtain exponential gain-per-pass and start-up from vacuum.

INTRODUCTION

The recent years have seen rising interest in a possible novel regime of FEL operation: the so-called Quantum FEL. Bonifacio *et al.* [1] have proposed the implementation of this realm – despite experimental difficulties – because they expect better temporal coherence properties and a narrower linewidth of the radiation in SASE operation. Due to these prospects the Helmholtz-Zentrum Dresden-Rossendorf and Ulm University have started a collaboration to gain deeper insight into the emergence and the properties of the Quantum FEL. In a single-electron model we have identified the quantum regime of the FEL as an effective two-level system for the electron's momentum states [2] and have established a connection to the Jaynes-Cummings model [3].

In this article, we examine a situation where many electrons interact simultaneously with the laser and the wiggler field. Based on collective projection operators we develop a formalism which allows us to identify the two-level behaviour of the Quantum FEL. However, since we are dealing with many electrons, the suitable analogy is the Dicke [4] – describing a collection of two-level atoms interacting with a radiation field – rather than the Jaynes-Cummings model.

In the two-level approximation we find start-up from vacuum and exponential gain-per-pass in the short-time limit which are essential for SASE operation. Moreover, we calculate higher order corrections to this deep quantum regime and thus find analytical expressions which match the numerical results of [1].

MODEL

We start from the one-dimensional, quantized single-mode and many-particle Bambini-Renieri Hamiltonian [5,6]

$$\hat{H} \equiv \sum_{j=1}^N \frac{\hat{p}_j^2}{2m} + \hbar g \left(\hat{a}_L \sum_{j=1}^N e^{i2k\hat{z}_j} + \text{h.c.} \right) \quad (1)$$

where \hbar and m stand for the reduced Planck constant and for the electron mass, respectively and we already have eliminated the free dynamics of the laser field. The Bambini-Renieri frame – in which a nonrelativistic treatment of the FEL dynamics is possible – is defined by the condition that the wave numbers of the laser (subscript L) and the wiggler field (subscript W) are equal, i.e. $k_L = k_W \equiv k$ [5]. The position operator \hat{z}_j for the j -th of the N electrons and its conjugate momentum operator \hat{p}_j fulfill the canonical commutation relation $[\hat{z}_j, \hat{p}_j] = i\hbar$. While the laser field is quantized with the bosonic commutation relation $[\hat{a}_L, \hat{a}_L^\dagger] = 1$ for the photon annihilation and creation operators \hat{a}_L and \hat{a}_L^\dagger , the wiggler is treated as an external classical field due to its high intensity. The coupling constant $g \equiv e^2 \mathcal{A}_L \tilde{\mathcal{A}}_W / (\hbar m)$ is given by the product of the amplitudes \mathcal{A}_L and $\tilde{\mathcal{A}}_W$ of the vector potentials of the laser and the wiggler field, respectively with e being the elementary charge.

An essential ingredient for recognizing the two-level behaviour of the Quantum FEL in the single-particle case is the occurrence of different time scales in the Schrödinger equation [2]. This feature stands out by expanding the state vector of the system in the scattering basis $|n + \mu, p - \mu q\rangle$ as introduced in [7] which is characterized by the number μ of scattered photons, that is, the number of times the electron experiences the quantum mechanical recoil $q \equiv 2\hbar k$ with n being the initial number of photons in the laser field and p the initial momentum of the electron.

This expansion is not possible in the many-particle case, since complicated entangled states are created by the Hamiltonian Eq. (1) as apparent from the case $N = 2$

$$\left(e^{2ik\hat{z}_1} + e^{2ik\hat{z}_2} \right) |p_1, p_2\rangle \sim |p_1 + q, p_2\rangle + |p_1, p_2 + q\rangle. \quad (2)$$

Therefore, we try to see the occurrence of the relevant time scales directly in the Hamiltonian and not from a particular

representation of the state-vector. We achieve this goal by introducing the collective projection operators

$$\hat{\Upsilon}_{p',p''} \equiv \sum_{j=1}^N \hat{\sigma}_{p',p''}^{(j)} \equiv \sum_{j=1}^N |p'\rangle^{(j)} \langle p''| \quad (3)$$

where $|p\rangle^{(j)}$ is the momentum eigenstate of the j -th electron.

With the help of the completeness relation

$$\sum_{p'} |p'\rangle^{(j)} \langle p'| = \mathbb{1} \quad (4)$$

we rewrite the Hamiltonian Eq. (1) in terms of these collective operators as

$$\sum_{j=1}^N \hat{p}_j^2 = \sum_{p'} p'^2 \hat{\Upsilon}_{p',p'} \quad \text{and} \quad \sum_{j=1}^N e^{\pm i 2k \hat{z}_j} = \sum_{p'} \hat{\Upsilon}_{p' \pm q, p'} \quad (5)$$

where we have made use of ${}_{(j)} \langle p' | \hat{p}_j^2 | p'' \rangle_{(j)} = p'^2 \delta_{p',p''}$ and ${}_{(j)} \langle p' | e^{\pm i 2k \hat{z}_j} | p'' \rangle_{(j)} = \delta_{p',p'' \pm q}$. Note that we do not sum over the particles any longer, but over the momenta, which in our formalism are numbers instead of operators.

In order to further simplify our approach we note that due to the discreteness of the recoil μq each electron can only be in momentum states separated by the recoil q . Assuming that initially all electrons have the same momentum p , i.e. $|\Psi(t=0)\rangle = |p, p, \dots, p\rangle \otimes |n\rangle$ (with the laser field being initially in the Fock state with photon number n) we can change the summation index in Eq. (5) to the integer number μ according to $p' \rightarrow p - \mu q$ (with p fixed) so that $\hat{\Upsilon}_{p' \pm q, p'} \rightarrow \hat{\Upsilon}_{\mu \mp 1, \mu}$.

The last step in recognizing the different time scales is to transform the Hamiltonian into the interaction picture which yields the expression

$$\hat{H}_{\text{Int}} = \epsilon \left(\hat{a}_L e^{i\Delta\tau} \sum_{\mu} \hat{\Upsilon}_{\mu, \mu+1} e^{-i2\mu\tau} + \text{h.c.} \right). \quad (6)$$

Here, we have introduced the scaled time $\tau \equiv \omega_r t$, the coupling constant $\epsilon \equiv g/\omega_r$, the recoil frequency $\omega_r \equiv q^2/(2m\hbar)$ and the momentum deviation from resonance $\Delta \equiv p/(q/2) - 1$. Moreover, we have made the transformation to the interaction picture with the help of the commutation relation

$$[\hat{\Upsilon}_{\mu, \nu}, \hat{\Upsilon}_{\rho, \lambda}] = \delta_{\nu, \rho} \hat{\Upsilon}_{\mu, \lambda} - \delta_{\lambda, \mu} \hat{\Upsilon}_{\rho, \nu} \quad (7)$$

which can be easily verified using the definition Eq. (3). We emphasize that we have defined the resonant electron momentum at $p = q/2$, which is the reasonable definition for the Quantum FEL [2] as we will see in the next section.

DEEP QUANTUM REGIME

The Hamiltonian Eq. (6) consists of terms oscillating with integer multiples of the recoil frequency ω_r and a contribution due to the deviation Δ from resonance. When we choose

the initial momentum p of the electrons in the vicinity of the quantum resonance $q/2$, i.e. $\Delta \ll 1$, the terms $e^{\pm i\Delta\tau}$ will be slowly varying. In contrast, the phase factors with $e^{i\mu\tau}$ are rapidly oscillating for $\mu \neq 0$ and we can neglect them in the weak-coupling limit performing a rotating-wave-like approximation. This quantum regime is determined by the quantum parameter [2]

$$\alpha \equiv \epsilon \sqrt{N} = \frac{g \sqrt{N}}{\omega_r} \quad (8)$$

given by the ratio of the coupling and the recoil frequency and has to be small to fulfill the weak-coupling condition, i.e. $\alpha \ll 1$.

If we perform this rotating-wave-like approximation, we arrive at the Quantum FEL Hamiltonian

$$\hat{H}_{\text{QFEL}} \equiv \epsilon \left\{ \hat{a}_L e^{+i\Delta\tau} \hat{\Upsilon}_{0,1} + \hat{a}_L^\dagger e^{-i\Delta\tau} \hat{\Upsilon}_{1,0} \right\} \quad (9)$$

which governs the dynamics of the FEL in the deep quantum regime. Here, the electrons can only have the momenta p and $p - q$ and we observe the same two-level behaviour as in the single-particle case [2]. This limit is analogous to the Jaynes-Cummings model [3] in quantum optics, which describes the dynamics of a *single* two-level atom interacting with a quantized radiation field.

However, the algebra of the collective operators $\hat{\Upsilon}_{\rho, \lambda}$ with $\rho, \lambda = 0, 1$ is more complicated and therefore richer than that of the Pauli matrices which appear in the Jaynes-Cummings Hamiltonian. This distinctive difference originates from the fact that the collective operators create entangled superposition states as exemplified by Eq. (2) and products of these operators cannot be cast in a closed form. Indeed, the Hamiltonian Eq. (9) is equivalent to the Dicke Hamiltonian [4] which describes the simultaneous interaction of a *collection* of two-level atoms with a quantized electromagnetic field. Thus, the projection operators $\hat{\Upsilon}_{\rho, \lambda}$ are equivalent to the pseudo angular momentum operators of the Dicke model.

The time evolution of the system follows from the Heisenberg equation of motion

$$\frac{d}{d\tau} \hat{O} = i [\hat{H}_{\text{QFEL}}, \hat{O}] \quad (10)$$

for an operator \hat{O} and we obtain a system of coupled nonlinear differential equations, for which no analytical solution is known. However, for short times we can linearize this set of equations in the parametrical approximation [8].

For this purpose, we notice the appearance of the operator $\hat{\Upsilon}_z \equiv \hat{\Upsilon}_{0,0} - \hat{\Upsilon}_{1,1}$ in the equations for $\hat{\Upsilon}_{1,0}$ and \hat{a}_L . This operator describes a kind of inversion of the number of electrons in the excited and ground state denoted by p and $p - q$, respectively. For an initial state $|p, p, \dots, p\rangle \otimes |n\rangle$, with all electrons in the excited state, the expectation value of $\hat{\Upsilon}_z$ gives the number of electrons $N \gg 1$. We assume that for short times comparatively few electrons change to the ground state and we can replace $\hat{\Upsilon}_z$ by its expectation value at $\tau = 0$, i.e. $\hat{\Upsilon}_z \approx \langle \hat{\Upsilon}_z \rangle_0 = N$. Thus, we arrive at the

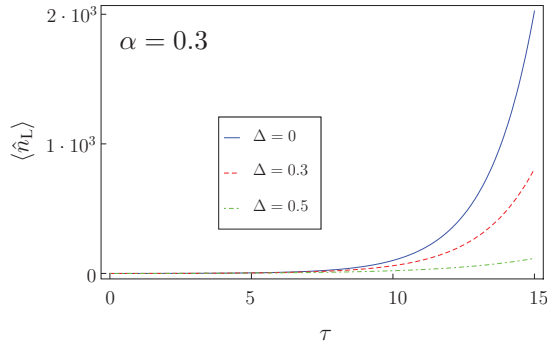


Figure 1: Mean number of photons $\langle n_L \rangle$ for the Quantum FEL as a function of the scaled time τ according to Eq. (13) with $\alpha = 0.3$ - for resonance $\Delta = 0$ (blue line), $\Delta = 0.3$ (red dashed line) and $\Delta = 0.5$ (green dashed/dotted line).

linearized set of equations

$$i \frac{d}{d\tau} \begin{pmatrix} \tilde{Y}_{1,0} \\ \tilde{a}_L \end{pmatrix} = \alpha \begin{pmatrix} 0 & -1 \\ 1 & \kappa \end{pmatrix} \begin{pmatrix} \tilde{Y}_{1,0} \\ \tilde{a}_L \end{pmatrix} \quad (11)$$

for the operators $\tilde{Y}_{1,0} \equiv \hat{Y}_{1,0} / \sqrt{N}$ and $\tilde{a}_L \equiv \hat{a}_L$. Here, we have already transformed to a frame where the time dependence due to the detuning $\Delta \equiv \kappa\alpha$ has been eliminated.

Searching for a solution of the kind $\sim e^{-i\lambda\tau}$ we easily find the frequencies

$$\lambda_{\pm} = \frac{\kappa\alpha}{2} \pm i\alpha \sqrt{1 - (\kappa/2)^2}. \quad (12)$$

The non-vanishing imaginary part – which has its maximum at resonance – leads to an exponential gain-per-pass. Indeed, the time evolution of the mean photon number

$$\langle \hat{n}_L(\tau) \rangle = \frac{1}{1 - (\kappa/2)^2} \sinh^2 \left[\alpha\tau \sqrt{1 - (\kappa/2)^2} \right] \quad (13)$$

with the photon number operator $\hat{n}_L \equiv \hat{a}_L^\dagger \hat{a}_L$ confirms this claim, where we have started with the laser field in vacuum, i.e. $n = 0$. Hence, with the start-up from vacuum and the exponential gain-per-pass we have obtained two important ingredients for the realisation of a SASE-FEL [9]. In Fig. 1 we show the photon number versus time τ for different detunings from resonance $q/2$. We note that the photon number grows more slowly, the further away the electrons are from resonance.

At resonance, the photon number increases exponentially with $e^{2\alpha\omega_\tau t}$, thus we find the gain length

$$L_g^{(q)} = \frac{c}{2\alpha\omega_\tau} \quad (14)$$

for the Quantum FEL where we have used $t \approx z/c$ with c being the speed of light.

We have to keep in mind that the length given by Eq. (14) is measured in the co-moving reference frame and we have to include the effects of relativistic length contraction to

compute the gain length in the laboratory frame. Note that the scaling with α^{-1} is not very different from the classical regime where $L_g^{(cl)} \sim \alpha^{-2/3}$ [10]. However, since in the quantum regime $\alpha \ll 1$ the gain length $L_g^{(q)}$ is very large. Hence, the suggestion of an optical undulator in [11], where more undulator periods can be passed within the same absolute wiggler length, seems reasonable.

We note that the connection between the Quantum FEL and the Dicke model – at least for exact resonance – was already found in [12] starting from a second-quantized Hamiltonian [13]. The link to our model can be established by applying Schwinger's representation [14] of angular momentum $\hat{Y}_{1,0} = \hat{c}_1^\dagger \hat{c}_0$, where \hat{c}_1^\dagger and \hat{c}_0 are bosonic operators. In the next section we present the first proof for the two-level behaviour of the Quantum FEL within a many-electron model, at least in the linearized regime.

HIGHER ORDER CORRECTIONS

A very useful technique to treat Hamiltonians of the type Eq. (6) is the Bogoliubov-Mitropolskii method of averaging [15] which is well-known in non-linear mechanics and has recently found its application in the field of atomic Bragg diffraction [16]. Since we now apply this method to the Hamiltonian and not to the equations of motion, we use a variation of the original technique: the so-called "Canonical Averaging" [17].

For this purpose we first cast our Hamiltonian in the form

$$\hat{H}'(\tau) = \epsilon \sum_{\mu} \hat{H}_{\mu} e^{i2\mu\tau} \quad (15)$$

with

$$\begin{cases} \hat{H}_0 & \equiv \hat{a}_L^\dagger \hat{Y}_{0,1} + \hat{a}_L^\dagger \hat{Y}_{1,0} - \kappa \sqrt{N} \hat{n}_L \\ \hat{H}_{\mu} & \equiv \hat{a}_L^\dagger \hat{Y}_{-\mu, -\mu+1} + \hat{a}_L^\dagger \hat{Y}_{\mu+1, \mu} \end{cases} \quad (16)$$

where we have already eliminated the time-dependence due to the detuning $\Delta = \kappa\alpha$ which again is assumed to be small, i.e. $\Delta \ll 1$.

Following the procedure of [17] we search for a transformation of the density operator $\hat{\rho}(\tau)$ in the form of $e^{\hat{A}(\tau)} \hat{\rho}(\tau) e^{-\hat{A}(\tau)}$ where $\hat{A}(\tau)$ itself can be expanded into a power series of ϵ and every term of this series again is expressed as a Fourier series similar to Eq. (15). Using the Liouville equation

$$i \frac{d}{d\tau} \hat{\rho}(\tau) = [\hat{H}'(\tau), \hat{\rho}(\tau)] \quad (17)$$

we choose $\hat{A}(\tau)$ in such a way that all secular growing terms vanish order by order and we arrive at a time-independent effective Hamiltonian

$$\hat{H}_{\text{eff}} = \epsilon \hat{H}_{\text{eff}}^{(1)} + \epsilon^2 \hat{H}_{\text{eff}}^{(2)} + \epsilon^3 \hat{H}_{\text{eff}}^{(3)} + \dots \quad (18)$$

The first order gives $\hat{H}_{\text{eff}}^{(1)} = \hat{H}_0$ in accordance with the discussion of the preceding section. We do not want to show the cumbersome expressions [17] for the higher orders. Instead we sketch the procedure: After calculating the Heisenberg

equations of motion for $\hat{Y}_{1,0}$ and \hat{a}_L up to third order in ϵ we again linearize these equations by setting $\hat{Y}_{0,0} \approx N$. Here, the largest terms behave as $\epsilon^k N^{k/2} = \alpha^k$ for the k -th order. Keeping only these contributions we arrive at the linear set of equations

$$i \frac{d}{d\tau} \begin{pmatrix} \tilde{Y}_{1,0} \\ \tilde{a}_L \end{pmatrix} = \alpha \mathbf{M} \begin{pmatrix} \tilde{Y}_{1,0} \\ \tilde{a}_L \end{pmatrix} \quad (19)$$

with the matrix

$$\mathbf{M} \equiv \begin{pmatrix} 0 & -\left(1 - \frac{\alpha^2}{8}\right) \\ 1 - \frac{\alpha^2}{8} & -\left(\kappa + \frac{\alpha}{2} - \frac{\kappa\alpha^2}{4}\right) \end{pmatrix}. \quad (20)$$

Using again the ansatz $e^{-i\lambda\tau}$ we find the expression

$$\text{Im}\lambda = \pm \alpha \sqrt{1 - \frac{\kappa^2}{4}} \left[1 - \frac{\kappa/2}{1 - \frac{\kappa^2}{4}} \frac{\alpha}{4} - \frac{5 - 3\kappa^2 + \kappa^4/2}{\left(1 - \frac{\kappa^2}{4}\right)^2} \frac{\alpha^2}{32} \right] \quad (21)$$

for the imaginary part of the frequency which is responsible for the exponential gain. For $\alpha \ll 1$ terms of higher order yield only small corrections to Eq. (12). Note, that for exact resonance $\kappa = 0$ the second order term vanishes and we have to go to the next higher order to see the corrections.

At last we compare our results for the Quantum FEL with the ones of Bonifacio *et al.* in [1]. Starting from a description in terms of collective bunching operators, they have derived the cubic equation

$$(\lambda^2 - 1)(\lambda + 1 + \Delta) - 2\alpha^2 = 0 \quad (22)$$

for the frequencies λ , which for $\alpha \gg 1$ give asymptotically the correct results for the classical high-gain FEL [9].

We now study Eq. (22) in the quantum regime $\alpha \ll 1$ by expanding λ in powers of α , that is

$$\lambda = \lambda^{(0)} + \alpha \lambda^{(1)} + \alpha^2 \lambda^{(2)} + \alpha^3 \lambda^{(3)} + \dots \quad (23)$$

and solve the resulting equations order by order. Here, we have set $\Delta = \kappa\alpha \ll 1$. Indeed, we obtain – apart from an unimportant rapidly oscillating solution – two solutions whose imaginary part match with Eq. (21).

Hence, we have found a perfect correspondence between our solution for the Quantum FEL and the one of [1], at least up to third order in α and a small momentum detuning Δ . This agreement is shown in Fig. 2 where we compare our analytical results with the numerical solution of Eq. (22) for two different values of α . Moreover, we see that the maximum of $\text{Im}\lambda$ is shifted from $p = q/2$ to the left for increasing α . This feature is in accordance with the fact that for the classical high-gain FEL the resonance is at $p = 0$ [10].

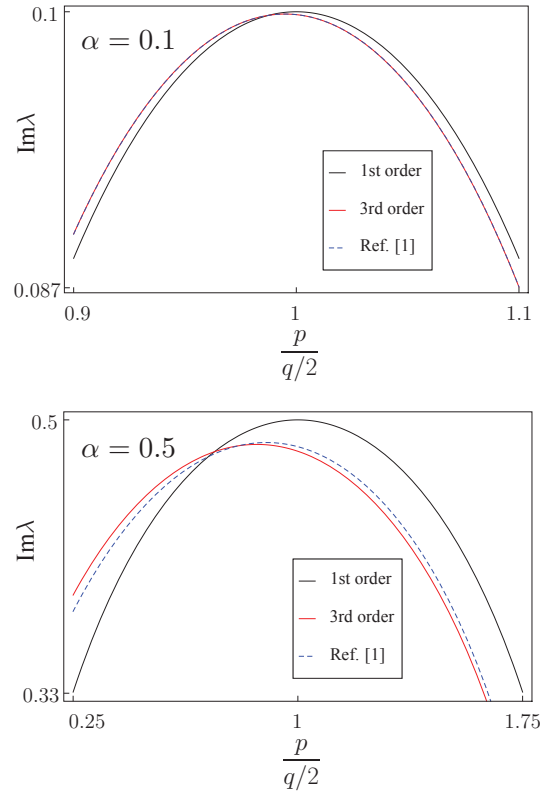


Figure 2: Imaginary part $\text{Im}\lambda$ of the scaled frequency λ , which governs the dynamics of the Quantum FEL vs. the initial momentum p of the electrons in units of $q/2$. Our results, first order in the quantum parameter α , Eq. (12), (black line), and third order in α , Eq. (21), (red line), are compared with the numerical solution of the cubic equation Eq. (22) of [1] (blue dashed line) for $\alpha = 0.1$ (above) and $\alpha = 0.5$ (below).

CONCLUSION

We have proposed a many-electron theory of the Quantum FEL based on collective projection operators. This analysis brings out most clearly that the underlying dynamics is not governed by the Jaynes-Cummings but the Dicke Hamiltonian. In particular, the linearized Heisenberg equations of motion for the lowest collective electron operator and the annihilation operator of the field predict an exponential gain starting from the vacuum. This result is crucial for the realization of the SASE-FEL. Moreover, the method of canonical averaging has allowed us to calculate higher order corrections which are in complete agreement with the results of Ref. [1]. A more detailed study of the quantum properties of the radiation of the Quantum FEL is in preparation.

ACKNOWLEDGMENT

We thank M. Bussmann, A. Debus and K. Steiniger for many helpful discussions. WPS is grateful to Texas A&M University for a Texas A&M Institute for Advanced Study (TIAS) Faculty Fellowship.

REFERENCES

- [1] R. Bonifacio *et al.*, Phys. Rev. STAB **9**, 090701 (2006).
- [2] P. Preiss *et al.*, Proceedings of the 34th International Free-Electron Laser Conference, 93 (2012).
- [3] E. T. Jaynes and F. W. Cummings, Proceedings of the IEEE **51**, 89 (1963).
- [4] R. H. Dicke, Phys. Rev. **93**, 99 (1954).
- [5] A. Bambini, A. Renieri and S. Stenholm, Phys. Rev. A **19**, 2013 (1979).
- [6] W. Becker and J. K. McIver, Phys. Rev. A **27**, 1030 (1983).
- [7] F. Ciocci *et al.*, Physics Reports **141**, 1 (1986).
- [8] W. H. Louisell, A. Yariv and A. E. Siegman, Phys. Rev. **124**, 1646 (1961).
- [9] R. Bonifacio, C. Pellegrini and L. Narducci, Optics Communications **50**, 373 (1984).
- [10] P. Schmüser, M. Dohlus and J. Rossbach, "Ultraviolet and Soft X-Ray Free-Electron Lasers." Springer (2008).
- [11] R. Bonifacio, G. R. M. Robb and A. Schiavi, Proceedings of the 27th International Free-Electron Laser Conference, 71 (2005).
- [12] R. Gaiba, "Quantum Aspects of the Free Electron Laser." PhD-Thesis (2007).
- [13] G. Preparata, Phys. Rev. A **38**, 233 (1988).
- [14] J. Schwinger in "Quantum Theory of Angular Momentum.", Edited by L. C. Biedenharn and H. Van Dam, 229, Academic Press (1965).
- [15] N. M. Bogoliubov and I. A. Mitropolskii, "Asymptotic Methods in the Theory of Non-Linear Oscillations." Vol. 10. Taylor & Francis (1961).
- [16] E. Giese *et al.*, Phys. Rev. A **88**, 053608 (2013).
- [17] L. L. Buishvili, E. B. Volzhan and M. G. Menabde, Theoretical and Mathematical Physics **46**, 166 (1981).

QUANTUM FEL I: MULTI-MODE THEORY

R. Endrich, E. Giese, Institut für Quantenphysik , Universität Ulm, D-89069 Ulm, Germany
 P. Kling, Helmholtz-Zentrum Dresden-Rossendorf eV, D-01328 Dresden, Germany
 and Institut für Quantenphysik , Universität Ulm, D-89069 Ulm, Germany
 R. Sauerbrey, Helmholtz-Zentrum Dresden-Rossendorf eV, D-01328 Dresden, Germany
 W.P. Schleich, Institut für Quantenphysik and Center for Integrated Quantum Science
 and Technology (IQST), Universität Ulm, D-89069 Ulm, Germany;
 Texas A&M University Institute for Advanced Study (TIAS),
 Institute for Quantum Science and Engineering (IQSE)
 and Department of Physics and Astronomy,
 Texas A&M University, College Station, Texas 77843-4242 USA

Abstract

The quantum regime of the FEL in a single-mode, single-particle approximation is characterized by a two-level behaviour of the center-of-mass motion of the electrons. We extend this model to include all modes of the radiation field and analyze the effect of spontaneous emission. In particular, we investigate this scattering mechanism to derive experimental conditions for realizing an FEL in the quantum regime.

INTRODUCTION

In [1] the existence of the so-called quantum regime of the FEL was predicted and in [2] a quantum optics approach to the Quantum FEL (QFEL) was developed. Before we extend our model of the QFEL to a multi-mode theory, we briefly recapitulate its essential ingredients.

We start with the Hamiltonian of the FEL, i.e. an electron of mass m and charge e coupled to a single mode of the radiation field of frequency ω by the wiggler of amplitude \mathcal{A}_W . This Hamiltonian expressed in the Bambini-Renieri frame [3], which is a comoving non-relativistic frame of reference reads [4] in the interaction picture

$$\hat{H} \equiv \hbar g \hat{a}_L^\dagger e^{-2ik\hat{z}} e^{-i\hat{\Delta}(\hat{p})t} + \text{h.c.} \quad (1)$$

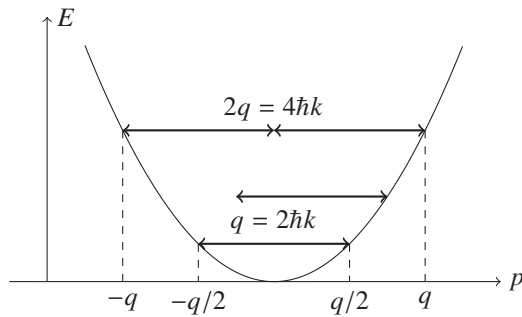


Figure 1: Momentum-energy parabola of the electron, that is $E = E(p)$. Only resonant photon transitions are of interest, the off-resonant ones can be neglected. Higher order photon transitions are on resonance as well, but they are suppressed by the quantum parameter α , defined by Eq. (5).

The coupling constant [2]

$$g \equiv \frac{e^2}{\hbar m} \sqrt{\frac{\hbar}{2\varepsilon_0 V \omega}} \mathcal{A}_W, \quad (2)$$

with the quantization volume V , Planck's constant \hbar , and the vacuum permittivity ε_0 couples the photon creation operator \hat{a}_L^\dagger to the center-of-mass motion of the electron represented by the position and momentum operator, \hat{z} and \hat{p} , respectively, where the detuning

$$\hat{\Delta}(\hat{p}) \equiv \hat{p}(2k/m) - \omega_r \quad (3)$$

contains the recoil frequency $\omega_r \equiv q^2/2m\hbar$. The operator $\exp[-2ik\hat{z}]$ shifts the electron momentum by the recoil

$$q \equiv 2\hbar k \quad (4)$$

determined by the wave number k .

At this point the Hamiltonian is exact for a strong classical wiggler field. In the classical regime the electron recoil is a negligible quantity, whereas in the quantum domain it enters in a crucial way into the detuning, which suppresses off-resonant photon transitions. This effect is illustrated in Fig. 1 where the initial and final momentum on the energy parabola are on resonance. For a single photon exchange, only the momentum states $|q/2\rangle$ and $|-q/2\rangle$ are on resonance.

Higher-order photon transitions, as seen in Fig. 1, are on resonance for higher momenta as well. However, it has been shown in [2] that a j -photon transition with $j > 1$ is proportional to α^j where

$$\alpha \equiv \frac{g \sqrt{n+1}}{\omega_r} \quad (5)$$

is the quantum parameter and n the photon number.

For $\alpha \ll 1$ only the single-photon transition remains, while higher-order transitions are suppressed. This feature represents the main criterion for the QFEL and the momentum states $|\pm q/2\rangle$ undergo a Rabi oscillation with the frequency

$$\Omega \equiv g \sqrt{n+1}. \quad (6)$$

This frequency determines the timescale on which a QFEL is operational, and will play a key role in our considerations.

MULTI-MODE HAMILTONIAN

Since a QFEL behaves very much like a two-level system, a natural assumption is that spontaneous emission will also occur similar to that of a two-level atom [5], rather than to spontaneous undulator radiation in a classical FEL. Hence, we expect the probability $P(\mathbf{p}_0; t)$ to find the electron in its initial momentum state $|\mathbf{p}_0\rangle$ to decay exponentially as a function of time, that is

$$P(\mathbf{p}_0; t) = e^{-\Gamma t} P(\mathbf{p}_0; 0) . \quad (7)$$

Our goal is to find an expression for the decay constant Γ . In order to do so, we extend the Hamiltonian, Eq. (1), and couple a single electron to all modes. The resulting Hamiltonian then reads [6]

$$\hat{H}_{sp} \equiv \sum_{j,\lambda} \left(\mathbf{e}_{j,\lambda}^* \cdot \mathbf{e}_W \right) \left(\hbar g_j \right) \hat{a}_j^\dagger e^{-\frac{i}{\hbar} \mathbf{q}_j \cdot \hat{\mathbf{r}}} e^{-i \hat{\Delta}_j(\hat{\mathbf{p}}) t} + \text{h.c.} , \quad (8)$$

where $\mathbf{e}_{j,\lambda}$ and \mathbf{e}_W denote the polarization vectors of the mode of the radiation field characterized by the mode indices j and λ , and of the wiggler field, respectively, and the coupling constant g_j between the electron and the j th mode.

The Hamiltonian \hat{H}_{sp} differs from \hat{H} , Eq. (1), by the interaction of the electron with all modes, manifesting itself in a sum over all modes, and subsequently by the sum over all possible polarizations for each mode. The recoil

$$\mathbf{q}_j \equiv \hbar (\mathbf{k}_j - \mathbf{k}_W) \quad (9)$$

depends, in contrast to Eq. (4), on the wave vectors \mathbf{k}_j of the j th mode and \mathbf{k}_W of the wiggler. Moreover, the detuning

$$\hat{\Delta}_j(\hat{\mathbf{p}}) \equiv \frac{\hat{\mathbf{p}} \cdot \mathbf{q}_j}{\hbar m} - \frac{\mathbf{q}_j^2}{2m\hbar} - (\omega_j - \omega) \quad (10)$$

is now a slightly more complicated operator with the frequency ω_j of the j th mode.

Since in the one-mode Hamiltonian, Eq. (1), the angles in $\hat{\Delta}_j$ between \mathbf{p} and \mathbf{q}_j only take on the values 0 or π it corresponds to one space dimension Eq. (3). This restriction is no longer true for Eq. (8) and we have to take into account the directions of the involved wave vectors. The expression for the detuning is now dependent not only on the absolute value of the electron momentum, but also on its direction as well as the wave vectors \mathbf{k}_j of all modes.

In order to find a resonance condition, we now simplify Eq. (10) significantly. The initial momentum is aligned with the z -axis, i.e. $\mathbf{p}_0 \equiv (q/2) \mathbf{e}_z = (\hbar\omega/c) \mathbf{e}_z$ to match the excited state of the QFEL, as discussed in the first section. When we apply the detuning operator $\hat{\Delta}(\hat{\mathbf{p}})$ defined by Eq. (10) onto the initial momentum state, we find,

$$\hat{\Delta}_j(\hat{\mathbf{p}}) |\mathbf{p}_0\rangle = \left\{ \frac{\hbar}{mc^2} \left[\omega (\omega_j \cos \delta - \omega) - (\omega_j - \omega)^2 \right] - (\omega_j - \omega) \right\} |\mathbf{p}_0\rangle , \quad (11)$$

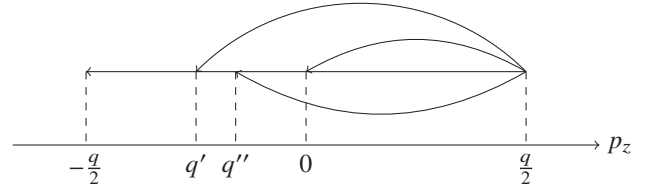


Figure 2: Additional resonances in the quantum regime of the FEL due to the presence of a reservoir. Whereas in Fig. 1 there is only a single resonance between $|\pm q/2\rangle$ remaining, with a reservoir any transition where the projection on the z -axis of the electron momentum $\mathbf{p}' \equiv \mathbf{p} - \mathbf{q}_j$ lies within $\pm q/2$ is possible.

where δ denotes the angle between \mathbf{q} and \mathbf{k}_j .

The term associated with the square brackets scales with $\hbar\omega/mc^2 \ll 1$ and can therefore be neglected, which means that the frequency difference $(\omega_j - \omega)$ between mode and wiggler will determine the resonance condition. We recall that in Eq. (1) the electron momentum p determines the detuning and the frequency difference in the detuning vanishes due to only a single mode being present. This is no longer the case when many modes are relevant and it is indeed this frequency difference that dictates the resonance condition. We can therefore make the approximation

$$e^{-i \hat{\Delta}_j(\hat{\mathbf{p}}) t} |\mathbf{p}\rangle \cong e^{i(\omega_j - \omega) t} |\mathbf{p}\rangle . \quad (12)$$

These additional resonances can be seen in Fig. 2. Once the electron has spontaneously emitted a photon and has therefore a new momentum \mathbf{p}' , then there is another mode on resonance due to Eq. (12), and the electron can spontaneously emit another photon, and so on. Indeed, the electron can spontaneously emit an infinite amount of photons since the wiggler, which we consider to be a classically device, is an external field.

When we now try to find the expression for the decay constant Γ the resulting differential equations will not decouple due to this cascade. We therefore have to find the point where this photon cascade stops.

PHOTON CASCADE

In order to cope with this problem we recall the relevant timescale of the QFEL as well as the condition for the strong coupling regime. For optimal gain the electron has to spend a time τ in the wiggler that allows for half of a Rabi cycle, that is

$$\Omega \tau = \frac{\pi}{2} . \quad (13)$$

In a conventional atom-reservoir interaction, we have for the strong-coupling regime the condition [7]

$$\frac{\Gamma}{g \sqrt{n+1}} \ll 1 , \quad (14)$$

which yields with Eqs. (6) and (13) the inequality

$$\Gamma\tau \ll 1. \quad (15)$$

Next we introduce the probability N_ℓ for an electron to spontaneously emit ℓ photons. The initial condition is that at $t = 0$ there are only electrons with momentum $\mathbf{q}/2$. When they are coupled to a reservoir, N_0 decays exponentially while $N_{\ell \neq 0}$ is increasing. For example, for a two-level atom, denoted with \tilde{N}_ℓ , with the decay constant Γ_{at} we find [6]

$$\tilde{N}_0(t) = e^{-\Gamma_{at}t} N_0(0) \approx (1 - \Gamma_{at}t) N_0(0) \quad (16)$$

$$\tilde{N}_1(t) = (1 - e^{-\Gamma_{at}t}) N_0(0) \approx (\Gamma_{at}t) N_0(0) \quad (17)$$

where we have used the condition Eq. (14) for the strong coupling regime.

Since we are interested in more than a single spontaneous emission process, we now examine two subsequent spontaneous emission processes of the same electron. The respective set of differential equations read

$$\dot{N}_0(t) = -\Gamma N_0(t) \quad (18)$$

$$\dot{N}_1(t) = +\Gamma N_0(t) - \Gamma N_1(t) \quad (19)$$

$$\dot{N}_2(t) = +\Gamma N_1(t). \quad (20)$$

Here we have assumed that the decay constant Γ is equal for all scattering events, which is reasonable since Γ , as we will show later, depends on the resonance condition which is independent on the electron momentum Eq. (12).

This set of equations is easily solved and with Eq. (15) we have $\exp[-\Gamma\tau] \approx 1 - \Gamma\tau$, and thus the solution reads

$$N_0(t) \approx (1 - \Gamma\tau) N_0(0) \quad (21)$$

$$N_1(t) \approx [1 - (\Gamma\tau)] (\Gamma\tau) N_0(0) \approx (\Gamma\tau) N_0(0) \quad (22)$$

$$N_2(t) \approx (\Gamma\tau)^2 N_0(0) \approx 0. \quad (23)$$

In comparison to Eqs. (16) and (17) we note only a small difference of the order of $\Gamma\tau$ which is not relevant on the timescale of our problem. This feature can be seen in Fig. 3 where the quantities N_0, N_1, N_2 are solved exactly and are plotted in comparison to the Rabi oscillations. The difference to \tilde{N}_1 , Eq. (17), which represents only one spontaneously emitted photon does not matter until the first full Rabi cycle, but by that time the electron has already left the wiggler. We therefore conclude that we can neglect all further spontaneous emissions once the electron has emitted a photon. This behavior coincides perfectly with the two-level dynamics of the QFEL since in the quantum regime the electron can only emit a single photon.

DECAY CONSTANT: EXPLICIT FORM

With this information we now address the Schrödinger equation for the QFEL in the presence of a reservoir. The state vector $|\Psi(t)\rangle$ contains the electron momentum \mathbf{p} as well as all possible photon numbers $\{n\}$ of all modes denoted by curly brackets, and reads

$$|\Psi(t)\rangle \equiv \int d\mathbf{p}' \sum_n c(\mathbf{p}', \{n\}; t) |\mathbf{p}', \{n\}\rangle \quad (24)$$

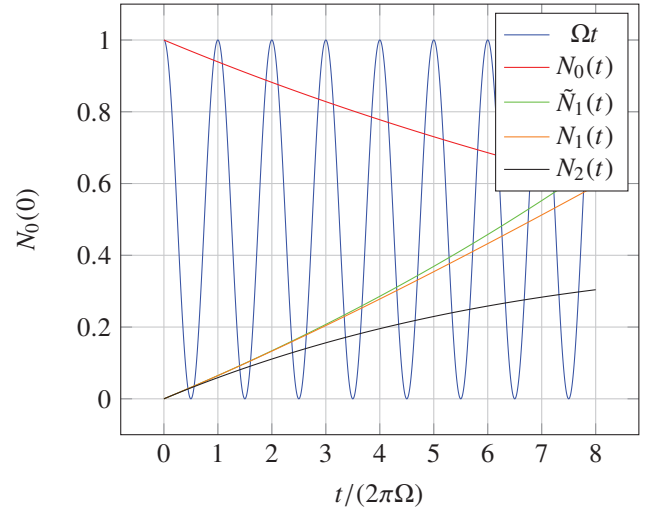


Figure 3: Timescale of the random scattering in the QFEL together with the corresponding Rabi oscillations for comparison. The value of the decay constant Γ was set to 1% of $g\sqrt{n+1}$, giving rise to the strong coupling regime. The quantity $\tilde{N}_1(t)$ represents only a single scattering event and is the counterpart of the decay of a two-level atom.

Since we want to connect this state vector to Eq. (7) we calculate

$$P(\mathbf{p}_0; t) = |c(\hbar k_W \mathbf{e}_z, \{0\}; t)|^2. \quad (25)$$

With the Hamiltonian, Eq. (8), the simplified detuning, Eq. (12) as well as the results Eqs. (17), (22) and (23) from the third section we arrive at the set of differential equations

$$\begin{aligned} \dot{c}(\hbar k_W \mathbf{e}_z, \{0\}; t) = & -i \sum_{j,\lambda} (\mathbf{e}_W \cdot \mathbf{e}_{j,\lambda}^*) g_j e^{i(\omega_j - \omega)t} \\ & \times c(\hbar k_W \mathbf{e}_z - \mathbf{q}_j, \{1\}_j; t) \end{aligned} \quad (26)$$

$$\begin{aligned} \dot{c}(\hbar k_W \mathbf{e}_z - \mathbf{q}_j, \{1\}_j; t) = & -i (\mathbf{e}_W^* \cdot \mathbf{e}_{j,\lambda}) g_j e^{-i(\omega_j - \omega)t} \\ & \times c(\hbar k_W \mathbf{e}_z, \{0\}; t) \end{aligned} \quad (27)$$

which can be solved by formally integrating Eq. (27) and substituting it into Eq. (26). The integral over time will result in a Dirac delta function that allows us to evaluate the sum. The resulting differential equation reads [7]

$$\dot{c}(\mathbf{p}_0, \{0\}; t) = 2\pi g^2(\omega) \mathcal{D}(\omega) c(\mathbf{p}_0, \{0\}; t) \quad (28)$$

with the mode density $\mathcal{D}(\omega) \equiv \omega^2 / (\pi^2 c^3)$ of the electromagnetic field [7].

The coupling constant g , defined in Eq. (2), and the classical electron radius [8]

$$r_e \equiv \frac{e^2}{4\pi\epsilon_0 mc^2} \quad (29)$$

together with the reduced Compton wavelength [8]

$$\lambda \equiv \frac{\hbar}{mc} \quad (30)$$

allows us to express Eq. (28) as

$$\dot{c}(\mathbf{p}_0, \{0\}; t) = -\frac{2}{3} \frac{r_e}{\lambda} a_0^2 \omega \cdot c(\mathbf{p}_0, \{0\}; t) \quad (31)$$

with the wiggler parameter [2]

$$a_0 \equiv \frac{\sqrt{2}e}{mc} \mathcal{A}_W. \quad (32)$$

Hence, we finally obtain the explicit expression

$$\Gamma \equiv \frac{1}{3} \frac{r_e}{\lambda} a_0^2 \omega \quad (33)$$

for the decay constant appearing in Eq. (7).

DECAY CONSTANT: ESTIMATES

Expression Eq. (33) suggests that we can tune the decay rate Γ by the wiggler parameter a_0 . In order to have a low decay the QFEL is best operational with

$$a_0 < 1. \quad (34)$$

Moreover, we have to ensure that we are in the strong coupling regime, that is the approximations from the third section hold true. Since $\Gamma = \Gamma(a_0, \omega)$ and $g = g(\alpha, \omega)$ we can directly calculate this ratio which reads

$$\frac{\Gamma}{g \sqrt{n+1}} = \frac{a_0^2}{\alpha} \frac{1}{\omega} \cdot 8.3 \times 10^{15} \frac{1}{s}. \quad (35)$$

However, we have to keep in mind that this ratio is still expressed in the Bambini-Renieri frame. We now connect this condition to the quantities in the laboratory frame and recall the transformation [3]

$$\omega = \frac{2\pi c}{\sqrt{\lambda_L \lambda_W}}. \quad (36)$$

of the resonance frequency to the laboratory system with the wiggler and laser wavelength, λ_W and λ_L , respectively.

The latter one is given by the identity [9]

$$\lambda_L = \frac{\lambda_W}{2\gamma^2} (1 + a_0^2) \quad (37)$$

with the Lorentz factor

$$\gamma = \frac{E}{mc^2}, \quad (38)$$

which is determined by the electron energy E .

When we now combine Eqs. (36), (37) and (38) in Eq. (35) and evaluate all constants of nature we arrive at the condition

$$\chi \equiv a_0^2 \sqrt{1 + a_0^2} \frac{\lambda_W}{E} \ll \alpha 14.5 \frac{\text{mm}}{\text{GeV}} \quad (39)$$

for the QFEL being in the strong coupling regime.

We compare the condition Eq. (39) in Table 1 for three FELs and see that none of them can fulfill it even for $\alpha \ll 1$. For an electron accelerator operating in the GeV regime, one does need at least a wiggler wavelength in the order of micrometers.

Table 1: The parameter χ defined by Eq. (39) providing the condition for a strong coupling regime of the QFEL for the FEL ELBE [10] at the HZDR as well as for the LCLS [11] at Stanford University. If χ exceeds the value of $\alpha 14.5 \text{ mm/GeV}$ with $\alpha \ll 1$, the coupling to the reservoir is too strong. The parameters a_0 and λ_W have been set to their possible minimum values and E to its possible maximum. Even if these devices are capable of reaching the quantum regime, none of them succeed at operating in the strong coupling regime.

FEL	χ in [mm/GeV]
ELBE U27	75.4
ELBE U100	82.2
LCLS	110.6

SUMMARY

In our previous model [2, 4] the ratio of the coupling constant g and the recoil frequency ω_r , i.e. the quantum parameter α , has served as the condition for the quantum regime of the FEL.

We are now in the position to incorporate decoherence due to a reservoir reflecting spontaneous emission as well. This extension has allowed us to derive a condition under which one does not only reach the quantum regime, but also the strong coupling regime of the QFEL which is best suited for a stable laser output.

ACKNOWLEDGMENT

We thank M. Bussman, A. Debus and K. Steiniger for many helpful discussions.

WPS is grateful to Texas A&M University for a Texas A&M University Institute for Advanced Study (TIAS) Faculty Fellowship.

REFERENCES

- [1] R. Bonifacio, N. Piovella and G. R.M. Robb, *Fortschr. Phys.* **57** (2009) 1041.
- [2] P. Preiss, *Theory of the Quantum Free-Electron Laser*, PhD thesis, Ulm University (2013).
- [3] A. Bambini, R. Renieri, and S. Stenholm, *Phys.Rev. A* **19**, 2013 (1975).
- [4] P. Preis, R. Endrich, E. Giese, P. Kling, M. Knobl, W.P. Schleich, R. Sauerbrey, *Theory of the Quantum FEL in a nutshell*, Proceedings of FEL2012, Nara, Japan.
- [5] V. Weisskopf and E. Wigner, *Z. Phys.* **63**, 54 (1930).
- [6] W.P. Schleich, *Quantum Optics in Phase Space* (Berlin: Wiley-VCH, Weinheim, 2001).
- [7] P. Meystre, M. Sargent III, *Elements of Quantum Optics*, (Springer, Heidelberg, 1990).
- [8] J. Sakurai, *Advanced Quantum Mechanics* (Addison-Wesley, 1987).
- [9] P. Schmüser, M. Dohlus, and J. Rossbach, *Ultraviolet and Soft X-Ray Free-Electron Lasers*, 3rd ed. (Springer, Heidelberg, 2009).

- [10] M. Gensch, *The Main Parameters of the Free-Electron Lasers at the ELBE-Center for High-Power Radiation Sources*, <http://www.hzdr.de/db/Cms?pNid=205>, (2014).
- [11] J. Arthur *et.al.*, *Linac Coherent Light Source (LCLS) Conceptual Design Report*, (2002).

TWO-COLOR FREE-ELECTRON LASER VIA TWO ORTHOGONAL UNDULATORS

N. S. Mirian*, School of Particle and Accelerator Physics,

Institute for Research in Fundamental Sciences (IPM), 19395-5531, Tehran, Iran

G. Dattoli, ENEA Centro Ricerche Frascati, via E. Fermi, 45, IT 00044 Frascati, Rome, Italy

V. Petrillo, Università degli Studi di Milano, via Celoria 16, IT 20133 Milano, Italy and

INFN-Mi, via Celoria 16, IT 20133 Milano, Italy

Abstract

An amplifier Free electron Laser (FEL) including two orthogonal polarized undulators with different periods and field intensities is able to emit two color radiations with different frequency and polarization while the total length of device does not change respect to usual single color FELs. The wavelengths of two different colors can be changed by choosing different periods, while variation in the magnetic strengths can be used to modify the gain lengths and saturation powers.

INTRODUCTION

Recently generation of free-electron laser radiation with two or more simultaneous colors opens new promising chapter in applications [1,2] and in the study of the underlying physics. The packets contain two different spectral lines with adjustable time separation between them. Applications exist over a broad range of wavelengths involving pump-probe experiments, multiple wavelength anomalous scattering, or any process where there is a large change in cross section over a narrow wavelength range [3].

In order to produce this type of radiation several schemes have been proposed, and many promising theoretical proposals have been so far investigated. Some of the initially proposed designs were based on the use of staggered undulator magnets having different values of deflecting parameters to achieve lasing at two distinct wavelengths [4–7]. In this way, the length of the FEL undulator is essentially doubled and a complex scheme is required to reach saturation and power levels comparable with the single color configuration. A different technique involving the use of either a chirped or a two-color seed laser, is recently demonstrated at the FERMI soft X-ray FEL. It initiates the FEL instability at two different wavelengths within the modulator gain bandwidth [8, 9]. Another option is relying on injection of multi-energy electron beam in the FEL undulator [10] resonating at two different wavelength, allowing the control of frequency and time separation ranges of the FEL pulses, while maintaining similar saturated power levels and minimal undulator length [11, 12]. In this configuration, the SASE lasing occurs from separated and nearly independent electron distributions [13].

Recently a new proposal with a further different scheme has been presented in reference [14, 15]. In this case the

FEL emission is obtained from two orthogonally polarized undulators with different polarized and field intensities. The two radiations have not only different frequencies, but also different polarizations, while the total length of the device does not change with respect to usual single color FELs. Producing two waves with orthogonal polarizations with comparable intensities is very important because it opens various possibilities to get insights into and to control the internal organization and orientation in space of molecules, taking advantage of the selective excitation of the molecular fluorescence by differently polarized beams.

This paper presents a brief overview over the main theory of the production and properties of two-color radiation generated by two orthogonal undulators.

MODEL EQUATION IN AN AVERAGED AND NON AVERAGED SVEA TREATMENT

The FEL undulator is assumed to be composed by two linear undulators orthogonally polarized with periods given respectively by λ_{01} and λ_{02} . and deflection parameters $K_{1,2} = |eB_{1,2}\lambda_{01,02}/mc^2|$. The undulator magnetic field, in the paraxial approximation, is described by the following expression

$$\mathbf{B}_w = -B_{w2} \sin(k_{02}z)\hat{e}_x + B_{w1} \sin(k_{01}z)\hat{e}_y, \quad (1)$$

where $k_{01,02} = 2\pi/\lambda_{01,02}$.

Following the Colson's analysis [16], the zero order dimensionless velocity components can be written as

$$\beta_{x,y} = -\frac{K_{1,2}}{\gamma_0} \cos(k_{01,02}z) \approx -\frac{K_{1,2}}{\gamma_0} \cos(\omega_{01,02}t), \quad (2)$$

$$\beta_z = -\frac{1}{4} \left[\left(\frac{K_1}{\gamma} \right)^2 \cos(2k_{01}z) + \left(\frac{K_2}{\gamma} \right)^2 \cos(2k_{02}z) \right] + \beta_0 \quad (3)$$

with $\beta_{x(y),j} = v_{x(y),j}/c$ and $\beta_0 = 1/\sqrt{1 - \gamma_0^2}$. From Eq (3) the following resonance conditions can be found.

$$\lambda_{1,2} = \frac{\lambda_{01,02}}{2\gamma_0^2} (1 + K_1^2/2 + K_2^2/2). \quad (4)$$

The trajectories of the electrons inside the undulator takes the form:

* najmeh.mirian@ipm.ir

$$\mathbf{r} = \beta_0 c t \hat{e}_z - \frac{K_1}{k_{01} \gamma_0} \sin(\omega_{01} t) \hat{e}_x - \frac{K_2}{k_{02} \gamma_0} \sin(\omega_{02} t) \hat{e}_y \quad (5)$$

$$- \frac{\lambda_{01}}{16\pi} \frac{K_1^2}{\gamma_0^2} \sin(2\omega_{01} t) \hat{e}_z - \frac{\lambda_{02}}{16\pi} \frac{K_2^2}{\gamma_0^2} \sin(2\omega_{02} t) \hat{e}_z.$$

The longitudinal motion at zero order is described by:

$$z = \beta_0 c t - \frac{\xi_1}{k_1} \sin(2\omega_{01} t) - \frac{\xi_2}{k_2} \sin(2\omega_{02} t), \quad (6)$$

with $\xi_{1,2} = \frac{K_{1,2}^2}{4(1+K_1^2/2+K_2^2/2)}$.

The the proportional one-dimensional vector potential is assumed as

$$\mathbf{A} = -i \left[A_1 e^{i(k_1 z - \omega_1 t)} \hat{e}_x + A_2 e^{i(k_2 z - \omega_2 t)} \hat{e}_y \right], \quad (7)$$

$A_{1,2}$ are slow complex amplitudes, $k_{1,2} = 2\pi/\lambda_{1,2}$. In the following, we will assume $n\lambda_{01} = m\lambda_{02}$; in this way, we will treat both the case of an harmonic relation between λ_1 and λ_2 , and the case where m/n is a generic rational number, describing all other situations.

In order to write the FEL equation in universal scaling notation [17], we define the normalized fields as $a_{1,2} = \frac{\omega_1}{\omega_p} \frac{e A_{1,2}}{\sqrt{\rho_1} \gamma_0} \frac{1}{mc^2}$ where

$$\rho_{1,2} = \frac{1}{\gamma_0} \left[\frac{\omega_p K_{1,2} \mathcal{F}_{1,2}}{8\omega_{01,02}} \right]^{2/3} \quad (8)$$

is the FEL parameter and ω_p is the plasma frequency. In terms of the scaled quantity $\Gamma_i = \frac{\gamma_i - \gamma_0}{\rho_i \gamma_0}$, and, the phases $\theta_{1,2} = \omega_{01,02} t + k_{1,2} \beta_z c t - \omega_{1,2} t$ the equations are therefore:

$$\frac{d\Gamma_i}{d\tau} = e^{i\theta_{1i}} a_1 + \frac{\mathcal{F}_2}{\mathcal{F}_1} \frac{K_2}{K_1} \frac{k_{w2}}{k_{w1}} e^{i\theta_{2i}} a_2 + cc. \quad (9)$$

$$\frac{\partial a_1}{\partial \zeta} + \frac{1}{c} \frac{\partial a_1}{\partial \tau} = \sum e^{-i\theta_{1i}}. \quad (10)$$

$$\frac{\partial a_2}{\partial \zeta} + \frac{1}{c} \frac{\partial a_2}{\partial \tau} = \frac{K_2 k_{w1}}{K_1 k_{w2}} \frac{\mathcal{F}_2}{\mathcal{F}_1} \sum e^{-i\theta_{2i}}, \quad (11)$$

where $\mathcal{F}_{1,2} = J_0(\frac{k_{1,2} \xi_{1,2}}{k_{2,1}}) [J_0(\xi_{1,2}) - J_1(\xi_{1,2})]$ are the Bessel factors modified for the case of two undulators. The phases in field equations are

$$\frac{d\theta_{1i}}{d\tau} = \Gamma_i, \quad \frac{d\theta_{2i}}{d\tau} = \frac{k_{02}}{k_{01}} \Gamma_i. \quad (12)$$

Therefore the gain length of the two polarization, when $m \neq n$ are

$$L_{g1} = \frac{\lambda_{01}}{4\pi \sqrt{3} \rho_1} = \left(\frac{\lambda_{01}}{\lambda_{02}} \right)^{1/3} \left(\frac{\mathcal{F}_2}{\mathcal{F}_1} \right)^{2/3} L_{g2}. \quad (13)$$

In a non averaged orbit approximation, Lorentz force equations are employed directly. Then the electron momentum equations for j^{th} electron are

$$\frac{dp_{x,y}}{dt} = e\beta_z B_{1,2} \sin k_{01,02} z - ek_{1,2} (1 - \beta_z) [A_{1,2} e^{i\alpha_{1,2}} + cc]$$

$$\frac{dp_z}{dt} = -e\beta_y B_2 \sin k_{02} z - ek_2 \beta_y [A_2 e^{i\alpha_2} + cc] \quad (14)$$

$$-e\beta_x B_1 \sin k_{01} z - ek_1 \beta_x [A_1 e^{i\alpha_1} + cc]$$

where $\alpha_{1,2} = k_{1,2} z - \omega_{1,2} t$. By writing the transverse current in terms of the particle density \bar{n} as $J_{x,y} = -\sum e c \beta_{x,y} \bar{n} \delta(z - z_j)$ in Maxwell's equation and by using the Slowly Varying Envelope Approximation (SVEA), we obtain the two following independent differential equations

$$\frac{\partial}{\partial z} A_{1,2} + \frac{1}{c} \frac{\partial}{\partial t} A_{1,2} = \frac{2\pi e \bar{n}}{k_{1,2}} \sum \beta_{x(y),j} \delta(z - z_j) e^{-i\alpha_{1,2}} \quad (15)$$

TWO PULSES SASE FEL EMISSION

In the approximation of the time independent scheme, the set of non averaged (14-15) and averaged (9-12) equations have been integrated numerically with independent codes. Both codes employ the forth-order Runge-kutta method to demonstrate the evaluations of FEL system. In non averaged code the Runge-Kutta step size must be small enough to demonstrate the particles motion in the wiggler. At the first step the particles are assumed to be unbunched and monoenergetic.

The parameters chosen for the simulations, similar to the SPARC's [18, 19], are: $\lambda_{01} = 2.8 \text{ cm}$, $K_1 = 2.1$, $\gamma_0 = 300$, and the electron current I has been fixed at 100 A, for a value of $\rho_1 = 5.47 \times 10^{-3}$. In simulation thermal and diffraction effect are ignored.

The comparison between the solutions of averaged (blue curves) and non averaged (red curves) equations is demonstrated in Fig. 1 for (a) $\lambda_{02} = 1.5\lambda_{01}$, (b) $\lambda_{02} = 2\lambda_{01}$ and (c) $\lambda_{01} = 10\lambda_{02}$, with the two magnetic strengths fixed at the same value $K_1 = K_2$.

The agreement is indeed significant along all the growth up to the onset of saturation. Discrepancies arise, instead, once that the saturation is reached, particularly when the two waves have similar intensity (case (a)), probably due to the differences in the sets of equations and to the different method of integration. Black curves, labeled with (T), indicate the logistic map proposed in [20], and given by

$$P_{1,2} = \frac{P_{01,2} A_{1,2} e^{(0.223t/Z_{1,2})}}{(1 + \frac{P_{01,2}}{P_{s1,2}} (A_{1,2} - 1))}. \quad (16)$$

$$A_{1,2} = \left(\frac{1}{3} + \frac{2}{9} \cosh\left(\frac{t}{L_{g1,2}}\right) + \frac{4}{9} \cos\left(\frac{\sqrt{3}t}{2L_{g1,2}}\right) \cosh\left(\frac{t}{2L_{g1,2}}\right) \right)$$

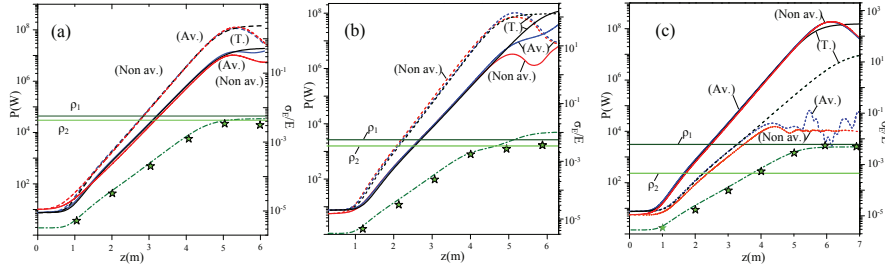


Figure 1: Power $P(W)$ in the x (solid curves) and y (dashed curves) polarizations vs $z(m)$. Comparison between non averaged (red curves) and averaged (blue) model for (a) $n/m = 1.5$ and (b) $n/m = 2$ and (c) $m/n = 10$. The black line is the logistic map, Eq (16). In green σ_E/E , as given by Eq (18). Green stars: energy spread computed by the phase spaces

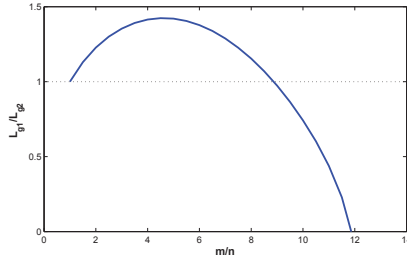


Figure 2: Ratio of gain length of both pulses vs m/n , $K_1 = K_2 = 2.1$

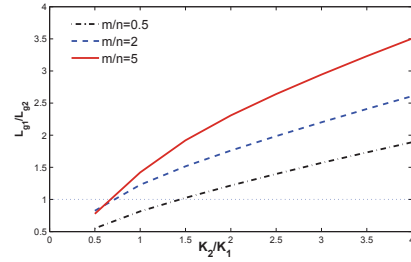


Figure 3: Ratio of gain length of both pulses vs K_2/K_1 , for different values of m/n .

with $Z_{1,2} = 1.066L_g \log(9 \frac{P_{s1,2}}{P_{01,2}})$ and $P_{s1,2} = 1.42\rho_{1,2}P_b$, being the saturation power as a function of the beam power P_b . As can be seen, formula (16) fits very accurately lethargy, growth and gain lengths of both waves, while the saturation value is of the same order only for one of the two polarizations. This is due to the interaction between the two waves occurring when the power in the two polarizations is large enough, an effect which is not accounted in Eq(16). In fact, through electron interaction an induced increase in the energy spread σ_E occurs, as can be seen in Fig. 1, where the relative value σ_E/E , computed by the phase space, is presented together with the analytical formula [20]

$$\frac{\sigma_E}{E} = \sqrt{\left[\frac{\sigma_1}{E}\right]^2 + \left[\frac{\sigma_2}{E}\right]^2} \quad (17)$$

where:

$$\frac{\sigma_{1,2}}{E} = \frac{3}{2} \sqrt{\frac{\rho_{1,2}P_{01,2}}{P_b}} \sqrt{\frac{A}{1 + 1.24 \frac{P_{01,2}}{P_{s1,2}} (A_{1,2} - 1)}}. \quad (18)$$

The growth of the energy spread continues up to the value of ρ_2 , and then, saturates, producing also the anticipated saturation of the radiation with the longer gain length.

The graph of the coefficient L_{g1}/L_{g2} versus different value of the m/n while the two magnetic strengths are fixed at the same value $K_1 = K_2$ is shown in Fig. 2. It shows from $m = 1$ to about $m = 9$ the largest frequency wave has a

shorter gain length, while for m larger than 9 the opposite occurs.

Figure 3 shows the ratio of gain length of both pulses versus K_2/K_1 with fixed $m/n = 0.5, 2, 5$. The slop of the ratios increases as well as the value of the m/n increases.

As a result the wavelengths of two different colors can be changed by setting different periods, while variations in the magnetic strengths have the effect of modifying the gain lengths.

According to general FEL theory the saturation power and length are dependent on the FEL parameter $\rho_{1,2}$, however the numerical simulations show that the interaction between the two waves can change the level of the saturation power. When one wave reaches saturation, the electrons are strongly influenced by its electric field, so the growth of the other one is affected. In order to balance the level of the power in the two different polarization at the end of the undulator, the magnetic strength of one of the two waves can be varied. We fixed the vertical undulator properties ($K_1 = 2.1$ and $\lambda_{01} = 2.8\text{cm}$), while K_2 is varied for different n/m . The ratio of the power of the pulses at the first saturation point is reported vs K_2 in Fig. 4 for various values of n/m between 0.5 and 2. When $n/m = 2$, since $\rho_1 > \rho_2$, the first wave going in saturation was the x -polarization and the power amount of $P_{s1} = 168\text{MW}$ is reached in $z_s = 7.2\text{m}$. The power of the y -polarization in this same point can be varied by using different values of K_2 . In the case $n/m = 1.5$, both x and y -polarizations saturate at $z_{1s} \approx 6\text{m}$, and the

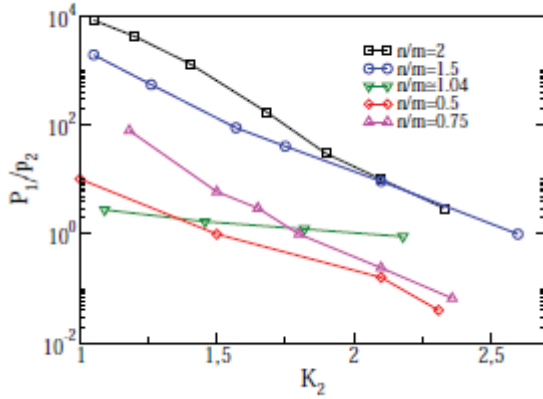


Figure 4: The power ratio of x-polarization to y-polarization for different value of n/m , while $K_1 = 2.1$ and $\lambda_{01} = 2.8\text{cm}$.

x-polarization reaches the value $P_{s1} = 168\text{ MW}$. In the case n/m close but not equal to 1, the waves saturate in close positions, the saturation length does not depend strongly on K_2 , while, instead, the power ratio depends on it. For $n/m = 1$, the gain length follows

$$L_{g1} = L_{g2} = \frac{\lambda_{01}}{4\pi\sqrt{3}\left(1 + \left(\frac{f_2}{f_1}\frac{K_2}{K_1}\right)^2\right)^{1/3}} \quad (19)$$

and the ratio between the powers has a different trend. For the cases $n/m < 1$, since the ratio between the FEL parameters is less than one ($\rho_1/\rho_2 < 1$), the first wave going to saturation is the y-polarization. If m/n is integer (as, for instance the case $n/m = 0.5$) the waves saturate in different points. In otherwise (like $n/m = 0.75$) both waves saturate in same position but in different power levels.

CONCLUSION

Emission of two pulses from two orthogonal undulators with different polarizations and periods have been discussed. Non averaged and averaged equations have been present. The agreement between these two models as regards lethargy, growth and gain length of the radiation, with discrepancies appear in saturation have been demonstrated. The advantage of this kind of device is production of two color radiation with an easy control of the frequencies and opposed polarizations, while the total length of the device does not change respect to usual single color FELs. The possibility of changing independently the strength of the two magnetic fields allows to control the final power and the saturation length.

REFERENCES

- [1] J. A. Rudenko, and R. Moshhammer, Annu. Rev. Phys. Chem. 63, 635 (2012).
- [2] C. M. Guenther, et al., Nature Photonics 5, 99 (2011).
- [3] H. P. Freund and P. G. O'Shea, Phys. Rev. Lett. 84, 2861 (2000).
- [4] D. Jaroszynski et al., Phys. Rev. Lett. 72, 2387 (1994).
- [5] S. G. Biedron, et al., SPIE paper N. 4632-35 LASE 2002 High-Power Lasers and Applications Directed Energy Laser and Beam Control Technologies.
- [6] G. Dattoli, L. Giannessi, et al., Nucl. Instr. and Meth. Res., Sect. A, 495, 48 (2002).
- [7] G. Dattoli, V. V. Mikhailin, P. L. Ottaviani and K. V. Zhukovsky J. Appl. Phys. 100, 084507 (2006).
- [8] B. Mahieu, E. Allaria, D. Castronovo, M. B. Danailov, et al., Optics Express 21, 22728 (2013).
- [9] E. Allaria, F. Bencivenga, R. Borghes, F. Capotondi et al., Nature Communications 4, 2476 (2013).
- [10] M. Ferrario et al., Nucl. Instr. and Meth. Res., Sect. A, A 637, S43-S46 (2010).
- [11] V. Petrillo, M. Anania, M. Artioli et al., Phys. Rev. Lett., 111, 114802 (2013).
- [12] F.-J. Decker et al., "Two-Color Self Seeding and Scanning the Energy of Seeded Beams at LCLS", In Proc. 35th Int. Free-Electron Laser Conf., New York, 2013, pp. 514-517.
- [13] F. Ciocci et al., Phys. Rev. Lett. 111, 264801, (2013).
- [14] G. Dattoli, N. S. Mirian, et al., Phys. Rev. ST Accel. Beams, 17, 050702 (2014).
- [15] N. S. Mirian, G. Dattoli et al., submitted for publication (2014).
- [16] W. B. Colson, IEEE J. Quantum Electron. 17, 1417 (1981).
- [17] R. Bonifacio, C. Pellegrini and L. Narducci, Opt. Commun. 50, 373 (1984).
- [18] M. Ferrario, D. Alesini, M.P. Anania et al., Nucl. Instrum. Methods Phys. Res., B 309,183 (2013).
- [19] L. Giannessi et al., Phys. Rev. ST Accel. Beams 14, 060712 (2011).
- [20] G. Dattoli, P.L. Otaviani, S. Pagnutti, "Booklet for FEL design: a collection of practical formulae", Report No. ENEA RT/2007/40/FIM.

SPECTRAL LIMITS AND FREQUENCY SUM-RULE OF CURRENT AND RADIATION NOISE MEASUREMENT*

R. Ianculescu, University of Tel-Aviv, Tel-Aviv and Shenkar College, Ramat Gan, Israel
A. Gover, A. Nause, University of Tel-Aviv, Tel-Aviv, Israel

Abstract

The current noise spectrum of an electron beam is generally considered white and expressed by the shot-noise formula (eI_0). It is possible to control the spectral energy of a random electron beam current by longitudinal space charge micro-dynamics and dispersive transport. Both noise suppression (relative to eI_0) and noise enhancement have been demonstrated, exhibiting sub/super-Poissonian particle distribution statistics, respectively. We present a general theory for the current noise of an e-beam and its radiation emission in the entire spectrum. The measurable current noise spectrum is not white. It is cut-off at high frequencies, limited by the measurement length and the beam axial momentum spread (fundamentally limited by quantum uncertainty). We show that under certain conditions the current noise spectrum satisfies a frequency sum-rule: exhibiting noise enhancement in one part of the spectrum when suppressed at another part and vice versa. The spontaneous emission (radiation noise) into a single radiation mode or single direction in any scheme (OTR, Undulator etc.) is sub-radiant when the beam current is sub-Poissonian and vice versa, but the sum-rule does not apply.

INTRODUCTION

Electron beam current-noise is an inherent property of any particulate current resulting from the microscopic discontinuity of charge flow in a charged particles beam. The conventional assumption regarding the current noise in an accelerated electron beam is that it is limited by the Shot-Noise formula:

$$S_{I_{\text{shot}}} = eI_0 \quad (-\infty < f < \infty), \quad (1)$$

where I_0 is the average current of a continuous coasting electron beam and $S_I(f)$ is the power spectral density (PSD) of the current. This expression is a direct consequence of the assumption that the beam particles positions are random uncorrelated uniform variables, so that the number of particles in each interval satisfies the Poisson statistics.

It has been known [1] that as an electron beam propagates, the Coulomb interaction between the particles results in correlation between the particle positions and therefore, the particles statistics, as well as their current PSD may deviate from the shot-noise formula (1). In particular it has been shown that Eq. (1), is not even a lower limit for random electron beam noise, and taking advantage of the Coulomb interaction effect, or the longitudinal space charge (LSC) interaction of random bunching, it is possible to suppress

the current noise below the shot-noise level (current noise suppression) at least in part of the spectrum.

Recently it has been shown theoretically [2–8] and experimentally [9, 10] that shot-noise suppression is possible in high quality e-beams at optical frequencies. This noise suppression process can be achieved by transport of the beam along a drift section of quarter plasma oscillation length [9] or by transport through a drift section and a subsequent dispersive section [10]. In the later case, if the dispersion effect (presented by the parameter R_{56}) is large, the opposite effect - noise gain - is achieved, at least in part of the spectrum (micro-bunching instability [11]).

Current noise is the source of incoherent spontaneous emission of radiation (radiation noise) in all electron-beam radiation sources, and in particular Undulator radiation and SASE (Self Amplified Spontaneous Emission) in FEL [8]. For this reason controlling radiation noise is one of the reasons of interest in controlling electron-beam current noise at short wavelengths. In innovative temporally coherent seed-injected FELs [12] incoherent SASE radiation limits the coherence of the FEL output and imposes stringent demands on the power level of the seed radiation source [8]. Hence current noise suppression of the e-beam before injection into the wiggler is desirable. On the other hand, control over the e-beam current shot-noise can also be useful for the opposite purpose: enhancing SASE radiation [13]. This process has been recently demonstrated by Marinelli et al [14] and may possibly be used to produce high power radiation in SASE FELs with shorter wigglers.

MEASUREMENTS OF CURRENT-NOISE SPECTRUM

Determining the spectral limits of noise-control, and particularly noise-suppression, is a task of prime interest in connection to electron-beam transport in applications of electron beams for emission of coherent radiation (FEL). Of primary importance is the short wavelength limit, as there is significant interest in developing coherent (low noise) X-UV FELs.

The short wavelength limit of current noise suppression by drift over a quarter plasma wavelength is the Debye condition: $\lambda > \lambda_D$, where the Debye wavelength λ_D is determined by the axial velocity spread of the beam due to finite emittance or energy spread [15]. A similar condition applies also to the drift/dispersion noise suppression scheme where the dispersive section enhances the optical phase-spread at short wavelength [15]. The LSC noise-suppression effect is also limited at low frequencies (though this limit is of less interest). The low frequency limitation of LSC interaction

* This research was supported by a grant from the United States-Israel Binational Science Foundation (BSF), Jerusalem, ISRAEL

is due to the 3-D fringing effect in a finite cross-section beam [3].

While the shot-noise formula (1) predicts a “white noise” spectrum for a continuous uncorrelated electron beam as a direct result from the assumption of Poisson statistics, the noise-suppressed (or noise-enhanced) electron beam is governed by more complex statistics, and its spectrum is certainly not “white”. To understand the nature of this spectrum we take a close look into the derivation of the current noise formulae, and in particular pay attention to physical limitations associated with the measurement of the spectrum.

Since optical frequency current cannot be measured directly, the only way to measure the current optical frequency noise spectrum is by measuring the radiation that the e-beam current emits in any kind of radiation scheme, in which the optical radiation spectrum is proportional to the current noise spectrum. Most measurements of this kind were done using Optical Transition Radiation (OTR) [16]. Another obvious scheme is Undulator radiation, which is the spontaneous emission radiation of an FEL. In any case it is important to point out that any physical measurement is done during a finite time, which in the present case is the transit time of the electron through the radiation device $T_{tr} = L_{tr}/(\beta c)$, where L_{tr} is the radiative emission length, namely the formation length $L_f = \beta\gamma\lambda$ in the case of OTR and the Undulator length L_u in the case of Undulator radiation.

The finite measurement time and the finite radiation emission length have implications on the applicability of the current noise spectral measurement of a correlated electron beam as well as an uncorrelated electron beam (shot-noise): the interaction length must be short enough in order to make sure that one measures spontaneous emission only and not SASE, and that the current noise stays constant along the transit length, and that transition of current noise to velocity noise through LSC micro-dynamic processes [8, 15] is negligible.

Under these limiting assumptions, a general formulation was presented in [17] for the calculation of the spectral radiation energy emission by a finite pulse of N_e electrons entering the radiative interaction region at ordered times (pre-bunched) or random times. The current of the electron pulse is represented by:

$$I(t) = -e \sum_{j=1}^{N_e} \delta(t - t_{0j}), \quad (2)$$

where t_{0j} is the time at which electron j is at $z = 0$. Its spectral components are

$$\check{I}(f) = -e \sum_{j=1}^{N_e} e^{i2\pi f t_{0j}} \quad (3)$$

where we define the Fourier transform

$$\check{I}(f) = \int_{-\infty}^{\infty} dt I(t) \exp(i2\pi f t), \quad (4)$$

The energy spectral density (ESD) of the finite pulse is

$$p_I(f) = \langle |\check{I}(f)|^2 \rangle = e^2 \left\langle \left| \sum_{j=1}^{N_e} e^{i2\pi f t_{0j}} \right|^2 \right\rangle, \quad (5)$$

here $\langle \rangle$ represents statistical average over the arrival times t_{0j} . For a continuous coasting beam one usually defines the power spectral density (PSD) by $S_I(f) = \lim_{T \rightarrow \infty} \frac{1}{T} \langle |\check{I}_T(f)|^2 \rangle$, where $\check{I}_T(f)$ is the Fourier transform in the time window T , which reduces for the case of a rectangular finite pulse of time T_b to

$$S_I(f) = \frac{1}{T_b} \langle |\check{I}(f)|^2 \rangle = \frac{p_I(f)}{T_b}, \quad (6)$$

The spontaneous emission formulation [17] is based on a modal expansion of the radiation field in terms of any complete set of eigenmodes, where the set may be discrete or continuous modes of free space (plane-waves).

The derivation leads to a general proportionality relation of the ESD of the emitted radiation energy per mode (in units of Joule/Hz) and the ESD of the current. The proportionality factor can be calculated specifically for any free electron radiation scheme like Undulator radiation and OTR [9, 17] then be used for the calculation of the current ESD as long as one measures the radiation energy per mode, or in the case of free space plane waves - the far field radiation ESD per unit solid angle.

As shown in the next sections the detailed analysis of the current noise and the consequent radiation noise shows that the ESD of the current and the radiation deviate from the simple white shot-noise of formula (1) even when the e-beam is random and uncorrelated. At low frequencies (long wavelengths)

$$f < 1/T_b \quad (7)$$

(where T_b is the pulse duration) one expects enhancement of the current noise due to the coherent contribution (DC part) of the pulse shape function to the Fourier transform. This effect gives rise to super-radiant emission at low frequencies [17].

Another effect colors the measurable spectral energy of the current noise, and cuts it off at high frequencies. This effect is associated with the inherent uncertainty in the particle position during the measurement of the current noise. Because noise measurement is never instantaneous and because there is always inevitable uncertainty in the position σ or crossing time $\sigma_t = \sigma/(\beta c)$, of the particles either because of initial axial velocity spread, or fundamentally, because of quantum (Heisenberg) momentum uncertainty, the position of each particle in the calculation of the current ESD (5) must be averaged over the probability function of the position uncertainty (or t_{0j}). This is done in the following sections, and also resolves the problem of a seemingly infinite noise energy when one integrates the ESD of point particles (5) over all frequencies.

An interesting observation, that was noted by Alex Chao [18] for current-noise spectrum, suggests a “sum-rule theorem”, namely that the integral of the noise spectrum stays constant even when the noise is suppressed or enhanced in some part of the spectrum. This theorem and its limitations are examined in the following sections, using our finite noise energy model. Simple examples for noise suppression or enhancement (sub-Poissonian or super-Poissonian distributions) are examined.

THE DERIVATION OF THE SHOT-NOISE FOR A CONTINUOUS COASTING BEAM OF POINT CHARGES

We consider a bunch of particles, each one of charge e , all moving with a uniform velocity $v = \beta c$ in the \hat{z} direction. The bunch length is $L_b \rightarrow \infty$, the number of charges is $N_e \rightarrow \infty$, so that N_e/T_b is finite, resulting in the average DC current $I_0 = eN_e/T_b$. Each charge is uniformly distributed in the interval $[0, L_b]$, i.e. has equal probability to be located anywhere in the bunch. To each space coordinate we associate a time interval coordinate, so that $T_b \equiv L_b/v$ is the time interval of the entire bunch. Hence counting charges in a space interval Δz at a given time is equivalent to counting charges that pass through a given point z during a time interval $\Delta t = \Delta z/v$. The bunch length T_b is divided in sub-intervals Δt , so that the current measured in the interval Δt is $I = en/\Delta t$, where n is a random variable representing the number of charges in the given interval Δt .

The probability to find a charge in an interval $\delta t \ll \Delta t$ is $p = N_e \delta t / T_b$. Because the probability p is extremely small, one may neglect the possibility of having 2 or more charges in the interval δt , considering the occurrence of the event of having a charge in δt as $N = \Delta t / \delta t$ Bernoulli trials, so that n is binomial distributed with N trials and probability p , with average $m_n = Np$ and variance $\sigma_n^2 = Np(1-p)$. Because N is very large and p is very small, n may be approximated by Poisson distribution with parameter $\lambda = Np = N_e \Delta t / T_b$, so that its average and variance are $m_n = \sigma_n^2 = \lambda$.

It follows that when the *location* is distributed *uniformly*, the number of charges in *any* interval Δt is *Poisson* distributed, i.e. having the mean equal to the variance.

So if one measures the current I in a time interval Δt , one obtains $I = en/\Delta t$, so that the current is the random variable n multiplied by $e/\Delta t$. Therefore the average current is $m_I = em_n/\Delta t = e\lambda/\Delta t \equiv I_0$ and its variance is $\sigma_I^2 = (e/\Delta t)^2 \sigma_n^2 = (e/\Delta t)^2 \lambda = eI_0/\Delta t$. Considering $\Delta t = 1/(2B)$ to be the Nyquist interval, where $2B$ is the two-sided bandwidth, we obtain $\sigma_I^2 = 2eI_0B$. For point charges, the current at time t is independent from the current at time $t + \tau$, so the auto-covariance matrix is diagonal $C_I(\tau) \equiv C_{I(t)I(t+\tau)} = eI_0\delta(\tau)$ and its Fourier transform is eI_0 having the area of σ_I^2 in the bandwidth range $-B < f < B$. Therefore the auto-covariance function is

$$C_I(\tau) = eI_0\delta(\tau), \quad (8)$$

and from random processes theory, the auto-correlation function is the DC square plus the auto-covariance function:

$$R_I(\tau) = I_0^2 + eI_0\delta(\tau), \quad (9)$$

and the PSD is the Fourier transform of the above

$$S_I(f) = I_0^2\delta(f) + eI_0 \equiv I_0^2\delta(f) + S_{I_{\text{shot}}}, \quad (10)$$

where the flat spectral density is $S_{I_{\text{shot}}}$ in formula (1).

We saw in this section that if the charges are *uniformly* distributed over the interval T_b , the *number* of charges is *Poisson* distributed in *each* sub-interval Δt . The opposite is not necessarily true: if the number of charges is Poisson distributed in a sub-interval Δt we only know that it is also Poisson distributed in any sub-interval *bigger* than Δt (i.e. for frequencies smaller than $1/(2\Delta t)$), but about smaller intervals (higher frequencies) we don't know anything, and this depends on how the charges are distributed inside Δt . It is to be mentioned that the beam drift dynamics establishes the distribution of the charges locations and this *location distribution* establishes the statistics of the current, i.e. the statistics of the random variable n . In this work we do not use beam dynamics, but we would examine how changes in the statistics of n influence the spectrum.

THE FINITE PULSE ESD AND THE SUM RULE

Expression (10) describes an ideal Shot noise PSD, for a coasting beam. In this section we analyze the energy spectral density (ESD) for a finite beam of duration T_b and the connection to the coasting beam PSD.

Expanding Eq. (5), we get

$$p_I(f) = e^2 \left\langle \sum_{j=1}^{N_e} \sum_{k=1}^{N_e} e^{i2\pi f(t_{0j}-t_{0k})} \right\rangle = e^2 N_e + e^2 \left\langle \sum_{j=1}^{N_e} \sum_{\substack{k=1 \\ k \neq j}}^{N_e} e^{i2\pi f(t_{0j}-t_{0k})} \right\rangle \quad (11)$$

The first part of the result was obtained by summing over $j = k$ and represents the independent frequency ESD Shot noise term:

$$p_{I(\text{shot})} \equiv e^2 N_e = T_b eI_0, \quad (12)$$

which results in the PSD Shot noise term eI_0 in Eq. (10) if divided by T_b . The second part should average to 0 for $f \neq 0$, but it has a contribution for $f \simeq 0$. This contribution may be approximated for $N_e \gg 1$ by replacing the sum by an integral on dt and setting $dt \simeq T_b/N_e$, as follows

$$e^2 \left\langle \sum_{j=1}^{N_e} \sum_{\substack{k=1 \\ k \neq j}}^{N_e} e^{i2\pi f(t_{0j}-t_{0k})} \right\rangle \simeq e^2 \left| \frac{N_e}{T_b} \int_0^{T_b} e^{i2\pi f t} dt \right|^2 = I_0^2 T_b^2 \text{sinc}^2(fT_b). \quad (13)$$

This part, divided by T_b represents the $\delta(f)$ in Eq. (10), given that $\lim_{T_b \rightarrow \infty} T_b \text{sinc}^2(fT_b) = \delta(f)$.

In addition, as mentioned before, there is always uncertainty in the particle axial momentum - either because of technical momentum spread of the electron beam, or fundamentally because of quantum limits (Heisenberg's uncertainty principle). Therefore we shall consider the size of the charge to be finite, so that $\delta(t - t_{0j})$ in Eq. (2) is replaced by $\frac{1}{\sqrt{2\pi}\sigma_t} \exp\left(-\frac{(t-t_{0j})^2}{2\sigma_t^2}\right)$, so that σ_t represents the uncertainty in the arrival time of a charge.

Repeating the Fourier transform on the current for charges of finite size, the $\exp(i2\pi f t_{0j})$ are replaced by $\exp(i2\pi f t_{0j}) \exp\left[-\frac{1}{2}f^2(2\pi\sigma_t)^2\right]$, so that the Fourier transform of the current should be multiplied by the factor $\exp\left[-\frac{1}{2}f^2(2\pi\sigma_t)^2\right]$.

This implies that the ESD in Eq (5) should be multiplied by the square of the above term: $e^{-f^2(2\pi\sigma_t)^2}$, so that the ESD of the current is described by:

$$p_I(f) = e^2[N_e^2 \text{sinc}^2(fT_b) + N_e]e^{-f^2(2\pi\sigma_t)^2}. \quad (14)$$

This means that very close in time measurements of current are *dependent*. For this purpose let us consider the $T_b \text{sinc}^2(fT_b) \approx \delta(f)$ in Eq. (14), divide by T_b and inverse Fourier the non delta part. This gives a more accurate auto-covariance function

$$C_{I(\text{finite size charges})}(\tau) = eI_0 \frac{1}{2\sqrt{\pi}\sigma_t} \exp\left(\frac{-\tau^2}{4\sigma_t^2}\right), \quad (15)$$

which means that neighbor measurements of current done on time intervals of the order of the arrival uncertainty σ_t are dependent.

The sum rule

The total energy in the ESD may be analyzed using Parseval theorem. If $f(t)$ and $\check{f}(f)$ are a Fourier transform pair

$$\int_{-\infty}^{\infty} |f(t)|^2 dt = \int_{-\infty}^{\infty} |\check{f}(f)|^2 df \quad (16)$$

Averaging on both sides and using the ESD definition in Eq. (5), we obtain from Parseval theorem

$$\left\langle \int_0^{T_b} I^2(t) dt \right\rangle = \int_{-\infty}^{\infty} p_I(f) df = 2 \int_0^{\infty} p_I(f) df \quad (17)$$

where the last equality uses the fact that the ESD is an even function. For point particles (canceling e^2 on both sides) it becomes:

$$\left\langle \int_0^{T_b} \left(\sum_{j=1}^{N_e} \delta(t - t_{0j}) \right)^2 dt \right\rangle = 2 \int_0^{\infty} \left| \sum_{j=1}^{N_e} \exp(i2\pi f t_{0j}) \right|^2 df \quad (18)$$

This sum rule, was noted by Alex Chao [18]. It implies that the LHS is insensitive to particles positions (being δ^2 for point particles), hence the RHS must be constant, and therefore if there is noise suppression (homogenization) in one part of the spectrum, there must be noise enhancement in another part.

However, the problem for point particles is that the above constant is infinite, because the δ^2 function is ill defined. The solution: any physical measurement of current noise spectrum (OTR, Undulator radiation) takes place during a finite beam transit time, so that during the measurement there is inherent uncertainty in the particle location (σ) either because of momentum spread or fundamentally because of quantum (Heisenberg) principle. This consideration sets the constant to be finite, but sets a limit on the validity of the sum-rule (particles overlap).

Therefore the sum-rule is valid under the limitations of the overlap condition, and we may evaluate both sides of (17) for the case of finite size charges. The LHS of Eq. (17) results in

$$\begin{aligned} \left\langle \int_0^{T_b} I^2(t) dt \right\rangle &= \int_0^{T_b} dt \left(\sum_{j=1}^{N_e} \frac{e^2}{\sqrt{2\pi}\sigma_t} \exp\left(-\frac{(t-t_{0j})^2}{2\sigma_t^2}\right) \right)^2 \\ &\approx \frac{N_e e^2}{2\sqrt{\pi}\sigma_t}, \end{aligned} \quad (19)$$

for any realization of $I(t)$, provided the gaussians do not overlap, i.e. if

$$\sigma_t \ll T_b/N_e. \quad (20)$$

or using the definition of I_0 the condition becomes

$$I_0 \ll e/\sigma_t, \quad (21)$$

hence is valid for low currents. The RHS of Eq. (17) results in

$$2 \int_0^{\infty} p_I(f) df \approx e^2 N_e \left(\frac{1}{2\sqrt{\pi}\sigma_t} + \frac{N_e}{T_b} \right), \quad (22)$$

provided the $T_b \text{sinc}^2(fT_b)$ in Eq. (14) is narrow enough to be approximated by $\delta(f)$ and hence not to be affected by the Gaussian decay $e^{-f^2(2\pi\sigma_t)^2}$. Indeed the results in Eqs (19) and (22) coincide if condition (20) is satisfied. It is easy to check that one full overlap of 2 charges increases the area by $\frac{1}{\sqrt{\pi}\sigma_t}$, so that partial overlaps increase by less than that.

SIMULATIONS OF THE SUM-RULE CONSERVATION

In Figure 1 we calculate the normalized ESD $p_I(f)/p_{I(\text{shot})}$ vs normalized frequency fT_b for a bunch of $N_e = 500$ charges, where the bunch duration is $T_b = 500$ time units and the arrival uncertainty is $\sigma_t = \frac{T_b/N_e}{80} = 0.0125$.

Next we examine sub and super Poissonian distributions. The interval T_b is divided into M sub-intervals, so given $N_e = 500$ the average number of charges in each sub-interval is N_e/M . Choosing for the number of charges in each sub-interval a Poisson random variable with average N_e/M , or a Gaussian random variable with average N_e/M and standard deviation $\sqrt{N_e/M}$, and spreading the charges by uniform distribution inside the sub-interval, gives a Poissonian realization. The PSD is calculated with Eq. 6, and the averaging is done over 200 realizations, resulting in Poissonian

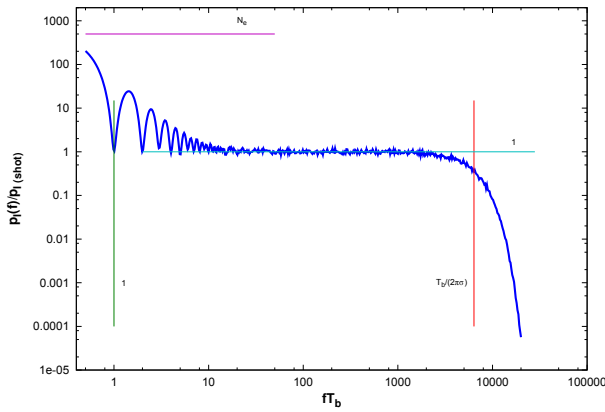


Figure 1: The normalized PSD of the current $p_I(f)/p_{I(\text{shot})}$. The location for each charge is randomly chosen by uniform distribution in the interval $[0, T_b]$, hence the number of charges in each sub-interval is Poisson distributed. The ESD is calculated with Eq. 5, and the averaging is done over 200 realizations. In the flat region we get 1 by definition. At $fT_b = 1$ we see the first 0 of the sinc^2 behavior for low frequencies, and for $fT_b \rightarrow 0$ (left to the plot) the normalized ESD tends to $I_0^2 T_b^2 / p_{I(\text{shot})} = N_e$. At $fT_b = T_b / (2\pi\sigma_t)$ the normalized ESD decays to e^{-1} . The total area under the curve is 11392, which compares well with $\frac{N_e e^2}{2\sqrt{\pi}\sigma_t} = 11284$.

PSD, which is identical to the PSD in Figure 1. Using the same procedure, with a Gaussian distribution of standard deviation $2\sqrt{N_e/M}$ or $0.5\sqrt{N_e/M}$, results in the super and sub-Poissonian PSDs. Because the number of charges in an interval cannot be negative, we cut the distribution below 0, and to keep the correct average we also cut the distribution over $2N_e/M$. Therefore the variances obtained are not exactly the ones chosen. The sub and super-Poissonian behaviors are in sub-intervals bigger or equal the basic sub-interval T_b/M (but not too big to compare with T_b !), i.e. for frequencies smaller than $M/(2T_b)$ but not 0.

Those sub and super-Poissonian PSDs are implemented in Figures 2 and 3 for $M = 50$ and 100 respectively.

In Figure 4 we check how the sum rule described above is satisfied. When creating sub or super-Poissonian distribution for frequencies below some threshold, to satisfy the sum rule, the distribution should be of the opposite type in the complementary range. Unfortunately, this is not easy to show, because for the super-Poissonian cases created here, the overlap between charges increases, hence increasing the total area under the PSD. In addition the frequency regions for the sub and super-Poissonian are very narrow (below normalized frequency $fT_b = 25$ or 50 for the cases described in Figures 2 and 3 respectively), relative to the whole normalized spectrum range of about $fT_b = 10000$, described in those cases. Hence in the complementary region one gets the opposite case, but very close to Poissonian. Also, the small fluctuations of the PSD make the comparison difficult. To show how the sum rule works we created a “very” sub Poissonian distribution in sub-intervals $T_b/50$, having

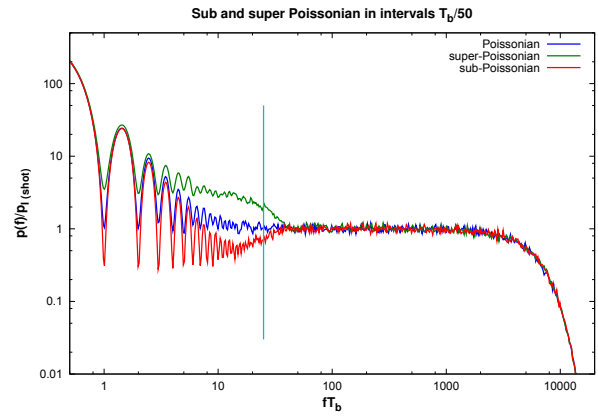


Figure 2: Super and sub-Poissonian statistics in sub-intervals $T_b/50$. The interval T_b is divided into 50 sub-intervals, so given $N_e = 500$ the average number of charges in each sub-interval is 10. The Poissonian, super-Poissonian and sub-Poissonian PSDs are shown by the blue, green and red curves respectively. The standard deviation for the super-Poissonian case is $1.8\sqrt{10}$ instead of the chosen $2\sqrt{10}$, while the sub-Poissonian case has a standard deviation very close to $0.5\sqrt{10}$. The sub and super-Poissonian behavior are for frequencies $fT_b < 50/2 = 25$ (marked with vertical line), and the super and sub Poissonian PSD values are established by the relative variances, i.e. 1.8^2 and 0.5^2 . The areas under the spectra are 11523, 11392, 11396 for the super-Poissonian, Poissonian, and sub-Poissonian, respectively.

a standard deviation close to 0 and compared it with the Poissonian distribution. The comparison required to smooth the lines, hence the crossing point is not accurate. We show the difference between the sub-Poissonian PSD and the Poissonian PSD around the crossing point. Left to the crossing point, the value is negative and right to the crossing point the value tends to be small positive.

CONCLUSION

We presented in this work a statistical and spectral analysis for the current of an electron beam. We showed that even for random and uncorrelated distribution of the electrons locations, the ESD is not exactly the shot-noise, but has super-radiant properties at low frequencies, and is cut off at high frequencies due to the uncertainty in the arrival time of the electrons. The last conclusion solves the “infinite” energy dilemma of the shot-noise.

We showed that under some conditions, the ESD satisfies a sum-rule, so when noise is suppressed in some spectral region it is enhanced in another region. However the validity of the sum-rule is limited to low current beam electron only (21), such that the overlap of the uncertainties of the particles location during transit is smaller than the average spacing between the particles.

We calculated ESD for different cases of sub or super Poissonian, and checked the sum-rule, i.e. the (partial) conservation of the total energy.

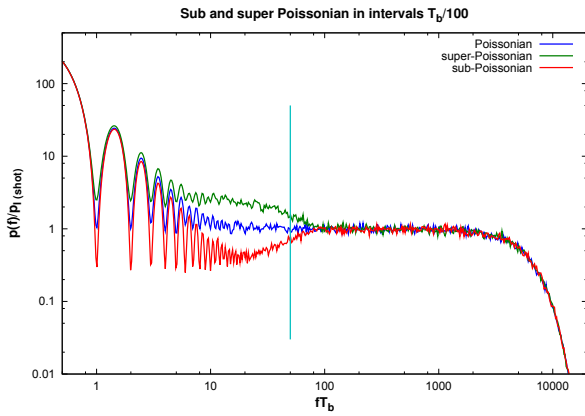


Figure 3: Super and sub-Poissonian statistics in sub-intervals $T_b/100$. The interval T_b is divided into 100 sub-intervals, so given $N_e = 500$ the average number of charges in each sub-interval is 5. The Poissonian, super-Poissonian and sub-Poissonian PSDs are shown by the blue, green and red curves respectively. The standard deviation for the super-Poissonian case is $1.54\sqrt{10}$ instead of the chosen $2\sqrt{10}$, while the sub-Poissonian case has a standard deviation very close to $0.5\sqrt{10}$. The sub and super-Poissonian behavior are for frequencies $fT_b < 100/2 = 50$ (marked with vertical line) and the super and sub Poissonian PSD values are established by the relative variances, i.e. 1.54^2 and 0.5^2 . The areas under the spectra are 11599, 11392, 11315 for the super-Poissonian, Poissonian, and sub-Poissonian, respectively.

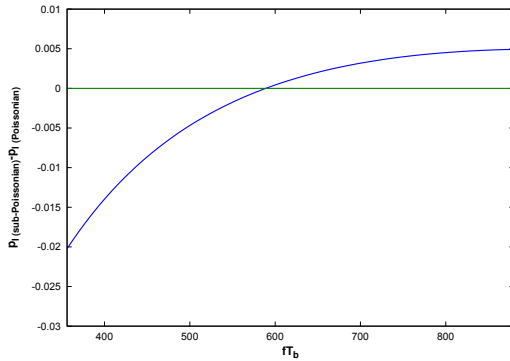


Figure 4: The difference between the PSD for a sub-Poissonian distribution (at low frequencies) and a Poissonian distribution. Because of the sum rule, sub-Poissonian spectrum becomes higher than the Poissonian spectrum at high frequencies.

REFERENCES

- [1] H. Haus and N. Robinson, “The minimum noise figure of microwave beam amplifiers”, Proc. IRE 43, 981 (1955).
- [2] A. Gover and E. Dyunin, “Collective-Interaction Control and Reduction of Optical Frequency Shot Noise in Charged-Particle Beams”, PRL 102, 154801, (2009).
- [3] A. Nause, E. Dyunin and A. Gover, “Optical frequency shot-noise suppression in electron beams: Three-dimensional analysis”, Jour. Appl. Phys. 107, 103101 (2010).
- [4] A. Marinelli and J. Rosenzweig, “Microscopic kinetic analysis of space-charge induced optical microbunching in a relativistic electron beam”, Phys. Rev. ST Accel. Beams, 13, 110703 (2010).
- [5] K.-J. Kim, R.R. Lindberg, “Collective and Individual Aspects of Fluctuations in Relativistic Electron Beams for Free Electron Lasers”, TUOA2, in Proc. 33th Int. Free-Electron Laser Conf., Shanghai, China, pp. 156-159 (2011).
- [6] D. Ratner, Z. Huang and G. Stupakov, “Analysis of shot noise suppression for electron beams”, Phys. Rev. ST-AB 14, 060710 (2011).
- [7] A. Gover, T. Duchovni, E. Dyunin, and A. Nause, “Collective microdynamics and noise suppression in dispersive electron beam transport”, Physics of Plasmas, 18 (2011).
- [8] A. Gover and E. Dyunin, Journal of Quantum Electronics 132166 (2010).
- [9] A. Gover, A. Nause, E. Dyunin, and M. Fedurin, “Beating the shot-noise limit”, Nature Physics, 8, 877 (2012).
- [10] D. Ratner and G. Stupakov, “Observation of shot noise suppression at optical wavelengths in a relativistic electron beam”, Phys. Rev. Lett., 109, 034801 (2012).
- [11] Z. Huang, J. Wu and T. Shafan “Microbunching Instability due to Bunch Compression” SLAC-PUB-1159, (December, 2005)
- [12] M. Labat et al., “High-Gain Harmonic-Generation Free-Electron Laser Seeded by Harmonics Generated in Gas”, Phys. Rev. Lett., 107, 224801 (2011).
- [13] E. L. Saldin, E. A. Schneidmiller, and M. V. Yurkov, “The physics of free electron lasers” (Springer, Berlin, 2000).
- [14] A. Marinelli, E. Hemsing, M. Dunning, D. Xiang, S. Weathersby, F. O’Shea, I. Gadjev, C. Hast, and J. B. Rosenzweig, “Generation of Coherent Broadband Photon Pulses with a Cascaded Longitudinal Space-Charge Amplifier”, Phys. Rev. Lett., 110, 264802 (2013).
- [15] A. Nause, E. Dyunin and A. Gover, “Short wavelength limits of current shot-noise suppression” to be published in Physics of Plasmas, (Sept. 2014)
- [16] V.L. Ginzburg and I.M. Frank. “Transition radiation” Zh. Eksp. Teor. Fiz., 16(1):15-22, 1946.
- [17] A. Gover, “Superradiant and stimulated-superradiant emission in prebunched electron-beam radiators. I. Formulation” Phys. Rev. Special Topics - Accelerators and Beams 8, 030701 (2005)
- [18] Alex Chao, Stanford Linear Accelerator, private communication, (2014)

AN ANALYSIS OF OPTIMUM OUT-COUPLING FRACTION FOR MAXIMUM OUTPUT POWER IN OSCILLATOR FEL

Jia Qika[#], NSRL, University of Science and Technology of China, Hefei, 230029, China

Abstract

The effect of the out-coupling fraction on the output power in oscillator FEL is analyzed. The formulas of the optimum out-coupling fraction and the corresponding maximum output power are given. They are dependent on the initial small signal gain and the passive loss rate of the light in the optical cavity. The initial comparison show that the result given by the formula agree well with the results in references.

INTRODUCTION

The basic working modes of free-electron lasers (FELs) include the amplifier, the oscillator and the self-amplified spontaneous emission (SASE). The oscillator FEL work in the low gain regime with the multi-amplifying. For oscillator FEL, one main goal of the design and optimization is to achieve the maximum output power. An important work is to optimize the out-coupling fraction of the light. It has been discussed by several authors [1-3], in this paper we analysis the optimization of the out-coupling fraction for maximum output power, here we don't consider what specific way of the out-coupling is used.

ANALYSIS

By expanding FEL equations and taking some approximation, the optical field gain at the pass n can be given as [4]

$$g_n \approx \frac{e^{g_{ss}} - 1}{1 + e^{g_{ss}} P_{n-1} / P_c}, \quad (1)$$

where P_{n-1} is the optical power at the pass $n-1$, the power of the optical pulse at the undulator exit during the n th passage, g_{ss} is initial small signal gain:

$$g_{ss} = -(2k_u \rho L)^3 \left\langle \frac{\partial}{\partial x} \frac{\sin^2(x/2)}{(x/2)^2} \right\rangle_{\phi_0}, \quad (2)$$

where ρ is FEL parameter, k_u and L is the wave vector and length of the undulator, $x = \phi_0' L$, the angular bracket represents the average over the electron's initial phase velocities (i.e. the tuning parameter) ϕ_0' ; and

$$P_c = \frac{g_{ss}}{\beta} \rho P_e. \quad (3)$$

P_e is electron beam power and [4, 5]

$$\beta = (2k_u \rho L)^7 \left\langle \frac{1}{x^7} \{ x(6-x^2) \sin x + 4(1-x^2) \cos x + \frac{3}{2} x \sin 2x + \frac{1}{2} \left(\frac{5}{2} - x^2 \right) \cos 2x - \frac{21}{4} \} \right\rangle_{\phi_0}. \quad (4)$$

When the power equal to P_c , i.e. $P_{n-1} = P_c$, from Eq. 1 it has

$$g_n = \frac{e^{g_{ss}} - 1}{e^{g_{ss}} + 1} = \text{cth}\left(\frac{g_{ss}}{2}\right) \approx g_{ss} / 2.$$

Therefore P_c is the value of the intensity halving the small signal gain of the device. The profiles of the angular bracket parts in the expressions of g_{ss} (Eq. 2) and β (Eq. 4) are given in Fig. 1, from which we have $g_{ss} / \beta \sim 100 / (2k_u \rho L)^4$. Therefore we can estimate the value of P_c : $P_c \sim 100(\sqrt{3}L_g / L)^4 \rho P_e$, for low gain regime $L < 3L_g$, thus we have $P_c \sim 10\rho P_e$. Notice the saturation power $P_s > P_c$ (Eq. 7), we can know that the saturation power of oscillator FEL is larger than that of SASE FEL ($\sim \rho P_e$).

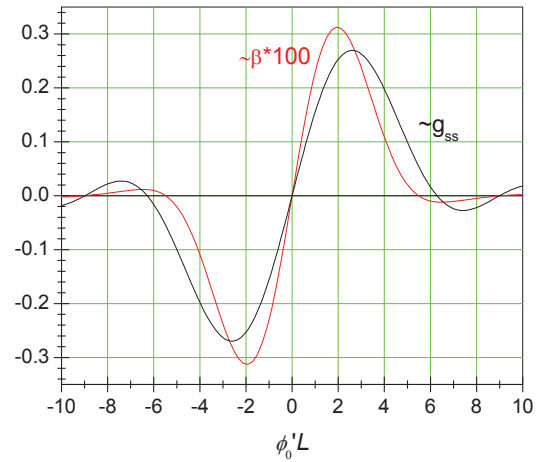


Figure 1: the angular bracket parts of g_{ss} and β in Eq. 2 and 4.

The intra-cavity power at pass n is

$$P_n = P_{n-1}(1 + g_n)(1 - \alpha) = P_0 \prod_{i=1}^n (1 + g_i)(1 - \alpha), \quad (5)$$

where α is the total loss ratio in optical cavity including the output coupling fraction and the passive loss. P_0 is the initial emission power, i.e. the spontaneous emission power [6]:

$$P_0 = (2k_u \rho L)^2 \frac{1}{N_{e,s}} \rho P_e. \quad (6)$$

N_{es} is the number of electrons in the slippage distance.

As the optical field intensity increase, the gain decrease, when the net gain equal to zero, it has $g_n = \alpha/(1-\alpha)$, the system reaches equilibrium, namely the optical field reaches saturation. From Eq. 1 we obtain the saturation power in cavity

$$P_s = \frac{1-\alpha-e^{-g_{ss}}}{\alpha} P_c \sim \frac{g_{ss}-\alpha}{\alpha} P_c. \quad (7)$$

The saturation powers given by Eq. 7 agree well with the one-dimensional numerical results [1].

With Eq. 7 the gain at the pass n (Eq. 1) can also be written as

$$g_n = \frac{(e^{g_{ss}}-1)\alpha}{\alpha + [e^{g_{ss}}(1-\alpha)-1]P_{n-1}/P_s}. \quad (8)$$

The time required to reach saturation can be estimated as

$$T_e \geq \frac{4L_c \ln(P_s/P_0)}{c(g_{ss}-\alpha-g_{ss}\alpha)}, \quad (9)$$

where L_c is the length of optical cavity, We denote the output coupling fraction and the passive loss of the cavity as α_{oc} and α_{lo} , respectively, and from $1-\alpha = (1-\alpha_{lo})(1-\alpha_{oc})$, we have $\alpha = \alpha_{lo} + \alpha_{oc} - \alpha_{oc}\alpha_{lo}$. Then the output power is $P_{out} = P_s(1-\alpha_l)\alpha_{oc}$. For a given intra-cavity optical power of oscillator FEL, the larger out-coupling fraction gives a larger fraction of the out-coupled power. But the larger out-coupling fraction means the smaller net gain, which leads to the optical field saturated earlier, i.e. the lower intra-cavity power. Therefore there exists an optimum output coupling fraction for maximum out-coupled power (Fig. 2).

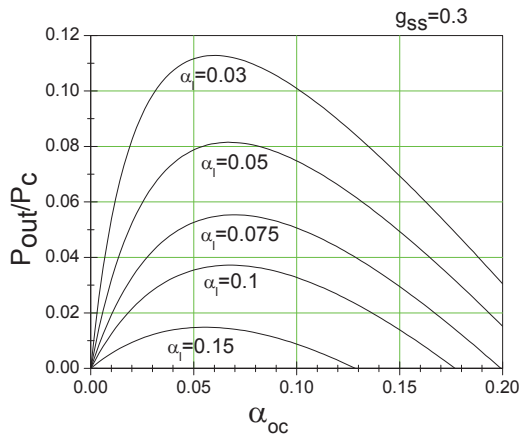


Figure 2: the output power with output coupling fraction for different cavity loss, the initial gain is 0.3.

Using Eq. 7 we differentiate the output power P_{out} with respect to α_{oc} , and set the derivative equal to zero, then we get the optimum out-coupling fraction

$$\alpha_{oc,m} = (\alpha - \alpha_{lo}) / (1 - \alpha_{lo}) = (\sqrt{(1-e^{-g_{ss}})\alpha_{lo}} - \alpha_{lo}) / (1 - \alpha_{lo}). \quad (10)$$

We can see that the optimal output coupling is determined by the passive losses and the initial small signal gain (Fig. 3).

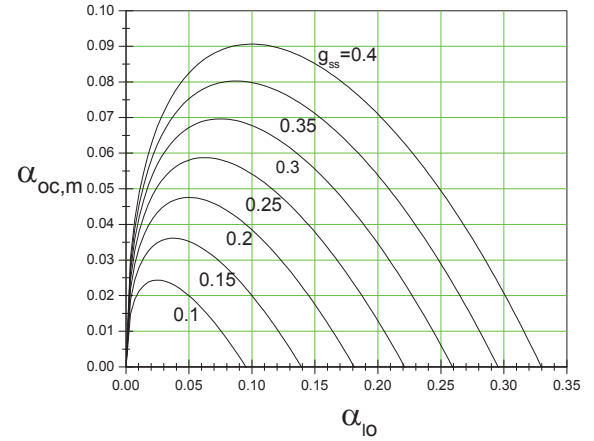


Figure 3: the variation of optimum out-coupling fraction with the cavity loss for different initial gain.

The corresponding maximum output power is:

$$P_{out,m} = (\alpha - \alpha_l)P_s = (\sqrt{1-e^{-g_{ss}}} - \sqrt{\alpha_{lo}})^2 P_c. \quad (11)$$

For comparison, an example of the output power with the out-coupling fraction is shown in Fig. 4, it is from ref. [2]. the optimum out-coupling fraction in the figure is 6%, while using Eq. 10 it is 5.8%. Comparing with the results in references [1,3], the results given by our formula (Eq. 10) are also in good agreement with them.

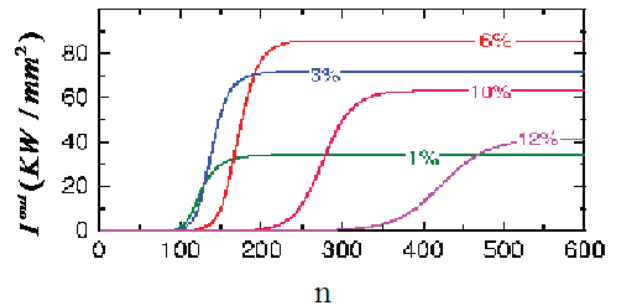


Figure 4: From ref. [2], the outcoupled intensity is shown as a function of the number of roundtrips calculated for different output couplers. The small-signal gain was assumed to be 25% and 5% losses were assumed.

The Eq.10 gives optimum out-coupling fraction 5.8%.

SUMMARY

In summary a simple formula is given for the optimum out-coupling fraction and the corresponding maximum output power of an oscillator FEL, it will be helpful to design and optimization of an oscillator FEL. The obtained formula show that the optimum out-coupling fraction is related with initial gain and the passive loss of the light in the optical cavity.

It should be pointed out that when we get the formula, we assumed that the passive loss is not varied with the out-coupling fraction, which holds under certain conditions. For example, in the hole-coupling mode when the hole is small. But if the hole is too large, the optical field mode will be changed that will have effect on the passive loss. Another assumption is that the initial gain is the small signal gain, which is applicable to the case of the undulator length less than the three gain length, i.e. in the low gain regime.

The results from the formula agree well with the results in the references. The more detail comparison with numerical simulation will be carried out to check the extent of its validity.

ACKNOWLEDGMENTS

This work is partly supported by the Major State Basic Research Development Program of China under Grant

No. 2011CB808301 and the National Nature Science Foundation of China under Grant No. 11375199.

REFERENCES

- [1] G. Dattoli, L. Giannessi, and A. Torre, "Saturation and cavity-loss optimization in free-electron lasers," *PHYSICAL REVIEW E* 48, No. 2, 1993, p1401-1403.
- [2] ELBE, <http://www.hzdr.de/db/Cms?pOid=10501&pNid=83>
- [3] Yehoshua Socol, "High-power free-electron lasers—technology and future applications," *Optics & Laser Technology*, 46, 2013, p111–126.
- [4] Jia Qika, "An analytical calculation for the laser gain in a long pulse FEL", *Chin. Phys. Lett. (China)*, Vol.6, No.12,1989, p533.
- [5] W.B.Colson and S.K.Ride, *Physics of Quantum Electronics*, eds. S.Jacobs,H.Pilloff, M.Sargent, M.Scully and R.Spitzer (Addison-Wesley, Reading, 1980) Vol.7, p377.
- [6] Jia Qika, "Analysis of spontaneous emission and its self-amplification in free-electron laser," *FLS 2006*, DESY Hamburg, <http://adweb.desy.de/mpy/FLS2006/proceedings/index.htm>

A SIMPLE METHOD FOR GENERATING A FEW FEMTOSECOND PULSES IN SEEDED FELS*

Li Heting#, Jia Qika, He Zhigang

NSRL, University of Science and Technology of China, Hefei, 230029, China

Abstract

We propose a simple method to generate a few femtosecond pulses in seeded FELs. We use a longitudinal energy-chirped electron beam passing through a dogleg where transverse dispersion will generate a horizontal energy chirp, then in the modulator, a seed laser with narrow beam radius will only modulate the centre part of electron beam and short pulses in high harmonics will be generated in the radiator. Using a representative realistic set of parameters, we show that 30 nm XUV pulse with duration of 8 femtoseconds (FWHM) and peak power of GW level can be generated from a 180 nm UV seed laser with beam waist of 75 μm .

INTRODUCTION

There is a rapidly growing interest in the availability of extremely short pulses, which have facilitated the rapid development of “ultrafast science”, including structural studies of single biomolecules, femtosecond chemistry, etc [1]. In recent years, free-electron lasers (FELs) researchers have explored various ways to produce high-power, ultrashort pulses at XUV and shorter wavelengths with a particular emphasis on temporal synchronism with external lasers to facilitate pump-probe experiments [2].

A definition of the ultra-short X-ray pulses in Ref. [3] is the pulse duration of the order of few femtoseconds and shorter. A rather natural way to obtain such pulses is to use ultra-short electron bunches. However, most of short pulse schemes rely upon manipulating one or more properties of an ultrashort temporal portion of a much longer electron bunch, such as transverse emittance, energy or current [4-7]. These manipulations generally use a few-cycle, near-IR laser pulse to energy-modulate the e-beam so that, when combined with other transport elements such as chromatic chicanes, foils, specially tuned undulators, the FEL emission will predominately arise from the modulated portion.

In this paper, we propose a new simple method to generate a few femtosecond pulses in seeded FELs. A both longitudinal and transverse energy-chirped electron beam is obtained from a dogleg section and modulated by a seed laser with a narrow beam radius, thus only the short centre portion of electron bunch is modulated and then generate short pulses emission in the radiator. This is an easy-to-implement scheme for an existed seeded FEL configuration.

METHODS

Our scheme, as shown in Fig. 1 in which we place a high-gain harmonic generation (HG) configuration as an example for seeded FELs, does not require any other hardware or special properties of electron beam. The unique difference is the use of dogleg, however, there usually be one or several doglegs in the transport line between the linac and undulators. This scheme can be combined with other kinds of seeded FELs, such as echo-enabled harmonic generation (EEHG) [8], phase-merging enhanced harmonic generation (PEHG) [9] and so on.

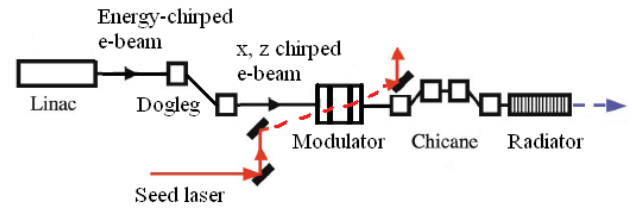


Figure 1: A schematic of the proposed scheme for short pulse production.

We assume an energy-chirped beam at the exit of Linac. The energy chirp parameter

$$h = \frac{d\gamma/\gamma}{dz} \quad (1)$$

is defined such that, for positive sign of h , electrons in the head of the bunch have larger energy than those in the tail, where γ is the relativistic factor and z is the bunch length coordinate. Using the electrons with the average energy γ_0 as the reference particles, for an electron (x_0, z_0) , after passing through the dogleg with a momentum compaction R_{56} and a transverse dispersion η , we have its new coordinates (x, z) as

$$z = z_0 + R_{56}(hz_0 + \delta\gamma_0) \approx (1 + hR_{56})z_0 \quad (2)$$

$$x = x_0 + \eta(hz_0 + \delta\gamma_0) \approx \eta h z_0 \quad (3)$$

Here, we use the condition that the initial slice energy spread $\delta\gamma_0$ is much smaller than the chirped energy deviation and the initial beam transverse size is much smaller than that after dogleg. This approximation is reasonable because here the dogleg has a considerable dispersion strength and, to obtain short pulse, we need to extend the transverse size to an enough big level.

In this case, we can give the RMS bunch length and x-plane beam size after dogleg as

$$\sigma_z \approx (1 + hR_{56})\sigma_{z0} \quad (4)$$

*Work supported by Major State Basic Research Development Program of China (2011CB808301) and the Fundamental Research Funds for the Central Universities of China (WK2310000045)

#liheting@ustc.edu.cn

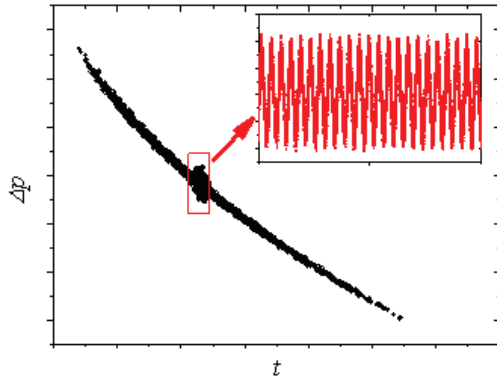


Figure 2: The longitudinal phase space of the electron bunch after modulated by a seed laser with narrow waist.

$$\sigma_x \approx \eta h \sigma_{z0} \quad (5)$$

where σ_{z0} means the RMS bunch length prior dogleg. In addition, the peak current of electron beam changes

$$I_p \approx \frac{1}{(1 + hR_{56})} I_{p0} \quad (6)$$

Till here the situation is very similar to that in Ref. [1] where a slotted foil will be used next and the manipulated electron beam will be accelerated again, while in our scheme, next the electron bunch will be sent through the HGHG configuration.

We assume a seed laser with a small beam radius of r_s to modulate the electron bunch. The transverse beam size of the seed laser is much smaller than the electron beam's, therefore only the electrons that locate in the optical field of the seed laser will be modulated as Fig. 2 shows, and then bunch at the fundamental wavelength and its harmonics after passing a chicane. The length of the modulated portion bunch can be written as

$$\sigma_{z\text{mod}} \approx (1 + hR_{56}) \frac{r_s}{\eta h} \quad (7)$$

In fact, we do not need a very accurate energy chirp from Linac, especially for the bunch head and tail. A roughly energy-chirped electron beam also can achieve that only the centre portion of bunch is modulated by the seed laser.

SIMULATIONS

To show the feasibility of the proposed scheme, as mentioned above, we take an HGHG scheme to generate XUV short pulses as an example. We consider a set of parameters based on Hefei soft x-ray FEL proposal [10]: $E=800$ MeV, $I_p=600$ A, $\varepsilon_n=2$ mm · mrad, slice energy spread: $\delta\gamma=0.01\%$, RMS bunch length $\sigma_{z0}=0.5$ ps, and initial energy chirp: $h=67$ at the exit of Linac. The HGHG process is simulated by the GENESIS code [11]

Assuming a dogleg with a momentum compaction $R_{56}=-7$ mm and a transverse dispersion $\eta=0.6$ m, after passing the dogleg, the electron bunch is compressed by a factor of 1.875, therefore, the peak current becomes to be about 1125 A. We have roughly designed the dogleg settings using the transport matrix method and the

assuming is reasonable and easy to be implemented. In addition, it is worth pointing out that we do not expect to compress the chirped bunch too much through the dogleg, because when the compression factor is large, the slice energy spread will grow dramatically and a large energy modulation will be needed, thus, a very powerful seed laser will be needed as the modulator is very short. Therefore, the bunch is only compressed by a factor less than two. The current profiles before and after the dogleg are given in Fig. 3. The elements R_{51} and R_{52} of the transport matrix are neglected here, as these two elements can be optimized to a very small level by adding one or several quadrupoles in the dogleg and we will discuss the affection in the next part.

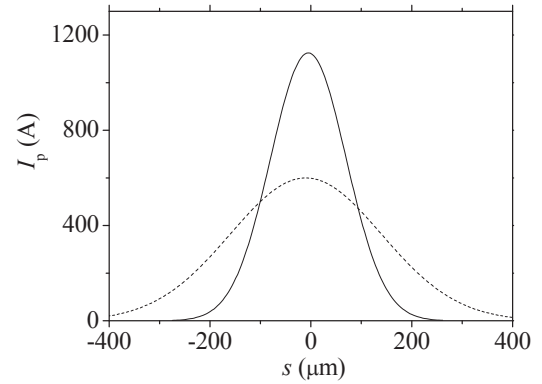


Figure 3: The current profiles at the entrance(dash line) and exit (line) of dogleg.

To generate short pulses, a 180 nm seed laser with a narrow beam waist of 75 μm is used. The rayleigh length of seed laser can be calculated as:

$$z_r = \pi \omega_0^2 / \lambda_s \quad (8)$$

where ω_0 is the radius of the optical beam waist. Here, z_r is about 0.1 m. Obviously, this short Rayleigh length will lead a rapid growth of the laser beam radius in the modulator. Considering this, we use a short undulator with 6 periods and period length $\lambda_u=5.4$ cm to provide period magnetic field for energy modulation. The waist position of the seed laser is the centre of the modulator. On this condition, the laser beam radius at the entrance and exit of the modulator is about twice beam waist. This will lead a spread of the length of the modulated portion. However, as the electrons in different transverse position will obtain different energy modulation, we can suppress this spread effect by carefully optimizing the dispersive strength of the chicane. The following simulation results imply that the modulated portion is much longer than that from Eq.(7), but when after chicane the bunched portion and radiation pulse have a nearly equal length with that from Eq.(7).

According to Eq.(7), we can roughly calculate the length of the modulated portion to be $\sigma_{z\text{mod}}=1\mu\text{m}$ (3.3 fs) and the FWHM length 7.8 fs. We take the sixth harmonic for the HGHG scheme. Figure 4 shows the bunching factor of 6th harmonic along the electron bunch at the exit of chicane. From Fig. 4, it can be found that the FWHM

length of the bunched portion is about 8 fs that is a little longer than the result of analytical calculation. We give the 30 nm radiation pulse in Fig. 5. The FWHM length of the radiation pulse is about 8 fs. The peak power is about 0.9 GW.

These results agree with the analysis very well. The little extending of radiation pulse length should be attributed to the rapid variation of the seed beam radius.

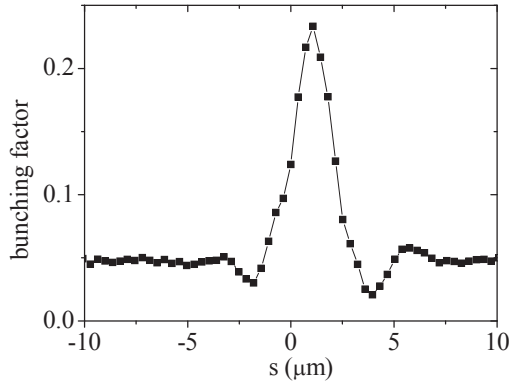


Figure 4: The bunching factor of 6th harmonic along the electron bunch at the entrance of radiator.

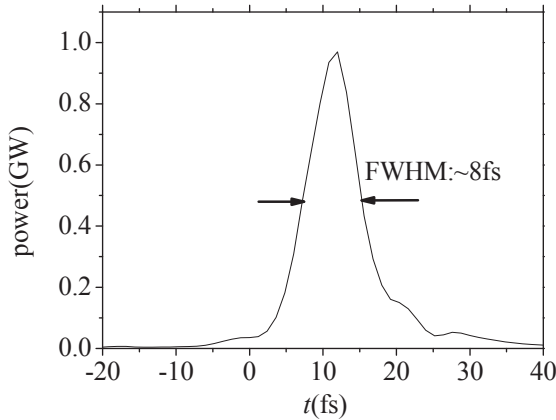


Figure 5: Pulse structure of 30 nm radiation. The pulse length is 8 fs (FWHM).

DISCUSSIONS

Obtaining the electron bunch chirped in both longitudinal and transverse directions is a critical issue in this scheme. The initial energy chirp is easy to be achieved from the Linac and as mentioned above, it does not need to be very accurate. We only care the properties of the centre portion bunch. When passing through the dogleg, the transport matrix elements R_{51} and R_{52} may extend the centre portion length by $\Delta z = R_{51}x + R_{52}x'$, and we should control $\Delta z \ll \sigma_{zmod}$. In a two-dipole dogleg, usually the first term is very small enough to be ignored, but in the second term, the element R_{52} is equal to η , and this may lead a degradation of the quality of the centre

portion bunch. We have simulated the physical process in the dogleg with full matrix, and the results show that it does not degrade the FEL performance too much with above parameter settings. However, one should optimize the transport matrix to minimize R_{52} for experiments.

Another important point is controlling the beam radius of seed laser, which directly determine the radiation pulse length. Limited to the seed wavelength, the seed beam radius is also limited since the rayleigh length will be too short if the seed beam radius is too small. Besides, due to the low up-frequency conversion efficiency, the radiation wavelength of the single stage HGHG scheme is limited and this may finally lead that the radiation pulse length can not be much shorter than the single spike condition. Maybe if we combine this scheme with the EEHG scheme, the radiation pulse length can be sub-femtosecond level.

CONCLUSION

In conclusion, we have described a simple scheme for generating sub 10 fs pulse in seeded FELs. This scheme is easy to be implemented because for an existing seeded FEL facility, the hardware requirement is already satisfied. An extra demand is a seed laser with narrow beam waist. Using the HGHG scheme as an example, we have shown that 30 nm XUV pulse with duration of 8 fs (FWHM) and peak power of GW level can be generated from a 180 nm seed laser with beam waist of 75 μm .

REFERENCES

- [1] P. Emma et al., "ATTOSECOND X-RAY PULSES IN THE LCLS USING THE SLOTTED FOIL METHOD", FEL'04, pp333-338.
- [2] W.M. Fawley, Nucl. Instr. and Meth. A 593 (2008) 111.
- [3] W.A. Barletta, et al., Nucl. Instr. and Meth. A 618 (2010) 69.
- [4] P. Emma, et al., Phys. Rev. Lett. 92 (2004) 074801.
- [5] E.L. Saldin, et al., Phys. Rev. ST Accel. Beams 9 (2006) 050702.
- [6] A.A. Zholents, W.M. Fawley, Phys. Rev. Lett. 92 (2004) 224801.
- [7] A.A. Zholents, G. Penn, Phys. Rev. ST Accel. Beams 8 (2005) 050704.
- [8] Stupakov G. Phys. Rev. Lett., 102 (2009) 074801.
- [9] Chao Feng, et al., New Journal of Physics, 16 (2014) 043021.
- [10] Concept Design Report of Hefei Soft X-ray FEL Facility, May 2006 (in Chinese).
- [11] S. Reiche et al., Nucl. Instr. and Meth. A 483 (2002) 70.

NUMERICAL SIMULATION OF A SUPER-RADIANT THz SOURCE DRIVEN BY FEMTOSECOND ELECTRON BUNCHES*

R. Chulkov, B.I. Stepanov Institute of Physics, NAS, Minsk, Belarus

V. Goryashko, Department of Physics and Astronomy, Uppsala University, Uppsala, Sweden

V. Zhaunerchyk, Department of Physics, University of Gothenburg, Sweden

Abstract

We summarize our studies for a super-radiant source operating in the THz frequency range. In particular, we focus on a single-pass planar undulator comprising no guiding structure. Using a numerical code that supports 3D time-dependent modeling of radiated fields as well as statistical properties of electron bunches, we analyze influence of electron bunch parameters on generated THz radiation and reveal some surprising results. More specifically, for the considered undulator configuration, we predict degradation in the angular divergence and spectral broadening of the generated radiation as the electron bunch emittance decreases. We also demonstrate how electron bunch lengthening associated with the electron energy spread can be suppressed.

INTRODUCTION

Pulsed THz free-electron lasers (FELs) are typically driven by radio-frequency linear accelerators (rf Linacs) able to produce intense electron bunches with a duration in the picosecond or even in the femtosecond range. When the bunch length is much shorter than the resonant wavelength of an excited electromagnetic field in an undulator, the bunch radiates like a point-charge giving rise to the so-called super-radiant regime of an FEL [1]. In this case, output intensity scales as a squared number of all electrons at the FEL start-up while for SASE (self-amplified spontaneous emission) it scales with a number of electrons [2]. The super-radiant regime enables realization of a relatively compact high-power THz FEL facility based on a single-pass undulator configuration. At the same time, the operation efficiency of such a super-radiant source is strongly affected by the quality of a driving electron bunch such that the source design requires a numerical modeling, which should take into account general statistical properties of electron bunches as well as the THz field diffraction. Below, we present results of such a modeling for a single-pass THz super-radiant source comprising a planar undulator.

MODEL DESCRIPTION

Our numerical model describes a single-pass interaction geometry without any guiding structure for generated THz field. A numerical code accounts for a non-zero bunch emittance and an electron energy spread and enables 3D modeling of radiated fields when electron bunches are comparable to or shorter than the FEL resonant wavelength. The key approach of the model is the expansion of a THz field into com-

plete sets of mutually orthogonal Hermite-Gaussian modes. The fast-varying field in a time domain is calculated via inverse Fourier transform of the frequency components. Details of our approach can be found in Refs. [3–8]. The model considers only a single linear polarization of the THz radiation lying in the plane of the wiggling motion of electrons. We also assume that the injected electron bunch is not astigmatic and its waist is located at the undulator center in the ballistic approximation. Then, the initial rms (root-mean-squared) bunch width $\sigma_{x,y}$ can be written as [9]:

$$\sigma_{x,y} = \sqrt{\epsilon \left(\beta_0 + \frac{L_u^2}{4\beta_0} \right)}, \quad (1)$$

where ϵ is the rms bunch emittance, β_0 is the geometrical β -function and L_u is the undulator length. An initial distribution of macroparticles in an electron bunch was simulated using a charge weighted algorithm based on the temporal Poisson statistical properties of electrons [10]. A Gaussian statistics is used to produce an initial energy spread and transverse distribution of the macroparticles. Their initial transverse velocities $[v_{0xj}, v_{0yj}]$ have been taken according to the relations [9, 11]:

$$v_{0xj} = -\vartheta x_{0j} v_{0zj}, \quad v_{0yj} = -\vartheta y_{0j} v_{0zj}, \quad (2)$$

$$\vartheta = \frac{1}{\beta_0} \left(\frac{L_u}{2\beta_0} + \frac{2\beta_0}{L_u} \right)^{-1}, \quad (3)$$

where $[x_{0j}, y_{0j}]$ are the initial transverse coordinates of the macroparticles. The numerical code has been implemented in the double precision arithmetic. The finite-difference integration scheme of the equations for electron motion as well as the equations for the Fourier amplitudes is the 4-th order Bashforth-Moulton predictor-corrector [12] with relative tolerance control on each integration step. Parameters of the simulations are listed in Table 1.

Table 1: Parameters of the Simulation

resonant frequency, THz	0.3	1.0	3.0
bunch charge, nC	1.0	1.0	0.5
mean e-energy, MeV	9.0	9.31	16.5
bunch duration, fs	150	150	100
bunch β_0 -function, m	3.0	3.0	3.0
magnetic flux, T	0.31	0.14	0.14
undulator period, cm	11.0	11.0	11.0
number of periods	9	9	9
undulator parameter K_u	2.26	1.0	1.0

* Work supported by the Swedish FEL center

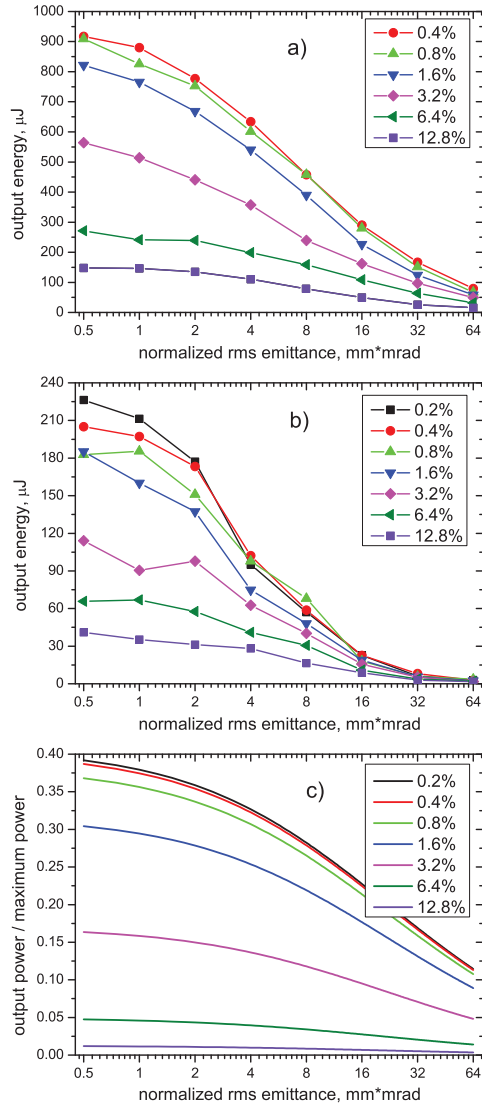


Figure 1: (Color online) The output energy of THz pulses as a function of ϵ_n for different δ -values at $f_R = 0.3$ THz (a) and $f_R = 3.0$ THz (b). The relative THz power is analytically evaluated for $f_R = 3.0$ THz (c).

RESULTS

Figure 1a shows the output energy E_{THz} of THz pulses calculated as a function of the normalized bunch emittance ϵ_n for different values of the relative energy spread δ and resonant frequency $f_R = 0.3$ THz. As one can see, the output energy E_{THz} is highly sensitive to both the bunch emittance and energy spread. For the high-quality electron bunch with $\epsilon_n < 1$ mm-mrad and $\delta < 1\%$, the model predicts an output energy up to 1 mJ that corresponds to the conversion of the electron bunch energy into radiation of more than 10%. This value is approximately an order of the magnitude higher than typical conversion efficiencies of short-pulse THz FEL oscillators [7, 8]. We explain this by the fact that in a super-radiant source, electrons lose their energy coherently as long as the bunch length is far less than

the resonant wavelength. Under these conditions, the electron energy loss results in shift of the resonant wavelength to lower frequencies according to the FEL resonant condition. This is the case of low emittance and energy spread. However, when the bunch quality degrades, the scatter in the longitudinal velocities of electrons leads to the bunch lengthening when electrons in different parts of the bunch oscillate with a different phase. The relative electron phase reaches π -value when the bunch length approaches a half of the resonant wavelength or exceeds it. Under such conditions, the mutual coherence between different part of the bunch gets broken and the output energy drops drastically (Fig. 1a). Thus, $E_{\text{THz}} < 100 \mu\text{J}$ for $\epsilon_n > 50$ mm-mrad regardless of the δ values. For $\epsilon_n \approx 5$ mm-mrad, the same E_{THz} values are also predicted when $\delta > 13\%$.

For resonant frequency $f_R = 1.0$ THz, our model predicts nearly the same level of the peak output energy, $E_{\text{THz}} > 0.8$ mJ. However, in this case, the energy is more sensitive to the bunch quality. This is because of a shorter resonant wavelength and more stringent requirements to a tolerable scatter in electron velocities. For $f_R = 3.0$ THz, we did not observe any noticeable output for a bunch duration of 150 fs since, under such conditions, the bunch length was close to the FEL resonant half-wavelength. Figure 1b shows numerical results obtained for 100 fs bunch duration. In comparison with the data shown in Fig. 1a, there is a noticeable decrease in E_{THz} , that does not exceed 0.3 mJ even if the super-radiant source is driven by high-quality electron bunches. For moderate-quality bunches ($\delta = 4\%$ and $\epsilon_n = 20$ mm-mrad), predicted E_{THz} value is only $\sim 8 \mu\text{J}$.

A comparison of the numerical data with the prediction of the analytical theory [14] (Fig. 1c) indicates that the numerical model is more sensitive to ϵ_n but it is less susceptible to δ . Specifically, the calculated output energy drops 8.2 times whereas the theoretical power does 2.3 times as ϵ_n increases from 0.5 to 32 mm-mrad. When δ increases from 0.2 to 6.4%, the calculated energy and the theoretical power gain drops 3.3 and 8.3 times, respectively. The discrepancy between the numerical and theoretical dependencies can be explained by the fact that at relatively low ϵ_n values, the electron bunch lengthening caused by a non-zero electron energy spread can be suppressed (Fig. 2). Such suppression is directly related to the bunching effect of the generated THz wave, which tends to group electrons in such a way that they are pulled into regions of the peaks of the electric field. This bunching enhances electromagnetic emission at low ϵ_n when the electron current density is relatively high. However, at high ϵ_n or low current density, the intensity of the THz field is insufficient for electron bunching, see Fig. 2(a).

Figure 3 shows the normalized THz spectra calculated at $f_R = 3.0$ and 1.0 THz. The undulator parameter K_u is equal to 1.0 for all the cases presented and no evident high-order spectral harmonics are observed. As is seen, all the spectral distributions are extended from the resonant frequency towards the low-frequency side. The resonant frequency appears as a cut-off value above which spectral intensities di-

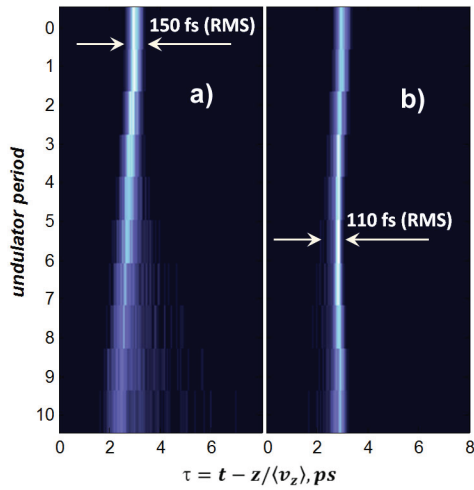


Figure 2: (Color online) The density maps of electron trajectories in a coasting frame calculated for $\epsilon_n=64$ mm·mrad (a) and $\epsilon_n=4$ mm·mrad (b) when $\delta=1\%$ and $f_R=1.0$ THz.

minish to almost zero. Causes of such spectral extension to low-frequencies will be discussed below and here we just mention that an increase in duration of a driving electron bunch leads to additional broadening of the spectrum and frequency down shift of its peak intensity. For instance, at $f_R=3.0$ THz the relative width of a super-radiant pulse exceeds 100% when the bunch duration is greater than 100 fs (Fig. 3a). The spectral broadening with an increase in the bunch duration is due to enhanced contribution of SASE for which an effective interaction length with the electron bunch is less than the undulator length due to diffraction walk-off out of the interaction region. Similar broadening is also observed when δ grows. In this case, however, the shift of the peak spectral intensity is negligible (Fig. 3b).

The spectral changes due to the variation in ϵ_n require a more detail discussion. Figure 3c demonstrates that a decrease in ϵ_n leads to both the shift in the peak intensity and spectral broadening. However, the cause of such a broadening is quite different from the above two cases. It turned out that this spectral behavior is directly related to spatial properties of the generated radiation. In order to reveal its physical origin, we calculated the output transverse energy density distributions of the THz radiation for low and high ϵ_n values, which are shown in Fig. 4a and Fig. 4b, respectively. The former exhibits a broad halo of more than the 50 mm width. In the second case, the THz beam width is several times narrower (~ 10 mm, FWHM) and despite pronounced astigmatism in its transverse profile, it is close to a Gaussian distribution both in vertical and horizontal directions. The spatially broadened THz field at the undulator output at the low ϵ_n value is due to the enhanced off-axis field contribution. This contribution grows with an increase in the diffraction angle $\alpha_d = c/(2\pi f w_0)$, which is in inverse proportion to the transverse width w_0 of the region where electrons emit coherently.

ISBN 978-3-95450-133-5

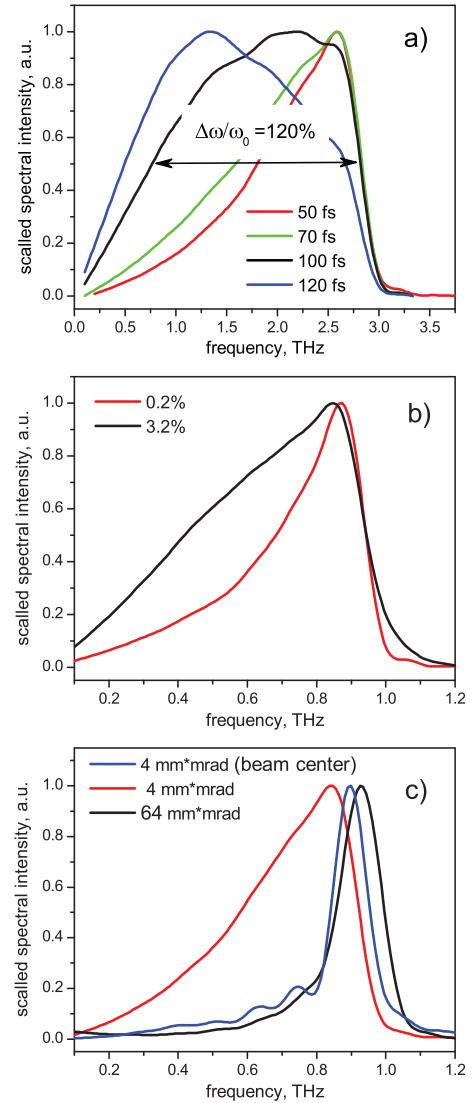


Figure 3: (Color online) The scaled output spectra calculated for different bunch durations at $f_R=3.0$ THz, $\delta=1\%$, and $\epsilon_n=4$ mm·mrad (a); for two δ values at $f_R=1.0$ THz and $\epsilon_n=8$ mm·mrad (b); for two ϵ_n values at $f_R=1.0$ THz and $\delta=1\%$ (c).

The off-axis FEL resonant condition shifts f_R to the lower values with an increase in the angle between observation direction and the undulator axis [13]. Thus, when ϵ_n decreases, the w_0 value decreases as well (Eq. 1c) giving rise to the spatial divergence of the THz radiation that leads to enhanced off-axis intensity and spectral broadening. Such a conclusion is supported by comparison of the THz spectra calculated at $\epsilon_n=4$ mm·mrad over the transverse region of 80×80 mm and a paraxial part, which is confined by 10×10 mm. The paraxial spectrum is considerably narrower and its peak intensity is close to the f_R value (Fig. 3c).

The spectra of the super-radiant THz radiation shown in Fig. 3 are given for the undulator parameter $K_u = 1$ such that no evident high-order harmonics are recognized.

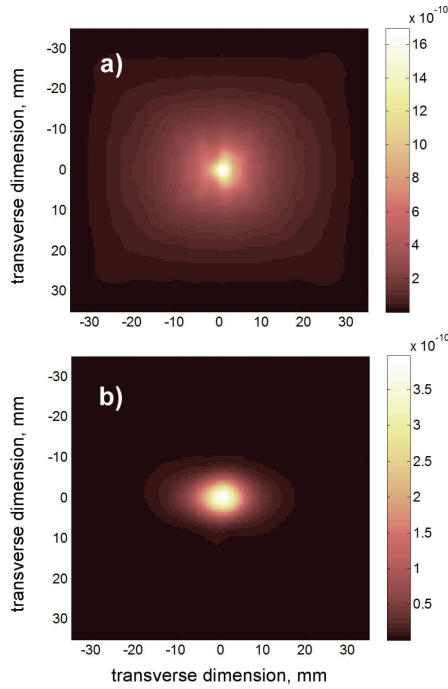


Figure 4: (Color online) The density map of a transverse distribution of radiated energy calculated for $f_R=1.0$ THz, $\delta=1\%$, $\epsilon_n=4$ mm·mrad (a) and $\epsilon_n=64$ mm·mrad (b).

Meanwhile Fig. 5 demonstrates the spectrum calculated for $f_R=0.3$ THz and $K_u \approx 2.3$. One can clearly see both odd and even frequency harmonics in the spectrum. Note that the paraxial spectrum is enriched by odd harmonics whereas even harmonics are more intensive in the integral spectrum. This observation agrees with the FEL theory for the off-axis light generation [13].

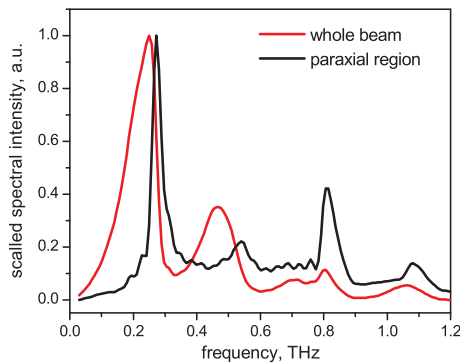


Figure 5: (Color online) The scaled output spectra of the whole super-radiant pulse and only of a paraxial region calculated for $f_R=0.3$ THz, $\delta=1\%$, $\epsilon_n=4$ mm·mrad.

CONCLUSION

We have analyzed radiation properties of a single-pass super-radiant THz source having a simple undulator with plane magnets. The comparison of the analytical and numerical results indicates that our numerical model predicts

the radiation output to be more sensitive to the bunch emittance but less susceptible to the electron energy spread. The discrepancy is related to the bunching effect of the THz field on electrons that enhances the FEL output at low emittance values. We have also investigated the impact of the electron bunch quality on spectral and spatial properties of the THz radiation and shown that the increase in the bunch duration and electron energy spread leads to the spectral broadening. The cause of such a spectral broadening is the enhanced contribution of SASE. For the considered interaction geometry, we predict degradation in angular divergence of the generated radiation and its spectral broadening as the electron bunch emittance decreases. Such degradation and broadening have been shown to be directly related to the diffraction and the FEL resonance condition for off-axis light generation.

ACKNOWLEDGMENT

We would like to acknowledge the financial support from the Swedish FEL center.

REFERENCES

- [1] A. Gover, F. V. Hartemann, G. P. Le Sage, N. C. Luhmann, R. S. Zhang, and C. Pellegrini, *Phys. Rev. Lett.*, **72**, 1192 (1994).
- [2] R. Bonifacio and F. Gasagrande, *Nucl. Instrum. Methods A*, **239**, 29 (1985).
- [3] Y. Pinhasi, V. Shterngartz, and A. Gover, *Phys. Rev. E* **54**, 6774 (1996).
- [4] Y. Pinhasi, Yu. Lurie, and A. Yahalom, *Nucl. Instrum. Methods Phys. Res., Sect. A* **475**, 147 (2001).
- [5] M. J. de Loos, C. A. J. van der Geer, S. B. van der Geer, A. F. G. van der Meer, D. Oepts, and R. Wünsch, *Nucl. Instrum. Methods Phys. Res., Sect. A* **507**, 97 (2003).
- [6] V. Zhaunerchyk, R. T. Jongma, Yu. Lurie, Y. Pinhasi, and W. J. van der Zande, *Appl. Phys. Lett.* **97**, 231109 (2010).
- [7] V. Zhaunerchyk *et al.*, *Phys. Rev. Spec. Top. Accel. Beams* **15**, 050701 (2012).
- [8] R. Chulkov, V. Goryashko, D. Arslanov, R. T. Jongmac, W. J. van der Zandec, and V. Zhaunerchyk, *Phys. Rev. Spec. Top. Accel. Beams*, **17**, 050703 (2014).
- [9] D. A. Edwards, M. J. Syphers, *An Introduction to the Physics of High Energy Accelerators*, Wiley (1993).
- [10] B.W. J. McNeil, M.W. Poole, and G. R.M. Robb, *Phys. Rev. Spec. Top. Accel. Beams*, **6**, 070701 (2003).
- [11] G. Mishra, V. Gupta, N. P. Rajput, B. Kuske, D. Kraemer, R. Bakker, *Nucl. Instr. Meth. Phys. Res. A* **527**, 233 (2004).
- [12] W. H. Press *et al.*, *Numerical recipes in FORTRAN* (second edition), Cambridge University Press (1992).
- [13] G. Dattoli, A. Renieri, A. Torre, *Lectures on the Free Electron Laser Theory and Related Topics*, World Scientific, 637 pages (1993).
- [14] R. Bonifacio, L. De Salvo Souza, B.W.J. McNeil, *Opt. Commun.* **93**, 179 (1992).

X-RAY SMITH-PURCELL RADIATION FROM A BEAM SKIMMING A GRATING SURFACE

D.Yu. Sergeeva, A.A. Tishchenko*, NRNU “MEPhI”, Moscow, Russia

Abstract

X-Ray Smith-Purcell radiation, i.e. the radiation from a beam of charged particles moving above a periodical target parallel to its surface, is considered for the case when a part of the beam crosses the target. The radiation arising is the superposition of Smith-Purcell radiation and transition radiation (TR) from the grating. The analytical expression for spectral-angular distribution of radiation is obtained. It is shown that characteristics of radiation in this case differ considerably from the characteristics of radiation for the bunch with uniform distribution. The incoherent form-factor of bunch with Gaussian distribution of particles has been obtained; it is proved to provide a considerable increase of the radiation intensity in conditions when bunch skims the grating.

INTRODUCTION

Smith-Purcell radiation as a base of Free Electron Lasers is actively studied experimentally and theoretically in recent years [1]-[3]. Usually the beam is supposed to move at some distance above the target surface. In practice this distance is chosen to be minimal in order to broaden the spectrum of radiation to high frequencies, therefore the beam passes very close to the target surface. Along with that, experimental data contains the information about grating heating, which is apparently caused by interaction of the beam with the grating. For example, authors of article [4] suppose that the beam skims the grating surface. There has been no theory of Smith-Purcell radiation for such conditions yet. We give the analytical description of X-Ray radiation arising when the beam of charged particles moves above the periodical target and a part of the beam crosses the target. The radiation arising is the superposition of Smith-Purcell radiation and transition radiation (TR) from the grating. This radiation determines the process of beam bunching and, consequently, gains of radiation.

Talking of SPR in this article we shall mean that this is the special case of DR – Diffraction radiation for periodical target, i.e. grating. So, sometimes we shall mention DR, meaning that lion share of the bunch goes above the target surface, and sometimes mention TR, when considerable part of the bunch intersects the edges of the target.

FIELD OF RADIATION

We consider Smith-Purcell radiation from the bunch of N particles. The grating consists of N_{st} strips with

dielectric permittivity $\varepsilon(\omega)$ and vacuum between the strips. The width of a strip is a , the grating period is d . We assume that each particle has the charge e and moves uniformly with the constant velocity $\mathbf{v} = (v_x, v_y, 0)$, α is the angle between the beam velocity and axis x , see Fig. 1. The center of the bunch is at a distance h above the grating surface ($h > 0$) or under the surface ($h < 0$). The radius-vector of m -th particle is $\mathbf{r}_m = (x_m, y_m, z_m)$. We would like to emphasize that these coordinates can be negative. To find the field of radiation we use the method of polarization, described for single-particle radiation in more detail in monograph [5] and developed for the radiation from the bunch in [6], [7].

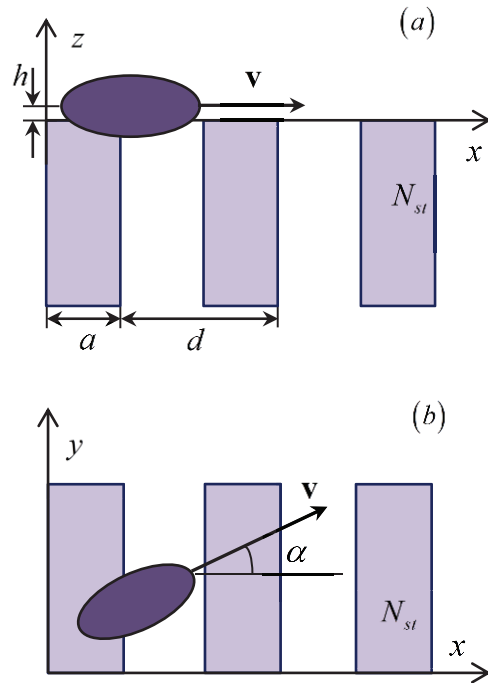


Figure 1: Bunch skimming a grating surface generates radiation (a) side view; (b) top view.

In X-Ray frequency range the dielectric permittivity has the form:

$$\varepsilon = 1 + \chi' + i\chi'', \quad (1)$$

where $\chi' = -\omega_p^2/\omega^2$, $\omega \gg \omega_p$, ω_p is the plasma frequency. Now we consider non-absorbing medium i.e. $\chi'' \ll |\chi'|$.

*tishchenko@mephi.ru

The Coulomb field of each particle polarizes the target and due to it the radiation is generated. The polarization current density has the form:

$$\mathbf{j}(\mathbf{r}, \omega) = \frac{\omega}{4\pi i} (\varepsilon(\omega) - 1) \mathbf{E}_0(\mathbf{r}, \omega). \quad (2)$$

Here $\mathbf{E}_0(\mathbf{r}, \omega)$ is the Coulomb field of the bunch. Its Fourier image can be written as:

$$\mathbf{E}_0(\mathbf{q}, \omega) = - \sum_{m=1}^N \frac{ie}{2\pi^2} \frac{\mathbf{q} - \mathbf{v}\omega/c^2}{q^2 - \omega^2/c^2} e^{-i\mathbf{q}\mathbf{r}_m} \delta(\omega - \mathbf{q}\mathbf{v}). \quad (3)$$

The field of radiation is defined by polarization current density [1]:

$$\mathbf{E}(\mathbf{r}, \omega) = \frac{i\omega}{c^2} \frac{e^{ikr}}{r} \left[\mathbf{n}' \left[\mathbf{n}' \int_V d^3r' e^{-ikr'} \mathbf{j}(\mathbf{r}', \omega) \right] \right]. \quad (4)$$

Here $\mathbf{k}' = \mathbf{n}' \sqrt{\varepsilon(\omega)} \omega/c$ and the prime means the value in the medium. In Eq. (4) it is integrated over the area of generation of the radiation, i.e. over the volume of the target V .

It should be noticed that if the problem contains the interference and coherence phenomena then it is needed to take into account the law of refraction even in high-frequency region [6]. In this paper we allow it for the upper edge:

$$\mathbf{n}' = \varepsilon(\omega)^{-1/2} (n_x, n_y, \sqrt{\varepsilon(\omega) - 1 + n_z^2}), \quad (5)$$

$\mathbf{n} = (n_x, n_y, n_z)$ - the unit vector of the wave-vector in vacuum: $\mathbf{k} = \mathbf{n}\omega/c$. It is easy to see that the minimal value of n_z exists:

$$n_z^{\min} = \sqrt{1 - \varepsilon(\omega)}, \quad (6)$$

for which the waves incident to the target edge are ordinary plane waves. For $n_z < n_z^{\min}$ the incident waves are evanescent. In this paper we shall consider only case of comparatively big angles $n_z > n_z^{\min}$, because the case of radiation at grazing incidence needs more the case, so, we have the limit for defined by Eq. (6).

Thus, after integrating in Eq. (4) using Eqs. (2), (3) and taking into account the law of refraction Eq. (5) one can obtain the field of Smith-Purcell radiation from the bunch skimming a grating surface:

$$\begin{aligned} \mathbf{E}(\mathbf{r}, \omega) = & -ie \frac{\varepsilon(\omega) - 1}{2\pi v_x} \frac{\omega^2}{c^2} \frac{e^{ikr}}{r} e^{i\frac{\varphi a}{2}} e^{i(N_{st}-1)\frac{\varphi d}{2}} F_1 F_{st} \times \\ & \times \sum_{m=1}^N e^{-i\xi x_m} e^{-ik_y y_m} e^{-ik'_z z_m} [\mathbf{n}' [\mathbf{n}' \mathbf{L}_m]]. \end{aligned} \quad (7)$$

$$\text{Here } F_1 = \frac{\sin(\varphi a/2)}{\varphi}, F_{st} = \frac{\sin(N_{st}\varphi d/2)}{\sin(\varphi d/2)}, \xi = \frac{\omega - k_y v_y}{v_x}$$

$$\mathbf{A} = \xi \mathbf{e}_x + k_y \mathbf{e}_y - \mathbf{e}_x v_x \omega/c^2 - v_y \mathbf{e}_y \omega/c^2, \quad \varphi = \xi - k_x,$$

$$\mathbf{L}_m = \frac{\mathbf{A}\rho^{-1} - i\mathbf{e}_z}{\rho - ik'_z} + \frac{\mathbf{A}\rho^{-1} \text{sgn}(z_m) - i\mathbf{e}_z}{\rho - ik'_z \text{sgn}(z_m)} \left[e^{-z_m \rho \text{sgn}(z_m) + ik'_z z_m} - 1 \right],$$

$$k'_z = \varepsilon(\omega)^{-1/2} \frac{\omega}{c} \sqrt{\varepsilon(\omega) - 1 + n_z^2}, \quad \rho^2 = \xi^2 + k_y^2 - \omega^2/c^2.$$

INCOHERENT AND COHERENT FORM-FACTORS

Knowing the field Eq. (7) one can obtain the spectral-angular distribution of radiation:

$$\frac{dW(\mathbf{n}, \omega)}{d\Omega d\omega} = \left\langle cr^2 |\mathbf{E}(\mathbf{r}, \omega)|^2 \right\rangle. \quad (8)$$

Angle brackets $\langle \dots \rangle$ mean the averaging over the locations of all the particles. Eq. (8) can be written as

$$\frac{dW(\mathbf{n}, \omega)}{d\Omega d\hbar\omega} = \frac{1}{137} \left(\frac{\varepsilon(\omega) - 1}{2\pi\beta_x} \right)^2 \frac{\omega^2}{c^2} F_1^2 F_{st}^2 G, \quad (9)$$

where

$$G = \left\langle \frac{\omega^2}{c^2} \left| \sum_{m=1}^N e^{-i\xi x_m} e^{-ik_y y_m} e^{-ik'_z z_m} [\mathbf{n}' [\mathbf{n}' \mathbf{L}_m]] \right|^2 \right\rangle. \quad (10)$$

The factor G determines the radiation from the bunch, that is why we will call it form-factor; however, it differs from what is usually called form-factor (see Eq. (19) or monograph [5] in more detail). The reason to use this new denomination is that in our case it is impossible to separate from G the multiplier usually contained in the spectral-angular distribution of the single particle. In the limiting cases of “pure” DR and TR our form-factor G (Eq. (10)) turns into the production of usual form-factor and the part of single-electron density of radiation.

Factor F_{st}^2 defines the dispersion relation of Smith-Purcell effect in Diffraction radiation (which is usually called mere Smith-Purcell radiation, SPR): it has sharp maxima at

$$\varphi d = 2\pi n_{sp}, \quad n_{sp} = 1, 2, \dots, \quad (11)$$

where

$$\varphi = (\omega - \mathbf{k}\mathbf{v})/v_x. \quad (12)$$

Using properties of sum and averaging in Eq. (10) one can obtain the form factor as the sum of coherent and incoherent form-factors (see also [6]-[10]):

$$G = NG_{inc} + N(N-1)G_{coh}. \quad (13)$$

Let us consider the bunch of non-interacting particles with Gaussian distribution. In this case the distribution function is

$$f = \frac{e^{\frac{(x_m \cos \alpha + y_m \sin \alpha)^2}{\sigma_x^2}} e^{\frac{(-x_m \sin \alpha + y_m \cos \alpha)^2}{\sigma_y^2}} e^{\frac{(z_m - h)^2}{\sigma_z^2}}}{\pi^{3/2} \sigma_x \sigma_y \sigma_z}, \quad (14)$$

where h is z -position of the bunch center, which can be both positive and negative. After some calculations it is possible to find G_{coh} and G_{inc} from Eq. (10):

$$\begin{aligned} G_{inc} = & [C_1 - \text{Re } C_2] [1 - \Phi(h/\sigma_z)] + \\ & + \frac{C_1}{2} e^{2h\rho} e^{\rho^2 \sigma_z^2} [1 - \Phi(h/\sigma_z + \rho\sigma_z)] + \\ & + \frac{C_1}{2} e^{-2h\rho} e^{\rho^2 \sigma_z^2} [1 + \Phi(h/\sigma_z - \rho\sigma_z)] - \\ & - \text{Re} \left(e^{h(\rho - ik'_z)} e^{\frac{\sigma_z^2 (\rho - ik'_z)^2}{4}} (C_1 - C_2) \right) + \\ & \text{Re} \left(e^{h(\rho - ik'_z)} e^{\frac{\sigma_z^2 (\rho - ik'_z)^2}{4}} (C_1 - C_2) \Phi \left(\frac{h}{\sigma_z} + \sigma_z \frac{\rho - ik'_z}{2} \right) \right) \\ C_1 = & \frac{\omega^2 \mathbf{A}^2 \rho^{-2} + 1 - (\mathbf{A}\mathbf{n}')^2 \rho^{-2} - (n'_z)^2}{c^2 \rho^2 + k_z'^2}, \\ C_2 = & -\frac{\omega^2 \mathbf{A}^2 \rho^{-2} - 1 - (\mathbf{A}\mathbf{n}')^2 \rho^{-2} + (n'_z)^2 + 2i(\mathbf{A}\mathbf{n}')\mathbf{n}'_z \rho^{-1}}{c^2 \rho^2 + k_z'^2 - 2i\rho k'_z}, \end{aligned} \quad (15)$$

and

$$\begin{aligned} G_{coh} = & \frac{1}{4} e^{-I} \left| e^{-h\rho} e^{\frac{\sigma_z^2 \rho^2}{4}} \left[1 + \Phi \left(\frac{h}{\sigma_z} - \frac{\rho\sigma_z}{2} \right) \right] \mathbf{C}_3^* - \right. \\ & \left. - e^{h\rho} e^{\frac{\sigma_z^2 \rho^2}{4}} \left[1 - \Phi \left(\frac{h}{\sigma_z} + \frac{\rho\sigma_z}{2} \right) \right] \mathbf{C}_3 + \right. \\ & \left. + e^{\frac{\sigma_z^2 k_z'^2}{4}} e^{-ik'_z h} \left[1 - \Phi \left(\frac{h}{\sigma_z} - \frac{ik'_z \sigma_z}{2} \right) \right] [\mathbf{C}_3 + \mathbf{C}_3^*] \right|^2, \end{aligned} \quad (16)$$

where $\Phi(x) = \frac{2}{\sqrt{\pi}} \int_0^x e^{-t^2} dt$ - is the Laplace function, * - means conjugate complex value;

$$\begin{aligned} \mathbf{C}_3 = & \mathbf{n}' \frac{\omega (\mathbf{A}\mathbf{n}') \rho^{-1} + in'_z}{c \rho + ik'_z} - \frac{\omega \mathbf{A} \rho^{-1} + i\mathbf{e}_z}{c \rho + ik'_z}, \\ I = & \sigma_x^2 \sigma_y^2 \frac{(sk_y - \sin \alpha \cos \alpha [\sigma_y^2 - \sigma_x^2] \xi)^2 + \sigma_x^2 \sigma_y^2 \xi^2}{4s^2}, \\ s = & \sigma_y^2 \cos^2 \alpha + \sigma_x^2 \sin^2 \alpha. \end{aligned}$$

We would like to draw reader's attention to the exponents in Eqs. (15) and (16) which are proportional to

the square of the radiation frequency (which is contained in ρ , for example). It may seem that these exponents increase indefinitely with $\omega \rightarrow \infty$. However, it is known that for $x \rightarrow \infty$ the asymptotic form of Laplace function is

$$\Phi(x \rightarrow \infty) \approx 1 - \frac{e^{-x^2}}{x\sqrt{\pi}}. \quad (17)$$

Thus, G_{coh} and G_{inc} decrease with growing of frequency (one can see it above in Fig. 2). Also, considering the limiting cases $\omega \rightarrow \infty$, $h > 0$ (Diffraction radiation) and $\omega \rightarrow \infty$, $h \rightarrow -\infty$ (Transition radiation) it is useful to keep in mind that $\Phi(-x) = -\Phi(x)$. The results obtained (Eq. (9) with Eqs. (13), (15) and (16)) for radiation of a single charged particle turn into results of article [11] in case of $h > 0$ (DR), and into results of [12] in case of $h < 0$ (TR).

ANALYSIS

To plot the figures we put:

$$\begin{aligned} n_x &= \sin \theta \cos \phi, \\ n_y &= \cos \theta, \\ n_z &= \sin \theta \sin \phi. \end{aligned} \quad (18)$$

In all figures with the exception of Figs. 2 and 4 the length of the bunch is too big to observe the coherent radiation and this is the incoherent radiation that makes the main contribution.

Figure 2 demonstrates the coherent and incoherent form-factors for Gaussian distribution of the particles in the bunch in dependence on the wavelength of radiation. It is plotted for parameters of SLAC (FACET, $E = 20 \text{ GeV}$). To compare this two function we have to choose very short bunches ($\sigma_x = 10 \text{ nm}$). Had we not use that order of the bunch length, the coherent form-factor would have been too small to be noticeable. This functional behaviour is different for the bunch with uniform distribution of the particles [6]. Moreover, as opposed to the uniform distribution of the particles in the bunch, the incoherent form-factor dominates starting from $\lambda \simeq \sigma_x$ and less, see Fig. 2. Nevertheless, both for Gaussian and uniform distributions the incoherent part of form-factor should be taken into account (see comparison between incoherent form-factors for Gaussian and uniform distributions in Fig. 3). Figure 3 is plotted until value of wavelength corresponding to $\omega = 3\omega_p$.

In Fig. 4 the dependence of coherent and incoherent factors on α is demonstrated. It is plotted for value of α satisfying to the Eq. (6). The values of viewing angles satisfy the third maximum from Smith-Purcell dispersion relation ($n_{sp} = 3$). One can see that the more the angle between the beam velocity and the rulings direction is, the

more intensive radiation can be obtain. We would like to stress that in case $\alpha \neq 0$ the radiation is distributed over the cone surface [13] with cone angle $\theta = \arccos(\beta^{-1} \sin \alpha)$. The features of this case demand the separate consideration. For clarity, all figures hereafter will be plotted at $\alpha = 0$, excluding Fig. 4.

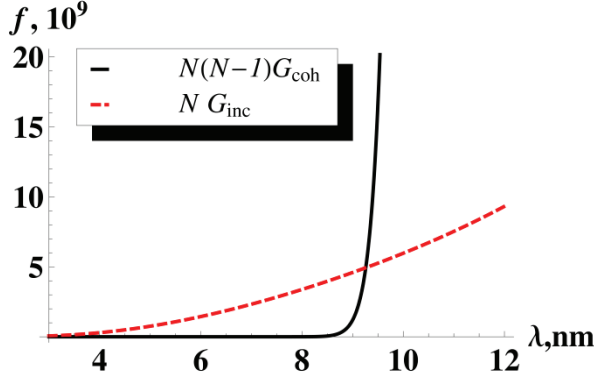


Figure 2: The coherent (solid black) and incoherent (dashed red) form-factors for Gaussian distribution of the particles in the bunch. Here $\hbar\omega_p = 26.3 \text{ eV}$ (beryllium), $\gamma = 4 \cdot 10^4$ (energy of FACET, SLAC), $N = 10^{10}$, $\alpha = 0$, $\phi = \pi/6$, $h = 60 \mu\text{m}$, $\sigma_x = 10 \text{ nm}$, $\sigma_y = \sigma_z = 5 \mu\text{m}$.

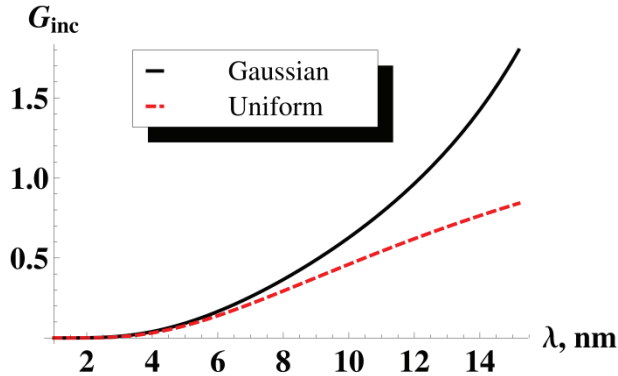


Figure 3: The incoherent form-factor for uniform (dashed red, results from [6]) and Gaussian (solid black) distribution. Here $\hbar\omega_p = 26.3 \text{ eV}$ (beryllium), $\gamma = 4 \cdot 10^4$ (energy of FACET, SLAC), $N = 10^{10}$, $\alpha = 0$, $\phi = \pi/6$, $h = 60 \mu\text{m}$, $\sigma_x = 20 \mu\text{m}$, $\sigma_y = \sigma_z = 15 \mu\text{m}$.

The spectral-angular distribution of Smith-Purcell radiation for different values of impact-parameter is shown in Fig. 5. Our results permit to see the transition of diffraction radiation (DR) into TR and, moreover, they describe the case when one half of the bunch is above the target surface, while the other is under it (see the black solid curve in Fig. 5).

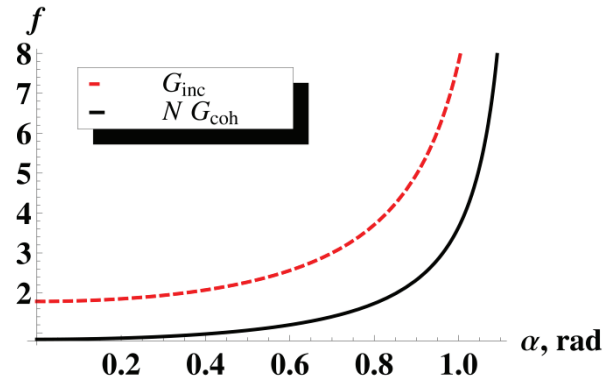


Figure 4: The coherent (solid black) and incoherent (dashed red) form-factors for Gaussian distribution of the particles in the bunch depending on α . Here $\hbar\omega_p = 26.3 \text{ eV}$ (beryllium), $\lambda = 9.1 \text{ nm}$, $\gamma = 4 \cdot 10^4$ (energy of FACET, SLAC), $N = 10^{10}$, $h = 60 \mu\text{m}$, $\sigma_x = 10 \text{ nm}$, $\sigma_y = \sigma_z = 5 \mu\text{m}$, $\theta = \arccos(\beta^{-1} \sin \alpha)$, $n_{sp} = 3$, $\phi = \arccos\left[\frac{1}{\beta} \frac{\cos \alpha - 2\pi c n_{sp} / (d\omega\beta)}{\sin \theta}\right]$.

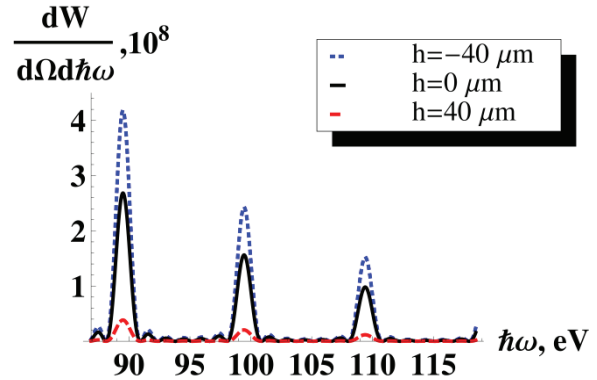


Figure 5: The spectral-angular distribution of radiation from the bunch when its center is above the target surface (dashed red), under it (dotted blue), on the surface (solid black). Here $N_{st} = 7$, $d = 0.9 \mu\text{m}$, $a = d/2$ and other parameters as in Fig. 3.

The spectral-angular distribution of the radiation from the bunch moved under the target surface for comparatively low energy of electrons is shown in Fig. 6. With growing of the distance between the bunch center and the target surface the differences in intensity of radiation becomes insignificant and goes to the distribution of TR from the infinity strips.

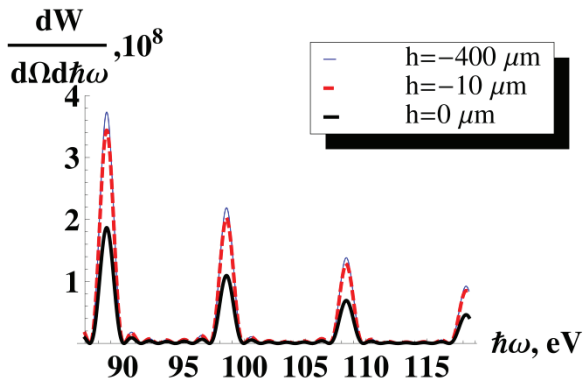


Figure 6: The spectral-angular distribution of radiation from the bunch when its center is under the target surface (dashed red and dotted blue) and on the surface (solid black). Here $\hbar\omega_p = 26.3 \text{ eV}$ (beryllium), $\gamma = 20$ (energy of LUCX (KEK, Japan)), $N_{st} = 7$, $N = 10^{10}$, $\alpha = 0$, $\phi = \pi/6$, $\sigma_x = 30 \mu\text{m}$, $\sigma_y = \sigma_z = 10 \mu\text{m}$, $d = 0.9 \mu\text{m}$, $a = d/2$.

Usually, the spectral-angular distribution of radiation from the bunch is written in the following form:

$$\frac{dW(\mathbf{n}, \omega)}{d\Omega d\hbar\omega} = \frac{dW_1(\mathbf{n}, \omega)}{d\Omega d\hbar\omega} [N + N(N-1)G'_{coh}], \quad (19)$$

where $dW_1(\mathbf{n}, \omega)/d\Omega d\hbar\omega$ is the spectral-angular distribution of radiation from a single particle; the designation G'_{coh} with prime is used in order to indicate that it does not coincide with the coherent form-factor G_{coh} from our expression (see Eqs. (13) and (16)).

We would like to stress, that form of Eq. (19) is, generally speaking, not correct. There are two reasons for this. First is that in Eq. (19) the incoherent form-factor has not been taken into account. Second, using Gaussian distribution we always deal with the polarization radiation, which is the mixture of Diffraction radiation and Transition radiation – there are the “tails” of distribution that are on the other side of the upper edge of the target. Therefore, we can tell about TR or DR only in limiting cases, when bunch is distant enough from the upper edge of the target.

In Fig. 7 we plot the correct distribution (solid black curve) and distribution from Eq. (19). As one can see, the difference can be considerable.

The spectral-angular distribution depending on impact-parameter is shown in Fig. 8. The angle ϕ corresponds to the third peak of SPR. Black solid curve corresponds to our results, red dashed - to the results obtained by usual way (see Eq. (19)). One can see that for impact-parameter $h \geq \sigma_z$ they are very close to each other, but for negative h situation changes.

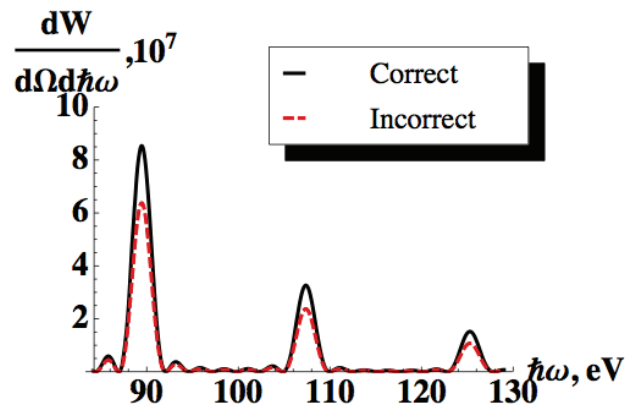


Figure 7: The spectral-angular distribution of incoherent radiation for correct (black solid, G_{inc} from Eq. (15)) and incorrect (red dashed, $G_{inc} = 1$) calculation of the form-factor. Here $N_{st} = 7$, $d = 0.5 \mu\text{m}$, $a = d/2$, $\omega = 3\omega_p$, $h = 17 \mu\text{m}$ and other parameters as in Fig. 3.

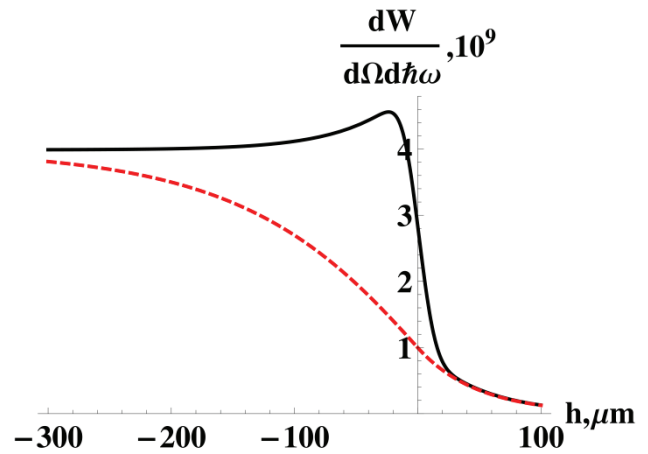


Figure 8: The spectral-angular distribution depending on impact-parameter: DR for $h > 0$, TR for $h < 0$. Black solid curve corresponds to our results, red dashed - to the usually considered results (see Eq. (19)). Here $N_{st} = 7$, $d = 0.5 \mu\text{m}$, $a = d/2$, $\phi = 24.6^\circ$ ($n_{sp} = 3$) and other parameters as in Fig. 3. The curves are plotted for $\omega = 3\omega_p$, i.e. $\lambda \ll \sigma_x = 20 \mu\text{m}$, which corresponds to incoherent radiation.

CONCLUDING REMARKS

The existence of incoherent form-factor was denoted more than a decade ago [9], [10], but for the first time it has been obtained in analytical form and analyzed only recently [6] for uniform distribution of the electrons in bunch.

In this work we obtain the incoherent form-factor for Gaussian distribution, along with the coherent one. It is proved, that for the case considered (particles of the bunch go both through the target and above it), spectral-angular distribution of radiation has the features both

resonant DR and resonant TR. Therefore, the resulting intensity of radiation coincides with habitual Eq. (19) in case of incoherent X-ray TR only when $|h| > \gamma\beta\lambda/4\pi$, and in case of DR only when $h > \min\{\sigma_z, \gamma\beta\lambda/4\pi\}$ - see Fig. 8. It is interesting to see, that Fig. 8 demonstrates the strong effect of the edge, and along with that shows the peak of transition radiation caused by incoherent form-factor.

The theory developed is valid for arbitrary energies of the particles, for Gaussian distribution and for UV and X-ray domain of photon energies ($\omega \gg \omega_p$, which in practice stands for $\omega > 3\omega_p$).

REFERENCES

- [1] D. Li *et al.*, "Growth rate and start current in Smith-Purcell free-electron lasers," *Appl. Physics Lett.*, vol. 100, p. 191101, 2012.
- [2] J. Gardelle *et al.*, "Start Current and Gain Measurements for a Smith-Purcell Free-Electron Laser," *Phys. Rev. Lett.*, vol. 102, no. 22, p. 224801, 2010.
- [3] J. D. Jarvis *et al.*, "Small-signal theory of a grating-based free-electron laser in three dimensions," *Phys. Rev. ST AB*, vol. 13, p. 020701, 2010.
- [4] H. L. Andrews *et al.*, "Observation of THz evanescent waves in a Smith-Purcell free-electron lase," *Phys. Rev. ST AB*, vol. 12, p. 080703, 2009.
- [5] A. P. Potylitsyn *et al.*, *Diffraction Radiation from Relativistic Particles*, Berlin: Springer-Verlag, 2011.
- [6] D. Yu. Sergeeva *et al.*, "UV and X-ray diffraction and transition radiation from charged particles bunches," *Nucl. Instruments and Methods B*, vol. 309, p. 189, 2013.
- [7] D. Yu. Sergeeva *et al.*, "UV and X-ray diffraction radiation for submicron noninvasive diagnostics," in *Proc. of IPAC 2013*, Shanghai, China, 2013, pp. 616-619.
- [8] H. L. Andrews *et al.*, "Longitudinal profile monitors using Coherent Smith-Purcell radiation," *Nucl. Instruments. and Methods A*, vol. 740, p. 212, 2014.
- [9] G. Doucas *et al.*, "Determination of longitudinal bunch shape by means of coherent Smith-Purcell radiation," *Phys. Rev. ST AB*, vol. 5, p. 072802, 2002.
- [10] J. H. Brownell *et al.*, "Spontaneous Smith-Purcell radiation described through induced surface currents," *Phys. Rev. E*, vol. 57, p. 1075, 1998.
- [11] A. A. Tishchenko *et al.*, "Diffraction radiation from an ultrarelativistic charge in the plasma frequency limit," *Phys. Rev. E*, vol. 70, p. 066501, 2004.
- [12] A. A. Tishchenko *et al.*, "X-ray transition radiation from an ultrarelativistic charge passing near the edge of a target or through a thin wire," *Nucl. Instruments and Methods B*, vol. 227, p. 63, 2005.
- [13] A. A. Tishchenko *et al.*, "Backward Smith-Purcell Radiation," in *Proc. of RREPS 2013*, Erevan, Armenia, 2013.

FORWARD X-RAY AND ULTRAVIOLET SMITH-PURCELL RADIATION FOR FEL

A.A. Tishchenko*, D.Yu. Sergeeva, NRNU “MEPhI”, Moscow, Russia

Abstract

Smith-Purcell radiation in X-Ray and UV frequency range is investigated. The particle is supposed to move at arbitrary angle to the rulings direction parallel to a grating surface. The radiation going both through the upper and forward target edges is taken into account. Spectral and angular characteristics of the forward radiation are discussed. The influence of oblique incidence of the particle to the grating in on the intensity of radiation is analyzed.

INTRODUCTION

The scheme of Free Electron Lasers based on Smith-Purcell effect is well known to describe the process of interaction between an electron beam and evanescent wave, which bunches this beam. In this work we concentrate on the process of generation of the radiation propagating at small angles. In terms of approach described in detail in [1]-[3], we investigate the Smith-Purcell radiation at oblique incidence of a single charged particle for X-Ray and UV frequency region. This forward radiation propagates through all region of the beam moving, whereas the usual surface waves existing in FELs [4] decrease exponentially with distance from the surface. Therefore, the forward radiation considered in this article is able to provide more close interaction between the beam and the radiation, than the surface waves.

FIELD OF RADIATION

Let the charge e moves with constant velocity $\mathbf{v} = (v_x, v_y, 0)$ at a distance h above the upper edge of a target. The target consists of N strips with dielectric permittivity $\varepsilon(\omega)$ with air between strips. The period of the grating is d . The size of a strip is (a, ∞, b) (see Fig. 1). We find the radiation field using the polarization current method. The essence of this method is following. The Coulomb field of a moving particle $\mathbf{E}_0(\mathbf{r}, \omega)$ acts upon material of the target and excites dynamically changed polarization currents in it. This leads to arising of the radiation determined by Fourier-image of the current density $\mathbf{j}(\mathbf{r}, \omega)$:

$$\mathbf{j}(\mathbf{r}, \omega) = \frac{\omega}{4\pi i} (\varepsilon(\omega) - 1) \mathbf{E}_0(\mathbf{r}, \omega). \quad (1)$$

For X-Ray frequency region

$$\omega \gg \omega_p \quad (2)$$

the dielectric function of a medium can be written as:

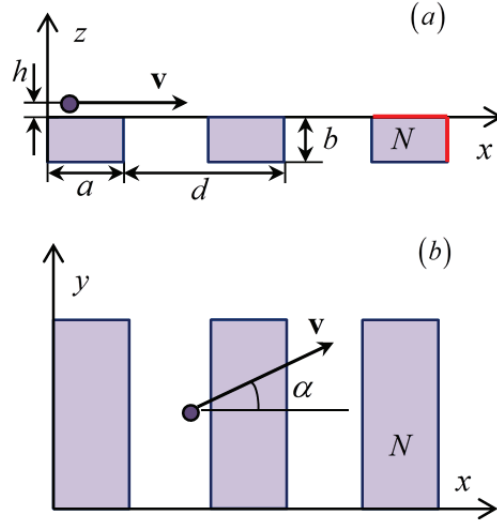


Figure 1: The geometry (a) side view, (b) top view.

$$\varepsilon = 1 + \chi' + i\chi'', \quad (3)$$

where $\chi' = -\omega_p^2 / \omega^2$, ω_p is the plasma frequency, which is usually in the range of 15 - 35 eV, in dependence on the target material. The case of absorbing medium can be of interest, for example, to deal with X-ray Cherenkov radiation [5], [6]; now we restrict our consideration to non-absorbing mediums only, i.e. $\chi'' \ll |\chi'|$. However, as the absorption in X-ray region plays a role mainly near narrow lines, our results remain valid in rather wide range of parameters.

The radiation field is determined by current density as

$$\mathbf{E}(\mathbf{r}, \omega) = \frac{i\omega}{c^2} \frac{e^{ikr}}{r} \left[\mathbf{n} \left[\mathbf{n} \int_V d^3r' e^{-ikr'} \mathbf{j}(\mathbf{r}', \omega) \right] \right], \quad (4)$$

where it is integrated over the region of existence of polarization currents, i.e. over the target volume V ; the prime in the designation of wave vector $\mathbf{k}' = \mathbf{n}' \sqrt{\varepsilon(\omega)} \omega/c$ stands for the value inside the matter.

To obtain the field of forward radiation we should take into account the refraction of radiation at two target edges: the upper one and the forward one (see the red lines in Fig. 1). Allowing for the law of refraction is important here because of periodicity of the target. The matter is that, despite the weakness of the effect of the refraction in X-ray range, for numerous periodic sources of radiation the effect of refraction is accumulated and becomes prominent.

*tishchenko@mephi.ru

In brief, we divide the effective area of integration V into two parts V_1 and V_2 in z -direction by plane $z = n'_z(x - a - sd)/n'_x$. Here s is the number of the strip. So, the radiation generated in the volume V_1 refracts at the upper edge, the radiation generated in the volume V_2 refracts at the forward edge.

The refraction laws for upper and forward edges give us the relations for the unit wave-vectors \mathbf{n}_1 and \mathbf{n}_2 of radiation propagating in V_1 and V_2 - inside the target, and \mathbf{n} - out of the target:

$$\begin{aligned}\mathbf{n}_1 &= \varepsilon(\omega)^{-1/2} \left(n_x, n_y, \sqrt{\varepsilon(\omega) - 1 + n_z^2} \right), \\ \mathbf{n}_2 &= \varepsilon(\omega)^{-1/2} \left(\sqrt{\varepsilon(\omega) - 1 + n_x^2}, n_y, n_z \right).\end{aligned}\quad (5)$$

Generally speaking, there are two different situations when the laws of refraction are allowed for:

I. without taking into account inhomogeneous plane waves;

II. taking into account only inhomogeneous plane waves.

The case I is realized if $n_z^2 > 1 - \varepsilon(\omega)$; then z -component of the wave-vector in medium n_{1z} is real, which corresponds to the ordinary plane waves. The case II takes place if $n_z^2 < 1 - \varepsilon(\omega)$; then z -component of the wave-vector in medium n_{1z} is imaginary and it corresponds to the inhomogeneous evanescent waves.

The same situation can arise with the x -component of wave-vector, but it will give radiation mainly at the big angles. Our goal in this work is to analyse forward radiation, which accompanies and acts upon the moving beam during a considerable part of its way. So, below the condition $n_x^2 \geq 1 - \varepsilon(\omega)$ is thought to be always satisfied.

Let us start with the **first** more general case of $n_z^2 > 1 - \varepsilon(\omega)$. After integrating in Eq. (4) the total field of radiation takes the form:

$$\begin{aligned}\mathbf{E}(\mathbf{r}, \omega) &= -i \frac{e(\varepsilon - 1)}{4\pi v_x} \frac{1}{\rho} \frac{\omega^2}{c^2} \frac{e^{ikr}}{r} e^{-h\rho} \times \\ &\times \left\{ \frac{[\mathbf{n}_1[\mathbf{n}_1\mathbf{L}]]}{t_1} \left[\frac{e^{i\varphi_1 a} - 1}{i\varphi_1} - \frac{e^{i\varphi_1 a} - e^{-\frac{n_{1z}}{n_{1x}} t_1 a}}{i\varphi_1 + \frac{n_{1z}}{n_{1x}} t_1} \right] \sum_{s=1}^N e^{i\varphi_1(s-1)d} - \right. \\ &\left. - \frac{[\mathbf{n}_2[\mathbf{n}_2\mathbf{L}]]}{t_2} \left[\frac{e^{i\varphi_2 a} - 1}{i\varphi_2} e^{-bt_2} - \frac{e^{i\varphi_2 a} - e^{-\frac{n_{2z}}{n_{2x}} t_2 a}}{i\varphi_2 + \frac{n_{2z}}{n_{2x}} t_2} \right] \sum_{s=1}^N e^{i\varphi_2(s-1)d} \right\},\end{aligned}\quad (6)$$

where

$$\mathbf{L} = \mathbf{A} - i\rho\mathbf{e}_z, \quad \mathbf{k} = \omega/c\mathbf{n}, t_{(1,2)} = \rho - i\sqrt{\varepsilon}k_{(1,2)z},$$

$$\mathbf{A} = \frac{\omega}{c\beta_x} \left\{ 1 - n_y\beta_y - \beta_x^2; \beta_x(n_y - \beta_y); 0 \right\},$$

$$\rho = \frac{\omega}{c\beta_x} \sqrt{(1 - n_y\beta_y)^2 + n_y^2\beta_x^2 - \beta_x^2}, \quad (7)$$

$$\varphi_1 = \frac{\omega}{c\beta_x} (1 - n_y\beta_y - n_x\beta_x),$$

$$\varphi_2 = \frac{\omega}{c\beta_x} \left(1 - n_y\beta_y - \beta_x \sqrt{\varepsilon(\omega) - 1 + n_x^2} \right).$$

Indexes 1, 2 are used for radiation generated in V_1 and V_2 correspondingly. Variable without the index means it is the same for radiation generated in V_1 and V_2 . Using well-known expression for spectral-angular distribution

$$dW(\mathbf{n}, \omega)/d\Omega d\omega = cr^2 |E(\mathbf{r}, \omega)|^2$$

we get:

$$\frac{dW(\mathbf{n}, \omega)}{d\Omega d\hbar\omega} = \frac{1}{137} \left(\frac{\varepsilon - 1}{4\pi\beta_x} \right)^2 \frac{e^{-2h\rho}}{\rho^2} \frac{\omega^4}{c^4} (q_1^{(j)} + q_2^{(j)} + q_3^{(j)}).$$

Here index $j = \text{I, II}$ corresponds to the cases I and II.

$$\begin{aligned}q_1^{(I)} &= \frac{\mathbf{A}^2 + \rho^2 - (\mathbf{A}\mathbf{n}_1)^2 - \rho^2 n_{1z}^2}{\rho^2 + \varepsilon n_{1z}^2 \omega^2 / c^2} \frac{\sin^2(N\varphi_1 d/2)}{\sin^2(\varphi_1 d/2)} \times \\ &\times \left\{ \frac{4\sin^2(a\varphi_1/2)}{\varphi_1^2} + \frac{1 + e^{-2\gamma_1 a} - 2e^{-\gamma_1 a} \cos(ax_1)}{x_1^2 + y_1^2} - \right. \\ &\left. - \frac{4\sin(a\varphi_1/2)}{\varphi_1(x_1^2 + y_1^2)} \left(\cos \frac{\varphi_1 a}{2} [y_1 - D_1] + \sin \frac{\varphi_1 a}{2} [x_1 - R_1] \right) \right\}, \\ q_2^{(I)} &= \frac{\mathbf{A}^2 + \rho^2 - (\mathbf{A}\mathbf{n}_2)^2 - \rho^2 n_{2z}^2}{\rho^2 + \varepsilon n_{2z}^2 \omega^2 / c^2} \frac{\sin^2(N\varphi_2 d/2)}{\sin^2(\varphi_2 d/2)} \times \\ &\times \left\{ \frac{4\sin^2(\varphi_2 a/2)}{\varphi_2^2} e^{-2b\rho} + \frac{1 + e^{-2\gamma_2 a} - 2e^{-\gamma_2 a} \cos(ax_2)}{x_2^2 + y_2^2} - \right. \\ &\left. - \frac{4\sin(a\varphi_2/2)}{\varphi_2(x_2^2 + y_2^2)} e^{-b\rho} \left[\cos \left(\sqrt{\varepsilon} k_{2z} b - \frac{\varphi_2 a}{2} \right) [y_2 - D_2] - \right. \right. \\ &\left. \left. - \sin \left(\sqrt{\varepsilon} k_{2z} b - \frac{\varphi_2 a}{2} \right) [x_2 - R_2] \right] \right\},\end{aligned}$$

$$\begin{aligned}q_3^{(I)} &= 8\text{Re} \left[\frac{\mathbf{n}_1(\mathbf{n}_1\mathbf{L}) - \mathbf{L}}{\rho - i\sqrt{\varepsilon}k_{1z}} F \frac{\mathbf{n}_2(\mathbf{n}_2\mathbf{L}^*) - \mathbf{L}^*}{\rho + i\sqrt{\varepsilon}k_{2z}} e^{i(\varphi_1 - \varphi_2) \left(a + (N-1)\frac{d}{2} \right)} \times \right. \\ &\times \left(\frac{\sin(\varphi_1 a/2)}{\varphi_1} e^{-\frac{ia\varphi_1}{2}} - \frac{1 - \exp[-a\gamma_1 - iax_1]}{2(y_1 + ix_1)} \right) \times \\ &\times \left(\frac{1 - \exp[-a\gamma_2 + iax_2]}{2(y_2 - ix_2)} - e^{-b(\rho + i\sqrt{\varepsilon}k_{2z})} e^{\frac{i\varphi_2 a}{2}} \frac{\sin(\varphi_2 a/2)}{\varphi_2} \right) \Bigg],\end{aligned}$$

$$\begin{aligned}
D_{(1,2)} &= e^{-y_{(1,2)}a} \left[y_{(1,2)} \cos ax_{(1,2)} - x_{(1,2)} \sin ax_{(1,2)} \right], \\
R_{(1,2)} &= e^{-y_{(1,2)}a} \left[x_{(1,2)} \cos ax_{(1,2)} + y_{(1,2)} \sin ax_{(1,2)} \right] \\
x_{(1,2)} &= \varphi_{(1,2)} - \frac{n_{(1,2)z}}{n_{(1,2)x}} \sqrt{\varepsilon} k_{(1,2)z}, \quad y_{(1,2)} = \frac{n_{(1,2)z}}{n_{(1,2)x}} \rho \\
F &= \frac{\sin(N\varphi_1 d/2)}{\sin(\varphi_1 d/2)} \frac{\sin(N\varphi_2 d/2)}{\sin(\varphi_2 d/2)}
\end{aligned}$$

Now let us consider the **second case**. Here $n_z^2 \leq 1 - \varepsilon(\omega)$, i.e. the wave in the matter is evanescent. The total field of radiation has the form of Eq.(6), the spectral-angular distribution has the form of Eqs.(8), but here:

$$\begin{aligned}
n_{1z} &= -im_{1z}, \quad y_1 = \frac{-m_{1z}}{n_{1x}} \rho, \quad x_1 = \varphi_1 + \sqrt{\varepsilon} m_{1z} \frac{\omega}{c} \frac{m_{1z}}{n_{1x}} \\
q_1^{(II)} &= \frac{Q}{(\rho - \sqrt{\varepsilon} m_{1z} \omega/c)^2} \frac{\sin^2(N\varphi_1 d/2)}{\sin^2(\varphi_1 d/2)} \times \\
&\times \left\{ \frac{4 \sin^2(a\varphi_1/2)}{\varphi_1^2} + \frac{4 \sin^2((y_1 + x_1)a/2)}{(y_1 + x_1)^2} - \right. \\
&\left. - \frac{8 \sin(a\varphi_1/2) \sin((y_1 + x_1)a/2)}{\varphi_1 (y_1 + x_1)} \cos\left(\frac{(\varphi_1 - x_1 - y_1)a}{2}\right) \right\},
\end{aligned}$$

$q_2^{(II)} = q_2^{(I)}$ and x_2, y_2 are the same as in first situation.

$$\begin{aligned}
q_3^{(II)} &= 8 \operatorname{Re} \frac{\mathbf{n}_1(\mathbf{n}_1 \mathbf{L}) - \mathbf{L}}{\rho - m_{1z} \sqrt{\varepsilon} \omega/c} F \frac{\mathbf{n}_2(\mathbf{n}_2 \mathbf{L}^*) - \mathbf{L}^*}{\rho + i \sqrt{\varepsilon} k_{2z}} e^{i(\varphi_1 - \varphi_2)(a + \frac{d}{2}(N-1))} \\
&\times \left(\frac{\sin(\varphi_1 a/2)}{\varphi_1} e^{-\frac{i\varphi_1 a}{2}} - \frac{1 - e^{-i(y_1 + x_1)a}}{2i(y_1 + x_1)} \right) \times \\
&\times \left(\frac{1 - \exp[-ay_2 + iax_2]}{2(y_2 - ix_2)} - e^{-b(\rho + i\sqrt{\varepsilon} k_{2z})} e^{\frac{i\varphi_2 a}{2}} \frac{\sin(\varphi_2 a/2)}{\varphi_2} \right),
\end{aligned}$$

$$Q = \mathbf{A}^2 + \rho^2 - 2[(\mathbf{A} \mathbf{n}_1)^2 - m_{1z}^2 \rho^2] + |\mathbf{n}_1|^2 [(\mathbf{A} \mathbf{n}_1) - m_{1z} \rho]^2$$

ANALYSIS OF THE RESULTS

To analyse the results we put

$$\begin{aligned}
n_x &= \sin \theta \cos \phi, \\
n_y &= \cos \theta, \\
n_z &= \sin \theta \sin \phi.
\end{aligned} \tag{9}$$

Moreover, we choose the value of angle $\theta = \arccos(\beta^{-1} \sin \alpha)$, because for it the exponent $e^{-2\varphi h}$ in Eq. (8) has maximum, and the maximal radiation is distributed near the cone surface with the cone opening equal $\arccos(\beta^{-1} \sin \alpha)$ (in more detail see [7], [8]).

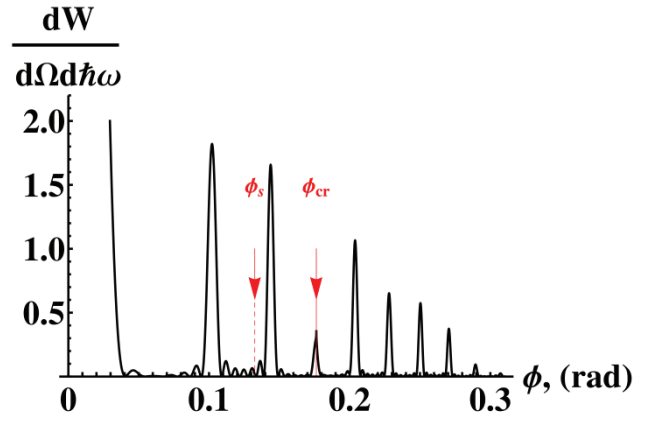


Figure 2: The total spectral-angular distribution of Smith-Purcell radiation. Here $\hbar\omega_p = 26.3 \text{ eV}$ (beryllium), $\gamma = 4 \cdot 10^4$ (energy of FACET, SLAC), $N = 7$, $\alpha = 30^\circ$, $\theta = \arccos(\beta^{-1} \sin \alpha)$, $d = 1.5 \mu\text{m}$, $a = d/4$, $b = 0.15 \mu\text{m}$, $h = 60 \mu\text{m}$, $\lambda = 6.75 \mu\text{m}$, $\phi_{cr} = \arcsin(\sqrt{1 - \varepsilon}/\sin \theta)$. For $\phi \leq \phi_{cr}$ there are inhomogeneous evanescent waves in the medium, for $\phi \geq \phi_{cr}$ there are usual plane waves in the medium. For $\phi < \phi_s = \arctan[b/(d-a)]$ it is needed to take into account the radiation refracted on the forward edge of the strip and propagating through the next strips.

Figure 2 demonstrates the spectral-angular distribution of the radiation depending on the angle ϕ . It represents the set of peaks like usual Smith-Purcell radiation. The value of $dW(\mathbf{n}, \omega)/d\Omega d\hbar\omega$ for $\phi = 0$ is maximal and equals ≈ 19.8 for parameters taken. Obtaining Eq. (8), we suppose rather big grating period:

$$(d-a)n_{2z}/n_{2x} \geq b. \tag{10}$$

We do so in order not to consider the radiation generated in one strip and going through the next strips, which would require much more complicated calculation.

Solving the inequality (10) relative to ϕ with help of Eq. (9), it is easy to get the restriction

$$\phi > \phi_s = \arctan[b/(d-a)]. \tag{11}$$

The minimal value ϕ_s is shown in Fig. 2 as red dashed line with arrow. To consider the area of $\phi < \phi_s$ one should take into account the radiation refracted on the forward edge of the strip and propagating through the next strips. As we said above, there is some critical value $n_z^{cr} = \sqrt{1 - \varepsilon(\omega)}$ or, using the third of Eqs. (9), there is

$$\phi_{cr} = \arcsin(\sqrt{1 - \varepsilon}/\sin \theta). \tag{12}$$

For $\phi \leq \phi_{cr}$ there are inhomogeneous plane (evanescent) waves in the medium, for $\phi \geq \phi_{cr}$ there are usual plane waves in the medium. The value ϕ_{cr} is shown in Fig. 2 as

thin red line with arrow. Figure 2 is plotted up to the value

$$\phi_{max} = \min \left\{ \arccos \left(\frac{\sqrt{1-\varepsilon(\omega)}}{\sin \theta} \right); \arctan \left(\frac{b}{a} \right) \right\}. \quad (13)$$

The first quantity in braces arises from the inequality $n_x^2 \geq \varepsilon(\omega) - 1$, the second one arises from the condition

$$b \geq a n_{2z} / n_{2x}, \quad (14)$$

which is of common sense for thick enough strips; for thin strips the independent calculations are required.

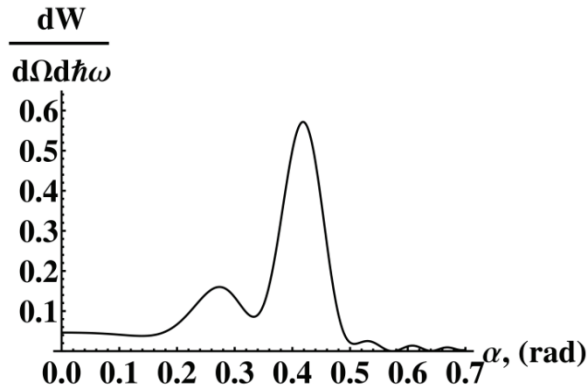


Figure 3: The total spectral-angular distribution of the Smith-Purcell radiation depending on α . Here $\phi = 0.2 \text{ rad}$ and other parameters the same as in Fig. 2.

Figure 3 demonstrates the spectral-angular distribution in dependence on the angle between trajectory of the particle and the grating rulings. We would like to notice that with the growing of α the angle $\theta = \arccos(\beta^{-1} \sin \alpha)$ changes. This graph shows the radiation in the plane perpendicular to the xz -plane and at constant angle to the grating plain. One can see that for fixed value of viewing angle ϕ and for $\alpha = 0$ the radiation is not maximal. It is possible to observe more intensive radiation turning the grating relative to z -axis. The different maxima in Fig. 3 correspond to the peaks of Smith-Purcell radiation (different diffraction orders).

CONCLUSION

We developed theory for the radiation from the single particle moving parallel to the grating surface at arbitrary angle to the rulings direction. Refraction of radiation on both target edges proves to influence significantly on Smith-Purcell radiation spectrum in UV and soft X-ray ranges of frequency.

It was shown that for fixed value of observation angle and for particle moving perpendicular to the ruling direction the radiation is not maximal: it is possible to observe more intensive radiation turning the grating relative to z -axis.

REFERENCES

- [1] A. P. Potylitsyn *et al.*, Diffraction Radiation from Relativistic Particles, Berlin: Springer-Verlag, 2011.
- [2] D. Yu. Sergeeva *et al.*, "UV and X-ray diffraction and transition radiation from charged particles bunches," *Nucl. Instruments and Methods B*, vol. 309, p. 189, 2013.
- [3] A. A. Tishchenko *et al.*, "Diffraction radiation from an ultrarelativistic charge in the plasma frequency limit," *Phys. Rev. E*, vol. 70, p. 066501, 2004.
- [4] H. L. Andrews *et al.*, "Reconstruction of the time profile of 20.35 GeV, subpicosecond long electron bunches by means of coherent Smith-Purcell radiation," *Phys. Rev. ST AB*, vol. 17, p. 052802, 2014.
- [5] W. Knulst *et al.*, "High brightness, narrowband, and compact soft x-ray Cherenkov sources in the water window," *Appl. Phys. Lett.*, vol. 83, p. 4050, 2003.
- [6] A. A. Tishchenko *et al.*, "X-ray diffraction radiation in conditions of Cherenkov effect," *Phys. Lett. A*, vol. 359, p. 509, 2006.
- [7] A. A. Tishchenko *et al.*, "Backward Smith-Purcell Radiation," in *Proc. of RREPS 2013*, Erevan, Armenia, 2013.
- [8] O. Haeberle *et al.*, "Smith-Purcell radiation from electrons moving parallel to a grating," *Phys. Rev. E*, vol. 55, p. 4675, 1997.

RADIATION AND INTERACTION OF LAYERS IN QUASI-PLANE ELECTRON BUNCHES MOVING IN UNDULATORS

N. Balal^{*} Ariel University, Ariel, Israel ^{*}, V.L. Bratman, Ariel University, Ariel, Israel and Institute of Applied Physics, Russian Academy of Sciences, Nizhny Novgorod, Russia

Abstract

A simple general 1-D theory of coherent spontaneous undulator radiation from dense bunches allows easily taking into account both Coulomb and radiation interaction of the particles in the bunches with arbitrary densities, velocity distributions and energy chirps. The theory can be applied for estimations of THz radiation sources.

RADIATION OF A MOVING PLANE

Generating powerful coherent THz radiation from dense and relatively low-energy electron bunches formed in compact laser-driven photo-injectors [1-8] is a fairly complicated task because of strong Coulomb repulsion of “insufficiently heavy” particles. To overcome it, one can apply energy chirping [6, 8] or/and formation of quasi-plane bunches with increased transverse size [4, 7]. The main properties of radiation and dynamics for such bunches may be found from the simplest 1-D model representing a bunch as a set of moving charged planes. The field of a plane that consists of electrons moving synchronously along arbitrary identical trajectories $\vec{r}(t)$ can be written in the form [3]

$$\vec{E}_z = -2\pi\sigma s, \quad \vec{E}_r = 2\pi\sigma\vec{\beta}_r(\tilde{r})[1 - s\beta_z(\tilde{r})]^{-1}, \quad \vec{H}_r = s\hat{z} \times \vec{E}_r.$$

Here, $-\sigma$ is a surface charge density, $\vec{\beta} = \vec{v}/c$ is the normalized electron velocity, $s = \text{sgn}[z - z(t)]$, \tilde{r} is the retarded time. Unlike the Lienard-Wiechert field of a point charge, the field of the plane is finite at the charges and determine both the self-action of the charged plane and its radiation. If the particles oscillate in the plane and move with a ultrarelativistic translational velocity β_z , the plane generates coherent spontaneous radiation that is contracted/stretched and increased/decreased by amplitude in the passing/counter $\pm z$ directions, respectively.

The motion of electrons in a linearly polarized undulator field $\vec{H}_u = \vec{y}_0 H \cos(2\pi z/d)$ and own field of the charged plane is described by self-consistent equations

$$\frac{dp_x}{d\zeta} = K \cos \zeta - q \frac{p_x}{p_z}, \quad \frac{dp_z}{d\zeta} = -K \frac{p_x}{p_z} \cos \zeta - q \frac{p_x^2}{1 + p_x^2}, \quad \frac{d\tau}{d\zeta} = \frac{\gamma}{p_z}.$$

Here, $\zeta = 2\pi z/d$, $\tau = 2\pi ct/d$ are the normalized axial coordinate and current time, $\vec{p} = \gamma\vec{\beta}$, γ are the normalized electron momentum and energy,

$K = eH/2\pi mc^2$, $q = e\sigma d/mc^2$ are the undulator and space charge parameters, respectively. For particles with the same energy and zero transverse velocities at the entrance into the undulator field the initial conditions are as follows

$$p_x = 0, \quad p_z = \sqrt{\gamma_0^2 - 1}, \quad \tau = 0.$$

For electron with ultrarelativistic axial velocity the transverse electric and magnetic radiation self-forces almost completely compensate each another, and because of it the transverse electron momentum differs from its unperturbed value $p_x = K \sin \zeta$ only on terms of the order of small parameter q/γ_0 . In the first approximation both the energy and Doppler up-conversion factor for radiating particles averaged by undulator oscillations linearly decrease along the axial coordinate:

$$\bar{\gamma} = \gamma_0(1 - \eta), \quad \Gamma = (1 - \bar{\beta}_z)^{-1} = \Gamma_0(1 - 2\eta),$$

where

$$\eta = (\gamma_0 - \bar{\gamma})/(\gamma_0 - 1) = \alpha \zeta$$

is the efficiency of radiation, $\alpha = (q/\gamma_0)(1 - 1/\sqrt{1 + K^2})$. The radiation field from the plane presents a signal with duration $\tau_r = 2\pi N \lambda_0/d$ and linear modulation of both amplitude, $E = 1 - \alpha\psi$, and frequency, $\omega = \omega_0 E$ (Fig. 1):

$$E_x/2\pi\sigma = (\Gamma_0 K/\gamma_0) E \sin \tilde{\zeta}$$

where $\omega_0 = \Gamma_0(2\pi c/d)$, $\psi = \Gamma_0(\tau - \zeta)$ are the non-perturbed radiation frequency and the phase at the point of observation, $\tilde{\zeta} = \psi(1 - \alpha\psi)$ is the retarded coordinate.

The above formulas provide very good coincidence with numerical calculations even for fairly large space charge parameters and undulator lengths. For example, using for the radiating plane the typical parameters of the Israeli THz source (currently under development) [8]: electron energy $E_0 = 5.5 \text{ MeV}$, surface density $\sigma_0 = 0.1 \text{ nC/mm}^2$ and $K=0.47$ demonstrates coincidence of analytical and numerical results with high precision; in order to show the differences the density in Fig.1a has been increased up to $3\sigma_0$.

^{*}nezahb@ariel.ac.il

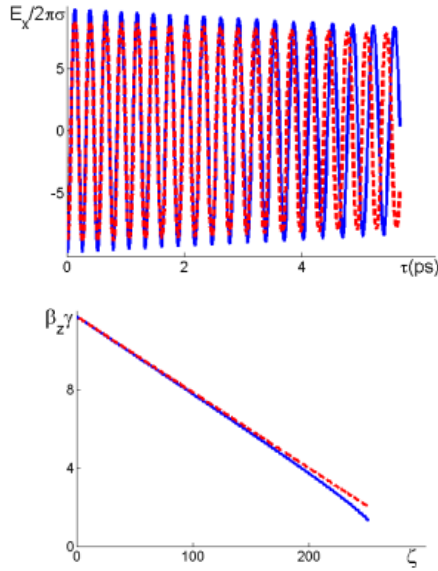


Figure 1: Radiation pulse (a) and electron axial momentum (b) for one plane: analytical (blue) and numerical (red) solutions.

INTERACTING LAYERS

The transverse electron momenta of the particles in a dense moving layer of a finite thickness is also basically determined by the undulator field, but strong axial Coulomb repulsion of sub-layers can quickly increase the axial electron momenta and size of the bunch. In order to mitigate this effect rear particles should be accelerated in a stronger RF field than the front ones during the bunch formation [6, 8] (energy chirp, $\Delta\gamma_0 > 0$). The averaged axial motion of particles in the combined undulator field and fields of all sub-layers is close to the relativistic uniformly accelerated motion. If longitudinal electron masses in sub-layers are close to each other, the particle separation is described by a quasi-nonrelativistic formula. Thus, in the case of two planes

$$\Delta\zeta = \Delta\zeta_0 - \frac{\Delta\gamma_0}{\gamma_0^3} \tau + \frac{(q_1 + q_2)\tau^2}{2\gamma_0^3}.$$

For example, the change in separation between two planes with electron energy E_0 and densities $\sigma_0/2$ is 0.1 mm at the length of 20 cm. The separation can be significantly decreased and then returns back to the initial value at the energy chirp $\Delta\gamma_0 \sim 1$.

Coulomb and radiation forces change the kinetic and potential energy of the particles. The radiation flux is equal to the change in the surface density of the total energy,

$$w = q_1(\gamma_1 - 1) + q_2(\gamma_2 - 1) - q_1 q_2 (\zeta_1 - \zeta_2),$$

and for two planes one has the approximate equation

$$\frac{dw}{d\tau} = -q_1^2 \frac{p_{1x}^2}{1 + p_{1x}^2} - 2q_1 q_2 \frac{p_{1x}}{\gamma_1} \left(\frac{\gamma_2 p_{2x}}{1 + p_{2x}^2} \right)_{\tilde{\tau}_2} - q_2^2 \frac{p_{2x}^2}{1 + p_{2x}^2}.$$

Here, $\tilde{\tau}_2$ is the retarded time corresponding to the radiation of the second plane which acts on the first one at the moment τ . If the separation between the planes is much smaller than the characteristic radiation wavelength, the planes radiate coherently. For significantly changing separations, regions of constructive and destructive interference quickly replace one another.

The front plane is decelerated by the self-radiation and accelerated by the Coulomb and radiation forces from the back plane. If the separation between them changes quickly, the latter force can be neglected. Then the self-radiation force for the first plane can compensate its Coulomb repulsion by the second plane and stabilize the axial velocity of the first plane if $q_2 \approx (1 - 1/\sqrt{1 + K^2})q_1$ (Fig. 2a). In this case, the radiation of the first plane can be powerful and narrowband while the radiation of the decelerated second plane provides a low-frequency part of the spectrum (Fig. 2b).

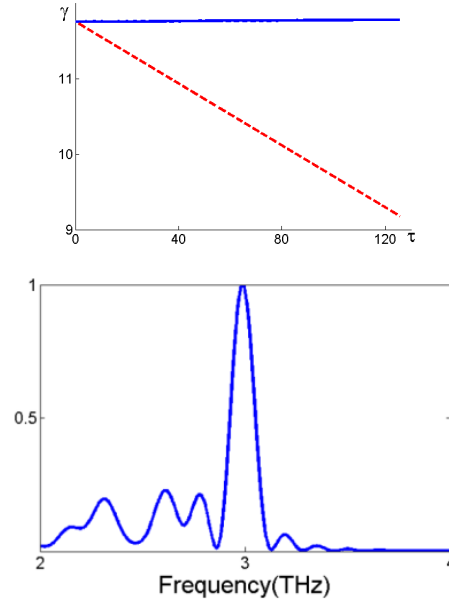


Figure 2: The Lorentz-factors and radiation spectrum for two planes with space charge parameters q_1 (blue) and q_2 (red). Coulomb acceleration of the front plane in the field of the rear one is compensated by the radiation deceleration.

In order to simulate radiation and dynamics of a quasi-plane electron bunch it is needed to provide a sufficient number of the electron sub-layers (moving planes) in each axial area with the scale of the order of the radiation wavelength at any time. If the initial thickness of the layer is much smaller than the wavelength and its changes during the motion in the undulator field are small, the resulting radiation is certainly close to that from one plane. However, at the layer surface density of the order

of σ_0 and particle energy of the order of E_0 without energy chirping the Coulomb repulsion increases the layer thickness many times (even for short interaction length). At the initial layer thickness 0.1 mm and fairly large optimum chirp $\Delta\gamma_0 \approx 2.7$ the minimum thickness is very small (Fig. 3).

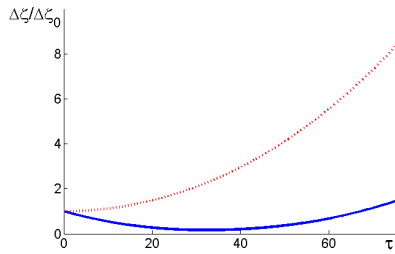


Figure 3: Change in the normalized pulse length of a moving layer with the surface density σ_0 and initial duration 0.3 ps (uniform initial charge distribution; red - without energy chirp, blue - $\Delta\gamma_0 = 2.7$).

Then the thickness increases up to the initial value at 11 undulator periods when the radiation is saturated with efficiency close to 1% (Fig. 4a). The corresponding radiation energy, pulse duration and power flux are 0.5 mJ/cm², 3.5 ps and 140 MW/cm², respectively. This radiation is distributed over a fairly broadband frequency spectrum with the central frequency 3.7 THz and width of the order of 30% (Fig. 4b).

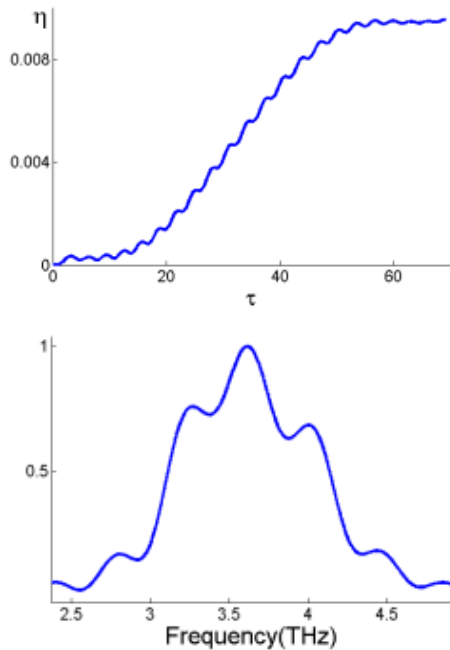


Figure 4: Current efficiency and radiation spectrum for a moving layer with initial duration 0.3 ps.

CONCLUSION

The developed 1-D approach for coherent spontaneous undulator radiation based on using the field of a moving charged plane is much simpler than the existing exact 3-D

methods which take into account finite transverse sizes of the bunches, transverse non-homogeneity of the undulator fields and influence of electrodynamic systems (waveguides) on the radiation. Due to compensation of transverse radiation forces there exists a small parameter of the problem even in the case of a very large charge density. Correspondingly, the field of a dense bunch weakly changes transverse undulator particle oscillations, and the particle dynamics can be easily studied using simple averaging of equations by undulator oscillations. The same method can be also used for essential simplification of equations in a 3-D approach. Though the 1-D approach provides only estimations and obviously overestimates the influence of the Coulomb particle repulsion, it gives a clear physical picture and demonstrates the problems associated with maintaining coherence and narrowband spectrum of the radiation for large charges and relatively low electron energy.

REFERENCES

- [1] A. Doria, R. Bartolini, J. Feinstein, G.P. Gallernao, R.H. Pantell, "Operation of a compact free-electron laser in the millimeter-wave region with a bunched electron beam", IEEE J. Quantum Electron., May 1993, 29, p.1428.
- [2] A. Gover, F. V. Hartemann, G. P. Le Sage, N. C. Luhmann, Jr., R. S. Zhang, and C. Pellegrini, "Time and frequency domain analysis of superradiant coherent synchrotron radiation in a waveguide free-electron laser", Phys. Rev. Lett., February 1994, 72, pp. 1192-1195.
- [3] V.L. Bratman, S.V. Samsonov, "Radiation and radiative damping of a charged plane, oscillating with a relativistic velocity", Phys. Letters A206, October 1995, pp. 377-382.
- [4] V.L. Bratman, D.A. Jaroszynski, S.V. Samsonov, A.V. Savilov, "Generation of ultra-short quasi-unipolar electromagnetic pulses from quasi-planar electron bunches", Nucl. Instrum. and Meth. in Phys. Research A 475, December 2001, pp. 436-440.
- [5] Y. Pinhasi, Yu. Lurie, A. Yahalom, "Space-frequency model of ultra wide-band interactions in free-electron lasers", Phys. Rev. E 71, March 2005, p. 036503.
- [6] Yu. Lurie and Y. Pinhasi, "Enhanced super-radiance from energy-modulated short electron bunch free-electron lasers", Phys. Rev. ST Accel. Beams 10, August 2007, p. 080703.
- [7] N. Balal, V.L. Bratman, A.V. Savilov, "Peculiarities of the coherent spontaneous synchrotron radiation of dense electron Bunches", Physics of Plasmas, February 2014, p. 023103.
- [8] A. Friedman et al., "Configuration and status of the Israeli THz Free Electron Laser", presented at this conference: 36th Int. Free-Electron Laser Conf., Basel, 2014.

QUASI-OPTICAL THEORY OF TERAHERTZ SUPERRADIANCE FROM AN EXTENDED ELECTRON BUNCH*

N.S. Ginzburg, A.M. Malkin, A.S. Sergeev, I.V. Zotova, V.Yu. Zaslavsky,
Institute of Applied Physics RAS, Nizhny Novgorod, Russia

Abstract

We consider the superradiance of an extended relativistic electron bunch moving over a periodically corrugated surface for the generation of multi-megawatt terahertz pulses. To study the above process we have developed a three-dimensional, self-consistent, quasi-optical theory of Cherenkov stimulated emission which includes a description of the formation of evanescent wave over a corrugated surface and its excitation by RF current induced in the electron bunch.

INTRODUCTION

In recent years, significant progress was gained in the generation of electromagnetic pulses in the centimeter and millimeter wavelength ranges based on the Cherenkov superradiance (SR) of high-current subnanosecond electron bunches with particle energies of 300–400 keV [1–5] propagating in periodically corrugated single-mode waveguides. In these frequency ranges SR pulses of subnanosecond duration with record-breaking gigawatt peak power were obtained by means of compact high-current accelerators. Typical duration of bunches employed in these experiments was, on the one hand, large compared to the wavelength and, on the other hand, it was limited by the so-called coherence length within which coherent emission of a single electromagnetic pulse from the entire bunch volume is possible due to the slippage of radiation relative to the particles. This SR emission includes electron self-bunching, and the peak power of SR pulse is approximately proportional to the square of the total number of particles in the electron pulse.

A natural continuation of this research is a development of Cherenkov SR sources operating at shorter wavelength values, including the terahertz frequency range. Technological advancements in the fabrication of spatially periodic microstructures also encourage such studies. In order to generate powerful single pulses in the THz range, it is necessary to reduce the duration of the electron bunches to several tens of picoseconds with corresponding increase in their densities. In turn, to obtain stable transverse focusing of dense electron bunches, it would be necessary to increase the particle energy up to several MeV. This increase is also a positive factor in view of improving the impedance of coupling to a surface wave. It should be recalled that for the Cherenkov radiation mechanism the spatial scale of the transverse field decay $L_{\perp} \sim \lambda\gamma/2\pi$ (where $\gamma = (1 - \beta_0^2)^{-1/2}$ is the relativistic Lorentz factor) increases with the particle energy due to a decrease in the requirements for the

waves deceleration. High brightness electron bunches generated by photoinjectors [6, 7] can satisfy the above conditions.

We should emphasize that the methods used for the theoretical description of stimulated Cherenkov radiation from relativistic electron beams in the short wavelength range must differ significantly from the approach developed previously for the microwave range. The existing theory of relativistic Cherenkov radiation sources operating in the regimes of both long-pulse (quasi-stationary) [8–10] and short-pulse (SR) [1–3] generation was based on an assumption that the transverse size of the microwave system is comparable to the radiation wavelength. Under these conditions, the Cherenkov radiation was described using a formalism according to which the electron beam interacted with a spatial harmonic of the volume waveguide mode possessing a fixed transverse structure.

For wavelengths shorter than one millimeter, the conditions of ensuring the electron beam transport and reducing Ohmic losses imply the use of oversized (or open) slow-wave systems. Accordingly, it is necessary to take into account the diffraction effects and to use a quasi-optical approach for the description of Cherenkov radiation from relativistic electron beams moving over periodically corrugated surfaces. In the case of a quasi-stationary electron beam such an approach was developed in [11] for consideration of surface-wave oscillators. In this letter we demonstrate that a similar method can be effectively used for analysis of stimulated emission of extended electron bunches moving above a corrugated surface. The validity of our consideration is confirmed by direct particle-in-cell (PIC) simulations based on CST STUDIO 3D code.

BASIC MODEL

We consider a three dimensional (3D) model of the Cherenkov SR from an extended electron bunch that moves rectilinearly at a velocity of $v_0 = \beta_0 c$ along guiding magnetic field $\vec{H}_0 = H_0 \vec{z}_0$ over a plane with a shallow periodic sinusoidal corrugation

$$b(z) = b_1 \cos(\bar{h}z), \quad (1)$$

where $b_1 \ll d$ is the corrugation amplitude, d is the period, and $\bar{h} = 2\pi/d$. We assume that an electron bunch has finite dimensions $l_{x,y,z}^e$ in three space coordinates (Fig. 1a).

Radiation field near the corrugated surface can be presented as a sum of two counter-propagating TM-

polarized wave beams with the following components of magnetic field

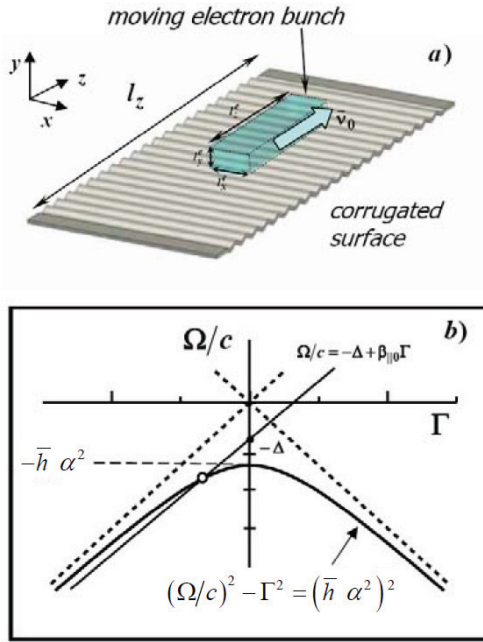


Figure 1: **(a)** Principal scheme of generation of SR pulses by an extended electron bunch moving over a periodically corrugated surface. **(b)** The dispersion diagram of the normal surface wave and resonance point in the case of a relativistic rectilinear electron beam.

$H_x = \text{Re} \left[A_+ (z, x, y, t) e^{i(\omega t - kz)} + A_- (z, x, y, t) e^{i(\omega t + kz)} \right], (2)$
 $k = \omega/c$. Correspondingly, the electric field satisfies the Maxwell equation $\vec{E} = -i/k \text{rot} \vec{H}$ and possesses components:

$$\begin{aligned} E_y &= -\text{Re} \left[A_+ e^{i(\omega t - kz)} - A_- e^{i(\omega t + kz)} \right], \\ E_z &= -\text{Re} \left[\frac{i}{k} \left(\frac{\partial A_+}{\partial y} e^{i(\omega t - kz)} + \frac{\partial A_-}{\partial y} e^{i(\omega t + kz)} \right) \right]. \end{aligned} \quad (3)$$

Under the Bragg resonance condition $\bar{h} \approx 2k$ coupling and mutual scattering of the counter-propagating wavebeams (2) takes place. To describe the waves coupling on the periodic structure located at $y=0$ we use the surface magnetic currents concept [12,13]. In the planar geometry under consideration, the surface current can be written as

$$j_x^m = -\frac{c}{4\pi} E_z = -\frac{c}{4\pi} \left(\frac{\partial (b(z) E_y)}{\partial z} + i\omega H_x \frac{b(z)}{c} \right). \quad (4)$$

In general form, field excitation by the surface magnetic j_x^m and volume electric j_z^e (see below) currents is described by the wave equation:

$$\Delta H_x - \frac{1}{c^2} \frac{\partial^2 H_x}{\partial t^2} = \frac{4\pi}{c^2} \frac{\partial j_x^m}{\partial t} \delta(y) - \frac{4\pi}{c} \frac{\partial j_z^e}{\partial y}. \quad (5)$$

Here, $\delta(y)$ is the delta function. In (2) and (3) we chose carrier frequency equal to the Bragg frequency $\bar{\omega} = \bar{h}c/2$. Taking into account the Bragg resonance condition after substituting the fields (2), (3) and the magnetic currents (4) into Eq.(5), we obtain a system of coupled parabolic equations (here we take $j_z^e = 0$)

$$\pm \frac{\partial A_{\pm}}{\partial z} + \frac{\partial A_{\pm}}{c \partial t} + \frac{i}{\bar{h}} \frac{\partial^2 A_{\pm}}{\partial x^2} + \frac{i}{\bar{h}} \frac{\partial^2 A_{\pm}}{\partial y^2} = i\alpha A_{\mp} \delta(y), \quad (6)$$

where $\alpha = \bar{h}b_1/4$ is the coupling parameter.

To demonstrate that Eqs.(6) describe formation of surface waves, let us derive a dispersion relation for normal wave propagating near the infinite corrugated surface. For simplicity we consider here a 2D model, neglecting the radiation diffraction in the x direction. We should present the solution of the above equations in the region $y > 0$ as $A_{\pm} \sim \exp i(\Omega t - \Gamma z - g_{\pm} y)$, where

$g_{\pm} = i\sqrt{-\bar{h}(\Omega/c \mp \Gamma)}$ are the transverse wave numbers. Taking into account the boundary conditions on the corrugated surface $(\partial A_{\pm}/\partial y - \alpha \bar{h} A_{\mp})|_{y=0} = 0$ which follow from Eqs. (6) we get the dispersion equation:

$$g_+ g_- = -\bar{h}^2 \alpha^2 \quad \text{or} \quad \frac{\Omega^2}{c^2} - \Gamma^2 = \bar{h}^2 \alpha^4. \quad (7)$$

As seen from Fig. 1b, a dispersion curve of the normal wave is located below the light cone and corresponds to an evanescent slow-wave with exponential decay of amplitude along the vertical y coordinate. For ultra-relativistic electrons and shallow corrugation the typical crossing point of the dispersion curve of the normal surface wave and the electron beam line $\Omega/c = -\Delta + \beta_0 \Gamma$ belongs to the slope where the group velocity of the surface wave is co-directed with the electron longitudinal velocity.

Under the conditions of Cherenkov interaction, the microbunching of electrons takes place under the action of the longitudinal electric field component E_z . This process is described by the equations

$$\left(\frac{\partial}{\partial Z} + \frac{1}{\beta_0} \frac{\partial}{\partial \tau} \right)^2 \theta = \text{Re} \left(\frac{\partial \hat{A}_+}{\partial Y} e^{i\theta} \right) \quad (8)$$

$$\theta|_{Z=0} = \theta_0 + r \cos \theta_0, \quad \theta_0 \in [0, 2\pi), \quad r \ll 1,$$

$$\left(\frac{\partial}{\partial Z} + \frac{1}{\beta_0} \frac{\partial}{\partial \tau} \right) \theta \Big|_{Z=0} = \hat{\Delta}, \quad (9)$$

where $\theta = \bar{\omega}(t - z/c)$ is the phase of electrons relative to the co-propagating partial wave A_+ , $\hat{\Delta} = 2\Delta/\bar{h}G$. The microbunching induces a high frequency electron current that can be presented in the form:

$$j_z^e = -\frac{Qv_0}{V} f(z - v_0 t, x, y) J, \quad (10)$$

where $J(z, x, y) = \frac{1}{\pi} \int_0^{2\pi} \exp(-i\theta) d\theta_0$, Q is the bunch total charge, V is its volume, and the function $f(z, x, y)$ defines the unperturbed bunch profile.

Substituting (10) in Eq.(5) we get equations that describe the excitation of a surface wave by the electron bunch:

$$\begin{aligned} \frac{\partial \hat{A}_+}{\partial Z} + \frac{\partial \hat{A}_+}{\partial \tau} + i \frac{\partial^2 \hat{A}_+}{\partial X^2} + i \frac{\partial^2 \hat{A}_+}{\partial Y^2} + \sigma \delta(Y) \hat{A}_+ \\ = i \hat{\alpha} \delta(Y) \hat{A}_- - \frac{\partial}{\partial Y} (J F(Z - \beta_0 \tau, X, Y)), \quad (11) \\ - \frac{\partial \hat{A}_-}{\partial Z} + \frac{\partial \hat{A}_-}{\partial \tau} + i \frac{\partial^2 \hat{A}_-}{\partial X^2} + i \frac{\partial^2 \hat{A}_-}{\partial Y^2} + \sigma \delta(Y) \hat{A}_- = i \hat{\alpha} \delta(Y) \hat{A}_+. \end{aligned}$$

Self-consistent system (8), (11) was written using the following normalization:

$$Z = G \bar{\omega} z / c, \quad X = \sqrt{2G} \bar{\omega} x / c, \quad Y = \sqrt{2G} \bar{\omega} y / c, \quad \tau = G \bar{\omega} t, \\ \hat{A}_{\pm} = \sqrt{2e} A_{\pm} / \left(mc \bar{\gamma}_0^3 G^{3/2} \right), \quad \hat{\alpha} = \sqrt{2/G} \alpha,$$

$$G = \left(\frac{e}{mc^3} \frac{\lambda^2}{\pi \gamma_0^3} \frac{Q \gamma_0}{V} \right)^{1/2} \text{ is the gain parameter. Below we}$$

assume for simplicity that the electron density has uniform distribution over all three space coordinates. It should be noted that in Eqs.(11) the Ohmic losses are also taken into account through being characterized by the parameter $\sigma = k \varepsilon \sqrt{2/G}$, where ε is the skin depth.

In the simulations we have used the following boundary conditions. In the longitudinal direction we assume that the corrugation has a finite length $L = G \bar{\omega} l / c$ and electromagnetic energy fluxes from outside are absent: $\hat{A}_{\pm}|_{Z=0} = 0$, $\hat{A}_{\pm}|_{Z=L} = 0$. In the vertical y direction we take into account that in practice the electron bunch should be transported in the vacuum channel formed by the planar waveguide. In this case Eqs.(11) should be supplemented by an additional boundary condition at the second regular plate of the waveguide: $\partial \hat{A}_{\pm} / \partial Y|_{Y=B} = 0$,

where $B = \sqrt{2G} \bar{\omega} b / c$ is the normalized gap between the plates. If this gap is sufficiently large ($B \gg 1$) the position of the second plate does not affect the characteristics of the electron-wave interaction due to the exponential decay of the surface wave in the y direction. Nevertheless it allows us to present the solution of Eqs.(11) as a sum of the modes of the regular planar

waveguide $\hat{A}_{\pm} = \sum_{n=0}^{\infty} \hat{A}_{\pm}^n(Z, X, \tau) \cos(n\pi Y/B)$ for the numerical simulation. In the horizontal x direction we used the artificial cyclical boundary conditions which were imposed at a large distance from the bunch.

SIMULATION RESULTS

Simulations of the Cherenkov SR were performed in the terahertz range for an electron bunch with a length of $l_z^e = 1.2$ cm, transverse dimensions of $l_x^e = 0.45$ mm and $l_y^e = 0.3$ mm, particle energies of 1.4 MeV and a total bunch charge of 2.2 nC. These parameters can be obtained for the electron bunches generated by photoinjectors [6,7]. The bunch was propagating over a plane with a corrugated region of length 13 cm, a corrugation period of 0.15 mm and a corrugation amplitude of 22 μ m. For a copper surface the skin depth in the terahertz range is $\varepsilon \approx 0.07 \mu$ m. These physical parameters correspond to the normalized quantities $G = 3.5 \cdot 10^{-3}$, $\hat{\alpha} = 5.5$, $\Delta = 10.5$, $L = 9.7$, $L_x^e = 0.8$, $L_y^e = 0.53$, $L_z^e = 0.9$, $\sigma = 0.035$. We used the initial small electron density fluctuations governed by the parameter $r \ll 1$ as initial conditions.

The results of these simulations showed that the main fraction of the radiation is emitted in the form of a short SR pulse in the positive direction of the axis z , i.e., in the direction of propagation of the electron bunch. The temporal dependence of the total radiation power

$$P_+ = G^2 \frac{\gamma_0^2}{32\pi} \frac{m^2 c^5}{e^2} \iint_0^{\infty} |\hat{A}_+(Z=L)|^2 dX dY \text{ is shown in}$$

Fig. 2. The process of pulse formation is illustrated by Fig. 3, where spatial structures of the partial waves are

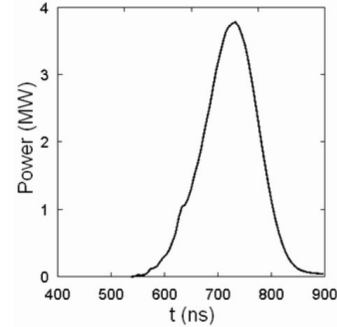


Figure 2: SR pulse temporal profile.

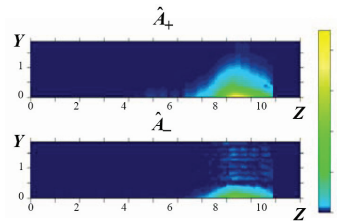


Figure 3: Spatial structures of the partial waves $\hat{A}_{\pm}(Y, Z)$ that corresponds to formation of normal surface wave ($X = 0$, $\tau = 10$).

presented. One can see that the amplitudes of both partial waves exponentially decay in the direction of the y axis with increasing distance from the corrugated surface. In Fig. 4, spatial profiles of the electric field on the cross-

section $Y = 0.6$ are shown in consecutive moments of time. As follows from the dispersion diagrams Fig. 1b the electron velocity in the resonance point exceeds the group velocity of the normal wave. It leads to formation of wake fields behind the electron bunch that is clearly observed in Fig. 4. The peak power of the SR pulse amounted to 3.5 MW at a pulse duration of ~ 100 ps.

Results obtained in the framework of a quasi-optical model were confirmed by direct CST STUDIO PIC simulations. Figure 5a,b shows the SR pulse and its spectrum with a central frequency of 0.8 THz obtained for

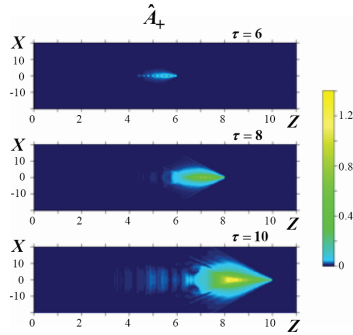


Figure 4: Formation of wake field after electron bunch. Profiles of electric field $\hat{A}_+(X, Z)$ on the surface $Y = 0.7$ in consecutive points in time.

the physical parameters of the periodic system and electron bunch indicated above. The total estimated radiation power was about 3.7 MW. The fields had the structures corresponding to a surface evanescent wave located near the corrugated surface. Figure 5c demonstrates the formation of the wake-field.

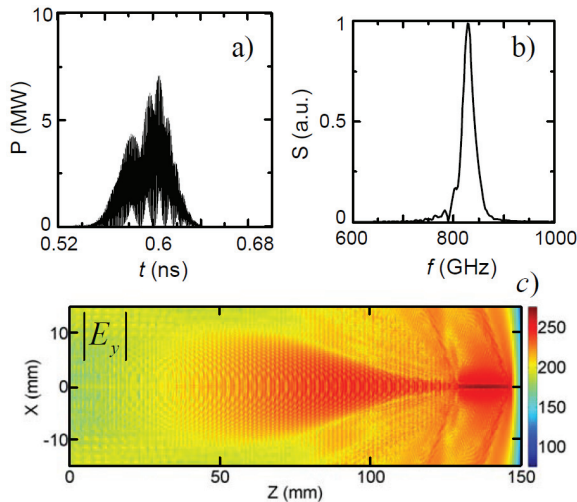


Figure 5: Results of 3D direct PIC simulations of Cherenkov SR in terahertz range for an electron bunch formed by a photoinjector gun. (a) – SR pulse, (b) – radiation spectrum, (c) – formation of wake field.

CONCLUSION

Thus, the results of our analysis show the possibility of generating single high-power terahertz pulses using the phenomenon of Cherenkov superradiance of extended electron bunches that move in free space over a corrugated surface. We believe that it is expedient to study the possibility of moving to still shorter wavelengths, which can be achieved by decreasing the period of the diffraction gratings and increasing the density and energy of the particles in the electron bunches.

ACKNOWLEDGMENT

The authors are grateful to I.Yu.Kostyukov and A.D.R. Phelps for fruitful discussions. This study was supported by the Russian Foundation for Basic Research (project no. 14-08-01180) and the Dynasty Foundation.

REFERENCES

- [1] N.S. Ginzburg, Yu.V. Novozhilova, I.V. Zotova et al., *Phys. Rev. E*, **60**, 3297 (1999).
- [2] S.M. Wiggins, D.A. Jaroszynski, B.W.J. McNeil et al., *Phys. Rev. Lett.* **84**, 2393 (2000); M.I. Yalandin, V.G. Shpak, S.A. Shunailov et al., *IEEE Trans. Plasma Sci.* **28**, 1615 (2000).
- [3] A.A. Elthaninov, S.D. Korovin, V.V. Rostov et al., *Laser and Particle Beams*, **21**, 187 (2003)
- [4] S.D. Korovin, A.A. Eltchaninov, V.V. Rostov et al., *Phys. Rev. E*, **74**, 016501 (2006).
- [5] V.V. Rostov, A.A. Elchaninov, I.V. Romanchenko, and M.I. Yalandin, *Appl. Phys. Lett.*, **100**, 224102 (2012).
- [6] J.G. Power, Overview of photoinjectors, *Proc. of 14th Adv. Accel. Concepts Workshop*, Annapolis, USA, AIP Conf. Proc. Vol.1299, Ed. by G. Nusinovich and S. Gold, 2010.
- [7] P. Piot, Y.E. Sun, and K.J. Kim, *Phys. Rev. ST-AB*, **9**, 031001 (2006).
- [8] N.S. Ginzburg, S.P. Kuznetsov, and T.N. Fedoseeva, *Quantum Electron.* **21**, 728 (1978).
- [9] B. Levush, T. Antonsen, A. Bromborsky et al., *Phys. Fluids B* **4**, 2293 (1992).
- [10] A.N. Vlasov, G.S. Nusinovich, and B. Levush, *Phys. Plasmas* **4**, 1402 (1997).
- [11] N.S. Ginzburg, A.M. Malkin, A.S. Sergeev, and V.Yu. Zaslavsky, *Appl. Phys. Lett.* **99**, 121505 (2011); *Appl. Phys. Lett.* **100**, 143510 (2011).
- [12] B.Z. Katsenelenbaum, *Theory of Irregular Waveguides with Slowly Varying Parameters* (Academic Press, M. 1961).
- [13] M.I. Fuks, M.B. Goikhman, N.F. Kovalev et al., *IEEE Trans. on Plasma Sci.*, **32**, 1323 (2004).

USING LORENTZ TRANSFORMATIONS FOR SIMULATIONS OF WIGGLER SUPERRADIANCE FROM THE PICOSECOND ELECTRON BUNCHES*

A.M. Malkin, I.V. Zotova, Institute of Applied Physics RAS, Nizhny Novgorod, Russia
N.S. Ginzburg, A.A. Golovanov, Institute of Applied Physics RAS, Nizhny Novgorod, Russia
and Nizhny Novgorod State University, Nizhny Novgorod, Russia
V.P. Tarakanov, Joint Institute for High Temperatures RAS, Moscow, Russia

Abstract

In this paper we present a theoretical analysis of superradiance (SR) from picosecond electron bunches wiggling in periodical undulator field based both on the method of averaged ponderomotive force and on a direct numerical PIC (particle-in-cell) simulation. Within both approaches the analysis takes place in the reference frame co-moving with electrons which allows simplifying the procedure of simulation significantly due to the fact that all the spatial scales including the radiation wavelength, the length of the beam and the length of the pump field packet into which the undulator field is transformed are of the same order. We show that in the reference frame the SR effect can be interpreted as a formation of the distributed Bragg mirror in the bulk of the electron beam which is effectively reflecting (scattering) the pump wave. A possibility of generation of multimewatt pulses in terahertz and far infrared wave ranges is demonstrated.

INTRODUCTION

Recently, a significant progress has been achieved in generation of ultrashort electromagnetic pulses in centimeter and millimeter waveband based on superradiance (SR) of high-current electron bunches [1]. Generated pulses are characterized by record-breaking (gigawatt) peak powers. As it was shown both theoretically and experimentally at particle energies of ~ 300 keV, currents ~ 1 kA and the bunch durations ~ 1 ns the most effective mechanism of SR pulses generation is the Cherenkov one, realized in a periodic slow-wave structure.

The advancement of SR sources further into short wave ranges can be obtained by using the emission of electron bunches moving in the undulator field. In this case the particles energy should be increased up to 4-5 MeV and the bunch duration should be about several picoseconds. The bunches formed by photo-injection guns possess the necessary characteristics [2]. In this paper under assumption that the electron bunch propagates in a planar waveguide a theoretical analysis and KARAT PIC code simulations of above process were performed. In both approaches we analysis SR effects in the co-moving with electrons reference frame K' [3]. In particular, this allows to simplify the numerical simulation procedure

significantly, because at relativistic factor values $\gamma \sim 10$ the length of undulator of about several meters according to Lorentz transformations turns into several tens of centimeters, whereas the length of picosecond electron bunch in the rest reference frame stretches up to several centimeters (see Fig. 1). Besides the radiated wavelength transforms from the submillimeter to millimeter range. Proportionality of all scales, including the transverse size of the bunch, allows us to simulate the processes without using significant computational resources, finding then the parameters of radiated pulses in the lab frame using again the relativistic transformations.

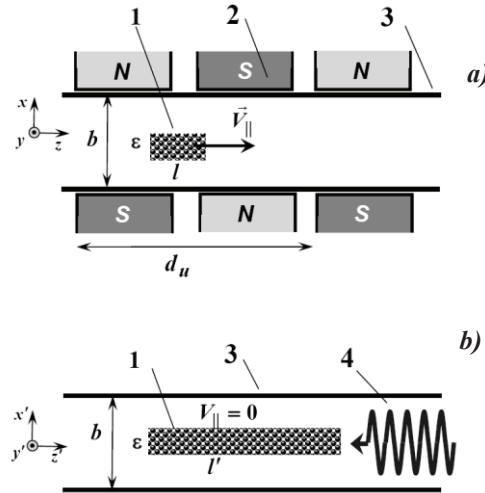


Figure 1: Scheme of generation of superradiance pulse (a) in the lab reference frame and (b) in the co-moving reference frame. (1) - electron beam, (2) - undulator, (3) - planar waveguide, (4) - electromagnetic TE wave, into which the undulator field transforms.

SIMPLIFIED MODEL

We consider here a two-dimensional model assuming that an electron bunch with a length of l moves in a planar waveguide with the gap between plates b_0 (See Fig. 1). Electrons oscillate in a planar undulator field with vector potential:

$$\vec{A}(z, t) = \text{Re}(\vec{y}_0 A_u \exp[ih_u z]), \quad (1)$$

*Work supported by Russian Foundation for Basic Research, grant No.12-02-01152

where $d = 2\pi/h_u$ is the undulator period, A_u is an amplitude. Further analysis will be conducted in the co-moving reference frame where the undulator field transforms into propagating pump wave

$$\vec{A}'(z', t') = \text{Re}(\vec{y}_0 A'_u \exp[i\omega' t' + ih' z']), \quad (2)$$

where $\omega' = \gamma V_{||} h_u$, $h' = \gamma h_u$. In K' the electron bunch (layer) of finite length l' can be divided into a set of macroparticles differing by initial location z'_0 .

Radiated field in the planar waveguide with a gap of b between the plates can be presented as a sum of TE modes with a frequency determined by the electron oscillations frequency and with different longitudinal wavenumbers $h'_n = \sqrt{k'^2 - g_n^2}$, $g_n = (2n-1)\pi/b$:

$$\vec{A}_s = \text{Re} \left[\dot{y}_0 \sum_n A_n(z') \cos(g_n x') e^{i\omega' t' \pm ih'_n z'} \right] \quad (3)$$

Mode amplitudes excited by one oscillating macroparticle in the instant of time when its coordinate is $z'(z'_0)$ can be found from Helmholtz equation:

$$\frac{d^2 A_n}{dz'^2} + h_n'^2 A_n = -4\pi\alpha_u \theta_n e^{ih'_n z'(z'_0)} \delta(z' - z'(z'_0)), \quad (4)$$

where $\theta_n = (2/b) \int_{-\varepsilon/2}^{\varepsilon/2} \cos(g_n x') dx'$. Solution of (4) can be

presented as a composition of two components propagating in $\pm z'$ directions:

$$A_n(x', z') = \frac{2\pi}{ih'_n} \alpha_u \sigma \theta_n e^{ih'_n z'(z'_0) - ih'_n |z' - z'(z'_0)|} \quad (5)$$

Fields (5) acting together with (1) lead to the emergence of the averaged ponderomotive force

$F_{pond} = -\frac{e^2}{2mc^2} \nabla \langle A^2 \rangle$ acting from one of the macroparticles on the other one. This force can be presented in the form:

$$\begin{aligned} F_{pond}(x', z') &= \\ &= \pi e \sigma \alpha_u^2 \sum_n \frac{k'}{h'_n} \theta_n f_n[k'(z' - z'(z'_0))] \cos(g_n x'), \\ f_n(\zeta) &= \mu_n^+ \cos(\mu_n^+ \zeta), \quad \zeta > 0, \\ f_n(\zeta) &= \mu_n^- \cos(\mu_n^- \zeta), \quad \zeta < 0, \end{aligned} \quad (6)$$

where $\mu_n^\pm = (h' \pm h'_n)/k'$, $k = \omega'/c$. This force is sign-variable and attracting near the particle. It is depicted in Fig. 2 for different values of the gap between the plates. We also take into account the Coulomb forces which can be written as:

$$\begin{aligned} F_c &= -4e\sigma f_c(z), \\ f_c(z) &= \frac{z}{\varepsilon} \left[R\left(\frac{\varepsilon}{z}\right) + \sum_{m=1}^{\infty} (-1)^m \left(R\left(\frac{mb-\varepsilon}{z}\right) + R\left(\frac{mb+\varepsilon}{z}\right) - 2R\left(\frac{mb}{z}\right) \right) \right] \end{aligned}$$

Thus the dynamics of particles can be described by the following equations:

$$\begin{aligned} \frac{\partial Z(Z_0, \tau)}{\partial \tau} &= P(Z_0, \tau), \\ \frac{\partial P(Z_0, \tau)}{\partial \tau} &= \hat{F}_{pond} + \hat{F}_c, \end{aligned} \quad (7)$$

$$\begin{aligned} \hat{F}_{pond} &= \\ &= -\sum_n \frac{\omega_p'^2}{4\omega' c h'_n} \theta_n^2 \frac{b}{2\varepsilon} \alpha_u^2 \int_0^L \chi(\tilde{Z}_0) f_n(Z(Z_0, \tau) - Z(\tilde{Z}_0, \tau)) d\tilde{Z}_0, \\ \hat{F}_c &= \frac{\omega_p'^2}{\pi \omega'^2} \int_0^L \chi(\tilde{Z}_0) f_c \left(\frac{Z(Z_0, \tau) - Z(\tilde{Z}_0, \tau)}{k'} \right) d\tilde{Z}_0. \end{aligned}$$

where $Z = \omega' z'/c$, $L = \omega' l'/c$, $\tilde{p} = p'/mc$, $\tau = \omega' t'$,

$\omega_p = \sqrt{4\pi e^2 \rho'/m}$, $\alpha_i = eA'_u/mc^2$. At initial moment all of the electrons are uniformly distributed over the longitudinal coordinate in the interval $[0, B]$. Normalized amplitudes of the component of scattered field which is radiated in the direction which is opposite to direction of pump wave are given by

$$|\alpha_s^+| = \frac{i\omega_p^2 \alpha_i}{2\omega^2} \left| \int_0^B \exp(2iZ(\tilde{Z}_0)) d\tilde{Z}_0 \right|.$$

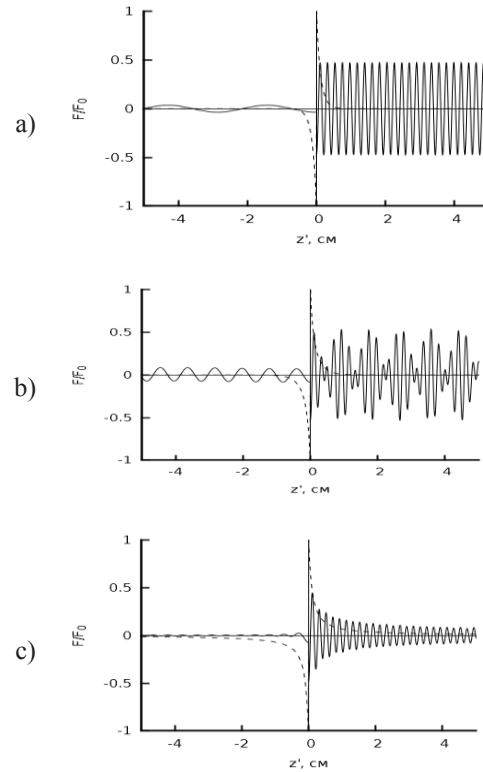


Figure 2: Dependence of the ponderomotive (solid line) and Coulomb (dotted line) forces on the longitudinal coordinate for a waveguide with one propagating mode (a, $b=0.4$ cm), with two propagating modes (b, $b=0.7$ cm) and in the free space (c, $b=60$ cm).

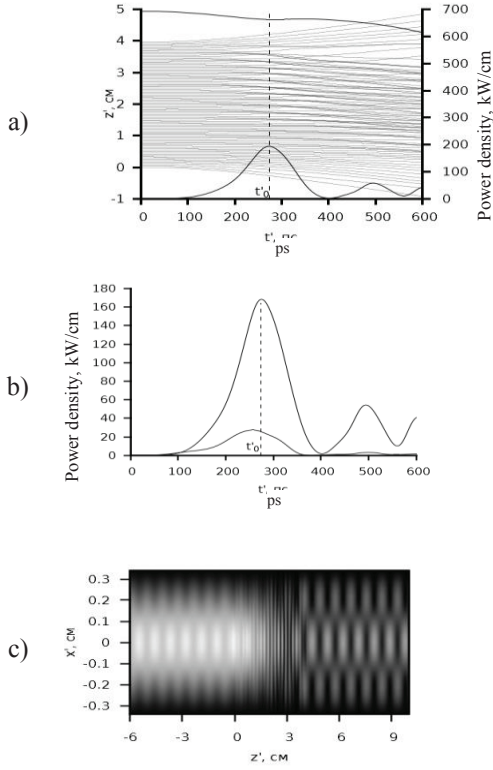


Figure 3: Simulation of the undulator SR process based on Eqs. (7): (a) bunching of electrons and time dependence of integral powers radiated forward and backward, (b) temporal dependencies of mode intensities with different transverse indices, (c) spatial distribution of a field at the instant of time corresponding to the peak amplitude. $L = 63$, $\alpha_u = 0.7$, $\varepsilon/b = 0.29$, $\omega'_p/\omega' = 0.024$

RESULTS OF SIMULATION WITHIN THE AVERAGED MODEL

Simulations of Eqs. (7) show that due to attracting feature of pondermotive force (6) the bunching of particles developed (Fig. 3a). Correspondingly at some instant of time (Fig. 3b) coherent summation of fields radiated by most of particles takes place and the generated field constitutes a short SR pulse. Initial level of signals corresponds to the level of radiation of the bunch without modulation and in fact is determined by the front edges of electron pulse. This radiation in the case under consideration is a seed initiating the further development of SR process.

We simulated the radiation of the electron bunch with particles energy of 5 MeV, with a length of ~ 4 mm, charge of 5 nC/cm (linear current density of 375 A/cm) and the transverse size $\varepsilon \sim 2$ mm oscillating in the field of undulator with period of 4 cm and field amplitude of 0.19 T. The radiation was assumed to take place in a planar waveguide with the gap between plates of 7 mm. In the rest frame K' the length of the bunch was 4 cm.

The undulator field transforms into a wave with a wavelength of 4 mm and the power density of 5.6 MW/cm.

As follows from Fig.3b the peak radiation power density is 0.17 MW/cm and the pulse duration of 120 ps. By means of Lorentz transformations we obtain the power density of the radiation of the forward propagating wave in the lab frame of 70 MW/cm. Radiation frequency is about 1.5 THz and the pulse duration decreases down to 6 ps. Note that in the rest frame the pump pulse was about 20 wavelength. In the lab frame it corresponds to 20 period undulator with a total length of about 0.8 m.

RESULTS OF PIC SIMULATIONS IN CO-MOVING REFERENCE FRAME

The analysis of SR process within the model that employed the averaged pondermotive force approach does not account for a number of important factors, including transverse inhomogeneity of the undulator field along the transverse coordinate. Another significant simplification is the assumption of relatively small undulator field leading to weak relativism of the electrons movement in co-moving reference frame. Thus, our semi-analytical consideration was supplemented by a direct PIC simulation in the rest frame, where, as we stated in the Introduction, different dimensions of the system are of the same scale.

We simulated the system dynamics using the KARAT PIC-code [4]. In the co-moving frame we simulated the situation when a pump pulse incidents on a stationary plasma bunch. Initial geometry of the interaction space is presented in Fig. 4a. Note that transverse stability of the beam is provided by transverse inhomogeneity of the undulator field which is illustrated by Fig. 4b where also the spatial modulation of the beam width with a period inversely proportional to the amplitude of the pump wave.

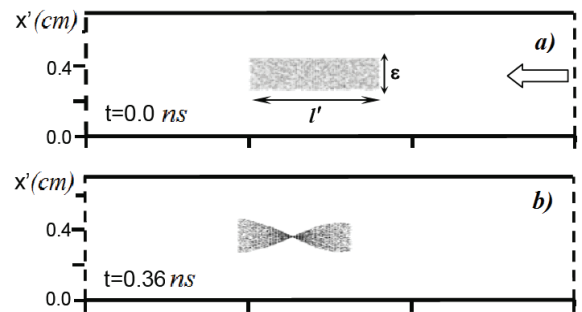


Figure 4: (a) Interaction space geometry and the initial position of the electron bunch. Arrow is the direction of the pump pulse propagation. (b) Electron bunch focusing under the transversely inhomogeneous pump field.

Simulation parameters correspond to those used in previous Section, although we took the larger undulator parameter $\alpha_u = 0.9$. Fig. 5a shows the SR pulse having in the rest frame power density 90 kW/cm and duration of 100 ps. Radiation spectrum is presented in Fig. 5b with a central frequency of 48 GHz. The frequency is

downshifted with respect to the pump frequency. This effect emerges due to the decrease of the average translational velocity with the rise of bounce oscillations.

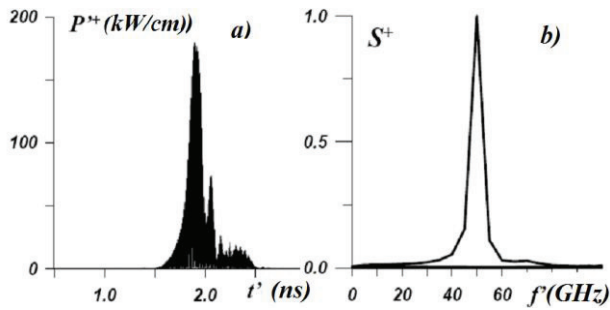


Figure 5: Results of PIC simulation of the undulator SR in co-moving reference frame: (a) pulse of superradiance propagating in the positive direction of the z axis, (b) it's spectrum.

After transformation into the lab frame the center frequency of the forward-radiated pulse increases up to 0.9 THz. It's power increases $4\gamma^2=400$ times reaching 36 MW/cm and the pulse duration decreases $\gamma=10$ times down to 10 ps. It is interesting to note that the time of development of the process in the rest frame is about 200-300, still the bunch moving with a velocity close to the speed of light passes the distance of about 1 m. Thus the simulation conducted is an example of unconventional use of relativity theory in applied problems.

CONCLUSION

Thus the analysis undertaken demonstrates the possibility of using the undulator SR for generation of

powerful (multi-MW) pulses in THz wave range based on bunches formed by photo-injecting guns. Obviously, increasing the particles energy leads to the radiation frequency increase alongside with peak power increase. One of the important results of the work is the development of approaches giving the general physical picture and allowing detailed simulation.

Note also that instead of the undulator field the wiggling of electrons can be provided by an electromagnetic wave in RF or optical range. In the electrons' rest frame the processes of stimulated scattering are close to the processes of undulator radiation. Correspondingly, the models developed here can be applied to the scattering problem.

REFERENCES

- [1] S.D.Korovin, et al., "Generation of Cherenkov superradiance pulses with a peak power exceeding the power of driving short electron beam", Phys. Rev. E. V. 74, P. 016501-016509 (2006).
- [2] Kurennoy S.S., et al., "Development of photoinjector RF cavity for high-power CW FEL", Nucl. Instr. & Meth. in Phys. Res. A. V.528, Iss 1-2, P. 392-396. (2004).
- [3] N.S.Ginzburg, A.S.Sergeev "Superradiance of an electron swarm in a periodic magnetic field", JETP Lett. V.54, P.446. (1991).
- [4] V.P.Tarakanov, "User's Manual for Code KARAT", Springfield: BRA (1992).

SENSITIVITY STUDY OF A TAPERED FREE-ELECTRON LASER

A. Mak*, F. Curbis, S. Werin, MAX IV Laboratory, Lund University, Sweden

Abstract

The output power of a free-electron laser (FEL) can be greatly enhanced by tapering the undulator line. In this work, a sensitivity study of a tapered FEL is presented. The study is conducted using the numerical simulation code GENESIS and a taper optimization method. Starting from a possible case for the future X-ray FEL at the MAX IV Laboratory in Lund, Sweden, a number of parameters are varied systematically and the impact on the FEL power is investigated. These parameters include the electron beam's initial energy, current, emittance, energy spread, as well as the seed radiation power.

INTRODUCTION

In a single-pass free-electron laser (FEL), the technique of undulator tapering involves the decrements in the deflection parameter a_w along the undulator line, thereby maintaining the resonance condition as the electrons lose energy to the radiation. This can increase the output power and the energy extraction efficiency, as has been demonstrated by experiments at the LLNL [1] and the LCLS [2].

The effectiveness of this technique relies on the proper optimization of the tapering profile $a_w(z)$. Two methods are the multidimensional scanning method by Jiao et al. [3] and the GINGER self-design taper algorithm [4] based on the Kroll-Morton-Rosenbluth (KMR) formalism [5]. In a previous work [6], we presented another method based on a modification of the KMR formalism and demonstrated, with numerical simulations, its higher efficiency of energy extraction than the GINGER algorithm.

Utilizing this method of taper optimization, we conduct a sensitivity study to determine the impact of various parameters on the power of a tapered FEL. The results shall provide insights into the development of an X-ray FEL at the MAX IV Laboratory [7], which is part of the laboratory's long-term strategic plan. The plan includes an extension of the MAX IV linear accelerator to 4–6 GeV, enabling the production of hard X-ray.

METHOD

Sensitivity Study

We carry out the sensitivity study using the numerical simulation code GENESIS [8] in the steady-state mode. The starting point is a possible case for the future X-ray FEL at the MAX IV Laboratory, with main parameters as shown in Table 1. We use this as the reference case for the purpose of our sensitivity study.

Based on the reference case, we vary five parameters systematically, one at a time. The parameters are the electron

Table 1: Main Parameters for the Reference Case

Parameter		Value
Electron beam energy	E	4 GeV
Beam current	I	4 kA
Normalized emittance	$\epsilon_{x,y}$	0.4 mm mrad
Average beta	$\bar{\beta}$	20 m
Energy spread	σ_E/E	1×10^{-4}
Undulator period	λ_w	20 mm
Radiation wavelength	λ	4 Å
Seed radiation power	P_{in}	5 MW

beam's energy, current, emittance, energy spread and the seed radiation power. For each parameter value, we apply our taper optimization method, so as to obtain the highest possible FEL power at the end of a 200-metre undulator line. Finally, we examine the impact that the variation of each parameter has on the FEL power.

Taper Optimization

The taper optimization method used in this sensitivity study is the Modified KMR Method, which has been elucidated in a previous work of ours [6]. The method considers a reference particle with phase-space coordinates (ψ_R, γ_R) subject to the following constraints:

$$\gamma_R(z) = \sqrt{\frac{\lambda_w}{2\lambda} [1 + a_w^2(z)]}$$

$$\psi_R(z) = gz \text{ for some } g > 0.$$

The energy γ_R is always on resonance throughout the undulator line, while the phase ψ_R is made to increase linearly with distance z along the undulator line at some desired gradient g . Imposing these constraints on the particle's equation of motion results in a taper profile $a_w(z)$. In numerical simulations, we scan over different values of g to obtain the maximum FEL output power.

RESULTS AND DISCUSSIONS

Sensitivity to Beam Energy

The initial energy of the electron beam is 4 GeV in the reference case. We examine the effects of increasing the energy from 4 GeV to 5, 6 and 7 GeV. For each energy, we apply the taper optimization method to maximize the final FEL power at $z = 200$ m. The resulting FEL power curves and the corresponding taper profiles are shown in Fig. 1. The optimum g -values resulting from the taper optimizations are specified in the figure legend.

The reference case, with initial beam energy 4 GeV, produces a final FEL power of 1.6 TW. Upon increasing the initial beam energy, the FEL power shows a higher growth

* alan.mak@maxlab.lu.se

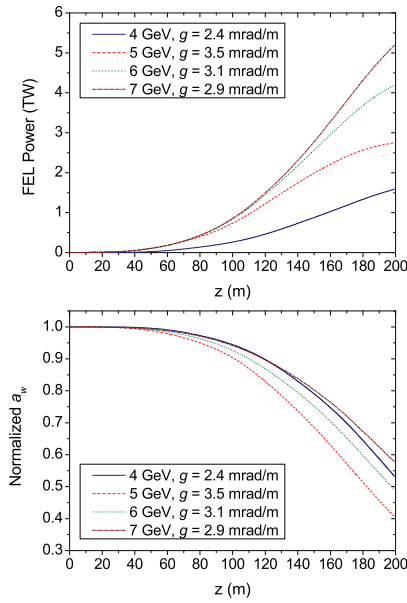


Figure 1: The FEL power curves (top) and the corresponding taper profiles (bottom) for different initial energies of the electron beam. In all the taper profiles, the a_w parameter is normalized to its initial value.

rate, hence a larger final value at $z = 200$ m (see Fig. 1). For every 1-GeV increase in the initial beam energy, there is at least an 1-TW increase in the final FEL power. In particular, an increase of initial beam energy from 4 GeV to 6 GeV results in an increase of final FEL power by 1.6 times.

Sensitivity to Beam Current

The initial current of the electron beam is 4 kA in the reference case. We vary the current around the reference-

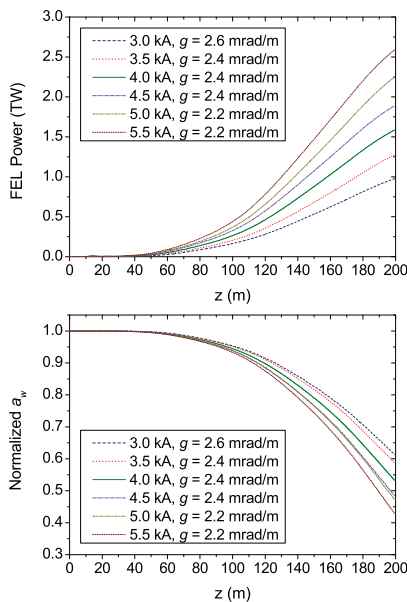


Figure 2: The FEL power curves (top) and the corresponding taper profiles (bottom) for different initial currents.

case value, from 3.0 kA to 5.5 kA at intervals of 0.5 kA. The FEL power curves and the corresponding taper profiles are shown in Fig. 2.

As seen in Fig. 2, a higher initial current results in a more rapid growth of FEL power. Also, the final FEL power at $z = 200$ m increases almost linearly with the initial current.

Sensitivity to Emittance

The initial emittance of the electron beam is 0.4 mm mrad (for both the x- and y-directions) in the reference case. We vary the emittance around the reference-case value. In particular, we decrease it to 0.2 and 0.3 mm mrad, and increase it to 0.6, 0.8 and 1.0 mm mrad. The FEL power curves and the corresponding taper profiles are given in Fig. 3.

The results show that a lower initial emittance yields a more rapid growth of FEL power. Also, the final FEL power at $z = 200$ m increases almost quadratically with the initial emittance. Reducing the initial emittance from 0.4 mm mrad to 0.2 mm mrad doubles the final FEL power.

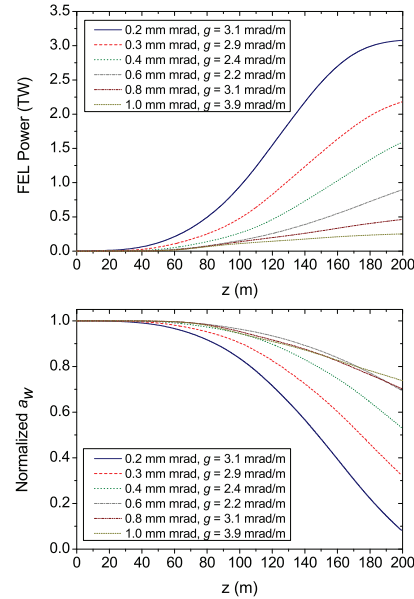


Figure 3: The FEL power curves (top) and the corresponding taper profiles (bottom) for different initial emittances.

Sensitivity to Energy Spread

The initial relative energy spread of the electron beam is 1×10^{-4} in the reference case. We examine the effects of increasing the value to 5×10^{-4} , as well as decreasing the value to 5×10^{-5} and 1×10^{-5} . The FEL power curves and the corresponding taper profiles are shown in Fig. 4.

There are two observations. First, increasing the energy spread from the reference-case value to 5×10^{-4} reduces the final FEL power almost by half. Second, decreasing the energy spread from the reference-case value has no appreciable impact on the FEL power.

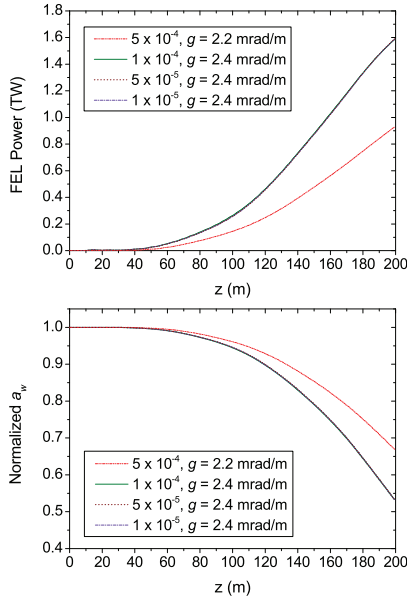


Figure 4: The FEL power curves (top) and the corresponding taper profiles (bottom) for different initial energy spreads. Note the overlapping of the curves for energy spread values 1×10^{-4} , 5×10^{-5} and 1×10^{-5} .

Sensitivity to Seed Power

The seeding of an FEL can be achieved by various methods [9], of which one example for hard X-ray FELs is self-seeding [10]. In this subsection, we study the sensitivity of

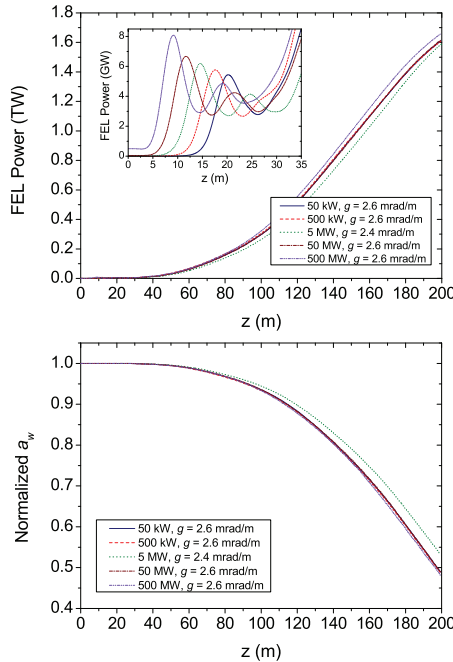


Figure 5: The FEL power curves (top) and the corresponding taper profiles (bottom) for different seed powers. The inset shows a magnification of the power curves for $z < 35$ m.

the FEL performance to the seed radiation power, regardless of the seeding method.

In the reference case, the seed power is 5 MW. We examine the effects of changing the seed power to the following values: 50 kW, 500 kW, 50 MW and 500 MW. The resulting FEL power curves and the corresponding taper profiles are shown in Fig. 5.

Upon varying the the seed power, the FEL power curves exhibit the expected behaviours in the region of initial exponential growth (see inset of Fig. 5). With a higher seed power, the initial exponential growth and the initial saturation of FEL power occur within a shorter distance z down the undulator line. The higher is the seed power, the higher is the FEL power at the initial saturation.

While the seed power has a strong influence on the initial saturation power, its impact on the final FEL power at $z = 200$ m is relatively small (see Fig. 5).

Taper Optimization

In each taper optimization, we scan over g for an optimum value that maximizes the final FEL power at $z = 200$ m, where g is the gradient of the linearly increasing phase $\psi_R(z) = gz$ of the reference particle. This subsection summarizes some general observations regarding the taper optimizations.

In general, a larger g leads to more rapid power growth beyond the initial saturation. However, the final saturation occurs at a lower power and at a smaller z . In contrast, a smaller g leads to slower power growth beyond the initial saturation. However, the final saturation occurs at a higher power and at a larger z , which is often beyond the undulator line simulated. The phase gradient g therefore serves as an independent adjustment knob for the final saturation power and the final saturation length of a tapered FEL. The optimum value of g depends on the length of the undulator line and the electron beam parameters.

From the sensitivity results presented in the previous subsections, we can also examine the dependence of the optimum g -value on the various parameters. First, the optimum g -value is largely unaffected by the seed power. Second, it remains the same for initial energy spread values below the reference-case value. Third, it decreases almost linearly with the initial beam current.

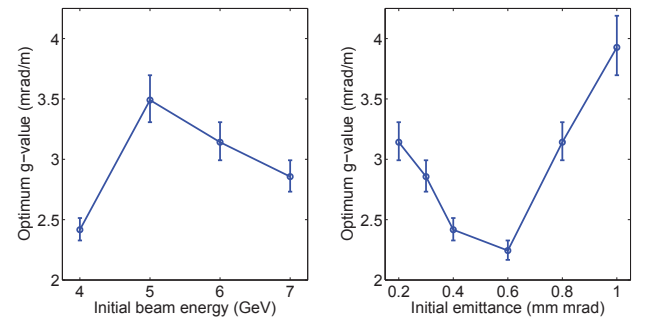


Figure 6: The dependence of the optimum g -values on the initial beam energy (left) and emittance (right).

However, it is worth taking a closer look at the dependence on the initial beam energy, as well as the initial emittance. As seen in Fig. 6, the optimum g -value has a local maximum at some initial beam energy and a local minimum at some initial emittance. The significance behind these turning points is unknown. Further investigation is needed to understand the physical meaning behind these g -dependences.

CONCLUSION

We have presented a sensitivity study on a tapered FEL, based on a reference case for the future X-ray FEL at the MAX IV Laboratory [7]. Using of the numerical simulation code GENESIS [8], we apply the Modified KMR Method [6] to optimize the taper profile $a_w(z)$ in a 200-metre undulator line. In this method, the phase gradient g of the reference particle acts as an independent adjustment knob for the final saturation length and the final saturation power.

We have examined the dependence of the FEL output power on the initial beam energy, current, emittance, energy spread and the seed power. The results show that final FEL power increases with the initial beam energy and current, but decreases with the emittance. Meanwhile, the initial energy spread and the seed power have very little influence on the final FEL power.

Beyond this work, we shall further our sensitivity study by considering the effects of break sections in the undulator line, which are required for beam focusing and diagnostics. We shall also explore the possibility of fine-tuning our taper optimization method by considering quadratic or cubic functions for the reference particle's phase $\psi_R(z)$.

REFERENCES

- [1] T.J. Orzechowski et al., "High-Efficiency Extraction of Microwave Radiation from a Tapered-Wiggler Free-Electron Laser", *Phys. Rev. Lett.* 57, 2172 (1986).
- [2] D. Ratner et al., "FEL Gain Length and Taper Measurements at LCLS", in *Proc. 31st Int. Free-Electron Laser Conf.*, Liverpool, 2009, pp. 221-224.
- [3] Y. Jiao et al., "Modeling and Multidimensional Optimization of a Tapered Free Electron Laser", *Phys. Rev. ST Accel. Beams* 15, 050704 (2012).
- [4] W.M. Fawley et al., "Tapered Undulators for SASE FELs", *Nucl. Instrum. Meth. A* 483, 537 (2002).
- [5] N.M. Kroll et al., "Free-Electron Lasers with Variable Parameter Wigglers", *IEEE J. Quantum Electronics* 17, 1436 (1981).
- [6] A. Mak et al., "Methods for the Optimization of a Tapered Free-Electron Laser", in *Proc. 5th Int. Part. Accel. Conf.*, Dresden, 2014, pp. 2909-2911.
- [7] S. Werin et al., "Towards an X-ray FEL at the MAX IV Laboratory", in *These Proceedings: Proc. 36th Int. Free-Electron Laser Conf.*, Basel, 2014, TUP080.
- [8] S. Reiche, "GENESIS 1.3: a Fully 3D Time-Dependent FEL Simulation Code", *Nucl. Instrum. Meth. A* 429, 243 (1999).
- [9] S. Reiche, "Overview of Seeding Methods for FELs", in *Proc. 4th Int. Part. Accel. Conf.*, Shanghai, 2013, pp. 2063-2067.
- [10] G. Geloni et al., "A Novel Self-Seeding Scheme for Hard X-Ray FELs", *J. Modern Optics* 58, 1391 (2011).

UPDATE ON THE FEL CODE GENESIS 1.3

S. Reiche, Paul Scherrer Institut, Villigen, Switzerland

Abstract

The widely used time-dependent code Genesis 1.3 has been modified to address new needs of users worldwide. The existing limitation of tracking isolated slices of the FEL beam has been overcome by keeping the entire electron beam in memory, which is tracked as a whole through the undulator. This modification allows for additional features such as allowing particles to migrate into other slices or applying self-consistent wakefield and space charge models.

INTRODUCTION

Since the first high gain Free-Electron Lasers [1–4] numerical codes have aided the users to understand experimental results and to design future facilities. Several codes are available [5–9] and have been benchmarked against each other and experiments [10]. With the ongoing development of the general computer technology and infrastructures the FEL codes can expand the complexity of the underlying models or operate with more particles for finer resolutions. Currently single-pass FELs at the Angstrom level can be run in a few hours or less.

However new FEL schemes, e.g. self-seeding [11], EEHG [12], high-brightness SASE FELs [13], are rather complex and very difficult to model for users of the FEL codes. The primary obstacle is that most codes have evolved from a single processor platform to a large scale parallel computer platform while preserving the ability to run on a single computer. Nevertheless a new algorithm, where a parallel computer network is deeply embedded, can offer new features beyond the capabilities of existing codes.

In this paper I present the current status of the code Genesis 1.3 [6], which has been modified under the assumption that the computer cluster is large enough to hold the entire electron beam and radiation field in memory. The beam and field is propagated through the undulator as a whole with a resolution down to each individual electron. The core algorithm is still based on the slowly varying envelope approximation (SVEA) [14], where the equations of motion are averaged over one undulator period. It allows one to choose integration step sizes larger than the undulator period to keep the number of integration steps within a reasonable limit even for very long hard-X-ray FELs such as LCLS or Swiss-FEL. A non-averaged approach is not pursued, but which has been successfully implemented by new codes such as PUFFIN [8].

CURRENT LIMITATION

During the development of Genesis in the late nineties one important factor was the available memory for the calculation. Keeping the entire radiation field and particle distribution was way beyond the practical limit of those days

and an extensive bookkeeping has to be done to reduce the required footprint in memory space. This was done by tracking a single electron slice through the undulator interacting with many radiation field slices which are slipping in from behind and then slipping out after a few integration steps, depending on the length of the electron slice. The bookkeeping is storing temporarily the field which slips out to feed it to the next electron slice once the tracking of the current slice has been done. Using this approach the memory needs to store only the data of a single electron slice and the radiation field over one slippage length compared to the entire time window which can be many times longer than a slippage length. However this restricts the algorithm to work sequentially through the electron bunch from the tail to the head. No information can propagate in the backward direction.

Recent ideas to improve longitudinal coherence in SASE FELs [13, 15, 16] are based on an enhancement of slippage to cover the entire bunch. That way the spectral brightness is improved. The consequence is that the record for storing the slippage field needs to be increased by a large factor. In fact, it would use the same memory size if the entire radiation field were kept in memory at all time. The latter approach has the advantage that one could calculate the spectrum during runtime and not, as it is now, as a post-processing step.

A second limitation arises from proposed schemes which are utilizing a large harmonic conversion, either by a multi-staged approach in HGHG cascades or a direct conversion with high efficiency in EEHG schemes [17]. Genesis particle distribution is based on a quiet loading where macro particle are mirrored and evenly distributed in longitudinal position to cancel out completely any Fourier component for a given wavelength. In an explicit step in the beam loading algorithm a controlled random offset is applied to the particle to give the correct statistics in the bunching factor [18]. To include more harmonics more mirror particles are needed, preferably at least twice the number than the highest harmonic considered. For the 100th harmonic this would be at least 200 mirror particles. If one used 1000 particle to generate the remaining 5 D distribution and then apply the mirroring process one slice would be filled with 200k macro particles or if sliced to the final harmonics 2000 particles. For an FEL operating at 1 nm with a 1 kA beam current that is almost of the same order as the real number of electrons to be modeled. With a moderate increase in the particle number then a real one-one simulation could be carried out with the advantage that no mirroring needs to be done and therefore the transverse distribution is much smoother (effectively filled with 200k particles rather than only 1k).

Last, Genesis is limited by restricting particles into a single slice and keep them over the entire undulator length. For SASE FELs and an electron beam with almost no energy spread it is a valid assumption but breaks down for over-compression schemes such as self-seeding or EEHG, where particles are moved into different slices even when they are initially grouped together with a distance shorter than the radiation wavelength. To move particles into a different slice would mean that a particle is taken out of the beamlet which is formed by the mirroring process to model the correct shot noise. To illustrate this a minimal beamlet has two particles, separated by half a radiation wavelength, and is split apart and moved into different slices. Prior to this step the phases of both particles are almost canceling and the overall emission level is low. After the splitting each particle is in a different slice and has no corresponding particle to cancel the bunching factor when evaluating the source term for the Maxwell equation. The emission level would be effectively enhanced and determined by the number of macro particles in the simulation and not by the number of electrons to be modeled.

CORE ALGORITHM

The fundamental change in the upcoming version of Genesis is the exchange of the loop order in the code. In the new version the inner loop cycles through all slices to advance them by one integration step along the undulator. This is repeated till the end of the undulator is reached. No record of a slippage field is needed because the entire radiation field is kept in memory at any time.

The code supports the distribution of the calculation over many computer nodes in a computer cluster, following the MPI standard of inter-node communication. Unlike in previous versions, where each node only holds a single slice (all adjacent to each other), the time window covers the entire bunch and radiation field and each node is assigned to a subdomain of the time window. Each node holds an array of many slices filling up the subdomain. Figure 1 illustrates the different approaches of the old and new version to assign the time domain to the nodes.

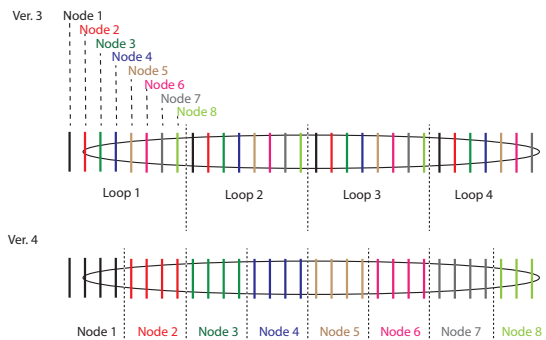


Figure 1: Assignment of radiation slices to the computer nodes in version 3 and 4 of Genesis.

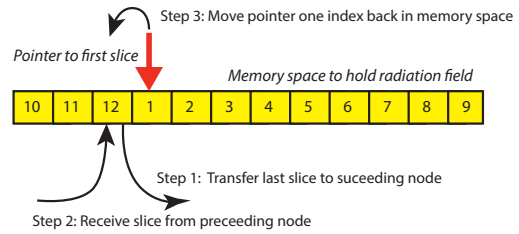


Figure 2: Indexing the radiation field when slippage is applied.

Management of the slices is done in the C++ part of the code, using the vector container of the C++ Standard Template Library (STL). One entry in the vector corresponds to a given slice. These containers are wrapped by the Beam and Field classes. Therefore harmonics and/or polarization can be modeled as an array of the field class avoiding the complicated and error-prone bookkeeping of a single array of the previous versions.

The most atomic algorithm advances a single slice of the electron distribution and the radiation field by one integration step. The particle tracker is based on a 4th order Runge-Kutta integrator [19] while the radiation field is advanced by an Alternating Direction Implicit (ADI) field solver [20]. This part is preserved from the Fortran code of the older version. Therefore the new version is still a hybrid version between C++ and Fortran albeit the Fortran part is significantly reduced. In a future release Genesis will move to C++ completely. Between the integration of the the beam and the field, Genesis now allows additional steps such as sorting the particle distribution and transition of particles between slices (see last section).

The code also differentiates between interaction within an undulator and the propagation through break sections. Also the integration step size can vary along the undulator. This avoids the restriction in older version that the undulator lattice has to fit to the granularity of a fixed integration step size. Slippage is now explicitly calculated and applied only once the field has advanced by more than the slice spacing of the electron slices. This corrects the bug in Genesis that slippage is enforced after each integration step even in undulator break section where the condition of one wavelength per undulator period no longer holds.

When slippage is applied then all wavefronts are advanced by one slice. However each node holds multiple wavefronts and shifting all data in memory is highly inefficient. Instead an index pointer, which indicates the first slice, is decreased. So when looping over all slices the loop starts at this index and ends at the final index, which is the start index plus the number of slices minus one. When the actual slice in the record is accessed the modulo of the loop index with the number of slices is taken. With this extra little bookkeeping very little data transfer is needed. Only one wavefront is sent to the next node in a 1D topology. Figure 2 shows the memory management of the radiation field for a node.

While calculating the slippage Genesis can also apply an autophasing for the drift section of two adjacent undulator modules, which simplifies the set up of new undulator lattices. The new element of a phase shifter allows adjusting the phase to the user's will.

CHANGES TO INPUT AND OUTPUT FORMAT

The latest version of Genesis breaks with the input format from the previous versions. Instead of a very long Fortran namelist with over 100 parameters the input is broken up into several smaller, thematically grouped namelists. The description of the undulator is completely removed from the main input deck and is now fully described by a lattice file. The overall structure is similar to the code Elegant [21], which needs also at least one input file and a lattice file. In the following the two files are briefly described.

Lattice File

The lattice files follow the syntax: *Label : Type = {Argument List}*; Elements are referred to by the label and can also be used to predefine new lattice elements by using the reference argument. They are basic elements such as undulators, drifts, quadrupoles and, as a new type, a line container, which can hold both types, elements and lines. The code unrolls references and nested lines up to 10 iterations. If at that level the element is not fully defined, the code will generate an error message and stop execution.

The line container allows also tagging each element with two features. One is the repetition of the element, which is indicated by a preceding integer number and the multiplication sign. Second, the absolute position of an element within the line can be specified by a succeeding @-sign and the position in meters. This feature is useful when quadrupoles are super-imposed onto an undulator.

An example of an input file is given below, which defines an undulator lattice with a FODO cell structure and 12 undulator modules.

```
QF1: Quadrupole = { l=0.15, k1= 1.1 };
QF2: Quadrupole = { ref=QF1, k1=-1.1 };
D1: Drift = { l=0.15 };
D2: Drift = { l=0.3 };
Un: Undulator = {lambdau=0.015,nwig=265,
                  aw=0.8485281};
FODO: LINE = {Un,D1,QF1,D2,Un,D1,QF2,D2};
SWISSFEL: LINE = {6*FODO};
```

The user must define at least on line, which is referred by the main input deck. Other lines, which are defined but not referred to, are ignored. Also this lattice can be regarded as a base lattice, from which modified lattices can be derived, such as taper profiles, quadruple misalignment etc. An explicit list of elements and the allowed syntax is given in the manual of the new version of Genesis.

Main Input File

The biggest change in the Genesis input is that the parsing of the input deck is event driven. So whenever a name list is closed by the *&end* statement, the content is parsed and, if needed, action is applied. The *setup* name list is mandatory and must come first. The *track* name list invokes the actual tracking of the particles and radiation field through the undulator. Before that the beam and field needs to be defined.

An example input file is listed below. Elements in namelist, which are not defined, are falling back to their default value. The complete list of all name lists and their elements is given in the manual.

```
&setup
  rootname=output-test
  lattice=SwissFEL.lat
  beamline=SwissFEL
  lambda0=1e-10
  gamma0=11357.8165
  delz=0.075
&end

&time
  slen=40e-6
  sample=10
&end

&lattice
  zmatch=9.15
&end

&sddsbeam
  file=inputdist.sdds
  match=true
  center=true
  output=true
&end

&field
  power=1000
  dgrid=0.3e-3
  ngrid=151
  waist_size=50e-6
&end

&track
  output_step=1
&end
```

The example shows some new features, such as automatic matching in the *lattice* name list. The matching point defines the end point in the cell of a periodic lattice (e.g. a FODO cell). With the given lattice definition and the reference energy *gamma0* Genesis calculates the matched β - and α -function values. These value can be used in the beam-

loading routine, but only if the match command/name list occurs before.

Genesis supports the direct import of Elegant output distributions by calling an external shell script which itself converts the SDDS format into an HDF5 format by using functions of the SDDS-Toolbox kit. The converted file is then read by Genesis and used to load the particle distribution within. If Elegant and the Toolbox Kit are not installed, Genesis will stop execution.

A field name list can occur multiple times to generate a superposition of field distributions. This can either be in the transverse direction (different Gauss-Hermite modes) or in longitudinal direction (different wavelengths). The latter is only possible in time-dependent simulations. In a similar way higher harmonics can be defined.

Output files

Only a few changes have been made to the output files. The format is still HDF5 but now the output for electron beam, undulator lattice and radiation field are grouped in the root level of the output file. Different harmonics will have different group names such as */field3* for the third harmonic. There are only particle and field dumps but the information can be dumped at various positions within the undulator lattice, reproducing the functionality of IPPART and IPRADI of the older versions.

POSSIBLE EXTENSION TO THE CODE

Based on the change of the core algorithm, keeping the entire radiation field and particle distribution in memory offers many possibilities which will expand the capability of Genesis 1.3. The following describes briefly the most significant features which will be added soon.

Sorting

Simulations, which resolve each individual electrons (also available in the older versions of Genesis), benefit from simpler algorithms avoiding the limitation of the quiet loading. The statistics are automatically correct at any harmonic which allows a very simple harmonic conversion in Genesis by simply slicing the particle distribution at the selected harmonics. Also particles can migrate into other slices without the restriction of a beamlet.

The sorting has to be done on all nodes simultaneously and tests have shown that a rather simple bubble sort algorithm is superior because the majority of electron motions is still limited and will end up in adjacent slices. Thus a single iteration of the bubble sort algorithm will be sufficient most of the time. The exceptions are strong mixing of particles such as in the chicanes of dispersive sections of laser-based or self-seeding schemes. Even here the motion is limited and the Bubble sort will be efficient, except in a very high harmonic conversion in EEHG schemes with particles shifted around on the scale of the total bunch length.

Self-Consistent Wakes and Space Charge Fields

In the older version a space charge field or wakefield has to be calculated externally and then added to the simulation as an effective potential. For that the current profile needs to be extracted from the input distribution. This can be done self-consistently in the new version because the current profile is known at any given time and can be broadcast to all nodes. Then each node calculates the resulting wakes over the given length of its assigned time-domain window based by the current profile ahead of the node. This makes the use of wake fields and space charge field less error prone (such as a mismatch in the wake potential and current profile in older versions because they are fed to Genesis by different files).

Self-Seeding Schemes

Similar to calculating wake fields from the entire bunch distribution dispersive effects in self-seeding configuration can be applied because the field content is known. As a prerequisite step the field is transferred into frequency domain by a 3D Fast Fourier Transformation. The field is now represented by plane waves with the total field vector k and the transverse wave numbers k_x and k_y . In frequency space the beam can easily be transported or the Green's function of a dispersive element can be applied. At the beginning of the next undulator section the field is converted back into the time domain.

Chicanes

In intra-undulator sections the electron transport is now completely decoupled from the field propagation and the electrons are no longer bound to the radiation field grid. This allows for more flexibility, in particular the implementation of chicanes. Here the particles are tracked by transport matrices and the total path lengths of the electrons are compared to the path lengths of the radiation field. The difference is compensated by shifting the radiation field in the forward direction.

CONCLUSION

Genesis 1.3 is currently adapted to large size computer clusters, utilizing the benefits of keeping the entire particle distribution and radiation field in memory, distributed over the nodes of the cluster. With the reverse in the looping order, collective effects such as wake fields, change in current profile due to magnetic chicanes and dispersive elements for the radiation field (e.g. self-seeding) can be modeled within a single run of Genesis, reducing the chances of error by manipulating input and output files for the electron distribution and radiation field.

The current status of Genesis allows reproducing the core features of the older version. Initial tests have shown an increase in the execution time by 10 to 20%. New features (magnetic chicanes, sorting, automatic harmonic conversion) will be added in the upcoming months.

REFERENCES

- [1] J. Andruszkow *et al*, Phys. Rev. Lett. **85** (2000) pp. 3825-3829
- [2] P. Emma *et al*, Nature Photonics **4**, (2010) pp. 641-647
- [3] T. Ishikawa *et al*, Nature Photonics **6** (2012), pp. 540-544
- [4] E. Allaria, *et al*, New Journal of Physics **14** 113009 (2012)
- [5] W.M. Fawley, LBNL-49625-Rev. I (2004)
- [6] S. Reiche, Nucl. Instr. & Meth. **A 429** (1999) 243.
- [7] E.L. Saldin, E.A. Schneidmiller, and M.V. Yurkov, Nucl. Instr. & Meth. **A 429** (1999) 233
- [8] L.T. Campbell and B.W.J. McNeil, Physics of Plasmas, **19** (2012) pp. 093119-093119-13
- [9] H.P. Freund and T.M. Antonsen, Phys. Rev. **E 52** (1995) 5401
- [10] G. Marcus *et al*, "FEL Code Comparison for the Production of Harmonics via Harmonic Lasing", presented at this conference: *36th Int. Free-Electron Laser Conf.*, Basel, 2014, TUP031.
- [11] G. Geloni, V. Kocharyan and E. Saldin, Journal of Modern Optics **58:16** 1391 (2011)
- [12] D. Xiang and G. Stupakov, Phys. Rev. STAB **12** (2009) 030702
- [13] N. R. Thompson and B. W. J. McNeil, Phys. Rev. Lett. **100** 203901 (2008)
- [14] A.E. Siegman, *Lasers*, (University Science Books, 1986, Sausalito)
- [15] J. Wu, A. Marinelli and C. Pellegrini, "Generation of Longitudinally Coherent Ultra High Power X-ray FEL Pulses by Phase and Amplitude Mixing" in *Proc. 34th Int. Free-Electron Laser Conf.*, Nara, 2012, pp. 237-240
- [16] D. Xiang *et al*, Phys. Rev. ST Accel. Beams **16**, 010703 (2013)
- [17] S. Reiche and M. Carla, "Detailed Modeling of Seeded Free-electron Lasers" in *Proc. 34th Int. Free-Electron Laser Conf.*, Nara, 2012, pp. 101-104
- [18] W.M. Fawley, Phys. Rev. STAB **5** (2002) 070701
- [19] P. Kaps and P. Rentrop, Numerische Mathematik, **33** (1979) 55
- [20] W.F. Ames, Numerical Methods for Partial Differential Equations (Academic Press, New York, 1977)
- [21] M. Borland, *elegant: a Flexible SDDS-Compliant Code for Accelerator Simulation* APS LS-287 (2000)

MINERVA, A NEW CODE TO MODEL FREE-ELECTRON LASERS

H.P. Freund, Department of Electrical and Computer Engineering, Colorado State University,
Fort Collins, USA

P.J.M. van der Slot[#], Mesa Institute for Nanotechnology, University of Twente,
Enschede, the Netherlands

Department of Electrical and Computer Engineering, Colorado State University, Fort Collins, USA

Abstract

Simulation codes modeling the interaction of electrons with an optical field inside an undulator are an essential tool for understanding and designing free-electron lasers (FELs). As there exists a large variety of FELs ranging from long-wavelength oscillators using partial wave guiding to soft and hard x-ray FELs that are either seeded or starting from noise, a simulation code should be capable of modeling this huge variety of FEL configurations. A new code under development, named MINERVA, will be capable of modeling such a large variety of FELs. The code uses a modal expansion for the optical field, e.g., a Gaussian expansion for free-space propagation, and an expansion in waveguide modes for propagation at long wavelengths, or a combination of the two for partial guiding at THz frequencies. MINERVA uses the full Newton-Lorentz force equation to track the particles through the optical and magnetic fields. To allow propagation of the optical field outside the undulator and interact with optical elements, MINERVA interfaces with the optical propagation code OPC. Here we describe the main features of MINERVA and give various examples of its capabilities.

INTRODUCTION

A variety of different free-electron laser (FEL) simulation codes have been developed over the past several decades such as GINGER [1], MEDUSA [2], TDA3D [3], and GENESIS 1.3 [4] among others. Typically, these codes undergo continuous development over their usable lifetimes. As a result, the codes become increasingly complex as new capabilities are added or older capabilities are deleted, and this tends to hobble their performance. It also renders it increasingly more difficult to make further modifications that might be needed. Because of this, we decided to develop a new code using a “clean-slate” approach having the properties and characteristics that we desired. We designate this new code as MINERVA.

The organization of the paper is as follows. The properties of MINERVA are described in the second section. We describe the comparison of MINERVA with the SPARC SASE FEL [5] in the third section, and a comparison with the long wavelength JLAB IR-upgrade FEL oscillator [6] in the fourth section. A summary and discussion follows.

PROPERTIES OF MINERVA

The formulation of MINERVA describes the particles and fields in three spatial dimensions and includes time dependence as well. Electron trajectories are integrated using the complete Newton-Lorentz force equation. No wiggler-averaged-orbit approximation is made. The magnetostatic fields can be specified by analytical functions for a variety of analytic undulator models (such as a planar or helical representations), quadrupoles, and dipoles. These magnetic field elements can be placed in arbitrary sequences to specify a variety of different transport lines. As such, MINERVA can set up field configurations for single or multiple wiggler segments with quadrupoles either placed between the undulators or superimposed upon the undulators to create a FODO lattice. Dipole chicanes can also be placed between the undulators to model various high-gain harmonic generation (HGHG) configurations. The fields can also be imported from a field map if desired.

The electromagnetic field is described by a modal expansion. For free-space propagation, MINERVA uses Gaussian optical modes, while waveguide modes are used when the wavelength is comparable to the dimensions of the drift tube. As a result, MINERVA can treat both long and short wavelength FELs. A combination of the Gaussian and waveguide modes is also possible when there is partial guiding at, for example THz frequencies.

The electromagnetic field representations are also used in integrating the electron trajectories, so that harmonic motions and interactions are included in a self-consistent way. Further, the same integration engine is used within the undulator(s) as in the gaps, quadrupoles, and dipoles, so that the phase of the optical field relative to the electrons is determined self-consistently when propagating the particles and fields in the gaps between the undulators.

Particle loading is done in a deterministic way using Gaussian quadrature that preserves a quiet start for both the fundamental and all harmonics. Shot noise is added following the procedure developed for MEDUSA [7], so that MINERVA is capable of simulating SASE FELs.

MINERVA has also been linked to the Optics Propagation Code (OPC) [8,9] for the simulation of FEL oscillators or propagating an optical field beyond the end of the undulator line to a point of interest.

MINERVA is written in Fortran 95 using dynamic memory allocation and supports parallelization using the Message Passing Interface.

[#]p.j.m.vanderslot@utwente.nl

THE SPARC SASE FEL

The parameters of the SPARC SASE FEL [5] are as follows. The electron beam had an energy of 151.9 MeV, a bunch charge of 450 pC, and a bunch width of 12.67 psec. The peak current was approximately 53 A. The x and y emittances were 2.5 mm-mrad and 2.9 mm-mrad respectively, and the rms energy spread was 0.02%. There were six undulators each of which was 77 periods in length (with one period for the entrance up-taper and another for the exit down-taper) with a period of 2.8 cm and an amplitude of 7.88 kG. The gap between the undulators was 0.4 m in length and the quadrupoles (0.053 m in length with a field gradient of 0.9 kG/cm) forming the FODO lattice were located 0.105 m downstream from the exit of the previous undulator. The resonance occurred at a wavelength of 491.5 nm, but the undulator line was not long enough to reach saturation over the six undulators.

The experimental measurement of the pulse energy versus position was compared with the predictions of four simulation codes: GINGER, MEDUSA, PERSEO [10], and GENESIS 1.3. The resulting comparison is shown in Fig. 1 and shows generally good agreement between the codes and between the codes and the experiment. It is not our purpose here to provide a detailed description of the experiment; rather, we want to demonstrate that MINERVA is also in good agreement with the other codes and, by extension, with the experiment. This is shown in Fig. 2 where we plot the predictions of MINERVA and MEDUSA for the parameters of the SPARC experiment, and which shows that MINERVA is in similarly good agreement with the measured pulse energies.

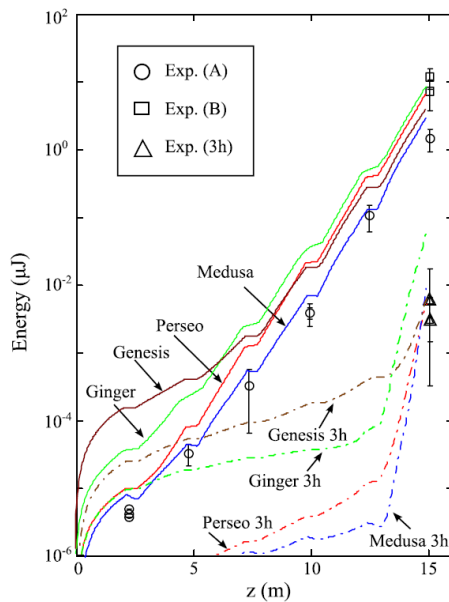


Figure 1: Comparison of GINGER MEDUSA, PERSEO, and GENESIS with the SPARC experiment [5], showing the optical pulse energy as a function of the distance z .

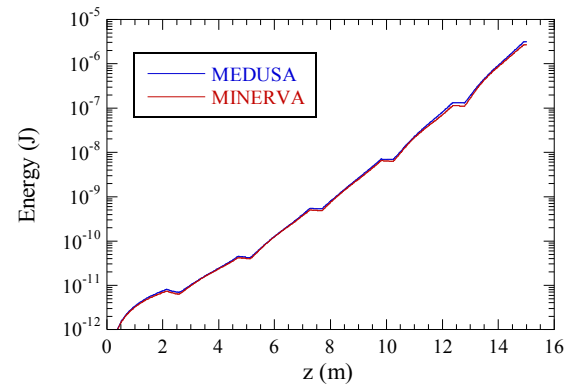


Figure 2: Comparison of MINERVA with MEDUSA for the SPARC experiment, showing the optical pulse energy versus the distance z .

THE JLAB IR-UPGRADE FEL OSCILLATOR

To further investigate the capabilities of MINERVA we also compared the code with an existing long-wavelength FEL oscillator, the IR-upgrade FEL oscillator of the Thomas Jefferson National Accelerator Facility (JLAB) [6]. The JLAB IR-upgrade has already successfully been modeled using MEDUSA [11] and we use the same parameters for MINERVA to model the IR-upgrade. These were a kinetic energy of 115 MeV, an energy spread of 0.3%, a bunch charge of 115 pC, a pulse length of 390 fs, a normalized emittance of 9 mm mrad in the wobble plane and 7 mm mrad in the plane orthogonal to the wobble plane, and a repetition rate of 74.85 MHz for the electron beam. The planar undulator was 30 periods long, had a period of 5.5 cm, and a peak on-axis magnetic field of 0.375 T. For a proper electron beam transport through the undulator, we used a one period up- and down taper. The electron beam was focused into the undulator with the focus at the center of the device. The resonator length was about 32 m and the cold-cavity Rayleigh length was 0.75 m. The total loss of the resonator was 21%. For these settings, the wavelength was 1.6 μm .

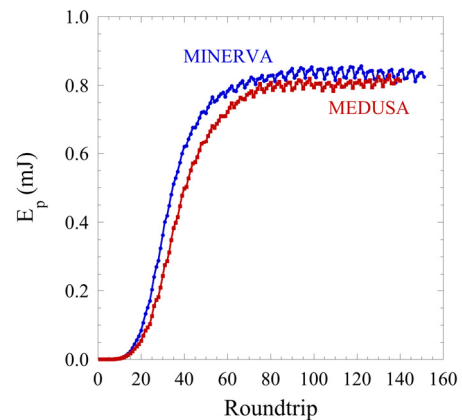


Figure 3: Comparison of MEDUSA and MINERVA for the JLAB IR-upgrade FEL oscillator, showing the intra-cavity pulse energy versus the roundtrip number.

To simulate the FEL oscillator, OPC takes the optical pulse at the exit of the undulator and propagates the pulse through the resonator to the entrance of the undulator. Both MEDUSA and MINERVA take this optical pulse and propagate it together with a fresh electron bunch through the undulator. This process repeats for a predefined number of roundtrips. The intra-cavity optical pulse energy E_p is shown in Fig. 3 as a function of the roundtrip number for both MEDUSA (red) and MINERVA (blue). Figure 3 shows that, although MINERVA predicts a slightly faster growth, the two codes are in good agreement with each other when the oscillator reaches a stationary state. MINERVA predicts a pulse energy that is 3% higher. Since MEDUSA showed a good agreement with the experiment [11], the same is true for MINERVA.

Each electron bunch contains a kinetic energy of 13.2 mJ. The optical energy extracted from the resonator is 0.16 mJ per pulse. Therefore, the FEL efficiency that follows from the simulation is 1.2%, which is close to the experimental value of 1.4%. The theoretical value is $1/2N_u = 1.7\%$.

The spectrum of the optical pulse extracted from the cavity at roundtrip 150 is shown in Fig. 4 and the center wavelength is, as expected, at $1.6 \mu\text{m}$ with a -3 dB bandwidth of 24 nm. The transverse spectral intensity is shown in Fig. 5 for the center wavelength and the distribution is close to Gaussian. For wavelengths around the center wavelength the energy distribution is similar to that shown in Fig. 5, however for wavelengths at the edge of the spectrum the transverse distribution changes as is shown in Fig. 6 for two wavelengths that are 60 nm below (Fig. 6a) and 60 nm above (Fig. 6b) the center wavelength and a wavelength of $1.70 \mu\text{m}$ (Fig. 6c). Although these wavelengths contain hardly any energy, the transverse spectral intensity shows characteristics that change rapidly with the wavelength.

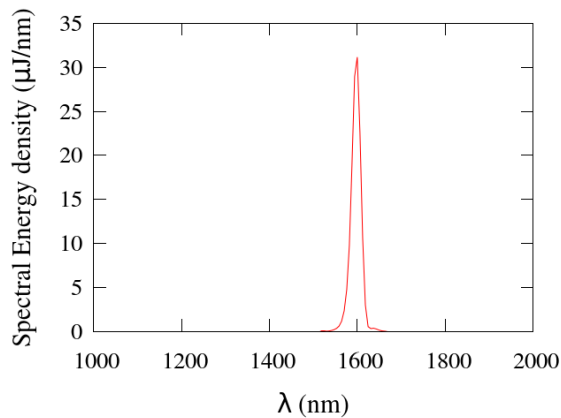


Figure 4: Spectral energy density of the optical output pulse for the IR-upgrade FEL oscillator.

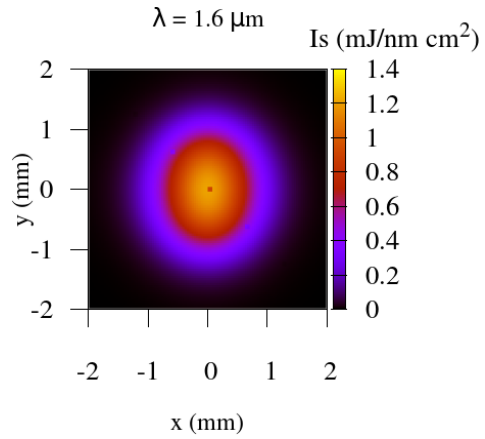


Figure 5: Transverse spectral intensity at the central wavelength of $1.6 \mu\text{m}$ for the optical pulse after $n=900$.

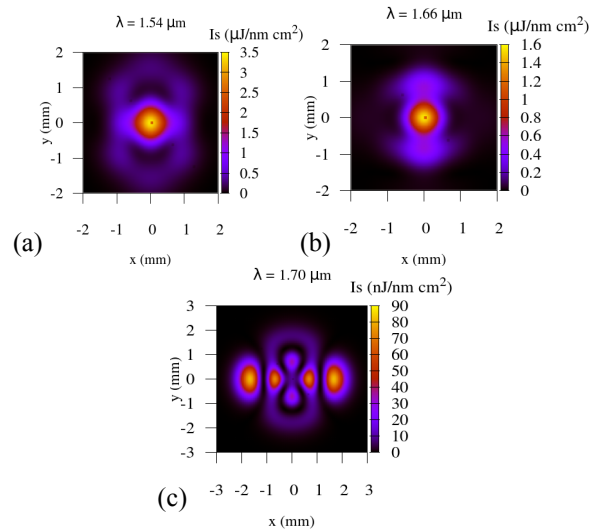


Figure 6: Transverse spectral intensity at wavelengths of $1.54 \mu\text{m}$ (a), $1.66 \mu\text{m}$ (b) and $1.70 \mu\text{m}$ (c) for $n=900$.

For example, at $\lambda = 1.7 \mu\text{m}$, the emission is predicted to be off-axis with four, about equal, strength maxima located on the x -axis ($y = 0$) and two lower maxima on the y -axis ($x = 0$). The origin of these characteristics is still under investigation, but is likely to consist in the generation of high order modes off the peak wavelength.

SUMMARY AND CONCLUSION

As shown in the paper, the current state of development of MINERVA and MINERVA/OPC yields good agreement for the two experiments studied thus far. Consequently, we feel that MINERVA can accurately, and with confidence, predict the performance of short wavelength FELs. MINERVA is currently in beta-test and development will continue. In particular, the inclusion of waveguide modes will permit the simulation of long wavelength THz FELs.

REFERENCES

- [1] W.M. Fawley, "An Informal Manual for GINGER and its' post-processor XPLOTGIN", LBID-2141, CBP Tech Note-104, UC-414, 1995.
- [2] H.P. Freund, Phys. Rev. E **52**, 5401 (1995).
- [3] T.M. Tran and J.S. Wurtele, Comput. Phys. Commun. **54**, 263 (1989).
- [4] S. Reiche, Nucl. Instr. Meth. A **429**, 243 (1999).
- [5] L. Giannessi *et al.*, Phys. Rev. ST-AB **14**, 060712 (2011).
- [6] G.R. Neil *et al.*, Nucl. Instr. Meth. A **557**, 9 (2006).
- [7] H.P. Freund, L. Giannessi, and W.H. Miner, Jr., J. Appl. Phys. **104**, 123114 (2008).
- [8] J. Karsenberg *et al.*, J. Appl. Phys. **100**, 093106 (2006).
- [9] <http://lpno.tnw.utwente.nl/opc.html>
- [10] L. Giannessi, "Overview of PERSEO, a system for simulating FEL dynamics in Mathcad", in Proceedings of the 28th Free Electron Laser Conference, Berlin, Germany, 91 (2006), <http://jacow.org/>
- [11] P.J.M. van der Slot *et al.*, Phys. Rev. Lett., **102**, 244802 (2009)

RECENT UPDATES TO THE OPTICAL PROPAGATION CODE OPC

P.J.M. van der Slot[#]

Mesa⁺ Institute for Nanotechnology, University of Twente, Enschede, The Netherlands
Department of Electrical and Computer Engineering, Colorado State University, Fort Collins, USA
K.-J. Boller

Mesa⁺ Institute for Nanotechnology, University of Twente, Enschede, The Netherlands

Abstract

In order to understand and design free-electron lasers (FELs), simulation codes modeling the interaction of electrons with a co-propagating optical field in the magnetic field of an undulator are essential. However, propagation of the optical field outside the undulator is equally important for evaluation of the optical field at the location of the application or to model FEL oscillators.

The optical propagation code OPC provides such capabilities and can interface with FEL gain codes like GENESIS 1.3, MEDUSA and MINERVA. Here we present recent additions and modifications to the code that improves the speed of the code and extends the modeling capabilities. These include amongst other, inline diagnostics that results in considerable faster runtimes, the ability to convert from free-space modes to guided modes (currently only cylindrical waveguides), and the possibility to determine the spectrum at each transverse location. The latter opens the possibility to include dispersion in the optical propagation.

INTRODUCTION

Simulation tools play an essential role in the design and understanding of free-electron lasers (FELs). In the last few decades, several codes have been developed to model the interaction of electrons with a co-propagating optical field inside the magnetic field of an undulator, amongst others, GENESIS 1.3 [1], GINGER[2], MEDUSA [3] and MINERVA [4] as a recent addition. These codes are used to calculate the spatio-temporal characteristics of the optical pulse coming out of the undulator. However, self-consistent modelling of an oscillator FEL also requires to model the propagation of the optical pulse outside the gain section, i.e., outside the undulator. Even for single pass systems, a system designer or user is typically interested in the characteristics of the optical pulse in the far field. The optical propagation code (OPC) [5] provides tools for propagating the optical field outside the gain section and interfaces with the FEL gain codes GENESIS 1.3, MEDUSA and MINERVA. The main properties of OPC are described in ref. [5], and we only summarize its main characteristics here. The propagation of the optical field is done using one of three methods, a spectral method, a Fresnel diffraction integral and a modified Fresnel diffraction integral. These methods propagate the complex phasor of the electric field of the optical pulse

from an input plane to an output plane, where the modified Fresnel integral allows for an expansion of the grid on which the optical field is defined, but not the number of grid points. OPC allows placement of various optical elements along the propagation path, such as apertures, lenses and mirrors. In this paper we describe the recent additions to the code that enhances its capabilities and increases the speed of the code. The remainder of the paper is organized as follows. We will first describe the addition of inline diagnostics, which is then followed by a description of waveguide modes and finally we discuss the possibility to propagate in the frequency domain, which allows the use of dispersive elements in the optical path. We conclude with a brief summary and outlook for future additions to OPC.

IN-LINE DIAGNOSTICS

In order for the user to analyze the optical properties of the light generated in the FEL, the user has the ability to execute a number diagnostics on the optical pulse, such as obtaining the intensity $I(x, y, s)$ as a function of the position (x, y) in the transverse plane for a specific longitudinal position s , the phase $\Theta(x, y, s)$ as a function of the position (x, y) for a specific s or $\Theta(x = x_0, y = y_0, s)$ as a function of s for a specific transverse location (x_0, y_0) , the power $P(s) = \iint I(x, y, s) dx dy$ in the pulse, the fluence $F(x, y) = \int I(x, y, s) ds$, a cross section $I(x, y = y_0, s)$ or $I(x = x_0, y, s)$ through the pulse, the “centre of gravity” (x_c, y_c) of the optical pulse and its rms radius r_{rms} (weighted with the intensity distribution). These diagnostics can be applied at any (intermediate) plane along the optical path where the optical field is evaluated. Until recently, OPC first propagates the optical from start to end of the optical path, while storing the optical field at the locations where diagnostics are requested. After the optical propagation has completed, the user can perform the diagnostic commands to the stored optical field. For this reason, we refer to this as off-line diagnostics.

The stored optical field consists of the complex phasor (amplitude and phase) of a linearly polarized electric field at each grid point for each of the time samples of the optical field, and the amount of data can become very large for large grid sizes ($N_x \times N_y = N_p^2$, for simplicity) and/or number of times samples N_s . For this reason, the optical field is stored on disk and the associated disk I/O can have an impact on the speed of the program when the files become large or a large number of diagnostics are requested.

[#]p.j.m.vanderslot@utwente.nl

To avoid a significant increase in run time due to diagnostic evaluations wanted by the user, OPC has been upgraded with so-called in-line diagnostics. Instead of dumping the optical field to the hard disk when diagnostics are requested, the user can now execute diagnostic commands during the propagation along the optical path. These new diagnostics commands are applied to the optical field while it is still in the memory of the computer and therefore avoids a large amount of relative slow disk I/O. Backward compatibility with off-line diagnostics is maintained to allow the user to use earlier work without modifications and to post-process optical fields produced at an earlier time.

In order to obtain an impression about the speed improvement, we created a script that times the speed of the calculations in three cases. In the first, a predefined optical field is propagated over a distance of 5 m using the Fresnel diffraction integral method. This provides the time t_p required to do the propagation. In the second case, the predefined field is again propagated using the same method and at the end of the path the optical field is dumped and processed with a diagnostic command after the propagation is completed (off-line diagnostic). This provides the time t_{pod} for the propagation and off-line diagnostic command. The third and last case propagates the same predefined optical field but now implements the same diagnostic command at the end of the propagation path (in-line diagnostic). This provides the time t_{pid} of the propagation plus the in-line diagnostic command. Each case is executed 20 times consecutively, to obtain an average execution time. The tests were run on a duo Xeon computer with a total of 12 cores. The results are summarized for the diagnostic commands total and statistics in Tables 1 and 2 for $N_s = 300$ and $N_s = 600$ time samples, respectively. The command to generate a cross section through the intensity profile shows a similar behavior.

Table 1: Average Execution Time for the Diagnostic Commands Total and Statistics, $N_s = 300$

N_p	total			statistics	
	t_p (s)	t_{pod} (s)	t_{pid} (s)	t_{pod} (s)	t_{pid} (s)
255	2.0	3.2	2.0	3.1	2.0
441	3.5	4.6	3.3	4.6	3.3
567	4.9	6.2	4.8	6.3	4.7
945	11.9	20.0	11.6	19.2	11.7

Table 2: Average Execution Time for the Diagnostic Commands Total and Statistics, $N_s = 600$

N_p	total			statistics	
	t_p (s)	t_{pod} (s)	t_{pid} (s)	t_{pod} (s)	t_{pid} (s)
255	2.4	4.1	2.9	3.1	2.0
441	5.8	7.1	5.3	7.1	5.3
567	8.8	16.2	8.2	20.6	8.4
945	22.0	57.1	49.9	61.6	51.6

The results in Table 1 show that a single in-line diagnostics command hardly effects the runtime of the

code compared to a single propagation step, while a single off-line diagnostic command can almost double the runtime of a single propagation step. Table 2 shows the runtimes when we increase the number of time samples from $N_s=300$ to $N_s=600$. For the three smallest number of grid points ($N_p = 255, 441$ and 567), a single in-line diagnostic command again hardly increase the run time while a single off-line diagnostic command can more than double the run time. Only for the combination of the largest value for $N_p = 945$ and $N_s = 600$, we observe a serious degradation in performance for the in-line diagnostics, although they still outperform the equivalent off-line diagnostic command. Note, for these parameters ($N_p = 945$ and $N_s=600$), the optical field corresponds to almost 9 GB of data.

WAVEGUIDE MODES

When the FEL emits light at THz or longer wavelengths, the natural diffraction of the light becomes so large that the effect of the vacuum tube, through which the electrons move, cannot be neglected any more. The electromagnetic wave becomes guided. The MINERVA gain code [4] will be able to model FELs with guided or partial guided wave propagation inside the undulator. In order to support cold cavity calculations and propagate the optical field back to the entrance of the undulator, OPC has been extended to include waveguide modes. Currently only cylindrical waveguides modes are supported.

An additional “waveguide” option as part of the optical path has been made available to the user. This option decomposes an incident optical field in free space into waveguide modes and obtains the complex phasor (amplitude and phase) for each mode [6]. These modes are then propagated to the other end of the waveguide, where they are combined into a new optical field that is emitted into free space. Typically, the wavelength is sufficiently far below the cut-off wavelength that reflection at the waveguide end can be neglected [6]. The user has access to the modal decomposition and obtain the energy and amplitude for each of the excited modes. Although one may start with a linear polarized optical field in free space, the optical field will possess two orthogonal polarization directions after propagating through a cylindrical waveguide. OPC has been extended to include two perpendicular polarizations to accurately model the optical field emitted into free space from a waveguide. This framework can in principle also be used to propagate circular polarized light along an optical path. As an example, Fig. 1 shows how much power is coupled in the fundamental TE_{11} mode and all TE modes together as a function of the waist w_0 of a fundamental Gaussian TEM_{00} mode when it is focused on the end of a cylindrical waveguide with an inner radius $R_{wg} = 3$ mm. Note, as the peak intensity of the incident TEM_{00} mode is kept constant, the total power in the incident field increases with the size of the focus. As the waist of the TEM_{00} mode increases from its minimal value of 1 mm, more power is coupled into the waveguide and between $w_0 = 2$ and 2.4 mm less than 1 % of the coupled power is

in higher order modes. At optimum coupling, w_0 is 2.4 mm and 87.5 % of the incident power is coupled into the fundamental TE_{11} mode. When the waist is further increased, less power is coupled into the waveguide and higher order modes are excited. This is because the incident optical field becomes too large and a considerable fraction of the field falls outside the aperture provided by the cylindrical waveguide.

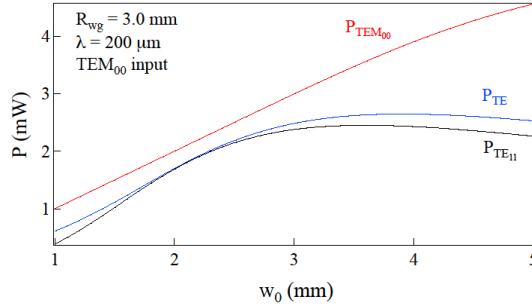


Figure 1: Coupling between free-space Gaussian TEM_{00} mode and the TE_{nm} modes in a cylindrical waveguide of radius $R_{wg} = 3$ mm.

SPECTRAL DOMAIN

Until recently, OPC assumed that the optical bandwidth of the pulse is sufficiently small that the center wavelength of the optical field can be used for the propagation and that dispersion along the optical path is not important. These assumptions break down when (ultra)short pulses need to be propagated or when the optical components used along the optical path have a significant dispersion over the bandwidth of the optical pulse. OPC has been upgraded to give the user the choice to propagate in the time domain where consecutive time samples are propagated one after the other along the optical path (using the center wavelength), or to transfer to the frequency domain where consecutive frequencies are propagated along the optical path.

The transformation to the frequency domain also allows users to inspect the transverse distribution of the various frequency components. As an example we show in Fig. 2 the energy at the exit of the undulator of an FEL oscillator [7] as a function of the roundtrip number. The system parameters are listed in the figure. Figure 2 suggests that the system becomes stationary, i.e., no changes from one pass to the next, after about 400 roundtrips. The power of the optical pulse as a function of the roundtrip n and the longitudinal internal coordinate $s = ct$, where c is the speed of light in vacuum and t is the time coordinate, is shown in Fig. 3 and although the pulse energy is almost constant, the temporal shape of the pulse still changes after $n = 400$. The spectrum of the optical pulse at $n = 900$ roundtrips is shown in Fig. 4. As the initial carrier wavelength was at 495 nm, Fig. 4 shows that the wavelength with maximum spectral energy density is at

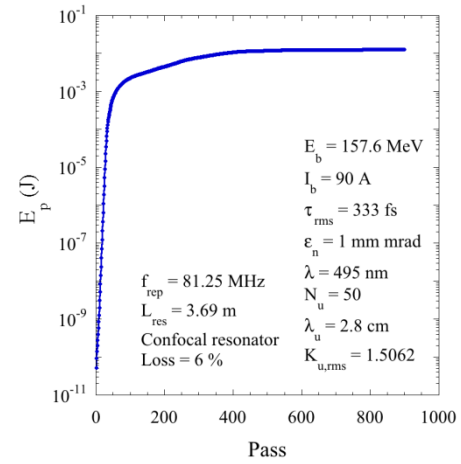


Figure 2: Pulse energy at the exit of the undulator in a FEL oscillator as a function of the roundtrip number.

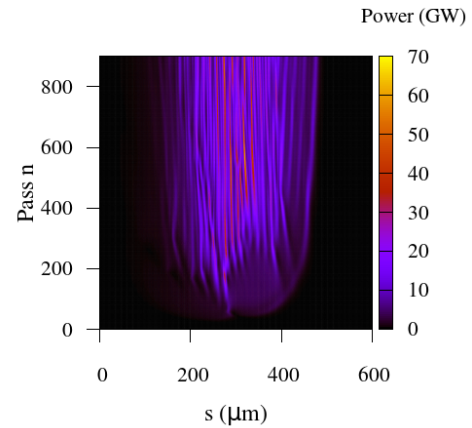


Figure 3: Power $P(n, s)$ as a function of the roundtrip number n and the internal longitudinal coordinate $s = ct$ for the parameters of Fig. 2.

499.8 nm, while the intensity weighted average wavelength is $\bar{\lambda} = 521$ nm, where $\bar{\lambda}$ is defined as

$$\bar{\lambda} = \frac{\int \lambda I(\lambda) d\lambda}{\int I(\lambda) d\lambda} \quad (1)$$

The rms bandwidth is defined as

$$\Delta\lambda_{rms} = \sqrt{\overline{\lambda^2} - \bar{\lambda}^2}, \quad (2)$$

where $\overline{\lambda^2}$ is defined similar as $\bar{\lambda}$. For the spectrum shown in Fig. 4, we find that $\Delta\lambda_{rms} = 35$ nm. Note, the -3 dB bandwidth $\Delta\lambda_{-3dB} = 0.81$ nm.

OPC also provides the possibility to inspect the transverse energy distribution of the frequency components. Examples are shown in Fig. 5, where we plot the transverse distribution for the initial carrier wavelength (495 nm), the wavelength with the highest spectral energy density (499.8 nm), close to the average wavelength (521.3 nm) and an arbitrary wavelength (530.2 nm).

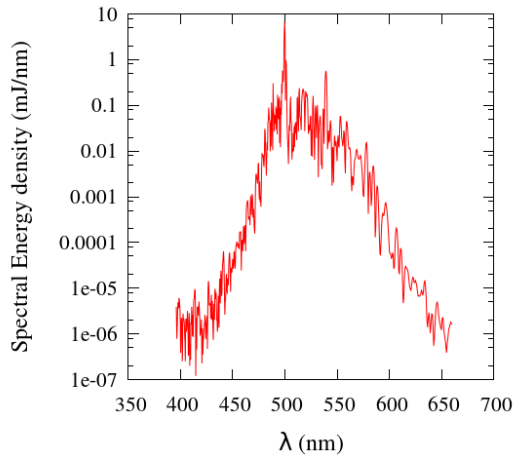


Figure 4: Spectrum of the optical pulse after 900 roundtrips. Parameters as in Fig. 2.

Figure 5 shows that not all frequency components in the spectrum have the same transverse distribution. For example, not all frequency components have their maximum spectral intensity on axis.

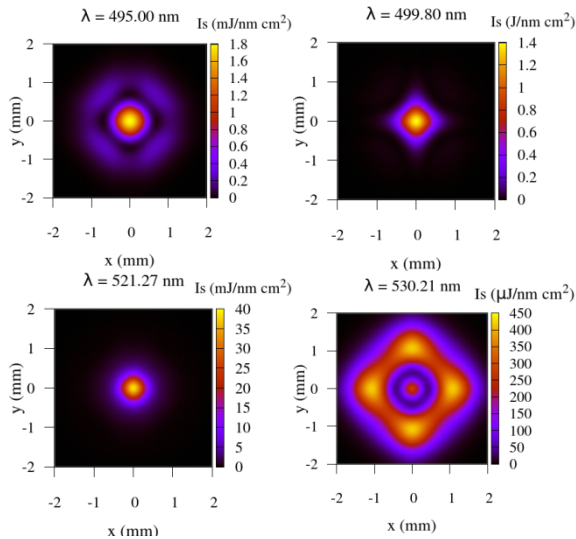


Figure 5: Transverse spectral intensity $I_s(x, y)$ for the wavelengths 495.0, 499.8, 521.3 and 530.2 nm. Note the difference in scale for $I_s(x, y)$ at the various frequencies.

So far, we have demonstrated the new diagnostics in the spectral domain. However, propagation in the frequency domain also allows the use of dispersive optical components along the optical path. For example, if we consider a multilayer mirror, then reflecting a short optical pulse from the mirror is problematic to implement in the time domain, as the pulse may temporally broaden. By transforming to the frequency domain and if the complex reflection coefficient (reflected amplitude and phase shift) of the mirror is available for the frequency range of interest (either measured or calculated), we can reflect each frequency component of the mirror. By

transforming back to the time domain, the pulse has been reflected from the mirror including broadening of the pulse due to the partial reflection at the layers of the mirror. Alternatively, if the optical pulse propagates through a material, a wavelength dependent refractive index can be included.

CONCLUSION

We have described the enhanced capabilities of OPC. In particular, the in-line diagnostics are considerably faster than the off-line diagnostics and a single in-line diagnostic command hardly changes the runtime of a single propagation step. Only for a very large number of grid points and a larger number of time samples do the in-line diagnostics significantly add to the total run time. The waveguide modes that have been added are a first step towards guided propagation and towards interfacing with FEL gain codes that can handle partial or complete wave guiding. Finally, the transformation to the frequency domain allows for a more accurate propagation and introduces added diagnostics to the package. A propagation in the frequency domain also allows the use of dispersive optical elements.

Further extensions that are planned for the immediate future are the use of the HDF5 library for storing data to remain compatible with the upcoming release of GENESIS 1.3 and to implement a number of dispersive optical elements.

ACKNOWLEDGMENT

This work has been supported in part by the Office of Naval Research Global, grant number, N62909-10-1-7151.

REFERENCES

- [1] S. Reiche, Nucl. Instr. Meth. A **429**, 243 (1999).
- [2] W.M. Fawley, An Informal Manual for GINGER and its' post-processor XPL0TGIN, LBID-2141, CBP Tech Note-104, UC-414, 1995.
- [3] H.P. Freund, Phys. Rev. E **52**, 5401 (1995).
- [4] H.P. Freund et al., "Minerva, a new code to model free-electron lasers", TUP020, these proceedings, FEL'14, Basel, Switzerland (2014).
- [5] J. Karsenberg et al., J. Appl. Phys. **100**, 093106 (2006).
- [6] P.J.M. van der Slot et al., "Design of a resonator for the CSU THz FEL" in *Proc. 35th Int. Free-Electron Laser Conf.*, New York, pp. 719-722 (2013).
- [7] See also G. Dattoli et al., "Free-electron laser oscillator: short pulses, mode locking, harmonic generation and tapering", WEA02, these proceedings, FEL'14, Basel, Switzerland (2014).

THE IMPLEMENTATION OF 3D UNDULATOR FIELDS IN THE UNAVERAGED FEL SIMULATION CODE *Puffin*

J. R. Henderson¹, L.T. Campbell^{1,2,3,4}, A.R. Maier^{3,4} and B.W.J. McNeil¹

¹SUPA, Department of Physics, University of Strathclyde, Glasgow, UK

²ASTeC, STFC Daresbury Laboratory and Cockcroft Institute, Warrington, UK

³Center for Free-Electron Laser Science, Notkestrasse 85, Hamburg, Germany

⁴Institut für Experimentalphysik, Universität Hamburg, Hamburg, Germany

Abstract

The FEL simulation code *Puffin* is modified to include 3D magnetic undulator fields. *Puffin*, having previously used a 1D undulator field, is modified to accommodate general 3D magnetic fields. Both plane and curved pole undulators have been implemented. The electron motion for both agrees with analytic predictions.

INTRODUCTION

Puffin [1] is an unaveraged 3D FEL code which does not make the Slowly Varying Envelope Approximation (SVEA) or period averaging in its analytical model. As such, it is capable of modelling the a broad radiation field spectrum, full longitudinal broadband electron beam transport through the undulator, and Coherent Spontaneous Emission (CSE) emerging from current gradients in the beam.

However, although *Puffin* models a 6D electron beam and 3D radiation field, it does not employ a 3D magnetic undulator field. Instead, it implements a 1D undulator field with no off-axis variation. Superimposed, is an external focusing channel which is an approximation of the natural focusing found in a helical undulator. This focusing channel may be strengthened or weakened through the use of a ‘focusing factor’ [2] to obtain a desired betatron frequency.

Such a model does not simulate the detuning of the resonance condition in the transverse dimensions. Nor does it allow the focusing to emerge naturally from the off-axis variation of the magnetic fields. The resulting electron motion is an approximation in the case of a helical or curved-pole undulator; it is inaccurate in the case of an undulator with plane poles. Furthermore, the betatron motion as derived in *Puffin* is only valid when the electron beam is close to mono-energetic.

There is a need to model more realistic undulator fields; in particular, plane pole and curved pole undulators are more common than helical undulators for UV/X-ray FELs. There is therefore a requirement that various 3D planar undulator types be implemented in *Puffin*.

In the following, the *Puffin* model is first generalized to include general undulator magnetic fields. This model also allows a helical field description to be developed. Note also that this general magnetic field description need not be limited to undulators, and may allow future alternative applications of the *Puffin* code, to solve other radiation-electron interactions in static magnetic fields.

This general description is then used to implement both a generic plane pole and curved (canted) pole undulator FEL. Results are presented to demonstrate the correct electron motion and radiation characteristics are being solved.

MODIFIED MATHEMATICAL MODEL

The derivation of the FEL system of equations modelled by *Puffin* is given in [1], using a magnetic undulator field

$\mathbf{B}_u = \frac{B_u}{2}(\mathbf{u}e^{ik_u z} + c.c.)$, where $\mathbf{u} = u_x \hat{\mathbf{x}} + iu_y \hat{\mathbf{y}}$ defines the polarization of the undulator. Following the same derivation, but using a general 3D magnetic field of the form $\mathbf{B} = B_x \hat{\mathbf{x}} + B_y \hat{\mathbf{y}} + B_z \hat{\mathbf{z}}$, one obtains the following system of equations:

$$\left[\frac{1}{2} \left(\frac{\partial^2}{\partial \bar{x}^2} + \frac{\partial^2}{\partial \bar{y}^2} \right) - \frac{\partial^2}{\partial \bar{z} \partial \bar{z}_2} \right] A_{\perp} = - \frac{1}{\bar{n}_p} \frac{\partial}{\partial \bar{z}_2} \sum_{j=1}^N \bar{p}_{\perp j} L_j \delta^3(\bar{x}_j, \bar{y}_j, \bar{z}_{2j}) \quad (1)$$

$$\frac{d\bar{p}_{\perp j}}{d\bar{z}} = \frac{1}{2\rho} \left[ib_{\perp} - \frac{\eta p_{2j}}{\alpha^2} A_{\perp} \right] - i\alpha \bar{p}_{\perp j} L_j b_z \quad (2)$$

$$\frac{dp_{2j}}{d\bar{z}} = \frac{\rho}{\eta} L_j^2 \left[\eta p_{2j} (\bar{p}_{\perp j} A_{\perp}^* + c.c.) - i(1 + \eta p_{2j}) \alpha^2 (\bar{p}_{\perp j} b_{\perp j}^* - c.c.) \right] \quad (3)$$

$$\frac{d\bar{z}_{2j}}{d\bar{z}} = p_{2j} \quad (4)$$

$$\frac{d\bar{x}_j}{d\bar{z}} = \frac{2\rho\alpha}{\sqrt{\eta}} L_j \Re(\bar{p}_{\perp j}) \quad (5)$$

$$\frac{d\bar{y}_j}{d\bar{z}} = -\frac{2\rho\alpha}{\sqrt{\eta}} L_j \Im(\bar{p}_{\perp j}). \quad (6)$$

where

$$\eta = \frac{1 - \bar{\beta}_z}{\bar{\beta}_z} = \frac{\lambda_r}{\lambda_u}, \quad (7)$$

$$\begin{aligned} \bar{p}_{\perp} &= \frac{p_{\perp}}{mca_u}, & A_{\perp} &= \frac{eua_u l_g}{2\sqrt{2}\gamma_r^2 mc^2 \rho} E_{\perp}, \\ \rho &= \frac{1}{\gamma_r} \left(\frac{a_u \omega_p}{4ck_u} \right)^{2/3}, & a_u &= \frac{eB_0}{mck_u}, \\ \alpha &= \frac{a_u}{2\rho\gamma_r}, & b_{\perp} &= b_x - ib_y, \end{aligned} \quad (8)$$

and $b_{x,y,z} = B_{x,y,z}/B_0$ are the scaled magnetic fields in x , y and z , respectively, and B_0 is the peak on-axis magnetic field. Other parameters remain as defined in [1]. The FEL parameter ρ above is defined using the peak undulator parameter, rather than the *r.m.s.* undulator parameter.

Using the above system of equations, one may use b_x , b_y and b_z to define a static 3D magnetic field with which to simulate the energy exchange between a co-propagating electron beam and radiation field. The model is still subject to the same limitations as in [1], *i.e.* the paraxial approximation and the neglect of the backwards propagating wave.

Currently, two 3D undulator fields have been implemented in Puffin using this model, both derived from [3, 4]. The first is an undulator field with canted, or curved, pole faces, providing beam focusing in both transverse dimensions:

$$\begin{aligned} b_x &= \frac{\bar{k}_x}{\bar{k}_y} \sinh(\bar{k}_x \bar{x}) \sinh(\bar{k}_y \bar{y}) \sin(\bar{z}/2\rho), \\ b_y &= \cosh(\bar{k}_x \bar{x}) \cosh(\bar{k}_y \bar{y}) \sin(\bar{z}/2\rho), \\ b_z &= \frac{\sqrt{\eta}}{2\rho\bar{k}_x} \cosh(\bar{k}_x \bar{x}) \sinh(\bar{k}_y \bar{y}) \cos(\bar{z}/2\rho), \end{aligned} \quad (9)$$

where $\bar{k}_{x,y}$ give the hyperbolic variation of the magnetic field in \bar{x}, \bar{y} , and must satisfy

$$\bar{k}_x^2 + \bar{k}_y^2 = \frac{\eta}{4\rho^2}. \quad (10)$$

The second undulator type is a planar undulator with plane pole faces, described by:

$$\begin{aligned} b_x &= 0, \\ b_y &= \cosh(\sqrt{\eta}\bar{y}/2\rho) \sin(\bar{z}/2\rho), \\ b_z &= \sinh(\sqrt{\eta}\bar{y}/2\rho) \cos(\bar{z}/2\rho). \end{aligned} \quad (11)$$

SIMULATIONS

The electron transport through both of these undulator types is well known. Some simple tests can therefore be designed to see if the electron motion in Puffin exhibits the correct behaviour.

As described in [3], a natural focusing channel arises from the off-axis variation of the magnetic field in the curved-pole undulator. From this so-called 'natural' focusing, one expects a slow oscillation characterised by betatron wavenumbers and corresponding matched beam radii in \bar{x} and \bar{y} , given, in the scaled notation, as:

$$\bar{k}_{\beta x} = \frac{a_u \bar{k}_x}{\sqrt{2\eta\gamma_r}}, \quad \bar{k}_{\beta y} = \frac{a_u \bar{k}_y}{\sqrt{2\eta\gamma_r}}, \quad (12)$$

$$\bar{\sigma}_x = \sqrt{\frac{\rho \bar{\epsilon}_x}{\bar{k}_{\beta x}}}, \quad \bar{\sigma}_y = \sqrt{\frac{\rho \bar{\epsilon}_y}{\bar{k}_{\beta y}}}. \quad (13)$$

respectively.

For the curved pole simulation, $\rho = 0.0017$, $a_u = 4.404$, $\bar{\epsilon}_{x,y} = 1$ and $\gamma_r = 575.63$. A small electron pulse is used to generate a significant amount of coherent spontaneous

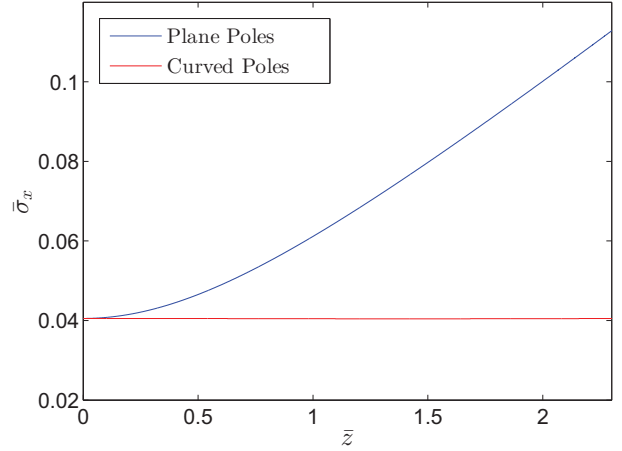


Figure 1: The electron pulse radius $\bar{\sigma}_x$ plotted as a function of distance through the undulator.

emission (CSE) [5], to avoid a noisy transverse intensity distribution, allowing a simple check of the emitted radiation properties.

The radii in \bar{x} and \bar{y} , matched at injection, are seen to be constant throughout propagation. $\bar{\sigma}_x$ is plotted against \bar{z} in Figure 1. In this case, $\bar{k}_x = \bar{k}_y$, which, from condition (10) and equation (12), results in

$$\bar{k}_{\beta x} = \bar{k}_{\beta y} = \frac{a_u}{4\rho\gamma_r}, \quad (14)$$

and, from (13), matched beam radii of $\bar{\sigma}_{x,y} = 0.039$, giving good agreement with Figure 1.

Similar to the curved-pole undulator, a natural focusing channel also arises in the plane-pole undulator, this time exclusively in the \bar{y} direction. For this simulation, the parameters used are identical to the curved pole case, except the beam energy and the undulator parameter are adjusted to $\gamma_r = 238.04$ and $a_u = 1.2876$, to give the same betatron wavelength and transverse radii for comparison to the curved pole case.

The betatron period and matched beam radius in \bar{y} are now:

$$\bar{k}_{\beta y} = \frac{a_u}{2\sqrt{2}\rho\gamma_r}, \quad (15)$$

$$\bar{\sigma}_y = \sqrt{\frac{\rho \bar{\epsilon}_y}{\bar{k}_{\beta y}}}, \quad (16)$$

and electron motion in the (\bar{x}, \bar{p}_x) dimension should undergo free space dispersion when averaged over an undulator period, resulting in an expansion of the beam in the \bar{x} dimension.

The radius in \bar{x} during propagation is plotted in Figure 1, showing the beam expansion. The initial radius in \bar{x} is here set to the matched radius in \bar{y} , so $\bar{\sigma}_x = \bar{\sigma}_y = 0.0327$. The radius in \bar{y} remains constant, as expected.

Another test which can be made on the electron motion is that, again from [4], $|\bar{p}_\perp|^2 = 0.5$ remains constant for all

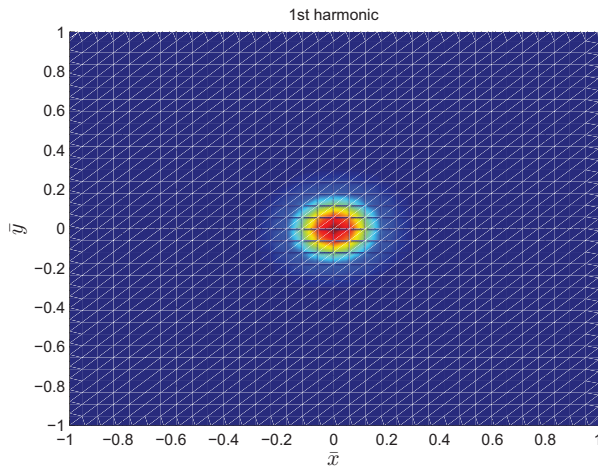


Figure 2: Transverse intensity profile of the 1st harmonic.

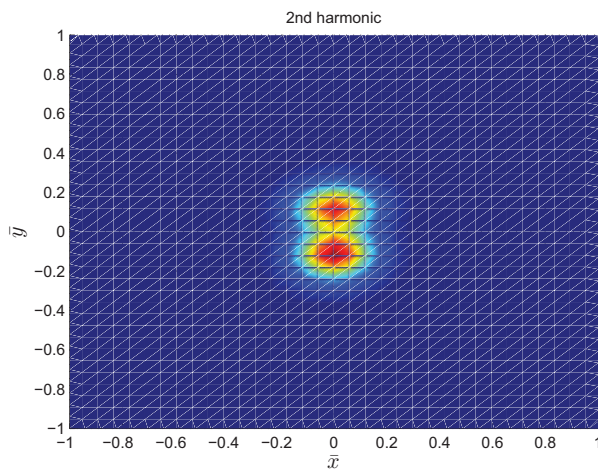


Figure 3: Transverse intensity profile of the 2nd harmonic.

electrons when averaged over an undulator period, which maintains a constant resonance condition throughout their betatron oscillations. This condition is seen to be satisfied in Puffin.

Puffin, being an unaveraged, non-SVEA code, is capable of the self-consistent simulation of the full radiation field spectrum in the FEL. The transverse intensity distributions of the first 2 harmonics in the plane-pole case from CSE is shown in Figures 2 and 3, showing the expected on-axis emission for the first harmonic and the off-axis emission for the second harmonic [6].

CONCLUSION

The system of equations (1 - 6) have been derived in order to implement more realistic 3D undulators in Puffin, increasing the scope of the code.

The betatron oscillation of each electron arises naturally and self-consistently from the motion of the electrons in the specified undulator fields - it is not an approximation of the motion, which would only be valid for electrons close

to a given energy, super-imposed on top of another system of equations. Consequently, the functionality reported here will allow the simulation of broadband electron beams transported correctly through the FEL.

The work here may be combined with the model presented in [7], which describes how to employ a taper in the equations, to taper an undulator module's magnetic fields to and from zero over the first and last few undulator periods in each module. As well as more closely modelling a 'realistic' undulator, this avoids the task of calculating the correct initial conditions of the electron beam macroparticles that ensures a stable propagation along the undulator. This calculation can non-trivial, particularly for beams with a large energy spread.

Other static magnetic fields, such as quadrupoles, may be added to the equations. They would be subject to the same scalings presented here, which are specific to the FEL - for example, z is scaled to l_g , the FEL gain length. It is intended this will be done in the future.

ACKNOWLEDGMENTS

We gratefully acknowledge the computing time granted by the John von Neumann Institute for Computing (NIC) and provided on the supercomputer JUROPA at Jülich Supercomputing Centre (JSC), under project HHH20; Science and Technology Facilities Council Agreement Number 4163192 Release #3; and ARCHIE-WeSt High Performance Computer, EPSRC grant no. EP/K000586/1

REFERENCES

- [1] L.T. Campbell and B.W.J. McNeil, *Physics of Plasmas* **19**, 093119 (2012)
- [2] R. Bonifacio, L. De Salvo Souza, and B.W.J. McNeil, *Opt. Commun.* **93**, 179-185 (1992)
- [3] E.T. Scharlemann, *J. Appl. Phys.* **58**, 2154 (1985)
- [4] E.T. Scharlemann, in *High Gain, High Power FELs* (edited by R. Bonifacio et al) (1989)
- [5] N. Piovella, *Phys. of Plasmas* **6**, 3358 (1999)
- [6] J.A. Clarke, *The Science and Technology of Undulators and Wigglers*, Oxford University Press (2004)
- [7] L.T. Campbell, B.W.J. McNeil and S. Reiche, *Investigation of a 2-Colour Undulator FEL Using Puffin*, MOPSO09, Proceedings of FEL 2013

MODELING CSR IN A VACUUM CHAMBER BY PARTIAL FOURIER ANALYSIS AND THE DISCONTINUOUS GALERKIN METHOD *

D. A. Bizzozero^{†1}, R. Warnock^{2,1}, J. A. Ellison¹

¹Department of Mathematics and Statistics, University of New Mexico
Albuquerque, New Mexico 87131, USA

²SLAC National Accelerator Laboratory, Stanford University
Menlo Park, California 94025, USA

Abstract

We continue our study [1–3] of CSR from a bunch on an arbitrary curved orbit in a plane. The vacuum chamber has rectangular cross section with possibly varying horizontal width. We make a Fourier transform in $s - ct$ and use the slowly varying amplitude approximation. We invoke a Fourier expansion in the vertical coordinate y , which meets the boundary conditions on the top and bottom plates and makes contact with the Bessel equation of the frequency domain treatment. The fields are defined by a PDE in s and x , first order in s , which is discretized in x by finite differences (FD) or the discontinuous Galerkin method (DG). We compare results of FD and DG, and also compare the computation speeds to our earlier calculations in 3D (paraxial) which did not use the Fourier series in y [4–8]. This approach provides more transparency in the physical description, and when only a few y -modes are needed, provides a large reduction in computation time.

STATEMENT OF THE PROBLEM

Statement of the Physical Problem

We start with the wave equation for the E_y and H_y fields in the Frenet-Serret coordinates (s, x, y, t) :

$$\nabla^2 E_y - \frac{1}{c^2} \frac{\partial^2 E_y}{\partial t^2} = Z_0 \left(\frac{1}{c} \frac{\partial J_y}{\partial t} + c \frac{\partial \rho}{\partial y} \right), \quad (1a)$$

$$\nabla^2 H_y - \frac{1}{c^2} \frac{\partial^2 H_y}{\partial t^2} = -\frac{R}{x+R} \frac{\partial J_x}{\partial s} + \frac{\partial J_s}{\partial x} + \frac{1}{x+R} J_s. \quad (1b)$$

We shall solve for the fields in a toroidal vacuum chamber with perfectly conducting walls at $x = x_{in}, x_{out}$ and $y = \pm h/2$. The bunch orbit is centered in the chamber and has bending radius R . We next apply a Fourier transform in $s - ct$ and a Fourier series in y . Now the fields and sources are expressed in the form

$$F(s, x, y, t) = \int_{-\infty}^{\infty} dk e^{ik(s-ct)} \sum_{p=1}^{\infty} \phi_p(y) \hat{F}_p(s, x, k), \quad (2)$$

$$\phi_p(y) = \begin{bmatrix} \cos \\ \sin \end{bmatrix} \left(\alpha_p (y + h/2) \right), \quad \alpha_p = \frac{\pi p}{h}.$$

* Work supported by DOE under DE-FG02-99ER41104 and DE-AC03-76SF00515.

[†] dbizzoze@math.unm.edu

If the vertical distribution of charge is an even function of y , which we assume, then only odd integers p are involved. For E_y, H_x, H_s, J_y the factor ϕ_p contains only cos terms whereas for $H_y, E_x, E_s, \rho, J_x, J_s$ it contains only sin terms. In the approximation of slowly varying amplitude (paraxial approximation) terms with $\partial^2/\partial s^2$ are neglected and the transformed equations (1) for $\hat{F}_p(s, x, k) = \hat{E}_{yp}, \hat{H}_{yp}$ become (with $\gamma_p^2 = k^2 - \alpha_p^2$):

$$\frac{2ikR^2}{(x+R)^2} \frac{\partial \hat{F}_p}{\partial s} = -\frac{\partial^2 \hat{F}_p}{\partial x^2} - \frac{1}{x+R} \frac{\partial \hat{F}_p}{\partial x} - \left(\gamma_p^2 - \frac{(kR)^2}{(x+R)^2} \right) \hat{F}_p + S. \quad (3)$$

For a charge density of the form $q\lambda(s-ct)H(y)\delta(x)$, where q is the charge, the source terms are:

$$S_{\hat{E}} = \sigma \delta(x), \quad S_{\hat{H}} = \tau \left(\delta'(x) + \delta(x)/R \right) \quad (4a)$$

$$\sigma = qZ_0\alpha_p c \hat{\lambda}(k)H_p, \quad \tau = q\beta c \hat{\lambda}(k)H_p, \quad (4b)$$

where $\hat{\lambda}$ and H_p are Fourier transforms of λ and H . For a Gaussian H with width $\sigma_y \ll h$ we have $H_p = (-1)^{(p-1)/2} (2/h) \exp(-(\alpha_p \sigma_y)^2/2)$.

The perfectly conducting boundary conditions are guaranteed by:

$$\hat{E}_{yp}|_{x=x_{in}, x_{out}} = 0, \quad \frac{\partial \hat{H}_{yp}}{\partial x}|_{x=x_{in}, x_{out}} = 0. \quad (5)$$

To construct initial conditions for $\hat{E}_{yp}, \hat{H}_{yp}$, we assume an infinite straight prior to the entrance of the bend and use the steady-state solutions $\hat{F}_{p0} = \hat{E}_{yp0}, \hat{H}_{yp0}$ which satisfy:

$$\frac{d^2 \hat{F}_{0p}}{dx^2} - \alpha_p^2 \hat{F}_{0p} = S \quad (6)$$

With the solutions $\hat{E}_{yp}, \hat{H}_{yp}$ to the initial value problem (3-6) for each p , we construct the remaining fields through additional relations in Eq. (30), then return to the space-time domain by (2).

Statement of the Mathematical Problem

To solve (3) numerically, we first introduce a transformation to treat the singularities of (4a):

$$V = \hat{E}_{yp} - \sigma x \Theta(x), \quad (7a)$$

$$W = \hat{H}_{yp} - \tau \Theta(x), \quad (7b)$$

with Θ being the Heaviside step function. Under these transformations, V, W still satisfy (3); however, the sources become:

$$S_V = -\sigma\Theta(x)\left(\frac{1}{x+R} + x\left(\gamma_p^2 - \frac{(kR)^2}{(x+R)^2}\right)\right), \quad (8a)$$

$$S_W = -\tau\Theta(x)\left(\gamma_p^2 - \frac{(kR)^2}{(x+R)^2}\right). \quad (8b)$$

We have eliminated δ and δ' from the source, gaining a big advantage for the numerical work. A jump in the sources at $x = 0$ remains, but that too can be removed by a second transformation, which will be described elsewhere.

The boundary conditions for V, W are:

$$\begin{aligned} V|_{x=x_{in}} &= 0, \quad V|_{x=x_{out}} = -\sigma x_{out}, \\ \frac{\partial W}{\partial x}|_{x=x_{in}, x_{out}} &= 0. \end{aligned} \quad (9)$$

Next, we condense (3) to the following for fixed k, p :

$$i \frac{\partial u}{\partial s} = a(x) \frac{\partial^2 u}{\partial x^2} + b(x) \frac{\partial u}{\partial x} + c(x)u + \tilde{S}_{V,W}(x) \quad (10)$$

with u representing V, W , and $\tilde{S}_{V,W} = (x+R)^2 S_{V,W}/2kR^2$. It is important to note that our Schrödinger-type equation (10) is only parabolic in the sense of infinite propagation speed. It is hyperbolic-like in the sense that initial conditions are not smoothed by the PDE evolution.

The solutions of (6) to provide initial conditions are found readily by variation of parameters:

$$\begin{aligned} \hat{E}_{yp0}(x) &= -\frac{\sigma}{\alpha_p} \frac{\sinh(\alpha_p x_{out}) \sinh(\alpha_p(x - x_{in}))}{\sinh(\alpha_p(x_{out} - x_{in}))} \\ &\quad + \frac{\sigma}{\alpha_p} \sinh(\alpha_p x) \Theta(x), \end{aligned} \quad (11a)$$

$$\begin{aligned} \hat{H}_{yp0}(x) &= -\tau \frac{\sinh(\alpha_p x_{out}) \cosh(\alpha_p(x - x_{in}))}{\sinh(\alpha_p(x_{out} - x_{in}))} \\ &\quad + \tau \cosh(\alpha_p x) \Theta(x). \end{aligned} \quad (11b)$$

NUMERICAL IMPLEMENTATION

In this section we describe our numerical algorithms for integrating (10) by finite difference (FD) and nodal discontinuous Galerkin (DG) numerical schemes. We use explicit time-stepping in s for both methods.

Finite Difference Scheme

We begin by discretization of $[x_{in}, x_{out}]$ into $N_{res} + 1$ equidistant nodes spaced by Δx . The nodal coordinates are defined by $x_i = x_{in} + (i-1)\Delta x$ and $u_i = u(x_i)$. We define the 4th order differentiation operators by:

$$\begin{aligned} \frac{du}{dx}\bigg|_{x_i} &\approx \frac{u_{i-2} - 8u_{i-1} + 8u_{i+1} - u_{i+2}}{12\Delta x}, \\ \frac{d^2u}{dx^2}\bigg|_{x_i} &\approx \frac{-u_{i-2} + 16u_{i-1} - 30u_i + 16u_{i+1} - u_{i+2}}{12\Delta x^2}. \end{aligned} \quad (12)$$

For points near the boundaries, i.e. $i = 1, 2, N_{res}, N_{res} + 1$, we use lopsided 5 point stencils. For explicit time stepping, we employ a leap-frog scheme. It is important to note: the leap-frog scheme is unstable for the heat equation [9] but stable for our Schrödinger-type equation in (10). The leap-frog scheme is:

$$u^{n+1} = u^{n-1} + 2\Delta s \Phi(u^n) \quad (13)$$

with $\Phi(u^n)$ denoting the right-hand-side of (10) with the discretizations (12) at $s = n\Delta s$. For stability, we take:

$$\Delta s = C_{CFL} k \Delta x^2. \quad (14)$$

In our tests, $C_{CFL} < 0.3$ results in a stable scheme for $p \lesssim 40$. Due to the oscillatory nature of the solution for large p , a smaller CFL constant must be taken if larger p -modes are desired.

The boundary conditions on V are imposed by setting $V_1 = 0$ and $V_{N_{res}+1} = -\sigma_p x_{out}$ while the boundary conditions for W are imposed with a one-sided derivative stencil and solving for W_1 and $W_{N_{res}+1}$ as functions of $W_{2,\dots,5}$ and $W_{N_{res}-3,\dots,N_{res}}$ respectively. The initial conditions on V, W are computed analytically from (11).

Discontinuous Galerkin Scheme

We derive our DG scheme in some detail since it is not as well known as FD. DG methods have features taken from finite element (FE) and finite volume methods (FV). Solutions are represented by polynomials local to each element as in FE; however, the PDE can be represented in an explicit semi-discrete form. The PDE is satisfied using fluxes between elements similar to FV. This results in a scheme which can maintain high-order accuracy (hp -adaptivity) and stability for wave-dominated problems [10].

We rewrite the PDE in (10) in first order form as

$$i \frac{\partial u}{\partial s} = a(x) \frac{\partial q}{\partial x} + b(x)q + c(x)u + f, \quad q = \frac{\partial u}{\partial x}. \quad (15)$$

To find an approximate solution, we begin by partitioning the domain $[x_{in}, x_{out}]$ into K elements of polynomial degree N . The total number of nodes is given by $(N+1)K$. We next focus on a particular element k (note, this k is *not* related to Fourier transform in (2)). We approximate the solution on this element in the Lagrange polynomial basis:

$$u^k(x, s) = \sum_{j=1}^{N+1} u_j^k(s) \ell_j^k(x), \quad (16)$$

$$q^k(x, s) = \sum_{j=1}^{N+1} q_j^k(s) \ell_j^k(x), \quad (17)$$

with $\ell_j^k(x_i^k) = \delta_{ij}$ for nodal coordinates x_i^k . The derivatives of u in (15) are given by differentiating (16). The terms f , cu and bq are replaced by their natural interpolating poly-

mials

$$(cu)^k = \sum_{j=1}^{N+1} c_j^k u_j^k(s) \ell_j^k(x), \quad (bq)^k = \sum_{j=1}^{N+1} b_j^k q_j^k(s) \ell_j^k(x), \quad (18)$$

$$f^k = \sum_{j=1}^{N+1} f_j^k(s) \ell_j^k(x)$$

and $a\partial_x q$ is replaced by

$$a^k \sum_{j=1}^{N+1} q_j^k(s) [\ell_j^k(x)]', \quad (19)$$

where a^k is the value of a at the midpoint of element k . Note that each of these is a polynomial of degree N (or less). Equation (19) assumes a does not vary much on element k , which is certainly true in our case, however, we are investigating alternatives which do not make such an assumption. Inserting (16), (18), (19) into (15) we obtain the following residuals $\mathcal{R}_{1,2}^k(x, s)$ defined by

$$\mathcal{R}_1^k(x, s) = i \frac{\partial u^k}{\partial s} - a^k \frac{\partial q^k}{\partial x} - (bq)^k - (cu)^k - f^k, \quad (20a)$$

$$\mathcal{R}_2^k(x, s) = q^k - \frac{\partial u^k}{\partial x}. \quad (20b)$$

We now require that the residuals $\mathcal{R}_{1,2}^k(x, s)$ be approximately orthogonal to the ℓ_i^k . This yields $N+1$ equations for each (u_j^k, q_j^k) of the form

$$\int_{\mathcal{D}^k} \mathcal{R}_1^k(x, s) \ell_i^k(x) dx \approx 0, \quad \int_{\mathcal{D}^k} \mathcal{R}_2^k(x, s) \ell_i^k(x) dx \approx 0, \quad (21)$$

for $i = 1, \dots, N+1$. Clearly, requiring these to be zero will not yield a viable algorithm, as there would be no coupling between elements. The heart of DG is to couple adjacent elements using the so-called flux condition. This is obtained by integrating the $[\ell_i^k(x)]'$ terms by parts, inserting the flux condition, and then reversing the integration by parts. We illustrate this on $\mathcal{R}_2^k(x, s)$.

$$\begin{aligned} \int_{\mathcal{D}^k} -\frac{\partial u^k}{\partial x} \ell_i^k dx &= \int_{\mathcal{D}^k} u^k \ell_i^k(x)' dx - [u^k \ell_i^k]_{x_1^k}^{x_{N+1}^k} \approx \\ \int_{\mathcal{D}^k} u^k \ell_i^k(x)' dx - [u^{k*} \ell_i^k]_{x_1^k}^{x_{N+1}^k} &= \\ \int_{\mathcal{D}^k} -\frac{\partial u^k}{\partial x} \ell_i^k dx + [(u^k - u^{k*}) \ell_i^k]_{x_1^k}^{x_{N+1}^k} \end{aligned} \quad (22)$$

but the calculation is identical for the x -derivative of q in (21). The approximation step introduces u^* (and q^*) which give rise to the numerical fluxes which combine boundary information from the two elements in contact at the interface at x_1^k or x_{N+1}^k . While many choices of numerical fluxes exist, we opt to use a local DG flux [10] of the form:

$$\begin{aligned} u^*(x_1^k) &= u_1^k, \quad u^*(x_{N+1}^k) = u_{N+1}^{k+1}, \\ q^*(x_1^k) &= q_{N+1}^{k-1}, \quad q^*(x_{N+1}^k) = q_{N+1}^k. \end{aligned} \quad (23)$$

The motivation for these fluxes is to model an upwind scheme as was done for parabolic equations and obtain an optimal order of convergence (see p.247-253 in [10]).

We define the vectors $\ell^k(x) = (\ell_1^k(x), \dots, \ell_{N+1}^k(x))^T$ and similarly for $\mathbf{u}^k(s)$ and $\mathbf{q}^k(s)$. We also introduce the mass and stiffness matrices

$$\mathcal{M}_{ij}^k = \int_{x_1^k}^{x_{N+1}^k} \ell_i^k \ell_j^k dx, \quad \mathcal{S}_{ij}^k = \int_{x_1^k}^{x_{N+1}^k} \frac{d\ell_i^k}{dx} \ell_j^k dx. \quad (24)$$

Thus (21) and (22) yield:

$$\mathbf{q}^k = (\mathcal{M}^k)^{-1} \mathcal{S}^k \mathbf{u}^k - (\mathcal{M}^k)^{-1} [(u - u^*) \ell^k]_{x_1^k}^{x_{N+1}^k}, \quad (25a)$$

$$\begin{aligned} i \frac{d\mathbf{u}^k}{ds} &= a^k (\mathcal{M}^k)^{-1} \mathcal{S}^k \mathbf{q}^k - a^k (\mathcal{M}^k)^{-1} [(q - q^*) \ell^k]_{x_1^k}^{x_{N+1}^k} \\ &\quad + \mathcal{B}^k \mathbf{q}^k + \mathcal{C}^k \mathbf{u}^k + \mathbf{f}^k. \end{aligned} \quad (25b)$$

Here $\mathcal{B}^k = \text{diag}(b_1^k, \dots, b_{N+1}^k)$ and similarly for \mathcal{C}^k .

In the code we combine all K elements, thus we can arrange the solution as an $(N+1) \times K$ array with mass and stiffness matrices common to all elements. This approach enables the right-hand-side operations to be done using dense matrix-matrix multiplication. Boundary conditions are handled by adjustment of the fluxes (23). Dirichlet conditions such as for V are imposed by:

$$\begin{aligned} u^*(x_1^1) &= u(x_{in}), \quad u^*(x_{N+1}^K) = u(x_{out}), \\ q^*(x_1^1) &= q_1^1, \quad q^*(x_{N+1}^K) = q_{N+1}^K, \end{aligned} \quad (26)$$

and Neumann conditions such as for W are imposed on q^* instead of u^* . The (\mathbf{u}, \mathbf{q}) systems for V and W are evolved in s separately using a Runge-Kutta scheme. The restriction for Δs scales as in (14) with Δx as the minimal distance between two nodes on an element. We use Legendre-Gauss-Lobatto quadrature nodes (see p.43-51 in [10]) due to advantages in matrix conditioning; however, this choice of nodes imposes severe restrictions on Δs at high orders N . A balance of K and N is needed for optimal efficiency.

NUMERICAL RESULTS

In this section we examine several aspects for a line charge model (i.e. $\sigma_y \rightarrow 0$). First we compare results for V in the FD and DG schemes of the previous section, emphasizing both computational accuracy and efficiency. Next, we examine the convergence of the Fourier series sum over p of \hat{E}_{yp} . Lastly, we compute the longitudinal impedance from a relation for \hat{E}_{sp} using V and W .

Finite Difference versus Discontinuous Galerkin

For our numerical tests, we use the following parameters (as in [3, 6, 8]):

$$\begin{array}{ll|ll} x_{in} & = -0.030 \text{ m} & x_{out} & = 0.030 \text{ m} \\ h & = 0.020 \text{ m} & R & = 1.000 \text{ m} \\ q & = 10^{-12} \text{ C} & \beta & = 1 \\ k & = 8 \cdot 10^3 \text{ m}^{-1} & p & = 1 \end{array}$$

A common grid of points in x is used for the error comparisons of both FD and DG methods. A reference solution for V at $s = 0.200$ m is computed by the FD scheme with $N_{res} = 5760$. The FD scheme errors are tabulated below.

N_{res}	240	480	960	1920
L^∞ Error	1.46e-4	1.06e-5	1.31e-6	4.58e-7
L^2 Error	1.24e-4	9.08e-6	1.40e-6	4.61e-7
Time	0.4 s	2.4 s	6.9 s	15.0 s

Our FD method exhibits almost optimal self-convergence (convergence with respect to a higher resolution solution), but tapers off at higher resolutions. We attribute this to the jump discontinuities at $x = 0$ of the source terms in (10).

Next, the DG scheme with the same parameters is compared for varying order N and elements K . A reference solution for V is computed using $(N, K) = (12, 80)$ which is compared on the set of nodes for $(N, K) = (2, 20)$, common to all solutions.

$K \backslash N$	2	4	6	8
20	2.91e-2	9.01e-3	5.67e-4	1.97e-5
	3.69e-2	5.22e-3	2.67e-4	8.49e-6
	0.04 s	0.22 s	1.0 s	2.8 s
40	8.89e-3	1.92e-4	2.18e-6	3.36e-8
	9.08e-3	2.03e-4	2.13e-6	3.10e-8
	0.10 s	1.0 s	4.4 s	14 s
80	1.88e-3	1.22e-5	3.64e-8	1.82e-9
	1.26e-3	7.98e-6	2.23e-8	1.96e-9
	0.50 s	5.0 s	24 s	77 s

Above, we list the L^∞ (top), L^2 (middle), and CPU times (bottom) for varying values of K and N . In both the FD and DG methods, the order of self-convergence becomes sub-optimal once the resolution is high enough. Again, this loss of self-convergence is attributed to the discontinuous sources as in FD. Both FD and DG methods display comparable efficiency by comparing the CPU times in the tables for similar errors.

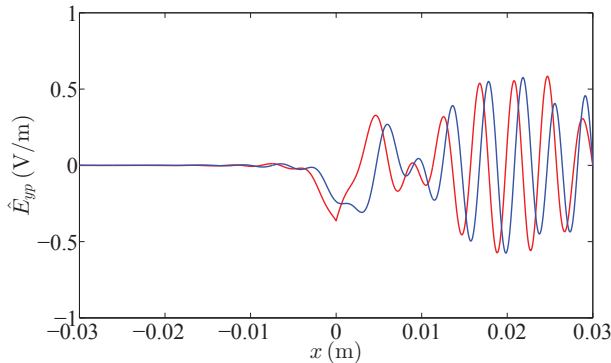


Figure 1: Real (red) and imaginary (blue) parts of DG reference solution for $\hat{E}_{y,p}$ using $N = 12$, $K = 80$, $p = 1$, $k = 8 \cdot 10^3 \text{ m}^{-1}$, at $s = 0.200$ m.

Fourier Series Convergence

To construct the solutions in y we use the Fourier series as defined in (2). We concentrate on \hat{E}_y defined as:

$$\hat{E}_y = \sum_{p=1}^{\infty} \hat{E}_{yp} \cos(\alpha_p(y + h/2)) \quad (27)$$

It is important to note that while each \hat{E}_{yp} is bounded, the infinite sum introduces a singularity at $(x, y) = (0, 0)$ for a line charge model. We wish to study the L^2 self-convergence of the partial sums in (27). Thus we subtract the singularity adopting the approach used in [4–8]. The singular term in \hat{E}_y , by the expression in [4], is:

$$\hat{E}_y^b = \frac{qZ_0 c \hat{\lambda}(k)}{2\pi} \frac{y}{x^2 + y^2}. \quad (28)$$

Defining $\hat{E}_y^r = \hat{E}_y - \hat{E}_y^b$, we obtain

$$\hat{E}_y^r = \sum_{p=1}^{\infty} [\hat{E}_{yp} - \hat{E}_{yp}^b] \cos(\alpha_p(y + h/2)), \quad (29)$$

with \hat{E}_{yp}^b as the Fourier series components of (28). Thus, we can examine the L^2 self-convergence of \hat{E}_y^r . We take the $p_{max} = 39$ partial sum ($p = 1, 3, \dots, p_{max}$) as a reference solution for (29) for $k = 8 \cdot 10^3 \text{ m}^{-1}$. This solution is compared to the partial sums for varying p_{max} .

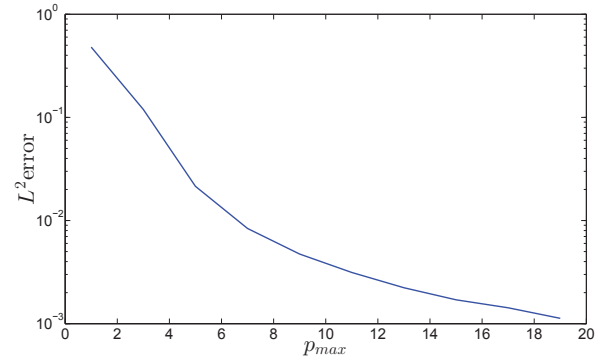


Figure 2: L^2 error \hat{E}_y^r for varying p_{max} , with 1441×481 (x, y) grid, $k = 8 \cdot 10^3 \text{ m}^{-1}$, and $s = 0.200$ m.

The self-convergence plot in Figure 2 shows only a few p -modes are necessary to obtain a solution accurate to 10^{-2} . The solutions were computed in ~ 100 seconds for $p_{max} = 19$ at this resolution. In contrast, in [3], this took ~ 1000 seconds for the same parameters using a 2D FD method. Thus, this 1D approach provides a large computational speed-up over the 2D FD method in [3] using the same computer hardware. The reference solution of \hat{E}_y^r as a surface plot is displayed in Figure 3.

CSR Impedance

In this section we compute the longitudinal impedance by examining the dependence of \hat{E}_s on kR . The \hat{E}_s field Fourier

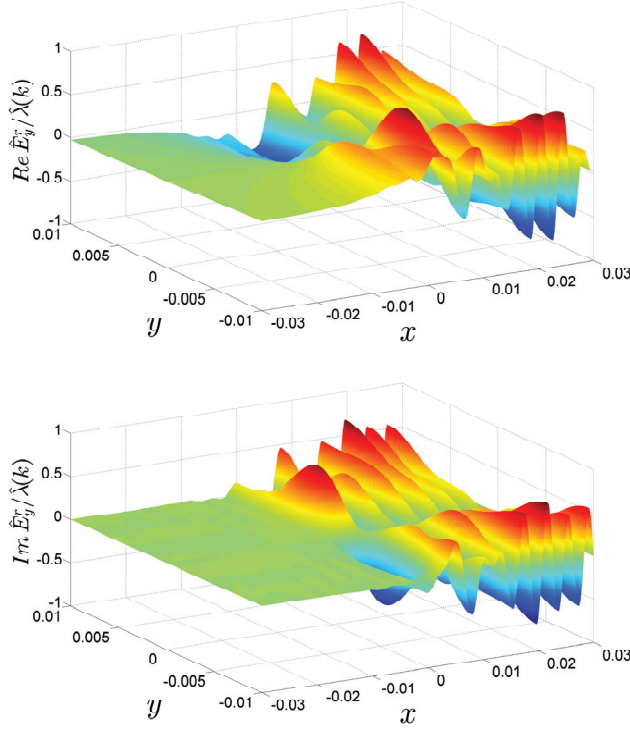


Figure 3: Reference solution for $Re(\hat{E}_y^r)/\hat{\lambda}(k)$ (top), $Im(\hat{E}_y^r)/\hat{\lambda}(k)$ (bottom) with $p_{max} = 39$, 1441×481 (x, y) grid, $k = 8 \cdot 10^3 \text{ m}^{-1}$, and $s = 0.200 \text{ m}$.

series components are given in terms of the p -dependent V and W by:

$$\hat{E}_{sp} = \frac{-1}{\gamma_p^2} \left[\frac{\alpha_p R}{x + R} \left(ik(V + \sigma x \Theta) + \frac{\partial V}{\partial s} \right) - ik Z_0 \frac{\partial W}{\partial x} \right]. \quad (30)$$

We mention here that the transforms in $s - ct$ and y also yield formulas for \hat{E}_{xp} , \hat{H}_{xp} , \hat{H}_{sp} which depend only on V and W and their s and x derivatives. The $\partial/\partial s$ terms in (30) are computed by the right-hand-sides of (10). Also of note, the imaginary part of the function \hat{E}_{sp} becomes very sharply peaked at $x = 0$ with increasing p and thus requires finer spatial resolution as the desired accuracy is increased. Numerical experiments suggest that the values of \hat{E}_s are inaccurate for $x \in [-\Delta x, 0, \Delta x]$ and that \hat{E}_s is smooth. Thus, we fit a spline to the points $x \in \{-3\Delta x, -2\Delta x, 2\Delta x, 3\Delta x\}$ and use this in the associated interval. For this numerical test we use the following parameters:

x_{in}	$= -0.032 \text{ m}$	x_{out}	$= 0.078 \text{ m}$
h	$= 0.032 \text{ m}$	R	$= 7.143 \text{ m}$
q	$= 10^{-12} \text{ C}$	β	$= 1$

We examine the value of \hat{E}_s at $(x, y) = (0, 0)$ at the end of the bend at $s = 2.00 \text{ m}$. This solution for \hat{E}_s is computed using $N_{res} = 480$ and $p_{max} = 9$ with the spline correction. The result is shown in Figure 4, where we see a smooth solution with no visual numerical artifacts.

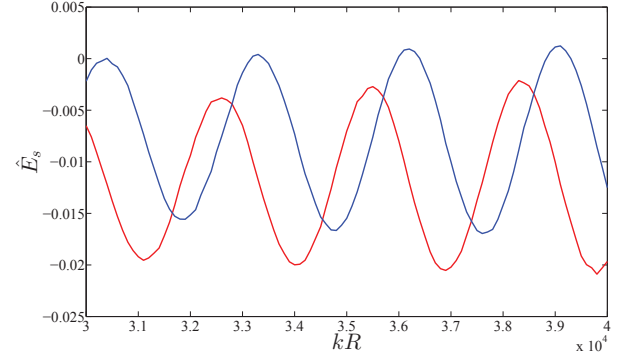


Figure 4: Above, $Re[\hat{E}_s]$ (red), $Im[\hat{E}_s]$ (blue) is plotted versus kR evaluated at $(x, y) = (0, 0)$ using $p_{max} = 9$ modes with $\hat{\lambda}(k)$ set to $1/(2\pi)$.

CONCLUSION

Summary

We have modeled CSR in a rectangular toroidal bend and achieved results similar to [3] in a fraction of the computation time. Our new method revolving around the Fourier series in y has greatly reduced the computational complexity of the system and resulted in reasonable approximations to the CSR fields using only a few p -modes.

The comparison between FD and DG methods enabled us to explore newer numerical techniques and make decisions on future codes based on the different methods. We have shown DG to be superior in the full 2D problem without the Fourier series in y [3].

Future Work

We aim to adjust our algorithms to allow for perturbations in the wall positions $x_{in}(s)$ and $x_{out}(s)$ to more accurately describe complex vacuum chambers. This adjustment must be made carefully as to not violate the paraxial approximation. We have currently developed an approach using a coordinate transformation to a constant-width chamber but need to examine computational limitations (particularly for complex chamber geometries with large excursions).

Another area of interest is in dropping the paraxial approximation to examine the fields in a chamber with arbitrary walls. Our ongoing analysis suggests the use of a time-domain (non-paraxial) approach to treat Maxwell's equations in that setting.

ACKNOWLEDGMENTS

We would like to thank the following people for their support on this project: Stephen Lau and Daniel Appelö for valuable insights on numerical algorithms, and Jack Bergstrom for valuable questions and discussions.

REFERENCES

- [1] G. Bassi, J. A. Ellison, K. Heinemann, R. Warnock, "Microbunching Instability in a Chicane: Two-Dimensional

- Mean Field Treatment”, Phys. Rev. ST Accel. Beams **12**, 080704 (2009).
- [2] K. Heinemann, D. Bizzozero, J. A. Ellison, S. R. Lau, G. Bassi, “Rapid integration over history in self-consistent 2D CSR modeling”, Proceedings of ICAP2012, Rostock-Warnemunde, Germany, August 2012. See jacow.org for the paper and slides at TUSDC2, i.e., <http://accelconf.web.cern.ch/AccelConf/ICAP2012/papers/tusdc2.pdf>
- [3] D. Bizzozero, J. A. Ellison, K. A. Heinemann, S. R. Lau, “Paraxial Approximation in CSR Modeling Using the Discontinuous Galerkin Method”, Proceedings of FEL13, New York, August 2013. See jacow.org for the paper at MOPSO06, i.e., <http://accelconf.web.cern.ch/AccelConf/FEL2013/papers/mopso06.pdf>
- [4] T. Agoh and K. Yokoya, “Calculation of coherent synchrotron radiation using mesh”, Phys. Rev. ST Accel. Beams **7**, 054403 (2004).
- [5] G.V. Stupakov and I.A. Kotelnikov, “Calculation of coherent synchrotron radiation impedance using the mode expansion method”, Phys. Rev. ST Accel. Beams **12**, 104401 (2009).
- [6] D. Zhou, K. Ohmi, K. Oide, L. Zang, and G. Stupakov, “Calculation of Coherent Synchrotron Radiation Impedance for a Beam Moving in a Curved Trajectory”, Jpn. J. Appl. Phys. **51**, 016401 (2012).
- [7] T. Agoh, *Dynamics of Coherent Synchrotron Radiation by Paraxial Approximation*, Ph.D. Dissertation, University of Tokyo, December (2004).
- [8] D. Zhou, *Coherent Synchrotron Radiation and Microwave Instability in Electron Storage Rings*, Ph.D. Dissertation, The Graduate University for Advanced Studies, September (2011).
- [9] J. Strikwerda, *Finite Difference Schemes and Partial Differential Equations* (Pacific Grove, CA: Wadsworth & Brooks/Cole Advanced Books & Software, 1989).
- [10] J. Hesthaven and T. Warburton, *Nodal Discontinuous Galerkin Methods* (New York: Springer, 2008).

TW X-RAY FREE ELECTRON LASER OPTIMIZATION BY TRANSVERSE PULSE SHAPING*

C. Emma, C. Pellegrini, UCLA, Los Angeles, CA 90095 USA
J. Wu, SLAC, Menlo Park, CA 94025, USA

Abstract

We study the dependence of the peak power of a 1.5 Å TW, tapered X-ray free-electron laser on the transverse electron density distribution. Multidimensional optimization schemes for TW hard X-Ray free electron lasers are applied to the cases of transversely uniform and parabolic electron beam distributions and compared to a Gaussian distribution. The optimizations are performed for a 200 m undulator using the fully 3-dimensional FEL particle code GENESIS. The study shows that the flatter transverse electron distributions enhance optical guiding in the tapered section of the undulator and increase the maximum radiation power from a maximum of 1.56 TW for a transversely Gaussian beam to 2.26 TW for the parabolic case and 2.63 TW for the uniform case.

INTRODUCTION

Radiation produced by Self Amplified Spontaneous Emission X-ray Free Electron Lasers (SASE X-FELs) [1] has been used to probe matter at the fastest timescales (fs) and the smallest dimensions (Å). LCLS and SACLA, the world's most powerful existing X-FELs deliver diffraction limited X-ray pulses of a few to a hundred femtoseconds in the energy range of 0.25 to 10 keV with peak power at saturation of 20-30 GW and a line-width on the order of 10^{-3} [2]. Pushing the capabilities of XFELs to TW peak power levels will have a great impact on future scientific endeavours, particularly in the fields of coherent X-ray diffraction imaging and nonlinear science. It is well known that the peak power of an FEL can be increased by tapering the undulator magnetic field to match the electron energy loss while preserving the synchronism condition [3]. The LCLS for example currently boosts its output power by a factor 2-3 using a limited taper capacity $\Delta K/K \sim 0.8\%$. For a SASE FEL this gain is limited due to the spiky nature of the radiation [4]. In a seeded or self-seeded FEL however, recent work has shown that a more flexible taper capacity can lead to much larger output powers, reaching levels of one TW or larger [5,6]. The analytic models developed in previous studies to obtain the optimal tapering profile have included three dimensional effects but only considered electron beams with Gaussian transverse density profile. In this work we examine the effect of using transversely parabolic and transversely uniform electron distributions in a tapered hard X-ray FEL with LCLS-II like parameters. The results are compared to the Gaussian beam case in both single frequency and time dependent simulations using the GENESIS code [7].

Table 1: GENESIS Simulation Parameters

Parameter Name	Parameter Value
Beam energy E_0	13.64 GeV
Beam peak current I_{pk}	4000 A
Normalized emittances $\epsilon_{x,n}/\epsilon_{y,n}$	0.3/0.3 $\mu\text{m rad}$
Peak radiation power input P_{in}	5 MW
Undulator period λ_w	32 mm
Normalised undulator parameter a_w	2.3832
Radiation wavelength λ_r	1.5 Å
FEL parameter ρ	7.361×10^{-4}

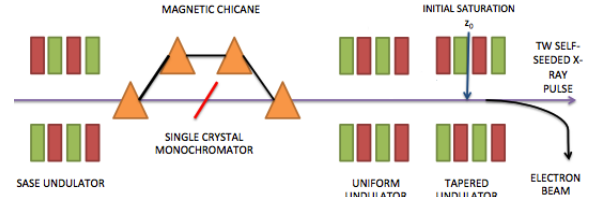


Figure 1: Schematic representation of a tapered X-ray FEL using a self-seeding monochromator and an optimised tapered section.

TAPERING OPTIMIZATION

Transverse Pulse Shaping in a Tapered FEL

In recent work [5] it has been pointed out that diffraction and refraction have an important impact on the peak power of TW X-FELs. Starting from conservation of energy and applying the same assumptions as in Ref. [5] we can write the radiation power as a function of the longitudinal position in the undulator:

$$P(z) = \frac{\pi r_s(z)^2 a_{s0}(z)^2}{4Z_0} \left(\frac{k_s m_e c^2}{e} \right)^2, \quad (1)$$

where $a_{s0}(z) = |e|A_s(z)/\sqrt{2}mc^2$ is the on-axis normalized vector potential of the radiation field for a linearly polarised undulator, $r_s(z)$ is the radiation beam size, k_s is the radiation wavenumber and Z_0 is the free space impedance. We must now optimize the growth of the radiation field inside the undulator in order to maximize the output radiation power. As described first in Ref. [3], this can be achieved by an adiabatic decrease in the resonant energy $\gamma_r(z)mc^2$, which is defined by the now z dependent resonance condition:

$$\gamma_r^2(z) = \frac{k_w}{2k_s} (1 + a_w(z)^2), \quad (2)$$

where $k_w = 2\pi/\lambda_w$ is the undulator wavenumber and $a_w(z) = |e|B_w(z)/\sqrt{2}k_w mc^2$ is the normalized vector po-

* Work supported by: DOE Grant Number DE-SC0009983

tential of the undulator field. The optimal taper profile can then be obtained by choosing a functional form for $a_w(z)$:

$$a_w(z) = a_w(z_0) \times [1 - c \times (z - z_0)^d], \quad (3)$$

where z_0 is the initial tapering location, and c and d are constants to be obtained through simulations that maximize the output radiation power. The quadrupole focusing gradient $K_q(z)$ is also similarly optimized (see Fig. 2). The importance of the transverse electron distribution becomes apparent when examining the FEL process post-saturation. After the exponential gain regime the FEL is dominated by refractive guiding of the radiation by the electron beam. For a bunched electron beam it has been shown that the guiding is described quantitatively by a refractive index proportional to the beam microbunching [8] $n \sim \langle e^{-i\Psi} \rangle$ where the average is over the beam electrons trapped in the ponderomotive potential and Ψ is the ponderomotive phase. It is thus important to maintain a sufficiently large microbunching throughout the tapered undulator as this increases the refractive index and boosts the coherent interaction between the electrons and the radiation [9].

In order to calculate the microbunching we follow Ref. [5] and first determine the fraction of trapped electrons trapped in the FEL bucket along the undulator:

$$F_t(z) = \frac{1}{N_e} \int_0^{r_{max}} F_t(r, z) f_0(r) 2\pi r dr, \quad (4)$$

where $f_0(r)$ is the transverse beam distribution and $F_t(r, z)$ is the *local* trapping fraction which is determined by the radially dependent maximum and minimum phases $\Psi(r, z)$ for which particles follow stable trajectories in phase space [3]. We make the resonant phase approximation, in which we assume the trapped electrons are uniformly distributed in the ponderomotive phase at each radial location r and their contribution to the microbunching is $\exp[-i\Psi_r(r, z)]$ and $\Psi_r(r, z)$ is the radially dependent resonant phase. Now the microbunching can be calculated simply by averaging the product $F_t(r, z) \exp[-i\Psi_r(r, z)]$ over the radial coordinate r . Examining Eq. 4 shows that by manipulating the transverse electron beam distribution it is possible to maximize the trapping fraction and consequently the microbunching throughout the tapered undulator. For the case of a transversely Gaussian electron distribution considered thus far, the electrons in the radial tail of the beam experience a smaller ponderomotive potential and thus can become detrapped from the FEL bucket. If however the electron distribution is flatter, as in the parabolic or uniform cases, it is possible to trap more electrons in the bucket, increasing the bunching factor throughout the undulator and thereby extracting more power. The following section examines these predictions using GENESIS simulations.

Simulation Results

The simulations are performed for a 200 m undulator with 3.4 m undulator sections, 1 m breaks and parameters similar

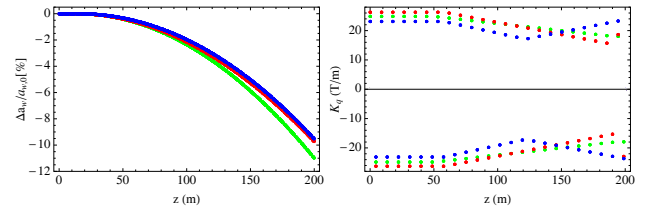


Figure 2: Optimal taper field and quadrupole focusing profile for the Gaussian (green), parabolic (red) and uniform (blue) transverse electron distributions obtained from multi-dimensional optimization using GENESIS single frequency simulations.

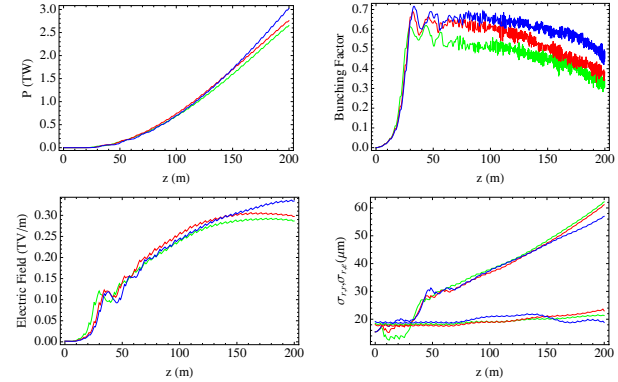


Figure 3: Comparison of time independent results for Gaussian (green), parabolic (red) and uniform (blue) transverse beam distributions at $\lambda_r = 1.5 \text{ \AA}$. X-ray pulse power, upper left and electric field, lower left, electron microbunching upper right, electron and radiation beam radii lower right.

to LCLS-II (see Table 1). After performing the multidimensional optimization, the taper profiles obtained for the three different transverse distributions are shown in Fig. 2. The corresponding evolution of the radiation field, power, electron beam microbunching and radiation size is illustrated in Fig. 3.

The main result is an increase in the bunching factor for the parabolic and uniform distributions as compared to the Gaussian. This is indicative of a larger trapping fraction and consequently a greater output power. Such a discrepancy is however only marginally observed in single frequency simulations with the Gaussian beam achieving $P_{max} = 2.65 \text{ TW}$ compared to $P_{max} = 2.76 \text{ TW}$ for the parabolic case and $P_{max} = 3.03 \text{ TW}$ for the uniform case. Using the same optimal undulator parameters found via time independent simulations, we performed time dependent simulations of the three different transverse distributions for 6.4 fs bunch lengths. Analyzing the results shown in Fig. 4 we notice that the uniform and parabolic distributions exhibit a steady growth in output power, and a slow decrease in the bunching factor throughout the tapered undulator. On the other hand the transversely Gaussian beam suffers a significant reduction in the bunching and power as well as an increased diffraction of the radiation. Furthermore, in the time dependent case the transversely Gaussian beam shows an early saturation of

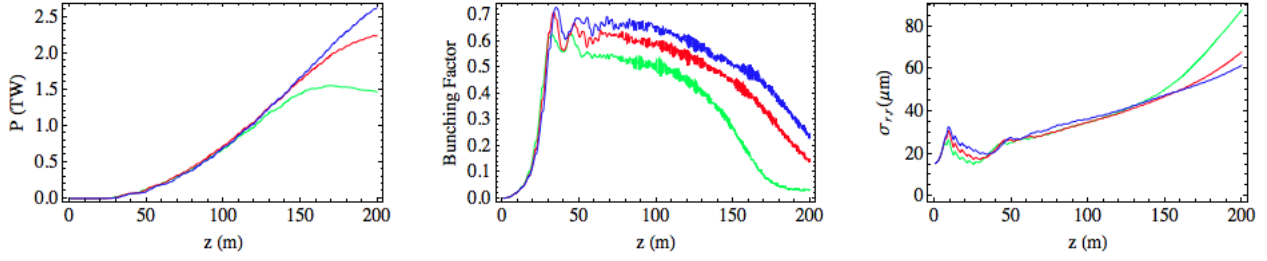


Figure 4: Power, bunching factor and radiation size as a function of longitudinal distance for transversely Gaussian (green), parabolic (red) and uniform (blue) beams. The results are shown for a wavelength $\lambda_r = 1.5 \text{ \AA}$ and bunch length of 16 fs. The optimized taper profiles are found in time independent simulations.

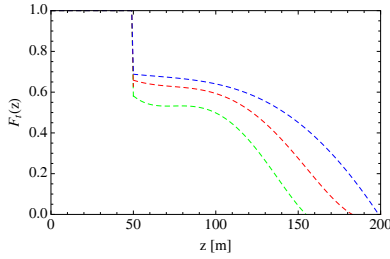


Figure 5: Evolution of the trapping function $F_t(z)$ for the Gaussian (green), parabolic (red) and uniform (blue) transverse electron distributions obtained from GENESIS single frequency (solid) and time dependent (dashed) simulations.

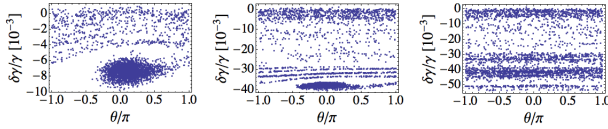


Figure 6: Longitudinal phase space evolution for a 6.4 fs bunch with Gaussian transverse electron distribution obtained from GENESIS time dependent simulations. The data is shown from left to right at $z = 50, 120, 180$ meters.

the power, a result previously reported in Ref. [5]. For the three different distributions the trapping fraction is displayed in Fig. 5 and the corresponding longitudinal phase space evolution for the Gaussian beam is shown in Fig. 6. The data shows significant detraping for the Gaussian case after $z = 120$ m which is consistent with the growth in the radiation size due to reduction in guiding observed in Fig. 4. The parabolic and uniform distributions maintain an improved trapping and guiding and this sustains the growth in output power allowing them both to reach over 2 TW of power at $z = 200$ m. Using the optimized taper profiles for each electron distribution the extraction efficiency reaches values between $\eta = 2.75\%$ and $\eta = 4.83\%$, an order of magnitude improvement compared to state of the art X-FELs such as the LCLS.

CONCLUSION

We evaluated the effect of changing the transverse electron distribution in an optimized tapered free electron laser. The

performances of FELs with transverse Gaussian, parabolic or uniform beam distributions are compared. The tapering profile as well as the quadrupole focusing is optimized to yield the maximum output power following the method described in Ref. [5]. Optimizations were performed for a 200-m long undulator with break sections using the three dimensional particle code GENESIS. Time independent results show that the effect of changing the transverse beam distribution is mostly marginal, yielding similar growth in the radiation power for the transversely Gaussian, parabolic and uniform distributions. This is not the case when multi-frequency effects are taken into account in time dependent simulations, where the transverse distribution has an important impact on the FEL process affecting the trapping fraction and consequently the maximum output power. For a resonant wavelength of $\lambda_r = 1.5 \text{ \AA}$ and a bunch length of 6.4 fs the maximal power increased from $P_{max} = 1.56$ TW for the Gaussian beam, to $P_{max} = 2.26$ TW for a parabolic beam and $P_{max} = 2.63$ TW for a uniform beam. An argument based on the reduction in the trapping fraction has been considered to explain this discrepancy in maximal power output. For all three transverse distributions, using the optimized taper profiles, the extraction efficiency is between $\eta = 2.8 - 4.8\%$, a factor of 20-40 improvement on current state of the art X-FEL facilities.

The study shows that transverse pulse shaping is an effective way to improve the performance and increase the output power of a tapered X-ray free electron laser. In light of the promising results found in this study we propose to investigate methods to transversely shape the electron beam distributions, like shaping the laser pulse on the FEL injector photocathode, using suitable masks inside the beamline or introducing nonlinear elements in the electron beam transport line.

REFERENCES

- [1] R. Bonifacio, C. Pellegrini, L. Narducci, Optics Communications, vol. 50, no. 6, p. 373, 1984
- [2] C. Pellegrini, N. A. Part Accel. Conf. Proceedings, California, 2013
- [3] N.M. Kroll, P.L. Morton, M. Rosenbluth, IEEE Journal of Quantum Electronics, vol. 17, p. 1436, 1981

- [4] W.M. Fawley, Z. Huang, K.-J. Kim, N.A. Vinokurov, Nucl. Instrum. Meth., vol. 483, p. 537, 2002
- [5] Y. Jiao, et. al., Phys. Rev. ST. AB., vol. 15, p. 050704, 2012
- [6] W. Fawley, et. al., FEL 2011 Conference Proceedings, p. 050704, 2011
- [7] S. Reiche, Nucl. Instrum. Meth., vol. 429, p. 243, 1999
- [8] E.T. Scharlemann, A.M. Sessler, J.S. Wurtele, Phys. Rev. Lett., vol. 54, p. 1925, 1985
- [9] D. Prosnitz, A. Szoke, V.K. Neil, Phys. Rev. A, vol. 24, p. 1436, 1981

TRANSVERSE COHERENCE PROPERTIES OF A TGU-BASED FEL

Panagiotis Baxevanis, Zhirong Huang, Ronald Ruth, SLAC National Accelerator Laboratory,
Menlo Park, CA 94025, USA

Carl B. Schroeder, Lawrence Berkeley National Laboratory, Berkeley, CA 94720, USA

Abstract

The use of a transverse gradient undulator (TGU) is considered an attractive option for FELs driven by electron beams with a relatively large energy spread. In this scheme, a dispersion is introduced in the beam while the undulator poles are inclined so that the undulator field acquires a linear dependence upon the transverse position in the direction of dispersion. By suitably selecting the dispersion and the field gradient, the energy spread effect can be significantly mitigated, thus avoiding a drastic reduction in the FEL gain. However, adding the dispersion typically leads to electron beams with large aspect ratios. As a result, the presence of higher-order modes in the output FEL radiation can become significant. To investigate this effect, we study the properties of the higher-order eigenmodes of a TGU-based, high-gain FEL, using both a simplified, analytically-solvable model and a variational technique. This formalism is then used to provide an estimate of the degree of transverse coherence for a representative soft X-ray, TGU FEL example.

INTRODUCTION

One of the most crucial parameters which affect the performance of a free electron laser (FEL) is the energy spread in the driving electron beam. A large value of the latter gives rise to a wide spread in the resonant wavelength, resulting in a substantially decreased FEL gain. Using a transverse gradient undulator (TGU) [1]- [2], it is possible to mitigate this problem. By dispersing the electron beam and tilting the undulator poles, both the electron energy and the undulator parameter acquire a linear transverse dependence. A suitable selection of the dispersion and the field gradient minimizes the impact of the energy spread upon the FEL resonance condition, leading to improved performance. This scheme has been shown to be attractive for FEL concepts that utilize the beam from laser-plasma accelerators (LPAs) [3]. However, a drawback of the TGU approach is the increased size of the electron beam in the direction of dispersion (typically the horizontal direction), which can cause the growth of multiple FEL modes in the exponential-gain regime, degrading the transverse coherence of the output radiation. In order to provide a theoretical framework for understanding this effect, we study the properties of the higher-order FEL modes for a TGU-based configuration. Our analysis is based on solving the FEL eigenmode equation for the parallel beam case (negligible emittance and focusing effects) by employing an exactly-solvable, approximate model and a variational approach. When applied to a specific LPA-based example, this formalism yields results

which agree with simulation and provide us with insight into the factors which affect transverse coherence in a TGU FEL.

THEORY

As mentioned earlier, our study is based on an analysis of the FEL eigenmodes, i.e. the solutions of the form $A(\mathbf{x})e^{i\mu z}$ for the complex amplitude of the electric field of the radiation - where $\mathbf{x} = (x, y)$ is the transverse position vector and z is the longitudinal coordinate along the undulator. Each eigenmode is thus characterized by a z -invariant transverse profile $A(\mathbf{x})$ and a constant, complex growth rate μ . According to our previous treatment of a TGU-based FEL [4], the equation that is satisfied by the profile and the growth rate of a growing mode (i.e. one with $\text{Im}(\mu) < 0$) in the parallel beam regime is

$$\left(\mu - \frac{\nabla_{\perp}^2}{2k_r}\right) A(\mathbf{x}) = U(\mathbf{x}, \mu) A(\mathbf{x}), \quad (1)$$

where

$$\begin{aligned} U(\mathbf{x}, \mu) = & -8\rho_T^3 k_u^3 \exp\left(-\frac{x^2}{2\sigma_T^2} - \frac{y^2}{2\sigma_y^2}\right) \\ & \times \int_{-\infty}^0 d\xi \xi e^{i(\mu - \Delta\nu k_u)\xi} e^{-2(\sigma_{\delta}^{ef})^2 k_u^2 \xi^2} \\ & \times \exp\left(-2ik_u C_p \frac{x}{\eta} \xi\right). \end{aligned} \quad (2)$$

Here, $\nabla_{\perp}^2 = \partial^2/\partial\mathbf{x}^2$, $k_r = 2\pi/\lambda_r$ and $k_u = 2\pi/\lambda_u$ - where λ_r is the resonant wavelength and λ_u is the undulator period - $\Delta\nu$ is a dimensionless detuning variable while σ_T and σ_y are the rms electron beam sizes in the x and y directions. The former of the last two parameters includes the contribution of the - constant - dispersion η and is given by $\sigma_T = (\sigma_x^2 + \eta^2\sigma_{\delta}^2)^{1/2}$, where σ_x is the non-dispersive horizontal beam size and σ_{δ} is the rms energy spread. Moreover, ρ_T and σ_{δ}^{ef} are, respectively, the effective Pierce parameter and energy spread of the FEL, quantities that are expressed by $\rho_T = \rho(1 + \eta^2\sigma_{\delta}^2/\sigma_x^2)^{-1/6}$ and $\sigma_{\delta}^{ef} = \sigma_{\delta}(1 + \eta^2\sigma_{\delta}^2/\sigma_x^2)^{-1/2}$, where ρ is the Pierce parameter for $\eta = 0$. This non-dispersive FEL parameter is in turn given by $\rho = (K_0^2[JJ]^2 I_p / (16I_A \gamma_0^3 \sigma_x \sigma_y k_u^2))^{1/3}$, where γ_0 is the average electron energy in units of its rest mass $m_0 c^2$, K_0 is the on-axis undulator parameter, $[JJ] = J_0(K_0^2/(4 + 2K_0^2)) - J_1(K_0^2/(4 + 2K_0^2))$, $I_A \approx 17$ kA is the Alfvén current and I_p is the peak current of the electron beam. On the other hand, $C_p = \sigma_x^2/\sigma_T^2 + \bar{\alpha}\eta - 1$ with $\bar{\alpha} = K_0^2\alpha/(2 + K_0^2)$, α being the transverse gradient of the

undulator field. The expression for C_p given above is a generalization of the one contained in [4], which only covered the case with $\bar{\alpha} = 1/\eta$. The latter describes the TGU resonance condition. To proceed, we introduce the scaled quantities $\hat{x} = x/\sigma_T$, $\hat{y} = y/\sigma_y$, $\hat{\mu} = \mu/(2\rho_T k_u)$, $\hat{\xi} = 2\rho_T k_u \xi$, $\hat{\nu} = \Delta\nu/(2\rho_T)$ and $\hat{\sigma}_\delta^{ef} = \sigma_\delta^{ef}/\rho_T$, in which case the eigenmode equation is cast into a fully dimensionless form:

$$\left(\hat{\mu} - p_{dx} \frac{\partial^2}{\partial \hat{x}^2} - p_{dy} \frac{\partial^2}{\partial \hat{y}^2}\right) A(\hat{\mathbf{x}}) = \hat{U}(\hat{\mathbf{x}}, \hat{\mu}) A(\hat{\mathbf{x}}), \quad (3)$$

where $\hat{\mathbf{x}} = (\hat{x}, \hat{y})$, $p_{dx} = (4\rho_T k_u k_r \sigma_T^2)^{-1}$ and $p_{dy} = (4\rho_T k_u k_r \sigma_y^2)^{-1}$ are the diffraction parameters,

$$\begin{aligned} \hat{U}(\hat{\mathbf{x}}, \hat{\mu}) = & -\exp\left(-\frac{\hat{x}^2}{2} - \frac{\hat{y}^2}{2}\right) \\ & \times \int_{-\infty}^0 d\hat{\xi} \hat{\xi} e^{i(\hat{\mu}-\hat{\nu})\hat{\xi}} e^{-(\hat{\sigma}_\delta^{ef})^2 \hat{\xi}^2/2} e^{-2i\hat{p}_0 \hat{\xi} \hat{x}} \end{aligned} \quad (4)$$

and $\hat{p}_0 = \sigma_T(C_p/\eta)/(2\rho_T)$.

Exactly Solvable Model

For $p_{dx}, p_{dy} \ll 1$, the radiation size in both the x and y directions is smaller than the corresponding size of the electron beam. In this case, we can expand the Gaussian term in the RHS of Eq. (4) according to $\exp(-\hat{x}^2/2 - \hat{y}^2/2) \approx 1 - \hat{x}^2/2 - \hat{y}^2/2$. Moreover, when $|\hat{p}_0| \ll 1$, the $\hat{\xi}$ -integral in the definition of \hat{U} can be approximated by $\hat{I}_0 - 2i\hat{p}_0 \hat{I}_1 \hat{x} - 2\hat{p}_0^2 \hat{I}_2 \hat{x}^2$, where $\hat{I}_n = \int_{-\infty}^0 d\hat{\xi} \hat{\xi}^{n+1} e^\Psi$ and $\Psi = i(\hat{\mu} - \hat{\nu})\hat{\xi} - (\hat{\sigma}_\delta^{ef})^2 \hat{\xi}^2/2$. Thus, by expanding \hat{U} up to second order in \hat{x} and \hat{y} , the mode equation is written in a simplified form as

$$\begin{aligned} & \left(\hat{\mu} - p_{dx} \frac{\partial^2}{\partial \hat{x}^2} - p_{dy} \frac{\partial^2}{\partial \hat{y}^2}\right) A(\hat{\mathbf{x}}) = \\ & (F_0 + F_1 \hat{x} + F_2 \hat{x}^2 + G_2 \hat{y}^2) A(\hat{\mathbf{x}}), \end{aligned} \quad (5)$$

where $F_0 = -\hat{I}_0$, $F_1 = 2i\hat{p}_0 \hat{I}_1$, $F_2 = \hat{I}_0/2 + 2\hat{p}_0^2 \hat{I}_2$ and $G_2 = \hat{I}_0/2$. It can be shown that the above equation admits exact analytical solutions [5], which are given by

$$\begin{aligned} A_{mn}(\hat{\mathbf{x}}) = & H_m(\sqrt{2\hat{a}_x}(\hat{x} - \hat{b}/(2\hat{a}_x))) e^{-\hat{a}_x \hat{x}^2 + \hat{b} \hat{x}} \\ & \times H_n(\sqrt{2\hat{a}_y} \hat{y}) e^{-\hat{a}_y \hat{y}^2}, \end{aligned} \quad (6)$$

where H_k are the Hermite polynomials and $m, n = 0, 1, 2, \dots$. The growth rate $\hat{\mu}$ and the mode parameters $\hat{a}_x, \hat{a}_y, \hat{b}$ satisfy the relations

$$\hat{\mu} + p_{dx}[(4m+2)\hat{a}_x - \hat{b}^2] + (4n+2)p_{dy}\hat{a}_y = -\hat{I}_0 \quad (7)$$

$$\hat{a}_x^2 = -\frac{\hat{I}_0 + 4\hat{p}_0^2 \hat{I}_2}{8p_{dx}}, \quad \hat{a}_x \hat{b} = \frac{i\hat{p}_0}{2p_{dx}} \hat{I}_1, \quad \hat{a}_y^2 = -\frac{\hat{I}_0}{8p_{dy}}. \quad (8)$$

In general, the modes described by Eqs. (6)-(8) are characterized by an asymmetric intensity profile (given by $|A(\hat{\mathbf{x}})|^2$), which is not invariant under the reflection $x \rightarrow -x$, though it is still invariant under $y \rightarrow -y$. The main advantage of this model is that it provides a simple way to estimate the mode properties even for high mode order.

ISBN 978-3-95450-133-5

Variational Calculation

Approximations for the growth rate and the profile of an FEL mode can also be obtained through a well-established variational technique [6]. In this case, we begin by constructing a so-called variational functional, expressed by

$$\begin{aligned} & \int d^2 \hat{\mathbf{x}} A(\hat{\mathbf{x}}) \left(\hat{\mu} - p_{dx} \frac{\partial^2}{\partial \hat{x}^2} - p_{dy} \frac{\partial^2}{\partial \hat{y}^2} \right) A(\hat{\mathbf{x}}) \\ & = \int d^2 \hat{\mathbf{x}} A^2(\hat{\mathbf{x}}) \hat{U}(\hat{\mathbf{x}}, \hat{\mu}). \end{aligned} \quad (9)$$

Given a trial function for the mode profile $A(\hat{\mathbf{x}})$, this functional yields an accurate estimate for the growth rate $\hat{\mu}$. Here, we seek to derive variational solutions for the first few eigenmodes. In order to make a judicious choice of the trial function for a specific mode, we each time try a form which has the same functional dependence on \hat{x} and \hat{y} as the exact solution given by Eq. (6). For example, we select a trial function of the form $A(\hat{\mathbf{x}}) = e^{-\hat{a}_x \hat{x}^2 + \hat{b} \hat{x}} e^{-\hat{a}_y \hat{y}^2}$ for the fundamental (00, i.e. $m = 0, n = 0$) mode while our choice for the 01 mode is $A(\hat{\mathbf{x}}) = \hat{y} e^{-\hat{a}_x \hat{x}^2 + \hat{b} \hat{x}} e^{-\hat{a}_y \hat{y}^2}$. Substituting these into Eq. (9), we obtain the result

$$\begin{aligned} & F(\hat{a}_x, \hat{a}_y, \hat{b}, \hat{\mu}) = \hat{\mu} + p_{dx} \hat{a}_x + \chi p_{dy} \hat{a}_y + (\hat{a}_x + 1/4)^{-1/2} \\ & \times \hat{a}_x^{1/2} \hat{a}_y^{1/2} (\hat{a}_y + 1/4)^{-\chi/2} \int_{-\infty}^0 d\hat{\xi} \hat{\xi} e^{i(\hat{\mu}-\hat{\nu})\hat{\xi}} e^{-(\hat{\sigma}_\delta^{ef})^2 \hat{\xi}^2/2} \\ & \times \exp\left(\frac{(\hat{b} - i\hat{p}_0 \hat{\xi})^2}{2\hat{a}_x + 1/2} - \frac{\hat{b}^2}{2\hat{a}_x}\right) = 0, \end{aligned} \quad (10)$$

where $\chi = 2n + 1$, n being the second index of the 00/01 mode. Using the stationary condition $\partial \hat{\mu} / \partial \hat{a}_x = \partial \hat{\mu} / \partial \hat{a}_y = \partial \hat{\mu} / \partial \hat{b} = 0$, we also obtain the additional relations $\partial F(\hat{a}_x, \hat{a}_y, \hat{b}, \hat{\mu}) / \partial \hat{a}_x = 0$, $\partial F(\hat{a}_x, \hat{a}_y, \hat{b}, \hat{\mu}) / \partial \hat{a}_y = 0$ and $\partial F(\hat{a}_x, \hat{a}_y, \hat{b}, \hat{\mu}) / \partial \hat{b} = 0$. These three derivative relations have to be solved simultaneously along with Eq. (10) in order to determine the properties of the 00/01 mode. As far as the 10 mode is concerned, we now use a trial function of the form $A(\hat{\mathbf{x}}) = (\hat{x} + \hat{\lambda}) e^{-\hat{a}_x \hat{x}^2 + \hat{b} \hat{x}} e^{-\hat{a}_y \hat{y}^2}$ while, for the 11 mode, we choose $A(\hat{\mathbf{x}}) = (\hat{x} + \hat{\lambda}) \hat{y} e^{-\hat{a}_x \hat{x}^2 + \hat{b} \hat{x}} e^{-\hat{a}_y \hat{y}^2}$. These manipulations yield the relation

$$\begin{aligned} & F(\hat{a}_x, \hat{a}_y, \hat{b}, \hat{\lambda}, \hat{\mu}) = (\hat{\mu} + \chi p_{dy} \hat{a}_y) \left[(\hat{\lambda} + \frac{\hat{b}}{2\hat{a}_x})^2 + \frac{1}{4\hat{a}_x} \right] \\ & + p_{dx} \hat{a}_x \left[(\hat{\lambda} + \frac{\hat{b}}{2\hat{a}_x})^2 + \frac{3}{4\hat{a}_x} \right] + \hat{a}_x^{1/2} (\hat{a}_x + 1/4)^{-1/2} \\ & \times \hat{a}_y^{1/2} (\hat{a}_y + 1/4)^{-\chi/2} \int_{-\infty}^0 d\hat{\xi} \hat{\xi} e^{i(\hat{\mu}-\hat{\nu})\hat{\xi}} e^{-(\hat{\sigma}_\delta^{ef})^2 \hat{\xi}^2/2} \\ & \times \left[(\hat{\lambda} + \frac{\hat{b} - i\hat{p}_0 \hat{\xi}}{2\hat{a}_x + 1/2})^2 + \frac{1}{4\hat{a}_x + 1} \right] \\ & \times \exp\left(\frac{(\hat{b} - i\hat{p}_0 \hat{\xi})^2}{2\hat{a}_x + 1/2} - \frac{\hat{b}^2}{2\hat{a}_x}\right) = 0, \end{aligned} \quad (11)$$

where χ is defined as before. In this last two cases, the variational solution is completed by the relations $\partial F / \partial \hat{a}_x = \partial F / \partial \hat{a}_y = \partial F / \partial \hat{b} = \partial F / \partial \hat{\lambda} = 0$.

Table 1: Undulator and Electron Beam Parameters

Parameter	LPA
Undulator parameter K_0	2
Undulator period λ_u	1 cm
Beam energy $\gamma_0 m_0 c^2$	1 GeV
Resonant wavelength λ_r	3.9 nm
Peak current I_p	10 kA
Energy spread σ_δ	10^{-2}
Normalized emittance $\gamma_0 \epsilon_x$	0.1 μm
Normalized emittance $\gamma_0 \epsilon_y$	0.1 μm
Horizontal size σ_x	11.3 μm
Vertical size σ_y	11.3 μm
FEL parameter ρ	6×10^{-3}

NUMERICAL RESULTS

The formalism presented in the previous section can provide an estimate of the mode content in the output radiation from a TGU-based FEL. An interesting example of such a concept refers to a machine which would utilize a 1 GeV/10 kA LPA beam with the aim of producing radiation within the so-called water window wavelength region [3]. The full set of parameters is listed in Table 1. This set was also used in [4] in order to demonstrate the optimization of the dispersion η using a variational calculation for the fundamental FEL mode. The main results are summarized in the graph of the frequency-optimized gain length vs the dispersion (Fig. 1). In terms of our present scaling, the power gain length L_g is given by $L_g = -\sqrt{3}L_T/(2\text{Im}(\hat{\mu}))$, where $L_T = \lambda_u/(4\pi\sqrt{3}\rho_T)$. This optimization scenario involves varying the dispersion while keeping the other parameters fixed (except - of course - the TGU gradient, which satisfies the condition $\bar{\alpha} = 1/\eta$) and maximizing the power growth rate with respect to the detuning for each dispersion value.

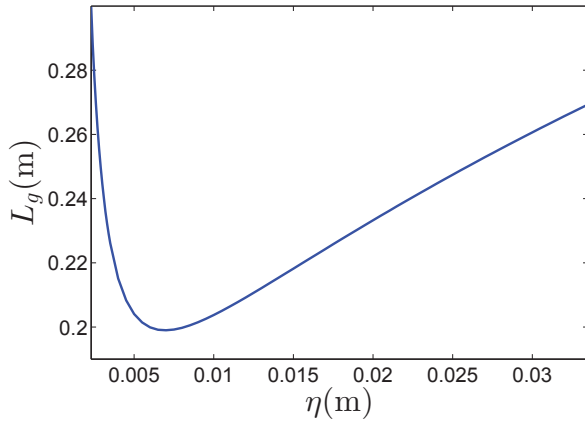


Figure 1: Frequency-optimized gain length of the fundamental mode as a function of the dispersion for the LPA parameters. The data shown were obtained using the variational solution.

The optimum gain length is about 20 cm, for a 7 mm dispersion.

From a practical point of view, it may be desirable to select a dispersion value appreciably larger than the optimum. By thus moving away from the steep part of the optimization curve, the sensitivity of the gain length with respect to unexpected variations of η is reduced at a modest cost in terms of FEL gain. However, operating at or to the right side of the optimum typically creates an electron beam with a large ratio of horizontal to vertical size. As has been shown in simulation studies [3], such a configuration can allow the growth of multiple FEL modes in the high gain regime, reducing the transverse coherence of the output radiation. To study this effect, we first select a dispersion $\eta = 1$ cm (quite close to the optimum) and employ the variational solution in order to ascertain what the ordering of the various FEL modes is with respect to the power growth rate. For this dispersion value, $p_{dx} = 0.008$, $p_{dy} = 0.63$, $\hat{\rho}_0 = 0.02$ and the e-beam aspect ratio σ_T/σ_y is about 9. The main results are presented in Fig. 2, which shows the negative imaginary part of the scaled growth rate as a function of the detuning for the 00, 10, 01 and 11 modes. For each mode, the power growth rate attains a maximum for some negative detuning value. The corresponding frequency-optimized gain lengths are, respectively, $L_g^{00} = 20.4$ cm, $L_g^{10} = 21.2$ cm, $L_g^{01} = 30.5$ cm and $L_g^{11} = 32.3$ cm. The other important observation is that modes with the same n -index (and, thus, similar vertical profile) form groups with closely spaced growth rates. As expected, most favored are the modes with $n = 0$, which are characterized by Gaussian-like profiles and maximum overlap with the electron beam.

To check whether this pattern holds when more higher-order modes are included, we use the truncated, parabolic-like model to obtain equivalent detuning curves for the modes already considered plus some additional ones

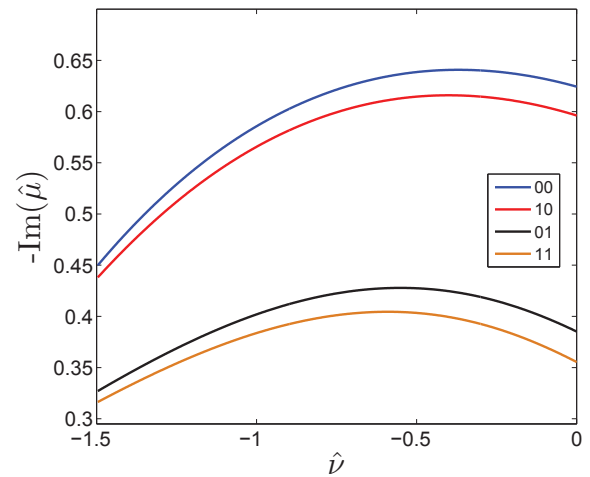


Figure 2: Negative imaginary part of the scaled growth rate $\hat{\mu}$ as a function of the scaled detuning $\hat{\nu}$ for various FEL modes (variational data for the $\eta = 1$ cm case).

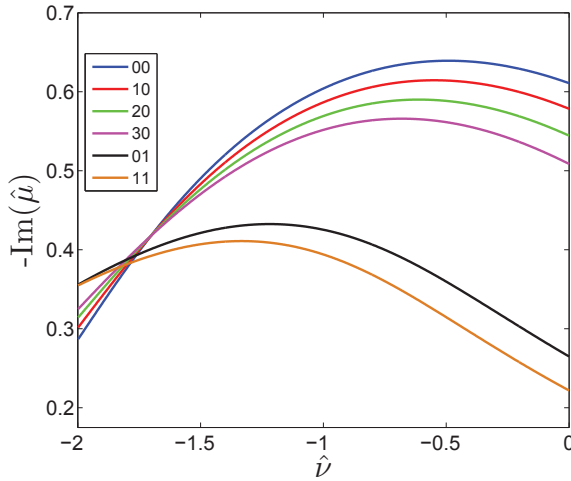


Figure 3: Negative imaginary part of the scaled growth rate $\hat{\mu}$ as a function of the scaled detuning $\hat{\nu}$ for several FEL modes (data from the analytical solution, for the $\eta = 1$ cm case).

(namely the 20 and 30 modes, see Fig. 3). We note that the data from the analytical solution are not identical to the variational results, as the detuning curves in the former case are shifted towards the left (i.e. the region of negative $\hat{\nu}$). This is due to the fact that, even though p_{dx} and \hat{p}_0 are much smaller than unity, p_{dy} is not quite so, with the result that the present parameters probably lie at the limit of the exact model's applicability. However, we can still verify that the mode spectrum has the same structure as in the variational case. Moreover, even though the detuning curves differ for the two approaches, both the variational and the exact solution actually give very similar estimates for the optimized gain lengths. For comparison, we now obtain $L_g^{00} = 20.4$ cm, $L_g^{10} = 21.2$ cm, $L_g^{20} = 22.1$ cm, $L_g^{30} = 23.1$ cm, $L_g^{01} = 30.2$ cm and $L_g^{11} = 31.8$ cm.

As a quantitative measure of the degree of transverse coherence, we use the quantities $f_{mn} = \exp(L_{sat}/L_g^{mn})/\exp(L_{sat}/L_g^{00})$. These express the ratio of the power amplification factor for the mn higher-order mode versus that of the fundamental at the saturation length L_{sat} . Since SASE - which is the operating mode assumed here - excites a range of frequencies, all gain lengths associated with this calculation are optimized with respect to the detuning. As an estimate of the saturation length, we use $L_{sat} = N_g L_g^{00}$, where $N_g \approx 20$. More precisely, we can use the formula $N_g \approx \log[P_{sat}/(P_{SASE}/9)]$, where $P_{sat} \approx 1.6\rho_T\gamma_0 m_0 c^2 I_p (L_T/L_g^{00})^2$ is the saturation power and $P_{SASE} \approx \rho_T^2 \gamma_0 m_0 c^3 / \lambda_r$ is the SASE power [7]. For the 1 cm dispersion, this calculation yields $L_{sat} \approx 4.4$ m, which agrees with the simulated saturation within a 5 m undulator shown in [3]. Using the variational values for the mode gain lengths, we obtain $f_{10} \sim 0.43$, $f_{01} \sim 8 \times 10^{-4}$ and $f_{11} \sim 3.6 \times 10^{-4}$ while the values from the analytical solution yield $f_{10} \sim 0.43$, $f_{20} \sim 0.19$, $f_{30} \sim 8.5 \times 10^{-2}$,

$f_{01} \sim 9.7 \times 10^{-4}$ and $f_{11} \sim 4.7 \times 10^{-4}$. These results would lead us to expect that at least 1-2 higher-order modes (10 and 20) would be visible in the radiation profile at saturation. Again, this is indeed what was observed in [3] for $\eta = 1$ cm. We have repeated this analysis for two additional dispersion values [5], namely $\eta = 2$ cm and $\eta = 4$ mm. The aspect ratios in these cases are ~ 18 and ~ 3.6 , respectively, while σ_y is the same as before (~ 10 μ m). In the first case, it was found that $f_{mn} \leq f_{10} \sim 0.68$ while the smaller dispersion yields $f_{mn} \leq f_{10} \sim 0.05$. This provides additional support for our main conclusion, which is that the transverse coherence for such TGU-based schemes is enhanced when the electron beam aspect ratio is decreased.

CONCLUSION

In this paper, we have developed a formalism that is suitable for investigating the higher-order mode properties of a TGU-based, high-gain FEL when emittance and focusing effects are negligible (parallel beam regime). We employ a variational approach along with an exactly solvable, parabolic-like model in order to obtain approximate solutions to the eigenmode equation, both for the fundamental and for the higher-order FEL modes. These solutions are then used in a study of the transverse coherence of the radiation from an LPA-based, TGU FEL example. Verifying earlier observations based on simulation, it is shown that a stronger TGU gradient (i.e. a smaller dispersion and thus less excessive horizontal beam size) enhances transverse coherence. This property is likely to be relevant in determining the operating parameters of a TGU FEL.

ACKNOWLEDGMENT

This work was supported by the Department of Energy Contract No. DE-AC02-76SF00515 and No. DE-AC02-05CH11231.

REFERENCES

- [1] T. Smith, J. M. J. Madey, L. R. Elias and D. A. G. Deacon, J. Appl. Phys. 50, 4580 (1979).
- [2] N. Kroll, P. Morton, M. Rosenbluth, J. Eckstein and J. Madey, IEEE J. Quantum Electron. 17, 1496 (1981).
- [3] Z. Huang, Y. Ding and C. B. Schroeder, PRL 109, 204801 (2012).
- [4] P. Baxevanis, Y. Ding, Z. Huang and R. Ruth, Phys. Rev. ST-AB 17, 020701 (2014).
- [5] P. Baxevanis, Z. Huang, R. Ruth and C. B. Schroeder, to be submitted to Phys. Rev. ST-AB.
- [6] M. Xie, Nucl. Instr. and Meth. A 507 (2003) 450.
- [7] M. Xie, Nucl. Instr. and Meth. A 445 (2000) 67.

INITIAL VALUE PROBLEM FOR AN FEL DRIVEN BY AN ASYMMETRIC ELECTRON BEAM

Panagiotis Baxevanis, Ronald Ruth

SLAC National Accelerator Laboratory, Menlo Park, CA 94025, USA

Abstract

FEL configurations in which the driving electron beam is not axially symmetric (round) are important in the study of novel concepts (such as TGU-based FELs, [1]- [2]) but also become relevant when one wishes to explore the degree to which the deviation from symmetry - inevitable in practical cases - affects the performance of more conventional FEL schemes [3]. In this paper, we present a technique for solving the initial value problem of such an asymmetric FEL. Extending an earlier treatment of ours [4], we start from a self-consistent, fully 3D, evolution equation for the complex amplitude of the electric field of the FEL radiation, which is then solved by expanding the radiation amplitude in terms of a set of orthogonal transverse modes. The numerical results from such an analysis are in good agreement with simulation and provide a full description of the radiation in the linear regime. Moreover, when the electron beam sizes are constant, this approach can be used to verify the predictions of the standard eigenmode formalism.

INTRODUCTION

In most theoretical treatments of the free electron laser (FEL), it is assumed that certain characteristics of the electron beam (such as size and angular divergence) and the undulator system (such as focusing strength) are the same in both transverse directions, a premise which defines the so-called round beam case. There exist, however, novel FEL concepts whose treatment requires a definite departure from the round beam scenario. A particularly intriguing example of the latter is an FEL based on a transverse gradient undulator (TGU), where the addition of dispersion may cause the horizontal size of the electron beam to become much larger than its vertical size. Moreover, non-symmetric FEL examples may become relevant even in the context of more conventional configurations since asymmetry is an inherent feature in many key FEL components (we note, for instance, the absence of horizontal focusing in a flat-pole undulator). In this work, we adopt a model that covers both cases and present a semi-analytical method for solving the initial value problem of the FEL in the linear regime.

THEORY

We begin our analysis by presenting a slightly generalized version of an already established analytical result regarding a TGU-based FEL. In particular, using the methods outlined in [4]- [5], one can derive a 3D equation which governs the evolution of the radiation amplitude $E_v(\mathbf{x}, z)$ throughout the linear regime of the interaction. The result -

in its most general form - can be stated as

$$\begin{aligned} & \left(\frac{\partial}{\partial z} + \frac{\nabla_{\perp}^2}{2ik_r} \right) E_v(\mathbf{x}, z) + \frac{8i\rho_T^3 k_u^3}{2\pi\sigma'_x\sigma'_y} \int_0^z d\zeta \xi e^{-i\Delta\nu k_u \xi} \\ & \times \exp \left[-2(\sigma_{\delta}^{ef})^2 k_u^2 \xi^2 \right] \int_{-\infty}^{\infty} dp_x dp_y E_v(x_+, y_+, \zeta) \\ & \times \exp \left[-2ik_u \xi \left(C_p \frac{x}{\eta} + \left(\bar{\alpha} \frac{\xi}{2} + \frac{\eta\sigma_{\delta}^2}{\sigma_T^2} z_x \right) p_x \right) \right] \\ & \times \exp \left[-\frac{(x - p_x z_x)^2}{2\sigma_T^2} - \frac{1}{2} \left(\frac{1}{\sigma_x'^2} + ik_r \xi \right) p_x^2 \right. \\ & \left. - \frac{1}{2} \left(\frac{1}{\sigma_y'^2} + ik_r \xi \right) (p_y^2 + k_n^2 y^2) \right] \equiv F E_v(\mathbf{x}, z) = 0. \end{aligned} \quad (1)$$

Here, F is meant as an operator, $\nabla_{\perp}^2 = \partial^2/\partial \mathbf{x}^2$, $\xi = \zeta - z$, $z_x = z - z_0$, $x_+ = x + p_x \xi$ and $y_+ = y \cos(k_n \xi) + (p_y/k_n) \sin(k_n \xi)$, where z_0 is a constant offset and k_n is the undulator natural focusing strength in the y -direction, $k_r = \omega_r/c = 2\pi/\lambda_r$ and $k_u = 2\pi/\lambda_u$ - where λ_r is the resonant wavelength, ω_r is the resonant frequency and λ_u is the undulator period - while $\Delta\nu = \nu - 1 = \omega/\omega_r - 1$ is the detuning (ω is a frequency variable). On the other hand, σ_y and σ_y' are the rms values for the vertical size and angular divergence of the electron beam while σ_T and σ_x' are their horizontal counterparts at $z_x = 0$. The former of the last two parameters includes the contribution of the - constant - dispersion η and is given by $\sigma_T = (\sigma_x^2 + \eta^2 \sigma_{\delta}^2)^{1/2}$, where σ_x is the non-dispersive horizontal beam size (at $z = z_0$) and σ_{δ} is the rms relative energy spread. It should be emphasized that - unlike the horizontal beam size, which attains a minimum at $z = z_0$ - the vertical beam size is assumed to be constant, so the matching condition $\sigma_y'/\sigma_y = k_n$ holds in the y -direction. Moreover, ρ_T and σ_{δ}^{ef} are, respectively, the effective Pierce parameter and energy spread of the FEL, quantities that are expressed by $\rho_T = \rho(1 + \eta^2 \sigma_{\delta}^2/\sigma_x^2)^{-1/6}$ and $\sigma_{\delta}^{ef} = \sigma_{\delta}(1 + \eta^2 \sigma_{\delta}^2/\sigma_x^2)^{-1/2}$, where ρ is the Pierce parameter for $\eta = 0$. The non-dispersive FEL parameter is in turn given by $\rho = (K_0^2 [JJ]^2 I_p / (16 I_A \gamma_0^3 \sigma_x \sigma_y k_u^2))^{1/3}$, where γ_0 is the average electron energy in units of its rest mass $m_0 c^2$, K_0 is the on-axis undulator parameter, $[JJ] = J_0(K_0^2/(4 + 2K_0^2)) - J_1(K_0^2/(4 + 2K_0^2))$, $I_A \approx 17$ kA is the Alfvén current and I_p is the peak current of the electron beam. As far as the remaining parameters are concerned, $C_p = \sigma_x^2/\sigma_T^2 + \bar{\alpha}\eta - 1$ with $\bar{\alpha} = K_0^2 \alpha / (2 + K_0^2)$, α being the transverse gradient of the undulator field. Finally, we should also note that the expression for C_p given above is a generalization of the one contained in [5], which only covered the case with $\bar{\alpha} = 1/\eta$.

The latter is referred to as the TGU resonance condition. In the limit of $\alpha \rightarrow 0$ and $\eta \rightarrow 0$, $\rho_T \rightarrow \rho$, $\sigma_\delta^{ef} \rightarrow \sigma_\delta$ and the exponent in the third line of Eq. (1) vanishes (note that $C_p/\eta \rightarrow 0$) so the evolution equation now describes a standard FEL with vertical - but not horizontal - natural focusing.

Mode Expansion

Our goal is to obtain a solution to Eq. (1) that is compatible with a given input amplitude $E_v(\mathbf{x}, 0)$. To this end, we introduce a set of orthogonal transverse modes [6] given by $\psi_{mn}(\mathbf{x}, z) = \chi_m(x, z)\varphi_n(y, z)$, where

$$\begin{aligned}\chi_m(x, z) &= (2^m m!)^{-1/2} H_m \left(\frac{\sqrt{2}\Delta x}{w_x} \right) e^{-imu_x} \chi_0(x, z), \\ \varphi_n(y, z) &= (2^n n!)^{-1/2} H_n \left(\frac{\sqrt{2}y}{w_y} \right) e^{-inu_y} \varphi_0(y, z)\end{aligned}\quad (2)$$

and

$$\begin{aligned}\chi_0(x, z) &= (k_r \beta_{xr} / \pi)^{1/4} (\beta_x + iz)^{-1/2} e^{-k_r \alpha_{xi}^2 / (2\beta_{xr})} \\ &\quad \times \exp \left(-\frac{k_r (x - \alpha_x)^2}{2(\beta_x + iz)} \right), \\ \varphi_0(y, z) &= (k_r \beta_{yr} / \pi)^{1/4} (\beta_y + iz)^{-1/2} \\ &\quad \times \exp \left(-\frac{k_r y^2}{2(\beta_y + iz)} \right).\end{aligned}\quad (3)$$

In the above definitions, $m, n = 0, 1, 2, 3, \dots$, H_k are the Hermite polynomials while β_x , β_y and α_x are complex-valued functions of z . The real parts of these quantities are denoted by β_{xr} , β_{yr} and α_{xr} - respectively - while their imaginary parts are β_{xi} , β_{yi} and α_{xi} . This convention - an index r/i denoting real/imaginary part - is adopted for other variables in this paper as well. Moreover, $w_x = (2/(k_r \beta_{xr}))^{1/2} |\beta_x + iz|$, $w_y = (2/(k_r \beta_{yr}))^{1/2} |\beta_y + iz|$, $u_x = \arctan((z + \beta_{xi})/\beta_{xr})$, $u_y = \arctan((z + \beta_{yi})/\beta_{yr})$ and $\Delta x = x - x_c$, where $x_c = \alpha_{xr} + \alpha_{xi}(z + \beta_{xi})/\beta_{xr}$. These modes satisfy the orthonormality condition $\int d^2\mathbf{x} \psi_{m'n'}^*(\mathbf{x}, z) \psi_{mn}(\mathbf{x}, z) = \delta_{mm'} \delta_{nn'}$ and form a complete set. Thus, the radiation amplitude $E_v(\mathbf{x}, z)$ can be expanded in terms of the generalized Gauss-Hermite modes described above. Our strategy is to construct an approximate solution to the initial value problem by retaining only the fundamental ($m = n = 0$ or 00) mode in such an expansion. In other words, we would like to have $E_v(\mathbf{x}, z) \approx E_v^{00}(\mathbf{x}, z) = a_{00} C_{00}(z) \psi_{00}(\mathbf{x}, z)$, where a_{00} is a constant and $C_{00}(z)$ is a dimensionless mode coefficient to be determined along with the basis parameters $\beta_x(z)$, $\alpha_x(z)$ and $\beta_y(z)$. Since $E_v^{00}(\mathbf{x}, z)$ is not an exact solution, $FE_v^{00}(\mathbf{x}, z)$ is a non-zero function. Our solution is based on imposing the condition that the projections of FE_v with respect to the 00, 10, 20 and 02 modes are zero i.e. $(\psi_{00}, FE_v^{00}) = (\psi_{10}, FE_v^{00}) = (\psi_{20}, FE_v^{00}) = (\psi_{02}, FE_v^{00}) = 0$, where we define the inner product $(f, g) = \int d^2\mathbf{x} f^* g$. The projections with respect to the 01 and 11 modes are identically zero. Using Eqs. (1)-(3) along with the aforementioned conditions, we can obtain a

set of four integro-differential equations for C_{00} , β_x , α_x and β_y . In order to cast these analytical results in a more useful form, we first introduce the scaled variables $\hat{z} = z/\beta_{ex}$, $\hat{\beta}_x = \beta_x/\beta_{ex}$, $\hat{\alpha}_x = \alpha_x/\sigma_x$ and $\hat{\beta}_y = \beta_y/\beta_{ey}$, where $\beta_{ex} = \sigma_x/\sigma'_x$ is the minimum horizontal electron beta and $\beta_{ey} = \sigma_y/\sigma'_y = 1/k_n$ the vertical beta function. The resulting equations are

$$\begin{aligned}\frac{dC_{00}}{d\hat{z}} &= i \left\{ \frac{1}{4\hat{\beta}_{xr}} \frac{d\hat{\beta}_{xi}}{d\hat{z}} + \frac{1}{4\hat{\beta}_{yr}} \frac{d\hat{\beta}_{yi}}{d\hat{z}} + B_x \frac{\hat{\alpha}_{xi}}{\hat{\beta}_{xr}} \right. \\ &\quad \times \left(\frac{d\hat{\alpha}_{xr}}{d\hat{z}} + \frac{\hat{\alpha}_{xi}}{2\hat{\beta}_{xr}} \frac{d\hat{\beta}_{xi}}{d\hat{z}} \right) \Big\} C_{00} \\ &\quad + \int_0^{\hat{z}} d\hat{\zeta} C_{00}(\hat{\zeta}) L_1(\hat{z}, \hat{\zeta}, \hat{\beta}_x, \hat{\beta}_{x,\zeta}, \hat{\alpha}_x, \hat{\alpha}_{x,\zeta}, \hat{\beta}_y, \hat{\beta}_{y,\zeta}),\end{aligned}\quad (4)$$

$$\begin{aligned}\frac{d\hat{\alpha}_x}{d\hat{z}} &= i \frac{\hat{\alpha}_{xi}}{\hat{\beta}_{xr}} \frac{d\hat{\beta}_x}{d\hat{z}} + C_{00}^{-1} \\ &\quad \times \int_0^{\hat{z}} d\hat{\zeta} C_{00}(\hat{\zeta}) L_2(\hat{z}, \hat{\zeta}, \hat{\beta}_x, \hat{\beta}_{x,\zeta}, \hat{\alpha}_x, \hat{\alpha}_{x,\zeta}, \hat{\beta}_y, \hat{\beta}_{y,\zeta}),\end{aligned}\quad (5)$$

$$\frac{d\hat{\beta}_x}{d\hat{z}} = \frac{\int_0^{\hat{z}} d\hat{\zeta} C_{00}(\hat{\zeta}) L_3(\hat{z}, \hat{\zeta}, \hat{\beta}_x, \hat{\beta}_{x,\zeta}, \hat{\alpha}_x, \hat{\alpha}_{x,\zeta}, \hat{\beta}_y, \hat{\beta}_{y,\zeta})}{C_{00}}\quad (6)$$

and

$$\frac{d\hat{\beta}_y}{d\hat{z}} = \frac{\int_0^{\hat{z}} d\hat{\zeta} C_{00}(\hat{\zeta}) L_4(\hat{z}, \hat{\zeta}, \hat{\beta}_x, \hat{\beta}_{x,\zeta}, \hat{\alpha}_x, \hat{\alpha}_{x,\zeta}, \hat{\beta}_y, \hat{\beta}_{y,\zeta})}{C_{00}}.\quad (7)$$

In the above equations (and elsewhere), an extra subscript ζ assigned to a variable denotes a dependence upon the integration variable $\hat{\zeta}$, i.e. $\hat{\beta}_{x,\zeta} = \hat{\beta}_x(\hat{\zeta})$, $\hat{\alpha}_{x,\zeta} = \hat{\alpha}_x(\hat{\zeta})$ and $\hat{\beta}_{y,\zeta} = \hat{\beta}_y(\hat{\zeta})$ etc. The functions L_1 - L_4 are given by

$$\begin{aligned}L_1 &= -8iA^3 \hat{\xi} \exp(-2iA\hat{v}\hat{\xi} - 2A^2(\hat{\sigma}_\delta^{ef})^2 \hat{\xi}^2) \\ &\quad \times (\hat{\beta}_{xr,\zeta}/\hat{\beta}_{xr})^{1/4} (\hat{\beta}_{yr,\zeta}/\hat{\beta}_{yr})^{1/4} (\hat{\beta}_x/\hat{\beta}_{x,\zeta})^{1/2} \\ &\quad \times (\hat{\beta}_y/\hat{\beta}_{y,\zeta})^{1/2} G_{pp}^{-1/2} \hat{T}_2^{-1/2} \exp(\hat{T}_0) C_{pp}^{-1/2} \hat{Y}_2^{-1/2}, \\ L_2 &= (\hat{\beta}_{xr}/B_x)^{1/2} e^{iu_x} (\hat{T}_1/\hat{T}_2) L_1, \\ L_3 &= 2\hat{\beta}_{xr} e^{2iu_x} [\hat{T}_2^{-1} (1 + \hat{T}_1/(2\hat{T}_2)) - 1] L_1, \\ L_4 &= 2\hat{\beta}_{yr} e^{2iu_y} (\hat{Y}_2^{-1} - 1) L_1,\end{aligned}\quad (8)$$

where $A = \rho_T k_u \beta_{ex}$, $\hat{\xi} = \hat{\zeta} - \hat{z}$, $\hat{v} = \Delta v/(2\rho_T)$, $\hat{\sigma}_\delta^{ef} = \sigma_\delta^{ef}/\rho_T$, $\hat{\beta}_x = \hat{\beta}_x + i\hat{z}$, $\hat{\beta}_y = \hat{\beta}_y + i(\beta_{ex}/\beta_{ey})\hat{z}$ and $B_x = k_r \sigma_x \sigma'_x$. Furthermore, $\hat{T}_1 = G_\theta + G_{\theta p} G_p / G_{pp}$, $\hat{T}_2 = (1/2)(G_{\theta\theta} - G_{\theta p}^2 / G_{pp})$, $\hat{Y}_2 = (1/2)(C_{tt} - C_{tp}^2 / C_{pp})$ and

$$\begin{aligned}\hat{T}_0 &= \frac{G_p^2}{2G_{pp}} + \frac{\hat{T}_1^2}{4\hat{T}_2} - \frac{\hat{x}_c^2}{2R^2} - 2i\hat{p}_0 \hat{\xi} \hat{x}_c \\ &\quad - \frac{B_x}{2} \left\{ \frac{\hat{\alpha}_{xi}^2}{\hat{\beta}_{xr}} + \frac{\hat{\alpha}_{xi,\zeta}^2}{\hat{\beta}_{xr,\zeta}} + \frac{(\hat{x}_c - \hat{\alpha}_x^*)^2}{\hat{\beta}_x^*} + \frac{(\hat{x}_c - \hat{\alpha}_{x,\zeta})^2}{\hat{\beta}_{x,\zeta}} \right\},\end{aligned}\quad (9)$$

Table 1: Undulator and Electron Beam Parameters

Parameter	LCLS	USR
Undulator parameter K_0	3.7	3.68
Undulator period λ_u	3 cm	2 cm
Beam energy $\gamma_0 m_0 c^2$	14.3 GeV	4.5 GeV
Resonant wavelength λ_r	0.15 nm	1 nm
Peak current I_p	3 kA	200 A
Energy spread σ_δ	10^{-4}	1.5×10^{-3}
Norm. emittance $\gamma_0 \sigma_x \sigma'_x$	0.5 μm	0.0123 μm
Norm. emittance $\gamma_0 \sigma_y \sigma'_y$	0.5 μm	1.23 μm
Horizontal size σ_x	23.1 μm	8.3 μm
Vertical size σ_y	30.2 μm	38.7 μm
FEL parameter ρ	5×10^{-4}	6×10^{-4}

where $R = \sigma_T / \sigma_x$, $\hat{x}_c = x_c / \sigma_x = \hat{\alpha}_{xr} + \hat{\alpha}_{xi}(\hat{z} + \hat{\beta}_{xi}) / \hat{\beta}_{xr}$ and $\hat{p}_0 = k_u \beta_{ex} \sigma_x (C_p / \eta)$. The remaining quantities to be defined are

$$\begin{aligned}
 G_{pp} &= 1 + \hat{z}_x^2 / R^2 + i B_x \hat{\xi} + B_x \hat{\xi}^2 / \hat{\beta}_{x,\zeta}, \\
 G_{\theta\theta} &= \hat{\beta}_x / \hat{\beta}_{xr} + \tilde{w}_x^2 [1 / \hat{\beta}_{x,\zeta} + (R^2 B_x)^{-1}], \\
 G_{\theta p} &= \tilde{w}_x [\hat{z}_x / (R^2 B_x^{1/2}) - B_x^{1/2} \hat{\xi} / \hat{\beta}_{x,\zeta}], \\
 G_p &= \hat{x}_c \hat{z}_x / R^2 - B_x (\hat{x}_c - \hat{\alpha}_{x,\zeta}) \hat{\xi} / \hat{\beta}_{x,\zeta} \\
 &\quad - 2i \hat{\xi} (\bar{Q}_1 \hat{\xi} / 2 + \bar{Q}_2 \hat{z}_x), \\
 G_\theta &= -\tilde{w}_x [B_x^{1/2} (\hat{x}_c - \hat{\alpha}_x^*) / \hat{\beta}_x^* + \hat{x}_c / (R^2 B_x^{1/2}) \\
 &\quad + B_x^{1/2} (\hat{x}_c - \hat{\alpha}_{x,\zeta}) / \hat{\beta}_{x,\zeta} + 2i \bar{p}_0 \hat{\xi} / B_x^{1/2}]
 \end{aligned} \tag{10}$$

where $\hat{z}_x = z_x / \beta_{ex}$, $\tilde{w}_x = |\hat{\beta}_x| / \hat{\beta}_{xr}^{1/2}$, $\bar{Q}_1 = k_u \beta_{ex}^2 \sigma'_x \bar{\alpha}$, $\bar{Q}_2 = k_u \beta_{ex}^2 \sigma'_x (\eta \sigma_\delta^2 / \sigma_T^2)$ and

$$\begin{aligned}
 C_{pp} &= 1 + i B_y \bar{\xi} + B_y \sin^2 \bar{\xi} / \hat{\beta}_{y,\zeta}, \\
 C_{tt} &= \hat{\beta}_y / \hat{\beta}_{yr} + \tilde{w}_y^2 [B_y^{-1} + i \bar{\xi} + \cos^2 \bar{\xi} / \hat{\beta}_{y,\zeta}], \\
 C_{tp} &= -B_y^{1/2} (\tilde{w}_y / \hat{\beta}_{y,\zeta}) \cos \bar{\xi} \sin \bar{\xi},
 \end{aligned} \tag{11}$$

with $B_y = k_r \sigma_y \sigma'_y$, $\bar{\xi} = (\beta_{ex} / \beta_{ey}) \hat{\xi}$ and $\tilde{w}_y = |\hat{\beta}_y| / \hat{\beta}_{yr}^{1/2}$. Two important special cases are worth mentioning. The first one refers to the limit $\alpha, \eta \rightarrow 0$, which describes a conventional FEL with a flat-pole undulator and an undispersed beam. In this case, we have $\bar{p}_0 = 0$, $\bar{Q}_1 = \bar{Q}_2 = 0$, $R = 1$ and - provided that $\hat{\alpha}_x(0) = 0$ - the radiation profile remains on-axis, i.e. $\hat{\alpha}_x = 0$ so $\hat{x}_c = 0$, $G_p = G_\theta = 0$, $\hat{T}_0 = \hat{T}_1 = 0$ and $L_2 = 0$ (Eq. (5) then becomes trivial). The second case is a TGU-based FEL in which the horizontal emittance effect can be neglected. This scenario can be accommodated by the general equations given above if we set $G_{pp} = 1$ and $G_{\theta p} = G_p = 0$.

NUMERICAL RESULTS

In the previous section, we presented a semi-analytical, approximate method for solving the initial value problem of an asymmetric FEL in the linear regime. Here, we test

this method by comparing numerical results derived from it with simulation data and the predictions of standard eigenmode analysis. In particular, we first consider the case of an FEL based on a conventional, LCLS-type undulator with a flat pole-face ($\bar{\alpha} = 0$) and no external focusing (Table 1). The driving electron beam is also characterized by LCLS-like parameters, namely a 14.3 GeV energy, a 3 kA peak current and a 0.5 μm normalized emittance in both x and y (of course, $\eta = 0$). The vertical natural focusing beta function $\beta_{ey} \approx \sqrt{2} \gamma_0 / (K_0 k_u)$ is approximately 51 m while - in the absence of horizontal focusing - we assume that the horizontal beta function attains a minimum value of $\beta_{ex} = 30$ m at $z = z_0 = 36$ m. For this configuration, we performed a steady-state GENESIS simulation [7] assuming a seed wavelength of 0.1500372 nm and an input Gaussian seed with a 9 m Rayleigh length and a waist located 6 m inside the undulator. At the same time, we derived the linearized solution by numerically solving Eqs. (4)-(7). Based on the seed parameters mentioned above, our initial values were $\hat{\beta}_x(0) = 0.3 - 0.2i$, $\hat{\alpha}_x(0) = 0$ and $\hat{\beta}_y(0) = 0.176 - 0.117i$. The comparison between the results obtained through the two approaches is shown in Figs. 1-2, where the FEL gain $G = \log(P/P_0) - P$ is the radiation power and P_0 its value at $z = 0$ - and the radiation beam size σ_r are plotted as functions of z . Since $P \propto \int d^2 \mathbf{x} |E_v(\mathbf{x}, z)|^2$, we find that $P = P_0 |C_{00}(z)|^2$ if we select $C_{00}(0) = 1$. The analytical expression for σ_r - defined in the context of GENESIS as the square root of the average value of $x^2 + y^2$ - is $\sigma_r = (\sigma_{rx}^2 + \sigma_{ry}^2)^{1/2}$, where $\sigma_{rx} = w_x / 2$ and $\sigma_{ry} = w_y / 2$. Very good agreement is observed in the first 50 m of undulator, which is the approximate extent of the linear regime.

On the other hand, whenever the z -dependent effects introduced by the horizontal emittance can be disregarded, the solution of the initial value problem can be expressed in terms of the guided, FEL eigenmodes. This corresponds to

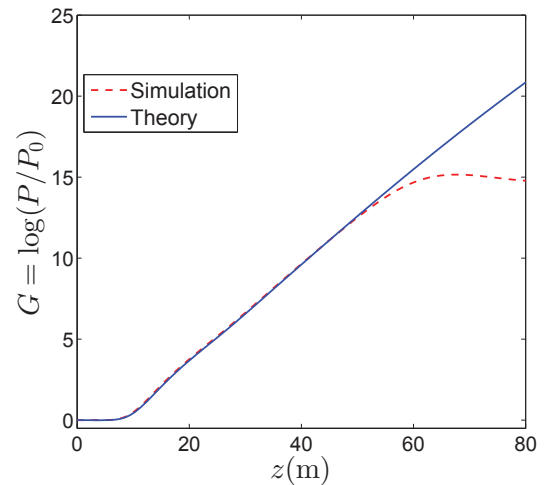


Figure 1: FEL gain as a function of z for the LCLS parameters (data from the linearized solution versus simulation results).

the previously mentioned model of a TGU-based FEL with $\sigma'_x = 0$ but $\sigma'_y \neq 0$. In this case, a single, Gaussian-like FEL mode typically dominates all the others in the high-gain part of the linear regime, i.e. $E_y(\mathbf{x}, z) \propto A_{00}(\mathbf{x})e^{i\mu_{00}z}$, where μ_{00} is the growth rate and $A_{00}(\mathbf{x})$ the transverse profile of the dominant, fundamental mode. As has been shown elsewhere [5], this fundamental growth rate can be accurately calculated through a variational technique. In view of this property, we should also expect the linearized solution to asymptotically converge into a guided mode. To facilitate a direct comparison with the results of the eigenmode formalism, we express the mode coefficient as $C_{00}(z) = \exp(i \int_0^z \mu(t) dt)$, where $\mu(z) = -iC_{00}^{-1}(dC_{00}/dz)$ is a z -dependent complex growth rate and compare the variational value of μ_{00} with the asymptotic value $\mu(\infty)$. For a specific example, we use the TGU parameters listed in Table 1, which refer to a concept based on the PEPX ultimate storage ring (USR). In this case, $\beta_{ey} \approx 11$ m and $\beta_{ex} = \sigma_x/\sigma'_x = 50$ m, though the latter quantity - like the horizontal emittance $\sigma_x\sigma'_x$ - is now merely a convenient scaling factor. We solve Eqs. (4)-(7) for $\eta = 3.5$ cm, $\tilde{\alpha} = 1/\eta$, $\hat{v} = -0.15$, $\hat{\beta}_x(0) = 0.238 + 0.086i$, $\hat{\alpha}_x(0) = 0.167 + 0.992i$ and $\hat{\beta}_y(0) = 0.896 + 0.543i$. These initial values are selected so that the transverse profile of the input radiation field roughly matches that of the fundamental FEL mode. As is evident from Fig. 3, the z -dependent growth rate indeed attains a constant value in the high-gain portion of the linear regime. The same conclusion can be established for $\beta_x + iz$, $\beta_y + iz$ and α_x , so that ψ_{00} evolves into a guided mode with a z -invariant transverse profile. Lastly, we point out that our solution yields $\hat{\mu}(\infty) = \mu(\infty)/(2\rho_T k_u) = 0.398 - 0.312i$, which is very close to the variational result $\hat{\mu}_{00} = \mu_{00}/(2\rho_T k_u) = 0.394 - 0.308i$.

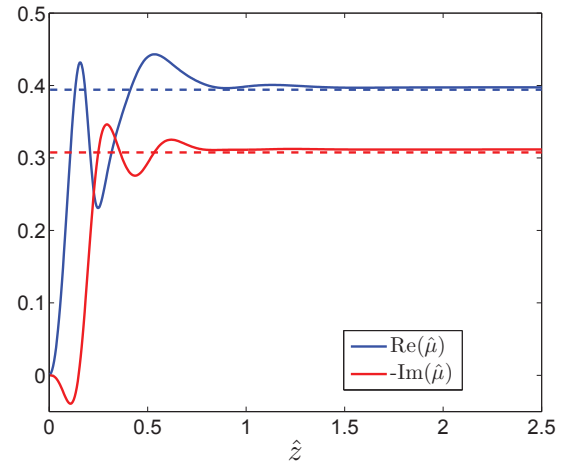


Figure 3: Real and imaginary part of the scaled growth rate $\hat{\mu} = \mu/(2\rho_T k_u)$ as a function of $\hat{z} = z/\beta_{ex}$ (USR parameters). The dashed lines correspond to the variational solution.

CONCLUSION

We have developed a technique for approximately solving the initial value problem of an asymmetric FEL in the linear regime of the interaction. Starting from a self-consistent, 3D evolution equation for the radiation amplitude, we constructed an approximation scheme in which the latter quantity can be adequately described by the fundamental (00) element in a basis of generalized Gauss-Hermite modes. In this way, the problem is ultimately reduced to a set of four integro-differential equations for a single mode coefficient and three basis parameters. Numerically solving this set yields results which provide a complete characterization of the radiation and are in good agreement both with simulation data and with the predictions of the eigenmode theory.

ACKNOWLEDGMENT

This work was supported by the Department of Energy Contract No. DE-AC02-76SF00515.

REFERENCES

- [1] N. Kroll, P. Morton, M. Rosenbluth, J. Eckstein and J. Madey, IEEE J. Quantum Electron. 17, 1496 (1981).
- [2] Z. Huang, Y. Ding and C. B. Schroeder, PRL 109, 204801 (2012).
- [3] M. Xie, Nucl. Instr. and Meth. A 507 (2003) 450.
- [4] P. Baxevanis, R. Ruth, Z. Huang, Phys. Rev. ST-AB 16, 010705 (2013).
- [5] P. Baxevanis, Y. Ding, Z. Huang and R. Ruth, Phys. Rev. ST-AB 17, 020701 (2014).
- [6] P. Baxevanis and R. Ruth, to be submitted to Phys. Rev. ST-AB.
- [7] S. Reiche, Nucl. Instr. and Meth. A 429 (1999) 243.

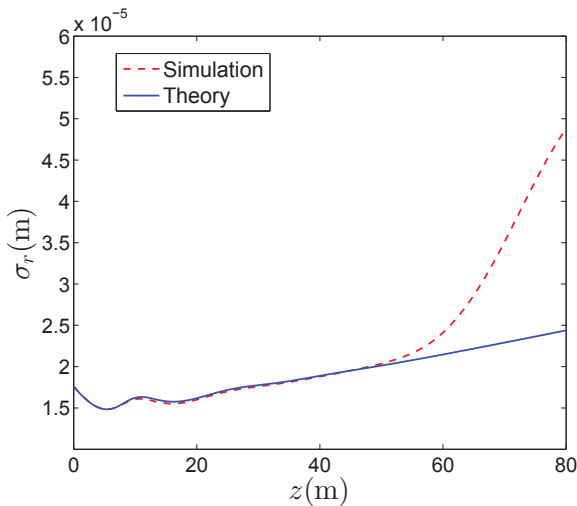


Figure 2: Radiation beam size as a function of z for the LCLS parameters (data from the linearized solution versus simulation results).

MODE DECOMPOSITION OF A TAPERED FREE ELECTRON LASER

S.D. Chen, K. Fang, X. Huang, C. Pellegrini, J. Wu, SLAC, CA 94025, USA

K. Fang, Indiana University, IN 47405, USA

C. Emma, C. Pellegrini, University of California, Los Angeles, CA 90095, USA

S.D. Chen, C.S. Hwang, NCTU, Hsinchu 30076, Taiwan

C.S. Hwang, NSRRC, Hsinchu 30076, Taiwan

S. Serkez, Deutsches Elektronen-Synchrotron, 22607 Hamburg, Germany

Abstract

For the ultimate use for the scientific experiments, the free electron laser (FEL) will propagate for long distance, much longer than the Rayleigh range, after exiting the undulator. To characterize the FEL for this purpose, we study the electromagnetic field mode components of the FEL photon beam. With the mode decomposition, the transverse coherence can be analyzed all along. The FEL here in this paper is a highly tapered one evolving through the exponential growth and then the post-saturation taper. Modes contents are analyzed for electron bunch with three different types of transverse distribution: flat-top, Gaussian, and parabolic. The tapered FEL simulation is performed with Genesis code. The FEL photon beam transverse electric field is decomposed with Gaussian-Laguerre polynomials. The evolutions of spot size, source location, and the portion of the power in the fundamental mode are discussed here. The approach can be applicable to various kind scheme of FEL.

INTRODUCTION

Free electron Laser (FEL) is one of the most powerful tools for frontier scientific research. Many experiments, especially for bioimaging [1, 2], will benefit greatly from the enhanced coherent light peak power at Terawatt (TW) level. To improve the efficiency of an FEL, in recent years, the tapered undulator scheme has gotten renewed attentions [3–5]. More recently, to further improve the taper efficiency, various transverse distributions of the electron bunch are investigated. In this paper, we study this topic by looking into the mode contents of the FEL in the exponential growth regime as well as in the post-saturation tapered regime.

As initiated in Ref. [5], the transverse effect is also an important aspect to be studied for boosting the FEL power into TW level. In this paper, three different types of transverse distributions of the electron beam, the flat-top, Gaussian, and parabolic distributions, are analyzed. Different transverse distributions can excite different kinds of high-order modes, which can in principle help trapping the electrons as the FEL interaction develops along the undulator field. Therefore, the FEL power can be further increased. With the mode contents analyzed, the transverse coherence can be studied naturally. The mode decomposition, which is to decompose a field to a set of complete orthonormal modes, is widely used on laser like high directional sources [6].

To compare with the decomposition method, a simple analytical extended “line source” model is developed. The

decomposition result and the evolution of the spot size, the source location and the power ratio of fundamental mode to the total power are presented.

LAGUERRE-GAUSSIAN EXPANSION

A complex E-field with the form of $\tilde{E}(x, y)$ can be expanded in a complete orthonormal basis. Here the Laguerre-Gaussian polynomials are chosen as the basis for expansion:

$$E(r) = \sum_{n=0}^{\infty} a_n e^{-\zeta r^2/2} L_n(\Re(\zeta) r^2), \quad (1)$$

where we assume that the modes have azimuthal symmetry $r = \sqrt{x^2 + y^2}$ with $\Re(\zeta)$ being the real part of ζ which characterizes the mode size and also the wave-front curvature. With the orthogonality condition, the coefficients a_n can be calculated, and the square of a_n gives the power of each mode.

We get the electric field as a numerical solution from GENESIS [7] simulation. The electric field output is a two-dimensional matrix with complex values, which is in the form of $\tilde{E}(\Delta x m_1, \Delta y m_2)$, where m_1 and m_2 are integers. The a_n should be integrated by discretized form of

$$a_n = \sum_{m_1} \sum_{m_2} \tilde{E}(\Delta x m_1, \Delta y m_2) \exp\left(\frac{-\zeta}{2} r^2\right) * L_n(\Re(\zeta) r^2) \Re(\zeta) \Delta x \Delta y, \quad (2)$$

where r^2 should be substituted by $(\Delta x m_1)^2 + (\Delta y m_2)^2$.

We have carefully chosen the grid size and simulation area such that the orthogonality between different Laguerre-Gaussian modes is well preserved. The grid size is small enough to represent the structure in Laguerre-Gaussian modes, while the simulation area is large enough so that the cutoff error is negligible.

Based on the above formalism, an electric field can be decomposed numerically by the mode series of a Laguerre-Gaussian polynomial. However, the set of mode series are not determined until the value ζ is fixed. Although conceptually the basis is complete for an arbitrary complex value of ζ , physics consideration has to be applied to find ζ . The details of our approach is given in next section.

DECOMPOSITION METHOD

The electric field expression in Eq. (1) is analogous to a standard Gaussian laser beam. For $n = 0$ in Eq. (1), at a certain z , we can have the relations:

$$\Re(\zeta) = \frac{2}{w^2(z)}, \quad (3)$$

and

$$\Im(\zeta) = \frac{k}{R(z)}, \quad (4)$$

where $\Im(\zeta)$ is the imaginary part of ζ . $R(z)$ and $w(z)$ stands for the wave-front curvature and the spot size, respectively. The above relations clearly expresses the physical and mathematical meaning of ζ , and the relations help us develop a brief approach of finding the value ζ .

Let's discuss the imaginary part of ζ first. For free space propagation of a divergent field $\tilde{E}(\Delta x m_1, \Delta y m_2)$ at z , the rms spot size (σ_r) increases as in the $+z$ -direction; and σ_r decreases as in the $-z$ -direction (and vice versa for a convergent photon beam). One special case is that σ_r increases in both propagation directions ($\pm z$ -directions), when the wave-front curvature is infinity. In other words, writing the electric field in the following form:

$$\tilde{E}(\Delta x m_1, \Delta y m_2) = \tilde{E}_0 e^{-i a} \exp[-i b r^2 - c r^2], \quad (5)$$

such a special case happens at $b = 0$. Normally, $b = \Im(\zeta) \neq 0$ for an arbitrary z . However, by multiplying a term, $\exp[i b' r^2]$ to Eq. (5), the propagation property will be changed. If $b' = b$, $\exp[i b' r^2] \times \tilde{E}(\Delta x m_1, \Delta y m_2)$ has the property of the special case, *i.e.*, σ_r increases in both the $+z$ and the $-z$ directions, then we have b' right equal to $\Im(\zeta)$. This is how we find $\Im(\zeta)$.

Now, let's discuss the real part of ζ . In Ref. [8], a Variational-Solution-Based (VSB) expansion method was adopted to solve the dispersion relation of an FEL system with a trial function in Gaussian form. The solution of the dispersion relation tells us that the fundamental eigenmode [$n = 0$ in Eq. (1)] has the largest growth rate and eventually the fundamental eigenmode dominates the electric field. So a simple rule could be adopted for choosing $\Re(\zeta)$, *i.e.*, the chosen $\zeta = \Re(\zeta) + i\Im(\zeta)$ should maximize the portion of the fundamental mode, while the $\Im(\zeta)$ should be fixed by the propagation approach described above.

Before we explain the details of the mode content, let us give the parameters of the simulation as in Tab. 1. For the particular example in this paper, we are simulating a seeded FEL in a highly tapered undulator and reaches TW level as shown in Fig. 1 for three different electron transverse distributions: Flattop, Gaussian, and Parabolic. Within about 180 meter long undulator, the FEL power can reach TW level for all the three different distributions, with the flattop distribution supporting the highest power. The seed is a Gaussian fundamental mode with 5 MW peak power.

Here is a brief description of the approach:

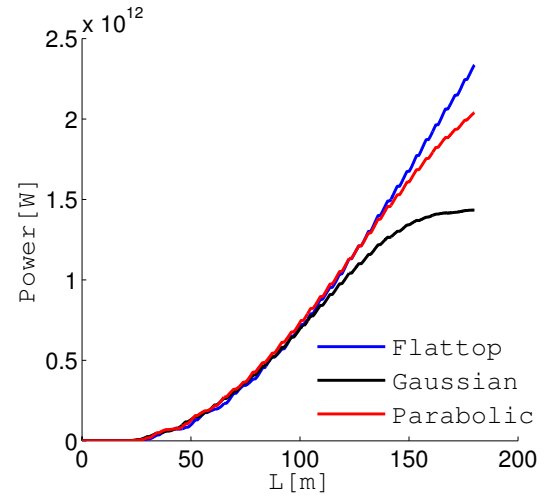


Figure 1: FEL power along the undulator for three different distributions: Flattop, Gaussian, and Parabolic.

Table 1: The Parameters Used in The Simulation in This Paper

Symbol	Value	Unit
Charge Q	150	pC
Centroid energy E_0	13.64	GeV
Peak current I_{pk}	4	kA
Temporal distribution	flattop	-
Slice normalized emittance ε_n	0.3	mm-mrad
Slice energy spread σ_δ	9.5	10^{-5}
Undulator period λ_w	3.2	cm
Length of undulator L_w	180	m
FEL wavelength λ_r	1.5	Å
FEL seed power P_{seed}	5	MW
Power gain length L_G	2.7	m

1. Get $\Im(\zeta)$ by studying the wave front curvature property via free space propagation.
2. Get $\Re(\zeta)$ by maximizing the portion of fundamental mode.

The summation of modes from decomposition calculation is then compared with the electric field from GENESIS output. Results for three typical values of z , namely: in the exponential growth region ($z = 20$ m), at the exponential growth saturation point ($z = 30$ m), and post exponential growth saturation region ($z = 150$ m), are presented in Fig. 2. The results show that the approach works well. Even though the curve inside the central parabolic region of the phase plot (right column in Fig. 2) deviates from a parabolic curve, it still gives a very nice match, which gives a strong proof that a_n calculated by Eq. (2) gives correct amplitude and phase

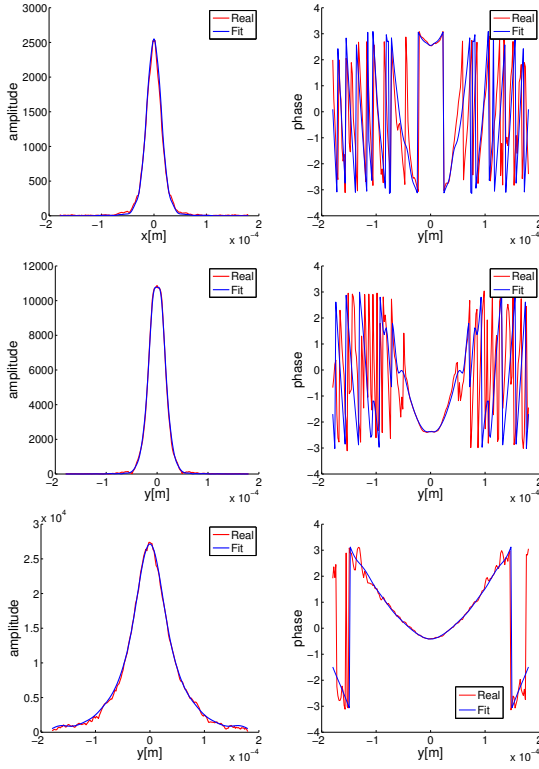


Figure 2: The absolute value and the phase of the $E(r) = \sum_{n=0}^{19} a_n e^{z_n}$ (from decomposition calculation) and $\tilde{E}(\Delta x m_1, \Delta y m_2)$ (from the GENESIS simulation) are plotted. Three cases with $z = 20, 30$, and 150 m represent the exponential growth region, the saturation point, and the post saturation region, respectively.

of the modes. According to the results, the electric field data can be well reconstructed with about twenty modes. The discrepancy of the phase in the large r -region is due to the numerical reflection field from the boundary in GENESIS simulation. Furthermore, there is very little FEL power in this large r -region. The evolution of the spot size and the source location is discussed after next section.

THEORETICAL MODEL: A LINE SOURCE

In the post-saturation region after the exponential growth, the FEL photon can be modeled as an extended line source. The light emitted from a long undulator in the post-saturation region is analogous to an extended line source containing infinite points from which a laser beam is emitted at its waist position. The line source points are weighted by the following function,

$$p^{\alpha, \beta}(z_s, z_{\text{sat}}) = 1 + \alpha(z_s - z_{\text{sat}})^{\beta}, \quad (6)$$

where z_s is the source location, and z_{sat} is the exponential growth saturation point. The weighting function in Eq. (6) as a physics consideration is to describe the fact that the local emitted power is varying along the undulator. For $\beta = 0$,

Eq. (6) describes a scenario that the local emitted power is the same along the undulator, so that the total power will be increasing linearly along the undulator. While for $\beta = 1$, Eq. (6) then describes that the local emitted power is increasing linearly along the undulator, so that the total power will be increasing quadratically along the undulator.

For the case that the observation point z is outside of the undulator, *i.e.* $z > L_u$, an integration from the exponential growth saturation point z_{sat} to the undulator exit L_u then describes how the spot size evolves in such a line source model,

$$w^2(z, L_u) = \frac{\int_{z_{\text{sat}}}^{L_u} w_0^2 \left[1 + \left(\frac{z - z_s}{z_R} \right)^2 \right] p^{\alpha, \beta}(z_s, z_{\text{sat}}) dz_s}{\int_{z_{\text{sat}}}^{L_u} p^{\alpha, \beta}(z_s, z_{\text{sat}}) dz_s}, \quad (7)$$

where the subscript in z_s means “source” which can be anywhere from the exponential growth saturation point, z_{sat} , to the end of undulator at L_u ; $z_R = \pi w_0^2 / \lambda_r$ is the Rayleigh range and w_0 is the beam waist size.

Normally, the second term in the weighting function as in Eq. (6) is much larger than the first term: “1”, so the first term is dropped in the following calculation for simplicity even though the integral in Eq. (7) can still lead to a closed form with the first term: “1”. With the first term dropped, the parameter α is canceled out, so the integral in Eq. (7) becomes:

$$w_{\beta}^2(z, L_u) = \frac{w_0^2 (1 + \beta) \Gamma(1 + \beta)}{z_R^2 \Gamma(4 + \beta)} \times \left[(1 + \beta)(3 + \beta)(z - L_u)^2 + (3 + \beta)(z - z_{\text{sat}})^2 - (1 + \beta)(L_u - z_{\text{sat}})^2 + (2 + \beta)(3 + \beta)z_R^2 \right]. \quad (8)$$

For $\beta = 0$ and $\beta = 1$, the expressions are:

$$w_{\beta=0}^2(z, L_u) = w_0^2 \left[1 + \frac{(z - L_u)^2}{2z_R^2} + \frac{(z - z_{\text{sat}})^2}{2z_R^2} - \frac{(L_u - z_{\text{sat}})^2}{6z_R^2} \right], \quad (9)$$

and

$$w_{\beta=1}^2(z, L_u) = w_0^2 \left[1 + \frac{2(z - L_u)^2}{3z_R^2} + \frac{(z - z_{\text{sat}})^2}{3z_R^2} - \frac{(L_u - z_{\text{sat}})^2}{6z_R^2} \right]. \quad (10)$$

Notice that the spot size is a function of both the observation point (z) and the undulator length (L_u). If on the other hand, the observation point is inside the undulator, *i.e.*, $z < L_u$, we can simply replace L_u by z in Eqs. (9) and (10), then the first term vanishes. The expression of $\beta = 1$ is used as the expected value for the “line source” curve in Fig. 3.

Based on the line source model, we can compute the effective source location:

$$w_{\text{line}}^2(z, L_u) = w_0^2 \left[1 + \left(\frac{z - z_{\text{eff}}}{z_R} \right)^2 \right], \quad (11)$$

where $w_{\text{line}}^2(z, L_u)$ is given in Eq. (7). The effective source location can be obtained by solving the above equation, $z_{\text{eff}}(z) = z - z_R \sqrt{w_{\text{line}}^2(z, L_u) / w_0^2 - 1}$.

For $\beta = 0$ and $\beta = 1$, the expression for z_{eff} can be simplified by proper approximations to get:

$$z_{\text{eff};\beta=0}(z) \approx \frac{(L_u + z_{\text{sat}})}{2} - \frac{(L_u - z_{\text{sat}})^2}{24z} - \frac{(L_u - z_{\text{sat}})^2 (L_u + z_{\text{sat}})}{48z^2}, \quad (12)$$

and

$$z_{\text{eff};\beta=1}(z) \approx \frac{(2L_u + z_{\text{sat}})}{3} - \frac{(L_u - z_{\text{sat}})^2}{36z} - \frac{(L_u - z_{\text{sat}})^2 (2L_u + z_{\text{sat}})}{108z^2}. \quad (13)$$

The above described model and expressions (for $\beta = 1$) will be compared to the numerical results below.

DECOMPOSING RESULT AND OPTIC PROPERTIES

A tapered undulator scheme is studied to achieve TW power level. Three different types of electron transverse distributions are considered in the study. The electric fields at several different observation points along the undulator are simulated with GENESIS. The electric fields are decomposed by the approach introduced in third section. The decomposition is applied to all three cases with different kind of transverse electron distributions. As shown in Fig. 1, for the Gaussian case, the tapered FEL saturates at about 150 m, hence in the following, we should results up to 150 m. The evolution of the portion of power in the fundamental mode can be clearly obtained after the mode decomposition. Before reporting the results, some related optic properties and FEL characteristics are discussed as in the follows.

The spot size can be calculated by Eq. (3), and the evolution of spot size is shown in Fig. 3. The simulation results are compared to the expected value ("line source") which is introduced above in above section. The expected spot size values of the FEL light are modeled by two physical considerations: one is the gain guiding effect in the exponential growth region, which gives a result that the spot size does not change before the exponential saturation point as the FEL develops along undulator; the other one is that the light emitted from the post saturation region is described by the extended line source model above.

The spot size from the decomposition calculation shows the gain guiding characteristic in all three cases of transverse distributions. The gain guiding effect is fully established at

around 20m as in Fig.3. Before 20m, there are modes not satisfying the azimuthal symmetry. Besides, the fundamental mode is not dominating yet before 20m.

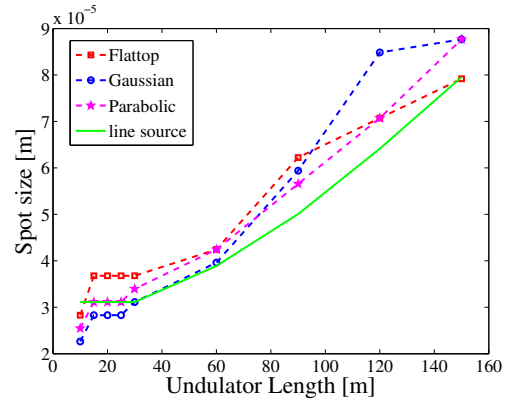


Figure 3: FEL beam spot size varies along the undulator distance.

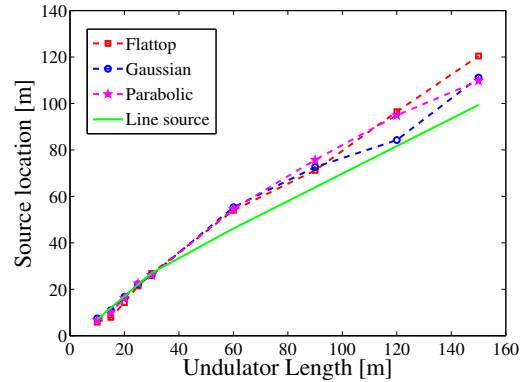


Figure 4: FEL source location varies along the undulator distance.

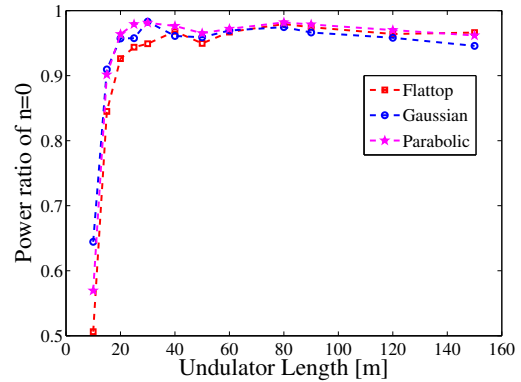


Figure 5: The portion of the fundamental mode power varies along the undulator distance.

The effective beam waist locations, also called the source locations, of all three cases are plotted in Fig. 4 and the expected value is shown together. The expected value is

defined by two rules. First, in the exponential growth region, the source location is at about one gain length before the observation point. For example: the electric field at 30m has a source location at 27.3m since the gain length here is 2.7m. Second, the extended “line source” model with $\beta = 1$ is adopted to get the effective source location.

For the numerical part, analogy to a laser beam, the FEL effective beam waist location z_s can be evaluated by the wave front curvature $R(z)$ and the spot size $w(z)$ at certain location z . Since we expand the electric field in the Laguerre-Gaussian basis as in Eq. (1), we can write the $R(z)$ and $w(z)$ with $\Re(\zeta)$ and $\Im(\zeta)$:

$$z_s = \frac{R(z)}{1 + \left[\frac{\lambda R(z)}{\pi w(z)^2} \right]^2} = \frac{2\pi}{\lambda} \frac{\Im(\zeta)}{\Im^2(\zeta) + \Re^2(\zeta)} \quad (14)$$

The results show that in the exponential growth region, the source location is very close to one gain length before the observation point, just as expected. In the post saturation region, the source location is very close to the expected values as in Fig. 4.

The discussion on the spot size and source location evolution reveals some expected FEL properties, which supports that the approach of mode decomposition is reliable. Next, we show how the power of the fundamental mode evolves along the undulator as in Fig. 5. In the plot, in the exponential growth region, the portion of the fundamental mode grows very fast and exceeds 95% at saturation point. In the post saturation region, after 80m, the ratio drops down slightly. However, it is still higher than 90%. This is a very important result. This means that when the TW FEL is achieved by utilizing taper undulator associated with various types of beam transverse distributions, the power portion in the fundamental mode remains high. This ensures that such an FEL light has high transverse coherence.

SUMMARY

The taper undulator scheme with three kinds of transverse electric beam distributions is investigated for a TW FEL. The transverse coherence property is discussed by mode decomposition. An approach of finding the mode contents of a complex electric field generated from GENESIS simulation is proposed and proven to be reliable. It is discovered that in the post saturation region, over 90% of the total power belongs to the fundamental mode. For the three different transverse distributions, the percentage of the fundamental mode power is higher in the flattop and parabolic cases than in the Gaussian case. The high percentage of the fundamental mode guarantees a high transverse coherence. With

the knowledge of the mode contents, the source location is also calculated, which provides information for downstream x-ray beam line design.

ACKNOWLEDGEMENT

The authors would like to thank Professor S.-Y. Lee of Indiana University for many stimulated discussions. K.F. would like to express his gratitude to Prof. Lee for many advices. The work was supported by the US Department of Energy (DOE) under contract DE-AC02-76SF00515 and the US DOE Office of Science Early Career Research Program grant FWP-2013-SLAC-100164. The work of K.F. was also supported by the US DOE grant DE-FG02-12ER41800 and National Science Foundation grant NSFPHY-1205431.

REFERENCES

- [1] H.N. Chapman, P. Fromme, A. Barty, T.A. White, R.A. Kirian, A. Aquila, M.S. Hunter, J. Schulz, D.P. DePonte, U. Weierstall, R.B. Doak, F.R.N.C. Maia, A. Martin, I. Schlichting, “Femtosecond X-ray protein nanocrystallography”, *Nature* **470**, 73-78 (2011).
- [2] M.M. Seibert, T. Ekeberg, F.R.N.C. Maia, M. Svenda, J. Andreasson, O. Jönsson, D. Odić, B. Iwan, A. Rocker, D. Westphal, M. Hantke, D.P. DePonte, “Single mimivirus particles intercepted and imaged with an X-ray laser”, *Nature* **470**, 78-81 (2011).
- [3] N.M. Kroll, P.L. Morton, M.R. Rosenbluth, “Free-Electron Lasers with Variable Parameter Wiggles”, *IEEE J. Quantum Electron.*, **QE-17**, 1436-1468 (1981).
- [4] X. Wang, H. Freund, D. Harder, W. Miner, J. Murphy, H. Qian, Y. Shen, and X. Yang, “Efficiency and Spectrum Enhancement in a Tapered Free-Electron Laser Amplifier”, *Phys. Rev. Lett.* **103**, 154801 (2009).
- [5] Y. Jiao, J. Wu, Y. Cai, A.W. Chao, W.M. Fawley, J. Frisch, Z. Huang, H.-D. Nuhn, C. Pellegrini, S. Reiche, “Modeling and multidimensional optimization of a tapered free electron laser”, *Phys. Rev. ST Accel. Beams*, **15**, 050704 (2012).
- [6] F. Gori, M. Santarsiero, R. Simon, G. Piquero, R. Borghi, and G. Guattari, “Coherent-mode decomposition of partially polarized, partially coherent sources”, *Journal of the Optical Society of America A*, **20**, 78-84 (2003).
- [7] S. Reiche, “GENESIS 1.3: a fully 3D time-dependent FEL simulation code”, *Nucl. Instrum. Methods A*, **429**, 243 (1999).
- [8] J. Wu and L.H. Yu, “Eigenmodes and mode competition in a high-gain free-electron laser including alternating-gradient focusing”, *Nucl. Instrum. Methods A*, **475**, 79-85 (2001).

ISASE STUDY

K. Fang, X. Huang, S.D. Chen, C. Pellegrini, J. Wu, SLAC, CA 94025, USA

K. Fang, Indiana University, IN 47405, USA

C. Emma, C. Pellegrini, University of California, Los Angeles, CA 90095, USA

S.D. Chen NCTU, Hsinchu 30076, Taiwan

S. Reiche Paul Scherrer Institut, 5232 Villigen PSI, Switzerland

Abstract

Improved Self Amplified Spontaneous Emission (iSASE) is a scheme that reduces FEL bandwidth by increasing phase slippage between the electron bunch and radiation field. This is achieved by repeatedly delaying electrons using phase shifters between undulator sections. Genesis 1.3 [1] is modified to facilitate this simulation. With this simulation code, the iSASE bandwidth reduction mechanism is studied in detail. A Temporal correlation function is introduced to describe the similarity between the new grown field from bunching factor and the amplified shifted field. This correlation function indicates the efficiency of iSASE process.

INTRODUCTION

Improved Self Amplified Spontaneous Emission (iSASE) [2, 3] is capable of improving spectrum by increasing cooperation length, and may have the potential to serve as a self-seeding scheme. With several phase shifters installed along the FEL lattice, optical field can be shifted and connection is built up between electrons that separated by several spikes width away. Then with proper interference between new grown field and optical field, bandwidth can be reduced.

Similar idea, known as phase locking of longitudinal spikes in SASE process, is first introduced by A. Gover [4]. Then phase locking FEL amplifier is studied to generate attosecond xray pulse trains by repeatedly delay electron bunch [5]. Similar configuration is then used to improve temporal correlation of SASE FEL [6, 7].

ISASE MECHANISM

SASE mode, radiation field slips one wave length after every undulator period. Slippage field stimulates electrons to radiate in the same phase. Coherent length is built up as electron bunch and radiation field interact through the undulator. One way to improve the temporal coherence is to provide additional slippage to the radiation field. As it's in the SASE mode, slippage field will stimulate electron bunch to generate similar wave package. Therefore it may improves the correlation function and potentially increase coherence length.

Phase shifters are installed after a few gain length. After phase shifters, radiation field is shifted by ϕ , here ϕ is in pondermotive phase. Shifted radiation field stimulates local electron bunch to radiate in similar pattern. Electron bunch,

on the other hand, has its own energy and density modulation will also generate radiation field accordingly. iSASE mechanism can be understood by viewing optical field as superposition of new grown field from bunching factor and amplified optical field,

$$E_1(\theta; z) = E_0(\theta; z) + aE_0(\theta + \phi; z). \quad (1)$$

Here θ is the pondermotive phase, z is the location along the undulator, $E_0(\theta; z)$ represents new grown field from electron bunch distribution, and $aE_0(\theta + \phi; z)$ is the amplified shifted radiation field, with a to be complex amplitude describing the amplitude and angle difference between these two field. The phase difference can come from radiation field propagation or electron bunch relative drift.

Then the power spectrum is

$$P(\nu; z) = |\tilde{E}_0(\nu; z)|^2 T(\nu, \phi, a), \quad (2)$$

where $\nu = \omega/\omega_s$ and

$$T(\nu, \phi, a) = 1 + |a|^2 + 2|a| \cos(\nu\phi + \varphi), \quad (3)$$

with φ to be the angle of complex amplitude a . Power spectrum is modulated by $T(\nu, \phi, a)$. Modulation of the original power spectrum $|\tilde{E}_0(\nu)|^2$ has potential to reduce bandwidth. The interference term can be written as $2|a| \cos(\Delta\nu\phi + x + \varphi)$, with $\Delta\nu = \nu - 1$ and x is the fractional phase of ϕ . Modulation function has the period determined by relative shift ϕ in frequency domain. The modulation period in frequency domain is $\frac{2\pi}{\phi}$.

The fractional phase x and complex amplitude phase φ contribute as a detuning factor $(x + \varphi)/\phi$ to the modulation since it shifts the modulation function. In order to maintain FEL power, we can choose $T(\nu, \phi, a)$ peak has to overlap with $|\tilde{E}_0(\nu)|^2$ center where the power is maximal. When the delay ϕ is small, then the modulation function is almost uniform across the FEL spectrum. Therefore the bandwidth is almost unchanged. When the modulation period $\frac{2\pi}{\phi}$ is comparable to the FEL bandwidth, modulation to the FEL spectrum becomes more obvious. Yet if the modulation period is too small, multi harmonics may occur in the spectrum. Choosing $\frac{2\pi}{\phi}$ to be close to the FEL bandwidth, modulated power spectrum may have maximal reduction.

Figure 1,2 shows the power spectrum at two different locations from Genesis simulation. To exclude possible contribution from fractional phase, a unbroken undulator is used. This guarantees no phase evolution in the radiation field. Slippage is assumed to be multiple number of wavelength. Effect of a phase shifter is like a modulation function to the power spectrum (Eq. 2). At $z = 20m$ (Fig. 1),

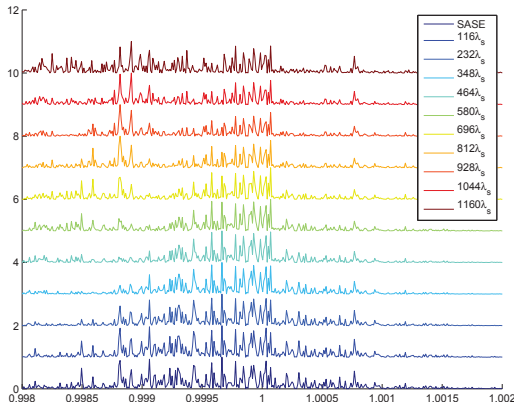


Figure 1: Figure plots the power spectrum at $z = 20m$ for different phase shifter strength. The phase shifter locates at $7m$.

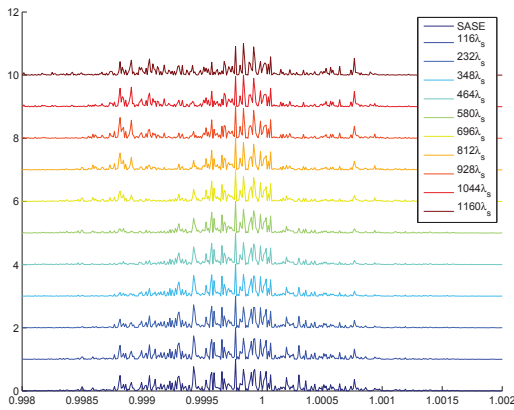


Figure 2: Figure plots the power spectrum at $z = 30m$ for different phase shifter strength. The phase shifter locates at $7m$.

the power spectrum is noisy (see SASE spectrum). Phase slippage $\phi = 348\lambda_s$ is able to clean up the skirt of SASE spectrum, and provide the quietest spectrum among all the cases. For those cases where $\phi > 348\lambda_s$, modulation period becomes smaller. Therefore several humps occur in these cases. At $z = 30m$ (Fig. 2), FEL bandwidth reduces due to FEL interaction. Phase slippage $\phi = 580\lambda_s$ gives the quietest spectrum in this case. $\phi = 348\lambda_s$ on the contrary has a slightly mild modulation across the SASE bandwidth, therefore less bandwidth reduction at this location. Again, side band occurs as phase slippage increases.

The effect of the fractional phase slippage can be translated into detuning in the modulation function. As the modulation function center shifts, different frequency will be amplified. Figure 3 plots the power spectrum at $z = 30m$ with one phase shifter locates at $z = 10m$. Phase error varies from 0° to 360° . As phase error increases, the modulation function starts to blue shift. As a result, some higher frequency signal get amplified. Moreover, since the modulation function is a periodic function, some lower frequency signals are also amplified. When the phase slippage is 180° out of phase, the valley of the modulation function locates

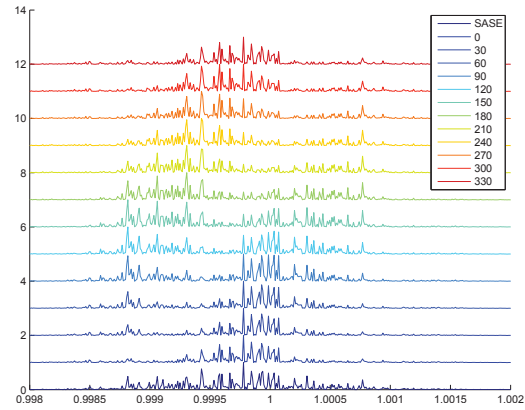


Figure 3: Figure plots the power spectrum at $z = 30m$ for phase shifters with different fractional phase. The phase shift slippage is $580\lambda_s$.

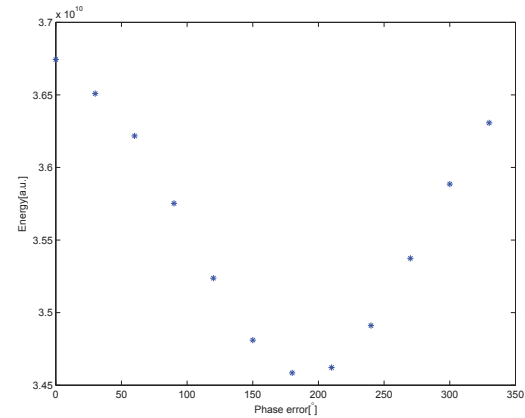


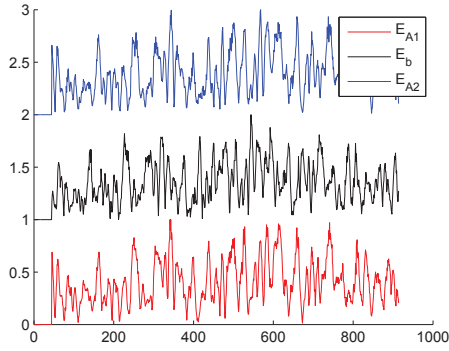
Figure 4: Figure plots the power at $z = 30m$ for phase shifters with different fractional phase. The phase shift slippage is $580\lambda_s$.

at the center of the SASE spectrum, and resulting in two humps with almost equal power in the spectrum. Figure 4 plots correspondingly the power with different phase shifter errors. When the modulation function peaks at the center of FEL natural gain band, FEL power is maximal corresponding to zero fractional phase error. FEL power is minimal if the valley of the modulation function coincides with the center of FEL natural gain band.

CORRELATION FUNCTION

A necessary condition for iSASE to have interference and then modulate the power spectrum is that the new grown radiation field and amplified slipped radiation field have similar distribution. The distribution of new grown field is determined by the prebunched beam. Therefore maintaining the electron bunching factor is essential. Phase shifters are usually dispersive, thus electrons are inevitably rotated in the longitudinal phase space.

To illustrate the interference mechanism, we force electron bunch to maintain its bunching factor distribution through the phase shifter. Figure 5 shows the field envelope

Figure 5: Temporal distribution of E_{A1}, E_b, E_{A2} .

for new grown field and amplified field are similar. The new grown field E_b is obtained by setting the radiation field to zero after passing phase shifter. Effectively this is equivalent to seeding the next undulator section with a prebunched electron bunch. The amplified field $E_A^{(1,2)}$, on the other hand, can be computed in two ways. The first way it's to keep both prebunched beam and shifted radiation field after phase shifter and simulate through the second undulator section. Subtracting E_b from the radiation field in the second section we obtain the amplified field $E_A^{(1)}$. The $E_A^{(2)}$ can be computed by smearing density modulation after passing the phase shifter. This is achieved by resampling macro particles as a fresh beam. Then the electron bunch are uniformly distributed within a wavelength.

Correlation function is used to quantify the similarity between the new grown field and amplified field,

$$g(\phi) = \frac{\langle E_\alpha(\theta) E_\beta^*(\theta + \phi) \rangle}{\sqrt{\langle |E_\alpha(\theta)|^2 \rangle \langle |E_\beta(\theta)|^2 \rangle}}. \quad (4)$$

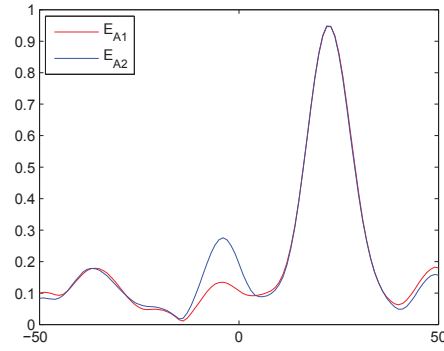
Figure 6 plots the correlation between the new grown field and the amplified field, i.e. correlation between E_b and $E_A^{(1,2)}$. The peak center denotes the relative shift, while height of the peak depicts the similarity. Correlation length can be deduced from the width of the peak. Having a strong correlation between $E_A(\theta)$ and $E_b(\theta)$ is a necessary condition for them to interfere.

CONCLUSION

In this paper, we study the iSASE mechanism with Genesis 1.3 simulation code. Phase shift is translated into a filter function to the power spectrum. Any phase difference between shifted field and new grown field generate a detuned filter function, and may amplify slightly different frequency. A correlation function is introduced to describe the correlation between new grown field and shifted field.

APPENDIX

A new package is being developed to facilitate Genesis to simulate insertion devices like phase shifters. An new

Figure 6: Correlation function between new grown field E_b and shifted field E_A .

element, insertion, is added to the element list. In this element electron bunch and optical field are processed independently. Electrons can be processed by a transfer map. Optical field will be processed according to the optical elements. Then the relative slippage between optical field and electron bunch is taken into account by swapping field.

ACKNOWLEDGEMENT

The authors would like to thank Professor S.-Y. Lee of Indiana University for many stimulated discussions. K.F. would like to express his gratitude to Prof. Lee for many advices. The work was supported by the US Department of Energy (DOE) under contract DE-AC02-76SF00515 and the US DOE Office of Science Early Career Research Program grant FWP-2013-SLAC-100164. The work of K.F. was also supported by the US DOE grant DE-FG02-12ER41800 and National Science Foundation grant NSFPHY-1205431.

REFERENCES

- [1] S. Reiche, "GENESIS 1.3: a fully 3D time-dependent FEL simulation code", Nucl. Instrum. Methods A, **429**, 243 (1999).
- [2] J. Wu et al, "Generation of longitudinally coherent ultra high power X-Ray FEL pulses by phase and amplitude mixing", in *Proceedings of the 32th International Free Electron Laser Conference, Nara, Japan, 2012* (JACoW,2012), p. 237.
- [3] J. Wu et al, "X-Ray spectra and peak power control with iSASE" in *Proceedings of the 4th International Particle Accelerator Conference, Shanghai, China, 2013* (JACoW,2013), p. 2068
- [4] A. Gover, "FEL Prize Lecture: Coherent Electron-Beam Radiation Sources and FELs: A Theoretical Overview", in *Proceedings of the 28th International Free Electron Laser Conference, Berlin, Germany, 2006* (JACoW,2006), p. 1.
- [5] N.R. Thompson and B.W.J. McNeil, "Mode Locking in a Free-Electron Laser Amplifier", Phys. Rev. Lett., **100**, 203901 (2008).
- [6] N.R. Thompson, D.J. Dunning, and B.W.J. McNeil, "Improved temporal coherence in SASE FELs", in *Proceedings of the 1st International Particle Accelerator Conference, Kyoto, Japan, 2010* (IEEE,Newyork,2010), p. 2257.

- [7] B.W.J. McNeil, N.R. Thompson, and D.J. Dunning, “Transform-Limited X-Ray Pulse Generation from a High-Brightness Self-Amplified Spontaneous-Emission Free-Electron Laser”, Phys. Rev. Lett., **110**, 134802 (2013).

MODE COMPONENT EVOLUTION AND COHERENCE ANALYSIS IN TERAWATT TAPERED FEL

K. Fang, S.D. Chen, X. Huang, C. Pellegrini, J. Wu, SLAC, CA 94025, USA

K. Fang, Indiana University, IN 47405, USA

C. Emma, C. Pellegrini, University of California, Los Angeles, CA 90095, USA

S.D. Chen, C.S. Hwang, NCTU, Hsinchu 30076, Taiwan

S. Serkez, Deutsches Elektronen-Synchrotron, 22607 Hamburg, Germany

Abstract

A fast and robust algorithm is developed to decompose FEL radiation field transverse distribution into a set of orthonormal basis. Laguerre Gaussian and Hermite Gaussian can be used in the analysis. The information of mode components strength and Gaussian beam parameters allows users in downstream better utilize FEL. With this method, physics of mode components evolution from starting stage, to linear regime and post saturation are studied with detail. With these decomposed modes, correlation function can be computed with less complexity. Eigenmodes of the FEL system can be solved using this method.

INTRODUCTION

Free Electron Laser (FEL) is a powerful source that generates high brightness radiation for scientific research. Radiation at TW level may be able to resolve a single molecule image [1,2]. One way to improve brightness is to increase total photon number by tapering the undulator. This scheme has been proposed in [3]. Now it is arousing the FEL community's interest [4,5]. Recently the effect different transverse electron distributions on taper efficiency is also studied.

The transverse content for a radiation is an important property of FEL. It may provide useful information in the downstream. Also as it's pointed out in [5], the transverse content plays an important role in tapered FEL. This paper may provide insight into transverse content by decomposing electric field transverse distribution generated from Genesis 1.3 [6] into Hermite Gaussian modes. With this decomposition, correlation function can be computed with less effort. Moreover, this method also provides a tool to study eigenmodes of the FEL system.

MODE DECOMPOSITION METHOD

In this study we decompose electric field into a set of Hermite Gaussian modes. Hermite Gaussian modes is a set of orthonormal basis. Two dimensional Hermite Gaussian modes allows x and y directions to have different distributions. The transverse radiation field along the undulator can be written as

$$E(\mathbf{r}; z) = \sum a_{mn}(z) H_m\left(\frac{\sqrt{2}}{w(z)}x\right) H_n\left(\frac{\sqrt{2}}{w(z)}y\right) \exp(-\zeta r^2). \quad (1)$$

Here $\zeta_r = \frac{1}{w^2}$, $\zeta_i = \frac{k}{2R}$. w is the spot size of fundamental Gaussian mode, while R describes the wave front curvature.

In this work, we use orthogonal condition to find amplitude a_{mn} for each Hermite-Gaussian mode. Wavefront curvature need to be eliminated before applying the orthogonal condition. To fit R , a lens with focal length f is applied to electric field. Then beam waist of the modified field is found through propagation. Curvature radius is found when the spot size of modified electric field diverges in both forward and backward propagation. After eliminating wavefront curvature, orthogonal condition is applied to extract mode amplitudes.

$$a_{mn} = \int E(\mathbf{r}; z) H_x\left(\frac{\sqrt{2}}{w}x\right) H_y\left(\frac{\sqrt{2}}{w}y\right) \exp(-\zeta r^2). \quad (2)$$

This integral has to be evaluated in a discrete form with finite cutoff, nevertheless good accuracy can still be achieved when w falls in some range.

To test the orthogonality, we define a matrix elements

$$C_{ij} = \sum_q H_m\left(\frac{\sqrt{2}x_q}{w}\right) H_n\left(\frac{\sqrt{2}y_q}{w}\right) H_k\left(\frac{\sqrt{2}x_q}{w}\right) H_l\left(\frac{\sqrt{2}y_q}{w}\right) \exp(-\zeta r_q^2) \frac{2\Delta x \Delta y}{w^2}, \quad (3)$$

where i and j has one to one correspondence with (m, n) and (k, l) . Fig. 1 describes how the orthogonality is maintained in this numerical method. In the region where w is small, there is not enough sampling rate to resolve structures in Hermite Gaussian modes. Therefore orthogonality condition is degraded. In large w region, numerical integral is inaccurate because of the cutoff error. Numerical integral could provide accurate expansion for electric field in basis with moderate w . To expand electric field in w where orthogonality condition is not preserved, we could first expand electric field with moderate w . Then expansion in other parameter w' can be computed by transformation method. The amplitudes in w' basis are connected with amplitudes in w basis with

$$a_{mn}(w') = \sum_{k,j} T_{m,k}(w'|w) T_{n,j}(w'|w) a_{kj}(w). \quad (4)$$

Here $T_{m,k}(w'|w) = \int H_m\left(\frac{\sqrt{2}}{w'}x\right) H_k\left(\frac{\sqrt{2}}{w}x\right) \exp\left(-\frac{x^2}{w'^2} - \frac{x^2}{w^2}\right) dx$.

Electric field can be decomposed into Hermite-Gaussian modes along the undulator in a tapered FEL. Yet, there

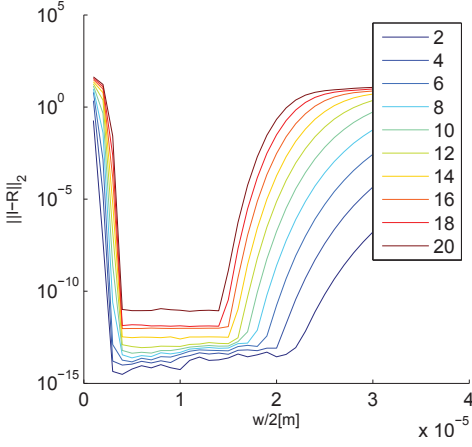


Figure 1: Figure plots how $R = \|I - C\|_2$ varies with w for general FEL simulation condition. 191 grid points are evenly distributed within a $[-180\mu\text{m}, 180\mu\text{m}]$ window in both directions. Different color corresponds to different maximal index number. For example, $N = 4$ corresponds to 16 modes with index $0 \leq m, n \leq 3$.

is free parameter w needs to be determined, for Hermite-Gaussian is a complete set of basis for different w . In linear regime, $w(z)$ describes the Gaussian mode that has the strongest coupling to the electrons, i.e. electric mode that has maximal growth rate. And in this regime, $w(z)$ can be computed using 3D FEL theory, e.g. [7]. In this work, we are going to obtain $w(z)$ by maximizing fundamental mode power. The same method can then be extended to post saturation regime where 3D theory is hard to solve. Fig. 2 plots the power of high order modes $\kappa = \sum_{mn \neq 0} |a_{mn}|^2 / |a_{00}|^2$ as a function of w at different locations of the undulator. κ for different locations have similar dependency on w , i.e. there is a w that could minimize κ . This could be explained as follows. For electric field with some radiation size σ_r , it can be described by fewer terms in Hermite-Gaussian basis with $w \approx 2\sigma_r$ than other w . For case w is significantly larger than $2\sigma_r$, high order modes are added destructively to construct the electric field. For case w is significantly smaller than $2\sigma_r$, high order modes are added constructively.

At the early stage of FEL process, about half of the FEL power is in the high order modes (minimal κ for $L = 10m$). This may also be seen from some structures in the core of the electric field distribution (Fig. 3). These structures indicate the existence of high order mode component. And the decomposition result (Fig. 4) is able to reconstruct these structures. High portion of high order mode is a result of the fact that the input seed is not the eigenmodes of the FEL interaction. Therefore it couples to many high order mode components. And as the FEL interaction proceeds, the fundamental mode, with the highest grow rate, starts to dominate. About 90% of the power is in the fundamental mode when FEL reaches saturation at $z = 30m$ (Fig. 2). As FEL interaction proceeds further into post saturation, high

order mode components start to increase, i.e. κ function has higher minimal value after saturation point after $30m$.

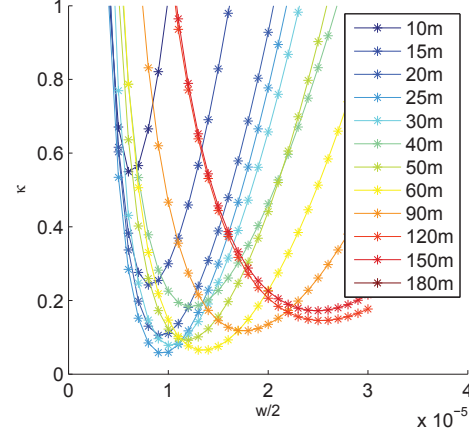


Figure 2: Here plots the total power of all the high order modes for different w . We choose w such $\kappa = \sum_{mn \neq 0} |a_{mn}|^2 / |a_{00}|^2$ is minimized.

COHERENCE ANALYSIS

With the decomposed electric field, coherence function can be computed with less effort.

$$\Gamma(\mathbf{r}_1, \mathbf{r}_2) = \frac{\langle E(\mathbf{r}_1) E^*(\mathbf{r}_2) \rangle}{\sqrt{\langle |E(\mathbf{r}_1)|^2 \rangle \langle |E(\mathbf{r}_2)|^2 \rangle}} \quad (5)$$

Then the time average can be computed as,

$$\begin{aligned} \langle E(\mathbf{r}_1) E^*(\mathbf{r}_2) \rangle &= \sum \langle a_{mn} a_{pq}^* \rangle H_m\left(\frac{\sqrt{2}}{w} x_1\right) H_n\left(\frac{\sqrt{2}}{w} y_1\right) \\ &\quad H_p\left(\frac{\sqrt{2}}{w} x_2\right) H_q\left(\frac{\sqrt{2}}{w} y_2\right) \exp\left(-\frac{\mathbf{r}_1^2 + \mathbf{r}_2^2}{w^2}\right), \end{aligned} \quad (6)$$

where $\langle a_{mn} a_{pq}^* \rangle = \int a_{mn}(s) a_{pq}^*(s) ds$. The advantage of this method is that the ensemble average $\langle \dots \rangle$ only need to compute once.

Fig. 5 plots the one point correlation function, i.e. $\mathbf{r}_1 = 0$ in Eq. 5, in different regimes. At the beginning, only the central area has high correlation. As FEL process evolves, radiation field is diffracted from the center, therefore phase information is brought to the outer region. There is some ring structure in the correlation function. These structures come from the diffraction in the undulator gap. As FEL reaches post saturation regime, diffraction effect becomes even more important, resulting in a large coherent area.

MODE EVOLUTION

In FEL process, electric field evolution can be expressed as

$$\begin{aligned} \hat{O}_{FEL}(\Psi_1 + \Psi_s) &= \tilde{\Psi}_1 \\ &= \Psi_2 + \hat{O}_{FEL} \Psi_s. \end{aligned} \quad (7)$$

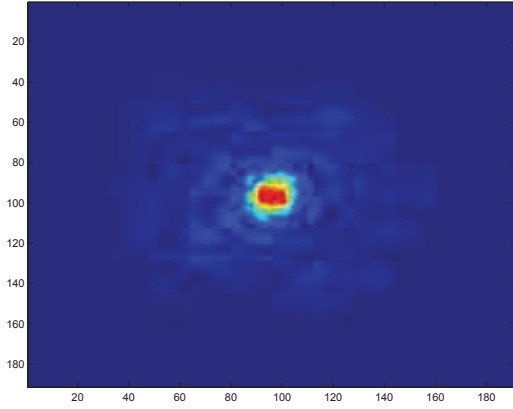


Figure 3: Electric field at 10m from Genesis simulation.

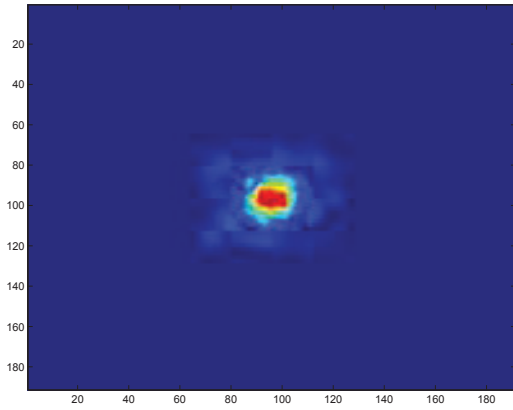
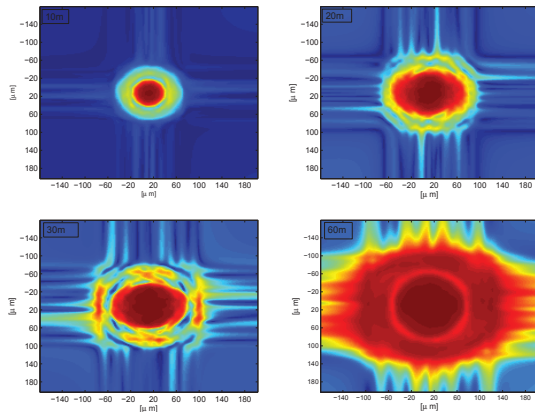
Figure 4: Reconstructed field from Hermite Gaussian modes, $E = \sum_{m,n=0} a_{mn} H_m(\frac{\sqrt{2}}{w}x) H_n(\frac{\sqrt{2}}{w}y) \exp(-\frac{x^2+y^2}{w^2})$.

Figure 5: One point correlation function is plotted at different locations of the undulator. Four plots represent initial stages, linear regime, saturation and postsaturation respectively. Coherence area is increasing as FEL process proceeds.

Here $\Psi_{1,2}$ are the state of transverse distribution at two different locations, while Ψ_s represents the state accounting for bunching at location one. \hat{O}_{FEL} is a non self-adjoint linear operator that evolves electric field from location 1 to location 2. Genesis is used to compute this evolution. Transverse electric field distribution Ψ_1 interacts with particle distribution Ψ_s in Genesis. The output electric field $\hat{\Psi}_1$ is then a linear superposition of both Ψ_2 and $\hat{O}_{FEL}\Psi_s$. Therefore the evolved state Ψ_2 from Ψ_1 is computed by $\hat{\Psi}_1 - \hat{O}_{FEL}\Psi_s$, where $\hat{O}_{FEL}\Psi_s$ is computed by simulating by setting input radiation zero.

Our simulation scheme using Genesis is described as follows,

- Simulate FEL process through an Undulator section $U1$ with the output electric field transverse distribution E_1 and electron distribution $f_1(\vec{x})$.
- Decompose transverse profile E_1 into Hermite Gaussian modes $\{HG_n\}$.
- Simulate each Hermite Gaussian modes HG_n independently with electron distribution $f_1(\vec{x})$ for another section $U2$ with output field E_{2n} .
- Simulate electron beam $f(\vec{x})$ without electric field for $U2$ with output field E_b .
- HG'_n is then obtained by subtracting E_b from E_{2n} .

Fig. 6 plots the evolution of the first four Hermite Gaussian modes from 10m to 30m. The first two columns plot the input Hermite Gaussian modes and final field. The third column plots the free propagation of each input mode over 20m. The modes in the second column deviate from both the first and third column indicating interaction with electron beam. Power amplification for each Hermite Gaussian mode is plotted in Fig. 7. For 10m to 30m, where is the linear regime, the fundamental mode has the strongest coupling to the electron beam and therefore the maximal power gain. Therefore the transverse distribution of electric field is able to maintain a Gaussian like distribution in linear regime. For the post saturation regime, e.g. from 50m to 70m, higher order modes $HG_{1,0}$ and $HG_{0,1}$ have stronger coupling to the electron beam than the fundamental mode (Fig. 7). This agrees with the increase of ratio of high order mode we find out in mode decomposition as FEL proceed to post saturation.

HG'_n is then decomposed into Hermite-Gaussian mode,

$$\hat{O}_{FEL}\phi_n = \sum \alpha_{pn} \phi_p. \quad (8)$$

Eigenmodes of \hat{O}_{FEL} can then be computed from this $\{\alpha\}$ matrix. Assuming the q th eigenmode is defined as $\sum \beta_n^q \phi_n$,

$$\hat{O}_{FEL} \sum_n \beta_n^q \phi_n = \lambda^q \sum_n \beta_n^q \phi_n \quad (9)$$

$$= \sum_{n,p} \beta_n^q \alpha_{pn} \phi_p. \quad (10)$$

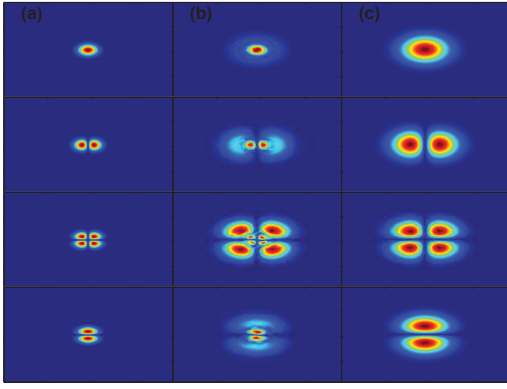


Figure 6: Column(a) plots the input Hermite Gaussian modes at the entrance of the undulator section. Column(b) plots the resultant field for each Hermite Gaussian mode at the end. Column(c) plots the free propagation result across the same distance as a comparison.

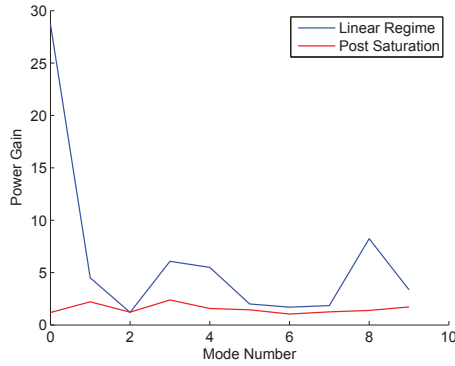


Figure 7: Power gain is computed by dividing the power of the input mode HG_n by the power of the output mode HG'_n .

Since \hat{O}_{FEL} is a non-self-adjoint operator, $\{\beta^q\}$ are not orthogonal vectors and $\{\lambda^q\}$ are complex eigenvalues. Fig. 8 plots the first four eigenmodes for the \hat{O}_{FEL} from $15m$ to $25m$. The first mode is a Gaussian like mode. The second and third mode are dipole mode like, and with different orientations. The fourth mode is azimuthal symmetric and has one node in radial direction. The first and fourth mode are usually found as the first and second mode in 3D FEL theory. In these theories, mostly an azimuthal symmetry in electric field is assumed. In our simulation, we are able to find modes that break this symmetry since the Hermite Gaussian basis has this degree of freedom. As a comparison, we plot the interaction of these eigenmodes with electron bunch and their free propagation results for the same distance. Eigenmodes maintain their distribution through interaction with electron beam. If the eigenmodes are propagated freely across the same distance, as is shown in column (c), distribution will be strongly diffracted.

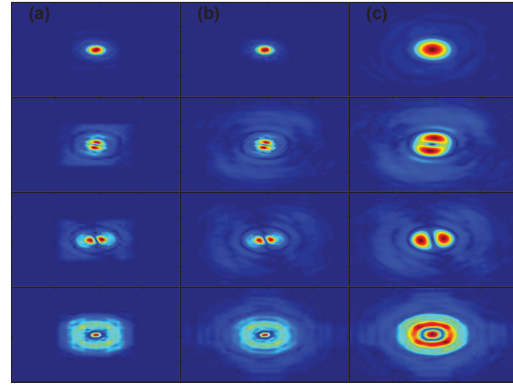


Figure 8: Column (a) plots the eigenmodes at the entrance of the undulator. Column (b) plots output field at the end of the undulator for each mode respectively. Column (c) shows the free propagation result across the same distance for each eigenmode.

CONCLUSION

In this paper, we propose a mode decomposition method using Hermite Gaussian mode as basis. We find that there are some region of w , within which the orthogonal condition is well satisfied. Wavefront curvature R is fitted by free propagation method. And w is chosen such that the fundamental Gaussian mode has the most dominating power. With this method, we are able to analyze mode component in different regimes. The fundamental mode is found to maintain a good portion of power in a tapered FEL. Coherence function is computed using the decomposed mode amplitude. Mode evolution is also studied based on this method. The eigenmodes of the FEL operator is computed by simulating Hermite Gaussian mode interacting with electron beam individually.

ACKNOWLEDGMENT

The authors would like to thank Professor S.-Y. Lee of Indiana University for many stimulated discussions. K.F. would like to express his gratitude to Prof. Lee for many advices. The work was supported by the US Department of Energy (DOE) under contract DE-AC02-76SF00515 and the US DOE Office of Science Early Career Research Program grant FWP-2013-SLAC-100164. The work of K.F. was also supported by the US DOE grant DE-FG02-12ER41800 and National Science Foundation grant NSFPHY-1205431.

REFERENCES

- [1] H.N. Chapman, P. Fromme, A. Barty, T.A White, R.A. Kirian, A. Aquila, M.S. Hunter, J. Schulz, D.P. DePonte, U. Weierstall, R.B. Doak, F.R.N.C. Maia, A. Martin, I. Schlichting, "Femtosecond X-ray protein nanocrystallography", *Nature* **470**, 73-78 (2011).
- [2] M.M. Seibert, T. Ekeberg, F.R.N.C. Maia, M. Svenda, J. Andreasson, O. Jönsson, D. Odić, B. Iwan, A. Rocker, D. Westphal, M. Hantke, D.P. DePonte, "Single mimivirus particles

- intercepted and imaged with an X-ray laser”, *Nature* **470**, 78-81 (2011).
- [3] N.M. Kroll, P.L. Morton, M.R. Rosenbluth, “Free-Electron Lasers with Variable Parameter Wigglers”, *IEEE J. Quantum Electron.*, **QE-17**, 1436-1468 (1981).
- [4] X. Wang, H. Freund, D. Harder, W. Miner, J. Murphy, H. Qian, Y. Shen, and X. Yang, “Efficiency and Spectrum Enhancement in a Tapered Free-Electron Laser Amplifier”, *Phys. Rev. Lett.* **103**, 154801 (2009).
- [5] Y. Jiao, J. Wu, Y. Cai, A.W. Chao, W.M. Fawley, J. Frisch, Z. Huang, H.-D. Nuhn, C. Pellegrini, S. Reiche, “Modeling and multidimensional optimization of a tapered free electron laser”, *Phys. Rev. ST Accel. Beams*, **15**, 050704 (2012).
- [6] S. Reiche, “GENESIS 1.3: a fully 3D time-dependent FEL simulation code”, *Nucl. Instrum. Methods A*, **429**, 243 (1999).
- [7] J. Wu and L.H. Yu, “Eigenmodes and mode competition in a high-gain free-electron laser including alternating-gradient focusing”, *Nucl. Instrum. Methods A*, **475**, 79-85 (2001).

FEL CODE COMPARISON FOR THE PRODUCTION OF HARMONICS VIA HARMONIC LASING*

G. Marcus[†], W. M. Fawley, SLAC, Menlo Park, CA, USA
E. A. Schneidmiller, M. V. Yurkov, DESY, Hamburg,
Germany S. Reiche, PSI, Villigen, Switzerland

Abstract

Harmonic lasing offers an attractive option to significantly extend the photon energy range of FEL beamlines. Here, the fundamental FEL radiation is suppressed by various combinations of phase shifters, attenuators, and detuned undulators while the radiation at a desired harmonic is allowed to grow linearly. The support of numerical simulations is extensively used in evaluating the performance of this scheme. This paper compares the results of harmonic growth in the harmonic lasing scheme using three FEL codes: *FAST*, *GENESIS*, and *GINGER*.

INTRODUCTION

Numerical simulation has been a critical tool both in the design and the commissioning of short wavelength free-electron lasers based upon the principle of self-amplified spontaneous emission (SASE) such as *FLASH* and the *LCLS*. In part due to the complex physics such as the varying exponential growth rates as a function of wavelength, the effective startup noise, and radiation-electron beam slippage effects that help develop longitudinal coherence, accurate numerical modelling for SASE configurations can be more challenging than that required for more simple time-steady FEL amplifiers. Over the past three decades, numerous simulation codes have been developed for FEL modelling purposes, ranging from 1D, time-steady approximations to fully 3D, time-dependent approaches. Some code-to-code benchmarking has been done for high gain FEL's. The study by Biedron *et al.* [1] in the very late 1990's compared results from five different codes for the linear growth rates and saturated power for a time-steady test case based upon parameters corresponding to the Argonne LEUTL FEL. A decade later Giannessi *et al.* [2] compared fundamental and harmonic power vs. z profiles for both single frequency and time-dependent, externally-seeded test cases, finding good agreement between the 1D *PERSEO* code and the 3D *GENESIS* and *MEDUSA* codes. However, apart from a comparison of SASE startup in the *GENESIS* and *GINGER* codes with theoretical predictions [3], there appear to be few if any code comparison studies in the literature for full SASE cases.

Here we give the results of a small SASE benchmarking study where we have concentrated upon cases with parameters related to the operating *LCLS*-1 FEL at SLAC and to the upcoming, soft x-ray *LCLS*-2 machine. The codes used were *FAST*, *GENESIS*, and *GINGER*, each of which has

been used extensively to model SASE-based FELs and each of which has sufficient dimensionality to examine the development of longitudinal and transverse coherence at both the fundamental FEL resonant wavelength and higher odd harmonics. Because of the recent interest in trying to reach higher output photon energies via use of harmonic emission (see, *e.g.*, [4, 5]), we also wanted to look reasonably carefully at the gain and saturation of the third harmonic in "lasing mode", *i.e.*, in situations where the fundamental is suppressed allowing the third harmonic to grow to much higher saturated powers than would be true otherwise. The remainder of this paper is arranged as follows. In §II, we give brief descriptions of each of the three codes concentrating on the features most relevant to SASE and harmonic emission. In §III we present the results of two LCLS-related cases: a) 6-keV fundamental and 18-keV third harmonic emission for a continuous (*i.e.*, non-segmented) *LCLS*-1 undulator initiated by shot noise b) 1.67-keV fundamental and 5-keV third harmonic emission for a hypothetical, segmented *LCLS*-II undulator with break sections in which there are special phase shifters tuned to suppress the fundamental via phase shifts of $2/3$ and $4/3$ wavelengths. We conclude in §IV with a short discussion of our findings.

CODE DESCRIPTIONS

In this section we describe some basic characteristics of the three codes used for this study. They share many common features including a 3D particle mover, an eikonal (*i.e.*, slowly varying envelope approximation) field solver and wiggle-period averaging for calculating the coupling between the radiation and the beam electrons. Each code works in the time domain (*i.e.* spectral decomposition is done only via post-processing) and also subdivides the electron beam into "slices" whose longitudinal centers are spaced uniformly.

FAST

FAST is the generic name for a set of codes developed for analysis of the FEL amplification process in the framework of 1-D and 3-D models using different techniques as described in [6–9]. Analytical techniques implemented in these codes allows analysis of beam radiation modes via an eigenvalue equation and the amplification process during the exponential growth stage (initial-value problem). The simulation codes can simulate the FEL process with both steady-state and time-dependent models and can also treat odd harmonic emission in planar undulator geometries [10]. The three-dimensional version of *FAST* [11] takes into ac-

* This work was supported at SLAC by the U.S. Department of Energy under Contract No. DE-AC02-76SF00515.

[†] gmarcus@slac.stanford.edu

count all important physical effects: diffraction, slippage effects, space charge, and emittance and energy spread in the electron beam. The field solver uses retarded potentials and expands the radiation via azimuthal modes. *FAST* has been thoroughly tested in the high gain exponential regime using analytical results for the beam radiation modes (complex eigenvalues and eigenfunctions) [6–8]. It has also been tested from shot noise start-up through the linear stage of amplification against three-dimensional analytical results for the initial-value problem [9]. Start-up from electron beam shot noise can be simulated either by an artificial macroparticle ensemble [12, 13] or by tracing the *actual* number of electrons in the beam [14], initially randomly distributed in the full 6D phase space. All the *FAST* results presented in this paper are calculated with actual number of electrons.

GENESIS

GENESIS [15] is a time-dependent 3D FEL simulation program where the radiation field and macroparticle source terms are discretized on a Cartesian mesh. As with *FAST* and *GINGER*, shot noise can be simulated by standard methods [12, 13]; since the latest *GENESIS* version runs on reasonably large computer clusters, in some situations the code can model the actual number of beam electrons, thus *a priori* providing the correct shot noise at any frequency. Harmonic emission has been implemented by using the effective coupling factors [16] for odd and even harmonics. The user can choose either to model the self-consistent interaction of the higher harmonics of the radiation field with the electron beam (*i.e.*, true lasing) or, alternatively, to calculate the so-called non-linear emission associated with the strong harmonic bunching factor that occurs as the fundamental approaches saturation.

GINGER

GINGER [17] differs from the previous two codes in that the standard field solver model employs 2D cylindrical axisymmetry. Thus any gain, energy spread and saturation effects due to modes with higher order azimuthal number will be neglected. The radial grid follows a mathematical *sinh* function giving a nearly constant spacing near the axis and exponentially-expanding spacing much farther out, thus permitting quite distant boundaries with reasonable numbers of grid cells (e.g., $nr = 128$). Recently, the *GINGER* field solver has been extended to handle true harmonic lasing (*i.e.*, not only the nonlinear harmonic emission that was discussed in [18]). The z -advance control algorithm is such that arbitrary length drift spaces are properly modelled (including vacuum field propagation); their length is not required to be an integer of the nominal z -step size.

BENCHMARK CASES

We looked at two cases that would test numerically various SASE physics at both the fundamental and third harmonic radiation wavelengths such as the effective input noise signal,

the growth rate in the linear regime, and the saturation level. We now discuss each of them in turn.

Table 1: Test Case e-Beam and Undulator Parameters

parameter	unit	LCLS-1	LCLS-2
Current	kA	3.0	1.0
Emittance	mm-mrad	0.40	0.40
Energy	GeV	11.62	4.0
σ_E	keV	1400	500
$\langle \beta_{x,y} \rangle$	m	26.0	12.0
λ_u	mm	30.0	26.0

LCLS-I Continuous Undulator

For our first study we chose a case that nominally corresponds to the LCLS-1 FEL at SLAC operating at a 6-keV fundamental. For purposes of simplification, we considered a continuous, unsegmented undulator, *i.e.*, one without any break sections. The electron beam and undulator parameters are shown in the third column of Table 1. For this and the other cases, energy loss and increased incoherent energy spread due to broadband spontaneous emission was artificially suppressed. Artificial harmonic focusing was applied resulting in a 26-m beta function, a value comparable to the average value due to the quadrupole focusing in the actual LCLS. Due to the low normalised emittance and high current, there is strong gain at the fundamental and power saturation occurs by $z \approx 45$ m. As shown in Fig. 1, each code shows a saturation level of about 30 GW. The initial noise levels depend upon the dimensionality of the field solver with *GINGER* and *FAST* with enforced axisymmetry showing good agreement as would be expected. The *GENESIS* results are nearly identical to those of *FAST* run that included up to $m = \pm 2$ azimuthal mode number. As pointed out in [3], the magnitude of the startup spontaneous emission is a function of the transverse gridding with finer spacing including more transverse modes and thus more power.

The results for the situation with third harmonic lasing only (fundamental emission artificially suppressed) are quite similar. Examining Fig. 2 one sees that *GINGER* saturates at a few percent higher power level and *GENESIS* slightly differs from *FAST* with $|m| \leq 2$ in the linear gain region from 25 to 55 m. But overall, the three independent codes agree strikingly well in both the effective noise level and final saturation power. We also found that the final saturation power in *FAST* is essentially independent of the maximum allowable azimuthal mode number, at least through $m = \pm 3$.

LCLS-II Optimized Third Harmonic Lasing with Phase Shifters

Our second benchmarking case corresponds to LCLS-2 operating in the soft x-ray regime. Compared with LCLS-1, the hypothetical LCLS-2 design has much lower current and energy but significantly stronger focusing. Here the

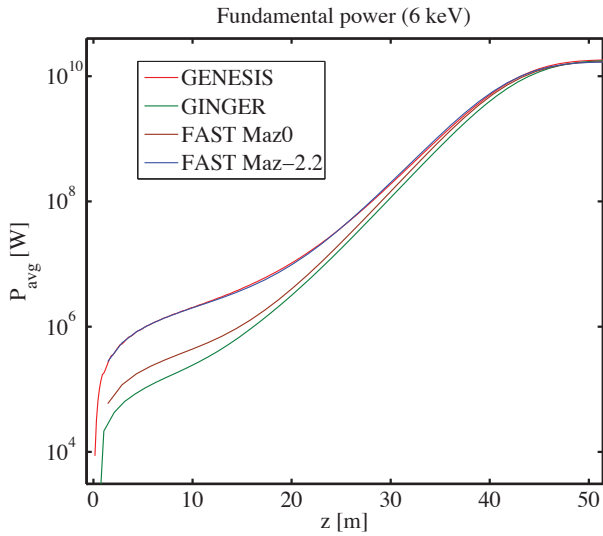


Figure 1: Growth of fundamental vs. z for LCLS-1 parameters. One FAST run corresponds to axisymmetry ("Maz0") while the other includes azimuthal modes in the interval $m = \pm 2$ ("Maz-2.2").

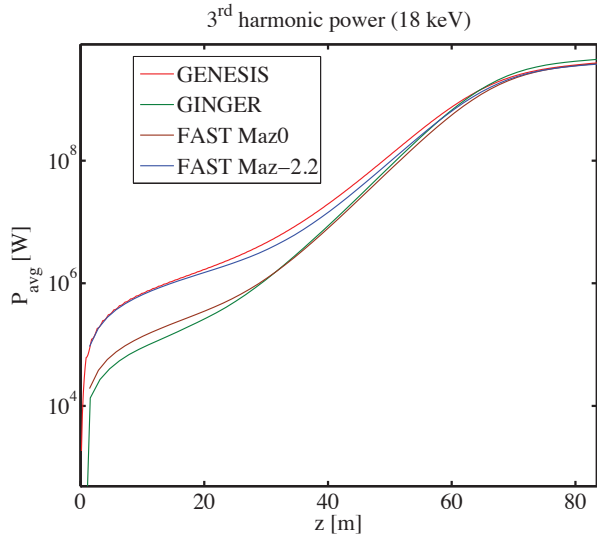


Figure 2: Growth of third harmonic vs. z for LCLS-1 parameters with the fundamental emission completely artificially suppressed.

26-mm period, planar-polarised, variable-gap undulator is segmented with a periodicity of two short break sections ($L = 0.13$ m) and one long break ($L = 0.78$ m) with the active undulator segments having lengths of 1.17 m. For focussing, the dominant term in the GENESIS run was provided by a FODO quadrupole lattice while FAST and GINGER adopted an artificial, continuous in z harmonic component.

Since LCLS-II will have wavelength tunability via a changing K , the break sections will have active phase shifters in order to keep the electron beam and radiation in phase. This capability gives the option of following suggestions by McNeil *et al.* [19] and Schneidmiller and Yurkov [5] to pur-

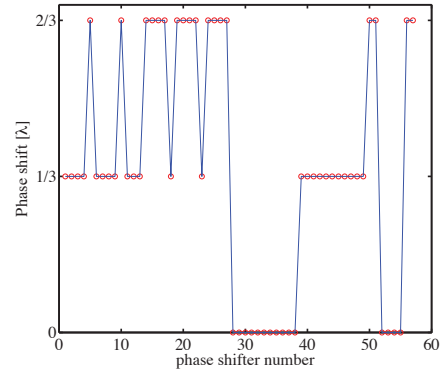


Figure 3: Graphical representation of phase shifter values (normalised to the radiation wavelength) versus break section position in the LCLS-II benchmark case. A positive value corresponds to an incremental increase of the electron beam's delay (and a decrease in ponderomotive phase) relative to what would give exact phase resonance with the electromagnetic field.

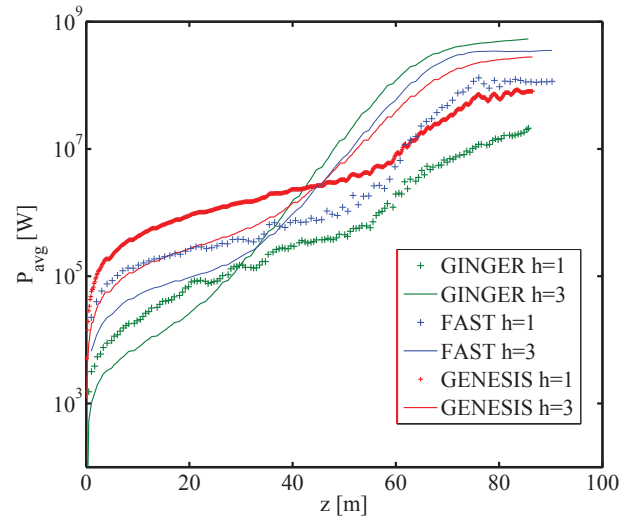


Figure 4: Growth of fundamental (1.67 keV; symbols and thick line) and third harmonic (5 keV; thin lines) vs. z for a hypothetical LCLS-II case in which phase shifters suppress growth at the fundamental.

posefully use combinations of $\Delta\Phi = 2\pi/3$ and $\Delta\Phi = 4\pi/3$ phase shifters to suppress the lasing of the fundamental while not affecting that of the third harmonic. In principle this scheme allows the harmonic to reach saturation without its gain being depressed by incoherent energy spread associated with growth in the fundamental power. We followed the general prescription of Ref. [5] for picking phase shifter values as a function of break position. Figure 3 shows the particular values chosen (but note that we plot the increase in electron beam delay, not $\Delta\Phi$ which has the opposite sign).

Our simulation results, as displayed in Fig. 4, show the variable phase shifter disruption succeeds quite well in suppressing the SASE growth of the fundamental at 1.67 keV

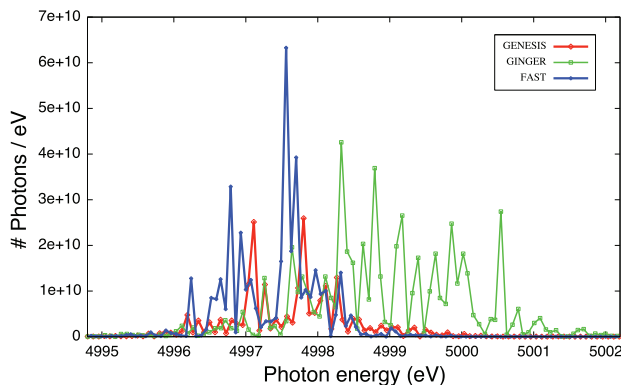


Figure 5: Output spectrum in 5 keV region for the hypothetical LCLS-II of the previous two figures. The spectral intensity corresponds to a pulse length of 54 fs. The difference in the mean wavelength between the GINGER run and the other codes is due to a slightly different K .

with barely any growth beyond the normal spontaneous component up to $z = 60$ m. In the next twenty meters there does appear to be some coherent exponential gain but by this point the third harmonic at 5 keV photon energy has saturated at a value of ~ 500 MW average power, nearly an order of magnitude greater than is true for the fundamental. The integrated output spectra from a single SASE run, as shown in Fig. 5, show an inverse normalized RMS bandwidth of about 5000.

While the code agreement is reasonably good with respect to the third harmonic power vs. z , FAST and especially GINGER show greater saturated power than does GENESIS. At present we do not fully understand the reasons for the discrepancy. Tests with FAST appear to rule out a dependence of the saturated output power on the number of included azimuthal modes. Both GENESIS and GINGER show some dependence of $P(z)$ on the macroparticle number per slice; the final power in GINGER at $z = 86$ m drops by 20% for a $4\times$ increase in particle number to 65K per slice. For GENESIS simulation of the LCLS-I case, the effective noise power in the fastest growing mode can change $2\times$ for a $8\times$ increase in macroparticle number although the asymptotic power is virtually unchanged.

DISCUSSION

In this study we have examined the predictions of three standard multi-dimensional FEL simulation codes, FAST, GENESIS, and GINGER, regarding SASE growth of the fundamental and third harmonic for two cases related to LCLS parameters. We have found for an LCLS-I like case the independent growth and saturation of the fundamental and third harmonic power are nearly identical in the three codes once the exponentially growing modes dominate the spontaneous background. The fully 3D codes GENESIS and FAST agree best in the "spontaneous regime" before the fastest growing modes dominate when the latter is limited to azimuthal modes with $|m| \leq 2$. GINGER and FAST also agree in this

regime when the latter is run with azimuthal symmetry, *i.e.*, only the $m = 0$ mode.

A second test case involving a segmented, LCLS-II like undulator with phase shifters shows that following the prescription of Ref. [5] introducing shifts of $\Delta\Phi = 2\pi/3, 4\pi/3$ successfully suppresses the fundamental growth so that the third harmonic at 5 keV reaches saturation at levels of 500 MW. While the code agreement is generally good, there are differences in the saturation regime that at present are not fully understood. The differences suggest that numerical modelling of higher harmonics is likely more sensitive to choices of shot noise algorithms, gridding, and macroparticle number.

We are pleased to acknowledge useful discussions with Z. Huang and T. Raubenheimer.

REFERENCES

- [1] S.G. Biedron *et al.*, "Multi-Dimensional Free-Electron Laser Simulation Codes: A Comparison Study", *Nucl. Instr. Meth. Phys. Res., Sect. A* **445**, 110 (2000).
- [2] L. Giannessi *et al.*, "Higher-Order Harmonics Coupling in Different Free-Electron Laser Codes", *Nucl. Instr. Meth. Phys. Res., Sect. A* **593**, 143 (2008).
- [3] Z. Huang, K.-J. Kim, "Spontaneous and Amplified Radiation at the Initial Stage of a SASE FEL", *Nucl. Instr. Meth. Phys. Res., Sect. A* **507**, 65 (2003).
- [4] D. Ratner *et al.*, "Harmonic Lasing at the LCLS", *Proc. FEL 2013*, <http://accelconf.web.cern.ch/AccelConf/FEL2013/papers/wepso53.pdf>
- [5] E.A. Schneidmiller, M.V. Yurkov, "A Possible Upgrade of FLASH for Harmonic Lasing Down to 1.3 nm", *Nucl. Instr. Meth. Phys. Res., Sect. A* **717**, 37 (2013).
- [6] E.L. Saldin, E.A. Schneidmiller, M.V. Yurkov, "The Physics of Free Electron Lasers" (Springer-Verlag, Berlin, 1999).
- [7] E.L. Saldin, E.A. Schneidmiller, M.V. Yurkov, "The general solution of the eigenvalue problem for a high-gain FEL", *Nucl. Instr. Meth. Phys. Res., Sect. A* **475**, 86 (2001).
- [8] E.A. Schneidmiller, M.V. Yurkov, "Harmonic lasing in x-ray free electron lasers", *Phys. Rev. ST Accel. Beams* **15**, 080702 (2012).
- [9] E.L. Saldin, E.A. Schneidmiller, M.V. Yurkov, "Diffraction effects in the self-amplified spontaneous emission FEL", *Opt. Comm.* **186**, 185 (2000).
- [10] E.A. Schneidmiller, M.V. Yurkov, "Coherence Properties of the Odd Harmonics", *Proc. FEL 2012*, <http://accelconf.web.cern.ch/AccelConf/FEL2012/papers/mopd08.pdf>
- [11] E.L. Saldin, E.A. Schneidmiller, M.V. Yurkov, "FAST: a three-dimensional time-dependent FEL simulation code", *Nucl. Instr. Meth. Phys. Res., Sect. A* **429**, 233 (1999).
- [12] C. Penman, B.W.J. McNeil, "Simulation of input electron noise in the free-electron laser", *Opt. Comm.* **90**, 82 (1992).
- [13] W.M. Fawley, "Algorithm for loading shot noise microbunching in multidimensional, free-electron laser simulation codes", *Phys. Rev. ST Accel. Beams* **5**, 070701 (2002).

- [14] E.L. Saldin, E.A. Schneidmiller, M.V. Yurkov, “Coherence properties of the radiation from X-ray free electron laser”, *Opt. Comm.* **281**, 1179 (2008).
- [15] S. Reiche, “GENESIS 1.3: a fully 3D time-dependent FEL simulation code”, *Nucl. Instr. Meth. Phys. Res., Sect. A* **429**, 243 (1999).
- [16] S. Reiche, P. Musumeci, K. Goldammer, “Recent Upgrade to the Free-electron Laser Code Genesis 1.3”, Proc. PAC 2007, Albuquerque, NM, USA, p 1269.
- [17] W.M. Fawley, “A User Manual for GINGER”, LBNL-49625-Rev. 1 (2004); see also http://www-ssrl.slac.stanford.edu/lcls/lcls_tech_notes.html/LCLS-TN-04-3.pdf
- [18] W.M. Fawley, “An Enhanced GINGER Simulation Code with Harmonic Emission and HDF5 IO Capabilities”, Proc. FEL 2006, <http://www.JACoW.org/AccelConf/f06/PAPERS/MOPPH073.PDF>
- [19] B.W.J. McNeil *et al.*, “Harmonic Lasing in a Free-Electron-Laser Amplifier”, *Phys. Rev. Lett.* **96**, 084801 (2006).

FEL SIMULATION AND PERFORMANCE STUDIES FOR LCLS-II

G. Marcus, Y. Ding, P. Emma, Z. Huang, T. Raubenheimer, L. Wang, J. Wu
SLAC, Menlo Park, CA 94025, USA

Abstract

The design and performance of the LCLS-II free-electron laser beamlines are presented using start-to-end numerical particle simulations. The particular beamline geometries were chosen to cover a large photon energy tuning range with x-ray pulse length and bandwidth flexibility. Results for self-amplified spontaneous emission and self-seeded operational modes are described in detail for both hard and soft x-ray beamlines in the baseline design.

INTRODUCTION

The LCLS-II is envisioned as an advanced x-ray FEL light source that will be fed by both a superconducting accelerator and the existing LCLS copper linac and will be capable of delivering electron beams at a high repetition rate, up to 1 MHz, to a collection of undulators [1–3]. In the initial phase, referred to as the baseline scenario, the CW linac will feed two independently tuned undulators capable of producing radiation covering a large spectral range with each beamline dedicated to either soft or hard x-ray photon energies. The soft x-ray (SXR) beamline will cover photon energies from 0.2 – 1.3 keV while the hard x-ray beamline will cover 1.0 – 5.0 keV. The copper linac will feed the hard x-ray beamline exclusively and will cover photon energies from 1 – 25 keV. Each of the beamlines will be capable of producing radiation in both the self-amplified spontaneous emission (SASE) and self-seeded (SS) operational modes [4, 5]. While various external seeding and other advanced FEL concepts are being explored for LCLS-II [6, 7], this paper reports the results of detailed FEL simulations in the baseline case for multiple start-to-end (S2E) charge distributions coming from the CW superconducting linac at the higher end of the individual undulator beamline tuning ranges. The simulation code ASTRA [8] was used to track the electron beams through the injector, ELEGANT [9] was used to transport the beams through the linac to the undulators, and GENESIS [10] was used for FEL simulations.

ELECTRON BEAM AND UNDULATOR PARAMETERS

The nominal LCLS-II electron beam and undulator design parameters can be found in Table 1. Both the HXR and SXR beamlines will employ a variable gap hybrid permanent magnet undulator broken into individual segments that are interspersed with strong focusing quadrupoles, adjustable phase shifters, and various other diagnostic elements. The vacuum chamber will be made of Aluminum and will have a rectangular cross section with a full height of 5 mm. The relaxation time for Aluminum is $\tau = 8$ fs and can be used to specify not only the DC but also the AC contributions to the

Table 1: Nominal Electron Beam and Undulator Parameters for the Baseline LCLS-II Scenario

Parameter	Symbol	Value SXR(HXR)	Unit
e-beam energy	E	4.0	GeV
emittance	ϵ	0.45	μm
current	I	1000	A
energy spread	σ_E	500	keV
beta	$\langle\beta\rangle$	12(13)	m
undulator period	λ_u	39(26)	mm
segment length	L_u	3.4	m
break length	L_b	1.0	m
# segments	N_u	21(32)	-
total length	L_{tot}	96(149)	m

resistive wall wakefield (RWW) in the FEL simulations [11]. The SXR beamline is envisioned to operate with a SASE and SS tuning range of 0.2 – 1.3 keV while the HXR beamline will operate from 1.0 – 5.0 keV in the SASE mode and will use the electron beam from the copper linac for self-seeding from 5.0 – 12.0 keV in the baseline case.

The slice parameters of a S2E 100 pC electron beam are illustrated in Figure 1. The core of the bunch, which is roughly 60 fs long, has a very flat phase space with a current of $I \sim 900$ A, slice energy spread of $\sigma_E \sim 450$ keV, and slice emittances of $\epsilon_n \sim 0.27 \mu\text{m}$, all of which satisfy the design requirements. It is also relatively well matched to the lattice where the matching parameter $B_{mag} = 1/2 (\beta_0\gamma - 2\alpha_0\alpha + \gamma_0\beta) \leq 1.3 - 1.4$ typically does not affect the performance [12, 13].

The slice parameters of a S2E 20 pC electron beam are illustrated in Figure 2. The core of the bunch, which is roughly 30 fs long, has a relatively flat phase space with a current of $I \sim 550$ A, slice energy spread of $\sigma_E \sim 280$ keV, and slice emittances of $\epsilon_n \sim 0.1 \mu\text{m}$. The significantly smaller slice emittance and energy spread are extremely beneficial to the performance of the HXR beamline at the high end of the tuning range, as will be illustrated shortly, where the FEL is most sensitive to these parameters. The 20 pC electron beam is also relatively well matched to the lattice with a similar matching parameter in the core of $B_{mag} \leq 1.3 - 1.4$.

The slice energy change over the length of both the HXR and SXR beamlines due to the RWW is illustrated in Figure 3 and Figure 4 for the 100 pC and 20 pC S2E electron beams respectively. It was shown in [14] that the FEL performance could be impacted, due to slowly varying electron beam or undulator parameters, if a slice energy change on the order of $\Delta E \sim 2\rho_{1D}E_0$ occurred before the FEL reached saturation.

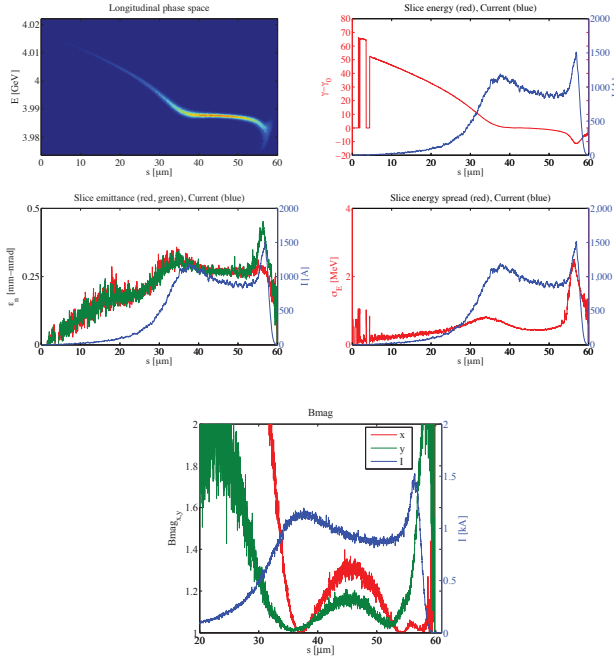


Figure 1: Longitudinal phase space (top left), slice energy (top right), x (green) and y (red) slice normalized emittance (middle left), slice energy spread (middle right), and matching parameter (bottom) for the 100 pC S2E electron beam. The blue curves are the current and assist in locating the slice properties within the electron beam longitudinal profile.

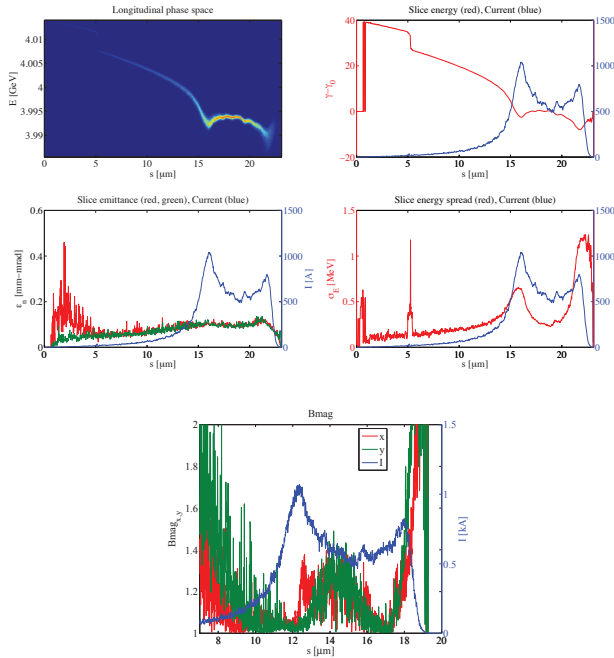


Figure 2: Longitudinal phase space (top left), slice energy (top right), x (green) and y (red) slice normalized emittance (middle left), slice energy spread (middle right), and matching parameter (bottom) for the 20 pC S2E electron beam. The blue curves are the current and assist in locating the slice properties within the electron beam longitudinal profile.

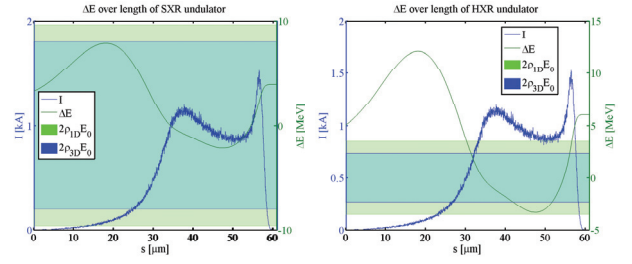


Figure 3: Slice energy change (green line) over the length of the SXR (left) and HXR (right) undulator for the 100 pC electron beam due to the RWW effect. The green (blue) shaded region indicates a tolerable slice energy change with respect to ρ_{1D} (ρ_{3D}) when the undulator is tuned to the higher end of the photon spectral range. The current is shown as the blue line.

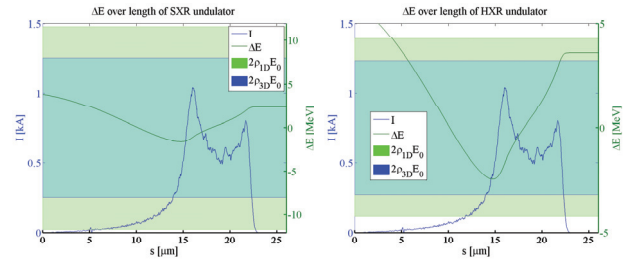


Figure 4: Slice energy change (green line) over the length of the SXR (left) and HXR (right) undulator for the 20 pC electron beam due to the RWW effect. The green (blue) shaded region indicates a tolerable slice energy change with respect to ρ_{1D} (ρ_{3D}) when the undulator is tuned to the higher end of the photon spectral range. The current is shown as the blue line.

Here, ρ_{1D} is the well known FEL Pierce parameter [15] while $\rho_{3D} = \lambda_u / 4\pi \sqrt{3} L_g^{3D}$ is an effective FEL parameter defined using the M. Xie formulas [16]. Figure 3 shows that while the SXR beamline is not affected by the RWW in the case of the 100 pC beam, the HXR beamline begins to suffer when the undulator is tuned to produce radiation at the higher end of the tuning range. It can also be seen that the RWW will produce a nonlinear curvature in the LPS of the 100 pC beam, which is often associated with spectral broadening in self-seeding and high-gain harmonic generation operational modes [17]. This particular effect, however, is not noticeable in the SXR beamline as shown below. Moving to a lower charge (and lower peak current) significantly reduces the RWW effect as illustrated in Figure 4, where the energy chirp imparted to the LPS is roughly linear across the beam.

The SXR beamline will incorporate a self-seeding system (SXRSS) to produce longitudinally coherent soft x-ray free electron laser pulses. The HXR beamline will also incorporate a self-seeded beamline. However, it will only operate with the electron beam coming from the copper linac in the baseline scenario, and thus is not presented here.

The SXRSS system consists of two undulators that are separated by a monochromator and a magnetic chicane. The first undulator consists of 7 independent segments while the second undulator consists of 14 independent segments. The monochromator design for the LCLS-II will be based on the existing LCLS SXRSS monochromator [18]. It has a compact footprint that is designed to allow both the chicane and monochromator to occupy the equivalent space of a single undulator segment along the strong focusing quadrupole FODO cell strongback. The resolving power is nominally specified to be $R = 5000$, but upgrade paths to $R \sim 10,000$ are being explored.

The SASE FEL process in the first undulator begins from shot-noise and is interrupted well before saturation in the linear regime. In this way, the slice properties of the electron beam are preserved for an additional FEL process downstream. The SASE FEL x-ray beam is sent through a monochromator which selects a narrow band of the radiation profile while the electron beam passes through the magnetic chicane. The specification of the individual components of both the monochromator and chicane are not yet established. As such, a phenomenological approach is used to model the bandwidth reduction of the seed. The nominal monochromator design relative bandwidth ($1/R$) and overall efficiency (2%) are used to specify the amplitude of a Gaussian filter function. The phase of the filter function is defined through Kramers-Kronig relations such that causality is not violated when the filter is applied to the fully three-dimensional FEL pulse exiting the seventh undulator section. The fields exiting the monochromator are then used to specify the seed into the next undulator. The magnetic chicane serves the dual role of compensating for the delay introduced by the monochromator and destroying any residual electron beam microbunching from the first undulator. This is important because the narrow bandwidth radiation from the monochromator would have a transmitted power much less than the effective power of the microbunching. The monochromatized radiation and the demodulated electron beam then interact in a seeded FEL process in the second undulator where the seed power dominates the electron beam shot noise. The narrow bandwidth (much narrower than the SASE bandwidth) seed radiation is amplified to saturation where the second undulator is tuned such that the seed is at the fundamental resonant frequency.

NUMERICAL SIMULATIONS

We begin with the results of SASE simulations in the SXR beamline tuned to produce radiation at the high end of the tuning range of $E_\gamma = 1.24$ keV or $\lambda_r = 1$ nm using the nominal 100 pC S2E electron beam. As illustrated in Figure 5, saturation is reached after 11 of 21 undulator sections at an energy of $E_{sat} = 220$ μ J. There is significant room to explore post-saturation tapering. The full width at half maximum (FWHM) temporal duration is $\Delta\tau \sim 60$ fs while the relative FWHM bandwidth is $\Delta E_\gamma/E_{0,\gamma} \sim 1.6 \times 10^{-3}$. Operating the SXR beamline without a taper at a repetition rate

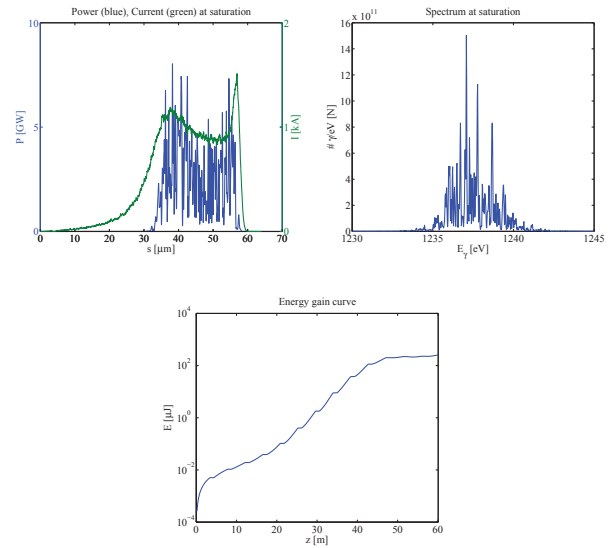


Figure 5: Energy gain curve for SASE FEL simulations using the 100 pC S2E electron beam (bottom). Power profile (blue) and current (green) (top left) and spectrum (top right) at saturation.

of 1 Mhz would deliver ~ 220 W of average power, which is more than the transport optics will be designed to accommodate in the baseline case. Therefore, methods to control this power, for example using electron beam energy chirp control at the undulator or time-dependent bunch manipulation at the injector, while still allowing the FEL to saturate are being explored.

The results for SXRSS simulations where the undulator was again tuned to produce radiation at $E_\gamma = 1.24$ keV is shown in Figure 6 for ten independent runs where only the random number seed for the generation of shot-noise in GENESIS was changed. The FEL pulse amplifies to just over $E = 1$ μ J in the first stage of amplification where single SASE spikes typically reach 10 – 20 MW. The monochromatized radiation had an average power of ~ 25 kW after the Gaussian filter function was applied, which is much larger than the estimated shot noise power of ~ 500 W. Because the pulse is rather long temporally, the monochromatized field contains a few SASE spikes in the spectral domain, which are amplified to saturation after 16 undulator segments. The pulse energy at saturation is $E_{sat} \sim 200$ μ J. This again leaves room to explore post-saturation tapering. On average (blue curve), however, the relative bandwidth of the SXRSS FEL at saturation approaches the monochromator bandwidth of $\Delta E_\gamma/E_{0,\gamma} \sim 2 \times 10^{-4}$. The bottom right plot of Figure 6 illustrates that there is no bandwidth growth from nonlinear energy curvature induced by the RWW. The red curve is the spectrum from a typical run showing the amplification of a few spikes that make it through the monochromator while the blue curve shows the results of the amplification of a perfectly monochromatic and temporally flat seed and shows very little broadening.

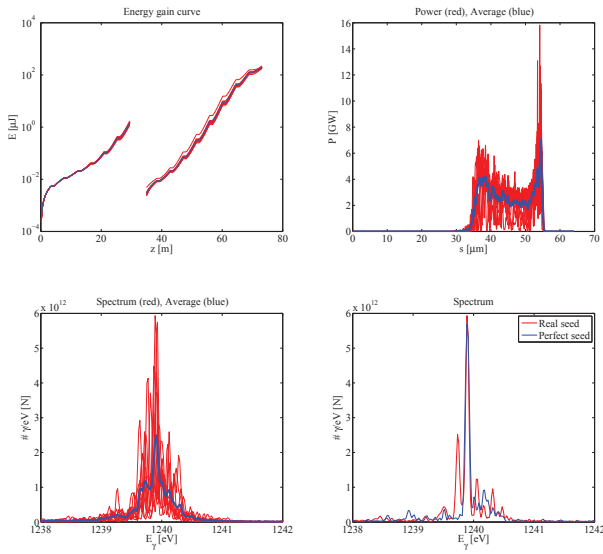


Figure 6: The energy gain curve (top left), power profile (top right) and spectrum (bottom left) for 10 independent runs (red) and their average (blue) using the 100 pC S2E electron beam. The bottom right figure shows the spectrum resulting from the amplification of a perfect seed (blue) and the real seed coming from the monochromator in the second state of the SXRSS beamline.

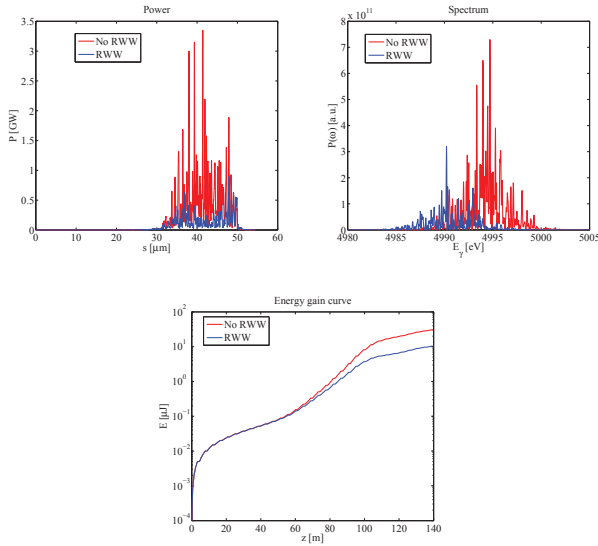


Figure 7: Power profile (top left) and spectrum (top right) at the end of the beamline and the energy gain curve (bottom). Results with the RWW on (off) are shown in blue (red).

The results for SASE simulations in the HXR beamline tuned to produce radiation at the high end of the tuning range of $E_\gamma = 5$ keV using the nominal 100 pC electron beam are shown in Figure 7 with both the RWW turned on in the simulation (blue) and turned off (red). There is a noticeable difference in performance. The RWW suppresses the final energy by about a factor of 3 from $E \sim 30$ μJ (off)

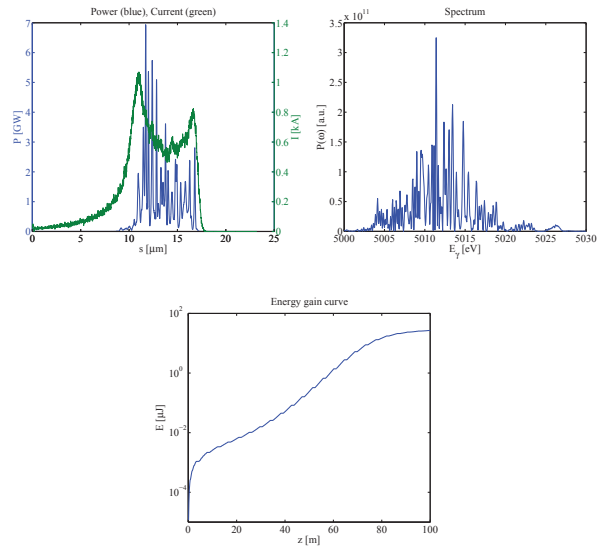


Figure 8: Energy gain curve for SASE FEL simulations using the 20 pC S2E electron beam (bottom). Power profile (blue) and current (green) (top left) and spectrum (top right) at saturation.

to $E \sim 10$ μJ (on), suppresses the amplification of radiation in the core of the beam from spikes that average $P \sim 1$ GW (off) to $P \sim 300$ MW (on) and redshifts the spectrum. There exists, however, some flexibility in tuning a linear taper to slightly mitigate the performance degradation. Either way, the FEL does not seem to reach full saturation by the end of the undulator. This leaves no room for post-saturation tapering and allows for no overhead. Better performance at $E_\gamma = 5$ keV can actually be obtained by going to lower charge where the drastically smaller emittance and smaller energy spread produce a much shorter gain length as illustrated in Figure 8, which shows the results for SASE simulations in the HXR beamline using the 20 pC S2E particle distribution. The FEL in this case reaches saturation after 24 of 32 undulator segments at an energy of $E_{sat} \sim 27$ μJ. This leaves significant room for post-saturation tapering. The FWHM temporal duration is $\Delta\tau \sim 20$ fs while the relative FWHM bandwidth is $\Delta E_\gamma/E_{0,\gamma} \sim 7 \times 10^{-4}$.

CONCLUSION

The LCLS-II baseline scenario has been extensively studied using S2E FEL simulations in both the HXR and SXR beamlines and for low and high charge distributions. A small sample of these studies are included here for electron beams coming from the CW superconducting linac to illustrate some of the challenges associated with the design. These include, but are not limited to, RWW effects in the undulator, heat load on the optics (both SXRSS monochromator and transport optics), and FEL power control. Identifying and understanding these challenges will enable the LCLS-II to more effectively deliver photon beams that will certainly push advanced x-ray science to new frontiers.

ACKNOWLEDGMENT

This work was supported by U.S. Department of Energy Contract No. DE-AC02-76SF00515.

REFERENCES

- [1] T. Raubenheimer *et al.*, “The LCLS-II, a New FEL Facility at SLAC”, in *These Proceedings: Proc. 36th Int. Free-Electron Laser Conf., Basel, 2014*, WEB01.
- [2] P. Emma *et al.*, “Linear Accelerator Design for the LCLS-II FEL Facility”, in *These Proceedings: Proc. 36th Int. Free-Electron Laser Conf., Basel, 2014*, THP025.
- [3] J. Schmerge *et al.*, “The LCLS-II Injector Design”, in *These Proceedings: Proc. 36th Int. Free-Electron Laser Conf., Basel, 2014*, THP042.
- [4] J. Feldhaus *et al.*, *Opt. Comm.* **140**, 341 (1997).
- [5] G. Geloni *et al.*, *Journ. Mod. Opt.* **58**, 16 (2011).
- [6] G. Penn *et al.*, “Laser Seeding Schemes for Soft X-rays at LCLS-II”, in *These Proceedings: Proc. 36th Int. Free-Electron Laser Conf., Basel, 2014*, MOP075.
- [7] G. Marcus *et al.*, “Harmonic Lasing Options for LCLS-II”, in *These Proceedings: Proc. 36th Int. Free-Electron Laser Conf., Basel, 2014*, MOP054.
- [8] K. Flottmann, ASTRA: A space charge tracking algorithm. User’s manual available at http://www.desy.de/mpyflo/Astra_dokumentation
- [9] M. Borland, Elegant, Advanced Photon Source LS-287, (2000).
- [10] S. Reiche, *Nucl. Instr. Meth. Phys. Res. Sec. A* **429**, 243 (1999).
- [11] K. Bane *et al.*, SLAC-PUB-10707 (2004).
- [12] F.-J. Decker *et al.*, SLAC-PUB-5484 (1991).
- [13] T. Raubenheimer *et al.*, SLAC-PUB-95-6850 (1995).
- [14] Z. Huang *et al.*, *Phys. Rev. ST Accel. Beams* **8**, 040702 (2005).
- [15] R. Bonifacio *et al.*, *Opt. Comm.* **50**, 373 (1984).
- [16] M. Xie, *Nucl. Instrum. Methods Phys. Res. Sect. A* **445**, 59 (2000).
- [17] A. Marinelli *et al.*, *Phys. Rev. ST Accel. Beams* **13**, 070701 (2010).
- [18] Y. Feng *et al.*, “System Design for Self-Seeded the LCLS at Soft X-ray Energies”, in *Proc. 34th Int. Free-Electron Laser Conf., Nara, 2012*, TUoBI01.

BROADLY TUNABLE FREE-ELECTRON LASER FOR FOUR-WAVE MIXING EXPERIMENTS WITH SOFT X-RAY PULSES

G. Marcus, SLAC, Menlo Park, CA 94025, USA
G. Penn, LBNL, Berkeley, CA 94720, USA
A. A. Zholents, ANL, Argonne, IL 60439, USA

Abstract

This paper examines a FEL design for the production of three soft x-ray pulses from a single electron beam suitable for four-wave mixing experiments. Independent control of the wavelength, timing and angle of incidence of the three ultra-short, ultra-intense pulses with exquisite synchronization is critical. A process of selective amplification where a chirped electron beam and a tapered undulator are used to isolate the gain region to only a short fraction of the electron beam is explored in detail. Numerical particle simulations are used to demonstrate the essential features of this scheme in the context of the LCLS-II design study.

INTRODUCTION

Hard and soft X-ray free-electron lasers (FELs) [1–4] have become essential tools for the investigation of dynamical systems as they have the ability to operate on the time and length scales natural to atomic and electronic motion in matter [5]. Many experiments envisioned for the exploration of the dynamical properties of matter, which leverage the unique capabilities of FEL facilities, will be based on a pump and probe technique. Extending this technique to include a broad variety of four-wave mixing (FWM) spectroscopies, which rely on the use of three fully coherent and independent pulses of light with unique carrier frequencies and wave vectors, is of critical importance.

A pathway for producing FEL pulses suitable for FWM experiments from a single electron beam has recently been proposed [6]. In that study, a process of selective amplification employing a strongly chirped electron beam and a tapered undulator is used to isolate the gain region of a self-amplified spontaneous emission (SASE) FEL allowing for a single longitudinally coherent pulse to amplify to saturation [7–9]. The taper also serves to suppress gain outside the chirped region, leaving the electron beam capable of producing additional radiation in a downstream FEL process. This energy modulation and undulator taper combination can be repeated in multiple stages to produce the three independent FEL pulses necessary for FWM experiments if a broad tuning range is necessary. Alternatively, a grating and mask can be used to split one of these large bandwidth pulses if two nearby frequencies are sufficient. A potential beamline for this scenario is shown in Figure 1.

This paper describes the electron beam energy modulation and undulator taper requirements for the production of longitudinally coherent FEL pulses from the selective amplification process in the context of the LCLS-II design study for photon energies of $E_\gamma = 250 - 1000$ eV. Numerical

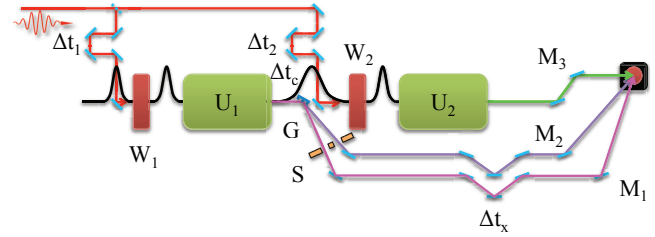


Figure 1: A possible beamline for a FWM FEL [6]: W_1 and W_2 are modulators, U_1 and U_2 are undulators, Δt_1 and Δt_2 are seed laser delay stages, Δt_c is the electron beam chicane delay, Δt_x is the x-ray delay line, G is the grating, S is the slit, and $M_{1,2,3}$ are adjustable x-ray mirrors.

simulations using the FEL code GENESIS [10] are used to illustrate the more impressive characteristics of this scheme at $E_\gamma = 1$ keV (see Table 1).

Table 1: Electron Beam, Undulator, and Modulator Laser Parameters for the Nominal LCLS-II Scenario

Paramter	Symbol	Value	Unit
e-beam energy	E	4.0	GeV
emittance	ϵ	0.45	mm-mrad
current	I	1000	A
energy spread	σ_E	500	keV
beta	$\langle\beta\rangle$	12	m
undulator period	λ_u	39	mm
segment length	L_u	3.4	m
break length	L_b	1.0	m
photon energy	E_γ	0.25 – 1	keV
seed wavelength	λ_s	2.1	μm

ELECTRON BEAM ENERGY CHIRP AND UNDULATOR TAPER

In the particular selective amplification scheme employed here, the electron beam is energy modulated by a carrier-envelope-phase-stable, single-cycle, mid-IR laser pulse within a single period modulator. This modulation takes the following idealized form [11]:

$$\gamma = \gamma_0 + \Delta\gamma \sin\left(\frac{2\pi}{\lambda_l}[s - s_0]\right) e^{-\frac{(s-s_0)^2}{2\sigma_l^2}}. \quad (1)$$

ISBN 978-3-95450-133-5

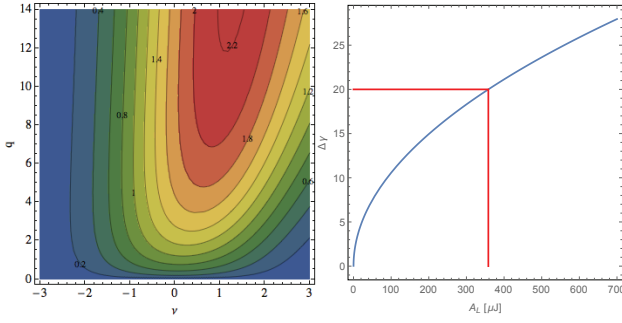


Figure 2: f as a function of q and v for $\hat{\sigma}_\tau = 0.42$ (left) and $\Delta\gamma$ as a function of A_L for the optimized f (right).

Here, γ is the electron beam energy normalized to its rest energy (mc^2), λ_l is the seed laser wavelength, s is the electron coordinate with respect to the center of the bunch, σ_l is the rms width of the gaussian envelope for the single-cycle laser pulse longitudinal electric field and

$$\Delta\gamma = \frac{2}{mc^2} \sqrt{A_L \alpha \hbar \omega_0 \frac{K^2}{2 + K^2}} [JJ] f(q, v, \hat{\sigma}_\tau), \quad (2)$$

where A_L is the seed laser energy, α is the fine structure constant, \hbar is Planck's constant, ω_0 is the mean frequency of the spontaneous radiation generated inside the modulator, $K = eB\lambda_u/2\pi mc$ is the undulator strength parameter, e is the electron charge, B is the peak magnetic field on axis, λ_u is the undulator period, $[JJ] = J_0 \left[K^2 / (4 + 2K^2) \right] - J_1 \left[K^2 / (4 + 2K^2) \right]$ is the Bessel form factor accounting for the coupling of electron motion to radiation emission in a planar undulator, and $f(q, v, \hat{\sigma}_\tau)$ depends in a complicated way on the undulator length, L_u , Rayleigh length ($q = L_u/z_R$), detuning ($v = 2L_u/\lambda_u(1 - \gamma/\gamma_r)$), and the electric field pulse width ($\hat{\sigma}_\tau = \sigma_l \lambda_u / L_u \lambda_l$). The dependence of f on q and v can be found in Figure 2 for a single-cycle seed laser of wavelength $\lambda_l = 2.1 \mu\text{m}$ and for a single period modulator.

An example of this energy modulation can be found in Figure 3 where the modulator parameters were optimized to produce an amplitude of $\Delta\gamma = 20$ with a laser energy of $A_L \sim 360 \mu\text{J}$. The choice in the seed laser wavelength, duration and number of modulator periods are crucial to differentiating the slope of the energy chirp near the zero crossing phase ($s \sim 6 \mu\text{m}$) from the slope of the chirp in the regions immediately adjacent ($s \sim 4, 8 \mu\text{m}$). Additionally, the choice in seed laser wavelength was motivated by the progress that has been made in recent years in obtaining carrier-envelope-phase-stable single-cycle pulses in this wavelength region [12]. There is a large and linear energy chirp around $s \sim 6 \mu\text{m}$ parameterized by $\alpha_c = d\gamma/ds \sim 2\pi\Delta\gamma/\lambda_l$. As previously mentioned, gain degradation due to an energy chirp along the electron beam longitudinal profile can be compensated by appropriately tapering the undulator. This taper is given analytically by:

$$\frac{dK}{dz} = \frac{1}{K_0} \left(1 + \frac{K_0^2}{2} \right)^2 \frac{\alpha_c}{\gamma_0^3}, \quad (3)$$

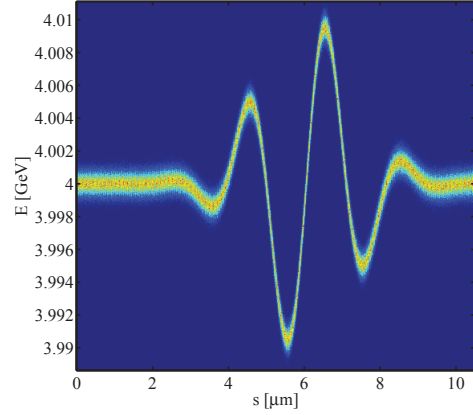


Figure 3: The longitudinal phase space near an energy modulation using a single-cycle $\lambda = 2.1 \mu\text{m}$ laser in a single period modulator.

where K_0 and γ_0 indicate the initial undulator parameter and e-beam energy respectively. This undulator taper also suppresses gain where there is no conjugate energy chirp, leaving ample real estate along the electron beam longitudinal profile for additional radiative processes. The taper that produced the optimal pulse characteristics (longitudinally coherent, single-spike, large contrast with remainder of pulse) is shown in Figure 4, which was $\sim 80\%$ of the theoretically predicted value.

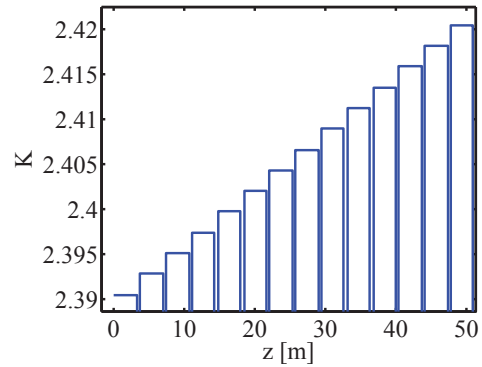


Figure 4: Undulator parameter along the undulator indicating the optimal taper to compensate for the energy modulation with $\Delta\gamma = 20$.

NUMERICAL SIMULATIONS

The FEL simulation code GENESIS was used to evaluate the performance of the chirp and taper combination in the context of the LCLS-II design project under ideal conditions. The results of twenty independent SASE simulations are shown in Figure 5 in the temporal and spectral domains. The longitudinal profile is dominated by a single spike of radiation in the gain compensation region that is > 2 orders

of magnitude larger than radiation that has been suppressed by the taper. There is a small time and energy jitter that

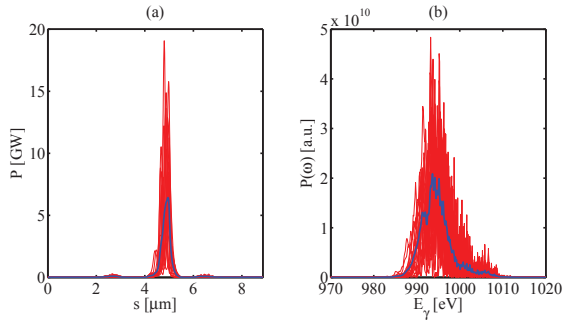


Figure 5: Power (left) and spectrum (right) of twenty independent simulations (red) and their average values (blue).

is associated with SASE and the start-up of radiation from shot-noise as illustrated in Figure 6. The left plot shows a “waterfall” of the longitudinal power profile for the twenty simulations separated on the y-axis by 10 GW. A small temporal jitter is evident. This is perhaps more clearly illustrated on the right, which is a scatter plot showing the pulse energy and arrival time deviations from the average value for the twenty independent SASE runs. The standard deviation for the temporal jitter distribution is only ~ 0.26 fs and for the energy jitter is $\sim 1.4 \mu\text{J}$.

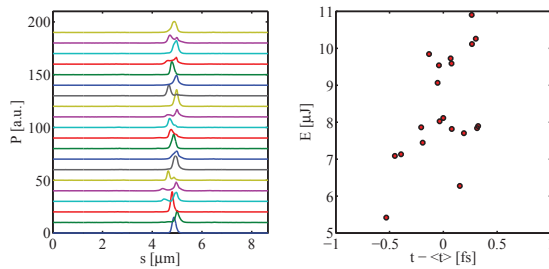


Figure 6: Longitudinal power (separated by 10 GW) (left) and a time and energy jitter distribution for twenty independent simulations.

It is useful, at this point, to analyze the pulse characteristics of a typical SASE simulation. The longitudinal profiles in the temporal and spectral domains are illustrated in Figure 7. The right plot shows the spectrum at saturation where the FWHM of $\Delta E_\gamma \sim 4.4$ eV is much larger than the nominal SASE bandwidth of an unmodulated electron beam in an untapered undulator. This is a result of the very large e-beam energy chirp, which produces a chirped FEL pulse and is manifested as a large quadratic spectral phase. The left plot shows the saturated FEL power (blue) in relation to the initial (green) and final (red) slice energies. The electrons clearly only give significant energy to the radiation where the undulator taper compensates for the electron beam energy chirp. This is also clearly illustrated in Figure 8, which

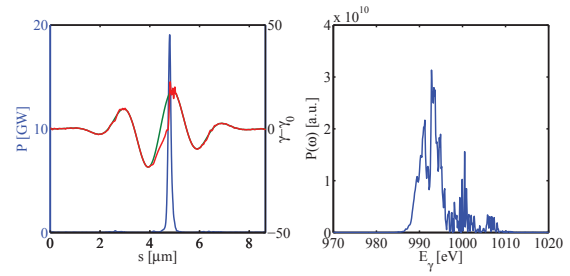


Figure 7: Power (blue), initial (green) and final (red) slice energy from the nominal resonance energy (left) and spectrum (right) of a typical simulation.

shows the power as a function of the electron beam coordinate (s , x-axis) and the distance along the undulator (z , y-axis). This figure also illustrates how the undulator taper suppresses the gain where it is not compensated by an appropriate energy chirp ($s \sim 0 - 2, 6 - 8 \mu\text{m}$). The peak power for the pulse illustrated in Figure 7 is $P_{pk} \sim 19$ GW while the FWHM temporal duration is $\Delta t \sim 0.42$ fs, corresponding to an energy of $E = 9.8 \mu\text{J}$ and $\sim 6 \times 10^{10}$ photons. The FWHM

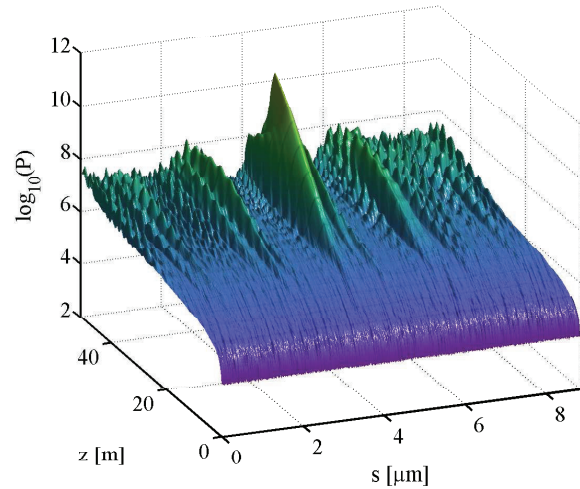


Figure 8: Power (\log_{10} scale) as a function of s (electron beam coordinate) and z (undulator distance) showing the amplification of a single longitudinally coherent mode.

time-bandwidth product of this pulse is $\text{TBP} \sim 1.9$ eV-fs and is very near the Fourier-transform limit. This pulse, however, is certainly not Gaussian, and so this number should be regarded carefully. Most pulses have a TBP of 3 – 5 times the Fourier-transform limit. This is a direct consequence of the chirped nature of the FEL radiation, which is clearly illustrated by the on-axis, near field Wigner transform slightly before (left) and at saturation (right) shown in Figure 9. It should be noted that the Wigner transform here is dominated by a single coherent region. This particular pulse shows bandwidth growth and pulse compression as the pulse reaches saturation and slips forward onto the crest of

the electron beam energy modulation (see Figure 7) where the energy chirp is smaller and nonlinear.

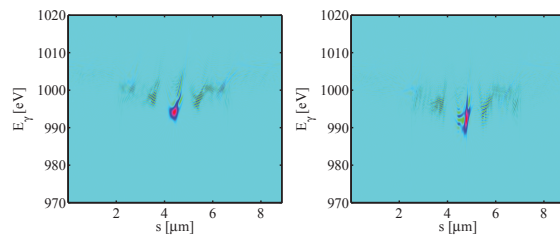


Figure 9: The on-axis, near field Wigner transform of the FEL pulse slightly before (left) and at saturation (right).

CONCLUSION

In conclusion, the selective amplification process initially proposed in [6] is easily adaptable to LCLS-II type parameters. An added benefit to working in this regime is that the optimal seed laser used for the energy modulation is based on technology that has been, and is continuing to be, well developed. The addition to an FEL facility of a beamline capable of delivering soft x ray pulses suitable for FWM spectroscopies is sure to revolutionize x ray science.

ACKNOWLEDGMENT

The authors would like to thank Y. Ding and Z. Huang for many helpful and insightful discussions. This work was supported by the Director, Office of Science, Office of Basic Energy Sciences, of the U.S. Department of Energy under Contracts No. DE-AC02-05CH11231, No. DEAC02-06CH11357, and No. DE-AC02-76SF00515.

REFERENCES

- [1] P. Emma *et al.*, *Nat. Photon.* **4**, 641 (2010)
- [2] T. Ishikawa *et al.*, *Nat. Photon.* **6**, 540 (2012)
- [3] W. Ackermann *et al.*, *Nat. Photon.* **1**, 336 (2007)
- [4] E. Allaria *et al.*, *Nat. Photon.* **6**, 699 (2012)
- [5] J. Marangos, *Cont. Phys.* **52**, 551 (2011)
- [6] G. Marcus, G. Penn, A. A. Zholents, *Phys. Rev. Lett.* **113**, 024801 (2014)
- [7] E. L. Saldin *et al.*, *Phys. Rev. ST Accel. Beams* **9**, 050702 (2006)
- [8] L. Giannessi *et al.*, *Phys. Rev. Lett.* **106**, 144801 (2011)
- [9] G. Marcus *et al.*, *Appl. Phys. Lett.* **101**, 134102 (2012)
- [10] S. Reiche, *Nucl. Instr. Meth. Phys. Res. Sect. A* **429**, 243 (1999)
- [11] A. A. Zholents, K. Holldack, in *Proceedings of the 28th International Free Electron Laser conference*, Berlin, Germany, 2008
- [12] Y. Deng *et al.*, *Opt. Lett.* **37**, 4973 (2012)

INVESTIGATION OF REVERSE TAPER TO OPTIMIZE THE DEGREE OF POLARIZATION FOR THE DELTA UNDULATOR AT THE LCLS*

J. MacArthur[†], A. Marinelli, A. Lutmann, T. Maxwell, H.-D. Nuhn, D. Ratner, Z. Huang
SLAC, Menlo Park, CA 94025, USA

Abstract

A 3.2 m adjustable phase Delta undulator will soon be installed on the last girder of the LCLS undulator line. The Delta undulator will act as an afterburner terminating the 33 undulator line, providing arbitrary polarization control to users. Two important figures of merit for users will be the degree of polarization and the x-ray yield. In anticipation of this installation, machine development time at the LCLS was devoted to maximizing the final undulator x-ray contrast and yield with a standard canted pole planar undulator acting as a stand in for the Delta undulator. Following the recent suggestion [1] that a reverse taper in the main undulator line could suppress linearly polarized light generated before an afterburner while still producing the requisite microbunching, we report on a reverse taper study at the LCLS wherein a yield contrast of 15 was measured along the afterburner. We also present 1D simulations comparing the reverse taper technique to other schemes.

INTRODUCTION

Circularly polarized soft x-ray radiation is used to probe a variety of material properties, from the electronic structure of magnetic substances [2] to the chirality of biomolecules [3]. Off plane synchrotron radiation [4] and helical undulator radiation [5] have supplied circularly polarized x-rays to synchrotron users for several decades. High quality circularly polarized radiation from FEL facilities is limited to energies at or below the XUV [6], though thin magnetized films have been used to produce circularly polarized soft x-rays at the cost of several orders of magnitude in intensity [7].

A Delta undulator [8] is currently being constructed [9] at the LCLS to address this shortcoming. Unlike canted pole or adjustable gap devices, the Delta is an adjustable phase undulator [10] wherein the longitudinal position of four opposing magnetic arrays is varied to adjust the axial magnetic field strength and helicity. The result is full polarization control – linear, circular, and elliptically polarized light can be produced. The Delta undulator at LCLS will operate in the 300-2000 eV region, extending availability of circularly polarized FEL sources into the soft x-ray. This 3.2 m device will replace the final planar undulator in the 33 undulator-line at LCLS.

The Delta undulator is only 1.5-2 gain LCLS gain lengths long, not nearly long enough reach FEL saturation. Instead, the Delta will act as an afterburner, as seen in Fig. 1. In this

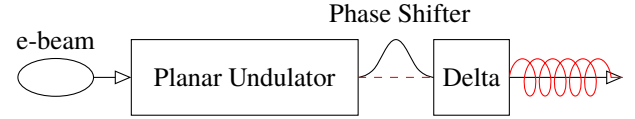


Figure 1: Schematic representation of the Delta undulator in the afterburner configuration. The beam is microbunched in the planar undulator, and a small amount of plane polarized radiation seeds the Delta after an optimum phase shift (red, dashed). The Delta produces circularly polarized x-rays (red, solid).

configuration, the electron beam is microbunched in a long planar undulator before entering the Delta.

If the Delta undulator is configured with a helical field, the degree of circular polarization will be dictated by the ratio of the power produced in the Delta and the power produced in the planar undulator. To be more precise, the polarization of light is commonly characterized by the four Stokes parameters. In terms of the complex electric field, these parameters are [11]

$$\begin{aligned} s_0 &= \langle E_x E_x^* + E_y E_y^* \rangle = I_x + I_y \\ s_1 &= \langle E_x E_x^* - E_y E_y^* \rangle = I_x - I_y \\ s_2 &= \langle E_x E_y^* + E_y E_x^* \rangle = I_{45^\circ} - I_{-45^\circ} \\ s_3 &= i \langle E_x E_y^* - E_y E_x^* \rangle = I_{\text{RCP}} - I_{\text{LCP}}, \end{aligned}$$

where $\langle \rangle$ indicates a time average over the pulse duration. The two figures of merit relevant to circularly polarized light from a helical undulator are the average power $P = \int s_0 dx dy$, and the degree of circular polarization, s_3/s_0 .

Several schemes have been proposed to maximize the average power and $|s_3|/s_0$. A reverse taper can be applied to the planar undulator to suppress background radiation [1], the longer undulator and afterburner may be placed in a crossed-undulator configuration [12, 13], and the resonant frequency of the afterburner may be tuned to the second harmonic of the planar undulator [14]. In this paper we compare the reverse taper scheme to others in a 1D framework and report on an experimental investigation of the reverse taper scheme at LCLS.

1D COMPARISON

The resonant wavelength λ_r in an FEL is given as

$$\lambda_r(z) = \frac{\lambda_u}{2\gamma^2} (1 + a_u^2(z)), \quad (1)$$

where λ_u is the undulator period and γ is the Lorentz factor. The rms undulator parameter $a_u = e\lambda_u B_{\text{rms}}/2\pi mc$ is given

* Work supported by U.S. DOE Office of Basic Energy Sciences under Contract No. DE-AC02-76SF00515.

[†] jmacart@slac.stanford.edu

in terms of the on-axis rms magnetic field strength B_{rms} . Eq. 1 is valid for planar and helical undulators.

Reverse Taper Review

The reverse taper technique for the suppression of background radiation relies on a large, positive detune [15]

$$\Delta\hat{\nu} = \Delta\nu/2\rho \gg 1, \quad (2)$$

where ρ is the FEL Pierce parameter and $\Delta\nu = (\lambda_r(z) - \lambda)/\lambda$. Note that $\Delta\hat{\nu}$ is the negative of the detune parameter \hat{C} used by Schneidmiller and Yurkov [1]. With Eq. 2 satisfied, the growth of the scaled field intensity $|a|^2 = P/\rho P_{\text{beam}}$ is suppressed in favor of the bunching b ,

$$|b|^2 \approx \Delta\hat{\nu}^2 |a|^2. \quad (3)$$

This relation is precisely what is desired of a planar undulator upstream from a helical afterburner – strong bunching allows the helical undulator to produce a significant amount of radiation, but background radiation is suppressed.

To satisfy Eq. 3 along the length of the planar undulator, a reverse linear taper ($da_u/dz = \text{constant} > 0$) is introduced so that

$$\Delta\hat{\nu}(\hat{z}) = \beta\hat{z} = \frac{\lambda_u}{4\pi\rho^2} \frac{a_u(0)}{1 + a_u(0)^2} \frac{da_u}{dz} \hat{z}, \quad (4)$$

where $\hat{z} = 4\pi\rho z/\lambda_u$ and $a_u(0)$ is the undulator parameter at the start of the planar undulator. The bunching spectrum evolution for a sample reverse taper configuration is shown in Fig. 2. The white line guides the eye by showing how $\Delta\hat{\nu}_0 = (\lambda_r(0) - \lambda_r(z))/2\rho\lambda_r(z)$ changes along a reverse taper, and the bunching intensity is shown to peak close to the initial resonant frequency rather than following the reverse taper. An afterburner would be placed at $z = 45$ and $\Delta\hat{\nu}_0 = -2$ for maximum gain.

1D Simulation Comparison

We have performed 1D simulations to compare the effectiveness of the reverse taper configuration relative to other afterburner schemes. Relevant simulation parameters are included in Table 1. Note that the Pierce parameter for a planar undulator is different than that of a helical undulator due to the presence of the [JJ] factor for planar undulators. The value of ρ_{planar} corresponds to gain length of 1.8 m, within the 1.5-2 m gain length range typically observed at LCLS for 1 keV operation.

Four different afterburner schemes were tested to optimize the degree of circular polarization. Each setup is modeled after the configuration in Fig. 1. A 1D SASE algorithm is used to calculate the beam and radiation conditions at the end of the the planar undulator. The beam is optimally phase shifted relative to the radiation, and both the beam and radiation are used as inputs for the Delta undulator. At the end of the Delta undulator, the power and degree of circular polarization are calculated. Planar undulator segments are assumed to produce plane polarized radiation, while helical undulators are assumed to produce circularly polarized radiation.

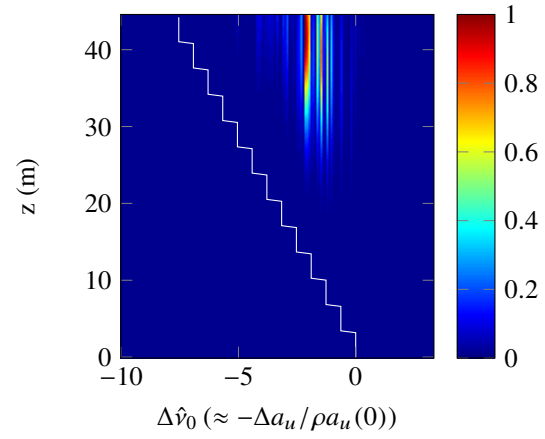


Figure 2: The bunching spectrum in arbitrary units along a reverse tapered 13 undulator line with $\rho = 7.5 \times 10^{-4}$, $\Delta E/E = 2.5 \times 10^{-4}$, and $\beta = 0.55$. The x-axis is the detune from $\lambda_r(0)$, and the white line indicates the detune of $\lambda_r(z)$ from $\lambda_r(0)$. Bunching increases with z , but peak bunching does not follow the taper. An afterburner would be placed at $z = 45$ and $\Delta\hat{\nu}_0 = -2$.

Table 1: 1D Simulation Parameters

Parameter	Value
x-ray energy	1 keV
beam energy	4.72 GeV
undulator period	3 cm
peak current	1.3 kA
planar undulator segment	3.42 m
Delta undulator	3.2 m
σ_E/E	2.5×10^{-4}
ρ_{planar}	7.5×10^{-4}
ρ_{helical}	9.1×10^{-4}

Figure 3 shows the comparative effectiveness of each scheme. In the first column, a reverse tapered planar undulator is followed by a helical afterburner. The reverse taper does an excellent job suppressing the field growth, and the afterburner is optimally positioned in a_u (c.f. Fig. 2) for rapid field growth. The second column shows a different scheme, wherein an \hat{x} planar undulator is followed by a carefully placed \hat{y} undulator. A $\pi/2$ phase shift between the two produces circularly polarized radiation, but s_3/s_0 is limited by beam slippage [13]. The third column shows the simplest scheme, where a planar undulator is followed by a helical undulator. Proper longitudinal placement of the helical undulator maximizes the power contrast. The final column shows an entirely different scheme, where the beam energy is decreased so that the 2nd harmonic is 1 keV. The bunched beam is sent into a helical afterburner tuned to 1 keV. A monochromator would be needed to remove the contaminant 500 eV radiation from the circularly polarized 1 keV radiation.

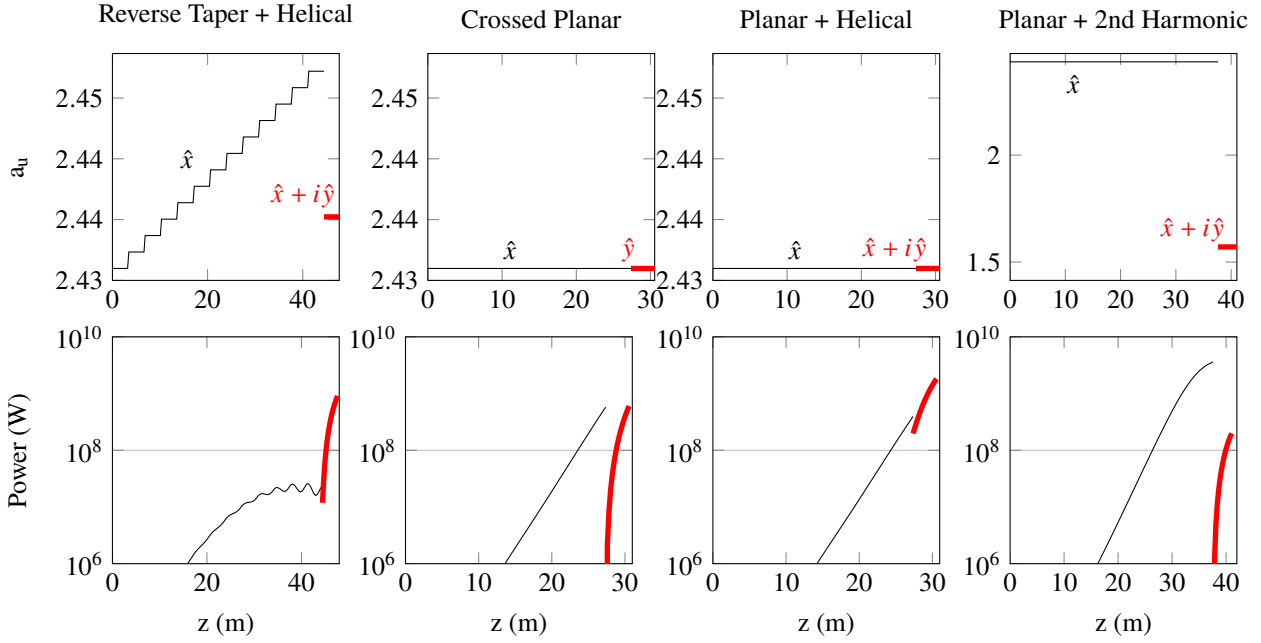


Figure 3: Several schemes for generating circularly polarized radiation are compared. The top row shows the undulator parameter a_u as a function of distance along the undulator for each scheme, with labels indicating whether the radiation produced in the undulator is planar or helical. The bottom row shows the z dependent power produced in the long planar undulator (black) and the afterburner (red).

Table 2 shows summary statistics for each of the afterburner schemes. The reverse taper arrangement provides an ideal balance of power and contrast. These apparent advantages were the basis for a machine study at LCLS, presented in the next section.

Table 2: Simulation Results

Configuration	Power (GW)	s_3/s_0
Reverse Taper + Helical	0.89	0.975
Cross Planar	0.85	0.829
Planar + Helical	1.80	0.797
Planar + 2nd Harmonic	0.19	1.0

REVERSE TAPER AT LCLS

The Delta undulator is not available to verify these 1D predictions, but the reverse taper concept has been tested at LCLS with a planar afterburner. While no circularly polarized radiation is produced, the x-ray yield contrast before and after the afterburner can verify whether the concept works.

The experimental parameters for the machine study are shown in Table 3. Several different taper slopes and lengths were attempted, and the best configuration is shown in Fig. 4. The contrast was maximized by scanning the afterburner along available a_u values.

The reverse taper was proven to be effective at suppressing unwanted radiation while enabling bunching. As seen in Fig. 5, a contrast of 15 was observed between the end of the

Table 3: Experimental Parameters

Parameter	Value
x-ray energy	1.017 keV
beam energy	4.72 GeV
undulator period	3 cm
peak current	1.3 kA
bunch charge	150 pC
σ_E/E	$\sim 2.5 \times 10^{-4}$
planar undulator segment	3.42 m
standard taper L_G	1.49 m

taper and the afterburner. Ignoring interference effects, a factor of 15 corresponds to $s_3/s_0 = 0.91$. If the afterburner were helical rather than planar, simulations predict a roughly factor of 2 increase in contrast, equivalent to $s_3/s_0 = 0.95$. This is not far from the prediction in Table 2.

We could not perform an exhaustive search for the best taper length and slope, and 1D simulations suggest we missed the mark on the ideal taper length. In Fig. 6, the z -dependent bunching spectrum along the undulator configuration of Fig. 4 is simulated using the parameters of Table 3. The ideal location for an afterburner is at peak bunching, which occurs after only 8 undulator segments in the simulation.

Subsequent machine time spent on improving upon these results were met by significantly different beam conditions. The standard taper gain length of the results presented here was 1.49 m, while gain lengths in subsequent experiments were ≥ 2 m. Similar contrast could not be achieved with

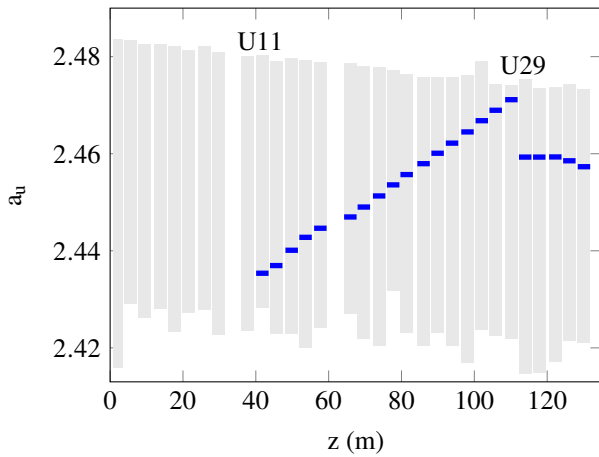


Figure 4: Undulator parameter values for the reverse taper experiment (blue), with available a_u in the background (gray). The reverse taper goes from U11-28 with a gap at U16 for hard x-ray self-seeding. The afterburner is U29. The optimum position of position of U29 was determined by scanning from $a_u = 2.44$ to 2.475.

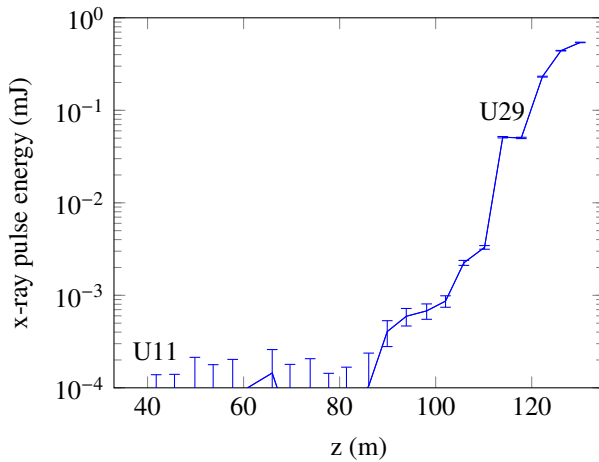


Figure 5: The cumulative pulse energy as a function of distance along the undulator averaged over 120 shots. Between the end of the reverse taper (U28) and the afterburner (U29) the pulse energy increases by a factor of 15.5.

these longer gain lengths in the time allocated to the machine studies. 1D simulations suggest the maximum contrast at acceptable yields is highly dependent upon the energy spread and gain length, so keeping these parameters low will be important during the operation of the Delta undulator.

CONCLUSION

In preparation for the commissioning of the Delta undulator at LCLS, we have performed 1D simulations of different schemes that attempt to maximize the degree of circular polarization and the radiation yield. Machine development time at the LCLS was spent investigating the most promising scheme, a reverse tapered undulator followed by an afterburner undulator. We have achieved a radiation yield contrast

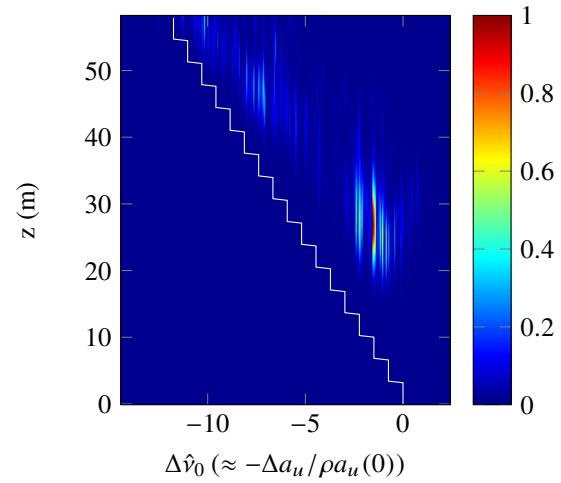


Figure 6: A simulated bunching spectrum to match the experimental parameters. The afterburner U29 would sit at 60 m, but the ideal location for an afterburner may have been earlier. The ideal undulator location is a rather narrow region in $z - \Delta\hat{v}_0$ space.

of 15 before and after the afterburner, verifying the utility of this technique. Finding the ideal taper orientation for variable beam conditions may be a challenge, though we expect to learn more during the commissioning of the Delta undulator.

REFERENCES

- [1] E. A. Schneidmiller and M. V. Yurkov, "Obtaining High Degree of Circular Polarization at X-ray Free Electron Lasers via a Reverse Undulator Taper," *Phys. Rev. ST Accel. Beams*, vol. 16, p. 110702, 2013.
- [2] J. Stöhr *et al.*, "Element-Specific Magnetic Microscopy with Circularly Polarized X-rays," *Science*, vol. 259, pp. 658–658, 1993.
- [3] U. Hergenhahn *et al.*, "Photoelectron Circular Dichroism in Core Level Ionization of Randomly Oriented Pure Enantiomers of the Chiral Molecule Camphor," *J. Chem. Phys.*, vol. 120, no. 10, pp. 4553–4556, 2004.
- [4] C. T. Chen *et al.*, "Soft-x-ray Magnetic Circular Dichroism at the $L_{2,3}$ Edges of Nickel," *Phys. Rev. B*, vol. 42, pp. 7262–7265, 1990.
- [5] S. Sasaki *et al.*, "First Observation of Undulator Radiation from APPLE-1," *Nucl. Instr. Meth. Phys. Res. A*, vol. 347, pp. 87–91, 1994.
- [6] T. Mazza *et al.*, "Determining the Polarization State of an Extreme Ultraviolet Free-Electron Laser Beam Using Atomic Circular Dichroism," *Nat. Commun.*, vol. 5, 2014.
- [7] T. Wang *et al.*, "Femtosecond Single-Shot Imaging of Nanoscale Ferromagnetic Order in Co/Pd Multilayers Using Resonant X-ray Holography," *Phys. Rev. Lett.*, vol. 108, p. 267403, 2012.
- [8] A. B. Temnykh, "Delta Undulator for Cornell Energy Recovery Linac," *Phys. Rev. ST Accel. Beams*, vol. 11, p. 120702, 2008.

- [9] H.-D. Nuhn *et al.*, “R&D Towards a Delta-Type Undulator for the LCLS,” in *FEL2013 Proceedings*, p. 348, 2013.
- [10] R. Carr, “Adjustable Phase Insertion Devices as X-ray Sources,” *Nucl. Instr. Meth. Phys. Res. A*, vol. 306, pp. 391–396, 1991
- [11] *Principles of Optics*, (New York: Permagon Press, 1964).
- [12] K. J. Kim, “A Synchrotron Radiation Source With Arbitrarily Adjustable Elliptical Polarization,” *Nucl. Instr. Meth. Phys. Res. A*, vol. 219, no. 2, pp. 425 – 429, 1984.
- [13] H. Geng, Y. Ding, and Z. Huang, “Crossed Undulator Polarization Control for X-ray FELs in the Saturation Regime,” *Nucl. Instr. Meth. Phys. Res. A*, vol. 622, no. 1, pp. 276 – 280, 2010.
- [14] Z. Huang and S. Reiche, “Generation of GW-Level, Sub-angstrom Radiation in the LCLS Using a Second-harmonic Radiator,” in *FEL2004 Proceedings*, pp. 201–204, 2004.
- [15] Z. Huang and K.-J. Kim, “Review of X-ray Free-Electron Laser Theory,” *Phys. Rev. ST Accel. Beams*, vol. 10, p. 034801, 2007.

OBSERVATION OF SMITH-PURCELL RADIATION AT 32 GHZ FROM A MULTI-CHANNEL GRATING WITH SIDEWALLS

J. T. Donohue, CENBG, CNRS/IN2P3, Université de Bordeaux, France
J. Gardelle, P. Modin, CEA, CESTA, Le Barp, France

Abstract

In a demonstration experiment at 5 GHz, we found copious emission of coherent Smith-Purcell (SP) radiation at the fundamental frequency of the evanescent surface wave, when the grating had sidewalls. Reaching higher frequencies requires a reduction in the size of the grating, which leads to a considerable reduction in power. To partially compensate this, we suggested superposing several copies of the reduced grating in parallel. A test of this concept has been performed with a seven-channel grating, at a frequency near 32 GHz. The SP radiation signals were observed directly with a fast oscilloscope. Power levels were of order 5 kW, in fair agreement with three-dimensional simulations made with the code "MAGIC".

INCREASE FREQUENCY BY REDUCING THE PERIOD AND WIDTH BETWEEN SIDEWALLS

A demonstration experiment in the microwave domain showed that a Smith-Purcell (SP) free electron laser (FEL), with conducting sidewalls placed at the ends of the grating's grooves, emitted intense radiation at the frequency of the surface wave on the grating [1]. In single shot operation, the ratio of emitted power to beam power exceeded 10 %. An earlier experiment, on a grating without sidewalls [2], had demonstrated emission of coherent SP radiation at the second harmonic of the surface wave. That experiment confirmed the scenario proposed in the two-dimensional (2-D) model of Andrews and Brau [3]. But the efficiency was only of order 0.1 %. In the presence of sidewalls the dispersion relation for the grating surface wave is modified [4]. In particular, the intersection of the beam line with the new dispersion relation may occur at an allowed SP frequency, which can't happen in the 2-D theory of Reference [3]. Since the beam bunching at the fundamental frequency is typically must greater than that on harmonics, the emission at the fundamental frequency is much stronger. Thus the use of sidewalls greatly increases the power. Of course, to be of practical interest, it is necessary to reach much higher frequencies, i.e., mm wavelength or less.

The well-known SP relation is [5],

$$\lambda = L(1/\beta - \cos \theta_{sp})/|n|,$$

where λ denotes the wavelength, L the grating period, n the order of diffraction, θ_{sp} the angle with respect to the beam, and β the relative velocity of the electron. In order to reach shorter wavelengths, it suffices to reduce the grating period. However, the component of the evanescent surface wave in resonance with the beam only

extends to a height proportional to the wavelength. In order to reach high frequencies, the beam must closely approach the grating surface. If the grating profile is preserved (groove-depth/period and groove-width/period constant), the 2D dispersion relation of Andrews and Brau in the dimensionless variables is unchanged. The scale reduction doesn't require a reduction in the overall size of the grating, although the task of propagating an intense and wide sheet beam at tiny distances above the grating would certainly be difficult. For the grating with sidewalls, the distance between sidewalls, w , must undergo the same reduction in scale as the period L . This rapidly leads to long thin gratings when the frequency is increased. Furthermore, our experiment requires an intense (0.5 T) longitudinal magnetic field to control the beam. At the portion of the beam nearest the grating, the image charges produce a moderately strong vertical electric field (a few kV/cm), which, combined with the magnetic field, generates a transverse $\vec{E} \times \vec{B}$ drift. If the number of periods is too great, most of the electrons will drift into the sidewalls. If the radiated intensity is proportional to the total surface of the grating, a grating with sidewalls will suffer a power reduction proportional to the square of the scale factor.

At FEL 2013 two of the authors suggested that it might be possible to superpose laterally N copies of the N -fold reduced gratings [6]. The beam used in the full-scale experiment would continue in use, except that it would be positioned to be flush with the grating top, and of 1 mm thickness. The hope was that the overall power reduction would be only $1/N$, instead of $1/N^2$. In support of this hypothesis, several simulations of multi-channel gratings were performed with the three-dimensional (3D) particle-in-cell code "MAGIC" [7]. These simulations, made with 2, 4, 6, 8 and 10 channels, indicated that the radiation at the bunching frequency (N times the original bunching frequency) occurred at the same SP angle, which was approximately 140° . On the upstream wall of the simulation volume, the azimuthal distribution grew more concentrated around the vertical direction with increasing N . A simple analysis using the theory of antenna arrays was proposed to explain this tendency. It indicated that the width of the azimuthal distribution would decrease as $1/N$, as would the radiated power in the principal lobe.

These results depend crucially on the existence of some coherence among the various channels. In the antenna theory this is assumed, but in the simulations, it is seen to be only a fair approximation. Although the simulated fields from each channel merge smoothly into the observed radiation pattern, there is no reason to expect this to occur in practice. It then becomes necessary to

confirm that enough coherence takes place to produce a well-collimated radiation pattern. To test this, we carried out an experiment on a seven-channel grating with sidewalls at a frequency of approximately 32 GHz.

DESCRIPTION OF THE EXPERIMENT

Our previous work at frequencies of order 5 GHz used standard microwave detectors and oscilloscopes that were available. To reach higher frequency, the possibility of using a 33 GHz bandwidth oscilloscope (DSA73304) suggested dimensioning the experiment to produce radiation near 32 GHz. The dimensions of our previous and new gratings are shown in the Table.

Table 1: Parameters of the Experiment

Parameters	Original grating	7-channel grating
Peak Voltage	60-120 kV	60-120 kV
Current	10-40 A	10-40 A
Pulse duration FWHM	300 ns	300 ns
Beam thickness	1 mm	1-2 mm
Beam height	0.5 mm	0-2 mm
Beam width	3.5 cm	5.2 cm
Period L	2 cm	3.3 mm
Groove depth H	1 cm	1.65 mm
Groove width A	1 cm	1.65 mm
Channel width w	4 cm	6.6 mm
Number of periods	20	40
Magnetic field	1 T	0.5 T

The dispersion relation (DR) for the grating is displayed in Fig. 1, along with the 2-D DR of Andrews and Brau. For beam energy of 80 keV, the operating point is at 33.2 GHz. The corresponding SP angle is 145° .

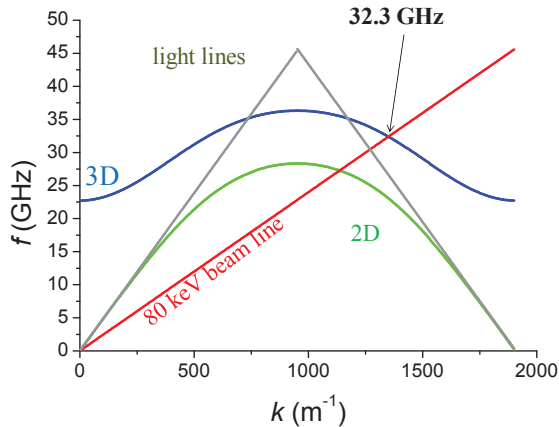


Figure 1: Dispersion relation: frequency f v. axial wave number k , for grating with $L = w/2 = 3.3$ mm. 2D green, 3D blue, 80 keV beam line red.

The set-up may be seen in Fig. 2. The radiation enters a section of WR 28 wave guide surrounded by a flange. A small B-dot probe is positioned near the grating so as to measure the magnetic field a few mm above the grating. The return current from the beam stop is monitored by a Rogowski coil.

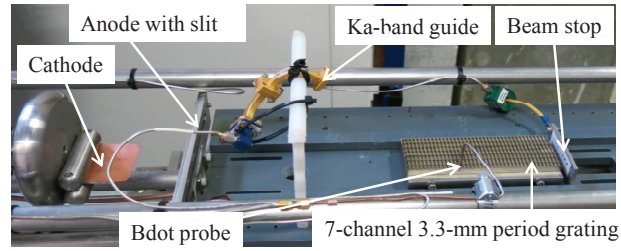


Figure 2: Photograph of set-up, showing essential elements. The vacuum box and solenoid are not shown.

The sheet beam is emitted from a knife-edge cathode, and passes through a slit on the anode, whose height and opening width may be adjusted. Thermally sensitive paper on the beam stop can be used to observe the beam shape. The experiment is inserted in a cylindrical vacuum box, which is surrounded by a pulsed solenoid.

A major concern is the efficiency of the wave guide and flange system for detecting the SP radiation. To investigate this 3D “MAGIC” were performed. One is displayed in Fig. 3.

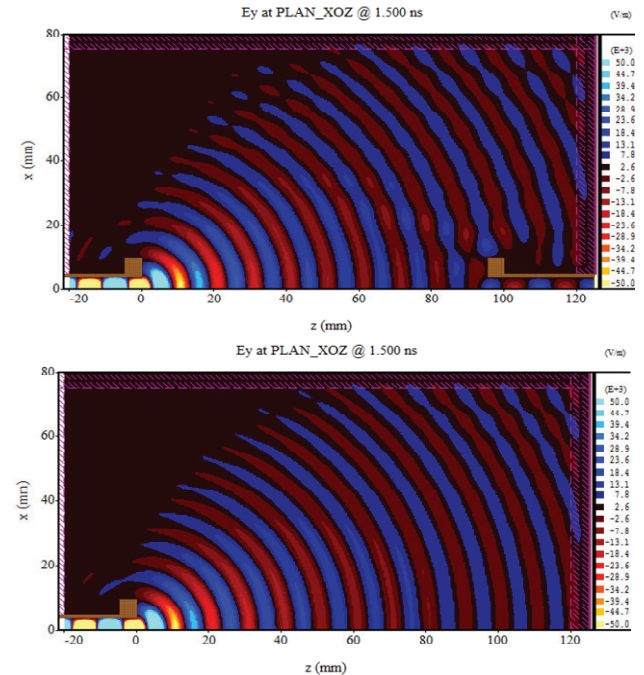


Figure 3: Waveguide efficiency “MAGIC” simulations: upper with and lower without wave guide receiver.

An input wave guide emits radiation at 33 GHz on the bottom left. The upper figure shows the propagation from the wave guide source to a similar detector at the bottom right. The lower shows the power flow in the absence of the receiver. We find that the power in the wave guide overestimates by a factor of 1.5 (at 33 GHz) the power arriving in the equivalent area in the second simulation. This correction factor was included in our power estimates.

The attenuation of the connecting cables and fixed attenuators was measured as a function of frequency by using a tunable source of known power connected to the oscilloscope. The response of the B-dot probe (located

just above a groove of the grating) was estimated from its calculated inductance and area, with an error of 20%.

In Fig. 4 contour map of B_x is displayed in order to show where the radiation is predicted to occur (145°). The Ka-band waveguide has been moved around this lobe.

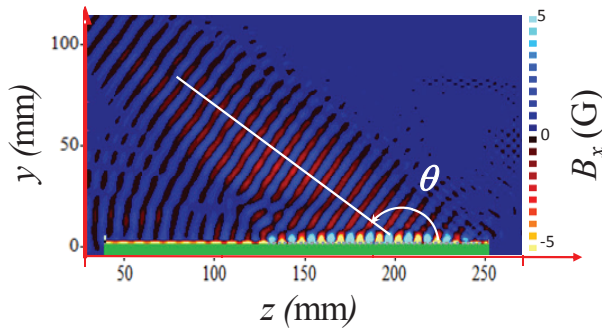


Figure 4: "MAGIC" contour map of B_x showing angle of emission.

RESULTS OF THE EXPERIMENT

In Fig. 5, we have plotted the two oscilloscope signals, B-dot (left scale) and Ka-band (right scale), for two shots. We observe a shot-to-shot variation due to fluctuations in beam current. There is considerable resemblance between the signals.

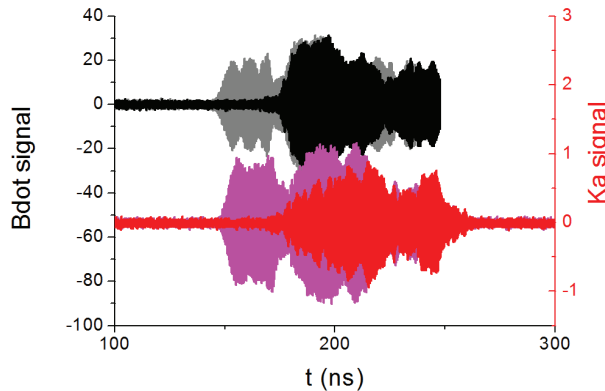


Figure 5: Comparison of the B-dot (left scale) and Ka-band signals (right scale) for two different shots.

By using our calibration of the B-dot probe, we show in Fig. 6 a typical magnetic component B_x as a function of time, along with its FFT. The maximum value is in good agreement with MAGIC predictions at the B-dot location. The measured frequency corresponds to that expected from the dispersion relation.

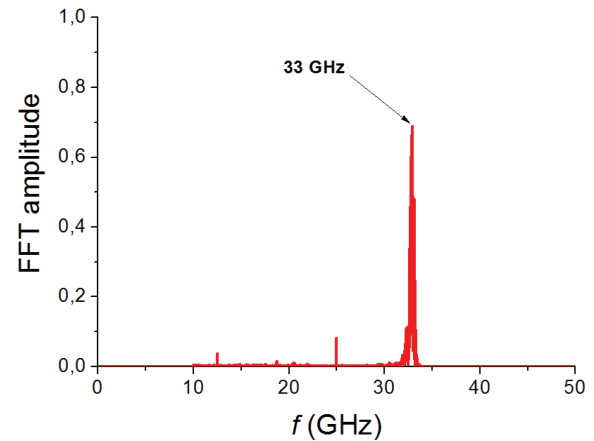
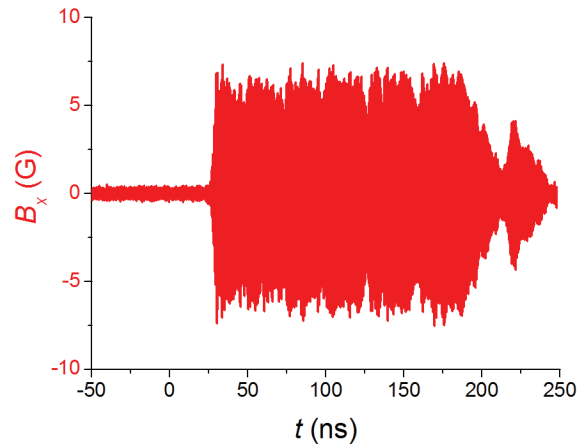
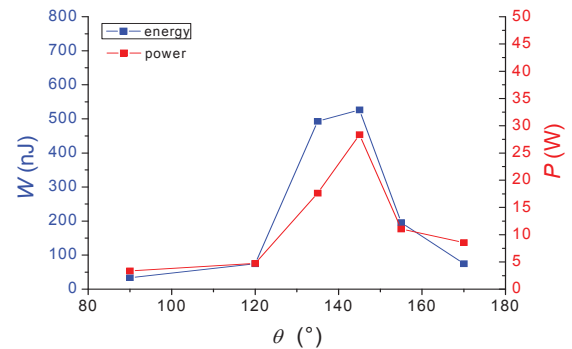


Figure 6: B_x field from the B-dot time signal and FFT.

The Ka-band wave guide was moved so as to explore the radiation pattern. We present in Fig. 7 some results of this exploration: the top figure gives the variation in θ at $\phi = 90^\circ$ whereas the lower figure gives the variation in ϕ at $\theta = 145^\circ$. Both the peak instantaneous power (red) and the energy (blue) are plotted. The energy is deduced by integrating the power over the duration of the pulse.



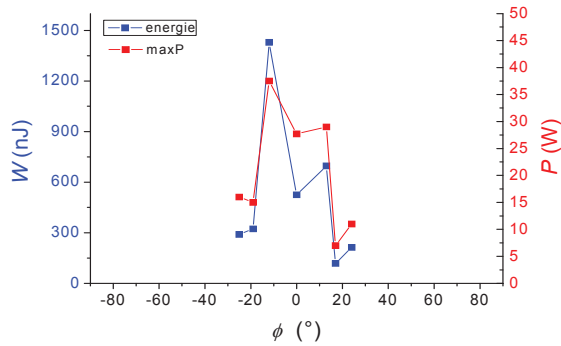


Figure 7: Angular distributions of energy and power.

We can compare this value to the MAGIC simulation which is displayed in Fig. 8. This 3D plot shows the power density in a plane at the position $z = 6$ cm (as shown in Fig. 4). In this simulation, which uses a perfect grazing beam at 20 A, the power density is of the same order of magnitude and leads to a total emitted power of approximately 20 kW.

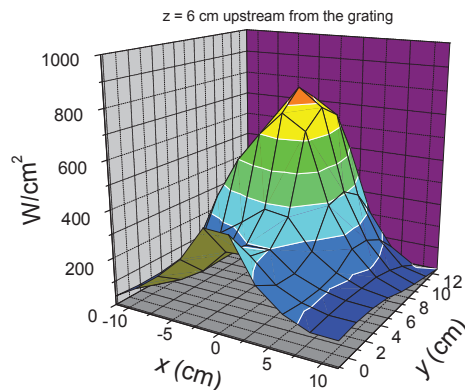


Figure 8: "MAGIC" prediction for power distribution on the rear wall of the simulation volume.

The radiation pattern depends strongly on the coherence among the different channels. If the coherence is high the radiation is confined to a relatively narrow lobe. However, we have no general argument that such coherence is to be expected, and we rely on simulations that suggest that a fair degree of coherence occurs. We varied the mesh size to see whether the coherence depended upon it. Unfortunately, it does. The results of this investigation are displayed in Fig. 9.

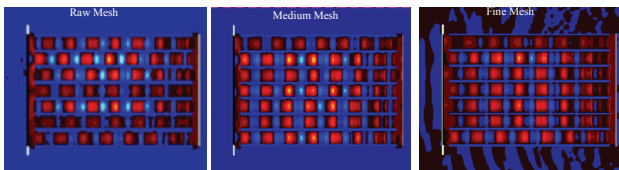


Figure 9: Influence of mesh-size on coherence.

Here we show the contour maps of B_x at the top of grating surface for three different mesh size in the

direction along the grooves (1330, 570 and 290 μm , from left to right). The smallest mesh size is the practical limit of the computer we used. We can see that the coherence is better for the smallest mesh size though not perfect. However, the effect of coherence is to concentrate the emission pattern into a narrow lobe by limiting the azimuthal angle ϕ to small values around 90° . The experimental results indicate that the power is indeed concentrated in such a small lobe

CONCLUSION

The results presented here lend support to the hypothesis that a multi-channel SP FEL with sidewalls has enough coherence to produce a reasonably narrow radiation pattern. The concentration around the SP angle with respect to the beam direction was to be expected, while the concentration in a narrow range of azimuthal angle happens only if substantial coherence among the different channels occurs. Although we know of no general argument in favour of such coherence, it appears to occur both in our somewhat rough experiment as well in the simulations with small transverse mesh-size. In the near future a 20 channel grating designed to produce radiation at 100 GHz will be tested.

REFERENCES

- [1] J. Gardelle, P. Modin and J. T. Donohue, "Observation of copious emission at the fundamental frequency by a Smith-Purcell free-electron laser with sidewalls", *Appl. Phys. Lett.* **100**, 111303 (2012).
- [2] J. Gardelle, L. Courtois, P. Modin and J. T. Donohue, "Observation of coherent Smith-Purcell radiation using an initially continuous flat beam", *Phys. Rev. ST Accel. Beams* **12**, 110701 (2009).
- [3] H. L. Andrews and C. A. Brau, "Gain of a Smith-Purcell free-electron laser", *Phys. Rev. ST Accel. Beams* **7**, 070701 (2004).
- [4] J. T. Donohue and J. Gardelle, *Phys. Rev. ST Accel. Beams* **14**, 060709 (2011).
- [5] S. J. Smith and E. M. Purcell, "Visible light from localized surface charges moving across a grating", *Phys. Rev.* **92**, 1069 (1953).
- [6] J. T. Donohue and J. Gardelle, "Towards high frequency operation with a multi-grating Smith-Purcell Fel" in *Proc. 35th Int. Free-Electron Laser Conf.*, New York, 2013, pp. 525-528.
- [7] B. Goplen, L. Ludeking, D. Smithe, and G. Warren, "User-configurable MAGIC for electromagnetic PIC calculations", *Computer Physics Communications* **87**, 54 (1995).

“FLYING” RF UNDULATOR *

I. V. Bandurkin, S. V. Kuzikov, A. V. Savilov[#], A. A. Vikharev,
Institute of Applied Physics, Nizhny Novgorod, Russian Federation

Abstract

A concept for the room-temperature rf undulator, designed to produce coherent X-ray radiation by means of a relatively low-energy electron beam and pulsed mm-wavelength radiation, is proposed. The “flying” undulator is a high-power short rf pulse co-propagating together with a relativistic electron bunch in a helically corrugated waveguide. The electrons wiggle in the rf field of the -1st spatial harmonic with the phase velocity directed in the opposite direction in respect to the bunch velocity, so that particles can irradiate high-frequency Compton’s photons. A high group velocity (close to the speed of light) ensures long cooperative motion of the particles and the co-propagating rf pulse.

INTRODUCTION

Typically, the undulator of an X-FEL is a periodic system of DC magnets with a magnetic field ~ 1 T and a period of several centimeters, where a wiggling relativistic electron bunch produces short wavelength radiation in the self-amplified spontaneous emission (SASE) regime [1-3]. In comparison with this traditional undulator, the so-called rf undulator, where an electron bunch flies toward a counter-propagating rf wave, introduces a strong appeal to use less energetic electron beam in order to produce the same wavelength of Compton’s scattered radiation [4-7]. In the case of weak electron wiggling, the wavelength of Compton’s photons produced by electrons with the same energy $W = mc^2(\gamma - 1)$, is determined by $\lambda \approx \lambda_{\text{rf}} / 4\gamma^2$ for the rf undulator (in contrast to $\lambda \approx \lambda_u / 2\gamma^2$ for the conventional undulator), where λ_{rf} and λ_u are the wavelength of microwaves for the rf undulator and the period of DC magnets for the conventional undulator, respectively. In order to reach the nanometer wavelength scale, one can use an electron bunch with an energy of several hundreds MeV in the rf undulator with a period of about ~ 1 cm instead of the 1-2 GeV beam in the conventional undulator with a period of several centimeters [8]. The effective undulator period can be as short as the wavelength of the used rf radiation, i.e., $\lambda_u = 2\pi/(h+k)$ (here, $k = \omega/c$ is the vacuum wavenumber, and h is the wave propagation constant). That is why millimeter and sub-millimeter radiation is preferable for the rf undulator.

The inevitable cost of these evident advantages is a necessity to provide a high power level of microwaves in order to ensure that an acceptable value of the undulator

parameter K is competitive with conventional undulators with $K \sim 1$. In the Ka-band, the necessary power of a wave (for it to be counter-propagating to electrons) in the waveguide with a radius of ~ 1 cm reaches a GW level. In order to provide such a power level, modern projects of rf undulators employ cavities with high Q-factors powered by existing high-power rf sources like klystrons or gyroklystrons, which are able to provide tens of megawatts. According to such a concept, the whole rf-undulator system should consist of many relatively short (~ 1 m) and mutually phased sections. As each section should be fed by its own rf source, the X-FEL consisting of tens of sections is very expensive.

Note that high-Q cavities bring a threat of destructive phenomena like rf breakdown and pulsed heating [9,10]. In order to avoid these undesirable phenomena, a short pulse of rf radiation of a high (GW) power level is preferable. In particular, experiments with particle accelerators show that nanosecond rf pulses of the GW level can travel through an electrodynamic structure without a breakdown [11].

There are necessary rf sources of the GW power level. In particular, these sources can be based on moderately-relativistic (hundreds of keV) BWOs [12-14]. Existing sources can deliver more than a 1 GW power in the X-band and about 1 GW in the Ka-band with a repetition rate as high as several kHz. It was proven experimentally that phases of these separate sources can be mutually locked [13]. The mentioned BWOs are able to produce rf radiation in short pulses only (usually shorter than 20 ns). If such a short rf pulse with the duration τ and the group velocity v_{gr} propagates counter to electrons in a waveguide, moving with a velocity close to the light velocity c then the effective undulator length for wiggling (the length of the intersection of electron path and rf pulse) is determined as follows

$$L_{\text{eff}}^{\text{count}} = \frac{v_{\text{gr}}\tau}{1 + v_{\text{gr}}/c}. \quad (1)$$

If $\tau=10$ ns, $v_{\text{gr}} \approx c$, then $L_{\text{eff}} \approx 1.5$ m. This is too short for the SASE XFEL, so that a lot of sections and rf sources are required to reach the saturation level.

CONCEPT OF THE FLYING UNDULATOR

We suggest an rf undulator based on co-propagation of an electron bunch and a short high-power rf pulse without a loss in Doppler’s up-conversion of the frequency [15]. This “flying” undulator has the following effective undulator length:

*Work supported by the Russian Foundation for Basic Research (Projects 14-08-00803 and 14-02-00691).

[#]savilov@appl.sci-nnov.ru

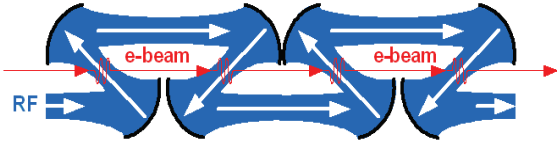


Figure 1: Periodic mirror transfer line with the “flying” rf undulator.

$$L_{\text{eff}}^{\text{co}} = \frac{v_{\text{gr}} \tau}{1 - v_{\text{gr}}/c}, \quad (2)$$

which is longer by factor $(1 + v_{\text{gr}}/c)/(1 - v_{\text{gr}}/c)$ than the interaction distance of the counter-propagating particles and the rf pulse with the same duration. The sectioned scheme shown in Fig. 1 illustrates the main idea of the “flying” undulator. Electrons and the rf pulse (which naturally contains counter-propagating wave subsections) can move together over a long distance. However, the length of the counter-propagating subsections is small as compared to the length of the whole undulator.

CORRUGATED WAVEGUIDE MODES

In a helical corrugated waveguide (Fig. 2), wiggling can be provided in the long section. The surface of this waveguide can be described in the cylindrical system of coordinates (z -axis coincides with waveguide center) by the formula $r(z, \varphi) = R_0 + a \sin(2\pi z/D + \bar{m}\varphi)$, where R_0 is the average waveguide radius, a is the corrugation amplitude, D is the period, and \bar{m} is the number of helical threads. In this corrugated waveguide, there is an infinite number of the so-called Floquet’s spatial harmonics with propagation constants $h_n = h_0 + 2\pi n/D$ (here n is the harmonic number) and phase velocities $v_{\text{ph}} = \omega/h_n$ (they could be either positive or negative relative to the electron velocity sign).

We consider the “flying” rf undulator, where the co-propagating 0-th harmonic has the positive propagation constant h_0 and phase velocity, but the -1-st harmonic has the negative propagation constant h_{-1} and the negative phase velocity. The group velocity is positive and constant for all spatial harmonics. Particles are assumed to oscillate in the transverse fields of the -1-st harmonic. In this case, the equivalent undulator period is given by the formula

$$\lambda_u = 2\pi / (|h_{-1}| + k). \quad (3)$$

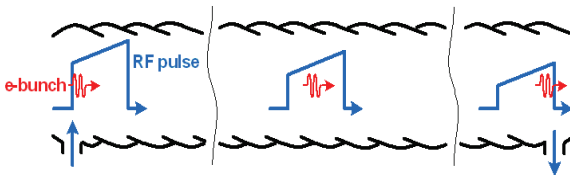


Figure 2: “Flying” rf undulator based on the helical waveguide.

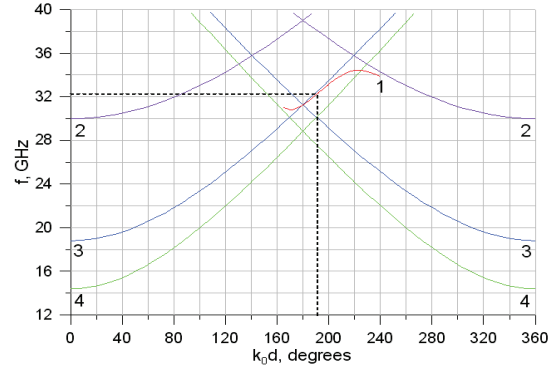


Figure 3: Dispersion characteristic of the normal TM_{01} - TM_{11} wave in the helical waveguide (curve 1); dispersion curves of TM_{11} (2), TM_{01} (3), and TE_{11} (4) partial waves in the smooth circular cross-section waveguide.

Note that $|h_{-1}|$ can be close to the vacuum wavenumber k , or even bigger (for slow -1st harmonic). Therefore, the equivalent undulator period might be favourably as short as it is in the case of the counter-propagating rf pulse (when the equivalent undulator period is close to the half-wavelength, $\lambda_u = 2\pi/(h+k) \approx \lambda_{\text{rf}}/2$).

Eigenmodes of a helical waveguide with a weak corrugation can be represented using partial waves of the smooth circular waveguide. Far from Bragg’s resonances, amplitudes of all non-zero harmonics are negligibly small. Nevertheless, if Bragg’s conditions ($h_1 \pm 2\pi/D = h_2$ and $m_1 \pm \bar{m} = m_2$, where h_1, h_2 are propagation constants of partial modes, and m_1 and m_2 are azimuthal indices) is satisfied for a certain pair of waves, the amplitudes of 0-th and ± 1 -st harmonics become comparable.

The co-propagating partial wave of the “flying” undulator can cause large-scale perturbation of electron motion and spoil the X-FEL radiation spectrum [8]. In order to avoid this, the 0-th and -1-st harmonics should be represented by modes with different transverse structures. The 0-th harmonic should be chosen so that it does not have transverse fields in the center, where a thin electron beam is injected. Waves like TE_{mn} or TM_{mn} with the azimuth index $m \neq 1$ satisfy this requirement. Of course, the operating (“wiggling”) fields of the -1-st harmonic should be as high as possible. Therefore, the -1-st harmonic should preferably be a wave with $m=1$. In particular, let us consider the rf undulator based on the helical corrugated waveguide, where the TM_{01} wave is actually the 0th harmonic, the rotating TM_{11} is the -1-st harmonic in the one-thread ($\bar{m} = 1$) helical waveguide.

We investigate the operating TM_{01} - TM_{11} wave. Figure 3 illustrates the dispersion curve of this normal wave (the eigenfrequency vs the phase h_0D in degrees) for the following waveguide parameters: $R_0=6.1$ mm, $D=6$ mm, and $a=0.3$ mm. Dispersion curves of the main partial modes in the smooth circular waveguide are also shown.

The dispersion curve of our normal wave is close to linear within the phase interval between 170° and 220° . At these points, the dispersion curve of the partial TM_{01} mode has intersections with the dispersion curves of the partial TM_{11} and TE_{11} waves, correspondingly. Thus, at these points one can observe the phenomenon of the dispersion curve's splitting caused by Bragg's resonance. Note that the operating point is placed approximately between the mentioned TM_{01} - TM_{11} and TM_{01} - TE_{11} Bragg's resonances, so that the TE_{11} fields contribute also to the field structure of the operating normal wave.

FLYING UNDULATOR OPTIMIZATION

The dimensionless magnitude of the momentum of electron oscillations (the undulator parameter, $K = \gamma V_\perp / c$) is proportional to the deflecting rf fields of the -1-st harmonic:

$$K = \frac{e(E_\perp + H_\perp)\lambda_u}{2\pi mc^2},$$

where E_\perp and H_\perp are the transverse fields at the waveguide axis. In a FEL, the amplitude of the optical radiation grows along the electron path on the z coordinate as $P_s = \exp(z/L_g)$, where the small-signal gain length, $L_g = (\sqrt{3}C/2)^{-1}$, is determined by the amplification parameter [16]

$$C = \left[K_{\text{eff}}^2 \frac{I}{I_A} \frac{4\pi}{\gamma^5 \sigma \lambda} \right]^{1/3}. \quad (4)$$

Here, I is the electron current, $I_A = 17 \text{ kA}$, and σ is the transverse rms size of the electron beam. In this formula, $K_{\text{eff}} = K$ in the case of a planar undulator. It is important that in the "flying" undulator, the wiggling component of the rf field has circular polarization; this makes the effective undulator parameter twice as high, $K_{\text{eff}} = 2K$.

Thus, the optical wave gain is $\exp(L_{\text{eff}}/L_g)$. At fixed parameters of the electron beam and rf pulse duration, L_{eff}/L_g is proportional to the factor

$$\eta = K^{2/3} \frac{v_{\text{gr}}/c}{1 - v_{\text{gr}}/c}, \quad (5)$$

which should be used to optimize parameters of the co-propagating "flying" rf undulator, as well as to compare the "flying" undulator with the rf undulator based on the counter-propagating wave [in the latter, factor η can be calculated by substituting the denominator in (5), namely, $\eta = K^{2/3} (v_{\text{gr}}/c)/(1 + v_{\text{gr}}/c)$].

Figure 4 shows the undulator parameter K , the normalized group velocity v_{gr}/c , and the gain parameter η calculated in accordance with Eq. 5 for the 1 GW rf power. The highest value of η (near 190° at $f=32 \text{ GHz}$) corresponds to $\lambda_u = 5.4 \text{ mm}$ and $v_{\text{gr}}/c \approx 0.7$. The maximum of η corresponds approximately to the maximum of v_{gr} , although K naturally grows up when the phase approaches to the Bragg's resonances mentioned above. The reason is that in accordance with Eq. 5 the vicinity of the group velocity to the light velocity is more vulnerable in comparison with the contribution of the rf field amplitude to the power of $2/3$. At the optimal point (190°) the ratio of the transverse electric field (32 MV/m) to the longitudinal one (102 MV/m) at the axis is 0.31. This value allows evaluating amplitudes of the partial TM_{11} wave ($E_z = 0, E_\perp \neq 0$) and the TM_{01} wave ($E_z \neq 0, E_\perp = 0$) in the normal wave.

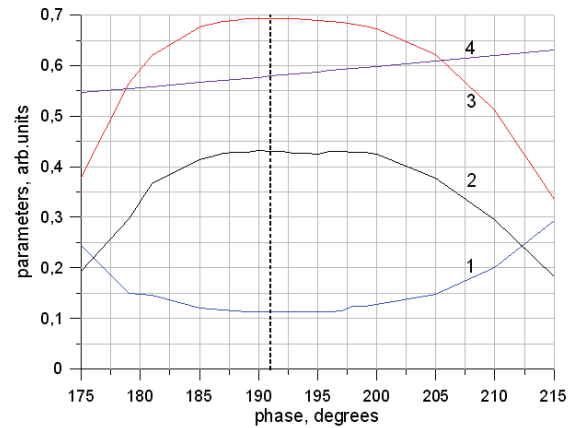


Figure 4: Normalized characteristics of the TM_{01} - TM_{11} normal wave in the helical waveguide undulator parameter K (curve 1), gain factor η (2), normalized group velocity v_{gr}/c (3), and the ratio of the effective undulator period to the rf wave wavelength radiation $\lambda_u/\lambda_{\text{rf}}$ (4).

Let us compare this "flying" rf undulator created on the basis of a 10 ns rf pulse with $\lambda_{\text{rf}} = 1 \text{ cm}$ and with the DC-magnet undulator ($K = 0.5$ and $\lambda_u = 3 \text{ cm}$). Due to $v_{\text{gr}} = 0.7c$, the "flying" undulator provides electron wiggling within the distance $L_{\text{eff}} \approx 10 \text{ m}$ (see Eq. 2) with the effective undulator period $\lambda_u = 0.58\lambda_{\text{rf}}$. At a fixed target radiation wavelength $\lambda \approx \lambda_u/2\gamma^2$, the ratio of the required electron energies is $\gamma^{\text{DC}}/\gamma^{\text{rf}} = \sqrt{\lambda_u^{\text{DC}}/\lambda_u^{\text{rf}}} = 2.3-2.5$. Since the amplification factor is proportional to $C \propto (K_{\text{eff}}^2/\gamma^5)^{1/3}$ and $K_{\text{eff}} = 2K$ for the circular polarized rf undulator,

one obtains $C^{\text{rf}}/C^{\text{DC}} = 2.3-2.6$. Thus, the “flying” rf undulator with $L_{\text{eff}} \approx 10$ m provides the gain, which is equally as high as the referenced DC undulator with the length $L \approx 25$ m, and requires significantly lower electron energy.

FOCUSSING PROPERTIES

We should mention an additional advantage of the “flying” undulator, namely, its focusing properties. The transverse fields of its co-propagating partial wave TM_{01} (0-th spatial harmonic) component have minimum (zero) at the waveguide axis (the e-beam position). Therefore, the pondermotive Miller force caused by this non-synchronous wave is directed to the centre (Fig. 5).

In contrast, the field of the operating undulator partial wave TM_{11} (-1-st spatial harmonics) possesses de-focusing properties (Fig. 5), as it has maximum in the centre of the operating waveguide. However, the estimated value of the de-focusing Miller force caused by this wave is significantly smaller as compared to the focusing force provided by the 0-th TM_{01} spatial harmonic.

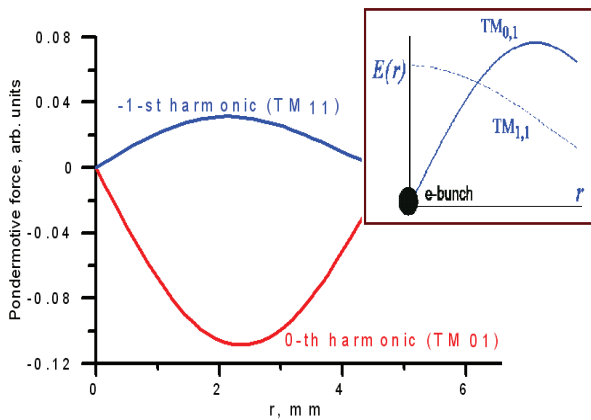


Figure 5: Transverse structures of the partial waves TM_{01} and TM_{11} forming the normal wave in the helical waveguide, and transverse structures of pondermotive Miller forces provided by these two partial waves.

RF SOURCE FOR THE FLYING UNDULATOR

As a prototype of the rf source for the flying undulator, a relativistic Cherenkov backward-wave oscillator is being under creation at the Institute of Applied Physics (Fig. 6). This rf source is based of the 550 kV / 4 kA electron beam provided by the SINUS-6 accelerator. A tubular beam of rectilinearly moving particles passes through the operating corrugated waveguide in a guiding magnetic field of 6 T and excites the backward far-from-cutoff operating mode TM_{01} . A special resonant reflector is placed at the waveguide input; this is needed to provide output of the rf power.

According to simulations, realization of the simplest scheme of such rf oscillator at the operating frequency of 35 GHz can be a way for creation of a source of a 20 ns rf

pulse with the peak power of about 0.5 GW; the corresponding electronic efficiency amounts $\sim 20\%$. According to simulations, the use of a sectioned operating cavity can enhance the output power up to 700-800 MW.

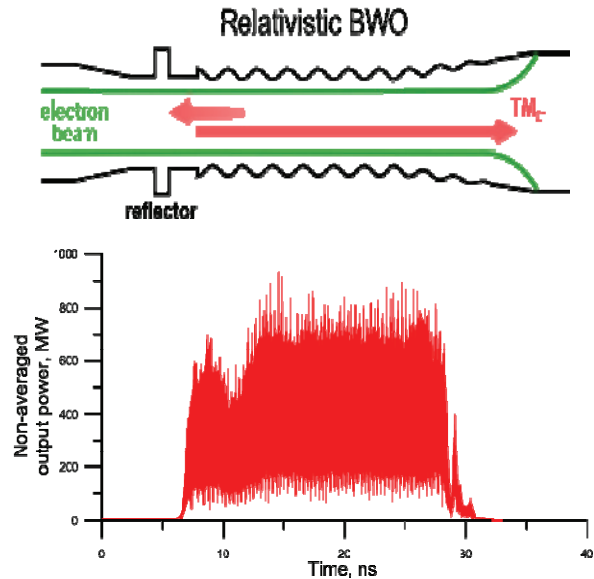


Figure 6: Relativistic Cherenkov BWO, and calculated non-averaged output power versus the time.

REFERENCES

- [1] L. Giannessi et al, Phys. Rev. Lett. 106, 144801 (2011).
- [2] C Bostedt et al., J. of Phys. B 46 , 164003 (2013).
- [3] G. Marcus et al., Appl. Phys. Lett. 101 , 134102 (2012).
- [4] V.L. Bratman, N.S. Ginzburg, M.I. Petelin, JETP Letters 28, 190 (1978).
- [5] T. Shintake et al, Japanese J. of Appl. Phys. 22, 844 (1983).
- [6] P. Sprangle, B. Hafizi and F. Mako, Appl. Phys. Lett. 55, 2559 (1989).
- [7] S. Tantawi et al, Phys. Rev. Lett. 112, 164802 (2014).
- [8] S. V. Kuzikov et al, Phys. Rev. ST Accel. Beams 16, 070701 (2013).
- [9] V. Dolgashev, S. Tantawi, Y. Higashi, and B. Spataro, Appl. Phys. Lett. 97, 171501 (2010).
- [10] L. Laurent et al, Phys. Rev. ST Accel. Beams 14, 041001 (2011).
- [11] M. C. Thompson et al, Phys. Rev. Lett. 100, 214801 (2008).
- [12] S. D. Korovin et al, Phys. Rev. E 74, 016501 (2006).
- [13] V.V. Rostov et al, Appl. Phys. Lett. 100, 224102 (2012).
- [14] A.V. Savilov, Appl. Phys. Lett. 97, 093501 (2010).
- [15] S.V. Kuzikov, A.V. Savilov, A.A. Vikharev, Appl. Phys. Lett. 105, 033504 (2014).
- [16] Zh. Huang and K.-J. Kim, Phys. Rev. ST AB 10, 034801 (2007).

HIGH EFFICIENCY LASING WITH A STRONGLY TAPERED UNDULATOR

J. Duris and P. Musumeci

Department of Physics and Astronomy, UCLA, Los Angeles, CA 90095, USA

Abstract

Typical electrical to optical energy conversion efficiencies for FELs are limited by the Pierce parameter to 10^{-3} or smaller. Undulator tapering schemes have enabled extraction of as much as 1 or 2% of the electron energy. Recently, the UCLA BNL helical inverse free electron laser (IFEL) experiment at ATF demonstrated energy doubling and acceleration of 30% of an electron beam from 52 to 93 MeV with a modest 10^{11} W power CO₂ laser pulse. By reversing and retuning the undulator, the electrons may be violently decelerated, thereby transferring energy from the beam to the laser pulse. Simulations show that by sending a 1 kA, 70 MeV electron beam and 100 GW laser into a prebuncher and the reversed undulator, 41% of the electron beam energy should be converted to radiation, allowing the laser pulse power to grow to 127 GW.

INTRODUCTION

Recent results of the UCLA BNL helical IFEL experiment demonstrated the possibility of doubling the energy of an electron beam with a high-power laser. Reversing the process, one could imagine the possibility of extracting half of the e-beam power and converting it into coherent radiation. The essence of this idea is described in another paper in these proceedings as the low gain regime of tapering enhanced stimulated superradiant amplification or TESSA [1]. FELs are typically limited by the Pierce parameter ρ to less than 1 percent electro-optical power conversion and even the best lasers don't exceed efficiencies of about 30% so converting nearly half of the e-beam power to coherent radiation would be significant achievement.

Inverse free electron laser acceleration has seen progress in recent years. The STELLA experiment at ATF demonstrated efficient IFEL acceleration with gradients similar to conventional RF-accelerating cavities and captured up to 80% of electrons with the use of a prebunched beam [2]. The UCLA Neptune IFEL experiment first achieved accelerating gradients surpassing that of conventional rf-accelerators [3]. The LLNL-UCLA IFEL experiment at Lawrence Livermore National Lab used a multi-TW Ti:Sa laser and produced significant peak gradients [4].

The UCLA BNL IFEL collaboration at ATF was conceived to improve the average IFEL accelerating gradient with the use of the first strongly period- and field-tapered helical undulator. Whereas electrons propagating through a linear undulator undergo sinusoidal motion thereby reducing to zero twice per period their transverse velocity, the helical trajectories of the electrons propagating through the undulator provide continuous transverse velocity which in

turn enables continuous energy transfer. The experiment accelerated electrons from 52 to 106 MeV with a TW class CO₂ laser, averaging a 100 MeV/m accelerating gradient along the 54 cm undulator, and accelerated up to 30% of electrons from 52 MeV to a stable 93 MeV final energy with <1.8% energy spread [5].

EXPERIMENTAL DESIGN

The IFEL decelerator project builds off of the experience of the helical IFEL experiment by retuning the existing helical undulator to decelerate electrons instead of accelerating them. The experimental setup is depicted in Figure 1. In order to further increase the strength of the stimulated radiation, compression and prebunching are necessary. The peak current of the beam will be increased from 100 A to 1 kA with ATF's compressor. Furthermore, a combination prebuncher and chicane phase delay module is currently being built at UCLA with the goal of increasing the fraction of the beam accelerated to full energy. The electron beam acquires an energy modulation at the resonant wavelength while the chicane module delays the modulated beam in order to phase lock to the ponderomotive wave at the entrance of the helical IFEL undulator. 3D simulations show that 70 to 90% of the injected beam should be accelerated to high energy. With a 30 MeV change in energy, 1 kA current, and 80% capture, an estimated 24 GW e-beam power should be transferred to the radiation field.

Helical Undulator Design

The tapering of the helical undulator was previously changed [5], enabling the first demonstration of IFEL resonant energy tuning. Since the undulator period is predetermined by the dimensions of the magnets in the undulator, the gap between magnets was changed in order to manipulate the field and resonant energy along the undulator. In order to reverse the effect of the accelerator, the undulator may be reversed and the gap tapered in order to reduce the resonant energy during the interaction. The highest stable energy electron beam that may be produced at the ATF is 70 MeV, and the final energy of the decelerated electron beam is 42 MeV. The experimental parameters are summarized in Table 1.

The undulator design follows closely the methods described in [1] but differs slightly since the undulator period is fixed (see Figure 2a). Equations 1 and 2 describe the approximate longitudinal dynamics of a particle undergoing helical IFEL interaction. Here, $K_l = \frac{eE_0\lambda}{m_0c^22\pi}$ and $K = \frac{eB\lambda_w}{m_0c2\pi}$ are the laser and undulator normalized vector potentials respectively.

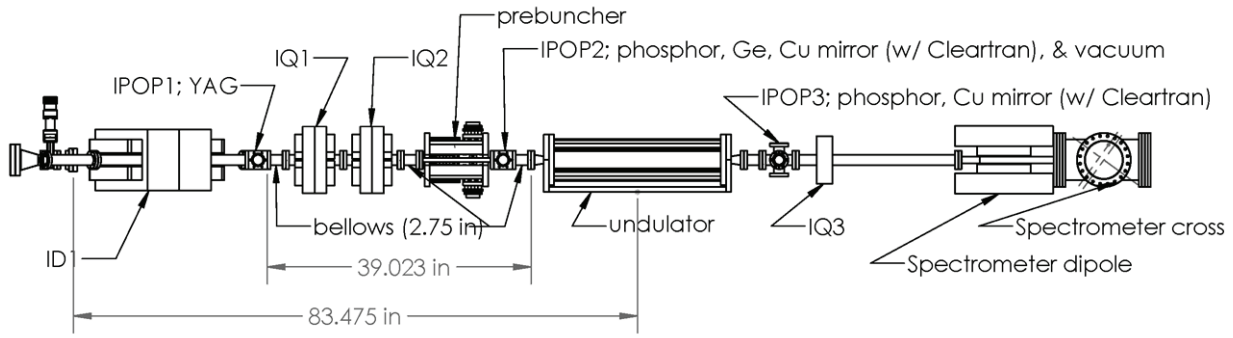


Figure 1: Diagram of the beamline setup for the IFEL decelerator project. The e-beam and laser both enter from the left side of the figure, and the dipole ID1 cancels dispersion as it kicks the electrons onto the beamline with the laser pulse. IQ1, IQ2, and IQ3 are focusing quadrupoles while IPOP1, IPOP2, and IPOP3 house beamline diagnostics. A prebuncher & phase delay stage located just upstream of the undulator prebunch and phase-lock the e-beam to the ponderomotive wave. Downstream of the undulator lies an energy spectrometer for the decelerated beam as well as a CO₂ laser pickout for laser diagnostics (joulemeter, spectrometer, and streak camera).

$$\frac{d\gamma}{dz} = \frac{kK_L K}{\gamma} \sin \psi \quad (1a)$$

$$\frac{d\psi}{dz} = k_w - k \frac{1 + K^2}{2\gamma^2} \quad (1b)$$

Equation 1b describes the ponderomotive gradient due to the combined interaction of undulator- and laser-fields as evident by the presence of K and K_L in the equation. For a stationary resonant phase, a resonant particle's energy is determined completely by zeroing the phase advance in Equation 1b, yielding the energy of a resonant electron:

$\gamma_r = \sqrt{\frac{\lambda_w}{2\lambda} (1 + K^2)}$. Matching the gradient in the resonant energy to the ponderomotive gradient from Equation 1b results in the tapering condition, Equation 2, determining K in terms of λ_w and K_L . A positive resonant phase ψ_r yields a tapering with increasing resonant energy along the undulator while $\psi_r < 0$ results in a tapering for deceleration.

$$\frac{dK}{dz} = \frac{8\pi K K_L \sin \psi_r - \frac{d\lambda_w}{dz} (1 + K^2)}{2\lambda_w K} \quad (2)$$

When the undulator period and laser parameters are specified along with the initial condition that K at the entrance be such that the resonant energy is equal to the input beam's 70 MeV energy, the differential equation yields K which in turn determines the on-axis field strength along the undulator. An undulator builder equation can then be used to estimate the gap along the undulator needed to create the designed on-axis field.

The laser and e-beam parameters used in the tapering design are specified in Table 1, and the calculated period and resonant energy as well as the solutions to the IFEL/FEL equations are shown in Figure 2. The initial seed power was chosen to be large enough for significant deceleration but small enough to increase the ratio between the signal (stimulated power) to background (seed power). The resonant

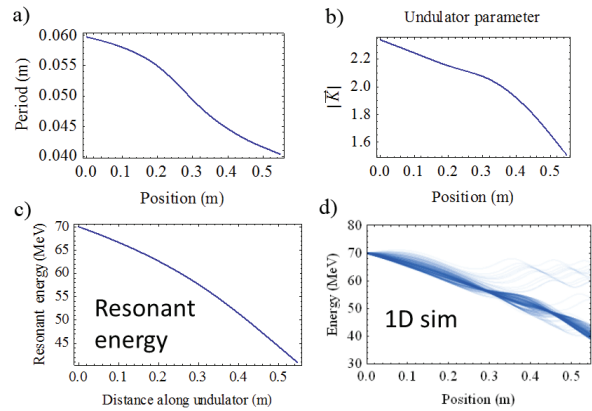


Figure 2: The a) period and b) normalized undulator vector potential decreases along the undulator causing c) the resonant energy to decrease. d) Solutions to Equation 1 describing the longitudinal IFEL dynamics were calculated with the design seed laser and undulator tapering.

phase was set to a constant $-\pi/4$ as a compromise between bucket depth and ponderomotive gradient.

Table 1: Design Parameters

E-beam energy	70 to 40 MeV
Laser focal intensity	4 TW/cm ²
Laser wavelength	10.3 μ m
Rayleigh range	30 cm
Laser waist	undulator midpoint
1/e ² spot size	0.99 mm
M ²	1.07
Resonant phase	$-\pi/4$

Time Resolved Laser Diagnostics

The setup of the beamline for the IFEL decelerator experiment is very similar to that of the IFEL accelerator experi-

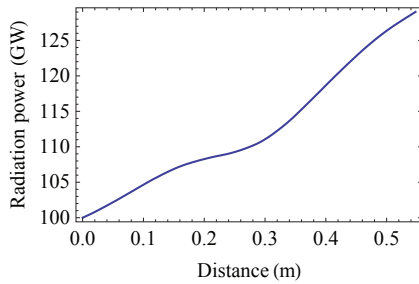


Figure 3: The radiation power grows along the undulator as the electrons are decelerated.

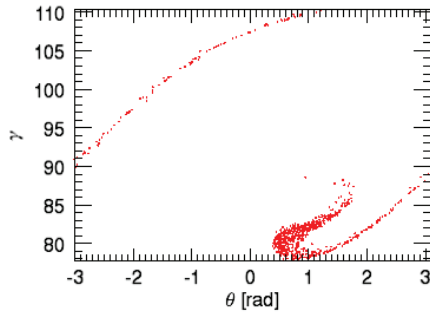


Figure 4: The e-beam longitudinal phase space is shown at the exit of the undulator. The beam loses 28 MeV as the particles are decelerated from 70 to 42 MeV.

ment with the exception of the laser diagnostics. While the peak power of the radiation is increased nearly 30% during the interaction, since the laser pulse duration of 4.5 ps is longer than the 1 ps e-beam duration, the total energy of the radiation field should only increase by a few percent, necessitating temporally resolved power measurements of the amplified pulse. In order to resolve the power gain, the amplified CO₂ laser pulse will be extracted from the beamline about 4 m from the undulator where intensities are below damage thresholds for transport optics and sent to a streak camera for time domain measurements and a grating for spectral measurements. Furthermore in order to understand better the laser evolution, small reflections from the laser will be split off up- and down-stream of the undulator and calibrated to yield relative energy measurements.

SIMULATIONS

Simulations were performed with the 3D FEL code Genesis 1.3 [6] for a 70 MeV input e-beam, laser focusing parameters listed in Table 1 and 100 GW seed laser power. The radiation power grows along the interaction as shown in Figure 3. Figure 4 shows the output beam's longitudinal phase space at the end of the undulator. Up to 43% of the beam is captured and decelerated from 70 to 42 MeV while the radiation power grows by nearly 30%. The transverse profile of the laser spot is also shown in Figure 5.

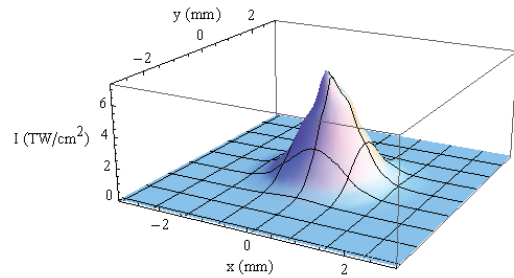


Figure 5: The transverse radiation profile is shown at the exit of the undulator. Growth of the radiation at the center of the seed is clearly visible.

CONCLUSIONS

While recent achievements in IFEL acceleration have focused on high-gradient acceleration, the UCLA-BNL helical IFEL decelerator experiment aims to achieve high-gradient deceleration in order to demonstrate high efficiency electro-optical conversion. The undulator tapering design achieves this by matching the resonant energy and ponderomotive accelerating gradients for decelerating resonant phases with the strongly tapered helical IFEL undulator. By compressing and prebunching the electron beam, significant power gain should be observable with time resolved laser measurements. For moderate laser intensities, over 40% of the e-beam energy is predicted to be converted to coherent radiation.

This work was supported by DOE grant DE-FG02-92ER40693, Defense of Threat Reduction Agency award HDTRA1-10-1-0073 and University of California Office of the President award 09-LR-04-117055-MUSP.

REFERENCES

- [1] J. Duris, A. Murokh, and P. Musumeci, in these proceedings.
- [2] W. Kimura et al., *Phys. Rev. Lett.*, 92:054801, 2004.
- [3] P. Musumeci et al., *Phys. Rev. Lett.*, 94:154801, 2005.
- [4] J. Moody et al. in Proceedings of the 2013 North American Particle Accelerator Conference, Pasadena, CA, 2013.
- [5] J. Duris, et al. *Nat. Commun.* 5:4928 doi: 10.1038/ncomms5928, 2014.
- [6] S. Reiche, K. Goldhammer, P. Musumeci in Proceedings of PAC07, Albuquerque, New Mexico, USA, IEEE, 2007.

IFEL DRIVEN MICRO-ELECTRO-MECHANICAL SYSTEM FREE ELECTRON LASER

N. Sudar, P. Musumeci, UCLA Particle Beam Physics Laboratory, Los Angeles, Ca 90024, USA

Abstract

The Free Electron Laser has provided modern science with a tunable source of high frequency, high power, coherent radiation. To date, short wavelength FEL's have required large amounts of space in order to achieve the necessary beam energy to drive the FEL process and to reach saturation of the output radiation power. By utilizing new methods for beam acceleration as well as new undulator technology, we can decrease the space required to build these machines. In this paper, we investigate a scheme by which a tabletop XUV FEL might be realized. Utilizing the Rubicon Inverse Free Electron Laser (IFEL) at BNL together with micro-electro-mechanical system (MEMS) undulator technology being developed at UCLA, we propose a design for a compact XUV FEL.

INTRODUCTION

Current short wavelength Free Electron Lasers (FEL) require long and expensive particle accelerators to produce the necessary high energy electron beams, limiting the housing of these machines to large scale national labs. In order to make this technology more readily available, it is necessary to investigate ways in which we can decrease these space and monetary constraints. In this paper, we investigate a compact design for an FEL that is driven by a beam that has been accelerated through the IFEL acceleration scheme. Furthermore, we investigate the use of micro-electromechanical system (MEMS) undulator technology to decrease both size and resonant wavelength of our FEL.

In an IFEL [1,2] a high power laser is copropagated with the electron beam in an undulator magnet. Through interactions with the undulator field, the beam undergoes transverse oscillations, allowing it to exchange energy with the laser. By tapering the undulator magnets, the beam's transverse oscillations will remain resonant with the laser frequency as it gains energy, maximizing the interaction. Utilizing laser intensities of 10-20 TeraWatts, the IFEL is capable of sustaining GeV/m acceleration gradients over meter scale distances, greatly decreasing the distance required to reach high beam energies [3]. The ability to also preserve an excellent output quality [4] makes the IFEL a great candidate for use in compact FEL design.

RUBICON IFEL

As input of our FEL amplifier we consider a beam accelerated by the Rubicon IFEL at Brookhaven National Laboratory. Rubicon utilizes a strongly tapered undulator driven by a high power 10.3 μm CO₂ laser. Utilizing 625 GigaWatt laser intensities we achieve acceleration gradients

up to 100 MeV/m, accelerating the beam from 53 MeV to an energy of 98 MeV in about 50 centimeters [3].

Particles in the beam will bunch around the periodic minima of the IFEL ponderomotive potential as they gain energy propagating in the undulator. This process creates periodically spaced, short bunches of electrons with RMS widths $\sim 1/10$ of the laser wavelength while increasing the peak current by about a factor of 5, Fig. 1. Simulations and measurements from the Rubicon IFEL[5] indicate that the IFEL process preserves the initial beam quality, keeping the normalized emittance of the accelerated bunch constant throughout the interaction.

To further enhance the Rubicon IFEL's performance, efforts are currently under way to install a pre-buncher before injection into the IFEL. Utilizing an undulator section tuned to the IFEL drive laser wavelength we impart a modulation on the beam, separating the beam into periodically spaced bunches. Utilizing a chicane to tune the resonant phase of the bunches relative to the IFEL ponderomotive potential, we can inject a large fraction of particles on crest of the accelerating wave, Figure 2. Initial simulations show trapping and acceleration of 74% of the injected particles, greatly increasing the peak current while also decreasing the final energy spread to $\sim 0.1\%$, providing us with a high quality, high brightness, high energy electron beam, ideal for seeding a high gain FEL amplifier.

MEMS UNDULATOR

The FEL process is achieved by sending a high energy electron beam through a magnetic undulator field with a period λ_u . The electrons wiggle in this field, and therefore radiate. When the wavelength of the radiation, λ_r slips ahead of the electron beam one period each cycle of transverse

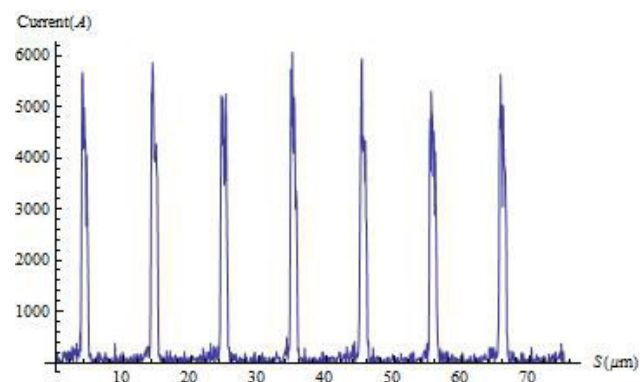


Figure 1: Current profile of Rubicon IFEL output beam.

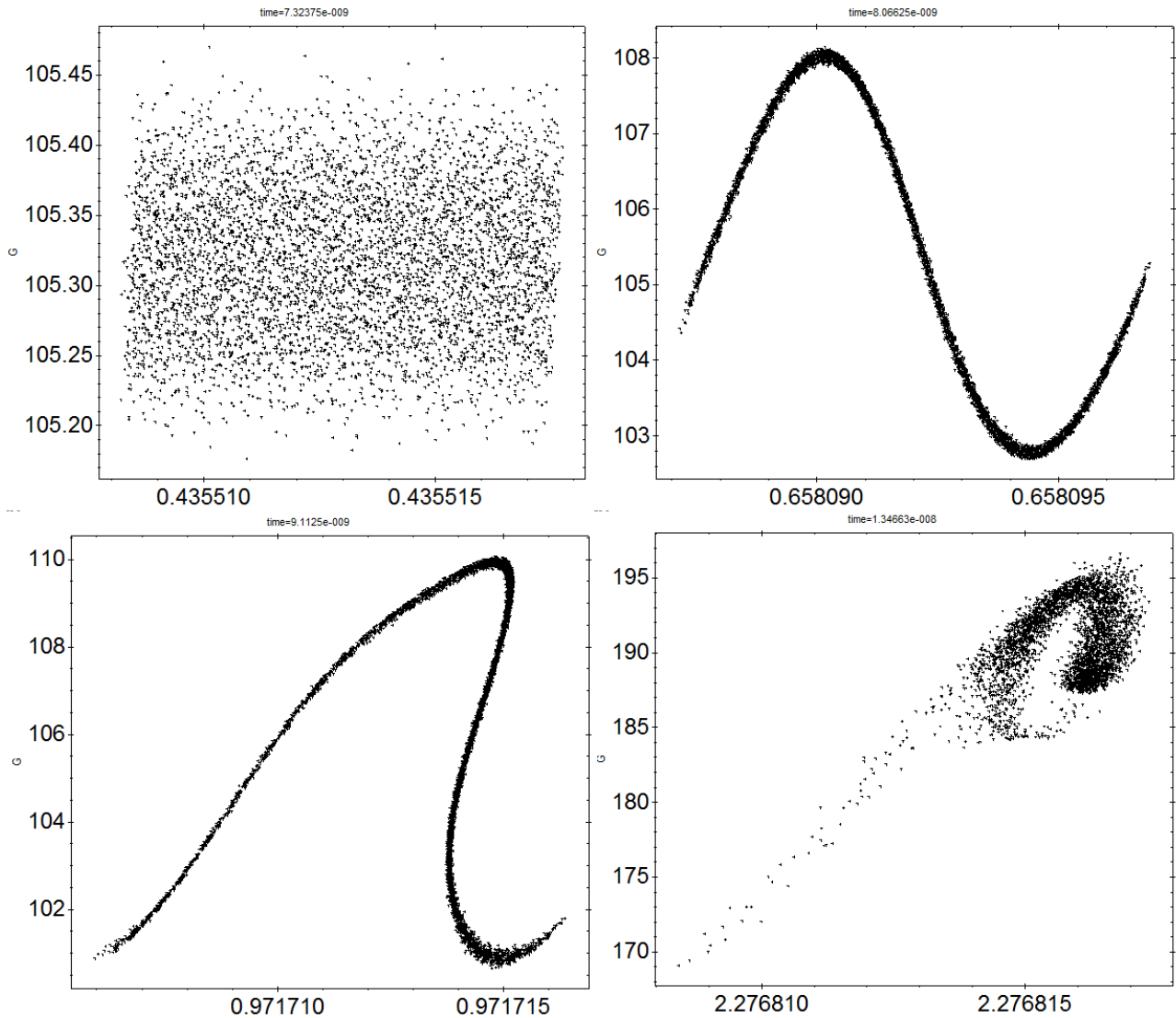


Figure 2: GPT simulation of single bunch γ vs. z phase space in Rubicon IFEL with pre-buncher. (Top Left) Incoming Beam. (Top Right) Beam after pre-buncher modulator. (Bottom Left) Beam after pre-buncher chicane phase shifter. (Bottom Right) Beam after IFEL acceleration.

oscillation, constructive interference occurs. This corresponds to the resonant condition:

$$\lambda_r = \lambda_u \frac{(1 + K^2)}{2\gamma^2}$$

where $K = eB_0/2\pi mc$ is the undulator normalized vector potential, B_0 is the peak undulator magnetic field, γ is the electron beam energy, and e and m are the charge and mass of the electron.

The FEL amplification induces a periodic energy modulation in the beam as the FEL radiation interacts back with the electron beam causing the electrons near the crest of the field to accelerate forward and those near the trough to decelerate. As the beam propagates in the undulator, this energy modulation is converted into density modulation, creating a train of micro bunches separated by the resonant wavelength. As the bunching becomes stronger, the

electrons in the bunch radiate in phase and the FEL exhibits exponential gain [6].

The main problem of directly using the output of an IFEL accelerator to seed an FEL is related to the spiky longitudinal structure of the beam as it exits the laser. With a beam energy of ~ 100 MeV, using conventional permanent magnet undulators, ($K \sim 1$, $\lambda_u \sim 0.01$ m) we exhibit a resonant wavelength of $\lambda_r \sim 300$ nm. With an IFEL drive laser wavelength of $10.3 \mu\text{m}$, we expect current spikes to have widths on the order of $1 \mu\text{m}$. We can see that after 1 or 2 periods the radiation will have slipped out of the current spike halting the gain process.

In order for us to utilize the outcoming beam from the Rubicon IFEL effectively it is necessary for us to use an undulator with a small period and a small K in order to

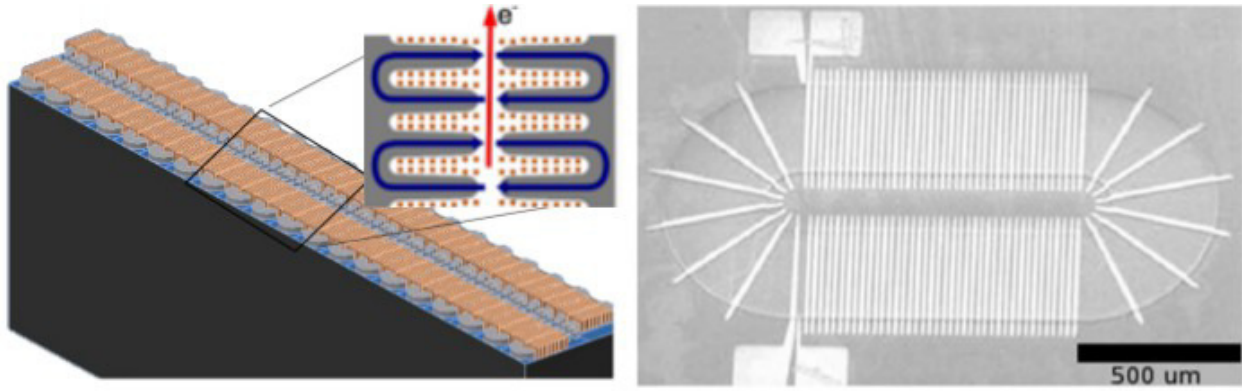


Figure 3: (Left) CAD of a MEMS undulator showing the yoke structure for flux direction in an undulator period. (Right) Racetrack solenoidal coil Scanning Electron Micrograph fabricated at UCLA. (image courtesy of Harrison et al.)

create radiation with a wavelength small compared to the width of the current spikes. In this paper we investigate the usage of MEMS technology being developed currently at UCLA [7]. In particular, we consider an undulator with $\lambda_u = 1 \text{ mm}$ and $K = 0.1$ allowing us to achieve $\lambda_r \sim 15 \text{ nm}$. With our current spikes now being $\sim 60\text{--}70 \lambda_r$ long, it is possible for the radiation created in the tail of the bunch to slip forward, driving the FEL feedback process responsible for gain.

MEMS technology requires three main components, a coil to produce magnetomotive force (MMF), a magnetic yoke to direct the created magnetic flux, and magnetic pole tips that increase the flux density. The MEMS devices being developed at UCLA utilize a racetrack solenoidal coil to generate the necessary flux, Figure 3. This particular design allows more coils to be fit in a given surface area, allowing a larger flux per period compared to typical planar designs. To maximize the peak field and decrease magnetic fringing, MMF flux is directed by yokes placed on both sides of the undulator. Initial studies show achievable undulator wavelengths, $\lambda_u = 25 \rightarrow 1000 \mu\text{m}$ with K ranging from $K = 0.0009$ to $K = 0.1$ respectively.

SIMULATION RESULTS

Simulations of the MEMS undulator FEL were done using the 3-D simulation code Genesis 1.3. The current profile input into Genesis was taken from General Particle Tracer simulations of the Rubicon IFEL as seen in Figure 1. Input parameters for the simulation can be found in Table 1.

Input beam parameters such as emittance, beam size, and energy spread were chosen based on Ming Xie optimization, noting that the beam quality entering the Rubicon IFEL will be conserved. We are able to achieve a 3-D gain length of ~ 0.018 . Knowing that the current spikes are $\sim 1 \mu\text{m}$ wide and that the radiation will slip ahead $\sim 15 \text{ nm}$ per 1 mm undulator period, we find that radiation from the tail will slip out of the beam after $\sim 70 \text{ mm}$, and thus experience about 4 3-D gain lengths before exiting the current spike. This allows radiation from the back of the current spike to gain as it slips ahead, driving the micro bunching process

Table 1: Genesis Simulation Input Parameters

γ	183.4
$\varepsilon_n \text{ (mm-mrad)}$	0.15
$\sigma_r \text{ (}\mu\text{m)}$	5.51
$\Delta\gamma/\gamma$	0.001
λ_u	1
K	0.1
λ_r	15.2
ρ	0.004
Lg3D	0.0176
Saturation (λ_u)	600
Power (MW)	13

responsible for the high gain FEL interaction. This process will continue until the particles in the current spike are maximally bunched, at which point saturation power is reached. In Figure 4, we see the radiation pulse from maximally bunched particles in the 4th current spike.

Looking at the power as a function of z in Figure 5, we can see that saturation is reached around 0.6 m . In Figure 6, we see the spectrum of the outgoing radiation centered around 15.2 nm .

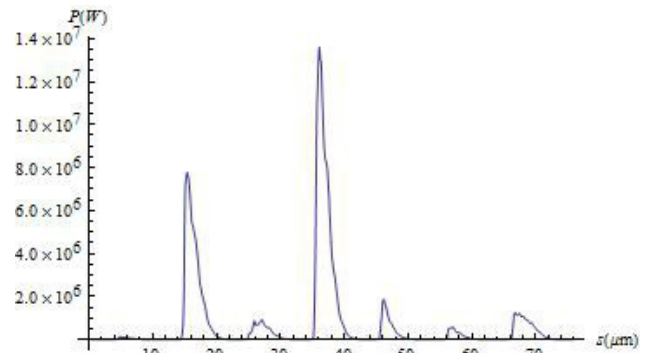


Figure 4: Power output of FEL after $600 \lambda_u$.

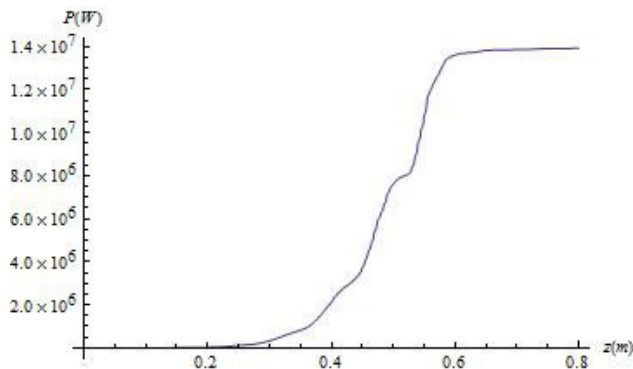


Figure 5: Maximum radiation power along undulator. Saturation is reached at $z \sim 0.6$ m.

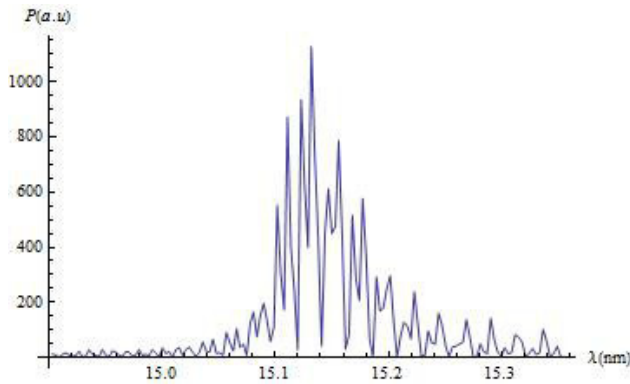


Figure 6: Spectrum of output radiation at saturation.

CONCLUSION

We have demonstrated a potential strategy for manufacturing a tabletop XUV FEL utilizing the Rubicon IFEL at BNL with modern MEMS technology. IFEL acceleration

acceleration gradients allow us to achieve the necessary beam energy in only 0.5 m and small undulator periods allow us to reach FEL saturation power in only 0.6 m, providing a cost and space effective alternative to modern FEL machines. Increases in the laser power driving the IFEL could lead to even higher acceleration gradients and thus higher beam energies, possibly allowing us to utilize the same technology to produce high power X-Rays.

REFERENCES

- [1] R.B. Palmer, "Interaction of relativistic particles and free electromagnetic waves in the presence of a static helical magnet" in *J. Appl. Phys.* **43**, 3014 (1972).
- [2] E.D. Courant, C. Pellegrini, W. Zakowicz, "High energy inverse free-electron-laser accelerator" in *Phys. Rev. A* **32**, 2813 (1985).
- [3] J.P. Duris, P. Musumeci, R.K. Li, "Inverse free electron laser accelerator for advanced light sources" in *Phys. Rev. STAB* **15**, 061301 (2012).
- [4] J.P. Duris et al., "High Quality Electron Beams from a Helical Inverse Free Electron Laser Accelerator" Submitted to *Nature Physics*
- [5] W.D. Kimura, P. Musumeci, et al., "A Helical Undulator Wave-guide Free-Electron Laser" in *AIP Conference Proceedings* **737** (2004).
- [6] R. Bonifacio, C. Pellegrini, "Collective instabilities and high-gain regime in a free electron laser" in *Optics and Comm.*, **50**, 373, (1984).
- [7] J. Harrison et al., "Surface-micromachined magnetic undulator with period length between 10 μ m and 1 mm for advanced light sources" in *Phys. Rev. STAB* **15**, 070703 (2012).

TERAHERTZ FEL BASED ON PHOTOINJECTOR BEAM IN RF UNDULATOR

I.V. Bandurkin, S.V. Kuzikov[#], M.E. Plotkin, A.V. Saviolov, A.A. Vikharev, Institute of Applied Physics, Russian Academy of Sciences, Nizhny Novgorod, Russia

Abstract

Photoinjectors, which can produce picosecond electron bunches of MeV-level, are attractive for THz generation. Fortunately, a long distance to reach scattering power saturation in FEL is not necessary, if bunch length is shorter than the produced THz half-wavelength. However, the energy of several MeVs does not allow providing long traveling of the flying bunch without longitudinal divergence. That is why, we suggest using specific rf undulator in a form of the normal wave in the helical waveguide at 3 GHz frequency. The mentioned wave has the -1st space harmonic with transverse fields and negative phase velocity (responsible for particle wiggling). This wave has also the 0th harmonic with longitudinal field and positive phase velocity equal to bunch velocity. Due to the synchronous 0th harmonic one can effectively channel low-energy bunches (due to longitudinal focusing field) as far as several meters distance. One might also inject electron bunches in slightly accelerating field, in this case the output THz pulse obtain nearly linear frequency modulation. Such long THz pulses with the mentioned modulation of the frequency can be efficiently compressed by pair of diffraction gratings.

CONCEPTS OF THz FEL BASED ON PHOTOINJECTOR ELECTRON BEAM

In order to produce THz radiation, we suggest to use short bunches of electrons with bunch length less than a half of THz wavelength. Such bunches can be easily produced by means of the existing rf photoinjectors which are driven by high-power picoseconds lasers [1]. Typically rf gun might release bunches of 5-10 MeV and charge up to 1 nC. In order to produce 1 THz radiation, bunch length should not exceed 0.15 mm. This bunch length means that all electrons radiate THz wave in the phased condition (coherently). Unfortunately, the desirable short bunches cannot keep longitudinal size at long distance because Coulomb force causes strong divergence of particles. That is why, one should provide longitudinal focusing of electron bunches at whole length of THz FEL. To solve this problem, we suggest to escort each bunch by slow TM_{01} wave which, being in Cerenkov synchronism with electrons, executes longitudinal focusing in proper phase (at zero longitudinal electric field) like it happens in accelerators (autophasing). Of course, longitudinal focusing inevitably makes whole FEL more complicated and expensive, because it assumes exact injection in proper rf phase. However, in rf

photoinjectors particles already are assumed to be synchronized with rf field. In our case we consider THz FEL as a prolonged rf gun. Second, due to focusing one might build long FEL and to produce long THz pulses. In order to multiply power of these long THz pulses, its are appealing to be compressed by means of special pulse compressor consisted of two gratings. Principles of the mentioned pulse compressor were elaborated for high power laser systems [2, 3]. In accordance with these principles, the pulse with the chirped frequency modulation is compressed in a system with frequency dispersion shaped by two gratings operated in non-mirror regime of the reflection [4]. In case of THz FEL the necessary frequency modulation can be provided by using non-equidistant periodicity of undulator's periods. There are two opportunities. The first concept (Fig. 1) can be based on DC-magnet undulator with slow focusing TM_{01} waveguide and pulse compressor.

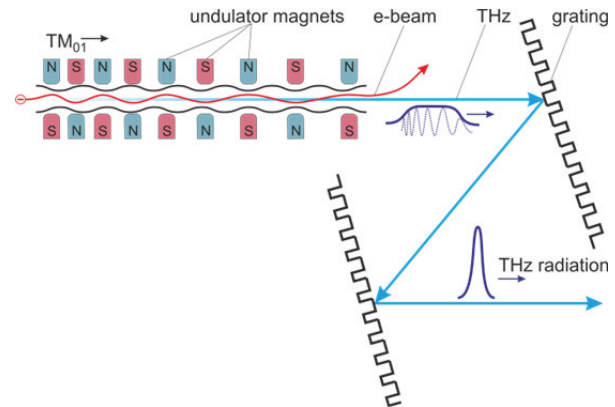


Figure 1: Concept of THz FEL with DC-magnet undulator, focusing TM_{01} waveguide, and built-in pulse compressor.

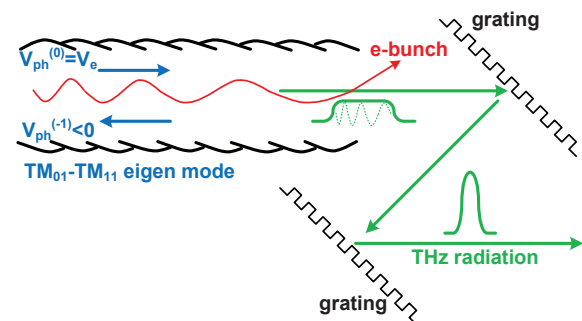


Figure 2: Concept of THz FEL with helical rf undulator and built-in pulse compressor.

In the second scheme (Fig. 2) the helical waveguide supports slow eigen mode consisted of two main space harmonics. The 0-th harmonic is represented by focusing

[#]kuzikov@appl.sci-nnov.ru

TM₀₁ wave, the -1st harmonic is TM₁₁ wave with negative phase velocity which causes wiggling of electrons. The chirped pulse in this case is obtained using injection of particles in slightly accelerating rf field so that particles with growing energy naturally radiate power with growing frequency.

BEAM DYNAMICS IN LONG WAVEGUIDE SECTION

Principle of longitudinal bunch focusing is shown in Fig. 3. Here slow TM₀₁ wave with phase velocity close to bunch velocity guides particles so that electrons near front are slightly decelerating, but back electrons are placed in slightly accelerating field.

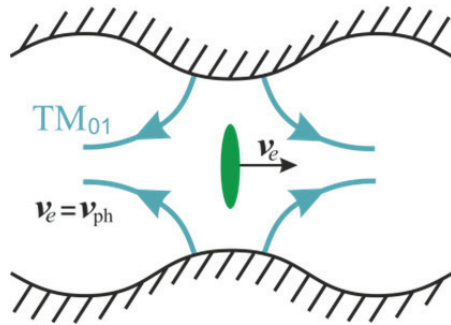


Figure 3: Scheme of bunch focusing in longitudinal direction.

As one can see in Fig. 3 there are no forces which prevent transverse expansion of particles in the bunch. Moreover, there are deflecting radial electric field component, E_r , which causes transverse defocusing. Although azimuth component of magnetic field, H_ϕ , mitigates the mentioned divergence, one should provide longitudinal DC magnetic field, in order to avoid loss of current density due to defocusing phenomenon. That is why, in simulations of bunch dynamics with parameters, shown in Table 1, we used 2.5 GHz TM₀₁ wave with 100 MV/m E_z amplitude (typical values for rf gun) and axial DC magnetic field as high as 1 T magnitude.

Table 1: Bunch Parameters

Parameter	Value
Charge, nC	0.1
Energy, MeV	5
Length, mm	0.15
Radius, mm	1.5

Results of simulations for this case are presented in Fig. 4 (XZ-plane) and in Fig. 5 (XY-plane) respectively. 250 particles were used in simulations. Red dots describe incident bunch, blue ones show particle distribution behind 0.5 m, the green particles corresponds to approximately 1 m distance behind photoinjector. Note that in DC magnetic field particles slowly rotate around z-axis (Fig. 5). The far an electron from axis, the bigger is

angle of the rotation. The Figures 4 and 5 confirm that high-charge bunches can be efficiently guided at long distances (>1 m) in longitudinally focusing TM₀₁ mode and in guiding DC magnetic field simultaneously.

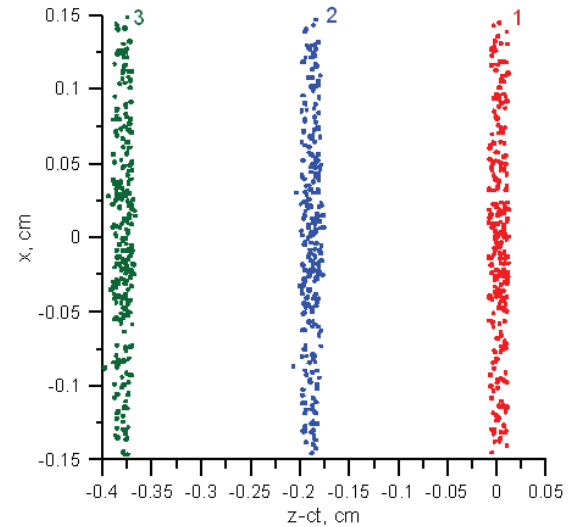


Figure 4: Space distribution of particles in plane XZ for bunch flying in waveguide with focusing TM₀₁ wave: 1 – $t=0$, 2 – $t=1.65$ ns, 3 – $t=3.33$ ns.

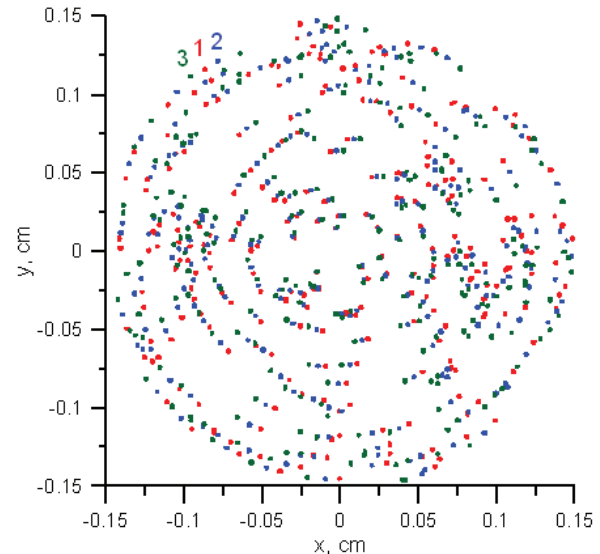


Figure 5: Space distribution of particles in plane XY for bunch flying in waveguide with focusing TM₀₁ wave: 1 – $t=0$, 2 – $t=1.65$ ns, 3 – $t=3.33$ ns.

The used amplitude of focusing TM₀₁ wave is comparable with fields in rf gun. This value means that necessary rf power is high enough. Therefore, it seems appealing to use this power for bunch guiding as well as for provision of particle's wiggling at once. Principles of such rf structure, which plays a role of an accelerator and undulator simultaneously, were investigated recently [5-7]. The mentioned periodic structure has helical corrugation (Fig. 6). One of the eigen modes in this corrugated waveguide is the mode consisted predominantly of the partial TM₀₁ wave (0th space harmonic) and partial TM₁₁ wave (-1st harmonic) as well.

In the slow eigen mode the phase velocity of the 0th harmonic is assumed to be equal (or close) to bunch velocity (Fig. 7). This harmonic does not have transverse deflecting fields exactly at axis so that perturbation of transverse bunch dynamics is minimized [8]. The -1st harmonic has negative phase velocity and strong transverse electric and magnetic fields at axis. This harmonic provides wiggling of electrons and production of radiation with essential Doppler's frequency up-shift. In particular, in the 2.5 GHz structure the bunch with parameters, shown in Table 1, can radiate photons with frequency close to 1 THz.

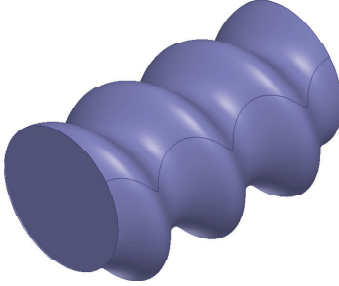


Figure 6: 3D view of helical accelerating section.

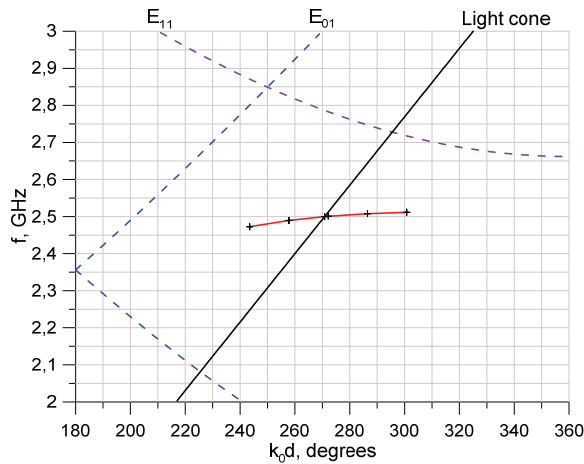


Figure 7: Dispersion of TM₀₁-TM₁₁ normal eigen mode in helical accelerating structure (solid red curve) and dispersion curves of partial waves in cylindrical waveguide (dashed curves).

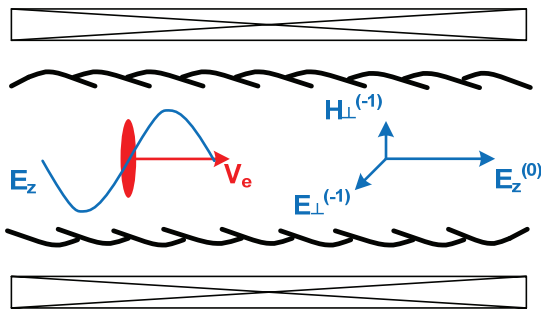


Figure 8: RF undulator based on helical waveguide.

The principal scheme of the described rf undulator is shown in Fig. 8. In the 2.5 GHz helical waveguide with parameters (average radius – 68.7 mm, period of corrugation – 90.2 mm, amplitude of corrugation – 14.1

mm) with $E_z=100$ MV/m longitudinal focusing field of the 0th (TM₀₁) harmonic the effective undulator parameter, determined by fields of the -1st harmonic, is as high as $K \approx 1$. This value allows to obtain ~5 MW power at 1 THz behind the undulator (about 1 MV/m field strength).

UNDULATOR WITH NONUNIFORM PERIODICITY AND THZ PULSE COMPRESSOR

We propose compression of a frequency modulated THz pulse by means of pair of diffraction gratings employed in the autocollimator regime [4]. The modulated input signal can be obtained from an undulator in which DC magnets are arranged with a variable spatial period. In rf undulator necessary frequency modulation is reached using bunch injection in slightly accelerating field (Fig. 9) or using slightly asynchronous wave relative to electron bunch.

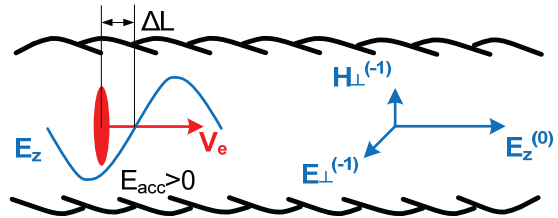


Figure 9: Injection of particle bunch in accelerating phase of E_z field component.

In accordance with pulse compression scheme after the first grating different frequency components of the wavebeam are reflected with different angles relative to the grating plane and travel different distances to the second grating (Fig. 10). After the second grating all frequency components propagate in the common direction and become phased ones, i.e. rf pulse is compressed.

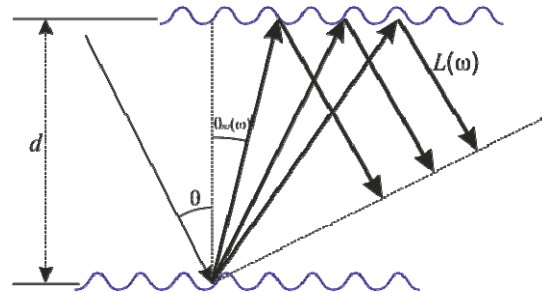


Figure 10: Paths of rays in system of two paired gratings.

In the proposed design, parameters of the gratings should be selected so to provide scattering to the -1st diffraction maximum only. Path length L in the compressor, defined according to Fig. 10, depends on frequency ω :

$$L(\omega) = \frac{d(1 + \cos(\theta + \theta_{-1}(\omega)))}{\cos(\theta_{-1}(\omega))}, \quad (1)$$

where d is the distance between the gratings, θ is the angle between the incident wave and the normal of the first grating, $\theta_{-1}(\omega)$ is the angle of the scattered wave which depends on frequency as follows:

$$\theta_{-1}(\omega) = \arcsin(\sin \theta - \frac{2\pi}{kD}), \quad (2)$$

where D – is a period of the corrugation, $k=\omega/c$, c – is the light velocity.

In the computer simulation initial pulse had the linear frequency modulation:

$$A_{in}(t) = A_0 \exp(-\frac{t^2}{2T^2}(1 - i\Delta\omega t) - i\omega t), \quad (3)$$

where t is current time, T is pulse length, $\Delta\omega$ is a difference of frequencies at the start and at the end of the input pulse (frequency modulation). Simple estimations in aberration-free approximation give the formula for compression coefficient:

$$C = \frac{T}{T_{out}} = 2\pi N \frac{\Delta\omega}{\omega}, \quad (4)$$

where T_{out} – is a length of the output pulse, N – is a number of field periods in the input pulse.

The Fig. 11 shows the input pulse and the output (compressed) pulse with central frequency 1 THz, $N = 50$ periods, $\theta = 45^\circ$, and $\Delta\omega/\omega = 0.1$. These parameters correspond to parameters of THz radiation which could be obtained by undulator discussed in the previous text. As it follows from Fig. 11, the power in output pulse is roughly 10 times more in comparison with power in input pulse. This means that already considered undulator supplemented with pulse compressor is able to reach 50 MW power level.

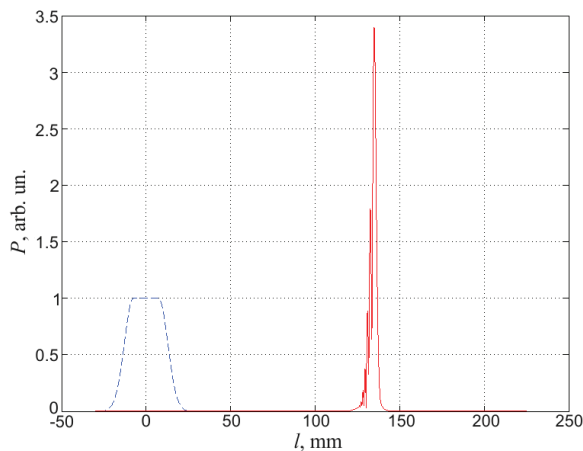


Figure 11: Pulse compression by means of two gratings: incident 1 THz pulse (blue dashed curve) and the compressed pulse (red solid curve).

Note that frequency modulation cannot be increased too much in comparison with the used value, because

autocollimation regime of diffraction grating has the limited bandwidth. Nevertheless, one is able to increase pulse length (N) in a more long undulator, in order to obtain more power. In addition, there is a possibility to focus output THz wavebeam by means of the metallic focusing mirror. In already considered example wavebeam waist is close to transverse bunch size (1.5 mm), so due to focusing to size $\sim \lambda \times \lambda$ one can multiply power by factor $\sim 10^2$. In particular, in wavebeam, produced by the undulator of 10 m length, the field strength in minimal possible size of the wavebeam can reach ~ 1 GV/m.

CONCLUSION

Short electron bunches with charge ~ 0.1 nC, injected from photocathode, can be efficiently guided in the long waveguide (>1 m) with focusing synchronous S-band TM_{01} mode. Such bunches do not require microbunching to saturate output power, because they are shorter than the half-wavelength of the produced THz radiation. Necessary focusing field magnitude is ~ 100 MV/m, which is comparable with accelerating field in the existing S-band photoinjectors. In order to increase output field and power of THz radiation, it is appealing to use undulator (DC-magnet or rf) which allows forming pulses with chirped frequency. Such pulses could be compressed by factor 10^1 - 10^2 by means of grating's pair. Using additional space focusing of THz wavebeam by mirror, one is able finally to reach in mirror focus more than 100 MV/m THz field.

REFERENCES

- [1] L. Faillace, Recent advancements of RF guns, Physics Procedia, 52, 2014, pp. 100 – 109. <http://www.sciencedirect.com/science/article/pii/S1875389214000261#>
- [2] Bahk S. W. et al., “Generation and characterization of the highest laser intensities”, Opt. Lett., 29, (24), 2004, pp. 2837–2839.
- [3] V. Yanovsky, et al. “Ultra-high Intensity-300-TW Laser at 0.1 Hz Repetition Rate”, Opt. Express, V.16. № 3. 2008, pp. 2109–2114.
- [4] Electromagnetic Theory of Gratings, Ed. by R. Petit. Berlin; Heidelberg: New York; Springer Verlag, 1980.
- [5] S.V. Kuzikov et al, Helical Self Focusing and Cooling Accelerating Structure, Proc. of of PAC2013, Pasadena, CA USA, 29 September -4 October 2013, pp. 1049-1051.
- [6] S.V. Kuzikov et al, Concepts for Short Period rf undulators, Proc. of of PAC2013, Pasadena, CA USA, 29 September -4 October 2013, pp. 1046-1048.
- [7] S.V. Kuzikov et al, “Flying radio frequency undulator, Applied Physics Letters”, Vol. 105, Issue: 3, 2014, pp. 033504 - 033504-4.
- [8] S.V. Kuzikov et al, “Configurations for Short Period rf Undulators”, Phys. Rev. ST Accel. Beams 16, Issue 7, 070701 (2013).

CHIRPED PULSE SUPERRADIANT FREE-ELECTRON LASER*

Yen-Chieh Huang[#] and Chia-Hsiang Chen, Institute of Photonics, National Tsinghua University, Hsinchu, Taiwan

Zhen Zhang and Juhao Wu, SLAC, Menlo Park, USA

Abstract

When a short electron bunch traverses an undulator to radiate a wavelength longer than the bunch length, intense superradiance from the electrons can quickly deplete the electron's kinetic energy and lead to generation of an isolated chirped radiation pulse. Here, we develop a theory to describe this chirped pulse radiation in such a superradiant FEL and show the opportunity to generate isolated few-cycle high-power radiation through chirped-pulse compression after the FEL.

INTRODUCTION

High power radiation is useful for applications requiring high energy density. In view of the high-power laser successfully demonstrated by optical chirped pulse amplification, a chirped-pulse FEL followed by a pulse compressor could be an ideal candidate to generate extremely high power radiation in the spectrum no readily accessible by a conventional laser source. It has been suggested previously the use of an energy-chirped electron beam to amplify a frequency-chirped seed laser in an FEL amplifier to obtain temporally compressed high-power radiation at one of the harmonics of the seed laser [1]. It was also suggested the use of an energy-chirped electron pulse to generate self-amplified chirped radiation, which is then filtered to seed a downstream self-amplified-spontaneous-emission (SASE) FEL [2]. Wu *et al.* [3,4] pointed out that manipulating chirps in seed radiation and electron beam to an FEL allows generation of attosecond few-cycle pulses. In this paper we propose a scheme to generate a chirped pulse radiation directly from fast energy depletion of a short electron bunch in an undulator. An external compressor is then used to compress the chirped pulse to achieve few-cycle radiation.

THEORY

From energy conservation, the loss rate of the total electron kinetic energy is equal to the radiation power. To take into account all radiation energy at the expense of the electron kinetic energy, we started from the expression of the coherent synchrotron radiation power of a tightly bunched charge. Given initial electron energy $\gamma = \gamma_0$ at the retarded time $t' = 0$, one can derive the Lorentz factor γ as a function of t' in the relativistic limit $\gamma \gg 1$

$$\gamma = \frac{\gamma_0}{1 + t' / \tau_d}, \quad (1)$$

where the pump depletion time τ_d is defined as

$$\tau_d = \frac{W_0}{P_{r,0}}, \quad (2)$$

with W_0 being the initial energy of the electron bunch and $P_{r,0}$ being the initial radiation power of the electrons.

The radiation power is proportional to the square of γ and can thus be expressed as

$$P_{r,N_e}(t') = \frac{P_{r,0}}{(1 + t' / \tau_d)^2}. \quad (3)$$

Furthermore, the wavelength of the dominant radiation mode at t' satisfies

$$\lambda_r = \lambda_u \frac{1 + a_u^2}{2\gamma^2(t')}, \quad (4)$$

where λ_u is the undulator period and $a_u = eB_{rms}/m_0ck_u$ is the undulator parameter with $k_u = 2\pi/\lambda_u$, m_0 the electron rest mass, e the electron charge, c the vacuum speed of light, and B_{rms} the rms undulator field. Given a known relationship between the retarded time t' and observation time t , the radiation power in (3) and wavelength in (4) can be expressed in terms of the observation time.

By using Eqs. (3,4), one can write the temporal-dependent radiation field as

$$E(t_n) = \frac{E_0}{(3r_\tau t_n + 1)^{2/3}} \exp[j\phi(t_n)] \quad (5)$$

where E_0 is the maximum or the initial radiation field, $r_\tau = \tau_u/\tau_d$ is the ratio of the electron transit time through the undulator τ_u to the electron energy depletion time τ_d , and $\phi(t_n)$ is the radiation phase as a function of time. The time variable $t_n = t/(N_u\lambda_{r,0}/c)$ is the observation time normalized to the unperturbed slippage time $N_u\lambda_{r,0}/c$ with N_u being the number of undulator periods, and $\lambda_{r,0}$ being the initial radiation wavelength. The time duration $t_n = 1$ is the radiation pulse width or the electron slippage length in the undulator without pump depletion. With pump depletion, the electron slows down when traversing the undulator and the time duration $t_n = 1$ gives the amount of thus increased radiation pulse width. Physically r_τ is a figure indicating the degree of pump depletion in a given undulator. The frequency chirp of the radiation is embedded in the radiation phase

$$\phi(t_n) = 2\pi \frac{N_u}{r_\tau} (3r_\tau t_n + 1)^{1/3} + \phi_0 \quad (6)$$

where ϕ_0 is an arbitrary initial phase.

Figure 1 plots the chirped radiation field as a function of the normalized observation time for $r_\tau = 1$ from a 20-period undulator. There are two important features in the plot; the field amplitude reduces and the radiation wavelength increases over time, both due to energy loss of electrons to superradiance in the undulator.

*Work supported by MoST of Taiwan under NSC 102-2112-M-007-002-MY3. #ychuang@ee.nthu.edu.tw

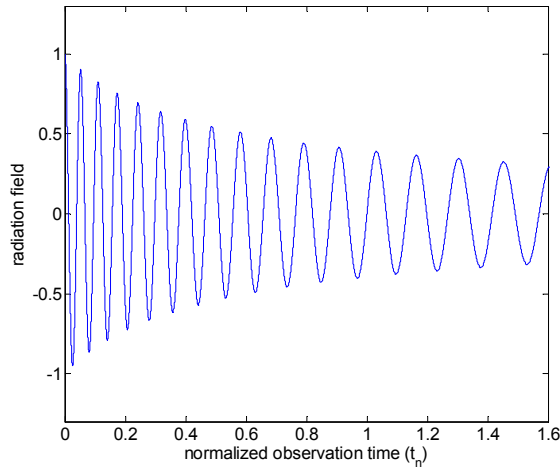


Figure 1: Frequency chirped radiation field from a CPS FEL with $r_r = 1$ and $N_u = 20$.

Previously we have assumed a particle-like electron bunch with zero size. To take into account the finite electron bunch length, the radiation power in Eq. (3) is multiplied by the so-called bunch form factor [5], which for a Gaussian electron bunch is given by

$$F(\nu_r) = e^{-(2\pi\nu_r\sigma_r)^2}, \quad (7)$$

where ν_r is the radiation frequency and σ_r is the rms temporal length of the electron bunch. As the electrons propagate down an undulator and radiate, the radiation frequency ν_r decreases due to slowdown of electrons and σ_r could increase due to debunching. If the multiplication $\nu_r\sigma_r$ remains approximately a constant in an undulator, the modification needed to be done for the above theory is to divide the pump depletion time τ_d in Eq. (2) by a constant form factor.

THZ AND EUV CPS FEL

In the following we first present a design example for a proof-of-principle experiment at THz frequencies using existing accelerator technologies and one at extreme-ultra-violet (EUV) frequencies driven by a future dielectric laser accelerator (DLA) [6].

For the first design example at THz frequencies, we choose an accelerator system consisting of an S-band photoinjector followed by linear accelerators for electron injection, velocity bunching, and particle acceleration. The accelerator system is expected to generate an electron beam with some nominal parameters: rms electron bunch length = 60 fs, bunch charge = 15 pC, mean electron energy $\gamma = 30$, rms relative energy spread $\Delta\gamma/\gamma = 0.5\%$, positive energy chirp with head-to-tail energy difference $\Delta\gamma = 0.8$, rms normalized emittance = 0.1 mm-mrad, and rms beam radius = 0.5 mm. The initial energy chirp is helpful to maintain a small electron bunch length and energy spread in the undulator. We assume here a 1.5 m long planar undulator with a period of 56 mm and undulator parameter of 1.7, permitting radiation generation at 2.5 THz for a beam with $\gamma = 30$. To confirm maintenance of a short electron bunch in the undulator,

we employ the simulation code, General Particle Tracer (GPT) [7], to simulate the propagation of the electron bunch through the undulator. Our simulation result shows that the electron bunch in the undulator undergoes compression first due to the initial positive energy chirp in the beam and is kept in a length of 58 ± 7 fs. The initial energy chirp in the beam also helps to partially compensate the space-charge induced energy spread. To predict the chirped radiation field, we first calculate the bunch form factor with $\sigma_r = 60$ fs and use it to modify the pump depletion time in our theory. At the undulator exit, the calculated degree of pump depletion is $r_r = 12\%$. Figure 2 shows the radiation pulse envelope before (blue curve) and after (red curve) pulse compression by using a standard quadratic phase filter [8] with a chirping parameter of 0.0524 in units of the inverse square of the normalized observation time. For comparison, the transform-limited pulse (black dashed line) is also shown in the figure. It is seen that almost all the compressed pulse energy is already in the width of the transform-limited pulse. The full width of the chirped pulse is 12 ps, containing 27 radiation cycles generated from the 27 periods of the undulator. The power of the chirped pulse gradually drops to about 63% of its initial value due to pump depletion. At the end of the undulator the percentage bandwidth of the chirped radiation is broadened to 20.4%. After compression, the peak power of the output radiation pulse is increased nearly 10 times. The half width of the compressed pulse is about 1.3 ps, containing approximately 3 radiation cycles.

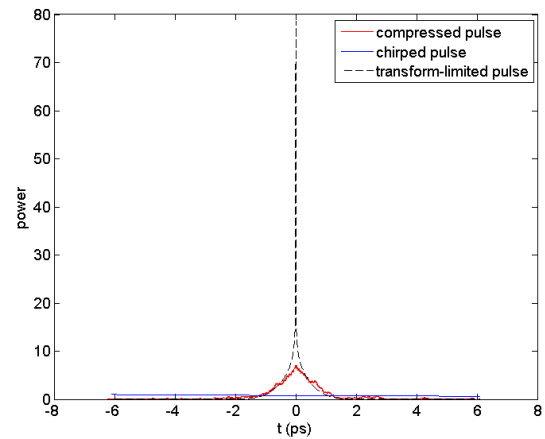


Figure 2: Power envelopes of the radiation pulse before (blue curve) and after (red) compression using an optimized quadratic phase filter for the proposed proof-of-principle CPS FEL at 2.5 THz. After pulse compression, the number of radiation cycles is reduced from 27 to just 3. For comparison, the transform-limited pulse is shown as a black dashed curve.

It is envisaged that a DLA, driven by a laser at $\sim 1 \mu\text{m}$, would generate electron bunches with a length in the nm range. Give the high repetition rate from the driver laser and the nm-bunched electrons, a CPS FEL could be useful to generate EUV and soft x-ray radiations with

both high average and peak powers. As a design example at the EUV wavelengths, we assume a DLA generating an electron bunch with initial energy of $\gamma = 200$ and bunch length of ~ 1 nm. Debunching of electrons in an undulator is much less concerned for a 100 MeV beam. To integrate with a DLA, a dielectric laser undulator [9] is selected for this design, having a peak undulator field of 3.3 T. The 3.3 T undulator field is consistent with a 1 GV/m laser field near the damage threshold of a dielectric for an incident fs laser pulse [10]. The undulator length is 157.5 mm long, consisting of 150 undulator periods with a period length of 1.05 mm. Therefore, the initial radiation wavelength is 13.5 nm. The bunch charge for injection is 75 fC, assuming the electron charge from an accelerator can be scaled by its driving wavelength. The calculated degree of pump depletion for this design is $r_\tau = 5.2\%$.

Figure 3 shows the radiation pulse envelope before (blue curve) and after (red curve) pulse compression by using a quadratic phase filter with a chirping parameter of 0.021 in units of the inverse square of the normalized observation time. The full length of the chirped pulse is 7.3 fs. There are 150 radiation cycles in the pulse, generated from the 150-period undulator. The power of the chirped pulse gradually drops to about 80% of its initial value of 760 W due to pump depletion. At the end of the undulator the percentage bandwidth of the chirped radiation is broadened to nearly 10%. After compression, the peak power is increased by 13 times, reaching a value of 1 kW. The half width of the compressed pulse is about 0.4 fs, containing 9 radiation cycles. The time-bandwidth product of the compressed pulse is ~ 0.5 , which is about the value for a transform-limited Gaussian pulse.

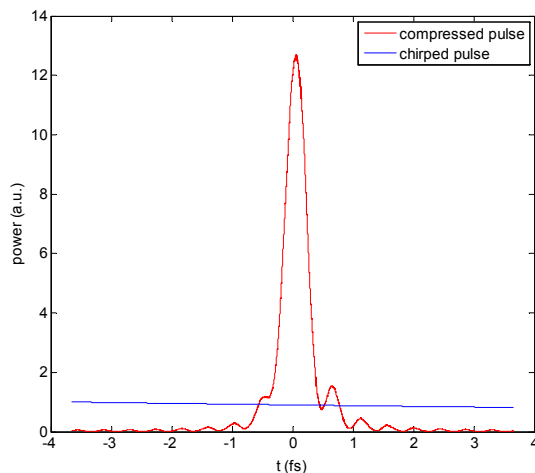


Figure 3: Power envelopes of the proposed EUV CPS FEL radiation pulse before (blue curve) and after (red) compression by a quadratic phase filter. After pulse compression, the peak power of the radiation pulse is increased by about 13 times and the number of the radiation cycles reduces from 150 to 9.

CONCLUSION

A short electron bunch emitting superradiance in an undulator can quickly lose its kinetic energy and generate

a chirp-pulse radiation. We have developed a theory to describe the radiation field of such a CPS FEL. The phase of the chirped field strongly depends on how fast the electron energy is depleted in an undulator. In the linear regime where the degree of pump depletion is kept below 10%, we show two design examples of CPS FEL in the THz and EUV spectra that generate few-cycle radiation after pulse compression by using standard quadratic phase filters. In the regime of strong pump depletion, we suggest to use tailor designed chirped mirrors or gratings to compensate the nonlinear chirp in the radiation field to achieve transform-limited pulse compression. A future effort would include numerical simulation of the CPS FEL subject to an arbitrary input beam.

ACKNOWLEDGMENT

Huang acknowledges a partial financial support from US DOE Office of Science Early Career Research Program grant FWP-2013-SLAC-100164 during a visit to SLAC to finalize the design of the THz CPS FEL.

REFERENCES

- [1] L. H. Yu, E. Johnson, and D. Li, "Femtosecond free-electron laser by chirped pulse amplification," *Physical Review E* **49**, 4480-4486 (1994).
- [2] Carl B. Schroeder, Claudio Pellegrini, Sven Reiche, John Arthur, and Paul Emma, "Chirped-beam two-stage free-electron laser for high-power femtosecond x-ray pulse generation," *J. Opt. Soc. Am. B* **19**, 1782-1789 (2002).
- [3] Juhao Wu, Paul R. Bolton, James B. Murphy, and Kelin Wang, "ABCD formalism and attosecond few-cycle pulse via chirp manipulation of a seeded free electron laser," *Optics Express* **15**, 12749-12754 (2007).
- [4] Juhao Wu, James B. Murphy, Paul J. Emma, Xiejie Wang, Tkahiro Watanabe, Xinming Zhong, "Interplay of the chirps and chirped pulse compression in a high-gain seeded free-electron laser," *J. Opt. Soc. Am. B* **24**, 484-495 (2007).
- [5] D. Xiang and W. H. Huang, "Investigations on collective behavior in radiation process with random walk model," *Nucl. Instrum. Methods. Phys. Res. B* **240**, 855-862 (2005).
- [6] Y. C. Huang and R. L. Byer, "A proposed high-gradient laser - driven electron accelerator using crossed cylindrical laser focusing", *Appl. Phys. Lett.* **69**, 2175 (1996).
- [7] <http://www.pulsar.nl/gpt/>
- [8] B. E. A. Saleh and M. C. Teich, *Fundamentals of Photonics*, 2nd Ed. (New Jersey, Wiley, 2007), 948.
- [9] T. Plettner and R. L. Byer., "Proposed dielectric-based microstructure laser-driven undulator," *Phys. Rev. ST Accel. Beams* **11**, 030704 (2008).
- [10] B. C. Stuart, M. D. Feit, A. M. Rubenchik, B. W. Shore, and M. D. Perry, "Laser-Induced Damage in Dielectrics with Nanosecond to Subpicosecond Pulses", *Phys. Rev. Lett.* **74**, 2248 (1995).

STORAGE RING XFEL WITH LONGITUDINAL FOCUSING

I. Agapov*, G. Geloni, European XFEL GmbH, Hamburg, Germany

Abstract

In present work we investigate the possibility of running a high gain FEL on a storage ring using a longitudinally focusing insertion to compress bunches passing an undulator. If integrated into a storage ring similar to PETRA III such device could potentially produce continuous ps pulses of photons in the nm range with peak pulse powers of tens of GW. Even without operating in FEL saturation mode the longitudinal focusing can provide means to increase the brightness and shorten the photon pulse length

INTRODUCTION

Low gain FELs with wavelength down to ~ 200 nm (6 eV) have been in operation at storage rings using optical cavities. Short wavelength FELs presently use linacs as drivers since they provide necessary electron beam quality. X-ray FELs such as LCLS, European XFEL or SwissFEL are now in operation or under construction worldwide. They use linacs as drivers to assure beam qualities necessary for a SASE process at those wavelengths. For a typical wavelength (1 keV–30 keV) the European XFEL requires emittances below 10^6 , energy spreads ~ 1 MeV and peak currents of several kA at electron beam energies up to 17.5 GeV. The saturation length (for basic definitions in the FEL theory see e.g. [1]) roughly defines the minimum practically sensible undulator length. At European XFEL, for the shortest wavelength, achieved with the maximum electron beam energy, the saturation length can be a hundred meters, but for soft X-rays it can be as short as 30 meters depending on the wavelength and electron beam parameters. This makes it in principle possible to fit such an undulator into a storage ring. Beam parameters in latest generation light sources such as PETRA III (see Table 1) are such that for UV photons the beam quality is not far removed from that required for an FEL. For shorter wavelength saturation length becomes larger and the possibility of using the stored beam for SASE FEL directly becomes limited. The interest in shorter wavelength storage-ring based FELs has recently been growing since they could combine extreme peak brightness and coherence of an FEL with continuous operation and lower power consumption of a storage ring (see e.g. [2] and references therein). An insertion device with longitudinal focusing would consist of a compression section, SASE undulator, and a decompression section. The rest of the ring could be passed with the usual bunch length. A design sketch is presented in Fig. 1. It could be used as an insertion or as a bypass subject to space availability. This scheme is in principle similar to a crab cavity type, discussed e.g. in [3], however longitudinal phase space only is manipulated. In the following some simulation studies for the possibility of integrating such an

insertion into PETRA III are presented. All calculations are performed with *Ocelot* [4].

Table 1: PETRA III Beam Parameters [5], assuming high bunch charge operation mode with 40 bunches

Parameter	Value
Beam energy	6 GeV
Circumference	2304 m
Emittance $\varepsilon_x, \varepsilon_y$	$10^{-9}, 10^{-11}$
Energy spread	10^{-3} (6 MeV)
Bunch charge	20 nC
Bunch length	44 ps or 13 mm
Peak current	170 A
Longitudinal damping time	10 msec

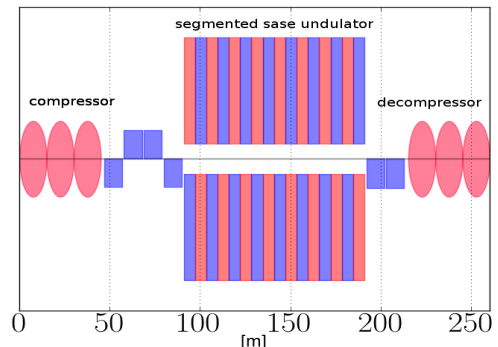


Figure 1: Insertion device layout. Going from left to right, the beam passes an RF module, a dispersive section (chicane or arc), a number of undulators, a dispersive section and finally another RF module.

POSSIBILITY OF AN FEL INSERTION DEVICE AT PETRA III

Longitudinal Phase Space Focusing

In a linac-based FEL bunch compression is a key factor, but can allow for certain beam distortion as long as it preserves the lasing bunch core. For a multiturn operation the margin for such distortions is much thinner. Space charge and Coherent Synchrotron Radiation (CSR) [6] effects play much smaller role for longer bunches and higher energies, so cleaner compression and decompression can be in principle expected than for a typical linac FEL. The requirement is that no beam instabilities and distortions should appear on the time scale faster than the longitudinal damping time which is about 1000 turns for PETRA III. Neglecting collective interactions, the longitudinal phase space map for the insertion is

* ilya.agapov@xfel.eu

$$M = M_{RF2} \cdot M_{C2} \cdot M_{C1} \cdot M_{RF1} \quad (1)$$

where the dispersive sections maps are given by matrices

$$M_{C1,C2} = \begin{pmatrix} 1 & R_{56}^{(1,2)} \\ 0 & 1 \end{pmatrix} \quad (2)$$

and the RF cavity maps are

$$M_{RF1,RF2} : \begin{pmatrix} t \\ p \end{pmatrix} \rightarrow \begin{pmatrix} t \\ p + V^{(1,2)} \sin(f_{RF} \cdot t) \end{pmatrix} \quad (3)$$

Here t and p are longitudinal coordinates usually measured in meters and relative energy units, R_{56} is the standard notation for dispersive time delay and $V^{(1,2)}$ are total RF voltages for the compressor and the decompressor. One easily checks that by choosing $R_{56}^{(1)} = -R_{56}^{(2)}$ and $V^{(1)} = -V^{(2)}$ the whole transfer map reduces to unity. So when collective self-interactions and diffusion are neglected the insertion has no theoretical footprint on longitudinal beam dynamics. The possible undulator parameters used in simulations are given in Tables 2 and 3, and the beam compressor parameters corresponding to PETRA III beam parameters are shown in Table 4 and 5. 800 MHz cavity was chosen for demonstration since it has the wavelength longer than the electron beam size. 1.3 GHz cavity of European XFEL type could also be used, but half its wavelength is shorter than the electron bunch length and the bunch tails will not be compressed fully (see Figs. 2, 3). The system length with undulator is of the order of 200 m. No optimization has been performed so far wrt. length, RF power, potential for using storage ring arcs etc., so this number could be sufficiently improved.

Table 2: Possible Parameters of a 20 mm Soft X-ray Undulator

Parameter	Value
Period	$l_w = 0.02m$
Field	$K = 0 - 10.0$
Radiation wavelength at 6 GeV	300 eV-17 keV
Section length	0.9 m
Optics	FODO with $\beta = 4m$

Table 3: Parameters of a 68mm Soft X-ray Undulator of European XFEL Type (for 6 GeV electron beam)

Parameter	Value
Period	$l_w = 0.068m$
Field	$K = 0 - 10.0$
Radiation wavelength at 6 GeV	100 eV-5 keV
Section length	0.9 m
Optics	FODO with $\beta = 4m$

An obvious drawback of the system is the large amount of RF power required. Since the longitudinal focusing is proportional to $V \cdot f_{RF}$ higher RF frequency will result in

Table 4: Parameters of the Bunch Compressor and Decompressor used in Simulations with 20x Compression for Nominal Bunch Length

Parameter	Value
RF frequency	800 MHz
Cavity length (at 35 MV/m gradient)	45 m x2
Chicane length	20-30 m
Dipole fields	0.2 T
R_{56} compressor	-0.15 m
R_{56} decompressor	0.15 m

shortening the section length. With 12 GHz cavities the length can be reduced to a few meters only. However the bunch length at PETRA III is longer than the RF wavelength for frequencies about $\geq 1GHz$. One can still achieve compression in that case, but it would result in a specific current shape 3. If low momentum compaction operation is assumed where the bunch length is shortened by a factor of say, 10, such high frequency cavities could be employed efficiently (see Table 5). Producing shorter bunches without loosing bunch current at PETRA III is however presently impossible.

Table 5: Parameters of the Bunch Compressor and Decompressor with 50x Compression for Short Bunch Operation

Parameter	Value
RF frequency	3.9 GHz
Cavity length (at 35 MV/m gradient)	9 m x2
Chicane length	~20 m
Dipole fields	~0.2 T
R_{56} compressor	-0.15 m
R_{56} decompressor	0.15 m

Undulator

The radiation wavelength is

$$\lambda_r = \frac{l_w}{2\gamma^2} \left(1 + \frac{K^2}{2} \right) \quad (4)$$

And the Pierce parameter is

$$\rho = \frac{1}{\gamma} \left(\left(\frac{KA_{JJ}l_w}{8\pi\sigma_b} \right)^2 \frac{I}{I_A} \right)^{\frac{1}{3}} \quad I_A = 17kA \quad (5)$$

gain length

$$L_G = l_w / (4\pi \sqrt{3} \rho) \quad (6)$$

So to increase the energy reach of a SASE FEL into the harder part of the spectrum one chooses possibly short undulator period. If using the FODO optics, decreasing the beam size is possible down to $\sqrt{2\epsilon L}$ where L is the period length. E.g. 4 m FODO optics will require short undulators of ~ 1 m length with quadrupoles between them. Power estimates assuming 0.02 mm and 0.068 mm period undulators are presented in Figs. 4-6.

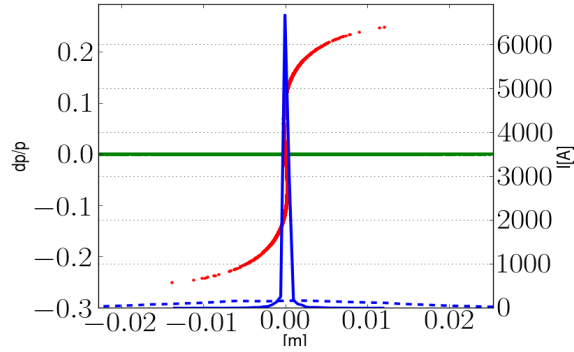


Figure 2: Simulated longitudinal phase space at the entrance (green), after the bunch compressor and at the exit (identical to the entrance phase space) of the insertion device, with 800 MHz cavity. Current profiles before (blue dashed line) and after (solid blue line) are shown.

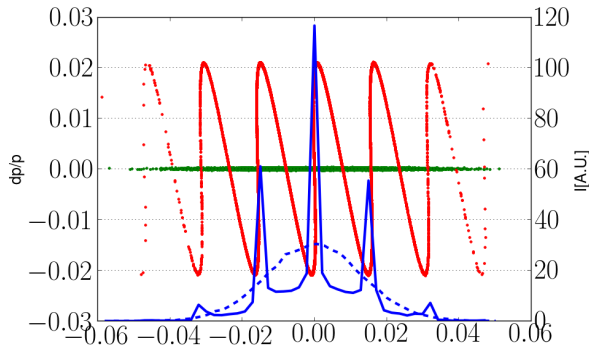


Figure 3: Simulated longitudinal phase space at the entrance (green) and after the bunch compressor (red) with 12 GHz cavity. Current profiles before (blue dashed line) and after (solid blue line) are shown.

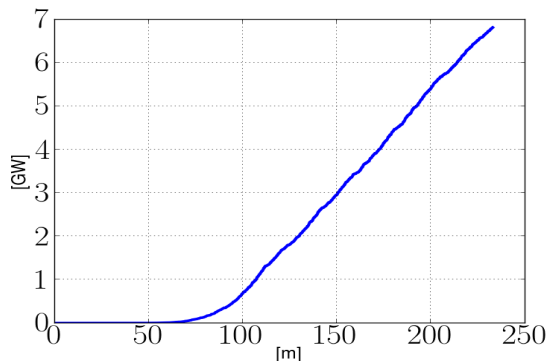


Figure 4: Steady state SASE simulations for $E_\gamma = 1266 \text{ eV}$, $K=5.0$, 50x compression.

Influence on Beam Dynamics

The feasibility question from the beam dynamics point of view reduces to the turn-to-turn preservation of beam quality. Synchrotron radiation induces bunch diffusion, mostly in the longitudinal phase space. Such diffusion is in principle a lim-

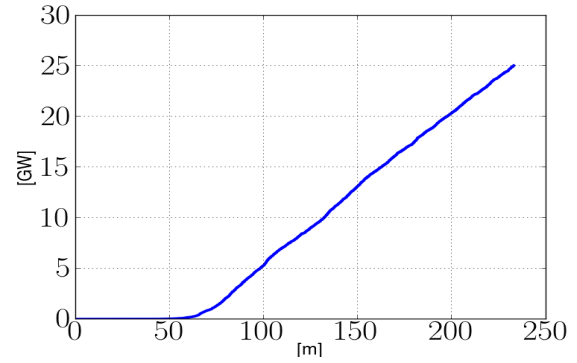


Figure 5: Steady state SASE simulations for $E_\gamma = 335 \text{ eV}$, $K=10.0$, 50x compression.

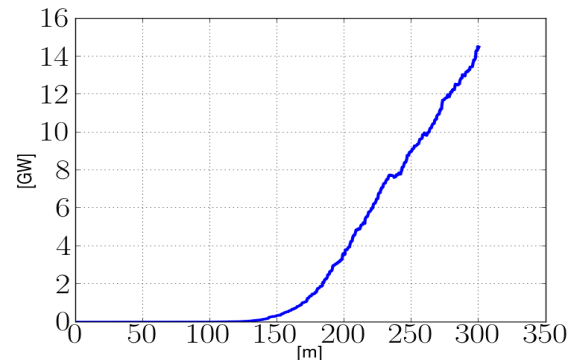


Figure 6: Steady state SASE simulations for $E_\gamma = 100 \text{ eV}$, $I_w = 0.068$, $K=10.0$, 50x compression.

iting factor even for linac-based FEL performance, however for the device in question the diffusion footprint is similar to that of standard ring insertion devices and is not in principle a limiting factor. Moreover, the FEL undulators can potentially be used in place of damping wigglers for reducing the emittance. The FEL-induced energy spread however is to be taken into account for more detailed studies. A major limiting factor in FELs is the coherent synchrotron radiation [6]. In the design discussed the bunch length (1 ps) is 5-6 orders of magnitude longer than the critical wavelength of the bending magnet radiation (2-20 keV for 0.1-1 T dipoles), whereas CSR manifests itself when the bunch length is comparable to the wavelength of the radiation emitted. Estimates based on taking into account the power enhancement factor

$$g(\lambda) = N \left| \int_{-\infty}^{\infty} n(z) \exp(2\pi i z / \lambda) dz \right|^2 \quad (7)$$

where N is the number of particles in the bunch, $n(z)$ the bunch form factor and λ the radiation wavelength, show negligible effect on the total emitted power of synchrotron radiation. Another SASE undulator effect on the beam is microbunching which is washed away in dispersive sections and should not present a problem.

CONCLUSION AND OUTSTANDING R&D NEEDS

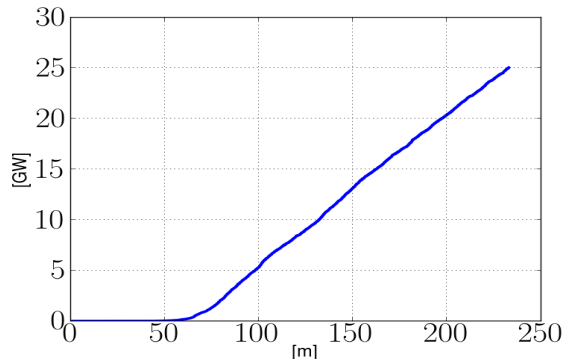


Figure 7: Steady state SASE simulations for $E_\gamma = 335\text{ eV}$, $K=10$, 50x compression assuming $\beta = 4\text{ m}$ optics equalizing vertical and horizontal emittance is possible.

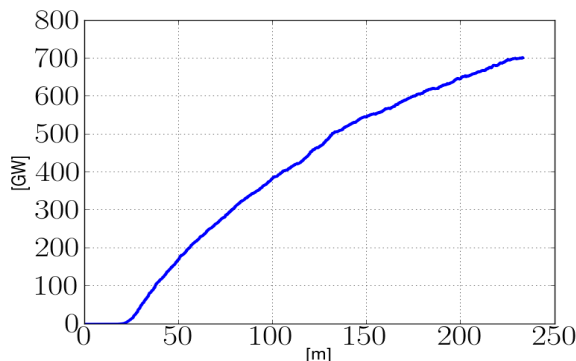


Figure 8: Steady state SASE simulations for $E_\gamma = 335\text{ eV}$, $K=10$, 20x compression assuming $\beta = 4\text{ m}$ optics equalizing vertical and horizontal emittance and bunch shortening down to 4 ps is possible.

Several issues need to be further addressed.

Although CSR should not be a limiting factor, possibilities for other instabilities need investigation.

Electron optics design has to be performed to match the existing beam transport. In this work power estimates were done based on standard FODO optics with $\langle\beta\rangle = 4\text{ m}$. Due to large difference in the vertical and horizontal emittances, special optics producing round beams will improve the performance. This could be achieved by emittance exchange between the vertical and the horizontal (see Fig. 7) plane or possibly by an asymmetric low- β_x optics. The energy spread after the first focusing RF cavity is significant (5%). This will require very large momentum acceptance optics in the insertion. On the other hand, the performance can be improved with a transverse gradient undulator [7]. Moreover, if same current short bunch operation ($\sim 4\text{ ps}$) of a storage ring could be achieved, the performance is improved significantly (see Fig. 8).

With proper optimization of the layout for the X-ray wavelength of interest to experiments, operation of $\sim 100\text{ m}$ long insertion device with longitudinal focusing as an FEL in the present or next [8] generation of light sources producing ps photon pulses of high peak power seems theoretically possible. The major problem is however due to the fact that straight sections of 100 m length are not feasible in present storage ring light sources. Thus a major step on the way to practically implementing the proposed FEL scheme is in R&D towards storing high current beams in storage rings.

ACKNOWLEDGEMENTS

The author is thankful to A. Kling, R. Wanzenberg, K.-J. Kim, A. Zholents and R. Lyndberg for useful discussions.

REFERENCES

- [1] E. Saldin et al., "The Physics of Free Electron Lasers", Springer-Verlag 2000
- [2] K. Huang et al., "Steady-state analysis of short-wavelength, high-gain FELs in a large storage ring", Nucl. Instr. and Meth. A 593 pp. 120-124 (2008)
- [3] A. Zholents, "Electron beam-based sources of ultrashort x-ray pulses", ANL/APS/LS-320 (2010)
- [4] I. Agapov, "Towards more accurate modeling of the FEL radiation for the European XFEL", in Proceedings of IPAC 2013, Shanghai, TUPEA006 (2013)
- [5] http://photon-science.desy.de/facilities/petra_iii/machine/parameters/index_eng.html
- [6] K. Biscari (ed), ICFA Beam dynamics newsletter no. 35 (2004)
- [7] Z. Huang et al., "Compact X-ray Free-Electron Laser from a Laser-Plasma Accelerator Using a Transverse-Gradient Undulator" Phys. Rev. Lett. 109, 204801 (2012)
- [8] M. Borland, "Progress Toward an Ultimate Storage Ring Light Source", Journal of Physics: Conference Series 425 (2013) 042016

STATUS OF ELECTRON BEAM SLICING PROJECT AT NSLS-II, BNL*

A. He, F. Willeke, L.H. Yu, BNL, Upton, NY 11973, USA

Abstract

The Electron Beam Slicing (e-beam slicing) at NSLS-II, Brookhaven National Laboratory, supported by the Laboratory Directed Research and Development (LDRD) Program, is focused on the development of the new method to generate ultra-short x-ray pulses using focused short low energy (~ 20 MeV) electron bunches to create short slices of electrons from the circulating electron bunches in a storage ring. The e-beam slicing activities are staged in 3 main phases. In Phases 0, the theory of e-beam slicing is developed, the low energy linac compressor is simulation designed, the radiation separation between the satellite and core is analyzed by simulation and the properties of the e-beam slicing system are discussed and compared with other ultra-short x-ray sources. In Phase I, the crucial parts of the e-beam slicing scheme will be tested experimentally which include the micro-focusing test of low energy electron beam in space charge dominated regime and the electron beam slicing test using the Accelerate Test Facility (ATF) electron beam as the high energy beam. The kick back system will be simulation designed to increase the repetition rate of e-beam slicing system. At Phase II, the design of e-beam slicing project at NSLS-II will be proposed. Phase 0 has completed successfully, Phase 1 is under way. This paper presents an update on the status of Phase 0.

The electron beam slicing method [12, 13] is a different approach to generate ultra-short x-ray pulses of the order of 100 fs pulse length. As shown in Fig. 1, when a short electron bunch from a low energy linac (for example, 20 MeV, 200 pC, 150 fs) passes 35 μm above a storage ring bunch (30 ps) at a right angle, it kicks a short slice (~ 160 fs) of electron bunch vertically. The radiation from the short slice is separated from the core bunch. This method has many advantages, i.e., small space in storage ring for interaction, very short radiation pulse length (~ 160 fs), high pulse flux, high repetition rate and high stability. We expect the new method may provide a complimentary approach to other ultra-short x-ray pulse sources.

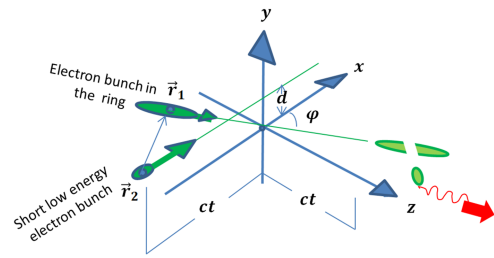


Figure 1: Illustration of electron beam slicing.

INTRODUCTION

The community interested in science using sub-picosecond x-ray pulses is growing rapidly. Laser slicing is one of the approaches to generate ultra-short x-ray pulse [1–6]. Typically, for laser slicing the x-ray pulses are of the order of 100 fs with repetition rate of order of 1 kHz and the number of photons per 0.1% bandwidth per pulse is of the order of 1000. To generate ultra-short x-ray pulses with many orders of magnitude higher repetition rate, another method is proposed by Zholents [7, 8] using a crab cavity which provides pulse length of order of a picosecond. It provides a continuous stream of x-ray pulses [9] with a much higher average flux. A new source of ultra-short x-ray pulses is x-ray free electron laser, with the pulse energy many orders of magnitude higher than storage ring and pulse width of 100 fs or less [10]. However, compared with the storage ring sources, the fluctuation of the intensity and wavelength from a SASE FEL is large, and, the repetition rate is low. For example, the repetition rate of LCLS SASE FEL is 120 Hz [11]. Hence, even though the single pulse energy is much lower than the SASE FEL pulse, the high repetition rate and high pulse to pulse stability of storage ring sources continue to attract a wide range of user interests.

THEORY OF E-BEAM SLICING

We explored the new method by calculating the angular kick received by a high energy electron (labeled as bunch 1), generated by a point charge in the low energy linac electron bunch (labeled as bunch 2) and integrated over the 3-D electron distribution of the low energy bunch. The result gives the angular kick as a function of the 3-D position of an electron in the storage ring bunch:

$$\Delta\theta_y = \frac{eq_2 Z_0 c}{2\pi E_1} \frac{\gamma_2 (1 - \beta_1 \beta_2 \cos \varphi)}{\sqrt{\gamma_2^2 (1 - \cos \varphi)^2 + \sin^2 \varphi}} \frac{1}{\sqrt{2}\sigma_y} \times f_y(\rho, \bar{u}_1, \bar{y}_1) \quad (1)$$

where f_y gives the profile as a function of the high energy electron's position

$$f_y(\rho, \bar{u}_1, \bar{y}_1) = \int_0^\infty \text{Re}[W(\bar{u}_1 + iy)] [e^{-(\rho y - \bar{y}_1)^2} - e^{-(\rho y + \bar{y}_1)^2}] dy \quad (2)$$

* Work supported by DOE under contract LDRD12-023 and LDRD14-022

with

$$\begin{aligned} \rho &\equiv \sqrt{\frac{\gamma_2^2}{\gamma_2^2(1 - \cos \varphi)^2 + \sin^2 \varphi} \cdot \frac{\sigma_x^2 \sin^2 \varphi + \sigma_z^2(1 - \cos \varphi)^2}{\sigma_y^2}} \\ \bar{y}_1 &\equiv \frac{d - y_1}{\sqrt{2}\sigma_y} \\ \bar{u}_1 &\equiv \frac{z_1 \sin \varphi + x_1(1 - \cos \varphi)}{\sqrt{2\sigma_x^2 \sin^2 \varphi + 2\sigma_z^2(1 - \cos \varphi)^2}} \end{aligned} \quad (3)$$

E_1 is the energy of the storage ring electron 1, φ is the crossing angle between the beam axis of the low energy bunch and the beam axis of the high energy bunch, while d is the vertical distance between the centres of the low energy beam and the high energy beam. x_1, y_1, z_1 are the coordinates of the high energy electron, $\sigma_x, \sigma_y, \sigma_z$ are the RMS beam size of the low energy bunch. q_2 is the charge of low energy bunch, γ_2 is its dimensionless energy, $Z_0 = 377 \Omega$ is the vacuum impedance. W is the error function: $W(u) = e^{-u^2} \text{erfc}(-iu)$. Eq. (1) gives the angular kick as a function of the electron's 3-D position x_1, y_1, z_1 in the storage ring bunch 1. The profile function Eq. (2) describes the profile of the slice bunch and can be used to estimate the pulse width of the slice [14].

BUNCH COMPRESSOR SIMULATION

The estimated examples [12–14] show to obtain the sufficient angular kick to separate the slicing from the core, very short (~ 150 fs), focused ($\sim 35 \mu\text{m} \times \sim 35 \mu\text{m}$), high charged (50 pC \sim 200 pC) bunch is required. To reduce the cost, we simulation designed a 5 MeV bunch compressor using BNL photo-cathode electron RF-gun to generate a low energy bunch with the 166 fs RMS bunch length, 28 μm and 31 μm RMS beam size in the vertical and horizontal direction separately, with 50 pC charge [15]. To increase the repetition rate of e-beam slicing system, we carried out a simulation study to design a system consisting of the LBNL's VHF gun operating at 186 MHz with repetition rate of 1 MHz [16], superconducting rf cavity at 1.3 GHz, several solenoids and a compressor chicane with a matching section. The simulation code used is IMPACT-T [17]. To check the effect of the Coherent Synchrotron Radiation (CSR), we compared the simulation results with the results when the CSR effect is turned off in IMPACT-T, and also compared with simulation using the code PARMELA which does not take CSR into account [15]. Our comparison shows that the CSR effect is negligible in our case. We carried out a multi-objective optimization procedure using the genetic algorithm [18]. Some optimized results are shown in Table. 1. For example, at 20 MeV with 200 pC charge and a 8.7 m compressor chicane, the optimization leads to 148 fs RMS bunch length at the focal point with 46 μm , and 25 μm for horizontal and vertical RMS beam size respectively. Fig. 2 shows the histograms of 6-D phase space at the final focus point of the compressor

with the color bar indicating the particle density. A more detailed description is to be found in [19].

Table 1: Performances of Compressor

Case	Charge [pC]	Energy [MeV]	σ_L^a [fs]	σ_H^b [μm]	σ_V^c [μm]
1	150	18	130	47	28
2	200	20	148	46	25
3	200	22	128	42	25

^a the longitudinal rms bunch length of the linac bunch

^b the horizontal rms beam size of the linac bunch

^c the vertical rms beam size of the linac bunch

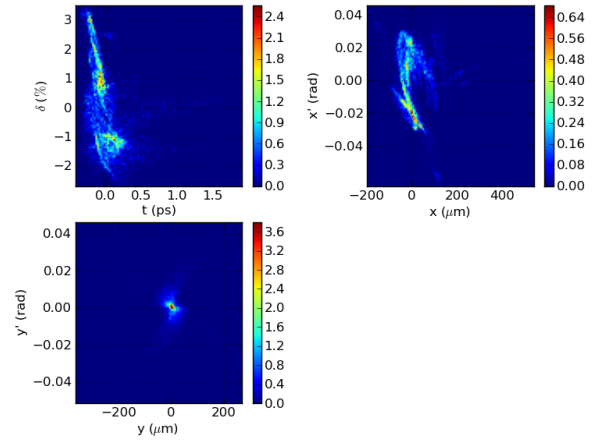


Figure 2: The histograms of 6-D phase space at the final focus point of the compressor. The color bar shows the particle density.

PHOTON FLUX AND REPETITION RATE

If we use a 20 mm period in-vacuum-undulator of NSLS-II as the radiator [20], the photon flux for 8 keV x-rays is 10^{15} photons/sec/0.1%BW for a beam current 500 mA. With about 1000 bunches, bunch current is 0.5 mA. As an estimate, for a slice of 0.3 ps out of the 30 ps core bunch length, the slice fraction is 0.3 ps/30 ps=1%. Since revolution time is about 2.6 μs , the single pulse photon flux is $10^{15} \times 0.3 \text{ ps}/30 \text{ ps} \times 2.6 \mu\text{s}/1000 = 2.6 \times 10^4$ photons/0.1%BW. If we choose a camshaft current of 3 mA, the flux can be increase to 15.6×10^4 photons/0.1%BW.

The emittance increase sets the limitation on the repetition rate. For a single bunch, the emittance increase due to angular kicks is equal to the emittance increase rate times the damping time. One angular kick of $5\sigma_y'$ with a slice of 300 fs in a 30 ps bunch increases ε_y by 12% ε_y . With a repetition rate of 100 Hz for a single bunch, and damping time of 10 ms, the emittance increase is 12% ε_y . If we distribute the kicks uniformly over all 1000 bunches, the repetition rate would be 100 kHz. For 100 kHz repetition rate, the photon flux is 2.6×10^9 photons/sec/0.1%BW for the example above.

For most synchrotron light source users, the requirement on vertical emittance is not very stringent. Thus depending on the tolerance of the vertical emittance increase, the repetition rate limit can be 100 kHz to 1 MHz at the expense of a slightly reduced separation for the same kick.

SPECIFIC EXAMPLE

Slice Profile at Licker and Radiator

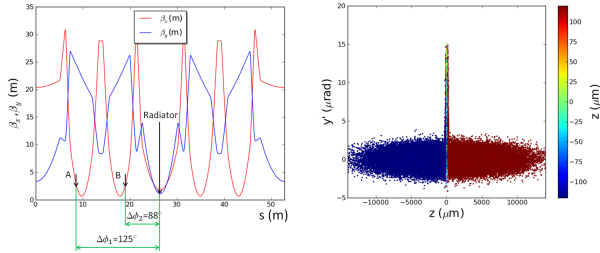


Figure 3: NSLS-II lattice (left). Phase space for y' versus z at the crossing point at 8.3 m right after the kick (right).

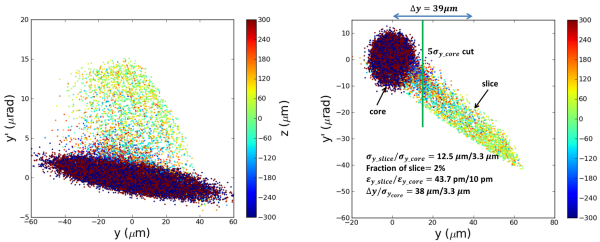


Figure 4: Phase space for (y, y') at the crossing point right after the kick (left) and at the radiator (right).

We use the 6-D phase space distribution shown in Fig. 2 for the low energy bunch from the linac compressor simulation as an example to calculate the slice profile. The formula for angular kick gives the optimum vertical distance from the linac beam to the storage ring beam as $35 \mu\text{m}$. To improve angular separation of the slice from the core, we should choose the crossing point in the storage ring with maximum β_y to minimize the core vertical divergence. In the meantime, to reduce the slice pulse length, we need to minimize β_x . This criterion leads us to choose the slicing point at the position of either about 8.3 m (point A) or 19.3 m (point B) in the left plot of Fig. 3 where $\beta_x = 3.8 \text{ m}$, $\beta_y = 25 \text{ m}$. These two positions have vertical betatron phase advances from the radiator U20 at position 26 m of about 125° and 88° respectively. Using the 6-D distribution of the linac bunch at the final focus point shown in Fig. 2, we calculate the angular kick received by particles in the storage ring bunch after the crossing and plot the phase space distribution. In the right plot of Fig. 3 we show the phase space for y' versus z right after the kick with crossing point at 8.3 m. In the left plot of Fig. 4, we show y' versus y at the crossing point at 8.3 m, right after the kick. The right plot of Fig. 4 gives the phase space plot of y versus y' at the radiator at 26 m. The right

plot of Fig. 3 shows a thin slice is kicked up right after the crossing, while the left plot of Fig. 4 shows how the slice is separated from the core in (y, y') phase space, right after the kick. The right plot of Fig. 4 shows the same phase space after a 125° phase advance at the radiator. The transport of phase space distribution is carried out by the tracking code "ELEGANT" [22]. The phase space rotation is such that the slice can be separated from the core both angularly and spatially.

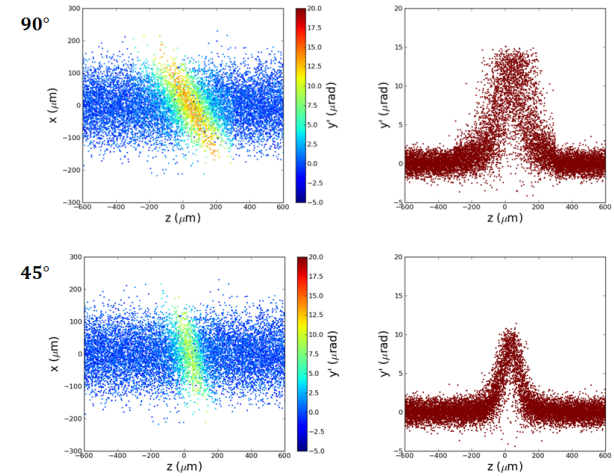


Figure 5: Compare phase space distribution in (z, x) plane and (z, y') plane for 90° and 45° respectively.

Table 2: Quantitative Comparison of 90° and 45° Crossing Angle

	σ_t [fs]	$\frac{\sigma_{y,\text{slice}}}{\sigma_{y,\text{core}}}$ [$\mu\text{m}/\mu\text{m}$]	slice fraction [%]	$\frac{\epsilon_{y,\text{slice}}}{\epsilon_{y,\text{core}}}$ [pm/pm]	$\frac{\Delta y}{\sigma_{y,\text{core}}}$ [pm/pm]
90°	320	12.5/3.3	2	43.7/10	38/3.3
45°	150	7.03/3.3	1	22/10	29/3.3

The RMS slice length in this case is 320 fs, much larger than the linac bunch length of 128 fs. This is because the horizontal crossing time at the interaction point at 8.3 m in Fig. 3. It is possible to reduce the pulse length due to the crossing time by reducing the crossing angle [14]. The simulation shows the bunch length is reduced to 150 fs at the expense of only a small reduction of spatial separation from $38 \mu\text{m}$ to $29 \mu\text{m}$. In Fig. 5 we compare the phase space distribution for the 90° crossing and 45° crossing. The left plot is for the (z, x) phase space with the colour scale representing the kick angle, clearly showing the tilted distribution for the case of 90° gives longer pulse length in z direction. In the right of the plot we give the distribution in (z, y') plane, showing clearly the reduction of pulse length for 45° crossing. Table 2 gives the comparison of quantitative analysis of these two cases. The RMS pulse length of the slice is reduced from 320 fs to 150 fs when crossing angle is 45° .

Table 3: Separation Performances of Hard X-ray Synchrotron Radiation from Electron Beam Slices

separate type		Flux/pulse ^a [photons/0.1%bw]	Flux ^b [photons/sec/0.1%bw]	Peak Intensity [photons/sec/0.1%bw/mm ²]	SNR	τ^c [fs]
90°	spatial+angular	10×10^3	10×10^8	2.1×10^{10}	12	320
	spatial	18×10^3	18×10^8	6.5×10^{10}	5	320
45°	spatial+angular	5×10^3	5×10^8	1.1×10^{10}	8 ^d (2.6)	150
	spatial	5×10^3	5×10^8	3.6×10^{10}	8 ^e (2.7)	150

^a assume NSLS-II's revolution time is about 2.6 μ s, then Flux/pulse= Power \times 2.6 μ s

^b assume the repetition rate of the low energy linac is 100 kHz, then Flux=Flux/pulse \times 100 kHz

^c radiation pulse length

^d with 10 ps of the detector's time resolution

^e with 10 ps of the detector's time resolution

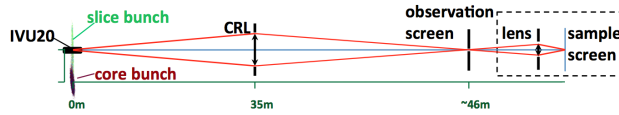


Figure 6: Optical scheme of e-beam slicing beamline.

Radiation Separation

The thin slice bunch and core bunch pass through the 3 m long U20 in-vacuum undulator and radiate x-ray pulses of length 150 fs–320 fs (depending on the crossing angle) and 30 ps respectively. Due to the spatial and angular differences in vertical phase space of the two bunches, the very short, satellite hard x-ray radiation can be separated from the core bunch radiation with sufficient signal to noise ratio (SNR). We propose a conceptual optical scheme [23] shown in Fig. 6 allowing for the separation of the satellite radiation from the core. To get reliable estimates of the separation performances, a wavefront propagation study was performed using the SSynchrotron Radiation WorkshopT (SRW) physical optics computer code [24].

Two methods are used to separate the radiations. One is the pure spatial separation, and the other one is the spatial and angular hybrid separation [13]. The separate performances on the observation screen is shown in Table. 3. For example, at 90° crossing angle, using spatial and angular hybrid separation, the separate SNR is 12 and the flux per pulse reaches 10000 photons/0.1%BW at the expense of relatively longer 320 fs pulse length. Since the repetition rate can reach 100 kHz, the average flux per second for this case can reach 1×10^9 photons/sec/0.1%BW. At 45° crossing angle, the satellite hard x-ray pulse 150 fs is much shorter. The smaller angular kick results in a smaller SNR at 2.7. However, If a fast detector with a time resolution around several picoseconds is used in the femtosecond x-ray diffraction experiment, SNR can increase significantly [13].

CONCLUSION

These results presented have clearly confirmed the feasibility of electron beam slicing approach as a new method of

the generation of short x-ray pulses. Experimental tests are scheduled in the next future.

REFERENCES

- [1] A. Zholents, M. Zolotarev, "Femtosecond x-ray pulses of synchrotron radiation" *Phys. Rev. Lett.* **76**, 916 (1996)
- [2] R.W. Schoenlain et al., "Generation of femtosecond pulses of synchrotron radiation" *Science* **287**, 2237 (2000)
- [3] S. Khan et al., "Femtosecond undulator radiation from sliced electron bunches" *Phys. Rev. Lett.* **97**, 074801 (2006)
- [4] G. Ingold et al., "Sub-picosecond optical pulses at the SLS storage ring" in *Proc. PAC01*, Chicago, IL, USA, 2001, pp. 2656-2658
- [5] C. Steier et al., "Accelerator physics challenges of the fs-slicing upgrade at the ALS", in *Proc. PAC03*, Portland, OR, USA, 2003, pp. 397-399
- [6] O. Chubar, P. Elleaume, "Accurate and efficient computation of synchrotron radiation in the near field region" in *Proc. EPAC98*, Grenoble, France, 1998, pp. 1177-1179
- [7] A. Zholents et al., "Generation of subpicosecond X-ray pulses using RF orbit deflection" *Nucl. Instrum. Methods Phys. Res., Sect. A* **425**, 385 (1999)
- [8] M. Katoh, "Ultra-short pulses of synchrotron radiation on storage rings" *Japan. J. Appl. Phys* **38**, L547 (1999)
- [9] M. Borland, "Simulation and analysis of using deflecting cavities to produce short x-ray pulses with the Advanced Photon Source" *PRSTAB* **8**, 074001 (Mar. 2005)
- [10] P. Emma "First lasing of the LCLS X-ray FEL at 1.5 Å" in *Proc. PAC09*, Vancouver, BC, Canada, 2009, pp. 3115-3119
- [11] J.N. Galayda, The Linac Coherent Light Source Project. No. SLAC-PUB-10115 (Aug, 2002)
- [12] F. Willeke, L.H. Yu, "Ultra-short x-ray pulses generation by electron beam slicing in storage rings" in *Proc. IPAC13*, Shanghai, China, 2013, pp. 1134-1136
- [13] A. He, F. Willeke, L.H. Yu, "Ultra-short x-ray pulses generation by electron beam slicing in storage rings" *PRSTAB* **17**, 040701 (2014)
- [14] A. He, F. Willeke, L.H. Yu, "Dependence on crossing angle of electron beam slicing in storage rings" to be submitted

- [15] A. He et al., “Simulation design of a low energy bunch compressor with space charge effect” in Proc. *IPAC13*, Shanghai, China, 2013, pp. 2307-2309
- [16] F. Sannibale et al., “Status of the APEX project at LBNL” in Proc. *IPAC12*, New Orleans, LA, USA, 2012, pp. 2173-2175
- [17] J. Qiang, ImpactT code, LBNL-62326 (2007)
- [18] M. Ehrgott, *Multicriteria Optimization*, (Springer, 2005)
- [19] A. He et al., “Low energy compressor design with high repetition rate for e-beam slicing” in *These Proceedings: Proc. FEL14*, Basel, Switzerland, 2014, THP036
- [20] S. Ozaki et al., “Philosophy for NSLS-II design with sub-nanometer horizontal emittance” in Proc. *PAC07*, Albuquerque, NM, USA, 2007, pp. 77-79
- [21] F. Lohl et al., “Electron bunch timing with femtosecond precision in a superconducting free-electron laser” *Phys. Rev. Lett.* **104**, 144801 (2010)
- [22] M. Borland, ANL APS Report No. LS-287 (2000)
- [23] A. He et al., “Separation of hard X-ray synchrotron radiation from electron beam slices” in Proc. *SPIE Optics + Photonics 2014*, San Diego, California
- [24] O. Chubar et al., “Physical optics computer code optimized for synchrotron radiation” in Proc. *SPIE 4769*, Seattle, WA, USA, 2002, pp. 145-151

DEVELOPMENT OF COMPACT THZ-FEL SYSTEM AT KYOTO UNIVERSITY

Suphakul Sikharin, Yusuke Tsugamura, Heishun Zen, Toshiteru Kii, and Hideaki Ohgaki,
Institute of Advanced Energy Kyoto University, Gokasho, Uji, Kyoto 611-0011, Japan
Qika Jia, University of Science and Technology China, Hefei, 230029, China

Abstract

We are developing a compact accelerator based terahertz (THz) radiation source by free-electron laser (FEL) at the Institute of Advanced Energy, Kyoto University. The system consists of a 1.6-cell S-band BNL-type photocathode RF-gun, a focusing solenoid magnet, a magnetic bunch compressor, focusing quadrupoles and an undulator. The system will generate an ultra-short electron pulse in a few hundred femtoseconds shorter than radiation wavelength, expecting for a super-radiant emission from the undulator. The target radiation wavelength is 100 to 300 μm . A tracking simulation and optimization are performed by using PARMELA and General Particle Tracer (GPT) code. The FEL radiations are analyzed by a 1 dimensional FEL theory. The design parameters, simulation results and status are reported and discussed in this paper.

INTRODUCTION

A new compact terahertz radiation source is under the development at the Institute of Advanced Energy, Kyoto University. The system was designed to be simple, compact and economical aimed using for scientific researches or industrial applications. The system consists of a 1.6-cell S-band BNL-type photocathode RF-gun, a focusing solenoid magnet, a 4-dipole magnetic bunch compressor, quadrupole magnets, a planar halfbach undulator and a photocathode drive laser system. Currently, the RF-gun, the undulator and the laser system have been prepared. The magnetic chicane and the quadrupoles are newly designed components. The system is located in the same accelerator room with Kyoto University Free-Electron Lasers (KU-FEL) [1]. The schematic view of the proposed system is shown in Fig. 1.

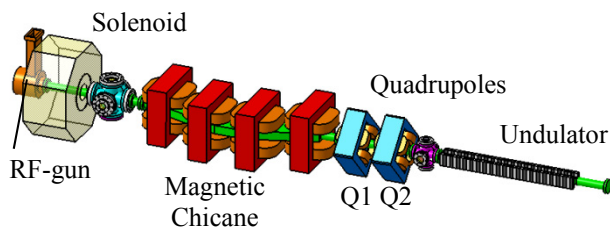


Figure 1: Schematic view of the compact THz-FEL system at Institute of Advanced Energy, Kyoto University.

BEAM DYNAMIC STUDY

The multi-particle beam dynamics was investigated by numerical simulation using PARMELA [2] and GPT [3]. Both codes track particles in the 6-dimensional phase space including the space-charge effect. The simulation of the RF-gun was performed by PARMELA. Then the results are converted to GPT file format and used as the input for the beam dynamics simulations from the RF-gun exit to the end of the undulator by GPT. The parameters of the system was optimized to provide the electron beam with a high peak current, a small beam size and a low energy spread suitable for the FEL radiation generation inside the undulator.

For the simulation of multi-particle beam dynamics, 10,000 macro particles per 2,856 MHz with the total charge of 100 pC are assumed to be emitted from photocathode plug illuminated by the lasers.

Photocathode RF-gun

The 1.6-cell S-band BNL-type photocathode RF-gun, which was manufactured by KEK since 2008, is a new adoption component of the laboratory. The RF-gun performances have been studied by numerical simulations in [4]. In this study, this RF-gun numerical model is used.

The photocathode RF-gun is illuminated by a picoseconds mode-locked Nd:YVO₄ UV laser system [5]. The laser system consists of an acousto-optic modulator, beam position stabilizer, two of double pass amplifiers, SHG and FHG crystals. The cathode plug was made from copper and loaded to the RF-gun by a load-lock system. The quantum efficiency (QE) of the cathode plans to be improved by coating the cathode surface with Cs and Te.

For the simulation, the RF-gun operates at a high accelerating condition with average accelerating voltage of 80 MV/m in order to reduce the space-charge effect. The accelerating field ratio between half-cell and full-cell are assumed to be 1:1. We made several calculations and concluded that the lasers are injected at a low accelerating phase which provides a lower energy spread and a better linearization of an energy chirp. The laser profiles are Gaussian distribution in both transverse and longitudinal with specified cut-off limits. The simulation parameters of the RF-gun are listed in Table.1.

Table 1: The Photocathode RF-gun Parameters

RF-Gun Parameters	Values
Type	1.6-cell S-band BNL type photocathode
Accelerating field	80 MV/m (avg)
Bunch charge	100 pC
Solenoid field strength	1,800 G
Laser type	Forth harmonics of pico-seconds mode-locked Nd:YVO ₄
Laser longitudinal length	rms 6.2 deg, max 12 deg
Laser transverse size	max radius 1 mm.
Laser injection phase	12 deg

Magnetic Chicane

The magnetic chicane bunch compressor which consists of 4-rectangular H-type dipole electromagnets is a newly designed. The chicane creates an energy dependent path inside where the path length of electrons with higher momentum is shorter than electrons with lower momentum. Consequently, the electron bunch become shortens in the longitudinal leading to increasing of the peak current. The schematic of the magnetic chicane is shown in Fig. 2.

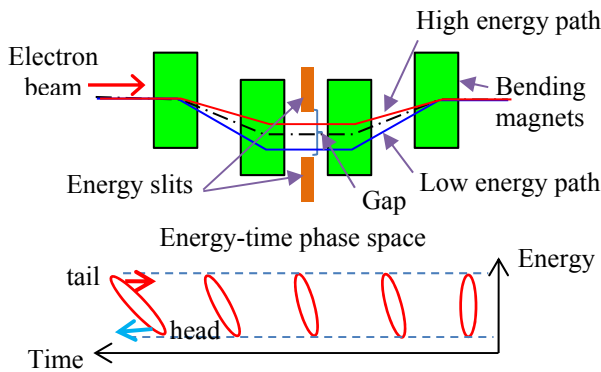


Figure 2: Schematic of the magnetic chicane.

Table 2: The Magnetic Chicane Parameters

Magnetic Chicane Parameters	Values
1 st order momentum compaction (R_{56})	-113.5 mm.
Deflection angle	29.5 deg.
Energy slits - Slit width	2 mm
- Offset from centre	112.2 mm
Magnets - Geometrical length	75 mm.
- Distance between magnets	125 mm
- Magnetic field	0.168 T
- Coil current	1969.6 A-turns

The energy slits consist of two metal plates whose positions can be adjusted in horizontal axis. The slits are placed between the 2nd and 3rd magnet to remove electrons which do not contribute to the FEL radiation. The deflection angle of the chicane can be varied from 0 to 35 degree. The optimized chicane parameters given by

simulation corresponding to the RF-gun parameters are shown in Table. 2.

Undulator and THz-radiation

The undulator for the compact THz-FEL is a planar Halbacht type, an adjustable gap and a deflection plane in vertical. Since the electron bunch will be shorter one and the radiation wavelength is very long in our case, the slippage effect is significant which cause FEL interaction only a few period of the undulator. Therefore the short undulator period of 10 has been chosen. The quadrupoles are installed upstream the undulator to focus an electron beam to the undulator. The undulator parameters are listed in Table. 3. The THz-radiations are generated by injecting an ultra-short electron bunch to the undulator. When the electron bunch length is significantly shorter than the FEL wavelength, each individual electron moves sinusoidal and emits the radiation in almost the same phase called "super-radiation". The power of super-radiation, P_{sr} , can be estimated by the 1-dimensional FEL theory [6]

$$P_{sr} < (4\pi \frac{l_b}{\lambda_s} b)^2 \rho^3 P_e ,$$

where l_b is the bunch length, λ_s is the undulator resonance wavelength, b is the bunching factor $b = |\langle e^{i\theta} \rangle|$ where θ is the phase of the electrons inside the FEL radiation wave, ρ is the FEL parameter and P_e is the power of the electron beam.

Table 3: The Undulator Parameters

Undulator Parameters	Values
Type	Plannar Halbacht
Number of period	10 periods
Period length	70 mm.
Undulator gap	40 mm.
Peak magnetic field	0.275 T
Undulator parameter (K)	1.802
FEL resonance wave length	244 μ m
Quadrupole magnetic field gradient (T/m)	Q1 = 1.4, Q2 = -2

SIMULATION RESULTS

For the RF-gun section, PARMELA simulation has been performed to obtain the electron bunch with a linear energy chirp which is suitable for the bunch compression by the chicane. The energy time phase-space, the current profile and the transverse phase-space the electron bunch at the RF-gun exit are shown in Figs. 3 and 4. The FWHM bunch length and the peak current are 4 ps and 24.4 A. The transverse phase spaces of both horizontal (x axis) and vertical (y axis) are the same.

At the undulator entrance, GPT simulation has been performed to optimize the chicane parameter. The FWHM bunch length reduces to 0.4 ps, the peak current is up to 90 A and the bunching factor is 0.26. The bunch

charge reduces to about half of the initial bunch charge because of the energy slits. The energy time phase-space, the current profile and the transverse phase-space at the undulator entrance are shown in Fig. 5, 6. The electron beam properties are listed in Table 4.

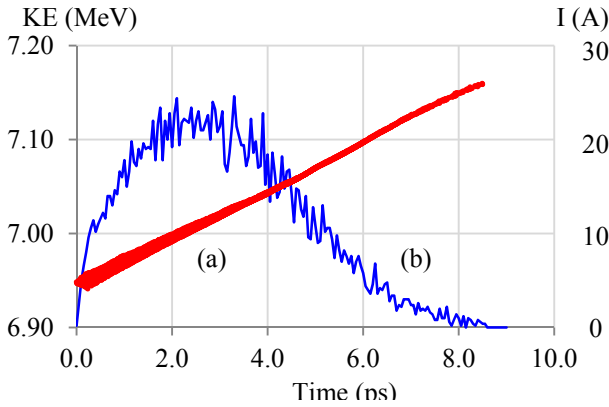


Figure 3: Energy time phase-space (a) and current profile (b) at the RF-gun exit (PARMELA simulation results).

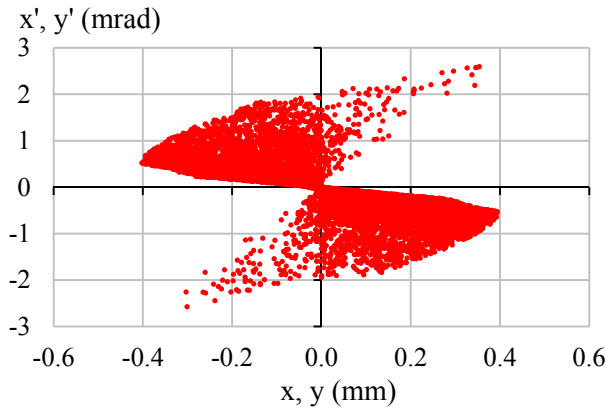


Figure 4: Transverse phase-space in x-x' and y-y' at the RF-gun exit (PARMELA simulation result).

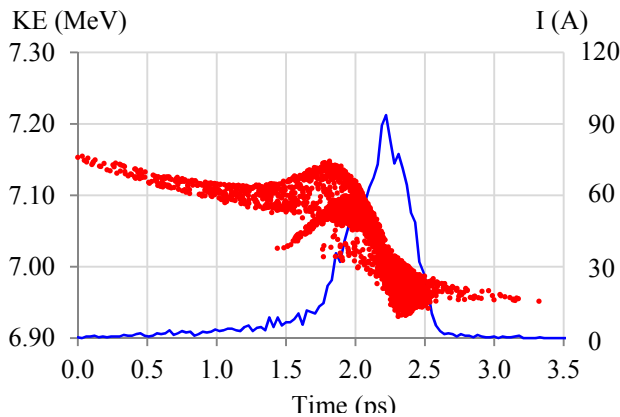


Figure 5: Energy time phase-space (a) and current profile (b) at the undulator entrance.

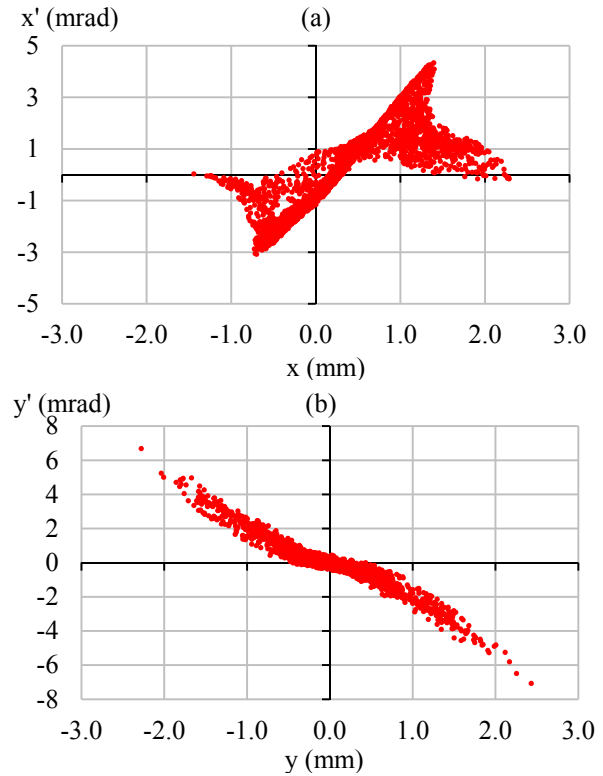


Figure 6: Transverse phase-space in x-x' (a) and y-y' (b) at the undulator entrance (GPT simulation result).

The rms beam size, transverse and longitudinal normalized rms emittances of the whole system are shown in Figs. 7, 8 and 9. The undulator has a strong focusing in horizontal (non-deflection plane) and no focusing in vertical (deflection plane). The average horizontal and vertical rms beam sizes of the beam inside the undulator are 0.59 mm and 0.32 mm, respectively.

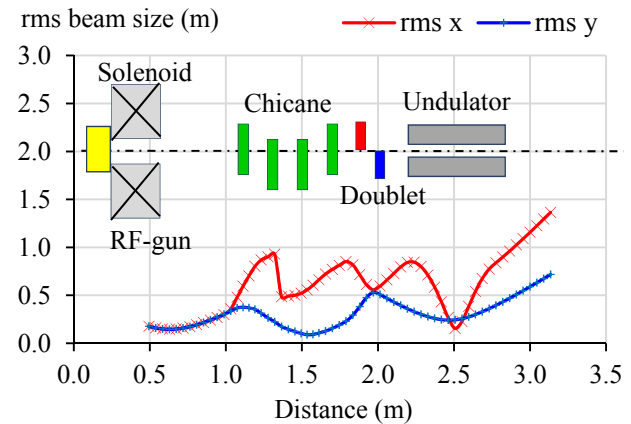


Figure 7: RMS beam size (GPT simulation results).

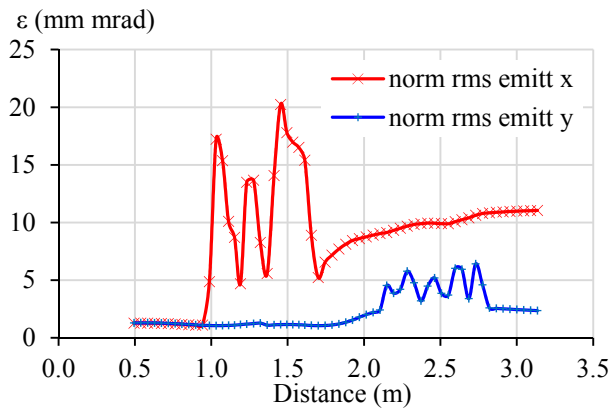


Figure 8: Transverse normalized rms emittance (GPT simulation results).

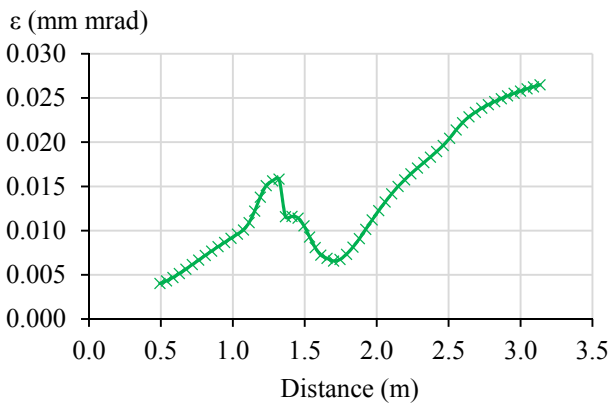


Figure 9: Longitudinal normalized rms emittance (90% of particles of the bunch, GPT simulation results).

Table 4: Summary of the Electron Beam and the THz Radiation Properties

Parameters	Values
<u>RF-gun exit</u>	
Beam energy - Average	7.02 MeV
- Maximum	7.15 MeV
- Minimum	6.94 MeV
RMS Energy spread	0.61 %
Bunch length (FWHM)	4 ps
Bunch charge	99.9 pC
Peak current	24.4 A
RMS beam size (mm)	$\sigma_x = 0.17$, $\sigma_y = 0.17$
Normalized RMS emittance (mm mrad)	$\bar{\epsilon}_x = 1.27$, $\bar{\epsilon}_y = 1.29$
<u>Undulator Entrance</u>	
Beam energy	
- Average	7.04 MeV
- Maximum	7.15 MeV
- Minimum	6.93 MeV
Energy spread	0.89 %
Bunch length (FWHM)	0.4 ps
Bunch charge	48.6 pC
Bunching factor	0.26

Peak current	93.7 A
RMS beam size (mm)	$\sigma_x = 0.66$, $\sigma_y = 0.46$
Normalized RMS emittance (mm mrad)	$\bar{\epsilon}_x = 8.9$, $\bar{\epsilon}_y = 2.2$

THz-radiation

Radiation wavelength	244 μm
FEL parameter	0.0243
Super-radiation power	0.078 MW

CONCLUSION

The multi-particle beam dynamics of the compact THz-FEL has been investigated by the numerical simulations. The electron bunch at the undulator entrance has the average energy of 7.04 MeV, the energy spread of 0.89%, the bunch length of 0.4 ps, the peak current of 93.7 A, the bunching factor of 0.26 and the average rms beam radius inside the undulator of 0.67 mm. The calculated FEL parameter is 0.0243. Such a beam will provide the super-radiation power of 0.078 MW for the wavelength of 244 μm . A seeding FEL scheme [7] is also under consideration to obtain a high power FEL.

REFERENCES

- [1] H. Zen et al., "Present Status of Mid-Infrared Free Electron Laser Facility in Kyoto University", in *Proc. 4th Int. Particle Accelerator Conf.*, Shanghai, 2013.
- [2] L.M. Young et al., "PARMELA", LANL Technical Note LA-UR-96-1835, 2002.
- [3] S.B. van der Geer et al., "General Particle Tracer: A 3D code for accelerator and beam line design", in *Proc. 5th European Particle Accelerator Conf.*, Stockholm, 1996, pp 1241.
- [4] H. Ohgaki et al., "Numerical Evaluation of Oscillator FEL with Multi-bunch Photo-cathode RF-Gun in Kyoto University", in *Proc. 29th Int. Free-Electron Laser Conf.*, Novosibirsk, 2007, pp 390-393.
- [5] H. Zen et al., "Development of Photocathode Drive Laser System for RF Guns in KU-FEL", in *These Proceedings: Proc. 36th Int. Free-Electron Laser Conf.*, Basel, 2014, THP045.
- [6] Q. Jia, to be submitted.
- [7] T. Kii et al., "Design Study on THz Seeded FEL Using Photocathode RF Gun and Short Period Undulator", in *Proc. 30th Int. Free-Electron Laser Conf.*, Gyeongju, 2008, pp.196-199.

POTENTIAL PHOTOCHEMICAL APPLICATIONS OF THE FREE ELECTRON LASER IRRADIATION TECHNIQUE IN LIVING ORGANISMS

F. Shishikura[#], K. Hayakawa, Y. Hayakawa, K. Nakao, M. Inagaki, K. Nogami, T. Sakai, T. Tanaka, Laboratory for Electron Beam Research and Application, Nihon University, Chiba, Japan
H. Zen, T. Kii, H. Ohgaki, Institute of Advanced Energy, Kyoto University, Kyoto, Japan
T. Sakae, Nihon University School of Dentistry at Matsudo, Chiba, Japan

Abstract

The free electron lasers (FELs) of the Laboratory for Electron Beam Research and Application (LEBRA), Nihon University and of Kyoto University (KU) were combined to produce tunable FEL wavelengths from the visible to the mid-infrared region (0.4–20.0 μm). We have previously verified that visible light from the LEBRA-FEL can control the germination of lettuce seeds, a well-known photochemical reaction in plants. We found that red light (660 nm FEL) promotes the germination and far-red light (740 nm FEL) inhibits it. In this article, we further examine the photochemical effects on lettuce seed germination of various wavelengths from visible to mid-infrared generated by combining the two FELs. The red spectra of FEL ranging from 600 to 680 nm (activity peak: 660 nm) promoted germination at an activity level of over 40%, whereas the far-red spectra of FEL from 700 to 760 nm (activity peak: 740 nm) inhibited germination at a similar activity level. For the other wavelengths examined, we did not observe the promotion or inhibition of seed germination at an activity level of more than 40%. However, the unique characteristics of the combination of two FELs may prove to be a useful tool because of its high pulse radiation energy, narrow spectral half-bandwidths, and tunable wavelengths from visible to mid-infrared. It may allow the identification of novel photochemical reactions in living organisms.

INTRODUCTION

In 2001, the Laboratory for Electron Beam Research and Application (LEBRA) achieved the first lasing of 0.9–6.5 μm , in the near- and a small part of the mid-infrared regions of free electron lasers (FELs), in which higher harmonics were generated by using nonlinear optical crystals. Now, the FELs cover a wide range of wavelengths from visible to mid-infrared regions from 400 nm to 6.5 μm [1]. In 2012, the Institute of Advanced Energy in Kyoto University (KU), succeeded in producing a FEL (KU-FEL) that covered a large part of the mid-infrared region, and its high-energy and tunable wavelengths have recently been extended from 5 to 20 μm [2]. Following these breakthroughs, we have focused on using both these FELs for investigating photochemical reactions in living organisms. In 2013, we verified that the visible LEBRA-FELs can control the germination of lettuce seeds, a well-known photochemical reaction in

plants [3, 4], and showed that red light (660 nm FEL) promotes germination, whereas far-red light (740 nm FEL) inhibits it [5]. We also found that the FEL treatment was still effective when using neutral density filters to reduce radiation energy at 660 nm and 740 nm to as low as about 0.05 $\mu\text{J/pulse}$ (10 min irradiation) and about 0.63 $\mu\text{J/pulse}$ (10 min irradiation), respectively [5].

The aim of this study is to determine the photochemical efficiency in lettuce seed germination tests of the tunable wavelengths of FEL from 400 nm to 20 μm , generated by combining the two FEL facilities at LEBRA and KU [1, 2]. The results showed that lettuce seed germination was promoted when the seeds were irradiated by the red FEL spectra from 600 to 680 nm and inhibited by the far-red FEL spectra from 700 to 760 nm. The activity levels that corresponded to the photochemical efficiency were more than 40% for the promotion and inhibition. For the more than 25 other FEL wavelengths examined, ranging from visible to mid-infrared regions, photochemical efficiencies of less than 40% activity was observed for promoting and inhibiting lettuce seed germination.

MATERIALS AND METHODS

Lettuce Seeds and Imbibition

Lettuce seeds (*Lactuca sativa* L.) from the Red Wave cultivar (a leaf lettuce) were obtained from a commercial supplier (Lot Nos. 546427 and 546430; Sakata Seed Co., Yokohama, Japan) and were used within the recommended period. Prior to irradiation experiments, the seeds were imbibed, as described in our previous report [5].

Setup of FEL Irradiation Systems

The setups of the LEBRA-FEL and KU-FEL irradiation systems are shown in Figure 1 (A-1 and B-1). The sample stages for the FEL irradiation experiments are shown in the magnified views (A-2 and B-2). In the sample stage, 5 or 6 lettuce seeds can be irradiated at once. A set of typical germination results at a wavelength of 690 nm is shown in Figure 2 (A and B).

Radiation Sources

We use the definitions in the Photonics Spectrum Reference Chart (Laurin Publishing, Pittsfield, MA) relating to ranges for the visible (400–750 nm), near-infrared (750 nm to 3 μm), and mid-infrared spectra (3–30

[#]shishikura@lebra.nihon-u.ac.jp

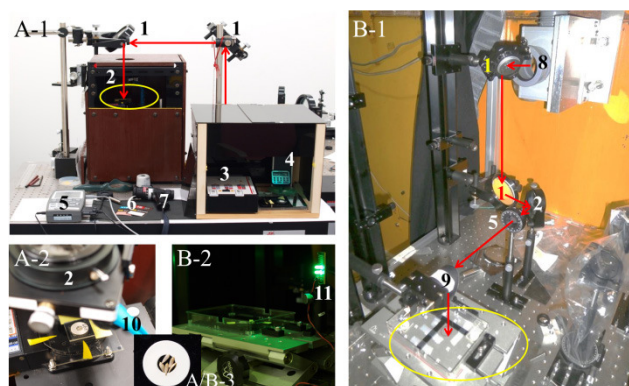


Figure 1: Setup of the two irradiation systems: LEBRA-FEL (A-1; view from front) and KU-FEL (B-1; view from top). Parts shown in yellow ovals in A-1 and B-1 are the sample irradiation stages, both of which are enlarged in A-2 and B-2, respectively. The inset (A/B-3) shows the hollow 6 mm in diameter where five lettuce seeds can be placed. Each path for the given wavelengths, indicated by red arrows, can irradiate the seeds on the sample stage. 1: flat mirror (Sigma-Koki); 2: lens (Sigma-Koki); 3: photo seed germination apparatus; 4: safety light-1; 5: laser power/energy meter (FieldMaxII-TOP); 6: detector cards (left: visible, right: infrared; Edmund Optics, Inc., Tokyo, Japan); 7: infrared conversion viewer (Newport Corp.); 8: output port of the FEL beam transport; 9: off-axis parabolic mirror (Sigma Koki); 10: safety light-2; 11: safety light-3.

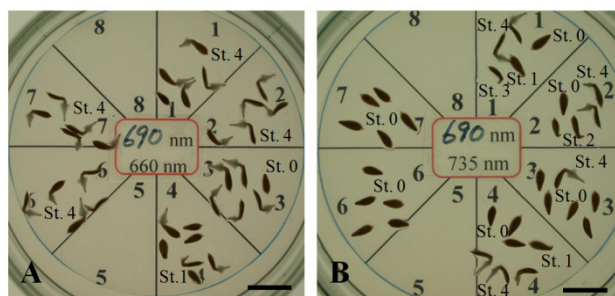


Figure 2: Examples of 690 nm FEL irradiation experiments. A: Inhibition experiment. B: Promotion experiment. Prior to 690 nm FEL irradiation, the seeds were depleted of active materials by exposure to LEDs. Agar plates were divided into eight blocks: No. 1–4 for irradiation experiments, No. 6 and 7 for controls. Five developmental stages (St. 0–4) defined previously [5] were used to evaluate the irradiation experiments. Scale bars = 10 mm

μm). The LEBRA-FEL can generate visible, near-infrared, and part of the mid-infrared spectra. The KU-FEL can produce a large part of the mid-infrared spectra. We collaborated closely on the specifications for the irradiation light sources, particularly for the longer wavelengths in the mid-infrared region. The typical beam parameters of the two FELs have been described previously [1, 2], in which the FEL radiation energies could be reduced by combined neutral-density glass filters (Kenko Tokina Co. Ltd., Tokyo, Japan) or a polarizing

filter (WP25H-K, Thorlabs Inc, Newton, NJ). The irradiation energies used here are listed in Table 1 and typical half-bandwidths have been reported previously [5]: 8 nm for the 660 nm FEL, and 16 nm for the 735 nm FEL. The radiation power is measured by a power meter (FieldMaxII-TOP, Coherent, Inc., Portland, OR), a pyroelectric energy detector (818E-20-50S, Newport Corp., Irvine, CA), or a multi-function optical meter (1835-C, Newport Corp.).

Depletion of Active Materials in Seeds

After imbibition for a given time (usually 50 min [5, 6]), the seeds were depleted of the naturally occurring active materials that accumulate during seed storage [7]. To deplete the active material produced in response to red light, the seeds were exposed to far-red FEL. Then to deplete the active material produced in response to far-red light, the seeds were exposed to red FEL [5]. These characteristics were manipulated by a 10 min exposure to 660 or 735 nm light-emitting diode (LED) light, both of which were installed in a photo seed germinating apparatus (GR-8, Shimadzu Rika Co., Tokyo, Japan). This apparatus is designed specifically for lettuce seed germination tests: it contains a row of small, divided sections with built-in LED lighting sources and each section can be separately illuminated by 735, 660, 505, or 470 nm LEDs. To deplete the naturally occurring active materials, conditions for pre-exposure to LEDs were chosen based on the manufacturer's instructions. After a 50 min imbibition, the seeds were sown on two layers of washed filter paper in glass Petri dishes (4.5 × 4.5 cm, 2 cm deep), and were immediately transferred to the chambers (6 × 6 cm, 3 cm deep) of the photo seed germination apparatus. The seeds were pre-exposed for 10 min to red or far-red light at 25.0 °C. The seeds were then irradiated for 5 min at a given FEL wavelength to determine whether the wavelength can promote or inhibit germination of the lettuce seeds.

FEL Irradiation Experiments and Germination Tests

About thirty-five seeds were exposed to red (660 nm) or far-red (735 nm) LED light for at least 10 min in the photo seed germination apparatus, and were then removed one by one from the Petri dishes with fine forceps. The seeds were immediately placed in a sample irradiation glass stage (1.5 × 1.5 cm) with a small hollow 6 mm in a diameter, which was large enough to place 5-6 seeds in without touching (Figure 1; enlarged view of A/B-3). The FEL irradiation experiments did not exceed 2 h [5, 6], including time for imbibition, pre-exposure with LED (usually 10 min), and irradiation time (5 min). These FEL irradiation experiments were repeated three or four times. Controls were taken at the beginning and the end of the irradiation experiments. To achieve continuous incubation under oxidative conditions, immediately following irradiation, the seeds were moved from the sample stage to a 7 cm Petri dish, which had been prepared with 0.4% agar in distilled water. Unirradiated control seeds were

also transferred. Each Petri dish was shielded from light by wrapping in a double sheet of aluminum foil, and then incubated at 25.0 ± 0.5 °C in a climatic test chamber (Atmos Chamber MTH-2200; Sanyo, Osaka, Japan) or an incubator (SLC-25A, Mitsubishi Corp., Tokyo, Japan). The germination processes were recorded and evaluated within 20–24 h of incubation under a dissection microscope. All handling was performed in darkness or carried out under safety lights (white lights) covered with band pass filters (BPB-45 or BPN-50, Fujifilm Corp., Tokyo, Japan), as well as green LEDs (4 units; 520 nm spectrum, half-bandwidth; 30 nm). Either of the two kinds of band pass filters was fixed on the front of a white light (0.5 W-LED, Panasonic Co., Tokyo, Japan). The safety lights had no effect on the seed germination for up to 20 min irradiation. This means that under the safety lights, the seeds can be manipulated without being affected by the light during the operations (usually not exceeding 5 min). The installation of the safety lights is shown in Figure 1.

Evaluation

Except for observing and evaluating the state of germination, all other operations were carried out in darkness or under the safety lights. To evaluate the irradiation experiment results, the seed germination processes were determined and divided into five developmental stages (St. 0–4) within 20–24 h of incubation [5]. Figure 2 shows an example of the irradiation experiments at a given FEL wavelength. To evaluate effectiveness of the FEL irradiation experiments simply, we further divided the five developmental stages into two groups: one includes seeds at stages St. 0–2, and the other includes seeds at stages St. 3 and 4. This made evaluating the efficiency of FEL easier, because almost all the seeds normally develop to St. 4 within 20–24 h incubation at 25 °C in the dark. The seeds in the first group (St. 0–2) showed little or no activation in the promotion experiments, whereas the seeds in the second group (St. 3 and 4) showed activation in the promotion experiments. This was reversed for the inhibition experiments.

RESULTS AND DISCUSSION

One of the most important prerequisites is to switch the seeds into either of the two active states of germination, promotion or inhibition, so that the seeds fully respond to the photo-potential of a given wavelength of light. In the promotion experiments, the active materials produced by red light were depleted by irradiating some of the seeds with far-red light, and then the response of the seeds to various wavelengths of light was examined. In contrast, in the inhibition experiments, the active materials produced by far-red light were depleted by irradiating some of the seeds with red light, and then the response of the seeds to different wavelengths was examined. The reversibility of the active states of promotion and inhibition produced by red light and far-red light, respectively, was repeatedly demonstrated by far-red FEL and red FEL in our previous

report [5]. Other studies have shown that LEDs can retrieve the reversibility of photoreactions in lettuce seed germination [8] in the same manner as fluorescent lights, sodium light illuminators, and incandescent lights. Therefore, instead of FEL irradiation, we prepared the two photosensitive states of lettuce seeds by exposing them to either red (promotion) or far-red (inhibition) LED light. Both the seed lots used here showed high photosensitive states: the activity levels of promotion or inhibition exceed 93%. This means that the seed were sufficient to determine whether the FEL spectra, ranging from visible to mid-infrared, affect the seeds.

Efficiencies of Visible Spectra

The results of the irradiation experiments at visible wavelengths are summarized in Table 1. The active wavelengths for promoting seed germination are 600–680 nm (>40% promoting activity) and those for inhibition are 700–780 nm (>40% inhibiting activity). The values of inhibition and promotion given in Table 1 are plotted to show the typical apparent patterns of the effectiveness of wavelengths for lettuce seed germination (Figure 3). Interestingly, there are two active peaks for inhibition, which resemble the typical color curve of red-absorbing materials, as reported by Hartmann and Mollwo [7], who used a xenon arc cinema projector as a lighting source. Furthermore, the wavelengths at 410 nm and 500 nm seemed to be effective in germination of the lettuce seeds, which are consistent with previous work [9] although further FEL experiments are required.

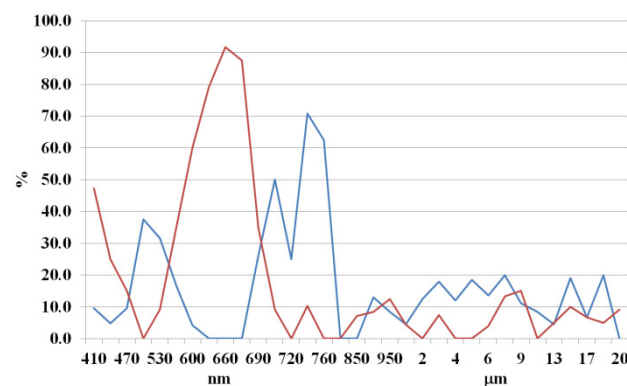


Figure 3: Action spectra for promotion (red line) and inhibition experiments (blue line) constructed from the data shown in Table 1. Activity levels over 40% are recognized as effective.

Efficiencies of Near- and Mid-Infrared Spectra

Based on reviews covering recent biological applications of infrared radiation sources [10], some studies of the biological and biomedical effects of infrared spectra have been published [10], and it is a promising treatment for certain medical and scientific fields [10]. We intend to use near- and mid-infrared radiation sources to identify the biological effects of radiation on cells, tissue, and small living organisms. Therefore, our initial work has focused on irradiating lettuce seeds, the germination

of which can be easily controlled by visible light exposure and can be evaluated within a day. Table 1 also summarize the efficiencies of near-infrared and mid-infrared irradiation, respectively. Even using high radiation energies, activities of over 20% for either promotion or inhibition were not detected. Under these conditions, heat effects are negligible because both LEBRA-FEL and KU-FEL use discontinuous pulsed spectra of 2 and 1 Hz, respectively, rather than continuous pulsed spectra. Even increasing the irradiation time from 5 min to 10 or 20 min for the 9 μm FEL and 20 μm FEL did not affect the spectra with over 20% activity (data not shown here).

Table 1: Effect of Visible, Near-Infrared and Mid-Infrared Spectra⁽¹⁾ on Lettuce Seed Germination

FEL μm	Inhibition		Promotion		Evaluation ⁽²⁾ %		Energy $\mu\text{J/pulse}$
	St. 0-2	St. 3-4	St. 0-2	St. 3-4	Inhi- bition	Promo- tion	
0.41	2	19	10	9	9.5	47.4	11.7
0.44	1	20	15	5	4.8	25.0	12.5
0.47	2	19	17	3	9.5	15.0	12.5
0.50	6	10	17	0	37.5	0.0	9.5
0.53	6	13	20	2	31.6	9.1	18.4
0.56	3	15	13	7	16.7	35.0	23.7
0.60	1	23	10	15	4.2	60.0	3.2
0.63	0	17	5	19	0.0	79.2	3.2
0.66	0	22	2	22	0.0	91.7	7.8
0.68	0	17	2	14	0.0	87.5	3.3
0.69	6	17	15	8	26.1	34.8	5.2
0.70	11	11	20	2	50.0	9.1	9.2
0.72	4	12	17	0	25.0	0.0	11.1
0.74	17	7	26	3	70.8	10.3	17.7
0.76	10	6	16	0	62.5	0.0	10.7
0.80	0	16	17	0	0.0	0.0	19.4
0.85	0	15	13	1	0.0	7.1	22.3
0.90	3	20	22	2	13.0	8.3	14.0
0.95	2	22	21	3	8.3	12.5	4.8
1.0	1	21	22	1	4.5	4.3	10.5
2.0	3	21	24	0	12.5	0.0	175
3.0	5	23	25	2	17.9	7.4	600
4.0	3	22	26	0	12.0	0.0	650
5.0	5	22	30	0	18.5	0.0	700
6.0	3	19	24	1	13.6	4.0	325
7.0	3	12	13	2	20.0	13.3	319
9.0	2	16	17	3	11.1	15.0	350
11.0	1	11	14	0	8.3	0.0	308
13.0	1	21	19	1	4.5	5.0	350
15.0	4	17	18	2	19.0	10.0	350
17.0	1	14	14	1	6.7	6.7	304
19.0	4	16	19	1	20.0	5.0	350
20.0	0	20	20	2	0.0	9.1	300

⁽¹⁾ Wavelengths from 0.41 to 3 μm were generated by LEBRA-FEL and those from 7 to 20 μm were generated by KU-FEL.

⁽²⁾ The effects of the irradiation experiments are denoted by numbers of seeds counted and evaluated by lettuce seed developmental stages [5], and expressed in percentages calculated by following formulas: Inhibition (%) = $a/(a + b) \times 100$, where a is the number of seeds at St. 0-2 and b is the number of seeds at St. 3-4. Promotion (%) = $c/(c + d) \times 100$, where c is the number of seeds at St. 0-2 and d is the number of seeds at St. 3-4.

Finally, we would like to propose here that new photochemical techniques with tunable wavelengths (0.4–20 μm) produced by combined use of LEBRA-FEL and KU-FEL (and other FELs in the future) may offer a useful tool for investigating photo-triggered biological systems, including the nervous system, in living organisms.

ACKNOWLEDGMENT

We thank Prof. T. Morii (Institute of Advanced Energy, Kyoto Univ.) and his staff (Dr. E. Nakada and Dr. S. Nakano) for helpful assistance. This work was supported by the “Joint Usage/Research Program on Zero-Emission Energy Research”, Institute of Advanced Energy, Kyoto University (ZE25 and ZE26C-2).

REFERENCES

- [1] K. Hayakawa et al., “The LEBRA 125 MeV electron linac for FEL and PXR generation”, in *Proc. 27th Int. LINAC Conf.*, Lubeck, Germany, 2004, pp. 90-92.
- [2] H. Zen et al., “Present status of Kyoto University free electron laser”, in *Proc. 35th Int. FEL Conf.*, New York, USA, 2013, pp. 711-714.
- [3] L.H. Flint, E.D. McAlister, *Smithson. Misc. Collect.* 94, 1-11 (1935).
- [4] H.A. Borthwick et al., *Proc. Natl. Acad. Sci. USA* 38, 662-666 (1952).
- [5] F. Shishikura et al., “LEBRA free electron laser as a radiation source for photochemical reactions in living organisms”, in *Proc. 35th Int. FEL Conf.*, New York, USA, 2013, pp. 675-679.
- [6] H. Ikuma, K.V. Thimann, *Plant Physiol.* 39, 756-767 (1963).
- [7] K.M. Hartmann, A. Mollwo, *Naturwissenschaften* 87, 398-403 (2000).
- [8] R.J. Bula et al., *HortScience* 26, 203-205 (1991).
- [9] J.G.C. Small et al., *Planta* 144, 133-236 (1979).
- [10] F. Vatansever, M.R. Hamblin, *Photonics Lasers Med.* 1, 255-266 (2013).

NARROW LINEWIDTH, CHIRP-CONTROL AND RADIATION EXTRACTION OPTIMIZATION IN AN ELECTROSTATIC ACCELERATOR FEL OSCILLATOR

H. Marks*, A. Gover, H. Kleinman, J. Wolowolsky, Tel Aviv University, Israel
D. Borodin, M. Einat, M. Kanter, Y. Lasser, Yu. Lurie, Ariel University, Israel

Abstract

In recent years the electrostatic accelerator FEL based in Ariel has undergone many upgrades. By varying the accelerating potential the resonator allows lasing between 95-110 GHz. It is now possible to remotely control the output reflectivity of the resonator and thereby vary both the power built up in the resonator and that emitted. This has allowed fine control over the power for different user experiments. A voltage ramping device has been installed at the resonator/wiggler to correct drops in voltage which occur due to electrons striking the walls of the beam line. This has allowed stable pulses of just over 50 μ s with a chirp rate of ~ 80 kHz/ μ s.

INTRODUCTION

The Israeli Electrostatic Accelerator FEL (EA-FEL) is one of the few FEL oscillators besides the UCSB FEL [1] that can operate quasi-CW. The Dutch FOM operated along similar principles and at higher power but has since been dismantled [2]. It is most fitting for studying the physics of single mode laser oscillation and developing narrow line-width high power applications in the mm-wave/THz regime, it has in an earlier configuration displayed particularly narrow line-width for an FEL [3].

The EA-FEL is a straight-line Van-de-Graaff ion accelerator. It was converted into an energy-retrieving electron accelerator. The electron beam is injected from a 50 keV electron-gun into the accelerator from ground potential. The beam is accelerated up to the positively charged high-voltage (HV) terminal in the center of the pressurised gas tank. An FEL wiggler/resonator assembly is installed in the HV terminal. After passing through the wiggler in the terminal, the beam is decelerated and transported in a straight line up to the collector. The mm-wave radiation, coupled out of the FEL resonator in the terminal, is guided through an optical transmission line

The laser was upgraded and is now providing longer higher power pulses (up to 50 μ s) to a user room. A variable cavity radiation out-coupler was installed as the front mirror of the laser cavity. It is useful for realizing the concept of radiation power extraction maximization of an FEL oscillator [4]. A voltage ramp generator that was installed in the accelerator terminal made it possible to stabilize the voltage of the resonator/wiggler assembly during the laser pulse, and in this way to attain longer laser pulse operation. It also makes it possible to attain narrow laser line-width and controlled frequency chirp that may be used for spectroscopy.

METHOD

In order to improve the parameters of FEL operation beyond those reported [3] a number of steps were taken. The wiggler was removed from the system and errors in the magnetic field were corrected [5]. Next a new resonator was installed that operates using the Talbot effect to separate the electron beam from the radiation (see Fig. 1). Section 1 is a Talbot (interference) wave splitter composed of a straight rectangular waveguide 10.7×25 mm². It allows passage of the electrons whilst fully reflecting the split radiation pattern.

Section 2 is a waveguide with two corrugated walls 10.7×15 mm². The third section begins with a section of smooth walled waveguide identical to that in the first section. After 145 mm there is a transition from a rectangular waveguide to a parallel plate waveguide. In one dimension the radiation is guided, in the other free diffraction occurs. The electron beam leaves this section via a hole in an inclined parabolic mirror, whilst the radiation which is split either side of the hole is reflected upwards to a second off-axis mirror. The second off-axis mirror reflects the radiation to an outcoupling element whose reflection and transmission properties can be remotely controlled. The outcoupling element consists of 3 polarisers, the wires of the first and third of which are held vertical, perpendicular to the electric field of the radiation excited in the resonator, whilst the middle polariser is free to rotate.

The accelerator is based on the build-up of positive static charge within the tank, electrons which hit the walls of the beam line cause the accelerating voltage to drop. To correct for this a remotely controlled voltage ramp generator was developed for stabilizing the resonator/wiggler potential during the laser pulse and for controlling laser frequency chirp. The ramp generator is connected between the resonator/wiggler assembly and the high voltage terminal (that are isolated from each other). The ramp voltage generator can produce a voltage ramp of up to 25 kV during the electron beam pulse duration.

Table 1: EA-FEL Parameters

Beam Energy:	1.34-1.44 MeV
Wiggler Period:	44.4 mm
Number of Periods (N_w):	26
Radiation Frequency:	95-110 GHz
Resonator Internal Loss:	30%
Cathode Current:	0.5-3 A

*harry_s_marks@hotmail.com

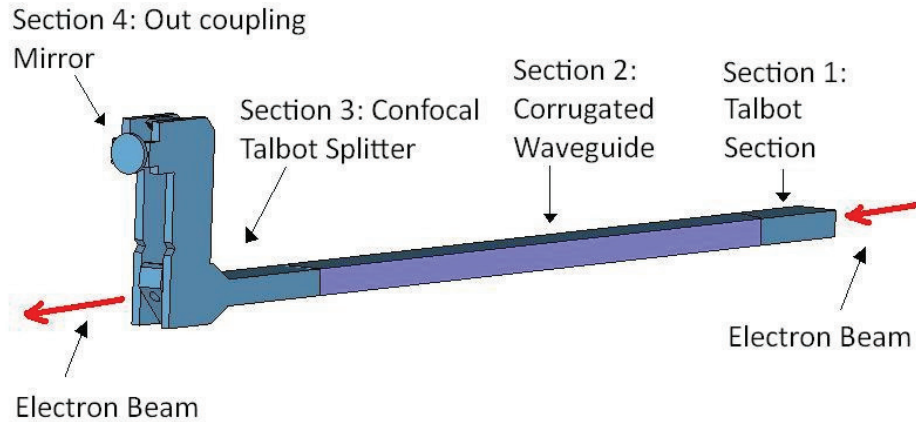


Figure 1: The mm-wave Talbot effect confocal resonator.

RESULTS

Changing the reflectivity of the outcoupling grids between pulses allows finding the maximum output power point for lasing (see Fig. 2). Power was measured in the user room (maximum 2 kW for a 0.93 A current) and extrapolated back to the resonator to compare with the simulation program FEL3D. Losses in the transmission line were measured to be $\sim 80\%$, this could be reduced to 30% fairly simply, but the work has not been prioritised. The pulse to pulse variation in power is due to the ever rippling voltage of the electrostatic accelerator.

Nw is the number of wiggler periods of which there are a total of 26, 20 of these encompass the corrugated waveguide. Due to the Talbot splitting we need to consider an effective Nw.

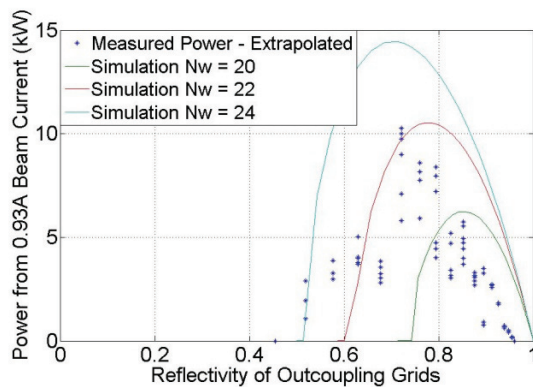


Figure 2: By changing the reflectivity of the outcoupling from the resonator it was possible to vary the power built up within and emitted from the resonator.

With imperfect transport and a consequent loss in the accelerating potential of ~ 0.5 kV/ μ s the longest pulse attainable was just over 30 μ s. By using the voltage ramping at 25 kV with a time constant of 3.34 μ s it was possible to attain pulses of just over 50 μ s. An example of such a long pulse measured at the end of the transmission line in the user room is shown in Fig. 3. The power reflectivity of the out-coupling grids was set to 0.87, the

Cathode current was 1.12 A. The total pulse energy in the user room was 39.5 mJ, which translates to 200 mJ at the resonator exit (~ 5 kW).

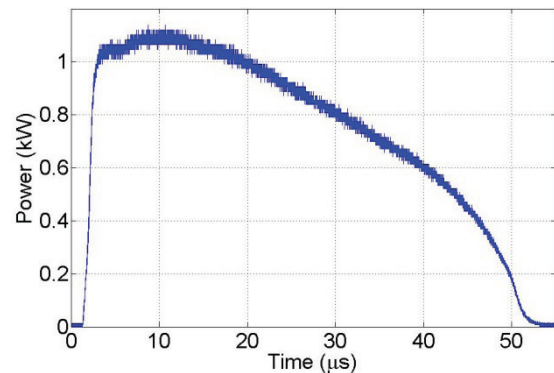


Figure 3: Sample long pulse obtained using the voltage ramping device installed within the accelerator.

To record the spectral lasing line of the FEL the laser output was mixed in the user room after attenuation with a local oscillator (LO) at a frequency close to the lasing frequency. The intermediate frequency (IF) signal out of the mixer was recorded, and the data was later processed using a Matlab spectrogram program. Single longitudinal mode operation of the FEL was verified over the course of many experiments. For the pulse shown in Fig. 3 single mode operation begins after 3.5 μ s. The spectrogram of this pulse after 3.5 μ s is shown in Fig. 4. The spectrogram of the ~ 50 μ s pulse was taken with time windows of 2.5 μ s whilst the oscilloscope was set to 500 MHz. The general trend in Fig. 4 is for the IF to increase in frequency, however, early in the pulse due to the voltage ramping the IF signal decreases before rising again. Due to the falling accelerating potential the IF frequency chirps over the 50 μ s from 10 MHz to ~ 14 MHz, a total chirp rate of 80 kHz/ μ s. In this case it is clear the LO was set above the lasing frequency, hence the increasing IF as the lasing frequency drops.

The rate of change of the frequency grows with time. In the first 10 μ s the linewidth is particularly narrow, $\Delta f/f =$

1.2×10^{-6} , which is close to the Fourier Transform limit. Were the chirp to be eliminated the entire signal would be Fourier Transform limited.

improving the diagnostic systems. By doing so it should be possible to increase lasing pulse times to be of the order of milliseconds.

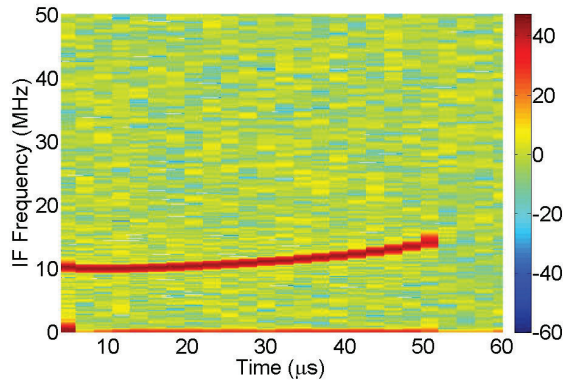


Figure 4: Spectrogram of the IF frequency of the sample pulse shown in Fig. 3.

CONCLUSION

An important milestone in the EA-FEL project has been reached demonstrating the great versatility of the system. Basic laser-oscillator physics effects can be studied in this system in the context of FEL oscillators. The record narrow linewidth achieved and the controlled chirp effect are promising features for fine single-pulse spectroscopic applications. All the new technological modifications were successfully operated. The main challenge left to overcome is to reduce beam leakage by

REFERENCES

- [1] L. R. Elias et al, "The UCSB electrostatic accelerator free electron laser: First operation", Nuclear Instruments and Methods in Physics Research Section A, Vol. 237, Issues 1–2, 15 June 1985, pp. 203–206.
- [2] A. G. A. Verhoeven et al, "First microwave generation in the FOM free-electron maser", Plasma Phys. Control. Fusion, Vol. 40, Issue 8A, August 1998, pp 139-156.
- [3] Y. Socol et al, "Physical Review ST Accelerators and Beams", Phys. Rev. ST Accel. Beams 8, 080701 August 2005, pp1-9.
- [4] A. Abramovich et al, "Efficiency Enhancement of a Pre-Bunched Free-Electron Maser Oscillator by Locking to a Single Eigen Frequency of the Resonator", Nuclear Instruments and Methods in Physics Research Section A, Vol. 429, 1999, pp 107-110.
- [5] H. S. Marks et al, "Wiggler improvement based on single axis magnetic measurement, synthesized 3-D field simulation of trajectories and sorting of lateral focusing magnets", Nuclear Instruments and Methods in Physics Research Section A, Vol. 660, (2011) pp. 15–21.

FACILITY FOR COHERENT THZ AND FIR RADIATION

A. Meseck, Helmholtz-Zentrum, Berlin, Germany
V. Ziemann, Uppsala University, Uppsala, Sweden

Abstract

Linac based THz sources are increasingly becoming the method of choice for a variety of research fields, justifying the increasing demand for high repetition rate THz FEL facilities world wide. In particular, pump and probe experiments with THz and FIR radiation are of major interest for the user community. In this paper, we propose a facility which accommodates an SRF-linac driven cw THz-FEL in combination with an FIR undulator which utilizes the micro-bunched beam. The layout permits almost perfect synchronization between pump and probe pulse as well as nearly independently tunable THz and FIR radiation.

INTRODUCTION

In recent years several accelerator based facilities for THz radiation started to operate. In order to extend the capability of these facilities toward pump-probe experiments a second radiation source synchronized on the femto-second level to the THz source is desirable. The second source could be an external conventional laser system. This option, however, requires complex synchronization of the accelerator based source and the laser. In this report we discuss a way to generate two frequencies from the same electron-beam, such that the synchronization is inherently given.

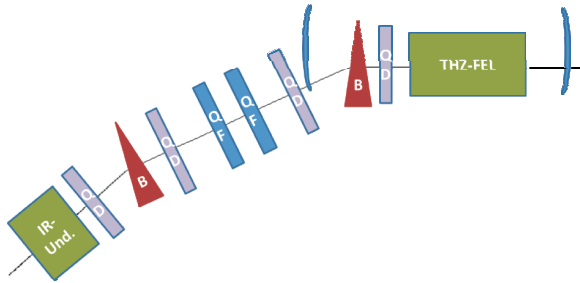


Figure 1: The geometry.

We base our proposal on a 10 MeV electron beam with a typical charge on the order of 300 pC that drives a conventional FEL in oscillator configuration with a frequency of 1 THz. The micro-bunching introduced in the oscillator is converted in a short beam line to a comb-like bunch with a spiked longitudinal distribution capable of generating high harmonics in a second undulator. In the remainder of the report we discuss first the conceptual design, followed by a numerical simulations and concluding remarks.

CONCEPTUAL

Initially we intended to consider an electron beam that had acquired a longitudinal correlation in a buncher cavity, bunch

it in an oscillator with a transverse-gradient undulator and then compress it in order to up-convert the micro-bunching to higher frequencies. This proved to be impossible, because the typical momentum spreads generated in THz oscillator destroyed the delicate structures in phase-space. In the process, however, we developed methods to analyze the propagation of distribution functions that proved useful in the analysis of even the simpler setup, we eventually had to settle for.

We started by considering a distribution in longitudinal phase space z_b, δ_b after the initial buncher given by

$$\Psi_b(z_b, \delta_b) = \frac{1}{2\pi\sigma_z\sigma_\delta} \times \exp \left[-\frac{1}{2} \left\{ \left(\frac{1}{\sigma_z^2} + \frac{h^2}{\sigma_\delta^2} \right) z_b^2 - 2 \frac{h}{\sigma_\delta^2} z_b \delta_b + \frac{\delta_b^2}{\sigma_\delta^2} \right\} \right] \quad (1)$$

where σ_z is the initial bunch length and σ_δ the initial relative momentum spread. The parameter h is the conventional chirp parameter $(dE/dz)/E_0$ of a buncher system, where dE/dz denotes the energy gain per unit length and E_0 the average energy of the beam, 10 MeV in our case.

After modulating the energy in the THz oscillator $\delta_u = \delta_b + a \cos(k_t z_b)$ with amplitude a and wavenumber k_t corresponding to 1 THz we get the distribution function

$$\Psi_u(z_u, \delta_u) = \int d\delta_b \int dz_b \Psi_b(z_b, \delta_b) \delta(z_u - z_b) \delta(\delta_u - \delta_b - a \cos(k_t z_u)) \quad (2)$$

and after ensuring that the Jacobian is unity and doing the integrals we obtain $\Psi_u(z_u, \delta_u)$. We can apply the same method for the propagation through the beam line with a given R_{56} and finally get the distribution function immediately upstream of the second undulator $\Psi_f(z_f, \delta_f)$ as

$$\Psi_f(z_f, \delta_f) = \frac{1}{2\pi\sigma_z\sigma_\delta} \exp \left[-\frac{1}{2} \left\{ \left(\frac{1}{\sigma_z^2} + \frac{h^2}{\sigma_\delta^2} \right) [z_f - R_{56}\delta_f]^2 - 2 \frac{h}{\sigma_\delta^2} [z_f - R_{56}\delta_f] (\delta_f - a \cos(k_t [z_f - R_{56}\delta_f])) + \frac{(\delta_f - a \cos(k_t [z_f - R_{56}\delta_f]))^2}{\sigma_\delta^2} \right\} \right] \quad (3)$$

This expression is easily coded in Matlab to produce contour plots of phase space and projections onto the longitudinal axis. The algorithm is extremely rapid. Each run only takes a few second and allows convenient parameter variations.

Playing with the parameters for chirp h , bunching amplitude a and R_{56} of the beam line resulted in the comb-like

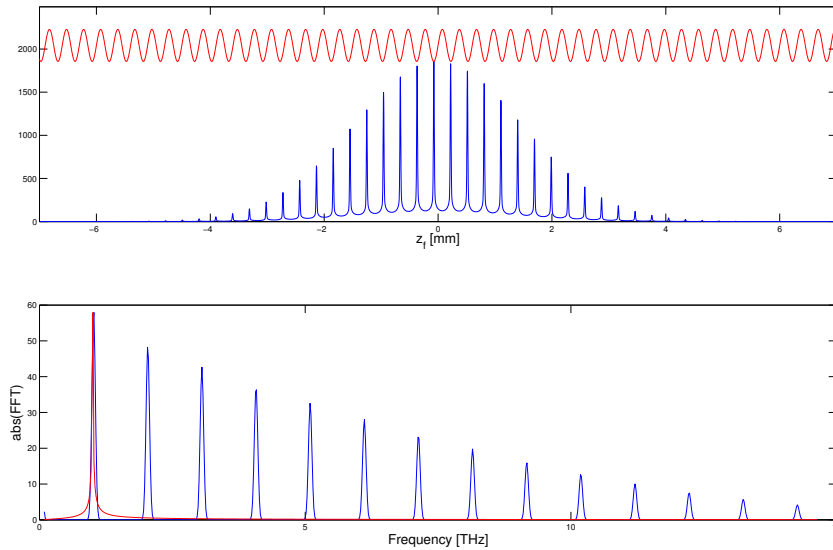


Figure 2: The final longitudinal distribution for a bunching system that is optimally set up according to the parameters given in the main text.

beam shown in the upper graph in Fig. 2. There we show a bunch with initial bunch length $\sigma_z = 1.5$ mm, momentum spread $\sigma_\delta = 10^{-3}$ propagated through a system with $h = 2.7/\text{m}$, $a = 0.01$, $R_{56} = -4.8$ mm. Note that we also show a 1 THz oscillation in red for comparison. The bottom graph shows the Fourier-transform of the comb-like bunch with harmonics extending way above the tenth harmonics. We need to point out that the modulation amplitude is rather large compared to the incoherent momentum spread.

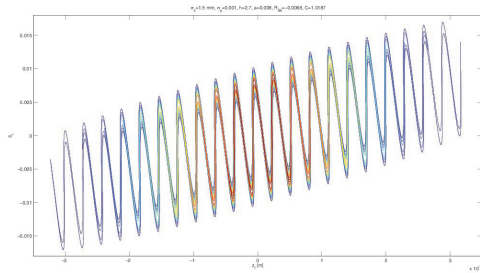


Figure 3: A contour plot of the longitudinal distribution corresponding to Fig. 2. Note that the left slopes of the distribution is rather steep resulting in high harmonics.

The optimum set of parameters to produce the most pronounced comb-like bunch can be understood intuitively by requiring that the modulation in phase space, as shown in Fig. 3 is distorted in such a way in the beam line that one side of the sine-like modulation becomes vertical. A simple linearized model leads to the relation $0 = 1 + R_{56}(h + k_t a)$ which resembles the requirement for maximum compression, but here the chirp is replaced by the chirp h and the slope of the modulation in the FEL $k_t a$. It turns out that with our

chosen parameters $k_t a$ is much larger than any reasonable h , such that an initial chirp will only affect the results in a minor way.

NUMERICAL

We tested the feasibility of the scheme with $h = 0$ by simulating the THz oscillator with an optical cavity length of 8.042 m, an undulator with 30 periods of 10 cm each and $K_{rms} = 1.14$ with FELO [1]. For the simulations we assumed the same beam parameters as in the previous section and equal horizontal and vertical normalized emittances of 5 mm mrad.

We found that in saturation the output power reached about 13 MW as shown in Fig. 4 and the modulation amplitude reached 2.6 % after an initial transient of about 300 pulses as

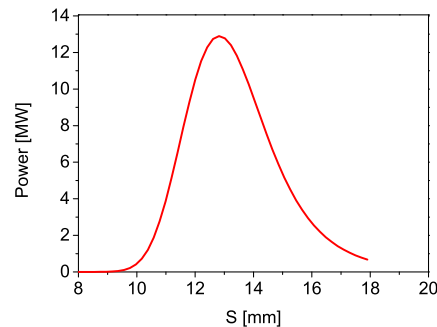


Figure 4: The radiation profile of the THz-FEL after 300 passes is shown

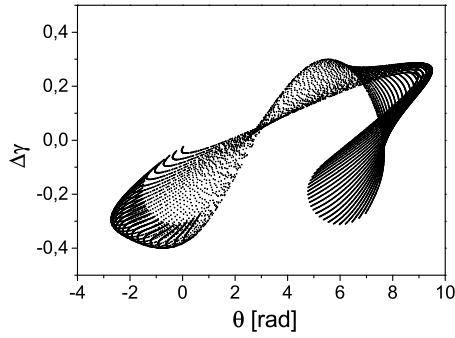


Figure 5: The energy deviation of electrons is plotted against electron phases. Phase space plots for each slice are overlaid on top of each other. There are 30 slices of 300 μm each.

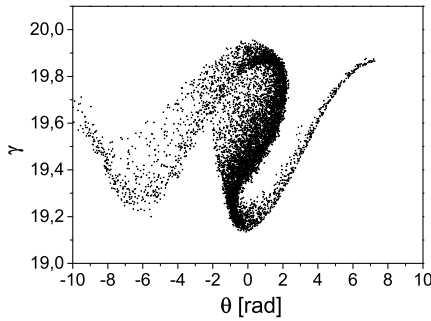


Figure 6: The electron energies as a function of electron phases is plotted for the central slice.

shown in Fig. 5. The gain settles to 15 % in the steady state. Since FELO is a one-dimensional code we verified the three-dimensional behavior of the system and in particular the micro-bunching of the electron beam using Genesis [2] while utilizing the THz photon intensity obtained in the previous FELO runs as well as the same electron beam parameters.

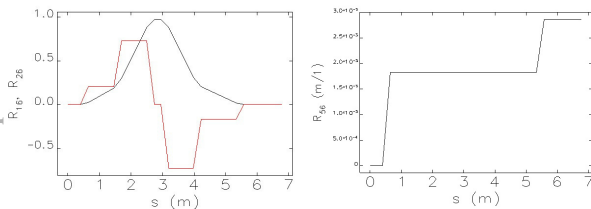


Figure 7: The dispersion and R_{56} for the beam line between the undulators.

Since the optimized THz-FEL saturates, the maximum bunching for the fundamental wavelength is already achieved at the exit of the THz-FEL. Figure 6 shows the longitudinal phase space of the central slice at the undulator exit. The imprinted energy modulation as well as the nonlinear shape of it, typical for saturation behavior, are clearly visible. Generally, in an FEL the maximum bunching of higher harmonics

is reached before the fundamental bunching saturates. Thus, the harmonics for which we are aiming in this study are somewhat over-bunched. Therefore it is crucial to adjust the bunching, following the discussion in the previous section, before the entrance of the second undulator which is tuned to the sixth harmonics. For this, we designed a simple beam line consisting of two identical weak dipole magnets and six small quadrupole magnets. The dipoles bend about 12 degree each in the same direction, while the quadrupoles take care of beam size and dispersion compensation. The R_{16} , R_{26} , and R_{56} of the beam line are depicted in Fig. 7. We expect a negligible incoherent synchrotron radiation from this beam line, however, there still might be a small contribution of coherent synchrotron radiation as the current profile is not smooth as discussed below.

For the simulation we modeled an electron distribution suitable for the code elegant [3] corresponding to the distribution obtained from GENESIS and propagated it through the beam line to the entrance of the second undulator. The longitudinal current profile at this position is shown in Fig. 8, while its corresponding spectrum is depicted in Fig. 9. The amount of micro-bunching which can be expected after the

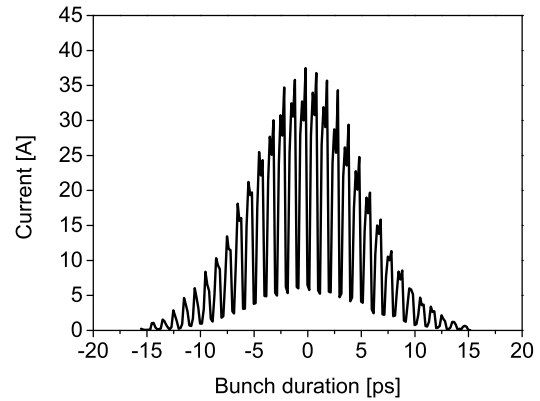


Figure 8: The longitudinal current distribution propagated to the entrance of the second undulator.

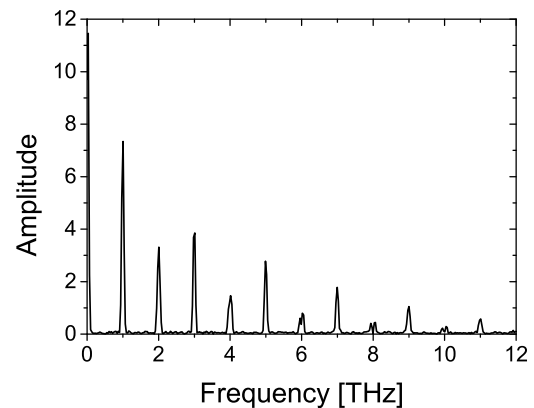


Figure 9: The spectrum corresponding to Fig. 8 obtained by Fourier-transformation.

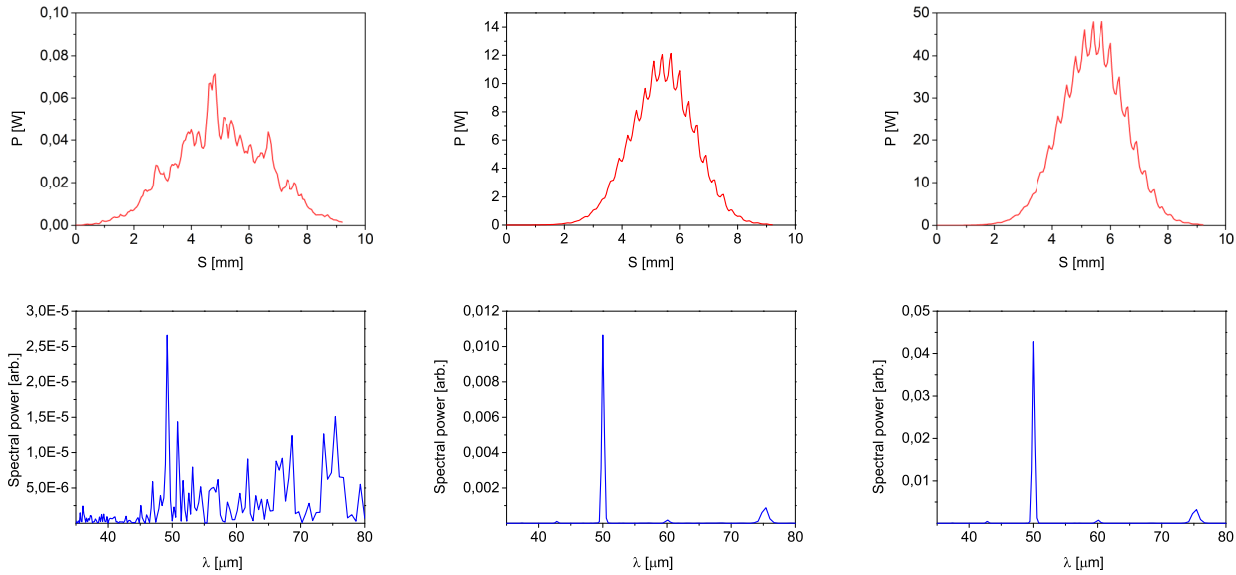


Figure 10: The output power profile (top row) and spectrum (bottom) from the second undulator that is driven by the current distribution from Fig. 8 with zero (left), 0.5 % (center), and 1 % (right) micro-bunching.

passage through the beam line depends on the effect of coherent synchrotron radiation and space charge forces. These effects need to be studied in full 3D and are subject to future studies. From our simple tracking simulations, we expect a maximum bunching of about 2 %. Assuming that the bunching will smear out, due the effects mentioned above, we perform simulations for initial micro-bunching of 0.5 % and 1 %. This longitudinal electron beam distribution is used as input to GENESIS simulations of the second undulator with 20 periods of 2.4 cm each and $K_{rms} = 0.76$. This corresponds to a resonant frequency of 6 THz or equivalently $\lambda = 50 \mu\text{m}$. We find that the initial bunching is crucial. In spite of the current profile with higher spikes, significant radiation output can only be achieved with an initial micro-bunching. Figure 10 demonstrates the effect of micro-bunching clearly. Dependent on the initial micro-bunching we obtain radiation with a peak power of 12 W to 45 W. Even if we do not expect to initiate the FEL process, we think that using GENESIS is justified as we study coherent emission of micro-bunched beam.

CONCLUSIONS

We discussed a scheme where the micro-bunching generated in a THz oscillator is preserved and optimized in a simple beam line to provide a comb-like longitudinal current distribution. This is used in a second undulator tuned to harmonics to generate radiation at the harmonic that is inherently synchronized with the THz radiation from the first undulator. The expected FIR peak output power of 12 W to 45 W is comparable to IR peak output powers from storage rings operating with similar bunch charges but at considerably higher energies.

REFERENCES

- [1] B. McNeill et al., *FEL0: A one-dimensional time-dependent FEL oscillator code*, Proceedings of the 28th FEL conference in Berlin, Germany, p.59, 2006.
- [2] S. Reiche, *GENESIS 1.3: A fully 3-D time dependent FEL simulation code*, Nucl.Instrum.Meth. A429 (1999) 243.
- [3] M. Borland, *elegant: A Flexible SDDS-Compliant Code for Accelerator Simulation*, Advanced Photon Source LS-287, 2000.

CAVITY LENGTH CHANGE VS. MIRROR STEERING IN A RING CONFOCAL RESONATOR*

S. Benson[#], Jefferson Lab, Newport News, VA 23606, USA

Abstract

In principle, a ring confocal resonator allows for the use of a short Rayleigh length without the extreme sensitivity to mirror steering typical in a near-concentric resonator [1]. One possible weakness of such a resonator is that the cavity length is no longer independent of the mirror steering. This is one of the strengths of a linear resonator. In this presentation, it is shown that, in a simple 2-dimensional corner cube type ring confocal resonator, the cavity length is, in fact, not dependent on the mirror steering to first order in the mirror angles. Thus the ring-confocal resonator might be a very easy-to-operate and stable resonator for short Rayleigh range operation in FEL oscillators.

INTRODUCTION

It is well known that the optical mode in a confocal resonator has much lower sensitivity to mirror steering than a near-concentric design. Since the mode size in the return path of the confocal resonator is rather large it is more practical to make the confocal resonator for an FEL in a ring configuration so that the mode does not have to pass through a narrow wiggler gap on the return leg. This may lead to a couple of problems. The first is astigmatism, which may be addressed using cylindrical or toroidal optics. The second is a potential coupling of mirror steering to cavity length changes. Decoupling of cavity length and mirror steering, a given in linear resonators, makes laser optimization very straightforward. A dependence of cavity length on mirror steering would greatly complicate operation of the FEL. This note will derive the change in cavity length as each mirror is steered in a ring confocal resonator. As will be seen, the properties of the ring resonator tend to make the cavity length extremely insensitive to mirror steering.

DEFINITION OF VARIABLES

Let us first describe the ring confocal resonator and define our variables. The resonator is shown in Fig. 1. The two flat mirrors that deflect the beam away from the electron beam axis are called the flat deflecting optics or FDOs. The curved mirrors that bring the beam back towards the wiggler are called the fold mirrors or FMs. The angle that the FDOs deflect the beam (twice the angle of incidence on the FMs) will be referred to as θ . The

transverse separation between the forward and reverse legs of the resonator will be represented by B . The distance between the FDO and the FM is equal to $B/\sin\theta=C$. The distance from the cavity center (assumed also to be the wiggler center) to the FDO is A . The FMs are concave mirrors that collimate the beam that emerges from the wiggler. The radius of curvature for a ring confocal resonator should be $R_{\text{eff}} = 2(A+C)$. The actual radius of curvature will be longer by $\sec(\theta/2)$. It is useful to know the effective radius of curvature as a function of the round trip distance in the resonator. Since the distance in the backleg between the FDO and the FM is $C\cos(\theta)$, the round trip cavity length $L_{\text{rt}}=2(2A+C(1+\cos(\theta)))$. Using this we have $R_{\text{eff}} = L_{\text{rt}}/2 + C(1-\cos(\theta))$.

NORMAL VIBRATION MODES

To calculate the change in cavity length for a given mirror angle tilt it is useful to define normal modes of the resonator that are linear combinations of all four mirrors. Since the angular shifts are all linear one can represent a change in the angle of any one mirror as a linear combination of these four modes. Since there are four mirrors, it is possible to define four normal modes related to the four angles via a non-singular matrix to be derived below. There is a default beam path that goes through the center of the wiggler, hits the centers of each mirror, and returns a distance B away from the wiggler in the backleg. The default beam path is parallel in the forward and backwards directions in the resonator. Define the following four modes of the beam path with respect to the default beam path. Assume that the mirrors rotate about the point that the default beam path intersects the mirror surface:

- Mode 1 – In this mode the light paths are still parallel in the forward and backward directions but they move either towards the center of the ring or away from the center.
- Mode 2 – In this mode the light path is parallel in the forward and backward directions but the two paths both move in the same direction with respect to the default beam path.
- Mode 3 – In this mode the light path goes through the center of the wiggler and is a distance B away in the backleg at that point. The path goes through the wiggler at an angle and returns with the opposite angle so the mode looks wedged from above.
- Mode 4 – In this mode the light path again goes through the center of the wiggler at an angle but the angle in the backleg is the same as in the forward leg. The mode as a whole is tilted.

*Authored by Jefferson Science Associates, LLC under U.S. DOE Contract No. DE-AC05-84-ER40150, the Office of Naval Research, and the Joint Technology Office. The U.S. Government retains a non-exclusive, paid-up, irrevocable, world-wide license to publish or reproduce this manuscript for U.S. Government purposes
#felman@jlab.org

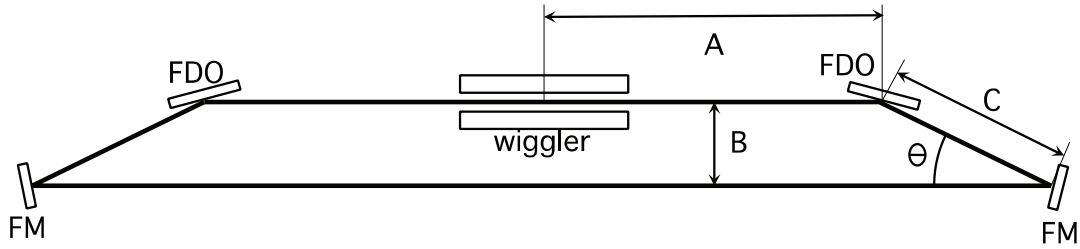


Figure 1: Layout of the ring confocal resonator with the leg lengths and mirror labels defined.

Any mode can be made from these four. It is possible to define a matrix that relates the modes to the individual mirror angles. This matrix can then be inverted to give the individual mode changes for a given tilt in one mirror.

In this note, the discussion is limited to one plane. Any changes in cavity length due to vertical steering should be second order in the angle (which is a very small quantity) and so should be negligible.

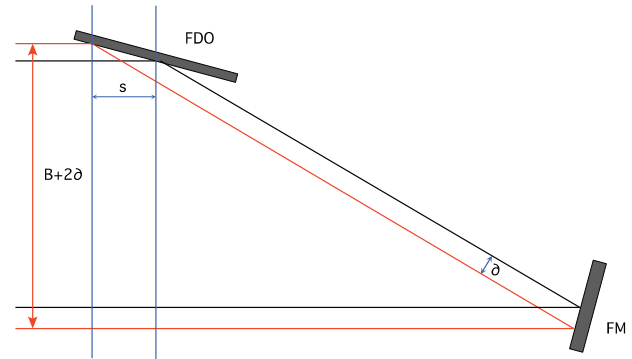
To derive the normal modes in terms of the mirror angles it is useful to review the nature of a two-dimensional corner cube. The beam will exit parallel to the input beam unless an angular error between the two mirrors is introduced. Movement of the beam to one side on the entrance automatically leads to movement in the same direction on the output (i.e. beam left motion stays beam left unlike a mirror where beam left turns into beam right). The curvature in the FM does lead to behavior different from a corner cube. Changes in position on the FM lead to a relative change in the angular orientation between the mirrors. This has the effect of stabilizing the mode so that it tends to move towards the position where the input and output angles are the same.

Mode 1

In this mode one only rotates the two FMs. If both of these mirrors turn the opposite direction then the separation between the forward and backward beams increases and decreases but the beam path is parallel to the default path. Devine the transverse shift as δ , where a positive δ is away from the ring center. To first order, the FDO and the FM act as a two-dimensional corner cube. Thus, the exit beam from the two mirrors is also shifted away from the center by the same amount. Since the beam has moved on the FM however, it is necessary to steer the FM slightly to maintain the exit beam parallel to the input beam to correct for the angle caused by the mirror curvature. The angle necessary to correct the angle is δ/R_{eff} . The geometry of this is shown in Fig. 2 where all offsets have been greatly exaggerated. In fact, the mirror steering angles are in μrad or less and the bend angles are in rad. The mode movements are in hundreds of microns while the beam separation is on the order of a meter.

To see how sensitive this is, let us consider an example. Assume a ring confocal resonator with an angle $\theta = 30^\circ$ and a distance $B = 68.6$ cm. Assume that the radius of curvature in the plane of the ring is given by the formula above and that $L_r = 64.084$ m. The effective ROC should therefore be 32.23 meters and the actual ROC must be

33.36 m. In this case a one microradian tilt in both FMs in the opposite directions will move the mode by $32.2 \mu\text{m}$ both in the wiggler and in the backleg (both away from the ring center). The $1/e^2$ waist size for a Rayleigh range of 70 cm and a wavelength of $1.06 \mu\text{m}$ is $486 \mu\text{m}$ so this is quite a small shift compared to the mode size.


 Figure 2: Geometry for Mode 1 shift. Both parallel rays move out from the center by a distance δ . The black curve is the default path and the red is the position for mode 1.

Mode 2

This mode requires all four mirrors to move. The mode is a bit unnatural since one is fighting the tendency of the mode to move the same direction on the output as at the input. One wants the FDO and the FM to both rotate approximately the same amount but the FM must rotate a bit less to account for its ROC. For a common axis shift of distance δ , the FDO must shift by an angle $\phi_{\text{FDO}} = \delta/C$. This actually moves the return leg up by 2δ so that the beam moves in the opposite direction instead of the same direction. It also changes the angle of the beam by $2\phi_{\text{FDO}}$ and this must be compensated for by also rotating the FM by about the same amount. Since we have moved up on the FM however, there is an extra angle provided by the curvature so the FM does not have to move quite so far. The net result is:

$$\phi_{\text{FM}} = \frac{\delta}{C} - \frac{\delta}{R_{\text{eff}}} = \frac{\delta}{C} \left(1 - \frac{C}{R_{\text{eff}}} \right) = \phi_{\text{FDO}} \left(1 - \frac{C}{R_{\text{eff}}} \right)$$

The final expression in parentheses is equal to 0.957 for the numerical example above. Thus the two mirrors move almost the same amount. The mirrors at the opposite end of the cavity rotate in the opposite direction, with the FM again rotating a bit less than the FDO. The geometry for

this configuration is shown in Fig. 3. Note that for the numerical example above, the distance in microns is close to the tilt angle of the mirrors in micro-radians. The mode moves by $1.37 \mu\text{m}$ for $1 \mu\text{rad}$ of mirror tilt. This is 23.5 times less sensitive than the movement in Mode 1.

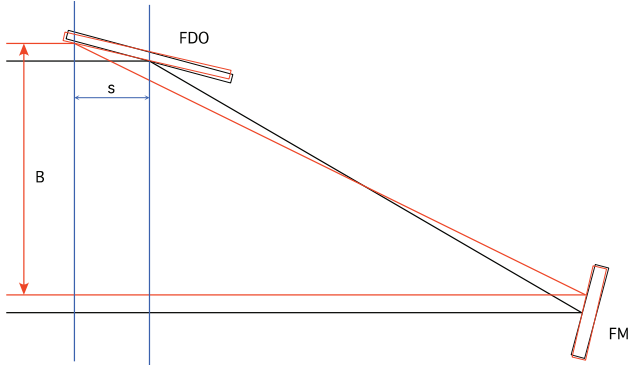


Figure 3: Geometry of Mode 2. Here both mirror rotate by a positive angle. The FM rotates slightly less than the FDO to account for the radius of curvature. The angles shown are exaggerated by about a factor of 1000 to show that they occur. The black path is the default position and the red path is the rotated position.

Mode 3

In this mode we again only need rotate the FMs. If they are rotated in the same direction we find that the separation between the forward and back branches is smaller on the upstream end than at the downstream end for a negative (clockwise) angle. The geometry looks the same as Fig. 2 except that the input and return ray for mode 3 are slightly converging so that they intersect with the default rays at the position of the center of the wiggler. If a ray leaves the wiggler center at an angle ψ with respect to the default ray, it will be offset by a distance $\psi R_{\text{eff}}/2$ at the FM. Since the purpose of this mirror is to collimate the beam, the exit ray will be parallel to the default ray if the FM is not rotated. To get the return ray to intersect the default ray at the position of the wiggler center one must rotate the FM by an angle:

$$\phi_{\text{FM}} = \frac{\psi R_{\text{eff}}}{4(A + C \cos \theta)} = \frac{\psi(A + C)}{2(A + C \cos \theta)}$$

So to create a mode with rays at an angle ψ_{Mode3} with respect to the default ray, one must rotate the FMs by a little more than half the mode angle

$$\phi_{\text{FM}} = \psi_{\text{Mode3}} \frac{A + C}{2(A + C \cos \theta)}$$

Remember that in this case the two FMs rotate in the same sense, i.e. both positive or both negative angles. For the numerical example above the fraction in this equation is 0.506 so the wedge angle is essentially twice the mirror rotation.

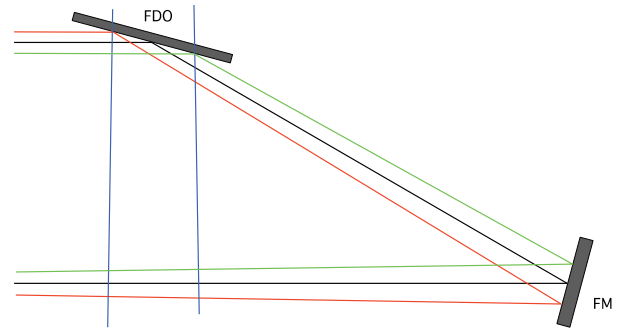


Figure 4: Geometry of Mode 3. The green rays are the upstream rays mirrored onto the downstream end. The red rays are the downstream rays. The blue lines are perpendicular to the return leg rays

Mode 4

Finally in Mode 4 all four mirrors rotate the same direction but the FMs rotate slightly less than the FDOs. This looks just like Fig. 3 except that the mode 4 rays are at a slight angle with respect to the default rays and they are in opposite directions on the upstream and downstream mirrors. The analysis is the same as for Mode 2 except that the quantity δ is equal to $\psi(A + C \cos \theta)$ where ψ is the angle of the mode with respect to the default mode. The ratio between the mode rotation ψ and the mirror tilt ϕ_{FDO} is found from

$$\psi = \frac{C \phi_{\text{FDO}}}{A + C \cos \theta}$$

For the parameters of the resonator detailed above, the ratio is about 12 to 1, so you have to tilt all the mirrors by $12 \mu\text{rad}$ to get $1 \mu\text{rad}$ of mode tilt.

CHANGE IN CAVITY LENGTH

Now that we have defined the modes let us derive the change in the cavity length for each mode compared to the default rays. The blue vertical lines in Fig. 2 show the intersections between a vertical line and the point where the rays hit the FDO. The distance between the left blue line and its corresponding line on the other end of the resonator is obviously the same for the default rays and the Mode 1 rays. Note that, by construction, the red lines are parallel to the black lines and therefore, all the angles of incidence and angles of reflection are the same. Any change in the cavity length would be due to a difference in the path length from the left blue line back to the left blue line. The distance along the red path is simply

$$L_{\text{Mode1}} = (B + 2\delta)(\csc \theta + \cot \theta)$$

The distance along the black path is the same but without the 2δ term and the extra distance $2s$ where $s = \delta \cot(\theta/2)$. The path difference is then:

$$L_{\text{Mode1}} - L_{\text{default}} = 2\delta \left[\csc \theta + \cot \theta - \cot \left(\frac{\theta}{2} \right) \right]$$

It can be shown that the expression in brackets is identically zero via trigonometric identities. Mode 1 therefore does not change the cavity length with respect to the default path.

Mode 2 is more complicated due to the fact that the angles are now not the same. The opening angle for the Mode 2 path in Fig. 3 (red lines) is now $\theta_{M2} \equiv \theta - 2\phi_{FDO}$. The distance along the path for Mode 2 is then:

$$L_{Mode2} = B(\csc\theta_{M2} + \cot\theta_{M2})$$

The path for the default ray from the left blue line back to the left blue line is

$$L_{default} = 2\delta \cot\left(\frac{\theta_{M2}}{2}\right) + B(\csc\theta + \cot\theta)$$

It is useful to use the relations (true for small η) $\csc(\theta - \eta) \cong \csc\theta + \eta \csc\theta \cot\theta$ and $\cot(\theta - \eta) \cong \cot\theta + \eta(\csc\theta)^2$.

The change in path length is then

$$L_{Mode2} - L_{default} = 2B\phi_{FDO} \left[\csc\theta \cot\theta + (\csc\theta)^2 - \csc\theta \cot\left(\frac{\theta}{2}\right) \right]$$

where we have used the expression $C=B \csc(\theta)$. We now have:

$$L_{Mode2} - L_{default} = 2C\phi_{FDO} \left[\cot\theta + \csc\theta - \cot\left(\frac{\theta}{2}\right) \right]$$

which is again zero. So the path length change for mode 2 is also zero to first order in the angular offsets.

For Mode 3 we can use the anti-symmetric nature of the mode to argue that any change in the mode orbit length in one half of the resonator is cancelled out in the other half. In Fig. 4 we show the geometry for Mode 3 with the upstream end reflected onto the downstream end. The upstream end is represented by the green rays and the downstream end is represented by the red rays.

One can see that each change from the default rays is mirrored in the opposite end. When the calculation is done carefully one finds, in fact, that the path difference from the default rays is $-B\psi_{Mode3}$ on the downstream end and $B\psi_{Mode3}$ on the upstream end to first order in ψ_{Mode3} so the net change in path is zero for Mode 3.

The same asymmetry argument can be used for Mode 4 to state that, since the path length change for Mode 2 is zero, the path length change for Mode 4 must also be zero.

Since any mode in the resonator can be derived from a linear combination of these four modes and since each of the modes has no change in the cavity length one comes to the startling conclusion that the ring confocal resonator

round trip path length is independent of the mirror steering to first order in the mirror tilt angles.

RELATION BETWEEN INDIVIDUAL MIRROR STEERING AND MODE SHIFTS

It is useful to derive the relation between the mode changes, which may involve a change in all four mirrors to the mode changes when only one mirror is shifted. Let us first number the mirrors as 1 through 4 with the upstream FDO being 1 and the upstream FM as mirror 4. Let us also define the quantities $G=(A+C\cos\theta)/(A+C)$, $H=(A+C)$, $F=(1-C/R_{eff})$ and $J=C/(A+\cos\theta)$. As noted above F and G are usually very close to but slightly less than unity. The quantity $2H$ is the same as the effective radius of curvature of the FMs and J is usually small compared to one. We can represent the modes by the following steering operator:

$$S = \begin{pmatrix} FH & -FH & H & -H \\ -C/4 & C/4 & 0 & 0 \\ -FG & -FG & G & G \\ J/4 & J/4 & 0 & 0 \end{pmatrix}$$

When the angle vector $(\theta_1, \theta_2, \theta_3, \theta_4)$ is multiplied by this matrix it will give a set of mode amplitudes. Modes 1 and 2 are defined by the distances that the axes move while Modes 3 and 4 are defined by the angles that the rays tilt. One can also invert this matrix to get the angles for a given combination of modes:

$$S^{-1} = \begin{pmatrix} 0 & -2/C & 0 & 2/J \\ 0 & 2/C & 0 & 2/J \\ 1/2H & 2F/C & 1/2G & 2F/J \\ -1/2H & -2F/C & 1/2G & 2F/J \end{pmatrix}$$

When this is multiplied by a vector of the mode amplitudes (M_1, M_2, M_3, M_4) we get the angle vector $(\theta_1, \theta_2, \theta_3, \theta_4)$.

It is worth noting some features of this resonator.

1. Modes 2 and 4 are suppressed due to the nature of the end mirrors as corner cubes. In fact the fold mirrors do not change modes 2 and 4 at all.
2. The resonator mode position in the wiggler (via mode 1) is fairly sensitive to the tilt of any of the 4 mirrors. For the example resonator, the beam moves 161 μm in the wiggler for a 10 μrad shift in either of the fold mirrors and 150 μm for a 10 μrad shift in either FDO.
3. The mode is extremely stable in angle. To get 100 μrad of mode tilt one needs 2.2 mrad of tilt in mode 4 and 50 μrad in mode 3.

CONCLUSION

The conclusion is a bit counter-intuitive but is consistent with the use of corner cubes in interferometers, where path length changes are critical. Since each of the

modes does not change the cavity length (to first order in the mirror tilts), and since any mode may be produced by a linear combination of the four modes, then the resonator mode is independent of the mirror tilts. The counter-intuitive nature comes from the nature of a corner cube. When one turns a corner cube, the beam comes back exactly along the original angle independent of the angle of the cube. The route through the cube also changes but in such a way that the length change in one leg is exactly compensated by the other. The net change is then exactly zero.

ACKNOWLEDGMENT

Michelle Shinn and Joe Gubeli were a valuable sounding board for this idea and checked the calculations.

Thanks also to Gwyn Williams for pointing out the use of corner cubes in interferometers. This work was supported by the Joint Technology Office, the Commonwealth of Virginia, and the Office of Naval Research.

REFERENCES

- [1] Stephen Benson, George Neil, Michelle Shinn, “Lasing with a Near-Confocal cavity in a high power FEL” in *Laser and Beam Control Technologies*, Santanu Basu, James Riker, Editors, Proceedings of SPIE Vol. 4632 (2002).

NUMERICAL CALCULATION OF DIFFRACTION LOSS FOR CHARACTERISATION OF A PARTIAL WAVEGUIDE FEL RESONATOR*

Q. Fu[#], K. Xiong, P. Tan, B. Qin, Y. Q. Xiong

State Key Laboratory of Advanced Electromagnetic Engineering and Technology(AEET)

School of Electrical and Electronic Engineering

Huazhong University of Science and Technology (HUST), Wuhan 430074, China

Abstract

Waveguide is widely used in long wavelength Free-Electron Lasers to reduce diffraction losses. In this paper the amplitude and phase transverse distribution of light emission produced in a partial-waveguide FEL resonator is calculated by Fresnel principle. To acquire high power out-coupled and optimize resonator structure of HUST THz-FEL, the characterisation of reflecting mirror is discussed to reduce diffraction loss.

OPTICAL MODES OF WAVEGUIDE FEL

The geometry of HUST THz-FEL waveguide resonator is shown in Fig. 1. A rectangular waveguide made of good conductor is located at the middle of two reflecting mirrors. The cross section of the waveguide is $a \times b$ and the length is L . Two mirrors are at a distance from waveguide entrance, therefore the optical beam propagates in free space during waveguide and mirrors.

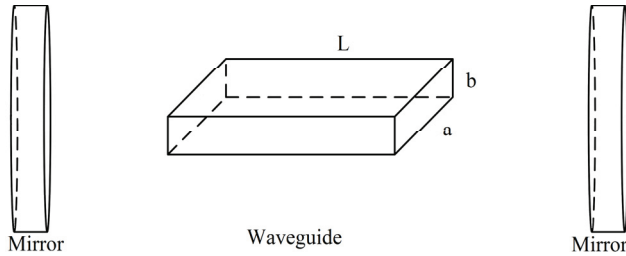


Figure 1: Layout of waveguide resonator.

To simplify this problem, the resistance of the metallic waveguide walls is neglected and the optical modes in the waveguide can be expressed as the solutions of a homogeneous Helmholtz equation [1]:

$$(\nabla^2 + k^2)\phi(x, y, z) = 0 \quad (1)$$

where k is the wavenumber of radiation.

Since this waveguide is adopted to a planar undulator with vertical periodic magnetic field, the eigenmodes in the waveguide is the pi modes with horizontal polarization, and it can be expressed as a combination of TE and Hermite-Gaussian mode:

*Work supported by the Fundamental Research Funds for the Central Universities : 2014TS146
#qfu@hust.edu.cn

$$E(x, y, z) = \cos\left(\frac{ny\pi}{b}\right) \exp\left(\frac{-x^2}{\omega^2(z)}\right) + i\left(\frac{k_n}{2R(z)} - \frac{1}{2} \tan^{-1} \frac{z}{z_R}\right) \quad (2)$$

where $k_n = \sqrt{k^2 - \frac{n^2 \pi^2}{b^2}}$, $\omega(z)$, $R(z)$ and z_R are the Gaussian beam x-radius, the x-radius of curvature of wave-fronts and the Rayleigh range. The distance z is measured with respect to the beam waist, in this case, the center of waveguide, then:

$$\begin{aligned} \omega(z) &= \omega_0 \sqrt{1 + \frac{z^2}{z_r^2}} \\ R(z) &= z \left(1 + \frac{z_r^2}{z^2}\right) \\ z_r &= \frac{\pi \omega_0^2}{\lambda} \end{aligned} \quad (3)$$

The solution describes an optical beam with a Gaussian amplitude distribution in horizontal direction and a cosine amplitude distribution in vertical.

DIFFRACTION LOSS

Optical beam is guided in waveguide so diffraction loss mainly occurs between waveguide and mirrors. In our case, the process starts from a given radiation field distribution out of waveguide, spreading to mirror and back to waveguide in free space. The shape of mirror work as diaphragm and the concave geometry will modulate the phase of optical wavefronts to focus the beam back into waveguide.

Propagation in Free Space

The Fresnel diffraction integral shows the electric field of diffraction pattern is given as a convolutional type function.

$$\begin{aligned}
E(x, y, z) &= -\frac{ie^{ikz}}{\lambda z} \int_S E(x', y', 0) \\
&\quad e^{\frac{ik(x-x')^2 + (y-y')^2}{2z}} dx' dy' \\
&= \psi_0(x, y) * h_z(x, y)
\end{aligned} \quad (4)$$

Analytical solution of this equation is difficult. For numerical computation, the wavefront of free space part is processed with 2D fast Fourier transformation.

The field can be calculated as a multiplication of initial optical field and a function related to free-space propagation length in the Fourier space [2].

$$\begin{aligned}
F\{\psi_z(x, y)\} &= F\{\psi_0(x, y) * h_z(x, y)\} \\
&= F\{\psi_0(x, y)\} \cdot F\{h_z(x, y)\}
\end{aligned} \quad (5)$$

where

$$h_z(x, y) = \frac{-ie^{ikz}}{\lambda z} e^{\frac{ik}{2z}(x^2 + y^2)} \quad (6)$$

Reflecting from Mirrors

The effect of reflecting mirrors can be expressed as below:

$$R(x, y) = rM(\rho)D(x, y) \quad (7)$$

The constant r is the amplitude reflection coefficient, $M(\rho)$ is the modulation of phase which is related to the concave type and curvature radius of mirrors, $D(x, y)$ represents the geometrical shape of mirrors, which can be regarded as a diaphragm. $D(x, y) = 1$ inside the mirror, and 0 outside.

For spherical mirror:

$$M(\rho) = e^{-ik \frac{x^2 + y^2}{\rho}} \quad (8)$$

Because of guiding effect, the curvature radius of the wavefront is different in vertical plane and horizontal plane. A pair of toroid mirror may fit the wavefronts better and retain more optical energy.

For toroid mirror, phase delay on mirror is separated in 2 directions according to various curvature radius in x , y axis. Hence the modulation of phase is defined as

$$M(\rho) = e^{-ik \left(\frac{x^2}{\rho_x} + \frac{y^2}{\rho_y} \right)} \quad (9)$$

Diffraction Loss

Since the energy inside a diaphragm is defined by [3]:

$$I = \iint_S E(x, y) E^*(x, y) dx dy \quad (10)$$

The diffraction loss of propagation from waveguide to mirror, and then reflected back to the entrance of waveguide can be determined.

$$\text{Loss Efficiency} = 1 - I_{\text{entrance}} / I_0 \quad (11)$$

SIMULATION AND RESULT

Out of waveguide, the laser beam will propagate through a distance in the free space to the mirror then back to the entrance of waveguide. The simulation will be started with the eigen mode at waveguide entrance. The propagation and the optical field back to waveguide will be calculated by using Fresnel diffraction principle.

In the numerical simulation, which has been performed using HUST THz-FEL resonator structure, the loss efficiency at different wavelength is calculated to optimize the curvature radii and geometry of mirror. The configuration of HUST FEL is listed below:

Table 1: Configurations of Resonator

Configurations	Size
Waveguide horizontal size/a	40mm
Waveguide vertical size/b	10mm
Free propagation distance	905mm
Waveguide length/L	1130mm
Wavelength range	50μm-150μm
Mirror diameter	60mm

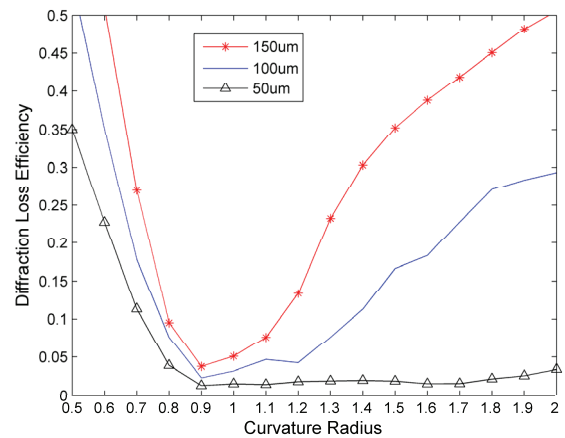


Figure 2: Diffraction loss efficiency as a function of curvature radius.

Here we take the first-order eigen mode at the opening of waveguide as initial field distribution, and calculate the diffraction loss efficiency between waveguide and reflecting mirror.

The diffraction loss of first-order eigen mode at different wavelength is plotted in Fig. 2 as a function of curvature radius of spherical mirrors. It is evident that diffraction loss is more significant at long wavelength range, which is the main reason why waveguide is widely adopted at long wavelength free electron lasers.

At various wavelength ranges, low loss situation occurs when curvature radius is 0.9m, and the loss efficiency at that spot is 3.8%. Diffraction loss at long wavelength is more sensitive, but loss efficiency at 50 μ m does not increase much while curvature radii rise above 0.9m.

In order to make further effort to reduce the diffraction loss, we also finished the computation of the performance of toroid mirrors. Since the radiation is guided in vertical direction and propagates freely in horizontal, the horizontal curvature radius of wavefronts would be larger than vertical ones to maintain more energy on the waveguide entrance.

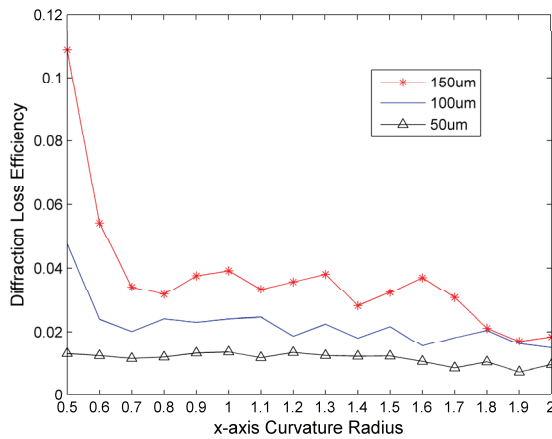


Figure 3: Vertical curvature radius at 0.9m, diffraction loss efficiency as a function of horizontal curvature radius.

Fig. 3 shows diffraction loss efficiency as a function of horizontal curvature radius when vertical curvature radius is 0.9m. The performance of toroid mirror in different wavelength is similar to spherical one: diffraction loss is higher and more sensitive at long wavelength.

The diffraction loss efficiency at different curvature radius in 2 directions is illustrated in Fig. 4.

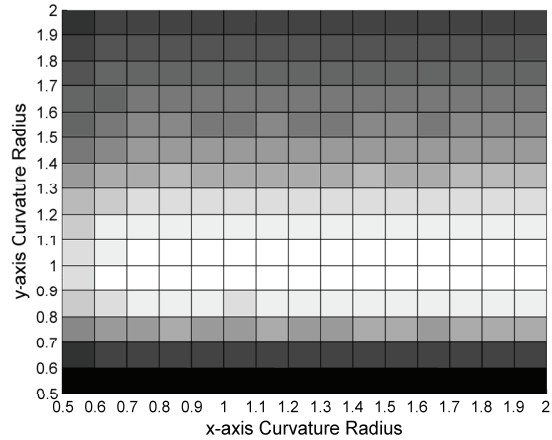


Figure 4: Wavelength at 150 μ m, diffraction loss efficiency as a function of 2-dimension curvature radius.

The best configuration at 150 μ m is a pair of toroid mirrors with $R_x=1.9$ m in horizontal, and $R_y=0.9$ m in vertical and the loss efficiency of that configuration is 1.7%, which is less than the loss with a pair of spherical mirror at $R=0.9$ m. This calculation proved that the optimization of mirror in concave type and curvature radius can indeed reduce diffraction loss in HUST THz-FEL resonator.

CONCLUSION

In general, toroid mirror can achieve a better performance than spherical mirror. By optimizing mirror concave, it can lower nearly a half of diffraction loss and allows larger room for concave mechanical error.

However, in practice, adoption of toroid mirror is more expensive and time-consuming to process, and more importantly, it will increase the difficulty when using He-Ne lasers for alignment mirrors [4]. The laser spot can not be well-focused in both directions and form a round dot. Alignment accuracy might be effected.

REFERENCES

- [1] L. R. Elias, J. C. Gallardo, Appl. Phys. B31(1983)
- [2] R. Prazeres, M. Billardon, Nucl. Instr. and Meth. A318 (1992)
- [3] X. Wang, Q. Xu, M. Xie, Z. Li, Opt. Commun. 131(1996)
- [4] S. Varro et al., *Free Electron Lasers*, (InTech, 2012).

PRESENT STATUS OF COHERENT ELECTRON COOLING PROOF-OF-PRINCIPLE EXPERIMENT*

I. Pinayev[#], F.Z. Altinbas, D.R. Beavis, S. Belomestnykh, I. Ben-Zvi, K.A. Brown, J.C. Brutus, A.L. Curcio, L. DeSanto, A. Elizarov, C.M. Folz, D.M. Gassner, H. Hahn, Y. Hao, C. Ho, Y. Huang, R. Hulsart, M. Ilardo, J. Jamilkowski, Y. Jing, F.X. Karl, D. Kayran, R. Kellermann, N.D. Laloudakis, R. Lambiase, V.N. Litvinenko, G. Mahler, M. Mapes, W. Meng, R. Michnoff, T.A. Miller, M. Minty, P. Orfin, A. Pendzick, F. Randazzo, T. Rao, J. Reich, T. Roser, J. Sandberg, B. Sheehy, J. Skaritka, K. Smith, L. Snydstrup, A. Steszyn, R. Than, C. Theisen, R.J. Todd, J. Tuozzolo, E. Wang, G. Wang, D. Weiss, M. Wilinski, T. Xin, W. Xu, A. Zaltsman, BNL, Upton, New York, USA
M.A. Kholopov, P. Vobly, BINP, Novosibirsk, Russia
G.I. Bell, J.R. Cary, K. Paul, I.V. Pogorelov, B.T. Schwartz, A. Sobol, S.D. Webb, Tech-X, Boulder, Colorado, USA
C. Boulware, T. Grimm, R. Jecks, N. Miller, Niowave Inc., Lansing, Michigan, USA
P. McIntosh, A. Wheelhouse, STFC, Daresbury Lab, Warrington, UK

Abstract

The status of FEL-based Coherent Electron Cooling Proof-of-principle Experiment at BNL is presented. The experimental set-up is comprised of a 2 MeV CW SRF electron gun and 20 MeV CW SRF linac and 8-m long helical FEL amplifier. The status of the accelerator commissioning, and progress in the construction of the helical undulator at Budker INP, is also reported.

nominal energy experience zero longitudinal electric field.

The dependence of time-of-flight on the ion's energy will insure that the off-energy ions will be accelerated or decelerated, depending on the sign of their energy error. Such interaction will lessen the energy spread in the ion beam [1]. The used electron beam will be bent away from the ions' path and then dumped.

PROJECT OVERVIEW

Figure 1 shows the overall layout of our experiment [1, 2]. A CsSb photocathode inside a 2 MeV 112 MHz SRF gun will generate the electron beam when illuminated with a 532 nm laser. Two 500 MHz copper cavities will provide energy chirp for the ballistic compression of the electron beam. The compressed bunches will be accelerated further to 22 MeV by a 704 MHz 5-cell superconducting RF linac.

After passing through a dogleg the electron beam will merge with 40 GeV/u gold ion beam. The ions will "imprint" their distribution on to the electron beam by modulating its density. This modulation will be amplified in a high-gain FEL comprising of three 2.5-m-long helical undulators.

The ions will co-propagate with electron beam through the FEL. Therein, the ion's average velocity is matched to that of the group velocity, e.g., to the propagation speed of the wave-packet of the electron beam's density modulation. A phase shifter, a system of four dipoles forming a chicane structure, follows each undulator. The phase shifters between the undulators will match the phase advance of the optical packet with electron density. The one at the exit of the FEL provides the means to tune the phase of the wave-packet such that the ions with the

RF SYSTEM

112 MHz RF Gun

The 112 MHz SRF cavity [3, 4], modified by Niowave, was installed into the RHIC tunnel. Modifications included cavity incorporation into a new cryomodule, addition of the two manual tuners for coarse adjusting of the cavity's resonant frequency. After the installation the cathode launching mechanism manufactured by Transfer Engineering was attached and after several attempts was aligned with cavity (see Fig.2). This mechanism will allow in place exchange of the multialkaline photocathodes planned for usage. The 112 MHz gun was equipped with a water-cooled fundamental power coupler, as shown in Fig. 3. It will be used to fine-tuning of the cavity's frequency. The cathode stalk, situated inside the cavity, is maintained at room temperature by circulating water. Both parts can freeze and piping can be damage if water flow stops. To protect the cavity we developed an emergency blow out system which we expel water with gaseous helium if water block is sensed.

Although its design accelerating voltage is 2 MV, during the test we were limited the maximal voltage to 1 MV by the increasing radiation levels in the semi-open test environment. The SRF gun will be tested at its full accelerating voltage during September 2012. The 112 MHz 2 kW amplifier for the gun is already in place.

After the cavity conditioning and reaching the design voltage we will test photocathode operation in the SRF environment

* Work supported by Stony Brook University and by Brookhaven Science Associates, LLC under Contract No. DE-AC02-98CH10886 with the U.S. Department of Energy.
#pinayev@bnl.gov

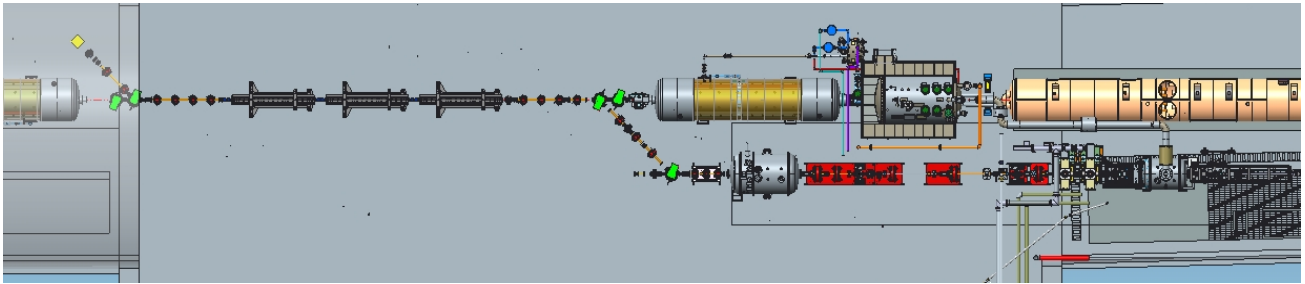


Figure 1: Layout of the coherent electron cooling proof-of-principle experiment in the RHIC tunnel.

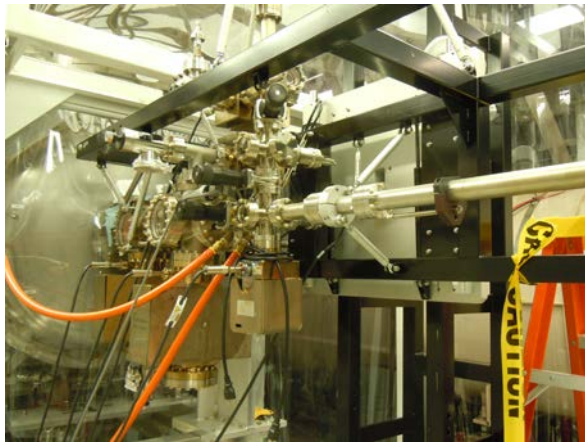


Figure 2: Cathode launch mechanism with 112 MHz gun inside the clean room.

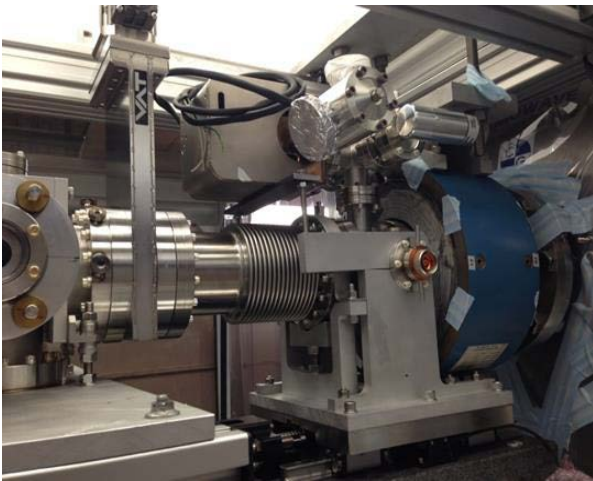


Figure 3: View of the 112 MHz power coupler mounted on the translation stage for tuning. On the left side viewport for the seed laser injection can be seen.

500 MHz System

The Daresbury Laboratory, UK provided two 500 MHz copper cavities on a long-term loan to BNL. Presently, the cavities are refurbished and are installed into the RHIC's tunnel (Fig. 4). The cavities are water cooled, and water

flow switches as well as four body temperature sensors are connected to the machine protection system. We are installing infrared temperature gauges of the ceramic RF windows, after this procedure the cavities will be ready for full power tests.

The cavities will be fed from an amplifier installed at the adjacent building. The output of the amplifier is connected to a circulator for protection. The power will be split using a special waveguide tee to avoid cavities crosstalk. A remotely controlled phase shifter is installed for the proper matching.



Figure 4: 500 MHz cavities with water manifold installed in the RHIC tunnel. The RF power is fed from the two waveguides on the top of the cavities.

704 MHz Accelerating Cavity

The BNL conducted the test of the two 20 MV 5-cell accelerating cavities (Fig. 5). One was fabricated by Advanced Energy Systems [4], and the other by Niowave.

After the test we selected the AES one for placing in the cryomodule, which is now is being built by Niowave. The main remaining issue is design of a fine cavity tuner, the testing of which is scheduled in September.



Figure 5: 704 MHz cavity manufactured by AES at vertical test facility.

DIAGNOSTICS

The diagnostics for the CeC system [5, 6] include nine beam position monitors (BPMs), two integrating current transformers (for measuring the current and the beam's transmission), four flags to measure the beam sizes (as well as the emittances and energy spread at 22 MeV), and one pepper pot (for measuring the emittance of the low-energy beam in the 2 MeV section). The view on the flag installed into the low energy section is shown in Fig. 6. Another flag is preceded with pepper-pot target. The target has three positions: fully retracted for the normal operations and two for the measuring of emittance in each plane. We will employ beam-loss monitors to control the beam losses in the CeC beam-line and the irradiation of the helical undulator. The longitudinal profile of ion beam will be observed using the existing RHIC wall-current monitor with a 6 GHz bandwidth.

The transvers beam position will be monitored with 4-buttons pick-up electrodes connected to Libera Brilliance BPM receiver manufactured by Instrumentation Technologies. Position of the electron beam will be used for fast interlock by MPS.

ISBN 978-3-95450-133-5

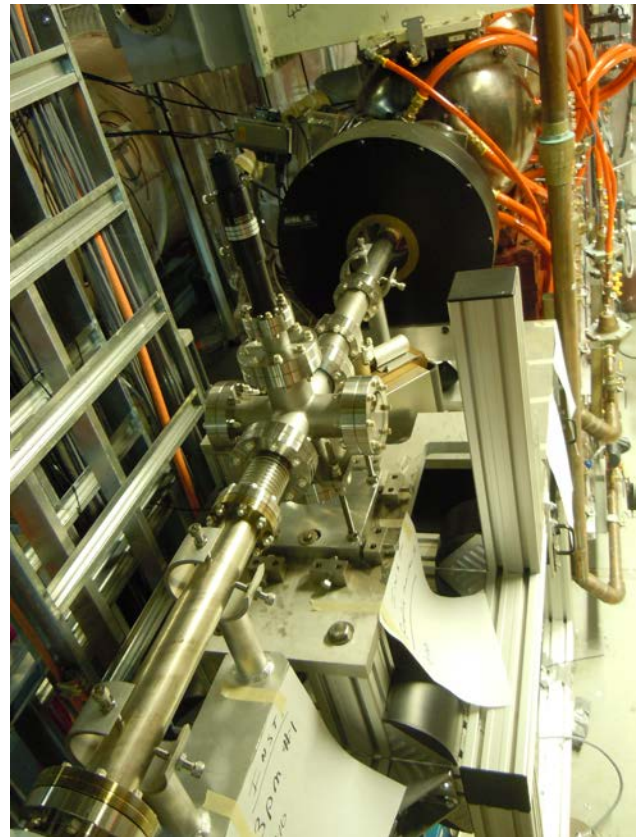


Figure 6: View of the vacuum cross with flag installed into the low energy beamline. The GigE camera will be added soon.

HELICAL UNDULATOR

Figure 7 shows the field integrals of the first out of three helical wigglers manufactured at BudkerINP. The wiggler was tuned to reach the requirements for CeC PoP project using 1D Hall probe. Fine tuning of the helical wiggler presently is being performed with a 3D Hall probe. The delivery of the first of the three helical undulators is scheduled for September.

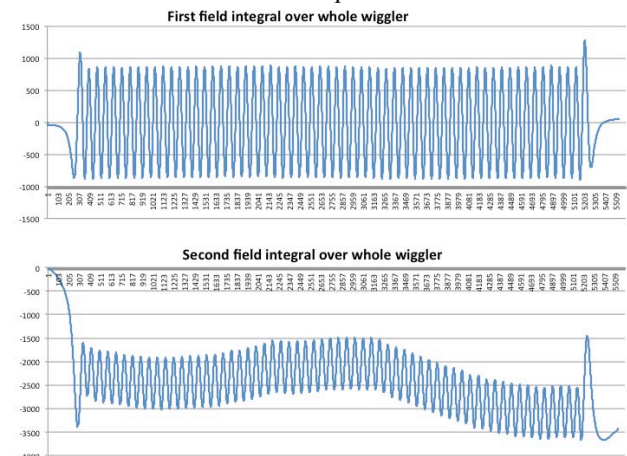


Figure 7: The first and second integral of the wiggler field after the initial tuning.

OTHER SYSTEMS

We are steadily progressing with installation the cryogenic system and the driver laser. The laser is acquired and will generate flat-top pulses of variable durations from 100- to 500-picoseconds, and with the leading- and the falling-edges below 50 picoseconds. The optical peak power should exceed 1 kW at 532 nm. The laser will be synchronized with the RHIC's timing system via a low-level RF system. The laser will be installed in the special shed outside RHIC tunnel and optical power will be transferred via optical fiber.

The solenoids are installed as well as most of the vacuum system for the low energy part as shown in Fig. 8. The RHIC personnel protection system was modified to include the components of the CeC PoP project and allow local run of the equipment without need to close the whole tunnel.



Figure 8: Solenoids and the vacuum chamber in the low-energy drift section. On the left side there is a portable clean room used for the particle free assembly. On the background the quiet helium source for the 112 MHz gun is placed on a platform

PLANS

We plan to commission the 500 MHz bunching cavities and 112 MHz gun in September this year. We plan to be install the linac, the helical undulators, the high power beam dump, and the balance of equipment during the RHIC shutdown in 2014 and commission the electron part of the equipment during Run 15.

REFERENCES

- [1] V.N. Litvinenko and Ya.S. Derbenev, Phys. Rev. Lett. 102, 114801 (2009).
- [2] V.N. Litvinenko et al., "Proof-of-principle Experiment for FEL-based Coherent Electron Cooling", in *Proc. 33rd Int. Free-Electron Laser Conf.*, Shanghai, 2011, pp. 322-325.
- [3] S. Belomestnykh et al., "Developing of Superconducting RF Guns at BNL", in *Proc. 26th Int. Linear Accelerator Conf.*, Tel-Aviv, 2012, pp. 324-326.
- [4] D. Kayran et al., "SRF Photoinjector for Proof-of-Principle Experiment of Coherent Electron Cooling at RHIC", in *Proc. 3rd Int. Particle Accelerator Conf.* New Orleans, 2012, pp. 622-624.
- [5] T.A. Miller et al., "Infrared Diagnostics Instrumentation Design for the Coherent Electron Cooling Proof of Principle Experiment", in *These Proceedings: Proc. 36th Int. Free-Electron Laser Conf.*, Basel, 2014, THP074.
- [6] D. Gassner et al., "Coherent Electron Cooling Proof of Principle Stage 1 Instrumentation Status", in *These Proceedings: Proc. 36th Int. Free-Electron Laser Conf.*, Basel, 2014, THP093.

HIGH POWER OPERATION OF THE THz FEL AT ISIR, OSAKA UNIVERSITY

K. Kawase[#], S. Suemine, R. Kato, A. Irizawa, M. Fujimoto, M. Yaguchi, S. Funakoshi,
R. Tsutsumi, K. Miyazaki, K. Furukawa, K. Kubo, A. Tokuchi, G. Isoyama,
ISIR, Osaka University, Osaka, Japan

Abstract

To enhance the power of the THz FEL, we have developed a 27 MHz grid pulser for the thermionic electron gun. It makes the bunch intervals 4 times longer and increases charge of the bunch 4 times higher than the dc-beam injection scheme whereas the beam loading is the same as that in the dc scheme. In this new operation mode, where a single FEL pulse lases in the cavity, we have succeeded in obtaining the micropulse energy exceeding 200 μJ at a wavelength of 67 μm .

INTRODUCTION

The THz FEL has been developed using the L-band electron linac system at the Institute of Scientific and Industrial Research (ISIR), Osaka University. The first lasing was demonstrated at wavelengths from 32 to 40 μm in 1994 [1]. Some years later, the linac system was substantially upgraded for higher stability and reproducibility of its operation. In addition, the pulse duration of the klystron modulator was expanded from 5 to 10 μs for FEL, so that the THz-FEL reached the power saturation first time at a wavelength of 70 μm [2]. The FEL currently operates over the wavelength range from 25 to 150 μm [3].

We pursue research on the upgrade of the FEL to expand the wavelength range and to increase the FEL power. One of the key factors to achieve such objectives is a higher beam current, which is expected to increase FEL gain and the saturation power of the FEL [4]. We are, therefore, developing a new operation mode of the linac system for higher bunch charge.

In the present scheme of the linac operation for the FEL, an electron pulse with a current of 0.6 A and a duration of 8 μs is extracted from the electron gun, and pre-bunched at the rf frequency of 108 MHz using the sub-harmonic buncher system. The electron beam that is a train of bunches at 9.2 ns intervals for the 8 μs duration is accelerated using the 1.3 GHz rf structures consisting of a pre-buncher, a buncher, and a 3 m long acceleration tube of the travelling wave type. The electron beam with the charge of 1 nC/bunch is transported via the FEL beamline to the THz-FEL. In this operation, the rf power measured at the exit of the traveling-wave acceleration tube is reduced to 24% of that without the electron beam. Therefore, the beam loading is too high to further increase the beam current [5].

On the other hand, the optical cavity of the FEL is 5.531 m long, and accordingly, the round-trip time of a light pulse is 36.9 ns, meaning that four FEL pulses independently arise and develop in the cavity. Because a single FEL pulse is sufficient to lase, we can increase the bunch charge four times higher by expanding the bunch interval to 36.9 ns whereas the beam loading in the acceleration tube is kept at the same level. Therefore, we have developed a simple and compact grid pulser system for the electron gun to generate a train of electron pulses with a peak current of 2.4 A and a duration of 5 ns at intervals of 36.9 ns, which corresponds to the repetition frequency of 27 MHz, continuing for 8 μs .

In this paper, we will report recent results of the THz-FEL in high power operation using the electron beam of 4 nC/bunch.

EXPERIMENTAL SETUP

The schematic drawing of the L-band linac and FEL system at ISIR is shown in Figure 1. The electron beam is extracted from the electron gun with the thermionic cathode operating at -100 kV DC and pre-bunched using the three-stage sub-harmonic buncher (SHB) system. The SHB system consists of two 108 MHz 1/4 wavelength resonators and one 216 MHz resonator. The electron beam is bunched and accelerated with 1.3 GHz travelling-wave RF structures, including a pre-buncher, a buncher, and a 3 m long acceleration tube. The accelerated electron beam is tuned using the diagnostic beamline with the analysing magnet and the Faraday cup so that the electron energy is constant over the pulse and the instantaneous energy spread is small. After beam tuning, the electron beam is transported via the FEL beamline to the FEL that consists of a planar type permanent magnet wiggler and an optical cavity. The THz-FEL beam is transported from the accelerator room through the shielding wall to the experimental station in the measurement room.

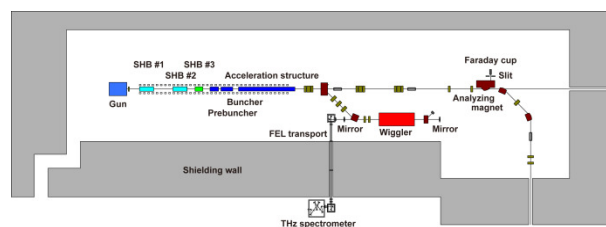


Figure 1: Schematic diagram of the L-band linac and the FEL system at the ISIR, Osaka University.

[#]kawase@sanken.osaka-u.ac.jp

Grid Pulser

To drive the electron gun at the repetition frequency of 27 MHz, we developed a simple and compact grid pulser system using a field effect transistor (FET). To extract electron pulses with a peak current of 2.4 A from the cathode (YU-156, Eimac), the output pulse height from the grid pulser is required to be over -150 V. For the efficient capture of electrons by the SHB system, the pulse duration is required to be less than 5 ns (FWHM), which corresponds to the half-period of the 108 MHz rf. To meet requirements for the voltage and the speed, we selected two candidates for the FEL (2SK408 and 2SK410, Hitachi), and developed a delayed shunt circuit for the gate of the FET to determine the pulse duration and to reduce the trail of the output pulse by grounding the gate and removing remaining charge in it. The schematic diagram of the grid pulser circuit is shown in Fig. 2. The input pulse train at the repetition frequency of 27 MHz for the duration of 8 μ s is amplified by the transistor amplifier and divided into two lines. A pulse in the main line triggers the FET on the gate stage and a high voltage pulse is generated on the drain stage. The pulse in the other line is delayed using a coaxial cable and turns the transistor to shunt the base stage of the FET.

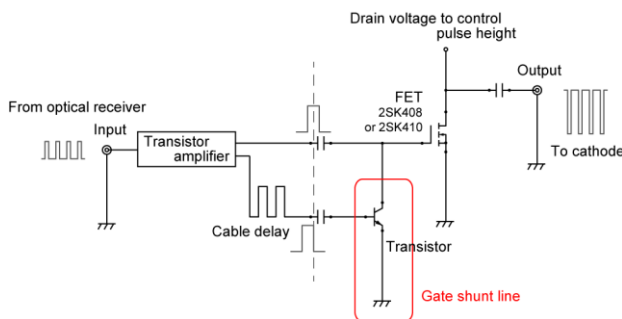


Figure 2: Schematic diagram of the grid pulser circuit.

In order to determine the optimal delay for shunting, the output signal of the grid pulse was measured for several cable lengths of the delay-line. The results of the measurement are shown in Fig. 3. As the results of these measurements, we select the delay-line length 40 cm longer than the length of main line.

Figure 4 shows the time profile of the electron beam generated using the grid pulser and measured with a core monitor at the exit of the electron gun system. The peak current of each bunch is almost constant, and the bunch repetition frequency is 27 MHz. The bunch duration of the electron beam is measured to be less than the specification, 5 ns.

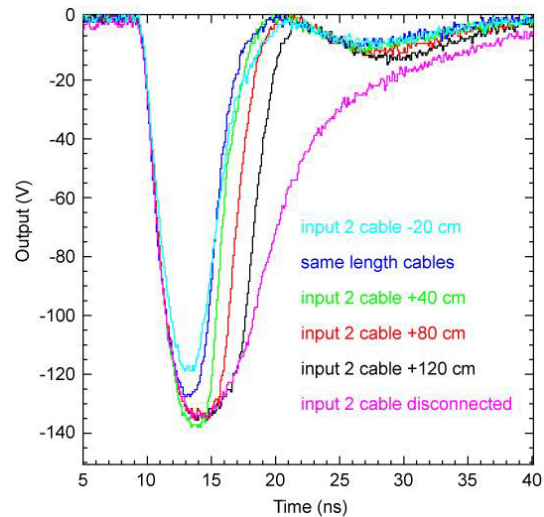


Figure 3: Tuning result of the delayed shunt timing.

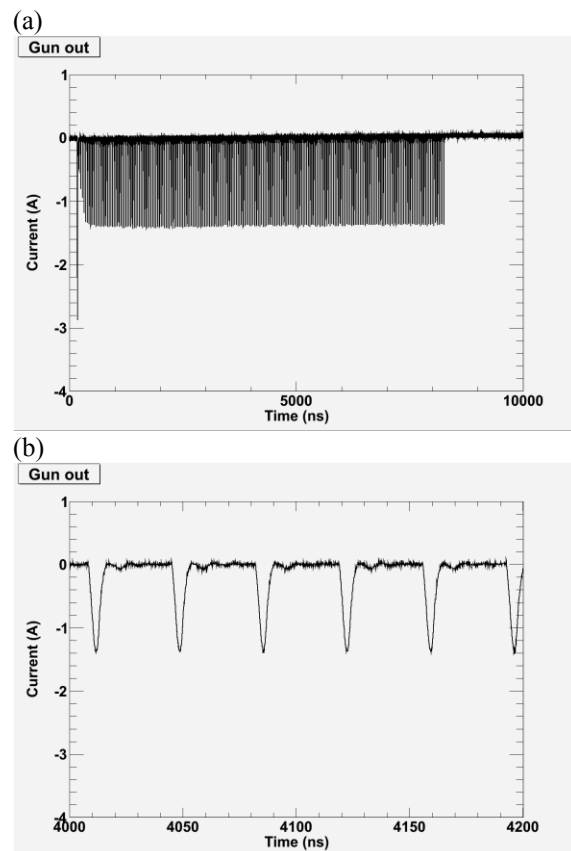


Figure 4: The waveform of the electron beam generated with the new grid pulser system. This waveform shows the core monitor signal measured at the exit of the electron gun. (a) full length waveform of the generated electron beam. (b) horizontal axis is expanded.

Beam Loading

Figure 5 shows the RF power exiting the acceleration tube in the 108 MHz operation with the beam current of 0.6 A (a) and that in the 27 MHz operation with a current of 2.0 A (b). As expected, the beam loading in in the 27 MHz operation with 2.0 A is lower than that in the 108 MHz operation with 0.6 A.

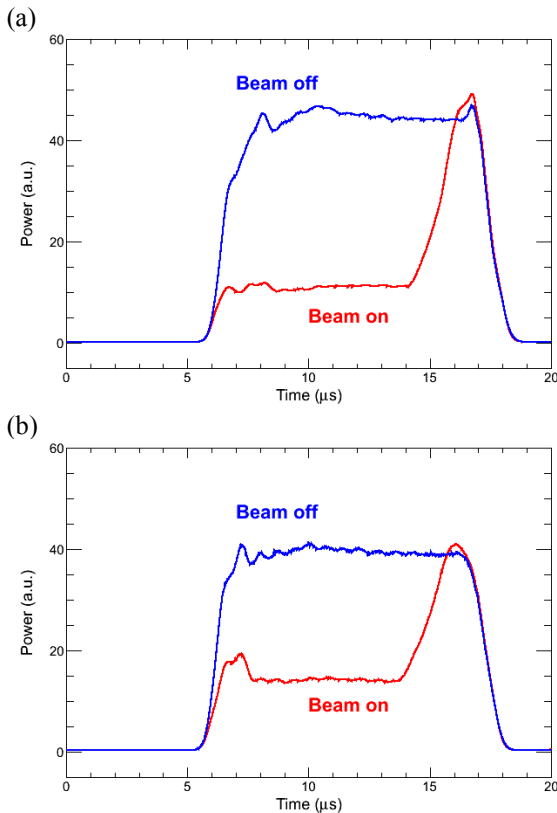


Figure 5: Beam loading at the acceleration tube for the dc-injection with the beam current of 0.6 A (a) and the 27 MHz operation with the peak current of 2.0 A (b).

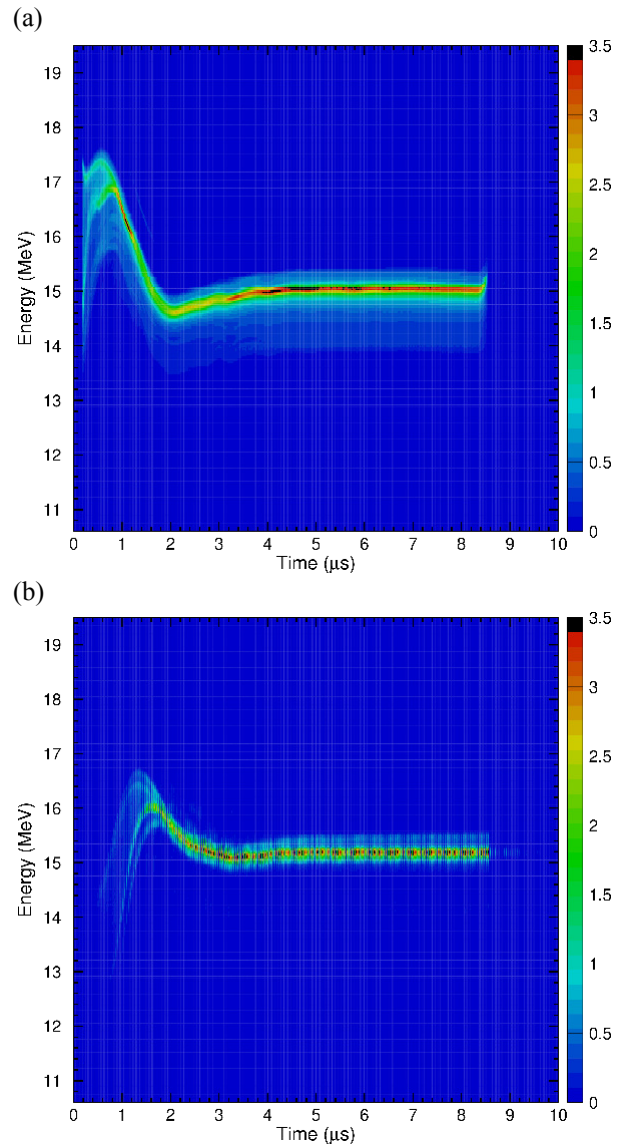


Figure 6: The typical energy spectra of the electron beam. (a) the dc-injection operation. (b) the 27 MHz operation.

Electron Beam Spectra

To generate a high quality and high intensity FEL, the electron beam with a constant energy and small energy spread is necessary.

The time-resolved energy spectrum of the electron beam was measured using an analysing magnet and the Faraday cup with a slit. The signal from the Faraday cup is measured with an oscilloscope by changing the magnetic field of the analysing magnet, so that a two-dimensional energy spectrum of the electron beam is obtained. The typical spectra in both operations are shown in Fig. 6. In both cases, the projected spectral width is about 1% and the r.m.s. uniformity of the peak energy through the macropulse after 2 μ s is estimated to be about 0.1%. After the beam tuning, we achieve a similar quality of the electron beam in the energy spectra.

RESULTS

By using the 27 MHz operation of the electron beam, we generate the THz-FEL with the pulse interval of 36.9 ns and with the macropulse length of a few microseconds. As the preliminary results, the maximum macropulse energy is achieved to 26 mJ for the wavelength of 67 μ m at the user area. The wavelength of the FEL is variable by changing the magnetic field strength of the wiggler, that is, by changing the gap length of the wiggler. Figure 7 shows the variation of the macropulse energy of the FEL by changing the gap length of the wiggler for the 27 MHz operation and the dc-injection (108 MHz operation) cases, respectively. At present, the macropulse energy of the FEL at the 27 MHz operation is two times larger than that at the 108 MHz operation. Roughly speaking, because the number of pulses is reduced in one-quarter, the

micropulse energy is increased eightfold in the 27 MHz operation.

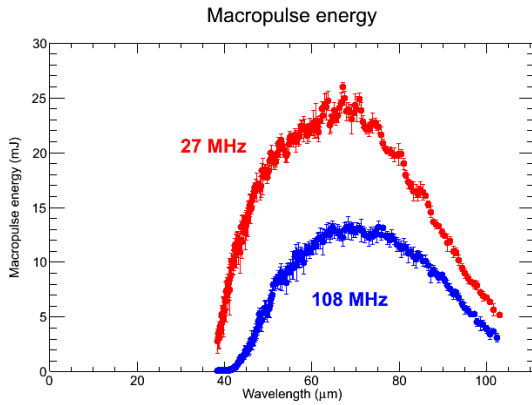


Figure 7: Macropulse energy of the FEL in the 27 MHz operation (red) and the 108 MHz operation (blue).

The time structure of the FEL macropulse is measured by using a fast response THz detector (Moletron, pyroelectric detector P-5). The typical waveform of the observed signal is shown in Fig. 8. From the measured waveform, the maximum micropulse energy is estimated to be 200 μJ for the wavelength of 67 μm. By assuming the pulse duration of 20 ps which is typical bunch duration of the electron beam accelerated by the L-band linac, the peak power of the THz pulse is estimated to be 10 MW, and by focusing it with the radius of 200 μm, the peak intensity is estimated to be 16 GW/cm².

The typical specifications of the THz-FEL at the ISIR are listed in Table 1.

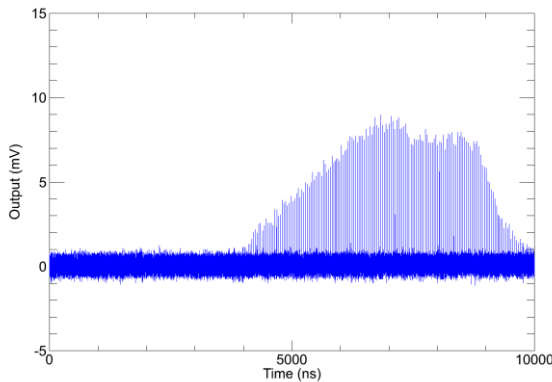


Figure 8: Typical waveform of the generated THz-FEL measured by a fast pyroelectric detector.

CONCLUSION

By increasing the bunch charge of the electron beam combining a new grid pulser system and the sub-harmonic buncher system, we achieve the

intensification of the micropulse energy of the FEL in eight times compared with the dc-beam injection scheme. As a preliminary result, the peak intensity is estimated to be 16 GW/cm² at the wavelength of 67 μm. This intense coherent and monochromatic THz radiation will open various research fields such as nonlinear responses of the materials in the THz region. The present results are not final ones. After optimization of various parameters and measurements of the THz pulse duration by the several methods, we will have more intense THz pulse and more precise characterization of that.

Table 1: Typical Specifications of the THz-FEL at the ISIR (Preliminary)

Parameter	value
Wavelength range	25 – 150 μm
(Frequency)	2 – 12 THz
Macropulse energy at user area	>10 mJ (70 μm)
Repetition rate of macropulse	5 Hz (max. 10 Hz)
Macropulse duration	2 ~ 6 μs
Bunch separation	9.2 ns or 36.9 ns
Energy stability of macropulse	3 ~ 7% (r.m.s.)

ACKNOWLEDGMENT

A part of this work was supported by JSPS KAKENHI Grant Numbers 24310069 and 24651102.

REFERENCES

- [1] S. Okuda et al., Nucl. Instrum. and Meth. in Phys. Res. A 358, 244 (1995).
- [2] R. Kato et al., “Re-commissioning of the Far-infrared Free Electron Laser for Stable and High Power Operation After the Renewal of the L-band Linac at ISIR, Osaka University”, FEL’07, Novosibirsk, Russia, August 2007, p. 521 (2007); <http://www.JACoW.org>
- [3] R. Kato et al., “High Power Terahertz FEL at ISIR, Osaka University”, IPAC’10, Kyoto, Japan, May 2010, p. 2209 (2010); <http://www.JACoW.org>
- [4] G. Dattoli et al., “Experimental and Theoretical Aspects of the Free-Electron Laser”, in: Laser Handbook vol. 4, eds. M.L. Stitch and M. Bass, North-Holland, Amsterdam (1985).
- [5] K. Kawase et al., Nucl. Instrum. and Meth. in Phys. Res. A 726, 96 (2013).

HIGH POWER COUPLED FEL OSCILLATORS FOR THE GENERATION OF HIGH REPETITION RATE ULTRASHORT MID-IR PULSES

M. Tecimer, THz-FEL Group, UHM, Honolulu, HI 96822, USA

Abstract

100-200 MeV range ERL driven high gain FEL oscillators generating few cycle short, high intensity mid-IR pulses with tens of MHz repetition rates might become attractive tools in various strong field applications. In a recent study a mode-locked, coupled FEL oscillator scheme has been presented to generate multi-mJ level, ultra-short (<10 cycles) output pulses tunable within the entire IR region. The current work elaborates on an improved FEL oscillator scheme that can cope with the high power levels accumulated within the coupled cavity while operating unidirectionally, eliminating the feedback in the reverse direction. The various operational regimes of the coupled laser system are discussed.

INTRODUCTION

The objective of the study is to draw on the potential of the ERL based FEL devices to produce multi tens of mJ level, ultra-short (≤ 10 cycles) output pulses tunable within the entire IR region (and beyond) with at least several tens of MHz repetition rates. The latter would be a major step in overcoming the performance limitations of the current ultra-short laser technology in the high-field applications, a domain that is being dominated by conventional NIR/MIR sources. The achieving of the goal relies on taking advantage of the high powers deposited in the beam (average as well as per bunch) by a 100-200 MeV range superconducting ERL system operating at high repetition rates and elaborating on schemes with high extraction efficiency that would enable the generation of few cycle long intense radiation pulses.

In a recent study a high gain FEL oscillator scheme is investigated that encompasses two coupled oscillator cavities [1]. In general terms the system operates as an injection locked laser system whereby the first FEL cavity (master oscillator) provides a strong ultrashort, wide-bandwidth seed signal that is transmitted through the coupler mirror (less than a few percentage coupling ratio) into the amplifier cavity. The latter can be driven in different operational regimes. The most straightforward manner is using the second cavity as a passive pulse stacker cavity. In this mode its finesse is set to optimize the outcoupled pulse energy (unless an intracavity application is considered). On the other hand injecting the spent beam into the second FEL oscillator cavity where it further interacts with the optical pulse that is coupled in and building up within this cavity leads to the injection locked operation. In this operational modus the resultant radiation field circulating in the amplifier cavity can be approximated in the first order by summing up the coupled fields that are coherently accumulating and boosting up the intracavity power in an enhancement

cavity (EC) and the field build up resulting from the injection locked FEL interaction. The extent of the latter contribution can be defined by adjusting the undulator and resonator parameters of the two cavities. In the studied cases the amplification effect based on the coherent pulse stacking of an EC turns out to be superior to the growth of the intracavity fields due to the FEL process. Note that unlike the latter, coherent pulse stacking does not suffer from a saturation mechanism that limits the amplification and the associated field build up over many roundtrips. (Reaching the *steady-state* in an EC is a different process than the FEL saturation.) It should also be emphasized here that prior to its injection into the amplifier cavity the beam already starts acquiring a relatively large energy spread since the master FEL oscillator is driven at zero cavity detuning and saturation is attained. Nevertheless, at the presence of the accumulating fields within the amplifier cavity and the broad band interaction with it, the spent beam's energy transfer into the radiation fields exceeds significantly the one due to the fresh injected beam's FEL interaction in the master oscillator, increasing accordingly the final beam energy spread.

In realizing the above mentioned operational regimes a nearly 100% percent coupling efficiency (in coupling the seed) is ensured while a decoupled, virtually reverse feedback free configuration is implemented. Our simulations that allow reverse feedback (bidirectional coupling) indicate a limit value for the coupling ratio back into the master oscillator at around 10^{-8} [2] in order to recover nearly the same performance that results from the fully decoupled case.

On the other hand the high intracavity power levels circulating particularly within the amplifier cavity necessitate designs that can cope with thermal related effects on the mirrors (distortion of the fields, damage at the mirror surfaces) by adopting proper measures in time and space. Whereas the average power can be controlled over the duty cycle (macropulses at lower duty cycle) it is also essential to increase the mode waist on the mirrors. In addition cryocooled laser optics developed for high power applications can be utilized to alleviate the thermally induced adverse effects.

COUPLED FEL OSCILLATORS

The composite resonator shown in Fig.1 is a special case of two coupled lasers in the weak coupling limit [1] (transmission of mirror B $\ll 1.0$). In order to incorporate the features that are briefly addressed in the introduction a hybrid cavity design is adopted. While the first cavity supports the Gaussian (fundamental) mode the second (amplifier) cavity is a Bessel-Gauss (BG) type cavity [3-5]. Here we take advantage of two salient features of the

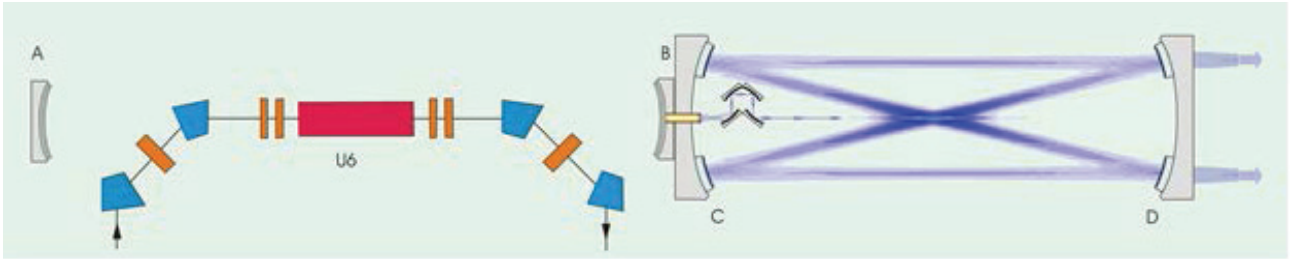


Figure 1: Schematic layout of the coupled cavities. Here the second cavity that supports the BG beam serves as a passive EC. The output is an annular beam.

BG cavities: i) the field distribution at mirrors C and D is an annulus with an approximately Gaussian radial intensity, ii) if an ordinary BG beam is imaged by a lens the outcome is a modified BG beam and vice versa [5]. All mirrors are dielectric mirrors with minimal absorption losses. The coupling mirror B has an optical waveguide/fiber optic placed at the beam axis that is terminated with an axicon on its tip. All transition surfaces (dielectric layer to fiber optic, axicon to free space) are individually impedance matched (coated) so to minimize any distortion of the reflected fields in the master oscillator (note that the coupling ratio is anyhow less than 0.01-0.02) and to maximize the coupling efficiency into the amplifier cavity (stressing here that this is not a hole coupling). The mirror lens set (optical delay line) incorporated into the amplifier cavity ensures the proper mode matching at the plane of coupling. Figure 2 shows the extent of the annular beam (normalized field Amplitude) at mirrors C and D for the wavelength range of interest and for a cavity length of ~ 26 m. One should also indicate at this point that the Gaussian cavity (master oscillator) too can be replaced by a BG type cavity. BG type cavities offer a wide range of beam manipulation means that however is not the topic of this report.

Mode-locking in FEL Oscillators Operating at Zero Cavity Detuning

A key aspect in our approach is that the master oscillator is driven in a single spike modus that is realized in a short pulse high gain FEL oscillator with perfectly synchronized optical cavity length (\sim zero cavity detuning) [6, 7]. In this regime that is dominated by high FEL gain, low cavity loss and optical pulse-electron beam slippage effects, the radiation stored in the cavity evolves into an ultrashort, intense spike. As demonstrated experimentally [7] this mode of operation enables also a high FEL extraction efficiency reaching up to many percentages which, along with a highly energetic electron beam, builds the first step towards achieving mJ level FEL pulses. The dynamics of an FEL operating in this regime is characterized by the so called short bunch limit [8]. As a result of the high gain FEL interaction, in the short bunch limit the spike width can become even shorter than the cooperation length $l_c = \lambda_r / 4\pi\rho$; λ_r and ρ denote the radiation wavelength and the FEL parameter [8], respectively. Furthermore, as was demonstrated in Ref. 7,

the FEL interaction induces a frequency chirp in the generated spike, making further compression of the pulse duration possible while bringing the pulse width ultimately down to a few cycles. Along with the mentioned high extraction efficiency, the generation of ultrashort (<10 cycles) spikes is an additional factor provided by the presented high gain FEL oscillator operated at perfect synchronism towards achieving high peak intensities.

Coherent pulse stacking as well as injection locked FEL amplification of the *frequency combs* in the seeded cavity are discussed in [1] and the references therein. It is worthwhile to turn the attention to the mode-locking process that leads to the formation of the described ultrashort, ultra-broad bandwidth, chirped optical pulses in the master oscillator. The fact that the high gain FEL operation at perfect synchronism enables the generation of ultrashort optical pulses that are propagating with a (nearly) self-similar shape from one roundtrip to the next indicates that the interaction can sustain and amplify a vast number of longitudinal cavity modes excited within an ultrabroad bandwidth (*frequency comb*) while a fixed phase relationship (phase locking) between all of them is established.

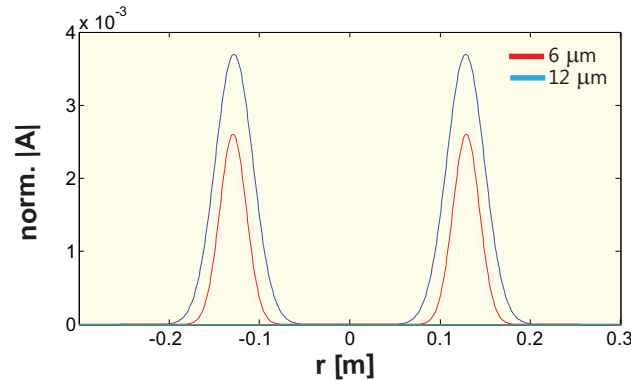


Figure 2: Plot of the norm. Amplitude cross section at the BG cavity mirrors. Keeping the tilt angle fixed annular beam's width and radius can be increased by lengthening the cavity.

The mode-locking process of frequency combs that is of interest here relies on a *self-starting* and *self-sustaining* phase and amplitude (loss) modulation. As already stated in [1], this *passive mode-locking* process is supported and sustained by the energy transfer from the radiation pulses to the particles that reach the bottom of the ponder-

omotive potential well as they execute synchrotron oscillations with frequency $\Omega_s \sim P^{1/4}$ [9] in the phase space. The time scale of the process is dominated by the slippage of the optical pulse during half a synchrotron oscillation period (electrons absorbing energy from the pulse tail) and as such it is a pulse intensity dependant process [1, 2]. The time scale and magnitude of the loss changes dynamically in response to the pulse intensity and vice versa. The slippage dominated interaction leads also to a phase modulation manifested by the induced chirp in the optical pulse. The complex index of refraction guiding of the optically bunched beam [10] is also pulse intensity dependant in the exponential gain regime. Its evolution in the course of the high gain FEL interaction is an additional effect that needs to be accounted for in the overall analysis. As indicated in [1], it would be useful to model the combined non-linear, self induced phase and amplitude modulation process by the master equation approach for mode-locking [11] relating and contrasting the described high gain FEL dynamics at zero cavity detuning to mode-locking in ultrafast optics.

Whereas constraints are imposed on the generation of few cycle high intensity pulses by using atomic lasers for high field applications (arising from power scaling limits due to material damage of the gain medium and artificial modelocking elements, (undesired) intensity dependent nonlinearities, restricted operational wavelength range) the mode-locking process exploited in this study allows to overcome these limitations, opening up ways for pertinent new applications. On the other hand major challenges inherent to the FEL interaction in realizing the envisaged operational modus in the mid-IR spectral region are described in [1].

SIMULATIONS

Simulations are carried out using the FEL modeling that is based on the multifrequency expansion of the fields with no averaging carried out in the source term [1]. Since the modeling employs transverse mode expansion too, adopting the optical guiding approach [12] would allow more accurate predictions of the high gain FEL dynamics, even an oscillator is treated in our case. The transverse guiding effects are not taken into account in the results presented in this report.

The considered FEL scheme is assumed to be driven by a 100 MeV rf linac, ~ 80 pC-150 pC bunch charge, 100 fs (σ_z) long bunches with 0.5% energy spread (σ_E). For the sake of simplicity in transporting and injecting the spent beam for the injection locked operation transverse emittance is neglected. Planar undulator modules consisting of 10 to 23 periods ($\lambda_u=6$ cm) with uniform fields are used in the respective resonators.

Figure 3 displays the temporal profile (at saturation) of the generated seed spike that is inherent to this low loss, ultrashort pulse, high gain FEL regime. Figure 4 displays the broadening of the spike's spectrum (at saturation) by increasing the bunch charge up to 150 pC. The spike duration shortens according to the scaling dependency $P^{-1/4}$ accompanied with a stronger chirp in the pulse. Note

the down shift of the initial resonance frequency ($\sim 6\mu\text{m}$) following the beam energy loss due the FEL interaction. In Fig.5, adjusting the loss and the slippage, the next satellite spike develops to a similar peak power level as the primary spike, exhibiting an evolution somewhat in analogy to the formation of limit cycle oscillations in the cavity detuned FEL oscillators at saturation.

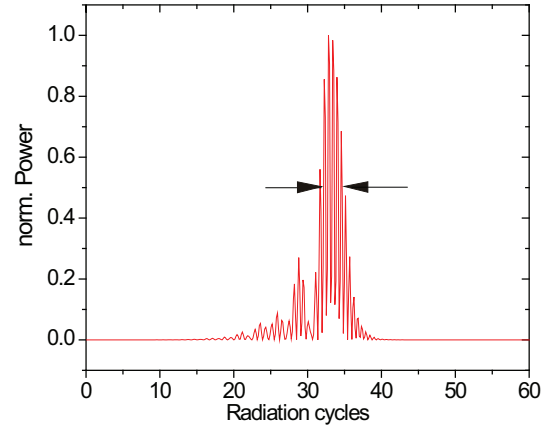


Figure 3: The seed spike's FWHM is around 3-4 radiation cycles.

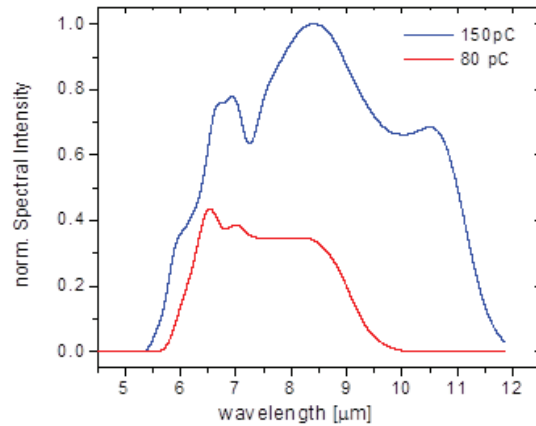


Figure 4: Pulse spectrum at saturation for 80 pC and 150 pC bunch charges.

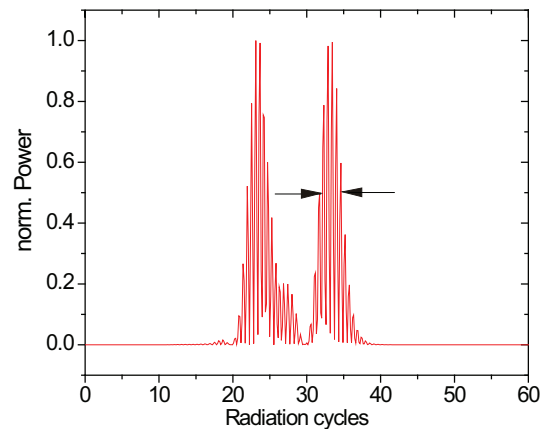


Figure 5: Double spike generation at saturation. The delay between the pulses amounts to ~ 200 fs.

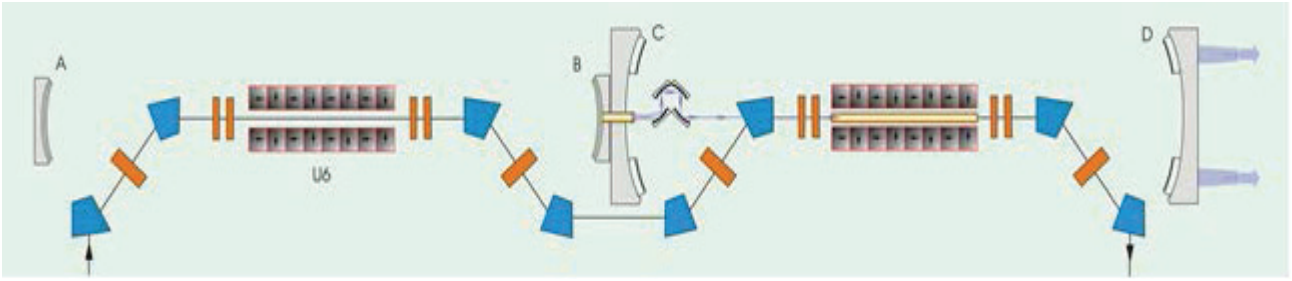


Figure 6: Schematic layout of the coupled injection-locked FEL cavities. By adjusting the settings of the resonator and the undulator modules in the respective cavities (basically cavity loss and slippage) the contribution arising from the injection locked FEL to the circulating power in the amplifier cavity can be varied. Note that the shown components are not scaled.

In order to amplify the BG beam (\sim truncated Bessel beam) injected into the coupled cavity we employ a technology already developed for high power fiber lasers/optical waveguides. Bessel-like beams can well be generated by selectively exciting high order LP_{0n} fiber modes. The adopted approach here involves the use of hollow core photonic band gap (or photonic crystal) fibers/optical waveguides (HC-PBF/HC-PCF) [13] with a large core aperture (5.5-6.0mm). The large core aperture favors the excitation of higher order modes (HOM), exhibiting extremely low attenuation as well as low dispersion for the wavelength range of interest. It is also beneficial for very high power applications. On top of it, the technology of HC-PCFs offer enormous design flexibility in tailoring broadband dispersion characteristics (controlling dispersion and its slope, achieving ultra-low, ultra-flattened dispersion) and the implementation of highly efficient ($>99\%$) grating based mode converters. The latter is crucial to enforce the gain medium (in addition to the injected Bessel beam) to couple selectively to the desired HOM along the interaction region. Matched doubled-chirped mirrors can be included into the resonator design for an additional dispersion control.

The injection locked FEL simulations carried out here assume the mode radial order ≥ 10 . The schematic layout of the coupled oscillator FEL is shown in Fig.6. The delay line mirrors ensure the proper synchronization between the electron and radiation pulses and the proper mode matching of the seeded Bessel beam at the entrance of the HC-PBF (undulator entrance). The aperture of ~ 5.5 -6 mm is chosen to allow a loss free transport along the undulator for a beam with 80 pC charge.

It is worthwhile to note at this point that the injected pulse's mode structure can be better matched by replacing the fiber optic/axicon configuration depicted in Fig.1 with a mode converter written HC-PBF of the desired radial order.

Figure 7 shows the pulse energy evolution of the outcoupled pulse at mirror D (The intracavity pulse energy amounts to nearly 1.5J). Here the contribution from the injection locked FEL interaction makes up less than 5% of the total pulse energy (which nevertheless exceeds by far the energy extracted from the electron

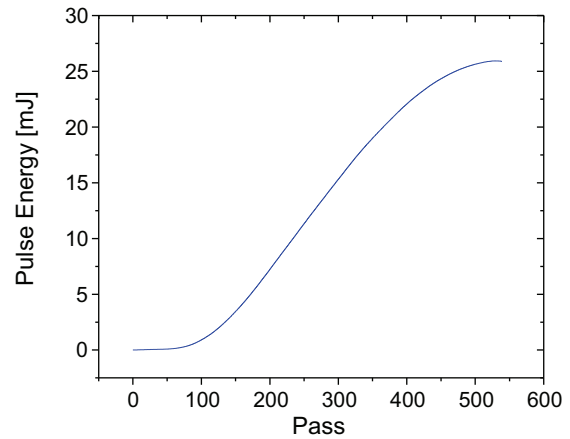


Figure 7: Outcoupled pulse energy evolution.

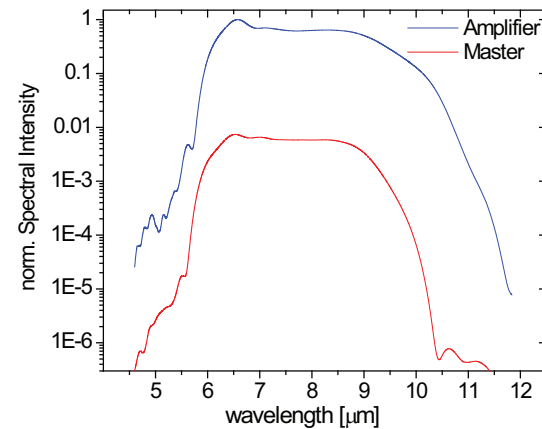


Figure 8: Frequency response of the injection locked amplifier cavity to the input seed wave whose temporal profile is shown in Fig. 3.

beam in the master oscillator). Figure 8 displays the frequency response of the injection locked amplifier cavity to the input seed wave. The truncation at 12 μm is due to the mirror reflectivity characteristics. By adjusting the undulator and resonator settings the contribution is increased up to $\sim 20\%$ for the BG beam as depicted in Fig. 9. Here, the pulse energy evolution of the BG beam, the Gaussian beam as well as the passive Enhancement

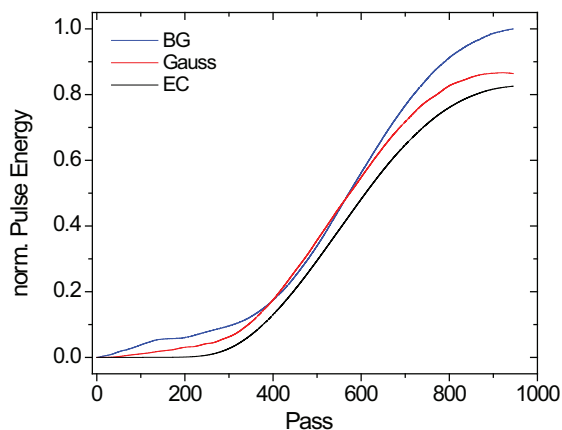


Figure 9: The pulse energy evolution in the amplifier cavity. BG refers to an FEL that is based on Bessel-like beam in the cavity. In the case of the Gaussian cavity it is assumed (hypothetically) that the reverse feedback vanishes.

Cavity are contrasted, respectively. The pulse energy is normalized to the maximum pulse energy attained by the BG beam.

A detailed description of the presented scheme along with the simulation results will be reported elsewhere.

CONCLUSION

In the presented study the used simulation model yields, under the described idealized conditions, Joule level intracavity as well as tens of mJ outcoupled high rep. rate ultrashort, broad bandwidth mid-IR pulses. The studied coupled FEL oscillator configuration enables efficient injection locked amplification of beams with large energy spread (dirty beams) at the presence of the accumulated, ultrashort, broad band, high intensity intracavity radiation pulses. Further studies focus on the following topics: i) rather than using the relatively low

charge spent beam, injection of high intensity 'dirty' beams (using a different beam source/accelerator system) into the second cavity will push up the FEL saturation power, ii) increasing the intensity of the seed pulses (and the extraction efficiency) by replacing the Gaussian master oscillator with a Bessel-like beam cavity. In the latter case it might be sufficient to drive the second cavity only as a passive EC while reaching pulse intensity levels still useful for high field applications that are presented in Ref. [2].

REFERENCES

- [1] M. Tecimer, PRSTAB 15, 020703 (2012).
- [2] M. Tecimer, Presentations,
http://accl.kek.jp/seminar/file/KEK_Tecimer.ppt
<http://www.phys.hawaii.edu/~mtecimer>
- [3] P. Pakkonen, J. Turunen., Opt. Commun. 156, 359 (1998).
- [4] J. Rogel-Salazar et al., Opt. Commun. 190, 117 (2001).
- [5] W.P. Putnam et al., Opt. Express. 20, 24429 (2012).
- [6] N. Nishimori, R. Hajima, R. Nagai, E.J. Minehara, Phys. Rev. Lett. 86, 5707 (2001).
- [7] R. Hajima, R. Nagai, Phys. Rev. Lett. 91, 5707 (2003).
- [8] R. Bonifacio et al., Phys. Rev. Lett. 73, 70 (1994).
- [9] N.M. Kroll et al., IEEE J. Quantum Electron. 17, 1436 (1981).
- [10] E.T. Scharlemann, A.M. Sessler, J.S. Wurtele, Nucl. Instrum. Methods Phys. Res., Sect. A 239, 29 (1985).
- [11] H.A. Haus, IEEE J. Sel. Topics Quantum Electron., 6, 1173 (2000).
- [12] P. Sprangle, A. Ting, C.M. Tang, Phys. Rev. E 36, 2773 (1987).
- [13] X.E. Lin, PRSTAB 4, 051301 (2001).

COMMISSIONING STATUS OF THE ASTA FACILITY AT FERMILAB*

A.H. Lumpkin[#], J. Ruan, D. Broemmelsiek, D. Crawford, D. Edstrom, N. Eddy, E. Harms, J. Hocker, J. Leibfritz, J. Santucci, G. Stancari, D. Sun, J. Thangaraj, R. Thurman-Keup, A. Warner, and J. Zhu

Fermi National Accelerator Laboratory, Batavia, IL 60510 USA

Abstract

Early commissioning results and status of the Advanced Superconducting Test Accelerator (ASTA) at Fermilab will be described. The ASTA facility will consist of an L-band rf photocathode (PC) gun, two superconducting L-band rf booster cavities, transport lines, and an 8-cavity TESLA style cryomodule. Early results include first photoelectrons from the Cs₂Te photocathode and operations at 3-5 MeV from the rf PC gun. Measurements of beam size, position, energy, and charge have been obtained with the beam profile station and Faraday cup at that low energy location. Diagnostics for the 20-50 MeV energy beam are also described as well as the first conditioning results for the cryomodule cavities.

INTRODUCTION

The Advanced Superconducting Test Accelerator (ASTA) facility [1] is currently being constructed at Fermilab with initial commissioning steps already in progress. The electron beam has been generated in a photoinjector based on a UV drive laser and the L-band rf photocathode (PC) gun cavity which is shown in Fig. 1. Low energy results at 3-5 MeV sampled after the gun are described. Initial commissioning of beam to the low energy beam dump will be done with one booster cavity. The beam line with one 4-dipole chicane, extensive diagnostics, and spectrometer has been installed in the linac for 20-50 MeV operations in the coming months. Downstream of this location is the 8-cavity cryomodule in which all cavities have been operated individually. Updated cryomodule results will be presented. The feasibility of using the commissioned linac and cryomodule to provide 300-MeV beams to drive EUV FEL oscillator tests at 120 nm was described previously [2].

EXPERIMENTAL ASPECTS

The injector portion of the facility, the first cryomodule, and the proposed FEL oscillator configuration are shown in Fig. 2. After the L-band rf pC gun, two L-band superconducting booster cavities will provide up to 50 MeV acceleration capability. At this time, the first cavity has been temporarily replaced by a spool piece, and

the second cavity has been installed and conditioned to 20 MV/m. Only results from the diagnostics after the rf gun and cryomodule conditioning will be presented.

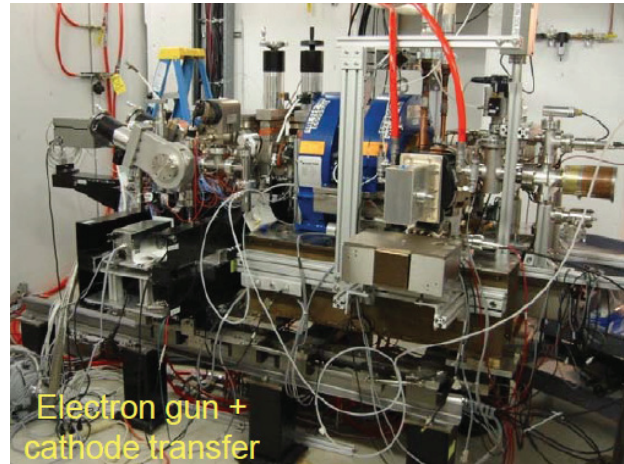


Figure 1: The L-band photoinjector with photocathode transfer hardware, and with two solenoid magnets.

The Drive Laser

The drive laser is based on an Yb fiber laser oscillator running at 1.3 GHz that is then divided down to 81.25 MHz and amplified. The four-stage origination and amplification is a set of commercial components from Calmar collectively referred to as the seed laser in the context of ASTA. The 81.25 MHz packets of IR laser, at a wavelength of 1053 nm is directed into a multi-pass amplifier (MPA), which provides amplified pulses at a 3 MHz rate that are then pulse cleaned with two sets of Pockels cells. The MPA has recently been replaced by a preamp composed of three single pass stages. A third Pockels cell, referred to as the pulse picker is not currently being used. Three YLF-based single-pass amplifiers (SPA) and a Northrup-Grumman SPA (NGA) boost the energy to several μ J per pulse before the two doubling crystal stages that generate the green and then the UV components at 3 MHz [3]. The UV is transported out of the laser lab through the UV transport line to the photocathode of the gun for generation of the photoelectron beams for the SC rf accelerator [1].

Base Electron Beam Diagnostics

The base beam profile imaging stations have been equipped with both YAG:Ce scintillators and optical transition radiation (OTR) screens, optical transport, and digital CCD cameras. The Gig-E vision protocol has been supported by selection of the Prosilica 5 Mpix cameras for

*Work supported under Contract No. DE-AC02-07CH11359 with the United States Department of Energy.
#lumpkin@fnal.gov

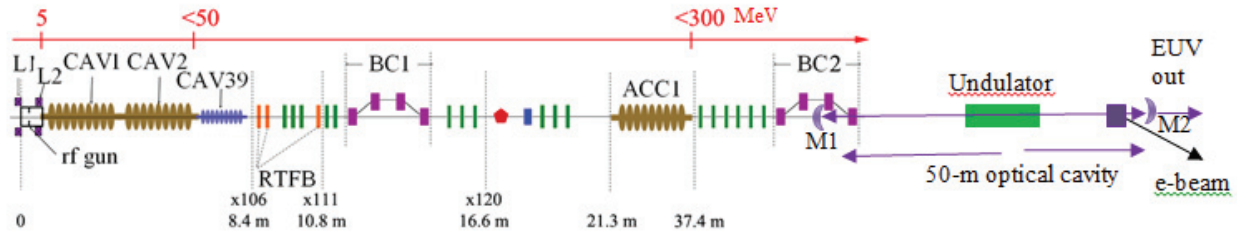


Figure 2: Schematic of the ASTA linac showing the rf gun, solenoids L1 and L2, the L-band booster cavities (CAV1 and CAV2), a proposed third harmonic linearizing cavity, chicane BC1, the first cryomodule (ACC1), and the proposed FEL oscillator configuration.

the beamline profiling stations and the 1.3 Mpixel camera with 2/3" format for the streak cameras. We have then used both the online Java-based ImageTool and the offline MATLAB-based ImageTool processing programs [4,5] in the commissioning of the system. The commissioning of the UV drive laser and the comprehensive measurements with the streak camera are described elsewhere in this conference [6]. A set of rf BPMs, wall current monitors, and toroids are also being implemented.

The Hamamatsu Streak Camera Systems

Commissioning of the laser lab streak camera system was facilitated through a new suite of controls centered around ACNET, the Fermilab accelerator controls network. This suite included operational drivers to control and monitor the streak camera, as well as Java-based programs to interface with the driver and retrieve images from the readout camera. This commissioning period allowed a number of improvements to be made to all aspects of interfacing with the C5680 streak camera, both in terms of software and hardware [6].

For the electron beam studies, the second streak camera is also a Hamamatsu C5680 mainframe with S20 PC streak tube and can accommodate a vertical sweep plugin unit and a horizontal sweep unit or blanking unit. The all-mirror input optics enables the assessment of the UV OTR component as well as the visible light OTR. These optics also mitigate the streak image blurring due to the inherent chromatic temporal dispersive effects of the lens-based input optics for broadband sources such as OTR. The studies will start with the M5675 synchroscan unit with its resonant circuit tuned at 81.25 MHz so the streak image would have jitter of less than 1 ps from the system itself.

Bunch Length Monitor at 20-50 MeV

We have developed plans for the bunch length monitor station that will be located after the chicane at X121 as shown in Fig. 3. An Al-coated Si wafer rotated at 45 degrees to the beam direction will serve as the converter screen (36 mm x 25 mm) for generation of coherent transition radiation (CTR), coherent diffraction radiation (CDR), and incoherent OTR. The three sources are schematically shown in Fig. 4. Initially, the lower screen edge will be moved above the beam center to allow the nonintercepting generation of CDR instead of using an aperture in a screen. The THz signals will be detected by

pyroelectric detectors, and the MPI will be employed for bunch length evaluation. The OTR will be transported in an enclosed pipe outside of the tunnel to the streak camera station.

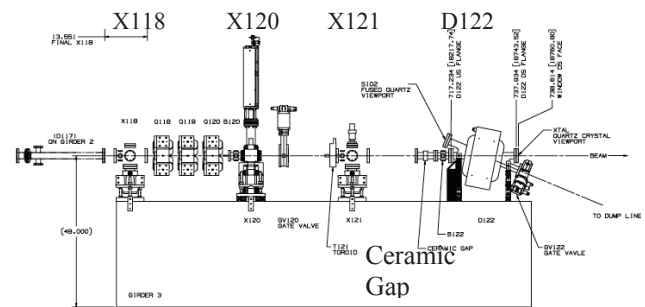


Figure 3: Post-chicane area (Girder 3) with quads and planned imaging stations X118, X120, and X121 and the ceramic gap.

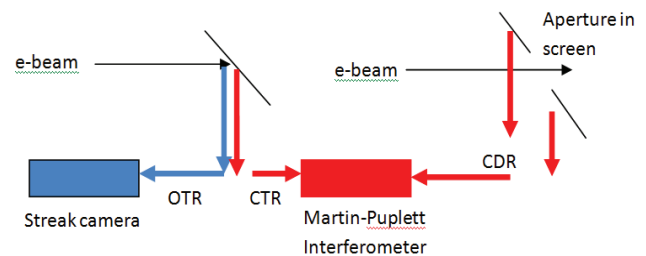


Figure 4: Schematic of a three-source option for OTR, CTR, and CDR diagnostics with the streak camera and MPI indicated. The OTR/CTR screen is at the left, and the CDR screen with aperture is at the right.

In addition a ceramic gap monitor located downstream of the X121 station as indicated in Fig. 3 will be used to assess bunch length. The expected temporal resolutions for the techniques are provided in Table 1 as compared to alternative rf deflector techniques. The rf deflector installations have been postponed. The streak camera viewing OTR and MPI via CTR will be used to evaluate the ceramic gap monitor performance with low power beam at the 1 ps level. With high power beam we will adjust the Al screen lower edge to be a few mm above the beam line center and use the CDR with MPI to compare to the ceramic gap results.

Table 1: Summary of Bunch Length Monitor Options with Technique, Resolution, and Estimated Charge Needed

Technique	Resolution	Charge needed
Streak camera	~0.6 ps sigma at 800 nm, range 0.5-25ps, phase stable*	8-10 nC
MPI	0.3 ps, range 0.3 to 1ps. CTR,CSR,CDR	10-50 nC, depends on σ_t
Ceramic gap	0.5 to 5ps	TBD
RF cavity, L-band	0.5 ps estimated	250 pC with scintillator screen
RF cavity, 3.9 GHz	TBD	250 pC with scintillator screen

EXPERIMENTAL RESULTS

Initial PC RF Gun Results

The rf PC gun studies were initiated last year on June 20, 2013 by using just the Mo substrate as a low quantum efficiency cathode. With a few μJ of energy per UV pulse, we generated a few pC per micropulse. Since that time the Cs_2Te coated cathodes with about 1 to 1.5 % Q.E. were installed in the transfer chamber, and one subsequently inserted into rf gun back plane. Micropulse charges of 20 to 1000 pC were generated for 100 μs at 3 MHz. One of the first images is shown in Fig. 5, and an early evaluation of beam energy versus the gun rf power is shown in Fig. 6. The plots show both data extracted from the solenoid field scan and the use of the corrector magnets to cause measurable beam deflections. The highest power gave a gradient of about 45 MV/m. A few runs were done with 3000 micropulses to exercise the laser system at the design macropulse length, but with reduced charge per micropulse as seen in Fig. 7. This kind of macropulse when accelerated by the linac and cryomodule and bunch compressed could support an FEL oscillator configuration at 120 nm. The schematic of this implementation is shown in Fig. 2, and the simulations are given in reference [2].

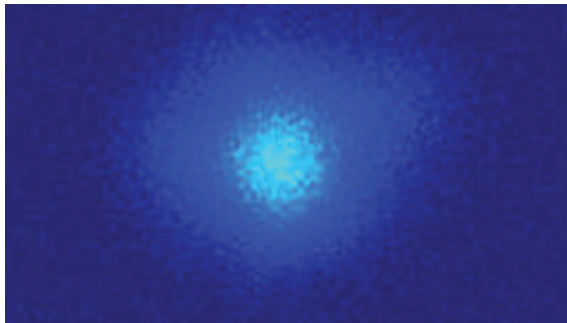


Figure 5: Image of beam at 4 MeV from the gun using the YAG:Ce converter screen and digital CCD camera. It was sub-mm (sigma) beam size [7].

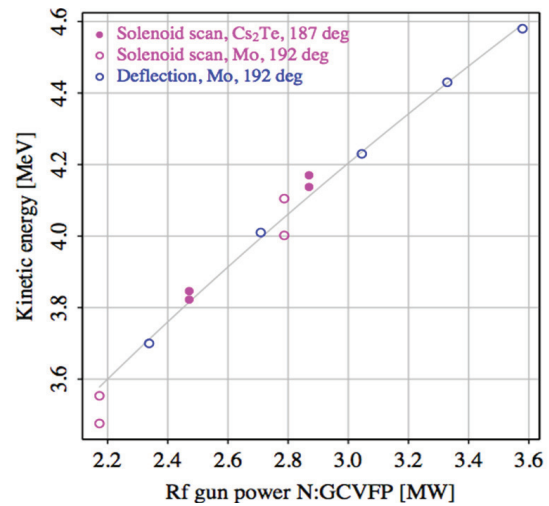


Figure 6: Electron beam energy after the gun vs. rf gun power [8].

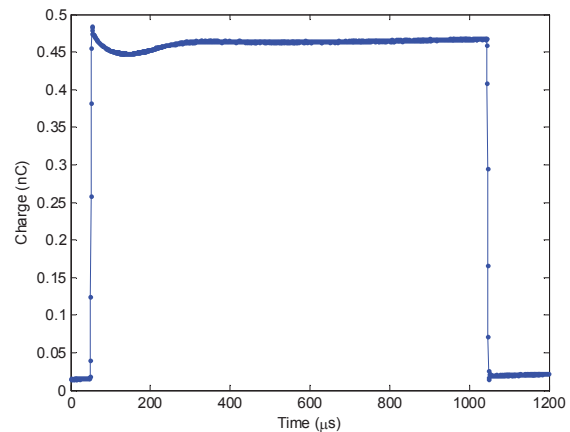


Figure 7: Demonstration of 1-ms-long macropulse of photoelectrons with about 0.45 nC per micropulse as measured at the low energy Faraday cup [8].

Cryomodule Cavity Conditioning Results

The eight cavities in the cryomodule presently installed in the tunnel as shown in Fig. 8 have been rf conditioned individually. All but one reached the targeted 31.5 MV/m gradient as shown in the plots of Fig. 9 [9]. The one reached 30.5 MV/m. The average of the eight cavity gradients is still 31.3 MV/m, which is the highest value demonstrated in a cryomodule to date. The plots of the cavity gradients in the vertical and horizontal test stands are also shown for comparison in Fig. 9. Details were presented at IPAC14 [9]. More recently cavities 1-7 have been powered at the same time through an rf power distribution system and attained > 30 MV/m average in initial conditioning tests.



Figure 8: Cryomodule as installed in the ASTA tunnel before the waveguide distribution system was installed.

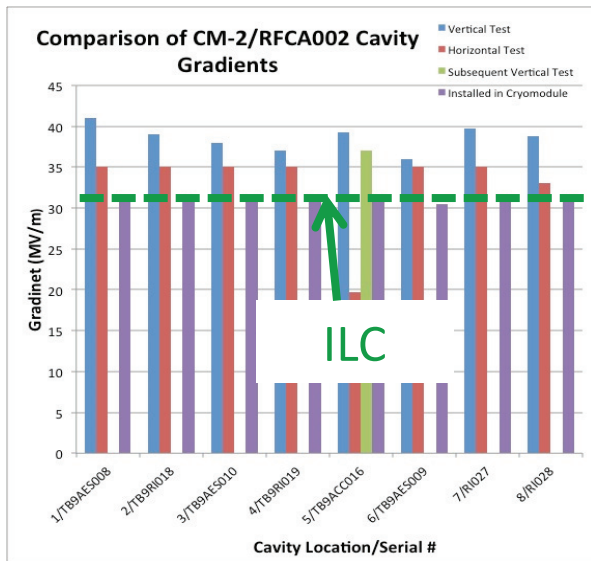


Figure 9: Plot of the cavity gradients attained in the vertical test stand (blue), horizontal test stand (red), and when installed in the CM-2 cryomodule (purple). The 31.5 MV/m value was a target and initial administrative limit in the cryomodule tests [9].

SUMMARY

In summary, we have described a series of commissioning results on first beam from the gun and first tests at high gradient of the SCRF cavities in the cryomodule. We are poised to accelerate beam to 20+ MeV and to begin full characterization of the beam properties. Eventually we will extend the beamline to the high energy beam dump and then inject beam into the cryomodule to evaluate higher order modes under beam loading conditions.

ACKNOWLEDGMENTS

The authors acknowledge the generation of ACNET controls for the various systems by C. Briegel; the development of the Java-based ImageTool code by J. Diamond, the 81.25 MHz rf source provided by B. Chase, and efforts of the mechanical support and clean room personnel of Fermilab's Accelerator and Technical Divisions.

REFERENCES

- [1] The ASTA User Facility Proposal, Fermilab-TM-2568, October 2013.
- [2] A.H. Lumpkin et al., "Feasibility of an XUV FEL Oscillator at ASTA", in *Proc. 35th Int. Free-Electron Laser Conf.*, New York, 2013, pp. 88-91.
- [3] J. Ruan, M. Church, D. Edstrom, T. Johnson, and J. Santucci, in *Proc. of Int. Particle Accel. Conf.*, Shanghai, 2013, WEPME057.
- [4] J. Diamond, FNAL, online Java-based ImageTool, (2013).
- [5] R. Thurman-Keup, FNAL, offline MATLAB-based ImageTool (2011).
- [6] A.H. Lumpkin, C. Edstrom, J. Ruan, and J. Santucci, "Commissioning of a Dual-Sweep Streak Camera with Applications to the ASTA Photoinjector Drive Laser", in *These Proceedings: Proc. 36th Int. Free-Electron Laser Conf.*, Basel, 2014, MOP021.
- [7] D. Crawford et al., "Assembly and Installation of Beam Instrumentation for the ASTA Front-end Diagnostic Table", in *Proc. of the Int. Particle Accel. Conf.*, Dresden, 2014, pp.3732-3734.
- [8] J. Ruan et al., "Commissioning Status of the Advanced Superconducting Accelerator at Fermilab", in *Proc. of the Int. Particle Accel. Conf.*, Dresden, 2014, WEPRI058.
- [9] E. Harms et al., "SRF Systems for ASTA at Fermilab", in *Proc. of the Int. Particle Accel. Conf.*, Dresden, 2014, WEPRI052.

CHARACTERISTICS OF TRANSPORTED TERAHERTZ-WAVE COHERENT SYNCHROTRON RADIATION AT LEBRA

N. Sei, H. Ogawa, Research Institute of Instrumentation Frontier, National Institute of Advanced Industrial Science and Technology (AIST), 1-1-1 Umezono, Tsukuba, Ibaraki 305-8568, Japan
K. Hayakawa, T. Tanaka, Y. Hayakawa, K. Nakao, T. Sakai, K. Nogami, M. Inagaki, Laboratory for Electron Beam Research and Application (LEBRA), Nihon University, 7-24-1 Narashinodai, Funabashi, 274-8501, Japan

Abstract

Nihon University and National Institute of Advanced Industrial Science and Technology have jointly developed terahertz-wave coherent synchrotron radiation (CSR) at Laboratory for Electron Beam Research and Application (LEBRA) in Nihon University since 2011. We have already observed intense terahertz-wave radiation from a bending magnet located above an undulator dedicated for an infrared free-electron laser (FEL), and confirmed it to be CSR. We have transported the CSR to an experimental room, which is next to the accelerator room across a shield wall, using an infrared FEL beamline. The power of the transported CSR was 50 nJ per macropulse, and it was available at frequencies of 0.1–0.3 THz. The transported CSR beam can be applied to two-dimensional imaging and spectroscopy experiments. From two-dimensional imaging performed with the THz-wave CSR, metallic structures concealed by plastic in a smart card were nondestructively detected at a spatial resolution of 1.4 mm.

INTRODUCTION

In order to obtain an FEL with high gain, the electron beam in FEL facilities has a short bunch length and a high charge. The electron beam in the FEL facilities can also generate intense terahertz waves by coherent radiation. Since 2011, then, Nihon University and National Institute of Advanced Industrial Science and Technology have jointly developed intense THz-wave CSR at Laboratory for Electron Beam Research and Application (LEBRA) in Nihon University. We have already observed intense coherent synchrotron radiation (CSR) in the THz-wave region using an S-band linac at LEBRA [1]. Because the CSR does not influence a process of infrared FEL oscillations, it is possible to use the THz-wave CSR and infrared FELs simultaneously. If a complex light source composed from the CSR and FEL are developed, we can conduct highly reliable material identifications.

Then, we transported the CSR to the experimental room, which was next to the accelerator room across a shield wall, using an infrared FEL beamline. We could obtain a CSR beam whose intensity was approximately 50 nJ per macropulse. The CSR beam could be used for

spectroscopy experiments at frequencies of 0.1–0.3 THz [2]. In this article, characteristics of the CSR transported to the experimental room are reported in detail.

THZ WAVE SOURCE BY CSR

The S-band linac at LEBRA consists of a 100 keV DC electron gun, prebuncher, buncher, and three 4 m long traveling wave accelerator tubes [3]. The electron beam accelerated by the linac is guided to an FEL undulator line by two 45° bending magnets. The electron-beam energy can be adjusted from 30 to 125 MeV, and the charge in a micropulse is up to 30 pC in full-bunch mode, where the electron beam is bunched in 350-ps intervals. The electron-beam energy was set to 100 MeV in the CSR observations. The macropulse duration determined by the flat-top pulse width of the 20 MW klystron output power is approximately 20 μ s. The bunch length is compressed from 3 to less than 1 ps by a magnetic compressor using two 45° bending magnets that guide the electron beam to an FEL undulator line [4]. However, there is no optical beam window to extract the CSR in the FEL undulator line. Thus, we developed the CSR emitted at the entrance of the second 45° bending magnet, where the calculated bunch length was approximately 2 ps in full-bunch mode. Although the CSR is emitted along the electron-beam orbit in a bending magnet chamber (internal height, 24 mm), its solid angle which was incident on an entrance of a transfer pipe (diameter, 20 mm; length, 265 mm) was 0.065 radians.

We observed intense sub-THz-wave radiation emitted from the second 45° bending magnet by using a Schottky D-band diode detector (Millitech Inc., DXP-06) [1]. The measured power of the intense sub-THz-wave radiation was proportional to the second power of the electron-bunch charge in full-bunch mode. The vertically polarized component of the intense sub-THz-wave radiation had roughly the same vertical distribution as the synchrotron radiation. Thus, the radiation was identified as CSR. The measured CSR power per macropulse was approximately 0.4 μ J in the D-band region.

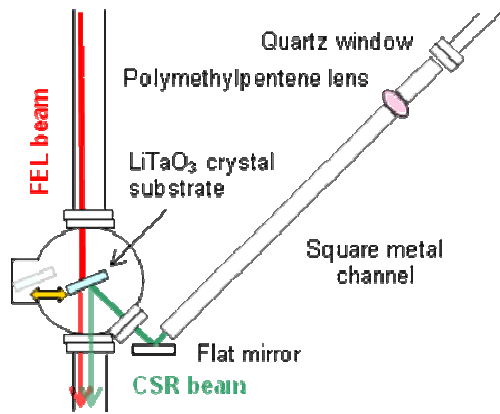


Figure 1: Relationship between the THz-wave source and the infrared FEL beamline.

TRANSPORTATION OF THE CSR

If the intense THz-wave CSR is transported to the same space as the infrared FEL, we can conduct complex imaging in the two wavelength regions and expect to realize highly reliable material identifications. Then, we planned to transport the CSR beam to an experimental room using the infrared FEL beamline. Outline of the THz-wave source of the CSR and the infrared FEL beamline is shown in Fig. 1. Because the infrared FEL beam is a plane wave in the beamline, the CSR beam should be converted to a plane wave to be transported to the experimental room. A Tsurupica lens (Pax Co., Ltd), which had a focal length of 800 mm and an effective diameter of 36 mm, was installed at a position 800 mm

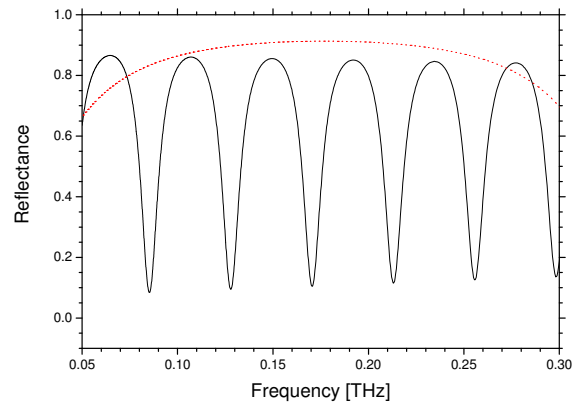


Figure 2: Calculated reflectance spectra of the LiTaO₃ substrate with thicknesses of 0.5 (solid line) and 0.06 (dotted line) mm.

from the upper end of the second 45° bending magnet, where the THz-wave CSR is generated. The CSR beam was converted to a plane wave by the Tsurupica lens, then it deflected 90° by a flat mirror and injected into the infrared FEL beamline through a quartz window. A square metal channel whose inner sides were 36 mm was set between the Tsurupica lens and the flat mirror.

To match the profile of the THz-wave CSR to the profile of the infrared FEL, we needed an optical device that would transmit the infrared FEL and reflect the THz-wave CSR by an angle of 22.5°. Because the optical device needed to maintain the wave front of the infrared FEL, a mesh mirror could not be used. Based on the difference in refractive indices in the THz-wave region

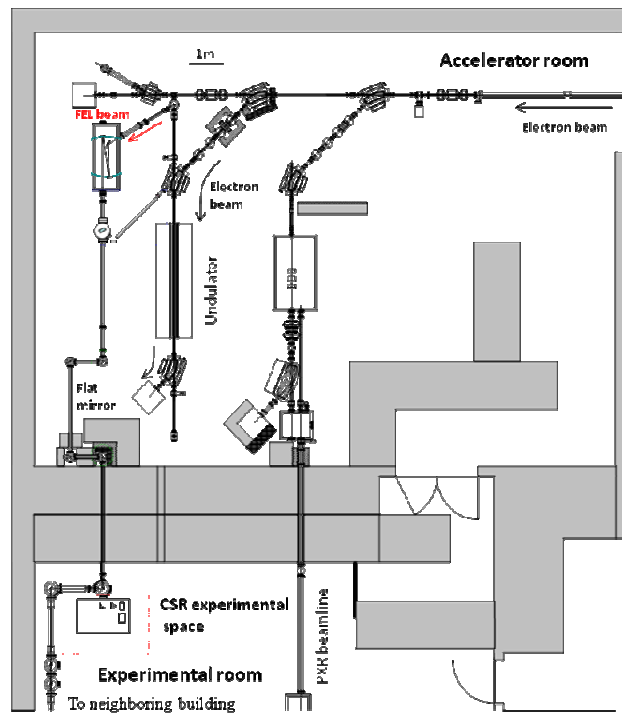


Figure 3: Schematic layout of the transportation of the CSR beam.

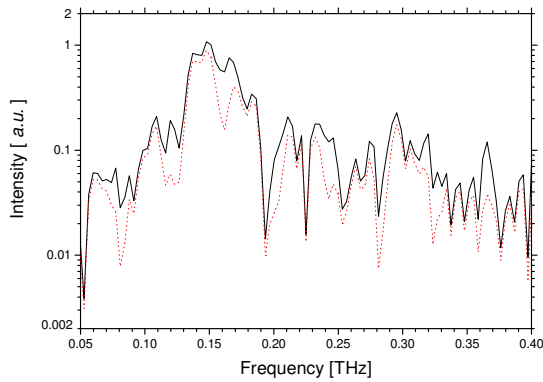


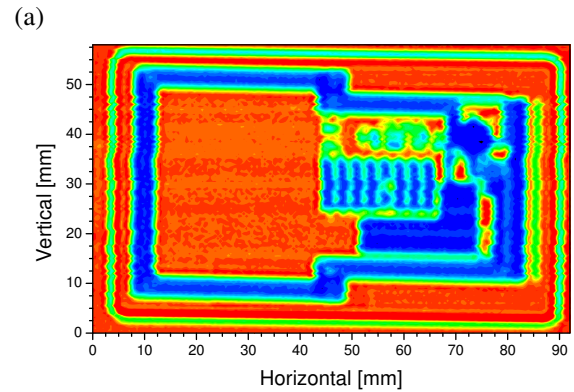
Figure 4: Calculated spectrum of the transported CSR (dotted line) and spectrum after removing the influence of the interference of the LiTaO_3 substrate (solid line).

and the infrared region, we used a flat substrate of LiTaO_3 crystal with a diameter of 76 mm and a thickness of 0.5 mm. The refractive index of the LiTaO_3 crystal is approximately 2.1 in the near-infrared region [5], and it has a transmittance of 75% in the wavelength region of 0.5–5 μm . On the other hand, the refractive index of LiTaO_3 crystal is approximately 6.5 around a frequency of 0.2 THz [6]. Figure 2 shows a calculated reflectance spectrum of the LiTaO_3 crystal substrate with a thickness of 0.5 mm. There are frequency regions of low reflectance every 42.8 GHz due to interference caused by the substrate. Based on this interference, the optimum thickness of the LiTaO_3 crystal substrate was estimated to be less than 70 μm for the reflectance spectrum; however, a thin film of LiTaO_3 crystal was not available. We expected this substrate to have an average reflectance of 67% in the frequency region of 0.1–0.3 THz.

Figure 3 shows the outline of the infrared FEL beamline. The CSR beam was transported by four flat mirrors installed in the infrared FEL beamline to the experimental room. The CSR beam was extracted from the infrared FEL beamline through a sapphire window that is attached to the first mirror chamber in the experimental room. The maximum CSR power per macropulse was estimated to be approximately 50 nJ in the D-band region in full-bunch mode. So, transportation efficiency for the CSR beam was 13%.

SPECTRUM OF THE THZ-CSR

In order to investigate the spectral characteristics of the transported CSR, we used a homemade Martin-Puplett type interferometer [7], which was used in step-scan mode with a maximum optical path difference of 50 mm. Metal wire grid mirrors, which had wire diameters of 15 μm and wire spacings of 60 μm , were used as a polarizer and a beam splitter in the interferometer. The CSR beam reflected by the polarizer was concentrated by a parabolic mirror that was then injected into a pyroelectric detector (Gentec Electro-Optics Inc., THZ-I-BNC) that was sensitive at frequencies above 0.1 THz. Figure 4 shows a



(b)

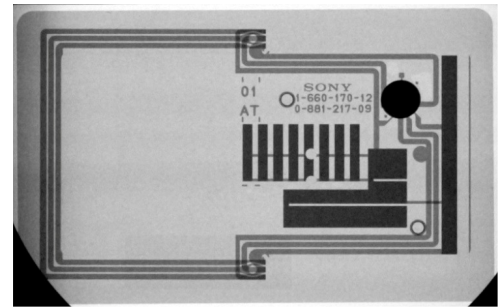


Figure 5: Transmission image of a smart card measured by the CSR beam with a D-band diode detector (a) and by the parametric x ray with an imaging plate (b).

typical spectrum of the transported CSR beam from calculating with interferograms measured by the interferometer. Note that a frequency region with low intensity appeared every 41 GHz in the CSR spectrum. The interference from the LiTaO_3 crystal substrate caused these periodic dips in the CSR spectrum. Based on the interval of the dips, the refractive index of the LiTaO_3 crystal was evaluated to be 6.9, which is almost the value of 6.5. As shown in Fig. 4, although some deep dips of unknown provenance remained in the spectrum after removing the influence of the interference, the transported CSR could be used at frequencies of 0.1–0.3 THz in full-bunch mode.

TWO-DIMENSIONAL IMAGING

We have developed a two-dimension imaging experiment by using the transported CSR beam. The CSR beam was extracted through the sapphire window and then concentrated by the parabolic mirror. We used a smart card as a sample. The dimensions of the smart card were 51 mm in height, 85.5 mm in width, and 0.8 mm in thickness. It was set on an acrylic board with a thickness of 2 mm, and the board was located at the focal point of the CSR beam. To limit the irradiated area of the CSR beam, a conical horn, which had a circular output with a diameter of 2 mm, was set at a position 2 mm above the

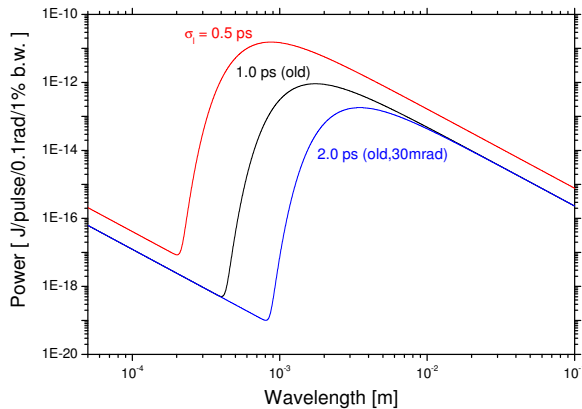


Figure 6: Calculated spectra of the CSR beam for the present light source (black and blue lines) and planning light source (red line).

smart card. To measure transmittance of the smart card, the D-band diode detector was set at a position 2 mm away from the acrylic board. The two-dimensional distribution of transmittance was measured by a raster scan at an interval of 0.5 mm. Figure 5 shows the imaging data for the smart card from the sub-THz-wave CSR and from a parametric X-ray, which was supplied by another beamline in LEBRA [8]. Comparing the CSR and X-ray imagings shows that the CSR beam could sense metals in the plastic body of the smart card. This CSR imaging system distinguished 1.5 mm wide metal plates and 1.0 mm wide gaps between metal plates at the center of the card. It could not distinguish 0.5 mm wide gaps of wires around the edge of the card. When a spatial resolution of the CSR imaging system was defined as a width where the transmittance is from 0.2 to 0.8 at an edge, it was evaluated to be 1.4 mm. However, a narrow wire with a width of 0.5 mm was detected at the right edge; therefore, we could sense a smaller metal piece in the plastic body when another metal structure did not exist around the wire.

FUTURE PLAN OF THz SOURCE

As mentioned above, the bunch length can be compressed to be less than 1 ps in the FEL straight section. Then, we plan to develop a new CSR source, which can supply more intense and shorter-wave THz beam, at the downstream bending magnet in the FEL straight section. A solid angle of the new CSR source will be 0.1 radians. Figure 6 shows a spectrum of the expected CSR beam at the exit of the bending magnet when the bunch length is 0.5 ps. The intensity of the new CSR

beam will be approximately 100 times than that of present CSR beam. We will remake the vacuum chamber of the bending magnet to extract the intense CSR and transport it to the experimental room with using the infrared FEL beamline.

CONCLUSIONS

We have successfully transported THz-wave CSR from an accelerator room to an experimental room by using an existing infrared FEL beamline at LEBRA. The intensity of the CSR in the experimental room was approximately one eighth of that near the second 45° bending magnet in the accelerator room. The CSR spectrum was measured by a Martin-Puplett type interferometer and a pyroelectric detector, and it was found that the CSR was available in the frequency region of 0.1–0.3 THz. In a two-dimensional imaging experiment on a smart card, the spatial resolution of the imaging system was 1.4 mm. We will investigate characteristics of the CSR at the downstream bending magnet in the FEL straight section and develop a new THz-wave CSR source.

ACKNOWLEDGMENTS

This work has been supported in part under the Visiting Researcher's Program of the Research Reactor Institute, Kyoto University, and ZE Research Program ZE25B-7 and ZE26B-1, Kyoto University.

REFERENCES

- [1] N. Sei et al., J. Phys. D: Appl. Phys. **46** (2013) 045104.
- [2] N. Sei et al., “Complex light source composed from sub-terahertz-wave coherent synchrotron radiation and an infrared free-electron laser at LEBRA”, J. Opt. Soc. Am. B (in press).
- [3] Y. Hayakawa et al., Nucl. Instrum. Methods Phys. Res., Sect. A, **483** (2002) 29.
- [4] K. Hayakawa et al., “Operation of near-infrared FEL at Nihon university” Proc. 29th Int. Free Electron Laser Conf., (Novosibirsk, Russia, 2007) p 114 (2007).
- [5] J. L. Casson et al., J. Opt. Soc. Am. B, **21** (2004) 1948.
- [6] M. Schall et al., Int. J. Infrared Millimet. Waves. **20** (1999) 595.
- [7] D. H. Martin and E. Puplett, Infrared Phys. **10** (1970) 105.
- [8] Y. Hayakawa et al., J. Inst., **8** (2013) C08001.

A SWEDISH COMPACT LINAC-BASED THz/X-RAY SOURCE AT FREIA

V.A. Goryashko*, Uppsala University, Uppsala, Sweden

A. Opanasenko, NSC/KIPT, Kharkiv, Ukraine

V. Zhaunerchyk, University of Gothenburg, Gothenburg, Sweden

Abstract

THz radiation enables probing and controlling low-energy excitations in matter such as molecular rotations, DNA dynamics, spin waves and Cooper pairs. In view of growing interest to the THz radiation, the Swedish FEL Center and FREIA Laboratory are working on the conceptual design of a compact multicolor photon source for multidisciplinary research. We present the preliminary design of such a source driven by high-brightness electron bunches produced by a superconducting linear accelerator. A THz source is envisioned as an FEL oscillator since this enables not only generation of THz pulses with a bandwidth down to 0.01% (with inter-pulse locking technique) but also generation of short pulses with several cycles in duration by detuning the resonator. For pump-probe experiments, the THz source will be complemented with an X-ray source. One of the most promising options is the inverse Compton scattering of quantum laser pulses from electron bunches. Such an X-ray source will operate from 1 to 4 keV with output intensity comparable to a second generation synchrotron. The envisioned THz/X-ray source is compact with a cost comparable to the cost of one beamline at a synchrotron.

INTRODUCTION

The energy of photons from the THz spectrum range corresponds to the energy of many types of excitations in matter such as low-frequency vibrations in large molecules, molecular rotations, lattice vibrations, spin waves, internal excitations of bound electron-hole pairs. A recent workshop “*The Science and Technology of Accelerator-Based THz Light Sources*,” Uppsala, November 18-19, 2013 clearly demonstrated a tremendous increase in applications of THz radiation in physics, material science and biomedicine. The analysis of literature and the presentations given at the workshop show that apart from a well-established time-domain THz spectroscopy [1], THz radiation allows coherent control of quantum transport in semiconductor superlattices [2], spin waves in antiferromagnets [3], quantum bits in semiconductors [4], high-Tc superconductivity [5]. The control was demonstrated experimentally.

THz radiation also finds a lot of applications in biophysics. In particular, it was reported that irradiation of mammalian stem cells with a THz field results in heterogenic changes in gene expression [6]. The proposed resonant mechanism of interaction of THz fields with stem cells predicts a creation of new open states in the double helix of DNA [7]. One more exciting application of THz radiation is connected to the study of chiral molecules, which are widely found in

biology, for example, amino acids. Chirality plays an important role in medicine since drugs containing different enantiomers have different biological activity [8] because receptors, enzymes, antibodies and other elements of the human organism also exhibit chirality. Fingerprints of biological molecules belong to the THz region and it is foreseen that circularly polarized THz radiation can be used for studying chirality of bio-molecules.

In view of growing interest to the THz radiation, the Swedish FEL Center together with the FREIA Laboratory is studying the national user interest in THz physics and working on the conceptual design of a versatile photon source. The ultimate goal is to build a versatile THz/X-ray source for a multidisciplinary national user facility at the FREIA laboratory of Uppsala University. The photon source will be driven by high-brightness electron bunches produced by a superconducting linear accelerator (SC linac). In particular, we aim to combine an envisioned THz FEL with a soft X-ray source and such a combination will provide an opportunity for the time-resolved pump(THz)–probe(X-ray) measurements. Implementation of superconducting technology would greatly enhance flexibility of the envisioned multi-color photon source. Specifically, a photon source based on a SC linac enables the best flexibility in terms of bandwidth and wavelength tunability as well as scalability both in repetition rate and pulse energy [9]. Superconducting linacs enable operation in continuous wave (CW) or quasi-CW mode, which implies higher average brightness of the source. With a high duty factor operation, a SC linac also reduces the overall size of the facility and is economically more efficient than its normal conducting counterpart.

THE COMBINED THz/X-RAY SOURCE

The conceptual layout of the combined THz/X-ray source is schematically shown in Fig. 1. A SC linac is followed by an X-ray source and a THz FEL oscillator.

One of the main challenges of the project is an electron source since high-brightness low-emittance electron bunches are needed for an efficient inverse Compton scattering process. Currently, only a SC photocathode RF gun can deliver bunches with the required parameters. However, this gun is complicated for fabrication and operation as well as expensive for a university facility. The search for an alternative lead us to a gun design, which is similar to the design proposed at Argonne [10]. The proposed gun utilizes a normal conducting (NC) 176 MHz re-entrant resonant cavity with an acceleration gradient of 20 MV/m. Note that an RF gun cavity of such geometry has been developed at the Lawrence Berkeley National Laboratory (USA) [11, 12] for the NGLS project. This cavity has a high thermal handling capability.

* vitaliy.goryashko@physics.uu.se; vitgor06@gmail.com

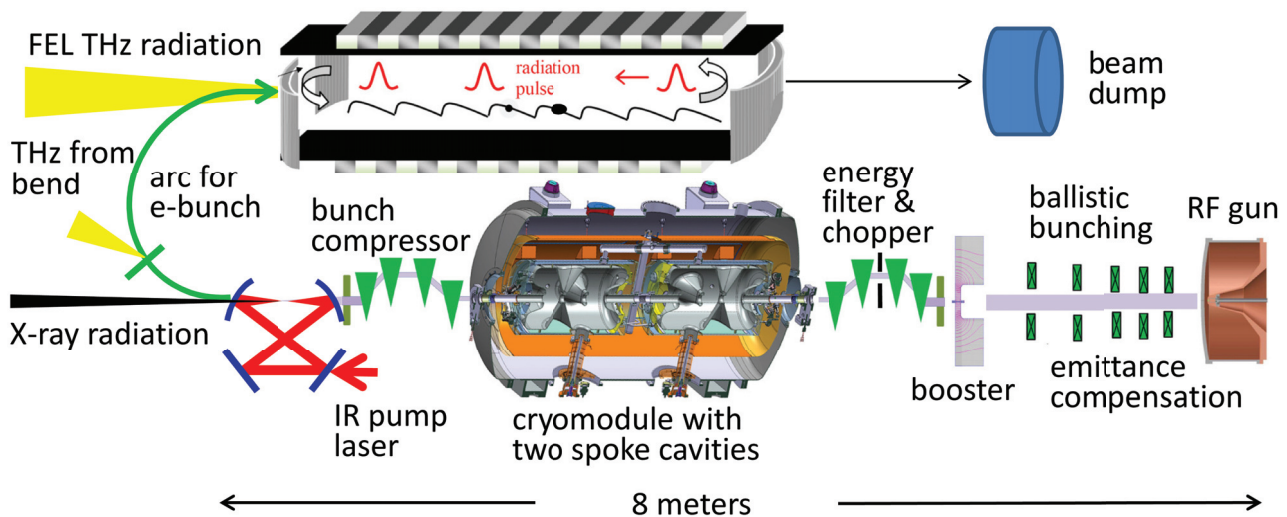


Figure 1: Schematic of a THz FEL complemented with an X-ray source.

ity and is suitable for CW operation. In order to achieve a low-emittance of 1 mm-mrad, the grid in our design is eliminated and electrons are injected into the gun cavity through a small aperture in the cavity wall. The thermionic cathode is located in the inner conductor of a stripline attached to the cavity walls. The cathode is isolated from RF fields of the gun cavity and 1 ns electron bunches are generated by applying RF pulses to the cathode via a stripline. Dark currents are suppressed by biasing. The gun is compatible with magnetic fields for emittance compensation and thermionic cathodes are capable of long-term, stable operation as this was demonstrated at Spring-8 (Japan) [13]. Simulations performed with the EGUN and PARMELA codes show that electron bunches with a charge of 0.7 nC, a duration of 1 ns, an energy of 0.4 MeV and an emittance of 1 mm-mrad can be generated. The shapes of the cathode and input/output apertures of the gun cavity were optimized in order to reduce the effects of electron beam aberration.

The NC thermionic gun has the advantages of long cathode life time (more than 20 000 hours in electron microscopes), the ease of operation and a robust and cost-efficient design. The disadvantage of such a gun is rather long electron bunches, which require an additional compression just after the RF gun. The longitudinal phase-space linearization will be done by means of the third harmonic of the gun cavity frequency. By using the third harmonic we also plan to create a non-linear energy chirp in order to compensate the non-linear dependence of the electrons transit time on their position in a bunch and obtain strong ballistic bunching [14].

The simulations performed with the simulation codes PARMELA and ASTRA show that 0.4 MeV, 0.7 nC bunches can be successfully compressed down to 10 ps within 2 meters by ballistic bunching. The use of the emittance compensation method with a solenoid allows us to keep the bunch emittance below 2 mm-mrad. A NC booster increases the bunch energy to 1 MeV for subsequent energy filtering. The

energy filter (the first, from right to left, chicane shown in Fig. 1) reduces the energy spread to around 20 keV and the bunch charge to 0.2 nC, which is sufficient for the photon source. The average power deposited in the energy filter is below 100 W.

After the energy filter, electrons will be accelerated by two double-spoke cavities operating at 352.21 MHz. A recent study on high-beta spoke cavities for electron linacs [15] strongly indicates that the energy gain in a double-spoke cavity can be as much as 10 MeV. In this case the surface electric and magnetic fields are around 30 MV/m and 55 mT, respectively, which make the cavity operation stable. The spoke cavities will be powered by two RF sources able to deliver 400 kW peak power at 352.21 MHz with a duty cycle of 10%. The sources are being built at the FREIA laboratory within the FREIA-ESS project and are potentially available for use after 2018. A turn-key cryomodule hosting two double-spoke cavities is being developed within the ESS project as well and it will be available from industry. Only minor adaptations will be required. However, the spoke cavities have to be slightly re-designed for a high phase velocity.

Downstream the cryomodule, electron bunches are compressed in a magnetic chicane down to a few ps and collided head-to-head with an IR pulse produced by an external laser in order to produce X-rays via the inverse Compton scattering. The latter technique was experimentally proven in many laboratories [16]. Scattering of laser pulses with a wavelength of 1 μm on electrons with energies from 8 to 15 MeV will result in X-ray radiation from 1 keV to 4.3 keV.

A successful implementation of inverse Compton scattering requires very intense IR pulses with a repetition rate of 176 MHz, see the electron beam temporal structure in Fig. 2. A potential solution to this problem is the use of a so-called optical enhancement cavity [17]. The experimental studies [18] already demonstrated stable cavity operation with

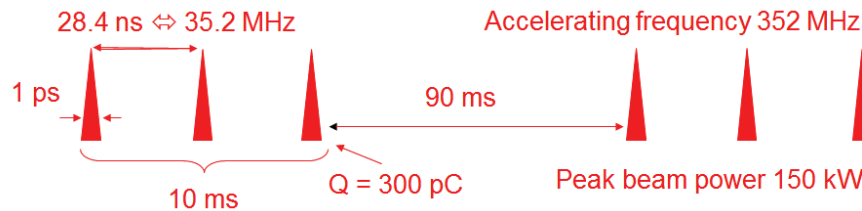


Figure 2: The proposed time structure of an electron beam at the end of the linac.

a power enhancement of around 1300 for average power of 670 kW at 1 μm wavelength and 250 MHz repetition rate. One should stress that the coherent enhancement of laser pulses in a passive cavity also provides ideal conditions for high-order HHG with multi-MHz repetition rate as it was recently demonstrated experimentally [19]. In our design, 1 mJ optical pulses will make a round trip with the repetition rate of electron bunches being equal to 176 MHz. This translates into 176 kW of average power circulating in the enhancement optical cavity during a 10 ms pulse. Note that a few ps laser pulses with a wavelength of 1 μm can be generated with up- to-date semiconductor lasers at the required power level.

Using results from the ref. [20], the analysis of X-ray emission predicts a peak and an average brightness of 5.7×10^{17} and 10^{13} photons/(s \times mm 2 \times mrad 2 \times 0.1% bw) respectively. The optical and electron beams are assumed to be tightly focused to a spot of around 60 μm . The coupling of the electron beam into the interaction region and of the X-rays out of it is currently planned through a 1 mm aperture in the cavity focusing mirrors. Another option for coupling of the electron beam would be to move one of the focusing mirrors into the centre of the magnetic chicane. This needs further investigation.

After the generation of X-rays, the electron beam is sent to a THz FEL configured as an oscillator located on top of the linac in order to make the system more compact. The latter allows not only generation of THz pulses with a bandwidth of 10^{-4} (with inter-pulse locking technique [21]) but also generation of short pulses with several cycles in duration by detuning the resonator [22]. The frequency will be tunable from 0.3 THz (1 mm) to 6 THz (50 μm) with a pulse energy 1-20 μJ . The temporal structure of the train of radiation pulses will reproduce the temporal structure of the electron beam presented in Fig. 2. For applications demanding a low repetition rate, a part of THz pulses will be re-directed to a different user station by inserting a mirror with changeable reflectivity in the THz transport line. Let us stress that in this case the THz FEL will serve two user stations.

By running the linac in a low-charge mode, one can generate short electron bunches, thus providing the possibility of generation of broadband THz pulses in the last dipole of the second chicane and/or in a dipole installed in the bending arc. The synchronization of THz and X-ray pulses for pump-probe experiments should be on a sub-ps scale and is quite

challenging but feasible. For example, the synchronization at FLASH (DESY, Germany) is on a 10 fs level [23].

SUMMARY

We present the design of a compact combined THz/X-ray source driven by a SC linac. A combination of THz and X-ray radiation shall make possible pump-probe experiments on probing and controlling low-energy excitations in matter such as molecular rotations, DNA dynamics, spin waves and Cooper pairs. In addition, the proposed Compton X-ray source can be used as a stand-alone source and provide local users of synchrotron radiation with a tunable source suitable for phase-contrast imaging and protein crystallography.

ACKNOWLEDGEMENTS

The authors would like to acknowledge the financial support from the Swedish FEL center.

REFERENCES

- [1] T. Kampfrath *et al.*, "Resonant and nonresonant control over matter and light by intense terahertz transients," *Nature Photonics*, vol. 7, pp. 680–690, May, 2013.
- [2] B.J. Keay *et al.*, "Dynamic Localization, Absolute Negative Conductance, and Stimulated, Multiphoton Emission in Sequential Resonant Tunneling Semiconductor Superlattices," *Phys. Rev. Lett.*, vol. 75, pp. 4102–4106, Nov., 1995.
- [3] T. Kampfrath *et al.*, "Coherent terahertz control of antiferromagnetic spin waves," *Nature Photonics*, vol. 5, pp. 31–34, May, 2011.
- [4] B. E. Cole *et al.*, "Coherent manipulation of semiconductor quantum bits with terahertz radiation," *Letters to Nature*, vol. 410, pp. 60–63, March, 2001.
- [5] A. Dienst *et al.*, "Optical excitation of Josephson plasma solitons in a cuprate superconductor," *Nature Materials*, vol. 12, pp. 535–541, March, 2013.
- [6] B.S. Alexandrov *et al.*, "Specificity and Heterogeneity of Terahertz Radiation Effect on Gene Expression in Mouse Mesenchymal Stem Cells," *Scientific reports*, vol. 3, p. 1184, Jan., 2013.
- [7] B.S. Alexandrov *et al.*, "DNA Breathing Dynamics in the Presence of a Terahertz Field," *Phys. Lett. A*, vol. 374, pp. 1214–1217, Feb., 2010.
- [8] T.S. Tracy, S.D. Hall, "Metabolic inversion of (R)-ibuprofen. Epimerization and hydrolysis of ibuprofenyl-coenzyme A," *Drug Metab. Dispos.*, vol. 20, pp. 322–327, March, 1992.

- [9] M. Gensch, "Super-radiant Linac-based THz Sources in 2013," Proc. of the 35th International Free-Electron Laser Conference, New York, USA, 2013, p. WEIBNO01.
- [10] R. Lindberg, "Thermionic cathode-based injector R&D at Argonne national Laboratory," Mini-Workshop on Compact X-Ray FELs Using High-Brightness Beams, Berkeley, USA, 2010.
- [11] K. Baptiste *et al.*, "Status of the LBNL Normal-Conducting CW VHF Photo-Injector," Proc. of the 23rd Particle Accelerator Conference, Vancouver, Canada, 2009, p. MO6RFP077.
- [12] F. Sannibale, RPM Seminar, "APEX: A Normal-Conducting Low-Frequency RF Photo-Injector for the Next Generation Light Source," LBNL Physics Division, Berkeley, USA, 2012.
- [13] H. Maesaka, "Low rep rate guns: SPRING 8," 48th ICFA Advanced Beam Dynamics Workshop on Future Light Sources, SLAC, California, USA, 2010.
- [14] A. Opanasenko *et al.*, "Fundamental limits of ballistic bunching of high-brightness electron beams," Proc. of the 5th International Particle Accelerator Conference, Dresden, Germany, 2014, p. MOPRO091.
- [15] C.S. Hopper, J.R. Delayen, "Superconducting spoke cavities for high-velocity applications," Phys. Rev. ST Accel. Beams, vol. 16, p. 102001, Oct., 2013.
- [16] Workshop on Compact Light Sources, Rockville, USA, 2010.
- [17] I. Pupeza, "Power Scaling of Enhancement Cavities for Non-linear Optics," Ph.D. dissertation, München, Germany, 2011.
- [18] H. Carstens *et al.*, "Megawatt-scale average-power ultrashort pulses in an enhancement cavity," Optics Letters, vol. 35, pp. 2595-2598, May, 2014.
- [19] I. Pupeza *et al.*, "Compact high-repetition-rate source of coherent 100 eV radiation," Nature Photonics, vol. 7, pp. 608-612, July, 2013.
- [20] F. V. Hartemann *et al.*, "High-energy scaling of Compton scattering light sources," Phys. Rev. ST Accel. Beams, vol. 8, p. 100702, Oct., 2005.
- [21] H.H. Weits and D. Oepts, "Continuously tunable, high-power, single-mode radiation from a short-pulse free-electron laser," Phys. Rev. E, vol. 60, pp. 946-957, Nov., 1999.
- [22] G.M.H. Knippels *et al.*, "Intense Far-Infrared Free-Electron Laser Pulses with a Length of Six Optical Cycles," Phys. Rev. Lett., vol. 75, pp. 1755-1759, Aug., 1995.
- [23] S. Schulz *et al.*, "Past, Present and Future Aspects of Laser-Based Synchronization at FLASH." Proc. of the International Beam Instrumentation Conference 2013, Oxford, UK, 2013, p. TUPSO23.

TOWARDS AN X-RAY FEL AT THE MAX IV LABORATORY

Francesca Curbis, Sverker Werin*, MAX IV Laboratory & MAX Nfak, Lund University, Lund, Sweden

Mikael Eriksson, Christoph Quitmann, Sara Thorin, MAX IV Laboratory, Lund, Sweden
Per Johnsson, Department of Physics, Lund University, Sweden

Abstract

The design of the 3 GeV linac for the MAX IV facility was done to provide the ability to host a future FEL in the hard X-ray as well as in the soft X-ray range. The linear accelerator, with its two bunch compressors, is now under commissioning. Through the years increasing details for the actual FEL have been discussed and presented. In parallel a steering group for the science case for a Swedish FEL has worked and engaged a large number of Swedish user groups. These two paths are now converging into a joint project to develop the concept of an FEL at MAX IV.

We will report on the paths to FEL performance based on the 3 GeV injector, FEL design considerations, the scientific preparation of the project, the linac commissioning and the strategy and priorities.

INTRODUCTION

The MAX IV Laboratory is in a strong phase of development with the completely new MAX IV facility which includes two ultra low emittance storage rings (3 and 1.5 GeV) [1] (Fig. 1). These rings are to be injected from a full energy (3 GeV) linac. The linac will from the start also drive the Short Pulse Facility (SPF) with the FemtoMAX beamline [2] for experiments using short (<100 fs) incoherent X-ray pulses. Currently the linac system is completely installed and under commissioning while the storage ring building is being finalized and magnet delivery has commenced.

From the very start of the MAX IV design around year 2000, it was envisaged that the future development would most likely be in the field of Free Electron Lasers. Thus the facility is prepared to be expanded into an X-ray FEL.

In the strategy of the MAX IV laboratory for the period 2013-2026 the two main goals after completing the MAX IV storage rings are a) the build-up of all 25 experimental stations at the storage rings and b) a FEL. Thus the work has been initialized both on the scientific applications of a FEL and the design of such a source. The first assumed opportunity to apply for funding is after the inauguration of the MAX IV facility (June 21st, 2016).

A FEL AT THE MAX IV LABORATORY

The design of a FEL at the MAX IV Laboratory has so far been driven by accelerator considerations. To realize the project the input from the scientific community in Sweden is being collected, leading to a science case for a FEL in Sweden (see below).

* corresponding author: sverker.werin@maxlab.lu.se



Figure 1: The MAX IV Facility in June 2014 with the Area for FEL Expansion to the Left. (photo P. Nordeng)

The 3 GeV linac at the MAX IV will be the base for a FEL project. It is in its base line design equipped with a photo cathode RF-gun [3], emittance compensating injection and two bunch compressors [4]. The performance is more or less on the level of a soft FEL driver, while expansion towards a hard X-ray FEL is well prepared. We foresee an expansion of the linac by approximately 3 GeV, total 6 GeV, following the second bunch compressor to reach a photon energy of about 9 keV (1.3 Å). The relatively low final electron energy indicates a FEL design with a low normalized emittance which is basically achieved by low charge, < 100 pC, operation.

General Layout

The general layout of the proposed facility is found in Fig. 2, where the necessary expansion is marked by the yellow field. Two FELs share the photon energy range 1.2-9 keV (1.3-10 Å) and 0.25-1.2 keV (10-50 Å) respectively. Table 1 summarizes the “Start-of-design” parameters for the FEL which represent a picture of the possible machine performance and a first match to the user requirements. We believe that the final design will come close to these performances but a full design analysis is not done yet, and we expect additional user input.

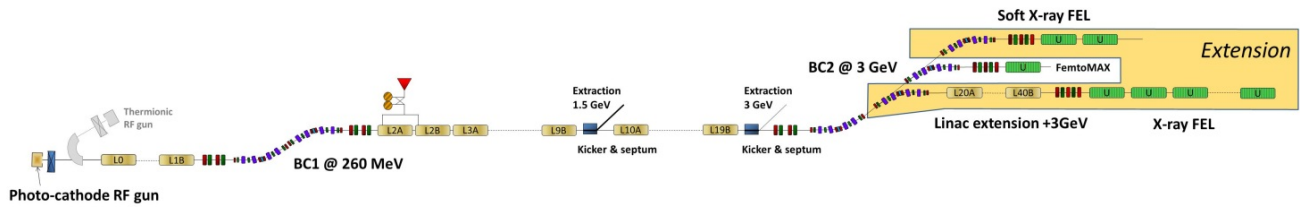


Figure 2: Overview of the MAX IV linac and the possible FEL. (White background: constructed and under commissioning. Yellow background: FEL extension.)

Hard X-ray FEL

The most demanding branch line for the MAX FEL will be the one reaching 9 keV/1.3 Å. With an electron energy around 6 GeV meeting the emittance requirements means retaining a low normalized emittance. This can be done by reducing the accelerated charge. To keep the gain length short the peak current has to be high. Meeting the user requirement of 10^{12} photons/pulse makes the design demanding and tapering is considered. Simulations of the injector [5] show that the peak current can be reached and combining proper seeding with tapering of the undulators we believe to meet the requirements.

The hard X-ray FEL will benefit from seeding based on the HXRSS, crystal based self-seeding, as operated at the LCLS [6] and SACLA [7]. We foresee difficulties in providing seeding in the complete photon energy range, especially between roughly 1 and 2.5 keV.

The undulators should reach 16 mm period and a K value between 1.5 and 2.1. An initial choice is in-vacuum devices, which are already under construction for the FemtoMAX beamline at MAX IV. As the operating gap has to be reduced below 5 mm in certain energy ranges, we will closely investigate the wake field effects, and thus also look for alternative insertion devices, such as the super conducting undulator technology developed for LCLS-II [8].

Soft X-ray FEL

A soft X-ray FEL can be built as a branch line in parallel to the linac extension. The maximum energy of the existing injector is 3 GeV which is more than adequate. A further consideration is the position of the second bunch compressor, which in this case is at full energy. Other concepts will be studied, such as adding a traditional chicane compressor at an earlier point in the lattice.

The undulators for the soft X-ray system are more relaxed with a 22.5 mm period and $K=2.5$. This can be achieved by in-vacuum devices at larger gaps, which simplifies the design. Here helical devices will be needed for the final radiation section.

There is a user demand for seeding and we believe that soft X-ray self seeding using a monochromator [9] will cover the upper part of the energy range, while laser seeding (HHG laser source or EEHG) could prove beneficial in the lower energy range, as well as helping time stamp/synchronization.

Simulations and Considerations

Modelling of the complete system is now being set-up and as first data from the pre-injector commissioning is coming in, this will be added to the model.

Seeding will be included into the modelling, but the tools for the different methods (HXRSS, SXRSS, HHG) are being developed [10].

Tapering is studied [11] to be able to reach to photon flux requirements. A modified algorithm is promising but still the length requirement is significant and would be a cost driver.

Wake fields and CSR effects act differently on the beam as the double achromat bunch compressors [4] operate on a different RF slope compared to chicane compressors. With low charge operation the compression needs to be hard to reach peak current able to drive the hard X-ray FEL, which further complicates the design. To this the effect of low gap in-vacuum undulators has to be added.

Injector tests have already started on the photo cathode gun in the gun test stand and with the first electrons in the pre-injector. As the system is commissioned data will be extracted and the system tuned to find optimum operating conditions and issues that need improvement for FEL operation up to 9 keV.

A key investigation is to explore the longitudinal phase space to assure that the peak current and energy spread can be reached while controlling the emittance growth. The MAX IV linac lacks this kind of diagnostics and thus a transverse deflecting system will be investigated.

THE MAX IV INJECTOR

Linac, Guns and BC

The pre-injector is built around two RF guns, one thermionic for storage ring injection and on one photo cathode for short pulse-low emittance operation. The thermionic gun [12] is similar to the guns developed at MAX-lab for injection of MAX I-III [13] and also operated as photo cathode gun for the MAX-lab FEL test facility [14]. The photo cathode gun is of a similar type as the system for Fermi@ELETTRA [15].

The linac is an S-band system (3 GHz) driven in pairs with one klystron and a SLED system per two structures. The operating energy is 3 GeV with a maximum energy

of 3.5-3.7 GeV. The maximum repetition rate is 100 Hz, though in principle higher repetition rates can be achieved by short circuiting the SLED system, shortening the RF pulse and thus reducing the final energy. The linac will inject the two storage rings in top-up mode which is assumed to require short (\approx second) interruptions every 2-5 minutes. With the double RF-gun system and the ability to change RF power and phase pulse-by-pulse both compression and final energy can be tuned separately for the two modes. A small limitation is that the optics has to be retained, but simulations show that this is feasible especially as the second bunch compressor is positioned after the extraction to the rings. Combining higher rep rates (>100 Hz) for FEL and top-up still needs to be investigated. Low field X-band structures could here become a solution.

The two bunch compressors (at 0.25 and 3 GeV) are double achromats with fixed first order momentum compaction but tuneable second order momentum compaction. Thus they can also passively linearize the longitudinal phase space. The compression is adjusted by the preceding linac phase.

FemtoMAX and SPF

The first station at the MAX IV facility is the FemtoMAX beamline in the Short Pulse Facility (SPF). The SPF will take compressed (<100 fs) electron pulses directly from the linac. The FemtoMAX will utilise incoherent undulator radiation based on these pulses to cover the range 1-8 keV with pulses of up to 10^7 photons/pulse. This station will not only be very special on the MAX IV, but also many of the techniques and operation modes for a FEL will be developed and tested here.

Commissioning of the Linac

The complete linac system has been installed during 2013-2014 and is now under commissioning. The two electron guns have previously been operated in a gun test stand and the gun laser system has been tested at the FEL test-facility at MAX-lab. First electrons have now been accelerated through the pre-injector on-site and the main linac is under RF power.

SWEDISH FEL SCIENCE

To date, Sweden has been very well represented at current FEL facilities.

Swedish groups made notable contributions to the science cases at LCLS and the European XFEL, and were also among the first users of FLASH and LCLS.

In addition, the Swedish user community has been very successful in obtaining beamtime at LCLS, and there are several Swedish in-kind contributions to both the preparatory and construction phases for the European XFEL.

In 2012 the work on a science case for a Swedish FEL was initiated by the formation of a steering committee at a meeting at the Swedish research council (VR) between

representatives from the main Swedish Universities [16]. Since then, several workshops have been organized to identify future possibilities and to collect input from the Swedish user community. To date, more than 40 proposals from Swedish scientists have been collected, making up a preliminary science case ranging from fundamental studies of femtosecond dynamics and non-linear spectroscopy of atoms and molecules, via clusters and nanosystems, to investigations of biomolecular systems and artificial photosynthesis.

The work with the Swedish science case is now continuing with the extraction of required FEL parameters from the received proposals, the identification and conceptual design of the needed end-stations, as well as the integration of these requirements into the FEL design.

Table2: FEL Parameters (“Start-of-design”) Yellow Fields Met in the Existing Linac Design

	FEL 1	FEL 2
Accelerator		
Energy	≈ 6 GeV	2-3 GeV
Rep rate	100 Hz	100 Hz
Linac	S-band	S-band
Bunch compressors	0.250 & 3 GeV	0.25 GeV
Electron beam		
Peak current	2-3 kA	
Charge	20-150 pC	
Beta function	7.5 m	
Emittance, norm	0.25-0.4 mmRad	
Pulse length	10 - 100 fs	10 - 100 fs
FEL undulator		
Undulator period	16 mm	22.5
Undulator K	1.5-2.1	1.5-2.5
Type	In-vac	(In-vac)
FEL performance		
Wavelength	1.3-10 Å	10-50 Å
Energy	1.2-9 keV	0.2-1.2 keV
Flux	10^{12} ph/pulse	

CONCLUSION/SUMMARY

For many years Swedish scientists have expressed need for an FEL. The recent work combining a scientific case with the appropriate accelerator design is pushing such a Swedish FEL closer to becoming a real option. With the MAX IV linac a firm platform to start an FEL project is

now at hand. It is clear that a multi station FEL in both the hard and soft X-ray is feasible.

Funding for studying the design, analysing the MAX IV injector in FEL mode and continued focusing of the scientific case is now being sought. The aim is to have a complete design ready by the time of the MAX IV storage rings start-up (June 2016), after which funding for the complete project can be sought.

REFERENCES

- [1] *Detailed Design Report - The MAX IV facility*, Available: https://www.maxlab.lu.se/sites/default/files/DDR_MAX_IV_First_Edition_2010-08-25.pdf
- [2] S. Werin, et al, "Short pulse facility for MAX-lab," *Nucl. Instr. and Meth. in Phys. Res. A* 601, pp. 98-107, (2009).
- [3] J. Andersson et al, "Beam performance of the photocathode gun for the MAX IV linac," presented at the Free Electron Laser Conference 2014, Basel, Switzerland, (2014).
- [4] S. Thorin et al, "Bunch compression by linearising achromats for the MAX IV injector," presented at the Free Electron Laser conference 2010, Malmö, Sweden, (2010).
- [5] S. Thorin et al, "The MAX IV linac and first design for an upgrade to 5 GeV to drive an X-ray FEL," presented at the Free Electron Laser conference 2013, New York, NY, USA, (2013).
- [6] J. Amann, et al., "Demonstration of self-seeding in a hard-X-ray free-electron laser," *Nature Photonics* 6, pp. 693-698, 2012, doi:10.1038/nphoton.2012.180
- [7] T. Inagaki, et al, "Stable generation of high power self-seeded XFEL at SACLA," presented at the International Particle Accelerator Conference 2014, Dresden, Germany, (2014).
- [8] *SCU R&D Review*, SLAC, US, 2014, Available: https://portal.slac.stanford.edu/sites/ad_public/review/s/scu_rd_jan_2014/presentations/Forms/AllItems.aspx
- [9] Y. Feng, "System design for self-seeding the LCLS at soft X-ray energies," presented at the Free Electron Laser conference 2012, Nara, Japan, (2012).
- [10] F. Curbis et al., "Simulation studies for an X-ray FEL based on an extension of the MAX IV linac," presented at the Free Electron Laser Conference 2013, New York, US, (2013).
- [11] A. Mak et al., "Sensitivity study of a tapered Free-Electron Laser," presented at the Free Electron Laser Conference 2014, Basel, Switzerland, (2014).
- [12] B. Anderberg, et al, "The design of a 3 GHz thermionic RF-gun and energy filter for MAX-lab," *Nucl. Instr. And Meth. In Phys. Res. A* 491, pp. 307, (2002).
- [13] M. Eriksson, "The MAX-lab story; from microtron to MAX IV," presented at the International Particle Accelerator Conference 2014, Dresden, Germany, (2014).
- [14] N. Čutić, et al, "Vacuum ultraviolet circularly polarized coherent femtosecond pulses from laser seeded relativistic electrons," *Phys. Rev. Spec. Top. - Acc. and Beams*, vol. 14, 030706, (2011).
- [15] M. Trovo et al., "Status of the FERMI@ELETTRA photoinjector", in Proceedings of European Particle Accelerator Conference 08, Genoa, pp 247 - 249, (2008).
- [16] Available: <http://www.llc.lu.se/sxlf>

CONFIGURATION AND STATUS OF THE ISRAELI THz FREE ELECTRON LASER*

A. Friedman, N. Balal, V. Bratman, E. Dyunin, Y. Lurie, E. Magory, Ariel University, Ariel, Israel
A. Gover, Tel Aviv University, Tel Aviv, Israel

Abstract

A THz FEL is being built in Ariel University. This project is a collaboration between Ariel University, and Tel Aviv University. Upon completion it is intended to become a user facility. The FEL is based on a compact photo cathode gun (60 cm) that will generate an electron beam at energies of 4.5 - 6.5 MeV. The pulses are planned to be of 300 pico Coulomb for a single pulse, and of up to 1.5 nano Coulomb for a train of pulses. The FEL is designed to emit radiation between 1 and 4 THz. It is planned to operate in the super radiance regime. The configuration of the entire system will be presented, as well as theoretical and numerical results for the anticipated output of the FEL, which is in excess of 150 KW instantaneous power. The bunching of the electron beam will be achieved by mixing two laser beams on the photo-cathode. The compression of the beam will be achieved by introducing an energy chirp to the beam and passing it through a helical chicane.

We plan on compressing the single pulse to less than 150 femto seconds. The status of the project at the time of the conference will be presented.

INTRODUCTION

At present there is an operating FEL in Ariel University, operated in collaboration with Tel Aviv University. We are in the process of building a new Tera Hertz Super Radiance FEL[1,2]. Figure 1 depicts the general layout of the system.

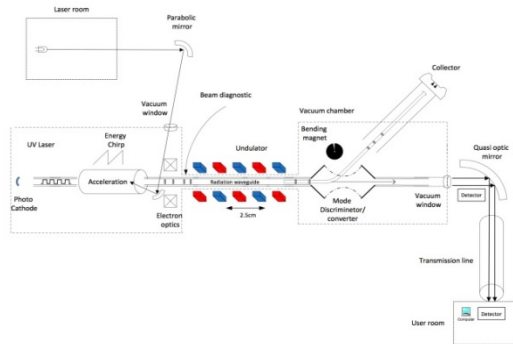


Figure 1: General layout of the Tera Hertz FEL.

The main components of the system are:

1. RF Structure.
2. Photo Cathode.
3. Laser for photo cathode.
4. Helical Chicane.
5. Wiggler.
6. Tera Hertz transmission line.

RF STRUCTURE

The RF structure is an integration of two sections: a standing wave section in which the electrons gain most of their energy, and a traveling wave section in which the energy is set to an energy chirp that would cause the pulse to shrink in time[3,4]. Figure 2 shows a simulation of the field inside the structure; the strong field is in the standing wave section, while the weaker field is in the traveling wave section.

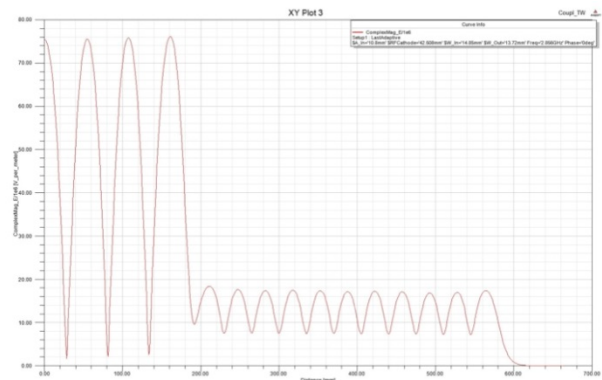


Figure 2: The electric field inside the RF structure

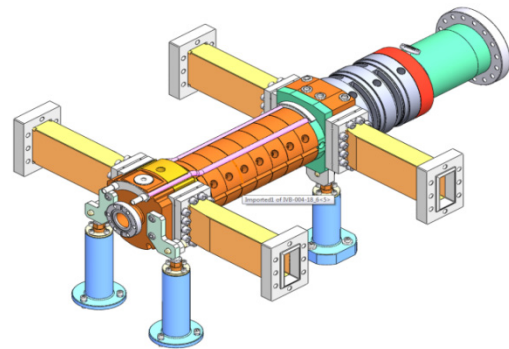


Figure 3: The mechanical design of the RF structure.

Figure 3 shows the 3D mechanical design of the RF structure including the photo cathode to the right of the picture and the input on output ports for the 3 GHz driving field.

LASER

The laser for the THz FEL is a Coherent Laser capable of producing 100 pulses per second with a width of 35 femto seconds. The energy per pulse is about 6 mJ. Currently, the laser has been ordered.

HELICAL CHICANE

Once the chirped electron beam exits the gun, it requires 6 meters to compress to 150 femto seconds. In order to shorten this length significantly, and maintain the energy chirp in the beam, while maintaining its emittance, we are designing a helical chicane.

WIGGLER

The design of the wiggler is a classical Halbach configuration as seen in Figure 4.

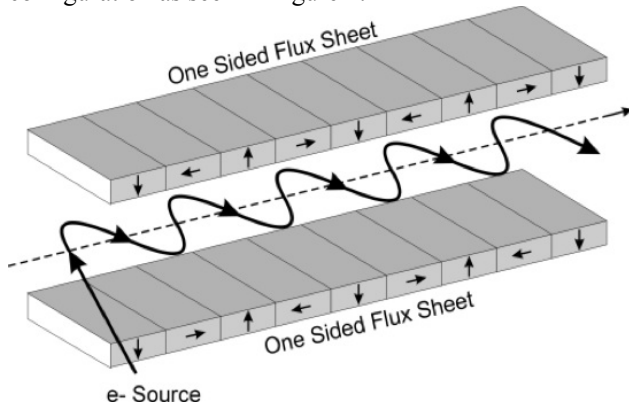


Figure 4: Halbach configuration

The design of the wiggler allows for changing the gap, with a typical gap of about 8 mm. For a wiggler period of 20 mm, this translates to a field strength on the axis of about 0.4 Tesla (Figure 5).

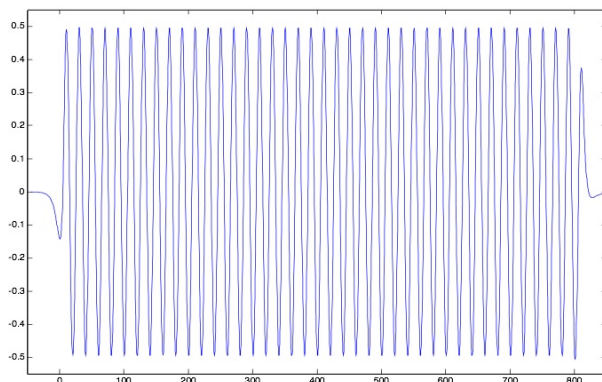


Figure 5: Wiggler field on axis

In order to make sure the electron beam does not hit the walls two magnetic bars are placed on wiggler side (see Figure 6). Currently we are still working on optimization of the placement of the two magnetic bars. However the result of an electron tracing simulation can be seen in Figure 7.

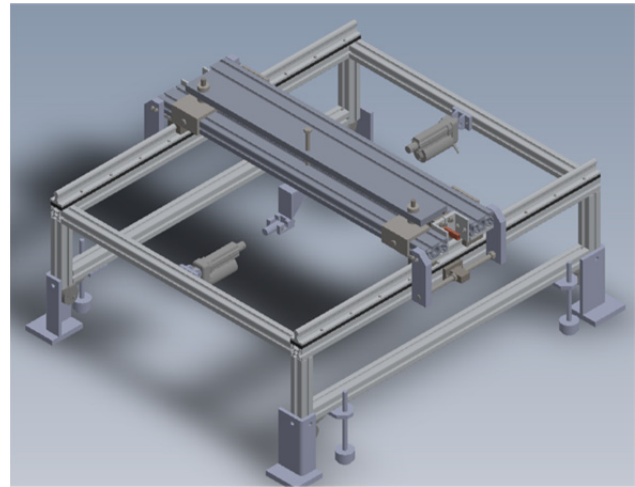


Figure 6: Wiggler structure. Note that the wiggler jaws are horizontal to each other. The transverse focusing magnet can be seen on top. The wiggler is built for a variable gap.

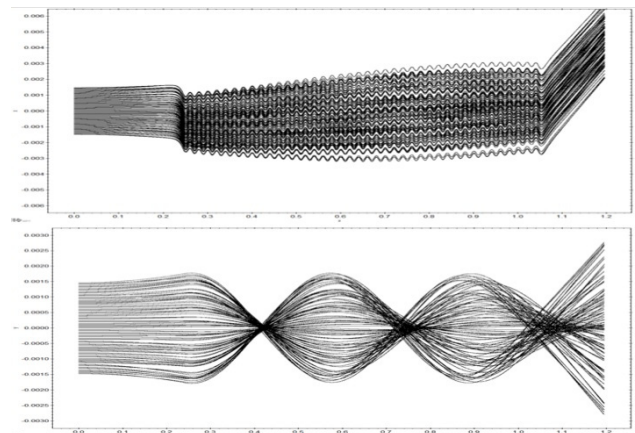


Figure 7: Electron tracing inside the wiggler using GPT. The top is the x-direction, bottom - y-direction.

We have also checked the tolerances for the electron beam entry as well as the alignment between the wiggler and the waveguide, and found to be within reason.

TERA HERTZ TRANSMISSION LINE

An electromagnetic field operating as the Tera Hertz range (1-9 THz) behaves closer to light than to millimeter waves. Thus, it is useful to use quasi optical methods to calculate its behaviour. We have written a Fourier Optics code that calculates its 3et incomplete, we have results for the free space propagation of the electric field as it exits the FEL.

In Figures 8 – 10 one can see the electric fields as it propagates away from the FEL. The field at the FEL exit was calculated with a home written code. Looking at the results it becomes obvious that we will have to use some mode conversion in order to assure that most of the energy goes into the TEM₀₀ mode.

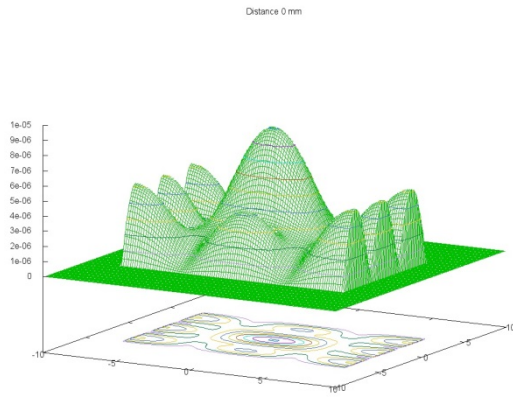


Figure 8: The electric field at the FEL exit

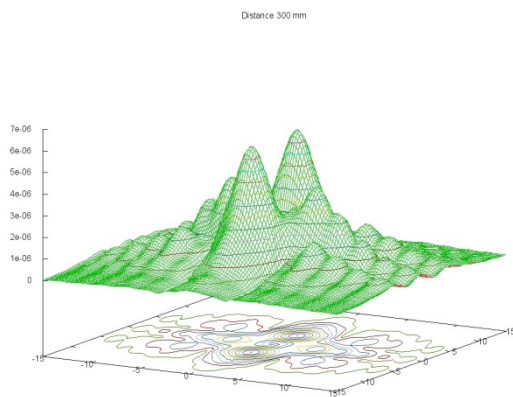


Figure 9: The electric field 30 cm from the FEL (diameter is doubled)

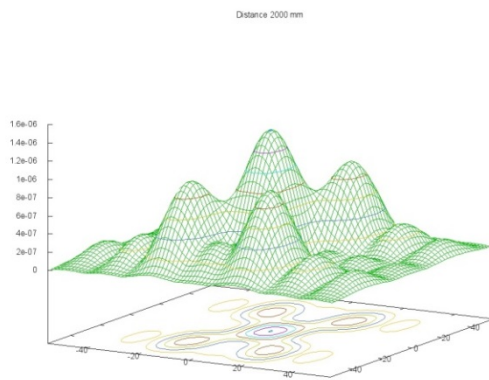


Figure 10: The electric field 2 meters from the FEL.

FEL CALCULATIONS

A code written locally is used to simulate the FEL[5]. The code calculates the excitation of the waveguide modes inside the FEL. It takes into account space charge effects, and is completely 3D. For a wiggler field of 0.4 T, and a charge of 300 pC the code yields an output of 150 KW. Figure 11 and Figure 12 show the results of the latest simulation.

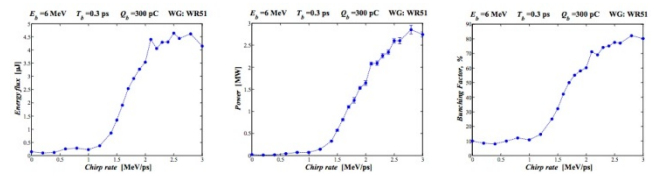


Figure 11: Energy flux (left), peak power during the pulse (in the center), and the bunching factor (right) as functions of the chirp rate. For 0.3ps e-beam pulse duration, each 1 MeV/ps of chirp rate corresponds to 300keV maximum difference of the electrons' energies.

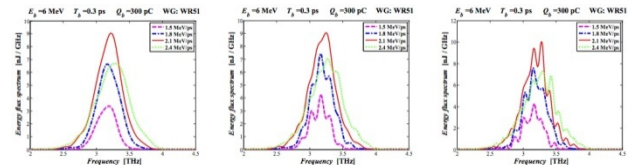


Figure 12: Spectrum of the radiation emitted after the first 20, 30 or 40 periods of the wiggler (the left, the center and the right pictures, respectively). An effective, enhanced coherent emission takes place at a first stage (first 20 periods) when a proper chirp rate is introduced (~ 2.1 MeV/ps), while incoherent, noisy radiation is present in the following.

CONCLUSIONS

The Israeli FEL is a multi-year project which is well on its way. The RF Gun and the Wiggler are being manufactured at present. Because of the extremely high space charge, the project poses several challenges which are yet to be fully resolved.

REFERENCES

- [1] E.Dyunin, Y.Lurie, Y.Pinhasi, A.Gover, 25th Convention of Electrical & Electronics Engineers in Israel, (2008) 825-829.
- [2] Y. Pinhasi, Yu. Lurie, and A. Yahalom, Nucl. Instrum. Methods Phys. Res., Sect. A 475, 147 (2001).
- [3] B. Spataro, et al., Nucl. Instr. And Meth. A 657 (2011) 99-106.
- [4] J. Rosenzweig, et al., Nucl. Instr. And Meth. A 657 (2011) 107-113.
- [5] Y. Pinhasi, Yu. Lurie, A. Yahalom, and A. Abramovich, Nucl. Instrum. Methods Phys. Res., Sect. A 483, 510 (2002).

COHERENT HARMONIC GENERATION AT THE DELTA STORAGE RING: TOWARDS USER OPERATION*

A. Meyer auf der Heide[†], S. Hilbrich, M. Höner, H. Huck, M. Huck,
S. Khan, C. Mai, R. Molo, H. Rast, A. Schick, P. Ungelenk,

Center for Synchrotron Radiation (DELTA), TU Dortmund University, Dortmund, Germany

Abstract

At DELTA, a 1.5-GeV synchrotron light source at the TU Dortmund University, a short-pulse facility based on Coherent Harmonic Generation (CHG) is in operation and shall soon be used for pump-probe experiments. Due to the interaction of ultrashort laser pulses with electron bunches in an undulator, CHG provides short and coherent pulses at harmonics of the laser wavelength. In this paper, recent progress towards user operation, pulse characterization studies such as transverse and longitudinal coherence measurements as well as CHG in the presence of an RF phase modulation are presented.

INTRODUCTION

High-gain free-electron lasers (FELs) are almost ideal radiation sources to study the structure and function of matter, combining short wavelength with femtosecond pulse duration and extremely high peak brilliance. However, to date only four of these machines are in user operation (FLASH, LCLS, SACLA, and FERMI), and being based on linear accelerators, their pulse repetition rate is low and they serve only one experiment at a time. In contrast to that, the pulse duration at synchrotron light sources based on storage rings is 30 to 100 ps, given by the bunch length, but there are about 50 of these facilities in operation [1], each providing up to 40 beamlines simultaneously with soft and hard x-rays at a rate of up to 500 MHz. For experiments that do not require or cannot even tolerate the high peak intensity delivered by high-gain FELs, methods to reduce the pulse length can significantly extend the scientific opportunities of conventional synchrotron light sources.

At synchrotron light sources, pulses in the femtosecond regime can be obtained by separating radiation from a small longitudinal part of the electrons from the rest. Such a ‘slice’ is defined by the interaction of electrons with a co-propagating ultrashort laser pulse in an undulator (the ‘modulator’) leading to a periodic modulation of the electron energy within the slice. In the case of incoherent radiation from a subsequent undulator (the ‘radiator’), a spatial separation of the short radiation component is required, a method known as femtoslicing [2–5].

Coherent Harmonic Generation

Another method based on the interaction of an ultrashort laser pulse with an electron bunch is called coherent harmonic generation (CHG) [6–9]. Here, the energy modulation

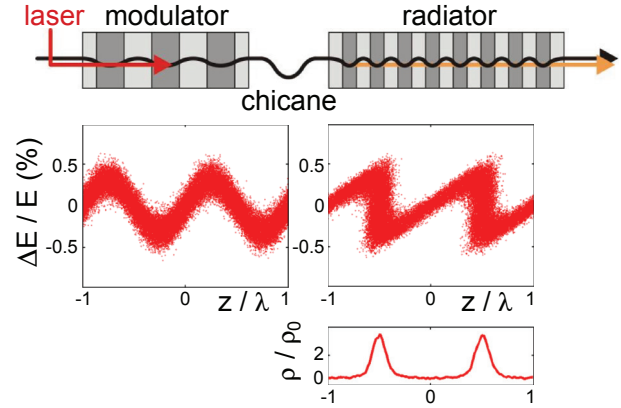


Figure 1: Sketch of the magnetic setup for CHG (top), the longitudinal phase space before and after the magnetic chicane (center), and the longitudinal electron density after the chicane (bottom).

is converted into a density modulation (‘micro-bunching’) using a magnetic chicane. This leads to the emission of a short coherent pulse in the radiator at harmonics of the laser wavelength. A sketch of this technique is depicted in Fig. 1.

Due to the coherent nature of this radiation mechanism, the CHG pulse can be more intense than the incoherent radiation from the rest of the bunch, such that no spatial separation is required. The radiated power is given by

$$P_{\text{inc}} = N_e \cdot P_e, \quad (1)$$

$$P_{\text{coh}} = \left(\frac{\tau_L}{\tau_b} \cdot N_e \right)^2 \cdot b_n^2 \cdot P_e, \quad (2)$$

where P_{inc} is the incoherent power emitted by an electron bunch with N_e electrons, P_e is the power emitted by a single electron, and P_{coh} is the CHG power emitted by the laser-modulated slice. The number of electrons contributing to the coherent emission is given by N_e times the ratio of laser pulse length τ_L and electron bunch length τ_b . The so-called bunching factor b_n is a measure for the degree of micro-bunching with a value between 0 and 1. It is given by [10]

$$b_n = e^{-\frac{1}{2}n^2 \cdot B^2} \cdot J_n(n \cdot A \cdot B), \quad (3)$$

with

$$A = \frac{\Delta E}{\sigma_E} \quad \text{and} \quad B = r_{56} \cdot \frac{2\pi}{\lambda_L} \cdot \frac{\sigma_E}{E},$$

and the harmonic number n of the laser wavelength λ_L to which the radiator is tuned. Here, J_n is the Bessel function

* Work supported by the DFG, the BMBF, and the state of NRW.

[†] arne.meyeraufderheide@udo.edu

of the order n , ΔE is the amplitude of the energy modulation, E is the beam energy, σ_E is the natural energy spread of the electron bunch, and the transfer matrix element r_{56} is the strength parameter of the magnetic chicane.

With a typical bunching factor of the order of $b_n \approx 0.1$, a fraction of contributing electrons of $\tau_L/\tau_b \approx 10^{-3}$, and $N_e \approx 10^{10}$, this leads to a power ratio of $P_{\text{coh}}/P_{\text{inc}} \approx 100$.

In contrast to femtoslicing, which suffers from an extremely low photon rate due to incoherent radiation from a small fraction of the bunch, the intensity of the CHG pulses is large. However, the wavelength is restricted to harmonics of the incident seed wavelength, and due to the dependence $\sim e^{-n^2}$ of the bunching factor, this method is only effective up to about $n = 5$. Instead of using the fundamental wavelength of a femtosecond laser (usually 800 nm from a titanium:sapphire laser system), frequency-doubled or -tripled laser pulses may be used for seeding in order to reach shorter CHG wavelengths.

In 2009, a new FEL seeding scheme was proposed, known as echo-enabled harmonic generation (EEHG) [11], in which a twofold laser-electron interaction leads to significant bunching at much higher harmonics. An implementation of the EEHG scheme to generate ultrashort coherent pulses is planned at DELTA [12].

SETUP AT DELTA

Following proof-of-principle experiments in the 1980s, e.g. [13], recent implementations of the CHG principle were undertaken at ELETTRA [8] in Trieste, Italy, at UVSOR [9] in Okazaki, Japan, and at DELTA [14, 15] in Dortmund, Germany.

DELTA is a 1.5-GeV electron storage ring operated as a light source by the Center for Synchrotron Radiation at the TU Dortmund University. In 2011, a short-pulse facility for coherent VUV and THz pulses based on the CHG principle was installed in the northern section of the storage ring (Fig. 2) [16, 17]. In contrast to other storage rings, the CHG facility at DELTA is fully compatible with standard user operation due to seeding at the nominal beam energy, and up to 50 days of dedicated machine time are available per year for characterization and optimization of the CHG source.

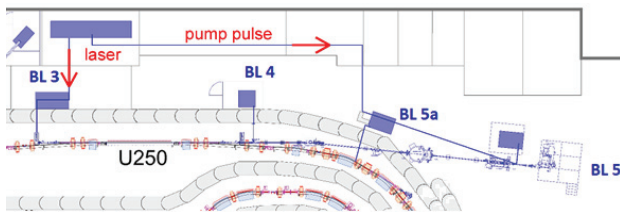


Figure 2: Sketch of the short-pulse facility in the northern section of the DELTA storage ring, including the seeding beamline BL 3, the electromagnetic undulator U250, the diagnostics beamline BL 4, the VUV beamline BL 5, and the THz beamline BL 5a (see text for details).

Laser System and Seeding Beamline

The seeding beamline BL3 features a titanium:sapphire laser system, which generates pulses with a duration of 40 fs (FWHM), a wavelength of 800 nm, and a pulse energy of 8 mJ at a repetition rate of 1 kHz. Using a second- and third-harmonic-generation unit (SHG, THG), the seeding wavelength can be converted to 400 nm or 267 nm, respectively. An optical parametric amplifier can be employed to continuously adjust the seeding wavelength between 470 nm and 1150 nm.

Thus far, seeding is performed with the fundamental wavelength of 800 nm and with 400 nm from the SHG unit. The 800-nm pulses are focused with a set of three lenses, two of which are motorized to adjust position and size of the laser waist in the modulator independently. In the case of 400 nm, the focusing is performed using one movable and one fixed curved mirror. Here, position and size of the waist are correlated.

A fraction of the focused beam is reflected back into the laser laboratory, where a ‘virtual beam waist’ is observed and optimized at the same distance from the telescopes as the actual modulator.

In future, also the third harmonic of the laser wavelength will be employed for seeding, and a common beam path will be used for all wavelengths (Fig. 3). For focusing, two consecutive telescopes with two curved mirrors each will be installed. Replacing lenses by curved mirrors will reduce pulse lengthening and self-phase modulation. Furthermore, a larger section of the beam path will be in vacuum to reduce pulse distortion in air, and therefore stabilize the CHG intensity. The first telescope (in air) increases the spot size on the vacuum window, while the second telescope (in vacuum) focuses the beam and both together allow to adjust waist size and position independently. Due to the wavelength-dependence of the Rayleigh length, the waist radius and the beam divergence cannot be both the same for each seeding wavelength. A solution has been found to achieve satisfactory waist parameters for all wavelengths using the same dielectric mirrors with a multi-wavelength coating.

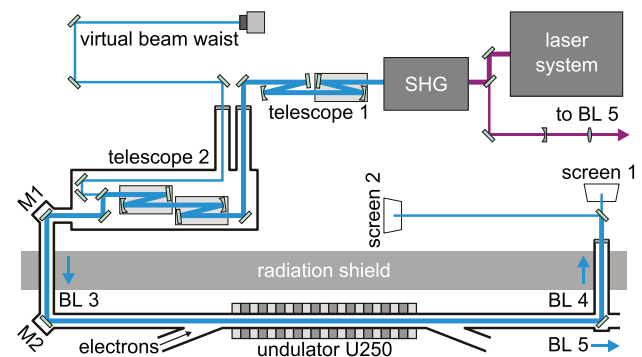


Figure 3: Sketch of the laser beam path, including the planned multi-wavelength reflective telescopes (see text for details).

The remotely controlled mirrors M1 and M2 (Fig. 3) and a digital RF phase shifter (vector modulator) allow to adjust the transverse and longitudinal overlap of the laser pulses and electron bunches.

Optical Klystron and Diagnostics Beamlines

The electromagnetic undulator U250 (Fig. 2) serves as modulator, dispersive chicane, and radiator by using three independent power supplies.

In-air diagnostics and characterization experiments are performed at the diagnostics beamline BL 4, while radiation with a wavelength below 200 nm is studied at the VUV beamline BL 5 operated by Forschungszentrum Jülich.

The diagnostics beamline BL 4 features fast photodiodes and a streak camera to optimize the temporal laser-electron overlap, as well as CCD cameras observing undulator and laser light at different distances from the modulator to optimize the transverse overlap. Characterization studies of the CHG radiation are performed using power meters, photodiodes, CCD spectrometers, a Czerny-Turner-type monochromator equipped with an avalanche photodiode (APD), and a fast-gated iCCD camera¹.

Following the laser-electron interaction in the undulator U250, the off-energy electrons travel on dispersive orbits through the subsequent magnets. Thus, path length differences lead to the formation of a sub-ps dip in the longitudinal electron density giving rise to coherent THz radiation pulses, which are extracted by the dedicated THz beamline BL 5a [17]. Besides serving as diagnostics for the laser-electron overlap, the THz beamline is used for machine studies [18] and offers intense and short pulses for time-resolved THz spectroscopy.

Pump-Pulse Beamline and User Experiments

For future pump-probe experiments, a fraction of each laser pulse is guided directly to the VUV beamline BL5. Here, the pulses are focused on the sample and transversely stabilized using a feedback system based on position-sensitive diodes and piezo-driven mirrors. The delay between pump and probe pulse is controlled with fs precision by mirrors on a motorized linear stage.

The transverse and temporal overlap between pump and probe pulses on the sample has been established. A first photoemission pump-probe experiment studying the phenomena in ferromagnetic systems using the linear magnetic dichroism [19] is under preparation.

EXPERIMENTAL RESULTS

Characterization of the CHG Pulses

In good agreement with Eqs. 1 and 2, the measured CHG radiation at the second harmonic of the seeding wavelength is up to 600 times brighter than the incoherent radiation, while the third harmonic is still 150 times brighter [14]. With a seeding wavelength of 400 nm, the fifth harmonic

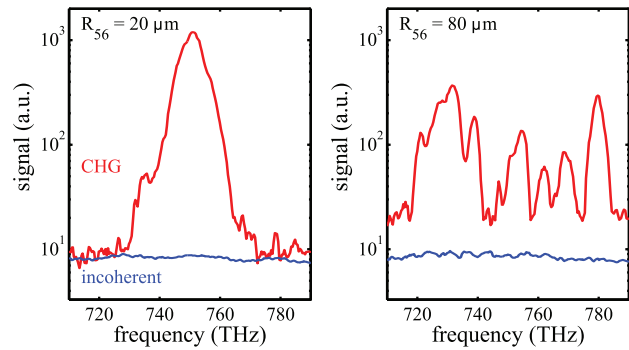


Figure 4: Spectra of CHG and spontaneous undulator radiation around 750 THz (wavelength 400 nm, second harmonic of 800 nm) measured using a Czerny-Turner monochromator with an APD as detector. With a chicane strength far above the optimum value (right), interference fringes in the CHG spectrum emerge [15].

(80 nm) could be observed, and during 800 nm seeding, the seventh harmonic (114 nm) was detected so far.

While seeding with 800 nm and 400 nm, the CHG spectra have been studied extensively under variation of several parameters such as the chicane strength (Fig. 4) or the chirp of the seed laser pulse. CHG spectra are measured with a linear CCD spectrometer, a Czerny-Turner monochromator with an APD, as well as by scanning the monochromator at the VUV beamline BL5. All measurements with optimized chicane strength (e.g. left part of Fig. 4) show a similar spectral width close to the Fourier limit [14].

The coherence of the laser-induced radiation has been studied both transversely and longitudinally [15]. The transverse coherence is measured using a classical double-slit experiment with variable slit separation and a fast-gated iCCD camera as detector. Given by the decreasing visibility of the interference fringes with increasing slit separation, coherence lengths of 1.5 mm and 0.8 mm for 400- and 200-nm

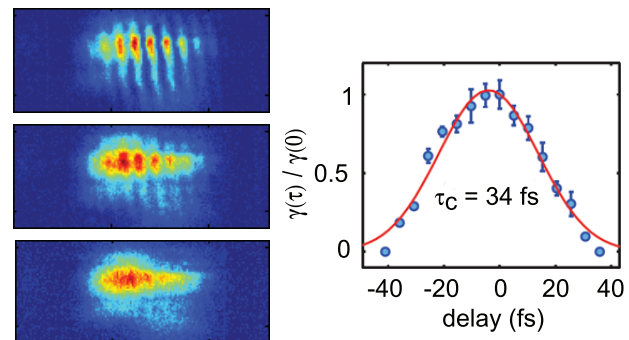


Figure 5: Interference patterns (left) of CHG pulses recorded with a fast-gated iCCD camera behind a double-slit. Using a combination of fused-silica wedges, a relative delay (increasing from top to bottom) between the light from both slits was introduced, leading to a decrease of the fringe visibility γ (right) [15], which allows to calculate of the longitudinal coherence time τ_c .

¹ The camera was generously provided by B. Schmidt and S. Wunderlich, DESY, Hamburg.

CHG radiation (seeding wavelength of 800 nm) have been measured. As part of an ongoing collaboration with the University of Siegen, the transverse coherence is also studied by analyzing speckle patterns generated by single CHG pulses scattered from a thin organic film [20].

The coherence time, or temporal coherence length, has been studied using both a Michelson interferometer and a double slit experiment, in which the light from one of the slits was delayed using a combination of fused-silica wedges [15]. First consistent results obtained with both setups yield a coherence time of 34 fs (see Fig 5), while the coherence time of spontaneous undulator radiation is only 10 fs partly given by a bandpass filter.

CHG in the Presence of an RF Phase Modulation

During standard user operation at DELTA, a phase modulation of the accelerating RF with twice the synchrotron frequency is routinely applied. The theory of RF phase modulation is described e.g. in [21]. Depending on the amplitude of the modulation, this leads to a longitudinal ‘breathing’ of the electron bunches (Fig. 6, center) or to the formation of two separate stable islands, which rotate in longitudinal phase (Fig. 6, right). As a consequence, the average electron density is reduced and the beam lifetime increases.

In general, the varying electron density would lead to a decreased CHG intensity with large fluctuations. However, adjusting the modulation frequency to a value close to a multiple of the laser repetition rate, the laser-electron interaction samples different phases of the bunch length oscillation at a slow rate of typically 2π per minute, and therefore the laser-induced CHG and THz signals exhibit a beating behaviour as shown in Fig. 7.

Surprisingly, the THz and CHG signals oscillate with 180 degree phase difference. This can be explained by assuming that the CHG signal primarily depends on the number of participating electrons according to Eq. 2 with the exponential factor in Eq. 3 being close to unity, while the THz signal

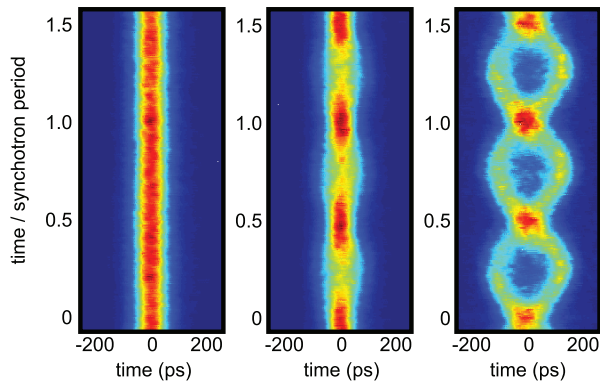


Figure 6: Streak camera images showing the evolution of the longitudinal bunch profile (horizontal axis) over 1.5 synchrotron periods (vertical axis) for an undisturbed beam (left) and in the presence of an RF phase modulation with increasing amplitude (center and right).

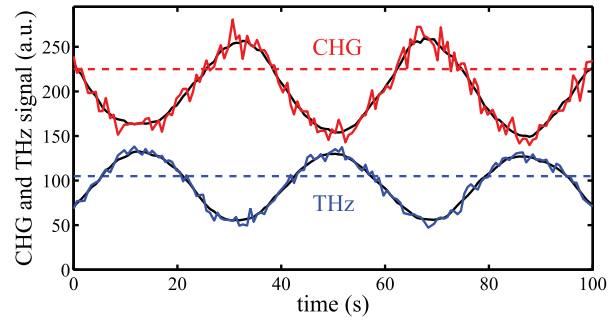


Figure 7: Slow oscillation of CHG and THz intensities due to an RF phase modulation in the ‘breathing regime’ (Fig. 6, center) close to a multiple of the laser repetition rate. The dashed lines indicate the signal intensities without RF phase modulation.

strongly depends on the energy spread, which is large when the bunches are short and vice versa.

For the intended user operation of the short-pulse facility in the presence of an RF phase modulation, a perfect synchronization between the laser pulses and the modulation phase is required. This is easily achieved at DELTA since most time-critical components receive a common 10-MHz signal from an atomic clock.

The CHG intensity and its fluctuations were recorded for different phases of the bunch length oscillation (Fig. 8). At an optimum phase within the ‘breathing regime’ (Fig. 6, center), a CHG intensity of up to 30% higher than without the RF phase modulation was observed indicating that the bunches are even slightly shorter at optimum phase than without modulation. However, the effect of an increased beam lifetime is more pronounced at larger modulation amplitudes (‘island regime’, Fig. 6, right).

Recent studies concentrate on a hybrid filling pattern with a high-current single bunch in the gap of a 3/4 multibunch pattern. Here, the RF phase modulation can be applied to all bunches, while the high-current single bunch is stabilized using a digital bunch-by-bunch feedback system [22]. First promising results show that it is possible to increase the beam lifetime without reducing the CHG intensity.

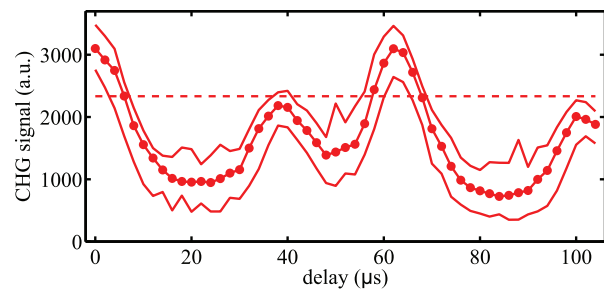


Figure 8: CHG intensity versus delay of the RF modulation phase (‘breathing regime’, Fig. 6, center) showing a minimum, maximum, and average (dots) intensity during a 20 second interval. The dashed line indicates the CHG intensity without RF phase modulation.

SUMMARY AND OUTLOOK

Since commissioning of the short-pulse facility in 2011, extensive characterization and optimization studies of the CHG and coherent THz radiation have been performed. CHG operation has already been performed during user shifts employing a hybrid filling pattern. Studies using an RF phase modulation have shown that the CHG signal can be significantly increased. Preparations for first user experiments are nearly completed. The final goal of the CHG facility is the generation of ultrashort pulses at 23 eV photon energy (53 nm, fifth harmonic of 266-nm seed), while a first pump-probe experiment will be performed at 9.3 eV photon energy (133 nm, third harmonic of 400-nm seed).

In addition, an upgrade of the short-pulse facility at DELTA using the echo-enabled harmonic generation (EEHG) scheme is in preparation [12].

ACKNOWLEDGEMENTS

We are pleased to thank our colleagues at DELTA and other institutes, particularly FZJ in Jülich, HZB in Berlin, DESY in Hamburg and KIT in Karlsruhe, for their continuous support and advice. The financial support provided by the DFG, the BMBF and the NRW Forschungsschule is gratefully acknowledged.

REFERENCES

- [1] For a list of synchrotron radiation sources see e.g. <http://www.lightsources.org>
- [2] A. A. Zholents and M. S. Zolotarev, "Femtosecond X-Ray Pulses of Synchrotron Radiation", *Phys. Rev. Lett.* 76, p. 912ff., 1996.
- [3] R.W. Schoenlein et al., "Generation of Femtosecond Pulses of Synchrotron Radiation", *Science* 287, p. 2237ff., 2000.
- [4] S. Khan et al., "Femtosecond Undulator Radiation from Sliced Electron Bunches", *Phys. Rev. Lett.* 97, p. 074801ff., 2006.
- [5] P. Beaud et al., "Spatiotemporal Stability of a Femtosecond Hard-X-Ray Undulator Source Studied by Control of Coherent Optical Phonons", *Phys. Rev. Lett.* 99, p. 174801ff., 2007.
- [6] R. Coisson and F. de Martini., "Free-electron relativistic scatterer for UV-generation," in *Physics of Quantum Electronics: Free-electron generators of coherent radiation*, vol. 9, S. Jacobs et. al., Eds. New York City, NY: Addison-Wesley, 1982, p. 939ff.
- [7] B. Girard et al., "Optical Frequency Multiplication by an Optical Klystron", *Phys. Rev. Lett.* 53, p. 2405ff., 1984.
- [8] E. Allaria et al., "Experimental Characterization of Nonlinear Harmonic Generation in Planar and Helical Undulators", *Phys. Rev. Lett.* 100, p. 174801ff., 2008.
- [9] M. Labat et al., "Optimization of a Seeded Free-Electron Laser with Helical Undulators", *Phys. Rev. Lett.* 101, p. 164803ff., 2008.
- [10] L. H. Yu, "Generation of intense uv radiation by subharmonically seeded single-pass free-electron lasers", *Phys. Rev. A* 44, p. 5178ff., 1991.
- [11] G. Stupakov, "Using the Beam-Echo Effect for Generation of Short-Wavelength Radiation", *Phys. Rev. Lett.* 102, p. 074801ff., 2009.
- [12] S. Hilbrich et al., "Upgrade Plans for the Short-Pulse Facility at DELTA", in *These Proceedings: Proc. 36th Int. Free-Electron Laser Conf.*, Basel, 2014, MOP087.
- [13] R. Prazeres et al., "Coherent harmonic generation in the vacuum ultraviolet spectral range on the storage ring ACO", *Nucl. Instr. and Meth. A* 272, p. 68ff., 1988.
- [14] S. Khan et al., "Generation of Ultrashort and Coherent Synchrotron Radiation Pulses at DELTA", *Sync. Rad. News* 26, issue 3, p. 25ff., 2013.
- [15] M. Huck et al., "Ultrashort and Coherent Radiation for Pump-Probe Experiments at the DELTA Storage Ring", in *Proc. 5th Int. Particle Accelerator Conf.*, Dresden, Germany, 2014, p. 1848ff.
- [16] A. Schick et al., "Ultrashort VUV and THz Pulse Generation at the DELTA Storage Ring", in *Proc. 2nd Int. Particle Accelerator Conf.*, San Sebastián, Spain, 2011, p. 2942ff.
- [17] M. Höner et al., "A Dedicated THz Beamline at DELTA", in *Proc. 2nd Int. Particle Accelerator Conf.*, San Sebastián, Spain, 2011, p. 2939ff.
- [18] P. Ungelenk et al., "Studies of Ultrashort THz Pulses at DELTA", in *Proc. 5th Int. Particle Accelerator Conf.*, Dresden, 2014, p. 1936ff.
- [19] D. Venus et al., "Magnetic dichroism in UV photoemission at off-normal emission: Study of the valence bands", *Phys. Rev. B* 55, p. 2594ff., 1997.
- [20] C. Gutt, "Single Shot Spatial and Temporal Coherence Properties of the SLAC Linac Coherent Light Source in the Hard X-Ray Regime", *Phys. Rev. Lett.* 108, p. 024801ff., 2012.
- [21] H. Huang et al., "Experimental determination of the Hamiltonian for synchrotron motion with rf phase modulation", *Phys. Rev E* 48, p. 4678ff., 1993.
- [22] M. Höner et al., "Investigation of Beam Instabilities at DELTA using Bunch-by-bunch Feedback Systems", in *Proc. 5th Int. Particle Accelerator Conf.*, Dresden, Germany, 2014, p. 3486ff.

ALPHA – THE THZ RADIATION SOURCE BASED ON AREAL*

T. Vardanyan[#], G. Amatuni, V. Avagyan, A. Grigoryan, B. Grigoryan, M. Ivanyan, V. Khachatryan, V. Petrosyan, V. Sahakyan, A. Sargsyan, A. Tsakanian, V. Tsakanov, A. Vardanyan, G. Zanyan, CANDLE SRI, Yerevan, Armenia

Abstract

Advanced Research Electron Accelerator Laboratory (AREAL) based on photo cathode RF gun is under construction at the CANDLE. The basic aim of this new facility is to generate sub-picosecond duration electron bunches with an extremely small beam emittance and energies up to 50 MeV. One of the promising directions of the facility development is the creation of ALPHA (Amplified Light Pulse for High-end Applications) experimental stations with coherent radiation source in THz region based on the concept of both conventional undulator and novel radiation sources. The status of the AREAL facility, the main features and outlooks for the ALPHA station are presented in this work.

INTRODUCTION

The generation and acceleration of low emittance ultrashort electron bunches present the origin for the development of new coherent radiation sources. The AREAL RF photogun electron linear accelerator is currently under construction at the CANDLE Synchrotron Research Institute [1]. The basic aim of this new facility is to generate electron bunches with extremely small beam emittance and with sub-picosecond pulse duration for advanced experimental study in the field of accelerator technology, new radiation sources and dynamics of ultrafast processes.

The first phase of the AREAL facility with the beam energy of about 5 MeV at the gun exit is completed recently [2]. The second phase foresees 20 MeV design energy with possible upgrade of up to 50 MeV.

After successful realization of AREAL phase 1 which was demonstrated during the machine run shifts in May 2014 [3], the second phase of the project implementation being in progress implies installation of two accelerating S-band modules with corresponding diagnostic equipment.

In the past decade the THz radiation has been of great scientific interest with a wide range of potential application in the field of life, material and environmental sciences, development of bio and nano-technologies [4]. One of the promising directions of the AREAL facility development is the creation of ALPHA experimental station with coherent radiation source in THz region. The project will focus on the development of THz coherent radiation sources based on 1) conventional periodic magnetic (undulator) system, 2) novel single mode slowly travelling waveguide concept and 3) modulated beam

plasma interaction. In this paper we present the main features of ALPHA THz Free Electron Laser option based on the planar undulator.

AREAL FACILITY

The schematic layout of the AREAL laser driven electron linear accelerator is presented in Fig. 1. The facility contains copper photocathode illuminated by 285 nm wavelength UV laser, 1.6 cell S-band cavity and two 1.5 m long S-Band accelerating sections.

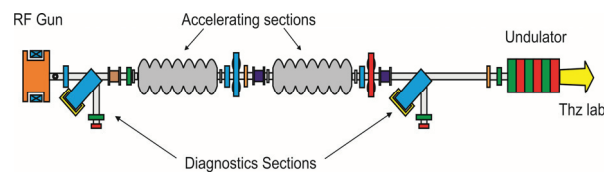


Figure 1: Layout of AREAL gun section with diagnostics.

The main design parameters of the AREAL facility electron beam are given in Table 1.

Table 1: AREAL Beam Parameters List

Energy	20-50 MeV
Bunch charge	10-200 pC
Transv. norm emit.	<0.3 mm-mrad
RMS bunch duration	0.5-8 ps
Energy spread at 20 MeV	0.2%

The ASTRA start-to-end tracking simulations are performed to optimize the acceleration phase and gradients to obtain minimum beam emittance and the energy spread. The results of the beam transverse size and normalized emittance for the beam energy of about 20 MeV is shown in Fig. 2 [5].

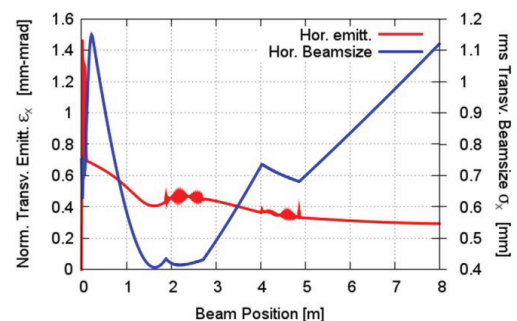


Figure 2: Transverse normalized emittance and beam size along the linac.

* Work supported by State Committee of Science MES RA in frame of the research project № SCS 13YR-1C0007.
#tvardanyan@asls.candle.am

ALPHA EXPERIMENTAL STATION

The tunability, high power and flexible picoseconds-pulse time structure of THz radiation turn the THz Free Electron Laser into a very attractive source of coherent radiation. The potential application can be carried out in the fields of imaging, material research, biology medicine, communication, diagnostics and others. THz FEL is already operating today and the vast majority of them operate in the infrared and far infrared regions. Several user facilities have been built to operate in the infrared region and most of them can reach or plan to extend into the THz region. As a first stage of ALPHA experimental station, the generation of coherent radiation in the range from 10 to 30 μm using FEL under Self-Amplified Spontaneous Emission (SASE) mode is considered.

THZ SASE FEL

A high-gain, single-pass FEL amplifier based on SASE is capable to produce a MW power THz pulse in a several meters long undulator. The SASE FEL radiation parameters strongly depend on the parameters of electron beam and undulator line. For the SASE process strong requirements are applied for the quality of electron beam. In the linac it is required to produce electron beam with small emittance to match diffraction limited photon beam, small energy spread to avoid gain degradation and high peak current. The electron beams produced in the AREAL linac meets these criteria and can be used for the generation of THz radiation using SASE FEL principle.

In order to get the THz radiation we consider the electron beam parameters listed in Table 2. With the current design of AREAL project the energy of 20-50 MeV will be reached by two 1.5 m long S-band travelling wave accelerating modules with 10-17MV/m acceleration gradient.

Table 2: Electron Beam Parameters

Parameter	Value	Unit
Energy	20-35	MeV
Energy spread	0.2	%
Bunch charge	250	pC
Emittance	0.3	mm-mrad
RMS bunch duration	2-3	ps

In our case we consider a 5 m long planar undulator with period of 3 cm. The electromagnetic undulator is under consideration as this type of undulator is cost-effective and very compact in structure. It also generates high magnetic field with very high precision. The field strength change depends on the electric current through the main coil. The undulator specifications for our case are listed in Table 3. Detailed study of undulator system performance and design is in progress.

Table 3: Undulator Parameters

Period length	3 cm
Total length	5 m
K	2.02
Peak field	0.72 T

The fundamental wavelength of undulator radiation is given by $\lambda = \lambda_u(1 + K^2/2)/2\gamma^2$, where λ_u is the undulator period, γ is the electron beam energy, K is the undulator parameters. For our parameters, the radiation wavelength is in the range of 10–30 μm that corresponds to 10-30 THz. The wavelength tuning will be performed via electron beam energy changes from 20 to 35 MeV.

NUMERICAL SIMULATION RESULTS

This section presents time-dependent numerical simulation results for radiation performances. Numerical simulations have been performed by GENESIS 3D simulation code [6] using parameters listed in Tables 2,3. Time-dependent simulations have been performed for the cases when radiation wavelength is 10 μm and 30 μm . In case of 30 μm radiation wavelength, rms bunch duration is assumed to be 3 ps with the energy of 20 MeV. For the case of 10 μm radiation wavelength, bunch rms duration is 2 ps and energy is 35 MeV. In Fig. 3 the average FEL power variation along the undulator line at 10 and 30 μm radiation wavelengths is shown.

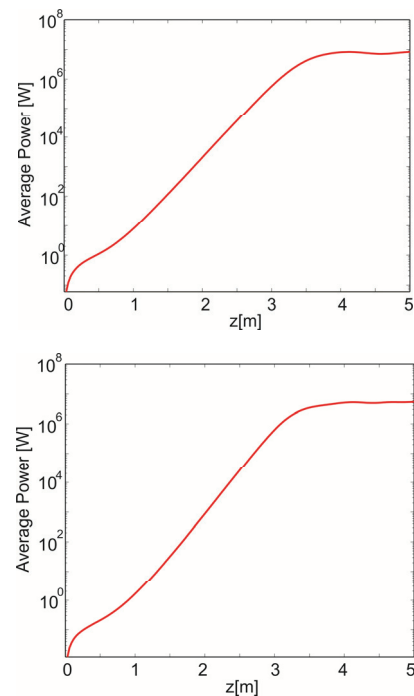


Figure 3: Average FEL power at 10 μm (top) and 30 μm (bottom) radiation wavelengths.

For this range of parameters the FEL saturates after 3.7 m at 10 μm radiation wavelengths and after 3.4m at 30 μm wavelengths. The peak power at saturation is about 27 MW and 14 MW for the 10 μm and 30 μm respectively. The pulse energy is about 40-60 μJ . Figure 4 presents the power distribution along the bunch at the saturation point for considered cases. In these simulations 20 initial seeds for the random number generator used for particle phase fluctuation (shot noise) have been considered.

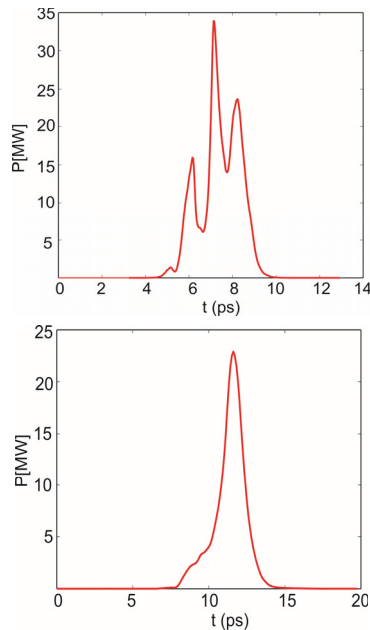


Figure 4: Power distribution along the bunch at the saturation point for 10 μm (top) and 30 μm (bottom) radiation wavelengths.

A single shot spectrum of the radiation for considered cases is shown in Fig. 5.

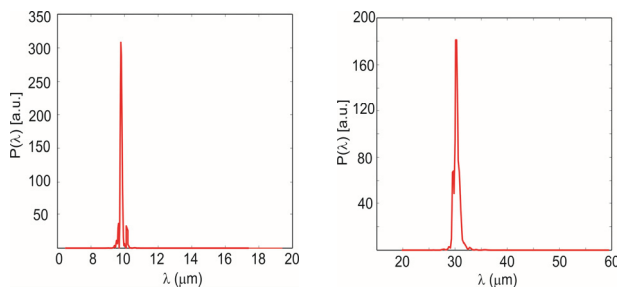


Figure 5: Spectrum of the FEL radiation at the saturation point at 10 μm (left) and 30 μm (right) wavelengths.

COHERENT THZ UNDULATOR RADIATION

In the AREAL linac, the laser system used for generation of ultra-short electron bunches can produce the pulses with the duration of 0.5-8 ps. The installation of the new module for the AREAL laser system that

compresses the laser pulse down to sub 30 fs pulse duration is under consideration. The form factor of the AREAL electron bunches is then close to unity at the radiation frequencies of about 1 THz that makes the AREAL electron bunches attractive for the coherent radiation in this range.

The study of the coherent radiation sources at the ALPHA station based on the conventional undulators, single mode travelling wave structures [7] and the beam-plasma interaction is underway.

We particularly consider the usage of helical undulator for generation of high power circular polarized radiation in order to apply in a wide range of research fields based on spin resolved photoelectron spectroscopy, the circular dichroism and etc. Figure 6 shows the discrete spectrum of single electron radiation in 1m long helical undulator section [8]. For the short bunch length option the THz circular polarised coherent radiation is expected for lower modes in radiation power spectrum.

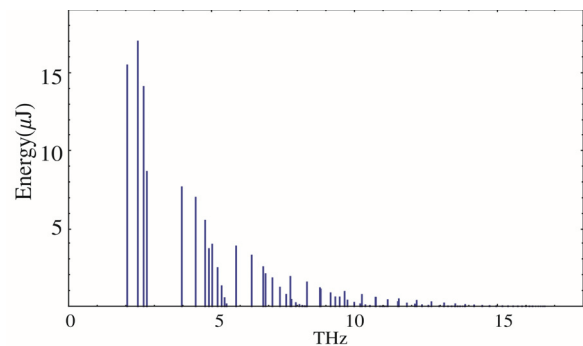


Figure 6: Discrete radiation energy spectrum for helical undulator.

SUMMARY

In this paper the status of the AREAL linear accelerator and the main features of ALPHA experimental station are presented. The SASE FEL scheme for the generation of the high power THz radiation at the wavelengths of 10 and 30 μm are considered. The options for the coherent THz radiation through short electron bunches are discussed.

REFERENCES

- [1] B. Grigoryan et al., IPAC'11, San Sebastián, Spain, p.1066 (2011).
- [2] B. Grigoryan et al., IPAC'14, Dresden, Germany, p. 620 (2014).
- [3] G. Amatuni et al., IPAC'14, Dresden, Germany, p. 3418 (2014).
- [4] T. Ping, et al., Sci. China Inf. Sci., Vol. 55 No. 1, p.1 (2012).
- [5] B. Grigoryan et al., IPAC'11, San Sebastián, Spain, p.1069 (2011).
- [6] S. Reiche, Nucl. Instrum. Meth. A 429, (1999) 243.
- [7] M. Ivanyan et al., Phys. Rev. ST Accel. Beams 17, 021302, (2014).
- [8] T.L. Vardanyan et al., IPAC'14, Dresden, Germany, p. 1989 (2014).

FERMI STATUS REPORT

M. Svandrlík[#], E. Allaria, F. Bencivenga, C. Callegari, F. Capotondi, D. Castronovo, P. Cinquegrana, M. Coreno, R. Cucini, I. Cudin, M.B. Danailov, G. D'Auria, R. De Monte, G. De Ninno, P. Delgiusto, A. Demidovich, S. Di Mitri, B. Diviacco, A. Fabris, R. Fabris, W. M. Fawley, M. Ferianis, E. Ferrari, P. Finetti, L. Fröhlich, P. Furlan Radivo, G. Gaio, D. Gauthier, F. Gelmetti, L. Giannessi, M. Kiskinova, S. Krecic, M. Lonza, N. Mahne, C. Masciovecchio, M. Milloch, F. Parmigiani, G. Penco, L. Pivetta, O. Plekan, M. Predonzani, E. Principi, L. Raimondi, P. Rebernik Ribic, F. Rossi, L. Rumiz, C. Scafuri, C. Serpico, P. Sigalotti, C. Spezzani, C. Svetina, M. Trovò, A. Vascotto, M. Veronese, R. Visintini, D. Zangrando, M. Zangrando, Elettra, Trieste, Italy

Abstract

FERMI, the seeded FEL located at the Elettra laboratory in Trieste, Italy, is now in regular operation for users with its first FEL line, FEL-1, which covers the wavelength range between 100 and 20 nm. We will give an overview of the typical operating modes of the facility for users and we will report on the status of beamlines and experimental stations. Three beamlines are now opened for users, three more are in construction. Meanwhile, the second FEL line of FERMI, FEL-2, a HGHG double stage cascade covering the wavelength range 20 to 4 nm is still under commissioning; we will report on the latest results in particular at the shortest wavelength, 4 nm in the fundamental.

extend the wavelength reach of FEL-2, as can be seen for instance in Fig. 1 that shows the spectrum at 10 nm, until the nominal performance at 4 nm was attained last June.

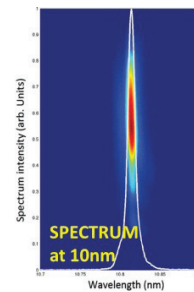


Figure 1: FEL-2 spectrum at 10 nm.

INTRODUCTION

The facility covers the photon energy range between 12 and 310 eV thanks to two seeded FEL lines. The low energy FEL line, FEL-1 reaching up to 62 eV, is made by a single stage HGHG scheme, with a modulator undulator and a radiator with six undulator elements [1]. The high energy FEL line, FEL-2 which generates photons down to 4 nm wavelength in the fundamental and 1.3 nm in the third harmonic, is made by a double stage HGHG cascade, in which the first stage is presently made by a modulator undulator and two radiator modules, and the second stage by a modulator undulator and six radiator modules; the “fresh bunch injection” mode is used [2].

FEL-1 started operation for users in December 2012 and since then welcomed scientists from Italy and from all over the world to perform experiments on the three experimental stations so far available, namely the Diffraction Projection Imaging (DiProI) station, the Elastic Inelastic Scattering TIMEX (EIS-TIMEX) station and the Low Density Matter (LDM) station.

FEL-2 produced the first coherent photons at 14.4 nm in October 2012; that was the first experimental demonstration of a high gain seeded free electron laser configured as a two stages cascade operating in the “fresh bunch injection” mode [3]. Since then FEL-2 commissioning runs were performed in-between user operation runs on FEL-1. They allowed to gradually

USERS OPERATION REPORT

Three calls for proposal of experiment on FERMI have been opened between 2012 and 2013. A total number of 125 proposals were received and 50 have been ranked by the FERMI Review Panel (FRP) for beamtime. In the 3rd call, 50 proposals have been submitted and 16 have been short listed in the FRP meeting of January 2014 for beamtime, that is, with an oversubscription rate of 3.13. Table 1 shows the standard parameters offered for experiments on FEL-1.

Table 1: FEL-1 Standard Parameters for User Operation

Parameter	FEL-1
Electron beam energy	1.0 - 1.4 GeV
Bunch charge	500 pC
Bunch Peak Current	400 – 600 A
Wavelength	100 – 20 nm
Energy per pulse*	30 – 200 μ J
Photons per pulse**	10^{13} at 20 nm
Intensity stability, rms	10%
Relative bandwidth	10^{-4}
Central wavelength stability	10^{-4} rms

*average, depending on wavelength and spectral purity.

**up to 10^{14} at longer wavelengths.

[#]michele.svandrlík@elettra.eu

The bar plot in Fig. 2 shows the natural increase of beamtime dedicated to users and the decrease of machine development (commissioning) time, as it has to be expected for a facility entering into its operational phase.

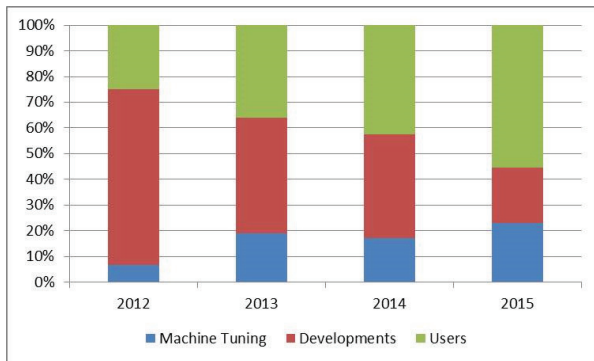


Figure 2: Operation hours distribution 2012-2015.

In 2013 the FERMI operation time attained almost 6500 hours, divided between time for linac, FEL-1 and FEL-2 commissioning and developments (55% of total hours) and time for users operation (45% of total). The latter includes machine tuning and beamline preparation time, beamtime for internal scientific groups and beamtime for external users assigned via the FRP. In total, during 2013 FERMI hosted 15 experiments that were peer reviewed by the FRP, pertaining to both the first and second call for proposals, equally divided between DiProI (5), EIS-TIMEX (5) and LDM (5). During 2014 the time for users operation will increase up to 60% of the total 6640 operation hours, leaving 40% for the developments still ongoing on FEL-2; 16 experiments will be hosted in 2014, namely 7 on DiProI, 2 on EIS-TIMEX and 7 on LDM. In 2015 the development time will be limited to 21% of the 6456 scheduled operation hours, while time for user operation will rapidly increase up to 79% of the total time, of which 55% is the portion of net time for experiments; 12 user experiments have been already allocated during the first semester of 2015.

The goal for the uptime of the FEL during user beamtime has been set at 80% of the scheduled operating hours. Figure 3 shows the actual achieved uptime during user runs, starting from run 14, December 2012, to run 20 that ended in July 2014. With the exception of run 17 in all other runs the uptime exceeded the goal; the recent trend is towards the 90% mark.

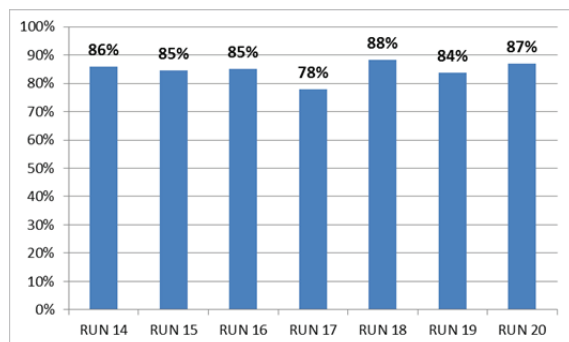


Figure 3: Uptime statistics December 2012 – July 2014.

Various actions have been launched to increase the reliability of some of the most critical systems, like the linac RF plants and the seed laser system, along with the aim to reduce the time needed for the optimization and fine tuning of the FEL parameters. For instance, after the installation of a new seed laser oscillator, with reduced phase noise, the seed laser system uptime is equal to 100%, along with a phase noise and jitter reduction by more than a factor of 3.

The time for optimization and fine tuning strongly depends on the FEL parameters requested by the users. For the standard operating conditions of FEL-1, listed in Table 1, the operability and reliability of the machine is very good and the uptime is close to 90%. However, a more complex set of FEL parameters can be requested by a given experiment. This is the case of the novel two colour FEL scheme, which is possible with a seeded FEL as FERMI [4], [5]. In this configuration, two FEL pulses, pump and probe, are generated by seeding the electron bunch with two laser pulses. Wavelength and intensity ratio between the two pulses, as well as the time delay between them can be controlled; the feature is that the two pump and probe pulses are practically jitter free. Figure 4 shows a typical spectrum of the two pulses. This configuration, of great interest for the FERMI users' community, may demand for longer machine preparation and optimization times, as it was the case in run 17 (see Fig. 3).

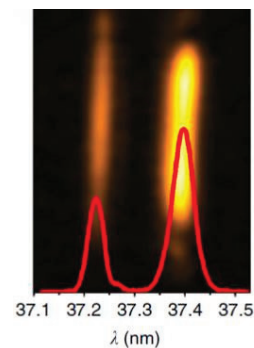


Figure 4: Typical double pulse spectrum.

Another way to perform time resolved experiments at FERMI is provided by transporting a portion of the IR seed laser pulse from the seed laser room down 150 m to the experimental stations. As shown in Fig. 5, low timing jitter is an intrinsic characteristic of the system, since the FEL is generated by the same seed pulse.

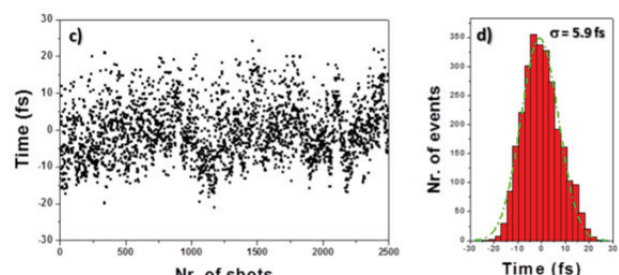


Figure 5: Typical jitter measurement at EIS-TIMEX.

Low jitter and high pointing stability along the transport line and in the distribution tables to the experimental stations are then ensured by advanced optical and mechanical design, along with sophisticated feedback loops. Figure 5 shows the measurement of the pump-probe time superposition at EIS-TIMEX, with an excellent jitter value of less than 7 fs rms [6].

FEL-2 ACHIEVES NOMINAL INTENSITY AT 4 NM

FEL-2 is based on a double stage cascaded HGHG scheme; the external seed laser, the third harmonic of a Titanium:Sapphire laser, seeds the first stage, made up of a modulator and a two segments radiator; the photon pulse generated in the first stage seeds the second stage, made up of a modulator and a six segments radiator. A delay line, made by a magnetic chicane after the first stage, allows to delay the electron beam with respect to the photon pulse. At the end of 2013, after three commissioning periods, FEL-2 was characterized at several harmonic transitions, in both stages, and at different electron beam energies, between 1.0 and 1.4 GeV. After first lasing at 14.4 nm in October 2012, later studies were carried out at 10.8 nm, where the energy per pulse achieved up to 100 μ J. Lasing was also observed at 6.5, 5.0 and 4.08 nm, even if at lower intensities. All studies were carried out with 500 pC electron bunch charge. Finally, in May 2014 it was possible to study the FEL-2 behaviour at the nominal electron beam parameters required for FEL-2 at 4 nm, as reported in what follows.

The run number 20 of FERMI started in May 2014. The first 7 weeks of the run are devoted to commission FEL-2 at its shortest wavelength, that is 4 nm (310 eV), with the electron beam parameters set to the nominal foreseen conditions, 1.5 GeV electron beam energy, 800 A peak current (800 pC extracted from the gun) and well controlled emittance and energy spread.

After few weeks of characterization and optimization, in particular of the beam trajectory across FEL-2, on the 6th of June we could produce FEL pulses at 4 nm with the expected average intensity of 10 μ J and some super-shots at 20 μ J. The first stage was tuned at the 13th harmonic of the seed laser, 20 nm, and the second stage at the 5th harmonic of the first stage (harmonic transition 13x5). Electron beam and FEL parameters are summarized in Table 2, while Fig. 6 shows the FEL-2 spot at 4 nm.

Table 2: FEL-2 Parameters, May – June 2014

Parameter	FEL-2
Electron beam energy	1.5 GeV
Bunch charge	800 pC
Bunch Peak Current	800 A
Wavelength	4 nm
Energy per pulse, average	10 μ J

In summary, a nicely optimized electron beam, with bunches of 800 pC charge and 800 A peak current allowed us to reach peak pulse intensities larger than, 10 μ J at nm. At wavelengths between 5 and 6 nm we could achieve even higher intensities, up to a peak of 80 μ J at 5.9 nm. Third harmonic spectra could be measured both at 5.9 nm and 4 nm.

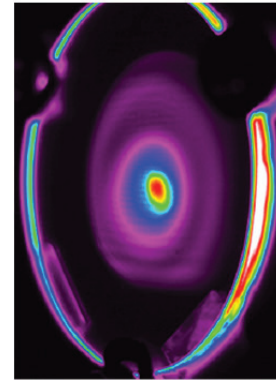


Figure 6: FEL-2 spot at 4 nm.

After the commissioning run, the first user experiment with photons generated by FEL-2 was performed at the EIS-TIMEX endstation [7]. FEL-2 was tuned at 12.4 nm central wavelength to study the Si $L_{2,3}$ -edge. The wavelength was tunable by ± 0.5 nm thanks to the OPA installed in the seed laser set-up; both the first and second stage of the cascade. Energy per pulse was around 15 μ J and the spectral bandwidth was 5×10^{-4} rms. Machine uptime for this first user experiment on FEL-2 attained 85%, i.e. similar to the value usually obtained on FEL-1.

This is a remarkable improvement compared to the results obtained in 2013; based on these results, FEL-2 will be available for users in the next call for proposals, the fourth of the series, which will be opened on October 1st, 2014. Beamtime will be assigned to the selected proposals in the second semester of 2015.

NEW BEAMLINES AT FERMI

Three more beamlines are presently under construction and will be available for users at the end of 2015. They are EIS-TIMER, a Four-Wave-Mixing instrument, MagneDyn, that will allow to perform time resolved magnetic dynamics studies, and finally TeraFERMI, that will use the spent electron beam in the Main Beam Dump to produce femtosecond, high intensity (MV/cm), broadband (0.1 to 10 THz) TeraHertz pulses.

In the first days of July 2014 a proof of principle experiment of the Four-Wave-Mixing technique was performed by the EIS-TIMER scientific team [8], in collaboration with the DiProI scientific team, by carrying out a transient grating experiment on the DiProI station.

In this successful experiment, a FEL pulse was split in two and recombined at the sample with a finite crossing angle. This allowed the generation of a dynamic XUV grating, which was probed in a pump-probe, four-wave-mixing scheme by an optical pulse coming from the user

laser, generated by the seed laser as previously explained. The coherent, non-linear, interaction of the three pulses originated a detectable coherent beam propagating along the phase matching direction, as shown in Fig. 7.

Such kind of non-linear XUV/soft x-ray wave-mixing experiments will be further developed in the EIS-TIMER dedicated beamline, also exploiting the unique capability of FERMI to radiate multi-colour seeded FEL pulses. The multi-colour transient grating approach will enable, for instance, to follow charge flows between constituent elements in molecules with femtosecond resolution, or to study energy transfer processes at the molecular scale.

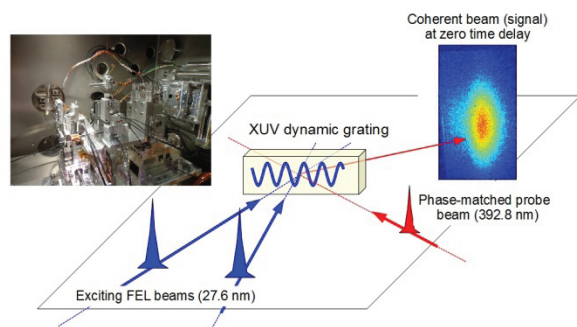


Figure 7: Four-Wave-Mixing experimental set-up and coherent beam signal.

MACHINE UPGRADE ACTIVITIES AND PLANS

Along with operation of FEL-1 and commissioning of FEL-2, the FERMI construction completion activities and the first upgrades are progressing. Three more beamlines are under construction and will be completed by 2015. Upgrades are now concentrated on the linac, which energy attained 1.56 GeV in September 2013. The new 50 Hz photocathode gun was installed and commissioned during 2013. Two more accelerating structures are in construction and will be installed during the winter shutdown 2015-2016, when also the final upgrade to 50 Hz operation will be completed. This will give operating margin on the nominal energy and is part of an upgrade program which has been launched to get an even more reliable and robust facility for our user's community.

The two new linac structures were designed to minimize phase and amplitude asymmetries in the coupler cells, in order to reduce the induced kick to the beam; they will gain 50 MeV each. They will replace the first two sections in the 100 MeV injector linac [9], that will then be relocated at higher energy where free spots in the layout and RF power plants are already available. This upgrade will increase the maximum linac energy to 1.65 GeV, beneficial both in terms of minimum wavelength achievable and of reliability and uptime. Furthermore, the beam quality at 100 MeV is expected to improve.

There is also a plan to profit of the free spots in the FEL-2 layout to upgrade it; namely there is space available to host a third undulator in the first stage radiator. This would bring advantages in terms of reliability and flexibility of FEL-2 operation. In fact, it

would provide a higher energy per pulse from the first stage at an equivalent seed power; alternatively it would allow to reduce the required seed power to reach an equivalent seed pulse energy for the second stage.

Energy per pulse at the level of 10-15 μJ at 20 nm is required from the first stage to seed in best conditions the second stage tuned at 4 nm. During run 20 this was obtained with about 40 μJ of seed energy.

For nominal electron beam parameters, the use of an additional undulator in the first stage would allow to reduce the required seed power level by 30-50% depending on the final FEL wavelength. This would allow to operate with a lower seed power, opening to the possibility of using the OPA amplifier on a wider range of seed wavelengths and to reduce phase distortions associated to non-linear effects due to high seed laser intensity. In general this upgrade relaxes also the requirements on the electron beam, allowing more freedom in the selection of the region in the electron beam longitudinal phase space where the first stage seeding occurs.

To implement this upgrade an undulator of the same type of the two existing ones is needed, i.e., 55 mm period APPLE-II type.

CONCLUSION

FERMI is routinely operating for users with FEL-1. The number of hours dedicated to user experiments has been steadily increasing between 2012 and 2015.

FEL-2 has achieved the nominal energy per pulse at 4 nm. At the end of June 2014 the first user experiment on FEL-2, at 12.4 nm, has been performed. The fourth call for users, which will be published on the 1st of October 2014, will accept proposals both on FEL-1 and on FEL-2, so covering the full energy range foreseen on FERMI that is from 12 eV up to 310 eV.

An upgrade program to widen the experimental opportunities and to further increase the reliability, the robustness and the flexibility of the facility is ongoing, and will particularly be focussed on the linac and on the FEL-2 first stage configuration.

REFERENCES

- [1] E. Allaria et al., "Highly coherent and stable pulses from the FERMI seeded free-electron laser in the extreme ultraviolet", *Nature Photonics* Vol 6, No 9 (2012); DOI:10.1038/nphoton.2012.233.
- [2] B. Liu et al., "Demonstration of a widely-tunable and fully-coherent high-gain harmonic-generation free-electron laser" *PRSTAB* 16, 020704 (2013)
- [3] W.M.Fawley, L. Giannessi et al., "Two-stage seeded soft-X-ray free-electron laser", *Nature Photonics* (2013); DOI:10.1038/nphoton.2013.277.
- [4] E. Allaria et al., "Two colour pump probe experiments with a twin-pulse-seed extreme ultraviolet FEL", *Nature Communications*, Vol. 4 (2013) doi: 10.1038/ncomms3476.

- [5] G. De Ninno et al., “Chirped Seeded Free-Electron Lasers: Self-Standing Light Sources for Two-Color Pump-Probe Experiments”, Phys. Rev. Lett. 110, 064801 (2013).
- [6] M.B. Danailov et al., “Towards jitter-free pump-probe measurements at seeded free electron laser facilities”, Optics Express, Vol. 22 Issue 11, pp.12869-12879 (2014).
- [7] E.Principi, private communication.
- [8] F. Bencivenga, private communication.
- [9] G. Penco et al., “Optimization of a high brightness photoinjector for a seeded FEL facility”, JINST, 8 P05015 (2013).

EXPERIMENT PREPARATION TOWARDS A DEMONSTRATION OF LASER PLASMA BASED FREE ELECTRON LASER AMPLIFICATION

M.-E. Couprie, C. Benabderrahmane, P. Berteaud, C. Bourassin-Bouchet, F. Bouvet, F. Briquez, L. Cassinari, L. Chapuis, M. El Ajjouri, C. Herbeaux, N. Hubert, M. Labat, A. Lestrade, A. Loulergue, J. Luning, O. Marcouillé, J.-L. Marlats, F. Marteau, C. Miron, P. Morin, F. Polack, K. Tavakoli, M. Valléau, D. Zerbib, SOLEIL, Gif-sur-Yvette, France
X. Davoine, CEA/DAM/DIF, Arpajon, France
I. Andriyash, G. Lambert, V. Malka, C. Thaury, LOA, Palaiseau, France
S. Bielawski, C. Evain, C. Szwaj, PhLAM/CERCLA, Villeneuve d'Ascq Cedex, France

Abstract

One direction towards compact Free Electron Laser is to replace the conventional linac by a laser plasma driven beam, provided proper electron beam manipulation to handle the value of the energy spread and of the divergence. Applying seeding techniques also enables to reduce the required undulator length. Rapidly developing Laser Wakefield Accelerators (LWFA) are already able to generate synchrotron radiation. With the presently achieved electron divergence and energy spread an adequate beam manipulation through the transport to the undulator is needed for FEL amplification. A test experiment for the demonstration of FEL amplification with a LWFA is under preparation in the frame of the COXINEL ERC contract in the more general context of LUNEX5. Electron beam transport follows different steps with strong focusing thanks to variable strength permanent magnet quadrupoles, demixing chicane with conventional dipoles, and a second set of quadrupoles for further focusing in the undulator. Progress on the equipment preparation and expected performance are described.

INTRODUCTION

More than 30 years after the first Free Electron Laser (FEL) [1], FEL based fourth generation light sources [2] presently offer femtosecond tuneable radiation in the X – ray domain with LCLS in USA [3], SACLA in Japan [4] and in the VUV- soft X-ray with FLASH in Germany [5] and FERMI in Italy [6]. FEL oscillators being limited to VUV [7], single optical pass FEL devices are preferred for short wavelength operation. After the first coherent harmonic generation experiments [8], seeding has demonstrated major advantages in terms of spectral purity [9-12]. Besides the preparation of additional FEL light sources for users around the world, new schemes are also under investigation. In view of the fifth generation light sources [13], several approaches are considered. One direction goes towards the improvement of FEL performance in a wide spectral range and with versatile properties and flexibility for users. Another one aims at reducing the size either by exploring further seeding and / or by replacing the conventional linear accelerator by a compact alternative one. Indeed, the rapidly developing Laser WakeField Accelerator (LWFA) [14, 15] are now

able to generate synchrotron radiation [16]. With an electron divergence of typically 1 mrad and an energy spread of the order of 1 %, an adequate beam manipulation through the transport to the undulator is required for FEL amplification. Different strategies have been proposed, such as a decompression chicane [17], or a transverse gradient undulator [18].

The studies presented here take place in the context of the LUNEX5 (free electron Laser Using a New accelerator for the Exploitation of X-ray radiation of 5th generation) collaboration, aiming at investigating the production of short, intense, coherent pulses in the 40-4 nm spectral range [19] with a 400 MeV superconducting linac and a LWFA both connected to a single FEL for advanced seeding configurations. Both accelerators are complementary: The conventional linac will enable studies of advanced FEL schemes, future upgrade towards high repetition rate and multi-user operation. The LWFA has first to be qualified by the FEL application. LUNEX5, after the completion of a Conceptual Design Report [20], is presently in a phase of R&D and complementary studies. In this frame, after transport calculation of longitudinal and transverse manipulation of a LWFA electron beam showing that theoretical amplification is possible, a test experiment is under preparation, with the support of different grants.

GENERAL DESCRIPTION

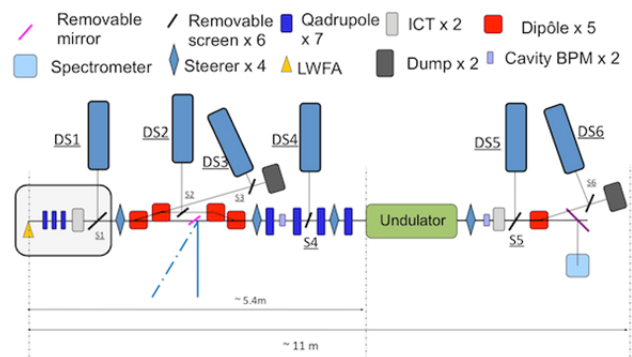


Figure 1: Scheme of the main components.

COXINEL grant aims at demonstrating FEL amplification with a LWFA. First, it intends to provide an appropriate electron beam transport from the source to the

undulator. Typical electron beam parameter sets are considered at 400 MeV : a 1π mm.mrad emittance with a beam size of $0.75 \mu\text{m}$ and a divergence of 1 mrad, a bunch duration of 3 fs and an energy spread of 1%, a bunch charge of 30 pC, leading to a peak current of 4 kA. The key concept relies on an electron beam longitudinal and transverse manipulation in the transport towards an undulator: a set of strong quadrupoles handle the large divergence of the electron beam, then a “demixing” chicane sorts the electrons in energy and reduces the spread from 1 % to a slice energy spread of 0.1 % and finally the transverse density is maintained constant all along the undulator (supermatching) by a proper synchronisation of the electron beam focusing and the progress of the optical wave along the undulator [21]. Calculations are carried out for an ultimate 40 nm wavelength and a 400 MeV electron beam. First tests will be performed at 200 nm with a 180 MeV electron beam, and a U20 undulator.

For this purpose, a transport line has been designed to be as compact as possible, as shown in Fig. 1. It comports a first set of strong permanent magnet based variable quadrupoles to handle the large electron beam divergence, a chicane with four dipoles for the electron beam decompression, a second set of four quadrupoles, an undulator, a beam dump dipole, and a series of diagnostics: two cavity BPMs (before and after the undulator), screens for the beam profile [22] and charge monitors.

THE ELECTRON SOURCE

Electrons are produced by an intense 2×60 TW laser of the “Laboratoire d’Optique Appliquée (LOA)” focused in a gas jet located in a dedicated chamber. The development of the best LWFA parameters for the FEL application is performed in the frame of the X-Five grant.

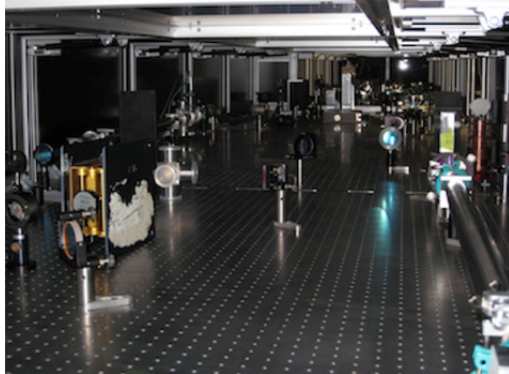


Figure 2: Picture of the LOA laser system.

THE TRANSPORT LINE

The equipment of the transport line is under preparation at Synchrotron SOLEIL.

The First Triplet of Highly Focusing Permanent Magnet Quadrupoles of Variable Strength

A gradient of 200 T/m is required, with an adjustment of the strength. Considering a bore diameter of 10 mm electromagnetic technology can’t be employed. In this scope, the design of a permanent magnet quadrupole with variable strength for the focusing of the LWFA diverging electron beam is presently finalised in the frame of the “Triangle de la Physique / Valorisation” QUAPEVA contract in collaboration with Sigmaphi company.

The Decompression Magnetic Chicane

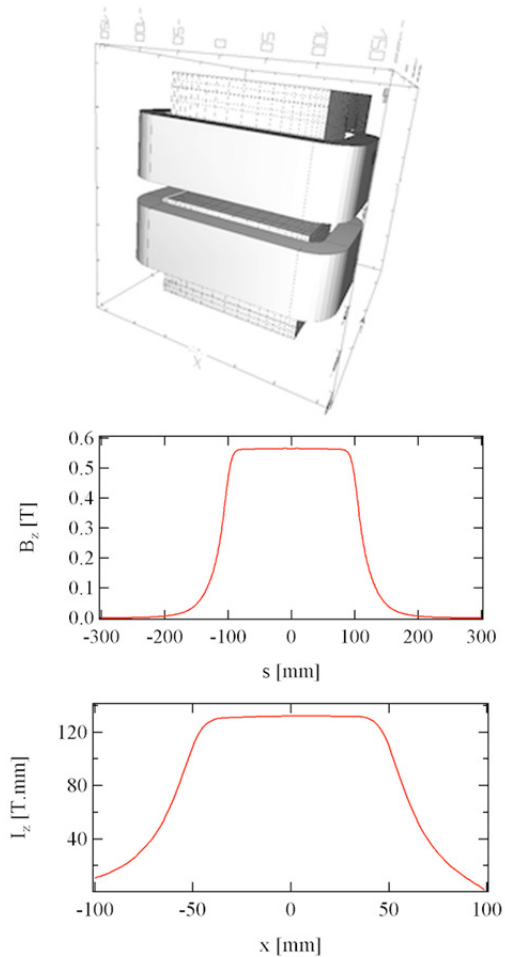


Figure 3: RADIA calculation of the chicane dipole: model, magnetic field versus longitudinal coordinate, field integral versus transverse direction. Gap: 25 mm.

The chicane is composed of four dipoles of 0.565 T for a 25 mm gap, on axis field integral of 132 T.mm enabling a 99 mrad deviation. The dipoles are variable and compact. A first design of air cooled dipole led to a coil heating. The design was then renewed to a cooled version, enabling also to get more compact components. The dipoles have been modelled both under TOSCA [23] and RADIA [24] software, as shown in Fig. 3. The power supplies of the dipoles provide 150 A, 8 V.

The beam pipe encloses the additional radial orbit displacement of 32 mm. In the chicane some diagnostics and the seeding mirror will also be installed, as shown in Fig. 4. They include a stopper for the infra-red laser generating the electrons, an electron beam profile monitor, a screen for the measurement of the electron beam energy. There is a special port for entering the seed laser with two possible angles, for either the 200 nm or the 40 nm seeding wavelengths.

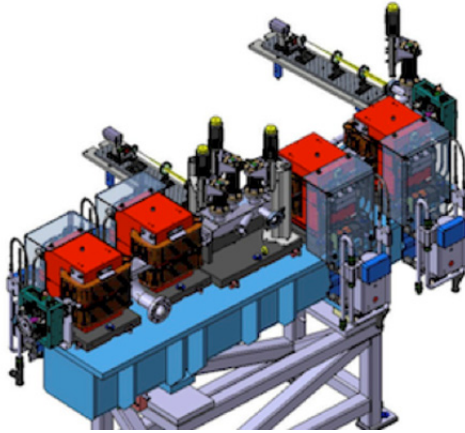


Figure 4: Catia view of the magnetic chicane with the seeding port and the diagnostics.

The Steerers

Two steerers (see fig. 5) are located at the entrance and at the exit of the chicane. They provide a 350 G magnetic field in both horizontal and vertical directions. The steerer power supply provides 10 A, 10 V.

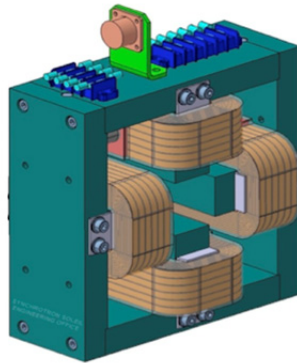


Figure 5: View of the beam transport steerers.

The Second Set of Quadrupoles (Quadruplet)

The quadrupoles are electromagnetic, air-cooled. The quadrupoles are modelled in TOSCA. They provide a 20 T/m gradient. The general view of the quadrupoles is shown in Fig. 6.

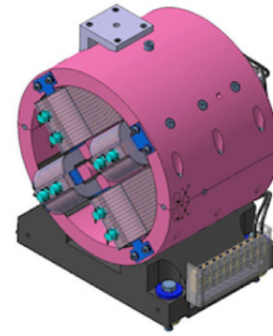


Figure 6: View of one air-cooled quadrupole.

THE FEL LINE



Figure 7: Example of SOLEIL U20 in-vacuum undulator.

Table 1: Characteristics of the Undulators

Characteristic	Unit	U20	U15
Period	mm	20	15
Technology		under vacuum	under vacuum, cryogenic
Permanent magnets		Nd ₂ Fe ₁₄ B	Pr ₂ Fe ₁₄ B
Poles		Vanadium-Permendur	Vanadium-Permendur
Number of periods		98	200
Minimum gap	mm	5.5	3
Peak field at 293 K	T	1.05	1.53
Peak field at 77 K	T		1.67
Deflection parameter (293 K)		1.96 at 293 K	2.4 at 77 K
Magnetic length	m	2	3

The FEL line comprises first the undulator with two beam steerers and two cavity BPM (of SwissFEL type [25]). Two different undulators will be used with first, a 2-m long typical U20 in-vacuum undulator of SOLEIL and then, a 3 m long cryo-ready undulator U15 (see Table

1 and Fig.7) thanks to the development of an existing U18 cryogenic undulator at SOLEIL [26].

A R&D program on the construction of a cryo-ready 3 m long 15 mm period undulator is under way in the frame of a French-Swedish collaboration. The choice (see Fig. 8) of the period has been studied regarding its use both for LUNEX5 -either with the superconducting linac or with the LWFA- and for its use on the SOLEIL 2.75 GeV storage ring.

The use of a specific grade of $\text{Pr}_2\text{Fe}_{14}\text{B}$ with poles in Vanadium-Permendur enables operation both at room temperature and at 77 K. The module scheme has been modified for using half-poles, enabling an easier swapping.

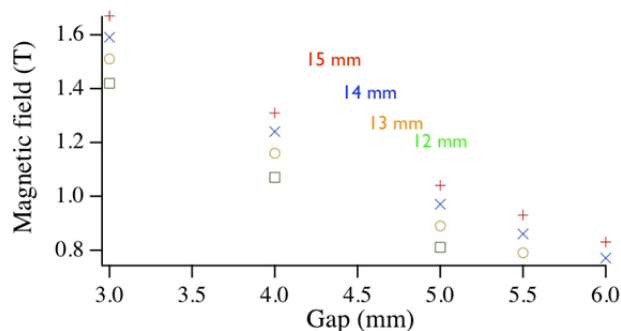


Figure 8: Peak magnetic field versus gap and period in the case of the cryogenic undulator.

A dipole, similar to the chicane one, will be pushed to higher current, providing a 1 T field for deflecting the electrons towards the dump.

A spectrometer for the spontaneous emission and Free Electron Radiation is under study. It will be installed at the exit of the undulator.

A resonant stripline BPM is also under study and it will be installed in the case of the 2 m undulator.

The general integration of the transport and FEL lines is shown in Fig. 9. The whole set occupies a length of the order of 11 m. For limiting the length, the cavity BPM and the steerer at the entrance of the undulator have been located inside the quadruplet of quadrupoles. Three pumping stations will also be installed (typically one in the chicane, one on the seeding port and one between quadrupoles of the second set).

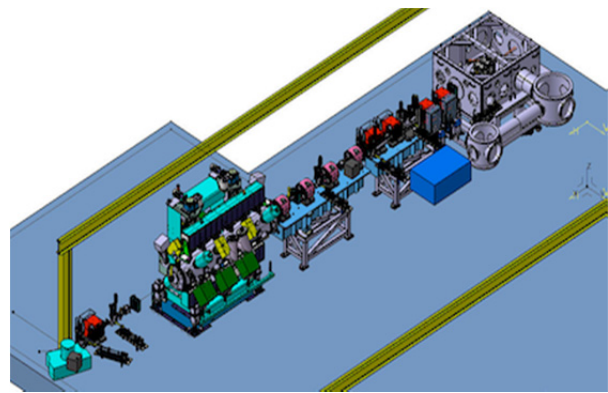


Figure 9: CATIA general integration view of the COXINEL LWFA demonstration set-up. General view of the COXINEL LWFA demonstration set-up (from right to left) : LWFA chamber (grey) with the first set of quadrupoles and a current beam transformer, magnetic chicane (red), quadruplet of quadrupoles (pink), undulator (case of 2 meter U20 undulator), dipole for beam dump (red), spectrometer (blue).

CONCLUSION

The preparation of the test experiment for a demonstration of LWFA based FEL amplification is in progress. Each different piece of equipment will be characterised independently prior to installation on the LOA site. Besides, tolerance and sensitivity parameters calculations are carried out in parallel.

ACKNOWLEDGMENT

M. E. Couprie and V. Malka are grateful to the support from the European Research Council for COXINEL and X-Five advanced grants. M. E. Couprie, C. Benabderrahmane, F. Briquez acknowledge the French-Swedish collaboration for the support on the U15 cryo-ready undulator. C. Benabderrahmane, M. E. Couprie, F. Briquez are thankful to the support from the “Triangle de la Physique” for the QUAPEVA valorisation contract and to J. L. Lancelot, F. Forest and O. Cosson from Sigmaphi for their involvement in the project.

REFERENCES

- [1] D.A.G. Deacon et al., “First Operation of a Free Electron Laser”, *Phys. Rev. Let.* 38, 892-894 (1977).
- [2] M. E. Couprie, J. M. Filhol, “X radiation sources based on accelerators”, *Compte-Rendus Physique*, 9, 5-6, 487-506 (2008).
- [3] P. Emma et al., “First lasing and operation of an ångstrom-wavelength free-electron laser”, *Nature Photonics* 4, 641 (2010)
- [4] S. T. Ishikawa et al., “A compact X-ray free-electron laser emitting in the sub-ångström region”, *Nature Photonics* 6, 540–544 (2012).
- [5] W. Ackermann et al. “Operation of a free-electron laser from the extreme ultraviolet to the water window”, *Nature Photonics* 1, 336-342 (2007).

- [6] E. Allaria et al., “Highly coherent and stable pulses from the FERMI seeded free-electron laser in the extreme ultraviolet”, *Nature Photon.* 6 699–704 (2012).
- [7] M. Trovò et al., “Operation of the European storage ring FEL at ELETTRA down to 190 nm”, *Nucl. Inst. Meth. A* vol 483, issue 1-2, 157-161 (2002).
- [8] R. Prazeres et al. “Coherent Harmonic Generation in VUV with the optical klystron on the storage ring Super-ACO”, *Nucl. Inst. Meth. A* 304 72-76 (1991).
- [9] L. H. Yu et al., “High-Gain Harmonic-Generation Free-Electron Laser”, *Science* 289, 032 (2000).
- [10] G. Lambert et al., “Injection of harmonics generated in gas in a Free Electron Laser providing intense and coherent extreme-UV light”, *Nature Phys.* 4, 296-300 (2008).
- [11] T. Tanikawa, G. Lambert, T. Hara, M. Labat, Y. Tanaka, M. Yabashi, O. Chubar, M.E. Couprie, “Nonlinear harmonic generation in a free-electron laser seeded with high harmonic from gas”, *EPL* 3 34001 (2011)
- [12] J. Amann et al., “Demonstration of self-seeding in a hard-X-ray free-electron laser”, *Nature Photonics* 6, 693–698 (2012).
- [13] ICFA-sponsored workshop series on Physics and Applications of High Brightness Beams, March 25-28, 2013, San Juan, Puerto Rico, chaired by J. B. Rosenzweig and M. Ferrario, <http://pbpl.physics.ucla.edu/HBEB2013/index.html>
- [14] T. Tajima and J. M. Dawson, “Laser Electron Accelerator”, *Phys. Rev. Lett.* 43, 267 (1979)
- [15] V. Malka et al., “Principle and applications of compact laser-plasma electron accelerator”, *Nature Phys.* 7, 219 (2011).
- [16] H. P. Schlenvoigt et al., “A compact synchrotron radiation source driven by a laser-plasma wakefield accelerator”, *Nature Physics*, 4, 130-133, 2008; M. Fuchs et al., “Laser-driven soft-X-ray undulator source”, *Nature Physics* 5, 826 (2009)
- [17] A. R. Maier et al., “Demonstration Scheme for a Laser-Plasma-Driven Free-Electron Laser”, *Phys. Rev. X* 2, 031019 (2012)
- [18] Z. Huang et al., “Compact X-ray free-electron laser from a laser-plasma accelerator using a transverse-gradient undulator” *Phys. Rev. Lett.* 109, 204801 (2012); T. Smith et al. *J. Appl. Phys.* 50, 4580 (1979)
- [19] M. E. Couprie et al., *Journal of Physics Conferences Series*, 2013, 425: art.n° 072001 - (SRI2012) (2013)
- [20] LUNEX5 CDR, <http://www.lunex5.com/spip.php?article33>
- [21] A. Loulergue et al., “Longitudinal and transverse beam manipulation for compact laser wakefield accelerator based free-electron lasers”, *Physics and applications of High Brightness Beams : towards a fifth generation light source*, Puerto-Rico, March 25-28, 2013; A. Loulergue, “Beam Manipulation for Plasma Accelerator Based Free Electron Lasers”, THP001, these proceedings, FEL’14, Basel, Switzerland (2014).
- [22] M. Labat et al., “Electron beam diagnostics for COXINEL”, THP087, these proceedings, FEL’14, Basel, Switzerland (2014).
- [23] TOSCA, OPERA-3d, www.cobham.com/design-simulation-software
- [24] O. Chubar, P. Elleaume and J. Chavanne, “A three-dimensional magnetostatics computer code for insertion devices”, *J. Synchrotron Radiat.* (1998). 5, 481-484
- [25] B. Keil et al., “Design of the SwissFEL BPM System”, TUPC25, IBIC2013, Oxford, UK (2013)
- [26] C. Benabderrahmane, P. Berteaud, M. Valléau, C. Kitegi, K. Tavakoli, N. Béchu, A. Mary, J. M. Filhol, M. E. Couprie, “Nd2Fe14B and Pr2Fe14B magnets characterisation and modelling for cryogenic permanent magnet undulator applications”, *Nuclear Instruments and Methods in Physics Research A* 669 1-6 (2012)

THE STATUS OF LUNEX5 PROJECT

M. E. Couprie, C. Benabderrahmane, P. Berteaud, C. Bourassin-Bouchet, F. Bouvet, F. Briquez, L. Cassinari, L. Chapuis, M. Diop, J. Daillant, M. El Ajjouri, C. Herbeaux, N. Hubert, M. Labat, P. Lebasque, A. Lestrade, A. Loulergue, P. Marchand, O. Marcouillé, J. L. Marlats, C. Miron, P. Morin, A. Nadji, F. Polack, F. Ribeiro, J. P. Ricaud, P. Roy, K. Tavakoli, M. Valléau, D. Zerbib, Synchrotron SOLEIL, France

S. Bielawski, C. Evain, E. Roussel, C. Sz waj, PhLAM/ CERLA, Lille, France

G. Lambert, V. Malka, R. Lehe, A. Rousse, C. Thaur y,

Laboratoire d'Optique Appliquée, Palaiseau, France

G. Devanz, C. Madec, A. Mosnier, CEA/DSM/IRFU/SACM, Saclay, France

D. Garzella, B. Carré, CEA/DSM/IRAMIS/ LIDyL, Saclay, France

N. Delerue, Laboratoire de l'Accélérateur Linéaire, Orsay, France

X. Davoine, CEA/DAM/DIF, Bruyère-Le-Châtel, France

A. Dubois, J. Lüning, LCPMR, Paris-VI, France

Abstract

LUNEX5 (free electron Laser Using a New accelerator for the Exploitation of X-ray radiation of 5th generation) aims at investigating the production of short, intense, coherent Free Electron Laser (FEL) pulses in the 40-4 nm spectral range. It comprises a 400 MeV superconducting Linear Accelerator for high repetition rate operation (10 kHz), multi-FEL lines and adapted for studies of advanced FEL schemes, a 0.4 - 1 GeV Laser Wake Field Accelerator (LWFA) for its qualification by a FEL application, a single undulator line enabling seeding with High order Harmonic in Gas and echo configurations and pilot user applications. Concerning the superconducting linac, the electron beam dynamics has been modified from a scheme using a third harmonic linearizer and a compression chicane to a dog-leg coupled to sextupoles. Besides, the choice of the gun is under revision for achieving 10 kHz repetition rate. A test experiment is under preparation in collaboration with the Laboratoire d'Optique Appliquée, aimed at validating the computed transport performance of longitudinal and transverse manipulation on a LWFA electron beam enabling to provide theoretical amplification.

INTRODUCTION

France has a long history in Free Electron laser, and has obtained the second worldwide FEL on ACO (first visible

radiation) in 1983 [1] and first FEL based short wavelength harmonic generation [2]. The Super-ACO FEL, commissioned in 1989 [3], delivered in 1993 the first UV FEL beam [4] to users [5, 6, 7, 8, 9] with first pump-probe two colour experiments. Extensive studies aiming at further understanding the FEL dynamics and at improving its own performance were performed, such as temporal structure [10], short pulse operation [11, 12, 13], interplay with the electron beam [14, 15]. Mirror performance and degradation have been also extensively analysed [16].

An infra-red FEL user facility, CLIO is in operation since 1992 [17].

Considering short wavelength single pass FEL, there have been active collaborations for seeding studies, in particular with high harmonics in gas (HHG) using a 160 nm seed providing radiation down to 27 nm [18] and recently with a 60 nm seed [19] at SCSS Test Accelerator and at SPARC [20]. Short wavelength FEL user facilities (LCLS [21], SACLA [22], FLASH [23] and FERMI [24]) are providing new tools for the investigation of matter.

New researches are going towards exploring how to approach closer the diffraction and Fourier limits in a wide spectral range and with versatile properties. Besides, some other trends are investigating how FEL can become more compact, by seeding schemes and replacing the conventional accelerator by LWFA [25].

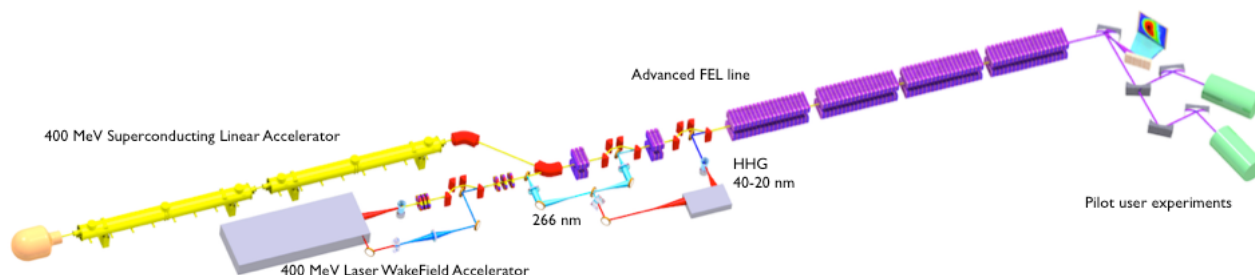


Figure 1: LUNEX5 sketch with two cryomodules (yellow), laser hutch for LWFA (grey), undulators (four radiators and two ECHO modulators) (purple), pilot user experimental sections (green).

DESCRIPTION OF LUNEX5 DEMONSTRATOR PROJECT

LUNEX5 [26, 27] aims at investigating the production of short, intense, and coherent pulses in the soft X-ray region, using two types of accelerators. On one hand, a 400 MeV superconducting linac will enable a cw operation for high repetition rate and multiple users. On the other hand, a LWFA is also coupled, for qualifying this type of acceleration concept with the FEL TW laser of LOA, before using a dedicated 400 TW laser system. The undulator line will be composed of different cryo-ready undulator segments of 15 and 30 mm period, enabling Echo Enable Harmonic Generation seeding (ECHO) [28] and HHG seeding to be compared. Two pilot user experiments in gas phase and condensed matter are also planned to qualify the FEL performances in the different cases. The LUNEX5 scheme is shown in Fig. 1. The planned spectral range (4-40 nm) from the fundamental, the third and the fifth harmonics is shown in Fig. 2, with CDR electron beam parameters, which are in particular quite optimistic in the LWFA case. On the fundamental wavelength, the FEL radiation ranges between 15 and 40 nm, with a peak power between 10 and 100 MW. With the superconducting linear accelerator, there are more than 10^{11} photons/pulse and 10^{27} peak brightness on the fundamental wavelength.

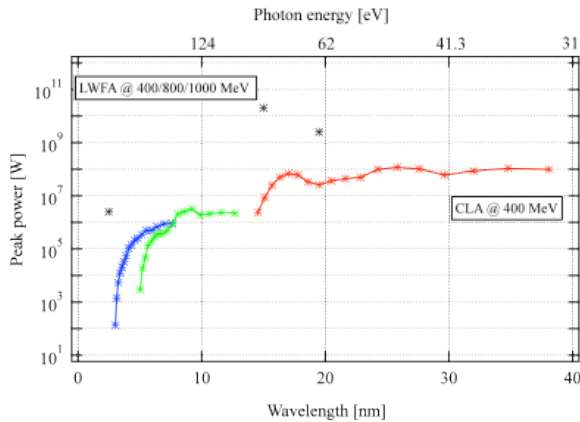
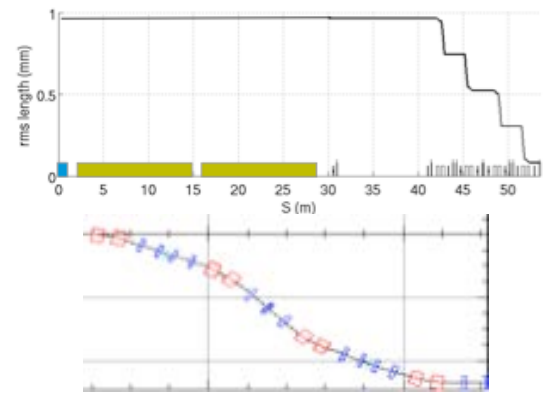


Figure 2: Photon peak power vs energy for a CLA (resp. LWFA) of 400 MeV, with slice energy spread of 0.02 % (resp. 0.1 %), emittance of 1.5π mm.mrad, peak current of 400 A (resp. 10 kA), bunch length of 1 ps (resp. 2 fs).

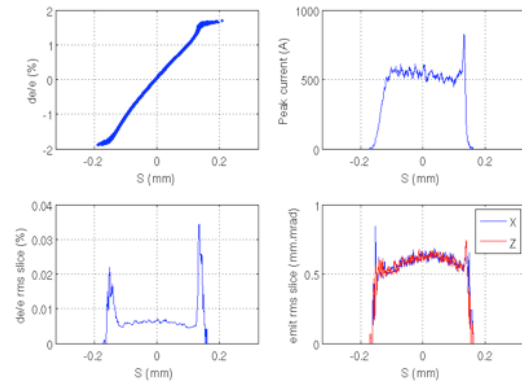
The conventional accelerator will be a 400 MeV superconducting L-band (1.3 GHz) Linac. It will enable achieving high average current, further upgrading towards CW [29] and multi-user operation. The 12 m long XFEL type cryomodule houses a string of eight 9-cell cavities, each equipped with an adjustable antenna input power coupler, two HOM dampers and a monitoring pick-up; their frequency tuning is ensured by a motor driven mechanism, which changes the cavity length and fast piezo-tuners, for the control of the microphonics. Initially, a pulsed operation (10 % duty cycle, i.e. 100 bunches per

macropulse of 500 μ s flat-top at 50 Hz repetition rate) of the linac was considered with two cryomodules operating at 24 MV/m (130 W of cryogenic power at 2 K). In the CW operation mode, a third cryomodule will reduce the accelerating gradient from 24 down to 16.5 MV/m, hence keeping the cryogenic load at a reasonable level (< 500 W at 2 K). Each cavity will have its own RF transmitter and LLRF system, for insuring a high stability in phase and amplitude. Solid state amplifiers, capable of delivering up to 20 kW CW at 1.3 GHz, providing modularity and low phase noise, will be developed at SOLEIL. The presently aimed temporal structure, 10 kHz repetition rate is of interest for coincidence, photo-emission and in a longer term, for imaging (Coherent diffraction Imaging). The superconducting linac choice will enable at term to dispatch electrons towards different FEL lines, for a reduced operating cost.

After considering a magnetic compressor combined to a harmonic cavity, a dogleg with sextupoles (Fig. 3a) is adopted. It enables to linearize the phase space, to compress the beam by typically a factor of 10, to increase the peak current and to cancel the second order dispersion (Fig. 3b). It is less versatile but cheaper than the harmonic cavity and chicane scheme.



a



b

Figure 3: a) Scheme of the dogleg b) Energy spread (top left), slice energy spread (bottom left), peak current (top right), slice emittance (bottom right).

The gun will be either a superconducting one [30] or an APEX type one [31]. The study and test of an elementary RF unit with sc cavity, low level RF and solid state amplifier for CW operation is also under discussion.

The best suitable regime of operation of the LWFA for the FEL application is currently under investigation. One can naturally foresee to operate in the colliding scheme [32, 33] or in the cold injection one [34]. First estimates of optimistic LWFA performance (1 μm transverse size, 1.25 mrad divergence, 1 π mm. mrad emittance, 2 fs duration, 0.1 % energy spread, 20 pC charge, i.e. 4 kA peak current) were first assumed. Now, one considers an electron divergence of typically 1 mrad and an energy spread of the order of 1%. In the transport to the undulator, adequate manipulation of the electron beam phase space is needed to handle the rather large energy spread and divergence.

The FEL line enables different configurations to be studied and compared: echo, HHG seeding [35]. The FEL saturation is generally achieved earlier in the echo case than in the HHG seeding. The FEL is tuned by varying the seeding wavelength and the undulator resonance wavelength, harmonic generation in gas providing a discreetly tunable source from 40 to 15 nm. Further manipulation of the FEL properties such as the two-colour operation, the optical post-compression (FELShaping, OPT2X contracts) are also considered.

LUNEX5 has two end stations for time resolved pump-probe studies of isolated species (TR-AMO) and for condensed matter imaging exploiting the coherence. The TR-AMO end station will consist in a high resolution VG-Scienta electron spectrometer allowing for spectroscopy of cold atoms/molecules, clusters or nanoparticles, issued from a multi-purpose source, combined with the full momentum characterisation of both electrons and ions (ion momentum spectrometers combining time-of-flight and 2D ion position detection in coincidence mode). Lensless imaging technique also relies on very stable setup and accurate algorithms to extract real space images. It is proposed to use an existing mobile setup of LCPMR. Magnetization dynamics will be triggered through intense fs laser irradiation and probed by x-ray magnetic linear dichroic images measurements.

After the preparation of the CDR, LUNEX5 project is presently under a phase of R&D and complementary studies. Different programs have been funded. Some of them are here further described.

TOWARDS THE DEMONSTRATION OF A LWFA BASED FEL AMPLIFICATION

COXINEL grant aims at demonstrating an appropriate electron beam transport from the source to the undulator. The key concept relies on an innovative electron beam longitudinal and transverse manipulation in the transport towards an undulator: a “demixing” chicane [36] sorts the electrons in energy and reduces the spread from 1 % to a slice one of 0.1 % and the effective transverse size is maintained constant along the undulator (supermatching)

by a proper synchronisation of the electron beam focusing with the progress of the optical wave [37]. An example of the baseline implementation is shown in Fig. 4.

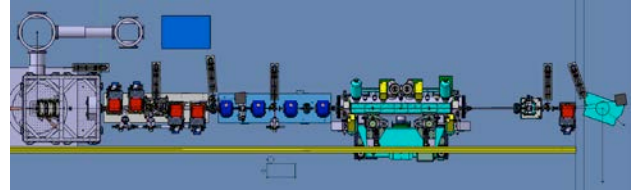


Figure 4: COXINEL transport line scheme.

Equipment is under preparation at Synchrotron SOLEIL. The magnetic design of a permanent magnet quadrupole with variable strength for the focusing of the LWFA diverging electron beam has been proposed in the frame of “Triangle de la Physique” contract QUAPEVA.

Besides, the X-Five grant concerns the optimisation of the LWFA electron beam with a 2x60 TW laser of the Laboratoire d’Optique Appliquée. Coupling both programs enables to prepare a demonstration experiment to observe FEL amplification at 200 nm first and then at shorter wavelength. After successful amplification, further study and potential control of the FEL properties will then follow.

R&D ON A CRYO-READY UNDULATOR

A cryogenic 15 mm period undulator is under design at SOLEIL in collaboration with MAX-LAB. The 3 m long device consists of vanadium-Permendur poles and $\text{Pr}_2\text{Fe}_{14}\text{B}$ magnets. The chosen grade is characterized by a remanence of 1.32 T and a coercitive force of 1900 kA/m at room temperature, leading to an on axis magnetic field peak value of 1.61 T at minimum gap of 3 mm. Once cold at 77 K, the remanence of this material should reach 1.57 T, increasing the undulator field up to 1.77 T at minimum gap. The magnets and poles are fixed on the girders by means of holders, each of them containing one magnet enclosed by two half-poles (see Fig. 5). This design ensures that all the holders are identical, in order to make easier the magnetic optimization steps of the undulator.

The undulator magnetic measurements, which must be performed at 77 K through the small gap of 3 mm and along about 5 m is a critical point. The measurement bench under design consists of a stretched wire and a Hall

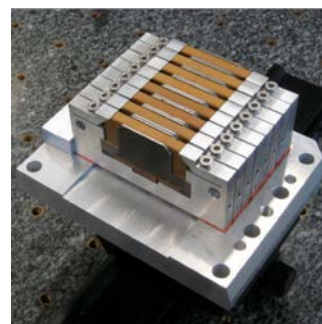


Figure 5: Four period assembly with half-poles.

probe both installed inside the vacuum chamber. The position and angle of the Hall probe will be controlled by lasers and interferometers and adjusted by piezo-motors in a similar way that the SAFALI system [38].

DEVELOPMENT ON ELECTRO-OPTICAL SAMPLING

The electro-optic detection technique offers the possibility to measure directly, in a non-destructive manner, the shape and the length of individual relativistic electron bunches with a sub-picosecond resolution [39, 40]. The technique relies on the Pockels effect induced by the electric field of a relativistic electron bunch in an electro-optic crystal. The induced birefringence in the crystal is probed using a polarized chirped laser pulse, the temporal pulse shape is retrieved by measuring the optical spectrum of the laser pulse (Fig. 6).

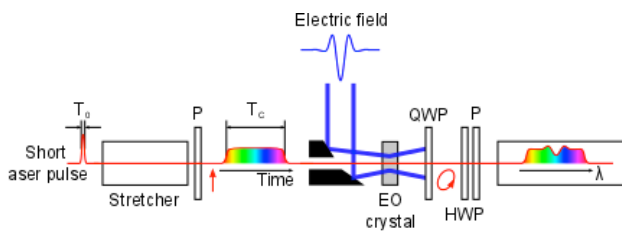


Figure 6: Schematic drawing of spectrally encoded electro-optic detection.

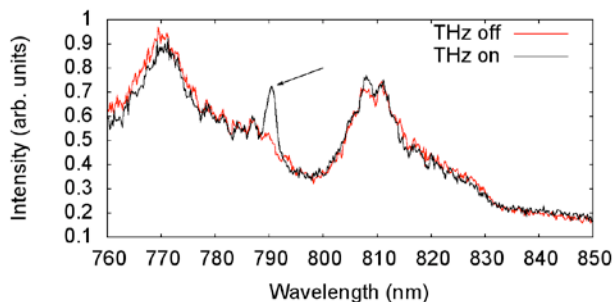


Figure 7: Optical spectrum of the probed laser pulse without (red) and with (black) external electric field in the EO crystal. The arrow indicates the peak corresponding to the THz pulse.

A preliminary experiment was realized at the PhLAM laboratory where a THz pulse was successfully detected in a ZnTe crystal using a 800-nm chirped laser pulse (Fig. 7). This detection technique [40,41] is known as the spectrally encoded electro-optic detection and allows for single-shot recordings of pulse shapes. However, in the future upgrade towards high-repetition rate FELs, single-shot recordings at high acquisition rate (MHz range) will be required and the present classical spectrally encoded technique is limited by the camera speed. Using a novel opto-electronic technique, based on the photonic time-stretch [42,43] well-known in optics and photonics, we demonstrated single-shot recordings up to 88 MHz of

CSR pulses on the AILES beamline at Synchrotron SOLEIL [44]. The temporal waveform containing the spectrally encoded signal is stretched in time so that it is slow enough to be detected using a photodetector instead of a spectrometer. This technique enables to overcome the current limitation in acquisition rate of the spectrally encoded electro-optic detection scheme.

CONCLUSION

Some R&D and complementary studies for the LUNEX5 project have been launched. The choice of the superconducting linac is confirmed by the need of high repetition rate operation for scientific application and for multi-FEL operation. Besides, a test experiment for the demonstration of FEL amplification with a LWFA is under preparation. Important funding is still necessary for the LUNEX5 demonstrator.

ACKNOWLEDGMENT

The authors are grateful to the support from the European Research Council for COXINEL and X-Five grants, the “Laboratoire d’Excellence Physique Atomes Lumière Matière” (LABEX PALM, ANR-10-LABEX-0039) for FELshaping and Ultrafast-X contracts, the IDEX Paris Saclay for OPT2X, the French-Swedish collaboration for the support on the U15 cryo-ready undulator, ANR for DYNACO and SP, the “Triangle de la Physique” for QUAPEVA, the European COST action CM1204 « XUV/X-ray light and fast ions for ultrafast chemistry » (XLIC). The CERLA is supported by the French Ministère chargé de la Recherche, the Région Nord-Pas de Calais and the FEDER.

REFERENCES

- [1] M. Billardon, P. Elleaume, J. M. Ortega, C. Bazin, M. Bergher, M. Velghe, Y. Petroff, D. A. G. Deacon, K. E. Robinson, and J. M. J. Madey, “First Operation of a Storage-Ring Free-Electron Laser”, *Phys. Rev. Lett.* 51, 1652, (1983).
- [2] B. Girard, Y. Lapierre, J. M. Ortéga, C. Bazin, M. Billardon, P. Elleaume, M. Bergher, M. Velghe, Y. Petroff, “Optical frequency multiplication by an optical klystron”, *Phys. Rev. Lett.* 53 (25) 2405-2408 (1984).
- [3] M. E. Couprie et al. , “Free Electron Laser oscillation on the Super-ACO storage Ring at Orsay”, *Nucl.Inst. Meth. A* 296, 13-19 (1990).
- [4] M. E. Couprie, D. Garzella, A. Delboulbé, M. Velghe, M. Billardon, “Operation of the Super-ACO FEL in the UV range at 800 MeV”, *Europhysics Letters* 21(9), 909-914 (1993).
- [5] M. E. Couprie, P. Tauc, F. Merola, A. Delboulbé, D. Garzella, T. Hara, M. Billardon, “Fluorescence decays and rotational dynamics of the NADH coenzyme, First use of the UV Super-ACO Free Electron Laser”, *Rev. of Scient. Inst.* 65 1495-1495, (1994).

- [6] M. Marsi, M. E. Couprie, L. Nahon, D. Garzella, A. Delboulbé, T. Hara, R. Bakker, G. Indlekofer, M. Billardon, A. Taleb-Ibrahimi, "Surface States and Space Charge Layer Dynamics on Si(111)2x1: a Free Electron Laser-Synchrotron radiation study", Appl. Phys. Lett. 70, 895-897, (1997).
- [7] M. Marsi, L. Nahon, M. E. Couprie, D. Garzella, T. Hara, R. Bakker, M. Billardon, A. Delboulbé, G. Indlekofer, A. Taleb-Ibrahimi, "Surface photovoltage in semiconductors under pulsed optical excitation, and its relevance to synchrotron radiation spectroscopy", Journal of Electron Spectroscopy and Related Phenomena 94, 149-157 (1998); M. Marsi, R. Belkhou, C. Grupp, G. Panaccione, A. Taleb-Ibrahimi, L. Nahon, D. Garzella, D. Nutarelli, E. Renault, R. Roux, M.E. Couprie, M. Billardon, "Transient charge carrier distribution at UV photoexcited SiO₂/Si interfaces", Phys. Rev. B 61, R5070-R5073 (2000).
- [8] L. Nahon, E. Renault, M.E. Couprie, F. Mérola, P. Dumas, M. Marsi, A. Taleb-Ibrahimi, D. Nutarelli, R. Roux and M. Billardon, "Applications of UV-Storage Ring Free Electron Lasers : the case of Super-ACO", Nuclear. Instr. Meth. A 429, 489-496 (1999).
- [9] E. Renault, L. Nahon, D. Garzella, D. Nutarelli, G. De Ninno, M. Hirsch, M. E. Couprie, "Transient Absorption Spectroscopy in biology using the Super-ACO storage ring FEL and the synchrotron radiation combination", Nucl. Inst. Meth. A 475 (1-3), 617-624 (2001).
- [10] M. Billardon, D. Garzella, M.E. Couprie, "Saturation mechanism for a storage ring Free Electron Laser", Phys. Rev. Lett. vol 69(16), 19 oct. 1992, 2368-2371
- [11] T. Hara, M. E. Couprie, A. Delboulbé, P. Troussel, D. Gontier, M. Billardon, "Observation of the super-ACO FEL micropulse with a streak camera", Nucl. Inst. Meth. A 341, 21-23 (1994).
- [12] M. E. Couprie, T. Hara, D. Gontier, P. Troussel, D. Garzella, A. Delboulbé, M. Billardon, "Temporal dynamics of storage ring free electron lasers", Phys. Rev E 53 (2), 1871-1889 (1996).
- [13] M. E. Couprie, D. Nutarelli, R. Roux, L. Nahon, B. Visentin, A. Delboulbé, G. Flynn, M. Billardon, "The Super-ACO FEL operation with shorter positron bunches", Nucl. Instr. Meth. A 407, 215-220 (1998).
- [14] R. Bartolini, G. Dattoli, L. Mezi, A. Renieri, M. Migliorati, M.E Couprie, R. Roux and G. De Ninno, "Suppression of the Saw-Tooth Instability in a Storage Ring by Free Electron Laser: an Example of non Linear Stabilisation by Noise", Phys. Rev. Lett. 87(13) 134801(4) (2001).
- [15] G. Dattoli, L. Mezi, A. Renieri, M. Migliorati, M. E. Couprie, R. Roux, D. Nutarelli, M. Billardon, "Storage Ring FEL dynamics and head-tail instability", Phys. Rev. E 58 (5), 6570-6574 (1998)
- [16] M. Velghe, M.E. Couprie, M. Billardon, "Specific Optical Properties of multilayer Mirrors for FEL experiments", Nucl. Inst. Meth. A 296, 666-671 (1990).
- [17] F. Glotin, J.M. Berset, R. Chaput, B. Kergosien, G. Lambert, D. Jaroszynski, J.M. Ortega, R. Prazeres, M. Velghe, J.C. Bourdon, M. Bernard, M. Dehamme, T. Garvey, M. Mencik, B. Mouton, M. Omeich, J. Rodier, P. Roudier, "First lasing of the CLIO FEL", Proc. of the 3rd European Particle Accelerator Conference, Berlin, Éd. Frontières, Gif-sur-Yvette, p. 620, (1992).
- [18] G. Lambert, T. Hara, M. Labat, T. Tanikawa, Y. Tanaka, M. Yabashi, D. Garzella, B. Carré, M.E. Couprie, "Seed level requirement for improving the temporal coherence of a Free Electron Laser", Europhysics Lett. 88, 54002 (2009)
- [19] T. Togashi, E. J. Takahashi, K. Midorikawa, M. Aoyama, K. Yamakawa, T. Sato, A. Iwasaki, S. Owada, T. Okino, K. Yamanouchi, F. Kannari, A. Yagishita, H. Nakano, M.E. Couprie, K. Fukami, T. Hatsui, T. Hara, T. Kameshima, H. Kitamura, N. Kumagai, S. Matsubara, M. Nagasono, H. Ohashi, T. Ohshima, Y. Otake, T. Shintake, K. Tamasaku, H. Tanaka, T. Tanaka, K. Togawa, H. Tomizawa, T. Watanabe, M. Yabashi, T. Ishikawa, "Extreme ultraviolet free electron laser seeded with high-order harmonic of Ti:sapphire laser", Optics Express, 1, 317-324 (2011)
- [20] M. Labat, M. Bellaveglia, M. Bougeard, B. Carré, F. Ciocci, E. Chiadroni, A. Cianchi, M. E. Couprie, L. Cultrera, M. Del Franco, G. Di Pirro, A. Drago, M. Ferrario, D. Filippetto, F. Frassetto, A. Gallo, D. Garzella, G. Gatti, L. Giannessi, G. Lambert, A. Mostacci, A. Petralia, V. Petrillo, L. Poletto, M. Quattromini, J.V. Rau, C. Ronsivalle, E. Sabia, M. Serluca, I. Spassovsky, V. Surrenti, C. Vaccarezza, and C. Vicario, "High-Gain Harmonic-Generation Free-Electron Laser Seeded by Harmonics Generated in Gas", Phys. Rev. Lett. 107, 224801 (2011).
- [21] P. Emma et al., Nature Photonics 4, 641 (2010).
- [22] S. T. Ishikawa et al., Nature Photonics 6, 540-544 (2012).
- [23] W. Ackermann et al., Nature Photonics 1, 336-342 (2007).
- [24] E. Allaria et al., Nature Photon. 6 699-704 (2012).
- [25] T. Tajima and J. M. Dawson, Phys. Rev. Lett. 43, 267 (1979); V. Malka, J. Faure, Y. A. Gauduel, E. Lefebvre, A. Rousse, K. Ta Phuoc, "Principle and applications of compact laser-plasma electron accelerator", Nature Physics 4 447-453 (2008); O. Lundh, J. Lim, C. Rechatin, L. Ammoura, A. Ben-Ismaïl, X. Davoine, G. Gallot, J-P. Goddet, E. Lefebvre, V. Malka, J. Faure, "Few femtosecond, few kiloampere electron bunch produced by a laser-plasma accelerator", Nature Physics 7, 219-222 (2011).
- [26] M. E. Couprie et al., Journal of Physics Conferences Series, 2013, 425: art.n° 072001 (2013).
- [27] <http://www.lunex5.com/spip.php?article34>
- [28] G. Stupakov, "Using the Beam-Echo Effect for Generation of Short-Wavelength Radiation", Phys. Rev. Lett., 102, 074801 (2009).

- [29] Technology Collaboration, <http://tesla-new.desy.de/>
- [30] A. Arnold, J. Teicher, PRSTAB 14, 024801 (2011), J. Teichert et al., Journal of Physics, Conf. series 298 (2013) 012008, J. Teichert et al. Proc. FEL 2013, New York, USA, 136 (2013).
- [31] D. Filippetto et al., Proceedings of FEL2012, Nara, Japan, 337-343 (2012).
- [32] E. Esarey, R. F. Hubbard, W. P. Leemans, A. Ting, P. Sprangle, "Electron injection into plasma wake fields by colliding laser pulses", Phys. Rev. Lett. 79, 2682 (1997).
- [33] J. Faure, C. Rechatin, A. Norlin, A. Lifschitz, Y. Glinec, V. Malka, "Controlled injection and acceleration of electrons in plasma wakefields by colliding laser pulses", Nature 444, 737-739 (2006)
- [34] X. Davoine, E. Lefebvre, C. Rechatin, J. Faure, V. Malka, "Cold Optical Injection Producing Monoenergetic, multi-GeV Electron Bunches", Phys. Rev. Lett. 102, 065001 (2009); Davoine, X, Beck, A., Lifshitz, V. Malka, E. Lefebvre "Cold injection for electron wakefield acceleration", NJP 12, 095010 (2010).
- [35] C. Evain et al., International Particle Accelerator Conference, New Orleans, USA, 2012, May 21-25, 1611-1613 (2012).
- [36] A. R. Maier et al., Phys. Rev. X 2, 031019 (2012).
- [37] A. Loulergue et al., Physics and applications of High Brightness Beams: towards a fifth generation light source, Puerto-Rico, March 25-28, (2013).
- [38] T. Tanaka, R. Tsusu, T. Nakajima, T. Seike and H. Kitamura, "In-situ undulator field measurement with the SAFALI system", Proceedings of FEL 2007, Novosibirsk, Russia, 468-471 (2007).
- [39] X. Yan et al. Phys. Rev. Lett. 85, 3404{3407 (2000).
- [40] I. Wilke et al. Phys. Rev. Lett. 88, 124801 (2002).
- [41] Z. Jiang and X.-C. Zhang, Applied Physics Letters 72, 1945{1947 (1998).
- [42] E. Roussel et al. Proceedings of IPAC2014, Dresden, Germany, THOBA01 (2014).
- [43] F. Coppinger et al., IEEE Transactions on Microwave Theory and Techniques 47, 1309 (1999).
- [44] Y. Han and B. Jalali, Journal of Lightwave Technology 21, 3085 (2003).

FREE ELECTRON LASERS IN 2014

J. Blau[#], K. Cohn, W. B. Colson, and W. Tomlinson

Physics Department, Naval Postgraduate School, Monterey CA 93943, USA

Abstract

Thirty-eight years after the first operation of the free electron laser (FEL) at Stanford University, there continue to be many important experiments, proposed experiments, and user facilities around the world. Properties of FELs operating in the infrared, visible, UV, and X-ray wavelength regimes are tabulated and discussed.

LIST OF FELS IN 2014

The following tables list existing (Table 1) and proposed (Tables 2, 3) relativistic free electron lasers (FELs) in 2014. The 1st column lists a location or institution, and the FEL's name in parentheses. References are listed in Tables 4 and 5; another useful reference is:

http://sbfel3.ucsb.edu/www/v1_fel.html.

The 2nd column of each table lists the operating wavelength λ , or wavelength range. The longer wavelength FELs are listed at the top and the shorter wavelength FELs at the bottom of each table. The large range of operating wavelengths, seven orders of magnitude, indicates the flexible design characteristics of the FEL mechanism.

In the 3rd column, t_b is the electron bunch duration (FWHM) at the beginning of the undulator, and ranges from almost CW to short sub-picosecond time scales. The expected optical pulse length in an FEL oscillator can be several times shorter or longer than the electron bunch depending on the optical cavity Q, the FEL desynchronism and gain. The optical pulse can be many times shorter in a high-gain FEL amplifier, or one based on self-amplified spontaneous emission (SASE). Also, if the FEL is in an electron storage-ring, the optical pulse is typically much shorter than the electron bunch. Most FEL oscillators produce an optical spectrum that is Fourier transform limited by the optical pulse length.

The electron beam kinetic energy E and peak current I are listed in the 4th and 5th columns, respectively. The next three columns list the number of undulator periods N , the undulator wavelength λ_0 , and the rms undulator

parameter $K = eB\lambda_0/2\pi mc^2$ (cgs units), where e is the electron charge magnitude, B is the rms undulator field strength, m is the electron mass, and c is the speed of light. For an FEL klystron undulator, there are multiple undulator sections as listed in the N-column; for example 2x7. Some undulators used for harmonic generation have multiple sections with varying N , λ_0 , and K values as shown. Some FELs operate at a range of wavelengths by varying the undulator gap as indicated in the table by a range of values for K . The FEL resonance condition, $\lambda = \lambda_0(1+K^2)/2\gamma^2$, relates the fundamental wavelength λ to K , λ_0 , and the electron beam energy $E = (\gamma-1)mc^2$, where γ is the relativistic Lorentz factor. Some FELs achieve shorter wavelengths by using coherent harmonic generation (CHG), high-gain harmonic generation (HHG), or echo-enabled harmonic generation (EEHG).

The last column lists the accelerator types and FEL types, using the abbreviations listed after Table 3.

The FEL optical power is determined by the fraction of the electron beam energy extracted and the pulse repetition frequency. For a conventional FEL oscillator in steady state, the extraction can be estimated as $1/(2N)$; for a high-gain FEL amplifier, the extraction at saturation can be substantially greater. In a storage-ring FEL, the extraction at saturation is substantially less than this estimate and depends on ring properties.

In an FEL oscillator, the optical mode that best couples to the electron beam in an undulator of length $L = N\lambda_0$ has a Rayleigh length $z_0 \approx L/12^{1/2}$ and has a fundamental mode waist radius $w_0 \approx (z_0\lambda/\pi)^{1/2}$. An FEL typically has more than 90% of its power in the fundamental mode.

At the 2014 FEL Conference, there were two new lasings reported: FLASH2 at DESY and a SASE FEL at the SwissFEL Test Facility at PSI. Progress continues on many other existing and proposed FELs around the world, from small terahertz FELs to large X-ray FEL facilities.

ACKNOWLEDGMENTS

The authors are grateful for support from the HEL-JTO.

[#]blau@nps.edu

Table 1: Existing Free Electron Lasers (2014)

LOCATION (NAME)	$\lambda(\mu\text{m})$	$t_b(\text{ps})$	E(MeV)	I(A)	N	$\lambda_0(\text{cm})$	K(rms)	Type
Frascati (FEL-CATS)	430-760	15-20	2.5	5	16	2.5	0.5-1.4	RF
UCSB (mm FEL)	340	25000	6	2	42	7.1	0.7	EA,O
Novosibirsk (FEL1)	120-240	50	12	8	2x33	12	0.71	ERL,O
Dresden (TELBE)	100-3000	0.15	15-34	15	8	30	≤ 5.7	RF,SU
Nijmegen (FLARE)	100-1400	3	10-15	50	40	11	0.5-3.3	RF,O
KAERI (THz FEL)	100-1200	20	4.5-6.7	0.5	80	2.5	1.0-1.6	MA,O
Osaka (ISIR, SASE)	70-220	20-30	11	1000	32	6	1.5	RF,S
Himeji (LEENA)	65-75	10	5.4	10	50	1.6	0.5	RF,O
UCSB (FIR FEL)	60	25000	6	2	150	2	0.1	EA,O
Osaka (ILE/ILT)	47	3	8	50	50	2	0.5	RF,O
Novosibirsk (FEL2)	40-80	20	20	20	33	12	1.0	ERL,O
Osaka (ISIR)	25-150	20-30	13-20	50	32	6	≤ 1.5	RF,O
Tokai (JAEA-FEL)	22	2.5-5	17	200	52	3.3	0.7	RF,O
Bruyeres (ELSA)	20	30	18	100	30	3.2	0.8	RF,O
Dresden (ELBE U100)	18-250	1-4	15-34	30	40	10	0.5-2.7	RF,O
Osaka (iFEL4)	18-40	10	33	40	30	8	1.3-1.7	RF,O
Kyoto (KU-FEL)	5-21.5	<1	20-36	17-40	52	3.3	0.7-1.56	RF,O
Darmstadt (FEL)	6-8	2	25-50	2.7	80	3.2	1.0	RF,O
Osaka (iFEL1)	5.5	10	33.2	42	58	3.4	1.0	RF,O
Beijing (BFEL)	5-25	4	30	15-20	50	3	0.5-0.8	RF,O
Daresbury (ALICE)	5-11	~ 1	27.5	80	40	2.7	0.35-0.9	ERL,O
Dresden (ELBE U27)	4-21	1-4	15-34	30	68	2.73	0.3-0.7	RF,O
Berlin (FHI MIR FEL)	4-50	1-5	15-50	200	50	4	0.5-1.5	RF,O
Tokyo (MIR-FEL)	4-16	2	32-40	30	43	3.2	0.7-1.8	RF,O
Nijmegen (FELIX)	3-250	1	50	50	38	6.5	1.8	RF,O
Orsay (CLIO)	3-150	10	12-50	100	38	5	≤ 1.4	RF,O
Nijmegen (FELICE)	3-40	1	60	50	48	6.0	1.8	RF,O
Hawaii (MkV)	2-10	2-5	30-45	30-60	47	2.3	0.1-1.3	RF,O
Osaka (iFEL2)	1.88	10	68	42	78	3.8	1.0	RF,O
Nihon (LEBRA)	1.5-6.5	1	58-100	10-20	50	4.8	0.7-1.4	RF,O
Tsukuba (ETLOK-III)	0.85-1.45	90	310	1-3	2x7	20	1-2	SR,O,K
UCLA-BNL (VISA)	0.8	0.5	64-72	250	220	1.8	1.2	RF,S
JLab (IR upgrade)	0.7-10	0.35	120	300	30	5.5	3.0	ERL,O
Osaka (iFEL3)	0.3-0.7	5	155	60	67	4	1.4	RF,O
JLab (UV demo)	0.25-0.7	0.35	135	200	60	3.3	1.3	ERL,O
Duke (OK-5)	0.25-0.79	5-20	270-800	10-50	2x30	12	3.18	SR,O,K
Okazaki (UVSOR-II)	0.2-0.8	6	600-750	28.3	2x9	11	2.6-4.5	SR,O,K
Tsukuba (ETLOK-II)	0.2-0.6	55	310	1-3	2x42	7.2	1-1.4	SR,O,K
SINAP (SDUV-FEL)	0.2-0.35	2-8	100-180	20-100	360	2.5	0.98	RF,A,H,E
DELTA (U250)	0.2	100	1500	40	2x7	25	7.3-10	SR,K,H
Duke (OK-4)	0.19-0.4	50	1200	35	2x33	10	4.75	SR,O,K
ELETTRA (SR-FEL)	0.09-0.26	70	1000	150	2x19	10	4.2	SR,A,K,H
PSI (SwissFEL Test)	0.07-0.8	0.5-3	100-220	20-160	265	1.5	0.5-1.3	RF,S
Frascati (SPARC)	0.066-0.8	0.15-8	80-177	40-380	450	2.8	0.5-1.55	RF,A,S,H
DESY (sFLASH)	0.038	0.5	700	1000	180 120	3.14 3.3	1.9 2.1	RF,S,H
SPRING-8 (SCSS)	0.03-0.06	1	250	300	600	1.5	0.3-1.06	RF,S
ELETTRA (FERMI-1)	0.02-0.08	0.7-1.2	1250	300-600	252	5.5	1-3	RF,A,H
ELETTRA (FERMI-2)	0.004-0.0144	0.7-1.6	1000-1400	300-700	396	3.5	0.85-1.6	RF,A,H
DESY (FLASH2)	0.004-0.08	0.05-0.5	500-1250	2500	768	3.14	0.5-2	RF,S
DESY (FLASH1)	0.004-0.045	0.05-0.5	370-1250	2500	981	2.73	0.87	RF,S
SLAC (LCLS)	0.12 nm	0.07	15400	3500	3696	3	2.5	RF,S
SPRING-8 (SACLA)	0.08-0.25 nm	0.02-0.03	8300	3000-4000	6300	1.8	1.52	RF,S

Table 2: Proposed Free Electron Lasers (2014)

PROPOSED FELs	$\lambda(\mu\text{m})$	$t_b(\text{ps})$	E(MeV)	I(A)	N	$\lambda_0(\text{cm})$	K(rms)	Type
KAERI (Table-top THz)	400-600	20	6.5	1	28	2.3-2.6	2.1-2.4	MA,O
Tokyo (FIR-FEL)	300-1000	5	10	30	25	7	1.5-3.4	RF,O
Colorado State University	200-800	5-15	6	100	50	2.5	1.0	RF,O
NPS-Niowave (THz)	170-550	1-2	3-5	3-7	10	3.3	0.5-1.2	RF,SU
India (CUTE-FEL)	50-100	1000	10-15	20	50	5	0.57	RF,O
Berlin (FHI FIR FEL)	40-500	1-5	20-50	200	40	11	1-3	RF,O
Novosibirsk (FEL3)	5-30	10	40	20-100	3x33	6	2.0	ERL,O
Beijing (PKU-FEL)	4.7-8.3	1	30	60	50	3	0.5-1.4	ERL,O
Turkey (TARLA U25)	3-20	0.4-6	15-40	12-155	60	2.5	0.25-0.7	RF,O
(TARLA U90)	18-250	0.4-6	15-40	12-155	40	9	0.7-2.3	
Tallahassee (Big Light)	2-1500	1-10	50	50	45	5.5	4.0	ERL,O
Daresbury (CLARA)	0.1-0.4	0.5	250	400	500	2.9	0.7-1.5	RF,A
Dalian (DCLS)	0.05-0.15	1	300	300	360	3.0	0.3-1.6	RF,A,H

Table 3: Proposed Short Wavelength Free Electron Lasers (2014)

PROPOSED FELs	$\lambda(\text{nm})$	$t_b(\text{ps})$	E(GeV)	I(kA)	N	$\lambda_0(\text{cm})$	K(rms)	Type
JLab (JLAMP)	10-100	0.1	0.6	1	330	3.3	1.0	ERL,O,A
SINAP (SXFEL)	8.8	0.26	0.84	0.6	720	2.5	0.95	RF,H,E
Glasgow (ALPHA-X)	2-300	0.001-0.005	0.10-1.0	1	200	1.5	0.5	PW,A
Groningen (ZFEL)	0.8	0.1	1-2.1	1.5	2600	1.5	0.85	RF,S,H
PSI (SwissFEL Athos)	0.7-7	0.002-0.015	2.5-3.4	1.5-2.7	1200	4	0.7-3.5	RF,S,SS
(SwissFEL Aramis)	0.1-0.7	0.002-0.015	2.1-5.8	1.5-2.7	3192	1.5	0.5-1.3	RF,S,SS
SLAC (LCLS-II SXR)	1.0-6.2	0.01-0.1	2.0-4.0	0.5-1.5	1827	3.9	1.4-3.9	RF,S,SS
(LCLS-II HXR)	0.05-1.2	0.01-0.1	2.5-15.0	0.5-4	4160	2.6	0.36-1.7	RF,S,SS
Pohang (PAL SXFEL)	1-4.5	0.06-0.18	2.6-3.2	1-3	1300	3.43	1.6-3.4	RF,S
(PAL HXFEL)	0.06-1	0.045-0.09	4-10	2-4	4100	2.44	1.3-2.1	
DESY (Europe XFEL)	0.4-5	0.002-0.18	8-17.5	5	1544	6.8	4-9	RF,S
	0.05-0.4				4375	4	1.65-3.9	
LANL (MaRIE)	0.03	0.03	12	3.4	3200	1.86	0.86	RF,S,H,E

Accelerator type:

MA - Microtron Accelerator
 ERL - Energy Recovery Linear Accelerator
 EA - Electrostatic Accelerator
 RF - Radio-Frequency Linear Accelerator
 SR - Electron Storage Ring
 PW - Laser Plasma Wakefield Accelerator

FEL type:

A - FEL Amplifier
 K - FEL Klystron
 O - FEL Oscillator
 S - Self-Amplified Spontaneous Emission (SASE)
 H - Harmonic Generation (CHG, HGHG)
 E - Echo-Enabled Harmonic Generation (EEHG)
 SS - Self-Seeded Amplifier
 SU - Super-radiant FEL

Table 4: References and Websites for Existing FELs

LOCATION (NAME)	Internet Site or Reference
Beijing (BFEL)	http://www.ihep.ac.cn/english/BFEL/index.htm
Berlin (FHI MIR)	http://fel.fhi-berlin.mpg.de
Bruyeres (ELSA)	P. Guimbal et al., Nucl. Inst. and Meth. A341 , 43 (1994).
Daresbury (ALICE)	http://www.stfc.ac.uk/ASTeC/Alice/projects/36060.aspx
Darmstadt (FEL)	M. Brunken et al., Nucl. Inst. and Meth. A429 , 21 (1999).
DELTA (U250)	H. Huck et al., Proceedings of FEL 2011, Shanghai, China. http://accelconf.web.cern.ch/AccelConf/FEL2011/papers/mooa5.pdf
DESY (FLASH, sFLASH)	http://flash.desy.de
Dresden (ELBE)	http://www.hzdr.de/FELBE
Duke (OK-4, OK-5)	http:// https://www.phy.duke.edu/duke-free-electron-laser-laboratory
ELETTRA (SR-FEL)	http://www.elettra.trieste.it/elettra-beamlines/fel.html
ELETTRA (FERMI)	http://www.elettra.trieste.it/FERMI
Frascati (FEL-CATS)	http://www.frascati.enea.it/fis/lac/fel/fel2.htm
Frascati (SPARC)	http://www.roma1.infn.it/exp/xfel
Hawaii (MkV)	M. Hadmack, Ph.D. Dissertation, University of Hawaii, December 2012.
Himeji (LEENA)	T. Inoue et al., Nucl. Inst. and Meth. A528 , 402 (2004).
JLab (IR upgrade)	G. R. Neil et al., Nucl. Inst. and Meth. A557 , 9 (2006).
JLab (UV demo)	S. V. Benson et al., Proceedings of FEL 2011, Shanghai, China. http://accelconf.web.cern.ch/AccelConf/FEL2011/papers/weoci1.pdf
KAERI (THz FEL)	Y. U. Jeong et al., Nucl. Inst. and Meth. A575 , 58 (2007).
Kyoto (KU-FEL)	H. Zen et al., Proceedings of FEL 2013, New York, NY, USA http:// https://accelconf.web.cern.ch/accelconf/FEL2013/papers/wepso84.pdf
Nihon (LEBRA)	K. Hayakawa et al., Proceedings of FEL 2007, Novosibirsk, Russia. http://accelconf.web.cern.ch/AccelConf/f07/papers/MOPPH046.pdf
Nijmegen (FELICE, FELIX)	http://www.ru.nl/felix
Nijmegen (FLARE)	http://www.ru.nl/flare
Novosibirsk (FEL1)	N. G. Gavrilov et al., Nucl. Inst. and Meth. A575 , 54 (2007).
Novosibirsk (FEL2)	N. A. Vinokurov et al., Proceedings of FEL 2009, Liverpool, UK. http://accelconf.web.cern.ch/AccelConf/FEL2009/papers/tuod01.pdf
Okazaki (UVSOR- II)	H. Zen et al., Proceedings of FEL 2009, Liverpool, UK. http://accelconf.web.cern.ch/AccelConf/FEL2009/papers/wepc36.pdf
Orsay (CLIO)	http://clio.lcp.u-psud.fr
Osaka (iFEL4)	T. Takii et al., Nucl. Inst. and Meth. A407 , 21 (1998).
Osaka (iFEL1,2,3)	H. Horiike et al., Proceedings of FEL 2004, Trieste, Italy. http://accelconf.web.cern.ch/AccelConf/f04/papers/THPOS17/THPOS17.pdf
Osaka (ILE/ILT)	N. Ohigashi et al., Nucl. Inst. and Meth. A375 , 469 (1996).
Osaka (ISIR)	R. Kato et al., Proceedings of IPAC 2010, Kyoto, Japan. http://accelconf.web.cern.ch/accelconf/IPAC10/papers/tupe030.pdf
PSI (SwissFEL Test)	S. Reiche, Proceedings of FEL2014, Basel, Switzerland.
SINAP (SDUV-FEL)	Z. T. Zhao and D. Wang, Proceedings of FEL 2010, Malmo, Sweden. http://accelconf.web.cern.ch/AccelConf/FEL2010/papers/moobi1.pdf
SLAC (LCLS)	http://lcls.slac.stanford.edu
SPring-8 (SCSS, SACLA)	http://xfel.riken.jp/eng/index.html
Tokai (JAEA-FEL)	R. Hajima et al., Nucl. Inst. and Meth. A507 , 115 (2003).
Tokyo (MIR-FEL)	http://www.rs.noda.tus.ac.jp/fel-tus/English/E-Top.html
Tsukuba (ETLOK-II)	K. Yamada et al., Nucl. Inst. and Meth. A528 , 268 (2004).
Tsukuba (ETLOK-III)	N. Sei, H. Ogawa and K. Yamada, Optics Letters 34 , 1843 (2009).
UCLA-BNL (VISA)	A. Tremaine et al., Nucl. Inst. and Meth. A483 , 24 (2002).
UCSB (mm, FIR FEL)	http://sbfel3.ucsb.edu

Table 5: References and Websites for Proposed FELs

LOCATION (NAME)	Internet Site or Reference
Beijing (PKU-FEL)	Z. Liu et al., Proceedings of FEL 2006, Berlin, Germany. http://accelconf.web.cern.ch/AccelConf/f06/papers/TUAAU05.pdf
Berlin (FHI FIR)	http://fel.fhi-berlin.mpg.de
Colorado State University	S. Milton et. al., Proceedings of IPAC 2014, Dresden, Germany. http://accelconf.web.cern.ch/AccelConf/IPAC2014/papers/thpri074.pdf
Dalian (DCLS)	T. Zhang et. al., Proceedings of IPAC2013, Shanghai, China http://accelconf.web.cern.ch/accelconf/IPAC2013/papers/weodb102.pdf
Daresbury (CLARA)	J. A. Clarke et. al., Proceedings of IPAC 2012, New Orleans, LA, USA. http://accelconf.web.cern.ch/AccelConf/IPAC2012/papers/tuppp066.pdf
DESY (Europe XFEL)	http://www.xfel.eu
Glasgow (ALPHA-X)	http://phys.strath.ac.uk/alpha-x/
Groningen (ZFEL)	J. P. M. Beijers et al., Proceedings of FEL 2010, Malmo, Sweden. http://accelconf.web.cern.ch/AccelConf/FEL2010/papers/mopc22.pdf
India (CUTE-FEL)	S. Krishnagopal and V. Kumar, Proceedings of FEL 2007, Novosibirsk, Russia. http://accelconf.web.cern.ch/accelconf/f07/papers/MOPPH074.pdf
JLab (JLAMP)	S. V. Benson et al., Proceedings of FEL 2009, Liverpool, UK. http://accelconf.web.cern.ch/accelconf/FEL2009/papers/mopc70.pdf
KAERI (Table-top THz)	Y. U. Jeong et al., J. Korean Phys. Soc., Vol. 59 , No. 5, 3251 (2011).
LANL (MaRIE)	http://marie.lanl.gov
Novosibirsk (FEL3)	N. G. Gavrilov et al., Nucl. Inst. and Meth. A575 , 54 (2007).
NPS-Niowave (THz)	http://www.niowaveinc.com
Pohang (PAL XFEL)	J.-H. Han et. al., Proceedings of IPAC 2012, New Orleans, LA, USA. http://accelconf.web.cern.ch/accelconf/IPAC2012/papers/tuppp061.pdf
PSI (SwissFEL Athos, Aramis)	http://www.psi.ch/swissfel
SINAP (SX-FEL)	Z. T. Zhao and D. Wang, Proceedings of FEL 2010, Malmo, Sweden. http://accelconf.web.cern.ch/AccelConf/FEL2010/papers/moobi1.pdf
Tallahassee (Big Light)	http://www.magnet.fsu.edu/usershub/scientificdivisions/emr/facilities/fel.html
Tokyo (FIR-FEL)	http://www.rs.noda.tus.ac.jp/fel-tus/English/E-Top.html
Turkey (TARLA U25,U90)	http://www.tarla.org.tr

THE TURKISH ACCELERATOR AND RADIATION LABORATORY IN ANKARA (TARLA) PROJECT*

A. Aksoy[†], Ö. Karşı, Ç. Kaya, Ö. Yavaş, Institute of Accelerator Technologies, Ankara, Turkey
S. Ozkorucuklu, Istanbul University, Istanbul, Turkey
P. Arıkan, Gazi University, Ankara, Turkey

Abstract

The Turkish Accelerator and Radiation Laboratory in Ankara (TARLA) which is proposed as a first facility of Turkish Accelerator Center (TAC) Project will operate two Infra-Red Free Electron Lasers (IR-FEL) covering the range of 3–250 microns. The facility will consist of an injector fed by a thermionic triode gun with two-stage RF bunch compression, two superconducting accelerating modules operating at continuous wave (CW) mode and two independent optical resonator systems with different undulator period lengths. The electron beam will also be used to generate Bremsstrahlung radiation. The facility aims to be first user laboratory in the region of Turkey in which both electromagnetic radiation and particles will be used. In this paper, we discuss design goals of the project, present status and road map of the project.

INTRODUCTION

TARLA, also called the Turkish Accelerator Center (TAC) IR FEL Oscillator facility, has been proposed as a sub-project of TAC in Turkey. TAC is an accelerator based research center project which consists of the conceptual design studies of a third generation synchrotron radiation facility based on 3.56 GeV positron ring, a SASE/X FEL facility based on multi GeV electron linac and a 1–3 GeV proton accelerator, a linac-ring type charm factory, since 2006 [1–3]. The construction phase of TARLA has been supported by Ministry Development (MD) of Turkey since 2010 and the laboratory has been still under construction [4, 5].

The main goal of TARLA is to provide FEL radiation between the ranges of 3–250 μm in the infrared region by using two undulator-resonator system. The facility will also have a bremsstrahlung production target and some fixed target applications using the available electron beam which is in the energy range of 15–40 MeV. The electron beam will be obtained by a thermionic triode electron source operating at 250 kV in continuous wave (CW) mode. And the beam will further be accelerated up to 40 MeV by two superconducting RF modules that are designed for ELBE project [6]. The electron beam will be transported to two independent optical resonator systems housing undulators with the different period lengths of 25 mm and 90 mm. The schematic view of the facility is given in Fig. 1 and the main electron beam parameters as well as some FEL parameters of TARLA are given in Tables 1 and 2 respectively.

TARLA laboratory building completed in May 2011 under Ankara University Institute of Accelerator Technologies in Golbasi Campus which is about 15 km south of the center of Turkey, Ankara.

Table 1: Electron Beam Parameters of TARLA

Parameter	Unit	Value
Beam energy	MeV	15–40
Max. average beam current	mA	1
Max. bunch charge	pC	77
Horizontal emittance	mm.mrad	<15
Vertical emittance	mm.mrad	<12
Longitudinal emittance	keV.ps	<85
Bunch length	ps	0.4–6
Bunch repetition rate	MHz	13
Macro pulse duration	μs	50 - CW
Macro pulse repetition rate	Hz	1 - CW

TARLA ACCELERATOR

TARLA will consists of three main parts: the injector, the main accelerator and the transport lines to the U25 and U90 undulators (Fig. 1). The high current (1 mA) CW electron beam from injector which provides the energy of 250 keV will be transported to two superconducting modules including two TESLA RF cavities that are separated by a bunch compressor. The maximum available energy of the electron beam with these accelerator modules will be between the range of 15–40 MeV and two independent optical resonator systems will support the generation of FEL radiation.

Injector

TARLA injector will have a thermionic triode DC electron gun, two buncher cavities operating at 260 MHz and 1.3 GHz, five solenoid lenses, one dipole magnet and several steerer magnets. The total length of the injector is about 5.75 m. Although the designs of electron gun and buncher cavities are the same with the ELBE Radiation Source [7], there will be a small difference with the beam line of ELBE by using a bend about 15° just after the gun, in order to avoid the field emission current from the SC cavities to back-bombard the cathode.

Main Accelerator

TARLA main accelerator will include two ELBE cryomodels (Linac-1, Linac-2) and a magnetic bunch compressor (BC) between them (see Fig. 1). Each cryomodel

* Work supported by Ministry of Development of Turkey

[†] avniaksoy@ankara.edu.tr

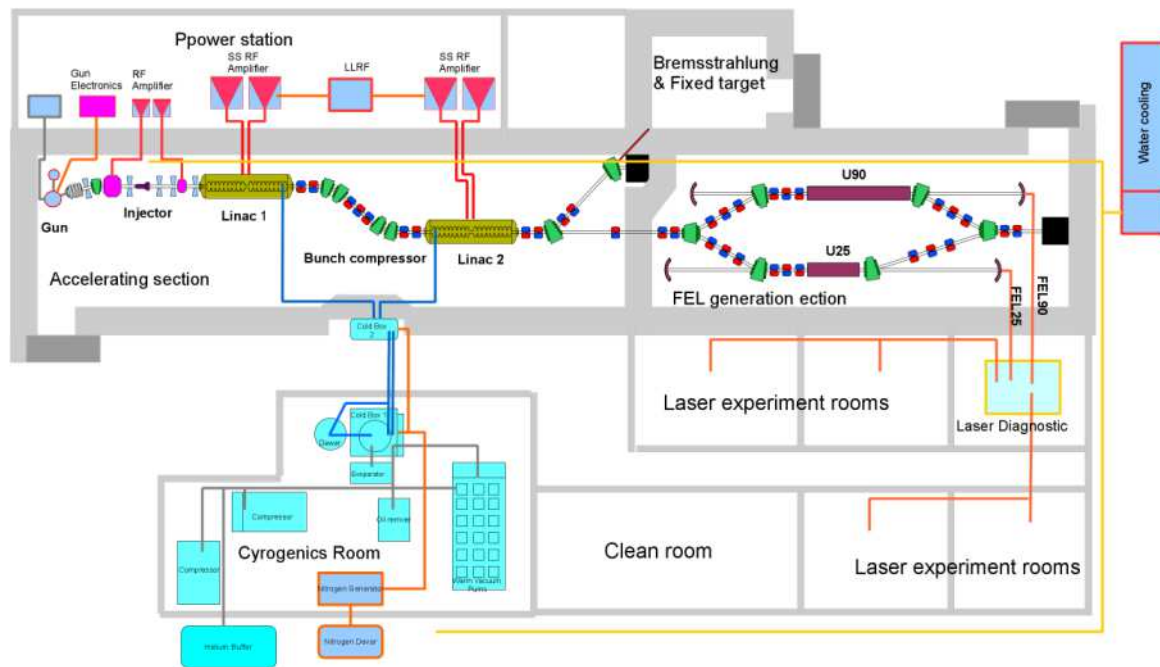


Figure 1: Layout of TARLA facility.

contains two nine-cell TESLA cavities with a maximum achievable accelerating gradient of 10 MV/m, thus, the total maximum reachable beam energy is about 40 MeV. The (fixed R_{56}) bunch compressor between the two modules will allow to optimize the micropulse duration and energy spread of the beam by tuning the phase of the cavities.

ELBE Cryomodule The cryomodules each contains two SC Nb cavities which are identical to the structures developed for the TESLA project at DESY [8]. The cryostat and mechanical tuning systems of the cryomodule have been developed and built for the ELBE project in close collaboration with the Stanford University [9]. For CW operation at 1 mA about 10 MV/m gradient have been demonstrated during long-term operation at ELBE using 10 kW RF sources. Recently it has been shown that the cavities are capable to accelerate 1.5 mA beam current using 16 kW power sources [10].

Bunch Compressor During the capture process from the injector into the first SC cavity the bunch acquires a chirp about 200 keV/ps with the leading electrons having higher energies. If one considers to use a chicane for compressing the bunch, the sign of the chirp would have to be changed operating the second cavity of Linac-1 off-crest. Such an operation would yield a large overall energy reduction. In order to have shortest bunch length at maximum energy we have designed an arc type bunch compressor with $R_{56} = 11$ cm. For increased dispersion we have used a pair of bending magnets each bending by 20° . If one wants to increase the length of the bunch using this type of bunch compressor one has to drive the second cavity of Linac-1 off-crest and change the sign of the chirp. The reduction of the maximum

achievable beam energy can here be accepted as the long-bunch mode is only of interest for long FEL wavelengths. Figure 2 shows the longitudinal phase space of beam before and after bunch compressor. As it can be seen the beam is compressed down to 0.4 ps.

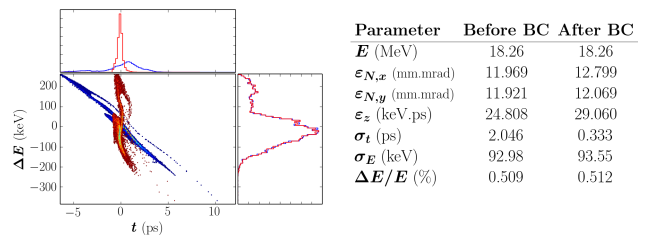


Figure 2: Longitudinal phase space of beam before and after bunch compressor.

TARLA RF System The two main control schemes which are Generator Driven Resonator (GDR) and Self Excited Loop (SEL) will be used for driving the RF structures at TARLA. Each cavity is individually driven with the independent low-level RF controllers and 16 kW saturated RF power sources (Solid states power amplifiers with 18 kW power) that allows easy control of the energy spread and beam energy at any location on beamline. It is planning that the RF system will be implemented for TARLA by the middle of 2015. Figure 3 shows the schematic view of RF system of TARLA.

FREE ELECTRON LASER

In order to cover all desired wavelength between 3–250 μm we plan to use two optical resonators which have two dif-

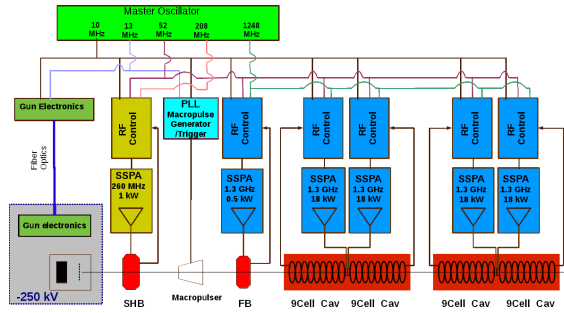


Figure 3: Schematic view of TARLA RF network.

ferent NdFeB hybrid undulators with periods of $\lambda_{U90} = 90$ mm and $\lambda_{U25} = 25$ mm.

FEL Transport Lines

For injecting the beam into the undulators a dogleg design consisting of two 30° bending magnets with a quadrupole triplet in between has been used for both FEL line. The quadrupole triplet and the symmetry of dipoles (including the pole face angles) are applied to obtain achromaticity in which the central quadrupole is free for tuning while side quadrupoles are used to minimize the dispersion. Three more degrees of freedom are provided by the triplet focusing the beam into the undulator. For instance for FEL25 line, Figure 7 shows that there exists matching covering the full energy range as well as the range of undulator's strengths suitable for lasing (given in Table 2). Figure 4 shows the bunch phase spaces at the entrance of U25 undulator for maximum beam energy and minimum undulator strength.

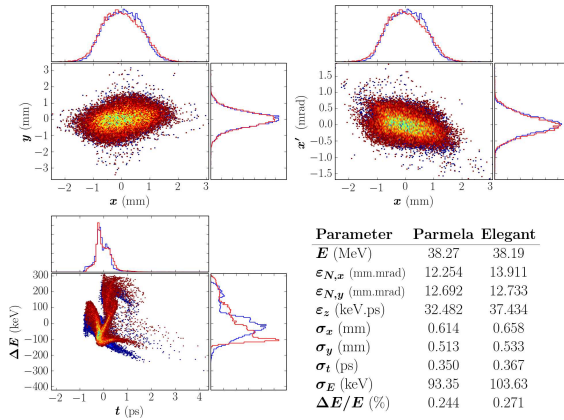


Figure 4: Bunch phase spaces at the entrance of U25 undulator for maximum beam energy and minimum undulator strength.

FEL Generation

The undulators have been chosen NdFeB with 2.5 cm and 9 cm periods in order to scan desired wavelength ranges. Expected FEL parameters are given in Table 2 and Figure 5 shows possible observable wavelengths for beam energy vs. undulator strengths.

Table 2: Some Resonator and Expected FEL Parameters of TARLA

Parameter	Unit	U25	U90
Period length	mm	25	90
Magnetic gap	mm	14	40
Number of poles	#	60	40
Undulator strength	#	0.25 - 0.72	0.7 - 2.3
Wavelength	μm	3 - 20	18 - 250
Max. peak power	MW	5	2.5
Max. average power	W	0.1 - 40	0.1-30
Max. pulse energy	μJ	10	8
Pulse length	ps	1 - 10	1 - 10

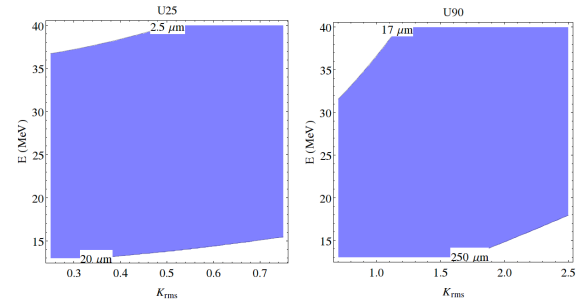


Figure 5: The possible wavelength range with respect to beam energy and undulator strength for U25 and U90.

Figure 6 shows laser pulse energy variation vs number of passes for various wavelengths obtainable from U25 and U90 undulators. As it can be seen the laser saturates around 200 round trip.

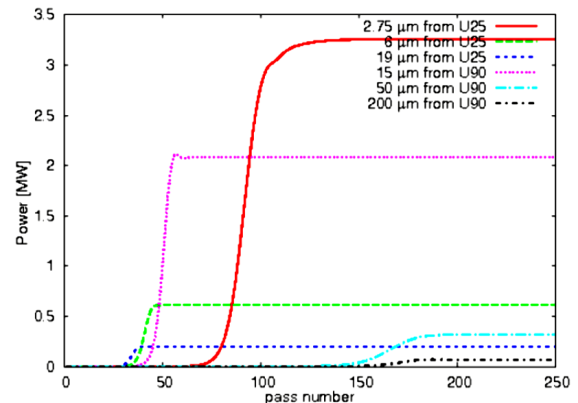


Figure 6: Laser saturation processes versus number of passes for various wavelengths obtainable from U25 and U90 undulators.

ELECTRON GUN TEST SETUP

The electron gun has been commissioning for more than 1 year at Institute of Accelerator Technologies of Ankara University (see Fig. 8). Fast pulsing electronics in order to create electron bunches with 500 ps has been developed by

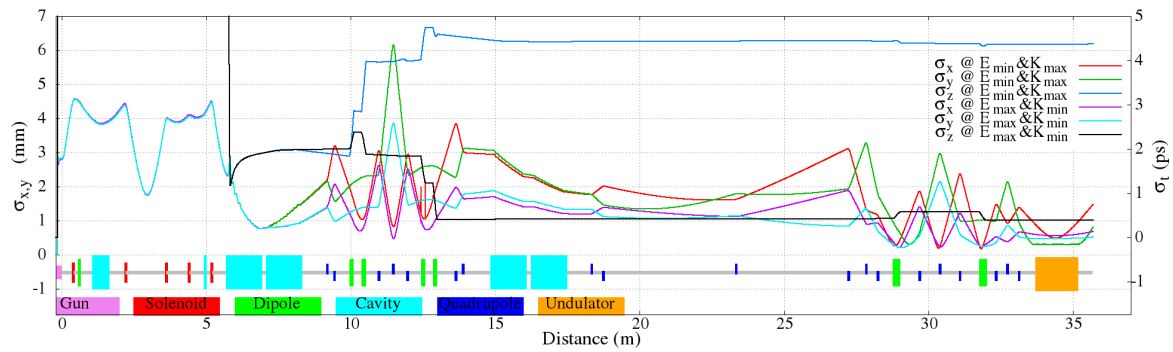


Figure 7: Beam envelope and bunch length variation along to U25 undulator.

TARLA team. It has been demonstrated that the beam can be created at 250 keV with more than 1 mA current in CW mode with required bunch length and emittance.

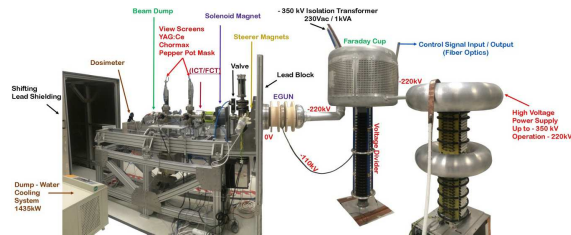


Figure 8: Test setup of TARLA electron gun.

CONCLUSION

First electron beam from TARLA gun has been observed in April 2013 and the injector is being installed and commissioned at present. The cryogenic plant is going to be installed by the end of 2014 and first cryomodule will be delivered by the beginning of 2015. We expect the first electron beam from first linac by the end of 2015 and from second linac not too much later. The first FEL beam is expected by beginning of 2018.

TARLA facility which is the first user laboratory in the region of Turkey will give good opportunities to the researchers in basic and applied science especially the ones who need high power laser in middle and far infrared region. Main purpose of TARLA-FELs is to use IR FEL for research in material science, nonlinear optics, semiconductors, biotechnology, medicine and photochemical processes. At the beginning, we plan to start up three of five experimental stations for laser diagnostic, IR spectroscopy and microscopy, material science. After taken some experiences and according to

our region needs the rest of the stations will be carried out including medical science and optics and chemistry laboratories as well.

REFERENCES

- [1] Ö. Yavaş et al., "Turkish Accelerator Center: The Status and Road map", at this conference.
- [2] Ö. Yavaş, A. K. Çiftçi, S. Sultansoy, EPAC 2000, p. 1008. (2000).
- [3] S. Sultansoy et al., "The Status of Turkic Accelerator Complex Proposal", PAC05 (2005), p.449.
- [4] S. Özkoşucuklu, A. Aksoy, "The Technical Design Report of Turkish Accelerator and Radiation Laboratory in Ankara", Ankara University, (2011).
- [5] A. Aksoy, et al., "The Turkish Accelerator Complex IR FEL Project", Infrared Physics & Technology, v:51, p:378-381, (2008).
- [6] A. Büchner, et al., "The ELBE Project at Dresden Rossendorf", EPAC 2000, Vienna, Austria, (WEP3B04), (2000).
- [7] F. Gabriel, et al., "The Rossendorf Radiation Source ELBE and its FEL Projects", Nucl. Instr. and Meth. B, v:161-163, p:143-1147, (2000).
- [8] B. Aune, et al., "Superconducting TESLA cavities", Phys. Rev. ST AB, v:3, p:092001, (2000).
- [9] J. Teichert, et al., "RF Status of Superconducting Module Development Suitable for CW Operation: ELBE Cryostats", Nucl. Instr. and Meth. A, v:557, p:239-242,(2006).
- [10] H. Büttig, et al., "Two Years Experience with the upgraded ELBE RF-System driven by 20 kW Solid State Amplifier Blocks", WEPME003, Proceedings of IPAC2014, Dresden, Germany, (2014).

DEVELOPMENTS IN THE CLARA FEL TEST FACILITY ACCELERATOR DESIGN AND SIMULATIONS

P. H. Williams[#], D. Angal-Kalinin, A. D. Brynes, J. K. Jones, B. P. M. Liggins, J. W. McKenzie, B. L. Militsyn, ASTeC, STFC Daresbury Laboratory, Cheshire, U.K
S. Spampinati, University of Liverpool & The Cockcroft Institute, Cheshire, U.K

Abstract

We present recent developments in the accelerator design of CLARA (Compact Linear Accelerator for Research and Applications), the proposed UK FEL test facility at Daresbury Laboratory. These comprise a revised front-end to ensure integration with the existing VELA (Versatile Electron Linear Accelerator) line, simulations of a magnetically compressed ultra-short mode and a post-FEL diagnostics section. We also present first considerations on the inclusion of final acceleration using X-band structures.

THE CLARA ACCELERATOR

CLARA (Compact Linear Accelerator for Research and Applications) is a proposed 250 MeV, 100-400 nm FEL test facility at Daresbury Laboratory [1]. The purpose of CLARA is to test and validate new FEL schemes in areas such as ultra-short pulse generation, temporal coherence and pulse-tailoring. The accelerator will comprise 4 S-Band, normal-conducting linacs with a medium-energy, variable bunch-compression scheme, feeding into a flexible arrangement of FEL modulators and radiators.

For seeding the accelerator includes a pre-FEL dogleg where laser light can be introduced. The accelerator will be driven by a high rep-rate RF photocathode S-Band (2998.5 MHz) gun, operating in single bunch mode at up to 400 Hz, and with bunch charges up to 250 pC. The accelerator is intended to be flexible, with seeded, ultra-short and multi-bunch train modes provided. Compression can be achieved via a variable magnetic bunch compressor between linacs 2 and 3 or velocity bunching in the injector. Linearisation can be provided by a harmonic X-band structure immediately prior to the magnetic compressor.

FRONT END

The VELA user facility, based on the ALPHA-X photocathode gun, has been commissioned and successfully delivered beam to users in 2013 [2]. The proposed FEL test facility, CLARA, is intimately linked to VELA with much common infrastructure. The design of the CLARA Front End (CLARA-FE) has been optimised to meet the requirements of the CLARA injector as well as to transport higher repetition rate, higher energy bunches to the presently operating VELA facility.

The proposed layout shown in Fig. 1 has been designed to use a common RF and drive laser infrastructure to feed two photo-injector RF guns. This will allow the flexibility of sending ~5 MeV high repetition rate bunches to

existing VELA user areas, and up to 50 MeV bunches transported through the S-bend placed after the first linac on the CLARA line to the VELA user areas at lower rep-rate. The layout assumes that the present VELA gun moves to CLARA when the front end is ready and installed. The ~55 MeV bunches after linac-1 can either be transported to (1) the CLARA line, (2) around the first dipole in the S-bend, then straight ahead to a diagnostic spectrometer line for characterising high energy bunches and (3) around the second dipole in the S-bend to the VELA user areas (the quadrupole triplet can be energised to eliminate dispersion in the VELA line). When the new High Repetition Rate Gun (HRRG) [3] is ready for commissioning and characterisation, it will be installed in the present VELA gun position. This is attractive as it provides a full set of dedicated diagnostics including the Transverse Deflecting Cavity (TDC). After this characterisation the HRRG will be moved to the CLARA line. Depending on the experimental programme either the original VELA gun or another new gun will be installed on the VELA line. This option will make low energy, short bunches available to proposed electron diffraction experiments on the VELA line [4]. At present, all simulations for the CLARA machine have been performed using a model of the existing VELA low rep-rate gun as it is assumed this will be installed before the HRRG.

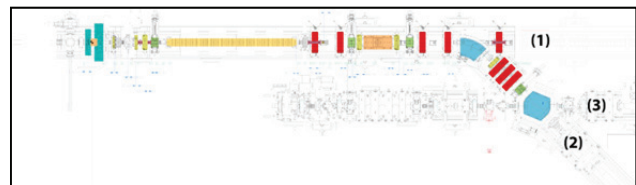


Figure 1: CLARA Front End Layout. The beam can be directed to (1) the rest of CLARA, (2) a diagnostic spectrometer line and (3) the existing VELA line with two user areas. The second “lozenge” dipole also admits beam from the existing VELA gun line allowing to be diverted to (2) or continue to (3).

ULTRA-SHORT MODE

One of the required modes of CLARA operation is transport of a medium charge (100 pC) bunch with length less than 25 fs RMS and corresponding high peak current in excess of 1 kA. This should have transverse normalised emittance of < 1 mm mrad and energy spread of < 150 keV RMS. This parameter set is specified for research into FEL schemes where the bunch length must be shorter than the typical SASE spike separation of $2\pi l_c$, with l_c the cooperation length. Previously, accelerator simulations

have concentrated on a velocity bunching scheme in the injector to achieve these parameters [5]. Here we present a preliminary tuning for the ultra-short mode using purely magnetic compression. The harmonic cavity was turned off and the variable bunch compressor set to maximum deflection, giving an R_{56} of -72 mm. Linacs 3 and 4 were set on crest and linac 2 scanned to find minimum bunch length. The resulting bunch properties are shown in Fig. 2.

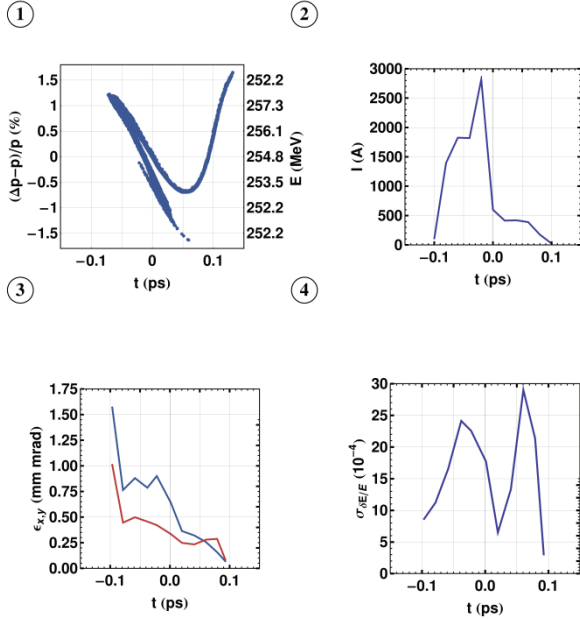


Figure 2: Preliminary beam properties for the magnetically compressed ultra-short mode. (1) Longitudinal phase space. (2) Current profile in 20fs bins. (3) Normalised transverse slice emittances (blue horiz., red vert.) in 20 fs bins. (4) Slice energy spread in 20 fs bins.

It is clear that this setup requires further optimisation as the slice energy spread and chirp exceeds specifications, and the RMS bunch length is 39 fs. However peak current is exceeded and so may be traded off through energising of the harmonic cavity and off-crest running in linacs 3 and 4. It is intended to refine this setup using multi-dimensional optimisation to minimise the energy spread and curvature, and to relax the compression somewhat as we exceed the required peak current by a factor of three. This should also mitigate the emittance degradation seen.

POST-FEL DIAGNOSTICS

Some of the advanced FEL schemes proposed depend on a manipulation of the electron beam properties with characteristic scales of several coherence lengths and shorter than the electron bunch [6,7,8]. To test mode locking and femto-slicing for the production of trains of short pulses [9,10,11] requires a 30 - 50 μm modulation of the beam energy, created via interaction with an IR laser beam in a short undulator.

The performances of these schemes depend on this energy modulation so monitoring the longitudinal phase

space is important. A transverse deflecting cavity (TDC) [12] installed in the last part of the FEL line allows the longitudinal beam distribution to be observed on a screen placed after the dipole leading to the beam dump. Figure 3 shows an initial layout of this diagnostic system, with a vertical TDC shown. This deflection maps the electron beam longitudinal coordinate to the vertical coordinate on a screen after the spectrometer dipole whilst the dipole converts energy to the horizontal coordinate.

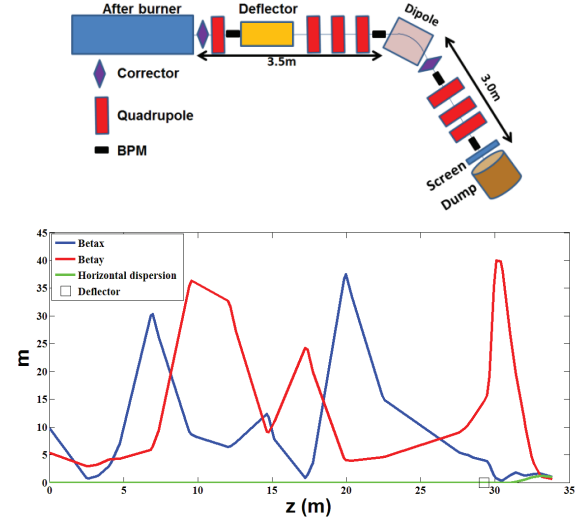


Figure 3: Layout of the phase space diagnostics (top) and potential optics solution (bottom) with transverse deflector and energy spectrometer.

The longitudinal resolution of the screen image can be written as:

$$\sigma_{L,r} = \frac{pc}{eV_0 k |\sin \Delta\Psi|} \sqrt{\frac{\varepsilon_n}{\gamma \beta_{y,D}} + \frac{(\sigma_{screen})^2}{\beta_{y,S} \beta_{y,D}}} \quad (1)$$

Here $k = 2\pi/\lambda$ and σ_{screen} is the screen resolution. V_0 is the deflecting voltage, $\beta_{y,D}$ and $\beta_{y,S}$ are vertical beta functions at the deflector and screen. $\Delta\Psi$ is the vertical phase advance between the deflector and screen, and $\lambda = 10.01\text{cm}$ for a 2.998 GHz S-band cavity. The energy resolution of the spectrometer can be written as [13]:

$$\sigma_E = \sqrt{\frac{E^2 \varepsilon_n \beta_{x,S}}{\eta^2 \gamma} + \frac{E^2 (\sigma_{screen})^2}{\eta^2} + (eV_0 k)^2 \frac{\beta_{y,S} \varepsilon_n}{\gamma}} \quad (2)$$

Here η is the horizontal dispersion at the screen. The first two terms represent the resolution of an energy spectrometer while the third term is the energy spread induced by the deflector [14].

The optimum phase advance between deflector and the screen is $\Delta\psi = 90^\circ$. Large values of V_0 and $\beta_{y,D}$ give good longitudinal resolution but decrease the energy resolution via the induced energy spread. A small value of $\beta_{x,S}$ and a large value of η are required for good energy resolution. Figure 3 also shows a possible optical solution from the modulator exit to the screen. The radiators are at maximum gap and the intra-undulator quadrupoles are used along with those shown in Fig. 3 to give the required

resolution. The optics shown is for a beam energy of 150 MeV and gives a longitudinal resolution of $6.5 \mu\text{m}$ and an energy resolution of 50 keV with a deflecting voltage of 5 MV, calculated using Eq. 1 & 2. The vertical RMS beam size on the screen is 1.8 mm. With a beam energy of 250 MeV, similar resolution can be achieved with similar optics but with a deflecting voltage of 7.5 MV. Simulations have been performed with the code elegant to test the analytic results. An example of the simulated phase space imaged on the screen is shown in Fig. 4. - this is from a beam modulated with a few (FWHM 500 fs) cycle $50 \mu\text{m}$ laser with a peak power of 30 MW. Two million particles were used in this simulation. The screen image clearly shows energy modulations as predicted by the analytical equations above.

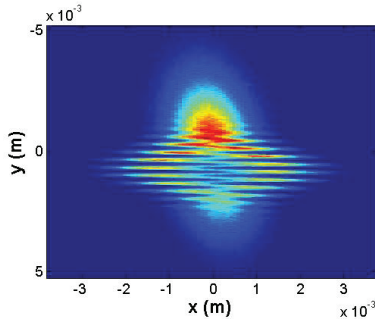


Figure 4: Beam imaged on the spectrometer screen.

X-BAND FINAL ACCELERATION

Recently interest has developed in using X-band (11994 MHz) CLIC structures as accelerating elements in a FEL [15]. To address this, we propose the replacement of the S-band linac 4 in CLARA with an equivalent length of such structures operating at 65 MV/m. We term this CLARA-X and will enable the beam energy to reach 426 MeV in the seeded mode. Figure 5 shows the optics for CLARA-X with the 4 S-band cavity replaced with an X-band equivalent. Almost no additional optimisation has been performed with the X-band cavity in-place.

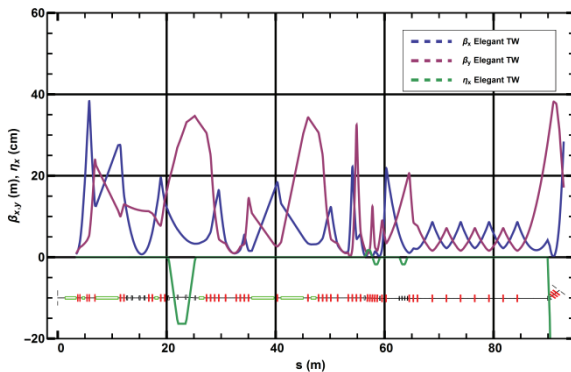


Figure 5: Optics for CLARA with X-band structures in the final linac. The energy reached is 426 MeV.

Figure 6 shows initial simulations of this mode at the same upstream configuration as in the S-band case with the X-band structures on crest. As the bunch is relatively long in this mode, additional curvature arising from the

stronger wakefields has only a small effect. This will be mitigated with a small reduction in the gradient of the harmonic linearising cavity prior to the bunch compressor.

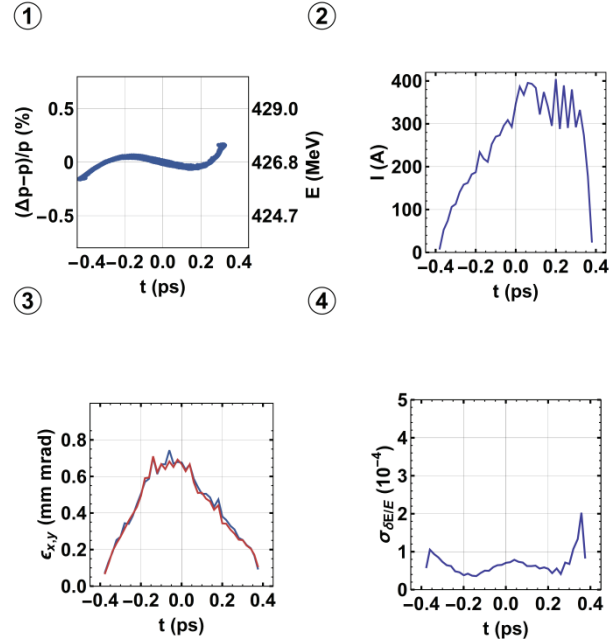


Figure 6: Beam properties, as described in Fig. 2, at the FEL for CLARA-X at 426 MeV in the seeded mode.

In order to confirm that the insertion of X-band structures does not compromise the nominal seeded operation mode of CLARA at 230 MeV tracking has also been performed in CLARA-X at reduced gradient. This is shown in Fig. 7. Again we see that the additional curvature from the stronger wakefields is a relatively

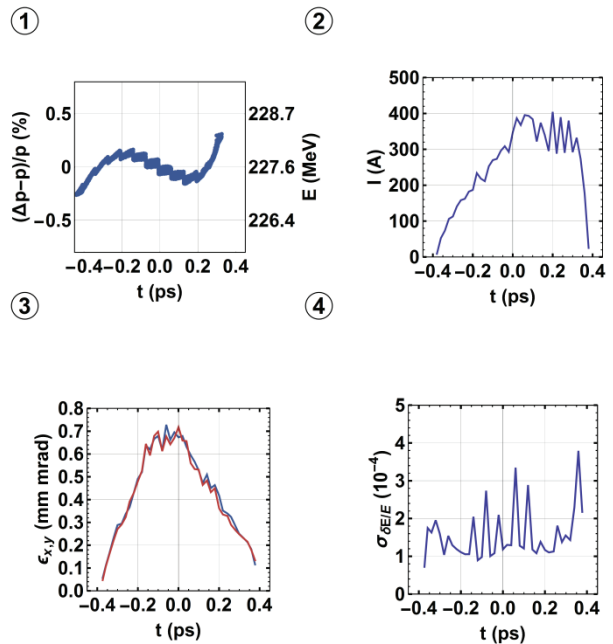


Figure 7: Beam properties, as described in Fig. 2, at the FEL for CLARA-X at 230 MeV in the seeded mode.

small effect and will be compensated for by a reduction in the gradient of the linearising cavity prior to the compressor. All other beam specifications for this mode are met adequately.

For completeness we reproduce the magnetically compressed ultra-short mode setup in the CLARA-X case. Results are shown in Fig. 8. We see that as in the S-band case a re-optimisation is required to compensate for the chirp and a relaxation in compression will mitigate the emittance growth seen.

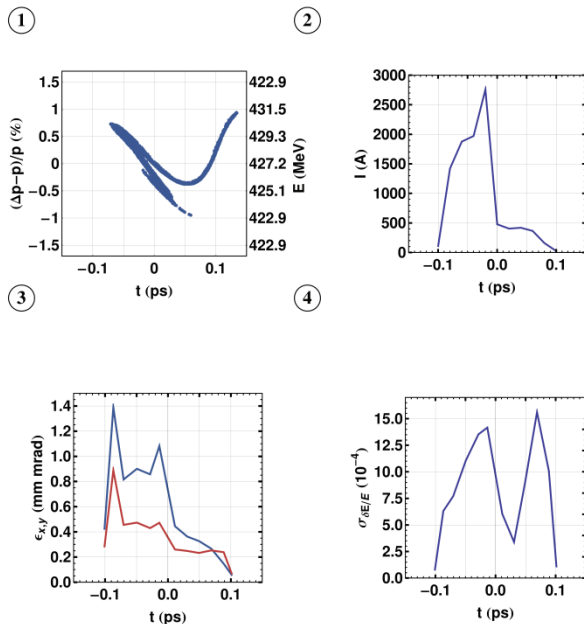


Figure 8: Beam properties, as described in Fig. 2, at the FEL for CLARA-X at 426 MeV in the magnetically compressed ultra-short mode.

CONCLUSION

Design work on the CLARA FEL test facility has been progressing throughout the year. The front end is now in procurement phase, correspondingly we have presented an updated layout taking into account engineering constraints. We have defined a preliminary tuning for the required ultra-short bunch mode using purely magnetic compression. We have presented results on the viability of post-FEL diagnostics on CLARA, and their expected performance. Finally, we have presented first considerations of performance upon replacing linac 4 with an equivalent length of X-band CLIC structures. With minimal optimisation of the machine design, we reproduce similar beam parameters to previous CLARA designs with either lower gradients and a similar energy, or higher gradients and a near-doubling of the CLARA beam energy. Initial studies also show we can maintain the newly-proposed magnetically compressed ultra-short bunch mode at this increased energy. Further optimisation of the machine design should lead to improvements of the beam parameters presented here.

REFERENCES

- [1] J. A. Clarke et al., JINST 9, 05 (2014): T05001.
- [2] B. Militsyn et al., “Beam Physics Commissioning of VELA at Daresbury Laboratory”, in: Proc. 5th Int. Particle Accelerator Conf., Dresden, 2014, THPRO052.
- [3] J. W. McKenzie et. al., “Cavity Design for an S-Band Photoinjector RF Gun with 400 Hz Repetition Rate”, in: Proc. 5th Int. Particle Accelerator Conf., Dresden, 2014, THPRO051.
- [4] M. Surman et. al., “Electron Diffraction on VELA at Daresbury”, in: Proc. 5th Int. Particle Accelerator Conf., Dresden, 2014, WEPRO108.
- [5] J. W. McKenzie et al., “Beam Dynamics Design of the CLARA FEL Test Accelerator” in: Proc. 35th Int. Free Electron Laser Conf., Nara, 2012, WEPD13.
- [6] A.A. Zholents, W.M. Fawley, Phys. Rev. Lett. 92, 224801 (2004).
- [7] E. Kur, D.J. Dunning, B.W.J. McNeil, J. Wurtele & A.A. Zholents, New J. Phys. 13 063012 (2011).
- [8] D.J. Dunning, B.W.J. McNeil and N.R. Thompson, Phys. Rev. Lett. 110, 104801 (2013).
- [9] E.L. Saldin, E.A. Schneidmiller and M.V. Yurkov, Phys.Rev. ST Accel. Beams 9, 050702 (2006).
- [10] N.R. Thompson and B.W.J. McNeil, Phys. Rev. Lett. 100,203901 (2008).
- [11] L. Giannessi et al., Phys. Rev. Lett. 106 ,144801 (2011).
- [12] G. A. Loew, O.H. Altenmueller, SLAC, PUB-135. Aug. 1965.
- [13] Y. Ding et al., “Commissioning of the X-band Transverse Deflector for Femtosecond Electron / X-Ray Pulse Length Measurements at LCLS”, in: Proc. 4th Int. Particle Accelerator Conf., Shanghai, 2013, WEOBB201.
- [14] M. Cornacchia and P. Emma, Phys. Rev. ST Accel. Beams 5, 084001 (2002).
- [15] A. Aksoy et al., “Conceptual Design of a X-FEL Facility using CLIC X-band Accelerating Structure”, in: Proc. 5th Int. Particle Accelerator Conf., Dresden, 2014, THPRO025.

A BEAM TEST OF CORRUGATED STRUCTURE FOR PASSIVE LINEARIZER

Heung-Sik Kang, Juho Hong, PAL, Pohang, Kyungbuk, Korea

Abstract

A dechirper which is a vacuum chamber of two corrugated, metallic plates with adjustable gap was successfully tested at Pohang, in August 2013. Another beam test was carried out to test the same structure to see if the flat geometry corrugated structure may work as a passive linearizer. The test result will be presented together with the simulation result.

PASSIVE LINEARIZER TO CORRECT QUADRATIC CHIRP

In August 2013, LBNL and SLAC experts were onsite at PAL-ITF to test a *dechirper*, an interesting instrument consisting of a vacuum chamber of two corrugated, metallic plates with an adjustable gap. One-meter long proto-type of dechirper was tested successfully to accurately measure the longitudinal, dipole, and quadrupole wakes [1]. And the linear chirp is well corrected by the linear longitudinal wake of dechirper.

An idea to use the same structure came up to see if the flat geometry corrugated structure may work as a passive linearizer replacing an expensive X-band linearizer system which consists of an X-band linearizer cavity and an X-band RF system. The total cost of that system is over 3 MUSD, and if including one spare of klystron and others, it goes to 5 MUSD. However, the passive wake structure is very cheap, below 200 kUSD even though the gap control system of two plates is included.

Figure 1 shows the flat geometry corrugated structure. The dimensions of the structure used at the experiment in August 2013 at PAL-ITF are: the corrugation period (p) is 0.5 mm, the corrugation depth (h) is 0.6 mm, the wall distance (t) is 0.3 mm, and the width of plate (w) 50 mm. Figure 2 shows the longitudinal wake of flat geometry corrugated structure.

For the passive wake structure to act like an X-band linearizer, quadratic part of longitudinal wake needs to be involved in the beam-wake interaction to correct quadratic chirp. So, the longitudinal wakefield wavelength, $\lambda = 2\pi\sqrt{ah/p}$, needs to be comparable to bunch length. Dechirper has two independent motors: jaws are always parallel and move vertically. The gap is adjustable from 1 to 30 mm. As the gap of the two plates goes close, the wavelength is decreased. With the corrugated structure parameters ($p=0.5$ mm, $h=0.6$ mm, $t=0.3$ mm), the calculated wakefield wavelengths are 7.5 mm, 5.3 mm, 3.8 mm for the gaps of 8 mm, 4 mm, 2 mm, respectively. To have the electron beam interact with the quadratic part of longitudinal wake, the electron beam

bunch needs to be longer than one fourth of the wake wavelength. But there is a limitation in the gap distance because the quadrupole wake of the flat geometry becomes very strong as the gap goes close.

Instead, we may increase the bunch length from 3 ps to 5 ps in rms in order to have the electron beam interact with the quadratic part of longitudinal wake. The simulation shows that the longitudinal wake at the gap of 6 mm can correct the quadratic chirp.

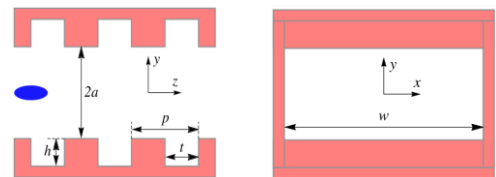


Figure 1: A flat geometry corrugated structure.

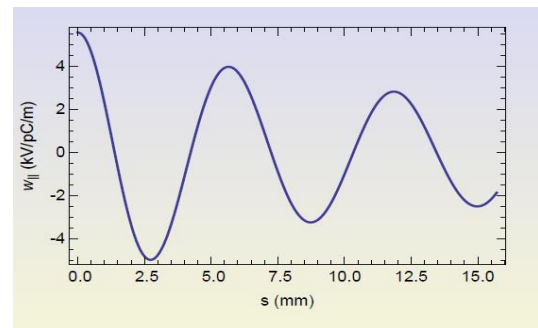


Figure 2: Longitudinal wake.

SIMULATION OF PASSIVE LINEARIZER AND BEAM TEST AT ITF

Figure 3 shows the layout of the PAL-ITF which consists of a PC RF-gun, two S-band Accelerating structures (L0a, L0b), a 1-m long S-band RF deflector, a 30-degree spectrometer, and three quads. A 1-m long corrugated chamber is located between L0b and the deflector. Six YAG screens are available, but Screen-6 is used for the analysis of the simulation and the experiment. In the simulation and measurement, all quads are turned OFF while the deflector is turned ON to allow the time-resolved measurement.

The beam energy is set at 80 MeV and the beam charge is 200 pC, and the pulse repetition rate is 10 Hz. Beam size and centroids measured on YAG screens, Spectrometer bend allows energy loss and energy spread measurements, and Dechirper offset is varied to guide the

beam at the center of the two plates to minimize the dipole wake of the flat geometry corrugated structure.

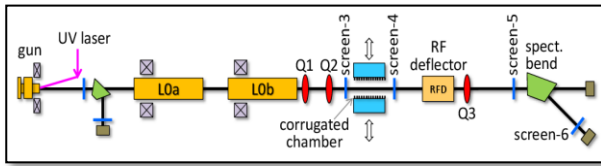


Figure 3: Layout of PAL-ITF.

Figure 4 shows the ELEGAT simulation result. Longitudinal phase space and x-y beam projection at Screen-6 are depicted for the gaps of (a) 30 mm, (b) 10 mm, and (c) 6 mm. The x-y beam projection at Screen-6 represents the energy-time phase space; x-axis represents the beam energy and y-axis represents the time streaked by the deflector. It is clearly seen that the quadratic energy chirp of Fig. 4(a) is well corrected by changing the gap to 6 mm in order to have a linear time-energy correlation as shown in Fig. 4(c).

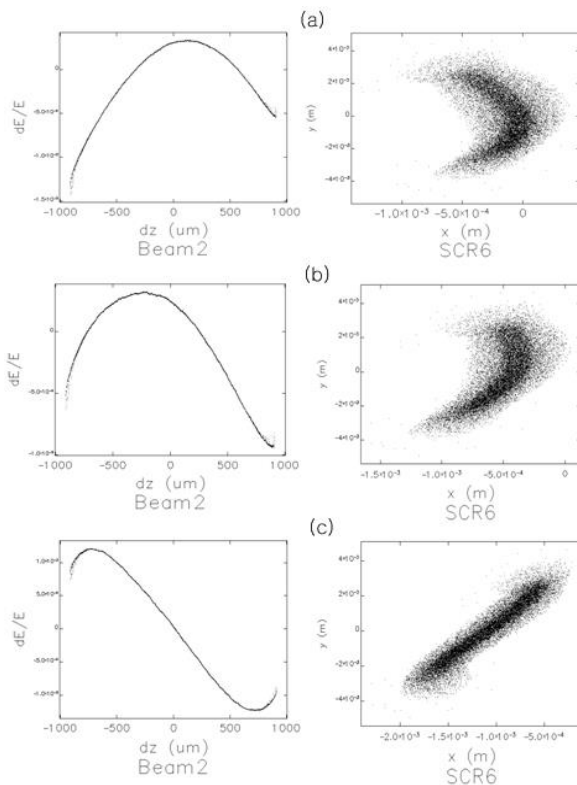


Figure 4: ELEGAT simulation result. Longitudinal phase space and x-y beam projection at Screen-6 for the gaps of (a) 30 mm, (b) 10 mm, and (c) 6 mm.

In the ELEGANT Simulation, the quadrupole wake of flat-geometry corrugation structure is not included because its effect is so strong that the linearization effect is not clearly seen. In the measurement, the beam shape at Screen-6 is altered due to a strong quadrupole wake (see

Fig. 5(c). But the beam shape of Fig. 5(b) is quite similar to that of Fig. 4(b) at the same gap of 10 mm.

The quadrupole wake effect is more clearly observed than the measurement of August 2013 because the bunch length is changed to 5 ps, longer than 3 ps of the previous measurement. The quadrupole wake effect goes strong as the bunch length is increased.

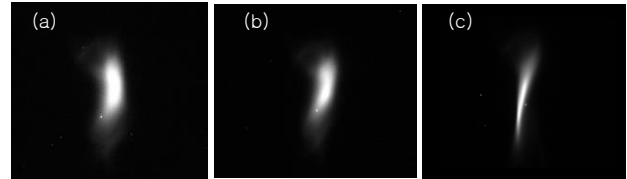


Figure 5: The measured beam images at Screen-6 for the gaps of (a) 15 mm, (b) 10 mm, and (c) 6 mm.

S2E SIMULATION OF PASSIVE LINEARIZER FOR PAL-XFEL

We carried out the S2E simulation of a passive linearizer for PAL-XFEL to look for a possibility of its use when the X-band linearizer happens to fail to work due to the system failure. The PAL-XFEL is a 0.1-nm hard X-ray XFEL facility (2011 ~ 2015) including a 10-GeV electron Linac (Normal Conducting S-band, 60 Hz) [2].

Figure 6 shows the layout of the PAL-XFEL. The X-band linearizer cavity, which is 0.6m long, is located between Linac-1 and BC1, where the beam energy is 330 MeV.

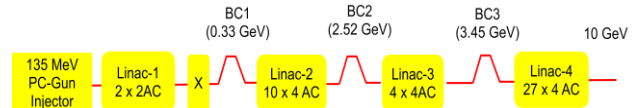


Figure 6: Layout of PAL-XFEL.

The corrugation parameters of passive linearizer used in this simulation are the same as ITF dechirper ($p = 0.5$ mm, $h = 0.6$ mm, $t = 0.3$ mm, $w = 50$ mm). But the structure length is increased to 2 m, and the gap is 3 mm. In the ELEGANT simulation, the quadrupole wake of flat-geometry corrugation structure is included. The simulation shows that the quadrupole wake does not give a big impact on the beam emittance.

Figure 7 and 8 show the S2E ELEGAT simulation results without X-band linearizer and with a passive linearizer, respectively. The current profile and the longitudinal phase spaces become bad when the X-band linearizer does not work (see Fig. 7). By using a passive linearizer, the current profile and the longitudinal phase space are well recovered enough to perform SASE FEL interaction in undulators (see Fig. 8). To get similar property as the X-band linearizer, RF phase of Linac-2 is only changed from -15.8 degrees to -16.0 degrees with other parameters unchanged.

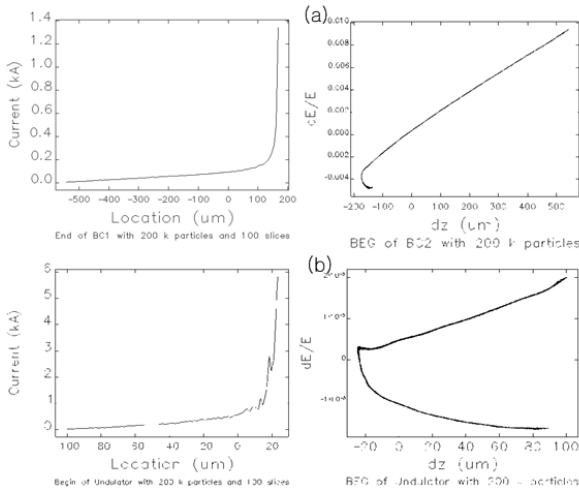


Figure 7: S2E ELEGAT simulation result without X-band linearizer. Current profile and longitudinal phase space (a) after BC1 and (b) at the entrance of undulators.

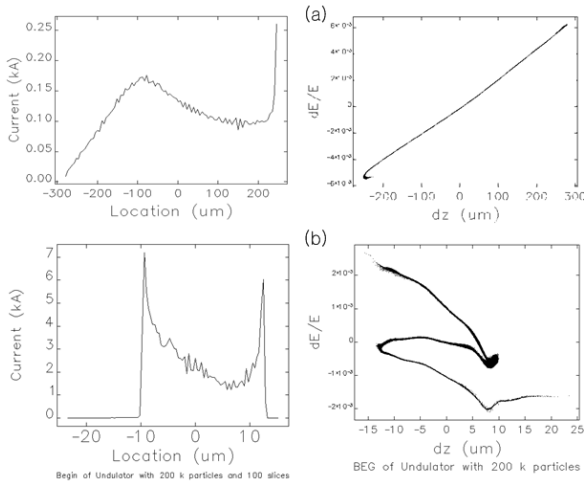


Figure 8: S2E ELEGAT simulation result with a passive linearizer. Current profile and longitudinal phase space (a) after BC1 and (b) at the entrance of undulators.

DISCUSSION

In the simulation, we found that it is impossible to get the exact same current profile and longitudinal phase space as an X-band linearizer system does. It is mostly because both the wake amplitude and the wake wavelength are dependent on the gap distance in the flat-geometry corrugated structure, so two parameters are correlated. Independent control of wake amplitude and wake wavelength is required for better linearization control.

The flat geometry structure is easy to change the gap, but it has a quadrupole wake effect. A round shape of wake structure is better in terms of quadrupole wake. But it lacks the controllability of wake amplitude and wake wavelength.

ACKNOWLEDGEMENT

I would like to thank K. Bane, G. Stupakov, P. Emma (SLAC), Marco Venturini (LBNL) for the use of figures and data that they made.

REFERENCES

- [1] Paul Emma et. al., PRL 112, 034801 (2014).
- [2] Kang, H.S. et al. Current Status of PAL-XFEL Project. *Proc. IPAC Conf. 2013* paper WEODB103 (2013).

DESIGN OF A COMPACT LIGHT SOURCE ACCELERATOR FACILITY AT IUAC, DELHI

S. Ghosh, B. K. Sahu, A. Rai, G. K. Chaudhari, P. Patra, J. Karmakar, A. Pandey, N. Kumar,
R. K. Bhandari, D. Kanjilal, Inter University Accelerator Centre, New Delhi, India
J. Urakawa, A. Aryshev, High Energy Accelerator Research Organization, KEK, Tsukuba, Japan
V. Naik, A. Roy, Variable Energy Cyclotron Center, Kolkata, India
A. Deshpande, T. Dixit, Society for Applied Microwave Electronics Engineering & Research,
Mumbai, India

Abstract

There is a growing demand for a high brightness light source with short pulse length among the researchers in the field of physical, chemical, biological and medical sciences in India. To cater to the experimental needs of multidisciplinary sciences, a project to develop a compact Light Source has been initiated at Inter University Accelerator Centre (IUAC). In the first phase of the project, pre-bunched electron beam of ~ 7 MeV energy will be generated by a photocathode RF gun and coherent THz radiation will be produced by a short undulator magnet. In the next phase, the energy of the electron beam will be increased up to 40 MeV by a pair of superconducting niobium resonators. The coherent IR radiation will be produced by using an undulator magnet (conventional method) and X-rays by Inverse Compton Scattering. To increase the average brightness of the electromagnetic radiation, fabrication of superconducting RF gun is going to be started in a parallel development. In this paper, the design of the accelerator system and the plan of producing THz radiation will be discussed.

INTRODUCTION

Inter University Accelerator Centre (IUAC), New Delhi, is a national accelerator facility equipped with many ion accelerators notably a 15UD Pelletron accelerator, a superconducting Linac booster [1], a 1.7 MV Pelletron and various low energy ion beam facilities. These accelerators are used to carry out research in the field of nuclear physics, materials science and radiation biology. Recently, to address the growing needs of the researchers from multidisciplinary fields like biological, chemical, medical and physical sciences, a project to develop a Free Electron Laser (FEL) facility named as Delhi Light Source (DLS) has been initiated at IUAC.

The development of the DLS project is being started with a room temperature (RT) photocathode RF electron gun which will produce a high quality electron beam of energy ~ 7 MeV. The beam will be then injected into a short undulator magnet to produce radiation in the THz range.

Simultaneously, to operate the RF gun in cw or quasi-cw mode, development of the superconducting (SC) RF photocathode electron gun is being explored. The SC RF gun will be either a three and half-cell niobium resonator similar to the structure being used at Rossendorf, Dresden

[2] or a Quarter Wave Resonator (QWR) similar to the design adopted by Brookhaven National Laboratory (BNL) [3]. Experience of IUAC in the fields of fabricating niobium resonators, cryostats and cryogenic systems will be useful in this development. The energy obtained from the 3.5 cell elliptical structure is estimated to be ~ 10 MeV. This beam will then be injected into an undulator magnet to produce THz radiation. However, if the QWR structure is adopted as RF gun, then the energy gain from the gun will be only a few MeV, so another 5 cell TESLA type SC resonator will be required to increase the energy upto ~ 10 MeV. Both the options of SC RF gun is shown in Fig. 1.

In the next phase of the development, two 9 cell TESLA type cavities will be installed to boost the energy from ~ 7 MeV (from RT RF gun) or 10 MeV (from SC RF gun) to ~ 40 MeV. This beam will be switched to three different beam lines. One beam line will be dedicated to produce infrared (IR) radiation with the help of a long undulator magnet. The second beam line will be for X-rays produced by the technique of Inverse Compton Scattering whereas the third one will be dedicated for experiments with THz/Far-IR and/or with 40 MeV electron beam. The layout of the complete project plan is shown in Fig. 1.

THE PROJECT – DELHI LIGHT SOURCE (DLS)

The compact light source project will make IUAC a unique national facility with the potential to deliver THz, IR, X-rays and electron beams as well as the energetic ion beams from different ion accelerators. The schematic of the layout of the Delhi Light Source is shown in Fig. 1. The project will be executed in three phases, namely:

- (a) Phase-I: to produce THz radiation from a RT photocathode RF gun.
- (b) Phase-II: to produce THz radiation from the SC photocathode RF gun
- (c) Phase-III: to increase the energy of the electron beam up to 40 MeV with the help of TESLA type resonators and to use this beam to produce THz, IR and X-rays.

The different phases are described in detail in the following sections:

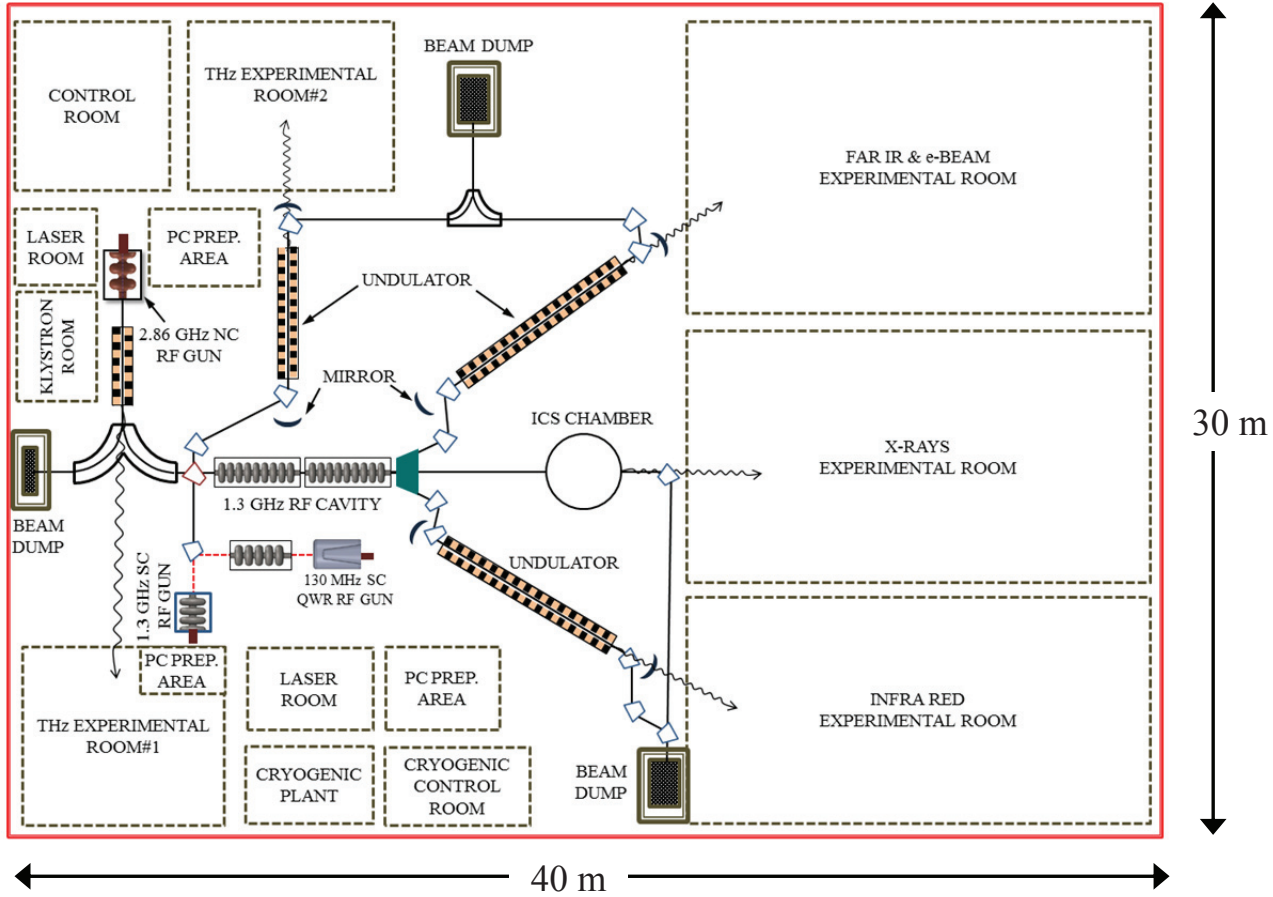


Figure 1: The complete layout plan of the Delhi Light Source (DLS).

Phase-I: To Produce THz Radiation from Room Temperature Photocathode RF Gun

The intense and ultrashort THz radiation can be produced by injecting pre-bunched [4] electron beam with FWHM of a few hundred femto-seconds (fs) into a short undulator magnet of a length of approximately ~ 700 mm. The wavelength of the electromagnetic radiation emitted from the undulator magnet depends on the electron beam energy and the undulator parameters. The equation relating to these parameters is as follows:

$$\lambda_R = \frac{\lambda_u}{2\gamma^2} \left[1 + \frac{K^2}{2} \right]$$

where

λ_R = Radiation wavelength

K = undulator parameter = $\frac{eB_u\lambda_u}{2\pi mc} = 93.4B_u(T)\lambda_u(m)$

λ_u = undulator wavelength

$\gamma = E/E_0$, ratio of electron energy to its rest mass energy in MeV

e = electronic charge (C)

B_u = Magnetic field of the undulator (T)

m = mass of electron (kg)

c = velocity of light (m/sec)

In the case of pre-bunched FEL, if the separation between the successive micro-bunches of the electron beam matches with the desired λ_R , then the emitted radiation from the micro-bunches passing through the undulator adds up in phase and the radiation power increases quickly.

The micro-bunching of the electrons takes place at the photocathode by the laser pulse stacking to generate a train of laser pulses ('comb' beam [4]) with a pulse repetition rate at THz frequency. The train of laser pulses is generated from a single laser pulse with the help of polarizing beam splitters (PBS), half wave plates and optical delay lines. The time spacing between the two successive pulses can be adjusted by carefully varying the path of the optical delay line. The variation of the time spacing ranges from ~ 333 fs to 3.3 ps (from $f = 3$ THz, $\lambda = 100 \mu m$ to $f = 0.3$ THz, $\lambda = 1$ mm). So by varying the time spacing between the laser pulses, the separation between the electron micro-bunches can be varied and a range of electromagnetic radiation will be produced when those microbunches will pass through a short undulator. However, due to space charge effect and relatively slow response time of production of electron from Cs_2Te photocathode, it is difficult to reduce the bunch length of the electron beam below ~ 300 fs.

Table 1: Parameter of the Ti:Sa Laser System

Wavelength	800 nm
Reference frequency	130 MHz
Oscillator frequency	130 MHz
Pulse duration	~ 40 fs
Repetition rate	10 Hz
Energy per pulse	~ 25 mJ

Table 2: Design Parameters of the Room Temperature (RT) Photocathode RF Gun

Electron energy (MeV)	7
Charge / micro-Pulse (pC)	100
E-beam bunch length (fs)	300
No. of micro-bunches (300fs each)	16
Frequency of micro-bunch trains (Hz)	10
Peak current (A)	333
Peak beam power (GW)	2.3
Average beam current (nA)	16
Average beam power (W)	0.112

The layout of the room temperature RF gun and the THz experimental room #1 is shown in Fig. 1. It has been decided, that DLS will have 2.6 cell copper resonator with a design similar to that of BNL and KEK [5]. This will be a S-band structure with resonance frequency of 2860 MHz. The energy obtained from 2.6 cell resonator is estimated to be ~ 7 MeV and RF pulse power requirement (peak) is calculated to be 18 MW (maximum).

The frequency of the copper resonator to be used as the RF gun is chosen to be 2860 MHz which is just a few MHz more than the commonly used frequency of 2856 MHz. The reason behind choosing 2860 MHz is that it is the 22nd harmonic of the reference frequency of 130 MHz as the frequencies of the SC cavities are chosen at 1300 MHz (3.5 cell TESLA type cavity) or 130 MHz (QWR).

A Cs₂Te photocathode inserted into the copper resonator would be used for the production of the electron beam. The development of the vacuum chamber to produce Cs₂Te photocathode, its vacuum transport system and load lock mechanism are being undertaken. With the remarkable success of GaN photocathode [6] and with its strong possibility for commercial availability, Cs₂Te may be substituted by GaN as photocathode material in future. To produce electrons from photocathode, a Ti:Sa femto-second (fs) laser system will be used. The laser parameters are given in Table 1.

The calculated design parameters of the room temperature RF gun and the THz radiation produced from the electron beam are given in Table 2 and 3.

Table 3: Expected Parameters of the 2.0 THz Radiation Emitted from the Electron Beam Produced by RT RF Gun

Radiation wavelength (μm)	150
K-parameter	0.8
Undulator period (cm)	3.4
RMS strength (T)	0.25
No. of periods (N) with 1m undulator	30
Peak radiation power (MW)	15
Average radiation power (mW)	0.75
Peak no. of photons /sec	10 ²⁸
Average no. of photons /sec	10 ¹⁷

Phase-II: To Produce THz Radiation from Superconducting Photocathode RF Gun

The second phase of the project will be started after witnessing a stable progress of Phase-I. In Phase-II, two possibilities are currently being explored. The first option is to develop a 3.5 cell 1.3 GHz niobium resonator [2] along with the provisions of (a) an independent tuning mechanism of gun and accelerating cells, (b) movement of the photocathode plug to optimise electron beam properties and (c) to generate a magnetic mode (TE) inside the cavity, predominantly around the last accelerating cell to reduce the transverse emittance of the beam. In addition, a resonant superconducting choke filter to prevent leakage of RF power from the cavity as well as the Higher Order Modes (HOM) and input couplers are to be designed.

In the second option, a niobium quarter wave resonator of 130 MHz will be developed and installed in the beam line (Fig. 1). This QWR would be similar to the existing QWRs for the heavy ion linac at IUAC [1]. The details of photocathode insertion mechanism inside the central conductor, set up for injecting the laser beam on the photocathode etc. are being worked out. The expected parameters of both the superconducting RF guns (1.3 GHz, 3.5 cell and 130 MHz QWR) are given in Table 4.

With the superconducting cavity, either with elliptical resonator or QWR, the THz radiation with the pre-bunched electron beam ('comb beam', similar to the case of room temperature RF gun) can be obtained in THz Experimental room#2 (Fig. 1). However, since this electron beam will have less average current, the total power of THz radiation will be low. So when quasi-cw electron beam will be produced from the superconducting RF gun, the beam will be injected into longer undulator magnet with optical cavity to produce THz radiation of much higher average power (Fig. 1).

Table 4: Design Parameters for the Superconducting Photocathode RF Gun

Frequency (MHz)	1300	130	
Type of operation	High Charge	High Current	
Electron energy (MeV)	10	10	2
Max bunch charge (nC)	1	0.05	4
Pulse duration (ps)	20	5	220
Bunch repetition (MHz)	1	39	13
Peak current (A)	50	10	18
Average current (mA)	1	2	52
Norm. transverse emittance (mm-mrad)	3	1	3
Photocathode material	Cs ₂ Te/ GaN	Cs ₂ Te/ CsK ₂ Sb	Cs ₂ Te/ GaN
Driving laser wavelength (nm)	266	266	266
Operating temp (K)	2	2	4.2

Phase-III: To Increase the Energy of the Electron Beam up to 40 MeV with the help of TESLA Type Resonators and to use this Beam to Produce Far-IR, IR and X-rays

The high quality electron beam from the room temperature RF gun and the SC RF gun can be injected into a couple of 9 cell TESLA type 1.3 GHz SC resonators which will further increase the energy of the electron beam from 7/10 MeV to ~ 40 MeV (Fig. 1). Frontline research experiments can then be carried out in three different beam lines. In the first beam line, far-IR radiation can be produced by long undulator magnet and experiments can be done with this radiation as well as with 40 MeV electron beam. In the second beam line, X-rays will be generated by the technique of Inverse Compton Scattering (ICS) by striking the electron beam with another laser [7]. In the third beam line, infrared radiation produced from the electron beam with the help of long undulator magnet, will be used for other set of experiments. The accelerator, the experimental facilities, the laser, the klystron, the control room and the shielded beam dumps will be accommodated in a hall of 40m x 30m (Fig. 1).

PRESENT STATUS OF THE PROJECT

Presently the phase-I of the project that aims at development of a RT RF gun to produce high quality electron beam of energy ~7 MeV has been started. For this, the fabrication of the copper resonator is being started with the help of KEK, Japan. The beam-line optics

design is going on and will be completed soon. The parameter finalization for the Klystron and the laser system is in progress and the purchase order for both the items will be placed shortly. The manufacturing and/or procurement of different beam diagnostic elements will be started once the beam optics design is finalised. Some preliminary work on the preparation procedure of the photocathode with the design of the preparation chamber has been started. The infrastructure for installing the RT RF gun is being developed and will be finished by the end of 2014. The low power tests of the RF gun are planned to be done by the end of 2014 followed by the high power tests in next 6 months.

To develop the SC RF gun, exploratory studies of SC photocathode RF gun based on Rossendorf type and 130 MHz QWR type based on BNL design are being carried out.

ACKNOWLEDGEMENT

The authors sincerely acknowledge the help and suggestions received from Prof. Ilan Ben-Zvi and Dr. Triveni Rao of Brookhaven National Laboratory, USA. The help received from Prof. S. Fukuda and Prof. Terunuma of KEK, Japan is also highly appreciated.

REFERENCES

- [1] S. Ghosh et. al., Physical Review Special Topic – Accelerator and Beams, 12.040101 (2009).
- [2] A. Arnold et. al. Nucl. Inst. Meth. A577, 2007, p. 440.
- [3] J. W. Lewellen, Proc. of ERL09, Ithaca, New York, p. 24.
- [4] S. Liu and J. Urakawa, Proc. of Free Electron Laser 2011, Shanghai, China, p 92-95.
- [5] X. J. Wang et. al., Nucl. Inst. Meth. A356, 1995, p. 159.
- [6] O. Siegmund et al. Nucl. Inst. Meth. A567, 2006, p. 89.
- [7] J. Urakawa, Nucl. Inst. Meth. A637, 2011, p. 547.

FAST, MULTI-BAND PHOTON DETECTORS BASED ON QUANTUM WELL DEVICES FOR BEAM-MONITORING IN NEW GENERATION LIGHT SOURCES

T. Ganbold, School of Nanotechnology, University of Trieste, P. le Europa 1, 34127, Trieste, Italy
 M. Antonelli, G. Cautero, R. Cucini, D. M. Eichert, W. H. Jark, R. H. Menk, Elettra – Sincrotrone Trieste S.C.p.A., S.S. 14 - km 163,5, 34149 Bazovizza, Trieste, Italy
 G. Biasiol, CNR-IOM, S.S. 14 - km 163,5, 34149 Bazovizza, Trieste, Italy

Abstract

In order to monitor the photon-beam position for both diagnostics and calibration purposes, we have investigated the possibility to use InGaAs/InAlAs Quantum Well (QW) devices as position-sensitive photon detectors for Free-Electron Laser (FEL) or Synchrotron Radiation (SR).

Owing to their direct, low-energy band gap and high electron mobility, such QW devices may be used also at Room Temperature (RT) as fast multi-band sensors for photons ranging from visible light to hard X-rays. Moreover, internal charge-amplification mechanism can be applied for very low signal levels, while the high carrier mobility allows the design of very fast photon detectors with sub-nanosecond response times.

Segmented QW sensors have been preliminary tested with 100-fs-wide 400 nm laser pulses and X-ray SR. The reported results indicate that these devices respond with 100 ps rise-times to such ultra-fast laser pulses. Besides, linear scan on the back-pixelated device has shown that these detectors are sensitive to the position of each ultra-short beam bunch.

INTRODUCTION

Several Free-Electron Lasers (FEL) and Synchrotron Radiation (SR) applications require radiation-hard and fast *in-situ* detectors for diagnostics and calibration purposes [1].

The opportunity to use QW devices for photon detection has been proposed in infrared region [2]. Recently, we have reported on QW detectors working in the ultraviolet (UV) and X-ray regions for FEL and SR sources [3, 4]. These QW devices give the possibility to detect a broad energy range of incoming photons, due to the low and direct band gap of the active layers. Furthermore, high carrier mobility at room temperature (RT) makes it possible to detect ultra-fast light pulses operating in either air or vacuum without cooling equipment. Therefore, epitaxially grown metamorphic InGaAs/InAlAs QW devices are here proposed as fast, solid-state detectors for beam monitoring applications.

These novel detectors are good candidates to sense the position and the intensity of a beam meeting the demanding time-resolution requirements posed by recent SR and FEL sources. To this aim, the performances of these detectors have been assessed by measuring their response to ultra-fast laser pulses.

Preliminary experiments have been carried out through a table-top Ti-sapphire laser delivering 100-fs-wide pulses with a 400 nm wavelength. The structure of the aforementioned QW devices and the main results of these tests are reported.

QUANTUM-WELL DEVICES

Device Structure and Characterization

These devices have been grown by Molecular Beam Epitaxy (MBE) at the CNR-IOM TASC Laboratory, Trieste. The starting material is a 500 μm thick epi-ready semi-insulating GaAs substrate. As shown in Fig. 1, in order to smooth the substrate surface a 200 nm thick GaAs layer was grown on its top, followed by a 200 nm thick GaAs/AlGaAs superlattice, which blocks the impurities from the bulk. Another 200 nm thick GaAs layer was introduced before an $\text{In}_x\text{Al}_{1-x}\text{As}$ step-graded buffer layer (BL) with increasing x from 0.15 to 0.75; this allows the lattice constant to be tuned in order to reduce the residual strain due to the lattice mismatch [5]. A 25 nm thick $\text{In}_{0.75}\text{Ga}_{0.25}\text{As}$ QW containing a 2D Electron Gas (2DEG) was placed in between 50 nm thick $\text{In}_{0.75}\text{Al}_{0.25}\text{As}$ barrier layers and a delta Si-doping was introduced in the upper barrier.

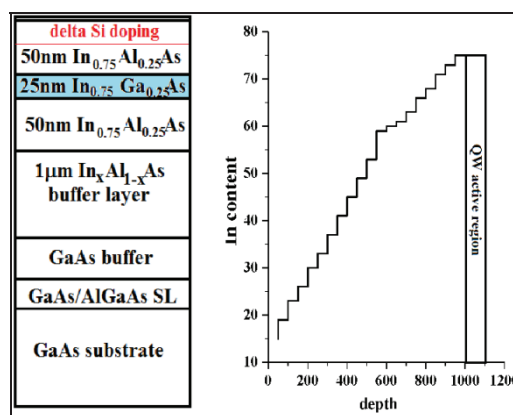


Figure 1: Layered structure of the samples and nominal profile of the In content in the step-graded buffer layer.

Hall-bar measurements were performed to characterize the charge density and the carrier mobility in the QW at room temperature, resulting in $n=7.7 \times 10^{11} \text{ cm}^{-2}$ and $\mu=1.1 \times 10^4 \text{ cm}^2\text{V}^{-1}\text{s}^{-1}$, respectively. Top-to-bottom resistance was found to be of the order of 100 M Ω at

ambient condition, mostly determined by the substrate resistivity.

Test-Dice Fabrication

Two types of samples (with a die area of $5 \times 5 \text{ mm}^2$) were prepared from $500 \text{ }\mu\text{m}$ thick InGaAs/InAlAs QW wafers and the structures on the surface were fabricated by using optical photolithography (Fig. 2). In the first sample, the QW region was segmented in three different pads, leaving a QW under each pad, while the rest of the surface was chemically etched by $1.5 \text{ }\mu\text{m}$ to reach the substrate. Ge/Ni/Au ($30/60/130 \text{ nm}$, respectively) ohmic contacts were provided as readout electrodes for currents from the pads. A single 400 nm Al electrode was deposited in the back side of the die for biasing.

In the second sample, the back side of the device was pixelated with $100 \text{ }\mu\text{m}$ wide clearances. Same readout electrodes were realized on each quadrant. The unsegmented QW side was covered by a single bias electrode identical to the one described above.

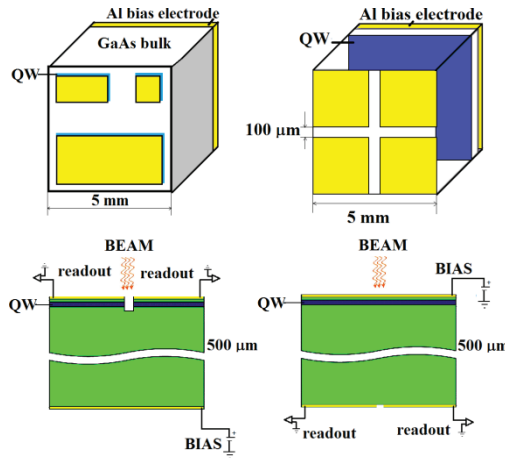


Figure 2: Schematic view of the fabricated devices.

EXPERIMENTAL DETAILS

Ultra-fast near UV pulsed laser sources are an efficient tool to characterize the presented QW detectors in terms of time response and position sensitivity. The reported experiments were carried out at the IUVS Support Laboratory of Elettra through a 400 nm titanium-sapphire laser emitting 100 fs wide pulses at a 1 kHz repetition rate. The laser beam was focused in order to obtain a $100 \text{ }\mu\text{m}$ spot on the surface of the QW sensor. The power of the impinging photon pulse was varied during the tests to check the dependence of photo-generated charges.

In order to perform mesh scans, the QW devices were mounted on a XY movable stage housed in a compact vacuum chamber. This stage is driven by stepper motors which are remotely controlled by a Labview-based software. The signals from the readout pads were acquired through a 40 GS/s oscilloscope.

RESULTS AND DISCUSSION

The first measurement was aimed at assessing the pulse response of the sensor. Therefore, the laser beam was focused on the surface of the first sample in proximity of the pads. The acquired signals (Fig. 3) show sub-ns response times with 100 ps rise/fall times to laser pulses.

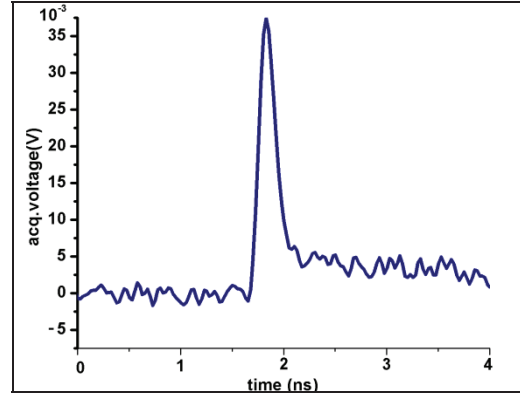


Figure 3: Response of device with segmented QW structure on the surface to the laser pulses.

Taking into account the small penetration depth of 400 nm photons, with a bias voltage as low as -10 V and electron mobility as high as $10^4 \text{ cm}^2 \text{ V}^{-1} \text{ s}^{-1}$, the charge collection time at readout pads should be of the order picoseconds, which is in agreement with the experimental results.

The area of the response pulse was estimated in terms of average incident power of the laser pulse and fitted by an allometric curve (Fig. 4), which could express the behaviour of the devices when dealing with low energy photons.

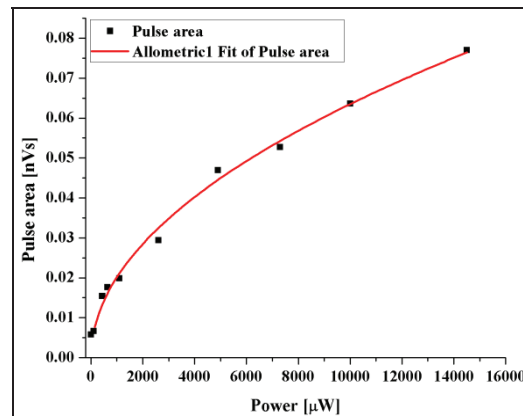


Figure 4: Peak area (time-integrated voltage pulse) dependence on incident power.

Figure 5 shows that the area of the acquired pulses is linearly proportional to the bias voltage applied from the back side of the device.

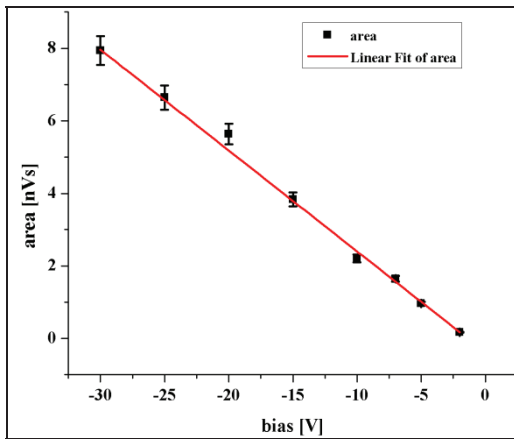


Figure 5: Area of response pulse VS bias voltage.

With the second device the position monitoring of each ultra-short laser pulse was tested by linear scans across the 100 μm clearance between the quadrants. As shown in Fig. 6a, when the beam hits one quadrant only, no current contribution from other channels is present.

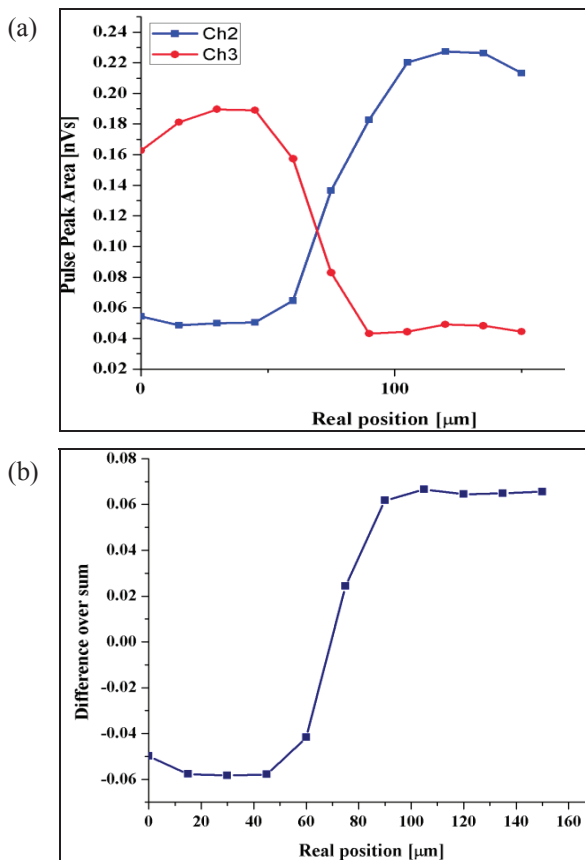


Figure 6: (a) Current switch from two channels during linear scan and (b) difference over sum.

It is evident how the two currents from each channel switch while the beam crosses the clearance. Furthermore, the difference-over-sum estimation [6] of the beam position results in a sigmoidal curve with a central linear

range of about 30 μm (Fig. 6b). This proves the capability of the detector for beam position monitoring. However, the number of steps in the transition region was not sufficient for a detailed estimation of the precision of the beam-position encoding.

CONCLUSION

The capabilities of the proposed QW devices were tested in terms of beam-position monitoring and fastness of signal detection in response to the short-pulsed laser light.

Thanks to their high carrier mobility and charge-amplification from 2DEG, these detectors responded with 100 ps rise times to ultra-short near UV pulses. Furthermore, beam-position sensing behaviour was confirmed by linear scan across the 100 μm clearance isolating two quadrants.

Alternative pixels strategies are under development to characterize other performances such as charge sharing behaviour of the pixels, energy resolution, charge collection efficiency of photo-generated current, etc.

ACKNOWLEDGMENT

T. Ganbold acknowledges support from the Training and Research in Italian Laboratories (TRIL) Programme at the International Centre for Theoretical Physics, Trieste.

REFERENCES

- [1] A. Galimberti, et al., 'A new detector for photon beam position monitoring designed for synchrotron radiation beamlines', Nuclear Instruments and Methods A 477 (2002) 317.
- [2] S.V. Bandara, et al., 'GaAs/AlGaAs multi-quantum-well based far infrared detectors for astronomy application', in Proc.Far-IR, Sub-mm & MM Detector Technology Workshop, Monterey, USA, 2002, id.86.
- [3] M. Antonelli et al., 'Bunch by bunch beam monitoring in 3rd and 4th generation light sources by means of single crystal diamond detectors and quantum well devices', in Proc.SPIE 8504, X-Ray Free-Electron Lasers: Beam Diagnostics, Beamline Instrumentation, and Applications, San Diego, USA, 2012, 85040D.
- [4] M. Antonelli et al., 'Fast synchrotron and FEL beam monitors based on single-crystal diamond detectors and InGaAs/InAlAs quantum well devices', Nucl. Instrum. Meth. A730 (2013) 164.
- [5] F. Capotondi et al., 'Strain induced effects on the transport properties of metamorphic InAlAs/InGaAs quantum wells', Thin Solid Films 484 (2005) 400
- [6] R.H. Menk et al., 'A Fast High Resolution Beam Position Monitor for Medium Hard and Hard X-Rays', in Proc. AIP Conference, Daegu, Korea, 2007, 879, 1109-1112.

HARD X-RAY SELF-SEEDING SETUP AND RESULTS AT SACLA

T. Inagaki[#], T. Tanaka, N. Adumi, T. Hara, R. Kinjo, H. Maesaka, Y. Otake, K. Togawa, M. Yabashi, H. Tanaka, T. Ishikawa, RIKEN SPring-8 Center, Sayo, Hyogo, Japan
Y. Inubushi, T. Kameshima, H. Kimura, A. Miura, H. Ohashi, T. Ohata, K. Tono, H. Yamazaki, S. Goto, Japan Synchrotron Radiation Research Institute, Sayo, Hyogo, Japan
T. Hasegawa, S. Tanaka, SPring-8 service Co. Ltd., Sayo, Hyogo, Japan

Abstract

A self-seeded XFEL system using a Bragg transmission scheme has been implemented at the compact XFEL facility SACLA, in order to generate a single-mode XFEL. The setup is composed of a small magnetic chicane that can delay the electron beam by up to 50 fs, and a diamond single crystal with the thickness of 180 μm . In the beam commissioning, intensity enhancement at 10 keV X-rays due to the self-seeding was observed with a single-shot spectrometer. A spectral bandwidth of the seeded FEL was reduced to 3 eV, being approximately 1/10 of that of SASE. After partial optimizations of the number of undulator segments, a temporal delay of the electron beam, and an rf phase of the pre-buncher cavity, the peak intensity of the seeded FEL signal in the averaged spectrum was 4 times higher than the SASE. Observation probability of the seeded FEL signal in the single-shot spectra was 42%. Although further optimization and improvement are still necessary to keep long-term stability, the initial step was successful to open up the routine operation in a near future.

INTRODUCTION

Self-seeding in the X-ray free electron laser (XFEL) is an important method to improve the temporal coherence of the self-amplified spontaneous emission (SASE) and to obtain high peak brilliance with narrow spectral bandwidth. In order to generate brilliant X-ray laser and supply to user experiments, the self-seeding system has been implemented in the Japanese XFEL facility, SPring-8 Angstrom Compact free electron LASer (SACLA) [1]. The scheme proposed at DESY [2] and firstly demonstrated in LCLS [3] was adopted, which uses a single diamond crystal in a forward Bragg diffraction (FBD) geometry to the initial SASE radiation from the first half of the undulators. It produces monochromatic tail components of transmitted X-ray pulses at a small time delay of several 10 fs. A compact magnetic chicane gives the delay to overlap the electron bunches and the monochromatic tail for seeding in the following undulators.

The hardware components were installed in parallel to the user operation from 2012. In August 2013, a vacuum chamber for housing a diamond single crystal was installed in the middle of the magnetic chicane. The commissioning started in October. After a number of tuning processes, significant spectral narrowing due to the self-seeding was confirmed at 10 keV. In the following

sections, the configuration, the tuning process and the experimental results are described.

SETUP

Figure 1 shows the configuration of SACLA and the self-seeding system. The electron beam from the thermionic cathode-type electron gun is sequentially accelerated and compressed at the accelerator section, to obtain high-density electron beam with the peak current of over several kA and the bunch length of several 10 fs. Then, the electron beam is led to the long undulator section composed of 21 segments of the in-vacuum undulators with the small periodic length of $\lambda_u=18$ mm and the maximum K-value (the magnetic deflection parameter) of 2.2.

Between the 8th undulator and the 9th undulator, the small magnetic chicane composed of 4 dipole magnets was inserted, in order to detour the electron beam from the diamond crystal and to provide a tunable time delay of maximum 50 fs. In the middle of the chicane, the diamond crystal chamber was installed, in order to generate the FBD of the SASE radiation from the upstream undulators. Figure 2 shows the schematic of the chamber. A diamond single crystal with the thickness of 180 μm is mounted on a holder in the vacuum chamber. The holder is attached on a multi-axis mechanical stage. The crystal is retracted from the beam axis during the usual SASE operation, while it is inserted for the self-seeding. The rotation of the crystal tuned the Bragg angle θ . The diffracted photon is measured by a photo-diode and a CCD detectors, attached on the 2 θ -rotational arm. Since the photon energy for our commissioning was 10 keV, the Bragg angle θ was set at about 44 degrees for 400 reflection of the diamond crystal. Under these configurations, monochromatic tail components in the transmitted radiation arise around 10 fs and 24 fs after the initial radiation, according to the theoretical calculation of FBD [3, 4]. The electron beam delaying at the chicane was overlapped to the radiation in the downstream undulators.

Properties of the FEL radiation were measured at the experimental hall. Thin-foil beam monitors in the optics hutch were used as the in-line monitors of the intensity and the center-of-mass position of the radiation [5]. The energy spectrum of the radiation was measured by the single-shot spectrometer [6]. The spectral resolution and the range are selected by changing the diffraction plane of the silicon crystal. The configuration using (220) plane has a wide measuring range of 100 eV, which was used

[#]inagaki@spring8.or.jp

for the measurement of the whole radiation spectrum. The configuration using (660) plane has a narrow measuring range of 6 eV, but it has a high energy resolution of about

70 meV, which was used for the precise measurement around the Bragg diffraction.

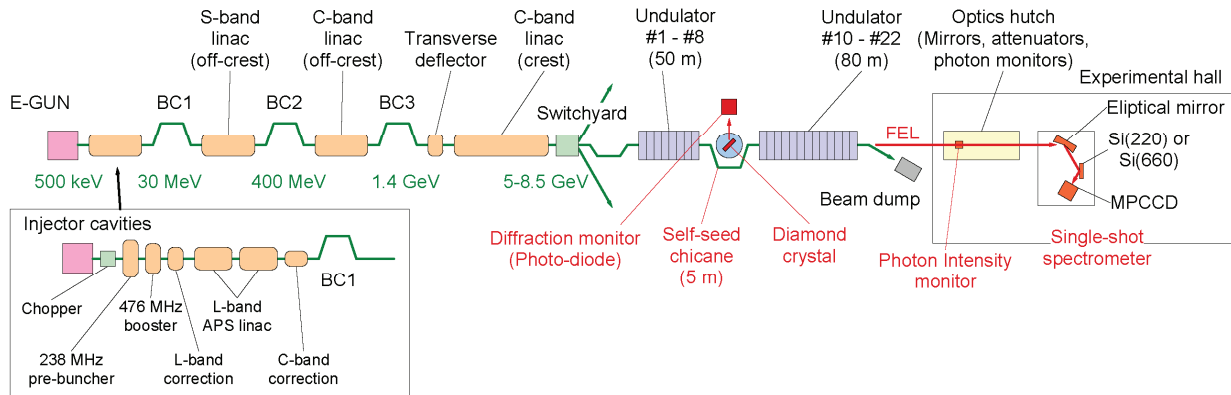


Figure 1: Configuration of the SACLA machine and the self-seeding system. BC1, BC2, and BC3 mean the three bunch compression chicanes.

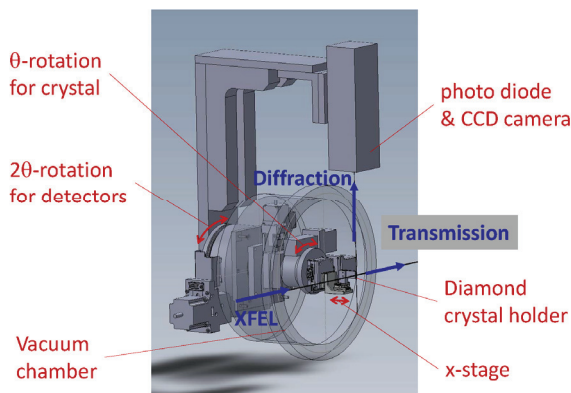


Figure 2: Diamond crystal chamber.

TEST RESULTS

Commissioning of the self-seeding was performed several times during the machine study period of SACLA operation. In November 2013, the first evidence of the seeded radiation was observed in the energy spectrum. After the electron beam stability was improved in May 2014, significant spectrum narrowing due to the self-seeding process was observed. In this section, we report the results of commissioning in June 2014.

The electron beam energy and the photon energy for the commissioning were 7.8 GeV and 10 keV, respectively. The K-value of the undulators was set at about 2.1, with a small taper of -0.002/segment for a compensation of the electron energy loss. The electron bunch charge was about 340 pC. The bunch length was about 30 fs, which was measured using the transverse deflector cavity located after the final bunch compression chicane (BC3). The electron beam quality was confirmed by measuring the SASE pulse energy of about 550 μ J/pulse, using all of 21 undulator segments and without the crystal insertion.

Adjustment of the SASE Photon Energy

Four undulator segments (#5-8) in the upstream of the diamond crystal were used to generate initial SASE radiation of about 30 μ J/shot in average. After the dipole magnets at the chicane were turned on to give a delay of 20 fs to the electron beam, the diamond crystal was inserted to the beam axis. The Bragg angle was set at 44 degrees in diamond 400 diffraction for 10 keV radiation. We optimized the undulator K values, to match the wavelength of the SASE radiation to the Bragg diffraction wavelength. Figure 3 shows the diffracted X-ray intensity as a function of the offset from the initial K values. We selected the offset of -0.002, which corresponds to the center of the SASE spectrum.

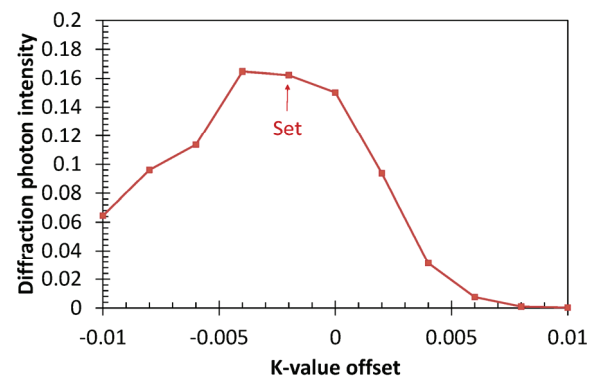


Figure 3: Bragg diffraction intensity measured by the photo-diode as a function of the K-value offset of the upstream undulators.

Spectrum of the Transmitted SASE Radiation

Energy spectrum of the transmitted SASE radiation was measured using the single-shot spectrometer. The diffraction plane of the silicon crystal was set to (660) for high-resolution measurement. Figure 4 shows the typical

spectrum. We found a clear dip due to the Bragg diffraction of the diamond crystal. The width of the dip was about 0.1 eV (2 pixels of the CCD detector), which was comparable to the measurement resolution. These results proved the diamond crystal has a good quality for raising the FBD and no radiation damage or degradation was observed during the commissioning.

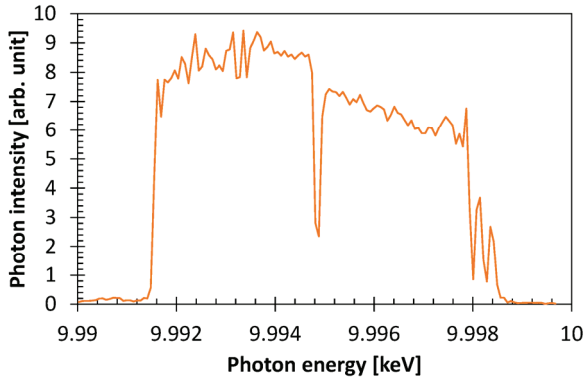


Figure 4: Energy spectrum of the transmitted SASE radiation from the upstream undulators, which was the integration of 100 shots. There was a clear dip at 9.995 keV due to the Bragg diffraction of the diamond crystal.

Observation of the Seeding

After the confirmation of the Bragg diffraction, we closed the gap of the downstream undulators. We measured the photon energy spectrum using the single-shot spectrometer with 220 diffraction plane for wide measuring range of 100 eV. Figure 5 shows the energy spectra with different number of downstream undulator segments. Clear peaks were observed at 9.99 keV photon energy. Increasing the number of undulator segments, the monochromatic X-ray component dominantly increased. With all of 13 undulator segments (blue line in Figure 5), the peak intensity of the monochromatic component was 4 times higher than the SASE background. The spectral bandwidth was 3 eV in FWHM, which was one order narrower than that for SASE. For the confirmation, we detached the diamond crystal from the SASE photon axis. Then the monochromatic component disappeared. We concluded the enhancement of the monochromatic component was surely due to the self-seeding from the FBD of the diamond crystal. Since Figure 4 and Figure 5 were measured with different configuration of the spectrometer, the photon energy difference between the Bragg diffraction in Figure 4 and the seeded FEL peak in Figure 5 was not obvious and they were within the measurement error.

In the following subsections, we describe the optimization of various parameters and the sensitivity study for the accelerator.

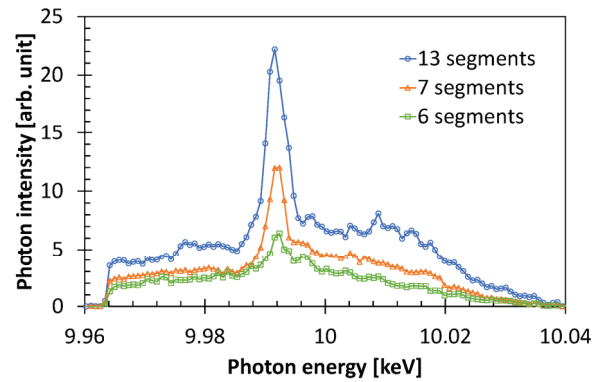


Figure 5: Energy spectra of the X-ray radiation with the seeding configuration. The three lines show the spectra with different number of active undulator segments at the downstream of the chicane. The spectra were the integration of 100 shots.

Number of Undulator Segments

Figure 6 shows the peak intensity of the seeded monochromatic components and the SASE background, as a function of the number of downstream undulator segments. When we increased the number of undulator segments, the seeded FEL signal also increased, while the SASE background was hardly increased. This result means the radiation from the downstream undulator was fairly monochromatic due to the seeding. In the Figure 6, slight decrease of the seeded FEL intensity with 9 undulator segments was not obvious, because the systematic error and the reproducibility were still larger than the discrepancy of the seeded FEL intensity.

Next we changed the number of upstream undulator segments, fixing the 13 downstream undulator segments. Figure 7 shows the seeded FEL intensity and the SASE background, with 3, 4, 5 or 6 undulator segments. With 3 undulator segments, the seeded FEL signal was not observed. We consider the initial SASE radiation was too weak for the seeding. With 6 undulator segments, the seeded FEL intensity was lower than the case with 4 or 5 undulator segments. It was considered that the SASE radiation process increased the energy spread of the electron beam and it suppressed the seeding. Therefore we concluded the optimum number of upstream undulator was 4 or 5 (corresponding SASE pulse energy was from 30 to 100 $\mu\text{J}/\text{pulse}$). For the following study, we used 4 and 13 undulator segments in the upstream and downstream, respectively.

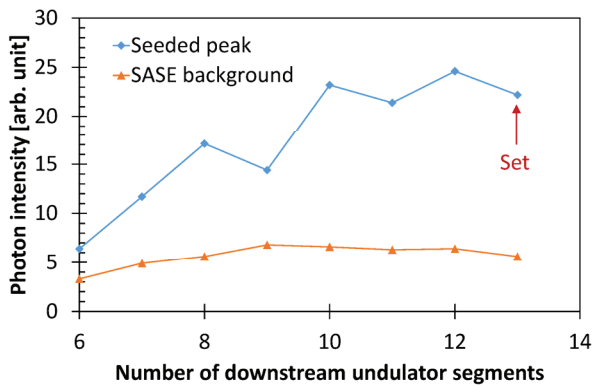


Figure 6: Peak intensity of the seeded monochromatic components and the intensity of the SASE background, as a function of the number of active undulator segments at the downstream of the chicane. For these measurements, 4 upstream undulator segments were used and the delay of the electron beam was set at 20 fs.

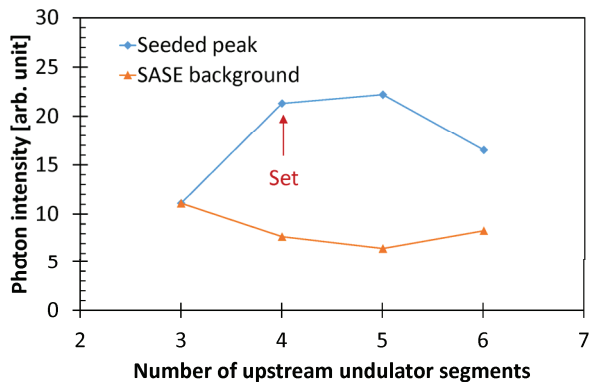


Figure 7: Peak intensity of the seeded monochromatic components and the intensity of the SASE background, depending on the number of active undulator segments at the upstream of the chicane. For these measurements, 13 downstream undulator segments were used and the delay of the electron beam was set at 20 fs.

Delay Time for Electron Beam

Figure 8 shows the seeded FEL signal and the SASE background, as a function of the temporal delay for the electron beam at the chicane. The seeded FEL signal was enhanced with the delay of about 25 fs and 45 fs, which was consistent with the theoretical calculation.

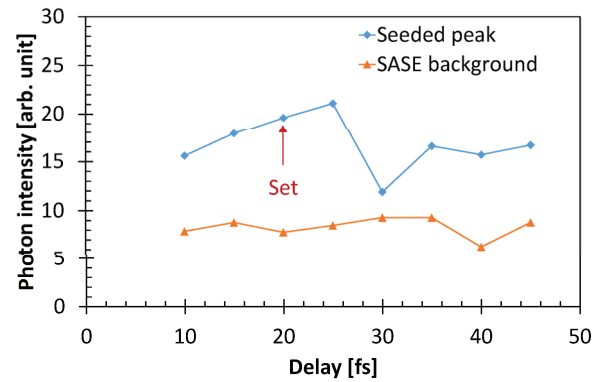


Figure 8: Peak intensity of the seeded monochromatic components and the averaged intensity of the SASE background, depending on the delay time at the chicane.

RF Phase of the Accelerator

In order to optimize the electron beam properties and to check the sensitivity for the rf phase variation, we performed a systematic study changing the rf phase of each accelerator section. Figure 9(d) shows the spectra with different rf phase of the 238 MHz pre-buncher. Only the change of 0.05 degree caused the significant effect for the seeded amplification. Figure (a) (b) and (c) show the variation of the seeded FEL intensity and the overall pulse energy, changing the rf phase of C-band linac between BC2 and BC3 (off-crest acceleration section), L-band APS-type linac and 238 MHz pre-buncher, respectively. They show the seeded FEL intensity was more sensitive to the rf phase variation than the SASE intensity. Table 1 summarizes the rf phase tolerance to maintain the seeded FEL intensity of more than half of the optimum peak intensity. These results indicate that the commissioning for the self-seeding requires higher operational stability and accuracy than the case of usual SASE operation. Actually, the observed spectrum and the peak intensity were sometimes changed during the several hours of the commissioning. These variations might be caused by tiny drifts of the accelerator condition, which were not recognized in usual SASE operation. We should study more to optimize and stabilize the accelerator condition.

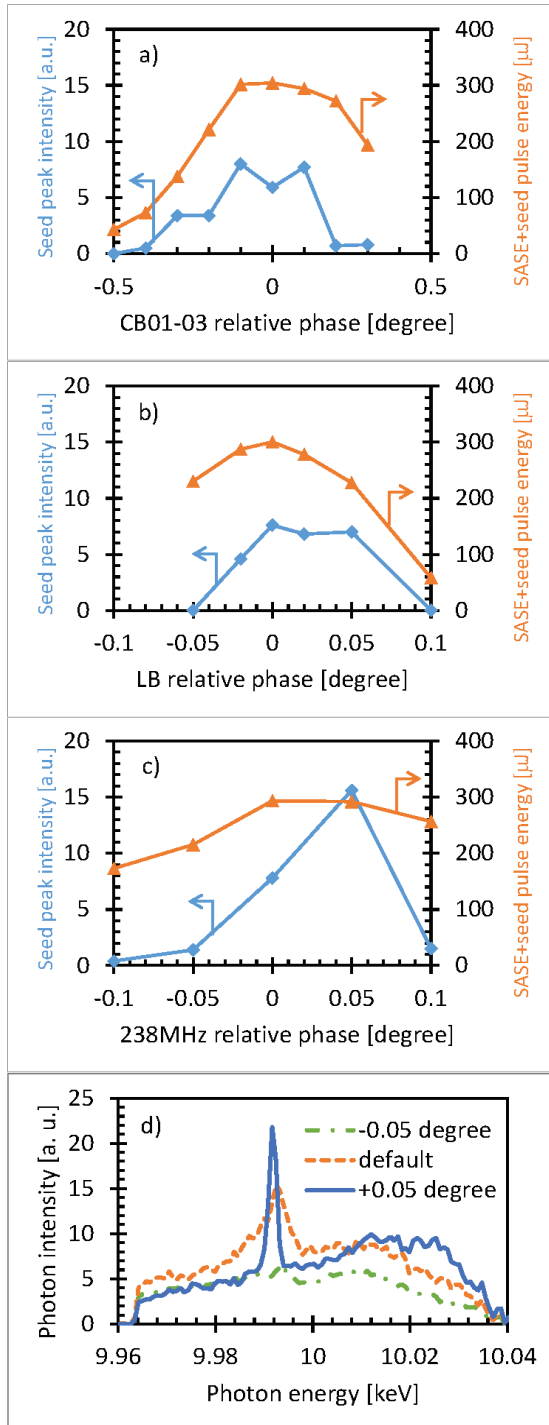


Figure 9: (Plot a, b, and c) Peak intensity of the seeded monochromatic components (Blue line), and the total pulse energy measured by the in-line beam monitor (Orange line), depending on the relative rf phase of the C-band linac before BC3, (a), the L-band APS-type linac (b) and the 238 MHz pre-buncher cavity (c), from the initial operating parameters. Plot d) shows the energy spectra for three rf phases of the 238 MHz pre-buncher cavity. The each spectrum is the integration over 100 shot, measured by the single-shot spectrometer.

Table 1: RF Phase Tolerances and the Corresponding Time Period for Each Accelerator Section. The tolerances in this table are defined as the rf phase difference made 50 % decrease of the seeded FEL intensity

Accelerator section	Tolerance (time)
238 MHz pre-buncher	$\pm 0.05^\circ$ (600 fs)
476 MHz booster	$\pm 0.1^\circ$ (600 fs)
L-band APS-type linac	$\pm 0.05^\circ$ (100 fs)
C-band correction cavity	$\pm 0.3^\circ$ (150 fs)
S-band linac	$\pm 0.5^\circ$ (500 fs)
C-band linac (before BC3)	$\pm 0.2^\circ$ (100 fs)

Single-Shot Spectrum

We analysed the single-shot spectrum data with optimum rf parameters, as shown in Figure 9 (d, blue line). Figure 10 shows the distribution of the peak photon energy (wavelength) and the peak intensity of each single-shot spectrum. Since the seeding wavelength is fixed by the Bragg diffraction angle of the diamond crystal, the “seeded” events are distributed around the photon energy of 9.99 keV. We defined the criteria of the “seeded” events, that the photon energy were 9.990 ± 0.005 keV and the peak intensity was more than 20,000 counts (blue dash line in Figure 10). The criteria for the peak intensity was required to distinguish the clear peak from the many small spikes due to the initial SASE background. Then, the probability for observation of the seeded FEL signal which satisfied above criteria was 42%. Averaged peak intensity for the seeded FEL signal was 9 times higher than the averaged intensity of SASE background. Shot-by-shot fluctuation of the peak intensity was 31% in rms. Fluctuation of the photon energy was less than 1 eV, which is comparable to the resolution of the spectrometer. These are promising results for the future practical use of self-seeding in SACLA.

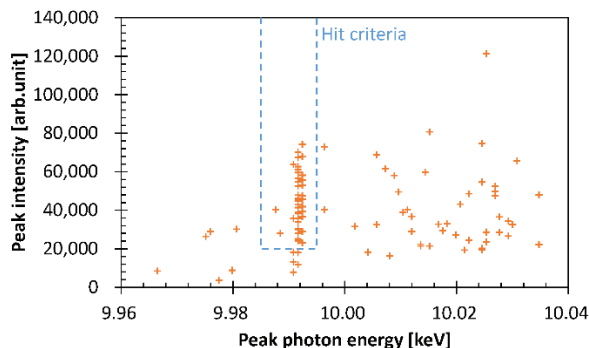


Figure 10: Distribution of the peak photon energy and the peak intensity for each single-shot spectrum, which is the same data set as “+0.05 degree” spectrum in Figure 9 d). Blue dash line box shows the criteria for “seeded” event.

CONCLUSION

In order to generate high-intense, monochromatic X-ray laser, self-seeded XFEL system with forward Bragg diffraction (FBD) of the diamond single crystal has been developed in SACLA. The monochromatic X-ray enhancement and the spectral narrowing due to the seeding were observed at a photon energy of 9.99 keV. The peak intensity of the seeded FEL signal was 4 times higher than the SASE. The probability for observation of the seeded FEL signal in the single-shot spectrum was 42% and the fluctuation of the intensity was 31% in rms. These are promising results for the future practical use of the self-seeding scheme. Since the seeding process is quite sensitive to the rf phase variation, high operational stability and accuracy is necessary for the seeding.

Further tuning efforts are continued for stable seeded FEL generation in order to provide seeded XFEL for users.

ACKNOWLEDGMENT

The authors give thanks to Dr. G. Geloni, Dr. J. Hastings, Dr. E. Allaria, Dr. F. Loehl, and Dr. K. Ohmi, for joining our commissioning and having useful discussions. The authors thank all of SACLA staffs for operation of SACLA and construction of self-seeding hardware and software.

REFERENCES

- [1] T. Ishikawa, et. al., “A compact X-ray free-electron laser emitting in the sub-angstrom region”, *Nat. Photonics* 6, 540-544 (2012).
- [2] G. Geloni, V. Kocharyan, and E. Saldin, “A novel self-seeding scheme for hard X-ray FELs”, *J. Mod. Opt.* 58, 1391-1403 (2011).
- [3] J. Amann, et. al., “Demonstration of self-seeding in a hard X-ray free-electron laser”, *Nat. Photonics* 6, 693-698 (2012).
- [4] R. Lindberg and Yu Shvydko, “Time dependence of Bragg forward scattering and self-seeding of hard x-ray free electron lasers”, *Phys. Rev. ST Accel. Beams* 15, 050706 (2012).
- [5] K. Tono, et. al., “Beamline, experimental stations and photon beam diagnostics for the hard x-ray free electron laser of SACLA”, *New J. of Phys.* 15, 083035 (2013).
- [6] Y. Inubushi, et. al., “Determination of the pulse duration of an x-ray free electron laser using highly resolved single-shot spectra”, *Phys. Rev. Lett.* 109, 144801 (2012).

GENERATION OF OPTICAL ORBITAL ANGULAR MOMENTUM USING A SEEDED FREE ELECTRON LASER*

P. Rebernik Ribič, D. Gauthier, Elettra, Trieste, Italy

G. De Ninno, Elettra, Trieste, Italy and University of Nova Gorica, Slovenia

Abstract

We propose an effective scheme for the generation of intense extreme-ultraviolet (XUV) light beams carrying orbital angular momentum (OAM). The light is produced by a high-gain harmonic-generation free-electron laser (HGFG FEL), seeded using a laser pulse with a transverse staircase-like phase pattern. The transverse phase modulation in the seed laser is obtained by putting a phase-mask in front of the focusing lens, before the modulator. The staircase-like phase pattern is effectively transferred onto the electron beam in the modulator and the microbunching structure is preserved after frequency up-conversion in the radiator. During light amplification in the radiator, diffraction and mode selection drive the radiation profile towards a dominant OAM mode at saturation. With a seed laser at 260 nm, gigawatt power levels are obtained at wavelengths approaching those of soft x-rays. Compared to other proposed schemes to generate OAM with FELs, our approach is robust, easier to implement, and can be integrated into already existing FEL facilities without extensive modifications of the machine layout.

INTRODUCTION

At present, the radiation modes of modern free-electron lasers (FELs) working at saturation are limited to a fundamental Gaussian-like mode with no azimuthal phase variation. This is true for FELs based on self-amplified spontaneous emission (SASE), where the amplification starts from electron shot-noise [1–6], as well as for seeded FELs, such as those based on high-gain harmonic-generation (HGFG), where the amplification process is triggered by a coherent input seed [7–9].

Generation of high-order radiation modes, however, is a subject of strong interest, not only from the fundamental point of view but also in practical applications. In particular, helically phased light beams or optical vortices with a field dependence of $\exp(il\phi)$, where ϕ is the azimuthal coordinate and l an integer referred to as the topological charge, are currently among intensively studied topics in optics. These light beams, which carry orbital angular momentum (OAM) [10] that can be transferred to atoms, molecules, and nanostructures [11–16], have already been utilized at visible and infrared wavelengths in a wide variety of applications, ranging from micromanipulation [17], detection of spinning objects [18], microscopy [19], and optical data transmission [20–22]. Perhaps the most promising applications of vortex beams at short wavelengths are in x-ray mag-

netic circular dichroism, where different OAM states allow the separation of quadrupolar and dipolar transitions [23], photoionization experiments, where the dipolar selection rules are violated giving rise to new phenomena beyond the standard effect [24], and in resonant inelastic x-ray scattering, where vortex-beam-mediated coupling to vibrational degrees of freedom could provide important information on a wide range of molecular materials [25].

Hemming and coworkers proposed two clever approaches to generate intense vortex beams at short wavelengths using FELs. The first one exploits the interaction of an electron beam (e-beam) with a seed laser in a helical undulator [26], while the second one is based on the echo-enabled harmonic generation (EEHG) scheme [27], where two seed lasers and two magnetic chicanes are used to produce harmonic microbunching of an e-beam with a corkscrew distribution [28]. A proof-of-principle experiment has recently been performed to demonstrate the first scheme using a single undulator section, generating optical vortices at 800 nm [29]. In this approach, however, OAM beams are produced at the fundamental frequency of the seed. Reaching short wavelengths would therefore require a coherent XUV or x-ray input signal, which is not trivial to obtain. On the other hand, the technique based on EEHG uses a relatively complex setup, which has yet to be thoroughly tested in experiments.

THE SCHEME TO GENERATE OAM WITH A SEEDED FEL

The scheme is shown in Fig. 1. The main difference with respect to the standard HGFG setup [30] is the use of an optical phase mask in order to create a transverse phase modulation in the seed laser profile. Naively, the simplest way to produce an XUV/x-ray optical vortex with this setup would be to seed the FEL directly with an OAM beam, by using a spiral phase plate as the phase mask. However, this approach fails at short wavelengths. The reason is that the topological charge l_n of higher harmonics is multiplied with the harmonic number n [28]; i.e., $l_n = ln$, where l is the topological charge of the seed. This results in a high-order OAM mode at the entrance of the radiator, which is tuned to $\lambda = \lambda_s/n$, where λ_s is the seed laser wavelength. Due to a lower coupling with the e-beam and stronger diffraction, this high-order OAM mode is not amplified in the radiator [28], leading to a dominant fundamental (non-OAM) mode at saturation.

The idea behind our approach is the following: instead of a helical transverse phase profile, a four quadrant staircase-like phase structure is imprinted onto an axially symmetric e-

* The research was in part funded by the TALENTS UP Programme (7th FP, Specific Programme PEOPLE, Marie Curie Actions - COFUND) G.A. 600204

beam in the modulator. The resulting transverse distribution of electrons in phase can be represented by the following matrix:

$$B_m = \begin{bmatrix} \frac{1}{2}\pi & 0 \\ \pi & \frac{3}{2}\pi \end{bmatrix}, \quad (1)$$

meaning simply that the electrons with the azimuthal coordinate between $-\pi/4$ and $\pi/4$ have a relative phase of 0, the electrons with $\pi/4 \leq \phi < 3\pi/4$ have a relative phase of $\pi/2$ and so on. Following frequency up-conversion at the radiator entrance, the phase distribution is multiplied by n , giving:

$$B_r = n \begin{bmatrix} \frac{1}{2}\pi & 0 \\ \pi & \frac{3}{2}\pi \end{bmatrix} \mod 2\pi, \quad (2)$$

which for odd $n = 2k + 1$, where k is an integer, becomes:

$$B_r = \begin{cases} \begin{bmatrix} \frac{1}{2}\pi & 0 \\ \pi & \frac{3}{2}\pi \end{bmatrix} = B_m, & \text{for even } k \\ \begin{bmatrix} \frac{3}{2}\pi & 0 \\ \pi & \frac{1}{2}\pi \end{bmatrix}, & \text{for odd } k. \end{cases} \quad (3)$$

The above equations show that the transverse microbunching structure is preserved for odd harmonics even after frequency up-conversion. The odd harmonics therefore carry the same staircase-like transverse phase pattern, which determines the spatial properties of the radiation at the radiator entrance. Because this initial bunching distribution contains a strong helical component, the radiation profile evolves into a dominant $l = 1$ OAM mode at saturation. With an initial Gaussian transverse seed profile with $\lambda_s = 260$ nm and e-beam parameters corresponding to modern seeded FELs, optical beams carrying orbital angular momentum at XUV wavelengths and gigawatt power levels can be generated.

The interested reader can find more details about the generation scheme together with numerical results using the parameters of modern generation FELs in PRL 112, 203602 (2014).

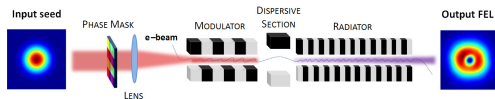


Figure 1: The scheme to generate XUV OAM beams using a HGHG free-electron laser.

ACKNOWLEDGMENT

We acknowledge fruitful discussions with A. Camper, S. Di Mitri, S. Reiche, A. Meseck, and the FERMI commissioning team.

REFERENCES

- [1] K.-J. Kim, Phys. Rev. Lett. **57**, 1871 (1986).
- [2] M. Xie, Nucl. Instrum. Meth. A **445**, 59 (2000a).
- [3] Z. Huang and K.-J. Kim, Phys. Rev. ST Accel. Beams **10**, 034801 (2007).
- [4] E. L. Saldin, E. A. Schneidmiller, and M. V. Yurkov, Opt. Commun. **186**, 185 (2000).
- [5] W. Ackermann *et al.*, Nature Photonics **1**, 336 (2007).
- [6] P. Emma *et al.*, Nature Photonics **4**, 641 (2010).
- [7] L.-H. Yu *et al.*, Nucl. Instrum. Meth. A **445**, 301 (2000).
- [8] Z. Huang and K.-J. Kim, Phys. Rev. E **62**, 7295 (2000).
- [9] E. Allaria *et al.*, Nature Photonics **6**, 699 (2012).
- [10] L. Allen, M. W. Beijersbergen, R. J. C. Spreeuw, and J. P. Woerdman, Phys. Rev. A **45**, 8185 (1992).
- [11] A. Picón, A. Benseny, J. Mompart, J. R. Vázquez de Aldana, L. Plaja, G. F. Calvo, and L. Roso, New J. Phys. **12**, 083053 (2010a).
- [12] R. Jáuregui, Phys. Rev. A **70**, 033415 (2004).
- [13] M. Babiker, W. L. Power, and L. Allen, Phys. Rev. Lett. **73**, 1239 (1994).
- [14] A. Alexandrescu, D. Cojoc, and E. Di Fabrizio, Phys. Rev. Lett. **96**, 243001 (2006).
- [15] M. Babiker, C. R. Bennett, D. L. Andrews, and L. C. Dávila Romero, Phys. Rev. Lett. **89**, 143601 (2002).
- [16] K. Toyoda, F. Takahashi, S. Takizawa, Y. Tokizane, K. Miyamoto, R. Morita, and T. Omatsu, Phys. Rev. Lett. **110**, 143603 (2013).
- [17] H. He, M. E. J. Friese, N. R. Heckenberg, and H. Rubinsztein-Dunlop, Phys. Rev. Lett. **75**, 826 (1995).
- [18] M. P. J. Lavery, F. C. Speirits, S. M. Barnett, and M. J. Padgett, Science **341**, 537 (2013).
- [19] A. Jesacher, S. Fürhapter, S. Bernet, and M. Ritsch-Marte, Phys. Rev. Lett. **94**, 233902 (2005).
- [20] J. Wang *et al.*, Nature Photonics **6**, 488 (2012).
- [21] X. Cai, J. Wang, M. J. Strain, B. Johnson-Morris, J. Zhu, M. Sorel, J. L. O'Brien, M. G. Thompson, and S. Yu, Science **338**, 363 (2012).
- [22] N. Bozinovic, Y. Yue, Y. Ren, M. Tur, P. Kristensen, H. Huang, A. E. Willner, and S. Ramachandran, Science **340**, 1545 (2013).
- [23] M. van Veenendaal and I. McNulty, Phys. Rev. Lett. **98**, 157401 (2007).
- [24] A. Picón, J. Mompart, J. R. Vázquez de Aldana, L. Plaja, G. F. Calvo, and L. Roso, Opt. Express **18**, 3660 (2010b).
- [25] A. S. Rury, Phys. Rev. A **87**, 043408 (2013).
- [26] E. Hemsing, A. Marinelli, and J. B. Rosenzweig, Phys. Rev. Lett. **106**, 164803 (2011).
- [27] G. Stupakov, Phys. Rev. Lett. **102**, 074801 (2009).
- [28] E. Hemsing and A. Marinelli, Phys. Rev. Lett. **109**, 224801 (2012).
- [29] E. Hemsing, A. Knyazik, M. Dunning, D. Xiang, A. Marinelli, C. Hast, and J. B. Rosenzweig, Nature Physics **9**, 549 (2013).
- [30] L. H. Yu, Phys. Rev. A **44**, 5178 (1991).

FIRST LASING FROM A HIGH POWER CYLINDRICAL GRATING SMITH-PURCELL DEVICE*

H.P. Bluem[#], R.H. Jackson, J.D. Jarvis, A.M.M. Todd, Advanced Energy Systems, Princeton, NJ, USA
J. Gardelle, P. Modin, CEA-CESTA, Le Barp cedex, France
J. T. Donohue, CENBG, Gradignan, France

Abstract

Many applications of THz radiation remain impractical or impossible due to an absence of compact sources with sufficient power. A source where the interaction occurs between an annular electron beam and a cylindrical grating is capable of generating high THz power in a very compact package. The strong beam bunching generates significant power at the fundamental frequency and harmonics. A collaboration between Advanced Energy Systems and CEA/CESTA has been ongoing in performing proof-of-principle tests on cylindrical grating configurations producing millimeter wave radiation. First lasing was achieved in such a device. Further experiments performed with a 6 mm period grating produced fundamental power at 15 GHz, second harmonic power at 30 GHz and, although not measured, simulations show meaningful third harmonic power at 45 GHz. Comparison with simulations shows very good agreement and high conversion efficiency. Planned experiments will increase the frequency of operation to 100 GHz and beyond. Ongoing simulations indicate excellent performance for a device operating at a fundamental frequency of 220 GHz with realistic beam parameters at 10 kV and simple extraction of the mode.

BACKGROUND & INTRODUCTION

The generation of tunable, narrowband, coherent, terahertz (THz) radiation is a topic of great interest across a wide variety of disciplines and applications. Although significant scientific and industrial opportunities exist, progress in the development of high-power compact sources has been frustrated by various technical and engineering challenges. AES is developing a flexible, compact, THz source architecture that addresses many of these historical challenges and aims to deliver high average power from 0.2 to 2 THz. The AES concept is a cylindrical extension of the so-called Smith-Purcell free-electron laser (SPFEL). The SPFEL is a type of backward-wave oscillator (BWO) that lases on an evanescent wave (surface wave) supported by an open slow-wave structure (SWS) [1].

When an electron passes in close proximity to an open, periodic, metallic grating, energy is transferred from the electron to radiative modes of the grating. This so-called Smith-Purcell radiation (SPR) is emitted over a broad spectrum with the wavelength of the emitted photons

being correlated to the angle of emission by the Smith-Purcell relation:

$$\lambda_{SP} = \frac{L}{|p|} \left(\frac{1}{\beta} - \cos \theta \right),$$

where L is the grating period, p is the diffraction order of the grating, β is the electron velocity normalized to the speed of light, and θ is the emission angle relative to the beam axis [2]. The SPR radiation is always at a higher frequency than the backward surface wave, except when the fundamental is confined laterally on a scale comparable to its wavelength [3]. When the electron beam is bunched by the backward wave interaction the SPR power is dramatically enhanced and is strongly peaked at angles corresponding to harmonics of the bunching frequency [4]. Under these conditions the SPR is said to be superradiant and significant power output can be generated at high frequencies.

The radiation output of a SPFEL is then a combination of the fundamental and the superradiant SPR at its harmonics. The power in the backward wave is much higher than the SPR power; however, because the backward wave is nonradiative, some form of outcoupling is required. Simple, although suboptimal, outcoupling is provided by scattering off of the discontinuities at the ends of the grating. Optimized structures can deliver efficient outcoupling in the forward or backward directions.

The SPFEL can easily be designed for a specific frequency by adjusting the grating geometry and the beam energy. A limited active-tuning range is possible via adjustment of the beam energy. Ultimately, the highest frequency achievable will be determined by current density, energy spread, and ohmic losses in the grating, and fabrication tolerances. This is highly dependent on the specifics of the system design. Higher frequency output, albeit at lower power, may be provided by the coherently enhanced SPR.

The AES concept, which utilizes a cylindrical SWS and a high-power annular electron beam, is compatible with established transport and compression techniques from the microwave-tube industry. Furthermore, the cylindrical geometry provides for maximum grating surface area in a compact package. The open grating design provides significant flexibility in the generation and extraction of fundamental and harmonic radiation; this is a major point of contrast with other e-beam driven sources.

The AES system is a significant departure from previous designs. As such, it was determined that the demonstration of key concepts at microwave frequencies

*Work supported by the Office of Naval Research and the Office of Naval Research Global
#bluem@aesprin.com

would provide an important reference point for theoretical and experimental efforts, and would help ensure the success of a THz prototype.

EXPERIMENT

Over the past year, a joint effort between AES and CEA-CESTA has successfully achieved first lasing of a cylindrical SPFEL. This collaboration leverages the existing infrastructure and capabilities of CEA-CESTA as well its previous successes in the demonstration of SPFEL technology [3, 5-7]. Experiments have been performed using two separate gratings: one designed for operation at 5-GHz, and one for 15 GHz. The initial 5-GHz experiments took place in September 2013 and the 15 GHz experiments followed shortly thereafter in January 2014. In this report we will focus primarily on the results of the 15-GHz experiment.

The basic experimental configuration is shown in Figure 1. An electron gun diode is situated at the end of a 200-kV, 500-A sub-microsecond cable generator. The electron source is an explosive electron emission cathode with an annular geometry. We have characterized the performance of the gun diode using a printed-circuit-board cathode (copper layer on phenolic) and a graphite cathode. The performance for these two sources is substantially the same. The electron beam is shaped, and its current reduced, using an adjustable aperture at the anode. Various beam currents, thicknesses, and beam-grating separations can be investigated in this way. The typical energy and current of the transmitted beam is 80 keV and 50 A. The grating is machined to the desired geometry from a single piece of aluminum, and the beam stop is attached at the downstream end. The entire apparatus is housed in a large plastic vacuum chamber operating at $\sim 10^{-4}$ Torr. A pulsed solenoid surrounds the vacuum chamber and provides a confinement field of approximately 5 kG during the beam pulse.

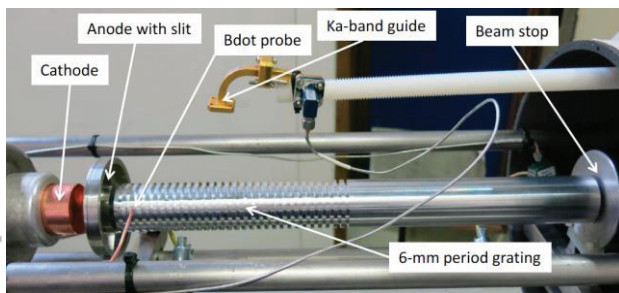


Figure 1: Basic experimental arrangement for the cylindrical SPFEL demonstrations.

The properties of the high voltage pulse, the electron beam, and the radiation output are measured with a variety of diagnostics. The diode voltage is monitored with a capacitive divider placed in the oil tank upstream from the diode. Two Rogowski coils are used to measure the beam losses during propagation and the current into the beam stop. The electron beam can be destructively imaged using thermal paper [as shown in Fig. 2], although the response is not believed to be linear. The surface

wave is measured using a B-dot probe that can be moved throughout the chamber. Depending on frequency, the SPR is collected using either a microwave horn on the exterior of the downstream end of the apparatus or a section of WR-28 waveguide positioned inside of the chamber. These radiation diagnostics are monitored directly using a 33-GHz fast oscilloscope. Particular attention was given to calibrating the microwave transmission lines. A few-kHz to 50-GHz synthesizer was used to calibrate all cables and fixed attenuators several times.

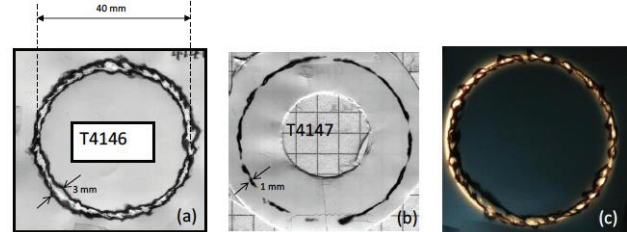


Figure 2: Beam imprint on thermal paper just before the anode aperture (left) and at the beam dump for a 0.5-mm aperture (center). Backside illumination of the anode aperture with an imprint of the beam (right).

The grating parameters for the 15-GHz experiment are as follows: 6-mm period, 3-mm groove width, 3-mm groove depth, 19.25-mm grating radius, and 30 grating periods. The dispersion relation for this grating, which is shown in Figure 3 indicates synchronicity at just below 15 GHz for an 80-keV beam energy. Using a small-signal SPFEL theory we estimate the start current for this grating and beam geometry to be on the order of 1 ampere. This includes the effects of ohmic losses, which are not significant at these frequencies, and the magnetic guide field. The typical beam current of 40-50 A is far in excess of this amount, leading to large oscillations of the SPFEL's power output.

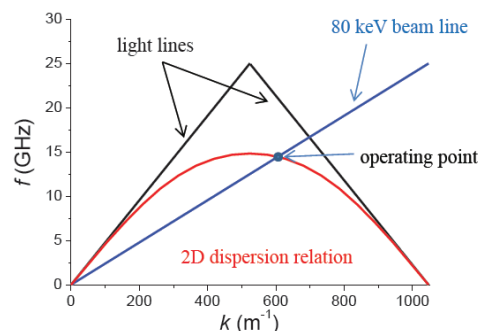


Figure 3: Dispersion curve for the 15-GHz grating. An 80-keV beam line is also shown and the synchronous point of just under 15 GHz is indicated.

Figure 4 shows a typical B-dot signal during one of the more than 100 shots that were taken. These data were taken with the probe located 3 mm above the third groove in the grating. Also shown in Figure 4 is a fast Fourier transform (FFT) of the signal and a sliding FFT. These analyses indicate a strong peak at ~ 14.6 GHz, which is

very close to the expected frequency of the evanescent mode. The frequency of the mode changes slightly with time due to variation of the accelerating voltage in the electron gun. Based on the probe's inductance and the calibration measurements of attenuation in the measurement system, we estimate a field strength of ~ 17 G at this location. The B-dot probe was subsequently placed at four different positions in azimuth to determine the homogeneity of the field strength; several shots were taken at each location. The field strength was nearly uniform in azimuth for this longitudinal position.

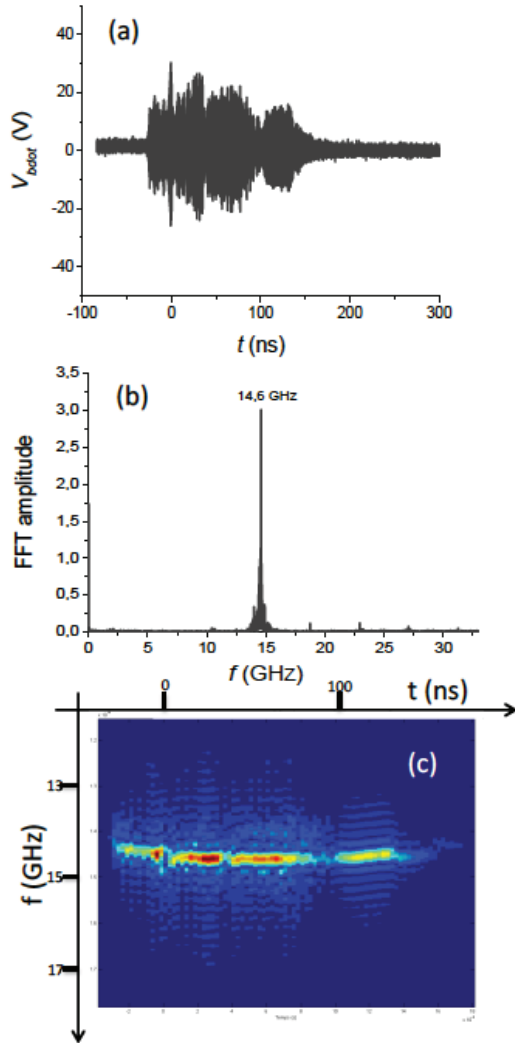


Figure 4: B-dot signal (top), FFT (center), and sliding FFT (bottom) for a typical shot.

The WR-28 waveguide used to collect the superradiant SPR is located ~ 65 mm above the grating surface and can be positioned arbitrarily along the length of the grating. Conveniently, the length of the waveguide is sufficient to place the fundamental radiation beyond the cutoff frequency. A sliding FFT of a typical signal is shown in Figure 5. As expected, the signal is dominated by a single frequency (~ 29.2 GHz) that is exactly twice the fundamental. Again, the frequency variation is consistent with that expected from the time dependence of the beam

energy. The superradiant SPR was also found to be uniform in the azimuthal coordinate. Estimates of the emitted SPR power and comparisons with simulations are given in the following section.

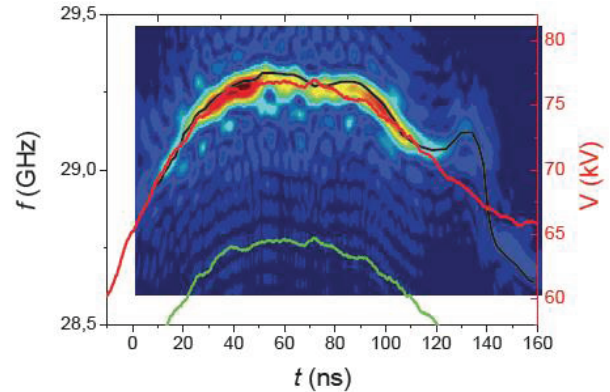


Figure 5: Sliding FFT of the radiation collected by the WR-28 waveguide. The intensity map shows the FFT vs time, the black line is the nominal centroid of the distribution, the red line shows the variation of the beam voltage, and the green line is the theoretical operating frequency multiplied by two.

SIMULATIONS

The simulations were carried out using two different PIC codes: MAGIC 3D and VORPAL, and the agreement between these codes was found to be excellent. Figure 6 shows an intensity map of the azimuthal magnetic field during the lasing process and after saturation. The second harmonic is clearly visible in the top image at $\sim 70^\circ$ above the horizontal. Ultimately, for this simple grating, the radiation output is dominated by scattered fundamental radiation from the upstream end of the grating. Figure 7 shows the simulated azimuthal magnetic field at the nominal position of the B-dot probe. The observed frequency, 14.3 GHz, is very close to the 14.6 GHz measured in the experiments. Also, the field strength is of the same order, as seen in Table 1.

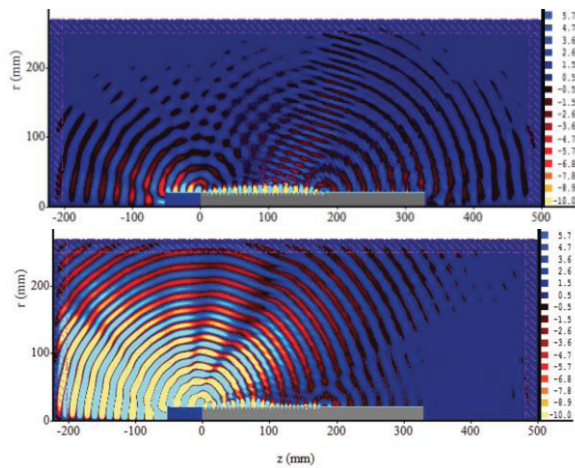


Figure 6: Intensity maps of the azimuthal magnetic field during lasing (top) and after saturation (bottom).

The collection efficiency of the WR-28 waveguide was determined using particle in cell (PIC) simulations in MAGIC 3D. The effective emitting area for the coherent SPR was estimated through simulations as well. Combining these simulated results with the experimental data, we estimate that the radiated power at 29 GHz is on the order of 8.5 kW. This compares well with the simulation estimates of ~ 5 kW. Although it was not measured in the experiments, the simulated third-harmonic power is ~ 0.5 kW.

Table 1: Comparison of Experimentally Estimated Field and Power Levels with Simulated Values from MAGIC and VORPAL

Results Table	Frequency (GHz)	Experiment	MAGIC	VORPAL
B-dot field (G)	15	17	33	35
Radiated Field (2nd) (W)	30	8500	5000	5000
Radiated Field (3rd) (W)	45		500	500

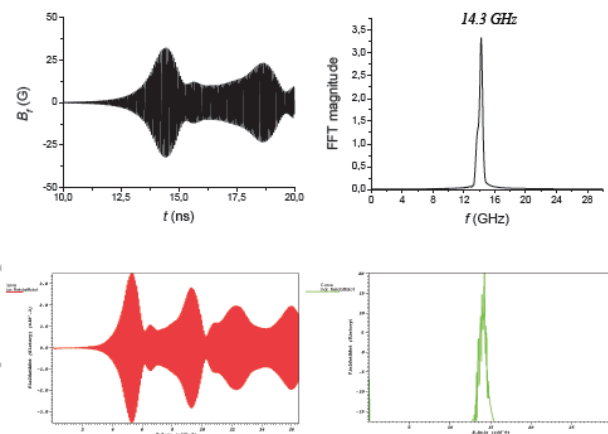


Figure 7: MAGIC (top) and VORPAL (bottom) simulations of the azimuthal magnetic field strength at the nominal location of the B-dot probe.

The simulated results can also be used to estimate the conversion efficiency between kinetic energy of the electron beam and energy in the fields. The energy loss

fluctuates wildly due to the excessively high beam current; however, the maximum rms kinetic energy lost by the beam is approximately 15 keV. This corresponds to a total power in the fields approaching a megawatt.

CONCLUSIONS AND FUTURE WORK

AES has been developing a cylindrical Smith-Purcell free-electron laser concept for the production of high-power THz radiation. Recently, a collaboration between AES and CEA-CESTA has successfully demonstrated first lasing of such a device at 5 and 15 GHz. Validation of key concepts in the microwave regime will help mitigate risk as system designs are pushed toward higher frequencies. Good agreement is obtained between experimental data, PIC simulations, and small-signal SPFEL theory. Building on these successes we are planning near-term demonstrations at 50 and 100 GHz (fundamental) using the same electron gun and power systems. Extensive simulations are being carried out to optimize grating structures according to various performance metrics, including start current, superradiant SPR production, and outcoupling efficiency for the evanescent fundamental. Additionally, AES is designing a 220-GHz prototype that will utilize existing cathode technology and a reliable, low-voltage, compressionless design.

ACKNOWLEDGMENT

This work was supported by the Office of Naval Research and the Office of Naval Research Global under contract No. N00014-10-C-0191 and grant No. N62909-13-1-N62.

REFERENCES

- [1] H. L. Andrews and C. A. Brau, Phys. Rev. ST Accel. Beams 7, 070701 (2004).
- [2] S. J. Smith and E. M. Purcell, Phys. Rev. 92, 1069 (1953).
- [3] J. Gardelle, P. Modin, and J. T. Donohue, Appl. Phys. Lett. 100, 131103 (2012).
- [4] H. L. Andrews, C. H. Boulware, C. A. Brau, and J. D. Jarvis, Phys. Rev. ST Accel. Beams 8, 110702 (2005).
- [5] J. Gardelle, L. Courtois, P. Modin, and J. T. Donohue, Phys. Rev. ST Accel. Beams 12, 110701 (2009).
- [6] J. Gardelle, P. Modin, and J. T. Donohue, Phys. Rev. Lett. 105, 224801 (2010).
- [7] J. T. Donohue and J. Gardelle, Appl. Phys. Lett. 99, 161112 (2011).

BEAM OPERATION OF THE PAL-XFEL INJECTOR TEST FACILITY*

J.-H. Han[†], J. Hong, J. H. Lee, M. S. Chae, S. Y. Baek, H. J. Choi, T. Ha, J. Hu,
W. H. Hwang, S. H. Jung, C. B. Kim, C. H. Kim, I. Y. Kim, J. M. Kim,
S. H. Kim, H. S. Lee, S.-J. Lee, Y. Y. Lee, C.-K. Min, G. Y. Mun, D. H. Na,
S.-J. Park, S.-S. Park, Y. J. Park, Y. K. Son, H. R. Yang, H.-S. Kang, I. S. Ko,
Pohang Accelerator Laboratory (PAL), Pohang, 790-834, Republic of Korea

Abstract

The Pohang Accelerator Laboratory X-ray Free electron Laser (PAL-XFEL) project was launched in 2011. This project aims at the generation of X-ray FEL radiation in a range of 0.06 to 6 nm for photon users with a bunch repetition rate of 60 Hz. The machine consists of a 10 GeV normal conducting S-band linear accelerator and five undulator beamlines. The linac and two undulator beamlines will be constructed by the end of 2015 and first FEL radiation is expected in 2016. As a part of preparation for the project, an Injector Test Facility was constructed in 2012. Since December 2012, beam commissioning is being carried out to find optimum operating conditions and to test accelerator components including RF, laser, diagnostics, magnet, vacuum and control. We present the status of beam commissioning and components tests at the test facility.

INTRODUCTION

The Pohang Accelerator Laboratory X-ray Free-Electron Laser (PAL-XFEL) project was started in 2011 [1–3]. This project aims at the generation of X-ray FEL radiation in a range of 0.06 to 6 nm for users. The machine consists of a 10 GeV electron linac and five undulator beamlines. The linac is based on the normal-conducting S-band technology, which has been used for the 3 GeV full energy injector linac of PLS-II, the 3rd generation light source at PAL, over 20 years [4]. As Phase-I of PAL-XFEL, one hard X-ray undulator beamline with two experiment stations and one soft X-ray undulator beamline with one experiment station are under preparation. Both hard and soft X-ray undulator systems are variable-gap, out-vacuum type.

This new machine is being built on the northern hill of the PAL campus (see Fig. 1). The building construction was started in autumn 2012. The building will be ready by December 2014. Accelerator components will be installed from January 2015 during the year. The machine is capable of 60 Hz operation with a single bunch initially. Upgrade to 120 Hz as well as two micro-bunch is foreseen as next phase in a few years. A fast kicker to divide electron pulses into the two undulator beamlines is considered as future upgrade as well. PAL-XFEL commissioning will be started from winter 2015. Beam commissioning will be carried out at a repetition rate of 10 Hz for the first year of operation mainly

due to the operation budget. First FEL is foreseen in early summer 2016.

At the beginning of the project in 2011, the construction of the Injector Test Facility (ITF) was started [5]. The facility was built in the extended building of the PLS-II full energy injection linac as shown in Fig. 1. The concrete tunnel, RF gallery, laser clean room and control room were prepared.

The RF system, accelerator components, laser system and control system were installed from summer to autumn 2012. The first beam was generated and transported to the beamline end in December 2012. Emittance measurement was started in spring 2013. Since then, beam test of diagnostics has been carried out.

In this paper, we describe the construction, component installation, beam test of diagnostics and beam property measurement. Some experiment results are shown even though empirical optimization is ongoing.

BUILDING

At the northwestern end of the PLS-II linac building, there has been a multi-purpose test area. This test area is now utilized as the Accelerator Test Facility (ATF) of PAL-XFEL. At ATF, high power modulators, klystrons, low level RF modules, accelerator structures, RF power doublers (SLAC energy doubler, SLED) and SiC loads are tested.

This test area was extended in 2012 for ITF. The extended floor area is about 30 m long and 14 m wide. A concrete tunnel with 1.5 m thickness was built in ITF. The inner area of the tunnel is 19.2 m long and 3.5 m wide. The view of the ITF tunnel and gallery is shown in Fig. 2. The roof of the tunnel is removed for installation work in the photograph. During the operation, the roof is covered with the concrete plates for radiation safety.

A laser clean room was constructed on the same floor of the tunnel and gallery. Temperature and humidity is controlled in the room. On top of the laser room, a control room was constructed.

ACCELERATOR DESIGN

The ITF accelerator was designed for the test of the first 9 m of the PAL-XFEL linac. An S-band (2.856 GHz) photocathode gun and two 3 m long S-band (2.856 GHz) constant-gradient traveling-wave structures are used for electron beam generation and acceleration. The layout is shown in Fig. 3.

Even though the PAL-XFEL injector will have three S-band accelerating structures, the design using two structures was adopted at ITF. After the two structures beam energy is

* Work supported by The Ministry of Science, ICT and Future Planning of the Korean Government

[†] janghui_han@postech.ac.kr



Figure 1: Areal view of the Pohang Accelerator Laboratory site in July 2014. The PAL-XFEL building under construction is shown at the left side. The circular building at the top right is the PLS-II ring. The full energy injector linac is connected to the ring. The end of the linac, the accelerator and injector test facilities (ATF and ITF) of PAL-XFEL are located. The insertion device test laboratory (IDL) is located in the storage building located at the north of PLS-II. In the PLS-II ring, the photon test facility (PTF) is located.

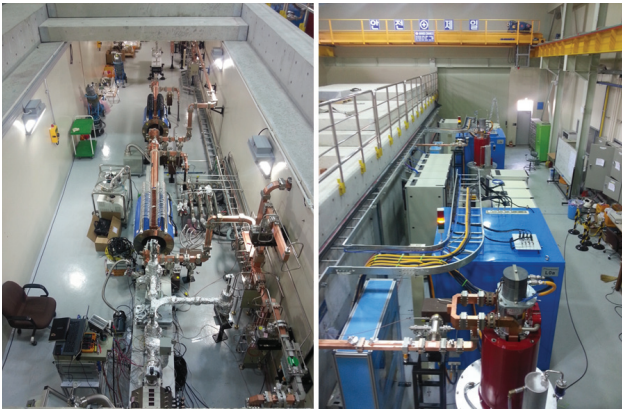


Figure 2: Injector Test Facility (ITF) of PAL-XFEL. The accelerator components are installed in the tunnel (left). The RF systems, magnet power supplies other facility control systems are installed in the gallery (right).

high enough for emittance measurements, diagnostics tests and laser heater test. With two structures a space for the installation of diagnostics and other test stands is allowed.

An electron beam is generated at the copper cathode, which is the central part of the gun cavity back plane, by a drive laser pulse. The beam is accelerated through the gun cavity with a 120 MV/m maximum field at the cathode on the beam axis. At the gun exit, the beam energy becomes 5.7 MeV. Immediate downstream of the gun a solenoid is positioned for beam focusing. Between the gun and first accelerating structure there are an integrating current transformer (ICT), a spectrometer dipole and screen, two screens

for beam image measurement, a stripline beam position monitor (BPM) and three sets of beam steerers.

The first accelerating structure starts at 2.2 m from the cathode. Between the structures a stripline BPM and a set of steerers are positioned. 0.92 m long solenoids are installed around the structures. The first solenoid is mainly for beam matching at the structures and the second for beta-function control at the components downstream. After further acceleration through two S-band structures, the beam energy becomes up to 140 MeV.

Table 1: Nominal Operation Parameters of ITF

Laser/cathode	
Laser profile	Gaussian
Fwhm length	3 ps
Rms size	0.2 mm
Gun	
Peak field at cathode	120 MV/m
Beam launch phase from 0-crossing	38°
Accelerating section	
Gradient of 1st section	21 MV/m
Gradient of 2nd section	24 MV/m
Phase of 1st section from on-crest	-10°
Phase of 2nd section from on-crest	0°
Nominal electron beam	
Bunch charge	200 pC
Fwhm bunch length	3 ps
Normalized transverse emittance	0.6 mm mrad
Mean energy	137 MeV

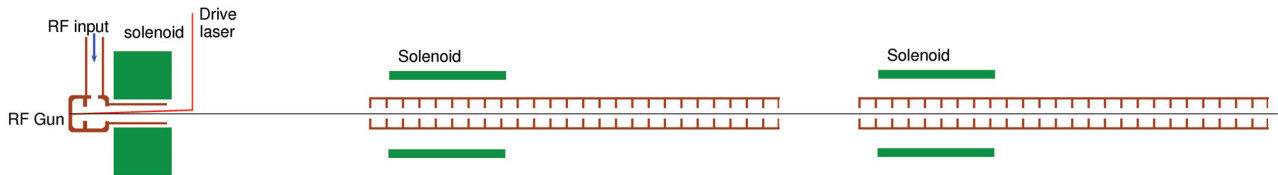


Figure 3: ITF accelerator layout with the gun and two accelerating structures.

ACCELERATOR COMPONENTS

RF Gun

The baseline gun has been developed at PAL, which consists of 1.6 cells and a high power RF coupler on the side of the second cell with a length of half a wavelength. Both cells have a round shape. Two RF input holes are made with mirror symmetry and two additional pumping holes reduce the high-order modes of the RF field [6]. The peak accelerating field at the cathode is designed to be 120 MV/m and the beam energy at the gun exit is 5.7 MeV [7].

The cavity body was made by diamond machining oxygen free copper. Machining was done at a local company, Hanatech. Cleaning and vacuum brazing were carried out in PAL. RF tuning was mainly done by controlling the cell length before the final brazing.

The first gun used for the Injector Test Facility (ITF) was the gun produced in 2011 for the test at the Gun Test Facility (GTF), which was located in the underground ATF area for the gun test far advance to the PAL-XFEL project [8]. This GTF gun was used for the first beam generation at ITF. An improved gun, named Gun1-0, in terms of brazing and tuning process was produced in spring 2013. Gun1-0 installed in the ITF tunnel is shown in Fig. 4. Gun1-0 was used for the ITF beam operation from summer 2013 to summer 2014. In September 2014, another gun, named Gun1-1, will be installed at ITF. This gun will be used later for PAL-XFEL beam commissioning as well.

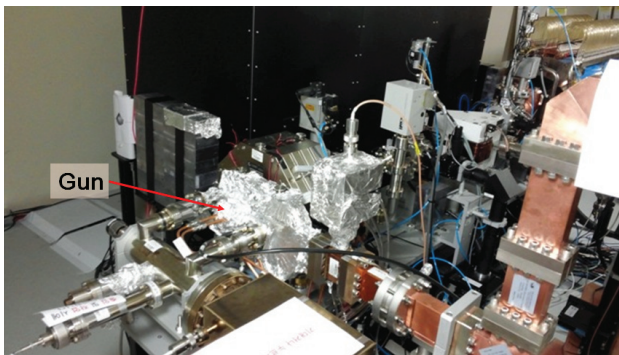


Figure 4: RF gun installed in the ITF tunnel.

High power RF test was done for Gun1-0 with the full peak power of 13 MW and repetition rate of 60 Hz. The RF pulse length was 2 μ s. RF breakdown did not take place even though the test period was only a few hours. At nominal operation the gun operates at 10 Hz, 12 MW and 1.75 μ s.

A focusing solenoid is positioned after the gun for the emittance compensation process. The solenoid was manufactured by RadiaBeam Technologies. Almost the same design of solenoids have been used for the GTF gun and for the gun of the femtosecond terahertz beamline in PLS-II.

A next stage gun development, targeting the achievement of a lower transverse emittance as well as a higher peak current, is ongoing [9]. This gun will provide an electron beam with a lower transverse emittance by optimizing the gun cell length and focusing solenoid position [10, 11]. With an exchangeable cathode plug, damaged cathodes can be replaced with a fresh one easily. Cathodes with high quantum efficiency and/or low thermal emittance will be tested at the gun.

Laser

The Ti:sapphire laser system is a commercial regenerative amplifier from Coherent Inc [12]. The pulsing rate of the seed laser (Coherent Mira) is set to 79.333 MHz which is synchronized to the master oscillator. A regenerative amplifier (Coherent Legend Elite) is used to generate pre-amplified output with about 150 ps and 120 Hz repetition rate. A post-power amplifier is employed to boost the output power up to 2.5 W with an rms noise of 0.24 %. The center wavelength is 770 nm. The wavelength is tripled for the beam generation at the gun.

Figure 5 shows the results of UV (257 nm) laser pulse length measurement using synchronized cross correlation with a femtosecond IR pulse. Various UV pulse length was used for electron beam generation. The transverse shape of a laser pulse and the effect to the beam parameter are discussed in Ref. [7]

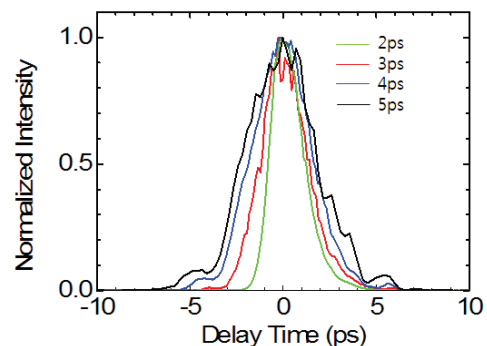


Figure 5: Pulse length measurement using cross correlation method.

The laser clean room is located at the north wall of the linac tunnel. Figure 6 shows the view of the laser room. Laser pulses generated in the laser room are transported through a hole in the ITF tunnel wall to the laser table in the tunnel. A pin hole and optics are installed on the laser table in the tunnel for the transverse beam shaping. The laser position at the cathode is remotely controlled using two mirrors.



Figure 6: Laser system in the laser clean room.

Photocathode

The oxygen-free copper which is part of the gun cavity back plane, is used as photocathode. At nominal operating condition, a quantum efficiency (QE) of order of 10^{-5} is measured. Laser cleaning was tried using an IR (760 nm) laser pulse as well as a UV (253 nm) laser pulse. An IR laser pulse with hundreds ps length was found to be most useful up to now. After the IR laser cleaning, the QE of the cathode was recovered from 4.0×10^{-5} to 1.3×10^{-4} and stayed without QE drop for a few months [13]. More systematic study is planned in September 2014.

Accelerating Structures

Two 3 m long S-band constant-gradient traveling-wave structures, manufactured by Mitsubishi Heavy Industries, are installed in the ITF tunnel (see Fig. 7). The structures have J-type high power RF coupler for reducing the dipole mode in the coupling cell [14]. Since the coupler cell has a round shape, the quadrupole mode remains. It seems to be the reason of beam emittance rise when the second structure is on. Study on the effect to a beam is ongoing.

Both structures have 0.9 m long focusing solenoids, which were manufactured by Keum Ryong Tech, a local company. These solenoids are used for beam matching at the structures and downstream components.

RF SYSTEM

Two S-band klystrons from Toshiba (E37320) feed high power RF to the gun, two accelerating structures and deflecting cavity. The maximum power of the klystron is 80 MW with a pulse length of $4 \mu\text{s}$. The first klystron feeds the gun and first accelerating structure. The second feeds the second structure and RF deflector (see Fig. 8). The maximum

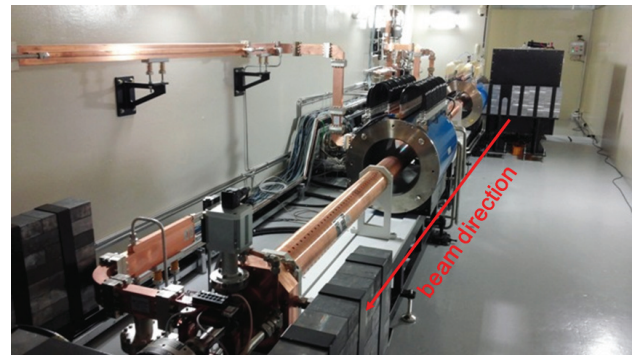


Figure 7: Accelerating structures and focusing solenoids installed in the ITF tunnel.

repetition rate of the RF systems is 60 Hz. 6 dB and 8 dB

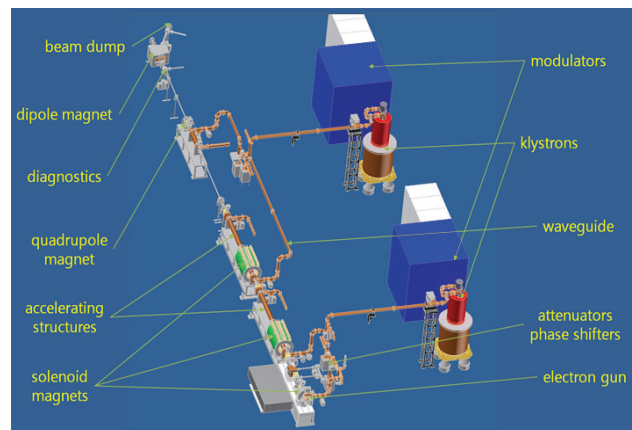


Figure 8: Main components of accelerator beamline and RF systems. The concrete tunnel wall between the accelerator beamline and RF stations is not shown.

RF power dividers are installed at the first and second RF stations, respectively. Higher power is sent to the accelerating structures. Lower power is delivered to the gun or RF deflector.

For the independent RF operation of the gun a high power RF attenuator and a phase shifter are installed in the waveguide to the gun. For the RF deflector, a vacuum gate valve is installed before the cavity coupler in addition to an attenuator and a phase shifter because only few kW RF power in the deflector can induce a transverse kick to a beam. Both attenuators and phase shifters were manufactured by Nihon Koshuha.

Two high power pulse modulators were manufactured by a Korean company, DAWONSY. The maximum power of the modulators is 200 MW (400 kV, 500 A) with a flat top width of $4 \mu\text{s}$.

Two low level RF (LLRF) modules consisting of both phase and amplitude detector (PAD) and phase and amplitude controller (PAC) units were manufactured by Mobeis, a Korean company. More detail on the LLRF modules is found in Ref. [15] The solid state pre-amplifiers amplify a 2.856 GHz pulse from the LLRF module to 800 W for the

klystron operation. The pre-amplifiers are manufactured by SUNGSAN, a Korean company.

DIAGNOSTICS

Screen Station

100 μm thick 1 inch YAG screens are installed normal to the beam direction. A 200 nm aluminum layer on a 100 μm silicon substrate, installed 45° to the beam axis, reflects beam images horizontally to the view port parallel to the beam axis. BAUMER TXG50 GigE cameras with 5M pixels and a 2/3 inch CCD sensor are used.

The original version of ITF screen station was manufactured by RadiaBeam Technologies. A new version of screen station is under preparation for the use at PAL-XFEL, with considering the European XFEL/DESY and SwissFEL screen station designs (see Fig. 9). The new version has a target geometry for the reduction of coherent optical transition radiation (COTR).

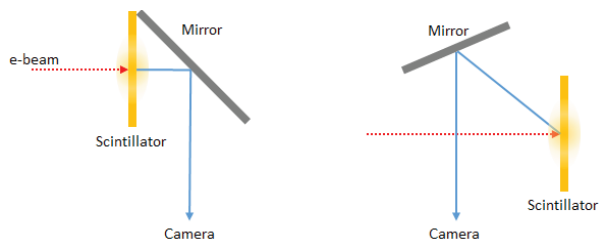


Figure 9: Geometry of screen station. The original design (left) manufactured by RadiaBeam Technologies and the new design (right) for reducing the COTR.

Spectrometer Dipole

Two spectrometer systems are installed for beam energy measurement. Both systems consist of a dipole for beam bending, a drift vacuum tube and a screen.

The first dipole is installed between the gun and first accelerator column for the gun commissioning. Beam launch phase of the gun is found with this spectrometer by means of beam energy measurement as function of gun RF phase. The dipole is a sector magnet which bends a beam by 90° .

The second dipole is installed at the end of the ITF beamline. The dipole is a sector magnet which bends a beam by 30° for a beam energy measurement up to 150 MeV.

Integrating Current Transformer

Two Bergoz integrating current transformers (ICTs) were installed, one after the gun and another before the beam dump at the end of the beamline. Since signal from the ICTs was interfered by high level of noise, it was difficult to read beam signal using the controller. The first ICT after the gun was replaced with Turbo-ICT from Bergoz Instrumentation. Bunch charge is now measured clearly using the Turbo-ICT without background noise problem.

Beam Position Monitor

Seven stripline beam position monitors (BPMs) are installed. One BPM is located before the first accelerating structure to monitor the position of a beam entering the accelerating structure. Three BPMs are located between the first and second structures, after the second structure, and before the RF deflector, respectively. These four BPMs are used for beam operation purpose.

Other three BPMs are installed on the BPM test stand at the rear part of the ITF beamline (see Fig. 10). Using this

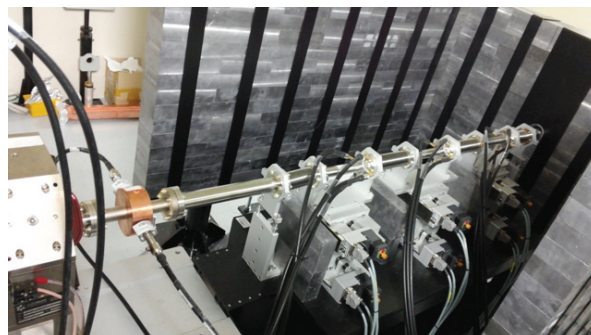


Figure 10: Diagnostics test stand at ITF.

BPM test stand, the performance of BPM electronics was evaluated. Libera Brilliance Single Pass and Libera Single Pass E from Instrumentation Technologies showed 3 μm and 1.5 μm resolution for 200 pC electron beam, respectively. μTCA based BPM electronics produced by SLAC showed about 3 μm resolution using a divided signal from a 200 pC beam. All tested BPM electronics satisfy the PAL-XFEL BPM resolution requirement, 5 μm at 200 pC.

This test stand will be used for the test and beam-based calibration of new BPM pick-ups as well. A new type of BPM pick-ups will be installed in this autumn.

Beam Arrival Time Monitor

A cavity type of beam arrival time monitors (BAMs) are installed before the BPM test stand as shown in the left side of Fig. 10. Resonance takes place when an electron passes through the single cell S-band cavity. The RF signal is collected with two pick-up antenna at the cavity cylindrical wall. The signal is analyzed using one channel of the LLRF module installed at the second RF station. The BAM resolution is about 10 fs. More detail on the BAM will be found in Ref. [16]. Figure 11 shows analyzed signal from the beam arrival time monitor. This measurement was carried out during the pulse optical timing test [17].

RF Transverse Deflector

An RF transverse deflecting cavity is installed about 2 m downstream of the second accelerating structure (Fig. 12). This 1 m backward traveling-wave structure deflects an electron bunch vertically. This deflector was used for the dechirper experiment [18] and slice emittance measurement. It will be used for laser heater test in winter 2014. This

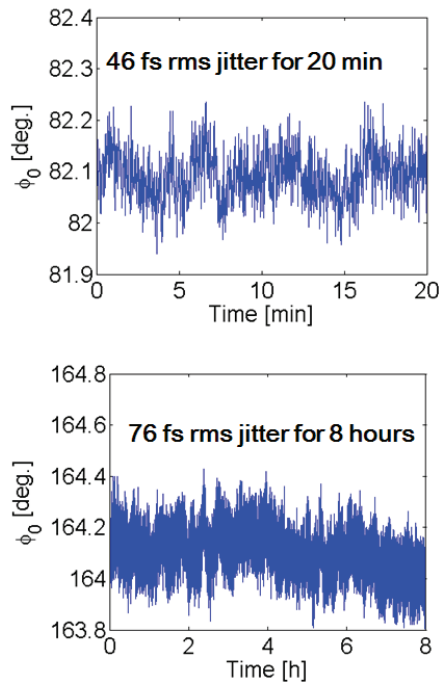


Figure 11: Measured signal from the beam arrival time monitor during the pulsed optical timing test for a short term (top) and a long term (bottom).

deflector will be moved to PAL-XFEL and installed after the first bunch compressor where the beam energy is 350 MeV.

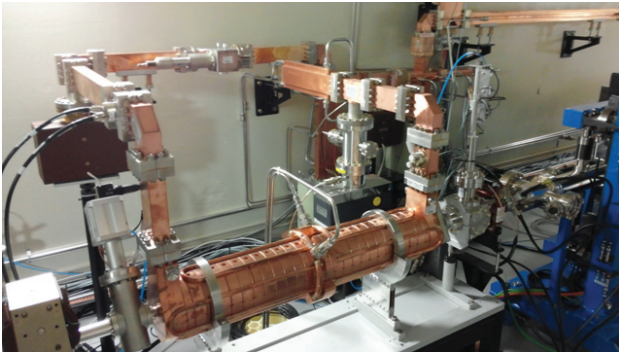


Figure 12: RF transverse deflector installed in the ITF tunnel.

EMITTANCE MEASUREMENT

Projected Emittance

Projected emittance was measured by scanning the strength of the third quadrupole [19, 20]. The beam image was measured using the screen immediate upstream of the second (high energy) spectrometer dipole. The distance between the quadrupole and screen is 2.6 m. Measured emittance was normalized by dividing with the beam energy measured with the second spectrometer dipole and screen downstream. An example scan of quadrupole strength for emittance measurement is shown in Fig. 13.

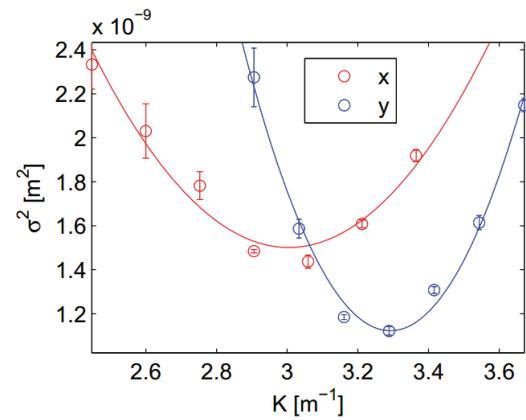


Figure 13: An example of single quadrupole scan for projected emittance measurement. Current of the third quadrupole was scanned and the beam image was measured with the screen 2.6 m downstream.

Figure 15 shows the history of emittance measurements at 200 pC bunch charge for the past 18 months. The values in the plot are the quadratic means of the horizontal and vertical emittance values. For each measurement point, gun solenoid field was optimized for best emittance compensation condition. For the measurements, various drive laser size and length, RF phases of the gun and first accelerating structure, RF amplitude of the gun, and current of the accelerating structure solenoid were used.

Figure 14 shows the emittance measurement with various radius and pulse length of drive laser. For each measurement, gun RF phase and gun solenoid current were optimized. This result does not agree with numerical simulation. An electron beam generated with a 5 ps laser pulse length has a smaller emittance compared to the 3 ps case according to numerical simulation using the ASTRA code [21]. The reason is under investigation.

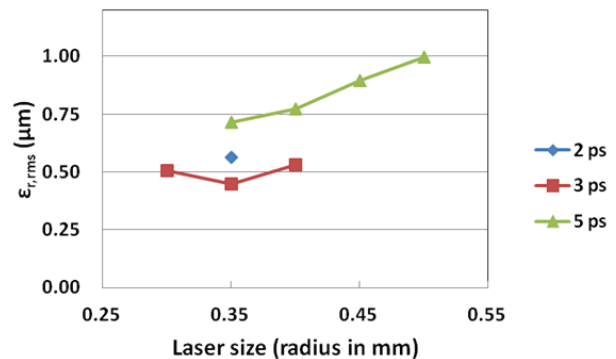


Figure 14: Projected emittance (95% rms) for various radius and pulse length of drive laser at 200 pC bunch charge.

During the first few months of ITF operation, measured emittance values varied much. However, at good measurement conditions emittance values below 0.5 mm mrad was measured (see Fig. 15). Recent measurements do not show

a low emittance. We are studying possible reason including components alignment.

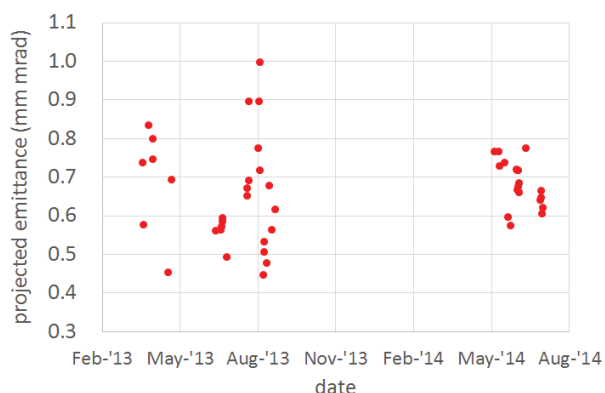


Figure 15: Projected emittance (95% rms) measured with 200 pC beams at ITF from early 2013 to summer 2014.

For the period of October 2013 to April 2014, beam test of stripline BPM, laser cleaning, and other maintenance were carried out instead of systematic emittance measurement.

Slice Emittance

Slice emittance for the horizontal direction was measured by streaking a bunch vertically using the RF deflector [22]. As for projected emittance, the third quadrupole was used for beam focusing and the last screen was used for beam image measurement. Figure 16 shows an example measurement at 200 pC. Slices were divided for equal charge. Each slice has a 10 pC charge. The measurement condition was not fully optimized yet.

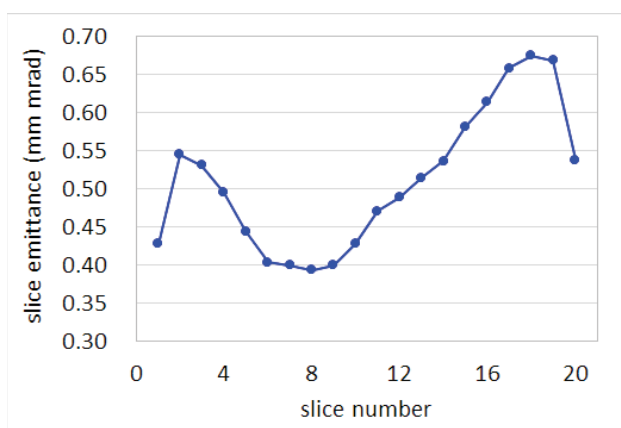


Figure 16: Slice emittance (95%) for the horizontal direction measured by streaking vertically using the RF deflector. The right side corresponds to the bunch head.

Systematic measurements of slice emittance as well as projected emittance are planned in September 2014.

OTHER BEAM TESTS

Dechirper

A 1 m long dechirper system was produced for the test of energy chirp control. The beam experiment was successfully carried out at ITF with SLAC and LBNL physicists in August 2013 [18, 23].

Laser Heater

A laser heater system will be installed in the ITF tunnel in September 2014. Beam commissioning will be carried out and operating condition will be found in winter 2014 for the efficient commissioning at PAL-XFEL. Laser heater components such as laser heater undulator (see Fig. 17), bending magnets and vacuum chamber are ready for installation. A small fraction of an IR pulse (770 nm) from the gun laser system will be sent to the laser heater.

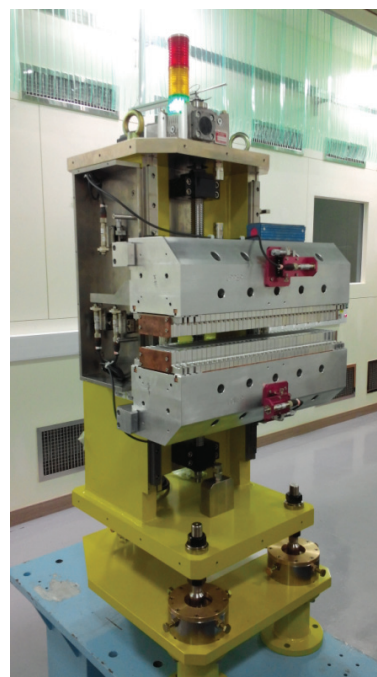


Figure 17: Laser heater undulator. The undulator magnetic field is being measured in the insertion device test lab.

Cavity BPM

Cavity BPM test is foreseen in autumn 2014. The cavity BPMs, which were fabricated at PAL, will be used in the undulator lines of PAL-XFEL for a position reading resolution better than 1 μm [24].

SUMMARY

The PAL-XFEL Injector Test Facility (ITF) was built in 2012 for beam commissioning of the injector in advance to the construction of the PAL-XFEL main linac. Beam test of the RF system, drive laser and diagnostics required for the PAL-XFEL main linac is also another important role of ITF.

ISBN 978-3-95450-133-5

Projected and slice transverse emittance is being measured with various machine parameters. Diagnostics test using electron beams was done successfully. Beam commissioning of the ITF accelerator including new guns and diagnostics will be continued.

REFERENCES

- [1] J.-H. Han et al., "Status of the PAL-XFEL project," in *Proceedings of 3rd Int. Particle Accelerator Conf.*, New Orleans, 2012, p. 1735.
- [2] H.-S. Kang et al., "Current status of PAL-XFEL project," in *Proceedings of 4th Int. Particle Accelerator Conf.*, Shanghai, 2013, p. 2074.
- [3] I. S. Ko and J.-H. Han, "Current status of PAL-XFEL project," in *Proceedings of 27th Linear Accelerator Conf.*, Geneva, 2014, MOIOB03.
- [4] S. H. Nam et al., "Upgrade of Pohang Light Source (PLS-II) and challenge to PAL-XFEL," *Synchrotron Radiation News* 26, p.24 (2013).
- [5] S. J. Park et al., "Construction of injector test facility (ITF) for the PAL XFEL," in *Proceedings of 4th Int. Particle Accelerator Conf.*, Shanghai, 2013, p. 2220.
- [6] M. S. Chae et al., "Emittance growth due to multipole transverse magnetic modes in an rf gun," *Phys. Rev. ST Accel. Beams* 14, 104203 (2011).
- [7] J. Hong et al., "Beam measurement of photocathode RF-gun for PAL-XFEL," in These Proceedings: Proc. 36th Int. Free-Electron Laser Conf., Basel, 2014, THP011.
- [8] J. Hong et al., "High-power Beam Test of an RF Gun for the PAL-XFEL," in *Proceedings of 3rd Int. Particle Accelerator Conf.*, New Orleans, 2012, p. 1539.
- [9] J. Hong et al., "Development of photocathode RF-gun at PAL," in *Proceedings of 35th Int. Free-Electron Laser Conf.*, New York, 2013, p. 279.
- [10] J.-H. Han et al., "Design of a high repetition rate S-band photocathode gun," *Nucl. Instr. and Meth. A* 647, 17 (2011).
- [11] J.-H. Han, "Design of a low emittance and high repetition rate S-band photoinjector," *Nucl. Instr. and Meth. A* 757, 1 (2014).
- [12] C.-K. Min et al., "Development of low-noise picosecond laser system for Cu photocathodes," PAL-PUB/2014-002, PAL, 2014.
- [13] C.-K. Min et al., "Recovering damaged Cu photocathodes by pulsed laser cleaning," PAL-PUB/2014-001, PAL, 2014.
- [14] S. Miura et al., "Development of S-band accelerating structure," in *Proceedings of 34th Int. Free-Electron Laser Conf.*, Nara, 2012, p. 153.
- [15] J. Hu et al., "Experimental test of the prototype LLRF systems for PAL-XFEL," in *Proceedings of 5th Int. Particle Accelerator Conf.*, Dresden, 2014, p. 2462.
- [16] J. Hong et al., "Bunch arrival time monitor for PAL-XFEL," in *Proceedings of 3rd Int. Beam Instrumentation Conf.*, Monterey, 2014, MOPOD016.
- [17] C.-K. Min et al., "Current status of development of optical synchronization system for PAL XFEL," in *Proceedings of 2nd Int. Beam Instrumentation Conf.*, Oxford, 2013, p. 772.
- [18] P. Emma et al., "Experimental demonstration of energy-chirp control in relativistic electron bunches using a corrugated pipe," *Phys. Rev. Lett.* 112, 034801 (2014).
- [19] M. Chae et al., "Simulation for new injector test facility of PAL-XFEL," in *Proceedings of 34th Int. Free-Electron Laser Conf.*, Nara, 2012, p. 117.
- [20] M. Chae, "Study on electron beam optimization at PAL-XFEL injector test facility," PhD Thesis, POSTECH, 2014.
- [21] K. Flöttmann, "ASTRA, A Space Charge Tracking Algorithm," ver. 3.0, http://www.desy.de/~mpyflo/Astra_dokumentation/
- [22] J. H. Lee et al., "Slice emittance measurement using rf deflecting cavity at PAL-XFEL ITF," in These Proceedings: Proc. 36th Int. Free-Electron Laser Conf., Basel, 2014, THP013.
- [23] H.-S. Kang and J. Hong, "A beam test result of corrugated structure for passive linearizer," in These Proceedings: Proc. 36th Int. Free-Electron Laser Conf., Basel, 2014, TUP093.
- [24] S. Lee et al., "Design of the X-band cavity beam position monitor," *J. Korean Phys. Soc.* 63, 1322 (2013).

EUROPEAN XFEL CONSTRUCTION STATUS

W. Decking*, DESY, Hamburg, Germany
F. Le Pimpec, European XFEL GmbH, Hamburg, Germany
for the European XFEL Project Team

Abstract

The European XFEL is presently being constructed in the Hamburg region, Germany. It aims at producing X-rays in the range from 260 eV up to 24 keV out of three undulators that can be operated simultaneously with up to 27000 pulses/second. The FEL is driven by a 17.5 GeV linear accelerator based on TESLA-type superconducting accelerator modules. This paper presents the status of major components, the project schedule and a summary of beam parameters that are adapted to the evolving needs of the users.

INTRODUCTION

The European XFEL [1] construction has started in 2009 with the ground-breaking for the underground buildings - about 5.5 km of tunnels, six access shafts, two underground dump halls, the injector building and the 4500 m² experimental hall. The underground construction is finished and the erection of the above ground buildings on three different sites is well underway. The series production of components is in full swing with many parts already being ready for installation. The completion of the construction phase was planned for end of 2015. Due to the delayed delivery of several components, a new schedule was adopted with the completion date shifted to end of 2016.

Encouraged by the successful operation of LCLS and SACLA and based on the small emittances measured for the XFEL photo-cathode RF-gun at PITZ (DESY/Zeuthen) [2], the European XFEL has adjusted its target parameters in 2011, see Table 1. The new parameter set enlarges the performance range of the facility [3], but puts a strain on different sub-systems, especially for operation at very low charge (20 pC). All beam diagnostics are affected as well as the RF stabilization and the beam-stabilizing feedback systems. As a rule, the original 1 nC-case specifications could be extended down to 0.1 nC and a limit to the deterioration in performance for even lower charges was set.

Table 1: European XFEL Electron Beam Properties

Quantity	Target Parameters
Electron Energy	8/12/14/17.5 GeV
Bunch Charge	0.02 - 1 nC
Norm. Slice Emittance at Und.	0.4 - 1.0 mm mrad
Slice Energy Spread at Und.	4 - 2 MeV
Peak Current	5 kA

* winfried.decking@desy.de

Figure 1 summarizes the photon energy reach of the European XFEL for different accelerator energies and undulator gap settings. The facility covers the photon energy range from the Carbon K-edge up to above 25 keV in the first SASE harmonic.

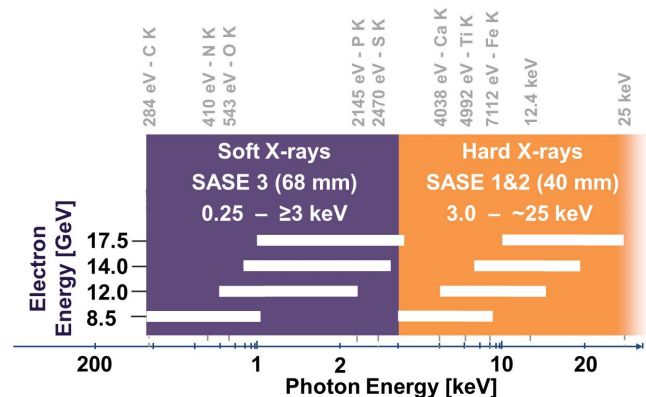


Figure 1: Photon energy reach of the two undulator types of the European XFEL at different electron energies.

ACCELERATOR

Injector and Bunch Compression

The XFEL RF gun is similar to the operating gun at FLASH, DESY. It has been conditioned at PITZ [4]. RF operation in the design configuration in the XFEL injector tunnel took place in December 2013 [5]. The photo-cathode laser - a Nd:YLF laser operating at 1047 nm converted to UV wavelength in two stages - has been delivered by the Max Born Institute, Berlin [6]. The RF gun should produce its first beam after the completion of the laser beam line in October 2014. The injector tunnel will host, in addition to the gun, one standard XFEL superconducting 1.3 GHz module, a superconducting 3.9 GHz module with an accelerating voltage of up to 40 MV, a laser heater and a diagnostic section. The final installation of all components is scheduled for mid 2015. The complete injector can be commissioned and operated independently from the ongoing installation work in the main accelerator tunnel.

The European XFEL employs a three-stage bunch compression scheme to reduce both micro-bunching and the required 3.9 GHz voltage. All magnetic chicanes are tunable within a wide range of R_{56} to allow for flexible compression scenarios, for instance balancing peak current and arrival time stability with LLRF performance. The tuning is achieved by means of large pole width dipole magnets and accordingly wide (400 mm) vacuum chambers. All

dipole magnets are produced and measured, fulfilling the stringent requirements on the field quality over the complete width of the pole. After the second and third compression stage, diagnostic stations similar to the one in the injector are placed.

Linear Accelerator

At the heart of the facility is the superconducting linear accelerator. 100 TESLA-type accelerator modules can deliver a 17.5 GeV electron beam with an average beam power of 600 kW. The linac will be operated in a pulsed mode with 10 Hz repetition rates and up to 2700 bunches per pulse. Production of cavities is in full swing, with more than 1/2 of the total of 800 industry-built cavities already being delivered to DESY. The average accelerating gradient is exceeding the specified 23.6 MV/m and 2/3 of the cavities are accepted for accelerator module assembly immediately after their initial rf test; the gradient reached for those cavities is almost 30 MV/m. About 1/3 of the cavities undergo an additional ultra pure, high pressure water treatment after test, boosting the achievable average gradient clearly above XFEL specifications. A forecast until the end of production gives a potential additional energy of 1.3 GeV in excess of the XFEL design energy of 17.5 GeV [7].

The tested cavities are then integrated into a string of eight cavities at CEA Saclay [8] and installed together with a quadrupole and beam position monitor into a cryostat, thus forming an accelerator module. So far nine series modules have been produced. Most of the sub-components are available in sufficient quantities to sustain the required production rate of 1 module/week. Still, to achieve the project goal of installation of the last of the 100 modules in the tunnel by mid 2016 an accelerated assembly is necessary.

The accelerator modules are supported from the ceiling with a beam height of about 2.2 m above the tunnel floor (see Figure 2). This allows for klystrons, pulse transformers as well as the LLRF and other electronics racks to be installed below the accelerator. The modulators are installed in one single hall above ground and the high-voltage pulse is fed to the pulse transformer by up to 2 km long cables. Almost all of the modulators and 2/3 of the klystrons are delivered and will be installed and put into operation following the installation of the modules in the tunnel.

The LLRF system is completely based on the MTCA.4 technology and is now successfully in operation at FLASH [9]. It is for instance capable of manipulating the RF phase and amplitude along one RF pulse, which would allow to deliver bunches with different properties to different users within one 600 μ s RF pulse. The beam dynamics potential and issues for this operation mode are under investigation [10].

Electron Beam Distribution and Dumps

After the linac almost 3 km of electron beam lines distribute the beam through the SASE undulators to three different beam dumps. Most of the electromagnets have already been delivered by the Efremov Institute, St. Petersburg,

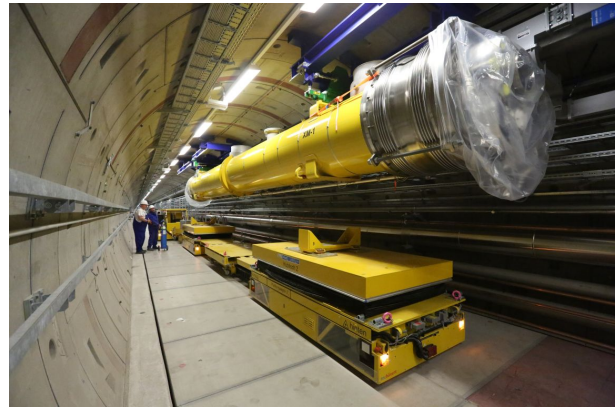


Figure 2: First accelerator module installed at its final position in the main accelerator tunnel [11].

while the vacuum system is under preparation at DESY and Budker Institute, Novosibirsk.

Downstream of the linac the electron beam line will also be supported from the ceiling, over a length of 600 m. This keeps the tunnel floor free for transports and installation of electronics. Especially at the end of the 5.4 m diameter tunnel, where 3 beamlines (to SASE1&3, SASE2 and into the linac dump) run in parallel, installation and maintenance of the components pose a considerable challenge.

The electrons are distributed with a fast rising flat-top strip-line kicker in one of the two electron beam lines. A similar system is already in operation at FLASH2 [12], the second undulator beamline recently being commissioned at FLASH, DESY. Another kicker system is capable of deflecting single bunches in a dump beam line [13]. This allows for a free choice of the bunch pattern in each beam line even with the linac operating with constant beam loading.

Three solid state beam dumps will be placed at the end of the accelerator beam lines, capable of absorbing 300 kW of beam power each, while the beam dump at the end of the injector (see Figure 3) allows to operate the injector stand alone up to full beam power. Two tuning dumps after the bunch compressors complete the beam absorbers. All beam dumps are manufactured by industry and the high power dumps come with a semi-automated exchange device, that allows replacement of the dumps in case of a failure.

Beam Diagnostics

State of the art electron beam diagnostics is of pivotal importance for the success of an FEL. 64 screens and 12 wire scanner stations, 460 beam position monitors of eight different types, 36 toroids and 6 dark-current monitors are distributed along the accelerator. Production of the sensors and read-out electronics is well underway and prototypes of all devices have been tested at FLASH. BPM electronics is developed by the Paul-Scherrer-Institut, Villigen and shows together with the DESY built pick-ups performance already exceeding the specifications [14, 15], of - for example - a single bunch resolution of 1 micron for the undulator cavity BPM's.



Figure 3: Test installation of the injector dump [11]. The dump is placed on the exchange device ready to be moved into its concrete housing to the right.

Energy measurement will be performed with dedicated beam position monitors in dispersive sections. In addition time of travel measurements through compressor chicanes using beam arrival time monitors, precision aligned screens and synchrotron radiation monitors [16] in the chicanes can be used.

Longitudinal and slice parameters of the bunches can be measured at dedicated diagnostic sections in the injector at 130 MeV, after the second bunch compressor BC1 at about 600 MeV and after the final bunch compression stage at 2400 MeV. The diagnostic sections rely on transverse deflecting structures and kicker systems to distribute single bunches onto off-axis screens to measure transverse slice beam parameters on-line during a bunch train [17]. The dispersive diagnostic beam lines at these positions can only be operated in a dedicated mode with a DC deflector that steers the beam in the tuning dumps. At high energies after the linac the bunch compression [18] and beam arrival time [19] will be measured.

PHOTON BEAM SYSTEM

The photon beam system (PBS) starts at the undulator sections and ends inside the experimental hutches. The layout of these sections is shown in Figure 4.

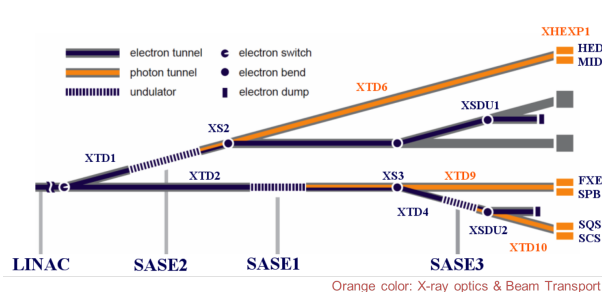


Figure 4: Photon Beam System layout

While the control systems DOOCS is used for the electron accelerator, Karabo controls the components related to the

transport and diagnostic of the photon beam to be delivered to the experimental areas. In addition to that, Karabo will be used for acquiring, manipulating and managing the huge amount of data to be collected by the multi mega-pixel detectors installed at the various instruments [20, 21]. The challenge of the photon system, which includes various state of the art optics and instrumentations, will be to cope with the structure of the electron beam and the peak power density per bunch. As a reminder, each electron bunch train is comprised of 2700 bunches distant of 220 ns (4.5 MHz) and 2 trains are distant by 100 ms (10 Hz).

We will in the following sections show some highlights of the various components of the photon beam system.

Undulator System

The undulator system consists of movable gap out-of vacuum undulator segments of 5 m length and intersections with a phase-shifter, a movable quadrupole, a photon absorber and a cavity beam position monitor. Undulator parameters are summarized in Table 2 [22]. In total 91 undulator segments have to be built and tuned. At the time of writing 81% of the undulators have been measured and tuned in three dedicated measurement labs (see Figure 5). Measured segments are placed into storage before the start of installation at the beginning of 2015. The phase shifters are produced by three different companies. Tight tolerances and a special shimming procedure [23] ensure that they can be operated over a wide range with no influence on the electron beam trajectory.

Table 2: European XFEL Undulator Parameters

Quantity	SASE1/SASE2	SASE3
System length	213.5 m	128.1 m
Number of segments	35	21
λ_0	40 mm	68 mm
K-Range	3.9 - 1.65	9.0 - 4.0
Operational Gap Range	10 - 20 mm	10 - 25 mm



Figure 5: Undulators in the measurement hall [11].

Photon Beam Transport

The photon bunches emitted at the end of an undulator section will have a high peak power density (20 GW/mm² for pulses of up to 150 fs). This is sufficiently high to damage any material placed in its way. The photon beam transport concept is to let the beam expand before cleaning and steering to the experimental areas could happen. Various mirrors are going to be installed in the 3 initial beam lines. Their properties are shown in Table 3. The mirrors will be in vacuum and coated with B₄C to sustain the beam power. The SASE2 mirror will be partially coated with B₄C and Pt. Pt coating is necessary to reflect higher harmonics of the FEL beam (>24 keV) to the samples. The substrate length is 900 mm for the flat mirrors and 950 mm for the bendable ones.

Table 3: Mirrors Specifications - All mirrors shape error (peak to valley) should be <2 nm; and the RMS roughness <3Å. The overall optical length for all mirrors is 850 mm [24]

Mirror	Type	Radius (km)	Heat Load (W)	Energy (keV)
M1 (SASE1)	flat	>600	7.0	3 - 24
M2 (SASE1)	bendable	54 to ∞	2.5	3 - 24
M3 (SASE1)	flat	>600	1.2	3 - 24
M1 (SASE2)	flat	>600	7.0	3 - 80
M2 (SASE2)	bendable	58 to ∞	2.5	3 - 80
M3 (SASE2)	flat	>600	1.2	3 - 80
M1 (SASE3)	flat	>600	140	0.26 - 3
M2 (SASE3)	bendable	10 to ∞	40	0.26 - 3
M5 (SASE3)	flat	>600	10	0.26 - 3

In addition to the mirrors described above, 2 curved mirrors and 3 flat monochromators for the soft-XR beam line will be provided.

Photon Beam Diagnostics

While being transported it is also important to know the quality of the photon beam, its pulse energy, position, wavelength, polarization and more photon parameters, see [25,26] and ref therein. X-ray Gas Monitors, designed and produced by DESY, will allow for non-invasive on-line monitoring of intensity and beam position. The first complete device was tested at the PTB (Physikalisch-Technische Bundesanstalt) beamlines at BESSY2, Berlin in July 2014. Photoelectron Spectrometers will, online and non-destructively, measure the photon wavelength and bandwidth as well as the beam polarization. Invasive diagnostics such as imagers are implemented throughout the beam transport for alignment of the optical elements. Special commissioning diagnostics like the undulator K-parameter spectrometers and MCP-based detectors were constructed and are ready for installation.

Delivering Sample

The first SASE experiment to be operating in 2017 for users will include advanced sample systems suited to meet the special requirements of the extremely high peak power density and the 4.5 MHz repetition rate within a pulse train. Sample environment systems include a fast solid sample scanner that will be able to swap micro scale targets fixed on surfaces within two pulse trains. For handling of liquid samples for biological imaging and crystallography and for spectroscopy of chemicals in liquid solvation, a versatile liquid jet system is under development. To provide a fresh stream of sample for each pulse of the European XFEL, the liquid jets need to have high speeds in the order of 100 m/s. With aerodynamic focusing of a liquid jet by a surrounding stream of supersonic helium gas, liquid jet diameters below a μ m can be reached. This results in low sample consumption and reduced background from evaporation [27].

Detectors and Laser systems in the Experimental Areas

After the sample interaction of the X-Ray, GB of data per photon pulse will be recorded by some fast imaging detectors, Figure 6. The challenge of the detectors is to acquire, pre-process the data and transmit them to a computing center before the next train of photon bunches arrives. The detectors will be either installed permanently or be movable from instruments to instruments, as well as allowing dismounting for re-calibration.

A significant amount of the experiments at the European XFEL (up to 75%) will require optical lasers for pump-probe experiments [29]. Naturally, such a laser must be adapted to the European XFEL bunch pattern. Some degree of freedom in the choice of pulse width and wavelength (around 800 nm) is also desirable. Energy requirements for single pulses usually range from μ J to mJ. Moreover, different experiments need different repetition rates and pulse patterns inside the burst. In consideration of such difficult demands, the European XFEL embarked on a development project to overcome the lack of commercial laser technology, capable of fulfilling them. The scheme consists a multi-stage non-collinear parametric amplifier, employing an Yb-based synchronized front-end, Yb:YAG Innoslab pump amplifiers and dispersion managed super-continuum seed [30–34]. With the exception of further scaling of pulse energy and average power, all essential features were achieved with the R&D prototype: pedestal-free 15 fs pulses at an intra-burst repetition rate of up to 4.5 MHz, a pulse energy of 180 μ J with an intra-burst repetition rate of 188 kHz, long pulse generation up to 75 fs, wavelength tuning over a range of more than 100 nm, random pulse selection and the production of a diffraction-limited laser beam. Current plans foresee the installation of one pump-probe laser per SASE beamline.

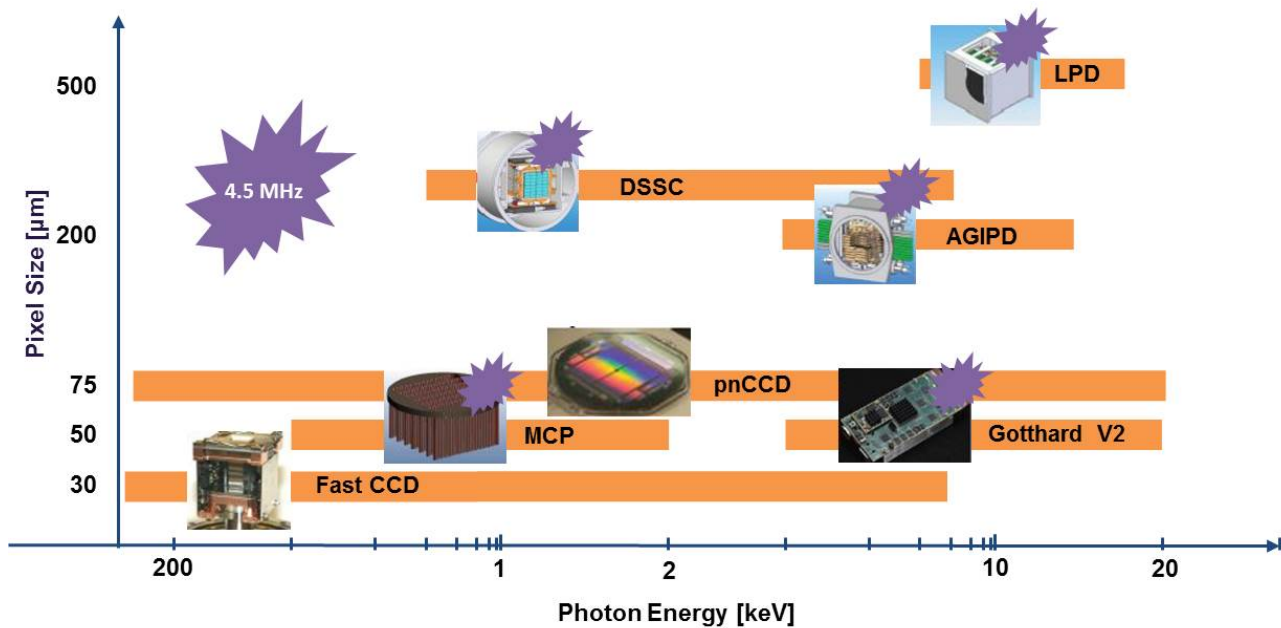


Figure 6: Planned photon detectors at the Soft and Hard X-ray beamlines. Most of them are capable of operating at the intra-bunch frequencies (4.5 MHz) [28]

CONCLUSION

The European XFEL is constantly evaluating its target beam parameters. Recent studies show the potential of the facility within [35–38] or even beyond its baseline design [39–41]. Fabrication and installation of components for the European XFEL is in full swing. The 6 scientific instruments serving the initial 3 SASE lines have now completed their Technical Design Reports hence completing a necessary milestone before the start of their construction [42]. The aim is to close the main accelerator tunnel by mid 2016. The subsequent beam commissioning follows an ambitious schedule with the goal to have the possibility of first lasing by end of 2016.

ACKNOWLEDGMENT

The authors would like to acknowledge the various work package leaders for their input.

REFERENCES

- [1] M. Altarelli et al., editor, *European XFEL Technical Design Report*, DESY 2006-097, DESY-European XFEL, 2007.
- [2] M. Krasilnikov et al., "Experimentally minimized beam emittance from an L-band photoinjector", *Phys. Rev. ST Accel. Beams*, 15 (10), 1000701, 2012.
- [3] E. Schneidmiller, M. Yurkov, "An Overview of the Radiation Properties of the European XFEL", In *FEL14, Basel, Switzerland*, 2014.
- [4] G. Vashchenko et al., "Recent Electron Beam Optimization at PITZ", In *FEL14, Basel, Switzerland*, 2014.
- [5] J. Branlard et al., "European XFEL RF Gun Commissioning and LLRF Linac Installation", In *IPAC14, Dresden, Germany*, 2014.
- [6] S. Schreiber et al., "Upgrades of the Photoinjector Laser System at FLASH", In *FEL2012, Nara, Japan*, 2012.
- [7] H. Weise, "How To Produce 100 Superconducting Modules for the European XFEL in Collaboration and with Industry", In *IPAC14, Dresden, Germany*, 2014.
- [8] S. Berry et al., "Clean Room Integration of the European XFEL Cavity Strings", In *IPAC14, Dresden, Germany*, 2014.
- [9] C. Schmidt et al., "Performance of the microTCA.4 based LLRF system at FLASH", In *IPAC14, Dresden, Germany*, 2014.
- [10] E. Kot et al., "Different Charges in the Same Bunch Train at the European XFEL", In *FEL14, Basel, Switzerland*, 2014.
- [11] Photograph courtesy D. Nölle, DESY.
- [12] M. Scholz et al., "Optics Measurements at FLASH2", In *FEL14, Basel, Switzerland*, 2014.
- [13] N. Golubeva et al., "Layout and Optics of the Dump Line at the European XFEL", In *IPAC14, Dresden, Germany*, 2014.
- [14] M. Stadler et al., "Beam Test Results of Undulator Cavity BPM Electronics for the European XFEL", In *IBIC2012, Tsukuba, Japan*, 2012.
- [15] D.M. Treyer et al., "Design and Beam Test Results of Button BPMs for the European XFEL", In *IBIC2013, Oxford, Great Britain*, 2013.
- [16] M. Sachwitz et al., "Synchrotron Radiation Monitor for Beam Energy Measurements at the European XFEL", In *FEL14, Basel, Switzerland*, 2014.
- [17] J. Wychowaniak et al., "Design of Multi-setup TDS-based Electron Beam Diagnostics for the European X-Ray Free Electron Laser", In *FEL14, Basel, Switzerland*, 2014.
- [18] P. Peier et al., "Coherent Radiation Diagnostics for Longitudinal Bunch Characterization at European XFEL", In *FEL14, Basel, Switzerland*, 2014.

- [19] M.K. Czwalińska et al., "Recent Developments for the Improved Bunch Arrival Time Monitors at FLASH and for the European XFEL", In *FEL14, Basel, Switzerland*, 2014.
- [20] M. Kuster et al., "Detectors and Calibration Concept for the European XFEL", *Synchrotron Radiation News*, 27 (4), 2014.
- [21] B. Heisen et al., "Karabo: An Integrated Software Framework Combining Control, Data Management, and Scientific Computing Tasks", In *ICALEPS2013, San Francisco, USA*, 2013.
- [22] J. Pflueger et al., "Status of the Undulator Systems for the European X-ray Free Electron Laser", In *FEL13, New York, USA*, 2014.
- [23] Y. Li et al., "Results of Shimming Strategy for the Phase Shifters of the European XFEL", In *FEL14, Basel, Switzerland*, 2014.
- [24] H. Sinn et al., "Design of Photon Beamlines at the European XFEL", In *FEL10, Malmö, Sweden*, 2010.
- [25] J. Grünert, Conceptual Design Report: Framework for X-Ray Photon Diagnostics at the European XFEL, Technical report, European XFEL, 2012, doi:10.3204/XFEL.EU/TR-2012-003.
- [26] J. Grünert et al., "Implementation Phase of the European XFEL Photon Diagnostics", In *FEL14, Basel, Switzerland*, 2014.
- [27] J. Schulz, "Sample refreshment schemes for high repetition rate FEL experiments", In *SPIE Optics + Optoelectronics 2013, Prague, Czech Republic*, 2013.
- [28] M. Kuster, private communication.
- [29] L. Wissmann et al., "Status of Pump-Probe Laser Development for the European XFEL", In *FEL14, Basel, Switzerland*, 2014.
- [30] M.J. Lederer et al., "Pump-probe laser development for the European X-Ray Free-Electron Laser Facility", In *SPIE Conference on Optics and Photonics, San Diego, CA, USA*, 2012.
- [31] K. Kruse et al., "Hall-fiber 1030nm burst-mode front-end amplifier for the European XFEL pump-probe laser development for the European X-Ray Free-Electron Laser Facility", In *Ultrafast Optics Conference IX, Davos, Switzerland*, 2013.
- [32] P. Russbuehler et al., "400 W Yb:YAG Innoslab fs-amplifier", *Optic Express*, 17:12230–12245, 2009.
- [33] M. Kellert et al., "High power femtosecond 1030nm burst-mode front-end and pre-amplifier for the European XFEL pump-probe laser development", In *CLEO 2013, Munich, Germany*, 2013.
- [34] M. Pergament et al., "High Power Burst-mode Femtosecond Non-collinear Parametric Amplifier with Arbitrary Pulse Selection", In *CLEO 2014, San Jose, CA, USA*, 2014.
- [35] E. Schneidmiller, M. Yurkov, "Circular Polarization Control by Reverse Undulator Tapering", In *FEL14, Basel, Switzerland*, 2014.
- [36] E. Schneidmiller, M. Yurkov, "Optimization of a High Efficiency FEL Amplifier", In *FEL14, Basel, Switzerland*, 2014.
- [37] I. Agapov et al., "SASE Characteristics from Baseline European XFEL Undulators in the Tapering Regime", In *FEL14, Basel, Switzerland*, 2014.
- [38] V. Kocharyan et al., "Purified SASE Undulator Configuration to Enhance the Performance of the Soft X-ray Beamline at the European XFEL", In *FEL14, Basel, Switzerland*, 2014.
- [39] E. Saldin et al., "Proposal to Generate 10 TW Level Femtosecond X-ray Pulses from a Baseline Undulator in Conventional SASE Regime at the European XFEL", In *FEL14, Basel, Switzerland*, 2014.
- [40] G. Geloni et al., "Perspectives of Imaging of Single Protein Molecules with the Present Design of the European XFEL", In *FEL14, Basel, Switzerland*, 2014.
- [41] E. Schneidmiller, "Prospects for CW Operation of the European XFEL in Hard X-ray Regime", In *FEL14, Basel, Switzerland*, 2014.
- [42] European XFEL Annual Report 2013, doi:10.3204/XFEL.EU/AR-2013.

THE NEW IR FEL FACILITY AT THE FRITZ-HABER-INSTITUT IN BERLIN

Wieland Schöllkopf, Sandy Gewinner, Wolfgang Erlebach, Heinz Junkes, Andreas Liedke, Gerard Meijer, Alexander Paarmann, Gert von Helden, Fritz-Haber-Institut der Max-Planck-Gesellschaft, Faradayweg 4-6, 14195 Berlin, Germany

Hans Bluem, David Dowell*, Ralph Lange*, John Rathke, Alan M.M. Todd, Lloyd M. Young*, Advanced Energy Systems, Inc., 27 Industrial Blvd., Medford, NY 11763, USA

Ulf Lehnert, Peter Michel, Wolfgang Seidel, Rudi Wünsch, Helmholtz-Zentrum Dresden-Rossendorf, Bautzner Landstraße 400, 01328 Dresden, Germany

Stephen C. Gottschalk, STI Optronics, Inc., 2755 Northup Way, Bellevue, WA 98004, USA

Abstract

A mid-infrared oscillator FEL has been commissioned at the Fritz-Haber-Institut. The accelerator consists of a thermionic gridded gun, a subharmonic buncher and two S-band standing-wave copper structures. It provides a final electron energy adjustable from 15 to 50 MeV, low longitudinal (<50 keV-ps) and transverse emittance ($<20\pi$ mm-mrad), at more than 200 pC bunch charge with a micro-pulse repetition rate of 1 GHz and a macro-pulse length of up to 15 μ s. Pulsed radiation with up to 50 mJ macro-pulse energy at about 0.5% FWHM bandwidth is routinely produced in the wavelength range from 4 to 48 μ m. Regular user operation started in Nov. 2013 with 6 user stations. The user experiments include nonlinear spectroscopy of solids, spectroscopy of bio-molecules (peptides and small proteins), which are conformer selected in the gas-phase or embedded in superfluid helium nano-droplets at 0.4 K, as well as vibrational spectroscopy of mass-selected metal-oxide clusters and protonated water clusters in the gas phase.

INTRODUCTION

In 2008 the Fritz-Haber-Institut (FHI) embarked on setting up an infrared FEL facility. The aim was to set up an FEL that is capable of providing intense, pulsed laser radiation, continuously tunable from a few micron in the near to mid-infrared (MIR) all the way to several hundred micron in the far-infrared (FIR), or Tera-Hertz (THz) regime. Installation of the FEL started in mid 2011 in a new, dedicated FEL building on the FHI campus in Berlin. We observed first lasing in 2012 [1–3] and started user operation in November 2013.

IR radiation in the spectral region from 3 to 100 μ m is often referred to as the molecular fingerprint region, because it is the region in which the fundamental vibrational modes of molecules, clusters or solid materials are located. The vibrational IR spectrum is intimately connected to the molecular structure and dynamics, which is why IR spectroscopy is one of the basic methods for molecular structure characterization. The highest energy vibrations, involving stretching motions of light atoms, are found around a wavelength of 3 μ m. Lower energy vibrations are found throughout the

IR region, down to the FIR region beyond 100 μ m. The vibrational frequencies in the FIR result from heavy atoms and/or weak bonds, or from soft modes that involve large amplitude motions and global geometry changes. Thus, FIR spectroscopy also allows to study the folding dynamics of (bio)molecules.

FIR radiation can also be used to directly probe surface-adsorbate vibrations. This allows to study the structure and dynamics of adsorbates on surfaces, to measure the properties of deposited or gas-phase cluster materials, or to investigate real-world catalysts in action. In addition, the intense FEL radiation can readily induce multiple photon excitation processes and is well suited for double-resonance experiments with other, table-top laser systems.

DESIGN OF THE FHI FEL

To cover the full wavelength range of interest from about 4 to 500 μ m the basic design of the FHI FEL includes two different undulator lines as outlined in Fig. 1 [1–5]. The MIR branch works for wavelengths up to about 50 μ m and the FIR branch covers the wavelength range from about 40 to 500 μ m. A normal-conducting linear accelerator provides electrons of up to 50 MeV energy with a beam transport system feeding either of the FEL branches or the diagnostics beamline (Fig. 1).

Electron Accelerator and Beamline

The electron accelerator and beamline system, designed, built, and installed by Advanced Energy Systems, Inc. (AES), has been described before [4–7]. In brief, the accelerator system is comprised of a gridded thermionic gun, a subharmonic buncher cavity and two standing-wave, $\pi/2$ copper linacs. The first of the two S-band (2.99 GHz) linacs accelerates the electron bunches to a nominal energy of 20 MeV, while the second one accelerates or decelerates the electrons to deliver any final energy between 15 and 50 MeV. A chicane between the linacs allows for adjustment of the electron bunch length as required.

Key performance parameters of the accelerator are low longitudinal (<50 keV-psec) and transverse emittance ($<20\pi$ mm-mrad) at more than 200 pC bunch charge with a micro-bunch repetition rate of 1 GHz. The maximum

* Consultants to Advanced Energy Systems, Inc.

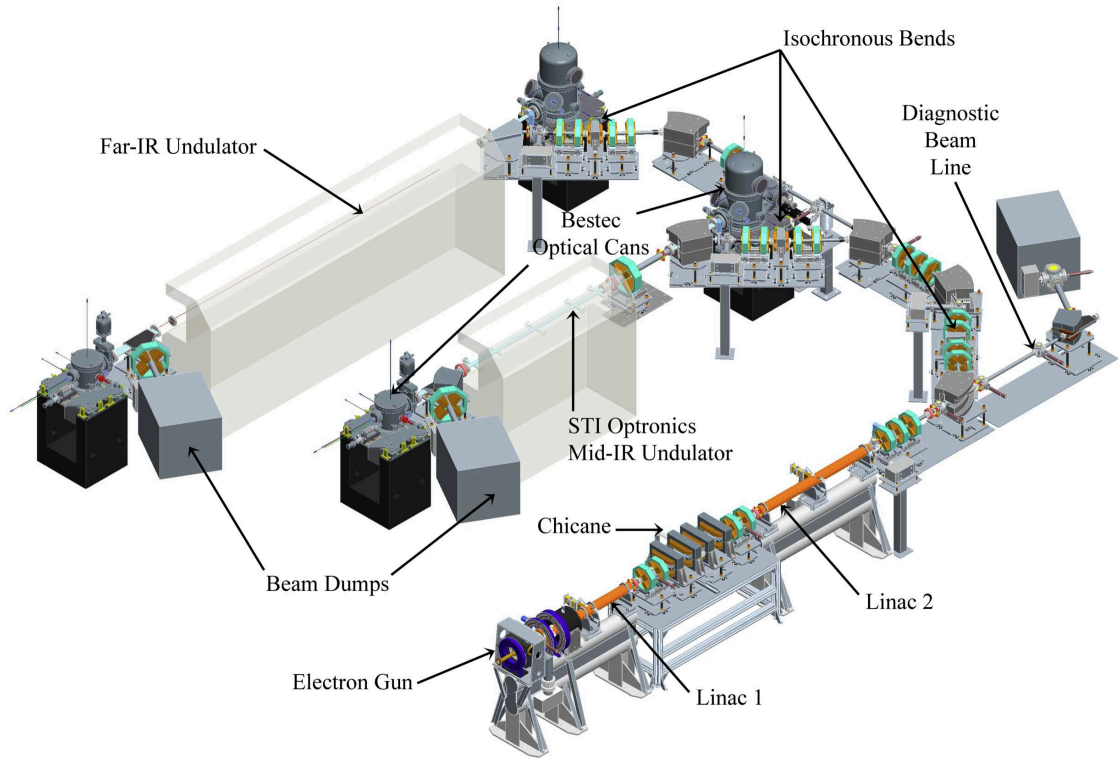


Figure 1: Overview of the FHI FEL installation showing the electron accelerator system and the MIR FEL (operational) and the FIR FEL (to be installed in the future).

Table 1: Summary of Electron Beam Parameters of the S-band Linear Accelerator

Parameter	Unit	Spec.	Target
Electron energy	MeV	20 - 50	15 - 50
Energy spread	keV	50	< 50
Energy drift per hour	%	0.1	< 0.1
Bunch charge	pC	200	> 200
Micro-bunch length	ps	1 - 5	1 - 10
Micro-bunch rep. rate	GHz	1	1
Micro-bunch jitter	ps	0.5	0.1
Macro-bunch length	μs	1 - 8	1 - 15
Macro-bunch rep. rate	Hz	10	20
Normalized rms transverse emittance	$\pi \mu\text{m rad}$	20	20

macro-bunch repetition rate is 20 Hz. Table 1 summarizes the top-level electron beam performance.

The beam is delivered from the accelerator to either the MIR or the FIR FEL by 90°-isochronous achromats that minimize the effect of the micro-bunch and macro-bunch jitter to ensure radiation wavelength stability and timing consistency for pump-probe experiments. A quadrupole triplet downstream of the second linac leads to the first dipole where the diagnostic beamline goes straight through. There is another quadrupole triplet in the back leg before the second

90° isochronous achromat delivers the beam to the MIR FEL. Downstream of the undulator the electrons are bent to the beam dump by a 60°-dipole.

MIR Oscillator FEL

Both the MIR and FIR FEL consist of an undulator placed within an IR cavity as summarized in Table 2. The MIR FEL includes a planar, radiation-resistant, high-field-strength, wedged-pole hybrid undulator, manufactured by STI Optronics, Inc., which has been described in detail elsewhere [8]. It is 2 m long containing 50 periods with a period length of 40 mm. At a minimum undulator gap of nominally 16.5 mm, a maximum root-mean-square undulator parameter K_{rms} of more than 1.6 is reached [8]. This, in combination with the minimum electron energy of 15 MeV corresponds to a theoretical maximum wavelength of more than 50 μm for the MIR system.

The 5.4 m long FEL cavity is formed by a cavity end mirror and the outcoupling mirror. These are gold-plated copper mirrors of spherical concave shapes with radius of curvature of 2.65 m and 3.51 m, respectively. As a result, the Rayleigh length of the cavity mode is 2 m, thereby matching the undulator length, and the location of the mode's waist is shifted by 50 cm away from the cavity center to coincide with the undulator center [3]. The cavity-end mirror is mounted on a precision translation stage to enable cavity length adjustment with a nominal precision of 1 μm. The

Table 2: Summary of Essential Parameters of the MIR (commissioned) and FIR (prospected) FEL Setups

Undulator	MIR	FIR
Type	Planar hybrid	Planar hybrid or PPM
Material	NdFeB	NdFeB or SmCo
Period (mm)	40	110
No. of periods	50	40
Length (m)	2.0	4.4
K_{rms}	0.5 - 1.6	1.0 - 3.0
IR-cavity	MIR	FIR
Length (m)	5.4	7.2

outcoupling mirror has a hole in its center. Each one of a set of mirrors with hole diameters of 0.75, 1.0, 1.5, 2.5, and 3.5 mm can be precisely positioned at the cavity end by an in-vacuum mirror changer. This allows to choose the out coupling-hole diameter best suited for the wavelength range of interest.

The FIR FEL has not yet been installed, but its design has been outlined. The right column of Table 2 gives the essential design parameters for the FIR undulator and cavity. The electron branch-off beamline has been included in the current system, thereby allowing for implementation of the FIR system at a later point of time.

CHARACTERIZATION OF THE MIR FEL RADIATION

To characterize the IR radiation different commercial IR detectors including a liquid-nitrogen cooled MCT (HgCdTe) detector (Judson J15D24) and a large area (46 mm diameter) pyroelectric detector (Ophir PE50BB) are used for IR power and pulse energy measurements. In addition, a vacuum Czerny-Turner grating spectrometer (Acton VM-504) equipped with a 0.5"-wide pyroelectric linear array detector (DIAS 128LT) allows online monitoring of the FEL spectrum (see Fig. 2). Further commercial diagnostics equipment includes a 5 stage IR beam attenuator (LASNIX Model 102). It is planned to set up additional equipment for characterizing and manipulating the IR beam in the future including a photo-acoustic cell and a polarization rotator.

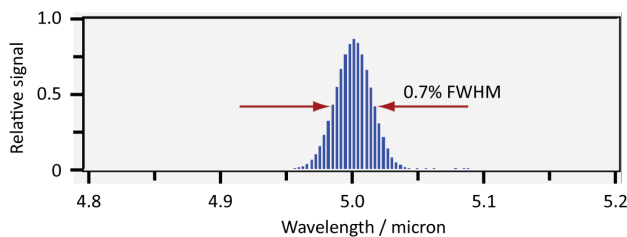


Figure 2: Spectrum of the FEL laser line centered at 5 μ m measured with the grating spectrometer.

Figure 2 shows a spectrum of the FEL line centered at a wavelength of 5 μ m obtained for an electron energy of

38 MeV. The spectral line FWHM (full width at half maximum) in this measurement is about 33 nm corresponding to a relative line width of less than 0.7%. As discussed in detail in the next section, the line width can be varied by adjusting the FEL cavity length. Most user experiments at the FHI FEL facility benefit from narrow line width, even at the expense of pulse energy. Therefore, the FEL is usually tuned to exhibit a narrow line width of typically 0.35% to 0.6% FWHM, when lasing at 10 μ m or less, increasing to 1.0% to 1.5% FWHM at the longest wavelengths close to 50 μ m. This corresponds to absolute FWHM bandwidths of 3.6 to 6 cm^{-1} and 2 to 3 cm^{-1} at 10 and 50 μ m central wavelength, respectively.

As of summer 2014 the accelerator is operated at either one of three electron energies of 38 MeV (regime I), 26.5 MeV (regime II), and 18.5 MeV (regime III). With these three energies lasing over the entire MIR wavelength range from 3.5 to 48 μ m is achieved. Figure 3 shows measurements of the macro-pulse energy for the three regimes, when the FEL is operated at narrow line width conditions. Largest macro-pulse energies of about 50 mJ are found at highest electron energy (regime I), decreasing to less than 10 mJ in regime III at wavelengths larger than 25 μ m. We expect lasing at even shorter or longer wavelengths once the accelerator is operated at its maximum and minimum electron energies of 50 and 15 MeV (see Table 1), respectively. So far, a maximum IR pulse energy of 130 mJ was observed with a broad spectrum centered around 9 μ m.

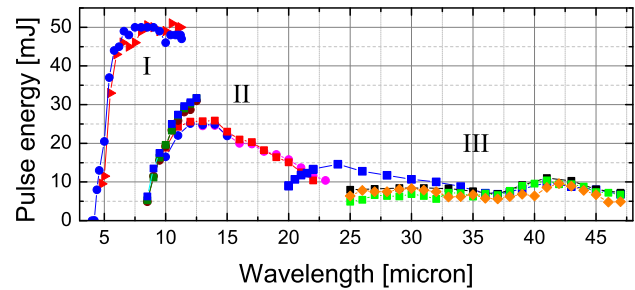


Figure 3: Macro-pulse energies measured at narrow bandwidth conditions for electron energies of 38 MeV (regime I), 26.5 MeV (regime II) and 18.5 MeV (regime III).

Micro-pulse Characterization by SHG Auto-correlation Measurements

To determine the micro-pulse time structure we implemented an auto-correlation measurement setup shown schematically in Fig. 4. The FEL beam is split in equal parts by a Ge-coated ZnSe beam splitter. Both partial beams are focused onto a 1 mm thick CdTe single crystal. The optical path-length difference of the beams is accurately controlled by a commercial precision translation. Non-linear interaction in the CdTe sample leads to second harmonic generation (SHG). Due to the angle between the incident beams, the generated SHG beam is separated from the reflected FEL beams, allowing to block the latter by an aperture. As a re-

sult, the relatively weak SHG signal can be detected free of the second harmonic background signal inherently present in the FEL beams.

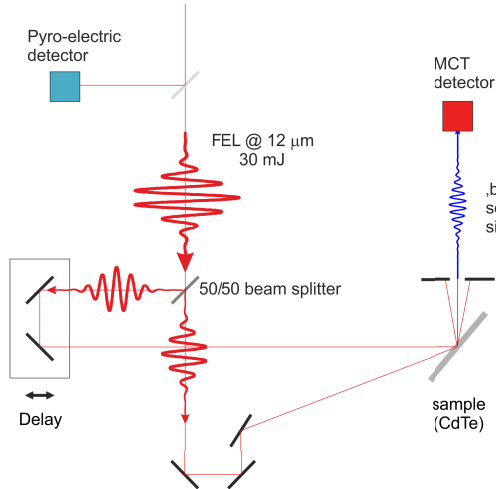


Figure 4: Setup to measure auto-correlation functions by second harmonic generation in a CdTe sample.

Auto-correlation data measured at a wavelength of 12 μm is shown in Fig. 5 for three different cavity length detunings of $\Delta L = -3, -16$, and $-50 \mu\text{m}$, where $\Delta L = L - L_0$ with L and $L_0 = 5.4 \text{ m}$ standing for the actual and nominal cavity length, respectively. The 2-D plots on the left of Fig. 5 show the SHG signal as a function of the delay time and real time. The former describes the micro-pulse arrival-time difference due to the optical path-length difference, while the latter refers to the time referenced to the beginning of the electron macro bunch. Thus, the plots show the evolution of the micro-pulse auto-correlation over the macro-pulse time window.

For the smallest cavity detuning of $-3 \mu\text{m}$ (Fig. 5A) micro-pulses occur rather late in the macro-pulse indicating a relatively small FEL gain. These pulses show very sharp auto-correlation functions with FWHM values down to 0.6 ps. The auto-correlation time structure changes significantly when the cavity detuning is increased to $-16 \mu\text{m}$ (Fig. 5B). Pulses now appear earlier within the macro-pulse indicating a larger FEL gain. In addition, the auto-correlation function exhibits multiple peaks separated by about 1 ps. Finally, at even larger cavity detuning of $-50 \mu\text{m}$ (Fig. 5C) the multiple-peak structure has evolved into a single broad peak with a relatively large FWHM increasing from 3 ps to about 8 ps over the course of the macro-pulse.

A multiple-pulse time structure of the micro-pulses in an oscillator FEL was observed at FELIX before and explained in terms of limit-cycle oscillations [9, 10]. Our observations agree well with those findings. The large variation of the micro-pulse time structure allows us to tune the temporal and spectral properties of the FEL radiation by changing the cavity length. In fact, in most FHI FEL user experiments, which will be described in the next section, a rather narrow spectral bandwidth is advantageous. Time resolved experi-

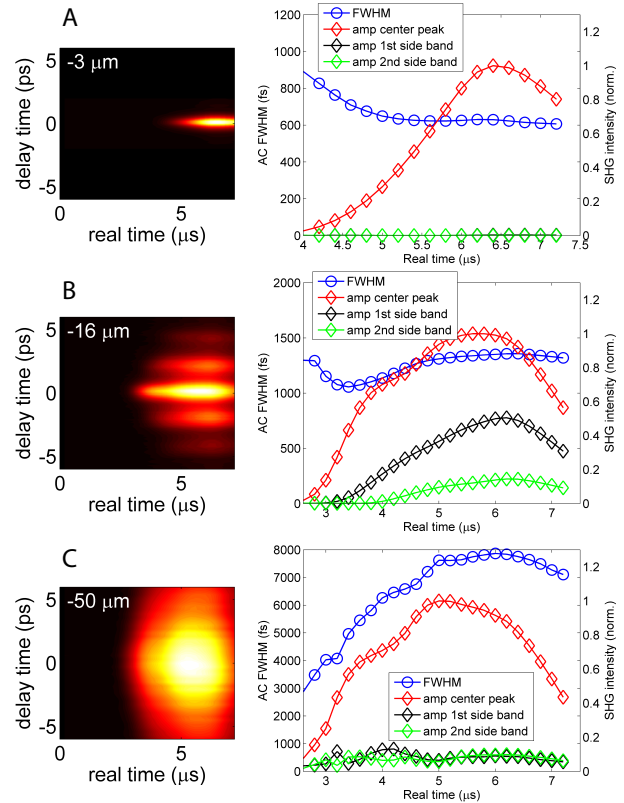


Figure 5: Auto-correlation measurements of FEL pulses at 12 μm wavelength for 3 different cavity length detunings of $\Delta L = -3 \mu\text{m}$ (A), $-16 \mu\text{m}$ (B), and $-50 \mu\text{m}$ (C), measured with the setup shown in Fig. 4. The plots on the left show the observed SHG signal as a function of delay time and real time within the electron macro-bunch time window with zero set by the beginning of the macro-bunch. The data analysis results shown on the right indicate the evolution of the micro-pulse structure over the macro-pulse.

ments, however, will benefit from short FEL pulses that can be achieved at small cavity length detuning. The FWHM of 0.6 ps observed in the auto-correlation function shown in Fig. 5A corresponds, assuming a Gaussian pulse shape, to a deconvoluted micro-pulse length of less than 0.43 ps FWHM.

FACILITY AND USER STATIONS

The IR pulses, extracted from the MIR FEL, enter the IR beamline through a CVD diamond window under Brewster angle. The window separates the ultra-high vacuum of less than 1×10^{-8} mbar in the undulator and cavity-mirror chambers from the high vacuum (10^{-5} mbar) in the IR beamline. The IR beamline consists of 10 cm inner-diameter stainless steel pipes interconnected at right angle by vacuum chambers housing 90° -deflection broadband IR mirrors. The mirrors are either flat or toroidal (focusing) and are made out of copper with a gold coating. The nominal mirror reflectivity is 99.2% over the entire IR range. A total of 6 such mirrors steer the IR beam from the FEL cavity in the vault to the

IR diagnostic station, located in the neighboring building, over a total length of 18 m (see Fig. 6). Another IR beam-line system (user beamlines) brings the FEL beam from the diagnostic station to either one of six experimental stations located in the basement and the ground floor as indicated in Fig. 6.

As of summer 2014 five experiments from the area of gas-phase spectroscopy of clusters and bio-molecules as well as one experiment from the field of solid-state physics have been using the MIR FEL radiation.

Station I: Chemistry of transition metal clusters

The group of André Fielicke (FHI & TU Berlin) has been using the FHI FEL radiation to investigate transition-metal clusters in the gas phase. For instance, vibrational spectra of CO attached to small cationic ruthenium and cobalt-manganese clusters have been measured. These studies allow to probe the effects of alloying on the d-band center that is controlling the strength of the p-backbonding to the CO. Further systems studied so far by FHI FEL radiation include: (i) neutral iron oxide clusters studied by IR-UV two color ionization; (ii) neutral gold clusters in search for O₂ activation in the presence of deuterated water; (iii) positively charged Rh_n⁺CH₄ clusters; and (iv) neutral Si_nB clusters.

Station II: Vibrational spectroscopy of gas phase clusters: catalysis, astrochemistry and new materials The

group of Knut Asmis (FHI & U Leipzig) has been using the FHI FEL radiation to study negatively charged aluminum oxide and iron oxide clusters in the gas phase. The small negatively charged metal oxide clusters are prepared in an ion trap, cooled to temperatures on the order of 20 K, and tagged with a few D₂ molecules per cluster. Mass-selective vibrational spectra are measured by way of IR photodissociation of the messenger-tagged complexes in order to probe (close to) the linear absorption regime.

Station III: Vibrational spectroscopy of gas phase clusters: atmospheric chemistry and ion solvation

Protonated gas-phase water clusters $\text{H}_3\text{O}^+(\text{H}_2\text{O})_n$ and

$\text{D}_3\text{O}^+(\text{D}_2\text{O})_n$ as well as $\text{Cs}^+(\text{H}_2\text{O})_n$ and $\text{Cs}^+(\text{D}_2\text{O})_n$ have been investigated by the Asmis group to elucidate their structural properties. Further systems studied at this beamline using the FHI FEL radiation include anionic ClMgCO_2^- molecules as well as $\text{NO}_3^-(\text{HNO}_3)_n(\text{H}_2\text{O})_m$ and $\text{NO}_3^-(\text{HNO}_3)_n$ clusters tagged with D_2 .

Station IV: Spectroscopy of conformer selected pro-

teins The group of Gert von Helden (FHI) has been using the FHI FEL to study the structure of bio-molecules in the gas phase. IR spectra of the protein Ubiquitin (76 amino acids) in different charge states $n+$ and crown-ether complexes thereof have been measured. Prior to the interaction with the FEL beam, the molecules are not only selected according to their mass-to-charge ratio but they are also conformer selected using gas-phase IMS (ion mobility spectrometry) methods. Surprisingly narrow amide-I bands near 1650 cm^{-1} and amide-II bands near 1500 cm^{-1} have been found. Further molecules studied by IR spectroscopy combined with IMS include the penta-peptide leucine-enkephalin.

Station V: Spectroscopy of bio-molecules embedded in superfluid helium nano-droplets

droplet isolation spectroscopy has been established as a method to record optical spectra of molecules at ultracold conditions. Charged bio-molecules, brought into the gas phase via electrospray ionization, are mass-to-charge selected in a mass spectrometer and stored in an ion trap. Suprafluid helium nano-droplets traversing the ion trap pick up the molecules. The IR spectra of the ions at 0.4 K in the helium droplet, measured with the FHI FEL radiation, reveal much narrower lines than those measured using conventional gas-phase methods. This is why the results are expected to improve the understanding of the peptide and protein structures. The von Helden group has so far observed spectra of leucine-enkephalin and of the proteins ubiquitin and angiotensin.

Station VI: Nonlinear spectroscopy of solids The

group of Alexander Paarmann (FHI) has embarked on a project to investigate ultrafast dynamics in solid state systems under MIR excitation with the FHI FEL. These experiments on the one hand allow micro-pulse temporal characterization using second harmonic generation in MIR nonlinear optical crystals like CdTe and GaSe. On the other hand, ultrafast time-resolved experiments using the FEL as pump pulse and applying various probes, such as visible reflectivity or sample magnetization allow detailed study of fundamental interactions among low-energy excitations. As part of the project, sub-ps time synchronization of a near-IR femtosecond laser with the FEL micro-pulses will be implemented.

Station under preparation: Surface science experiment A surface-science beamline station is currently un-

der construction by the group of Helmut Kühlenbeck (FHI). It is scheduled for commissioning in 2015. It will be used

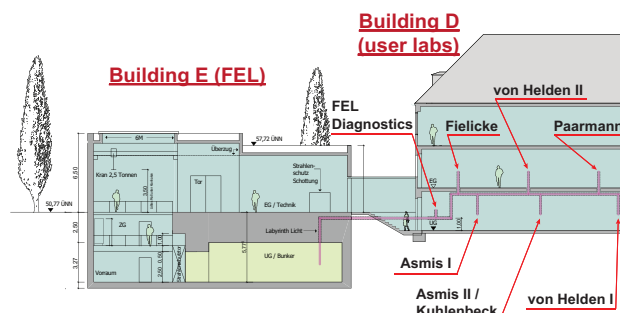


Figure 6: Cross sectional view of the new FEL building (left) and the spectroscopy-lab building (right) indicating the IR transport beamline system connecting the FEL with currently six user stations in the basement and ground floor, which are labelled by the principle investigator's name.

for vibrational spectroscopy of metal clusters deposited on flat ordered substrates, so-called model catalysts. Similar to the gas-phase experiments the clusters will be tagged with weakly bound rare-gas atoms. Upon vibrational excitation of the cluster by FEL radiation, the rare gas atoms will desorb due to the rapid resonant heating of the clusters, and vibrational spectra of the clusters can be measured by recording the desorption signal.

CONCLUSION

The IR FEL Facility at the Fritz-Haber Institute of the Max-Planck Society started regular user operation in November 2013. The MIR oscillator FEL, operated with 15 to 50 MeV electrons from an S-band copper accelerator made by AES, Inc., provides pulsed radiation from, currently, 4 μm to almost 50 μm . The temporal and spectral properties of the FEL radiation has been characterized using a grating spectrometer and by auto-correlation measurements. The width of the FEL's spectral line was determined to be as small as 0.35% (FWHM) for relatively large detuning of the FEL cavity length. For very small cavity detuning, IR pulses as short as 0.4 ps (FWHM) have been observed. As of now, 6 user stations have been applying the FHI FEL radiation for vibrational spectroscopy of charged and neutral cluster and bio-molecules in the gas-phase or embedded in helium-nanodroplets as well as for nonlinear spectroscopy of solids.

ACKNOWLEDGMENTS

We thank Johannes Bahrtdt, Andreas Gaupp, Klaus Ott, and Ernst Wehreter (Helmholtz-Zentrum Berlin) as well as Lex van der Meer (Radboud University Nijmegen) for their valuable support to the planning and commissioning of the FHI FEL. Furthermore, we thank the members of the FHI FEL user groups listed in this paper for fruitful discussions.

REFERENCES

- [1] W. Schöllkopf et al.. First Lasing of the IR FEL at the Fritz-Haber-Institut Berlin. In *Proceedings of FEL 2012, Nara, Japan*, MOOB01, 2013.
- [2] H.P. Bluem et al. Accelerator Beamline Performance for the IR FEL at the Fritz-Haber-Institut, Berlin. In *Proceedings of FEL 2012, Nara, Japan*, WEOC04, 2013.
- [3] W. Schöllkopf et al. The IR and THz Free-Electron Laser at the Fritz-Haber-Institut. In *Proceedings of FEL 2013, New York, NY, USA*, WEPSo62, 2013.
- [4] W. Schöllkopf et al. Status of the Fritz Haber Institute THz FEL. In *Proceedings of FEL 2011, Shanghai, China*, TUPB30, 2012.
- [5] A.M.M. Todd et al. Commissioning of the Fritz Haber Institute Mid-IR FEL. In *Proceedings of IPAC 2012, New Orleans, Louisiana, USA*, TUPPP087, 2012.
- [6] A.M.M. Todd et al. Commissioning Status of the Fritz Haber Institute THz FEL. In *Proceedings of IPAC 2011, San Sebastián, Spain*, THPC106, 2011.
- [7] H.P. Bluem et al. The Fritz Haber Institute THz FEL Status. In *Proceedings of FEL 2010, Malmö, Sweden*, MOPA09, 2010.
- [8] S.C. Gottschalk et al. Design and Performance of the Wedged Pole Hybrid Undulator for the Fritz-Haber-Institut IR FEL. In *Proceedings of FEL 2012, Nara, Japan*, THPD13, 2013.
- [9] D.A. Jaroszynski et al. Experimental observation of limit-cycle oscillations in a short-pulse free-electron laser. *Phys. Rev. Lett.* **70**, 3412 (1993).
- [10] G.M.H. Knippels et al. Formation of multiple subpulses in a free-electron laser operating in the limit-cycle mode. *Phys. Rev. E* **53**, 2778 (1996).

FLASH: FIRST SOFT X-RAY FEL OPERATING TWO UNDULATOR BEAMLINES SIMULTANEOUSLY

K. Honkavaara*, B. Faatz, J. Feldhaus, S. Schreiber, R. Treusch, M. Vogt,
DESY, Hamburg, Germany[†]

Abstract

FLASH, the free-electron laser user facility at DESY (Hamburg, Germany), has been upgraded with a second undulator beamline FLASH2. After a shutdown to connect FLASH2 to the FLASH linac, FLASH1 is back in user operation since February 2014. Installation of the FLASH2 electron beamline has been completed early 2014, and the first electron beam was transported into the new beamline in March 2014. The commissioning of FLASH2 takes place in 2014 parallel to FLASH1 user operation. This paper reports the status of the FLASH facility, and the first experience of operating two FEL beamlines.

INTRODUCTION

FLASH [1–4], the free-electron laser (FEL) user facility at DESY (Hamburg), delivers high brilliance XUV and soft X-ray FEL radiation for photon experiments.

The TESLA Test Facility (TTF) Linac [5], constructed at DESY in mid 1990's and operated until end of 2002, was originally dedicated to test the feasibility of high gradient superconducting accelerator technology in the framework of the TESLA linear collider project [6]. In addition, it was used to drive a SASE (Self Amplified Spontaneous Emission) free-electron laser pilot facility TTF-FEL [7, 8] at photon wavelengths from 80 nm to 120 nm [9, 10] to demonstrate the feasibility of SASE FELs in the VUV range. Based on the experience gathered from the TTF-FEL operation, FLASH – originally called VUV-FEL at TTF2 – was constructed in 2003–04.

The first lasing of FLASH at 32 nm was achieved in January 2005 [11]. Since summer 2005 FLASH has been operated as an FEL user facility, being the first facility in the world delivering VUV and XUV FEL radiation for photon experiments. During 2005–2007, FLASH delivered FEL radiation in wavelengths from 13 nm to 47 nm (fundamental), entering the water window with the 3rd and 5th harmonics [1]. An energy upgrade to 1 GeV in summer 2007 extended the range to the soft X-rays with wavelengths down to 6.5 nm [12, 13]. The next upgrade [14], accomplished in 2009/10, led to major modifications of the facility, including, for example, the installation of third harmonic RF cavities to linearize the longitudinal phase space and an energy upgrade to 1.25 GeV. This allowed lasing with wavelengths down to 4.1 nm [15], entering thus the water window also with fundamental wavelengths.

The most recent upgrade to include a second undulator beamline has been carried out in 2011–14, mostly parallel

Table 1: FLASH Parameters 2014

Electron beam		
Energy	MeV	380 - 1250
Bunch charge	nC	0.08 - 1
Bunches / train		1 - 500
Bunch spacing	μs	1 - 25
Repetition rate	Hz	10
FEL radiation		
Wavelength (fundamental)	nm	4.2 - 45
Average single pulse energy	μJ	10 - 500
Pulse duration (fwhm)	fs	< 50 - 200
Spectral width (fwhm)	%	0.7 - 2
Peak power	GW	1 - 3
Photons per pulse		10 ¹¹ - 10 ¹³
Peak brilliance	*	10 ²⁹ - 10 ³¹
Average brilliance	*	10 ¹⁷ - 10 ²¹

* photons / (s mrad² mm² 0.1 % bw)

to the FLASH user operation. After a shutdown in 2013 to connect the new beamline to the FLASH linac, the operation re-started in August 2013. Since February 2014, FLASH is back in user operation. The beam commissioning of the second undulator beamline (FLASH2) has started in March 2014.

This paper reports the status of the FLASH facility, and the first experience of operating two undulator beamlines. Part of the material discussed here has been presented in previous conferences, most recently in [4].

FLASH FACILITY

The layout of the FLASH facility is shown in Fig. 1. The first undulator beamline, being in operation since 2004, is referred to FLASH1, the new one to FLASH2. Table 1 shows typical FLASH operating parameters. These parameters are not all achieved simultaneously, but indicate the overall span of the performance.

A superconducting linac driven by an RF-gun based photoinjector provides a train of electron bunches: the maximum bunch train length is 800 μs, and it can be shared between the two undulator beamlines. Several discrete bunch spacings between 1 μs (1 MHz) and 25 μs (40 kHz) are possible. The bunch train repetition rate is 10 Hz. The typical bunch charge ranges from 80 pC to 1 nC.

The photocathode laser system has two independent lasers, both based on an actively mode-locked pulse train oscillator with a linear chain of fully diode pumped Nd:YLF ampli-

* katja.honkavaara@desy.de

[†] for the FLASH team

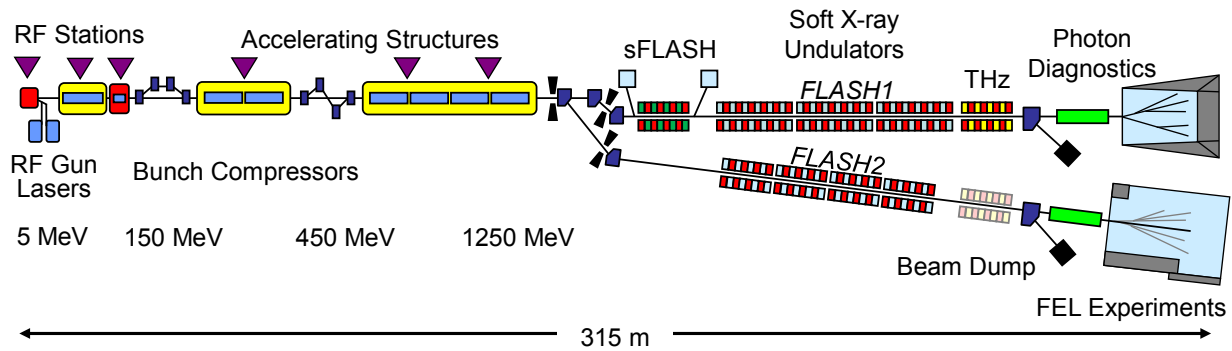


Figure 1: Layout of the FLASH facility (not to scale).

fiers followed by frequency quadrupling to the UV [16, 17]. During simultaneous operation, one of the lasers is used to produce the electron bunch train for the FLASH1 beamline, the other one for FLASH2. The duration of the Gaussian shaped laser pulse is fixed to 6.5 ± 0.1 ps (rms). For certain experiments, especially in order to produce very short electron bunches [18], a third laser system is in the testing phase. This laser provides UV-pulses with an adjustable duration of 0.8 ps to 2 ps (rms), easing thus the compression of electron bunches.

An exchangeable cathode, consisting of a thin Cs_2Te film on a molybdenum plug [19], is installed on the back-plane of the RF-gun. During the last years, severe hardware problems have occurred related to the RF-gun and its RF-window [4, 20]. During the 2013 shutdown, a new RF-gun has been installed and was successfully taken into operation in autumn 2013. Unfortunately, a vacuum leak developed at the RF-window, and the window had to be replaced in April 2014. New RF-gun design options and new RF-window types are being tested with a goal to increase their lifetime considerably.

The FLASH linac consists of seven superconducting TESLA type accelerating modules. Each module has eight 9-cell niobium cavities operated at 1.3 GHz. The maximum achievable electron beam energy is 1.25 GeV. A module with four 3.9 GHz (third harmonics of 1.3 GHz) superconducting cavities is installed downstream the first accelerating module to linearize the energy chirp in the longitudinal phase space. In order to achieve the peak currents required for the lasing process, electron bunches are compressed by two magnetic chicane bunch compressors at beam energies of 150 MeV and 450 MeV, respectively.

The RF-gun and the accelerator modules are regulated by a sophisticated low level RF (LLRF) system. During the 2013 shutdown, the LLRF system of the accelerator modules has been upgraded to a new powerful and fast digital system using MTCA.4 specifications [21]. The upgrade of RF-gun LLRF system is scheduled late 2014. Details of the new LLRF system and its performance at FLASH can be found in [22].

A kicker-septum system is now installed downstream the last accelerator module. Flat-top kickers with a total deflec-

tion angle of 2.2 mrad kick the FLASH2 part of the bunch train vertically into the deflecting channel of a Lambertson septum. The septum deflects the beam horizontally by 6.5° into the FLASH2 beamline. The FLASH1 part of the bunch train goes straight ahead to the FLASH1 collimator and undulator section. The septum magnet with the FLASH1 and FLASH2 beamlines is shown in Fig. 2.

The FLASH1 and FLASH2 bunch trains are within the same RF-pulse. This allows to serve both beamlines with a bunch train repetition rate of 10 Hz. The two trains, one for FLASH1 and the other one for FLASH2, are separated by a gap of some tens of μs . The minimum gap width is determined by the kicker pulse rise time, and is about 30 μs .

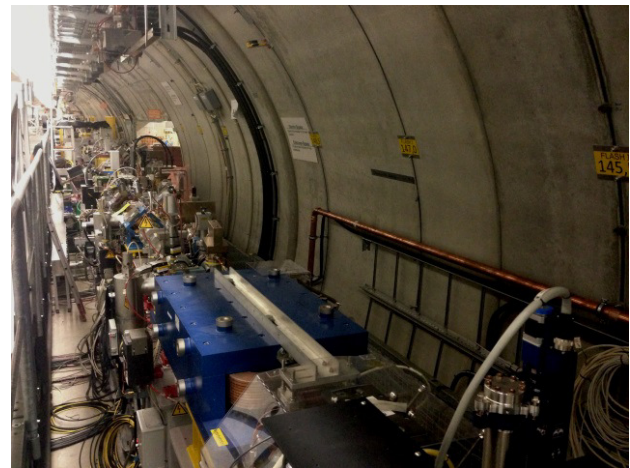


Figure 2: Separation of FLASH1 (straight) and FLASH2 beamlines (to the right). The blue magnet is the Lambertson septum.

The FLASH1 electron beam passes through six 4.5 m long fixed gap (12 mm) undulator modules producing FEL radiation based on the SASE process. The undulators consist of permanent NdFeB magnets, the undulator period is 27.3 mm, and the peak K-value 1.23. The FLASH2 beamline has twelve 2.5 m long variable gap undulators with an undulator period of 31.4 mm.

At FLASH1 a transverse deflecting structure is installed upstream of the SASE undulators. It serves together with a

kicker and an off-axis screen as an on-line monitor for the electron bunch length and shape [23]. This monitor is now in continuous use, especially during short pulse operation.

In the FLASH1 beamline, a planar electromagnetic undulator is installed downstream of the SASE undulators to produce, on request, THz radiation. Later, a THz undulator will also be installed into the FLASH2 beamline.

Both FLASH1 and FLASH2 have a sophisticated photon diagnostics section providing a possibility to measure and characterize the photon beam parameters. In the FLASH1 experimental hall, five photon beam lines are available for user experiments. Photon diagnostics and photon beamlines of FLASH1 are described in [2, 24]. Since FLASH1 is not yet equipped with permanent end-stations, each experiment has to provide and install its own measurement hardware. The first permanent end station (CAMP instrument) is under preparation at beamline BL1. The operation of FLASH2 starts initially with 2-3 photon beamlines, and the new experimental hall foresees place for finally up to seven beamlines. The aim is to provide several fixed end-stations for photon users. The FLASH2 photon beamlines and diagnostics are described in [24, 25].

A seeding experiment sFLASH [26], with four variable gap undulators, is installed between the collimation section and the SASE undulators in the FLASH1 beamline. In the FLASH2 beamline, a place for seeding hardware is reserved upstream of the undulators. Investigations of the optimal seeding scheme for FLASH2 are on-going. Initially the FLASH2 operation will start with SASE having similar parameters as FLASH1.

OPERATION STATUS OF FLASH1

After the shutdown to connect the FLASH2 beamline to the FLASH linac, the operation started in August 2013.

A ground settlement of the FLASH1 beamline of up to 10 mm was expected due to the heavy load of the new FLASH2 buildings, including a 6 m deep and 80 m long triangle-shaped space between FLASH1 and FLASH2 buildings, which was filled with some kilotonnes of sand for radiation safety reasons. Due to delays in FLASH2 civil construction, the settlement occurred late, mainly in summer 2013. As a consequence, the final survey and re-alignment of FLASH1 undulators coincided with the commissioning of the linac and caused a significant delay of about one month for beam commissioning. A stable FEL operation was established by end of 2013, including commissioning of the photon beamlines, which had to be re-adjusted as well.

A highlight of the commission phase was the successful increase of the average single FEL pulse energy up to 540 μJ . This is a new record at FLASH, and has been achieved at a photon wavelength of 8.7 nm. A new electron beam optics [27, 28], allowing simultaneous operation of FLASH1 and FLASH2, has been implemented. Substantial amount of time was used also to commission the new LLRF system, new magnet controls, and upgrades of the timing system.

The 5th user period started in February 2014. As in the previous user periods, the photon experiments have requested a large variety of beam parameters. Experiments requiring 400 pulses per train with 1 μs spacing at the wavelength of 7.8 nm, 50 pulses per train with 5 μs spacing at 42 nm, and a single pulse in the water window at 4.3 nm are examples of the diversity of beam parameters realized in the last months. In addition many experiments require photon pulses shorter than 50 fs (fwhm) or with a small bandwidth ($<1\%$). Arrival time stabilization to the 20 to 40 fs level is also often requested.

A vacuum leak on the RF-window of the RF-gun was detected in March 2014, and the window was promptly exchanged at the next opportunity in April. Due the required conditioning of the RF-window, one user experiment had to be postponed. Nevertheless, the the user run could be continued with shorter RF-pulses to serve users with a few bunches per train only. During the following weeks, the RF-gun pulse length has been slowly increased, and a length of 500 μs has been re-established. The user operation continued in June 2014 according to the schedule with a stable RF-gun operation.

COMMISSIONING STATUS OF FLASH2

The construction of the building hosting the new FLASH2 undulator line started in autumn 2011. The civil construction took significantly longer than expected and was finished only early summer 2013, almost half a year later than originally scheduled. The construction of the new experimental hall has been finalized in spring 2014.



Figure 3: FLASH2 undulator beamline with twelve variable gap undulators.

The installation of the FLASH2 extraction beamline and its connection to the FLASH linac took place in spring and early summer 2013. The mounting of the FLASH2 electron beamline, including the undulators (see Fig. 3), was finished in January 2014. Devices for basic photon diagnostics, such as an MCP detector to measure the photon pulse energy, a Ce:YAG crystal for beam profile and position measurements,

and a wavelength spectrometer, have also been installed already. Technical commissioning of FLASH2 components, for example, magnet power supplies and variable gap undulators, started early 2014. The control and timing systems have been upgraded to allow simultaneous operation of FLASH1 and FLASH2.

After connecting the FLASH2 personnel interlock system, the official permission for FLASH2 beam operation was given February 7, 2014. Due to the FLASH1 user operation, dedicated beam time for FLASH2 had been restricted to a few days only until simultaneous operation was established. The first electron beam was transported into the FLASH2 extraction beamline on March 4, 2014, and beam transport up to the dump was achieved on May 23, 2014.

Figure 4 shows the FLASH1 and FLASH2 electron beams on a screen at the septum entrance; the upper one is the kicked beam to be deflected to FLASH2, the lower one the beam going straight to FLASH1.

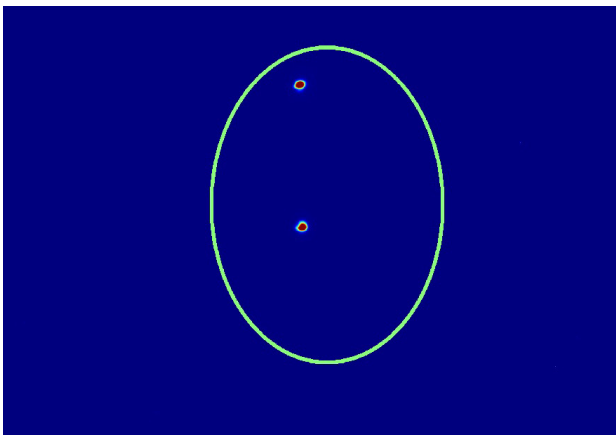


Figure 4: FLASH1 (lower) and FLASH2 (upper) electron beams on a screen at the septum entrance. The beam separation is 16 mm.

End of May 2014, the simultaneous operation of FLASH1 and FLASH2 has been established, and starting with June, the FLASH2 beam commissioning has taken place, whenever possible, parallel to the FLASH1 user operation. This increases significantly the time available for FLASH2 beam commissioning.

The on-going commissioning is mainly related to the electron beam diagnostics and to the beam loss and machine protection systems. The setting up of the beam optics to provide a stable, loss-free beam transport is under way [29]. In order to avoid radiation damage on the permanent undulator magnets, the first beam operation has been carried out with open undulator gaps. First lasing is expected soon.

OPERATION OF TWO UNDULATOR BEAMLINES

The FLASH linac uses superconducting accelerator technology, which allows operation with long RF-pulses, i.e. with long electron bunch trains. The bunch train can be

shared between the two undulator beamlines, giving the possibility to serve simultaneously two photon experiments, both at 10 Hz pulse train repetition rate. Since roughly half of the photon experiments request operation with a few pulses per train only, it is feasible to organize experiments such that both undulator beamlines are efficiently used.

Two separate injector lasers are used in parallel to produce two electron bunch trains within the same RF-pulse with different parameters. The two trains are separated by a gap of some tens of μs (kicker pulse rise time). The number of bunches as well as the bunch spacing can be selected independently for both trains, taking into account the total available RF-pulse length of 800 μs . In addition, the electron bunch charge can be different in the two trains. This feature, together with the flexible LLRF system, which is able to provide in certain limits different accelerating amplitude and phase for the two trains, allows FLASH1 and FLASH2 experiments with different pulse durations. Since the electron bunches are accelerated and compressed by the same linac, the practical feasibility of different parameters is constrained by beam dynamics of the bunch compressors (space charge related collective effects) and the acceptance of the beam optics in terms of beam energy.

FLASH1 has fixed gap undulators, and therefore the electron beam energy of the FLASH linac is defined by the wavelength of the FLASH1 experiment. Thanks to the variable gap undulators, the FLASH2 wavelength can be typically tuned by a factor of 2-3 and hence be adapted, at a fixed electron beam energy, to the requirements of the FLASH2 experiment. In the future, it is planned to exchange the FLASH1 undulators to variable gap ones as well.

During the last months, we have gathered our first experience to operate the FLASH1 and FLASH2 beamlines simultaneously. We have successfully established FLASH2 electron beam operation during FLASH1 photon user experiments. For example in July 2014, FLASH1 delivered a photon beam to a user experiment at 4.3 nm, while the FLASH2 electron beam was simultaneously transported up to the dump and used for commissioning of electron beam diagnostics, without disturbing the FLASH1 operation.

Operation with two injector lasers is well-established and applied routinely. The control and timing systems as well as operation procedures have been upgraded and commissioned. In order to allow smooth simultaneous operation of both beamlines, it is important to set up the FLASH linac at the same time for FLASH1 and FLASH2 operation. This includes, for example, the beam orbit in the common beamline between the kicker and the septum. In the first meters downstream of the septum, the two electron beamlines are very close to each other (Fig. 2), and cross-talk through stray fields of the magnets has to be taken into account as well.

SUMMARY AND OUTLOOK

After connecting the FLASH2 beamline to the FLASH linac, the 5th period of user FEL experiments at FLASH1 started in February 2014, continuing until April 2015.

The FLASH2 beam commissioning started in March 2014 and mainly takes place in parallel to the FLASH1 user operation. First lasing and SASE operation is expected soon. The first FLASH2 pilot photon experiments are expected in 2015, and regular user operation in 2016.

With FLASH2 in operation, the user capacity of FLASH will be significantly increased. The variable gap undulators will ease photon wavelength changes in FLASH2, and, together with two injector lasers and the flexible LLRF system, allow parallel operation of FLASH1 and FLASH2 with to a certain extent independent parameters.

ACKNOWLEDGMENT

We like to thank all colleagues participating in the successful operation, meticulous maintenance, and continuous upgrading of the FLASH facility. Special thanks are due to the DESY technical groups for their formidable effort to accomplish the FLASH II Project and to commission the new beamline. We appreciate the crucial contribution of Sven Ackermann, Matthias Scholz, and Johann Zemella to the first FLASH2 beam operation.

REFERENCES

- [1] W. Ackermann *et al.*, “Operation of a free-electron laser from the extreme ultraviolet to the water window”, *Nature Photonics* **1**, 336 (2007).
- [2] K. Tiedtke *et al.*, “The soft x-ray free-electron laser FLASH at DESY: beamlines, diagnostics and end-stations”, *New J. Phys.* **11**, 023029 (2009).
- [3] K. Honkavaara *et al.*, “Status of the FLASH Facility”, in *Proc. 35th Free-Electron Laser Conf.*, New York, 2013, pp. 550-553.
- [4] M. Vogt *et al.*, “Status of the Free Electron Laser User Facility FLASH”, in *Proc. 5th Int. Particle Accelerator Conf.*, Dresden, 2014, pp. 938-940.
- [5] D. A. Edwards, Ed., “TESLA Test Facility Linac, Design Report”, DESY, Hamburg, Rep. TESLA-1995-01, March 1995.
- [6] R. Brinkmann *et al.*, Eds., “TESLA Technical Design Report. Part II: The Accelerator”, DESY, Hamburg, Rep. DESY-01-011, March 2001.
- [7] J. Rossbach, “A VUV free electron laser at the TESLA test facility at DESY”, *Nucl. Instrum. Meth. A* **375**, 269 (1996).
- [8] J. Andruszkow *et al.*, “First Observation of Self-Amplified Spontaneous Emission in a Free-Electron Laser at 109 nm Wavelength”, *Phys. Rev. Lett.* **85**, 3825 (2000).
- [9] V. Ayvazyan *et al.*, “Generation of GW Radiation Pulses from a VUV Free-Electron Laser Operating in the Femtosecond Regime”, *Phys. Rev. Lett.* **88**, 104802 (2002).
- [10] V. Ayvazyan *et al.*, “A new powerful source for coherent VUV radiation: Demonstration of exponential growth and saturation at the TTF free-electron laser”, *Eur. Phys. J. D* **20**, 149 (2002).
- [11] V. Ayvazyan *et al.*, “First operation of a free-electron laser generating GW power radiation at 32 nm wavelength”, *Eur. Phys. J. D* **37**, 297 (2006).
- [12] J. Rossbach, “First Lasing below 7 nm Wavelength at FLASH/DESY, Hamburg”, in *Proc. 30th Int. Free-Electron Laser Conf.*, Gyeongju, 2008, pp. 1-3.
- [13] S. Schreiber *et al.*, “Operation of FLASH at 6.5 nm Wavelength”, in *Proc. 11th European Particle Accelerator Conf.*, Genoa, 2008, pp. 133-135.
- [14] S. Schreiber *et al.*, “Status of the FEL User Facility FLASH”, in *Proc. 33rd Int. Free-Electron Laser Conf.*, Shanghai, 2011, pp. 267-270.
- [15] S. Schreiber *et al.*, “First Lasing in the Water Window with 4.1 nm at FLASH”, in *Proc. 33rd Free-Electron Laser Conf.*, Shanghai, 2011, pp. 164-165.
- [16] I. Will *et al.*, “Photoinjector drive laser of the FLASH FEL”, *Optics Express* **19**, 23770 (2011).
- [17] S. Schreiber *et al.*, “Upgrades of the Photoinjector Laser System at FLASH”, in *Proc. 34th Int. Free-Electron Laser Conf.*, Nara, 2012, pp. 385-388.
- [18] J. Roensch-Schulenburg *et al.*, “Operation of FLASH with Short SASE-FEL Radiation Pulses”, in *These Proceedings: Proc. 36th Int. Free-Electron Laser Conf.*, Basel, 2014, TUB04.
- [19] S. Schreiber *et al.*, “Photocathodes at FLASH”, in *Proc. 3rd Int. Particle Accelerator Conf.*, New Orleans, 2012, USA, pp. 625-627.
- [20] S. Schreiber *et al.*, “Status of the FLASH Facility”, in *Proc. 34th Int. Free-Electron Laser Conf.*, Nara, 2012, pp. 37-40.
- [21] MicroTCA® (Micro Telecommunications Computing Architecture) is a trademark of PICMG, MTCA.4 specifications: <http://www.picmg.org>
- [22] C. Schmidt *et al.*, “Performance of the MicroTCA.4 Based LLRF System at FLASH”, in *Proc. 5th Int. Particle Accelerator Conf.*, Dresden, 2014, pp. 2433-2435.
- [23] M. Yan *et al.*, “First Realization and Performance Study of a Single-Shot Longitudinal Bunch Profile Monitor Utilizing a Transverse Deflecting Structure”, in *Proc. 2nd Int. Beam Instrumentation Conf.*, Oxford, 2013, pp. 456-459.
- [24] K. Tiedtke *et al.*, “Challenges for Detection of Highly Intense FEL Radiation: Photon Beam Diagnostics at FLASH1 and FLASH2”, in *Proc. 35th Free-Electron Laser Conf.*, New York, 2013, pp. 417-420.
- [25] E. Ploenjes *et al.*, “FLASH2 Beamline and Photon Diagnostics Concepts”, in *Proc. 35th Free-Electron Laser Conf.*, New York, 2013, pp. 614-617.
- [26] S. Ackermann *et al.*, “Generation of Coherent 19- and 38-nm Radiation at a Free-Electron Laser Directly Seeded at 38 nm”, *Phys. Rev. Lett.* **111**, 114801 (2013).
- [27] M. Scholz *et al.*, “Extraction Arc for FLASH II”, in *Proc. 34th Int. Free-Electron Laser Conf.*, Nara, 2012, pp. 305-307.
- [28] J. Zemella *et al.*, “Measurements of the Optical Functions at FLASH”, in *Proc. 5th Int. Particle Accelerator Conf.*, Dresden, 2014, pp. 1141-1143.
- [29] M. Scholz *et al.*, “Optics Measurements at FLASH2”, in *These Proceedings: Proc. 36th Int. Free-Electron Laser Conf.*, Basel, 2014, THP073.

THz STREAK CAMERA FOR FEL TEMPORAL DIAGNOSTICS: CONCEPTS AND CONSIDERATIONS

Pavle Juranić, Rafael Abela, Rasmus Ischebeck, Luc Patthey, Claude Pradervand, Milan Radović,
Volker Schlott, Andrey Stepanov, PSI, Villigen PSI, Switzerland
Ishkhan Gorgisyan, Christoph P. Hauri, Leonid Rivkin,
PSI, Villigen PSI, Switzerland, and EPFL, Lausanne, Switzerland
Balazs Monoszlai, PSI, Villigen PSI, Switzerland, and University of Pécs, Hungary
Rosen Ivanov, Peter Peier, DESY, Hamburg, Germany
Jia Liu, XFEL.EU, Hamburg, Germany
Kanade Ogawa, Shigeki Owada, Tadashi Togashi, Makina Yabashi,
RIKEN Spring-8 Center, Sayo-cho, Sayo-gun, Hyogo, Japan

Abstract

The accurate measurement of the arrival time of a hard x-ray free electron laser (FEL) pulse with respect to a laser is of utmost importance for pump-probe experiments proposed or carried out at FEL facilities around the world. This paper presents the latest device to meet this challenge, a THz streak camera, and discusses the challenges in its design, use, and analysis of results.

INTRODUCTION

Laser pump, x-ray probe experiments performed at FEL facilities around the world [1, 2, 3, 4, 5] typically want to use short pulse length and intense coherent x-ray radiation to perform experiments with sub-picosecond time resolution. As they go towards improved temporal resolutions, the experiments require accurate measurements of the arrival times of the FEL pulses relative to a laser pump on the sample they are probing. This measurement must also be non-invasive, allowing the experimenters the maximum use of the X-ray beam for their work rather than for diagnostics.

Several methods have been proposed and implemented in the past to meet this diagnostics challenge: transmission/reflectivity spatial and spectral encoding used for soft and hard x-rays at FLASH, SACLA, and LCLS [6, 7, 8, 9], the THz streak camera for soft x-rays at FLASH [10, 11] and other methods [12, 13, 14]. These methods all have their advantages and drawbacks, and the only one that has been attempted for hard x-ray arrival time measurement is the spatial/spectral encoding setup, which has an arrival time accuracy of on the order of 10 fs RMS [6, 9]. The potentially more accurate THz streak camera has not been attempted for use at hard x-ray sources due to the small photoionization cross-section of the gas target and the difficulties in differentiating jitters in the photon energy of the FEL beam from an arrival time signal of the FEL beam by electron spectroscopy. The Photon Arrival and Length Monitor (PALM) prototype chamber [15] developed at the Paul Scherrer Institute (PSI) for the future SwissFEL facility mitigates both of these problems, measuring the pulse length, and the arrival times of hard x-ray FEL pulses relative to a THz pulse and the laser it is generated from.

CONCEPTS

The concept of the THz streak camera has been explained in the past in literature [16, 17, 18], and has shown itself capable of measuring pulse lengths of high-harmonic-generation (HHG) soft x-rays in table-top laser laboratories. The device can also be used to measure the arrival time of the x-ray relative to the THz pulse.

The THz streak camera uses a gas that is photoionized by the x-ray light as an electron emitter. The electrons are then subject to a time-varying vector potential generated by co-propagating THz radiation, the duration of which is longer than the pulse length of the x-ray pulse. A shift in the arrival time of the x-ray pulse translates to a shift in the kinetic energy gained by the electrons in the vector potential. The final kinetic energy of the photoelectrons K_f streaked by the vector potential U_p is

$$K_f = K_0 + 2U_p \sin^2(\varphi_0) \pm \sqrt{8K_0 U_p} \sin(\varphi_0) \quad (1)$$

where K_0 is the initial kinetic energy of the electrons at the time of ionization, φ_0 is the phase of the vector potential at the time of the ionization, and

$$U_p = \frac{e^2 E_{THz}^2(t)}{4m_e \omega_{THz}^2} \quad (2)$$

$E_{THz}(t)$ is the (sinusoidal) THz electric field, e is the electron charge, m_e is the mass of the electron, and ω_{THz} is the frequency of the THz f in radians/s.

The time delay between the external THz field and the FEL pulse was controlled by a translation stage, and time of flight of the electrons under different time delays were recorded, forming a two dimensional (2D) streaked spectrogram. As shown in Eq. 1, the shape of the spectrogram is determined by the THz frequency, initial electron kinetic energy and the vector potential. The time-to-energy map can be extracted by recording the center of mass (COM) kinetic energy of each time delay and shot-to-shot arrival time of the FEL pulses related to the THz pulse are retrieved by recording the single-shot electron kinetic energy when the stage is set at the middle of the time-to-energy slope. The pulse lengths are measured by looking at the change in spectral width of

the kinetic energy of the electrons. A longer pulse will give a longer width, as described in [10, 11].

Since x-ray photoionization cross sections decrease as the x-ray photon energy increases [19], fewer electrons are thus expected to generate from single-shot ionization of the noble gas atoms for hard x-rays. However, the PALM setup counterbalanced this effect by using gas from a supersonic pulsed valve [20] that is synchronized to the FEL pulse that increases the sample density in the interaction region, while in the other hand decrease the gas load in the streaking chamber.

SETUP CONSIDERATIONS

The flight path of electrons, and especially low-kinetic-energy electrons, can be affected by magnetic fields, yielding flight times inconsistent with their real kinetic energy. To counteract this issue, the chamber was built out of μ -metal and described in [15]. As schematically shown in Figure 1, two ETF20 Kaesdorf electron time-of-flight (eTOF) spectrometers measured the strength of the streak induced on the photoelectrons by the vector potential of the THz field. This tandem measurement is used to eliminate the photon energy jitter common at FELs from the observed spectra. The pressure near the sensor element of the eTOFs, the multi-channel plates (MCPs) should not be on the order of 10^{-6} mbar to prevent sparking and damage to the MCPs. Small pumps are attached to the eTOFs to keep the drift tube under low pressure despite a higher gas load in the chamber. Despite this precaution, the pressure in the main chamber is limited by the tolerance of the MCPs, and should always be checked before the device is started.

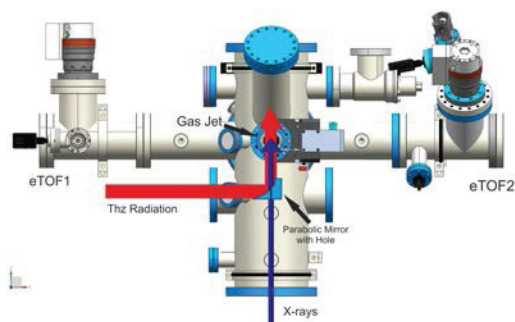


Figure 1: Schematic drawing of the PALM prototype chamber.

The two e-TOF spectrometers, positioned opposite each other, measure exact opposite streaking effects, but measure the same electron kinetic energy shift due to photon energy jitter. The resolution of the eTOFs over the dynamic range of the measurement is controlled by adjusting their drift tube and electrostatic lens settings. By subtracting the average of the two mean kinetic energies from each individual measurement, the photon energy jitter contribution is eliminated, leaving only the clean measurement of the FEL relative pulse arrival time.

The Xe gas is injected into the interaction region by a LaserLab Amsterdam piezo cantilever valve [21] synchronously with the FEL repetition rate. The valve has a 40° conical nozzle with a diameter of $150\ \mu\text{m}$ with a backing pressure of about 3.5 bar above atmospheric pressure. The valve was placed 10 to 12 mm away from the center of the interaction region to deliver the largest amount of gas in the smallest volume possible while not interfering with the flight path of either the THz beam or the FEL pulse. The estimated diameter of the gas target in the interaction region was between 1.2 and 1.5 mm. The average pressure in the chamber while the valve was working was 1.1×10^{-5} mbar, with a background pressure of about 3×10^{-7} mbar.

The THz radiation has thus far been generated in a LiNbO_3 crystal via the tilted pulse-front pumping method [22] optimized for a high-energy pump [23] by 800 nm laser 5-10 mJ system outside of the chamber and then introduced into vacuum through a z-cut quartz window. The laser intensity should be monitored on a shot-to-shot basis to compensate for the change in the THz field's power in the data analysis. A three inch parabolic mirror focuses the THz radiation 170 mm downstream, 20 mm behind the interaction region to avoid Gouy phase shift [24] effects across the diameter of the gas target. The unfocused x-ray FEL pulses are transmitted through the 3-5 mm hole in the middle of the parabolic mirror and co-propagate with the THz field. High humidity or temperature variations can have an effect on the laser power or the strength of the THz field, so utmost care should be taken to stabilize both in the room the PALM is placed in. A larger streaking slope gives better results and time resolution.

The setup of the device requires a calibration of the eTOFs to find an accurate electron flight-time to kinetic energy scale. This is done by either scanning the photon energy of the FEL beam over several hundred electron volts, a hard and time-consuming process for the operators, or by tweaking the retardation voltage settings on the eTOFs to simulate an effective lower photon energy by directly reducing the kinetic energy of the electrons in the flight tube. The latter method works best for high kinetic energy electrons (>1000 eV) so that the flight time from the interaction region to the entrance of the eTOF is as short as possible. Lower energies have larger variations in flight times over this field-free region, and would not be well-simulated by altering only the flight time in the flight tube.

The calibration scan should also record the measured spectral width as a function of retarded energy. The eTOF lensing and retardation systems are usually optimized around one energy—large variations from this sweet spot cause de-focusing effects from the electrostatic lenses, yielding larger measured electron kinetic energy spectral widths than what the FEL delivered. This effect can be corrected for by measuring the response of the spectral width as a function of electron kinetic energy for a single photon energy, and then accounted for in analysis later. One such scan is shown in Figure 2.

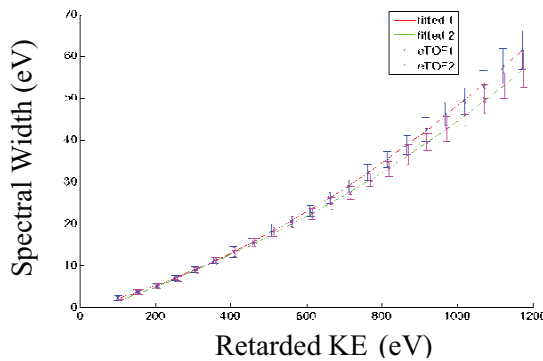


Figure 2: ETOF spectral width scan for 7 keV with a monochromator done at SACLA.

Further tests need to be done to check the accuracy of measurement of the mean kinetic energy of a peak, performed by having to eTOFs measure the same beam at the same time without the THz streak and comparing the variations of the kinetic energies they measure. This measurement is typically accurate to about 0.3-1% of the retarded kinetic energy of the electrons.

ANALYSIS CONSIDERATIONS

There are several effects that have to be accounted for when evaluating the data from a THz streak camera measurement. Some of the most important ones are listed below, along with some suggestions mitigate them. Spectral width drift and jitter is the tendency of the FEL beam to change the width of its spectrum with time or on a shot-to-shot basis. If a calibration measurement was done with one spectral width, and the beam changes this width, the final evaluation for pulse length can be erroneous. The addition of another e-TOF that would measure the non-streaked beam would rectify this problem, seeing any drifts or jitters in the on a shot-by-shot basis.

Space charge is generated in the interaction region as the thousands or millions of atoms are photoionized by the FEL beam. The effect is most easily observed for electrons of low kinetic energies, where even a small space charge can retard the flight of an electron to a measurable degree. High energy electrons, however, are much less sensitive to the space-charge effect, and the few-eV space charge contribution to the streaking strength of a multi-keV electron is negligible.

A large number of electrons flying together through the drift tube of the eTOF have mutual Coulomb repulsions which could distort the original imprint the FEL pulse created at the time of photoionization. This can cause the perceived spectral width to be larger than the real one. However, simulations done with SimION have shown that the contribution from such repulsions for 1000-2000 high-KE electrons flying simultaneously through the drift tube, a number that is typical for a single peak observed by the eTOFs, is small, on the level of a percent or less of the spectral width. The effect is noticeable for low kinetic energy electrons (few eV-10s of eV) since they have more time to separate themselves in the drift tube.

CONCLUSIONS

The PSI-developed PALM device will measure the arrival time and pulse length of hard x-rays at SwissFEL. Because it is a gas-based measurement method, it is also less intrusive than most other methods and allows for the use of the FEL pulse for experiments further downstream with a minimal loss of intensity or wavefront distortion.

REFERENCES

- [1] W. Ackermann et. al., "Operation of a free-electron laser from the extreme ultraviolet to the water window," *Nature Photonics*, vol. 1, p. 336, 2007.
- [2] P. Emma et. al., "First lasing and operation of an angstrom-wavelength free-electron laser," *Nature Photon*, vol. 4, p. 641, 2010.
- [3] D. Pile et. al., "X-rays first light from SACLA," *Nature Photon*, vol. 5, p. 436, 2011.
- [4] E. Allaria et. al., "The FERMI@Elettra free-electron-laser source for coherent x-ray physics: photon properties, beam transport system and applications," *New J. Phys*, vol. 12, p. 075002, 2010.
- [5] P. Oberta et. al., "The SwissFEL facility and its preliminary optics beamline layout," *Proceedings of SPIE*, vol. 8079, p. 807805, 2011.
- [6] M. Bionta et. al., "Spectral encoding of x-ray/optical relative delay," *Optics Express*, vol. 19, p. 21855, 2011.
- [7] M. Beye et. al., "X-ray pulse preserving single-shot optical cross-correlation method for improved experimental temporal resolution," *Appl. Phys. Lett.*, vol. 100, p. 121108, 2012.
- [8] O. Krupin et. al., "Temporal cross-correlation of x-ray free electron and optical lasers using soft x-ray pulse induced transient reflectivity," *Optics Express*, vol. 20, p. 11396, 2012.
- [9] M. Harmand et. al., "Achieving few-femto second time-sorting at hard X-ray free-electron lasers," *Nature Photon.*, vol. 7, pp. 215-218, 2013.
- [10] I. Grguras et. al., "Ultrafast X-ray pulse characterization at free electron lasers," *Nature Photon*, vol. 6, p. 852, 2012.
- [11] U. Fröhling et. al., "Single-Shot Terahertz-Field-Driven X-ray Streak Camera," *Nature Photon*, vol. 3, p. 353, 2009.
- [12] F. Tavella et. al., "Few-femtosecond timing at fourth-generation X-ray light sources," *Nature Photon*, vol. 5, p. 162, 2011.
- [13] S. Duesterer et. al., "Femtosecond x-ray pulse length characterization at the Linac Coherent Light Source free-electron laser," *New J. Phys*, vol. 13, p. 093024, 2011.
- [14] R. Riedel et. al., "Single-shot pulse duration monitor for extreme ultraviolet and X-ray free electron lasers," *Nature Comm.*, vol. 4, p. 1731, 2013.

- [15] P. Juranic et. al., "A scheme for a shot-to-shot, femtosecond-resolved pulse length and arrival time measurement of free electron laser x-ray pulses that overcomes the time jitter problem between the FEL and the laser," *JINST*, vol. 9, p. P03006, 2014.
- [16] M. Hentschel et. al., "Attosecond Metrology," *Nature*, vol. 414, p. 509, 2001.
- [17] M. Drescher et. al., "X-ray pulses approaching the attosecond frontier," *Science*, vol. 291, p. 1923, 2001.
- [18] M. Uiberecker et. al., "Attosecond Metrology with Controlled Light Waveforms," *Laser Physics*, vol. 15, p. 195, 2005.
- [19] B. L. Henke, E. M. Gullikson and J. C. Davis, "X-ray interactions: photoabsorption, scattering, transmission, and reflection at $E=50\text{-}30,000$ eV, $Z=1\text{-}92$," *At. Data Nucl. Data Tables*, vol. 54, pp. 181-342, 1993.
- [20] G. N. Makarov and A. N. Petin, "Investigation of Atomic and Molecular Clustering in a Pulsed-Gas Dynamic Jet with a Pyroelectric Detector," *Journal of Experimental and Theoretical Physics*, vol. 107, pp. 725-733, 2008.
- [21] D. Irimia et. al., "A short pulse (7msFWHM) and high repetition rate (dc-5kHz) cantilever piezovalve for pulsed atomic and molecular beams," *Rev. Sci. Instr.*, vol. 80, p. 113303, 2009.
- [22] J. Hebling et. al., "Velocity matching by pulse front tilting for large area THz-pulse generation," *Opt. Express*, vol. 10, pp. 1161-1166, 2002.
- [23] A. G. Stepanov et. al., "Mobile source of high-energy single-cycle terahertz pulses," *Appl. Phys. B*, vol. 101, pp. 11-14, 2010.
- [24] A. B. Ruffin et. al., "Direct Observation of the Gouy Phase Shift with Single-Cycle Terahertz Pulses," *Phys. Rev. Lett.*, vol. 17, p. 3410, 1999.

EXPERIMENTAL CHARACTERIZATION OF FEL POLARIZATION CONTROL WITH CROSS POLARIZED UNDULATORS

E. Ferrari^{1,2}, E. Allaria¹, J. Buck³, G. De Ninno^{1,4}, B. Diviacco¹, D. Gauthier^{1,4}, L. Giannessi^{1,5}, Z. Huang⁶, M. Ilchen^{3,7}, G. Lambert⁸, A.A. Lutman⁶, B. Mahieu⁸, G. Penco¹, C. Spezzani¹, J. Viefhaus⁹

¹Elettra – Sincrotrone Trieste S.C.p.A, Basovizza, Italy

²Università degli Studi di Trieste, Dipartimento di Fisica, Trieste, Italy

³European XFEL, Hamburg, Germany

⁴Laboratory of Quantum Optics, University of Nova Gorica, Ajdovscina, Slovenia

⁵ENEA C.R. Frascati, Frascati (Roma), Italy

⁶SLAC National Accelerator Laboratory, Menlo Park, CA, USA

⁷Stanford PULSE Institute, Menlo Park, CA, USA

⁸Laboratoire d'Optique Appliquée, ENSTA, Palaiseau, France

⁹DESY, FS-PE, Hamburg, Germany

Abstract

Polarization control of the coherent radiation is becoming an important feature of recent and future short wavelength free electron laser facilities. While polarization tuning can be achieved taking advantage of specially designed undulators, a scheme based on two consecutive undulators emitting orthogonally polarized fields has also been proposed. Developed initially in synchrotron radiation sources, crossed polarized undulator schemes could benefit from the coherent emission that characterizes FELs. In this work we report the first detailed experimental characterization of the polarization properties of an FEL operated with crossed polarized undulators in the Soft-X-Rays. Aspects concerning the average degree of polarization and the shot to shot stability are investigated together with a comparison of the performance of various schemes to control and switch the polarization.

INTRODUCTION

FEL sources naturally produce radiation with precise polarization states as they use undulators. The polarization of light is in fact directly correlated to the symmetry of the electron trajectory in the magnetic device where radiation and electrons couple in the FEL process. Self Amplified Spontaneous Emission (SASE) FELs, which require several tens of meters of undulators, normally use linearly polarized undulators. The choice was mainly driven by the users' request. Moreover, linear undulators ensure high field quality and reduced cost. Otherwise, if different states of polarization are to be provided, elliptical polarized undulators [1,2] have been demonstrated to be suitable for both low and high gain FELs in the VUV and XUV wavelength range [3]. These devices implement a variable arrangement of the magnetic poles such that the magnetic field can assume a circular, elliptical or planar symmetry and so does the emitted radiation. Unfortunately they are not capable of fast variations of the polarization state as requested, for

example, by circular dichroism experiments [4].

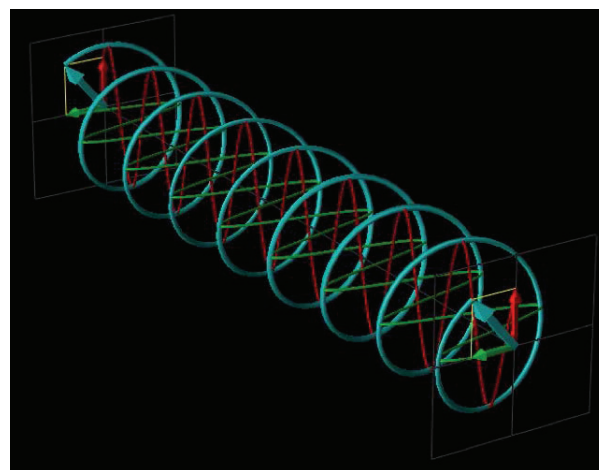


Figure 1: Crossed undulator scheme. One undulator is emitting horizontal polarization (green curve) while the other vertical polarization (red curve) to produce circularly polarized light (blue curve). Image obtained with [5].

CROSSED POLARIZED UNDULATORS

Other possible approaches for fully controlling the output polarization of the emitted radiation have been studied. One is the crossed undulator scheme [6,7].

Synchrotron Sources

Originally demonstrated on synchrotron light sources, the scheme relies on two undulators emitting orthogonally polarized light, e.g., one linear horizontal and one linear vertical undulator, see Figure 1. A suitable phase shifter separates the undulators in order to carefully control the relative phase between the two emitted waves. In this way the scheme is capable of producing linearly polarized light with an arbitrary direction as well as elliptically and circularly polarized light with arbitrary chirality.

In general the source used for this kind of devices must have a high degree of coherence and narrow bandwidth spectrum, so that the two electro-magnetic waves emitted by the undulators can interfere between each other in correspondence of the sample to be studied. In the case of synchrotron light, the bandwidth is too large, so the scheme needs a monochromator to be effective. Still, due to the limited coherence, the maximum degree of polarization that has been demonstrated is in the 40% range [8]. Nevertheless the light has been successfully used to perform experiments [9], demonstrating the viability of the method for full polarization control.

FEL Sources

FEL sources, characterized by a narrow bandwidth emission and high degree of coherence, are most suitable for the crossed undulator setup.

A number of studies have been carried out for SASE, based on FLASH, XFEL [10] and LCLS [11,12] setups. While in the case of synchrotrons the intensity emitted by the two undulators has the same intensity, for FELs the gain determines a possible unbalance between the two undulator emissions. For overcoming this difficulty the scheme can be implemented using a first undulator that acts as a buncher for the electrons that, just before reaching saturation, are injected in the crossed undulators emitting the same intensity for both undulators. In the case of SASE the maximum theoretical limit for the degree of polarization of the output radiation is thought to be in the 80 to 90% range, mainly limited by the spiky structure of the SASE pulse [10-12].

A seeded FEL can therefore be the right choice for the crossed undulator scheme for its higher degree of temporal coherence, inherited by the external seed source used. A theoretical maximum degree of polarization in this case can exceed the 90% [13].

The scheme has been successfully demonstrated at the SDUV FEL [14], using a bunched beam and two orthogonal undulators emitting visible light at 523 nm,

corresponding to the second harmonic of the external 1047-nm seed. The balancing of the emission from the two undulators has been achieved by using short undulators in order to have a nearly rigid bunching in both of them.

CROSSED POLARIZED UNDULATORS AT FERMI

Despite of the aforementioned demonstration [14], the demonstration of the scheme in presence of FEL gain in the VUV spectral range was still missing up to now. In the following we provide a description of the measurements carried on at FERMI FEL facility [15], on the FEL-1 beamline.

FERMI is a seeded FEL based on the High-Gain harmonic generation (HGHG) scheme [16]. It features two FEL beamlines, a single stage cascade FEL-1 [17] and a double-stage for FEL-2 [18]. The necessary electron beam for the production of the photons is provided by a normal conducting linac [19].

All the presented results were obtained with FEL-1 tuned at the 8th harmonic of the 260 nm Ti:Sa seed laser, corresponding to HGHG FEL emission at 32 nm. Contrary to the visible spectral range, the measurement of the polarization of light in the VUV and X-ray range is an experiment in itself [20].

FERMI is based on variable polarization APPLE-II type radiator undulators [17]. The polarization of the FEL radiation can be linear horizontal, linear vertical, circular left and right and can be changed arbitrarily. Phase shifters are installed in between each undulator and are used to modify the phase variation of the light emitted by each module.

These features open up the possibility of different implementations of the crossed undulator scheme. We can in fact superimpose a horizontal linear polarization with a vertical linear polarization, in order to produce circular polarization with different chirality and linear polarization

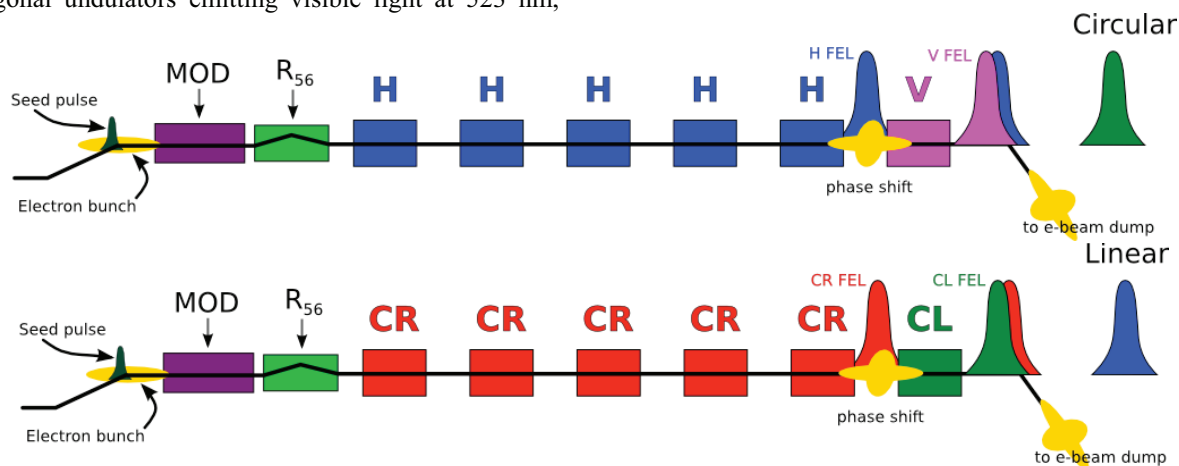


Figure 2: Two different ways to achieve the crossed undulator scheme at FERMI. By taking advantage of the variable polarization undulators, the crossed polarization scheme can be implemented with linear horizontal and linear vertical polarization in order to produce circular or linear polarization with variable direction (top). It is also possible to couple circular right and circular left polarized light to produce linearly polarized light with an arbitrary direction of polarization (bottom).

at an arbitrary direction of the polarization angle depending on the phase shift in between the orthogonal undulators, see Figure 2 (top panel).

Another possibility is to implement the crossed polarization scheme by superimposing two circular polarized emissions with opposed chirality to produce linearly polarized light with arbitrary polarization angle, as shown in Figure 2 (bottom panel).

EXPERIMENTAL DESCRIPTION

During a dedicated beam time, different polarimeters have been installed and used to characterize the radiation produced by FERMI in the different pure polarization states. In all the cases a degree of polarization up to 99% has been measured at different wavelengths [21]. The machine was then tuned to explore the crossed undulator scheme. One of the concerns for the scheme is its stability from one shot to another, so a shot-to-shot diagnostics was needed.

e-TOF Polarimeter

The only polarimeter capable of characterizing the polarization state of the radiation on a shot-to-shot basis is the *e*-TOF polarimeter [20]. The device uses angle-resolved electron spectroscopy to determine the degree of linear polarization of the incident light. It is composed of an array of 16 time-of-flight electron spectrometers arranged in a circular symmetry with respect to the photon beam axis.

A 3D rendering of the device is shown in Figure 3. It is capable of detecting the degree of linear polarization as well as its direction, by analysing the angular distribution of electrons photoemitted by a rare gas injected in the centre of the device.

The circular polarization signal is instead indistinguishable from the unpolarized one, but it can be inferred by assuming the source to be fully polarized and subtracting in quadrature the measured degree of linear polarization.

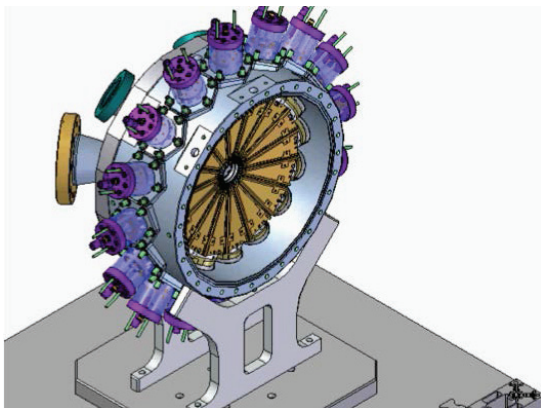


Figure 3: 3D rendering of the *e*-TOF polarimeter used for the shot-to-shot measurements.

Balancing The Intensities in Presence of Gain

As already mentioned, a key point for obtaining a high degree of polarization in the case of the cross polarized undulators is balancing the intensity of the two sources. This is critical not only to avoid the production of elliptically polarized light, which in principle can be compensated by a proper tuning of the phase shifter between the two sources, but also because unbalanced sources can lead to a degradation of the maximum polarization degree obtainable.

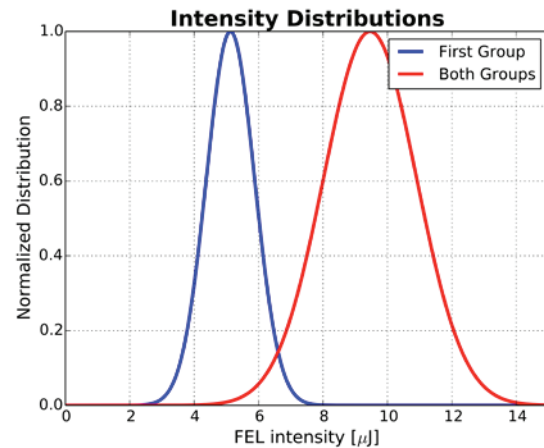


Figure 4: Distribution of the FEL pulse intensities for the first group of undulators (blue curve) and when both groups are emitting radiation (red curve).

While in the case of SDUV-FEL [14] the emission was balanced by using short undulators, so that the FEL gain was not playing any role, in the case of FERMI we wanted to exploit if the balancing of the two crossed sources was possible. This has been achieved by properly tuning the seed laser intensity and dispersive section strength in order to have that the first group of undulators (radiators 1-5 in Figure 2) emits the same FEL energy per pulse as the last undulator alone.

The balancing of the two sources can be fast checked during the experiment either via a gain curve scan or just by recording the intensity distribution with the last undulator tuned and detuned. In Figure 4 the emitted intensities per FEL pulse are reported in the case of all the undulator tuned (red curve) and for the last undulator detuned (blue curve). One can notice that the two groups of undulators are emitting $\sim 5 \mu\text{J}$ pulse energy each, for a total emission of $10 \mu\text{J}$.

EXPERIMENTAL RESULTS

In the following the data acquired for the circular left and circular right crossed polarization scheme are presented. This configuration has been chosen in order to take full advantage of the *e*-TOF polarimeter characteristics, in particular its sensitivity to linear polarization. In the circular left plus circular right scheme, in fact, the output polarization should be linearly polarized, with arbitrary direction of the polarization direction depending on the phase shifter setting. The

machine was tuned as described above in order to have the two undulators emitting similar intensities. The data have been acquired via the FERMI control system and analysed using DART [22].

Direction of Polarization

In Figure 5 the measured direction of the linear polarization, as a function of the shot number (top panel) and the corresponding statistical histogram (bottom panel) are reported in case of zero phase between the two orthogonally polarized sources. One can see that the direction of the linear polarization is compatible with horizontally polarized light, as expected. The rms of the distribution is instead a factor 2 to 3 larger than the one found for the pure horizontal polarization state, cfr. [21]. The obtained result is probably due to shot-to-shot variations of the balance between the intensity of the two sources.

Degree of Linear Polarization

In Figure 6 the degree of linear polarization as a function of the shot number (top panel) and the corresponding statistical histogram (bottom panel) is reported. The rms of the distribution has a value compatible with what found in the pure polarization case, cfr [21], showing that the crossed undulator scheme can be stable enough for performing experiments. The average degree of linear polarization has been found to be ~65%, lower than what expected and reported in [14].

The result can be explained by considering the fact that each of the two crossed polarized sources is diverging due to propagation effects. In Figure 7 a schematic representation of the propagation from the two undulators (red and blue lines) to the detector is provided. At large distances from the sources, compatible with the position of the detector along the beamline, the wavefronts (represented in black) exhibit different behaviours for the on-axis and off-axis regions.

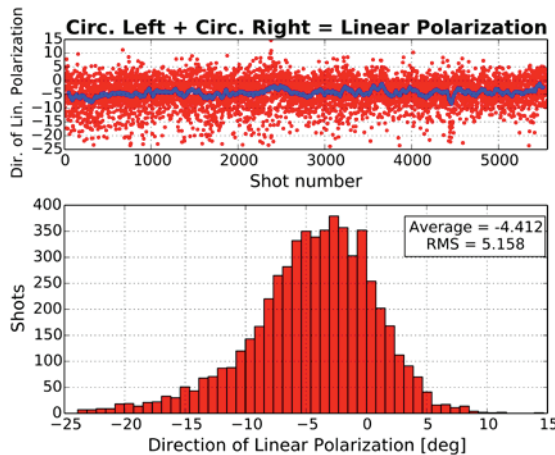


Figure 5: Shot-to-shot distribution of the measured direction of the linear polarization vector in the case of circular left and circular right crossed undulators.

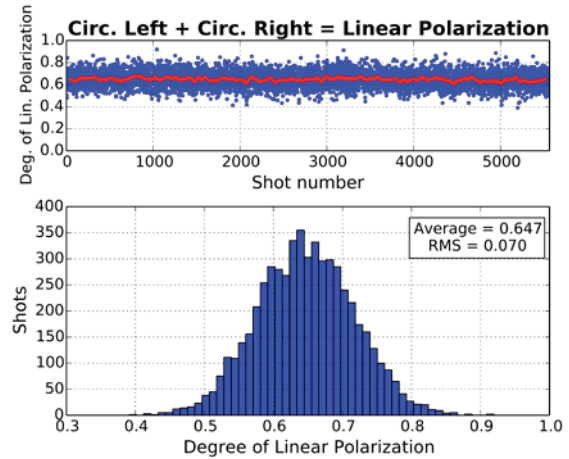


Figure 6: Shot-to-shot statistics of the degree of linear polarization in the case of circular cross polarized undulators that produce linear polarization.

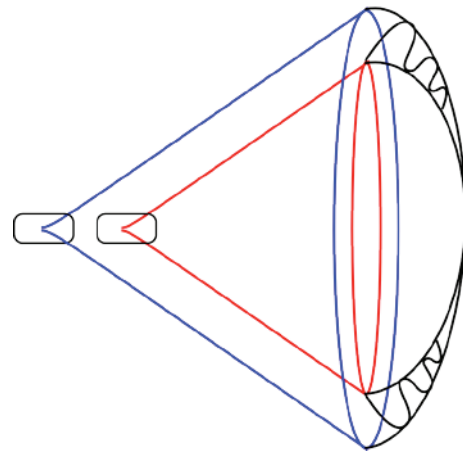


Figure 7: Schematic description of two undulators with different source position (red and blue lines). The wavefronts of the two sources are represented in black.

The on-axis radiation has a smooth phase relation between the two sources, so the resulting field has a definite polarization. Instead, the off-axis emission exhibits rapid phase variations (represented by the oscillating ripples) due to the different divergence of the two sources. This means that, while small regions have a definite polarization state, the latter is changing with the changes of the radiation phase, leading to an overall loss of polarization.

CONCLUSION

Crossed polarized undulator scheme has been demonstrated on a seeded high gain FEL in the VUV. The maximum degree of linear polarization obtained was 65%. Polarization control, both in direction and type, is possible by properly tuning the phase shifter in between the two undulator groups. Other schemes were proposed and have been implemented in order to further improve the degree of polarization obtainable with the crossed undulator scheme [23,24].

A more detailed analysis on the acquired data for the crossed polarized undulator experiment at FERMI is on going [15].

Future activities will focus on studying the possibility of performing fast polarization switching via implementation of an electromagnetic phase shifter.

ACKNOWLEDGMENT

Authors are grateful to the FERMI team for the valuable support received during the experiment for: operating the FEL (FERMI commissioning and laser teams), the installation and alignment of the polarimeter (PADReS), integration of the polarimeter within the FERMI control system (FERMI control team) and assistance with the beamline operation (DIPROI team).

REFERENCES

- [1] S. Sasaki, Nucl. Instrum. Meth. Phys. Res. A 347, 83 (1994).
- [2] A. B. Temnykh, Phys. Rev. ST Accel. Beams 11, 120702, (2008).
- [3] C. Spezzani et. al., Phys. Rev. Lett. 107, 084801 (2011).
- [4] M. H. M. Janssen and I. Powis, Phys. Chem. Chem. Phys. 16, 856 (2014).
- [5] <http://www.enzim.hu/~szia/emanim/emanim.htm>
- [6] K.-J.Kim, Nucl. Instrum. Meth. Phys. Res. A 219, 425 (1984).
- [7] K.-J.Kim, Nucl. Instrum. Meth. Phys. Res. A 445, 329 (2000).
- [8] J. Bahrtdt et. al., Rev. Sci. Instr. 63, 339 (1992).
- [9] R. David et. al., Nucl. Instrum. Meth. Phys. Res. A 343, 650 (1994).
- [10] Y. Li et. al, “Study of controllable polarization SASE FEL by a crossed-planar undulator”, Proceedings of the 2008 European Particle Accelerator Conference, WEPC118, Genoa, Italy, (2008).
- [11] Y. Ding and Z. Huang, Phys. Rev. ST Accel. Beams 11, 030702 (2008).
- [12] G. Geloni, et. al., arXiv:1101.4085v1, (2011).
- [13] H. Geng, et. al., “Polarization analysis for seeded FELs in a crossed-planar undulator”, Proceedings of the 2010 International Particle Accelerator Conference, TUPE068, Kyoto, Japan, (2010).
- [14] H. Deng et. al., Phys. Rev. ST Accel. Beams 17, 020704 (2014).
- [15] E. Allaria, et. al, in preparation.
- [16] L. H. Yu, Phys. Rev. A 44, 5178 (1991).
- [17] E. Allaria et al., Nat. Photonics 6, 699 (2012).
- [18] E. Allaria et al., Nat. Photonics 7, 913 (2013).
- [19] S. Di Mitri et. al., Nucl. Instrum. Meth. Phys. Res. A 608, 19 (2009).
- [20] E. Allaria, et. al., “Control of the polarization of a vacuum- ultraviolet, high-gain, free-electron laser”, in press.
- [21] E. Allaria, et. al., “Measurements of FEL polarization at FERMI”, MOP078, these proceedings.
- [22] E. Allaria et. al., “A Tool for Real Time Acquisitions and Correlation Studies at FERMI”, THP070, these proceedings.
- [23] G. Geloni, et. al., “Improvement of the crossed undulator design for effective circular polarization”, Proceedings of the 2011 Free-Electron Laser Conference, MOPB25, Shanghai, China, (2011).
- [24] T. Tanaka and H. Kitamura, “Improvement of crossed undulator for higher degree of polarization”, AIP Conference Proceedings, 705, 231 (2004).

A PLAN FOR THE DEVELOPMENT OF SUPERCONDUCTING UNDULATOR PROTOTYPES FOR LCLS-II AND FUTURE FELS

P. Emma, N. Holtkamp, H.-D. Nuhn, SLAC, Stanford, CA 94309, USA

D. Arbelaez, J. Corlett, S. Myers, S. Prestemon, R. Schlueter, LBNL, Berkeley, CA 94720, USA

C. Doose, J. Fuerst, Q. Hasse, Y. Ivanyushenkov, M. Kasa, G. Pile, E. Trakhtenberg, E. Gluskin, ANL, Argonne, IL 60439, USA

Abstract

Undulators serve as the primary source of radiation for modern storage rings, and more recently for the advent of Free-Electron Lasers (FELs). The performance of future FELs can be greatly enhanced using the much higher magnetic fields of superconducting undulators (SCU) [1]. For example, the LCLS-II hard x-ray undulator can be shortened by up to 70 m using an SCU in place of a PMU (permanent magnet undulator), or its spectral performance can be critically improved when using a similar length. In addition, SCUs are expected to be orders of magnitude less sensitive to radiation dose; a major issue at LCLS-II with its 1-MHz electron bunch rate. We present a funded R&D collaboration between SLAC, ANL, and LBNL, which aims to demonstrate the viability of superconducting undulators for FELs by building, testing, measuring, and tuning two 1.5-m long planar SCU prototypes using two different technologies: *NbTi* at ANL and *Nb₃Sn* at LBNL. Our goal is to review and reassess the LCLS-II HXR baseline plans (PMU) in July of 2015, after the development and evaluation of both prototypes, possibly in favor of an SCU for LCLS-II.

INTRODUCTION

The LCLS-II [2] FEL project at SLAC aims to construct a new continuous wave (CW), 4-GeV superconducting linac (SC-linac) [3], to feed either of two new undulators: 1) the Soft X-ray Undulator (SXU), or 2) the Hard X-ray Undulator (HXU). The HXU replaces the existing LCLS-I fixed-gap undulator and can be optionally fed by the existing 3-15-GeV copper (Cu) linac (120 Hz), presently used to drive the LCLS-I FEL. The spectral requirements for the SXU are 0.2-1.3 keV (SASE and self-seeded), while the HXU requires 1 keV to ≥ 5 keV (SASE, and self-seeded where possible) when driven by the SC-linac. The HXU spectral range, when driven by the Cu-linac (3-15 GeV), requires 1-25 keV.

The present (2014) baseline design uses two adjustable-gap, planar PMUs (NdFeB) with 39-mm (SXU) and 26-mm (HXU) periods and a 7.2-mm full magnetic gap, g_m . At 4 GeV (limited by SC-linac costs) the PMUs reach these requirements, but with little margin, especially in the HXU which barely produces 5 keV SASE, and cannot exceed 4 keV when self-seeded (limited hall length).

To remove these performance limitations, we propose an SCU undulator, at least for the HXU system, which significantly extends the spectral range when driven by the SC-linac, outperforms the presently foreseen PMU, and can even provide > 1 TW peak power when self-

seeded, tapered, and driven by the Cu-linac. It also offers much less magnetic field sensitivity to radiation dose, an issue greatly magnified by the high-rate, high power linac.

Unresolved technical risk issues for SCU systems, such as field correction, and limited experience with SCUs in operating machines [4], [5], have led to an R&D plan with a goal of building, testing, and correcting two 1.5-m long prototype FEL undulators by July 2015 which meet LCLS-II HXU specifications using two different conductors: *NbTi* (21 mm period), and *Nb₃Sn* (19 mm period), each with an 8-mm magnet gap.

FEL PERFORMANCE MOTIVATION

The motivations for SCUs, especially in comparison to PMUs (“in” or “out” of vacuum), are listed below.

- Higher magnetic fields allow superior FEL performance, or reduced undulator length.
- No permanent magnetic material to be damaged by radiation, allowing long life and smaller gaps.
- Reduced resistive wakefield with a cold bore? [6].
- Much lower vacuum pressure limits gas scattering.
- Smaller footprint and simpler *K*-control than the typical massive adjustable-gap PMU.
- Easily oriented for vertical polarization, if desired.

Figure 1 shows LCLS-II (HXU, SC-linac) calculations [7] of the full undulator system length (2-m magnet segments and 0.7-m breaks; each with a BPM, quadrupole, and phase shifter) versus the upper-limit SASE photon energy that saturates within 80% of that undulator length at 4 GeV (beam parameters in Table 1).

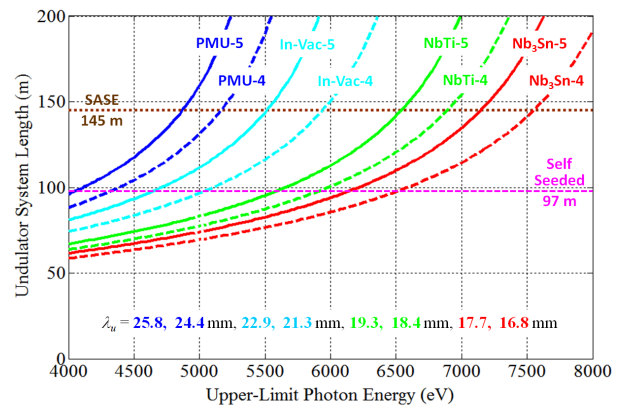


Figure 1: Undulator system length (with breaks) versus upper-limit SASE photon energy saturating in 80% of that undulator length at 4 GeV. Existing 145-m und. hall length is indicated.

The lower-limit photon energy is chosen at 1.5 keV for all curves (at 4 GeV), so once the magnet gap and undulator technology (e.g., NdFeB-PMU, NbTi-SCU, or Nb₃Sn-SCU) are chosen, the period is then exactly given from the FEL resonance condition,

$$\lambda_r = \frac{\lambda_u}{2\gamma^2} (1 + K^2/2),$$

where λ_r is the FEL wavelength, λ_u is the period, γ is the electron energy in units of rest mass, and K is the undulator parameter ($K \approx 0.93 \cdot B_{pk}[\text{T}] \lambda_u[\text{cm}]$), where the peak field, B_{pk} , is a known function of the magnet gap, g_m , period, and the precise undulator technology used.

All “5” labels (e.g., “PMU-5”) in Figure 1 have 5-mm vacuum gaps (7.3-mm magnet gaps), while “4” labels (e.g., “PMU-4”) are 1-mm smaller. The “in-vacuum” is the same PMU technology and has the same (4-mm and 5-mm) vacuum gaps for fair comparison, but 2-mm smaller magnet gaps. Periods are shown for all 8 cases.

The SCU performance is superior to the PMU (both “in-vac” and “out-of-vac”) allowing up to 7.6 keV SASE saturation in a 145-m undulator (whereas LCLS-II baseline design allows just 5 keV). Clearly the “in-vacuum” performs better than the “out-of-vacuum”, but neither reaches the attractive performance levels of the SCUs. The Nb₃Sn promises the best performance, but involves more risk with a 650°C heat treatment cycle required. Note that self-seeding requires 50% more undulator, so the highest self-seeded photon energy is the intersection of these curves with the 97-m line (e.g., 6.5 keV for Nb₃Sn-4). The parameters used in these calculations (and TW discussion below) are in Table 1.

Table 1: Parameters used for FEL Calculations (SC & Cu-linac)

Parameter	Sym.	SC-linac	Cu-linac	unit
Electron energy	E_0	4.0	6.6	GeV
Emittance	$\gamma \mathcal{E}_{x,y}$	0.4	0.4	μm
Energy spread, rms	σ_E	0.5	1.5	MeV
Peak current	I_{pk}	1	4	kA
Und. period	λ_u	16.8	16.8	mm
Und. magnet gap	g_m	6.3	6.3	mm
Und. vacuum gap	g_v	4.0	4.0	mm

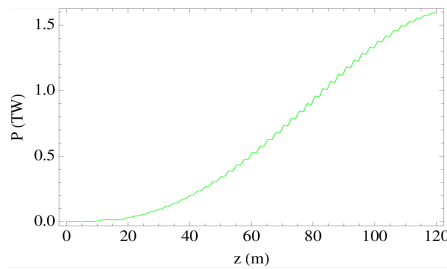


Figure 2: Peak power (1.6 TW) at 4 keV using same “Nb₃Sn-4” undulator of Figure 1, but now self-seeded, tapered, and driven by the Cu-linac at 6.6 GeV with 4 kA (see Table 1). Segment lengths are 2 m long, which is optimal for this 1-m gain length.

In addition to this spectral range extension, when the same “Nb₃Sn-4” undulator (or similar for “NbTi-4”) is driven by the Cu-linac at 6.6 GeV (120 Hz), with self-seeding [8], and a step-wise field taper applied to each 2-m undulator segment (20% total taper), a peak FEL power of 1.6 TW at 4 keV is possible (see Figure 2 and Table 1). Here the self-seeding monochromator is at $z = 0$.

SCU R&D PLAN

The goal of this R&D effort is to demonstrate the viability of SCU technology for FEL undulators by building, measuring, testing, and correcting two prototype SCUs. The parameters, such as magnetic field strength for the chosen period and gap, and field quality over the undulator length, must be demonstrated. The parameter selection is dictated by the desired spectral range of x-rays and the electron energy of LCLS-II. As a result, with an 8-mm prototype gap, the undulator period lies between 19 and 21 mm, depending on the superconductor. The vacuum gap is 5.7 mm. The undulator segment length should not be too long, in order to avoid practical difficulties, and is chosen as 1.5 m for the prototype, representing a reasonable building block for a long undulator line. This length also conveniently fits the existing 2-m long test cryostat at ANL [4] for prototype testing. A full-scale SCU system may use a longer segment and smaller gap, but this needs more study.

We will build two 1.5-m long superconducting planar undulator magnetic structures, one from NbTi (ANL) and another from Nb₃Sn (LBNL), with independent cryogenic testing on each using the same (existing) APS 2-m cryostat, verifying the magnetic performance of each undulator using the same magnet measurement bench. It will also employ a unique magnetic tuning approach developed at LBNL [9] (see below). The project design and execution relies heavily on well-established designs of the cryostat, undulator magnet core, and magnetic measurement systems developed and implemented for shorter undulators at the APS [10].

The APS SCU magnetic measurement system incorporates Hall-probe and rotating coil sensors modified for the smaller vacuum pipe diameter. The system will also incorporate a pulsed-wire technique developed at LBNL [11]. The project deliverable will be two fully functional superconducting undulators that meet LCLS-II undulator specifications by July 2015. Prototype undulator parameters are listed in Table 2, showing the slightly different period for each magnet.

Table 2: SCU Prototype Parameters

Parameter	Symbol	NbTi	Nb ₃ Sn	Unit
Magnetic full gap	g_m	8	8	mm
Vacuum chamber gap	g_v	5.7	5.7	mm
Und. period	λ_u	21	19	mm
Magnet length	L_m	1.5	1.5	m
Peak magnetic field	B_{pk}	1.66	1.86	T
Max. K value	K_{max}	3.27	3.31	-

PROTOTYPE MAGNET DESIGNS

Two 1.5-m long magnets are being developed, with NbTi conductor at ANL and Nb₃Sn at LBNL, each based on recent SCU development experience [4], [12]. The magnet designs are described for each technology below.

The Niobium-Titanium Magnet (NbTi)

The NbTi magnet is a scaled up version of the 1.1-m long SCU1 magnet, the second superconducting undulator currently being built at the Advanced Photon Source (APS) of ANL. The magnetic design is similar to that of SCU0 [13], the first SCU currently in operation at the APS. It consists of a pair of identical magnets, or jaws, separated by a gap where a beam chamber is accommodated. Each jaw is a series of vertical racetrack superconducting coil packs (53 turns) wound with a round 0.7-mm wire, and separated by magnetic poles, with currents flowing in opposite directions in adjacent coil packs. The winding form is made of low carbon steel to increase the undulator peak field. Each jaw has a main coil and there are two pairs of correction coils that are wound on top of the main coil in the first and last two end grooves. The correction coils are separately powered and are used mainly for tuning the second field integral since the first integral is automatically zeroed due to a chosen asymmetric magnetic configuration.

The design model of the magnet is shown in Figure 3. The superconducting coils are indirectly cooled by liquid helium passing through the channels in the cores; the flanges of the *LHe* circuit are visible in the Figure.

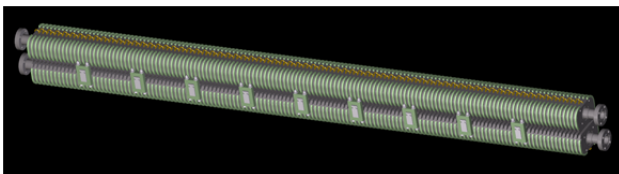


Figure 3: NbTi prototype undulator magnet design.

The Niobium-3-Tin Magnet (Nb₃Sn)

A prototype using Nb₃Sn superconductor is being fabricated at LBNL. The high transport current provided by Nb₃Sn conductors is leveraged in order to attain the highest possible magnetic field in the undulator. Nb₃Sn is an intermetallic compound with an A15 lattice structure, and is very brittle in nature. To avoid damage, the material is drawn in an unprocessed state and wound prior to subjecting the material to a heat treatment cycle that produces the intermetallic Nb₃Sn. This reaction process, which occurs at ~650 °C, adds an additional processing step to the fabrication when compared to NbTi.

The magnetic design is based on a solid low carbon steel mandrel structure into which grooves are machined to accommodate the coils. The result is a single structure that provides all of the magnetic and structural characteristics of a half-undulator. The half-undulator is wound from a single continuous length of wire (0.6-mm diameter) with alternating wire directions in neighboring coil packs (56 turns). Insulation in the form of a glass

braid with a thickness of less than 60 μm will be used to electrically isolate the wire. Two sets of end correction coils are used to cancel dipole fields inside the undulator and to correct for end kicks. The 2nd field integral is zero by choice of a symmetric magnetic configuration.

The Nb₃Sn prototype is shown in Figure 4, including the single-piece undulator core, an end corrector that is decoupled from the main core, and a joint section where the brittle Nb₃Sn conductor is soldered to NbTi cable.

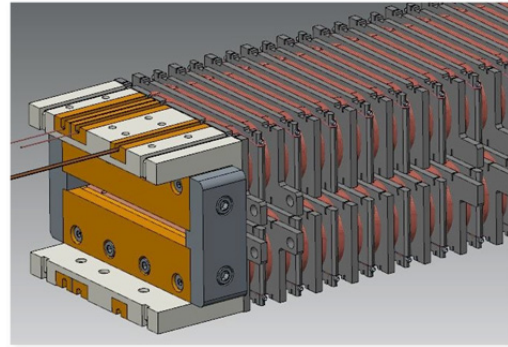


Figure 4: Nb₃Sn prototype undulator magnet design.

MAGNETIC MEASUREMENTS

The APS SCU horizontal magnetic measurement system incorporates Hall probe mapping for determining local field and phase errors, and a stretched-wire rotating coil system for measuring both static and dynamic field integrals and integrated multipole coefficients. The horizontal measurement system incorporates a heated warm-bore Ti tube inside a cold beam chamber. This design allows switching between the Hall probe and the rotating coil measurement system while the SCU is at cryogenic temperatures. The Hall sensor is housed in a small carbon fiber tube and is driven by a 3.5-m long linear stage. The carbon fiber tube slides inside the Ti tube during a field measurement [14]. For integrated field measurements, the integral coil (which is inside the Ti tube) is continuously rotated by two precision rotary stages and uses a lock-in amplifier technique for improved sensitivity and noise rejection [15]. The effective resolution of the Hall probe measurement scan is 0.1 Gauss with five measurement points per millimeter. Repeatability of the measured 1st and 2nd field integrals are ±0.5 G-cm and ±100 G-cm² respectively, well below the LCLS-II HXU FEL tolerances.

Wire-based methods, such as pulsed wire or vibrating wire techniques, can readily be used in small gap devices or where space restrictions make other measurement methods more difficult. For both methods, a wire is stretched along the length of the undulator and current is passed through the wire, generating either a local disturbance (pulsed wire method) or a global wire vibration (vibrating wire method) due to the Lorentz force. For the pulsed wire technique, the shape of the disturbance can be related to the first and second field integrals of the magnetic field (depending on the length of the current pulse), making this an attractive candidate for

field-integral measurements. A pulsed-wire measurement system has been constructed at LBNL and will be applied to the measurement of the superconducting undulators. Significant effort has been placed in the improvement of the pulsed wire method in order to obtain accurate measurements in undulators, especially those with short period lengths. Specifically, algorithms that correct for finite pulse width and dispersive effects in the wire motion have been developed in order to obtain accurate field integral and phase error measurements [11].

MAGNETIC CORRECTIONS

In order to reduce magnetic field errors, much of the focus will be placed on accurate winding methodologies and machining processes. Nevertheless, for long devices, corrections may be necessary for the stringent tolerances on trajectories and phase errors in an FEL. The methods include end corrections, and phase error and trajectory corrections in the periodic section of the undulator. A tuning scheme using YBCO tape-based single-turn coils and superconducting switches will be implemented for corrections in the periodic section of the device. The coils can be activated by using heater switches, which divert the current from a bypass path to individual coils. Since all of the coils are wired in series, the current through all active coils is equivalent. Therefore, the correction is performed with a single variable current source with variable *on/off* single-turn coils which can be activated at desired locations along the device. It can then be used to tune the undulator in-situ while magnetic measurements are performed. Figure 5 shows the concept, including the main tape, the soldered single-turn coil tapes, and the switching heaters. When a heater is *off*, the current bypasses its single-turn coil. When a heater is *on*, a majority of the current ($> 95\%$) passes through that single-turn coil for field correction.

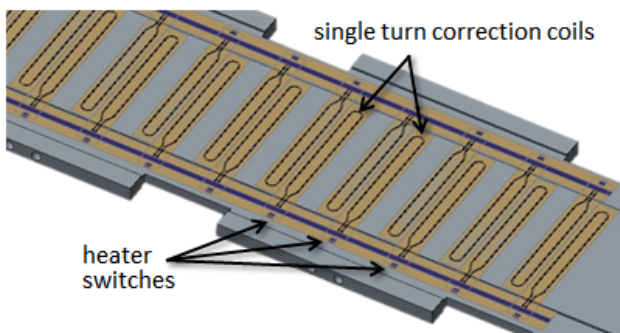


Figure 5: Periodic section field tuner on both sides of chamber.

The single-turn correction coils (0.1 mm thick) will be placed on each side of the vacuum chamber under the undulator poles. The coils will be placed in a pattern that allows for positive and negative kick corrections as well as positive and negative phase error corrections. A switching network and corrector scheme using patterned superconducting (YBCO) tapes and sputtered heaters has been developed at LBNL [9]. A new scheme that uses

resistive joints is being developed for the tuning of the undulator prototypes.

THE CRYOSTATS

Two 4-K *LHe* cryostats are being prepared for the R&D program, with a small tuning cryostat developed at LBNL to allow early testing of field measurement and correction techniques. In addition, a larger 2-m long cryostat, based on the existing design in Ref. [4], is being constructed at ANL. This larger cryostat will be used to do the full SCU testing for each magnet in sequence. The details of each cryostat are described in the two sections below.

The Small Tuning-Cryostat at LBNL

A small cryogen-free cryostat will be used for the field tuning R&D at LBNL. This cryostat can accommodate the full-length (1.5 m) field corrector (Figure 5) and its supporting vacuum chamber. The cold components in the cryostat are cooled with two pulsed tube cryocoolers. A radiation shield is cooled with the first stage of cryocoolers, while the tuner system will be cooled with the second stage of cryocoolers. Current leads with a 100-A capacity will be used to power the tuning system.

The 2-m Test-Cryostat at ANL

The 2-m test cryostat shown in Figure 6 is a copy of the SCU0 cryostat which has been in service in the APS storage ring since January 2013 [16]. Refrigeration at 4.3K is provided by a pair of cryocoolers thermally linked to a 100-liter *LHe* reservoir piped to the magnets. Since the available cooling power exceeds the heat load, the system operates in full recondensation mode with zero helium boil-off. Cold mass, thermal shield, and vacuum vessel geometry are large enough to accommodate both the ANL and LBNL magnet designs, including instrumentation and magnetic measurement systems.



Figure 6: ANL cryostat for testing each of the SCU magnets.

FULL SYSTEM CONCEPT FOR LCLS-II

A concept for a full LCLS-II undulator system is being developed simultaneously with the prototype program. A possible layout is shown in Figure 7, with two 2-m long

SC-undulator sections making up one 5-m cryostat with 0.5-m “cold” magnetic breaks. The system is composed of (up to) 29 cryostats for a full length of (up to) 145 m. Each break includes a cold cavity BPM with $\sim 1\ \mu\text{m}$ rms position resolution, a cold quadrupole focusing magnet, steering coils, and a cold adjustable phase shifter. The undulator parameters will be similar to those of Table 1.

System layout could follow the “minimal segmentation” concept used for the SC-linac, with cold cryostat interconnects, common insulating vacuum, and internal cryogenic distribution throughout the undulator string. Segmentation at some level may be desirable from a maintenance or functional standpoint although the packing factor (0.8), heat load, and cryogenic distribution system cost would be adversely impacted. Cooling would likely be provided by a small closed-cycle 4-K cryogenic refrigerator in the several-hundred Watt class, providing both magnet and thermal shield cooling. The refrigerator would be separate and independent from the SC-linac cryoplant for reasons of operational flexibility, differences in cooling requirements, and physical system location.

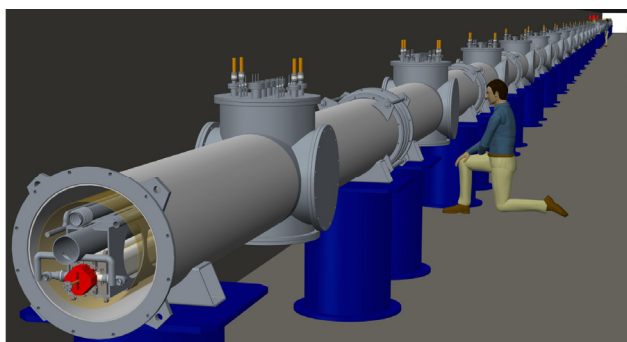


Figure 7: Conceptual SCU system layout for LCLS-II HXU.

DISCUSSION

The performance of the LCLS-II HXR FEL can be greatly improved by choosing superconducting undulators, allowing a much wider photon tuning range, a far longer undulator lifetime, and the possibility of generating terawatt peak power levels from a tapered, self-seeded FEL. Practical development of this technology is the key to making this decision. A baseline LCLS-II design change is possible, but not before completion of the R&D prototypes (July 2015) and a fully developed plan with LCLS-II project impact estimated.

ACKNOWLEDGMENT

Work supported by the Director, Office of Science, of the U.S. Department of Energy under Contract No. DE-AC02-76SF00515, DE-AC02-05CH11231, and DE-AC02-06CH11357.

REFERENCES

- [1] J. Bahrddt, Y. Ivanyushenkov, “Short Period Undulators for Storage Rings and Free Electron Lasers”, *Journal of Physics, Conf. Series*, **425** (2013), 032001.
- [2] T. Raubenheimer, “The LCLS-II, a New FEL Facility at SLAC”, in *Proc. of 36th Int. Free-Electron Laser Conf.*, Basel, 2014, WEB001.
- [3] P. Emma *et al.*, “The Linear Accelerator Design for the LCLS-II FEL Facility”, in *Proc. of 36th Int. Free-Electron Laser Conf.*, Basel, 2014, THP025.
- [4] Y. Ivanyushenkov *et al.*, “Experience of Operating a Superconducting Undulator at the Advanced Photon Source”, In *Proc. of 2011 Part. Acc. Conf.*, New York, NY, pp. 2053-2055, WEP0049.
- [5] R. Rossmanith *et al.*, “A Year’s Experience with a Superconducting Undulator in the Storage Ring ANKA”, in *Proc. of 2006 EPAC*, Edinburgh, Scotland, pp. 3571-3573, THPLS123.
- [6] B. Podobedov, “Resistive Wall Wakefields in the Extreme Anomalous Skin Effect Regime”, *Phys. Rev. ST - AB*, **12**, 044401, 2009.
- [7] M. Xie, “Design Optimization for an X-Ray Free Electron Laser Driven by SLAC Linac”, in *Proc. of 1995 Part. Acc. Conf.*, Dallas, TX, pp. 183-185, (1995), TPG10.
- [8] J. Amann *et al.*, “Demonstration of Self-seeding in a Hard-X-ray Free-electron Laser”, *Nature Photonics*, **6**, 693-698, 2012.
- [9] D. Arbelaez *et al.*, *IEEE Transactions on Applied Superconductivity*, Vol. **23**, No. 3, June 2013.
- [10] K. Harkay *et al.*, “APS Superconducting Undulator Beam Commissioning Results”, in *Proc. of 2013 Part. Acc. Conf.*, Pasadena, CA, pp. 703-705, WEOAA3.
- [11] D. Arbelaez *et al.*, “A Dispersion and Pulse Width Correction Algorithm for the Pulsed Wire Method”, *NIM A*, Vol. **716**, pp. 62-70.
- [12] D. Dietderich *et al.*, “Fabrication of a Short-Period Nb₃Sn Superconducting Undulator”, *IEEE Trans. on Applied Superconductivity*, Vol. **17**, No. 2, June 2007, pp. 1243-1246.
- [13] Y. Ivanyushenkov *et al.*, “Development of a Planar Superconducting Undulator for the Advanced Photon Source”, *IEEE Trans. on Applied Superconductivity*, Vol. **22**, No. 3, June 2012.
- [14] Y. Ivanyushenkov *et al.*, “Development Status of a Magnetic Measurement System for the APS Superconducting Undulator”, In *Proc. of 2011 Part. Acc. Conf.*, New York, NY, pp. 1286-1288, TUP243.
- [15] C. Dose, M. Kasa, “Magnetic Measurements of the First Superconducting Undulator at the Advanced Photon Source”, in *Proc. of 2013 Part. Acc. Conf.*, Pasadena, CA, pp. 1238-1240, THPBA06.
- [16] J. Fuerst *et al.*, “Cryogenic Performance of a Cryocooler-Cooled Superconducting Undulator”, *Adv. Cryo. Eng., AIP Conf. Proc.*, **1573**, pp. 1527, 2014.

SIMULTANEOUS MEASUREMENT OF ELECTRON AND PHOTON PULSE DURATION AT FLASH

S. Düsterer, DESY, Hamburg, Germany

Abstract

One of the most challenging tasks for extreme ultraviolet, soft and hard X-ray free-electron laser photon diagnostics is the precise determination of the photon pulse duration, which is typically in the sub 100 fs range. In a larger campaign nine different methods, which are able to determine such ultrashort photon pulse durations were compared at FLASH [1]. Radiation pulses at a wavelength of 13.5 nm and 24.0 nm together with the corresponding electron bunch duration were measured by indirect methods like analyzing spectral correlations, statistical fluctuations and energy modulations of the electron bunch, and also direct methods like autocorrelation techniques, THz streaking or reflectivity changes of solid state samples. A detailed description of the measurement campaign can be found in Ref. [2].

THE IDEA

One of the main characteristics of the new generation XUV to X-ray free-electron lasers is their ultrashort pulse duration in the femtosecond range. With these new sources ultra-fast reaction dynamics on the femtosecond time scale [3–5] can be investigated. It also allows the investigation of multi-photon processes in the XUV [6] to the X-ray range [7] which has not been possible before. The accurate knowledge of the FEL key parameters such as pulse peak power, radiance, and on-target irradiance for example is crucial for the analysis of experimental data. It turns out that the number of photons, the focal spot size and the spectral content in such short pulses can be measured reliably [8–11], while the pulse duration is still the most difficult parameter to be determined.

At FLASH [1] the duration of the generated photon pulses can be varied over a range of few tens of femtoseconds up to several 100s of fs. Still, a reliable method to measure pulse durations for the entire parameter range is not yet available. Although a variety of methods have been proposed, they all need to be set-up and tested experimentally to find out the best suited technique. In a campaign nine different techniques – three electron bunch duration measurements and six photon based methods – have been used to determine the photon pulse duration. They are either performed in a *direct* way by measuring the photon pulse duration at the experimental end stations or on the other hand by *indirect* methods measuring only parameters which are linked – by theoretical models – to the actual pulse duration. From the measured information the actual XUV pulse duration can be calculated using these models. From the experimental point of view, indirect methods are typically simpler to realize as compared to the direct approaches. However, they have to be verified and calibrated by direct methods. So

far only photon pulse duration measurement campaigns using one (or two) measurement technique have been undertaken at FLASH in the last years [12–17]. Up to now there were no studies at FLASH or at any other XUV/X-ray FEL where many different methods were compared within one dedicated pulse duration measurement campaign as shown in Fig. 1.

The main motivation for this study was three-fold. Firstly, we wanted to address the question how well the results measured by the indirect methods agree with the direct ones. What are the error bars when comparing the different methods? How much information about the photon pulse duration can we deduce from the electron beam parameters in contrast to the photon based methods? Secondly, the realization of all nine techniques together under the same beam conditions allows a direct comparison of advantages and disadvantages of the individual techniques. Thirdly, the aim of the campaign was to identify sensitive parameters of the electron bunch compression and to develop recipes for routine operation to reliably establish a specific user requested XUV pulse duration at FLASH, especially for ultrashort pulses below 50 fs. The detailed description of all methods and the comparison of the various approaches can be found in the extended paper Ref. [2].

CONCLUSION

The FEL was tuned such that all pulses in the bunch train had roughly the same electron bunch and XUV pulse parameters for the measurements that were performed at 13.5 nm. For this case a remarkably good agreement between all methods was found. Most of all it was shown that all used indirect methods reveal the same results as the direct methods and thus the assumptions made for the analysis of the indirect methods seem to be valid for this case. On the other hand, when the electron pulse and thus the XUV parameters were significantly changing within the bunch train, as in the case when the FEL was running at 24 nm, a strong deviation between different methods was observed. Here it is difficult to judge which method can be trusted to what extend.

While in SASE mode of operation the photon pulse is shorter than the total length of the electron bunch from which it is generated, the assumption of a factor 0.6 [2, 17] between the two can only be used as a very simple rule of thumb for first estimations. The measurements as well as start-to-end simulations showed, the factor can be substantially smaller depending on the accelerator settings. Due to the complicated beam dynamics in the energy range FLASH is working in, parameters like slice emittance and energy spread also have to be taken into account as well. Up

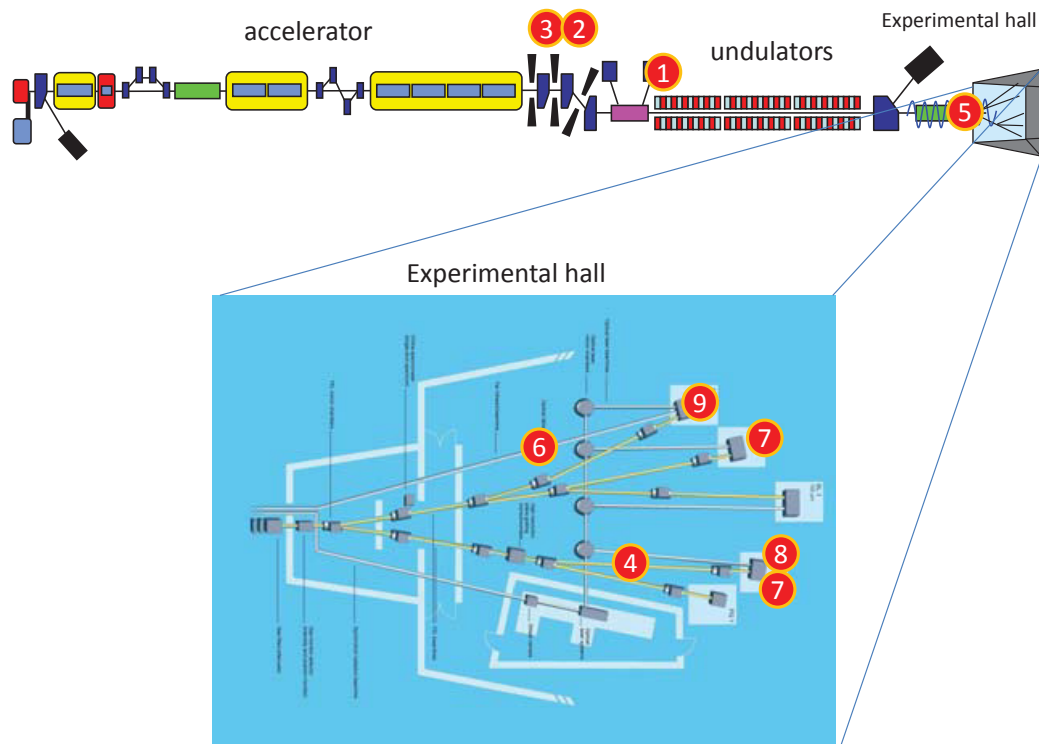


Figure 1: Schematic layout of the FLASH accelerator and the experimental hall (not to scale). The total length of the facility is 315 m. The positions of the various techniques for electron bunch or photon pulse duration measurements are indicated by numbers: (1) Transverse Deflecting RF Structure (TDS), (2) Bunch Compression Monitors (BCM), (3) THz Spectrometer CRISP, (4) XUV Spectra, (5) XUV Statistics, (6) Optical Replica (Afterburner), (7) XUV Autocorrelation (gas phase), (8) XUV Autocorrelation (solid state), (9) THz Streaking. A detailed description of the measurements can be found in Ref. [2].

to now we can only state that a universal scaling factor between electron and photon pulses could not be determined for FLASH.

ACKNOWLEDGEMENTS

The author wishes to acknowledge the work of the scientific and technical team at FLASH. The presented work was performed by the participants of the pulse duration campaign: M. Rehders, A. Al-Shemmary, C. Behrens, G. Brenner, O. Brovko, M. DellAngela, M. Drescher, B. Faatz, J. Feldhaus, U. Fröhling, N. Gerasimova, N. Gerken, C. Gerth, T. Golz, A. Grebentsov, E. Hass, K. Honkavaara, V. Kocharian, M. Kurka, Th. Limberg, R. Mitzner, R. Moshhammer, E. Plönjes, M. Richter, J. Rönsch-Schulenburg, A. Rudenko, H. Schlarb, B. Schmidt, A. Senftleben, E. Schneidmiller, B. Siemer, F. Sorgenfrei, A. Sorokin, N. Stojanovic, K. Tiedtke, R. Treusch, M. Vogt, M. Wieland, W. Wurth, S. Wesch, M. Yan, M. Yurkov, H. Zacharias, and S. Schreiber.

REFERENCES

- [1] W. Ackermann *et al.*, "Operation of a Free Electron Laser in the Wavelength Range from the Extreme Ultraviolet to the Water Window," *Nature Photonics* **1**, 336 (2007).
- [2] S. Düsterer, M. Rehders, A. Al-Shemmary, C. Behrens, G. Brenner, O. Brovko, M. DellAngela, M. Drescher, B. Faatz, J. Feldhaus, U. Fröhling, N. Gerasimova, N. Gerken, C. Gerth, T. Golz, A. Grebentsov, E. Hass, K. Honkavaara, V. Kocharian, M. Kurka, Th. Limberg, R. Mitzner, R. Moshhammer, E. Plönjes, M. Richter, J. Rönsch-Schulenburg, A. Rudenko, H. Schlarb, B. Schmidt, A. Senftleben, E. Schneidmiller, B. Siemer, F. Sorgenfrei, A. Sorokin, N. Stojanovic, K. Tiedtke, R. Treusch, M. Vogt, M. Wieland, W. Wurth, S. Wesch, M. Yan, M. Yurkov, H. Zacharias, and S. Schreiber "Development of experimental techniques for the characterization of ultrashort photon pulses of XUV free-electron lasers", submitted
- [3] Y.H. Jiang, A. Rudenko, O. Herrwerth, L. Foucar, M. Kurka, K.U. Kuehnel, M. Lezius, M.F. Kling, J. van Tilborg, A. Belkacem, K. Ueda, S. Düsterer, R. Treusch, C.D. Schroeter, R. Moshhammer, and J. Ullrich, "Ultrafast Extreme Ultraviolet Induced Isomerization of Acetylene Cations", *Phys. Rev. Lett.* **105**, 263002 (2010).
- [4] C.M. Günther, B. Pfau, R. Mitzner, B. Siemer, S. Roling, H. Zacharias, O. Kutz, I. Rudolph, D. Schöndelmaier, R. Treusch and S. Eisebitt, "Sequential Femtosecond X-Ray Imaging", *Nature Photonics* **5**, 99-102 (2011).

- [5] K. Schnorr *et al.*, "Time-Resolved Measurement of Inter-atomic Coulombic Decay in Ne₂", Phys. Rev. Lett. **111**, 093402 (2013).
- [6] M. Richter, S. V. Bobashev, A. A. Sorokin, and K. Tiedtke, "Multiphoton ionization of atoms with soft x-ray pulses", J. Phys. B: At. Mol. Opt. Phys. **43**, 194005 (2010).
- [7] L. Young *et al.*, "Femtosecond electronic response of atoms to ultra-intense X-rays", Nature **466**, 56 (2010).
- [8] M. Richter *et al.*, "Measurement of gigawatt radiation pulses from a vacuum and extreme ultraviolet free-electron laser", Appl. Phys. Lett. **83**, 2970 (2003).
- [9] K. Tiedtke *et al.*, "Gas detectors for X-ray lasers", J. Appl. Phys. **103**, 094511 (2008).
- [10] G. Brenner *et al.*, "First results from the online variable line spacing grating spectrometer at FLASH" Nucl. Instrum. Meth. A **635** S99 (2011).
- [11] A.A. Sorokin *et al.*, "Method based on atomic photoionization for spot-size measurement on focused soft x-ray free-electron laser beams," Appl. Phys. Lett. **89**, 221114 (2006).
- [12] R. Mitzner, A.A. Sorokin, B. Siemer, S. Roling, M. Rutkowski, H. Zacharias, M. Neeb, T. Noll, F. Siewert, W. Eberhardt, M. Richter, P. Juranic, K. Tiedtke and J. Feldhaus, "Direct autocorrelation of soft-x-ray free-electron-laser pulses by time-resolved two-photon double ionization of He", Phys. Rev. A **80**, 025402 (2009).
- [13] Y.H. Jiang, T. Pfeifer, A. Rudenko, O. Herrwerth, L. Foucar, M. Kurka, K.U. Kühnel, M. Lezius, M.F. Kling, X. Liu, K. Ueda, S. Düsterer, R. Treusch, C.D. Schröter, R. Moshhammer, and J. Ullrich, "Temporal coherence effects in multiple ionization of N₂ via XUV pump-probe autocorrelation", Phys. Rev. A **82**, 041403(R) (2010).
- [14] U. Fröhling, M. Wieland, M. Gensch, T. Gebert, B. Schütte, M. Krikunova, R. Kalms, F. Budzyn, O. Grimm, J. Rossbach, E. Plönjes and M. Drescher, "Single-shot terahertz-field-driven X-ray streak camera", Nature Photonics **3**, 523-528 (2009).
- [15] I. Grguras, A.R. Maier, C. Behrens, T. Mazza, T. J. Kelly, P. Radcliffe, S. Duesterer, A.K. Kazansky, N.M. Kabachnik, Th. Tschentscher, J.T. Costello, M. Meyer, M.C. Hoffmann, H. Schlarb and A.L. Cavalieri, "Ultrafast X-ray pulse characterization at free-electron lasers", Nature Photonics **6**, 852-857 (2012).
- [16] R. Riedel, A. Al-Shemmary, M. Gensch, T. Goltz, M. Harmand, N. Medvedev, M.J. Prandolini, K. Sokolowski-Tinten, S. Toleikis, U. Wegner, B. Ziaja, N. Stojanovic and F. Tavella, "Single-shot pulse duration monitor for extreme ultraviolet and X-ray free-electron lasers" Nature Communications **4**, 1731 (2013).
- [17] C. Behrens, N. Gerasimova, Ch. Gerth, B. Schmidt, E. A. Schneidmiller, S. Serkez, S. Wesch, and M.V. Yurkov, "Constraints on photon pulse duration from longitudinal electron beam diagnostics at a soft x-ray free-electron laser", Phys. Rev. ST Accel. Beams **15**, 030707 (2012).

EXPERIMENTAL RESULTS OF DIAGNOSTICS RESPONSE FOR LONGITUDINAL PHASE SPACE

F. Frei*, V. Arsov, H. Brands, A. Saa Hernandez, R. Ischebeck, F. Löhl, B. Kalantari, R. Kalt, B. Keil, W. Koprek, G.L. Orlandi, T. Schilcher, V. Schlott, PSI, Villigen, Switzerland

Abstract

At SwissFEL, electron bunches will be accelerated, shaped, and longitudinally compressed by different radio frequency (RF) structures (S-, C-, and X-band) in combination with magnetic chicanes. In order to meet the envisaged performance, it is planned to regulate the different RF parameters based on the signals from numerous electron beam diagnostics. Here we will present experimental results of the diagnostics response on RF phase and field amplitude variations that were obtained at the SwissFEL Injector Test Facility.

INTRODUCTION

The SwissFEL free electron laser [1] is currently under construction at the Paul Scherrer Institut. To obtain a proper and stable bunching process, certain stability requirements of different sub-systems (Laser, RF, magnets etc...) have to be reached. Diagnostics should be available to measure the related beam parameters and possibly provide this information to feedback systems, which then can be used to stabilize the beam.

In order to develop and optimize different components and procedures for SwissFEL, the 250 MeV SwissFEL Injector Test Facility (SITF) [2] is currently in operation.

To investigate the current status of the systems, a diagnostics response measurement was performed at SITF. Each RF parameter was varied separately around previously chosen initial settings. The measured responses of the diagnostics then allow conclusions on the achievable sensitivities at these initial settings. Additionally, corresponding simulations performed using the code LiTrack are presented in a separate contribution [3]. The post analysis has been done following the concept already described in detail in [4].

It is worth emphasizing that the present paper provides a snapshot of the work presently done at SITF. The systems are under continuous development and optimization to reach the ultimate goals for SwissFEL.

After a first brief overview of the systems installed at SITF, the initial settings of the RF and the diagnostic elements will be described in more detail. Based on this information, the diagnostic response measurement is described in a third section followed by a section discussing the analysis of the deduced response matrix.

SWISSFEL INJECTOR TEST FACILITY

As depicted in Fig. 1, SITF is based on an S-band radio frequency (RF) photoinjector (FINSS). A booster

LINAC consisting of normal conducting S-band RF structures (FINSB01-FINSB02-FINSB03/04) is simultaneously generating the acceleration up to 250 MeV and the necessary energy chirp for the magnetic compression in the bunch compressor (BC). To linearize the longitudinal phase space for optimal bunch compression, a fourth harmonic X-band cavity (FINXB) phased for deceleration is located in front of the bunch compressor.

Jitter and drift of field amplitude and phase of each of these accelerating cavities (subsequently referred to as actuators) affect the longitudinal phase space of the electron bunches. To measure the effect on the electron beam, SITF is equipped with longitudinal instrumentation (subsequently referred to as diagnostics) which is illustrated in Fig. 1.

For the present measurements, the bunch charge is measured with stripline beam position monitors (BPMs) that were previously calibrated against a Faraday cup and a wall-current monitor [5]. Two of these stripline BPMs (BPM-E₁, BPM-E₂) are located between the first and the second dipole of the bunch compressor, where the horizontal beam position is a measure of the mean particle energy. Furthermore, a synchrotron radiation monitor (SRM) [6] after the third dipole of the bunch compressor provides the energy distribution by imaging the incoherent synchrotron radiation onto a camera. While the position of the centroid is also a measure of the mean particle energy, the width is related to the relative energy spread.

After the bunch compressor, relative bunch length changes are measured by the bunch compression monitor (BCM). This monitor is based on coherent diffraction radiation (CDR) generated as the electron bunch passes through a hole of radius 3 mm in a 1 μ m thick titanium foil. The CDR is thereafter filtered by two different "thick grid" high pass THz filters. The two different spectral bands are individually detected by two Schottky diodes. Additionally, the absolute bunch length can be measured destructively using an S-band transverse deflecting cavity (TDC). Thereby, the longitudinal profile gets vertically deflected. The bunch profile is then measured by imaging the electron distribution onto a subsequent screen.

A bunch arrival time monitor (BAM) after the bunch compressor is based on a Mach-Zehnder type modulator [7]. A high bandwidth pickup signal [8] is sampled at the zero crossing by a laser pulse. This laser pulse provides the timing reference. It is delivered in the accelerator tunnel through single-mode fiber links stabilized in length with femto second precision. The arrival time change results in deviation from the zero crossing, thus creating a modulation voltage for the electro optical modulator, which encodes the arrival time into the amplitude of the reference laser pulse.

* franziska.frei@psi.ch

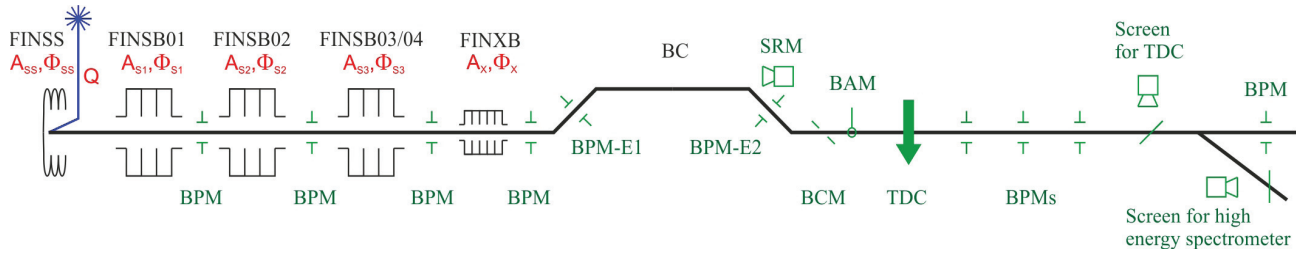


Figure 1: Scheme of the SwissFEL Injector Test Facility. The longitudinal diagnostics used through the measurement is shown in green, whereas the actuators varied are colored in red.

Ideally, one would like to have one diagnostic related to a single actuator (or vice versa). However, in reality, these beam based measurements are not independent. For example, the total CDR energy detected at the BCM is not only a measure of the relative bunch length, but is also affected by the bunch charge.

THE INITIAL SETTINGS

To investigate the diagnostic response to the different actuators, namely the RF phase, RF amplitude, and charge, the actuators are varied one by one around the initial settings (IS) listed in Table 1.

For a bunch charge of 20.5 pC, the RF parameters at the initial settings were optimized for a mean particle energy of 200 MeV and a compression factor of roughly 7 resulting in a bunch duration of 260 fs rms (see Fig. 2).

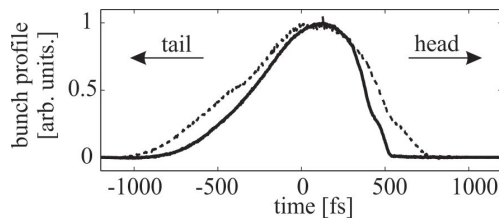


Figure 2: Solid line: Longitudinal electron bunch profile (260 fs rms) at the initial settings, measured by the TDC. Dashed line: Longitudinal electron bunch profile for a smaller compression phase.

The phase of FINSS Φ_{SS} is at the initial settings, typically set to minimize the energy spread, and the on-crest energy gain of the particle is estimated to 7 MeV. For maximal energy gain, FINSB01 is operated on-crest (phase = 0°), with an estimated energy gain of a particle of 53.7 MeV. For the current compression scheme, the phase of FINSB02 Φ_{S2} was set slightly off-crest to -2.5° . For this RF station, the on-crest energy gain of a particle is estimated to 70.8 MeV. However, the main energy chirp was introduced by FINSB03 at an off-crest phase of -37.5° with an on-crest energy gain of a particle estimated to 102.7 MeV. To linearize the compression, the fourth harmonic field FINXB with an estimated on-crest energy gain of the particle of 14.2 MeV is operated anti-on-crest with $\Phi_{XB} = 180.0^\circ$.

The particle energy gains for an on-crest phase are estimated based on the forward RF power at the entrance of each RF structure for the initial settings.

An RF feedback stabilizes the vector sum of the input and output RF fields measured with directional couplers. It stabilizes the RF amplitudes and phases, which might fluctuate due to temperature changes in the accelerating structures. In these measurements of the vector sum, the amplitudes are given in arbitrary units (see Table 1), while the phases are given in deg.

Table 1: Initial Settings (IS) and Variation Range of the Actuators (their stability was determined at the IS values)

Act.	IS	Var. Range	Stability
Q	20.5 pC	18.6 - 21.9 pC	0.18 pC
Φ_{SS}	148.5 $^\circ$	$\pm 1.5^\circ$	0.039 $^\circ$ (36 fs)
A_{SS}	0.4990 arb units	-2.64 - 2.04 %	0.04 %
Φ_{S1}	-0.02°	$\pm 1.5^\circ$	0.022 $^\circ$ (21 fs)
A_{S1}	0.3000 arb units	$\pm 1.67\%$	0.011 %
Φ_{S2}	-2.5°	$\pm 1.5^\circ$	0.026 $^\circ$ (24 fs)
A_{S2}	0.5950 arb units	$\pm 0.51\%$	0.0072 %
Φ_{S3}	-37.53°	$\pm 1.5^\circ$	0.035 $^\circ$ (32 fs)
A_{S3}	0.3309 arb units	$\pm 6.0\%$	0.056 %
Φ_{XB}	180.04 $^\circ$	$\pm 1.5^\circ$	0.18 $^\circ$ (42 fs)
A_{XB}	0.3500 arb units	$\pm 8.6\%$	0.13 %

The variation ranges of the actuators are chosen large enough to measure a clear effect on the diagnostics, but small enough to ensure linear dependencies. The resulting experimentally defined variation ranges are summarized in Table 1.

For each actuator, the stability value listed in Table 1 is the standard deviation of the measured values of 300 bunches over one minute at the initial settings. For the whole measurement, SITF was operating at the standard repetition rate of 10 Hz, but only every second bunch was measured.

For the chosen initial settings, the resolutions of the different diagnostics are listed in Table 2.

The resolution of the SRM is derived from the pixel size (40 μm) of the camera and the nominal dispersion at that position (330.9 mm). By cross calibrating the BPM-E1 and BPM-E2 in the bunch compressor with respect to the SRM, the dispersion at the position of these BPMs can be derived (172.6 mm). For the initial settings of 200 MeV, their spatial resolution of 8 μm results in an energy resolution roughly

Table 2: SITF Longitudinal Diagnostics and Their Resolution at the Initial Settings

Diagnostics	Quantity measured	Resolution (Δ)
BPM-E ₁	energy diff. to the IS	9.3 keV
SRM-E	energy diff. to the IS	24 keV
SRM- $\Delta E/E$	relative energy spread	$1.2 \cdot 10^{-4}$
BPM-E ₂	energy diff. to the IS	9.3 keV
BCM-D1r	CDR, integr. 0.6-2 THz	1.6 mV (0.8 %)
BCM-D2r	CDR, integr. 0.26-2 THz	2.4 mV (0.6 %)
BPM-Q	mean of all BPMs	62 fC (0.3 %)
BAM-t	bunch arrival time after BC	52 fs
TDC- σ_t	bunch length	40 fs

2.6 times better than the estimated energy resolution of the SRM-E.

The resolution of the BCM is estimated according to previous correlation measurements using two identical frequency ranges for the integration. For smaller signal levels, the relative noise is slightly larger, resulting in a different relative noise for BCM-D1r and BCM-D2r.

For the BAM, the resolution is intrinsically measured from the pickup slope and the instantaneous amplitude jitter of the reference laser pulses. While the present BAM resolution at high charges (200 pC) is in the order of 10 fs, at a charge of 20.5 pC it drops to 52 fs [7].

The resolution of TDC- σ_t is a rough estimate of comparing the measurements at the two zero-crossings in the present measurements.

Since values of actuators and diagnostics might differ by many orders of magnitude and units, the measured quantities are subsequently divided by the listed stabilities resp. resolutions.

DIAGNOSTICS RESPONSE

During the diagnostics response measurement, the actuators are varied one by one in five steps around the initial setting. For each step, all the diagnostics and actuators are read out bunch synchronously with the exception of the SRM and the TDC. While the data from the SRM was acquired simultaneously at the same five steps, the TDC measurements were done separately after all the actuators were varied since the TDC is destructive.

Throughout the measurement, the RF actuators are changed through a vector modulator via low level RF electronics and the charge was varied by rotating a polarizer in the gun-laser beam path.

As an example, the procedure is described in detail for the variation of Φ_{S3} , the phase of FINSB03 and illustrated in Fig. 3. By varying Φ_{S3} , there is not only a change in compression and bunch length expected, but also a change in energy. Furthermore, since a phase change implies a change of the curvature in phase space, this affects the energy spread as well as the bunch shape.

For the five points around the initial settings, Φ_{S3} was nominally set to $[-39.03^\circ, -30.28^\circ, -37.53^\circ, -36.78^\circ, -36.03^\circ]$.

The diagnostics and read back values of the actuators are recorded at 5 Hz during one minute for each set phase.

To simplify the comparison between the different measured quantities, the actuator values Φ_{S3} are divided by their rms stability of 0.035° and the diagnostics values are divided by the expected corresponding rms resolution, mentioned in Fig. 3 as Δ as well as in Table 2.

For each diagnostic element, Figs. 3a)-i) show the mean and standard deviation at each scan point with respect to the mean and the barely visible standard deviation of the also measured actuator Φ_{S3} .

As expected, the charge shown in g) is not affected by any change of Φ_{S3} . A very weak response might be seen for the relative energy spread by the SRM- $\Delta E/E$ in c). However the main change is observed by the diagnostics most sensitive to energy which are BPMs in the bunch compressor a) and d) and the SRM-E b). These diagnostics only show a difference from the actual energy to the original energy at the initial settings. The convention of the axis for these diagnostics is chosen to show a positive difference for an increase in energy. Since an energy change is affecting the transit time through the bunch compressor, also the BAM h) is sensitive to energy changes. While Φ_{S3} is moved towards the on-crest phase, the mean particle energy is increasing and the beam is less deflected by the dipoles in the bunch compressor. This implies a slightly shorter trajectory through the bunch compressor and therefore a negative deviation of the arrival time with respect to the measurement at the initial settings.

Furthermore, a variation in Φ_{S3} results in a change of compression that is detected by the BCMs e) and f) and the TDC i). While the phase is shifted towards the on-crest phase, the electron bunch is less compressed and the integrated energy in the two frequency ranges of the BCMs is decreased, because the coherent diffraction radiation is shifting towards lower frequencies. This is seen in Figs. 3e) and f).

The responses of individual diagnostics on the actuators are confirmed to be linear within the scan ranges. The response R_{ij} of diagnostics i with respect to the actuator j is approximated by the slope of a linear fit.

A slope of 1 corresponds to the situation where the value of the diagnostics is changing by one rms resolution, if the actuator is changed by an amount corresponding to its rms stability. This means that slopes smaller than 1 can not be measured reliably in single shot. However, slow drifts might still be detected by averaging over an appropriate number of bunches. The measured response matrix is depicted in Table 3.

DISCUSSION OF THE RESPONSE MATRIX

A very rough inspection of the response matrix in Table 3 shows, that only the charge measurement by BPM-Q is clearly sensitive to only one actuator, namely to the charge. All the other diagnostics are sensitive to more than one actuator.

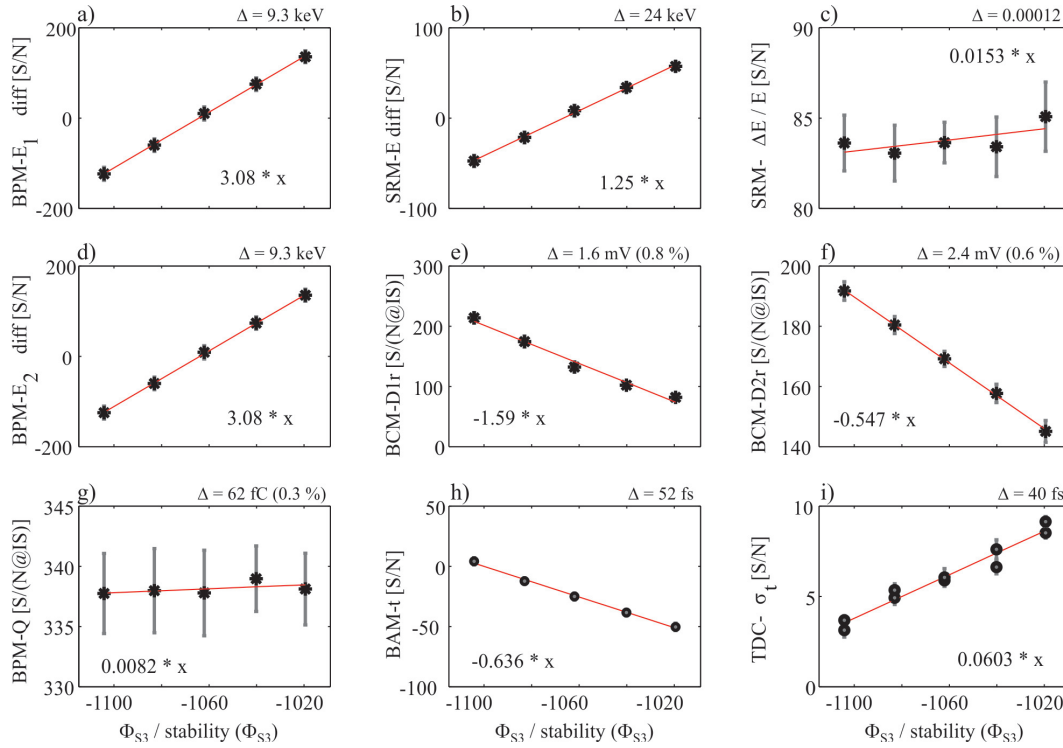


Figure 3: Phase scan of the off-crest operated accelerating structure FINSB03. Φ_{S3} is varied for 5 different settings around its IS value. The resulting measurements of the SITF longitudinal diagnostics are depicted in a) to i). The middle points correspond to the initial settings and the bars shown indicate the standard deviation. Therefore, the quantity is divided by the resolution Δ of the corresponding detector, and the RF actuator by its rms stability 0.035° .

Table 3: Response matrix R of the experimentally measured values as a function of the actuators. The values measured have been divided by the measured stability of the actuators and the expected (resp. measured) resolution of the diagnostics. The bold numbers indicate the most sensitive diagnostic for each actuator according to the measurement.

	Q	Φ_{SS}	Φ_{S1}	Φ_{S2}	Φ_{S3}	Φ_{XB}	A_{SS}	A_{S1}	A_{S2}	A_{S3}	A_{XB}
BPM-E ₁	0.11	-1.03	-0.07	0.07	3.08	0.08	-2.93	0.57	0.38	3.73	-1.55
SRM-E	-0.02	-0.38	-0.03	0.03	1.25	0.02	-1.13	0.23	0.16	1.50	-0.63
SRM- $\Delta E/E$	0.08	0.05	-0.02	-0.03	0.02	0.18	-0.05	0.01	0.01	0.10	-0.03
BPM-E ₂	0.25	-1.03	-0.07	0.07	3.08	0.05	-2.94	0.57	0.39	3.72	-1.56
BCM-D1r	0.98	-0.04	-0.45	-0.66	-1.59	3.37	0.57	-0.14	-0.08	-0.16	0.31
BCM-D2r	1.12	0.01	-0.14	-0.22	-0.55	1.01	0.20	-0.04	-0.02	-0.04	0.10
BPM-Q	2.89	0.09	0.01	0.00	0.01	0.04	0.08	0.00	-0.00	0.01	-0.01
BAM	-0.32	-0.02	0.01	-0.01	-0.63	0.01	-0.13	-0.12	-0.07	-0.72	0.31
TDC - σ_t	-	0.00	0.02	0.02	0.06	-0.17	-0.01	0.00	0.01	0.00	-0.01

Since the responses of each diagnostic on each actuator is linear, simultaneous variations of all parameters can be represented as a linear combination of the individual variations. Therefore, the response matrix can be analyzed using the method of singular value decomposition (SVD) [9].

For this purpose, the response matrix R can be decomposed into three matrices according to

$$R = U \cdot \Sigma \cdot V^T, \quad (1)$$

where the matrix Σ is a diagonal matrix, containing the singular values of R . By convention, they are sorted by descending order, as depicted in Table 4. Each singular value corresponds to the weighting factor of the related mode. The corresponding mode is derived from the left singular vectors of R contained in U (describing the diagnostics in Table 5) and the right singular vectors of R contained in V (describing the actuators in Table 6). Since the singular values for mode 7-9 are very small compared to the first 6 modes, in

Table 5 and 6 only the first 7 singular vectors are shown for better understanding.

Table 4: Matrix Σ , containing the singular values of R. They describe the importance of the corresponding singular vectors in U, resp. V.

	1	2	3	4	5	6	7	8	9
1	8.96	0	0	0	0	0	0	0	0
2	0	4.22	0	0	0	0	0	0	0
3	0	0	2.70	0	0	0	0	0	0
4	0	0	0	0.62	0	0	0	0	0
5	0	0	0	0	0.08	0	0	0	0
6	0	0	0	0	0	0.06	0	0	0
7	0	0	0	0	0	0	0.01	0	0
8	0	0	0	0	0	0	0	0.01	0
9	0	0	0	0	0	0	0	0	0.01

Table 5: Matrix U, containing the first seven left singular vectors of R as columns. They describe the diagnostics and are sorted according to their importance.

	1	2	3	4	5	6	7
BPM-E ₁	-0.67	0.11	-0.07	-0.06	-0.03	-0.10	0.37
SRM-E	-0.27	0.03	-0.04	0.06	0.17	0.06	0.42
SRM- $\Delta E/E$	-0.01	0.05	-0.02	0.03	0.89	0.39	-0.10
BPM-E ₂	-0.67	0.12	-0.02	-0.10	-0.05	0.07	-0.54
BCM-D1r	0.17	0.82	-0.46	0.03	0.06	-0.26	-0.09
BCM-D2r	0.06	0.36	0.11	-0.05	-0.36	0.81	0.22
BPM-Q	0.00	0.40	0.87	-0.10	0.11	-0.24	-0.01
BAM	0.09	-0.05	-0.11	-0.98	0.06	-0.01	0.04
TDC - σ_t	-0.01	-0.03	0.04	0.00	-0.14	0.20	-0.57

Mode number 1 is primarily acting on the mean particle energy. The first row in U implies that this mode is basically measured by the BPM-E. The corresponding actuators are mainly A_{S3} , Φ_{S3} and A_{SS} . A slightly lower impact on the energy is given by A_{XB} . Since FINXB is operated anti-on-crest, this coefficient has the opposite sign compared to the coefficient for the amplitude of FINSB03.

Mode number 2 is describing a combined compression-charge mode, mainly detected by the BCM-D1r and the BPM-Q (column 2 in U). The leading actuators (column 2 in V) are the phase of FINXB and the charge. A smaller influence is given by the phases of FINSB03 and FINSB02 as well as the amplitude of FINSB03.

Since BCM-D1r is integrating the CDR energy in a narrower spectral range starting at a higher frequency than BCM-D2r (see Table 2), the relative change of the detected CDR is higher than for BCM-D2r, thus resulting in a higher sensitivity with respect to compression.

Table 6: Matrix V, containing the first seven right singular vectors of R as columns. They describe the actuators and are sorted according to their importance.

	1	2	3	4	5	6	7
Q	-0.00	0.57	0.82	-0.06	-0.02	-0.01	-0.00
Φ_{SS}	0.16	-0.05	0.08	0.23	0.86	0.41	0.04
Φ_{S1}	0.00	-0.10	0.08	-0.01	0.08	-0.08	-0.07
Φ_{S2}	-0.03	-0.14	0.10	-0.02	0.13	-0.35	0.84
Φ_{S3}	-0.53	-0.18	0.14	0.33	0.28	-0.60	-0.27
Φ_{XB}	0.06	0.75	-0.52	0.07	0.21	-0.30	0.02
A_{SS}	0.48	-0.03	0.07	0.82	-0.27	-0.10	0.02
A_{S1}	-0.10	0.00	0.00	0.06	-0.07	0.10	-0.01
A_{S2}	-0.06	0.00	-0.00	0.04	-0.00	0.09	0.02
A_{S3}	-0.61	0.19	-0.11	0.35	-0.19	0.46	0.35
A_{XB}	0.26	-0.02	0.00	-0.16	0.02	-0.13	0.29

Mode number 3 is also describing a combined charge-compression mode with the same contributors as mode number 2, but now primarily acting on the charge. In contrast to mode 2, the relative signs of charge and compressions are opposite.

Mode number 4 with a singular value already more than 10 times smaller than the first one, is describing the arrival time. This is exclusively detected by the BAM. The corresponding main actuator is given by the amplitude of FINSS and, much weaker, by the phase and amplitude of FINSB03.

Mode number 5 having a singular value which is roughly 100 times smaller than the first mode, is only contributing very little to the overall response. However, column 5 in U is indicating that mainly the relative energy spread is affected with a slight contribution of also BCM-D2r by the corresponding main actuator of the phase of FINSS (column 5 in V).

The remaining singular values are so small, that they are probably dominated by noise and have no constructive impact on the response matrix. Therefore, columns 8 and 9 of the matrices U and V are not shown for better understanding.

CONCLUSION AND OUTLOOK

A diagnostics response matrix was successfully measured at one working point of the SITF. As expected, the beam based measurements of the different diagnostics are not decoupled. This implies that different beam parameters can only be stabilized by using an appropriate procedure based on different diagnostics.

This can be seen for example in mode number 1, dedicated to energy. There is not only one actuator mainly affecting the energy, but the gun amplitude A_{SS} as well as the amplitude of the accelerating S-band cavity A_{S3} and the compression

phase Φ_{S3} are contributing in the same order of magnitude relative to their stability.

It is worth underlining that the specific responses R_{ij} are determined based on the measured stabilities of the actuators. These stabilities vary from RF station to RF station as listed in Table 1. If these stabilities change, for example because the temperature stabilisation of an RF cavity is improved, this would affect all entries in the response matrix. In particular the relative importance of the different actuators might then change in the present representation.

The charge and compression modes (modes number 2 and 3) might be disentangled by compensating the influence of varying charge on the bunch compression monitor in the data processing. This would lead to zeros in the response matrix for $R_{BCM-D1r,Q}$ and $R_{BCM-D2r,Q}$. In consequence, mode number 2 would be dedicated to compression, with the leading actuator of the X-band phase followed by the S-band compression phase and the S-band amplitude. Mode number 3 would be purely sensitive to charge.

As can be seen from the response matrix R , the two BPMs in the bunch compressor as well as the centroid of the synchrotron radiation monitor SRM-E are redundant measurements with a higher accuracy for the BPMs. However, the BPMs only allow to measure the center of mass of the particle energy distribution in the electron bunch. In contrast, the synchrotron radiation monitor provides additional information on the longitudinal phase space projected onto the energy axis. The width of this distribution (the relative energy spread) is the main measure used in mode number 5.

According to the response matrix, the BCMs, sensitive to bunch length changes, do not allow for a clear distinction between a change in the compression phase Φ_{S3} and Φ_{XB} . To solve this ambiguity, the choice of spectral filters could probably be improved further, or a more direct measure of the curvature in phase space could be beneficial. This could possibly be implemented using not only the centroid and the width at the synchrotron radiation monitor, but also some information about the measured shape and their asymmetry.

As a further option, instead of measuring the asymmetry of the longitudinal phase space projected onto the energy axis, the equivalent information is expected for a direct measure of the asymmetry in the temporal profile of the electron bunch.

It is worth noting that there are further effects affecting a proper and stable bunching process not accounted for in these measurements presented here. Among others these are laser arrival time on the cathode, fluctuations in the longitudinal laser pulse profile or the stability of the magnetic fields.

The presented diagnostic response measurement serves first and foremost as a response study of the current diagnostics installed at SITF. In particular, there were more actuators than linear independent diagnostics available. If this approach of SVD would be used for regulation, the different weighting factors would probably need to be optimized experimentally. Furthermore, for slow regulations, it could be important to account for drifts of the diagnostics which were neglected throughout this paper.

ACKNOWLEDGMENT

The authors would like to thank Thomas Schietinger and Eduard Prat for carefully setting up the SwissFEL Injector Test Facility at the initial settings. A further thank belongs to Daniel M. Treyer for fruitful discussions and his work concerning read out electronics.

REFERENCES

- [1] R. Ganter (ed.), "SwissFEL Conceptual Design Report", PSI Bericht, 10-04, 2010, ftp://ftp.psi.ch/psi/SwissFEL_CDR/SwissFEL_CDR_V20_23.04.12.pdf
- [2] M. Pedrozzi (ed.), "SwissFEL Injector Conceptual Design Report", PSI Bericht, 10-05, 2010, http://www.psi.ch/swissfel/CurrentSwissFELPublicationsEN/SwissFEL_Injector_CDR_310810.pdf
- [3] A. Saa Hernandez et al., "Longitudinal Response Matrix Simulations for the SwissFEL Injector Test Facility", in *These Proceedings: Proc. 36th Int. Free-Electron Laser Conf.*, Basel, 2014, THP097.
- [4] R. Ischebeck et al., "Response Matrix of Longitudinal Instrumentation in SwissFEL", in *Proc. 33rd Int. Free-Electron Laser Conf.*, Schanghai, 2011, FROA4.
- [5] B. Keil et al., "Commissioning of the Resonant Stripline BPM System of the SwissFEL Test Injector", in *Proc. 33rd Int. Free-Electron Laser Conf.*, Shanghai, 2011, pp. 652-655.
- [6] G.L. Orlandi et al., "Bunch-Compressor Transverse Profile Monitors of the SwissFEL Injector Test Facility", in *Proc. Int. Beam Instrumentation Conf.*, Tsukuba, 2012, pp. 271-275.
- [7] V. Arsov et al., "Commissioning and Results from the Bunch Arrival-time Monitor Downstream the Bunch Compressor at the SwissFEL Test Injector", in *These Proceedings: Proc. 36th Int. Free-Electron Laser Conf.*, Basel, 2014, THP085.
- [8] A. Angelovski et al., "High bandwidth pickup design for bunch arrival-time monitors for free-electron laser", in *Phys. Rev. ST Accel. Beams* 15, 112803, 2012.
- [9] I. Bronstein et al., *Taschenbuch der Mathematik*, (Verlag Harri Deutsch, 2008), 7th edition.

FEMTOSECOND-STABILITY DELIVERY OF SYNCHRONIZED RF-SIGNALS TO THE KLYSTRON GALLERY OVER 1-km OPTICAL FIBERS

Kwangyun Jung, Jungwon Kim[#], Jiseok Lim, Junho Shin, Heewon Yang,
KAIST, Daejeon, South Korea
Heung-Sik Kang, Chang-Ki Min, PAL, Pohang, South Korea

Abstract

We present our recent progress in optical frequency comb-based remote optical and RF distribution system at PAL-XFEL. A 238 MHz mode-locked Er-laser is used as an optical master oscillator (OMO), which is stabilized to a 2.856 GHz RF master oscillator (RMO) using a fiber-loop optical-microwave phase detector (FLOM-PD). We partly installed a pair of 1.15 km long fiber links through a cable duct to connect an OMO room to a klystron gallery in the PAL-XFEL Injector Test Facility (ITF). The fiber links are stabilized using balanced optical cross-correlators (BOC). A voltage controlled RF oscillator (VCO) is locked to the delivered optical pulse train using the second FLOM-PD. Residual timing jitter and drift between the two independently distributed optical pulse train and RF signal is measured at the klystron gallery. The results are 6.6 fs rms and 31 fs rms over 7 hours and 62 hours, respectively. This is the first comb-based optical/RF distribution and phase comparison in the klystron gallery environment.

INTRODUCTION

Time-resolved X-ray-optical pulse pump-probe experiments with femtosecond time resolution and sub-nm spatial resolution can reveal molecular dynamics and accelerate natural and medical science. Therefore, the future most advanced X-ray Free Electron Lasers (XFELs) require femtosecond-precision synchronization of several lasers and RF signals in tens of accelerator units over km length scale [1]. In the last decade, optical timing and synchronization techniques, based on CW lasers or pulsed mode-locked lasers, have been intensively investigated.

Optical pulsed fiber link stabilization technique based on a balanced optical cross-correlator (BOC) resulted in unprecedented performance. Sub-10 fs in rms long-term stability and short-term jitter were achieved for standard single mode fiber link stabilization in well-controlled laboratory environment [2]. This technique has been already installed in operating FEL facilities (such as FERMI and FLASH), and currently shows <100 fs in peak-to-peak long-term stability over several hours [3,4]. This amount of drift is caused by the polarization mode dispersion (PMD) of the fiber link. Recently, in order to deal with the PMD problem, a polarization maintaining (PM) fiber link was used, and sub-femtosecond long-term timing link stability [5] and remote optical-to-optical

synchronization [6] in the laboratory environment was reported.

Synchronization techniques of local RF signals to a mode-locked laser have been also developed in the last decade. A balanced optical-microwave phase detector (BOM-PD) with sub-10 fs long-term stability and short-term jitter was demonstrated [2]. It detects timing error between optical pulse trains and RF signals directly in the optical domains based on electro-optic sampling in the fiber Sagnac-loop interferometer. The BOM-PD is being used in FEL facility (FERMI) for the mode-locked laser stabilization to the RF master oscillator in the well-controlled laser room [3]. In 2012, a fiber-loop optical-microwave phase detector (FLOM-PD) was developed with both sub-femtosecond short-term jitter and long-term stability [7]. It showed ultra-low short-term residual phase noise floor (-158 dBc/Hz) between two 10 GHz microwave oscillators which were locked to a common mode-locked laser locally [8]. The basic principle of the FLOM-PD is very similar with the BOM-PD, but the FLOM-PD is based on balanced photodetection instead of synchronous detection, and it is much simpler and easy to build.

The combination of these two modular methods (BOC + BOM-PD or BOC + FLOM-PD) may lead to a great performance in remote RF transfer or remote synchronization between a mode-locked laser and a RF oscillator. However, the full implementation of such remote laser-RF synchronization has not been demonstrated so far.

In this paper, we show remote synchronization between a 238 MHz mode-locked laser and a 2.856 GHz RF source by combining FLOM-PD-based local laser-RF synchronization units and BOC-based stabilized fiber links in the real accelerator klystron gallery environment [9]. We installed a pair of 1.15 km long fiber links in an accelerator building and measured the relative phase drift between the optical pulse train and the RF signal at the link outputs in a klystron gallery, which resulted in 6.6 fs and 31 fs rms timing drift maintained over 7 hours and 62 hours, respectively [9]. To our knowledge, this is the first demonstration of maintaining few-fs-level drift over hours of operation in the remote synchronization between a femtosecond mode-locked laser and a RF source over a kilometer in distance. This shows the possibility to distribute RF signals, all tightly locked to a master mode-locked laser, to remote locations with femtosecond stability, not only in the well-controlled laboratory but also in the accelerator environment.

[#]Jungwon.kim@kaist.ac.kr

TEST OF REMOTE LASER-RF SYNCHRONIZATION IN ACCELERATOR ENVIRONMENT

In order to assess the feasibility of applying remote laser-RF synchronization in a real large-scale scientific facility outside the well-controlled laboratory, we installed a pair of 1.15 km dispersion compensated fiber links in an accelerator building [Injector Test Facility (ITF) in the Pohang Accelerator Laboratory (PAL)]. Figure 1 shows the schematic of the experiment at the PAL-ITF.

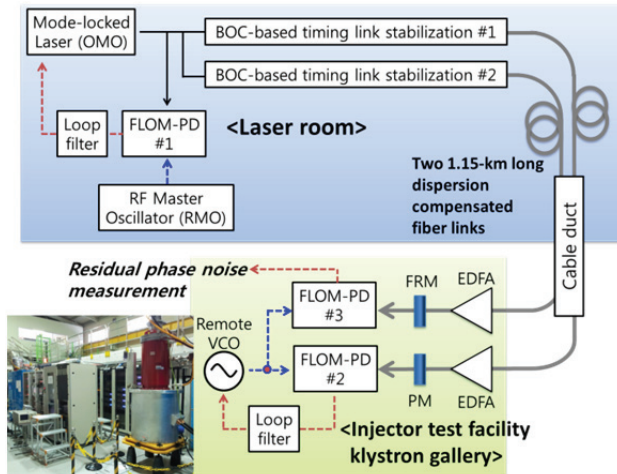


Figure 1: Remote laser-RF synchronization test set-up in an accelerator building (PAL-ITF). BOC, balanced optical cross-correlator; FLOM-PD, fiber-loop optical-microwave phase detector; FRM, Faraday rotating mirror; PM, partial mirror; VCO, voltage-controlled oscillator [9].

In a laser room, a 238 MHz repetition rate, 120 fs pulsewidth, soliton mode-locked Er-laser (OneFive, Origami-15) is stabilized to the 2.856 GHz RF master oscillator (Agilent, N5181B) with 6 kHz locking bandwidth using a fiber-loop optical-microwave phase detector (FLOM-PD) for a long-term stable operation. The 6 kHz feedback bandwidth is selected, because the laser phase noise is higher than the RF master oscillator phase noise below the 6 kHz Fourier frequency region. The output from the laser is split into two independent fiber links. Each link is composed of 1.05 km standard SMF-28 fiber and 100 m DCF (OFS LLWB), and part of each fiber link is installed in a cable duct between the laser room and the klystron gallery. The outputs of the fiber links are installed in an instrument rack in the klystron gallery (photograph in Fig. 1). Part of the delivered optical pulse trains is reflected back, and is applied to the balanced optical cross-correlator (BOC) in the laser room. The detected fiber link timing fluctuations are compensated by a pzt fiber stretcher and a fiber coupled motorized stage. In the klystron gallery rack, a 2.856 GHz voltage-controlled RF oscillator (VCO, INWAVE AG, DRO-2856A) is synchronized with the

output from one link using the FLOM-PD (FLOM-PD #2 in Fig. 1). Finally, to assess the out-of-loop synchronization performance between the locked VCO and the delivered pulse train via the other fiber link, another FLOM-PD (FLOM-PD #3 in Fig. 1) is used. Thus, we can evaluate the relative phase stability between the RF signal regenerated from a fiber link output and the optical pulse train from another independently timing-stabilized fiber link output.

Figure 2 shows the residual phase noise measured in the klystron gallery rack. The rms timing jitter between the RF source and the optical signal is 7.3 fs integrated from 1 Hz to 10 MHz. The VCO is locked to the delivered optical signal with 300 kHz bandwidth. Outside the locking bandwidth, the VCO phase noise follows the free-running VCO absolute phase noise itself. Note that the measured VCO absolute phase noise data from the vendor was limited by a measurement instrument at the high offset frequency (>300 kHz). To figure out the residual phase noise floor inside the locking bandwidth, we also measured the residual phase noise between the two delivered fiber links output optical pulse trains using an out-of-loop balanced optical cross-correlator (BOC). The result shows that the BOC is more sensitive to the gallery environment than the FLOM-PD, because the residual phase noise measured by the BOC is even higher. Thus, the origin of the -128 dBc/Hz noise floor below 1 kHz offset frequency measured by the FLOM-PD was not revealed yet. However, it might be caused by the link stabilization performance. In fact, the noise floor from 30 kHz to 100 kHz is the balanced photodetector voltage noise floor of the in-loop BOC for the fiber link stabilization.

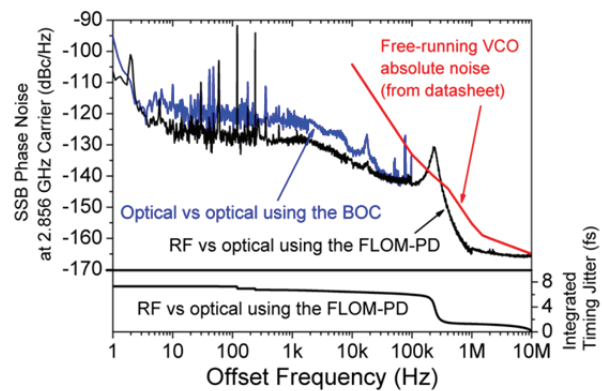


Figure 2: Residual phase noise measurement at the klystron gallery rack after transferring over 1.15 km long fiber link.

Figure 3 shows the relative phase drift measured in a klystron gallery rack. The best 7 hours result (indicated as the red box in Fig. 3) shows 6.6 fs rms timing drift integrated over 7 hours. To our knowledge, this is the first time to show that maintaining sub-10 fs long-term RF phase stability in operating klystron gallery environment is possible by remote laser-RF synchronization via

kilometer-scale fiber links. Over the full measurement span of 62 hours, the integrated rms timing drift is 31 fs. There are several possible reasons for this drift. First reason is that the gallery temperature change by ~ 3 K with a period of ~ 1 day, which can influence the excess phase drift in FLOM-PDs themselves (note that the instrument rack used in the gallery did not have an active temperature controller in this experiment). The previously measured temperature coefficient of the FLOM-PD with an active temperature change of several Kelvin was ~ 20 fs/K [7]. Secondly, PMDs in the two independent 1.15 km long fiber links may have caused the relative phase drift between them that cannot be compensated by the timing stabilization method. Similar amount of PMD-limited timing drift (~ 100 fs) has been observed in other fiber links with hundreds meters to few kilometers scale [4,10,11]. In addition, harsh environments in the klystron gallery with high voltage, high current pulsed signals, and high vibration might lead to additional timing noise to the local laser-RF synchronization system. However, as this is a very early stage demonstration in the gallery environment, more careful investigation on the exact origins and noise-coupling mechanisms is required.

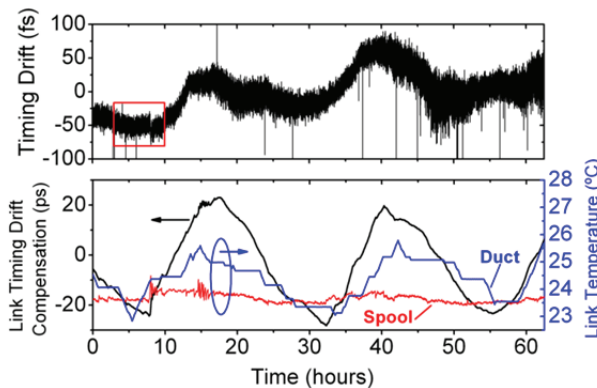


Figure 3: Residual phase drift measurement at the klystron gallery rack after transferring over 1.15 km long fiber link. The best 7 hours result (indicated by red box) shows 7.7 fs rms drift integrated over 7 hours. For the entire 62 hours measurement, 31 fs rms drift was measured [9].

CONCLUSION

We demonstrate remote fiber link-based synchronization between a mode-locked laser and a 2.856 GHz RF source with sub-10 fs rms timing drift over >7 hours, in the accelerator environment. The longer-term synchronization performance is limited to 31 fs rms drift during 2-3 days, by combined effects of the fiber link PMD, gallery rack temperature change, and harsh vibration environment. As this is a very early stage demonstration in the gallery environment, more careful

investigation on the exact origins and noise-coupling mechanisms is required.

ACKNOWLEDGMENT

This work was supported by the PAL-XFEL Project and the National Research Foundation (Grant number 2012R1A2A2A01005544) of South Korea.

REFERENCES

- [1] Basic Energy Sciences Advisory Committee (BESAC), "Report of the BESAC Subcommittee on Future X-ray Light Sources" website: http://science.energy.gov/~media/bes/besac/pdf/Reports/Future_Light_Sources_report_BESAC_approved_72513.pdf
- [2] J. Kim et al., "Drift-free femtosecond timing synchronization of remote optical and microwave sources," *Nat. Photon.* **2**, 733 (2008).
- [3] M. Ferianis, "State of the Art in High-Stability Timing, Phase Reference Distribution and Synchronization Systems," in *Proceedings of IEEE Particle Accelerator Conference (PAC) 2009*, May 2009.
- [4] S. Schulz et al., "Past, Present and Future Aspects of Laser-Based Synchronization at FLASH," in *Proceedings of IBIC 2013*, Paper WEPC32, September 2013.
- [5] M. Y. Peng et al., "Long-term stable, sub-femtosecond timing distribution via a 1.2-km polarization-maintaining fiber link: approaching 10^{-21} link stability," *Opt. Express*, **21**, 19982 (2013).
- [6] M. Xin et al., "One-femtosecond, long-term stable remote laser synchronization over a 3.5-km fiber link," *Opt. Express*, **22**, 14904 (2014).
- [7] K. Jung and J. Kim, "Subfemtosecond synchronization of microwave oscillators with mode-locked Er-fiber lasers," *Opt. Lett.* **37**, 2958 (2012).
- [8] K. Jung et al., "Ultralow phase noise microwave generation from mode-locked Er-fiber lasers with subfemtosecond integrated timing jitter," *IEEE Photon. J.* **5**, 5500906 (2013).
- [9] K. Jung et al., "Remote Laser-Microwave Synchronization over Kilometer-Scale Fiber Link with Few-Femtosecond Drift," *J. Lightwave Technol.* Early Access Article DOI: 10.1109/JLT.2014.2312400 (2014).
- [10] J. A. Cox et al., "Sub-femtosecond timing distribution of an ultrafast optical pulse train over multiple fiber links," in *Proceedings of Conference on Lasers and Electro Optics 2008*, Paper CML1, May 2008.
- [11] K. Jung et al., "Frequency comb-based microwave transfer over fiber with 7×10^{-19} instability using fiber-loop optical-microwave phase detectors," *Opt. Lett.* **39**, 1577 (2014).

ELECTRON BEAM DIAGNOSTICS AND FEEDBACK FOR THE LCLS-II*

Josef Frisch, Paul Emma, Alan Fisher, Patrick Krejcik, Henrik Loos, Timothy Maxwell,
Tor Raubenheimer, Stephen Smith, SLAC, Menlo Park CA 94305, USA

Abstract

The LCLS-II is a CW superconducting accelerator driven, hard and soft X-ray Free Electron Laser which is planned to be constructed at SLAC. It will operate with a variety of beam modes from single shot to approximately 1 MHz CW at bunch charges from 10 to 300 pC with average beam powers up to 1.2 MW. A variety of types of beam instrumentation will be used, including stripline and cavity BPMs, fluorescent and OTR based beam profile monitors, fast wire scanners and transverse deflection cavities. The beam diagnostics system is designed to allow tuning and continuous measurement of beam parameters, and to provide signals for fast beam feedbacks.

LCLS-II

The LCLS-II uses a 4 GeV, CW superconducting LINAC to drive two variable gap undulators to generate soft and hard X-rays (see Fig. 1). The hard X-ray undulator and some of the electron beam line are shared with the LCLS-I room temperature LINAC in order to allow operation with either accelerator. The SC LINAC will operate at bunch rates up to approximately 1MHz, and uses fast kickers (“beam spreader”) to direct selected bunches to each undulator, or to the beam dump.

The LCLS-II includes a low rate (120Hz) diagnostic line at an energy of 100 MeV. A kicker can select single bunches for diagnostics without interfering with the rest of the bunch train.

The LCLS-II can operate in a variety of modes with varying bunch charge and pulse structure, a representative operating mode is shown in Table 1.

Table 1: LCLS-II Electron Beam Parameters (Nominal)

Beam energy	4 GeV
Bunch Charge	10 – 300 pC
Bunch rate	< 0.93 MHz
Average beam power	<1.2 MW
Peak current	500-1500 A
Bunch length (RMS)	0.6 – 52 μ m
Energy spread	125-1500 keV
Energy stability RMS	<0.01%
Emittance (at 100pC, normalized)	~0.3 μ m

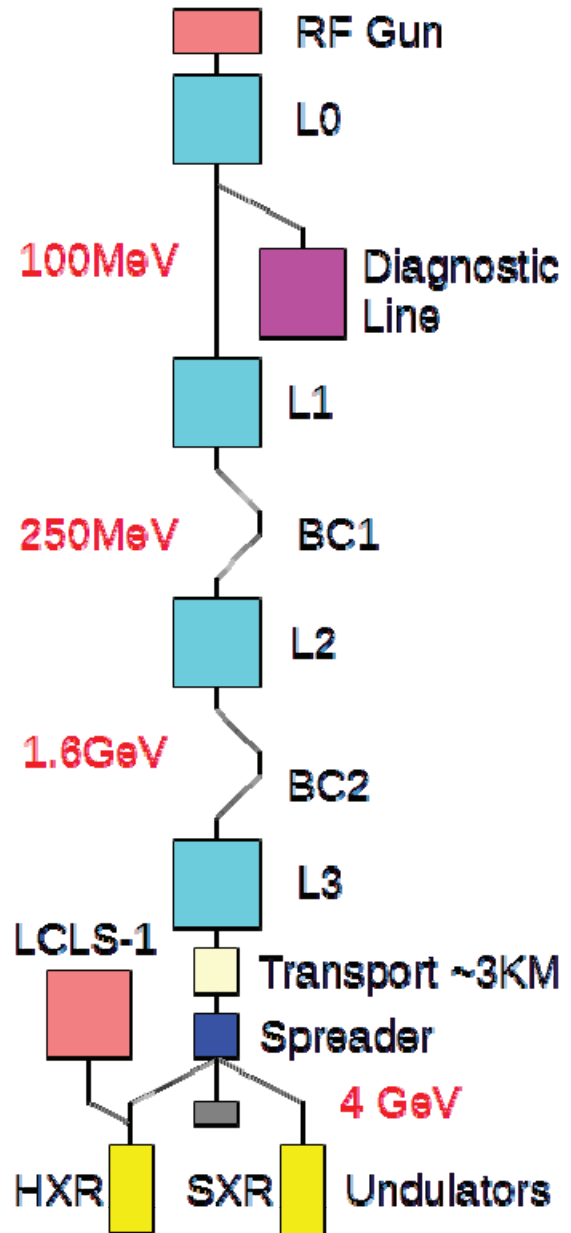


Figure 1: LCLS-II Layout.

DIFFERENCES FROM LCLS-I

Beam Rate / Average Power

The single bunch properties for LCLS-II are similar to those for the existing LCLS-I; however the high average bunch rate and beam power result in new requirements for

*Work Supported by DOE contract DE-AC-02-76-SF00515

the diagnostics systems. The high average power prevents the use of continuously intercepting beam diagnostics in the main beam lines. However, OTR and YAG profile monitors can be used in the lower rate diagnostic line. High speed wire scanners can be used in the full 1MHz rate beam provided they operate above a minimum scan velocity.

The high beam rate results in high data rates and necessitates the use of processing in FPGAs. Feedbacks which operate at or near full beam rate will also require FPGA processors. In addition some devices with slow response times (for example cavity BPMs) will require additional signal processing to isolate individual bunch signals.

Low Charge / Short Bunch Operation

The LCLS-II will operate with bunch charges as low as 10pC with pulse lengths as short as 600nm RMS. The requirement for high position resolution for low bunch charges will require the use of cavity BPMs in locations where single bunch resolution below 20 microns is required.

At the shortest bunch lengths (600nm) the temporal structure of the bunch will have significant frequency components in the visible spectrum. This will result in substantial optical coherent emission that is strongly dependent on details of the bunch temporal profile, and prevent the use of optical imaging diagnostics for the compressed beam.

DIAGNOSTICS CONTROLS

Common Platform

The beam diagnostics system will largely be built from a common controls hardware / firmware / software platform. The same platform is expected to also be used for the LLRF system (see Fig. 2).

- **Analog Front End:** This converts raw sensor signals into a bandwidth and amplitude that can be directly digitized. An example would be the variable gain amplifiers and RF downmixers for a cavity BPM.
- **A-D:** The specifications have not been finalized but this is expected to be a commercial high performance A-D, roughly 150Ms/s, 16 bit.
- **FPGA:** This converts raw data from the A-D into “physics” parameters such as X, and Y position at the 1 MHz beam rate.
- **Timing Network:** This provides beam time clock and pulse ID with <1ns stability
- **EPICS Network:** Conventional TCP/IP network for communication and configuration
- **MPS Network:** Machine protection network to provide low latency (<100usec), high reliability beam trip signals if pre-defined beam limits are violated
- **Fast Feedback Network:** A low latency (~5 μ sec + cable speed) network to transmit data from sensors to feedback actuators.

- **DAC:** The specifications have not been finalized but this is expected to be a commercial high performance D-A, roughly 100Ms/s at 16 bits. Note that the D-A is not required for many diagnostics devices but may be included on the FPGA board for commonality of parts.
- **Analog Driver:** This converts the D-A output to the signal levels / types required to drive the beam actuator (kicker, deflection cavity etc.).

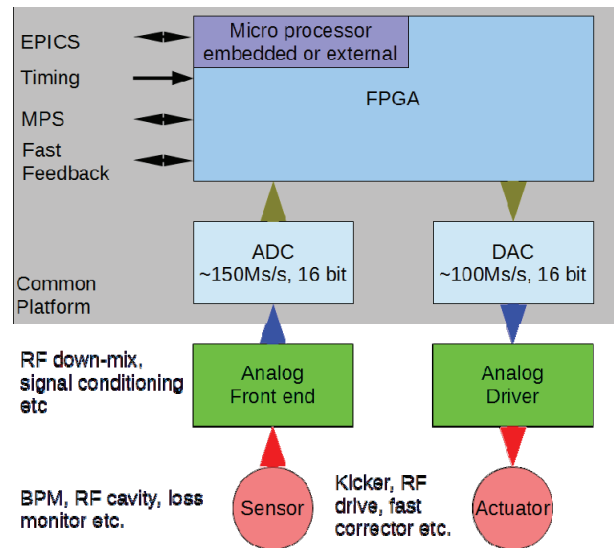


Figure 2: Common controls platform.

Other Devices

Some devices, including profile monitors and wire scanners, which cannot operate at the 1MHz beam rate will be controlled directly through EPICS rather than the “common platform”. These will be triggered to operate on specific beam pulses by the timing system.

BEAM POSITION

The LCLS-II contains approximately 360 BPMs of a variety of types:

Stripline BPMs

Standard strips: Most of the LCLS-II uses 12cm strips in a 2.5 cm diameter pipe

Bypass Line: The LCLS-II uses the existing PEP-II 2-kilometer bypass line. This line has stripline BPM pickups with 61cm long strips in a 7.3cm diameter pipe.

The stripline BPM electronics will be similar to that used for LCLS-I: the strip signals will be bandpass filtered, then digitized. A strip-to-strip calibration system will correct for variations in channel gains (see Fig. 3). LCLS-II will use a 300MHz BPM processing frequency compatible with both strip lengths. The high beam rate will require processing in an FPGA to extract single bunch data. Note that for installations with long cables, reflections from previous bunches may interfere with measurements and so will need calibration and correction.

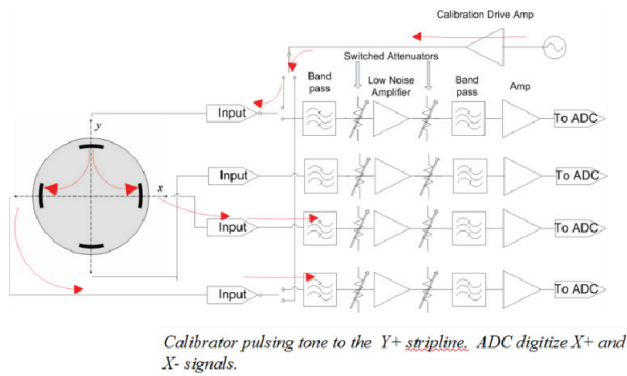


Figure 3: Stripline BPM front end electronics.

Cavity BPMs

Cavity BPMs are used in locations where high resolution is required. Three different types of cavity BPMs will be used:

- **Undulator BPMs:** These are required to provide a resolution of $<1\mu\text{m}$ at a 10pC charge. They will operate at X-band (11.424 GHz).
- **LINAC Feedback BPMs:** These are used in locations where single bunch resolution that is better than that which can be obtained with striplines is required. The design has not been finalized but will likely be S-band in order to provide sufficient aperture.
- **Dispersion Region BPMs:** The bunch compressors and dispersive regions in the beam transport system require large aperture ($\sim 100\text{ mm}$) with high resolution ($20\mu\text{m}$) at 10pC. This will require low frequency (L-band) cavity BPMs.

The cavity BPM front end electronics will use a conventional filter and downmix to an IF frequency that can be digitized. The IF frequency has not been selected yet, but is probably near 50MHz.

All of the cavity BPMs will be high “Q” and single bunch measurements will be performed by subtracting the vector amplitude of the fields that are present in the cavity from the previous bunch time. In the simulation in figures 4, and 5, the fields for measurement time “B” from bunch “A” in the absence of a bunch in “B” are subtracted from the measured “B” signal. The subtraction is done on the vector amplitudes of the RF signals. Note that the simulation was done at 10X the real bunch rate in order to exaggerate the effect that needs correction.

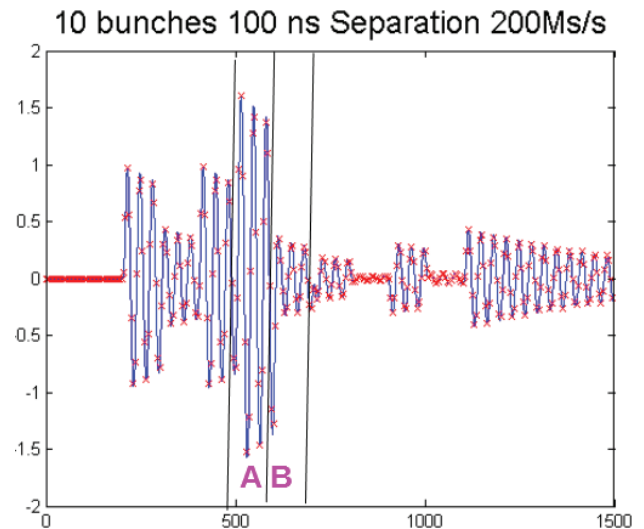


Figure 4: Simulation: The signal for bunch “B” is corrected for the ringing signal for bunch “A”.

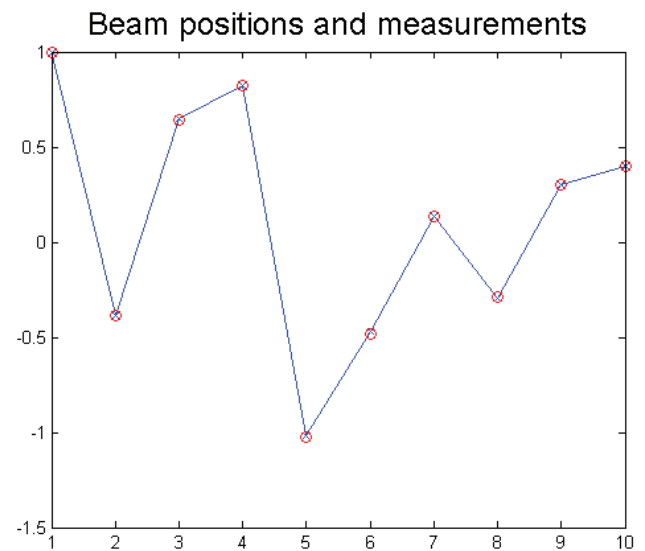


Figure 5: Simulation: Corrected BPM position (red circles) plotted with the correct beam position (blue line).

Cold Button BPMs

The cryo-modules will use button BPMs: the single bunch resolution requirements are $100\mu\text{m}$ RMS at 10pC, with multi-bunch averaging to obtain better resolution. The buttons will be similar to the XFEL design with 20mm diameter buttons in a 70mm beam pipe (see Fig. 6). Processing electronics will operate below beam pipe cutoff and will downmix $\sim 1\text{GHz}$ button signals to an IF that is digitized by the standard controls digitizer.

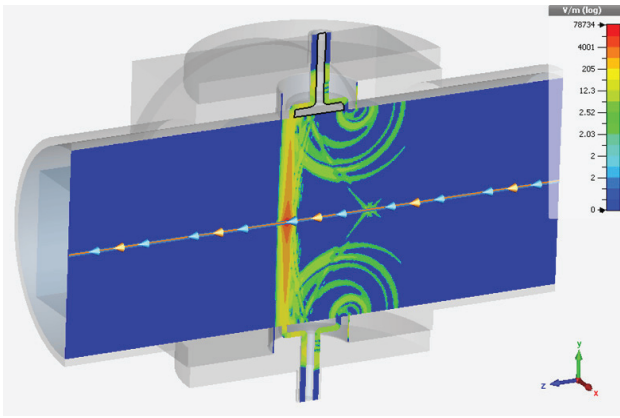


Figure 6: Cryo button BPM based on European XFEL design.

Note that LCLS-II has chosen a somewhat simpler but lower performance processing scheme than that used by XFEL [1].

HOM BPMs

The signals from the SC cavity HOM ports are brought out to room temperature. The first cavity in the injector and possibly others will be instrumented with HOM based position readouts similar to those described in [2].

TRANSVERSE PROFILE

Profile Monitors

The short bunch operating modes (0.6um RMS) of LCLS-II will result in substantial enhancement of optical emission from the longitudinal bunch form factor in addition to the coherent emission from CSR induced current modulation. This is expected to make imaging based on optical radiation impractical in the fully compressed beams.

OTR type profile monitors will be used in the injector at reduced beam rates, and in the low rate diagnostic line (120Hz, 100MeV). We are investigating the use of a profile monitor design developed at PSI using YAG:Ce crystals that is less susceptible to coherent emission than standard designs [3].

OTR profile monitors will also be used in the dump lines. The OTR foils will be located away from the main beam axis and the beam will be kicked onto the foil at low rate for energy spread measurements.

Wire Scanners

The LCLS-II will rely on wire scanners for most beam profile measurements. Wire scanners can be used on the full rate beam as long as the scan rate is high enough to prevent overheating of the wires. Calculations were done to estimate the wire temperature rise under varying beam conditions and scan rates [4]. For uncooled carbon wires, 34um in diameter (same as for LCLS-I wire scanners), and 100pC and a 600kHz beam with a 40um spot size, a scan speed > 250mm/s is required to avoid thermal damage. A prototype fast wire scanner based on a linear

motor has been tested at SLAC and operates at and above that speed (see Fig. 7).

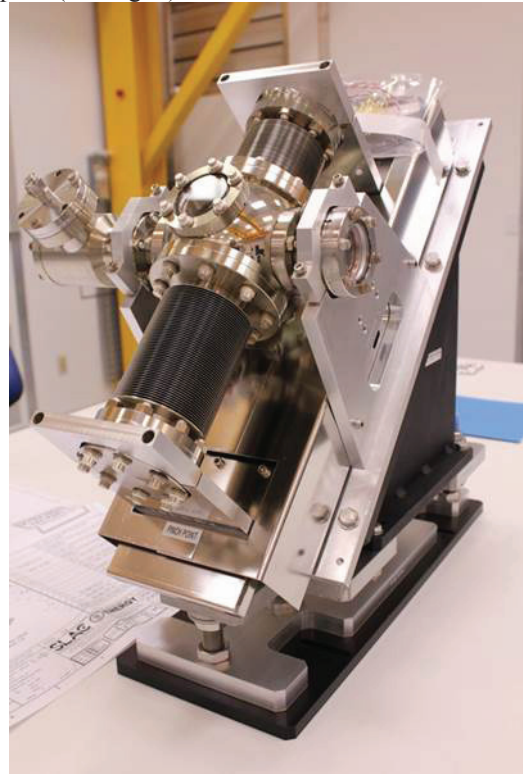


Figure 7: Fast wire scanner tested at SLAC.

Thermal radiation does not provide significant cooling; however heat diffusion along the length of the wire can substantially reduce the wire temperature. Figure 8 shows the reduction in temperature rise as a function of thermal diffusivity in the range of values expected for different carbon wire types.

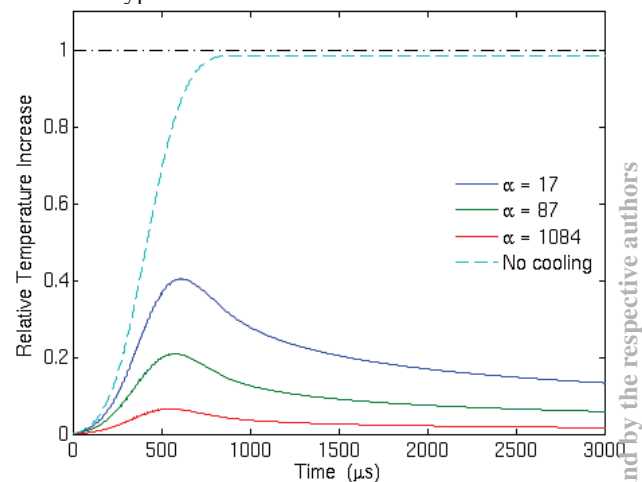


Figure 8: Wire temperature rise (normalized) as a function of wire thermal diffusion in mm²/sec.

The signals from the wire scanners will be detected by measuring the degraded energy particles lost from the beam. The wire scanner data will be correlated with beam position data from one or more nearby cavity BPMs to correct the scans for beam position jitter.

Halo Monitors

The high average beam power in LCLS-II requires measurements of the beam halo to prevent beam loss. The wire scanners will include thick wires that can be moved close to, but not in the main beam to allow sensitive halo measurements.

LONGITUDINAL MEASUREMENTS

Beam Energy / Energy Spread

BPMs in locations with known dispersion are used to measure the beam energy. BPMs in nearby non-dispersive regions are used in combination with the optics model to correct for incoming beam orbit variations.

Due to the requirement for high energy resolution ($<0.01\%$ single bunch), and the large aperture requirements (several cm), cavity BPMs are used for the energy measurements.

Wire scanners are used in the dispersive regions to measure the beam energy spread. As with other wire scanners, the average beam position is measured and corrected with BPMs to remove beam jitter.

Bunch Length – Relative

The electron bunch length is measured with coherent radiation monitors in the bunch compressors. This measurement is not calibrated but is used for bunch length control feedback. The concept is similar to LCLS-I however there are additional technical challenges:

- The wide range of operating charge and bunch length requires a large dynamic range from the detectors.
- The high beam rate can result in high average powers on the detectors.
- The high beam rate requires firmware to correct for multi-bunch effects in the detectors.

For BC2, pyroelectric detectors similar to the LCLS-I design will be used. As the maximum average coherent radiation power could exceed 10 Watts, and the detector average power limit is estimated at 25mW, the beam will be attenuated. The maximum allowed single bunch energy on the detector at a 1MHz beam rate is 25nJ. However the estimated detector noise is 6nJ which only provides a very limited single bunch signal to noise. In addition the charge amplifiers used for the LCLS-I bunch length monitors do not have sufficient bandwidth to measure a 1 MHz beam. This is an area of active development and several approaches are being considered:

- Cooled pyroelectric detectors that can be used at higher average power
- Improved charge amplifiers designed for lower noise and higher bandwidth
- Use of alternate detector technology

For BC1 at low charges and long bunch lengths the signals can be as low as 1.5nJ. Here the bunch lengths are

longer so the coherent emission peak frequency is in the 100s of GHz. High sensitivity millimeter wave diodes are available commercially in this frequency range [5]. High frequency diodes measuring signals from a ceramic gap have been tested successfully as bunch length monitors in the first bunch compressor in LCLS-I.

Bunch Length Monitor – Transverse Cavity

Calibrated bunch length and longitudinal profile measurements will be performed with transverse deflection cavities similar to those used on LCLS-I. Transverse deflection cavities will be installed in the following locations:

- Injector 100MeV diagnostics line, combined with a spectrometer bend: S-band
- After BC1: S-band
- After BC2: X-band
- After each undulator, combined with a spectrometer bend: X-band

The transverse cavities will use room temperature structures operated at a maximum of 120Hz. The fill time of the structures is substantially shorter than the 1 microsecond bunch spacing so the deflectors can be used to measure single bunches without disturbing the remainder of the 1MHz bunch train.

Downstream of the undulators the combination of a TCAV and spectrometer bend allows a measurement of the E vs. T profile of the electron bunch after the lasing interaction (see Figs. 9 and 10).

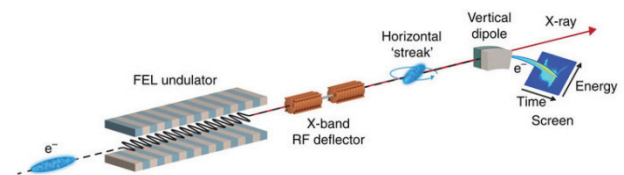


Figure 9: Transverse deflection cavity and spectrometer.

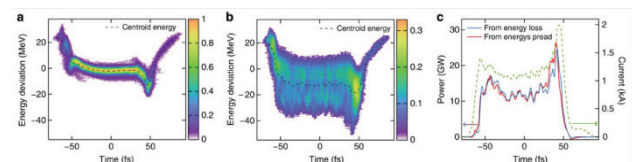


Figure 10: TCAV measurements at LCLS-I showing energy spread / change from FEL interaction.

The X-band transverse deflection structure at LCLS-I has used time-dependent energy loss to measure X-ray pulses with a temporal resolution of 3 femtoseconds FWHM [6].

Arrival Time Monitor

The X-ray experiments performed at LCLS-II will require measurement and control of the bunch arrival time. A RF cavity based bunch length monitor similar to

that used at LCLS-I will provide pulse by pulse bunch timing information.

Electron bunches excite a longitudinal cavity whose output is down-mixed and digitized. The measured RF phase is then corrected for cavity frequency drifts (primarily due to temperature changes) by using the cavity frequency measured on each pulse.

The existing LCLS-I monitor operates at <10fs RMS jitter and 40fs drift [7]. Based on initial tests, improvements to the processing algorithm are expected to improve the measurement jitter to <7fs RMS.

FEEDBACK

Slow Feedback

The measurements from all diagnostic devices are available through EPICS channel access. The diagnostics electronics firmware will provide data averaged by beam destination as well as single pulse data selected by pulse-ID. The beam control devices (magnets, kickers and RF stations) are controllable through EPICS, with control of pulsed / fast devices available on a pulse-ID or beam destination aware fashion.

Feedbacks will be programmed in Matlab [8] operating through channel access in a similar fashion to that used in LCLS-I. Based on LCLS-I experience, loop speeds of up to approximately 5 Hz are expected, sufficient for beam drift correction.

Transverse beam feedbacks will control the trajectory throughout the accelerator / FEL systems. Most of the controls will be slow correctors, but fast (1MHz) correctors are available upstream of the undulators and feedbacks can control the kickers used for the diagnostic line and beam spreader. A total of 15 transverse feedbacks are planned.

Longitudinal feedbacks use the measured beam energy and bunch length at various locations to control the RF fields in the SC cavities in a manner similar to that used for LCLS-I. A total of 11 longitudinal feedbacks are planned.

The LCLS-II uses a single SC linac to drive two variable gap undulators. Undulator gap tuning is used for wavelength changes; however there is a need for fine independent control of the operating wavelength of the two undulators.

A single SC structure at the end of the LINAC will be operated off frequency so that the electron bunches directed to the two undulators see opposite phase accelerating fields. The amplitude of this structure controls the difference in the X-ray energies while the remainder of the RF controls the sum allowing for independent X-ray energy feedback in both undulators.

Fast Feedback

The LLRF systems for the SC structures are expected to control the fields to maintain short term variations below 0.01% amplitude and 0.01 degrees phase. Slow variations will be corrected by the slow beam feedbacks

described above. This is expected to meet the LCLS-II beam stability requirements.

There may be high frequency beam disturbances that are not controlled by the RF system, including:

- Interference in cavity probe signals from beam fields
- Mechanical vibration of the SC structures
- The microbunching instability can cause variations in the longitudinal profile which will result in variations in CSR energy losses
- Variations in drive laser pointing

The LCLS-II will include a fast feedback system that allows selected devices to be attached to a low latency feedback network. Initial design studies suggest that a latency of 5 μ s in addition to the cable delays is practical.

The final design and implantation of the fast feedback system will be finished after early beam commissioning when the requirements are understood.

The “common platform” FPGA interface described earlier will include a SFP (small form pluggable transceiver) port that can be connected to the low latency feedback network.

REFERENCES

- [1] D.M. Treyer et al., “Design and Beam Test Results of Button BPMs for the European XFEL” DESY Report DESY-2041-01447, 2013.
- [2] S. Molloy et al., “High Precision SC Cavity Alignment Measurements with Higher Order Modes”, SLAC-PUB-12349, 2007.
- [3] R. Ischebeck et al., “SwissFEL Beam Profile Monitor”, to be published in the proceedings of the 2014 International Beam Instrumentation Workshop, ID 1113, Monterey California, 2014.
- [4] H. Loos et al., “LCLS Beam Diagnostics”, to be published in the proceedings of the 2014 International Beam Instrumentation Workshop, ID 1113, Monterey California, 2014.
- [5] www.vadiodes.com
- [6] C. Behrens et al, “Few-femtosecond Time-resolved Measurements of X-ray free-electron Lasers”, Nature Communications 5, 3762, 2014.
- [7] A. Brachmann et al: “Femtosecond Operation of the LCLS for User Experiments.”, SLAC-PUB-14234, 2010.
- [8] www.mathworks.com

BEAM ENERGY MANAGEMENT AND RF FAILURE COMPENSATION SCENARIOS FOR THE EUROPEAN XFEL

Bolko Beutner, DESY, Hamburg, Germany

Abstract

Total beam delivery time to user stations is a key parameter for FEL user facilities. Therefore downtime due to RF issues, among other things, should be minimized. Specifically in case of a RF failure machine operation and beam delivery should be maintained as long as the next scheduled maintenance day. This is achieved by increasing the power in all remaining klystrons to recover the lost beam energy. These modification of the beam energy profile along the machine induces an optics perturbation which is typically compensated by a rescaling of the quadrupole magnet gradients to maintain a constant focusing strength. However, we would like to resume operation at the next macro-pulse after a RF event. While, in general, the RF systems can handle such changes the magnets can not. In this paper we will explore optics perturbations for the case that we do not change the magnets at all, to estimate the feasibility of fast beam recovery after klystron failure. In addition corrections to the RF setup are calculated with the goal of avoiding changes in the bunch compression dynamics of the machine.

BEAM ENERGY MANAGEMENT FOR THE EUROPEAN XFEL

Superconducting technology used at the European XFEL allows for RF pulses as long as $600\ \mu\text{s}$ supporting bunch trains with an internal repetition rate of up to 4.5 MHz. These pulses are, which are refereed to as *macro-pulses* are triggered with 10 Hz. The European XFEL is driven in total by 26 1.3 GHz multi-beam klystrons [1] [2]. These RF stations are distributed along European XFEL as shown in Fig. 1.

The energy gain ΔE , number of RF stations N , and individual voltages per klystron $\Delta E/N$ and cavity V are summarized in Table 1. Each klystron in the Linac 1-3 sections drives four accelerator cryo-modules consisting of eight cavities with a total energy gain up to 755 MeV. Design gradient of the niobium cavities is 23.6 MV/m. Since the assembly of the cryo-modules is work in progress we do not have final numbers on the actual available gradient. After final testing and should the situation arise re-treatment of all modules we assume an available gradient of 23.6 MV/m with an average overhead of 10% [3]. Linac 3 is configured to achieve nominal final beam energy of 17.5 GeV at the nominal gradient of 23.6 MV/m using 20 instead of 21 RF stations as beam energy reserve.

In the following the name *klystron* refers to the full RF station including modulator, pulse cables, pulse transformers, klystrons, waveguides, down to the cavities, and failures in each of these components are refereed to as *klystron failure*.

From the point-of-view of electron beam energy management the machine is conveniently separated into three parts. First the Injector and Linac 1 section. In this region of the machine each section is essentially driven by one klystron. Klystron failures in this part are fatal and can not be compensated, immediate repair is required to resume operation. The second part is Linac 2. A reduction of acceleration voltage can be recovered by reserves in Linac 3. This Linac 2 however is upstream of the last bunch compressor chicane. Voltage changes effectively modify the energy chirp at BC2 and therefore the final longitudinal beam profile. In addition to energy profile reorganization the off-crest phases needs modification to maintain the final current profile. Linac 3, the main linac, is the last part. Here the majority of the beam energy is generated and here beam energy variations are corrected. The nominal energy gain of Linac 3 is 15.1 GeV. Since we only rely on 20 instead of 21 klystron stations and assume an 10% energy overhead the total voltage capacity of Linac 3 is 17.4 GeV. This additional energy reserve of about 2.3 GeV can be used to compensate the outage of about three klystron stations.

Table 1: XFEL Energy Gain Configuration

Linac Section	ΔE [GeV]	N	$\Delta E/N$ [MeV]	V [MV/m]
Injector	0.13	1	130	16.5
Linac 1	0.57	1	570	17.8
Linac 2	1.7	3	567	17.7
Linac 3	15.1	21/20	719/755	22.5/23.6

MAIN LINAC ENERGY MANAGEMENT

To redistribute the energy gain along we propose an iterative procedure. We start with an index set I which includes all klystrons used for energy correction. Typically I contains all stations except the failed one. The voltages of modules not in I $\Delta V_{j \notin I}$ are not necessarily set to zero, to allow modeling of reduced gradients in individual stations, e.g. detuned cavities within a module or reduced voltage operations as quench prevention. The voltage of each module in operation is modified according to:

$$\Delta V'_i = \frac{E_{\text{nominal}} - \sum_{j \notin I} \Delta V_j}{|I|} \frac{w_i}{\langle w_i \rangle}, i \in I. \quad (1)$$

The positive weight factors w_i are chosen to set priorities according to the performance and reliability of the individual RF stations. After voltage scaling according to Eq. 1 each ΔV_i is compared with the individual maximum. If the maximum is exceeded it is set to this maximum and the station

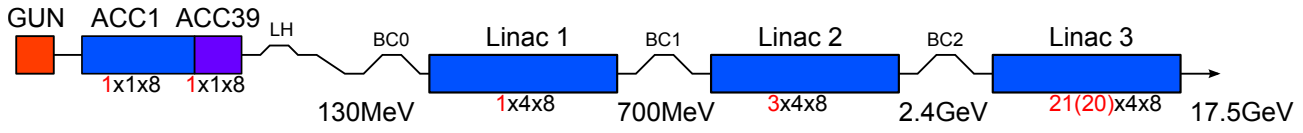


Figure 1: Overview of the XFEL linac and bunch compressor sections. The beam energy at different positions along the machine is given together with the number of RF stations per linac section. For instance Linac 2 consists of 3 klystrons driving 4 modules each containing 8 cavities. Linac 3 consists of 21 klystron stations.

removed from the set I to have these stations not modified in further iterations. Such iterations continue until the nominal energy gain is retained or all available structures are set to maximum voltage. Examples of such energy profile corrections are shown in Fig. 2, 3, and 4. As mentioned earlier

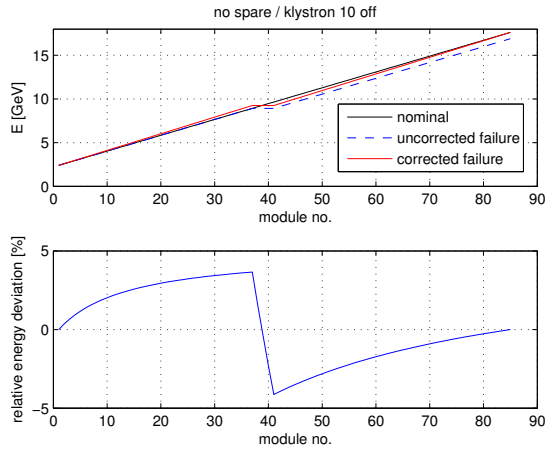


Figure 2: Example of energy correction in Linac 3 of XFEL. In the upper plot the nominal energy profile (black solid), reduced energy after RF failure in station 10 (blue dashed), and the corrected energy profile (red solid) are shown. The relative deviation, the corresponding quadrupole field deviation, along the linac indicated by the module number is shown in the lower plot. In this example no dedicated spare is used, all cavities nominally are operated at $23.6 \text{ MV/m} \cdot 20/21 = 22.5 \text{ MV/m}$.

the main linac is driven by 21 RF stations while only 20 are required for nominal operation. Basically two options can be considered to use this reserve, either all stations are operated at 20/21 of the nominal gradient or one RF station is not used in nominal operation and activated as needed. In the latter case this "spare" can be located at different positions along the linac.

In the following we consider four scenarios, all stations are in operation, the most downstream station, the middle station or the klystron in the beginning of the main linac are deactivated. Comparing this first two options in Fig. 2 and Fig. 3 we see that in the first case we have an energy deviation at all positions while in the second case the deviation is somewhat localized.

The exact shape of the energy deviation depends on the position of the broken RF station. An overview of the energy

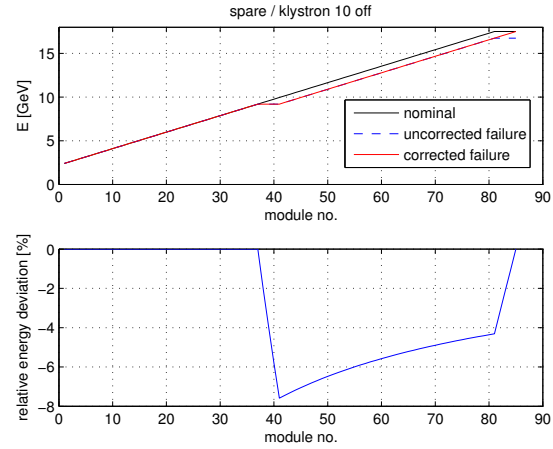


Figure 3: As in Fig. 2. In this example a reserve klystron station is located at the end of the main linac.

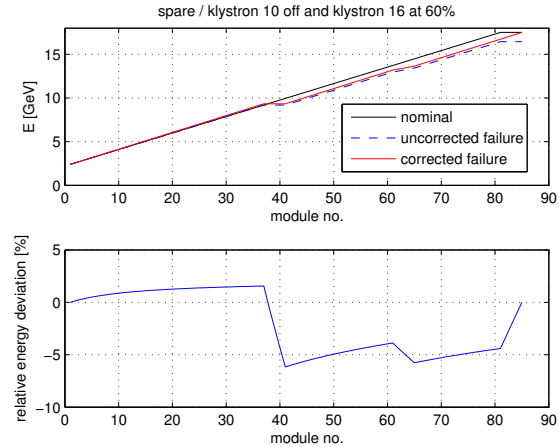


Figure 4: As in Fig. 3. In this example RF station 10 is off and station 16 is set to 60% of nominal gradient.

deviations along the linac for the different scenarios is given in Fig. 5.

The impact on the beam optics mismatch amplitude $\text{BMAG} = \xi + \sqrt{\xi^2 - 1}$ with $\xi = 1/2 \cdot (\beta\gamma_0 - 2\alpha\alpha_0 + \gamma\beta_0)$ at the end of the linac with respect to the design optics is summarized in Fig. 6.

Overall optics mismatch amplitude is optimized in the case with all klystrons in operation and the "spare in the middle" case. In all these situations the maximum deviation from the design optics occurs if the first RF station is out of operation. In general this behavior is expected. As shown

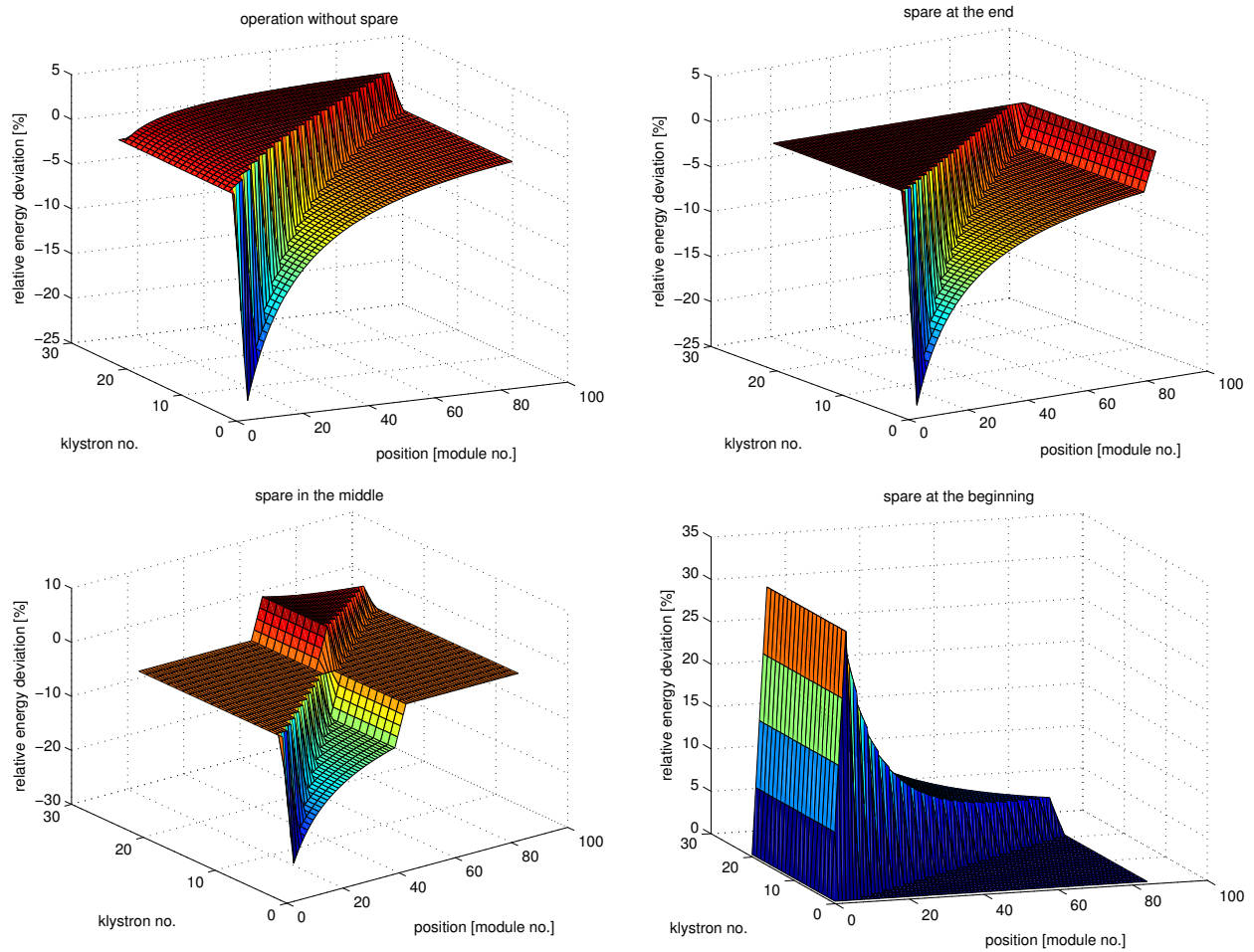


Figure 5: A summary of the energy deviations caused by module failures is shown here. Each plot contains the energy deviation as in the lower plot of Fig. 2 as a function of the klystron which is assumed to be not operational. Different spare scenarios are compared. No dedicated spare is used in the upper left plot. In the remaining scenarios the spare position is at the end, in the middle, or at the beginning of the linac.

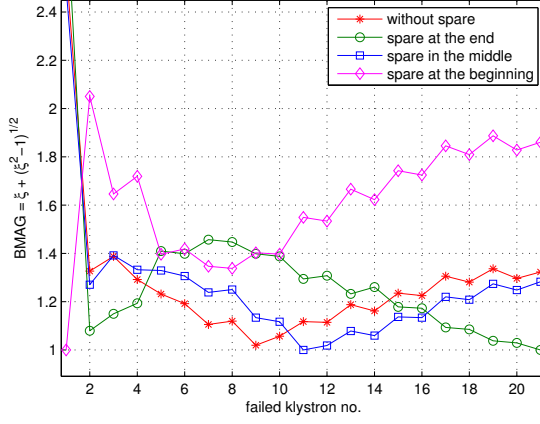


Figure 6: Summary of the optics impact of the different spare scenarios. The optics mismatch at the end of Linac 3 with respect to the nominal optics is plotted vs. the position of a non-operating klystron. In all scenarios excluding the spare at the beginning case the optics deviation caused by the first RF stations in the linac are as high as $\text{BMAG} = 2.9$.

in Fig. 3 the range in which the quadrupole are "detuned" depends on the distance between the broken Klystron and the average position of the reserve. While the impact on the relative energy deviation is obviously lower at higher energies. Studies on operation with simultaneous operation at different bunch charges indicate that a BMAG of about 1.9 ($\xi = 1.2$) is tolerable [4]. However further studies are required on the effects from this optics mismatch on the FEL performance.

I would conclude that all stations should be in operation all the time with reduced gradient. This optimizes robustness of the beam optics and is, in routine operation, less demanding because of the lower gradient.

BUNCH COMPRESSOR LINAC

Above we discussed energy management in Linac 3 of the European XFEL. In Linac 2 we face a different situation. The relative impact of a RF station is larger due to the lower number of independent RF stations, 3 compared to 21. Therefore the energy of BC2 can not be maintained if a RF station is not operational, which calls for a rescaling of the magnets in BC2 inhibiting fast recovery at the next macropulse. Final energy is corrected in Linac 3 as described in the last section. In addition any change in the acceleration upstream of BC2 affects the energy chirp and thus the compression. One way to treat this problem would be a complete redesign of the longitudinal dynamics of XFEL for different energies at BC2 covering reasonable situations. Such a design strategy is covered in [5], but beyond the scope of this paper.

If only Linac 2 is affected we can find a corrected RF phase which compensates the compression analytically. Two effects play a role here. First of all the voltage changes so the generated energy chirp is affected and has to be corrected by

a phase offset. And since the relative energy chirp is relevant for compression the beam energy at BC2 E_{BC} , which is affected by the Linac 2 phase, has to be taken into account as well.

The energy at the chicane E_{BC} reads

$$E_{\text{BC}} = E_0 + eV \cos(\varphi) \quad (2)$$

with the initial energy E_0 at the beginning of Linac 2 section and the voltage V of Linac 2.

For the energy along the bunch at position s holds

$$E(s) = eV \cos\left(\varphi + \frac{2\pi}{\lambda}s\right) + E_0 \quad (3)$$

$$= E_0 + eV \left(\cos(\varphi) - \frac{2\pi}{\lambda} \sin(\varphi)s + \dots \right) \quad (4)$$

$$\approx E_{\text{BC}} + As, \quad (5)$$

with an linear energy chirp $A = -2\pi eV \sin(\varphi)/\lambda$. If we assume that the initial acceleration upstream to E_0 is not on-crest an additional initial chirp term $A_0 s$ has to be added to Eq. 5.

The normalized relative energy deviation $\delta = \frac{E(s) - E(0)}{E(0)} = \frac{A_0 s + As}{E_{\text{BC}}}$ at the bunch compressor is required to be constant to maintain the compression. Therefore

$$\frac{A_0 s + As}{E_{\text{BC}}} = \frac{A_0 s + A's}{E'_{\text{BC}}} \quad (6)$$

$$\frac{A_0 + A}{E_{\text{BC}}} = \frac{A_0 + A'}{E'_{\text{BC}}} \quad (7)$$

$$\frac{A_0 - \frac{2\pi eV}{\lambda} \sin(\varphi)}{E} = \frac{A_0 - \frac{2\pi eV'}{\lambda} \sin(\varphi')}{E'} \quad (8)$$

$$\frac{A_0 - \frac{2\pi eV}{\lambda} \sin(\varphi)}{E_0 + eV \cos(\varphi)} = \frac{A_0 - \frac{2\pi eV'}{\lambda} \sin(\varphi')}{E_0 + eV' \cos(\varphi')} \quad (9)$$

$$a = \frac{A_0 - \frac{2\pi eV'}{\lambda} \sin(\varphi')}{E_0 + eV' \cos(\varphi')} \quad (10)$$

$$a(E_0 + eV' \cos(\varphi')) = A_0 - \frac{2\pi eV'}{\lambda} \sin(\varphi') \quad (11)$$

with the initial chirp A_0 , additional chirp generated in a downstream linac section A , and a convenient constant a defines the corrected phase φ' for a given modified voltage V' . For convenience V' is scaled with a linear energy factor from V . An energy factor of 1 would be nominal operation while 2/3 corresponds to operation with one klystron out of operation in Linac 2 of XFEL.

In the following example we apply Eq. 11 on the 250 pC case of European XFEL with a peak current of 5 kA. It is convenient to solve Eq. 11 numerically which is illustrated in Fig. 7.

The corrected phase φ' and the resulting energy at BC2 E_{BC} are plotted in Fig. 8 and Fig. 9 respectively. Due to this phase changes the energy at BC2 does not scale linearly with the voltage in Linac 2. Especially in the case of reduced Linac 2 voltage we actually lose less energy than expected.

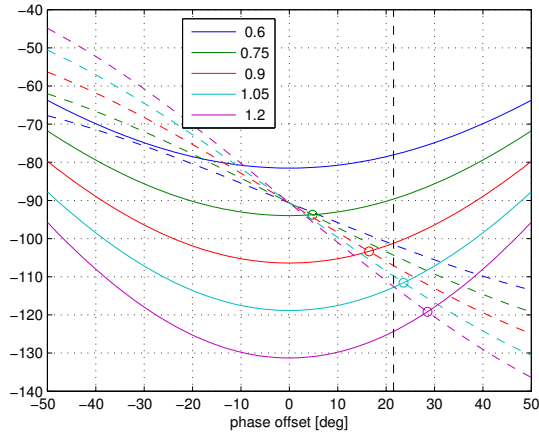


Figure 7: An example of a numerical solution of Eq. 11. The l.h.s (solid lines) and the r.h.s of Eq. 11 (dashed lines) are shown over a range of possible phases φ' . The intersections (circles) indicating the solutions for φ' for different energy factors indicated by a color code. The nominal phase φ (energy factor 1) is indicated by the dashed black vertical line. The case 0.6 has no solution.

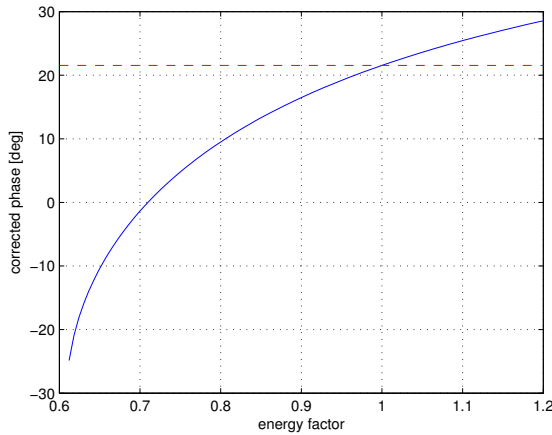


Figure 8: Solution for φ' of Eq. 11. The nominal phase φ (energy factor 1) is indicated by the dashed red line.

Please note that below an energy factor of about 0.61 no solution can be found. Outside of the presented analysis this can be avoided by either a modified R_{56} of the chicane or an upstream modification of the energy chirp A_0 .

These solutions are used in numerical simulations of the longitudinal dynamics done with *RF Tweak 5* [6]. The results of these calculations Fig. 10 confirm the validity of Eq. 11. Minor differences in the current profiles can be attributed to self-field effects which depend on the beam energy and are not covered by Eq. 11. Slow beam-based feedback systems which are anyhow foreseen to stabilize the peak current will correct for these effects.

ISBN 978-3-95450-133-5

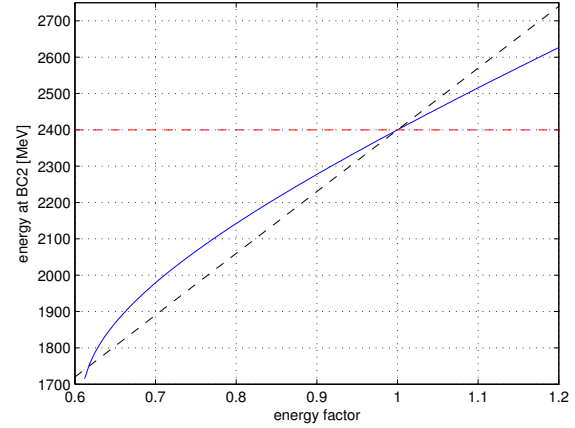


Figure 9: Energy at BC2 E'_{BC} after phase correction is applied. Energy scaled with the energy factor is indicated by the black dashed line. The nominal energy E_{BC} (energy factor 1) is indicated by the dashed red line.

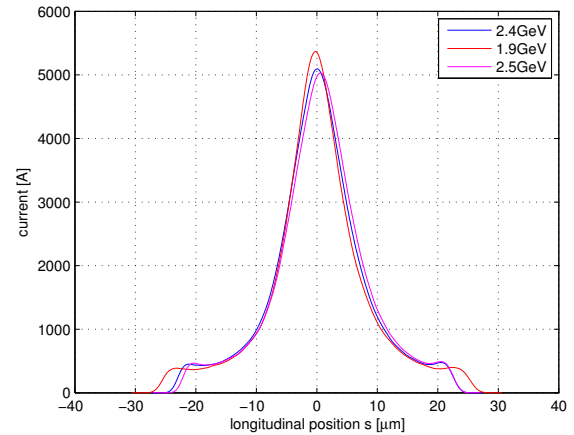


Figure 10: Longitudinal current profiles for different operation points using V' and φ' in Linac 2. The nominal current profile (BC2 at 2.4 GeV) is compared to operation with one klystron less (BC2 at 1.9 GeV) and 10% more energy (BC2 at 2.5 GeV).

CONCLUSION AND OUTLOOK

The presented analysis outlines the strategy of the energy management of the European XFEL, which covers 24 of the 26 1.3 GHz RF stations. It seems feasible to aim for "next shot" compensation of RF issues in Linac 3 even without magnet rescaling. Since the required quadrupole field changes are typically on the order of a few percent we could think of advanced corrections were the RF compensation is done immediately and the magnets following ignoring hysteresis effects. Such an approach would in general result in a lower optics mismatch than presented in Fig. 6. If hysteresis effects are critical the conclusion would be to use a reserve RF station at the end of Linac 3. In such a situation all field changes go in the same direction (compare Fig. 3) which by

using the correct branch of the hysteresis curve avoids field ambiguities. This investigation needs to be completed by an detailed look on how beam mismatch impacts the FEL performance.

An simple technique to stabilize compression was presented. Although magnet rescaling is required in case of Linac 2 RF problems. We will investigate more detailed compression fall-back scenarios including phase corrections in RF stations upstream of Linac 2.

A reliable automatized implementation of these procedures can even be used for temporary RF trips which are typically recovered on the order of minutes. Even thou this studies were conducted with the European XFEL in mind the basic principles are applicable for other facilities as well.

ACKNOWLEDGMENT

I would like to acknowledge helpful discussions and contributions from Winfried Decking, Martin Dohlus, Torsten Limberg, and Sascha Meykopff.

REFERENCES

- [1] Massimo Altarelli et al., "The European X-Ray Free-Electron Laser Technical design report", DESY 2006-097, DESY, Hamburg, 2007
- [2] W. Decking and T. Limberg, "European XFEL Post-TDR Description", XFEL.EU TN-2013-004-01, Hamburg, 2013
- [3] H. Weise, "How To Produce 100 Superconducting Modules for the European XFEL in Collaboration and with Industry", Proceedings of IPAC2014, Dresden, 2014, WEIB03
- [4] Yauhen Kot, Torsten Limberg and Igor Zagorodnov, "Different Charges in the Same Bunch Train at the European XFEL", DESY 13-215, Hamburg, 2013
- [5] Igor Zagorodnov and Martin Dohlus, "Semianalytical modeling of multistage bunch compression with collective effects", Phys. Rev. ST Accel. Beams 14, 014403 – Published 13 January 2011
- [6] Martin Dohlus, private communication.

TWO CHARGES IN THE SAME BUNCH TRAIN AT THE EUROPEAN XFEL

Y. Kot, T. Limberg, I. Zagorodnov, DESY, Hamburg, Germany

Abstract

The European XFEL has been initially designed for the operation with bunch charge of 1 nC [1] which was later extended down to 20 pC [2]. An important upgrade of this extension might be the ability to operate different bunch charges in the same RF pulse. In this paper we assume the nominal design of the XFEL injector which means in particular that both charges in the same RF pulse experience the same solenoid field and are generated by the laser of the same rms size. We discuss the requirements which the combined working points of the injector have to fulfil and show the results of the complete start to end (S2E) and SASE simulations for the simultaneous operation of 250 pC and 500 pC bunch charges.

INTRODUCTION

We report about the simulations on the operation of two different bunch charges at the European XFEL. From the beam dynamics point of view the most essential issue there is to achieve the similarity of the beam optical functions keeping emittance growth of the bunches reasonably low. In the next section we give an overview about the XFEL injector with respect to the beam optical functions which is followed by the presentation of the combined working points for the solenoid field and laser beam profile if the injector is operated with two charges in the same RF pulse. Finally we discuss the results of the S2E and SASE simulations for the bunch pair of 250/500 pC.

BEAM OPTICS ISSUES OF THE XFEL INJECTOR

The injector of the European XFEL may be divided into three sections from the beam optical functions point of view. The first section begins at the cathode and is 14.48 m long. Since it doesn't contain quadrupole magnets manipulation of the beam optical functions is achieved here indirectly by the choice of the solenoid field strength as well as gun gradient, RF focussing effects in ACC1 or laser beam size at the cathode.

The next (matching) section begins right after the first accelerating module which is followed by the first quadrupole. It contains six quadrupoles which are used for the matching of the beam optical functions.

The third part of the injector begins after the matching point at 29.51 m where the beam optics is expected to be the same for any bunch charge and any initial settings of the gun.

Since both bunches in the train experience the same magnetic field in the quadrupoles one has to guarantee that they arrive the matching section with similar twiss

functions in order to avoid effects of the beam optics distortion like beta beat downstream the matching point.

The ability of the XFEL injector to obtain two different charges in the same RF train with similar beam optical functions has been discussed in [3]. It was shown that it is possible on cost of emittance growth of lower charge if the difference between charges is not too large. Once the suitable value of the peak solenoid field has been found the choice of the laser beam size should be then on the ascending branch for higher charge and on the descending branch for lower charge (see Fig. 1).

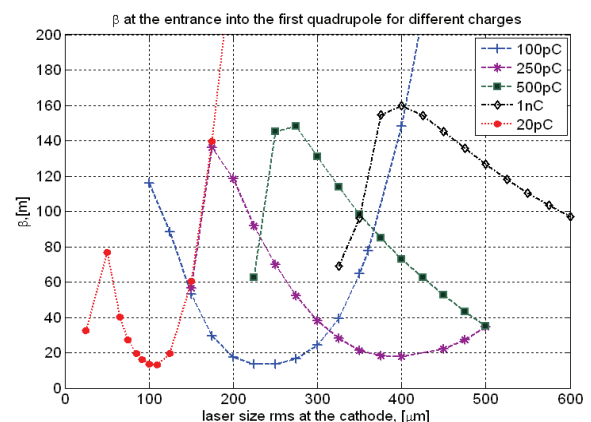


Figure 1: Dependence of the β -function at the beginning of the matching section on laser beam rms size for different bunch charges. Simulations are done for the peak solenoid field of 0.2220 T.

COMBINED WORKING POINTS FOR TWO CHARGES IN THE SAME TRAIN

Under combined working points we define the choice of the settings of the solenoid peak field and rms laser beam size at the cathode. These settings are valid for each particular RF pulse so that they can't be adjusted separately for any bunch in the same RF pulse.

The determination of the combined working points has been also performed under the assumption of the same parameters of the gun and longitudinal gun laser profile for both bunches. These parameters are summarized in the Table 1. The energy of the beam has been fixed to 150 MeV at the exit of the first accelerating module ACC1 and to 130 MeV after the third harmonic module

Table 1: Gun Parameters

Peak Gun Gradient, [MV/m]	Gun Phase	Laser Pulse and Form
60	-1.9	Flat Top 20 ps, rise and fall time 2 ps

ACC39. In order to make use of the computed working points for the later start to end simulations a compression scenario with the phase of 17.8 degrees of the ACC1 was assumed.

In order to find the combined working points we have analysed the intersections of the operation windows for bunch charges of 20, 100, 250, 500 and 1000 pC. Except of the bunch charge pair of 250/500 pC a combined operation appeared possible also for pairs 100/250 pC and 500/1000 pC. It is also possible to find settings which provide similar beam optical functions for some other bunch pairs though, but the match of the twiss functions by means of the quadrupoles which are foreseen in the matching section is no longer feasible.

As mentioned in the previous section the condition of similarity of the beam optical functions can be fulfilled on cost of the emittance growth of the lower bunch charge. For example, the comparison of the scans for 250 pC and 500 pC bunch charges has shown a perfect agreement of beam optical functions for peak solenoid field of $\text{MaxB}=0.2235$ T and rms laser beam size at the cathode of $\text{XY}=0.325$ mm but the emittance growth of the 250 pC bunch compared to the possible minimum has achieved already 160% which reduces significantly the SASE generation with this bunch.

On the other hand recent tests at FLASH [4] related to the operation of the two bunch charges in the same RF train have shown that the distortion of the beam optical functions which has been introduced by the change of the energy gain by 5% and keeping at the same time the currents in the quadrupole magnets unchanged leads though to a SASE drop of 10-20% but operation and generation of SASE remain acceptable.

In order to find a suitable combined working point we introduce the penalty function which takes into account not only the mismatch between beam optical functions $\xi_{1 \rightarrow 2}$ but also the relative emittance growth of both charges:

$$\text{pen} = \frac{\Delta\epsilon_1}{\epsilon_{10}} + \frac{\Delta\epsilon_2}{\epsilon_{20}} + 2(\xi_{1 \rightarrow 2} - 1)$$

Detailed description of the two dimensional scans over the combined working points can be found in [3]. The combined working points which minimize the penalty function and resulting relative emittance growth of the corresponding bunches are summarized in the Table 2.

Table 2: Combined Working Points for Different Bunch Charge Pairs

Bunch Charges Q_1/Q_2 , [pC]	Combined WP		Emittance Growth		Pen
	MaxB, [T]	XY, [mm]	$\frac{\Delta\epsilon_1}{\epsilon_{10}}$, %	$\frac{\Delta\epsilon_2}{\epsilon_{20}}$, %	
100/250	0.2220	0.205	74.8	1.7	1.487
250/500	0.2224	0.285	50.1	0.0	0.887
500/1000	0.2226	0.400	51.7	4.1	0.957

OPERATION WITH 250/500 pC BUNCH CHARGES WITHIN THE SAME TRAIN

RF Rough Adjustment

We consider an operation of 250 pC and 500 pC bunches within the same RF pulse for the nominal design of the XFEL injector.

The first rough definition of the RF settings has been accomplished by means of RF tweak tool [5]. The tool simulates the dynamics of the particle distribution mainly in the longitudinal phase space, takes into account some collective effects like the longitudinal space charge and CSR and gives also a simple approximation of transverse dynamics. It is based on the semi analytical approach which has been described in [6]. This way it becomes possible to find the first guess of the proper RF settings which would provide the chosen compression scheme.

The input parameters which make possible to achieve this way a Gaussian-like profiles with the peak current of several kA for each charge are shown in the Table 3.

Table 3: Input Parameters for the Compression Scheme

R ₅₆ at Bunch Compressors, [m]			Energy at Bunch Compressors, [GeV]		
R _{56_0}	R _{56_1}	R _{56_2}	E ₀	E ₁	E ₂
0.065	0.043	0.020	0.13	0.65	2.3

RF Fine Adjustment

Once the “first guess” for the RF settings was found the expected reference distributions after each bunch compression stage have been saved and a start to end run has been performed for each bunch charge from the first quadrupole at $s=14.48$ m up to the end of the linac 3 at $s=1629$ m. Since the longitudinal particle distributions after the start to end run normally differ from the reference distributions due to more accurate calculation of the collective effects and taking into account of the wake fields an additional RF adjustment was performed to provide the required longitudinal distributions. In the Table 4 the results for the final RF settings are shown which lead to reasonable 6D distributions with a peak current of 7.75 kA for 250 pC and 5.34 kA for 500 pC bunch charges.

Table 4: RF Settings for the Simultaneous Compression of 250 pC and 500 pC Bunch Charges

	ACC1	ACC39	L1	L2	L3
ΔE_{max} , [GeV]	0.157	0.026	0.657	1.667	11.76
Phase, [deg]	17.79	186.1	37.69	6.57	0.00

Bunch Parameters after S2E Simulations

The results for the main bunch parameters at the beginning and at the end of the S2E simulations are summarized in the Tables 5a and 5b.

Table 5a: Projected Emittance of the 250 pC and 500 pC Bunches Operated at the Combined WP at the Beginning and at the End of S2E Section

	250 pC		500 pC	
	$\epsilon_{x,pr}$ [μm]	$\epsilon_{y,pr}$ [μm]	$\epsilon_{x,pr}$ [μm]	$\epsilon_{y,pr}$ [μm]
Start	0.336	0.325	0.424	0.422
End	0.391	0.509	0.486	1.367

Table 5b: Rms Energy Spread, Peak Current, FWHM Bunch Length and Total Compression at the Beginning and at the End of S2E Section for 250 pC and 500 pC Bunches Operated at the Combined WP

	250 pC			
	$\delta_{E,rms}$ [MeV]	I_p , [A]	τ , [fs]	C
Start	2.74e-4	16.12	11225	196
End	0.765	7.75e+3	19	
	500 pC			
Start	7.58e-4	26.14	13890	136
End	0.553	5.34e+3	78	

SASE SIMULATIONS FOR THE BUNCH CHARGE PAIR 250/500 pC

Lasing simulations for the SASE 1 section of the European XFEL has been performed by means of the Genesis tracking code [7]. The beam input files have been generated from the output files of the S2E simulations while the evolution of the beam optical functions between Linac 3 and undulator section has been approximated by formulas of the linear optics using the XFEL lattice file.

The results of the simulations indicate the resulting SASE pulse energy of 618 μJ for 250 pC and 708 μJ for 500 pC bunch charge. Though both bunch charges demonstrate comparably equal pulse energy they differ at the same time in pulse length and average laser power. The part of the bunch which contributes to the SASE process is three times longer for 500 pC bunch than that for 250 pC bunch (approximately 30 μm compared to 10 μm). On the other side the 500 pC bunch has smaller peak current and also significantly smaller maximum averaged power (12.5 GW compared to 31 GW for 250 pC bunch). Moreover it is to mention that the 250 pC bunch demonstrates not only high peak current but also a double horn longitudinal structure while 500 pC bunch

retains a stable “flat top” pulse with moderate laser power over the entire length of 30 μm (see Fig. 2 and 3).

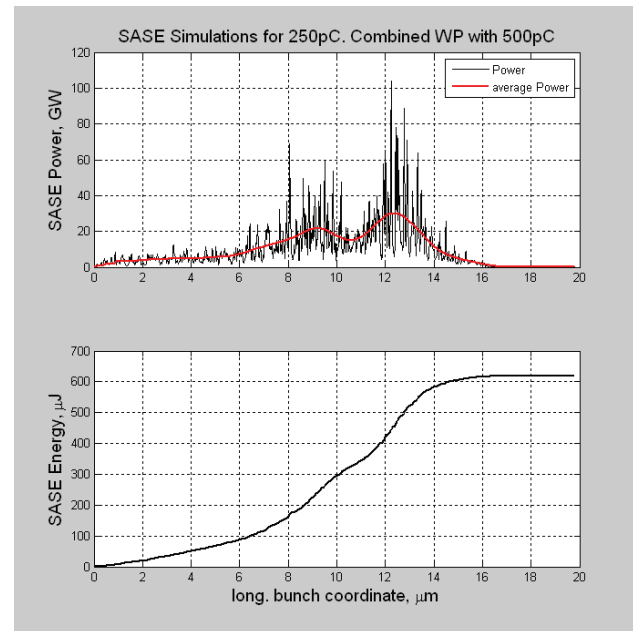


Figure 2: SASE Simulations for 250 pC Bunch.

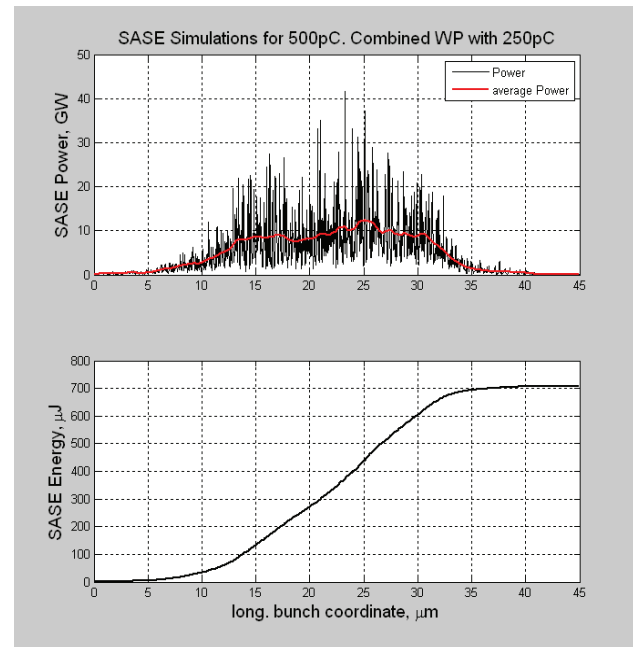


Figure 3: SASE Simulations for 500 pC Bunch.

SUMMARY AND DISCUSSION

Crucial point for the simultaneous operation of the European XFEL with two different bunch charges is the ability to achieve similar beam optical functions of both bunches after the first accelerating module. Simulations have shown that it is possible for nominal design of the XFEL injector on cost of the emittance growth of the bunch with smaller charge. In order to get suitable bunch parameters it is reasonable however to look for a compromise between emittance growth and mismatch of

the beam optical functions between bunches. Combined working points have been derived by means of the simulations with ASTRA code as ones which minimize the penalty function proposed in this paper.

A complete S2E simulations consisting of the particle tracking from the cathode to the undulator section has been performed for 250/500 pC bunch pair. It was shown that it is possible to find combined working points for the operation of the solenoid, injector laser and RF settings of the accelerating modules which lead to suitable for lasing 6D particle distributions of both charges.

Subsequent SASE simulations with Genesis code revealed that both charges deliver laser pulses of similar energy but different longitudinal structure, length and average power.

A very tempting upgrade of the nominal design of the XFEL injector with respect to the simultaneous operation of two different bunch charges can be an installation of an additional laser system at the cathode. The benefit of it would be more flexibility by the choice of the combined working points since the rms laser beam size becomes adjustable for each bunch separately and only solenoid field remains the same for both bunches. Detailed analysis of this case can be found in [3]. Another promising improvement could be the ability to change the RF settings during the RF pulse which has been already successful tested at FLASH [4].

REFERENCES

- [1] DESY XFEL Project Group “The European X-Ray Free-Electron Laser. Technical Design Report” July 2007.
- [2] W. Decking and T. Limberg, “European XFEL. Post-TDR Description”, February 2013.
- [3] Y. Kot, T. Limberg, I. Zagorodnov, “Different Charges in the Same Bunch Train at the European XFEL”, DESY 13-215, November 2013.
- [4] S. Ackermann “The Results from FLASH II Tests” FEL Seminar 23.04.2013, DESY, Hamburg.
- [5] M. Dohlus, Personal Communication.
- [6] I. Zagorodnov, M. Dohlus “A Semi-Analytical Modelling of Multistage Bunch Compression with Collective Effects”, Phys. Rev. ST Accel. Beams 14 (2011) 014403.
- [7] S. Reiche, “Genesis 1.3: a Fully 3D Time-Dependent FEL Simulation Code”, Nuclear Instruments and Methods in Physics Research A 429 (1999) 243-248.

START-TO-END ERROR STUDIES FOR FLUTE

M. Weber*, A.-S. Müller, S. Naknaimueang, M. Schuh, M. Schwarz, P. Wesolowski
KIT, Karlsruhe, Germany

Abstract

FLUTE, a new linac based test facility and THz source, is currently under construction at the Karlsruhe Institute of Technology (KIT) in collaboration with DESY and PSI. With a repetition rate of 10 Hz, electron bunches with charges from 1 pC to 3 nC will be accelerated up to 40-50 MeV and then compressed longitudinally in a magnetic chicane to generate intense coherent THz radiation. Since the stability and repeatability of longitudinal bunch profiles are essential for optimum compression and THz radiation properties, simulation-based start-to-end error studies using the tracking code ASTRA have been performed to determine the influence of the machine elements on the bunches. Thus, critical parameters are identified and their respective tolerance ranges defined. In this contribution a summary of the error studies will be given.

INTRODUCTION

The "Ferninfrarot Linac- Und Test-Experiment" (FLUTE) [1], [2] is a new compact linear accelerator facility, aimed at the generation of coherent THz radiation with fs electron bunches. Additionally, it will serve as a test stand for the study of different generation mechanisms of THz radiation (CSR, CTR and CER) as well as for the development of diagnostics for the ultra-short bunches.

Figure 1 shows the baseline design of FLUTE. In a 3 GHz RF photo gun the initial bunches with charges from 1 pC to 3 nC are generated and accelerated to about 7 MeV. In order to compensate the strong space charge forces acting within the bunches at low energy, a solenoid is used for transverse focusing right after the gun. A travelling wave linac accelerates the bunches to their final energy of 40-50 MeV. In addition, a negative correlated energy spread is induced to longitudinally compress the bunches in the D-shaped bunch compressor (chicane). To control and optimize the transverse bunch size, a focusing quadrupole doublet is used before the chicane.

BEAM DYNAMICS SIMULATIONS

For the design of FLUTE and the optimization of the machine parameters, different simulation tools including the tracking code ASTRA [3] have been used [4] in order to get a minimum RMS bunch length after compression. For the error studies the tracking has been done with ASTRA for the entire machine. Table 1 shows the current design values for the machine parameters applied in the simulations. Depending on the bunch charge, RMS bunch lengths between 220 fs (3 nC) and 5 fs (1 pC) after compression can be achieved. CSR effects inside the chicane are neglected in this case.

Simulations including CSR effects result in bunch lengths of about 270 fs for the 3 nC bunches, while for 1 pC CSR leads to about 5% longer bunches. Especially in this highly sensitive low charge regime further optimization is ongoing.

Table 1: Design Values for the FLUTE Machine Parameters used in the ASTRA Simulations

Parameter	Unit	Value
Bunch charge	nC	0.001 - 3
Laser spot size (RMS)	mm	0.5 - 2.25
Laser pulse length (RMS)	ps	0.5 - 4
Gun peak field	MV/m	120
Solenoid peak field	T	0.14 - 0.18
Linac peak field	MV/m	10
Quadrupole strength	m ⁻²	11.88 - 12
Dipole bending radius	m	1.12 - 1.006

ERROR STUDIES

A solid understanding of the influence of the machine parameters on the 3D bunch shape is a prerequisite for a stable operation with ultra-short bunches. These parameters include the ones shown in Table 1, as well as the alignment of the different machine components. Two simulation procedures have been applied. On the one hand, systematic scans of individual machine parameters have been performed. On the other hand, randomly generated deviations have been added on the design values of these parameters. This has been done for each machine component separately, as well as for the whole machine at once. The errors follow a Gaussian distribution and each entry in the distribution corresponds to one simulation run. For that purpose an internal routine included in ASTRA has been used. Observing the distribution of the output bunch parameters (such as RMS bunch length and transverse bunch size) after multiple simulation runs then gives information about the average influence of the errors on the bunch. Table 2 shows the RMS values for the error distributions on the considered machine parameter values. A cut-off after three sigma has been made, meaning that deviations of the input values do not exceed this range. So values that are too far off from the design value of the respective machine parameter (with probabilities below 0.3%) are avoided within the random distributions.

Regarding the laser, errors have been added on the laser pulse length, timing offset (jitter), spot size and position at the cathode, as well as on the bunch charge (laser amplitude). Out of these, the timing offset has the strongest influence on the bunch profiles. Figure 2 shows a systematic scan of the laser timing between ± 500 fs and the impact on the bunch

* manuel.weber@partner.kit.edu

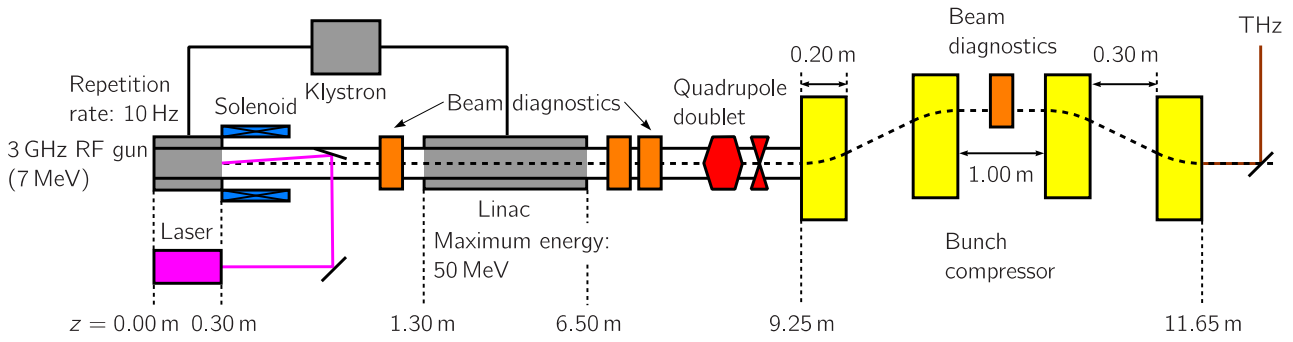


Figure 1: Baseline layout of FLUTE as used for the error studies. The initial bunches are generated in an RF photo gun, accelerated to 40-50 MeV in the linac and then longitudinally compressed in a four dipole chicane. Gun and linac are powered both by the same klystron.

Table 2: RMS Values for the Gaussian Distributed Errors (added on the design value of the respective machine parameter)

Parameter	Unit	Value
Bunch charge	%	0.25
Laser spot size	%	1
Laser pulse length	%	0.1
Laser timing	ps	0.5
Phase (laser, gun, linac)	degree	0.1
Peak field (gun, solenoid, linac, chicane)	%	0.1
Position of machine component	mm	0.25
Rotation of machine component	mrاد	0.5

length after compression for a 1 pC bunch. A 500 fs timing offset equals a phase error of

$$\phi(t) = \omega t = 2\pi \times 3 \text{ GHz} \times 500 \text{ fs} \approx 0.5^\circ \quad (1)$$

in gun and linac. So the electrons gain a different amount of energy compared to the case without jitter. This leads to a deviation of mean energy and energy spread of the bunch and disturbs the optimum bunch compression in the chicane.

In Fig. 3, Gaussian distributed errors have been added on all machine parameters simultaneously in 150 simulation runs (this number has been chosen concerning reasonable computation times since one simulation run takes more than two hours). Although the overall fluctuations increase, the effect of the laser timing offset on lengthening the bunch can still be observed. Also, the horizontal RMS bunch size after compression is strongly affected (see Fig. 4). Particles travelling off axis through the linac are influenced by transverse components of the accelerating RF wave. This has a focusing or defocusing effect on the bunch, depending on the linac phase. So the bunch size increases or decreases, while in both cases the RMS bunch length grows.

Further start-to-end simulations concerning the deviations on the values of gun, solenoid, linac, quadrupole doublet and bunch compressor parameters as listed in Table 2 have been

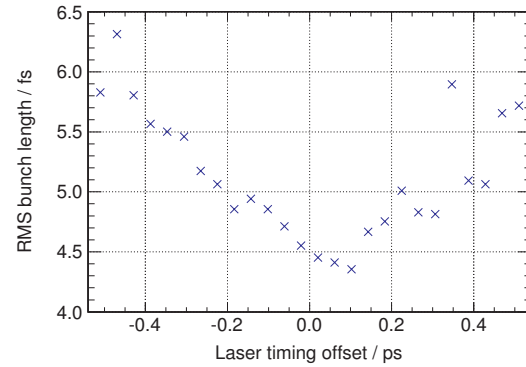


Figure 2: Systematic scan of the laser timing offset for a 1 pC bunch. Timing deviations lead to longer bunches after compression. A stability of ± 200 fs is required to keep the fluctuations in bunch length in the range of 0.5 fs.

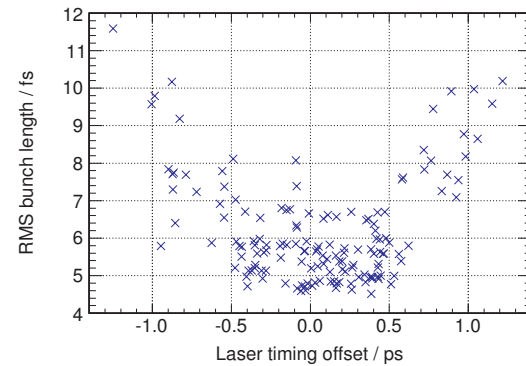


Figure 3: Influence of the laser timing on the RMS bunch length after compression. Gaussian distributed errors are added on all machine parameters simultaneously (1 pC, 150 simulations). Compared to Fig. 2 there is still a correlation between laser timing and compressed bunch length.

performed. The histograms in Fig. 5 and Fig. 6 show the effect of all errors on bunch length and horizontal bunch size for a 1 pC bunch along the machine axis (after 150 simulation runs). The overall relative fluctuations in bunch length around the mean rise from about 5% before compression to about 20% after compression. Looking at the impact of

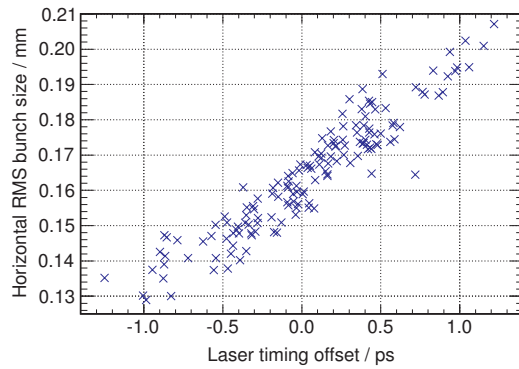


Figure 4: Impact of the laser timing on the horizontal RMS bunch size after compression. Similar to Fig. 3, Gaussian distributed errors are added on all machine parameters simultaneously (1 pC bunch). Transverse components of the accelerating RF wave inside the linac are focusing or defocusing the bunch, depending on the phase. Due to the timing-related phase errors, this has the effect of increasing or decreasing transverse bunch sizes.

the deviations on the horizontal bunch size, the maximum fluctuations around the mean are in the order of 10%. For higher bunch charges up to 3 nC, the relative fluctuations in bunch length before compression are in the same order of magnitude as for 1 pC. After compression the fluctuations are decreasing with higher charges. Because of the very short RMS lengths of the 1 pC bunches, small variations in absolute numbers lead to large deviations in relative numbers. Concerning this sensitive case, also numerical influences on the bunch parameter fluctuations are currently under investigation.

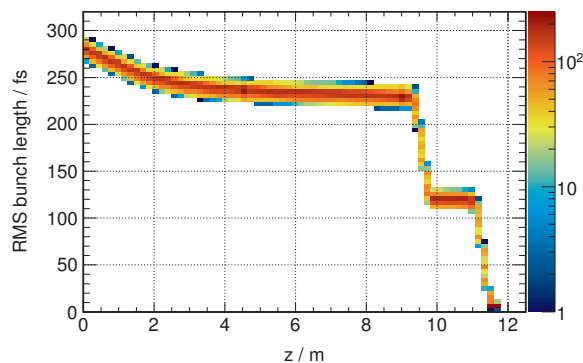


Figure 5: Histogram of the RMS value of the bunch length along the machine axis (1 pC, 150 simulations). Gaussian distributed errors have been added on all machine parameters simultaneously. Fluctuations around the mean value rise from about 5% before compression to about 20% after compression.

SUMMARY

FLUTE, a new accelerator test facility, is currently under construction at KIT. Simulation-based error studies using

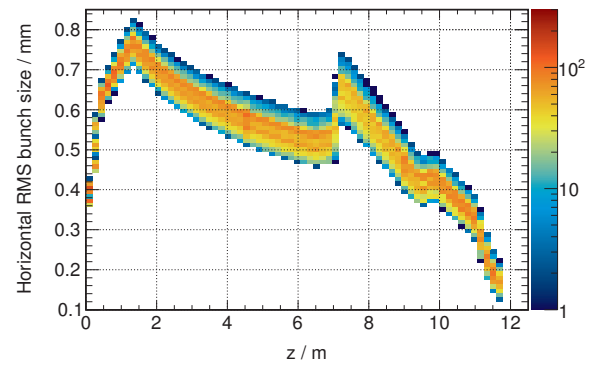


Figure 6: Histogram of horizontal RMS bunch size along the machine axis after 150 simulations with Gaussian distributed errors (1 pC). After compression fluctuations around the mean rise to about 10%.

the tracking code ASTRA have been performed. The laser timing jitter is identified as the most crucial machine parameter in terms of influencing bunch length and bunch size after compression. Its deviations should be kept below ± 200 fs. In this case the RMS compressed bunch length (5 fs, 1 pC bunch charge) fluctuates about 0.5 fs. The average fluctuations increase to about 1 fs when adding Gaussian distributed errors on all machine parameters simultaneously. These parameters include the alignment of the FLUTE machine components, as well as electric and magnetic peak fields and the phases in gun and linac. In general, alignment errors should not exceed 0.25 mm in position and 0.5 mrad in rotation, which is possible with present machining precision. The same applies for deviations up to 0.1% of the electric and magnetic peak fields. The jitter of gun and linac phases should not be larger than 0.1° . The overall relative fluctuations of bunch size and bunch length after compression then amount to about 10-20% for the 1 pC bunches (which is the most sensitive case). The relative fluctuations for higher charges are decreasing due to the larger absolute values of their bunch parameters.

In the next steps the influence of CSR effects inside the chicane will be included in the error studies, especially for the higher charges. Also the impact of the errors on the generated THz radiation will be investigated.

REFERENCES

- [1] M. J. Nasse et al., "FLUTE: A versatile linac-based THz source", *Rev. Sci. Instrum.* 84, 022705 (2013), doi: <http://dx.doi.org/10.1063/1.4790431>
- [2] M. Schuh et al., "Status of FLUTE", in *Proc. 5th Int. Particle Accelerator Conf.*, Dresden, 2014, pp. 231-233.
- [3] K. Flöttmann. (2013). "ASTRA - A Space Charge Tracking Algorithm" (Version 3.0). <http://www.desy.de/~mpyf10/>
- [4] S. Naknaimueang et al., "Design Studies for FLUTE, A Linac-based Source of Terahertz Radiation", in *Proc. 35th Int. Free-Electron Laser Conf.*, New York, 2013, pp. 598-601.

OPTIMIZATION OF THE PITZ PHOTO INJECTOR TOWARDS THE BEST ACHIEVABLE BEAM QUALITY*

M. Khojoyan[#], M. Krasilnikov, F. Stephan, G. Vashchenko, DESY Zeuthen, Zeuthen, Germany

Abstract

Uniform 3D ellipsoids are proven to be the best distributions for high brightness charged particle beam applications due to the linear dependence of the space charge fields on the position within the distribution [1]. Such electron bunches have lower emittance and are less sensitive to the machine settings and, therefore, should allow more reliable operation, which is one of the key requirements for single-pass free-electron lasers (FELs). The Photo Injector test facility at DESY, Zeuthen site (PITZ) is optimizing high brightness electron sources for linac based FELs such as the European XFEL. Recent measurements at PITZ using a photocathode laser with a flat-top temporal profile have revealed record low transverse emittance values at different bunch charges [2]. As a next step towards the further improvement of the high quality beams, a cathode laser system, capable of producing quasi-3D ellipsoidal bunches is intended to be used at PITZ. In this work the beam dynamics optimization results for various bunch charges and for flat-top and 3D ellipsoidal cathode laser shapes are presented. For each working point the relative emittance growth is estimated due to possible deviations of the machine parameters.

INTRODUCTION

The Photo Injector test facility at DESY, Zeuthen site (PITZ) is one of the leading laboratories on generation and optimization of high brightness electron bunches of different charges for free-electron laser (FEL) machines such as FLASH [3] and the European XFEL [4]. At PITZ electron beams of excellent quality are created utilizing the photo effect and are accelerated in an L-band RF gun up to several MeV energies. A pair of solenoid coils surrounding the gun is used for beam transverse focusing meanwhile providing zero remnant magnetic fields at the cathode. The final as high as 25 MeV beam energy is reached after passing through a second accelerating structure. The electron beam transverse properties are usually measured with the help of the emittance measurement systems (EMSY), where a single slit scan technique [5] is used to measure the electron beam emittance. Additionally, there are many diagnostics available for full characterization of high brightness electron beams. A more detailed description of the PITZ setup can be found elsewhere [6].

*Work supported by the German Federal Ministry of education and Research, project 05K10CHE "Development and experimental test of a laser system for producing quasi 3D ellipsoidal laser pulses" and RFBR grant 13-02-91323.

[#]martin.khojoyan@desy.de

Optimization of the photocathode laser shape is one of the key issues on generating high quality bunches. Recent measurements performed at PITZ by applying a nominal flat-top longitudinal laser shape have revealed unprecedented transverse emittance values for different bunch charges [2]. To further improve the achievable beam quality a laser system capable of producing quasi-3D ellipsoidal laser pulses is under development at the Institute of Applied Physics (IAP, Nizhny Novgorod). The project is being realized in the frame of a joint German-Russian research activity including the Joint Institute of Nuclear Research (JINR, Dubna) and PITZ (DESY).

In this contribution, an optimization of the transverse beam emittance is performed for different bunch charges comparing a cylindrical (flat-top temporal profile) and 3D ellipsoidal cathode laser distributions. A new linac setup with shifted (optimized) positions of the second accelerating cavity and the first emittance measurement system (EMSY1) is used in the simulations. The tolerance studies are performed for each optimized machine setup to predict the transverse emittance dilution due to possible mismatch of the machine parameters during the experiments. Finally, the influence of possible imperfections coming from the 3D laser shape on the electron beam emittance is estimated for different bunch charges.

SIMULATION SETUP FOR EMITTANCE OPTIMIZATION

The ASTRA [7] simulation code has been used to optimize the electron beam quality at various bunch charges assuming flat-top and 3D ellipsoidal cathode laser pulse shapes. Previously performed studies have revealed a much better injector performance of a 1 nC electron beam for the 3D ellipsoidal laser profile with a shifted position (40 cm closer to the gun) of the second accelerating cavity as compared to the current setup [8]. In this work the position of the first emittance measurement system (EMSY1) is shifted accordingly by ~ 45 cm upstream towards the cathode. The simulation setup is shown in Fig. 1. The following values of machine parameters were used during the optimization. A flat-top temporal laser shape with fixed FWHM length of 21.5 ps and 2 ps rise and fall times was considered in simulations for different charges. The transverse laser profile was assumed to be homogeneous. For each bunch charge the longitudinal size of the 3D ellipsoidal laser was tuned accordingly to get the same electron bunch rms length at EMSY1 (Z=5.28 m) as it is for the flat-top case. The gun

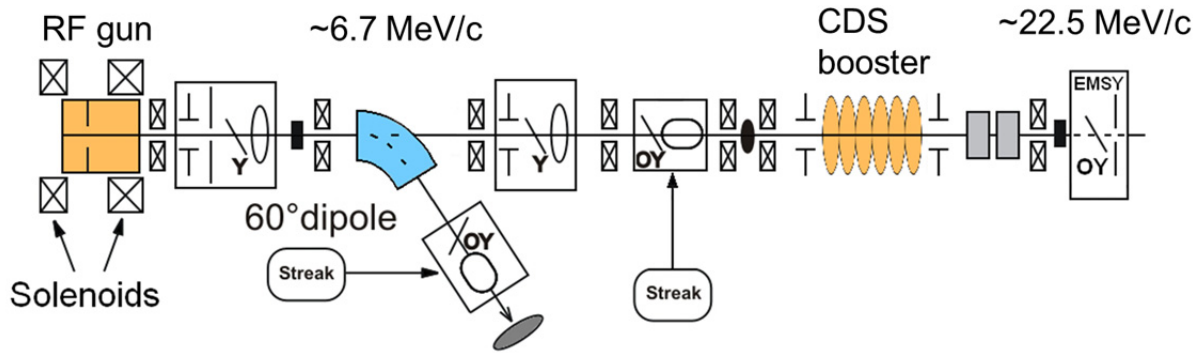


Figure 1: Part of the PITZ setup used in simulations for the emittance optimization. Starting position of the CDS booster is at $Z=2.675$ m and the first emittance measurement screen is located at 5.28 m downstream the cathode.

peak electric field at the cathode was kept constant to a value that corresponds to ~ 6.7 MeV/c beam momentum at the phase of maximum acceleration. The accelerating field gradient in the booster was 18 MV/m yielding to ~ 22.5 MeV/c final beam momentum. For different bunch charges (from 20 pC to 1 nC) the transverse normalized rms emittance was optimized at the position of EMSY1 by simultaneously tuning the laser rms spot size, gun phase and the main solenoid current. The obtained results are shown in Fig. 2, where the normalized rms projected emittance as a function of bunch charge is shown for flat-top (blue dots) and 3D ellipsoidal (red dots) cathode laser profiles. As seen from the plot, there is ~ 30 -35 % improvement in transverse emittance for the case of 3D ellipsoidal laser profile in a wide range of bunch charges. It should be mentioned that this dependence was obtained for fixed laser pulse length and fixed beam energy and can be modified after retuning of the above mentioned parameters.

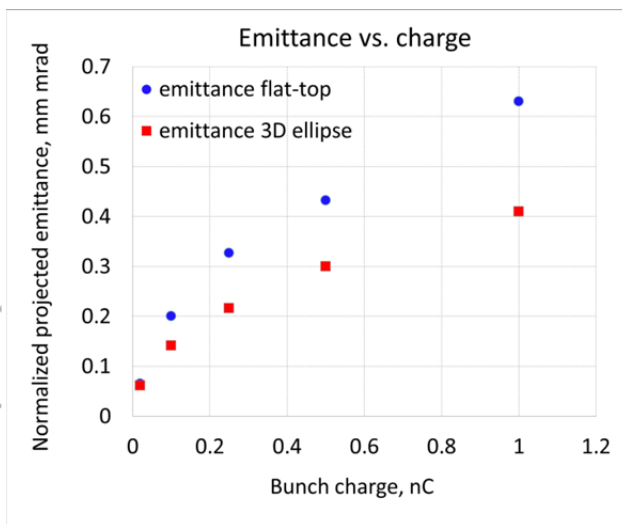


Figure 2: Electron beam transverse emittance as a function of bunch charge for flat-top and 3D ellipsoidal laser profiles.

EMITTANCE DILUTION DUE TO VARIOUS IMPERFECTIONS

Different sources of emittance dilution during the experimental measurements are described in the following sections.

Jitter of Optimized Machine Parameters

During the experiments one of the possible sources of emittance growth is a deviation / jitter of optimized machine parameters from their optimal values. In this section, the influence of the jitter of various machine parameters on the transverse emittance is estimated for different charges. At each working point the maximum possible deviations of three parameters, namely main solenoid current (± 0.5 A), laser rms spot size on the cathode (± 10 μm) and the gun phase (± 1 deg) were considered as a possible source of emittance overestimation during the experiments. The first parameter justifies the step of the solenoid scan during the emittance measurements. The second parameter is chosen taking into account the measurement precision of the laser spot size on the virtual cathode. The third parameter is taken with safety margins combining the impacts of gun phase jitter and limited accuracy of momentum measurements. For each bunch charge and cathode laser profile the above mentioned parameters were simultaneously scanned in the specified ranges. The difference between the highest emittance value obtained from the scan and the initial emittance value without any jitter considerations was assumed to be the possible influence of the jitter of machine parameters on the emittance. The result is summarized in Tab. 1, where the relative emittance growth caused by the jitter of optimized machine parameters is shown for various bunch charges and two laser profiles. One can notice a rather strong jitter influence on the emittance for the flat-top laser profile at low charges. A possible explanation can be that the absolute optimum emittance predicted from the simulations at such low charges is not obtained at high beam energies (22.5 MeV/c beam momentum as fixed in our simulations) but at fairly low energies [9]. More

detailed studies are still needed for a better understanding of beam physics at such low charges. For other bunch charges the estimated error on the emittance is less than 10 % for both laser shapes. In addition, less sensitivity on machine parameters was observed for 3D ellipsoidal laser profile as compared to the flat-top case.

Table 1: Summary of Beam Tolerance Studies for Two Laser Profiles. The values in the table represent the emittance overestimation due to the possible jitter of optimized machine parameters: main solenoid current (± 0.5 A), laser rms spot size (± 10 μm) and gun phase (± 1 deg).

Charge / laser profile	Estimated error on the emittance, %
20pC / flat-top	21
20 pC / 3D ellipse	9
100 pC / flat-top	17
100 pC / 3D ellipse	5.5
250 pC / flat-top	5
250 pC / 3D ellipse	4.5
500 pC / flat-top	6
500 pC / 3D ellipse	4
1 nC / flat-top	5.5
1 nC / 3D ellipse	5

Non-perfectness of the 3D Laser Shape

Another possible source of emittance dilution is the imperfections of the quasi-3D ellipsoidal laser shape, which was observed lately during the tests at IAP [10]. In order to study how a non-perfect ellipsoidal cathode laser shape (spatial and temporal imperfections in 3D laser shape) impacts on the electron beam transverse emittance, a modelling of the non-perfect 3D laser shape has been implemented into the beam dynamics simulations. For that purpose, temporal (δ_t) and radial (δ_r) border sharpness parameters have been introduced into the laser intensity distribution, describing the fraction of spatial and temporal distortions with respect to the perfect 3D shape [11]. Figure 3 depicts the intensity distribution of a perfect 3D laser pulse (a), likewise the distribution which is modified due to bounded sharpness of ellipsoid edges (b). The transverse emittance growth was estimated at the position of EMSY1 for different values of border sharpness parameters and for different bunch charges. In Fig. 4, the transverse emittance is given as a function of border sharpness parameter. In this example, the case of the 1 nC bunch charge is shown. It can be concluded, that overall 30 % spatial and temporal distortions in the 3D

ellipsoidal shape yield to a transverse emittance growth, where the resulting emittance value is comparable to the optimized emittance value for the flat-top laser profile. Similar results were obtained for other charges as well.

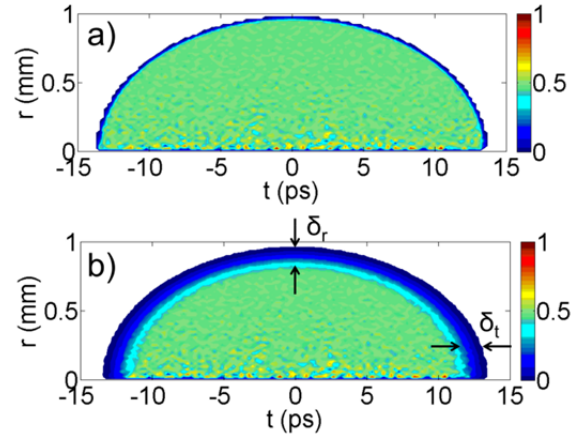


Figure 3: An example from border sharpness modelling in ASTRA. a) Intensity distribution of a perfect 3D shape, b) 20 % distortion in temporal and radial directions. The range of the intensity values (0 \rightarrow the lowest, 1 \rightarrow the highest) is shown by colour bars on the right part of each figure.

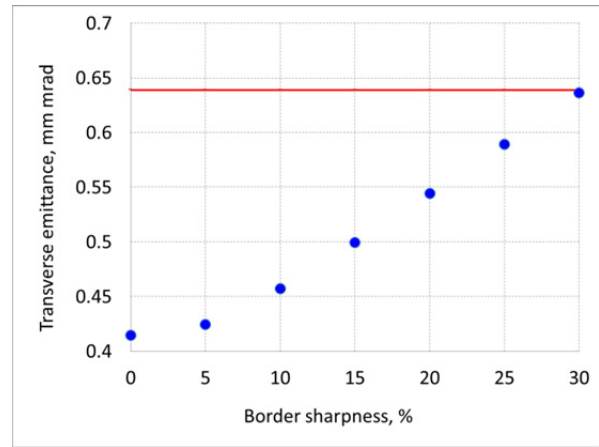


Figure 4: Transverse emittance at EMSY1 as a function of border sharpness parameter ($\delta_r=\delta_t=\delta$) for 1 nC bunch charge (blue dots). The red line on the graph emphasizes the optimized transverse emittance value for the case of the flat-top temporal laser profile at the same charge.

CONCLUSION

A transverse emittance optimization has been performed for different bunch charges with a modified PITZ setup, including shifted (optimized) positions of the second accelerating cavity and the first emittance measurement station. 30-35 % improvement in transverse emittance was obtained for almost all charges when using quasi 3D ellipsoidal laser pulses with respect to flat-top laser pulses. The alteration of the electron beam quality, namely the dilution of the beam transverse emittance was

estimated taking into account two possible sources of systematic errors: the impact of possible deviation of the optimized machine parameters from their optimal values during the experiments and the non-perfectness of the 3D ellipsoidal cathode laser shape. The studies for the first case have revealed $< 10\%$ emittance overestimation for different laser profiles and for charges higher than 100 pC. Much less sensitivity of the transverse emittance depending on the 3D ellipsoidal cathode laser shape imperfections has been obtained with the new linac setup. More extended investigations are necessary to study the precision of the emittance measurements while operating at low bunch charges.

REFERENCES

- [1] I.M. Kapchinskij, V.V. Vladimirskij, Conference on High Energy Accelerators and Instrumentation, CERN, Geneva, 1959, pp. 274-288.
- [2] M. Krasilnikov et al., “Experimentally minimized beam emittance from and L-band photoinjector”, *Physical Review Special Topics - Accelerators and Beams*, vol. 15, p. 100701 (2012).
- [3] M. Ackermann et al., *Nature Photon.* 1, pp. 336-342, 2007.
- [4] M. Altarelli et al., DESY, Report No. 2006-097, 2006.
- [5] L. Staykov, “Characterization of the transverse phase space at the photo-injector test facility in DESY, Zeuthen site”. PhD thesis, Hamburg University, 2012.
- [6] F. Stephan et al., “Detailed characterization of electron sources yielding first demonstration of European X-ray Free-Electron Laser beam quality”, *Physical Review Special Topics – Accelerators and Beams*, vol. 13, p. 020704 (2010).
- [7] K. Flöttmann, ASTRA, <http://www.desy.de/~mpyflo>
- [8] M. Khojyan et al., “Studies on the Application of the 3D Ellipsoidal Cathode Laser Pulses at PITZ”, in *Proc. 5th Int. Particle Accelerator Conf.*, Dresden, 2014, pp. 2958-2961.
- [9] G. Vashchenko, “Transverse phase space studies with the new CDS booster cavity at PITZ”, PhD thesis, Hamburg University, 2013.
- [10] M. Krasilnikov et al., “Development of a photo cathode laser system for quasi ellipsoidal bunches at PITZ”, in *Proc. 35th Int. Free-Electron Laser Conf.*, New York, 2013, pp. 303-308.
- [11] M. Khojyan et al., “Beam dynamics optimization for the high brightness PITZ photo injector using 3D ellipsoidal cathode laser pulses”, in *Proc. 35th Int. Free-Electron Laser Conf.*, New York, 2013, pp. 298-302.

RECENT ELECTRON BEAM OPTIMIZATION AT PITZ

G. Vashchenko*, G. Asova†, P. Boonpornprasert, J. D. Good, M. Gross, I. Isaev,
D. Kalantaryan, M. Khojayan, G. Kourkafas, M. Krasilnikov, D. Malyutin,
D. Melkumyan, A. Oppelt, M. Otevrel, T. Rublack, F. Stephan,
Deutsches Elektronen-Synchrotron, Zeuthen site, Zeuthen, Germany
G. Pathak, Hamburg University, Hamburg, Germany
D. Richter, Helmholtz-Zentrum Berlin, Berlin, Germany

Abstract

High brightness electron sources for linac based free-electron lasers operating at short wavelength such as FLASH and the European XFEL are characterized and optimized at the Photo Injector Test Facility at DESY, Zeuthen site (PITZ). In the last few years PITZ mainly was used to condition RF guns for their later operation at FLASH and the European XFEL. Only limited time could be spent for beam characterization. However, recently we have performed emittance measurements and optimization for a reduced gun accelerating gradient which is similar to the usual operation conditions at FLASH. The results of these measurements are presented in this paper.

INTRODUCTION

The Photo Injector Test facility at DESY, Zeuthen site (PITZ) is developing, characterizing and optimizing high brightness electron sources for free-electron lasers like FLASH [1] and the European XFEL [2]. One of the most important parameters, influencing the FEL process, is the normalized transverse projected emittance, hereinafter called emittance, of the electron beam. A normal conducting 1.6-cell L-band RF gun cavity with a Cs₂Te photocathode, which is illuminated by cylindrically shaped UV laser pulses, is used to produce high quality electron beams of different charges. The produced electron beam is focused with a pair of solenoids installed around the gun and accelerated further by the cut disc structure booster, hereinafter called CDS booster, after which numerous diagnostic devices are installed. The emittance of the electron beam is measured using the conventional slit scan method based on a direct measurement of the electron beam size and angular spread [3]. As the energy of the electron beam after the final acceleration is not sufficient to prevent a space-charge induced emittance growth, several emittance measurement stations are installed along the beamline to monitor the emittance evolution. More details about the PITZ setup can be found elsewhere [3–5]. All the data presented in this work were obtained using the first emittance measurement station installed just downstream the CDS booster.

In the last few years PITZ was mainly focused on conditioning of electron guns required by FLASH and the European XFEL without the possibility to perform comprehensive electron beam characterization and optimization due to the

tight time schedule. However, recently we got the possibility to partially perform electron beam characterization with an RF gun which was conditioned at PITZ and will be delivered for further usage at the European XFEL. Due to lack of time, the measurements were performed only for 1 nC and 100 pC electron beam charges. Only emittance dependencies on the most sensitive machine parameters were measured. In the following section, measured data compared to the results of numerical simulations using the ASTRA code [6] are presented.

EMITTANCE SIMULATIONS AND MEASUREMENT RESULTS

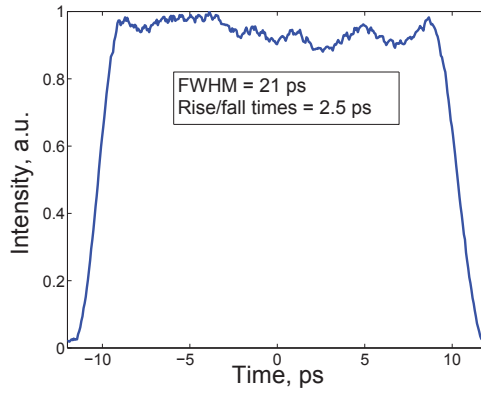
Emittance dependencies on the main solenoid current, gun launching phase and rms laser spot size on the cathode were measured for electron beams with 100 pC and 1 nC charges. A flat-top temporal UV laser profile with a FWHM of about 21 ps was used and is presented together with the transverse laser profile in Fig. 1. The gun on-axis peak field on the cathode was reduced to about 53 MV/m, as compared to the nominal 60 MV/m which is planned for the European XFEL, in order to combine the electron beam characterization with gun stability tests at long RF pulses. This yields an accordingly reduced electron beam momentum after the gun of about $p_z \sim 5.9$ MeV/c as compared to about $p_z \sim 6.8$ MeV/c at 60 MV/m. Further acceleration by the CDS booster operated at the maximum allowed accelerating gradient and tuned to the maximum mean momentum gain phase, hereinafter called MMMG phase, resulted in a final electron beam momentum of about $p_z \sim 21.2$ MeV/c. The emittance of the electron beam was measured using the first emittance measurement station installed 5.74 m from the cathode [3]. For both probed electron bunch charges emittance dependencies on the main solenoid current were measured for various rms laser spot sizes on the cathode and an MMMG gun launching phase (an optimum gun phase according to the simulations, see e.g. [3, 4]). Additionally, for the electron beam with 1 nC bunch charge, the emittance dependence on the gun launching phase was measured for the rms laser spot size on the cathode delivering the minimum emittance at the MMMG phase.

Emittance Data for 1 nC Electron Bunch Charge

As it was mentioned, emittance dependencies on the rms laser spot size on the cathode and gun launching phase were measured for electron beams with a bunch charge of 1 nC.

* Grygorii.Vashchenko@desy.de

† BAS INRNE, 1784 Sofia, Bulgaria.



(a) Temporal profile.

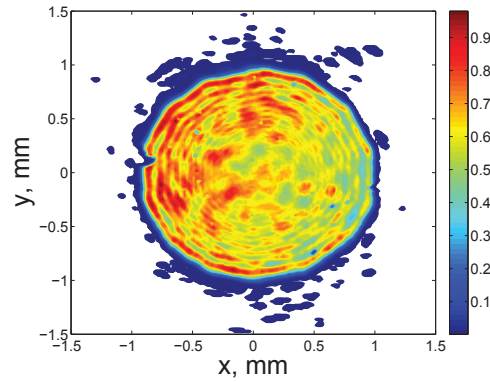
(b) Transverse profile. $\sigma_{xy} = 0.48$ mm.

Figure 1: Examples of UV laser profiles used for emittance measurements. The temporal profile was tried to be kept constant for measurements with different electron bunch charges while the transverse spot size was varied.

For each laser spot size, a solenoid scan was performed in order to find the minimum emittance value. For the main solenoid current value delivering the minimum emittance, several statistical emittance measurements were done. The result of these measurements is presented in Fig. 2 and yield a minimum emittance value of $1.01 \pm 0.01 \mu\text{m}$ for an rms laser spot size at the cathode of 0.38 mm. Corresponding simulations were performed and yield a minimum emittance value of $0.77 \mu\text{m}$ for an rms laser spot size on the cathode of 0.45 mm. The measurement and simulation curves do not include data points for the rms laser spot sizes of less than 0.38 and 0.43 mm, respectively, since the 1 nC bunch charge could not be extracted anymore due to space-charge limitations at the cathode. As compared to the nominal gun on-axis peak field of 60 MV/m the obtained emittance values are higher by 26 % and 42 % in the simulations and measurements, respectively [3,4]. The difference between

measurements can be caused by Schottky-like effects which were not taken into account in the simulations [3]. An additional cause of the discrepancy is the deviation of the laser profiles which were used for the measurements from the ideal profiles used in simulations. As one can see in Fig. 1, there is a significant deviation of the transverse laser profile from the ideal uniform profile used in the simulations, caused by interference effects. The temporal laser shape is also not perfectly flat.

The emittance dependence on the gun launching phase was measured for a fixed laser spot size on the cathode. The rms laser spot size of 0.38 mm, which gives the smallest emittance (see Fig. 2) for the MMMG phase, was chosen. Like in the previous case, emittance solenoid scans were performed for each gun launching phase. For the solenoid current providing the minimum emittance value, several statistical emittance measurements were performed additionally. The result of these measurements is presented in Fig. 3. Emittance decrease for the gun launching phases of 6 and 9 deg during the measurements is not yet fully understood. It might be connected to the higher electric fields on the cathode during emission which yield accordingly enhanced Schottky-like effects which are not included in the simulations, as well as to the general limitations of the photoemission model used in the simulations at the conditions close to the space-charge limit [4]. Besides the above discussed parameters like the laser spot size, main solenoid current and the gun launching phase, the emittance is also influenced by the electron beam transport through the beamline. As shown in [3], there is a significant influence of the electron beam transport through the CDS booster on the emittance. Optimization of the transport through the CDS booster can be done based on direct emittance measurements. Magnetic fields of several steerer magnets upstream the CDS booster were varied in order to change the inclination and offset of the electron beam. The measured emittance as a function of steerers settings is presented in Fig. 4. As one can see, an improper electron beam transport has a significant influence

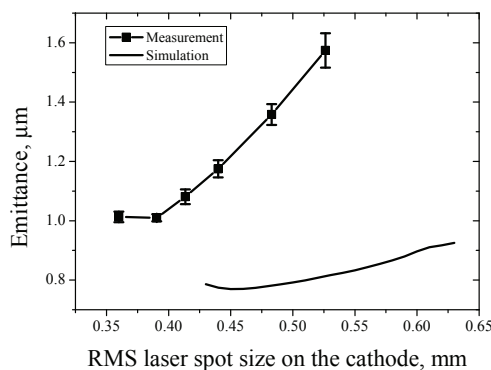


Figure 2: Emittance dependence on the rms laser spot size on the cathode for an electron beam with 1 nC bunch charge.

this measurement and earlier experimental results is larger than the difference between the corresponding simulations. The reason for this might be, that due to the tight schedule, not all machine parameters have been fully optimized. The strong discrepancy between the machine parameters delivering the minimum emittance in the simulations and

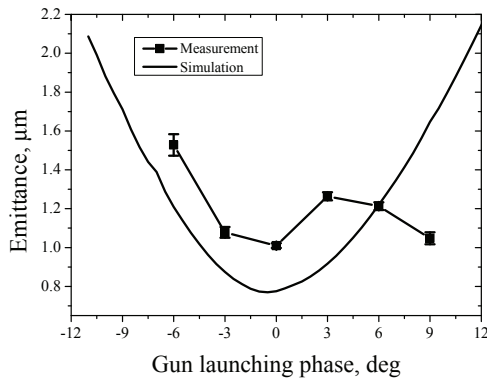


Figure 3: Emittance dependence on the gun launching phase, with respect to the MMMG phase, for an electron beam with 1 nC bunch charge.

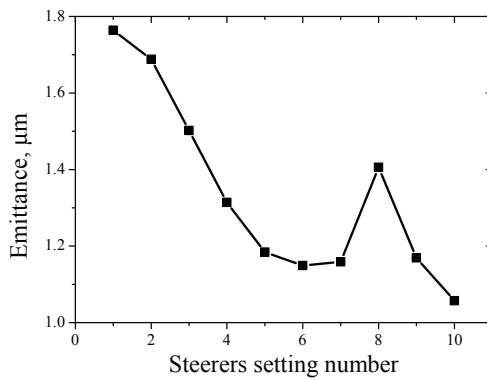


Figure 4: Emittance as a function of the steerer settings upstream the CDS booster.

on its quality due to consequent inhomogeneous acceleration of the electron beam in the CDS booster.

Emittance Data for 100 pC Electron Beam Charge

Due to lack of time, only the emittance dependence on the rms laser spot size was measured for electron beams with 100 pC charge. During these measurements the gun launching phase was fixed to the MMMG phase. As for previous measurements with 1 nC electron bunch charge, the main solenoid current scan was performed for each rms laser spot size on the cathode. For the main solenoid current delivering the minimum emittance, several statistical emittance measurements were performed. The result is presented in Fig. 5. A minimum emittance value of $0.26 \pm 0.01 \mu\text{m}$ was found for an rms laser spot size on the cathode of 0.16 mm during the measurements. In the simulations a minimum emittance value of $0.18 \mu\text{m}$ was found for an rms laser spot size on the cathode of 0.17 mm. Similar to the measurements with 1 nC electron beams, there is a significant discrepancy between the emittance values obtained in measurements and simulations. As in 1 nC case it might be partially explained by Schottky-like effects, imperfections of the real laser profiles and by possible systematic errors during the emittance measurements which are not taken into account. For a pre-

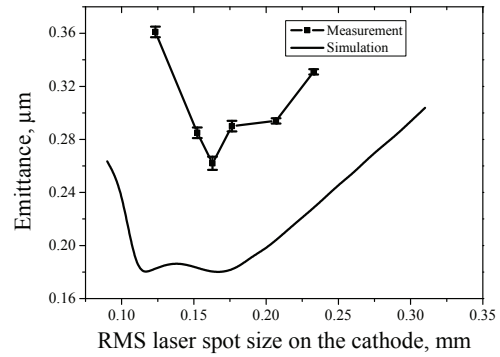


Figure 5: Emittance dependence on the rms laser spot size on the cathode for an electron beam with 100 pC bunch charge.

vious similar measurement but at a peak field of 60 MV/m at the cathode, the systematic emittance overestimation was estimated to be at the level of about 10 % [3]. For a reduced field of 53 MV/m one can expect a larger emittance overestimation due to a stronger sensitivity of the emittance on machine parameters.

SUMMARY

After a long period devoted mainly to the conditioning of photo electron guns for their future usage at FLASH and the European XFEL, PITZ finally got the possibility to characterize the quality of the electron beam in terms of its emittance. The measurements with bunch charges of 1 nC and 100 pC were performed for the gun on-axis peak field at the cathode of 53 MV/m. Although this gun peak field is smaller than 60 MV/m foreseen for the European XFEL and the experimental beam optimization has been incomplete due to lack of time, the obtained emittance value of $1.01 \pm 0.01 \mu\text{m}$ for an electron beam of 1 nC bunch charge is only 10 % higher than the required $0.9 \mu\text{m}$ for the European XFEL. Therefore one can expect that by bringing the gun to the nominal European XFEL operating gradient the emittance is expected to improve accordingly below the design value of $0.9 \mu\text{m}$.

ACKNOWLEDGMENT

The authors would like to thank S. Schreiber for his valuable comments and careful proof-reading of this paper.

REFERENCES

- [1] W. Ackermann et al., *Nature Photon.* 1, 336 (2007)
- [2] M. Altarelli et al., DESY, Hamburg Report No. DESY 2006-097, 2007
- [3] G. Vashchenko, *Transverse phase space studies with the new CDS booster cavity at PITZ*. PhD thesis. DESY-THESIS-2013-043, 2013
- [4] M. Krasilnikov et al., *Phys. Rev. ST Accel. Beams* 15, 100701 (2012)
- [5] F. Stephan et al., *Phys. Rev. ST Accel. Beams* 13, 020704 (2010)
- [6] K. Floetmann, A Space charge TRacking Algorithm, <http://www.desy.de/~mpyf10>

EVOLUTION OF A WARM BUNCHED BEAM IN A FREE DRIFT REGION

B. Maly, A. Friedman, Ariel University - Schlesinger Family Center for Compact Accelerators, Radiation Sources, and Applications, Ariel, Israel

Abstract

The state of the art of FELs development at present is "Table-Top X Ray Free Electron Lasers". Many such schemes involves a pre-bunched electron beam [1]. In this paper we will analyze the evolution and "survivability" of bunching introduced into the beam in the free drift region prior to the wiggler [2-6]. We examined analytically the first order degradation in beam bunching due to space charge effect. It will be shown that there is a limited interaction region, characterized by an exponential decay of the bunching factor, having a length inversely proportional to the square of the electron beam normalized temperature, followed by a stable bunch region. We will present examples of the effect for several schemes of X Ray and Tera Hertz FELs considered or being constructed presently.

INTRODUCTION

First, we present a solution for the evolution of a cold bunched continuous electron beam in a free drift region, based on a one-dimensional first order Vlasov equations including space charge effects [3-5]. Based on the first order cold beam solution, we expand the analysis for the evolution of a warm bunched electron beam in a free drift region, by assuming normal distributions for both transversal and longitudinal components of the momentum, independently [2,6]. Analytical solution is achieved by using a second order two-dimensional Taylor expansion of the exponent argument in the previously derived cold beam solution.

EVOLUTION OF A COLD BUNCHED ELECTRON BEAM IN A FREE DRIFT REGION

The analysis for cold electron beam is based on relativistic Vlasov equation for plasma:

$$\frac{\partial f}{\partial t} + \vec{v} \cdot \nabla f + \frac{d\vec{p}}{dt} \cdot \nabla_p f = 0 \quad (1)$$

where $f(\vec{r}, \vec{p}, t)$ is the distribution function of the plasma, \vec{p} and \vec{v} are the momentum and velocity vectors, respectively.

The time derivative of the momentum can be replaced by Lorentz force in the absence of an external magnetic field:

$$\frac{d\vec{p}}{dt} = -e\vec{E} \quad (2)$$

where e is the absolute value of the electron charge, and \vec{E} is the electric field vector. In the current model there is no external electric field and no radiation field (since there is no external acceleration/deceleration, this is a good assumption). Therefore only the self-induced Coulomb

field is considered (space charge). Thus the electric field can be derived out of the electric scalar potential:

$$\vec{E} = -\nabla\psi \quad (3)$$

where ψ is the electric scalar potential.

Substituting (2) and (3) into (1) results in:

$$\frac{\partial f}{\partial t} + \vec{v} \cdot \nabla f + e\nabla\psi \cdot \nabla_p f = 0 \quad (4)$$

where

$$\nabla_p \triangleq \hat{x} \frac{\partial}{\partial p_x} + \hat{y} \frac{\partial}{\partial p_y} + \hat{z} \frac{\partial}{\partial p_z} \quad (5)$$

In this formulation we restrict ourselves to a single (longitudinal) dimension. Hence, equation (4) becomes:

$$\frac{\partial f}{\partial t} + v_z \frac{\partial f}{\partial z} + e \frac{\partial \psi}{\partial z} \frac{\partial f}{\partial p_z} = 0 \quad (6)$$

p_z and v_z are the longitudinal components of the momentum and velocity, respectively.

Space charge effects are derived from the Poisson equation:

$$\nabla^2 \psi = -\frac{\rho}{\epsilon_0} \quad (7)$$

ρ is the charge density (per unit volume), and ϵ_0 is the permittivity of free space.

The charge density can be integrated out of the distribution function:

$$\rho(z, t) = -e \int_{-\infty}^{\infty} f(p_z, z, t) dp_z \quad (8)$$

Substituting (8) into (7) results in:

$$\frac{\partial^2 \psi}{\partial z^2} = \frac{e}{\epsilon_0} \int_{-\infty}^{\infty} f(p_z, z, t) dp_z \quad (9)$$

The charge density of the electron beam is modulated at the origin ($z = 0$), hence the distribution function at the origin can be expressed as:

$$f(z = 0) = n_0(1 + \alpha e^{j\omega t})\delta(p_z - \bar{p}_z) \quad (10)$$

where n_0 is the electrons density per unit volume, α is the modulation factor, ω is the angular frequency of the modulation, δ is the Dirac delta function, and \bar{p}_z is the average longitudinal momentum; since the electron beam is cold, the spread in longitudinal momentum is described by a Dirac delta function.

Using perturbation theory, we assume that both the distribution function and the electrical scalar potential can be expressed as an infinite series of terms, each proportional to a higher power of the modulation factor, α :

$$f = f_0 + \alpha f_1 + \alpha^2 f_2 + \dots, \quad \psi = \alpha \psi_1 + \alpha^2 \psi_2 + \dots \quad (11)$$

$\psi_0 = 0$, since in a free drift region there is no external electrical scalar potential applied to the electron beam.

In this section we are interested only in terms that are proportional to the modulation factor itself, i.e. linear to α .

Assuming that the perturbation is propagating along the electron beam in the positive longitudinal direction with an angular frequency equals to that of the modulation, ω , and a propagation coefficient k , then the form of the first order terms in (11) can be expressed as:

$$f_1 = f_{1\omega} e^{j(\omega t - kz)} \quad , \quad \psi_1 = \psi_{1\omega} e^{j(\omega t - kz)} \quad (12)$$

where $f_{1\omega}$ and $\psi_{1\omega}$ are the frequency dependent amplitudes of the first order distribution function and the electrical scalar potential, respectively.

Substituting (12) in (6) and neglecting any terms that are not first order in α results in:

$$f_{1\omega} = \frac{k \cdot e \cdot n_0}{\omega - v_z \cdot k} \psi_{1\omega} \frac{\partial}{\partial p_z} [\delta(p_z - \bar{p}_z)] \quad (13)$$

Substituting (12), (13) in (9) and neglecting non-linear α -dependent terms results:

$$1 + \frac{e^2 \cdot n_0}{k \cdot \epsilon_0} \int_{-\infty}^{\infty} \frac{1}{\omega - v_z \cdot k} \cdot \frac{\partial}{\partial p_z} [\delta(p_z - \bar{p}_z)] dp_z = 0 \quad (14)$$

In order to proceed from (14) we calculate the derivatives of the following expressions:

$$v_z = \frac{p_z}{m \cdot \gamma} \Rightarrow \frac{dv_z}{dp_z} = \frac{1}{m \cdot \gamma^3} \quad ,$$

$$\gamma = \left(1 + \frac{p_z^2}{m^2 c^2}\right)^{\frac{1}{2}} \Rightarrow \frac{d\gamma}{dp_z} = \frac{p_z}{m^2 c^2 \gamma} \quad (15)$$

The integral in (14) is carried by parts and the result is:

$$\begin{aligned} \int_{-\infty}^{\infty} \frac{1}{\omega - v_z \cdot k} \cdot \frac{\partial}{\partial p_z} [\delta(p_z - \bar{p}_z)] dp_z &= \\ &= -\frac{k}{m \gamma^3} \cdot \frac{1}{(\omega - \bar{v}_z \cdot k)^2} \end{aligned} \quad (16)$$

where $\bar{\gamma} \triangleq \gamma(p_z = \bar{p}_z)$ and $\bar{v}_z \triangleq v_z(p_z = \bar{p}_z)$.

Substitute (16) in (14) leads to the dispersion relation:

$$k = \frac{\omega \pm \tilde{\omega}_p}{\bar{v}_z} \quad (17)$$

where $\omega_p \triangleq \left(\frac{e^2 n_0}{m \epsilon_0 \gamma^3}\right)^{\frac{1}{2}}$ is the plasma frequency and $\tilde{\omega}_p \triangleq \omega_p(p_z = \bar{p}_z)$.

Therefore the first order distribution function for the cold electron beam is:

$$f = n_0 \left\{ 1 + \frac{\alpha}{2} \left[e^{j(\omega t - \frac{\omega + \omega_p}{v_z} p_z)} + e^{j(\omega t - \frac{\omega - \omega_p}{v_z} p_z)} \right] \right\} \cdot \delta(p_z - \bar{p}_z) \quad (18)$$

The physical interpretation of (18) is that the modulation in the charge density of the electron beam propagates in two waves, having phase velocities higher and lower than the longitudinal velocity of the electron beam, with no degradation in amplitude along the longitudinal direction. Superimposed these two waves results in a standing wave, having a wave number of $\frac{\omega_p}{v_z}$

and acting as an "envelope" (amplitude modulation) of a propagating wave (carrier), having an angular frequency ω , and a propagation coefficient $\frac{\omega}{v_z}$:

$$\begin{aligned} \left[e^{j(\omega t - \frac{\omega + \omega_p}{v_z} p_z)} + e^{j(\omega t - \frac{\omega - \omega_p}{v_z} p_z)} \right] &\approx \\ &\approx e^{j(\omega t - \frac{\omega}{v_z} p_z)} \cdot \cos\left(\frac{\omega_p}{v_z} p_z\right) \end{aligned} \quad (19)$$

EVOLUTION OF A WARM PRE-BUNCHED BEAM

Calculation of Terms

Based on the first order cold beam solution for the distribution function, we expand the analysis for the evolution of a warm bunched electron beam in a free drift region, by replacing the one-dimensional Dirac delta function in (18) with normal distributions for both transversal and longitudinal components of the momentum, independently:

$$f_1 = \frac{1}{2} n_0 \cdot \left[e^{j(\omega t - \frac{\omega + \omega_p}{v_z} p_z)} + e^{j(\omega t - \frac{\omega - \omega_p}{v_z} p_z)} \right] \cdot \left[\frac{1}{\sqrt{2\pi} \Delta p_{\perp}} e^{-\frac{(p_{\perp})^2}{2(\Delta p_{\perp})^2}} \right] \cdot \left[\frac{1}{\sqrt{2\pi} \Delta p_z} e^{-\frac{(p_z - \bar{p}_z)^2}{2(\Delta p_z)^2}} \right] \quad (20)$$

where p_{\perp} is the transversal component of the momentum, Δp_{\perp} and Δp_z are the standard deviations of the transversal and longitudinal normal distributions, respectively; the average transversal momentum component is zero: $\bar{p}_{\perp} = 0$.

In expression (20) only terms that are proportional to the modulation factor itself, i.e. linear to α , are considered.

The influence on the charge density along the electron beam, caused by the perturbation, is given by the two-dimensional integration over the transversal and longitudinal components of the momentum:

$$\rho_1 = -e \int_{-\infty}^{\infty} dp_{\perp} \int_{-\infty}^{\infty} f_1 dp_z \quad (21)$$

ρ_1 is the first order approximation of the charge density: $\rho = \rho_0 + \alpha \rho_1 + \alpha^2 \rho_2 + \dots$

In order perform the integration in (21), we use a second order two dimensional Taylor expansion for the core of the cold beam solution, centered at the average values of the transversal and longitudinal components of the momentum; we define:

$$g^{\pm}(p_{\perp}, p_z) \triangleq \frac{\omega \pm \omega_p}{v_z} \quad (22)$$

The second order approximation of the function g^{\pm} is given by:

$$\begin{aligned} g^{\pm}(p_{\perp}, p_z) &\approx g^{\pm}(0, \bar{p}_z) + \\ &+ \left[\frac{dg^{\pm}}{dp_{\perp}} \right]_{(0, \bar{p}_z)} \cdot p_{\perp} + \left[\frac{dg^{\pm}}{dp_z} \right]_{(0, \bar{p}_z)} \cdot (p_z - \bar{p}_z) + \\ &+ \frac{1}{2} \left[\frac{d^2 g^{\pm}}{dp_{\perp}^2} \right]_{(0, \bar{p}_z)} \cdot p_{\perp}^2 + \end{aligned}$$

$$+ \left[\frac{d^2 g^\pm}{dp_\perp dp_z} \right]_{(\mathbf{0}, \bar{\mathbf{p}}_z)} \cdot \mathbf{p}_\perp \cdot (\mathbf{p}_z - \bar{\mathbf{p}}_z) + \frac{1}{2} \left[\frac{d^2 g^\pm}{dp_z^2} \right]_{(\mathbf{0}, \bar{\mathbf{p}}_z)} \cdot (\mathbf{p}_z - \bar{\mathbf{p}}_z)^2 \quad (23)$$

Basic relations:

$$v_z = \frac{p_z}{m \gamma} ; \quad \gamma = \left(1 + \frac{p_\perp^2 + p_z^2}{m^2 c^2} \right)^{\frac{1}{2}} ; \quad \omega_p = \left(\frac{e^2 n_0}{m \epsilon_0 \gamma \gamma_z^2} \right)^{\frac{1}{2}} \quad (24)$$

$$\gamma = (1 - \beta^2)^{-\frac{1}{2}} ; \quad \gamma_z = (1 - \beta_z^2)^{-\frac{1}{2}} ; \quad \gamma_z = \gamma \cdot \left(1 + \frac{p_\perp^2}{m^2 c^2} \right)^{-\frac{1}{2}} \quad (25)$$

First order derivatives:

$$\frac{d\gamma}{dp_\perp} = \frac{p_\perp}{m^2 c^2 \gamma} ; \quad \frac{d\gamma}{dp_z} = \frac{p_z}{m^2 c^2 \gamma} ; \quad \frac{d\gamma_z}{dp_\perp} = -\frac{p_\perp p_z^2 \gamma_z^3}{m^4 c^4 \gamma^4} ; \quad \frac{d\gamma_z}{dp_z} = \frac{p_z \gamma_z}{m^2 c^2 \gamma^2} \quad (26)$$

$$\frac{dv_z}{dp_\perp} = -\frac{p_\perp p_z}{m^2 c^2 \gamma^3} ; \quad \frac{dv_z}{dp_z} = \frac{1}{m \gamma \gamma_z^2} ; \quad \frac{d\omega_p}{dp_\perp} = \frac{\omega_p p_\perp}{m^2 c^2 \gamma^2} \left(\gamma_z^2 - \frac{3}{2} \right) ; \quad \frac{d\omega_p}{dp_z} = -\frac{3}{2} \frac{\omega_p p_z}{m^2 c^2 \gamma^2} \quad (27)$$

$$\frac{dg^\pm}{dp_\perp} = \frac{p_\perp}{m c^2 \gamma p_z} \left[\omega \pm \omega_p \left(\gamma_z^2 - \frac{1}{2} \right) \right] ; \quad \frac{dg^\pm}{dp_z} = -(\pm) \frac{3}{2} \frac{\omega_p}{m c^2 \gamma} - \frac{m \gamma}{p_z^2 \gamma_z^2} (\omega \pm \omega_p) \quad (28)$$

Second order derivatives:

$$\frac{d^2 g^\pm}{dp_\perp^2} = \frac{1}{m c^2 p_z} \cdot \frac{p_\perp^2}{m^2 c^2 \gamma^2} \cdot \left[\pm \omega_p \left(\frac{5}{4} - \gamma_z^2 - \gamma_z^4 \right) - \omega \right] + \frac{1}{m c^2 p_z} \cdot \left[\omega \pm \omega_p \left(\gamma_z^2 - \frac{1}{2} \right) \right] \quad (29)$$

$$\frac{d^2 g^\pm}{dp_\perp dp_z} = \frac{p_\perp}{m^3 c^4 \gamma^3} \left[\pm \omega_p \left(\frac{7}{4} - \frac{3}{2} \gamma_z^2 \right) - 2\omega \right] - \frac{p_\perp}{m c^2 \gamma \gamma_z^2 p_z^2} \left[\omega \pm \omega_p \left(\gamma_z^2 - \frac{1}{2} \right) \right] \quad (30)$$

$$\frac{d^2 g^\pm}{dp_z^2} = \pm \frac{15}{4} \frac{\omega_p p_z}{m^3 c^4 \gamma^3} + 2 \frac{m \gamma}{p_z^3 \gamma_z^2} (\omega \pm \omega_p) + \frac{\omega \pm \frac{5}{2} \omega_p}{m c^2 \gamma \gamma_z^2 p_z} \quad (31)$$

Substituting the average values of the transversal and longitudinal components of the momentum in expressions (24)-(31) leads to the following definitions of constants:

$$\tilde{\gamma} \triangleq \gamma(\mathbf{p}_\perp = \mathbf{0}, p_z = \bar{p}_z) = \left(1 + \frac{\bar{p}_z^2}{m^2 c^2} \right)^{\frac{1}{2}} ; \quad \tilde{\gamma}_z \triangleq \gamma_z(\mathbf{p}_\perp = \mathbf{0}, p_z = \bar{p}_z) = \tilde{\gamma} \quad (32)$$

$$\tilde{\omega}_p \triangleq \omega_p(\mathbf{p}_\perp = \mathbf{0}, p_z = \bar{p}_z) = \left(\frac{e^2 n_0}{m \epsilon_0 \tilde{\gamma}^2} \right)^{\frac{1}{2}} ; \quad \tilde{v}_z \triangleq v_z(\mathbf{p}_\perp = \mathbf{0}, p_z = \bar{p}_z) = \frac{\bar{p}_z}{m \tilde{\gamma}} \quad (33)$$

$$A^\pm \triangleq g^\pm(\mathbf{0}, \bar{\mathbf{p}}_z) = \frac{\omega \pm \tilde{\omega}_p}{\tilde{v}_z} \quad (34)$$

$$\left[\frac{dg^\pm}{dp_\perp} \right]_{(\mathbf{0}, \bar{\mathbf{p}}_z)} = \mathbf{0} ; \quad B^\pm \triangleq \left[\frac{dg^\pm}{dp_z} \right]_{(\mathbf{0}, \bar{\mathbf{p}}_z)} = -(\pm) \frac{3}{2} \frac{\tilde{\omega}_p}{m c^2 \tilde{\gamma}} - \frac{m}{\tilde{p}_z^2 \tilde{\gamma}} (\omega \pm \tilde{\omega}_p) \quad (35)$$

$$C_1^\pm \triangleq \left[\frac{d^2 g^\pm}{dp_\perp^2} \right]_{(\mathbf{0}, \bar{\mathbf{p}}_z)} = \frac{1}{m c^2 \tilde{p}_z} \left[\omega \pm \tilde{\omega}_p \left(\tilde{\gamma}^2 - \frac{1}{2} \right) \right] ; \quad \left[\frac{d^2 g^\pm}{dp_\perp dp_z} \right]_{(\mathbf{0}, \bar{\mathbf{p}}_z)} = \mathbf{0} \quad (36)$$

$$C_2^\pm \triangleq \left[\frac{d^2 g^\pm}{dp_z^2} \right]_{(\mathbf{0}, \bar{\mathbf{p}}_z)} = \pm \frac{15}{4} \frac{\tilde{\omega}_p \tilde{p}_z}{m^3 c^4 \tilde{\gamma}^3} + 2 \frac{m}{\tilde{p}_z^3 \tilde{\gamma}} (\omega \pm \tilde{\omega}_p) + \frac{\omega \pm \frac{5}{2} \tilde{\omega}_p}{m c^2 \tilde{\gamma}^3 \tilde{p}_z} \quad (37)$$

Using the above definitions of the constants, the second order approximation of g^\pm as given in (23) becomes:

$$g^\pm(\mathbf{p}_\perp, \mathbf{p}_z) \approx A^\pm + B^\pm \cdot (\mathbf{p}_z - \bar{\mathbf{p}}_z) + \frac{1}{2} [C_1^\pm \cdot \mathbf{p}_\perp^2 + C_2^\pm \cdot (\mathbf{p}_z - \bar{\mathbf{p}}_z)^2] \quad (38)$$

With the definition:

$$h(\mathbf{p}_\perp, \mathbf{p}_z, \mathbf{z}) \triangleq \frac{p_\perp^2}{2 \Delta p_\perp^2} + \frac{(p_z - \bar{p}_z)^2}{2 \Delta p_z^2} + j \mathbf{z} \cdot g^\pm(\mathbf{p}_\perp, \mathbf{p}_z) \quad (39)$$

The integration in (21) can be written as:

$$\rho_1^\pm = -\frac{e n_0}{4 \pi \Delta p_\perp \Delta p_z} e^{j \omega t} \cdot \int_{-\infty}^{\infty} d\mathbf{p}_\perp \int_{-\infty}^{\infty} e^{-h(\mathbf{p}_\perp, \mathbf{p}_z, \mathbf{z})} d\mathbf{p}_z \quad (40)$$

Substituting (38) in (39) results in:

$$h(\mathbf{p}_\perp, \mathbf{p}_z, \mathbf{z}) \approx \frac{p_\perp^2}{2 \Delta p_\perp^2} + \frac{(p_z - \bar{p}_z)^2}{2 \Delta p_z^2} + j \mathbf{z} A^\pm + j \mathbf{z} B^\pm \cdot (\mathbf{p}_z - \bar{\mathbf{p}}_z) + \frac{1}{2} [j \mathbf{z} C_1^\pm \cdot \mathbf{p}_\perp^2 + j \mathbf{z} C_2^\pm \cdot (\mathbf{p}_z - \bar{\mathbf{p}}_z)^2] \quad (41)$$

We examine the coefficients of the terms p_\perp^2 , p_z^2 and \mathbf{p}_z ; we suggest the following definitions:

$$\sigma_\perp(\mathbf{z}) \triangleq \frac{\Delta p_\perp}{\sqrt{1 + j \mathbf{z} C_1^\pm \cdot \Delta p_\perp^2}} ; \quad \sigma_z(\mathbf{z}) \triangleq \frac{\Delta p_z}{\sqrt{1 + j \mathbf{z} C_2^\pm \cdot \Delta p_z^2}} ; \quad \bar{\mathbf{p}}(\mathbf{z}) \triangleq \bar{\mathbf{p}}_z - j \mathbf{z} B^\pm \cdot [\sigma_z(\mathbf{z})]^2 \quad (42)$$

Substitute (42) in (41) results in:

$$h(\mathbf{p}_\perp, \mathbf{p}_z, \mathbf{z}) \approx \frac{p_\perp^2}{2 [\sigma_\perp(\mathbf{z})]^2} + \frac{[p_z - \bar{p}(\mathbf{z})]^2}{2 [\sigma_z(\mathbf{z})]^2} + j \mathbf{z} A^\pm + \frac{1}{2} \mathbf{z}^2 (B^\pm)^2 [\sigma_z(\mathbf{z})]^2 \quad (43)$$

The first order charge density can now be calculated in (40) by using the approximation for $h(\mathbf{p}_\perp, \mathbf{p}_z, \mathbf{z})$ in (43):

$$\rho_1^\pm = -\frac{e n_0 \sigma_\perp(\mathbf{z}) \sigma_z(\mathbf{z})}{2 \Delta p_\perp \Delta p_z} e^{j \omega t} e^{-\{j \mathbf{z} A^\pm + \frac{1}{2} \mathbf{z}^2 (B^\pm)^2 [\sigma_z(\mathbf{z})]^2\}} =$$

$$= -\frac{en_0}{\sqrt{(1+jzC_1^\pm \cdot \Delta p_z^2)(1+jzC_2^\pm \cdot \Delta p_z^2)}} \cdot \frac{1}{2} \cdot e^{j\left(\omega t - \frac{\omega \pm \tilde{\omega}_p}{\tilde{v}_z} z\right)} \cdot e^{-\frac{(B^\pm)^2 \Delta p_z^2}{2} \cdot \frac{z^2}{1+jzC_2^\pm \cdot \Delta p_z^2}} \quad (44)$$

Physical Interpretation and Significance for Low Energy X-Ray FEL

The factor $\frac{1}{2} e^{j\left(\omega t - \frac{\omega \pm \tilde{\omega}_p}{\tilde{v}_z} z\right)}$ is proportional to the cold beam solution.

In order to evaluate the degradation in amplitude of the first order charge density along the longitudinal direction, we separate the other exponential expression in (44) into real and imaginary parts:

$$e^{-\frac{(B^\pm)^2 \Delta p_z^2}{2} \cdot \frac{z^2}{1+jzC_2^\pm \cdot \Delta p_z^2}} = e^{-\frac{j^3 \cdot C_2^\pm \cdot (B^\pm)^2 \cdot \Delta p_z^4}{2[1+z^2 \cdot (C_2^\pm)^2 \cdot \Delta p_z^4]}} \cdot e^{-\frac{(B^\pm)^2 \Delta p_z^2}{2} \cdot \frac{z^2}{1+z^2 \cdot (C_2^\pm)^2 \cdot \Delta p_z^4}} \quad (45)$$

The physical interpretation of the result in (45) is that there is a limited length region, at the vicinity of the modulation starting point, characterized by an exponential decay in the charge density modulation, described by the

expression $e^{-\frac{(B^\pm)^2 \Delta p_z^2}{2} z^2}$, with typical length of $\Delta z \approx \frac{1}{|C_2^\pm| \cdot \Delta p_z^2}$, followed by a stable modulation region.

If the frequency of the modulation divided by the factor $\tilde{\gamma}^2$ is significantly higher than the plasma frequency, i.e. $\frac{\omega}{\tilde{\gamma}^2} \gg \tilde{\omega}_p$, the terms $(B^\pm)^2$ and C_2^\pm are simplified:

$$(B^\pm)^2 \approx \frac{\omega^2}{m^2 c^4 \tilde{\gamma}^6} \quad ; \quad C_2^\pm \approx \frac{3\omega}{m^2 c^3 \tilde{\gamma}^4} \quad (46)$$

Note that $\frac{\omega}{c} = \frac{2\pi}{\lambda}$ and for $\tilde{\gamma} > 10$ the average longitudinal momentum is approximately: $\tilde{p}_z = m\tilde{\gamma}\tilde{v}_z \approx m\tilde{\gamma}c$; it is convenient to define the normalized temperature of the electron beam:

$$T_n \triangleq \frac{\Delta p_z}{\tilde{p}_z} \quad (47)$$

The expression describing the exponential decay in (45) becomes:

$$\exp\left[-\frac{(B^\pm)^2 \Delta p_z^2}{2} \cdot \frac{z^2}{1+z^2 \cdot (C_2^\pm)^2 \cdot \Delta p_z^4}\right] \approx \exp\left[-\frac{2\pi^2}{\tilde{\gamma}^4} \cdot T_n^2 \cdot \frac{z^2}{\lambda^2} \cdot \frac{1}{1+\frac{36\pi^2}{\tilde{\gamma}^4} T_n^4 \cdot \frac{z^2}{\lambda^2}}\right] \quad (48)$$

Therefore, the typical length of region characterized by the exponential decay, normalized with respect to the wavelength, is inversely proportional to the square of the normalized temperature:

$$\frac{\Delta z}{\lambda} \approx \frac{\tilde{\gamma}^2}{6\pi} \cdot \frac{1}{T_n^2} \quad (49)$$

The attenuation in the amplitude of the first order charge density in the stable region, with respect to the initial modulation factor is:

$$\left|\frac{\rho_1^\pm(z \gg \Delta z)}{\rho_1^\pm(z=0)}\right| \approx e^{-\frac{1}{18T_n^2}} \quad (50)$$

Typical normalized length for the attenuation in the amplitude of the first order charge density (the point where the attenuation decreases down to about $\frac{1}{e}$ of its initial value) is no less than:

$$\left|\frac{\rho_1^\pm(z=\Delta z)}{\rho_1^\pm(z=0)}\right| \approx \frac{1}{e} \Rightarrow \frac{\Delta z}{\lambda} > \frac{\tilde{\gamma}^2}{\sqrt{2}\pi} \cdot \frac{1}{T_n} \quad (51)$$

The actual normalized length in (51) may increase for high values of the normalized temperature, due to the term in the denominator of (48), which becomes:

$1 + 18T_n^2$ at that point.

The table below depicts the estimate typical normalized lengths of the attenuation in the amplitude of the first order charge density, as calculated in (51). This was calculated for two different operating ranges, (Tera Hertz and X Ray) in various cases:

λ	$\tilde{\gamma}$	T_n	Δz
100 μm	10	0.1	22.5mm
10nm	80	0.001	14.4mm
10nm	400	0.01	36mm

CONCLUSIONS

For a cold electron beam in a free drift region, a first order perturbation in charge density was calculated. The result is shown to be a propagation wave in the longitudinal direction at the excitation frequency. The phase velocity of the density wave equals to that of the beam velocity plus an amplitude modulation caused by a standing wave acting as a slow-varying "envelope". The standing wave has a wave number equals to the plasma frequency divided by the beam velocity, but with no attenuation in charge density modulation along the longitudinal direction.

Introducing two dimensional velocity spreads causes the first order charge density modulation of a warm electron beam in a free drift region to decrease rapidly (exponential decay) in the longitudinal direction. The decrease has a typical normalized length proportional to $\tilde{\gamma}^2$, and inversely proportional to the normalized temperature.

In the Tera Hertz range, a typical normalized length (the effective length without losing the bunching) of the order of tens of millimeters can be achieved with $\tilde{\gamma} \approx 10$ and a normalized temperature of **0.1**; the same order of magnitude of typical normalized length in the X Ray range can be achieved with $\tilde{\gamma} \approx 80$ and a normalized temperature of **0.001**, or $\tilde{\gamma} \approx 400$ and a normalized temperature of **0.01**.

REFERENCES

- [1] I. Schnitzer and A. Gover, "The Prebunched Free Electron Laser in Various Operating Gain Regimes", Nuclear Instruments and Methods in Physics Research A237 124-140 (1985).
- [2] B. Steinberg, A. Gover, S. Ruschin, "Three Dimensional Theory of Free Electron Lasers in the Collective Regime", Phys. Rev. A36, 147-163 (1987).
- [3] A. Gover, E. Dyunin, T. Duchovni, A. Nause, "Collective Microdynamics and Noise Suppression in Dispersive Electron Beam Transport", Physics of Plasmas, 18, 123102 (2011).
- [4] Z. Huang, M. Borland, P. Emma, J. Wu, C. Limborg, G. Stupakov, J. Welch, "Suppression of Microbunching Instability in the Linac Coherent Light Source", Phys. Rev. ST. Accel. Beams 7, 074401 (2004).
- [5] R. A. Bosch, K. J. Kleman, J. Wu, "Modeling Two-Stage Bunch Compression with Wakefields: Macroscopic Properties and Microbunching Instability", Phys. Rev. ST Accel. Beams 11, 090702 (2008).
- [6] D. Ratner, A. Chao, Z. Huang, "Three-Dimensional Analysis of Longitudinal Space Charge Microbunching Starting from Shot Noise", FEL Conference 2008, Gyeongju, Korea, SLAC-PUB-13392.

ANALYSIS OF BEAM STABILITY IN THE KAERI ULTRASHORT PULSE ACCELERATOR

H. W. Kim[#], S. Bae, B. Gudkov, K. H. Jang, Y. U. Jeong, Y. Kim, K. Lee, J. Mun, S. H. Park, S. J. Park, KAERI, Daejeon, Republic of Korea, UST Accelerator and Beam Nano Engineering, Daejeon, Republic of Korea
N. Vinokurov, S. V. Miginsky, Budker INP SB RAS, Novosibirsk, Russia and KAERI, Daejeon, Republic of Korea, and UST Accelerator and Beam Nano Engineering, Daejeon, Republic of Korea

Abstract

An RF-photogun-based linear accelerator for the Korea Atomic Energy Research Institute (KAERI) ultra-short pulse facility is under construction [1]. It has a symmetry structure with four different beamlines. The UED beamlines will generate ultra-short electron pulses with over 10^6 electrons per pulse for the single-shot measurements on femtosecond dynamics of atomic or molecular structures. Electron bunches with an energy of ~ 3 MeV from the RF photogun can be compressed up to less than 50 fs by achromatic and isochronous bends. The intrinsic r.m.s. timing jitter of the pulses through the bends is estimated to be less than 30 fs with the r.m.s. energy fluctuation of 0.1%. In the THz pump and X-ray probe beamline, two successive laser pulses with a time interval of ~ 10 ns are used to generate two electron bunches having more than 100 pC bunch charges. Two electron bunches are accelerated by a linac up to ~ 25 MeV and separated into individual beamlines by a fast kicker.

to various users. The beam dynamics in the KAERI ultra-short pulse accelerator have been calculated with code ASTRA [2] and ELEGANT [3].

UED BEAMLINE

A third harmonic of a Ti:sapphire femtosecond laser, with a 200-fs-pulse full width at half maximum (FWHM) and the RF photogun are used to generate femtosecond electron bunches. The simulated beam parameters are listed in Table 1.

Table 1: Simulated UED Beam Parameters

Bunch charge	1 pC
Beam energy	2.6 MeV
Bunch length (FWHM)	< 50 fs
Norm. Emittance	0.3 mm mrad
Energy spread (r.m.s.)	0.3%

The power supply usually have overall stability about 10~100 ppm. It is causative of magnet errors. Two bending magnets and six quadrupole magnets comprise the UED beamline. The effects of the magnet errors estimated with an accuracy of the power supply of 0.1% (r.m.s.), are shown in Fig. 2 and Fig 3.

The time resolution of UED depends on the bunch length and timing jitter. The timing jitter depends mostly on the time of flight of the electron bunches from the RF photogun to the sample. MeV UEDs [4-7] are built in all over the world. All they have straight beamline. By comparison, KAERI facility is longer than the other facility but it is expected to have low timing jitter because of the 90-degree achromatic and isochronous bend. We estimate the timing jitter, which is caused by the energy fluctuation at the sample when the electron beam has 0.1% of the energy fluctuation, are shown in Fig. 4. The calculated r.m.s. timing jitter with the isochronous bend (red) is 16 fs, and that with the straight beamline (green) is 54 fs.

BEAM SEPARATION

Two bunches of electron generated at about 10 ns intervals by the RF photogun are accelerated to 25 MeV in the same linac. After that, two bunches are separated into individual beamlines by a fast kicker.

Two bunches are vertically deflected by the steering coil. The first bunch is deflected downward about 10 mm after traveling 0.92 m of drift space. It goes straight for generating intense terahertz pulse.

INTRODUCTION

The KAERI ultra-short pulse accelerator consists of a 1.5-cell S-band (2856 MHz) RF photogun and a 3-m-long travelling-wave-type linac. The scheme of the facility is shown in Fig. 1.

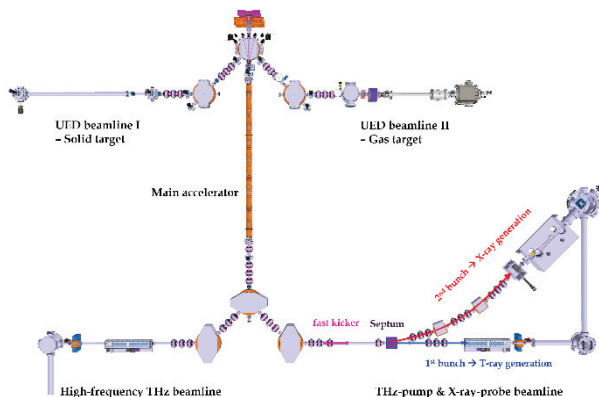


Figure 1: Scheme of the facility.

This facility can be operated in high repetition rate (maximum 500 Hz) and it will provide the ultrafast electron diffraction (UED) and pump-probe experiments

[#]This work was supported by the World Class Institute (WCI) Program of the National Research Foundation of Korea (NRF) funded by the Ministry of Science, ICT and Future Planning. (NRF Grant Number: WCI 2011-001) #khw8412@kaeri.re.kr

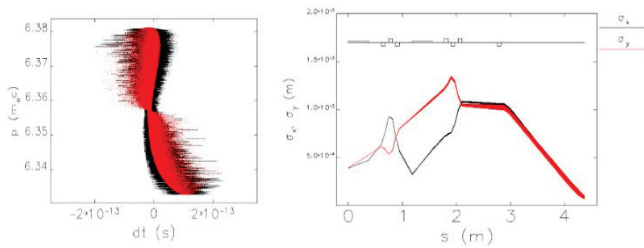


Figure 2: Longitudinal phase space (left) and beam size (right) change due to magnet errors.

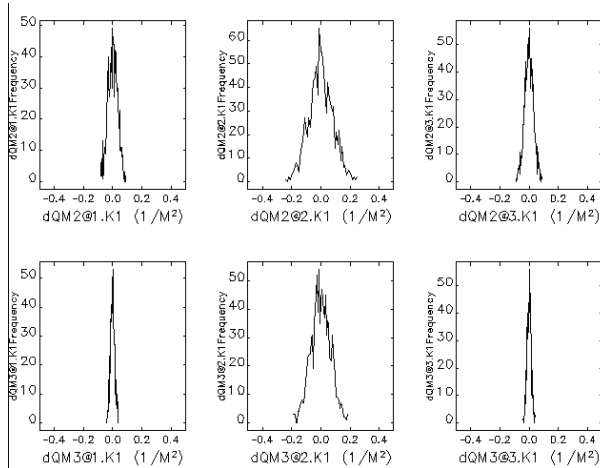


Figure 3: Variation of quadrupole strengths by power supplies with a fluctuation of 0.1%.

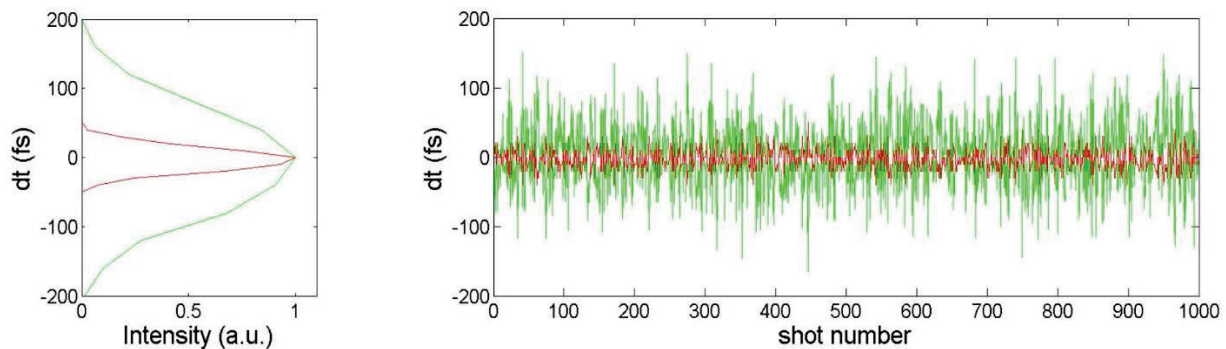


Figure 4: Calculated timing jitter (red – in a 90-degree achromatic and isochronous bend, green – straight beamline) at the target when the beam has 0.1% of an energy fluctuation. (without space charge effect).

After 10 ns the second bunch is kicked upward by the fast kicker. The length of kicker is 0.5 m and the bending angle is 1.7° . The two bunches have a 20 mm vertical distance in front of a septum and the second bunch is deflected to horizontal direction by the septum magnet. The septum has a 0.2 m length and 15° bending angle. The achromatic bend of the two-bunch beamline consists of the septum, a rectangular dipole, and a triplet. The second bunch is focused to the metal target for generating an x-ray pulse by a triplet after the achromatic bend.

REFERENCES

- [1] N. Vinokurov, et al., in: Proceedings of the Free Electron Laser Conference 2013, New York, 2013, p. 287.
- [2] K. Floettmann, A Space Charge Tracking Algorithm ASTRA, <http://www.desy.de/~mpyflo/>.
- [3] M. Borland, "elegant: A Flexible SDDS-Compliant code for Accelerator Simulation." Advanced Photon Source LS-287, Sep. 2000.
- [4] X.J. Wang, et al., J. Korean Phys. Soc. 48 (2006) 390.
- [5] J.B. Hastings, et al., Appl. Phys. Lett. 89 (2006) 184109.
- [6] P. Musumeci, J.T. Moody, C.M. Scoby, Ultramicroscopy 108 (2008) 1450.
- [7] R.K. Li, et al., Chin. Phys. C 33, Suppl. II. to appear.

BEAM MEASUREMENT OF PHOTOCATHODE RF-GUN FOR PAL-XFEL

J. Hong*, J.-H. Han, C.-K. Min, M.S. Chae, Y.-J. Park, S.-J. Park, H.-S. Kang, PAL, Pohang, Korea
I. S. Ko, POSTECH, Pohang, Korea

Abstract

The Injector Test Facility (ITF) at Pohang Accelerator Laboratory (PAL) was constructed to develop an injector for the PAL X-ray free-electron laser (PAL-XFEL) project. The PAL-XFEL design requires the injector to produce an electron beam with a slice emittance of 0.4 mm-mrad at the charge of 200 pC. A 4-hole type RF-gun has been successfully fabricated and tested at ITF. In this paper we report the recent beam-measurement results using the RF-gun at ITF. Emittance measurements have been carried out by changing laser and RF parameters.

INTRODUCTION

Pohang Accelerator Laboratory X-ray Free Electron Laser (PAL XFEL) is now under construction [1]. This construction will be finished at the end of 2015. There will be a hard X-ray (0.1nm) beamline with self-seeding scheme with 10 GeV electron beam. There is a 3 GeV branch also to make 1 nm soft X-ray radiation. As part of the PAL-XFEL project, the Pohang Accelerator Laboratory (PAL) constructed the Injector Test Facility (ITF) [2].

The schematic diagram of the ITF beam-line is shown in Fig. 1. The ITF beam-line consists of the RF-devices, magnets and several diagnostic devices. In the 4-hole type RF-gun ('GUN') an electron beam is generated [3]. Downstream of the 'GUN', the emittance compensation solenoid ('S1') which enables the correction of space charge emittance growth is mounted. Downstream of the solenoid, the Turbo Integrating Current Transformer ('ICT1') is installed to measure electron bunch charge. YAG screen #1 ('Y1') is located at the downstream of 'ICT1' to measure the transverse beam profile. Then the electron beam is accelerated by two 3-meter J-type S-band linacs ('ACC1' and 'ACC2') for which enough to accelerate the beam up to 140 MeV. After acceleration the emittance will be measured using the quadrupole #3 ('Q3') and screen #5 ('Y5'). Finally the electron beam will be dumped at the end of the beam-line or after screen #6 ('Y6'). All diagnostic devices are synchronized to the electron beam. The important device for each measurements is described in Table 1. The control system of ITF is based on the Experimental Physics and Industrial Control System (EPICS).

EXPERIMENTAL RESULT

Image

The beam size, position and profile are measured using YAG crystals imaged with CCD cameras for image processing. The screen system is manufactured from RADIA

Table 1: Electron Beam Diagnostics

Measurement	Main Divice	Additional Divice
Size	Y1 to Y5	-
Position	B1 to B5	Y1 to Y5
Charge	ICT1	B1
Energy	D2 + Y6	D1 + Y7
Bunch Length	T-CAV + Y5	-
Arrival Time	BA	-
Emittance	Q3 + Y5	-

BEAM. The images were acquired with an 14-bit CCD camera synched to the electron beam. The lens was set to give a calibration of 8 μm per pixel to allow a compromise between capturing the full variation of the beam size and maximizing the resolution of smallest spot size. Typically five images of the beam are taken at each processing. Typical image of the each screens as shown in Fig. 2.

Charge

Bunch charge is measured using the Turbo Integrating Current Transformer ('ICT1') which is made by BERGOZ. The quantum efficiency (QE) of the photocathode is defined by the ratio of photons hitting the cathode surface and generated electrons. This ratio is expressed as

$$QE = 4.47 \times 10^{-6} \frac{Q_{e\text{-beam}}(\text{pC})}{U_{\text{laser}}(\mu\text{J})}, \quad (1)$$

where $Q_{e\text{-beam}}$ is the photoelectron charge, and U_{laser} is the laser pulse energy. In this case the wavelength of laser is 256 nm. Measurement of bunch charge versus laser energy is shown in Fig. 3. The slope of fitting line gives the quantum efficiency of the copper cathode, which is 1.26×10^{-4} . We also measure bunch charge as a function of laser injection phase as shown in Fig. 4.

Energy

Beam energy and energy spread are measured using the dipole spectrometer. In ITF, there are two types of spectrometers. One is the 90° dipole spectrometer ('D1'+'Y7') for low-energy measurement. The other is the 30° dipole spectrometer ('D2'+'Y6') for high-energy measurement. The electron energy, U and the energy spread, $\frac{\Delta U}{U}$ at the exit of the RF-gun can be written as [4, 5]

$$U = m_e c^2 \left[1 + \frac{\alpha}{2} \left(kL \sin(\phi_f) + \sin(kL) \sin(\phi_f + kL) \right) \right], \quad (2)$$

$$\frac{\Delta U}{U} = \frac{1}{U} \frac{dU}{d\phi_0} \Delta\phi_0, \quad (3)$$

* npwinner@postech.ac.kr

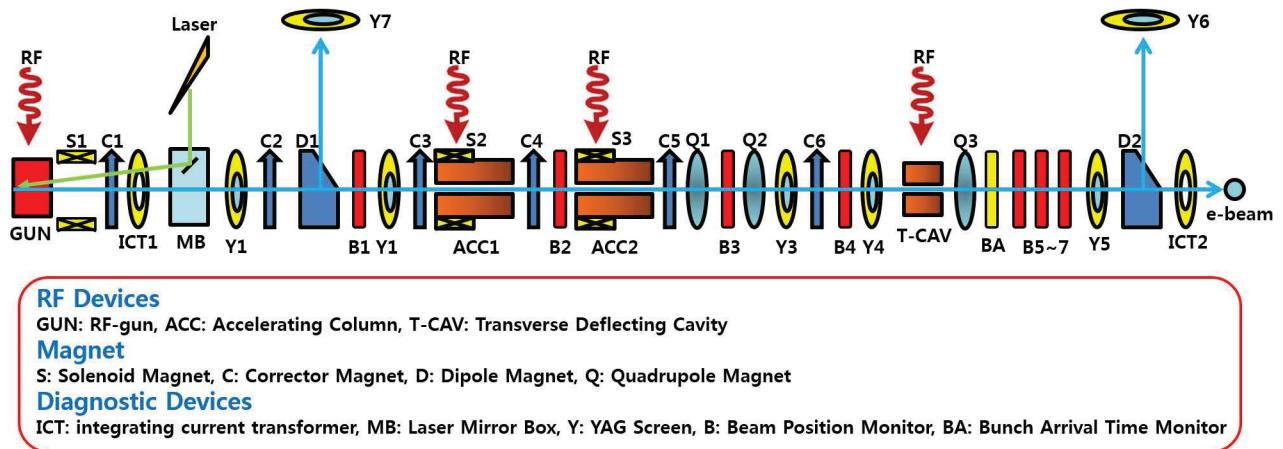


Figure 1: Schematic diagram of the ITF beam-line.

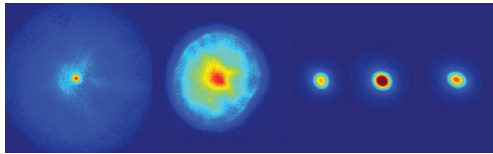


Figure 2: Typical image of the each screens (Left to right: 'S1' to 'S5').

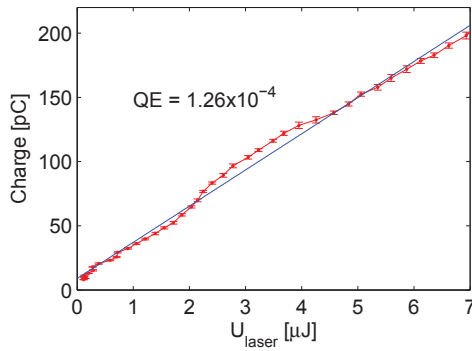


Figure 3: Measured bunch charge versus laser pulse energy. The solid line represents a linear fit.

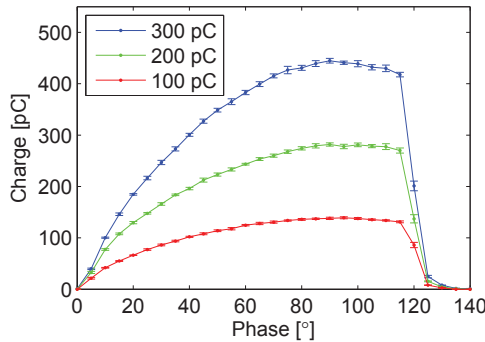


Figure 4: Measured bunch charge versus laser injection phase.

where m_e is the electron mass, and c is the speed of light, k is the wavenumber. $L = 0.105$ m is the length of the rf gun cavity, $\Delta\phi_0$ is the laser pulse length. In these equations, α and ϕ_f are seen the reference [4]. Measured energies and their spreads as a function of injection phase at the high-energy spectrometer ('D2'+ 'Y6') are shown Fig. 5. In these figures, dashed lines are just guides to the eye and solid lines represent the calculated values from Eqs. (3). These solid lines show a good agreement with the experiment results.

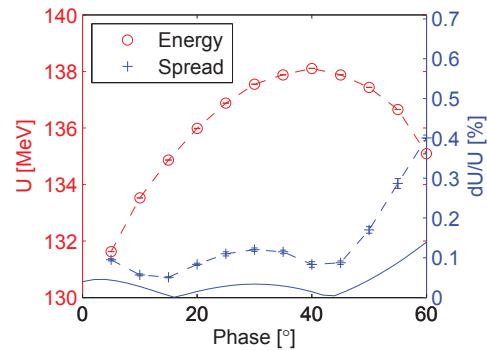


Figure 5: Measured electron energy and energy spread versus laser injection phase at the high-energy spectrometer.

Emittance

Downstream of the 'ACC2' the projected emittance of the electron beam is measured using the single quad-scan technique whereby the rms beam size, σ is measured on 'Y5' and the quadrupole strength, k of 'Q3'. To calculate the emittance, we use formula;

$$\epsilon = \frac{1}{dL^2} \sqrt{ac - \frac{b^2}{4}}, \quad (4)$$

where $d = 0.147$ m is the effective length of 'Q3', $L = 2.64$ m is the distance between 'Q3' and 'Y5', and a , b , c are determined by following equation;

$$\sigma^2 = ak^2 + bk + c. \quad (5)$$

Emittance measurements were made with 200 pC of charge using a longitudinal Gaussian pulse with a FWHM of 3 ps, at a laser phase of 40° , a gun energy of 5.75 MeV, and -10° off crest in ‘ACC1’ with an accelerating field gradient of 21 MV/m and ‘ACC2’ is not used. The square of σ versus k for one of the scans is shown in Fig. 6 as an example. The

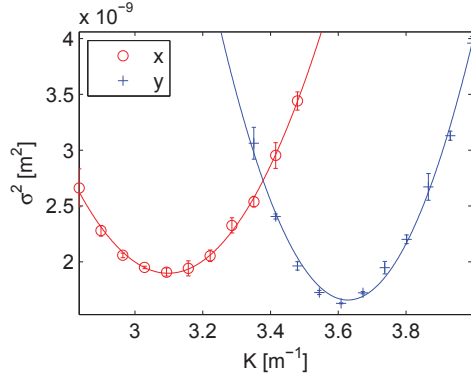


Figure 6: The square of σ versus k for one of the scans.

emittance as a function of ‘S1’ current when the laser shape are shape #1, #2, and #3 are shown in Fig. 7.

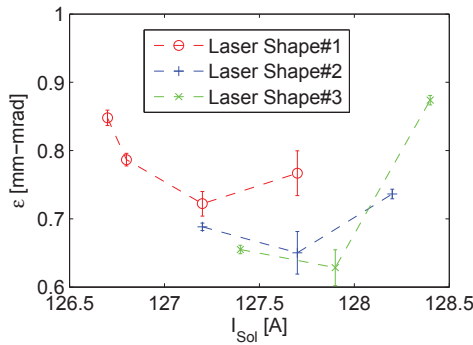


Figure 7: The emittance as a function of the solenoid current.

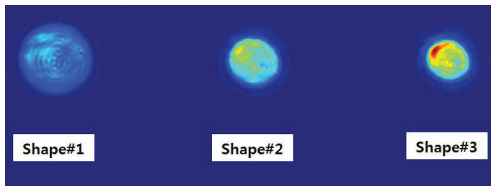


Figure 8: The laser images of the ‘Shape#1’, ‘Shape#2’, and ‘Shape#3’.

Figure 8 shows the laser images of ‘Shape#1’, ‘Shape#2’, and ‘Shape#3’. The emittance as a function of ‘S1’ current when laser shape are shape #1, #2, and #3 are shown in Fig. 9. The emittance as a function of ‘S1’ current when RF-gun energies of 5.25 MeV, 5.5 MeV, and 5.75 MeV are shown in Fig. 10. The emittance as a function of ‘S1’ current when laser pulse length of 2 ps, 3 ps, and 4 ps are shown in Fig. 11. Slice emittance for the horizontal direction was

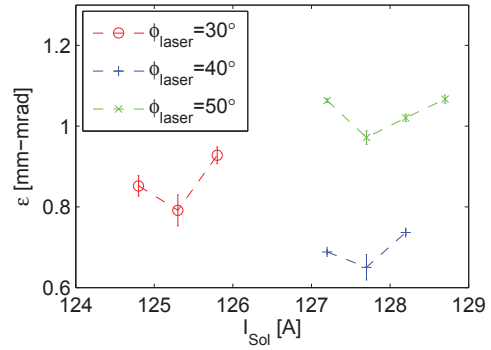


Figure 9: The emittance as a function of the solenoid current.

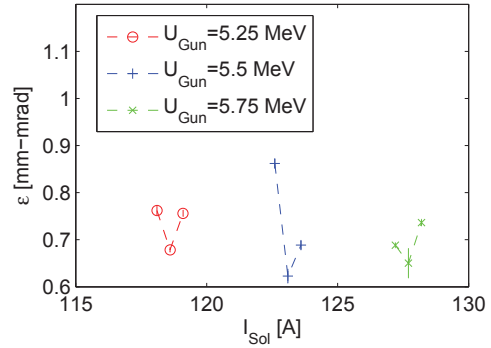


Figure 10: The emittance as a function of the solenoid current.

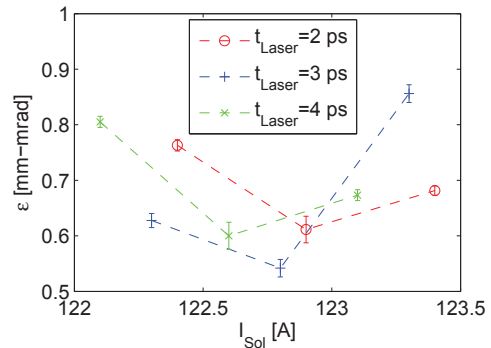


Figure 11: The emittance as a function of the solenoid current.

measured by streaking a bunch vertically using ‘T-CAV’ [6]

SUMMARY

This paper summarizes the current status of ITF gun operation. The detailed system parameters and typical electron beam parameters are described in Table 2. In these measurement, the quantum efficiency of the copper cathode is 1.26×10^{-4} . The relative beam energy spread for a laser injection phase around 40° is about 0.1% rms. The lowest transverse emittances are $\epsilon_x = 0.481 \pm 0.010$ mm-mrad and $\epsilon_y = 0.597 \pm 0.020$ mm-mrad. For the lowest trans-

Table 2: ITF System and Electron Beam Parameters

Parameter	Value	Unit
RF-gun		
Operating Frequency	2856	MHz
Mode Separation	17	MHz
Quality Factor	13200	
RF-pulse Width	2	μs
Repetition Rate	10	Hz
Laser		
Laser spot size	$\sigma = 0.14$	mm (rms)
Laser Pulse Length	2.9	ps (FWHM)
Laser pulse energy	7	μJ
Laser injection phase	38	$^{\circ}$
Electron Beam		
Energy	70	MeV
Energy Spread	0.1	% (rms)
Charge	200	pC
Length	3	ps

verse emittance, we need more optimization of various parameters. Studies to improve the laser profile and more optimization of various parameters will be conducted in the future. Measured results also will be compared with simulation results.

REFERENCES

- [1] H. S. Kang et al., “X-ray Free Electron Laser Project of Pohang Accelerator Laboratory”, FEL’10, Malmo, Sweden, August 2010, MOPC19 (2010), <http://www.JACoW.org>
- [2] J.-H. Han et al., “Operation of PAL-XFEL injector test facility”, WEB02, *These Proceedings*, FEL’14, Basel, Switzerland (2014).
- [3] J. Hong et al., “New RF-gun Design for the PAL-XFEL”, FEL’12, Nara, Japan, August 2012, MOPD43 (2012), <http://www.JACoW.org>
- [4] K. J. Kim, Nucl. Instrum. Methods Phys. Res., Sect. A **275**, 201 (1989).
- [5] Y. W. Parc and I. S. Ko, J. Korean Phys. Soc. **54**, 2247 (2009).
- [6] J. H. Lee et al., “Slice emittance measurement using rf deflecting cavity at PAL-XFEL ITF”, THP013, *These Proceedings*, FEL’14, Basel, Switzerland (2014).

ERROR ANALYSIS FOR LINAC LATTICE OF HARD X-RAY FEL LINE IN PAL-XFEL*

H. Yang[#], J. H. Han, H. -S. Kang, and I. S. Ko
Pohang Accelerator Laboratory, Pohang 790-784, Korea

Abstract

PAL-XFEL consists of the hard x-ray line for 0.06 – 1-nm FEL and the soft x-ray line for 1 – 10-nm FEL. The linac of hard x-ray line is designed to generate 10-GeV, 200-pC, and 3-kA electron beam. It consists of S-band accelerating columns, an X-band linearizer, three bunch compressors (BC). We conduct error simulation in order to evaluate the tolerances of machine parameters and alignments. First, the machine tolerances and beam jitter levels are calculated in the simulations with dynamic errors and we find out the optimized lattice to satisfy the target tolerance of machine. Second, we conduct simulations with misalignment. We quantify the emittance dilution by misalignments, especially those of BCs. In order to compensate the misalignments, the methods of beam correction like Beam Based Alignment (BBA) are presented and the effects of emittance improvements are calculated.

INTRODUCTION

PAL-XFEL is designed to provide the hard x-ray (HX) FEL and the soft x-ray (SX) FEL with the branch line on the middle of the linac lattice, as shown in Fig. 1 [1]. The linac for HX generates 10-GeV, 200-pC, and 3-kA electron beam for 0.06 – 1-nm FEL, as shown in Table 1. The HX linac lattice consists of four sections of accelerating columns, three bunch compressors (BC), an X-band linearizer, and dog-leg line, as shown in Fig. 1. The linac lattice is optimized by the Multi-Objective Genetic Algorithm (MOGA) optimizer whose objectives are the FEL saturation power and length [2]. The parameters of optimized linac lattice are presented in Fig. 2 and the optimized beam parameters are summarized in Table 2. The performance of FEL deteriorates by the dynamic and static errors of the system. The instability of FEL operation is arisen by the dynamic errors of machine like the jitter of the RF phase and voltage. Also, the emittance dilution by static errors should be compensated to achieve the target of FEL performance.

We conducted error simulations for dynamic and static errors with ELEGANT. Two methods were used in the dynamic error simulations, which are the linear interpolation method and the random error simulation with machine parameters. In the first method, not only the machine tolerances were calculated, but also the significant parameters for the stable operation were identified. In the random error simulations, machine tolerances obtained by the previous method were confirmed and beam jittering levels were calculated. The

misalignments were applied in the linac lattice for the static error simulations. First, the emittance dilution by the misalignments of bending magnets in BCs was obtained and alignment tolerances of these magnets were calculated. Second, we obtained the emittance dilution by misalignments of all elements in the linac lattice. It was identified that the emittance with best alignment by the developed technology is not enough for FEL operation. In order to suppress the emittance dilution, we conducted two types of the beam correction which are the one-to-one beam correction and the local Beam Based Alignment (BBA) in simulations. In this paper, we present the details of the setting and results in error simulations. Also, we discuss the improvement of the emittance with various beam correction methods.

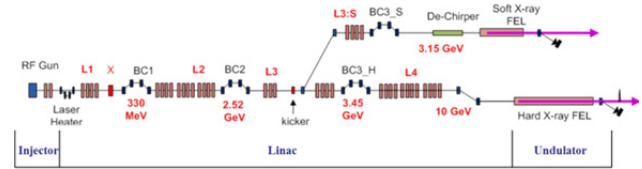


Figure 1: Schematic diagram of PAL-XFEL. The SX branch line is on the middle of the linac lattice.

Table 1: Parameters for HX FEL

Parameters (unit)	Values
Beam energy (GeV)	10
Beam charge (nC)	0.2
Slice emittance (mm-mrad)	0.4
Injector gun	Photocathode RF-gun
Peak current at undulator (kA)	3.0
Repetition rate (Hz)	60
Linac structure	S-band
Hard x-ray wavelength (nm)	0.06 ~ 1

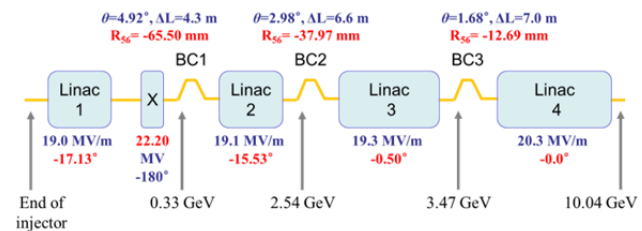


Figure 2: The optimized parameters of the linac lattice for HX line.

*Work supported by MSIP, Korea.

[#]highlong@postech.ac.kr

Table 2: The Optimized Beam Parameters of HX Line

Parameters (unit)	Values
Beam energy (GeV)	10.04
Beam charge (pC)	200
Peak beam current (kA)	2.91
Bunch length (fs)	65
Normalized projected emittance_H (μm)	0.337
Normalized projected emittance_V (μm)	0.257
Saturation power (GW)	12.0
Saturation length (m)	52.8

DYNAMIC ERROR SIMULATION

We conducted the linear interpolation method to calculate the machine tolerance and find out significant machine parameters for the beam stability. Then, simulations of random machine errors were conducted in order to verify previous results.

Linear Interpolation Method

The target beam tolerances (T) were determined under $\pm 10\%$ of the current variation, $\pm 0.02\%$ of the energy variation, ± 20 fs of the arrival time variation, and 10% of the horizontal normalized projected emittance variation [2]. The machine tolerances (M) were calculated with the beam tolerances and the equation which is represented by [3]

$$\sqrt{\sum_{i=1}^N \left\{ \frac{\sigma(\Delta x_i/x_{i0})}{P_{\text{sen}}} \right\}^2} < 1, \quad (1)$$

where, $P_{\text{sen}} = T/[\partial(f/f_0)/\partial(\Delta x_i/x_{i0})]$, x is machine parameter, f is beam parameter. The machine parameters used in simulations are summarized in Table 3. $\partial(f/f_0)/\partial(\Delta x_i/x_{i0})$ were obtained by the linear interpolation of simulation results.

The machine tolerances were determined by the criterion of $\sum [M/P_{\text{sen}}]^2 < 0.56$, as shown in Table 3. 0.44 remained for other variables in the injector and $\sigma(x_i) = \sqrt{N}\sigma(x)$ (N : number of klystrons) was applied for multi-klystron in this calculation [3]. It was verified that the RF phase and voltage of the L1 and L2, and the RF phase of the linearizer are significant parameters for the beam stability.

Random Error Simulation

We conducted the simulations with random machine errors about 2 cases. The machine tolerances obtained by the previous method were applied in Case 1 and the relatively loosened tolerances than the previous results were applied in Case 2, as shown in Table 4. As a result, both of cases were verified to satisfy target beam tolerances, as shown in Table 5.

Table 3: Machine Tolerances of HX Linac Lattice

Parameter	# of kly.	symbol	[(machine tolerance / P_{sen}) ²]				Tolerance (rms)	unit
			$\Delta I/I_0 = \pm 10\%$	$\Delta E/E_0 = \pm 0.02\%$	$\Delta t_f = \pm 20\text{fs}$	$\Delta \epsilon_{\text{nx}}/\epsilon_{\text{nx0}} = \pm 10\%$		
Mean L1 rf phase	2	ϕ_1	0.090	0.000	0.122	0.084	0.03	deg.
Mean X rf phase	1	ϕ_X	0.308	0.019	0.000	0.364	0.07	deg.
Mean L2 rf phase	10	ϕ_2	0.007	0.005	0.100	0.007	0.03	deg.
Mean L3 rf phase	4	ϕ_3	0.000	0.000	0.000	0.000	0.1	deg.
Mean L4 rf phase	27	ϕ_4	0.000	0.000	0.000	0.000	0.1	deg.
Mean L1 rf voltage	2	V_1	0.009	0.005	0.043	0.006	0.01	%
Mean X rf voltage	1	V_X	0.004	0.002	0.022	0.000	0.05	%
Mean L2 rf voltage	10	V_2	0.000	0.005	0.188	0.000	0.02	%
Mean L3 rf voltage	4	V_3	0.000	0.014	0.020	0.000	0.05	%
Mean L4 rf voltage	27	V_4	0.000	0.099	0.000	0.000	0.05	%
B.C.-1 angle	-	θ_1	0.000	0.000	0.000	0.000	0.002	%
B.C.-2 angle	-	θ_2	0.000	0.000	0.000	0.000	0.002	%
B.C.-3 angle	-	θ_3	0.000	0.000	0.000	0.000	0.002	%
Sum			0.418	0.149	0.495	0.461		

Table 4: Error Setting of Random Error Simulations

Element	Errors (Gaussian, 3- σ cutoff)	Value		Unit
		Case 1	Case 2	
RF strucs.	phase errors	0.03 (L1) 0.07 (X) 0.03 (L2) 0.1 (L3~4)	0.05 (L1) 0.1 (X) 0.05 (L2) 0.1 (L3~4)	deg.
	relative voltage errors	100 (L1) 400 (X) 200 (L2) 500 (L3~4)	200 (L1) 400 (X) 200 (L2) 1000 (L3~4)	ppm
Bends	bending angle errors	20	20	ppm
Drift	length errors (\rightarrow timing errors)	10 (66)	10 (66)	μm (fs)
e^- beam	random charge error	1	1	%

Table 5: Beam Jitters by Random Machine Errors

Beam jitter (standard deviation)	$\Delta I/I_0$	$\Delta E/E_0$	Δt_f	$\Delta \epsilon_{\text{nx}}/\epsilon_{\text{nx0}}$
Target	10%	0.02%	20 fs	10%
Case 1	8.7%	0.009%	14.0 fs	6.5%
Case 2	10.1%	0.015%	19.1 fs	8.1%

SIMULATION WITH MISALIGNMENTS

Alignment Tolerance of BC

The dispersive emittance dilution is arisen by the misalignments of magnets and beam position monitors (BPM) [4]. Since the main source of the dispersion is the errors in BCs, we calculated the alignment tolerances of bending magnets in BCs. In this calculation, we applied multipole components to the sixth order in the magnetic field, as shown in Table 6 [5]. The tolerances for horizontal (x), vertical (y), longitudinal (z) distance, and azimuthal (ϕ) tilt were obtained.

The transverse emittance dilution by magnets of BC1 is presented in Fig. 3. These components are dominant for the whole of the emittance dilution. The alignment tolerances of bending magnets in BCs were determined by the limitation of 2% emittance growth, as shown in Table 7. The values are achievable except the longitudinal alignment tolerances (Δz) of BC1, but it is able to be compensated by the trim coil in each bending magnet whose maximum magnetic field is 10% of the main field.

Emittance Dilution by Misalignments and Compensation with Beam Correction

In order to quantify the emittance dilution by the misalignment, it was applied to all elements of magnets, RF structures, and diagnostics in the linac lattice. It distributes Gaussian distribution which σ is 0 – 400 μm for offsets and 0 – 2.5-mradian for tilt, as shown in Table 8. Figure 4 is the result of 50 random seeds. Since the target alignment tolerance of the linac lattice is $\sigma = 70 - 80 \mu\text{m}$, the horizontal normalized projected emittance is about 2.1 μm and the vertical one is about 1.5 μm , as shown in Fig. 4. These are about 500% of emittance dilutions from the ideal values in Table 2.

In order to compensate it, the beam corrections with 98 sets of correctors and BPMs in the HX linac lattice were applied. It was applied that $\sigma = 80\text{-}\mu\text{m}$ misalignments of quadrupoles and RF structures, the BPM resolution of 5 μm , and the BPM misalignment of $\sigma = 50 \mu\text{m}$ relative to the quadrupole because the quadrupole and BPM are in the same structure.

Table 6: Multipole Strengths of Bending Magnets in BC

HOM	BC1	BC2	BC3
b_1/b_0	-	-1.60×10^{-16}	-1.60×10^{-16}
b_2/b_0	-0.93×10^{-4}	-0.80×10^{-4}	-0.80×10^{-4}
b_3/b_0	-	-	-
b_4/b_0	3.68×10^{-4}	-0.57×10^{-4}	-0.57×10^{-4}
b_5/b_0	-	-	-
b_6/b_0	2.57×10^{-4}	0.58×10^{-4}	0.58×10^{-4}

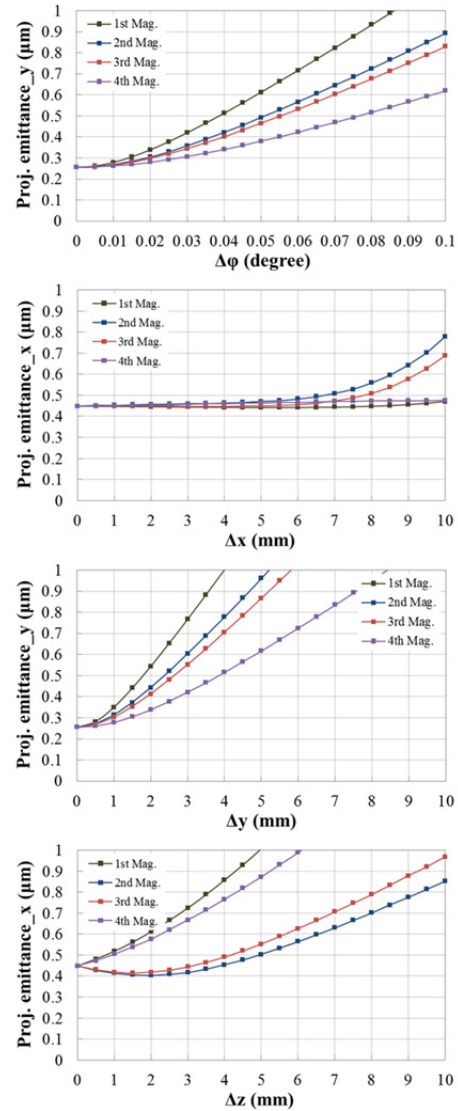


Figure 3: The emittance dilution by misalignments of bending magnets of BC1.

Table 7: Alignment Tolerances of BC Magnets

BC1	Unit	1 st Mag.	2 nd Mag.	3 rd Mag.	4 th Mag.
$\Delta\phi$	deg.	0.005	0.005	0.005	0.010
Δx	mm	9.0	2.5	6.0	3.0
Δy	mm	0.20	0.30	0.35	0.50
Δz	mm	0.1	4.0	3.0	0.2

BC2	Unit	1 st Mag.	2 nd Mag.	3 rd Mag.	4 th Mag.
$\Delta\phi$	deg.	0.010	0.015	0.020	0.020
Δx	mm	10	7.5	6.0	10
Δy	mm	2.5	4.0	4.5	6.0
Δz	mm	7.5	1.5	2.0	6.0

BC3	Unit	1 st Mag.	2 nd Mag.	3 rd Mag.	4 th Mag.
$\Delta\phi$	deg.	0.030	0.040	0.045	0.060
Δx	mm	10	10	10	10
Δy	mm	10	10	10	10
Δz	mm	10	8.5	9.5	10

The one-to-one correction and local BBA were conducted in simulations. The one-to-one correction is to correct the beam passing through the BPM center. The misalignments of BPMs are not considered in this correction. The local BBA is conducted by scanning of a quadrupole magnet and a corrector before a BPM. It takes much time, but the BPM position which beams pass through the quadrupole center is found out by this sequence. The emittance improvement by beam corrections is presented in Fig. 5, which each plot is average of 200 random seeds. The normalized projected emittances are 0.55 of x-axis and 0.34 of y-axis by the one-to-one correction and 0.51 of x-axis and 0.30 of y-axis by the local BBA at the end of the linac. In the other word, the emittance dilution is suppressed to 60% for x-axis and 30% for y-axis by the one-to-one correction, and 50% for x-axis and 15% for y-axis by the local BBA. For more emittance improvement and less time of the beam correction, it is required to apply other correction methods like dispersion-free steering (DFS) and wakefield-free steering (WFS) [6, 7].

Table 8: The Misalignment Setting of All Elements

error distribution: gaussian
error amplitude = σ
cutoff = 3σ

of samples = 50
Error factor: 0.05 ~ 5

Element	rms errors (Gaussian, 3- σ cutoff)	Value	Unit
Quads	misalignment	80 (dx, dy) 1 (dz)	μm mm
	tilt	0.5	mrاد.
Bends	tilt	0.5	mrاد.
RF struc.	misalignment	80 (dx, dy)	μm

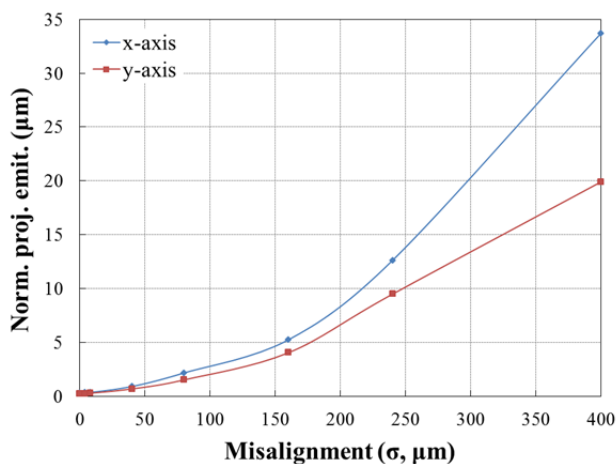


Figure 4: The emittance dilution by misalignments of all elements in the linac lattice.

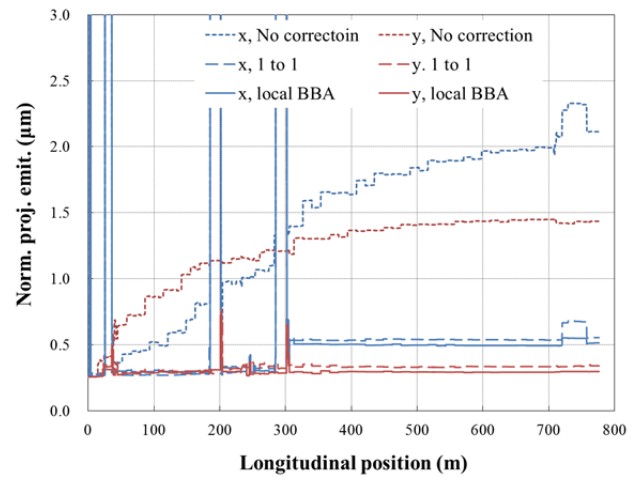


Figure 5: Emittance improvements by beam corrections.

SUMMARY

We conducted the error analysis of HX linac lattice in PAL-XFEL. Machine tolerances and beam jittering level were obtained by dynamic error simulations, which are achieved the beam tolerances under $\pm 10\%$ of the current variation, $\pm 0.02\%$ of the energy variation, ± 20 fs of the arrival time variation, and 10% of the projected emittance variation. It was found out that the significant machine parameters for the beam stability are the RF phase and voltage of the L1 and L2, and the RF phase of the linearizer. Alignment tolerances of bending magnets of BCs were calculated and verified to be achievable. The emittance dilution was 500% from the ideal emittance in $\sigma = 80\text{-}\mu\text{m}$ misalignments of all elements in the linac lattice. It was suppressed to 60% for x-axis and 30% for y-axis by the one-to-one correction, and 50% for x-axis and 15% for y-axis by the local BBA.

REFERENCES

- [1] H. S. Kang et al., "Start to End Simulation of Three Bunch Compressor Lattice for PAL-XFEL", in *Proc. IPAC2012, New Orleans, Louisiana, USA, 2012*, pp. 1738-1740.
- [2] H. Yang et al., "Linac Lattice Optimization for PAL-XFEL Hard X-ray FEL Line", in *Proc. IPAC2014, Dresden, Germany, 2014*, pp. 2900-2902.
- [3] J. Arthur et al., Conceptual Design Report: Linac Coherent Light Source, SLAC-R-593 (2002).
- [4] T. O. Raubenheimer, *Phys. Rev. ST Accel. Beams* **3**, 121002 (2000).
- [5] K. Flottmann et al., "Tolerances of TTF-2 First Bunch Compressor", in *Proc. PAC2003, Portland, Oregon, USA, 2003*.
- [6] A. Latina et al., *Phys. Rev. ST Accel. Beams* **17**, 042803 (2014).
- [7] A. Latina et al., "Tests of Beam-based Alignment at FACET", in *Proc. IPAC2014, Dresden, Germany, 2014*, pp. 1186-1188.

SLICE EMITTANCE MEASUREMENT USING RF DEFLECTING CAVITY AT PAL-XFEL ITF

Jae Hyun Lee, Jang-Hui Han, Juho Hong, Sung-Ju Park, In Soo Ko,
Pohang Accelerator Laboratory, Pohang, 790-834, Korea

Abstract

One of key characteristic for operating PAL-XFEL is the time-dependent transverse properties of a bunch, slice emittance. To achieve the design FEL performance of PAL-XFEL a slice emittance of 0.4 mm mrad at 0.2 nC is required. An Injector Test Facility (ITF) was constructed to study beam properties. In addition to projected emittance measurement, slice emittance measurement is being done using a transverse RF deflecting cavity. We presents results of slice emittance measurement at ITF and future plan for the optimization of operating condition.

INTRODUCTION

The aim of ITF is to study beam dynamics and to produce low emittance electron beams for required future operating condition of PAL-XFEL. The required slice emittance for PAL-XFEL at the exit of injector is 0.4 mm-mrad at 0.2 nC and the acceptable emittance is 0.6 mm-mrad [1]. ITF has been operated to measure emittance and to optimize the elements of injector required for designed condition of PAL-XFEL. Maintaining a low emittance is necessary and one of the principal challenges. The ITF accelerator consists of an S-band 1.6-cell photocathode RF gun, two S-band accelerating columns, solenoids and diagnostic components including quadrupoles and transverse RF deflector [2]. The laser heater is planned to be installed in September 2014. A schematic layout of current ITF elements map is shown in Fig. 2. The Quadrupole for quad scan and YAG screen are located at 13.22 m and 15.86 m from the cathode, respectively. Using the transverse RF deflecting cavity, we can observe an image of the streaked beam at the YAG screen and then measure the slice emittance by the technique of quad scan. The details of the transverse RF deflecting cavity is introduced in the next section. Recently slice emittance has been measured at ITF. In this paper, the results of the slice emittance measurement are described.

EXPERIMENTAL SETUP

The measurements of slice emittance have been performed at the end of ITF with 81.7 MeV of the beam energy at 0.2 nC. The phase of RF photocathode gun is set to 34 ± 0.05 degree. The acceleration phase of two S-band accelerating columns located at 2.14, 5.72 m from cathode is set to on crest. Using the transverse RF deflecting cavity the beam can be streaked at YAG screen. The measurement is carried out by quad scan. The

calculation of the slice emittance is fulfilled by using MATLAB code.

Transverse RF Deflecting Cavity

The RF deflecting cavities have been widely studied and used in the accelerator field for the high energy physics research and beam diagnostics of Free Electron Laser and many others. In RF deflecting cavity, as the transverse kick varies sinusoidally in time, each part of the bunch receives a different kick due to finite bunch width. Generally the phase of transverse RF deflecting cavity is chosen to have a zero crossing of RF phase at the middle of the bunch. According to this principle, the bunch gets no net deflection but is streaked vertically at a zero crossing phase of RF field [3]. Therefore we can observe a longitudinal image of the beam. The S-band transverse RF deflecting cavity is described in Fig. 1 and the specifications of it is in Table 1.

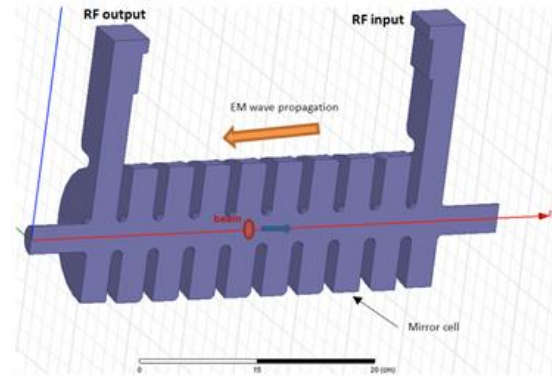


Figure 1: Schematic diagram of Transverse RF Deflecting Cavity.

Table 1: Specifications of Transverse RF Deflecting Cavity

RF parameter	Value	Unit
Frequency f	2.856	GHz
Transverse shunt impedance	28.7	MΩ/m
Unloaded Q	13,400	
Number of cells N	28 (L~1m)	
Attenuation constant α	0.158 (m ⁻¹)	
Group velocity v_g	0.014 c	
Kick/ $\sqrt{\text{power}}$	2.7	MV/ $\sqrt{\text{MW}}$

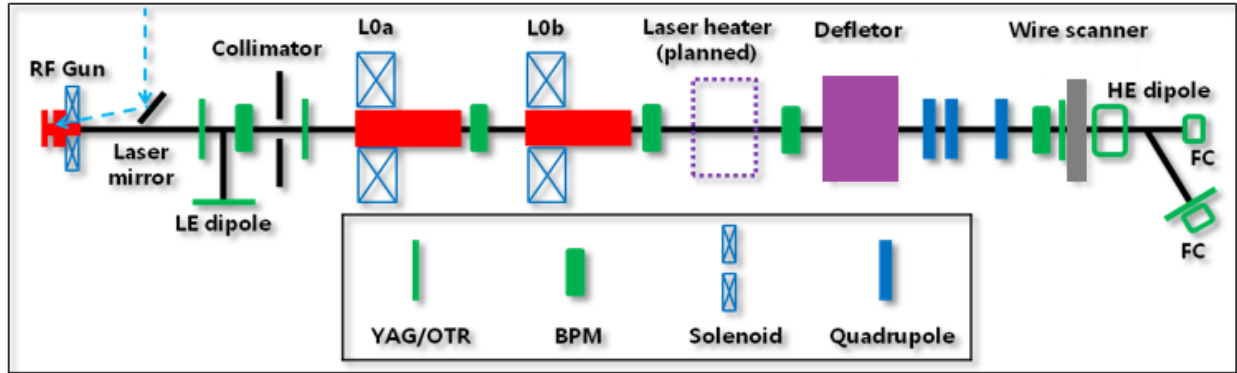


Figure 2: Schematic layout of Injector Test Facility at Pohang Accelerator Laboratory.

Quadrupole Scan

The emittance of beam can be obtained from both the beam size and beam divergence which are not able to be directly measured. While the beam size can be measured by using quadrupoles [4]. The method of emittance measurement is based on the quadrupole scan technique using a matrix [5]. It is a destructive way to measure beam emittance and can be affected by the nonlinear field of the quadrupole thus they have to be properly arranged [2]. The Quadrupole for quad scan is the third quadrupole shown in Fig. 2. The transformation matrix can be described as follows:

$$R = \begin{pmatrix} R_{11} & R_{12} \\ R_{21} & R_{22} \end{pmatrix}. \quad (1)$$

Using the matrix form, the propagation matrix from the quadrupole to the screen can be written as:

$$\sigma^s = R \sigma^q R^T. \quad (2)$$

where σ is the beam matrix describing drifts, quadrupole, etc. q, s stand for entrance of the quadrupole and screen respectively. The beam size at screen is $\sqrt{\sigma_{11}^s}$, then the equation can be written in accordance with $\sigma_{11}^q, \sigma_{12}^q = \sigma_{21}^q$ and σ_{22}^q :

$$\sigma_{11}^s = R_{11}^2 \sigma_{11}^q + 2R_{11}R_{12} \sigma_{12}^q + R_{12}^2 \sigma_{22}^q. \quad (3)$$

The transformation matrix R is altered by the quadrupole strength k , subsequently the normalized beam emittance is easily obtained by using relation, $\epsilon = \gamma\beta\sqrt{\det(\sigma^q)}$, where γ and β are the energy and the velocity of beam respectively. The beam size can be obtained from image on the YAG screen. We have performed to measure slice emittance by a single quadrupole scan technique. The specification of quadrupole is shown in table 2.

Table 2: Specifications of the Quadrupole for Quad Scan

Quadrupole parameter	Value	Unit
Effective length	14.7	cm
Max. quadrupole strength	27.97	/m ²

Measurement

Before performing measurements, the phase of the RF photocathode gun set up to experiment phase first. The phase of two accelerating columns is adjusted step by step. The orbit of beam can be aligned using several of corrector magnets which also are used to control the bunch to centre on the YAG screen located at 15.86 m. The bunch is properly focused to have round shape on YAG screen by RF gun solenoid current. For quad scan, a sufficient current range should be found by varying the quadrupole current. The total charge of the bunch is checked at all times through a turbo ICT and should be kept as 0.2 nC during measurements. The bunch passes through the RF deflecting cavity with close to a zero crossing phase of RF field. The streaked beam image is presented on YAG screen. In order to examine how to be affected the slice emittance by gun solenoid current, the slice emittance is measured by changing RF gun solenoid with four or five step. Moreover the beam energy can be altered by adjusting the modulator power of first accelerating column. The five beam images take at each quadrupole current step and are averaged without noise background by MATLAB code. The noise background is eliminated before taking a beam image. The bunch is divided by twenty slices. We can obtain the beam size calculated from each slice image and gain a value of the slice emittance.

EXPERIMENTAL RESULTS

The slice emittance has been measured at 0.2 nC with 81.7 MeV of the beam energy. Figure 3 shows the beam images vertically streaked by transverse RF deflecting cavity on the YAG screen. The top of the bunch is head.

The electron bunch at the YAG screen is divided by twenty slice.

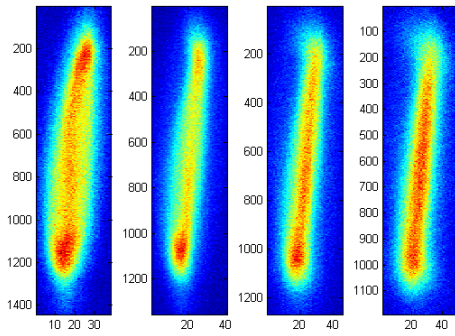


Figure 3: Streaked beam image on YAG screen located 15.86 m with different quadrupole strength k . The upper side is the head of electron bunch.

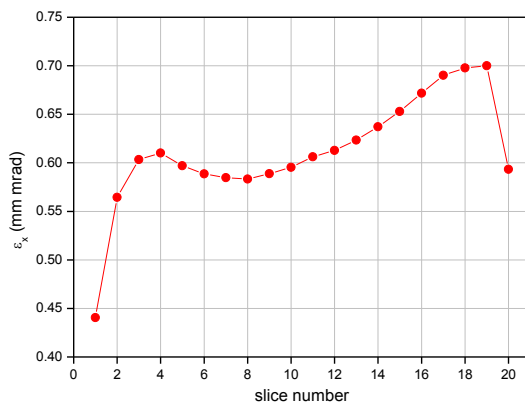


Figure 4: An example of measured slice emittance (95%).

The slice emittance is shown in Fig. 4 and its value is about 0.65 mm mrad (95%) for 0.2 nC at core of the electron bunch. However it is not enough for the designed slice emittance of PAL-XFEL performance. It needs to be analysed and adjusted the elements of injector. The optimization of machine parameters as the gun solenoid current, the phase of each elements and the position of elements in injector should be carried out more precisely for meeting the design emittance of PAL-XFEL.

CONCLUSION

The understanding of slice emittance plays a significant role in the optimization of high brightness electron sources. The measurements of the slice emittance at ITF of PAL have been successfully done. While we have problem to optimize the elements of injector for the requirements of PAL-XFEL. We will accelerate the electron beam later up to 135 MeV after passing two accelerating columns and the laser heater system will be installed in September this year. These are possible to lower projected and slice emittance. Furthermore we expect that the emittance is close to the design emittance of PAL-XFEL.

ACKNOWLEDGMENT

We would like to thank all the staff of ITF for their valuable support.

REFERENCES

- [1] H.-S. Kang et al., "Current Status of PAL-XFEL Project", in *Proc. 4th Int. Particle Accelerator Conf.*, Shanghai, 2013, pp. 2074-2076.
- [2] M. Chae et al., "Simulation for New Injector Test Facility of PAL-XFEL", in *Proc. 34th Int. Free Electron Laser Conf.*, Nara, 2012, pp. 117-119.
- [3] M. Huening et al., "Observation of Femtosecond Bunch Length Using a Transverse Deflecting Structure", in *Proc. 27th Int. Free Electron Laser Conf.*, California, 2005, pp. 538-540.
- [4] H. Wiedemann, *Particle Accelerator Physics 3rd edition*, (Springer, 2007), pp. 164.
- [5] J. Rossbach, P. Schmüser, "Basic Course on Accelerator Optics", CAS-CERN Accelerator School : *5th General Accelerator Physics Course*, Finland, 1992, pp. 38-46.

CYCLOTRON-UNDULATOR COOLING OF A FREE-ELECTRON-LASER BEAM*

I.V. Bandurkin, S.V. Kuzikov, A.V. Savilov[#], Institute of Applied Physics, Nizhny Novgorod, Russian Federation

Abstract

We propose methods of fast cooling of an electron beam, which are based on wiggling of particles in an undulator in the presence of an axial magnetic field. We use a strong dependence of the axial electron velocity on the oscillatory velocity, when the electron cyclotron frequency is close to the frequency of electron wiggling in the undulator field. The abnormal character of this dependence (when the oscillatory velocity increases with the increase of the input axial velocity) can be a basis of various methods for fast cooling of moderately-relativistic (several MeV) electron beams. Such cooling may open a way for creating a compact X-ray free-electron laser based on the stimulated scattering of a powerful laser pulse on a moderately-relativistic (several MeV) electron beam.

INTRODUCTION

Fast development of the technique of photo-cathode electron photoinjectors has resulted in creation of compact and accessible sources of moderately-relativistic (several MeV) dense (~ 1 nC in a ps pulse) bunches [1-3]. Methods for decrease of the energy spread (cooling) are actual from the point of view of various applications of such beams, including free-electron lasers (FELs). However, cooling methods are developed now basically for electron beams of significantly higher energies [4,5]. As for a moderately-relativistic high-dense short e-bunches, the strong Coulomb interaction of the particles results in a requirement for a short (~ 1 m and even less) length of a cooling system. In this situation, the cooling system should possess resonant properties, namely, a strong dependence of parameters of the particles inside the cooling system on their input energies.

We propose to provide cooling by the use of electron wiggling in a circular polarized “cooling” undulator in the presence of an axial magnetostatic field zB_0 (Fig. 1). If the bounce-frequency of electron oscillations in the undulator, $\Omega_u = V_{||}h_u$ is comparable with the electron cyclotron frequency, $\Omega_c = eB_0/\gamma mc$ (here $V_{||}$ is the electron axial velocity, h_u is the undulator wavenumber, and γ is the relativistic electron mass factor). In this situation, the velocity of undulator oscillations V_u depends strongly on the initial axial velocity.

*Work supported by the Russian Scientific Foundation (grant # 14-19-01723).

[#]savilov@appl.sci-nnov.ru

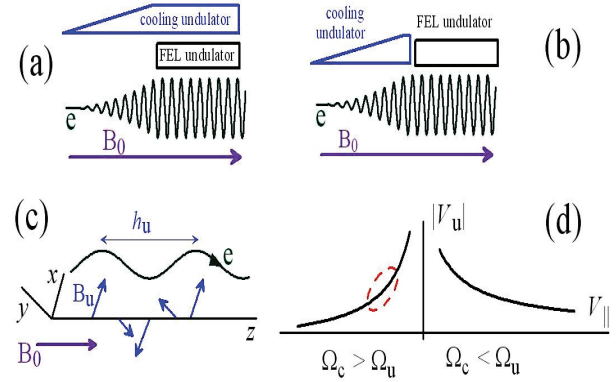


Figure 1: (a) and (b): Schematics of non-radiative cyclotron-undulator cooling systems with the operating FEL undulator placed inside and outside of the cooling system. (c): Electron motion in the circular polarized undulator with the uniform axial field. (d): Characteristic dependence of the undulator velocity on the axial electron velocity (the optimal range is shown schematically).

NON-RADIATIVE “AXIAL” COOLING

Non-radiative “axial” cooling is based on the fact that the axial velocity spread is the only factor important for the FEL operation. This spread can be decreased due to its “transformation” into the spread in the velocity of electron rotation in the cooling system. Electrons move along axial magnetic field and enter the cooling undulator with the adiabatically growing field in the input section, where each electron gets its own rotatory velocity (Fig. 1a). If at the input of the system every particle possesses only the axial velocity $V_0 = \bar{V} + \delta V$, then the axial velocity in the regular region of the undulator is determined by the energy conservation law:

$$V_{||}^2 \approx V_0^2 - V_u^2. \text{ Thus,}$$

$$V_{||}^2 \approx \bar{V}^2 + 2\bar{V}\delta V - V_u^2(\bar{V}) - \alpha\delta V, \quad \alpha = \partial V_u^2 / \partial V_{||}.$$

If $\alpha = 2\bar{V}$, then the spread in $V_{||}$ disappears. This condition is independent of the initial spread, δV . Evidently, we should use the range of parameters, where $\partial|V_u|/\partial V_{||} > 0$ (Fig. 1d), so that the initial axial velocity excess, δV , is compensated by the greater rotatory velocity, V_u .

If such a cooling system is used in a FEL, then the operating FEL undulator designed to produce optical radiation can be placed inside the regular section of the cooling undulator (Fig. 1a). Another way is to “switch off” the field of the cooling “undulator” sharply (Fig. 1

b). Then, forced undulator oscillations of the particles are just transformed into free cyclotron oscillations possessing the same rotatory velocities, $V_{\perp} = V_u$ (and, therefore, the same axial velocities).

In the case of the adiabatically smooth entrance of electrons into the cooling undulator, the normalized velocity of the forced oscillations of the particles, $\beta_u = V_u / c$, is determined as follows:

$$\beta_u = K / \gamma \Delta. \quad (1)$$

Here, $K = eB_u / h_u mc^2$ is the undulator factor (the normalized transverse electron momentum, $K = \gamma V_u / c$ in the case, when the axial magnetic field is absent), and $\Delta = 1 - \Omega_c / \Omega_u$ is the mismatch between the electron cyclotron frequency and the bounce-frequency of electron oscillations in the undulator.

In the simplest situations, when electrons enter into an ideal cooling undulator along ideally rectilinear trajectories (so that they have no input transverse velocity), then the condition of axial velocity cooling has the following form [6]:

$$K^2 \approx -\Delta^3. \quad (2)$$

In order to describe this spread, it is convenient to introduce the axial gamma-factor, $\gamma_{\parallel} = 1 / \sqrt{1 - \beta_{\parallel}^2}$, and

use the spread $D(\gamma_{\parallel}) \approx \gamma^2 D(\beta_{\parallel})$, where D denotes the relative dispersion. The uncompensated axial spread is determined by three factors. First, there is the initial spread in transverse velocity, $0 < \beta_{\perp 0} < \bar{\beta}_{\perp 0}$. This leads to the following uncompensated axial spread:

$$D_{\perp}(\gamma_{\parallel}) \approx \gamma_0^2 \beta_u \bar{\beta}_{\perp 0} / 2. \quad (3)$$

Second, there is the spread in the transverse electron position, $0 \leq r \leq r_e$. As the undulator field is not uniform, $B_u(r) \approx 1 + (h_u r / 2)^2$, this spread induces the corresponding spread in the undulator velocity $0 \leq \delta \beta_u \leq 2 \beta_u (h_u r / 2)^2$. This leads to estimation similar to the previous one:

$$D_r(\gamma_{\parallel}) \approx \gamma_0^2 \beta_u^2 (r_e / \lambda_u)^2 / 2. \quad (4)$$

The third source of the uncompensated spread is the non-ideal transformation of the axial spread [6]:

$$D_{\parallel}(\gamma_{\parallel}) \approx [D_0(\gamma_{\parallel})]^2 (1 + \Delta^{-1}). \quad (5)$$

Let us notice that an increase in the undulator parameter leads to the reduction in the Doppler frequency up-conversion factor $\sim \gamma_{\parallel}^2$ due to the increase in the transverse electron velocity. However, according to Eqs. (1) and (2), β_u depends on K weakly in the optimal cooling regime, $\beta_u \approx K^{1/3} / \gamma$. At the same time, the undulator factor is related by Eq. (2) to the mismatch between the cyclotron undulator frequencies, $|\Delta| \approx K^{2/3}$.

Evidently, K should be great enough to avoid the close-to-resonance situation, when it is difficult to provide the adiabatically smooth entrance into the undulator [7,8]. In addition, in the case of $|\Delta| \ll 1$ the system is very critical to the initial spread [see Eq. (5)].

Let us consider a 5 MeV electron bunch with the parameters typical for modern photo-injectors: energy spread $D_0(\gamma) \approx D_0(\gamma_{\parallel}) \sim 1\%$, normalized emittance $\varepsilon \approx \pi$ mm mrad, and the bunch radius $r_e \sim 1$ mm. In the case of a cooling undulator with $\lambda_u = 5$ cm and $K = 0.2$, the condition (2) leads to $\Delta \approx 0.3$ and $\beta_u \approx 0.06$. In this case, the estimations (3)-(5) result in the similar uncompensated spreads in axial velocity

$$D_{\perp}(\gamma_{\parallel}) \approx 3 \times 10^{-4}, \quad D_r(\gamma_{\parallel}) \approx 1 \times 10^{-4}, \quad D_{\parallel}(\gamma_{\parallel}) \approx 4 \times 10^{-4}.$$

According to simulations of motion of a 5 MeV electron bunch in a cooling undulator with the period $\lambda_u = 5$ cm and with the adiabatically tapered entrance, the undulator length should amount tens cm. In this case, the non-relativistic cyclotron wavelength $\lambda_c = 2\pi c / (\gamma \Omega_c) \approx \lambda_u / \gamma = 5$ mm corresponds to the axial magnetic field $B_0 \approx 2$ T.

CYCLOTRON RADIATION COOLING

A disadvantage of the non-radiative ‘‘axial’’ cooling is that the operating undulator of the FEL should be placed inside the cooling system. Moreover, the uncompensated axial velocity spread is limited by the transverse velocity spread. Since the cooling system does not remove the transverse spread, it is impossible to improve axial cooling by the use of the additional second stage of the cooling system. An alternative method of cooling, namely, cyclotron radiation cooling, might be more attractive. In this case, the cooling system consists of two sections (Fig. 2), namely, the undulator section with the adiabatically tapered entrance, and the cyclotron radiation section (the region of the uniform magnetic field). The non-adiabatic exit of electrons from the undulator section is accompanied with transformation of the forced

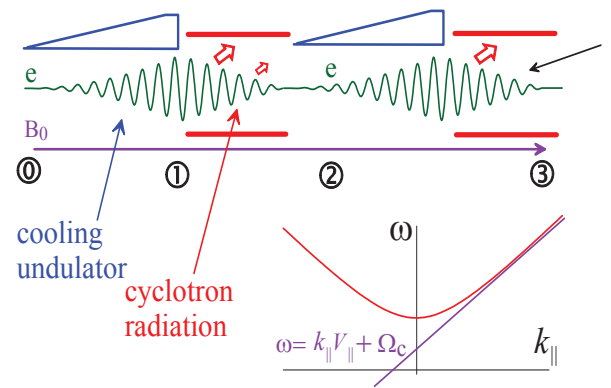


Figure 2: Schematic of the two-stage cooling system with cyclotron radiation sections, and electron-wave dispersion characteristics in the radiation sections.

oscillations into the free cyclotron oscillations with the same oscillatory velocity. Then, in the radiation section, electrons lose their transverse momentums due to the cyclotron radiation. Optimally, at the output of the cooling system, electrons possess only the axial velocity.

Let us consider radiation of a particle, which performs free cyclotron rotations in the radiation section. We suppose that this section represents a waveguide, and the cyclotron resonance condition, $\omega = \Omega_c + k_{\parallel}V_{\parallel}$, is fulfilled for the lowest transverse mode in the so-called grazing regime, when the wave group velocity, $V_{gr} = c^2 k_{\parallel} / \omega$, coincides approximately with the axial electron velocity (Fig. 2). The elementary act of radiation of this wave is emission of a photon with the energy $\hbar\omega$ and the axial momentum $\hbar k_{\parallel}$. Thus, a radiation loss in the electron energy is related to the change in axial momentum as follows [9]: $dp_{\parallel} / d\gamma = \beta_{gr}$, where $\beta_{gr} = V_{gr} / c$. Therefore, the cyclotron radiation does not perturb the axial velocity, $d\beta_{\parallel} / d\gamma = \beta_{gr} - \beta_{\parallel} = 0$. Thus, the radiation cooling operates similar to the non-radiative axial cooling, namely, the spread in β_{\parallel} is minimized due to its transformation into the spread in velocity of electron rotation in the undulator section, β_u . Then, in the radiation section, the rotatory velocity disappears.

As the cyclotron radiation does not perturb the axial electron velocity, the condition of cooling (2) and estimations (3)-(5) stay true for this scheme. Thus, from the viewpoint of the uncompensated spread, the single-stage radiation scheme has no advantages as compared to the non-radiative scheme. However, the important advantage of the radiation scheme is that the rotatory velocity is absent at the output. Therefore, a further decrease in the spread can be provided by organizing the downstream second cooling section (Fig. 2). Let us consider a situation, when at the entrance of the first cooling section the electron bunch possesses the axial spread $D_0(\gamma_{\parallel}) = 1\%$ and a relatively large transverse

velocity spread $\bar{\beta}_{\perp 0} = 5 \times 10^{-4}$ (points 0 in Fig. 2). According to estimations (3)-(5) and simulations, in this case at the output of the first section (point 1) the axial spread is $D(\gamma_{\parallel}) \sim 10^{-3}$. Therefore, at the input of the second section (points 2), the electrons have the axial spread $D_0(\gamma_{\parallel}) = 0.1\%$ and a small transverse velocity spread. According to simulations, when the electrons have passed the second section (point 3 in Fig. 2), the uncompensated spread in axial velocity can be decreased down to the level of $D(\gamma_{\parallel}) \sim 10^{-5}$.

The length of the radiation section can be estimated on the basis of the theory of the cyclotron autoresonance maser [9]. If the radiated electromagnetic pulse and the electron bunch propagate together, then one can use the amplifier equations, when the wave amplitude grows with

the bunch coordinate. If the phase velocity of the wave is close to the speed of light, $\beta_{ph} = 1 / \beta_{gr} \rightarrow 1$, then the phase of electrons with respect to the synchronous wave, $\theta = \omega t - k_{\parallel}z - \int \Omega_c dt - \theta_{c0}$, varies slowly due to the autoresonance effect, so that $\theta(z) \approx \theta_0$. At the input of the radiation section, initial phases of different electrons are determined by their initial cyclotron phases and time of the entrance into the section. $\theta_0 = \omega t_0 - \theta_{c0}$. Cyclotron oscillations have sin-phase character [10], as they have arisen due to the transformation of the forced undulator oscillations. Thus, the phase size of the electron bunch, $\delta\theta_0 = 2\pi l_e / \lambda$, is less than 2π , if the length of the electron bunch, l_e , is smaller than the wavelength of the synchronous wave. The latter can be estimated by formula $\lambda \approx \lambda_u / \gamma^2$ following from $\omega \approx \gamma^2 \Omega_c \approx \gamma^2 \Omega_u$. As an example, in the case of $\lambda_u = 5\text{cm}$ and $\gamma = 10$, the wavelength is $\lambda = 0.5\text{mm}$, whereas for a 1 ps electron bunch $l_e = 0.3\text{mm}$. In this case, cyclotron radiation has the spontaneous character, as the electron bunch has a ready-to-radiate size. Estimations predict that the radiation section can be as short as tens of cms.

UBITRON RADIATION COOLING

The abnormal dispersion of the undulator velocity of electrons, $\partial|V_u| / \partial V_{\parallel} > 0$, can be used to provide also a cooling method based on the ubitron radiation of electrons inside the regular part of the undulator with guiding axial magnetic field (Fig. 3). In this situation, electrons with higher initial energies have bigger undulator velocities and, therefore, lose more energy due to the radiation.

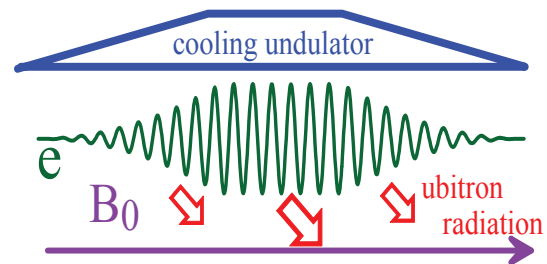


Figure 3: Ubitron radiation cooling system.

Let us assume, that at the input of the cooling undulator there is a spread in electron energy, so that the initial electrons mass-factors can be expressed as follows: $\gamma_0 = \bar{\gamma}_0 + \Delta\gamma_0$, where $\bar{\gamma}_0$ describes the averaged value of the initial electron energy and $\Delta\gamma_0$ describes the spread. Evidently, at the output of the cooling system, the electron energies become lower due to the ubitron radiation inside the undulator:

$$\gamma = \bar{\gamma}_0 + \Delta\gamma_0 - \Delta\gamma_{rad}. \quad (6)$$

Here $\Delta\gamma_{rad}$ is the radiation loss. Similar to the cyclotron radiation cooling considered above, we assume

that the radiated wave propagates together with the bunch ($V_{gr} = V_{||}$), and the bunch length is shorter than the wavelength of the radiated wave ($l_e < \lambda$). In this situation, the amplitude of the co-propagated wave increases in the process of the radiation (similar to the SASE FEL regime). The energy radiated during the trip of the e-bunch through the cooling undulator is proportional to the square of the undulator velocity: $\Delta\gamma_{rad} = \alpha V_u^2$, where $\alpha \propto IL^2$ is a coefficient proportional to the electron current and to the square of the undulator length. Since the undulator velocity depends of the initial electron energy, $\gamma_0 = \bar{\gamma}_0 + \Delta\gamma_0$, Eq. (6) can be represented as follows:

$$\gamma = \bar{\gamma}_0 + \Delta\gamma_0 - \alpha V_u^2(\bar{\gamma}_0) - \Delta\gamma_0 \times \alpha \frac{\partial V_u^2}{\partial \gamma_0} \bigg|_{\gamma_0 = \bar{\gamma}_0}.$$

Thus, in the case of the abnormal dispersion of the undulator velocity, $\partial|V_u|/\partial\gamma_0 > 0$, the ubitron radiation leads to the decrease of the energy spread. Let us notice, that the condition of the cooling, $\alpha \times \partial V_u^2 / \partial \gamma_0 = 1$, is independent on the value of the initial spread, $\Delta\gamma_0$. According to estimations, in the case of a 5 MeV e-bunch with radius $r_e \sim 1$ mm, the optimal cooling condition (2) is true for the undulator length amounting tens cm.

RF UNDULATOR COOLING

Finally, we discuss the possibilities to use cyclotron-undulator cooling schemes for electron bunches with higher energies. Since in the case of a magnetostatic cooling undulator the non-relativistic cyclotron wavelength is estimated as $\lambda_c \sim \lambda_u / \gamma$, an increase in the electron gamma-factor results in an increase of the axial magnetic field required. However, for high-energy electrons, instead of the magnetostatic cooling undulator, one can use an rf undulator (a powerful rf pulse), which co-propagates together with the bunch (Fig. 4). In this case, the condition of closeness of the cyclotron and undulator frequencies,

$$\Omega_c \sim \omega_u - k_{||u} V_{||} \approx \omega_u (1 - \beta_{gr,u} \beta_e),$$

leads to the following estimation: $\lambda_c \sim \lambda_u / \gamma(1 - \beta_{gr,u} \beta_e)$. If the group velocity of the undulator wave is close to the speed of light, $\beta_{gr,u} \rightarrow 1$, the optimal conditions for the cooling can be provided at a moderate magnetic field.

Let us consider axial cooling of electrons with $\gamma = 100$ in a rf pulse with $\lambda_u = 3$ cm (Fig. 4). A super-radiant GW-power-level Cherenkov backward-wave oscillator [11] can be used as a source of such pulse. If this pulse is formed by the $TE_{1,1}$ transverse mode of a waveguide with the radius $R \approx \lambda_u$, then $\beta_{gr} \approx 0.95$, and the non-relativistic cyclotron wavelength $\lambda_c \approx \lambda_u / 5 = 0.6$ cm

corresponds to the axial magnetic field $B_0 \approx 1.8$ T. In this case, the rf pulse power $P_u = 0.5$ GW corresponds to the undulator parameter $K = 0.25$, whereas the rf pulse duration of 0.5 ns corresponds to the cooling system length of about 3 m only.

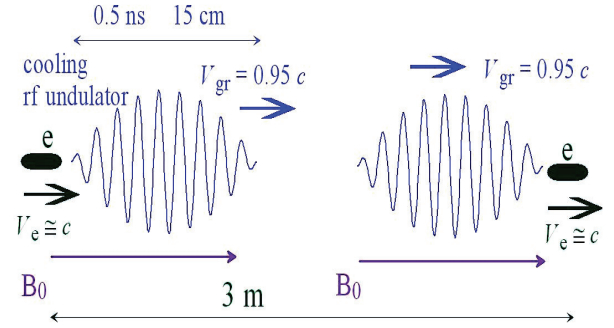


Figure 4: Schematic of the cooling system based on a short powerful rf pulse co-propagating with the e-bunch.

REFERENCES

- [1] J.G. Power, Proc. of 14th Advanced Accelerator Concept Workshop, Annapolis, USA, 2010, p.163.
- [2] B. Dunham et al, Appl. Phys. Lett. 102, 034105 (2013).
- [3] F. Stephan et al, Phys. Rev. ST Accel. Beams 13, 020704 (2010).
- [4] J. L. Hirshfield and G. S. Park, Phys. Rev. Lett. 66, 2312 (1991).
- [5] H. Deng and C. Feng, Phys. Rev. Lett. 111, 084801 (2013).
- [6] I.V. Bandurkin, S.V. Kuzikov, A.V. Savilov, Appl. Phys. Lett. 105, No. 7 (2014).
- [7] H.P.Freund, T.M.Antonsen, Principles of free-electron lasers (Chapman & Hall, London, 1996).
- [8] N.S.Ginzburg, N.Yu.Peskov, Phys. Rev. ST Accel. Beams 16, 090701 (2013).
- [9] V. L. Bratman et al, Int. J. Electron. 51, 541 (1981).
- [10] A.V. Savilov et al, Phys. Rev. E 63, 4207 (2000).
- [11] S. D. Korovin et al, Phys. Rev. E 74, 016501 (2006).

OPTIMIZATION OF FEL PERFORMANCE BY DISPERSION-BASED BEAM-TILT CORRECTION

Marc W. Guetg*, Sven Reiche

Paul Scherrer Institut, CH-5232 Villigen PSI, Switzerland

Abstract

In Free Electron Lasers (FEL) the beam quality is of crucial importance for the radiation power. A transverse centroid misalignment of longitudinal slices in an electron bunch reduces the effective overlap between radiation field and electron bunch. This leads to a reduced bunching and decreased FEL performance.

The dominant sources of slice misalignments in FELs are the coherent synchrotron radiation within bunch compressors as well as transverse wake fields in the accelerating cavities. This is of particular importance for over-compression, which is required for one of the key operation modes for the SwissFEL under construction at the Paul Scherrer Institute in Switzerland.

The slice centroid shift can be corrected using multi-pole magnets in dispersive sections, e.g. the bunch compressors. First and second order corrections are achieved by pairs of sextupole and quadrupole magnets in the horizontal plane while skew quadrupoles correct to first order in the vertical plane.

INTRODUCTION

An FEL strives to have a relative bandwidth of the photon energies of the order of 10^{-4} . For specific applications like powder diffraction, Bragg imaging, or single-shot absorption spectroscopy much larger bandwidths are desirable to increase the chance of hitting resonances [1, 2]. A special configuration of the FEL under construction at PSI Switzerland, SwissFEL [3], will yield a bandwidth of up to 3% at 1 Å to fulfill these needs. In the following we refer to it as the large-bandwidth mode of SwissFEL.

This mode uses a high energy chirp along the bunch to increase the photon bandwidth. The longitudinal wake-fields [4] originating in the cavities of the last linac and an over-compression in the final bunch compressor (BC) to revert the sign of the incoming energy correlation create the needed chirp. Because of over-compression coherent synchrotron radiation (CSR) considerably deteriorates the transverse profile by introducing beam distortion in the bending plane.

A beam slice misalignment reduces the overlap between the electron beam and its radiation field. This leads to a reduction of SASE performance in the offset regions. CSR, being a major contributor to the beam tilt, is of concern at small bunch lengths within the bending magnets. Therefore correction of the tilt is of special importance for the large-bandwidth mode of SwissFEL utilizing over-compression.

This work implements an alternative description of the beam tilt [5] and quantifies its effect on the lasing through genesis [6] simulations. In addition we address the induced orbit and bunch length jitter.

THEORY

This section describes the beam tilt and how to manipulate it. In this work x stands for both transverse planes and z the longitudinal direction. The Taylor approximation of the beam tilt μ is:

$$\tilde{x}(z) = x + \sum_{i=1}^n \mu_i (z^i - \langle z^i \rangle), \quad (1)$$

$$\tilde{x}'(z) = x' + \sum_{i=1}^n \mu'_i (z^i - \langle z^i \rangle), \quad (2)$$

where n corresponds to the highest order to be considered. Misaligned beam parameters are denoted by a tilde. This description has the benefit of adjustable abstraction without losing analytical correctness if n reaches infinity.

This work uses the statistical emittance (ε) defined as:

$$\varepsilon_x^2 = \langle x^2 \rangle \langle x'^2 \rangle - \langle x x' \rangle^2. \quad (3)$$

The parameter x' denotes the momentum normalized by the total momentum. The beam tilt μ alters the emittance as follows:

$$\tilde{\varepsilon} = \varepsilon \sqrt{1 + M_n + M_n^*}, \quad (4)$$

where M corresponds to the pure and M^* to the mixing term. They are both expressed through

$$M_n = \frac{1}{\varepsilon_x} \sum_{i,j=1}^n (\beta_x \mu'_i \mu'_j + \gamma_x \mu_i \mu_j - 2\alpha_x \mu_i \mu'_j) Z_{i,j}, \quad (5)$$

$$M_n^* = \frac{1}{\varepsilon_x^2} \sum_{i,j,k,l=1}^n (\mu_i \mu_j \mu'_k \mu'_l - \mu_i \mu'_j \mu_k \mu'_l) Z_{i,j} Z_{k,l}, \quad (6)$$

where α, β, γ are the Twiss parameters and $Z_{i,j}$ is the reduced mean, defined as:

$$Z_{i,j} = \langle z^{i+j} \rangle - \langle z^i \rangle \langle z^j \rangle. \quad (7)$$

For a linear longitudinal phase-space correlation, considering μ up to only first-order ($n = 1$), M^* vanishes and M simplifies to

$$M_1 = \frac{\varepsilon_z \beta_z}{\varepsilon_x} (\mu_1'^2 \beta_x + \mu_1'^2 \gamma_x + 2\mu_1 \mu_1' \alpha_x), \quad (8)$$

where ε_z corresponds to the longitudinal emittance and β_z to the longitudinal beta function.

* marc.guetg@psi.ch

The beam tilt leads to a deviation of slice and projected parameters like emittance and mismatch parameter, therefore making it harder to operate the machine in places where the slice beam parameters cannot be measured. More importantly the beam tilt reduces the FEL power, specifically at the tails of the bunch. The slices are offset to the undulator axes and undergo betatron oscillations, thereby reducing the overlap between radiation and electrons. In addition does μ changes the optics making it more difficult to match the beam (core) due to the mismatch along the bunch. A series of genesis simulations demonstrate this behaviour (figure 1). The far-field is used as performance benchmarks, since it

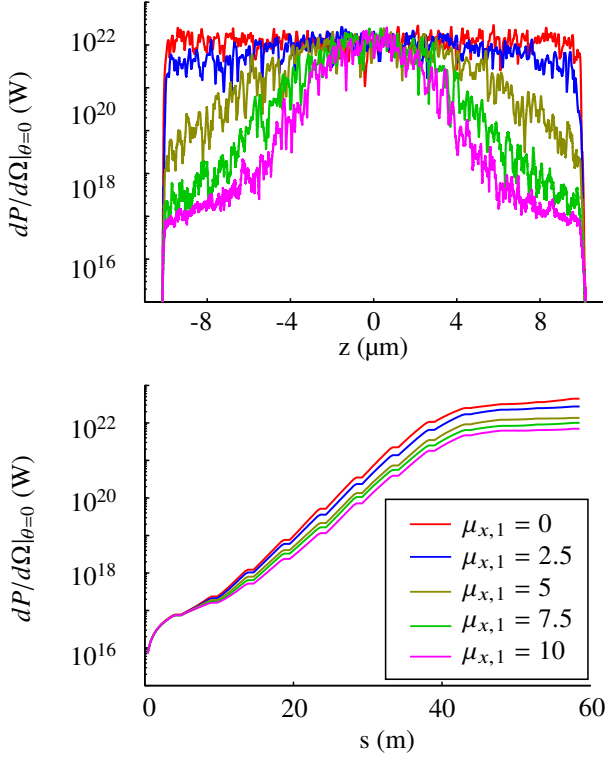


Figure 1: Scan of $\mu_{x,1}$. The bottom graph shows the radiation growth along the SwissFEL undulator line whereas the top one represents a snapshot along the FEL pulse at the end of the undulator line.

possess a clearer start up signal and lower contribution by higher transverse modes at the power level of spontaneous radiation.

CORRECTION ALGORITHM

Static fields cannot act differently on electrons in a bunch, as long as the electrons have the same orbit. This changes in a dispersive section (η) with a strictly monotonic chirp along the bunch: here a given longitudinal position is mapped uniquely to a transverse position. A superposition of multipole fields allows acting independently on these positions.

In the following we distinguish between lattice and beam dispersion and tilt. The lattice parameters only depend on the beam line and do not take into account any self interaction.

The beam parameters on the other hand are derived from the higher-order moments in the beam independent from their source.

For a linear longitudinal phase space and an energy chirp with $|\alpha_z| \gg 0$, μ and η are directly linked by:

$$\mu_i \approx \left(\frac{-\alpha_z}{\beta_z} \right)^i \eta_i, \quad (9)$$

where μ_i and η_i correspond to the Taylor approximation terms of the beam tilt or the dispersion, respectively.

The condition of a strictly monotonic chirp is fulfilled at the bunch compressors. Therefore by adjusting the lattice dispersion the beam tilt can be controlled by changing the beam dispersion. The existing energy chirp vanishes in the subsequent C-band linac due to longitudinal wakefields thereby unlinking lattice dispersion and beam tilt because $\alpha_z \approx 0$. Any applied correction will now be independent of magnetic multipoles as long as there is no energy correlation along the bunch. The leaking lattice dispersion is then independent from any corrected bunch dispersion. This means that the orbit of the bunch is still energy dependent but the phase space coverage in momentum and space is not.

Due to the large lattice dispersion at the correction locations weak corrector magnet strengths are sufficient to achieve the desired manipulation of η . This has the benefit of only marginally disturbing the optics.

CORRECTION IMPLEMENTATION

To measure the beam tilt μ the beam is streaked by a transverse deflecting cavity or by a (skew) quadrupole magnet within the BC. Since the longitudinal phase space at the BC is strictly monotonic both methods are equivalent. The tilt in momentum (μ') is reconstructed by measuring μ for several phase advances.

The perturbation matrix is measured using all available corrector magnets as knobs and measurements of μ , R_{56} and chromaticity. To suppress low impact contributions the matrix elements not mentioned in table 1 are forced to zero. By measuring several phase advances it is then

Table 1: Pairing for Perturbation Response Matrix (not mentioned elements are set to zero to increase stability)

Knobs	Quad	Skew quad	Sextupole	Dipole
	$\mu_{1,x}$	$\mu_{1,y}$	$\mu_{2,x}$	R_{56}
Penalties	$\mu_{1,x'}$	$\mu_{1,y'}$	$\mu_{2,x'}$	
			Chromaticity	

possible to reconstruct μ as well as μ' at any given point. The implementation of the correction algorithm is discussed in more detail in [5].

SIMULATIONS

The simulations of this work focus on the large bandwidth mode of SwissFEL [3] utilizing over-compression. The

resulting strong CSR kick makes the need for the correction most critical for this mode.

For correction both BC's in SwissFEL are equipped with a pair of (skew) quadrupole and sextupole magnets. These 12 corrector magnets are used to correct for the beam tilt while keeping chromaticity at bay. The change in R_{56} is then adjusted by the bending angle of the bunch compressors.

Elegant [7] simulations up to the undulator entrance were done followed by genesis simulations to quantify the gain in FEL power. Figure 2 shows the increase in power through the applied correction. The correction increases the power

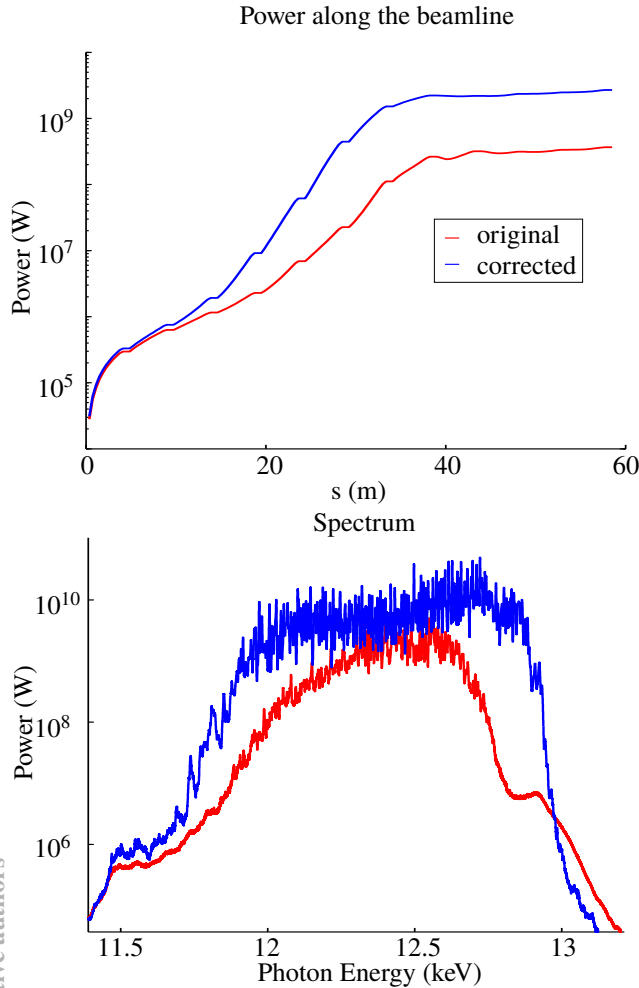


Figure 2: Genesis simulations for the SwissFEL large bandwidth mode at $\lambda_{\text{photons}} = 1 \text{ \AA}$. The top picture shows the FEL power for the corrected and the uncorrected case. The resulting increase in FEL power is about one order of magnitude. Uncorrected configuration exhibits narrower spectra, counteracting the goal of the large bandwidth mode.

by one order of magnitude at saturation. Furthermore the correction increases the photon bandwidth, which is a critical parameter for the large-bandwidth mode. This is mainly because the tails are now contributing stronger in the overall SASE process. This leads to a broadening of the spectrum due to the strong energy chirp which is translated into a frequency chirp of the FEL pulse.

ISBN 978-3-95450-133-5

JITTER

The leakage of lattice dispersion out of the bunch compressors leads to energy induced orbit jitter. An orbit offset within the undulator leads to subsequent orbit oscillations reducing FEL power.

Since it is not possible to correct the leakage of this lattice dispersion without introducing new bunch dispersion, it is important to investigate the sensitivity to energy jitter.

In addition to the orbit jitter T_{566} is enlarged, which in case of an energy jitter $\Delta\delta$ leads to an altered \tilde{R}_{56} of

$$\tilde{R}_{56} = R_{56} + 2T_{566}\Delta\delta, \quad (10)$$

considering up to second order matrix elements [8].

The SwissFEL tolerance of an acceptable beam orbit jitter is 10% of its rms beam size in momentum and space. The bunch length jitter is tolerable up to 10% of its length. The jitter study shows that the orbit as well as the bunch length jitter stay well within their respective tolerance levels. Figure 3 shows their distributions by jittering the RF klystrons at their respective tolerance values in phase and amplitude [3].

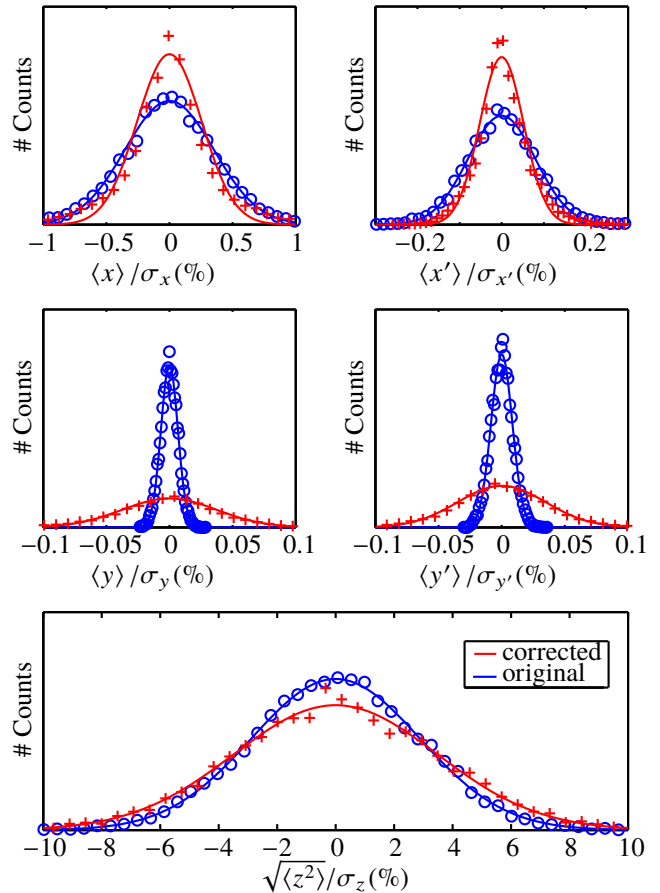


Figure 3: 10'000 Jitter runs for both corrected and uncorrected cases. The additional orbit jitter originating from the leaking dispersion is minimal and is well within tolerances of SwissFEL. The points correspond to the actual data points and the lines correspond to Gaussian fits.

The gun laser jitter was studied by varying the charge of the electron bunch and proved to be of no significance.

Other sources of orbit jitter [3] in the machine are stronger than the contribution from the leaked lattice dispersion. The same holds true for the bunch length jitter. The increase in orbit and bunch length jitter stays within the acceptable limits and does therefore not restrict the applied correction.

DISCUSSION

We have proposed a correction scheme for slice misalignment and validated it in simulation and with measurements. In simulations we see an tremendous increase of nearly one order of magnitude in FEL power for a strongly misaligned beam. The correction is of particular importance for the large-bandwidth mode because of the strong CSR kick due to over-compression and the spectral broadening. The experiment delivered a proof-of-principle of feasibility of the introduced method as presented in [5].

The proposed iterative correction method implementing a perturbation matrix is applicable in practice because it respects tolerance values in terms of mismatch and jitter of the machine.

Concerns about the energy induced orbit and bunch-length jitter are addressed and are well below the tolerance level for the expected jitter budget for SwissFEL.

We conclude that the presented method is feasible to correct μ and make the large-bandwidth mode viable for SwissFEL.

REFERENCES

- [1] S. P. Collins, R. J. Cernik, B. Fell, C. C. Tang, N. W. Harris, M. C. Miller, and G. Oszlanyi. Station 16.3: a High-Resolution Single-Crystal Diffraction Facility at the SRS, Daresbury. *Journal of Synchrotron Radiation*, 5(5):1263–1269, Sep 1998.
- [2] D. B. Turner, P. Wen, D. H. Arias, K. A. Nelson, H. Li, G. Moody, M. E. Siemens, and S. T. Cundiff. Persistent exciton-type many-body interactions in GaAs quantum wells measured using two-dimensional optical spectroscopy. *Phys. Rev. B*, 85:201303, May 2012.
- [3] R. Ganter, editor. *SwissFEL Conceptual Design Report*. PSI, 2012.
- [4] Karl Bane. Short-range dipole wakefields in accelerating structures for the NLC. *LCC-Note-0116*, 2003.
- [5] M. W. Guetg, B. Beutner, E. Prat, and S. Reiche. Dispersion based beam tilt correction. In *Proc. 34 th Int. Free-Electron Laser Conf.*, number TUPSO24, New York, 2013.
- [6] S. Reiche. GENESIS 1.3: a fully 3D time-dependent FEL simulation code. *Nuclear Instruments and Methods in Physics Research Section A: Accelerators, Spectrometers, Detectors and Associated Equipment*, 429:243–248, 1999.
- [7] M. Borland. Elegant: A flexible SDDS-compliant code for accelerator simulation. Technical report, Argonne National Lab., IL (US), 2000.
- [8] K. L. Brown. A first-and second-order matrix theory for the design of beam transport systems and charged particle spectrometers. Technical report, SLAC, 1971.

THE SEED LASER SYSTEM FOR THE PROPOSED VUV FEL FACILITY AT NSRRC

M.C. Chou[#], N.Y. Huang, A.P. Lee, W.K. Lau, NSRRC, Hsinchu, Taiwan

Abstract

The possibility of establishing a free electron laser (FEL) facility in Taiwan has been a continuing effort at National Synchrotron Radiation Research Center (NSRRC) in the past several years. The Baseline design of the envisioned NSRRC FEL is a high gain harmonic generation (HG) FEL seeded by a 266 nm laser. The seed laser is produced by adding an optical parametric amplification (OPA) system pumped by upgrading the existing IR laser system. To provide broad tunability of the FEL radiation, the seed laser will be tunable. The spectrum considered for seeding the FEL is between 266 - 800 nm with peak power of 200 MW. The spatial and temporal overlap between the sub-100 fs electron bunch and the 100 fs UV seed laser is under study.

INTRODUCTION

An FEL facility aimed for VUV and THz radiation is being studied at NSRRC in Taiwan [1]. To fulfil the user needs, this facility is designed to be operated in two modes, one for VUV applications and the other for THz applications. Recently, there are growing interests in applications like spectroscopy, elementary excitations, and NMR spectroscopy, etc., requiring high power THz radiation from the accelerator-based devices. The non-invasive and non-ionizing nature of THz spectroscopy is vital for medicine and biology applications from the safety point of view. On the other hand, this proposed facility will provide intense, fully coherent ultrafast light sources up to the extreme VUV region. Direct VUV photoionization is a key approach to probe properties of valence electrons of molecules and materials, which mostly lie at about 6 - 20 eV below the ionization limit. The Baseline FEL lies in this exact energy region and is therefore most suitable to study the transformation of molecules and materials that are important in many research fields. This proposed VUV FEL light source will provide scientists a promising tool to develop more sensitive experimental methods to prove important chemical and physical processes in energy, biological and environmental sciences.

Strong consideration has been given to minimize the cost by making maximum use of existing hardware at NSRRC. One unique consideration is to use an existing undulator for the dual functions of the THz radiator and the modulator of an HG section. Design emphasizes versatility of operation and beam quality control and compensation of nonlinearities, with an envision that it will allow as much as possible future upgrades as well as later R&D of FEL physics. The possibility of establishing a free electron laser facility in Taiwan has been a

continuing effort at NSRRC in the past several years. With the installation of a new 3-GeV storage ring, the Taiwan Photon Source (TPS), it is a good time to renew this effort on the feasibility of an FEL facility. We consider it to serve two purposes:

1. To develop a technology platform for FEL researches in Taiwan. This FEL platform will provide a technology base to pursue a wide range of future possibilities beyond TPS, including industrial applications such as high brightness electron gun technology, and lithography manufacturing.
2. To initiate an FEL science research, and to provide a training ground for FEL researchers in Taiwan. This facility will allow the researchers to gain experience and accumulate credentials, and prepare to compete in the FEL world stage.

In the beginning of 2013, the first operation of the 2998 MHz photoinjector at NSRRC has been successfully preformed after high power microwave processing of the photoinjector cavity up to 60 MV/m. A 266-nm, 300-μJ ultra-violet (UV) laser system has been installed as the drive laser for the photocathode RF gun. A stable electron beam with energy of 2.6 MeV at 250 pC bunch charge has been achieved. Beam transverse emittance of ~3 mm mrad is measured at 250 pC with Gaussian laser pulse [2]. A new photo-cathode rf gun cavity is in fabrication for higher field gradient operation. Laser shaping technique can be employed to further reduce the beam emittance.

THE PROPOSED FEL FACILITY

The System Layout

The Baseline design of the envisioned NSRRC FEL is an HG FEL seeded by a 266 nm laser. With the existing linac sections and the high power klystron systems, an accelerated beam with beam energy of ~325 MeV at the linac end can be expected. With the existing hardware and the possible upgrades in the limited space, we consider the Baseline design of the envisioned NSRRC FEL as an HG FEL seeded by a 266 nm laser to generate the VUV radiation at 66.5 nm which is 4th harmonic of laser wavelength. The resonant condition is satisfied when the radiator strength is tuned as $K = 1.98$. The performance of HG FELs has been discussed widely in recent 10 years [3]. In addition to being much stable and tunable with narrow bandwidth, the HG source also offers fully temporally coherent radiation pulse. A schematic of the overall layout is shown in Fig. 1. The length of the accelerator system from the gun to L3 exit is 27 m. The length of the diagnostics and FEL stations is 6 m. Including a 4 m × 5 m experimental area for users, the whole facility tightly fits into the existing 38 m × 5 m long tunnel in the TPS Linac Test Laboratory.

[#]chou.mc@nsrrc.org.tw

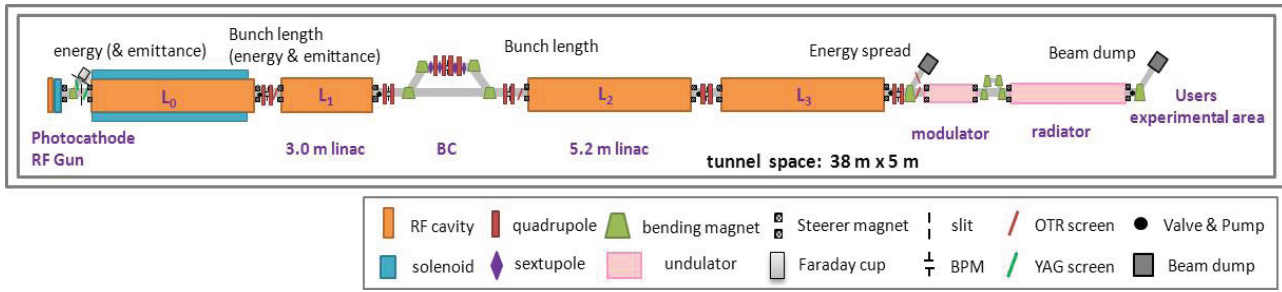


Figure 1: Layout of the proposed FEL facility at NSRRC.

FEL Performance

In the HGHG operation, the seed laser interacts with the electron bunch in the 1-m EPU56 modulator to imprint energy modulation on the electron bunch. The seed laser is shared with the RF gun ($\lambda = 266\text{nm}$). The peak power of the upgrade laser is 200 MW, the laser pulse energy is 300 μJ and FWHM pulse width is 1.5 ps. Through a small chicane (total length 40 cm, $R_{56} = 30\text{ }\mu\text{m}$), the energy modulation is converted into density modulation. This pre-bunched electron beam will readily radiate coherently in the radiator undulator leading to an exponential growth and reach saturation in its 3-m length as shown in Fig. 2. The FEL resonant wavelength in the radiator is $\lambda = 66.5\text{ nm}$, which is the 4th harmonic of the 266 nm seed laser. The saturated peak power near the 2-m position is 200 MW for the fundamental mode and 2 MW and 200 kW respectively for the 3rd and the 5th harmonics.

To provide broad tunability of the FEL radiation, the seed laser will be tunable. Linac energy and undulator strength K are then adjusted accordingly to maintain FEL resonance. The existing seed laser will be upgraded by adding an OPA system, followed by an appropriate nonlinear crystal and laser splitting schemes. Radiation with wavelength range between 66.5 – 200 nm and the brightness of $3.3 - 5.7 \times 10^{28}$ photons/ $\mu\text{m}^2/0.1\%$ is expected when an appropriate laser system is included.

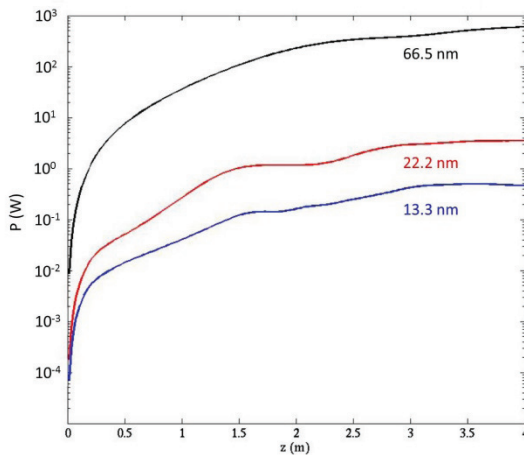


Figure 2: The growth of the radiation power in the undulator. The fundamental (66.5 nm), the 3rd harmonic (22.2 nm), and the 5th harmonic (13.3 nm) radiations are marked as black, red and blue lines respectively.

The seeding laser with wavelength between 266 – 800 nm with peak power of $\sim 100 - 200\text{ MW}$ is adopted in this estimation.

As mentioned above, the EPU56 will serve the dual functions as an HGHG modulator and a THz coherent undulator radiation (CUR) undulator. When the THz radiation is desired from the undulator, the accelerated beam exiting L_0 will traverse through the beam line and reach the undulator to generate THz CUR. In such operation, L_0 will be optimized to generate 100 pC, 100 fs electron bunches at 27.3 MeV through velocity bunching. The radiation frequency is 4.5 THz when the undulator strength K is 3.4. The total radiated energy is 2.74 μJ , and the corresponding peak power is 0.7 MW. This undulator can provide variable polarization, allowing adjustable polarization in its THz CUR. This unique property can support additional novel applications for the users.

Table 1: Estimated Beam Performance and Radiation of the VUV/THz FEL at NSRRC

Electron beam	
Energy [MeV]	325
Repetition rate [Hz]	10
Slice emittance [mm-mrad]	0.8
Bunch length [fs]	51.3
Peak current [A]	500
Slice energy spread [keV]	1.7
VUV radiation	
Wavelength [nm]	66.5
Peak power [MW]	200
Gain length [m]	0.17
Photons/pulse [10^{13}]	1.1
Brightness [photons/ $\mu\text{m}^2/0.1\%$]	3.34×10^{28}
Temporal coherence modes	~ 1
Spatial coherence M^2	~ 2
THz radiation	
Frequency [THz]	4.5
Total radiated energy [μJ]	2.7
Peak power [MW]	0.7

THE ULTRAFAST LASER SYSTEM

The Existing Laser System

The ultrafast laser system used to drive the photocathode rf gun was purchased from Coherent Corporation and it is a Ti:sapphire laser system based on the chirped-pulse amplification technique [4]. This system

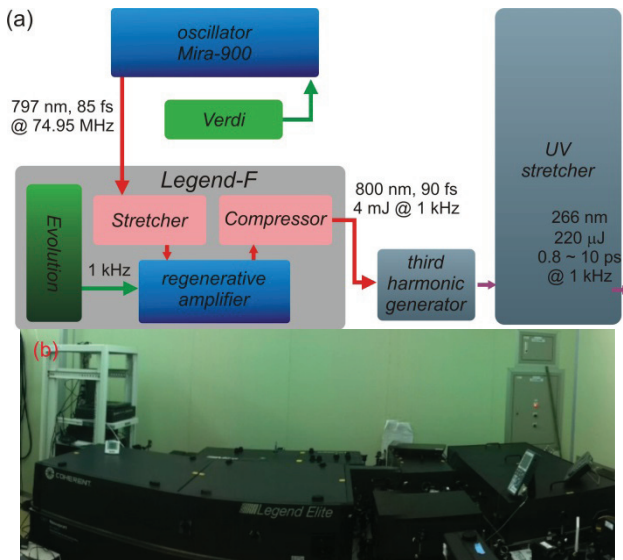


Figure 3: (a) Layout and (b) photo of the ultrafast laser system.

consists of an oscillator (Mira-900), an amplifier (Legend-F), a third harmonic generator (THG), and a UV stretcher. The layout of the laser system is shown in Fig. 3. The oscillator is an 85-fs passively mode-locked oscillator pumped by Verdi, a 5-W cw frequency-doubled Nd:YVO₄ laser. It delivers 16 nJ energy per pulse, 74.95 MHz repetition rate and a central wavelength of 797 nm. The seed laser from the oscillator is then conveyed into the Legend-F amplifier. It is composed of three essential elements, an optical pulse stretcher, a regenerative amplifier and an optical pulse compressor. Before entering the amplifier, the laser pulses are stretched with an Öffner-type all-reflective stretcher. After stretched, the laser pulses are amplified by a regenerative amplifier while the energy is raised from nJ to mJ level and meantime the repetition rate of the laser is modulated to 1 kHz by a frequency-doubled diode-pumped Nd:YLF laser (Evolution). The amplified laser pulse is further compressed with a grating compressor. Currently the IR laser output from the Legend is 4 mJ per pulse with energy stability <0.5% RMS, which is lower than that of factory specifications due to the degradation of optics such as the compressor grating.

In order to extract photoelectrons from the Cu photocathode RF gun efficiently, the photon energy of the laser pulse should be higher than the work function of Cu ~ 4 eV. For this reason the laser frequency from the Legend is tripled by a THG, which mainly consists of two nonlinear crystals. After the THG, a UV laser pulse with 266 nm, corresponding to photo energy of 4.5 eV, is generated. The UV laser pulse can be further stretched from 800 fs to 10 ps by a UV stretcher, which is consisted of four fused silica prisms. We set the pulse duration of the UV laser at 8 ps for initial gun test. Similarly, the UV laser energy of 220 μJ at the exit of the UV stretcher is a little lower, compared to that of factory specifications due to the degradation of the nonlinear crystals and prisms.

Although the UV energy attenuates to about 100 μJ after propagating to the Cu cathode due to mirror loss and absorption of the air, it is sufficient for the photocathode RF gun.

The Upgraded Laser System for FEL Seeding

As mention above, in order to provide broad tunability of the FEL radiation, the part of the spectrum considered for seeding the FEL is between 266 – 800 nm with peak power of 100 – 200 MW. We aimed to cover wavelengths in the range 66.5 – 200 nm with the expected performance. One method to obtain such light sources with broad spectra is using an OPA system, followed by appropriate non-linear crystals and laser splitting schemes. A feasible OPA system is a TOPAS as was chosen at FERMI@Elettra [5]. The signal and idler waves of TOPAS span from 800 nm to 2.4 μm. Through a sequence of nonlinear harmonic generation and mixing, the frequency is up-converted to UV. Figure 4 shows the tuning spectra of the TOPAS. The desired FEL seed laser wavelength is 266 nm, laser pulse energy is 300 μJ, and FWHM pulse width is 1.5 ps, corresponding to the peak power of 200 MW. It means that when using the TOPAS system, the 800-nm pump energy should be larger than 40 mJ. The laser energy of the existing laser system is too low to be used as the pump source for producing such high energy of 266 nm from the OPA process. Furthermore, the seed laser should be shared with (a much smaller need of) the RF gun. Therefore we plan to add a 4-pass amplifier after the existing laser system to boost the laser energy.

Figure 5 shows the layout of the upgraded laser system. First, a beam splitter will be inserted after the regen amplifier. The stretched, expanded 800-nm laser pulse with 4 mJ (80% output of the regen amplifier) is then compressed to 100 fs and used to generate the UV laser pulse by the THG. Then the UV laser pulse is used as the drive laser of the photocathode RF gun as mentioned above. The residual laser pulse (20% output of the regen amplifier) will be used as the seed pulse for the 4-pass amplifier. This 4-pass amplifier will be pumped by a frequency-doubled Q-switched Nd:YAG laser from both ends. This amplifier is made of a 10-mm-long, 1.5-cm diameter, 0.25% doping, normal-cut Ti:sapphire crystal with anti-reflective coating, and seven folding mirrors in a bow-tie configuration. At the Ti:sapphire crystal, the pump beam diameter is 3.9 mm FWHM and the laser beam diameter is 2.6 mm FWHM. With pump energy of

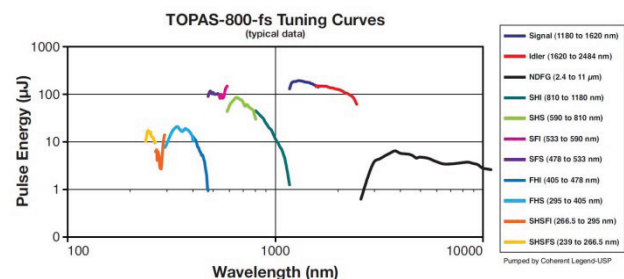


Figure 4: Spectra of the TOPAS.

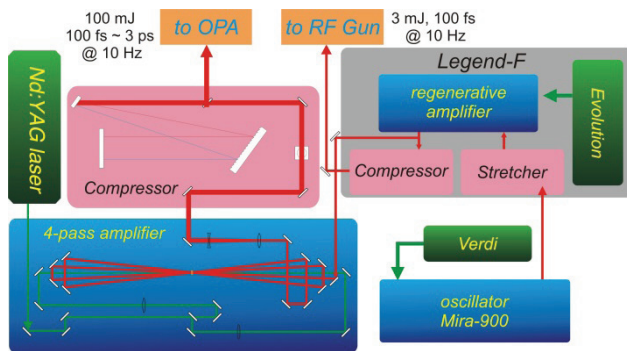


Figure 5: Layout of the upgraded laser system.

600 mJ, the laser pulses are amplified to 130 mJ. After the 4-pass amplifier the laser beam is expanded to 20-mm diameter in clear aperture. The amplified laser pulse is further compressed to 100 fs with 100-mJ energy by another grating compressor. Pulse durations of the laser pulse can be varied from 100 fs to 3 ps with either sign of chirp by adjusting the grating separations. In addition, in order to match the repetition rate of the RF system, the repetition rate of the upgraded laser system will be tuned from 1 kHz down to 10 Hz by adjusting the Pockels' cell timing inside the regen amplifier. The amplified 800-nm laser pulse with 100 mJ, 1.5 ps can be used to pump the OPA system to generate the UV laser for the FEL seeding.

In the initial stage of this FEL project our objective is to generate the ultrashort electron beam via velocity bunching in L_0 for THz CUR before next summer. Before installing the existing EPU56 undulator at the exit of L_0 , it is a good opportunity to produce ultrashort x-ray sources through the Thomson scattering once the 100 MeV electron beam and the 100 mJ laser pulse are ready. Furthermore, high-order harmonic generation (HHG) will be investigated as well when the laser system is upgraded to support the HHG FEL. We will for example try to optimize the 5th harmonic to reach the EUV regime using this facility. With HHG seed down to 66.5 nm directly, the 3 m long undulator can be used as direct amplifier. A comparison between a HHG seed amplifier and a HHG FEL can be an interesting topic.

Synchronization

To generate and accelerate electron bunches from the photocathode RF gun, one has to make synchronization between the laser and the RF system. The fine synchronization with the RF reference can be carried out at the level of the laser oscillator. The laser oscillator can be locked with the signal generator by a Synchrolock which was also bought from Coherent [6]. Coherent specifies a time jitter is less than 250 fs RMS when the Synchrolock is used to lock two laser oscillators. Since the oscillator phase noise may have variations, we think the time jitter is < 1 ps RMS when an external RF signal is used to drive the Synchrolock. In order to make sure the good synchronization between the UV pulse and the electron beam during seeding process, we will set the pulse duration of the UV pulses at 1.5 ps since the time jitter of the current system is < 1 ps. The proposed FEL

facility will provide intense, fully coherent ultrafast light sources up to the extreme VUV region. The femtosecond VUV pulses and IR laser pulses can be used to do some time-resolved pump-probe experiments. But a time jitter of < 1 ps is still too long for the VUV pulses with respect to the experimental pump lasers. An optical timing system based on stabilized fiber links has been developed for the LCLS to provide synchronization at the sub-20 fs level [7]. We will improve the time jitter of our system by referring to what has been done at LCLS. We will also plan a full series of measurements to characterize the overall timing stability of the VUV and laser pulses.

CONCLUSION

In this proceeding, we report the feasibility of building a new light source at NSRRC which delivers the VUV radiation from a 4th harmonic HHG FEL which will be seeded externally by a tunable laser. Installation of the photoinjector system including the beam diagnostics tools and the first linac section is in progress. The seed laser will be produced by adding OPA system pumped by upgrading the existing IR laser system with installing a 4-pass amplifier. We expect the energy upgrade of the laser system will start in the beginning of 2015 and the first lasing of VUV FEL will be in 2016. This FEL facility allows us to pursue a wide range of future possibilities beyond TPS, the newly constructed 3rd generation light source, and it will serve as the foundation for FEL researchers in Taiwan.

REFERENCES

- [1] N.Y. Huang, *et al.*, "Study of a THz/VUV Free Electron Laser Facility in Taiwan", in *Proc. 5th Int. Particle Accelerator Conf.*, Dresden, Germany, 2014, pp. 2980-2982.
- [2] A.P. Lee, *et al.*, "Operation of the NSRRC 2998 MHz Photo-cathode RF Gun", in *Proc. 4th Int. Particle Accelerator Conf.*, Shanghai, China, 2013, pp. 2247-2249.
- [3] L.-H. Yu, *et al.*, "High-Gain Harmonic-Generation Free-Electron Laser", *Science* **289**, 932 (2000).
- [4] D. Strickland, G. Mourou, "Compression of Amplified Chirped Optical Pulses", *Opt. Comm.* **56**, 219 (1985).
- [5] E. Allaria, *et al.*, "FERMI@Elettra: A Seeded FEL Facility for EUV and Soft X-Rays", in *Proc. 28th Int. Free-Electron Laser Conf.*, BESSY, Berlin, Germany, 2006, pp. 166-169.
- [6] M.C. Chou, *et al.*, "Operation of the Drive Laser System for the 2998 MHz NSRRC Photoinjector", in *Proc. 4th Int. Particle Accelerator Conf.*, Shanghai, China, 2013, pp. 2250-2252.
- [7] J. M. Byrd, *et al.*, "Femtosecond Synchronization of Laser Systems for the LCLS", in *Proc. 1st Int. Particle Accelerator Conf.*, Kyoto, Japan, 2010, pp. 58-60.

HIGHER-ORDER MOMENT MODELS OF LONGITUDINAL PULSE SHAPE EVOLUTION IN PHOTOINJECTORS*

C. Mitchell[†], J. Qiang, F. Sannibale, M. Venturini, C. Papadopoulos, D. Filippetto, H. Qian, R. Huang
LBNL, Berkeley, CA 94720, USA

Abstract

The presence of longitudinal asymmetry, sometimes in the form of a one-sided tail, in the current profile emerging from low-energy photoinjectors can strongly impact the beam quality downstream of the compression region of an FEL beam delivery system. To understand the origin of this feature, an approximate model for the evolution of higher-order longitudinal beam moments is developed in the presence of nonlinear kinematic effects and longitudinal space-charge. This model is applied to investigate the evolution of beam skewness in injector systems with parameters similar to the APEX Injector under investigation at Lawrence Berkeley National Laboratory.

INTRODUCTION

Careful control of the longitudinal phase space distribution of each electron bunch exiting an FEL beam delivery system is critical to optimizing the FEL radiation brightness and coherence. Previous studies have shown that, in some cases, an asymmetric tail may appear in the beam current profile out of the injector [1], limiting the portion of charge that contributes to the lasing process. To understand this feature, we attempted to develop a simple model of the longitudinal pulse shape evolution in low-energy photoinjectors using a moment description.

The utility of the second-order rms beam envelope equations [2] has led to the study of systems of such equations for higher-order beam moments [3,4]. Our approach is based on the Hamiltonian formulation of the Vlasov-Poisson equation as described in [5], which provides a systematic framework for constructing moment equations through a given order [6]. The resulting system of equations describes the longitudinal beam moments through fourth order, using a 1D wakefield model of the longitudinal space-charge interaction.

This model was applied to an LCLS-II type injector system based on the design of the Advanced Photoinjector Experiment (APEX) at Lawrence Berkeley National Laboratory [7], whose layout is shown in Fig. 1. After photoemission from a 186 MHz RF gun, each bunch passes through a 1.3 GHz buncher cavity operated near 90° off-crest, which introduces an energy-bunch length correlation. The bunch then undergoes ballistic compression in a drift before entering the first of several 9-cell 1.3 GHz TESLA accelerating cavities.

In the following section, we characterize the longitudinal pulse shape in the injector using a moment description. In

the remainder of the paper, this characterization is used to investigate the origin and evolution of longitudinal beam asymmetry in the presence of ballistic compression.

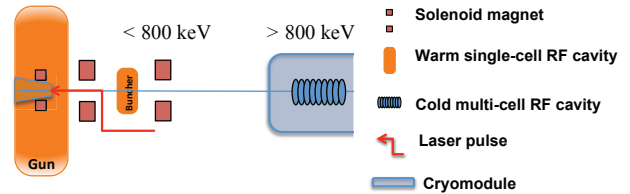


Figure 1: The low-energy portion of the photoinjector for an FEL beam delivery system based on the APEX design.

PULSE SHAPE CHARACTERIZATION

It is useful to characterize the shape of the electron bunch current profile in terms of the sequence of standardized moments:

$$\mu_n = \left\langle \left(\frac{z - \langle z \rangle}{\sigma_z} \right)^n \right\rangle, \quad n = 0, 1, 2, \dots, \quad (1)$$

where z denotes the longitudinal coordinate within the bunch and σ_z the rms bunch length. The quantities μ_3 and μ_4 define the beam skewness and kurtosis, respectively, which must satisfy the inequality [8]:

$$\mu_4 \geq \mu_3^2 + 1. \quad (2)$$

The skewness is a measure of bunch asymmetry: for a bunch with a unimodal density profile, a value $\mu_3 > 0$ denotes that a low-density tail appears for $z > \langle z \rangle$, while $\mu_3 < 0$ denotes that a low-density tail appears for $z < \langle z \rangle$. The kurtosis is often described as a measure of “peakedness”, and for a Gaussian profile takes the value $\mu_4 = 3$. Note that many authors use the excess kurtosis, defined by $\mu_4 - 3$.

An approximation to the shape of the beam current profile can be obtained by matching the centroid location, rms bunch length, and the moments (μ_3, μ_4) to a corresponding probability distribution from the Pearson family [9]- [12]. Figure 2 illustrates the current profile of a 300 pC, 99 MeV electron bunch at the exit of a proposed LCLS-II injector system based on the APEX design (Fig. 1), together with a Pearson distribution of matching skewness and kurtosis. Note the asymmetry of the current profile, with a slight tail appearing for $z < 0$.

Figure 3 illustrates the evolution of the skewness and kurtosis of this bunch during the first 3.5 m of the injector system of Fig. 1 as simulated using IMPACT-T [13]. The beam is nearly symmetric at the exit of the buncher, with

* Work supported by the U.S. Department of Energy under Contract No. DE-AC02-05CH11231.

[†] ChadMitchell@lbl.gov

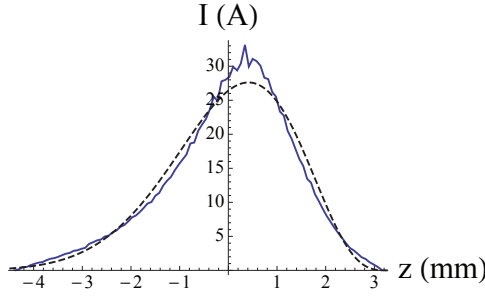


Figure 2: The simulated current profile of a 300 pC, 99 MeV bunch at the exit of a proposed LCLS-II injector (solid) is shown together with a Pearson Type I distribution (dashed) with matched $(\mu_3, \mu_4) = (-0.521, 3.132)$.

$\mu_3 = 0.06$, and the values (μ_3, μ_4) change significantly in the drift region between the buncher exit (1 m) and the pre-booster entrance (2.2 m). These values remain nearly unchanged from 10 cm beyond the pre-booster entrance through the remainder of the acceleration system. As a result, the final pulse shape appears to be set primarily by the dynamics in the ballistic compression region, which will be the focus of this paper.

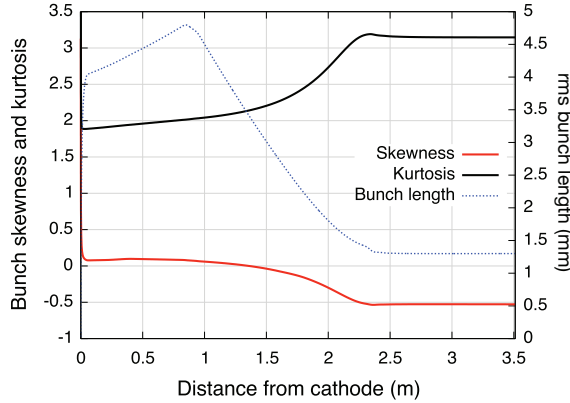


Figure 3: The skewness μ_3 , kurtosis μ_4 , and bunch length σ_z are shown as a function of bunch centroid distance from the cathode for the layout shown in Fig. 1.

NONLINEAR BALLISTIC COMPRESSION

The Hamiltonian describing longitudinal single-particle motion within a drifting beam relative to a nominal reference particle can be written in terms of the canonical variables $z = -c\Delta t$, $\delta = \Delta\gamma/\gamma$ in the form:

$$H_1(z, \delta) = -\sqrt{(1 + \delta)^2 - 1/\gamma^2} + (1 + \delta)/\beta, \quad (3)$$

where

$$\gamma = 1/\sqrt{1 - \beta^2} \quad (4)$$

denotes the nominal relativistic gamma factor, the drift distance s is taken as the independent variable, and Δt , $\Delta\gamma$ denote deviations from the nominal trajectory.

The Taylor map associated with (3) is given through terms of degree 3 by:

$$z = z_i + R_{56}\delta_i + T_{566}\delta_i^2 + U_{5666}\delta_i^3, \quad \delta = \delta_i \quad (5)$$

where

$$R_{56}(s) = \frac{s\gamma}{(\gamma^2 - 1)^{3/2}}, \quad T_{566}(s) = -\frac{3}{2} \frac{s\gamma^3}{(\gamma^2 - 1)^{5/2}},$$

$$U_{5666}(s) = \frac{1}{2} \frac{s(4\gamma^2 + 1)\gamma^3}{(\gamma^2 - 1)^{7/2}}.$$

Consider a beam with a linear relative energy chirp $h = d\delta/dz < 0$ and small uncorrelated energy spread $\sigma_\delta \ll |h\sigma_z|$ entering a drift region. Using (5), one can obtain the evolution of the standardized moments (1) as functions of the initial moments $\mu_{n,i}$ and the two dimensionless parameters:

$$\alpha = h^2 T_{566} \sigma_{z,i} C, \quad \beta = h^3 U_{5666} \sigma_{z,i}^2 C, \quad (6)$$

where $C = 1/(1 + hR_{56})$ is the linear compression factor. In the typical case when $|\beta| \ll |\alpha| \ll 1$, so that nonlinear effects are moderately weak, we find that:

$$\mu_3 = \mu_{3,i} + 3\alpha(\mu_{4,i} - \mu_{3,i}^2 - 1) + O(\alpha^2). \quad (7)$$

It follows from (7) and (2) that an initially symmetric beam (with $\mu_{3,i} = 0$) is driven toward values of increasingly negative skewness through the nonlinear effect of nonzero T_{566} .

Eliminating h in favor of the compression factor C gives an approximate expression for the final beam skewness exiting a ballistic compression region of length L in the absence of space-charge:

$$\mu_3 = \mu_{3,i} + \frac{9}{2} \frac{(C - 1)^2}{C} \left(\frac{\sigma_{z,i}}{L} \right) (1 + \mu_{3,i}^2 - \mu_{4,i}) \gamma (\gamma^2 - 1)^{1/2}. \quad (8)$$

The development of beam asymmetry in a drift is a relativistic effect that grows with increasing beam energy, as apparent in (8).

A MOMENT MODEL OF LONGITUDINAL SPACE-CHARGE

The 2D relativistic Vlasov equation for a drifting beam takes the form:

$$\frac{\partial f}{\partial s} + \frac{\partial H_1}{\partial \delta} \frac{\partial f}{\partial z} + \frac{qE_z}{mc^2\gamma} \frac{\partial f}{\partial \delta} = 0, \quad (9)$$

where E_z is the longitudinal space-charge electric field and H_1 is given in (3). Following the formalism of [14]- [15], (9) possesses the Lie-Poisson structure of a continuous Hamiltonian system with the collective Hamiltonian given by:

$$H_{\text{coll}} = \int H_1(\zeta) f(\zeta) d\zeta + \frac{1}{2} \frac{q}{mc^2\gamma} \int \phi(z) f(\zeta) d\zeta, \quad (10)$$

where $\zeta = (z, \delta)$ and the potential ϕ satisfies:

$$E_z(z) = -\frac{\partial \phi}{\partial z}. \quad (11)$$

We use a simple model of the longitudinal space-charge wakefield, given in terms of the line-charge density ρ by [16, 17]:

$$E_z(z) = -\frac{g}{4\pi\epsilon_0\gamma^2}\rho'(z), \quad \phi(z) = \frac{g}{4\pi\epsilon_0\gamma^2}\rho(z), \quad (12)$$

where g is a geometrical factor that depends on the boundary conditions. Writing

$$\rho(z) = qN_b\lambda(z), \quad \lambda(z) = \int f(z, \delta)d\delta, \quad (13)$$

where N_b is the number of particles in the bunch and λ is a probability density describing the longitudinal profile of the beam, the second term in (10) then takes the form:

$$H_{\text{int}} = \frac{g}{2} \frac{N_b r_c}{\gamma^3} \int \lambda(z)^2 dz, \quad (14)$$

where r_c is the classical electron radius.

Given any basis of polynomials $\{P_\alpha : \alpha = 1, 2, \dots, n\}$ of degree 1- N in the phase-space variables $\zeta = (z, \delta)$, we define a set of moments associated with the distribution function f by:

$$m_\alpha = \int P_\alpha(\zeta) f(\zeta) d\zeta \quad (\alpha = 1, 2, \dots, n). \quad (15)$$

If H_{coll} can be expressed as a function of the moments m_α , then the system of equations for the moments through order N takes the form [6]:

$$\frac{dm_\alpha}{ds} = \sum_{\beta=1}^n \frac{\partial H_{\text{coll}}}{\partial m_\beta} \langle \{P_\alpha, P_\beta\} \rangle, \quad (16)$$

where $\{, \}$ denotes the usual Poisson bracket.

Working through order $N = 4$, there are 14 such equations. The single-particle term in (10) is expressed as a function of the moments m_α by expanding H_1 as a Taylor series of degree 4. The interaction term H_{int} is expressed as a function of the moments by evaluating (14) when λ is taken to be the unique Pearson distribution that has the specified moments through fourth order [11]. This allows (14) to be written in the form:

$$H_{\text{int}} = \frac{g}{2} \frac{N_b r_c}{\gamma^3 \sigma_z} \tilde{H}_{\text{int}}(\mu_3, \mu_4), \quad (17)$$

where \tilde{H}_{int} is a function of the beam skewness and kurtosis only. Figure 4 shows the contours of \tilde{H}_{int} , indicating a global minimum at $(\mu_3, \mu_4) = (0, 2.14286)$, which corresponds to a parabolic current profile.

As is typical of the hierarchy of moment equations [3], the system (16) couples the desired set of moments (through order 4) to moments of higher order (through order 6). We close the system by substituting analytical expressions for the 5-6th order moments that are obtained in the absence of space-charge using the single-particle map (5). This procedure is expected to introduce significant error when the effects of space-charge are sufficiently large.

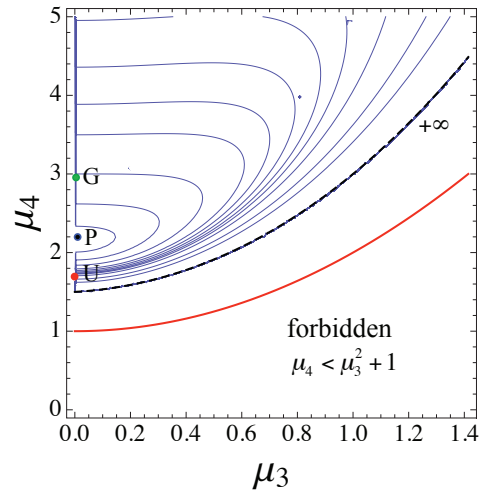


Figure 4: Contours of the space-charge interaction Hamiltonian (17) in the Pearson plane, showing the locations corresponding to Gaussian (G), parabolic (P), and uniform (U) current profiles. The quantity \tilde{H}_{int} is minimum for a parabolic profile and diverges along the solid black curve. The figure is symmetric about the line $\mu_3 = 0$.

APPLICATION

The moment model of the previous section was used together with the code IMPACT-Z to investigate the evolution of beam skewness and kurtosis in the ballistic compression region of an APEX-type photoinjector (Fig. 1). For each simulation, a bunch with an initially symmetric current profile and a linear energy chirp (at the buncher exit) was modeled during its 1.2 m drift between the buncher and the entrance of the first accelerating cavity. In order to study the beam longitudinal dynamics using IMPACT's 3D Poisson solver, only the longitudinal component of the space-charge electric field is included. In each case, the initial rms bunch length is fixed at 4.36 mm and the initial energy chirp of the beam is adjusted to produce a compression factor of 3.

Figure 5 shows the trajectory of a bunch in the plane (μ_3, μ_4) at a kinetic energy of 821 keV for several values of bunch charge. The initial longitudinal current profile is Gaussian, corresponding to $(\mu_3, \mu_4) = (0, 3)$. In the absence of space-charge, the magnitude of both the skewness and kurtosis increase along the drift, with the final skewness given correctly by (8). The effect of space-charge appears to be to drive the skewness and kurtosis values toward those of a parabolic profile, consistent with minimizing the interaction energy shown in Fig. 4.

Figure 6 shows the beam skewness at the exit of the drift as a function of the beam kinetic energy for a fixed bunch charge of 300 pC. Results are shown for a bunch with an initially Gaussian longitudinal profile and for an initially parabolic longitudinal profile. As is predicted in the absence of space-charge (8), the skewness increases with the beam energy. Note that the final skewness depends significantly on the details of the initial longitudinal profile of the beam.

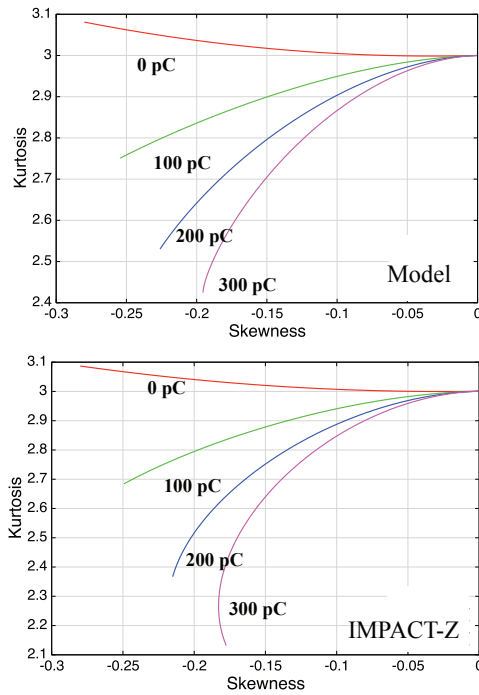


Figure 5: Beam skewness and kurtosis evolution predicted by the moment model (16) (upper) and by IMPACT-Z (lower) for an initially Gaussian 821 keV beam undergoing ballistic compression by a factor of 3 over a 1.2 m drift.

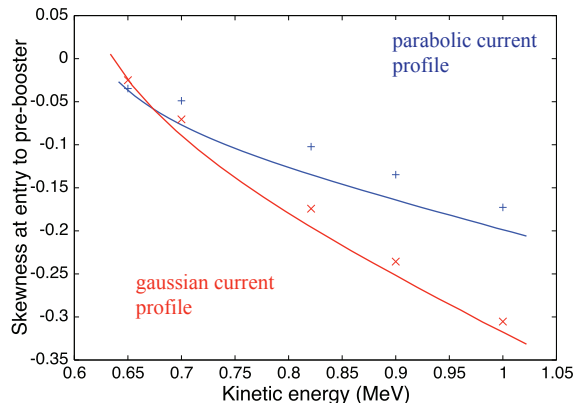


Figure 6: Final beam skewness as a function of beam energy at the exit of 1.2 m drift. Curves are results from the moment model (16), while points are taken from IMPACT-Z simulation.

CONCLUSIONS

A fourth-order moment model was developed for modeling longitudinal beam dynamics in the ballistic compression region of an FEL photoinjector, using a simple model of the longitudinal space-charge wakefield (12). The model predicts scaling of the final beam skewness with the bunch charge and beam energy that is consistent with simulation in IMPACT-Z in the presence of 1D space-charge. The transverse dynamics of the beam are not considered here. In particular, the transverse beam size appears only through the

factor g governing the strength of the space-charge wakefield, which is held fixed for these studies.

It is expected that a more accurate model could be obtained by replacing the wakefield (12) by the wakefield obtained from an appropriate longitudinal space-charge impedance [18]. Alternative schemes for closing the set of moment equations are also under consideration.

ACKNOWLEDGEMENT

This work is supported by the Office of Science of the U.S. Department of Energy under Contract No. DE-AC02-05CH11231 and made use of computer resources at the National Energy Research Scientific Computing Center.

REFERENCES

- [1] C. Papadopoulos *et al.*, “Injector Design Studies for NGLS”, FEL’13, New York, August 2013, TUPSO69 (2013), <http://www.JACoW.org>
- [2] F. J. Sacherer, IEEE Trans. Nucl. Sci. NS-18, 1105 (1971).
- [3] P. J. Channell, IEEE Trans. Nucl. Sci. NS-30, 2607 (1983).
- [4] W. P. Lysenko, AIP Conf. Proc. 297, 516 (1993).
- [5] P. J. Morrison, Phys. Lett. 80A, 383 (1980).
- [6] B. A. Shadwick and J. S. Wurtele, “General Moment Model of Beam Transport”, PAC’99, New York, March 1999, 2888 (1999), <http://www.JACoW.org>
- [7] F. Sannibale *et al.*, Phys. Rev. ST Accel. Beams 15, 103501 (2012).
- [8] V. K. Rohatgi and G. J. Székeley, Stat. and Prob. Lett. 8, 297 (1989).
- [9] K. Pearson, Phil. Trans. Royal Soc. London A 216, 429 (1916).
- [10] C. C. Craig, Annals Math. Stat. 7, 16 (1936).
- [11] A. Stuart and J. K. Ord, *Kendall’s Advanced Theory of Statistics*, vol. 1, 6th ed., (Oxford: Oxford University Press, 1994), 215.
- [12] H. Jeffreys, *Theory of Probability*, 3rd ed., (Oxford: Oxford University Press, 1961), 74.
- [13] J. Qiang, S. Lidia, and R. Ryne, Phys. Rev. ST - Accel. Beams 9, 044204 (2006).
- [14] J. E. Marsden and A. Weinstein, Physica 4D, 394 (1982).
- [15] I. Bialynicki-Birula and J. C. Hubbard, Physica 128A, 509 (1984).
- [16] M. Reiser, *Theory and Design of Charged Particle Beams*, 2nd ed., (Weinheim: Wiley-VCH, 2008), 398.
- [17] A. Chao, *Physics of Collective Instabilities in High Energy Accelerators*, (New York: John Wiley, 1993), 23.
- [18] M. Venturini, Phys. Rev. ST Accel. Beams 11, 034401 (2008).

ELECTRON BEAM DYNAMICS OPTIMIZATION USING A UNIFIED DIFFERENTIAL EVOLUTION ALGORITHM*

J. Qiang[†] and C. E. Mitchell, LBNL, Berkeley, CA 94720, USA

Abstract

Accelerator beam dynamics design depends heavily on the use of control parameter optimization to achieve the best performance. In this paper, we report on electron beam dynamics optimization of a model photoinjector using a new unified differential evolution algorithm. We present the new unified differential evolution algorithm and benchmark its performance using several test examples. We also discuss the application of the algorithm in the multi-objective optimization of the photoinjector.

INTRODUCTION

The photoinjector is a key component in the accelerator beam delivery system of next generation light sources, generating a high brightness electron beam into the accelerator. The goal of photoinjector beam dynamics design is to achieve a high peak current while maintaining low transverse emittances at the same time. This requires optimizing a number of physical control parameters such as accelerating RF cavity amplitudes and phases, focusing solenoid strengths and locations, and the initial distribution of the electron beam. In previous studies, multi-objective optimization based on genetic algorithms has been used in the photoinjector beam dynamics optimization [1–3]. In this paper, we apply a new unified differential evolution algorithm for multi-objective beam dynamics optimization.

The differential evolution algorithm is a relatively new method in evolutionary algorithms [4]. It is a simple but powerful population-based, stochastic, direct-search algorithm with self-adaptive step size to generate next-generation offspring for global optimization. In a number of comparison studies, it has been shown to be efficient in comparison to simulated annealing method, controlled random search, evolutionary programming, and genetic algorithms [4–6]. However, the standard differential evolution algorithm includes multiple strategies during the mutation stage. This could complicate the use of the algorithm. In this paper, we have adopted a unified differential algorithm recently proposed by the authors [7] in a newly developed variable population multi-objective differential evolution algorithm [8] in a photoinjector beam dynamics optimization.

STANDARD DIFFERENTIAL EVOLUTION

In the standard differential evolution algorithm, a population with size NP in control parameter space is randomly generated at the beginning. This population defines the first

generation of the control parameters. After this initialization, the differential evolution algorithm consists of three stages to produce a new generation: mutation, crossover, and selection. During the mutation stage, for each parameter vector $\vec{x}_{i,G}, i = 0, 1, 2, \dots, NP - 1$ in a population of size NP at generation G , a perturbed vector \vec{v}_i is generated using one of the following mutation strategies [4, 9]:

$$\text{DE/rand/1} : \vec{v}_i = \vec{x}_{r_1} + F_{xc}(\vec{x}_{r_2} - \vec{x}_{r_3}) \quad (1)$$

$$\text{DE/rand/2} : \vec{v}_i = \vec{x}_{r_1} + F_{xc}(\vec{x}_{r_2} - \vec{x}_{r_3}) + F_{xc}(\vec{x}_{r_4} - \vec{x}_{r_5}) \quad (2)$$

$$\text{DE/best/1} : \vec{v}_i = \vec{x}_b + F_{xc}(\vec{x}_{r_1} - \vec{x}_{r_2}) \quad (3)$$

$$\text{DE/best/2} : \vec{v}_i = \vec{x}_b + F_{xc}(\vec{x}_{r_1} - \vec{x}_{r_2}) + F_{xc}(\vec{x}_{r_3} - \vec{x}_{r_4}) \quad (4)$$

$$\text{DE/current-to-best/1} : \vec{v}_i = \vec{x}_i + F_{cr}(\vec{x}_b - \vec{x}_i) + F_{xc}(\vec{x}_{r_1} - \vec{x}_{r_2}) \quad (5)$$

$$\text{DE/current-to-best/2} : \vec{v}_i = \vec{x}_i + F_{cr}(\vec{x}_b - \vec{x}_i) + F_{xc}(\vec{x}_{r_1} - \vec{x}_{r_2}) + F_{xc}(\vec{x}_{r_3} - \vec{x}_{r_4}) \quad (6)$$

$$\text{DE/current-to-rand/1} : \vec{v}_i = \vec{x}_i + F_{cr}(\vec{x}_{r_1} - \vec{x}_i) + F_{xc}(\vec{x}_{r_2} - \vec{x}_{r_3}) \quad (7)$$

$$\text{DE/current-to-rand/2} : \vec{v}_i = \vec{x}_i + F_{cr}(\vec{x}_{r_1} - \vec{x}_i) + F_{xc}(\vec{x}_{r_2} - \vec{x}_{r_3}) + F_{xc}(\vec{x}_{r_4} - \vec{x}_{r_5}) \quad (8)$$

$$\text{DE/rand-to-best/1} : \vec{v}_i = \vec{x}_{r_1} + F_{cr}(\vec{x}_b - \vec{x}_i) + F_{xc}(\vec{x}_{r_2} - \vec{x}_{r_3}) \quad (9)$$

$$\text{DE/rand-to-best/2} : \vec{v}_i = \vec{x}_{r_1} + F_{cr}(\vec{x}_b - \vec{x}_i) + F_{xc}(\vec{x}_{r_2} - \vec{x}_{r_3}) + F_{xc}(\vec{x}_{r_4} - \vec{x}_{r_5}) \quad (10)$$

where the integers r_1, r_2, r_3, r_4 and r_5 are chosen randomly from the interval $[1, NP]$ and are different from the current index i , F_{xc} is a real scaling factor that controls the amplification of the differential variation, \vec{x}_b is the best solution among the NP population members at the generation G , and F_{cr} is a weight for the combination between the original target vector and the best parent vector or the random parent vector. In order to increase the diversity of the parameter vectors, crossover between the parameter vector $\vec{x}_{i,G}$ and the perturbed vector \vec{v}_i is introduced with an externally supplied crossover probability Cr to generate a new trial vector $U_{i,G+1}, i = 0, 1, 2, \dots, NP - 1$. For a D dimensional control parameter space, the new trial parameter vector $U_{i,G+1}, i = 0, 1, 2, \dots, NP - 1$ is generated using the following rule:

$$\vec{U}_i = (u_{i1}, u_{i2}, \dots, u_{iD}) \quad (11)$$

$$u_{ij} = \begin{cases} v_{ij}, & \text{if } \text{rand}_j \leq CR \text{ or } j = \text{mbr}_i \\ x_{ij}, & \text{otherwise} \end{cases} \quad (12)$$

where rand_j is a randomly chosen real number in the interval $[0, 1]$, and the index mbr_i is a randomly chosen in-

* Work supported by the U.S. Department of Energy under Contract No. DE-AC02-05CH11231.

[†] jqiang@lbl.gov

teger in the range $[1, D]$ to ensure that the new trial vector contains at least one parameter from the perturbed vector. During the selection stage, the new trial solution $U_{i,G+1}$ is checked against the original parent $x_{i,G}$. If the new trial solution produces a better objective function value, it will be put into the next generation $(G + 1)$ population. Otherwise, the original parent is kept in the next generation population. The above procedure is repeated for all NP parents to populate a new generation. This completes one new generation. Many generations are used to attain the final global optimal solution.

THE UNIFIED DIFFERENTIAL EVOLUTION ALGORITHM

The presence of multiple mutation strategies can complicate the use of the differential evolution algorithm. A new single mutation expression that can unify most conventional mutation strategies used by the differential evolution algorithm was proposed by the authors [7]. This single unified mutation expression can be written as:

$$\vec{v}_i = \vec{x}_i + F_1(\vec{x}_b - \vec{x}_i) + F_2(\vec{x}_{r_1} - \vec{x}_i) + F_3(\vec{x}_{r_2} - \vec{x}_{r_3}) + F_4(\vec{x}_{r_4} - \vec{x}_{r_5}) \quad (13)$$

Here, the second term on the right hand of the equation (13) denotes the contribution from the best found solution in the current generation, the third term denotes the rotationally invariant contribution from the random solution, and the fourth and fifth terms are the same terms as those used in the original differential evolution algorithm to account for the contributions from the difference of parent solutions. The four parameters F_1 , F_2 , F_3 and F_4 are the weights from each contribution. This unified mutation expression represents a combination of exploitation (from the best found solution) and exploration (from the random solutions) to generate a new mutant solution.

From the above equation, one can see that for $F_1 = 0$, $F_2 = 1$, and $F_4 = 0$, this equation reduces to DE/rand/1; for $F_1 = 0$, $F_2 = 1$, and $F_3 = F_4$, it reduces to DE/rand/2; for $F_1 = 1$, $F_2 = 0$, and $F_4 = 0$, it reduces to DE/best/1; for $F_1 = 1$, $F_2 = 0$, and $F_3 = F_4$, it reduces to DE/best/2; for $F_2 = 0$ and $F_4 = 0$, it reduces to DE/current-to-best/1; for $F_2 = 0$ and $F_3 = F_4$, it reduces to DE/current-to-best/2; for $F_1 = 0$, and $F_4 = 0$, it reduces to DE/current-to-rand/1; for $F_1 = 0$, and $F_3 = F_4$, it reduces to DE/current-to-rand/2; for $F_2 = 1$, and $F_4 = 0$, it reduces to DE/rand-to-best/1; for $F_2 = 1$, and $F_3 = F_4$, it reduces to DE/rand-to-best/2. Using the single equation (13), ten mutation strategies in the standard differential evolution algorithm can be written as a single mutation expression. Meanwhile, this new expression provides an opportunity to explore more broadly the space of mutation operators. By using a different set of parameters F_1, F_2, F_3, F_4 , a new mutation strategy can be achieved. For example, from our experience, we found that using $F_1 = 0.25$, $F_2 = 0.25$, $F_3 = 0.2$, $F_4 = 0.2$, and $CR = 0.8$ in the uDE can give better performance in some test studies than the conventional mutation strategy [4, 9]

(shown in the following section). If these parameters can be adaptively adjusted during the optimization evolution, then multiple mutation strategies and their combinations can be used during different stages of optimization. Thus, the unified mutation expression has the virtue of mathematical simplicity and also provides the user with flexibility for broader exploration of different mutation strategies.

BENCHMARK EXAMPLES

One of the exploratory unified differential evolution algorithms (uDE) ($F_1 = 0.25, F_2 = 0.25, F_3 = 0.2, F_4 = 0.2, CR = 0.8$) is tested with several numerical test functions together with the conventional differential evolution algorithm. These test functions are [10, 11]:

- (1) Sphere function

$$F_{\text{sph}}(\vec{x}) = \sum_{i=1}^N x_i^2; \quad -100 \leq x_i \leq 100;$$

- (2) Schwefel's problem 1.2

$$F_{\text{sch2}}(\vec{x}) = \sum_{j=1}^N \left(\sum_{i=1}^j x_i \right)^2; \quad -100 \leq x_i \leq 100;$$

- (3) Quartic function with noise

$$F_{\text{qrt}}(\vec{x}) = \sum_{i=1}^N i x_i^4 + \text{rand}[0, 1]; \quad -1.28 \leq x_i \leq 1.28;$$

- (4) Ackley's function

$$F_{\text{ack}}(\vec{x}) = 20 + \exp(1) - 20 \exp \left(-0.2 \sqrt{\frac{1}{N} \sum_{i=1}^N x_i^2} \right) - \exp \left(\frac{1}{N} \sum_{i=1}^N \cos(2\pi x_i) \right); \quad -32 \leq x_i \leq 32;$$

The sphere function is a continuous, unimodal and separable function. The Schwefel's problem 1.2 is a non-separable unimodal function. The noisy quartic function is a unimodal function with random noise in the objective value. The Ackley's function is a multimodal non-separable problem and has many local minima and a narrow global minimum.

In Figs. 1-4, we show the evolution of the error relative to the true global minimum objective function value of these test functions for the algorithms with dimension $N = 50$. At each generation, the objective function value has been averaged over 25 random seeds. It is seen that the unified differential algorithm performs quite well in these test examples quickly converging to the true minimum.

A PHOTOINJECTOR BEAM DYNAMICS OPTIMIZATION

We applied the above exploratory unified differential evolution algorithm together with a particle-in-cell code [12]

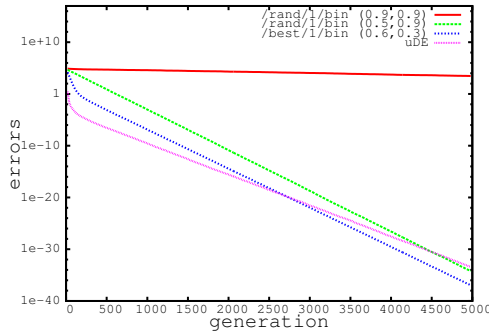


Figure 1: Evolution of the average error in the test sphere function.

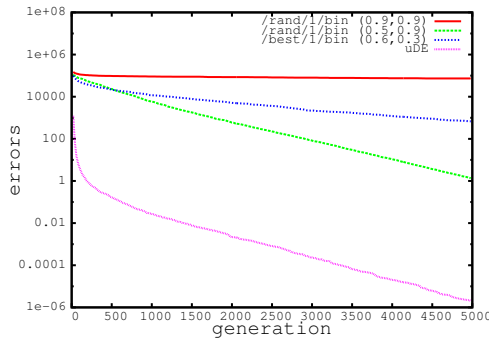


Figure 2: Evolution of the average error in the test Schwefel's problem 1.2 function.

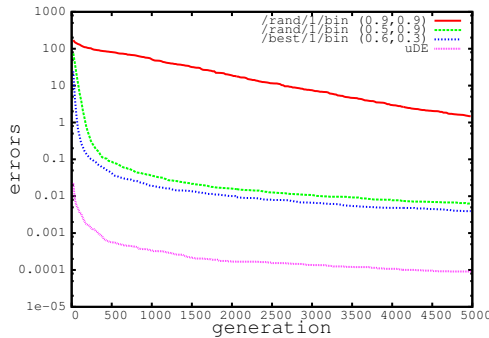


Figure 3: Evolution of the average error in the noisy quartic function.

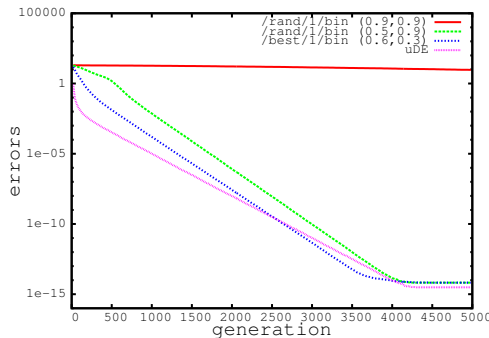


Figure 4: Evolution of the average error in the Ackley function.

in a photoinjector beam dynamics optimization. This unified differential algorithm was implemented in the recently developed multi-objective differential evolution algorithm based on the variable population and external storage for beam dynamics optimization [8]. A schematic plot of the photoinjector is shown in Fig. 5. It consists of a 187 MHz

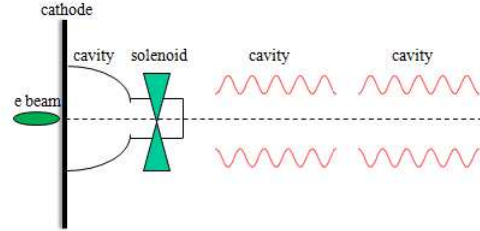


Figure 5: A schematic plot of a photoinjector for multi-objective optimization application.

RF gun [13, 14], a solenoid, and two 1.3 GHz boosting cavities. The objective functions to be optimized are the transverse rms emittances and the longitudinal rms bunch length that is directly related to the peak current of the beam. There are 9 control parameters that are used in the optimization. Those are the initial electron beam transverse size and bunch length, strength of the solenoid field, starting location of the boosting RF cavity, and amplitudes and phases of the two RF cavities. The maximum amplitude of the RF field inside the gun is set as about 38 MV/m. The charge for the electron beam is 300 pC. Some optimal solutions of the rms bunch length and the transverse emittance are shown in Fig. 6. There is a sharp change of the rms bunch length around rms emittance 1.4 mm-mrad. This sharp reduction of the rms bunch length is due to the over compression of the electron beam longitudinally. In the photoinjector design, one normally tries to keep the final transverse emittance below 1 mm-mrad. Here, we choose a working point with transverse emittance around 0.9 mm-mrad. Figure 7 shows the rms projected emittance evolution inside the injector. At the end of the second boosting RF cavity, the transverse rms emittance reaches 0.9 mm-mrad, but still decreases. The kinetic energy of the beam at the exit of the second cavity is about 13 MeV with a final peak current of 20 A.

SUMMARY AND DISCUSSION

In this paper, we used a new unified differential evolution algorithm in the multi-objective photoinjector beam dynamics optimization. The unified differential evolution algorithm has the virtue of mathematical simplicity and the capability to explore a broader mutation strategy space. Using a new exploratory mutation strategy, we have done beam dynamics optimization for a photoinjector consisting of a low RF frequency gun, a solenoid and two boosting cavity. Our preliminary optimization results suggest that below 1 μm transverse emittance is achievable out of this injector. More detailed study is needed to understand the space-charge

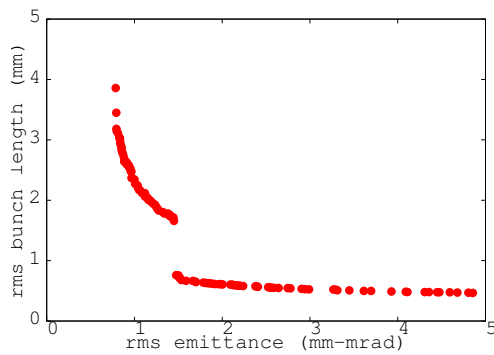


Figure 6: Optimal rms bunch length and transverse emittance solutions of the photoinjector beam dynamics optimization.

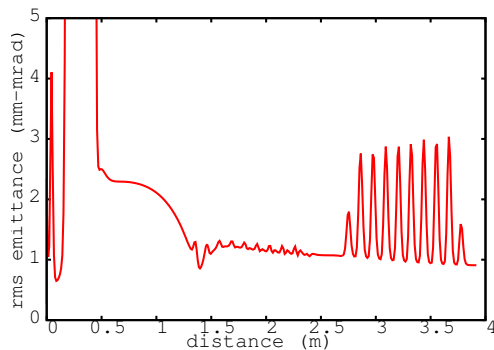


Figure 7: Transverse rms projected emittance evolution inside the photoinjector.

emittance compensation, the jump in the Pareto front, and the extension to include more RF accelerating cavities.

ACKNOWLEDGEMENT

This research used computer resources at the National Energy Research Scientific Computing Center and at the National Center for Computational Sciences.

REFERENCES

- [1] I.V. Bazarov and C.K. Sinclair, Phys. Rev. ST Accel. Beams 8, 034202 (2005).
- [2] C. E. Papadopoulos et al., in *Proc. 35th Int. Free Electron Laser Conf.*, Malmö, Sweden, 2010, p. 479.
- [3] A. Hofler et al., Phys. Rev. ST Accel. Beams 16, 010101 (2013).
- [4] R. Storn and K. Price, Journal of Global Optimization 1a1:341-359, (1997).
- [5] K. Price, R. Storn, and J. Lampinen, Differential Evolution - A Practical Approach to Global Optimization, Springer, Berlin, 2005.
- [6] M. M. Ali and A. Torn, Computers and Operations Research, Elsevier, no. 31, p. 1703, 2004.
- [7] J. Qiang and C. Mitchell, "A Unified Differential Evolution Algorithm for Global Optimization," LBNL-6703E, 2014.
- [8] J. Qiang et al., in *Proc. 4th Int. Particle Accelerator Conf.*, Shanghai, China, 2013, p. 1031.

- [9] F. Neri and V. Tirronen, Artif. Intell. Rev. 33, p. 61, 2010.
- [10] J. Brest et al., IEEE Transactions on Evolutionary Computation, vol. 10, no. 6, pp. 646-657, 2006.
- [11] J. Zhang and A. C. Sanderson, IEEE Transactions on Evolutionary Computation, vol. 13, no. 5, pp. 945-958, 2009.
- [12] J. Qiang et al., Phys. Rev. ST Accel. Beams 9, 044204 (2006).
- [13] K. Baptiste et al., Nucl. Instrum. Methods Phys. Res., Sect. A 599.
- [14] F. Sannibale et al., Phys. Rev. ST Accel. Beams 15, 103501 (2012).

THEORETICAL INVESTIGATION OF COHERENT SYNCHROTRON RADIATION INDUCED MICROBUNCHING INSTABILITY IN TRANSPORT AND RECIRCULATION ARCS*

C. -Y. Tsai[#], Department of Physics, Virginia Tech, Blacksburg, VA 24061, USA
D. Douglas, R. Li, and C. Tennant, Jefferson Lab, Newport News, VA 23606, USA

Abstract

The coherent synchrotron radiation (CSR) of a high brightness electron beam traversing a series of dipoles, such as recirculation or transport arcs, may lead to the microbunching instability. We extend and develop a semi-analytical approach of the CSR-induced microbunching instability for a general lattice, based on the previous formulation with 1-D CSR model [1] and apply it to investigate the physical processes of microbunching amplification for two example transport arc lattices. We find that the microbunching instability in transport arcs has a distinguishing feature of multistage amplification (e.g. up to 6th stage for our example arcs in contrast to two stage amplification for a 3-dipole chicane [2]). By further extending the concept of stage gain as proposed by Huang and Kim [2], we developed a method to quantitatively characterize the microbunching amplification in terms of iterative or staged orders that allows the comparison of optics impacts on microbunching gain for different lattices. The parametric dependencies and Landau damping for our example lattices are also studied. Excellent agreement of the gain functions and spectra from Vlasov analysis with results from ELEGANT is achieved which helps to validate our analyses.

INTRODUCTION

As is well known, CSR effects have been one of the most challenging issues associated with the design of magnetic bunch compressor chicanes for X-ray FELs and linear colliders. Typically, CSR is emitted not only for a wavelength range comparable or longer than the bunch length duration but also for shorter wavelengths if the bunch charge density is modulated at such wavelength range (so called microbunching). Such coherent radiation effects, which have been confirmed both in numerical simulation and experiments, can result in undesirable beam quality degradation. The aforementioned works were, however, mostly focused on studies of magnetic bunch compressor chicanes. Recently the superconducting radio frequency recirculation linac facilities (e.g., free-electron laser facility or electron cooler for collider machine) have been brought to attention [3-5]. The recirculation or transport arcs are necessary elements in such facilities. However, similar studies on such systems with multiple modular dipoles as in a transport or recirculation arc were mostly focused on transverse beam dynamics while longitudinal phase space

degradation has very limited discussions. In this paper, we pay attention to the CSR effects on the longitudinal beam dynamics as beam traversing around the recirculation arcs, particularly on the CSR-induced microbunching issues. The reasons to be concerned about the microbunching instability are based on the two facts: first, such system is characteristic of long transport lines with many dipole magnets whether in a single or multiple pass operation; the other, the system typically delivers the beam which features high beam quality, i.e. high brightness, for the use in next-generation light sources or hadron cooling in high-energy electron recirculating cooling rings. Thus, the seeds that cause density modulation, derived from either the density ripples from upstream injector or longitudinal space charge especially for low energy beam, would be extremely possible to lead to microbunching instability. Therefore further investigation of CSR-induced microbunching effects and its detailed physical processes are of critical importance and may shed light on how to improve designs for future lattices.

METHODS

The CSR-induced microbunching instability can be formulated with the linearized Vlasov equation in typical bunch compressors [1]. This model makes coasting-beam approximation and assumes steady-state 1-D CSR [6] with negligible shielding (boundary) effects. By the method of characteristics, the linearized Vlasov equation can be rewritten as the general form of Volterra integral equation below [1]:

$$g_k(s) = g_k^{(0)}(s) + \int_0^s K(s, s') g_k(s') ds' \quad (1)$$

$$K(s, s') = \frac{ikr_e n_b}{\gamma} C(s) C(s') R_{s_6}(s' \rightarrow s) Z(kC(s'), s') \\ \times [\text{Landau damping}]$$

where the [Landau damping] term can be expressed as

$$\exp \left\{ \frac{-k^2}{2} \left[\frac{\epsilon_{x0} \left(\beta_{x0} R_{s1}^2(s, s') + \frac{R_{s2}^2(s, s')}{\beta_{x0}} \right)}{\sigma_s^2 R_{s6}^2(s, s')} \right] \right\} \quad (2)$$

Here the kernel function $K(s, s')$ describes the CSR interaction, $g_k(s)$ the resultant bunching factor as a function of the longitudinal position given the wavenumber k , and $g_k^{(0)}(s)$ is the bunching factor without CSR.

* Authored by Jefferson Science Associates, LLC under U.S. DOE Contract No. DE-AC05-06OR23177.

[#] jcysai@vt.edu

In this work, we have extended the formulation to a general transport line by input of the transport functions of a lattice from a common particle tracking code, e.g. ELEGANT [7] and developed a program to solve Eq. (1) self-consistently or Eq. (3) (below) iteratively [8]. For the latter approach, we adapt, motivated by [2], the above integral equation (Eq. (1)) by iteratively finding the staged solutions. The advantage of using this method is to facilitate us exploring up to which stage the overall CSR process can be described, by direct comparison with the self-consistent solutions. The staged iterative solution for n -th order can be defined as

$$\mathbf{g}_k^{(n)} = \left(\sum_{m=0}^n \mathbf{K}^m \right) \mathbf{g}_k^{(0)} \quad (3)$$

where we have already expressed the bunching factors in vector form for discrete s values and the kernel $K(s, s')$ in matrix form, denoted as \mathbf{K} . It can be easily shown that Eq. (1) and Eq. (3) are equivalent, i.e. $g_k(s)$ is a component of $\mathbf{g}_k^{(n)}$ at some specific location when $n \rightarrow \infty$ provided the sum converges. With a given wavenumber k , the CSR-induced microbunching gain is then defined, based on Eq. (1), as $G(s) = |g_k(s)/g_k^{(0)}(0)|$. Note that g_k is in general a complex quantity, or a phasor in complex domain. Setting $\tilde{G}^{(n)}(s) = \mathbf{g}_k^{(n)}(s)/\mathbf{g}_k^{(0)}(0)$, we define the stage gain as the amplitude of the phasor $\tilde{G}^{(n)}(s)$, i.e. $G^{(n)}(s) = |\tilde{G}^{(n)}(s)|$.

To compare the CSR gains contributed from individual stages, we further define the final stage gain phasor up to a certain order M as

$$\tilde{G}_f^{(M)} = \tilde{G}^{(M)}(s = s_f) = \tilde{G}_0 + \tilde{G}_1 I_b + \dots + \tilde{G}_M I_b^M = \sum_{m=0}^M \tilde{G}_m I_b^m$$

In order to extract the net effect caused by lattice optics, the above expression can be further formulated as

$$\tilde{G}_f^{(M)} = \sum_{m=0}^M A^m d_m^{(\lambda)} \left(\frac{I_b}{\gamma} \right)^m \quad (4)$$

where $A = -0.94 + 1.63i$, I_b the beam current, γ the relativistic factor of beam energy, and $d_m^{(\lambda)}$ (given some modulation wavelength $\lambda = 2\pi/k$) now reflects the effects from lattice optics at m -th stage and Landau damping through beam emittance and energy spread. Again we remind the connection between Eq. (3) and Eq. (4) $G_f^{(M)} = |\tilde{G}_f^{(M)}| = G^{(M)}(s = s_f)$. As mentioned, we implement the above semi-analytical methods (self-consistent and iterative approach) by input of the transport functions from ELEGANT [7], and then solve Eq. (1) and/or Eq. (3) for the gain function $G(s)$ or gain spectrum $G_f(\lambda)$.

SIMULATION RESULTS

CSR Microbunching Gain Analysis

To demonstrate how our new methods can be used to calculate of microbunching gain spectrum for general arc lattices, we take two 180° transport arc lattices as our study examples. For the detailed description of the two

example lattices, we refer the interested reader to [9]. The first example lattice, a 1.3 GeV recirculation arc with large momentum compaction function (Example 1), is a second order achromat and globally isochronous with a large dispersion modulation across the entire arc. This allows an assessment of the impact of large momentum compaction oscillation, large dispersion, and the absence of multiple periodic isochronicity on CSR microbunching gain. In contrast to the first example, the second example, a 1.3 GeV recirculation arc with small momentum compaction function (Example 2), is also a second order achromat but designed to be a locally isochronous lattice within superperiods which insure that the bunch length is the same at phase homologous CSR emission sites. The small dispersion and its slope result not only in a small momentum compaction in each superperiod but the modulation of the momentum compaction through the system is also small; thus potentially providing some limitation on CSR gain.

Table 1: Initial Beam and Twiss Parameters for the Two Example Arc Lattices

Name	Example 1 (large R_{56})	Example 2 (small R_{56})	Unit
Beam energy	1.3	1.3	GeV
Bunch current	65.5	65.5	A
Normalized emittance	0.3	0.3	μm
Initial beta function	35.81	65.0	m
Initial alpha function	0	0	
Energy spread (uncorrelated)	1.23×10^{-5}	1.23×10^{-5}	

Table 1 summarizes the initial beam and Twiss parameters of the two high-energy recirculation arcs based on [9]. The CSR-induced microbunching gains for the two recirculation arcs are shown in Figs. 1 and 2. The two upper figures demonstrate the evolution of the self-consistent gain as a function of s for three different modulation wavelengths. One can see in Fig. 1 the shorter wavelengths enhance the Landau damping through Eq. (2) while longer wavelengths feature negligible CSR effect [6]. The two bottom figures show the gain spectra $G_f(\lambda)$ at the exits of the lattices as a function of modulation wavelength, from which one can obviously see the difference between them: Example 1 is vulnerable to CSR effect while Example 2 is not. To validate our semi-analytical approach, we also simulate the two example lattices by ELEGANT [7]. Extensive convergence studies were performed for ELEGANT tracking [10], and the gain spectra from ELEGANT show good agreement with our semi-analytical results (see Figs. 1 and 2). Because of very high gain for Example 1 lattice,

we notice that ELEGANT simulations encounter a big challenge for microbunching gain calculation based on particle tracking algorithm, so special cares are required [10]. From the iterative approach in Eq. (3), we also find an interesting feature of microbunching in the two example arcs: in contrast to the 2-stage amplification exhibited in a conventional bunch compressor chicane [2], the CSR-induced microbunching gain in the recirculating arcs (each consisting of 24 dipoles) requires up to 6th stage amplification, as shown in bottom figures of Figs. 1 and 2.

To further examine the feature of multistage CSR gain for such systems, we extract the coefficients $d_m^{(\lambda)}$ (here λ is chosen that corresponds to the maximal gain; for Example 1 and 2 lattices, $\lambda_{opt} = 36.82$ and $19 \mu\text{m}$, respectively) in Eq. (4) by fitting each staged solutions obtained from Eq. (3) so that we can quantify and compare the individual stage gains with inclusion of lattice optics effects and beam parameters ε_{x0} and σ_δ associated with Landau damping. Figure 3 shows the bar charts representing the final gains as functions of beam current and stage index for both arcs. Since $d_m^{(\lambda)}$ are independent of beam current and energy, they can be used to obtain a current scaling law of CSR gain for each given wavelength. Figure 4 compares the final overall gain from Eq. (4) and Eq. (1) for different currents in the case of Example 1 lattice, at a selected wavelength that is in the vicinity of optimal wavelength for maximal gain.

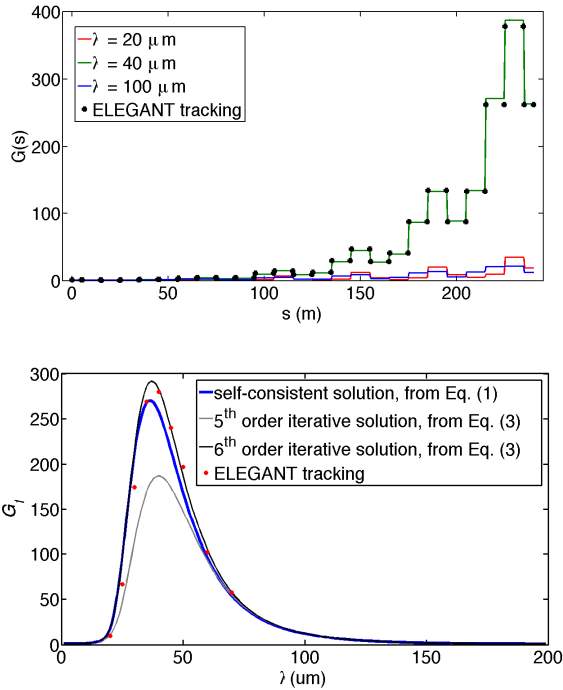


Figure 1: (top) CSR gain functions $G(s)$, where dots are for $\lambda = 40 \mu\text{m}$; (bottom) gain spectrum $G_f(\lambda)$ as a function of initial modulation wavelength for Example 1 lattice.

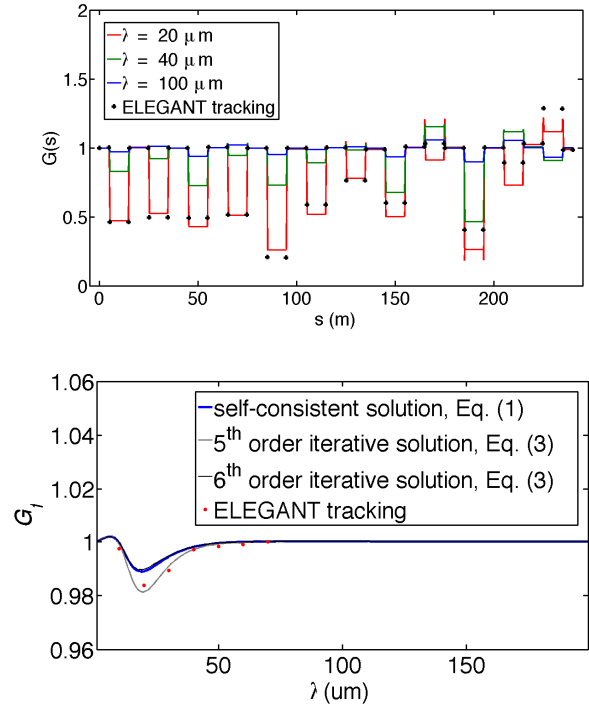


Figure 2: (top) CSR gain functions $G(s)$, where dots are for $\lambda = 20 \mu\text{m}$; (bottom) gain spectrum $G_f(\lambda)$ as a function of initial modulation wavelength for Example 2 lattice.

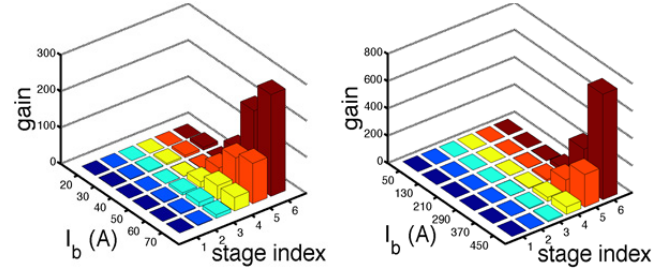


Figure 3: Bar chart representation of staged gains (at the exit of lattice) for several different beam currents for the two example arcs, (left) Example 1 lattice; (right) Example 2 lattice, where for Example 1 and 2 lattices, $\lambda_{opt} = 36.82$ and $19 \mu\text{m}$, respectively. Note the current scale (I_b) and vertical scale are different.

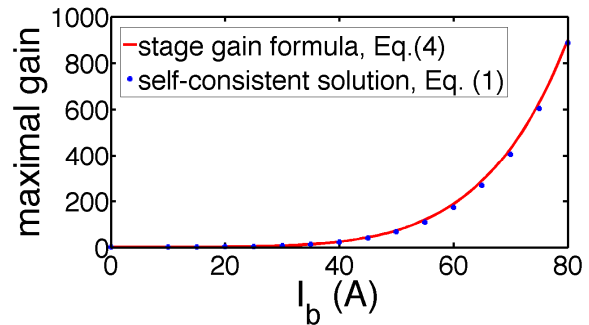


Figure 4: The current dependence of maximal CSR gain for the Example 1 lattice. Solid red line from Eq. (4) with $M = 6$, and blue dots from Eq. (1).

Parametric Dependencies and Landau Damping

For a gain spectral curve, we are most interested in the maximal gain and the corresponding optimum wavelength. Figure 5 shows the parametric dependencies of maximal gains and optimum wavelengths as functions of energy spread (for zero beam emittance) and beam emittance (for zero beam energy spread) for Example 1 lattice. We can see that both larger energy spread and beam emittance result in more Landau damping and the optimum wavelength drifts toward longer wavelengths to compensate the overall damping. It is also found in the two top figures the optimum wavelengths scale linearly and radically for beam energy spread and emittance, respectively. In the two bottom figures the maximal gains behave proportionally to σ_δ^{-8} and ε_{x0}^{-4} .

After carefully examining the parametric dependencies for Example 2 lattice and combining the results of the two lattices [8], we find the behaviour of optimum wavelength λ_{opt} features a linear relationship to beam energy spread σ_δ (for zero beam emittance) as

$$\lambda_{opt} \propto \sigma_\delta \quad (5)$$

Here we note that Ref. [11] gives a linear expression on how the optimum wavelength relates to beam energy spread assuming 2-stage amplification in a typical bunch compressor for zero-emittance beam. Although our example lattices feature 6th stage amplification, the optimum wavelength is also characteristic of linear relation to beam energy spread (Eq. (5)). Whether such observations reflect the general behaviour for multistage amplification and/or arbitrary lattice is still a question for further investigation. Similarly, we obtain a relation for the dependence of the optimum wavelength on beam emittance (for zero energy spread beam) as

$$\lambda_{opt} \propto \sqrt{\varepsilon_{x0}} \quad (6)$$

Furthermore, we simulate and analyse several lattices with varying amplification stages [8] and find the maximal gain can be scaled in the case of zero beam emittance at M -th stage as,

$$G_{f,max} \propto \frac{1}{\sigma_\delta^{(4/3)M}} \quad (7)$$

and in the case of zero energy spread at M -th stage as,

$$G_{f,max} \propto \frac{1}{\varepsilon_{x0}^{(2/3)M}} \quad (8)$$

For the two Example lattices, $M \approx 6$. The observation of such scaling (Eq. (5) and Eq. (6)) also corresponds well to the gain behaviour in a typical bunch compressor chicane featuring two-stage amplification ($M = 2$) [10].

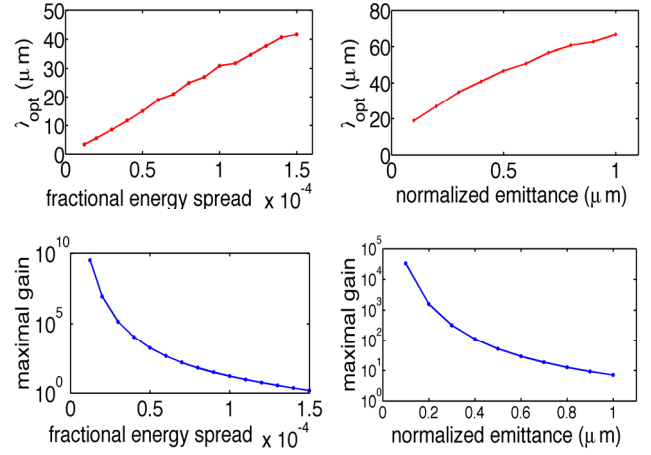


Figure 5: Optimum wavelengths (upper) and maximal CSR gains (lower) as functions of beam energy spread with zero emittance and finite beam emittance with vanishing energy spread for Example 1 lattice.

To further illustrate how the multi-stage amplification contributes to and how the lattice optics impacts on the microbunching development, we create in Fig. 6 the “quilt” patterns of $R_{s6}(s' \rightarrow s)$ (shown in the kernel of Eq. (1)) behaviour for the two example lattices in order to clearly identify the enhancement or suppression of microbunching along the beamline by lattice optics. For a planar and uncoupled lattice, the term $R_{s6}(s' \rightarrow s) = R_{s6}(s) - R_{s6}(s') + R_{s1}(s')R_{s2}(s) - R_{s1}(s)R_{s2}(s')$. The upper left area in the figures has vanishing value due to causality. It is obvious that in the left figure the block areas with large amplitude of $R_{s6}(s' \rightarrow s)$, particularly the bottom right deep red blocks, exist and can accumulate the CSR gain. To be specific, for Example 1 lattice (left figure), energy modulation at $s' \approx 15$ m will cause density modulation at $s \approx 60$ m, that causes CSR-induced energy modulation at this location. Then such modulation propagate by $R_{s6}(s' \rightarrow s)$ from $s' \approx 60$ m to $s \approx 100$ m, and so on. It is this situation that causes multi-stage CSR amplification. Here we note that more complete analysis needs to take Landau damping factor into account (Eq. (2)) [8]. In contrast, the situation in the right figure for Example 2 lattice is more alleviated because of the smaller amplitudes of $R_{s6}(s' \rightarrow s)$.

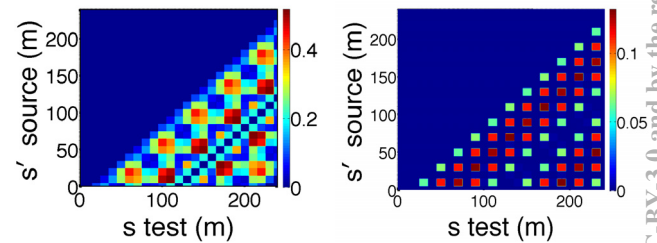


Figure 6: $R_{s6}(s' \rightarrow s)$ “quilt” patterns for the two Example lattice arcs: Example 1 (left) and Example 2 (right).

SUMMARY

In this paper we extended previous work [1, 2] to study the CSR-induced microbunching gain in transport and recirculation arcs, by finding both the self-consistent [Eq. (1)] and iterative [Eq. (3)] solutions. Different from that of typical bunch compressor chicane, CSR gain is characteristic of multistage amplifications, e.g. up to 6-th stage in our two example lattices (Figs. 1 and 2). Then we quantified and compared the CSR gains contributed from individual stages for the two lattices with exclusion of beam current and energy dependence (Fig. 3) and demonstrate a current scaling law for close-to-maximum CSR gains for a fixed wavelength in the vicinity of optimal one (Fig. 4).

The parametric dependencies of optimum wavelength and maximal gain on beam energy spread and beam emittance are summarized in Eq. (5-8) from our semi-analytical simulations for Example 1 lattice. We also note that whether such semi-analytical observations reflect the general behavior for multistage amplification and/or arbitrary lattice is still a question for further investigation.

We finally presented in Fig. 6 the $R_{s_6}(s' \rightarrow s)$ impact on the overall CSR gain for both example lattices and found that for Example 1 lattice there exist several cumulated large-amplitude areas so that the gain eventually builds up (i.e. multi-stage amplification) while for Example 2 this situation is well controlled at the same range of beam current scale. As shown in Fig. 3, with the same current range, Example 1 can reach much larger gain than Example 2. This demonstrates the impact of lattice design on the control of microbunching.

ACKNOWLEDGMENT

This work is supported by Jefferson Science Associates, LLC under U.S. DOE Contract No. DE-AC05-06OR23177.

REFERENCES

- [1] S. Heifets *et al.*, Coherent synchrotron radiation instability in a bunch compressor, Phys. Rev. ST Accel. Beams **5**, 064401 (2002)
- [2] Z. Huang and K. -J. Kim, Formulas for coherent synchrotron radiation microbunching in a bunch compressor chicane, Phys. Rev. ST Accel. Beams **5**, 074401 (2002)
- [3] R. C. York, 5 upgradable to 25 keV free electron laser facility, Phys. Rev. ST Accel. Beams **17**, 010705 (2014)
- [4] Y. Zhang and J. Bisognano Eds., Scientific requirements and conceptual design for a polarized medium energy electron-ion collider at Jefferson Lab, arXiv: 1209.0757v2 [physics.acc-ph]
- [5] P. Piot *et al.*, Longitudinal phase space manipulation in energy recovery linac-driven free-electron lasers, Phys. Rev. ST Accel. Beams **6**, 030702 (2003)
- [6] Ya. S. Derbenev *et al.*, Microbunch radiative tail-head interaction, TESLA-FEL-Report 1995-05
- [7] M. Borland, elegant: A Flexible SDDS-Compliant Code for Accelerator Simulation, Advanced Photon Source LS-287 (2000)
- [8] C. -Y. Tsai *et al.*, to be published
- [9] D. R. Douglas *et al.*, Control of coherent synchrotron radiation and microbunching effects during transport of high brightness electron beams, arXiv: 1403.2318v1 [physics.acc-ph]
- [10] C.-Y. Tsai and R. Li, Simulation of coherent synchrotron radiation induced microbunching gain using ELEGANT, JLAB-TN-14-016
- [11] E. L. Saldin *et al.*, Klystron instability of a relativistic electron beam in a bunch compressor, Nucl. Instrum. Methods Phys. Res. Sect. A **490**, 1 (2002)

SIMULATION OF ALPHA MAGNET ELEMENTS IN DIPOLE-ONLY TRACKING CODES^{*,†}

J.W. Lewellen[#] and F. Krawczyk, AOT-AE, LANL, Los Alamos, NM 87544 USA

Abstract

Alpha magnets [1] are useful in a variety of ion-beam and low-energy (< 5 MeV) electron-beam transport systems as both “switchyard” elements and as bunch compressors [2,3]. A unique feature of the alpha-magnet is its broad-band achromatic transport. Particles of different energies, injected at a specific location and angle, will exit at the same location and (symmetry-reflected) angle but with a different time-of-flight.

Despite the general usefulness of alpha magnets in low-energy beam transport and compression schemes, few simulation codes support them as native elements. The (arguably) most-commonly-used codes used for injector design, PARMELA [4], ASTRA [5] and GPT [6] (listed in order of their release) support tracking of space-charge-dominated beams through dipole magnets, but do not support alpha magnets. As a result, these codes are unable to directly model a useful and interesting beam transport device.

We present an approximate method for simulating an alpha magnet in a tracking code using dipole elements. As the simulation code **elegant** [7] supports alpha magnets as well as multiple dipole models, it is used to provide a basic check of the approximation and a means of estimating the induced errors.

INTRODUCTION

Alpha magnets refer to a general class of achromatic bending magnets [1]. They are so-named because a particle beam traversing a properly aligned alpha magnet follows a trajectory reminiscent of the Greek letter α as shown in Figure 1. While alpha magnets in general can have a field dependence $B_z \sim G x^n$, $n \geq 1$, quadrupolar alpha magnets ($n=1$) are the most practical to construct. Unless explicitly stated otherwise, the rest of this paper refers only to quadrupolar alpha magnets.

Figure 1 illustrates the achromatic nature of the alpha magnet: over a $\pm 20\%$ energy spread, electrons injected at the proper angle exit at the same point and angle; the trajectories are self-similar but have different overall length, facilitating the alpha magnet’s use as a bunch compressor or stretcher, depending upon the chirp of the incoming beam. All particles cross the midplane, or $x=0$, line three times: at injection, at their maximum depth Δy within the alpha magnet, and at exit.

Using Borland’s notation [8], the included half-angle of the alpha magnet θ_α is 40.71° . The general scaling factor for particle trajectories in an alpha magnet is

$$\alpha^2 = 5.867 \cdot 10^{-4} \text{ cm}^{-2} \frac{g[\text{G/cm}]}{\beta\gamma}, \quad (1)$$

where g is the magnetic field gradient in Gauss cm^{-1} , γ is the particle’s Lorentz factor, β is the particle’s normalized velocity, and the product $\beta\gamma$ is the normalized momentum. The total path length of the particle’s trajectory is

$$s_\alpha = \frac{\Lambda_\alpha}{\alpha} = 191.655 \text{ cm} \cdot \sqrt{\frac{\beta\gamma}{g[\text{G/cm}]}} \quad (2)$$

the maximum depth the particle reaches is

$$\Delta y = \frac{\Delta Q_1}{\alpha} = 75.0513 \text{ cm} \cdot \sqrt{\frac{\beta\gamma}{g[\text{G/cm}]}} \quad (3)$$

and the trajectory width is

$$\Delta x = \frac{\Delta Q_2}{\alpha} = 49.212 \text{ cm} \cdot \sqrt{\frac{\beta\gamma}{g[\text{G/cm}]}} \quad (4)$$

$\Lambda_\alpha=4.642$, $\Delta Q_1 = 1.818$ and $\Delta Q_2 = 1.192$ are the normalized path length, path depth and path width, respectively, and along with θ_α are invariants for quadrupole-type alpha magnets.

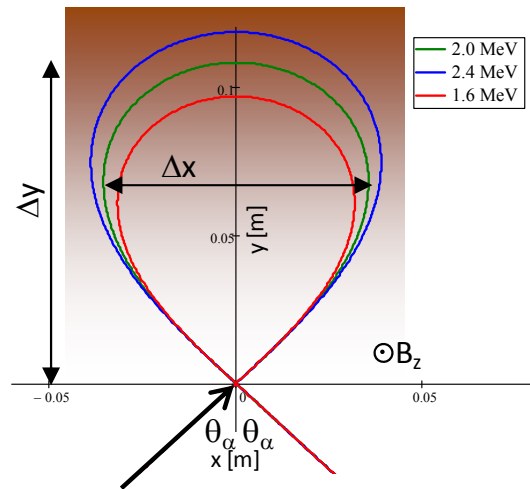


Figure 1: Three electron beam trajectories in an ideal quadrupolar alpha magnet: 2 MeV (green), 2.4 MeV (blue) and 1.6 MeV (red), all injected at the ideal injection angle along the line indicated by the black arrow. Background shading indicates relative magnetic field strength. The magnetic field gradient is 2.32 T/m.

The trajectory is self-similar for all choices of gradient and momentum, providing broadband achromaticity. For a fixed magnetic field gradient g and small variations of normalized momentum $\beta\gamma$ around a central value, the path

* Work supported by the Los Alamos Accelerator Code Group

† Approved for public release: LA-UR-14-26276

jwlewellen@lanl.gov

length varies approximately linearly with momentum, thus allowing the alpha magnet to be used as a chirper or stretcher; $R_{56} = s_\alpha/2 = \Lambda_\alpha/2\alpha$.

ALPHA MAGNET APPROXIMATION

Several approaches suggest themselves as means of implementing alpha magnets in accelerator tracking codes that do not natively support them, without needing to modify the source code.* For instance, one could export the beam distribution immediately before the alpha magnet, transform it by the transport matrix described in [8] via Matlab or another general-purpose numerical code, reimport it and continue with the simulation. However, this is awkward, generally non-portable and does not provide for including space-charge effects within the alpha magnet. One could also attempt to define an appropriate field map, but as the alpha magnet effectively redefines the z-axis for the beam, depending on the code this would also require exporting, processing and reimporting the beam distribution. Rather, one would prefer a method implementable completely within a single simulation code, and relatively easily translated from code to code.

An alpha magnet's magnetic field can be approximated by a series of $N+1$ dipoles with edges parallel to the x- (or the normalized-coordinate Q_2) axis, as illustrated in Figure 2. Since most beam dynamics code make at least some provision for modelling the effects of dipoles, this is our preferred method for emulating alpha magnets.

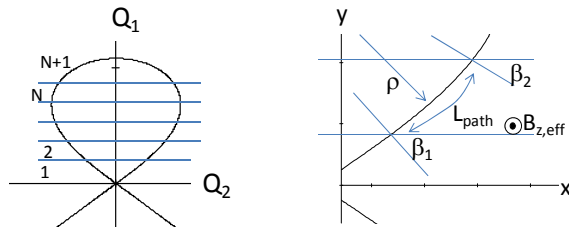


Figure 2: division of the alpha magnet into multiple dipole "slices" (left), and a close-up of some important parameters for a given slice (right).

Our approach, in essence, breaks the alpha magnet up into N slices plus an $(N+1)^{th}$ "runout" or "turn-around" region encompassing the maximum, or midplane, depth reached by all particles in the beam.

To an extent, the number of slices, and thus slice width, is an arbitrary parameter. In a physical alpha magnet, particles entering with different energies will have differing maximum depths as they cross the midplane. In most beam dynamics codes, if a dipole is present in the beamline, every particle in the beam is constrained to enter it. Therefore, when approximating an alpha magnet with dipoles, the "deepest" slice must be arranged to

ensure that the lowest-energy particle in the beam would in fact reach it.

For each slice, and the $(N+1)^{th}$ "runout" region, the dipole parameters required by the specific beam-dynamics code (e.g. entrance / exit angles, magnetic field, bend radius, net bending angle, path length) are calculated via numerical integration of the normalized equations of motion through an ideal alpha magnet.

Once this exercise has been completed, so long as the number of slices does not change and certain other constraints are met, the edge angles remain constant and all other quantities scale with the α parameter, allowing for easy reuse of the model. Also, from symmetry, we need only calculate these parameters for one-half of the alpha magnet trajectory.

METHODOLOGY

Trajectory Calculation and Parameterization

A standalone numerical code, for instance MathCAD (used for this work), Matlab or Mathematica, is used to calculate the ideal trajectory of a particle from injection to the alpha magnet midplane using normalized coordinates as described in [8], allowing parameterization of the normalized transverse position (Q_2) and path length (L) as a function of normalized depth into the alpha magnet (Q_1). In turn, these permit us to define the angle θ of the particle's momentum vector with respect to the Q_1 (y) axis, as a function of depth. Figure 3 shows $Q_2(Q_1)$, $L(Q_1)$ and $\theta(Q_1)$ for the ideal trajectory from entrance point to maximum depth. Note that the horizontal axes on these plots corresponds to the vertical axis in Figure 2.

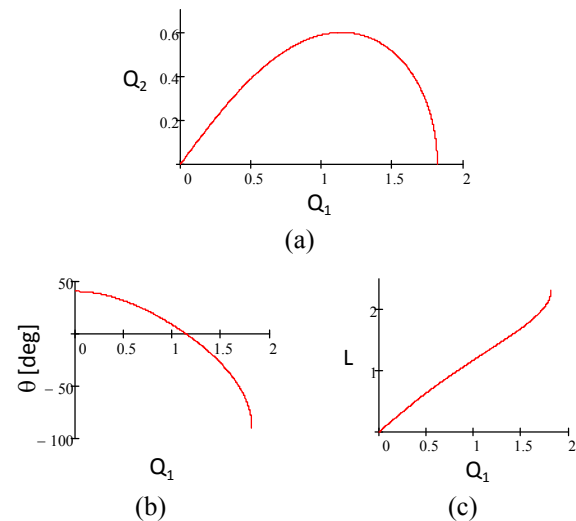


Figure 3: Normalized alpha magnet trajectory (a) transverse coordinate Q_2 vs. depth Q_1 ; (b) angle to the Q_1 axis vs. Q_1 ; (c) path length as a function of Q_1 .

Dipole Slice Parameters

The magnetic field gradient g , the central momentum $\beta\gamma_0$, and the maximum depth Δy of the central trajectory within the alpha magnet are related by Equation 2; two

* One of GPT's unique features is the ability to add user-defined elements without risking corruption of its core algorithms (particle stepping, space-charge, etc.). Directly implementing an alpha magnet with GPT is thus relatively straightforward.

out of three of these parameters must be specified to compute the dipole slice parameters. The ratio of the minimum to the central momentum, $\beta\gamma_{\min}/\beta\gamma_o$, is also required. Then the width of the slices in normalized coordinates along the Q_1 axis, is given by

$$w_{\text{slice}} = \frac{\Delta Q_1}{N} \cdot \sqrt{\eta \frac{\beta\gamma_{\min}}{\beta\gamma_o}}, \quad (5)$$

where η is a safety factor to allow for some variation in the injected beam momentum spread due to, for instance, optimization of upstream components.

Using $N=8$ slices, $\beta\gamma_{\min}/\beta\gamma_o=0.95$, and $\eta=0.9$, $w_{\text{slice}} = 0.21$; the distance along the Q_1 axis between the start of the runout region and the depth of the central trajectory is $\Delta Q_1 - Nw_{\text{slice}} = 0.138$. The slice width is therefore on the same order as the width of the runout region (assuming a symmetric momentum distribution), a condition we have empirically found works well.

Parameterization of the curves in Figure 3 yields the entrance and exit angles for each dipole slice (following the TRANSPORT [9] sign convention), and the normalized path length through each slice. These are presented in Table 1. Note that the “runout” slice is adjusted to transport the beam to the midplane of the alpha magnet.

Table 1: Slice Entry/Exit Angles and Path Lengths

Slice	From $Q_1=$	To $Q_1=$	β_1 [deg]	β_2 [deg]	$\delta\Lambda_\alpha$
1	0	0.210	40.71	-39.06	0.2749
2	0.210	0.420	39.06	-34.33	0.2630
3	0.420	0.630	34.33	-26.79	0.2450
4	0.630	0.840	26.79	-17.40	0.2275
5	0.840	1.051	17.40	-5.76	0.215
6	1.051	1.261	5.76	8.19	0.2107
7	1.261	1.471	-8.19	25.43	0.2201
8	1.471	1.681	-25.43	49.5	0.2657
runout	1.681	-	-49.5	0	0.3991

For an N -slice alpha magnet model, either $2N+1$ or $2(N+1)$ dipoles must be defined, depending on whether one wishes to access the beam distribution at the midplane of the alpha magnet. Assuming the latter case, and using the nomenclature shown in Figure 4 as a reference, the following relationships exist between dipoles prior to and following the midplane:

- Dipoles on the same slice have the same magnetic field, bending radius and path length: $B_{n,e}=B_{n,i}$, $\rho_{n,e}=\rho_{n,i}$ and $L_{n,e}=L_{n,i}$ for $n=1..N$ and runout.
- The dipole entrance and exit edge angles are related as: $\beta_{1,n+1,(i,e)} = -\beta_{2,n,(i,e)}$ for $n=1..N$ and runout; $\beta_{2,R,i}=\beta_{1,R,e}=0$; and $\beta_{(2,1),n,e}=\beta_{(1,2),n,i}$ for $n=1..N$.

The magnetic field B_n for each slice is given by

$$B_n = \left(n - \frac{1}{2}\right) g \frac{w_{\text{slice}}}{\alpha}, \quad n \leq N \quad (6)$$

Following the N^{th} slice, the field in the runout section is taken to be

$$B_R = \frac{\Delta Q_1}{\alpha} g, \quad (7)$$

the nominal field at the central momentum trajectory midpoint. The physical path length and bending radius within each dipole slice is given by

$$L_n = \frac{\delta\Lambda_\alpha}{\alpha} \text{ and }, \quad (8)$$

and the bending radius of the central trajectory is

$$\rho_n = \frac{\beta\gamma_o m_e c}{q_e B_n} \quad (9)$$

for all slices as well as the runout region.

The bend angle per slice can be set via two ways:

$$\theta_{FA,n} = \frac{L_n}{\rho_n}, \quad (10a)$$

bases the bend angle per slice on the slice magnetic field and path length through the slice (the “field average” method), while

$$\begin{aligned} \theta_{EM,n} &= \beta_{1,n} + \beta_{2,n}, \quad n \leq N \\ \theta_{EM,R,i} &= \beta_{1,n} + 90^\circ \\ \theta_{EM,R,e} &= \beta_{2,R} + 90^\circ \end{aligned} \quad (10b)$$

bases the bend angle per slice on the edge angles, using the relationship that, for a rectangular bend magnet, the bend angle equals the sum of the edge angles. (The runout dipoles are special cases because their entrance and exit planes are perpendicular, not parallel.)

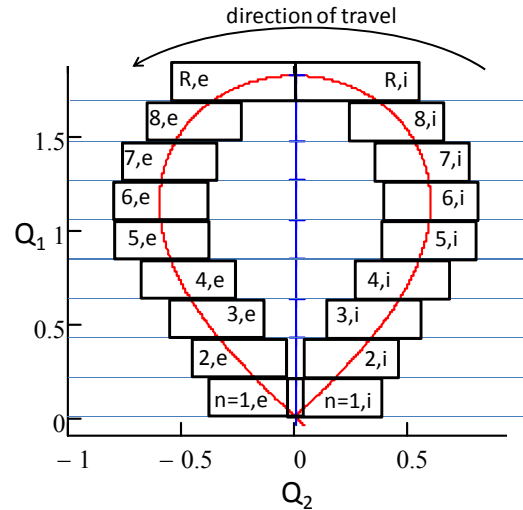


Figure 4: Dipole reference nomenclature; the beam passes through dipoles (n,i) before crossing the midplane, and dipoles (n,e) after passing the midplane.

ELEGANT TESTING

We use the beam dynamics code **elegant** to check the model: it has a built-in model for alpha magnets for reference; it has several dipole models and fine control over how they are implemented; and it can generate an R-matrix directly for a defined beamline.

For our test, we use a pencil electron beam with $\beta\gamma_0=4.811$ (2 MeV kinetic) and a $\pm 5\%$ hard-edge momentum spread, and a magnetic field gradient $g = 1 \text{ T/m}$, so $\alpha=11.04 \text{ m}^{-1}$. The other parameters are chosen to be consistent with the values given in Table 1, e.g. $N=8$ and $\eta=0.9$. Global default tracking was set to 2nd order, and both canonical sector bends (csbend element) and numerically integrated dipoles (nibend elements) were used to test the method.

Equations 11-13 show, respectively, the 1st-order transport matrices for **elegant**'s alpha magnet model (R_α), and csbend dipoles using edge-angle (R_{EM}) and field-average methods (R_{FA}) for calculating slice bend angles. Figure 5 and 6 plot x and x' vs $\beta\gamma$ at the exit of the alpha magnet for the test cases using csbend and nibend dipole models, respectively.

$$R_\alpha = \begin{pmatrix} -1 & -0.21 & 0 & 0 & 0 & 0 \\ 0 & -1 & 0 & 0 & 0 & 0 \\ 0 & 0 & -0.74 & 0.69 & 0 & 0 \\ 0 & 0 & -0.66 & -0.74 & 0 & 0 \\ 0 & 0 & 0 & 0 & 1 & 0.21 \\ 0 & 0 & 0 & 0 & 0 & 1 \end{pmatrix} \quad (11)$$

$$R_{EM} = \begin{pmatrix} -1 & -0.2 & 0 & 0 & 0 & 0 \\ 0 & -1 & 0 & 0 & 0 & 0.02 \\ 0 & 0 & -0.82 & 0.49 & 0 & 0 \\ 0 & 0 & -0.66 & -0.82 & 0 & 0 \\ 0 & 0.02 & 0 & 0 & 1 & 0.25 \\ 0 & 0 & 0 & 0 & 0 & 1 \end{pmatrix} \quad (12)$$

$$R_{FA} = \begin{pmatrix} -0.88 & -0.19 & 0 & 0 & 0 & 0.01 \\ 1.22 & -0.88 & 0 & 0 & 0 & -0.01 \\ 0 & 0 & -0.80 & 0.53 & 0 & 0 \\ 0 & 0 & -0.67 & -0.80 & 0 & 0 \\ -0.01 & 0.1 & 0 & 0 & 1 & 0.24 \\ 0 & 0 & 0 & 0 & 0 & 1 \end{pmatrix} \quad (13)$$

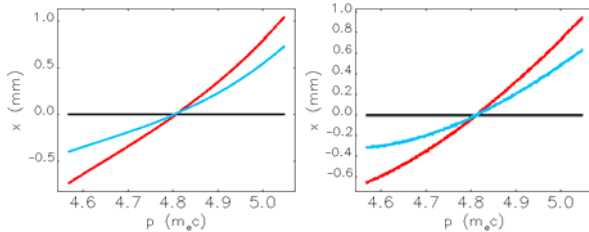


Figure 5: p - x space at the exit of the alpha magnet, for the built-in model (black), edge-angle method (red) and field-average method (blue) using **elegant**'s canonical sector bend (left) and numerically integrated bend (right) models.

CONCLUSIONS

A series of dipoles can be used to model the behavior of an alpha magnet in codes that do not natively include

such elements. The “edge-angle” method for calculating dipole slice bend angle arguably provides somewhat more accurate first-order transport in the transverse planes, but the “field-average” method provides lower anomalous p - x coupling. Higher-order terms are more strongly dependent upon the details of the dipole model used.

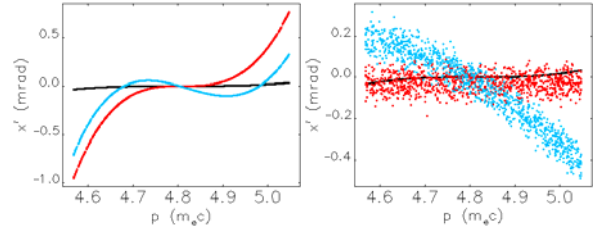


Figure 6: as in Figure 5, but plotting x' vs p .

This approach to approximating an alpha magnet was tested only using **elegant**. While the approach in general appears to be valid, the specifics of the dipole model a given beam dynamics code uses may have a significant impact upon the transverse dynamics, and in particular p - x and p - x' coupling. For instance, **elegant**'s numerically integrated dipole model, Nibend, produces notably different p - x' coupling than the canonical sector bend dipole model. Therefore, when using this approach with any beam dynamics code, we suggest at minimum determining the 1st-order transport matrix elements for comparison with **elegant**'s predictions for an equivalent momentum and trajectory depth.

REFERENCES

- [1] H.A. Enge, “Achromatic Magnetic Mirror for Ion Beams,” Rev. Sci. Instrum. **34**, p. 385 (1963). DOI: 10.1063/1.1718372
- [2] S.V. Bensen et al., “The Stanford Mark III Infrared Free Electron Laser,” Nucl. Instrum. Meth. A, vol 250, p. 39 (1986). DOI: 10.1016/0168-9002(86)90857-0
- [3] J.W. Lewellen et al., “A Hot-Spare Injector for the APS Linac,” Proc. 1999 Part. Accel Conf, New York, NY, p. 1979 (1999).
- [4] J.H. Billen and L. Young, “Pamela User's Manual,” LA-UR-96-1835 (1996).
- [5] K. Floettmann, ASTRA User's Manual, 2000, http://www.desy.de/~mpyflo/Astra_dokumentation/
- [6] M.J. de Loos and S.B van der Geer, “General Particle Tracer: a New 3D Code for Accelerator and Beam Line Design,” Proc. 5th European Part. Accel. Conf., Sitges, Barcelona, p. 1241 (1996).
- [7] M. Borland, “elegant: a Flexible SDDS-Compliant Code for Accelerator Simulation,” Advanced Photon Source Light Source Note LS-287 (2000). DOI: 10.2172/761286
- [8] M. Borland, “A High-Brightness Thermionic Microwave Electron Gun,” Ph.D. thesis, Stanford University, 1991.
- [9] D.C. Carey, K.L. Brown and F. Rothacker, “Third-Order TRANSPORT with MAD Input,” SLAC-R-530, page 126 (1998).

HIGH-GRADIENT CATHODE TESTING FOR MaRIE^{*,†}

J.W. Lewellen[#], N.A. Moody and F.L. Krawczyk, AOT-AE, LANL, Los Alamos, NM 87544 USA

Abstract

X-ray free-electron lasers (X-FELs) provide unprecedented capabilities for characterizing and controlling matter at temporal, spatial and energetic regimes which have been previously inaccessible. The quality of the electron beam is critical to X-FEL performance; a degradation of beam quality by a factor of two, for instance, can prevent the X-FEL from lasing at all, rather than yielding a simple reduction in output power.

The beam source for the world's first X-FEL, the LCLS at SLAC [1], defines the current state-of-the-art. Next-generation X-FELs such as MaRIE [2], intended to lase at 40 kV and beyond, will demand much higher quality electron beams, delivered at higher repetition rates, than present-generation injectors can deliver.

While conceptual designs for new beam sources exist [3], they incorporate assumptions about the behavior of the photocathode under extreme operating conditions. The combined requirements for high bunch charge, short bunch duration, and small emission area, dictate the use of high-efficiency photocathodes operating at electric field gradients of ~ 140 MV/m and durations of > 10 μ s. No suitable cathode has been operated under these conditions, however, so the success of next-generation X-FELs rests on a series of untested assumptions. We present our plans to address these knowledge gaps, including the design of a high-gradient RF cavity specifically designed for testing cathodes under MaRIE-relevant conditions.

INTRODUCTION

The MaRIE X-ray free-electron laser is intended to produce coherent X-ray photons at energies of 40 kV and higher. MaRIE requires a 12-GeV electron beam at the undulator with a normalized emittance of ~ 0.1 μ m RMS, a duration of 12 fs, an energy spread of $< 0.015\%$, and a bunch charge of 100 pC. Further, the MaRIE linac must deliver a pulse train to the undulator, with RF macropulse-average currents up to ~ 100 mA. These requirements, in turn, place extreme demands upon the MaRIE beam source and, in particular, the cathode.

Cathode-Related Considerations

The beam emission radius on the cathode must be small, on the order of a fraction of a millimeter, to satisfy the transverse beam quality requirements; an emission time on the order of a few ps is also required. This combination generally precludes the use of a metallic photocathode because the low quantum efficiency would

require a drive laser pulse with power densities approximating the ablation threshold.

The high emission current density requires extremely high electric field gradients at the cathode's surface to overcome the bunch's self-fields, which would otherwise limit the emitted current density or otherwise degrade the beam quality.

Gun-Related Considerations

The cathode must be removable from the injector to allow introduction, replacement and refurbishment of the selected cathode. This means the cathode-to-gun RF joint must also withstand RF fields up to 140 MV/m for durations of at least 10 μ s, and potentially much longer if the MaRIE baseline linac design is made superconducting. [4]

DESIGN REQUIREMENTS

Our initial experiments will characterize the effects of a MaRIE-relevant operating environment upon cathode dark current emission and quantum efficiency.

In broad terms, our research will address two questions: What will operating at the high gradients required over long RF pulses do to a semiconductor or multi-alkali cathode; and What will the cathode, operating at high gradient, do to the linac?

The former question relates primarily to the potential damage to the cathode from field-emission electrons and ions within the gun cavity, and to the nature and extent of changes to the surface and emission properties of the emitting surface from exposure to high gradients, both instantaneous and long-term.

The latter question relates to characterization of dark current from the cathode (and candidate RF joint designs), and to the potential for the cathode constituent elements to degrade the gun's ability to generate and sustain the required electric field gradients.

The cathode test cell design, therefore, must meet several primary design objectives:

- It must provide MaRIE-relevant RF gradients (140 MV/m) and pulse durations (10 μ s or longer);
- It must provide multiple viewports to both image and direct a photocathode drive laser onto candidate cathodes; and
- It must facilitate ready removal and replacement of candidate photocathodes.

Secondary design objectives include:

- It must be modular, to allow rapid and inexpensive modifications, upgrades or repairs; and
- It must demonstrate successful, low-field-emission operation of the cathode-to-gun RF joint.

* Work supported by the US Department of Energy

† Approved for public release: LA-UR-14-26438

jwlewellen@lanl.gov

CATHODE TEST CELL DESIGN

RF Cavity Design

While initial baseline for the MaRIE linac was a normal-conducting S-band (2.856 GHz) design, recent discussions have centered around using a superconducting L-band (1.3 GHz) linac as a means of providing longer RF macropulses. Either frequency choice raises issues for the MaRIE cathode test cell design. The design gradient should be more readily achievable at higher frequencies, particularly using a simple “pillbox” cavity. Klystrons capable of producing 10+ μ s pulses are more readily available at lower frequencies, however, they are often limited in RF power output, which would require using a re-entrant geometry to obtain the desired gradient.

The MaRIE cathode test cell frequency has been downselected to L-band, based primarily upon the availability of L-band klystrons capable of producing both the required macropulse duration, and sufficient RF power to produce the design gradient in a simple pillbox-type cavity. [5] The potential change to the MaRIE baseline RF frequency is a point in its favour, but not a decisive one.

The initial RF design of the test cell was completed using SUPERFISH [6] and is shown in Figure 1; the final RF design will be tuned and validated using CST Microwave Studio [7] after the mechanical design has been completed.

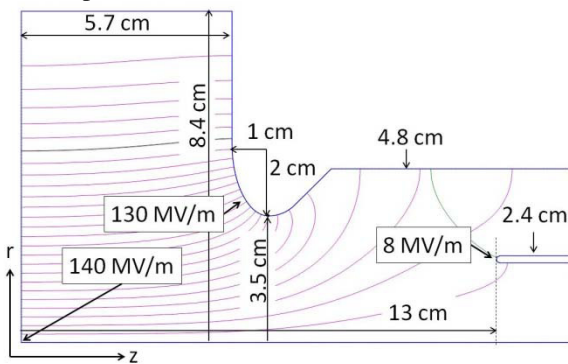


Figure 1: SUPERFISH model of MaRIE cathode test cell RF geometry, showing primary dimensions and selected field gradients.

The test cell makes use of an elliptical cross-section iris, and an on-axis RF power coupler. The iris radius has been selected as a compromise between shunt impedance and peak surface field. The coaxial RF power coupler radii have been chosen to transmit only the TEM coaxial waveguide mode at 1.3 GHz; other modes are cut off. While this is not, strictly speaking, necessary for the test cell itself, designing the coupler to transmit only the TEM mode allows us the potential of using the test cell to support measurements for which field symmetry is important, i.e. emittance measurements. Some of the cavity's RF properties are listed in Table 1.

Table 1: RF Properties of the MaRIE Cathode Test Cell

Parameter	Value	Units
Shunt impedance	7.27	M Ω /m
Q	14,334	
P_{in}	11.1	MW
$E_{max, cath}$	140	MV/m
$E_{max, iris}$	130	MV/m
H_{max}	225,202	A/m

Beam Transport

While the test cell is not intended to be a high-brightness beam source in and of itself, we are interested in characterizing both field-emission and photoemission as a function of applied gradient. To that end, we have performed a series of simple beam transport simulations on the test cell to characterize electron trajectory as a function of launch phase and starting radial position, in the absence of space charge. Figure 2 shows the trajectories for launch phases of 35° and 60° past the zero-crossing, corresponding to “conventional” launch phase selections.

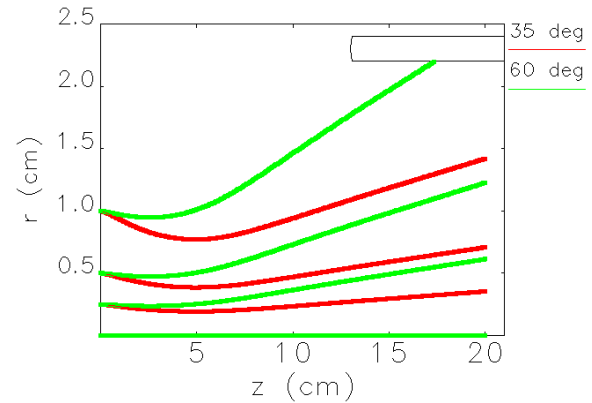


Figure 2: Trajectories for particles launched at 35 and 60 degrees past the zero crossing, emitted at 0.25, 0.5 and 1 cm radii.

Figure 3 shows trajectories for launch phases of 10°, 90° and 115°, corresponding to a very early laser pulse, to the field-emission peak, and to close the the cutoff phase beyond which emitted particles cannot leave the test cell. In both figures, the bar in the upper right of the plot is the RF power coupler inner conductor. Finally, Figure 4 shows the kinetic energy of the particles as a function of position along the z-axis, for the launch phases shown in Figures 2 and 3.

Figure 5 shows anticipated field emission trajectories for electrons emitted at -90° from the iris and from the end of the RF power coupler inner conductor. Impact energies on the cathode are anticipated to be at approximately 3 – 3.5 MeV when the on-cathode gradient is 140 MV/m.

Mechanical Design

The design requirements for the MaRIE cathode test cell include a high degree of modularity. This reflects the

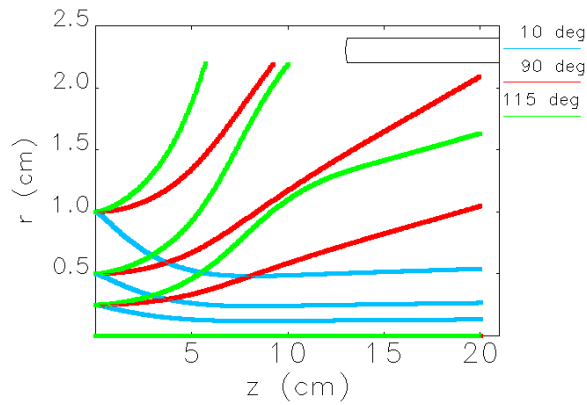


Figure 3: Trajectories for particles launched at 10, 90 and 115 degrees past the zero crossing.

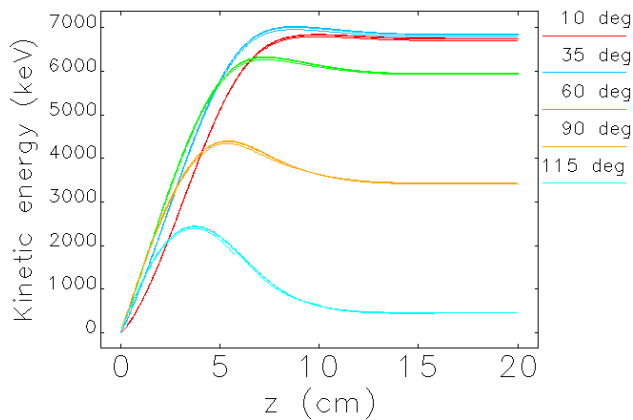


Figure 4: Kinetic energy vs. position for various launch phases.

challenging nature of the experiment, in particular the potential need to test multiple iterations of critical features such as the gun-to-cathode joint. It also drove the choice of on-axis RF power coupling, since separating the RF power feed from the body of the gun allows a lower-cost replacement of the entire cathode test cell proper, should this become necessary.

Figure 6 shows an overview of the design (left) and a close-up cut-away view of the interior of the RF cavity (right).

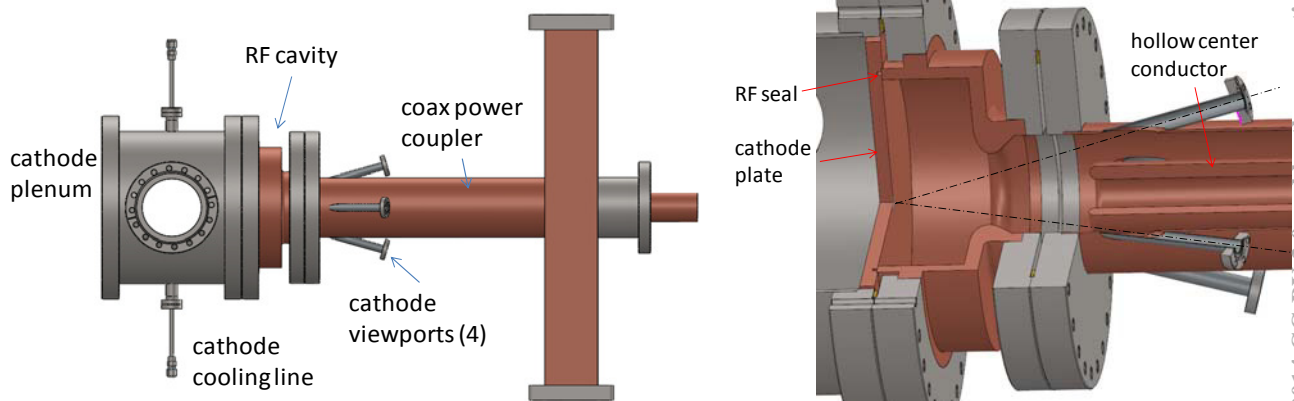


Figure 6: Mechanical design of the MaRIE cathode test cell: overall view (left) and closeup cut-away view (right).

The entire back wall of the RF cavity is removable, and has its RF seal separated from the vacuum seal. The removable back wall provides an inexpensive and easily modified platform for testing different cathode-to-gun joint designs.

The four cathode viewports are located symmetrically around the RF power coupler, with axes 16° from the axis of the power coupler. Each provides approximately a 1-cm diameter field of view at the cathode surface.

To characterize photoemission and dark current from the cathode, we envision placing an isolated viewscreen within the hollow center conductor of the RF power coupler approximately 20 cm from the cathode. The beam dynamics simulations suggest that a collector larger than ~ 2.5 cm in diameter should collect all electrons emitted during “normal” launch phases from emission radii out to ~ 5 mm (see Figure 2), the area we can address via the four viewports. Field emission (at 90°) from radii less than ~ 0.75 mm should be collected as well; this suggests that placing the cathode-to-gun RF seal at a radius of 1 cm or greater should help to isolate our diagnostics from field emission from the seal.

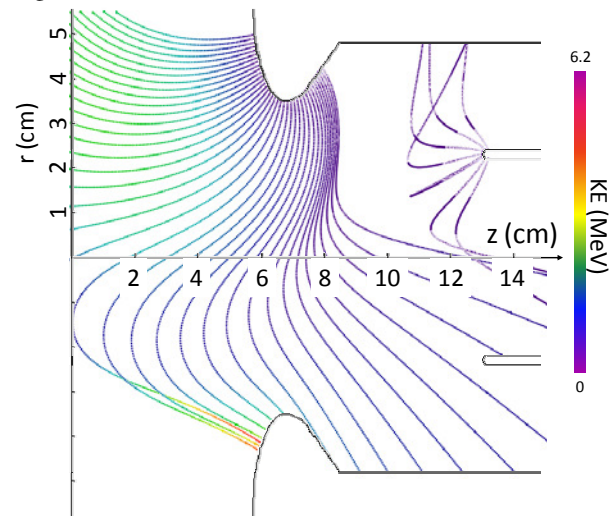


Figure 5: Field emission tracks from the iris and coupler end.

Each 10- μ s, 11-MW RF pulse will deliver energy sufficient to raise the body of the gun, on average, by 0.04 K, so active water cooling is not required, but a water system (not shown) will be provided to temperature-stabilize the test cell as well as to permit frequency tuning.

The cathode plenum provides an interface to a cathode fabrication, characterization and loadlock system, not shown here. It also provides means for pumping the area around the cathode plate, and to provide water cooling to the cathode plate if necessary.

Design Alternatives

The primary design risk, other than the cathode-to-gun RF seal, is achieving the design gradient with available RF power. At present, we intend to partner with the Argonne Wakefield Accelerator (AWA) to perform these tests. AWA includes among its facilities an L-band klystron capable of producing a 20-MW RF pulse for ~ 10 μ s, which easily meets our baseline design's requirements.

If required, however, a re-entrant nosecone and / or cathode plate should provide the design gradient with as little as 4 MW of RF power. Implementing this alternative scheme should require re-fabricating only the cathode cell body and cathode plate and, potentially, a redesign of the in-coupler electron diagnostics.

SCHEDULE AND VENUE

The mechanical and RF design is presently at approximately the 80% completion level, and we anticipate beginning construction of the test cell in late 2014. Initial RF testing will concentrate on achieving the design gradient in the gun, including validation of the cathode-to-gun RF seal. This shall be followed by characterizing the quantum efficiency and field-emission behavior of candidate cathodes as a function of their exposure to RF fields at various gradients and pulse durations. Finally, we intend to perform in-situ characterization of cathode performance within the MaRIE cathode test cell.

At present, we intend to perform the tests in collaboration with the Argonne Wakefield Accelerator group, starting in early- to mid-2015. In addition to the klystron mentioned above, the AWA facility incorporates vault space and photocathode drive laser options; and the personnel have extensive familiarity with related accelerator and cathode physics issues.

DISCUSSION AND CONCLUSIONS

Next-generation X-ray free-electron lasers, including the MaRIE 40-kV X-FEL, will place increasing demands on the performance of the electron beam source arising from increasingly tight beam-quality requirements at the undulator. The beam sources, and cathodes in particular, will be required to operate at higher gradients, for longer RF pulse durations, with higher laser pulse energies and emitted charge densities.

We have designed a cathode test cell to help evaluate the performance of candidate cathode materials under conditions similar to those expected within a notional MaRIE-class injector. The test cell has been designed using a modular approach, so all major components are separately replaceable. We have elected to have a completely removable back wall for the RF cavity, allowing us the ability to test different cathode-to-gun RF seal methods without replacing the entire cavity.

Four viewports placed on the RF power coupler permit observation of the center of the cathode plate over a field-of-view of approximately 1 cm. The viewports can be used for imaging, photocathode drive laser introduction, or arc monitoring.

An electrically isolated imaging screen, can be placed within the hollow inner conductor of the RF power coupler. This placement will help us to separate out photocurrent and dark current arising from the cathode, from dark current from the RF seal, providing the RF seal radius is greater than 1 cm.

ACKNOWLEDGEMENTS

We wish to thank the Argonne Wakefield Accelerator group, in particular John Power, for insightful discussions regarding L-band klystron capabilities and currently operating high-gradient L-band structures.

REFERENCES

- [1] Y. Ding et al., "Measurements and Simulations of Ultralow Emittance and Ultrashort Electron beams in the Linac Coherent Light Source," *Phys. Rev. Lett.* 102, 254801, 24 June 2009.
DOI: 10.1103/PhysRevLett.102.254801
- [2] B.E. Carlsten et al., "MaRIE X-Ray Free-Electron Laser Pre-Conceptual Design," *Proc. 2011 Part. Accel. Conf.*, p. 799, New York, NY.
- [3] Private communication, S. Russell, LANL, 2014.
- [4] Private communication, B.E. Carlsten, LANL, 2014.
- [5] Private communication, J. Power, ANL, 2014.
- [6] J.H. Billen and L.M. Young, "Poisson Superfish," LA-UR-96-1834, revised 13 January 2006.
- [7] <https://www.cst.com/Products/CSTMWS>

LINEAR ACCELERATOR DESIGN FOR THE LCLS-II FEL FACILITY

P. Emma, J. Frisch, Z. Huang, A. Marinelli, T. Maxwell, H. Loos, Y. Nosochkov, T. Raubenheimer, J. Welch, L. Wang, M. Woodley, SLAC, Stanford, CA 94309, USA
A. Saini, N. Solyak, FNAL, Batavia, IL 60510, USA
J. Qiang, M. Venturini, LBNL, Berkeley, CA 94720, USA

Abstract

The *LCLS-II* is an FEL facility proposed in response to the July 2013 BESAC advisory committee, which recommended the construction of a new FEL light source with a high-repetition rate and a broad photon energy range from 0.2 keV to at least 5 keV. A new CW 4-GeV electron linac is being designed to meet this need, using a superconducting (SC) L-band (1.3 GHz) linear accelerator capable of operating with a continuous bunch repetition rate up to 1 MHz at ~ 16 MV/m. This new 700-m linac is to be built at SLAC in the existing tunnel, making use of existing facilities and providing two separate FELs, preserving the operation of the existing FEL, which can be fed from either the existing copper or the new SC linac. We briefly describe the acceleration, bunch compression, beam transport, beam switching, and electron beam diagnostics. The high-power and low-level RF, and cryogenic systems are described elsewhere.

INTRODUCTION

The LCLS-II [1] high-repetition rate FEL project at SLAC aims to construct a new superconducting linac composed of TESLA-like RF cavities in continuous wave (CW) operation, in order to accelerate a 1-MHz electron beam to 4 GeV. This new superconducting linac (SC-linac), driven by a new high-rate injector [2], will replace the existing SLAC copper linac in sectors 1-7 (101.6 m/sector), while the remaining Cu RF structures in sectors 7-10 will be removed and replaced with a simple beam pipe and focusing lattice (the “linac extension”). The existing 2-km PEP-II bypass line (suspended from the tunnel ceiling) will be modified to transport electrons from the linac extension in sector 10 through more than 2.5 km and into either of two undulators in the existing LCLS undulator hall. The layout is shown in Figure 1 with the SC-linac in blue at far left and the SXU and HXU undulators at far right. The “linac extension” and “bypass line” are also shown.

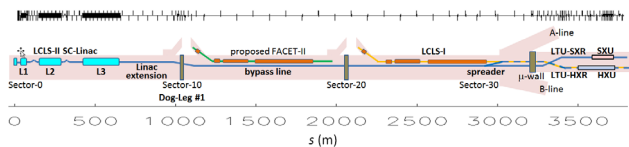


Figure 1: LCLS-II layout in existing SLAC tunnels (3.8 km).

LINAC AND RF LAYOUT

The *nominal* requirements of this new high-power linac are to accelerate a continuous rate of electron bunches,

with 100 pC per bunch, at a 0.6-MHz repetition rate (or higher with a reduced bunch charge to 10 pC, or lower with 300-pC, maintaining <120 kW in each of two electron dump lines). This new linac makes use of the ‘Tesla-Technology’ accelerating module, with thirty-five 13-m long cryomodules (CM), each including eight 9-cell L-band RF cavities (1.038 m/cavity) cooled to 2.0 K using liquid Helium. In addition, a short 3.9-GHz third-harmonic linac (HL) section is used to linearize the bunch compression process in two short cryomodules, each including eight special 9-cell, 3.9-GHz cavities (0.346 m/cavity) with up to 80 MV of on-crest voltage (decelerating). The linac design includes bunch compressors to nominally produce a 1-kA peak current at 100 pC/bunch without significantly increasing the transverse emittance. Finally, the design must reduce the final correlated energy spread to $<0.03\%$ rms and stabilize the beam against the microbunching instability by adding a small intrinsic energy spread (5-6 keV rms) at the injector, using a laser heater (LH) system [3] at 100 MeV.

The linac is segmented into several sections in order to include two magnetic chicanes to compress the bunch to a 1-kA peak current (8.6 micron rms bunch length at 100 pC). The linac segments and their various parameters are summarized in Figure 2, including the beam energy, rms bunch length, rms relative energy spread, chicane strength (R_{56}), RF phases, crest voltage, and cryomodule number. The RF parameters are in Table 1.

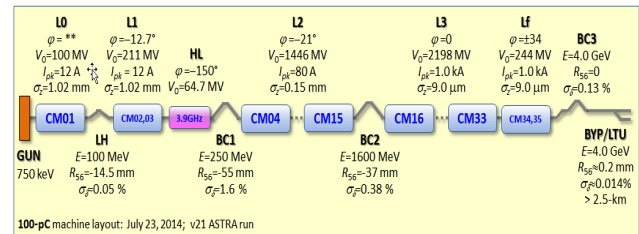


Figure 2: Linac layout with RF and compression parameters.

Table 1: SC-linac RF Parameters at 100 pC/bunch

Linac section	Phase (deg)	Gradient (MV/m)	No. of CM's	Avail. cavities	Powered cavities
L0	~ 0	16.3	1	8	7
L1	-12.7	13.6	2	16	15
HL	-150	12.5	2	16	15
L2	-21	15.5	12	96	90
L3	0	15.7	18	144	135
Lf	± 34	15.7	2	16	15

The average accelerating gradient (for most 1.3-GHz cavities) has been chosen at ~ 16 MV/m with an unloaded Q value of $\geq 2.7 \times 10^{10}$ at a temperature of 2.0 K. The RF parameters in Table 1 assume 6% of all cavities nominally unpowered as spares (or in maintenance), and the mean accelerating gradient is defined over the powered cavities only, and at crest phase. The “Lf” section is just the last two cryomodules arranged with a nominal $+34^\circ$ and -34° phasing, as opposed to L3 with 18 CM’s at crest phase. The Lf section provides an electron energy adjustment range of $\pm 1\%$, which will be controlled by an energy feedback loop. Keeping the two phases equal but opposite in sign (symmetric around crest phase) eliminates the induced energy chirp along the bunch, and provides energy control with these two phase settings.

ELECTRON BEAM PARAMETERS

A list of electron beam parameters is given in Table 2, including the *nominal* parameters and their ranges (range values are not simultaneous here).

Table 2: Electron Beam Parameters (Nominal and Range)

Parameter	sym.	nom.	range	unit
Final energy	E_f	4.0	2.0-4.1	GeV
Bunch charge	Q_b	100	10-300	pC
CW linac bunch rate	f_b	0.62	0-0.93	MHz
Avg. linac current	I_{av}	62	1-300	μ A
Avg. linac e^- power	P_{av}	0.25	0-1.2	MW
Emittance (norm., x & y)	$\gamma\epsilon_{1-2}$	0.45	0.2-0.7	μ m
Final peak current	I_{pk}	1.0	0.5-1.5	kA
Final rms bunch length	σ_{zf}	8.6	0.6-52	μ m
Compression factor*	C_T	85	25-150	-
Final slice E -spread, rms	σ_{Es}	500	125-1500	keV

* Total magnetic, from injector-end (100 MeV) to undulator.

FOCUSING LATTICE

The linac focusing lattice (L1, L2, and L3) is set using cold quadrupole magnets at the end of each 13-m CM, with some warm quadrupole magnets included around the bunch compressors to match the Twiss functions. The linac focusing lattice (30°/cell, L2 & L3), from cathode to HXR dump, is shown in Figure 3. The lines split in two (to HXR or SXR lines) at $s \approx 2776$ m (kicker).

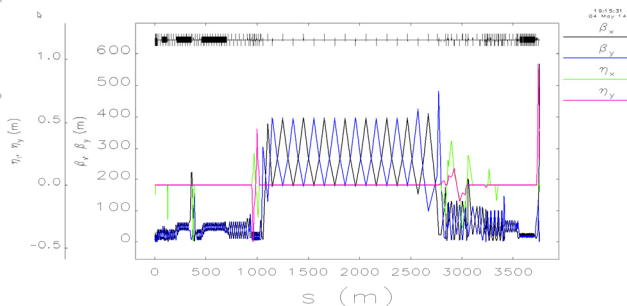


Figure 3: Focusing lattice from cathode to HXR dump. Large beta functions are in the existing, long bypass line,

while the HXR undulator is near the end of the line at $s \approx 3550$ -3700 m.

Similarly, the focusing over the full SXR-machine, from cathode to SXR dump, is shown in Figure 4. This plot is different from the previous plot only at $s > 2776$ m.

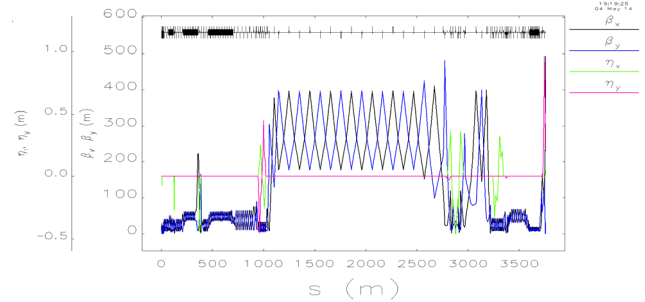


Figure 4: Focusing lattice from cathode to SXR dump at 4 GeV. The SXR undulator is near the end of the line at $s \approx 3600$ -3700 m. The two lines split (to HXR or SXR) at $s \approx 2776$ m.

ELECTRON DIAGNOSTICS

The high-rate and high-power electron beam in the SC-linac makes intercepting diagnostics (e.g., beam screens) difficult to use without damage. For this reason an off-axis (parallel) diagnostic section is tapped off the main linac just after the laser heater at 100 MeV using a fast kicker to steal pulses at up to 100 Hz (< 15 W). This post-LH diagnostic section includes a transverse RF deflector allowing both projected and slice measurements for emittance and energy spread continuously.

Existing strip-line BPMs are used in most locations with cold button-BPMs used at the end of each CM. Cavity BPMs are used in several key locations for feedback control and in the undulators where a 1-2 μ m rms position resolution is required. Relative bunch length monitors (coherent edge radiation) are included after each bunch compressor, similar to that used in LCLS-I [4]. Fast wire-scanners (~ 1 m/s) are envisioned for transverse beam profiles and emittance measurements at several in-line locations along the machine. YAG and OTR screens may be included, but are presently compromised in performance by coherent transition radiation. Finally, RF deflectors will be used to time-resolve key emittance and energy spread measurements, as allowed by budget.

LONGITUDINAL STABILITY

The jitter of the linac RF systems will cause the final bunch characteristics to vary, affecting the FEL performance. The variable bunch characteristics are primarily: 1) the final electron energy, 2) the final peak current, and 3) the arrival time of the bunch in the undulator. We therefore require specific stability tolerances for each RF system (phase and amplitude), bunch charge, drive-laser timing, and bunch compressor chicane power supplies, such that the final machine stability is within our chosen limits. These limits are as

follows: *a)* a final relative electron energy stability of $< 0.01\%$ rms, *b)* a final relative peak current stability of $< 4\%$ rms, and *c)* an arrival time of the electron bunch (assumed same as x-ray pulse timing) of < 20 fs rms.

To prescribe the necessary RF tolerances we first need to calculate the individual error sensitivities, defined as the level of error required to change each of the bunch characteristics by exactly the chosen limits. For example, we calculate the L2-linac RF phase error ($\Delta\phi_2$), assuming all 90 powered RF cavities in L2 vary in an uncorrelated and random way, which causes: 1) an energy change of 0.01% , 2) a peak current change of 4% , and 3) a timing change of 20 fs (each individually, not simultaneously).

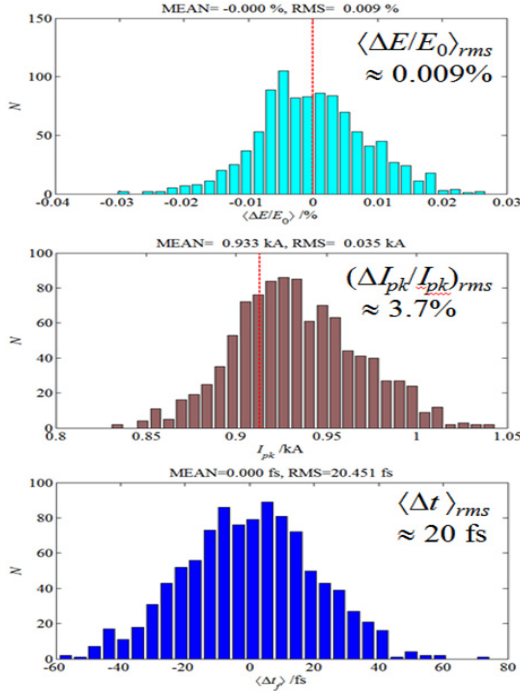


Figure 5: Jitter/tracking simulation using *LiTrack* [5] and rms (Gaussian) stability tolerances of Table 3, confirming the final expected stability of $(\Delta E/E)_{rms} \approx 0.009\%$, $(\Delta I_{pk}/I_{pk})_{rms} \approx 3.7\%$, and $\Delta t_{rms} \approx 20$ fs rms. It may be possible to improve this.

Of course the sensitivities are not applicable as system tolerances, since each one (by itself) consumes the entire stability budget. For this reason, we scale down each sensitivity such that the quadrature sum of all errors, assuming uncorrelated jitter from system to system, just reaches the beam stability limit for each item. The list of final rms tolerances as a full stability budget is given in Table 3, where we assume uncorrelated errors over the “ N cavities” in each linac section, assuming each cavity is powered by its own RF power amplifier. Note also that beam-based feedback systems will stabilize these errors at frequencies below ~ 1 Hz, so these tolerances represent the fast jitter levels that must not be exceeded by design. Final tracking simulations, with rms jitter on each item as listed in Table 3, are shown in Figure 5 as verification.

Table 3: Longitudinal Stability Tolerances at 100 pC/bunch

Parameter (rms)	symbol	Tol.	N cav's	unit
Phase error in L0	$\Delta\phi_0$	0.040	7	degL
Phase error in L1	$\Delta\phi_1$	0.039	15	degL
Phase error in HL	$\Delta\phi_H$	0.039	15	degH
Phase error in L2	$\Delta\phi_2$	0.095	90	degL
Phase error in L3-linac	$\Delta\phi_3$	1.8	150	degL
Amplitude error in L0	$\Delta V_0/V_0$	0.026	7	%
Amplitude error in L1	$\Delta V_1/V_1$	0.039	15	%
Amplitude error in HL	$\Delta V_H/V_H$	0.039	15	%
Amplitude error in L2	$\Delta V_2/V_2$	0.095	90	%
Amplitude error in L3	$\Delta V_3/V_3$	0.12	150	%
Laser timing error*	Δt_c	0.31	-	ps
Bunch charge error	$\Delta Q/Q_0$	1.5	-	%
Current reg. in LH	$\Delta I_H/I_H$	0.005	-	%
Current reg. in BC1	$\Delta I_1/I_1$	0.005	-	%
Current reg. in BC2	$\Delta I_2/I_2$	0.003	-	%

* The gun timing error is compressed by 3.85, from gun to 100 MeV, due to velocity compression.

WAKEFIELDS OF LONG TRANSPORT

The long transport lines following the LCLS-II linac also generate longitudinal wakefields which need to be included in the bunch compression system design, especially for cancellation of the energy chirp before entering the FEL. The wakefields are due to the resistive-wall effect and have contributions from each transport line section according to pipe radius, material, and length. The various wakefield section parameters are listed in Table 4, including pipe length, internal radius, internal plating material, and the material’s conductivity. The DC wakefield is accurate here, ignoring AC conductivity [6]. Beamline sections of Table 4 are labeled in Figure 1.

Table 4: Resistive-Wall Wakefields of Long Transport Lines

Beamline Section	Pipe Length (m)	Pipe Radius (mm)	Pipe Material	Cond. $/10^6$ (Ohm-m) $^{-1}$
Linac Exten.	250	24.5	stainless	1.37
Dog-Leg #1	78	19	stainless	1.37
Bypass Line	1734	24.5	stainless	1.37
LTU-SXR	827	24.5	Alum.	36.0
LTU-HXR*	778	20.6	Copper	58.0

* Much of this pipe exists and is copper plated to reduce wakes.

BEAM SPREADER AND BEAM DUMPS

To rapidly switch beam into one of two FEL undulators, a fast, bipolar, vertical magnetic kicker (0.75 mrad) is used at the end of the bypass line at up to a 1-MHz switching rate. The kicker requires 50 ppm rms field stability and < 40 nrad rms kick variation at baseline (no kick). Two 2-hole horizontal Lambertson magnets

(septa) then spread the beam to the HXR or SXR undulators as shown in Figure 6 and Figure 7.

Electron beam dumps at the end of each FEL line are limited to 120 kW of beam power. Therefore, at a 100-pC bunch charge and 4 GeV, the maximum repetition rate in each FEL line is 312 kHz. With a lower bunch charge (e.g., 30 pC) the rate can be increased to 1 MHz, but always power-limited to 120 kW in each FEL line.

The linac beam power can be twice this level (250 kW at 625 kHz for 100 pC/bunch) and a straight-ahead beam dump, “D10” in Figure 6, is included after the spreader (kicker off). This dump is rated for 250 kW and will reuse the existing MW-class dump presently in the linac.

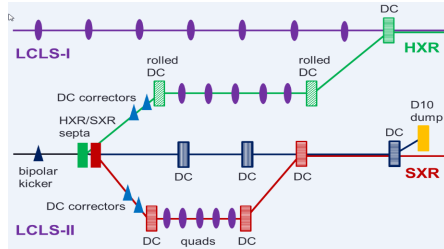


Figure 6: Fast beam spreader system (plan view) with vertical “kicker” and two “2-hole septa” magnets which bend horizontally. This schematic shows the geometry rather than the complete optics (e.g., not all quads are shown).

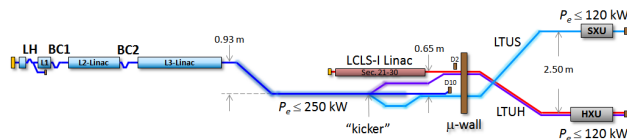


Figure 7: Full LCLS-II layout (plan view) with switching into the SXR undulator (top-right) and HXR undulator (lower-right) at up to a 1-MHz rate using a fast “kicker” and two septa.

BEAM COLLIMATION

Included in the linac layout is a system of adjustable-gap collimators designed to block undesirable beam halo which might otherwise be lost in radiation sensitive areas. It is designed to greatly reduce the rate of undulator demagnetization caused by beam-loss induced radiation, and to limit beam loss to below 1 W/m in areas with limited radiation shielding. The system employs multiple stages of collimation in x , x' , y , y' , and δ , phase space coordinates. Simulations show the gun-generated halo can be reduced by a more than factor of 10^7 . Touschek and beam-gas-generated halo, which are expected to be significant but at a much lower level than gun-generated halo, are also seen to be well collimated before reaching the undulator.

MICROBUNCHING INSTABILITY

The microbunching instability can have a significant impact on beam quality causing, in particular, an undesired growth in the sliced beam energy spread. The primary means to control the instability is the laser heater

(LH). The current LH design uses the same undulator as in LCLS-I ($\lambda_u = 5.4$ cm), but with longer laser wavelength ($\lambda_L = 1$ μm) to exploit the availability of high rep-rate, high-power systems. For the 100-pC baseline beam, an estimate based on linear theory for the microbunching instability indicates an optimum LH setting corresponding to 5-6 keV rms energy spread at 100 MeV, consistent with a 500-600 keV rms sliced energy spread at the FELs ($C_T \approx 100$). Preliminary results (to be reported elsewhere) from high-resolution macro-particle simulations with *IMPACT* [7], fully accounting for CSR and space charge fields, show a somewhat larger effect of the instability, which appears to be noticeably aggravated by the presence of the long transport sections between the SC-linac and the FELs. The *IMPACT* simulations also allow for an accurate characterization of the so-called “trickle-heating” effect [3], due to space charge and the micro-correlations induced by the electron/laser interaction in the LH. The effect (see Figure 8) may not necessarily be harmful but it interferes with the ability to control the induced energy spread by appropriate tuning of the laser power, especially at low settings. Possible remedies include a modification of the LH chicane, machine lattice, or less desirably, choice of the LH laser wavelength (shorter).

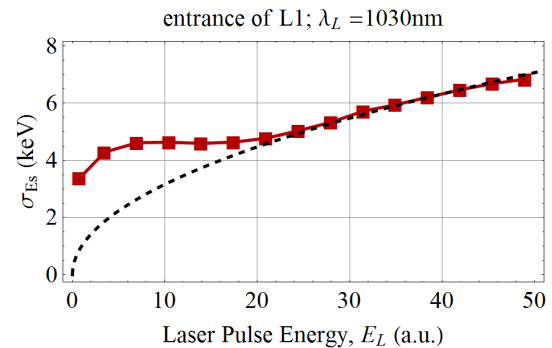


Figure 8: The beam slice energy spread ($Q = 100$ pC) as observed at the entrance of L1 (*IMPACT* simulations) deviates from $\sim \sqrt{E_L}$ (dashed line) because of the “trickle heating” effect. (Here, the beam time-slice is defined to be a few μm ’s long.)

START-TO-END TRACKING RESULTS

Start-to-end particle tracking simulations have been done using *Elegant* [8] and *ASTRA* [9], where *ASTRA* tracks from cathode through first CM at 100 MeV, including space-charge forces. *Elegant* takes this beam and continues tracking through the full linac, the long transport lines, and to the start of the undulators, including bunch compression, 2nd-order optics, longitudinal wakefields of the linac and long transport-lines, plus coherent radiation (CSR) in the bends using a transient 1D line-charge model. The final longitudinal phase space at 4 GeV is shown in Figure 9. The slice emittance (0.35 μm at 100 pC here) is not increased while the flat energy profile (middle) is the result of the resistive-wall wakefields in the long transport lines described above.

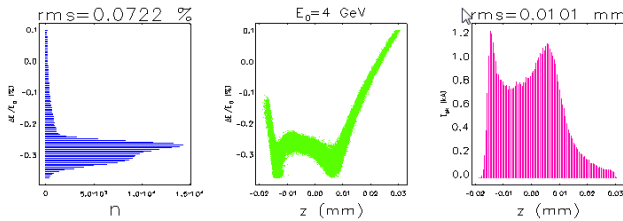


Figure 9: *Elegant* tracking results of longitudinal phase space (100 pC/bunch) including resistive-wall wakes and CSR in the bends. Space charge is only included in the *ASTRA* tracking.

SUMMARY

The baseline design of the LCLS-II CW, SC linear accelerator generates the appropriate beam power, rate, and quality for the two new FELs to be built at SLAC. The detailed particle tracking up to high energy has not yet included space-charge forces, which may be a beam quality limitation with regard to the micro-bunching instability. The design study continues.

REFERENCES

- [1] T. Raubenheimer, “The LCLS-II, a New FEL Facility at SLAC”, in *Proc. of 36th Int. Free-Electron Laser Conf.*, Basel, Switzerland, 2014, WEB001.
- [2] J. Schmerge *et al.*, “The LCLS-II Injector Design”, in *Proc. of 36th Int. Free-Electron Laser Conf.*, Basel, Switzerland, 2014, THP042.
- [3] Z. Huang *et al.*, “Measurements of the Linac Coherent Light Source Laser Heater and its Impact on the X-ray Free-Electron Laser Performance”, *Phys. Rev. ST - AB*, **13**, 020703 (2010).
- [4] H. Loos, “LCLS Accelerator Operation and Measurement of Electron Beam Parameters Relevant for the X-ray Beam”, *Proc. SPIE 8778, Advances in X-ray Free-Electron Lasers II: Instrumentation*, 87780J (May 3, 2013), doi:10.1117/12.2021569.
- [5] K. Bane, P. Emma, “*LiTrack*: A Fast Longitudinal Phase Space Tracking Code with Graphical User Interface”, in *Proc. of 2005 Part. Acc. Conf.*, Knoxville, TN, USA, pp. 4266-4268, 2005.
- [6] K.L.F. Bane, G. Stupakov, “Resistive Wall Wakefield in the LCLS Undulator Beam Pipe”, SLAC-PUB-10707, October 2004.
- [7] J. Qiang, *et al.*, “High Resolution Simulations of Beam Dynamics in Electron Linacs for X-ray Free-Electron Lasers”, *Phys. Rev. ST-AB*, **12**, 100792, (2009).
- [8] M. Borland, *Elegant*, APS LS-287, presented at ICAP 2000, Darmstadt, Germany.
- [9] K. Floettmann, “Astra”, DESY, Hamburg, <http://www.desy.de/~mpyflo>, 2000.

DESIGN STUDY OF LCLS CHIRP-CONTROL WITH A CORRUGATED STRUCTURE

Z. Zhang, K. Bane, Y. Ding, Z. Huang, R. Iverson, T. Maxwell, G. Stupakov, L. Wang
SLAC National Accelerator Laboratory, Menlo Park, CA 94025, USA

M. Ruelas, M. Harrison, P. Frigola
Radiabeam Systems, Santa Monica, CA 90404, USA

Abstract

The purpose of this paper is to investigate the use of flat metallic plates with small corrugations as a passive dechirper, studying its effects on beam dynamics. Similar systems have been tested in Pohang and Brookhaven at relatively low energies (100 MeV) and with relatively long bunches (>1 ps) [1, 2]. Four meters of such a structure are being machined by Radiabeam Systems for use in the LCLS with a high energy and femtosecond electron beam. In this paper we use a field matching program to obtain the longitudinal and transverse wakes for the purpose of the LCLS dechirper design. In addition, we fit the longitudinal wake to simple functions, so that one can obtain the wake without resorting to the field matching program. Since the transverse wakes—both dipole and quadrupole wakes—are strong, we include beam dynamics simulations to find the tolerances for injection jitter and misalignment in the LCLS.

INTRODUCTION

In a linac-based X-ray free electron laser (FEL) there is often a need for energy chirp control of the beam as the magnetic compression employed in such FELs typically leaves an undesired time-energy correlation in the bunch, which can broaden the FEL bandwidth. While the chirp can be removed by the off-crest acceleration in a following linac section, this solution can be costly or impractical, particularly for a superconducting linac-based FEL. For such cases, a dedicated structure that can intentionally generate a strong longitudinal wakefield was recently proposed to dechirp the beam. In Ref. [3], a round metallic structure with corrugated walls was suggested and analyzed as a passive dechirper. Compared to round geometry, the flat geometry of corrugated plates has the advantage of allowing the dechirper strength to be adjusted by changing the separation of the plates [4].

In both round and flat structures, the transverse wakes can be strong, with amplitude scaling as the -4th power of aperture (vs. the -2nd power for the longitudinal wake). In a flat structure, however, in addition to the usual dipole wakefield that is excited when the beam passes through the structure off axis, there is also a quadrupole wake excited, even when the structure and beam are perfectly aligned. These transverse wakes will, if not properly controlled, increase the projected transverse emittance and lead to a deterioration of FEL performance.

Similar dechirper systems have been tested in Pohang and Brookhaven at relatively low energies (100 MeV) [1, 2] and a new one is being machined for use at the LCLS [5, 6].

However, when this structure is used for high energy beam, such as found in the LCLS, in order to generate a significant dechirping effect, the gap between the two plates needs to be set very small (< 1 mm). And to relax the manufacture tolerance, the size of corrugations are chosen at 0.5 mm, which is comparable to the gap size. In this case, the analytical formulas of wakefields are not applicable. In this paper the longitudinal and transverse wakes of the flat corrugation structure are calculated by the field matching method [7] and a simplified fitting formula with corrugation parameters is obtained for the longitudinal wakefield. A detailed tolerance study including beam offset, alignment error and structure imperfection is also conducted for the designed device.

FIELD MATCHING AND FITTING FORMULA

Figure 1 gives a sketch of the dechirper, showing the parameters half-gap a , corrugation period p , corrugation slit t , corrugation depth h , and width w . The wakefields of the structure are characterized by these parameters.

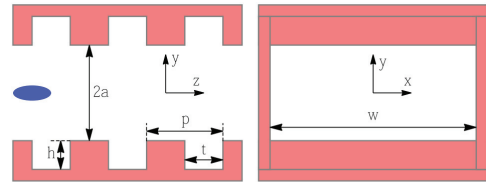


Figure 1: Geometry of dechirper structure parameters.

The analytical theory of wakefields in Ref. [3, 7, 8] is based on the assumption that all dimensions of the corrugations are much smaller than the gap size and the structures are deeply corrugated

$$p, h \ll a \quad \text{and} \quad h \gtrsim p \quad (1)$$

and also assuming large aspect ratio $w/2a$. The point charge wakefield for the flat pipe with small corrugations can be written as

$$W(z) = \frac{\pi^2}{16} \frac{Z_0 c}{\pi a^2} \cos(kz), \quad z > 0 \quad (2)$$

where $Z_0 = 377\Omega$ is the characteristic impedance of vacuum and c is the speed of light. The wave number, k , is well approximated by

$$k = \sqrt{\frac{p}{ah}} \quad (3)$$

Note that in Eq. 2, the amplitude of the wakefield is independent of the dimensions of corrugations.

However, for the LCLS dechirper, the half-gap a is very small and comparable with the corrugation size. So the analytical formulas above are not applicable in the parameter regime of interest. In order to obtain the wakefield for general case, we adopt the field matching method [7] of solving the Maxwell's Equations. The field matching program used for the numerical simulations is described elsewhere [9].

Fitting Formulas and Parameter Ranges

The form of the fitting formula for the longitudinal wakefield is assumed to be a damped cosine oscillation of the form

$$W(z) = \frac{\pi^2 Z_0 c}{16 \pi a^2} F e^{-\frac{kz}{2Q}} \cos(kz), \quad z > 0 \quad (4)$$

where the terms before F on the right side are the analytical amplitude of the flat metallic structure and F is the amplitude factor; k and Q are the wave number and quality factor, respectively. The three parameters are all functions of h, p, a , which will be shown in detail in the following subsections.

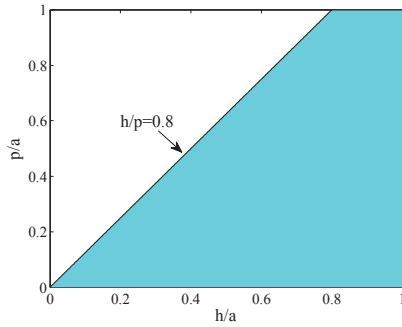


Figure 2: Validity range (colored) of the fitting formula of longitudinal wakefield.

The fitting formula Eq. 4 is valid in a specific range of interest shown in Fig. 2. We assume the dimensions of corrugations are not larger than the gap size

$$p, h \leq a \quad (5)$$

and the corrugation is "deeply corrugated" to have a strong dominant mode

$$h/p > 0.8 \quad (6)$$

The factor 0.8 is chosen based on the results of numerical calculation. The applications of this structure focus on the short-range wakefields, so the longitudinal range of the fitting formulas is limited to

$$kz \leq 3\pi \quad (7)$$

We also keep $t = p/2$ for simplicity.

Fitting Results

The field matching results for F , k and Q are shown in Figs. 3, 4 and 5. Each line in Fig. 3 corresponds to a value of p/a from 0.1 to 1 and h/a is determined by the valid range requirement. The double-arrow line in Figs. 4 and 5 signify that for a given h/a , we plot all wave numbers under different p/a values ranging from 0.1 to 1. Based on these results, we can obtain the fitting formulas for these three parameters. We found that k and Q have little dependence on p/a . Actually in the analytical theory, the wave number is dependent on t/p . But we keep $t/p = 1/2$, as a constant, in the field matching calculations. The fitting forms for these three parameters of Eq. 4 are given in the following equations.

$$F\left(\frac{h}{a}, \frac{p}{a}\right) = b_1\left(1 - \frac{p}{a}\right)\left(1 - \frac{h}{a}\right) + b_2\left(1 - \frac{h}{a}\right) + b_3\left(1 - \frac{p}{a}\right)^2 + b_4\left(1 - \frac{p}{a}\right) + b_5 \quad (8)$$

$$k = \frac{1}{a} \left(\frac{c_1}{\sqrt{h/a}} + c_2 \right) \quad (9)$$

$$Q\left(\frac{h}{a}\right) = d_1 \left(\frac{h}{a}\right)^2 + d_2 \frac{h}{a} + d_3 \quad (10)$$

where $b_i (i = 1, \dots, 5)$, c_1, c_2 , d_1, d_2, d_3 are the fitting coefficients. The best fit result for these coefficients are given in Tab.1.

Table 1: Coefficients of Best Fit for Eqs. 8,9,10 to the Field Matching Algorithm

Coefficient	Value	Coefficient	Value
b_1	0.1483	c_1	1.7096
b_2	0.1418	c_2	-0.5026
b_3	-0.0437	d_1	3.2495
b_4	0.1460	d_2	-9.1830
b_5	0.5908	d_3	10.2230

The results of the fitting formulas are also indicated in the corresponding figures by red dashed lines. It can be seen that for the amplitude factor F and wave number k the fitting formulas agree well with the results of the field matching program. The sum of the five coefficients $\sum_{i=1}^5 b_i \approx 1$ indicates that the new formula is consistent with the analytical formula as $p/a \ll 1, h/a \ll 1$. For the quality factor Q , the precision is also good enough for applications which focus on the short-range wakefields, such as energy chirp control.

Example Longitudinal Wakefields

In this subsection, we sample some values of p, h to compare wakefields of the fitting formulas and of field matching calculations. The results are presented in Fig. 6 with the specific values of p, h written in each figure.

The wakefields are normalized by $W(0^+)$ of the analytical wakefield. It can be seen that the fitting formula Eq. 4

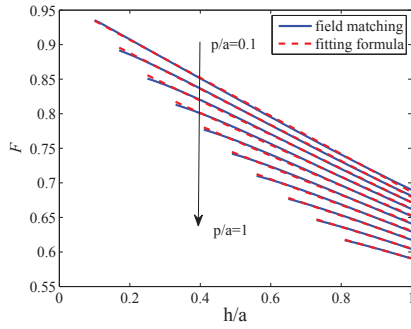


Figure 3: Amplitude factor F from field matching solution (blue solid line) and corresponding best fit to Eq. 8 (red dashed line).

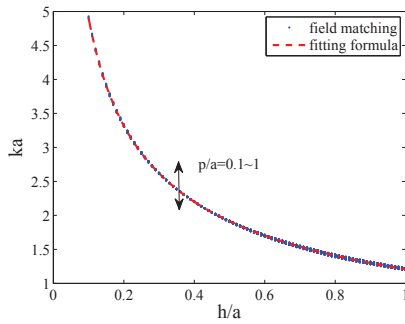


Figure 4: Wave number by field matching algorithm (blue dots) and corresponding best fit to Eq. 9 (red dashed line).

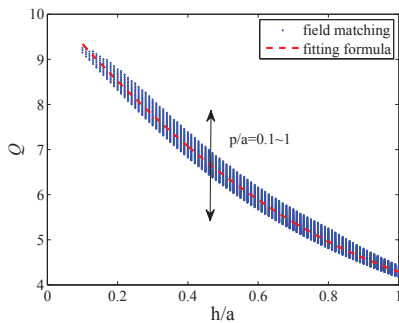


Figure 5: Quality factor by field matching algorithm (blue dots) and corresponding best fit to Eq. 10 (red dashed line).

agrees well with the results of the field matching calculation at least within the longitudinal range of $kz \leq 3\pi$. There is a little deviation in the wavelength between the two wakefields, especially when p/a and h/a are close to 1. This is because the wakefield may not behave like a cosine oscillation. If we choose other fitting forms of wave number, e.g. $k_1 z + k_2 z^2$, we can get perfect fitting results including the wave number. In that case, we need to introduce more fitting coefficients throughout, complicating the formulas. However, for the parameters under consideration, the fit as described is found to yield wakefields sufficiently consistent with all field matching solutions.

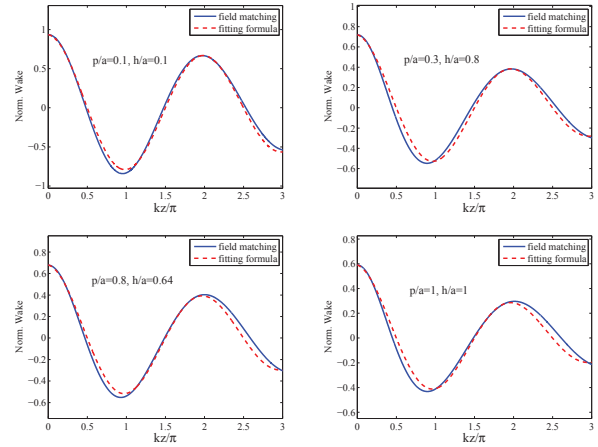


Figure 6: Examples of wakefields calculated using field matching (blue solid line) and Eq. 4 with fitting formulas Eqs. 8,9,10 (red dashed lines).

SIMULATION STUDY OF LCLS DECHIRPER

As a demonstration experiment of chirp-control for high energy beams, the dechirper will be installed at the linac-to-undulator (LTU) area of the LCLS. Essential diagnostics for the proposed dechirper experiment are shown in Fig. 7. The dechirper will be located in a low β region of the LCLS LTU. Neighboring BPMs will be used to ensure alignment through the device. A distant downstream BPM will be used to detect any deflection due to the dipole wake that may be introduced by centering errors of the dechirper. Transverse emittance measurements will be performed using LTU quads (not shown) along with the COTR-mitigated transverse profile monitor [10] at the end of LTU or, alternatively, LTU wire scanners (not shown). Finally, slice energy spread measurements will be performed in the LCLS electron dump using an X-band transverse deflecting cavity (XTCAV) [12] in conjunction with the final spectrometer bend.

The beam energy is ~ 6.6 GeV, which will generate soft x-ray photons of 2 keV energy. The peak current after compression is ~ 1.5 kA and the energy chirp induced by the RF off-crest acceleration is not canceled fully by the wakefield of the downstream linac. The relevant parameters of the beam are given in Tab.2.

Table 2: Beam Parameters for Proposed Dechirper Experiment

Parameter	Value	Units
Charge Q	150	pC
Peak current I_p	~ 1.5	kA
Energy E	6.6	GeV
Emittance ϵ_x	0.77	μm
Emittance ϵ_y	0.39	μm
β_x	5	m
β_y	19	m

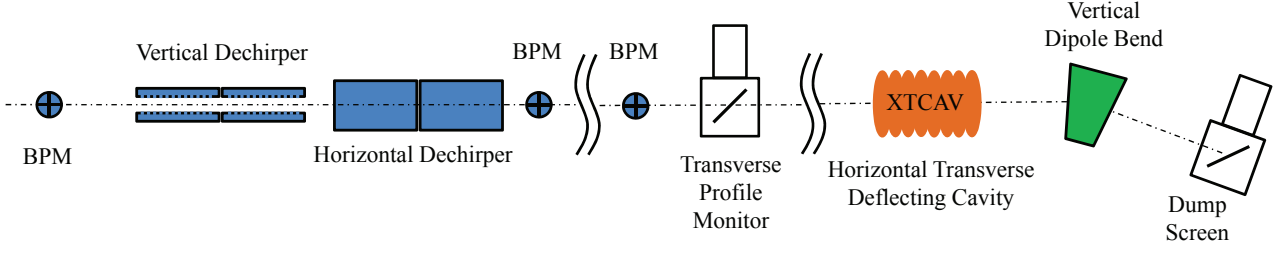


Figure 7: Schematic of the proposed dechirper experiment (not to scale). See text for description.

The total length of the dechirper is 4m in the latest design. However, the following analysis for transverse wakefields is based on Elegant [11] simulations of a 2-m-long dechirper. A longer dechirper will benefit the experiment as it allows a larger gap to achieve the same integrated longitudinal wake, while the transverse wakefields decrease more quickly with gap size. The strength of the longitudinal wake varies as $1/a^2$, while that of the transverse wakes as $1/a^4$. Thus the tolerance requirements for the new 4-meter-long dechirper will be relaxed. The structure parameters of the dechirper in the simulations are given in Tab.3.

Table 3: Structure Parameters of LCLS Dechirper in the Simulation

Parameter	Value	Units
Half-gap a	0.5/0.7	mm
Period p	0.5	mm
Depth h	0.5	mm
Slit t	0.25	mm
Width w	12	mm
Total length L	2*	m

* The total length is 4 meters in the latest design.

When $a = 0.7$ mm, the longitudinal wakefield of the structure fully cancels the remaining energy chirp. The wakefield amplitude will increase by a factor of 2 if a is set to 0.5 mm, which means over-dechirping of the beam. Figure 8 presents the longitudinal, dipole and quadrupole wakefields of the dechirper obtained by the field matching program assuming $a = 0.5$ mm and other parameters in Tab.3. The simulated longitudinal phase space before and after the dechirper with $a = 0.5$ mm are shown in Fig. 9.

In the experiment of the LCLS, we can use the x-band deflecting cavity (XTCV) located at the end of the LCLS beamline to measure longitudinal phase space [12] in Fig. 9. The final simulated images at the screen OTRDMP are given in Fig. 10, corresponding to the longitudinal phase space w/ and w/o dechirper in the beamline. The expected effect of the dechirper is clearly measurable.

Quadrupole Wakefield

The choice of dechirper parameters is determined by the following considerations. A smaller dechirper gap generates

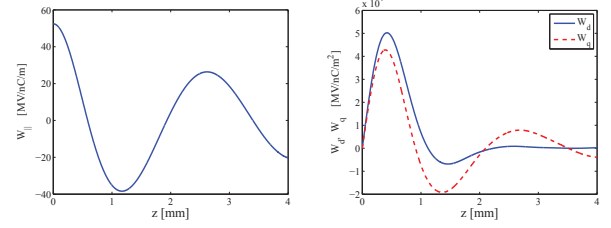
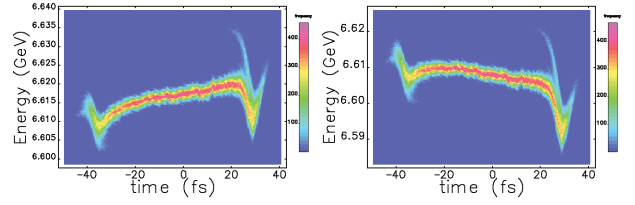
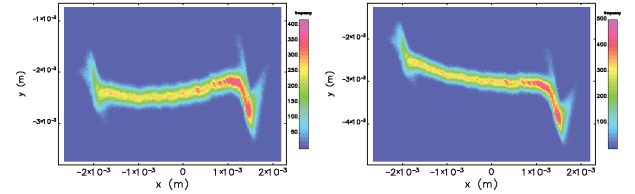

 Figure 8: Longitudinal (left) and transverse (right) wakefields of the LCLS dechirper when the gap size $a = 0.5$ mm and other parameters are shown in Tab.3.

 Figure 9: Longitudinal phase space before (left) and after (right) the dechirper with half-gap size $a = 0.5$ mm.


Figure 10: Simulated images on the screen at OTRDMP to measure the longitudinal phase space w/o(left) and w/ (right) dechirper in the beamline.

a stronger longitudinal wakefield (which scales as $1/a^2$), and allows one to shorten the device for the required size of the energy chirp. However, an extremely small gap makes the transverse dipole and quadrupole wakefields stronger and leads to projected emittance growth and tight tolerances on the beam position jitter and dechirper alignment. Note that the transverse wakefields used in the following tolerance study are also calculated by the field matching program.

In this subsection, we consider the effect of the quadrupole wakefield, which can introduce time-dependent focusing or

defocusing on the beam to increase projected emittance. In the design, the whole dechirper will be divided into two sections of equal length. The two sections are oriented orthogonally, one with vertical plates and the other with horizontal ones. (Here the direction of dechirper is determined by the direction of the gap, e.g. the dechirper structure shown in Fig. 1 is a vertical dechirper.) Then there are four combinations for these two sections. We compare different combination types together in Fig. 11 with projected emittance increase, which is defined as

$$\frac{\delta\epsilon}{\epsilon_0} = \frac{\epsilon}{\epsilon_0} - 1 \quad (11)$$

where ϵ_0 and ϵ are the emittance before and after the dechirper, respectively. The smaller increase in the horizontal plane is due to the smaller β value ($\beta_y = 19m, \beta_x = 5m$) and larger initial emittance before dechirper due to the CSR effect during upstream magnetic compression. It can be observed that if the two sections are oriented in the same direction, the projected emittance growth in vertical plane ($\delta\epsilon_y$) will be larger than 10% even when the beam and the device are both aligned perfectly. However, if we rotate the second section by 90° with respect to the first one, the emittance increase in both planes will become small. This verifies that the quadrupole wakefield effect can be canceled if the two sections are crossed by 90° . It is also noticed in the simulations that we need to keep similar or symmetric β values to cancel the quadrupole wakefield.

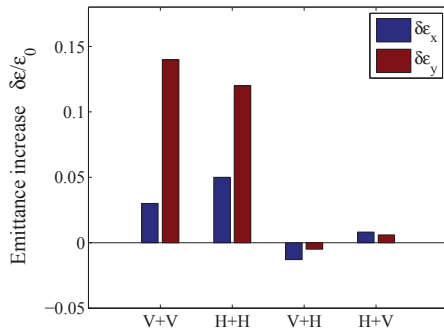


Figure 11: Projected emittance increase for different combinations of the two dechirper sections. "V" means vertical dechirper and "H" means horizontal dechirper.

Dipole Wakefield

If the beam enters the structure offset from the axis, it will excite the dipole wakefield. The tail of the beam will be kicked, increasing the projected emittance. In Fig. 12 we present the emittance growth versus the beam offset. Vertical (horizontal) offset leads to vertical (horizontal) emittance growth.

The asymmetric effect in the two planes is due to the different β value and ϵ_0 in the two planes. The analytical formula is derived based on Ref. [4] with the fitting formula of longitudinal wakefields Eq. 4. It can be observed that

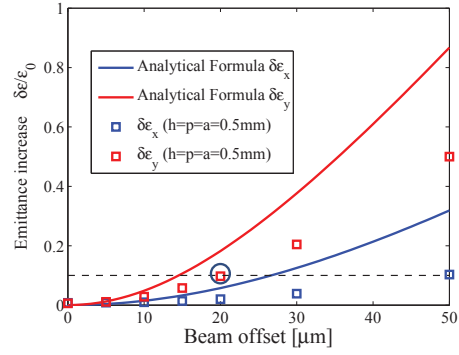


Figure 12: Projected emittance growth versus the beam offset. Vertical (horizontal) offset leads to vertical (horizontal) emittance growth.

emittance growth is more sensitive in the vertical plane and that the offset should be controlled to within $20\mu m$ if the allowed emittance growth is to be less than 10%.

Tolerance Study

In this subsection, we consider the structure tolerance of the dechirper for the experiment. We adopt the analytical methods in Ref. [4] to analyze the dipole wakefield induced by the structure error. First is the rotation error in the x direction as shown in Fig. 13. In this device, each plate has a certain angle (θ_1, θ_2) with respect to the beam path.

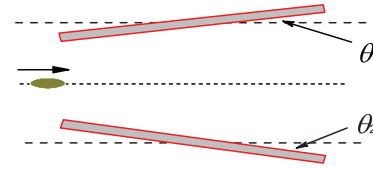
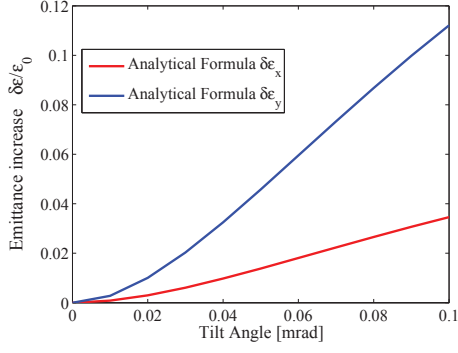


Figure 13: Dechirper with x-rotation error. Anticlockwise (clockwise) rotation corresponds to positive (negative) angle.

The emittance increase can be calculated by the method in Ref. [4] with infinitely small steps integrated along the beam path for a 1 m-long structure.

$$\left(\sqrt{\left(\frac{\epsilon}{\epsilon_0} \right)^2 - 1} \right)_{s \rightarrow s+\Delta s} = 0.375 Z_0 c \cdot \frac{\eta Q \beta \sigma_z \Delta s}{(a + s(\theta_1 - \theta_2)/2)^4 E} \cdot \frac{s(\theta_1 + \theta_2)}{2\sigma_0} \quad (12)$$

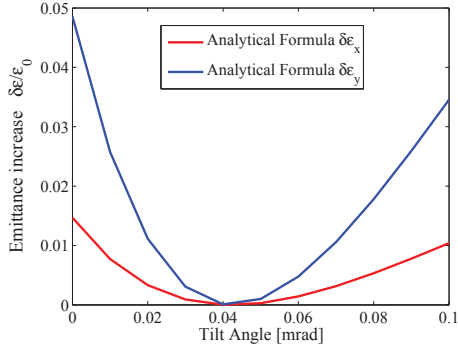
where Q is bunch charge, σ_z bunch length, σ_0 transverse beam size, E beam energy and η the amplitude factor of dipole wakefield. θ_1, θ_2 are the angles of the plates shown in Fig. 13. For simplicity, we choose θ_1 as the variable and set $\theta_2 = 0$. We plot the projected emittance increase versus the tilt angle θ_1 in Fig. 14. The dipole wake from the tilt angle leads to the increase of projected emittance and 0.1 mrad ($\theta_1 = 0.1\text{mrad}, \theta_2 = 0$) misalignment over 1 m length results in more than 10% emittance growth.


 Figure 14: Emittance increase versus the tilt angle θ_1 .

However, for a certain tilt angle we can cancel the effect of dipole wakefield by offsetting the beam at the entrance. When the beam is offset by Δ , Eq. 12 can be written as

$$\left(\sqrt{\left(\frac{\epsilon}{\epsilon_0} \right)^2 - 1} \right)_{s \rightarrow s + \Delta s} = 0.375 Z_0 c \cdot \frac{\eta Q \beta \sigma_z \Delta s}{(a + s(\theta_1 - \theta_2)/2)^4 E} \cdot \frac{s(\theta_1 + \theta_2)/2 - \Delta}{\sigma_0} \quad (13)$$

For example, if we offset beam by $10 \mu\text{m}$, the new curve of emittance increase and the tilt angle is shown in Fig. 15. For a tilt angle, we can always find an offset value that cancels the effect of dipole wakefield.


 Figure 15: Emittance increase versus the tilt angle θ_1 with offset $10 \mu\text{m}$.

Another error we consider here is the rotation angle about the longitudinal (z) axis. In the design, we cross the two sections by 90° to cancel the quadrupole wakefield. In Fig. 16, we present the emittance growth versus the crossing angle of the two sections of the dechirper. The scheme of the dechirper is the third combination type in Fig. 11: the first section is vertical and the second one is horizontal. Based on these simulations, the tolerance for the crossing angle is very relaxed, with 1% or less emittance increase even with 10° deviation from nominal.

Optimizing Beam Optics at the Dechirper

From the simulations and analysis given above, we find the tolerance requirements in y are much tighter than the

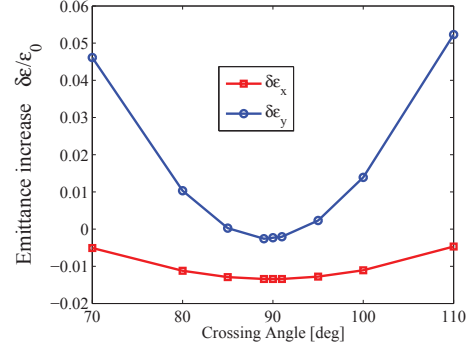


Figure 16: Emittance increase versus the crossing angle of two sections.

ones in x . One reason for the difference is that β_y is much larger than β_x . In the simulations, we use the nominal twiss parameters of the LTU area with $\beta_y = 19\text{m}$, $\beta_x = 5\text{m}$ at the location of dechirper. If we optimize the twiss parameters for the dechirper experiment, making the β small in both planes, the tolerance introduced by the transverse wakefield can be loosened. Indeed after careful design, we can keep the β of the two planes both small ($\sim 7\text{m}$). In this case, the tolerance requirements for the vertical plane can be loosened by a factor ~ 2 , and the experiment will be easier to carry out.

CONCLUSION

In this paper we investigated the use of a pair of flat metallic plates with small corrugations as a passive dechirper for the LCLS. We studied dechirper wakefield and fit the numerically-obtained longitudinal wake to simplified formulas, so that anyone can easily obtain the wake over a large parameter region without access to the field matching program. The fitting formulas agree well with the results of the field matching calculation. We simulated the application of the dechirper to the LCLS beam and studied the effect of the transverse wakefields. The quadrupole wakefield effect can be largely canceled out by crossing the two sections of dechirper by 90° . The dipole wakefield gives the tolerance on beam position jitter. If the expected emittance growth is to be limited to 10%, the beam position jitter should be controlled to within $20 \mu\text{m}$. In the tolerance study, the x -rotation error introduces a dipole kick, but its effect can be eliminated by offsetting the beam at the entrance of dechirper. Constraints on the error in the crossing angle are found to be quite relaxed. Smaller β values yield looser tolerances. After optimizing the twiss parameters of the LTU area, mechanical stability and positioning requirements are found to be acceptable for the current beam parameters and available diagnostics.

ACKNOWLEDGMENT

This work was supported under US Department of Energy contract DE-AC02-76SF00515.

REFERENCES

- [1] P. Emma *et al.*, PRL 112, 034801.
- [2] M. Harrison *et al.*, "Removal of Residual Chirp in Compressed Beams Using a Passive Wakefield Technique" in *Proc. North American Particle Accelerator Conf.*, Pasadena, CA, USA, 2013, pp. 291-293.
- [3] K. Bane and G. Stupakov, Nucl. Inst. Meth. A 690, 106 (2012).
- [4] K. Bane and G. Stupakov, SLAC-PUB-15852 (2013) and LCLS-II TN-13-01.
- [5] K. Bane *et al.*, SLAC-PUB-15853 (2013) and LCLS-II TN 13-02.
- [6] M. Ruelas *et al.*, "Mechanical Design for a Corrugated Plate Dechirper System for LCLS", in *These Proceedings: Proc. 36th Int. Free-Electron Laser Conf.*, Basel, Switzerland, 2014, THP033.
- [7] K. Bane and G. Stupakov, Phys. Rev. ST Accel. Beams 6, 023301 (2003).
- [8] G. Stupakov and K. Bane, Phys. Rev. ST Accel. Beams 15, 124401 (2012).
- [9] Z. Zhang *et al.*, report in preparation.
- [10] R. Ischebek *et al.*, "Instrumentation and Results at the Swiss-FEL Injector Test Facility", in *Proc. 2nd Int. Beam Instrumentation Conf.*, Oxford, UK, 2013, pp. 12-18.
- [11] M. Borland, ELEGANT, Advanced Photon Source LS-287, 2000.
- [12] C. Behrens *et al.*, Nature Comm. 5, 3762 (2014).

LCLS-II BUNCH COMPRESSOR STUDY: 5-BEND CHICANE*

D.Z. Khan[#], T.O. Raubenheimer, SLAC, Menlo Park, CA 94025, USA

Abstract

In this paper, we present a potential design for a bunch compressor consisting of 5 bend magnets which is designed to compensate the transverse emittance growth due to Coherent Synchrotron Radiation (CSR). A specific implementation for the second bunch compressor in the LCLS-II is considered. The design has been optimized using the particle tracking code, ELEGANT [1]. Comparisons of the 5-bend chicane's performance with that of a symmetric 4-bend chicane are shown for various compression ratios and bunch charges. Additionally, a one-dimensional, longitudinal CSR model for the 5-bend design is developed and its accuracy compared against ELEGANT simulations.

INTRODUCTION

The Linac Coherent Light Source (LCLS) at SLAC has shown tremendous success in its scientific capabilities in the biological, chemical, atomic and material sciences [2, 3, 4]. To build upon the success of the LCLS, a myriad of upgrades will be made to push the limits of current x-ray free-electron laser (X-FEL) design and technology to meet the ever growing demands of the scientific community. LCLS-II is an upgrade of the LCLS based on a 4 GeV superconducting RF linac [5]. Among the many upgrades being researched, one of particular interest is the bunch compression system.

Compression of electron beams is important in FELs to minimize the gain length [6]. A successful compression system is one that compresses the bunch longitudinally while preserving the beam's transverse emittance. The currently planned compression system of LCLS-II, and many current X-FEL facilities such as FLASH (DESY) [7] and SACLA (RIKEN) [8], uses a sequence of magnetic chicane to compress the bunch length by orders of magnitude [5]. LCLS-II's two-stage compression (Fig. 1) is simple and effective but poses problems towards the end of its compression cycle via CSR's dilution of horizontal emittance.

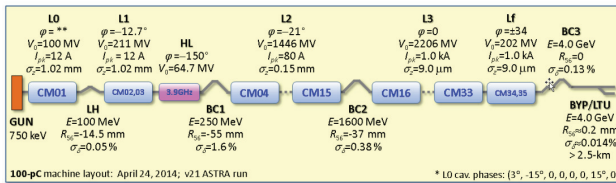


Figure 1: A diagram of the LCLS-II beamline with relevant component details. LCLS-II plans to utilize a two-stage magnetic chicane compression system; BC1 and BC2. The topic of this paper focuses on the self-radiative effects of the electron beam experienced in BC2.

*Work supported by Department of Energy Contract No. DE-AC02-76SF00515.

[#]donish@SLAC.stanford.edu

On the curved sections of an FEL beamline the electron beam can interact with itself. The synchrotron radiation from the electrons in the tail of the bunch can interact with the electrons in the head under the right conditions. The phenomenon becomes highly disruptive when the phase difference between the radiating electrons is small i.e. when the bunch length becomes comparable to the radiation wavelength. Under this regime, the synchrotron radiation becomes coherent and its power scales as N^2 , where N is the electron population of the bunch. In the coherent regime, the radiation causes a strong non-linear longitudinal energy chirp. This chirp can be estimated using a simple 1-D model [9]:

$$\frac{dE}{ds}(z) = \int_{-\infty}^z \frac{d\lambda(z')}{dz'} \left(\frac{1}{(z-z')^{\frac{1}{3}}} \right) dz' \quad (1)$$

$$\sigma_{RMS-\delta} = 0.22 \frac{r_e N L_B}{\gamma \rho^{2/3} \sigma_z^{4/3}} \propto [L_B^{\frac{1}{3}}][\theta^{\frac{2}{3}}][\sigma_z^{-\frac{4}{3}}] \quad (2)$$

where z is the longitudinal position along the bunch, λ is the normalized electron distribution, L_B is the magnet length, ρ is the bending radius and σ_z is the RMS bunch length. Equations 1 and 2 are derived from a 1-D model of the steady-state CSR wakefield. The CSR effect can create a number of unwanted effects on the electron beam [10, 11]. In this paper, we concern ourselves namely on CSR's influence on the bend plane's projected emittance growth.

Novel techniques have been developed to mitigate and nullify the CSR effect. Adjusting the linac optics to provide a $-I_{2 \times 2}$ transfer matrix between two sequential bends (such as in doglegs) has shown to provide excellent cancellation of CSR induced emittance growth [12]. A main assumption of this method is that the bunch length of the beam is constant between successive bends and therefore, the CSR RMS energy spread can be assumed to be identical at each location. The matter becomes highly complicated when the bunch length between the two successive bends is evolving, such as that of the bunch compressor. For an evolving bunch length, studies have shown that a minimization of the \mathcal{H} -function in CSR significant bends results in significant reduction of emittance growth [13]. Compressor designs based on matched chicanes or large period wigglers can also reduce the emittance growth [14, 15]. Utilizing asymmetry in a chicane design (allocating more R_{56} in the first half of a, for example, 4-bend chicane) has shown success in partial nullification of emittance dilution when compared to the standard symmetric designs [16, 17]. Additionally, it has been shown that, in multi-stage compression systems, allocating more R_{56} to the initial bunch compressors, while maintaining final compression, dampens the CSR effect in the final compressor where CSR is most detrimental [13]. Though the techniques cited

demonstrate effective reduction of the CSR induced emittance dilution, they tend to require many additional magnetic elements that can lead to further degradation of the longitudinal phase space and fall short of complete nullification.

LCLS-II CURRENT BUNCH COMPRESSOR

The currently planned compression scheme of LCLS-II consists of a two-stage magnetic chicane system. Each compressor is comprised of the standard 4-bend chicane (Fig. 2). We focus our attention on the second bunch compressor (BC2) where the CSR is most influential. Pertinent details of the BC2 are included in table 1.

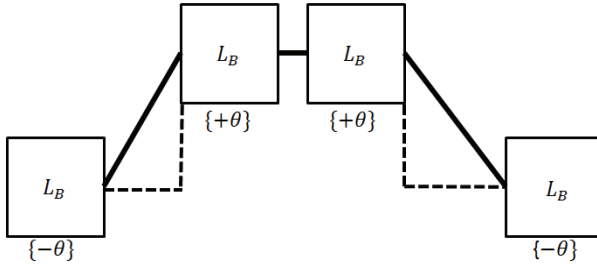


Figure 2: A cartoon of the 4-bend chicane being used for BC1 and BC2 at LCLS and currently planned for LCLS-II.

Table 1: Various Design Parameters of BC2 in LCLS-II

Parameter	Symbol	BC2	Unit
Electron Energy	E_0	1.6	GeV
Momentum Compaction	$ R_{56} $	59.9	mm
Chicane Total Length	L_T	23.0	m
Bend Angle Per Dipole	$ \theta $	0.05	Rad
Eff. Length Of Each Bend	L_B	0.54	m
Dispersion At Center	$ \eta_x $	562	mm

To gain greater insight on the CSR mechanism of BC2 we used ELEGANT to generate phase space plots of the longitudinal momentum change along the bunch as it evolves through BC2. From Figure 3, we see the CSR

wakefield begins to become significant in the third bend and fourth bends.

For a simplistic understanding of the emittance growth, we employ a linear kick model for the CSR [12]. The linear kick model provides a useful approximation of the CSR's effect on the bend plane emittance in terms of first-order energy kicks (Eq. 2) to the beam's centroid at each dipole's center. With the energy kicks, one can calculate the associated spatial (Δx) and angular ($\Delta x'$) kicks at the i th dipole given the local dispersion and dispersion's slope:

$$\Delta x_i = \eta_i \delta_P = \int R_{16i}(s) \delta_i ds \quad (3)$$

$$\Delta x'_i = \eta'_i \delta_P = \int R_{26i}(s) \delta_i ds \quad (4)$$

For coherent processes, the spatial and angular kicks can be summed linearly at each bend location and the final projected emittance is described by [18]:

$$\epsilon^2 = \epsilon_0^2 + \epsilon_0 \sqrt{\beta (\sum \Delta x'_i)^2 + 2\alpha \sum \Delta x_i \sum \Delta x'_i + \gamma (\sum \Delta x_i)^2} \quad (5)$$

Applying the linear kick model to the 4-bend chicane of BC2 allows us to see the limitations of the compressor and investigate a new compressor set up in regards to full emittance growth cancellation. Naturally, from equation 5, we see that a route to emittance growth cancellation is to have the kick sums cancel. With equations 3 and 4, we can develop a relation for the sum of spatial and angular kicks in the final two bends of BC2 where CSR is significant:

$$\sum \Delta x = \theta_B (L_B + L_D) \delta_{P3} \quad (6)$$

$$\sum \Delta x' = \theta_B (\delta_{P3} + \delta_{P4}) \quad (7)$$

where θ_B , L_B , L_D , δ_{P3} , and δ_{P4} is the bend angle, bend length, drift length between the 3rd and 4th bend, and the CSR RMS spread in bend 3rd and 4th bend, respectively. From equations 6 and 7, we see that the kick sums mathematically cannot cancel for the 3rd and 4th bends; they can only be minimized. Though, with the design constraints of maintaining R_{56} and having no residual dispersion at the exit of the 4th bend (achromatic condition), we begin to realize the limitations of the CSR emittance growth cancellation of the 4-bend chicane.

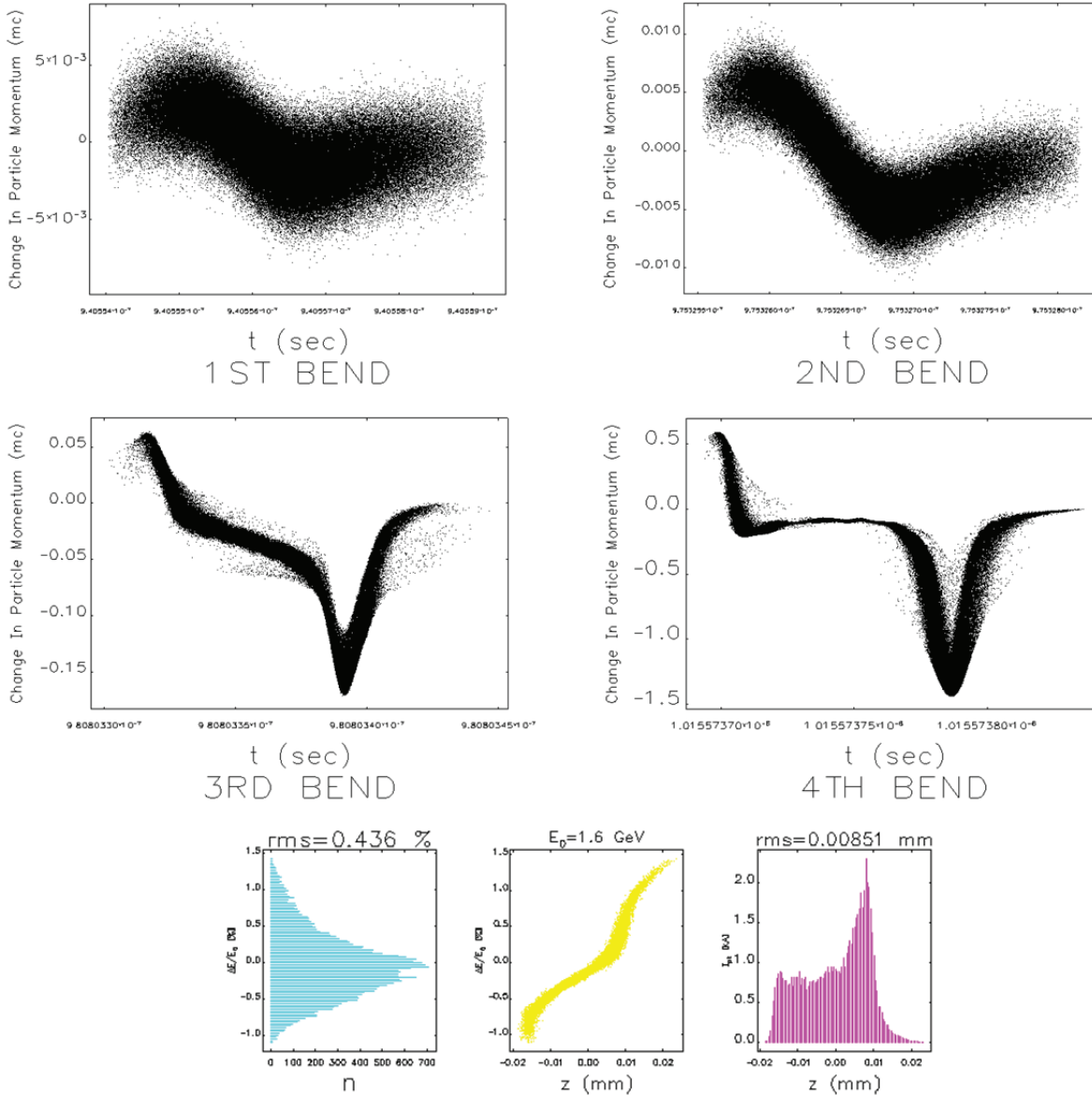


Figure 3: Top/Middle: The momentum difference for each particle in each bend in the planned LCLS-II BC2 4-bend chicane generated with ELEGANT. The CSR wake begins to take form in the third bend where the bunch is compressed to 7 microns. Bottom: (From left to right) The normalized energy spread, longitudinal energy phase space, and the current profile of the beam at the exit of BC2.

LCLS-II PROSPECTIVE BUNCH COMPRESSOR

The prospective chicane design (Fig. 4) is based on the aforementioned studies in this paper. If we are to design a compressor that has transverse spatial and angular kicks cancel, we consider the following:

1. The CSR energy kick is heavily weighted by the bunch length. As the bunch length decreases, the CSR energy kick increases to the inverse 4/3 power (Eq. 2).
2. The bend length and angle play a secondary role in the CSR energy kick. Decreasing either

parameter will decrease the CSR energy kick to the 1/3 and 2/3 power, respectively (Eq. 2).

3. The spatial and angular kick directions are entirely dependent on the local dispersion. The 4-bend chicane creates a solely polarized dispersive region which limits the cancellation potential of the kicks. An extra, oppositely directed dispersive region should be added to the chicane to allow the kicks to cancel.
4. The large bunch length makes the CSR nearly negligible in the first two bends in comparison to the last two. The angles of the first two

bends can be increased, while maintaining R_{56} , without much CSR induced consequences.

With these tenants in mind, we implement changes to the 4-bend chicane with the goal of completely cancelling the CSR induced emittance dilution.

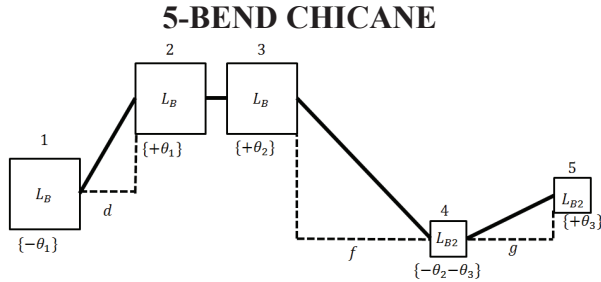


Figure 4: The 5-Bend Chicane. A second stage bunch compressor exhibiting full CSR induced emittance growth cancellation.

Table 2: The Various Characteristic Parameters of the 5-Bend Chicane Compared with the 4-Bend Chicane for BC2

Parameter	Symbol	5-Bend Chicane	4-Bend Chicane	Unit
Electron Energy	E_0	1.6	1.6	GeV
Momentum Compaction	$ R_{56} $	59.9	59.9	mm
Chicane Total Length	L_T	17.0	23.0	m
First Chicane Drift Length	L_D	3.3	9.8	m
Second Chicane Drift Length	L_F	8.7	N/A	m
Third Chicane Drift Length	L_G	1.7	N/A	m
Magnet Angle 1	$ \theta_1 $	0.103	0.05	Rad
Magnet Angle 2	$ \theta_1 $	0.103	0.05	Rad
Magnet Angle 3	$ \theta_2 $	0.046	0.05	Rad
Magnet Angle 4	$ \theta_2 + \theta_3 $	0.060	0.05	Rad
Magnet Angle 5	$ \theta_3 $	0.014	N/A	Rad
Eff. Length Of Magnet 1, 2, 3	L_B	0.54	0.54	m
Eff. Length Of Magnet 4 & 5	L_{B2}	0.25	0.54	m
Dispersion After Magnet 2	$ \eta_x $	401	562	mm
Dispersion After Magnet 4	$ \eta_x $	25	N/A	mm

We decreased the last two bend lengths and angles to account for the decreasing bunch length and to decrease the CSR effect (Table 2). Consequently, we increased the first bend angles to preserve the original compression and R_{56} . An extra bend is added in between the 4-bend's third

and fourth bend to create an extra oppositely directed dispersive region that improves the potential for kick cancellation (Fig. 5b).

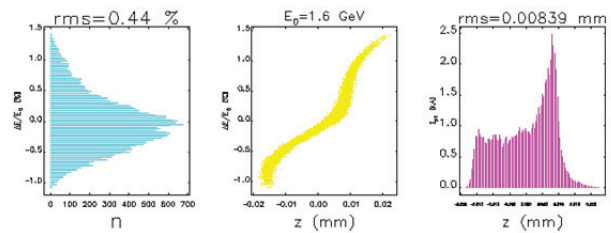
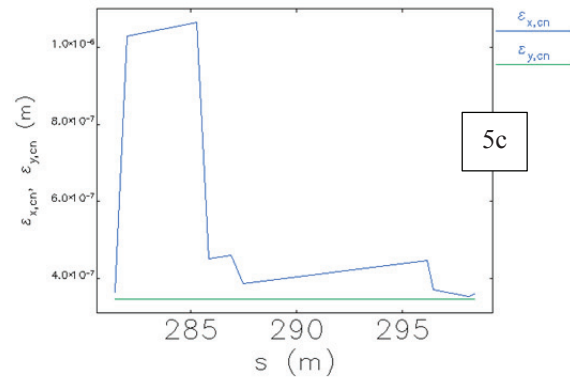
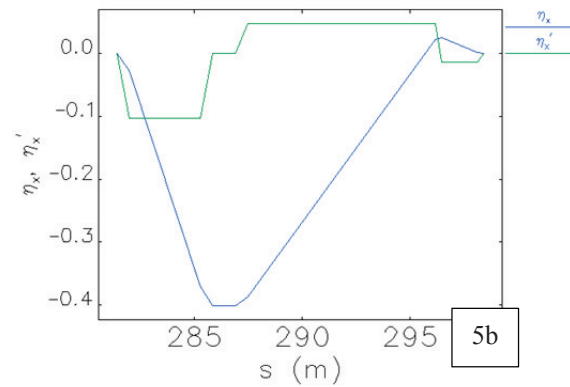
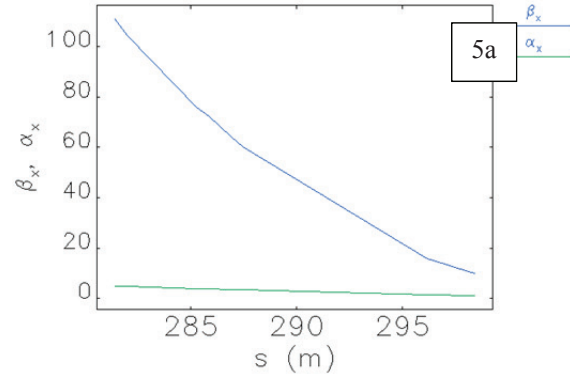


Figure 5 (Top to bottom): 5-bend chicane's: (a) The transverse x-plane β and α functions; (b) The dispersion and slope of dispersion function; (c) The dispersive corrected normalized transverse emittances ($\epsilon_{x,ec}$, $\epsilon_{y,ec}$); (d) The normalized energy spread, longitudinal energy phase space, and the current profile.

A first order approximation of the spatial and angular kicks, such as one previously performed for the 4-bend chicane (Eq. 3 and 4), provides us with the mathematical insight of the 5-bend chicane's emittance dilution suppression:

$$\sum Kicks' = \theta_1(L_B + d)(\delta_{P3} + \delta_{P4}) - \frac{1}{2}\theta_2\left(2f + L_B + \left\{\frac{\theta_2}{\theta_2 + \theta_3}\right\}L_{B2}\right)\delta_{P4} \quad (8)$$

$$\sum Kicks' = \theta_2(\delta_{P3} + \delta_{P4}) - \theta_3(\delta_{P4} + \delta_{P5}) \quad (9)$$

where, respectively, θ_1 , θ_2 and θ_3 are the 1st, 2nd and 3rd bend angles. L_B , L_{B2} , d , and f are the large and small magnet lengths and the 1st and 2nd drift spaces. And, δ_{P3} , δ_{P4} and δ_{P5} are the CSR RMS energy spread for the 3rd, 4th and 5th bending magnets. As with the 4-bend chicane case, the CSR wakefield begins to become significant in the 3rd magnet, so the kicks from the 3rd magnet and onward have been included in the linear kick model calculation. The form of equations 8 and 9, although more complicated than the 4-bend chicane, show more potential in having the kicks cancel.

Simulations performed in ELEGANT, with CSR turned on in the magnets and drifts, show that the 5-bend chicane provides excellent transverse emittance preservation (Fig. 5c). In fact, it has remarkably cancelled all transverse emittance growth due to CSR in the bunch compressor.

DESIGN IMPLEMENTATION & ENGINEERING CONSIDERATION

Although the benefits of the 5-bend chicane is clearly evident, its complexity does provide some difficulties in actually engineering the design [19, 20]:

1. The small magnets in the 4th and 5th bends require large field strengths to achieve their desired bend angle. The 4th bend, in particular, is highly problematic. With a 0.25 m magnet length and 0.060 rad bending angle, it would require a 13 kG field strength.
2. The three unique bending angles of the 5-bend chicane require a complicated powering scheme. A benefit afforded by the 4-bend chicane's simple design is it requires only a single power supply to power all four magnets amounting to a small $\frac{\Delta\theta}{\theta_B}$ deviation error throughout the system. Such is not the case for the 5-bend chicane. The first two magnets can be powered in series, while the three subsequent magnets would require their own power source, greatly increasing the $\frac{\Delta\theta}{\theta_B}$ of the system.

To ease the design and engineering efforts of the 5-bend chicane, we applied the following modifications [19, 20]:

1. Decrease the magnet strengths to provide a 50% overhead on the field requirements (Table 3):

Table 3: Revised Field Strength for each Magnet of the 5-Bend Chicane

Parameter	Symbol	5-Bend Chicane	Unit
Magnet 1	B_1	8.5	kG
Magnet 2	B_2	8.5	kG
Magnet 3	B_3	4.0	kG
Magnet 4	B_4	5.1	kG
Magnet 5	B_5	1.1	kG

2. Use identical magnets for each bend to allow the system to be powered in series just as in the 4-bend case.
3. Alter the coil number and gap size of each magnet to achieve the desired field strength; trim coils can further provide fine tuning.

Implementing these design revisions into the 5-bend design (Table 4) we then have:

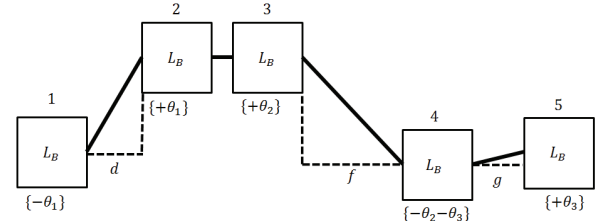


Figure 6: The revised 5-bend chicane with identical magnet lengths and overall decreased bend angles.

Table 4: The Various Characteristic Parameters of the Revised 5-Bend Chicane Compared with the 4-Bend Chicane for BC2

Parameter	Symbol	5-Bend Chicane	4-Bend Chicane	Unit
Electron Energy	E_0	1.6	1.6	GeV
Momentum Compaction	$ R_{56} $	59.9	59.9	mm
Chicane Total Length	L_T	17.8	23.0	m
First Chicane Drift Length	L_D	4.4	9.8	m
Second Chicane Drift Length	L_F	9.4	N/A	m
Third Chicane Drift Length	L_G	1.3	N/A	m
Magnet 1 Angle	$ \theta_1 $	0.087	0.05	Rad
Magnet 2 Angle	$ \theta_1 $	0.087	0.05	Rad
Magnet 3 Angle	$ \theta_2 $	0.046	0.05	Rad
Magnet 4 Angle	$ \theta_2 + \theta_3 $	0.060	0.05	Rad
Magnet 5 Angle	$ \theta_3 $	0.014	N/A	Rad
Eff. Length Of Each Bend	L_B	0.54	0.54	m
Dispersion After Magnet 2	$ \eta_x $	445	562	mm
Dispersion After Magnet 4	$ \eta_x $	22	N/A	mm

The performance of this revised 5-bend chicane (Fig. 6) is successful in greatly reducing the transverse emittance growth, but not in complete cancellation like before (results in 2.9% increase). Below, in Figure 7, are the relevant emittance and phase space plots of the revised 5-bend chicane from ELEGANT simulations. Comparing the phase space plots to that of the emittance dilution cancelling 5-bend (Fig. 5d) and 4-bend (Fig. 3) chicane, we see that the revised 5-bend chicane preserves the beam phase space extremely well.

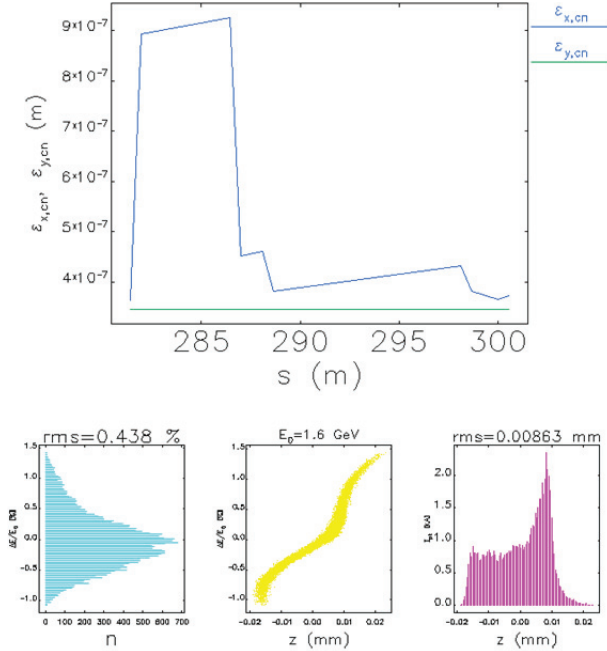


Figure 7: Top: The projected normalized corrected transverse emittance throughout the revised 5-bend chicane. Bottom (From left to right): The normalized energy spread, longitudinal energy phase space, and the current profile.

All discussions leading up this point has been in regards to nominal operations; 100pC bunch compressed to approximately 8.5 microns at the exit of BC2. For a comprehensive performance evaluation of the revised 5-bend chicane we compared its performance with that of the currently planned 4-bend chicane for two common bunch distributions and various compression ratios [21]. The results are displayed in table 5(a, b). The revised 5-bend chicane clearly outperforms the 4-bend chicane in emittance preservation for all cases.

Table 5a: “1.5kA” Chicane Test of BC2 in LCLS-II

Momentum Compaction $ R_{56} $ (mm)	Final Bunch Length (μm)	4-Bend ϵ_x Growth (%)	5-Bend ϵ_x Growth (%)
45.3	5.5	239	8
45.1	6.5	171	5
44.9	7.5	113	3
44.7	8.5	71	3
44.5	9.5	45	2

Table 5b: “1.0kA” Chicane Test of BC2 in LCLS-II

Momentum Compaction $ R_{56} $ (mm)	Final Bunch Length (μm)	4-Bend ϵ_x Growth (%)	5-Bend ϵ_x Growth (%)
36.6	5.5	178	23
36.3	6.5	135	13
36.0	7.5	91	8
35.7	8.5	59	5
35.4	9.5	37	4

LINEAR CSR MODEL

In this section, we develop a numerical treatment of the linear kick model for the emittance dilution cancelling 5-bend chicane, and test its results with that of ELEGANT. We have included the effects of bunch compression by approximating the bunch length as a linear function of angle traversed through the bending magnets [19]:

$$\sigma_z(\theta) \rightarrow \frac{\sigma_{z\text{beg}} - \sigma_{z\text{end}}}{\theta_B} \theta + \sigma_{z\text{beg}} \quad (10)$$

where $\sigma_{z\text{beg}}$, $\sigma_{z\text{end}}$, θ_B and θ is the bunch length at the entrance of the magnet, the bunch length at the exit of the magnet, the total bend angle of the magnet and the angle traversed by the bunch into the magnet, respectively. On the treatment of the CSR self-interaction in the system we employ two methods.

Steady State Regime

The CSR self-interaction is considered to be constant throughout the bunch’s trajectory in the magnet (the slippage length approaches infinity) and follows the form of equation 1 and its RMS Energy change following equation 2. We can calculate the RMS spatial and angular kicks by integrating the CSR RMS energy change with the dispersion function through the bending magnet as so [18]:

$$\langle \Delta x_i \rangle = \int R_{16i}(s) \delta_{RMS-i} ds \quad (11.a)$$

$$\langle \Delta x_i^2 \rangle = (\int R_{16i}(s) \delta_{RMS-i} ds)^2 \quad (11.b)$$

$$\langle \Delta x'_i \rangle = \int R_{26i}(s) \delta_{RMS-i} ds \quad (12.a)$$

$$\langle \Delta x'^2_i \rangle = (\int R_{26i}(s) \delta_{RMS-i} ds)^2 \quad (12.b)$$

The additive spatial kicks for coherent processes affect the transverse projected emittance according to equation 5. Then, the emittance growth is a simple matter to calculate.

Transient State Regime

We now account for the transient effects of the CSR self-interaction as the beam is entering and exiting the magnet. The phenomena can be described with two wakefield equations [22, 23]:

$$\begin{aligned} \frac{dE}{ds}(z, \phi) = W_{ENTERING}(z, \phi) = \\ -\frac{4}{R\phi}\lambda(z - S_L) + \frac{4}{R\phi}\lambda(z - 4S_L) - \\ \frac{2}{(3R^2)^{\frac{1}{3}}}\int \frac{d}{dz'}[\lambda(z')]\left(\frac{1}{(z-z')^{\frac{1}{3}}}\right)dz' \end{aligned} \quad (13)$$

where z is the coordinate along the bunch, R is the bending radius of the magnet, ϕ is the angle traversed into the magnet by the bunch, λ is the normalized linear charged density, and S_L is the slippage length ($\frac{R\phi^3}{24}$), and

$$\begin{aligned} \frac{dE}{ds}(z, x, \psi) = W_{EXITING}(z, x, \psi) = \\ \frac{4}{R}\lambda\left(z - \frac{R\phi_M^3}{24}\left[\frac{\phi_M + 4x}{\phi_M + x}\right]\right) + \\ \frac{4}{R}\left[\int \frac{d}{dz'}[\lambda(z')]\left(\frac{1}{(\psi+2x)^{\frac{1}{3}}}\right)dz'\right] \end{aligned} \quad (14)$$

where x is the position of the bunch past the exit of the bending magnet (the observed time) and ψ is the angle of the bunch at which the radiation was emitted (the retarded time). The wakefields are complicated in their dependence of ϕ and ψ when comparing them to the steady state form.

The RMS energy spread throughout the bunch can then be found:

$$\sigma_{W_i} = \left[\int_{-\sigma_z}^{+\sigma_z} [W_i(z)]^2 \lambda(z) dz - \langle W_i(z) \rangle^2 \right]^{1/2} \quad (15)$$

where $W_i(z)$ is either the entering or exiting wake and $\langle W_i(z) \rangle = \int_{-\sigma_z}^{+\sigma_z} W_i(z) \lambda(z) dz$ is simply the mean. Finally, the same procedure for finding the emittance growth from equation 5 can be applied.

For each method, the transverse projected emittance growth at the exit of chicane was calculated while scanning through various values of theta 1, 2 and 3 (and preserving R_{56}) and the results compared with ELEGANT. The results are shown in Figure 8.

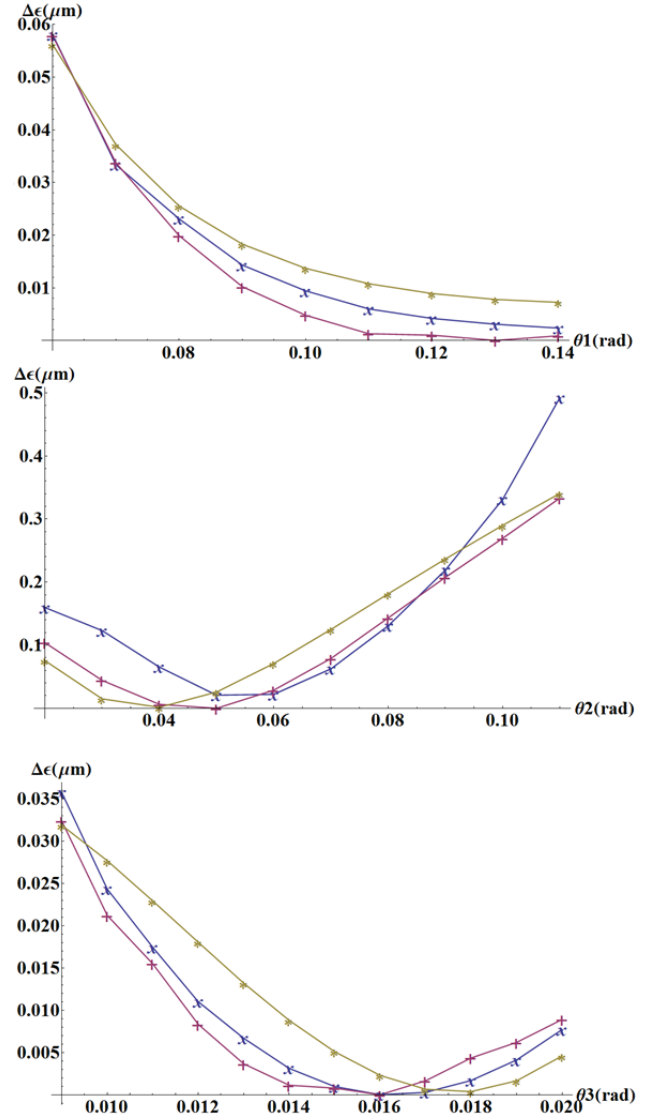


Figure 8: Plots of change in emittance at the exit of the 5-bend chicane for various bend angle scans. For each plot, the “+” is data collected with ELEGANT, the “*” is numerical data using the steady-state linear model, and the “x” is numerical data using the transient-state linear model. Top: Displays the emittance change at the exit of the 5-bend chicane while scanning θ_1 . Middle: Displays the emittance change while scanning θ_2 . Bottom: Displays the emittance change while scanning θ_3 .

The plots above show great agreement between ELEGANT and the steady and transient state linear CSR models. The steady state model is numerically simple to implement and can be calculated with limited resources. While the steady state behaviour agrees well with ELEGANT, we cannot ignore its failure to properly locate the emittance change minimum for scans of θ_2 and θ_3 (Fig. 8). The transient state model, on the other hand, properly locates the emittance change minimum for all angle scans while still maintaining agreement in behavior with ELEGANT. Conversely, the mathematics of the transient state model is far more complicated than that of the steady state. The transient state CSR wakefield

integrals must be evaluated numerically and require considerable resources and computation time.

CONCLUSION

Magnetic bunch compressors are a source of CSR induced emittance growth. New CSR mitigation techniques must be researched and developed to continue pushing X-FEL performance to the forefront.

In this paper, we have introduced a 5-bend chicane as a prospective bunch compressor for final stage compression at LCLS-II. In terms of emittance preservation, the 5-bend chicane is an attractive option with highly reduced CSR emittance growth, and in some cases, full cancellation. We will look to continue researching the 5-bend chicane as, potentially, the new standard in bunch compression and develop its analytical model to the extent of applying its CSR nullification to all relevant bending systems.

ACKNOWLEDGMENT

We would like to extend thanks to Paul Emma, Gennady Stupakov, Lanfa Wang and Mark Woodley for useful discussions.

REFERENCES

- [1] M. Borland, "Elegant: A Flexible SDDS-Compliant Code for Accelerator Simulation," Advanced Photon Source LS-287, September 2000.
- [2] N. Rohringer, D. Ryan, R. London, M. Purvis et al., Nature (London) 481, 488 (2012).
- [3] H. N. Chapman, P. Fromme, A. Barty, T. A. White, R. A. Kirian et al., Nature (London) 470, 73 (2011).
- [4] M. M. Seibert, E. T., F. Maia, M. Svenda et al., Nature (London) 470, 78 (2011).
- [5] Raubenheimer, Tor. "LCLS-II Parameters". LCLSII-1.1-PR-0133-R0.
- [6] Huang, Zhirong. "Brightness And Coherence Of Synchrotron Radiation And FELs", SLAC-PUB 15449.
- [7] W. Ackermann, G. Asova, V. Ayvazyan, A. Azima, N. Baboi, J. Ba"hr, V. Balandin, B. Beutner, A. Brandt, A. Bolzmann et al., Nat. Photonics 1, 336 (2007).
- [8] T. Ishikawa, H. Aoyagi, T. Asaka et al., Nat. Photonics 6, 540 (2012).
- [9] Y. S. Derbenev, E. L. S. J. Rossbach, and V. D. Shiltsev, Microbunch Radiative Tail-Head Interaction, Tech. Rep. TESLA-FEL 95-5, Deutsches Elektronen-Synchrotron, Hamburg, Germany (Sep 1995).
- [10] Microbunches Workshop, E.B. Blum, M. Deines and J.B. Murphy, AIP Conf. Proc. No. 367 (1996).
- [11] Z. Huang, J. Wu, T. Shafan. "Microbunching Instability Due To Bunch Compression". SLAC-PUB-11597. Dec. 2005.
- [12] S. Di Mitri, M. Cornacchia, and S. Spampinati, Phys. Rev. Lett. 110, 014801 (2013).
- [13] S. Di Mitri, M. Cornacchia. "Merit Functions For The Linac Optics Design For Colliders & Light Sources". NIMA 735, (2014) 60-65.
- [14] T. Raubenheimer, P. Emma, S. Kheifets, "Chicane and Wiggler Based Bunch Compressors for Future Linear Colliders", Proc. of 1993 IEEE PAC, Washington D.C. (1993) 635.
- [15] Y. Jing, Y. Hao, V.N. Litvinenko. "Compensating Effect of the Coherent Synchrotron Radiation in Bunch Compressors". Phys. Rev. ST Accel. Beams 16, 060704, June 2013.
- [16] P. Emma, V. Bharadwaj, Bunch Compressor Options for the LEUTL Facility at the APS, June 1999, unpublished.
- [17] M. Borland, J. W. Lewellen, S. V. Milton, "A highly flexible bunch compressor for the APS LEUTL FEL", in proceedings of LINAC2000, Monterey, USA, August 2000.
- [18] P. Emma, R. Brinkmann. "Emittance Dilution Through Coherent Energy Spread In Bend Systems". SLAC-PUB-7554, May 1997.
- [19] Raubenheimer, Tor. Private communications.
- [20] Amann, John. Private communications.
- [21] Wang, Lanfa. Private communications.
- [22] E. L. Saldin, E. A. Schneidmiller, and M. V. Yurkov, Nuclear Instruments and Methods, Sec. A 398, 373, 1997.
- [23] G. Stupakov, P. Emma. "CSR Wake For A Short Magnet In Ultra-Relativistic Limit". LCLS-TN-01-12, Dec. 2001.

MOGA OPTIMIZATION DESIGN OF LCLS-II LINAC CONFIGURATIONS*

L. Wang[#], P. Emma, Y. Nosochkov, T. Raubenheimer, M. Woodley and F. Zhou,
SLAC, Stanford, CA 94309, USA
C. Papadopoulos, J. Qiang and M. Venturini, LBNL, Berkeley, CA 94720, USA

Abstract

This paper briefly summarizes the preliminary optimization study on the configurations of LCLSII with superconducting cavity. The setup of each configuration is first optimized using Multi-Objective Genetic Algorithm (MOGA) with LiTrack which includes the longitudinal phase space only. For each operation mode, MOGA is applied to optimize the machine parameters in order to get flat top current profile and zero energy chirp at the beginning of the undulator. The geometric wake of the RF cavities and resistive wall wake of the beam pipe are included, but the coherent synchrotron radiation (CSR) wake is not included. Finally, ELEGANT code is used to do full 3-dimension particle simulation, which includes the CSR and ISR effect. Therefore, the emittance growth due to CSR can be checked. A new code has been recently developed to integrate all the wake field and CSR in the MOGA optimization.

INTRODUCTION

The new LCLS-II high-repetition rate FEL project at SLAC [1] will use a new superconducting linac composed of TESLA-like RF cavities in continuous wave (CW) operation, in order to accelerate a 1-MHz electron beam to 4 GeV. Figure 1 shows the optics (top) of the hard x-ray beam and the layout of LCLS-II linac (bottom). The new superconducting linac is driven by a new high-rate injector [2], will replace the existing SLAC copper linac in sectors 1-7 (101.6 m/sector), while the remaining Cu RF structures in sectors 7-10 will be removed and replaced with a simple beam pipe and focusing lattice (the “linac extension”). The existing 2-km PEP-II bypass line (large β section in Fig.1) will be modified to transport electrons from the linac extension in sector 10 through more than 2.5 km and into either of two undulators in the existing LCLS undulator hall. The overall design of the linac can be found in [3]. The resistive wall wake field along this long bypass beam line play an important role in the linac design as discussed later. The current design has two bunch compressors (BCs), which are located at the 2nd and 3rd non-zero horizontal dispersion sections in Fig. 1. The 1st dispersion section is laser heater. The injector beam is optimized at beam energy of 98MeV [4] to give a small transverse emittance and certain peak current. This paper describes the optimizations afterwards to the beginning of the FEL undulator.

The main parameters to be optimized include the phase and voltage of linac 1 (L1), linearizer (before BC1), linac 2 (L2) (between BC1 and BC2) and the R56 of BC1/BC2.

The beam energies at BC1 and BC2 are 250MeV and 1.6GeV, respectively. The beam is accelerated to 4.0 GeV by linac 3 (L3).

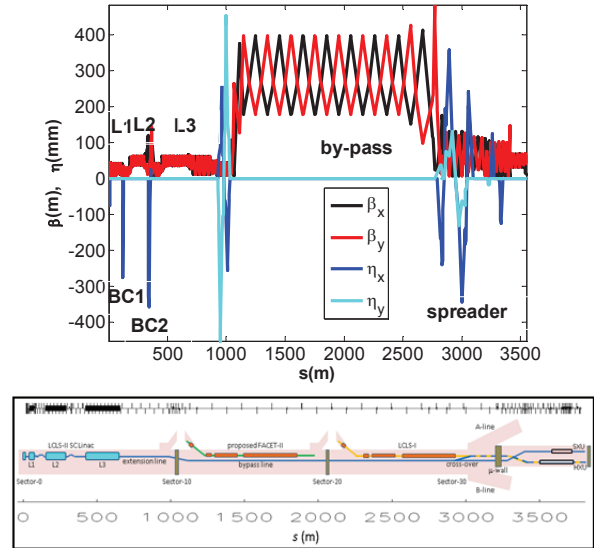


Figure 1: Optics (HXR)(top) and Layout (bottom) of the LCLS-II linac. The BC1 and BC2 are located at the 2nd and 3rd non-zero horizontal dispersion section, respectively.

NONLINEAR BEAM FROM INJECTOR

In the current design, the injector of LCLS-II uses CW normal conducting RF gun [2]. The strong space charge effect at the injector induces large nonlinearity in the longitudinal phase space. The dominant one is cubic term, which is the fundamental term of the longitudinal space charge effect. The high order terms also have large contributions to the linac beam dynamics. These nonlinear effects are amplified throughout the linac when the bunch is compressed. The strong space charge effect makes LCLS-II beam largely different from the existing LCLS beam where the nonlinear term (cubic term dominant) is mainly induced by the strong geometric wake in the normal conducting RF structures. As a result, the design of LCLS-II beam has strong dependence on the injector.

The longitudinal phase space, current profile and $Bmag = 0.5 \left(\frac{\beta_0}{\beta} + \frac{\beta}{\beta_0} + \left(\alpha \sqrt{\frac{\beta_0}{\beta}} + \alpha_0 \sqrt{\frac{\beta}{\beta_0}} \right)^2 \right)$ along the bunch at linac with 98MeV beam are shown in Fig. 2 for three bunch charges: 20pC, 100pC and 300pC. The overall bunch profile is similar: there is a long bunch tail. The nonlinearity can be clearly seen after extracting the linear chirp and RF curvature as shown in Fig. 3. The high order terms are comparable to the cubic term. The

*Work supported by Department of Energy Contract No. DE-AC02-76SF00515

[#]wanglf@SLAC.stanford.edu

nonlinearity is about proportional to the peak current. A 20pC bunch charge with 10A peak current has too large nonlinearity, which makes it difficult to provide good quality beam for FEL. For this reason, a lower peak current of 4.5A is chosen for 20pC to reduce the space charge effect.

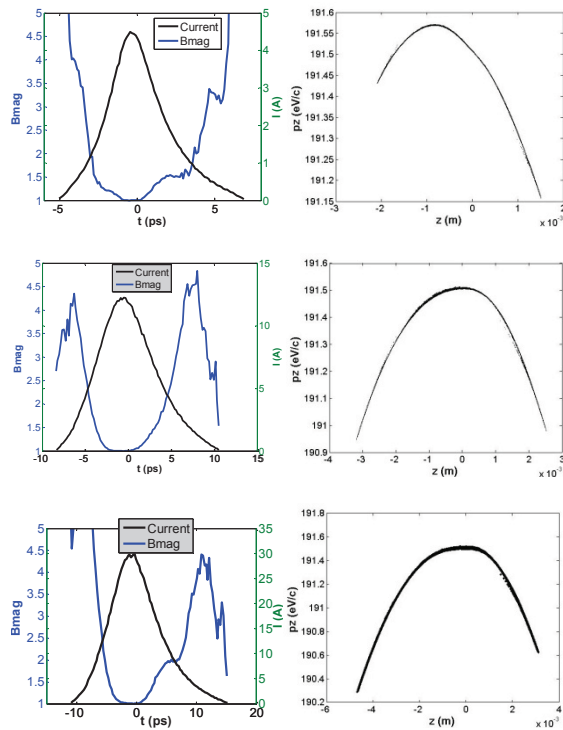


Figure 2: Current profile (left) and Phase space (right) at the exit of injector linac (98MeV) for 20pC (top), 100pC (middle) and 300pC (bottom) bunch charge. Bunch head is to the left.

The strong space charge also causes mismatching along the bunch, especially for 20pC case where the space charge is stronger. However, the core bunch still has good matching. When the beam passes through the linac, the collective effects add more mismatching to the beam. The mismatched beam can affect the FEL performance [5,6].

STRONG RESISTIVE WALL WAKE AS A NATURAL DE-CHIRPER

The wake fields play an important role in the beam dynamics: de-chirper the beam and increase the nonlinearity.

Figure 4 shows the longitudinal wake in the 1.3GHz and 3.9GHz SC cavity, which is used to linearize the phase space before BC1. The linearizer has much stronger wake.

On the other hand, the resistive wall (RW) wake plays an important role to de-chirper the beam. Table 1 lists the contributions of the resistive wall wake, which is dominant by the 2km-long bypass line. The beam is chirped along Linac 1 and Linac 2 by the RF cavities in order to compress the beam. This positive chirped beam is naturally de-chirped by the resistive wall wake after Linac

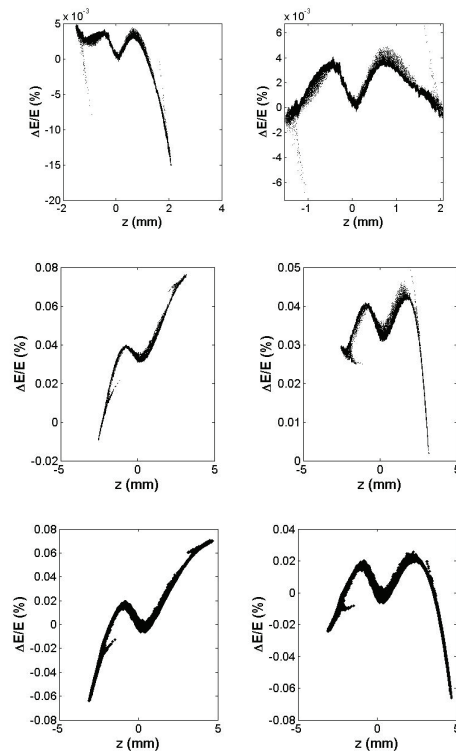


Figure 3: 3rd-order term (left column) and high order terms (right column) at the exit of injector linac (98MeV) for 20pC (top), 100pC (middle) and 300pC (bottom) bunch charge.

3 if the design is optimal. This is a nice feature of LCLSII design. However, this also puts a strong constraint on the design since the RW wake field cannot be adjusted. The large de-chirp effect due to the resistive wall wake requires enough chirper to be provided by the RF cavities. For 1kA peak current of flat beam, the energy loss due to the resistive wall wake are 4.8MV, 18MV and 34MV for 20pC, 100pC and 300pC, respectively. Figure 5 shows the evolution of longitudinal phase space where the de-chirper by the RW wake is clear seen.

The strong de-chirp of RW wake sets a tight constraint in the linac design. It is too strong for high charge so that it leads to a large bunch compression factor at the second bunch compressor, and therefore a large R_{56} . In most cases, there is no need for additional de-chirper. Instead, it requires the linac RF to provide large enough energy chirp to compensate the RW effect, which adds a constraint in the set-up of the bunch compressor systems. Indeed, the design of the BCs strongly depends on the RW wake. The design has more flexibility for a small RW wake.

Besides the energy loss due to the resistive wall wake, the RW wake also can spoil the phase space. The nonlinear wake field for a longer bunch ($>100\mu\text{m}$) causes strong distortion in phase space. This makes it difficult to provide high quality long bunch, for instance, 300pC bunch charge with peak current 500A. The RW wake with Aluminum pipe has stronger nonlinearity and it would be good to replace it with stainless steel material or surface

coating. Furthermore, when the beam has strong double horn in current profile, the RW wake also induces strong nonlinear de-chirper.

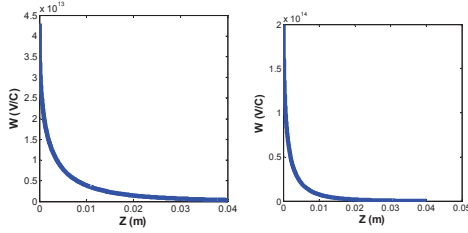


Figure 4: Longitudinal wake field in the 1.3GHz (left) and 3.9GHz (right) cavities.

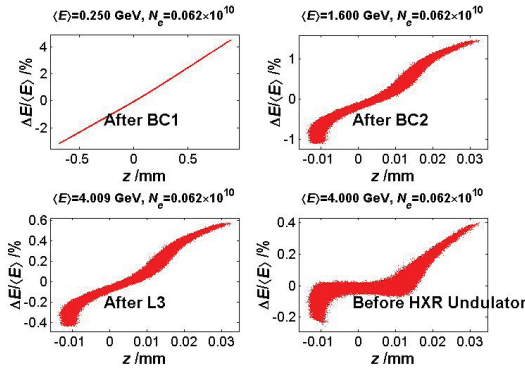


Figure 5: Longitudinal phase spaces for 100pC 1kA beam.

VARIOUS CONFIGURATIONS OF THE LINAC

The fast speed of Litrack code is used in the MOGA optimization [7] in this section. The CSR is not included. Table 2 summarizes the main parameters of the optimized configurations. The strategy of the optimization aims to reduce the RF power while providing a similar beam quality: flat current profile and smaller energy spread (zero energy chirper). A new baseline, which tends to reduce the R56 at BC2 by increasing the compression factor at BC1 in order to mitigate the CSR at BC2, is also added in Table 2 to show the range of the parameters. It uses a reduced RW wakes compared with the one listed in Table 1.

The energy losses due to CSR at BC2 are also listed in the Table (detail see next section). The power is calculated for a repetition rate of 929 kHz for all bunch charges. The energy loss in BC1 is about 1W for 100pC and 3W for 300pC. The maximum power loss in BC2 is about 117 W for 300pC charge, which can become even larger when larger peak currents are applied in the future.

Figure 6 shows the phase space and current profile at the beginning of the undulator by Litrack. The current profiles are all flat except 100pC 1.5kA case. These flat current profiles are essential for the self-seeding. There are also always near zero energy chirp for the core part of bunches.

Table 1: Resistive Wake along the Linac

Beam line Section	Pipe Length(m)	Pipe Radius(mm)	Material	Conductivity (Ohm-m)	Time Constant (fs)	Peak Energy Loss (MeV)
Linac Extension	353	24.5	S.S	1.37×10^6	5	1.2
Rolled DogLeg #1	50	12.7	S.S	1.37×10^6	5	0.5
Bypass Line	2193	24.5	S.S	1.37×10^6	5	12.06
DL<U to Und.	382	12.7	AL	3.60×10^7	5	4

Table 2: Configurations for BC1 Energy 250MeV and BC2 Energy 1.6GeV, without Dechirper

	20pC, 500A	100pC, 1kA	100pC, 1kA, New baseline [3]	100pC, 1.5kA	300pC, 1kA	300pC, 600A
$\phi_{L1} (^{\circ})$	-21	-21	-12.2	-21.9	-19.85	-20
$\phi_{Linearizer} (^{\circ})$	-165	-165	-150	-164.5	-162.2	-162
$\phi_{L2} (^{\circ})$	-21.1	-21	-21.1	-28.4	-28.86	-29
$\phi_{L3} (^{\circ})$	0	0	0	0	0	0
V_{L1} (MV)	219.6	219.6	216	225	222	222
$V_{Linearizer}$ (MV)	54.78	54.78	64.90	58.7	59.58	59.58
BC1 R_{56} (mm)	-53	-55	-55	-53.46	-47.4	-44.7
BC2 R_{56} (mm)	-61.8	-60	-37.5	-45.5	-49.2	-49.2
σ_{z0} (mm)	0.627	1.02	1	1.02	1.30	1.30
I_{pk0} (A)	4.5	12	12	12	31	31
σ_z^{BC1} (mm)	0.187	0.283	0.15	0.246	0.43	0.48
I_{pk}^{BC1} (A)	15	43	82	50	91	82
$\sigma_E^{BC1} (%)$	0.835	1.36	1.6	1.469	1.857	1.857
σ_z^{BC2} (μm)	5.16	8.85	9.2	5.516	29	48
I_{pk}^{BC2} (kA)	0.515	1.355	1.36	2.723	1.18	0.75
$\sigma_E^{BC2} (%)$	0.295	0.458	0.378	0.53	0.822	0.884
$\sigma_E^{UndBEG} (%)$	0.055	0.065	0.066	0.079	0.239	0.346
P_E^{BC2CSR} (W)		42		88	117	84

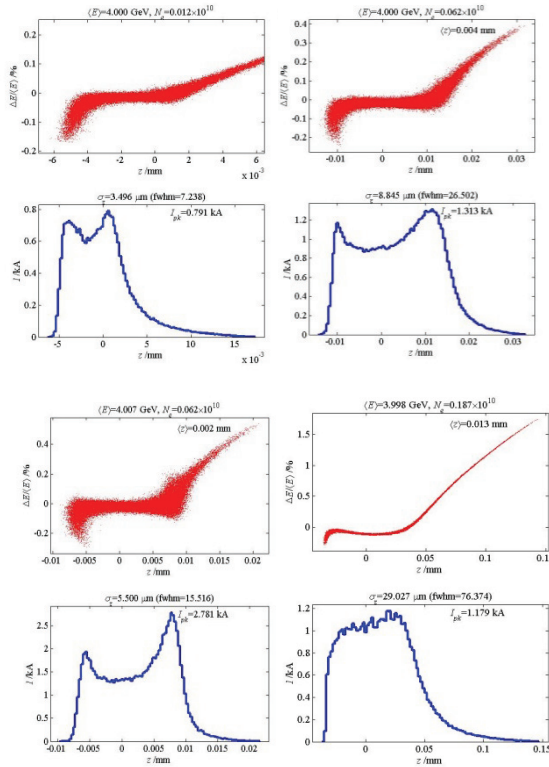


Figure 6: Phase space and current profile before the undulator for different configurations (from top/left to bottom/right: 20pC@500A, 100pC@1kA, 100pC@1.5 kA, 300pC@1kA).

CSR EFFECT ON THE BEAM

After getting satisfactory solutions from MOGA optimization, we use ELEGANT to track particles 3-dimensionally. Besides the wake fields, the CSR and ISR are included. The CSR changes the beam current profile and some parameters are tweaked to get flat top current profile.

BC1 and BC2 are located along the Superconducting Linac. Therefore, the energy loss there due to CSR needs to be evaluated. The energy loss due to CSR at the 2nd bunch compressor (BC2) is large due to the high peak current there. The radiation can propagate to the downstream and heat the superconducting RF cryomodule. The ISR in general is much smaller compared with the CSR. Unlike a true wake, each particle is affected only by those behind it. Also unlike true wakes, the effects of CSR depend on the slope of the bunch distribution. The steady status CSR model largely underestimates the CSR since the bending magnets are short in our case.

The reality of CSR in a bunch compressor is much more complicated than the 1-D steady state result. The transient effects entering bend magnets and the propagation of CSR through drifts following the bending magnets and the variation of bunch profile are all important. Furthermore, the CSR affects the transverse dynamics throughout the bunch compressor where the

transverse beam size and beam optics vary. The estimation of CSR in the paper includes all above factors by tracking the particles through the bunch compressors. The total energy loss at BC2 for various configurations is listed in Table. 2.

Figure 7 shows total CSR kicker along the bunch through BC2 for 300pC. The energy loss is up to 0.7MeV. The CSR kicker in this case acts like a linear de-chirper for the core part of bunch. However, when the bunch profile is not flat, the CSR kicker has strong nonlinearity.

Figures 8-11 shows the longitudinal phase space and current profile at the beginning of the undulator for various configurations. The simulations are done with ELEGANT code which includes the geometric wake fields, resistive wakes, ISR and CSR. The CSR has large impact on the beam. For instance, the current profile with CSR is different from the ones without CSR as shown in the previous sections. The phase space can also vary a lot due to the CSR. It is better to optimize the beam with CSR so that the solutions are the final ones.

The CSR can increase the projected emittance. The configuration of 300pC bunch charge with 700A is very good, which has zero emittance growth. The 20pC beam also has very small emittance growth. Figure 12 shows the slice emittance of 100pC 1kA beam and 300 pC 1kA beam. The emittance growth for 100pC charge 1kA beam is very small. However, the emittance at head of bunch for 300pC 1kA bunch is spoiled by CSR in the spreader (at 3000meter in Fig. 1). This emittance growth can be minimized by optimizing the optics there. We haven't applied any emittance cancellation schemes [8-11] yet. Overall, the emittance growth can be controlled by optimizing the current profile, reducing R56 and applying cancellation schemes.

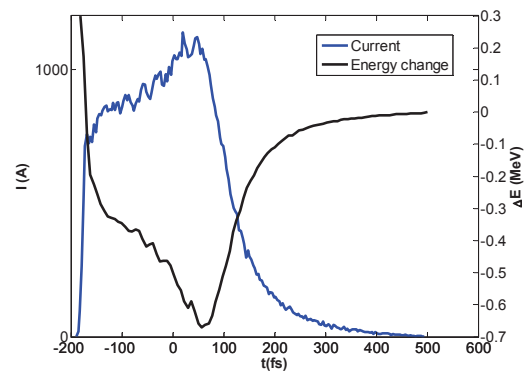


Figure 7: Energy loss due to CSR at whole BC2 for 300pC beam. The bunch shape is also shown, with the head to the left (the blue curve).

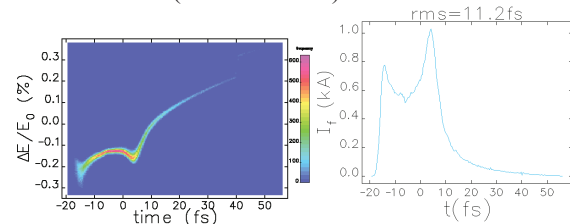


Figure 8: Phase space before undulator from Elegant simulation for 20pC beam with 600A peak current.

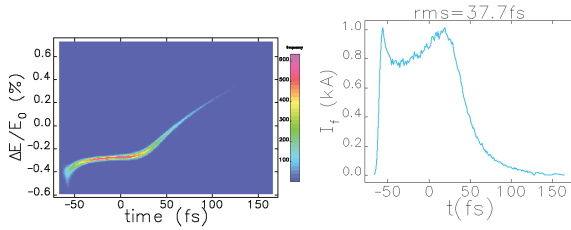


Figure 9: Phase space before undulator from Elegant simulation for 100pC beam with 1.0kA peak current.

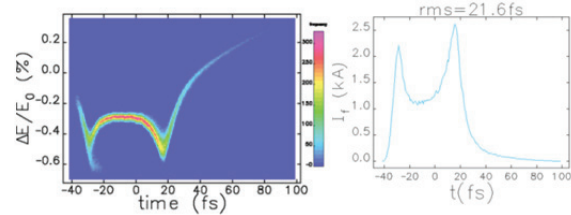


Figure 10: Phase space before undulator from Elegant simulation for 100pC beam with 1.5kA peak current.

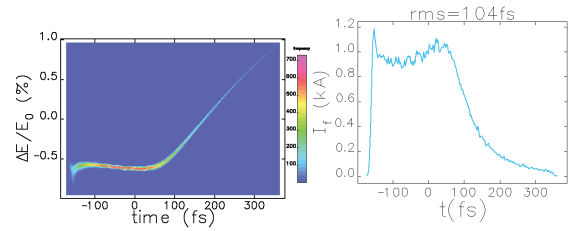


Figure 11: Phase space before undulator from Elegant simulation for 300pC beam with 1kA peak current.

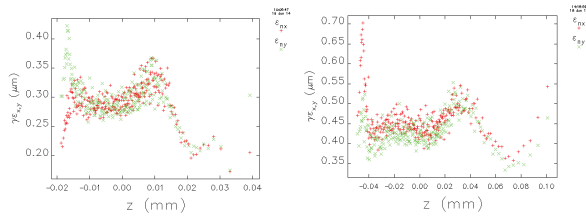


Figure 12: Slice emittance at the beginning of undulator for 100pC 1.0kA (left) and 300pC 1kA (right).

TOWARDS HIGH PEAK CURRENT

Preliminary study shows that it is a bit of a challenge to set-up high peak current configuration. Besides the projected emittance growth due to CSR, the large energy loss can distort the phase space. The emittance growth can be mitigated or cancelled by optics design, however, there is no simple mitigation for the latter. For instance, the peak current at 20pC can be easily above 3kA. Figure 13 shows an example of the ELEGANT simulation. However, the collective effect largely distorts the phase space. This makes the high peak current configuration difficult.

A new program is recently developed to include the CSR in the MOGA optimization. The studies show we are able to increase the peak current more than 1kA as what we have now. Figure 14 shows one example of the preliminary result for 300pC. A peak current of 1.5kA

with flat current profile is achieved, which is much better than the 1.5kA beam shown in Fig. 6 where there is a large horn in the current profile. Further careful studies including the emittance growth are under the way.

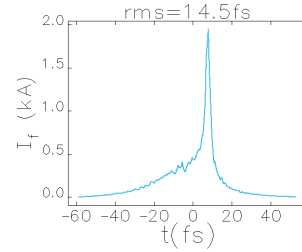


Figure 13: Current profile of 20pC bunch before the Undulator. Elegant simulation.

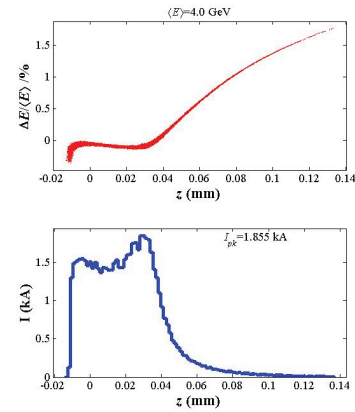


Figure 14: Example of high peak current solution for 300pC charge. Wake fields and CSR are included.

SUMMARY AND OUTLOOK

MOGA is applied to optimize the LCLSII in order to get flat top current profile and zero energy chirp. Small energy spread, zero energy chirp and flat current profile are achieved for different bunch charges. MOGA provides a very useful tool in the design.

One kA flat beams with good emittance are obtained for both 100 pC and 300 pC bunch charge. 20pC bunch has very small emittance, however the peak current with a flat current profile is below 1kA. Although a single spike with high peak current (>2kA) is possible, the beam quality is largely spoiled by the CSR.

In short summary, the resistive wall provides a strong de-chirper and has large impact on the design of LCLSII linac. The new proposed RW wake is about 30% smaller compared to what we used in Table 1 [3]. This allows more freedom in the design. For instance, a smaller compression factor at BC2 (therefore a small R56) is possible. A small R56 reduces the CSR there. However, a large R56 may provide stronger damping to the micro-bunch instability which is a concern now.

The emittance growth due to CSR can be well controlled for 1kA beams. However, the CSR can spoil the longitudinal phase space. Low charge modes are difficult and require more work. It is promising to have a high peak current 1.5 kA with flat current profile.

Studies show that there is a strong micro-bunch instability driven by the longitudinal space charge (LSC) impedance, especially along the long bypass beam line. This may have an impact on the linac design. The studies in this paper haven't included LSC, we are working on it.

ACKNOWLEDGEMENTS

We thank our colleagues M. Agostino, Y. Ding, M. Gabriel, Z. Huang, J. Wu at SLAC and G. Penn at LBNL for supporting the FEL simulations and fruitful discussions. This work is supported by Department of Energy Contract No. DE-AC02-76SF00515.

REFERENCES

- [1] T. Raubenheimer, "The LCLS-II, a New FEL Facility at SLAC", in Proc. of 36th Int. Free-Electron Laser Conf., Basel, 2014, WEB001.
- [2] J. Schmerge et al., "The LCLS-II Injector Design", in Proc. of 36th Int. Free-Electron Laser Conf., Basel, 2014, THP042.
- [3] P. Emma, et al., "Linear Accelerator Design for the LCLS-II FEL Facility", in Proc. of 36th Int. Free-Electron Laser Conf., Basel, 2014, THP025.
- [4] C.F. Papadopoulos, et al., "RF Injector Beam Dynamics Optimization for LCLS-II", in Proceedings of IPAC'14, Germany, June 2014, WEP0015 (2014).
- [5] G. Penn, T.O. Raubenheimer, L. Wang, P. Emma, E. Hemsing, Z. Huang, "LASER SEEDING SCHEMES FOR SOFT X-RAYS AT LCLS-II", in Proc. of 36th Int. Free-Electron Laser Conf., Basel, 2014, MOP075.
- [6] G. Marcus, Y. Ding, P. Emma, Z. Huang, T. Raubenheimer, L. Wang, J. Wu, "FEL SIMULATION AND PERFORMANCE STUDIES FOR LCLS-II", in Proc. of 36th Int. Free-Electron Laser Conf., Basel, 2014, TUP032.
- [7] L. Wang and T. O. Raubenheimer, "Multi-Objective Genetic Optimization for LCLSII X-Ray FEL", Proceedings of FEL 2013, August 2013, p.12 (2013); Journal of Mechanics Engineering and Automation 4 (2014) 632-638.
- [8] E.L. Saldin, E.A. Schneidmiller, M.V. Yurkov, "On the coherent radiation of an electron bunch moving in an arc of a circle", Instrum. Methods Phys. Res., Sect. A 398, p373 (1997).
- [9] D. Douglas, "Suppression and Enhancement of CSR-Driven Emittance Degradation in the IR-FEL Driver", Thomas Jefferson National Accelerator Facility Report No. JLAB-TN-98-012, 1998.
- [10] S. Di Mitri, M. Cornacchia, and S. Spampinati, "Cancellation of Coherent Synchrotron Radiation Kicks with Optics Balance", PRL 110, 014801 (2013).
- [11] Yichao Jing, Yue Hao, and Vladimir N. Litvinenko, "Compensating effect of the coherent synchrotron radiation in bunch compressors", Phys. Rev. STAccel. Beams 16, 060704 (2013).

RECENT PHOTOCATHODE R&D FOR THE LCLS INJECTOR*

F. Zhou, J. C. Sheppard, T. Vecchione, E. Jongewaard, A. Brachmann,
J. Corbett, M. Ferreira, S. Gilevich, J. Lewandowski, S. Vetter, S. Weathersby,
SLAC, Menlo Park, CA 94025, USA

Abstract

The Linac Coherent Light Source (LCLS) has used three copper photocathodes since its commissioning in 2007. Two of three copper cathodes had low initial quantum efficiency (QE) ($<1 \times 10^{-5}$) in the LCLS radio frequency (RF) gun. The two cathodes were exposed to the plasma cleaning in the cathode test chamber before installation in the RF gun. Recent studies at the SLAC RF gun test bed at the Accelerator Structure Test Area (ASTA) reveals that the pre-cleaning in the test chamber followed by cathode exposure to air for installation in the gun is the major factor leading to the low initial QE. All four cathodes, without the plasma pre-cleaning prior to the installation in the gun, have demonstrated initial $QE > 4 \times 10^{-5}$ at the ASTA. Systematic studies also demonstrate that high-power RF gun operation provides an initial QE boost. In-situ laser cleaning for three new cathodes in the RF gun is extensively investigated, and a robust laser cleaning procedure is established at the ASTA with improvements of previous cleaning recipe for the LCLS cathode. The QE was shown to reproducibly evolved to $>1 \times 10^{-4}$ from about 4×10^{-5} immediately following the laser cleaning over ~ 3 weeks, a time much shorter than a few months for the previous laser cleaning for the present LCLS cathode. The intrinsic emittance of copper cathodes is recovered to the normal value within 1-2 days following the laser cleaning, much shorter than 3 weeks for previous laser cleaning for the present LCLS cathode. The experimental results at the ASTA, including comparison with the previous cleaning for the present LCLS cathode, are presented in the paper. Physics of the laser cleaning process and the evolution of the QE is discussed.

INITIAL QE WITHOUT IN-SITU CLEANING IN THE RF GUN

An RF gun test bed located at the SLAC's Accelerator Structure Test Area (ASTA) has been constructed [1] to study photocathodes for the Linac Coherent Light Source (LCLS) injector cathode operations. The beamline of the ASTA gun test bed duplicates the existing LCLS injector gun system [2], consisting of a chirp-pulse-amplifier laser tripled to 253 nm wavelength, LCLS-type RF gun, a solenoid for emittance compensation, one pair of magnet correctors, a Faraday cup to measure the bunch charge, and a YAG screen to measure beam size and intrinsic emittance. Similar to the LCLS injector, the drive laser is configured for normal incident injection to the photocathode surface using a 45° in-vacuum mirror. The final electron beam energy from the RF gun is about 5.5 MeV.

*The work is supported by DOE under grant No. DE-AC02-76SF00515.

The Cause for Low Initial QE in the RF Gun

The LCLS located at the SLAC National Accelerator Laboratory has been successfully operated for users for about 5 years. Its copper-based photo-injector has produced an ultra-low emittance and ultra-fast electron beam for the x-ray free electron laser (XFEL). Since its commissioning in 2007, three identical copper cathodes have been used for the LCLS injector operations with different initial quantum efficiency (QE) values. As illustrated in Fig.1, the first and third (present) LCLS cathodes had unexpectedly very low initial QE [3], about 5×10^{-6} , while the second one had 6.5×10^{-5} of initial QE as expected. Lately, it is realized that both the first and third LCLS cathodes were exposed to the plasma cleaning in the test chamber before cathode exposure to air for installation in the RF gun, while the second one did not have this cleaning process. Very low QE measured in the test chamber drives to proceed to plasma cleaning for the cathode prior to the installation in the gun. During the cathode installation in the LCLS RF gun, the cathodes have to be exposed to air for about 3 minutes for the cathode change due to the lack of loadlock system. The recent observations at the ASTA RF gun reveal that the laser-cleaned areas are much more susceptible to the air exposure than the non-cleaned areas do. The ASTA RF gun is vented to nitrogen and then exposed to air for about 3 minutes to mimic the LCLS cathode change before its vacuum starts to be pumped down. Figure 2 (left) and (right) shows the QE maps before and after the RF gun vacuum venting to air, respectively. Before the RF gun vacuum venting, areas A, B, C, D, E, F, G and H on the cathode have been cleaned by the intensive laser, while the circled center area is not exposed to any laser cleaning. In Fig. 2 (left), bunch charge from areas A, B and C have been evolved to about 7500 units for a given laser energy, equivalent to 1×10^{-4} of QE, while the cathode center area has about 3500 units of the bunch charge for the same laser energy, equivalent to about 4×10^{-5} of QE. After gun vacuum venting, bunch charge productions from the previously cleaned areas A, B, C, D, E, F, G, and H were dropped to 1500-2000 units shown in Fig. 2 (right), equivalent to about $1-2 \times 10^{-5}$ of QE, but the QE of the cathode center area still remains unchanged, at 4×10^{-5} . The observations indicate that the cleaned or activated surface is susceptible to the air-exposure, revealing the pre-cleaning is the cause for low initial QE measured in the RF gun.

Total four cathodes are characterized, which are not exposed to the pre-cleaning prior to the installation in the ASTA RF gun. All four ASTA cathodes have good initial QE in the RF gun ranging from 4×10^{-5} to 8×10^{-5} , as illustrated in Fig. 1. We conclude that the pre-cleaning

process activates the cathode surface, extremely susceptible to the contaminations, such as air-exposure. Without plasma cleaning in the test chamber, high initial QE can be routinely achieved in the RF gun.

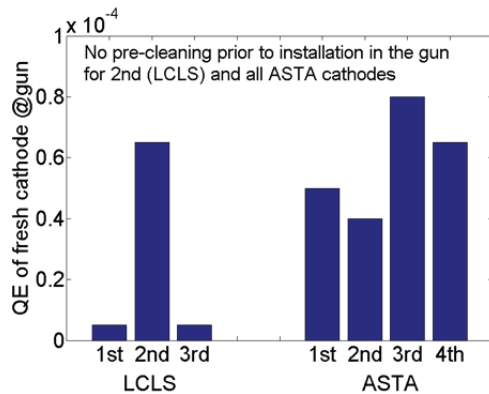


Figure 1: Original QE of cathodes in the LCLS and ASTA RF guns.

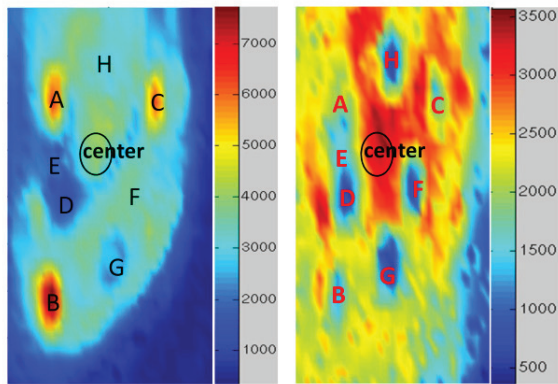


Figure 2: QE map before (left) and after (right) the gun vacuum venting. Before the gun venting, areas A to H are processed by laser cleaning while the center area is not cleaned by intensive laser.

QE Impact from the High-Power RF Processing

For LCLS operations all three photocathodes were characterized in a test chamber prior to the installation in the RF gun. The test chamber utilizes a broadband UV light source followed by a narrow-band monochromator to select the desired photon energy. The photoemission from the cathode under 2.6 kV/m of electric field is measured with nanometer. The QE measured in the test chamber is typically on the order of 1×10^{-7} at the desired photon energy of 4.91 eV (253 nm). The cathodes with the low QE observed in the test chamber are then directly installed in the ASTA RF gun. Surprisingly, following high-power RF processing all four cathodes in the gun have demonstrated an initial QE $> 4 \times 10^{-5}$ under normal operation conditions, two orders of magnitude higher than in the test chamber. The Schottky effect enhances QE by less than an order of magnitude for a copper work function between 4.3-4.7 eV. The two orders of magnitude of QE enhancement in the RF gun therefore cannot be explained by the Schottky effect alone. It is noticed that the high-power RF operation boosts QE at the

ASTA RF gun, as shown in Fig. 3. For a new cathode installed in the ASTA RF gun, the initial QE is 3×10^{-5} for the first day of electron beam operation. Then the QE increases by 50% after a few days of RF operations. It is logical to assume the RF processing conditions the cathode by removing surface contamination. In combination with the Schottky effect, a much higher QE is observed relative to measurements in a test chamber.

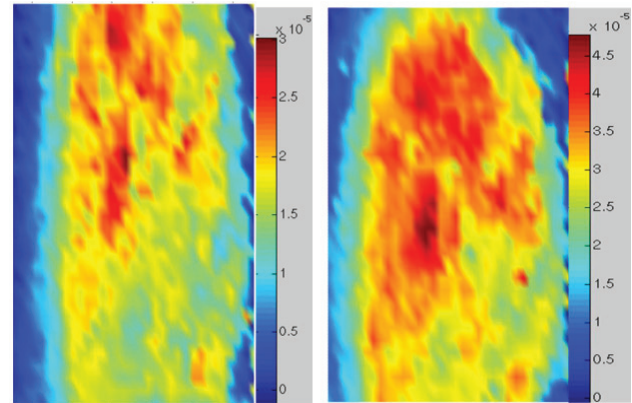


Figure 3: QE map for a new cathode in the ASTA RF gun: 3×10^{-5} of peak QE for first day with turn-on electron beam (left), 4.5×10^{-5} for a week later (right).

IN-SITU LASER-ASSISTED CLEANING DEVELOPMENTS IN THE ASTA RF GUN

Laser-based cleaning techniques have been widely used to clean metal photocathodes, such as copper and Mg, for more than two decades. A high-intensity laser beam, interacting with the metal cathodes, may ablate the cathode surface, removing surface contamination and possibly changing the cathode reflectivity, thereby resulting in a QE increase. However, the laser cleaning may change cathode's QE uniformity, thereby electron beam emittance, and also generate unwanted dark current or even deteriorate cathode's crystal quality, if the laser cleaning process is too aggressive.

The laser cleaning was performed for the present LCLS cathode in July 2011 [4]. The QE was evolved to 1×10^{-4} from 3×10^{-5} over a few months following the laser cleaning. Since then, 1×10^{-4} of the QE is essentially unchanged for three years to date for 24/7 users operation. The emittance was recovered to the normal value within three weeks following the laser cleaning. Although the previous LCLS laser cleaning was successful, two major concerns still remain. One concern is the reproducibility of the laser cleaning for different spots on the same cathodes and different cathodes. The other is the need to reduce emittance-recovery time and QE-evolution time following the laser cleaning with refinements of laser leaning process. These concerns are particularly important to deliver reliable and high quality electron beam for a high-impact machine for users, like the LCLS, which drives further studies at ASTA.

Improvements of Laser Cleaning at the ASTA RF Gun

The laser energy for the previous laser cleaning of the current LCLS cathode performed in 2011 was fully determined by the vacuum activity in the RF gun [4]. In that case, the laser energy was set to a value for each round of the laser cleaning in order that about 0.5×10^{-10} Torr of the RF gun vacuum rise can be observed. It took 2-3 rounds of laser cleaning to increase QE to the desired value, $(3-5) \times 10^{-5}$. For a better laser cleaning process, the laser energy should be set to a value with which QE is increased but with minimum gun vacuum rise. In this case, the copper crystal quality and cathode uniformity may not be affected. Ideally any minor surface change by the laser cleaning may cause a vacuum change. But in practice, observation of the RF gun vacuum rise depends on the resolution of the RF gun vacuum gauge and its controls, and the distance of the vacuum gauge to the cathode. To consider these practical factors, at the ASTA we start the laser cleaning with a laser-energy below the observable small gun vacuum activity. For example, if a small RF gun vacuum activity of 0.5×10^{-10} Torr is observed with 8 μJ of laser energy in about 40 μm rms of spot size, the actual laser energy for the first round is set to 6-7 μJ . Using this technique it was found that the QE could be reliably enhanced with only small amounts of vacuum activity.

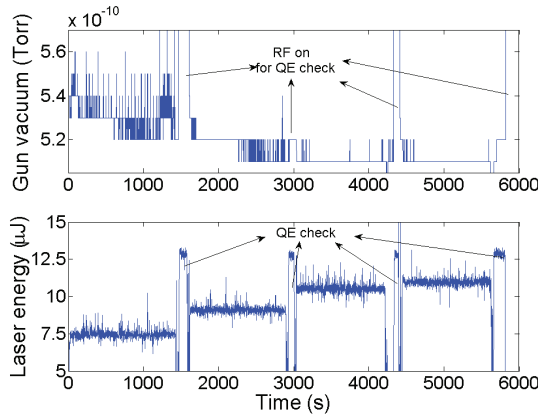


Figure 4: Laser energy and gun vacuum activities for the laser cleanings at ASTA.

Laser energy for subsequent rounds is increased in small, 0.5-1 μJ step. Typical RF gun vacuum activity and laser energy for each round are shown in Fig. 4. The vacuum activity during the laser cleaning for each round at the ASTA is much less than at the LCLS [4]. The laser cleaning raster step size is 30 μm for 40 μm of the focused laser size. For three of the four cathodes installed in the ASTA gun, about ten 1.2 mm \times 1.2 mm areas each cathode are processed by the laser cleaning. QE increases to $(3-5) \times 10^{-5}$ after a few rounds of laser cleaning. The QE and emittance evolutions following the laser cleaning are consistent and reproducible for different areas and cathodes. Table 1 lists the standard laser cleaning parameters developed at the ASTA, in comparison to the

previous laser cleaning recipe for the LCLS cathode. Note the required laser energy for the laser cleaning is proportional to the laser pulse length. The laser fluence for the single laser shot at ASTA is less than at the LCLS. The laser shots for the laser cleaning at the ASTA are only half the previous cleaning at the LCLS. The integrated laser fluence for laser cleaning at the ASTA is much less than the previous cleaning at the LCLS. It results in a much better QE evolution and quicker emittance recovery following the laser cleaning at the ASTA than the previous cleaning at the LCLS.

Table 1: Laser Cleaning Parameters at ASTA and LCLS

	ASTA (LCLS)
Laser pulse energy (μJ)	7-10 (17-20)
Laser size on cathode (μm)	40 (30)
Laser scan step size (μm)	30 (30)
Laser shots on each spot	60 (120)
Laser pulse length (ps)	1.6 (3)
Base gun vacuum range with RF power off (Torr)	$4-12 \times 10^{-10}$ ($4-7 \times 10^{-10}$)
Gun vacuum rise during the cleaning (Torr)	$<0.25 \times 10^{-10}$ (0.5×10^{-10})
Gun power during cleaning	RF off
QE after cleaning	$3-5 \times 10^{-10}$ (4×10^{-5})

QE and Emittance Evolution Following the Laser Cleaning

Using the standard laser cleaning process, the QE can be reliably increased to $(3-5) \times 10^{-5}$ from 10^{-6} - 2×10^{-5} after 3-8 rounds of the gentle cleaning. Following the laser cleaning, the QE is gradually increased, and eventually evolved to $>1 \times 10^{-4}$ over 2-3 weeks, as illustrated in Fig. 5, much shorter than a few months for previous LCLS cleaning. It shows all five areas A-E cleaned by the intensive laser have similar QE evolution over time, while the QE of the center area, which is not exposed to the laser cleaning, is kept unchanged over the time as expected. Note that the five areas A, B, C, D and E are cleaned on different dates, on 10th, 18th, 25th, 32nd and 32nd respectively, as illustrated in the plot.

At ASTA, the beam energy is determined by measuring the beam rotation angle through the solenoid, and the beam size is measured at a YAG screen downstream of the solenoid. The measured beam energy is 5.5 MeV, with which the space charge dominates the beam. Thus, only the intrinsic emittance with very low charge 1-2 pC can be measured using the solenoid scan. The measured intrinsic emittance for non-cleaned center area at ASTA is about 0.7 μm per mm-rms, close to the measured value in the LCLS, 0.9 μm per mm-rms. It indicates the emittance measurements at ASTA are reliable. Figure 6 shows the measured intrinsic emittance before the cleaning, immediately after the cleaning, and next day after the laser cleaning. For the emittance measurements, laser spot

on the cathode is 1 mm in size with about 3 mm offset in x-plane from the cathode center. The intrinsic emittance is increased immediately following the laser cleaning but in the next day the emittance is recovered to the one before the cleaning. The High power RF operation helps to smoothen out the surface's non-uniformity thereby improving the emittance. The emittance recovery time at the ASTA is only 1-2 days, much shorter than 2-3 weeks for the previous cleaning at the LCLS. The fewer laser cleaning fluence for the ASTA results in a better QE and emittance evolution than the previous laser cleaning at the LCLS.

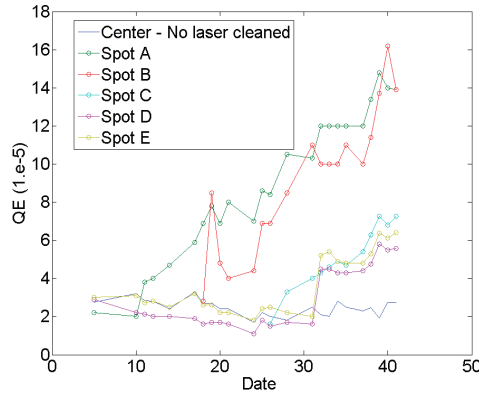


Figure 5: QE evolution for the areas with and without laser cleaning. Areas A, B, C, D and E are exposed to the laser cleaning while the center area is not cleaned by intensive laser.

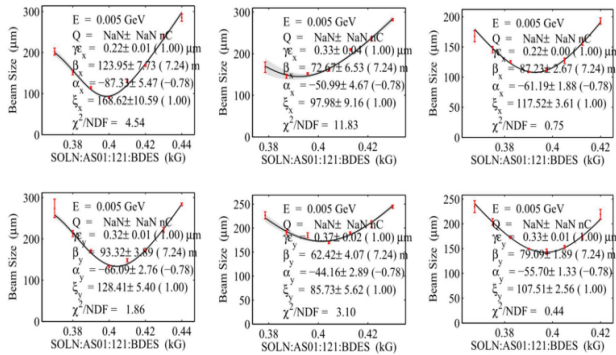


Figure 6: Intrinsic emittance 0.22-μm (x)/0.32-μm (y) before laser cleaning (left), 0.33-μm (x)/0.37-μm (y) immediately after laser cleaning (middle), and 0.22-μm (x)/0.33-μm (y) on the second day after laser cleaning (right).

Laser Pointing Requirements for the Laser Cleaning

Reasonable good laser pointing stability on the cathode is required for the application of laser cleaning technique to the cathode cleaning. The focused laser size for the laser cleaning of the ASTA cathodes is about 40 μm rms. According to the standard laser cleaning procedures, QE starts to be increased when the laser energy is increased to 7 μJ with continuous 60 shots for each location. However, for one time the QE was not changed at all, even if the

laser energy had been increased to 28 μJ with nominal 60 shots for each location. Eventually QE was increased through doubling laser shots for each location. Later, we realized the laser pointing stability on the cathode was bad during the laser cleaning, about 10 μm rms double the normal pointing jitter, as shown in Fig. 7. The bad laser pointing causes the failure of the laser cleaning. Melting the cathode surface needs certain amount of laser shots. Unstable laser pointing significantly reduces the actual laser shots for the same location. The laser cleaning works again with the nominal laser shots, when the laser pointing stability is improved to the normal value. According to the observations, laser pointing stability $\Delta\sigma_{x,y}/\sigma_{x,y}$ is required better than 10% to make laser cleaning work. This laser pointing requirement can be met readily for laser user facilities.

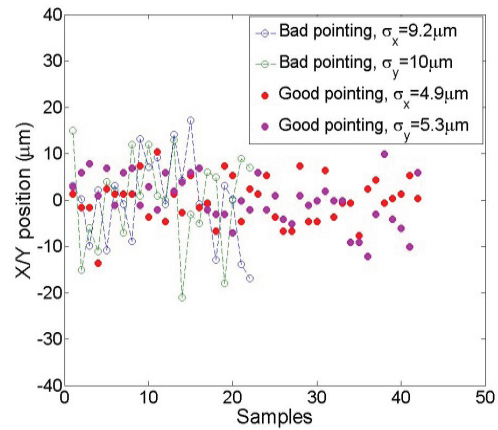


Figure 7: Laser pointing stability requirements during the laser cleaning. Laser cleaning fails with the bad laser pointing.

Discussion of the Laser Cleaning Process and the QE Evolution

Laser cleaning was thought as pure chemical processing to remove surface contaminations, thereby reducing work function and increasing the photoemission. During the process, the reflectivity was thought unchanged. Reducing work function increases the intrinsic emittance. Relations of QE to work function ϕ_w and intrinsic emittance ϵ_x are expressed by the following equations [5]:

$$QE(\omega) = \frac{1 - R(\omega)}{1 + \frac{\lambda_{opt}(\omega)}{\lambda_{e-e}(\omega)}} \frac{(h\nu - \phi_{eff})^2}{8\phi_{eff}(E_F + \phi_{eff})}$$

$$\frac{\epsilon_n}{\sigma_x} = \sqrt{\frac{h\nu - \phi_{eff}}{3mc^2}}$$

with $\phi_{eff} = \phi_w - 0.037947\sqrt{E_0}$, where R is the cathode optical reflectivity = 0.43, $h\nu$ is the photon energy, about 4.91 eV for 253 nm of wavelength, λ_{opt} is the photon absorption length of 116 angstroms, λ_{e-e} is electron-electron mean-free path about 22 angstroms, E_F is the

Fermi energy, about 7 eV, ϕ_{eff} is the effective work function, mc^2 is the rest mass energy of electron, E_0 is the applied RF electric field on the cathode, expressed by $E_{\text{peak}} \cdot \sin(\phi)$ in units of MV/m, E_{peak} is gun's peak accelerating gradient, 110 MV/m, ϕ is the gun phase from zero-crossing, 15° for intrinsic emittance measurement. Substituting these parameters into Eqs. 1 and 2, the intrinsic emittance should be changed by about 20% when the QE doubles from 6×10^{-5} to 1.2×10^{-4} . For the LCLS, the intrinsic emittance is expected to have been changed from 0.9 $\mu\text{m}/\text{mm}$ -rms to 1.08 $\mu\text{m}/\text{mm}$ -rms, when the QE doubles from 6×10^{-5} to 1.2×10^{-4} . However, no noticeable change of intrinsic emittance is observed at the LCLS, as shown in Fig. 8, when the QE is increased by a factor of 2 following the laser cleaning. The result indicates the laser cleaning process may not change the work function. Instead, the images of LCLS [4] and ASTA cathodes using the white light, as illustrated in Fig. 9, suggest that the reflectivity for the laser cleaned areas is decreased after the laser cleaning. The two squares subject to the laser cleaning have lower reflectivity than other areas without laser cleaning. It is believed a change in the reflectivity of cathode surface is one of the major factors for the observed QE enhancement following the laser cleaning.

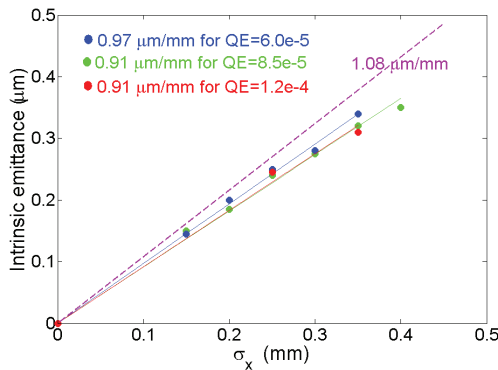


Figure 8: Measured intrinsic emittance with the different QE following the laser cleaning at the LCLS.

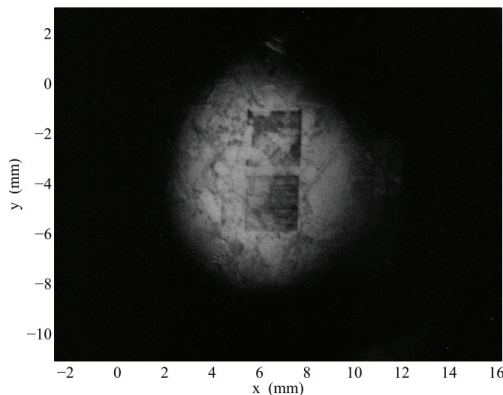


Figure 9: Image of the copper cathode using the white light. Two square areas are processed by the laser cleaning.

SUMMARY

LCLS cathodes have to be exposed to air for the installation in the RF gun due to the lack of loadlock system. Experimental studies indicate that the plasma cleaning for the cathodes in the test chamber results in a very low initial QE in the LCLS RF gun. All four cathodes, without the plasma cleaning in the test chamber, have reliably demonstrated initial $QE > 4 \times 10^{-5}$ in the ASTA gun. Laser cleaning procedures are improved at the ASTA, resulting in a better QE and emittance evolution than the previous cleaning at the LCLS. Physics of the laser cleaning process and its QE evolution is discussed. It is believed that the work function is not changed during the laser cleaning process and the QE evolution over time. The change of cathode surface reflectivity is considered as one of factors for the QE enhancement for the laser cleaning. A more complete picture of understanding the complex laser-cleaning process is under investigation.

REFERENCES

- [1] E. Jongewaard *et al.*, "RF Gun Photocathode Research at SLAC", in Proc. of 3rd International Part. Accel. Conference, New Orleans, Louisiana, 2012, pp. 664-666.
- [2] R. Akre *et al.*, "Commissioning the Linac Coherent Light Source Injector", Phys. Rev. ST Accel. Beams 11, 030703 (2008).
- [3] A. Brachmann *et al.*, "LCLS RF Gun Cathode Performance", in Proc. of 2nd International Part. Accel. Conference, San Sebastian, Spain, 2011, pp. 3200-3202.
- [4] F. Zhou *et al.*, "High-brightness Electron Beam Evolution following Laser-based Cleaning of a Photocathode", Phys. Rev. ST Accel. Beams 15, 090703 (2012).
- [5] D. Dowell and J. Schmerge, "Quantum Efficiency and Thermal Emittance of Metal Photocathodes", Phys. Rev. ST Accel. Beams 12, 119901 (2009).

FURTHER UNDERSTANDING THE LCLS INJECTOR EMITTANCE*

F. Zhou, K. Bane, Y. Ding, Z. Huang, and H. Loos, SLAC, Menlo Park, CA 94025, USA

Abstract

Coherent optical transition radiation (COTR) from the laser heater chicane is recently observed at the OTR screen used for the injector emittance measurements at the Linac Coherent Light Source (LCLS). The injector emittance measured at the OTR screen is under-estimated by 30% due to the COTR effect. Slice emittance upstream of the first LCLS magnetic bunch compressor (BC1) is measured, 0.45 μm for a central slice beam, using a traditional transverse s-band radio frequency deflector. Slice x- and y-emittances downstream of the BC1 are measured using a recently developed technique. It makes use of a collimator in the BC1 center to select a small portion of beam as a time-sliced beam. The measured projected emittance for the slice beam is considered as the slice emittance. With the technique, the measured central slice y-emittance is 0.45 μm after the BC1, similar to the injector emittance before the BC1, but the measured so-called central slice x-emittance has about 20% of increase after the BC1. Further measurements and analyses reveal that the parasitic effects, including collimator wakes, longitudinal space charge and dispersion due to the introduction of the beam collimation, do not impact the measured slice x- and y-emittance but coherent synchrotron radiation (CSR) deteriorates the projected x-emittance of the slice beam. The measured projected x-emittance of a slice beam under the CSR condition cannot be considered as a slice x-emittance. The technique is capable of reliable measurements of a slice emittance in non-bending plane instead of the bending plane, when a beam transports through magnetic bunch compressors.

EMITTANCE AT 135 MEV, PRIOR TO THE BC1

The Linac Coherent Light Source (LCLS), located at the SLAC National Accelerator Laboratory, has been successfully operated for users for more than five years [1]. Accurately characterizing emittance particularly the injector emittance is of importance for the x-ray Free Electron Laser (FEL) operations. Figure 1 shows the major components of the LCLS injector and its first magnetic bunch compressor (BC1) [2]. It begins with a copper cathode s-band RF gun and two s-band linac sections producing an electron beam with energy of 135 MeV. The 135-MeV beam then passes through a small laser heater (LH) chicane, followed by an s-band transverse RF deflector for time-resolved beam measurements. The 135-MeV beam is measured by the emittance station consisting of three optical transition radiation (OTR) screens or wire scanners. Then the beam is transported into the main linac and accelerated to 240

MeV through the LIS before entering the BC1. Located between these two structures is the x-band RF structure to linearize the longitudinal phase space before the bunch compression. There are three wire scanners downstream of the BC1 for emittance measurements. The quadrupole scan is used to measure emittance for a 135 MeV beam with one OTR screen or wire-scanner, and for a 220 MeV compressed beam after the BC1 with one wire scanner. The bunch charge is 150 pC for all emittance measurement discussed in the context.

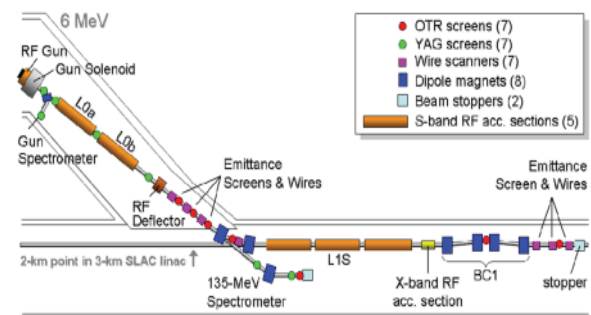


Figure1: Schematic layout of the LCLS injector including the BC1. The laser heater chicane is located in between the L0b and the RF deflector.

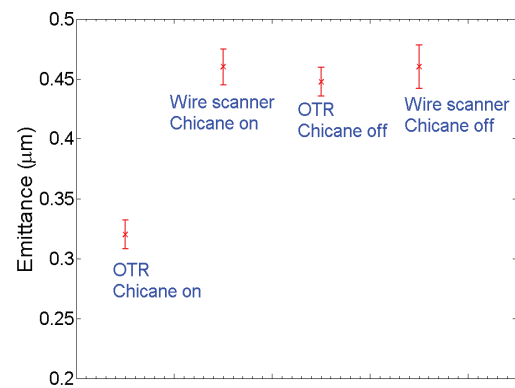


Figure 2: Projected emittance with the OTR screen and the wire-scanner for the LH chicane on and off at 135 MeV for 150 pC.

The LH chicane is to accommodate a short undulator for interaction of the laser beam with the electron beam to introduce an uncorrelated energy modulation of the electron beam to suppress the micro-bunching instability. The interaction of the electron beam with the laser beam in the LH chicane also induces micro-bunching at the laser wavelength and its harmonics, leading to coherent optical transition radiation (COTR) effects on the OTR screen [3] thereby impacting the accuracy of the emittance measurement. Therefore, the laser beam for the LH was always turned off but the LH chicane is normally

* The work is supported by U.S. DOE under grant No. DE-AC02-76SF00515.

turned on during routine emittance measurements using the OTR screen. However, with the LH chicane-on, we recently observed that the integrated charge at the OTR screen is still changed by a factor of 2 during the quadrupole scan. The micro-bunching from the cathode and drive laser could be amplified through the small R_{56} (5 mm) of the LH chicane itself. It makes optical transition radiation coherently at the OTR screen downstream of the chicane. The coherent optical transition radiation (COTR) light makes the core of electron beam denser thereby resulting in smaller electron beam. Turning off the LH chicane the integrated charge at the OTR screen is similar for different quadrupole strength. Using the wire scanner, the integrated charge for different quadrupole strength is similar, for both the LH chicane-on and -off. It indicates the wire scanner is not subject to the COTR light. Figure 2 shows the emittance comparisons for the LH chicane-on and -off using the OTR screen and the wire scanner for 150 pC. It shows that the emittance using the wire scanner is similar to the one using the OTR with the LH chicane-off. The OTR emittance with the LH chicane-on is underestimated by about 30%. The slice emittance is measured using the transverse RF deflector with the OTR screen at 135 MeV, prior to the BC1, as shown in Fig. 3. It shows the central slice beam emittance is about $0.45 \mu\text{m}$ for 150 pC with the LH chicane-off, and the measured slice emittance is underestimated by 30% with the LH chicane-on. Presently, the wire scanner replaces the OTR screen for emittance measurements at the 135-MeV LCLS injector.

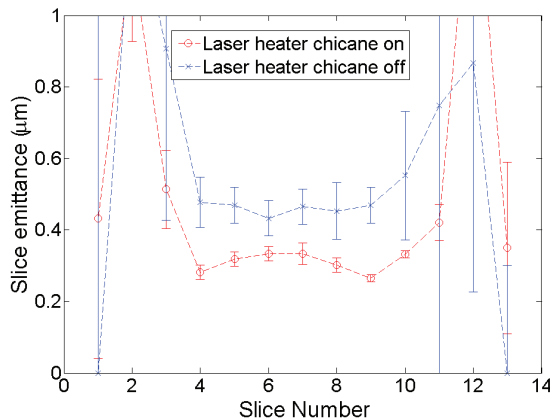


Figure 3: Slice emittance measured at the LCLS injector with the LH chicane-on and -off at 135 MeV, using the transverse RF deflector.

SLICE EMITTANCE MEASUREMENTS AND ANALYSES FOR THE BC1

It is crucial to measure and preserve the time-sliced beam emittance along the accelerator beamline particularly through the magnetic bunch compressors (BCs) for x-ray FEL operations. The transverse phase space volume of a slice beam may blow up, when an electron beam experiences non-linear fields along the beamline. Due to the lack of valid diagnostics for the time-sliced emittance measurements after the BCs at the

LCLS, we used to assume that the slice emittance is kept unchanged from the injector to the undulator for prediction of the LCLS FEL performance. Recently, a simple collimation technique is developed to measure the time-sliced emittance at the FERMI [4] and the LCLS, which provides a possible solution to measure the slice emittances through the BCs.

The schematic layouts of the LCLS BC1 and the 2nd magnetic bunch compressor (BC2) are very similar, as shown in Fig. 4. The BC1 is used for the following descriptions. The electron beam is bent in the x-plane. The electron beam is chirped with an off-crest RF phase of L1S linac before entering the BC1 chicane. In the BC1, the beam is time-horizontal position correlated, when the energy-time correlated chirped beam passes through the horizontally dispersive region. The nominal chirped beam width at the middle of the LCLS BC1 is about 11 mm for nominal operation with 150 pC of bunch charge. A horizontally-flat collimator is situated in the middle of the BC1 chicane to scrape the electrons by changing the horizontal collimator gap. Figure 5 (top) shows the full chirped-beam image taken at the OTR screen immediately after the BC1 collimator. The dispersive beam size at the center of the BC1 is 2.3 mm, much larger than the betatron beam size of $90 \mu\text{m}$. Thus, different width of time-sliced beams can be selected using the horizontal collimator jaws shown in Fig. 5 (middle and bottom). The projected emittance of selected time-sliced beam passing through the collimator is measured at 220 MeV, with a wire-scanner downstream of the BC1 using a quadrupole scan. The measured projected emittance of a small portion of the full beam is considered as the slice emittance with this technique.

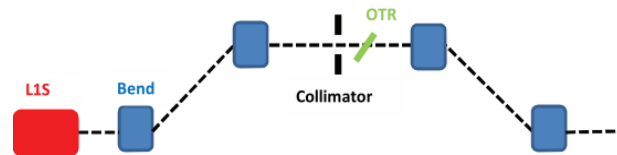


Figure 4: Schematic layout of the LCLS BC1. The collimator is situated in the center of the BC1 chicane and the OTR screen is next to the collimator. L1S is the linac used to introduce the energy-time correlation for the bunch compression.

Figure 6 shows the measured slice emittances in x- and y-plane through the BC1 with the collimation technique. The bunch charge before the collimation is 150 pC. The central slice beam charge is about 10 pC with 0.5 mm of the collimator gap. The measured central slice y-emittance through the BC1 is about $0.45 \mu\text{m}$ similar to the one before the BC1, while the measured so-called slice x-emittance is increased by about 20%. Similar phenomena are observed at the LCLS BC2, although the relatively large energy jitter makes the slice measurements jittery with the sub-mm collimator gap. This paper focuses on the measurements and analyses for the LCLS BC1. The following sections are to evaluate the parasitic effects of

using the collimation technique and discuss the so-called slice x-emittance growth.

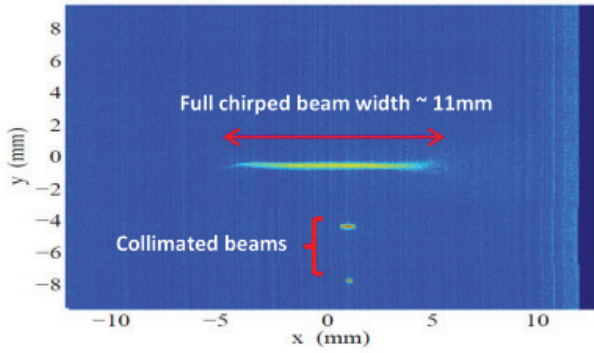


Figure 5: Example of the measured full chirped beam image at the OTR near the BC1 center (top) and sliced beams with different length after beam collimation (middle and bottom) at the LCLS BC1 with 150 pC.

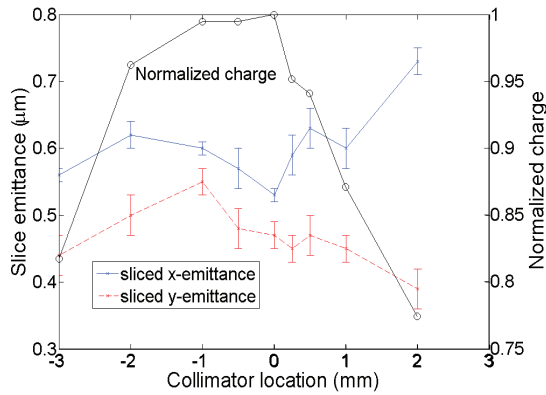


Figure 6: Time-sliced x- and y-emittances measured downstream of the LCLS BC1 at 220 MeV.

Impact of the X-Band Linearizer

The x-band linearizer, located upstream of the LCLS BC1, is used to linearize the longitudinal phase space of the chirped beam. A local x-bump is usually generated around the x-band cavity to reduce the wake effects, caused by the misalignments in the x-band structure. Figure 7 shows the measured projected and slice x-emittance as a function of transverse offset in the x-band cavity. In the full open state (10 cm of collimator gap), the measured emittance is for the full beam - projected emittance. For the mm or sub-mm of the collimator gap, a small portion of the beam is transported through the collimator. Thus the measured projected emittance is for a slice beam - slice emittance. The measurements show that the slice emittance is very similar for 0 mm, 0.5 mm and 1 mm of the transverse offsets in the x-band cavity, although the projected emittances of the full beams are very different with these transverse offsets. It is understood that the transverse wake of the x-band cavity generates a time-dependent head-tail force, which only impacts the projected emittance of the full beam, rather than its slice emittance.

ISBN 978-3-95450-133-5

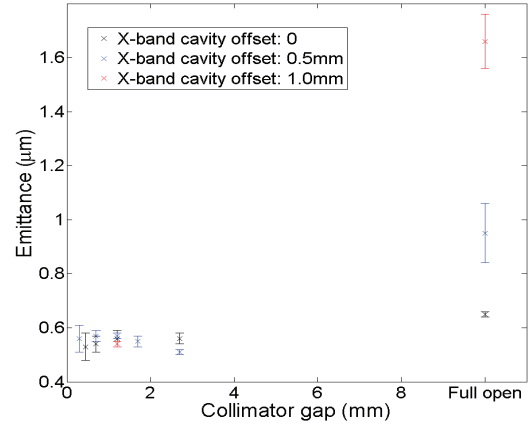


Figure 7: Measured projected and time-sliced x-emittance vs. transverse offset of the x-band linearizer.

Collimator Wakes

As discussed in the previous section, the typical full chirped beam width at the LCLS BC1 chicane center is about 11 mm with 150 pC for nominal operations. To evaluate the collimator geometrical wake effects, the collimator gap is set to different values, from a few mm to sub-mm, for emittance measurements. Figure 8 shows the measured emittance with variable collimator gaps. The slice x- or y-emittance is similar with different gaps below 6 mm. During the emittance measurements, the beam optics matching parameters are not changed at all for different gaps. It indicates no additional focusing is introduced by the collimator wake. For the case of very short bunches $\sigma_z \ll b$ (b is the half gap of the collimator), valid for our case, the flat collimator wake can be predicted with the optical model [5-6]. With the beam centered between the collimator jaws, the collimator wake induced beam defocusing is estimated with:

$$\frac{1}{f} = \frac{Z_0 c \pi}{24} \frac{eN}{b^2 (E/e)} \quad (1)$$

where f is the effective optical focal length caused by the collimator wake (defocusing is in the plane of the collimation), $Z_0 \approx 377 \Omega$, c is the speed of light, eN is the transmitted bunch charge through the collimator, and E is the electron beam energy. The focusing depends on position within the bunch, with the bunch head experiencing no effect and the tail experiencing the wake effect described by Eq. 1. With the LCLS BC1 parameters, beam energy $E=220$ MeV, the typical transmitted charge $eN=10$ pC through the minimum gap of 0.5 mm (half gap $b=0.25$ mm), the focal length created by the collimator wake is about 90 m, much larger than the few meters of the focal length of the magnetic lattice optics. It confirms that the measured beam matching parameters are not changed for different collimator gaps. The emittance growth in the x- and y-plane due to the collimator's quadrupole wake is approximately expressed by:

$$\frac{\varepsilon_{nx,ny}}{\varepsilon_{nx0,ny0}} = \sqrt{1 + \left(\frac{\beta_{x,y}}{f} \right)^2} \quad (2)$$

where $\varepsilon_{nx0,ny0}$ and $\varepsilon_{nx,ny}$ are the original and final emittances respectively, and $\beta_{x,y}$ is the betatron function at the collimator. With nominal $\beta_{x,y}=7$ m, the emittance growth caused by the collimator quadrupole wake is $<1\%$. Further calculations find that the resistive wall wake effect of the collimator is even weaker than the collimator's geometrical wake. The measurement and analysis lead to the conclusion that the contribution of the collimator wakes to the projected x- and y-emittance of a slice beam is negligible.

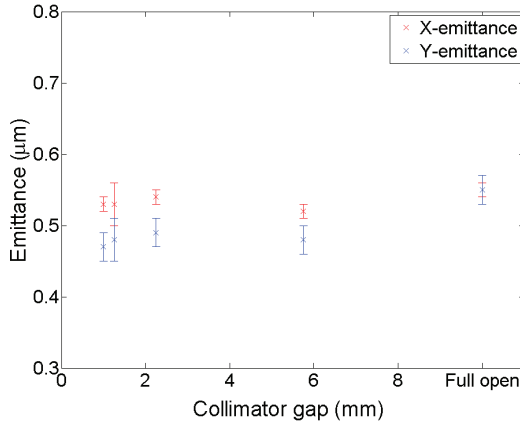


Figure 8: Measured x- and y-emittance vs. collimator gap. Full open means 100 mm of the collimator gap.

Dispersion Effect

In practice, <1 cm of the x-dispersion leakage from the LCLS BC1 chicane is possible. The dispersion induced x-emittance growth is estimated by:

$$\frac{\Delta\varepsilon_x}{\varepsilon_{x0}} \approx \frac{1}{2} \frac{(\eta_x \cdot \delta_E)^2}{\beta_x \cdot \varepsilon_{x0}} \quad (3)$$

where $\Delta\varepsilon_x$ is the emittance growth, ε_{x0} is the initial unnormalized emittance, β_x is the betatron function at the emittance measurement station, η_x is dispersion and δ_E is the rms energy spread. For the BC1 collimation measurements, only $<5\%$ of the full beam is selected for one slice beam measurement. Thus, the rms energy spread of a slice beam is about 0.05% for 1% of the rms energy spread for a full beam. Substituting the parameters into the Eq. 3 gives 1% of x-emittance growth for a slice beam with the 0.45 μm of the initial normalized slice x-emittance.

Longitudinal Space Charge and Coherent Synchrotron Radiation Effects

The longitudinal space charge (LSC) can degrade longitudinal phase space and transverse phase spaces in both x- and y-plane simultaneously. In the collimation scheme, the electron beam is truncated in the dispersion region or energy dimension, which makes the collimated beam current profile to a flat-top shape but with certain

slope on both edges. For this change, the LSC effect [7] is evaluated. Using the simulated temporal profile, we calculated the LSC and the emittance growth with the beam collimation and found the effects are negligible. The measured well-preserved slice y-emittance from the 135-MeV injector to the BC1, as stated in the previous sections, verifies the LSC is not the cause of the slice x- and y-emittance growth.

Short electron bunches traversing a dipole with bending radius ρ can emit coherent synchrotron radiation (CSR) [8-9] at wavelengths longer than the bunch length. Figure 9 shows the measured projected x- and y-emittance and slice y-emittance as function of the L1S phase for different bunch compressions. The CSR causes significant projected x-emittance growth at -30° , with which the beam is near full compression. It also shows that the measured central slice y-emittance using the collimator technique is similar for different bunch compressions, close to 0.45 μm measured at 135 MeV before the BC1. 0.5 mm of the collimator gap is used for all slice beam measurements. The selected slice beam length basically matches with FEL process in the undulator. The measured projected x-emittance of a collimated slice beam is grown by about 20% for the under-compression (-27°). Similar projected x-emittance growth for a slice beam was observed in Ref. [4] with the same collimation technique. The CSR caused x-emittance growth for a collimated slice beam can be estimated with 1D steady-state model:

$$\varepsilon_{xn} = \varepsilon_{xn0} \sqrt{1 + \left(\frac{\theta \delta_{CSR}}{2 \sigma_{x0}'} \right)^2} \quad (4)$$

where ε_{xn} and ε_{xn0} are the final and initial emittances respectively, θ is the bending angle, 0.1 rad, σ_{x0}' is the original beam divergence, and δ_{CSR} is the CSR caused rms energy spread expressed by:

$$\delta_{CSR} \approx 0.532 \frac{Q}{E} \frac{Z_0 c L}{2 \times 3^{4/3} \pi \rho^{2/3} \sigma_z^{4/3}} \quad (5)$$

where L is the bend length, 0.2 m, and ρ is the bending radius, 2 m, E is the beam energy at the BC1, 220 MeV, Q and σ_z are the bunch charge and bunch length respectively after the collimation, $Z_0 = 377 \Omega$, and c is the speed of the light. With 0.5 mm of the collimation, the bunch charge Q and bunch length σ_z are about 11 pC and 5 μm rms for under-compression (-27°). The calculations of the CSR for the last bend, applying above parameters into Eqs. 4-5, show that the projected x-emittance of the slice beam is grown by about 8%. The simulations using Elegant code predicts similar emittance growth with introducing 0.5 mm of beam collimation. Theoretical estimate and simulations verify the observed projected x-emittance growth for a collimated slice beam due to the CSR effect. Further simulations show that, without introducing the beam collimation, the time-sliced x-emittance is not changed for different bunch compressions. In the case of without beam collimation, the CSR only impacts the head-tail of the electron beam (projected emittance of the full beam), and thus the slice

emittance is not impacted. We conclude that under the CSR condition the measured projected x-emittance of a slice beam with the collimation technique cannot be considered as a slice x-emittance.

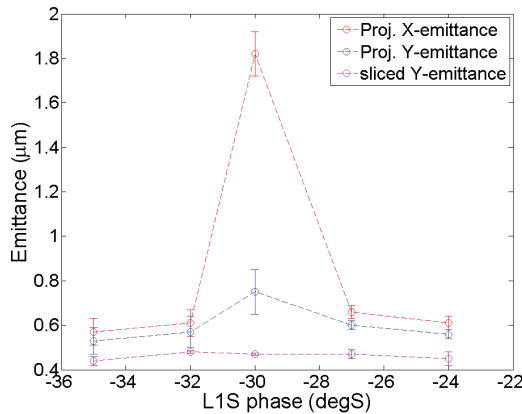


Figure 9: Projected x- and y-emittance and slice y-emittance for different bunch compressions with 150 pC.

SUMMARY

The LCLS injector emittance is under-estimated by 30% using the OTR screen due to the COTR effects from the LH chicane. With the transverse s-band RF deflector, the central slice emittance at 135 MeV prior to the BC1 is measured, about 0.45 μm for 150 pC. Emittances in the x- and y-plane for a slice beam through the BC1 are measured using a collimator located in the BC1 chicane center. With the collimation technique, the measured projected emittance for a slice beam is considered as the slice emittance. The measured so-called central slice x-emittance is increased by about 20% through the BC1, while the measured central slice y-emittance is about 0.45 μm similar to the one before the BC1. The further measurements and analyses reveal that the parasitic effects, including collimator wakes, longitudinal space charge and dispersion due to the introduction of the beam collimation, do not impact the measured projected x- and y-emittance of a slice beam but CSR effect deteriorates the projected x-emittance of the slice beam. Under the CSR condition, the measured projected x-emittance of a slice beam cannot be considered as a slice x-emittance. The technique is capable of reliable measurements of a slice emittance in non-bending plane instead of the bending plane, when a beam transports through magnetic bunch compressors.

REFERENCES

- [1] P. Emma *et al.*, “First Lasing and Operation of an Angstrom-wavelength Free Electron Laser”, *Nature Photon.* 4, 641 (2010).
- [2] R. Akre *et al.*, “Commissioning the Linac Coherent Light Source Injector”, *Phys. Rev. ST Accel. Beams* 11, 030703 (2008).
- [3] H. Loos *et al.*, “Observation of Coherent Optical Transition Radiation in the LCLS Linac”, in *Proc. of*

30th International Free Electron Laser conference, Gyeongju, Korea, 2008, pp. 485-489.

- [4] S. Di Mitri, D. Castronovo, I. Cudin, and L. Frohlich, “Electron Slicing for the Generation of Tunable Femtosecond Soft X-ray Pulses from a Free Electron Laser and Slice Diagnostics”, *Phys. Rev. ST Accel. Beams* 16, 042801 (2013).
- [5] G. Stupakov, K.L.F.Bane, and I. Zagorodnov, “Optical Approximation in the Theory of Geometric Impedance”, *Phys. Rev. ST Accel. Beams* 10, 054401 (2007).
- [6] K.L.F.Bane, G. Stupakov, and I. Zagorodnov, “Impedance Calculations of Nonaxisymmetric Transitions using the Optical Approximation”, *Phys. Rev. ST Accel. Beams* 10, 074401 (2007).
- [7] A. Chao and M. Tigner (eds.), “Handbook of Accelerator Physics and Engineering”, world scientific, Singapore, 1999. ISBN: 978-981-4415-84-2.
- [8] J. Murphy, S. Krinsky, and R. Gluckstern, “Longitudinal Wakefield for an Electron Moving on a Circular Orbit”, *Particle accelerator* 57 (1997), pp. 9-64.
- [9] H. Braun *et al.*, “Emittance Growth and Energy Loss due to Coherent Synchrotron Radiation in a Bunch Compressor”, *Phys. Rev. ST Accel. Beams* 3, 124402 (2000).

EFFECTS OF POTENTIAL ENERGY SPREAD ON PARTICLE DYNAMICS IN MAGNETIC BENDING SYSTEMS *

R. Li , Jefferson Lab, Newport News, VA 23606, USA

Abstract

Understanding CSR effects for the generation and transport of high brightness electron beams is crucial for designs of modern FELs. Most studies of CSR effects focus on the impacts of the longitudinal CSR wakefield. In this study, we investigate the impact of the initial retarded potential energy of particles, due to bunch collective interaction, on the transverse dynamics of particles on a curved orbit. It is shown that as part of the remnants of the CSR cancellation effect when both the longitudinal and transverse CSR forces are taken into account, this initial potential energy at the entrance of a bending system acts as a pseudo kinetic energy, or pseudo energy in short, because its effect on particle optics through dispersion and momentum compaction is indistinguishable from effect of the usual kinetic energy offset from the design energy. Our estimation indicates that the resulting effect of pseudo energy spread can be measurable only when the peak current of the bunch is high enough such that the slice pseudo energy spread is appreciable compared to the slice kinetic energy spread. The implication of this study on simulations and experiments of CSR effects will be discussed.

INTRODUCTION

When a high brightness electron beam is transported through a curved orbit in a bending system, the particle dynamics is perturbed by the coherent synchrotron radiation (CSR) forces, or the collective Lorentz force as a result of the Lienard-Wiechert fields generated by particles in the bunch. The longitudinal CSR interaction takes place when the fields generated by source particles at bunch tail overtake the motion of the test particles [1] at bunch head and cause changes of kinetic energy for the head particles. For parameters currently used in most machine designs and operations, the approximation of the longitudinal CSR force by that calculated using 1D rigid-line bunch model [2] often gives good description of the observed CSR effects [3].

In addition to the longitudinal CSR force, the transverse CSR force [4] can directly perturb transverse particle dynamics. This force features energy independence and, due to divergent contribution from nearby-particle interaction, has strong nonlinear dependence on the transverse (and longitudinal) positions of particles inside the bunch. Meanwhile, the potential energy change, as a result of both longitudinal and radial CSR or Coulomb forces, can cause change of kinetic energy of the particles and impact transverse particle dynamics via dispersion. The joint effects of both the transverse CSR force and the kinetic energy change on bunch

transverse dynamics have been analyzed earlier [5–7], and it is found that their harmful effects related to the potent feature of strong transverse dependence are cancelled. After the cancellation, the transverse dynamics of particles is perturbed by the remaining driving factors such as the effective longitudinal CSR force and the centrifugal force related to particles' initial potential energy.

In this study, we present the role of potential energy in the particle transverse dynamics after the cancellation effect is taken into account. We will show that the initial slice potential energy spread of a bunch, which we call pseudo slice energy spread, is indistinguishable from the usual slice kinetic energy spread in its perturbation to the transverse particle optics via both dispersion and momentum compaction. This effect is measurable only when the peak current of the bunch is high enough such that the pseudo slice energy spread is appreciable compared to the slice kinetic energy spread. The implication of this study on simulations and experiments of CSR effects will be discussed.

ROLE OF POTENTIAL ENERGY IN BUNCH TRANSVERSE DYNAMICS

In this section the CSR cancellation effect is briefly reviewed. We show how a centrifugal force term, which is related to the initial potential energy of particles, emerges as one of the remnant of the cancellation. We also discuss the role of initial potential energy in transverse particle dynamics.

Consider an ultrarelativistic electron bunch moving on a circular orbit with design radius R and design energy $E_0 = \gamma_0 mc^2$. Let $x = r - R$ be the radial offset of particles from the design orbit. The single particle optics is determined by the configuration of the external magnetic fields, while for a bunch with high peak current, this design optics will be perturbed by the Lorentz force \mathbf{F}^{col} resulting from the collective electromagnetic interaction amongst particles within the bunch. For transverse dynamics, such perturbation is expressed in terms of the first order equation

$$\frac{d^2 x}{c^2 dt^2} + \frac{x}{R^2} = \frac{\Delta E}{RE_0} + \frac{F_x^{\text{col}}}{E_0}, \quad (1)$$

with F_x^{col} being the radial component of the collective Lorentz force $\mathbf{F}^{\text{col}} = F_s^{\text{col}} \mathbf{e}_s + F_x^{\text{col}} \mathbf{e}_r$, and $\Delta E = E - E_0$ being the deviation of the kinetic energy from the design energy. The existence and effect of transverse CSR force F_x^{col} were first pointed out by Talman [4] when he analyzed F_x^{col} for space charge interaction of a bunch on a circular orbit using Lienard-Wiechert fields. His study shows that

* Work supported by Jefferson Science Associates, LLC under U.S. DOE Contract No. DE-AC05-06OR23177.

as a result of logarithmic divergence of nearby-particle interaction, this force is dominated by a term with the potent undesirable feature of strong nonlinear dependence over particles' transverse position within the bunch. Besides its role in the second driving term on the RHS of Eq. (1), the CSR force also causes change of particle's kinetic energy

$$\Delta E(t) = \Delta E(t=0) + \int_0^t \mathbf{F}^{\text{col}} \cdot \mathbf{v} dt', \quad (2)$$

which impacts the beam optics via dispersion as depicted by the first driving term in Eq. (1). As an example, the case of zero bunch charge corresponds to $F_x^{\text{col}} = F_s^{\text{col}} = 0$ and $\Delta E = E(0) - E_0$, when Eqs. (1) and (2) are reduced to equations for single particle dynamics. For the case of 1D CSR model as used in ELEGANT simulation, one has (1) $F_x^{\text{col}} = 0$ and (2) F_s^{col} in Eq. (2) is obtained for a 1D bunch moving along the design orbit with its line-charge density distribution obtained by projecting the actual 3D bunch distribution (at the time of force calculation) onto the design orbit, with the assumption that this 1D projected distribution has been frozen as it is for all retarded times. In general, however, the kinetic energy can be changed by the usual longitudinal CSR force acting on the bunch as well as by the potential energy change caused by various ways of particle-bunch interaction. Examples of such particle-bunch interaction include (1) betatron motion in the potential well set by the radial CSR force for a coasting beam [8], (2) noninertial space charge force related to the radiative part of the longitudinal Lienard-Wiechert electrical field experienced by off-axis particles interacting with a line bunch on a circular orbit [9], (3) longitudinal space-charge interaction for a converging bunch on a straight section right before the bunch entering into the last dipole of a bunch compression chicane [10]. In all these examples, the collective-interaction-induced potential energy $e\Phi^{\text{col}}$ shares the same feature of strong nonlinear dependence of particles' transverse position as that shown in the Talman's force.

The relation between the two driving terms in Eq. (1) becomes clear when both F_x^{col} and ΔE for the test particle are written in terms of retarded potentials [5]. The Talman's force is written as

$$F_x^{\text{col}} = F_x^{\text{eff}} + F^{\text{CSCF}}, \quad (3)$$

with the centrifugal space charge force F^{CSCF} term and the effective transverse force F_x^{eff} term defined respectively as

$$F^{\text{CSCF}} = \frac{e\beta_s A_s^{\text{col}}}{r}, \quad (4)$$

$$F_x^{\text{eff}} = -e \left(\frac{\partial \Phi^{\text{col}}}{\partial x} - \beta \cdot \frac{\partial \mathbf{A}^{\text{col}}}{\partial x} \right) - e \frac{dA_x^{\text{col}}}{cdt}. \quad (5)$$

Meanwhile the change of kinetic energy for the test particle is

$$\Delta E(t) = \Delta E(0) - e[\Phi^{\text{col}}(t) - \Phi^{\text{col}}(0)] + \int_0^t F_v^{\text{eff}}(t') c dt', \quad (6)$$

with the longitudinal effective force term F_v^{eff} defined as

$$F_v^{\text{eff}} = e \left(\frac{\partial \Phi^{\text{col}}}{c \partial t} - \beta \cdot \frac{\partial \mathbf{A}^{\text{col}}}{c \partial t} \right). \quad (7)$$

For a bunch with phase space density distribution $f(\mathbf{r}, \mathbf{v}, t)$, the retarded potentials $(\Phi^{\text{col}}, \mathbf{A}^{\text{col}})$ in the above expression are given by

$$\begin{aligned} \Phi^{\text{col}}(\mathbf{r}, t) &= e \int \frac{f(\mathbf{r}', \mathbf{v}', t')}{|\mathbf{r} - \mathbf{r}'|} d\mathbf{r}' d\mathbf{v}', \\ \mathbf{A}^{\text{col}}(\mathbf{r}, t) &= e \int \frac{\mathbf{v}' f(\mathbf{r}', \mathbf{v}', t')}{|\mathbf{r} - \mathbf{r}'|} d\mathbf{r}' d\mathbf{v}' \end{aligned} \quad (8)$$

for $t' = t - |\mathbf{r} - \mathbf{r}'|/c$, and with N_e electrons in the bunch,

$$\int f(\mathbf{r}, \mathbf{v}, t) d\mathbf{r} d\mathbf{v} = N_e. \quad (9)$$

The advantage of Eqs. (3)-(7) is that the potent term in F_x^{col} of Eqs. (1) and (3), contributed from the divergent local interactions, is now cleanly represented by the centrifugal space charge force F^{CSCF} in Eq. (4), leaving the remaining effective radial force F_x^{eff} free from the energy-independent local divergence of the order of F^{CSCF} . Similarly, all the local-interaction contributions to $\Delta E(t)$ are summarized by $-e[\Phi^{\text{col}}(t) - \Phi^{\text{col}}(0)]$ in Eq. (6), leaving the remaining contributions from the effective longitudinal force F_v^{eff} also free from the energy-independent local divergence. Substituting Eqs. (3) and (6) into Eq. (1), one obtains the transverse dynamical equation

$$\frac{d^2 x}{c^2 dt^2} + \frac{x}{R^2} = \frac{\delta \mathcal{E}(0)}{R} + \hat{G}^{\text{cor}} \quad (10)$$

with $\delta \mathcal{E}(0)$ the relative *total* energy deviation from design energy

$$\delta \mathcal{E}(0) = \frac{\mathcal{E}(0) - E_0}{E_0}, \quad \text{for } \mathcal{E}(0) = E(0) + E_\phi(0) \quad (11)$$

with

$$E_\phi(0) = e\Phi^{\text{col}}(0), \quad (12)$$

and \hat{G}^{cor} contains all the terms related to the interaction Lagrangian [7] that has negligible energy-independent local-interaction contributions

$$\hat{G}^{\text{cor}} = \frac{1}{E_0} \left(\frac{1}{R} \int_0^t F_v^{\text{eff}}(t') dt' + F_x^{\text{eff}} \right) + G_{\text{res}} \quad (13)$$

with the residual of cancellation

$$\begin{aligned} G_{\text{res}} &= -e \frac{\Phi^{\text{col}}(t) - \beta_s A_s^{\text{col}}(t)}{RE_0} \\ &\simeq -\frac{e^2}{R} \int \frac{\gamma_0^{-2} + \theta^2/2}{|\mathbf{r} - \mathbf{r}'|} f(\mathbf{r}', \mathbf{v}', t') d\mathbf{r}' d\mathbf{v}', \end{aligned} \quad (14)$$

for $\theta = [s(t) - s'(t')]/R$ being the angular distance between the test particle at the observation time and the source particle at retarded time. As we can see, the terms with

potent local-divergence contributions in both F_r^{col}/E_0 and in $\Delta E/(RE_0)$ of Eq. (1) are collected in G_{res} in Eq. (14). Moreover, since $\theta \rightarrow 0$ when $\mathbf{r}' \rightarrow \mathbf{r}$, the local divergence of the two terms cancels, leaving the residual with no energy-independent contributions from local interaction for any bunch distribution, as indicated by Eq. (14) [7, 11, 12].

Unlike the usual longitudinal CSR force, which is the result of EM field generated by tail of the bunch overtaking the head of the bunch [1], analyses of the radial CSR force based on Lienard-Wiechert fields show [11, 13] that F_x^{col} is dominated by contributions from head-tail interaction that has a sudden turn-on behavior as the bunch moves from straight section onto a circular orbit. It can be shown the dominant head-tail contributions in F_x^{col} are all included in F^{CSCF} of Eq. (4), and it turns on suddenly when the bunch moves from straight section $r \rightarrow \infty$ to $r = R$. Likewise the head-tail contributions are equally important for $-e\Phi^{\text{col}}(t)$ term in ΔE of Eq. (6). Since the perturbation of ΔE on optics in Eq. (1) is via the driving term $\Delta E/(E_0 R)$ in Eq. (1), its effect on the transverse dynamics also has a sudden turn-on behavior as the bunch enters from straight section ($R \rightarrow \infty$) to a circular arc (R finite). Consequently the two terms involved in the cancellation in Eq. (14) share common behavior and the residual of the cancellation is orders of magnitude smaller than each of the two terms [12].

As the two potent terms $-e\Phi^{\text{col}}(t)/(RE_0)$ and $e\beta_s A_s^{\text{col}}(t)/(RE_0)$ —contained in the first and second driving terms of Eq. (1) respectively—are cancelled, a centrifugal force term $e\Phi^{\text{col}}(0)/RE_0$ emerges as the remnant of the cancellation. The effect of this term on particle dynamics is the focus of this paper. One important observation [11, 13] is that similar to features of the centrifugal space charge force, $e\Phi^{\text{col}}(0)$ in Eq. (11) also contains contribution from the head-tail particle interaction with local divergence, and its effect on the transverse dynamics has the sudden turn-on behavior which is not cancelled away. On the other hand, it was noted [6, 12] that since $\delta_H(0)$ in Eq. (10) acts as the initial relative energy offset, so unlike the $e\Phi^{\text{col}}(t)$ term, here $e\Phi^{\text{col}}(0)$ in Eq. (11) does not cause emittance growth when the bunch is transported through an achromatic bending system such as a magnetic bunch compression chicane.

Another residual term left from the cancellation is \hat{G}^{cor} in Eq. (10). It is dominated by effects from the longitudinal tail-head CSR interaction, for which 1D CSR model is usually a good approximation. Exceptional situations occur when the Derbenev's criteria [5] for the validity of 1D CSR model is violated. Such situations include CSR interaction during roll-over compression [14] and cases of CSR-induced microbunching instability when either the modulation wavelength is very short or the bunch transverse size is very large. The correct evaluation of retarded potentials/fields in such situations requires extra care in identifying the source particles by finding the intersection of the past light cone of test particles with the 2D/3D bunch distribution in the history of bunch motion [14].

Let $(\Delta x_c, \Delta x'_c, \Delta z_c, \Delta \delta_c)$ be the phase space perturbation generated by \hat{G}^{cor} in Eq. (10). Then after combining Eq. (10) (for $s \simeq ct$) with $dz/ds = -x/R(s)$, one finds that the initial kinetic energy offset and potential energy of a particle at the entrance of a bending system always work together, as the joint entity $\delta_{\mathcal{E}0}$, in causing transverse and longitudinal chromatic effects for single particle optics, namely,

$$\begin{pmatrix} x \\ x' \\ z \\ \delta_H \end{pmatrix} = \begin{pmatrix} R_{11} & R_{12} & 0 & R_{16} \\ R_{21} & R_{22} & 0 & R_{26} \\ R_{51} & R_{52} & 1 & R_{56} \\ 0 & 0 & 0 & 1 \end{pmatrix} \begin{pmatrix} x_0 \\ x'_0 \\ z_0 \\ \delta_{H0} \end{pmatrix} + \begin{pmatrix} \Delta x_c \\ \Delta x'_c \\ \Delta z_c \\ \Delta \delta_c \end{pmatrix}, \quad (15)$$

for

$$\delta_{\mathcal{E}0} = \delta_{k0} + \delta_{\phi0}, \quad (16)$$

with $\delta_{k0} = (E(0) - E_0)/E_0$ the usual relative kinetic energy offset, and $\delta_{\phi0} = E_{\phi0}/E_0$. The significance of the impact of $\delta_{\phi0}$ on beam dynamics depends on the comparison of the initial potential energy spread with the initial kinetic energy spread. The discussion of Lorentz gauge as the natural choice of gauge for exhibiting the CSR cancellation effect can be found in Ref. [7].

THE SLICE TOTAL ENERGY SPREAD FOR A GAUSSIAN BUNCH

As a simplest example, we consider the impact of E_{ϕ} on the slice spread of total energy for an electron bunch with an idealistic cylindrically symmetric 3D Gaussian density distribution

$$P(r, z) = \frac{1}{(2\pi)^{3/2} \sigma_r^2 \sigma_z} \exp\left(-\frac{r^2}{2\sigma_r^2} - \frac{z^2}{2\sigma_z^2}\right). \quad (17)$$

The bunch arrives at the entrance of a bending system at $t = 0$ (we drop t dependence in the following discussion) after moving ultrarelativistically on a straight path with $v_s = \beta c$ and $v_x = v_y = 0$. Here we have $\sigma_x = \sigma_y = \sigma_r$ and $r^2 = x^2 + y^2$. The probability distribution of particles over the total energy offset $\Delta \mathcal{E} = \Delta E + E_{\phi}$, with $\Delta E, E_{\phi}$ and $\Delta \mathcal{E}$ being random variables, is

$$P_{\mathcal{E}}(\Delta \mathcal{E}) = \int P_E(\Delta \mathcal{E} - E_{\phi}) P_{E_{\phi}}(E_{\phi}) dE_{\phi}, \quad (18)$$

where we assume a Gaussian distribution for the kinetic energy

$$P_E(\Delta E) = \frac{1}{\sqrt{2\pi}\sigma_E} \exp\left(-\frac{(\Delta E)^2}{2\sigma_E^2}\right). \quad (19)$$

In this section we summarize how the distribution of total energy $P_{\mathcal{E}}(\Delta \mathcal{E})$, for the central slice ($z = 0$) of the bunch, deviates from the usual kinetic energy distribution $P_E(\Delta E)$ as a result of the potential energy distribution $P_{E_{\phi}}(E_{\phi})$ of the particles. We note that $P_{\mathcal{E}}(\Delta \mathcal{E}) = P_E(E)$ when the potential energy vanishes, i.e., $P_{E_{\phi}}(E_{\phi}) = \delta(E_{\phi})$.

The potential energy distribution $P_{E_{\phi}}(E_{\phi})$ can be uniquely determined from the probability distribution of

particles in the bunch $P(\mathbf{r}, t)$ and the dependence of potential energy on the particle spatial distribution $E_\phi(\mathbf{r}, t)$. For our example of cylindrical Gaussian distribution, with $(\tilde{r}, \tilde{z}) = (r/\sigma_r, z/\sigma_z)$ and $w = \tilde{r}^2$, the probability for particles to lie between w and $w + dw$ for the central $z = 0$ slice is deduced from Eq. (17)

$$P_w(w) = e^{-w/2}/2, \quad \text{with} \quad \int_0^\infty P_w(w)dw = 1. \quad (20)$$

The potential energy of a test particle at (\mathbf{x}, t)

$$E_\phi(\mathbf{x}, t) = e \int \frac{\rho(x_r, t - |\mathbf{x} - \mathbf{x}_r|/c)}{|\mathbf{x} - \mathbf{x}_r|} d^3\mathbf{x}_r \quad (21)$$

can be obtained [15] by applying Lorentz transformation on the scalar potential from the bunch comoving frame to the lab frame. For our example, with $\alpha = (\sigma_r/\gamma\sigma_z)^2$, this yields

$$E_\phi(r, z) = E_{\phi 0} f(\tilde{r}, \tilde{z}), \quad \text{with} \quad E_{\phi 0} = mc^2 I_p / I_A \quad (22)$$

for the peak current $I_p = N_e ec / (\sqrt{2\pi}\sigma_z)$ and Alfven current $I_A = e/(r_e c) = 17$ kA, and

$$f(\tilde{r}, \tilde{z}) = \int_0^\infty \frac{d\tau}{(1+\tau)\sqrt{1+\alpha\tau}} \exp\left(-\frac{\tilde{r}^2}{2(1+\tau)} - \frac{\tilde{z}^2}{2(1+\alpha\tau)}\right). \quad (23)$$

The dependence of the form function $f(\tilde{x}, \tilde{y}, \tilde{z})$ is shown in Fig. 1.

For the central slice at $z = 0$, we have from Eq. (22)

$$E_\phi(r, 0) = E_{\phi 0} U(w) \quad (24)$$

for the normalized potential energy

$$U(w) = \int_0^\infty \frac{d\tau}{(1+\tau)\sqrt{1+\alpha\tau}} \exp\left(-\frac{w}{2(1+\tau)}\right). \quad (25)$$

Combining $U(w)$ with $P_w(w)$ in Eq. (20), one gets the probability for the value of potential energy of a particle to reside between \mathcal{E}_ϕ and $\mathcal{E}_\phi + d\mathcal{E}_\phi$

$$P_{\mathcal{E}_\phi}(\mathcal{E}_\phi) d\mathcal{E}_\phi = P_U(U) dU = P_w(w) dw \quad (26)$$

or

$$P_U(w) \equiv P_{\mathcal{E}_\phi}(\mathcal{E}_\phi) \mathcal{E}_{\phi 0} = \frac{P_w(w)}{|dU(w)/dw|}. \quad (27)$$

The semi-analytical results of probability distribution P_U on U is then obtained from the parametric dependence of $(U(w), P_U(w))$ on w [15], as shown in Fig. 2, which automatically satisfies $\int P_U(U) dU = 1$. The probability of distribution for the total energy of particles in Eq. (18) then becomes

$$P_{\mathcal{E}}(\Delta\mathcal{E}) = \int P_{\mathcal{E}}(\Delta\mathcal{E} - E_{\phi 0} U) P_U(U) dU. \quad (28)$$

For the example in Fig. 1, the average and rms of particle distribution over U are respectively $\langle U \rangle = 15.0$ and $\sigma_U =$

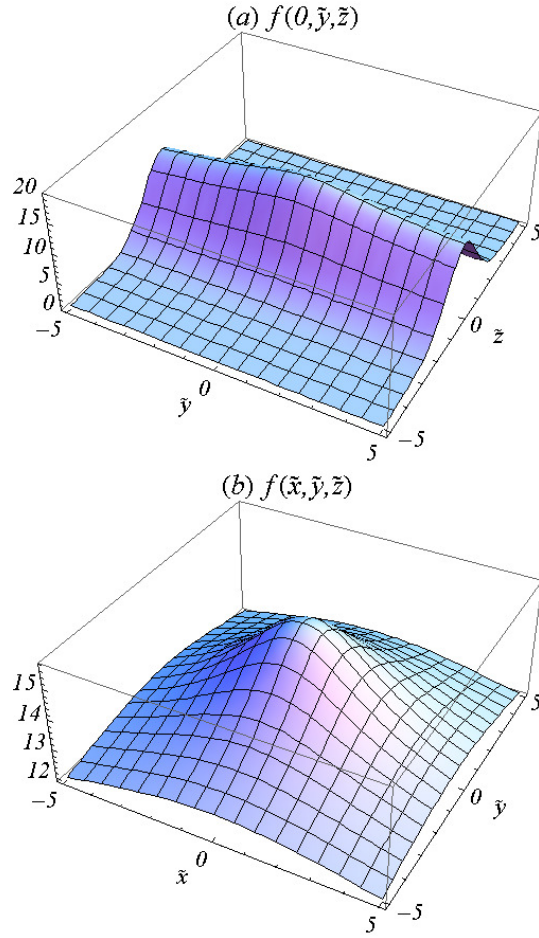


Figure 1: Behavior of $f(\tilde{x}, \tilde{y}, \tilde{z})$ in Eq. (23) for a cylindrical bunch over (a) the $\tilde{x} = 0$ plane and (b) the $\tilde{z} = 0$ plane for $\alpha = 5.7 \times 10^{-7}$.

0.51. An estimation of the rms spread of the total energy resulted from Eq. (18) is given by

$$\sigma_{\mathcal{E}} \simeq \sqrt{\sigma_E^2 + (E_{\phi 0} \sigma_U)^2}. \quad (29)$$

This relation shows that the rms of the total energy can be appreciably larger than that of the kinetic slice energy spread when

$$\xi \equiv \frac{E_{\phi 0} \sigma_U}{\sigma_E} \geq 1 \quad (30)$$

implying simultaneously both high peak current I_p and small kinetic energy spread σ_E .

To quantitatively compare the slice potential energy spread with the usual slice kinetic energy spread, and in particular, to compute the slice spread of the *total* energy, here we use the following parameters for the bunch [16, 17]

$$E_0 = 135 \text{ MeV}, \quad \sigma_z = 750 \mu\text{m}, \quad \epsilon_{x,y}^n = 1 \mu\text{m}, \quad \beta_{x,y} = 6 \text{ m}, \quad (31)$$

which corresponds to $\alpha = 5.7 \times 10^{-7}$. We further choose $I_p = 120$ A and thus $E_{\phi 0} = 3.6$ keV. Substituting the semi-analytical results $P_U(U)$ as shown in Fig. 2 into Eq. (28), one gets the distribution of total energy spread $P_{\mathcal{E}}(\Delta\mathcal{E})$ for cases

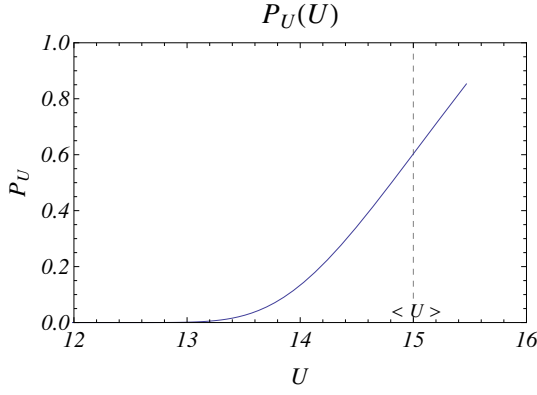


Figure 2: Probability distribution $P_U(U)$ for the central slice of a cylindrical Gaussian bunch with $\alpha = 5.7 \times 10^{-7}$.

when the slice kinetic energy spread takes (1) the typical value $\sigma_E = 3$ keV [18] when $\xi = 0.6$ and (2) $\sigma_E = 1$ keV when $\xi = 1.8$. The final results are shown in Fig. 3. It confirms our expectation that when $\xi \leq 1$ the potential energy has negligible effect on the slice total energy spread σ_E , as displayed by Fig. 3a, yet when $\xi \geq 1$ the potential energy spread can cause appreciable widening of the total energy spread, as indicated by Fig. 3b in which the red curve for $P_E(\Delta E)$ is much wider than the green curve for $P_E(E)$. Numerical evaluation using $P_E(\Delta E)$ of Eq. (28) yields $\sigma_E = 2.09$ keV for Fig. 3b, which agrees well with the estimation by Eq. (29) for $\sigma_E = 1$ keV. The semi-analytical results of $P_E(\Delta E)$, shown by the red curves in Fig. 3, are also in good agreement with results from the Monte Carlo approach presented by the red dots in Fig. 3. Here for the Monte Carlo approach we populate $N = 10^4$ particles with random Gaussian distributions in both the 2D configuration space (in the $z = 0$ plane) and in the kinetic energy offset ΔE . One then evaluates the total energy $\Delta E^i = \Delta E^i + E_\phi^i$ of the i -th ($i = 1, N$) particle by using E_ϕ^i in Eq. (22), and further obtain the histogram of particle distribution in ΔE .

DISCUSSIONS

In this paper, after a brief review of the cancellation effect in the CSR-induced perturbation on bunch transverse dynamics for an ultrarelativistic electron bunch moving through a magnetic bending system, it is shown how, after cancellation, the effective CSR forces and the potential-energy related centrifugal force emerge as the net driving factors for particle transverse dynamics. The behavior of longitudinal effective CSR force for an energy-chirped Gaussian bunch has been studied earlier [14], and in this presentation we summarized that role and behavior of the initial potential energy term. The main conclusion is that the initial potential energy always works together with the initial kinetic energy in perturbing the particle transverse dynamics, and for the example of a Gaussian bunch, we find that the potential energy effect is important only when the peak current of the bunch is high and the slice kinetic energy spread is small, i. e., $\xi \geq 1$. Note that ξ in Eq. (30) should remain

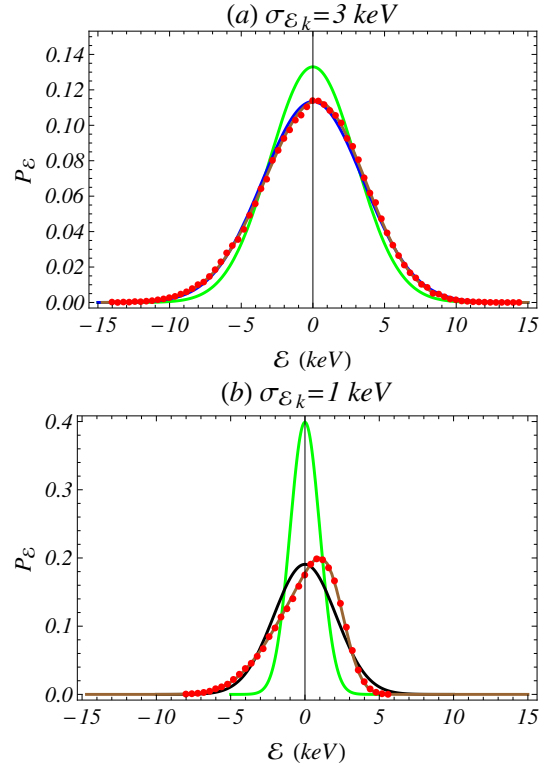


Figure 3: $P_E(\Delta E)$ for $z = 0$ slice of a cylindrical Gaussian bunch with $E_{\phi 0} = 3.6$ keV, $\alpha = 5.7 \times 10^{-7}$ for (a) $\sigma_E = 3$ keV and (b) $\sigma_E = 1$ keV. Green line: Gaussian distribution for kinetic energy $P_E(E)$; Brown line: semi-analytical results for distribution of total energy $P_E(\Delta E)$; Solid black line: Gaussian distribution using the estimated rms in Eq. (29); Red dots: Monte Carlo results of $P_E(\Delta E)$.

approximately a constant when the bunch gets compressed by a magnetic chicane with compression factor C , since both $E_{\phi 0}$ in Eq. (22) and the slice kinetic energy spread σ_E are increased by C . The potential energy spread for a general 3D bunch distribution requires careful numerical calculations.

For beam and machine parameters used in present designs, the 1D CSR model adopted by ELEGANT simulation often gives results in good agreement with measured CSR effects [3]. From the point of view of cancellation effect in CSR, the explanation of such success resides in the fact that in the 1D model both parts of the cancellation—the radial CSR force F_r^{col} and the potential energy change $-e[\Phi^{\text{col}}(t) - \Phi^{\text{col}}(0)]/R$ —are set to be zero, and only the impact resulted from the dominant longitudinal CSR force F_v^{eff} is being kept. The 2D/3D CSR effects are expected to show up in experiments for the unusual cases when the bunch distribution in x - z plane does not satisfy the Derbenev criteria $\sigma_x/(\sigma_z^2 R)^{1/3} \ll 1$, thence the behavior of F_v^{eff} will deviate [14] from that for a 1D rigid-line bunch, and when the bunch parameters are such that Eq. (30) is satisfied, thence the effect of potential energy will appear as enlargement of the measured slice energy spread or lengthening of bunch

length for a bunch at maximum compression as compared to results from the 1D CSR model.

Correct modeling of the cancellation effect poses significant challenge for 2D/3D CSR simulations, since it requires the two parts involved in the cancellation, $-e[\Phi^{\text{col}}(t) - \Phi^{\text{col}}(0)]/R$ and the radial CSR force F_r^{col} , be calculated with the same accuracy. Because $e[\Phi^{\text{col}}(t) - \Phi^{\text{col}}(0)]$ is an integrated effect of longitudinal and transverse CSR force on the circular orbit or Coulomb forces on a straight path, the cancellation effect can be taken care automatically only when both the CSR and space charge interaction are fully taken into account and the dynamics are advanced self-consistently. In addition, all the potential terms $\Phi^{\text{col}}(t)$, $\Phi^{\text{col}}(0)$ and $A_s^{\text{col}}(t)$ have sensitive dependence on the 3D bunch density distribution, as shown in Fig. 1. Without adequate care, incomplete modeling could result in partial or none cancellation and cause artificial errors. More detailed discussions can be found in Ref. [15].

REFERENCES

- [1] Ya. S. Derbenev et al., DESY-TESLA-FEL-95-05 (1995).
- [2] E. Saldin, E. Schneidmiller and M. Yurkov, Nucl. Instrum. Methods Phys. Res. Sect. A 398, 373 (1997).
- [3] K. L. F. Bane et al., Phys. Rev. ST Accel. Beams 12, 030704 (2009)
- [4] R. Talman, Phys. Rev. Lett. 56, 1429 (1986).
- [5] Ya. S. Derbenev and V. D. Shiltsev, SLAC-Pub-7181 (1996).
- [6] R. Li, Proceedings of the 2nd ICFA Advanced Accelerator Workshop, p.369 (1999).
- [7] R. Li and Ya. Derbenev, JLAB-TN-02-054 (2002).
- [8] E. Lee, Part. Accel. 25, 241 (1990).
- [9] B. E. Carlsten, Phys. Rev. E 54, p.838 (1996).
- [10] K. L. F. Bane and A. W. Chao, Phys. Rev. ST Accel. Beams 5, 104401, (2002).
- [11] G. Geloni *et al.*, DESY 02-48, (2002).
- [12] R. Li and Ya. Derbenev, Proceedings of 2005 Particle Accelerator Conference, Knoxville (2005).
- [13] G. Geloni et al., DESY 03-44 (2002)
- [14] R. Li, Phys. Rev. ST Accel. Beams 11, 024401 (2008).
- [15] R. Li, arXiv:1401.2868 (2014)
- [16] R. Akre et al., Phys. Rev. ST Accel. Beams 11, 030703 (2008).
- [17] Z. Huang et al., Phys. Rev. ST Accel. Beams 13, 020703 (2010).
- [18] D. Ratner, A. Chao, and Z. Huang, Proceedings of FEL08, Gyeongju, Korea, (2008).

MECHANICAL DESIGN FOR A CORRUGATED PLATE DECHIRPER SYSTEM FOR LCLS

M. Harrison*, P. Frigola, D.W. Martin, A. Murokh,
M. Ruelas, RadiaBeam Systems, Santa Monica, California, USA
Z. Huang, R. Iverson, T. J. Maxwell, Z. Zhang, SLAC, Menlo Park, California, USA

Abstract

RadiaBeam Systems is developing a novel passive chirp removal system using corrugated plates as studied by Bane and Stupakov [1]. Following on from low-energy experiments at BNL-ATF [2], RBS will install a much larger and powerful system for removing the chirp from the 3 GeV beams in the LTU section at LCLS. The larger plates will present new challenges in the areas of manufacturing and mechanical control. In this paper we review the requirements for the dimensions of the corrugated plates for proper operation and the infrastructure necessary for precisely placing the plates so as not to adversely disrupt the beam.

INTRODUCTION

Following the successful proof-of-concept dechirper experiment at Brookhaven National Laboratory [2], RadiaBeam Systems presents here plans for a scaled-up corrugated plate dechirper system for use in the 3 GeV Linac-To-Undulator (LTU) section at Linac Coherent Light Source (LCLS). The system will be designed to completely remove the residual chirp left over from the earlier compression sections. Prior beamlines required up to hundreds of meters of accelerating cavities running off-crest in order to lower the energy spread of the beam bunch enough for use in undulator light sources. The system described in this study will completely remove the chirp from the LCLS beamline with only two two-meter sections

CORRUGATED PLATES

The wakefield of a single electron is approximated by

$$W(z) = \left(\frac{\pi^2}{16} \right) \frac{Z_0 c}{\pi a^2} \cos \left(\frac{2\pi z}{\lambda} \right), \quad (1)$$

where Z_0 is the impedance of free space (377 Ω), c is the speed of light, and z is the bunch longitudinal coordinate. The wavelength of the wakefield, λ , given by

$$\lambda = 2\pi \sqrt{\frac{a\delta g}{p}}. \quad (2)$$

The rest of the dimensions (a , δ , g , and p) refer to dimensions of the corrugations, detailed in Table 1 and Fig. 1.

The total wakefield of the bunch forms a linear region over the bunch. The slope of this region determines the dechirping strength, h , is given by

$$h = \left(\frac{\pi^2}{16} \right) \frac{Z_0 c Q L}{\pi a^2 l}, \quad (3)$$

* harrison@radiabeam.com

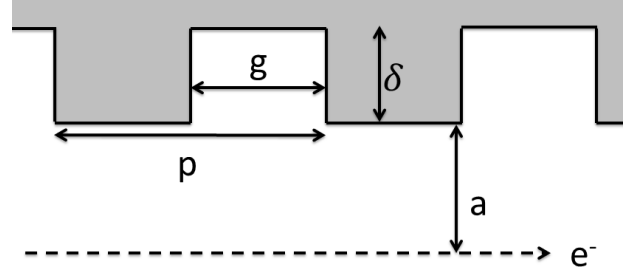


Figure 1: Dimensions of corrugated plates. See Table 1.

Table 1: Corrugated Plate Dimensions

Length	L	4.0 m
Width		12.7 mm
Period	p	0.51 mm
Depth	δ	0.51 mm
Gap	g	0.25 mm
Plate separation	a	1–30 mm
Material		Aluminum

where Q is the bunch charge, L is the length of the dechirper, and l is the bunch length. More accurate simulations of the wakefield ([3, 4]) show this to be an overestimation by factor of about 1.5, but Equation 3 serves to motivate the dimensions of the corrugated plates.

From Equation 3, the most important dimension in the corrugated plate dechirper is the gap between the plates and the total length. Dechirping power scales proportionally with L and $1/a^2$. Balancing beamline space and the minimum size of the beam determines the overall size constraints. The other dimensions—period, depth, and gap—are only constrained by the wakefield equations to being much smaller than a [1]. Specifically,

$$\delta, p \ll a \quad h \geq 0.8p \quad t = p/2. \quad (4)$$

For the LCLS dechirper, a total length of four meters (split into two equal length sections) was chosen to have a design gap ($2a$) of 1.4 mm [3]. A two-section dechirper also allows for cancellation of unwanted transverse quadrupole effects (to be discussed in the Other Considerations section).

The material of the corrugated plates was chosen to be aluminum because of its light weight and easy machinability. As long as the fundamental mode of the wakefield is dominant, the conductivity of the metal is unimportant [5]. To ease manufacturing and installation, the corrugated plates will be made in several sections each 0.5 meters long. Numerous simulations have been run to determine the tolerances

on manufacturing and they are within range of convention CNC machines with end mills and slit saws [6].

IN-VACUUM ASSEMBLY

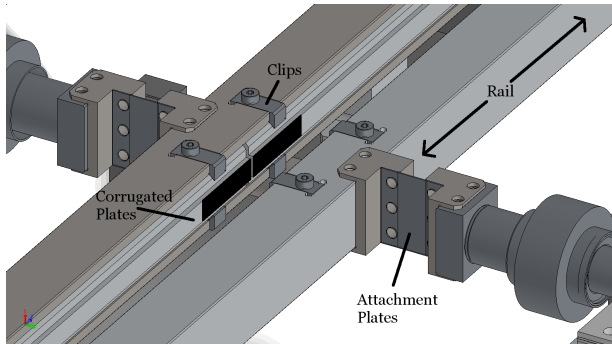


Figure 2: Drawing of the in-vacuum dechirper system.

The machined corrugated plates will be attached to 2 meter long aluminum rails which will also serve to keep the plates aligned with each other and the beamline (see Fig. 2). The plates will be held with clips to facilitate installation and replacement in case of damage to one plate. The rail will be attached to support shafts by means of attachment plates that will be slightly flexible to allow for the adjustment of the parallelism of the plates. The entire system will be housed in 6 inch (150 mm) diameter vacuum nipples. The support shafts are attached to flanges mounted on edge-welded bellows for motion feedthrough.

MOTION

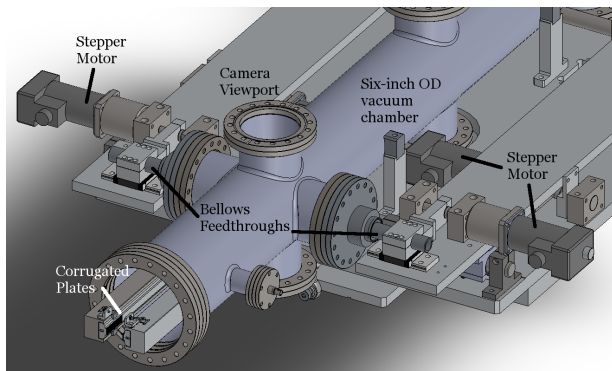


Figure 3: Drawing of dechirper system showing the vacuum chamber than will contain the corrugated plates, stepper motors, and bellows.

The edge-welded bellows are actuated by by NEMA 23 stepper motors, two per rail. The stepper motor nearest the vacuum chamber (middle of Fig. 3) controls the separation of the plate, while the far motor (right of Fig. 3) adjusts the parallelism of the plates. The stepper motors will act through a gear-reducer to lessen the torque required, reduce the linear travel per step, and provide a natural brake in case of power or motor failure. Position feedback will be provided by

Daytronic DS2000LC LVDTs, two per rail, with an accuracy of 50 μm . An Aerotech Epaq MR motion controller will control the actuation of two of these dechirper systems. Two cameras mounted on viewports at either end of the vacuum chamber will provide visual assessments of the separation and alignment of the corrugated plates.

OTHER CONSIDERATIONS

One of the consequences of using flat plates instead of the cylindrical geometry as originally proposed in Bane and Stupakov's paper [1] is that additional transverse wakefield components will be generated by the passing beam with magnitude that scales as $1/a^4$ [3]. Dipole wakefields, which have a similar effect to transverse deflecting cavities, arise due to the beam being off-center between the plates. This can be mitigated through careful positioning and alignment of the plates during installation and with the motors. Quadrupole wakefields can be greatly reduced in magnitude by operating two dechirpers, one with horizontal actuation (vertically-oriented corrugated plates) as in Figs. 3 and 2, and one with vertical actuation (horizontally-oriented plates). This arrangement is similar to a FODO arrangement of quadrupole magnets and minimizes the effect of the induced quadrupole wakefield.

The beam to be used in the commissioning of the new dechirper system at LCLS is described in Table 2.

Table 2: LCLS Beam Parameters

Beam energy	6.6	GeV
Beam charge	250	pC
Peak current	1.2	kA
Rep rate	120	Hz

In case of beam loss that hits the dechirper plates, the upstream sides of the dechirper rails will be fitted with shields of tungsten or lead.

While an active cooling system will not be necessary for the LCLS system, it will almost certainly be necessary for high-power CW systems like the planned LCLSII. Radia-Beam is studying methods of actively cooling the dechirper plates as they may have to dissipate kilowatts of power.

CONCLUSION

RadiaBeam Systems plans to install this dechirping system at LCLS in August 2015. There, it will undergo a battery of tests to determine its dechirping efficacy as well as its transverse effects on the beams transverse profile, motion, and emittance.

ACKNOWLEDGMENTS

This work is supported by Department of Energy grant number DE-SC0009550.

REFERENCES

- [1] K. Bane et al., "Corrugated Pipe as a Beam Dechirper", SLAC-PUB-14925, 2012
- [2] M. Harrison et al., "Removal of Residual Chirp in Compressed Beams Using a Passive Wakefield Technique", in *Proc. North American Particle Accelerator Conf.*, Pasadena, 2013, pp. 291–293
- [3] Z. Zhang et al., "Design Study of LCLS Chirp-Control with a Corrugated Structure", in *These Proceedings: Proc. 36th Int. Free-Electron Laser Conf.*, Basel, 2014, THP026.
- [4] M. Harrison et al., "Further Analysis of Corrugated Plate Dechirper Experiment at BNL-ATF." in *These Proceedings: Proc. 36th Int. Free-Electron Laser Conf.*, Basel, 2014, THP034
- [5] A. W. Chao, "Physics of collective beam instabilities in high energy accelerators" (John Wiley & Sons, New York, NY, 1993) 47–48.
- [6] SLAC Internal Reports

FURTHER ANALYSIS OF CORRUGATED PLATE DECHIRPER EXPERIMENT AT BNL-ATF

M. Harrison*, G. Andonian, P. Frigola, M. Ruelas, A. Murokh,
A. V. Smirnov, RadiaBeam Systems, Santa Monica, California, USA
M. Fedurin, BNL, Upton, Long Island, New York, USA

Abstract

RadiaBeam Systems successfully completed testing of a proof-of-concept corrugated plate dechirper at the Brookhaven National Laboratory Accelerator Test Facility. [1] Such passive devices should prove indispensable for the efficient operation of future XFEL facilities. These experiments demonstrated a narrowing of the energy spectrum in chirped beam bunches at 57.6 MeV. In this paper, we compare these results with results from Elegant simulations of the BNL-ATF beam. We also compare GdfidL simulations of the wakefield with the analytic results of Bane and Stupakov. [2]

GdfidL WAKEFIELD SIMULATION

The analytic equation for the wakefield [2] used to determine the dimensions of the corrugated plates is given by convolving the bunch charge density with the single electron wakefield:

$$W(z) = \frac{\pi^2 Z_0 c}{16 \pi a^2} \cos\left(\frac{2\pi z}{\lambda}\right), \quad (1)$$

where Z_0 is the impedance of free space (377Ω), c is the speed of light, z is the bunch longitudinal coordinate, λ is the wavelength of the wakefield given by

$$\lambda = 2\pi \sqrt{\frac{a\delta g}{p}}. \quad (2)$$

The other variables describe the dimensions of the corrugated plates and are listed in Table 1.

To check the accuracy of the analytic equations used in designing the plates, a numerical simulation of the wakefield was run using the program GdfidL. A 500-pC, 1-ps beam bunch with Gaussian longitudinal profile was simulated passing through the corrugated structure defined in Table 1 and the resulting wakefield calculated. A comparison between these two calculations is seen in Fig. 1. The GdfidL simulation reports a wakefield about 64% the magnitude of the analytic equations inside the electron bunch. This factor will be used in simulating the effect of the bunch's wakefield as it passes through the corrugated structure. Note that this factor matches field-matching simulations performed by SLAC with $F\left(\frac{h}{a} = 1, \frac{p}{a} = 1\right)$. [3]

ELEGANT SIMULATION

Using the beam simulation software package Elegant, a bunch was propagated through ATF's beamline to the chamber housing the dechirper. Bane and Stupakov's analytic

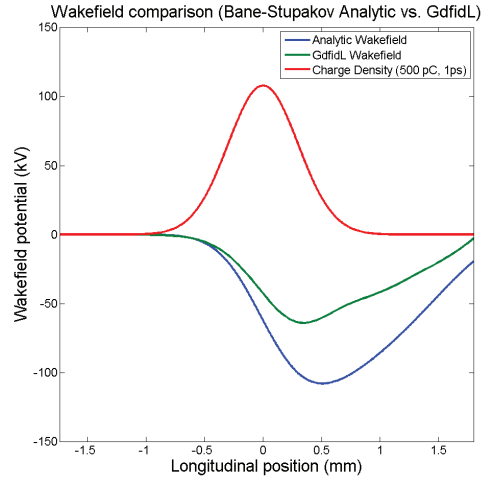


Figure 1: Comparison of the wakefield given by the analytic equations [2] and GdfidL simulations. The bunch charge density is also plotted for longitudinal position reference.

expression of the wakefield with the correction factor determined by the GdfidL simulation was directly applied to the bunch to determine the total dechirping power. Representative phase space plots at various plate gaps are shown in Fig. 2.

Table 1: Corrugated Plate Dimensions

Length	L	181	mm
Width		38.1	mm
Period	p	1.15	mm
Depth	δ	1.15	mm
Gap	g	0.77	mm
Plate separation	a	1–30	mm
Material		Aluminum	

Table 2: BNL ATF Beam Parameters

Beam energy	E	57.6	MeV
Bunch charge	Q	340	pC
Initial chirp		400	keV/mm
Transverse beam size		100	microns
Pulse length (full width)	l	3.4	ps
Longitudinal profile		Rectangular	

* harrison@radiabeam.com

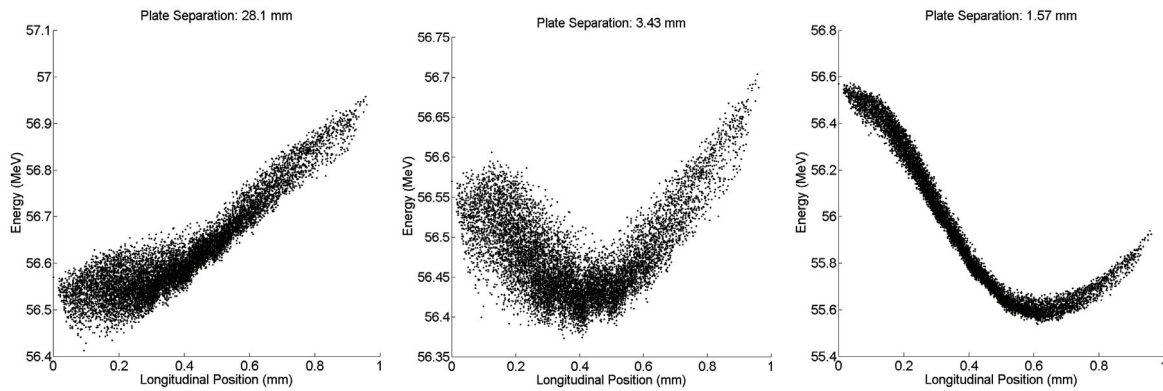


Figure 2: Longitudinal phase space plots at various plate gaps as simulated in Elegant. Note that the smallest gap causes an overdechirp that results in a larger energy spread.

BROOKHAVEN LAB EXPERIMENT RESULTS

To demonstrate the efficacy of a passive corrugated plate system, RadiaBeam Systems installed an 18 cm long test piece in the BNL ATF and ran beam through it with properties given in Table 2. The dimensions of the corrugated plates are given in Table 1 and illustrated in Fig. 3.

The experiment consisted of running the beam through the corrugated plates at various gaps while measuring the energy spread of the bunch with a downstream dipole spectrometer. The dechirping power, defined as the difference in energy spread before and after the dechirper divided by the bunch length, was calculated and plotted in Fig. 4 along with the predicted dechirping power calculated from the Elegant simulations.

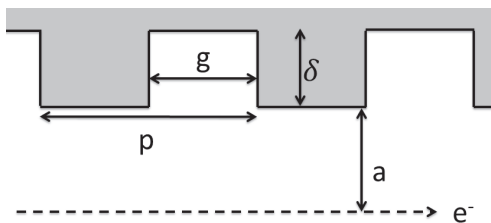


Figure 3: Dimensions of corrugated plates. See Table 1.

CONCLUSION

RadiaBeam Systems has successfully demonstrated a prototype dechirping system that requires no power or RF input. The simple device made of machined aluminum reduced and even reversed the longitudinal energy chirp of the BNL ATF beam. The agreement between the measurements and simulations in this experiment is an encouraging sign that scaling this system up to meters in length for GeV-energy systems such as LCLS, SwissFEL, PAL-XFEL, and many others.

In light of the success of this experiment, RadiaBeam Systems is currently designing a larger, multi-module dechirper for installation at LCLS. [4] The corrugated structures will be two meters long and there will be two sections: one with

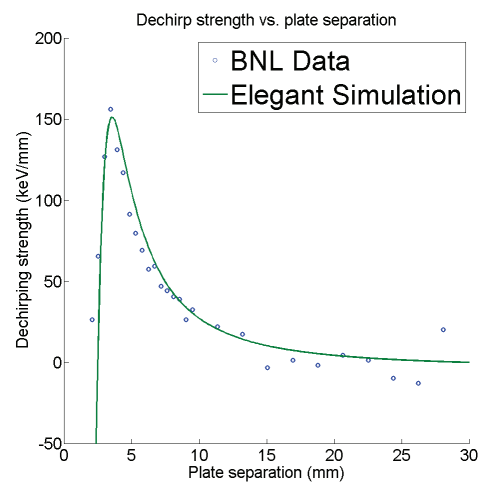


Figure 4: Comparison of measured and theoretical dechirping power of corrugated plates.

horizontal plates and one with vertical plates. The differing orientations will limit the unwanted quadrupole focusing effects seen in simulations. [3]

ACKNOWLEDGMENTS

This work is supported by Department of Energy grant number DE-SC0009550.

REFERENCES

- [1] M. Harrison et al., "Removal of Residual Chirp in Compressed Beams Using a Passive Wakefield Technique", in *Proc. North American Particle Accelerator Conf.*, Pasadena, 2013, pp. 291–293.
- [2] K. Bane et al., "Corrugated Pipe as a Beam Dechirper", SLAC-PUB-14925, 2012.
- [3] Z. Zhang et al., "Design Study of LCLS Chirp-Control with a Corrugated Structure", in *These Proceedings: Proc. 36th Int. Free-Electron Laser Conf.*, Basel, 2014, THP026.
- [4] M. Harrison et al., "Mechanical Design for a Corrugated Plate Dechirper System for LCLS," in *These Proceedings: Proc. 36th Int. Free-Electron Laser Conf.*, Basel, 2014, THP033.

RELATIVISTIC EFFECTS IN MICRO-BUNCHING

Vladimir N. Litvinenko, Stony Brook University, Stony Brook, USA
Gang Wang, Brookhaven National Laboratory, Upton, USA

Abstract

In this paper we present our theoretical studies of limits on bunching using magnetic systems. We discuss the connection of this limit with plasma oscillations in electron beams and present simple formulae for an additional limit of micro-bunching amplification.

INTRODUCTION

Bunching and microbunching are very popular beam manipulation techniques. They are used (or planed to be used) for creating high peak current beams for X-ray FELs [1-4], for controlling or amplifying the shot noise in electron beams [5-12], or even using it for cooling of hadron beams [13-14].

Majority of these applications rely on magnetic bunchers providing time-of-flight dependence on particle energy, which is usually described by the R_{56} coefficient of the transport matrix. One underlying assumption in many of these papers is that the bunching parameters are limited by kinematics of the motion, e.g. by R_{56} and the beam energy spread. For example, there is no assumed limit on the maximum amplification of the shot noise (micro-bunching) in electron beam.

On other hand, it is known from plasma physics that in ballistic compression case the energy oscillates between the space charge and the kinetic energy of the particles. Specifically, it is shown in [15,16], placing an external point charge q into a cold plasma (an electron beam) or warm plasma with κ -2 velocity distribution [16] will cause oscillations of the screening charge with maximum value not exceed $-2q$. This limit does not depend on the value of R_{56} or beam energy spread. It also means that in such system the shot noise can not be amplified. Nevertheless, the micro-bunching using magnetic chicanes with gain exceeding unity was both predicted theoretically and demonstrated experimentally [5-12].

Hence, there are fundamental questions about the attainable bunching in electron beam:

- (a) what energy is available to compensate for the space charge energy acquired during the process?
- (b) what is the maximum attainable microbunching gain?

In this paper we show that this is purely relativistic effect and are given a simple answer on the maxim amplification for micro-bunching.

We are not considering here any dynamic issues related to bunching such as coherent synchrotron radiation and focus only on the fundamental limit.

STANDARD APPROACH

Standard approach used on modern theory of micro-bunch (see for example [11]) uses the bunching and energy modulation factors, defined as follows:

$$b_k = \frac{1}{N} \sum_{n=1}^N e^{-ikz_n}; \mu_k = \frac{i}{N} \sum_{n=1}^N \eta_n e^{-ikz_n}; \eta_n = \frac{\delta\gamma_n}{\gamma_o}, \quad (1)$$

to describe the microbunching process using matrix formalism [7]:

$$\begin{bmatrix} b_k(s_2) \\ \mu_k(s_2) \end{bmatrix} = R(s_1|s_2) \begin{bmatrix} b_k(s_1) \\ \mu_k(s_1) \end{bmatrix} \quad (2)$$

Propagation through a straight section is described as a simple (plasma) oscillation between the bunching and the energy modulation, which is a good approximation:

$$R(s_1|s_2) = \begin{bmatrix} \cos\varphi_p & -\alpha \sin\varphi_p \\ \alpha \sin\varphi_p & \cos\varphi_p \end{bmatrix}; \quad (3)$$

$$\varphi_p = k_p(s_2 - s_1); k_p = \sqrt{4\pi r_e n_e / \gamma^3}; \alpha = k / \gamma^2 k_p.$$

The other, and much stronger approximation, is used for propagating the beam through a chicane (buncher) with longitudinal compaction factor, R_{56} , yielding in case of longitudinally cold e-beam [7]:

$$R_b = \begin{bmatrix} 1 & -kR_{56} \\ 0 & 1 \end{bmatrix}. \quad (4)$$

Taking into account Gaussian energy spread, yields an exponential suppression factor, which is well know from theory of optical klystron [17,18]:

$$R_b = \begin{bmatrix} 1 & -kR_{56} \cdot e^{-\frac{1}{2} \left(\frac{kR_{56}\sigma_\gamma}{\gamma} \right)^2} \\ 0 & 1 \end{bmatrix}. \quad (5)$$

formally limiting amplification to $g_{mn} \leq \gamma / \sqrt{e}\sigma_\gamma$. With high quality e-beam having $\sigma_\gamma / \gamma \sim 10^{-3} \div 10^{-4}$, Eq. (5) predicts a possibility if very high microbunching gain. Hence, standards treatment assumes that the bunching amplification in a chicane is determined by the values of R_{56} and is limited by the relative energy spread in the

beam. We will show that there is a fundamental limitation, which require reconsidering the use of Eqs. (4) and (5).

A SIMPLE CHICANE MODEL

Let's simplify the buncher into a chicane with short magnets, as illustrated in Fig.1. In this case interaction between particles and the bunching occurs in the legs of the chicane where their trajectories are straight. The later allows to simplify the model and to get an analytical expression for limits of attainable compression.

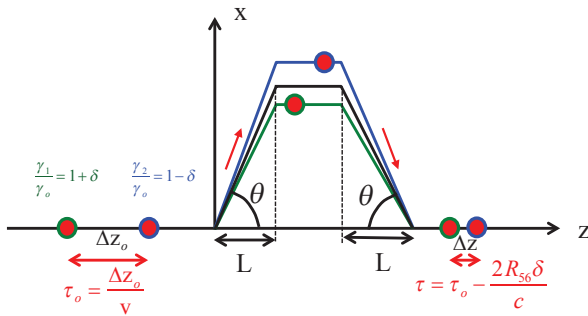


Figure 1: A simplified schematic of a chicane buncher with short dipole magnets, $R_{s6} \cong L\theta^2$, where L is the length of each leg of the chicane. Some distances, sizes and angles are exaggerated for visibility: for example, in practice $\theta \ll 1$, $\Delta z \ll L$.

Let's also choose magnets with translation symmetry in x-direction whose the magnetic field can be represented by a simple one-component vector potential (see Fig. 2):

$$A_x(x, 0, z) = \begin{cases} A_o; & 0 < z < L \\ -A_o; & L + l < z < 2L + l \\ 0; & z < 0, z > 2L + l \\ & L < z < L + l \end{cases}; \quad A_o = \frac{p_o c}{e} \sin \theta; \quad (6)$$

where we took into account that electron has negative charge $-e$. For the rest of the paper we are interested in plane trajectories and, unless specified otherwise, we assume $y=0$. Since the vector potential (and the Hamiltonian) does not depend on x , in the absence of other forces the x component of the canonical momentum is an invariant. It gives us a change of the horizontal momenta when electron passes each dipole

$$P_x = p_x - \frac{e}{c} A_x = inv;$$

$$p_x(0+\varepsilon)-p_x(0-\varepsilon)=+\frac{eA_o}{c}=p_o\sin\theta; \quad 0<\varepsilon\ll L \quad (7)$$

$$p_x(2L+l+\varepsilon)-p_x(2L+l-\varepsilon)=p_o \sin \theta.$$

Our model uses a very short kicks and drifts whose length much longer than the distance between charges. Hence, we neglect the interaction of the charges at the corners of the trajectory. We intentionally the conse-

vation law (7) at the boundaries of the vector potential dependence, with $0 < \varepsilon \ll L$, to identify the change imposed by the dipole magnet, and to separate it from the EM fields induced by beam itself. Specifically, Eq. (7) states, that the change of the horizontal momentum by a dipole does not depend neither on particle's energy nor its horizontal position.

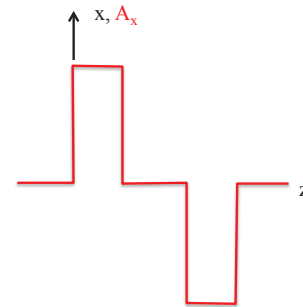


Figure 2: Sketch of beam trajectory and horizontal component of the vector potential of a simplified chicane.

We are using simple energy conservation law for deriving our limit. Naturally, we use the fact that magnetic field does not changes neither energy of the particle not the energy of the beam. It also applies to the total particle momentum. It means that changes of the horizontal momentum will cause corresponding change in the z-component of the momentum:

$$p_z = \sqrt{p^2 - p_x^2}. \quad (8)$$

Quite naturally, we focus on a second leg of chicane, where the bunch becomes shorter and the beam-induced field is increased.

CM ENERGY

To illustrate the method, we start from a simple model of two identical charged particles (electrons) interacting with each other. The idea is to find how close particles can approach each other (e.g. a minimum Δz) with a given energy deviation δ . In other words, when “space charge” stops “the bunching”?

The simplest way of finding this is use the center of mass system where the total momentum of two particles is zero and they approaching each other:

$$\pi_{1,2} = \pm \gamma_c \beta_c m c; \quad \varepsilon_c = \gamma_c m c^2. \quad (9)$$

Then the total kinetic energy

$$E_k = 2(\varepsilon_c - mc^2) = 2(\gamma_c - 1)mc^2 \quad (10)$$

can be transferred into the potential energy, when electrons approach each other to the distance in c.m. frame of:

$$r_f = \frac{r_e}{2(\gamma_c - 1)}, \quad r_e = \frac{e^2}{mc^2}, \quad (11)$$

and stop. Here we neglect initial electrostatic energy assuming $r_f \ll r_i$. The exact solution is

$$\frac{1}{r_f} = \frac{2(\gamma_c - 1)}{r_e} + \frac{1}{r_i} \rightarrow r_f = \frac{r_e}{2(\gamma_c - 1) + r_e/r_i}.$$

We note that since we are considering momentum along z-axis, this distance is compressed by factor γ_o .

Let's start from the case of ballistic compression, when the in c.m. two electrons have equal and opposite momenta along z-axis. Generally, their motion in c.m. is non-relativistic, but here we will use exact notations in order not to miss possible high order effects. In the lab frame boosted along the momenta of the electrons with $\gamma \equiv (1 - \beta^2)^{-1/2}$ we have:

$$p_{1,2} = \gamma_o (\beta \pm \beta_c) mc; \quad E_{1,2} = \gamma_o (1 \pm \beta\beta_c) mc^2; \quad (12)$$

$$\gamma_o = \gamma\gamma_c; \quad \delta = \beta\beta_c; \quad \beta_o^2 = \beta^2 + \beta_c^2 - \delta^2.$$

Hence, the total energy available for “bunching” is

$$E_k = 2 \frac{1 - \sqrt{1 - \delta^2 / \beta^2}}{\sqrt{1 - \delta^2 / \beta^2}} mc^2 \quad (13)$$

which for small relative energy deviations $\delta \ll 1$, typical for example in microbunching, becomes:

$$E_k \cong \frac{\delta^2}{\beta^2} mc^2. \quad (14)$$

We note that for relativistic beams, which are of interest for this paper, $1 - \beta \ll 1$, e.g. for $\delta \cdot 10^{-3}$ we would have only about quarter of eV of kinetic energy per electron available for bunching. When the bunching is completed both electrons stop in the c.m. frame, and their energies in the lab-frame become equal:

$$p_{1,2} = \gamma\beta mc; \quad E_{1,2} = \gamma mc^2; \quad \delta = 0. \quad (15)$$

The “beam” of two electrons then loses some energy, which can be calculated by subtracting Eq. (15) from Eq. (12):

$$\Delta E = \gamma \cdot 2mc^2(\gamma_c - 1), \quad (16)$$

which is naturally equal to the energy of electrostatic field (potential energy) of electrons, Eq. (11), boosted into the lab-frame – hence the factor γ . Thus, as expected the total energy of the system is conserved.

Let's now consider how the chicane changes this situation. The processes in the both legs are similar to a degree, but bunching of interest is happening in the second leg where particles come closer in both the transverse and longitudinal directions. As we discussed in previous section, the translation invariance in x direction preserves the x -component of the Canonical momentum:

$$P_x = p_x - \frac{e}{c} A_x(z)$$

Let's start from the same initial conditions as in Eq. (12) and propagate particles through first dipole to get (using Eq. (8)):

$$\vec{p} = \hat{x} \frac{eA_o}{c} + \hat{z} \sqrt{p^2 - \left(\frac{eA_o}{c}\right)^2}; \quad (17)$$

$$\frac{\vec{p}_{1,2}}{mc} = \hat{x} \frac{eA_o}{mc^2} + \hat{z} \sqrt{\gamma_o^2 (\beta \pm \beta_c)^2 - \left(\frac{eA_o}{mc^2}\right)^2},$$

with energies unchanged. The c.m. energy of the system is easiest to calculate using standard 4D product to the systems 4-momentum [19]:

$$E_{c.m.}^2 = c^2 p_i p^i = (p_1 + p_2)^2 = 2(mc^2)^2 + 2c^2 p_1 p_2; \quad (18)$$

$$c^2 p_1 p_2 = E_1 E_2 - c^2 \vec{p}_1 \vec{p}_2,$$

where we used know 4D product [19] $p_1^2 = p_2^2 = m^2 c^2$. Using Eqs. (12) and (17), $\gamma_o = \gamma\gamma_c$ and $\delta = \beta\beta_c$:

$$E_1 E_2 = (\gamma_o mc^2)^2 (1 - \delta^2);$$

$$\vec{p}_1 \vec{p}_2 = (\gamma_o mc)^2 \left\{ \left(\frac{eA_o}{\gamma_o mc^2} \right)^2 + \sqrt{(\beta + \beta_c)^2 - \left(\frac{eA_o}{\gamma_o mc^2} \right)^2} \cdot \sqrt{(\beta - \beta_c)^2 - \left(\frac{eA_o}{\gamma_o mc^2} \right)^2} \right\};$$

yields final

$$\frac{E_1 E_2 - c^2 \vec{p}_1 \vec{p}_2}{(\gamma_o mc^2)^2} = 1 - \delta^2 - a_o^2 - \sqrt{(\beta_o^2 + \delta^2 - a_o^2)^2 - 4\delta^2}; \quad (19)$$

$$E_{c.m.} = mc^2 \sqrt{2 + 2 \cdot \gamma_o^2 \left(1 - \delta^2 - a_o^2 - \sqrt{(\beta_o^2 + \delta^2 - a_o^2)^2 - 4\delta^2} \right)}.$$

where we used and introduced dimensionless vector potential (see (6)):

$$a_o = \frac{eA_o}{\gamma_o mc^2} = \beta_o \sin \theta. \quad (20)$$

Expanding (19) with $\gamma_o \gg 1$, $\delta^2 \ll 1$ to the leading order we obtain:

$$\frac{E_{c.m.}}{mc^2} \cong 2 + \delta^2 (1 + \gamma^2 tg^2 \theta). \quad (21)$$

with the kinetic energy available for the bunching of

$$\frac{E_k}{mc^2} = \frac{E_{c.m.}}{mc^2} - 2 \cong \delta^2 (1 + \gamma^2 tg^2 \theta) \quad (22)$$

For ballistic bunching with $\theta = 0$ we get already known result (14) $E_k \cong mc^2 \delta^2$. In a chicane it is amplified by a factor of $1 + \gamma^2 tg^2 \theta \sim 1 + (\gamma\theta)^2$. It is well known in accelerator theory is that factor $K = \gamma tg \theta$ is a measure of the relativity of the transverse motion:

$$\frac{p_x}{mc} = \gamma \beta \sin \theta \sim \gamma \theta.$$

For ultra-relativistic particles K -factor can be large even for modest bending angles. Hence, using a buncher with $K = \gamma\theta \gg 1$ will boost by $(1 + K^2)$ -fold the energy available to compensate the space charge potential energy accrued during the bunching.

Repeating similar calculations for an ensemble of particles gives an expected result:

$$E_k \cong (1 + (\gamma\theta)^2) \sum_{n=1}^N \delta_n^2 mc^2, \quad (23)$$

where δ_n is a relative energy deviation of n^{th} particle. Thus, the available kinetic energy available in an ensemble of particles is also amplified by the same factor.

DISCUSSIONS AND CONCLUSIONS

From analogy with plasma oscillation during ballistic transport (where microbunching gain of shot noise can not exceed unity), one should expect that a buncher could provide a shot noise gain $\sim K$. Qualitatively this can be concluded from following observations:

- in case of ballistic motion after a half of a plasma oscillation any unshielded electric charge will be surrounded by a cloud of electron with about twice the external charge with the cloud size defined by Debye radius [15,16]. The potential energy of such cloud is naturally proportional to the square of its charge. At this moment all kinetic energy is exhausted and electrons starting moving in opposite direction. In terms of the bunching factor, it is the same a gain not exceeding unity;
- since the potential energy if a charge collected in a given pattern is proportional to the square of its value, means that its maximum value is proportional to the square root of the available kinetic energy;
- since the chicane amplifies the available kinetic energy (K^2+1) fold when compared with the ballistic

motion, the charge which can be collected in the similar pattern could be $\sqrt{K^2+1} \sim K$ -fold larger than in a case of ballistic compression.

Hence, the conservation of the energy gives us a very straightforward way of limiting micro-bunching gain in a single chicane. First, we should notice that in the drift section the bunching is oscillating and “maximum gain” is simply equal 1. In the chicane, the available kinetic energy is amplified and hence the microbunching gain can exceed unity. Since the potential energy is proportional to the square of the bunching factor, the maximum micro-bunching gain (per chicane) must be limited by:

$$g_{\max} \leq \sqrt{(1 + (\gamma\theta)^2)} \sim \gamma\theta, \quad (24)$$

We want to underline that this boost has pure relativistic nature and depends on the product of the Lorentz factor and the bending angle, but not on the value to R_{56} .

Overall, Eq. (24) represents an additional, frequently overlooked, limit on micro-bunching amplification.

REFERENCES

- [1] P.Emma et al., “First lasing and operation of an ångstrom-wavelength free-electron laser”, Nature Photonics 4, 2010, pp. 641-647.
- [2] W. Ackermann et al., “Operation of a free-electron laser from the extreme ultraviolet to the water window”, Nature Photonics 1, 2007, pp. 336-342.
- [3] H.Tanaka, “The SPring-8 Angstrom Compact Free Electron Laser (SACLA)” In Proc. of IPAC 2012, May 2012, New Orleans, LA, USA, 2012, pp. 2106-2110.
- [4] H.H. Braun, “The Future of X-ray FELs)” In Proc. of IPAC 2012, May 2012, New Orleans, LA, USA, pp. 4180-4184.
- [5] A. Gover, A. Nause, E. Dyunin, and M. Fedurin, “Beating the shot-noise limit”, Nature Physics 8, 2012, pp. 877-880.
- [6] D. Ratner and G. Stupakov, “Observation of Shot Noise Suppression at Optical Wavelengths in a Relativistic Electron Beam”, Phys. Rev. Lett. 109, 2012, 034801.
- [7] A. Gover and E. Dyunin, “Collective-Interaction Control and Reduction of Optical Frequency Shot Noise in Charged-Particle Beams”, Phys. Rev. Lett., 102, 2009, 154801.
- [8] A. Nause, E. Dyunin, and A. Gover, “Optical frequency shot-noise suppression in electron beams: Three-dimensional analysis”, J. Appl. Phys. 107, 2010, 103101.
- [9] D. Ratner, Z. Huang, and G. Stupakov, “Analysis of shot noise suppression for electron beams”, Phys. Rev. ST Accel. Beams 14, 2011, 060710.

- [10] E. A. Schneidmiller and M.V. Yurkov, “Using the longitudinal space charge instability for generation of vacuum ultraviolet and x-ray radiation”, *Phys. Rev. ST Accel. Beams*, 13, 2010, 110701.
- [11] A. Marinelli, E. Hemsing, M. Dunning, D. Xiang, S. Weathersby, F. O’Shea, I. Gadjev, C. Hast, and J. B. Rosenzweig, “Generation of Coherent Broadband Photon Pulses with a Cascaded Longitudinal Space-Charge Amplifier” *Phys. Rev. Lett.* 110, 2013, 264802.
- [12] A. Marinelli, J. B. Rosenzweig, “Microscopic kinetic analysis of space-charge induced optical microbunching”, *Phys. Rev. ST Accel. Beams*, 13, 110703 (2010).
- [13] V.N. Litvinenko, “Suppression of Short Noise and Spontaneous Radiation in Electron Beams”, In *Proc. of the 2009 FEL Conference*, Liverpool, UK, 2009, p. 204.
- [14] D.F. Ratner, “Microbunched Electron Cooling for High-Energy Hadron Beams”. *Phys. Rev. Lett.* 111, 2013, 084802.
- [15] V.N. Litvinenko and Y.S. Derbenev, “Coherent Electron Cooling”, *Phys. Rev. Lett.* 102, 2009, 114801.
- [16] G. Wang, M. Blaskiewicz, “Dynamics of ion shielding in an anisotropic electron plasma”, *Phys. Rev. E* 78, 2008, 026413.
- [17] N.A. Vinokurov, A.N. Skrinsky, “Theory of Optical Klystron”, *MW Rel. Electronics*, Gorky. 1981, p. 204.
- [18] N.A. Vinokurov, A.N. Skrinsky, “Optical Klystron”, Preprint 77-59, BINP, Novosibirsk, Russia, 1977.
- [19] L.D. Landau and E.M. Lifshitz, *The classical Theory of Fields*, Pergamon, New York, 1975.

BENCHMARK AND SIMULATION DESIGN OF A LOW ENERGY BUNCH COMPRESSOR

A. He, F. Willeke, L.H. Yu, L. Yang BNL, Upton, NY 11973, USA
J. Qiang LBNL, Berkeley, CA 94720, USA

Abstract

In the electron beam slicing method [1], a low energy bunch with very short and focused beam size is required to interact with the storage ring bunch. We have designed a low energy bunch compressor with BNL photo-cathode electron RF-gun [2] by applying simulation code PARMELA [3].

In this paper, in order to confirm the simulation result, we benchmark the simulation result from PARMELA with that from IMPACT-T [4] for our compressor with BNL RF-gun. In order to increase the repetition rate of the electron beam slicing system, and change the compressor's RF gun from BNL RF-gun to LBNL's VHF gun [5] to redesign the compressor by applying IMPACT-T with both space charge effects and CSR effects considered. The benchmark between PARMELA and IMPACT-T has produced excellent agreement. The comparison of the CSR effects also shows the bunch can be compressed and focused to our desired size after optimization using code IMPACT-T with CSR effects turned on. The new compressor with high repetition rate still works in space charge dominated domain and the bunch with a negative energy chirp at the entrance of the chicane is compressed by a chicane with positive R_{56} . After the optimization, we have achieved a low energy bunch with the 128 fs RMS bunch length, 42 μm and 25 μm RMS beam size in the vertical and horizontal directions respectively, at 22 MeV with 200 pC charge.

INTRODUCTION

The electron beam slicing method [1] generates ultra-short x-ray pulses using focused short low energy (~ 20 MeV) electron bunches to create short slices of electrons from the circulating electron bunches in a synchrotron radiation storage ring. When a low energy electron bunch crosses from top of a high energy storage ring electron bunch, its Coulomb force will kick a short slice from the core of the storage ring electron bunch. The separated slices, when passing through an undulator, will radiate ultra-short x-ray pulses at about 100 fs. In order to minimize the cost of the electron beam slicing system and to explore the lower limit of the compressor's bunch energy, a low energy bunch compressor [2] without acceleration after the RF-gun exit has been designed to achieve the desired bunch compression and focusing. The RF gun used in this compressor is BNL RF-gun and the simulation code applied is PARMELA with space charge effects considered. Some optimized results for the BNL RF-gun compressor are given in Table 1.

In this paper, to verify the simulation results, we benchmark the simulation results from PARMELA with the results from IMPACT-T for the low energy compressor with BNL

RF-gun. To study the coherent synchrotron radiation (CSR) effects, we compare the simulation results when CSR effects is turned on with those when CSR is turned off in IMPACT-T. In order to increase the repetition rate of the electron beam slicing system, we change the compressor's RF gun from BNL RF-gun to LBNL's VHF gun [5] and redesign the compressor by applying IMPACT-T with both space charge effects and CSR effects considered.

BENCHMARK AND CSR EFFECTS

Both Linac tracking codes PARMELA [3] and IMPACT-T [4] can track relativistic particles taking into account space charge effects in the 6D space, whereas the space-charge solver is 2D r-z or 3D depending on the code. IMPACT-T also considers the coherent synchrotron radiation (CSR) effects which are not included in PARMELA.

To verify our simulation results from PARMELA, taking the compressor of case 3 in Table 1 as an example we benchmark the results with PARMELA against those with IMPACT-T. By applying IMPACT-T, we also discuss CSR effect which is not considered in code PARMELA. The CSR effects are related to the bunch energy, bunch charge and bunch length. To check the CSR effects, we compare the simulation results when CSR effects being turned on with the results when CSR effects being turned off in IMPACT-T. The results of the benchmark and comparison is shown in Table 2, Fig. 1 and Fig. 2.

Data in Table 2 show the RMS bunch length difference between PARMELA and IMPACT-T with CSR off is less than 6%. The difference of the transverse RMS beam size between the two codes is larger than 20% when all the results are calculated for 90% particles, with 10% longitudinal tails cut-off. If the transverse RMS beam size are calculated for 100% particles as shown in Fig. 1, the difference of those between the two codes decrease to $\sim 10\%$. Fig. 1 show the 6-D phase space at the final focus point for the three simulation results: PARMELA (the 1st row), IMPACT-T with CSR effects off (the 2nd row) and IMPACT-T with CSR effects on (the 3rd row). The color bar indicates the particle density.

Due to the space charge forces the particle energy is no longer constant, and the dispersion function and beta functions both lose their original meaning. We redefine the equivalent dispersion and the equivalent beta functions as described in [1]. To show the agreement between the two codes and the difference of the calculations with and without the CSR effects considered, we plot the evolution of the newly defined beta functions and the dispersion function along the dispersive chicane section of the compressor for the three simulation results in Fig. 2. Although the exact

Table 1: Performances of Compressors with Different Charge and Different Energy

compressor ^a	RF-gun	accelerate	length	Charge	Energy	σ_L^b	σ_H^c	σ_V^d
case		cavity	[m]	[pC]	[MeV]	[fs]	[μm]	[μm]
1	BNL	no	6.75	50	5	166	31	28
2	RF-gun	yes	6.75	100	12	110	34	31
3		yes	6.75	150	12	145	35	24
4	LBNL	yes	8.5	150	18	130	47	28
5	VHF-gun	yes	8.5	200	20	148	46	25
6		yes	8.5	200	22	128	42	25

^a The simulation results for the BNL RF-gun compressor come from PARMELA with CSR effects ignored. The simulation results for the LBNL's VHF gun compressor come from IMPACT-T with CSR effects considered.

^b the longitudinal RMS bunch length at final focal point

^c the horizontal RMS beam size at final focal point

^d the vertical RMS beam size at final focal point

value of these functions in Fig. 2 lose their original meaning with space charge effects increasing, these function curves still can be used to compare the simulation results.

The simulated results of IMPACT-T with CSR off (green curve) show good agreement with those of PARMELA (red curve) with slightly difference in the newly defined RMS beam size. The agreement between the two codes (the red and green curve) in the newly defined dispersion is excellent. The green curves (CSR off) and the blue curves (CSR on) are completely overlapped before the chicane's third bending magnet which is located at 4.6 m of the beamline. The green and blue curves appear separated after the third dipole. The separation indicates the CSR effects and also shows the CSR effects mainly take place at the 3rd and 4th dipole of the chicane. Analysis show the bunch length is significantly compressed from 800 fs to 300 fs when passing through the 3rd dipole and the bunch length has been compressed to 235 fs at the entrance of the 4th dipole. Although the CSR effects induce some minor difference, the results in Table 2 indicate it is promising that the final bunch can be further optimized.

The benchmark between PARMELA and IMPACT-T has produced excellent agreement. The comparison of the CSR effects also shows the bunch can be compressed and focused to our desired size after optimization using code IMPACT-T with CSR effects turned on.

Table 2: Benchmark Results of PARMELA Against IMPACT-T and Comparison of CSR Turning Off with CSR Turning On in IMPACT-T

code	CSR effects	σ_L^a	σ_H^a	σ_V^a
		[fs]	[μm]	[μm]
PARMELA	off	145	35	24
IMPACT-T	off	137	45	32
IMPACT-T	on	157	41	26

^a σ_L , σ_H , σ_V are the longitudinal RMS bunch length, the horizontal RMS beam size, the vertical RMS beam size at the final focal point respectively.

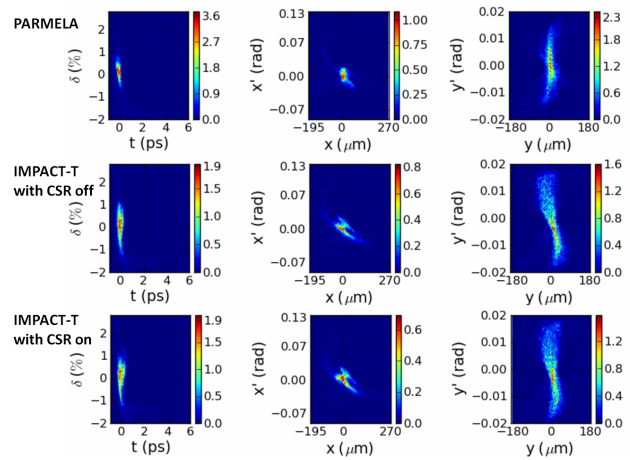


Figure 1: The histograms of bunch's 6-D phase space at the final focus point of the compressor. Data come from different simulation codes for the same compressor of case 3 in Table 1: PARMELA (the 1st row), IMPACT-T with CSR off (the 2nd row), IMPACT-T with CSR on (the 3rd row). The color bar shows the particle density.

HIGH REPETITION RATE LOW ENERGY COMPRESSOR

In order to increase the repetition rate of the electron beam slicing system to increase the photon flux, we change the RF gun of the compressor from BNL photo-cathode RF gun to LBNL's VHF gun which operates at 186 MHz with repetition rate of 1 MHz [5] and redesign the compressor by applying simulation code IMPACT-T with both space charge effects and CSR effects considered.

Matching by Manual Adjustment

We use the simulation result for the benchmarked compressor with BNL RF gun at 13 MeV as a starting point to study the compressor with VHF gun. First, we keep the same magnet sections as those of the benchmarked compressor which include the matching magnets, chicane magnets and final focusing magnets. We change the gun from BNL RF

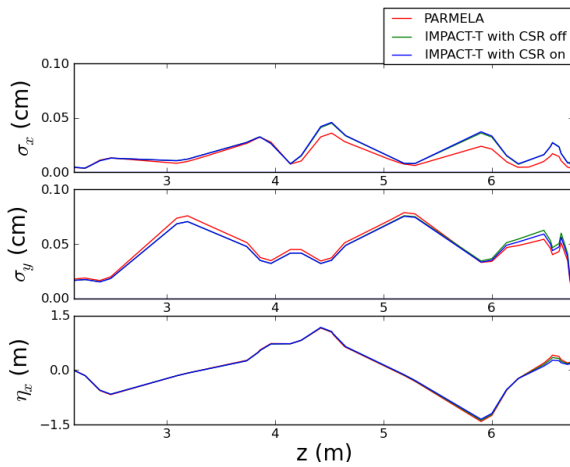


Figure 2: The evolution of the newly defined beta functions and the newly defined dispersion function along the dispersive section of the compressor. The red, green and blue curves correspond to the simulation results by PARMELA, IMPACT-T with CSR off, IMPACT-T with CSR on respectively.

gun to LBNL VHF gun and we also add several RF cavities between the gun and the matching magnets to accelerate the bunch. Then with the space charge effects turned on, we adjust the gun and the accelerating section to make the bunch's energy chirp and the transverse beam size after the acceleration to match with those at the entrance of the first matching quadruple of the benchmarked compressor.

At the photocathode, we set the bunch longitudinal distribution as flat-top with linear ramp at two ends and the total length from head to tail is 8 ps. The bunch transverse distribution is a uniform ellipse with hard cut edge and the diameter of the ellipse in x and y is 1.5 mm. The 3-D momentum distribution of the bunch is Gaussian. The bunch charge is set at 150 pC. Simulation shows the beam energy after LBNL's VHF gun is 730 keV. In order to avoid large betatron oscillation and beam blowing up, we move the accelerating cavity very close to the photocathode gun.

While keeping the bunch energy at 13 MeV after acceleration, we adjust the phases and gradients of the RF cavities manually to match the energy chirp of the bunch after acceleration with the energy chirp at the entrance of the first matching quadruple of the benchmarked compressor. At the same time, We adjust the intensity of focusing coils manually to make the bunch's transverse beam size match with those at the entrance of the first matching quadruple of the benchmarked compressor. We iterate the adjustments of the focusing coils and the RF cavities to optimize the matching. After the matching, the total length of the compressor system consisting of the LBNL's VHF gun, two focusing coils, two RF cavities and the matching, dispersive and focusing magnets section is 8.5 m. At the entrance of the first matching quadruple, the bunch's energy spread is increased to $\pm 9\%$ and the longitudinal bunch length is about 25 ps.

Global Optimization by Genetic Algorithm

With the previous matched compressor of LBNL VHF gun, we carry out a multi-objective optimization procedure [6] using a genetic algorithm to optimize the compressor with the bunch energy fixed at 13 MeV. After optimization, the RMS bunch length is still larger than 1 ps and the transverse RMS beam size are also very large around $150 \mu\text{m}$. Analyzing the longitudinal phase space of the final focused bunch colored by the initial emittance after acceleration and the initial energy spread after acceleration shown in Fig. 3 (I,II), we find the bunch length increase is not directly related to the initial emittance, but is related to the initial energy spread. If we artificially cut off those bunch particles with the initial energy spread larger than $\pm 2\%$, the RMS bunch length at the final focal point decreases from 1.26 ps to 0.38 ps as shown in Fig. 3 (III).

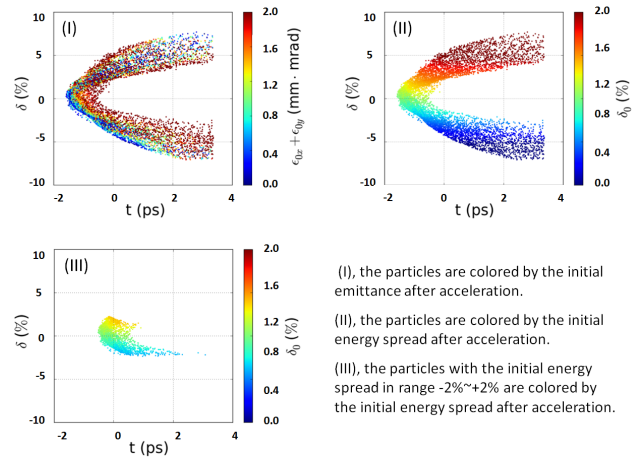


Figure 3: The longitudinal phase spaces at the final focal point for one optimized result of the VHF-gun compressor at 13 MeV. Simulation code is IMPACT-T with both space charge effects and CSR effects being turned on.

Based on the previous observation, in order to reduce the final bunch length, we increase the bunch energy to decrease the relative energy spread after the RF cavity acceleration. At the same time, in order to increase the kick angle and shorten the slice width in electron beam slicing method [1], we also increase the bunch charge. Using IMPACT-T with CSR effects turning on, we iterate to carry out the global optimization and gradually increase the bunch's charge and energy. Some optimized results are shown in Table 3. For example in Table 3, the 22 MeV, 200 pC charged bunch is longitudinally compressed from 6.8 ps head to tail bunch length at photocathode to 128 fs RMS bunch length by the 8.5 m compressor. The transverse beam size are focused from the diameter ellipse of 2 mm at photocathode to $42 \mu\text{m}$ and $25 \mu\text{m}$ for horizontal and vertical RMS beam size respectively. Figure 4 shows the histograms of 6-D phase space at the final focus point of the 22 MeV compressor with the color bar indicating the particle density.

Table 3: Performances of the 8.75 m LBNL's VHF Gun Compressor

bunch performance	initial bunch	focused ^a bunch
longitudinal bunch length [fs]	6783 ^b	128 ^c
horizontal beam size [μm]	1994 ^b	42 ^c
vertical beam size [μm]	1971 ^b	25 ^c
energy spread [%]	0.0014 ^d /0.98 ^e	1.38
average kinetic energy [MeV]	0.73 ^d /22 ^e	22
horizontal emittance [μm]	59 ^d /0.143 ^e	0.71
vertical emittance [μm]	58.5 ^d /0.142 ^e	0.19
charge [pC]	200	200
current [A]	30	1563

^a be calculated for 90% particles, with 10% longitudinal tails cut-off.

^b at cathode

^c RMS value

^d at gun exit

^e after RF acceleration

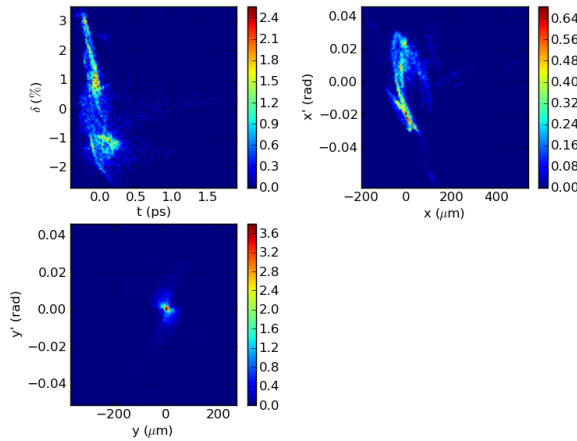


Figure 4: The histograms of 6-D phase space at the final focus point of the 22 MeV compressor with VHF gun. The color bar shows the particle density. Simulation code is IMPACT-T with both space charge effects and CSR effects being turned on.

CONCLUSION

The benchmark between PARMELA and IMPACT-T has produced excellent agreement. The comparison of the CSR effects also shows the bunch can be compressed and focused to our desired size after optimization using code IMPACT-T with CSR effects turned on. Our simulation shows that electron bunch with high charge can be compressed to very high current bunch at very low energy with both space charge effects and CSR effects included. This low energy compressor with repetition rate about 1 MHz significantly increases the repetition rate of the electron beam slicing system, and hence increases the photon flux of the ultrashort x-ray source.

ISBN 978-3-95450-133-5

ACKNOWLEDGMENT

We appreciate Dr. Simone Di Mitri for discussing about the CSR effects, and providing the cost estimate of our system's magnets. We wish to acknowledge the support of our colleagues of the accelerator group in NSLS-II BNL. This work was funded by DOE under contract LDRD12-023 and LDRD14-022.

REFERENCES

- [1] A. He, F. Willeke, L.H. Yu, "Ultra-short x-ray pulses generation by electron beam slicing in storage rings" *PRSTAB* **17**, 040701 (2014).
- [2] A. He et al., "Simulation design of a low energy bunch compressor with space charge effect" in *Proc. IPAC13*, Shanghai, China, 2013, pp. 2307-2309.
- [3] J.H. Billen, PARMELA, LA-UR-98-4478 (2001).
- [4] J. Qiang et al., "Three-dimensional quasistatic model for high brightness beam dynamics simulation" *PRSTAB* **9**, 044201 (2006).
- [5] F. Sannibale, B. Bailey, K. Byrd, C. Cork, J. Corlett, S. De Santis, S. Dimaggio, L. Doolittle et al., "Status of the APEX project at LBNL" in *Proc. IPAC12*, New Orleans, LA, USA, 2012, pp. 2173-2175.
- [6] L. Yang, D. Robin, F. Sannibale, C. Steier, W. Wan, "Global optimization of an accelerator lattice using multiobjective genetic algorithms" *Nucl. Instrum. Methods Phys. Res., Sect. A* **609**, 50 (2009).

BEAM PERFORMANCE OF THE PHOTOCATHODE GUN FOR THE MAX IV LINAC

J. Andersson*, F. Curbis, D. Kumbaro, F. Lindau, S. Werin
MAX IV Laboratory, Lund University, Lund, Sweden

Abstract

The MAX IV facility in Lund (Sweden) is under construction and conditioning of the electron guns for the injector is ongoing. There are two guns in the injector, one thermionic gun for storage ring injection and one photocathode gun for the Short Pulse Facility. In this paper we report on the beam performance tests of the photocathode gun. The measurements were performed at the MAX IV electron gun test stand [1] during spring 2014. Parameters that were studied includes quantum efficiency, emittance and emittance compensation. Results from the measurements are also compared to particle simulations done with ASTRA.

INTRODUCTION

The MAX IV facility [2] is under construction in Lund, Sweden and includes two storage rings for production of synchrotron radiation and a short pulse facility (SPF) [3]. Both storage rings and the SPF are injected from a full energy LINAC and the injector for the LINAC has two different guns, a thermionic gun and a photocathode gun. The thermionic gun is used for ring injection but due to the requirements of short bunches and the long tail of low energy electrons, the thermionic gun is unsuitable for injection to the SPF. A 1.6 cell photocathode gun will be used instead, based on the FERMI@Elettra [4] gun operating at a frequency of 2.9985 GHz.

One part of the commissioning of the facility is conditioning of the photocathode gun and measurement of basic beam properties to find the performance of the gun. The gun was conditioned during last part of 2013 and the measurements of beam parameters were done during the first half of 2014. In this article the results from these measurements will be presented and we compare some of them to simulated values. The goal of these measurements is to verify that the gun can perform well enough for the commissioning of the LINAC and the SPF operations. The requirement of the SPF is a beam energy of 3 GeV and a transverse normalised rms emittance of 1 mm mrad at the undulator entrance.

GUN TEST STAND

The photocathode gun was operated in the gun test stand at MAX IV. Measurements of beam energy were performed using a magnetic energy filter installed at the end of the test stand. The magnetic energy filter consists of two dipoles that bend the beam 120°. The setup in the gun test stand

used for measurements of spot size, emittance and phase-charge curves is displayed in Fig. 1. The pepperpot used for the emittance measurements is installed between the beam viewers YAG1 and YAG2, at a distance of 1.45 m from the cathode.

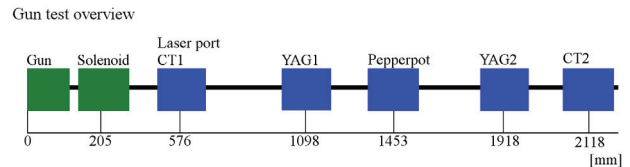


Figure 1: Schematic overview of the gun test stand.

The gun is powered by a klystron with a connected SLED cavity at 2.9985 GHz. The laser system is based on a Ti:Sapphire laser and the pulses are stretched, split and tripled to give a FWHM laser pulse length of 8 ps at 263 nm wavelength. The laser oscillator is locked to the 3 GHz signal of the RF system and the energy of the laser pulse can be changed during operation. The transport of the laser beam from the laser hutch to the cathode is done through air, the beam is then focused on the cathode through an aperture of 2 mm diameter. The laser is triggered to hit the cathode when the RF pulse has lasted long enough for the cavity to be filled, the precise injection phase is then controlled using a motorized optical delay stage.

SIMULATIONS

Simulations were made using ASTRA [5] with 10 000 particles, and the fields used to describe the gun and the solenoid are based on measured fields. The beam properties depend on the laser phase, the spot size, the electric field in the gun, as well as other parameters, so a number of different simulations were run for different settings to understand the behavior of the gun. The results for simulations of beam energy as function of the electric field for an injection phase of 10°, corresponding to the setting for the energy measurement, can be seen in Fig. 2.

To understand the phase-charge relation for the gun, simulations were made with a maximum electric field strength at the cathode of 90 MV/m to determine the charge as a function of the injection phase. ASTRA was used to determine the number of accelerated electrons as a function of the injection phase and this result combined with a field dependent charge curve gives an estimate of the phase-charge relation. These simulations do not fully account for the Schottky effect and shielding effects, so the amount of charge is

* joel.andersson@maxlab.lu.se

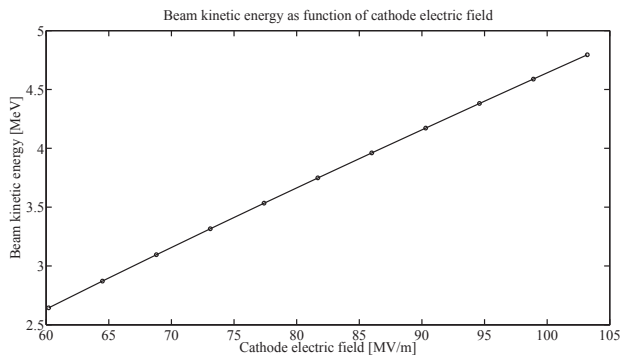


Figure 2: Simulated beam kinetic energy as function of cathode electric field.

an approximation. One result from the simulation for 90 MV/m and 100 μJ laser energy can be seen in Fig. 5 together with the results from the measurements.

To investigate the emittance dependence on the injection phase, simulations were made with an electron beam corresponding to a gaussian transverse symmetric beam size with a FWHM of 0.8 mm. These simulations were made with the same setting for the solenoid field strengths as the measurements, 0.198 T at 90 MV/m and 0.190 T at 86 MV/m, to be able to compare the results. The results at two different beam charges can be seen in Fig. 3 and Fig. 4.

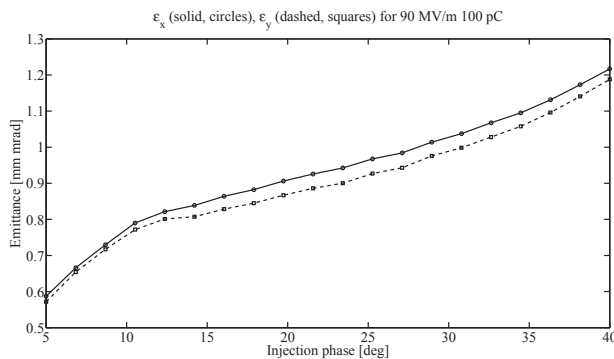


Figure 3: Simulated transverse normalised rms emittance for 90 MV/m and 100 pC charge.

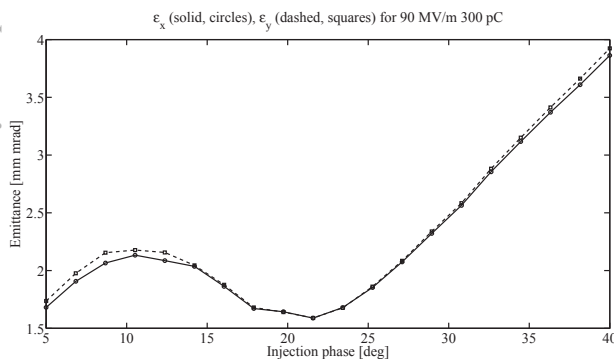


Figure 4: Simulated transverse normalised rms emittance for 90 MV/m and 300 pC charge.

MEASUREMENTS

Charge is measured using 250 MHz integrated current transformers (CT1 and CT2) connected to an oscilloscope, or using a Faraday cup. The beam viewers used were YAG crystals and CCD cameras and all measurement devices were triggered by the same signal and individual delays.

Energy

The energy of the electrons was measured using the magnetic energy filter. For a given RF power to the gun [setting of the modulator], the corresponding beam energy could be found by the current provided to the dipoles in the energy filter. The results are in Table 1 at an injection phase of approximately 10° .

Table 1: Energy Measurements

Modulator voltage [kV]	Kinetic energy [MeV]	Max E-field at cathode [MV/m]
22	3.4	77
23	3.8	82
23.5	4.0	86
24	4.2	90

The maximum electron energy in these measurements was 4.2 MeV. The total energy spread is about 0.6 MeV in all measurements but it is uncertain to what degree dark current electrons contribute to this energy spread. Compared to simulations this matches to a maximum electric field in the main cell for 23.5 kV of around 100 MV/m and for 24 kV of around 105 MV/m. This corresponds to a maximum electric field on the cathode of 86 MV/m and 90 MV/m.

Laser Phase - Charge

The injection phase is set using an optical delay stage in the laser system. To calibrate this setting a step-charge scan was made, the charge was measured using CT1 for different injection phases. The result can be seen in Fig. 5.

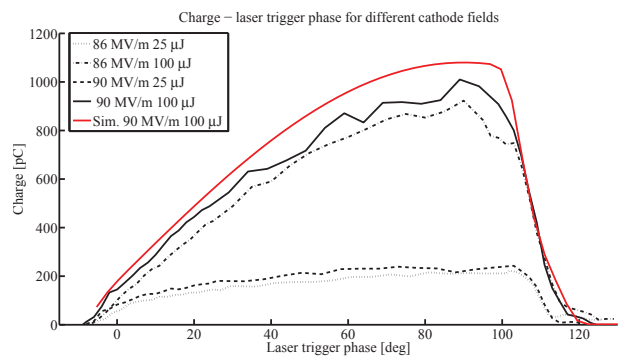


Figure 5: Measured charge as function of laser phase.

Comparing the measurements with simulations, they correspond with an offset of about 10° . The phase setting where beam charge is first measurable is approximately an injection phase of -10° , $\pm 2^\circ$. Since the laser pulse is

about 10° in length, the phase where charge is first measured should correspond to an injection phase of around -10° . These settings for the laser trigger could then be used to set the phase for the following simulations. It was noted during the experiments that this setting is not stable over time, it seems to be moving $\pm 2^\circ$ over a period of 5-10 minutes, so the calibration was remade for each new measurement to keep it as close as possible to the correct values.

Quantum Efficiency

Scans of the beam charge as a function of laser energy were performed for different electric field strengths in the gun to determine the quantum efficiency. The result is displayed in Fig. 6, for four different field settings.

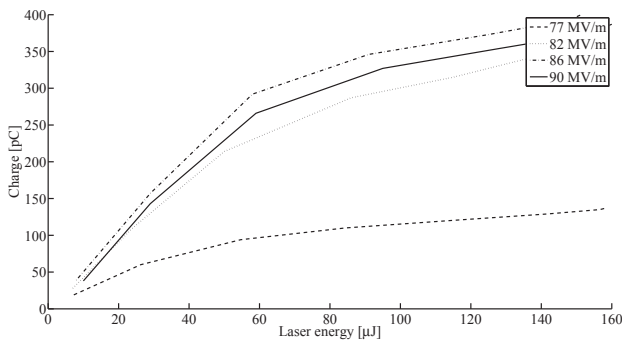


Figure 6: Measured charge as function of laser energy.

The emitted charge from the cathode will shield the cathode, and the lower electric field on the cathode leads to lower emission. This can be seen from the non-linear behavior of the charge in Fig. 6, the dependence of emitted charge of laser energy should in principle be linear without the effect from the space charge limitation.

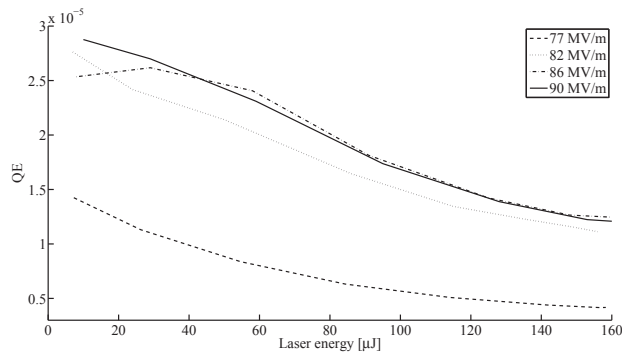


Figure 7: Measured quantum efficiency as function of laser energy.

The quantum efficiency is plotted in Fig. 7 for different field strengths. As can be seen the QE seems to be dependent both on the field in the gun and on the laser energy. The dependence of the QE on the electric field is the result from the Schottky effect. The Schottky effect will reduce the work function of the material in the cathode. A more detailed discussion can be found for example in [6].

On average the QE for the cathode turns out to be around $2 \cdot 10^{-5}$ for an electric field on the cathode in the 86 - 90 MV/m range.

Emittance

The beam transverse normalised rms emittance was measured using the pepperpot technique, using a with the mask set at 1.45 m from the cathode and 0.47 m from YAG2. The pepperpot used in the measurements had a grid size of 1 mm, a hole diameter of $100 \mu\text{m}$ and a thickness of 0.5 mm. Pepperpots with finer masks and holes were manufactured but could not be used due to inadequate quality.

The solenoid field was adjusted so the image of the pepperpot on YAG-2 contained at least 9 beamlets from the pepperpot. Due to the large grid size of the available pepperpot we had to set the solenoid to give a spot size of around 4 mm at the pepperpot plane, this is a non-optimal working point. This means the emittance measured is not properly optimized. The charge is kept constant for each measurement, that is the laser energy is adjusted for each injection phase setting in the measurements to keep the charge independent of the injection phase.

The background was subtracted from the images, though the signal was still quite noisy after filtering. There were also quite large shot to shot fluctuations in the images, and to minimize this effect the images chosen for the analysis have a good number of beamlets. The analysis was made using the method presented in Zhang [7], where beamlets are summed in the x- respective y-direction.

The dependence of the emittance on the injection phase was measured for two different fields and two different charges. The emittance is measured at electric fields on the cathode of 86 MV/m and 90 MV/m, corresponding to a maximum electric field amplitude of 100 MV/m and 105 MV/m in the main cell. The results can be seen in Figs. 8, 9 and 10.

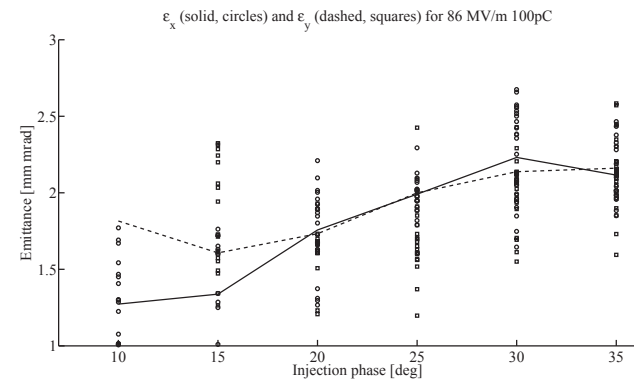


Figure 8: Measured emittance as function of injection phase for a maximum electric field on the cathode of 86 MV/m and 100 pC charge.

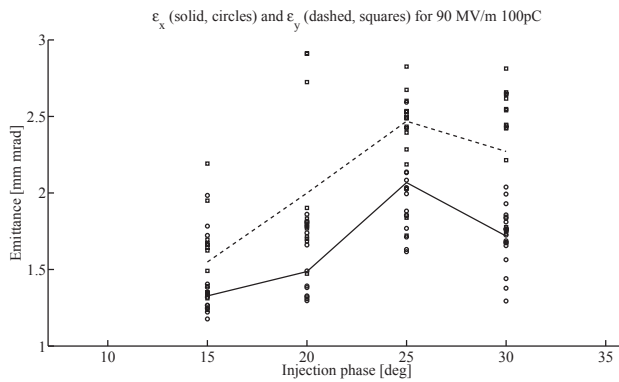


Figure 9: Measured emittance as function of injection phase for a maximum electric field on the cathode of 90 MV/m and 100 pC charge.

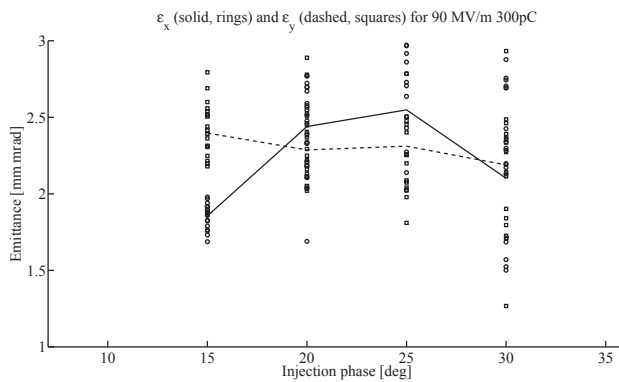


Figure 10: Measured emittance as function of injection phase for a maximum electric field on the cathode of 90 MV/m and 300 pC charge.

These measurements show little similarities with the simulations in Figs. 3 and 4. There might be many causes for this for example uncertainty of the effective laser spot size, energy and emission properties of the cathode. Future experiments and measurements will be done to try to match the simulations and measurements.

SUMMARY

The gun can provide a beam of around 4 MeV energy with an non-optimized emittance at likely injection phases of 1.5 - 2.5 mm mrad. We believed that the emittance at the optimized setting will be below 1 mm mrad. The quantum efficiency for the cathode in the gun with electric fields at the cathode between 85 and 90 MV/m is approximately $2 \cdot 10^{-5}$.

There are large shot to shot fluctuations in the measurements, affecting among other things the emittance measurements. These fluctuations are probably caused by fluctuations in the laser energy or timing issues.

FUTURE WORK

For the current gun design the next planned step is to put an existing emittance meter [8] into operation to character-

ize the emittance along the injector. The goal is to be able to measure the emittance and the spot size along the first 2-3 meters of the injector to be able to match the gun settings to the Ferrario working point [9].

The slits in the emittance meter have smaller dimensions than the pepperpot used in these measurements so the new setup will be able to measure the emittance at a more optimal working point of the gun.

Parallel to the work with the emittance meter, the collection and analysis of the measured data will be improved. It will also be investigated if there are possible ways to limit the shot to shot fluctuations in the setup and if so, how to implement these.

The models used in the simulations will be reviewed to see if there is anything that can be improved, and once the emittance meter is operational data from measurements will be used to improve the matching to simulations.

REFERENCES

- [1] E. Elafifi et al., "An electron gun test stand to prepare for the Max IV Project", in proceedings of International Particle Accelerator Conference, New Orleans, 2012, pp 1551-1553.
- [2] M. Eriksson et al., "The MAX-IV Design: Pushing the envelope", in Proceedings of Particle Accelerator Conference, Albuquerque, 2007, pp 1277-1279.
- [3] S. Werin et al., "Short pulse facility for MAX-lab", Nucl. Instr. and Meth. A, Volume 601, 2009, Pages 98-107.
- [4] M. Trovo et al., "Status of the FERMI@ELETTRA photoinjector", in Proceedings of European Particle Accelerator Conference, Genoa, 2008, pp 247 - 249.
- [5] K. Flöttman, ASTRA, <http://www.desy.de/~mpyflo>
- [6] D. H. Dowell, J. F. Schmerge, "Quantum efficiency and thermal emittance of metal photocathodes", Phys. Rev ST Accel. Beams 12, 074201, 2009.
- [7] M. Zhang, "Emittance formula for slits and pepper-pot measurements", Fermilab, Fermilab-tm-1988, Oct. 1996.
- [8] M. Ferrario et al., "Design study of a movable emittance meter device for the SPARC photoinjector", in Proceedings of European Particle Accelerator Conference, Lucerne, 2004, p. 2622-2624.
- [9] M. Ferrario et al., "HOMDYN Study for the LCLS RF photoinjector", SLAC, SLAC-PUB-8400, Mar 2000.

COMMISSIONING OF THE PHOTO-CATHODE RF GUN AT APS*

Y. Sun[#], J. Dooling, R. Lindberg, A. Nassiri, S. Pasky, H. Shang, T. Smith, A. Zholents
Advanced Photon Source, ANL, Argonne, IL 60439, USA

Abstract

A new S-band Photo-Cathode (PC) gun is recently commissioned at the Advanced Photo Source (APS), Argonne. In this paper we report the high-power RF conditioning process of the gun. Dark current is monitored during the RF conditioning. Following the RF conditioning, photo-electron beams are generated from the gun. The quantum efficiency of the copper cathode is monitored. Normalized beam emittance at different drive-laser sizes is measured as a function of solenoid strength, RF gradient and phase. Beam energy is also measured in a spectrometer.

THE APS PC GUN

The APS PC gun is a LCLS type gun [1-3] fabricated by SLAC. The gun is delivered to APS Oct. 2013 and installed at the Injector Test Stand (ITS) Dec. 2013.



Figure 1: The S-band photo-cathode RF gun and solenoid as installed at the ITS.

HIGH POWER RF CONDITIONING

High power RF conditioning of the PC gun started on March 5, 2014. Forward RF power of 12 MW, pulse length 2.5 μ s and 30 Hz repetition rate were successfully achieved on March 20, 2014.

To protect the gun from damaging during RF conditioning, three types of interlocks are implemented: reflected RF power, vacuum pressure and arc detector installed on the view port of the cathode cell.

The waveforms of the forward and reflected RF at the gun waveguide are saved at different RF power levels. An example is shown in Figure 2. Furthermore, waveforms of the field probes of the half-cell and full-cell are also collected, see Figure 3.

*Work supported by U.S. Department of Energy, Office of Science, under Contract No. DE-AC02-06CH11357.

[#]yinesun@aps.anl.gov

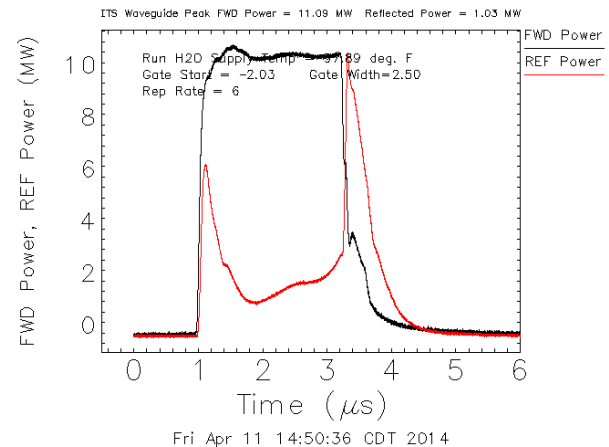


Figure 2: The forward and reflected RF waveforms at the gun waveguide.

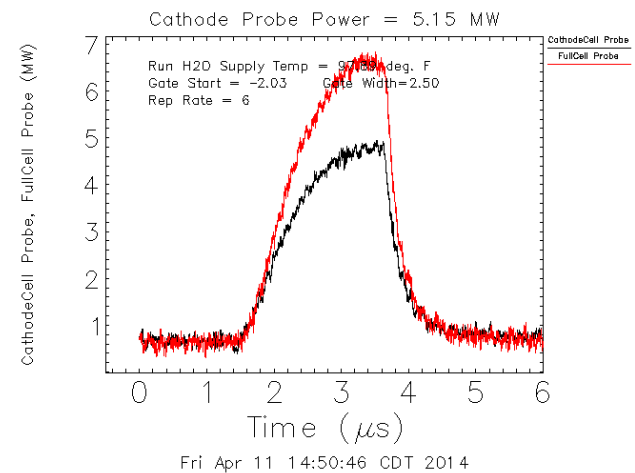


Figure 3: The cathode half-cell and the full cell field probe waveforms.

Dark currents are measured using the ICT at different solenoid strengths and RF power levels. A set of ICT measurements at 12 MW forward RF power, solenoid current ranging [20 ~ 240] A are plotted in Figure 4.

The total charge is calculated from integrating the current monitor waveforms. At different RF repetition rate, the dark current collected by the ICT varies as the solenoid current is changed, see Figure 5. The maximum dark current per RF pulse observed during the RF conditioning is less than 150 pC.

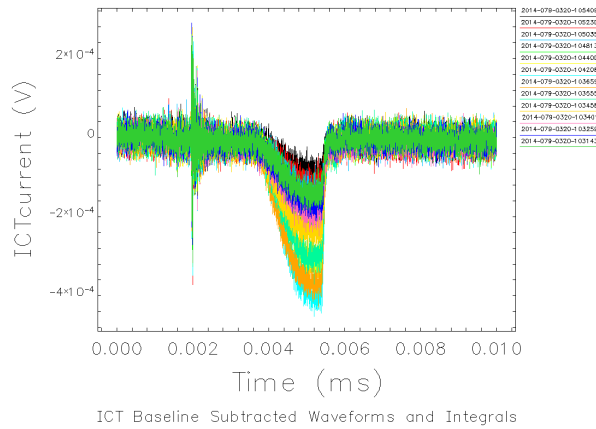


Figure 4: ICT waveforms as solenoid current is varied from 20A to 240A in 20A steps.

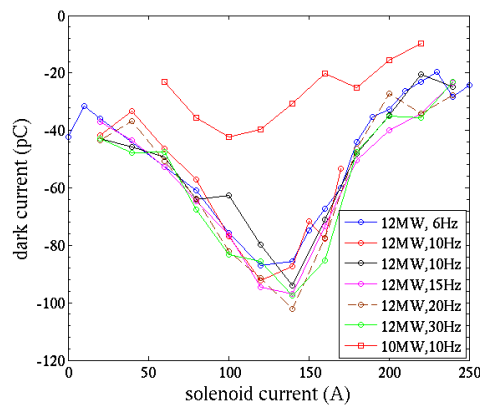


Figure 5: Dark current measured during RF conditioning of the PC gun.

ELECTRON BEAM COMMISSIONING

Following the successful high power RF conditioning, photo-electron beam commissioning of the PC gun in ITS started on April 10, 2014.

The ITS Beamline

The ITS beamline starts with the photocathode RF gun, followed by its main solenoid embedded with its quadrupole and dipole corrector magnets [4]. The major components of the beamline elements are illustrated in Figure 6. Three quadrupoles and three horizontal/vertical steering magnets, an integrated current monitor (ICT), a YAG screen and a Faraday cup are available in the straight-ahead beamline. The transverse emittance is measured by scanning one or two of the three quadrupole strengths and measure the beam size on the straight line YAG screen. Photo-electron bunch charge as well as dark current are measured by the calibrated ICT. The Faraday cup signal is used to maximize the beam transmission to the end of the beamline.

A spectrometer dipole magnet bends the beam by 45° and forms the bend line for beam energy and energy spread measurements. The bend line consists of two quadrupoles, a YAG screen and a Faraday cup.

The Injector Test Stand PC Gun Beamline

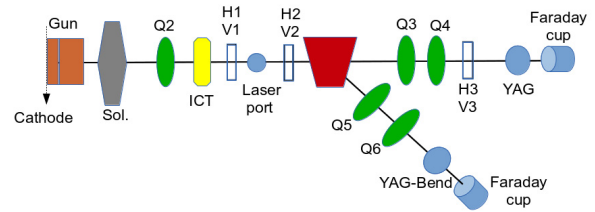


Figure 6: Layout of the Injector Test Stand photo-cathode RF gun beamline.

Cathode Quantum Efficiency

On the optical table inside the ITS, the drive-laser goes through a splitter, 85% of the laser is transported to photo-cathode and the rest is used for laser beam diagnostics including transverse profile monitoring on a virtual cathode, and laser energy measurement on a calibrated energy meter (EM3); see Figure 7.

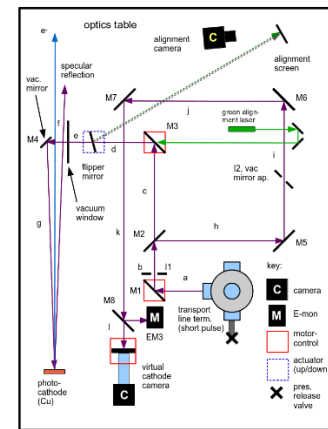


Figure 7: PC gun drive laser path on the optical table inside the ITS room.

As the gun RF phase is scanned, the photo-electron charge emitted is recorded to form a phase scan curve. Varying RF power s from 1 ~ 11 MW, the phase scan curves in Figure 8 are obtained. We see from Figure 8 that at RF power above 4.9 MW, the Schottky enhancement of the quantum efficiency is very pronounced.

The quantum efficiency (QE) is the number of emitted electrons per photon. In practical units for 263 nm drive-laser wavelength, the QE of cathode can be calculated via Eq. (1),

$$QE = \frac{Q(pC)}{U(\mu J)} \times 4.7 \times 10^{-6}, \quad (1)$$

where Q is the bunch charge in pC, U is the UV energy on cathode. For example, for 10 μJ UV laser, 21 pC bunch charge, the QE is 1×10^{-5} . The measured QE as a function of the accelerating gradient is shown in Figure 9.

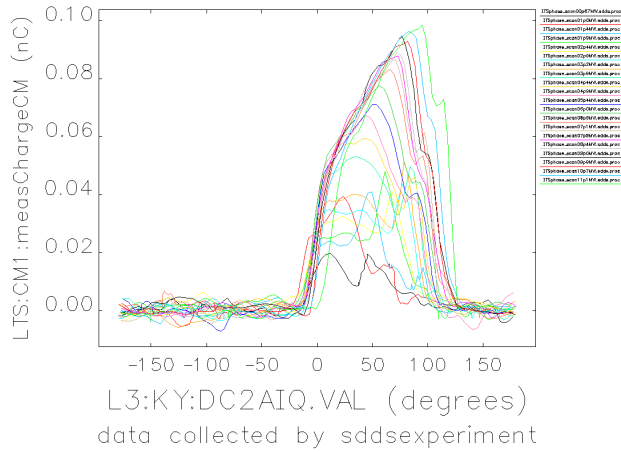


Figure 8: RF phase scan of the gun. Horizontal axis is the RF phase of the gun klystron, and vertical is the bunch charge measured by the ICT.

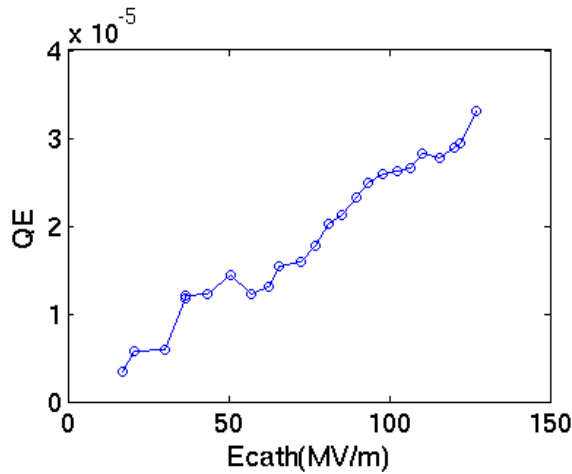


Figure 9: Quantum efficiency at different accelerating gradients on the cathode, UV laser energy at 16 μ J.

A quantum efficiency mapping of the cathode in a 2.5 mm by 2.5 mm square area was performed. The drive-laser position is controlled by a stepping motor and its location on the virtual cathode is recorded. The QE ranges from 3.2×10^{-5} to 3.8×10^{-5} , see Figure 10.

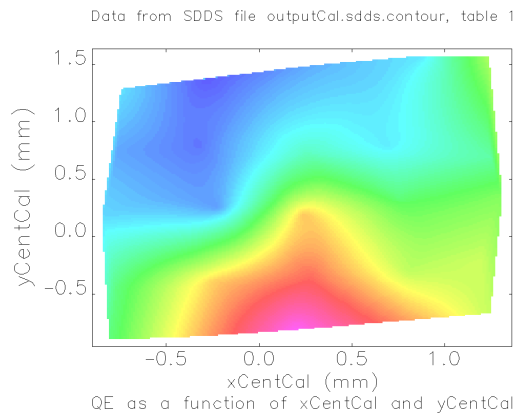


Figure 10: Quantum efficiency mapping of the cathode.

Transverse Emittance

The transverse emittance is measured using a quadrupole scan technique. The strengths of one or two quadrupoles in the straight beamline are varied while transverse beam size is measured on the YAG screen. The YAG screen is a 100 μ m thick YAG crystal with a 0.5" diameter holder.

Emittances are measured for different bunch charges and drive-laser spot sizes, as the gun accelerating gradient, phase and solenoid current are varied systematically. The laser spot size is controlled by inserting a pinhole in the laser path. Images of the drive-laser on the virtual cathode are shown in Figure 11.

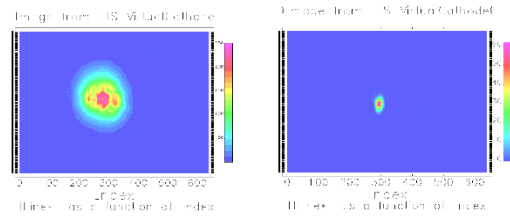


Figure 11: Virtual cathode images of the photo-cathode drive-laser. In the left image, the rms spot size is ~ 0.6 mm; on the right image, a 0.8 mm pin hole and a focusing telescope are used to create an rms spot size of 92 μ m by 179 μ m. The cause for the asymmetry in the right image is under investigation.

The best emittance obtained for bunch charge ~ 25 pC is ~ 0.8 μ m; see Figure 12 for measured emittances at different RF power and phase as the solenoid current is varied.

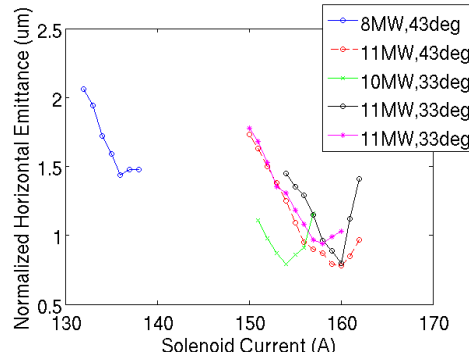


Figure 12: Normalized emittance measured for bunch charge ~ 25 pC.

To get higher bunch charge, the 0.8 mm pin hold was replaced by a 1.0 mm pin pole. An UV attenuator is used to control the drive-laser intensity to further control the bunch charge. At a bunch charge of ~ 100 pC, the smallest normalized emittance measured is ~ 2.1 μ m with 0.6 mm rms drive laser size; see Figure 13.

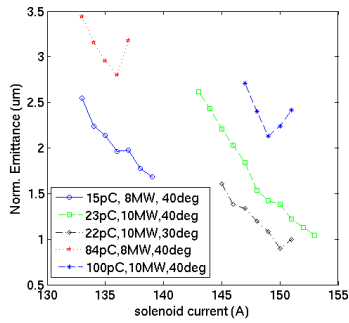


Figure 13: Normalized emittance measured with the 1 mm diameter pin hole inserted in the drive laser path.

Energy and Energy Spread

Beam energy is measured using a 45° sector spectrometer dipole magnet. Beam-based alignment is performed to ensure that the beam goes through the electrical and magnetic center of the PC gun, solenoid and the quadrupole upstream of the spectrometer dipole. At proper current of the spectrometer dipole, the beam goes through the center of the quadrupoles downstream of the dipole in the bend line, and beam centroid location on the bend line YAG is recorded.

As we change the gun gradient and phase, the beam energy is can be obtained from the magnetic field given the excitation current of the spectrometer dipole. Beam energy > 6 MeV is achieved. An example of measured beam energy at different RF phase and 10MW forward power is shown in Figure 14; corresponding energy spread is shown in Figure 15.

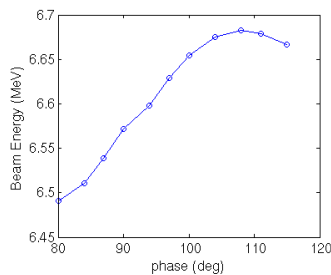


Figure 14: Measured beam energy at 10 MW forward power as the gun rf phase is varied

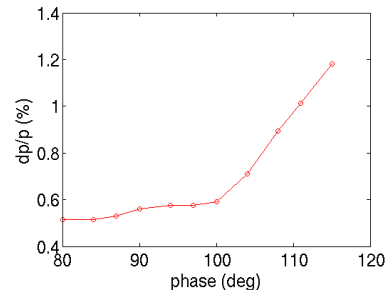


Figure 15: Measured relative energy spread for a ~35 pC bunch charge at 10 MW forward power as the gun rf phase is varied.

ACKNOWLEDGMENT

We wish to thank Norbet Holtkamp, Erik Jongewaard, Feng Zhou, Juwen Wang and Jim Lewandowski from SLAC for providing helpful information related to the PC gun. The many useful discussions with John Power from the AWA group of Argonne, Nicholas Sereno and Michael Borland at APS, Alex Lumpkin of Fermilab, are greatly appreciated. The installation and commissioning of the PC gun at ITS would not be possible without the support from the mechanical, survey and alignment, vacuum, water, electrical power, diagnostics and controls group.

REFERENCES

- [1] C. Limborg et al., "RF Design of the LCLS Gun," LCLS-TN-05-3, Feb. 2005.
- [2] D. H. Dowell et al., "Results of the SLAC LCLS Gun High-Power RF Tests," WEPMS036, PAC'07, Albuquerque, New Mexico (2007).
- [3] D. H. Dowell et al., "Commissioning Results of the LCLS Injector," WEAAU0, FEL'07, Novosibirsk, Russia (2007).
- [4] J. Schmerge, "LCLS Gun Solenoid Design Considerations," LCLS-TN-05-14, June 2005.

STATUS OF PUMP-PROBE LASER DEVELOPMENT FOR THE EUROPEAN XFEL

L. Wißmann[#], M. Emons, M. Kellert, K. Kruse, G. Palmer, M. Pergament, G. Priebe, J. Wang, U. Wegner, and M. J. Lederer, European XFEL GmbH, Notkestrasse 85, 22607 Hamburg, Germany

Abstract

The European XFEL is under construction and is designed to become a multi-user facility. Three SASE beam lines with two experimental areas each are foreseen to guarantee a high user throughput. In order to enable the full scientific potential of the facility, optical laser pulses for either pumping or probing samples will be deployed regularly.

We are presenting the pump-probe laser concept and the current status of the development, showing some experimental results of the prototype laser, achieved to date. The main emphasis of the presentation lies on the integration of the laser system into Karabo, the emerging control system of the European XFEL.

INTRODUCTION

The requirements for the pump-probe laser system (In the following: ‘PP laser’) are given by the XFEL accelerator (burst repetition rate 10 Hz, intra-burst pulse repetition rate 4.5 MHz, burst length 600 μ s, high arrival time stability) and the needs of experimentalists (pulse energy, pulse length, arbitrary pulse picking, wavelength tunability). Machine operation demands a high uptime while long-time planning and different experimentalists’ needs require high flexibility of the design. The general concept relies on a burst-mode, ps-pumped non-collinear optical parametric amplifier (NOPA), which draws on commercially available components where possible, and utilizes collaborative or in-house developments where needed.

The most important subsystems of the PP laser are described first, as depicted in Fig. 1. In the second half of this paper the integration of the laser into the control system is outlined, covering the necessary hardware, software, and machine timing issues.

PP LASER SUBSYSTEMS

A stable seed oscillator (OneFive Origami10), which is locked to the XFEL laser master oscillator via the optical synchronization system, emits a 54 MHz pulse train at 1030 nm. The timing jitter of the oscillator itself is specified to be <20 fs (rms, [1kHz-10Mhz]). The endpoint-to-endpoint stability of the synchronization systems is envisioned to reach 20 fs after XFEL commissioning [1]. Passive and active measures are taken to maintain this arrival time stability unto the exit of the PP laser.

For laser/x-ray overlap search, a long delay stage is implemented (Feinmess PMT 240). It supports a travel range of 400 mm (5 ns, quadruple pass) with an encoder resolution of 100 nm (stable 200 nm or 2.5 fs steps shown). Coupling the laser pulses into a single mode fiber for front end seeding has been successfully tested and yields less than 3% deviation over the full travel range.

The All-Fibre Front-End has multiple tasks [2]. It consists of several fibre amplifier stages, pulse picking devices, chirped fiber bragg gratings for dispersion management and extensive timing and control electronics. The laser pulse train from the seeder is split after pre-amplification and pre-stretching into two paths, XF1 (for power amplification and NOPA pumping) and XF2 (for supercontinuum generation and NOPA seeding). The output of the XF2 path is a 5 ms long burst with 4.5 MHz intra-burst repetition rate and a burst power of 20 W. An acousto-optic modulator (AOM) enables the selection of arbitrary pulse patterns inside the burst, before the pulses are compressed to 300 fs for supercontinuum generation.

In the XF1 path, the front-end output pulse train can be chosen to have different intra-burst repetition rates at constant burst power (of 4 W). This constant power mode enables different working points of the whole PP laser (incl. burst mode pump-pulse amplifiers). The tested repetition rates are 4.5 MHz, 1 MHz, and 0.2 MHz. The output burst length is again 5 ms, the pulse duration being 1.3 ns, and the spectral properties are optimized for the subsequent power amplifiers.

Further down the XF1 path, an InnoSlab multi-pass amplifier enhances the burst power to 400 W [3]. Two double-pass booster stages are planned to sequentially reach power levels of 7 kW and 20 kW. The currently achieved performance includes burst powers of 600 W (400 W specified), and with settable intra-burst frequencies of 0.2 MHz to 4.5 MHz this corresponds to 0.09 mJ to 2.1 mJ at 400W. The spectral width of the output pulses is measured to be $\Delta\lambda = 2.5$ nm, the beam quality factor M^2 equals 1.5, and the constancy of the pulse energy over the burst (in a 600 μ s window) is better than 1%. Intra-burst variations of beam shape and pointing have been measured to be negligible.

A Pockels cell arrangement, suited for high laser energies, is used to enable arbitrary pulse picking also in the pump path. Alternative, user selectable, beam exits before the XF1 compressor (pulse length ~ns) and after the XF1

[#]laurens.wissmann@xfel.eu

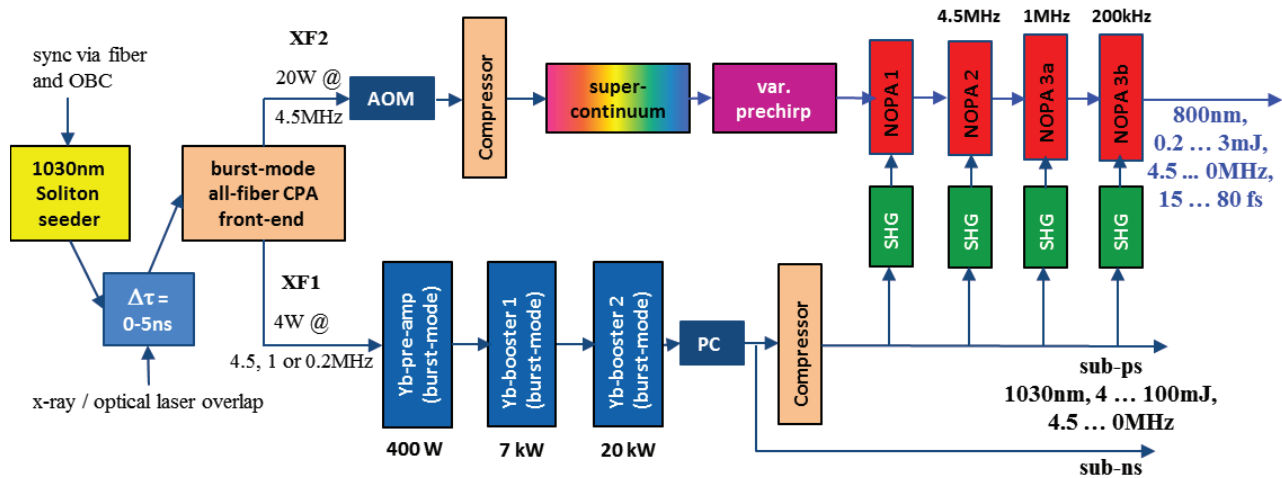


Figure 1: The planned PP laser system. The prototype is equipped with only 2 NOPA stages and one 400 W amp.

compressor (pulse length ~ 800 fs) are foreseen to enable the use of the 1030 nm, high power beam as alternative to the 800 nm short pulse output from the NOPA. To pump the NOPA with 515 nm light, frequency doubling is installed with an efficiency of $\sim 65\%$.

In the XF2 path, following supercontinuum generation in YAG, the pulses have a spectral content ranging from 600 nm to 1000 nm, and an energy of 7.2 nJ under stable conditions. Pairs of compensated chirped mirrors imprint a negative chirp on the pulses to enable fused silica for compression after parametric amplification. With different setups of the chirped mirrors and usage of the two available NOPA stages, a range of output pulse parameters is accessible. The shortest pulses, compressible to 14.9 fs, have a spectral bandwidth of 155 nm at 10% of maximum and are centered at 810 nm. At 200 kHz, a pulse energy of 180 μ J was achieved, corresponding to 34 W burst power. In the long pulse mode (up to 75 fs), only a fraction of the white light is selected through dispersive amplification filtering, allowing a wavelength tuning over 100 nm by shifting the seed temporally against the pump pulse. A detailed overview is given in [4].

For power scaling to a pump pulse energy level of 100 mJ, the envisioned booster amplifiers have already been installed and are being commissioned at this time. With the first booster, beam characterization at a power level of up to 4.5 kW is taking place. In order to exploit the pump power of the booster amplifiers, further NOPA stages need to be set up.

ACTIVE AND PASSIVE STABILITY

Environmental influences will impact on the pulse arrival time stability of the seed and pump pulses in the NOPA stages. This temporal stability is crucial as otherwise the NOPA output becomes unstable. Typical causes for drifts are temperature and humidity changes. Passive means to ensure stability include choice of materials and the use of sound principles. Nonetheless, due to the long optical paths, drifts of >100 fs are to be expected, which call for active means of stabilisation. For instance, highly

stable air conditioning ($\pm 0.1^\circ\text{C}$, $\pm 2.5\%$ rel. hum.) for the laser table area and active timing drift compensation are implemented. The latter consists of two optical balanced cross correlators, which measure the arrival time drift between the seeder and XF2 as well as XF2 and XF1, respectively at the input of the NOPA. A clocked and triggered readout of the arrival time change of single pulses in the burst is fed to a control loop which acts on piezo delay stages (see below).

Furthermore, active beam pointing stabilisation (TEM) has been implemented yielding pointing deviations as low as $1/40$ of the beam divergence.

PP LASER INTEGRATION

The PP laser is not a stand-alone R&D laser system. Three copies of it shall be installed in three laser hutches to serve six experimental areas as laser source. Experimentalists will have the control over crucial parameters of the laser system remotely (output power, pulse pattern, pulse arrival time). To this end and to receive status info of this XFEL subsystem, full integration of the PP laser into the emerging XFEL control system Karabo is desired. The installation of a diagnostic & control rack has been completed to host the required hardware (see Fig. 2). Its contents are, from top to bottom:

- A Beckhoff programmable logic controller (PLC) controls motors of differing kind and also features analogue and digital in- and outputs. This hardware is used for slow data exchange, as it is neither clocked nor triggered.
- A piezo driver to amplify the signals from the analogue PLC outputs before they are fed to piezo actuators (pulse arrival time stabilisation and oscillator locking to an RF reference).
- The driver for the seeder oscillator.
- The controller for the beam pointing stabilisation.
- Two delay generators to multiply triggers.
- A large rack mounted PC serving control purposes.
- A multi-purpose laboratory DC power supply.

- For fast data taking and computing, a μ TCA.4 crate has been set up, equipped with a card for timing purposes and a fast ADC (Struck SIS8300, 125 MS/s, 10 channels), beside the standard components (power supply, CPU, MCH). The μ TCA.4 standard has been developed to support extended backplane features (clock and trigger support) and flexible designs for rear transition modules (RTMs), of which full use is made.
- A HV driver for the Pockels cell, some RF circuitry and network switches.

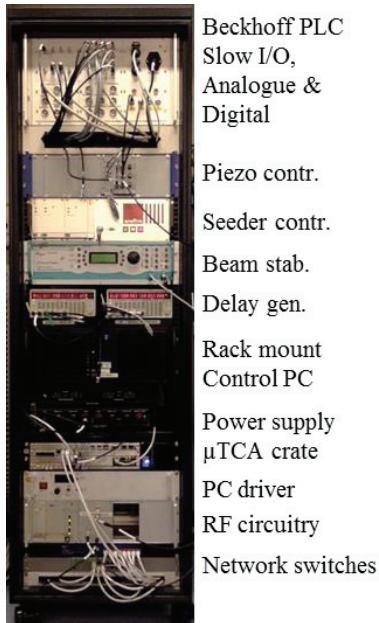


Figure 2: Fully equipped control and diagnostics rack.

KARABO

Karabo, the emerging control system of the photonic part of the XFEL, is a modular software framework designed for control, data acquisition, data management, and scientific computing [5]. The PP laser integration is quite advanced and serves as a test bed for the software stability and performance. Karabo devices as plug-in modules form the interface to any hardware or software. Many devices exist already, tested or regularly used are

- The remote client for front-end control
- An imaging tool for small CCD cameras (Basler), with a computing tool extracting beam positions
- A spectrometer and an energymeter tool
- Motor devices for small linear and rotary stages
- A motor control device for the long delay stage
- Analogue and digital I&O devices, among these also temperature sensors
- A sophisticated ADC firmware interface to allow for data reduction in the arrival time stabilisation
- A generic PID device to create control loops.

On the way are more software devices, allowing

- Remote control of the beam stabilisation (TEM)
- Interfacing the InnoSlab amplifiers
- Computing pulse lengths from single-shot autocorrelator images
- Use of a large CCD camera (36 x 24 mm sensor).

For Karabo, a graphical and a command line interface exist, the latter featuring full iPython compatibility. The GUI allows for distributed and remote access, use of individualised panels, access to history data, and project definition (easy device handling, process control).

TIMING

The PP laser has to be fully synchronised to the XFEL. A sophisticated μ TCA.4 based machine timing system has evolved from the system used at FLASH [6]. It relies on length stabilised optical fibre links between timer cards (x2 timer) to synchronise the distributed 1.3 GHz clocks. Before every burst the clocks in every timer board are reset. With this resync pulse, information on the burst filling at each PP laser position is spread, as well as the request for a PP laser pulse for each possible position in the burst. Each timer card has 6 front trigger outputs with settable delay, width, and internal trigger source. Also each card features an extension slot (RTM) with 6 more independent trigger outputs. Beside the network based modes, a timer card can also be operated stand-alone. Currently, the reference clock of the prototype system is derived from the seed laser oscillator. All triggers (amplifiers, diagnostics, ADCs) are then created inside the timer card. Varying pulse patterns have been realised remotely using the full capabilities of the timer card.

CONCLUSION

A fully operational prototype system of the envisioned PP laser has been set up. Extensive measurements of the system performance have shown all desired parameters can be reached. An upgrade to scale power to the final specifications is under way.

The hardware assembly needed for the integration of the PP laser into the emerging control system is completed. Corresponding software devices are largely available.

REFERENCES

- [1] C. Sydlo et al., "Development Status of Optical Synchronization for the European XFEL", IBIC 2013, Oxford, MOPC32, <http://www.JACoW.org>
- [2] K. Kruse, et al., "All-fiber 1030nm burst-mode front-end amplifier for the European XFEL pump-probe laser development for the European X-Ray Free-Electron Laser Facility," Paper Mo4.5, Ultrafast Optics Conference IX, 04–08 March 2013, Davos
- [3] M. Kellert et al., "High power femtosecond 1030nm burst-mode front-end and pre-amplifier for the European XFEL pump-probe laser development," Poster CA-P.23, CLEO 2013, 12–16 May 2013, Munich

- [4] M. Pergament et al., “High power burst-mode optical parametric amplifier with arbitrary pulse selection”, tbp 2014, submitted to Optics Express.
- [5] B.C. Heisen et al., “Karabo: an integrated software framework combining control, data management and scientific computing tasks”, 14th Intern. Conf. on Accelerator & Large Experimental Physics Control Systems, ICALEPCS 2013, San Francisco, U.S.A.
- [6] K. Rehlich et al., “The New Timing System for the European XFEL”, 14th Intern. Conf. on Accelerator & Large Experimental Physics Control Systems, ICALEPCS 2013, San Francisco, U.S.A.

DEVELOPMENT OF ALL-METAL STACKED-DOUBLE GATE FIELD EMITTER ARRAY CATHODES FOR X-RAY FREE ELECTRON LASER APPLICATIONS *

P. Das Kanungo, Y. Oh, C. Lee, M. Paraliyev, V. Guzenko, H.-H. Braun, S. Tsujino[#]
Paul Scherrer Institut, Villigen, Switzerland
T. Feurer, University of Bern, Bern, Switzerland

Abstract

Design, fabrication, and characterization of all-metal double-gate field emitter array cathodes at the Paul Scherrer Institute are reported. The beam characterization at low beam energies, combined with the neon gas conditioning for improving the beam uniformity indicated more than an order of magnitude reduction of the emittance. A combination of the proposed double-gate structure with the surface-plasmon-enhanced near infrared laser-induced field emission for ultrafast, high charge bunch generation is discussed.

INTRODUCTION

Realization of a high current and high brightness cathode using field emission has been proposed based on an array of metal nanotip emitters [1,2]. Comparing with conventional etched-wire needle-shaped field emitters, field emitter arrays (FEAs) produced by micro- and nanofabrication methods with an on-chip electron extraction electrode are advantageous for high acceleration gradient operation since the switching of the electron emission can be controlled independently from the acceleration gradient by applying a electron extraction potential in the order of 100 V to the electron extraction gate electrode G_{ex} . Using the all-metal single-gate FEAs developed at PSI, stable operation of FEAs in a combined diode-RF cavity electron gun with gradient up to 30 MV/m [3,4], and electrical pulsing of the FEAs down to ~200 ps [5] were demonstrated. Generation of 5 ps electron bunches was also demonstrated by exciting the FEAs by 50 fs near infrared laser pulses [6]. Although the curved shape of the emitter tip apex leads to a relatively large angular beam spread [7], the transverse emittance of array beam can be reduced by collimating the individual beamlet with a second beam collimation electrode G_{col} fabricated on top of G_{ex} [1,2]. One of the challenges to use double-gate FEAs for practical applications has been the large reduction of the emission current with the application of the beam collimation potential [8]. This was however in part solved with the recently reported double-gate structures with large collimation gate aperture diameters [9,10]. Such double-gate FEAs are promising for advanced accelerator applications including the compact X-ray free-electron lasers (FELs) when an extremely low emittance below 0.1 mm-mrad is required [11] or by utilizing the spatial beam structure combined

with the emittance exchange [12]. Double-gate FEAs with low emittance can also be key to realize compact THz vacuum electronic oscillators and amplifiers [13]. Our recent report showed the fabrication of up to 4×10^4 tip stacked-double-gate FEAs and their excellent beam collimation characteristics at low current level [14]. Here we report recent progress of the double-gate FEAs and the numerical study of the emission characteristics for a high density FEAs excited by near infrared laser pulses for X-ray free electron laser applications [15,16].

BEAM CHARACTERISTICS OF SINGLE- AND DOUBLE-GATE FIELD EMITTER ARRAYS

The FEAs used in the experiments consist of pyramidal shaped molybdenum nanotip emitters with the height of ~1 μm and the tip apex radius of curvatures of 5-10 nm. The emitter pitches are equal to 5 μm or 10 μm . The emitters are supported on metal substrates and equipped with G_{ex} and G_{col} electrodes. The gate electrodes and emitters are insulated each other by 1.2 μm -thick SiON layers [14,17,18]. Electron emission characteristics of the all-metal single-gate FEAs have been studied previously [3-6,15,17] including the intrinsic transverse emittance. In Figure 1, we summarize the experimentally observed emittance of *single-gate* FEAs with the FEA diameters between 0.2 and 2.3 mm. The upper boundary of the target emittance with the double-gate FEAs equal to 0.1 mm-mrad with the FEA diameter of 1 mm is also indicated in Figure 1.

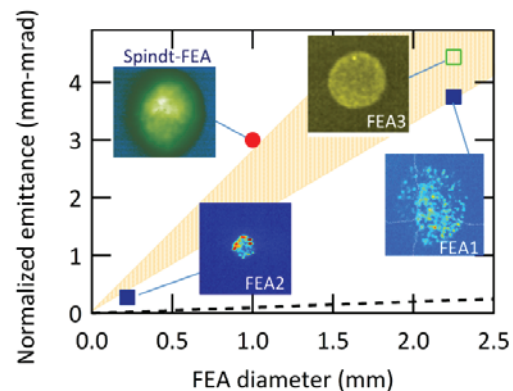


Figure 1: Normalized rms emittance of *single-gate* FEAs. The shaded area corresponds to the rms beam divergence of 20-30°. The broken line is the upper boundary of the target emittance with double-gate FEAs equal to 0.1 mm-mrad with the FEA diameter of 1 mm.

*Work partially supported by the Swiss National Science Foundation, No. 200020_143428 and 2000021_147101.

[#]E-mail: soichiro.tsujino@psi.ch

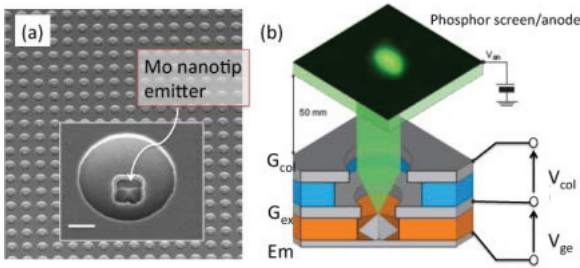


Figure 2: (a) SEM image of all-metal double-gate FEA with 10 μm pitch. The inset is the magnified view of single emitter (the scale bar is 2 μm). (b) Schematic diagram of beam characterization experiment.

The emittance of the single-gate devices FEA1 and 2 was measured using a pulsed diode gun [3] with a beam energy of ~200 keV and an emission current of ~100 μA. The emittance was evaluated from the fitting of the solenoid scan. Other single-gate FEAs, FEA3 and Spindt-FEA, were measured in the dc teststand [5,19] with a beam energy of 50 keV and an emission current of ~1 mA. For these experiments, a FEA holder compatible with the pulsed-diode gun and the dc teststand under high gradient conditions was developed [3-5]. Emittance values in the range of 2-3 mm-mrad for 1 mm diameter FEAs were observed. This corresponds to a rms beam divergence of 20-30° (shaded area in Fig. 1) of the field emission beam at the emitter tip apex [16, 19]. The here observed values are in the same order of magnitude as the emittance of the diamond FEAs without gate electrode [20]. The beam images of FEA1 and 2 are granular due to the emission from the sharpest emitters caused by the non-uniform tip apex radius. The beam uniformity can be significantly improved by applying in-situ neon gas conditioning [5,21] as demonstrated by the uniform beam image of FEA3. Since the emittance values of FEA2 and 3 are approximately the same, the beam non-uniformity appears to be not important in the present experiment [7].

Figure 2 shows the SEM of a double-gate FEA and its schematic operation principle. Application of a positive electron extraction potential V_{ge} to G_{ex} with respect to the emitters (Em) produces a field emission current. When a negative beam collimation potential V_{col} is applied to G_{col} with respect to G_{ex} , the field emission beamlets are individually collimated. Figure 3 (a) shows, the relation between the field emission current and V_{ge} at zero V_{col} after the FEA was in-situ conditioned for 30 min in the neon gas environment with a pressure of 1×10^{-4} mbar [5,21]. The field emission current increases exponentially with V_{ge} , following the Fowler-Nordheim characteristics [22].

We observed the field emission beam by a phosphor screen at the potential of 2.5 kV separated from the FEA by 50 mm. Figure 3 (c) shows the beam images at three different V_{col} values at V_{ge} equal to 100 V. V_{col} is indicated by the collimation parameter k_{col} equal to $|V_{col}|/V_{ge}$. The reduction of the rms beam radius R_{rms} and the increase of the beam brightness with the increase of k_{col} are visible. At the maximally collimated condition with k_{col} equal to

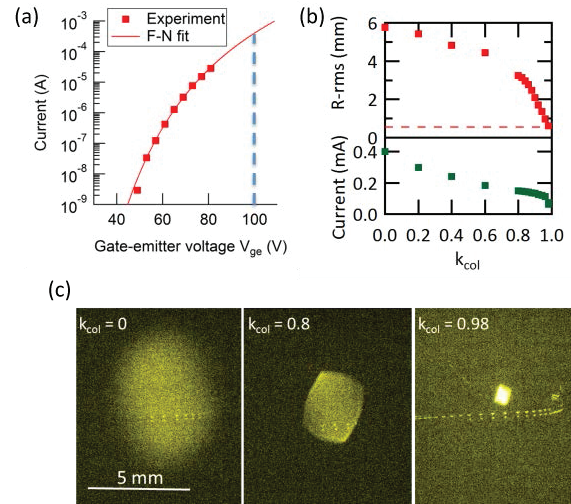


Figure 3: Beam characteristics of a double-gate FEA (a) Field emission current I vs V_{ge} at zero V_{col} . The curve is a fitting by Fowler-Nordheim equation, $I = A (V_{ge}/B)^2 \exp(-B/V_{ge})$. (b) Variation of the rms beam radius R_{rms} and the emission current with k_{col} equal to V_{col}/V_{ge} at V_{ge} of 100 V (marked by the vertical line in (a)). The horizontal broken line indicates the rms FEA radius. (c) Beam image for three k_{col} values with V_{ge} equal to 100 V.

0.98, R_{rms} approached the rms FEA radius R_0 (equal to 0.56 mm indicated by the broken line in Fig. 3(b) upper panel) and the beam brightness was enhanced by a factor of ~10. At k_{col} equal to 0.98, the emission current was ~60 μA and approximately 20% of the emission current of 0.4 mA at zero k_{col} was retained. Assuming free propagation of the electrons in the transverse direction, we evaluated the rms transverse velocity u_t from $(R_{rms} - R_0)$ and found u_t to be equal to $\sim 3 \times 10^{-4} c$ (c is the light velocity) at k_{col} equal to 0.98; the estimated emittance is below 0.1 mm-mrad for a 1 mm-diameter FEAs [23]. Recently, the same beam collimation characteristics was also observed using single-tip double-gate device [24]. The adaptation of the single-gate FEA holder for the double-gate FEAs and the emittance measurement of the double gate FEAs using the dc teststand is under way.

SURFACE-PLASMON POLARITON ENHANCED TIP-LASER INTERACTION

Next we discuss the strategy and design to realize a double-gate FEA compatible for X-FEL applications that can generate short electron pulses with high charge and low emittance. Experiments [6] with 5 μm-pitch single-gate FEA indicated that one can generate short high current pulses by exciting the FEA with the excitation of near infrared laser pulses. The observed electron yield was in the order of 10^{-7} . Therefore to generate high charge electron pulses e.g. 200 pC of the nominal bunch charge of the SwissFEL at the Paul Scherrer Institut, an order of magnitude increase of the electron yield is required. A possible strategy is to reduce the array pitch to sub-micron range by scaling down the double-gate structure

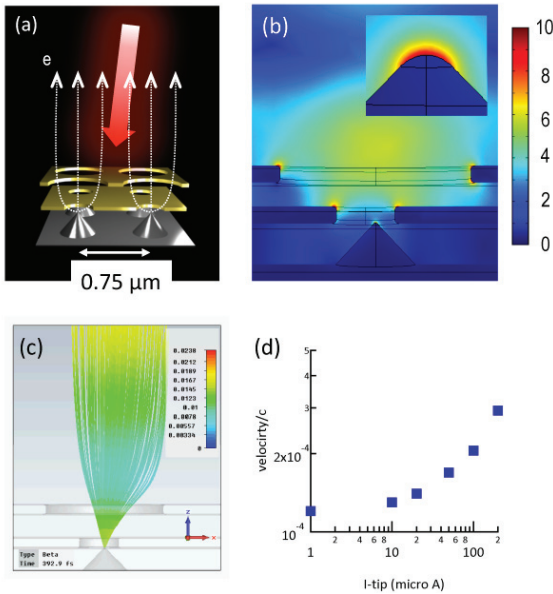


Figure 4: (a) Schematic of sub-micron-pitch double-gate FEAs with Mo emitters and Cu gates excited by near infrared laser pulses at 7° incident angle. (b) Optical electric field distribution calculated for the resonant wavelength equal to 800 nm. (c) Particle tracking simulation of the same structure at 100 MV/m external gradient with V_{ge} equal to 70 V and V_{col} equal to -76 V. (d) Tip current dependence of the rms transverse velocity.

described in the previous section, that can however reduce the tip excitation efficiency because of the concomitant reduction of the gate aperture diameters to sub-wavelength dimension for the excitation of near infrared pulses. We therefore proposed [15,16] to use copper as the gate material and to utilize the surface-plasmon-polariton (SPP) excitation of the gate electrode and the associated extraordinary optical transmission (EOT) of the plasmonic nano-aperture arrays [25]. Figure 4 (b) shows the optical electric field distribution of a 0.75 μm-pitch copper double-gate FEAs calculated by a finite element electromagnetic simulation tool with periodic boundary conditions in the lateral direction at the EOT resonance condition with 1.6 eV incident photon energy. We found that not only the EOT resonance is preserved in the presence of the molybdenum nanotip in the aperture cavity, but the optical electric field at the emitter tip apex is nearly a factor of 10 enhanced when the G_{ex} is shifted from the axis of the emitter tip by 5 nm [15,16]. Interestingly, with the normal incident excitation with the field along the lateral direction, the enhanced tip optical field is in the direction perpendicular to the tip apex surface. To extract electrons, it is however practical to irradiate the laser pulses at an angle slightly tilted from the surface normal direction. Although such oblique incidence angle excites SPP at a difference resonance photon energy [25], we found that when the incident angle is limited within $\sim 10^\circ$, see Figure 4 (b), the shift of the resonance photon energy is below ~ 10 meV, and not relevant for the present application [26].

To evaluate that the impact of the G_{ex} shift on the beam characteristics, we calculated the rms transverse velocity by a particle tracking simulator (CST Particle Studio) with the same double-gate emitter structure as the one used for the electromagnetic simulation in Figure 3. We assumed V_{ge} of 100 V, V_{col} of -76 V, the acceleration gradient of 100 MV/m, and the tip current between 1 and 200 μA. The initial current distribution at the emitter apex was calculated from the optical intensity obtained from Figure 4 (b) and assuming the field emission of the excited electrons that absorbed one photon with the energy of 1.6 eV [16]. The result is shown in Figure 4 (c) and (d). We found that despite the shift of G_{ex} , the field emission beam is well collimated with the rms transverse velocity below $2 \times 10^{-4} c$ for the tip current below ~ 100 μA.

These results show the capability a 10^6 -tip, 1 mm-diameter sub-micron-pitch double-gate FEA to generate 200 pC, electron pulses with the emittance well below 0.1 mm-mrad by exciting the FEA with 0.1 mJ near infrared laser pulses. The near infrared photon electron yield is increased to $\sim 2 \times 10^{-6}$ by using the SPP enhanced tip-laser coupling.

Test sub-micron-pitch FEAs fabricated by using the high-through-put electron beam lithography method [17,27] showed that the accuracy of the lithography and the sample uniformity are compatible to the proposed double-gate device, Figure 4 (a). Fabrication of the test device to demonstrate the SPP enhanced field emission is under way.

REFERENCES

- [1] C.-M. Tang, A. C. Ting, T. Swyden, "Field-emission arrays — a potentially bright source", Nucl. Instrum. Meth. A **318**, 353 (1992).
- [2] M. Dehler, A. Candel, E. Gjonaj, "Full scale simulation of a field-emitter arrays based electron source for free-electron lasers", J. Vac. Sci. Technol B **24**, 892 (2006).
- [3] S. Tsujino, M. Paraliyev, E. Kirk, T. Vogel, F. Le Pimpec, C. Gough, S. Ivkovic, H.-H. Braun, "Nanosecond pulsed field emission from single-gate metallic field emitter arrays fabricated by molding", J. Vac. Sci. Technol. B **29**, 02B117 (2011).
- [4] S. Tsujino, M. Paraliyev, E. Kirk, C. Gough, S. Ivkovic, H.-H. Braun, "Sub-nanosecond switching and acceleration to relativistic energies of field emission electron bunches from metallic nano-tips", Phys. Plasmas **18**, 064502 (2011).
- [5] S. Tsujino, M. Paraliyev, "Picosecond electrical switching of single-gate metal nanotip arrays", J. Vac. Sci. Technol. B **32**, 02B103 (2014).
- [6] A. Mustonen, P. Beaud, E. Kirk, T. Feurer, S. Tsujino, "Five picocoulomb electron bunch generation by ultrafast laser-induced field emission from metallic nano-tip arrays", Appl. Phys. Lett. **99**, 103504 (2011).
- [7] K. L. Jensen, P. G. O'Shea, D. W. Feldman, J. L. Shaw, "Emittance of a field emission electron source" J. Appl. Phys. **107**, 014903 (2010).
- [8] S. Tsujino, P. Helfenstein, E. Kirk, T. Vogel, C. Escher, H.-W. Fink, "Field-emission characteristics of molded molybdenum nanotip arrays with stacked collimation gate electrodes" IEEE Electron Device Letters **31**, 1059 (2010).

- [9] Y. Neo, T. Soda, M. Takeda, M. Nagao, T. Yoshida, C. Yasumuro, S. Kanemaru, T. Sakai, K. Hagiwara, N. Saito, T. Aoki, H. Mimura, “Focusing Characteristics of Double-Gated Field-Emitter Arrays with a Lower Height of the Focusing Electrode”, *Appl. Phys. Express* **1**, 053001 (2008).
- [10] P. Helfenstein, E. Kirk, K. Jefimovs, T. Vogel, C. Escher, H.-W. Fink, S. Tsujino, “Highly collimated electron beams from double-gate field emitter arrays with large collimation gate apertures” *Appl. Phys. Lett.* **98**, 061502 (2011).
- [11] B. Patterson, R. Abela, H.-H. Braun, U. Flechsig, R. Ganter, Y. Kim, E. Kirk, A. Oppelt, M. Pedrozzi, S. Reiche, L. Rivkin, Th. Schmidt, B. Schmidt, V. N. Strocov, S. Tsujino, A. F. Wrulich, “Coherent science at the SwissFEL X-ray laser”, *New J. Physics* **12**, 035012 (2010).
- [12] W. S. Graves, F. X. Kärtner, D. E. Moncton, P. Piot, “Intense superradiant X rays from a compact source using a nanocathode array and emittance exchange”, *Phys. Rev. Lett.* **180**, 263904 (2012).
- [13] J. H. Booske, “Plasma physics and related challenges of millimeter-wave-to-terahertz and high power microwave generation”, *Phys. Plasmas* **15**, 055502 (2008).
- [14] P. Helfenstein, V. A. Guzenko, H.-W. Fink, S. Tsujino, “Electron beam collimation with 40,000 tip metallic double gate field emitter arrays and in-situ control of nanotip sharpness distribution”, *J. Appl. Phys.* **113**, 043306 (2013).
- [15] A. Mustonen, P. Beaud, E. Kirk, T. Feurer, and S. Tsujino, “Efficient light coupling for optically excited high-density metallic nanotip arrays”, *Scientific Reports* **2**, 915 (2012).
- [16] P. Helfenstein, A. Mustonen, T. Feurer, S. Tsujino, “Collimated Field Emission Beams from Metal Double-Gate Nanotip Arrays Optically Excited via Surface Plasmon Resonance” *Appl. Phys. Express*, **6**, 114301 (2013).
- [17] E. Kirk, S. Tsujino, T. Vogel, K. Jefimovs, J. Gobrecht, A. Wrulich, “Fabrication of all-metal field emitter arrays with controlled apex sizes by molding” *J. Vac. Sci. Technol. B* **27**, 1813 (2009).
- [18] V. A. Guzenko, A. Mustonen, P. Helfenstein, E. Kirk, S. Tsujino, “High-density large-scale field emitter arrays for X-ray free electron laser cathodes”, *Microelectronic Engineering* **111**, 114 (2013).
- [19] S. C. Leemann, A. Streun, A. F. Wrulich, “Beam characterization for the field-emitter-array cathode-based low-emittance gun” *Phys. Rev. STAB* **10**, 071302 (2007).
- [20] J. D. Jarvis, B. K. Choi, A. B. Hmelo, B. Ivanov, C. A. Brau, “Emittance measurements of electron beams from diamond field emitter arrays” *J. Vac. Sci. Technol. B* **30**, 042201 (2012).
- [21] S. Tsujino, M. Paraliyev, E. Kirk, H.-H. Braun, “Homogeneity improvement of field emission beam from metallic nano-tip array by noble-gas conditioning” *Appl. Phys. Lett.* **99**, 073101 (2011).
- [22] R. G. Forbes, J. H. B. Deane, “Reformulation of the standard theory of Fowler–Nordheim tunnelling and cold field electron emission”, *Proc. R. Soc. A* **463**, 2907–2927 (2007).
- [23] P. Das Kanungo, P. Helfenstein, V. A. Guzenko, C. Lee, S. Tsujino, “Pulsed field emission imaging of double-gate metal nanotip arrays: effect of emission current and noble gas conditioning”, S3-C6, Technical digest, 27th International Vacuum Nanoelectronics Conference, Engelberg, Switzerland (2014).
- [24] C. Lee, P. Das Kanungo, V. Guzenko, P. Helfenstein, S. Tsujino, G. Kassier, A. Casandru, R. J. D. Miller, “Field emission beam characteristics of a double-gated single emitter”, P2-11, Technical digest, 27th International Vacuum Nanoelectronics Conference, Engelberg, Switzerland (2014).
- [25] T. W. Ebbesen, H. J. Leec, H. F. Ghaemi, T. Thio, P. A. Wolff, “Extraordinary optical transmission through sub-wavelength hole arrays” *Nature* **391**, 667 (1998).
- [26] A. Mustonen, Y. Oh, P. Helfenstein, T. Feurer, S. Tsujino, “Plasmon assisted double-gate field emitter arrays”, S1-C1 Technical digest, 27th International Vacuum Nanoelectronics Conference, Engelberg, Switzerland (2014).
- [27] A. Mustonen, V. Guzenko, C. Spreu, T. Feurer, S. Tsujino, “High-density metallic nano-emitter arrays and their field emission characteristics”, *Nanotechnology* **25**, 085203 (2014).

THE LCLS-II INJECTOR DESIGN*

J.F. Schmerge[#], A. Brachmann, D. Dowell, A. Fry, R.K. Li, Z. Li, T. Raubenheimer, T. Vecchione, F. Zhou, SLAC, Menlo Park, CA 94025, USA

A. Bartnik, I. Bazarov, B. Dunham, C. Gulliford, C. Mayes, Cornell University, Ithaca, NY 14853, USA

A. Lunin, N. Solyak and A. Vivoli, FNAL, Batavia, IL 60510, USA

D. Filippetto, R. Huang, C. Papadopoulos, G. Portmann, J. Qiang, F. Sannibale, S. Virostek, R. Wells, LBNL, Berkeley, CA 94720, USA

Abstract

The new LCLS-II project will construct a 4 GeV continuous wave (CW) superconducting linear accelerator to simultaneously feed two undulators which will cover the spectral ranges 0.2-1.2 keV and 1-5 keV, respectively. The injector must provide up to 300 pC/bunch with a normalized emittance $< 0.6 \mu\text{m}$ and peak current $> 30 \text{ A}$ at up to 1 MHz repetition rate. An electron gun with the required brightness at such high repetition rate has not yet been demonstrated. However, several different options have been explored with results that meet or exceed the performance requirements of LCLS-II.

The available technologies for high repetition-rate guns, and the need to keep dark current within acceptable values, limit the accelerating gradient in the electron gun. We propose a CW normal conducting low frequency RF gun for the electron source due to a combination of the simplicity of operation and the highest achieved gradient in a CW gun, potentially allowing for lower beam emittances. The high gradient is especially significant at the 300 pC/bunch charge where beam quality can suffer due to space charge. This paper describes the design challenges and presents our solutions for the LCLS-II injector.

INTRODUCTION

LCLS-II [1] is a proposed FEL user facility driven by a 4 GeV CW superconducting linac under construction at SLAC. The injector must simultaneously deliver high repetition rate up to 1 MHz and high beam brightness with normalized emittance of $< 0.6 \mu\text{m}$ at 300 pC/bunch and peak current $> 30 \text{ A}$. An injector capable of delivering the desired parameters has not yet been demonstrated. This paper describes one possible design for the LCLS-II injector.

The preferred LCLS-II electron gun is a normal conducting, CW, rf gun operating at 186 MHz (7th sub-harmonic of 1.3 GHz) like the APEX gun at LBNL [2]. Multiple gun technologies with different advantages and disadvantages were considered and the APEX gun was ultimately adopted for LCLS-II largely due to the high

achieved gradient of 20 MV/m and the demonstrated reliable CW operation. The gradient is especially important at 300 pC/bunch where beam quality can suffer due to space charge. The nominal values as well as the range of all the injector parameters are listed in Table 1. Parameters are specified at the injector exit unless otherwise indicated. The layout of the full injector is shown in Figure 1 including the gun, buncher, superconducting accelerator, laser heater for microbunching instability suppression and diagnostics. The accelerator is comprised of a single standard TESLA cryo-module with eight 9-cell SRF cavities which accelerates the beam from < 1 to approximately 100 MeV.

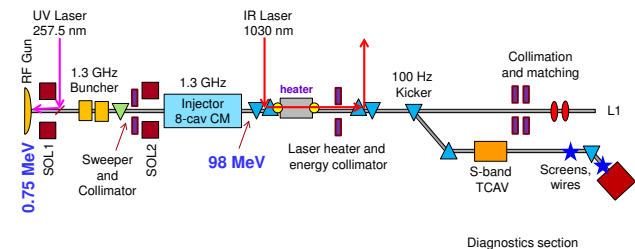


Figure 1: Injector layout.

GUN TECHNOLOGY

Three gun technologies, each with distinct advantages and disadvantages, were considered for LCLS-II.

1. DC guns
2. VHF rf gun at linac sub-harmonic
3. Superconducting high gradient multi-cell gun

The DC gun at Cornell has nearly demonstrated the nominal LCLS-II parameters as shown in Figure 2 [3]. These results were obtained with the DC gun operating at 350 kV corresponding to about 4 MV/m at the cathode but the gun will need to be operated at closer to 500 kV to meet the LCLS-II emittance requirements at 300 pC. The Cornell DC gun has recently been operated at 400 kV but no DC gun has yet demonstrated reliable e-beam operation at 500 kV including guns with segmented insulators. One advantage of the DC gun is to allow for arbitrary pulse separation which can fill adjacent linac buckets and is desired for multi-bunch operation. However, LCLS-II is currently designed to operate with only a single bunch.

*Work supported by U.S. Department of Energy under Contract DEAC03-76SF00515

[#]schmerge@slac.stanford.edu

Table 1: LCLS-II Injector Specifications

Parameter	Nominal	Range	Units
Electron energy at gun exit	750	500-800	keV
Electron energy	98	95-120	MeV
Bunch charge	100	10-300	pC
Bunch repetition rate	620	0-929	kHz
Dark current		0-400	nA
Peak current	10	5-30	A
Average current	0.062	0-0.3	mA
Average beam power	6.1	0-36	kW
Normalized slice emittance (rms)	0.4	0.2-0.6	μm
Bunch length (rms)	1	0.3-10	mm
Slice energy spread (rms)	1	1-5	keV
Vacuum pressure in gun	1	0.1-1	nTorr
Cathode quantum efficiency	2	0.5-10	%
Laser (UV) energy at cathode	0.02	0-0.3	μJ
Laser (IR) energy at laser heater	1	0-15	μJ
Average CW RF gradient	16	15-18	MV/m

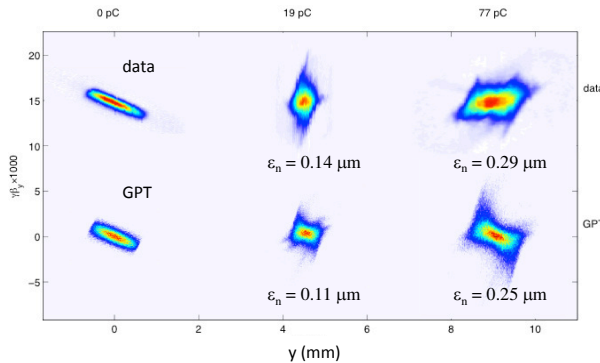


Figure 2: Cornell DC gun phase space measurements and comparison with GPT simulations at three charges. Emittances listed are for 90% of the particles.

The low frequency rf guns can reach high gradients including 20 MV/m for normal conducting and over 30 MV/m for superconducting [4]. While neither technology has demonstrated the desired brightness it is expected that they will perform similar to the DC guns because these guns operate near crest and the transit time plus laser pulse length is much shorter than the rf period. While the superconducting guns can produce higher gradient they have not yet demonstrated reliable operation and thus were not yet considered suitable for a user facility.

The multi-cell superconducting rf guns operate similar to the existing LCLS rf gun at GHz frequencies and high gradient. This combination produces shorter pulses requiring less compression downstream. Like the DC guns they permit multi-bunch FEL operation because they can fill every linac bucket. However, problems such as optimizing emittance compensation due to magnetic field

locations, multi-pacting and cathode exchanges still exist and require additional R&D. While we believe the superconducting guns (both low and high frequency) have the greatest potential to deliver the brightest beams due to the high gradients achievable, they are not yet ready for operation in a user facility requiring > 99% injector reliability. A SRF gun is considered an upgrade path in the future.

Based on the technology reliability and potential for high charge operation, we concluded the best candidate for the LCLS-II injector was the low frequency normal conducting rf gun. The gun cross-section is shown in Figure 3 and the basic parameters are listed in Table 2.

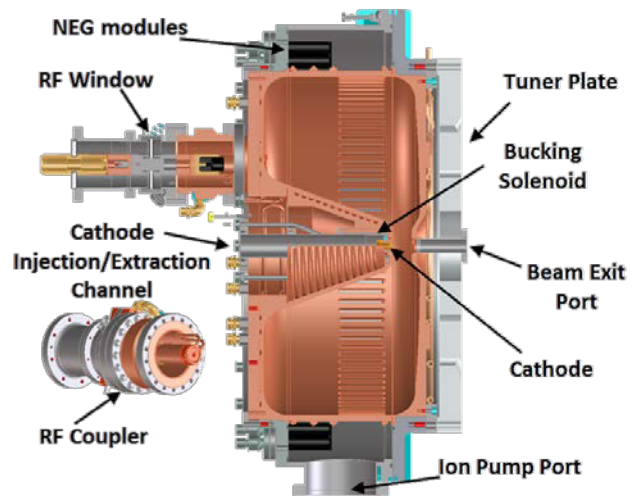


Figure 3: Cross section of the APEX CW rf gun.

Table 2: Measured APEX Gun Parameters

Parameter	Value
Frequency	186 MHz
Gap Voltage	750 kV
Field at Cathode	19.5 MV/m
Q_0	26500
Shunt Impedance	6.5 M Ω
RF Power	100 kW
Peak Surface Field	24 MV/m
Peak Wall Power Density	25 W/cm ²
Accelerating Gap	4 cm
Diameter	69.4 cm
Length	35 cm
Operating Pressure	0.1-1 nTorr

CHALLENGES

The primary challenge for the LCLS-II injector is the demonstration of the desired brightness at MHz repetition rate. Other challenges include the laser and cathode performance, dark current generation and preservation of the high brightness beam as the beam is accelerated to higher energies. Each of these challenges and our proposed mitigation is briefly described below.

High Brightness Demonstration

SLAC is collaborating with both Cornell and LBNL to demonstrate high repetition, high brightness beams with up to 300 pC/bunch charges at up to 1 MHz rate in 2015. The Cornell gun will be operated at a maximum energy of 400 keV and the APEX gun will operate at a maximum of 800 keV. Beam characterization will be performed at 10 and 30 MeV respectively. Layouts of the two machines are similar but not identical. Details on the optimization of various layouts and performance over a range of gun energies are reported elsewhere [5].

Laser and Cathode

The laser and cathode are extremely important components of the injector. We have adopted the conservative approach using a Cs₂Te cathode operating in the UV with QE > 0.5%. This leads to the spec of 0.3 μ J of laser energy at the cathode assuming the maximum charge of 300 pC. The measured lifetime as a function of QE is shown in Figure 4. The lifetime is especially important for user facilities and this measurement shows cathodes can easily deliver QE > 0.5% for more than the required 7 days. Alternative cathodes operating in the visible such as K₂CsSb and NaKSb will be considered in the future as they are further characterized and developed.

At 1 MHz rate and assuming 10% IR to UV conversion plus 90% losses in the transport and conditioning components leads to a 30 W IR laser power specification. The best candidate for the required laser system is a fiber oscillator/amplifier. They have the combination of average power scalability, beam quality, power and timing stability. Fiber-based laser systems with >10 W output power, MHz repetition rate, and high transverse and longitudinal beam quality are commercially available [6].

We anticipate improvements in commercially available systems in the next few years prior to ordering the LCLS-II laser. However, some R&D may be necessary to simultaneously deliver temporal and transverse shaping with the desired power and pointing stability.

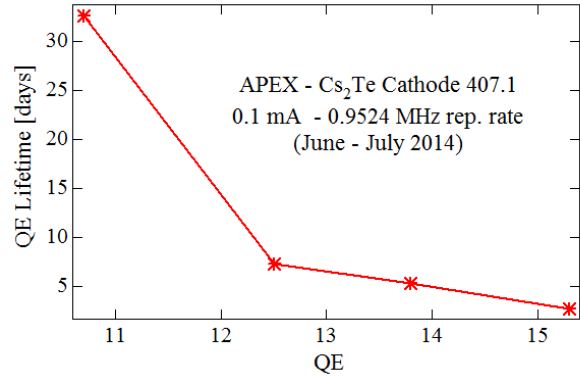


Figure 4: Measured Cs₂Te lifetime versus QE.

The laser also needs the capability to switch continuously between single shot and 1 MHz in order to allow different machine operation modes. A pulse picker system such as an Electro-Optic Modulator or Acousto-Optic Modulator will be used to vary the rate.

Dark Current

Dark current can be detrimental to the performance of a SRF based FEL due to possible quench of SRF cavities and radiation damaging of permanent magnet undulators. The dark current from the APEX gun has been characterized [7] with roughly 350 nA measured at the location of the first LCLS-II SRF cavity as shown in Figure 5. The dark current is dominated by field emission around the cathode plug outer diameter where the plug meets the gun “nose”. The “nose” has a small radius which enhances the field and generates the majority of the dark current. Figure 6 shows an image of the cathode on a downstream screen clearly showing the dark current dominated at the plug to gun boundary.

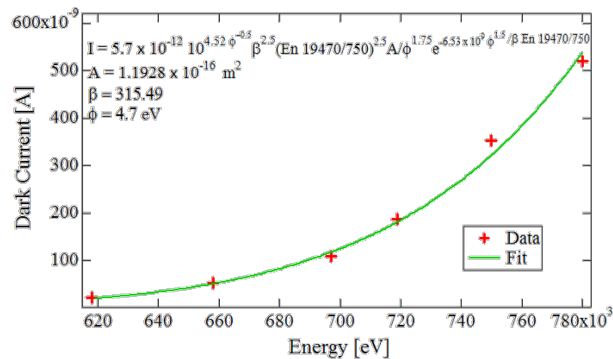


Figure 5: Measured Dark Current at location of first LCLS-II superconducting accelerator cavity.

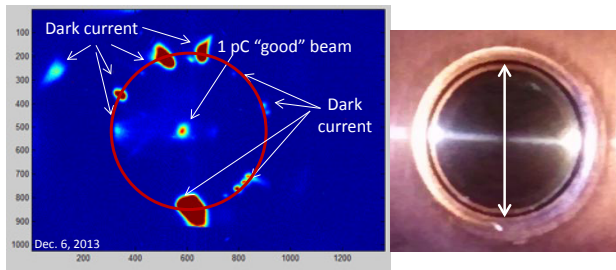


Figure 6: Measured dark current imaged onto a screen at left and the cathode plug on the right. The diameter of the ring of dark current matches the diameter of the plug.

Although the measurements shown already meet the LCLS-II spec we realize the dark current can increase with time and cathode exchanges so we have developed several methods for mitigation. An obvious method to reduce dark current is to reduce the gradient at the cathode. Figure 5 shows nearly an order of magnitude reduction is possible by operating at 650 keV instead of 750 keV. This method will clearly work but at the expense of beam quality so other methods are preferred. One method will be to clean the cathode and gun surface with CO₂ snow as demonstrated on the PITZ L-band gun [8] which resulted in an order of magnitude reduction in dark current. This method is effective at removing particulates and will be tested shortly on the APEX gun. Another possibility is to use a collimator to scrape the dark current electrons emitted from the gun “nose” since they originate at a much larger diameter than the photoelectrons. This method can potentially decrease the dark current an order of magnitude without scraping photoelectrons. A collimator will be tested soon and is described in more detail in reference 7.

Emittance Preservation

The standard TESLA SRF cavities include one Higher Order Mode (HOM) coupler at the upstream and downstream ends to damp higher order mode power plus the rf power feed coupler at the downstream end. These couplers produce field perturbations that break the field symmetry and cause beam deflection and emittance growth. The perturbation strength is largest at large radius and thus predominantly impacts the high charge cases. Figure 7 shows the emittance for both transverse planes at 300 pC with perfectly symmetric fields (no couplers), the standard TESLA cavity case with 2 HOMs and a single power coupler and a TESLA cavity modified to eliminate only the upstream HOM. The emittance for the standard TESLA cavity is approximately 30% larger than the symmetric case but most of the emittance is recovered by eliminating the upstream HOM. The difference between x and y plane emittances in the figure are due to a small quadrupole term that can be corrected. Additional information and discussion is included elsewhere [9].

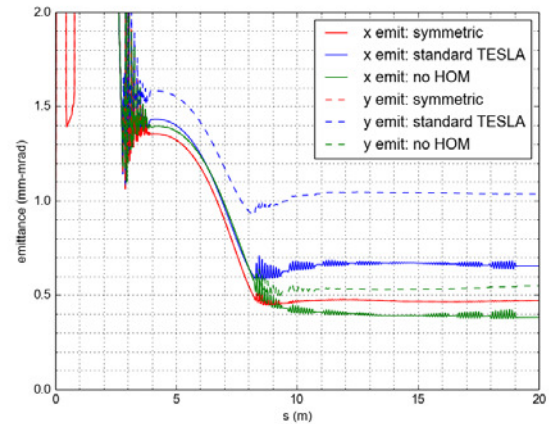


Figure 7: Horizontal and vertical emittance for 300 pC as a function of distance from the cathode for three cases; 1) ideal case with perfectly symmetric cavity fields, 2) 3-D fields from standard TESLA cavity including HOM couplers and 3) 3-D fields from standard TESLA cavity with upstream HOM coupler removed.

While it would be desirable to minimize the perturbations from all the couplers in the injector, the simulations show that only the first SRF cavity requires modification to the upstream HOM coupler to preserve the emittance since the beam energy increases an order of magnitude in the first cavity. Modification of the couplers existing design requires significant effort and expense so we are planning to modify only the first cavity.

We have considered three methods for eliminating the upstream HOM. The first method moves the upstream HOM to the downstream end so there are two HOMs and one power feed downstream. The couplers are arranged to minimize dipole and quadrupole perturbation terms. A second method is to add a second HOM at the upstream end approximately 180 degrees apart to minimize the dipole term. A third method completely eliminates the HOM and instead uses a coaxially symmetric beam absorber as described in reference 3. Simulations indicate that all three methods are equally effective. We are currently evaluating the engineering implications and other potential risks and benefits for the three options and will adopt a final choice in the near future.

Optimizing the brightness will require diagnostics to characterize the full 6-D phase space. Thus we plan to include transverse rf deflectors as shown in Figure 1 to measure the time dependent transverse phase space as well as longitudinal phase space. A pulsed kicker will operate up to 100 Hz to divert single pulses onto the diagnostic beamline. Continuous monitoring of the injector beam quality will allow implementation of feedbacks as necessary. Diagnostics will be critical to deliver the emittance values described here and in reference 5.

CONCLUSION

Simulations show the APEX gun, a normal conducting, 186 MHz rf gun, can deliver the desired LCLS-II electron beam parameters including $<0.6 \mu\text{m}$ normalized emittance with 300 pC/bunch at 1 MHz repetition rate. Demonstrations of high repetition, high brightness beams with up to 300 pC/bunch charges are expected at both APEX and Cornell in 2015. In addition the APEX gun with Cs_2Te cathode has demonstrated reliable CW operation, with the required dark current, QE, thermal emittance and lifetime. Additional R&D may be needed for the laser to simultaneously deliver the desired temporal and transverse pulse shapes with the required pulse energy and stability. In order to preserve the emittance downstream of the gun, modification of the rf HOM coupler in the first superconducting rf cavity will be necessary.

REFERENCES

- [1] T. Raubenheimer et al., "The LCLS-II, a New FEL Facility at SLAC," WEB01 these proceedings, FEL'14, Basel, Switzerland (2014).
- [2] D. Filippetto et al., "APEX: A Photo-injector for High Average Power Light Sources and Beyond," TUA01 these proceedings, FEL'14, Basel, Switzerland (2014).
- [3] C. Guilliford, et al, PRST-AB **16**, 073401 (2013).
- [4] J. Bisognano et al., "Wisconsin SRF Electron Gun Commissioning," NAPAC'13, Pasadena, USA, p. 622 (2013); <http://www.JACoW.org>
- [5] C. Papadopoulos et al., "RF Injector Beam Dynamics Optimization for LCLS-II," THP057 these proceedings, FEL'14, Basel, Switzerland (2014).
- [6] See for example IMRA website: <http://www.imra.com/products/product-lines/fcpa-microjewel/>
- [7] R. Huang et al., "Dark Current Studies at the APEX Photoinjector," THP054 these proceedings, FEL'14, Basel, Switzerland (2014).
- [8] A. Brinkmann et al., "Various Applications of Dry-Ice Cleaning in the Field of Accelerator Components at DESY," LINAC'08, Victoria, Canada, p. 803 (2008).
- [9] A. Vivoli et al., "Effect of Cavity Couplers Field on the Beam Dynamics of the LCLS-II Injector," THPP060 proceedings of Linac'14, Geneva, Switzerland (2014).

MODEL-BASED KLYSTRON LINEARIZATION IN THE SwissFEL TEST FACILITY

Amin Rezaeizadeh*, Paul Scherrer Institut, Villigen, Switzerland
and Automatic Control Laboratory, ETH, Zürich, Switzerland

Roger Kalt, Thomas Schilcher, Paul Scherrer Institut, Villigen, Switzerland
Roy Smith, Automatic Control Laboratory, ETH, Zürich, Switzerland

Abstract

An automatic procedure is developed to provide the optimal operating point of a klystron. Since klystrons are non-linear with respect to the input amplitude, a model-based amplitude controller is introduced which uses the klystron characteristic curves to obtain the appropriate high voltage power supply setting and amplitude, such that the operating point is close to the saturation. An advantage of the proposed design is that the overall open-loop system (from the input to the RF station to the klystron output amplitude) is linearized. The method has been successfully tested on a full scale RF system running at nominal power.

INTRODUCTION

The Swiss Free Electron Laser is currently being constructed at PSI [1]. The SwissFEL injector and the Linac Radio Frequency drives operate in a pulsed mode at the rate of 100 Hz. The pulse-to-pulse stability of the electron beam characteristics, such as beam energy, are crucial for the quality of laser pulses. As the RF phase and amplitude stability plays a significant role in this goal, an automatic procedure is developed to obtain the operating point of a klystron such that the output amplitude is close to its saturation level so that the pulse-to-pulse amplitude jitter is minimized. The procedure is model-based, using the klystron (AM/AM) characteristic curves. The major advantage of the design is that the overall system from the Low Level RF input to the vector modulator to the output of the klystron is linearized. Moreover, from the system dynamics standpoint, the closed-loop system can be treated as a linear system. A recent contribution [2], uses a third order polynomial function to correct the nonlinearity of the klystron. The method is open-loop and for constant high voltage.

Throughout this paper, the klystron and the upstream RF and LLRF subsystems such as the pre-amplifier and the vector modulator are referred to as the “drive chain”. The high voltage power supply setting and the input amplitude to the klystron are automatically determined according to the desired output power and the predefined headroom to the saturation. For the case where the demand power is obtainable via slight change in the input amplitude, the high voltage is kept unchanged. For precise control, a pulse-to-pulse feedback loop is closed around the operating point.

In the following section, we discuss the klystron amplitude-to-amplitude (AM/AM) modeling, followed by a pulse-to-pulse amplitude feedback scheme.

KLYSTRON MODELING

For fixed and constant high voltage, the klystron can be characterized by Rapp’s model used for solid-state power amplifiers (SSPA) [3] (which was initially introduced by Cann in 1980 [4]). The model is suitable for systems that are approximately linear with gradual saturation. We generalize the formulation of the model as follows,

$$y(a_{in}) = \frac{p_1 a_{in} + p_2}{\sqrt{1 + \left(\frac{a_{in}}{p_0}\right)^2}} + p_3, \quad (1)$$

where, y denotes the output amplitude of the klystron, a_{in} is the input amplitude and p_i ’s are constant parameters. This model describes the saturation and over-saturation characteristics of a klystron for constant high voltage.

Figure 1 illustrates the data of a klystron in the SwissFEL test facility and the fitted model from (1). In the original form [3, 4], the p_2 term is zero which does not capture the power drop in the over-saturation region.

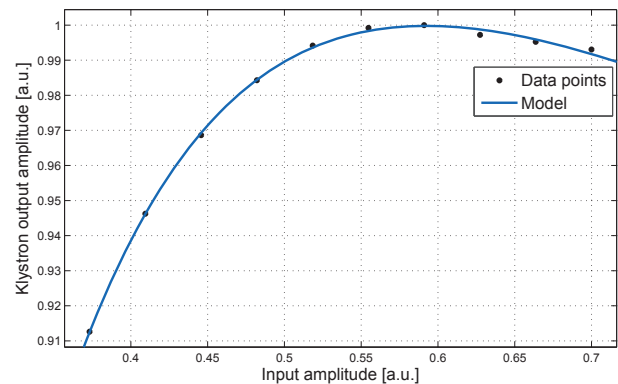


Figure 1: The klystron input-amplitude to output-amplitude (AM/AM) conversion curve. The output amplitude is normalized to the maximum amplitude. The regression of fitting is $R^2 = 0.999$.

According to the experiments, the output amplitude change is approximately linear with respect to high voltage changes. Therefore, the following formulation is introduced, connecting the input, output amplitude and the high voltage

* aminre@ee.ethz.ch

value.

$$y = f(a_{in}, h) := \frac{p_1 a_{in} + p_2 h + p_3 a_{in} h + p_4}{\sqrt{1 + \left(\frac{a_{in}}{p_0}\right)^2}} + p_5 h + p_6, \quad (2)$$

where y is the output amplitude, h denotes the high voltage power supply value, and p_i 's are constant parameters. Figure 2 shows the characteristic curves of the same klystron for different high voltage levels of h . The fitted curves are plotted in red. The output power, P , is directly calculated from (2) by squaring the output amplitude and multiplying by a power factor.

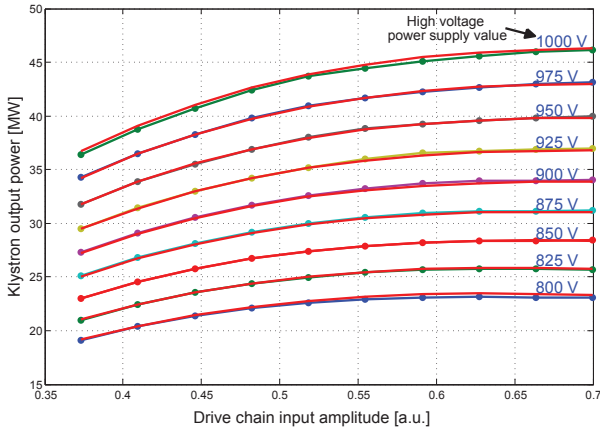


Figure 2: The klystron output power, P , for different input amplitudes and high voltage power supply levels, h (numbers in blue). The models are depicted in red. The fitting regression is $R^2 = 0.9996$. The standard deviation of the error between the fit and the data for the saturating powers is $\sigma \approx 0.19 \text{ MW}$ which corresponds to 0.65% headroom.

OPERATING POINT DETERMINATION

The operating point of the klystron is defined by the output power, P^* , the high voltage power supply setting, h^* , and the drive chain input amplitude, a_{in}^* (see Fig. 3).

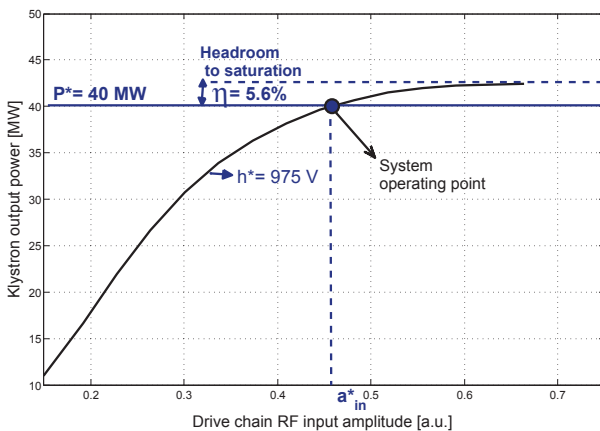


Figure 3: The operating point definition of the klystron.

For output amplitude stability (repeatability), it is preferable to operate the klystron very close to its saturation. The amount of the headroom to saturation level is given in percent and it is normally around 1 to 5 %. The maximum output amplitude, y_{max} , can be readily determined from (2):

$$y_{max} = \sqrt{(p_2 h + p_4)^2 + p_0^2 (p_3 h + p_1)^2} + p_5 h + p_6. \quad (3)$$

Since the desired headroom is specified, the desired output amplitude can be expressed in terms of y_{max} ,

$$y^* = (1 - \eta) y_{max}, \quad (4)$$

where y^* is the desired output amplitude which corresponds to P^* , and where η denotes the headroom.

From Eqs. 3 and 4, the corresponding setpoint value for high voltage power supply, h^* , can be easily calculated. In practice, equation (3) is close to linear with respect to the high voltage power supply, h .

Once h^* is determined, the calculation of the corresponding input amplitude, a_{in}^* , is straightforward. Substituting h^* and y^* into the model defined in (2), leads to,

$$y^* = \frac{p_1 a_{in}^* + p_2 h^* + p_3 a_{in}^* h^* + p_4}{\sqrt{1 + \left(\frac{a_{in}^*}{p_0}\right)^2}} + p_5 h^* + p_6. \quad (5)$$

Equation 5 is a simple quadratic algebraic equation with respect to a_{in}^* , and it has two solutions. Since over-saturation is not permitted, only the smaller solution is considered. Figure 4 depicts the schematic of open loop operation of the klystron. Since the model is not exact, the actual output amplitude, y , differs from y^* . Hence, a pulse-to-pulse feedback is needed to achieve the desired amplitude more precisely. The properties of the feedback are discussed in the following section.

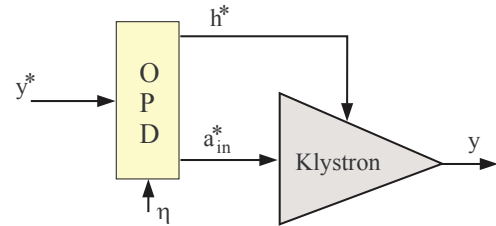


Figure 4: The schematic of open-loop operation of a klystron. The OPD-box denotes the operating point determination.

PULSE-TO-PULSE FEEDBACK

The term “pulse-to-pulse” refers to the fact that the system runs in a pulsed mode and there is no intra pulse feedback to compensate the error. The closed loop diagram of the system is illustrated in Fig. 5. The controller is an integrator with the gain C . For slight changes of the setpoint, the high voltage remains constant and the desired amplitude is reached by

varying the headroom and thus the input amplitude, a_{in}^* . This threshold of the amplitude setpoint is determined by the allowed range of the klystron output, which is defined to be $\pm\eta$ around the operating point (i.e. from the saturation level down to $1 - 2\eta$ below the saturation, where η is the specified headroom). For the case where the setpoint change is beyond the threshold, a new set value for the high voltage power supply is determined with the default headroom, η , and the integrator resets, which leads to $u = 0$.

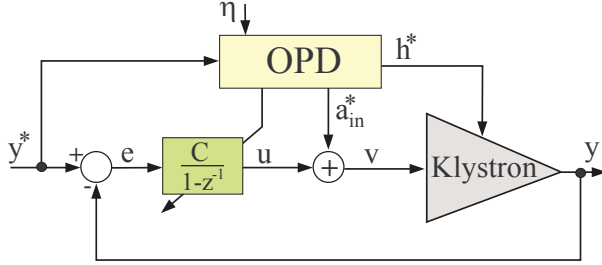


Figure 5: The schematic of closed loop operation of a klystron.

For the output y , we have the following expressions,

$$y_k = f(v_k, h^*) = f(a_{in}^* + u_k, h^*), \quad (6)$$

where f is model of the system response defined in (2), and where subscript k denotes the pulse index.

Approximating by Taylor's expansion implies,

$$y_k \approx f(a_{in}^*, h^*) + \left. \frac{\partial f(a_{in}, h^*)}{\partial a_{in}} \right|_{a_{in}=a_{in}^*} u_k, \quad (7)$$

For simplicity in notation, we define

$$f' := \left. \frac{\partial f(a_{in}, h^*)}{\partial a_{in}} \right|_{a_{in}=a_{in}^*} \text{ and } f_0 := f(a_{in}^*, h^*).$$

The controller signal, u_k is generated as follows,

$$\begin{aligned} u_k &= u_{k-1} + C(y^* - y_{k-1}) \\ &= u_{k-1} + C(y^* - f_0 - f' u_{k-1}), \end{aligned} \quad (8)$$

with a certain upper bound, to prevent excessive control-output and over-saturation of the klystron. In the case where the actuator hits the limit, a_{in}^* and h^* are recalculated for slightly larger headroom.

Substituting Eq. 8 into (7) leads to,

$$y_k = (1 - C f') y_{k-1} + f' C y^*. \quad (9)$$

Taking the term $C f'$ constant and neglecting higher order terms in the Taylor series approximation, make the klystron system linear from the setpoint y^* to the output y . Notice that f' is a function of a_{in}^* , which itself is a function of y^* .

For fast transient response, the controller gain is chosen such that $C = \frac{1}{f'}$. However, in practice, the model is not exact, therefore the local gain of the actual system, $g' = \frac{\partial y_k}{\partial a_{in}}$, differs from f' . Thus, the system dynamics are,

$$y_k = (1 - \frac{g'}{f'}) y_{k-1} + \frac{g'}{f'} y^*. \quad (10)$$

To ensure the stability of the closed-loop [5], we have the following constraint,

$$|1 - \frac{g'}{f'}| \leq \beta < 1, \quad (11)$$

which implies that the error decays at a rate of β^k .

The stability criterion in (11), leads to

$$\frac{1}{1 + \beta} < \frac{f'}{g'} < \frac{1}{1 - \beta}, \quad (12)$$

which indicates that the derivative of the model, f' , should be within a limit with respect to the true system.

EXPERIMENTAL RESULTS

In the following experiment which is done on a klystron in a C-band RF station, different power setpoints are applied and the headroom is set to be $\eta = 3\%$ from the saturation level.

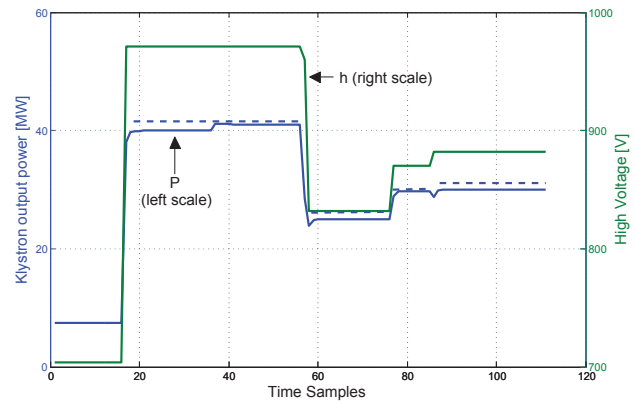


Figure 6: Closed-loop experiment result of applying different power setpoints. The high voltage power supply value is determined by the OPD unit and the pulse-to-pulse feedback gain, C , is modified accordingly. The dashed lines indicate the maximum power (saturation level).

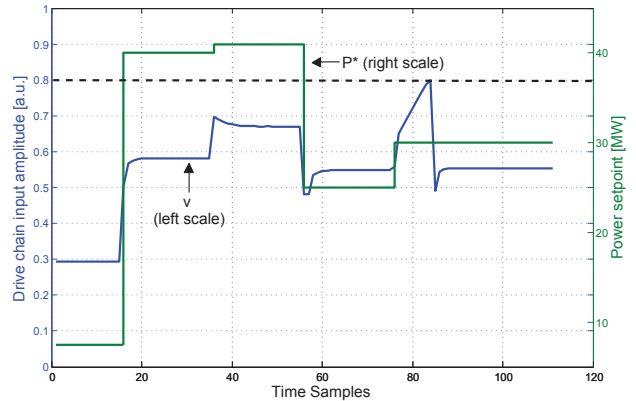


Figure 7: The input signal, v , to the klystron and the power setpoint, P^* . The dashed line denotes the maximum drive chain input.

Figure 6 illustrates the output power and high voltage power supply of the klystron for a series of step changes in the

setpoint. At time $k = 16$ the setpoint jumps to $P^* = 40\text{MW}$. The OPD provides the new integrator gain, C , as well as the corresponding high voltage power supply set value for the modulator which is 972V . The high voltage setting of the modulator responds relatively quickly, but it may take one or two pulses to reach the set value. During this time, the integrator value is set to zero and the feedback is still inactive. At time $k = 36$ the setpoint is slightly increased by 1MW . Since the new setpoint can be reached within the current headroom, the high voltage is kept unchanged and only the input amplitude is increased (by reducing the headroom to 1%).

At time $k = 56$, the setpoint drops almost to half of the power, 25MW , and the corresponding high voltage power supply value is set to 832V . At time $k = 76$, the headroom is manually reduced to $\eta = 1\%$ to observe the accuracy of modeling and the setpoint is set to 30MW . Because of model-mismatch, and specifically due to the small headroom, the klystron saturates and the actuator signal, v , hits the limit of the drive chain input (see Fig. 7). In this case, the OPD unit is notified and the new operating point is determined with a new larger headroom. As we can see, at $k = 85$ a new high voltage power supply set value is introduced with a new headroom (as default 3%) and the output power has reached the setpoint of 30MW .

CONCLUSION

This paper has illustrated the klystron AM/AM modeling and its applicability in the model-based automation of a klystron. Using the klystron models also gives an opportunity to operators to monitor the operating point of klystrons, as well as the saturation levels. As a result of such automation, the open-loop drive chain from the vector modulator to the klystron output is linearized, and the closed-loop system reaches the setpoint more quickly. The minimum amount of headroom to the saturation is limited by the error between the models and the data as given in Fig. 2. A model-based pulse-to-pulse feedback is tested successfully on the Swiss-FEL full scale C-band RF system. The feedback approach is based on an integrator with an adaptive gain, depending on the setpoint.

ACKNOWLEDGMENT

The authors would like to thank the LLRF and the RF team who made this research possible.

REFERENCES

- [1] Romain Ganter et al., SwissFEL Conceptual Design Report, PSI, Villigen, Switzerland, 2010.
- [2] M. Omet et al., “Development and Test of Digital LLRF Control Procedures and Techniques in Scope of ILC”, presented at the LLRF2013 workshop, Lake Tahoe, USA, October 1 - 4, 2013.
- [3] Ch. Rapp, “Effects of HPA-Nonlinearity on a 4-DPSK/OFDM-Signal for a Digital Sound Broadcasting System”, *Proc. of 2nd European Conference on Satellite Communications*, Liege, Belgium., Oct. 1991, pp. 179–184.
- [4] A. J. Cann, “Nonlinearity Model With Variable Knee Sharpness”, *IEEE Trans. Aerosp. Electron. Syst.* vol. 16, no. 6, pp. 874–877, Nov. 1980.
- [5] G.F. Franklin et al., *Digital Control of Dynamic Systems*, Addison Wesley, 1998.

RF PULSE FLATTENING IN THE SWISSFEL TEST FACILITY BASED ON MODEL-FREE ITERATIVE LEARNING CONTROL *

Amin Rezaeizadeh[†], Paul Scherrer Institut, Villigen, Switzerland
and Automatic Control Laboratory, ETH, Zürich, Switzerland

Thomas Schilcher, Paul Scherrer Institut, Villigen, Switzerland
Roy Smith, Automatic Control Laboratory, ETH, Zürich, Switzerland

Abstract

This paper introduces an iterative approach to producing flat-topped radio frequency (RF) pulses for driving the pulsed linear accelerators in the Swiss free electron laser (SwissFEL). The method is based on model-free iterative learning control which iteratively updates the input pulse shape in order to generate the desired amplitude and phase pulses at the output of the RF system. The method has been successfully applied to the klystron output to improve the flatness of the amplitude and phase pulse profiles.

INTRODUCTION

The SwissFEL project at PSI will develop a Free Electron Laser capable of generating extremely bright and short X-ray pulses [1]. The SwissFEL injector and linac RF drives operate in a pulsed mode at the rate of 100 Hz, using normal conducting RF accelerating structures. The input RF pulse length is relatively short (in the order of 1-3 μ s) and there is no RF digital feedback running within a pulse. In the two-bunch operating mode of the SwissFEL, each electron bunch is separated by 28 ns, and it is often required that the two bunches see the same amplitude and phase in the accelerating structure. To achieve this goal, an Iterative Learning Control (ILC) technique is introduced to generate a flat-topped (or generally any desired shape) RF pulse.

Iterative Learning Control is a method for controlling systems that operate in a repetitive, or trial-to-trial mode [2, 3]. In this method, the measured trajectory is compared to the desired trajectory to give an error estimate which is then used to update the input for the next trial. A model-based ILC algorithm has been previously introduced in [4] which uses an intra-pulse state feedback and it has been implemented in several systems [5] including accelerators [6]. However, this approach is not applicable in the SwissFEL since no intra pulse digital feedback is feasible. A new version of ILC has been recently developed which is not based on the model of the system and thus the usual system identification procedure is not required [7]. The recent method has been modified and successfully tested on a C-band RF station in the SwissFEL test facility.

RF STATION LAYOUT

The RF and low-level RF layout of the SwissFEL C-band station is illustrated in Fig. 1. The discrete waveforms of

the in-phase, I, and quadrature, Q, components of the RF signal are fed into the vector modulator to be up-converted to the carrier frequency (5.712GHz). Each waveform contains 2048 samples with the sampling time of $T_s = 4.2$ ns. The RF signal drives the klystron which delivers high power RF at the output. In C-band stations, an RF pulse compressor (Barrel Open Cavity) is placed after the klystron, followed by four accelerating structures.

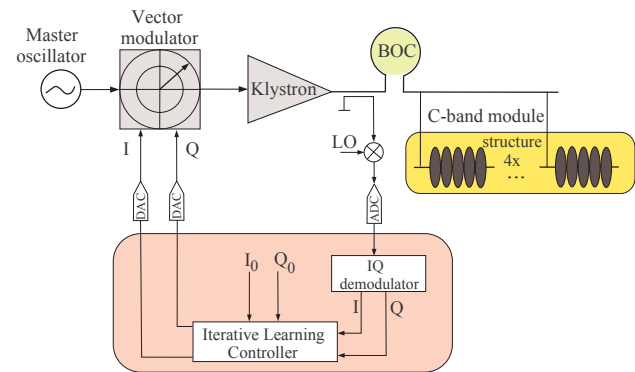


Figure 1: The RF layout of the SwissFEL C-band station.

For our experiment, we take the output of the klystron as the measured pulse whose shape is to be controlled. The signal is measured by a directional coupler and then down converted to the intermediate frequency (IF) of 39.67 MHz. The resulting signal is then sampled at the rate of 238 MHz, followed by a demodulation algorithm to obtain discrete waveforms of I and Q. The measured waveforms are compared to the desired ones and the ILC controller generates the next I and Q inputs to the DAC.

ITERATIVE LEARNING CONTROL SCHEME

The ILC is a technique to manipulate the input pulse shape iteratively until the output pulse shape fulfills the requirement. Model-free ILC methods are rarely investigated in literature, in contrast to a variety of model-based methods. Model-free ILC algorithms have the advantage that no system identification experiments are required. The idea behind our approach was developed by Janssens *et al.* [7].

Figure 2 illustrates the initial output signals of the klystron as a response to a rectangular input pulse. The colored area which is after filling time of the structures, denotes the region in which the electron bunches are fired. We refer to it as

* Work supported by Paul Scherrer Institut.

[†] aminre@ee.ethz.ch

the “flat-top” region, where ideally the pulse amplitude and phase should be constant.

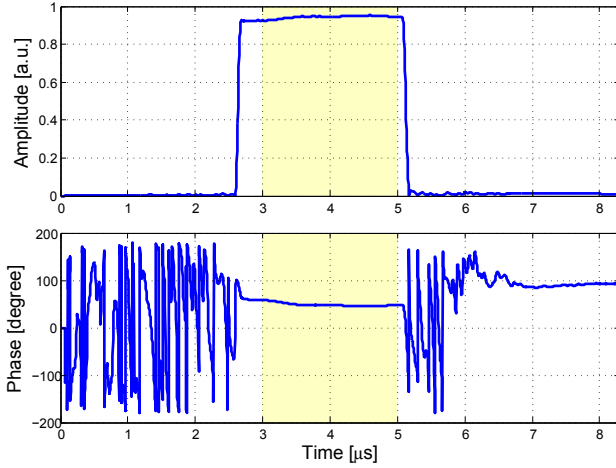


Figure 2: A typical pulse generated by the klystron. The measurement window consists of 2048 samples with sampling time of $T_s = 4.2$ ns. The electron-bunches are fired after filling time of the structures somewhere in the colored area, which we refer it to as the flat-topped region. The amplitude is normalized with respect to the saturation level (with 5% headroom).

For the notation throughout this paper, subscript i denotes the iteration counter, whereas index k captures the discrete time instants within one RF pulse. The following input update law is considered for an LTI SISO system,

$$u_{i+1}(k) = u_i(k) + u_{lc,i}(k) * \alpha_i(k), \quad (1)$$

where $u_i(k) \in \mathbb{R}$, $k \in \{1, 2, \dots, N\}$, and $u_{lc,i}$ denotes any linear combination of the previous trials' input signals $u_0(k), u_1(k), \dots, u_i(k)$, and where $\alpha_i(k)$ is a trial-varying but LTI FIR filter of length N . The asterisk denotes convolution. Since the system is assumed to be LTI, the corresponding output $y_{i+1}(k)$ is predicted to be

$$\hat{y}_{i+1}(k) = y_i(k) + y_{lc}(k) * \alpha_i(k), \quad (2)$$

where y_{lc} represents the corresponding linear combination of the previous trials' output signals $y_0(k), y_1(k), \dots, y_i(k)$.

Equation 1 can be extended to MIMO systems by using the lifted system representation,

$$u_{i+1} = u_i + U_{lc} \tilde{\alpha}_i, \quad (3)$$

where

$$u_i := \begin{pmatrix} u_{Ii} \\ u_{Qi} \end{pmatrix}, \quad u_{Ii}, u_{Qi} \in \mathbb{R}^N,$$

and where,

$$u_{Ii} = \begin{pmatrix} u_{Ii}(1) \\ u_{Ii}(2) \\ \vdots \\ u_{Ii}(N) \end{pmatrix}, \quad u_{Qi} = \begin{pmatrix} u_{Qi}(1) \\ u_{Qi}(2) \\ \vdots \\ u_{Qi}(N) \end{pmatrix}, \quad (4)$$

and N denotes the number of samples in the flat-top region. Moreover,

$$U_{lc} = \begin{pmatrix} U_{lcI} & U_{lcQ} & \mathbf{0} & \mathbf{0} \\ \mathbf{0} & \mathbf{0} & U_{lcI} & U_{lcQ} \end{pmatrix}, \quad \tilde{\alpha}_i = \begin{pmatrix} \alpha_{Ii} \\ \alpha_{Ii} \\ \alpha_{Qi} \\ \alpha_{Qi} \end{pmatrix}$$

where U_{lcI} and U_{lcQ} denote the lower-triangular Toeplitz matrices of $u_{lcI}(k)$ and $u_{lcQ}(k)$, respectively.

A similar relationship can be derived for y ,

$$\hat{y}_{i+1} = y_i + Y_{lc} \tilde{\alpha}_i, \quad (5)$$

where,

$$Y_{lc} = \begin{pmatrix} Y_{lcI} & Y_{lcQ} & \mathbf{0} & \mathbf{0} \\ \mathbf{0} & \mathbf{0} & Y_{lcI} & Y_{lcQ} \end{pmatrix},$$

and similarly, Y_{lcI} and Y_{lcQ} are the lower-triangular Toeplitz matrices of $y_{lcI}(k)$ and $y_{lcQ}(k)$, respectively.

Model-free ILC begins with the following optimization problem to determine the optimal filter $\tilde{\alpha}_i$,

$$\begin{aligned} \underset{\tilde{\alpha}_i}{\text{minimize}} \quad & \|\hat{y}_{i+1} - y_d\|_2^2 + r \|\tilde{\alpha}_i\|_2^2 \\ \text{subject to} \quad & \hat{y}_{i+1} = y_i + Y_{lc} \tilde{\alpha}_i \end{aligned} \quad (6)$$

where r is a weight on the input changes, and where y_d denotes the desired output vector which is expressed in terms of the desired I and Q waveforms:

$$y_d = \begin{pmatrix} y_{dI} \\ y_{dQ} \end{pmatrix} = \begin{pmatrix} a_d \cos \varphi_d \\ a_d \sin \varphi_d \end{pmatrix}, \quad (7)$$

where a_d and φ_d are respectively the desired output amplitude and phase trajectories in the flat-topped region (colored area in Fig. 2). We choose a smoothed amplitude trajectory as follows,

$$a_d(k) = a_0 e^{-(k-1)/k_0} + a_{ref} (1 - e^{-(k-1)/k_0}), \quad 1 \leq k \leq N, \quad (8)$$

where a_{ref} is the desired amplitude at the flat-top, and a_0 and k_0 are constants. A similar trajectory is defined for the phase. The reason for selecting such smooth trajectories is to avoid discontinuity which may result in large actuation to obtain flatness. The limits on the input signals are excluded from the constraints since they are inactive and can be treated separately.

As stated in [7], the following specific linear combination reduces the prediction error and allows Y_{lc} to be of full rank at every trial throughout the learning process,

$$U_{lc} = U_i - U_{i-1} + \gamma U_0, \quad (9)$$

and the linear combination matrix for the output would be

$$Y_{lc} = Y_i - Y_{i-1} + \gamma Y_0, \quad (10)$$

where γ is a tuning factor, and where U_i and U_0 are Toeplitz matrices of u_i and u_0 , respectively, with u_0 denoting the initial input signal. Similar definitions apply for Y_i and Y_0 .

The explicit solution to the optimization problem (6) can be readily calculated,

$$\tilde{\alpha}_i^* = (rI + Y_{lc}^T Y_{lc})^{-1} Y_{lc}^T (y_i - y_d). \quad (11)$$

Therefore, the input I and Q sequences are updated as

$$u_{i+1} = u_i + U_{lc} \tilde{\alpha}_i^*, \quad (12)$$

with defined bounds on the inputs.

EXPERIMENTAL RESULTS

As stated at the beginning, the control objective is to generate flat pulses at the klystron output. The actuation and measurement are based on I and Q waveforms, however we are mostly interested in amplitude and phase due to their physical meaning. Before running the ILC, the loop phase of the RF system was calibrated and set to zero, such that I and Q channels were approximately decoupled. Since the klystron is nonlinear with respect to amplitude, the inputs u_i are small signals around the operating point of the klystron. The algorithm begins with slightly exciting the input I and Q channels by small steps u_{I0} and u_{Q0} , respectively, which are constant over the whole pulse length.

Figure 3 shows the RF amplitude and phase waveforms after 30 iterations compared to the initial waveforms. The variance of the pulse over the flat-topped region is used as a measure of flatness. Figure 4 illustrates the standard deviation of the amplitude and phase pulses as the iteration advances. The iteration number “0” corresponds to the initial waveforms. The flatness has been improved by a factor of 3 and 5 for the amplitude and phase pulse, respectively. After around 20 iterations, the tracking error converges to the residual error which comes from the pulse to pulse noise through the system. The corresponding generated input waveforms are depicted in Fig. 5. As we can see, the resulting input signal is different from the nominal rectangular pulse.

SUMMARY

For multi-bunch operation of a pulsed mode FEL, in which several electron bunches are accelerated within an RF pulse, it is often required that the amplitude and phase remain constant over the pulse length so that the bunches achieve the same energy level. For pulsed mode machines, like the SwissFEL, where the pulse length is relatively short and no intra-pulse digital feedback is feasible, Iterative Learning Control is applicable to achieving the control objectives. In this paper, we investigated a model-free ILC approach and its application in RF pulse flattening of the klystron output. The proposed algorithm is applicable to RF waveform control in the other parts of the system, such as the RF pulse compressor and the Cavity pickups.

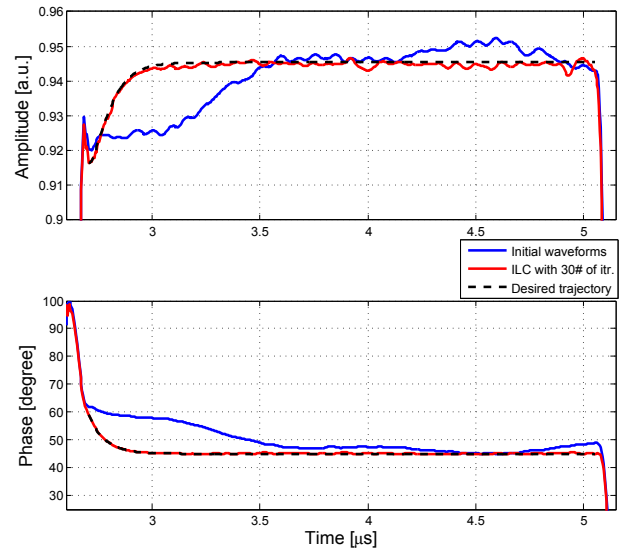


Figure 3: The klystron output amplitude and phase waveforms after 30 iterations (in red). The blue signal denotes the initial output waveforms (iteration #0).

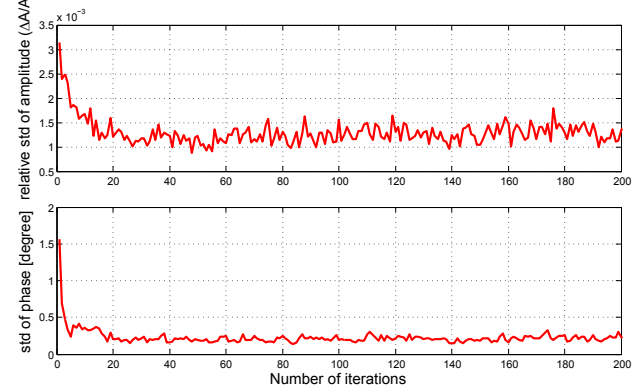


Figure 4: The standard deviation of flat-top amplitude and phase versus number of iterations.

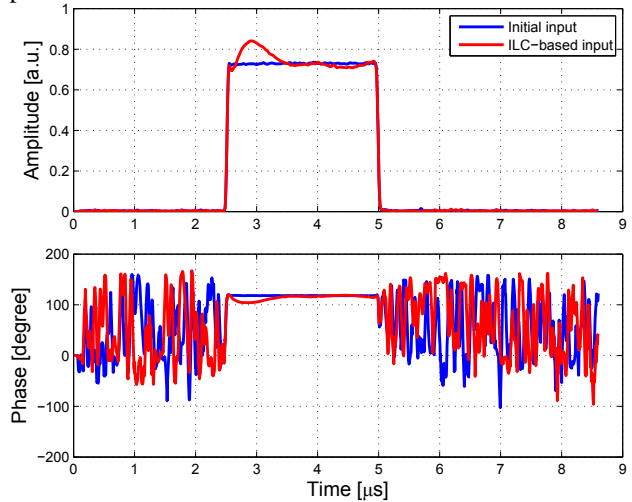


Figure 5: The input amplitude and phase waveforms generated by ILC (in red). The blue signal denotes the initial input waveforms (iteration #0).

ACKNOWLEDGMENT

The authors would like to thank the LLRF and the RF team who made this research possible, and special thanks goes to Roger Kalt for his help and support.

REFERENCES

- [1] Romain Ganter et al., SwissFEL Conceptual Design Report, PSI, Villigen, Switzerland, 2010.
- [2] M. Uchiyama, “Formulation of high-speed motion pattern of a mechanical arm by trial”, *Trans. SICE (Society of Instrument and Control Engineers)*, vol.14, no. 6, pp.706-712, 1978 (in Japanese).
- [3] D. A. Bristow et al. “A survey of iterative learning control”, *IEEE Control Systems Magazine*, vol.26, no.3, pp.96–114, June 2006.
- [4] N. Amann et al., “Iterative learning control using optimal feedback and feedforward actions”, *International Journal of Control*, vol. 65, no. 2, pp.277–293., 1996.
- [5] J.D. Ratcliffe et al., “Fast norm optimal iterative learning control for industrial applications”, *American Control Conference, 2005. Proceedings of the 2005*, pp.1951–1956 vol. 3, 8-10 June 2005.
- [6] S. Kichhoff et al., “An Iterative Learning Algorithm for Control of an Accelerator Based Free Electron Laser”, *Proc. of the 47th IEEE Conference on Decision and Control*, Cancun, Mexico, Dec. 9-11, 2008.
- [7] P. Janssens et al., “Model-free iterative learning control for LTI systems with actuator constraints”, *Proc. of the 18th IFAC World Congress*, pp.11556-11561, Milano, Italy, August 28–September 2, 2011.

DEVELOPMENT OF PHOTOCATHODE DRIVE LASER SYSTEM FOR RF GUNS IN KU-FEL*

H. Zen[#], S. Suphakul, T. Kii, H. Ohgaki, Institute of Advanced Energy, Kyoto University, Gokasho, Uji, Kyoto, 611-0011, Japan

R. Kuroda, Y. Taira, National Institute of Advanced Industrial Science and Technology (AIST), 1-1-1 Umezono, Tsukuba, Ibaraki 305-8568, Japan

Abstract

A photocathode drive laser system has been developed for RF guns in Institute of Advanced Energy, Kyoto University. Those RF guns require single-bunch and multi-bunch operation. Therefore, single-pulse and multi-pulse performances of the drive laser system have been examined for our laser system. As the result of test experiment, we have succeeded in generating UV laser pulses with micro-pulse energy of 205 μJ /micro-pulse in the single-pulse condition. On the other hand, in the multi-pulse condition, UV pulse lasers having flat macro-pulse shape with micro-pulse energy of 3.9 μJ and macro-pulse duration of 5 μs were successfully generated. Those values satisfy our target value required for the photocathode drive laser system and developed drive laser system will be used for electron beam generation.

INTRODUCTION

We have been developing an oscillator type mid-Infrared free electron laser (MIR-FEL) to contribute energy related sciences in Kyoto University [1]. The facility utilizes a 4.5-cell thermionic RF gun for its electron source. The gun can provide us high energy (~ 9 MeV) and multi-bunch electron beam with relatively long macro-pulse duration (~ 7 μs). However, the bunch charge is limited to less than 40 pC because of serious backbombardment effect [2]. Even with the limited bunch charge, we could provide MIR-FEL beam in the wavelength region from 5 to 20 μm . In addition to the MIR-FEL, development of THz-FEL has been started [3].

Two upgrade projects of MIR-FEL by modifying the thermionic RF gun have been carried out as well. One is a triode RF gun project [4] and the other is a photocathode project [5]. The triode RF gun uses a thermionic cathode and additional small cavity around the cathode. A numerical simulation predicted that the backbombardment effect could be solved by the proposed triode configuration [4]. The photocathode project is much simpler than the triode one. The photocathode RF gun driven by pico-second laser is completely free from the backbombardment effect and can produce electron beams with higher bunch charge and longer macro-pulse duration than the thermionic one. Initially we planned to install a modified BNL-type 1.6-cell RF gun to upgrade the MIR-FEL [6]. The gun cavity was manufactured in 2008. However, because of growing scientific interest in

THz region, we changed our plan and decided to use the manufactured 1.6-cell gun as an electron source of compact single pass THz-FEL [3].

For the photocathode upgrade project of existing MIR-FEL device, we need to develop multi-pulse laser for oscillator FEL. On the other hand, single-pulse laser is enough for single pass THz-FEL. Our early work on the multi-pulse laser system was reported in the proceedings of FEL2012 [7]. At that time, we tried to develop a four-pass amplifier using a laser diode (LD) pumped amplifier module. In this scheme, however, we suffered from a self-oscillation of the amplifier module. Therefore we modified the amplifier configuration to have two double-pass amplifiers and installed nonlinear crystals for second harmonic generation and fourth harmonic generation. In this paper we will report the performance of our photocathode drive laser system.

PHOTOCATHODE DRIVE LASER SYSTEM

In this section, target values of our photocathode drive laser system and system configuration are described.

Target Values

There are so many choices for photocathode material and then the required performance of its drive laser strongly depends on the quantum efficiency (QE) of the photocathode. In this work, we assume usage of high QE photocathode (e.g. Cs-Te: $\text{QE} > 1 \times 10^{-2}$) for the RF gun of multi-bunch operation and copper photocathode ($\text{QE} \sim 1 \times 10^{-4}$) for the RF gun of single-bunch operation. Then we set the target bunch charge as 1 nC for both cases. Therefore the target micro-pulse energy of drive laser can be calculated as 0.47 μJ for the multi-bunch case and 47 μJ for the single-bunch case at the laser wavelength of 266 nm. The main parameters are shown in Table 1.

The maximum repetition rate of macro-pulse is given by the maximum repetition rate of RF power source used to drive the RF gun, which is 10 Hz in KU-FEL. The repetition rate of micro-pulse must be harmonics of 29.75 MHz which is a roundtrip frequency of optical cavity used for MIR-FEL. The number of micro-pulse determines the number of FEL amplification in the FEL optical cavity. A numerical simulation predicted that very high FEL gain ($\sim 300\%$) could be achieved with photocathode operation of 4.5-cell RF gun [5]. Therefore, not so large number of amplification is required but here we set the target number of micro-pulse to have more

*Work supported by the "ZE Research Program, IAE (ZE26A-22)."

[#]zen@iae.kyoto-u.ac.jp

than 100 FEL amplifications in the cavity even it may be too much for MIR-FEL experiment.

Table 1: Target Values of Photocathode Drive Laser System

Bunch Charge		1 nC/micro-pulse
Laser Micro-pulse Energy @266 nm	Multi-bunch	0.47 μ J (QE > 0.01)
	Single bunch	47 μ J (QE $\sim 1 \times 10^{-4}$)
Macro-pulse Repetition Rate		≤ 10 Hz
Micro-pulse Repetition Rate		$n \times 29.75$ MHz
Number of Micro-pulse (Multi-bunch case)		$> n \times 100$

System Configuration

We used a mode-locked Nd:YVO₄ laser (GE-100-VAN-89.25MHz-CLX-Flexible AOM, Time-Bandwidth) as a laser oscillator. This laser's specifications are summarized in Table 2. The repetition frequency 89.25 MHz is one thirty second of the RF frequency of KU-FEL linac (2856 MHz) and third harmonics of roundtrip frequency of the FEL resonator cavity. The laser system was designed to synchronize the phase timing between the RF signal of KU-FEL and the repetition frequency of the drive laser by controlling the resonator length of the mode-locked laser. This oscillator has a built-in Acousto-optic modulator (AOM) for multi-pulse laser generation. The amplitude of pulse train generated from the oscillator can be arbitrary modulated by the AOM combined with an arbitrary waveform generator (AFG3251, Tektronix).

A beam alignment feedback system (Aligna4D, TEM) has been installed in the downstream of the AOM to stabilize both the laser beam position and angle whose drift can be caused by temperature drift of the AOM [7]. After that, two double-pass amplifier using a laser diode (LD) pumped amplifier (REA5006-2P1, CEO) which contains a Nd:YAG rod ($\phi 5 \text{ mm} \times 12.6 \text{ cm}$) is employed. Finally, amplified laser pulses are injected to nonlinear crystals for second harmonic generation (SHG) and fourth harmonic generation (FHG). In this work, we used KTP

crystal for SHG and KDP crystal for FHG. The photographs and schematic diagram of the multi-bunch laser system are shown in Fig. 1 and 2, respectively.

Table 2: Specification of Laser Oscillator

Wavelength	1064 nm
Repetition Rate of Micro-pulse	89.25 MHz (3 × 29.75 MHz)
Average output power	~600 mW
Pulse Duration	7.5 ps-FWHM
M ² value	< 1.13 (x and y)

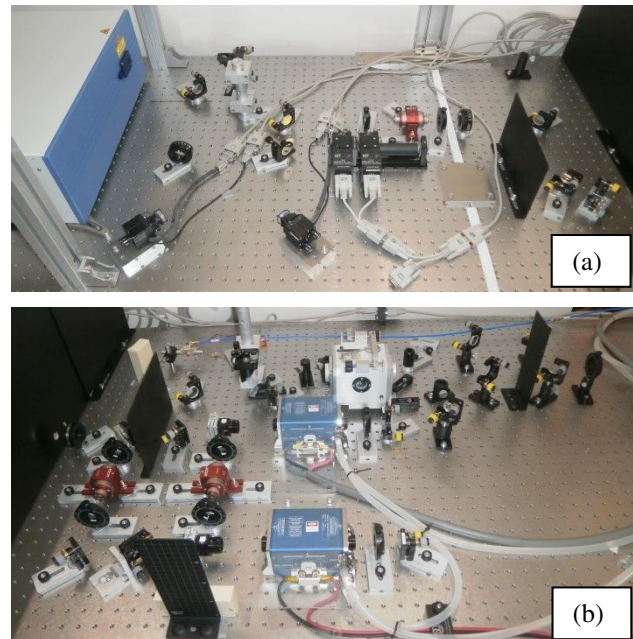


Figure 1: Photographs of the developed drive laser system. (a) Upstream side including the Nd:YVO₄ oscillator and the beam alignment feedback system. (b) Downstream side including the double-pass amplifiers and harmonic generation crystals.

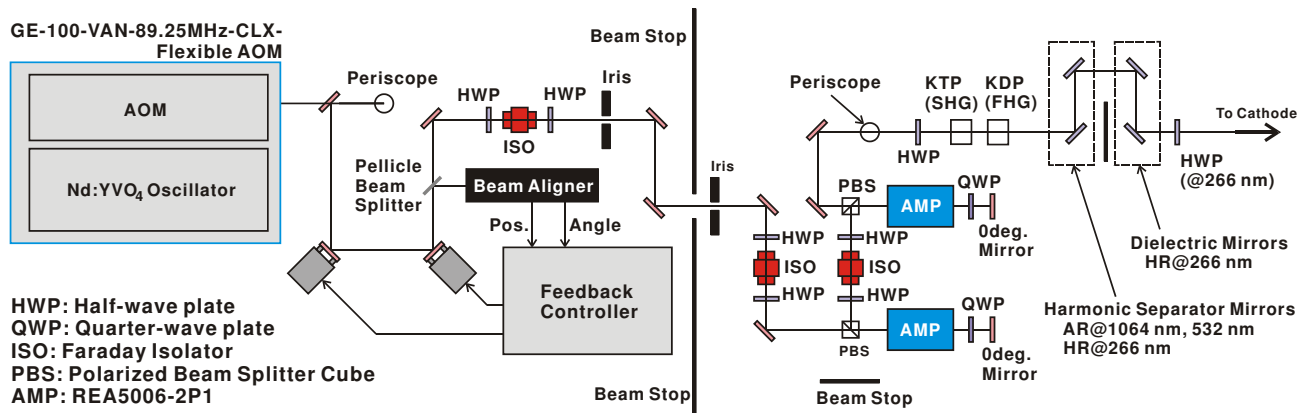


Figure 2: Configuration of photocathode drive laser system.

PERFORMANCE TEST

The performances of developed laser system were tested under the single-pulse and multi-pulse conditions.

Single-pulse Condition

Single optical pulses were selected by AOM from 89.25-MHz pulse train generated by the mode-locked oscillator and sent to the two double-pass amplifiers. Figure 3 shows the observed laser pulse energy after two double-pass amplifiers as a function of LD current of 2nd amplifier with fixed LD current of 1st amplifier (80A). The laser pulse energy was measured by pyroelectric energy meter (PE10BB, Ophir). At the low LD current condition up to 65 A, the laser pulse energy exponentially increased on the LD current and its gain was 3 times/10 A. With the higher LD current than 65 A, the laser pulse energy shows saturation tendency, i.e. departure from exponential curve. The maximum fundamental pulse energy recorded was 2.5 mJ/micro-pulse. At the same time, the pulse energies after the second and the fourth harmonic generation crystals were measured. The results plotted with SHG and FHG conversion efficiencies are shown in Fig. 4. The maximum pulse energy after SHG and FHG were 686 and 205 μJ , respectively. The highest conversion efficiencies of SHG and FHG in this system were 38% at the fundamental pulse energy of 890 μJ and 38% at the second harmonic pulse energy of 338 μJ , respectively. The maximum overall conversion efficiency from IR to UV was around 14% at the fundamental pulse energy of 890 μJ . The achieved maximum pulse energy after FHG was much higher than our requirement, 47 μJ /micro-pulse. Here we conclude that the developed laser system has enough high performance for single bunch operation with copper photocathode whose quantum efficiency is around 1×10^{-4} .

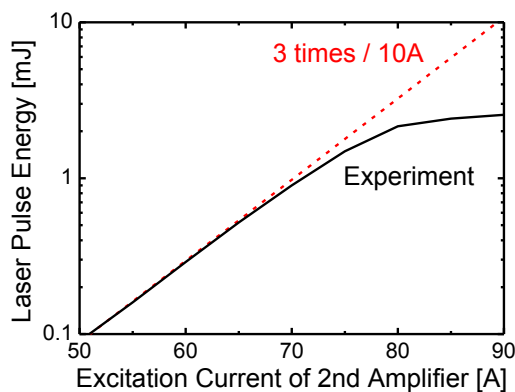


Figure 3: Laser pulse energy after two double-pass amplifiers as a function of LD excitation current of 2nd amplifier in case of single-pulse condition. The excitation current of LD in the 1st amplifier is fixed to 80 A.

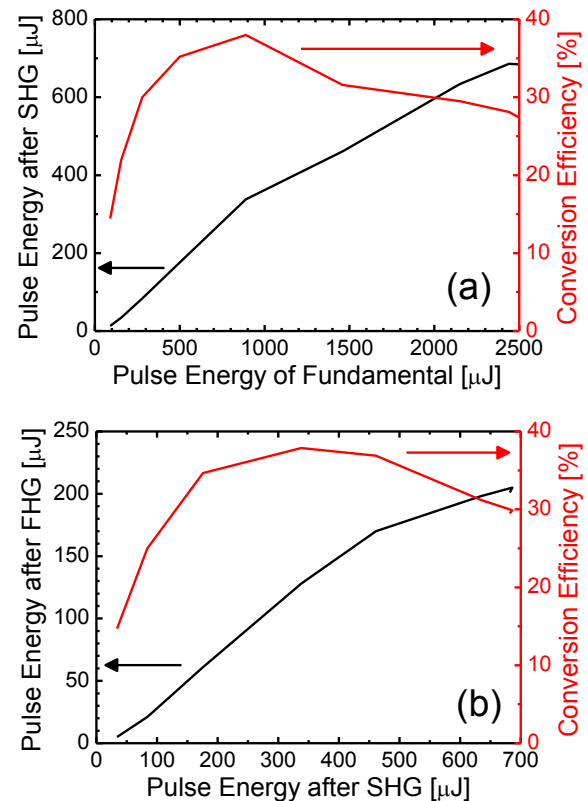


Figure 4: Laser pulse energy after SHG and FHG plotted with their conversion efficiencies as a function of incident laser pulse energy to the crystals. (a) Pulse energy after SHG and conversion efficiency of SHG. (b) Pulse energy after FHG and conversion efficiency of FHG.

Multi-pulse Condition

We tried to generate multi-pulse UV laser with a rectangular macro-pulse shape by modulating the built-in AOM. The macro-pulse structure and the macro-pulse energy was measured by an ultrafast photodetector (UPD-300-UD, ALPHALAS) and the pyroelectric energy meter (PE10BB, Ophir), respectively. A result is shown in Fig. 5. The pulse shape of UV laser is plotted with the control voltage of the AOM. As shown in Fig. 5 (a), almost flat macro-pulse could be generated by providing optimized control voltage to the AOM. The macro-pulse energy and the macro-pulse duration were 1.75 mJ and 5 μs , respectively. Then the micro-pulse energy was calculated as 3.9 μJ from those values and micro-pulse repetition rate of 89.25 MHz. The micro-pulse energy and macro-pulse duration satisfy our target values which listed in Table 1. With this condition, we can generate electron beam with bunch charge of 1 nC from a photocathode having QE of 1.2×10^{-3} . In order to show the importance of optimization of the AOM modulation pattern, a result of UV pulse shape measurement under the condition of rectangular AOM modulation pulse is shown in Fig. 5 (b). Since the micro-pulse energy of IR laser pulses in the second amplifier module were very high, the optical pumping power given by the LD in amplifier module was insufficient to maintain laser gain

during the macro-pulse. Therefore the micro-pulse energy after second amplifier rapidly decreased during the macro-pulse. Therefore we need to optimize the modulation of AOM for generating UV laser pulse train having the rectangular macro-pulse structure.

In the optimized condition, the overall conversion efficiency from IR to UV can be estimated as 3% from the achieved UV micro-pulse energy (3.9 μ J/micro-pulse) and result of conversion efficiency measurement in single pulse condition shown in Fig. 4. By adding focusing optics before the nonlinear crystals and reducing the laser beam size on the crystals, the conversion efficiency in the multi-bunch condition can be increased. If we cannot use high QE photocathode, we need to optimize the laser beam size on the nonlinear crystals to have higher UV micro-pulse energy in the multi-pulse condition.

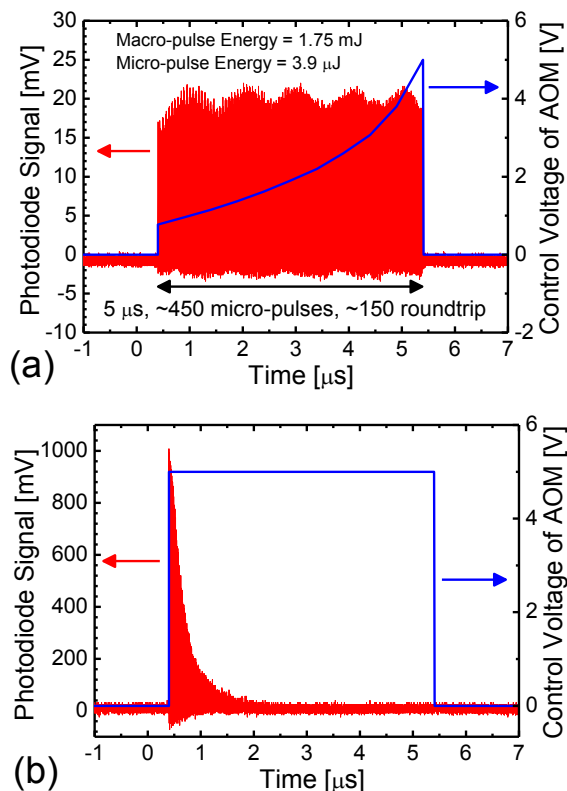


Figure 5: Measured UV pulse train with optimized amplitude modulation of AOM (a) and rectangular modulation of AOM (b). The periodic oscillation of peak value seen in figure (a) was caused by insufficient sampling speed of oscilloscope.

CONCLUSION

A photocathode drive laser system has been developed for photocathode RF guns in Institute of Advanced Energy, Kyoto University. The developed system consists

of an Nd:YVO₄ mode-locked oscillator with a built-in AOM, beam position stabilization system, two double-pass amplifiers and nonlinear crystals for harmonic generation. Performance tests have been conducted with single-pulse and multi-pulse conditions. In case of the single-pulse condition, the maximum IR micro-pulse energy and maximum UV micro-pulse energy were 2.5 mJ and 205 μ J, respectively. In the experiment, the maximum overall conversion efficiency from IR to UV was around 14%. In case of multi-pulse condition, we have succeeded in generating UV laser pulses having flat macro-pulse shape with 3.9- μ J micro-pulse energy and 5- μ s macro-pulse duration by applying optimum control voltage to the built-in AOM. Those values satisfies our requirements, i.e. generation of electron beams having 1-nC charge per bunch, and the developed laser will be used as the photocathode drive laser of RF guns in Institute of Advanced Energy, Kyoto University.

ACKNOWLEDGMENT

This research was supported by ZE Research Program, IAE, Kyoto University (ZE26A-22).

REFERENCES

- [1] H. Zen, et al., "Present Status of Kyoto University Free Electron Laser," in *Proc. 35th Int. Free-Electron Laser Conf.*, New York, 2013, pp. 711-714
- [2] H. Ohgaki, et al., "First Lasing of MIR-FEL at Kyoto University," in *Proc. 30th Int. Free-Electron Laser Conf.*, Gyeongju, 2009, pp. 4-7.
- [3] S. Suphakul, et al., "Development of Compact THz-FEL system at Kyoto University," in *These Proceedings: Proc. 36th Int. Free-Electron Laser Conf.*, Basel, 2014, TUP057.
- [4] T. Shiiyama, et al., "A Triode-type Thermionic RF Gun for Drastic Reduction of Back-streaming Electrons," in *Proc. 29th Int. Free-Electron Laser Conf.*, Novosibirsk, 2008, pp. 398-401.
- [5] H. Ohgaki, et al., "Upgrade Design of KU-FEL Driver Linac Using Photo-cathode RF-Gun," in *Proc. 26th Int. Free-Electron Laser Conf.*, Trieste, 2004, pp. 454-457.
- [6] H. Ohgaki, et al., "Numerical Evaluation of Oscillator FEL with Multibunch Photo-Cathode RF-Gun in Kyoto University," in *Proc. 29th Int. Free-Electron Laser Conf.*, Novosibirsk, 2008, pp. 390-393.
- [7] K. Shimahashi, et al., "Development of Multi-Bunch Laser System for Photocathode RF Gun in KU-FEL," in *Proc. 34th Int. Free-Electron Laser Conf.*, Nara, 2013, pp. 173-176.

Cu AND Cs₂Te CATHODES PREPARATION AND QE HISTORY AT THE SwissFEL INJECTOR TEST FACILITY

J. Bossert, R. Ganter, M. Schaer, T. Schietinger, PSI, Villigen, Switzerland

Abstract

The installation of a load-lock chamber attached to the RF photoinjector gives the possibility to carefully prepare the metallic cathodes under vacuum and also to use semiconductor cathodes like Cs₂Te cathodes which cannot be transported through air. An annealing procedure of copper cathodes to desorb water guarantees a good reproducibility of the initial quantum efficiency (QE) above 10^{-4} . Cs₂Te cathodes were tested in the same gun and showed that they also fulfill the emittance requirements of SwissFEL but with a much higher QE (1-2%). In order to better understand and improve the deposition procedure at PSI (based on a CERN recipe), surface analysis were performed and are discussed in the paper (SEM, EDX, interferometry, microscopy).

INTRODUCTION

The main advantage of semi-conductor cathodes (like Cs₂Te) over metallic cathodes (copper) is the increase in quantum efficiency by several orders of magnitudes (QE). The laser energy required for photoemission can then be reduced and invested elsewhere like in a better shaping (which always consumes laser power) or in multi bunch operation. The main drawbacks of Cs₂Te cathodes is however the increase in slice emittance and the short lifetime (rapid decrease of QE). At SwissFEL we would like to have both cathode options (Cu and Cs₂Te) ready for the future operation. In this paper we present the preparation procedures for both cathode materials together with their QE performances.

EXPERIENCE WITH COPPER CATHODES AT THE SITF

The SwissFEL Injector Test Facility (SITF) is a 250 MeV accelerator to test components and beam quality for SwissFEL. SITF produces beam since 2009 using copper cathode plugs installed in a RF photo-injector [1]. Cathodes are illuminated with laser pulses at 262 nm with a duration of $\sigma_t = 4$ ps rms (Gaussian), a nominal diameter of $\sigma_r = 250 \mu\text{m}$ (flat top transverse profile) and a repetition rate of 10 Hz. The electric field at the cathode surface during illumination is about 52 MV/m.

Until 2013, SITF was operated without any load-lock system and the QE directly after cathode installation was not reproducible and sometimes below the specification threshold of $\text{QE}_{\min} \sim 7 \cdot 10^{-5}$, see for example Cu₇ and Cu₈ in Fig. 1. Only cathode Cu₃ has behaved exceptionally well for a very long period. After the installation of the load-lock chamber in July 2013, we have established a cleaning and annealing procedure with temperature as high as 250°C [1] which guarantees a

starting QE always above 10^{-4} . This could be demonstrated on more than 5 cathodes. The duration until the QE decreases below $7 \cdot 10^{-5}$, is between 50 and 150 days (see Cu₁₉ and Cu₁₇ in Fig. 1).

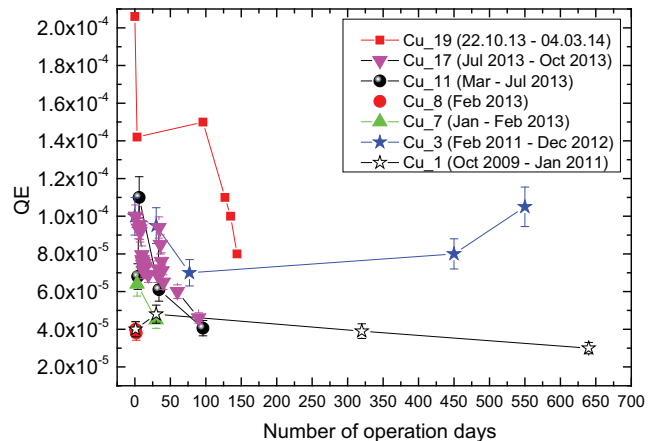


Figure 1: Evolution of the QE of copper cathodes installed in the injector since 2009. The load-lock chamber has been installed in July 2013.

The future laser system of SwissFEL (Yb:CaF₂ crystal) will be more powerful so that the minimum required QE will be as low as $4 \cdot 10^{-5}$. In view of Fig. 1, this would mean that the duration between two consecutive cathode exchanges should exceed 100 days. This would correspond to one shift shutdown every 100 days. Indeed, the exchange of cathodes with the load-lock takes only a few minutes but the RF conditioning of a new cathode still takes several hours.

Cs₂Te PREPARATION AND PERFORMANCES AT THE SITF

Cs₂Te Cathode Preparation

The deposition procedure used at PSI is copied from a CERN [2,3] recipe where 15 nm of tellurium and 25 nm of caesium are successively evaporated directly on the copper cathodes [4]. The copper cathodes undergo beforehand the same annealing procedure as for operation with pure copper cathode. An aperture mask limits the deposition area to a disc of 1cm diameter (Fig. 2). The cathodes can then be transferred from the evaporation chamber to the gun load-lock via a vacuum suitcase. The initial pressure in the evaporation chamber is around $3 \cdot 10^{-10}$ mbar going up to $1 \cdot 10^{-8}$ mbar during evaporation. The base pressure in the gun during operation is around $1 \cdot 10^{-9}$ mbar when RF is powered.



Figure 2: Evaporation chamber with the cathode holder and micro balance on the left and the Cs evaporation source on the right. (Top); Two cathodes with a 1 cm diameter disc of Cs₂Te (Bottom).

Cs₂Te Cathode Performances

Five Cs₂Te cathodes were prepared at PSI based on the above mentioned procedure. The two cathodes tested in the SITF gun started with a QE above 1% (Fig. 3). The laser energy had to be attenuated from typically 5 - 15 microjoules (in the case of normal copper cathode) to few tens of nanojoules showing the enormous spare potential in terms of laser energy. This laser energy could then be invested in a better shaping of the transverse and longitudinal profile of the laser pulses.

Two Cs₂Te cathodes were tested in the gun during one week with a few months interval. The first cathode produced and tested in the RF photoinjector (Cu(Cs₂Te)₁₃) had already a drop of the QE after 50 hours operation which might be related to a local surface contamination. For the second cathode (Cu(Cs₂Te)₈) the level of vacuum during deposition was improved and the QE stayed above 2 % during the whole week of operation.

The main goal of these tests was to compare the slice emittance obtained with Cs₂Te to the one obtained with copper in the same RF photoinjector. In fact, for both Cs₂Te cathodes the measured slice emittance increased only by 20 to 30% in comparison to what is typically obtained with copper cathodes. These results are presented in a companion paper [5].

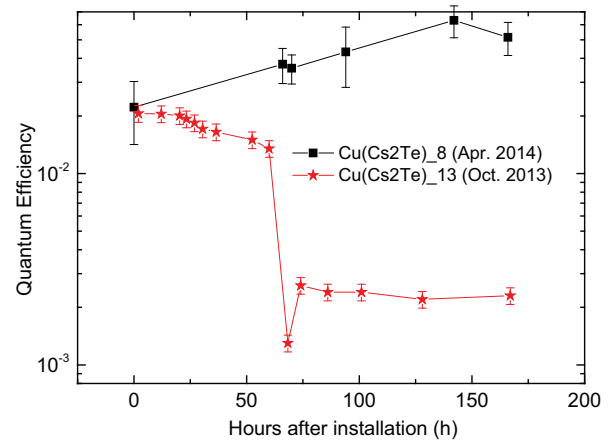


Figure 3: Evolution of the QE of Cs₂Te cathodes installed in the RF photo injector of the SITF in two different periods. (262 nm; 200 pC; $\sigma_{t,laser}=4$ ps rms; 10 Hz).

Cs₂Te SURFACE ANALYSIS

The QE maps taken during the tests of Cu(Cs₂Te)₁₃ and Cu(Cs₂Te)₈ present non uniformities as shown in Fig. 4 (bottom). Such non-uniformities are not good for beam quality and might be related to the deposition procedure.

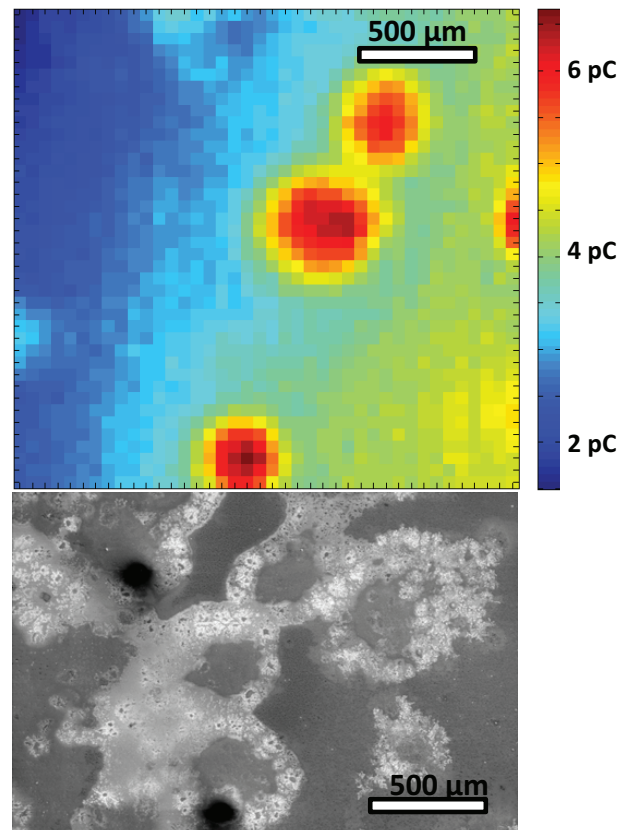


Figure 4: QE map of Cu(Cs₂Te)₁₃ measured in the gun by scanning small laser spots with constant energy (Top). SEM picture (with secondary electrons) of the same cathode after exposure to air (Bottom).

In order to better understand what causes these non-uniformities a series of surface analysis of the cathode were performed. As soon as the cathode is brought to air for surface analysis the oxidation is changing the surface so that the interpretations given below are only hypothesis. The scanning electron microscope picture of Fig. 4 exhibits many structures present on the surface with about the same size as the non-uniformities seen on the QE map.

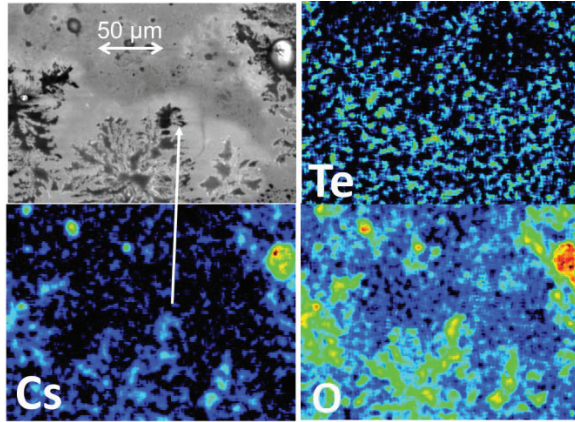


Figure 5: EDX analysis of $\text{Cu}(\text{Cs}_2\text{Te})_{13}$ cathode showing the distribution of Cs (caesium), O (oxygen) and Te (Tellurium). The SEM reference picture (with back scattered electrons) is in the upper left corner.

EDX analysis (energy dispersive X-ray spectroscopy) revealed that these bright structures observed in Fig. 4 top picture correspond to high concentration of caesium Cs and oxygen. Indeed the structure indicated by the arrow on Fig. 5 corresponds to Cs and oxygen. Oxygen is just going preferentially to the area with high Cs content when cathode is brought to air. At the difference of Cs the Te is much more spread over the entire area (see upper right picture of Fig. 5). This is consistent with the way Cs_2Te layer grows on copper substrate (island type of formation) [6].

Further SEM analysis of Cs alone deposited on copper and Te alone deposited on copper (Fig. 6) confirm this tendency that Cs does not spread over copper surface but rather grow by island on specific nucleation sites (see Fig. 6, center). Te is much more uniformly distributed even if some granularity is also visible (Fig. 6, Top). The SEM picture of the Cs_2Te layer is then a combination of the island with granularity (Fig. 6, Bottom).

These SEM pictures were however taken after exposure to air and it is not clear what comes from the air oxidation and what was the Cs non uniformity just after deposition in vacuum.

Finally, interferometry analysis of the Cs_2Te deposited layer where performed to quantify the increase in roughness in comparison to the copper substrate. In fact we observed a rise of the dark current from 1.5 nC to 1.6 nC when going from copper to Cs_2Te . This increase can either come from a lowering of the work function or from the increase of the surface roughness.

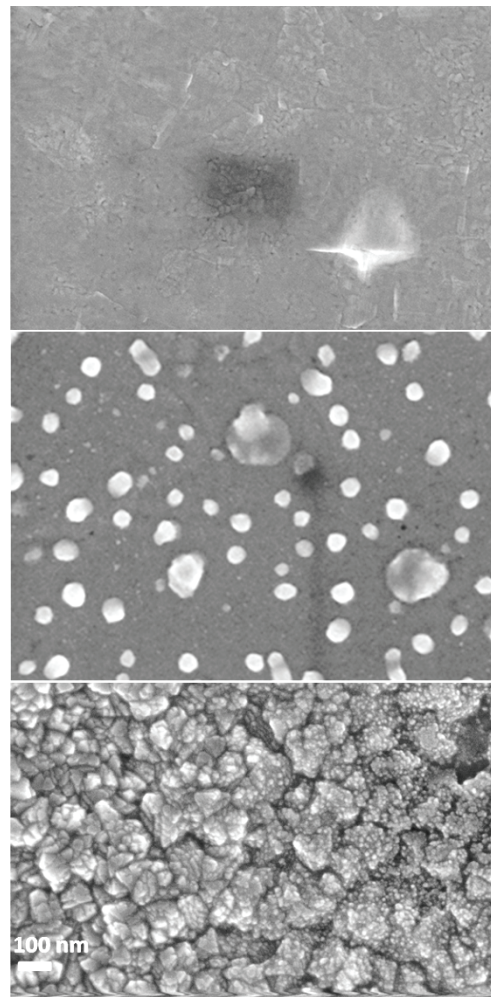


Figure 6: SEM pictures of 15 nm Te deposited on Cu (Top), 25 nm of Cs deposited on Cu (middle) and 40 nm of Cs_2Te compound on copper.

The interferometry analysis have shown that the average roughness R_a went from $R_a \sim 3$ nm for pure copper to $R_a \sim 15$ nm once Cs_2Te was deposited (Fig. 7). It is however not clear which part of the roughness is due to oxidation due to exposure to air and what was already present under vacuum. Nevertheless an increase of the roughness could well explain the observed increase of dark current.

Cs_2Te LIFETIME AND REJUVENATION

In order to be compatible with SwissFEL operation the Cs_2Te cathodes need to maintain a QE above 0.1 % for at least one week and this at a repetition rate of 100 Hz. Exchanging the cathode every week (4 cathodes can be stored in advance) should be possible for standard operation. The measurements done in the SIFT gun and shown in Fig. 3 were for 10 Hz repetition rate. Cs_2Te cathodes are much more sensitive to contamination than copper, especially to oxygen contamination [6] [7]. Lifetime measurements were done in a test chamber where the applied electric field was only 1 kV/cm so that

space charge limited regime was already observed for charges above a few pC.

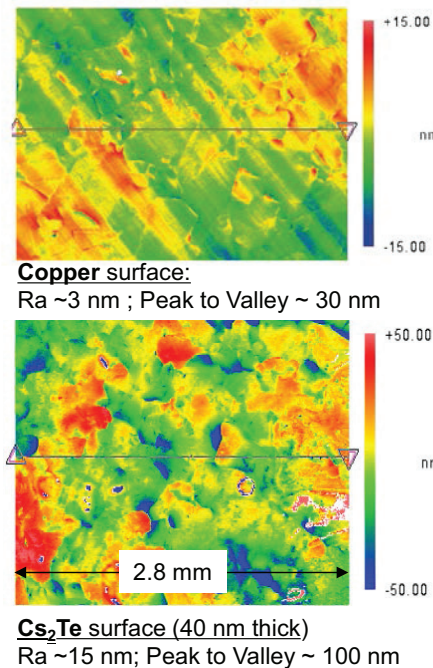


Figure 7: Interferometry measurements of a copper cathode surface (top) and of the Cs₂Te layer surface (bottom).

That is to say for laser energies above 1 nJ, the QE started to decrease due to space charge screening effect (Fig. 8). In addition the Schottky effect which influences the QE by lowering the barrier of potential is much less important for 1 kV/cm than in the RF gun where the extracting field is around 52 MV/m.

Nevertheless Fig. 8 shows that a QE of 0.1% is reached after 200 hours of operation at a pressure of 1.4e-8 mbar (the initial QE was around 1%). After 200 hours, an annealing procedure of 10 hours at 250°C has been applied to the cathode. This had the effect to bring back the QE to its initial value. This treatment was tested on a second cathode with the same result so that such annealing could be a sort of rejuvenation procedure to retrieve QE. It is however not clear what is the effect of annealing on the QE map and also how many times it could be applied. Most probably, the heating of the cathode helps to remove contaminants (oxygen based) present in vacuum and which accumulate on the cathode surface.

CONCLUSION

With the load-lock chamber installed at the RF photo-injector of SITF, one could clean copper cathode under vacuum and get QE above 1.e-4 and prepare Cs₂Te with QE above 1%. Using Cs₂Te photocathodes instead of copper improves the QE by a factor 100 at the cost of 20 % emittance increase which is still within the requirements of SwissFEL operation. QE maps of Cs₂Te

cathodes showed however non uniformities which might be explained by non-uniform spreading of Cs over the Te layer. Lifetime test at 100 Hz still need to be carried out but Cs₂Te is a valid cathode candidate for SwissFEL operation.

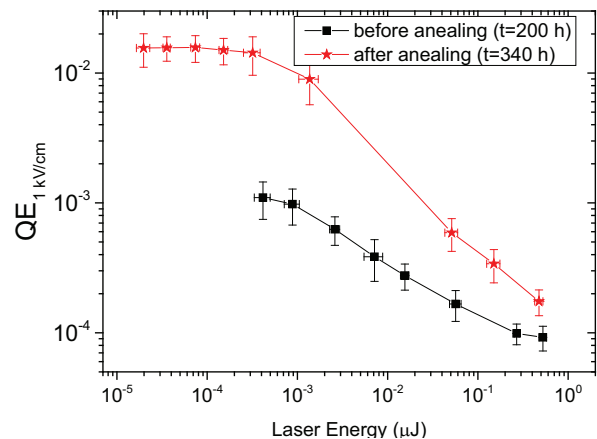


Figure 8: QE versus illuminating laser energy (266 nm, $F_{\text{cathode}}=1$ kV/cm DC; annealing temperature = 250 °C, $P=1.4\text{e-}8$ mbar).

ACKNOWLEDGMENTS

The authors would like to acknowledge Sybille Spielmann-Jäggi, Roland Bruetsch-Sutter and Anja Weber of PSI for the interferometry, EDX and SEM measurements. The authors are very grateful to Eric Chevallay from CERN for the detailed explanation of the Cs₂Te deposition procedure.

REFERENCES

- [1] R. Ganter *et al.*, "SwissFEL Cathode Load-lock System" in *Proc. 35th Int. Free-Electron Laser Conf.*, New York, USA, 2013, pp. 259-262.
- [2] E. Chevallay, Private Communication.
- [3] E. Chevallay *et al.*, "Photo-cathodes for the CERN CLIC Test Facility" in *Proc. 19th Int. Linear Accelerator Conf.*, Chicago, USA, 1998, TH4046.
- [4] R. Ganter *et al.*, SwissFEL Cs₂Te Cathode Preparation Procedure, Report No. FEL-GR16-173, 2013.
- [5] E. Prat *et al.*, "Thermal Emittance Measurements at the SwissFEL Injector Test Facility" in *These Proceedings: 36th Int. Free-Electron Laser Conf.*, Basel, Switzerland, 2014, THC02.
- [6] A. D. Bona *et al.*, *Appl. Phys.* **80** (1996).
- [7] D. Sertore *et al.*, *Nucl. Inst. And Meth. In Phys. Research A* **445**, 422 (2000).

PHOTOEMISSION STUDIES OF NIOBIUM AND LEAD PHOTOCATHODES USING PICOSECOND UV LASER*

R. Xiang[#], A. Arnold, P. Lu, P. Murcek, J. Teichert, H. Vennekate, HZDR, Dresden, Germany
R. Barday, HZB, Berlin, Germany

Abstract

We present the results of our investigations on superconducting photocathodes for superconducting rf injectors. Bulk niobium and lead film on niobium have been considered as the best candidates. The quantum efficiency (QE) at room temperature has been measured with 258 nm UV laser pulses of 14 ps duration. A QE of 10^{-4} has been obtained for the lead film. In order to improve the photoemission yield of niobium, new treatment methods, like Cs-activation and implantation with alkali metals, have been applied and the results are reported.

INTRODUCTION

In the past two decades, superconducting RF photoinjectors (SRF gun) have drawn a lot of attention because of their continuous-wave (CW), low emittance and high bunch charge operation. Different research projects have been launched at a growing number of accelerator laboratories [1-3]. A lot of efforts have been spent on solving the conflict between the normal conducting photocathodes and the superconducting cavity. The most direct and easiest way is to use superconducting materials as photocathodes. Previous experimental results showed that lead and niobium are the most promising candidates [4,5].

At HZDR, Cs_2Te is the standard photocathode material, and the drive laser has the wavelength of 258 nm in CW mode with adjustable repetition rate 100-500 kHz, and the pulse length is 14 ps FWHM. In this work, we used the present drive laser to investigate the photoemission properties of lead layer and bulk niobium, and tried to find a new recipe to improve the QE for niobium photocathode.

THIN LEAD LAYER

Lead is an attractive option for a low to moderate average current source. Arc deposition technique has been proved to be the best choice for coating [5]. QE investigation was done with the SRF gun drive laser for the lead layer produced at National Centre for Nuclear Research (NCBJ) of Poland [6].

Experimental Setup

The vacuum chamber used to measure the QE of

cathodes is shown in Fig. 1. It consists of an anode ring and a cathode in a parallel geometry with a spacing of 10 mm. The anode ring can be biased up to 400 V. The cathode is connected to a picoammeter Keithley6485 for the photocurrent measurement. The laser used for photoemission was focused on the cathode surface with a diameter of 1 mm, illuminating at normal incidence through the anode ring. A turbo-pump was used to keep the vacuum inside the chamber at a level of 10^{-7} mbar.

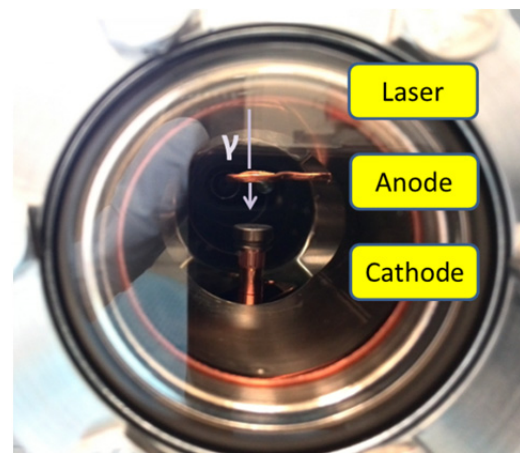


Figure 1: The experimental setup for QE measurement.

Preparation Progress

The 2 μm thick lead layer was coated on polycrystal niobium plugs. The mirror-like \varnothing 10 mm Nb plugs were mechanically polished with diamond suspension, resulting in a mean roughness of 25 nm.

The lead layer deposition was done at NCBJ (Swierk) using an UHV arc device equipped with a 30° bent plasma duct for droplets filtering at a deposition rate of 200 nm/min. Sample #C2 was additionally treated with three Ar plasma pulses in the IBIS rod plasma injector at NCBJ. Energy-dispersive X-ray spectroscopy (EDX) measurement showed 86 – 93 % lead in the 2 μm layer [6].

For all samples, the lead layers were briefly exposed to air between deposition, post-processing, SEM studies and QE measurement.

QE Measurement and Laser Cleaning

The QE of the layer was determined by measuring the laser power on the cathode and the current leaving the cathode. The bias on anode was adjustable from 30 V to 400 V.

*Work supported by the European Community under the FP7 programme (EuCARD-2, contract number 312453, and LA3NET, contract number 289191), and by the German Federal Ministry of Education and Research (BMBF) grant 05K12CR1.

[#]r.xiang@hzdr.de

For the sample #C1 the initial QE before laser cleaning was measured as 2×10^{-5} at 258nm (4.8 eV). Then a serious laser cleaning was performed with various laser power for different positions on the surface (Fig. 2). The maximum QE reached 1×10^{-4} after laser cleaning with laser intensity up to $1.2 \mu\text{J}/\text{mm}^2$. This is lower than the QE for the arc deposited Pb in the former work [5], where the authors obtained about 7×10^{-4} for 4.8 eV photons after cleaning with 248nm excimer laser up to $200 \mu\text{J}/\text{mm}^2$. The reason can be the lower laser density and shorter laser pulse duration in our experiment. The action time between the ps laser pulse and the metal surface may be too short for the cleaning task.

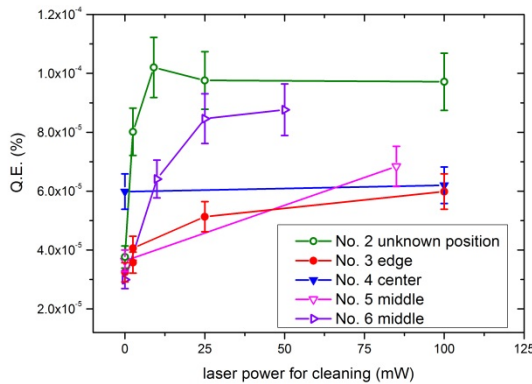


Figure 2: The laser cleaning for the Pb layer on #C1.

For the sample #C2, the original QE before laser cleaning was slightly more than that of #C1, 2.7×10^{-5} , and after cleaning with laser intensity up to $3.2 \mu\text{J}/\text{mm}^2$, the QE was limited to 6×10^{-5} @ 258nm (4.8 eV), lower than in case of #C1. Figure 3 shows the cleaning procedure vs. laser power. The photocurrent was measured with a weak laser of 0.6 mW for diagnostics. The higher power does not lead to much efficiency as expected.

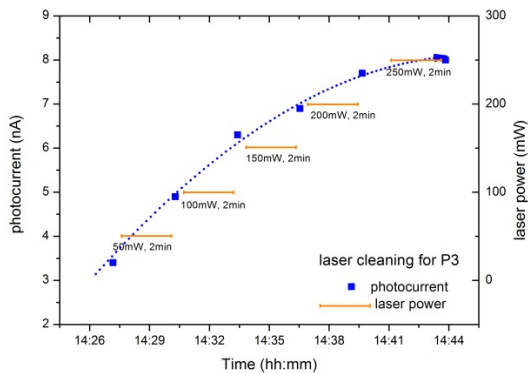


Figure 3: Laser cleaning progress for sample #C2. Photocurrent was measured by a weak laser with power of 0.6 mW. The anode was biased up to 200 V.

Test in SRF Gun

One Pb-coated Nb plug has been tested in the ELBE SRF gun. In this experiment, the cathode bias was -5kV, and the accelerating rf field of 5.2 MV/m was launched. A 4 nA beam current was achieved with 200 mW drive laser in repetition rate of 125 kHz. No obvious dark current was detected from the Pb layer.

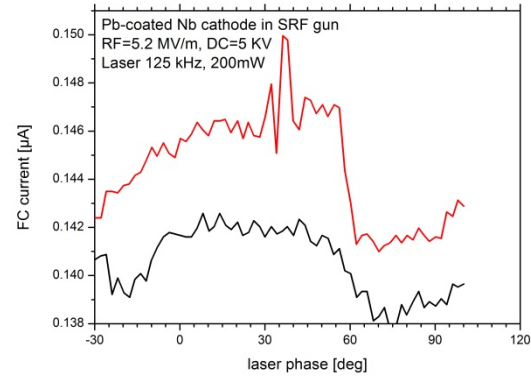


Figure 4: Phase scan during the beam test with Pb layer on Nb plug in ELBE SRF gun. The two curves were measured with the drive laser spot on different cathode positions.

BULK NIOBIUM CATHODE

Previous studies of photoemission in niobium have shown a small initial QE in level of 10^{-6} at 248 nm [7] and an exciting value of 10^{-4} for 248 nm though the high energy laser cleaning up to $0.84 \text{ mJ}/\text{mm}^2$ [4]. Here in our study, effort is made to look for a recipe to improve the QE for this wavelength range by reducing the work function of the bulk surface.

Niobium samples are 0.5mm thick bulk material of 99.9% purity, with a size $4.5 \text{ mm} \times 4.5 \text{ mm}$, mechanical polished to roughness of 10 nm, washed in solvents, ultrasonically cleaned and stored in dry air.

QE Measurement

The QE of virgin Nb after polishing and solvent cleaning was measured as 5.72×10^{-6} at 258 nm. This result is similar to the reported results [7]. In our measurement, the anode was set up to 5 kV (the electric field on cathode surface was 500 kV/m), lower than that in Smedley's experiments [4]. A range of bias values was used for QE measurement to establish the dependence of the QE on the electric field (Fig. 5). After one hour illumination, the QE increased slightly and the dependence changed also. The improvement may be caused by the laser cleaning effect.

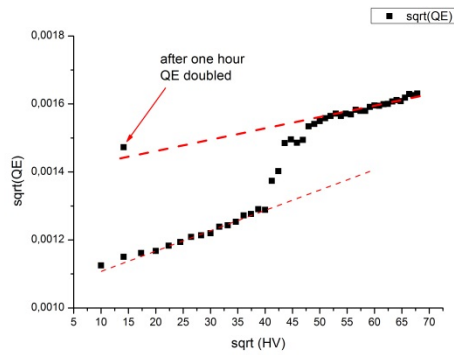


Figure 5: $(QE)^{1/2}$ vs $(bias)^{1/2}$ for mechanically polished Nb. The red lines are only used to guide viewer's eyes.

Activation with Cesium

In order to improve the QE, we tried to use low work function coating to reduce the surface barrier of the metal, therefore to assure more photo-excited electrons passing through the surface barrier. Cesium was our primary choice. In Fig. 6, the QE rose from 5×10^{-6} to 3×10^{-5} , which was achieved without any further treatment methods and the vacuum conditions were rather poor. With a better vacuum environment, the QE could be possibly even more. However, cesium coating is not the best approach to lower the surface barrier: (1) It has the potential pollution risk in case of practical SRF gun tests, because it is actually difficult to obtain properly clean surface; (2) The low laser damage threshold of the alkali layer on surface will impede its application.

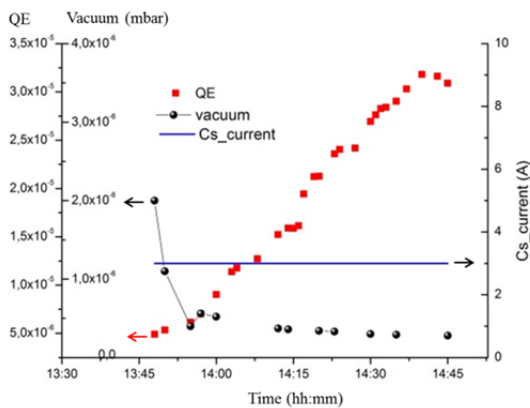


Figure 6: QE improvement, the vacuum condition, and the cesium dispenser current during the cesium activation of niobium.

Implantation with Alkali Metals

Another technique used for reducing the work function of metal cathodes is ion implantation with lower work function alkali metals or alkaline-earth metals. This technique is known to enhance the photoelectric emission of tungsten up to a factor of 50 [8] and to improve the QE of magnesium cathode up to 10 times [9].

Simulation was done with the code SRIM [10] to search for proper implantation energy, angle, density, and

then perform the implantation at ion beam centre (IBC), HZDR. The first test was done with 10 samples. Among them, five pieces were implanted with $^{133}\text{Cs}^+$ to a theoretical depth of 24 nm – 59 nm and cesium atom content of about 1%; other five samples were implanted with $^{39}\text{K}^+$ to the same depth and density. No post-annealing was performed after the implantation.

The samples were exposed to air after the implantation and stored in dry air till QE measurement was performed. The QEs of the samples were measured with 258 nm, 14 ps, 3 mW laser in vacuum, and the attracting electric field on surface was 40 kV/m. However, the results did not show improvement to the virgin niobium. The reason for that could be (1) the long waiting period in air, and (2) the weak electric field on the surface and the strong laser in picosecond pulse duration.

SUMMARY

In conclusion, the quantum efficiency of superconducting photocathodes, thin lead layer and bulk niobium, was investigated under DC field and RF field by using the picosecond UV drive laser of the ELBE SRF gun at HZDR. Lead layer on Nb plug has been applied in ELBE SRF gun for one beam test, 2 nA beam has been detected with the Faraday cup.

In order to search a recipe to improve the QE of niobium, cesium coating and alkali ion implantation have been performed on the mechanical polished niobium samples. The study of the effect of implantation on the photoemission of niobium will be continued.

ACKNOWLEDGMENT

The authors would like to thank all our colleagues at ELBE center and R. Aniol at IBC, HZDR for their support in this work. We acknowledge Jerzy Lorkiewicz, Robert Nietubyć from National Centre for Nuclear Research (NCBJ), Poland for the lead layer preparation on niobium plugs.

REFERENCES

- [1] A. Arnold, and J. Teichert, Phys. Rev. ST Accel. Beams 14, 024801 (2011).
- [2] J. Teichert, et al., "Free-electron laser operation with a superconducting radio-frequency photoinjector at ELBE", Nucl. Instr. and Meth. A. 743 (2014) pp. 114–120.
- [3] A. Neumann, et al., "SRF photoinjector test at HOBICAT", Proc. of SRF2011, July 2011, pp. 962-968; <http://www.JACoW.org>
- [4] J. Smedley, T. Rao, Q. Zhao, "Photoemission studies on niobium for superconducting photoinjectors", J. Appl. Phys. 98, 043111 (2005).
- [5] J. Smedley, T. Rao, J. Sekutowicz, "Lead photocathodes", Phys. Rev. ST Accel. Beams 11, 013502 (2008)
- [6] J. Lorkiewicz, et al., "Deposition and optimization of thin lead layers for superconducting accelerator photocathodes.", Phys. Scr. T161 (2014) 014071.
- [7] L.N. Hand, U. Happek, "Photoelectric quantum efficiency of niobium for $\lambda = 193$ nm and $\lambda = 248$ nm", Nucl. Instr. and Meth. A 372 (1996) pp.335-338.

- [8] J.P. Girardeau-Montaut, et al., "Enhancement of photoelectric emission sensitivity of tungsten by potassium ion implantation", Appl. Phys. Lett. ett., Vol. 66, No. 15, 1995, pp 1886-1888.
- [9] K. Zhao, et al. "Researches on new photocathode for RF electron gun." Nucl. Instr. and Meth. A. 445.1 (2000), pp. 394-398.
- [10] J.F. Ziegler, J.P. Biersack, & M.D. Ziegler, "SRIM, the stopping and range of ions in matter", Lulu. com, 2008.

FORMATION OF THE ELECTRON BUNCH LONGITUDINAL PROFILE FOR COHERENT ELECTRON COOLING EXPERIMENT*

I. Pinayev[#], D. Kayran, V.L. Litvinenko, BNL, Upton, NY 11973, USA

Abstract

Proof-of-principle experiment of the coherent electron cooling (CeC) is ongoing at Brookhaven National Lab. CeC mechanism utilizes amplification of density modulation, induced by hadrons, by an FEL structure. To fully utilize electron beam cooling capacity we need uniform longitudinal beam profile. In this paper we present two frequency injector system tuned for this requirement.

INTRODUCTION

The principle of the coherent electron cooling is the following [1]. The hadrons imprint their distribution onto the co-propagating electron beam thus creating a density modulation of the electron bunch. This modulation is amplified by a FEL structure and electric field is significantly increased. Due to the longitudinal dispersion a hadron arrives into the accelerating or decelerating phase of the field depending on its energy. With properly tuned system a net reduction of energy spread is obtained.

The cooling rate depends on the strength of the longitudinal space charge field, i.e. on the FEL gain, which depends exponentially on the peak current distribution of the electron bunch. Therefore it is desirable to have as much gain as possible. However, reaching saturation regime leads to the loss of the phase coherence and hence cooling. For this reason the FEL should operate under the saturation threshold but as close as possible. To fully utilize the electron beam cooling capacity we need to have flat longitudinal profile.

SYSTEM DESCRIPTION

The electron accelerator for the CeC proof of principle experiment [2] comprises a 112 MHz superconducting RF gun [3, 4], two normal conducting 500 MHz buncher cavities and 20 MeV five-cell 704 MHz accelerating cavity. In order to reduce project cost the RF equipment was chosen from the available hardware and no optimization of the frequencies values was available. The design voltage of the gun cavity is 2 MV, and each copper cavity is capable of the producing 300 kV voltage.

The electrons will be generated by a multialkaline cathode, illuminated by a fiber laser with frequency doubling to 530 nm wavelength. Laser, manufactured by NuPhoton, is capable to produce 78 kHz pulses (RHIC revolution frequency) with regulated pulse width from 100 to 550 picoseconds. The rise/fall time is around 50 picoseconds. The peak power is not less 1 kW. With 1%

quantum efficiency the extracted photocurrent is 4 Amperes, which is much less below of the required 80 A. Due to the low energy of electron beam we chose ballistic bunching of the beam, when compression is obtained in the drift space due to the velocity modulation. The energy chirp is eliminated in the 704 MHz cavity with slightly off-crest accelerating.

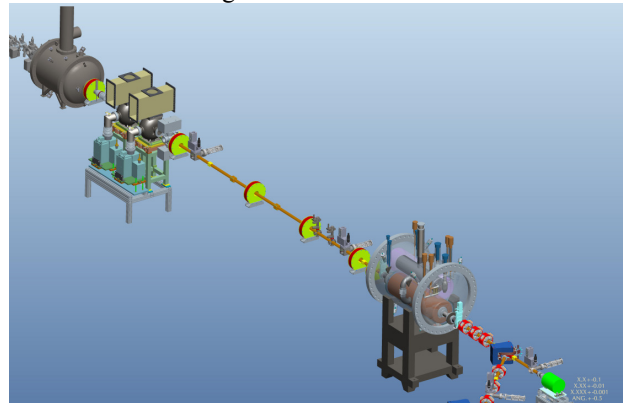


Figure 1: General layout of the electron accelerator for the coherent electron cooling proof-of-principle experiment. Electrons are generated in the 112 MHz SRF gun shown in the upper-left corner, proper velocity modulation is provided by the two copper cavities, the electron bunch is compressed in the drift section and further accelerated in the superconducting 704 MHz cavity shown in the lower-right corner.

The high degree of the desired compression makes significant high order terms such as δ_{566} , which causes unevenness of compression. Such effect is well known [5, 6] and there are two approaches to overcome it. The first approach, utilized in [5], is to modulate the initial beam current and non-linear compression will provide a flat top pulse. The second approach utilizes the second order (parabolic) energy chirp, which cancels the non-linearity. We have chosen the second approach in order to fully utilize the available laser power and have the ability with ease to adjust the pulse length. In our set-up the electron beam will be generated off-crest of the gun voltage to have the compressing chirp. The normal conducting cavities along with additional chirp will provide a parabolic compensation term.

SIMULATIONS RESULTS

The simulations were performed using code ASTRA. The initial electron beam has 2 nC charge distributed in a plateau with 0.4 ns FWHM and 80 ps rise/fall time. The transverse distribution was a uniform round beam with 2 mm radius and zero emittance. Total 50000 particles were generated. The gun cavity voltage was to provide 2 MeV

*Work supported by DoE program on Research and Development for Next Generation Nuclear Physics Accelerator Facilities
#pinayev@bnl.gov

electron beam (maximal field of 22.5 MV/m). The center of the beam was at -14.2° phase. The resulting longitudinal energy distribution is shown in Fig. 1.

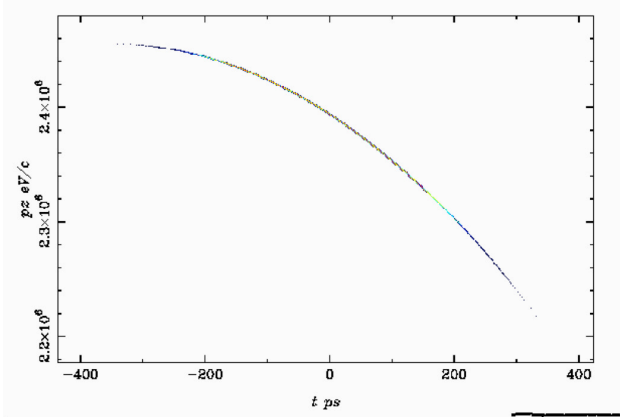


Figure 2: Distribution of the momentum along the electron bunch after the gun.

Further energy of the beam was modulated at the copper cavities with maximal field of 1.15 MV/m, which corresponds to 194 kV. The phase was -140° what allows provide both additional chirp and compensation term. The resulting energy distribution is shown in Fig. 3.

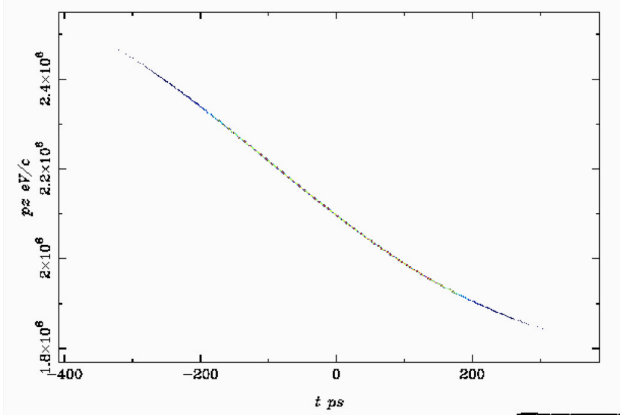


Figure 3: Distribution of the momentum along the electron bunch after the 500 MHz cavities. Note reduction of the beam energy due to the deceleration.

The resulting reduction of the r.m.s. bunch length is shown in Fig. 4.

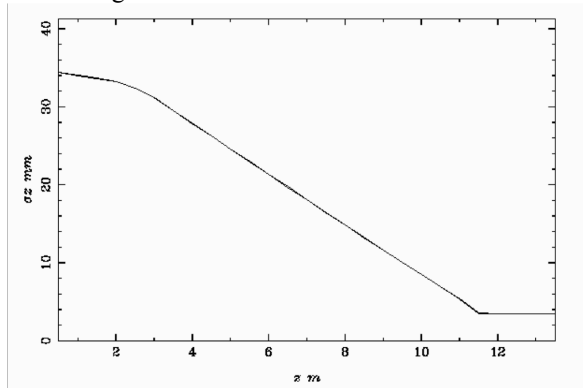


Figure 4: Reduction of the bunch length along the accelerating structure.

In the result of the velocity compression the beam profile evolves as illustrated in Fig. 5.

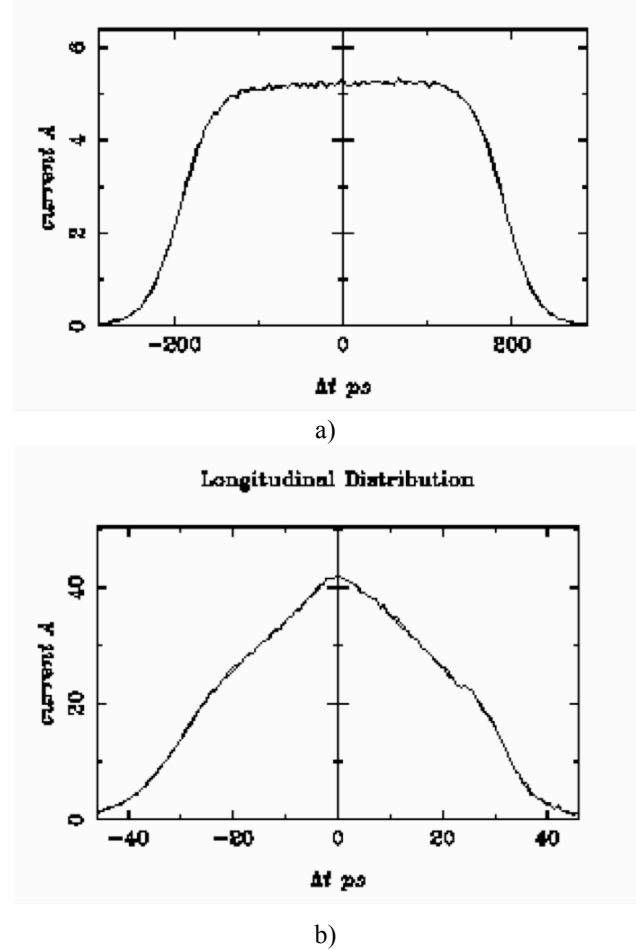


Figure 5: Longitudinal beam profiles: a) just after the gun, b) before the entrance into the 704 MHz cavity (11 meters from the cathode).

The final compression occurs inside the accelerating 704 MHz cavity where electron beam reaches minimal energy due to the fringe fields, which decelerate bunch.

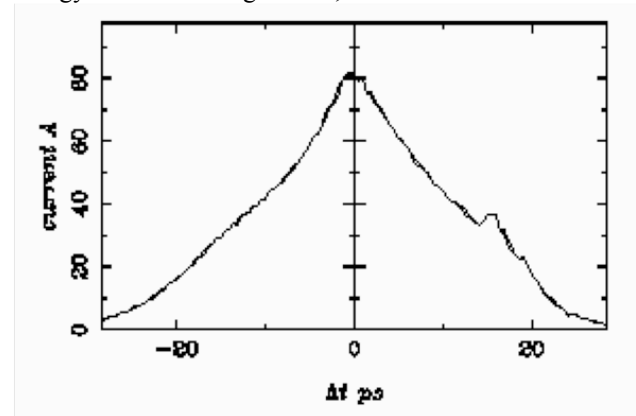


Figure 6: Final distribution of beam charge.

Flat distribution was achieved for beam without space charge but for the substantial space charge forces and

relatively low beam energy prevented achieving the same result for a real beam.

The electron beam was injected in the 704 MHz cavity at 8.5° phase to eliminate previously introduced energy chirp. The resulting momentum distribution is shown in Fig. 7.

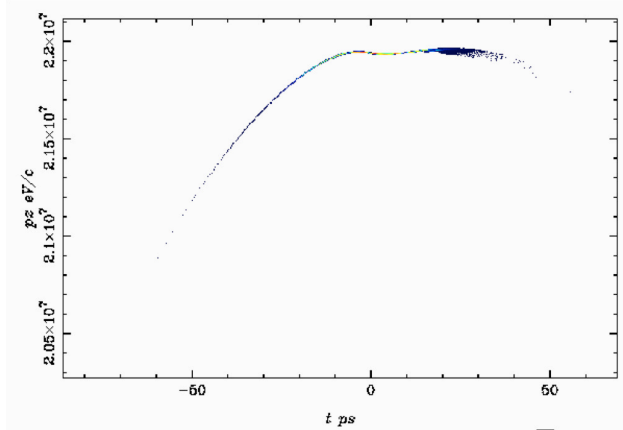


Figure 7: Momentum distribution along the electron bunch at the exit of accelerator.

CONCLUSION

The RF compensation method improved uniformity of the electron beam compression for the coherent electron cooling. Significant space charge forces prevented

complete uniform beam profile achieved with relativistic beams.

REFERENCES

- [1] V.N. Litvinenko and Ya.S. Derbenev, Phys. Rev. Lett. 102, 114801 (2009).
- [2] I. Pinayev *et al.*, “Present Status of Coherent Electron Cooling Proof-of-Principle Experiment”, in *Proceedings: Proc. 36th Int. Free-Electron Laser Conf.*, Basel, 2014, TUP072.
- [3] S. Belomestnykh *et al.*, “Developing of Superconducting RF Guns at BNL”, in *Proc. 26th Int. Linear Accelerator Conf.*, Tel-Aviv, 2012, pp. 324-326.
- [4] D. Kayran *et al.*, “SRF Photoinjector for Proof-of-Principle Experiment of Coherent Electron Cooling at RHIC,” in *Proc. 3rd Int. Particle Accelerator Conf.* New Orleans, 2012, pp. 622-624.
- [5] R.J. England, J.B. Rosenzweig, M.C. Thompson, “Longitudinal Beam Shaping and Compression Scheme for UCLA Neptune Laboratore”, in *Proc. 10th Workshop on Advanced Accelerator Concepts*, AIP Proceedings CP647, 2002, pp. 884-892.
- [6] K. Togawa, T. Hara, and H. Tanaka, “Electron-bunch compression using a dynamical nonlinearity correction for a compact x-ray free-electron laser,” PRST-AB 12, 080706 (2009).

HIGH POWER RF TEST AND ANALYSIS OF DARK CURRENT IN THE SwissFEL-GUN

P. Craievich*, S. Bettoni, M. Bopp, A. Citterio, C. Ozkan, M. Pedrozzi, J.-Y. Raguin, M. Schaer, A. Scherer, T. Schietinger, L. Stingelin, PSI, Villigen, Switzerland

Abstract

To fulfill the beam quality and operational requirements of the SwissFEL project, currently under construction at the Paul Scherrer Institut, a new RF photocathode gun for the electron source was designed and manufactured in house. A 2.6 cell S-band gun operating with near-perfect rotationally symmetric RF field was designed to operate with a 100 MV/m cathode field at a repetition rate of 100 Hz with average power dissipation of 0.9 kW with pulse duration of 1 μ s. The first SwissFEL-gun is now fabricated and installed in the SwissFEL Injector Test Facility (SITF). The frequency spectrum and field balance, through bead-pulling, have been directly verified in-situ and then the gun has been operated with high-power RF. The results of bead-pull measurements and high-power tests are presented and discussed. In addition the emitted dark current was also measured during the high-power tests and the charge within the RF pulse was measured as a function of the peak cathode field. Faraday cup data were taken for cathode peak RF fields up to 100 MV/m for the case of a diamond-milled polycrystalline copper cathode.

INTRODUCTION

The SwissFEL free electron laser project currently under construction at the Paul Scherrer Institut will be composed of a 5.8 GeV accelerator and two undulator beam lines which will cover the photon energy ranges from 12.4 keV to 1.8 keV and from 1.8 keV to 0.18 keV for Aramis and Athos lines, respectively [1]. To fulfill the beam quality and operational requirements a new RF photocathode gun for the electron source was designed [2] and manufactured in house [3]. It is composed of 2.6 cell operating with a near-perfect rotationally symmetric π -mode at the S-band frequency. The middle cell is coupled to two rectangular waveguides symmetrically arranged to cancel the dipolar component of the field. The racetrack interior shape of this coupling cell is optimized to minimize the quadrupolar field component. It is designed to operate with a 100 MV/m cathode field at a repetition rate of 100 Hz with average power dissipation of 0.9 kW and a pulse duration of 1 μ s. The first SwissFEL-gun is now fabricated and installed in the SwissFEL Injector Test Facility (SITF) [4]. In order to have the possibility to exchange cathode without breaking the vacuum the back-plane of the RF gun has a hole where a cathode plug can easily be inserted through a load-lock system [5]. Figure 1 shows a 3-D view of the SwissFEL-gun where the cathode-plug is visible in the back-plane. Measurements at

room temperature in the clean room showed that the resonant frequency depends on the force with the cathode-plug is pushed into the gun and thus the frequency spectrum and field balance, through bead-pulling, have been directly verified in SITF before starting with RF conditioning. Table 1 lists a comparison between RF simulations with HFSS [6] and measurements of the SwissFEL-gun RF parameters. In addition the emitted dark current was also measured during the high-power tests. Past measurements on the previous installed CTF3 gun showed quite high value of the dark current [7], thus the charge within the RF pulse of the SwissFEL-gun was measured as a function of the peak cathode field at different pulse durations. Faraday cup data were taken for different cathode peak RF fields for the case of a diamond-milled polycrystalline copper cathode with surface roughness $R_a=5$ nm.

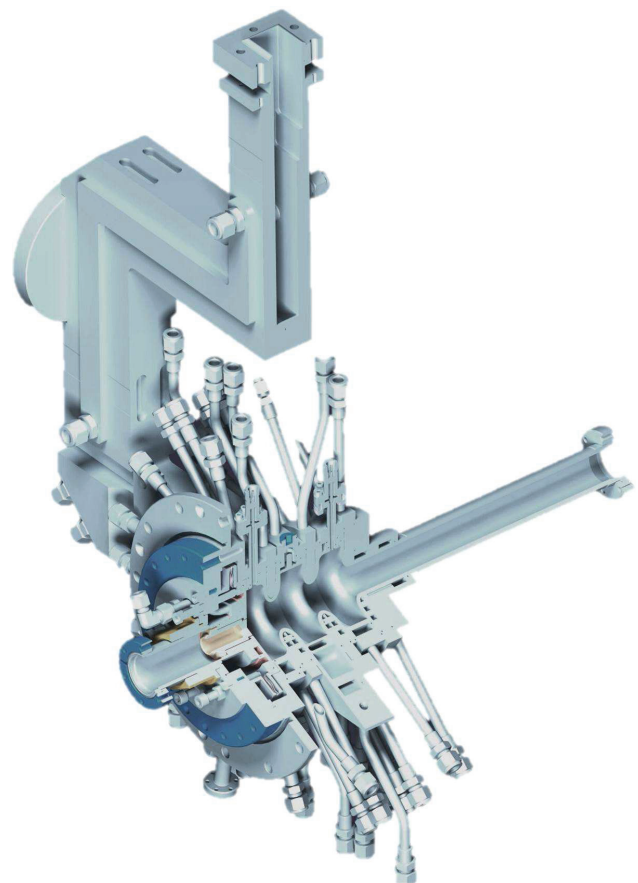


Figure 1: 3-D view of the SwissFEL-gun.

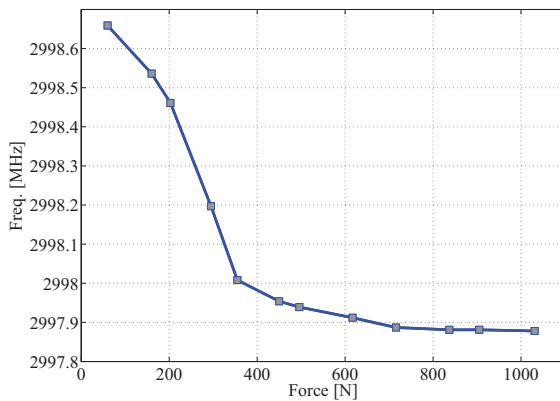
* paolo.craievich@psi.ch

Table 1: SwissFEL-gun RF Parameters for the SwissFEL Injector Test Facility (SITF)

Parameter	HFSS	Measured	unit
π -mode freq.	2997.912	2997.912	MHz
β -coupling	1.98	2.02	
Q_0	13630	13690 \pm 100	
Filling time	485	481	ns
Mode sep.	16.36	16.20	MHz
Field balance	>98	>98	%
Operational temp.	57.7	53.0	°C

CATHODE-PLUG TUNING

In order to perform the frequency tuning of the RF gun through the cathode-plug, the manipulator of the plug was equipped with a calibrated pressure gauge. Figure 2 reports the result of the measurements for different force. RF gun is tuned at nominal SITF frequency of 2997.912 MHz when a force of more than 600 N is applied. Figure 3 shows electric field profiles on-axis at position of the cathode-plug obtained from bead-pulling with a ceramic bead of 3 mm diameter. At nominal frequency the ratios (field balance) are $E_2/E_c = 1.02$ and $E_1/E_c = 1.01$ where E_c is the field at cathode and E_2 and E_1 are the fields in the middle and last cell, respectively. The frequency spectrum at operational conditions is shown in Fig. 4. Frequency separation with adjacent mode is 16.2 MHz, in a good agreement with the simulation result.

Figure 2: Resonant frequency of the π -mode as a function of the applied force on the cathode plug.

HIGH POWER RF TEST

The gun was tested at full power in the SITF bunker using actual RF distribution system of the injector with a TH2100 35 MW klytron, 35 MW peak power and 5 kW average power circulator and an active temperature control of the gun body temperature. The gun was conditioned over a period of one week and a typical processing curve to high power is given in Fig. 5. The RF conditioning process has

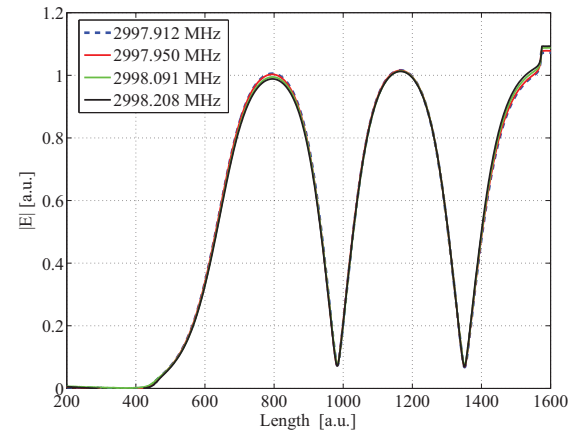


Figure 3: Electric field profile on-axis for different position of the cathode plug.

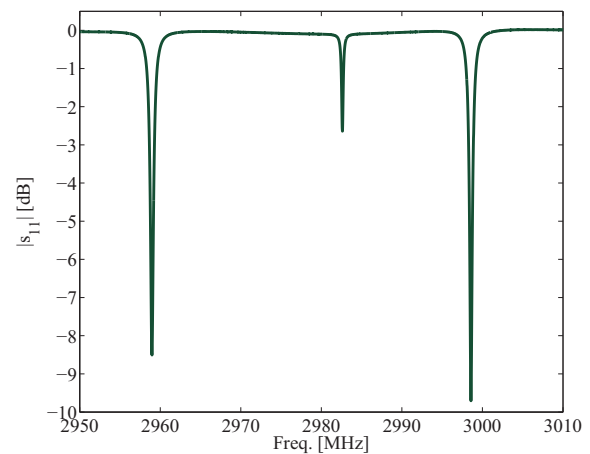


Figure 4: Frequency spectrum of the SwissFEL-gun. Operating frequency in vacuum 2997.912 MHz at 53 °C, frequency separation with adjacent mode is 16.2 MHz.

been performed with a pulse repetition rate of 100 Hz, by gradually increasing the RF power through an automatic conditioning tool and changing the pulse width from 0.3 to 1.0 μ s. After the conditioning period the vacuum level with RF power was around 1×10^{-10} mbar. It is worthwhile to note that nominal RF power of 18 MW with the RF pulse width of 1 μ s in the first week of operation was reached.

Beam Energy Jitter

The momentum and momentum spread of the electron beam can be measured through the energy spectrometer arm placed after the RF gun and before the first traveling wave structure. It consists of a 30° dipole magnet and in order to maximize the momentum resolution of the spectrometer, a quadrupole in front of the bending magnet was used to have the contribution of the dispersion to beam size larger than the contribution of the natural beam size. Energy resolution at the spectrometer was 4 keV rms and a systematic error

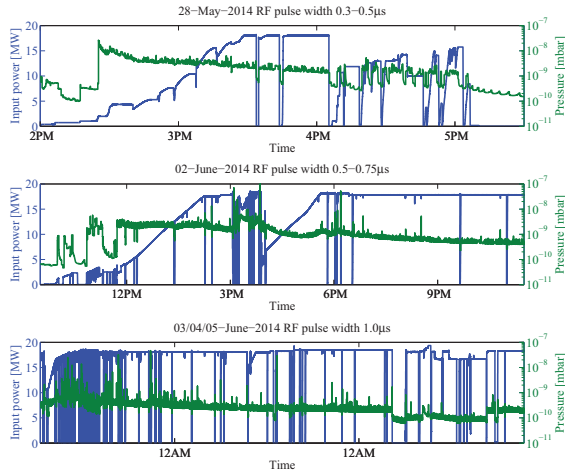


Figure 5: RF conditioning to high power.

due to uncertainties from dipole magnetic field of 1 %. Figure 6 shows an example of non-Gaussian horizontal profile at the spectrometer YAG screen which is fitted with a confi function [8]. The horizontal axis is converted in MeV according to the dipole dispersion of 0.387 m. Figure 7 shows the bunch mean energy and energy spread jitters at the gun exit measured on 49 not consecutive shots over 30 sec with laser at 10 Hz and RF repetition rate 10 Hz and 100 Hz. It is worthwhile noting that the rms relative mean energy jitters are 0.023 % and 0.020 % for 100 Hz and 10 Hz, respectively. Rms jitter of the energy spread is 0.5 keV for both repetition rates.

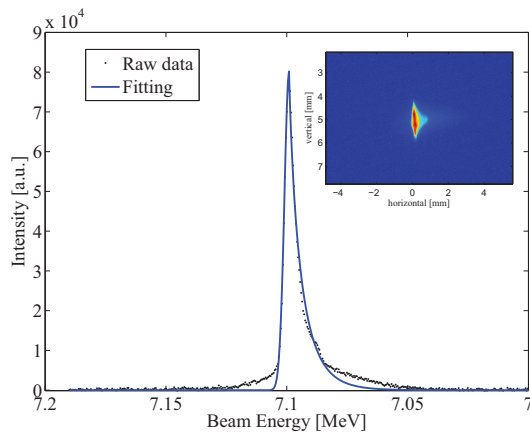


Figure 6: Example of non-Gaussian horizontal profile at the spectrometer at 7.1 MeV (black points) which is fitted with a confi function (blue line).

DARK CURRENT ANALYSIS

The low energy beam transport line between the RF gun and the first S-band accelerating structure has a length of approximately 3.3 m. At the gun exit there is a solenoid, followed by the laser ports and a coaxial Faraday cup that

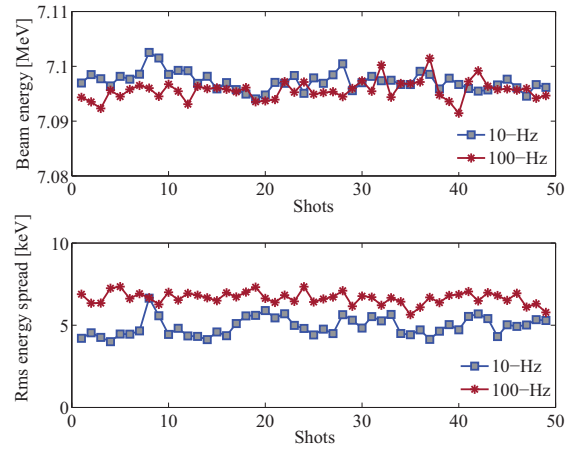


Figure 7: The bunch mean energy jitter (top) and bunch rms energy spread (bottom) at the gun exit measured on 49 not consecutive shots over 30 sec with laser repetition rate 10 Hz and RF repetition rate 10 Hz and 100 Hz.

allows the observation and measurement of the dark current from the RF gun and cathode. Figure 8 shows the typical signals on the scope connected to the Faraday cup once the gun solenoid was adjusted to maximize charge collection in the cup itself. Dark current signals show a plateau due to the amplitude modulation of the RF input power, which will be used to maintain a constant amplitude of the accelerating field for a two-bunch operation with a 28 ns spacing in SwissFEL [1]. At nominal operating conditions with

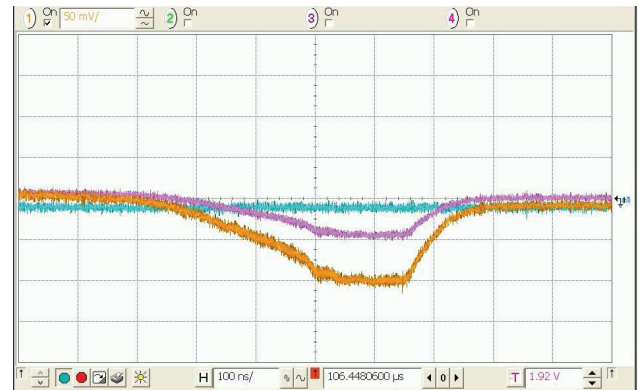


Figure 8: display on scope of signals from the Faraday cup during the measurement. Yellow trace: raw signal. Blue trace: background. Pink trace: signal after background subtraction.

peak electric field at the cathode of 100 MV/m, the integrated dark current collected by the Faraday cup is approximately 50 pC. The dark charge was also imaged using a 200 μ m thick YAG crystal scintillator placed in the same housing of the Faraday cup. Figure 9 shows a comparison between images of the dark currents in the CTF3-gun and SwissFEL-gun both focused with the gun solenoid on the same YAG screen. At nominal operating condition of the

gun (85 MV/m on the cathode surface), the dark current in the CTF3 gun collected by the Faraday cup was about 1.4 nC [7]. The observed scaling of integrated dark current with cathode field is plotted in Fig. 10 before and after alignment of the solenoid and at 10 Hz and 100 Hz. Basically the emission of electrons in a period of the RF field is generated by the field emission which can be described by the well-known Fowler-Nordheim (F-N) equation. Using such equation, and taking into account the transient behavior due to the filling time of the gun, the field enhancement factor β can be estimated in the range 63–68 with the assumption

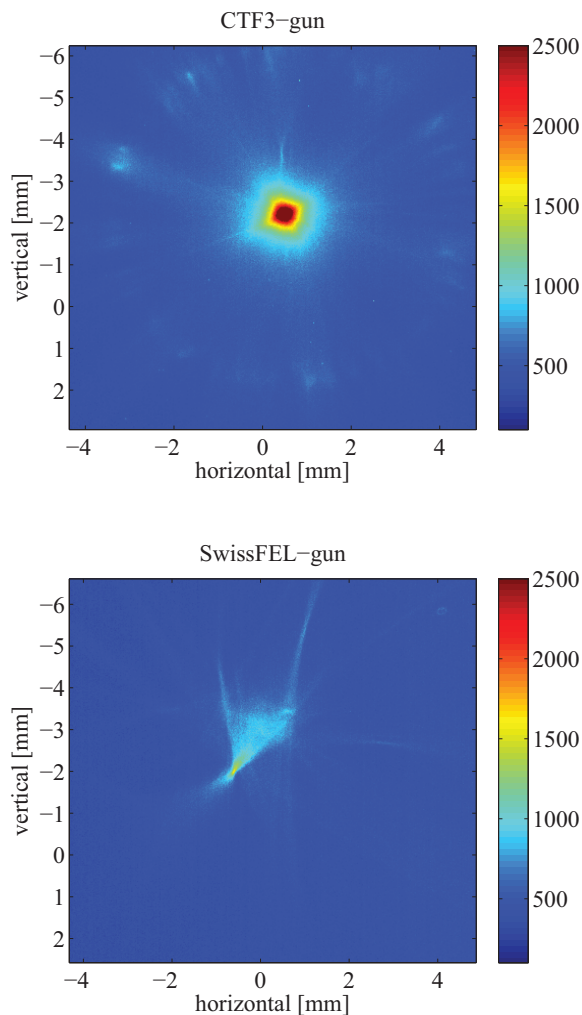


Figure 9: Reference images of dark current at nominal condition on the YAG screen in the CTF3 gun (top) and SwissFEL-gun (bottom).

CONCLUSION

The frequency tuning of the SwissFEL-gun based on the cathode-plug was possible applying a force larger than 600 N. The field imbalance was around 2 % and the frequency separation equal to 16.2 MHz, in good agreement with the simulations. The gun was smoothly conditioned to full power at 100 Hz over a period of one week and at the

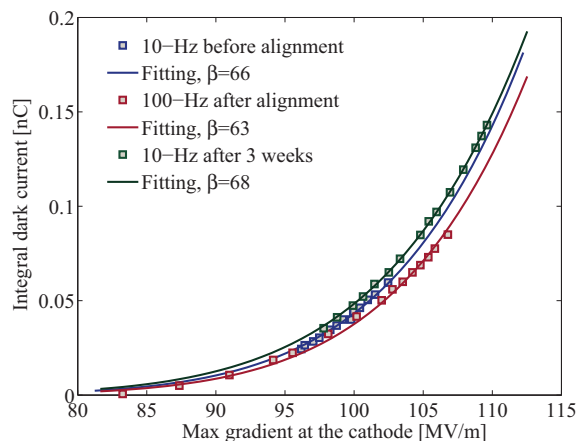


Figure 10: Integrated dark current on RF pulse as a function of the peak electric field at cathode before and after alignment of the RF gun and solenoid and at 10 Hz and 100 Hz.

end the vacuum level was around 1×10^{-10} mbar. We compared the relative mean energy and energy spread jitters at the gun exit at 10 Hz and 100 Hz. Rms relative mean energy jitters were 0.023 % and 0.020 % for 100 Hz and 10 Hz respectively, while the rms jitter of the energy spread was 0.5 keV for the both cases. Furthermore, we measured the emitted dark current within the RF pulse as a function of the peak cathode fields. At nominal operating conditions of the gun, peak electric field at cathode of 100 MV/m, the integrated dark current collected by the Faraday cup was approximately 50 pC. Using F-N equation and taking into account the transient behavior due to the filling time of the gun we estimated a field enhancement factor β in the range 63–68. As conclusion the SwissFEL-gun fulfilled RF specifications and is suitable for the SwissFEL injector.

REFERENCES

- [1] R. Ganter et al., SwissFEL CDR, PSI Bericht Nr. 10-04, April 2012.
- [2] J.-Y. Raguin et al., “The SwissFEL RF gun: RF design and thermal analysis”, LINAC’12, Tel-Aviv, September 2012, TUPLB01 (2012).
- [3] U. Ellenberger et al., “The SwissFEL RF Gun: Manufacturing and Proof of Precision by Field Profile Measurements”, LINAC’14, Geneva, Switzerland, September 2014, THPP114 (2014).
- [4] T. Schietinger et al., “Progress report on the SwissFEL injector test facility”, IPAC’12, New Orleans, May 2012, TUPPP065 (2012).
- [5] R. Ganter et al., “SwissFEL cathode load-lock system”, FEL’13, New York, August 2013, TUPSO21 (2103).
- [6] Ansys HFSS website: <http://www.ansys.com>
- [7] S. Bettoni et al., “Dark current transport and collimation studies for SwissFEL”, FEL’13, New York, August 2013, TUPSO21 (2103).
- [8] G. Penco et al., “Optimization of a high brightness photoinjector for a seeded FEL facility”, J. Instrum. 8, 05015 (2013).

THYRATRON REPLACEMENT*

Dr. Ian Roth, Dr. Marcel P.J. Gaudreau, PE, Michael Kempkes,
Diversified Technologies, Inc., Bedford, MA 01730, USA

Abstract

Thyratrons in high-power, short-pulse accelerators, have a limited lifetime. It would be desirable to replace the thyratrons with solid-state devices. One possibility, thyristors, are being developed for this application; however, they have not, to date, demonstrated the reliability needed for installation in the short pulse, high peak power RF stations used in many pulsed electron accelerators. An alternate solid-state device, the insulated-gate bipolar transistor (IGBT), can readily operate at the speed needed for accelerators, but commercial IGBTs cannot handle the voltage and current required. It is, however, possible to assemble these devices in arrays to reach the required performance levels without sacrificing their inherent speed. Diversified Technologies, Inc. (DTI) has patented and refined the technology required to build these arrays of series-parallel connected switches. Under a DOE contract, DTI is currently developing an affordable, reliable, form-fit-function replacement for the klystron modulator thyratrons at SLAC.

INTRODUCTION

The Stanford Linear Collider (SLC) has used thyratrons in its klystron modulators since its inception in 1963. While the thyratrons function, they need replacement every 10,000 hours at a cost of \$13,000 each, plus labor. Furthermore, periodic maintenance is required to adjust their reservoir heater voltage over the thyratron lifetime. As the Stanford Linear Accelerator Center (SLAC) continues to run its accelerator over the next two decades, replacing the thyratrons with a solid-state switch that would last 25 years or more, and does not need maintenance, would provide significant savings – both in the avoided cost of thyratrons as well as the labor in replacing and adjusting them.

SLAC is presently funding the development of a solid-state switch, based on thyristor technology, to replace the thyratrons (Figure 1). The difficulty is that a fast rising current in a thyristor tends to be carried in a small region, rather than across the whole device, and this localized current concentration can cause a short circuit failure.

APPROACH

An alternate solid-state device, the insulated-gate bipolar transistor (IGBT), can readily operate at the speed needed for the accelerator, but commercial IGBTs cannot handle the voltage and current required. It is, however, possible to assemble these devices in arrays to reach the required performance levels without sacrificing their

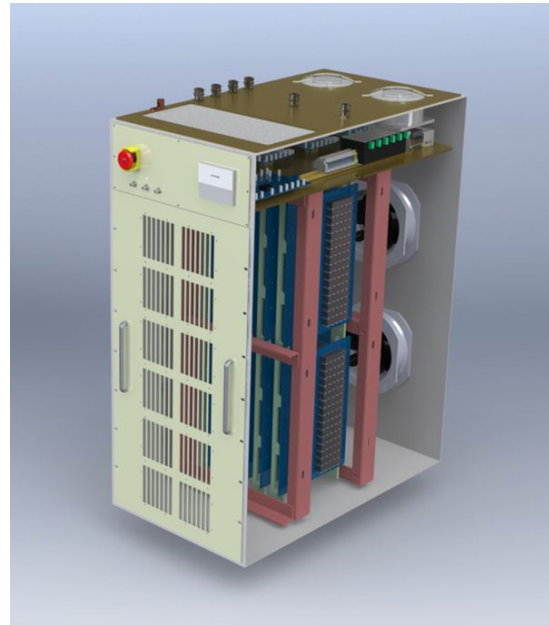


Figure 1: Artist's conception of thyratron-replacement solid-state switch array. Target specifications are detailed in Table 1.

inherent speed. Diversified Technologies, Inc. (DTI) has patented and refined the technology required to build these arrays of series-parallel connected switches. DTI has shipped more than 500 systems leveraging this technology, which have been operating in facilities around the world for many years.

DTI has begun this effort with careful consideration of potential candidate IGBTs, identifying the optimal device based on price and performance in single-device tests, determining the gate drive performance necessary to allow high-current operation, and targeting the development of a multi-device switch plate. In the second Phase of this SBIR, DTI will develop the gate drive for the system, then design, build, and test a complete switch that is small enough to be integrated into the existing cabinet. These switches will be delivered to SLAC, and their performance and reliability will be demonstrated in a SLC modulator.

MOTIVATION

The market for thyratrons is in decline. As newer solid-state modulators are deployed, and older thyratron systems are taken out of service, the demand for thyratrons has diminished significantly. In response, several vendors have either gone out of business or stopped manufacturing thyratrons, further diminishing their availability. It is not clear how long the supply of thyratrons for these legacy systems will continue, making

*Work supported by U.S. Department of Energy SBIR Award DE-SC0011292

a solid-state thyatron replacement critical for their continued operation and support.

For this and other reasons, the thyatrons in many klystron modulators represent a major expense in operation – not only from the increasing cost of replacement, but from the labor involved both in such annual replacement and in the need to adjust them for proper operation during their relatively short life.

Most of these systems, including commercial medical accelerators, were designed decades ago, before solid-state switches were available. Even today, the cost of transitioning from thyatrons and pulse-forming networks to solid-state modulators remains prohibitive for many of these systems, despite the declining availability of thyatrons. Consequently, DTI anticipates a wide range of benefits from the development of a cost-effective, drop-in replacement for the thyatrons in operation in commercial and scientific systems around the world.

CURRENT LIMITS

The current in the application is large, so to minimize the size and cost of the modulator, each IGBT should carry the maximum current possible. The IGBT chosen will have the highest current possible consistent with the risetime; higher current devices have a longer risetimes.

Another limit to the current is the gate voltage; this should be as high as possible, consistent with reliability. The gate voltage also needs to have a fast risetime to minimize the switching losses.

The current rate-of-rise in an IGBT is limited mainly by the inductance in the emitter lead of the device. As dI/dt is increased, the inductive voltage drop on the emitter lead increases, reducing the gate voltage on the device itself. This raises the conduction voltage drop, increasing the power dissipated in the device. Higher power dissipation raises the device temperature, which in turn limits device reliability. Therefore, low inductance in the emitter lead is required for both speed and reliability.

DTI is investigating the following steps to increase the ability of the devices to handle dI/dt :

- Use of more devices in a smaller package. Since both the current per device and the package inductance are lower, there will be a smaller inductive decrease in the

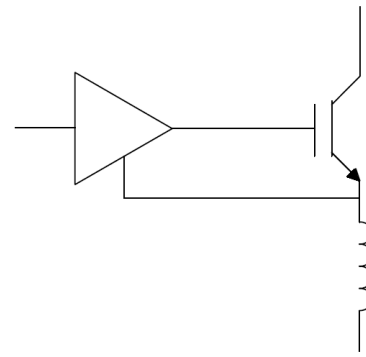


Figure 2: Schematic diagram of a Kelvin connection.

gate voltage. The tradeoff is that the overall switch will use more components; however, these smaller parts are cheaper.

- Development of a gate drive that produces an initially-high voltage to overcome the dI/dt drop, then decreases to keep the device gate voltage below the maximum allowed.

- Packaging the devices with a Kelvin connection (Figure 2), where the lead between the emitter and the gate drive does not carry current. This substantially reduces the inductive voltage drop.

MECHANICAL DESIGN

For this effort to be practical and cost-effective, the thyatron replacement switch must readily fit in the existing cabinet with minimum modifications required for its installation. The volume available for the new switch is that of the existing thyatron chassis which includes the thyatron and heater supplies. Applying this 17" x 17" x 37" volume to the new switch with 2080 devices, the volume per device would be 5.1 in³. This means that the switch will need to be very tightly packed. There is certainly room for the devices themselves, but providing the required cooling and voltage standoff (preferably with air) presents a challenge.

Forced air cooling will be used to cool the thyatron replacement switch. Twin fans mounted in the back will be used to draw outside air into the front of the unit thru grill-air filter into the ten switchplates shown in Figure 1. Air baffles (not shown) will direct air over either extrusion or pin fin heat sinks attached to each IGBT. After passing over the heatsinks on the switchplates, the air exits the cabinet through the two fans at the rear of the cabinet.

FUTURE PLANS

DTI will continue testing candidate devices and drives while being mindful of final cost. Following successful development, fabrication, and demonstration of the thyatron replacement switches for SLAC, DTI plans to make the switch assembly commercially available, targeting other legacy systems still using thyatron pulse-forming network pulse modulators.

Table 1: Solid-State Switch Specifications

Pulse Voltage	48 kV
Pulse Current	6.3 kA
Fault Current	17.8 kA
Pulse Width	6.0 us
Risetime	1 us
Repetition Rate	120 Hz
Lifetime	20 Years

AFFORDABLE SHORT PULSE MARX MODULATOR*

Robert Phillips, Gerard DelPriore, Dr. Marcel P.J. Gaudreau, PE, Michael Kempkes,
Diversified Technologies, Inc., Bedford, MA 01730, USA
Dr. Jeffery Casey, Rockfield Research, Inc., Las Vegas, NV 89135, USA

Abstract

Under a U.S. Department of Energy grant, Diversified Technologies, Inc. (DTI) is developing a short pulse, solid-state Marx modulator. The modulator is designed for high efficiency in the 100 kV to 500 kV range, for currents up to 250 A, pulse lengths of 0.2 to 5.0 μ s, and risetimes <300 ns. Key objectives of the development effort are modularity and scalability, combined with low cost and ease of manufacture. For short-pulse modulators, this Marx topology provides a means to achieve fast risetimes and flattop control that are not available with hard switch or transformer-coupled topologies.

INTRODUCTION

Under a DOE SBIR grant and based on research begun under the Next Generation Linear Collider (NLC) program, high energy, short-pulse modulators are being re-examined for the Compact Linear Collider (CLIC) and numerous X-Band accelerator designs. At the very high voltages required for these systems, however (Table 1), all of the existing designs are based on pulse transformers, which significantly limit their performance and efficiency. There is not a fully optimized, transformer-less modulator design capable of meeting the demanding requirements of very high voltage pulses at short pulsewidths.

MARX GENERATOR

A Marx generator is a system with energy storage capacitors which are charged in parallel at low voltage and discharged in series to provide high voltage output (Figure 1). This is a legacy idea, practiced for decades using resistor charging networks and spark-gaps for discharge. Constrained by the limits of closing switches, such systems required pulse forming networks and crowbars, with their attendant limitations.

The Marx topology allows a new degree of freedom unavailable to other architectures – DTI can intentionally underdamp the series snubbing within the pulse circuit. This cannot be done conventionally – the reactive overshoot endangers the load. In a Marx, we can compensate for the overshoot by initially firing only a subset of the switches – thus “sling-shotting” the leading edge faster than otherwise possible. We can tune the number and timing of subsequent module firings to counter the reactive ringing, and hold a flattop pulse to the desired voltage and accuracy.

Similarly, additional modules may be added to fire

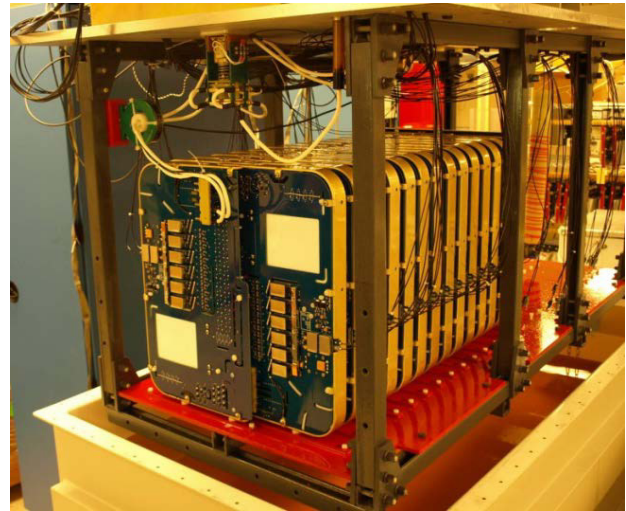


Figure 1: The Yale Marx 500 kV modulator charges many stages in parallel at low voltage, then discharges in series at high voltage. Each 12.5 kV, 250 A “flat pack” module is identical, providing for low fabrication and assembly cost.

sequentially later in the pulse to compensate for capacitor droop. This is a critical enabling technology motivating Marx use for long-pulse accelerators (such as ILC), and yields valuable optimization even for very short-pulse systems. The reduction of capacitor size afforded by this flexibility further reduces parasitic capacitance, and thus reduces equipment size and cost while increasing power efficiency.

DESIGN BENEFITS

Reduced Module Costs

Through the use of PC board trace shielding and RF cans in sensitive areas of the circuit, we were able to colocate controls directly on the board within reasonable proximity to pulsed current sections of the same board. By exposing the IGBTs directly to the oil, we can cool the devices effectively while eliminating machined parts and hardware, further reducing the module parts count, associated materials, and assembly costs. Since the flat-pack design significantly reduces voltage gradients from module to module within the Marx bank, the only significant need for corona and field reduction geometry is at the interface between the Marx bank stack and the walls of the tank. We anticipate more than a four-fold reduction in module mechanical costs, with the potential for additional reductions in manufacturing costs, compared to earlier designs.

*Work supported by U.S. Department of Energy SBIR Award DE-SC0004251

Simpler Interconnect

Each module in the redesigned Marx bank plugs directly into the two adjacent modules. We oriented the connectors and offset the board components and corona shields to allow any individual module to be added or removed from the stack, much like a book on a shelf, without any significant disassembly of support structures or disruption of the rest of the Marx bank. Since all module electrical connections and buswork are integral to the modules, only the fiber-optic control line (and optional fiber-optic monitor) needs to be externally connected. The first module in the stack plugs into a connector supplying charging HV, core bias current, auxiliary housekeeping power, and ground. A connector on the final module is connected to the Marx output coaxial cable, and includes a loopback for the common-mode choke bias current.

Scalability

The flat-pack Marx design is inherently modular and scalable, as additional plates may be added for a wide range of voltages. Whether at 100 or 500 kV, a Marx bank can use the same modules. The primary impact of additional plates is an increase in the charging current at the first plate, since it carries the current for all subsequent plates as well. Stray capacitance is also greatest at higher voltages, assuming constant spacing to the tank.

PROTOTYPE TESTING

During testing of the prototype bank, we ran four modules with all four modules simultaneously switched for a 1.5 μ s pulse, with a 10 kV pre-charge into the system, resulting in a 40 kV output. The prototype modules performed flawlessly into high voltage, with none of the chatter or jitter that would otherwise be

associated with gate drives impacted by noise coupling at high voltage. Most recently, DTI has tested a stack of 29 plates into a resistive load (Figure 2). The result was a 2 μ s pulse output of approximately 280 kV and 185 A. DTI will continue carefully constructing and testing modules to ensure the reliability and safety of the equipment.

Table 1. Yale Marx Design Parameters

Pulse Voltage	500 kV
Pulse Current	250 A
Pulse Width	1.8 μ s
Repetition Rate	20 Hz
Module Voltage	12.5 kV
Module Capacitance	0.6 μ F
# Modules for Base Pulse	40
Total # Modules in System	48 – 50
Expected Risetime	300 ns
Heater Voltage	24 VDC
Heater Current	21 A
Insulation	Oil

PLANS/CONCLUSION

In Phase III, DTI will extend this design to future short-pulse, high voltage modulators for the next generation of planned accelerators, as well as transition this design to industrial / medical accelerators. We believe that the same combination of modular, low cost elements demonstrated in this Phase II effort will allow solid-state modulators to finally reach a price level that will supplant traditional (but low cost) thyatron / PFN designs currently used in these systems.

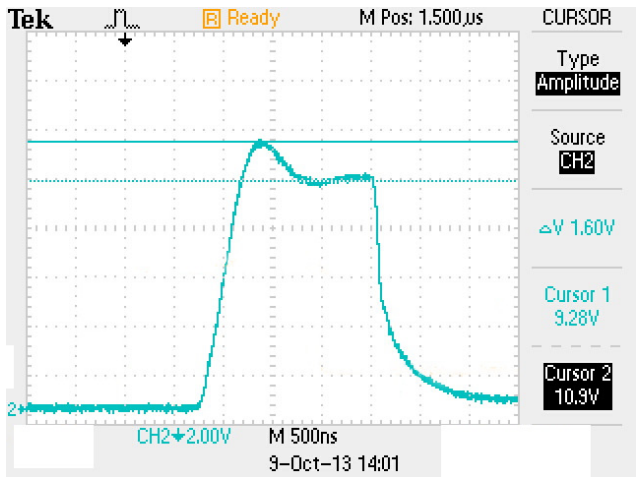


Figure 2: 280 kV, 185 A pulse from 29 Yale Marx modules into 1500 Ohm load, with intentional initial overshoot to reduce risetime. Ch2 (Blue): Current, 40A/div.

STEADY STATE MULTIPACTING IN A MICRO-PLUSE ELECTRON GUN

Zhou Kui*, Lu Xiangyang†, Quan Shengwen, Luo Xing, Yang Ziqin, Zhao Jifei

State Key Laboratory of Nuclear Physics and Technology, Peking University, Beijing 100871, China

Abstract

Multipacting is a resonant electron discharge phenomenon via secondary electron emission, while micro-pulse electron gun (MPG) utilizes the multipacting current in a radio-frequency (RF) cavity to produce short pulse electron beams. The concept of MPG has been proposed for many years. However, the unstable operating state of MPG vastly obstructs its practical applications. This paper presents a study on the steady state multipacting in a MPG. The requirements for steady state multipacting are proposed through the analysis of the interaction between the RF cavity and the beam load. Accordingly, a MPG cavity with the frequency of 2856 MHz has been designed and constructed. Various kinds of grid-anodes are tested in our primary experiments. Both the unstable and stable multipacting current have been observed. Presently, the stable output beam current has been detected at about 12.2 mA. Further experimental study is under way now.

INTRODUCTION

Multipacting is a resonant electron discharge phenomenon via secondary electron emission [1], which is frequently observed in microwave systems. When the multipacting effect occurs, it usually causes some undesirable problems, such as deteriorating the vacuum, absorbing incident power, leading to quenching of superconducting cavity, etc. So, most studies on multipacting focus on how to suppress or eliminate it. Until 1993, Fredrick M. Mako and William Peter proposed the concept of MPG [2], which utilized the multipacting current in a RF cavity to produce pulsed electron beams. Due to its self-bunching property, MPG is capable of providing high current and short pulse electron beams. In addition to that, its simple structure and high tolerance to contamination make it a potential electron source for accelerators and microwave systems.

The main problem in the development of MPG is the stability of the output beam current. To get high beam current and low emittance, previous studies on MPG always tried to feed high power into the cavity to get high surface field [3,4]. The stable multipacting current in the MPG was considered to be formed as the equilibrium result of the self-bunching effect and the space charge effect [1]. However, we believe the beam loading effect also plays an important role in the forming process of stable multipacting current.

This paper presents a study on the steady state multipacting in a micro-pluse electron gun with theory and experiments. In the second section, a MPG model is setup to show the basic characteristics of the MPG. The requirements for

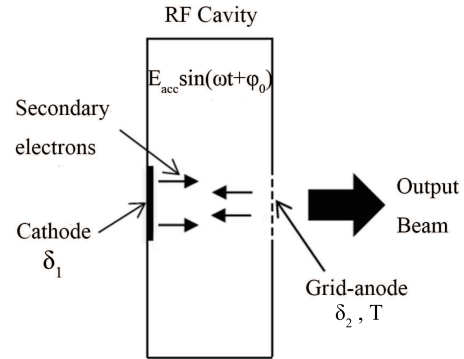


Figure 1: The schematic diagram of the MPG model [3].

the steady state multipacting is proposed through the analysis of the interaction of the RF cavity and electron beams. In the third section, a MPG cavity with the frequency of 2856 MHz has been designed and constructed. Different kinds of grid-anodes are tested in our experiments. Both the unstable and stable multipacting current have been observed successfully. The detected stable output beam current has reached 12.2 mA. Finally, a conclusion of this paper is given.

ANALYSIS OF STEADY STATE MP

The MPG Model

The MPG model (Fig. 1) consists of three parts: an RF cavity working in the TM_{010} mode, a secondary emission surface and a grid, which is opaque to the microwave electric field but partially transparent to the electrons in order to extract the electron beams [3]. We suppose the secondary emission surface to be the cathode with secondary emission yield (SEY) δ_1 and the grid to be the grid-anode with SEY δ_2 and transmission coefficient T . Here, we adopt Vaughan's empirical formula for δ_1 and δ_2 [5].

$$\delta_1(E_i) = \delta_{\max 1} (v_1 e^{1-v_1})^k \quad (1a)$$

$$\delta_2(E_i) = \delta_{\max 2} (v_2 e^{1-v_2})^k \quad (1b)$$

Where E_i is the electrons impact energy, $\delta_{\max 1}$ and $\delta_{\max 2}$ is the maximum value of δ_1 and δ_2 , $v_1 = (E_{i1} - E_0)/(E_{\max 1} - E_0)$, $v_2 = (E_{i2} - E_0)/(E_{\max 2} - E_0)$, in which $E_{\max 1}$ and $E_{\max 2}$ are the impact energy corresponding to $\delta_{\max 1}$ and $\delta_{\max 2}$, E_0 being the initial energy of secondary electrons and $k = 0.62$ for $v < 1$; $k = 0.25$ for $v > 1$. For one RF period, the total effective secondary electron emission yield δ is:

* Email: zhoukui@pku.edu.cn

† Corresponding author, email: xylu@pku.edu.cn

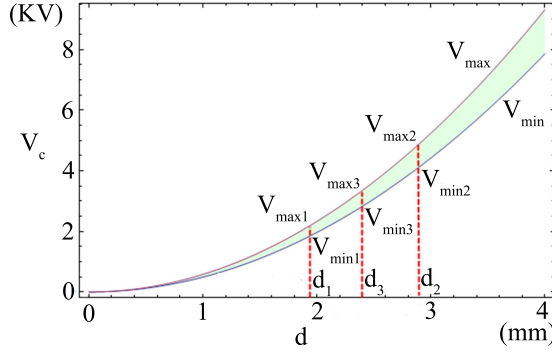


Figure 2: The resonant gap voltage range versus the gap d when the cavity frequency is 2856 MHz.

$$\delta = \delta_1(E_i)\delta_2(E_i)(1 - T) \quad (2)$$

Now, we consider a RF cavity operating at the resonant frequency ω_0 . The gap distance between the cathode and the grid-anode is d . Under the force of the electric field, electrons in the cavity move back and forth between the cathode and the grid-anode. The transit time from one anode to the other is just one-half RF period [1]. We obtain the resonant condition:

$$V_c = \frac{m}{e} \frac{\omega_0 d (\omega_0 d - \pi v_0)}{2 \sin \varphi_0 + \pi \cos \varphi_0} \quad (3)$$

In which, m is the mass of electron, e is the elementary electric charge, v_0 is the initial velocity of the emitted electrons and φ_0 is the initial phase of the RF field.

The MPG also needs to satisfy the requirement of the self-bunching property. The self-bunching property demands the secondary electrons emitted within an appropriate initial phase range. For electrons with emitted energy $E_0 = 0$, the appropriate initial phase range is 0 to $\arctan 2/\pi$ ($\approx 32.5^\circ$) [1]. Substituting the phase range into the resonant condition (Eq. 3), we get the corresponding resonant gap voltage range:

$$V_{min} = \frac{m}{e} \frac{\omega_0^2 d^2}{\sqrt{\pi^2 + 4}} \quad (4a)$$

$$V_{max} = \frac{m}{e} \frac{\omega_0^2 d^2}{\pi} \quad (4b)$$

Figure 2 shows the resonant gap voltage region (light green area) varying with the gap distance d when the cavity frequency is 2856 MHz. If the gap voltage is outside of this resonant range, the electrons cannot gather together in the longitudinal direction so that the electron beam will break up.

Requirements for Steady State Multipacting

Basically, the higher the gap voltage is, the more energy will be gained. According to the secondary emission prop-

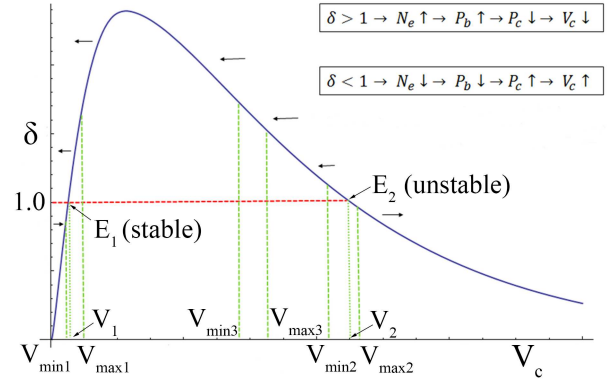


Figure 3: The total effective SEY curve versus the gap voltage V_c . (E_1 is the first crossover point and E_2 is the second one. V_1 and V_2 are the gap voltages corresponding to E_1 and E_2 . $[V_{min1}, V_{max1}]$, $[V_{min2}, V_{max2}]$ and $[V_{min3}, V_{max3}]$ are the corresponding resonant gap voltage ranges when the gap distance d takes different values. In addition, $V_1 \in [V_{min1}, V_{max1}]$ and $V_2 \in [V_{min2}, V_{max2}]$.)

erty of common materials, we can map the total effective SEY curve versus the gap voltage qualitatively (Fig. 3).

Supposing that the resonant gap voltage range is $[V_{min1}, V_{max1}]$, if the gap voltage V_c is greater (less) than V_1 , more (fewer) secondary electrons will be released, so the number of electrons N_e will increase (decrease). As a result, more (less) microwave power will be drained from the cavity as it accelerates more (fewer) secondary electrons. This leads to a higher (lower) P_b and lower (higher) P_c as well as a lower (higher) gap voltage V_c , which makes V_c closer to V_1 in subsequent RF periods. Similarly, V_c will move far away from V_2 automatically if $[V_{min2}, V_{max2}]$ is the resonant gap voltage range. Thus E_1 is the steady state operating point for the MPG, not E_2 . This conclusion is consistent with R. Kishek and Y.Y. Lau's theoretical analysis on multipactor discharge in a closed RF cavity [6, 7].

However, if the resonant gap voltage range is set to be $[V_{min3}, V_{max3}]$ as many previous studies did, δ will be always greater than 1. When the gap voltage reaches the resonant range, the multipacting current will grow to a very large value in a very short time. A great deal of microwave power will be drained from the cavity to accelerate these multiplied electrons. So the gap voltage will eventually fall outside of the resonant range and the electron beam will break up due to the longitudinal debunching. Therefore, there is no stable working point in $[V_{min3}, V_{max3}]$. This explains why previous MPGs could not work stably.

To obtain steady state multipacting, the working point should be set in the vicinity of the first crossover point E_1 and $[V_{min1}, V_{max1}]$ should be set as the resonant gap voltage range. Meanwhile, V_1 must be included in this resonant range. Noting that the value of E_1 depends on the secondary emission property of the cathode and the grid-anode as well as the transmission factor T (Eq. 2), while the resonant gap voltage range $[V_{min1}, V_{max1}]$ is determined by ω_0 and d .

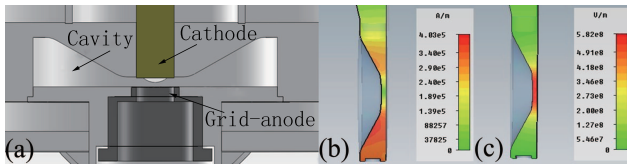


Figure 4: (a) the cross section of the MPG, (b) the magnetic field distribution, (c) the electric field distribution.

Table 1: The Designed RF Parameters of the MPG Cavity

RF parameters	Designed Value
Resonant frequency f_0 (MHz) :	2856
Gap distance d (mm)	1.75
Unloaded quality factor Q_0	653
Shunt impedance r_{shunt} ($M\Omega$)	0.036
Unloaded coupling coefficient β_0	1.25

So, as long as the above requirements are satisfied, it is possible to get steady state multipacting in the MPG.

PRIMARY EXPERIMENTS

The MPG Cavity and the Test Stand

According to the requirements for steady state MP, a micro-pulse electron gun working in the TM_{010} mode with the frequency of 2856 MHz has been designed and constructed. Table 1 lists the designed RF parameters of the MPG cavity. The micro-pulse electron gun (Fig. 4a) consists of a RF cavity made of stainless steel, a cathode made of Cu-Al-Mg alloy and a grid-anode. The impact energy corresponding to the maximum secondary emission yield δ_{max} is about 1 KeV for Cu-Al-Mg alloy [8]. The gap distance between the cathode and the grid-anode is adjustable with the precision of 0.01 mm. The cathode and the grid-anode are also dismountable and can be replaced easily. The distribution of the magnetic field and the electric field are shown in Fig. 4b and Fig. 4c. Obviously, the electric field is mainly concentrated in the region between the cathode and the grid-anode.

The test stand is shown in Fig. 5. The microwave power is supplied by a solid-state power amplifier with 1 kW maximum output power. The output electron beams from the grid-anode are collected by a faraday cup parallelly connected to a 50 Ω resistance and the beam current is measured by a HP 54503A oscilloscope with 1 $M\Omega$ input resistance.

Table 2: The Measured Output Beam Currents (I_b) with Various Grid-anodes

Grid-anode No.	1	2	3	4
Material	SS	SS	OFC	OFC
T	6%	18.3%	18.3%	25%
Measured I_b (mA)	≈ 0.2	3.8	4.2	12.2

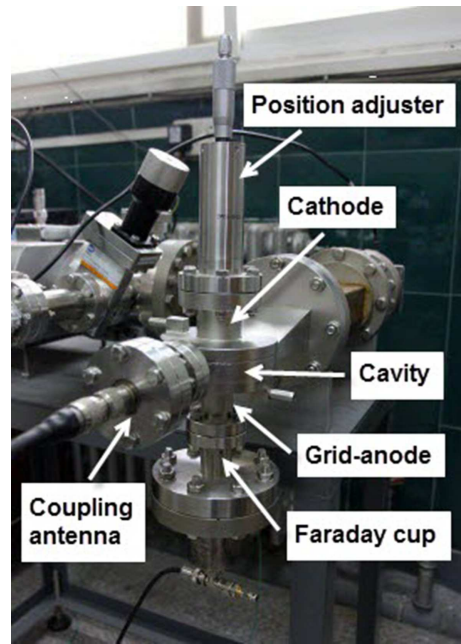


Figure 5: Photograph of the test stand.

Experiment Results and Discussions

Various grid-anodes are tested in our experiments. Table 2 lists the measured output beam currents corresponding to four kinds of grid-anodes with different material and transmission coefficient (T). In Table 2, SS refers to stainless steel and OFC represents oxy free copper. Figure 6 shows our primary experimental results. The macro-pulse width is 15 μs and the repetition rate is about 100 Hz. Figure 6a shows the output beam current when No.1 grid-anode is used. The output signal is very small and unstable on the oscilloscope. The waveform is fluctuating with the "spikes" on the pick-up signal and reflected signal in Fig. 6b. Figure 6c performs a very stable output beam current when the grid-anode is No.2. The signal waveform can remain unchanged for more than half an hour, which reveals that we have already obtained the steady state multipacting in the MPG. The output beam current is about 1.7 mA. Moreover, it can be adjusted up to 3.8 mA, which is shown in Fig. 6d. We also obtained the stable output beam current successfully, when No.3 and No.4 grid-anode are tested (Fig. 6e and Fig.6f). The output beam current measured in the experiments are about 4.2 mA ($T=18.3\%$) and 12.2 mA ($T=25\%$) respectively.

The spikes appearing on the pick-up signal and the reflected signal in Fig. 6b indicate the typical unstable multipacting processes in the cavity. In this situation, the total effective SEY is above 1, but the actual working point is not in the vicinity of E_1 . So, the electrons in the cavity grows rapidly without restraint. The multiplied electrons absorb plenty of RF power, leading to the cavity voltage falling out of the resonant gap voltage range, so the electron beam collapses. After that, the cavity voltage returns to the initial state. The remaining electrons in the cavity will begin

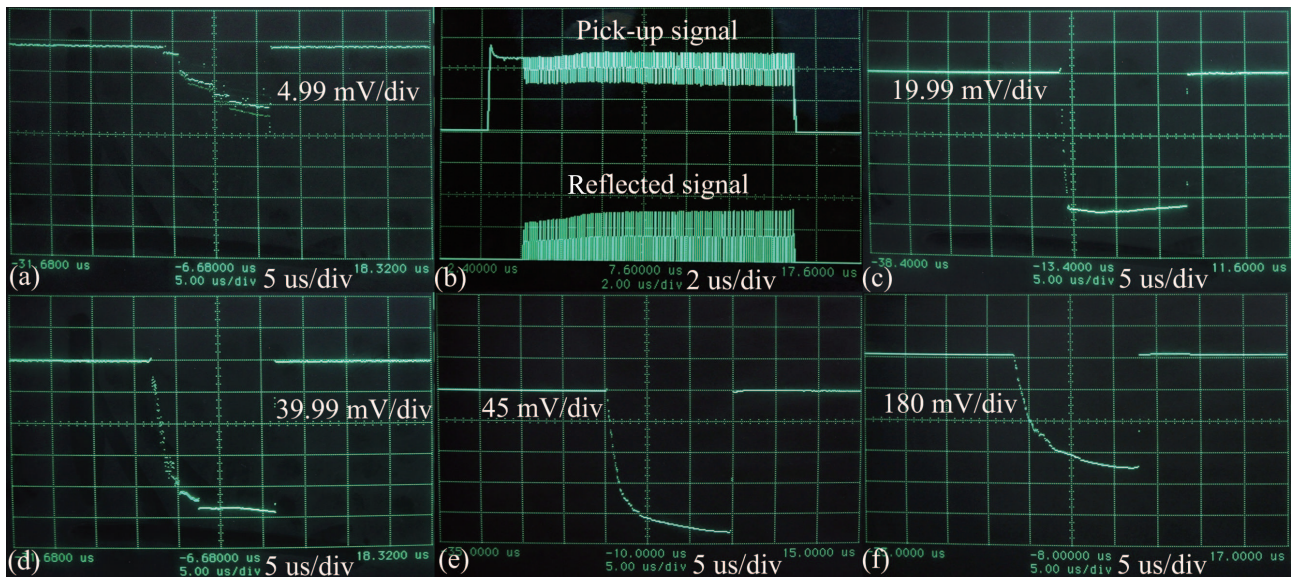


Figure 6: Primary experimental results. (a) is the output beam current (≈ 0.2 mA) when the grid-anode is No.1; (b) is the pick-up signal and reflected signal corresponding to (a); (c) is the output beam current (≈ 1.7 mA) when the grid-anode is No.2; (d) is the maximum detected output beam current (≈ 3.8 mA) when the grid-anode is No.2; (e) is the output beam current (≈ 4.2 mA) when No.3 grid-anode is tested; (f) is the output beam current (≈ 12.2 mA) when No.4 grid-anode is tested.

the multiplication again and a new cycle keeps on. So the "spikes" appears on the pick-up signal successively as well as the reflected signal due to the variation of the loaded coupling coefficient.

CONCLUSION

In summary, this paper presents a study on the steady state multipacting in a micro-pulse electron gun with theory and experiments. In theory, the requirements for steady state multipacting is proposed. The working point should be set in the vicinity of the first crossover point E_1 and $[V_{min1}, V_{max1}]$ should be set as the resonant gap voltage range. Meanwhile, V_1 must be included in this range. As for experiments, a MPG cavity with the frequency of 2856 MHz has been designed and constructed. Various kinds of grid-anodes are tested in our experiments. Both the unstable and stable multipacting current have been observed. Presently, the measured stable output beam current has reached 12.2 mA. Further experimental study is under way now.

ACKNOWLEDGMENT

We gratefully acknowledge the assistance of Li Ming and Yang Xingfan in providing the solid-state power amplifier.

We also thank Wang Xinping for preparing the Cu-Al-Mg alloy.

REFERENCES

- [1] J. R. M. Vaughan, IEEE Trans. Electron Devices 35(7), 1172-1180 (1988).
- [2] F. M. Mako and W. Peter, PAC'93, Washington, 4, 2702-2704 (1993).
- [3] L. K. Len and F. M. Mako, PAC'99, New York, 1, 70-74 (1999).
- [4] J. Y. Zhai, C. X. Tang, S. X. Zheng, EPAC'06, Edinburgh, 3203-3205 (2006).
- [5] J. R. M. Vaughan, IEEE Trans. Electron Devices 36(9), 1963-1967 (1989).
- [6] R. Kishek and Y. Y. Lau, Phys. Rev. Lett. 75(6), 1218-1221 (1995).
- [7] R. Kishek, Y. Y. Lau et al., Phys. Plasmas 5(5), 2120-2126 (1998).
- [8] Q. H. Pan, The Chinese Journal of Nonferrous Metals 10(3), 374-377 (2000).

DARK CURRENT STUDIES AT THE APEX PHOTOINJECTOR*

Ruixuan Huang[†], NSRL, University of Science and Technology of China
Hefei, Anhui, 230029, China

Daniele Filippetto, Christos Frantzis Papadopoulos, Fernando Sannibale
Lawrence Berkeley National Laboratory, Berkeley, CA 94720, USA

Abstract

The increasing scientific demand for a high repetition rate FEL light source is driving the development of electron sources with high beam quality, delivering electron bunches at rates in the MHz range. An ongoing project to develop such a source is the Advanced Photoinjector Experiment (APEX) at LBNL. High brightness electron beams require high fields at the cathode during the electron emission. Such high fields associated with imperfections on the cathode surface area can induce undesired electron field emission (dark current). Excessive dark current can generate quenching of SRF structures and undesired radiation doses activating accelerator components and damaging undulator structures. In the present paper, we discuss the dark current studies performed at APEX. Field emitters in the cathode area have been localized and characterized, and techniques for minimizing dark current emission and to passively remove it have been investigated.

INTRODUCTION

APEX aims to demonstrate the capability of a new concept RF gun, the CW 186 MHz VHF-Gun [1, 2], of delivering electron beams with quality required by X-ray FEL applications at MHz-class repetition rates. Figure 1 shows a cross section of the VHF-Gun. The requirements of CW operation and high accelerating field cause many technical challenges, and dark current control is one of them. Here we report on the dark current studies at APEX, with experimental measurements and simulation results. Based on the specific position of dark current emitters, a scheme for a passive collimation is proposed which could significantly reduce the dark current amount transported downstream.

DARK CURRENT MEASUREMENTS AND SIMULATIONS

Dark current measurements in APEX included the imaging of field emission sources located in the cathode area, and the measurement of dark current versus accelerating field at the cathode (for a single emitter and integrated over all emitters).

Sources of Dark Current in the VHF-Gun

In APEX the photo-emitting material is deposited on a molybdenum plug that can be inserted into the gun by the vacuum loadlock system located in the rear side of the gun.

* Work supported by Director of the Office of Science of the US Department of Energy under Contract no. DEAC02-05CH11231

[†] ruixuanhuang@lbl.gov

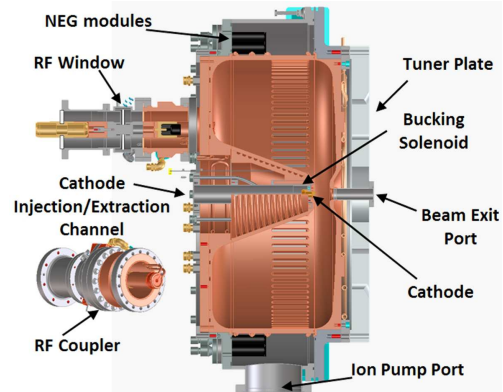


Figure 1: CAD cross-section of the VHF-Gun, with main components in evidence. The gun copper RF cavity resonates at 186 MHz and operates in continuous wave (CW) mode accelerating beams at a nominal energy of 750 keV with a gradient at the cathode of ~ 19.5 MV/m.

When inserted, see Fig. 2, only the tip part of the plug is exposed to the RF fields in the gun. This part has a radius of 5 mm and is surrounded by the copper of the cavity nose.

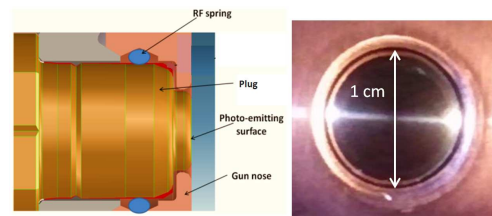


Figure 2: Left: CAD side view of the molybdenum cathode plug inserted in the gun nose. Right: picture showing the plug tip inside the gun viewed from the beam exit pipe.

By properly tuning two solenoids downstream, dark current electrons were used to create an image of the field-emitters at the cathode on a screen located downstream of the second solenoid. In the left side of Fig. 3 one of those images is shown. Several field emitting points are located with good accuracy along a ring are clearly visible. The image magnification was calibrated with the help of ASTRA simulations [3], revealing a ring radius of ~ 5.3 mm, implying the source to be located just outside the molybdenum plug, on the copper side surrounding the plug itself. The right side of Fig. 3 shows the dark current in the same imaging conditions, but the picture is taken with a much higher dynamic range, unveiling also the weakest sources.

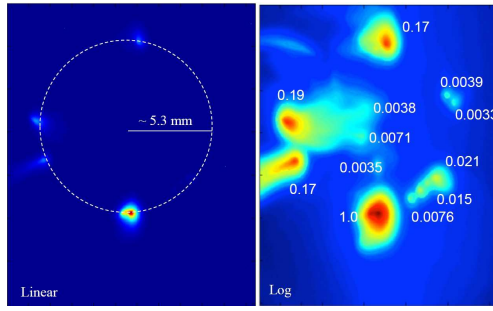


Figure 3: Left: image of the field emitters in the cathode area. Right: the same image with the intensity plotted in logarithmic scale shows the relative intensity of the peaks.

Dark Current Propagation Along the Beamline

Using the information from the experimental observation above, it was possible to simulate the dark current propagation from the emitters downstream the beamline. We represented the dark current source by 4 field emitters laying on the 5.3 mm radius circle, and separated by 90 degrees.

The temporal distribution was retrieved from the Fowler-Nordheim (FN) fit of data taken using a Faraday cup mounted at the exit flange of the gun (see Fig. 4), and the nominal accelerating field of 19.5 MV/m was used. For each gun RF phase the instantaneous dark current was calculated using the value from the fit in the figure. The resulting longitudinal distribution is shown in Fig. 5, together with the Gaussian fit approximation that was used in simulations.

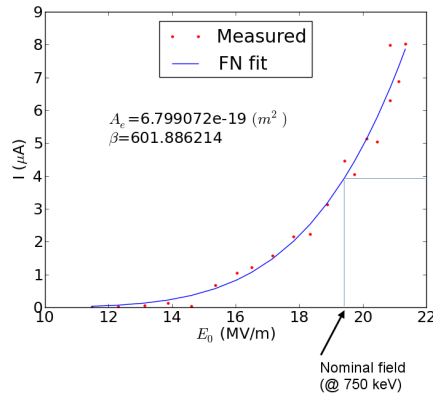


Figure 4: Dark current vs. electric field at the cathode measured by a Faraday cup directly attached to the gun beam exit pipe. A FN fit is also showed. A_e refers to the area of the emitting site and β is a local field enhancement factor that depends on the emitter geometry.

For the longitudinal and transverse momenta, a rectangular distribution with r.m.s. value equal to the momentum equivalent to $E_F / \sqrt{12}$ was used (with E_F the Fermi energy of the metal where the field emitters are located, 7 eV for Cu in our case). Such a choice overestimates the actual energy distribution width, but represents a conservative approximation for our simulations. Simulations showed that, regardless

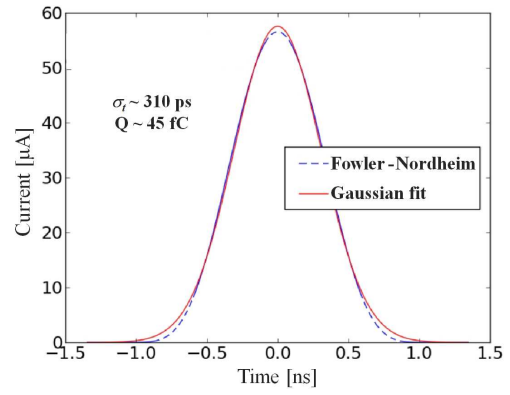


Figure 5: Longitudinal distribution calculated using the FN fit in Fig. 4. Also shown is the Gaussian fit used for the simulations.

of the emitter size, most particles were lost inside the gun and electrons within such initial distribution are not transported through the beamline to the screen position. This is mostly due to the significant RF defocusing kick that off-axis particles experience at the gun exit.

Single particle simulations also showed that the only way for the electrons to be transported downstream the beamline, is for them to have a sizeable net transverse momentum radially directed towards the center of the cathode and pre-compensating the RF kick, see Fig. 6. A further investigation of the field configuration in the cathode area showed that the orientation of the electric field in the interface area between the cathode plug and the surrounding copper, see Fig. 7, can indeed generate the radial momentum component required for transporting the electrons. It also appears evident that any field-emitter eventually present on the edge of the cathode plug would imprint on the electrons an opposite net transverse velocity, not allowing them to exit the gun. The net radial momentum value (within the range shown in Fig. 6) that an emitted electron has, depends on the radial position of that particular emitter along the rounded copper edge surrounding the cathode plug. That position is not known and, in order to overcome this uncertainty, multiple simulations with different initial transverse momentum distributions were performed. The initial distributions were assumed to be Gaussian with the same r.m.s. value, equivalent to $E_F / \sqrt{12}$, but with a variable mean value, equi-distributed over the range of transmitted radial momenta defined by the single particle simulations shown in Fig. 6.

By comparing the experimental image in Fig. 3 with the simulated ones, obtained using the same magnet settings, it was possible to significantly reduce the range of possible radial momenta to values between 20 and 40 keV/c.

In addition, the knowledge of the field emitter's locations in the VHF-Gun, allow to develop an effective strategy for reducing dark current. Details of the proposed methods will be presented below.

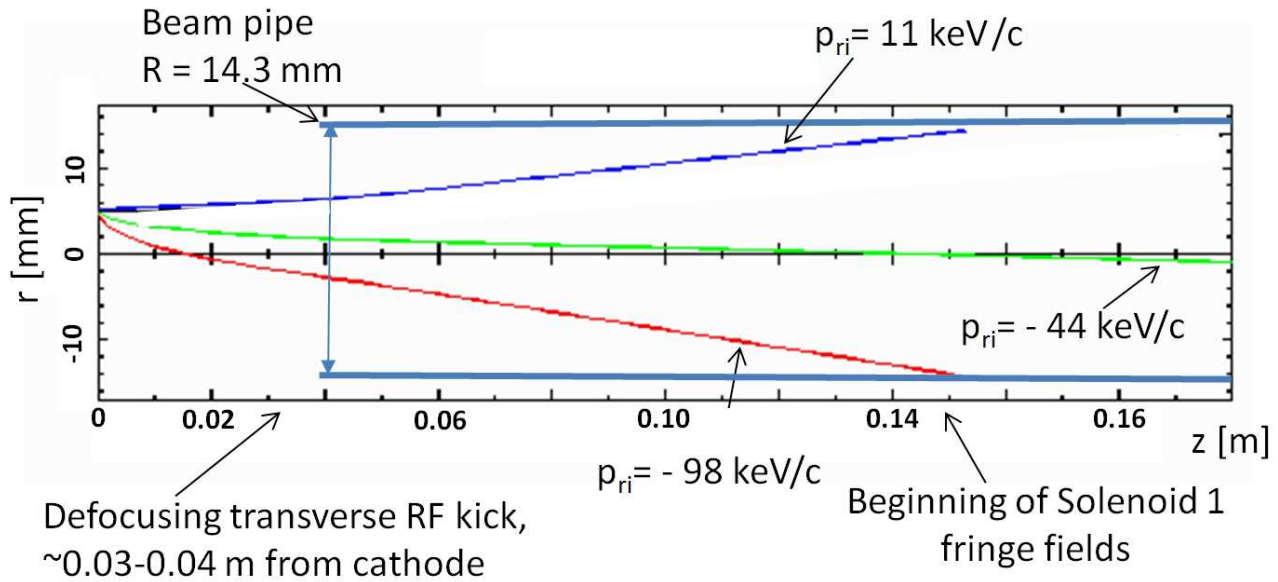


Figure 6: Single particle tracking showing the range of radially oriented transverse momenta required for electrons to be transmitted along the downstream beamline.

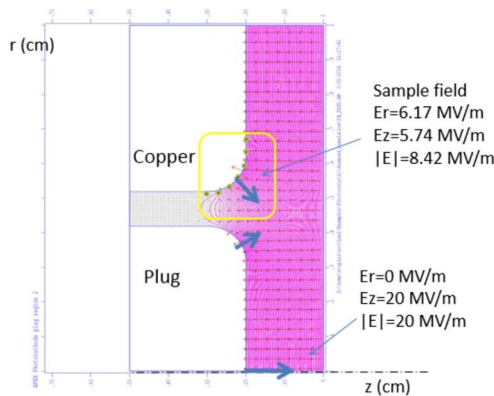


Figure 7: Simulation showing the electric field configuration in the interface area between the cathode plug and the gun cavity nose.

DARK CURRENT MITIGATION METHODS

The use of experimentally tested cleaning techniques such as dry-ice [4] or ethanol rinsing [5] applied to the gun cavity can drastically reduce the number of particulates and hence of potential field emitters. Dry-ice cleaning of the cathode area of the VHF-Gun, where the dark current sources are located, will be tested in APEX in the near future.

The position of the emitters around the VHF-Gun cathode plug can potentially be exploited for a passive collimation, drastically reducing amount of transported dark current. Such a scheme is described in more detail in the next section.

If necessary, by moderately reducing the gun operation energy it is possible to significantly reduce dark current with a minimal impact on the beam brightness performance [6].

An alternative to the passive collimation is represented by an active sweeper system composed by a transverse kicker followed by a collimator. A possible configuration for such a system is presently under study at APEX.

Passive Removal

Based on the experimental and simulation results discussed above, the possibility for a passive collimation scheme system to reduce dark current is studied here. The idea is based on the observation that for a given setting of the solenoids, there could be an optimum position along the beamline where the dark current spots are transversely well separated from the photo-emitted beam, as in the case of Fig. 3. By placing a circular collimator (circular aperture) with the proper diameter in such a position, it is possible in principle to remove most of the dark current without affecting the photo-emitted beam.

In order to evaluate the feasibility of such a scheme in APEX, a number of simulations were performed using the nominal beamline settings for the emittance compensation. The optimal longitudinal position for the collimator along the beamline is the one where the separation between the main beam and the dark current spots is maximum. For each longitudinal position along the beamline, the minimal acceptable radius for the collimator was assumed to be three times the r.m.s. transverse size of the photo-emitted beam in order to minimize losses of such beam. Simulations using the initial distributions described previously allowed to define the position for the collimator that maximizes the reduction in dark current.

Figure 8 shows the simulated dark current transmission vs. the longitudinal position of a collimator of length 1 cm and radius three times the r.m.s. transverse beam size of the photo-emitted beam at that particular longitudinal

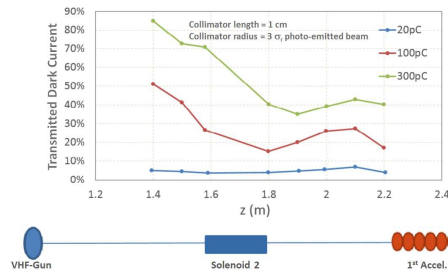


Figure 8: Dark current transmission vs. the longitudinal position of a collimator for three different charges per bunch. The simulations assume a collimator length of 1 cm and a radius three times the r.m.s. transverse beam size of the photo-emitted beam at that particular longitudinal position.

position. The cases for charges per bunch of 20, 100 and 300 pC are shown. It is worth remarking that at any given longitudinal position, the collimator radii used to obtain the results in the figure were not the same between the different charges. Indeed, the photo-emitted beam size depends on the charge per bunch and larger sizes are typically associated with larger charges per bunch. The optimal position for the collimator is the one where the transmitted dark current has a minimum. From Fig. 8, it can be seen that the region right downstream Solenoid 2 represents a good location for a collimator for all the three different charge cases. Additional studies showed that a collimator with 20 cm length inside Solenoid 2 represents a simple and effective solution for all the different charge cases.

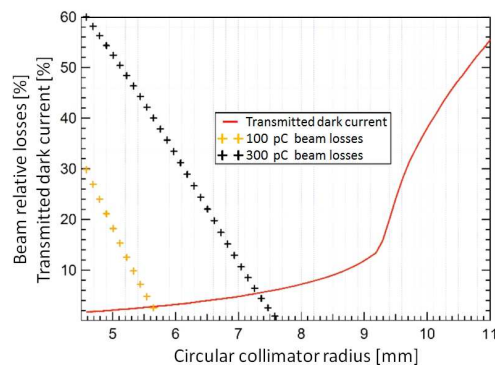


Figure 9: Beam losses vs circular collimator radius. The collimator used in the simulation has a length of 20 cm and is located inside Solenoid 2. It can be seen that with a radius of ~ 8.3 mm no losses are generated in the 100 and 300 pC (20 pC case is not shown in the figure), while $\sim 90\%$ of dark current is lost.

A summary of the results is reported in Fig. 9 where the relative dark current transmission and the relative beam losses vs. the radius of the collimator are shown. One can see from the figure that, for example, with a radius of 8.3 mm more than 90% of dark current is suppressed with no losses for the photo-emitted beams for both the 300 and 100 pC case. For the 20 pC case, not shown in the figure, the collimator does not generate losses even for much smaller radii. Figure 9 also shows that in the most challenging case of 300 pC an orbit stability of few hundreds microns is required to avoid photo-emitted beam losses.

The dark current heat load on the collimator is minimal and can be estimated of the order of 1 W. Such a value does not represents a challenge in terms of cooling, but in order to avoid damage to the collimator from the several hundreds of W if the photo-emitted beam is misteered, a proper cooling or a fast machine protection system is required.

A possible issue that needs to be further analyzed and investigated is represented by the effects on vacuum and cathode lifetime that scattered shower products induced by the dark current impinging on the collimator can potentially generate.

An experimental test is planned at APEX in the near future.

CONCLUSION

Dark current in APEX VHF-Gun has been characterized and point-like field emitters were localized in the cathode area. A passive collimation located at the second solenoid along the APEX beam line is proposed to reduce transported dark current by a factor of ten. The collimation system will be tested at APEX.

REFERENCES

- [1] J.W. Staples, F. Sannibale, and S. Virostek, CBP Tech Note No. 366 (2006).
- [2] K. Baptiste, et al., "A CW normal-conductive RF gun for free electron laser and energy recovery linac applications", Nucl. Instrum. Methods Phys. Res., Sect. A 599, 9 (2009).
- [3] K. Flottman, <http://www.desy.de/~mpyflo/astradokumentation/>
- [4] S. Rimjaen, et al., Proceedings of EPAC2008, Genoa, Italy (2008).
- [5] M. Kuriki, et al., Proceedings of IPAC2011, San Sebastián, Spain (2011), page 92.
- [6] C. F. Papadopoulos et al, "Longitudinal and Transverse Optimization for a High Repetition Rate Injector", In These Proceedings: Proc. 36th Free Electron Laser Conf., Basel, 2014, THP057.

THE SWISSFEL C-BAND RF PULSE COMPRESSOR: MANUFACTURING AND PROOF OF PRECISION BY RF MEASUREMENTS

Urs Ellenberger, Heinrich Blumer, Markus Bopp, Alessandro Citterio, Mathias Heusser, Max KleeB, Ludwig Paly, Markus Probst, Thomas Stapf, Riccardo Zennaro,
Paul Scherrer Institut, 5232 Villigen PSI, Switzerland

Abstract

A pulse compressor is required to compress the RF power distributed to the four accelerating structures of a single C-band (5.712 GHz) module of the SwissFEL. The pulse compressor is of the barrel open cavity (BOC) type. A total of 26 BOC devices are necessary to operate the linear accelerator (26 modules or 104 C-band structures) of SwissFEL X-ray laser. The C-band BOC combines the advantages of compactness and large RF efficiency i.e. large compression factor. Key features of the BOC are described and how they have been implemented in the manufacturing and tuning processes. RF measurements of the BOC are presented to account for the mechanical precision reached by manufacturing. So far 4 BOCs have

been manufactured in-house and one has been high power tested in a RF test stand to simulate the operation in SwissFEL.

INTRODUCTION AND OVERVIEW

The linear accelerator (LINAC) of the SwissFEL consists of 26 C-band modules each of 4 pieces of 2m long C-band structures made of copper discs and supported on two granite girders. The waveguide system of each module is fed through a pulse compressor made of the barrel open cavity (BOC) type [1]. It is mounted on top of one end of the module as depicted in Fig. 1.

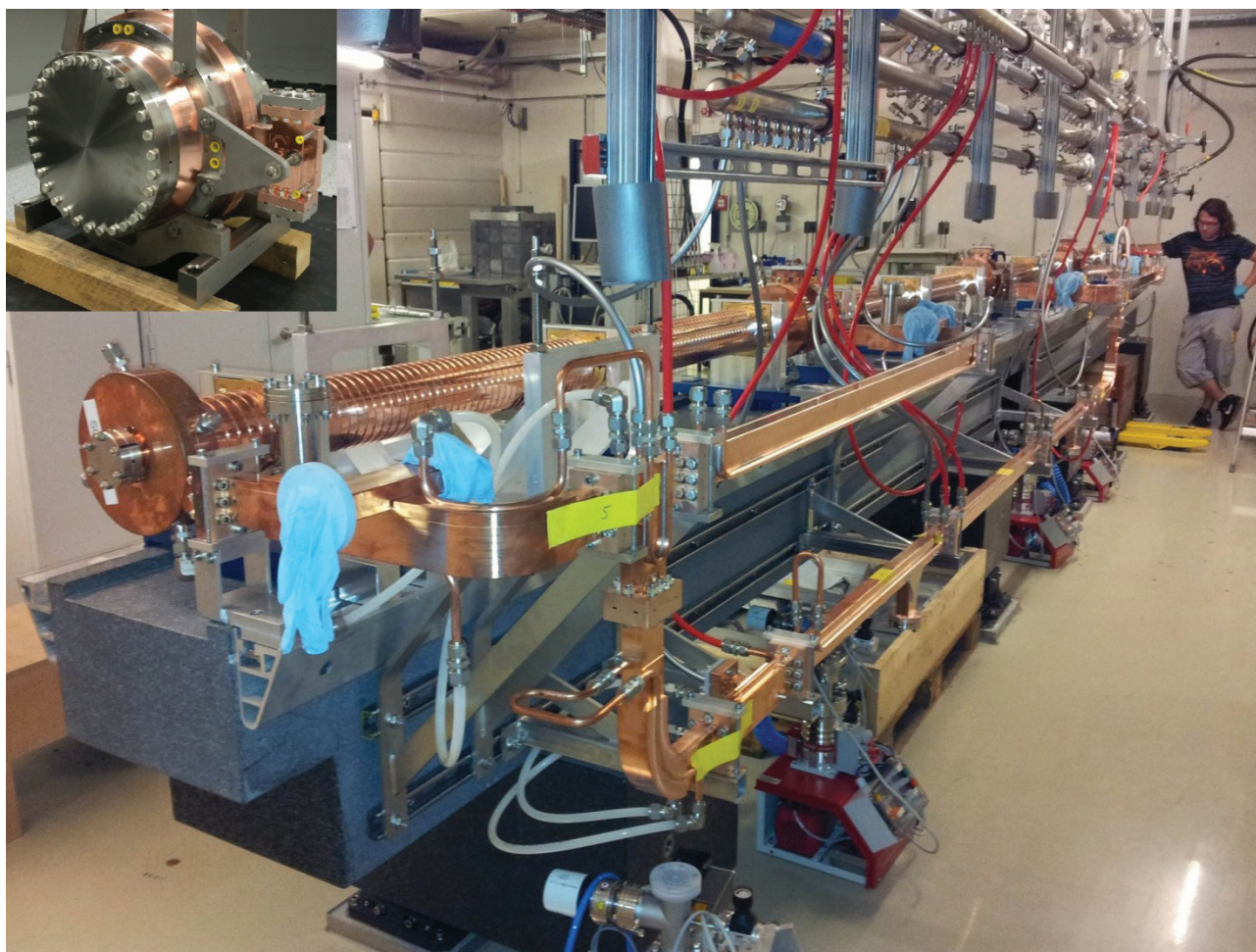


Figure 1: One C-Band module consists of 4 C-band structures made of copper discs and supported on two granite girders. The waveguide system is attached laterally on the girders. On the top left side of the module the pulse compressor BOC will be mounted (note inset photography on top, left).

The design and construction have been thoroughly tested on a prototype BOC made by VDL company in Netherlands. As a result the RF and the mechanical design of the BOC resonator have been qualified for the series production of at least 26 units. An on/off mechanism and an absorber inside the prototype BOC have been removed because they were unessential during testing and because of outgassing problems of silicon carbide parts [2].

The BOC for the SwissFEL is of a new design and uses the whispering gallery resonant mode TE_{18,1,1}. The RF efficiency is determined by the quality factor Q (the ratio of stored energy and power loss in a pulse compressor) and by the coupling factor β (between RF field of external waveguide and of resonance body of compressor). The β value has been optimized to maximize the multiplication factor M for a given klystron pulse length, Q_0 value and filling time of the accelerating structures [2]. For the main design parameters see Table 1.

Table 1: Main Parameters of BOC

Pulse Compressor	Design Parameter
Frequency	5.712 GHz
Quality Factor Q	216'000
Coupling Factor β	10
Energy Multiplication Factor M	2.13

The mechanical setup of the BOC is depicted in Fig. 2:

- The inner copper ring (large copper body of diameter 492 mm and height 290 mm) fully confines the resonator with 72 coupling slits.
- The outer copper ring composes part of the waveguide coupled to the inner cavity.
- Two stainless steel rings provide the water cooling to the cavity and make the body stiffer.
- One T-shaped copper piece for input and output RF signal and 2 C flanges close the inner copper ring.

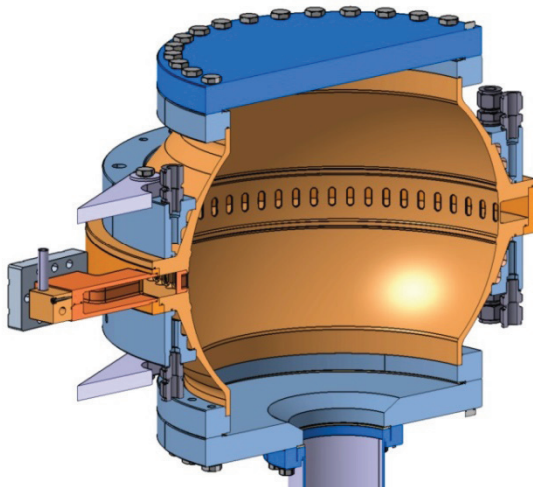


Figure 2: Cross section through the BOC and its parts.

The BOC is mounted on a frame on top of the C-band module. The total weight is about 80 kg. It has a very small impedance for vacuum which allows one vacuum pump to be directly connected to the bottom of the cavity.

MANUFACTURING

The manufacturing of C-band RF pulse compressors BOC has to conform to stringent requirements to minimize cost and to achieve a stable process for an economical industrial series production over years:

- Target precision on the inside of the copper body of $\pm 10 \mu\text{m}$ with a surface roughness R_a of $0.2 \mu\text{m}$
- After milling and final brazing the resonant frequency of the BOC (in whispering gallery mode) match the specified klystron frequency (5.712 GHz)
- The tuning range is $\pm 7 \text{ MHz}$ and is provided by machining two tuning rings placed symmetrical from the mid plane while measuring the resonant frequency achieved through a network analyzer.
- Each month a complete C-band module with one BOC has to be manufactured until spring 2016.

Encouraged by the results of a test BOC [2] we have developed, built and improved the equipment necessary to produce in-house the 26 units of BOC's and to meet the requirements as summarized above. Whenever possible we use pre-machined components to start with and work in parallel when appropriate. In this paper we report on the procedures and handling equipment of the manufacturing process and on the mechanical test results to meet the stringent requirements.

Manufacturing Process

The copper for the BOC pulse compressor is oxygen free, high-conductivity and forged in three-dimensions. Because of the forging-process we have a homogenous distribution of only small pores (not detectable with ultrasonic probes), a stress-free and inherently stable material due to the additional heat-treatment (forging) with a rather large grain size of about $400 \mu\text{m}$. To achieve the precision required for the inner and for the outer copper ring the stress-free material is mandatory even if chip formation is less favourably for large grain size. On the other hand this is related to large grain boundaries which are less prone to breakdowns in high-voltage RF fields (from the klystron, i.e. 50 MW for $3 \mu\text{s}$ at 100 Hz).

The BOC production steps are summarized as follows:

- Pre-turning, annealing and cleaning of inner copper ring and stainless steel rings and flanges
- Precise turning after annealing of the outer surface of the inner copper ring and of the stainless steel rings and flanges to fit the contour of the inner copper ring
- In-house turning, milling and cleaning of the outer copper ring, copper pieces and stainless steel plates for the T-shaped RF coupler
- Brazing of the inner copper ring with stainless steel rings and flanges (vacuum furnace, 850°C)

- Brazing of the copper and stainless steel parts to the T-shaped RF coupler (vacuum furnace, 850°C)
- Precise milling and turning of the inner surface of the inner copper ring and of the coupling slits (with a wall thickness of only 3 mm)
- Cleaning and final brazing the BOC body with the outer copper ring and with the T-shaped RF coupler in a vacuum furnace at 780°C.
- Tuning by turning the two tuning rings (symmetrically located above and below the mid-plane of the inner copper ring) to match the target frequency of 5.712 GHz
- Final cleaning, annealing and mounting on a frame ready for installation on a C-band module

Equipment used for Manufacturing

For the precise milling and turning of the copper we use a sturdy 5-axis CNC machining center (Hermle C42 U MT) with an actively driven swivelling rotary table as depicted in Fig. 3.

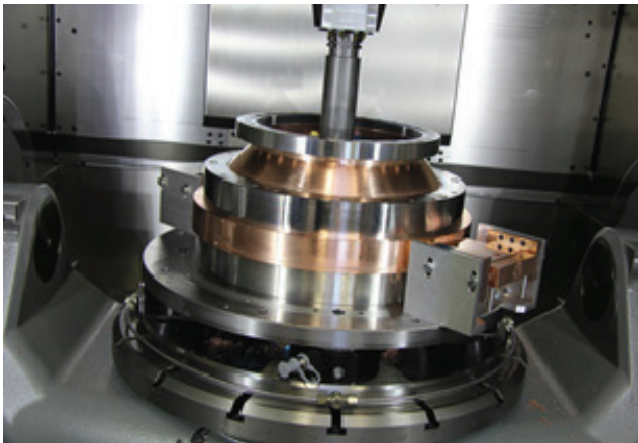


Figure 3: Pulse compressor BOC mounted in a zero-point clamping system on the swivelling rotary table of the CNC machining center Hermle C42 U MT.

The milling is based on a gantry construction type. The turning tools were adapted to fully reach the inner surface of the inner copper ring. A defined sequence of cuts (each cut prepares the next one) with poly- and mono-crystalline diamond (PCD, MCD) tools is required in a temperature and humidity controlled machining compartment of the milling-machine. With this we finally reach a measured precision of $\pm 10 \mu\text{m}$ on the inner copper surface with an estimated surface roughness of R_a of $0.2 \mu\text{m}$.

For quality control of shape and position tolerance we use a precise coordinate measuring machine Mitutoyo Legex with a base precision of $0.35 \mu\text{m}$. The BOC has a reference plane and a lateral surface area. The quality assurance is performed always related to the same reference plane. For the brazing fit we need to know the shapes of the inner and outer copper rings, of the flanges and of the stainless steel cooling rings and of the T-shaped

RF coupler. For the radio frequency application of the BOC we need to know the inner surface shape of the inner copper ring (equal to two displaced spheres) and position and shape of the tuning rings.

We use ultrasonic cleaning (with degreasing, de-oxidisation and prevention of re-oxidisation in separate baths) at 80 kHz and 60°C (see Fig. 4). After flushing with tap and de-ionized water and hot dry air drying the copper and stainless steel parts are stored in dry nitrogen gas or the BOC is filled with dry nitrogen gas and closed.



Figure 4: Ultrasonic cleaning of a BOC pulse compressor in one of the aqueous chemical liquids.



Figure 5: For the first brazing at 850°C three BOC pulse compressors in their solder gauges are arranged in a frame (total weight 640 kg) which is on a stationary table.

For heat treatment (annealing for stress relief at 250°C for 2 hours) and brazing we use a vacuum brazing furnace. The furnace is a full metal construction and operates up to 1'250°C in UHV vacuum ($< 10^{-6}$ mbar). It has been custom made by the PINK company (Germany). It has a rigid platform and a vertical movable dome with 9 programable heating elements. The total height is 8.5 m and the working height inside is 2.8m when the furnace is open. The usable working diameter is 0.8 m. The resulting working volume can accommodate up to three BOC's fixed in solder gauges and placed in a frame on top of each other (see Fig. 5). A series of thermocouples measures process temperatures along the copper bodies while operating the vacuum furnace for brazing. Because of the total mass and the brilliant surface finish of the copper the brazing process is rather slow (18 h).

For adequate handling of the BOC and its parts we have constructed and built a number of tools in-house. Among others the most important are:

- Zero-point clamping system for the BOC body to ensure reproducible setups within 10 μm
- Special lathe tool (280 mm long) to fix diamond tools and to allow turning of the full inside surface of the inner copper ring of the BOC
- Round supports with three-point bearings for levelling the BOC on the coordinate measuring

machine to ensure proper measurements with respect to the reference plane of the BOC

- Positioner with a controlled center of rotation for crane operation to allow a defined and safe rotation of the BOC by 90° to its final mounting position

TUNING

The RF (cold) measurements check the frequency mismatch of the structure with respect to the nominal frequency f_{nom} of 5.712 GHz at the nominal operating conditions after turning a defined sequence of the two tuning rings (see Fig. 6).

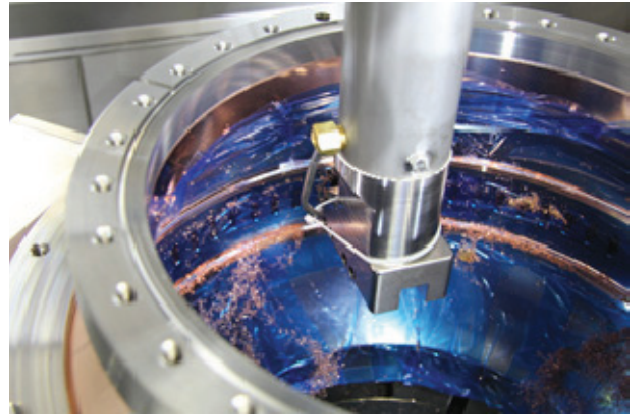


Figure 6: Turning on tuning rings with diamond tool.

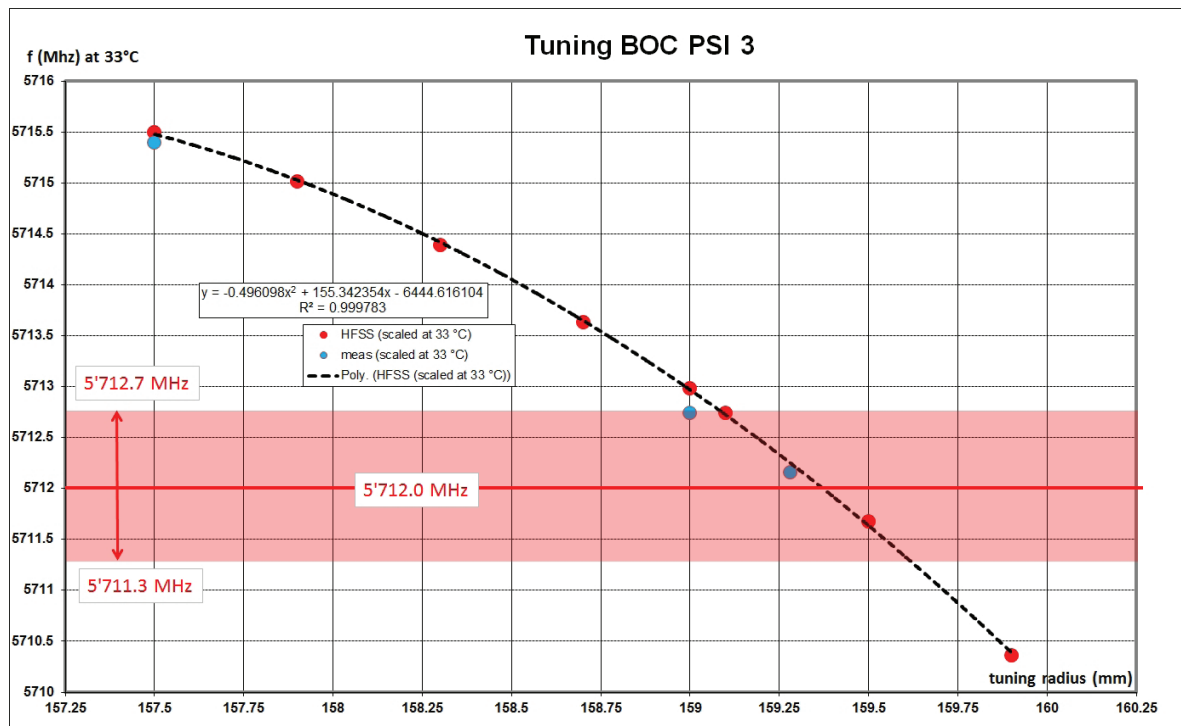


Figure 7: Measured tuning radius and resonant frequencies of BOC (blue dots) and calculated tuning radius and resonant frequencies (red dots). The range of tuning accessible through water cooling of the BOC (corresponds to 5'712 MHz \pm 0.7 MHz) is dashed in red and needs no further turning of the tuning rings.




#	Maker	Tuning steps	f (MHz)	Q ₀	Power test	Breakdown rate ¹⁾
0	VDL	4	5711.952	219000±4000		3 · 10 ⁻⁸ (35 MW; phase jump) (1) 2·10 ⁻⁸ (40 MW phase modulation) (1)
1	PSI	4	5712.061	226000±4000		1·10 ⁻⁷ (40 MW phase jump) (2)
2	PSI	3	5711.944	225000±4000	-	-
3	PSI	2	5712.159	218000±4000	-	-
4	PSI	0	5711.979	217000±4000	Next test	 No tuning
5-8	PSI	0	Under production			
9-30	PSI	0	Series production			

Figure 8: Measured parameters of resonance frequencies, quality factor Q_0 and power test with breakdown rates.

Referring to Fig. 7 this is expressed by increasing the radius of the tuning rings as a measure of increasing volume of the inner copper ring. The measurements are plotted against simulated data (code HFSS in ANSYS) to determine the next sequence of milling until the resulting frequency is sufficiently close to f_{nom} . In this case, quality factor Q_0 and coupling factor β are determined as well as the resulting frequency f_{meas} by the network analyzer. In practice no mechanical tuning can be performed for $f_{\text{meas}} - f_{\text{nom}} < 0.2$ MHz since this corresponds to a dimensional change of $< 34 \mu\text{m}$ or equivalent to a 2°C change.

The RF cold measurements are given below (Fig. 8):

- The values for Q_0 and β agree well within 1% to the designed values. This confirms the high precision machining and brazing of BOC pulse compressors.
- The frequency mismatch can be easily compensated by changing the operating temperature within $\pm 7^\circ\text{C}$ (corresponds to ± 0.7 MHz or to $\pm 50 \mu\text{m}$).
- Starting with BOC number 4 we have verified that the manufacturing is precise enough that no extra mechanical tuning (turning of tuning rings) is necessary. The tuning to resonance frequency f_{nom} (5.712 GHz) is performed by adjusting the cooling temperature within $\pm 7^\circ\text{C}$.

Referring to Fig. 9 for power testing of the BOC pulse compressor the input power from the modulator is 15 kW at 5.712 GHz. Peak power at the output of the BOC is 53 MW for $3 \mu\text{s}$ at 100 Hz. We have observed breakdown rates of $3 \cdot 10^{-8}$ at 100Hz (1 breakdown in 93 h).

CONCLUSIONS

Up to now 4 BOC pulse compressors have been manufactured and tested on site one of which has no tuning rings. This makes the manufacturing process

shorter and less risky for possible break-downs (no chips and no additional cleaning after chip production due to tuning). The mechanical precision required as well as the very good results of RF and power-testing are very well accomplished through the manufacturing processes. The next power test with a complete C-band module and with BOC number 4 is planned in spring 2015 when a new modulator becomes available.

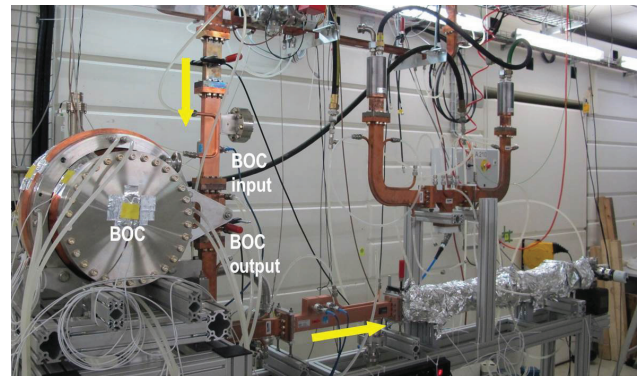


Figure 9: Setup for power testing of the BOC.

ACKNOWLEDGMENT

For helpful discussions and for supporting we wish to thank Hansrudolf Fitze and Tom Kleeb of the RF group as well the engineering group (Haimo Joehri) and the machine shop (Laila Kueng, Michael Kleeb).

REFERENCES

- [1] I. V. Syratchev, "The Progress of X-Band Open Cavity RF Pulse Compression Systems", EPAC 1994, London, England.
- [2] R. Zennaro et. al., "C-Band RF Pulse Compressor for SwissFEL", IPAC 2013, Shanghai, China.

LONGITUDINAL AND TRANSVERSE OPTIMIZATION FOR A HIGH REPETITION RATE INJECTOR¹

C. F. Papadopoulos, D. Filippetto, R. Huang, G. J. Portmann, H. Qian, F. Sannibale, S. Virostek,
R. Wells, LBNL, Berkeley, California, USA

A. Bartnik, I. V. Bazarov, B. Dunham, C. Gulliford, C. Mayes,
Cornell University (CLASSE), Ithaca, New York, USA

A. Vivoli, Fermilab, Batavia, Illinois, USA

A. Brachmann, D. Dowell, P. J. Emma, Z. Li, T. Raubenheimer, J. Schmerge, T. Vecchione, F. Zhou,
SLAC, Menlo Park, California, USA

Abstract

The injector is the low energy part of a linac, where space charge and non relativistic kinematic effects may affect the electron beam quality significantly, and in the case of single pass systems determines the brightness in the downstream components. Following the increasing demand for high repetition rate user facilities, a normal conducting, high repetition rate (1 MHz) RF gun operating at 186 MHz has been constructed at LBNL and is under operation. In the current paper, we report on the status of the beam dynamics studies. For this, a multi-objected approach is used, where both the transverse and the longitudinal phase space quality is optimized, as quantified by the transverse emittance and the bunch length and energy spread respectively. We also report on different bunch charge operating modes, as well as the effect of different gun gradients.

INTRODUCTION

LCLS-II [1] is a proposed user facility based on a superconducting RF linac driving a high repetition rate FEL, at SLAC. One of the important components of the project that have been identified is the injector part, which needs to accommodate the simultaneous objectives of high repetition rate and high beam brightness. For this reason, the Advanced Photoinjector Experiment (APEX) [2], an R&D project, is under way at LBNL, and is currently the baseline for LCLS-II. APEX is based on a normal conducting, continuous wave (CW) VHF electron gun, operating at 186 MHz. Another option being investigated in parallel is a photoinjector based on DC gun technology at Cornell University [3]. In the rest of the paper, the injector beam dynamics based on the VHF gun will be presented.

LCLS-II Injector Requirements

In order to accommodate the scientific requirements of LCLS-II [1], the requirements on the electron beam at the injector exit are given in Table 1.

A number of these requirements have already been demonstrated at APEX [2], specifically the ones related to the op-

eration of the gun only, such as quantum efficiency, bunch charge and electron energy at the gun exit.

Simulations of the APEX and LCLS-II injectors, discussed later in this paper, show that the brightness requirements can be achieved by APEX. For the experimental verification of this, the installation of APEX phase II is required, which will bring the energy of the beam higher (30 MeV) and allow for the demonstration of beam emittance, bunch compression and the conservation of 6D beam brightness.

INJECTOR LAYOUT

A schematic of the baseline design of the LCLS-II injector, based on the NCRF VHGE electron gun, is shown in Fig. 1

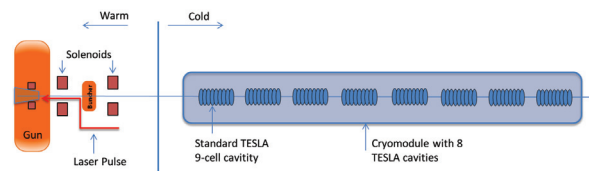


Figure 1: Schematic of LCLS-II injector. The beam energy at the warm-to-cold transition is nominally 750 keV.

The main difference with APEX is the cold part of the injector. In the case of LCLS-II, superconducting TESLA cavities [4] are used, while APEX will be using 3 normal conducting cavities, at 1.3 GHz like the TESLA ones. The final energy of APEX will be lower than 95 MeV, at approximately 30 MeV, enough to demonstrate the main dynamical processes of emittance compensation and bunch compression. The warm part of the LCLS-II injector [5] is essentially identical to the APEX layout.

As discussed below, for some bunch charges and especially the high (300 pC) case, the optimization requires relatively low gradient in the second and third TESLA cavities. This opens the possibility of having a single capture cavity in a stand-alone cryomodule followed by a drift and then a standard, 8 cavity cryomodule. Such a layout has the advantage of allowing more diagnostics as well as easing the maintenance procedure. The implications of using different layouts is discussed in a later section.

¹ This work was supported in part by the Work supported, in part, by the LCLS-II Project and by the Director of the Office of Science of the US Department of Energy under Contract no. DEAC02-05CH11231

Table 1: LCLS-II Injector Requirements

Parameter	Symbol	nominal	range	units
Electron energy at gun end	E_{gun}	750	500 - 800	keV
Electron energy at injector end	E_{inj}	98	95 - 120	MeV
Bunch Charge	Q_b	100	10 - 300	pC
Bunch Repetition Rate in Linac	f_b	0.62	0 - 0.93	MHz
Dark current in injector	I_D	0	0 - 400	nA
Peak current in injector	I_{pk}	12	4-50	A
Average current in injector	I_{avg}	0.062	0.0 - 0.3	mA
Avg. beam power at injector end	P_{av}	6.1	0 - 36	kW
Norm. rms slice emittance at injector end	$\gamma\epsilon_{\perp}$	0.4	0.2 - 0.6	mm
Vacuum Pressure	P_G	1	0.1 - 1	nTorr
Cathode quantum efficiency	QE	2	0.5 - 10	%
Laser Energy at cathode	E_{laser}	0.02	0.0 - 0.3	mJ
Avg. CW RF gradient (powered cavities)	E_{acc}	16	-	MV/m

OPTIMIZATION PROCEDURE

As shown in Table 1, the two main requirements on the brightness of the beam at the injector exit is the transverse emittance $\gamma\epsilon_{\perp}$ and the peak bunch current I_{pk} . In the case of transverse emittance, the goal is to achieve low values. The injector system described here is essentially cylindrically symmetric, which allows us to use the normalized emittance in one transverse plane ϵ_{nx} as one of the objectives to be minimized. Effects that break the symmetry, most importantly dipole and quadrupole components of the RF field in the RF cavities are beyond the scope of this paper, but are currently under evaluation. In the case of the current, I_{pk} is inverse to the bunch length σ_z for reasonably symmetric beams, and an alternative way to perform the optimization is to minimize σ_z .

Space charge at the low energy of the injector couples the longitudinal and transverse planes, and hence the two goals of minimizing the emittance and the bunch length are essentially competing. For such multi-objective, non-linearly coupled problems, the method of multi-objective genetic optimization has been applied with great success [6, 7]. In our approach, we employ the NSGA-II algorithm, with ϵ_{nx} and σ_z being the competing objectives. In this case, the result is not a single solution, but a population of solutions, a so-called Pareto front. This way, trade-offs between the two competing objectives can be evaluated easily. Also, the effect of varying certain aspects of the injector system (such as bunch charge, gun energy and injector layout) can also be evaluated visually, as will be discussed below.

In addition to these two objectives, certain constraints are also placed in the optimizer. The most obvious ones are the constraints on the knobs used in the optimizer, which are described in Table 2.

Other, secondary constraints that are placed on the beam quantities themselves are a) the total energy > 90 MeV, b) the correlated rms energy spread < 1% (in order to accommodate the energy acceptance of the laser heater) and c) the high order, correlated momentum spread $\sigma_{pHO} < \sigma_{max,Q}$,

Table 2: Knobs Used for Injector Optimization. All cavity fields refer to on-axis, peak electric field. Phase of 0 is taken to mean peak acceleration and -90 is zero crossing.

Knob	Value	Function
Gun Phase	-15-15 deg	Control bunch length
Buncher field	0-4 MV/m	Compression, Emit. comp.
Sol 1 B field	0.01-0.2 T	Emit. comp.
Sol 2 B field	0.01-0.2 T	Emit. comp.
CAV 1 field	5-30.5 MV/m (2.6 - 16 MV/m avg)	Emit. comp.
CAV 2 field	5-30.5 MV/m (2.6 - 16 MV/m avg)	Emit. comp.
RMS spot size at the cathode	0.05-2 mm	Control space charge effects
Bunch length at cathode	10-60 ps	Control space charge effects

where $\sigma_{max,Q}$ is a limit that depends on the downstream compression, which is different for different bunch charges.

The high order momentum spread is defined by the relation $\sigma_{pHO}^2 = \langle p_{HO}^2 \rangle$, where the momentum p_{HO} is constructed from the original momentum distribution $p(z) = p_0 + c_1 z + c_2 z^2 + O(z^3)$. The variable z refers to the longitudinal position in the bunch and p_{HO} is given by the $p_{HO} = O(z^3)$ terms. Physically, this can be justified since the p_0 term is the average momentum which doesn't affect beam brightness, and the terms corresponding to c_1 and c_2 can be removed by dephasing the downstream linac and by using a third harmonic cavity downstream respectively. Both of these are standard practices in linac driven FEL facilities. The precise value of the limit imposed on σ_{pHO} depends on the downstream linac dynamics [8,9].

Finally, the assumption of a thermal emittance coefficient of 0.65 mm-mrad/mm is made in the following simulations.

The exact value of this coefficient will of course be determined by measurements, currently underway, and may affect the final emittance of the beam. We should note here, that due to the optimization procedure we follow, the emittance is not the minimum possible achievable by the injector, since we also need to compress the beam. Hence, the effect of the thermal emittance coefficient is reduced, as other effects such as space charge, solenoid aberrations etc, increase the emittance. In addition to this, the subsequent plots correspond to simulations with a relatively low number of macroparticles (10k) and a relatively small number of grid points (30×50), in order to allow for a large number of solutions. This gives typically a larger number for the projected and slice emittance of the beam than finer simulations. Once a solution is picked, more accurate simulations (250k particles, 50×100 grid points) are used for start-to-end runs.

In the next sections, the effect of varying different aspects of the injector is discussed, and simulation results based on multi-objective optimization of the injector are presented, using the particle-in-cell code ASTRA [10].

DEPENDENCE ON BUNCH CHARGE

The bunch charge is the most fundamental characteristic of the electron bunch, and determines the emittance and transverse size of the beam. Different operational modes of the downstream FEL require different bunch charges, with specs described in Table 1.

In Fig. 2 we compare different bunch charges, at 20, 100 and 300 pC. As discussed previously, the result is not a single solution, but a front of solutions. Hence, for each case we can pick a solution that meets the specs of the specific run, while at the same time we are able to easily compare the performance of different charges.

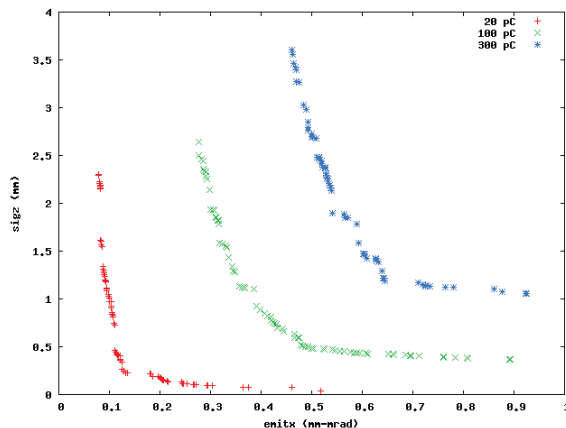


Figure 2: Comparison of Pareto fronts for different charges. Simulations for injector layout of Fig. 1 at gun energy 750 keV

One important point for beam dynamics is that, especially in the case of 300 pC, the optimization algorithm sets the gradient of the 2nd and 3rd cavities to very low gradients and effectively results in a long drift between the 1st and the 4th accelerating cavities. In Fig. 3, we compare the emittance

evolution for 3 of the solutions corresponding to Fig 2, with a finer grid. We see that the emittance compensation process is complete by the exit of the injector, and that a significant part of the process is done while the beam is in the 2nd and 3rd accelerating cavities, at a distance of 4-6 meters from the cathode, corresponding to energies 10-30 MeV (different for each charge optimization).

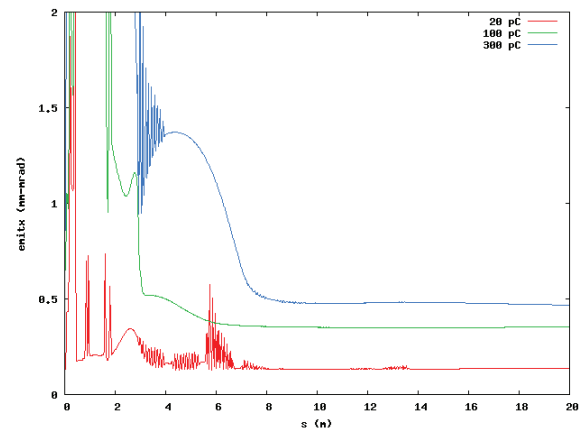


Figure 3: Comparison of emittance evolution for solutions corresponding to Fig. 2. Note that the emittance compensation is finalized at about 8 m.

EVALUATING DIFFERENT INJECTOR LAYOUTS

As mentioned in the previous section, the emittance compensation process is not finalized until after the 1st TESLA cavity in the cryomodule. This implies that it may be better to avoid accelerating the beam too quickly after the 1st cavity, in order to avoid freezing-in the emittance before the compensation process is finalized. In addition to this, a single cryomodule for the 1st cavity has other advantages, as it allows easier maintenance and additional diagnostics. For this reason, a “layout 2” case, which comprises of a single cavity cryomodule, a drift and then the standard 8 cavity cryomodule is also considered, in addition to “layout 1” shown in Fig. 1.

Beam dynamics considerations, especially for lower gun energy, may also require additional gradient and phase knobs in the first few MeV. For this reason, “layout 3” and “layout 4” are also considered, where the single cavity cryomodule is replaced by 5 2-cell cavities based on a Cornell design [3] or by 2 2-cell cavities and a standard TESLA cavity, respectively.

The different options are summarized schematically in Fig. 4.

The Pareto fronts corresponding to the layouts described are shown in Fig. 5, where we can compare the brightness performance of the different schemes, for the same gun energy.

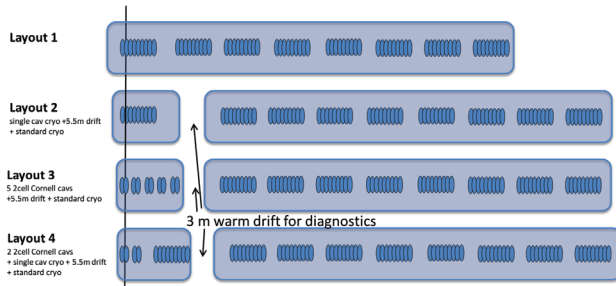


Figure 4: Different layout options for the cold part of the LCLS-II injector. Layout 1 is the baseline option.

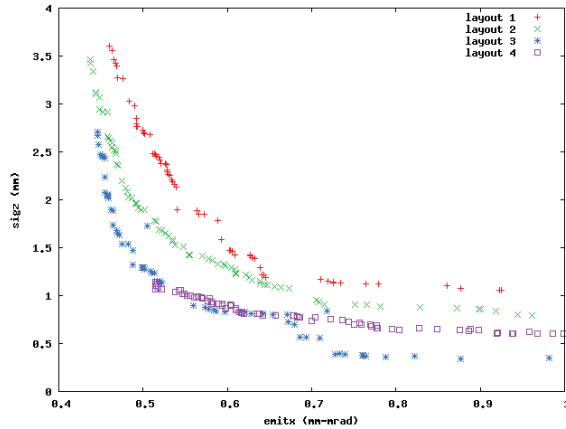


Figure 5: Comparison of Pareto fronts for different injector layouts. Gun energy is 750 keV, bunch charge 300 pC.

DEPENDENCE ON GUN ENERGY

One of the most important quantities that has a great effect on the beam brightness is the gun gradient. In general, higher gradients improve the beam quality, and in the case of the VHF gun this corresponds to higher energies at the gun exit. One potential reason to limit the gradient at the cathode is to reduce the dark current emitted from the gun, although a passive collimation system has also been proposed [11].

We should also point out that the peak energy measured at the exit of the VHF gun is 800 keV, while the nominal, operational energy is 750 keV.

In Fig. 6, a comparison of Pareto fronts for different energies is presented, for 100 pC. The layout in this case is very similar to layout 1 discussed previously, and more studies are under way for all the layouts.

CONCLUSIONS

We report on the status of beam dynamics simulations for the LCLS-II injector. A multi-objective optimization strategy is employed, which allows the simultaneous optimization of transverse and longitudinal phase space.

By using this approach, comparisons of varying different aspects of the injector, such as bunch charge, injector layout and gun energy are presented.

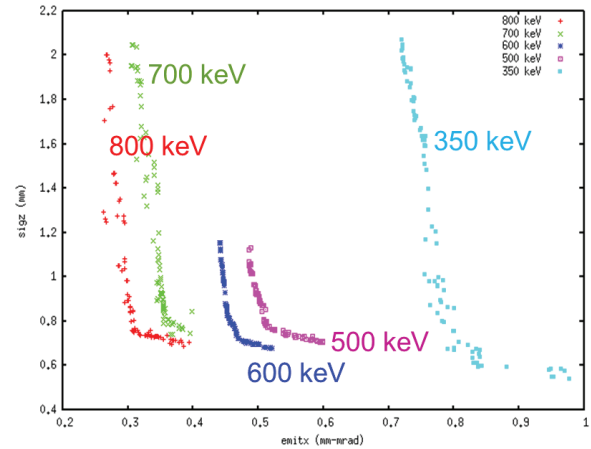


Figure 6: Comparison of Pareto fronts for different energies of the gun.

REFERENCES

- [1] Tor Raubenheimer. The LCLS-II, a New FEL Facility at SLAC. In *Proc. 36th Int. Free-Electron Laser Conf., Basel, 2014*, 2014. WEB01.
- [2] Daniele Filippetto et al. APEX: A Photo-injector for High Average Power Light Sources and Beyond. In *Proc. 36th Int. Free-Electron Laser Conf., Basel, 2014*, 2014. TUA01.
- [3] Colwyn Gulliford et al. Demonstration of low emittance in the cornell energy recovery linac injector prototype. *Phys. Rev. ST Accel. Beams*, 16:073401, Jul 2013.
- [4] B. Aune et al. Superconducting tesla cavities. *Phys. Rev. ST Accel. Beams*, 3:092001, Sep 2000.
- [5] John Schmerge et al. The LCLS-II Injector Design. In *Proc. 36th Int. Free-Electron Laser Conf., Basel, 2014*, 2014. THP042.
- [6] Ivan V. Bazarov and Charles K. Sinclair. Multivariate optimization of a high brightness dc gun photoinjector. *Physical Review Special Topics - Accelerators and Beams*, 8(3):034202, Mar 2005.
- [7] K. Deb. *Multi-objective optimization using evolutionary algorithms*. Wiley, 2001.
- [8] Lanfa Wang et al. Multi-objective Genetic Optimization for LCLS-II X-ray FEL. In *Proc. 36th Int. Free-Electron Laser Conf., Basel, 2014*, 2014. THP029.
- [9] Paul Emma et al. Linear Accelerator Design for the LCLS-II FEL Facility. In *Proc. 36th Int. Free-Electron Laser Conf., Basel, 2014*, 2014. THP025.
- [10] K. Flöttmann. ASTRA: A space charge tracking algorithm. *user's manual available at http://www.desy.de/~mpyflo/Astra_dokumentation*.
- [11] Ruixuan Huang et al. Dark Current Studies at the APEX Photoinjector. In *Proc. 36th Int. Free-Electron Laser Conf., Basel, 2014*, 2014. THP054.

SOLID-STATE SWITCH FOR A KLYSTRON MODULATOR FOR STABLE OPERATION OF A THZ- FEL

G. Isoyama[#], M. Fujimoto, S. Funakoshi, K. Furukawa, A. Irizawa, R. Kato, K. Kawase, K. Miyazaki, A. Tokuchi, R. Tsutsumi, M. Yaguchi, ISIR, Osaka University, Osaka, Japan
F. Kamitsukasa, Graduate School of Science, Osaka University, Osaka, Japan

Abstract

A solid-state switch using static induction (SI) thyristors has been developed for a klystron modulator of the L-band electron linac at Osaka University to enhance stability of a THz-FEL based on the linac. The switch meets the maximum specifications such that the holding voltage is 25 kV with the switching time of 270 ns, that the current is 6 kA for a pulse duration of 10 μ s, and that the repetition frequency is 10 Hz. The fluctuations of the klystron voltage are considerably reduced compared to those with a thyratron. The FEL is operated with the solid-state switch and the macropulse energy of the FEL at a wavelength of ~ 70 μ m are measured with an energy meter for infrared lasers. The fractional variation of the macropulse energy measured in successive 500 pulses is 2.4 % for the solid-state switch (standard deviation), which is much smaller than 5.4 % for the thyratron.

INTRODUCTION

We are conducting basic studies on the THz-FEL and its applications using the L-band electron linac at the Institute of Scientific and Industrial Research (ISIR), Osaka University. The FEL has been operated in the wavelength range from 25 to 150 μ m (2~12 THz). Performance of the FEL depends strongly on the accelerator providing the electron beam for the FEL. One of the crucial factors affecting such studies is stability of the FEL macropulse energy. To obtain a highly intense and stable FEL beam, the energy and the intensity of the electron beam must be constant in an electron pulse of a several microsecond duration, and pulse-to-pulse intensity fluctuations are required to be small. To enhance the stability of the electron beam, the klystron modulator was upgraded, in such a way that the fluctuations of the charging voltage of the PFN are reduced to 0.008% (peak-to-peak). Nevertheless, pulse-to-pulse fluctuations of the height of the high voltage pulse applied to the klystron are measured to be almost ten times larger than those of the charging voltage. Because the source of the instability is considered to be the thyratron, which is a fast high voltage and high current switch for a PFN in the klystron modulator, we have developed a solid-state switch that is expected to be more stable.

The first klystron modulator with a solid state switch for an electron linac was developed, to our knowledge, in the early 1990s at the FOM Institute for Plasma Physics for the FEL facility, FELIX [1]. The switch is made of 32 thyristors that are connected in a series to operate at the

maximum voltage of 40 kV and the maximum current of 2.6 kA. The following activities to develop solid-state switches and to use them began increasing at approximately 2000 in Europe, America, and Japan using semiconductor devices, including thyristors, IGBTs, and MOS-FETs. These devices, however, have both advantages and disadvantages for meeting the specifications and requirements for various klystron modulators.

Another candidate for a semiconductor device that is suitable for the solid state switch is the Static Induction Thyristor (SI-thyristor) because it has fast switching characteristics as well as a high holding voltage and a high current [2]. Two types of solid state switches with different types of SI thyristors were developed for the JLC project and were successfully tested at KEK. These switches, however, have not been used in operation of linacs.

In this paper, we will describe the development of the solid-state switch using SI thyristors and the evaluation of its performance in terms of the stability of the klystron voltage, the RF power and phase, and energy of the FEL macropulses. More detailed report on the solid-state switch will be published elsewhere.

STATIC INDUCTION THYRISTOR

The SI thyristor is a type of PIN diode that is equipped with the gate. The characteristics that are measured from a test sample for pulsed-power applications are reported to be as follows: the hold-on voltage is 5.5 kV, and the turn-on time is 35 ns, with $di/dt = 95$ kA/ μ s [2]. Because these values are sufficient for our purpose, we decided to develop a solid-state switch using SI thyristors. Although they are not available on the market, we obtain SI thyristors by courtesy of Shindengen Electric Manufacturing Co., Ltd., which is developing such devices. Figure 1 shows an SI thyristor manufactured by the company.

Two important specifications of the SI thyristors that we use are the maximum blocking voltage of 3.2 kV and the maximum average current of 50 A (root-mean-square), although the details are not available yet from the manufacturer. It is, however, expected that a much higher current can flow if the pulse duration is short and the repetition rate is not so high that the average power consumption in the SI thyristor does not exceed the value in the slow operation. Characteristics of a SI thyristor measured with square pulses of 2 kV, 1 kA, and a 2 μ s duration are the switching time of 360 ns (90%-to-10% change) and the turn-on resistance of 0.12 Ω . To evaluate

[#]isoyama@sanken.osaka-u.ac.jp

the holding voltage of the SI thyristor, the leak current is measured as a function of the applied voltage at several temperatures of the thyristor from 20 up to 80 °C because the leak current increases as the temperature becomes higher. The measurement shows that the leak current increases gradually with increasing temperature at lower voltages, whereas it increases sharply above 2.6 kV at any of the temperatures. Although the maximum value of the holding voltage written in the manufacturer's specifications is 3.2 kV, we assume that the maximum holding voltage of the SI thyristors is 2.5 kV for this purpose.

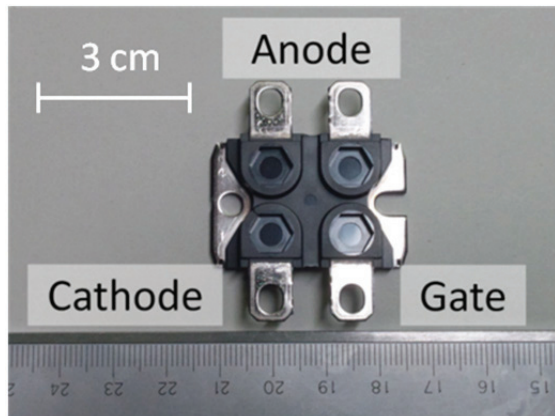


Figure 1: Static induction (SI) thyristor.

SOLID-STATE SWITCH

The modulator currently provides square pulses of 218 kV and 186 A, with a duration of 10 μ s, or those of 236 kV and 210 A with a 5 μ s duration to a klystron (Thales, TV2022D) at a repetition rate of 10 Hz using a 1:24 step-up transformer. Because the charging voltage of the PFN is shared almost equally by the PFN and the klystron when it is on, the switch is operated at 20 kV and 4.5 kA in the long-pulse mode or at 22 kV and 5.0 kA in the short-pulse mode. To fulfill the conditions for the voltage and the current with sufficient margins, the specifications of the switch are determined to be the maximum holding voltage of 25 kV and the maximum current of 6 kA; as a result, ten thyristors are connected in series, and six such series are connected in parallel for the solid-state switch using 60 SI thyristors with the measured characteristics of 2.5 kV and 1 kA at the maximum. Figure 2 shows the external views of the solid-state switch. The main frame consists of five 8-cm thick aluminum-alloy frames with a parallel lattice for air cooling. They are vertically stacked with bakelite frames in between for insulation. Three sets of two serially connected thyristors are installed directly on each longer side of each frame, and a control board with six trigger circuits for gates, a set of error detection circuits, and a power supply are installed on each shorter side, which means that six sets of two serially connected thyristors with peripheral circuits are on each frame. Thus, five such frames comprise a solid state switch with six parallel circuits of ten serially connected SI thyristors.

These frames are placed on a base box, which has two fans installed that send air upward through the five frames, a trigger circuit that sends trigger signals to the ten control boards via optical links, and a 5 V, 100 kHz insulated DC-DC converter that sends power to the boards. The dimensions of the solid-state switch are approximately 0.35 m wide, 0.25 m deep and 0.54 m high, which can be replaced with a thyatron switch in the klystron modulator.

The switching time of the solid-state switch was measured to be 270 ns at a PFN charging voltage of 20 kV using a dummy load.

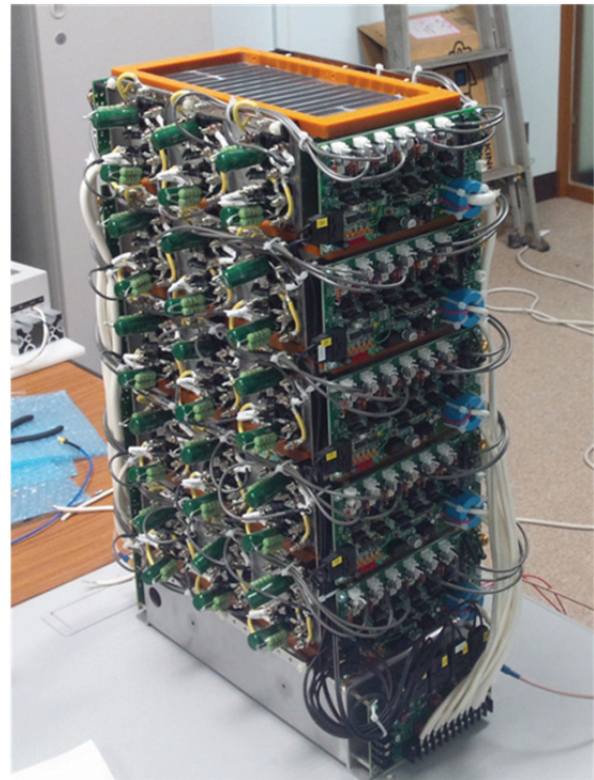


Figure 2: Solid-state switch using the SI thyristors.

OPERATION TEST

In the next step, an operations test of the solid-state switch was conducted to generate high power RF pulses using the klystron modulator at a charging voltage of 20 kV and a repetition rate of 10 Hz in the long pulse mode. The pulse height with the solid-state switch is slightly lower than that measured with a thyatron (L3 Communications, L-4888B) for comparison, because the turn-on resistance of the solid-state switch is slightly higher. Pulse-to-pulse fluctuations of the klystron voltage are obtained by measuring plateaus of 100 pulses using a differential amplifier (Tektronix, ADA400A) and a digital oscilloscope. The voltage fluctuation with the solid-state switch is constant in the pulse duration of $\sim 8 \mu$ s and it is $\delta V_k/V_k = 1.45 (\pm 0.12) \times 10^{-4}$, which is very close to the noise level of $1.27 (\pm 0.09) \times 10^{-4}$. If the noise contribution is subtracted from the measured value, the true value of

the fluctuation is estimated to be $7.0 (\pm 3.0) \times 10^{-5}$. The fluctuation with the thyatron is similar in the front of the pulses but it increases toward the rear part up to $\sim 3.2 \times 10^{-4}$. The variation in the RF power with the solid-state switch is similarly measured using a diode detector to be $\delta P/P = 1.52 (\pm 0.11) \times 10^{-3}$ and is constant over the pulse, which should be compared to the noise level of $1.42 (\pm 0.07) \times 10^{-3}$, and the true value of the power fluctuation is estimated to be $(5.4 \pm 3.6) \times 10^{-4}$, whereas the variation with the thyatron is also the same as that with the solid-state switch in the front part, but it increases in the latter half to $\sim 3 \times 10^{-3}$, which is similar to the behavior of the klystron voltage. The phase variation with the solid-state switch is $\delta\phi = 0.102 \pm 0.008$ degrees over the pulse, and the true value is estimated to be 0.056 ± 0.017 degrees using the noise level of 0.085 ± 0.006 degrees. The phase variation with the thyatron varies slowly over the range from 0.13 to 0.18 degrees in the pulse and is larger than that with the solid-state switch.

The FEL was operated with the solid-state switch to measure the energy of the FEL macropulse using an energy meter for infrared lasers. The operating conditions of the FEL are such that the electron energy is 15 MeV, that the gap of the wiggler is 36 mm, which yields the maximum macropulse energy and the FEL wavelength of $\sim 70 \mu\text{m}$ or 4.3 THz, and that the detuning of the optical cavity is close to zero. Figure 3 shows such measurements of 500 successive pulses with the solid-state switch (a) and with the thyatron (b). The red lines show mean values of the FEL energy and the broken lines indicate ranges of standard deviations of the variations. The fractional variation for the solid state switch is 2.4 % whereas that for the thyatron is 5.4 %, indicating that the solid state switch can significantly reduce the pulse-to-pulse fluctuations of the FEL intensity, though these variations are neither the best ones nor the worst ones.

The results of these measurement are summarized in Table 1.

REFERENCES

- [1] B.J.H. Meddens, et al., NIM A **372**, 446 (1996) .
- [2] S. Ishii, et al., Chemistry for Sustainable Development **9**, 57 (2001).

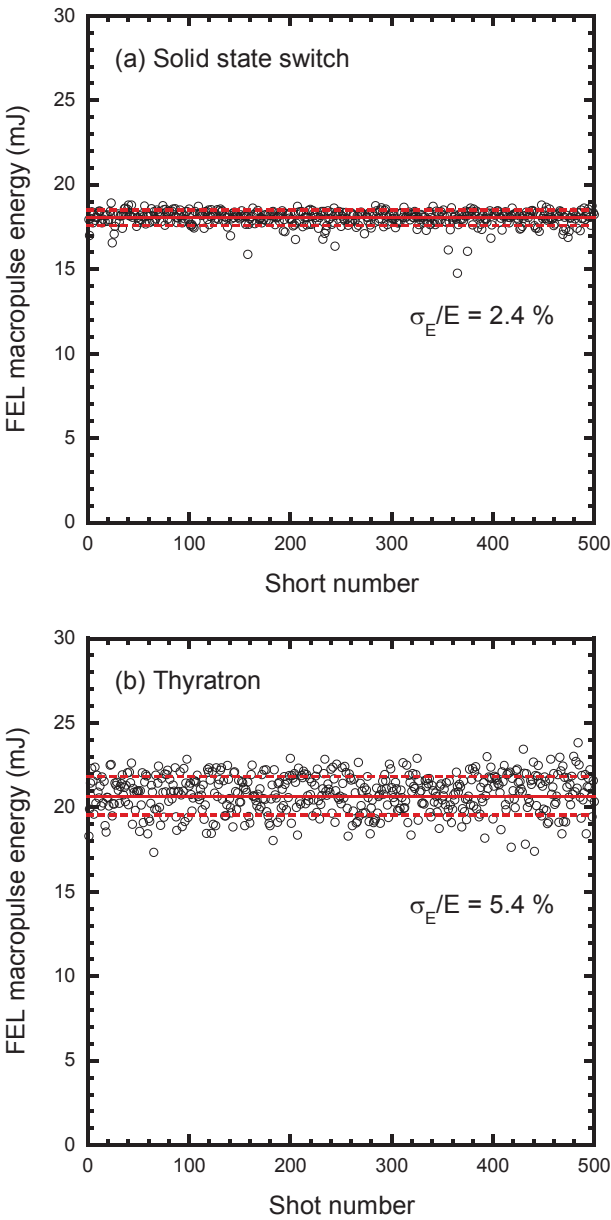


Figure 3: Fluctuations of macropulse energy measured with an energy meters. The red lines show mean values and the broken line indicate standard deviations.

Table 1. Summary of the Measured Variations

	Thyatron	Solid-state switch		
	measured	measured	noise	noise-subtracted
		<i>Fractional variations ($\times 10^{-4}$)</i>		
Klystron Voltage	~ 3.2	1.45 ± 0.12	1.27 ± 0.09	0.70 ± 0.30
RF power	~ 30	15.2 ± 1.1	14.2 ± 0.7	5.4 ± 3.6
		<i>Variations ($\times 10^{-2}$ degs.)</i>		
RF phase	~ 18	10.2 ± 0.8	8.5 ± 0.6	5.6 ± 1.7
		<i>Fractional variations (%)</i>		
FEL macropulse	5.4	2.4	-	-

THE LASER HEATER SYSTEM OF SWISSFEL

M. Pedrozzi, M. Calvi, R. Ischebeck, S. Reiche, C. Vicario, PSI, Villigen, Switzerland
B. D. Fell, N. Thompson, STFC/DL/ASTeC, Daresbury, UK

Abstract

Short wavelength FELs are generally driven by high-brilliance photo-cathode RF-guns which generate electron beams with an uncorrelated energy spread on the order of 1 keV or less. These extremely cold beams can easily develop micro-bunching instabilities caused by longitudinal space charge forces after the compression process. This can result in a blow up of the energy spread and emittance beyond the tolerable level for SASE emission. It has been demonstrated theoretically and experimentally [1] that a controlled increase of the uncorrelated energy spread to typically a few keV is sufficient to strongly reduce the instability growth. In the laser heater system, one achieves a controlled increase of the beam energy spread by a resonant interaction of the electron beam with a transversally polarized laser beam inside of an undulator magnet. The momentum modulation resulting from the energy exchange within the undulator is consequently smeared out in the transmission line downstream of the laser heater system. In SwissFEL, the laser heater system is located after the first two S-band accelerating structures at a beam energy of 150 MeV. This paper describes the layout and the sub-components of this system.

INTRODUCTION

SwissFEL is the hard X-ray free-electron laser presently under construction at PSI in Switzerland [2-3]. Table 1 summarizes the main beam parameters at the injection in the undulator section specified for SASE operation at 1 Å radiation.

Table 1: Beam Parameters - SASE Hard X-Ray Line

Parameter		units
Energy	5.8	GeV
Charge	200/10	pC
Uncorrelated RMS slice energy spread	350/250	keV
RMS normalized projected emittance	< 0.65/0.25	mm.mrad
RMS normalized slice emittance	<0.43/0.18	mm.mrad
Peak current	2.7/0.7	kA
Bunch length	25/6	fs

The final electron beam energy of roughly 6 GeV was defined according to the state of the art accelerator and

undulator technology in order to maximize compactness and minimize costs. The energy is relatively low with respect to other facilities of this class resulting in tighter beam quality requirements. The mitigation of emittance and energy spread growth during the acceleration and compression of the electron beam, caused in particular by micro-bunching instabilities [4-5], are therefore of primary importance for this facility [6]. It should be noted that for efficient self-seeding operation one aims to reach a normalized slice emittance of ~ 0.3 mm.mrad. The SwissFEL injector complex includes a laser heater (LH) system which will allow a controlled enhancement of the uncorrelated energy spread of the electron beam. Carefully adjusted, the energy spread can drastically reduce the gain of the micro-bunching instability without affecting the FEL performances.

SYSTEM DESCRIPTION

General Layout

Figure 1 shows a schematic of the SwissFEL injector facility. The PSI RF Photo-injector [7] produces 7.1 MeV high brightness electron bunches with an intrinsic emittance of 0.55 mm.mrad/mm [8] and a peak current of 20 A. The normalized slice emittance at the end of the injector with uncompressed beam will be typically around 0.2 mm.mrad for a bunch charge of 200 pC [9]. In Booster 1 two S-band traveling-wave cavities accelerate on crest the electron beam up to 150 MeV. After this first acceleration stage a set of 5 quadrupoles allows matching the optical functions through the laser heater chicane and 5 additional quadrupoles follow the LH modulator undulator to control the matching in booster 2. This section consists of two S-Band RF modules including each one klystron amplifier and two accelerating cavities. In booster 2 one accelerates off crest (up to 345 MeV) to provide the necessary energy-time correlation needed for the compression. Enough space has been reserved to allow future energy upgrades with a third RF accelerating module. The focusing along booster 2 consists of three FODO cells with 11m period. To suppress the second order energy-time correlation two X-band RF cavities (S-band 4th harmonic) running in decelerating mode precede the 13.5 m long compression chicane which is typically operated at compression factors between 10 and 15. The final nominal energy of the injector is 320 MeV.

Laser Heater Basic Specifications and Layout

As schematically illustrated in Figure 2 the LH consists of 3 main parts:

- A small magnetic chicane required for the laser coupling which corresponds to the first dispersive section of the accelerator complex.

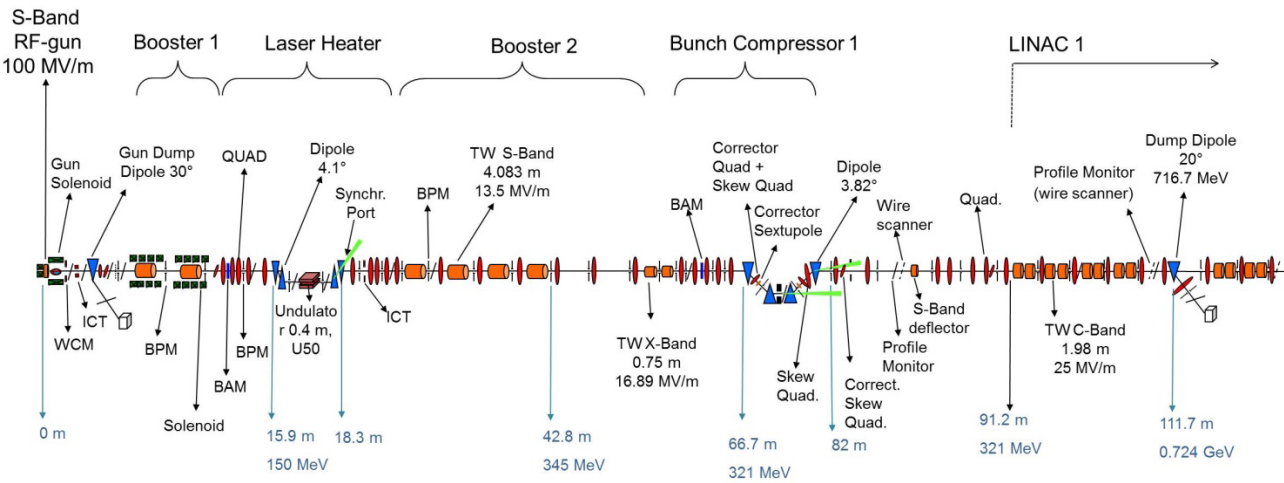


Figure 1: SwissFEL injector facility, schematic layout.

- An undulator modulator to allow a resonant energy exchange between laser and electron beam.
- The diagnostics elements for setting and monitoring the laser-beam overlap.

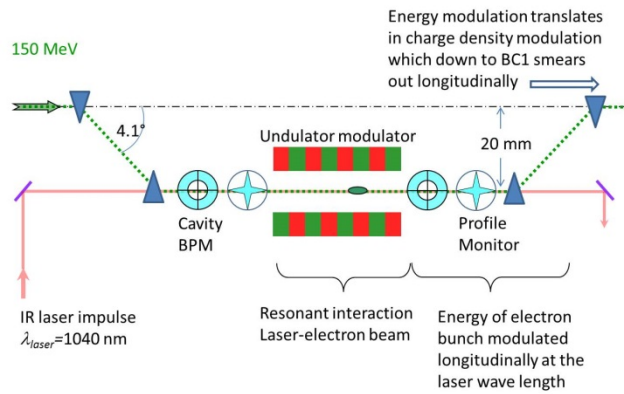


Figure 2: Laser heater basic principle.

The basic parameter of chicane, electron beam and laser are reported in table 2. The relatively low R56 was chosen in order to facilitate the matching for testing alternative compression schemes at low energy with velocity bunching.

The nominal electron beam energy was set as high as possible to allow an efficient power distribution between RF plants without compromising the emittance compensation process and keeping a safety margin on the RF power plants. The laser wavelength is defined by the Yb:CaF₂ photo cathode laser system. The choice of this technology is mainly driven by stability consideration. As described later in this paper, a fraction of the IR radiation produced by this system is used for the LH system.

Mechanically the LH beam line sits on three independent support girders as illustrated in Figure 3. At the entrance of the LH section a Beam Arrival Monitor (BAM) [10] delivers precise measurements of longitudinal drifts and jitter of the electron beam. During operation this tool helps surveying and maintaining the longitudinal laser-beam overlap.

ISBN 978-3-95450-133-5

Table 2: Laser Heater Parameters

Beam parameters		
Charge (pC)	10	200
Beta function @ undulator X/Y (m)	42 / 18	42/18
Proj. norm. emittance (mm.mrad)	0.15	0.3
RMS beam size (μm)	146	207
Nominal energy (MeV)	150 ± 1.5 %	
Pulse length flat top (ps)	10	3
Chicane dispersion (mm)	20.14	
Chicane parameters		
Bend angle (deg)	4.1	
Dipole 1/3 & 3/4 separation (mm)	280	
Dipole 2-3 separation (m)	1.82	
Dipole yoke length (mm)	120	
Off axis separation (mm)	20	
R56 (mm)	2.4	
Laser main parameters		
Wavelength (nm)	1040	
FWHM pulse lengths (ps)	50	
Waist at Focus (μm)	400	
Max. laser energy at LH (μJ)	100	

The undulator modulator and the magnetic chicane sit on the central girder. Two diagnostic modules consisting of one BPM followed by a screen are located upstream and downstream the undulator. Standard SwissFEL cavity BPMs and screens with chamber aperture of 16 mm are used. These monitors are required for adjusting and monitoring the transverse laser-beam overlap. As shown

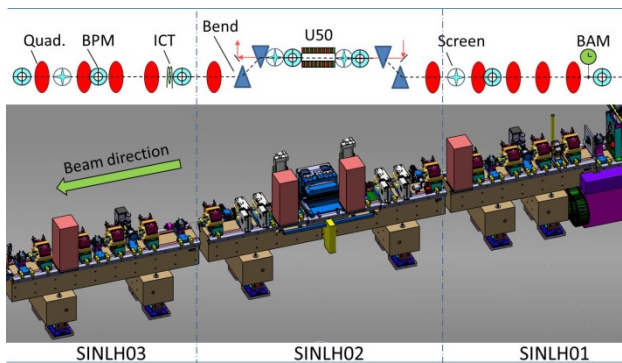


Figure 3: 3D Model of the LH beam line with schematic description of the main components.

in Figure 4 the central section of the chicane vacuum chamber, including screens and BPMs, is movable allowing a straight orbit with dipole OFF and with 20 mm off axis operation. Additionally the undulator can be remotely retracted from its nominal position by 100 mm to become invisible for the beam.

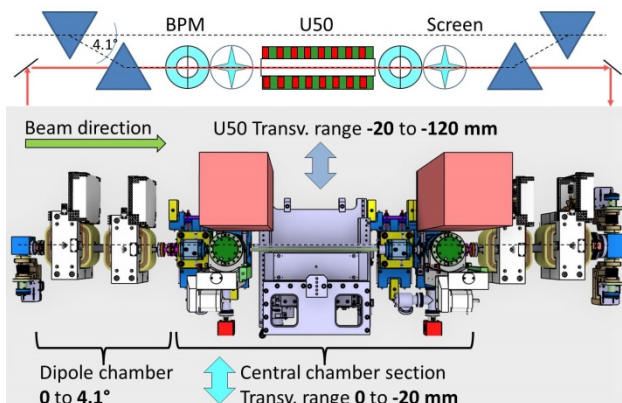


Figure 4: Movable parts in the LH chicane, with undulator in retracted position and chicane at 4.1°.

Laser System and Transfer Line

An infrared Yb-CaF₂ laser amplifier from the company Amplitude Système (Bordeaux) is used to generate by frequency multiplication the UV radiation for the RF-gun photocathode while the fundamental wavelength is used to drive the LH system. Figure 5 shows a schematic layout of the laser components that will be located in the SwissFEL laser room sitting alongside the accelerator tunnel near the gun region.

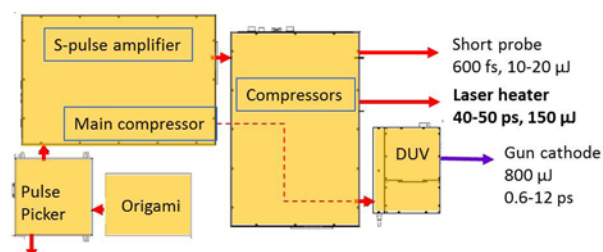


Figure 5: Layout of the laser system.

With a typical FWHM pulse length of 50 ps, the nominal operation of the LH would require moderate laser energy up to $\sim 1.1 \mu\text{J}$ (22 kW). For diagnostic purposes the system can deliver up to $150 \mu\text{J}$ at the source which should correspond to $100 \mu\text{J}$ (2 MW) at the LH undulator modulator. Driving the resonant interaction with laser powers between 200 kW and 2 MW should allow a fine adjustment of the longitudinal overlap by observing a broadening of the electron beam energy spread between 20 and 65 keV. The energy spectrometer can typically resolve a couple of keV.

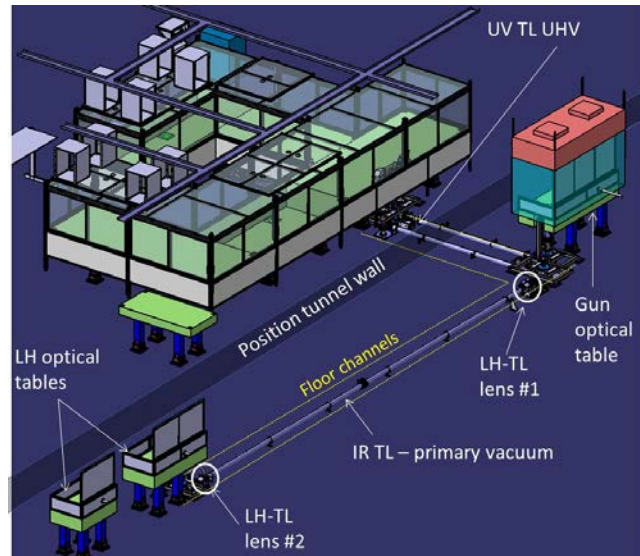


Figure 6: 3D model of the laser infrastructure with hidden accelerator components and building elements.

An independent in vacuum Transfer Line (TL) sitting in a floor channel assures the transport of the beam from the laser room down to the LH as shown in Figure 6. All mirrors of the TL are motorized and sit on supports directly fixed on the concrete floor and decoupled from the vacuum chamber to minimize pointing jitter due to vibrations. As shown in Figure 7 two lenses in the TL are used to image the laser beam from the laser room and to minimize the beam displacement due to laser angular jitter to few μm .

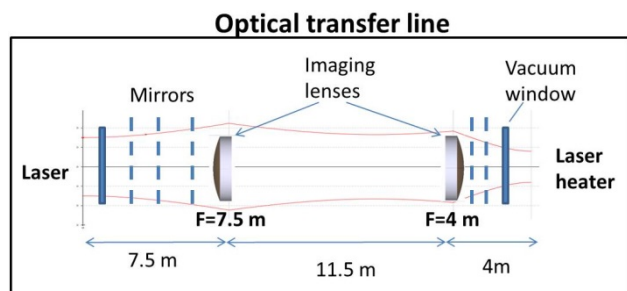


Figure 7: Schematic of the laser transfer line.

On the laser heater table (Figure 8) a set of motorized mirrors and a variable telescope are used to control the position and the beam size of the laser for optimal overlap with the electron beam. A variable attenuator will be used

to continuously adjust the laser energy. Finally a motorized delay stage will control the laser arrival time at the laser heater.

Electron and Laser Diagnostic Systems

The main functionalities to be investigated while designing the diagnostic system are:

- Adjustment: setting of the transverse and longitudinal laser-electron beam overlap
- Operation: monitoring of laser and electron beam parameters, and in particularly feedback on the longitudinal and transverse Overlap

Multiple laser heater diagnostics are needed to address the two above functionalities. Offline energy meters and online calibrated photodiodes will monitor the laser pulse energy at different locations. A camera system movable along a “virtual undulator” will record the laser beam shape and size. Cromox screens are suited as common in vacuum profile monitors for laser and electron beam to adjust the transverse overlap. Position sensitive detectors will be installed on the input and output optical laser heater table for precise laser alignment in the undulator. These sensors, in combination with the BPM placed in front and after the undulator, will allow surveying the transverse overlap during operation. For rough longitudinal synchronization, the laser arrival time will be measured with few tens ps resolution using a fast photodiode and a large bandwidth oscilloscope. For fine adjustment of the longitudinal overlap the LH will be overdriven up to ~2 MW laser power. At this intensity level the uncorrelated energy spread will be approximately ~65 keV, which should easily measurable in the energy spectrometer at 320 MeV. Since we do not expect large longitudinal fluctuation of the laser system, the BAM measurements of electron arrival should suffice for monitoring the longitudinal overlap during operation.

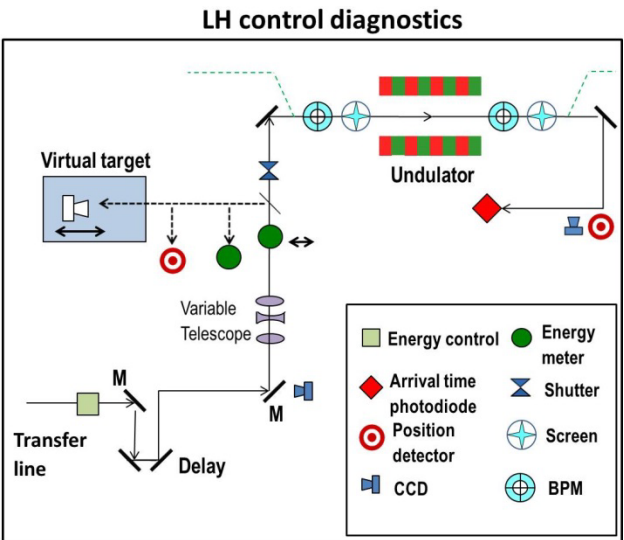


Figure 8: Schematic layout of diagnostic and control instrumentation.

ISBN 978-3-95450-133-5

Undulator System

The SwissFEL LH undulator is a planar permanent magnet Halbach array with 8 full periods of period length $\lambda_u=50\text{mm}$. The magnetic structure is longitudinally antisymmetric (the longitudinal centre of the undulator coincides with a zero crossing of the vertical magnetic field) so that the electron trajectory is centred on the magnetic axis. Table 3 summarizes the parameters of the magnetic blocks while Figure 9 shows the characteristic block shape.

Table 3: Properties of the Magnet Blocks

66 full length blocks (12.35 mm)	
Material	NdFeB
Grade	VACODYM 863 TP
Remanent field	1.25 T
Magnetisation	34 in +z, 32 in +y
Field tolerance	1%
Magnetisation angle tolerance	± 1 deg
12 end blocks	
Length 9.26mm $\pm 25\mu\text{m}$	4 magnetized +y
Length 6.18mm $\pm 25\mu\text{m}$	4 magnetized +z
Length 3.24mm $\pm 25\mu\text{m}$	4 magnetized +y

The undulator has been modelled in RADIA [11]. The computed variation of peak K versus full gap is shown in Figure 10. At gap 20mm (full closed), $K = 2.54$, and at gap 40mm (full open), $K = 0.667$.

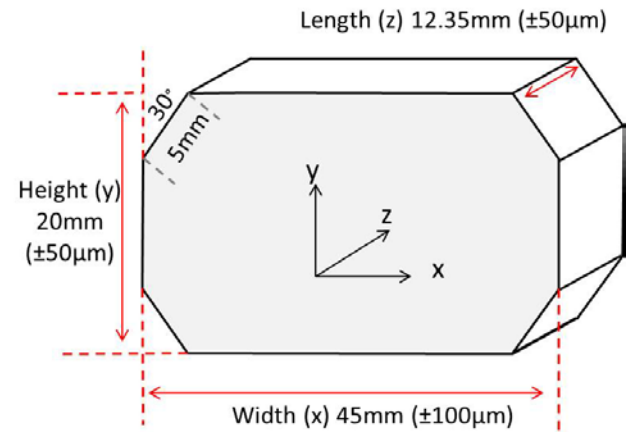


Figure 9: Shape of the magnetic blocks.

The undulator strength and period are linked to the laser wavelength and the beam energy via the resonance relation:

$$\lambda_{laser} = \frac{\lambda_u}{2\gamma^2} \left(1 + \frac{K^2}{2} \right) \quad (1)$$

$$K = \frac{eB_0\lambda_u}{2\pi m_e c}$$

where λ_u is the undulator period and K the undulator parameter. At the nominal energy of 150 MeV the resonance condition requires $K=2.28$ which corresponds to a gap of approximately 22 mm but the tuning range of the undulator allows operating the LH at energies ranging from 87 to 162 MeV.

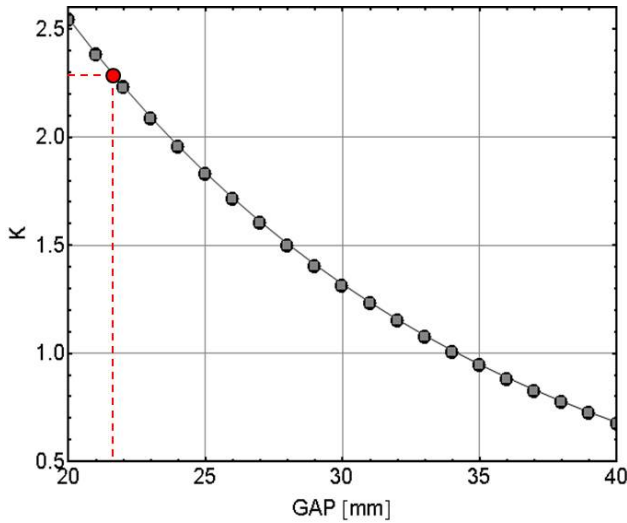


Figure 10: Tuning range of the U50 undulator factor K versus gap. In read the nominal K for 150 MeV.

Figure 11 shows calculated horizontal and vertical good field regions ($\Delta K/K_0 \leq 10^{-4}$) versus the undulator parameter K . At the nominal K the expected good field region are respectively ~ 620 and $\sim 150 \mu\text{m}$. These values determine the alignment tolerances of the electron bunch orbit along the undulator.

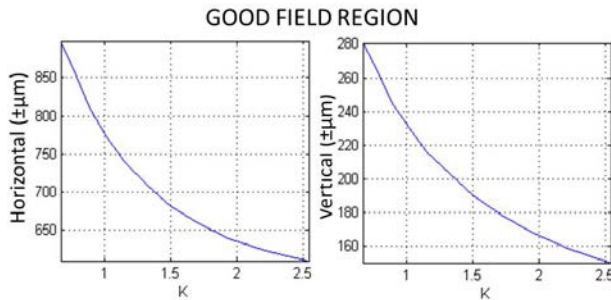


Figure 11: Horizontal and Vertical good field regions ($\Delta K/K_0 \leq 10^{-4}$) versus K .

STFC/ASTeC is in charge of the design, engineering and mechanical realization of the undulator assembly. Figure 12 shows the undulator during the assembly phase in the workshop at Daresbury Laboratory and the 3D model of the device mounted on the girder.

To set the exit position of a 150MeV beam exactly on axis (or to minimise the field 2nd integral) the end 1/4 length blocks are increased in length by $150 \mu\text{m}$. Because the design is antisymmetric the 1st integral (hence exit angle) is automatically zero for all gaps.

The specification for on-axis field quality is that the maximum relative variation in K is 1% rms. This is calculated from the maximum positive and negative B_z for each period, so is an average of 16 data points. The tolerances on block dimensions, field strength and field angle have then been specified so that the average of a set of unshimmed, perfectly constructed undulators, with errors added to each randomly in a uniform distribution, is within specification by factor of two, and all the unshimmed random undulators satisfy the specification.



Figure 12: U50 during assembly at Daresbury Laboratory and 3D model of the undulator on the support girder in extracted position.

BEAM DYNAMICS CONSIDERATIONS

Energy Spread Enhancement and FEL Operation

The final rms slice energy spread at the FEL undulator line scales proportionally to the compression factor with the uncorrelated energy spread after the LH. To avoid diluting the FEL performances, the relative energy spread must stay below the relative Bandwidths (BW) of the FEL. When operating SwissFEL at 5.8 GeV, and with the characteristic SwissFEL BW of 0.05% (corresponding to 2.9 MeV) one can tolerate at best $\sim 1 \text{ MeV}$ energy spread before starting to degrade the FEL efficiency. With a compression factor of 150, this value corresponds to a maximum tolerable uncorrelated energy spread after the LH of $\sim 7 \text{ keV}$. Running a few simulations with ASTRa from the gun up to the end of booster 1 and then ELEGANT in the LH section using the “laser modulator” element and assuming a laser waist of $400 \mu\text{m}$ one finds the approximate scaling relation between laser intensity and uncorrelated energy spread after the LH as:

$$\sigma_E (\text{keV}) \approx \sqrt{2.15 P_{laser} (\text{kW})} \quad (2)$$

Figure 13 illustrated the energy spread dependency described by equation (2) in the region of interest for the nominal operation of the LH up to a level compatible for overlap diagnose purposes.

As anticipated in this paper, a nominal laser power up to 22 kW should be sufficient to drive the LH at its nominal operation point. It should be noted that the LCLS measurements [1] show a weak FEL power dependency versus the laser intensity around the optimum operating point, relaxing the amplitude jitter tolerances of the IR laser source.

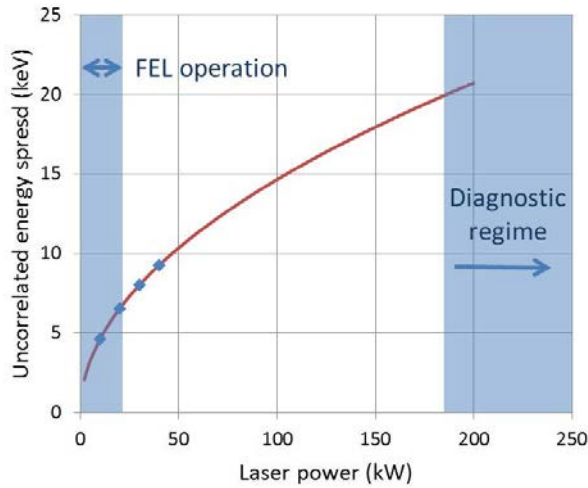


Figure 13: RMS uncorrelated energy spread versus Laser power. Blue dots from Elegant simulations assuming 150 MeV, 1040 nm laser wavelength, 400 μm laser waist, read equation 2.

Consideration on Trickle Heating

At LCLS an unexpected increase of the electron heating after the LH was clearly observed for very low laser powers. While the 1 D theory predicts negligible contributions of the Longitudinal Space Charge (LSC) to the energy spread growth, Z. Huang demonstrated the 3D nature of the observed phenomenon occurring when tilted μ -bunches are transported after the LH chicane applying strong horizontal focusing [1]. Basically the x-s density modulation doesn't smear completely after the half LH chicane but remains hidden in the x'-s plane. After a 90 deg phase advance this correlations develops again in x-s which, if associated with strong focusing, can considerably enhance the contribution of LSC. In SwissFEL the phase advance from the LH down to the first accelerating cavity of booster 2 is only 23° (see Figure 14) while the beta function remains relatively large (>10m) getting smaller only at the entrance of the linac where the energy rapidly boosts up.

In LCLS the beam propagate 11 m before injection in the next accelerating cavity experiencing phase advances larger than 90°. In SwissFEL this distance is only 2.5 m.

Figure 15 shows the longitudinal slice phase space at three different locations between the exit of the LH chicane and the first accelerating structure of Booster 2. From these measurements one can deduce the correlation factor R and evaluate the 3D electric field enhancement of LSC with respect to the 1D theory given by the following relation:

ISBN 978-3-95450-133-5

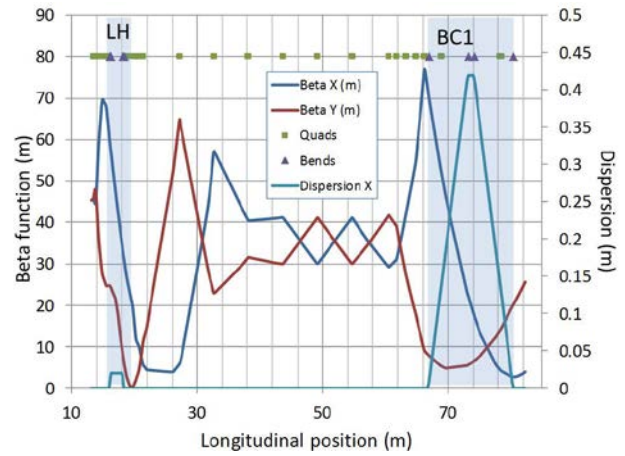


Figure 14: SwissFEL injector optics from the LH section up to the first bunch compressor.

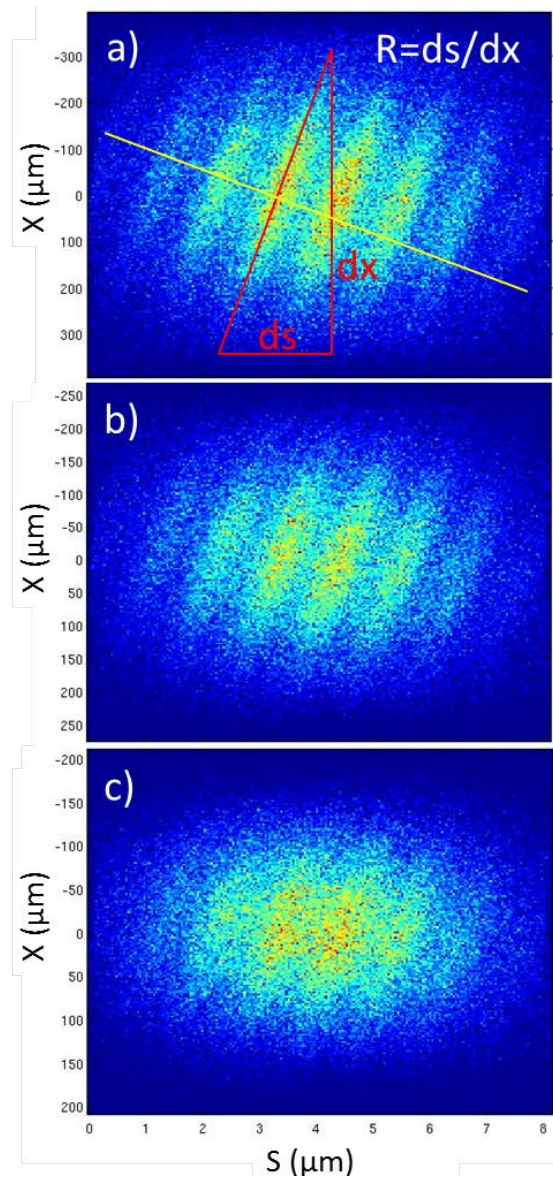


Figure 15: x-s phase space at a) 19.21 m, b) 20.46 m and c) 21.59 m.

$$\frac{E_k^{3D}}{E_k^{1D}} = \frac{e^{k^2 R^2 \sigma_x^2 / 2}}{1 + \gamma^2 R^2} \quad (3)$$

where $k=2\pi/\lambda_{laser}$, R the correlation factor, σ_x the horizontal rms beam size and γ the Lorenz factor.

Table 4: LSC Enhancement after the LH Chicane

$S(m)$	$\sigma_x(\mu m)$	R	LCS
19.21	153	0.00325	48
20.46	101	0.0046	18.5
21.59	71	0.0058	5.6

Table 4 summarizes the LSC enhancement in the case of SwissFEL at the location described in Figure 15 assuming 150 MeV beam energy and 1040 nm laser wavelength. Directly at the LH exit the enhancement factor is approximately 50 but it rapidly drops toward booster 2.

One can notice that these values are consistently lower than the enhancement factor of ~250 estimated for the LCLS in [1]. It should be noted in addition that the relaxed optic following the LH section allows maintaining the bunching factor predicted by the 3D theory well below his maximum preventing over-bunching as observed with the nominal optic at LCLS.

CONCLUSION

The SwissFEL baseline layout includes a Laser Heater system placed at 150 MeV. This system allows a controlled increase of the uncorrelated energy spread to fight micro-bunching instabilities possibly developing in the compression stages of the accelerator. The tuning range of the 50 mm period undulator allows in principle operating the LH beam for energies ranging from 87 up to 162 MeV, well matching the operational range of the accelerating cavities in booster 1. The LH system can be made completely invisible to the beam by extracting the undulator to an off axis position. The relaxed optic functions in the short transport line after the LH should efficiently cope with trickle heating at the nominal operational conditions of the laser heater.

ACKNOWLEDGMENT

The authors express their gratitude to Paul Emma and Zhirong Huang for their contribution to the discussion and theoretical analysis on trickle heating.

REFERENCES

- [1] Z. Huang, et al., Measurements of the coherent light source laser heater and its impact on the x-ray free-electron laser performance, Phys. Rev. Special Topics – Accelerator and beams 13, 020703 (2010).
- [2] SwissFEL Conceptual Design Report, Paul Scherrer Institut, Villigen, Switzerland, Report: 10-04.
- [3] H. H. Braun, in Proc. 34th Int. Free-Electron Laser Conf., Nara, Japan, 2012, pp. 9-12.
- [4] M. Borland, Coherent Synchrotron Radiation And Microbunching In Bunch Compressors, in Proc. 21st Int. Linac Conference, Gyeongju, Korea, pp. 11-15, 2002.
- [5] Z. Hunag et al., Microbunching Instability due to Bunch Compression, ICFA Beam Dynamics Newsletter No. 38, 2005, pp. 37-51.
- [6] S. Bettoni et al., Microbunching Instability Studies In SwissFEL, in Proc. 2nd Int. Particle Accelerator Conf. New Orleans, Louisiana, USA, 2012, pp. 1744-1746.
- [7] J.-Y. Raguin et al., The SwissFEL RF Gun: Design and Thermal Analysis, in Proc. 26th Linac Conference, Tel-Aviv, Israel, 2012, pp. 442-444.
- [8] E. Prat, et al., Thermal Emittance Measurements at the SwissFEL Injector Test Facility, in These Proceedings: Proc. 36th Int. Free-Electron Laser Conf., Basel, Switzerland, 2014, THC02.
- [9] E. Prat, et al., Slice Emittance Optimization at the SwissFEL Injector Test Facility, in Proc. 35th Free-Electron Laser Int. Conf, New York, 2013, pp. 200-204.
- [10] V. Arsov, et al., First Results from the Bunch Arrival-Time Monitor at the SwissFEL Test Injector, in Proc. 2nd Int. Beam Instrumentation Conf., Oxford, UK, 2013, pp. 8-11.
- [11] P. Elleaume, et al., Computing 3D Magnetic Fields From Insertion Devices, in Proc. 17th Particle Accelerator Conference, Vancouver, 1997, pp. 3509-3511.

DESIGN OF A SPATIO-TEMPORAL 3-D ELLIPSOIDAL PHOTOCATHODE LASER SYSTEM FOR THE HIGH BRIGHTNESS PHOTOINJECTOR PITZ*

T. Rublack[#], J. Good, M. Khojayan, M. Krasilnikov, F. Stephan, DESY, Zeuthen, Germany
 I. Hartl, S. Schreiber, DESY, Hamburg, Germany
 A. Andrianov, E. Gacheva, E. Khazanov, S. Mironov,
 A. Poteomkin, V. V. Zelenogorskii, IAP/RAS, Nizhny Novgorod, Russia
 E. Syresin, JINR, Dubna, Russia

Abstract

Minimized emittance is crucial for successful operation of linac-based free-electron lasers. Simulations have shown that 3-D ellipsoidal photocathode laser pulses are superior to the standard Gaussian or cylindrical laser pulses in this manner. Therefore, in collaboration with the Joint Institute of Nuclear Research (JINR, Dubna, Russia) and the Photo Injector Test facility at DESY, Zeuthen site (PITZ), a prototype laser system capable of producing spatio-temporal 3-D ellipsoidal pulses has been constructed at the Institute of Applied Physics of the Russian Academy of Science (IAP / RAS, Nizhny Novgorod, Russia). It is expected to receive the finalized prototype at PITZ within this year.

The laser system to create such 3-D ellipsoidal laser pulses will be introduced. Also the procedure of pulse shaping will be described in detail.

INTRODUCTION

The operation of modern free-electron lasers (FELs) necessitates high brightness electron bunches with small energy spread. As the electron beam parameters along the beam line depend strongly on initial conditions at the photocathode, a minimized emittance is crucial for a successful FEL operation. An important parameter crucial for the initial conditions is given by the characteristics of the cathode laser.

In the following paragraphs the influence of different laser pulse parameters on the initial electron beam quality will be briefly discussed. While some of the parameters are well known due to previous experience, others have to be simulated and/or empirically determined.

If the photon energy is below the vacuum energy level (where an electron is free) of the photocathode material, it is impossible to generate emission of free electrons with single photon excitation [1]. The vacuum energy level is defined as the sum of the electron affinity and the band gap energy for semi-conductors, or equivalently as the work function in metals.

Due to scattering processes within the material the (quasi) free electrons can lose enough energy (thermalize)

before reaching the cathode surface and therefore produce an electron beam with small mean transverse energy [2]. In contrast, higher incident photon energies lead to increased energy spread and to a reduction of the ablation threshold intensity of the photocathode material [3].

This naturally leads to the second important parameter which has to be considered – the laser pulse energy (or to be more precise the number of photons within a laser pulse). By first approximation the number of generated free electrons is proportional to the number of photons. However, space charge shielding effects and depletion of electrons at the surface of the photocathode as well as electron-hole recombination within the material – only to mention a few processes - reduce the quantum yield defined as the number of generated free electrons at the cathode per number of incident photons. At high laser pulse energies the space-charge shielding effect can even lead to saturation (Fig. 1).

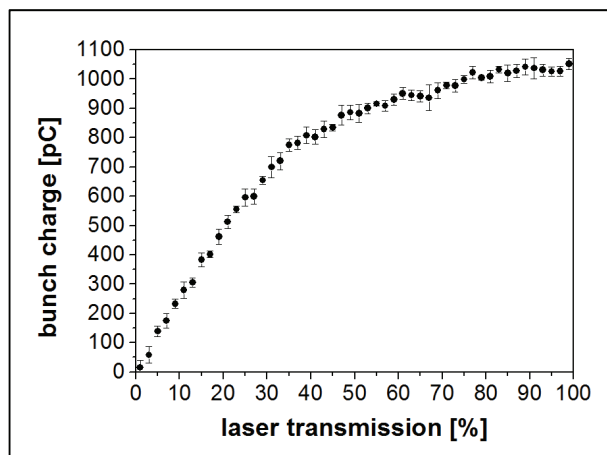


Figure 1: Example of measurement of the electron bunch charge with a Faraday cup as a function of laser energy 80 cm downstream the cathode. The laser energy is given in per cent of the maximum.

High pulse energies combined with high photon energies also risk thermal laser ablation of the photocathode material, which would destroy the characteristics of the photocathode and hence the properties of the electron bunch.

There are two more crucial laser pulse parameters – pulse duration and pulse shape. The latter has to be considered in three dimensions (spatially and temporally).

*Work supported by the German Federal Ministry of education and Research, project 05K10CHE “Development and experimental test of a laser system for producing quasi 3D ellipsoidal laser pulses” and RFBR grant 13-02-91323.

[#]Tino.Rublack@desy.de

While the pulse duration defines the electron bunch length the pulse shape defines the electron distribution within the electron bunch – as mentioned earlier, the higher the number of photons at a specific time and position the larger the generated electron density.

ELECTRON BUNCH OPTIMIZATION

The influence of the laser pulse parameters on electron emission are well known [4], so the next step for cathode laser optimization is the simulation of the optimized electron bunch properties to get maximum brightness and small energy spread.

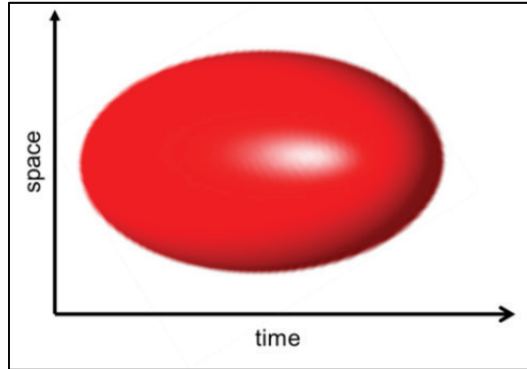


Figure 2: Illustration of a 3-D ellipsoidal laser pulse.

Simulations using PARMELA respectively ASTRA code show that the ideal electron bunch profile is ellipsoidal in both time and space (3-D) [5,6]. To generate such electron bunches the cathode laser beam must also be 3-D ellipsoidal (Fig. 2), assuming a one-to-one correlation between the incident laser pulse and the photocathode emission process. Simulations based on the PITZ photoinjector layout have shown a significant decrease of projected emittance of about 60 % compared to cylindrical Gaussian laser pulses and 32 % compared to cylindrical flat-top laser pulses [7]. A full description of this simulation procedure has been published by Khojayan et al. [8].

3-D ELLIPSOIDAL PHOTOCATHODE LASER SYSTEM

Motivated by the simulations, a laser system capable of producing 3-D ellipsoidal laser pulses is under investigation at IAP / RAS in collaboration with JINR. It is planned to install the laser system at PITZ in autumn this year. The PITZ photoinjector uses an L-band RF gun with a Cs₂Te photocathode. With a work function of 3.3 eV these cathodes require a laser wavelength in the UV (about 260 nm) [9]. Simulation studies at PITZ show that, depending on the bunch charges, a RMS pulse duration of about 4 – 8 ps and a transverse RMS size of the laser beam between 0.25 and 0.75 mm at the cathode generates very low emittance and at the same time very high peak currents.

The schematic set-up of the laser system is shown in Fig. 3. It consists of a dual-output fiber laser, a diode pumped Yb:KGW disk amplifier, a 3-D pulse shaper, and a frequency conversion unit for second and fourth harmonic generation. A scanning cross-correlator system has also been developed and built for the diagnostic channel to measure the spatial and temporal distribution of the shaped laser pulses.

The dual-output fiber laser generates 1030 nm laser pulses at a repetition rate of 45 MHz. The pulse duration of the laser pulses is about 150 fs. It also comprises a fiber-based pulse stretcher, a preamplifier and a system for pulse train (macropulse) formation. For a precise tuning of the laser pulse timing with respect to the RF phase, which is crucial for optimized operation of the photo injector, a piezo ceramic cylinder has been integrated inside the optical fiber coil of the oscillator.

The laser beam is then split into two beams at the output of the fiber laser – one is used for generation of electrons at the photocathode, after 3-D shaping and frequency conversion, the other one for temporal laser pulse characterization using the cross correlator technique.

After the fiber laser, the pulses of the primary output (working channel) are amplified using a multi-pass (10 passes to date) Yb:KGW disk amplifier. As pump source a LDM 2000-100 (Laserline GmbH) is used. Recently,

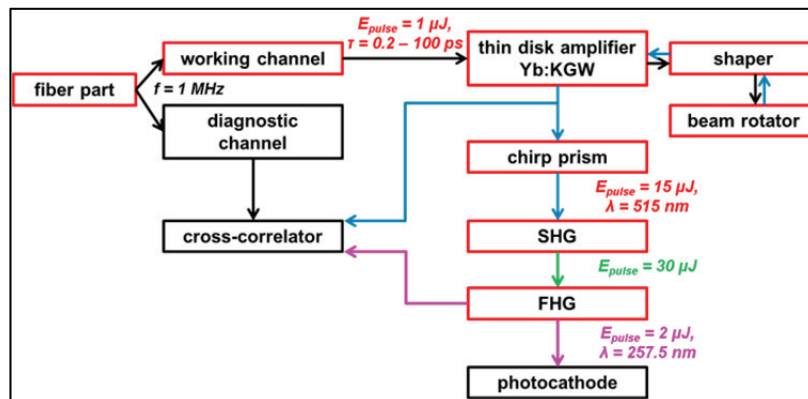


Figure 3: Schematic set-up of the actual 3-D ellipsoidal laser system.

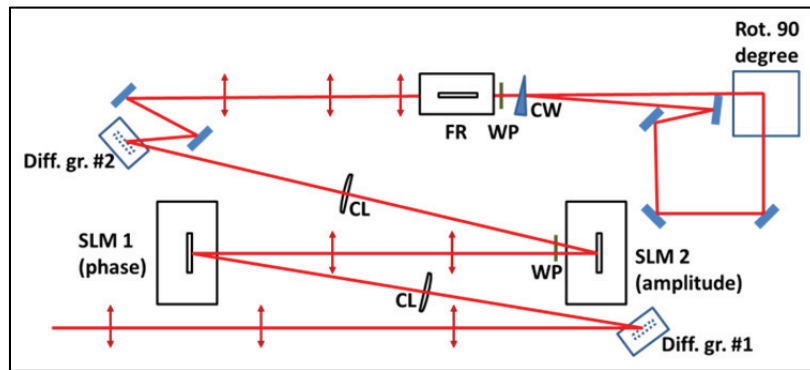


Figure 4: Setup of the 3-D pulse shaper: Diff. gr. – diffraction gratings, SLM – spatial light modulator, WP – half-wave plates, CL – cylindrical lens, FR – Faraday rotator, CW – calcite wedge, Rot. 90 degree – laser beam rotator (90°).

laser pulses up to 120 μJ have been obtained. After the multi-pass amplifier the laser pulses are shaped both temporally and spatially. This is realized by a scheme based on two spatial light modulators (currently SLM HES 6010 NIR by Holoeye Photonics AG). The principal set-up of the 3-D pulse shaper is shown in Fig. 4.

The pulse shaper is based on a zero dispersion optical compressor. Among other things, it consists of two diffraction gratings, two cylindrical lenses, two half-wave plates, and two liquid crystal based SLMs. The SLMs are positioned on the focal planes of both cylindrical lenses. So, one diffraction grating is imaged onto the other in the horizontal plane. There is no such imaging in the vertical plane which implies corresponding diffraction. However, these effects can be neglected for the current 3-D pulse shaper set-up, with beam diameter of about 8 mm and focal length of the cylindrical lenses of 405 mm.

The first SLM manipulates the phase of the laser pulse. A half-wave plate installed before the second SLM introduces a 45° rotation of the laser pulse polarization and therefore the second SLM becomes an amplitude manipulator. As one single pass through the pulse shaper only forms the laser profile in one, the laser pulses are passing the set-up twice – in the second pass, the laser pulses are rotated by 90°.

After the pulse shaper a LBO and a BBO crystal are used, respectively, for second and forth harmonic generation.

A cross-correlation with the beam from the diagnostics channel is used to characterize the laser pulses before and after higher harmonic generation. For this, a high-speed delay line is implemented, which allows measurement of the spatial and temporal profile of the laser pulses with high precision [10]. A full description of the cross-correlator can be found elsewhere [7].

CONCLUSION

Simulations have shown that 3-D ellipsoidal laser pulses instead of cylindrical pulses with Gaussian or flat-top temporal profiles can significantly reduce the emittance of electron bunches generated by a photoinjector. On the basis of these simulations a laser system capable to create 3-D ellipsoidal laser pulses is

under development. Thereby a description of the actual set-up and the principal procedure of pulse shaping have been given.

REFERENCES

- [1] R.A. Powell et al., “Photoemission Studies of Caesium Telluride”, *Phys. Rev. B*, 8(8), p. 3987 (1973).
- [2] S. Karkare et al., “Monte Carlo charge transport and photoemission from negative electron affinity GaAs photocathodes”, *J. Appl. Phys.* 113, p. 104904 (2013).
- [3] T. Rublack et al., “Laser ablation mechanism of transparent layers on semiconductors with ultrashort laser pulses”, *Proc. SPIE 8190, Laser-Induced Damage in Optical Materials*, Boulder, USA, 2011.
- [4] E.M. Logothetis and P.L. Hartman, “Laser-Induced Electron Emission from Solids: Many-Photon Photoelectric Effects and Thermionic Emission”, *Phys. Rev.* 187, p. 460 (1969).
- [5] C. Limborg-Deprey and P.R. Bolton, “Optimum electron distribution for space charge dominated beams in photoinjectors”, *Nuclear Instruments and Methods in Physics Research*, A557, p. 106 (2006).
- [6] M. Khojayan et al., “Beam dynamics optimization for the high brightness PITZ photo injector using 3D ellipsoidal cathode laser pulses”, TUPSO36, *Proc. 35th International Free Electron Laser Conference*, Manhattan, USA, 2013.
- [7] T. Rublack et al., “Development of a quasi 3-D ellipsoidal photo cathode laser system for PITZ”, WEPRO055, *IPAC’14, Dresden, Germany* (2014).
- [8] M. Khojayan et al., “Studies on the Application of the 3D Ellipsoidal Cathode Laser Pulses at PITZ”, THPRO043, *IPAC’14, Dresden, Germany* (2014).
- [9] S. Schreiber et al., “Photocathodes at FLASH”, *Proceedings 3rd Int. Particle Accelerator Conf.*, p. 625, New Orleans, USA, 2012.
- [10] V. V. Zelenogorskii et al., “Scanning cross-correlator for monitoring uniform 3D ellipsoidal laser beams”, *Quantum Electron* 44(1), p. 76 (2014).

COMMISSIONING OF AN IMPROVED SUPERCONDUCTING RF PHOTO INJECTOR AT ELBE

J. Teichert[#], A. Arnold, M. Freitag, P. Lu, P. Michel, P. Murcek, H. Vennekate, R. Xiang,
HZDR, Dresden, Germany
P. Kneisel, JLab, Newport News, USA
I. Will, MBI, Berlin, Germany

Abstract

In order to produce high-brightness electron beams in a superconducting RF photo injector, the most important point is to reach a high acceleration field in the cavity. For this reason two new 3.5-cell niobium cavities were fabricated, chemically treated and cleaned in collaboration with Jlab. The first of these two cavities was shipped to HZDR and assembled in a new cryomodule. This new gun (SRF Gun II) was installed in the ELBE accelerator hall in May 2014 and replaces the previous SRF Gun I. Beside the new cavity the ELBE SRF gun II differs from the previous gun by the integration of a superconducting solenoid. The paper presents the results of the first test run with a Cu photocathode.

INTRODUCTION

At the superconducting (SC) electron linear accelerator of the ELBE radiation facility [1] a new superconducting electron photo injector (SRF gun) has been installed in May 2014. The new gun (SRF Gun II) replaces the previous one which had been in operation from 2007 until April 2014. For the old SRF gun the handicap was the low acceleration gradient. Due to strong field emission of the cavity the maximum gradient (peak field) was only 17.5 MV/m in CW belonging to a kinetic energy of 3.3 MeV of the emitted electrons. Although SRF gun I could not reach the design specifications, it was successfully operated for R&D purposes and also for some dedicated user experiments at ELBE.

Table 1: Design Parameters of the ELBE SRF Guns at HZDR

Operation mode	FEL mode	High charge mode
Laser rep. rate	13 MHz	100-500 kHz
Laser pulse length	3 ps fwhm	12 ps fwhm
Peak field	50 MV/m	50 MV/m
Bunch charge	77 pC	1 nC
CW beam current	1 mA	≤ 0.5 mA
Kinetic energy	9.5 MeV	9.5 MeV
Transv. emittance	1 μm	2.5 μm

[#]j.teichert@hzdr.de

In a collaboration of HZDR and Jlab two new niobium cavities for the next ELBE SRF gun have been built, treated and tested at JLab. At the same time a new cryomodule has been designed and built at HZDR. One of the two new cavities was shipped to HZDR in November 2013. After arrival the assembly of the cryomodule was completed and the gun was installed in the ELBE accelerator hall in May 2014. The gun has been running since June 2014 for first RF and beam tests

The aim for ELBE SRF gun II is to approach the beam specification as given in Table 1. At ELBE an electron gun with high-brightness beam, high average current, and high bunch charge is needed to fulfill the future user requirements and provide high-flux neutron and positron beams as well as to operate the THz facility and the CBS x-ray source for users.

CAVITY AND CRYOSTAT DESIGN

The design of the new cryomodule for SRF gun II is shown in Fig. 1. The 1.3 GHz Nb cavity consists of three TESLA cells and a specially designed half-cell. Another superconducting cell, called choke filter, prevents the leakage of the RF field towards the cathode support system. The normal conducting (NC) photocathode is installed in this system, which is isolated from the cavity by a vacuum gap and cooled with liquid nitrogen. This design allows the application of NC photocathodes with high quantum efficiency (QE) like Cs₂Te.

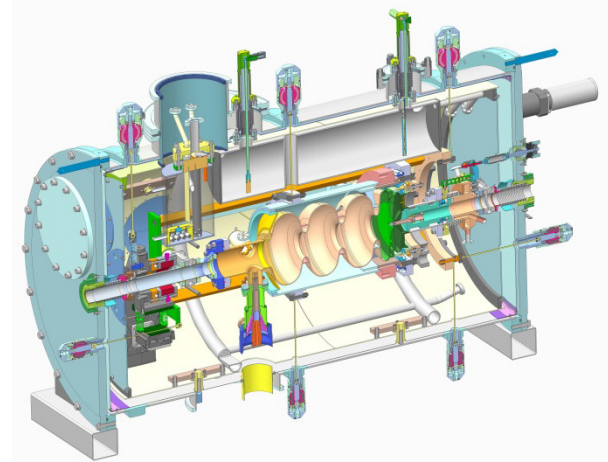


Figure 1: CAD view of the SRF Gun II cryomodule.

Similar to cavity and cathode support system, most of the cryomodule components, the cavity tuners, and the fundamental power coupler are identical in the design

with that of the previous SRF gun I [2]. The new cavity differs in the improved half-cell stiffening and some other minor modification [3].

New is the integration of a SC solenoid in the cryomodule for emittance preservation purposes. Compared to the NC solenoid of SRF gun I which was placed downstream the gun, the new design is much more compact and the distance to the cavity is smaller. The SC solenoid is placed on a remote-controlled x-y table to align its center to the electron beam axis. The cryogenic design of the assembly is sophisticated: The solenoid is cooled with 2 K He by means of a bypass from the cavity. The in-vacuum step motors and translation tables are on 77 K to reduce the heat load to the liquid He bath. Additional μ -metal shields hold the solenoid remanence field and the step motors fields on a 1 μ T level near the cavity. Details of the SC solenoid design and testing are published in ref. [4].

GUN COMMISSIONING

Installation

The installation of SRF Gun II is organized in two phases. The first step was the replacement of the gun cryomodules in the ELBE hall during the spring shutdown in May 2014. At once the cathode transfer system of SRF Gun I was dismantled for revision and cleaning. The commissioning started with a copper photocathode mounted in SRF Gun II during the clean-room assembly. The second step is the installation of the refurbished cathode transfer system. This work is scheduled for the ELBE autumn shutdown in October 2014. In the following run, the SRF Gun II can be operated with Cs₂Te photo cathodes.

RF Measurements

At first the cavity was undertaken a testing and conditioning program with pulsed RF. After that the cavity was tested and measured in CW. The preliminary results of the cavity performance (intrinsic quality factor versus acceleration gradient) are presented in Fig. 2. For comparison, the figure shows also the results of the final vertical test at Jlab (blue), as well as the best (after a high power processing), and the latest results for the old SRF gun I cavity. The acceleration gradient of about 10 MV/m, obtained up to now as the maximum, belongs to a peak field of 27 MV/m in the TESLA cells of the cavity. In the final vertical test this cavity reached 38 MV/m peak field. Remarkable for the new gun is, that the high quality factor of $>10^{10}$ could be retained after assembly and installation.

Superconducting Solenoid

The SC solenoid was already tested and its field distribution measured before (see Ref. [5]). In the gun the proper operation of the x-y table, the magnetic shielding, and the cryogenic behavior has been checked. The maximum design value for the current of 10 A could be reached without quenching. Moving the solenoid an

increased microphonics level is visible in the RF control system. But it is small enough that it does not cause an RF trip. The solenoid position has been arranged by beam based alignment. There is evidence for a small horizontal tilt of the solenoid axis. The fluxgate magnetometer in the cryomodule allows to monitor the fringe field value near the cavity. A degaussing procedure will be developed and implemented in the computer control system.

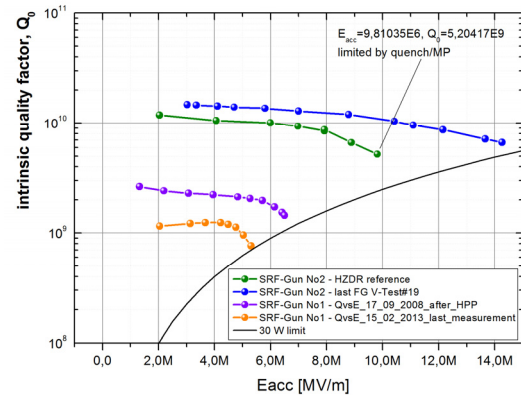


Figure 2: Comparison of cavity performance for the ELBE SRF guns.

Beam Parameter Measurements

In the following we present preliminary results of beam parameter measurements together with ASTRA [6] results. The measurements should confirm that all subsystems, like RF control, drive laser, timing and synchronization work well.

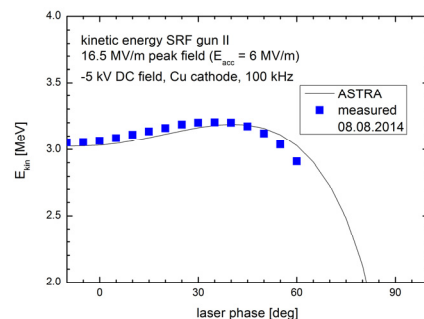


Figure 3: Measured kinetic energy versus laser phase.

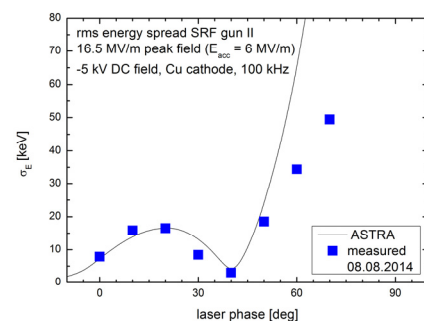


Figure 4: Measured rms energy spread versus laser phase.

The beam characterization was performed in CW with an acceleration gradient of 6 MV/m (16.5 MV/m peak field). At this gradient the cavity RF losses are about 3 W. The dark current measured in the Faraday cup, which is about 1 m downstream of the gun, was less than 1 nA. The low QE of the Cu photo cathode of less than 10^{-4} allows typical CW beam currents of 10-20 nA with the 258 nm UV drive laser operated with a repetition rate of 100 kHz. Due to the very low bunch charge the beam parameters are RF field dominated. An exception is the transverse emittance which is determined by the thermal emittance of the photo cathode of about $0.5 \mu\text{m}$ per mm laser spot.

Before each measurement the laser arrival phase was calibrated with a laser phase scan (0° corresponds to the zero-crossing of the RF field.) and the laser spot was centered on the photo cathode by means of beam based alignment.

The energy and energy spread of the beam was measured with the 180° dipole magnet in the diagnostics beamline [7] and are presented in Fig. 3 and 4. The kinetic energy has a maximum at a phase of 40° which leads to a change in the sign of correlation, and a minimum in the energy spread at this phase.

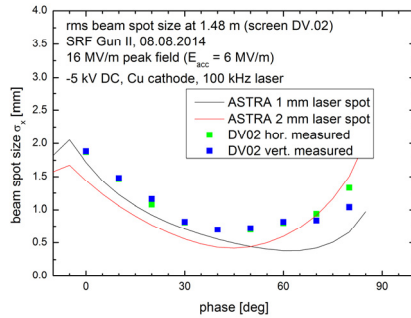


Figure 5: Measured rms beam spot size.

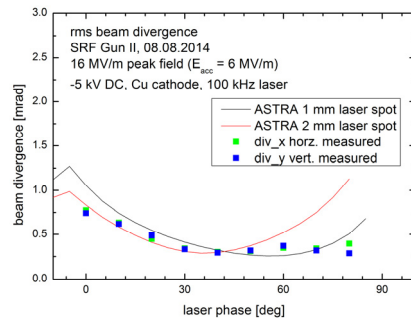


Figure 6: Measured rms beam divergence.

The absence of space charge effects leads to a nearly collimated beam which needs no further focusing. The spot size measured on a screen with 1.42 m distance to the cathode is shown in Fig. 5. Performing beam size measurements on two consecutive screens delivers the divergence of the beam coming out of the gun (Fig. 6).

Transverse emittance measurements were carried out using the moving slit scan technique. Results are shown in Fig. 7. A first determination of the bunch length was obtained from the phase scan method (Fig. 8). Thereto the beam was guided into the ELBE accelerator and then through the first linac module. For one of the accelerator cavities the phase was varied and a following dipole magnet was used to measure the energy spread as function of this phase.

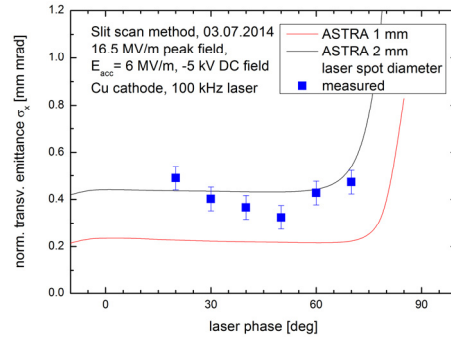


Figure 7: Measured normalized transverse rms emittance.

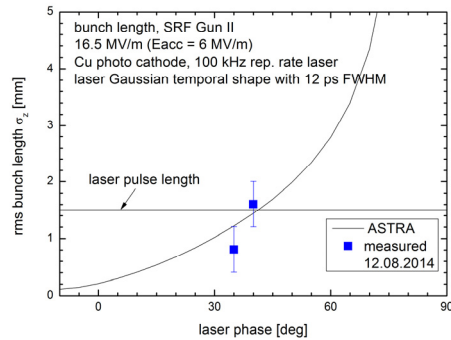


Figure 8: Measured rms bunch length.

CONCLUSION

The results of the first commissioning period of SRF Gun II are very promising. The RF performance measurements show that the intrinsic quality factor is still at 10^{10} after gun assembly and the cavity does not suffer under field emission. Compared to SRF Gun I an improvement of about a factor two in the maximum gradient could be achieved. First beam parameter measurements with the Cu cathode show good agreement with simulations and confirm the proper operation of all subsystems.

ACKNOWLEDGMENT

We would like to thank the whole ELBE team for their help and assistance with this project. The work is supported by the European Community under the FP7 programme (EuCARD-2, contract number 312453, and LA3NET, contract number 289191), and by the German Federal Ministry of Education and Research grant 05K12CR1.

REFERENCES

- [1] P. Michel, et al., “The Rossendorf IR-FEL ELBE”, in *Proc. 28th Int. Free-Electron Laser Conf., Berlin*, 2006, pp. 488-491.
- [2] A. Arnold, et al., *Nuclear Instruments and Methods A* 577 (2007) 440.
- [3] P. Murcek, et al., “Modified SRF Photoinjector for the ELBE at HZDR”, in *Proc. 16th Int. Conf. on RF Superconductivity, Chicago*, 2012, pp. 39-42.
- [4] P. Murcek, et al., “The SRF Photoinjector at ELBE – Design and Status 2013”, in *Proc. 16th Int. Int. Conf. on RF Superconductivity, Paris*, 2013, pp. 148-150.
- [5] H. Vennekate, et al., “Emittance Compensation for an SRF Photo Injector”, in *Proc. 16th Int. Int. Conf. on RF Superconductivity, Paris*, 2013, pp. 151-154.
- [6] K. Flöttmann, “ASTRA”, DESY Hamburg, www.desy.de/~mpyflo, 2000.
- [7] T. Kamps, et al., *Review of Scientific Instruments* 79 (2008) 093301.

PRODUCTION OF C-BAND DISK-LOADED TYPE CG ACCELERATING STRUCTURES

N. Shigeoka, D. Suzuki[#], S. Miura, Mitsubishi Heavy Industries, Ltd., Mihara, Hiroshima, Japan
T. Sakurai, T. Inagaki, Y. Otake, RIKEN SPring-8 Center, Kouto, Sayo, Hyogo, Japan
H. Ego, T. Asaka, JASRI, Kouto, Sayo, Hyogo, Japan

Abstract

Mitsubishi Heavy Industries, Ltd. manufactured six C-band disk-loaded type and quasi-constant gradient (CG) accelerating structures for the XFEL facility, SACLA (SPring-8 Angstrom Compact free electron LAsers). These structures were newly designed by RIKEN for operation at an acceleration gradient of over 45 MeV/m and a repetition rate of 120 pps. We report the production and low-power RF properties of these accelerating structures.

INTRODUCTION

In April 2013, Mitsubishi Heavy Industries, Ltd. contracted with RIKEN to manufacture six C-band disk-loaded type and CG accelerating structures for the XFEL facility, SACLA. The first structure was delivered in August 2013 to RIKEN and the other five were delivered in March 2014.

Devices of the accelerator system operable at a high repetition rate are being developed by RIKEN, as one of the possibilities to grow in the performance of SACLA. The C-band disk-loaded type structures were designed to enable us operation at a high repetition rate of more than 120 pps and a highly acceleration gradient of more than 50 MV/m. We paid attention to reduction in manufacturing cost and compatibility with the C-band choke-mode type accelerating structures in use as the main accelerators of the SACLA [1, 2].

We will report the results of the production and low-power RF test of these newly manufactured six accelerating structures in this paper.

FEATURES OF THE ACCELERATING STRUCTURES

The disk-loaded accelerating structure is a quasi-constant gradient (Quasi-CG) type. Its resonant frequency is 5712 MHz (30 deg. C in vacuum) and its total length is 1.8 m. Figure 1 shows the outline view of the accelerating structure. Table 1 shows required specifications.

The resonant frequency, total cavity length, attenuation constant τ , filling time t_F , and position of cooling pipe are designed to be compatible with the present choke-mode type structure [3, 4] for SACLA. There are two major modifications from the choke-mode type structures. One is that the regular accelerating cells have no choke structure but tuning holes and the other is that the accelerating mode was changed from $3\pi/4$ to $2\pi/3$. As a result of the former, the phase shift can be tuned after the

[#]daisuke4_suzuki@mhi.co.jp

Table 1: Requirements Specifications of the C-band Disk-Loaded Type Accelerating Structure

Items	Requirements Specifications
Resonance frequency	5172 MHz +/- 0.2 MHz 30 deg. C in vacuum
Coupler type	J-type double-feed coupler
Number of cells	100 + 2 coupler cell
Total cavity length	1.8 m
Structure type	Quasi-constant gradient
Phase shift	$2\pi/3$
Integrated phase error	$\leq \pm 3\text{deg.}$
VSWR	≤ 1.1
Q factor	$8000 \leq$
Average shunt impedance	$55 \text{ M}\Omega/\text{m} \leq$
Attenuation constant τ	0.56
Filling time t_F	270 ns
Material of cells	OFC-CLASS1 HIP
Brazing process	Vacuum brazing

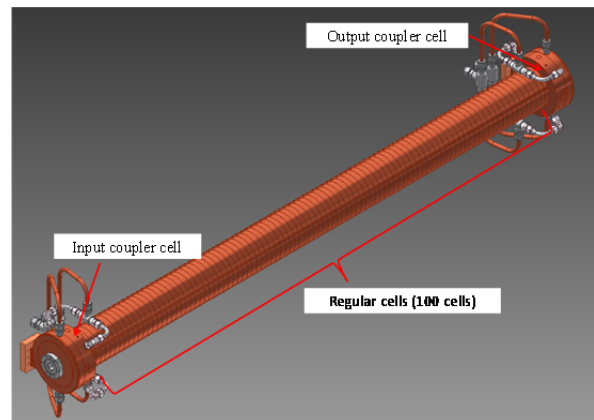


Figure 1: C-band disk-loaded type accelerating structure.

resonance frequency shift of each accelerating cell due to brazing process cannot be compensated by tuning, because of accelerating cells cannot equip tuning hole due to the choke structure surrounding the accelerating cell. As a result of the latter, the shunt impedance and the axial electric field can increase so the break down probability seemed to increase due to increase of the surface electric field. To reduce the risk of breakdown, the beam-hole edge, where the maximal surface electric field takes place, has ellipsoidal shape shown in Figure 2 to reduce the strength of the surface electric field.

PRODUCTION

Regular Accelerating Cell

Regular accelerating cells consist of disks and cylinders to simplify the geometry of them and improve workability. The beam-hole edge of each disk was ellipsoidally filleted, as noted in the preceding section. The place around each cylinder has eight holes arranged axisymmetrically to form cooling pipes and four holes for tuning by dimpling. The inner surfaces of the cells were mirror finished by using an ultraprecision lathe. The surface roughness is below $0.1\ \mu\text{m}$ except the beam-hole edge with a roughness of $0.3\ \mu\text{m}$. Figure 2 and Figure 3 show schematic views and pictures of the disk and the cylinder, respectively.

The inner diameter of the cylinder was oversized so that the frequency of the regular cells was tuned by approximately 2 MHz lower than an operating frequency of 5712 MHz, since the frequency was shifted high by the final brazing process.

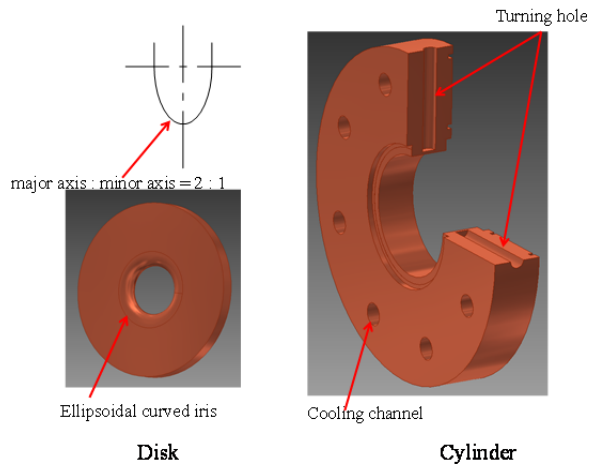


Figure 2: Schematic views of the disk and the cylinder.

Coupler Cell

The J-type double-feed coupler is integrated with the structure as with the choke-mode type structure. The coupler consists of a coupler cell, a square flange, a waveguide (WR-184), and a beam flange. Figure 4 and Figure 5 show a schematic view and a picture of the coupler cell, respectively.

The frequency and the phase shift of the coupler temporally assembled were measured by the nodal shift method and adjusted by modifying the internal diameter of the coupler cavity cell and the size of irises connecting the cell to the J-feeder. Figure 6 shows the measurement layout for the coupler cell. The coupler was brazed in a vacuum furnace after the RF adjustment.

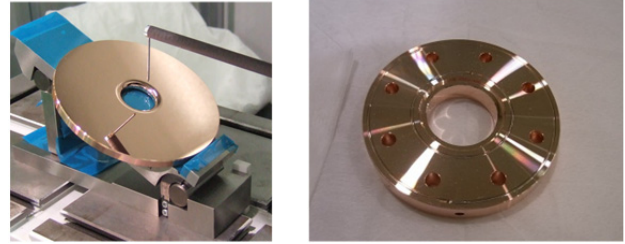


Figure 3: Disk and cylinder.

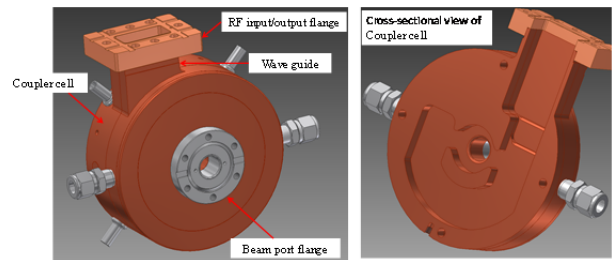


Figure 4: Schematic view of the coupler cell.

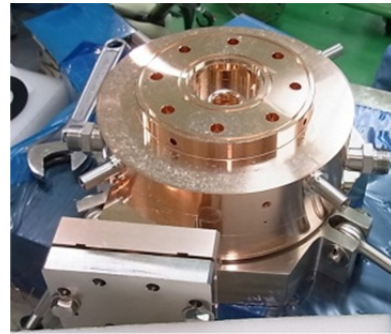


Figure 5: Coupler cell.

Brazing and Tuning

The couplers, disks and cylinders were stacked vertically with upstream side up and were brazed in the same position in a vacuum furnace. Figure 7 shows vacuum brazing layout for the accelerating structure. After the brazing, a phase shift of the each cell was measured by the nodal shift method and was tuned to a 120 deg. phase advance among the cells. by dimpling as mentioned above. We conducted the RF tuning for the structures in a condition of a temperature stabilized within $\pm 0.5\ \text{K}$ in order to improve accuracy of the RF measurement. In addition, temperature deviation of the accelerating structure during the tuning was controlled within $\pm 0.05\ \text{K}$ in the entire length of the structure by running temperature-stabilized water to the cooling channels of the accelerating structure.

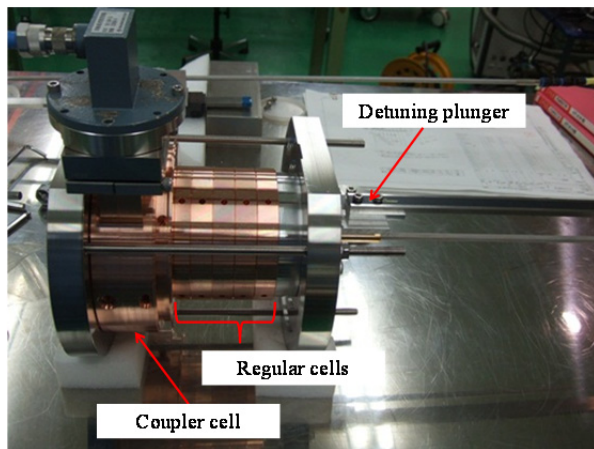


Figure 6: Measurement layout of the coupler cell.

After the tuning, a phase shift of each cell was measured by using the bead-pulling method [5] and the tuning was conducted again as necessary.

In the brazing process, cells are vertically stacked as already mentioned, so the cells on the downstream side of the structure were subjected to the higher load than that of the upstream side. In addition, material strength of the copper greatly decreases at the brazing temperature. As a result, the cells on the downstream side were slightly deformed after the brazing and their resonant frequency shifted high beyond our original expectations. Therefore, an integrated phase error was seemed to exceed the range of ± 3 deg. as required even after the tuning by the nodal shift method. To fix this problem, tuning of the cells by the bead-pulling method was conducted so that the integrated phase error was improved and reflections from the cells were reduced.

Results of the Low-power RF Test

Table 2 shows the measured RF properties of the accelerating mode of the structures after tuning.

In the case of the first structure labelled with #001, its integrated phase error of 3.2 deg. did not slightly meet the required specification. In the case of #003-#006, the further oversized diameter was given to the cells on the downstream side against their large phase shift by the brazing, and tuning accuracy was improved so the integrated phase error was below 2.8 deg. and the VSWR was below 1.05. Figure 8 shows the results of the integrated phase error of #003 by way of example.

Table 2: Results of the Low-power RF Test for Each Product

	#001	#002	#003	#004	#005	#006
Resonance frequency [MHz]	5712	5712.02	5712	5712	5712	5712
Integrated phase error [deg.]	3.2	2.8	2.7	2.8	2.8	2.8
Input VSWR	1.02	1.09	1.01	1.04	1.03	1.05
Attenuation constant τ	0.54	0.54	0.54	0.54	0.54	0.55
Filling time t_F [ns]	273	271	273	269	272	272
Q factor	8981	8969	9023	8944	8979	8950

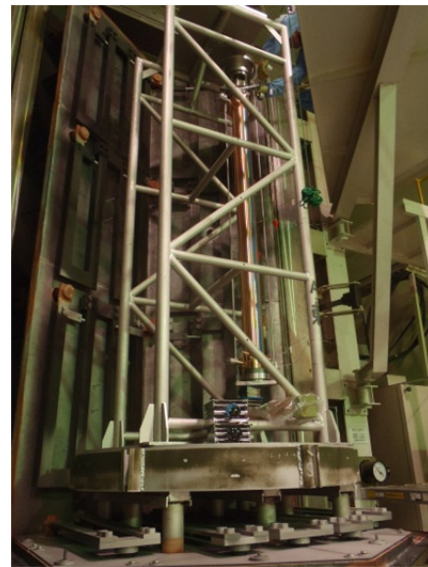


Figure 7: Vacuum brazing layout of the accelerating structure.

RESULTS OF THE HIGH-POWER RF TEST

A high-power RF test for #001 has already been conducted by RIKEN in the test bench of SACLA. An acceleration gradient of 50.1 MeV/m was achieved for 0.5 μ s in RF pulse width and at 60 pps in repetition rate. The operation with 42MV/m at 120 pps was possible for 24 hours or more without stopping due to the electric discharge etc. It was also verified that no thermal side effect was observed during operation at 120 pps. The detailed discussions on the results of the high-power RF test are described in the proceeding written by T. Sakurai et al.[6].

CONCLUSION

Six C-band disk-loaded type and CG accelerating structures were manufactured and the low-power RF tests of the accelerating structures were conducted. As a result, the first structure has a slight deviation in integrated phase-shift error but the others are fulfilled the required specifications. Consequently, the manufacturing method of the C-band disk-loaded type accelerating structures was established.

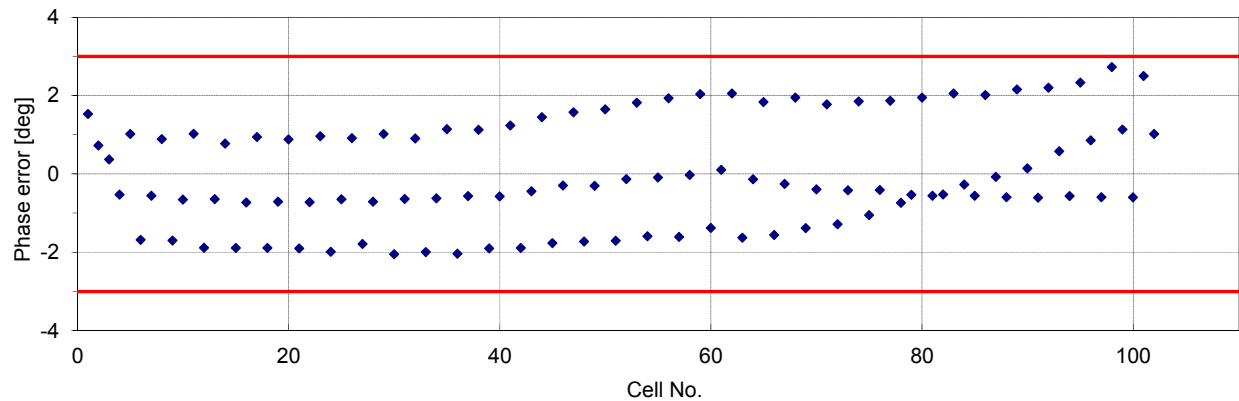


Figure 8: Results of the integrated phase error of #003.

REFERENCES

- [1] T. Sakurai al., "Design of a C-Band Disk-Loaded Type Accelerating Structure for a Higher Pulse Repetition Rate in the Sacla Accelerator", Proceedings of LINAC2012.
- [2] T. Sakurai al., "RF characteristic measurement of the model cavities towards development of the C-band disk-loaded type accelerating structure", Proceedings of the 10th Annual Meeting of Particle Accelerator Society of Japan, 2013.
- [3] T. Shintake. "The Chork Mode Cavity", Jpn. J. Appl. Phys. Vol. 31 (1992) pp.L1567-L1570, Part2, No.11A, 1 Nov. 1992.
- [4] S. Miura et al., "Manufacturing of the C-band Chork-Mode Type Accelerating Structure for SASE-FEL of RIKEN", Proceedings of the 28th Linear Accelerator Meeting in Japan, 2003.
- [5] T. Khabiboulline, et al., "A New Tuning Method for Travelling Wave Structures", 1996 IEEE.
- [6] T. Sakurai et al., "High power RF conditioning of C-band disk-loaded type accelerating structure", Proceedings of the 11th Annual Meeting of Particle Accelerating Society of Japan, 2014 (to be submitted).

HIGH REPETITION RATE S-BAND PHOTOINJECTOR DESIGN FOR THE CLARA FEL

J.W. McKenzie, P.A. Goudket, T.J. Jones, B.L. Militsyn, STFC/DL/ASTeC, UK
 L.S. Cowie, STFC/DL/ASTeC & Lancaster University, Cockcroft Institute, UK
 G. Burt, Lancaster University, Cockcroft Institute, UK
 V.V. Paramonov, INR of RAS, Moscow, Russia

Abstract

We present the design of a 1.5cell S-band photoinjector RF gun intended to be operated at repetition rates up to 400 Hz in single bunch mode. This gun is intended for use at the proposed CLARA (Compact Linear Accelerator for Research and Applications) FEL test facility at Daresbury Laboratory in the UK and will first be tested and characterised on VELA (Versatile Electron Linear Accelerator) in 2015. The final cavity design is presented including optimisation for CLARA beam dynamics, and choice of a novel coaxial H-shaped coupler.

INTRODUCTION

CLARA (Compact Linear Accelerator for Research and Applications) is a proposed 250 MeV, 100-400 nm FEL test facility at Daresbury Laboratory in the UK [1]. The electron source for CLARA needs to be able to operate in various regimes to meet the different FEL operational modes. In single bunch modes it needs to deliver bunch charges up to 250 pC at repetition rates of up to 400 Hz. In multi-bunch mode it needs to deliver 16×25 pC bunches with a bunch separation of 100 ns.

To meet this requirement, a 1.5 cell, 2.9985 GHz photocathode RF gun, shown in Fig. 1, has been designed. The gun is intended to operate with a peak field of 120 MV/m for the 100 Hz modes, which will be reduced to 100 MV/m for the 400 Hz modes to moderate the average power in the gun and thus heat loads. The gun will initially be tested on VELA [2] which contains a suite of diagnostics to fully characterise the 6D phase space of the emitted electron beam.

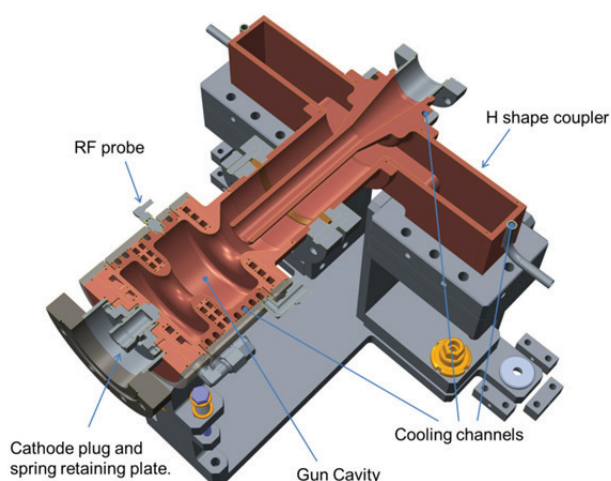


Figure 1: Overview of the gun design.

OVERVIEW AND COOLING

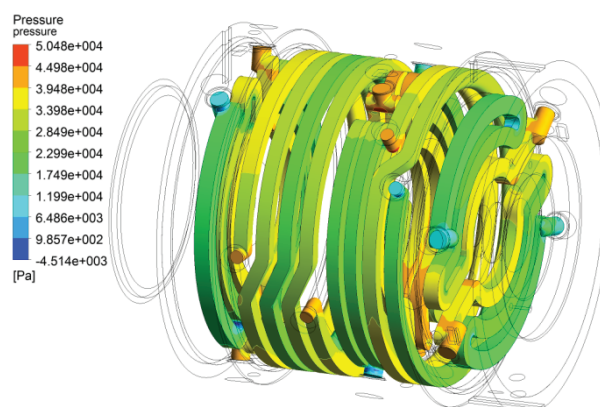


Figure 2: Pressure profiles at the surface of the cooling channels.

A 1.5 cell gun was chosen over 2.5 cells as, although this reduces the final energy of the electron bunch, it reduces the power requirements to the gun. Power fed into the gun manifests as heat deposited into the cavity walls and needs to be extracted by the cooling system. The expected average power for a 2.5 cell gun is almost double that of a 1.5 cell cavity, and for 100 MV/m at 400 Hz was estimated to be 6.8 kW for the 1.5 cell case.

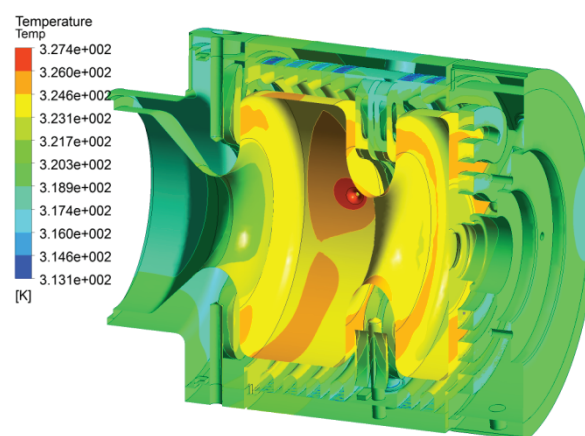


Figure 3: Temperature profile with the proposed cooling system with the gun operating at 100 MV/m at a 400 Hz repetition rate.

The magnetic field distribution of the cavity was converted into a heat flux and computational fluid dynamics simulations carried out in ANSYS. This showed that the proposed cooling, shown in Fig. 2,

consisting of nine channels cut into the bulk of the cavity, was sufficient to extract this power. More details of the cooling can be found in [3] and the temperature profile of the gun can be seen in Fig. 3.

To provide feedback, which is particularly needed for the multi-bunch operation mode, an RF probe is included in the second cell to monitor the fields, as shown in Fig. 1. A dimple is placed opposite for symmetry reasons. Although the probe aperture is blended, this local distortion to the magnetic fields causes it to be the area with the largest temperature increase, as shown in Fig. 3.

The gun will be equipped with a photocathode exchange system to accept 10 mm plugs of the INFN/DESY type [4]. The cathode is inserted through a plug in the back-plate of the first cell. Such a system allows for cathode changeover without breaking the cavity vacuum, and enables different metal and alkali photocathodes to be tested.

The gun cavity will be surrounded by a solenoid for emittance compensation and transverse focussing, and a bucking coil behind the cavity to cancel the magnetic field on the cathode plane. A coaxial coupler was chosen over side-coupling in order to preserve symmetry of the fields in the cavity and to minimise the effects of the dipole mode. This also allows the main solenoid to be placed around the cavity itself, rather than after, which is desirable from a beam dynamics standpoint.

More details on the overall gun design can be found in [5].

CAVITY DESIGN

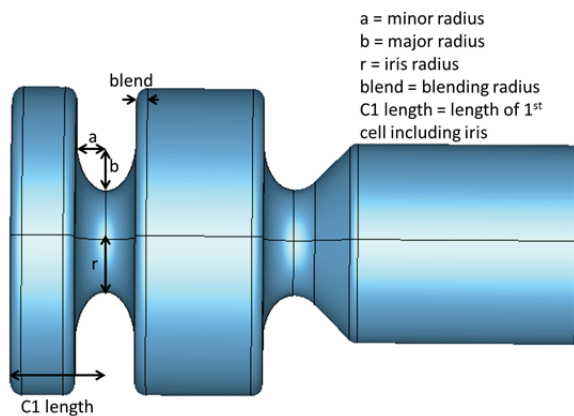


Figure 4: Parameterised 2D gun cavity model.

The cells are cylindrical with rounded edges to allow for a better distribution of the magnetic field and, as result, heat load. For the purpose of RF and beam dynamics optimisation, the cavity was parameterised as shown in Fig. 4 and modelled in Superfish via a custom Mathematica interface. This allowed each parameter to be varied individually, and a script automatically adjusted the radii of both cells to compensate for any changes in frequency or field flatness. Overall frequency will be set with operational water temperature with a scale factor of 50 kHz/°C, typical for S-band cavities. Tuning range is

therefore limited by reasonable temperature ranges of about 10 K, leading to a 500 kHz tolerance in frequency.

The iris radius, r , was chosen as a trade-off between geometrical quality factor, R/Q , and mode separation. The iris profile was chosen to be elliptical to minimise the maximum surface electric field. The ellipse minor radius, a , was fixed to 8 mm to give room for the cooling channels the ellipse major radius, b , and iris radius, r , optimised to give maximum R/Q for a minimum mode separation of 20 MHz.

FIRST CELL LENGTH OPTIMISATION

The parameter which has the largest effect on the beam dynamics is the first cell length. For optimisation the cell length was varied in Superfish and on-axis electric field distribution exported into ASTRA to simulate the beam dynamics. The beam, generated with a 76 fs rms laser pulse, as is currently used on the VELA photoinjector, was tracked from the photocathode through to the exit of the first linac module of CLARA as detailed in [1] and the beamline components optimised to give the minimum transverse emittance for each case.

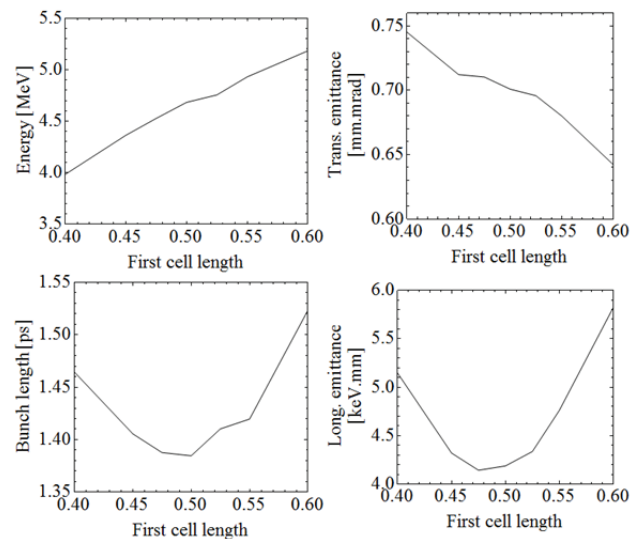


Figure 5: Beam parameters at the exit of the CLARA first linac for different gun first cell lengths for a 250 pC bunch and a gun peak field of 120 MV/m.

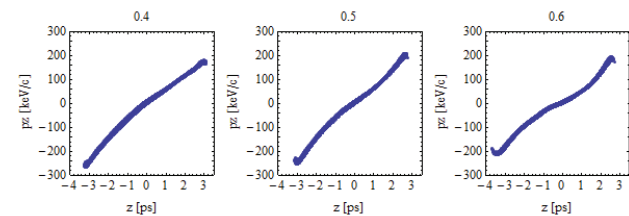


Figure 6: Longitudinal phase space of a 250 pC bunch at the exit of the CLARA first linac for gun first cell lengths marked above, for a gun peak field of 120 MV/m.

Operating with such a short laser pulse means that essentially the gun is operating in the “blow-out” regime [6] where the longitudinal beam distribution, instead of being determined by the laser pulse shape, is determined

by the space-charge, which forces the beam to expand longitudinally very rapidly after emission. The resulting beam is thus highly depending on the bunch charge, and the initial acceleration. Thus the electric fields in the first cell are critical for obtaining the best beam properties.

The first linac in CLARA will operate in two modes – firstly near crest in the modes where the beam will be compressed via a magnetic chicane downstream, and secondly, near the zero-crossing which uses velocity bunching to compress the bunch longitudinally. The simulations in this paper show only the case on the near-crest acceleration mode.

Figure 5 shows the results of the cell length scan for a 250 pC bunch with a peak on-axis electric field of each cavity of 120 MV/m. The first cell length is given as a fraction of the full cell length, which is set to half a wavelength. Increasing the cell length increases the final energy of the gun and reduces the transverse emittance.

However, looking at the longitudinal properties, there is an optimum cell length for minimising bunch length and longitudinal emittance. Figure 6 shows that for longer cell lengths there is more curvature in the longitudinal phase space of the beam – this makes the beam more difficult to manipulate downstream to provide the required bunch length for the FEL. Given that there is no requirement for higher gun energy and the transverse emittance in all cases meets the requirements of less than 1 mm.mrad for the FEL, a first cell length of 0.5 times that of the full cell provides optimum longitudinal beam properties.

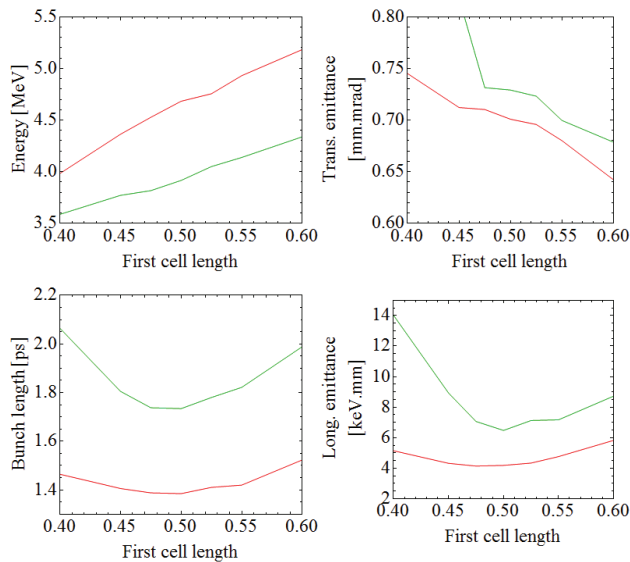


Figure 7: Beam parameters at the exit of the CLARA first linac for different gun first cell lengths for a 250 pC bunch and a gun peak field of 120 MV/m (red) and 100 MV/m (green).

The cell length scan was also carried out for a gun peak field of 100 MV/m and the results shown in Figs. 7 and 8. As can be seen, this lower gun gradient reduces the quality of the beam in all respects but the trends are the same. It is still apparent that a first cell length of 0.5 times that of the full cell gives good longitudinal properties. A shorter cell has clear first order curvature in the

longitudinal phase space, whilst a longer cell gives rise to higher order curvature.

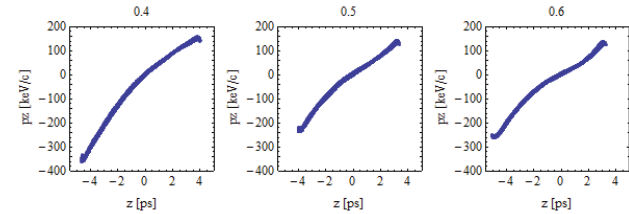


Figure 8: Longitudinal phase space of a 250 pC bunch at the exit of the CLARA first linac for gun first cell lengths marked above, for a gun peak field of 100 MV/m.

The cell length scan was also repeated for the 120 MV/m case at reduced bunch charges of 100 pC and 25 pC. The 100 pC case is shown in Figs. 9 and 10. It can be seen that the minimums for longitudinal emittance and bunch length are not for the same cell length as in the 250 pC cases. However, both of these parameters are much lower over all cell lengths due to the vastly reduced space-charge influence. Figure 9 also shows that the longitudinal phase-space doesn't vary as much as the high charge regime.

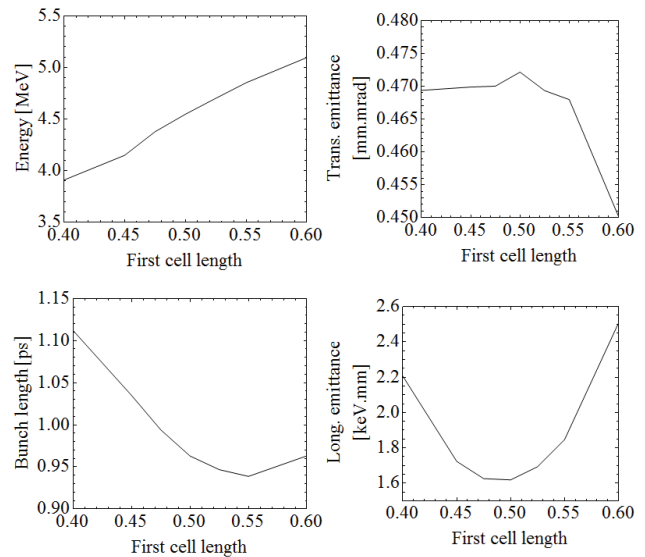


Figure 9: Beam parameters at the exit of the CLARA first linac for different gun first cell lengths for a 100 pC bunch and a gun peak field of 120 MV/m.

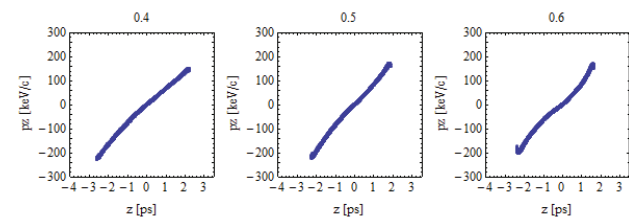


Figure 10: Longitudinal phase space of a 100 pC bunch at the exit of the CLARA first linac for gun first cell lengths marked above, for a gun peak field of 120 MV/m.

For the nominal case of 120 MV/m and 250 pC, the evolution of beam properties for CLARA is shown in Fig. 11.

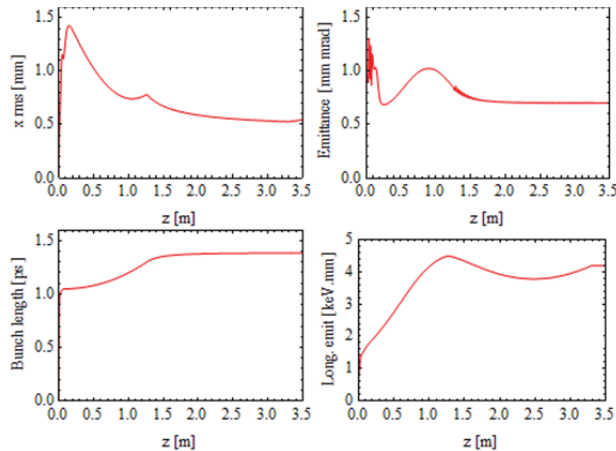


Figure 11: Evolution of parameters of a 250 pC bunch through linac 1 for the nominal case of 120 MV/m.

COUPLER DESIGN

Studies carried out on single-feed asymmetric designs show that they lead to a TE₁₁ dipole mode that can propagate to the cavity, as shown in Fig. 12. Due to the aperture size required for the laser, the cut-off frequency of the TE₁₁ mode in the coax section was below 3 GHz, resulting in up to 16% of the input power being transmitted to the TE₁₁ mode at the doorknob. While the coaxial length can be modified to cancel this out it still leads to a standing wave in the coupler which could cause a 50 kV transverse kick to the beam and cause asymmetric coupler and cavity heating, coupler mismatch and multipactor conditions. In order to allay that risk, it was decided to use a dual-feed system whereby the RF arrives to the cavity symmetrically.

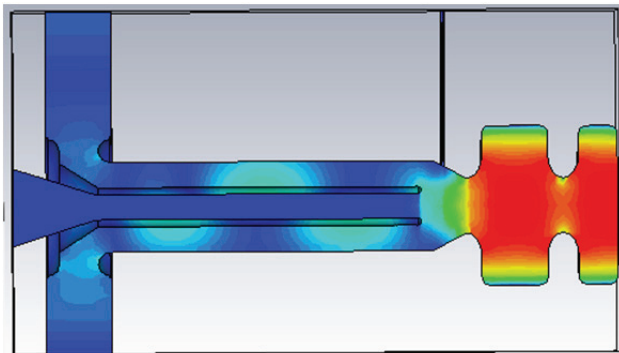


Figure 12: Dipole mode in the coaxial coupler of a single-feed asymmetric design.

A capacitive match at the doorknob is the solution commonly chosen for similar designs. However, it is a major risk in terms of multipactor and breakdown due to its geometry. An inductive iris would allow matching while removing the additional vulnerabilities presented by the capacitive coupling. The inductive iris is, however,

not tuneable, and reduces vacuum conductivity of the gun.

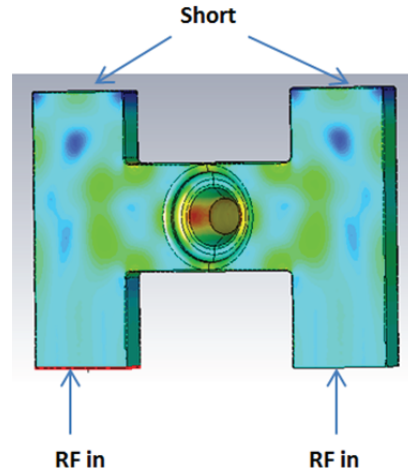


Figure 13: Electrical fields in the H-feed coupler.

In order to allow the coupler to be tuned to achieve the best possible match, we propose an alternative H-feed design, shown in Fig. 13. Movable shorts allow fine tuning of each arm separately, allowing the best possible compensation of phase errors in the two arms as well as the overall match of the transition. The shorts also give good access for pumping should this be required.

CONCLUSIONS

A 1.5 cell S-band RF gun cavity equipped with a novel H-feed coaxial coupler has been designed with cavity properties optimised to provide beam for the CLARA FEL test facility and operate at repetition rates up to 400 Hz.

REFERENCES

- [1] J. A. Clarke *et al.*, “CLARA Conceptual Design Report”, 2014 JINST 9 T05001.
- [2] P. McIntosh *et al.*, “VELA: A New Accelerator Technology Development Platform for Industry”, in *Proc. 5th Int. Particle Accelerator Conf.*, Dresden, 2014, pp. 2471-2463.
- [3] B. L. Militsyn *et al.*, “Design of the High Repetition Rate Photocathode Gun for the CLARA Project”, in *Proc. 27th Linear Accelerator Conf.*, Geneva, 2014, THPP126.
- [4] S. Schreiber *et al.*, “On the Photocathodes used at the TTF Photoinjector”, *Proc. 2003 Particle Accelerator Conf.*, (2003), pp 2071-2073, see also <http://www.lasa.mi.infn.it/ttfcathodes>
- [5] J. W. McKenzie *et al.*, “Cavity Design for a S-Band Photoinjector RF Gun with 400 Hz Repetition Rate”, in *Proc. 5th Int. Particle Accelerator Conf.*, Dresden, 2014, pp. 2983-2985.
- [6] L. Serafini, “The short bunch blow-out regime in RF photoinjectors”, in *AIP Conf.Proc.* **413** (1997) 321-324.

PERFORMANCE STUDY OF HIGH BANDWIDTH PICKUPS INSTALLED AT FLASH AND ELBE FOR FEMTOSECOND-PRECISION ARRIVAL TIME MONITORS

M.K. Czwalińska*, Ch. Gerth, H. Schlarb, C. Sydlo, DESY, Hamburg, Germany
 A. Angelovski, R. Jakoby, A. Penirschke, IMP, TU Darmstadt, Darmstadt, Germany
 T. Weiland, TEMF, TU Darmstadt, Darmstadt, Germany
 M. Kuntzsch, TU Dresden, Dresden, Germany and HZDR, Dresden-Rossendorf, Germany
 M. Gensch, HZDR, Dresden-Rossendorf, Germany

Abstract

At today's free-electron lasers, high-resolution electron bunch arrival time measurements have become increasingly more important in fast feedback systems for a timing jitter reduction down to the femtosecond level as well as for time-resolved pump-probe experiments. This is fulfilled by arrival time monitors which employ an electro-optical detection scheme by means of synchronised ultrashort laser pulses. Even more, at FLASH and the European XFEL the measurement has to cover a wide range of bunch charges from 1 nC down to 20 pC with equally sub-10 fs resolution. To meet these requirements, recently a high bandwidth pickup electrode with a cut-off frequency above 40 GHz has been developed. These pickups are installed at the macro-pulsed SRF accelerator of the free-electron laser FLASH and at the macro-pulsed continuous wave SRF accelerator ELBE. In this paper we present an evaluation of the pickup performance by direct signal measurements with high bandwidth oscilloscopes and by use of the electro-optical arrival time monitor.

INTRODUCTION

FLASH at the Deutsches Elektronen-Synchrotron is a free-electron laser with pulsed superconducting RF acceleration. Beam energies of up to 1.25 GeV correspond to FEL wavelengths down to 4.2 nm. THz sources and an optical laser are provided for pump-probe experiments. In addition, with the second FEL beamline, FLASH 2, the facility offers the possibility to apply or test different seeding schemes, i.e. HGHG, EEHG and HHG [1, 2]. Recently, increasingly more often user experiments demand for short FEL pulse lengths down to few 10 fs duration, which is achieved by decreasing the bunch charge well below 100 pC. Thus, the charge operation regime of FLASH now expands from a few 10 pC up to 3 nC.

ELBE at the Helmholtz-Zentrum Dresden-Rossendorf is a superconducting electron accelerator with a quasi-continuous wave (quasi-CW) mode of operation achieving beam energies up to 40 MeV. Bunches with up to 1 nC, after the next upgrade, and durations down to 200 fs are accelerated and transported to different beamlines, where they are used for various purposes, e.g. FEL pump-probe exper-

iments, THz generation or for experiments with Thomson back-scattering, with positron or neutron radiation [3, 4].

At both facilities, all of the diverse applications rely on stable beam conditions, which concerns electron bunch parameters such as charge, energy, compression and arrival time.

Arrival time drift and jitter are imprinted onto the electron bunch from instabilities in the electron source and from RF field fluctuations in the accelerating modules.

Besides delivering information to experiments, bunch arrival time monitors (BAMs) with femtosecond resolution also offer the possibility of feedback systems to actively stabilise the arrival time at different locations of the facility.

At FLASH e.g., such a beam-based feedback system has been implemented and has already proven a jitter reduction within the MHz repetition rate bunch train to below 20 fs (RMS) at a moderate bunch charge of 200 pC [5].

Bunch Arrival Time Monitor

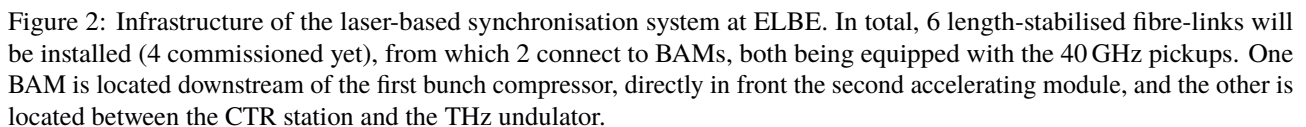
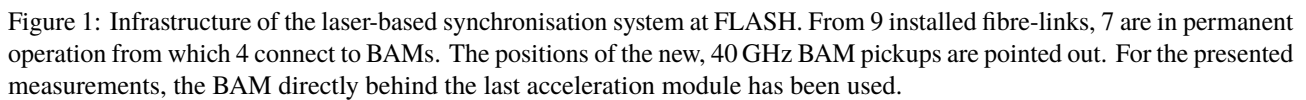
At both facilities, the same basic layout of the arrival time monitor is implemented. Making direct use of timing-stabilised laser pulses, which are provided by an optical synchronisation system [6], the BAM measures the electron bunch timing with an electro-optical detection scheme by means of integrated-optics devices.

For this, a broadband RF pickup delivers a transient beam-induced voltage signal, which is transported through phase-stable cables to the electro-optical modulator (EOM). In this Mach-Zehnder type EOM the voltage magnitude is translated into an amplitude modulation of the laser pulses, depending on the relative timing between optical and electrical signal. The optical, amplitude modulated signal then is detected and processed in high-speed, FPGA-based electronics. The arrival time is derived from an according time calibration showing a sensitivity of the monitor in the range of a few 10 fs per percent of amplitude modulation, which offers the possibility of sub-10 fs resolution [7].

In order to extend this high resolution operation of the BAMs also to low bunch charges, a broadband, cone-shaped pickup has recently been developed in cooperation with the Technical University of Darmstadt [8]. The RF feedthrough part has been produced by Orient Microwave and the mechanical vacuum parts were designed and built by DESY.

At FLASH and at ELBE, these new pickups with a cut-off frequency above 40 GHz have been installed lately.

* marie.kristin.czwalińska@desy.de



In this paper, we present first results from an extensive performance evaluation at both facilities. Two different approaches have been chosen, on the one hand a direct sampling of the RF signal with broadband oscilloscopes and on the other hand signal scanning by use of the electro-optical BAM setup.

BAMs at FLASH

At FLASH, the laser-based synchronisation system with individually length-stabilised fibre links has been in permanent operation since 2008 and, currently, serves 10 end stations [9]. From the 7 BAMs at FLASH, 4 locations are already equipped with the new high-bandwidth pickups (Fig. 1), each with a set of 4 pickups arranged symmetrically around the beampipe, aligned to in the horizontal and vertical plane. The pickup evaluation presented here, was performed at the BAM location directly behind the last accelerating module.

BAMs at ELBE

At ELBE, a pulsed optical synchronisation system has been implemented in 2012 in cooperation with DESY, and is now being extended to six remote stations [10, 11]. Figure 2 gives an overview of the synchronisation system infrastructure, pointing out the locations of the BAMs, which are connected via individual, length-stabilised fibre-links. One BAM is located behind the bunch compressor, directly in front of second accelerating module, the other is installed between the CTR station and the THz undulator.

The arrival time information will be used to enable a feedback on phase and amplitude values in the low-level RF control to continuously minimise deviations in the accelerating RF fields benefitting from the quasi-CW operation mode.

MEASUREMENTS AT FLASH

The RF pickup signals were connected through short (2 m) phase-stable RF cables (Phasemaster 160, Teledyne-Storm Microwave) to a Tektronix DSA8300 sampling oscilloscope with a 80E10 electrical sampling module, using an attenuation of 30 dB for an over-voltage protection. In addition, the device was covered with lead to be protected from radiation.

In this setup, we simultaneously measured the voltage signals from a single pickup on channel 2 and a combined signal from two opposing pickups in the horizontal orientation on channel 1. The signal from the remaining single pickup (vertical, top) has been low-pass filtered to trigger the oscilloscope, compare Figure 3.

For a thorough performance evaluation, extensive scans of electron bunch parameter have been performed, including various bunch compression settings, charge sweeps from 20 pC up to 250 pC and beam orbit scans.

As can be seen from Figure 4, the amplitude (corrected for the level of attenuation) shows the expected linear dependence on the total bunch charge, with up to 1 V peak at

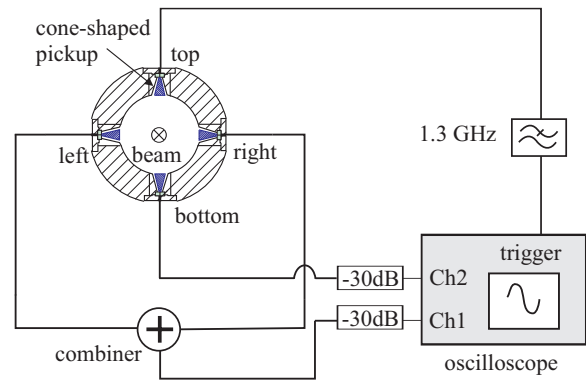


Figure 3: Measurement setup at FLASH with a sampling oscilloscope.

25 pC. This includes losses through 2 m of high quality RF cable and connector losses.

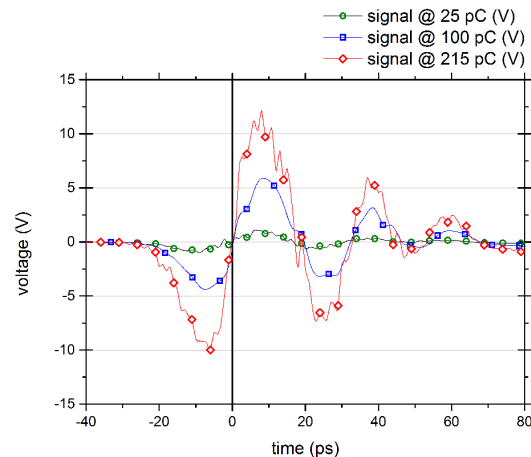


Figure 4: Voltage signals from the single pickup measured at 3 different bunch charges.

Simulations during the pickup design process indicated a linear scaling of voltage amplitude with bunch charge, while a peak voltage of 1 V has been expected for a charge of 20 pC [8], and has now been measured to 1.1 V at 25 pC.

The plots in Figures 5 and 6 reveal the orbit dependency of the linear signal slope (around the zero-crossing between the first two peaks), recorded at a fixed bunch charge of 150 pC.

In Fig. 5, the signal from the single pickup (lower vertical position) reflects the expected behaviour of a linear response to beam orbit changes in the vertical plane: with decreasing distance between bunch and pickup, the magnitude of the induced signal increases, thus the slope increases as well.

In Fig. 5, a remaining orbit dependency of about 20 % in total can be seen. However, the slope values from the other measurement channel, clearly displays the benefit of a signal combination in terms of a reduced sensitivity to orbit changes.

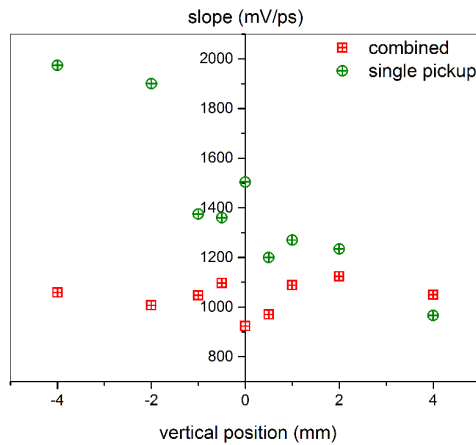


Figure 5: Variation of signal slopes under vertical beam orbit scans, at a bunch charge of 150 pC.

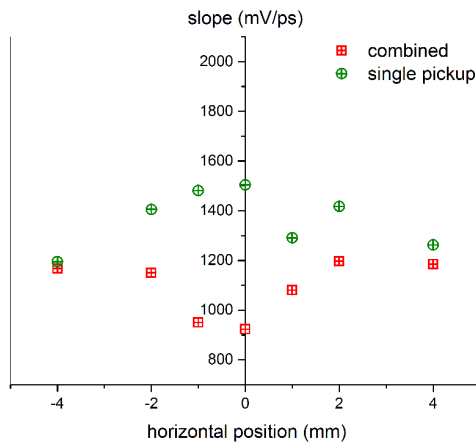


Figure 6: Variation of signal slope under horizontal beam orbit scans, at a bunch charge of 150 pC

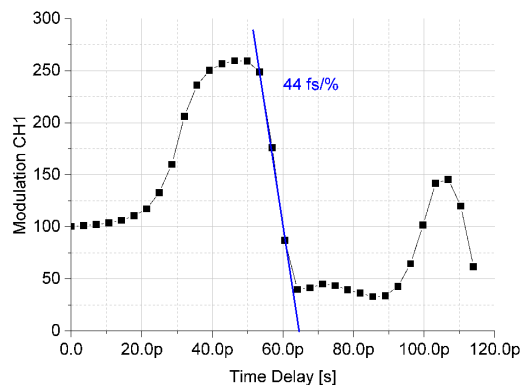


Figure 7: Calibration curve of the BAM signal at a charge of 50 pC. The time calibration of 44 fs/% yields the opportunity to achieve the targeted sub-10 fs resolution in the low charge regime down to 20 pC.

Any remaining orbit dependency can be removed from the arrival time data by using feedback from beam position monitors, ideally mounted in direct vicinity of the BAM pickup. This has been shown for the lower bandwidth BAMs in [12].

Due to this, at FLASH and also at the European XFEL, it is foreseen to install high-resolution bunch position monitors directly behind the BAM pickup mount. The signals will be transmitted through low-latency links to the BAM electronics and will be processed online in the FPGA-based board firmware.

MEASUREMENTS AT ELBE

At ELBE, the pickup performance has been evaluated in two different ways. The RF signal quality was verified in a similar setup as at FLASH, but a high bandwidth, real time oscilloscope Agilent Infiniium 90000 Q-Series has been used, which provides two 63 GHz channels at a sampling rate of 160 GS/s. With bunch charge sweeps between 5 pC and 95 pC the behaviour of amplitude and slope has been examined to prove the expected linearity.

The voltage slope at 20 pC bunch charge was measured with 380 mV/ps and thus complies with the results at FLASH and with simulations.

The data presented here, has been recorded with the BAM setup, which makes use of a 35 GHz semiconductor-based EOM (U2T, MZMO 2130). The combined signal from opposing RF pickups is transmitted through SiO₂ cables (Anritsu, with 35 GHz bandwidth), and fed into the modulation input of the EOM, including an RF limiter (Agilent N9355F) protecting the EOM against high peak voltages.

Using an optical delay line, the laser pulse timing has been scanned relative to the electron bunch timing, to obtain the transmission curve through the EOM depending on the input RF modulation voltage. Figure 7 shows the percentage amplitude modulation of the laser signal. The time calibration, thus sensitivity of the BAM, is given by the inverse linear slope around the operation point around 100 %, and was calculated to 44 fs/%.

This curve reveals the potential to achieve femtosecond-precise arrival time measurements also at lower bunch charges. With high quality electronics, which offer an amplitude detection with a noise level below 0.1 %, this BAM yields an achievable detection resolution of below 5 fs at a bunch charge of 50 pC.

CONCLUSION

Presented in this paper, as well as in former published studies, it has been shown that for achieving femtosecond-precise electron bunch arrival time measurements using the described monitor, several conditions must be met:

- a broad-band pickup with a voltage slope higher than 350 mV/ps for the envisioned lowest bunch charge regime,

- low-loss, high bandwidth RF transmission line with components which meet the bandwidth of the pickups
- a suitable, broad-band EOM with an E/O bandwidth similar to the RF components, and low V_{π} for a modulation depth close to 100 % over the full region of the linear voltage slope
- a high-precision, low-noise laser amplitude detection in analogue and digital electronics.

With the sensitivity of the BAM setup in the range of few 10 fs/%, we are convinced to reach the envisioned sub-10 fs resolution in the bunch charge regime of below 50 pC. With the optimised RF part of the BAM, the measurement accuracy itself is now predominantly limited by the overall amplitude noise in the system.

A more thorough evaluation of the obtained data from the extensive studies is in preparation, underlining the very good agreement with signal simulations, and showing that the design values of the cone-shaped, broadband RF pickup design are met.

ACKNOWLEDGMENT

The authors would like to thank the company Agilent Technologies Sales & Services GmbH & Co. KG for technical support and for providing the real time 63 GHz oscilloscope Agilent Infiniium 90000 Q-Series. We thank the FLASH and the ELBE team for the technical support and for the opportunity to perform these measurements. The work of A. Angelovski is supported by the German Federal Ministry of Education and Research (BMBF) within Joint Project - FSP 302.

REFERENCES

- [1] B. Faatz, N. Baboi, V. Ayvazyan, et. al., "FLASH II: a Seeded Future at FLASH", IPAC'10, Kyoto, Japan, 2010, TUPE005 (2010), <http://www.JACoW.org>
- [2] J. Bödewadt, C. Lechner, "Results and Perspectives on the FEL Seeding Activities at FLASH", FEL2013, New York, NY, USA, 2013 WEPSO02 (2013) <http://www.JACoW.org>
- [3] J. Teichert, A. Arnold, H. Büttig, et al., Nuclear Instruments and Methods in Physics A 743(2014), 114-120
- [4] M. Gensch, B. Green, S. Kovalev, et al., "THz Facility at ELBE: A Versatile Test Facility for Electron Bunch Diagnostics on Quasi-CW Electron Beams" IPAC'14, Dresden, Germany, TUZA02 (2014) <http://www.JACoW.org>
- [5] Ch. Schmidt, M.K. Bock, S. Pfeiffer, et al., "Feedback Strategies for Bunch Arrival Time Stabilization at FLASH Towards 10 fs" FEL'11, Shanghai, China THPA26 (2011), <http://www.JACoW.org>
- [6] F. Löh, V. Arsov, M. Felber, et al., Physical Review Letters 104, 144801 (2010)
- [7] M.K. Bock, M. Bousonville, M. Felber, et al., "Benchmarking the Performance of the Present Bunch Arrival Time Monitors at FLASH", DIPAC'11, Hamburg, Germany TUPD28 (2011) <http://www.JACoW.org>
- [8] A. Angelovski, A. Kuhl, M. Hansli, et al., Physical Review Letters Special Topics – Accelerators and Beams 15, 112803 (2012)
- [9] S. Schulz, M. Bousonville, M.K. Czwalińska, et al., "Past, Present and Future Aspects of Laser-Based Synchronization at FLASH", IBIC'13, Oxford, UK, 2013, WEPC32 (2013) <http://www.JACoW.org>
- [10] M. Kuntzsch, A. Buechner, M. Gensch, et al., "Status of the Femtosecond Synchronization System at ELBE" BIW'12, Newport News, VA USA, MOBP03 (2013) <http://www.JACoW.org>
- [11] M. Kuntzsch, S. Findeisen, M. Gensch, et al., "Electron Bunch Diagnostic at the Upgraded ELBE Accelerator: Status and Challenges" IBIC'13, Oxford, UK, MOBL3 (2013) <http://www.JACoW.org>
- [12] M.K. Bock, "Measuring the Electron Bunch Timing with Femtosecond Resolution at FLASH", DESY-THESIS-2013-008 (2013) <http://www-library.desy.de/>

A TOOL FOR REAL TIME ACQUISITIONS AND CORRELATION STUDIES AT FERMI*

Enrico Allaria, William M. Fawley, Elettra-Sincrotrone Trieste S.C.p.A., Basovizza, Italy[#]
Eugenio Ferrari, Elettra-Sincrotrone Trieste S.C.p.A., Basovizza, Italy and Università degli Studi di Trieste, Trieste, Italy

Abstract

In this work we report the recent implementation of a Matlab-based acquisition program that, exploiting the real time capabilities of the TANGO control system, can be used at FERMI for acquiring various machine parameter and electron beam properties together with most FEL signals on a shot-by-shot basis. Analysis of the saved datafiles is performed with a second code that can retrieve correlations and study dependence of FEL properties on machine parameters. An overview of the two codes is reported.

THE REAL TIME CAPABILITIES AT FERMI

The control system of FERMI uses the Tango [1] toolkit to provide an effective integration of technical systems and the software controlling them. A distributed real-time framework is integrated into the control system and provides the capability to measure the seed laser, electron and FEL output photon properties on a pulse-to-pulse basis [2]. With this framework, a unique “bunch number” time-stamp is distributed to all of the low level computers. Most of the measurement system detectors (e.g., electron and photon diagnostics) and actuators (e.g., power supplies) are synchronized with the bunch trigger and can have the “bunch number” associated to their measurements.

Using the Tango bindings, the FERMI control system allows interfacing the accelerator instrumentation to Matlab. This capability has been used to develop various scripting procedures and GUIs to permit user interaction with the machine and has been extensively used for the commissioning of both FEL-1 [3] and FEL-2 [4].

THE ACQUISITION PROGRAM

In this section we describe the MATLAB code implemented at FERMI for real time acquisition of relevant machine and FEL output signals. A brief description of the main features and components of the code will be presented.

Acquisitions are first setup from the RT MATLAB graphical user interface (GUI) (see Fig. 1) that allows the user to define the type of acquisition and select some of the device signals to be acquired. Before the main acquisition begins, a one shot record of the most important machine parameters (e.g., undulator gap settings, dipole and quadrupole magnet currents, lasers

intensities, ...) is acquired to provide a snapshot of the machine and FEL configuration. This information is stored and saved in the final achival data file. The predefined list of the acquired devices in principle saves all the relevant information that will allow reconstruction of the linac and FEL state during the data analysis phase. When needed, the list of saved signals can be changed on a case-by-case basis via a user-defined configuration file.

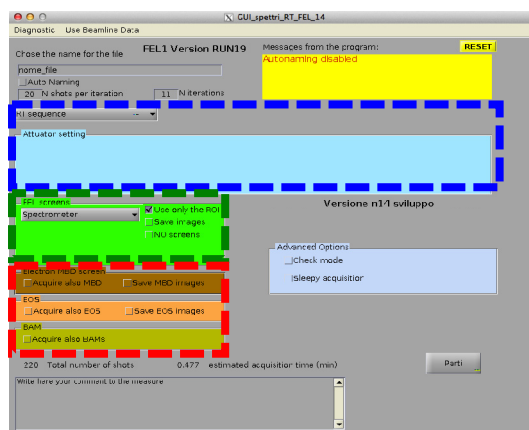


Figure 1: Graphical user interface for RT acquisition of FERMI machine instruments.

Types of Acquisition

The region highlighted in blue in Fig. 1 is used to select the type of acquisition. At present three possible acquisition types are available: “RT sequence” and “actuator scan” and “script scan”.

The **RT sequence** is the standard acquisition of the specified list of the machine devices, without any linac or FEL parameter being purposefully changed (i.e., “scanned”). The type of sequence is normally used to collect large quantities of data for statistical studies (e.g. correlations). The user can decide the length of the acquisition by deciding the number of shots acquired.

The **actuator scan** allows the user to actively change a particular machine parameter (e.g., the seed laser power or a dispersion section magnet strength) in order to map the response of the FEL. The parameter is selected from a predefined list as shown in Fig. 2.

*Work partially supported by the Italian Ministry of University and Research under grants FIRB-RBAP045JF2 and FIRB-RBAP06AWK3

[#]enrico.allaria@elettra.eu

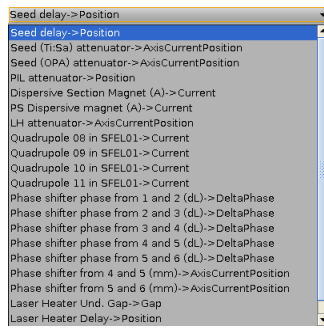


Figure 2: List of available machine parameters that can be used for a scan.

Further options for defining the parameters of the scan (number of shots per individual scan parameter value acquired, the total range and number of parameters values scanned, accuracy, ...) are also available to the user (see Fig. 3). At present standard actuator scans involve a linear change of actuator value.

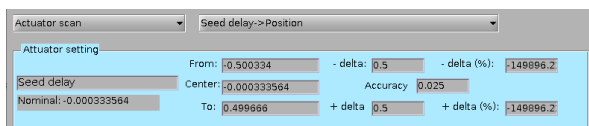


Figure 3: Details of the scan settings section of the data acquisition GUI.

A MATLAB-based **script scan** can be used in those cases where a simple scan cannot be defined with a single actuator or a simple linear value change. With the script scan option it is possible to use an external MATLAB script that controls the changes of one or more machine parameters during the data scan. One commonly used scan using this option measures the FEL gain curve by acquiring the FEL intensity as the number of on-resonance undulators is changed one-by-one.

Data Acquired During Scans

During the acquisition, the program reads data from the machine devices contained in a predefined list. This second list only accounts for devices that can be acquired on a shot-to-shot basis and will have the associated “bunch number” tag. The list of acquired instruments is defined in an external text file and is highly inclusive in order to have available in the final achival file all the possible information that might be useful to study possible correlation between the FEL intensity and other parameters. Examples of such measured quantities are the electron beam charge both before and after the undulator, the beam compressor pyrometer signals, transverse beam position monitor signals at a large number of locations both before, in, and beyond the undulators.

In addition to the predefined list of machine parameters the user can add to the acquisition few more instruments that may be of interest depending on the purposes of the measure. This includes the possibility to add data from one or more CCD cameras at various locations in the machine (see the green highlighted region in Fig. 1). The CDDs image either an intercepting LINAC e-beam screen

or an FEL diagnostics (e.g.: photon spectrometer). The acquisition can be limited to only the projections (1D vectors) or include the full 2D matrix. Additional special devices can be acquired in synchronization with all the other diagnostics for those case they are needed and are made available (see the red highlighted region in Fig. 1). This includes the bunch arrival monitors (BAMs), electro-optical sampling (EOS) station and the main electron beam dump.

After the acquisition is started, both messages about the scan’s progress are reported on the dedicated space in the GUI and selected data are shown within a dedicated figure. After acquisition is concluded, a logbook-ready image is displayed together with a summary of the acquisition, showing a small subset of the acquired data. An example is reported in Fig. 4 where the FEL intensity and the FEL spectra are plotted as a function of the actuator used during the acquisition (in this case the seed laser delay). The plot also reports the name of the file that is saved at the end of the acquisition.

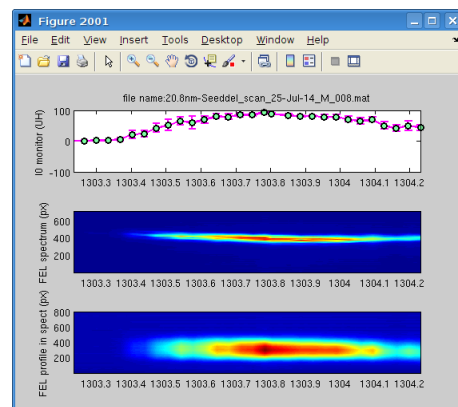


Figure 4: Details of the scan settings section of the data acquisition GUI.

The data file is saved in a MATLAB format, which allows a reasonably good compression, and contains all the acquired data as well as additional information such as the version of the code used, an optional user-defined comment to the acquisitions that can be inserted from the dedicated panel in the GUI, and the time of the acquisition.

THE ANALYSIS PROGRAM

After the data is taken and stored, a separate MATLAB-based program (Fig.5) is available to analyse the information.

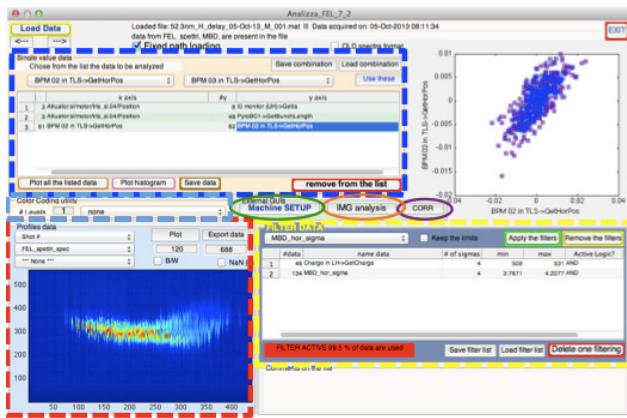


Figure 5: Details of the scan settings section of the data acquisition GUI.

Data Selection

After a file is loaded, all the acquired “single value” devices present in file are recognized and listed in the two tab-listed region highlighted in blue in Fig. 5. The two tab-lists allow the user to select an x-y combination whose preview is then shown in the side image. When the chosen x-y pair is considered acceptable, the user can add it to a table below. The data listed in the table is then considered for the final plotting, statistics computation and data exporting according to the user’s interests.

Vector-like quantities (e.g., spectra profiles) are listed in a separate tab (the red highlighted region in Fig. 5) and are visualized as false colors images. The vertical axis corresponds to 1D vector coordinate of each single profile while the horizontal direction corresponds to the different acquired bunches. A preview plot can also be done either by ordering bunches with time or according to the settings of a third device. This option is very useful for identifying correlation between the FEL spectra and other machine parameters as shown in Fig. 6.

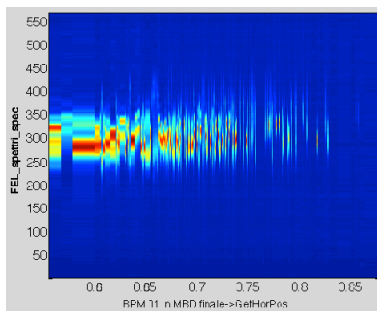


Figure 6: FEL spectral profiles ordered as a function of the transverse electron beam position in a dispersive region.

Data Filtering

Filter tools are available to improve the effective S/N ratios and to weed out bad shots. The user can define filter parameters by mean of the dedicated panel (yellow highlighted region in Fig. 5). The tab-list allows the user to select any of the acquired “single value” data and use it for filtering bad shots. In the particular case shown in

Fig. 5 the charge at the beginning of the LINAC and the position at the last e-beam screen are considered. The acceptance filter can be set by specifying extremes or by defining number of RMS sigmas. The program indicates to the user the amount of data that are rejected both in tota and from each individual filter. Once the user has defined a filter configuration, it can be applied resulting in only the good shots will be used for all further analysis and plots. In in the graphs generated by the code, a label is inserted to emphasize the use of the filter and the percentage of used data (Figs. 7,8,10).

Data Analysis and Plot

The data selected and listed in the table can be visualized in separate MATLAB figures. Various plots are generated depending on the type of acquisition and the user’s particular interests. In case of an “actuator scan” acquisition, if the actuator is selected for horizontal axis independent variable, an average and error bar are also calculated and plotted (Fig. 7).

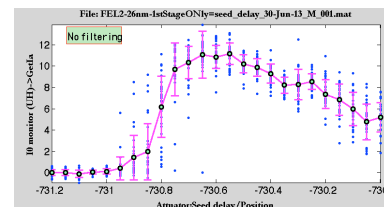


Figure 7: Plot generated for a scan acquisition.

Because the acquired data are synchronized by bunch number, they can be used to visualize correlations between different parameters. This can be done by plotting as an example, the FEL intensity as a function of electron beam parameters. It can also be exploited to show the correlation in FEL-2 between the first stage emission and the second stage emission (Fig. 8).

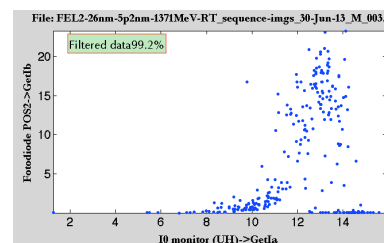


Figure 8: Intensity of second stage vs the first stage emission from FEL-2 operated at 5nm.

A visualization of the correlation between three separate machine parameters is also possible by using the dedicated “color coding” panel (the light blue highlighted region in Fig. 5). An example is shown in Fig. 9

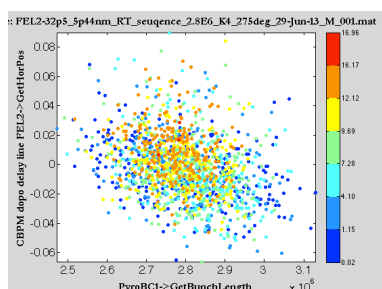


Figure 9: FEL intensity in color code as a function of the beam compression and position signals.

A statistical analysis of the selected data is also possible and the distribution of the variable values can be plotted together with the calculated average and standard deviation values (Fig. 10).

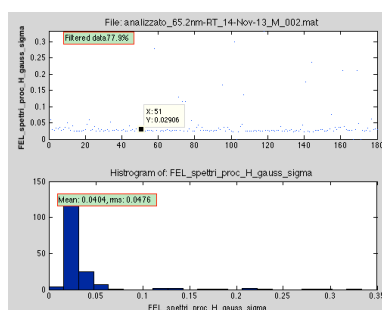


Figure 10: Histogram distribution of the data selected.

The plotting of the profiles (1D vectors) is handled by the Profile Viewer utility (red highlighted region in Fig. 5). A typical image showing the analyzed FEL spectrum as a function of on scanned parameter (dispersive section) together with the trend of the FEL intensity is shown in Fig. 11.

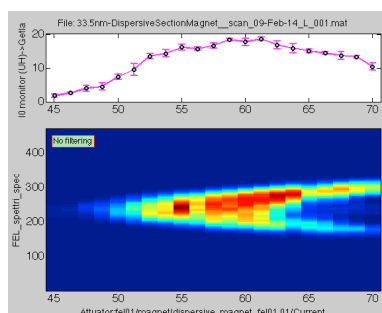


Figure 11: Plot generated for a scan acquisition.

If needed the data selected and listed in the table can be exported in ascii format for further analysis or processing with external programs.

Image Analysis

For those data files where diagnostic screen data were taken with images or profiles, an external program can be used by means of the dedicated button (orange circle in Fig.5) to determine various quantities such as the centroid and RMS size in the two transverse planes. For files with spectra, Gaussian fits to the output are used to determine

bandwidth and central wavelength. These quantities can then be added to the list of “single value” data and correlated against individual machine signals in the case of RT sequences or against the scan parameter in actuator scans.

Machine Setup

The machine configuration snapshot produced by the acquisition program at the moment of the acquisition can be easily visualized by using a dedicated tool that is launched from the main GUI (green circle in Fig.5). The tool automatically recognizes the devices and produces a user-friendly table with their names and corresponding values divided by machine sectors as shown in Fig. 12.

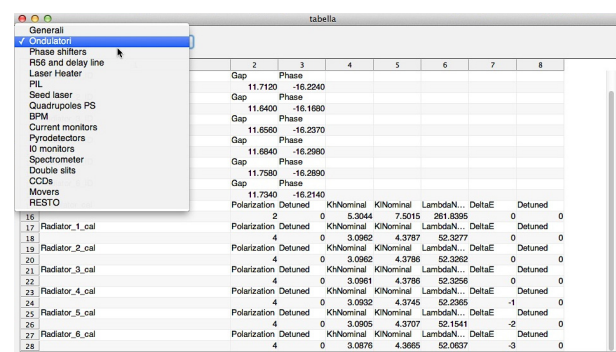


Figure 12: Tool to visualize the machine snapshot showing the setting for the FEL undulators at the moment of the acquisition.

CONCLUSION

Over the past two years we have steadily improved the acquisition and analysis programs. Currently, more than half of all FERMI commissioning data is taken with them. Moreover, many scientific users on FERMI are also using the acquisition program (or specially modified versions) for their studies. Since the acquired data is archived and is more-or-less self-describing in terms of contents, as the analysis program is improved, we are able to extract additional information from older data runs.

ACKNOWLEDGMENT

We are pleased to acknowledge the extensive assistance we have received from the FERMI controls team in developing these programs. We also thank M. Trovo, G. Gaio and L. Froehlich for additional assistance with the construction of the various MATLAB/TANGO/machine interfaces.

REFERENCES

- [1] TANGO Controls: <http://www.tango-controls.org/>
- [2] M. Lonza *et al.*, “Status report of the FERMI@Elettra control system” Proceedings of ICALEPCS2011, TUDAUST02, Grenoble (F) 2011.
- [3] E. Allaria *et al.*, Nat. Photonics **6**, 699 (2012).
- [4] E. Allaria *et al.*, Nat. Photonics **7**, 913 (2013).

OPTICS MEASUREMENTS AT FLASH2

M. Scholz*, B. Faatz, M. Vogt, J. Zemella, DESY, Hamburg, Germany

Abstract

FLASH2 is a newly build second beam line at FLASH, the soft X-ray FEL at DESY, Hamburg. Unlike the existing beam line FLASH1, it is equipped with variable gap undulators. This beam line is currently being commissioned. Both undulator beam lines of FLASH are driven by a common linear accelerator. Fast kickers and a septum are installed at the end of the linac to distribute the electron bunches of every train between FLASH1 and FLASH2. A specific beam optic in the extraction arc with horizontal beam waists in the bending magnets is mandatory in order to mitigate CSR effects. Here we will show first results of measurements and compare to simulations.

INTRODUCTION

The existing superconducting single-pass high-gain SASE FEL FLASH (Free-electron LASer in Hamburg) at DESY, Hamburg [1] delivers photons in the wavelength range from 4.2 nm to 45 nm. The photons generated in the fixed gap SASE undulators can be delivered to five experimental stations one at a time. A second undulator beam line was attached to the linac during the last three years and is now under commissioning [2]. The FEL will continue to be referred as FLASH and the two beam lines are named FLASH1 and FLASH2. Fast kickers and a DC Lambertson-Septum are installed behind the FLASH linac allow to distribute the beam either to FLASH1 or to the extraction arc leading to FLASH2. The final angle between FLASH1 and FLASH2 is 12°. Strong bending magnets in the extraction arc require specific Twiss functions in order to mitigate emittance growth due to coherent synchrotron radiation (CSR) [2, 3]. The FLASH2 undulator beam line is equipped with variable gap undulators [4] for SASE and reserves space for future seeding options. The extraction to a proposed third beam line hosting a plasma wake field experiment is considered in the beam line layout at the end of the FLASH2 arc.

In this paper, we will describe the first optics and dispersion measurements and the matching of these functions to the design values in a diagnostic section upstream of the FLASH2 undulators.

DISPERSION MEASUREMENT AND MATCHING

The dispersion describes the dependence of the transverse position on the relative momentum offset.

$$\eta_{x,y} = \frac{\Delta(x,y)}{\Delta p/p_0} \quad (1)$$

With the dispersions $\eta_{x,y}$, the positions x, y and the relative momentum offset p/p_0 . The design dispersion functions

* matthias.scholz@desy.de

of FLASH2 can be found in Fig. 2. In order to minimize the distortion of the centroid trajectory through non-linear dispersion, the measurement should be performed using bunches with minimized energy spread. Since the RF systems are capable of splitting their 800 μ s long flat tops between FLASH1 and FLASH2, this can be achieved to a large extent for FLASH2 while FLASH1 is in SASE operation [5]. We measured the horizontal beam offset at four different BPMs [6–10] downstream the extraction while changing the beam energy with the accelerating Module ACC45 of the linac. A MATLAB [11] script was used to control the measurement, to change the gradients of the accelerating module and to read the beam positions from the BPMs. The beam energy was changed during the procedure in 10 steps from 551.7 MeV to 554.7 MeV. The dispersion matching was carried out with a linac version of MAD8 [12, 13]. First, a setting of η_x and η'_x upstream the second last quadrupole in the extraction arc was searched fitting the measured dispersions at the four BPMs using the current machine settings. These values were then be used to close the dispersion in an optimization run using the last two quads in the extraction arc. After five iterations the procedure had converged. The data from the last measurement is presented in Fig. 1.

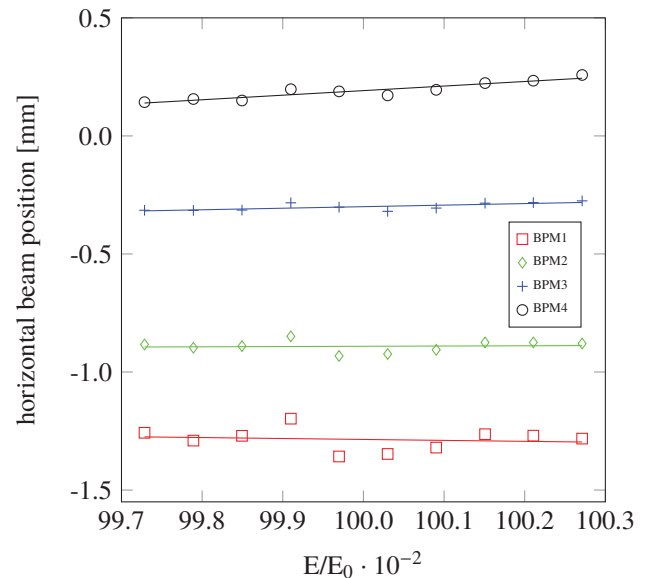


Figure 1: Results of the last dispersion measurement. This plot shows the horizontal beam positions at four different BPMs for different relative beam energies. The energy is normalized to $E_0 = 552$ MeV.

The final dispersion at the four positions was $\eta_{x,i} = [-4, 1, 7, 20]$ mm and the dispersion prime at the first BPM was calculated as $\eta'_{x,1} = 3.8 \cdot 10^{-4}$.

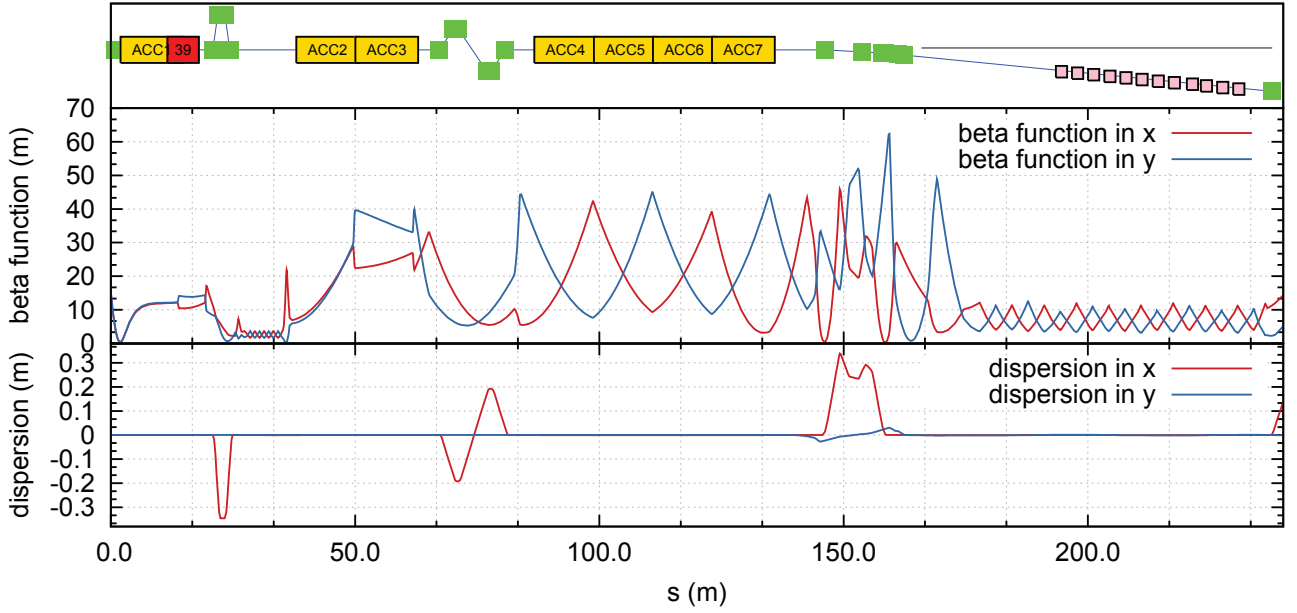


Figure 2: The upper plot shows the design optics of the FLASH2 beam line including the linac, the extraction arc and the undulator section. In the lower plot one can find the horizontal and vertical design dispersions in the two bunch compressors and in the FLASH2 extraction arc.

OPTICS MEASUREMENT AND MATCHING

We used four OTR screens in a periodic FODO structure between extraction and the SASE undulators with about 30° phase advance in between to measure the Twiss functions and the transverse emittances of the beam [14]. The upper plot in Fig. 2 shows the design optics of the new beam line including the linac and the arc. The beam was on-crest for this measurement and the dispersion was closed as good as described above. The optics measurements were carried out using a suite of shell scripts for the communication with the control system of the FEL. The fits of the measurement data were made with gnuplot [15] and the matching of the Twiss parameters was again carried out with a linac version of MAD8. The match between the design optics and the measured beam optics can be described by the mismatch amplitude [2]:

$$m_{\text{amp}} = m_{\text{par}} \sqrt{m_{\text{par}}^2 - 1} \quad \text{and} \quad (2)$$

$$m_{\text{par}} = \frac{1}{2} (\tilde{\beta}\gamma - 2\alpha\tilde{\alpha} + \beta\tilde{\gamma}),$$

with the mismatch parameter m_{par} , the design Twiss parameters α , β and γ and $\tilde{\alpha}$, $\tilde{\beta}$ and $\tilde{\gamma}$, the Twiss parameters of the measured beam. The mismatch amplitude describes the amplitude of the oscillation of an unmatched beta function around the design beta function. The range of the oscillation is $1/m_{\text{amp}} \beta \leq \tilde{\beta} \leq m_{\text{amp}} \beta$. After five iterations, the beam optics measurement procedure had converged. The start and end values for the mismatch amplitude can be found in Table 1. The beta functions in the matching section before and after the optimization as well as the design beta functions are

Table 1: Mismatch Amplitude of the Horizontal and Vertical Plane at Start and End of Matching Procedure

Mismatch Amplitude	Start	End
Horizontal	1.86	1.07
Vertical	1.99	1.07

shown in Fig. 3. The measured normalized transverse emittances were $\epsilon_{nx} = 6.9 \mu\text{m rad}$ and $\epsilon_{ny} = 3.0 \mu\text{m rad}$ and thus larger than expected. The first idea was to explain this with the remaining dispersion in the FLASH2 seed section but the following estimation shows that this effect is smaller. The effective emittance ϵ_{eff} including $\epsilon_\beta = \sigma^2/\beta$ as well as the contribution of the dispersion η can be calculated as follows [16]:

$$\epsilon_{\text{eff}} = \epsilon_\beta + \frac{1}{2} (\gamma\eta^2 + 2\alpha\eta\eta' + \beta\eta'^2) \delta^2 \quad (3)$$

with the Twiss functions α , β and γ , the dispersion and dispersion prime η and η' as well as with the relative momentum deviation $\delta = \Delta p/p_0$. Using the matched Twiss parameters and the dispersion measured at the OTR, $\epsilon_\beta = 2 \mu\text{m rad}$ and $\delta = 5 \cdot 10^{-3}$ one obtains the expected normalized horizontal effective emittance which is $\epsilon_{nx,\text{eff}} \approx 3 \mu\text{m rad}$. This apparent inconsistency suggests that either the energy spread of the beam or the initial emittance of the beam is larger than estimated.

CONCLUSIONS

We presented the results of the first dispersion and optics measurements in the new undulator beam line FLASH2

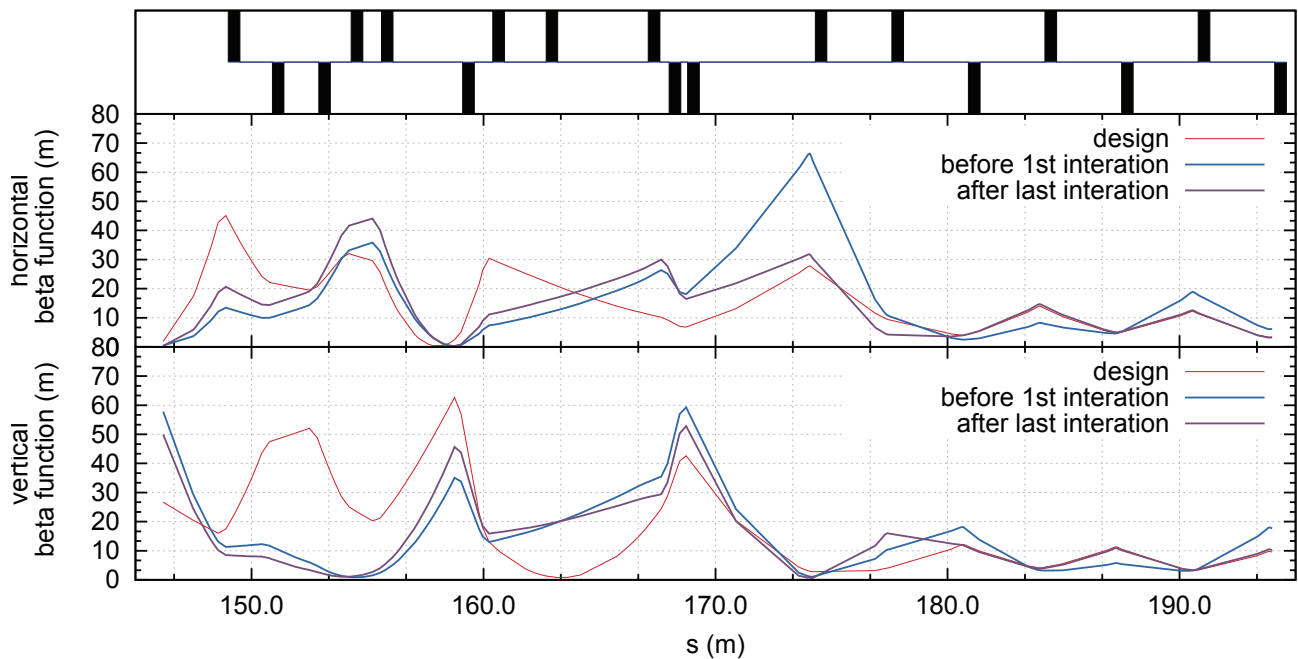


Figure 3: These plots show the design beta functions, the beta functions at the start of the matching and those at the end of this procedure. The latter match the design beta functions at the end of the seed section. The upper plot shows the horizontal plane and the lower plot the vertical plane.

and we showed that the used measurement and optimization tools work. The results were obtained while FLASH1 was in SASE operation. At the time of the measurement we did not have the diagnostic tools to verify during SASE operation in FLASH that the energy spread was completely minimized. This might had a certain degrading effects on the dispersion measurement. The closed dispersion and the matched beam in the FLASH2 beam line lead also to very small losses in the undulator section. With this beam we will start first lasing tests in the following weeks.

- [12] H. Grote et al., CERN/SL/90-13 (AP) (Rev. 4).
- [13] H. Grote et al., Proceedings of EPAC 2000, Vienna, Austria.
- [14] J. Zemella et al., Proceedings of IPAC2014, Dresden, Germany.
- [15] Gnuplot, a portable command-line driven graphing utility for different operating systems, www.gnuplot.info
- [16] N. Merminga et al., SLAC-PUB-55 11 May 1991.

REFERENCES

- [1] K. Honkavaara et al., Proceedings for the FEL2014, Basel, Switzerland.
- [2] M. Scholz, DESY-Thesis-2014-002
- [3] M. Scholz et al., Proceedings of FEL2012, Nara, Japan.
- [4] A. Schöps et al., Proceedings of IPAC2014, Dresden, Germany.
- [5] S. Ackermann et al., Proceedings of FEL2012, Nara, Japan.
- [6] B. Lorbeer et al., Proceedings of IBIC2012, Tsukuba, Japan.
- [7] F. Schmidt-Föhre et al., Proceedings of IPAC2014, Dresden, Germany.
- [8] B. Keil et al., Proceedings of IPAC'10, Kyoto, Japan.
- [9] D. Lipka et al., to be presented at IBIC2014, Monterey, California, USA.
- [10] B. Keil et al., to be presented at IBIC2014, Monterey, California, USA.
- [11] MathWorks MATLAB, high-level language and interactive environment for numerical computation, visualization, and programming, www.mathworks.com.

INFRARED DIAGNOSTICS INSTRUMENTATION DESIGN FOR THE COHERENT ELECTRON COOLING PROOF OF PRINCIPLE EXPERIMENT*

T. Miller[#], D. M. Gassner, V. Litvinenko, M. Minty, I. Pinayev, B. Sheehy,
C-AD, BNL, Upton, NY, 11973, U.S.A.

Abstract

The Coherent Electron Cooling Proof-of-Principle experiment [1] based on an FEL is currently under construction in the RHIC tunnel at BNL. Diagnostics for the experimental machine [2] are currently being designed, built and installed. This paper focuses on the design of the infrared diagnostic instrumentation downstream of the three tandem 2.8 m long helical wiggler sections that will act on a 22 MeV 68 uA electron beam co-propagating with the 40GeV/u RHIC gold beam. The 14 μm FEL radiation, or wiggler light, will be extracted from RHIC via a viewport in a downstream DX magnet cryostat and analysed by instrumentation on a nearby optics bench. Instruments concentrating on three parameters, namely intensity, spectral content, and transverse profile, will extract information from the wiggler light in an attempt to quantify the overlap of the electron and ion beams and act as an indicator of coherent cooling.

INTRODUCTION

The success of Coherent Electron Cooling (CeC) experiment will depend largely on the effectiveness of the instrumentation available. This paper focuses on those instruments associated with measuring and characterizing the infrared light emitted by the wiggler that functions as an FEL and amplifier [3] in this arrangement of modulator, amplifier, and kicker sections. See reference [4] for an update of CeC beam cooling theory using this three-step process. Presented in this paper are details of the instruments that will be employed to measure the wiggler light. Also presented are low cost alternatives to readily available off the shelf instruments and some other low cost alternative solutions.

The construction of the CeC experiment is underway and has been segmented into three phases, each requiring an increasing number of electron beam instruments. As elaborated on elsewhere at this conference [4], the instrumentation for the wiggler's infrared radiation, or wiggler light, will only be installed as part of phases two and three (see Fig. 1). The wiggler sections will be appended to the injector beamline after the injector is commissioned in Phase 1. Phase 2 allows for the wiggler sections to be tested with the electron beam as a stand alone experiment in the RHIC tunnel, independent of RHIC operations, except for use of the cryogenic system.

*Work supported by U.S. DOE under contract No DE-AC02-98CH10886 with the U.S. DOE

[#]tmiller@bnl.gov

During this phase, a local optical bench will be installed downstream of the three wiggler sections. The instruments located there will receive the wiggler light through a ZnSe viewport in a downstream auxiliary port of the dipole magnet that brings the electron beam to the beam dump. The optics bench will be located in the RHIC tunnel to avoid the upfront cost of an optical beam transport back to the laser building, approximately 60m away. When the experiment moves into Phase 3, the wigglers will be installed into the RHIC beam path to allow co-propagation of the electron beam and the Yellow ion beam. In this phase, the optical instrumentation table may be relocated to a laser trailer installed outside the RHIC tunnel to avoid further exposure to high radiation levels in the tunnel. A modification of the DX magnet cryostat, responsible for splitting and recombining the RHIC blue & yellow counter circulating beams, will be made so that the wiggler light can propagate straight out between the two emerging (blue & yellow) beam pipes via a viewport. A sealed optical beam transport could be installed to bring the light from the viewport to the laser trailer.

WIGGLER

The three helical permanent magnet wiggler sections are being constructed by the Budker Institute of Nuclear Physics. Table 1 summarizes the parameters of the electron beam and the wigglers.

Table 1: Wiggler & e-beam Parameters

e-Beam	Value
Energy	21.8 MeV
Charge per bunch	0.5 – 1 nC
Current (1nC), Avg / Pk	78 μA / 60 – 100 A
Beam Power	1.7 kW
Bunch Length	10 ps
Repetition Rate	78.3 kHz
Wiggler	Value
Length (3 sections)	3 x (2.5 + 0.30 m)
Period (λ_u) / poles	4 cm / 60 + 2.5 ea. section
Strength (K)	0.50
Wavelength (λ)	14 μm
Optical Power	250 nW – 250 mW

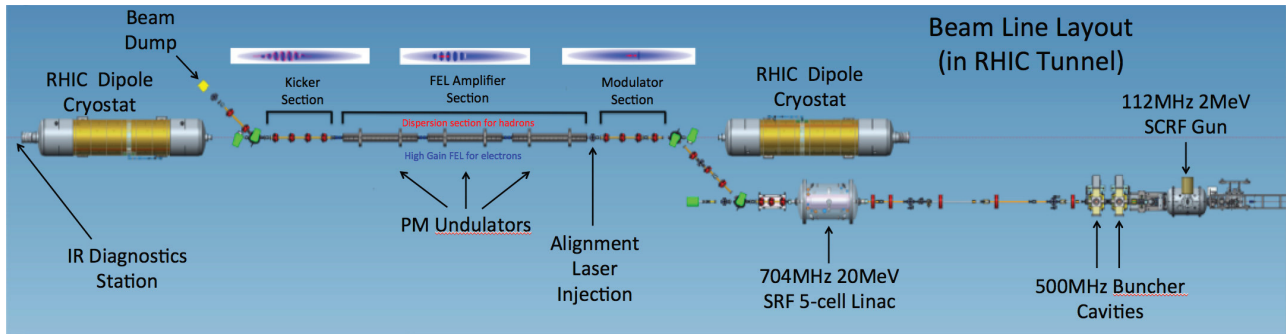


Figure 1: Layout of Phase 3 for implementation of the CeC experiment with the RHIC ion beam.

The three wigglers are due to arrive at BNL later this year. Window-frame corrector coils and 3-pole wiggler (phase shifter) coils are being provided to match the beam trajectory and the phase of the electron beam from one Wiggler section to the next. The position measurement of the electron beam is critical for sufficient overlap with the ion beam. Moreover, the phase of the electron beam entering each wiggler section must be adjusted to ensure proper alignment of the electron wave packets [5] created in the modulator section with the ion energy centers during the amplification process through the FEL.

To provide enough amplification of the imprinted pattern on the electron beam, an wiggler of a length surpassing fabrication capabilities was required. Therefore, three separate sections were proposed, each consisting of 60 poles, plus $2\frac{1}{2}$ poles for matching; thereby comprising the 2.8 m length. The wigglers will receive an electron beam of ~ 10 ps pulses at a repetition rate of 78 kHz, corresponding to the revolution frequency of the RHIC beams. This will allow a single bunch in RHIC to be cooled for comparison to the uncooled bunches during this proof of principle experiment.

The wiggler peak magnetic field strength, required to give the specified wiggler K parameter of 0.50 is calculated to be 0.134 T by the well-known equation (1) for the deflection parameter, K , below.

$$K = 0.934B(T)\lambda_u \text{ (cm)} \quad (1)$$

The coherent electron cooling theory calls for a dispersion section that imposes a time-of-flight dependence on the hadrons' energy in order for the kicker section to cool it [6]. As this proof of principle experiment is budget conscious, the experiment is designed such that the ion beam shares the same path as the electron beam through the wigglers where the effect on the ions is negligible. As the dispersion is still necessary, RHIC will operate its run with gold ions at an energy, less than typical, of 40 GeV/u for this dispersion to occur as the ions drift from the modulator section towards the kicker section.

As the electron beam passes through the wigglers, coherent radiation occurs and the system begins to behave as an FEL. The light emitted by the FEL will be an important feedback of both the position of the electron beam in the wiggler as well as the degree of overlap of the

electron and hadron beams. The light from the wiggler has a predictable wavelength that is given by equation (2) below.

$$\lambda = \frac{\lambda_u}{2\gamma^2} (1 + K^2) \quad (2)$$

Calculating γ based on the fact that the electrons must have the same velocity as the ions, at 40G eV/u, and using the K from (1), the expected wavelength is $14\mu\text{m}$. Moreover, numerical simulations were performed and presented earlier [2] showing the full spectrum. The viewport allowing the FEL IR light to exit the vacuum for analysis shall be constructed of ZnSe, allowing 70% transmission in the $0.6 - 20\mu\text{m}$ infrared region. Also, the simulations predict a radiation pattern, 15 m from the FEL, to be circular with a 40mm diameter. Figure 2 below shows this result, also presented earlier [2].

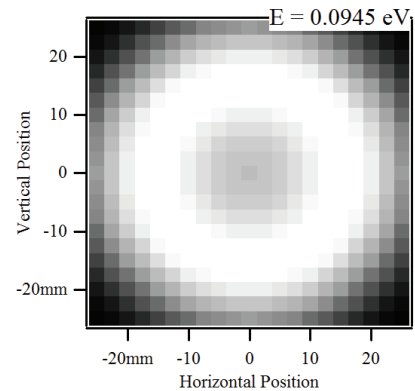


Figure 2: The transverse distribution of the optical power at wavelength corresponding to the maximum. The dip in the middle is due to the spiral electron motion.

IR INSTRUMENTATION

Measuring the characteristics of the wiggler light will be made in the far infrared region, as the wavelength is $14\mu\text{m}$. Qualities such as intensity, position, and spectral content of the light contain information about the lasing and cooling process. Moreover, a widening of the fundamental spectral line in the wiggler light is expected during the cooling process.

The optical table down stream of the last dipole supports devices to measure optical power, optical beam

profile, and optical beam spectrum. A 5 mW HeNe alignment laser with a 10X adjustable beam expander, located 65 ft upstream, will be used with a surveyed monument on the table to align the optical components to beam center. The laser beam is injected into the beam pipe using a mirror on the backside of a beam profile monitor just upstream of the wiggler section.

IR Power Measurements

The power from the IR light is expected to range from the 250 nW to 250 mW (spanning ~6 orders of magnitude depending on the amount of amplification, seeding, etc.). Two detectors will be used interchangeably during commissioning of the wigglers. A high bandwidth IR photodetector will be used, likely with a lock-in amplifier to improve S/N, to measure down to $\sim 1 \mu\text{W}$ with a 1 MHz BW so as to capture the optical power measurements and look for variations from pulse to pulse in the 78 kHz beam. The other detector is a slower but offers a wider range of thermal power sensitivity.

The IR photodetector is from Vigo Systems, model PC-3TE, optimized for 2 – 14 μm and based on a (HgCd)Te semiconductor with optimized doping and sophisticated surface processing with a three-stage thermoelectric cooler and optically immersed to a high refractive index GaAs hyperhemispherical lens. This detector is packaged in a sealed TO-8 case with a BaF₂ lens and integrated into model MIPAC-F-1 ac coupled transimpedance amplifier with a bandwidth of 1 MHz, shown in Fig. 3a.

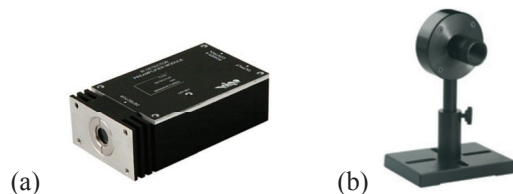


Figure 3: (a) 1MHz IR photodetector, (b) wide range thermal power sensor.

The thermal power IR detector, shown in Fig. 3b, is Ophir model 3A-UA-RS232_AO-V-FC, with a power input range of 10 μW – 3 W, over 3 selectable gain settings on an integrated calibrated amplifier and 16-bit DAC with remote connection via serial link. It has a spectral range of 0.19 – 20 μm , with a 9.5 mm aperture and is used for average power measurements in CW mode with a response time of 1.8 seconds.

These power measurement sensors will likely be employed after the electron beam has been commissioned to operate in CW mode. The thermal power sensor signal will be digitized, asynchronously at a rate 1 Hz; whereas the photodetector will require synchronous digitization to acquire the measurements with each beam pulse.

Direct Profile Measurements

We are considering using a pyroelectric crystal based digital camera to measure the IR beam profile. Spiricon offers a PyrocamTM III, as shown in Fig. 4, with a 124

x124 array of 100 μm pixels on a 11.5x11.5 mm sensor. The IR beam transverse profile at the exit of the DX magnet cryostat viewport is expected to have a 40 mm diameter, as shown in Fig. 2. Thus a large LWIR lens (7 – 14 μm typ.) will be required to image the 40mm diameter beam. The model Pyrocam IV, as shown in Fig. 4, is a better option with a 320x320 mm array of 80 μm pixels on a 25x25 mm sensor but at a much higher price. The pyroelectric crystal in the integrating sensor is sensitive to very short pulses. However, once CeC begins operating in CW mode, the internal chopper option of the Pyrocam would be needed.

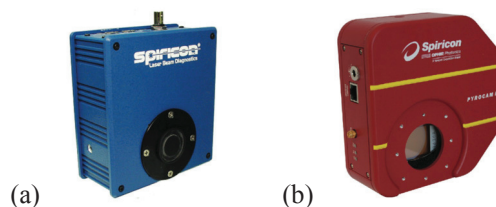


Figure 4: (a) Pyrocam III IR profile monitor, (b) Pyrocam IV IR Profile Monitor.

Scanning Profile Measurements

In order to be conscientious of cost, an alternative scanning method of profiling is proposed using the IR power measurement detectors already purchased. Leveraging off of software development completed for the “pin-hole” e-beam profile measurements made at RHIC’s Electron Lens (eLens) project [7]; a two-axis scanner could move the power detector, covered by a pinhole mask, to create a map of the beam’s transverse profile. In the eLens, the electron beam is scanned over a pin-hole masked Faraday cup. Software controls the steering magnets and recreates the image from the array of collected charge data. Here, similar software can run stepper motors to scan the detector through the beam and reconstruct the image from the array of collected IR power data. Thus scan time for a 300 x 300 point array would be require ~35 sec (accounting for stepper motor drive speed and integrator & digitizer triggering). This will require a stable beam over the full scan period.

The scanning algorithm produces arrays of data in alternating horizontal line directions to avoid retrace time. Thus the software must massage the data back into a proper array and apply the step size scale factors to recreate the image with the proper scale. The existing software was developed to analyse the image intensity by identifying axes (X, Y & θ) through which to section the data for a profile plot. A sample beam image from eLens is shown in Fig. 5, representative of the round beam profile expected from CeC’s helical wiggler. A radius feature is implemented to find the full field of the beam based on a settable threshold (3 % typ.). This is shown as the satellites around the beam spot in Fig 4.

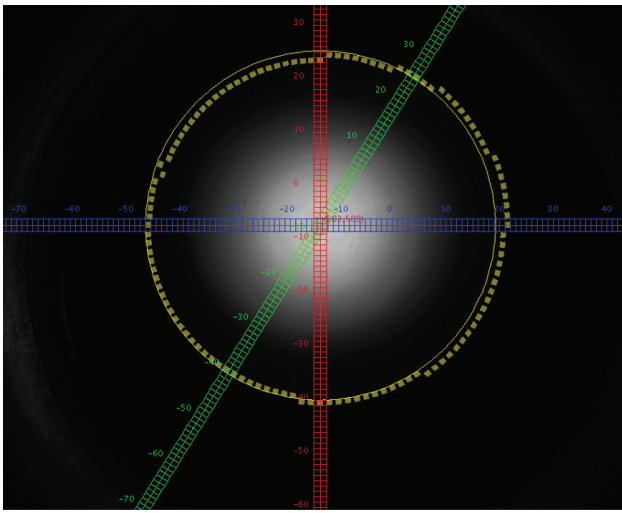


Figure 5: Representative beam spot for demonstrating profile measuring software.

Figure 6 shows the profile plots through one of the axes. The blue delimiting lines correspond to the full field (3 % typ.) point in the Gaussian tails. Each axis plot displays the calculated sigma, radius, and χ^2 .

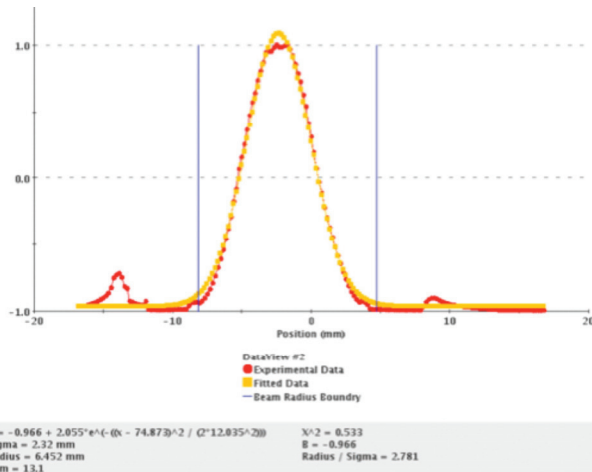


Figure 6: Screen shot of profile generated from the x-axis.

FUTURE PLANS

Once the Phase 1 configuration is commissioned during the next several months and stable e-beam from the photocathode is measured by the instrumentation, we will proceed with Phase 2 where the 5-cell superconducting LINAC is added as well as the three wiggler sections and the high power beam dump, and associated instrumentation [4]. Once the full power of the FEL is demonstrated and the IR light is measured with the power meters, and optional profiling system, the dog-leg beam transport section will be added to allow the three FEL be relocated into the RHIC beam for Phase 3; where the coherent electron cooling process will be demonstrated with the RHIC ion beam.

Spectral Measurements

As we advance in optimizing the coherent electron cooling process, it may become interesting to investigate, not only changes in the intensity and shape of the wiggler light, but also any changes in the spectrum. We expect to see variations in the spectral line width during the cooling process. We have considered the Acton VM-504 Spectrometer from Princeton Instruments configured with a 75-groove/mm grating centered around our 14 μm wavelength. If we find that spectral changes occur in a manner that has some distribution over the 2D image, we may consider an imaging spectrograph, such as Princeton's IsoPlane SCT 320 with cutting edge resolution due to its zero astigmatism design.

ACKNOWLEDGMENT

The authors would like to thank CeC community for the years of concept development, and especially the members of the C-AD Instrumentation Systems Group, and G. Miglionico for the layout drawings.

REFERENCES

- [1] V. Litvinenko, et al., "Proof-of-Principle Experiment for FEL-Based Coherent Electron Cooler", WEOA3, proceedings of FEL2011, Shanghai, China, 2011.
- [2] D. M. Gassner, et al., "Coherent Electron Cooling Proof of Principle Instrumentation Design", WEAP01, proceedings of BIW2012, Newport News, VA, 2012.
- [3] V. Litvinenko, et al., "High Gain FEL Amplification of Charge Modulation Caused by a Hadron" MOPPH026, Proceedings of FEL08, Gyeongju, Korea, 2008.
- [4] D. Gassner, et al., "Coherent Electron Cooling Proof of Principle Stage 1 Instrumentation Status" THP093, These proceedings, FEL2014, Basel, Switzerland, 2014.
- [5] G. Wang, et al., "Influence of Electron Beam Parameters on Coherent Electron Cooling", THYB02, proceedings of IPAC 2012, New Orleans, LA, USA, 2012.
- [6] V. Litvinenko, et al., "Advances in Coherent Electron Cooling" THAM2HA02, Proceedings of COOL2013, Murren, Switzerland, 2013.
- [7] T. Miller, et al., "RHIC Electron-Lens Beam Profile Monitoring" TUPG039, Proceedings of BIW2012, Newport News, VA, USA 2012.

DESIGN OF TDS-BASED MULTI-SCREEN ELECTRON BEAM DIAGNOSTICS FOR THE EUROPEAN XFEL

J. Wychowaniak*

DMCS, Technical University of Łódź, Łódź, Poland

Ch. Gerth, M. Yan

Deutsches Elektronen-Synchrotron DESY, Hamburg, Germany

Abstract

Dedicated longitudinal electron beam diagnostics is essential for successful operation of modern free-electron lasers. Demand for diagnostic data includes the longitudinal bunch profile, bunch length and slice emittance of the electron bunches. Experimental setups based on transverse deflecting structures (TDS) are excellent candidates for this purpose. At the Free-Electron Laser in Hamburg (FLASH), such a longitudinal bunch profile monitor utilizing a TDS, a fast kicker magnet and an off-axis imaging screen, has been put into operation. It enables the measurement of a single bunch out of a bunch train without affecting the remaining bunches. At the European X-ray Free-Electron Laser (XFEL) multi-screen stations in combination with TDS are planned to be installed. In order to allow for flexible measurements of longitudinal bunch profile and slice emittance, a configurable timing and trigger distribution to the fast kicker magnets and screen stations is required. In this paper, we discuss various operation patterns and the corresponding realization based on MTCA.4 technology.

INTRODUCTION

The performance of a hard X-ray free-electron laser (FEL), such as the European XFEL, depends critically on the transverse emittance of the electron beam [1]. Hence, it is important to generate electron beams with lowest possible emittance [2, 3] and efficiently preserve the emittance through acceleration and longitudinal bunch compression. Measurement and control of the transverse emittance is crucial for the optimisation and operation of the FEL as the beam emittance may be degraded due to non-linear effects, e.g. emission of coherent synchrotron radiation (CSR) or micro-bunching instabilities [4].

As the FEL amplification process takes place locally within longitudinal bunch slices, measurements of time-resolved properties, i.e. slice emittance, rather than time-averaged properties, i.e. projected emittance, are of interest. Excellent candidates for the measurement of the slice emittance with single-bunch resolution are transverse deflecting structures (TDS) [4, 5]. The electron bunch is streaked in transverse direction by the TDS and imaged with an imaging screen. The slice emittance can then be measured in the plane perpendicular to the streak direction by changing the phase advance between the TDS and the imaging screen. This can be achieved by either changing quadrupole currents

between the TDS and imaging screen (quad-scan method) or by employing several screens (multi-screen method) [6]. A disadvantage of this direct time-domain method is that the emittance of the diagnosed bunch is drastically degraded due to the scatter process in the imaging screen and the bunch cannot be used for FEL operation.

CONCEPTUAL LAYOUT OF THE SLICE EMITTANCE MONITOR SETUP

The super-conducting accelerator of the European XFEL will operated with RF macro pulses of up to $650 \mu\text{s}$ at a repetition rate of 10 Hz. Each RF macro pulse can be filled with a train of up to almost 3000 bunches at a maximum repetition rate of 4.5 MHz. This offers the possibility of using several bunches of each bunch train for on-line measurements. A generic layout of a slice emittance monitor, employing a TDS followed by four fast kicker magnets and four screen stations equipped with off-axis screens, is depicted in Fig. 1. Four electron bunches out of the bunch train are streaked by the TDS and then deflected by the fast kicker magnets onto the off-axis screens without disturbing FEL operation of the remaining bunches in the bunch train. A longitudinal bunch profile monitor, comprising one kicker magnet and one off-axis screen, has been commissioned successfully at the Free-Electron Laser in Hamburg (FLASH) [7].

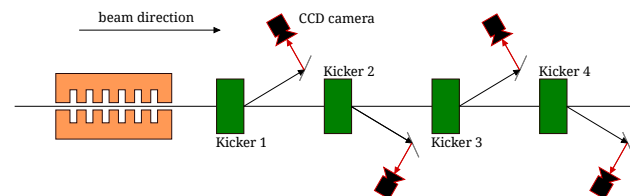


Figure 1: Generic layout of a slice emittance monitor.

At the European XFEL, installation of slice emittance monitors is foreseen at three different locations (see Fig. 2): in the injector and after the second and third bunch compressor chicane. Each TDS is followed by a matching section and a FODO lattice in which four screen stations are incorporated [8]. The screen stations will be equipped with off-axis scintillation screens made of $200 \mu\text{m}$ thick LYSO:Ce [9]. The scintillation screens will be installed at an angle of 0° with respect to the beam axis and imaged under 45° by a CCD camera in Scheimpflug arrangement. Micro-bunching instabilities can lead to the emission of coherent optical transition radiation (COTR) at the boundary of vacuum and the scintillator [10]. The imaging angle has been chosen to sup-

* jan.wychowaniak@desy.de

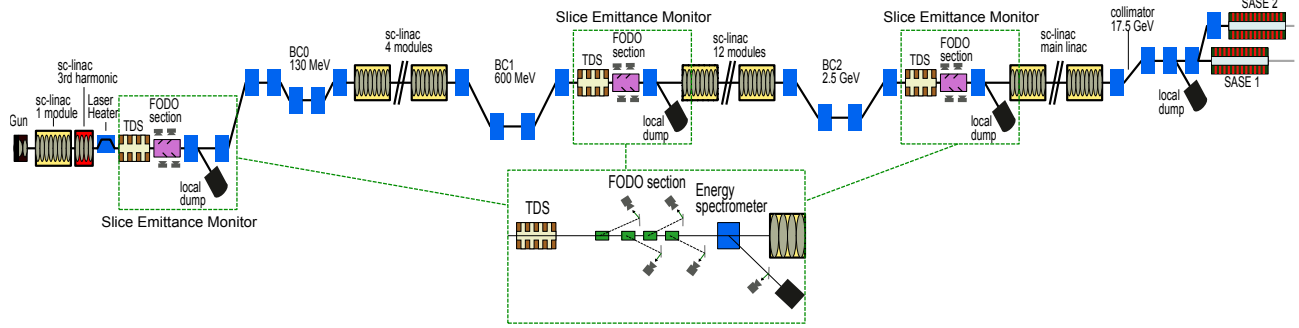


Figure 2: Accelerator layout of the European XFEL. Installation of TDS-based multi-screen slice emittance monitors is foreseen at three different locations along the accelerator.

press COTR, which has a strong angular dependence, while the incoherent isotropic scintillation light can be used for bunch profile measurements [4].

In order to deflect bunches out of the bunch train onto the off-axis screens, fast kicker magnets with a length of 350 mm will be installed downstream of each TDS. The kicker magnet consists of a ceramic vacuum chamber that has been sputtered at the inside with a layer of 1 μm thick stainless steel and a single air coil made of flat copper bars outside the vacuum. A pulser that generates a half cycle of a sine wave with a pulse duration of $t_p = 380$ ns is directly

attached to the kicker magnet. The maximum pulse current and high voltage generated by the pulser are $I_p = 5$ kA and $U_p = 20$ kV, respectively. The kick strength has been determined with a prototype kicker installed at FLASH and amounts to $k(\text{mrad}) = 0.1 U_p(\text{kV})/E(\text{GeV})$. The trajectories of the bunch centres induced by the four kickers and the respective positions on the imaging screens have been modelled for slice emittance monitor downstream of the second bunch compressor and are shown in Fig. 3. The kick directions alternate. As can be seen, the bunch deflected by the first kicker onto the first imaging screen also hits the third screen. As the screen stations will be equipped with CCD cameras (Basler aviator avA2300-25gm) with a minimum shutter time of 18 μs , the bunches deflected by the first and third kicker will overlap in the image of the third screen station.

OPERATION MODES

A slice emittance monitor that includes 4 pairs of kickers and screens allows for configurable operation modes, so that multiple bunch kick patterns can be employed.

Figure 4 illustrates a mode with four consecutive bunches being kicked out from a single bunch train for diagnostics. The kicked bunches hit the consecutive screens of the slice emittance monitor. They are marked in blue in the picture. This procedure is repeated for every bunch train. This is the typical kick pattern configuration for slice emittance measurements where the maximum data rate is required. Such configuration is used e.g. during the machine tuning phase, which requires the best possible operation statistics to be produced.

However, as mentioned above, the bunch deflected by kicker 1 (and designated for screen 1) hits also screen 3, which may result in disturbance of the beam size measurement. Here, simultaneous use of kickers 1 and 3 may be unwanted.

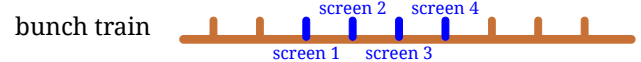


Figure 4: Typical bunch kick pattern for slice emittance measurements with maximum data rate.

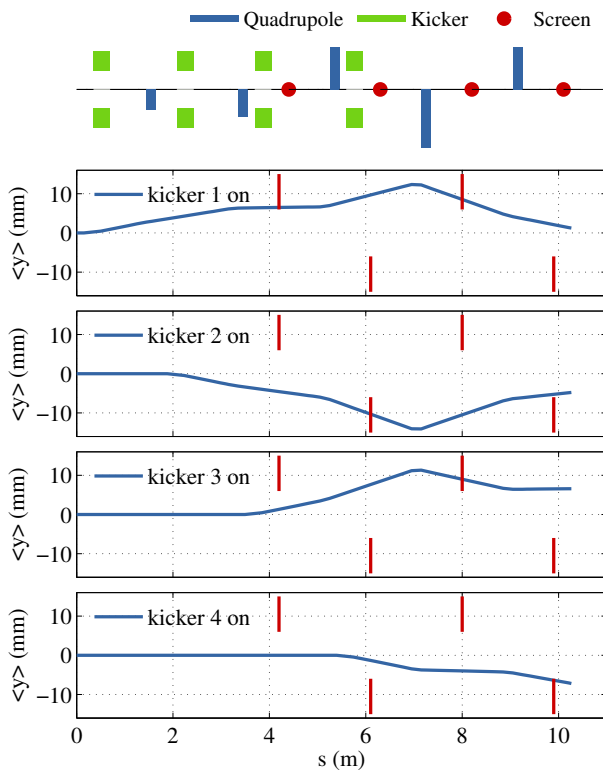


Figure 3: Top: Schematic layout of the beam line for on-line slice emittance measurements downstream of the second bunch compressor at European XFEL. Bottom: Trajectories of the bunch centres induced by for the four kicker magnets and respective beam positions on the off-axis screens.

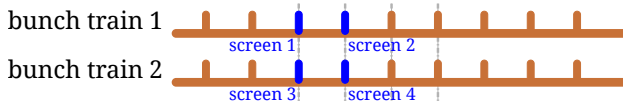


Figure 5: Possible pattern for kicking two bunches from a bunch train.

For such cases it is desirable to have the possibility of reducing the number of kicked bunches per bunch train. An example of such variation can be seen in Fig. 5. The number of bunches kicked per bunch train is reduced to two. This kick pattern can be seen as composed of two sub-patterns. One of them involves selected bunches designated together for being kicked from a bunch train with the use of kickers 1 and 2 (i.e. going towards screens 1 and 2). The other sub-pattern similarly (the same bunches), but with kickers 3 and 4 (towards screens 3 and 4). These two sub-patterns are then being applied alternately to consecutive bunch trains. Technically this means that for every sub-pattern only two out of four kickers are being triggered, and also two corresponding cameras collect images.

If even less data statistics is sufficient, then only one single bunch out of a bunch train may be taken out. As it can be seen in Fig. 6, the four kickers are configured with timing for the same single bunch in the bunch train, but triggered successively in four consecutive bunch trains. Such scenario is applicable e.g. to normal machine operation, where less statistics is required and the number of bunches sacrificed for beam diagnostics could be reduced.

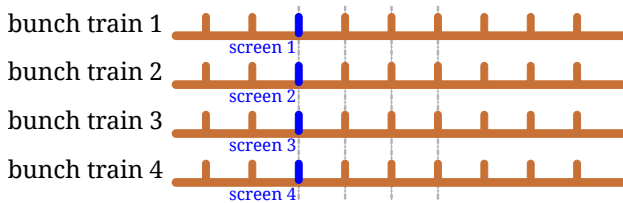


Figure 6: Possible pattern for kicking a single bunch from a bunch train.

Figure 7 provides a summary of the scenarios described above. They are just selected examples of how a TDS-based slice emittance monitor can be set up, in terms of its kicker and camera trigger configurations, in order to accommodate diverse patterns of kicked bunches. This configuration scheme is flexible and, as a result, numerous combinations of bunches designated for kicking are possible to be configured.

BUNCH PATTERN CONCEPT

The machine operation allows for a configurable number of bunches within a bunch train. Also, the spacing between bunches can vary, depending on the operating frequency that is configured. The maximum operating frequencies for FLASH and the European XFEL are 1 MHz and 4.5 MHz, respectively, while lower frequencies (wider bunch spacing) are also configurable. The description of number of bunches within a bunch train and their spacing in the machine timing

bunch nr	1	2	3	4	5	6	7	8	9
	Screen 1 a) / b) / c)			Screen 2 a) / b) / c)			Screen 3 a) / b) / c)		
bunch train 1	3	3	3	4	4	-	5	-	-
bunch train 2	3	-	-	4	-	3	5	3	-
bunch train 3	3	3	-	4	4	-	5	-	3
bunch train 4	3	-	-	4	-	-	5	3	-

Figure 7: Summary of most typical operation modes of slice emittance monitor.

system is referred to as bunch pattern. The bunch pattern concept is based on a 9 MHz structure, so that maximum operating frequencies of both XFEL and FLASH can be accommodated (see Fig. 8).

The bunch pattern concept is implemented in a form of a table of integer numbers (referred to as pattern table words), and as such is exchanged across the machine timing system. The number of bunches within a bunch train and their spacing are described by appropriate values within a table word corresponding to a given time position. As illustrated in Fig. 8 (lower part) for the European XFEL, values indicating bunch presence (red) are set for every second word which corresponds to an operation frequency of 4.5 MHz.

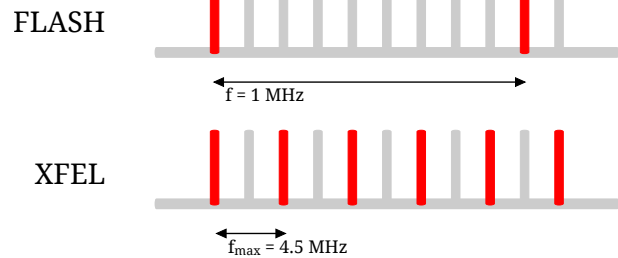
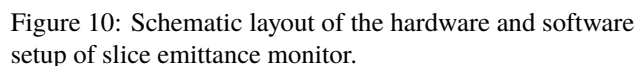
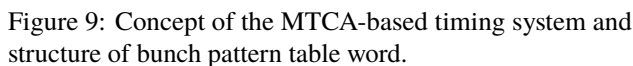


Figure 8: Bunch pattern describing maximum frequencies for FLASH (top) and XFEL (bottom).

The information contained in a pattern table word is composed on a bit basis (see Fig. 9). Appropriate bits within a word have meanings determined by the design of the timing system. Three most significant bits serve for the purpose of marking a given bunch to be kicked by one of the slice emittance monitor stations (TDS injector, TDS BC1 or TDS BC2). In Fig. 9 (middle) the pattern table words corresponding to presence of a bunch at given time position are marked with brown boundary. The pattern table words indicating bunches to be kicked by one of the slice emittance monitors (color code blue in the top), are marked red.

If a particular bunch is intended to be kicked, the pattern word corresponding to this bunch has one of its TDS bits set, depending on which slice emittance monitor is configured to take the bunch out.



The timing system is implemented in MTCA.4 standard [11]. It is designed as double size AMC modules, referred to as X2Timer cards. Each slice emittance monitor is provided with a dedicated MTCA.4 crate equipped with a X2Timer receiver, together with custom DOOCS server software [12] for controlling the card and slice emittance monitor hardware (see Fig. 10). For each bunch train the card:

- sets the TDS bits for the bunches to be kicked. This information is then propagated to the interested parties, e.g. the machine protection system (which needs to be aware that this beam loss is intentional),
- supplies the correct trigger to the kickers and cameras for bunches to be kicked.

By means of the DOOCS control software, a machine operator can configure the kick pattern for a given slice emittance monitor.

TDS-based multi-screen slice emittance monitors employing fast kicker magnets in combination with off-axis screens will be installed at the European XFEL. A flexible design of the timing system for the kickers and cameras, which allows for configuring different kick patterns depending on the desired operation modes, has been presented. The appliances based on the slice emittance monitor concept are presently in the design and construction phase. The required control software for the MTCA.4-based monitor hardware is under development, with corresponding laboratory tests being performed.

Commissioning of the injector of the European XFEL will start in mid 2015. This will provide the opportunity to operate the slice emittance monitor in the injector and gather experience with the concept presented in this paper under real operating conditions.

- [1] F. Zhou et al., Phys. Rev. Lett. 102, 254801 (2009).
- [2] F. Stephan et al., Phys. Rev. ST Accel. Beams 13, 020704 (2010).
- [3] F. Zhou et al., Phys. Rev. ST Accel. Beams 15, 090701 (2012).
- [4] Z. Huang et al., Phys. Rev. ST Accel. Beams 13, 020703 (2010).
- [5] M. Röhrs et al., Phys. Rev. ST Accel. Beams 12, 050704 (2009).
- [6] M. Yan et al., “Comparison of Quadrupole Scan and Multi-screen Method for the Measurement of Slice Emittance at SwissFEL Injector Test Facility”, THP088, *These Proceedings*, FEL’14, Basel, Switzerland (2014).
- [7] M. Yan et al., “First Realization and Performance Study of a Single-Shot Longitudinal Bunch Profile Monitor utilizing a Transverse Deflecting Structure”, IBIC’13, Oxford, September 2013, TUPC36, p. 456, <http://www.JACoW.org>
- [8] M. Röhrs, Ch. Gerth, "Electron beam diagnostics with transverse deflecting structures at the European X-ray free electron laser", FEL’08, Gyeongju, August 2008, MOPPH049, p. 90, <http://www.JACoW.org>
- [9] Ch. Wiebers et al., “Scintillating Screen Monitors for the Transverse Electron Beam Profile Diagnostics at the European XFEL”, IBIC’13, Oxford, September 2013, WEPF03, p. 807, <http://www.JACoW.org>
- [10] C. Behrens et al., Phys. Rev. ST Accel. Beams 15, 062801 (2012).
- [11] PICMG - MTCA.4 and other xTCA standards homepage, <http://www.picmg.org>
- [12] DOOCS homepage, <http://doocs.desy.de>

MEASUREMENTS OF THE TIMING STABILITY AT THE FLASH1 SEEDING EXPERIMENT*

C. Lechner[†], A. Azima, M. Drescher, L. L. Lazzarino, Th. Maltezopoulos, V. Miltchev, T. Plath, J. Rönsch-Schulenburg, J. Rossbach, M. Wieland, University of Hamburg, Hamburg, Germany
K. E. Hacker, S. Khan, R. Molo, DELTA, TU Dortmund University, Dortmund, Germany
S. Ackermann, J. Bödewadt, H. Dachraoui, N. Ekanayake, B. Faatz, M. Felber, K. Honkavaara, T. Laarmann, J. Müller, H. Schlarb, S. Schreiber, S. Schulz, DESY, Hamburg, Germany
P. Salen, P. van der Meulen, FYSIKUM, AlbaNova, Stockholm, Sweden
G. Angelova Hamberg, Uppsala University, Uppsala, Sweden

Abstract

For seeding of a free-electron laser, the spatial and temporal overlap of the seed laser pulse and the electron bunch in the modulator is critical. To establish the temporal overlap, the time difference between pulses from the seed laser and spontaneous undulator radiation is reduced to a few picoseconds with a combination of a photomultiplier tube and a streak camera. Finally, for the precise overlap the impact of the seed laser pulses on the electron bunches is observed. In this contribution, we describe the current experimental setup, discuss the techniques applied to establish the temporal overlap and analyze its stability.

INTRODUCTION

For the operation of an externally seeded free-electron laser (FEL), relative beam-beam jitter between the electron bunch and the laser pulse initiating the FEL gain process is only acceptable to a certain extent. Inhomogeneities in the electron beam slice parameters will directly translate into fluctuating performance of the seeded FEL. The duration of the region of the bunch with suitable electron beam parameters, such as slice energy spread, beam current, and emittance, is limited, which defines the timing jitter budget. Large jitter will naturally result in poor overlap quality. For instance, a major limitation of the studies of direct seeding with an high-harmonic generation (HHG) source at FLASH was the quality of the temporal overlap [1, 2].

EXPERIMENTAL LAYOUT

Electron Beamline

The seeding experiment is installed at the FLASH1 beamline of FLASH [3], the free-electron laser user facility in Hamburg, delivering high-brilliance SASE FEL radiation in the extreme ultra-violet (XUV) and soft x-ray range wavelength ranges. The superconducting linear accelerator of the FLASH facility generates trains of high-brightness electron bunches at a maximum energy of 1.25 GeV. These bunch trains, accelerated at 10 Hz repetition rate, consist of up

to 800 electron bunches at an intra-train repetition rate of 1 MHz.

The seeding experiment is installed between the collimation section of FLASH1 and the FLASH1 main undulator system. The electron beamline, shown schematically in Fig. 1, can be divided into three parts: (i) the modulator section, (ii) the variable-gap undulator system, and (iii) the photon extraction and diagnostics section. Of these, however, only the modulator section was used for the measurements presented in this paper. It comprises two electromagnetic undulators (5 periods of 20 cm, maximum K value 10.8) that originally had been installed for a longitudinal electron bunch diagnostics experiment [4]. At the exit of each electromagnetic undulator, a magnetic chicane is installed.

Downstream of the seeding experiment, a combination of a transverse-deflecting structure (TDS) and a dipole energy spectrometer is installed. First, an arrival-time-dependent transverse kick is applied in the TDS, an RF structure operated at 2856 MHz. After this conversion of longitudinal to spatial position, the contents of the longitudinal phase space of the electron bunch can be measured on the observation screen in the dispersive section downstream of the energy spectrometer.

Laser System

The laser system used for seeding experiments at FLASH1 was originally installed for direct-HHG seeding experiments at FLASH and consists of a 108.3 MHz Ti:sapphire oscillator used as seed in a classical chirped pulse amplification (CPA) scheme with 35 mJ maximum pulse energy at 35 fs FWHM minimal pulse duration. As described in the following section, the oscillator is electronically synchronized to a reference signal derived from an optical reference. The amplifier is pumped by a frequency-doubled Nd:YAG laser operating at 10 Hz allowing to seed one electron bunch per train [5].

For high-gain harmonic generation (HG) seeding at short wavelengths, a conversion of the $\lambda = 800$ nm laser pulses to UV wavelengths is required. For this, an in-vacuum arrangement of two non-linear optical crystals in the accelerator tunnel is employed: While the first one converts the laser light into its second harmonic, the second one emits its third harmonic at 267 nm when overlapping the 800 nm and 400 nm pulses [6].

* Work supported by Federal Ministry of Education and Research of Germany under contract No. 05K10PE1, 05K10PE3, 05K13GU4, and 05K13PE3 and the German Research Foundation programme graduate school 1355.

[†] christoph.lechner@desy.de

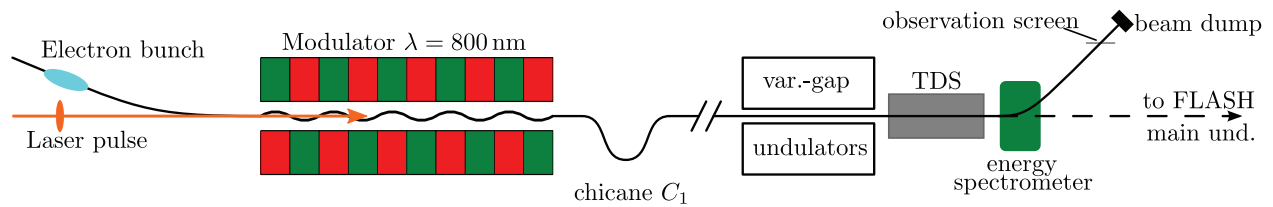


Figure 1: Layout of the hardware used in these measurements. The electron bunches arrive from the energy collimator of FLASH1, the seed laser pulses are injected into the accelerator vacuum upstream of the last dipole of the energy collimator. After modulation, the electron bunches are density-modulated in chicane C_1 . Finally, the longitudinal phase space of the electron bunch is analyzed by the combination of a TDS and an energy spectrometer.

Synchronization System

For pump-probe experiments to benefit from femtosecond XUV pulses delivered by FELs, synchronization of laser systems and the electron bunch timing on the same time scale is essential. The synchronization system at FLASH is implemented with length-stabilized optical fibers distributing trains of laser pulses with a repetition rate of 216.667 MHz [7]. These trains of optical pulses can be directly applied in electron beam diagnostics like bunch arrival monitors (BAMs) [8] or used for the synchronization of optical lasers using balanced optical cross-correlators (OXCs).

MEASUREMENT OF THE BEAM-BEAM JITTER

Establishing Laser-electron Overlap

For the measurements, we used mildly compressed electron bunches with a peak current of 0.3 kA and an rms bunch duration of about 0.3 ps at an energy of 700 MeV. The electron bunches and the laser pulses from the seeding laser are brought into spatial and temporal overlap in the modulator. To establish the spatial overlap, OTR screen stations close to the entrance and the exit of the modulator are used to image the spatial profiles of both the electron beam and the seed laser beam.

To establish the temporal overlap, the spontaneous undulator radiation emitted by the electron bunches as well as the seed laser pulses are extracted from the electron beamline. The light is sent to a fast photomultiplier tube to reduce the temporal offset of both signals to a few hundred picoseconds. Next, the longitudinal phase space of the uncompressed electron bunch is measured by the above described TDS and the laser timing is scanned electronically in sub-picosecond steps. The laser-induced modulation can then be directly observed on the TDS once the overlap is established. The camera images of the observation screen in the dispersive section were acquired using the FLASH data acquisition (DAQ) system. For this measurement, the variable-gap undulators were open and chicane C_1 after the modulator was set to $R_{56} = 295 \mu\text{m}$.

For time calibration of the longitudinal phase space measurement, we determined the centroid position of the

streaked electron bunch for a set of phases of the 2856 MHz RF driving the TDS. From this data, the time calibration was found to be $(-4.58 \pm 0.21) \text{ fs/pixel}$.

Data Analysis

The acquired images are analyzed using standard image processing techniques: After subtracting of a background image, which has been recorded without electron beam, a region of interest (ROI) is determined. As the contour of the longitudinal phase space cannot be predicted, the ROI is determined by an image analysis algorithm. As the actual image of the streaked electron bunch defines the ROI for further analysis, the impact of fluctuations of the RF driving the TDS is greatly reduced.

A series of 200 images was used for this analysis. From the part of the image selected by the ROI, the slice energy spread is determined. The local maximum of the slice energy spread marks the center of the laser-electron interaction. Figure 2 shows the arrival time information extracted from the analyzed TDS images; the corresponding histogram is in the right panel of this figure. From this data set, the relative beam-beam jitter is determined to be $(57.8 \pm 5.0) \text{ fs}$. For the error analysis, the effects introduced by the image analysis procedure, the uncertainty determining the slice with maximum slice energy spread, and the uncertainty of the time calibration of the TDS have been taken into account.

Discussion

The contributions to the total beam-beam jitter that can be measured independently are (i) jitter contribution of laser amplifier in the seeding laser system, (ii) electron beam jitter measured on the bunch arrival monitor (BAM), (iii) jitter of the optical synchronization system (however, negligible with $\sim 1 \text{ fs rms}$ [9]), and (iv) contributions of the synchronization of the laser oscillator.

Using the bunch arrival monitor (BAM) downstream of the second bunch compressor chicane of the FLASH linac, the arrival time jitter of the electron bunches has been measured. In the time interval under consideration, the rms arrival time jitter was 31 fs with the typical uncertainty for the electron bunch parameters being 13 fs. This measurement was performed in single-bunch operation after the upgrade of the FLASH low-level RF (LLRF) control sys-

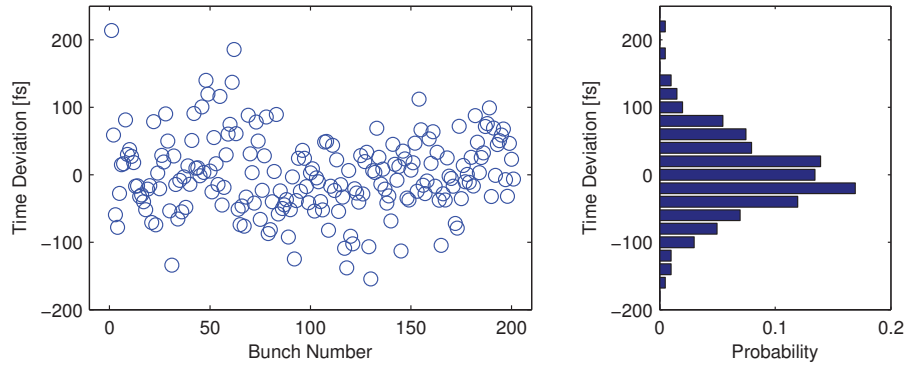


Figure 2: Timing of the laser signatures for a series of 200 images of the longitudinal phase space. In the right panel, the corresponding histogram is shown.

Table 1: Compilation of the Independently Measured rms Jitter Values. After subtraction of the contributions (i) – (iii), we obtain (48 ± 10) fs. In this beamtime, the typical in-loop measured jitter of the RF-synchronization of the oscillator of the seeding laser system was 55 fs, which is somewhat overestimated due to the noise floor in the phase noise measurement.

rms timing jitter	[fs]
beam-beam jitter (on TDS)	57.8 ± 5.0
(i) beam arrival time (on BAM)	31 ± 13
(ii) laser amplifier	10 ± 1
(iii) synchronization system	~ 1

tem to a MicroTCA.4-based solution [10]. The typical jitter introduced by the amplifier of the seeding laser system is (10 ± 1) fs.

Subtracting contributions (i) – (iii) from the total beam-beam jitter extracted from the TDS images, we obtain (48 ± 10) fs. This value includes the jitter of the RF-synchronization of the oscillator of the seeding laser system, for which the typical in-loop measured value in this beamtime was 55 fs. We note that due to the noise floor in the phase noise measurement, which originates from the photodetector, the result of this in-loop measurement of the timing jitter is somewhat overestimated. The measured timing jitter values are compiled in Table 1.

Assuming a desired minimum hit rate of $p = 0.9$, a beam-beam jitter of 60 fs rms would require the homogeneous region in the electron bunch to be at least 198 fs long. Practical minimum durations would be longer as we did not consider the finite duration of the seed pulse or budget for small temporal drifts.

Measurements at Other Facilities

A similar measurement of the relative beam-beam jitter was performed at the seeded FEL user facility FERMI@Elettra [11, 12]. There, a linearly chirped electron bunch is used to extract the jitter from electron energy

spectra measured at the beam dump. The laser-electron interaction in the modulator changes the energy of the electrons in the modulated region, corresponding to a relocation of charge density in the energy distribution. Measured energy distributions are compared with those of a reference bunch, determining the energy of the electrons before modulation. In a linearly chirped electron bunch, the beam energy at which this current reduction is observed can be related to a longitudinal position. Time calibration was found to be (0.22 ± 0.02) pixel/fs by deliberately changing the laser timing by ± 100 fs about the working point. At FERMI, the analysis of 200 consecutive modulated electron bunches resulted in an rms timing jitter of 68 fs [11].

SUMMARY AND OUTLOOK

In this paper, we show measured values for the relative beam-beam jitter in the FLASH1 seeding experiment that have been obtained from an analysis of the laser-electron interaction that will also be used in seeding experiments. Currently, the jitter is dominated by the RF-synchronization of the laser oscillator of the seeding laser system. An all-optical synchronization of this laser oscillator with a sub-10 fs (rms) timing jitter to the optical reference has already been tested. An upgrade of the laser synchronization to this solution based on a balanced optical cross-correlator (OXC) is expected for this year.

ACKNOWLEDGEMENTS

We thank DESY and the FLASH team for the opportunity to perform our experiment. We thank M. K. Czwilina for useful discussions. Supported by Federal Ministry of Education and Research of Germany under contract No. 05K10PE1, 05K10PE3, 05K13GU4, and 05K13PE3 and the German Research Foundation programme graduate school 1355.

REFERENCES

- [1] S. Ackermann, et al., *Generation of Coherent 19- and 38-nm Radiation at a Free-Electron Laser Directly Seeded at 38 nm*,

ISBN 978-3-95450-133-5

- Phys. Rev. Lett. 111, 114801 (2013).
- [2] J. Bödewadt and C. Lechner, *Results and perspectives on the FEL seeding activities at FLASH*, Proc. 35th Int. Free-Electron Laser Conf., New York, NY, USA, 2013, 491–495.
 - [3] K. Honkavaara, et al., *FLASH: First Soft X-ray FEL Operating Two Undulator Beamlines Simultaneously*, These Proceedings: Proc. 36th Int. Free-Electron Laser Conf., Basel, 2014, WEB05.
 - [4] G. Angelova, et al., *Observation of two-dimensional longitudinal-transverse correlations in an electron beam by laser-electron interactions*, Phys. Rev. ST Accel. Beams 11, 070702 (2008).
 - [5] Th. Maltezopoulos, et al., *A high-harmonic generation source for seeding a free-electron laser at 38 nm*, Appl. Phys. B, 115, 45–54 (2014).
 - [6] K. Hacker et al., *Progress towards echo-seeding in the FLASH ORS section*, TESLA-FEL 2011-06 (2011).
 - [7] S. Schulz et al., *Past, present and future aspects of laser-based synchronization at FLASH*, Proc. 2nd Int. Beam Instrumentation Conf., Oxford, UK, 2013, 753–756.
 - [8] M.K. Bock, et al., *Benchmarking the performance of the present bunch arrival time monitors at FLASH*, Proc. 10th European Workshop on Beam Diagnostics and Instrumentation for Particle Accelerators (DIPAC2011), Hamburg, Germany, 2011, 365–367.
 - [9] S. Schulz, et al., *Femtosecond-precision synchronization of the pump-probe optical laser for user experiments at FLASH*, Proc. SPIE Vol. 8778 (Advances in X-ray Free-Electron Lasers II: Instrumentation), Prague, Czech Republic, 2013, 87780R.
 - [10] C. Schmidt, et al., *Performance of the MicroTCA.4 based LLRF system at FLASH*, WEPME067, Proc. 5th Int. Particle Accelerator Conf., Dresden, Germany, 2014, 2433–2435.
 - [11] E. Allaria, et al., *Energy slicing analysis for time-resolved measurement of electron-beam properties*, Phys. Rev. ST Accel. Beams 17, 010704 (2014).
 - [12] E. Allaria, et al., *Measurement of electron-beam and seed laser properties using an energy chirped electron beam*, Proc. 35th Int. Free-Electron Laser Conf., New York, NY, USA, 2013, 24–26.

A LOW-COST, HIGH-RELIABILITY FEMTOSECOND LASER TIMING SYSTEM FOR LCLS*

Karl Gumerlock, Josef Frisch, Bruce Hill, Justin May, David Nelson, Stephen Smith,
SLAC National Accelerator Laboratory, Menlo Park, CA, USA

Abstract

LCLS has developed a low-cost, high-reliability radio-frequency-based (“RF”) locking system which provides phase locking with sub-25-femtosecond jitter for the injector and experiment laser systems. This system does not add significantly to the X-ray timing jitter from the accelerator RF distribution. The system uses heterodyne RF locking at 3808 MHz with an I/Q vector phase shifter and variable event receiver triggers to control the timing of the emission of the amplified laser pulse. Controls software provides full automation with a single process variable to control the laser timing over a 600 microsecond range with up to 4 femtosecond resolution, as well as online diagnostics and automatic error correction and recovery. The performance of this new locking system is sufficient for experiments with higher-precision timing needs that use an X-ray/optical cross-correlator to record relative photon arrival times.

LASER TIMING REQUIREMENTS

Lasers in the LCLS experiment hutch require sub-picosecond timing relative to the X-ray beam, originating as an electron beam from the SLAC linear particle accelerator (“linac”). The LCLS X-ray beam operates at a maximum repetition rate of 120 Hz and has a pulse-to-pulse timing jitter of approximately 60 fs RMS [1]. The relative timing of the laser and X-rays is measured in the experimental chamber by an X-ray/optical cross-correlator with approximately 10 fs resolution [2]. This cross-correlator is used to order the experimental data based on relative X-ray and laser arrival time. Any laser locking system must not substantially add to the total uncorrected experiment timing jitter. This corresponds to a target timing jitter of less than 75 fs RMS. The need to improve locking system jitter at LCLS was originally identified by Glowina *et al.* [3].

The cross-correlators used at LCLS include an optical delay stage to allow for high resolution timing measurements over a wide range of laser/X-ray time delays. The measurement range of the cross-correlator itself is approximately 1 picosecond. The timing jitter, drift, and the accuracy of laser time delay changes are required to keep the laser timed within that range, so that the cross-correlator is able to return good shot-to-shot timing data.

The range of timing scans required for experiments vary from sub-picosecond to 600 microseconds. The laser

system timing needs to be adjustable over that range without additional user intervention or expert knowledge.

TIMING SYSTEM ARCHITECTURE

X-ray pulse timing is determined by the electron beam timing, which is in turn controlled by the RF fields in the accelerator cavities. The accelerator RF sources are locked to a 476 MHz RF coaxial cable phase distribution system (“RF reference”). This reference is re-stabilized to the electron beam with each shot using electron arrival time measured at RF phase cavities (Fig. 1) in the LCLS undulator hall [1]. The RF reference is then transmitted through a stabilized coaxial cable to the experiment hutch, where it is used as a phase reference for the laser locking systems described in this text.

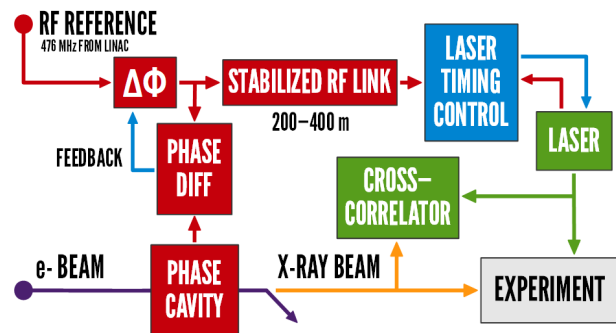


Figure 1: Laser timing system overview.

LASER TIME CONTROL

The experiment laser systems use a mode-locked Ti:sapphire laser oscillator which feeds a regenerative amplifier (“regen”). In some systems, a multipass amplifier is also used, however, the principle of operation remains the same.

The mode-locked laser oscillator (Fig. 2) operates at 68 MHz, 1/7th of the 476 MHz RF reference frequency. A commercial regenerative amplifier just after the oscillator is designed to accept an external trigger input: upon triggering, the regen selects and amplifies the next pulse from the mode-locked laser. A similar system also triggers any multipass amplifiers used downstream of the regen.

A frequency counter continuously measures the mode-locked laser cavity frequency. Controls software moves a stepper motor to coarsely control the cavity length to within 1 Hz of 68 MHz.

*Work supported by DOE Contract DE-AC02-76-SF00515

* Linac Coherent Light Source (“LCLS”)

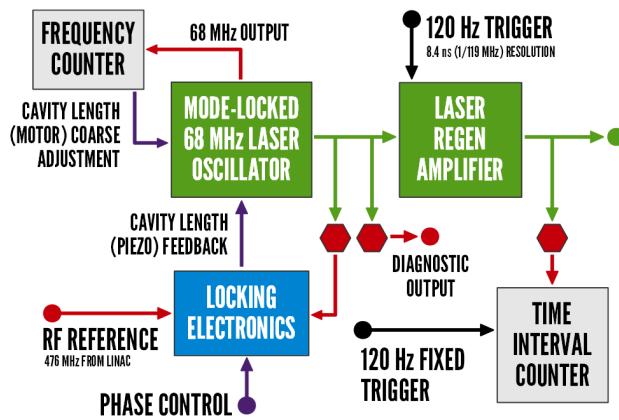


Figure 2: Basic laser timing control.

Phase locking electronics compare the phase of a photodetector on the mode-locked laser output with the accelerator reference and adjust a piezoelectrically-driven mirror (“piezo actuator”) to finely control the cavity length in a phase-locked loop.

The regenerative amplifier is triggered by an event receiver connected to the LCLS event timing system. This event system uses a 119 MHz base clock (1/4 of the 476 MHz RF reference) which allows trigger outputs to be set with 8.4 nanosecond resolution.

If the phase of the mode-locked laser is adjusted by more than one cycle of 119 MHz, the regen will jump to selecting a pulse on the next 68 MHz cycle of the mode-locked laser (“regen jump”). At initial timing system setup and calibration, the output of a time interval counter (Fig. 2) is used to determine when these regen jumps occur, by sweeping the phase control while monitoring the output timing relative to a fixed trigger. This information is then used to determine how to manipulate the timing of the regenerative amplifier trigger and the 68 MHz mode-locked laser phase to obtain the desired output timing.

Because the phase locking of the mode-locked laser is performed at 3808 MHz (8×476 MHz, or 56×68 MHz), it is possible for the laser timing to jump by ~ 262 ps ($1/3808$ MHz) periods. The time interval counter is also used to detect such jumps (“bucket jumps”), which are corrected automatically by software adjustment of the locking phase and regen trigger.

OPERATING MODES

Calibration

Normally, calibration is only performed at initial installation, or after a hardware change.

The 3808 MHz vector phase shifter is dialed through approximately 30 nanoseconds of phase shift while the time interval counter reading is recorded. This determines the points in the phase shift at which regen jumps occur. The measured timing is then fit to a sawtooth curve to

determine the correct settings for the regen trigger and phase shifter for normal locked operation. Both the 3808 MHz phase locking frequency, as well as the 119 MHz event timing system base clock from which the 120Hz event triggers are driven, are directly derived from the 476 MHz RF reference. This makes the time interval counter measurement more robust, as any jitter in the RF reference affects both the “start” and “stop” edges for the counter equally.

Unlocked Frequency Search

When the laser is unlocked, its free-running frequency is set by a stepper motor which coarsely controls the length of its mode-locked oscillator cavity. In this operating mode, a frequency counter measurement is used to drive a software feedback loop which moves the cavity length motor to adjust the cavity frequency to within 1 Hz of 68 MHz. The accelerator frequency and the reference for the frequency counter are each clocked by 10 MHz rubidium (Rb) references with $< 1e-9$ stability, making the frequency search process accurate and repeatable.

Normal Locked Operation

During normal operation, the oscillator is phase-locked to the RF reference at 3808 MHz. Timing changes are made by shifting the phase of the 3808 MHz RF and, where necessary, changing the trigger delay for the regenerative amplifier in 8.4 ns ($1/119$ MHz) steps to avoid regen jumps while shifting phase.

The feedback voltage on the piezo cavity length actuator for the mode-locked laser is monitored. If that voltage exceeds a set range, indicating that the piezo actuator is nearing the edge of its travel range, the cavity length control stepper motor is adjusted to allow the piezo actuator to be centered within its range of movement. This control is important to avoid saturating the piezo amplifier.

If the locking system loses phase lock, a hardware reset in the feedback circuitry will attempt to re-establish lock.

The phase lock error signal and the frequency counter are monitored in software to determine if the locking system has both lost lock and failed to recover. In this case, the system will switch back “unlocked frequency search” mode.

Bucket Jump Correction

If the phase locking of the mode-locked laser oscillator is disturbed, it can briefly lose lock and then re-lock to the 3808 MHz, sometimes ending up at an overall different time relative to the X-ray—a jump of one or more 3808 cycles, referred to as a “bucket jump”. This is uncommon, occurring on average less than once per day. However, it needs to be detected and corrected when it occurs.

In normal locked operation, the time interval counter is used to monitor the delay of the regen optical output relative to a fixed trigger. If a timing jump that is close to

an integer multiple of ~ 262 ps ($1/3808$ MHz) is detected, then the 3808 MHz phase shifter is directed to move by a corresponding integer number of cycles, returning the laser to the correct timing.

Note that because the time interval counter has a noise of ~ 20 ps, it is only used to detect bucket jumps (that are multiples of ~ 262 ps). Bucket jumps are corrected by adjusting the 3808 MHz vector phase shifter, which has a resolution of up to 4 fs and noise of a few femtoseconds RMS.

LASER PHASE DETECTION

The laser-RF phase detection system measures the relative timing of the mode-locked laser pulses and the 476 MHz linac RF reference. A high-bandwidth (10 GHz) photodiode converts the 68 MHz train of femtosecond laser pulses into a series of electrical pulses. A narrow bandpass filter then selects the 56th harmonic at 3808 MHz.

In parallel, the 476 MHz reference is multiplied in diode frequency multipliers to 3808 MHz, then shifted in phase by a software-controlled I/Q vector phase shifter. This output from the phase shifter, and the laser signal of the same frequency, are both downmixed against a 3807.75 MHz local oscillator to 250 kHz intermediate frequencies ("IF").

A higher frequency than 476 MHz was chosen for a phase detection frequency in order to reduce the dynamic range of the phase detector. Power of 2 harmonics are simple to generate with $\times 2$ multipliers, and 3808 MHz was the highest power of two harmonic of 476 MHz that did not have a reduced response due to limited photodetector bandwidth, and which could easily be processed with conventional printed circuit board ("PCB") electronics and fabrication techniques.

The 250 kHz IF signals are compared in phase using a precision analog multiplier operating as a mixer. The phase error output is then used as the input error term in a phase-locked loop ("PLL") which controls the cavity length piezo actuator.

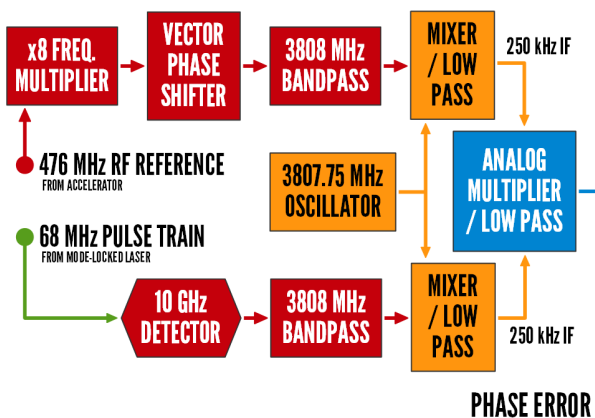


Figure 3: Laser phase detection.

LASER PHASE FEEDBACK

The laser phase locking system operates as a PLL where the output of the phase detector is used to control the frequency of the laser. An op-amp-based feedback loop with infinite gain at DC, and a second-order roll-off is used as described in Brennan [4]. If the feedback output saturates, the loop integrator capacitor is shorted by an analog switch, which resets the loop and allows the laser to re-lock.

The overall loop gain is adjustable with an analog-voltage-based gain control. The loop bandwidth is set in hardware by the resistors and capacitors in the feedback loops. Loop bandwidths between 1 kHz and 4 kHz are used depending on the dynamic response of each laser installation.

HARDWARE DESIGN

The timing system hardware is constructed from a set of independent modules to allow for easy upgrades and maintenance. These modules are also used for other RF systems at SLAC, and are based on the Stanford Research Systems ("SRS") "Small Instrumentation Module" platform ("SIM900"). The SIM900's ± 5 V and ± 15 V power supplies are used extensively, however, its built-in RS-232 communication is not.

The custom locking electronics are fabricated using surface mount components on inexpensive FR-4 PCB substrate (Fig. 4). This combination provides good performance at the desired 3808 MHz RF frequency at a much lower price point compared to PTFE substrate.

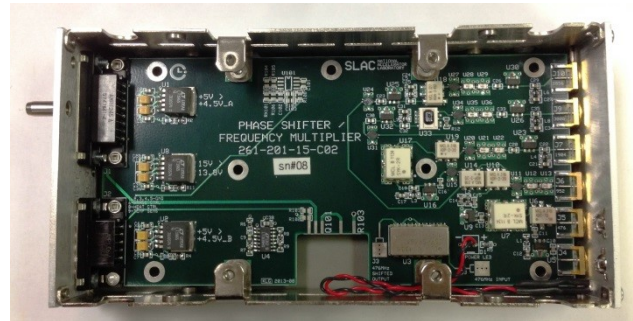


Figure 4: Frequency Multiplier PCB mounted in SRS SIM9B1 enclosure.

The full SIM900 instrumentation crate (Fig. 5, center) contains:

- **Frequency Multiplier:** Multiplies the 476 MHz RF reference from the accelerator $\times 8$ to obtain a 3808 MHz reference.
- **Phase Shifter:** Adjusts the phase of the 3808 MHz reference signal based on two analog input voltages using an I/Q vector modulator.
- **Phase Controller:** Generates the analog-voltage-based I/Q vector to drive the phase shifter. Accepts commands from governing software to shift phase by fractions of the I/Q circle. Uses stepper motor

controller firmware to provide a trapezoidal velocity profile to the phase shift, and is capable of moves of $> 1e5$ cycles of displacement ($34 \mu\text{s}$ at 3808 MHz) at a slow rate of $\sim 1 \text{ ms/s}$ with $\sim 16 \text{ fs}$ typical resolution.

- **Laser Receiver:** Selects the 3808 MHz harmonic from the 68 MHz pulse train from the laser detector, and downmixes it to a 250 kHz IF. The 3808 MHz reference from the frequency multiplier is processed in the same way along a parallel path with identical components.
- **Phase Detector:** Compares the phases of the two 250 kHz IF signals with a precision analog multiplier (Analog Devices AD734) operating as a mixer.
- **PLL:** Provides the lead / lag feedback for locking the laser loop. The loop parameters are programmed by resistors and capacitors on an externally-swappable daughter-card.
- **Laser Interface:** Contains photodiode signal conditioning circuitry used for diagnostics.

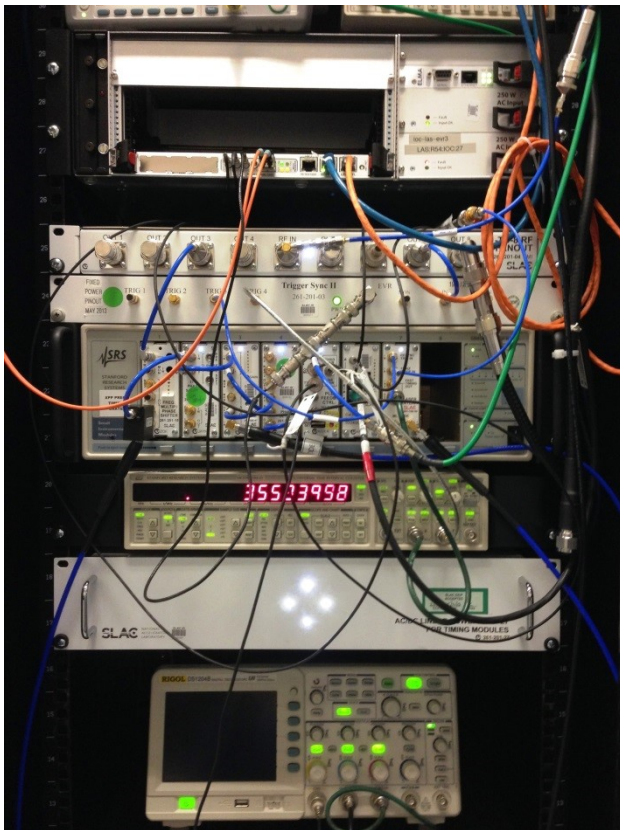


Figure 5: Full laser locking system inside rack enclosure.

The locking electronics within the SIM900 crate are further assisted by a trigger resynchronization module (Fig. 5, above SIM900) which uses the 476 MHz linac RF reference to reduce jitter on trigger signals originating from the LCLS event timing system.

Hardware Cost

The per-laser total cost of the new LCLS locking system hardware, including all off-the-shelf-components,

is approximately US\$40,000. This is very cost-competitive with commercial locking systems, with the additional benefit of modularity and flexibility in setup/upgrading.

SOFTWARE DESIGN

The entirety of the controls for the locking hardware system are exposed through process variables ("PV") in the LCLS installation of the Experimental Physics and Industrial Control System ("EPICS"). A layer of EPICS-based software interprets and archives system data and runs the slow loops governing the movement of the oscillator cavity length coarse adjustment motor.

Running on top of the EPICS code is a Python command & control script which consumes locking system data as well as user input from EPICS channel access ("CA"). This program coordinates movement of the event triggers and of the phase controller in the locking system crate to achieve the desired timing, based on the desired laser delay as requested by the user.

The command & control program also monitors timing data for anomalies such as bucket jumps, or other indications that the system cannot operate as designed, for example, if a photodiode becomes misaligned. Users are alerted through output EPICS PVs, and if necessary, the script disables locking system operation pending check-out and calibration.

Both EPICS and Python are open source frameworks, making the software for the locking system portable without the need for commercial licensing of any software tools.

LOCKING SYSTEM PERFORMANCE

The noise performance of the LCLS laser locking system was measured using an Agilent E5052 signal source analyzer (Fig. 6).

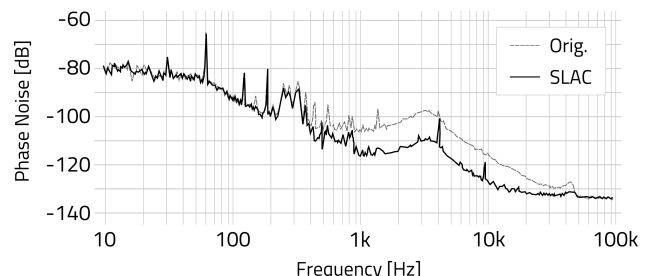


Figure 6: Trace of Agilent E5052 phase noise measurement of LCLS locking system.

When compared to the original fiber-based LCLS laser timing system [5-6], phase noise between 1 kHz and 10 kHz is improved by more than 10 dB . This results in an RMS laser / RF reference timing jitter of $\sim 25 \text{ fs}$ between 100 Hz and 10 kHz . Below 100 Hz , phase noise is dominated by the noise of the linac RF reference. Future efforts to reduce jitter will require improvements to the RF

reference, however, the performance of the system in its current state is sufficient to fall well within the 1-picosecond-wide arrival time window of the X-ray/optical cross-correlator.

Drift of the RF-based locking system has been measured at less than 1 ps/day. This is suboptimal when compared to a fiber-based system, and future upgrade paths to the LCLS laser locking system include drift correction using a parallel fiber distribution system.

As of the writing of this text, the new locking system has been operating for a cumulative total of 57 system-months with only a single hardware failure, and no major downtime. When problems occur, they are straightforward to address due to the modularity inherent in the design of the locking system, and easy to debug using the online diagnostics as well as numerous external RF connections on the system crate itself.

CONCLUSION

LCLS has created a low-cost, modular, RF-based laser locking system. The cost and performance of this custom system are very competitive with commercial locking solutions. The modularity of the system makes it easily repairable and upgradable. The software control for the system runs on open source frameworks and does not depend on commercial code.

The resulting laser timing jitter of ~25 fs RMS, when combined with the X-ray timing jitter of ~60 fs RMS, ensures that the optical and X-ray pulses arrive within the 1 ps window needed for the cross-correlator, which gives users shot-to-shot timing offsets used to order data during analysis.

The new system has also met reliability expectations with only one hardware failure in 57 system-months of operation.

ACKNOWLEDGEMENTS

The Linac Coherent Light Source is a U.S. Department of Energy Office of Science-funded facility located at SLAC National Accelerator Laboratory. LCLS is the world's first hard X-ray free-electron laser, allowing researchers to see atomic-scale detail on ultrafast timescales. The LCLS enables groundbreaking research in physics, chemistry, structural biology, energy science and many other diverse fields.

REFERENCES

- [1] A. Brachmann *et al.*, "Femtosecond operation of the LCLS for user experiments," in *Proc. of Int. Particle Accelerator Conf.*, Kyoto, Japan, 2010, pp. 2287-2289.
- [2] N. Hartmann *et al.* (2014, July 27), "Sub-femtosecond precision measurement of relative X-ray arrival time for free-electron lasers," *Nature Photonics* [Online]. Available: <http://dx.doi.org/10.1038/nphoton.2014.164>
doi: 10.1038/nphoton.2014.164
- [3] J. M. Glowia *et al.*, "Time-resolved pump-probe experiments at the LCLS," *Optics express*, vol. 18, no. 17, pp. 17620-17630, Aug 2010. Available: <http://dx.doi.org/10.1364/OE.18.017620>
doi: 10.1364/OE.18.017620
- [4] P. V. Brennan, *Phase-Locked Loops: Principles and Practice*, McGraw-Hill Professional, 1996
- [5] J. M. Byrd *et al.*, "Femtosecond Synchronization of Laser Systems for the LCLS," in *Proc. of the 2010 Int. Particle Accelerator Conf.*, Santa Fe, NM, USA, pp. 58-62.
- [6] G. Huang *et al.*, "Synchronize Lasers to LCLS e-Beam," in *Proc. of 2011 Particle Accelerator Conf.*, New York, NY, USA, 2011, pp. 636-638.

MEASUREMENTS OF COMPRESSED BUNCH TEMPORAL PROFILE USING ELECTRO-OPTIC MONITOR AT SITF *

Y. Ivanisenko[†], V. Schlott, PSI, Villigen, Switzerland
P. Peier, DESY, Hamburg, Germany

Abstract

The SwissFEL Injector Test Facility (SITF) is an electron linear accelerator with a single bunch compression stage at Paul Scherrer Institute (PSI) in Switzerland. Electro-optic monitors (EOM) are available for bunch temporal profile measurements before and after the bunch compressor. The profile reconstruction is based upon spectral decoding technique. This diagnostic method is non-invasive, compact and cost-effective. It does not have high resolution and wide dynamic range of an RF transverse deflecting structure (TDS), but it is free of transverse beam size influence, what makes it a perfect tool for fast compression tuning.

We present results of EOM and TDS measurements with down to 150 fs short bunches after the compression stage at SITF.

INTRODUCTION

Hard X-ray FEL facilities are based upon multi-stage compression of electron bunches. Bunch temporal profile monitoring is normally done after each compression stage. The most common approach is to use an RF transverse deflecting structure (TDS) [1].

Electro-optic monitor (EOM) represents another method for bunch temporal profile measurements [2]. The transverse electric field component of a moving charged particle is enhanced by the Lorentz factor. For an ultra-relativistic particle the field lines are concentrated in a thin disk, approaching zero thickness with Lorentz factor growing to infinity. The disk circumference lies in a plane perpendicular to the propagation direction. An ultra-relativistic bunch of particles will induce an electric field which is localized in the longitudinal extent of the bunch itself. The bunch length can be measured by sampling the distribution of its electric field. In electro-optic monitor a traveling electric field pulse can be converted into a laser pulse modulation of the same duration in a non-linear crystal. A modulation is produced on the top of a chirped laser pulse (with time-to-wavelength correlation) by using the electro-optic spectral decoding (EOSD) method. It is sufficient to know the spectrum of the pulse and its chirp to reconstruct the temporal profile of a bunch.

Although achievable time resolution is limited, an EOM has some advantages when compared to a TDS, since it is an alternative non-invasive technique to measure the longitudinal bunch profile. It requires much less beamline space and it

is only sensitive to a longitudinal distribution of charge. Both are time domain measurement approaches with absolute calibration. A TDS allows to measure bunch longitudinal profile in a larger dynamic range by changing the deflecting gradient. TDS has the best resolution achieved to date [3]. But it needs a separate RF system, and destroys the measured bunch.

EOM SETUP AT SITF

The SwissFEL Injector Test Facility (SITF) is a 250 MeV linear accelerator with a single bunch compression stage. There are two EOMs installed at SITF: one in front of and one behind the bunch compressor. A TDS is installed 1 meter downstream of the second EOM.

The EOSD measurement scheme is shown in Fig.1. An in-house developed fiber laser oscillator generates about 1 nJ pulses with the wavelength of 1030 nm and the spectral bandwidth of 25 nm at 40 MHz. A pulse picker lowers repetition rate to 1 MHz in front of an amplifier, that boosts up the pulse energy to 5-10 nJ. A grating compressor pre-compensates dispersion caused broadening of the pulse in the long fiber to the tunnel.

A 2 mm thick GaP crystal is installed in the vacuum beam pipe on a specially designed actuator platform with all other optical elements responsible for laser transport and polarization control. In case the crystal is put in the whole assembly moves not disturbing the internal alignment. The laser enters the vacuum through an optical view port and is directed to the crystal by a mirror. Then it propagates through the crystal, and it is reflected back at the end facet. After this it moves against the direction of the electron bunch and is guided out of the beam pipe to a spectrometer.

The linearly polarized laser beam is almost blocked by nearly crossed polarizers configuration without external electric fields. The laser light polarization is changed due to the electro-optic effect in the crystal in presence of an electron beam. In perfect case laser pulse has to propagate in the crystal synchronously to the electric field envelope of an

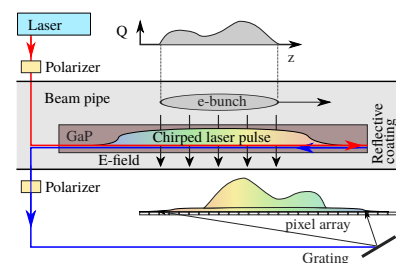


Figure 1: EOM setup scheme.

* The research leading to these results has received funding from the European Community's Seventh Framework Programme (FP7/2007-2013) under grant agreement n.°290605 (PSI-FELLOW/COFUND)

[†] yevgeniy.ivanisenko@psi.ch

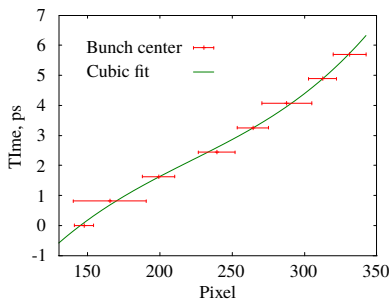


Figure 2: Spectrum to time calibration curve.

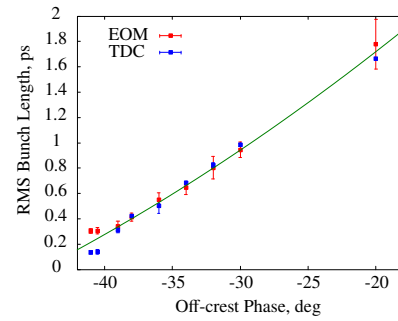


Figure 3: Bunch length measurements with EOM and TDS.

electron bunch. On practice the crystal bandwidth is substantially limited, hence the synchronicity with respect to the laser cannot be supported for the entire spectral range of the envelope.

The electron bunch temporal profile is now imprinted into a polarization modulation of the chirped laser pulse. It is converted into an intensity modulation after the second polarizer. An optical spectrometer is used to record the modulated laser spectrum. The laser pulse chirp calibration is required to map the spectrum into time. It is done by shifting the laser pulse arrival time by a known amount and registering the modulation shift in terms of wavelength. The final calibration (Fig. 2) is derived from a fit of time versus wavelength data with at least 3-4 points, generally depending on the fit model.

EXPERIMENTAL RESULTS

All bunch duration values are root mean square (RMS) values of a fitted gaussian distribution. Error bars indicate statistical error of 10 consequent measurements for TDS and 100 for EOM both at 2-3 Hz repetition rate with stable operation conditions. Bunch charge was kept at 100 pC during the entire period of measurements. Profile plots are showing the amplitude of the relative laser pulse modulation of the EOM, the TDS signal is normalized to match its peak with the EOM data. EOM and TDS do not have synchronous readout and the corresponding measurements are done in sequence one after the other.

RMS bunch length after the electron gun is 2.9 ps and down to about 100 fs after compression. Bunch energy is 200 MeV for all of the experiments described below. The phase of the last acceleration module is varied to control the bunch length. The energy reduction due to stronger off-crest phases is compensated by a higher gradient of another accelerating module.

Comparison with TDS

The aim is to study the dynamic range and resolution of the EOM behind the SITF bunch compressor. Reference measurements are done using the TDS. The measurement overview is in Fig. 3 in terms of bunch duration. The EOM bunch length results agree with the TDS in the range from 340 fs to 1.8 ps. The measured bunch profile is strongly distorted beyond the lower margin. Frequency mixing effect is

responsible for laser pulse spectrum deformations in case the frequency content induced by EO modulation is comparable with that of the probing laser pulse [4]. One solution is to reduce the laser pulse chirp at the crystal. In our experiment the full available compression of the laser pulses was applied to achieve the minimum chirp. Each additional grating compressor reduces the pulse energy by one third, therefore it would need more pulse energy from the laser. A feasible way is to reduce dispersion by using a shorter fiber to the tunnel.

The longest bunch was measured with stronger chirped laser pulses. Signal to noise ratio falls down to one in this case and no reliable fitting can be applied for bunches longer than 1.8 ps. The laser spectrum stability can be improved to increase signal to noise ratio. The situation becomes better for the nominal 200 pC bunch charge. Thicker EO crystal would result in larger modulations, but it would decrease the resolution due to stronger THz envelope dispersion. One could equip a in-vacuum actuator with several EO crystals of different thickness to cover broader bunch length range.

Three single shot profile pairs are shown in Fig. 4 (a,b,c) and one profile taken with a bunch after non-linear compression (Fig. 4(d)). Figure 4(a) indicates the situation when frequency mixing distorts the profile shape and limits the EOM resolution to about 300 fs. Bunch profiles of a gaussian shape were obtained in the measurement with 310 ± 20 fs pulses (plot (b)). The EOM bunch length value is 10% higher with respect to the value acquired by TDS. The profile peculiarities are completely smeared out by frequency mixing. Plots (c) and (d) represent bunch temporal profiles in case of linear and non-linear compression correspondingly. The triangular shape in the second plot has more high frequency content, which is more sensitive to broadening by frequency mixing.

EOM profiles in Fig. 5(a) are obtained from single shot measurement series. Bunch arrival time jitter is excluded by matching centers of all distributions to make comparison easier. The spread of amplitudes is 12 %, the bunch charge stability is better than 1 %. The modulation amplitude is clearly correlated to arrival time (Fig. 5(b)), but the modulation duration is not as much correlated. Therefore it cannot be related to the bunch current fluctuation, but rather some internal EOM modulation efficiency which drops towards the trailing part of the laser pulse.

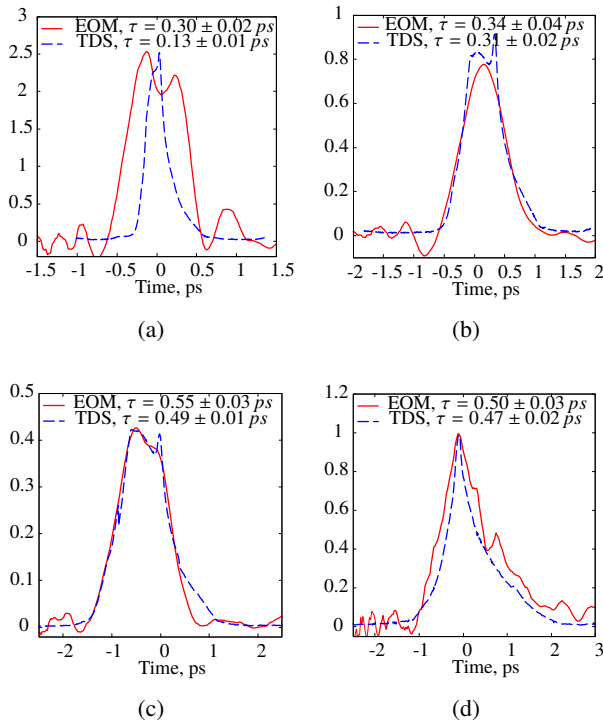
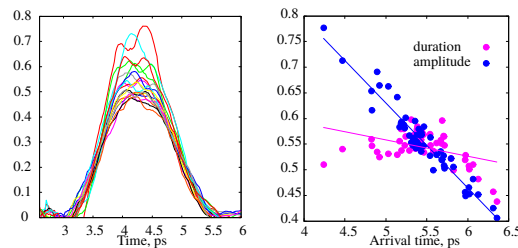


Figure 4: Bunch temporal profiles.

Role of Transverse Beam Size

The EOM measures longitudinal charge distribution and should not be influenced by transverse beam parameters. This assumption was tested by measuring with transversely defocused bunches after compression. The quadrupole magnet to the EOM distance is 1.6 m, the magnet to TDS distance is 2.5 m. TDS measurements are presented with and without beam size subtraction. This procedure subtracts a transverse profile of unstreaked beam from the streaked beam size quadratically. The results are summarized in Fig. 6.

Blue line and points represent TDS results without beam size subtraction. The unstreaked beam contribution is negligible when the beam optics is optimized for the best temporal resolution at the TDS screen ($I_{quad} = 1$ A). Now we change the quadrupole magnet current and observe the growth of the unstreaked distribution up to almost 3 times the streaked beam size matched to the screen. The value measured with EOM goes only slightly down. It can be caused by transverse-longitudinal coupling of the bunch due



(a) Set of 15 bunch profiles (b) Correlated amplitude

Figure 5: 15 consequent shots, settings like in Fig.4(c).

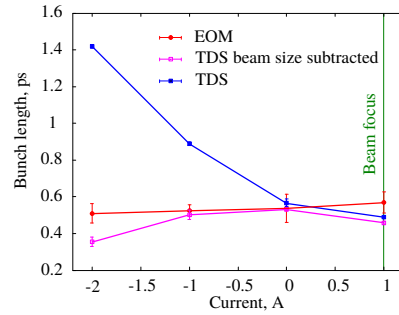


Figure 6: Bunch duration versus transverse size.

to residual dispersion. The main conclusion is that EOM measurements do not require transverse matching in very broad range of transverse parameters.

CONCLUSIONS

EOM measurements of temporal profile with compressed bunches were successfully carried out at SITF. A direct comparison to TDS has shown that in current state the EOM system is capable to cover the range between 300 fs and 1.8 ps. Measured temporal profiles agree well with TDS in the mentioned range. Frequency mixing deforms spectrum already at the modulation length of 340 fs and it also smears out shorter profile features of longer bunches.

SwissFEL will require to resolve about 200 fs pulses after the first bunch compressor in nominal mode, which is not yet covered by the EOM. The resolution can be improved by using 3 times as small pulse chirp as currently.

An experimental test was performed to demonstrate that EOM requires no transverse optics matching prior to bunch length measurements. This fact makes it a perfect tool for fast tuning of bunch compression, while transverse re-matching time can be spared for the final setup.

An electro-optic monitor possesses several advantages over TDS. It is a compact, non-invasive, much cheaper diagnostic equipment for bunch temporal profile measurements. Nowadays it can be built utilizing a reliable commercial femtosecond laser. It certainly lacks the dynamic range and resolution of TDS, but better laser spectrum stability and a shorter fiber to the tunnel can already contribute significantly to improving the resolution range.

REFERENCES

- [1] R. Akre, L. Bentson, P. Emma, P. Krejcik, "A Transverse Rf Deflecting Structure for Bunch Length and Phase Space Diagnostics", in *Proc. Particle Accelerator Conf.*, Chicago, 2001, pp. 2353-2355.
- [2] B. Steffen *et al.*, *Phys. Rev. ST Accel. Beams* 12, 032802 (2009).
- [3] Y. Ding *et al.*, *Phys. Rev. ST Accel. Beams* 14, 120701 (2011).
- [4] F. Müller, *Electro-Optical Bunch Length Measurements at the Swiss Light Source*, PhD Thesis, Bern University, 2011.

COHERENT RADIATION DIAGNOSTICS FOR LONGITUDINAL BUNCH CHARACTERIZATION AT EUROPEAN XFEL

P. Peier, H. Dinter, and Ch. Gerth, DESY Hamburg, Germany

Abstract

European XFEL comprises a 17.5 GeV linear accelerator for the generation of hard X-rays. Electron bunches from 20 pC to 1 nC will be produced with a length of a few ps in the RF gun and compressed by three orders of magnitude in three bunch compressor (BC) stages. European XFEL is designed to operate at 10 Hz delivering bunch trains with up to 2700 bunches separated by 222 ns. The high intra-bunch train repetition rate offers the unique possibility of stabilizing the machine with an intra-bunch train feedback, which puts in turn very high demand on fast longitudinal diagnostics. Two different systems will be installed in several positions of the machine. Five bunch compression monitors (BCM) will monitor the compression factor of each BC stage and be used for intra-bunch train feedbacks. A THz spectrometer will be used to measure parasitically the longitudinal bunch profile after the energy collimator at 17.5 GeV beam energy. We will present concepts for fast longitudinal diagnostics for European XFEL based on coherent radiation, newest developments for high repetition rate measurements and simulations for the feedback capability of the system.

INTRODUCTION

European XFEL will be a linac-driven hard X-ray free electron laser operating at wavelength down to 0.1 nm [1]. The machine will produce up to 2700 short (2-100 fs) X-ray pulses per macro pulse (10 Hz) with a repetition rate of up to 4.5 MHz. The X-ray pulse generation requires kA peak current of the electron bunches which will be achieved by three stages of bunch compression (BC0, BC1 and BC2 in Fig. 1). The corresponding bunch lengths are indicated in Table 1 (source: start-to-end simulations [2]). A high power laser

Table 1: RMS electron bunch lengths in European XFEL for three different charges. Highlighted row: used in simulations.

Charge	Gun	BC0	BC1	BC2
20 pC	4.5 ps	1.5 ps	180 fs	5 fs
100 pC	4.8 ps	1.6 ps	200 fs	12 fs
1000 pC	6.8 ps	2.2 ps	300 fs	84 fs

will generate 4 ps - 7 ps rms long electron bunches in the normal conducting photocathode gun. In the subsequent super conducting acceleration module (1.3 GHz) and the longitudinal phase space linearizer (3.9 GHz) the beam gets an energy of 130 MeV. In BC0 the bunches are compressed by a factor of three before they are accelerated to 700 MeV in the

first part of the linear accelerator (L1). In the second compression stage (BC1) the length of the bunches is reduced by a factor of eight and they are accelerated to 2.5 GeV in L2. In BC2 the bunches are compressed to their final length (fs level) and in L3 they are accelerated to the maximum energy of 17.5 GeV. The electrons are then transported through an energy collimator to the distribution area and to SASE1 or SASE2 undulator beamlines, respectively.

Stable X-ray SASE output requires among other parameters precise control of the longitudinal shape of the electron bunches. The longitudinal shape is tailored only in the BCs. Bunch compression is achieved with an accelerating module running off-crest to induce an energy chirp in the electron beam and a magnetic chicane. In operation the compression level is mainly defined by the phase setting of the corresponding acceleration module. Five bunch compression monitors (BCM), three independent and two redundant, will measure at full repetition rate a quantity that is directly related to the current profile. The independent BCs are the monitors of a feedback system controlling the RF phase settings. In addition one broadband infrared spectrometer is used to resolve accurately the final longitudinal bunch profile with single bunch resolution. It will be installed after the energy collimator where the electrons are fully compressed and have their final energy of 17.5 GeV. The spectrometer works best for short bunches producing short wavelength diffraction radiation.

In this paper, we will describe the requirements on the BCs and feedback system in European XFEL as well as design considerations for the monitors. The performance of the whole system is estimated using simulation tools and operation experiences gained at the VUV Free-electron-LASer-Hamburg (FLASH).

MONITORING THE LONGITUDINAL BUNCH SHAPE

Requirements and Concepts

Table 2: Longitudinal diagnostic requirements overview (numbers in brackets: injector).

Charge	20 - 1000 pC
Energy	(0.005)0.13 - 17.5 GeV
Bunchlength	5 - 2000(7000) fs rms
RF phase stability	0.01 deg
Bunch spacing	min. 222 ns
Repetition rate	10 Hz

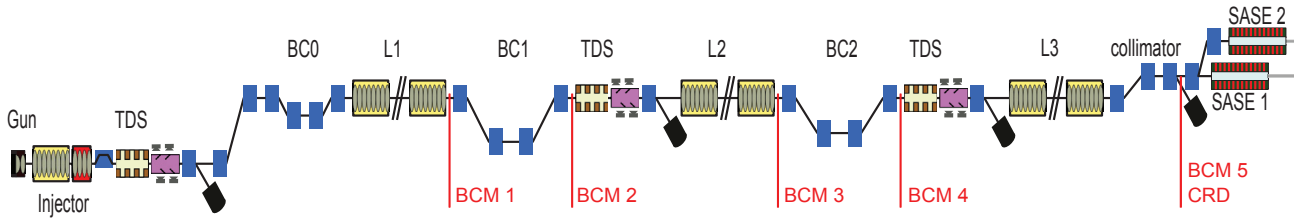


Figure 1: Main components of European XFEL.

Several longitudinal diagnostic systems have to be installed in European XFEL to cover the complete parameter range listed in Table 2. The current profile can be accurately monitored with a longitudinal profile monitor [3] consisting of a transverse deflecting structure (TDS, [4]) in combination with fast kicker magnets and off-axis screens. One bunch out of the bunch train is streaked in the TDS and kicked to the profile monitor where it is recorded by a camera. The TDS system offers direct profile measurement of a single bunch with femtosecond resolution. However, the system is destructive to the electron bunch and not capable of measuring all bunches in a bunch train. It is not sensitive to variations over the bunch train which may be caused by phase drifts of the low level RF (LLRF). The TDS based longitudinal profile monitor will be the reference system.

The longitudinal bunch shape determines the spectral content of the coherent radiation emitted by the electrons when passing a discontinuity such as Coherent Synchrotron Radiation (CSR), Coherent Diffraction Radiation (CDR), and Coherent Transition Radiation (CTR). The spectral density distribution of the coherent radiation emitted by a bunch composed of N electrons is given by Eq. 1, where $d^2P_0/d\omega d\Omega$ denotes the single electron spectrum for the process under consideration and $F(\omega, \Omega)$ the longitudinal bunch form factor. F is the normalized Fourier transform of the longitudinal current profile.

$$\frac{d^2P}{d\omega d\Omega} = \frac{d^2P_0}{d\omega d\Omega} (N + N(N-1)|F(\omega, \Omega)|^2) \quad (1)$$

Spectrally resolved measurements of the coherent radiation with a spectrometer directly yield the absolute value of the (complex) formfactor (CRISP4). The actual longitudinal bunch shape can be derived by making certain assumptions and using mathematical reconstruction methods [5]. By integrating the spectral intensity in a certain frequency range, we get a single signal that is correlated to the current profile of the bunch (BCM). Small variations in bunch shape lead to variations in the detected signal and can be used as monitor signal for the feedback system.

The longitudinal current profiles of a bunch with 100 pC bunch charge at several positions in the machine are depicted in Fig. 2. The corresponding formfactors are shown in Fig. 3. Analyzing the curves in Fig. 3 we find that THz detectors have to be used after BC0, BC1 and BC2. There will be no system to measure the coherent radiation between the electron gun and BC0 (10 GHz range).

ISBN 978-3-95450-133-5

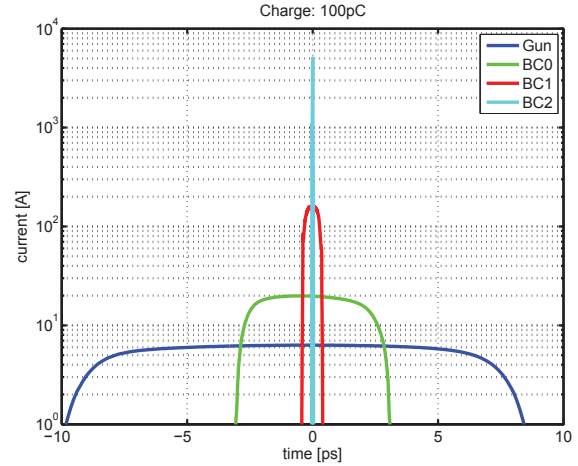


Figure 2: Longitudinal bunch profile from beam dynamics simulations.

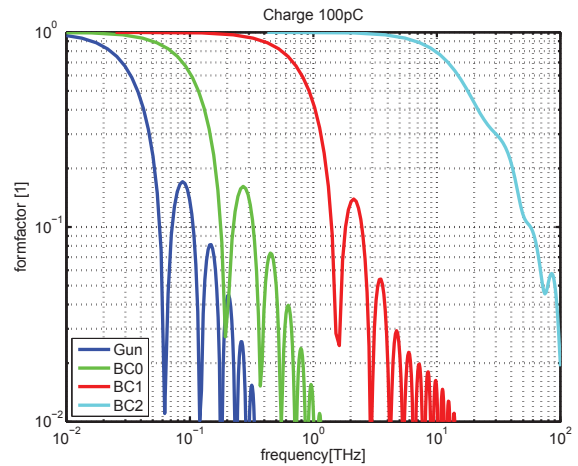


Figure 3: Longitudinal form factor derived from beam dynamics simulations.

Bunch Compression Monitor (BCM) and 4stage Coherent Radiation Infrared Spectrometer (CRISP4)

The BCMs have to be simple and reliable monitors providing robust signals from each bunch to be used for the RF phase feedback system. The signal generation should not depend on the beam orbit and must not disturb the beam itself. The monitors are composed of a cubic vacuum chamber, a screen mover and an in-vacuum diffraction radiation

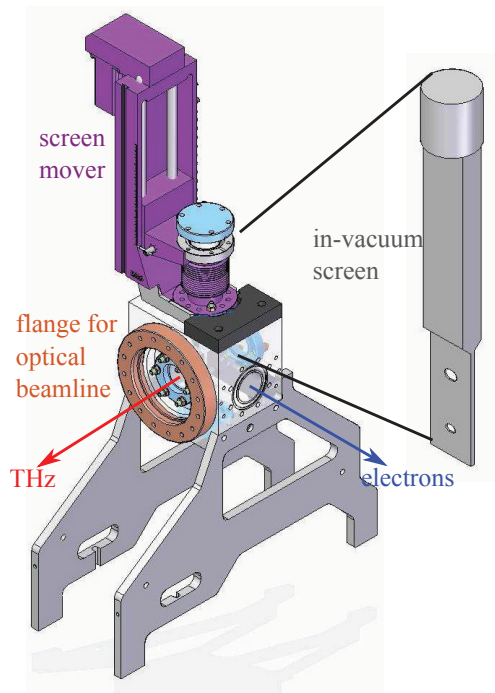


Figure 4: 3D CAD model of screen station for BCMs and CRISP4. Courtesy of N. Leuschner, DESY.

screen. The image export of the 3D CAD model of the vacuum station is shown in Fig. 4. The generated THz/infrared radiation is transported through an optical beamline to the detectors. The BCMs for European XFEL will be very similar to the proven systems installed at FLASH [6]. There the BCMs are used for slow RF phase feedback.

CRISP4 was also developed for FLASH [5] and a copy will be installed in European XFEL. The grating spectrometer was designed to cover the wavelength range from $4\text{ }\mu\text{m}$ to $440\text{ }\mu\text{m}$ with two sets of gratings. 120 pyro-electric sensors convert the radiation in the respective frequency band into an electrical signal. At FLASH, CRISP4 is mainly operated with an off-axis transition radiation screen and fast kicker magnets. CTR is much more intense than CDR for the same electron beam parameters but it is destructive to the electron bunch. Therefore, the system is limited to measure one single bunch of the bunch train. At European XFEL, CRISP4 will get the radiation of each bunch of the bunch train from a diffraction screen. Sufficient intensity is generated by coherent diffraction due to the high energy and the high peak current of the electron bunches. CRISP4 will provide CDR spectra taken with one set of gratings at full repetition rate.

SIMULATIONS AND RESULTS

In order to design each monitor station and to choose the most appropriate detectors, the longitudinal bunch properties, radiation process, radiation transport and detector response have to be taken into account. We developed a simulation tool which combines different codes and inputs. We are now able to calculate the expected signal depending on the RF phase of the accelerating modules and the BC chi-

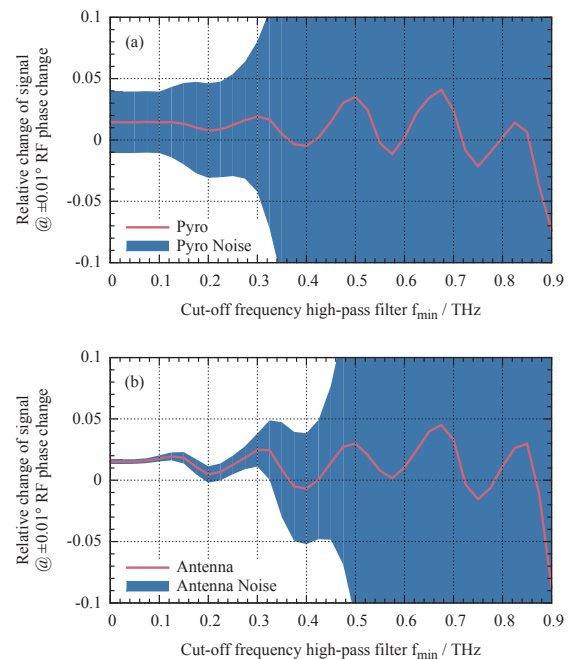


Figure 5: Simulation of relative detector response when changing RF phase by ± 0.01 deg versus edge frequency of THz high-pass filter. (a) pyro-electric sensor, (b) quasi optical detector (Schottky-diode with antenna).

cane setting. And therefore we are able to assess the required sensitivity of the sensors in order to provide reliable monitor signals to the feedback system.

Starting from the nominal acceleration module phase and amplitude settings we varied the phases by a small amount and calculated the according BCM response for two different detectors: pyro-electric sensor (Fig. 5 (a)) and quasi optical detector based on a Schottky-diode with antenna (Fig. 5 (b)). The scan range was chosen ± 0.01 deg. The expected signal change was then compared to the noise of the detectors. With intent to improve the response of our systems, we also include spectral THz filters into our simulations [7]. The longitudinal formfactors (Fig. 3) are close to one for low frequencies and therefore small changes in bunch length will only affect the slope of the formfactors at higher frequencies. In order to increase the sensitivity of the BCMs to small changes in bunch length at the expense of lower signal amplitude, a high-pass spectral THz filter is used to suppress the low frequencies. The results of the calculations for BC0 are summarized in Fig. 5. The red curves in both plots denote the relative change of the signal of the respective detector when changing the acceleration phase by ± 0.01 deg versus the edge frequency of a high-pass THz filter. The blue band denotes the absolute signal divided by the noise of the detector.

The relative signal change can slightly be improved when introducing THz filters, but the noise grows much more. The signal to noise ratio cannot be improved significantly. In addition we find that the Schottky-diode with antenna is

the detector of choice at this location. The oscillations of the signals correspond to the structure of the longitudinal formfactor depicted in Fig. 3.

CONCLUSION

The coherent radiation diagnostics for European XFEL is based on the monitors installed in FLASH. Several properties have to be improved or adapted. The main improvement necessary is the modification towards the higher bunch repetition rate (4.5 MHz). The mechanical design is completely new and has to comply with European XFEL design and vacuum specifications. A rigid full metal diffraction radiation screen (-holder) will be integrated in all monitors.

Several software tools are available to simulate the complete path: from RF phase setting to detector signal. Simulation results and experience from FLASH showed that uncooled detectors like pyro-electric elements (all wavelengths) and Schottky-diodes with antennas (long wavelengths) are well suited to provide feedback capable signals for a fast intra-bunch train feedback.

ACKNOWLEDGMENTS

We would like to thank ACST GmbH for providing us the quasi optical Schottky-diode detector. Moreover we are grateful to F. Ahr from CFEL/DESY for her help during detector tests with laser generated THz.

REFERENCES

- [1] M. Altarelli et al., “The European X-Ray Free-Electron Laser Technical design report,” (DESY 2006-097).
- [2] G. Feng et al., “Beam Dynamics Simulations for European XFEL,” (TESLA-FEL 2013-04).
- [3] M. Yan et al., “First Realization and Performance Study of a Single-Shot Longitudinal Bunch Profile Monitor utilizing a Transverse Deflecting Structure”, IBIC’13, Oxford, September 2013, TUPC36, p. 456, <http://www.JACoW.org>
- [4] P. Emma, J. Frisch, and P. Krejcik, “A Transverse RF Deflecting Structure for Bunch Length and Phase Space Diagnostics,” LCLS Technical Note, 12, (2000).
- [5] S. Wesch et al., “A multi-channel THz and infrared spectrometer for femtosecond electron bunch diagnostics by single-shot spectroscopy of coherent radiation,” Nuclear Instruments and Methods in Physics Research Section A 665.0, pp. 40 to 47 (2011).
- [6] H. Delsim-Hashemi et al., “Single-Shot Longitudinal Diagnostics with THz Radiation,” WG512, Proc. FLS2006, Hamburg, Germany (2006).
- [7] F. Frei et al., “Development of Electron Bunch Compression Monitors for SwissFEL”, IBIC’13, Oxford, September 2013, WEPC36, p. 769, <http://www.JACoW.org>

LONGITUDINAL DIAGNOSTICS OF RF ELECTRON GUN USING A 2-CELL RF DEFLECTOR*

M. Nishiyama[#], T. Takahashi, T. Toida, K. Sakaue, M. Washio, Waseda University, Tokyo, Japan
T. Takatomi, J. Urakawa, KEK, Ibaraki, Japan

Abstract

We have been studying a compact electron accelerator based on an S-band Cs-Te photocathode rf electron gun at Waseda University. We are using this high quality electron bunch for many application researches. It is necessary to measure the bunch length and temporal distribution for evaluating application researches and for improving an rf gun itself. Thus, we adopted the rf deflector system. It kicks the electron bunch with resonated rf electromagnetic field. Using this technique, the longitudinal distribution is mapped into the transverse space. The rf deflector has a 2-cell standing wave π -mode structure, operating in TM_{210} dipole mode at 2856 MHz. It provides a maximum vertical kick of 1.00MV with 750 kW input rf-power which is equivalent to the temporal resolution of around 58 fs bunch length. In this conference, we report the details of our rf deflector, the latest progress of longitudinal phase space diagnostics and future prospective.

INTRODUCTION

A photocathode rf electron gun is now widely utilized for an accelerator system in many facilities due to its controllability of initial beam profile and ability to generate low emittance beam. In Waseda University, we built a compact electron accelerator system based on an S-band Cs-Te photocathode rf electron gun. The rf gun is an improved BNL type IV 1.6 cell rf gun. It is applied to many researches, such as a pulse radiolysis experiment for tracing rapid initial chemical reactions by ionizing radiation [1], a laser Compton scattering for generating soft X-ray [2] and synchrotron radiation and transition radiation for generating coherent THz wave [3][4]. In these experiments, it is necessary to measure the bunch length and temporal distribution for evaluating temporal resolution, luminosity and coherence, respectively. The measurement of the bunch length is also helpful for studying the effect of rf acceleration. Thus, we adopt the rf deflector system.

THE METHOD OF BUNCH LENGTH MEASUREMENT USING RF DEFLECTOR

Figure 1 shows a principle of measuring the bunch length and temporal profile using an rf deflector. An rf deflector is one of rf cavities. It has been used as a strong tool for bunch length and temporal profile measurements in FELs and other facilities recently. Electromagnetic

field of its own resonates in an rf deflector when rf power is supplied. In Waseda University, the rf deflector generates the electromagnetic field of the TM_{210} mode. Lorentz force gives the transverse momentum on the electron beam by the high frequency time variation of the magnetic field and the beam is “kicked” horizontally. The electric field has no effect on the beam in the rf deflector, because it doesn't exist on the axis of the beam. Thus, the rf deflector can convert the longitudinal information of the electron beam into the transverse one. Using this technique, the temporal profile of an electron beam can be obtained directly as an image on screen.

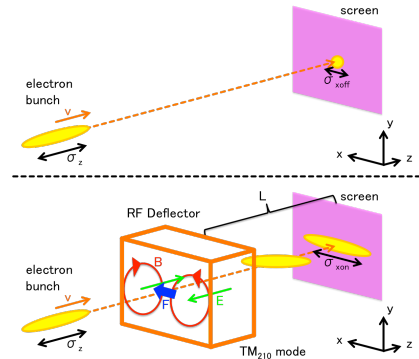


Figure 1: Bunch length measurement using an rf deflector.

Considering the transfer matrix between the rf deflector and the screen, the transverse position of each relativistic electron on the screen, Δx , as a function of longitudinal position from the bunch centroid along the bunch, Δz , is given approximately by

$$\Delta x = \frac{eV_T}{p_z c} L \sin(k\Delta z + \varphi) \cong \frac{eV_T}{p_z c} L [k\Delta z \cos \varphi + \sin \varphi] \quad (1)$$

where c is the light velocity, p_z is the longitudinal momentum, V_T is the deflecting voltage, L is the drift length between the rf deflector and the screen, k is the rf wave number, and φ is the rf phase [5]. The approximation is made that $|\Delta z| \ll 1/k$ because the longitudinal position is much shorter than the rf wavelength of 0.105 m. Operating at the zero-crossing phase like Figure 2, we can substitute $\varphi=0$ to Eq. (1),

$$\Delta x = \frac{eV_T}{p_z c} L k \Delta z \quad (2)$$

This phase gives the best kicking effect with the horizontal beam size corresponding to the bunch length ($\sigma_x \propto c\sigma_t$).

* Work supported by JSPS Grant-in-Aid for Scientific Research (A) 10001690 and the Quantum Beam Technology Program of MEXT.
[#]masa.hero@ruri.waseda.jp

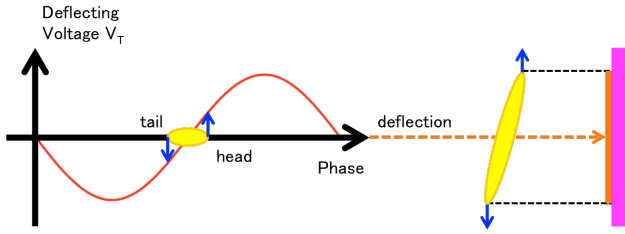


Figure 2: The schematic of rf deflection by rf zero-crossing phase.

Considering the beam size, from Eq (2), the bunch length σ_t is given by

$$\sigma_t = \frac{p_z c}{e V_T \omega L} \sqrt{\sigma_{x_{on}}^2 - \sigma_{x_{off}}^2} \quad (3)$$

and the temporal resolution σ_{t0} is given by

$$\sigma_{t0} = \frac{p_z c}{e V_T \omega L} \sigma_{x_{off}} \quad (4)$$

where ω is the rf angular frequency, $\sigma_{x_{on}}$ and $\sigma_{x_{off}}$ are beam sizes when the rf deflector is on and off, respectively. From Eq (4), it is clear that the temporal resolution can be better when we increase the deflecting voltage V_T , the angular frequency ω and the drift length L , and it can be worse when we increase the beam size $\sigma_{x_{off}}$ and the momentum p_z . ω is unique to the power supply and L is limited by the size of the facility. Thus, it is necessary to increase the deflecting voltage V_T and to decrease the beam size $\sigma_{x_{off}}$ for better temporal resolution.

DESIGN AND MANUFACTURE OF RF DEFLECTOR [6]

We used HFSS (High Frequency Structure Simulator) for the design of the rf deflector cavity and GPT (General Particle Tracer) for the evaluation of its performance. We carried out a simulation imposing the boundary condition which generates the electromagnetic field of TM_{210} mode in the cavity. Comparing an rf deflector of a rectangular geometry with that of a pillbox geometry, magnetic field on the axis of the beam in the rectangular rf deflector was stronger than the pillbox one. From the viewpoint of the Q value, the length in the x direction should be 1.4 times longer than the length in y directions. As for the length in the z direction, we started to study the length of time which the beam in the cavity was the half cycle of the magnetic field cycle, assuming that the beam has the light velocity. To increase the Q value of the cavity, we optimized while reducing as much as possible the energy losses in the cavity wall, increasing the most magnetic field strength in the cavity by reducing the surface of the cavity with rounded corners of a rectangular rf deflector. However, it became clear that this rf deflector could not measure the bunch length of 100 fs with any design because the power supply from the Klystron is limited in

our accelerator system. Therefore, to achieve much better temporal resolution, we started to design the 2-cell rf deflector. The deflecting voltage V_T of the 2-cell rf deflector is 1.41 times higher than that of 1-cell rf deflector. After all, we designed the impedance matching with the waveguide using HFSS and adjusted the length in the z direction by evaluating the deflection of an electron beam using GPT. Figure 3 shows the photograph of the rf deflector. The parameters of the manufactured rf deflector and the designed rf deflector are given in Table 1. The parameters of the manufactured rf deflector are almost as designed. Figure 4 and Figure 5 shows the result of magnetic field distribution measurement by bead perturbation method and that of rf resonant frequency measurement by reflecting method using the network analyzer respectively. The ratio of magnetic field peak in the 2-cell was almost 1:1 as designed and the electromagnetic field of π -mode is resonated around 2856 MHz. It provides the deflecting voltage of 1.00MV with 750 kW input rf power which is equivalent to the temporal resolution of around 58 fs bunch length with beam size of $\sigma_{x_{off}}$.

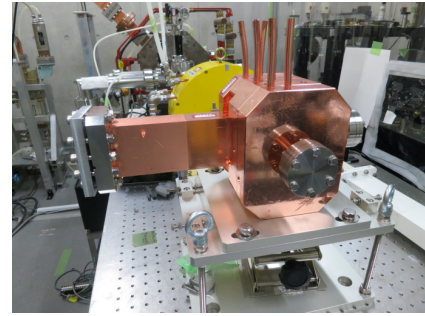


Figure 3: The photograph of the rf deflector.

Table 1: Parameters of RF Deflector

Parameters	Results	Design value
π -mode	2855.348 MHz	2855.372 MHz
0-mode	2859.874 MHz	2859.922 MHz
Δf	4.526 MHz	4.55 MHz
Q value on π -mode	16298	17282
Ratio of magnetic field	1:0.9875	1:1
Coupling constant β	0.839	1.000

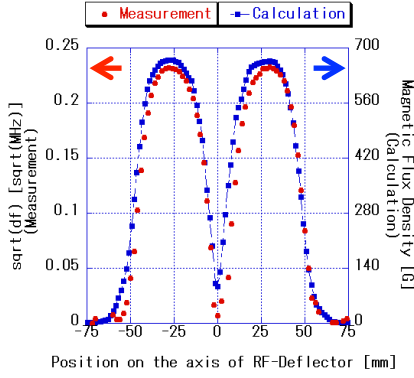


Figure 4: Result of magnetic field distribution measurement.

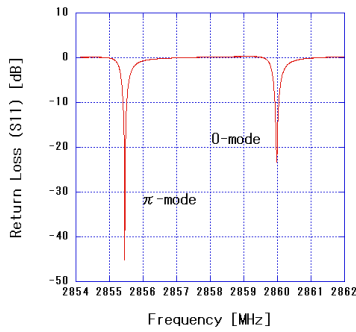


Figure 5: Result of rf resonant frequency measurement.

MEASUREMENT OF BUNCH LENGTH AND TEMPORAL PROFILE USING RF DEFLECTOR

Confirming the rf deflector was manufactured almost as designed, we installed the rf deflector in the accelerator system at Waseda University and carried out the measurement of the bunch length and temporal profile. Figure 6 shows the setup for the measurement.

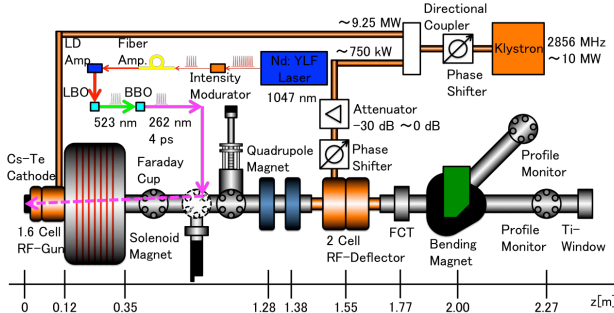


Figure 6: Setup for the bunch length measurement.

In the accelerator system, Nd: YLF laser is used as the seed laser for the rf gun. It oscillates infrared pulsed laser of which the wavelength is 1047 nm. Then the required number of pulses are picked up, amplified, and converted to ultraviolet pulses. These pulses have the pulse width of about 4 ps and the wavelength of 262 nm. They are irradiated to the Cs-Te cathode of an rf gun almost

perpendicularly. The rf gun is the uppermost of the beamline and a solenoid magnet is after the rf gun to compensate the emittance increase due to space charge effect. Two quadrupole magnets to focus the beam size σ_{xoff} are 1.28 m and 1.38 m away from the cathode. The rf deflector is 1.55 m and is supplied rf power of 750 kW separated from the Klystron output of 10MW using the directional coupler. Proper amount of rf power can be supplied with the attenuator so that all of the electron beam is projected on the screen. The rf phase of the deflector is determined independently from the rf phase of the gun with the phase shifter put after the directional coupler. 2.27 m away from the cathode, the screen is installed for measuring the beam profile. Therefore, the drift length L is 0.72 m.

At the measurement of the bunch length, we first calibrated the deflecting voltage V_T . From Eq. (1), the centroid of the electron beam ($\Delta z=0$) with rf phase shift is given by

$$\Delta x = \frac{eV_T}{p_z c} L \sin \varphi \quad (5)$$

Thus, we can calculate the deflecting voltage V_T by measuring the amplitude of a sinusoidal curve which the centroid of an electron beam draws with the rf phase shift. Figure 7 shows the result of the centroid shift. The deflecting voltage is calculated to be about 0.40 MV with the rf power of 192 kW from the amplitude of 12.195 mm using Eq. (5).

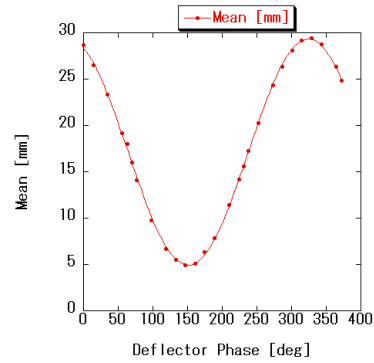


Figure 7: Deflecting voltage calibration.

Then we carried out the measurement of the bunch length and temporal profile. Figure 8 shows the typical electron beam profiles with rf deflector “off” (left) and “on” (right). The bottom line profiles show the projection to x direction. The charge of the electron beam was about 200 pC in this experiment. Temporal information is clearly projected on the screen. From the beam size $\sigma_{xoff}=365 \mu\text{m}$ when the rf deflector was “off”, and the beam size $\sigma_{xon}=4.20 \text{ mm}$ when the rf deflector was “on”, the bunch length was calculated to be about 3.79 ps using Eq. (3). This result is consistent with the pulse width of ultraviolet laser, 4 ps, irradiated to the cathode.

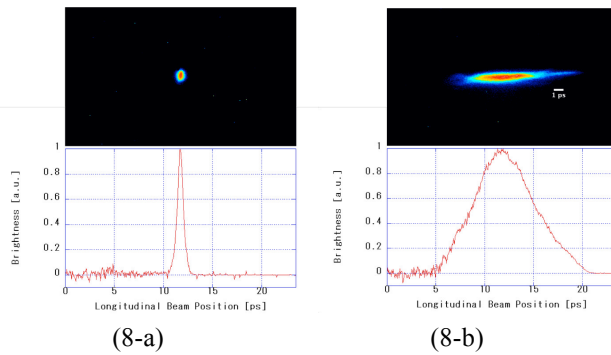


Figure 8: Electron beam profiles with rf deflector “off” (8-a) and “on” (8-b). The bottom line profiles show the projection to x direction.

Changing the charge to 1 nC by controlling the intensity of ultraviolet laser, we also carried out the measurement. Figure 9 shows the result.

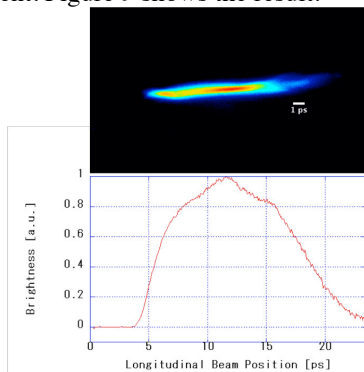


Figure 9: Electron beam profile. The bottom line profiles show the projection to x direction.

Comparing Fig. 9 with Fig. 8-a, the beam profile and the projection to x direction of both figures are different. The profile and projection in Fig. 9 are expanded due to the space charge effect with higher charge of 1 nC.

We also changed the rf phase of rf gun and carried out the bunch length measurement when the charge is 200 pC and 1 nC. Figure 10 and Figure 11 are the results of bunch length measurement when the charge is 200 pC and 1 nC respectively.

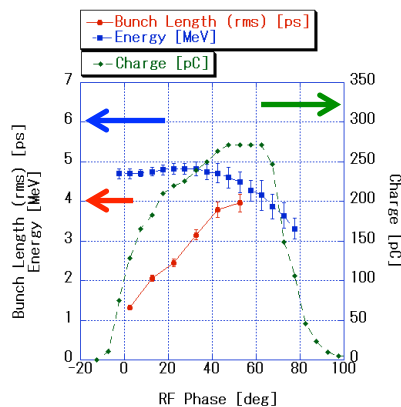


Figure 10: RF phase dependence of the bunch length, beam energy, and charge (200 pC).

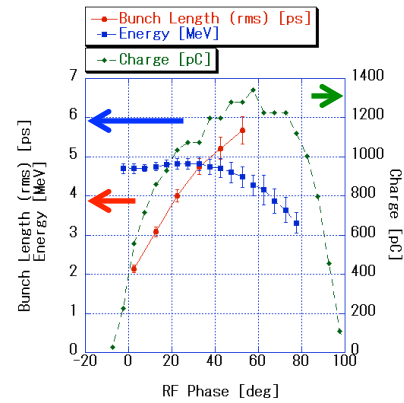


Figure 11: RF phase dependence of the bunch length, beam energy, and charge (1 nC).

Comparing Fig. 10 with Fig. 11, the bunch length increases in both figures with the increase of the rf phase. This is because the charge of electron beam increases with the increase of the rf phase. Considering the bunch length in detail, not only the absolute value but also the variation of the bunch length is larger when the charge is 1 nC due to the space charge effect.

SUMMARY AND PROSPECTS

Using the rf deflector, which we designed for our accelerator system, we succeeded in measuring the bunch length and temporal profile of an electron beam generated from the photocathode rf gun at Waseda University. For the measurement, the deflecting voltage was calculated to be about 0.40 MV with the rf power of 192 kW experimentally. The bunch length dependence on the charge of the electron beam and on the rf phase of the gun was obtained from this measurement. The charge is the key factor in the bunch length measurement. In near future, we will carry out the experiment to obtain the phase space of the electron beam using the rf deflector and a bending magnet. Through these experiments, we will examine the dynamics of the electron beam generated from the rf gun in Waseda University and utilize the rf deflector to cater to applied researches.

REFERENCES

- [1] Y. Hosaka, et al., Radiat. Phys. Chem. 84, 10, 2013.
- [2] K. Sakaue, et al., Radiat. Phys. Chem. 77, 1136–1141, 2008.
- [3] K. Sakaue, et al., Phys. Rev. S. T. Accel. Beams, 17, 023401, 2014.
- [4] Y. Koshiba, et al., Vibrat. Spectroscopy, to be published.
- [5] K. Sakaue, et al., Nucl. Instrum. Meth., under review.
- [6] Y. Nishimura, et al., Nucl. Instrum. Meth., to be published.

COMMISSIONING AND RESULTS FROM THE BUNCH ARRIVAL-TIME MONITOR DOWNSTREAM THE BUNCH COMPRESSOR AT THE SwissFEL INJECTOR TEST FACILITY

V. Arsov[#], M. Aiba, M. Dehler, F. Frei, S. Hunziker, M. Kaiser, A. Romann, V. Schlott, PSI, Villigen, Switzerland

Abstract

A high bandwidth Bunch Arrival-Time Monitor (BAM) has been commissioned downstream the bunch compressor at the SwissFEL Injector Test Facility (SITF). A new acquisition front end allowing utilization of the ADC full dynamic range was implemented. The resolution was measured as a function of the bunch charge for two different electro-optical intensity modulators (EOM). BAM measurements of machine relevant parameters were made. A comparison with the results from other diagnostics shows good agreement.

INTRODUCTION

SwissFEL is planned to start user operation in 2017 at charges between 10 pC - 200 pC [1]. To secure stable machine operation by applying feedbacks, as well as for decoupling of error sources manifested as bunch arrival time jitter, the latter should be measured non-destructively with resolution of 10 fs. In addition, BAM should have a low drift in the order of 10 fs/day. Such requirements are fulfilled for a scheme based on Mach-Zehnder type electro-optical modulator (EOM) [2], interfaced to a single-mode optical fiber link, through which reference laser pulses from a mode locked laser (few 100 fs pulse duration) are distributed [3]. These fiber links are stabilized in length via optical cross-correlation. A pick-up signal generated from the electron bunch is sampled at zero crossing with one of the reference laser pulses. At zero crossing this pulse is not modulated, but any temporal-offset of the beam produces a modulation voltage, which is converted in the EOM to amplitude modulation. With proper calibration, this amplitude modulation is interpreted in terms of arrival-time. An advantage of the method is that when acquiring the BAM signal with a fast ADC by sampling the amplitude and baseline points of the laser pulse-train, not only the pulse which interacts with the electron bunch is measured, but also multiple pulses preceding it, thus obtaining online information about the instantaneous BAM resolution. The technical difficulty is, that for the low charges foreseen for Swiss FEL, the pick-up response is small, thus limiting the resolution, as demonstrated with the first BAM prototype installed in SITF upstream the bunch compressor [4]. This paper describes the commissioning of a second BAM downstream the bunch compressor, for which several improvements were implemented, aiming for higher resolution at low charge.

IMPROVEMENTS IN THE BAM SETUP

The general system topology and schematic layout was already described in [4]. The new BAM front-end is located close after the last dipole of the SITF bunch compressor. Among the improvements aiming to increase the resolution is the use of higher bandwidth components. The EOMs are 40 GB/s (33 GHz), PowerBit SD40 (Oclaro) and MXAN-LN40 (Photline) installed in the first and the second BAM channels. All the RF cables are PhaseMaster160 from Teledyne with 40 GHz band width, low-drift at 24°C and with low sensitivity to radiation [5]. The pick-up Type KX00-0258 with cone-shaped buttons and 40 GHz bandwidth was developed by DESY and TU-Darmstadt for the European XFEL and produced by Orient Microwave [6]. The design is for the European XFEL beam pipe diameter of 40.5 mm. The vacuum chamber is adapted on both sides to the 38 mm beam pipe of the SITF with 20 cm long tapers. For SwissFEL the same cone-shaped button pick-up feedthroughs were adapted for 16 mm beam pipe diameter. A prototype KX00-0293 has been ordered at Orient Microwave and is expected to arrive for test at PSI at the beginning of September. It is expected that the smaller beam pipe diameter of SwissFEL will provide for stronger RF signals, thus improving the resolution at low charge.

The only low bandwidth components inherited from the first BAM are the limiters N9356C (25dBm threshold, 26.6 GHz bandwidth, Agilent), which allow higher voltages and full utilization of the EOM half-wave voltage range. A higher bandwidth limiter Type N9355F (50 GHz, 10 dBm) was also tested, but for higher input voltages than the nominal 10 dBm it starts to distort the signal, thus spoiling the resolution.

The next modification aiming the achievement of higher resolution at low charge is the combination of a photoreceiver and an offset-DAC. The photoreceiver accepts higher input optical powers (~2mW) and has 3V pk-pk output at 0.5mW optical input. The amplification stage is externally accessible, allowing optimal adjustment of the RF signal thresholds, thus preventing saturation. The offset-DAC shifts the RF signal by a DC voltage to optimally match it to the acquisition ADC input thus utilize the full resolution (presently 12 bit). The use of this combination showed considerable improvement in the BAM resolution, which otherwise was unsatisfactory despite the high bandwidth components [7]. A 16 bit ADC which is expected to further improve the resolution was recently installed and beam tests are pending.

[#]vladimir.arsov@psi.ch

Another improvement for BAM is the implementation of continuous bunch synchronous acquisition. The concept is described in [8], therefore it will only be summarized shortly here. The raw BAM traces from the two BAM channels are stamped with the bunch ID within the 10 Hz cycle and passed to the server as a single EPICS structured record. On the server side there are two buffers, which continuously exchange – while the first one is filled with data, the second one is slowly read at about 1 Hz with a high level application, e.g. Matlab. There the traces are split back and converted to bunch stamped arrival-time and instantaneous BAM resolution values. The continuous stamping has 100% reliability (no invalid events) with occasional slippage, i.e. omission of a following event (<0.1 % occurrence).

BAM MEASUREMENTS

BAM Charge Sensitivity

Figure 1 shows the pick-up charge response of the first BAM channel when the reference laser pulse is swept across the RF transient with a vector modulator.

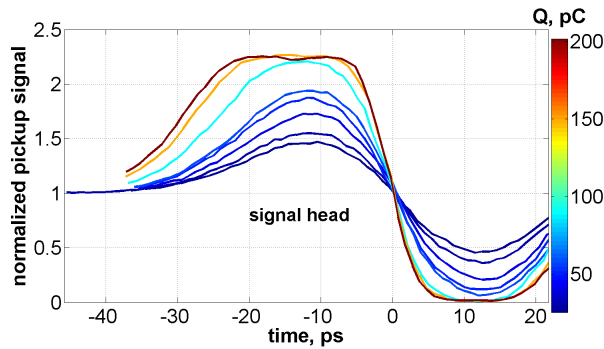


Figure 1: BAM pick-up signal sensitivity on the charge for the EOM1: PowerBit SD40 (Oclaro).

In the range 90 pC – 200 pC the pick-up response was strong enough to engage the limiter and to completely utilize the EOM half-wave voltage range ($V\pi = 4.6$ V). In this charge range the measured BAM resolution was 10 fs – 13 fs (Figure 2, red circles), which at these conditions is solely limited by the 12 bit ADC. For lower charges the pick-up response was weaker and 100% modulation could not be achieved. The resolution was correspondingly lower, reaching 40 fs at 25 pC (Figure 2, red circles).

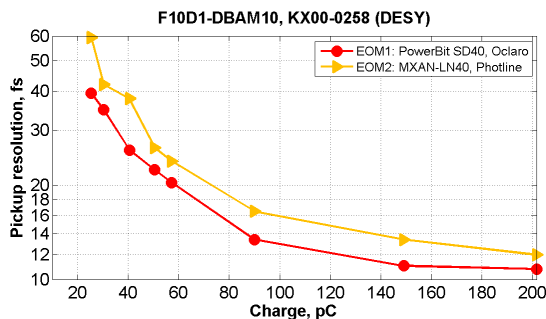


Figure 2: BAM resolution for the two EOM channels as a function of the bunch charge.

The EOM of the second BAM channel (MXAN-LN40, Photline) has a half-wave voltage in the order of 9 V. The pick-up response was similar to the one of Figure 1 (same type of pick-up), but due to the larger $V\pi$ the slope steepness is smaller and so is the measured resolution (Figure 2, yellow triangle). For EOM2 the resolution in the range 90 pC – 200 pC varied between 12 fs – 16 fs and for 25 pC was reduced to 60 fs.

Measurement of the Bunch Compressor Dispersion Parameter R_{56} with BAM

The bunch compressor (BC) dispersion parameter R_{56} was measured in two ways. An established method is to use a transverse deflecting structure (TDS) and measure the position offset on a BPM when the energy is varied in a small range ΔE . This method is destructive for the beam. The alternative non-destructive method is to measure the arrival time offset δt with BAM for the same small energy change. All cavities were operated on-crest (no compression), including the one used normally to produce an energy chirp on the beam for compression. This cavity will be called FINSB03 further in the text.

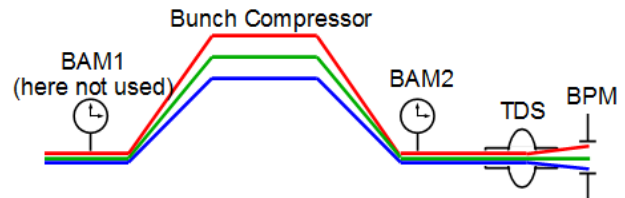


Figure 3: Scheme of the R_{56} measurement with the TDS and BAM. Beam energy E_1 (red) < E_2 (green) < E_3 (blue).

The measurement is schematically shown on Figure 3. The higher energy beams (blue) take the shorter path in the bunch compressor and arrive earlier at the detector (BAM2). On contrary, the lower energy beams (red) take the longer path in the bunch compressor and arrive later at BAM2. Similarly, the time-dependent transverse deflection from the TDS results in different beam positions on the BPM, which are proportional to the small relative energy variation. A measure for the strength of the effect is the BC dispersion parameter R_{56} . Equation (1) shows the dependence between the arrival time change and the energy change:

$$\delta t = \frac{R_{56}}{c_0} \cdot \frac{\Delta E}{E} \quad (1)$$

Prior to the R_{56} measurement, the beam energy was precisely measured as a function of the low-level RF input to FINSB03 with a dipole spectrometer situated at the end of the machine. A set value variation between 0.2584 and 0.2784 (a.u.) corresponded to bunch energy variation of (200.70 ± 2.95) MeV.

R_{56} was calculated from equation 1, where the arrival time was measured with BAM. For this particular measurement the charge was 45 pC for which the BAM resolution was 24 fs. An example for one such measurement is shown on Figure 4, where the arrival time

is plotted as a function of the above mentioned FINSB03 set energy variation. R_{56} is determined from the slope of the linear fit by accounting of all calibration constants.

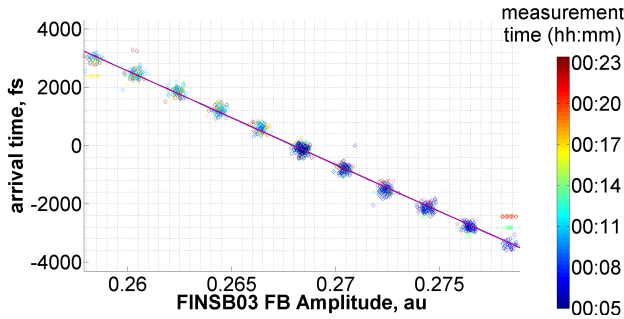


Figure 4: Example of the BAM sensitivity on FINSB03 amplitude change at on-crest operation corresponding to energy variation of (200.70 ± 2.95) MeV.

Several sets of such measurements were made for a fixed BC angle to evaluate the statistical errors. The BC angle was varied between 1° and 5° . The results are shown on Figure 5 for the TDS and BAM. The error bars are the rms values from the multiple measurements at a fixed angle. Both methods show good agreement with the theoretical curve (solid line).

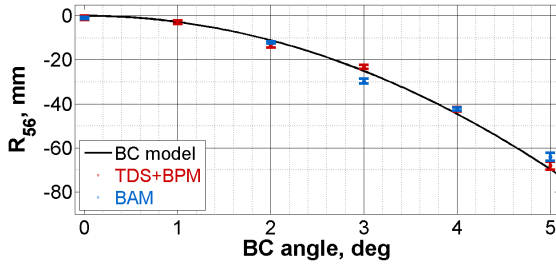


Figure 5: Measurement of the R_{56} for different BC angles with TDS and BAM.

Measurement of the Energy Jitter with BAM

For this measurement, the FINSB03 cavity, normally used to produce an energy chirp on the beam for compression, is operated at the negative zero-crossing, thus decompressing the beam. The principle is shown on Figure 6 schematically.

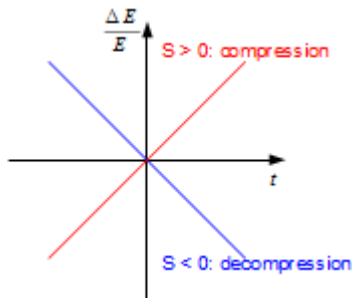


Figure 6: Arrival time dependence on the energy change $\Delta E/E$ caused by the RF field $U = \pm U_0 \sin(2\pi ft)$ at zero-crossing with a gradient slope

$$S = \frac{\Delta E}{E} \frac{1}{t} = \frac{1}{E} \frac{dU(t)}{dt} \Big|_{t=0}$$

Usually for bunch compression, FINSB03 is set off-crest on the positive slope S to create an energy chirp, such that the beam head gains less energy than the beam tail, leading to compression in the magnetic chicane.

In the proposed measurement, FINSB03 was operated at zero-crossing at the negative slope, thus decompressing the beam. At these conditions, the initial arrival time jitter is enhanced. To quantify the effect, the reciprocal compression factor F_C is introduced:

$$F_C = \frac{t + \delta t}{t} = 1 + \frac{\delta t}{t} \quad (2)$$

The compression factor is the ratio between the rms bunch lengths before and after the bunch compressor, with a larger compression factor meaning shorter bunch. In equation (2) the reciprocal compression factor F_C is expressed in terms of arrival time t and arrival time offset δt behind the bunch compressor and measured with respect to the bunch centre. $F_C > 1$ means bunch arrival-time delay and timing jitter increase (decompression), whereas $F_C < 1$ means earlier bunch arrival-time and timing jitter decrease (compression).

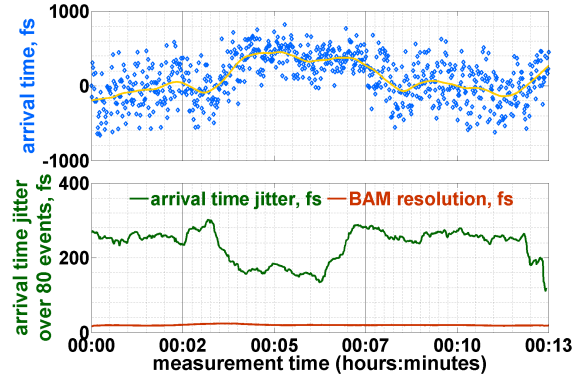


Figure 7: Arrival-Time jitter change when the FINSB03 cavity is cycled between on-off-on state. A clear decrease of the arrival time jitter (lower plot, green trace) to roughly 150 fs in the off-state is visible. The red curve on the lower plot is the instantaneous BAM resolution.

The effect of the timing jitter increase is illustrated in Figure 7, showing the arrival time (upper plot) and the arrival time jitter (lower plot). The lower plot shows also the instantaneous BAM resolution, measured online and simultaneously with the arrival time traces. The average BAM resolution was 20 fs at 50 pC.

Initially FINSB03 was turned on and set at the negative zero-crossing slope, leading to a large arrival time jitter band in the order of 250 fs (rms). When FINSB03 was switched off, no additional energy chirp was induced to the beam and the jitter band shrunk to roughly 150 fs (rms). Eventually FINSB03 was turned on again, recovering the large jitter band.

F_C can be directly measured with BAM as a jitter enhancement at given RF settings compared to the jitter without compression. F_C can be also calculated from equations (1) and (2) with $R_{56} = -46.9$ mm.rad² (nominal

BC angle 4.1°) and $E = 130$ MeV. The slope S of the field gradient (Figure 6) is calculated from the FINSB03 forward power P by using the calibration for the field amplitude U_0 from [9]:

$$U_0 [\text{MeV}] = 12.6 \cdot \sqrt{P [\text{MW}]} \quad (3)$$

The measurements were made at three FINSB03 settings: 0 MW (FINSB03 was off), 4.5 MW and 9.4 MW. The timing jitter values were normalized to the one corresponding to FINSB03 switched off, at which the slope S was constant and the reciprocal compression factor F_C equals one. The results are shown on Figure 8.

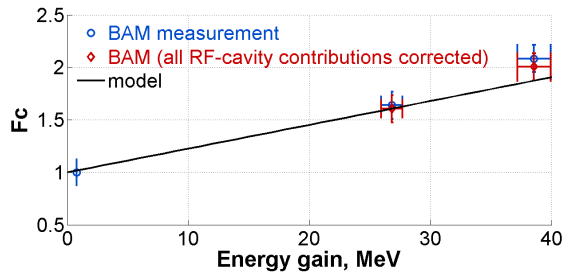


Figure 8: Beam decompression measured with BAM as rms arrival time jitter increase when the FINSB03 cavity is on (cavity powers 4.5 MW and 9.4 MW) at negative zero-crossing of the RF compared to the uncompressed state (FINSB03 RF-off).

The blue markers are the BAM measurements. The red markers are the arrival-time measurements corrected with the energy jitter contribution of all RF-cavities to the arrival-time. The error bars are calculated from the rms RF-cavity power change and the arrival-time resolution. The solid line is the model dependence. There is a good agreement between the measurement and the theoretical value. This measurement was dominated by the timing jitter upstream the bunch compressor, which was properly measured with BAM by accounting the influence of the RF-cavity phases and amplitudes.

Diagnostics Response Measurement

The diagnostics response measurements are thoroughly described in [10]. The BAM downstream the BC was among the used longitudinal diagnostics components. During runtime BAM was acquiring bunch ID stamped traces at 10 Hz simultaneously with the actuators used in the diagnostic response – bunch charge, cavity phases and amplitudes. After splitting and conversion into bunch-stamped arrival time the data were available for

correlation with the other parameters. The measurements were made at 20 pC for which the BAM resolution was 50 fs, presently still limited by the ADC resolution and the insertion loss of the offset-DAC. With the new triple photoreceiver having more amplification and less saturation at high optical powers, a resolution of 40 fs was achieved at this charge (Figure 2).

CONCLUSION

10fs BAM resolution was demonstrated for 200 pC, thus meeting the specifications for the initial phase of SwissFEL at high charge. With the use of a 16 bit ADC card and a pick-up with 16 mm beam pipe diameter, it is expected to achieve an even better resolution. The measurements are pending before the decommissioning of SITF. The BAM downstream the bunch compressor was successfully used to measure SITF machine parameters. Presently the BAM server runs with Matlab, with the possibility to export the bunch stamped events in structured EPICS records. The goal is eventually the whole data processing to be done on the FPGA.

REFERENCES

- [1] R. Ganter (ed.) “SwissFEL conceptual design report”, PSI V20 (2012)
- [2] F. Loehl, “Optical synchronization of a free-electron laser with fs precision”, DESY-THESIS-2009-031, (2009)
- [3] J. Kim et al., Nature Photonics **2**, pp. 733-736 (2008)
- [4] V. Arsov et al. “First results from BAM at the SwissFEL test injector”, MOAL4, Proc. IBIC'13, Oxford UK, pp. 8-11, (2013)
- [5] V. Arsov, unpublished, “Radiation tests of the PhaseMaster160 RF-cables in the PSI Ring Cyclotron (HIPA)”, PSI internal report 2013.
- [6] A. Angelovski, et al. Phys. Rev. ST. Accel. Beams **15**, 112803 (2012)
- [7] V. Arsov, “The SwissFEL BAM”, 3rd Mini-Workshop on Longitudinal Diagnostics, KIT, Karlsruhe, 03-04.07.2014
- [8] M. Dach et al. “Continuous data acquisition at runtime”, Internal Report on Bunch ID stamping for BAM, PSI, 2014.9
- [9] P. Craievich, unpublished, “Energy gains in SITF”, SwissFEL RF Meeting, 17.10.2013.
- [10] F. Frei et al. “Experimental results of diagnostics response for longitudinal phase space”, These Proceedings: FEL2014, Basel, Switzerland, THB02.

ELECTRON BEAM DIAGNOSTICS FOR COXINEL

M. Labat, N. Hubert, M. El Ajjouri, L. Cassinari,
C. Bourrassin-Bouchet, A. Loulergue, M.E. Couprie,
Synchrotron SOLEIL, France

Abstract

On the path towards more compact free electron lasers (FELs), the project COXINEL was recently funded: a transfer line will be installed to adapt a plasma accelerated beam (from LOA) into an in-vacuum undulator built by SOLEIL. This experiment should enable to demonstrate the first FEL based on a plasma accelerator. Because plasma beams are intrinsically very different from RF accelerator beams (much shorter, divergent and smaller with a higher energy spread and energy jitter), their transport and matching in the undulator is critical if willing to obtain a significant amplification. This is why special care has to be taken in the design of the beam diagnostics to be able to measure the transverse beam sizes, energy spread and jitter, emittance and bunch length. For these purposes, several diagnostics will be implemented from the plasma accelerator exit down to the undulator exit. In each station, several screen types will be available and associated to high resolution imaging screens. In this paper, we present the experimental layout and associated simulation of the diagnostics performances.

COXINEL LAYOUT

COXINEL project [1] was recently funded by the European Research Council. This project aims at demonstrating the operation of a plasma accelerator based Free Electron Laser. The key concept relies on an innovative electron beam longitudinal and transverse manipulation in between the plasma accelerator and the undulator. Indeed, typical plasma accelerator beams exhibit percent level energy spread which intrinsically disables any FEL amplification. The very small transverse dimensions and very large divergence of those beams also tend to dramatically spoil the initial emittance along the transport to the undulator. We proposed to use a "demixing" chicane to sort the electrons in energy and reduce the slice energy spread from 1 % to 0.1 %. Following the chicane, a set of quadrupoles is used to maintain the transverse density seen by the FEL radiation constant all along the undulator.

The COXINEL layout is illustrated in Figure 1. COXINEL will use the plasma accelerator of the Laboratoire d'Optique Appliquée (Palaiseau, France). The downstream equipments are under preparation at Synchrotron SOLEIL. They consist, following the electron beam path, in a triplet of quadrupoles, a demixing four dipoles chicane, a second set of quadrupoles, an undulator and a final beam dump. The expected electron beam and FEL parameters are summarized in Table 1. The targetted wavelength is 200 nm in first phase and 40 nm in second phase. The FEL will be operated in seeded mode.

Table 1: COXINEL Expected Parameters. (*) At the plasma accelerator exit.

Parameter	Value
Electron beam	
Energy	400 MeV
Energy spread (*)	1 %
Charge	10 pC
Peak current (*)	500 A
Electron beam duration in ID	15 fs-FWHM
Undulator	
Period	20 mm
Length	2 m
Peak magnetic field	0.9 T

Since the experiment relies on a refine manipulation of the electron beam phase space, beam diagnostics are vital on this project. Their location is indicated in Figure 1.

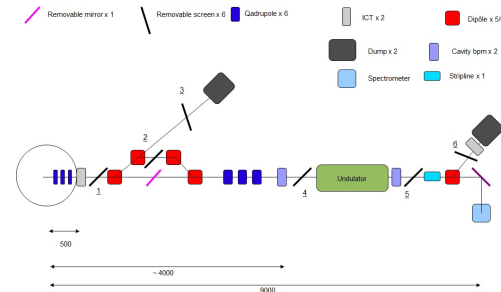


Figure 1: COXINEL layout.

DIAGNOSTICS STATIONS

Six diagnostics stations (DS) will be implemented on COXINEL. They are all designed on the same principle to ease their operation and reduce their cost. The first one will be installed just after the first triplet, the second one in the demixing chicane, the third one on the first beam dump, the fourth and fifth at entrance and exit of the undulator and the last one will be on the final beam dump. They consist in:

- a motorized tree than can position on the beam axis three different targets at 45° (see Figure 2),
- three targets: OTR screen, YAG:Ce or LYSO:Ce screen and calibration grid,
- an extraction viewport,
- an optical system to image the targets' surface,

- a ccd camera for image acquisition.

Those stations enable position, transverse dimensions, energy, energy spread and emittance measurements.

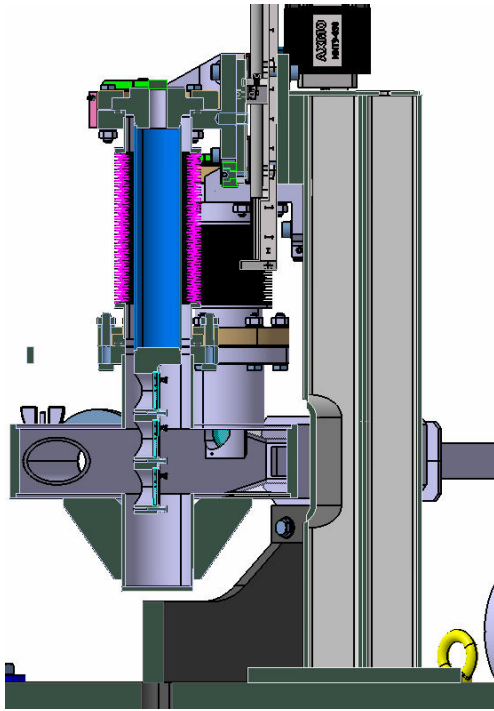


Figure 2: Motorized tree for the insertion of the diagnostics station screens.

Position and Transverse Size Measurement

To measure the electron beam position and transverse dimensions, a screen is inserted on the electron beam path at 45° incidence. OTR, YAG:Ce or LYSO:Ce screens can be used. The screen surface is then imaged thanks to an optical system on to a CCD camera. All diagnostics stations are identical and all mounted screens are 1" diameter. The imagers specifications are summarized in Table 2.

To be imaged on a 4 mm large CCD, a field of 20 mm has to be reduced by a factor 5. Assuming standard pixel size of $7 \mu\text{m}$, this would give a resolution of $35 \mu\text{m}$ in the image plane. To satisfy the requirements both in terms of field and resolution, we decided to equip the optical system with two possible magnifications, swapping one to the other using a translation stage. In each case, the system consists of a set of four focussing lenses of fixed focal length. The distance between the second and the third lens is simply changed to adapt the magnification. The final performances of the systems are summarized in Table 3.

But the imaging of electron beams using OTR or scintillator screens can be compromised when the electron beam (or some internal structures) becomes typically as long as optical wavelengths. In such cases, coherent OTR (COTR) is emitted with an intensity far above the incoherent OTR or the fluorescence in the case of the scintillator screens, and with a transverse distribution which no longer corresponds

to the initial electron beam one. Such effects have been extensively observed on several machines [2, 3].

On COXINEL, the electron beam duration will vary from a few fs at the source up to ≈ 20 fs inside the undulator, corresponding to a spectral range of 300 nm up to $10 \mu\text{m}$, allowing strong coherence effects in the visible range. First simulations of the COTR electric field distribution imaged on the CCD are presented in Figure 3, revealing the presence of a ring.

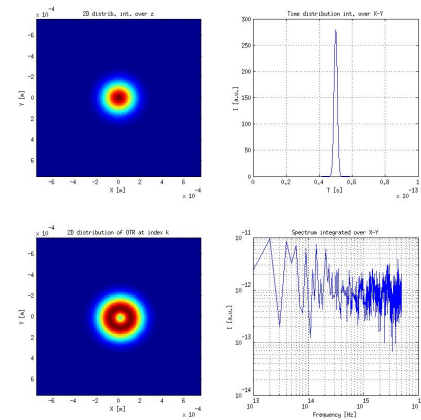


Figure 3: Calculation of the 3D OTR electric field in the image plane using [3]. Electron beam parameters are those of Table 1. Beam duration: 1 fs-rms.

For accurate transverse size measurements, COTR has to be mitigated. Several methods have been proposed, relying on spectral, temporal or spatial separation. We will test spectral and spatial selection and compare their efficiency.

But we will also use the COTR emitted for other electron beam diagnostic. Measuring the COTR spectrum or performing autocorrelation will provide some information on the electron bunch length. COTR measurement in the far field could also be an other way to measure the electron beam energy.

Energy Measurement

The electron beam energy and energy spread will be measured at DS2, DS3 and DS6. Indeed, those three DS are located in a dispersive section of the transport beam line. In all DSs, the electron beam deviation is ensured by the same type of dipole magnets. The maximum available field is 1 T while the nominal field is 0.53 T in the demixing chicane i.e. before DS2 and DS3 and XX T before DS6. Basic equations of electron beam deviation in a magnetic field enable to simulate the electron beam distribution expected at DS2, DS3 and DS6 and therefore to predict the measurable energy range as illustrated in Figure 4.

With the nominal field in DS2, the measurable energy range is 330 - 520 MeV with a resolution of 0.32 MeV to 0.1 MeV depending on the zoom which is used.

Table 2: COXINEL Imagers Specifications. *: horizontal x vertical plane. ?: last imagers specifications are not defined yet.

Imager	1	2	3	4/5	6
σ_x [mm - rms]	0.4	0.35	0-20	0.15	?
σ_z [mm - rms]	0.2	0.2	0.2	0.15	?
Field [mm]*	15x15	20x20	20x20	20x20	20x20
Res. [μ m - rms]	40	5	5	10	10
f_{acq} [Hz]	10	10	10	10	10
Charge min [pC]	10	10	10	10	10
Charge max [pC]	100	100	100	100	100

Table 3: COXINEL Imagers Expected Performances. Res. is the resolution in μ m.

Imager	1	2	3	4/5	6
Zoom 1					
M	0.18	0.18	0.18	0.18	0.18
Field [mm]	20	20	20	20	20
Res. [μ m]	41	41	41	41	41
Zoom 2					
M	-	1.5	1.5	0.74	0.74
Field [mm]	-	2.4	2.4	4.9	4.9
Res. [μ m]	-	5	5	10	10

Beam Position Measurement

The beam position can be measured on the diagnostics stations but not on-line. This is why other diagnostics are used for this purpose: cavity Beam Position Monitors (cBPM) and a stripline.

Two cBPM will be installed at the entrance and exit of the undulator, to ensure accurate orbit measurement and control where the amplification will occur. Both are systems provided by the Paul Scherrer Institute [4] which will be first tested on the SOLEIL's linac. The expected resolution is below 1 μ m even at low charge.

The stripline is designed at SOLEIL as illustrated in Figure 5. The expected resolution is higher, 30 μ m at 1 pC but more simple of operation. It will be installed at the exit of the undulator.

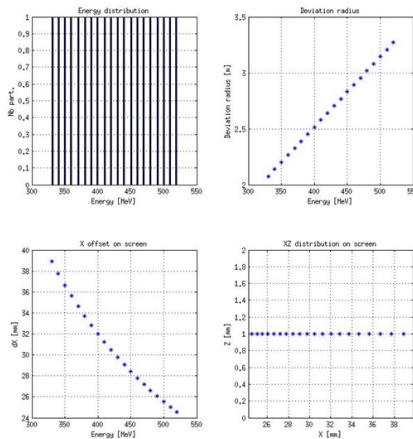


Figure 4: Calculation of the electron beam distribution on the target plane at DS2, DS3 and DS6 as a function of energy.

OTHER ELECTRON BEAM DIAGNOSTICS

Charge Measurement

The electron beam charge will be measured just after the first triplet, i.e. close to the plasma source, and at the undulator exit. We will use commercial Integrated Current Transformer from Bergoz, which allow accurate measurement even at the low expected charge of 10 pC.

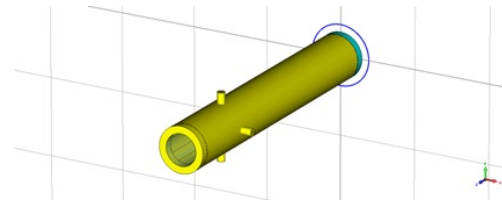


Figure 5: 3D modeling of the COXINEL stripline. Courtesy M. El Ajjouri.

DIAGNOSTICS FOR SEEDING

Because of space constraints, one single undulator will be used for the experiment. So that to see some amplification, the FEL has to be operated in seeded configuration. The seed will be generated via Harmonic Generation in gas using a leak of the drive laser used for plasma acceleration. It will be injected via a viewport using a mirror located in the middle of the chicane (where the electron beam deviation is the largest: few 30 mm).

Seeding requires accurate alignment of the seed on the electron beam in the spatial, temporal and spectral domain.

Spatial Alignment

The seed will be aligned on the electron beam trajectory using DS4 and DS5. Indeed, the electron beam position can be recorded at these two locations and then used as reference to steer the seed. The screens reflectivity at the

seed wavelength (200 nm) has been measured and any type of screen could be used.

Temporal Alignment

Temporal alignment is a more serious issue. Both electron beam and seed will be ≈ 10 fs long, requiring a few fs temporal diagnostic. One way could be to make an auto-correlation between the two infra-red lasers generating the electron beam and the seed at the exit of DS4 or 5. In this case, an appropriate setup has to be implemented to allow propagation of the drive laser through out DS4. An other way could be to use a streak camera at DS4 or 5. The temporal resolution could be 300 fs-fwhm meaning that a final scanning will be required to find the synchronism condition.

Spectral Alignment

The spectral alignment will be done using a spectrometer located at the undulator exit. We plan to install a commercial system with a spectral range of 300 - 30 nm at least. The device will then enable to visualize both the seed and the synchrotron radiation spectra. Again, space constraints require the use of a short focal length spectrometer, but resolution below 0.1 % could still be reached.

CONCLUSION

The COXINEL project aims at demonstrating FEL amplification on a plasma accelerator, relying on a refine manipulation of the electron beam phase space. The experiment will take place at Laboratoire d'Optique Appliquée which provides the plasma source. SOLEIL is preparing the downstream equipments: essentially magnets, undulator and diagnostics. The electron beam will be characterized all along the FEL line in terms of charge, position, transverse dimensions, emittance, energy and energy spread. Installation and first experiments are scheduled in 2015.

REFERENCES

- [1] M.E. Couprie et al., "Progress of the LUNEX5 project", IPAC'2014, Dresde, Germany, May 2014, THPRO003(2014).
- [2] S. Matsubara et al., "Improvement of screen monitor with suppression of coherent-OTR effect for SACLA", IBIC'2012, Tsukuba, Japan, Septembre 2012, MOCC04 (2012).
- [3] H. Loos et al., "Observation of coherent optical transition radiation in the LCLS linac", FEL'08, Gyeongju, Korea, August 2008, THBAU01 (2008).
- [4] B. Keil et al., "Design of the Swiss FEL BPM system", IBIC'2013, Oxford, UK, Septembre 2013, TUPC25 (2013).

COMPARISON OF QUADRUPOLE SCAN AND MULTI-SCREEN METHOD FOR THE MEASUREMENT OF PROJECTED AND SLICE EMITTANCE AT THE SwissFEL INJECTOR TEST FACILITY

M. Yan*, Ch. Gerth, DESY, Hamburg, Germany
B. Beutner†, R. Ischebeck, E. Prat, PSI, Villigen, Switzerland

Abstract

High-brightness electron bunches with small transverse emittance are required to drive X-ray free-electron lasers (FELs). For the measurement of the transverse emittance, the quadrupole scan and multi-screen methods are the two most common procedures. By employing a transverse deflecting structure, the measurement of the slice emittance becomes feasible. The quadrupole scan is more flexible in freely choosing the data points during the scan, while the multi-screen method allows on-line emittance measurements utilising off-axis screens in combination with fast kicker magnets. The latter is especially the case for high-repetition multi-bunch FELs, such as the European X-ray Free-Electron Laser (XFEL), which offer the possibility of on-line diagnostics. In this paper, we present comparative measurements of projected and slice emittance applying these two methods at the SwissFEL Injector Test Facility and discuss the implementation of on-line diagnostics at the European XFEL.

INTRODUCTION

Control and optimization of the transverse emittance as well as the slice emittance of the driving electron bunch are crucial to the performance of X-ray free-electron lasers (FEL). The principle of emittance measurement is described, for instance, in detail in Ref. [1]. The emittance to be reconstructed at a reference point is based on the second-order beam moments with $\epsilon^2 = \langle x_0^2 \rangle \cdot \langle x_0'^2 \rangle - \langle x_0 x_0' \rangle^2$. Transportation of the beam moments to a downstream position using the transport matrix R yields the relation

$$\langle x^2 \rangle = R_{11}^2 \langle x_0^2 \rangle + 2R_{11}R_{12} \langle x_0 x_0' \rangle + R_{12}^2 \langle x_0'^2 \rangle. \quad (1)$$

The squared beam size $\langle x^2 \rangle$ can be accessed directly using observation screens. At least three measurements for three different transport matrices R are required to obtain the second-order beam moments at the reference point. Commonly, linear least squares method is employed for the fit to the equation system. The same procedure can be adapted for the y -plane.

Variation of the transport matrices can be achieved with the quadrupole scan or multi-screen method. In the quadrupole scan method, the measurement point is fixed and the strengths of the quadrupoles between the reconstruction and measurement point are changed. In the multi-screen

method, the measurement point is chosen at different downstream locations to provide various transport lattices.

The quadrupole scan is more flexible in arranging data points, but cannot be performed in parallel to the FEL operation. The multi-screen method requires more space and diagnostic stations, but provides the possibility of parasitic emittance measurements utilizing off-axis screens. Such online diagnostics are highly demanded at high repetition multi-bunch FEL, such as the European XFEL [2]. A comparison of different aspects of these two methods is studied in Ref. [3].

Combined use of a transverse deflecting structure (TDS) with these two methods allows for measurement of the slice emittance. The longitudinal coordinate of the bunch is translated by the TDS to one transverse direction. The emittance in the other transverse plane perpendicular to the streak direction can then be determined in a time-resolved domain. Careful consideration in the accelerator optics has to be taken into account for the time resolution, which is correlated inversely to the TDS streak parameter [4]

$$S \sim \frac{eV_0 k}{pc} \sqrt{\beta_{y,TDS}} \cdot \sin(\Delta\mu_y). \quad (2)$$

Comparative measurements of projected and slice emittance using these two methods have been conducted at the SwissFEL Injector Test Facility (SITF) at PSI in Switzerland. In this paper, the experimental setup is described and the results are discussed.

DIAGNOSTIC SECTION

One main purpose of the SITF [5] is to demonstrate the feasibility of the SwissFEL. A schematic layout of the SITF is shown in Fig. 1. The nominal beam energy is 250 MeV and the charge can be varied from 10 pC to 200 pC.

The diagnostic section for the comparative emittance measurement is located downstream of the bunch compressor at a nominal energy of 250 MeV. An S-band TDS streaks the bunch in the vertical direction and enables slice emittance measurement in the horizontal plane. The TDS is followed by several matching quadrupoles, a 3.5-cell FODO section with multiple standard screen stations and a high-resolution transverse profile monitor [6]. The screen stations inside the FODO section are equipped with optical transition radiation (OTR) screens. The high-resolution profile monitor, which employs a scintillator screen, is designed in a special configuration to achieve resolution much smaller than the thickness of the scintillator and more robust than the OTR screen for operation with low charge bunches due to its higher light

* minjie.yan@desy.de

† Now at Deutsches-Elektronen Synchrotron DESY

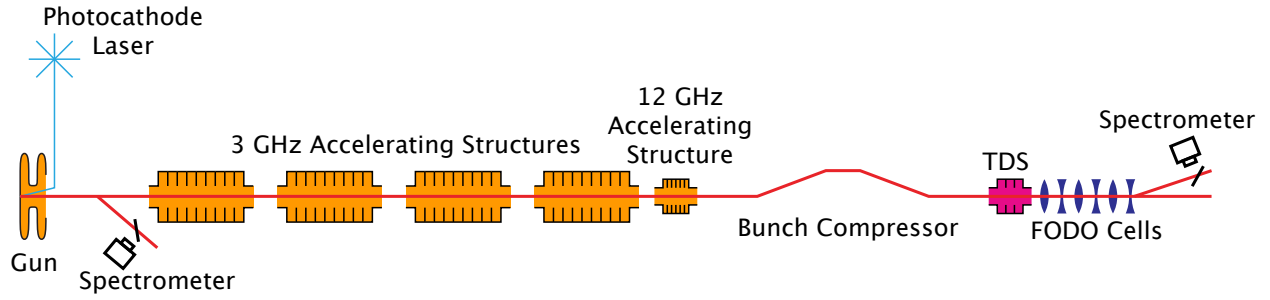


Figure 1: Schematic layout of the SwissFEL Injector Test Facility. The diagnostic section for emittance measurement, comprising S-band TDS, matching quadrupoles and FODO section, is located downstream of the bunch compressor.

yield. Hence, the high-resolution profile monitor was chosen for the quadrupole scan method, which has flexibility in selecting the measurement screens.

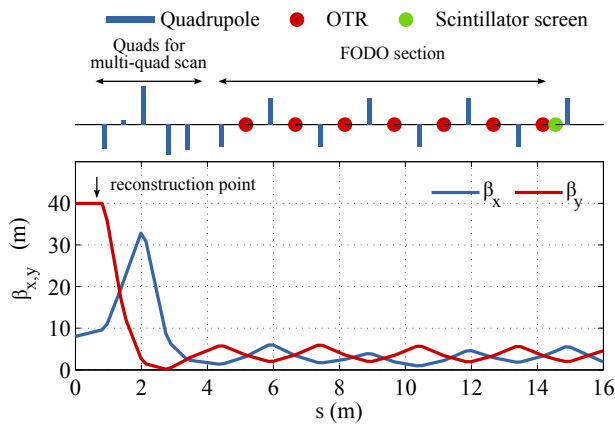


Figure 2: Accelerator optics (starting from the TDS) used for the multi-screen method. The same optics is used for both projected and slice emittance measurement.

Figure 2 shows the beamline layout of the diagnostic section starting from the TDS (top) and the design optics for the multi-screen method (bottom). The same optics is used for both projected and slice emittance measurement. From the TDS, where a large β_y in the streaking direction is essential to a good time resolution (see Eq. 2), the beam is matched with help of five quadrupoles into the 3.5-cell quasi-symmetric FODO section with phase advances of 72° and 52° in each cell in x and y plane, respectively. The reconstruction point is marked in the figure, and seven OTR screens (i.e. seven data points) are available for each measurement. The phase advances in x and y from the TDS to the individual OTR screens are shown in Fig. 3 (left). For the measurement of projected emittance, a total of 206° and 153° are covered in the x and y plane, respectively. Only five OTR screens are utilized for the measurement of slice emittance as bunches imaged at the first and last OTR screen in the FODO cell with phase advances of $\Delta\mu_y = 189^\circ$ and $\Delta\mu_y = 342^\circ$, respectively, lack sufficient streaking from the TDS due to the $\sin(\Delta\mu_y)$ term in Eq. 2.

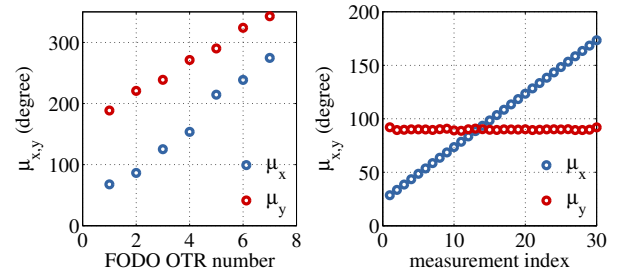


Figure 3: Phase advances from TDS to the individual measurement point for (left) projected and slice emittance measurement using multi-screen method, and (right) slice emittance measurement using quadrupole scan method.

The high-resolution profile monitor used for the quadrupole scan method is installed at the end of the FODO section and denoted with a green dot in Fig. 2. One single quadrupole (the fifth quadrupole in Fig. 2) is scanned for the measurement of projected emittance, covering phase advances in total of about 180° in both x and y planes [7]. Five quadrupoles (the first five quadrupoles in Fig. 2) are employed together for the measurement of slice emittance. The reconstruction point for the slice emittance and its value of twiss parameters are the same as those in the multi-screen method, which makes additionally a comparison of the reconstructed optics using these two methods possible. The phase advances for the measurement of slice emittance are illustrated in Fig. 3 (right). With the combined use of the five quadrupoles, the horizontal phase advance $\Delta\mu_x$ covers from 30° to 180° with equal steps and a constant $\Delta\mu_y = 90^\circ$ for the maximum streaking effect of TDS can be achieved. The multi-quadrupole scan has been used routinely for optimizing the slice emittance at the SITF [8].

EXPERIMENTAL RESULTS

The comparative measurements were performed using electron bunches with an energy of 200 MeV. All accelerating modules were operated on-crest. A bunch charge of 200 pC was chosen in order to get enough light emission from the streaked bunch using OTR screens. The beam sizes are defined using Gaussian fit to the transverse profiles. The

errors given in this paper include only statistical errors and are determined according to error propagation.

Projected Emittance

During the measurement using multi-screen method, the images taken with the fourth OTR screen display clear features affected by the OTR point spread function and therefore are omitted for the reconstruction of emittance.

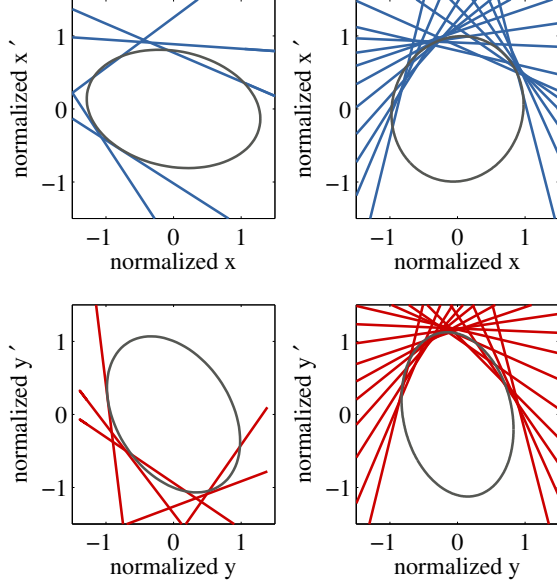


Figure 4: Fits of the beam ellipses using multi-screen method (left) and single quadrupole scan (right) for the measurement of projected emittance. The lines represent each measured beam size.

The results of the projected emittance measurements are shown in Fig. 4, and the reconstructed normalized projected emittances ϵ_N together with the mismatch parameters B_{mag} [1] are summarized in Table 1. The results obtained with these two methods are comparable, but the normalized emittances derived using the multi-screen method are slightly larger than that using single quadrupole scan in both planes. Errors from optics mismatch are minimized in the single quadrupole scan method, while the mismatch parameters of 1.12 and 1.07 in the multi-screen method indicate that there's still some errors coming from the optics mismatch.

Table 1: Summary of Projected Emittance Measurements

	Multi-screen method	Single quad-scan
$\epsilon_{N,x}$	513 ± 8 nm	486 ± 2 nm
$\epsilon_{N,y}$	495 ± 6 nm	458 ± 3 nm
$B_{\text{mag},x}$	1.12	1.00
$B_{\text{mag},y}$	1.07	1.06

Slice Emittance

The machine was operated with the same settings as for the projected emittance measurement. Several matching

iterations were performed to match the core slice to the design optics. The rms bunch length was determined to be approximately 3 ps. Each slice has a width of one fifth of the bunch length. The core slice is defined as the one at the longitudinal mean position of the bunch.

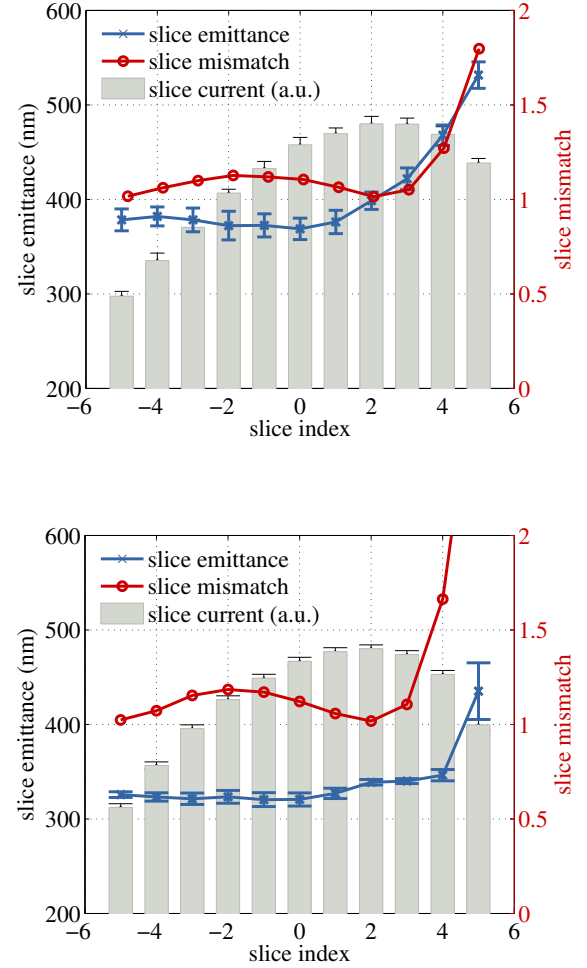


Figure 5: Normalized horizontal slice emittance and slice mismatch parameter obtained with (top) multi-screen method and (bottom) quadrupole scan method. The grey bars with errorbars represent the current in each slice.

Figure 5 shows the normalized horizontal slice emittance and slice mismatch parameter obtained with (top) multi-screen method and (bottom) quadrupole scan method with the TDS operated around the RF zero-crossing. The grey bars with errorbars represent the current in each slice. The reconstructed slice emittance from these two methods shows the same tendency in the slices, with relative constant emittance in the slices with negative indices and increasing emittance values towards the positive indices. The slice mismatch parameters from these two methods show the same feature as well. The slice emittances from the multi-screen method are in general larger than that from the quadrupole scan method, which has been observed in the projected emittance measurement as well.

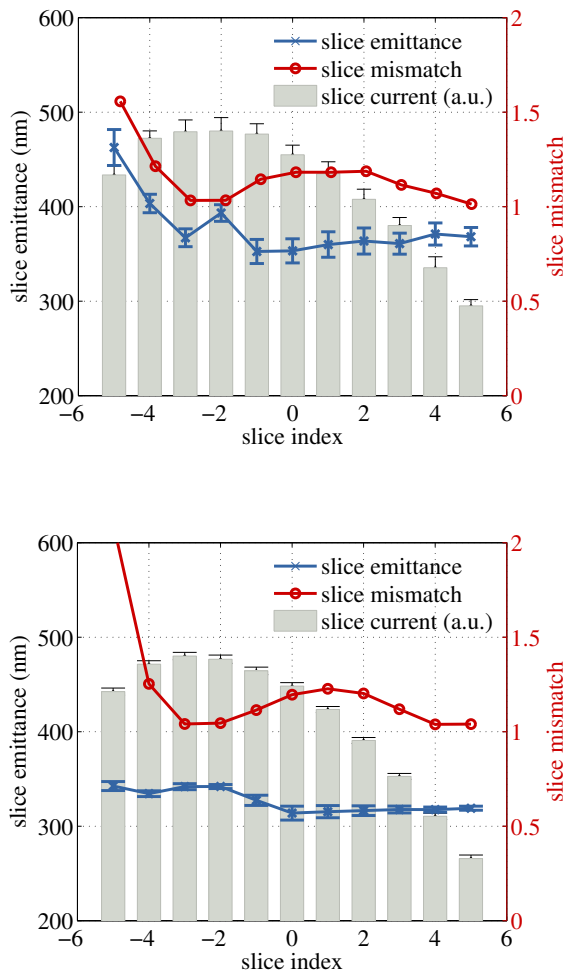


Figure 6: Normalized horizontal slice emittance and slice mismatch parameter obtained with (top) multi-screen method and (bottom) quadrupole scan method with the TDS operated around the other RF zero-crossing, i.e. with 180° phase shift compared to Fig. 5. The grey bars with errorbars represent the current in each slice.

In order to examine the influence of the TDS streak and the initial bunch correlation in (y', z) on the reconstructed longitudinal distribution, we repeated the slice emittance measurement at the other TDS RF zero-crossing (see Fig. 6), i.e. with 180° phase shift compared to Fig. 5. The consistency of the reconstructed slice emittance and slice mismatch parameter derived at these two TDS RF zero-crossings is a good confirmation of our measurements and excludes the influence of an initial bunch correlation. The feature of measuring larger slice emittance from the multi-screen method than the quadrupole scan method is still observed.

Since the design twiss parameters at the reconstruction point are the same in these measurements, they can be compared as well. Table 2 summarizes the reconstructed parameters of the core slice using these two methods. Though the slice emittance measured with the multi-screen method is

larger than that with quadrupole scan, there is a good agreement between the twiss parameters, which may indicate a possible calibration error of the OTR screens. Another possible explanation for this discrepancy is the worse emittance resolution of the multi-screen method due to the smaller β -function at the OTR screens in the FODO cell.

Table 2: Summary of Core Slice Emittance

TDS phase	1st.	2nd.
Multi-screen method		
$\epsilon_{N,x}$ (nm)	369 ± 11	353 ± 13
β_x (m)	6.58 ± 0.32	6.23 ± 0.31
α_x	-0.95 ± 0.05	-1.03 ± 0.04
$B_{\text{mag},x}$	1.10	1.18
Quadrupole scan method		
$\epsilon_{N,x}$ (nm)	321 ± 7	314 ± 7
β_x (m)	6.19 ± 0.21	5.73 ± 0.18
α_x	-0.86 ± 0.02	-0.90 ± 0.02
$B_{\text{mag},x}$	1.12	1.19
$\beta_{\text{Design},x}$ (m)	9.43	
$\alpha_{\text{Design},x}$	-1.02	

CONCLUSION

We have compared the projected and slice emittance using the multi-screen and quadrupole scan method at the SITF. The results are comparable and verified further by measurements at both TDS RF zero-crossings. The fact that the multi-screen method obtains generally slightly larger emittance might result from a calibration error of the OTR screens or a worse emittance resolution due to smaller β -function in the FODO cell.

REFERENCES

- [1] M. Minty and F. Zimmermann, *Measurements and Control of Charged Particle Beams*, Springer, Berlin, Heidelberg, New York (2003).
- [2] J. Wychowaniak et al., “Design of TDS-based Multi-Screen Electron Beam Diagnostics for the European XFEL”, THP075, *These Proceedings, FEL'14*, Basel, Switzerland (2014).
- [3] E. Prat and M. Aiba, *Phys. Rev. ST Accel. Beams* 17, 052801 (2014).
- [4] M. Roehrs, PhD thesis.
- [5] M. Pedrozzi et al., “250 MeV Injector Conceptual Design Report”, PSI Report No. 10-05 (2010).
- [6] R. Ischebeck and V. Thominet, “Transverse Profile Imager for Ionizing Radiation”, European Patent Application, EP2700979A1 (2014).
- [7] E. Prat, *Nucl. Instrum. Meth. A* 743, p103 (2014).
- [8] E. Prat et al., “Slice Emittance Optimization at the Swiss-FEL Injector Test Facility”, FEL'13, New York, August 2013, TUOCNO06, p. 200, <http://www.JACoW.org>

FEMTOSECOND TIMING DISTRIBUTION FOR THE EUROPEAN XFEL

C. Sydlo*, F. Zummack, M. K. Czwalinna, M. Felber, T. Lamb,
S. Schulz, Ch. Gerth, H. Schlarb, DESY, Hamburg, Germany
S. Jablonski, Warsaw University of Technology, Warsaw, Poland

Abstract

Accurate timing synchronization on the femtosecond time-scale is an essential installation for time-resolved experiments at free-electron lasers (FELs) such as FLASH and the upcoming European XFEL. To date the required precision levels can only be achieved by a laser-based synchronization system. Such a system has been successfully deployed at FLASH and is based on the distribution of femtosecond laser pulses over actively stabilized optical fibers. Albeit its maturity and proven performance this system had to undergo a major redesign for the upcoming European XFEL due to the enlarged number of stabilized optical fibers and an increase by a factor of up to 10 in length. The experience and knowledge gathered from the operation of the optical synchronization system at FLASH has led to an elaborate and modular precision instrument which can stabilize polarization maintaining fibers for highest accuracy as well as economic single mode fibers for shorter lengths. This paper reports on the laser-based synchronization system focusing on the active fiber stabilization units for the European XFEL, discusses the most recent performance results, which already meet the stringent requirements for operation.

INTRODUCTION

The optical synchronization system for the European XFEL will adopt to the greatest possible extent the proven and reliable system from FLASH. The long term experience with the optical synchronization system at FLASH has led to numerous enhancements and deeper understanding of the issues involved in such a complex and sensitive precision arrangement. Consequently, for the European XFEL an inimitable possibility arises to incorporate all the gathered knowledge from the bottom up into a new benchmark setting synchronization system.

A schematic representation of the synchronization system is shown in Figure 1. The master-oscillator (MO) distributes a stabilized 1.3 GHz reference to which the master laser-oscillator (MLO), with a repetition rate of 216.7 MHz (a sixth of the MO frequency), is locked. While this MLO lock still employs a simple homodyne scheme at FLASH, the locking of the MLO at the European XFEL will benefit from a more robust and drift-free approach [1]. The stabilized pulse train from the MLO is split into multiple channels and guided to the individual link stabilization units (LSUs) through the free-space distribution (FSD). Each LSU actively stabilizes the effective length of its assigned optical link fiber, which can be conveniently guided through the entire FEL to stations obliged to femtosecond timing stability.

* cezary.sydlo@desy.de

The optical synchronization supplies 12 stations the stabilization of the RF reference [1], 7 laser-to-laser locking stations (L2L) [2] and 7 stations with direct usage of the pulse train for bunch arrival-time measurement (BAM) [3]. One notable feature in this optical synchronization system is the slave laser-oscillator (SLO) at the end of the FEL. A sub-synchronization will be located in the experimental hall at the end of the beamlines to facilitate all the synchronization needs for the pump-probe lasers on-site. Additionally, it will stabilize all stations between 2.1 km and the end of the experimental hall. Hence, two more links with a length of 3.5 km are provided for SLO to MLO locking. On the one hand this serves as a redundancy improving reliability and robustness. On the other hand these two long links can be cross-correlated in-situ for diagnostics providing numbers for the actual synchronization accuracy. One more LSU is included in this planning to reserve space for later use yielding 24 LSUs in total for the main synchronization.

The latest status of the LSUs deployed at FLASH is described in [4], while a redesigned LSU has been introduced in [5] and is shown in Figure 2.

MEASUREMENTS

Set-up

The set-up for measuring the residual error of the fiber-link stabilization is kept as close as possible to the operation conditions at the European XFEL. A 1.3 GHz signal source is used as the Master-Oscillator (MO) to lock the Laser-Oscillator at its repetition frequency of 216.7 MHz, which is a sixth of the 1.3 GHz. The 200 fs pulses of the MLO centred around an optical wavelength of 1553 nm are distributed to the Link-Stabilization-Unit (LSU) and the out-of-loop (OOL) optical cross-correlator (OXC). The LSU is connected to 3.6 km of polarization maintaining fiber (PMF) with a partly reflecting fiber mirror at its end, which reflects a part of the light back to the LSU for timing detection. The transmitted part is fed into the OOL-OXC for timing error measurement. All components are placed in a climatized laboratory except for the fiber. The fiber is installed in a large hall at the DESY campus next to the laboratory to emulate completely uncontrolled ambient influence. As temperature and humidity do influence optical fibers [6] only such a test environment can guarantee proper test conditions. Identical to the installation in the European XFEL only the 3.6 km PMF is subjected to changes of temperature and humidity. All complementary fibers such as the dispersion compensating fiber, the piezo fiber stretcher, erbium doped fiber amplifier, etc., are left in the climatized laboratory. The deviation between the fiber length of 3.6 km and the European XFEL length of 3.4 km is

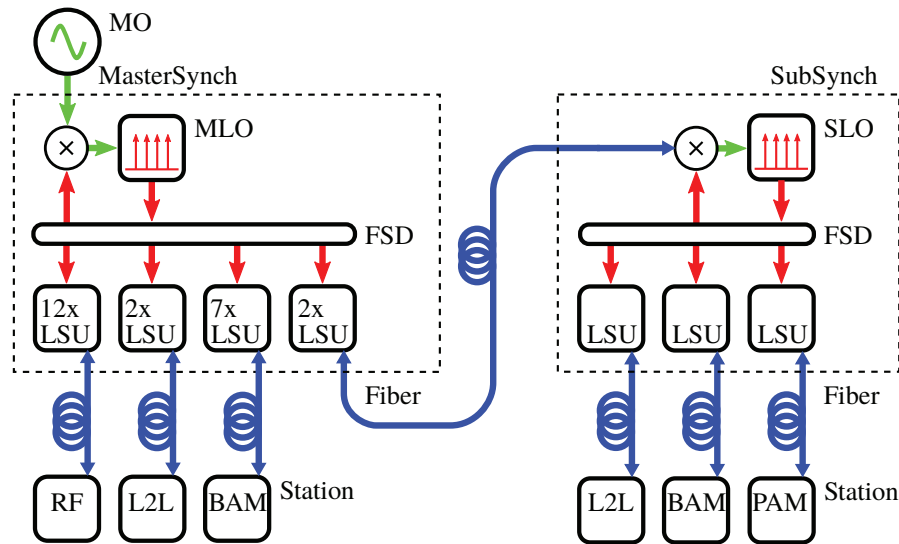


Figure 1: Schematic representation of the optical synchronization system for the European XFEL. The master synchronization will be located close to the injector and stabilize all stations up to 2.1 km. Also the slave laser oscillator of the sub-synchronization will be synchronized in the experimental hall 3.4 km downstream. All the stations between 2.1 km and the experimental hall will be synchronized from there.

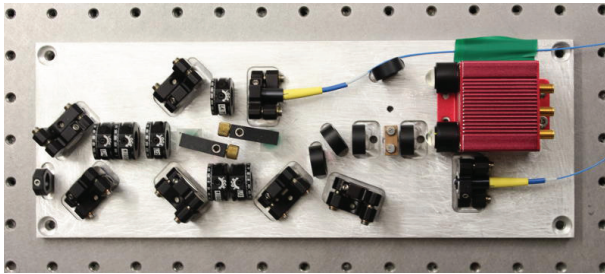


Figure 2: Laboratory prototype of the new Link Stabilization Unit for the European XFEL. This very prototype has been deployed for the stabilization of the 3.6 km link and the corresponding out-of-loop timing error measurements.

Discussion of Results

The set-up described before has been aligned, calibrated and measured for about one day. The measurement results are shown in Figure 4. Most noticeable from 25 h of operation is the large jitter of about 15 fs peak-to-peak (Gray color).

The residual drift observed over this time range has been calculated by a convolution of the raw data with a Hanning-window of 1 h full length and is about 8 fs represented by the black colored curve in Figure 4. The standard deviation for the raw data is calculated to 3.3 fs while subtracting the drift it reduces to 2.8 fs.

Especially the work on this drift is quite delicate as these levels of timing error are easily obtained from temperature and humidity dependence of pretty much everything. Table 1 contains temperature and relative humidity coefficients of materials which are commonly used in optics set-ups. These numbers already suggest that even small temperature variations can very easily cause the observed drifts. For this reason an optical table made out of superinvar (compare Table 1) has been installed in the synchronization room of the European XFEL to reduce these effects. However, tests in the laboratory do not benefit from this type of material as standard steel tables are used there. Also, for these lengths of stabilized fibers another effect has been observed. The temperature of the fiber does not only affect its effective length, but also its chromatic dispersion [7]. This effect changes the optical pulse shapes in the OXCs and therefore affects timing detection. Distinguishing between all these temperature effects on the femtosecond level has become a quite tedious task. Nevertheless, this work is ongoing and promises to further enhance the timing stability.

chosen to account for the fiber cabling paths. Consequently, the overall fiber length is longer and the response time of the fiber link is about 40 μ s in total. A schematic of the set-up is depicted in Figure 3.

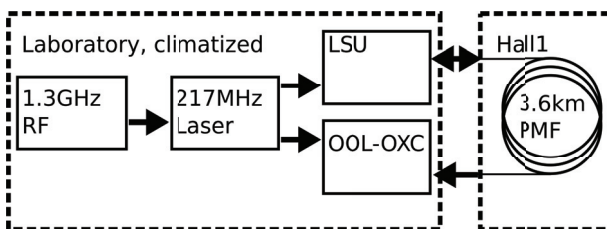


Figure 3: Schematic of the used setup to measure out-of-loop timing error. The Master-Oscillator (MO) delivers a stable 1.3 GHz signal to lock the Master-Laser-Oscillator at a sixth of its frequency. The Link-Stabilization-Unit (LSU) stabilizes the 3.6 km PMF, which is installed in an adjacent hall. The residual error is measured out-of-loop (OOL) with an Optical Cross Correlator (OXC).

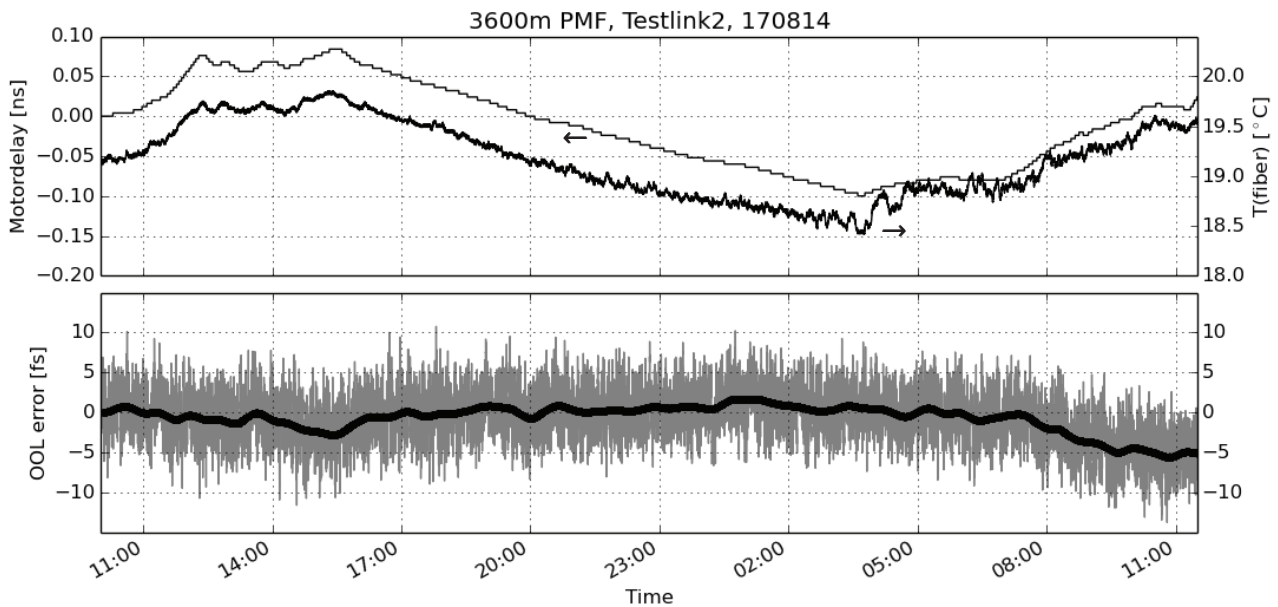


Figure 4: In the top graph the compensated length change of the fiber and the corresponding temperature is shown. The delay is given for one-way and therefore represents the drift of 3.6 km polarization maintaining fiber. The steps in this curve are 1.2 mm or 4 ps for each motor tuning step. The lower graph presents the measured residual out-of-loop timing error at the end of the stabilized fiber. Gray color shows the raw data, while the black line is a convolution with a Hanning-window of 1 h full length to distinguish between jitter and drift.

Table 1: Temperature and Humidity Influence of Various Materials

Material	Temperature fs / K / m	Rel. humidity fs / %RH / m
Aluminum	≈ 77	-
Steel [8]	33	-
SMF28e [6]	40	2.5
Furukawa PSOF [6]	3.2	0.4
Air (at 1550nm)	3	0.03
Superinvar [8]	<1	-

CONCLUSION

The results presented in this work are already well in agreement with the synchronization requirements for the European XFEL. We obtained jitter levels of 15 fs peak-to-peak and overall 3.3 fs RMS over 25 h. The design state for the LSUs has already been frozen and is ready for production.

However, for each systematic error there is also a systematic solution. The limits of achievable synchronization errors with reasonable complexity are not reached yet. Further work will concentrate on these limits to be prepared for potentially increased requirements in the future.

REFERENCES

- [1] T. Lamb et al., “Femtosecond Stable Laser-to-RF Phase Detection for Optical Synchronization Systems”, IBIC 2013, Oxford, Sept. 2013, TUPC33, <http://www.JACoW.org>
- [2] S. Schulz et al. “Femtosecond-precision synchronization of the pump-probe optical laser for user experiments at FLASH”, Proc. SPIE 8778, Advances in X-ray Free-Electron Lasers II: Instrumentation, 87780R (May 3, 2013); doi:10.1117/12.2021572
- [3] M.K. Czwalinna et al. “New Design of the 40 GHz Bunch Arrival Time Monitor Using MTCA.4 Electronics at FLASH and for the European XFEL”, IBIC 2013, Oxford, Sept. 2013, WEPC31, <http://www.JACoW.org>
- [4] F. Zummack et al., “Status of the Fiber Link Stabilization Units at FLASH”, IBIC 2013, Oxford, Sept. 2013, MOPC33, <http://www.JACoW.org>
- [5] C. Sydlo et al. “Development Status of Optical Synchronization for the European XFEL”, IBIC 2013, Oxford, Sept. 2013, WEPC31, <http://www.JACoW.org>
- [6] M. Bousonville “Fiber Drift Measurement”, DESY Internal Measurement Protocol, 2011, DESY, Hamburg, Germany
- [7] Hamp et al. “Temperature dependence of chromatic dispersion in optical fiber”, IEEE PHOTONICS TECHNOLOGY LETTERS, VOL. 14, NO. 11, NOVEMBER 2002
- [8] Newport Corporation, <http://www.newport.com>

DESIGN AND TEST OF WIRE-SCANNERS FOR SwissFEL

G.L. Orlandi*, M. Baldinger, H. Brands, P. Heimgartner, R. Ischebeck, A. Kammerer, F. Löhl, R. Lüscher, P. Mohanmurthy†, C. Ozkan, B. Rippstein, V. Schlott, L. Schulz, C. Seiler, S. Trovati, P. Valitutti, D. Zimoch, Paul Scherrer Institut, 5232 Villigen PSI, Switzerland

Abstract

The SwissFEL light-facility will provide coherent X-rays in the wavelength region 7-0.7 nm and 0.7-0.1 nm. In SwissFEL, view-screens and wire-scanners will be used to monitor the transverse profile of a 200/10 pC electron beam with a normalized emittance of 0.4/0.2 mm mrad and a final energy of 5.8 GeV. Compared to view screens, wire-scanners offer a quasi-non-destructive monitoring of the beam transverse profile without suffering from possible micro-bunching of the electron beam. The main aspects of the design, laboratory characterization and beam-test of the SwissFEL wire-scanner prototype will be presented.

INTRODUCTION

SwissFEL will provide coherent X-rays light in the wavelength region 7-0.7 nm and 0.7-0.1 nm [1]. Electron bunches with charge 200/10 pC and normalized emittance of 0.4/0.2 mm.mrad will be emitted by a photocathode at a repetition rate of 100 Hz according to a two-bunches train structure with a temporal separation of 28 ns. Thanks to a RF kicker switching the second electron bunch of the beam train into a magnetic switch-yard, the SwissFEL linac will simultaneously supply two distinct undulator chains at a repetition rate of 100 Hz: the hard-Xrays line Aramis and the soft-Xrays line Athos. The electron beam will be accelerated up to 330 MeV by a S-band RF Booster and to the final energy of 5.8 GeV by a C-band RF linac. Thanks to an off-crest acceleration in the RF Booster, the electron beam will experience a two-stages longitudinal compression from an initial bunch length of 3/1 ps (RMS) down to 20/3 fs (RMS) in two magnetic chicanes. Two X-band RF cavities will compensate the quadratic distortion of the longitudinal phase space due to the off-crest accelerating scheme of the beam and the non-linear contribution of the magnetic dispersion. A laser-heater in the Booster section will smooth down possible micro-structures affecting the beam longitudinal profile of the beam. Macro-bunching can be detrimental to the monitoring of the beam profile based on scintillator or OTR screens (Optical Transition Radiator) because of the emission of coherent OTR. As an alternative to view screens, wire-scanners (WSC) can be used to monitor the beam transverse profile. Moreover, the quasi-non-invasive feature of the WSCs - compared to view screens - can be beneficial to monitoring the beam transverse profile during FEL operations of the machine. In the following, results on design, characterization and beam test of wire-scanners for SwissFEL will be presented.

WSC DESIGN

Wire-Scanners can be used to measure the transverse profile of the electron beam in a particle accelerator [2–4]. Carbon or metallic wires with different diameter (D) - stretched on a wire-fork - can be vertically inserted at a constant velocity into the vacuum chamber by means of a motorized UHV linear stage to scan the beam transverse profile with an intrinsic resolution $D/4$ (rms). An encoder mounted on the linear stage allows the relative distance of the wire from the axis of the vacuum chamber to be measured at each machine trigger event. The interaction of the electron beam with the wire produces a "wire-signal" - scattered primary electrons and secondary particles (mainly electrons, positron and bremsstrahlung photons) - which is proportional to the number of the electrons sampled by the wire in the bunch. The Beam Synchronized Acquisition (BS-ACQ) - over a sufficient number of machine trigger shots - of the wire position and the wire-signal - detected by a loss monitors downstream the wire - allows the beam transverse profile along the horizontal or the vertical direction to be reconstructed. In SwissFEL, view screens and WSCs will be used to monitor the transverse profile of the electron beam which varies between 500 μm and 5 μm (rms) along the entire machine. View-screens will be mainly equipped with YAG crystals. In SwissFEL, only WSCs are in principle able to discriminate the 28 ns time structure of the two-bunches emitted at 100 Hz by the photocathode. The SwissFEL WSCs are designed according to the following criteria, see Fig. 1: use a single UHV linear stage to scan the beam profile in the X, Y and X-Y directions; use Tungsten wire with different diameters from 5 to 13 μm to ensure a resolution in the range 1.5-3.5 μm ; equip each wire-scanner station with spare/different-resolution wires; detect the wire losses in the bunch charge range 10-200 pC and resolve the 28 ns time two-bunches structure of the electron beam; BS-ACQ of the read-out of both the encoder wire position and the loss-monitor; wire-fork suitably designed for routine scanning of the beam profile during FEL operations (no beam interception with the wire-fork); wire-fork equipped with different pin-slots where the wires can be stretched at different relative distances so that the scanning time can be minimized and optimized according to the WSC position in the machine, see Fig. 1. In SwissFEL the wire losses will be measured by means of scintillator fibers (PMMA, Poly-Methyl-Methyl-Acrylate, Saint Gobain BCF-20, emission in the green) winding up the beam pipe. The fiber are directly connected to a photomultiplier (PMT, Hamamatsu H10720-110). For more information on the detection sys-

* gianluca.orlandi@psi.ch

† presently at Massachusetts Institute of Technology, MA, USA

tem of the wire-signal in SwissFEL, see these conference proceedings [5].

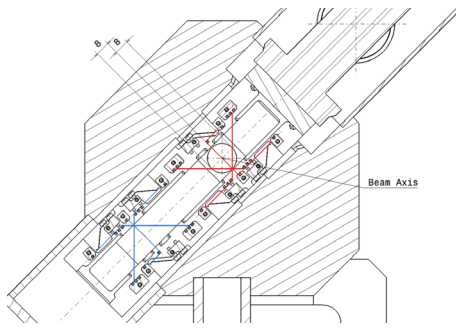


Figure 1: View of the Transverse section of the WSC vacuum chamber and, in particular, of the wire-fork and of the CF16 vacuum chamber. The wire-fork is equipped with 3 different pin-slots where the wire can be stretched. The distance of the "wire-vertex" from the vacuum-chamber axis can be set at 8, 5.5 and 3 mm in correspondence of the 3 different pin-slots.

WSC SIMULATIONS

Most part of the primary and secondary particles resulting from the interaction of a relativistic electron beam with a metallic wire are emitted within a narrow cone with respect to the direction of incidence. Since, only a small fraction of the solid angle of emission of the wire-signal can be covered by a loss-monitor, the efficiency of the wire-losses detection strongly depends on the relative distance between the wire and loss-monitors. In order to determine the most suitable distance of a loss-monitor from a wire in SwissFEL, the particle composition and the related energy and angular distribution of the particle shower has been evaluated with the Monte Carlo code FLUKA [6]. In FLUKA simulations, Tungsten wires with a diameter of 13 μm and 25 μm and beam energies of 340 MeV, 1.33 GeV, 2.99 GeV and 5.2 GeV are considered. The electron beam is modelled as a pencil beam (no energy spread) travelling along the axis of a CF16 vacuum-chamber (inner diameter 16 mm, outer diameter 18mm). Both the angular and the energy distributions - expressed as number of particles per unit primary particle - of the primary and secondary particles are calculated in FLUKA, see Figs. 2,3. Electrons and photons mainly contribute to the wire-signal, see Fig. 2. Moreover, 95% of the particle shower is emitted within a polar angle less than 0.1 rad, i.e., intercepts the CF16 vacuum chamber within 80 mm and 4000 mm from the wire, see Fig. 3.

Beam tests of WSCs and loss-monitor response were carried out at the 250 MeV SwissFEL Injector Test Facility (SITF) [7]. For such a purpose, a scintillator fiber winding around the vacuum chamber was installed just before the high energy bending dipole of the machine [5]. The loss-monitor response was tested intercepting alternatively with several OTR screens - 300 μm thick Si Wafer with a 200 nm Al coating - a 180 pC electron beam with energy 245 MeV and recording the corresponding time-integration

of the fiber-signal read-out (instead of WSCs, OTR screens were used in this measurement in order to avoid any dependence of the loss-monitor response on the variation of the beam profile along the machine). The loss-monitor response measured as a function of the different OTR screen - i.e., as a function of the relative distance OTR screen loss-monitor - is shown in Fig. 4. The curve in Fig. 4 shows a maximum of the signal for a distance between OTR-screen and loss-monitor of about 2.5 m in agreement with previous measurements [8]. Taking into account the radius of the CF40 vacuum-chamber of SITF, from this measured value of the optimum distance screen-loss-monitor a mean emission polar angle of about $\theta_{Si,300 \mu\text{m}} = 7.6 \text{ mrad}$ can be estimated for the particle shower produced by the interaction beam-screen. In order to rescale this result to the case of a Tungsten foil, the Rossi-Greisen formula [9] can be used. The Rossi-Greisen formula allows to calculate the rms scattering angle of a charged particle experiencing multiple Coulomb interaction while crossing a block of material. The resultant average scattering angle scales down with the charge energy and is proportional to the square-root of the normalized material thickness per radiation length of the material. According to the Rossi-Greisen formula, the mean emission polar angle for Tungsten foils 13 μm and 25 μm thick can be extrapolated from the previous result $\theta_{Si,300 \mu\text{m}} = 7.6 \text{ mrad}$: $\theta_{Si,300 \mu\text{m}}/\theta_{W,25 \mu\text{m}} = 0.67$ and $\theta_{Si,300 \mu\text{m}}/\theta_{W,13 \mu\text{m}} = 0.93$. Taking into account the scaling formulae above, the following optimum distances of a loss-monitor from a 25 μm and a 13 μm thick Tungsten wire can be estimated: 0.7 m and 1 m, respectively. Under the limit of applicability of this extrapolation method, an optimum distance between wire and loss-monitor of about 1m can be estimated (in agreement with FLUKA results).

WSC BENCH AND BEAM TESTS

Reliable WSC measurements require a precise knowledge of the relative position of the wire with respect to the centroid of the beam at each machine trigger event. For such a purpose, the read-out of both the encoder wire-position and the loss-monitor must be acquired in a BS-ACQ mode. The encoder read-out can provide a precise position of the wire provided that appreciable vibrations are not affecting the wire during the scan. The mechanical stability of a scanning wire can be measured in a test-bench by imaging the moving wire with a high speed camera. The wire vibration during a scan can be evaluated from the analysis of the centroid and the sigma of the projected images of the moving wire. Wire vibration measurements have been performed for different WSC set-ups, i.e., for different wire diameters, stepping motors and motor controllers. The mechanical stability of a Tungsten wire (25 μm diameter) stretched on a wire-scanner fork was measured for different velocities (0.1-10 mm/s) of a 3-phase stepping motor. Measurements were performed by imaging the wire by means of a high speed camera (camera frame rate 1kHz) and a microscope 10X (resolution 1px=1 μm). Appreciable vibrations of the wire

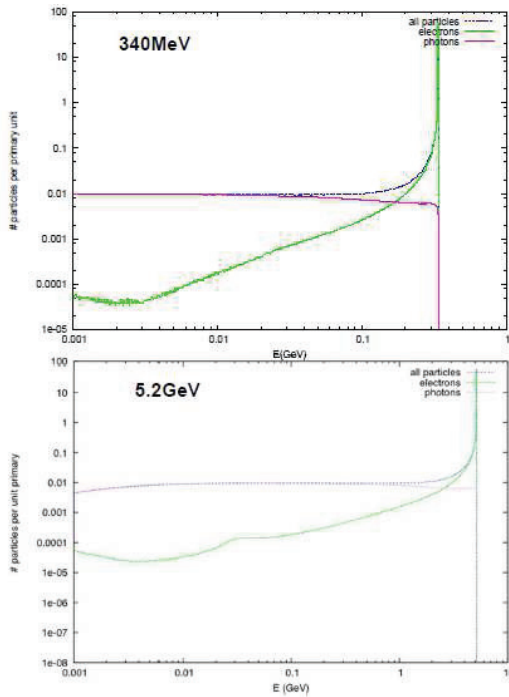


Figure 2: FLUKA results of the energy distribution of the wire losses for a beam energies of 340 MeV and 5.2 GeV.

were observed only for a wire velocity larger than 1 mm/s. For a wire speed of 2 mm/s, a vibration amplitude of about $0.6 \mu\text{m}$ (rms) was measured. A second series of vibration measurements have been performed in vacuum (10^{-4} mbar) on a prototype of the SwissFEL WSCs (2-phase stepping motor) for a velocity range of the wire 0.2–2 mm/s, see Fig. 1. A back-illuminated Tungsten wire ($13 \mu\text{m}$) was imaged by a camera with a frame rate of 500 fps equipped with a 200 mm lens (projected pixel size $9.7 \mu\text{m}$). In Figs. 5, the relative variation of the centroid and the sigma of the projected image of a $240 \mu\text{m}$ long portion of the wire in motion at a velocity of 2 mm/s is shown. After subtracting in quadrature from the rms values of the centroid and sigma distributions - Figs. 5 - the corresponding rms values measured with the wire at rest, it results that, for a wire velocity of 2 mm/s, the centroid vibration is about $1.3 \mu\text{m}$ and the apparent enlargement of the sigma due to possible oscillation of the wire at a frequency higher than 500 Hz is about $0.1 \mu\text{m}$. In conclusion, the results of the measurements of the mechanical stability of the SwissFEL WSCs indicate that, for the wire velocity range of interest for SwissFEL 0.2–2 mm/s, the measured vibration of the wire is less than the resolution limit which can be achieved in a measurement of the beam profile with a Tungsten wire with a diameter of $5 \mu\text{m}$.

Several WSC tests on the electron beam have been also carried out in SIF. Two different techniques were adopted to detect the wire-signal produced by a Tungsten wire with a diameter of $25 \mu\text{m}$. In the former case, the wire-signal was retrieved as the difference of the charge read-out of two Beam-Position-Monitors (BPM), the one upstream the wire

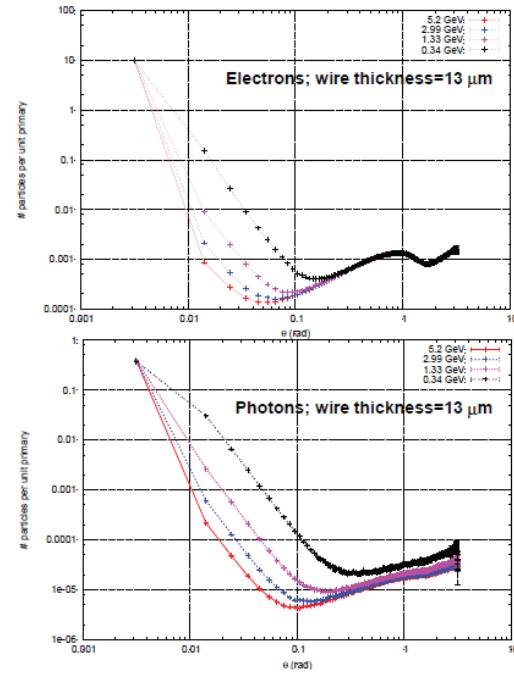


Figure 3: FLUKA results of the angular distribution of photons and electrons composing the wire losses.

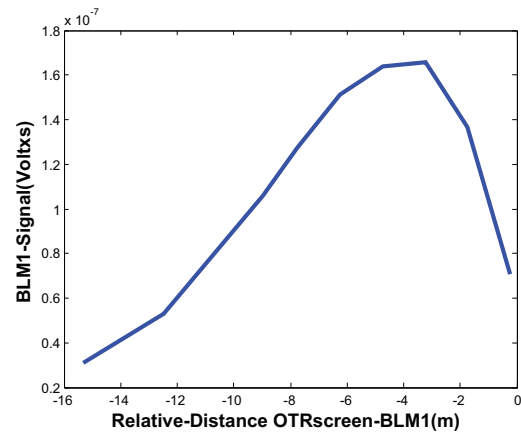


Figure 4: Measured beam losses as a function of the distance of the loss monitor from the single OTR screen intercepting the beam (charge 180 pC, energy 245 MeV).

and the other downstream the wire just behind the bending dipole of the high energy spectrometer. In this case a 10 Hz BS-ACQ of both the BPMs and encoder position of the wire was possible. In the latter case, the wire-signal was directly measured by a loss-monitor (scintillator fiber); no BS-ACQ available in this case. In both cases, the vertical profile of the beam measured by the WSC was compared with the beam profile measured by an OTR screen placed at the same longitudinal position of the wire. Results of both campaigns of measurements are shown in Fig. 6 (BPM read-out of the wire-signal) and in Fig. 7 (loss-monitor read-out of the wire-signal). Taking into account that the WSC data are not corrected by the transverse jitter of the beam, the OTR

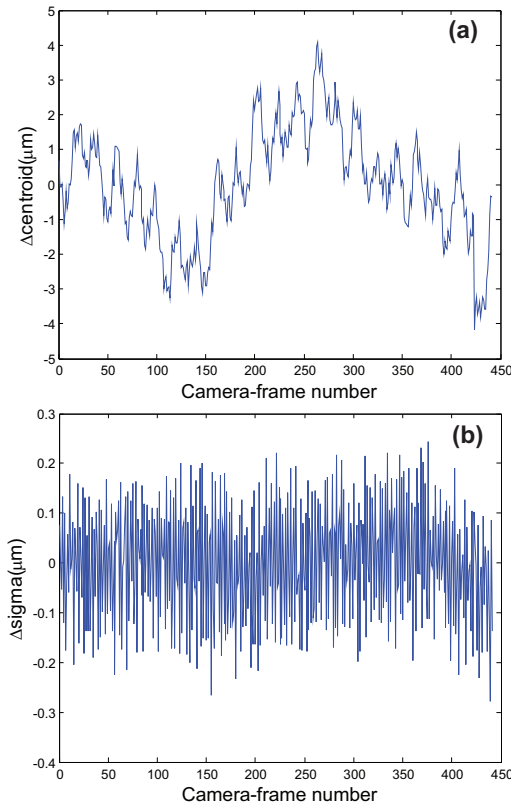


Figure 5: Wire vibration measurements results: relative variation of the centroid (a) and the sigma (b) of the projection of the camera image of the wire vs. camera frames number.

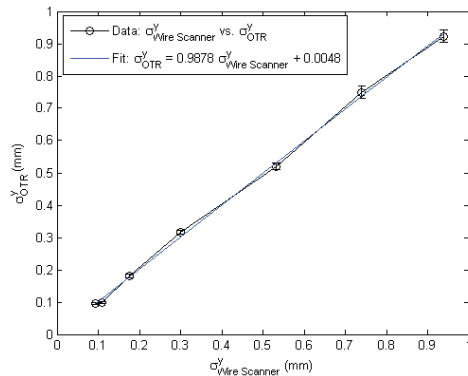


Figure 6: Measurements of the vertical profile of the electron beam: OTR vs. WSC results.

measurements vs. WSC measurements - see Fig. 6 - show an excellent linearity (less than 2% deviation) as well as the comparison of the WSC-loss-monitor and OTR measurements shows a good agreement within 8%, $\sigma_Y = 0.244 \pm 0.002$ mm (OTR), $\sigma_Y = 0.265 \pm 0.008$ mm (WSC).

CONCLUSIONS

Design and tests of the SwissFEL WSCs are presented. Results of the test-bench measurements of the mechanical stability of the prototype system indicate that, for the wire ve-

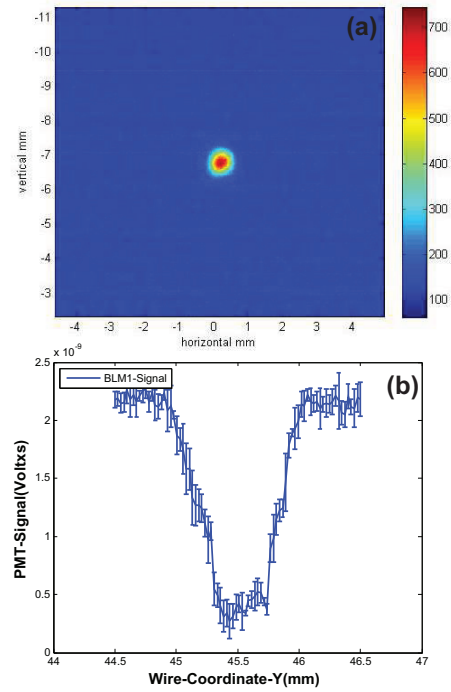


Figure 7: Measurements of the vertical profile of the electron beam with OTR screen and loss-monitor read-out of the WSC signal.

locities of interest for SwissFEL (0.2-2 mm/s), the measured wire vibration is less than the intrinsic resolution expected for a 5 μ m thick Tungsten scanning the transverse profile of the electron beam. WSC tests on the beam indicate that WSC measurements of the beam transverse profile are consistent with analogous measurements performed with OTR screens.

REFERENCES

- [1] SwissFEL Conceptual Design Report, PSI Bericht Nr. 10-04 April 2012.
- [2] R. Fulton et al., Nucl. Instr. Meth. in Phys. Res. A **274** (1989) 37-44.
- [3] M.C. Ross et al., Particle Accelerator Conference (PAC) 1991.
- [4] C. Field, Nucl. Instr. Meth. in Phys. Res. A **360** (1995) 467-475.
- [5] C. Ozkan et al., these proceedings.
- [6] S. Trovati, SwissFEL beam losses in wire scanners: energy and angular distributions, PSI Internal Note, FEL-TS96-001-0.
- [7] SwissFEL Injector Conceptual Design Report, PSI Bericht Nr. 10-05 July 2010.
- [8] E. Hohmann et al., to be published in Progress in Nuclear Science and Technology.
- [9] R.C. Fernow, Introduction to Experimental Particle Physics, Cambridge University Press, 1986.

TRANSITION RADIATION OF AN ELECTRON BUNCH AND IMPRINT OF LORENTZ-COVARIANCE AND TEMPORAL-CAUSALITY

Gian Luca Orlandi*,
Paul Scherrer Institut, 5232 Villigen PSI, Switzerland

Abstract

The study of Transition Radiation (TR) of a bunch of N electrons offers a precious insight into the role that Lorentz-covariance and temporal-causality play in an electromagnetic radiative mechanism of a relativistic beam. The contributions of the N single electrons to the radiation field are indeed characterized by emission phases from the metallic surface which are in a causality relation with the temporal sequence of the N particle collisions onto the radiating screen. The Lorentz-covariance characterizing the virtual quanta field of the relativistic charge is also expected to imprint the radiation field and the related energy spectrum. The main aspects of a Lorentz-covariance and temporal-causality consistent formulation of the TR energy spectrum of an electron bunch will be described.

INTRODUCTION

The electromagnetic field of a relativistic charge in a rectilinear and uniform motion can induce the boundary interface between two media with different dielectric properties to emit radiation, the so called Transition Radiation (TR) [1, 2]. Forward and backward radiation is emitted with an angular distribution scaling down with the Lorentz factor γ of the relativistic charge ($\gamma = E/mc^2$) and a frequency bandwidth determined by the plasma frequency and the finite dimension of the radiating surface. TR finds various application in beam diagnostics of a particle accelerator: to monitor the beam transverse profile by imaging the visible light spot (OTR, Optical Transition Radiation) emitted by the charged beam while crossing a metallic foil [3] or to measure the length of the charged beam via spectroscopic analysis of the coherent enhancement of the radiation intensity [4]. For observation condition of the radiation in the visible or in the far infrared, the interface vacuum-metal practically behaves like an ideal conductor. The modelling of the radiator surface as an ideal conductor allows a better comprehension of the dynamics of the charged distributions involved in TR emission and of the attribute as "polarization radiation" that is sometimes given to TR. An ideal conductor surface can be indeed schematized as a double layer of charge. The collision of a bunch of N relativistic electrons with the metallic surface can be modelled as the interaction of an incident relativistic charge with a double layer of charge (a beam collision at a normal angle of incidence onto the radiator surface is supposed in the present paper). At the same time, the radiation emission can be interpreted as the result of the dipolar oscillation of the double layer of charge which is induced by the relativistic electron bunch, see Fig. 1. The

observation of a backward emitted component in the TR can be indeed explained as the result of a dipolar oscillation of a double layer of charge. The propagation of the radiation field from the metallic surface can be interpreted in terms of the Huygens-Fresnel principle and formally expressed in terms of the Helmholtz-Kirchhoff integral theorem. Under far-field approximation, the Helmholtz-Kirchhoff integral theorem allows to express the single harmonic component of the radiation field as the Fourier transform - calculated with respect to the coordinates of the radiator surface - of the transverse component of the electric field of the relativistic charge, the so called *virtual quanta* field. The density-like Lorentz-covariance characterizing the electric field of the incident electron bunch is expected to characterize both the TR field and the corresponding energy spectrum. Signature of the Lorentz-covariance is the dependence of the radiation energy spectrum on the Lorentz-invariant distribution of the transverse coordinates of the N electrons. Besides Lorentz-covariance, the TR field and the related energy spectrum of the N electron bunch are also expected to bear the imprint of the temporal-causality constraint: the emission phases of the N single electron amplitudes composing the radiation field must be causality related to the temporal sequence of the N electron collision onto the metallic screen, which only depends on the distribution of the longitudinal coordinates of the N electrons. Lorentz-covariance and temporal-causality are physical constraints an electromagnetic radiative mechanism by a relativistic charged beam must fulfill. Both these two constraints are expected to imprint the TR energy spectrum of a bunch of N electrons. The failure in implementing the one of the two physical constraints in the formula of the TR energy spectrum of a bunch of N electrons implies necessarily also the defect of the other and vice-versa. In the present paper, a Lorentz-covariance and temporal-causality consistent formulation of the TR energy spectrum of a relativistic bunch of N electrons is presented and the agreement of the presented model with well-known results of the TR theory of a single electron is demonstrated [5–7]. The breaking point between a Lorentz-covariance and temporal-causality consistent or inconsistent theoretical model of TR of a bunch of N electrons is discussed.

TR ENERGY SPECTRUM

Causality and Covariance

The case of a bunch of N relativistic electrons at normal incidence onto a metallic screen is considered in the present paper. The N electrons are supposed to move with a common rectilinear and uniform velocity $\vec{w} = (0, 0, w)$ along the z -axis of the laboratory reference frame. The radiator

* gianluca.orlandi@psi.ch

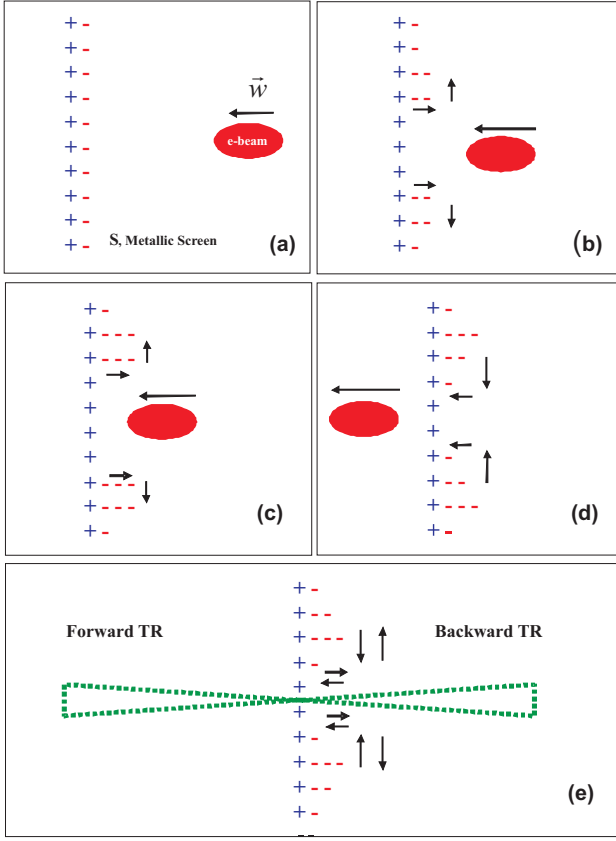


Figure 1: In the picture sequence [(a) → (e)], a simplified representation of the TR emission is sketched. The incident relativistic charge induces a dipolar oscillation on the double layer of charge, i.e., the metallic surface. With the charge approaching the metallic foil, the conduction electrons, initially at rest on the metallic surface, undergo a tangential displacement due to the electric component of the Lorentz force (the transverse component of the electric field is γ times stronger than the longitudinal one). Subsequent to the initial transverse motion, the conduction electrons are also displaced along the longitudinal direction because of the magnetic component of the Lorentz force. As a result of the dipolar oscillation, the double layer of charge generates the TR emission. Due to the simplicity of this pictorial representation, charge oscillation and radiation emission are artificially distinct in two different phases. In reality, such two phases are intrinsically and temporally indistinguishable.

surface is supposed to behave as an ideal conductor in the radiation frequency range of interest. The Fourier transform of the electric field travelling with the electron bunch reads

$$\vec{E}(\vec{k}, \omega) = -i(8\pi^2 e) \frac{[\vec{k} - (\omega \vec{w}/c^2)]}{[k^2 - (\omega/c)^2]} \times \left(\sum_{j=1}^N e^{-i\vec{k} \cdot \vec{r}_{0j}} \right) \delta(\omega - \vec{w} \cdot \vec{k}), \quad (1)$$

where $[\vec{r}_{0j} = (x_{0j}, y_{0j}), z_{0j}]$ ($j = 1, \dots, N$) are the spatial coordinate vectors of the N electrons at the reference time

$t = 0$. The (x, y) components of the Eq.(1) are normally referred as *virtual quanta* field. The harmonic component of the radiation field of the N electrons can be obtained by applying the Helmholtz-Kirchhoff integral theorem [1] to the electric field of the incident charge on the boundary metallic surface. Under far-field approximation, this reads

$$E_{x,y}^{tr}(\vec{k}, \omega) = \frac{k}{2\pi D} \int_S d\vec{\rho} E_{x,y}^{vq}(\vec{\rho}, \omega) e^{-i\vec{k} \cdot \vec{\rho}}, \quad (2)$$

where $\vec{\rho} = (x, y)$ are the spatial coordinates of the radiator surface S having an arbitrary size and shape, $k = \omega/c = 2\pi/\lambda$ is the wave number, $\vec{k} = (k_x, k_y) = k \sin \theta (\cos \phi, \sin \phi)$ is the transverse component of the wave-vector and D is the distance from the radiator surface to the observation point. From Eqs.(1,2), the harmonic component of the TR field of the N electrons reads [5–7]

$$E_{x,y}^{tr}(\vec{k}, \omega) = \sum_{j=1}^N H_{x,y}(\vec{k}, \omega, \vec{\rho}_{0j}) e^{-i(\omega/w)z_{0j}} \quad (3)$$

where, with $\alpha = \frac{\omega}{w\gamma}$,

$$H_{x,y}(\vec{k}, \omega, \vec{\rho}_{0j}) = \frac{iek}{2\pi^2 D w} \times \int_S d\vec{\rho} \int d\vec{\tau} \frac{\tau_{x,y}}{\tau^2 + \alpha^2} e^{-i\vec{\tau} \cdot \vec{\rho}_{0j}} e^{i(\vec{\tau} - \vec{k}) \cdot \vec{\rho}}. \quad (4)$$

TR energy spectrum can be finally obtained

$$\frac{d^2 I}{d\Omega d\omega} = \frac{cD^2}{4\pi^2} \sum_{\mu=x,y} \left(\sum_{j=1}^N |H_{\mu,j}|^2 \right) + \sum_{j,l(j \neq l)=1}^N e^{-i(\omega/w)(z_{0j} - z_{0l})} H_{\mu,j} H_{\mu,l}^*. \quad (5)$$

where $H_{\mu,j} = H_{x,y}(\vec{k}, \omega, \vec{\rho}_{0j})$ ($\mu = x, y$), see Eq.(4). The evidence of the temporal-causality constraint in the expression of the TR field stays in the emission phases from the radiator of the N single electron radiation field amplitudes $H_{\mu,j}$ which are in a causality relation with the temporal sequence of the N electron collisions onto the metallic screen, only dependent on the distribution of the N electron longitudinal coordinates z_{0j} ($j = 1, \dots, N$), see Eqs.(3,4). Temporal-causality consistent is the formula of the TR energy spectrum - see Eqs.(5) - where the reciprocal interference of N single electron radiation field amplitudes only depends on the reciprocal emission delays $(z_{0j} - z_{0l})$, $j, l = 1, \dots, N$. The covariant dependence of the TR energy spectrum - see Eqs.(3,4,5) - on the distribution of the N electron transverse coordinates (x_{0j}, y_{0j}) ($j = 1, \dots, N$) appears evident after performing the integral calculus in the Eq.(4) [5]. In fact, for a round radiator surface S with a radius R larger than the beam transverse size ($R \gg \rho_{0j} = \sqrt{x_{0j}^2 + y_{0j}^2}$), the TR

field - Eqs.(3,4) - reads

$$E_{x,y}^{tr}(\vec{k}, \omega) = \sum_{j=1}^N \frac{2iek}{Dw} \frac{\kappa}{\kappa^2 + \alpha^2} e^{-i[(\omega/w)z_{0j} + \vec{k} \cdot \vec{\rho}_{0j}]} \times \begin{pmatrix} \cos \phi \\ \sin \phi \end{pmatrix} \left[\rho_{0j} \Phi(\kappa, \alpha, \rho_{0j}) - (R + \rho_{0j}) \Phi(\kappa, \alpha, R + \rho_{0j}) \right], \quad (6)$$

where, with (J,K) Bessel function of 1st and 2nd kind,

$$\Phi(\kappa, \alpha, \rho_{0j}) = \alpha J_0(\kappa \rho_{0j}) K_1(\alpha \rho_{0j}) + \frac{\alpha^2}{\kappa} J_1(\kappa \rho_{0j}) K_0(\alpha \rho_{0j}). \quad (7)$$

From Eqs.(5,6,7), the formula of the TR energy spectrum of a N electron bunch at normal incidence onto a circular radiator with a finite radius R ($0 \leq R < \infty$) follows

$$\frac{d^2 I}{d\Omega d\omega} = \frac{d^2 I_e}{d\Omega d\omega} \left(\sum_{j=1}^N |A_j|^2 + \sum_{j,l(j \neq l)=1}^N A_j A_l^* e^{-i[(\omega/w)(z_{0j} - z_{0l}) + \vec{k} \cdot (\vec{\rho}_{0j} - \vec{\rho}_{0l})]} \right) \quad (8)$$

where

$$\frac{d^2 I_e}{d\Omega d\omega} = \frac{(e\beta)^2}{\pi^2 c} \frac{\sin^2 \theta}{(1 - \beta^2 \cos^2 \theta)^2} \quad (9)$$

is the well-known Frank-Ginzburg formula and

$$A_j = \rho_{0j} \Phi(\kappa, \alpha, \rho_{0j}) - (R + \rho_{0j}) \Phi(\kappa, \alpha, R + \rho_{0j}). \quad (10)$$

In Eqs.(8,9,10), the N electron transverse coordinates (x_{0j}, y_{0j}) ($j = 1, \dots, N$), on the one hand, contribute to determine the well-known three-dimensional form factor, on the other hand, leave a covariant mark on both the temporal incoherent and coherent components of the TR energy spectrum. The case of the TR emission from an infinite metallic surface ($S = \infty$) can be obtained from the results above under the limit $R \rightarrow \infty$. Under the limit $R \rightarrow \infty$, Eq.(10) - see also Eq.(12) - reads

$$A_j \rightarrow \rho_{0j} \Phi(\kappa, \alpha, \rho_{0j}). \quad (11)$$

Finally, with reference to Eqs.(8,9,11), the formula of the TR energy spectrum of N electrons hitting an infinite radiator ($S = \infty$) can be obtained. It is worth to stress that, in order to obtain the results of TR from an infinite radiator ($S = \infty$) - Eqs.(8,9,11) - the following formal procedure is applied: first, in the implicit expression of the TR field - see Eq.(3,4) - the integral calculus with respect to the radiator surface S is performed for a round screen with a finite radius R ; finally, the limit $R \rightarrow \infty$ is applied to the resultant expression of the TR field. In the following subsection, the consequences of applying directly the limit $S \rightarrow \infty$ to the implicit expression of the radiation field - Eq.(3,4) - will

be described. Numerical simulations of the angular distribution of the TR intensity - refer to the temporal incoherent part of the TR energy spectrum, see Eqs.(8,9,11) - are shown in Fig. 2 for a given value of the beam transverse size and different values of the observed wavelength and beam energy. A beam transverse size dependent diffractive cut-off clearly affects both the angular and spectral distributions of the TR intensity [5-7], see Fig. 2. Some relevant results already well-known in literature can be derived from the results reported above, see Eqs.(8,9,10). In the case of a single electron travelling along the z -axis, it can be indeed demonstrated [5] that under the limit $R \rightarrow \infty$ and $\rho_{01} \rightarrow 0$

$$\begin{cases} (R + \rho_{0j}) \Phi(\kappa, \alpha, R + \rho_{0j}) \rightarrow 0 \\ \rho_{0j} \Phi(\kappa, \alpha, \rho_{0j}) \rightarrow 1 \end{cases} \quad (12)$$

the TR field - Eq.(6) - tends to

$$E_{x,y}^{tr,e}(\vec{k}, \omega) = \frac{2iek}{Dw} \frac{\kappa}{\kappa^2 + \alpha^2} \begin{pmatrix} \cos \phi \\ \sin \phi \end{pmatrix} \quad (13)$$

from which the Frank-Ginzburg formula follows, see Eq.(9). Furthermore, in the case of a single electron with $\rho_{01} \rightarrow 0$ and a radiator with a finite radius R the well-known result of the TR field of a single electron hitting a round radiator can be obtained from Eq.(6,7,12)

$$E_{x,y}^{tr}(\vec{k}, \omega) = \frac{2iek}{Dw} \frac{\kappa}{\kappa^2 + \alpha^2} \begin{pmatrix} \cos \phi \\ \sin \phi \end{pmatrix} \times \left[1 - \alpha R J_0(\kappa R) K_1(\alpha R) - \frac{\alpha^2 R}{\kappa} J_1(\kappa R) K_0(\alpha R) \right]. \quad (14)$$

See Eq.(14) and compare it with Eqs.(8,9) in [8].

Causality and Covariance Defect

In previous section, the formula of the TR energy of an N electron beam normally hitting an infinite metallic surface ($S = \infty$) - see Eqs.(8,9,11) - was derived according to the following procedure: first, the integral calculus in Eq.(3,4) with respect to a finite screen size ($S < \infty$) is performed; finally, the limit $S \rightarrow \infty$ is applied to the so obtained result. If this procedure is inverted, i.e., if the limit $S \rightarrow \infty$ is directly applied to the implicit expression of the TR field - see Eq.(3,4) - before the integral calculus with respect the radiator surface S is performed, then the TR field reads [7]

$$E_{x,y}^{tr}(\vec{k}, \omega) = \sum_{j=1}^N E_{x,y}^{tr,e}(\vec{k}, \omega) e^{-i[(\omega/w)z_{0j} + \vec{k} \cdot \vec{\rho}_{0j}]}, \quad (15)$$

and the related formula of the TR energy spectrum reads:

$$\frac{d^2 I}{d\Omega d\omega} = \frac{d^2 I_e}{d\Omega d\omega} \left(N + \sum_{j,l(j \neq l)=1}^N e^{-i[(\omega/w)(z_{0j} - z_{0l}) + \vec{k} \cdot (\vec{\rho}_{0j} - \vec{\rho}_{0l})]} \right) \quad (16)$$

where $E_{x,y}^{tr,e}(\vec{k}, \omega)$ is given in Eq.(13). Looking at Eqs.(15,16), it appears evident the covariant role of the

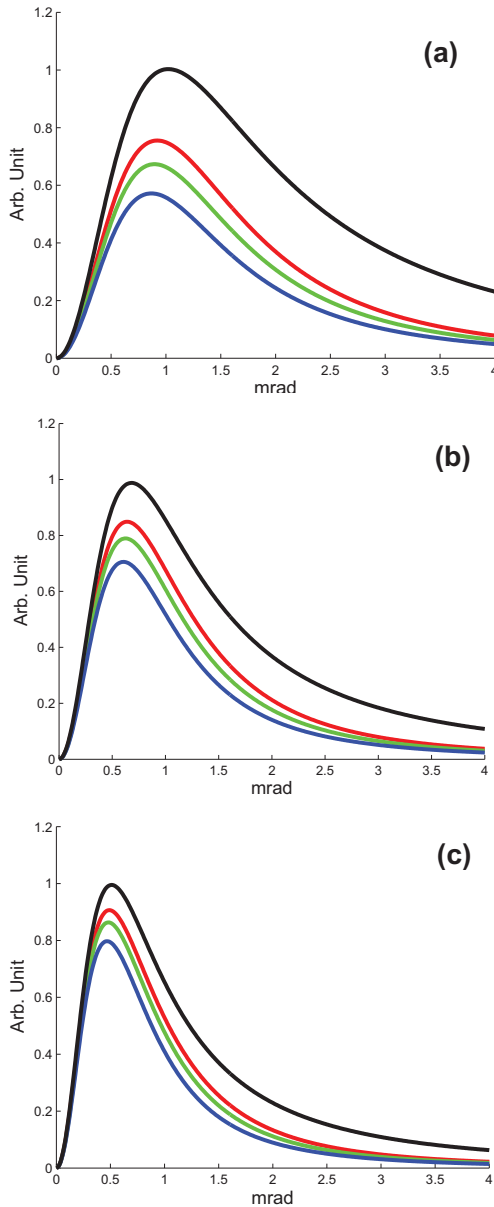


Figure 2: TR angular distribution for different beam energy: (a) 500, (b) 750 and (c) 1000 MeV; wavelength $\lambda = 680$ nm (Red curve), $\lambda = 530$ nm (Green curve), $\lambda = 400$ nm (Blue curve); Gaussian bunch of $N = 10^5$ electrons with $\sigma = 50$ μ m. Blue, Red and Green curves from Eqs.(8,9,11), (Black curve) from Eq.(9).

transverse coordinates of the N electrons is completely missed. In fact, in both the N single electron radiation field amplitudes and the temporal incoherent part of the TR energy spectrum any dependence on the Lorentz-invariant distribution of the N electron transverse coordinates (x_{0j}, y_{0j}) ($j = 1, \dots, N$) disappeared. Moreover, looking at the formula of the TR field - Eq.(15) - it turns out that the causality role played by the N electron longitudinal coordinates z_{0j} ($j = 1, \dots, N$) in determining the emission phases of the N single electron radiation amplitudes is completely mixed

up (indistinguishable) with the role of the N electron transverse coordinates (x_{0j}, y_{0j}) ($j = 1, \dots, N$). The transverse coordinates of the N electrons indeed do not determine the emission phases but only contribute to determine the observation phases as a function of the N electron distances from the z -axis of the reference frame. But, according to the formulation given in Eq.(15), the transverse coordinates of the N electrons seem to play the same causal role played by the N electron longitudinal coordinates.

CONCLUSIONS

Transition radiation (TR) emission of a bunch of N electrons is ruled by Lorentz-covariance and temporal-causality as other electromagnetic radiative mechanism by relativistic charged beams. In case of normal incidence, the Lorentz-covariance consistency for a model of TR means that the Lorentz-invariant dependence on the transverse coordinates of the N electrons is transmitted from the electric field of the relativistic bunch to the TR energy spectrum. At the same time, the clear and strict dependence of the emission phases of the N single electron radiation field amplitudes from the radiator surface on the distribution of the N electron longitudinal coordinates - i.e., on the temporal sequence of the N electron collision onto the metallic screen - is the signature of the temporal-causality in a model of TR. The formal procedure how to implement in the radiation field expression the integral calculus with respect to the radiator surface represents the breaking-point between a Lorentz-covariance and temporal-causality consistent or inconsistent model of TR.

REFERENCES

- [1] M.L. Ter-Mikaelian, *High-Energy Electromagnetic Processes in Condensed Media*, Wiley, New York (1972).
- [2] V.L. Ginzburg, V.N. Tsytovich, *Transition Radiation and Transition Scattering*, Adam Hilger, Bristol (1990).
- [3] L. Wartski, S. Roland, J. Lasalle, M. Bolore, G. Filippi, J. Appl. Phys. **46** (1975) 8.
- [4] U. Happek, A.J. Sievers, E.B. Blum, Phys. Rev. Lett. **67**, 21 (1991) 2962-2965.
- [5] G.L. Orlandi, Optics Communications 311 (2013) 180-185.
- [6] G.L. Orlandi, Paul Scherrer Institut Preprint PSI-PR-12-03, arXiv:1207.0644 [physics.acc-ph].
- [7] G.L. Orlandi, Paul Scherrer Institut Preprint PSI-PR-13-10, arXiv:1306.0768 [physics.acc-ph].
- [8] S. Casalbuoni, B. Schmidt, P. Schmüser, V. Arsov, S. Wesch, Phys. Rev. ST-AB **12**, 030705 (2009).

COHERENT ELECTRON COOLING PROOF OF PRINCIPLE PHASE 1 INSTRUMENTATION STATUS*

D. M. Gassner[#], J. C. Brutus, R. Hulsart, V. Litvinenko, R. Michnoff, T. Miller, M. Minty, I. Pinayev, M. Wilinski, Brookhaven National Laboratory, Upton, NY 11973, USA

Abstract

The purpose of the Coherent electron Cooling Proof-of-Principle (CeC PoP) [1] experiment being designed at RHIC is to demonstrate longitudinal (energy spread) cooling before the expected CD-2 for eRHIC. The scope of the experiment is to longitudinally cool a single bunch of 40 GeV/u gold ions in RHIC. The cooling facility will be installed inside the RHIC tunnel in 3 phases. The status of the instrumentation systems planned for phase 1 commissioning efforts will be described. This paper will also describe updates to the instrumentation systems proposed to meet the diagnostics challenges during the final phase of cooling commissioning [2]. These include measurements of beam intensity, emittance, energy spread, bunch length, position, and transverse alignment of electron and ion beams.

INTRODUCTION

Cooling of ion and hadron beams at collision energy is of critical importance for the productivity of present and future Nuclear Physics Colliders, such as RHIC, eRHIC and ELIC. An effective cooling process would allow us to cool the beams beyond their natural emittances and also to either overcome or to significantly mitigate limitations caused by the hour-glass effect and intrabeam scattering. It also would provide for longer and more efficient stores, which would result in significantly higher integrated luminosity. The scaled down economic version called

CeC PoP does not offer optimal cooling conditions, but it includes the most critical and untested elements (from modulator to kicker) and is sufficient for demonstration. The diagnostics systems described here are based on the requirements determined by the latest simulations; additional systems may be added as further simulations look more closely at non-ideal conditions. The CeC PoP phase 1 beam line is presently in the construction phase. The primary goals of this first phase are to test the 112 MHz SRF gun [3] and 500 MHz buncher cavities and to measure low power 2 MeV electron beam characteristics. Initial system commissioning is planned for early FY15.

ELECTRON BEAM DIAGNOSTICS

During the initial commission phase the electron beam diagnostics will provide the necessary measurements to commission the 112 MHz SRF Gun, then transport the 2 MeV beam through the 11m straight beam line to a low power dump as shown in Fig. 1. During the next phase the low power dump will be replaced with a 704 MHz SRF Linac and the wigglers and associated beam lines will be installed. The 21.8 MeV beam will be transported through the Linac and the FEL wigglers to the high power (10 kW) dump as shown in Fig. 2. During the following RHIC run the wigglers will be relocated into the nearby RHIC transport to allow electron co-propagation with the gold ion bunches and allow initial cooling studies as shown in Fig. 3.

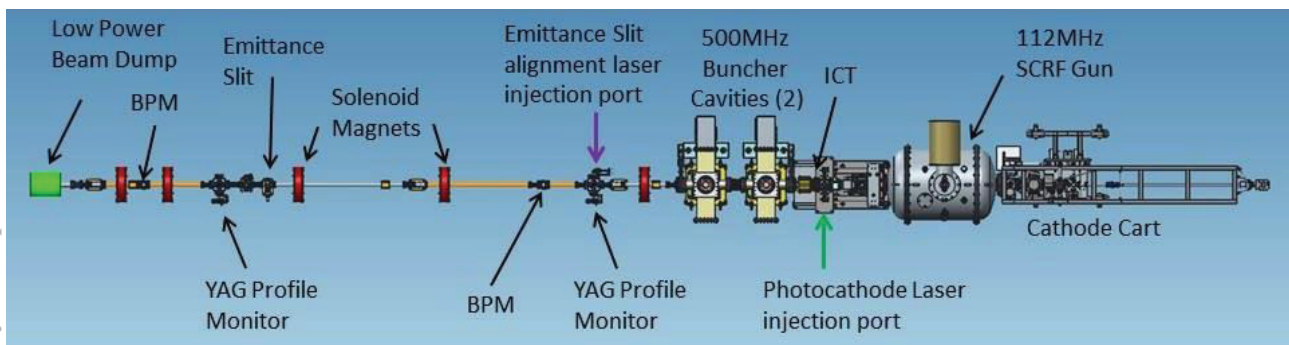


Figure 1: Plan view of the phase 1 electron beam line (2 MeV), the commissioning goals include SRF gun and buncher testing and beam parameter measurements.

*Work supported by U.S. DOE under contract No DE-AC02 98CH10886 with the U.S. DOE

[#]gassner@bnl.gov

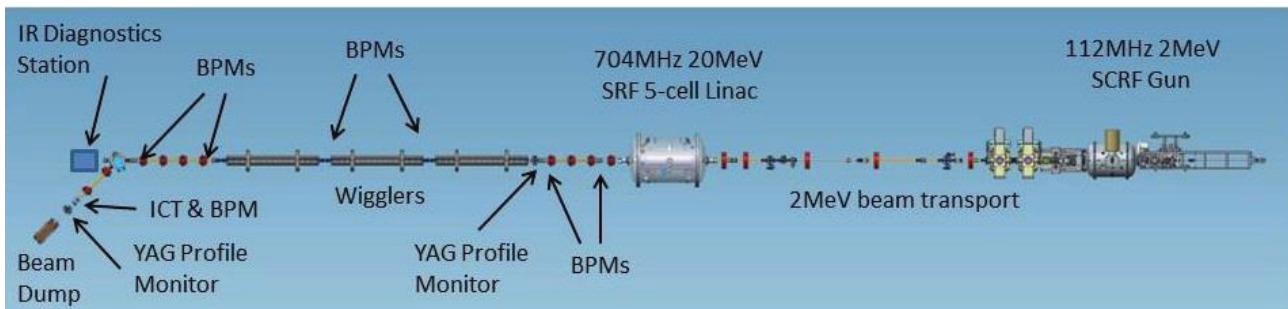


Figure 2: Plan view of the phase 2 electron beam line, the goals are to test 704 MHz 20 MeV Linac and wigglers.

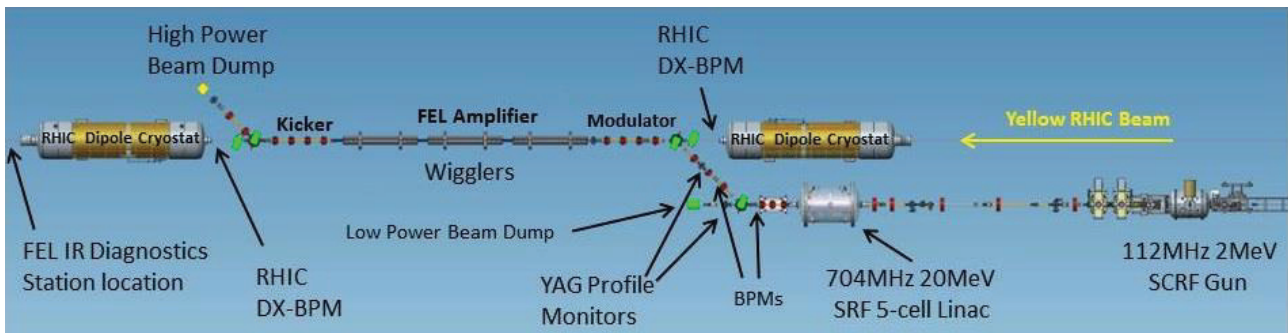


Figure 3: Plan view of the final phase 3 configuration to demonstrate cooling of RHIC gold beam.

Bunch Charge and Current

Electron bunch and bunch train charges will be measured by a Bergoz [4] in-flange Integrating Current Transformer (ICT-CF6-60.4-040-020:1-H-UHV-THERMOE) with 1.25V/C sensitivity and the AISI 316LN option. Beam charge signals will be processed by Bergoz BCM-IHR Integrate-Hold-Reset electronics with the 10 kHz option feeding a beam synched triggered digitizer. An ICT will be installed in the upstream portion of the 2 MeV transport and another just upstream of the high power dump to allow monitoring of the overall transport efficiency. Due to the 10 kHz measurement rate limitation only a subset of the planned 78 kHz bunches will be measured.

The low and high power beam dumps will be electrically isolated to allow measurement of the collected electron beam.

Beam Position Monitors

There are 11 dual plane button style BPM pick-ups in the 40 meter electron beam line. All of the 15mm diameter BPM buttons and associated housings are provided by MPF Products Inc.[5], except for the housings downstream of each wiggler that are provided with the wiggler structures from BINP as shown in Fig. 4.

During phase 1 commissioning Libera Brilliance Single Pass electronics from Instrumentation Technologies will process signals from the two BPMs downstream of the gun. We plan to utilize new in-house VME based BPM electronics modules presently in development for the remaining downstream BPMs. These modules are based on a Xilinx Zynq processor/programmable logic array combination which allows for great flexibility in designing custom processing algorithms for a variety of

bunch frequencies and types. The current design incorporates 500 MHz and 707 MHz band pass RF filters in the analog input section which are suited for electron beam measurements. A different configuration also allows the use of a 39 MHz low pass filter instead for hadron beam measurements. A set of four A/D converters can be clocked at rates up to 400 MHz and provide four channels of measurement on each hardware board which will correspond to each dual-plane BPM module. Each VME module has its own Ethernet connection to the network which allows direct access to data from standard controls software tools. The first series of hardware boards have been received at BNL and are currently under testing and evaluation.

During the phase 3 cooling demonstration an electron bunch will co-propagate with a 40 GeV/u gold bunch in the yellow RHIC ring. The electron-ion alignment strategy utilizes the button DX BPMs (ions only) located at the ends of the RHIC warm section in addition to the button BPMs in the common cooling region. Filters will be used to separate the analog beam position signals of the long 10ns ion bunch and the short 10ps electron bunch to allow separate BPM electronics modules to measure both beam positions in the common region.

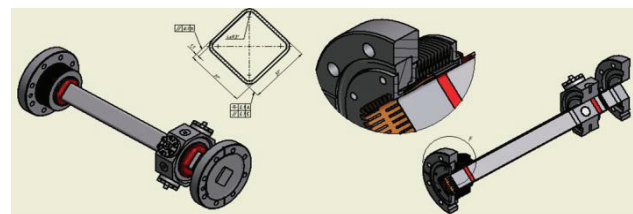


Figure 4: Beam Position Monitor pick-up assembly downstream of each Wiggler section provided by BINP.

Electron Beam Emittance

There are several techniques planned to measure beam emittance. The expected normalized emittance range is 2-10 mm-mrad. An emittance slit station will be used to measure the space-charge dominated 2 MeV beam emittance in the injection transport. This station consists of a 3-position plunging 2 mm thick tungsten mask located 0.5 m upstream of a YAG profile monitor. The 0.2 mm wide slits are 2 mm apart as shown in Fig 5.



Figure 5: Emittance slit 3-position plunger on left, and tungsten mask with 0.2mm horizontal and vertical slits.

The profile monitor upstream of the emittance slit is configured with a green diode laser and adjustable 3X beam expander to allow convenient alignment of the slit mask to ensure quality measurements can be made on the downstream profile monitor as shown in Fig. 6. A mirror mounted in the vacuum chamber on the back of the YAG mirror is used to direct the alignment laser towards the emittance downstream slit mask as shown in Fig. 7.

The 21.8 MeV beam emittance can be measured in the auxiliary beam line transport straight out of the SRF Linac using the traditional quad scan technique using image data from the downstream YAG profile monitor. The energy spread can be measured using the profile monitor located after the first dipole downstream of the Linac.

Longitudinal Profile Measurement

Longitudinal bunch length measurements will be made by varying the Linac rf phase and analyzing the images on the downstream profile monitor after the first dipole magnet. To fully utilize the electron beam cooling capacity a uniform longitudinal beam profile is needed [6]. A two frequency injector system tuned for this requirement will be utilized.

Transverse Profile Monitors

Transverse beam profiles will be measured using pneumatic plunging 0.1 X 30 mm YAG:Ce screens mounted in profile monitor stations as shown in Fig. 6 and 7. There will be six located of these stations installed at key locations in the beam transport.

Images from the YAG screen that is oriented orthogonal to the electron beam are transported by two mirrors and fixed lens to a GigE CCD camera. Software was developed that allows line-out profile data at any angle cut through the image as shown in Fig. 8.

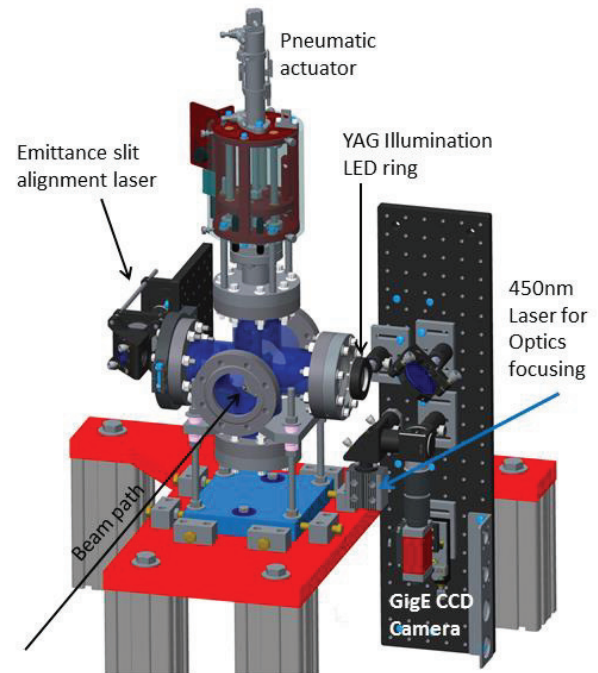


Figure 6: YAG Profile Monitor with emittance slit alignment diode laser injection port and 450 nm diode laser used for optics focusing.

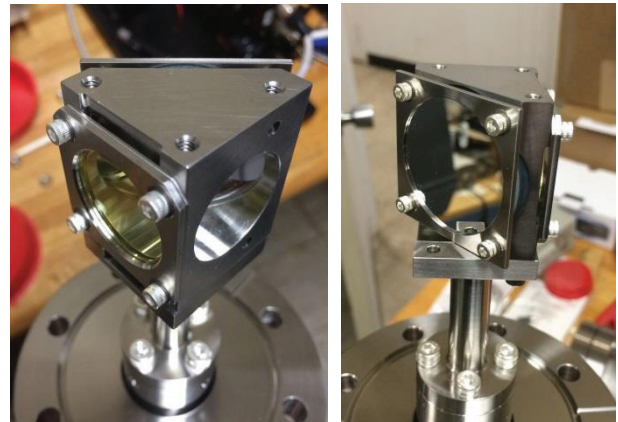


Figure 7: YAG screen head with 45 degree beam image mirror at left, at right the other side is shown with 45 degree laser alignment mirror behind the image mirror.

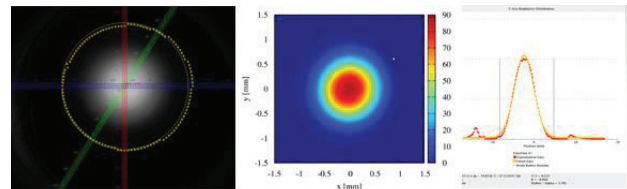


Figure 8: Beam profile monitor image signal processing examples.

Electron Beam Loss Monitors

Beam loss detectors will be distributed at 14 key locations throughout the beam line to provide a tuning aid

and will be used to optimize transport efficiency. Elevated radiation doses need to be avoided especially in the wiggler sections where they can lead to a partial demagnetization of the permanent magnets with a detrimental effect on the free-electron laser process. The primary loss sensor will be a photomultiplier tube based loss detector. The design of this detector is based on ones developed at Jefferson Lab and used at CEBAF. CeC PoP will plan to use the Hamamatsu R11558 PMT in the detectors.

Loss signals will be processed using a VME module developed at JLAB that provides dual parallel analog circuits for each detector. An integrating channel provides fast response (<1 us) with configurable interlock threshold comparison for machine protection, a second channel which employs a log-amp provides wide dynamic range (>50 dB) for tuning [7].

FEL WIGGLER DIAGNOSTICS

The laser light from the FEL wiggler will be used for monitoring the lasing and cooling process. Characteristics of the spontaneous radiation will be an indication of the electron beam trajectory and the quality of the electron and ion bunch overlap. The positively charged ions will attract the electrons and each cloud surrounding the ion will radiate coherently in the wiggler, thus substantially increasing the optical power due to the effective increasing of shot noise. FEL tuning will include alignment of the electron trajectory and proper relative phase adjustments of the three wiggler sections using separately powered phase shifters and dipole correctors downstream of each 2.8 m wiggler (2.5 m of 60 poles + 30 cm for $2\frac{1}{2}$ matching poles). The phase between the wigglers needs to be precise, and the relative electron-ion phase in the kicker region is critical to demonstrate cooling. The FEL gain needs to remain in the linear range for effective cooling and is expected to be on the order of 100, therefore the IR power will rise by four orders of magnitude. The wiggler radiation will be concentrated around a 14 micron wavelength. There will be a dedicated FEL IR diagnostics station located downstream of the wigglers [8].

ACKNOWLEDGMENTS

The authors would like to thank CeC community for the many years of concept development, and especially members of the C-AD Instrumentation Systems Group and G. Miglionico for the layout drawings.

REFERENCES

- [1] V. Litvinenko et al., “Proof-Principle Experiment for FEL-Based Coherent Electron Cooler”, in *Particle Accelerator Conference 2011*, New York, NY, THOBN3
- [2] D. M. Gassner et al., “Coherent Electron Cooling Proof of Principle Instrumentation Design” in *Beam Instrumentation Workshop 2012*, Newport, Virginia, USA, WEAP01
- [3] S. Belomestnykh et al., “Superconducting 112 MHz QWR electron Gun” in *15th International Conference on RF Superconductivity*, July 2011, Chicago, Illinois, USA, MOPO054
- [4] Bergoz Instrumentation website: www.bergoz.com
- [5] MPF Products Inc website: <http://mpfpi.com/>
- [6] I. Pinayev et al., “Formation of the Electron Bunch Longitudinal Profile for Coherent Electron Cooling Experiment”, in *These Proceedings: Proc. 36th Int. Free-Electron Laser Conf.*, 2014, Basel, THP048
- [7] J. Yan and K. Mahoney, “New Beam Loss Monitor for the 12GeV Upgrade” in *The International Conference on Accelerator and Large Experimental Physics Control Systems*, ICALEPCS2009, Kobe, Japan, WEP092
- [8] T. Miller et al., “Infrared Diagnostics Instrumentation Design for the Coherent Electron Cooling Proof of Principle Experiment”, in *Proceedings: Proc. 36th Int. Free-Electron Laser Conf.*, Basel, 2014, THP074

EVOLVEMENT OF THE LASER AND SYNCHRONIZATION SYSTEM FOR THE SHANGHAI DUV-FEL TEST FACILITY*

B. Liu[†], X.T. Wang, X.Q. Liu, S.P. Zhong, W.Y. Zhang, T.H. Lan, L. Feng, D. Wang
SINAP, CAS, Shanghai 201800, China

Abstract

Many attractive experiments including HGHG, EEHG, cascaded HGHG, chirped pulse amplification etc. are carried out or planned on the Shanghai Deep- Ultraviolet Free-Electron Laser test facility. These experiments are all utilizing a laser as seed, and need precise synchronization between the electron beam and the laser pulse. We will describe the history and current status of the seeding and synchronization scheme for the SDUV-FEL together with some related measurement results in this paper.

INTRODUCTION

High gain free-electron lasers (FELs) are being developed to serve as high-intensity coherent radiation sources for advanced user applications. One of the most feasible ways for delivering short-wavelength FEL is self-amplified spontaneous emission (SASE) [1, 2]. However, SASE radiation starts from shot noise of the electron beam, and results in a poor temporal coherence. With the growing interest in fully coherent sources, various seeded FEL schemes have been proposed on the basis of harmonic generation and seeding of external lasers. A typical scheme is high-gain harmonic generation (HGHG) [3], which has been demonstrated from the infrared to the soft X-ray spectral region [4–7].

Seeded FEL schemes need precise synchronization of laser and beam. Usually the electron beam duration for FEL is from picosecond down to femtosecond, and pulse length of the seed laser is at the same level. Thus the synchronization precision should be sub-picosecond and sometimes even down to femtosecond level. Such stringent requirement could be fulfilled with various ways, such as high harmonic phase-locked loop (PLL) and optical cross-correlation [8].

FEL experiments of HGHG, echo-enabled harmonic generation (EEHG) [9–11] and cascaded HGHG [12–14] have been carried out, and chirped pulse amplification [15, 16] are underway at Shanghai Deep-Ultraviolet Free-Electron Laser test facility (SDUV-FEL) [17], which is consisting of an injector, a main accelerator, a bunch compressor, two laser modulation stages, and a long undulator section. The seed laser interacts with the electron beam in the two modulator undulators.

All these experiments are externally seeded, and precise synchronization between the seed laser and electron beam is necessary. In this paper, the history and current status of related laser and synchronization systems are reviewed. Some measurement results are also presented.

* work supported by the National Natural Science Foundation of China (Grant No. 11175241)

[†] liubo@sinap.ac.cn

LASER SYSTEMS

The SDUV-FEL was originally a SASE test facility, and had only one Nd:YLF laser system serving as the drive laser. With some modification on the laser transport system, it had been successfully turned into a HGHG test facility since 2009. One Ti:Sapphire laser system was put into operation as the dedicated seed laser in 2010 and an optical parametric amplifier (OPA) system was added to extend the capability in 2011. Currently, a rather complicated laser transport system has been established to fulfill different requirements, which is shown in Figure 1.

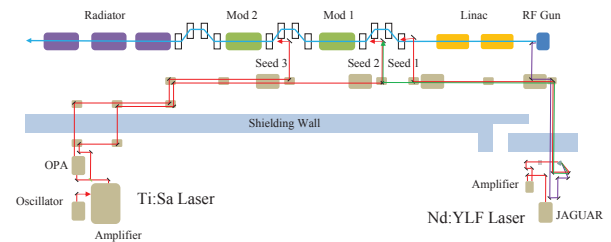


Figure 1: Layout of the laser transport system.

There are three laser injection points and two modulation sections along the beam line. The seed laser could be coming either from the Nd:YLF system or from the Ti:Sa system depending on the requirement of the planned experiment.

Nd:YLF Laser

The basic parameters of the Nd:YLF laser system is shown in Table 1.

Table 1: Parameters of the Nd:YLF Laser System

Parameter	Value	Remark
Wavelength	1047 nm	fundamental
Pulse length	8.7 ps	FWHM
Repetition rate	119 MHz	oscillator
Repetition rate	2 Hz (100 Hz max.)	amplifier
	>5 mJ@1047 nm	amplifier
Pulse energy	>2 mJ@523 nm	2nd harmonic
	>1 mJ@262 nm	4th harmonic

The Nd:YLF laser is mainly used to drive the RF gun at its fourth harmonic through two BBO crystals, while the residual fundamental and second-harmonic light could be used as the seed laser.

Ti:Sapphire Laser

The basic parameters of the Ti:Sapphire laser system is shown in Table 2.

Table 2: Parameters of the Ti:Sa Laser System

Parameter	Value	Remark
Center wavelength	750 --860 nm	
	1160 --1600 nm	OPA signal
	1600 --2600 nm	OPA idler
Pulse length	35 fs, 130 fs, 1 ps	FWHM
Repetition rate	79.333 MHz	oscillator
Repetition rate	1 kHz	amplifier
Pulse energy	>3.5 mJ @800 nm	amplifier
	>400 μ J	OPA signal
	>300 μ J	OPA idler

The Ti:Sapphire laser system is utilized as a dedicated seed to provide various wavelength output at different pulse length. With the OPA system, the laser seed could be tuned continuously from 1160 nm to 1600 nm or from 1600 nm to 2600 nm, thus we could continuously tune the FEL output without varying the electron beam energy.

SYNCHRONIZATION SYSTEM

Tuning of the Synchronization

At first, the seed laser and the electron beam are adjusted to be transversely overlapped through two frosted YAG screens which are placed upstream and downstream the modulator, respectively.

The longitudinal overlap of the seed laser and the beam is accomplished in two steps. Coarse synchronization is tuned with a PD and an oscilloscope. The beam and the seed laser could be observed by detecting the undulator radiation signal of the electron beam and the seed laser simultaneously by a PD downstream the modulator. By using a 1 GHz PD and a high resolution oscilloscope with 6 GHz bandwidth and 25 GS/s sampling rate, the electron beam and the seed laser could be temporally overlapped with a precision better than 100 ps.

Final precise synchronization is achieved by observing the radiation signals from the radiator while fine tuning the seed laser delay. When the seed laser does not interacts with the electron beam, only the spontaneous emission could be observed in the radiator undulator, which is rather weak. While one adjusts the laser delay with femtosecond level precision to the right direction, the stronger and stronger radiation signal will indicate final synchronization of the seed laser and the electron beam.

After longitudinal position is tuned to be fully coincident, the optimal interaction between the laser and the beam could be found by fine tuning of the transverse position while observing the radiation. Other parameters, such as the modulator gap, chicane strength and the radiator gap, could also

be optimized to fulfill the resonant condition, and hence increase the signal to noise ratio.

Original Scheme

The first HGHG experiment on SDUV-FEL is accomplished with a seed laser coming from the drive laser, which is actually the residual fundamental output after the first BBO crystal. The distribution system for the reference signals is shown in Figure 2. The frequency of master RF oscillator is 119 MHz, which is the same as the repetition rate of the drive laser oscillator, while the 2856 MHz reference for low-level RF systems is generated by a multiplier. Path length of the IR laser from the source to the interaction point inside modulator is designed almost equal to that of the UV laser plus electron bunch, and can be finely adjusted remotely by a motorized delay stage.

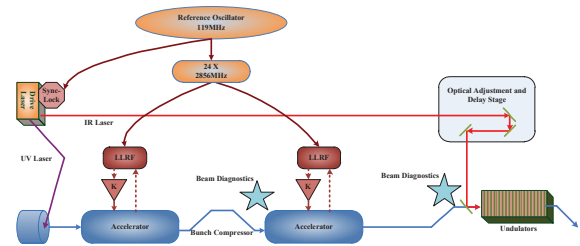


Figure 2: Original reference distribution system for the SDUV-FEL.

The auto-correlation measurement demonstrates that the pulse length of the drive laser is 8.7 ps (full width at half maximum, FWHM). In this experiment, the electron beam is accelerated on crest and the bunch compressor is off. That is to say, the electron beam and the laser will be of the similar length.

The coherent radiation intensity versus the laser delay is shown in figure 3. The FWHM is about 15 ps, which agrees with the laser pulse length measurement result.

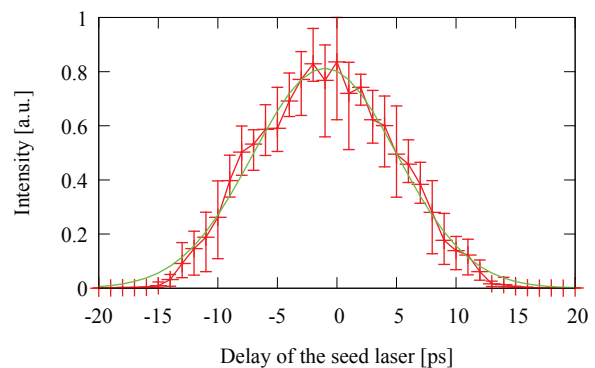


Figure 3: Measurement result of the seed laser scanning.

Current Scheme

In 2010, a Ti:Sapphire system was integrated into the SDUV-FEL to do some more sophisticated experiments.

The new laser oscillator is working at 79.333 MHz, which is $2/3$ of the drive laser. To make the laser pulse synchronized to the electron bunch, the timing and synchronization system must be upgraded to adapt to the changes, which is shown in Figure 4. A new customized master source based on crystal oscillator was built to provide phase-locked 119 MHz and 79.333 MHz references with very low phase noise. A commercial delay generator is used to scale down the reference frequency and provide triggers with different delays.

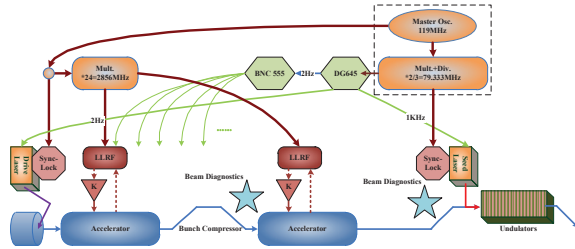


Figure 4: Current synchronization scheme for the SDUV-FEL.

After the new dedicated Ti:Sapphire seed laser is put into use, it's able to measure the beam profile directly. The new seed laser is 130 fs FWHM, and can resolve the bunch profile easily in sub-picosecond level.

Two different cases are demonstrated in Figure 5. One is for the uncompressed bunch (Fig. 5(a)), while the other is for the compressed bunch with the theoretical compression ratio of 2 (Fig. 5(b)). The results agree well with the theory and the simulation. The intensity fluctuations observed are mainly contributed by the beam energy instability and the timing jitter between the seed laser and the beam.

A rough estimation of the timing jitter between the laser and the beam could also be done from the scanning result. From the measurement data, one could estimate that the timing jitter during a short time period is about 1.0 ps. Further optical cross-correlation experiments are considered to verify these estimations.

Direct measurement of the relative phase between the laser and reference signal could also give some information of the synchronization system, as shown in Figure 6. Short time jitter is at sub-picosecond level, however, the drift is rather large. Further measurements are planned in order to determine which part contributes most, the reference distribution or the laser locking box.

Future Plan

For the SDUV-FEL, the bunch length of electron beam is at picosecond level, thus jitter and drift is not a big problem during various FEL experiments. However, for future FEL facilities, especially for user experiments, jitter and drift will be of great concern. Based on the pulsed laser technologies, a high performance synchronization system has been developed [18] to fulfill the requirements for future XFELs. Development of such kind of system is also planned in China and some key technologies will be tested on the SDUV-FEL,

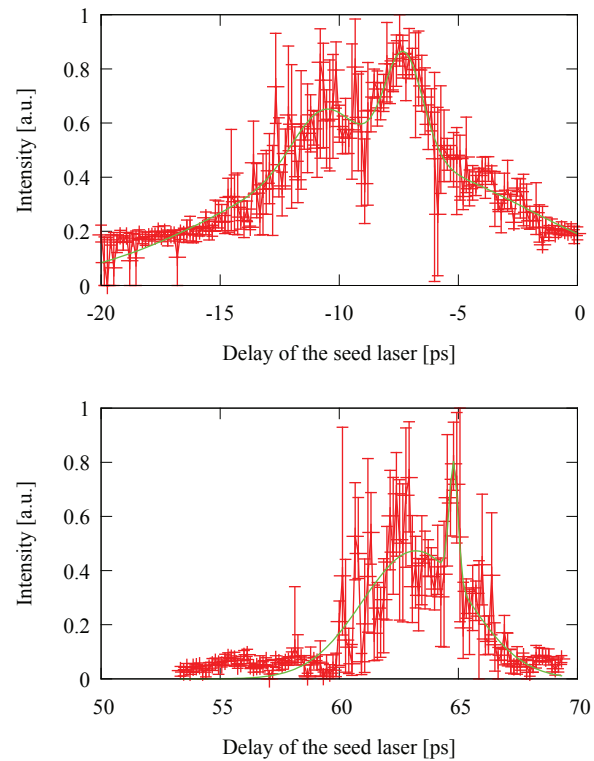


Figure 5: Seed laser delay scan for (a) the uncompressed beam and (b) the compressed beam.

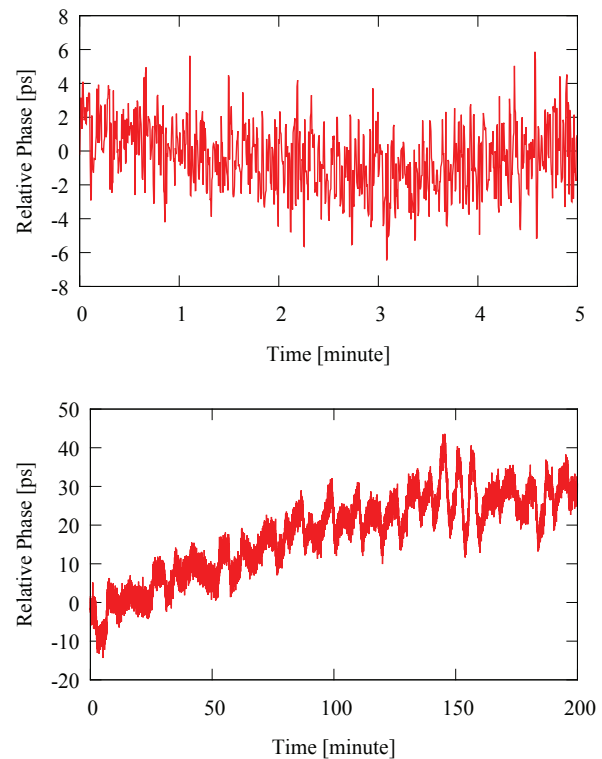


Figure 6: Jitter between the seed laser oscillator and the reference signal for (a) 5 minutes and (b) 200 minutes.

as shown in Figure 7. An Er-doped fiber laser locked to the RF oscillator will generate femtosecond laser pulses as reference. Through a phase stable fiber distribution subsystem, the reference optical pulses will be sent to different locations along the facility. The drive and seed lasers can be locked to the reference with laser-laser synchronization device which is based on optical cross-correlation, while the low noise RF signals for LLRF systems will be regenerated from the reference with the RF-laser synchronization device based on balanced optical-microwave phase detector. The stable reference can also be used for beam diagnostics directly.

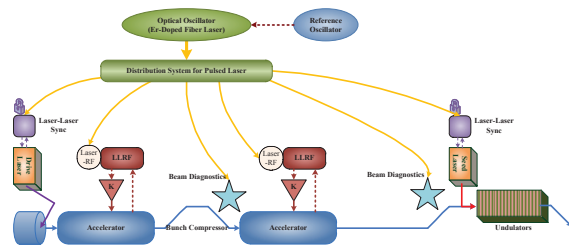


Figure 7: Future upgrade plan for the SDUV-FEL synchronization system.

CONCLUSION

Two solid-state laser systems serving as the drive and seed lasers have operated at SDUV-FEL for a few years. Kinds of seeding schemes are developed to fulfill different requirements of various FEL experiments. The pulse energy has been increased to provide more electron charge and more modulation power through several upgrades. Energy stability and pointing stability are main concerns in the future.

Precise synchronization between the laser and the beam is achieved, which is a necessity for seeded FEL experiments. A general approach is established to make the synchronization process easy and regular. The electron bunch profile is measured with the laser scanning technique, and the results agree with the theoretical expectation and the simulation.

Current synchronization is obtained by RF phase-locked loop, and all reference signals are derived from the same crystal oscillator. However, RF phase-locked loop has some limitations, such as low precision and large long-term drift, which is not a big problem for the long electron bunches and single-stage HGHG operation. But for cascaded HGHG and very short bunches, it requires much more stringent synchronization down to a few femtoseconds. A pulsed laser based optical synchronization system is under consideration for the SDUV-FEL, which will improve the synchronization precision and stability.

ACKNOWLEDGMENT

The authors would like to thank the operation staffs in the Shanghai Institute of Applied Physics for the excellent support during the SDUV-FEL experiments.

REFERENCES

- [1] A. M. Kondratenko and E. L. Saldin, "Generating Of Coherent Radiation By A Relativistic Electron beam In An undulator", Part. Accel. 10, 207 (1980).
- [2] R. Bonifacio, C. Pellegrini, and L. Narducci, "Collective instabilities and high-gain regime in a free electron laser", Opt. Commun. 50, 373 (1984).
- [3] L.H. Yu, "Generation of intense uv radiation by subharmonically seeded single-pass free-electron lasers", Phys. Rev. A 44, 5178 (1991).
- [4] L.H. Yu, M. Babzien, I. Ben-Zvi, et al., "High-Gain Harmonic-Generation Free-Electron Laser", Science 289, 932 (2000).
- [5] L.H. Yu, L. DiMauro, A. Doyuran, et al., "First Ultraviolet High-Gain Harmonic-Generation Free-Electron Laser", Phys. Rev. Lett. 91, 074801 (2003).
- [6] E. Allaria, R. Appio, L. Badano, et al., "Highly coherent and stable pulses from the FERMI seeded free-electron laser in the extreme ultraviolet", Nature Photonics 6, 699 (2012).
- [7] E. Allaria, D. Castronovo, P. Cinquegrana, et al., "Two-stage seeded soft-X-ray free-electron laser", Nature Photonics 7, 913-918 (2013).
- [8] S. Schulz, V. Arsov, A. Winter, et al., "An optical cross-correlation scheme to synchronize distributed laser systems at FLASH", THPC160, in *Proc. 11th European Particle Accelerator Conf.*, Genoa, Italy, pp. 3366-3368.
- [9] G. Stupakov, "Using the Beam-Echo Effect for Generation of Short-Wavelength Radiation", Phys. Rev. Lett. 102, 074801 (2009).
- [10] J.H. Chen, H.X. Deng, Q. Gu, et al., "Operating the SDUV-FEL with the echo-enabled harmonic generation scheme", Chinese Physics C 33, 706 (2009).
- [11] Z.T. Zhao, D. Wang, J.H. Chen, et al., "First lasing of an echo-enabled harmonic generation free-electron laser", Nature Photonics 6, 360 (2012).
- [12] L.H. Yu, I. Ben-Zvi, "High-gain harmonic generation of soft X-rays with the 'fresh bunch' technique", Nucl. Instr. and Meth. A 393, 96-99 (1997).
- [13] C. Feng, M. Zhang, G.Q. Lin, et al., "Design study for the cascaded HGHG experiment based on the SDUV-FEL", Chinese Science Bulletin 57, 3423-3429 (2012).
- [14] B. Liu, W.B. Li, J.H. Chen, et al., "Demonstration of a widely-tunable and fully-coherent high-gain harmonic-generation free-electron laser", Phys. Rev. ST Accel. Beams 16, 020704 (2013).
- [15] L.H. Yu, E. Johnson, D. Li, D. Umstadter, "Femtosecond free-electron laser by chirped pulse amplification", Phys. Rev. E 49, 4480-4486 (1994).
- [16] C. Feng, L. Shen, M. Zhang, et al., "Chirped pulse amplification in a seeded free-electron laser for generating high-power ultra-short radiation", Nucl. Instr. and Meth. A 712, 113-119 (2013).
- [17] Z.T. Zhao, Z.M. Dai, X.F. Zhao, et al., "The Shanghai high-gain harmonic generation DUV free-electron laser", Nucl. Instr. and Meth. A 528, 591 (2004).
- [18] J. Kim, J.A. Cox, J. Chen and F.X. Kärtner, "Drift-free femtosecond timing synchronization of remote optical and microwave sources", Nature Photonics 2, 733-736 (2008).

LONGITUDINAL RESPONSE MATRIX SIMULATIONS FOR THE SWISSFEL INJECTOR TEST FACILITY

A. Saa Hernandez*, B. Beutner†, F. Frei, R. Ischebeck, PSI, Villigen, Switzerland

Abstract

The Singular Value Decomposition (SVD) method has been applied to the SwissFEL Injector Test Facility to identify and better expose the various relationships among the possible jitter sources affecting the longitudinal phase space distribution and the longitudinal diagnostic elements that measure them. To this end, several longitudinal tracking simulations have been run using the Litrack code. In these simulations the RF and laser jitter sources are varied one-by-one within a range spanning several times their measured stability. The particle distributions have been dumped close to the diagnostic locations and the measured quantities analyzed. A matrix has been built by linearly fitting the response of each measured quantity to each jitter source. This response matrix is normalized to the stability of the jitter source and the instrumentation accuracy, and it is inverted and analyzed using SVD. From the eigenvalues and eigenvectors the sensitivity of the diagnostics to the jitters can be evaluated.

INTRODUCTION

The SwissFEL free electron laser [1] is currently being constructed at the Paul Scherrer Institute. The SwissFEL Injector Test Facility (SITF) has been operated since 2010 as a platform to develop and test the different components and optimize the procedures necessary to operate later SwissFEL.

Several sources of jitter and drift affect the longitudinal phase space dynamics of the SITF. In order to identify and better expose the various relationships among the error sources and the longitudinal diagnostics that measure them, longitudinal response matrix simulations have been performed for the SITF in a similar manner as previously realized for SwissFEL [2]. These simulations have been used to predict the response matrix later measured at SITF during two shifts. A detailed description and analysis of the experimental results is given on a separate contribution [3].

A scheme of the SITF showing the longitudinally relevant elements is sketched in Figure 1. The electrons emerge from an S-band RF photoinjector and are accelerated by a booster linac based on normal conducting S-band RF technology, which simultaneously generates the necessary energy chirp for the magnetic compression. In front of the magnetic chicane a fourth harmonic X-band cavity, phased for deceleration, linearizes the longitudinal phase space for optimal bunch compression. The last drift section is dedicated to the beam characterisation.

The bunch charge is measured with stripline beam position

monitors (BPM), that were calibrated via a Faraday cup and a wall-current monitor [4]. BPMs in dispersive sections measure the horizontal beam position from which the mean particle energy is inferred, while the energy distribution is measured by imaging the incoherent synchrotron radiation with a monitor (SRM) [5]. The bunch arrival time monitor (BAM) samples the deviation of a RF pick-up signal from the electron bunch with a pulsed reference laser [6]. The absolute bunch length is measured in a destructive manner using a transverse deflective cavity (TDC) and imaging the bunch at a screen, while the relative bunch length variations are measured with a bunch compression monitor (BCM) based on coherent diffraction radiation (CDR) generated as the electron bunch passes through a hole in a foil. After passing through THz filters, the emitted CDR is detected by Schottky diodes [3]. An overview of the longitudinal diagnostics relevant for the response matrix studies is also shown in Figure 1.

SIMULATIONS

To analyze the sensitivity of the electron beam to RF-phase, RF-amplitude, and charge errors the entire beamline must be considered. The beamline is modeled in *LiTrack* [7], a one-dimensional tracking code which includes the effect of longitudinal wakefields. The physics model of Litrack is more appropriate for highly-relativistic beams. For this reason the following trick is applied to study the entire beamline; initially a low-energy high space-charge 3D tracking simulation is done with *Astra* [8] and a particle distribution at 130 MeV (after FINSB02) is generated. The energy and longitudinal coordinates of these particles are used as a 1D input distribution for the LiTrack simulation, where it is firstly tracked backwards to the photocathode and afterwards tracked forward including the error sources. A total of 11 error sources have been studied in this work; the phase and amplitude of the photoinjector RF gun (ϕ_{SS} , A_{SS}), the phase and amplitude of the three S-band accelerating cavities (ϕ_{S1} , A_{S1} , ϕ_{S2} , A_{S2} , ϕ_{S3} , A_{S3}), the phase and amplitude of the linearizer X-band cavity (ϕ_X , A_X) and bunch charge (Q) due to laser fluctuations. The nominal settings of the charge and RF parameters in the simulations, presented in Table 1, are taken such to match those of the experiments performed at SITF. Thus, bunches of 20 pC are accelerated to a final energy of 200 MeV and compressed approximately 7 times their original length, from 1.9 ps (570 μm) down to 266 fs (79 μm) in the experiment, and only down to 85 μm , approximately 10% less compression, in the simulations with the same RF settings.

The tracking simulations are run varying the error sources one by one, in five steps, within the range shown in Table 1.

* angela.saa-hernandez@psi.ch

† presently at DESY, Hamburg

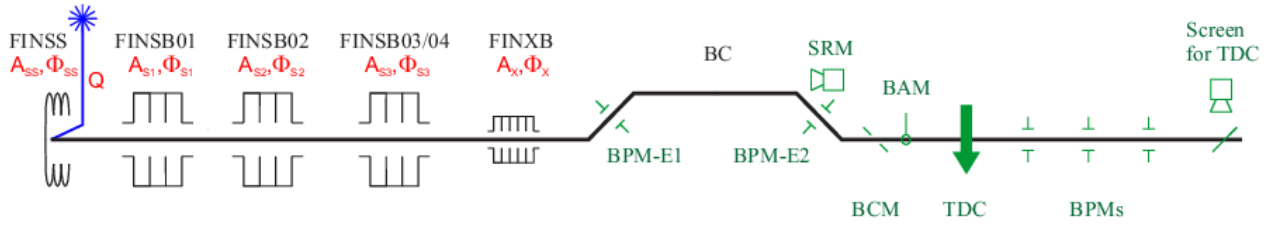


Figure 1: Scheme of the SwissFEL Injector Test Facility. In green the longitudinal diagnostics sketched at their positions, in red the error sources studied in this work.

Table 1: Initial settings and variation range of the longitudinal error sources that match the experimental conditions. The stability was measured during the experiments.

Parameter	Settings	Variation Range	Stability
ϕ_{SS}	4.3 °	± 1.5 °	0.039 °
A_{SS}	7.02 MV	± 7.4 %	0.041 %
ϕ_{S1}	-0.02 °	± 1.5 °	0.022 °
A_{S1}	53.57 MV	± 1.7 %	0.011 %
ϕ_{S2}	-2.5 °	± 1.5 °	0.026 °
A_{S2}	70.80 MV	± 0.5 %	0.007 %
ϕ_{S3}	-37.5 °	± 1.5 °	0.035 °
A_{S3}	102.65 MV	± 6.0 %	0.056 %
ϕ_X	180.04 °	± 1.5 °	0.18 °
A_X	14.21 MV	± 8.6 %	0.13 %
Q	20 pC	± 9 %	0.9 %

This range was defined experimentally. An example of the particle distribution tracked along the beamline for the five steps of the ϕ_{S3} variation range is shown in figure 2. The particle distribution is projected along the longitudinal position axis and the energy axis. The variation in arrival time and bunch compression is clearly visible for the different steps.

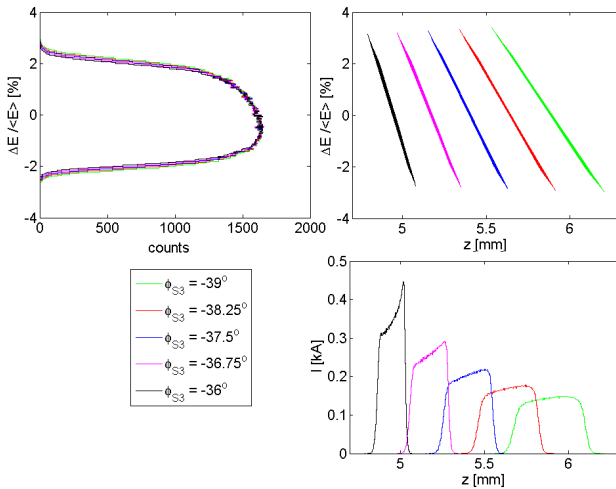


Figure 2: Particle distribution tracked with Litrack along the entire beamline, for the five steps variation of ϕ_{S3} .

The particle distributions are dumped close to the diagnostic locations and analyzed such to extract the parameter that would be measured by each diagnostic element. In this

manner, most of the diagnostic elements are not yet modeled in this first approximation to the response matrix problem. Thus, to get the energy at the position of the SRM and of the BPMs in the bunch compressor (BPM-E1, BPM-E2) the energy outputs provided by the LiTrack code close to those positions are simply taken. Similarly, to get the charge from the stripline BPMs the charge output of the LiTrack code after the bunch compressor is taken. To get the bunch length at the screen which images the bunch deflected by the TDC the particle distribution is projected along the longitudinal position axis and the rms is taken. Similarly, for the energy spread measurements at the SRM the rms from the particle distribution projected along the energy axis is taken. The BCM is the only diagnostic element which had to be modeled in order to be able to extract from the particle distribution the parameter it measures. To get the relative bunch length variations the current profile was generated from the projection of the particle distribution along the longitudinal position axis. From this, the power spectrum was derived and subsequently multiplied by the single electron spectrum and the spectral responsivity of the detectors used. The single electron spectrum was simulated by the numerical code *THz Transport* [9], taking into account the experimental geometry. For the two BCMs, the CDR is thereafter integrated in two spectral bands (BCM-D1r: 0.6 – 2 THz, BCM-D2r: 0.26 – 2 THz). The cut-on frequency of the high pass THz filter determines the sensitivity of the BCM.

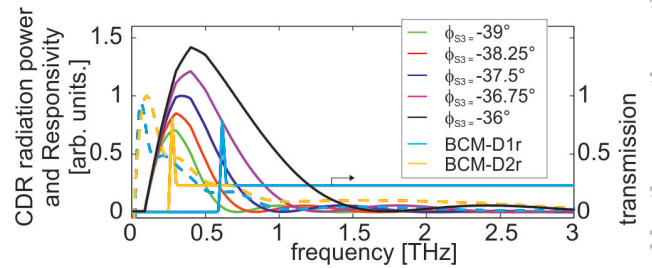


Figure 3: CDR radiation power corresponding to the ϕ_{S3} phase variation range and transmission of the THz filters and the spectral responsivities of the corresponding detectors (blue and yellow).

An example of the CDR generated for the five steps of the ϕ_{S3} variation range is shown in Figure 3. All the diagnostics elements, the corresponding measured parameters and

Table 2: Longitudinal Diagnostics and Their Resolution

Diagnostics	Quantity measured	Resolution
BPM-E ₁	energy	0.013 MeV
SRM-E	energy	0.024 MeV
SRM-ΔE	energy spread	0.024 MeV
BPM-E ₂	energy	0.013 MeV
BCM-D1r	CDR, integr. 0.6–2 THz	1.6 mV (0.8 %)
BCM-D2r	CDR, integr. 0.26–2 THz	2.4 mV (0.6 %)
BPM-Q	charge	0.062 pC (0.3 %)
BAM-t	bunch arrival time	52 fs
TDC-σ _z	bunch length	40 fs

its resolution, estimated experimentally, are presented in Table 2.

The quantities measured by the diagnostics are plotted for the error variation range. The response of the diagnostic to the error is defined by the slope of the linear fit. An example of the ϕ_{S3} variation measured by the 9 available diagnostic elements is shown in Figure 4.

The same is done for each of the 11 error sources, such that a 11×9 response matrix is obtained. To convert it into a dimensionless matrix where the terms can be compared, the responses are multiplied by the stability of the error sources and divided by the diagnostic resolution, shown in Tables 1 and 2, respectively. The resulting dimensionless response matrix is presented in Table 3. It can be observed that while the charge measurement using BPM-Q is only sensitive to the charge variation, all other diagnostics are sensitive to a combination of error sources.

Thus, in order to analyze the response matrix R the SVD method has been used. For this purpose R is decomposed into three matrices according to:

$$R = U \cdot \Sigma \cdot V^T \quad (1)$$

where the matrix Σ , presented in Table 4, contains the square roots of the singular values ordered from greatest to least along its diagonal. With the aim to account for the most significant correlations, we have restricted Σ to the first five singular values, and neglected the remaining ones. In order for the matrix multiplication to be consistent we have eliminated the corresponding column vectors of U and V . From the resulting matrices U and V with reduced dimensionality, shown in Tables 5 and 6, we can observe:

- The first singular value indicates a mode acting mainly on the bunch compression, which relates the variations of ϕ_{S3} and ϕ_X with the measurements from BCM-D1r and BCM-D2r. It is worth emphasizing that for the simulations the bunch length was roughly 10% longer and the bunch shape showed steeper rising and falling edges than the profile measured during the experiments. These deviations affect the resolution of the BCM, and since the resolution from the experimental measurement is used for normalization, this leads to an increase of the sensitivity of the BCM in the present simulations.
- The second singular value indicates a mode acting on the mean energy of the particles. The diagnostics BPM-E₁, BPM-E₂ and SRM-E measure energy changes caused mainly by variations of the phases ϕ_{S3} and ϕ_X and the amplitudes A_{S3} and A_X .
- The third singular value indicates a mode acting on the charge, which is measured by BPM-Q and in a smaller scale by the BCM monitors that measure variations of the bunch charge.
- The fourth singular value, almost 10^3 times smaller than the first one, indicates a combined mode acting on energy spread, bunch compression and charge, caused by the phase and amplitude of FINSB03 (ϕ_{S3} and A_{S3}) and the phase and amplitude of FINXB (ϕ_X and A_X).
- The fifth singular value is already so small, more than 10^5 times smaller than the first singular value, that is just dominated by noise and has no constructive impact on the response matrix.

CONCLUSIONS

A diagnostics response matrix for the SwissFEL Injector Test Facility has been simulated and afterwards experimentally measured. The simulation work used to predict the measurement results has been presented here. Because this simulation work does not yet include modeling of the different diagnostics including the detector responses, no quantitative comparison is yet to be done between the simulated and experimental response matrices. Still, the predicted sensitivities of some diagnostics to certain error sources and also the coupling between them have been later experimentally confirmed.

ACKNOWLEDGEMENTS

Initial particle distributions for the simulations in Litrack were provided by Simona Bettoni.

REFERENCES

- [1] R. Ganter (ed.) “SwissFEL Conceptual Design Report”, PSI Bericht, 10-04, 2010.
- [2] R. Ischebeck et al., “Response Matrix of Longitudinal Instrumentation in SwissFEL”, in Proc. 33rd Int. Free-Electron Laser Conf., Shanghai, 2011, pp. 652-655.
- [3] F. Frei et al., “Experimental Results of Diagnostics Response for Longitudinal Phase Space”, in These Proceedings: Proc. 36th Int. Free-Electron Laser Conf., Basel, 2014, THB02.
- [4] B. Keil et al., “Commissioning of the Resonant Stripline BPM System of the SwissFEL Test Injector”, in Proc. 32nd Int. Free-Electron Laser Conf., Malmö, 2010, pp. 429-432.
- [5] G.L. Orlandi et al., “Characterization of Compressed Bunches in the SwissFEL Injector Test Facility”, in Proc. Int. Beam Instrumentation Conf., Oxford, 2013, pp. 515-518.
- [6] V. Arsov et al., “Commissioning and Results from the Bunch Arrival-time Monitor Downstream the Bunch Compressor at the SwissFEL Test Injector”, in These Proceedings: Proc. 36th Int. Free-Electron Laser Conf., Basel, 2014, THP085.

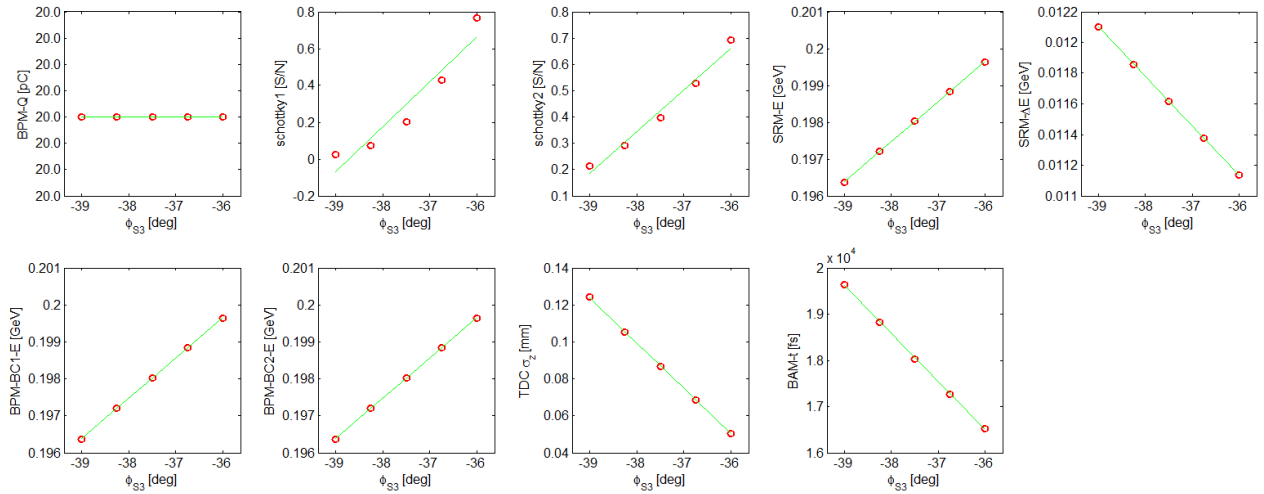


Figure 4: Variation of the ϕ_{S3} in five steps measured by each of the diagnostic measurements. A linear fit gives the response of the different diagnostics to this RF actuator.

Table 3: Response Matrix of the Diagnostics to the RF Variation (Matrix R).

	Q	ϕ_{SS}	ϕ_{S1}	ϕ_{S2}	ϕ_{S3}	ϕ_X	A_{SS}	A_{S1}	A_{S2}	A_{S3}	A_X
BPM- E_1	-0.01	-0.03	0	0.10	2.75	0	0.20	0.46	0.35	3.26	-1.31
SRM-E	-0.01	-0.01	0	0.06	1.60	0	0.12	0.27	0.21	1.90	-0.76
SRM- ΔE	-0.02	-0.04	-0.16	-0.24	-0.47	1.34	-0.01	-0.02	-0.01	0.15	0.05
BPM- E_2	-0.01	-0.03	0	0.10	2.75	0	0.20	0.46	0.35	3.26	-1.31
BCM-D1r	2.41	0.28	1.29	2.07	5.39	-11.09	0.17	0.36	0.26	0.37	-0.98
BCM-D2r	3.07	0.12	0.57	0.92	2.36	-4.90	0.08	0.16	0.12	0.16	-0.44
BPM-Q	3.00	0	0	0	0	0	0	0	0	0	0
BAM-t	0	0.01	0	-0.03	-0.73	0	-0.05	-0.12	-0.09	-0.87	0.35
TDC- σ_z	0	0	-0.02	-0.03	-0.07	0.15	0	0	0	-0.01	0.01

Table 4: Matrix Σ

	1	2	3	4	5
1	14.52	0	0	0	0
2	0	6.59	0	0	0
3	0	0	3.41	0	0
4	0	0	0	0.02	0
5	0	0	0	0	0.001

Table 5: Matrix U

	1	2	3	4	5
BPM- E_1	0.12	0.63	0.04	-0.02	-0.03
SRM-E	0.07	0.37	0.02	-0.01	-0.02
SRM- ΔE	-0.10	0.05	0.11	0.60	0.77
BPM- E_2	0.12	0.63	0.04	-0.02	-0.03
BCM-D1r	0.88	-0.14	-0.26	0.35	-0.11
BCM-D2r	0.42	-0.10	0.45	-0.62	0.47
BPM-Q	0.05	-0.06	0.85	0.36	-0.39
BAM-t	-0.03	-0.17	-0.01	0	-0.12
TDC- σ_z	-0.01	0	0.01	0.06	0.06

Table 6: Matrix V

	1	2	3	4	5
Q	0.25	-0.13	0.96	0	0
ϕ_{SS}	0.02	-0.01	-0.01	-0.02	0.08
ϕ_{S1}	0.10	-0.04	-0.03	-0.12	0.23
ϕ_{S2}	0.16	-0.04	-0.04	-0.17	0.02
ϕ_{S3}	0.45	0.48	-0.05	0.66	-0.31
ϕ_X	-0.82	0.33	0.26	0.20	-0.15
A_{SS}	0.02	0.04	0	-0.04	0.11
A_{S1}	0.04	0.10	0	-0.08	0.22
A_{S2}	0.03	0.07	0	-0.06	0.17
A_{S3}	0.09	0.74	0.08	-0.28	0.49
A_X	-0.10	-0.27	-0.01	0.63	0.70

[7] K.L.F. Bane and P. Emma, "Littrack: A Fast Longitudinal Phase Space Tracking Code with Graphical User Interface", in Proc. 2005 Particle Accelerator Conf., Knoxville, 2005, pp. 4266-4268.

[8] K. Flötman, "ASTRA A Space Charge Tracking Algorithm", user manual available at: <http://www.desy.de/~mpyflo/Astradokumentation/>

[9] THz Transport, developed by B. Schmidt, DESY.

CAMERALINK HIGH-SPEED CAMERA FOR BUNCH PROFILING

Daniel Llorente, Rasmus Ischebeck, Helge Brands, Patrick Pollet, Volker Schlott
Paul Scherrer Institut, Villigen, Switzerland

Abstract

In the context of upcoming SwissFEL linear accelerator, we are working on a high-speed high-resolution instrument capable of delivering good sensitivity even in dark conditions. The camera selected is a PCO.Edge with sCMOS technology and an ultra-low noise sensor with 2560x2160 pixel resolution working at 100Hz. This allows for single bunch monitoring in SwissFEL, allowing eventually for on-the-fly inter-bunch image processing.

The communication between the PCO.Edge camera and a last-generation Kintex7 FPGA has been demonstrated using a prototyping evaluation board and an 850-nm optical link connected to a 10Gbit SFP+ transceiver. Rudimentary packet processing has been implemented to confirm the satisfactory operation of the new link-layer protocol X-CameraLinkHS, specifically development for high-speed image transmission. We aim for online image processing and investigating the feasibility of achieving inter-bunch feedback (< 10 ms).

SYSTEM DESIGN FOR PROCESSING IMAGE AT ON-THE-FLY

The system is designed to monitor bunches of electrons with a high-resolution high-speed camera, capturing frames at 100Hz, the working frequency of the SwissFEL laser gun [1]. A last-generation FPGA will process such frames at a high speed, extracting the relevant parameters, comparing these values to programmable thresholds and eventually allowing for fast feedback to the machine without the intervention of the operator (see Fig. 1).

Frames need to be transmitted from the camera to the processing system over a distance of up to 1km, using for this purpose an 860-nm multimode optic fiber, which comfortably allows for the 10Gbps data rate of the camera. The preference of optic fiber over copper cabling is advised due to the long distances and noisy environment in which the system will be deployed.

Data is formatted in the camera according to the Camera-Link High Speed (CLHS) Protocol [2], which has been designed to provide low latency and low jitter in real-time signals for high-bandwidth image transmission. This is a proprietary link-layer protocol which can be implemented over commodity Ethernet connectors, thus benefiting in terms of price and availability of hardware. Particularly in our design, we use two Small form-factor pluggable transceivers (SFP+), a widely-spread standard in the communication industry for optic fibers.

The frame grabber has been implemented on a KC705 Prototyping Platform from Xilinx. This board includes a last-generation Kintex7 FPGA, which is the targeted device for the final design implementation. On this board,

DDR3 memory and one PCI connector are available, which are a powerful asset for further expanding the system capabilities. For deploying the instrument in the accelerator tunnel, we will transfer the firmware to a General Purpose Carrier Board v.3.0 (GPAC), which is expected to be the workhorse electronic board for future SwissFEL instruments.

The embedded system includes the Frame Grabber (an Intellectual Property (IP) Core) running along many other modules. For instances, the 10GBASE-KR core from Xilinx conveys the physical signals into CLHS packets (it is actually our PHY layer). The CLHS packets are decoded and transformed into frames by the X-Protocol decoder, provided by PCO, the camera manufacturer [3]. From this point on, the data format is presented as rows and columns of pixels. Together with the corresponding context data, the frame can be rebuilt.

At this point, we have two options. Data can be either processed at wire-speed on the FPGA in order to extract the relevant parameters or it can be alternatively stored on a temporary local buffer, waiting for retrieving from the control system an eventually processed offline. Both options present its advantages and drawbacks. Buffering large amounts of information require of fast big buffers, which can only be implemented with a reasonable cost on DDR memories. Even in this case, only some ms of video streaming can be stored.

A second option consists in processing the frames on-the-fly using a set of Hardware Accelerators specifically designed for this purpose (*Schwerpunkt* Extractor, Gradient Machine...). If fast enough, this early extraction of information from the frames may allow for inter-bunch feedback to the actuators, greatly speeding up the precise calibration of the machine. In this last case, the need for a large buffer would be overcome, though at the price of increasing design effort while flexibility for later modifications becomes more difficult.

sCMOS SENSORS

Many scientific imaging applications demand multi-megapixel focal plane sensors that can operate with very high sensitivity and wide dynamic range. Scientific CMOS technology delivers a very large high field, together with a low noise figure, that can be up to one degree of magnitude smaller [4]. This is especially the case when the number of photons is very low, as it is in our case, when only a handful of photons (~ 200) excite the sensor.

This high performance is obtained without reducing the fps rate, so the sensor is capable of capturing frames at 100 Hz without the traditional trade-off in CCD cameras that requires reducing resolution to increase frames per

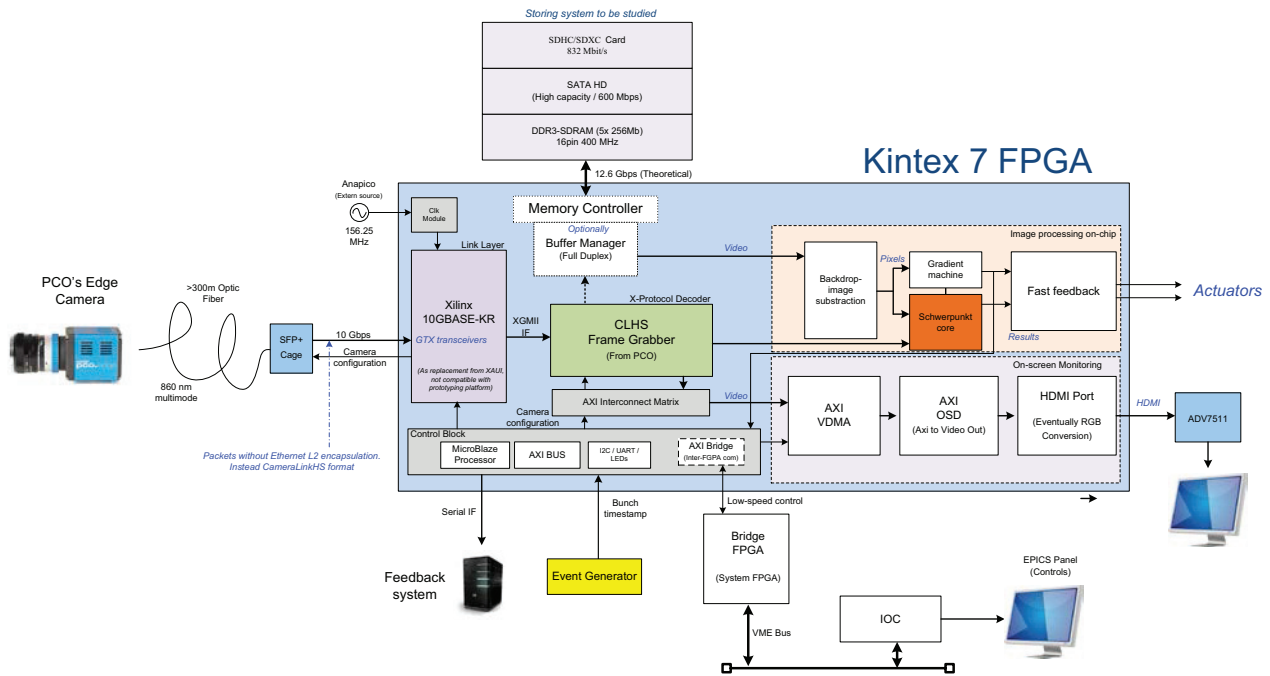


Figure 1: Prototype being implemented on a Xilinx's Kintex7 Prototyping Platform (KC705) with a K7 FPGA (xc7k325-2).

second or alternatively increasing fps but reducing the noise-to-signal figure.

In our case, one particularly interesting option is dynamically selecting a region of interest (ROI) and so capturing only a small portion of the image. The bunch usually excites less than 10% of the sensor, being its position variable before setup but quite stable during machine normal operation. This provides us with higher resolution and reduces the amount of data to be transmitted/processed to/in the FPGA.

STATUS AND NEXT STEPS

At the moment, the Frame Grabber is up and running on our test environment, being able to communicate with a camera prototype (the final camera is not yet available). Frames are received over optic fiber, and the PHY and Link Layer cores are up and working. The CLHS frames have been observed using a logic analyser. Together with this, a Test *Schwerpunkt* Extractor has been implemented to begin experimenting with data manipulation and control of the video streaming. This part of the system (which we could describe as data plane) is configured and monitoring by the control plane. For this purpose, a full-fledged on-chip Microblaze processor system together with its AXI communication matrix has been implemented to support the data plane.

In the coming months, we aim at extending the set of hardware accelerators. Priority has been given to communicating via PCI-Express with a fast PC to monitor the video stream on-the-fly on a screen, hence validating the correct setting of the camera. Alternatively, we study the option of using the VDMA cores included in the

Xilinx Vivado programming suite, directly driving a HDMI Port from the FPGA without the need of a supporting PC.

Eventually, the system will be transferred from the current prototyping platform to a General Purpose Analog Carrier board (GPAC v3.0). This PSI board will include different last generation FPGAs, including several seven series. Taking advantage of existing Firmware, the system will connect to a control board over a VME bus and from there to the SwissFEL network. Monitoring and control will be done over EPICS panels in the same way as the rest of the instrumentation on the accelerator.

ACKNOWLEDGMENT

The authors would like to thank specially Martin Schwarzbauer of PCO. His insights and collaboration during the firmware development were crucial to adapt the camera interface to the XAUI IP Core. He also developed the CLHS Frame Grabber IP Core.

REFERENCES

- [1] SwissFEL Conceptual Design Report 2012, PSI
- [2] Vision Online Standard: Camera Link HS Standard - <http://www.visiononline.org/vision-standardsdetails.cfm?type=10>
- [3] PCO Edge cameras; <http://www.pco.de/scmoscameras/pcoedge-55/>
- [4] New sCMOS vs. Current Microscopy; <http://www.andor.com>

THERMAL EMITTANCE MEASUREMENTS AT THE SwissFEL INJECTOR TEST FACILITY

E. Prat*, S. Bettoni, H. H. Braun, M. C. Divall, R. Ganter, T. Schietinger, A. Trisorio, C. Vicario
PSI, Villigen, Switzerland

C. P. Hauri, EPFL, Lausanne, Switzerland and PSI, Villigen, Switzerland

Abstract

In a laser-driven RF gun the ultimate limit of the beam emittance is the transverse momentum of the electrons as they exit the cathode, the so-called intrinsic or thermal emittance. In this contribution we present measurements of the thermal emittance at the SwissFEL Injector Test Facility for electron beam charges down to a few tens of fC. We have studied the dependence of thermal emittance and quantum efficiency on the laser wavelength, the RF-gun gradient and the cathode material (copper and cesium telluride).

INTRODUCTION

The electron beam emittance is of great importance for Free-Electron Laser (FEL) facilities. First, transversely coherent FEL radiation is generated if $\varepsilon_n/\gamma \approx \lambda/4\pi$, where ε_n is the normalized beam emittance, γ is the Lorentz factor and λ is the FEL radiation wavelength. This condition entails that by reducing the normalized emittance the final beam energy can be decreased, which translates into a more compact and affordable accelerator. Second, for a given beam energy, a smaller emittance implies a higher radiation power and a shorter undulator beamline to reach FEL saturation.

As accelerator technology advances and the emittance of the electron source is preserved downstream of the injector, the source becomes a significant contributor to the final emittance and brightness of the electron beam. The intrinsic or thermal emittance, which is proportional to the transverse momentum of the electrons exiting the cathode, is related to the initial kinetic energy or effective temperature of the electrons.

The thermal emittance for both metal and semiconductor photo-cathodes can be expressed as [1, 2].

$$\varepsilon_{th} = \sigma_l \sqrt{\frac{\phi_l - \phi_e}{3m_0c^2}}, \quad (1)$$

where ϕ_l is the laser photon energy, σ_l is the RMS laser beam size, m_0c^2 is the electrons rest mass energy, and ϕ_e is the effective work function. We call $\varepsilon_{th}/\sigma_l$ the normalized thermal emittance, expressed in nm/mm, as it is independent of the laser beam size. We note that the above expression is correct if tilted-surface effects related to the surface roughness of the cathode are negligible [3].

To illustrate the effect of the thermal emittance on the final FEL performance, Fig. 1 shows the dependence of the FEL power on the normalized thermal emittance for the 200 pC charge operation mode of SwissFEL [4]. For each

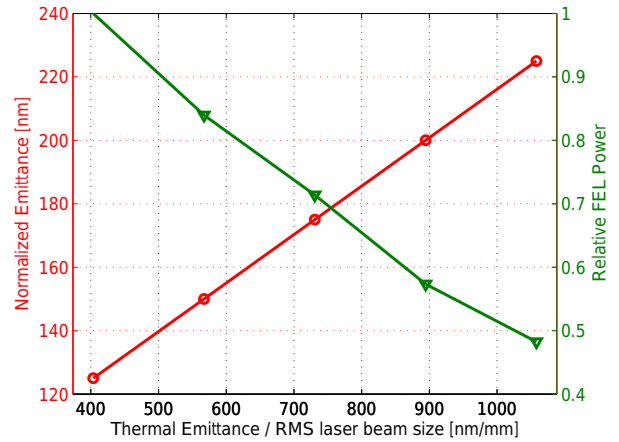


Figure 1: Relative FEL power as function of the normalized thermal emittance. Normalized core slice emittance is simulated for the 200 pC charge operation mode of SwissFEL for different normalized thermal emittance values. The corresponding normalized emittance for optimized laser beam size (red circles) is then used to calculate the relative FEL power (green triangles).

normalized thermal emittance value we performed numerical simulations to optimize the emittance at the end of the injector, from which the FEL power was calculated. For instance, the FEL power increases by about 25% for a normalized thermal emittance reduction from 600 nm/mm to 400 nm/mm.

The effective work function is defined as the material work function ϕ_w , reduced by the Schottky effect ϕ_s [5]:

$$\phi_e = \phi_w - \phi_s = \phi_w - \sqrt{\frac{e^3}{4\pi\varepsilon_0} \beta E_c(\varphi)}, \quad (2)$$

where e is the charge of the electron, ε_0 is the vacuum permittivity, β is the local field enhancement factor that depends on the cathode surface properties, and $E_c(\varphi)$ is the applied field on the cathode at the injection phase φ .

When $E_c(\varphi)$ varies in a small range, the quantum efficiency (QE) of a metal photo-cathode is linked to the laser photon energy and the effective work function as follows [1, 6]:

$$QE \propto (\phi_l - \phi_e)^2. \quad (3)$$

Equations 2 and 3 allow the determination of the effective work function of the employed cathodes directly from measurements in the RF gun in two independent ways: by measuring the emitted charge as a function of the injection

* eduard.prat@psi.ch

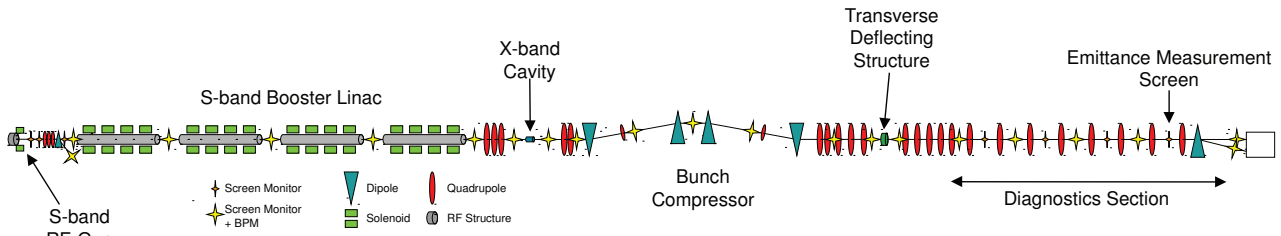


Figure 2: Schematic layout of the SwissFEL Injector Test Facility (not to scale). The total length is about 60 m.

phase (Schottky scan) and as a function of the laser energy (wavelength scan).

Extensive worldwide research and development have been performed in the last years to measure the thermal emittance for metal and semiconductor photo-cathodes, see for example Refs. [6–10]. We have experimentally studied at the SwissFEL Injector Test Facility [11] the normalized thermal emittance and QE dependence on the laser wavelength λ_l ($\phi_l = hc/\lambda_l$), the RF field at the cathode E_c , and the photo-cathode material (related to ϕ_w). These studies are presented for copper and cesium telluride.

We note that most of the results presented in this conference contribution will soon be published in a peer-reviewed journal [12].

THE SwissFEL INJECTOR TEST FACILITY

The SwissFEL Injector Test Facility is the principal test bed and demonstration plant for the SwissFEL project, which is presently under construction and aims at realizing a hard-X-ray FEL by 2017. Figure 2 shows a sketch of the SwissFEL Injector Test Facility.

Electron bunches of charges between 10 pC and 200 pC are generated in a 2.6-cell standing-wave S-band RF photo-injector gun, originally developed for high-current operation at the CLIC test facility (CTF) at CERN [13]. There are two gun drive lasers. The main one is based on a Ti:Sapphire chirped pulse amplification system [14], which allows the variation of the 3rd harmonic emission between 260 and 280 nm. This is further extended by the use of an optical parametric amplifier (OPA) and a conversion stage to 250–310 nm. The second laser system is a compact, turn-key Nd:YLF amplifier, with a fixed wavelength of 262 nm. A longitudinal Gaussian profile of 9.9 ps FWHM is used for the measurements presented here and a selection of different size circular apertures cut the central homogeneous part of the laser beam, which is imaged onto the cathode for each wavelength at close to normal incidence.

The total beam energy at the gun exit is 7.1 MeV. A solenoid close to the gun cavity is used for initial focusing. Additional individually powered windings inside the gun solenoid allow for correction of normal- and skew-quadrupole field components.

Four S-band accelerating structures bring the beam energy up to the nominal value of 250 MeV. Additional solenoid

magnets around these structures allow for further control of the transverse optics. After some space, which is used for an X-band linearizing system and a bunch-compressor chicane, an S-band transverse deflecting cavity is used for longitudinally resolved measurements such as bunch length and slice emittance. A dedicated beam diagnostic section downstream of the deflecting cavity allows us to characterize the accelerated beam. Several quadrupole magnets and beam screens measuring the transverse beam profile are available for emittance measurements. The final beam energy is measured by a spectrometer at the end of the diagnostic section.

More details on the SwissFEL Injector Test Facility can be found in Ref. [11].

MEASUREMENT PROCEDURES

When the emittance measurements are performed with sufficiently low charge to avoid space charge effects, the emittance of a selected longitudinal slice of the bunch corresponds to the thermal emittance. In our case we choose the central slices of the bunch, what we call the core slice emittance. The normalized thermal emittance $\varepsilon_{th}/\sigma_l$ can be reconstructed by measuring the thermal emittance as a function of the RMS laser beam size, which is varied by changing the laser aperture.

It is crucial to establish a reliable and high-resolution method to be able to precisely measure the thermal emittance of the electrons. Core slice emittance measurements are performed by streaking the bunch and visualizing it on a high-resolution YAG screen [15] at the high energy section of the machine. We can streak the beam either with a RF transverse deflector or by introducing dispersion to an energy-chirped beam. The normalized emittance resolution is about 2–3 nm for a final beam energy of 250 MeV. The longitudinal resolution is about 13 fs when the transverse deflector is used. With the dispersion method we can resolve more than 5 slices per RMS bunch length (if the RMS energy chirp of the beam is 1%). The statistical and systematic errors of the emittance are estimated to be below the 5% level. A more detailed description of the slice emittance measurements can be found in Refs. [16, 17].

The YAG screen has allowed measurements for bunch charges of 1 pC and less, where space charge effects are negligible for our laser beam sizes. The critical surface charge density in our case is ≈ 30 pC/mm² at 50 MV/m field on the cathode with a 9.9 ps FWHM pulse and has been

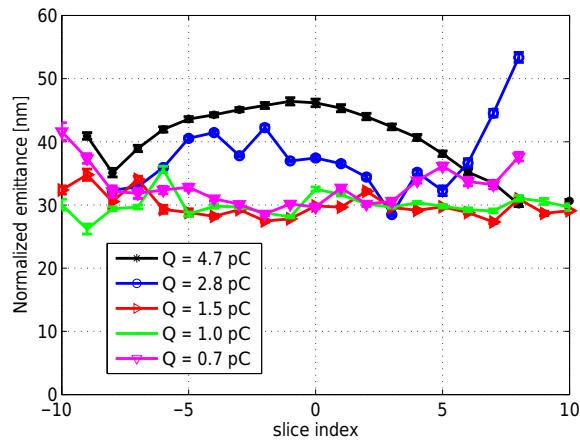


Figure 3: Measured slice emittance as a function of bunch charge to find the space-charge limit. Measurements for a bunch charge of 1 pC and less give the same core slice emittance values within the accuracy of the measurement, while at higher charge the presence of a space charge effect is clearly visible.

identified by reducing the bunch charge at fixed laser beam size until the emittance was no longer reduced, as shown in Figure 3. Once the space-charge limit is found, the charge surface density is kept constant during the aperture scan to avoid space charge effects.

The QE is measured by recording the charge at a calibrated beam position monitor 2.6 m downstream of the gun while changing the laser intensity.

MEASUREMENT RESULTS

We used four cathodes for our measurements, two made of pure copper, labeled Cath₃ and Cath₁₉, and two coated with cesium telluride labeled Cath₁₃ and Cath₈. The cesium telluride cathodes are prepared by depositing about 15 nm of tellurium and about 25 nm of cesium on a copper cathode. All the photocathodes were mounted in a load-lock chamber. More details on the cathode preparation can be found in Ref. [18].

We measured the dependence of the thermal emittance on the laser wavelength for the copper cathode Cath₃ and the influence of the gun gradient for the copper cathode Cath₁₉. The wavelength dependence measurements were carried out with the Ti:Sapphire laser, while all the rest of the measurements presented here were performed with the Nd:YLF laser.

Laser Wavelength

Figure 4 shows the core slice emittance measurements as a function of the laser beam size (aperture scan) for two different wavelengths (260.1 nm and 267.6 nm).

We observed a linear growth of the normalized thermal emittance as a function of the laser beam size (bottom plot of Fig. 4). This is in contradiction with Eq. 1, but can be explained by our present gun design, which exposes the

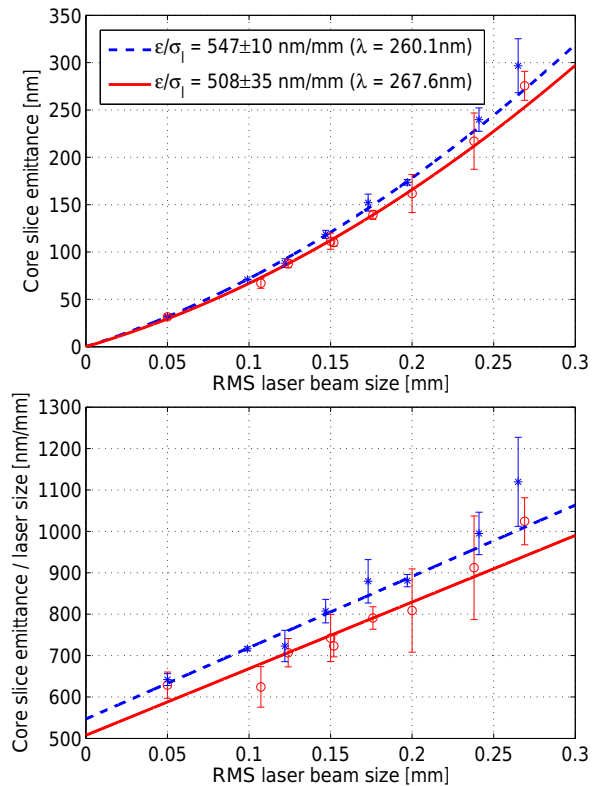


Figure 4: Core slice emittance as a function of the laser beam size for two laser wavelengths — 260.1 nm (dashed blue) and 267.6 nm (red solid) – for cathode Cath₃.

electron beam to a quadrupole field component due to non-coaxial RF feeds from opposing sides. Indeed, the inhomogeneity of the cathode was ruled out as an explanation by measuring the core slice emittance at the smallest aperture, while moving the laser beam across the cathode. The non-linear dependence of the asymmetric field in the gun was verified by aperture scans at different gun gradients (see next subsection). Taking the quadratic component into account the normalized thermal emittance can be determined as the extrapolation of the quadratic fit to an infinitely small laser beam size. The normalized thermal emittance corresponds to the linear term of a second-order fit to the emittance data, which gave 547 ± 10 nm/mm for a wavelength of 260.1 nm and 508 ± 35 nm/mm for a wavelength of 267.6 nm.

One month later we performed measurements at four different wavelengths using the same cathode (Cath₃). These measurements were realized with a charge of 1 pC and at the smallest laser aperture, corresponding to about 50 μ m RMS laser beam size on the cathode. We note that measurements performed with only the smallest aperture overestimate the normalized thermal emittance by 10–20%.

We measured the QE for different laser wavelengths, as shown in Fig. 5. The measurements were taken with the Ti:sapphire and the OPA, covering a wavelength range of 248–301 nm. By using Eq. 3 the best fit found for Cath₃ corresponds to an effective work function of 3.93 ± 0.03 eV (see inset of Fig. 5).

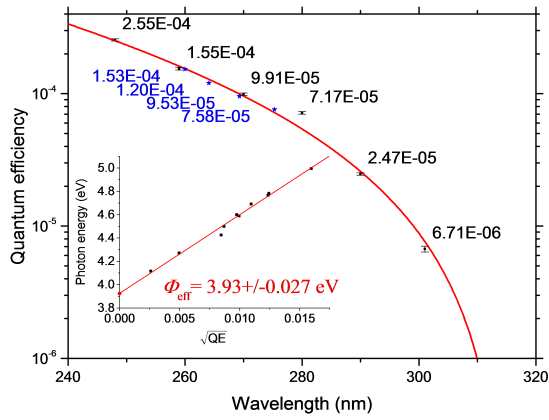


Figure 5: QE as a function of wavelength with cathode Cath₃. Measurements were performed with both the OPA (black points) and the 3rd harmonic of the Ti:sapphire laser (blue stars). The fit based on Eq. 3 (inset) gives an effective work function of 3.93 eV (red line).

Alternatively we estimated the effective work function by performing a Schottky scan, i.e., by measuring the emitted charge as a function of the gun phase. By using Eqs. 2 and 3 and fitting the points around the operational phase, the best fit was found with a work function of 4.56 eV for this cathode, giving an effective work function of 4.06 ± 0.09 eV. This value is close to the one from the wavelength scan. A Schottky scan done at the same time of the measurements shown in Fig. 4 gave an effective work function of 4.33 ± 0.10 eV.

Figure 6 summarizes the thermal emittance measurements performed as a function of the laser wavelength. There is a good agreement between the thermal emittance determined from the core slice emittance measurements and from the wavelength and Schottky scans.

Gun Gradient

Figure 7 shows an aperture scan measurement for the copper cathode Cath₁₉ for three different gun gradients corresponding to the following fields on the cathode $E_c(\varphi)$: 49.4 MV/m (nominal value), 34.8 MV/m and 16.4 MV/m. As expected from the RF-induced effect, the quadratic component decreased as a function of the gradient: it was 716 ± 84 nm/mm² at 49.9 MV/m, 508 ± 137 nm/mm² at 34.8 MV/m, and 321 ± 105 nm/mm² at 16.4 MV/m. The fitted normalized thermal emittances diminished for lower field on the cathode, following the dependence indicated in Eqs. 1 and 2: the normalized thermal emittance was 428 ± 16 nm/mm at 49.9 MV/m, 370 ± 25 nm/mm at 34.8 MV/m, and 346 ± 25 nm/mm at 16.4 MV/m.

For the lowest gun gradient it was possible to measure the slice emittance for a total bunch charge of about 30 fC. This was possible thanks to the high sensitivity of our profile monitor and due to the smaller amount of dark current produced by the gun with the lower RF gradient. The measurement for this ultra-low charge is shown in Figure 8. The core slice emittance was below 25 nm. This measurement was done

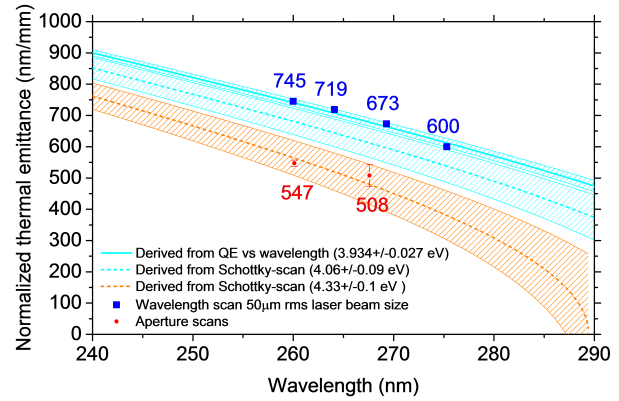


Figure 6: Normalized thermal emittance as a function of wavelength for cathode Cath₃. Measurements with the smallest aperture below the space charge limit, at 1 pC (blue squares). Reconstructed thermal emittance calculated from the effective work functions determined from the QE measurements as a function of wavelength shown in Fig. 4 (cyan solid) and from the Schottky measurements (cyan dashed). Two points derived from the aperture scan a month earlier shown on Fig. 4 (red dots) with the reconstruction from the Schottky scan performed at the same time (orange dashed).

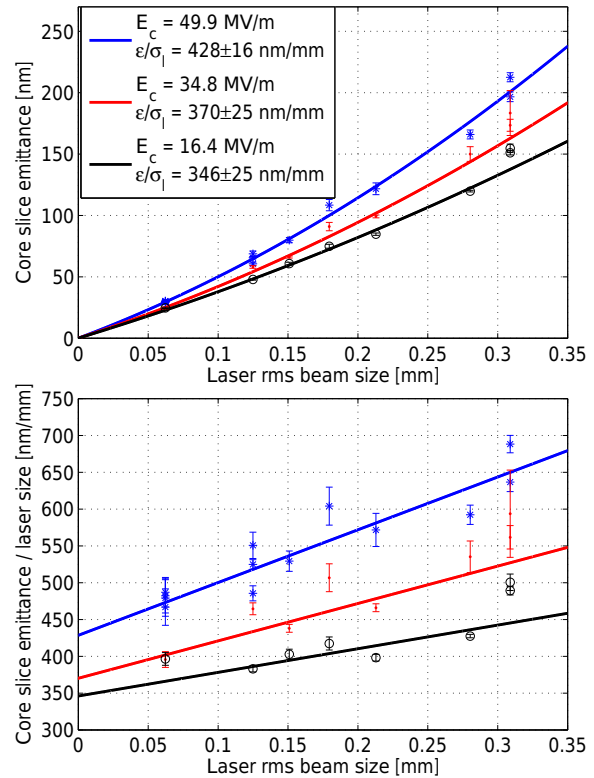


Figure 7: Core slice emittance as a function of beam size for three different fields on the cathode. The nonlinear effect was strongly reduced at lower field and the normalized thermal emittance varied as expected from theory.

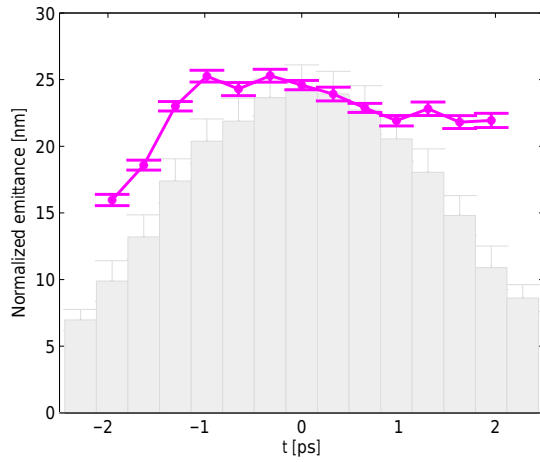


Figure 8: Normalized slice emittance in the horizontal plane for a bunch charge of 30 fC (magenta). The error bars are obtained by error propagation of the statistical beam-size errors. The longitudinal bunch charge profile is shown in gray bars.

by employing the smallest aperture, corresponding to about 50 μm RMS laser beam size at the cathode.

Cathode Material

We have tested each of the two cesium telluride cathodes for one week of operation. The thermal emittance of both cathodes was measured with aperture scans. For the cesium telluride cathode Cath₈ only measurements at the three smallest laser apertures were considered to be valid, due to the inhomogeneities of the QE outside the cathode center. The value of the thermal emittance for the cesium telluride cathodes Cath₁₃ and Cath₈ was 713 ± 88 nm/mm and 549 ± 29 nm/mm, respectively. We measured the thermal emittance for the copper cathode Cath₁₉ with the same machine conditions as when we performed the measurement with the cesium telluride Cath₈. The thermal emittance in this case was 430 ± 20 nm/mm, a value about 25% lower than for cesium telluride.

We have performed, for the two photo-cathode materials (with Cath₃ and Cath₁₃), an emittance optimization for an electron bunch with a 200 pC beam charge. We have achieved a slice emittance of about 200 nm for copper [16] and of about 250 nm for cesium telluride. Again, the degradation of the emittance when moving from copper to cesium telluride is about 25%.

Figure 9 shows the QE evolution of all the four cathodes tested at the SwissFEL Injector Test Facility. The copper cathodes were operated for several months (Cath₃ for about 5 months and Cath₁₉ for about 18 months), while the two cesium telluride cathodes (Cath₁₃ and Cath₈) could be tested only for one week each. The copper cathodes show a stable value of the QE around the 10^{-4} level. Both cesium telluride cathodes provided a QE of about 2% at the beginning of their operation. Whereas on the third day of operation the QE of Cath₁₃ suddenly dropped to about 2×10^{-3} , the QE

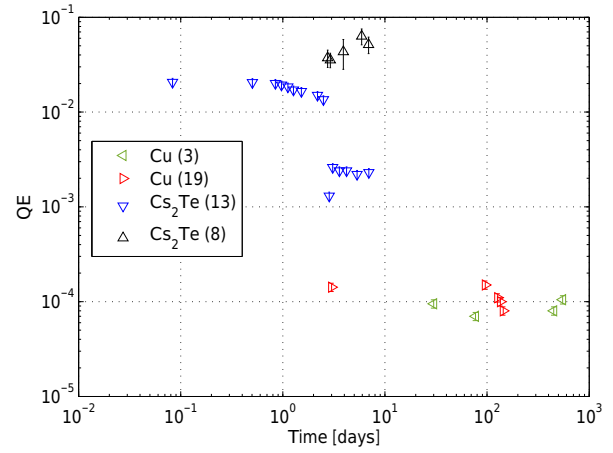


Figure 9: QE evolution of the four photocathodes tested at the SwissFEL Injector Test Facility, two copper (Cath₃ and Cath₁₉) and two cesium telluride (Cath₁₃ and Cath₈).

of Cath₈ stayed above 2% for the whole week. The reason for the QE deterioration of Cath₁₃ is not understood.

For the copper cathodes the QE, measured with the smallest available laser beam size, varied by about 15% across the area of measurements shown here. The cesium telluride cathodes were less homogeneous, with QE changing by up to a factor of two.

CONCLUSION

Table 1 displays all the normalized thermal emittance measurements presented in this contribution. To our knowledge, this is the first time that measurements for copper and cesium telluride are performed under the same conditions and that thermal emittance measurements agree well with theoretical expectations [1, 2]. Moreover, our measured normalized thermal emittances follow the expected dependence on the laser wavelength and field at the cathode: the emittance is smaller for longer wavelengths ($\varepsilon_{th}/\sigma_l \propto \phi_l^{1/2}$) and for reduced field on the cathode ($\varepsilon_{th}/\sigma_l \propto E_c^{1/4}$). We have verified, as suggested by Ref. [1], that a longer wavelength provides a smaller thermal emittance but gives also a lower QE. We have shown that the thermal emittance can be estimated from Schottky scans (charge as a function of the RF phase) or wavelength scans (charge as a function of the laser wavelength).

Cesium telluride provides a QE which is about two orders of magnitude higher than for the standard copper cathodes, while the emittance deterioration is only about 25%. This indicates that cesium telluride could be a viable alternative for SwissFEL. For a firm conclusion, however, more work on improving the surface homogeneity as well as long-term operation tests to evaluate the QE evolution with time are still needed.

For a reduced field at the cathode of 16.4 MV/m we have measured a normalized thermal emittance of about 350 nm/mm. This is, to our knowledge, the smallest normal-

Table 1: Measured Normalized Thermal Emittances at the SwissFEL Injector Test Facility

Label	Material	Measurement day	Normalized thermal emittance [nm/mm]	Laser wavelength [nm]	Field on the cathode [MV/m]
Cath ₃	copper	31-10-2012	547±10	260.1	49.9
	copper	30-10-2012	508±35	267.6	49.9
Cath ₁₉	copper	25-09-2013	428±16	262.0	49.9
	copper	25-09-2013	370±25	262.0	34.8
	copper	27-09-2013	346±25	262.0	16.4
	copper	04-04-2014	430±20	262.0	49.9
Cath ₁₃	cesium telluride	28-10-2013	713±88	262.0	49.9
Cath ₈	cesium telluride	04-04-2014	549±29	262.0	49.9

ized thermal emittance ever measured in an accelerator. The experimental verification of such small values was made possible through our reliable, high-resolution measurement procedure.

ACKNOWLEDGMENTS

We would like to thank the Beam Diagnostics team of PSI, in particular Rasmus Ischebeck, for developing and implementing the SwissFEL profile monitor used in our measurements. We acknowledge the extensive contributions of all the other PSI expert groups and the SwissFEL team to the construction and operation of the SwissFEL Injector Test Facility. We finally thank Masamitsu Aiba, Florian Müller, Sven Reiche and Mattia Schär for fruitful discussions that helped to improve the quality of the manuscript.

REFERENCES

- [1] D. H. Dowell and J. Schmerge, Phys. Rev. ST Accel. Beams **12**, 074201 (2009).
- [2] K. Flöttmann, TESLA FEL Report 1997-01 (1997).
- [3] D. H. Dowell, in *Photocathode Physics for Photoinjectors Workshop*, Ithaca, USA (2012).
- [4] R. Ganter (ed.), PSI Report 10-04 (2012).
- [5] Z. M. Yusof, M. E. Conde, and W. Gai, Phys. Rev. Lett. **93**, 114801 (2004).
- [6] H. J. Qian et al., Phys. Rev. ST Accel. Beams **15**, 040102 (2012).
- [7] D. Sertore, D. Favia, P. Michelato, L. Monaco, and P. Pierini, Proc. EPAC'04, Lucerne, Switzerland, 408–410 (2004).
- [8] Y. Ding et al., Phys. Rev. Lett. **102**, 254801 (2009).
- [9] F. Stephan et al., Phys. Rev. ST Accel. Beams **13**, 020704 (2010).
- [10] C. P. Hauri et al., Phys. Rev. Lett. **104**, 234802 (2010).
- [11] M. Pedrozzi (ed.), PSI Report 10-05 (2010).
- [12] M. Divall et al., to be published.
- [13] R. Bossart and M. Dehler, Proc. EPAC'96, Sitges, Spain 1544-1546 (1996).
- [14] A. Trisorio, P. M. Paul, F. Ple, C. Ruchert, C. Vicario, and C. P. Hauri, Optics Express **19**, 20128 (2011).
- [15] R. Ischebeck and E. Prat, to be published.
- [16] E. Prat et al., Proc. FEL'13, New York, NY, USA, 200–204 (2013).
- [17] E. Prat and M. Aiba, Phys. Rev. ST Accel. Beams **17**, 032801 (2014).
- [18] R. Ganter et al., these Proceedings Proc. 36th Int. Free-Electron Laser Conf., Basel, 2014, MOA02

SUPPRESSION OF THE CSR-INDUCED EMITTANCE GROWTH IN ACRHOMATS USING TWO-DIMENSIONAL POINT-KICK ANALYSIS*

Y. Jiao[#], X. Cui, X. Huang, G. Xu, IHEP, Beijing, China

Abstract

Coherent synchrotron radiation (CSR) effect causes transverse emittance dilution in high-brightness light sources and linear colliders. Suppression of the emittance growth induced by CSR is essential and critical to preserve the beam quality and to help improve the machine performance. To evaluate the CSR effect analytically, we propose a novel method, named “two-dimensional point-kick analysis”. In this method, the CSR-induced emittance growth in an n -dipole achromat can be evaluated with the analysis of only the motion of particle in (x, x') two-dimensional plane with n -point kicks, which can be, to a large extent, counted separately. To demonstrate the effectiveness of this method, the CSR effect in a two-dipole achromat and a symmetric TBA is studied, and generic conditions of suppressing the CSR-induced emittance growth, which are independent of concrete element parameters and are robust against the variation of initial beam distribution, are found. These conditions are verified with the ELEGANT simulations and can be rather easily applied to real machines.

INTRODUCTION

Electron beams with low transverse normalized emittance (at the $\mu\text{m}\cdot\text{rad}$ or sub- $\mu\text{m}\cdot\text{rad}$ scale), short bunch length (at the sub-picosecond scale), and high peak current (up to thousands of Amperes) are generated or expected in high-brightness light sources and linear colliders. In these machines as beams pass through bending magnets, the emission of the coherent synchrotron radiation (CSR) leads to beam quality degradation, by inducing increased beam energy spread and causing transverse emittance dilution. Suppressing this effect is necessary and important to preserve the expected machine performance that is evaluated without considering the CSR effect. This has stimulated extensive analytical, numerical, and experimental studies [1-20] on the CSR effect in the past few decades. One important topic among these studies is to suppress the CSR-induced emittance growth. It has been shown that the CSR effect can be suppressed through optical balance method [4, 19], CSR-kick matching [12, 13], shielding [17], and pulse shaping [18].

In this paper we present a novel method of analysing the net CSR kick after passage through an achromatic cell, named “two-dimensional (2D) point-kick analysis” [20]. With this method, the CSR-induced emittance growth in a n -dipole achromat can be evaluated with the analysis of only the motion of particle in (x, x') 2D plane with n -point kicks, which can be, to a large extent,

counted separately. In addition, the beam line between adjacent dipoles is treated as a whole and is formulated with a 2-by-2 transfer matrix. As a result, general CSR-cancellation (in linear regime) conditions can be obtained with this method. In the following, we will introduce the CSR point-kick model, and then use the 2D point-kick analysis to study the CSR effect in a two-dipole achromat and a symmetric TBA, respectively.

CSR 2D POINT-KICK MODEL

It has been shown that for an electron bunch of Gaussian temporal distribution, the rms energy spread caused by CSR is [12, 13]

$$\Delta E_{rms} = 0.2459 \frac{eQ\mu_0 c_0^2 L_b}{4\pi\sigma_z^{4/3} \rho^{2/3}}, \quad (1)$$

where Q is the bunch charge, μ_0 is the permeability of vacuum, c_0 is the speed of light, L_b is the particle bending path in a dipole, σ_z is the rms bunch length, and ρ is the bending radius. Note that ΔE_{rms} is proportional to both L_b and $\rho^{2/3}$, or namely, $\Delta E_{rms} \propto \rho^{1/3} \theta$, with θ being the bending angle. Therefore the CSR effect can be linearized by assuming $\delta(csr) = k\rho^{1/3} \theta$, where $\delta(csr)$ is the CSR-induced particle energy deviation, k depends only on the bunch charge Q and the bunch length σ_z , and is in unit of $m^{-1/3}$. It reveals [20] through ELEGANT simulations that this relation applies well to the cases with θ ranging from 1 to 12 degrees and ρ ranging from 1 to 150 m. With the so-called R-matrix method [12], the coordinate deviations of a particle relative to the ideal path after passage through a sector bending magnet can be evaluated,

$$\Delta X = \begin{pmatrix} D \\ D' \end{pmatrix} \delta_i + \begin{pmatrix} \zeta \\ \zeta' \end{pmatrix} k, \quad (2)$$

where $D = \rho(1-\cos\theta)$ and $D' = \sin\theta$ are the momentum dispersions, and $\zeta = \rho^{4/3}(\theta-\sin\theta)$ and $\zeta' = \rho^{1/3}(1-\cos\theta)$ are the “CSR-dispersions”.

Through theoretical derivations, we find that the CSR effect in a dipole can be simplified as a point-kick. This kick occurs at the center of the dipole, and is in the form of [20]

$$X_k = \begin{pmatrix} \rho^{4/3} k [\theta \cos(\theta/2) - 2 \sin(\theta/2)] \\ \sin(\theta/2) (2\delta + \rho^{1/3} \theta k) \end{pmatrix}. \quad (3)$$

After each kick, the particle coordinates increase by X_k , and in addition, the particle energy deviation increases by $kL_b/\rho^{2/3}$ (or $k\rho^{1/3} \theta$).

*Work supported by the National Natural Science Foundation of China (No. U1332108)

[#]jiaoyi@ihep.ac.cn

Next we will show that with this point-kick model, the analysis of the CSR-induced emittance growth can be greatly simplified.

TWO-DIPOLE ACRHOMAT

For a two-dipole achromat, as illustrated in Fig. 1, one needs only to consider two CSR kicks at the dipole centers. To avoid dependency of the analysis on concrete optics design, the beam line between two dipoles (actually the beam line between the centers of the two dipoles) is treated as a whole and is formulated in a general form

$$M_{c2c} = \begin{pmatrix} m_{11} & m_{12} \\ m_{21} & m_{22} \end{pmatrix}. \quad (4)$$

For simplicity, it is assumed that the particle starts from the entrance of the achromat with initial energy deviation of δ_0 and with initial coordinates of $x_0 = x'_0 = 0$. The coordinates remain zero until the particle experiences the CSR kick at the center of the first dipole.

Right after the first kick,

$$\begin{aligned} X_{1+} &= X_{1-} + X_{k,1} \\ &= \begin{pmatrix} 0 \\ 2S_1 \end{pmatrix} \delta_0 + \begin{pmatrix} \rho_1(C_1\theta_1 - 2S_1) \\ S_1\theta_1 \end{pmatrix} \rho_1^{1/3} k, \\ \delta_{1+} &= \delta_0 + k\rho_1^{1/3}\theta_1, \end{aligned} \quad (5)$$

where $S_1 = \sin(\theta_1/2)$ and $C_1 = \cos(\theta_1/2)$.

Similarly one can obtain the particle coordinates and energy deviation right after the second kick,

$$\begin{aligned} X_{2+} &= M_{c2c} X_{1+} + X_{k,2} = M_{c2c} X_{k,1} + X_{k,2}, \\ \delta_{2+} &= \delta_0 + k\rho_1^{1/3}\theta_1 + k\rho_2^{1/3}\theta_2, \end{aligned} \quad (6)$$

where X_{2+} is just the orbit deviation of particle relative to the ideal path, i.e., $\Delta X = X_{2+}$. It contains two terms, $\Delta X(\delta_0)$ and $\Delta X(k)$, which are omitted here due to lengthy expressions. The achromatic condition can be derived by solving $\Delta X(\delta_0) = 0$, and then the CSR-cancellation conditions are obtained by solving $\Delta X(k) = 0$.

The achromatic condition is

$$M_{c2c} = \begin{pmatrix} -S_1/S_2 & 0 \\ m_{21} & -S_2/S_1 \end{pmatrix}, \quad (7)$$

where $S_2 = \sin(\theta_2/2)$, $C_2 = \cos(\theta_2/2)$.

And the CSR-cancellation conditions are in the form

$$\begin{aligned} L_1\theta_1^2 &\cong L_2\theta_2^2, \\ m_{21} &\cong \frac{12}{L_1} \frac{S_2}{S_1}. \end{aligned} \quad (8)$$

In an actual circumstance, due to various reasons (e.g., random errors, other optics constraints), $M_{c2c}(2, 1)$ may be close to, rather than at the exact optimal value. Therefore it is useful to investigate the scaling of the emittance growth when the first condition in Eq. (8) is fulfilled while the second is not satisfied. It is in the form of

$$\begin{aligned} \Delta\epsilon_n|_{r=r^*} &\approx 2\gamma\beta k_{rms}^2 S_1^2 \theta_1^2 \rho_1^{2/3} \beta_1 \cdot \\ &[1 - M_{c2c}(2, 1) / M_{c2c}^*(2, 1)]^2. \end{aligned} \quad (9)$$

where $r \equiv \rho_2/\rho_1$, γ is the Lorentz factor, β is the particle velocity relative to the speed of light, β_1 is the horizontal beta function at the center of the first dipole, and an asterisked quantity means the quantity leads to a zero emittance growth in linear regime.

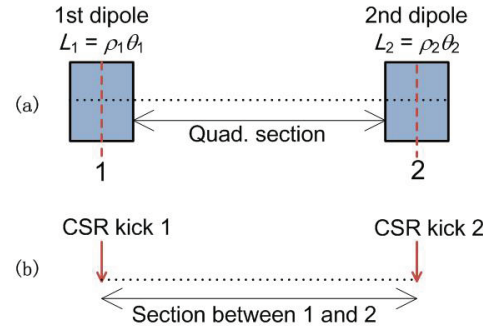


Figure 1: Schematic layout of a two-dipole achromat (a) and physical model for the 2D point-kick analysis of the CSR effect (b). The points 1 and 2 indicate the centers of the first and the second dipole, respectively.

To verify the found conditions, a two-dipole achromat with θ_1 of 6 degrees, ρ_1 of 8 m and θ_2 of 4 degrees, is considered. From Eq. (8), the optimal parameters resulting in zero emittance growth in linear regime can be determined, such as $\rho_2^* \cong 27$ m, and $M_{c2c}^*(2, 1) \cong 30/\pi$. Such an achromat is designed with four families of quadrupoles located between the dipoles, whose optics can be varied flexibly. The emittance growth in presence of the CSR wake is simulated with the ELEGANT program, where an electron bunch with typical parameters of initial normalized emittance of 2 $\mu\text{m}\cdot\text{rad}$, mean energy of 1 GeV, energy spread of 0.05%, bunch charge of 500 pC, and bunch length of 30 μm is tracked.

The variation of the growth in normalized emittance, $\Delta\epsilon_n$, with $M_{c2c}(2, 1)$ (while fixing $r = r^*$) and r [while fixing $M_{c2c}(2, 1) = M_{c2c}^*(2, 1)$] is investigated. The results are presented in Fig. 2. It shows that the found conditions result in a minimum $\Delta\epsilon_n$, and are quite robust against the variation of the initial Courant-Snyder (C-S) parameters (or namely, the initial beam distribution in phase space). In addition, the variation of $\Delta\epsilon_n$ with $M_{c2c}(2, 1)$ agrees pretty well with the analytical prediction from Eq. (9) with k_{rms} of 0.0012 $\text{m}^{-1/3}$ (dashed lines in Fig. 2), which indicates the validity of the 2D point-kick analysis.

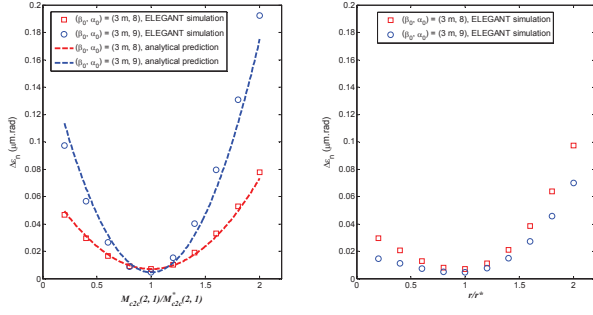


Figure 2: Variation of the emittance growth $\Delta\epsilon_n$ due to CSR with r and $M_{12}(2,1)$ for the cases with initial C-S parameters (β_0, α_0) of (3 m, 8) and (3 m, 9) in a two-dipole achromat, obtained by ELEGANT simulations. The dashed lines are the analytical prediction from Eq. (9) and with a shift of the minimum $\Delta\epsilon_n$.

Note that only the linear effect of the CSR wake in the dipole is considered in the 2D point-kick analysis. It is necessary to investigate the effects of the nonlinear components of the CSR wake in a dipole (denoted by *n.c. CSR*), the transient CSR at the edges of the dipole (denoted by *tr. CSR*), and the CSR wake in drift spaces following dipoles (denoted by *d.s. CSR*). Simulation results are summarized in Table 1. It shows that these effects are very weak relative to the linear effect of the CSR wake in dipoles, and rarely affect the performance of the proposed cancellation conditions.

Table 1: Emittance Growth in Presence of the Effects of *n.c. CSR*, *tr. CSR*, and *d.s. CSR* at the Optimal Condition

CSR effects	$\Delta\epsilon_n/\epsilon_{n0}$
<i>n.c. CSR</i>	1.5×10^{-3}
<i>n.c. CSR</i> + <i>tr. CSR</i>	2.8×10^{-3}
<i>n.c. CSR</i> + <i>tr. CSR</i> + <i>d.s. CSR</i>	5.95×10^{-3}

TBA WITH SYMMETRIC LAYOUT

The schematic layout of a TBA and the corresponding physical model of the CSR effect in a TBA are presented in Fig. 3. To control the number of the variables and to obtain explicit formulation of the net CSR kick, a TBA with symmetric layout (where all the dipoles have the same bending radii ρ , while the first and the third bending angles are θ_1 and the second bending angle is θ_2) is considered.

For such a TBA, the transfer matrix of the section between point 1 and 2 can be given by

$$M_{12} = \begin{pmatrix} m_{11} & m_{12} \\ m_{21} & m_{22} \end{pmatrix}, \quad (10)$$

and the transfer matrix of the section between point 2 and 3 is in the form [21]

$$M_{23} = \begin{pmatrix} m_{22} & m_{12} \\ m_{21} & m_{11} \end{pmatrix}. \quad (11)$$

With similar procedure to that in the above section, the particle coordinates deviation after passage the TBA can be evaluated by

$$\Delta X = M_{23}(M_{12}X_{k,1} + X_{k,2}) + X_{k,3}, \quad (12)$$

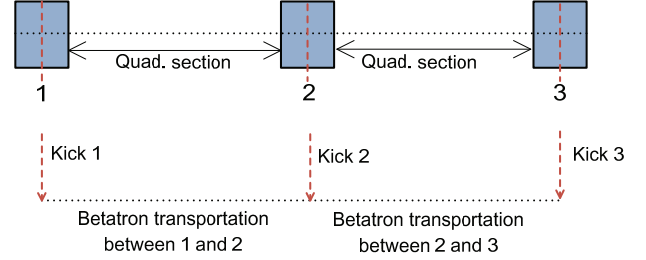


Figure 3: Schematic layout of a symmetric TBA and the corresponding physical model of the CSR effect in a TBA with three point-kicks.

Thorough straightforward derivations, the achromatic and the CSR-cancellation condition require the transfer matrix M_{12} in the form of

$$M_{12} = \begin{pmatrix} -\frac{q_2\rho + 2m_{12}(\theta_1 + \theta_2)S_1}{2q_1\rho} & m_{12} \\ \frac{1}{m_{12}}\left(\frac{q_2S_2}{4q_1S_1} + \frac{m_{12}(\theta_1 + \theta_2)S_2}{2q_1\rho} - 1\right) & -\frac{S_2}{2S_1} \end{pmatrix}, \quad (13)$$

where $q_1 = 2S_1 - C_1\theta_1$ and $q_2 = 2S_2 - C_2\theta_2$.

To verify the found conditions, we consider a TBA consisting of three identical dipoles with the bending radii of 7 m and bending angles of 3 degrees. The dependency of $\Delta\epsilon_n$ on m_{11} is investigated by fixing $m_{12} = -0.261$ and -1.058 , respectively. The results are shown in Fig. 4. It shows that $\Delta\epsilon_n$ reaches minimum as m_{11} is on or close to the optimal value, which agrees reasonably well with the analytical prediction.

Furthermore, in the case with $\theta_2 = 0$, the TBA reduces to a DBA, and the transfer matrix between the first and the third dipole centers turns out to be

$$\begin{aligned} M_{13}|_{\theta_2=0} &= M_{23}M_{12}|_{\theta_2=0} \\ &= \begin{pmatrix} 0 & m_{12} \\ -1/m_{12} & -m_{12}\theta_1S_1/q_1\rho \end{pmatrix} \begin{pmatrix} -m_{12}\theta_1S_1/q_1\rho & m_{12} \\ -1/m_{12} & 0 \end{pmatrix} \\ &= \begin{pmatrix} -1 & 0 \\ 2\theta_1S_1/q_1\rho & -1 \end{pmatrix} \cong \begin{pmatrix} -1 & 0 \\ 12/L_1 & -1 \end{pmatrix}, \end{aligned} \quad (14)$$

which is the same as the CSR-cancellation conditions for a DBA [see Eqs. (7) and (8) with $\theta_1 = \theta_2$].

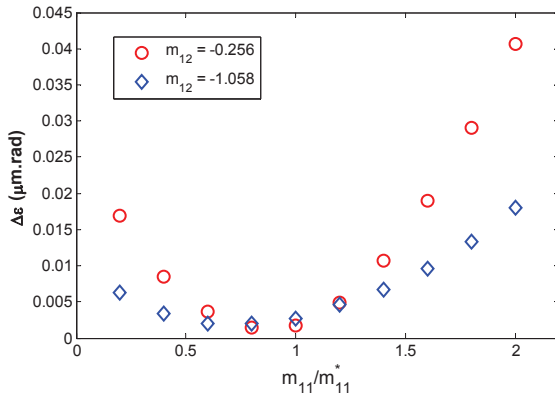


Figure 4: Variation of the emittance growth $\Delta\epsilon_n$ through TBA with respect to m_{11}/m_{11}^* , for the cases with m_{12} fixed as -0.261 (red points) and -1.058 (blue points).

CONCLUSION

In this paper we introduce the 2D point-kick method, and with this method we obtain conditions to cure the linear effect of the CSR wake in a two-dipole achromat and a symmetric TBA. The found conditions impose general rather than specific constraints on the optics of the beam line between adjacent dipoles and can be easily achieved by tuning the strengths (and the position if necessary) of the quadrupoles. In addition, the found conditions are quite robust against the variation of the initial beam distribution. The presented results are useful and easily followed in the optical design of the future FEL/ERL light sources and linear colliders.

At last it is worth mentioning that it assumes constant bunch charge and bunch length in the analysis, the results presented in this paper are more appropriate to the transport system with a small momentum compaction (R_{56}) than to that with a large R_{56} , e.g., a specified functional bunch compressor. Further study is being carried out to cover the cases where the bunch length has a large variation.

ACKNOWLEDGMENT

The authors appreciate J.Q. Wang and S.H. Wang of IHEP for their encouragement and support on this study, and also A. Chao of SLAC for helpful discussions.

REFERENCES

[1] T. Nakazato, M. Oyamada, N. Niimura, S. Urasawa, O. Konno, A. Kagaya, R. Kato, T. Kamiyama, Y. Torizuka, T. Nanba, Y. Kondo, Y. Shibata, K. Ishi, T. Ohsaka, and M. Ikezawa, Phys. Rev. Lett. 63, 2433 (1989).

[2] Ya.S. Derbenev, J. Rossbach, E.L. Saldin, and V.D. Shiltsev, Deutsches Elektronen-Synchrotron Report No. TESLA-FEL 95-05, 1995.

[3] E.L. Saldin, E.A. Schneidmiller, and M.V. Yurkov, Nucl. Instrum. Methods Phys. Res., Sect. A 398, 373 (1997).

[4] Ya.S. Derbenev and V.D. Shiltsev, Stanford Linear Accelerator Center Report No. SLAC-PUB-7181, 1996.

[5] P. Emma and R. Brinkmann, Stanford Linear Accelerator Center Report No. SLAC-PUB-7554, 1997.

[6] M. Dohlus and T. Limberg, Nucl. Instrum. Methods Phys. Res., Sect. A 393, 494 (1997).

[7] D. Douglas, Thomas Jefferson, National Accelerator Laboratory Technical Note, JLAB-TN-98-012 (1998)

[8] H. Braun, F. Chautard, R. Corsini, T.O. Raubenheimer, and P. Tenenbaum, Phys. Rev. Lett. 84, 658 (2000).

[9] M. Borland, Phys. Rev. ST Accel. Beams 4, 070701 (2001).

[10] S. Heifets, G. Stupakov, and S. Krinsky, Phys. Rev. ST Accel. Beams 5, 064401 (2002).

[11] Z. Huang and K.J. Kim, Phys. Rev. ST Accel. Beams 5, 074401 (2002).

[12] R. Hajima, Nucl. Instrum. Methods Phys. Res., Sect. A 528, 335 (2004).

[13] G. Bassi, T. Agoh, M. Dohlus, L. Giannessi, R. Hajima, A. Kabel, T. Limberg, and M. Quattromini, Nucl. Instrum. Methods Phys. Res., Sect. A 557, 189 (2006).

[14] M. Shimada, M. Okazaki, K. Harada, O. Tsukuba, in Proceeding of ERL07, Daresbury, UK, 2007, pp. 108-110.

[15] D. Sagan, G. Hoffstaetter, C. Mayes, and U. Sae-Ueng, Phys. Rev. ST Accel. Beams 12, 040703 (2009).

[16] C. Mayes and G. Hoffstaetter, Phys. Rev. ST Accel. Beams 12, 024401 (2009).

[17] V. Yakimenko, M. Fedurin, V. Litvinenko, A. Fedotov, D. Kayran, and P. Muggli, Phys. Rev. Lett. 109, 164802 (2012).

[18] C. Mitchell, J. Qiang, and P. Emma, Phys. Rev. ST Accel. Beams 16, 060703 (2013).

[19] S. Di Mitri, M. Cornacchia, and S. Spampinatic, Phys. Rev. Lett. 110, 014801 (2013).

[20] Y. Jiao, X. Cui, X. Huang, G. Xu, Phys. Rev. ST Accel. Beams 17, 060701 (2014).

[21] H. Wiedemann, *Particle Accelerator Physics I* (Springer-Verlag, Berlin, 1999), 123.

BEAM SIMULATIONS OF HIGH BRIGHTNESS PHOTOCATHODE DC GUN AND INJECTOR FOR HIGH REPETITION FEL LIGHT SOURCE

T. Miyajima*, Y. Honda, M. Yamamoto, X. Jin, T. Uchiyama,
KEK, Tsukuba, Ibaraki 305-0801, Japan

N. Nishimori, R. Nagai, R. Hajima, JAEA, Tokai-mura, Ibaraki 319-1195, Japan

Abstract

As a next generation FEL light source based on linac, high repetition rate operation to increase average FEL power has been proposed, e.g. LCLS-II project. The injector, which generates high brightness and high average current beam, is one of key components. A photocathode DC gun and superconducting RF cavities, which are developed for ERL light source, can be employed for the high repetition rate injector. For high repetition rate operation of FEL light source, injector simulations were carried out based on ERL injector with demonstrated hardware performance by the cERL beam operation in KEK. The optimization results show that the gun voltage of 500 kV is helpful to achieve low emittance. In addition, to estimate optimum gun voltage and cavity acceleration gradient for the FEL operation, two optimizations with different injector layouts were carried out. The results show that the both different layouts have potential to achieve target emittance for FEL operation. Under the realistic operation condition, the transverse normalized rms emittance of 0.8 mm mrad with the rms bunch length of 3 ps, the bunch charge of 325 pC, and the beam energy of 10 MeV is obtained from the optimizations.

INTRODUCTION

To increase average FEL power, high repetition rate operation of FEL light source based on linac is important for the next generation FELs, e.g. LCLS-II project [1]. In order to achieve the high repetition rate operation, the injector, which generates high brightness and high average current beam, is one of key components. The target emittances of high repetition rate FEL are 0.45 mm mrad and 0.7 mm mrad with the bunch charges of 100 pC and 300 pC, respectively [2]. A photocathode DC gun and superconducting RF cavities, which are developed for ERL light source, can be employed for the high repetition rate injector. The performance of ERL injector has been demonstrated at Cornell University, and 90 % transverse normalized emittance has been reached to 0.51 mm mrad with 77 pC/bunch [3]. In KEK, a high repetition rate and high brightness injector, whose repetition rate is 1.3 GHz, is being operated for compact ERL (cERL), which is a test ERL accelerator [4, 5]. In the beam operation, the hardware performance has been demonstrated. In the cERL operation, although the design gun voltage and the injector acceleration gradient are 500 kV and 15 MV/m, respectively, to keep stable beam operation we reduced them and demonstrated the beam operation with 390 kV and 7 MV/m. Based

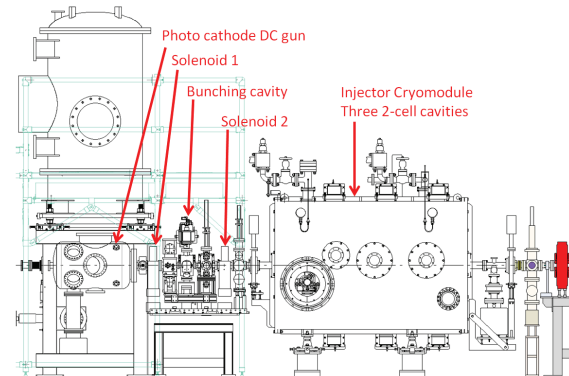


Figure 1: Layout of cERL injector.

Table 1: Center Positions of Injector Elements from Cathode Surface

Element	Original cERL (m)	New layout (m)
SL0	-	0.294
SL1	0.445	0.494
BC	0.809	0.752
SL2	1.218	0.909
SC1	2.221	1.519
SC2	2.781	2.079
SC3	3.341	2.639
SC4	-	4.519
SC5	-	5.079
SC6	-	5.639

on the demonstrated performance of the cERL injector, particle tracking simulations and optimizations of it with several hundred pC/bunch for the FEL injector were carried out. In addition, to estimate optimum gun voltage and acceleration gradient of cavity for FEL operation, we carried out two optimizations with different injector layouts.

PERFORMANCE OF CERL INJECTOR

The cERL injector consists of a photocathode DC gun, two solenoids, a bunching cavity, and three 2-cell superconducting cavities inside an injector cryomodule. Figure 1 shows the layout of the cERL injector. In this paper, SL, BC, SC denote that the solenoid magnet, the bunching cavity, and the 2-cell superconducting cavity, respectively. The element positions of the cERL injector are shown in Table 1. For ERL operation, the target maximum bunch charge is 77 pC, which corresponds to 100 mA average current. The cERL injector layout was optimized for 77 pC operation.

* tsukasa@post.kek.jp

Photocathode DC Gun

The photocathode DC gun, which was employed for the cERL, was developed by JAEA. The first design of the electrode with the gap of 100 mm is shown in Fig. 2. Before the installation of it to the cERL in KEK, high voltage processing was carried out at JAEA, and generating a 500 keV electron beam with currents up to 1.8 mA was demonstrated [6]. To achieve 500 kV, the design of the electrode was modified, and the gap was expanded to 160 mm to avoid discharge problem [7]. The expanded electrode shape is shown in Fig. 3. Due to the modification, the electric field on the cathode surface with the voltage of 500 kV was reduced from 6.7 MV/m to 5.8 MV/m as shown in Fig. 4. The lowest normalized emittance from a photocathode DC gun depends on the surface electric field on the cathode [3,8]. It is estimated to be

$$\epsilon_n \propto \sqrt{q \cdot \frac{k_B T}{E_{\text{cath}}}}, \quad (1)$$

where q is bunch charge, $k_B T$ is effective transverse energy of photoelectrons, and E_{cath} is electric field on the cathode surface. The relation shows that the electric field on the cathode is important to reduce the emittance. Therefore, the emittance for longer gap layout becomes worse compared with shorter gap layout, even if the gun voltage is same. To generate high brightness electron beam, the surface electric field on the cathode is one of important parameters.

On autumn 2012, the photocathode DC gun was transferred from JAEA to ERL development hall in KEK, and connected to the cERL injector beamline. However, in high voltage processing at KEK, a trouble about a ceramic insulator was found. To avoid serious damage of the ceramic insulator, we decided that to decrease the gun voltage from 500 kV to 390 kV in the beam operation.

In order to reduce the emittance growth caused by space charge effect, not only the gun voltage but also the surface electric field on the cathode are important as shown in Eq. (1). However, the relation of them is not so simple. In order to estimate the effects, we carried out beam simulations with different gaps and different gun voltages. Especially, to estimate the optimum gun voltage and the surface electric field on the cathode for FEL injector, the beam simulations with the bunch charges of 100 pC and 300 pC were carried out.

Injector Cavity

In the injector cryomodule, there are three 2-cell superconducting cavity. The RF frequency is 1.3 GHz. The design maximum acceleration gradient E_{acc} was 15 MV/m, and it was enough to accelerate the beam to 10 MeV. Before the beam operation, high voltage processing of the injector cavity was carried out. In the processing, the acceleration gradient of 8 MV/m was demonstrated in CW operation. Based on the results, we decided that the operation E_{acc} was 7 MV/m, and the injector beam energy was 5 MeV.

From April 2013, we started the beam operation of the injector, and demonstrated stable beam operation with the

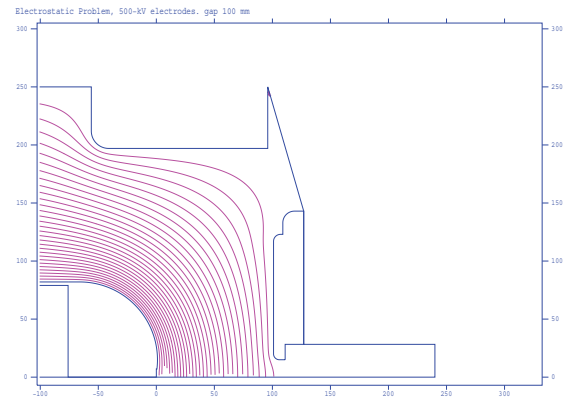


Figure 2: Electrode of a photocathode DC gun with gap of 100 mm. The horizontal and vertical axes are longitudinal and radial directions, respectively.

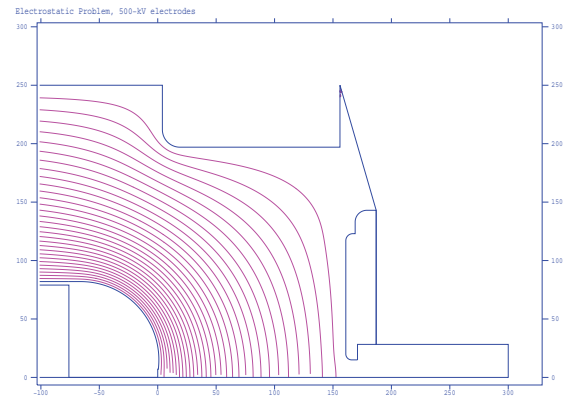


Figure 3: Electrode of a photocathode DC gun with gap of 160 mm.

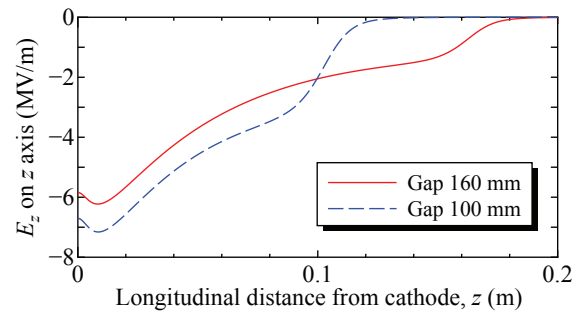


Figure 4: Longitudinal electric field of photocathode DC guns with different gaps.

gun voltage of 390 kV and the acceleration gradient of 7 MV/m [4]. However, to reduce emittance growth caused by space charge effect, higher beam energy at the exit of the injector is required. To increase the beam energy keeping the demonstrated E_{acc} of 8 MV/m, we proposed a new injector layout with two injector cryomodules. The simulations for the new layout, which contains six 2-cell cavities, were carried with the bunch charge of 325 pC.

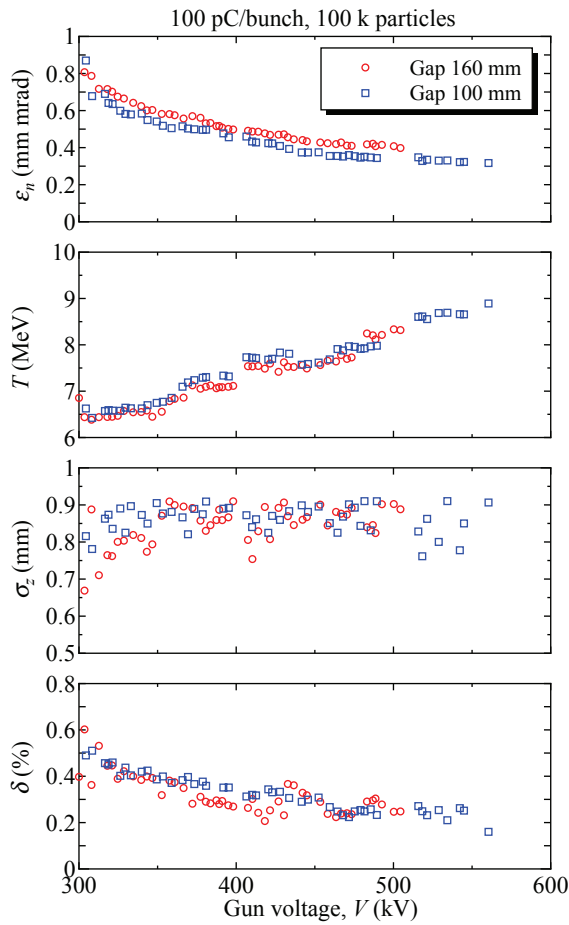


Figure 5: Optimization results with bunch charge of 100 pC for original injector layout.

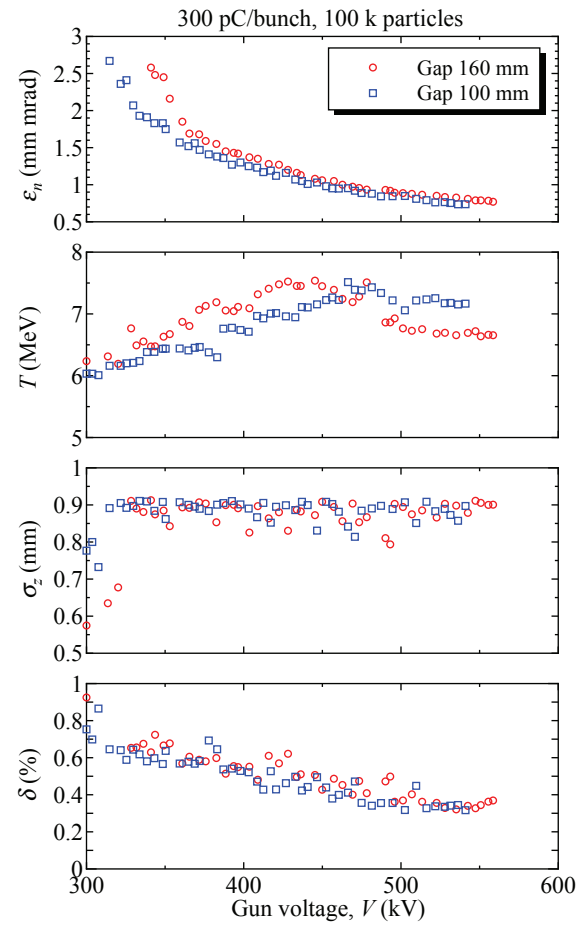


Figure 6: Optimization results with bunch charge of 300 pC for original injector layout.

INJECTOR OPTIMIZATION FOR HIGH BUNCH CHARGE OPERATION

In the simulations, we used General Particle Tracer with 3D mesh space charge routine [9]. As an initial parameter, $k_B T$ of 90 meV was assumed in the simulation. Initial emittance just after a cathode is calculated to be $\epsilon_{nx} = \sigma_x (k_B T / mc^2)^{1/2}$, where σ_x is rms laser spot size. As an initial laser distribution, beer-can shape was assumed. For the transverse direction, the particle distribution is radial uniform distribution described by laser diameter. The longitudinal distribution is flat-top distribution described by laser pulse length. To reproduce the measured beam dynamics of the cERL injector, the model of the photocathode gun was modified [10].

Effect of Gun Voltage for Original Layout

In order to estimate optimum gun voltage and gap of electrode, optimizations of injector parameters were carried out using Multi Objective Genetic Algorithm [11]. The original layout of the cERL injector as shown in Table 1 was used, and the element positions were fixed. The beam parameters were calculated at 6 m from the cathode surface, and we treated space after the exit of SC3 as pure drift space

without any magnet. In the optimization, gun voltage and projected normalized rms emittance were minimized. Free parameters are laser diameter, laser pulse length, gun voltage, two solenoid magnetic fields, buncher voltage and phase, and acceleration gradients and phases of SC1, SC2 and SC3. The maximum E_{acc} is 15 MV/m. The definition of cavity phase is the difference from the on-crest acceleration phase. The rms bunch length was limited to be less than 0.9 mm, which corresponds to 3 ps. The bunch charges are 100 pC and 300 pC. The number of macro-particles are 100,000 particles. In the optimizations, two different gaps of gun electrode, 100 mm and 160 mm, were used to estimate the effect of the surface electric field of the cathode.

For the bunch charge of 100 pC, the optimized results are shown in Fig. 5. The projected normalized emittance is 0.4 mm mrad for the gun voltage of 500 kV. The results shows that the cERL injector with E_{acc} of 15 MV/m can achieve the target emittance of 0.45 mm mrad for FEL operation. As shown in Fig. 5, the gap of 100 mm gives lower emittance comparing with the gap of 160 mm. However, the effect of the gap on the emittance is less than 0.1 mm mrad.

For the bunch charge of 300 pC, the optimized results are shown in Fig. 6. For the gun voltage of 500 kV, the projected

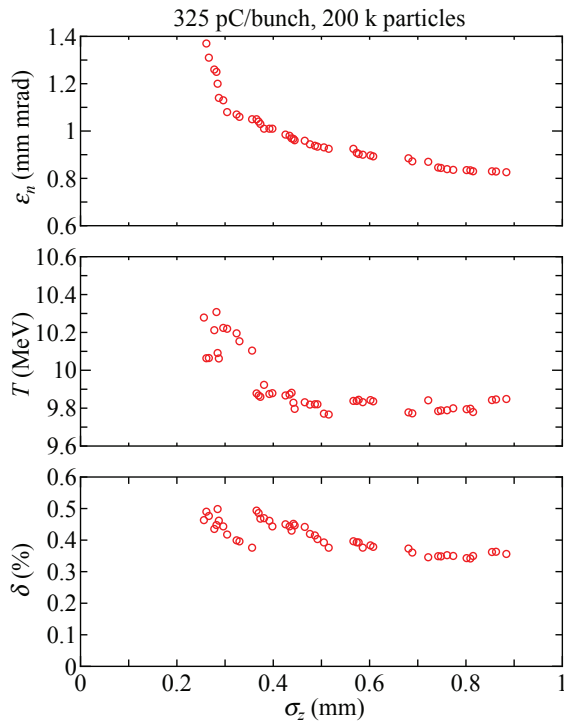


Figure 7: Optimization results with bunch charge of 325 pC for new layout with two injector cryomodules.

normalized emittance is 0.8 mm mrad. Compared with the results for 100 pC, the difference of emittance caused by the gap is smaller. The minimum emittance of 0.8 mm mrad is close to the target emittance of 0.7 mm mrad for FEL operation. The results show that higher gun voltage is better to achieve the target emittance.

Effect of Cavity Acceleration Field for New Layout

In order to estimate the effect of E_{acc} , we optimized a new layout of injector beam line with maximum E_{acc} of 8 MV/m, which is demonstrated value. The new layout contains two cryomodules, and total number of 2-cell cavities is six. In order to compensate emittance growth caused by space charge effect, we added a solenoid magnet, SL0, between the gun and the 1st solenoid, SL1. The beam parameters were calculated at 8 m from the cathode surface. In the optimization, projected normalized rms emittance and rms bunch length were minimized. Free parameters are laser diameter, laser pulse length, three solenoid magnetic fields, buncher voltage and phase, and acceleration gradients and phases of SC1, SC2 and SC3. The maximum E_{acc} is 8 MV/m. The gun voltage and the gap of electrode are fixed to be 500 kV and 160 mm, respectively. The bunch charge is 325 pC. The number of macro-particles are 200,000 particles.

The optimized results are shown in Fig. 7. For the bunch length of 0.9 mm, the projected normalized emittance is 0.8 mm mrad. The optimized injector parameters and element positions are shown in Table 2 and Table 1, respectively. The results show that the new layout with two cryomodules and the maximum E_{acc} of 8 MV/m can also achieve

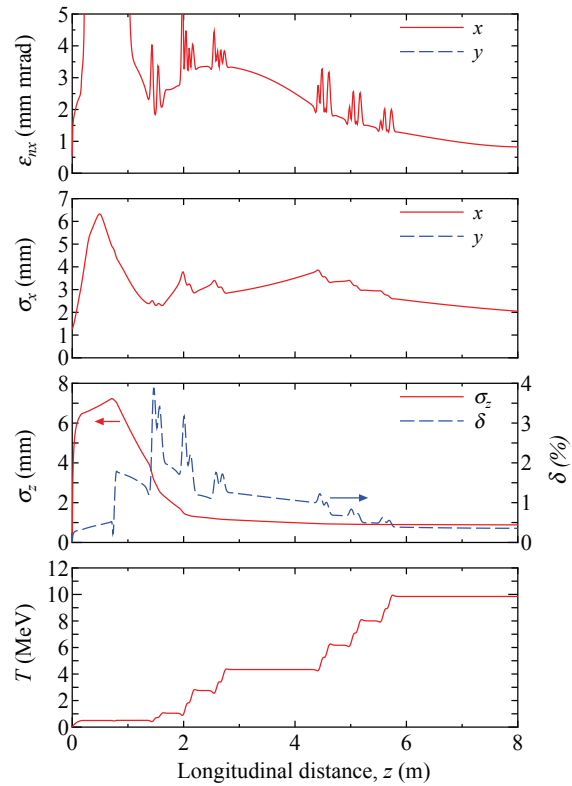


Figure 8: Time evolutions of beam parameters with optimized parameter for new injector layout. The bunch charge is 325 pC.

0.8 mm mrad. This value is close to the target emittance of 0.7 mm mrad.

The time evolutions of the beam parameters with the optimized parameters in Table 2 are shown in Fig 8. The emittance reduced to be 0.8 mm mrad at 8 m from the cathode surface. The rms beam size is 2 mm after the injector cryomodules. It is slightly larger to connect the beam envelope to downstream the injector. In the next step, to reduce the beam size and the envelope matching is required.

The both optimizations for the original and new injector layouts show that an ERL injector, which consists of a photocathode DC gun and superconducting cavities, has potential to achieve the low emittance beam, which is required for FEL operation.

SUMMARY

For high repetition rate operation of FEL light source based on linac, injector simulations were carried out based on ERL injector, which consists of a photocathode DC gun and superconducting RF cavities. The performance of the injector components were already demonstrated on the cERL beam operation in KEK. Based on the demonstrated hardware performance, we optimized the injector parameters to achieve the requirement for high repetition rate FEL, and investigated the effects of gun voltage and acceleration gradient of injector cavity using the original injector layout and

Table 2: Optimized Parameters for New Injector Layout with 325 pC

Parameter	Value
Laser diameter	5.06 mm
Laser pulse length (FWHM)	73.4 ps
Gun voltage	500 kV
Magnetic field of SL0	0.0356 T
Magnetic field of SL1	0.0299 T
Magnetic field of SL2	0.0109 T
Buncher voltage	115 kV
E_{acc} of SC1	2.98 MV/m
E_{acc} of SC2	7.98 MV/m
E_{acc} of SC3	7.97 MV/m
E_{acc} of SC4-6	8.00 MV/m
Buncher phase	-89.0 degree
Phase of SC1	-25.8 degree
Phase of SC2	-14.4 degree
Phase of SC3	-29.7 degree
Phases of SC4-6	0 degree

new layout with two injector cryomodels. The optimization results show that the gun voltage of 500 kV is helpful to achieve low emittance, and the both original and new layouts have potential to achieve target emittance for FEL operation.

REFERENCES

- [1] J. Galayda *et al.*, "The Linac Coherent Light Source-II Project", in Proc. of IPAC'14, Dresden, Germany, 2014, pp. 935-937.
- [2] C.F. Papadopoulos *et al.*, "RF Injector Beam Dynamics Optimization for LCLS-II", in Proc. of IPAC'14, Dresden, Germany, 2014, pp. 1974-1976.
- [3] Colwyn Gulliford *et al.*, Phys. Rev. ST Accel. Beams **16**, 073401 (2013).
- [4] S. Sakanaka *et al.*, "Construction and Commissioning of the Compact ERL Injector at KEK", in Proc. of ERL13, Novosibirsk, Russia, 2013, pp. 16-21.
- [5] N. Nakamura *et al.*, "Present Status of the Compact ERL at KEK", in Proc. of IPAC'14, Dresden, Germany, 2014, pp. 353-355.
- [6] N. Nishimori *et al.*, Appl. Phys. Lett. **102**, 234103 (2013).
- [7] N. Nishimori *et al.*, Phys. Rev. ST Accel. Beams **17**, 053401 (2014).
- [8] Ivan V. Bazarov *et al.* PRL **102**, 104801 (2009).
- [9] GPT, <http://www.pulsar.nl/gpt/>
- [10] T. Miyajima *et al.*, "Low Emittance Electron Beam Transportation in Compact ERL Injector", in Proc. of IPAC'14, Dresden, Germany, 2014, pp. 3104-3106.
- [11] Ivan V. Bazarov *et al.*, Phys. Rev. ST Accel. Beams **8**, 034202 (2005).

WAVE-MIXING EXPERIMENTS WITH MULTI-COLOUR SEEDED FEL PULSES

F. Bencivenga[#], A. Battistoni, F. Capotondi, R. Cucini, M. B. Danailov, G. De Ninno, M. Kiskinova, C. Masciovecchio, Elettra-Sincrotrone Trieste S.C.p.A., SS 14 km 163,5 in AREA Science Park, 34149 Basovizza, Trieste, Italy

Abstract

The extension of wave-mixing experiments in the extreme ultraviolet (EUV) and x-ray spectral range represents one of the major breakthroughs for ultrafast x-ray science. Essential prerequisites to develop such kind of non-linear coherent methods are the strength of the input fields, comparable with the atomic field one, as well as the high temporal coherence and stability of the photon source(s). These characteristics are easily achievable by optical lasers. Seeded free-electron-lasers (FELs) are similar in many respects to conventional lasers, hence calling for the development of wave-mixing methods. At the FERMI seeded FEL facility this ambitious task is tackled by the TIMER project, which includes the realization of a dedicated experimental end-station. The wave-mixing approach will be initially used to study collective atomic dynamics in disordered systems and nanostructures, through transient grating (TG) experiments. However, the wavelength and polarization tunability of FERMI, as well as the possibility to radiate multi-colour seeded FEL pulses, would allow to expand the range of possible scientific applications.

INTRODUCTION

Non-linear coherent methods based on wave-mixing processes are nowadays used in the optical domain to study a vast array of dynamical processes, taking place over a wide timescale range, with high time resolution as well as energy and wavevector selectivity [1]. In a typical wave-mixing experiment two or more coherent optical fields (input fields) interfere into the sample giving rise to a signal field. The large number of combinations between the parameters of the input fields (wavelength, polarization, bandwidth, arrival time, angle of incidence, etc.) allows to obtain selective information on very different dynamical processes occurring into the sample, some of them non achievable by linear methods [1].

The possibility to extend the wave-mixing approach at wavelengths shorter than the optical ones have attracted the interest of the scientific community and resulted into several theoretical and perspective works and also practical discussions on how to achieve this goal [2-5]. The only experimental report on a wave-mixing process stimulated by EUV/x-ray radiation is an optical/x-ray second order (three-wave-mixing) process, reported in [6]. More recently, we used a specially designed setup [7] to demonstrate the occurrence of a four-wave-mixing

(FWM) process stimulated by the EUV coherent photon pulses radiated by FERMI [8].

Some of the major advantages in using EUV/x-ray photons with respect to optical ones are related to the possibility to: (i) achieve element selectivity through the exploitation of core resonances [2,4], (ii) probe high energy collective excitations, as valence band excitons or plasmons [2,4], (iii) exploit a much larger wavevector range, which can compare or even exceed the inverse inter-atomic/molecular distances and may thus allow for atomic/molecular-scale resolution [4,9].

WAVE-MIXING: BASIC CONCEPTS

On formal grounds, non-linear radiation-matter interactions can be described by replacing the basic relation $\mathbf{P} = \epsilon_0 \chi \mathbf{E}$ (where \mathbf{P} , ϵ_0 , χ and \mathbf{E} are the polarization vector, the vacuum permittivity, the linear susceptibility tensor and the electric field vector impinging into the sample, respectively) with a power expansion in \mathbf{E} , i.e. [1]:

$$\mathbf{P} = \mathbf{P}^L + \mathbf{P}^{NL} = \epsilon_0 \chi \mathbf{E} + \epsilon_0 \sum_{n \geq 2} \chi^{(n)} \mathbf{E}^n, \quad (1)$$

where \mathbf{P}^L and \mathbf{P}^{NL} are the linear and non-linear terms of the induced polarization, while $\chi^{(n)}$ is the n^{th} -order susceptibility tensor (of rank $n+1$), associated to $(n+1)$ -wave-mixing processes. When Eq. 1 is inserted into the Maxwell equations one obtains an inhomogeneous wave equation, in which each “ $\chi^{(n)} \mathbf{E}_1 \mathbf{E}_2 \dots \mathbf{E}_n$ ” term plays the role of a driving force. These can be regarded as radiation sources at frequency $\omega_{\text{nm},p} = \pm \omega_1 \pm \omega_2 \dots \pm \omega_n$, where ω_i ($i=1-n$) are the frequencies of the n input fields while p labels the possible $\pm \omega_i$ permutations. It is worth noticing that $\omega_{\text{nm},p}$ are not necessarily equal to any ω_i .

Momentum conservation implies that the radiation emitted at $\omega_{\text{nm},p}$ (wave-mixing signal) is localized into a well defined region of space, centered around a $\mathbf{k}_{\text{nm},p}$ vector defined by the phase matching condition: $\Delta \mathbf{k} = |\mathbf{k}_{\text{nm},p} - (\pm \mathbf{k}_1 \pm \mathbf{k}_2 \dots \pm \mathbf{k}_n)| = 0$, where \mathbf{k}_i ($i=1-n$) are the wavevectors of the input fields. In real experiments $\Delta \mathbf{k} \neq 0$, also in light of the finite bandwidth and divergence of the input beams. However, as long as the coherence length ($L_c = \pi / \Delta k$) of the non-linear process exceeds the size of the illuminated region of the sample (L_{int}), the fields generated at different locations sample interfere constructively, leading to a N^2 increase of the non-linear signal (where N the number of elementary emitters).

[#]filippo.bencivenga@elettra.eu

Such a coherent addition of the non-linear emission is essential for the observation of the wave-mixing signal. Indeed, the total intensity radiated by non-linear processes is much lower than that due to linear processes. This is necessary condition to ensure the convergence of the power series shown in Eq. 1. However, since wave-mixing signals are localized in space while those arising from linear processes are much more isotropic, the latter

are usually much smaller than the former in a small spatial region centered around \mathbf{k}_{nwm} . Other two important consequences of the phase matching constraint are: (i) \mathbf{k}_{nwm} can be different from any \mathbf{k}_i (see, e.g., Figs. 1c and 1e), thus largely enhancing the signal-to-noise ratio [4] and (ii) in many cases different n-wave-mixing processes cannot be simultaneously realized since their phase-matching conditions are mutually exclusive [1].

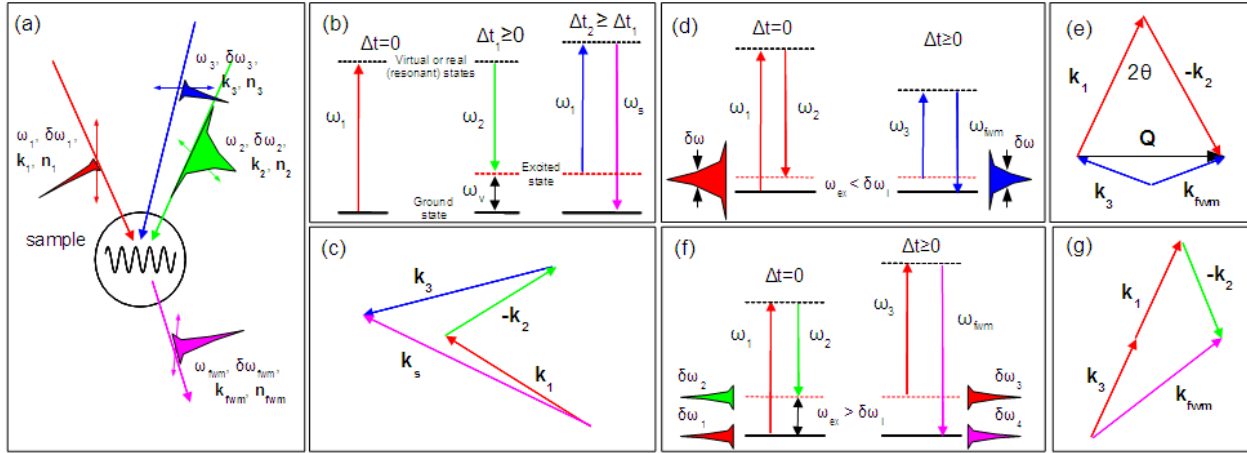


Figure 1: (a) sketch of a generic FWM experiment. ω_i , $\delta\omega_i$, \mathbf{k}_i and \mathbf{n}_i are the central frequency, bandwidth, wavevector and polarization of the input ($i=1-3$) and signal ($i=\text{fwm}$) fields; different colours mean different frequencies (i.e., the difference in central frequencies is larger than the bandwidth). Panels (b) and (c) are the level scheme and phase matching diagram of a generic wave-mixing experiment. Horizontal full black, dashed black and dashed red lines are the ground state, the excited state (of energy $\hbar\omega_{\text{ex}}$) and virtual or real resonant states, respectively, while Δt_1 and Δt_2 are the time delays of ω_2 and ω_3 pulses with respect to ω_1 . Panels (d) and (e) are the level scheme and phase matching diagram for SBS and SRS processes; here 2θ and \mathbf{Q} are the crossing angle and the excitation wavevector, respectively. (f) and (g) are, respectively, as (d) and (e) for the CARS process.

The signal intensity of a given wave-mixing process is thus related to the phase matching, usually accounted for by a $\text{sinc}^2(\Delta k L_{\text{int}})$ factor, and to the magnitude of the corresponding element of the $\chi^{(n)}$ tensors. In the optical domain the latter decay as a power law of the non-linear order, i.e.: $\chi^{(n)} \sim E_a^{-(n-1)}$ [1], where $E_a = e/(4\pi\epsilon_0 a_0^2) \sim 5 \cdot 10^{11}$ V/m (being a_0 the Bohr radius) is the atomic field strength. Furthermore, on general grounds second order processes cannot occur (i.e. $\chi^{(2)}=0$) in all centrosymmetric samples, such as liquids, glasses, polycrystals and most of crystalline structures. In most of the cases the lowest order non-vanishing coherent non-linear interactions are hence the third order ones (i.e. FWM); second-order processes are indeed mostly used to study surfaces and interfaces, since here the inversion symmetry is broken by definition. FWM is related to the $\chi^{(3)}$ tensor and are usually much weaker than any second order process, except the cases in which $\chi^{(2)}=0$. A typical FWM experiment is sketched in Fig. 1a-1c, while Figs. 1d-1g report the level schemes and phase matching diagrams for stimulated Brillouin/Raman scattering (SBS/SRS) and coherent antistokes Raman scattering (CARS) processes [1,10]. It is interesting to note how a given excitation (e.g., Raman modes in the example shown in Fig. 1) can be stimulated and probed either through SRS or CARS, depending on whenever the excitation energy ($\hbar\omega_{\text{ex}}$) is within the pulse bandwidth of the input fields or not.

ISBN 978-3-95450-133-5

Generally, the values of $\chi^{(3)}$ are expected to substantially decrease on increasing the input field frequency [1-4,11]. However, if some of the input frequencies are close to core atomic resonances, the $\chi^{(3)}$ values may be similar to (or just a few orders of magnitude lower than) those found in the optical regime [1-4,11]. On the other hand, we stress that the use of input field strength ($|E_i|$) comparable or larger than E_a to compensate for the drop in the $\chi^{(3)}$ values is questionable, at least as far as one is going to use wave-mixing methods to study samples under well defined conditions. Indeed, high-field processes (as, e.g., ionization potential depression [1]) might hamper the possibility to probe the dynamics of samples in well defined thermodynamic equilibrium states.

According to [2-4,11] we have estimated a significant drop in the overall efficiency of the FWM process on going from the EUV to the x-ray regime. On such grounds we cannot exclude that in the x-ray region the signal from most of FWM processes can be appreciated and/or be hidden by that due to linear processes [4].

EUV TRANSIENT GRATING

In transient grating (TG) experiments the interference between the two equal-frequency input fields ($\omega_1=\omega_2$)

impinges into the sample in time coincidence conditions and with a finite crossing angle (2θ); see also Figs. 1d-1e. The interference between these two pulses induces a transient standing electromagnetic wave with wavevector $\mathbf{Q}=\mathbf{k}_1-\mathbf{k}_2$ ($Q=|\mathbf{Q}|=4\pi \sin(2\theta/2)/\lambda_1$), which imposes a given modulation of many sample parameters, such as density, temperature or excited state populations [10]. All the excitations that may be stimulated in TG experiments are thus characterized by the same spatial periodicity, i.e. by the same Q -value. The latter can be experimentally set by 2θ and λ_1 . Such a Q -selection rule allows to select a given excitation out of the Q -dispersion relations of collective modes (phonons, spin waves, polarons, etc.) or a given Q -component in the Fourier spectrum of diffusion and/or relaxation processes.

The main aim of the TIMER project is to develop EUV/soft x-ray TG methods to study the aforementioned dynamical processes through SBS and SRS experiments in the $Q=0.1$ - 1 nm^{-1} range (extendable up to $Q\sim 2$ - 3 nm^{-1} in the near future) [9]. Such a “mesoscopic” Q -range is of the highest relevance for the study of collective atomic dynamics in disordered systems, such as glasses or liquids, as well as in systems, as gels or nanostructures, characterized by spatial periodicity or pseudo-periodicity in the ~ 1 - 100 nm range. To date, the 0.1 - 1 nm^{-1} Q -range is inaccessible by optical methods based on table-top or synchrotron sources [12], that are limited to $Q < 0.1 \text{ nm}^{-1}$. Conversely, x-ray and thermal neutron spectroscopy cannot (with the required energy resolution) Q -values lower than ~ 1 - 2 nm^{-1} .

These experiments will be mainly carried out at the EIS-TIMER end-station [9], which is featured by an all-reflective split-delay-and-recombination system [13]. This system will be able to control both the crossing angles and arrival times of the three FEL pulses impinging into the sample. TG experiments at EIS-TIMER can also exploit the wavelength/polarization tunability of FERMI [14] and the “jitter-free” FEL/optical pump-probe system available at the facility [15]. Recently, we used the latter system and a specially designed setup to carry out FEL-based TG experiments, that demonstrated the occurrence of appreciable SBS/SRS processes stimulated by EUV radiation [8]. The experimental setup to split and recombine the FEL pulse with a finite crossing angle (2θ) is sketched in Fig. 2b and will be described in details elsewhere [7]; an image of the FEL-induced FWM signal is shown in Fig. 2c. Our setup was placed inside the DiProI experimental end-station [16], downstream an adaptive KB mirror system. The system is based on three carbon coated EUV mirrors of 70 mm length, mounted on translational and tip-tilt stages. These permit to independently vary 2θ and the time delay between the two FEL pulses (Δt_{F-F}) in the 2° - 9° and $-1 \text{ ps} + 1 \text{ ps}$ range, respectively; see Figs. 2d-2e. An optical setup, external to the experimental chamber, allows to use an ultrafast “jitter-free” optical pulse [15] as third input beam for FWM experiments (TG in Ref. [8]). The arrival time (Δt) and crossing angle (θ_c) of such pulse with respect to the

FEL one labeled as FEL_A in Fig. 2b can be varied in the $-10 \text{ ps} + 200 \text{ ps}$ and 43° - 47° range, respectively. The external laser was also used to calibrate Δt_{F-F} vs $d1/d2$ (see Fig. 2e) through FEL-pump/optical-probe transient reflectivity measurements. The main limitation of our setup is the maximum Q -value, which is limited to $Q < 0.04 \text{ nm}^{-1}$ (i.e. below the “mesoscopic” range of interest) by the wavelength ($> 230 \text{ nm}$) of the optical pulse involved in the FWM process.

We finally note that the present setup could be alternatively used as a compact “split-and-delay” stage for FEL-pump/FEL-probe experiments. In this case the main advantage of our setup is the possibility to have a finite crossing angle between pump and probe pulses, thus allowing for a spatial discrimination between pump and probe pulses downstream the sample.

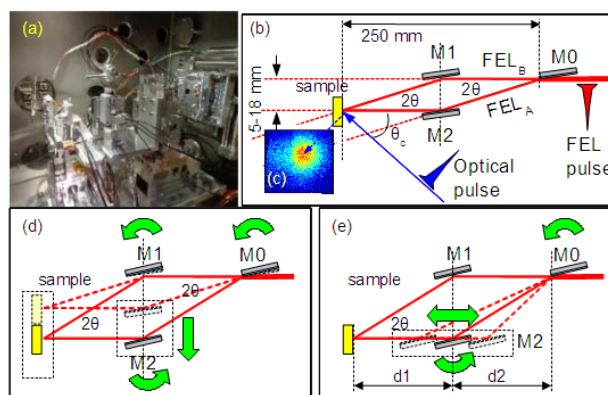


Figure 2: (a) picture of the experimental setup placed inside the DiProI experimental end station. (b) Sketch of the experimental setup: M0, M1 and M2 are C-coated plane mirrors; the relevant distances are indicated. (c) CCD image of the FWM beam. Panels (d) and (e) show how to vary 2θ and Δt_{F-F} independently (green arrows are the involved degrees of freedom for the three mirrors), the latter task is achieved by changing the ratio $d1/d2$.

MULTI-COLOUR WAVE-MIXING EXPERIMENTS

The two-colour (easily upgradable at three-colour) seeded FEL emission demonstrated at FERMI [17] can be used to further develop EUV/soft x-ray TG experiments. In particular, our setup in combination with the two-colours emission in principle allows for EUV/soft x-ray coherent Raman scattering (CRS) experiments, like the ones based on the CARS process. A possible experiment of such kind was discussed in [11] and shown in Fig. 3. In this case the interference between the crossed FEL pulses (of frequency ω_1 and ω_2) gives rise to a transient grating with ‘beatings’ at $|\omega_1-\omega_2|$. The latter may stimulate excitations with energy ($\hbar\omega_{ex}$) exceeding the pulse bandwidth ($\hbar\delta\omega$), in contrast to TG experiments discussed in the previous section, in which $\omega_1=\omega_2$. Furthermore, since the crossing angle and the photon energy difference can be independently set, it is possible to simultaneously achieve both Q and ω_{ex} selectivity.

More generally, in optical CRS ω_{ex} is limited to the sub-eV range, typical of vibrational modes and low-energy electronic excitations, by the low optical photon energy ($< 4\text{-}5$ eV). Conversely, the much larger ω_i -values of EUV/soft x-ray photons permits to probe ω_{ex} -values of several eV's, thus allowing to study ultrafast dynamics of high-energy excitations, as valence excitons. Moreover, since the FEL-based CARS experiment shown in Fig. 3 does not involve optical pulses, the wavevector $Q=|\mathbf{k}_1-\mathbf{k}_2|$ of the probed excitation is not limited to the sub- 0.1 nm^{-1} range by the (long) optical wavelength. This allows to probe dynamics at Q 's comparable with the inverse molecular dimensions and intermolecular separations, and thus to gain molecular-scale spatial resolution [2]. Finally, in EUV/x-ray CRS atomic selectivity can be attained by tuning some ω_i -values to atomic resonances [2,4,11]. In these cases the high-energy (resonant) states shown in Figs. 1b, 1d and 1f correspond to real core transitions of selected elements within the sample. In light of the localization of core shells, the resonant FWM signal carry out information on the coherences between resonant atomic sites [2] and might be used, e.g., to study ultrafast charge and energy transfer processes between different atoms in molecular solids [4].

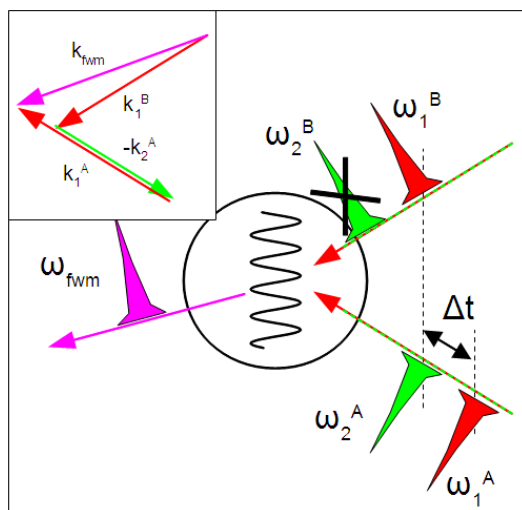


Figure 3: (main panel) sketch of a CRS experiment that may be performed at the FERMI facility exploiting the two-colour seeded FEL emission. The suffixes “A” and “B” correspond to the beam paths labelled in Fig. 1b as FEL_A and FEL_B, respectively. The crossed pulse (ω_1^B) is not involved in the FWM process. The phase matching geometry is shown in the inset.

The two-colour emission reported in [17] does not allow for $|\omega_1-\omega_2|$ values much larger than 1 eV, similarly to optical CRS, still with the possibility to exploit atomic selectivity in the excitation or probing process, not both [11]. This definitely calls for the development of novel multi-colours seeded FEL emission schemes, as these can substantially enhance the potentiality of wave-mixing experiments.

CONCLUSIONS

We reported on the development of EUV/soft x-ray wave-mixing methods at FERMI. In this context we obtained two relevant experimental results, i.e.: the demonstration of FEL-stimulated FWM processes [8] and a reliable multi-colour seeded FEL emission [17]. The combination of these two achievements opens up the possibility for a broad range of FWM applications, ranging from phonon spectroscopy to the study of low-energy coherent electronic excitations.

In the near future such studies will be carried out a more systematic way at the EIS-TIMER beamline [9]. However, it is worth mentioning that in a short term perspective FWM experiments can be in principle carried out at the DiProI end-station exploiting a specially designed setup [8].

ACKNOWLEDGEMENT

The authors acknowledge support from the European Research Council through the grant N. 202804-TIMER, the Italian Ministry of University and Research through grants FIRB-RBAP045JF2 and FIRB-RBAP06AWK3 and the Regional Government of Friuli Venezia Giulia through grant Nanotox 0060-2009.

REFERENCES

- [1] R. Boyd, *Non linear optics* (Oxford: Elsevier, 2008).
- [2] S. Tanaka and S. Mukamel, “Probing Exciton Dynamics Using Raman Resonances in Femtosecond X-Ray Four Wave Mixing”, *Phys. Rev. A* 67, 033818 (2003); “Coherent X-Ray Raman Spectroscopy: A Nonlinear Local Probe for Electronic Excitations”, *Phys. Rev. Lett.* 89, 043001 (2002); “X-ray four-wave mixing in molecules”, *J. Chem. Phys.* 116, 1877 (2002).
- [3] B. D. Patterson, “Resource Letter on Stimulated Inelastic X-ray Scattering at an XFEL”, SLAC Technical Note, SLAC-TN-10-026 (2010).
- [4] F. Bencivenga et al., “Nanoscale dynamics by short-wavelength four wave mixing experiments”, *New J. Phys.* 15, 123023 (2013).
- [5] G. Marcus, G. Penn, and A. A. Zholents, “Free-Electron Laser Design for Four-Wave Mixing Experiments with Soft-X-Ray Pulses”, *Phys. Rev. Lett.* 113, 024801 (2014).
- [6] T. E. Glover et al., “X-ray and optical wave mixing”, *Nature* 488, 603 (2012).
- [7] F. Capotondi et al., in preparation.
- [8] F. Bencivenga et al., in preparation.
- [9] F. Bencivenga and C. Masciovecchio, “FEL-based transient grating spectroscopy to investigate nanoscale dynamics”, *Nucl. Instrum. and Meth. A* 606, 785 (2009).
- [10] L. Dhar, J. A. Rogers and K. A. Nelson, “Time-resolved vibrational spectroscopy in the impulsive limit”, *Chem. Rev.* 94, 157 (1994).

- [11] F. Bencivenga et al., “Multi-colour pulses from seeded free-electron-lasers: towards the development of non-linear core-level coherent spectroscopies”, Faraday Discuss. DOI: 10.1039/c4fd00100a (2014)
- [12] C. Masciovecchio, F. Bencivenga and A. Gessini, “Water dynamics at the nanoscale”, Cond. Matt. Phys. 11, 47 (2008).
- [13] R. Cucini, F. Bencivenga and C. Masciovecchio, “All-reflective femtosecond optical pump-probe setup for transient grating spectroscopy”, Opt. Lett. 36, 1032 (2011).
- [14] R. Cucini et al., “Determination of dynamical parameters in liquids by homodyne transient grating spectroscopy at large angles”, Opt. Lett. 39, 5110 (2014).
- [15] M. B. Danailov et al., “Towards jitter-free pump-probe measurements at seeded free electron laser facilities”, Opt. Express 22, 12869 (2014).
- [16] F. Capotondi et al., “Coherent imaging using seeded free-electron laser pulses with variable polarization: First results and research opportunities”, Rev. Sci. Instrum. 84, 5 (2013).
- [17] E. Allaria et al., “Two-colour pump-probe experiments with a twin-pulse-seed extreme ultraviolet free-electron-laser”, Nat. Commun. 4, 2476 (2013).

OPTIMIZATION OF HIGH AVERAGE POWER FEL BEAM FOR EUV LITHOGRAPHY APPLICATION *

A.Endo, K.Sakaue, M.Washio, RISE, Waseda University, Tokyo, Japan
H.Mizoguchi, Gigaphoton Inc, Oyama, Japan

Abstract

EUV source community is interested in evaluating an alternative method based on high repetition rate FEL, to avoid a risk of the potential source power limit by the plasma based technology. Present SASE FEL pulse (typically 0.1mJ, 100fs, 1 mm diameter) has higher beam fluence than the resist ablation threshold, and high spatial coherence which results in speckle and interference patterns, and random longitudinal mode spikes of high peak power micro pulses, which is not favourable to resist chemistry. This paper discusses on the required technological assessment and lowest risk approach to construct a prototype, based on superconducting linac and cryogenic undulator, to demonstrate a MHz repetition rate, high average power 13.5nm FEL equipped with specified optical components, for best optimization in EUVL application, including a scaling to 6.7nm wavelength region.

INTRODUCTION

Extreme Ultraviolet Lithography (EUVL) is entering into the high volume manufacturing (HVM) stage, after intensive research and development of various component technologies like Mo/Si high reflectivity mirror, chemically amplified resist, and especially high average power EUV source from laser produced plasma at 13.5nm. Semiconductor industry road map requires a realistic scaling of the source technology to 1kW average power, and further wavelength reduction to 6.7nm. It is recently recognized by the community of the necessity to evaluate an alternative approach based on high repetition rate FEL, to avoid a risk of the source power limit by the plasma based technology.

It is discussed by several papers on the possibility to realize a high repetition rate (superconducting) FEL to generate a multiple kW 13.5nm light [1,2]. We must notice that the present SASE FEL pulse (typically 0.1mJ, 100fs, 1 mm diameter) has higher beam fluence than the resist ablation threshold [3], and high spatial coherence which results in speckle and interference patterns in resist, and random longitudinal mode beat which leads to high peak power micro spikes. The interaction of the SASE pulses with chemically amplified resist is not known, because the typical EUV (13.5nm) pulses from Tin plasma has a characteristics of continuous spectrum of 2% bandwidth with 10ns pulse width. The emission is fully non coherent, and the pulse energy is typically mJ level at 100 kHz repetition rate.

This paper discusses on the scaling of the FEL technology to kW average power level, optical technology

to optimize the FEL beam for lithography application, and scaling to 6.7nm wavelength region.

SCALING TO KW AVERAGE POWER

We start to evaluate a general perspective of high average power 13.5nm generation by SASE mode from recent typical operational parameters and future projects like LCLS2 etc. Genesis calculation was performed to estimate available single shot pulse energy by the electron beam and undulator parameters shown in the table 1. Pulse length was assumed as 100fs and 200fs to evaluate the difference of the output pulse energy depending on the pulse lengths. The calculation result is shown in the Figure 1, which indicates the saturation distance is nearly 20m with 0.1mJ pulse energy for short and long pulse lengths. The average power is 100W level with MHz repetition rate, and 1kW is obtained by 10MHz repetition rate with cryogenic superconducting linac and undulator. There are indeed various engineering challenges for this operation ahead.

Table 1: Parameters for Genesis Calculation

Charge	300pC
Emittance	1mm•mrad
Energy Spread	10^{-4}
Bunch Length	100fs/200fs
E-beam Energy	331.13MeV
Undulator Period	9mm
K Value	1
EUV Wavelength	13.5nm

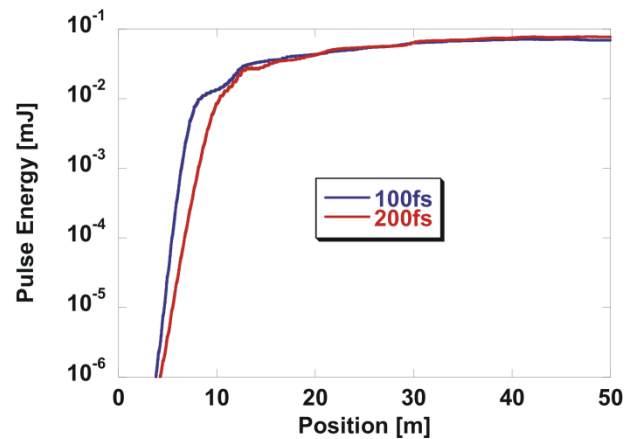


Figure 1: FEL pulse energy growth along Undulator.

*Work supported by NEDO

RESIST CHEMISTRY UNDER FEL PULSE IRRADIATION

Chemically amplified resists were first deployed in the mass-production lines of semiconductor devices during the transition of the exposure tool from Hg lamp to KrF excimer laser, and modified to be used by plasma EUV source. After EUV photons are absorbed by molecules, photoelectrons are emitted. The photoelectrons (I_e) with excess energy ($E > E_{th}$) induce further ionization and electronic excitation as shown in Fig.2. The inelastic mean free path of photoelectrons generated by EUV photons is less than 1 nm [4]. Therefore, the ionization and electronic excitation points are distributed narrowly around the photoabsorption point. This is one of the reasons why a higher resolution is expected for EUV lithography than for EB and X-ray lithography, in which the generation of high-energy secondary electrons is a concern. However, the problem associated with the thermalization distance of secondary electrons is the same as that in EB lithography.

One of the remarkable differences of SASE FEL EUV source is its pulse length typically as 100fs, which is 10^5 times shorter than that of plasma source. The EUV photoabsorption / initial ionization and secondary process are regarded as temporally separated under FEL pulses, but this is convoluted in the case of 10ns EUV pulse irradiation. Resist sensitivity is typically $10\text{mJ}/\text{cm}^2$ and the ablation threshold is 10 times higher for the case of 10ns 13.5nm pulses. An experiment by FLASH reported the ablation threshold of PMMA as less than $10\text{mJ}/\text{cm}^2$ with 13.5nm 25fs SASE FEL pulses [5]. It is desirable to make a systematic research on the resist chemistry under such FEL EUV fluence in advance.

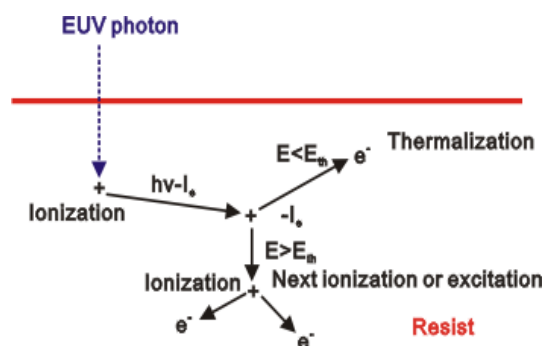


Figure 2: Resist reaction under EUV photon.

SPATIAL COHERENCE

Excimer lasers operating in the Deep Ultra-Violet (DUV) have been used in lithographic systems for over a decade. Their high brightness and limited spatial and temporal coherence make them an attractive source for circuit patterning. However, the wide bandwidth of excimer lasers caused problems in designing DUV

photolithographic optics. Line-narrowing processes reduce chromatic aberration in refractive optical systems, but have the disadvantage of increasing coherence and causing problems with interference and speckle. Increased spatial coherence brings problems with interference in conventional beam homogenization systems. Optical modelling of such partially coherent sources was beneficial in the design of efficient beam homogenization techniques, based on micro lens array.

Spatial coherence measurements were reported by illuminating a $10\text{ }\mu\text{m}$ pinhole array with a KrF excimer laser operating at 248 nm. An estimate of the spatial coherence of the source can be taken at a reference level of 50 % visibility, and gave a coherence length of 285 μm . An experimental characterization of the spatial and temporal coherence properties of FLASH at a wavelength of 8.0 nm is reported [6]. Double pinhole diffraction patterns of single femtosecond pulses focused to a size of about $10 \times 10\text{ }\mu\text{m}^2$ were measured. A transverse coherence length of $6.2 \pm 0.9\text{ }\mu\text{m}$ in the horizontal and $8.7 \pm 1.0\text{ }\mu\text{m}$ in the vertical direction was determined. The mutual coherence function K is given as 0.42, and a measurement of K by a laser plasma source is 3.2×10^{-9} . It is concluded from these measurements that a beam homogenization is required at EUV wavelength by using total reflection optics.

Multi foil optics (MOF) is a EUV optics which consists of two perpendicular sets of very thin reflecting mirrors, where photons are reflected at grazing incidence. Figure 3 shows an example of a MOF focusing element.

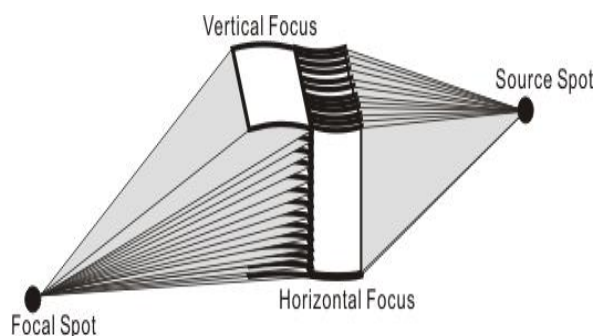


Figure 3: MOF EUV optics to compose FEL beam expander and beam homogenizer.

TEMPORAL COHERENCE AND SPIKE

Temporal coherence was also reported by using a split and delay unit. The coherence time of the pulses produced in the same operation conditions of FLASH was measured to be 1.75fs. The measured coherence time has a value, which corresponds to about 65.5 ± 0.5 wave cycles ($c\tau/\lambda$). It is well known that the SASE FEL pulses are composed of many small spikes and random spectrum due to SASE process. It is reported that the averaged spectrum has a 1.4% bandwidth typically.

LASER TECHNOLOGY FOR HGHG AT MHZ REPETITION

Seeding a FEL with an external coherent source has been studied together with SASE operation to enhance the radiation brightness and stability compared to SASE. An efficient scheme for seeding a VUV-soft x ray FEL uses a powerful, long wavelength external laser to induce on the electron beam coherent bunching at the harmonics of the laser wavelength. When the bunching is further amplified by FEL interaction in the undulator, the scheme is called as high gain harmonic generation (HGHG). A successful demonstration is reported from FERMI as double stage seeded FEL with fresh bunch injection technique [7]. High power seed sources and small electron beam energy spread are at the main limits for direct extension of the HGHG scheme to short wavelengths. The fresh bunch scheme was proposed as a way to overcome these limitations, namely the FEL radiation produced by one HGHG stage acts as an external seed for a second HGHG stage. A 10Hz demonstration is reported by using an electron beam parameters in Table 1 except the beam energy as 1 GeV. The following Table 2 compares the wavelength of the HGHG operation in the case of FERMI FEL-2 and EUV FEL.

Table 2: Comparison of Wavelengths for HGHG Operation in FERMI FEL-2 and EUV FEL

	Fermi FEL-2	EUV FEL
Seed	260nm	324nm
1 st FEL	32nm	40.5nm
2 nd FEL	10.8nm	13.5nm

The external seed laser was the third harmonic of a Titanium:Sapphire laser with a duration of ~ 180 fs (FWHM) and up to $20 \mu\text{J}$ energy per pulse. Its transverse size in the modulator was made larger than the electron beam size to ensure as uniform as possible the electron beam energy modulation. Once the same laser energy is required for 100W EUV FEL, 20W average power is required for 324nm with 180fs at MHz repetition rate. There are two approaches to generate such laser pulses, the first is based on MHz repetition rate Ti:Sapphire laser with 100 μJ level pulses, and the second one is based on OPCPA.

The short pulse, short wavelength laser technology is now advancing due to the new suitable laser configuration as thin disc laser, and efficient wavelength conversion method. Second harmonics of the Yb:YAG thin disc laser is employed to pump the Titanium:Sapphire laser or OPCPA with typically 1mJ pulse energy. It is reported recently that a thin disc multi pass amplifier generated 1.1 kW average power at 800kHz with 1.4mJ pulse energy of 6.5 ps[8]. It was also demonstrated to convert to the

second harmonics efficiently with more than 400W average power.

SUMMARY AND CONCLUSION

Discussion is presented in this paper on the EUV FEL perspective to the kW scaling with 13.5nm wavelength with suitable beam characteristics. It is pointed out that the EUV FEL pulse is available with 100W by MHz repetition rate, and kW by 10MHz. Suitable compensation technology is required to overcome the negative effects of the spatial and temporal coherence, and pulse spikes. These are beam expansion and homogenization by reflective optics, and external seeding by HGHG. Advanced EUV optics technology and short pulse high average power laser technologies are the fundamental tools for this research subjects. Wavelength extension to 6.7nm is one of the options of the future EUV lithography, and the plasma source is expected to supply by Gd plasma. The usable mirror has a narrower band width at this particular wavelength, and the resulting lower efficiency is the main problem for the Gd plasma approach. FEL EUV has a possibility to generate narrower band width, 1kW 6.7nm wavelength at relatively comparable source size and cost at this wavelength.

REFERENCES

- [1] E.A. Schneidmiller, V.F. Vogel, H. Weise, and M.V. Yurkov, "A kilowatt-scale free electron laser driven by L-band superconducting linear accelerator operating in a burst mode", 2011 International Workshop on EUV and Soft X-ray Sources, November 7-9, 2011, Dublin, Ireland
- [2] G. Stupakov and M. S. Zolotarev, "FEL oscillator for EUV lithography", SLAC-PUB 15900, January 2014
- [3] J. Chalupský, L. Juha et.al, "Characteristics of focused soft X-ray free-electron laser beam determined by ablation of organic molecular solids", OPTICS EXPRESS 15, 6036 (2007)
- [4] T.Kozawa and S.Tagawa, "Radiation chemistry in chemically amplified resists", J.J. Appl. Phys. 49 (2010) 03001
- [5] L.Juha, private communication
- [6] A.Singer et.al. "Spatial and temporal coherence properties of single free electron laser pulses" Opt.Express. 20, (2012) 17480
- [7] E.Allaria et.al. "Double stage seeded FEL with fresh bunch injection technique at FERMI", Proc. FEL2013, THIAN01
- [8] J.P.Negel et.al "Thin disc amplifier for ultrashort laser pulses with kilowatt average output power and mJ pulse energies", Proc. SPIE vol. 9135 1D, Laser sources and applications II, Brussels, 14-17 April 2014

A COLLINEAR WAKEFIELD ACCELERATOR FOR A HIGH REPETITION RATE MULTI BEAMLINE SOFT X-RAY FEL FACILITY*

A. Zholents[#], W. Gai, R. Lindberg, J.G. Power, Y. Sun, ANL, Argonne, IL 60439, USA
 C. Jing, A. Kanareykin, Euclid Techlabs LLC, Solon, OH 44139, USA
 C. Li, C.X. Tang, Tsinghua University, Beijing, China
 D. Yu. Shchegolkov, E.I. Simakov, LANL, Los Alamos, NM 87545, USA

Abstract

A concept is presented for a multi beamline soft x-ray free-electron laser (FEL) facility where several FEL undulator lines are driven by an equal number of high repetition rate single-stage collinear wakefield accelerators (CWA). A practical design of the CWA, extending over 30 meters and embedded into a quadrupole wiggler, is considered. The wiggler's structure of alternating focusing and defocusing quadrupoles is used to control single-bunch breakup instability. It is shown that practical restrictions on the maximum attainable quadrupole field limit the maximum attainable charge in the drive bunch whose sole purpose is to produce a high accelerating field in the CWA for the following main bunch. It is also pointed out that the distance between drive and main bunches varies along the accelerator, causing a measurable impact on the energy gain by the main bunch and on the energy spread of electrons in it. Means to mitigate these effects are proposed and results are presented for numerical simulations demonstrating the main bunch with plausible parameters for FEL application including a relatively small energy spread. Finally, results are presented for the expected FEL performance using an appropriately chosen undulator.

INTRODUCTION

A number of FEL facilities are currently in operation [1-4] and more have been planned. While tremendously effective in providing extreme photon fluxes, these machines can only accommodate a small number of users at a time. To address this limitation, multi-user FEL facilities have been recently proposed (see, for example, [5]). The mainstream approach is to accelerate electron bunches in a few GeV cw superconducting rf (SRF) linac and send them to a switchyard of ten or more FELs at a high bunch repetition rate. Here, we consider a different approach where a single cw SRF linac of a much lower energy (~400 MeV) and ten CWAs are used to provide ten FELs with a few GeV electron bunches. It is expected that the construction and operational costs of the facility, which are largely defined by the large SRF linac, can be significantly reduced. A high-gradient room-temperature CWA structure is the key to this proposal. Advanced accelerator studies aimed at a future high-energy collider

have shown impressive results, achieving multiple-GV/m energy gradients in various wakefield acceleration schemes [6,7].

A CWA SCHEME FOR FEL

In a collinear wakefield accelerator [8,9], the field generated by a leading, high-charge drive bunch is used to accelerate a trailing low-charge main bunch. The collinear configuration has the two beams traversing the accelerator along the same trajectory so that the energy is directly transferred from the drive bunch to the main bunch. There are two main candidates for a CWA structure. The corrugate pipe wakefield accelerator (CPWA) [10] structure consists of a metallic pipe with wall corrugations where traveling on the pipe's axis relativistic electrons excite a synchronous monopole mode whose amplitude and frequency is defined by the pipe radius and geometry of corrugations. The dielectric wakefield accelerator (DWA) [11] structure consists of a cylindrical dielectric tube with an axial vacuum channel inserted into a copper outer jacket. The dielectric constant and the inner and outer radii of the dielectric tube are chosen to adjust the fundamental monopole mode (TM_{01}) frequency excited by the relativistic electrons. The phase velocity of the mode equals the beam velocity $\sim c$.

The overall facility layout is shown in Figure 1. The scheme consists of 10 parallel FELs and ten parallel CWAs that supply FELs with a ~ 2 GeV electrons. The CWAs share a single 650 MHz cw SRF linac that accelerates 8-nC drive and 250-pC main bunches to ~400-MeV. Because of a need for the tight synchronization between drive and main bunches (of the order of 250 fs), both bunches are obtained from one source bunch as discussed below. The repetition rate of duets of drive and main bunches in the CWA is limited to ~ 50 kHz. This keeps the average wakefield power dissipation in the accelerating structure at a manageable level, as shown later. Thus, the bunch repetition rate in the cw SRF linac is ~ 500 -kHz. A spreader switchyard distributes electron bunches to the ten CWAs on a rotating basis (or as needed). The drive bunch has a special double triangular current profile, shown in Figure 2. The bunch current shape is tailored to maximize the transformer ratio R , defined as the ratio of the maximum accelerating field behind the drive bunch over the maximum decelerating field inside the bunch. Obtaining short drive bunch ~ 3.3 ps requires off-crest acceleration of the already pre-shaped bunch in SRF linac producing $\sim 10\%$ energy chirp

*Work supported by U.S. Department of Energy, Office of Science, under Contract No. DE-AC02-06CH11357 and by the U.S. Department of Energy through the Laboratory Directed Research and Development (LDRD) program at Los Alamos National Laboratory.

[#]azholents@aps.anl.gov

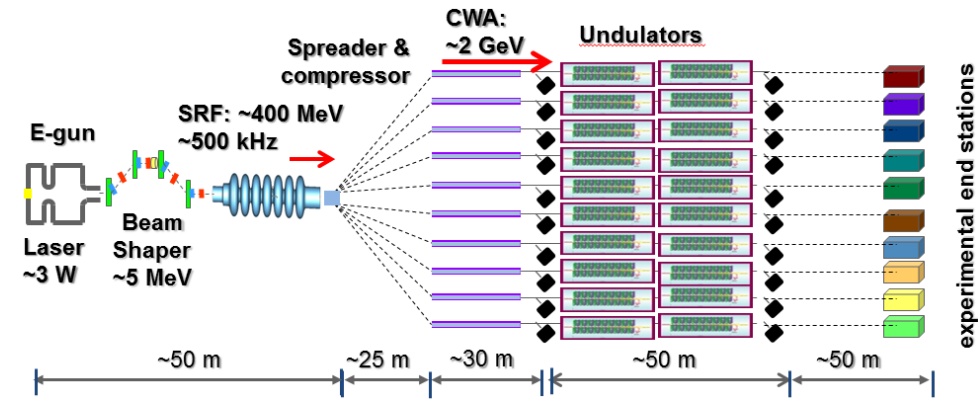


Figure 1: A schematic of the FEL facility showing (not to scale) an electron gun, bunch shaping section, cw superconducting linac, spreader and transport lines, an array of collinear wakefield accelerators, undulator arrays, and x-ray beamlines.

at the end and ~ a tenfold bunch compression in each spreader beam line. The energy chirp that remains after the compression assists in suppression of single-bunch breakup instability as discussed later in this paper.

The effective acceleration length of the CWA is ~30 m, over which distance the drive bunch loses ~80% of its energy and the main bunch gains ~ 1.6 GeV. As presently considered, each CWA has 40 half-meter-long acceleration sections followed by shorter break sections that include beam diagnostics, vacuum ports and a THz frequency directional coupler. In the case of the DWA, the vacuum chamber of the acceleration section consists of a quartz-based tube with copper cladding. A ceramic with DC conductivity [12] will be used in the dielectric layer allowing discharging of the erroneous charges produced by the electromagnetic showers induced by stray electrons. The inner surface can also be coated by a few nanometer metallic or TiN layer [13]. Cooling is provided to remove the heat load produced by the wakefields which is calculated to be 10.8-W per cm of a linear length of the DWA structure for the Case 2 of beam parameters discussed below. This chamber is embedded into a quadrupole wiggler with soft-iron magnetic poles excited by permanent magnets, as shown in Figure 3. The same chamber can be used in the case of the CPWA except corrugations on the inner wall instead of the dielectric layer. The chamber has a small 2-mm diameter hole, essential for achieving a high acceleration gradient using CWA.

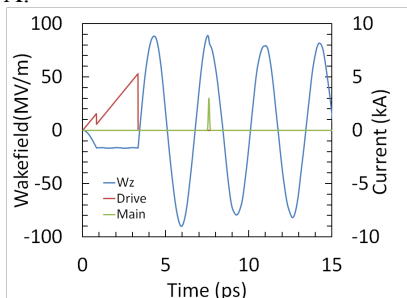


Figure 2: Drive bunch double triangle current profile and the wakefield due to drive and main bunches.

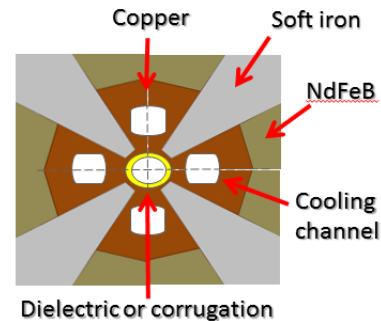


Figure 3: A cut-out part of the central area of the CWA showing the quadrupole wiggler and the vacuum chamber with cooling channels and either dielectric or corrugated inner part (marked by yellow colour). Electron beam propagates on the axis of the central cross.

DRIVE BUNCH SHAPING

The main plan for obtaining a double triangle current profile of the drive bunch is to use the mask with a special form shown in Figure 4. The same mask is also used to shape the low charge main bunch and fix it at a precisely defined distance behind the drive bunch.

The mask is placed in front of the transverse-to-longitudinal emittances exchange (EEX) beamline [14-21] which converts the red-coloured transverse image in Figure 4 into the double triangle longitudinal profile at the end of the beamline shown in Figure 2. The transmission efficiency of the mask is only ~45% and, therefore, we consider carrying out bunch shaping at a low beam energy ~5-MeV below a threshold energy for the material activation for copper. With a 500 kHz bunch repetition rate, approximately 25-kW of a source beam power is absorbed by the mask.

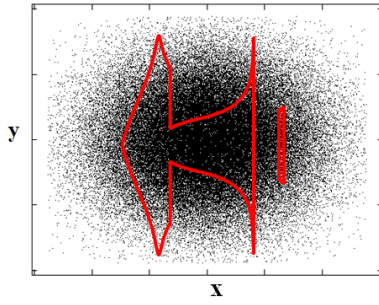


Figure 4: The outline of the mask boundary (red curve) on a background of Gaussian distribution of electrons of the source bunch in transverse coordinates [14].

A different approach is proposed in [22] where a near triangular bunch current profile is obtained using a combination of a wakefield producing dielectric tube and a compact magnetic chicane. It is therefore possible to use a double emittance exchange beamline [23] in order to convert the longitudinal profile obtained in [22] into the transverse distribution using the first emittance exchange leg, to apply the mask, and to use the second emittance exchange leg to convert the transverse distribution after the mask into the double triangle longitudinal profile at the end. Here, starting with the pre-shaped longitudinal distribution, the transmission efficiency of the mask is expected to be at ~80-90% level.

As discussed above, final compression of the drive and main bunches is planned after acceleration to 400 MeV utilizing the energy chirp acquired through bunch shaping manipulations and off-crest acceleration in the SRF linac and the spreader beamline beam transport time-of-flight properties.

A proof-of-principle experiment for beam shaping is in preparation at the AWA facility [24,25] with a 5-nC Gaussian bunch and plausible transverse and longitudinal emittances at 75 MeV electron beam energy.

MAIN PARAMETERS

Since physics of beam acceleration in CPWA and DWA is practically identical, we only discuss here the main beam parameters for a case of DWA. In order to inform design choices and evaluate sensitivities of the DWA to the key parameters of the dielectric channel and parameters of the drive and main bunches, we consider two hypothetical cases summarized in Table 1. The Case 2 is currently selected as our preferred scenario. In this case a ~90-MeV/m acceleration gradients is achieved at the wakefield maximum with the transformer ratio $R=5$ using a 8-nC drive bunch. A drive-beam-to-main-beam energy transfer efficiency is calculated to be ~15% using a 250-pC main bunch. All the values are calculated using four longitudinal structure modes, but the fundamental mode gives the dominant contribution because each structure is designed to minimize the loss factor of higher-order modes (HOMs). This is very important for achieving a high transformer ratio, as well as to mitigate the self-wakefield induced disturbances inside the main

bunch as discussed later. Stable propagation of a drive bunch with energy varying from 400-MeV to 80-MeV along the CWA through this hole presents a significant challenge and is discussed later.

While the structure is optimized to maintain a single-mode excitation for the drive beam, multiple modes are excited by the main beam due to its shorter bunch length. But the self-wakefield inside the main bunch will converge very fast because the loss factor of HOMs becomes negligible beyond the first few modes. A 250-pC per bunch and 10- μ m rms main bunch length were chosen in the design to allow a 3-kA peak current with a reasonable beam loading in the CWA.

Table 1: DWA and Beam Parameters

Parameter	Case 1	Case 2	Units
Fundamental mode frequency	400	300	GHz
ID/OD/Length	1.5/1.59/100	2/2.12/100	mm
Drive bunch charge	3.5	8	nC
Drive bunch energy	300	400	MeV
Double triangular bunch length	1	1	mm
Peak acc. field	42	90	MV/m
Bunch rep. rate	100	50	kHz
Power dissipation without/with THz field coupler*	19/5.4	55/10.8	W
Transformer ratio	8	5	
Main bunch charge/length	50/5	250/10	pC/ μ m
Drive beam dump energy	70	80	MeV
Total DWA length	40	20	m
Drive-to-main beam efficiency	8.6	15.5	%
Main beam energy	1.9	2.0	GeV

* per unit length, 100% THz field coupling efficiency is assumed

BEAM BREAKUP INSTABILITY

The small aperture of the CWAs structures makes the drive bunch particularly vulnerable to the single-bunch breakup (BBU) instability predominantly driven by transverse HEM₁₁ mode [26,27]. We consider using BNS damping [28] to control the BBU and, thus, surround the CWA by a quadrupole wiggler (composed of alternating focusing and defocusing quadrupole schematically shown in Figure 5) and use the energy chirp in the drive bunch entering the CWA.

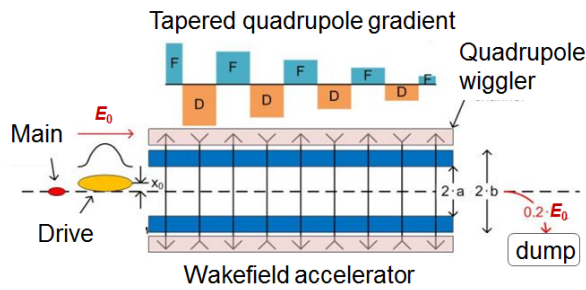


Figure 5: Schematic of a CWA. The quadrupole field is tapered to match the energy loss of the drive bunch along the accelerator. The final energy of the drive bunch at the end of the structure is 20% of its initial energy.

In order to better understand main parameter dependencies, we developed a simple two-particle model [29] that was later found to correctly represent the BBU for the drive bunch with a Gaussian longitudinal distribution. Using this model we determine the maximum achievable acceleration gradient as a function of the accelerating structure inner radius a shown in Figure 6. A grey area on this plot represents a stable region and a white area represents the unstable region. The border curve scales as \sqrt{a} in a good agreement with results of multiparticle tracking shown by red circles. In this simple model, the ultimate extent of the stability region is limited by a maximum attainable strength for the quadrupole field (that in this study was scaled as a^{-1} from the value of 1-T/mm at $a = 1$ mm). The dashed lines show scaling of the acceleration gradient when BBU is ignored.

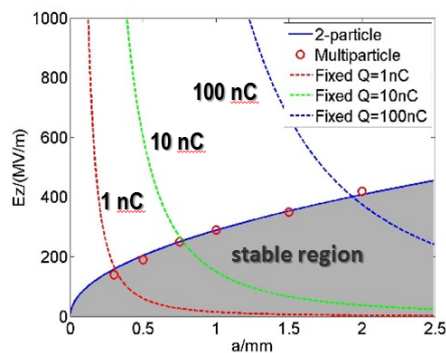


Figure 6: Maximum attainable energy gain in the CWA limited by BBU as a function of accelerating structure inner radius.

The remaining studies we did using the drive bunch with a double triangular current distribution. In this case when electrons lose much of their energy, the tail electrons begin to lag behind the head electrons to the extent that they even move into the region of the accelerating wakefield [30]. At the same time, the main bunch that gains a lot of energy begins to approach the tail of the drive bunch and goes out of the region with the maximum accelerating field. This effect is more pronounced when the drive's bunch energy is mostly used, and the energy of the tail electrons therefore

becomes very low. One option to reduce relative slippage of drive and main bunches is to increase the energy of a drive bunch which has prompted us to use 400 MeV SRF linac.

Another technique to mitigate slippage of the drive and main bunches with respect to each other is to position the main bunch at the second maximum of the wake field behind the drive bunch. One can also increase the frequency of the wakefield along the dielectric channel—either by decreasing the tube's radius or thickness of the dielectric layer, or depth of corrugations — and keep the main bunch at or near the second wakefield maximum. Ideally, this wakefield frequency adaptive CWA will be insensitive to the main bunch shifts closer to the drive bunch during the acceleration.

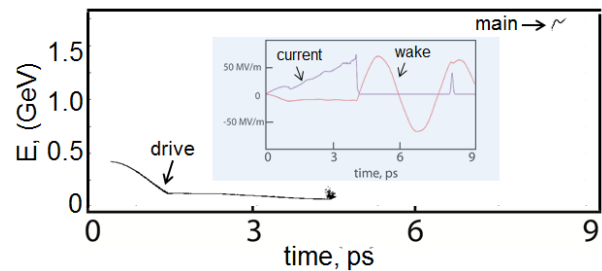


Figure 7: The result of the particle tracking showing energy variation in the drive and main bunches at a location of 18 m downstream of the DWA. The inset in the middle shows current in the drive and main bunches and the wakefield produced by the drive bunch with this current distribution.

The simulation result for the DWA with parameters given in Table 1 for the Case 2 is shown in Figure 7. Here we plot electron energy in drive and main bunches versus distance from the head of the drive bunch at the accelerator location of 18 m downstream from the accelerator entrance. The inset in the middle shows current in the drive and main bunches, and the wakefield produced by the drive bunch with this current distribution. It is approximately at this location that some tail electrons in the drive bunch begin to be accelerated by the wake produced by head electrons. In this simulation Gaussian distribution in the main bunch was used. A combination of the main bunch self-wakefield and the drive bunch wakefield produce a noticeable correlated energy variation along the main bunch. However, this energy variation can be tolerated in the FEL, as shown later. Calculations show that the main bunch with an inverse triangular current distribution proposed in [31] will have the self-wakefield canceling the drive bunch wakefield and significantly reduced correlated energy variation.

The straightness of the beam trajectory in the quadrupole wiggler is critical for maintaining the beam stability. Preliminary simulations point out that it should be at a micrometer level. This requirement presents significant challenges, but is feasible in principle, as demonstrated in dipole undulators of modern FELs.

FEL CONSIDERATIONS

Results of particle tracking for a main beam presented above and a particle distribution obtained there were used as an input particle distribution for modelling of the self-amplified spontaneous emission (SASE) process in the undulator line. Undulator parameters and other key parameters of this modelling are given in Table 3.

Table 3: SASE FEL Parameters

Parameter	Value	Units
Undulator period	1.8	cm
Undulator parameter, K	1.0	
Main beam mean energy	1.88	GeV
Main bunch charge	250	pC
Main bunch peak current	3	kA
Normalized emittance	1	μm
Main bunch relative energy spread, rms	0.3	%
FEL Pierce parameter, ρ	0.01	
X-ray wavelength	1	nm
X-ray peak power*	5	GW
FWHM x-ray pulse bandwidth, $\Delta\omega/\omega$	3.8	%

* averaged over the x-ray pulse length

Plots in Figure 8(a)-(d) show (a) the peak current and electron energy distribution in the main bunch, (b) the nonlinear saturation of SASE FEL gain in approximately 20 gain lengths, (c) peak x-ray power after the saturation, and (d) the x-ray spectrum. The slice energy spread of the electron beam is less than the FEL Pierce parameter ρ and no undulator tapering is used. However an additional undulator with tapering can be used beyond the saturation to increase the output power by a factor of 3 to 5.

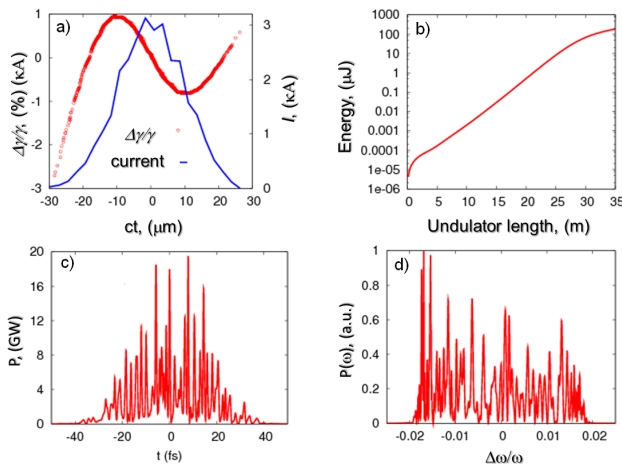


Figure 8: Current and energy distribution of the main bunch (a) and results of the FEL modeling described in the text (b)-(d).

Some applications may not be able to use FEL output with large frequency spread as in the above case, while others may benefit from it. For example, the time-resolved x-ray Laue diffraction actually requires a relatively large spectral bandwidth. A more ambitious plan would use a soft-x-ray self-seeding similar to one presented in [32] to obtain a narrow bandwidth radiation with significantly increased peak power. The feasibility of this option is yet to be determined in future studies.

CONCLUSION

It has been shown that the collinear wakefield accelerator is a viable candidate to be used in a synchrotron light source facility with multiple FELs. The accelerator is reasonably compact, flexible, and can support the FEL producing up to 5×10^4 x-ray pulses per sec. The entire facility can consist of up to ten independent FELs, each with its own collinear wakefield accelerator. The emphases have been given to finding regimes with stable beam operation at a high bunch repetition rate. The important component of the collinear wakefield accelerator is a quadrupole wiggler that allows suppression of the single-bunch breakup instability using BNS damping. Maintaining straightness of the beam trajectory through the wiggler at a few micrometer level presents significant challenges, but is feasible in principle. While we focused here on round structures, note however that flat geometries both for corrugated and dielectric structures were also proposed [33,34] that may offer specific advantages for a practical realization of the CWA. For example, the quadrupole wakefield, that is present in the planar geometry, may actually help to improve beam stability.

The strawman FEL facility design considered here only establishes the feasibility of this approach, but leaves many questions for future R&D.

REFERENCES

- [1] P. Emma et al., "First lasing and operation of an ångstrom-wavelength free-electron laser," *Nat. Photonics*, vol. 4, pp. 641-647, Aug. 2010.
- [2] W. Ackermann et al., "Operation of a free-electron laser from the extreme ultraviolet to the water window," *Nat. Photonics*, 1, 336-442, Jun. 2007.
- [3] T. Ishikawa et al., "A compact X-ray free-electron laser emitting in the sub-ångström region," *Nat. Photonics*, vol. 6, pp. 540-544, Feb. 2012.
- [4] E. Allaria et al., "Highly coherent and stable pulses from the FERMI seeded free-electron laser in the extreme ultraviolet," *Nat. Photonics*, vol. 6, pp. 699-704, Aug. 2012.
- [5] J. Corlett et al., "A Next Generation Light Source Facility at LBNL," *Proceedings of 2011 Particle Accelerator Conference*, New York, NY, 2011, pp. 775-777.
- [6] I. Blumenfeld et al., "Energy doubling of 42 GeV electrons in a metre-scale plasma wakefield accelerator," *Nature*, vol. 445, pp. 741-744, Feb. 2007.

- [7] M. C. Thompson et al., “Breakdown Limits on Gigavolt-per-Meter Electron-Beam-Driven Wakefields in Dielectric Structures,” *Phys. Rev. Lett.*, vol. 100, no. 21, pp. 214801, May 2008.
- [8] G. A. Voss and T. Weiland, “Particle Acceleration by Wake Field”, DESY report M-82-10, April 1982.
- [9] K. L. F. Bane, P. Chen, P. B. Wilson, “On collinear wake field acceleration”, SLAC - PUB – 3662, April 1985.
- [10] H. Figueroa et al. “Direct Measurement of Beam-Induced Fields in Accelerating Structures.” *Phys. Rev. Lett.*, vol 60, 2144, 1988.
- [11] W. Gai et al. Experimental Demonstration of Wake-Field Effects in Dielectric Structures. *Phys. Rev. Lett.*, vol 61, 2756, 1988.
- [12] C.K. Sinclair. *Nuclear Instruments and Methods in Physics Research A*, vol 557, p. 69 (2006).
- [13] Jing et al., “High Power Testing of a Fused Quartz-Based Dielectric- Loaded Accelerating Structure”, SLAC-PUB-12958, 2007.
- [14] D. Shchegolkov and E. Simakov, “Design of an emittance exchanger for production of special shapes of the electron beam current,” *Phys. Rev. ST Accel. Beams*, vol. 17, pp. 041301, Apr. 2014.
- [15] M. Cornacchia and P. Emma, “Transverse to longitudinal emittance exchange,” *Phys. Rev. ST Accel. Beams*, vol. 5, pp. 084001, Aug. 2002.
- [16] P. Emma et al., “Transverse-to-longitudinal emittance exchange to improve performance of high-gain free-electron lasers,” *Phys. Rev. ST Accel. Beams*, vol. 9, pp. 100702, Oct. 2006.
- [17] B. Jiang et al., “Emittance-Exchange-Based High Harmonic Generation Scheme for a Short-Wavelength Free Electron Laser,” *Phys. Rev. Lett.*, vol. 106, no. 11, pp. 114801, Mar. 2011.
- [18] Y.-E. Sun, et al., “Tunable Subpicosecond Electron-Bunch-Train Generation Using a Transverse-To-Longitudinal Phase-Space Exchange Technique,” *Phys. Rev. Lett.*, vol. 105, no. 23, pp. 234801, Dec. 2010.
- [19] P. Piot et al., “Generation of relativistic electron bunches with arbitrary current distribution via transverse-to-longitudinal phase space exchange,” *Phys. Rev. ST Accel. Beams*, vol. 14, no. 2, pp. 022801, Feb. 2011.
- [20] B. E. Carlsten et al., “Using an emittance exchanger as a bunch compressor,” *Phys. Rev. ST Accel. Beams*, vol. 14, no. 2, pp. 084403 Aug. 2011.
- [21] D. Xiang and A. Chao, “Emittance and phase space exchange for advanced beam manipulation and diagnostics,” *Phys. Rev. ST Accel. Beams*, vol. 14, no. 11, pp. 114001, Nov. 2011.
- [22] G. Andonian, “Bunch profile shaping using beam self-wakefields in a dielectric structure” *Proceedings of the 16th Advanced Accelerator Concepts Workshop*, to be published.
- [23] A. Zholents and M. Zolotarev, “A New Type of Bunch Compressor and Seeding of a Short Wave Length Coherent Radiation,” ANL/APS/LS-327, (May 2011)
- [24] G. Ha et al., “Start-to-end beam dynamics simulation of double triangular current profile generation in Argonne Wakefield Accelerator,” *Advanced Accelerator Workshop*, Austin, TX, 2012, pp. 693-698.
- [25] J. G. Power et al., “Longitudinal Bunch Shaping with a Double Dogleg based Emittance Exchange Beam Line,” *Proceedings of IPAC2014*, Dresden, Germany, 2014 pp. 1506-1508.
- [26] A. Chao, “Instabilities in Linear Accelerators,” in *Physics of collective beam instabilities in high energy accelerators*, New York: Wiley & Sons, 1993, ch. 3, pp. 127-160.
- [27] W. Gai et al., “Numerical simulations of intense charged-particle beam propagation in a dielectric wake-field accelerator,” *Phys. Rev. E.*, vol. 55, no. 3 pp. 3481-3488, Mar. 1997.
- [28] V. Balakin et al., “VLEPP: Transverse Beam Dynamics,” *Proceedings of the 12th International Conference on High Energy Accelerators*, Fermi National Acceleratory Laboratory, Batavia, IL, 1983, p. 119.
- [29] C. Li et. al., “High Gradient Limits due to Single Bunch Beam Breakup in a Collinear Dielectric Wakefield Accelerator,” *Phys. Rev. ST Accel. Beams*, to be published.
- [30] D. Shchegolkov et al., “Suppressing Parasitic Effects in a Long Dielectric Wakefield Accelerator” *Proceedings of the 16th Advanced Accelerator Concepts Workshop...*, to be published.
- [31] T. Katsouleas et al., “Beam loading in plasma accelerators,” *Particle Accelerators*, vol. 22, pp.81-99, 1987.
- [32] D. Ratner et al., “Soft X-ray Self-Seeding Setup and Results at LCLS,” *Proceedings of 36th International Free Electron Laser Conference...*, to be published, 2014.
- [33] A. Tremaine et al. “Electromagnetic wake fields and beam stability in slab-symmetric dielectric structures”, *Phys. Rev. E*, vol 56, p. 7204, 1997.
- [34] K. Bane, G. Stupakov, “*Impedance of a Rectangular Beam Tube with Small Corrugations*”, *Phys. Rev. ST Accel. Beams*, vol 6, 024401, 2003

DIVERGENCE REDUCTION AND EMITTANCE CONSERVATION IN A LASER PLASMA ACCELERATION STAGE

I. Dornmair, A. R. Maier*,

CFEL, Center for Free-Electron Laser Science, 22607 Hamburg, Germany

University of Hamburg, Institute for Experimental Physics, 22761 Hamburg, Germany

K. Floettmann, DESY, 22607 Hamburg, Germany

Abstract

In laser-plasma accelerators, very high acceleration gradients are reached, which makes them promising candidates for high-energy applications as well as as drivers for next-generation light sources. Yet, conserving the beam quality when coupling the beam into and extracting it from the plasma is very challenging. The concept presented here employs tapered matching sections to increase the matched beamsizes at the plasma entrance and to adiabatically reduce the beam divergence at the plasma exit, which suppresses chromatic emittance growth.

INTRODUCTION

The electric fields present in the wakefield of a driver laser or beam in a plasma accelerator [1,2] are far larger than in conventional cavities. Acceleration of electron bunches to GeV energies over cm-scale distances has been shown [3,4,5]. However, the focusing forces provided by the transverse field components are very strong.

An electron bunch whose transverse beam size is not matched to these focusing forces will perform betatron oscillations. The betatron frequency depends on the phase in the wake and on the bunch energy. Finite bunch length and (acquired correlated) energy spread then lead to emittance growth. The bunch size therefore needs to be matched, requiring extremely strong focusing optics both for injection into and extraction out of the plasma [6]. The combination of large divergence and large energy spread also leads to strong emittance growth in the drift following the plasma target [7,8].

ADIABATIC MATCHING IN PLASMA ACCELERATORS

We include adiabatic matching sections at the start and end of a plasma stage to increase the beta function needed to match an external beam into the plasma and to reduce the divergence before the plasma-vacuum transition. Adiabatic profiles are characterized by the changes of focusing strength being slow enough so the bunch envelope can follow its changes and stay matched. Since no betatron oscillations are performed, the emittance is conserved. Here, we derive with simulations ideal profiles for both plasma density and driver laser evolution.

We use the linear wakefield model with

$$E_z(r, \zeta) \propto a^2 k_p^2 \exp(-k_p^2 \sigma_z^2 / 2 - 2r^2 / w^2) \cos \Psi,$$

$$E_r(r, \zeta) \propto -a^2 k_p r / w^2 \exp(-k_p^2 \sigma_z^2 / 2 - 2r^2 / w^2) \sin \Psi,$$

that we implemented in the particle tracking code Astra [9] and cross-checked for short plasma targets with the PIC code VSim (formerly Vorpil) [10]. Here, $\Psi = k_p \zeta$ is the phase, $\zeta = z - v_g t$ the co-moving variable, v_g the laser group velocity and $k_p c = \sqrt{ne^2 / m_e \epsilon_0}$ the plasma frequency. The normalized vector potential a of the Gaussian laser pulse is given by $a^2 = a_0^2 \exp(-2r^2 / w^2) \exp(-\zeta^2 / 2\sigma_z^2)$. The model is valid for $a_0 < 1$ and includes changes of bunch phase due to the laser group velocity and due to changes in density. It does not include pump depletion and changes of the wakefield caused by transverse density profiles.

We consider a plasma stage separated into injection, acceleration and extraction section and has a peak density of $n_0 = 1 \cdot 10^{17} \text{ cm}^{-3}$. An electron beam of 100 MeV kinetic energy, normalized emittance $\epsilon_{nx} = 1 \text{ mmrad}$ and $\sigma_z = 1 \mu\text{m}$ is injected externally. The laser with $a_0 = 1.3$, fwhm length 130 fs and a spot size of $w_0 = 26 \mu\text{m}$ is focused at the start of the acceleration section. In the injection section it follows the Gaussian beam evolution while it is assumed to be guided throughout the acceleration section.

The matching condition reads $\beta_m = 1/\sqrt{K}$ for K the focusing strength of the wakefield given by

$$K = \frac{e}{\gamma m_e c^2} \frac{\partial E_r}{\partial r} \Big|_{r=0} \quad (1)$$

$$\propto -\frac{a^2 k_p}{w^2} \exp(-k_p^2 \sigma_z^2 / 2) \sin \Psi.$$

For a sharp plasma edge, i.e. no injection section, the laser focus and the electron focus coincide and a matched beta function of $\beta_m = 0.5 \text{ mm}$ is required.

In an injection section, the bunch experiences slowly increasing focusing forces. This lensing effect leads to a decrease of bunch size till the start of the acceleration section. The bunch therefore can be injected with a virtual focus in the injection section that can be much larger than without this section. The section length is naturally limited by the Gaussian evolution of the laser leading to much weaker fields in the wake away from the focus.

* andreas.maier@desy.de

We choose a linear plasma up ramp as the simplest function and match the electron beam by backpropagating it from the start of the acceleration section using the differential envelope equation $\sigma_x'' + K(z)\sigma_x - \varepsilon^2\sigma_x^{-3} = 0$. The beta function in the virtual focus depends on the length of the upramp l_{inj} as can be seen in Figure 1. It saturates for long plasma upramps when the laser evolution becomes the limiting factor.

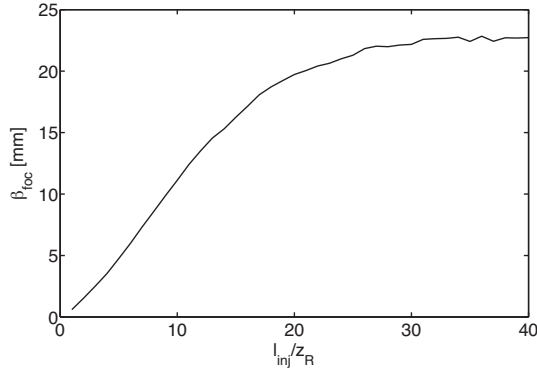


Figure 1: The beta function in the virtual focus depends on the length of the linear density upramp l_{inj} and saturates for very long injection sections since here the contribution of the laser very far away from the focus becomes negligible.

In the acceleration section the density is constant and the laser is assumed to be guided. We end this section when the bunch has reached dephasing at $k_p\zeta = -\pi/2$, that is after 79 cm. The bunch acquires a large energy chirp of $\Delta E/E/\sigma_z = 7\%/ \mu\text{m}$ which is mainly caused by off-crest acceleration combined with the finite bunch length compared to the plasma wavelength. After the acceleration, the bunch has a kinetic energy of 8.8 GeV. The emittance is conserved since changes of K are only caused by phase slippage which is a slow, adiabatic process.

In the extraction section, the divergence needs to be reduced for two reasons: Firstly, to relax the requirements on beam capturing optics behind the plasma and secondly to damp chromatic emittance growth in the drift following the plasma vacuum transition.

The general profile for the focusing strength [11]

$$K = \frac{K_0}{(1 + gz)^4} \quad (2)$$

provides largest adiabatic bunch size increase over the shortest distance. Since the emittance is conserved due to adiabaticity, the divergence is reduced. Here, g is a taper parameter that has to fulfill $g\beta_0 \ll 1$ with β_0 the beta function at the start of the extraction section.

We derive profiles in terms of laser and plasma parameters for two extreme cases, separating the contributions of laser and density. Assuming constant density and neglecting slippage between laser and bunch,

equation (1) simplifies to $K \propto a^2/w^2 \propto 1/w^4$. The ideal transverse laser profile evolution is then

$$w(z) = w_0(1 + gz). \quad (3)$$

Assuming the laser to be guided at constant $w(z) = w_0$, equation (1) gives $K \propto -k_p \exp(-k_p^2\sigma_z^2/2) \sin(k_p\zeta)$. We find a fit to the numerical solution for k_p of this equation together with equation (2) as

$$n = \frac{n_0}{(1 + agz + bg^2z^2)^2} \quad (4)$$

where $a = 3.45$ and $b = 1.59$ are fit parameters and g is the taper parameter. This fit is valid for starting the density downramp at dephasing.

Even though these profiles are optimized for the purpose of divergence reduction, their exact shape leaves room for variation as long as K is changed slow enough to still be adiabatic.

Astra simulations have been done to compare a plasma profile with a sharp end to a profile including the proposed ideal extraction section. Over a length of 53 cm K is tapered according to eq. (3) with $g = 30 \text{ m}^{-1}$. The plasma density is constant while the laser is assumed to be guided in such a fashion that its envelope increases linearly. As can be seen in Figure 2 the divergence is drastically reduced to only $15 \mu\text{rad}$ compared to $160 \mu\text{rad}$ for the sharp plasma end. This suppresses emittance growth in the drift to only $\Delta\varepsilon_{nx}/\Delta z = 0.06 \text{ mmmrad/m}$, whereas the emittance increases by $\Delta\varepsilon_{nx}/\Delta z = 33 \text{ mmmrad/m}$ without extraction section.

CONCLUSION

We have shown in simulations that by including dedicated matching sections for coupling a beam into and extracting it from a plasma stage, it is possible to drastically relax the requirements on beam optics before and after the stage. The beta function needed to match into the stage was increased by more than an order of magnitude, while the divergence after extraction was decreased by a similar amount. This minimizes chromatic emittance growth after the plasma and is of interest also for schemes employing internal injection.

Compared to PIC codes, the linear wakefield model used here is simplified in order to concentrate on the underlying beam dynamics, and does not include effects like beam loading or pump depletion.

ACKNOWLEDGMENT

We gratefully acknowledge the computing time provided on the supercomputer JUROPA under project HHH20. I. Dornmair acknowledges support by the IMPRS UFAST. We would like to thank N. Delbos (CFEL/UHH) and C. Werle (CFEL/UHH) for stimulating discussions and useful suggestions.

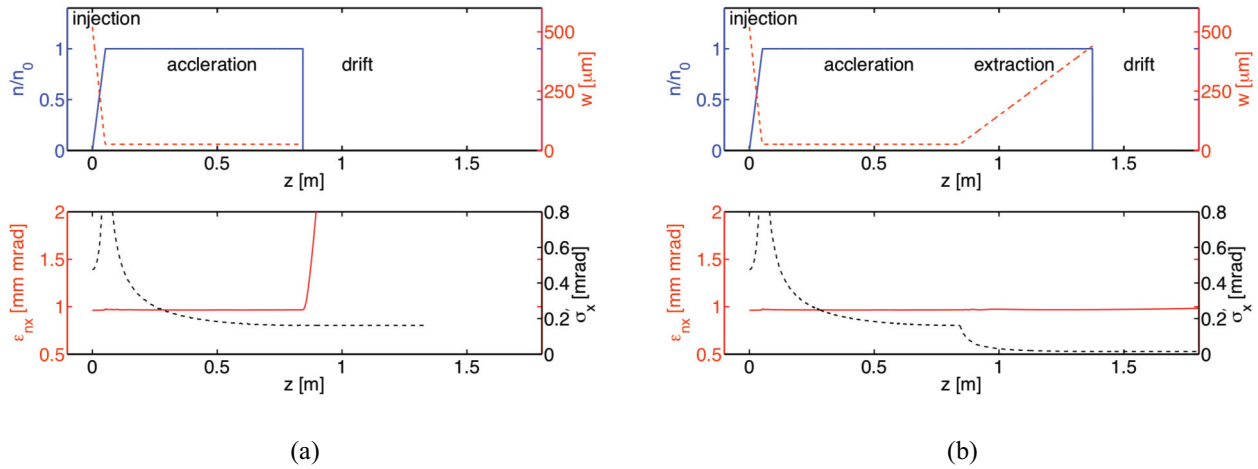


Figure 2: Top: Plasma profile (blue) and laser envelope (dashed red) for a case including a extraction section employing laser tapering (b) and a case with sharp plasma end (a) for comparison. Bottom: Normalized emittance (red) and beam divergence (black) of the electron beam throughout the complete stage. The extraction section drastically reduces the divergence and thus also suppresses chromatic emittance growth in the drift.

REFERENCES

- [1] T. Tajima, J. M. Dawson, Phys. Rev. Lett. 43, 267 (1979).
- [2] E. Esarey et al., Rev. Mod. Phys. 81, 1229 (2009).
- [3] W. P. Leemans et al., Nature Phys. 2, 696 (2006).
- [4] H. T. Kim et al., Phys. Rev. Lett. 111, 165002 (2013).
- [5] X. Wang et al., Nat. Commun. 4, 1988 (2013).
- [6] T. Mehrling et al., Phys. Rev. ST. Accel. Beams 15, 111030 (2012).
- [7] P. Antici et al., J. Appl. Phys. 112, 044902 (2012).
- [8] M. Migliorati et al., Phys. Rev. ST. Accel. Beams 16, 011302 (2013).
- [9] K. Floettmann, "Astra - a space charge tracking algorithm", <http://www.desy.de/~mpyflo/>.
- [10] C. Nieter, J. R. Cary, J. Comput. Phys. 196, 448 (2004).
- [11] K. Floettmann, Phys. Rev. ST. Accel. Beams 17, 054402 (2014).

List of Authors

Bold papercodes indicate primary authors

— A —	
Abdolvand, A.	THP086
Abela, R.	THA01
Abramovich, A.	MOP017
Ackermann, S.	MOP060, MOP083, MOP089, MOP094, THP076
Adachi, M.	THP079
Adams, B.W.	WEA03
Adli, E.	MOP062
Adumi, N.	TUC01
Agaker, M.	FRA01
Agapov, I.V.	MOP056, MOP058, TUP049
Ageev, E.I.	TUP063
Aiba, M.	MOP040, MOP041, THP085
Aksoy, A.A.	MOP062, TUP089
Al-Shemmary, A.	THA04
Alesini, D.	MOP080
Alex, J.	TUA04
Allaria, E.	MOP073, MOP077, MOP078, TUB02, TUP085, THA02, THP070
Altinbas, Z.	TUP072
Amann, J.W.	TUC02
Amatuni, G.A.	TUP083
Anania, M.P.	MOP080
Andersson, J.	THP037
Andonian, G.	THP034
Andrianov, A.V.	THP060
Andriyash, I.A.	TUP086
Angal-Kalinin, D.	MOP062, TUP091
Angelova Hamberg, G.	THP076
Angelovski, A.	THP069
Anghel, A.	MOP043
Anisimov, P.M.	TUP071
Antonelli, M.	TUP097
Arbelaez, D.	THA03
Arikan, P.	TUP089
Arnold, A.	THP047, THP061
Arslanov, D.	TUP065
Arsov, V.R.	THB02, THP085
Artioli, M.	MOP080
Aryshev, A.S.	TUP095
Asaka, T.	THP063
Asgekar, V. B.	MOP006
Asova, G.	THP007
Aßmann, R.W.	MOP089
Attwood, D.T.	TUT01
Audebert, P.	FRA03
Avagyan, V.S.	TUP083
Azima, A.	MOP060, MOP089, THP076

— B —	
Bacci, A.	MOP080
Bader, M.	THP062
Bae, S.	THP010, THP096
Baek, I.H.	THP009
Baek, S.Y.	WEB02
Balal, N.	TUP015, TUP081
Baldinger, M.	THP091
Bandurkin, I.V.	TUP040, TUP046, THP014
Bane, K.L.F.	THP026, THP031
Barday, R.	THP047
Bartnik, A.C.	THP042, THP057
Battistoni, A.	FRA02
Baxevanis, P.	TUP026, TUP027
Bazarov, I.V.	THP042, THP057
Beavis, D.R.	TUP072
Behrens, C.	TUP056
Bell, G.I.	TUP072
Bellaveglia, M.	MOP080
Belomestnykh, S.A.	TUP072
Ben-Zvi, I.	TUP072, TUP076
Benabderrahmane, C.	TUP086, TUP087, THP001
Bencivenga, F.	TUP085, FRA02
Benson, S.V.	TUP069
Berteaud, P.	TUP086, TUP087
Bettoni, S.	THP015, THP049, THC02
Beutner, B.	THP002, THP088, THP097
Bhandari, R.K.	TUP095
Biasiol, G.	TUP097
Biedron, S.	MOP085, TUP048, WEA02
Biela, J.	THP062
Bielawski, S.	TUP086, TUP087, THP078, THP079
Bizzozero, D. A.	TUP023
Blau, J.	TUP034, TUP051, TUP088
Blokesch, G.	THP062
Bluem, H.	WEA04, WEB04
Blumer, H.	THP056, TUA04
Bödewadt, J.	MOP060, MOP083, MOP089, THP076
Boehler, P.	MOP043
Bohler, D.K.	TUC02
Boland, M.J.	MOP062
Boller, K.J.	TUP021
Boonpornprasert, P.	MOP055, THP007
Bopp, M.	TUA04, THP049, THP056
Borodin, D.	MOP017, TUP064
Bossert, J.	THP046
Bostedt, C.	FRA01
Bou Habib, S.	THP068
Boulware, C.H.	TUP051, TUP072
Bourassin-Bouchet, C.	TUP002, TUP086, TUP087, THP087

Bouvet, F. TUP086, TUP087
 Boyes, M. TUC02
 Bozek, J.D. FRA01
 Brachmann, A. THP030, THP042, THP057
 Brands, H. THB02, THP091, THP098
 Bratman, V.L. TUP081, TUP015
 Braun, H.-H. MOP039, TUA04, WEB06,
 THP041, THC02
 Breede, H.F. MOP015
 Brenner, G. MOP060, TUB04
 Breukers, M. THP055
 Brinkmann, R. MOP067
 Briquez, F. MOP004, TUP086, TUP087
 Broemmelsiek, D.R. TUP075
 Brown, K.A. TUP072
 Brubach, J.B. THP078
 Brügger, M. MOP040, MOP041, MOP043
 Brutus, J.C. TUP072, THP093
 Brynes, A.D. TUP091
 Buck, J. MOP012, MOP014, THA02
 Burt, G. THP064
 Butkowski, Ł. THP089
 Butler, N. MOP044

— C —

Callegari, C. TUP085
 Calvi, M. MOP040, MOP041, MOP043,
 THP059, THP081
 Cammarata, M. FRA03
 Campbell, L.T. MOC04, TUB01, TUP022
 Capotondi, F. TUP085, FRA02
 Carlsten, B.E. TUP071
 Carpanese, M.C. MOP080
 Carré, B. TUP087
 Carron Montero, S. FRA01
 Cary, J.R. TUP072
 Casey, J.A. THP052
 Cassinari, L. TUP086, TUP087, THP078,
 THP087
 Castellano, M. MOP080
 Castronovo, D. TUP085
 Cautero, G. TUP097
 Cha, H.K. TUP059
 Chae, M.S. WEB02, THP011
 Chao, F.H. MOP086
 Chapuis, L. TUP086, TUP087
 Charitonidis, N. MOP062
 Charles, T.K. MOP062
 Chaudhari, G.K. TUP095
 Chen, C.H. MOP086, TUP047
 Chen, Q.S. MOP028
 Chen, S.D. MOP045, MOC03, TUP028,
 TUP029, TUP030
 Chiadroni, E. MOP080
 Chiu, Y.C. MOP086
 Cho, M.-H. MOP033, MOP031

Choi, H. J. WEB02
 Chou, M.C. THP018
 Chow, K. TUC02
 Chulkov, R.V. TUP012
 Cianchi, A. MOP080
 Cinquegrana, P. TUP085
 Ciocci, F. MOP080
 Ciricosta, O. FRA03
 Citterio, A. TUA04, THP049, THP056
 Clarke, J.A. MOP062
 Cocco, D. TUC02
 Coffee, R.N. FRA01
 Cohn, K. R. TUP034, TUP051, TUP088
 Colson, W.B. TUP034, TUP051, TUP088
 Corbett, W.J. THP030
 Coreno, M. MOP020, TUP085
 Cork, C.W. TUA01
 Corlett, J.N. THA03
 Couprie, M.-E. MOP004, TUP002, TUP086,
 TUP087, THP001, THP078,
 THP087
 Cowie, L.S. THP064
 Craievich, P. THP015, THP049, THP050
 Crawford, D.J. TUP075
 Cucini, R. TUP085, TUP097, FRA02
 Cudin, I. MOP073, TUP085
 Cui, X. THC03
 Curbis, F. TUP018, TUP080, THP037
 Curcio, A.J. TUP072
 Czwilinnia, M.K. THP068, THP069, THP090

— D —

D'Auria, G. MOP062, TUP085
 Dacasa, H. MOP073
 Dachraoui, H. THP076
 Daillant, J. TUP087
 Danailov, M.B. MOP073, MOP077, TUP085,
 FRA02
 Danner, S. MOP040, MOP041, MOP043
 Das Kanungo, P. THP041
 Dattoli, G. MOP080, MOP091, TUP006,
 TUP048, WEA02
 David, Ch. MOP042
 Davidyuk, I. MOP037
 Davoine, X. TUP086, TUP087
 De Monte, R. TUP085
 De Ninno, G. MOP073, TUB02, TUP085,
 TUC03, THA02, FRA02
 De Santis, S. TUA01
 Decker, F.-J. TUB03, TUC02
 Decking, W. MOP083, WEB03
 Dehler, M.M. THP085
 Delerue, N. TUP087
 Delgiusto, P. TUP085
 DelPriore, G. THP052
 Demidovich, A.A. MOP073, TUP085

Deneuve, F. FRA03
 Deng, H.X. MOP026, MOP070, MOP072, TUC04, FRB01
 DeSanto, L. TUP072
 Deshpande, A. TUP095
 Devanz, G. TUP087
 Di Cicco, A. MOP020
 Di Giovenale, D. MOP080
 Di Mitri, S. MOP062, MOP073, TUP085
 Di Palma, E. MOP080, TUP048
 Di Pirro, G. MOP080
 Dietrich, F. MOP012, MOP014
 Ding, Y. MOP054, MOP090, TUB03, TUP032, TUC02, THP026, THP031
 Dinter, H. THP068, THP083
 Diop, M. TUP087
 Divall, M.C. THC02
 Diviacco, B. TUP085, THA02
 Dixit, T.S. TUP095
 Dohlus, M. MOP060, MOP083
 Donohue, J.T. TUP036, WEA04
 Dooling, J.C. THP039
 Doolittle, L.R. TUA01
 Doose, C.L. THA03
 Dorchies, F. FRA03
 Dordevic, S. MOP039
 Dornmair, I. FRB04
 Douglas, D. THP022
 Dowd, R.T. MOP062
 Dowell, D. WEB04, THP042, THP057
 Drescher, M. MOP060, MOP089, THP076
 Dubois, A. TUP087
 Düsterer, S. THB01
 Dunham, B.M. THP042, THP057
 Dunn, J. FRA03
 Dunning, D.J. TUB01
 Duris, J.P. TUP042, TUP045, FRB03
 Dyunin, E. TUP081
 Dziarzhyski, S. MOP010, TUB04

— E —

Eddy, N. TUP075
 Edstrom, D.R. MOP021, TUP075
 Ego, H. THP063
 Eichert, D.M. TUP097
 Einat, M. TUP064
 Einstein, J. TUP048
 Ekanayake, N. MOP060, MOP089, MOP094, THP076
 El Ajjour, M.E. TUP086, TUP087, THP087
 Elizarov, A. TUP072
 Ellenberger, U. THP056, TUA04
 Ellison, J.A. TUP023
 Emma, C. MOC03, TUP025, TUP028, TUP029, TUP030

Emma, P. MOP075, TUP032, THA03, THB04, THP025, THP029, THP057
 Emons, M. THP040
 Endo, A. FRA04
 Endrich, R. TUP003, TUP004
 Epp, A. THP062
 Eriksson, M. TUP080
 Erk, B. FRA01
 Erlebach, W. WEB04
 Esarey, E. TUP053
 Espeloer, D. THA04
 Evain, C. TUP002, TUP086, THP001, THP078, THP079, TUP087
 Evtushenko, P.E. THP099

— F —

Faatz, B. MOA03, MOP006, MOP089, WEB05, THP073, THP076
 Fabris, A. TUP085
 Fabris, R. TUP085
 Fairley, D. TUC02
 Fajardo, M. MOP073, FRA03
 Fan, M. MOP028
 Fang, K. MOP045, TUP028, TUP029, TUP030, MOC03
 Fang, W. MOP062
 Fawley, W.M. MOP077, TUP085, THP070, TUP031
 Fedurin, M.G. TUP076, THP034
 Feifel, R. FRA01
 Felber, M. THP076, THP089, THP090
 Feldhaus, J. WEB05
 Fell, B.D. THP059
 Feng, C. MOP070, MOP072, TUC04, FRB01
 Feng, G. MOP056, MOP083, MOP089
 Feng, L. MOP026, THP095
 Feng, Y. TUC02
 Ferianis, M. TUP085
 Ferrari, E. MOP073, MOP077, TUB02, TUP085, THA02, THP070
 Ferrario, M. MOP080
 Ferreira, M.J. THP030
 Feurer, T. THP041
 Field, R.C. MOP046, MOP049
 Filippetto, D. TUA01, THP019, THP042, THP054, THP057
 Filippi, F. MOP080
 Finetti, P. MOP020, TUP085
 Fisher, A.S. THB04, THP065
 Fitze, H. TUA04
 Flechsig, U. MOP042, TUC02
 Flöttmann, K. FRB04
 Foerst, M. THA04
 Folz, C. TUP072

Fourment, C. FRA03
 Frassetto, F. **MOP019, MOP020, MOP073**
 Frei, F. **THB02, THP085, THP097**
 Frei, M. THP062
 Freitag, M. THP061
 Freund, H. **TUP020**
 Freund, W. **MOP009, MOP012, MOP013, MOP014**
 Friedman, A. **MOP017, TUP081, THP008**
 Frigola, P. **THP026, THP033, THP034**
 Frisch, J.C. **THB04, THP025, THP080**
 Fritz, D.M. FRA03
 Fröhlich, L. TUP085
 Fry, A.R. THP042
 Fu, Q. **MOP028, TUP070**
 Fuchs, J. FRA03
 Fuerst, J.D. **THA03**
 Fujimoto, M. **TUP065, TUP073, THP058**
 Fukami, K. **MOP022**
 Funakoshi, S. **TUP073, THP058**
 Furlan Radivo, P. **TUP085**
 Furukawa, K. **TUP073, THP058**

— G —

Gacheva, E. THP060
 Gai, W. FRB02
 Gaio, G. TUP085
 Gallo, A. **MOP080**
 Gan, Y.K. **MOP086**
 Ganbold, T. **TUP097**
 Ganter, R. **MOA02, MOP040, MOP041, THP046, THC02**
 Gardelle, J. **TUP036, WEA04**
 Garzella, D. TUP087
 Gassner, D.M. **TUP072, THP074, THP093**
 Gatti, G. **MOP080**
 Gaudin, J. FRA03
 Gaudreau, M.P.J. **MOP044, THP051, THP052**
 Gauthier, D. **MOP073, TUP085, TUC03, THA02**
 Gauthier, M. FRA03
 Gazis, E.N. **MOP062**
 Geddes, C.G.R. TUP053
 Gelmetti, F. TUP085
 Geloni, G. **MOP006, MOP056, MOP057, MOP058, MOP082, TUP049**
 Gensch, M. **MOP006, THA04, THP065, THP069**
 Gerasimova, N. **MOP010, MOP011**
 Gerber, D. THP062
 Gerth, C. **MOP016, THP068, THP069, THP075, THP083, THP088, THP089, THP090**
 Gewinner, S. WEB04
 Ghosh, S. **TUP095**
 Giangrisostomi, E. **MOP020**

Giannessi, L. **MOP073, MOP077, TUB02, TUP085, THA02, MOP01, MOP079, MOP080**
 Giese, E.A. TUP003, TUP004
 Gilevich, S. THP030
 Gillespie, W.A. THP086
 Ginzburg, N.S. **TUP016, TUP017**
 Giribono, A. **MOP080**
 Gluskin, E. **THA03**
 Golovanov, A.A. TUP017
 Golz, T. **MOP006, MOP060, TUB04, THA04, THP065**
 Good, J.D. THP007, THP060
 Gorgisyan, I. **MOP048, THA01**
 Goryashko, V.A. **TUP079, TUP012**
 Goto, S. TUC01
 Gottschalk, S.C. WEB04
 Goudket, P. THP064
 Gough, C.H. **MOP039**
 Gover, A. **TUP007, TUP064, TUP081**
 Grabosch, H.-J. **MOP015**
 Graf, A. FRA03
 Grazioli, C. **MOP020**
 Grebenyuk, J. TUP056
 Green, B.W. **THP065**
 Grigoryan, A. **MOP003, TUP083**
 Grigoryan, B. TUP083
 Grimm, T.L. TUP051, TUP072
 Groß, M. THP007
 Grudiev, A. **MOP062**
 Grünert, J. **MOP009, MOP012, MOP013, MOP014**
 Gu, Q. **MOP062**
 Gudkov, B.A. THP010
 Guetg, M.W. **THP016**
 Gulliford, C.M. THP042, THP057
 Gumerlock, K. **THP080**
 Guzenko, V. THP041

— H —

Ha, T. WEB02
 Hacker, K.E. **MOP018, MOP060, MOP083, MOP089, MOP094, MOP095, MOP096, MOP097, THP076**
 Hage, A. **MOP081**
 Hahn, H. TUP072
 Hajima, R. THC04
 Han, B. THP009
 Han, J.H. **WEB02, THP011, THP012, THP013**
 Hao, Y. TUP072
 Hara, T. **MOP022, TUC01**
 Harms, E.R. TUP075
 Harrison, M.A. THP026, **THP033, THP034**
 Hartl, I. **MOP089, THP060**
 Hasegawa, T. TUC01

Hass, E. MOP060, TUB04
 Hasse, Q.B. THA03
 Hastings, J.B. TUC02
 Hauri, C.P. MOP048, THA01, THC02
 Hayakawa, K. TUP060, TUP077
 Hayakawa, Y. TUP060, TUP077
 He, A. TUP054, THP036
 He, Z.G. TUP009
 Heimann, P.A. TUC02
 Heimgartner, P. THP091
 Hemsing, E. MOP075, MOC02
 Henderson, J. MOC04, TUB01, TUP022
 Herbeaux, C. TUP086, TUP087
 Heusser, M. THP056
 Hilbrich, S. MOP087, TUP082
 Hill, B.L. THP080
 Ho, C. TUP072
 Hocker, A. TUP075
 Höner, M. MOP087, TUP082
 Holtkamp, N.R. THA03
 Honda, Y. MOP088, THC04
 Hong, J.H. TUP093, WEB02, THP011, THP013
 Honkavaara, K. MOP060, WEB05, THP076
 Hosaka, M. THP079
 Hovakimyan, L.V. MOP003
 Hu, J. WEB02
 Hu, T. MOP028
 Huang, G. TUA01
 Huang, K.Y. MOP086
 Huang, N.Y. THP018
 Huang, R. TUA01, THP019, THP042, THP057, THP054
 Huang, X. TUP028, TUP029, TUP030
 Huang, X.Y. THC03
 Huang, Y. TUP072
 Huang, Y.-C. MOP086, TUP047
 Huang, Z. MOP054, MOP090, TUB03, TUP026, TUP032, TUP035, TUC02, WEA03, THA02, THP025, THP026, THP031, THP033
 Huber, P. MOP043
 Hubert, N. TUP086, TUP087, THP087
 Huck, H. MOP087, TUP082
 Huck, M. MOP087, TUP082
 Huegelmann, H. MOP016
 Hulsart, R.L. TUP072, THP093
 Hunziker, S. THP085
 Hwang, C.-S. MOP045, TUP028, TUP030
 Hwang, W.H. WEB02

— I —

Ianconescu, R. TUP007
 Iesari, F. MOP020
 Ilardo, M. TUP072

Ilchen, M. THA02, FRA01
 Ilin, K.S. THP079
 Inagaki, M. TUP060, TUP077
 Inagaki, T. MOP022, TUC01, THP063
 Innocenti, L. MOP080
 Inubushi, Y. TUC01
 Irizawa, A. TUP073, THP058
 Isaev, I.I. THP007
 Ischebeck, R. MOP040, MOP048, THA01, THB02, THP059, THP081, THP088, THP091, THP097, THP098
 Ishikawa, T. TUC01
 Isoyama, G. TUP073, THP058
 Ivanisenko, Ye. THP082
 Ivanov, R. MOP048, MOP089, THA01
 Ivanyan, M. MOP003, TUP083
 Ivanyushenkov, Y. THA03
 Iverson, R.H. TUB03, THP026, THP033

— J —

Jabłoński, S. THP090
 Jacewicz, M. MOP062
 Jackson, R.H. WEA04
 Jakoby, R. THP069
 Jamilkowski, J.P. TUP072
 Janas, E. THP089
 Jang, K.H. MOP030, THP009, THP010, THP038, THP096
 Janssen, X.J.A. THP055
 Jaouen, N. MOP004
 Jark, W.H. TUP097
 Jarvis, J.D. WEA04
 Jecks, R. TUP072
 Jeon, M.Y. MOP030
 Jeong, S.-H. MOP032, MOP033
 Jeong, Y.U. MOP02, MOP030, TUP059, THP009, THP010, THP096
 Jia, Q.K. TUP008, TUP009, TUP057
 Jiao, Y. THC03
 Jin, X. THC04
 Jing, C.-J. FRB02
 Jing, Y.C. TUP072
 Jöhri, H. TUA04
 Johnsson, P. TUP080
 Jones, J.K. TUP091
 Jones, T.J. THP064
 Jongewaard, E.N. THP030
 Jongma, R.T. TUP065, TUP067
 Jung, K. THB03
 Jung, S.H. WEB02
 Jung, Y.-G. MOP031, MOP033
 Junkes, H. WEB04
 Juranic, P.N. MOP048, THA01

— K —

Kaesler, W. THP062
 Kagamihata, A. MOP023
 Kaiser, M.G. THP085
 Kalantari, B. THB02
 Kalantaryan, D.K. THP007
 Kalt, R. THB02, THP043
 Kameshima, T.K. MOP042, TUC01
 Kamitsukasa, F. THP058
 Kammerer, A. THP091
 Kanareykin, A. FRB02
 Kang, H.-S. MOP031, MOP032, MOP033, THP093, WEB02, THB03, THP011, THP012
 Kanjilal, D. TUP095
 Kanter, M. TUP064
 Karabekyan, S. MOP031
 Karl, F.X. TUP072
 Karmakar, J. TUP095
 Karsli, Ö. TUP089
 Kasa, M. THA03
 Katayama, T. MOP042
 Kato, R. TUP073, THP058
 Katoh, M. THP079
 Kawase, K. THP073, THP058
 Kaya, Ç. TUP089
 Kayran, D. TUP072, THP048
 Kayser, Y. MOP042
 Keil, B. THB02
 Keller, A. MOP043
 Kellermann, R. TUP072
 Kellert, M. THP040
 Kempkes, M.K. MOP044, THP051, THP052
 Khachatryan, V.G. MOP001, TUP083
 Khan, D. THP027
 Khan, S. MOP060, MOP084, MOP087, MOP089, TUP082, THP076
 Khazanov, E. THP060
 Khojoyan, M. MOP055, THP006, THP007, THP060
 Kholopov, M.A. TUP072
 Kierspel, T. FRA01
 Kii, T. TUP057, TUP060, TUP063, THP045
 Kim, C. WEB02
 Kim, C.H. WEB02
 Kim, D.E. MOP031, MOP032, MOP033
 Kim, E.-S. THP096
 Kim, H.W. THP009, THP010, THP096
 Kim, I.Y. WEB02
 Kim, J. THB03
 Kim, J.M. WEB02
 Kim, K.-J. TUP024, WEA03
 Kim, S.H. WEB02
 Kim, Y. TUP059, THP010
 Kimberg, V. FRA01

Kimura, H. TUC01
 Kimura, S.I. THP079
 Kinjo, R. MOP023, TUC01
 Kiskinova, M. TUP085, FRA02
 Kivimaki, A. MOP020
 Kleeb, M. THP056
 Kleeb, T. TUA04
 Klein, A. MOP017
 Kleinman, H. TUP064
 Kling, P. TUP003, TUP004
 Kneisel, P. THP061
 Ko, I.S. MOP032, MOP033, WEB02, THP012, THP013, MOP031, THP011
 Koch, A. MOP009, MOP012, MOP013
 Kocharyan, V. MOP056, MOP057, MOP058, MOP082
 Kondo, C. MOP022
 Konomi, T. THP079
 Koprek, W. THB02
 Kot, Y.A. MOP083, THP003
 Kourkafas, G. THP007
 Kovalev, S. THP065
 Kozak, T. THP089
 Kraemer, D. THP062
 Krasilnikov, M. MOP055, THP006, THP007, THP060
 Krawczyk, F.L. THP023, THP024
 Krecic, S. TUP085
 Krejcik, P. THB04
 Kruse, K. THP040
 Krzywinski, J. MOP090, TUB03, TUC02, FRA01
 Kube, G. THP071
 Kubo, K. TUP073
 Küpper, J. FRA01
 Kuhlmann, M. MOP019
 Kumar, N. TUP095
 Kumbaro, D. THP037
 Kuntzsch, M. THP069, THP065
 Kuroda, R. THP045
 Kuzikov, S.V. TUP040, TUP046, THP014

— L —

La Civita, D. MOP011
 Laarmann, T. MOP060, MOP089, THP076
 Labat, M. TUP086, TUP087, THP001, THP078, THP087
 Laloudakis, N. TUP072
 Lamb, T. THP090
 Lambert, G. TUP086, TUP087, THA02
 Lambiase, R.F. TUP072
 Lan, T. MOP072, THP095
 Lange, R. WEB04
 Lasser, Y. TUP064
 Latina, A. MOP062

[illegible]

Marinelli, A.	MOC02, MOT01, TUB03, TUP035, TUC02, THP025, THC01	Montanez, P.A.	TUC02
Marks, H. S.	MOP017, TUP064	Moody, N.A.	THP024
Marlats, J.L.	TUP086, TUP087	Morin, P.	TUP086, TUP087
Marteau, F.	TUP086	Morton, D.S.	TUC02
Martin, D.W.	THP033	Mosnier, A.	TUP087
Martinez de la Ossa, A.	TUP056	Mostacci, A.	MOP080
Masciovecchio, C.	TUP085, FRA02	Mucke, M.	FRA01
Mavrič, U.	THP089	Mücke, O.D.	FRA01
Maxwell, T.J.	TUB03, TUP035, TUC02, THB04, THP025, THP026, THP033, FRA01	Müller, A.-S.	THP004
May, J.	THP080	Mueller, J.M.	MOP089, THP076
Mayes, C.E.	MOP050, THP042, THP057	Mullins, T.G.	FRA01
McIntosh, P.A.	TUP072	Mun, G.	WEB02
McKenzie, J.W.	TUP091, THP064	Mun, J.	MOP030 , THP010, THP096
McKisson, J.E.	THP099	Murcek, P.	THP047, THP061
M ^c Neil, B.W.J.	MOC04, TUB01 , TUP022	Murokh, A.Y.	FRB03, THP033, THP034
Mehrling, T.J.	TUP056	Musumeci, P.	TUP042, TUP045, FRB03
Meijer, G.	WEB04	Myers, S.A.	THA03
Melkumyan, D.	THP007	— N —	
Meng, W.	TUP072	Na, D.H.	WEB02
Menk, R.H.	TUP097	Nadji, A.	TUP087
Meseck, A.	TUP066	Nagai, R.	THC04
Meyer auf der Heide, A.	MOP087, TUP082	Nagler, B.	FRA03
Meyer, M.	MOP014	Naik, V.	TUP095
Michel, P.	WEB04, THP061	Nakajima, T.	TUP063
Michnoff, R.J.	TUP072, THP093	Nakao, K.	TUP060, TUP077
Miginsky, S.V.	THP010	Naknaimueang, S.	THP004
Militsyn, B.L.	TUP091, THP064	Nassiri, A.	THP039
Miller, N.	TUP072	Nause, A.	TUP007
Miller, T.A.	TUP072, THP074 , THP093	Nelson, D.J.	THP080
Millich, M.	TUP085	Nergiz, Z.	MOP062
Milne, C.J.	THT01	Nguyen, D.C.	TUP071
Miltchev, V.	MOP060, MOP089, THP076	Niell, F.M.	MOP044
Milton, S.V.	MOP085, TUP048, WEA02	Niknejadi, P.	MOP063
Min, C.-K.	WEB02, THB03, THP011	Nishimori, N.	THC04
Mincigrucci, R.	MOP020	Nishiyama, M.	THP084
Minty, M.G.	TUP072, THP074, THP093	Nogami, K.	TUP060, TUP077
Miotti, P.	MOP020	Noh, S.Y.	THP096
Mirian, N.S.	TUP006 , MOP080	Nordgren, J.	FRA01
Miron, C.	TUP086, TUP087	Norum, W.E.	TUA01
Mironov, S.	THP060	Nosochkov, Y.	THP025, THP029
Mitchell, C.E.	THP019 , THP020	Nuhn, H.-D.	MOP045, MOP046 , TUB03, TUP035, TUC02, THA03
Miura, A.	TUC01	— O —	
Miura, S.	THP063	Ogawa, H.	TUP077
Miyajima, T.	THC04	Ogawa, K.	MOP048, THA01
Miyazaki, K.	TUP073, THP058	Oh, B.G.	MOP031, MOP032, MOP033
Mizoguchi, H.	FRA04	Oh, Y.	THP041
Modin, P.	TUP036, WEA04	Ohashi, H.	MOP042, TUC01
Moeller, S.P.	TUC02	Ohata, T.	TUC01
Mohanmurthy, P.	THP091	Ohgaki, H.	TUP057, TUP060, TUP063, THP045
Molo, R.	MOP060, MOP087, MOP089, TUP082, THP076	Opanasenko, A.	TUP079
Monoszalai, B.	MOP048, THA01	Oppelt, A.	THP007
		Orfin, P.	TUP072

Orlandi, G.L. THB02, THP081, **THP091**,
THP092
Osemann, M. THP062
Osterhoff, J. TUP056
Otake, Y. MOP022, TUC01, THP063
Otevřel, M. THP007
Ouyang, Z. MOP028
Owada, S. MOP048, THA01
Ozkan, C. MOP041, THP049, **THP081**,
THP091
Özkorucuklu, S. TUP089

— P —

Paarmann, A. WEB04
Palmer, G. THP040
Paly, L. THP056, TUA04
Pandey, A. TUP095
Papadopoulos, C. F. TUA01, THP019, THP029,
THP042, THP054, **THP057**
MOP039, THP041
Paraliev, M. THP064
Paramonov, V.V. TUP059
Parc, Y.W. FRA03
Park, J. MOP031, MOP032, MOP033
Park, K.-H. THP009, THP010
Park, S. MOP030, THP009, THP010,
THP096
Park, S.J. WEB02, THP011, THP013
Park, S.S. WEB02
Park, Y.J. WEB02, THP011
Parmigiani, F. TUP085
Pasky, S.J. THP039
Pathak, G. THP007
Patra, P. TUP095
Patthey, L. MOP040, MOP048, THA01
Paul, K. TUP072
Pedrozzi, M. THP015, THP049, **THP059**
Pei, Y.J. MOP028
Peier, P. THA01, THP082, **THP083**,
THP089
Pellegrini, C. MOP045, MOC03, **MOT01**,
TUP025, TUP028, TUP029,
TUP030
Penco, G. MOP073, **TUB02**, TUP085,
THA02
Pendzick, A. TUP072
Penirschke, A. THP069
Penn, G. MOP054, **MOP075**, TUP033
Pergament, M. THP040
Perlick, F. MOP016, **THP071**
Petràlia, A. MOP080
Petrillo, V. TUP006, TUP048, WEA02,
MOP080, MOP091
Petrosyan, V.H. MOP001, TUP083
Peyrusse, O. FRA03
Pflüger, J. MOP007, MOP031

Phillips, R.A. **THP052**
Pile, G. THA03
Pinayev, I. **TUP072**, **THP048**, THP074,
THP093
Pivetta, L. TUP085
Planas, M. MOP012
Plath, T. **MOP018**, MOP060, MOP083,
MOP089, MOP094, TUB04,
THP076
Plekan, O. TUP085
Plönjes, E. MOP019
Plotkin, M.E. TUP046
Pogorelov, I.V. TUP072
Pogue, C.M. TUP051
Polack, F. TUP086, TUP087
Poletto, L. P. MOP019, MOP020, MOP073
Pollet, P. THP081, THP098
Pompili, R. MOP080
Portmann, G.J. TUA01, THP042, THP057
Poteomkin, A. THP060
Power, J.G. FRB02
Pradervand, C. MOP048, THA01
Prandolini, M.J. **TUA02**
Prat, E. **MOP052**, THP088, **THC02**
Prędkie, P. THP089
Predonzani, M. TUP085
Prestemon, S. THA03
Price, M.J. TUP034
Priebe, G. THP040
Priem, J.M.A. THP055
Principi, E. MOP020, TUP085
Probst, M. THP056
Przygoda, K.P. THP089
Purvis, M. FRA01

— Q —

Qian, H.J. TUA01, THP019, THP057
Qiang, J. THP019, **THP020**, THP025,
THP029, THP036, THP042
MOP028, TUP070
Qin, B. THP053
Quan, S.W. TUP080
Quitmann, C.

— R —

Raasch, J. THP079
Radovic, M. MOP048, THA01
Raguin, J.-Y. TUA04, THP049, **THP050**
Rai, A. TUP095
Raimondi, L. MOP073, TUP085
Randazzo, F. TUP072
Rao, T. TUP072
Rast, H. MOP087, TUP082
Rathke, J. WEB04
Ratner, D.F. TUB03, TUP035, **TUC02**
Rau, J.V. MOP080, TUP048
Raubenheimer, T.O. MOP050, MOP054, MOP075,

	TUP032, WEB01 , THB04, THP025, THP027, THP029, THP042, THP057 MOP073 , TUP085, TUC03 TUB04, MOP059 TUP072 MOP052 , MOP053 , MOP061, TUP019 , TUP029, TUP031, THP016, THP059 THP043 , THP044 TUP087 TUP087, THP078 THP007 THA04, TUA02 MOP055 THP091 THA01 FRA01 TUC02 MOP059 , MOP060, TUB04 , THP076 FRA01 FRA01 THP085 MOP080 TUP072 MOP059 , MOP060, MOP089, TUB04, THP076 MOP080 TUP085 THP051 TUP087 THP078 , THP079 , TUP087 TUP095 TUP087, THP078 MOP021, TUP075 FRA01 MOP062 THP007, THP060 THP026, THP033, THP034 TUP085 TUP026, TUP027 MOP042 FRA01 TUP053	Sakaue, K. Sakurai, T. Saldin, E. Salen, P.M. Samoylova, L. Sanchez-Gonzalez, A. Sandberg, J. Sannibale, F. Santana-Leitner, M. Santucci, J.K. Sargsyan, A. Sathe, C. Sauerbrey, R. Savilov, A.V. Scafuri, C. Schaefer, M. Scherer, A. Scheuring, A. Schick, A. Schietinger, T. Schilcher, T. Schlarb, H. Schleich, W.P. Schlott, V. Schlueter, D. Schmerge, J.F. Schmidt, B. Schmidt, T. Schmitz, M. Schneidmiller, E. Schöllkopf, W. Schöps, A. Scholz, M. Schreiber, S. Schroeder, C.B. Schuh, M. Schulte, D. Schulz, L. Schulz, M. Schulz, S. Schwartz, B.T. Schwarz, M. Sei, N. Seidel, W. Seike, T.	THP084, FRA04 THP063 MOP056, MOP057 , MOP058, MOP082 THP076 MOP011 FRA01 TUP072 TUA01, THP019, THP042, THP054, THP057 MOP046, MOP050 MOP021, TUP075 TUP083 FRA01 TUP003, TUP004 TUP040 , TUP046, THP014 TUP085 THP046, THP049 THP049 THP079 TUP082 MOP040, THP046, THP049, THC02 THB02, THP043, THP044 TUB04, THP068, THP069, THP076, THP089, THP090 TUP003, TUP004 THA01, THB02, THP081, THP082, THP085, THP091, THP098 THA03 THP042 , THP057 TUB04 MOP040, MOP041, MOP043 , THP081 THP071 MOP055, MOP060, MOP064 , MOP065 , MOP066 , MOP067, MOP068 , MOC01 , TUB04, TUP031, THA04 WEB04 MOP008 MOP083, THP073 MOA03 , MOP059, TUB04, WEB05, THP060, THP076 TUP026, TUP053 THP004 MOP062 TUA04, THP091 TUA02 THP076, THP090 TUP072 THP004 TUP077 WEB04 MOP023
— S —			
Saá Hernández, Á. Sabia, E. Sachwitz, M. Sahakyan, V. Sahu, B.K. Saini, A. Sakae, T. Sakai, T.	THB02, THP097 MOP080, MOP091, TUP048, WEA02 MOP015, MOP016 , THP071 TUP083 TUP095 THP025 TUP060 TUP060, TUP077		

Seiler, C. THP091
 Sekutowicz, J.K. MOP067
 Seletskiy, S. MOP079
 Sergeev, A. TUP016
 Sergeeva, D.Yu. TUP013, TUP014
 Serkez, S. MOP056, MOP057, MOP058,
 MOP082, MOP090, MOC03,
 TUP028, TUP030, TUC02
 Serpico, C. TUP085
 Sexton, D.W. THP099
 Shang, H. THP039
 Shchegolkov, D.Y. FRB02
 Sheehy, B. TUP072, THP074
 Shepherd, R. FRA03
 Sheppard, J. THP030
 Shevchenko, O.A. MOP037, MOP038
 Shigeoka, N. THP063
 Shin, J. THB03
 Shishikura, F. TUP060
 Shpakov, V. MOP080
 Shu, D. WEA03
 Shvyd'ko, Yu. MOP092, WEA03
 Siegel, M. THP079
 Sigalotti, P. TUP085
 Simakov, E.I. FRB02
 Sinn, H. MOP010, MOP011
 Sipahi, N. MOP085
 Skaritka, J. TUP072
 Smirnov, A.V. THP034
 Smith, K.S. TUP072
 Smith, R. THP043, THP044
 Smith, S.R. THB04, THP080
 Smith, T.J. TUB03
 Smith, T.L. THP039
 Snedden, E.W. THP086
 Snydstrup, L. TUP072
 Sobol, A.V. TUP072
 Sokolov, N.A. MOP036
 Solyak, N. THP025, THP042
 Son, Y.G. WEB02
 Spampinati, S. TUP091
 Spassovsky, I.P. MOP080, TUP048
 Spezzani, C. MOP073, TUP085, THA02
 Squibb, R. FRA01
 Stagira, S. MOP020
 Stancari, G. TUP075
 Stapf, T. THP056
 Staples, J.W. TUA01
 Steel, A. FRA03
 Steffen, B. TUB04, THP089
 Stepanov, A.G. MOP048, THA01
 Stephan, F. MOP055, THP006, THP007,
 THP060
 Steszyn, A.N. TUP072
 Stingelin, L. THP049
 Stojanovic, N. MOP006, MOP060, TUB04,

Stupakov, G.V. THA04, THP065
 Sturari, L. THP026
 Sudar, N.S. MOP073
 Suemine, S. TUP045
 Suh, H.S. TUP073
 Sun, D. MOP031, MOP032, MOP033
 Sun, Y.-E. TUP075
 Suphakul, S. THP039, FRB02
 Suzuki, D. TUP057, THP045
 Svandrlik, M. THP063
 Svetina, C. TUP085
 Sydlo, C. MOP073, TUP085
 Syratcev, I. THP069, THP090
 Syresin, E. MOP062
 Szewiński, J. THP060
 Szwaj, C. THP068
 TUP086, THP078, THP079,
 TUP087

— T —

Taira, Y. THP045
 Takahashi, T. THP084
 Takashima, Y. THP079
 Takatomi, T. THP084
 Takebe, H. MOP022
 Tan, P. MOP028, TUP070
 Tanaka, H. MOP022, TUC01
 Tanaka, S. TUC01
 Tanaka, T. MOP023, TUC01
 Tanaka, T. TUP060, TUP077
 Tang, C.-X. FRB02
 Tang, T. MOP047
 Tanikawa, T. MOP081, MOP089
 Tantawi, S.G. MOP047
 Tarakanov, V.P. TUP017
 Tavakoli, K. TUP086, TUP087
 Tavella, F. THA04, TUA02
 Tcheskidov, V.G. MOP037
 Tecimer, M. TUP074
 Teichert, J. THP047, THP061
 Tennant, C. THP022
 Than, R. TUP072
 Thangaraj, J.C.T. TUP075
 Thaur, C. TUP086, TUP087
 Theisen, C. TUP072
 Thoma, P. THP079
 Thompson, N. MOP061, TUB01, THP059
 Thorin, S. TUP080
 Thurman-Keup, R.M. TUP075
 Tischer, M. MOP006, MOP008
 Tishchenko, A.A. TUP013, TUP014
 Todd, A.M.M. WEA04, WEB04
 Todd, R.J. TUP072
 Togashi, T. MOP048, THA01
 Togawa, K. TUC01
 Toida, T. THP084

Tokuchi, A. TUP073, THP058
 Tomlinson, W.W. TUP088
 Tono, K. TUC01
 Tordeux, M.-A. THP078
 Toufexis, F. MOP047
 Trakhtenberg, E. THA03
 Treusch, R. MOP010, WEB05
 Trisorio, A. THC02
 Trovati, S. THP091
 Trovò, M. TUP085
 Tsai, C.-Y. THP022
 Tsakanian, A.V. MOP003, TUP083
 Tsakanov, V.M. MOP003, TUP083
 Tsugamura, Y. TUP057
 Tsujino, S. THP041
 Tsutsumi, R. TUP073, THP058
 Tuozzolo, J.E. TUP072
 Turner, J.L. MOP049, TUB03
 Tyrk, M.A. THP086

— U —

Uchiyama, T. THC04
 Ungelenk, P. MOP087, TUP082
 Urakawa, J. TUP095, THP084

— V —

Vaccarezza, C. MOP080
 Vagin, P. MOP006, MOP008
 Valitutti, P. THP091
 Valléau, M. MOP004, TUP086, TUP087
 van der Meer, A.F.G. TUP065
 van der Meulen, P. THP076
 van der Slot, P.J.M. TUP020, TUP021, WEA02
 van der Zande, W.J. TUP067
 Vannoni, M. MOP011
 Vardanyan, A. TUP083
 Vardanyan, T.L. MOP001, MOP003, TUP083
 Vascotto, A. TUP085
 Vashchenko, G. THP006, THP007
 Vecchione, T. THP030, THP042, THP057
 Vennekate, H. THP047, THP061
 Venturini, M. THP019, THP025, THP029
 Vermeulen, M.A. TUP065
 Veronese, M. TUP085
 Vetter, S. THP030
 Vicario, C. THP059, THC02
 Vieffhaus, J. THA02
 Vikharev, A.A. TUP040, TUP046
 Villa, F. MOP080
 Vinko, S.M. FRA03
 Vinokurov, N. MOP036, MOP037, MOP038,
 THP010, MOP030, THP009,
 THP096
 Virostek, S.P. THP042, THP057
 Visintini, R. TUP085
 Vivoli, A. THP042, THP057

Vobly, P. MOP006, TUP072
 Vogt, M. MOP006, WEB05, THP073
 von Helden, G. WEB04
 Vu, L.V. MOP015

— W —

Wacker, V. TUP056
 Walz, D.R. TUC02
 Wang, D. MOP070, MOP072, TUC04,
 THP095, FRB01
 Wang, E. TUP072
 Wang, G. TUP072, THP035
 Wang, H. TUA03
 Wang, J. THP040
 Wang, L. MOP075, TUP032, THP025,
 THP026, THP029
 Wang, X.T. MOP070, MOP072, THP095
 Wang, Y.B. MOP028
 Wang, Y.C. MOP086
 Wark, J.S. FRA03
 Warner, A. TUP075
 Warnock, R.L. TUP023
 Washio, M. THP084, FRA04
 Weathersby, S.P. THP030
 Webb, S.D. TUP072
 Weber, M. THP004
 Wegner, U. THP040
 Weiland, T. THP069
 Weiss, D. TUP072
 Welch, J.J. MOP046, MOP050, TUB03,
 TUC02, THP025
 Wells, R.P. TUA01, THP042, THP057
 Weninger, C. FRA01
 Werin, S. TUP018, TUP080, THP037
 Wesolowski, P. THP004
 Wheelhouse, A.E. TUP072
 White, G.R. MOP050
 Wieland, M. THP076
 Wilinski, M. TUP072, THP093
 Will, I. THP061
 Willeke, F.J. TUP054, THP036
 Williams, G. FRA03
 Williams, P.H. TUP091
 Wißmann, L.-G. THP040
 Wittenburg, K. THP071
 Wohlenberg, T. THP071
 Wolf, Z.R. MOP046
 Wolowelsky, J. TUP064
 Woodley, M. THP025, THP029
 Wu, D. TUA03
 Wu, J. MOP045, MOC03, TUP025,
 TUP028, TUP029, TUP030,
 TUP032, TUP047, TUC02
 Wu, Y.K. WEA01
 Wünsch, R. WEB04
 Wuensch, W. MOP062

Wunderlich, S. TUB04
Wychowaniak, J. THP075

— X —

Xiang, D. MOB03, MOC02
Xiang, R. THP047, THP061
Xiao, D.X. TUA03
Xin, T. TUP072
Xiong, K. TUP070
Xiong, Y.Q. MOP028, TUP070
Xu, G. THC03
Xu, W. TUP072

— Y —

Yabashi, M. MOP042, MOP048, TUC01, THA01
Yaguchi, M. TUP073, THP058
Yamamoto, M. THC04
Yamamoto, N. THP079
Yamamoto, S. MOP023
Yamazaki, H. TUC01
Yan, M. THP075, THP088
Yang, H. WEB02, THP012
Yang, H. THB03
Yang, J. MOP028
Yang, L. THP036
Yang, L. MOP028
Yang, X. TUA03
Yang, X. MOP079
Yang, Z.Q. THP053
Yatsyna, V.O. TUP065, TUP067
Yavaş, Ö. MOP062, TUP089
Yefanov, O. MOP082
Young, L.M. WEB04
Young-Gyu, Y.G. MOP032
Yu, L.-H. MOA01, TUP054, THP036
Yurkov, M.V. MOP055, MOP060, MOP064, MOP065, MOP066, MOP067, MOP068, MOC01, TUB04, TUP031, THA04

— Z —

Zagorodnov, I. MOP056, MOP057, MOP058, MOP082, MOP083, THP003
Zaltsman, A. TUP072
Zangrando, D. TUP085
Zangrando, M. MOP073, TUP085
Zanyan, G.S. TUP083
Zaslavsky, V.Yu. TUP016
Zeitoun, P. MOP073
Zelenogorsky, V. THP060
Zemella, J. THP073
Zen, H. TUP057, TUP060, TUP063, THP045, THP079
Zennaro, R. TUA04, THP056
Zerbib, D. TUP086, TUP087
Zhang, M. MOP070, TUC04
Zhang, T. MOP026, MOP070, TUC04
Zhang, W. MOP070
Zhang, W.Y. THP095
Zhang, Z. TUP047, THP026, THP033
Zhao, J. THP053
Zhao, Z.T. MOP070, MOP072, TUC04, FRB01
Zhaunerchyk, V. TUP012, TUP067, TUP079, TUP065, FRA01
Zholents, A. TUP033, THP039, FRB02
Zhong, S.P. THP095
Zhou, F. TUB03, THP029, THP030, THP031, THP042, THP057
Zhou, K. THP053
Zhu, J. TUP075
Zhu, L. MOP045
Ziemann, V.G. MOP062, TUP066
Zimoch, D. THP091
Zolotovskaya, S.A. THP086
Zotova, I.V. TUP016, TUP017
Zumbach, C. TUA04
Zummack, F. THP090

Institutes List

AES

Medford, New York, USA

- Bluem, H.
- Dowell, D.
- Jackson, R.H.
- Jarvis, J.D.
- Lange, R.
- Rathke, J.
- Todd, A.M.M.
- Young, L.M.

AIST

Tsukuba, Ibaraki, Japan

- Kuroda, R.
- Ogawa, H.
- Sei, N.
- Taira, Y.

Ampegon AG

Turgi, Switzerland

- Bader, M.
- Blokesch, G.
- Epp, A.
- Frei, M.
- Kaesler, W.
- Kraemer, D.
- Osemann, M.

Ankara University, Accelerator Technologies Institute

Golbasi / Ankara, Turkey

- Aksoy, A.A.
- Karsli, Ö.
- Kaya, Ç.
- Yavaş, Ö.

ANL

Argonne, Illinois, USA

- Adams, B.W.
- Dooling, J.C.
- Doose, C.L.
- Fuerst, J.D.
- Gai, W.
- Gluskin, E.
- Hasse, Q.B.
- Ivanyushenkov, Y.
- Kasa, M.
- Kim, K.-J.
- Lindberg, R.R.
- Nassiri, A.
- Pasky, S.J.
- Pile, G.
- Power, J.G.
- Shang, H.
- Shu, D.
- Shvyd'ko, Yu.
- Smith, T.L.

- Sun, Y.-E.
- Trakhtenberg, E.
- Zholents, A.

Ariel University Center of Samaria, Faculty of Engineering

Ariel, Israel

- Abramovich, A.
- Borodin, D.
- Einat, M.
- Kanter, M.
- Lasser, Y.
- Lurie, Yu.

Ariel University

Ariel, Israel

- Balal, N.
- Borodin, D.
- Bratman, V.L.
- Dyunin, E.
- Friedman, A.
- Lurie, Yu.
- Magori, E.
- Maly, B.

Automatic Control Laboratory, ETH Zurich

Zurich, Switzerland

- Režaeizadeh, A.
- Smith, R.

B.I. Stepanov Institute of Physics

Belarus, Russia

- Chulkov, R.V.

BINP SB RAS

Novosibirsk, Russia

- Kholopov, M.A.
- Miginsky, S.V.
- Shevchenko, O.A.
- Tcheskidov, V.G.
- Vinokurov, N.
- Vobly, P.

BNL

Upton, Long Island, New York, USA

- Altinbas, Z.
- Beavis, D.R.
- Belomestnykh, S.A.
- Ben-Zvi, I.
- Brown, K.A.
- Brutus, J.C.
- Curcio, A.J.
- DeSanto, L.
- Elizarov, A.
- Fedurin, M.G.
- Folz, C.
- Gassner, D.M.

- Hahn, H.
- Hao, Y.
- He, A.
- Ho, C.
- Huang, Y.
- Hulsart, R.L.
- Ilardo, M.
- Jamilkowski, J.P.
- Jing, Y.C.
- Karl, F.X.
- Kayran, D.
- Kellermann, R.
- Laloudakis, N.
- Lambiase, R.F.
- Litvinenko, V.
- Mahler, G.J.
- Mapes, M.
- Meng, W.
- Michnoff, R.J.
- Miller, T.A.
- Minty, M.G.
- Orfin, P.
- Pendzick, A.
- Pinayev, I.
- Randazzo, F.
- Rao, T.
- Reich, J.
- Roser, T.
- Sandberg, J.
- Seletskiy, S.
- Sheehy, B.
- Skaritka, J.
- Smith, K.S.
- Snyderstrup, L.
- Steszyn, A.N.
- Than, R.
- Theisen, C.
- Todd, R.J.
- Tuozzolo, J.E.
- Wang, E.
- Wang, G.
- Weiss, D.
- Wilinski, M.
- Willeke, F.J.
- Xin, T.
- Xu, W.
- Yang, L.
- Yang, X.
- Yu, L.-H.
- Zaltsman, A.

Budker INP & NSU

Novosibirsk, Russia

- Sokolov, N.A.

CAEP/IAE

Mianyang, Sichuan, People's Republic of China

- Li, K.
- Li, M.
- Wang, H.

- Wu, D.
- Xiao, D.X.
- Yang, X.

CANDLE SRI

Yerevan, Armenia

- Amatuni, G.A.
- Avagyan, V.S.
- Grigoryan, A.
- Grigoryan, B.
- Hovakimyan, L.V.
- Ivanyan, M.
- Khachatryan, V.G.
- Petrosyan, V.H.
- Sahakyan, V.
- Sargsyan, A.
- Tsakanian, A.V.
- Tsakanov, V.M.
- Vardanyan, A.
- Vardanyan, T.L.
- Zanyan, G.S.

CCPMR

Paris, France

- Dubois, A.
- Lüning, J.

CEA/DAM/DIF

Arpajon, France

- Davoine, X.

CEA/DSM/DRECAM/SPAM

Gif-sur-Yvette, France

- Carré, B.
- Garzella, D.

CEA/DSM/IRFU

France

- Devanz, G.
- Mosnier, A.

CEA/IRFU

Gif-sur-Yvette, France

- Madec, C.

CEA

LE BARP cedex, France

- Gardelle, J.
- Modin, P.

CELIA

Talence, France

- Deneuve, F.
- Dorchie, F.
- Fourment, C.
- Peyrusse, O.

CENBG

Gradignan, France
• Donohue, J.T.

CERN

Geneva, Switzerland
• Charitonidis, N.
• Grudiev, A.
• Latina, A.
• Schulte, D.
• Syrathev, I.
• Wuensch, W.

CFEL

Hamburg, Germany
• Dornmair, I.
• Foerst, M.
• Maier, A.R.
• Mücke, O.D.
• Rönsch-Schulenburg, J.
• Yefanov, O.

Chiang Mai University

Chiang Mai, Thailand
• Rimjaem, S.

Chungnam National University

Daejeon, Republic of Korea
• Jeon, M.Y.

CNR-IFN & Dipartimento di Fisica - Politecnico di Milano

Milano, Italy
• Stagira, S.

CNR-IFN

Padova, Italy
• Frassetto, F.
• Miotti, P.
• Poletto, L. P.

CNR-IMIP

Monterotondo Stazione RM, Italy
• Coreno, M.

Cockcroft Institute, Lancaster University

Lancaster, United Kingdom
• Burt, G.

Cockcroft Institute

Warrington, Cheshire, United Kingdom
• Spampinati, S.

Cornell University (CLASSE), Cornell Laboratory for Accelerator-Based Sciences and Education

Ithaca, New York, USA
• Bartnik, A.C.
• Bazarov, I.V.
• Dunham, B.M.
• Gulliford, C.M.
• Mayes, C.E.

CSU

Fort Collins, Colorado, USA
• Biedron, S.
• Einstein, J.
• Freund, H.
• Milton, S.V.
• Purvis, M.
• Rocca, J.J.
• Ryan, D.P.
• Sipahi, N.
• van der Slot, P.J.M.

DELTA

Dortmund, Germany
• Hacker, K.E.
• Hilbrich, S.
• Huck, H.
• Huck, M.
• Höner, M.
• Khan, S.
• Mai, C.
• Meyer auf der Heide, A.
• Molo, R.
• Rast, H.
• Schick, A.
• Ungelenk, P.

DESY Zeuthen

Zeuthen, Germany
• Boonpornprasert, P.
• Breede, H.F.
• Good, J.D.
• Grabosch, H.-J.
• Groß, M.
• Isaev, I.I.
• Kalantaryan, D.K.
• Khojoyan, M.
• Kourkafas, G.
• Krasilnikov, M.
• Leuschner, N.
• Malyutin, D.
• Melkumyan, D.
• Oppelt, A.
• Otevřel, M.
• Perlick, F.
• Rublack, T.
• Sachwitz, M.
• Stephan, F.
• Vashchenko, G.
• Vu, L.V.

DESY

Hamburg, Germany

- Ackermann, S.
- Al-Shemmary, A.
- Asgekar, V. B.
- Aßmann, R.W.
- Behrens, C.
- Beutner, B.
- Böldewadt, J.
- Brenner, G.
- Brinkmann, R.
- Butkowski, Ł.
- Czwalińska, M.K.
- Dachraoui, H.
- Decking, W.
- Dinter, H.
- Dohlus, M.
- Dziarzhytski, S.
- Düsterer, S.
- Ekanayake, N.
- Erk, B.
- Espeloer, D.
- Faatz, B.
- Felber, M.
- Feldhaus, J.
- Feng, G.
- Flöttmann, K.
- Geloni, G.
- Gerth, C.
- Golz, T.
- Grebenyuk, J.
- Hage, A.
- Hartl, I.
- Hass, E.
- Honkavaara, K.
- Huegelmann, H.
- Ivanov, R.
- Kocharyan, V.
- Kot, Y.A.
- Kube, G.
- Kuhlmann, M.
- Laarmann, T.
- Lamb, T.
- Li, Y.
- Limberg, T.
- Marchetti, B.
- Martinez de la Ossa, A.
- Mavrič, U.
- Mehrling, T.J.
- Mueller, J.M.
- Osterhoff, J.
- Peier, P.
- Plönjes, E.
- Riedel, R.
- Rolles, D.
- Saldin, E.
- Schlarb, H.
- Schmidt, B.
- Schmitz, M.
- Schneidmiller, E.
- Scholz, M.

- Schreiber, S.
- Schulz, M.
- Schulz, S.
- Schöps, A.
- Sekutowicz, J.K.
- Serkez, S.
- Steffen, B.
- Stojanovic, N.
- Sydlo, C.
- Tanikawa, T.
- Tischer, M.
- Treusch, R.
- Vagin, P.
- Viefhaus, J.
- Vogt, M.
- Wacker, V.
- Wittenburg, K.
- Wohlenberg, T.
- Wunderlich, S.
- Yan, M.
- Yurkov, M.V.
- Zagorodnov, I.
- Zemella, J.
- Zummack, F.

Diversified Technologies, Inc.

Bedford, Massachusetts, USA

- Butler, N.
- DelPriore, G.
- Gaudreau, M.P.J.
- Kempkes, M.K.
- Niell, F.M.
- Phillips, R.A.
- Roth, I.

Elettra-Sincrotrone Trieste S.C.p.A.

Basovizza, Italy

- Allaria, E.
- Antonelli, M.
- Battistoni, A.
- Bencivenga, F.
- Callegari, C.
- Capotondi, F.
- Castronovo, D.
- Cautero, G.
- Cinquegrana, P.
- Coreno, M.
- Cucini, R.
- Cudin, I.
- D'Auria, G.
- Danailov, M.B.
- De Monte, R.
- De Ninno, G.
- Delgiusto, P.
- Demidovich, A.A.
- Di Mitri, S.
- Diviacco, B.
- Eichert, D.M.
- Fabris, A.
- Fabris, R.

- Fawley, W.M.
- Ferianis, M.
- Ferrari, E.
- Finetti, P.
- Fröhlich, L.
- Furlan Radivo, P.
- Gaio, G.
- Gauthier, D.
- Gelmetti, F.
- Giangrisostomi, E.
- Giannessi, L.
- Jark, W.H.
- Kiskinova, M.
- Krecic, S.
- Lonza, M.
- Mahne, N.
- Masciovecchio, C.
- Menk, R.H.
- Milloch, M.
- Mincigrucci, R.
- Parmigiani, F.
- Penco, G.
- Pivetta, L.
- Plekan, O.
- Predonzani, M.
- Principi, E.
- Raimondi, L.
- Rebernik Ribič, P.
- Rossi, F.
- Rumiz, L.
- Scafuri, C.
- Serpico, C.
- Sigalotti, P.
- Spezzani, C.
- Sturari, L.
- Svandrlik, M.
- Svetina, C.
- Trovò, M.
- Vascotto, A.
- Veronese, M.
- Visintini, R.
- Zangrando, D.
- Zangrando, M.

ENEA C.R. Frascati

Frascati (Roma), Italy

- Carpanese, M.C.
- Ciocci, F.
- Dattoli, G.
- Di Palma, E.
- Giannessi, L.
- Petralia, A.
- Sabia, E.
- Spassovsky, I.P.

ENEA-Bologna

Bologna, Italy

- Artioli, M.

EPFL

Lausanne, Switzerland

- Gorgisyan, I.
- Hauri, C.P.
- Rivkin, L.

ETH

Zurich, Switzerland

- Biela, J.
- Gerber, D.

Euclid TechLabs, LLC

Solon, Ohio, USA

- Jing, C.-J.
- Kanareykin, A.

FEL/Duke University

Durham, North Carolina, USA

- Wu, Y.K.

Fermilab

Batavia, Illinois, USA

- Broemmelsiek, D.R.
- Crawford, D.J.
- Eddy, N.
- Edstrom, D.R.
- Harms, E.R.
- Hocker, A.
- Leibfritz, J.R.
- Lumpkin, A.H.
- Lunin, A.
- Ruan, J.
- Saini, A.
- Santucci, J.K.
- Solyak, N.
- Stancari, G.
- Sun, D.
- Thangaraj, J.C.T.
- Thurman-Keup, R.M.
- Vivoli, A.
- Warner, A.
- Zhu, J.

FHI

Berlin, Germany

- Erlebach, W.
- Gewinner, S.
- Junkes, H.
- Liedke, A.
- Meijer, G.
- Paarmann, A.
- Schöllkopf, W.
- von Helden, G.

FYSIKUM, AlbaNova, Stockholm University

Stockholm, Sweden

- Salen, P.M.
- van der Meulen, P.

Gazi University, Faculty of Arts and Sciences

Teknikokullar, Ankara, Turkey

- Arıkan, P.

Gigaphoton Inc

Hiratsuka, Kanagawa, Japan

- Mizoguchi, H.

HIJ

Jena, Germany

- Prandolini, M.J.
- Riedel, R.
- Tavella, F.

Huazhong University of Science and Technology, State Key Laboratory of Advanced Electromagnetic Engineering and Technology,

Hubei, People's Republic of China

- Liu, X.
- Ouyang, Z.
- Wang, Y.B.

HUST

Wuhan, People's Republic of China

- Chen, Q.S.
- Fan, M.
- Fu, Q.
- Hu, T.
- Lei, X.
- Liu, K.F.
- Liu, X.
- Qin, B.
- Tan, P.
- Xiong, K.
- Xiong, Y.Q.
- Yang, J.
- Yang, L.

HZB

Berlin, Germany

- Barday, R.
- Meseck, A.
- Richter, D.

HZDR

Dresden, Germany

- Arnold, A.
- Freitag, M.
- Gensch, M.
- Green, B.W.
- Kling, P.
- Kovalev, S.
- Kuntzsch, M.
- Lehnert, U.
- Lu, P.N.
- Michel, P.
- Murcek, P.

- Sauerbrey, R.
- Seidel, W.
- Teichert, J.
- Vennekate, H.
- Wunsch, R.
- Xiang, R.

IAP/RAS

Nizhny Novgorod, Russia

- Andrianov, A.V.
- Bandurkin, I.V.
- Bratman, V.L.
- Gacheva, E.
- Ginzburg, N.S.
- Golovanov, A.A.
- Khazanov, E.
- Kuzikov, S.V.
- Malkin, A.
- Mironov, S.
- Plotkin, M.E.
- Poteomkin, A.
- Savilov, A.V.
- Sergeev, A.
- Vikharev, A.A.
- Zaslavsky, V.Yu.
- Zelenogorsky, V.
- Zotova, I.V.

IHEP

Beijing, People's Republic of China

- Cui, X.
- Huang, X.Y.
- Jiao, Y.
- Xu, G.

Imperial College of Science and Technology, Department of Physics

London, United Kingdom

- Sanchez-Gonzalez, A.

Indiana University

Bloomington, Indiana, USA

- Fang, K.
- Lee, S.-Y.

INFN-Roma II

Roma, Italy

- Cianchi, A.

INFN-Roma

Roma, Italy

- Filippi, F.
- Giribono, A.

INFN/LNF

Frascati (Roma), Italy

- Alesini, D.
- Anania, M.P.

- Bellaveglia, M.
- Castellano, M.
- Chiadroni, E.
- Di Giovenale, D.
- Di Pirro, G.
- Ferrario, M.
- Gallo, A.
- Gatti, G.
- Pompili, R.
- Romeo, S.
- Shpakov, V.
- Vaccarezza, C.
- Villa, F.

INRNE

Sofia, Bulgaria

- Asova, G.

IOM-CNR

Trieste, Italy

- Biasiol, G.
- Kivimaki, A.

IPFN

Lisbon, Portugal

- Fajardo, M.

IPM

Tehran, Iran

- Mirian, N.S.

ISIR

Osaka, Japan

- Fujimoto, M.
- Funakoshi, S.
- Furukawa, K.
- Irizawa, A.
- Isoyama, G.
- Kato, R.
- Kawase, K.
- Kubo, K.
- Miyazaki, K.
- Suemine, S.
- Tokuchi, A.
- Tsutsumi, R.
- Yaguchi, M.

ISM-CNR

Rome, Italy

- Rau, J.V.

Israeli Free Electron Laser

Ariel, Israel

- Klein, A.

Istanbul University

Istanbul, Turkey

- Özkorucuklu, S.

Istituto Nazionale di Fisica Nucleare

Milano, Italy

- Bacci, A.
- Rossi, A.R.

IST

Lisboa, Portugal

- Williams, G.

IUAC

New Delhi, India

- Bhandari, R.K.
- Chaudhari, G.K.
- Ghosh, S.
- Kanjilal, D.
- Karmakar, J.
- Kumar, N.
- Pandey, A.
- Patra, P.
- Rai, A.
- Sahu, B.K.

JAEA

Ibaraki-ken, Japan

- Hajima, R.
- Nagai, R.
- Nishimori, N.

Japan Synchrotron Radiation Research Institute

(JASRI/SPRING-8)

Hyogo, Japan

- Kimura, H.
- Miura, A.
- Ohashi, H.
- Yamazaki, H.

JASRI/RIKEN

Hyogo, Japan

- Owada, S.

JASRI/SPRING-8

Hyogo-ken, Japan

- Ego, H.
- Fukami, K.
- Goto, S.
- Inubushi, Y.
- Kagamihata, A.
- Kameshima, T.K.
- Katayama, T.
- Ohata, T.
- Seike, T.
- Tono, K.

JINR

Dubna, Moscow Region, Russia

- Syresin, E.

JLab

Newport News, Virginia, USA

- Benson, S.V.
- Douglas, D.
- Evtushenko, P.E.
- Kneisel, P.
- Li, R.
- McKisson, J.E.
- Sexton, D.W.
- Tennant, C.

KAERI

Daejeon, Republic of Korea

- Bae, S.
- Baek, I.H.
- Cha, H.K.
- Gudkov, B.A.
- Han, B.
- Jang, K.H.
- Jeong, Y.U.
- Kim, H.W.
- Kim, Y.
- Lee, B.C.
- Lee, K.
- Miginsky, S.V.
- Mun, J.
- Park, S. H.
- Park, S.
- Vinokurov, N.

KAIST

Daejeon, Republic of Korea

- Jung, K.
- Kim, J.
- Lim, J.
- Shin, J.
- Yang, H.

KEK

Ibaraki, Japan

- Aryshev, A.S.
- Honda, Y.
- Jin, X.
- Miyajima, T.
- Takatomi, T.
- Uchiyama, T.
- Urakawa, J.
- Yamamoto, M.
- Yamamoto, S.

KIT

Karlsruhe, Germany

- Ilin, K.S.

- Müller, A.-S.
- Naknaimueang, S.
- Raasch, J.
- Scheuring, A.
- Schuh, M.
- Schwarz, M.
- Siegel, M.
- Thoma, P.
- Weber, M.
- Wesolowski, P.

Kyoto University

Kyoto, Japan

- Ageev, E.I.
- Kii, T.
- Nakajima, T.
- Ohgaki, H.
- Suphakul, S.
- Tsugamura, Y.
- Zen, H.

Kyungpook National University

Daegu, Republic of Korea

- Kim, E.-S.
- Noh, S.Y.

LAL

Orsay, France

- Delerue, N.

LANL

Los Alamos, New Mexico, USA

- Anisimov, P.M.
- Carlsten, B.E.
- Krawczyk, F.L.
- Lewellen, J.W.
- Moody, N.A.
- Nguyen, D.C.
- Shchegolkov, D.Y.
- Simakov, E.I.

LBNL

Berkeley, California, USA

- Arbelaez, D.
- Chow, K.
- Cork, C.W.
- Corlett, J.N.
- De Santis, S.
- Doolittle, L.R.
- Esarey, E.
- Filippetto, D.
- Geddes, C.G.R.
- Huang, G.
- Huang, R.
- Leemans, W.
- Mitchell, C.E.
- Myers, S.A.

- Norum, W.E.
- Papadopoulos, C. F.
- Penn, G.
- Portmann, G.J.
- Prestemon, S.
- Qian, H.J.
- Qiang, J.
- Rodes, L.N.
- Rykovanov, S.G.
- Sannibale, F.
- Schlueter, D.
- Schroeder, C.B.
- Staples, J.W.
- Venturini, M.
- Virostek, S.P.
- Wells, R.P.

LEBRA

Funabashi, Japan

- Hayakawa, K.
- Hayakawa, Y.
- Inagaki, M.
- Nakao, K.
- Nogami, K.
- Sakai, T.
- Shishikura, F.
- Tanaka, T.

LLNL

Livermore, California, USA

- Dunn, J.
- Graf, A.
- Park, J.
- Shepherd, R.
- Steel, A.

LOA

Palaiseau, France

- Andriyash, I.A.
- Dacasa, H.
- Lambert, G.
- Lehé, R.
- Mahieu, B.
- Malka, V.
- Rousse, A.
- Thaury, C.
- Zeitoun, P.

LPI

Moscow, Russia

- Tarakanov, V.P.

LULI

Palaiseau, France

- Audebert, P.
- Fuchs, J.
- Gauthier, M.

Lund University

Lund, Sweden

- Johnsson, P.

LUXOR

Padova, Italy

- Frassetto, F.
- Poletto, L. P.

Max Planck Institute for the Physics of Complex Systems

Dresden, Germany

- Kimberg, V.
- Rohringer, N.
- Weninger, C.

MAX-lab

Lund, Sweden

- Andersson, J.
- Curbis, F.
- Eriksson, M.
- Kumbo, D.
- Lindau, F.
- Mak, A.W.L.
- Quitmann, C.
- Thorin, S.
- Werin, S.

MBI

Berlin, Germany

- Will, I.

MEPhI

Moscow, Russia

- Sergeeva, D.Yu.
- Tishchenko, A.A.

Mesa+

Enschede, The Netherlands

- Boller, K.J.
- van der Slot, P.J.M.

MHI

Hiroshima, Japan

- Miura, S.
- Shigeoka, N.
- Suzuki, D.

Nagoya University

Nagoya, Japan

- Hosaka, M.
- Takashima, Y.
- Yamamoto, N.

National Technical University of Athens

Athens, Greece

- Gazis, E.N.

NCBJ

Świerk/Otwock, Poland

- Szewiński, J.

NCTU

Hsinchu, Taiwan

- Chen, S.D.
- Hwang, C.-S.

Nigde University

Nigde, Turkey

- Nergiz, Z.

Nihon University School of Dentistry at Matsudo

Matsudo-shi, Japan

- Sakae, T.

Niowave, Inc.

Lansing, Michigan, USA

- Boulware, C.H.
- Grimm, T.L.
- Jecks, R.
- Miller, N.
- Pogue, C.M.

NNGU

Nizhny Novgorod, Russia

- Savilov, A.V.

NPS

Monterey, California, USA

- Blau, J.
- Cohn, K. R.
- Colson, W.B.
- Price, M.J.
- Tomlinson, W.W.

NSC/KIPT

Kharkov, Ukraine

- Opanasenko, A.

NSRRC

Hsinchu, Taiwan

- Chou, M.C.
- Huang, N.Y.
- Hwang, C.-S.
- Lau, W.K.
- Lee, A.P.

NSU

Novosibirsk, Russia

- Davidyuk, I.

NTHU

Hsinchu, Taiwan

- Chao, F.H.
- Chen, C.H.
- Chiu, Y.C.
- Gan, Y.K.
- Huang, K.Y.
- Huang, Y.-C.
- Wang, Y.C.

Osaka University, Graduate School of Science

Osaka, Japan

- Kamitsukasa, F.

PAL

Pohang, Kyungbuk, Republic of Korea

- Baek, S.Y.
- Chae, M.S.
- Cho, M.-H.
- Choi, H. J.
- Ha, T.
- Han, J.H.
- Hong, J.H.
- Hu, J.
- Hwang, W.H.
- Jeong, S.-H.
- Jung, S.H.
- Jung, Y.-G.
- Kang, H.-S.
- Kim, C.H.
- Kim, C.
- Kim, D.E.
- Kim, I.Y.
- Kim, J.M.
- Kim, S.H.
- Ko, I.S.
- Lee, H.-G.
- Lee, H.-S.
- Lee, J.
- Lee, S.B.
- Lee, S.J.
- Lee, W.W.
- Min, C.-K.
- Mun, G.
- Na, D.H.
- Oh, B.G.
- Parc, Y.W.
- Park, K.-H.
- Park, S.J.
- Park, S.S.
- Park, Y.J.
- Son, Y.G.
- Suh, H.S.
- Yang, H.
- Young-Gyu, Y.G.

Paul Scherrer Institute

Villigen PSI, Switzerland

- Blumer, H.

- Ellenberger, U.
- Heusser, M.
- Kleeb, M.
- Paly, L.
- Probst, M.
- Stapf, T.

PhLAM/CERCLA

Villeneuve d'Ascq Cedex, France

- Bielawski, S.
- Evain, C.
- Le Parquier, M.
- Roussel, E.
- Szwaj, C.

PhLAM/CERLA

Villeneuve d'Ascq, France

- Evain, C.
- Roussel, E.
- Szwaj, C.

PKU

Beijing, People's Republic of China

- Lu, X.Y.
- Luo, X.
- Quan, S.W.
- Yang, Z.Q.
- Zhao, J.
- Zhou, K.

Politecnico/Milano

Milano, Italy

- Stagira, S.

POSTECH

Pohang, Kyungbuk, Republic of Korea

- Cho, M.-H.
- Ko, I.S.
- Lee, J.

Private Address

Uppsala, Sweden

- Goryashko, V.A.

PSI

Villigen PSI, Switzerland

- Abela, R.
- Aiba, M.
- Alex, J.
- Anghel, A.
- Arsov, V.R.
- Baldinger, M.
- Bettoni, S.
- Blumer, H.
- Boehler, P.
- Bopp, M.

- Bossert, J.
- Brands, H.
- Braun, H.-H.
- Brügger, M.
- Calvi, M.
- Citterio, A.
- Craievich, P.
- Danner, S.
- Das Kanungo, P.
- David, Ch.
- Dehler, M.M.
- Divall, M.C.
- Dordevic, S.
- Ellenberger, U.
- Fitze, H.
- Flechsig, U.
- Frei, F.
- Ganter, R.
- Gorgisyan, I.
- Gough, C.H.
- Guetg, M.W.
- Guzenko, V.
- Hauri, C.P.
- Heimgartner, P.
- Huber, P.
- Hunziker, S.
- Ischebeck, R.
- Ivanisenko, Ye.
- Jöhri, H.
- Juranic, P.N.
- Kaiser, M.G.
- Kalantari, B.
- Kalt, R.
- Kammerer, A.
- Kayser, Y.
- Keil, B.
- Keller, A.
- Kleeb, T.
- Koprek, W.
- Lee, C.
- Llorente Sancho, D.
- Locher, M.
- Löhl, F.
- Lüscher, R.
- Milne, C.J.
- Mohanmurthy, P.
- Monoszlai, B.
- Oh, Y.
- Orlandi, G.L.
- Ozkan, C.
- Paly, L.
- Paraliev, M.
- Patthey, L.
- Pedrozzi, M.
- Pollet, P.
- Pradervand, C.
- Prat, E.
- Radovic, M.
- Raguin, J.-Y.
- Reiche, S.
- Režaeizadeh, A.

- Rippstein, B.
- Rivkin, L.
- Romann, A.
- Rutishauser, S.
- Saá Hernández, Á.
- Schaer, M.
- Scherer, A.
- Schietinger, T.
- Schilcher, T.
- Schlott, V.
- Schmidt, T.
- Schulz, L.
- Seiler, C.
- Stepanov, A.G.
- Stingelin, L.
- Trisorio, A.
- Trovati, S.
- Tsujino, S.
- Valitutti, P.
- Vicario, C.
- Zennaro, R.
- Zimoch, D.
- Zumbach, C.

Radboud University

Nijmegen, The Netherlands

- Arslanov, D.
- Jongma, R.T.
- van der Meer, A.F.G.
- van der Zande, W.J.
- Vermeulen, M.A.

RadiaBeam Systems

Santa Monica, California, USA

- Andonian, G.
- Frigola, P.
- Harrison, M.A.
- Martin, D.W.
- Murokh, A.Y.
- Ruelas, M.
- Smirnov, A.V.

RadiaBeam

Santa Monica, California, USA

- Frigola, P.
- Harrison, M.A.
- Murokh, A.Y.
- Ruelas, M.

RAS/INR

Moscow, Russia

- Paramonov, V.V.

RIKEN SPring-8 Center

Sayo-cho, Sayo-gun, Hyogo, Japan

- Adumi, N.
- Asaka, T.

- Hara, T.
- Inagaki, T.
- Ishikawa, T.
- Kinjo, R.
- Kondo, C.
- Maesaka, H.
- Ogawa, K.
- Otake, Y.
- Sakurai, T.
- Takebe, H.
- Tanaka, H.
- Tanaka, T.
- Togashi, T.
- Togawa, K.
- Yabashi, M.

RIKEN/SPring-8

Hyogo, Japan

- Yabashi, M.

Rockfield Research Inc.

Las Vegas, Nevada, USA

- Casey, J.A.

Rome University La Sapienza

Roma, Italy

- Mostacci, A.

SAMEER

Mumbai, India

- Deshpande, A.
- Dixit, T.S.

SES

Hyogo-pref., Japan

- Hasegawa, T.
- Tanaka, S.

Shanghai Jiao Tong University

Shanghai, People's Republic of China

- Xiang, D.

SINAP

Shanghai, People's Republic of China

- Deng, H.X.
- Fang, W.
- Feng, C.
- Feng, L.
- Gu, Q.
- Lan, T.
- Li, B.
- Liu, B.
- Liu, X.Q.
- Wang, D.
- Wang, X.T.
- Zhang, M.

- Zhang, T.
- Zhang, W.Y.
- Zhang, W.
- Zhao, Z.T.
- Zhong, S.P.

SLAC

Menlo Park, California, USA

- Amann, J.W.
- Bane, K.L.F.
- Baxevanis, P.
- Bohler, D.K.
- Bostedt, C.
- Boyes, M.
- Bozek, J.D.
- Brachmann, A.
- Cammarata, M.
- Carron Montero, S.
- Chen, S.D.
- Cocco, D.
- Coffee, R.N.
- Corbett, W.J.
- Decker, F.-J.
- Ding, Y.
- Dowell, D.
- Emma, P.
- Fairley, D.
- Fang, K.
- Fawley, W.M.
- Feng, Y.
- Ferreira, M.J.
- Field, R.C.
- Fisher, A.S.
- Frisch, J.C.
- Fritz, D.M.
- Fry, A.R.
- Gilevich, S.
- Gumerlock, K.
- Hastings, J.B.
- Heimann, P.A.
- Hemsing, E.
- Hill, B.L.
- Holtkamp, N.R.
- Huang, X.
- Huang, Z.
- Iverson, R.H.
- Jongewaard, E.N.
- Khan, D.
- Krejcik, P.
- Krzywinski, J.
- Lee, H.J.
- Lee, R.W.
- Lemke, H.
- Levashov, Yu.I.
- Lewandowski, J.R.
- Li, R.K.
- Li, Z.
- Lindahl, A.
- Loos, H.
- Lutman, A.A.
- Lutmann, A.

- Mao, X.S.
- Marcus, G.
- Marin, E.
- Marinelli, A.
- Maxwell, T.J.
- May, J.
- Moeller, S.P.
- Montanez, P.A.
- Morton, D.S.
- Nagler, B.
- Nelson, D.J.
- Nosochkov, Y.
- Nuhn, H.-D.
- Pellegrini, C.
- Ratner, D.F.
- Raubenheimer, T.O.
- Ruth, R.D.
- Santana-Leitner, M.
- Schmerge, J.F.
- Sheppard, J.
- Smith, S.R.
- Smith, T.J.
- Stupakov, G.V.
- Tang, T.
- Tantawi, S.G.
- Tavella, F.
- Toufexis, F.
- Turner, J.L.
- Vecchione, T.
- Vetter, S.
- Walz, D.R.
- Wang, L.
- Warnock, R.L.
- Weathersby, S.P.
- Welch, J.J.
- White, G.R.
- Wolf, Z.R.
- Woodley, M.
- Wu, J.
- Zhang, Z.
- Zhou, F.
- Zhu, L.

SLSA

Clayton, Australia

- Boland, M.J.
- Charles, T.K.
- Dowd, R.T.
- LeBlanc, G.

SOLEIL

Gif-sur-Yvette, France

- Benabderrahmane, C.
- Berteaud, P.
- Bourassin-Bouchet, C.
- Bouvet, F.
- Briquez, F.
- Brubach, J.B.
- Cassinari, L.
- Chapuis, L.

- Couprie, M.-E.
- Daillant, J.
- Diop, M.
- El Ajouri, M.E.
- Herbeaux, C.
- Hubert, N.
- Jaouen, N.
- Labat, M.
- Lebasque, P.
- Lestrade, A.
- Louergue, A.
- Lüning, J.
- Manceron, L.
- Marchand, P.
- Marcouillé, O.
- Marlats, J.L.
- Marteau, F.
- Miron, C.
- Morin, P.
- Nadji, A.
- Polack, F.
- Ribeiro, F.
- Ricaud, J.P.
- Roy, P.
- Tavakoli, K.
- Tordeux, M.-A.
- Valléau, M.
- Zerbib, D.

Stanford University

Stanford, California, USA

- MacArthur, J.P.

STFC/DL/ASTeC

Daresbury, Warrington, Cheshire, United Kingdom

- Angal-Kalinin, D.
- Brynes, A.D.
- Clarke, J.A.
- Cowie, L.S.
- Dunning, D.J.
- Fell, B.D.
- Goudket, P.
- Jones, J.K.
- Liggins, B.P.M.
- McIntosh, P.A.
- McKenzie, J.W.
- Milityn, B.L.
- Snedden, E.W.
- Thompson, N.
- Wheelhouse, A.E.
- Williams, P.H.

STFC/DL

Daresbury, Warrington, Cheshire, United Kingdom

- Jones, T.J.

STI

Washington, USA

ISBN 978-3-95450-133-5

1030

- Gottschalk, S.C.

Stony Brook University

Stony Brook, USA

- Litvinenko, V.

Tech-X

Boulder, Colorado, USA

- Bell, G.I.
- Cary, J.R.
- Paul, K.
- Pogorelov, I.V.
- Schwartz, B.T.
- Sobol, A.V.
- Webb, S.D.

TEMF, TU Darmstadt

Darmstadt, Germany

- Weiland, T.

TU Darmstadt

Darmstadt, Germany

- Angelovski, A.
- Jakoby, R.
- Penirschke, A.

TU Dresden

Dresden, Germany

- Kuntzsch, M.

TUB

Beijing, People's Republic of China

- Li, C.
- Tang, C.-X.

TUL-DMCS

Łódź, Poland

- Kozak, T.
- Prędkie, P.
- Przygoda, K.P.
- Wychowaniak, J.

UCB

Berkeley, California, USA

- Attwood, D.T.

UCLA

Los Angeles, California, USA

- Duris, J.P.
- Emma, C.
- Musumeci, P.
- Nause, A.
- Pellegrini, C.
- Sudar, N.S.

Uni HH

Hamburg, Germany

- Ackermann, S.
- Azima, A.
- Drescher, M.
- Hass, E.
- Lazzarino, L.L.
- Lechner, C.
- Lockmann, N.M.
- Maier, A.R.
- Maltezopoulos, Th.
- Miltchev, V.
- Pathak, G.
- Plath, T.
- Rehders, M.
- Rönsch-Schulenburg, J.
- Roßbach, J.
- Wieland, M.

Uni Ulm

Ulm, Germany

- Endrich, R.
- Giese, E.A.
- Schleich, W.P.

Universita Degli Studi di Trieste

Trieste, Italy

- Grazioli, C.

Universita' degli Studi di Milano & INFN

Milano, Italy

- Mirian, N.S.
- Petrillo, V.

Universita' degli Studi di Milano

Milano, Italy

- Petrillo, V.

University of Dundee

Nethergate, Dundee, Scotland, United Kingdom

- Abdolvand, A.
- Gillespie, W.A.
- Tyrk, M.A.
- Zolotovskaya, S.A.

University of Gothenburg

Gothenburg, Sweden

- Yatsyna, V.O.
- Zhaunerchyk, V.

University of Hamburg

Hamburg, Germany

- Kierspel, T.
- Küpper, J.
- Mullins, T.G.
- Rehders, M.

University of Hawaii at Manoa

Honolulu, USA

- Tecimer, M.

University of Hawaii

Honolulu, USA

- Madey, J.
- Niknejadi, P.

University of Nova Gorica

Nova Gorica, Slovenia

- De Ninno, G.
- Gauthier, D.

University of Oslo

Oslo, Norway

- Adli, E.

University of Oxford, Clarendon Laboratory

Oxford, United Kingdom

- Ciricosta, O.
- Vinko, S.M.
- Wark, J.S.

University of Pécs

Pécs, Hungary

- Monoszlai, B.

University of Tel-Aviv, Faculty of Engineering

Tel-Aviv, Israel

- Gover, A.
- Ianculescu, R.
- Kleinman, H.
- Marks, H. S.
- Wolowelsky, J.

University of Trieste, School of Nanotechnology

Trieste, Italy

- Ganbold, T.

Università degli Studi di Trieste

Trieste, Italy

- Ferrari, E.

Università di Camerino

Camerino, Italy

- Di Cicco, A.
- Iesari, F.

Università di Roma II Tor Vergata

Roma, Italy

- Innocenti, L.

Universität Bern, Institute of Applied Physics

Bern, Switzerland

- Feurer, T.

- Katoh, M.
- Kimura, S.I.
- Konomi, T.

UNM

Albuquerque, New Mexico, USA

- Bizzozero, D. A.
- Ellison, J.A.

UW-Madison/PD

Madison, Wisconsin, USA

- Lawler, J.E.

UPMC

Paris, France

- Levy, A.

VDL ETG

Eindhoven, The Netherlands

- Breukers, M.
- Janssen, X.J.A.
- Priem, J.M.A.

Uppsala University

Uppsala, Sweden

- Agaker, M.
- Angelova Hamberg, G.
- Feifel, R.
- Goryashko, V.A.
- Jacewicz, M.
- Mucke, M.
- Nordgren, J.
- Rubensson, J.E.
- Ruder, R.J.M.Y.
- Sathe, C.
- Squibb, R.
- Zhaunerchyk, V.
- Ziemann, V.G.

VECC

Kolkata, India

- Naik, V.
- Roy, A.

Virginia Polytechnic Institute and State University

Blacksburg, Virginia, USA

- Tsai, C.-Y.

Warsaw University of Technology, Institute of Electronic Systems

Warsaw, Poland

- Bou Habib, S.
- Jabłoński, S.
- Janas, E.

USTC/NSRL

Hefei, Anhui, People's Republic of China

- He, Z.G.
- Huang, R.
- Jia, Q.K.
- Li, H.T.
- Pei, Y.J.

Waseda University

Tokyo, Japan

- Endo, A.
- Nishiyama, M.
- Sakaue, K.
- Takahashi, T.
- Toida, T.
- Washio, M.

USTRAT/SUPA

Glasgow, United Kingdom

- Campbell, L.T.
- Henderson, J.
- McNeil, B.W.J.

XFEL. EU

Hamburg, Germany

- Agapov, I.V.
- Buck, J.
- Dietrich, F.
- Emons, M.
- Freund, W.
- Gaudin, J.
- Geloni, G.
- Gerasimova, N.
- Grünert, J.
- Ilchen, M.
- Karabekyan, S.
- Kellert, M.
- Koch, A.
- Kruse, K.
- La Civita, D.
- Le Pimpec, F.
- Lederer, M.

UST

Daejeon City, Republic of Korea

- Jang, K.H.
- Jeong, Y.U.
- Kim, H.W.
- Lee, K.
- Miginsky, S.V.
- Park, S. H.
- Vinokurov, N.

UVSOR

Okazaki, Japan

- Adachi, M.

ISBN 978-3-95450-133-5

- Liu, J.
- Meyer, M.
- Palmer, G.
- Pergament, M.
- Pflüger, J.
- Planas, M.
- Priebe, G.
- Samoylova, L.
- Sinn, H.
- Vannoni, M.
- Wang, J.
- Wegner, U.
- Wißmann, L.-G.

Participant List

Family Name	Name	Institute	City	Country
Abela	Rafael	Paul Scherrer Institut	Villigen	Switzerland
Afif	El Mehdi	National Instruments		United States of America
Agapov	Ilya	European XFEL GmbH	Hamburg	Germany
Aksoy	Avni	Ankara University	Ankara	Turkey
Allaria	Enrico	Elettra - Sincrotrone Trieste	Trieste	Italy
Andersson	Joel	Max IV Laboratory	Lund	Sweden
Angelovski	Aleksandar	Technische Universität Darmstadt	Darmstadt	Germany
Arnold	Walter	TRANSTECH Hochfrequenz AG	Wettingen	Switzerland
Arsov	Vladimir	Paul Scherrer Institut	Villigen	Switzerland
Attwood	David	University of California	Berkeley	United States of America
Balal	Nezah	Ariel University	Ariel	Israel
Banine	Vadim	ASML Netherlands	Veldhoven	Netherlands
Bartolini	Riccardo	Diamond Light Source	Oxfordshire	United Kingdom
Baxevas	Panagiotis	SLAC	Stanford	United States of America
Bayle	Hervé	Bergoz Instrumentation	Saint Genis Pouilly	France
Beeckman	William	SIGMA PHI Accelerator Technologies	Vannes	France
Bencivenga	Filippo	Elettra - Sincrotrone Trieste	Trieste	Italy
Benson	Stephen	Jefferson Laboratory	Newport News	United States of America
Bettoni	Simona	Paul Scherrer Institut	Villigen	Switzerland
Beutner	Bolko	DESY	Hamburg	Germany
Biedron	Sandra	Colorado State University	Fort Collins, Colorado	United States of America
Bischofberger	Eduard	TEL Mechatronics AG	Trübbach	Switzerland
Bizzozero	David	University of New Mexico	Albuquerque	United States of America
Blau	Joseph	Naval Postgraduate School	Monterey, CA	United States of America
Bodker	Franz	Danfysik A/S	Taastrup	Denmark
Boonpornprasert	Prach	DESY	Zeuthen	Germany
Borodin	Dmitri	Ariel University	Ariel	Israel
Bourassin-Bouchet	Charles	Soleil Synchrotron	Giv-sur-Yvette Cedex	France
Bovier	Joel	IOxOS		
Brandenburg	Sytze	University of Groningen, KVI-CART	Groningen	Netherlands
Braun	Hans-Heinrich	Paul Scherrer Institut	Villigen	Switzerland
Breede	Heiko	DESY	Zeuthen	Germany
Breukers	Mathieu	VDL Enabling Technologies Group		Netherlands
Brinkmann	Reinhard	DESY	Hamburg	Germany
Briquez	Fabien	Synchrotron SOLEIL	Saint-Aubin	France
Broschinski	Yvonne	Oerlikon Leybold Vakuum Schweiz AG		Switzerland
Cadoppi	Andrea	SAES getters		
Calvi	Marco	Paul Scherrer Institut	Villigen	Switzerland
Cavellier	Matthieu	SIGMA PHI Accelerator Technologies	Vannes	France
Chen	Shuo	Ludwig institute for Cancer Research	Oxford	United Kingdom
Chen	Chiahsiang	National Tsinghua University	Hsinchu	Taiwan
Chen	Sei-Da	SLAC	Stanford	United States of America
Chou	Ming-Chang	National Synchrotron Radiation Research Center	Hsinchu	Taiwan
Chrin	Jan	Paul Scherrer Institut	Villigen	Switzerland
Chulkov	Ruslan	National Academy of Science of Belarus	Minsk	Belarus
Cohn	Keith	Naval Postgraduate School	Monterey, CA	United States of America
Coleman	Russell	Edwards Vacuum	Burgess Hill	United Kingdom
Colson	William	Naval Postgraduate School	Monterey, CA	United States of America
Coupré	Marie-Emmanuelle	Synchrotron SOLEIL	Gif sur Yvette	France
Craievich	Paolo	Paul Scherrer Institut	Villigen	Switzerland
Curbis	Francesca	Max IV Laboratory	Lund	Sweden
Czwalinna	Marie Kristin	DESY	Hamburg	Germany
Dattoli	Giuseppe	ENEA	Frascati	Italy
Dauner	Bernhard	Laser 2000 GmbH	Wessling	Germany
Davidyuk	Igor	Novosibirsk State University, BINP	Novosibirsk	Russia
Davis	Eric	Institute for Advanced Studies at Austin	Austin, Texas	United States of America
Decking	Winfried	DESY	Hamburg	Germany
Deng	Haixiao	Shanghai Institute of Applied Physics	Shanghai	Peoples Republic of China
Dinter	Hannes	DESY	Hamburg	Germany
Divall	Marta	Paul Scherrer Institut	Villigen	Switzerland
Diviacco	Bruno	Kyma Srl	Trieste	Italy
Dodge	William	Buckley Systems International	Rowley	United States of America
Donohue	John	Centre d'Etudes Nucléaires de Bordeaux	Gradignan	France
Dorchain	Geoffroy	Oerlikon Leybold Vakuum Schweiz AG		Switzerland

Proceedings of FEL2014, Basel, Switzerland

Duesterer	Stefan	DESY	Hamburg	Germany
Dunkel	Kai	RI Research Instruments GmbH	Bergisch-Gladbach	Germany
Dunning	David	STFC Daresbury Laboratory	Warrington	United Kingdom
Dupire	Pascal	SIGMA PHI Accelerator Technologies	Vannes	France
Duris	Joseph	University of California Los Angeles	Los Angeles	United States of America
Eaton	Douglas	ScandiNova Systems AB	Uppsala	Sweden
Ellenberger	Urs	Paul Scherrer Institut	Villigen	Switzerland
Emma	Paul	SLAC	Stanford	United States of America
Emma	Claudio	UCLA	Los Angeles	United States of America
Emmerichs	Hans-Ulrich	Coherent Deutschland GmbH	Dieburg	Germany
Endo	Akira	Waseda University, RISE	Tokyo	Japan
Endrich	Rainer	Institut für Quantenphysik, Uni U Im	Ulm	Germany
Eriksson	Harri	Luvata Pori Oy	Pori	Finland
Evain	Clement	PhLAM / University of Lille	Villeneuve d'Ascq	France
Evtushenko	Pavel	Jefferson Laboratory	Newport News	United States of America
Fan	Mingwu	Huazhong University of Science and Technology	Wuhan	Peoples Republic of China
Fawley	William	Sincrotrone Trieste	Oakland	United States of America
Fedurin	Mikhail	Brookhaven National Laboratory	Upton	United States of America
Feng	Lie	Shanghai Institute of Applied Physics	Shanghai	Peoples Republic of China
Feng	Chao	Shanghai Institute of Applied Physics, CAS	Shanghai	Peoples Republic of China
Ferrari	Eugenio	Elettra-Sincrotrone	Trieste	Italy
Filippetto	Daniele	Lawrence Berkeley National Laboratory	Berkeley	United States of America
Finetti	Paola	Elettra - Sincrotrone Trieste	Trieste	Italy
Flechsigg	Uwe	Paul Scherrer Institut	Villigen	Switzerland
Follath	Rolf	Paul Scherrer Institut	Villigen	Switzerland
Franceskin	Mojca	Kyma Srl	Trieste	Italy
Frassetto	Fabio	CNR-INFN	Padova	Italy
Frei	Franziska	Paul Scherrer Institut	Villigen	Switzerland
Frei	Marcel	Ampegon AG	Turgi	Switzerland
Freund	Wolfgang	European XFEL GmbH	Hamburg	Germany
Frey	Paul	Elma Electronic AG	Wetzikon	Switzerland
Friedman	Aharon	Ariel University	Ariel	Israel
Frisch	Josef	SLAC	Menlo Park	United States of America
Fruit	Byron	Aerotech, Inc.	Pittsburgh	United States of America
Fu	Qiang	Huazhong University	Wuhan	China
Fujii	Satoshi	Toshiba Electron Tubes & Devices Co., Ltd	Omiya-ku	Japan
Fujisawa	Masanobu	NEOMAX Engineering Co., Ltd.	Tokyo	Japan
Gabard	Alexander	Paul Scherrer Institut	Villigen	Switzerland
Ganbold	Tamiraa	School of Nanotechnology, University of Trieste	Trieste	Italy
Ganter	Romain	Paul Scherrer Institut	Villigen	Switzerland
Gantner	Markus	MEWASA		
Garvey	Terence	Paul Scherrer Institut	Villigen	Switzerland
Gassner	David	Brookhaven National Laboratory	Upton	United States of America
Geloni	Gianluca	European XFEL GmbH	Hamburg	Germany
Geometrante	Raffaella	Kyma Srl	Trieste	Italy
Gerasimova	Natalia	European XFEL GmbH	Hamburg	Germany
Gerth	Christopher	DESY	Hamburg	Germany
Gewinner	Sandy	Fritz-Haber-Institut	Berlin	Germany
Ghosh	Subhendu	Inter University Accelerator Centre	New Deli	India
Giannessi	Luca	Elettra - Sincrotrone Trieste	Trieste	Italy
Giguet	Eric	IRELEC & ALSYOM	Argenteuil	France
Gillespie	Allan	University of Dundee	Dundee	United Kingdom
Ginzburg	Naum	Institute of Applied Physics	Nizhny Novgorod	Russia
Golz	Torsten	DESY	Hamburg	Germany
Gorgisyan	Ishkhan	Paul Scherrer Institut / EPFL	Villigen	Switzerland
Goryashko	Vitaliy	Uppsala University	Uppsala	Sweden
Gough	Christopher	Paul Scherrer Institut	Villigen	Switzerland
Gover	Avraham	Tel Aviv University	Tel Aviv	Israel
Green	Bertram	Helmholtz Zentrum Dresden Rossendorf	Dresden	Germany
Grünert	Jan	European XFEL GmbH	Hamburg	Germany
Guertg	Marc	Paul Scherrer Institut	Villigen	Switzerland
Gumerlock	Karl	SLAC National Accelerator Laboratory	Menlo Park	United States of America
Gustin	Mitja	CAEN ELS d.o.o.	Sezana	Slovenia
Hacker	Kirsten	TU Dortmund	Dortmund	Germany
Hama	Hiroyuki	Tohoku University	Sendai	Japan
Han	Jang-Hui	Pohang Accelerator Laboratory	Pohang	Republic of Korea
Hara	Toru	RIKEN Spring-8 Center	Sayō-cho	Japan

Proceedings of FEL2014, Basel, Switzerland

Hauri	Christoph	Paul Scherrer Institut	Villigen	Switzerland
He	Zhigang	NSRL, Univ. of Science and Technology of China	Hefei	Peoples Republic of China
He	An	Brookhaven National Laboratory	Upton	United States of America
Heerwagen	Arndt	Newport Spectra-Physics	Darmstadt	Germany
Hemsing	Erik	SLAC	Menlo Park	United States of America
Henderson	James	Strathclyde University	Glasgow	United Kingdom
Hiekkänen	Ilppo	Luvata Pori Oy	Pori	Finland
Hilbrich	Svenja	DELTA	Dortmund	Germany
Holen	Paul	Stangenes Industries, Inc.	Palo Alto	United States of America
Homma	Akira	Mitsubishi Heavy Industries Ltd	Mihara	Japan
Honda	Yosuke	KEK	Tsukuba	Japan
Hong	Juho	Pohang Accelerator Laboratory	Pohang	Republic of Korea
Honkavaara	Katja	DESY	Hamburg	Germany
Huang	Senlin	IHIP, Peking University	Beijing	Peoples Republic of China
Huang	Zhirong	SLAC	Menlo Park	United States of America
Ianconescu	Reuven	Shenkar College of Engineering and Design	Ramat Gan	Israel
Ikeda	Naoaki	Mitsubishi Heavy Industries Ltd	Mihara	Japan
Inagaki	Takahiro	RIKEN Spring-8 Center	Hyogo	Japan
Ischebeck	Rasmus	Paul Scherrer Institut	Villigen	Switzerland
Isoyama	Goro	ISIR / Osaka University	Osaka	Japan
Ivanisenko	Yevgeniy	Paul Scherrer Institut	Villigen	Switzerland
Iwazumi	Toshiaki	Osaka Prefecture University	Sakai	Japan
Janežič	Elvis	Instrumentation Technologies d.d.	Sokan	Slovenia
Jang	Kyuha	KAERI	Daejeon	Republic of Korea
Jeong	Young Uk	KAERI	Daejeon	Republic of Korea
Jia	Qika	NSRL, USTC	Hefei	Peoples Republic of China
Jiang	Can	Hubei University of Science and Technology	Xianning	Peoples Republic of China
Jiao	Yi	Institute of High Energy Physics	Beijing	Peoples Republic of China
Jung	Kwangyun	KAIST	Daejeon	Republic of Korea
Juranic	Pavle	Paul Scherrer Institut	Villigen	Switzerland
Kaesler	Wolfgang	Ampegon AG	Turgi	Switzerland
Kanareykin	Alexei	Euclid Techlabs LLC	Gaithersburg	United States of America
Kang	Heung Sik	Pohang Accelerator Laboratory	Pohang	Republic of Korea
Kawase	Keigo	Osaka University	Osaka	Japan
Kayser	Yves	Paul Scherrer Institut	Villigen	Switzerland
Keens	Simon	Ampegon AG	Turgi	Switzerland
Keil	Boris	Paul Scherrer Institut	Villigen	Switzerland
Kempkes	Michael	Diversified Technologies	Bedford	United States of America
Kessler	Marcel	TEL Mechatronics AG	Trübbach	Seit
Khan	Shaukat	DELTA	Dortmund	Germany
Khodykin	Oleg	KLA-Tencor	Milpitas	United States of America
Khojayan	Martin	DESY Zeuthen	Zeuthen	Germany
Kilinc	Ahmet F.	HVP High Voltage Products GmbH	Martinsried	Germany
Kim	Kwang-Je	Argonne National Laboratory	Lemont	United States of America
Kim	Yujong	KAERI	Daejeon	Republic of Korea
Kim	Seung Jun	Korea Research Inst. of Bioscience & Biotechnology	Dae-Jeon	Republic of Korea
Kim	Kyung-Ryul	Pohang Accelerator Laboratory	Pohang	Republic of Korea
Kim	Hyun Woo	KAERI	Daejeon	Republic of Korea
Kim	Dong-Eon	Pohang Accelerator Laboratory (PAL)	Pohang	Republic of Korea
Kim	Chul Hoon	Pohang Accelerator Laboratory (PAL)	Pohang	Republic of Korea
Kinjo	Ryota	RIKEN Spring-8 Center	Hyogo	Japan
Kirsch	Matthias	Struck Innovative Systeme GmbH	Hamburg	Germany
Klein	Hans-Udo	Management&		Germany
Klein	Avi	Ariel University	Ariel	Israel
Kling	Peter	Helmholtz Zentrum Dresden Rossendorf	Dresden	Germany
Knopp	Gregor	Paul Scherrer Institut	Villigen	Switzerland
Ko	In Soo	POSTECH	Pohang	Republic of Korea
Koch	Andreas	European XFEL GmbH	Hamburg	Germany
Kocharyan	Vitali	DESY	Hamburg	Germany
Kokole	Mirko	Bruker Advanced Supercon GmbH	Cologne	Germany
Kot	Yauhen	DESY	Hamburg	Germany
Krawczyk	Frank	Los Alamos National Laboratory	Los Alamos	United States of America
Kropotov	Grigory	TYDEX J.S.Co.		
Kuzikov	Sergey	Institute of Applied Physics	Nizhny Novgorod	Russia
Labat	Marie	Soleil Synchrotron	St. Aubin	France
Lanaro	Andrea	Alca Technology S.r.l.		Italy
Lang	Alexander	Onefive GmbH	Zürich	Switzerland

ISBN 978-3-95450-133-5

Proceedings of FEL2014, Basel, Switzerland

Lazzarino	Leslie Lamberto	University of Hamburg	Hamburg	Germany
Le Pimpec	Frederic	European XFEL GmbH	Hamburg	Germany
Lechner	Christoph	University of Hamburg	Hamburg	Germany
Lee	Ki Tae	KAERI	Daejeon	Republic of Korea
Lee	SangBong	Pohang Accelerator Laboratory	Pohang	Republic of Korea
Lee	Jae Hyun	POSTECH	Pohang	Republic of Korea
Lehnert	Ulf	ELBE Radiation Source	Dresden	Germany
Lerch	Philippe	Paul Scherrer Institut	Villigen	Switzerland
Levy	Anna	Université Pierre et Marie Curie	Paris	France
Li	Yuhui	European XFEL GmbH	Hamburg	Germany
Li	Heting	National Synchrotron Radiation Laboratory	Hefei	Peoples Republic of China
Li	Rui	Jefferson Laboratory	Newport News	United States of America
Limberg	Torsten	DESY	Hamburg	Germany
Lindau	Ingolf	Max IV Laboratory	Lund	Sweden
Lindholm	Mikael	ScandiNova Systems AB	Uppsala	Sweden
Litvinenko	Vladimir	Stony Brook university	Mt Sinai	United States of America
Liu	Jia	European XFEL GmbH	Hamburg	Germany
Liu	Bo	Shanghai Institute of Applied Physics	Shanghai	Peoples Republic of China
Llorente Sancho	Daniel	Paul Scherrer Institut	Villigen	Switzerland
Loehl	Florian	Paul Scherrer Institut	Villigen	Switzerland
Loopstra	Erik	ASML Netherlands	Veldhoven	Netherlands
Lumpkin	Alex	Fermilab	Batavia	United States of America
MacArthur	James	Stanford University	Stanford	United States of America
Maccallini	Ernico	SAES getters		
Maier	Andreas	CFEL	Hamburg	Germany
Mak	Alan	Max IV Laboratory	Lund	Sweden
Malkin	Andrey	IAP RAS	Nizhny Novgorod	Russia
Maly	Benny	Ariel University	Ariel	Israel
Marcus	Gabriel	SLAC	Menlo Park	United States of America
Marinelli	Agostino	SLAC	Menlo Park	United States of America
Marks	Harry	Tel Aviv University	Tel Aviv	Israel
Marot	Gerard	IRLEC-ALCEN	St. Martin d'Heres	France
Maucher	Charly	PI MiCos GmbH	Eschbach	Germany
Mc Kenzie	Julian	STFC Daresbury Laboratory	Daresbury, Warrington	United Kingdom
Mc Neil	Brian	University of Strathclyde	Glasgow	United Kingdom
Mella	Fredrik	ScandiNova Systems AB	Uppsala	Sweden
Meseck	Atoosa	HBZ	Berlin	Germany
Meyer auf der Heide	Arne	DELTA	Dortmund	Germany
Michel	Peter	HZDR	Dresden	Germany
Miller	Toby	Brookhaven National Laboratory	Upton	United States of America
Milne	Christopher	Paul Scherrer Institut	Villigen	Switzerland
Milton	Stephen	Colorado State University	Fort Collins, Colorado	United States of America
Miotti	Paolo	CNR-IFN	Padova	Italy
Mirian	Najmeh Sadat	Insitute for Research in Fundamental Sciences	Teheran	Iran
Mita	Masahiro	NEOMAX Engineering Co., Ltd.		
Mitchell	Chad	Lawrence Berkeley National Laboratory	Berkeley, CA	United States of America
Moellers	Ralf	Elma Electronic AG	Pforzheim	Germany
Mohamed	Ahmed	Utrecht University	Utrecht	Netherlands
Mok	Iksu	Pohang Accelerator Laboratory	Pohang	Republic of Korea
Molo	Robert	DELTA	Dortmund	Germany
Mun	Jungho	Korea Atomic Energy Research Institute	Daejeon	Republic of Korea
Munderville	Matthew	Diversified Technologies	Bedford	United States of America
Murokh	Alex	RadiaBeam Technologies	Santa Monica	United States of America
Nakao	Keisuke	Nihon University	Funabashi	Japan
Neil	George	Jefferson Laboratory	Newport News	United States of America
Nguyen	Dinh	Los Alamos National Laboratory	Los Alamos	United States of America
Nielsen	Gunver	Danfysik A/S	Taastrup	Denmark
Nielsen	Louis	CML Eninegeering		
Niknejadi	Pardis	University of Hawaii	Honolulu	United States of America
Nishiyama	Masahiro	Waseda University	Tokyo	Japan
Nuhn	Heinz-Dieter	SLAC	Menlo Park	United States of America
Nussbaum	Christian	MDC Daetwyler AG	Bleienbach	Switzerland
O'Hara	Patrick	UHV Design Ltd.	Laughton	United Kingdom
Opara	Nadia	Paul Scherrer Institut / Uni Basel	Villigen	Switzerland
Orlandi	Gianluca	Paul Scherrer Institut	Villigen	Switzerland
Ozkan	Cigdem	Paul Scherrer Institut	Villigen	Switzerland
Paraliev	Martin	Paul Scherrer Institut	Villigen	Switzerland

Proceedings of FEL2014, Basel, Switzerland

Parker	Tyler	UC Irvine	Irvine	United States of America
Patterson	Bruce	Paul Scherrer Institut	Villigen	Switzerland
Patthey	Luc	Paul Scherrer Institut	Villigen	Switzerland
Pedrozzi	Marco	Paul Scherrer Institut	Villigen	Switzerland
Peier	Peter	DESY	Hamburg	Germany
Penco	Giuseppe	Elettra - Sincrotrone Trieste	Trieste	Italy
Penirschke	Andreas	Technische Universität Darmstadt	Darmstadt	Germany
Perlick	Florian	DESY	Zeuthen	Germany
Pernter	Michael	Elma Electronic AG	Wetzikon	Switzerland
Petit-Jean-Genaz	Christine	CERN	Geneva	Switzerland
Petralia	Alberto	ENEA Frascati	Frascati	Italy
Petrillo	Vittoria	Università di Milano	Milano	Italy
Pflueger	Joachim	European XFEL GmbH	Hamburg	Germany
Piel	Christian	RI Research Instruments GmbH	Bergisch-Gladbach	Germany
Pinayev	Igor	Brookhaven National Laboratory	Upton	United States of America
Plath	Tim	University of Hamburg	Hamburg	Germany
Plesko	Mark	Cosylab		
Pradervand	Claude	Paul Scherrer Institut	Villigen	Switzerland
Prandolini	Mark	Helmholtz-Institut Jena	Hamburg	Germany
Prat Costa	Eduard	Paul Scherrer Institut	Villigen	Switzerland
Pretrelli	Miguel	OCEM Energy Technology	Valsamoggia	Italy
Priem	Hans	VDL Enabling Technologies Group		Netherlands
Qin	Bin	Huazhong University of Science and Technology	Wuhan	Peoples Republic of China
Ratner	Daniel	SLAC	Menlo Park	United States of America
Raubenheimer	Tor	SLAC	Menlo Park	United States of America
Ravindran	Murali	National Instruments		United States of America
Rebernik Ribic	Primoz	Elettra - Sincrotrone Trieste	Trieste	Italy
Rechsteiner	Dominik	Ferrovac GmbH	Zürich	Switzerland
Reed	Jeffrey	Pearson Electronics Inc	Palo Alto	United States of America
Rehders	Marie	University of Hamburg	Hamburg	Germany
Reiche	Sven	Paul Scherrer Institut	Villigen	Switzerland
Rezaeizadeh	Amin	Paul Scherrer Institut	Villigen	Switzerland
Richardson	Carl	Toyama Co.		Japan
Rivkin	Leonid	Paul Scherrer Institut	Villigen	Switzerland
Roensch-Schulenburg	Juliane	University of Hamburg	Hamburg	Germany
Rohringer	Nina	Max Planck Inst. for the Physics of Complex Systems	Dresden	Germany
Romann	Albert	Paul Scherrer Institut	Villigen	Switzerland
Rosbach	Joerg	University of Hamburg	Hamburg	Germany
Roussel	Eleonore	PhLAM	Villeneuve d'Ascq	France
Rublack	Tino	DESY Zeuthen	Zeuthen	Germany
Ruelas	Marcos	RadiaBeam Technologies	Santa Monica	United States of America
Saa Hernandez	Angela	Paul Scherrer Institut	Villigen	Switzerland
Sabia	Elio	ENEA Frascati	Frascati	Italy
Sablic	Oliver	CPI	Palo Alto	United States of America
Sachwitz	Martin	DESY	Zeuthen	Germany
Saikatendu	Kumar	Takeda California	San Diego	United States of America
Sakaue	Kazuyuki	Waseda University	Tokyo	Japan
Saldin	Evgeny	DESY	Hamburg	Germany
Sanborn	William	MEGA Industries LLC	Gorham, Maine	United States of America
Savilov	Andrei	Institute of Applied Physics	Nizhny Novgorod	Russia
Schaa	Volker	GSI	Darmstadt	Germany
Schaer	Mattia	Paul Scherrer Institut	Villigen	Switzerland
Schietinger	Thomas	Paul Scherrer Institut	Villigen	Switzerland
Schlott	Volker	Paul Scherrer Institut	Villigen	Switzerland
Schmerge	John	SLAC	Menlo Park	United States of America
Schmidt	Thomas	Paul Scherrer Institut	Villigen	Switzerland
Schneidmiller	Evgeny	DESY	Hamburg	Germany
Schoellkopf	Wieland	Fritz-Haber-Institut	Berlin	Germany
Scholl	Caitlin	Brookhaven National Laboratory	Upton	United States of America
Scholz	Matthias	DESY	Hamburg	Germany
Schreiber	Siegfried	DESY	Hamburg	Germany
Schroeder	Carl	Lawrence Berkeley National Laboratory	Berkeley	United States of America
Schuh	Marcel	KIT	Karlsruhe	Germany
Seddon	Elaine	The Photon Science Institute	Manchester	United Kingdom
Seidel	Wolfgang	Helmholtz-Zentrum Dresden-Rossendorf	Dresden	Germany
Sergeeva	Daria	National Research Nuclear University	Moscow	Russia
Serkez	Svitozar	DESY	Hamburg	Germany

ISBN 978-3-95450-133-5

Proceedings of FEL2014, Basel, Switzerland

Shevchenko	Oleg	Budker INP	Novosibirsk	Russia
Shigeoka	Nobuyuki	Mitsubishi Heavy Industries Ltd	Mihara	Japan
Shirkov	Grigori	Joint Institute for Nuclear Research	Dubna	Russia
Shishikura	Fumio	LEBRA, Nihon University	Funabashi	Japan
Shvyd'ko	Yuri	Argonne National Laboratory	Argonne	United States of America
Singh	Mandeep	Newport Spectra-Physics BV	Delft	Netherlands
Sinram	Klaus	Buckley Systems International	Rowley	United States of America
Siv	Julie	Amplitude Technologies	Evry	France
Smith	Todd	Stanford University	Stanford	United States of America
Sostmann	Giselher	Edwards Vacuum	Crawley	United Kingdom
Spasic	Sasa	SENIS AG	Baar	Switzerland
Stephan	Frank	DESY Zeuthen	Zeuthen	Germany
Stojanovic	Nikola	DESY	Hamburg	Germany
Sudar	Nicholas	UCLA	Los Angeles	United States of America
Suh	Hyung Suck	Pohang Accelerator Laboratory	Pohang	Republic of Korea
Suphakul	Sikharin	Kyoto University	Kyoto	Japan
Svandrlík	Michele	Elettra - Sincrotrone Trieste	Trieste	Italy
Sydlo	Cezary	DESY	Hamburg	Germany
Tabeling	Joesph	Applied Diamond Inc.	Wilmington	United States of America
Tanaka	Hitoshi	RIKEN Spring-8 Center	Hyogo	Japan
Tanikawa	Takanori	DESY	Hamburg	Germany
Tappola	Paula	Luvata Pori Oy	Pori	Finland
Tecimer	Müfit	THz FEL Group UHM	Honolulu	United States of America
Teichert	Jochen	HZDR	Dresden	Germany
Termoellen	Michael H.	Aerotech GmbH		
Thompson	Neil	STFC Daresbury Laboratory	Warrington	United Kingdom
Tiedtke	Kai	DESY	Hamburg	Germany
Tischer	Markus	DESY	Hamburg	Germany
Tishchenko	Alexey	National Research Nuclear University MEPhI	Moscow	Russia
Todd	Alan	Advances Energy Systems	Princeton	United States of America
Tomlinson	Warren	Naval Postgraduate School	Monterey, CA	United States of America
Toufexis	Filippos	SLAC	Menlo Park	United States of America
Tsujino	Soichiro	Paul Scherrer Institut	Villigen	Switzerland
Turner	James	SLAC	Menlo Park	United States of America
Tyrk	Mateusz Amadeusz	University of Dundee	Dundee	United Kingdom
Ushankova	Olga	TYDEX J.S.Co.	St. Petersburg	Russia
Vagin	Pavel	DESY	Hamburg	Germany
van den Oetelaar	Louis	ASML Netherlands	Veldhoven	Netherlands
van der Meer	Lex	Radboud University Nijmegen	Nijmegen	Netherlands
van der Slot	Peter	University of Twente	Enschede	Netherlands
Vardanyan	Tigran	CANDLE	Yerevan	Armenia
Vashchenko	Grygorii	DESY	Zeuthen	Germany
Venkataraman	Chitra	Bruker ASC	Köln	Germany
Vicario	Carlo	Paul Scherrer Institut	Villigen	Switzerland
Villa	Fabio	INFN	Frascati	Italy
Vinokurov	Nicolay	Budker INP and KAERI	Novosibirsk	Russia
Vogel	Hanspeter	RI Research Instruments GmbH	Bergisch-Gladbach	Germany
Vogel	Dietmar	Toshiba Electron Tubes & Devices Co., Ltd	Omiya-ku	Japan
Wacker	Violetta	DESY	Hamburg	Germany
Walker	Richard	Diamond Light Source	Oxfordshire	United Kingdom
Walter	Thomas	DESY	Hamburg	Germany
Wang	Hanbin	CAEP/IAE	Hmianyang	Peoples Republic of China
Wang	Dong	Shanghai Institute of Applied Physics	Shanghai	Peoples Republic of China
Waters	Christopher	Pearson Electronics Inc	Palo Alto	United States of America
Weber	Martin	MDC Daetwyler AG	Bleienbach	Switzerland
Weichenthal	Reinhold	Mitutoyo (Europe GmbH)	Neuss	Germany
Welch	James	SLAC	Menlo Park	United States of America
Werin	Sverker	Max IV Laboratory	Lund	Sweden
Williams	Peter	STFC Daresbury Laboratory	Warrington	United Kingdom
Wissmann	Laurens	European XFEL GmbH	Hamburg	Germany
Wu	Ying	Duke University	Durham	United States of America
Wychowaniak	Jan	DESY	Hamburg	Germany
Xiang	Rong	Helmholtz-Zentrum Desden-Rossendorf	Dresden	Germany
Xiang	Dao	Shanghai Jiao Tong University	Shanghai	Peoples Republic of China
Xiong	Yongqian	Huazhong University of Science and Technology	Wuhan	Peoples Republic of China
Yan	Minjie	DESY	Hamburg	Germany
Yang	Xi	Brookhaven National Laboratory	Upton	United States of America

Proceedings of FEL2014, Basel, Switzerland

Yang	Haeryong	Pohang Accelerator Laboratory	Pohang	Republic of Korea
Yang	Jeongmu	Pohang Accelerator Laboratory	Pohang	Republic of Korea
Yatsyna	Vasyl	University of Gothenburg	Gothenburg	Sweden
Yeckel	Christopher	Stangenes Industries, Inc.	Palo Alto	United States of America
Yongaci	Oezkan	Mitutoyo (Schweiz) AG		
Yu	Li Hua	Brookhaven National Laboratory	Upton	United States of America
Yu	Tiaoqin	Huazhong University of Science and Technology	Wuhan	Peoples Republic of China
Yurkov	Mikhail	DESY	Hamburg	Germany
Yushiro	Osamu	Toshiba Electron Tubes & Devices Co., Ltd	Omiya-ku	Japan
Zambelli	Mauro	Kyma Srl	Trieste	Italy
Zen	Heishun	Kyoto University	Uji	Japan
Zeutschel	Tilo	NEOMAX Engineering Co., Ltd.		
Zhang	Shukui	Jefferson Laboratory	Newport News	United States of America
Zhao	Zhentang	Shanghai Institute of Applied Physics, CAS	Shanghai	Peoples Republic of China
Zholents	Alexander	Argonne National Laboratory	Argonne	United States of America
Zhou	Feng	SLAC	Menlo Park	United States of America
Zhou	Kui	Peking University	Beijing	Peoples Republic of China
Zielinski	Kamil	Lodz University of Technology	Lodz	Poland
Znidarcic	Matjaz	Instrumentation Technologies d.d.	Sokan	Slovenia